天津大学
Tianjin University

1895·2025
天津大学(北洋大学)
建校130周年

2025 40th CUS-EPSA

第40届中国高等学校电力系统及其自动化专业学术年会

The 40th Annual Conference on Chinese University Society for Electric Power System and Automation (CUS-EPSA)

论文集



2025.10.24–26 | 中国·天津

委员会成员

1. 学术委员会

委　员	单　位	委　员	单　位
李　斌	天津大学	文劲宇	华中科技大学
甘德强	浙江大学	郝治国	西安交通大学
梅生伟	清华大学	段献忠	湖南大学
刘玉田	山东大学	顾　伟	东南大学
谢开贵	重庆大学	严　正	上海交通大学
刘俊勇	四川大学	毕天姝	华北电力大学
唐文虎	华南理工大学	王懿杰	哈尔滨工业大学
严干贵	东北电力大学	邵振国	福州大学
鲁军勇	海军工程大学	何正友	西南交通大学
程　显	郑州大学	刘　辉	广西大学
鞠　平	河海大学	丁立建	合肥工业大学
唐　巍	中国农业大学	曹一家	长沙理工大学
符　杨	上海电力大学	卢志刚	燕山大学
李卫东	大连理工大学	黄悦华	三峡大学
和敬涵	北京交通大学	董旭柱	武汉大学
仉志华	中国石油大学(华东)	孙宏斌	太原理工大学
蔡　蔚	哈尔滨理工大学	刘广忱	内蒙古工业大学
丁晓峰	北京航空航天大学	肖朝霞	天津工业大学
周雪松	天津理工大学	韩　旭	河北工业大学
夏明超	沈阳工业大学	张化光	东北大学
李洪珠	辽宁工程技术大学	向　川	大连海事大学
李　刚	吉林大学	金立军	同济大学
施伟锋	上海海事大学	李　雪	上海大学
阮新波	南京航空航天大学	梁　睿	中国矿业大学
朱孝勇	江苏大学	王群京	安徽大学
徐丙垠	山东理工大学	和　萍	郑州轻工业大学
张晓星	湖北工业大学	黄　琦	电子科技大学
张　靖	贵州大学	束洪春	昆明理工大学
李伟林	西北工业大学	段建东	西安理工大学
汤旻安	兰州交通大学	李凤婷	新疆大学

孟安波	广东工业大学	裴　玮	中科院电工所
严剑峰	中国电力科学研究院		

2. 程序委员会

主任委员	**单　位**	**副主任委员**	**单　位**
贾宏杰	天津大学	肖先勇	四川大学
		刘　洪	天津大学
委　员	**单　位**	**委　员**	**单　位**
胡家兵	华中科技大学	丁　一	浙江大学
李更丰	西安交通大学	闵　勇	清华大学
李　勇	湖南大学	丁　磊	山东大学
胡秦然	东南大学	胡　博	重庆大学
程浩忠	上海交通大学	刘　念	华北电力大学
管　霖	华南理工大学	徐　英	哈尔滨工业大学
姜　涛	东北电力大学	陈飞雄	福州大学
张　晓	海军工程大学	廖　凯	西南交通大学
金　阳	郑州大学	黎静华	广西大学
张　犁	河海大学	向念文	合肥工业大学
杨德昌	中国农业大学	杨洪明	长沙理工大学
米　阳	上海电力大学	马　锴	燕山大学
李卫星	大连理工大学	唐　波	三峡大学
王小君	北京交通大学	徐　箭	武汉大学
康忠健	中国石油大学(华东)	叶　鹏	沈阳工程学院
薛屹洵	太原理工大学	雷　霞	西华大学
吕艳玲	哈尔滨理工大学	曾平良	杭州电子科技大学
刘广忱	内蒙古工业大学	陈　伟	兰州理工大学

3. 组织委员会

主　任	贾宏杰		
副主任	王守相		
	刘洪		
	穆云飞		
秘书长	徐弢		
副秘书长			
冀浩然		靳小龙	何星瑭
侯　恺		宋关羽	孙　冰

孙　强	温伟杰	徐正阳
赵倩宇	何佳伟	李博通
刘　博	于　浩	富晓鹏
雷　鸣	李　超	李霞林
肖　迁		

目录

001 基于大数据的电力设备状态监测与故障诊断方法 1

002 Modeling for Efficient Impulse Resistance Assessment of Transmission Tower Grounding Systems 4

003 PV Output Forecasting Based on the Combinations of Scene-Adaptive Decomposition and SENet-reweighted Informer 17

004 基于灰狼优化算法的同步调相机 PID 参数优化 32

005 基于等式残差抗差总体最小二乘法的谐波状态估计与定位 37

006 基于多变量模态分解与 BiLSTM 的超短期光伏功率概率预测 42

007 Comprehensive assessment of normal operational benefit and extreme event responsiveness for distribution systems 47

008 课堂、科创、实习基地融合的电力系统专业建设 67

009 Active Fault Location Method for Interphase Short Circuit of Distribution Network with Distributed Generation 72

010 Transient Fault-Current Characteristics and Second-Order Equivalent Modeling of Grid-Following Converters under Low-Voltage Ride-Through 86

011 High voltage overhead line insulator breakage detection technology based on lightweight DETR 100

012 Multi-Time Scale Optimal Scheduling of Hydrogen Integrated Energy Systems Considering Seasonal Fluctuations in Wind-Solar Power 108

013 电力系统混合振荡源定位的模态耗散能量流方法 128

014 一种微电网分层能量协调控制策略研究 134

015 Research on Frequency Stability of a New Power System Considering Inertia Constraints 141

016 灵活检修策略下的矿山柔性资源运行优化研究 156

017 Oscillation Sppression of Permanent Magnet Synchronous Motor Based on RTDS Hardware-in-the-Loop 162

018 基于滑模自抗扰控制的光伏并网次同步振荡抑制方法研究 176

019 Evaluation System and Assessment Method for Distributed New Energy Hosting

Capacity of Multi-Dimensional Observable Distribution Networks 181

020 基于 KJ-Kano-模糊综合评价模型的新一代集控站智能运维功能提升策略 198

021 风光氢储系统综述 206

022 Research and practice of LLM agent for human resource business of large enterprises 210

023 Deep Reinforcement Learning based Emergency Control of Cyber-Physical Power System 218

024 Low-Carbon Economic Scheduling of CCHP Microgrids Based on Two-stage Scenario Generation and Stepwise Carbon Trading 236

025 Research on Co-optimization Strategies Based on Cooperative Game in the Electricity Supply Chain 252

026 A Reactive Power Optimization Method for Substations Based on PSO-Genetic Fusion Algorithm 269

027 Risk Assessment of Power System Restoration Considering the Uncertain State of Lines to Be Restored 281

028 A two-layer optimal scheduling method for active power regulation of electric vehicle cluster power system 294

029 Coordinated Optimal Planning of Stations and Networks in Hydrogen-Integrated Energy Systems 309

030 面向量子通信设备部署的电力系统信息安全强化策略 325

031 A Coordinated Robust Volt_VAR Optimization for Distribution Systems with High Renewable Penetration 332

032 平抑风电波动的电氢储能容量优化配置 348

033 超声辅助固化对抑制环氧树脂/金属嵌件界面残余应力的作用 354

034 基于产教融合培养适应新型电力系统发展的新质生产力人才 361

035 基于 MATLAB 构建传输线集中参数模型 369

036 A Distributionally Robust Optimization Method for Operational Risk Analysis and Power Outage Warning in Unbalanced Distribution Networks 375

037 GIS/GIL 支柱绝缘子界面缺陷的超声频谱特征 383

038 Parameters Design of Controller for DFIG Grid-connected System and Analysis of

Oscillation Influencing Factors 388

039 基于 RF 特征优选的 DGA 电力变压器故障诊断 396

040 基于深度强化学习的综合能源系统优化运行研究 422

041 Reliability Planning of High-penetration Renewable Power Systems Considering Extreme Stagnant Meteorological Scenarios 427

042 Analysis and Modeling of Grounding Characteristics of Transmission Tower Based on Method of Moments 440

043 Research on Pre-Synchronization Control Strategy of VSG-Based Energy Storage Converter Without Phase-Locked Loop 455

044 柔性接地装置注入信号的配电网单相接地故障测距方法 461

045 Analysis on Equivalent Impedance Characteristics for VSG-Controlled Wind Farms. 467

046 考虑不确定性的新型电力系统优化调度研究 481

047 防止输电断面连锁过载的新能源电力系统鲁棒性控制方法 487

048 两相旋转坐标系下的可调度虚拟振荡器虚拟惯性控制 492

049 虚拟同步发电机的改进自适应控制策略 497

050 含分布式电源的油田井场综合负荷建模方法研究 503

051 基于广义 S 变换-FIR 的油田井场混合储能容量配置方法 508

052 面向新能源消纳能力提升的油田井场源荷动态匹配策略研究 513

053 Method for Two-Point Ground Fault Location with Different Phases on the Same Line Based on Load-Side Phase Voltage 518

054 Research of Full Sequence Impedance Equivalent Modeling of Wind Farm 531

055 规模化新能源接入的电力现货市场出清模型及仿真 542

056 Optimization Method for Energy Storage Operation of New Energy Station Accessories Considering Multiple Benefits 548

057 Study on Return Current Distribution Mechanism and Abnormal Return Mitigation in Heavy Haul Railway Traction Systems Considering Train Operation 557

058 基于云边协同的多微网分布式优化调度策略 576

059 A Robust Regression-Based Approach for Node Inertia Index Estimation in Power

Systems 582

060 Research Impact on Electrolytic Water Hydrogen Production on SSO in Wind-PV Complementary System 591

061 Control Parameter Identification Method for Grid-Following Converters Based on Multi-Disturbance Response 600

062 Low-Frequency Oscillation Analysis and Active Damping Suppression Strategy for Multi-Machine Parallel Grid-Forming Energy Storage Systems 615

063 电动飞机对机场电力系统的挑战 631

064 An MILP framework for Demand Response Incentive Design with NILM-based Potential Estimation 637

065 Parameter Identification of Photovoltaic Cells Based on Cardinal Curves and Improved AHO 646

066 An Adaptive Adjustment Method of Reclosing Time Based on Estimation of the Off-grid Time 666

067 一种融合已知类识别和未知类诊断的配电变压器故障诊断方法 677

068 小电流接地系统单相接地故障暂态零序特征分析及应用 684

069 Research on a PI-LADRC Hybrid Control Strategy for Grid-Forming Inverters in Strongly Series-Compensated Power Grids 689

070 Control Technology Based on Integration of Grid-Forming Flywheel Energy Storage and New Energy Power Stations 703

071 Research on Photovoltaic Power Ultra-Short Term Prediction Model Optimized by IQPSO for LSTM 711

072 Distributed Economic Dispatch of Integrated Transmission and Distribution Systems towards Reserve Sharing 720

073 Multi-Time-Scale Economic Dispatch Model and Method for Active Distribution Networks Driven by Complex Network Algorithms 736

074 Research on Optimal Scheduling of Photovoltaic-Hydrogen-Storage-Electric Vehicle Microgrids Based on the NGO-MOGWO Algorithm 748

075 Physics-Constrained Neural network Co-Design for Integrated Modeling and Control of DC/DC Power Converters 762

076 Optimal Capacity Configuration of Large-Scale Wind-Solar Hydrogen Production

Systems with Dynamic Hydrogen Production Efficiency 771

077 配电系统的可用供电能力 783

078 构网型储能联合风光火打捆低电压穿越控制 788

079 Post-disaster Recovery Strategy of Distribution Network Considering Uncertainty of V2G Response Potential 793

080 Flexible Arc Suppression Method Based on Voltage Current Mutual Compensation Using Fuzzy PI Control for Distribution Networks 806

081 Analysis of Fault Suppression Performance of Flexible Arc Suppression Methods in Distribution Networks 816

082 基于藤蔓优化算法并考虑需求侧响应的直流电网最优潮流计算 824

083 覆冰灾害下考虑多手段协同的柔性互联配电网增韧策略 829

084 Wave-Velocity-Free Single-Phase Grounding Fault Location in Distribution Networks Using Modal Traveling Waves and Tower Distances 839

085 A Day-Ahead Optimization Control Method Considering the Ramping Capability of Energy Storage Systems 855

086 Research on Efficiency Optimization Control of Off-grid Photovoltaic Electrolysis System Considering Multi-energy Coupling 863

087 基于级联扩张观测器自抗扰控制的双馈风机次同步振荡抑制策略 879

088 基于简化模型 MPC 的双馈风机有功功率控制 886

089 基于改进滑模观测器的永磁同步电机无传感器控制研究 891

090 基于小波分析的煤矿多级供电网单相接地故障选线方法 897

091 基于 Transformer-BiGRU 的双阶段风电功率预测 902

092 基于 SimuNPS 的储能电站并网振荡预测 907

093 离网型柔性合成氨系统各装置优化配置 912

094 A Life Cycle Assessment Model for Energy Storage Considering Multiple Benefit Factors 917

095 面向风电场通信的融合边缘计算与协作中继的成本优化策略研究 924

096 基于 MILP 模型的配电网可靠性评估方法研究 929

097 台风-滑坡灾害链下输电杆塔多荷载空间耦合故障模型 934

098 Research on the Fault Diagnosis Architecture of Secondary Equipments in Intelligent Substation Driven by Holographic Transparency 939

099 变流器主导的电力系统宽频振荡模型及能量转换过程分析 950

100 基于时域卷积功率的柔性直流输电线路单端量保护方案 955

101 Research and Development of a Fault Self-Healing Experimental Device for Shipboard Zonal Distribution Power System 961

102 基于二次分解与 GJO-KELM 的短期光伏功率预测 977

103 基于对比学习的极端天气电力负荷预测方法 985

104 行业企业导师权益保障与创新激励的协同机制研究 991

105 Collaborative Planning for Interconnected Offshore Wind Farms Using Mixed-Variable Bayesian Optimization 995

106 新工科背景下“电力系统”英文课程教学改革探索 1009

107 Research on Long-Horizon Model Predictive Control and Seamless Switching of Grid-Forming Converters in Hybrid Systems 1014

108 基于改进高压直挂级联 H 桥拓扑的储能变流器构网穿越控制 1033

109 Transient induced voltage and current analysis during ice-melting operations on double-circuit lines on the same tower 1039

110 基于动态任务对齐的电力场景小目标缺陷检测方法 1051

111 考虑热回收的寒地电算协同中心综合能源系统运行控制 1065

112 基于可控避雷器的直流送端换流站暂态过电压抑制措施 1075

113 An Optimization Method for Energy-Intensive Industrial Loads Participating in Demand Response Considering Energy-Material Flow Coupling 1080

114 Optimization of Isolation Measures for Single-phase Faults in the Collection Systems of New Energy Stations 1091

115 Impact of Voltage Measurement Errors on Voltage Control Performance of VSCs During Low-Voltage Ride-Through 1101

116 HVDC Operational Constraints in High-Penetration Wind-PV-Storage Hybrid Systems 1117

117 双碳目标下电磁场课程改革：新型电力系统工程案例贯穿的教学探索 1126

118 基于节点边际电价信号的主配网协同光伏接入容量评估模型..... 1131

119 A State Inference Method for Distribution Networks Utilizing Minimally Acquired Operational Data and Its Application..... 1139

120 Specific-Area-Level Charging Demand Forecasting and Analysis for Electric Vehicles Using iTransformer..... 1146

121 AC-side Oscillation Suppression of MMC-based Deicing Devices..... 1155

122 Energy Storage Control for Transient Stability Based on Power Angle Feedback..... 1167

123 Multi-mode Compound Control of Full-bridge MMC-based De-icing Devices.....1178

124 基于 V-I 轨迹颜色编码与特征优选的 NILM 方法..... 1191

125 Coordinated Wind-Storage Control Strategy for Enhancing Frequency Regulation Characteristics in Power System..... 1199

126 基于模型设计的光伏模拟器控制系统代码生成.....1211

001 基于大数据的电力设备状态监测与故障诊断方法

王　伟　　胡庆娥

（国网天津滨海供电分公司　天津市滨海新区营口道 394 号）

Method for Condition Monitoring and Fault Diagnosis of Power Equipment Based on Big Data

Wei WANG　Qinge HU

(State Grid Tianjin Binhai Electric Power Supply Branch　No.394,Yingkou Road,Binhai New Area, Tianjin)

ABSTRACT: Based on the multi-source collection of power equipment condition data, this paper explores big data-driven condition monitoring and intelligent fault diagnosis methods. It analyzes the application of mainstream technical models, such as machine learning and deep learning, in power industry scenarios, and proposes corresponding optimization strategies. Research demonstrates that big data-driven intelligent diagnostic systems can significantly enhance fault identification efficiency and equipment operational maintenance levels.

KEY WORDS: Big data; Power equipment; Condition monitoring; Fault diagnosis; Intelligent operation and maintenance; Machine learning

摘要：近年来，随着智能电网向数字化、智能化方向快速发展，电力设备监测数据呈现指数级增长态势。传统阈值报警和统计分析方法在应对海量异构数据时，普遍存在实时性差、误报率高的问题，尤其难以有效融合设备历史运维记录与环境参数等非结构化数据[1]。本研究认为电力设备监测亟须构建基于多模态数据融合的智能分析体系，通过引入大数据技术可以实现设备运行状态的多维度特征提取与关联分析，并且结合自然语言处理技术挖掘设备历史工单文本中的隐性知识，通过构建电力设备知识图谱，实现环境参数、运行数据与运维经验的多源信息融合。

关键词：大数据；电力设备；状态监测；故障诊断；智能运维；机器学习

0　电力设备状态监测的技术基础

0.1 多源数据采集与融合技术

电力设备状态监测依赖多源数据的采集与融合技术，实现对设备运行状态的全面感知。SCADA 系统实时采集设备的运行参数。主变压器监测点位包括油温、绕组温度、顶层油色谱、局部放电、铁芯振动五项关键参数，采用高精度传感器进行实时数据采集；断路器监测重点关注操作机构特性、触头温度、SF6 气体压力等运行参数，并配置相应的传感设备进行数据采集[2]。基于当前电力设备多源监测数据的特点，本研究认为构建智能化的数据融合与分析平台是提升设备状态监测效能的关键，通过建立统一的数据中台架构，能够有效整合 SCADA 系统、传感器网络、智能终端和历史运维数据，实现设备状态的立体化感知与协同分析。

0.2 大数据平台架构与处理流程

目前的大数据平台架构都是由电力设备状态以及监测数据提供整体框架的，平台架构中主要由数据采集层、预处理层、分析层、可视化层组成；多个层级负责不同的功能模块，各类数据源若想汇聚到平台需要数据采集层进行对接；而原始数据的数据格式统一，以及清洗、转换和集成，则是需要预处理层来完成；针对于数据的海量存储特征，存储层更加能够保障其安全性；后续的数据深度分析需要分析层采用多种算法完成，才能将设备当前的特征以及故障细化出规律；最后的可视化层则是将整体数据分析后呈现图表、仪表盘的形式，更加便捷于维修人员辨别故障、进行解决。

0.3 状态监测指标体系构建

电力设备状态监测的指标体系构建，是整体设备关键运行的环节。其中核心指标由电压、电流、维度、振动等性能数据组成，一旦这些指标出现异常则说明设备存在故障；电压、电流指标存在波动说明设备面临着绝缘、抑或负载异常，而设备发热情况则是由温度指标进行观察，接触不良或者运行过载等原因都是由于温度过高导致的；旋转类设备更多需要查看的是振动指标，机械磨损、部件松动等情况都要根据异常振动来确定。

1 基于大数据的故障诊断方法

1.1 基于机器学习的故障识别模型

基于大数据的电力设备状态监测，需要通过有效的机器学习故障识别模型分类；针对于电力设备故障类型可以采用决策树算法的方式，以树形结构来直观进行故障判断呈现，更加方便检修人员理解。而在高位空间中对于超平面进行分类，则需使用 SVM（支持向量机），才能将过于复杂的非线性故障进行特征有效出来。在后续的多个决策树的集成学习过程中，若想提高故障识别的准确率，则可以通过随机森林进行故障检测。

1.2 深度学习在故障预测中的应用

深度学习技术为电力设备故障预测提供了强大的特征提取与趋势分析能力。深度学习模型，如卷积神经网络（Convolutional Neural Network, CNN）和长短期记忆网络（Long Short-Term Memory，LSTM），已被证明在处理大量复杂数据方面极为有效，LSTM 模型在循环神经网络（Recurrent Neural Network，RNN）模型的基础上改进而来，均使用链式循环结构，RNN 模型的链式结构如下图所示。

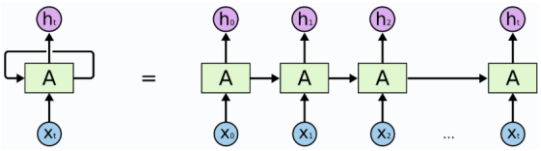


图 1 循环神经网络模型结构

Figure 1: Structure of Recurrent Neural Network Model

从上图可以看出，链式循环结构使得每个时刻的隐藏状态不仅取决于当前时刻的输入向量，还取决于上一时刻的隐藏状态，然而，RNN 模型内部仅由一个隐藏状态，状态更新主要依赖 tanh 激活函数，这是使得 RNN 模型难以同时处理长期特征与短期特征，尤其是在 RNN 模型训练的阶段，在基于误差反向传播算法优化模型参数时，极易出现梯度爆炸、梯度消失的现象，降低了模型对电力设备故障预测的能力。因此，本文建立基于 LSTM 的电力设备故障预测模型，LSTM 模型内部包含了输入门、遗忘门和输出门，通过特殊的门控机制保留了长期特征与短期特征，LSTM 的模型基本结构如图 2 所示。

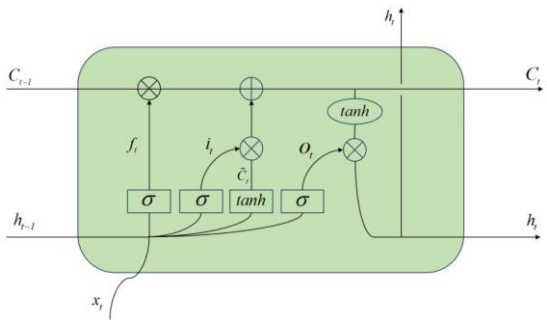


图 2 长短期记忆网络模型基本结构

Figure 2: Basic Structure of Long Short-Term Memory (LSTM) Network Model

由上图可知，输入门、遗忘门和输出门会有选择的删减、弱化次要特征，突出主要的特征，遗忘门会适时的丢弃次要、冗余特征，输入门会将最新的信息添加进信息流中，输出门将挑选适当的特征传递给下一层神经网络，LSTM 基于上述门控机制，提升了模型对电力设备故障的预测能力。同时，为充分捕捉电力设备故障之间的耦合关系，本文利用双向长短期记忆网络（Bi-directional Long Short-Term Memory，Bi-LSTM）模型捕捉电力设备故障之间的耦合关系，Bi-LSTM 的模型架构如下所示。

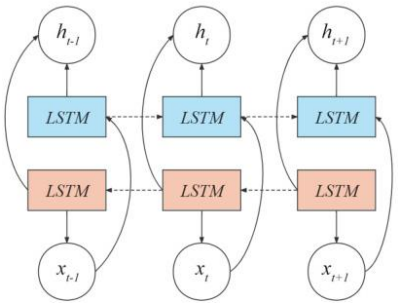


图 3 双向长短期记忆网络模型架构

Figure 3: Architecture of Bidirectional Long Short-Term Memory (BiLSTM) Network Model

Bi-LSTM 模型主要包含前向层和反向层，在前向层中，正向 LSTM 按照时间顺序依次读取电力设备故障事件，在反向层中，反向 LSTM 按照逆序捕捉故障事件耦合特征，前向层和反向层相互独立，不共享模型参数，但使用相同的输入向量，这样的模型结构使得 Bi-LSTM 能够充分捕捉电力设备故障事件的耦合关系，提升模型对电力设备故障的预测能力，这为从海量的设备运行数据中提取关键信息，预测设备的未来状态和维护需求提供了可能[3]。尽管深度学习在电力设备故障预测中展现出巨大潜力，但其实际应用仍面临模型可解释性不足、小样本场景下泛化能力有限等挑战。本研究认为，

将深度学习与传统机理模型相结合，构建“数据驱动+知识引导”的混合预测框架是未来的发展方向。

1.3 异常检测与自学习机制构建

电力设备状态监测与故障诊断需要构建高效的异常检测、以及自学习机制，方能保证系统持续具有适应数据能力。在监测过程中需要建立基准模型保障设备的正常运行，不仅能及时将潜在的故障隐患挖掘出来，还能有效识别偏离精准的异常设备行为，对于尚未记录储存的故障类型有良好的识别能力。针对于新出行的故障案例以及运行数据，自学习机制可以根据模型功能进行不断的吸收、学习，将自身的故障特征库不断自动更新，有效提升未知故障的逐步识别能力。

2 应用挑战与优化策略

2.1 数据质量与模型训练问题

当前阶段电力设备故障监测与诊断面临的最大挑战是如何建立数据质量、以及模型训练；由于电力设备监测与诊断的过程中，常常容易遭遇采集数据不稳定的情况，最终会导致模型训练的学习效果不佳。而且，正常数据的样本数量要远远多于故障数据，导致模型训练只能收集到极少数的故障类型，后期真正需要识别的时候能力较弱。针对于以上诸多情况，本文建议在模型训练过程中加入数据清洗技术，用以有效增强数据的真实性，并且同步将故障样本平衡分布；对于不敏感数据无法有效收集的情况，可以采用集成学习方法将模型训练的泛化能力提升，最终实现复杂数据环境下还能保障诊断性能的稳定性。

2.2 模型实时性与部署效率问题

模型的实时性与部署效率是制约大数据故障诊断技术落地应用的关键因素。电力设备状态数据实时产生，要求模型能够快速处理并给出诊断结果，而复杂的深度学习模型计算量大，难以满足实时性需求；同时，不同电力设备的运行环境与硬件条件差异较大，模型部署面临兼容性与效率问题。如基于时间序列分析法，实现对电力设备远程精准诊断、故障预警。在众多模型中，长短期记忆网络（LSTM）凭借独特结构、强大处理长期依赖关系的能力脱颖而出，现已广泛应用于电力设备相关数据的深度分析之中[4]。针对电力设备故障诊断中模型实时性与部署效率的挑战，可以通过将 LSTM 等时序模型进行知识蒸馏和量化压缩，在边缘侧实现毫秒级故障初筛，同时依托云端强大的计算能力完成复杂故障的精准分析。

2.3 标准化建设与系统集成难题

近年来，基于大数据技术的电力设备状态监测与故障预警系统逐渐成为研究热点，通过对设备运行数据的实时监测与分析，能够及时发现潜在故障，避免事故发生，提升设备的安全性和运行效率[5]。目前，电力行业不同设备厂商的数据格式、接口规范不统一，导致数据共享与融合困难；不同诊断模型的输出形式与应用场景存在差异，难以实现系统间的协同工作。解决这些问题需要推动行业数据标准的制定，统一数据采集、存储与传输的格式；规范模型接口与输出标准，促进不同模型的集成与协同。

3 结语

大数据技术为电力设备的智能运维提供了强有力的技术支撑。通过构建高效的数据采集体系、应用先进的数据挖掘与建模技术，可以实现电力设备状态的全面感知与故障的精准预测。未来，应进一步完善数据平台建设、优化模型性能，并推动行业标准化落地，构建“感知—分析—预测—决策”一体化的电力设备智能诊断体系，为智慧电网建设提供坚实保障。

参考文献

[1] 王长安，周苗苗. 基于大数据的电力设备状态监测与故障诊断方法[J].中国高新科技，2025,(10):63-65.

[2] 宋宏冰，袁克立，袁辉. 基于深度学习的电气设备运行状态预测和健康管理研究[J].电气技术与经济,2024,(05):01-03.

[3] 李平. 电力设备运行状态监测技术的优化与应用[J].中国机械，2025,(13):94-97.

[4] 苏曼丽，门茂臣. 基于物联网的电力设备状态监测与故障预警技术研究[J].家电维修，2025,(05):137-139.

[5] 姚海峰. 基于大数据技术的电力设备运行状态监测与故障预警系统[J].电工技术，2025,(02):105-108.

收稿日期：2025-08-25。

作者简介：



王伟

王伟(1985 年)，女，硕士研究生，高级工程师，运维检修部变电运检室技术员，E-mail：wei.wangd@tj.sgcc.com.cn；



胡庆娥

胡庆娥(1993 年)，女，硕士研究生，中级工程师，运维检修部变电运检室正值监控员，E-mail：qinge.hu@tj.sgcc.com.cn。

002 Modeling for Efficient Impulse Resistance Assessment of Transmission Tower Grounding Systems

Xingyu Meng[1], Wei Xu[1], Caitang Sun[1] and Gang Li[1]

[1] the College of Instrumentation and Electrical Engineering ,
Jilin University, Changchun 130061, China
ligang2013@jlu.edu.cn

Abstract. The accelerated deployment of ultra-high-voltage (UHV) transmission systems necessitates enhanced lightning protection reliability, where the transient characteristics of tower grounding systems under lightning impulses directly determine power system security. While conventional impulse resistance models incorporate soil nonlinear ionization effects, their practical implementation is constrained by intricate parameter calibration and prohibitive computational demands, failing to meet requirements for rapid engineering design and real-time assessment. To address the critical need for efficient estimation of conductor impulse resistance in field applications, this paper proposes a linear model-based computational methodology. By integrating convolution techniques with finite element methods, this study establishes circuit models via Simulink and finite element models with COMSOL to comprehensively investigate grounding system response under lightning currents. Model validity is demonstrated through comparative verification. Furthermore, our framework develops impulse resistance mitigation strategies addressing key parameters: capacitive-inductive properties, soil resistivity, conductor spatial arrangements, and grounding grid topologies. This provides theoretical foundations for optimizing analytical approaches, streamlining engineering design, and enhancing computational efficacy in UHV projects.

Keywords: Grounding System, Impulse Resistance, Convolution Method, Finite Element

1 Introduction

Transmission lines constitute the primary infrastructure of power grids. As grid construction scales expand, the requirements for transmission line safety and stability become increasingly stringent. Tower grounding resistance serves as a critical indicator of transmission line safety, encompassing both power-frequency grounding resistance and impulse grounding resistance, which typically exhibit significant differences [1]. Accurately analyzing the impulse resistance characteristics of tower grounding systems and precisely calculating the impulse resistance magnitude are of paramount importance for enhancing tower lightning protection capability and transmission line safety [2].

2

When lightning current flows through a grounding conductor into the soil, it induces a rapid increase in the soil's electric field intensity. Once the internal electric field intensity exceeds a certain threshold, spark discharge occurs, known as the soil ionization effect [3]. Accounting for soil ionization significantly complicates the analysis of grounding conductor impulse characteristics, leading to complex parameter calibration and higher computational costs, which hinders meeting the demands for rapid engineering design, estimation, and assessment. Therefore, establishing simplified models of grounding conductors is necessary to simulate their behavior, enabling convenient and accurate measurement of impulse grounding resistance [4].

Currently, extensive research has been conducted domestically and internationally on the impulse characteristics of grounding conductors. Visacro S. et al. [5] investigated the dependence of grounding electrode resistance on various parameters, primarily focusing on soil resistivity and permittivity. Simulation tests were conducted on six typical tower grounding bodies by Professor He Jinliang's team, providing recommendations for selecting practical grounding device structures. They also derived empirical formulas for the impulse coefficient and effective length of different grounding device configurations [6]. A soil ionization model based on energy conservation during the ionization process was proposed by S. Sekioka and M.I. Lorentzou, where soil electrical parameters depend on the energy stored within the ionized zone post-ionization [7]. This model was compared with the A.C. Liew model [8][9], and it concisely elucidates the physical process of soil ionization, explaining the fundamental reason for the lag in grounding device impulse impedance changes relative to current variations. Professor Sima Wenxia's team at Chongqing University has conducted substantial research on impulse resistance measurement. Based on dimensional similarity principles, they performed impulse grounding simulation tests on grounding grids in homogeneous and two-layer soils using impulse current generators. The influence patterns of factors such as current injection point location, grid burial depth, and soil structure on the impulse grounding characteristics of grids were established through analysis of impulse grounding resistance and potential distribution under various test conditions [10]. Furthermore, the team[11] investigated the impact of short conductors on impulse resistance characteristics and proposed related impulse resistance reduction methods.

This paper employs a methodology integrating circuit theory with electromagnetic field theory. By establishing grounding system models in Simulink and COMSOL, a refined characterization of the grounding system is achieved. The research investigates the influence of multiple factors on the impulse characteristics of grounding conductors and explores resistance reduction methods tailored to different factors. The findings provide valuable references and theoretical support for the convenient, accurate measurement, assessment, and optimization of tower grounding resistance in engineering practice.

2 Model Building

2.1 Circuit Theory — Equivalent Circuit Models for Grounded Conductors

In the theoretical analysis of impulse grounding resistance, the conventional power-frequency grounding resistance model is insufficient to accurately characterize the dynamic response characteristics of grounding devices, due to the high-frequency transient effects induced by the steep-fronted characteristics of lightning currents (with rise times on the order of microseconds). Based on electromagnetic field theory analysis, and neglecting the nonlinear effects of soil ionization, the grounding conductor network can be abstracted into a circuit model of a linear time-invariant (LTI) system. Building upon this foundation, this paper equivalently models the grounding system as a Π-type circuit. The Circuit is as Fig. 1. In subsequent simulation experiments, the circuit can be further simplified as shown in Fig. 2.

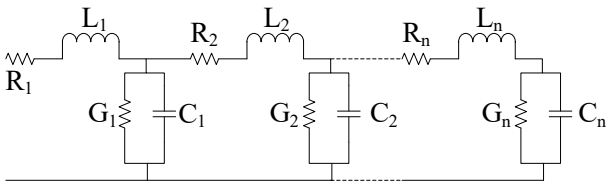


Fig. 1. Equivalent Circuit Diagram of Grounding System

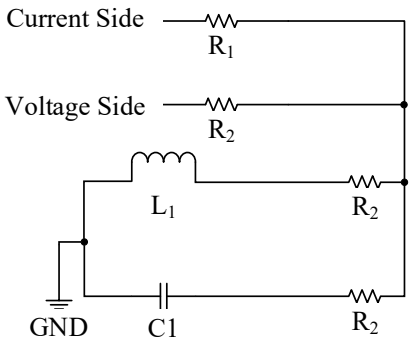


Fig. 2. Equivalent Circuit Diagram of Grounding System

As depicted in Fig. 2, resistor R_1 represents the current pole grounding resistance, while R_2 corresponds to the voltage pole grounding resistance, with both parameters specified as 100 Ω. This circuit model explicitly incorporates the influence of capacitance and inductance on impulse resistance characteristics, enabling simulation and analysis of grounding system behavior under non-ionizing soil conditions.

2.2 Convolutional Models

The convolution method enables indirect determination of impulse grounding resistance through application of readily obtainable, low-frequency, low-magnitude impulse currents.

For the previously defined linear time-invariant (LTI) system, the input impedance transfer function Z(s) = V(s)/I(s) exhibits time-domain convolution properties. When both excitation and response functions are measured at the same system port, the transfer function corresponds to either input impedance or admittance. Under these conditions, the system function remains invariant. Consequently, injection of a gradual-rise, low-magnitude impulse current into the grounding system, coupled with measurement of the resultant voltage response, permits indirect computation of the conductor's impulse grounding resistance.

Define the input/output function as follows:

Let the input current signal be $i_1(t)$, the low-frequency output voltage signal be $u_1(t)$, the input inrush current signal be $i_2(t)$, the output signal at the time of inputting inrush current be $u_2(t)$, and the system function be h(t).

According to the invariance of the system function, there is the following relation:

$$H(s)=\frac{U_1(s)}{I_1(s)}=\frac{U_2(s)}{I_2(s)} \tag{1}$$

$$U_1(s)\cdot I_2(s)=U_2(s)\cdot I_1(s) \tag{2}$$

Application of the inverse Laplace transform to the preceding equation yields the continuous time-domain convolution integral governing the system dynamics.

$$u_1(t)*i_2(t)=u_2(t)*i_1(t) \tag{3}$$

$$\int_0^t u_1(\tau)i_2(t-\tau)d\tau=\int_0^t u_2(\tau)i_1(t-\tau)d\tau \tag{4}$$

Exploiting the inherent discretization property of convolution operators, the continuous convolution integral may be transformed into a discrete-time representation through sufficiently fine temporal sampling, yielding:

$$u_1(n)*i_2(n)=u_2(n)*i_1(n) \tag{5}$$

Among them, $i_1(n)$, $i_2(n)$ for the input signal sampling value sequence, can be obtained directly, $u_1(n)$ for the low-frequency output voltage signal sampling value sequence, which is easier and more accurate to measure, so the sequence of $u_2(n)$ can be based on the other three sequences of the value of solving out.

Consequently, the output sequence $u_2[n]$ can be computationally derived from the other three sequences via the system invariance relation. The impulse grounding resistance magnitude is then determined by the ratio of peak values [12].

2.3 Finite Element Model

The finite element method (FEM) is a numerical analysis technique capable of effectively addressing boundary value problems. Its fundamental principle can be elaborated as follows: the solution domain is discretized into a multitude of small elements; within each element, an approximate function is assumed, and the combination of these functions is employed to represent the unknown field function to be solved. Through this process, the solution domain is transformed from a continuous system with infinite degrees of freedom to a discrete system with finite degrees of freedom. The solution of the entire system is approximated by a finite set of unknown coefficients of the interpolating functions defined on each subdomain. Subsequently, by applying either the Ritz transformation or the Galerkin method to process the unknown functions of the subdomains, a system of algebraic equations is derived. Solving this system of equations yields the solution to the boundary value problem [13].

When a lightning impulse current is injected into the grounding device, the potential equation can be derived based on electromagnetic field theory.

$$\varepsilon \frac{\partial}{\partial t}\left(\nabla^2 \varphi\right) + \nabla(\gamma \nabla \varphi) = 0 \tag{6}$$

This formulation satisfies the following boundary conditions:

1) Potential approaches zero at infinity

2) Normal component of current density vanishes at the ground surface

3) Continuity of potential and current density across material interfaces

Significant resistivity discontinuities at soil-conductor interfaces induce pathological matrix conditioning, leading to convergence impairment or failure in solving the potential equation. The finite element method effectively mitigates these numerical instabilities.

The solution domain encompassing both soil and grounding structures is discretized using four-node isoparametric tetrahedral elements. Application of the Galerkin weighted residual method to the potential equation yields.

$$R_i^e = \int_{V_e} N_i^e \left[\varepsilon \frac{\partial}{\partial t}\left(\nabla^2 \varphi^2\right) + \nabla\left(\gamma \nabla \varphi^e\right) \right] dV \tag{7}$$

Where V_e is the unit integration interval, N_i^e is the weight function of the i-th node in unit e, φ^e is the interpolation function, and R_i^e corresponds to the residue weighted integration.

The potential on the e-region of the discretized resulting cell can be expressed by the following equation.

$$\varphi^e = \sum_{j=1}^{10} N_j^e(x, y, z)\varphi_j^e \tag{8}$$

A simplification of the above equation yields the equation for the unit associated with the current injection surface:

$$R_i^e = \sum_{j=1}^{10} \varphi_j^e \int_{V_e} \left[\left(\varepsilon \frac{\partial}{\partial t} + \gamma \right) \nabla N_i^e \nabla N_j^e \right] dV - \int_{\partial V_e} N_i^e \sigma ds = 0 \tag{9}$$

σ is the current surface density at the boundary where the current injection point is located.

The unitary equation not associated with the current injection surface is given by:

$$R_i^e = \sum_{j=1}^{10} \varphi_j^e \int_{V_e} \left[\left(\varepsilon \frac{\partial}{\partial t} + \gamma \right) \nabla N_i^e \nabla N_j^e \right] dV = 0 \tag{10}$$

On this basis, the finite element model can be iteratively calculated.

3 Circuit-convolution Modeling Calculations

3.1 Lightning Current Generation Circuit

The transient current associated with the lightning discharge process exhibits prominent high-frequency spectral characteristics, nonlinear time-domain distribution features, and a large current amplitude. Taking the 4μs/10μs current specified in the international standard IEC 61000-4-5 as an example, its wavefront time (defined as the time interval from the virtual origin to reaching 90% of the peak value) is 4±0.4μs, and the half-peak time (defined as the time interval from the wavefront origin to reaching 50% of the peak value) is 10±1μs. Its dynamic process demonstrates significant nonlinear time-varying behaviors.

Based on the aforementioned current definition and circuit theory, this study constructs an RCL series circuit to generate the above-described lightning current. The corresponding circuit diagram is presented in Fig. 3:

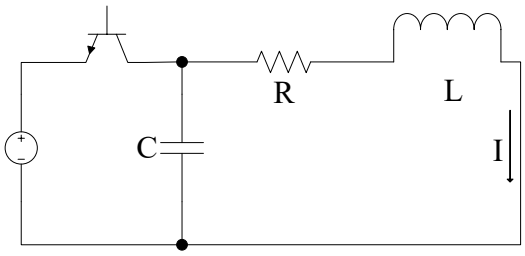


Fig. 3. Lightning Current Generator Circuit Diagrams

Within the circuit, the initial voltage dictates the pulse amplitude, the inductance parameter L governs the wavefront steepening effect, the capacitance C regulates the energy release rate, and the distributed resistance R, approximated via piecewise linearization, endows the wave tail with an exponential decay characteristic.

For instance, to generate a 4μs/10μs current waveform with a peak value of 10kA, the circuit parameters are configured as follows: capacitor charging voltage of 519kV,

capacitance of 1.5 μF, resistance of 3 Ω, and inductance of 12 μH. This parameter configuration enables the generation of the aforementioned lightning current waveform, which is illustrated in Fig. 4.

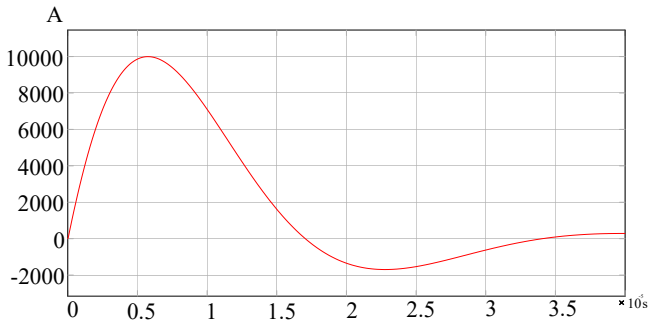


Fig. 4. 4μs/10μs lightning current waveforms

The waveform characteristics meet the requirements of the national standard, and subsequent current waveforms of different frequencies and peaks can be generated by changing the values of the circuit component parameters.

3.2 Simulation Circuit Construction

Based on the theoretical foundation of RLC series circuit model and convolution method, a high-precision lightning inrush current simulation system is built on Simulink platform, and the circuit block diagram of the simulation system is shown in Fig. 5:

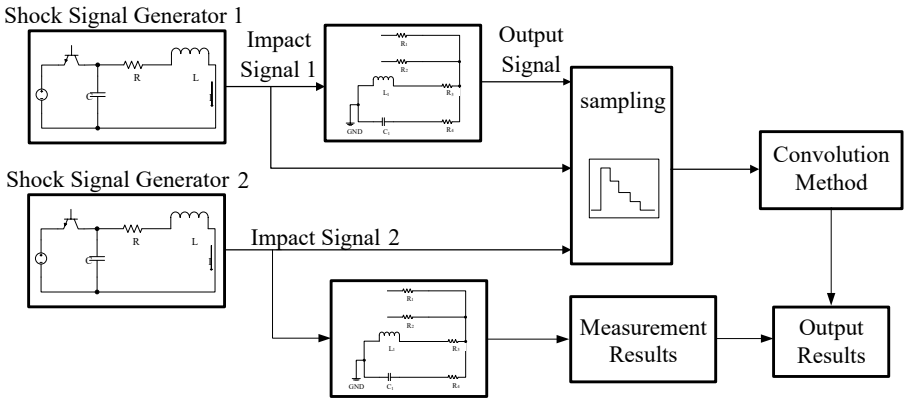


Fig. 5. Block diagram of the simulation system circuit

Two sets of inrush current generating circuits are used in the figure, where Shock Signal Generator 1 is used to generate inrush current with a slower wave head and

smaller peak which is readily available in the engineering, and the other set is used to generate lightning currents. After sampling the required signals, the convolution calculation can be converted into a matrix operation, so as to solve the impulse resistance of the grounding system according to the convolution theory interval.

3.3 Impulse Characterization under Convolutional Modeling

Three standardized lightning impulse currents (4μs/10μs, 8μs/20μs, and 30μs/80μs per IEC 62305-1) were applied to validate the simulation circuit. Each waveform featured a 100μs wavefront time and 1000A peak magnitude injected at the grounding system input terminal. The resultant output voltage waveform was recorded, and convolution operations were performed between these voltage measurements and the corresponding lightning current waveforms. This enabled computational determination of the grounding system's impulse resistance (CMR), which was subsequently compared against direct measurements of surge impulse resistance (SMR) obtained through conventional injection methods. The comparative results are presented in Table 1:

Table 1. Convolutional model test results.

Current type	CMR (Ω)	SMR (Ω)	Error
4μs/10μs	7.121	7.144	0.32%
8μs/20μs	7.540	7.211	4.56%
30μs/80μs	9.194	8.930	2.96%

Comparative analysis between computational results and simulation data demonstrates close agreement, with convolution-derived impulse resistance values deviating within 5% of simulated measurements. To evaluate parameter sensitivity, a 4μs/10μs lightning current waveform was applied to the grounding system while systematically varying its inductive and capacitive components. Under controlled conditions where inductance and capacitance were maintained at 20 μH and 1 μF respectively, the correlation between computed impulse resistance and simulated values is quantified in Fig. 6:

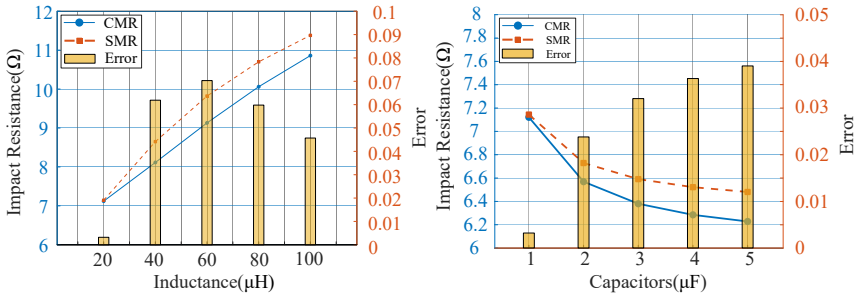


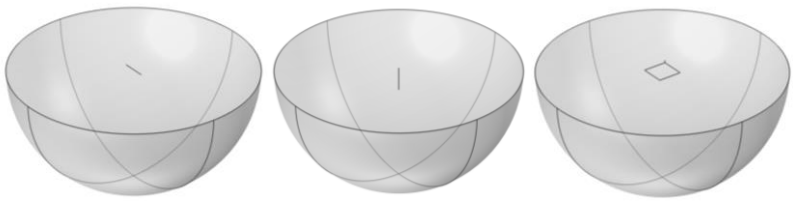
Fig. 6. Output results under different parameter conditions. (a) different inductance values, (b) different capacitance values

Analysis of these results demonstrates that the convolution method achieves higher computational accuracy for grounding systems exhibiting predominantly capacitive characteristics, with relative errors under 5%. Conversely, systems dominated by inductive properties show reduced accuracy when applying this methodology.

4 Finite Element Modeling

4.1 Simulation Model Building

The grounding conductor model was developed in COMSOL Multiphysics. Representative configurations, specifically a single vertical grounding electrode and a square grounding grid, were employed for this study. The corresponding models are presented in Fig. 7:



(a) (b) (c)

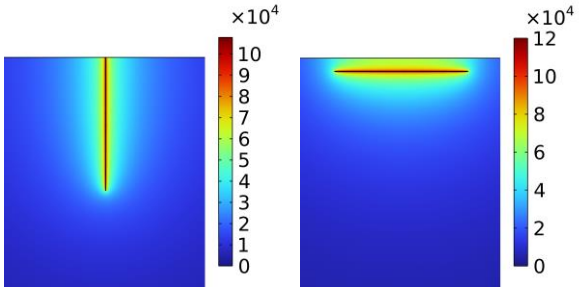
Fig. 7. Grounding conductor models. (a) Single horizontal conductor, (b) Single vertical conductor, (c) Square grounding grid model.

The grounding conductor is modeled as a cylindrical steel element with an electrical conductivity of 5.8×10^6 S/m. Geometrical parameters are defined as follows: a base radius of 0.1 m, with both the single-electrode length and grounding grid edge length set to 10 m. A standard 8μs/20μs lightning impulse current waveform (10 kA peak magnitude) is applied at the excitation point. The computational domain employs the following boundary conditions: (1) Zero potential at infinity; (2) Zero normal current density at the ground-air interface; (3) Continuity of electric potential and current density across all material interfaces.

4.2 Impulse characterization of a single conductor

Under the assumption of negligible soil ionization effects, the soil is modeled with constant electrical conductivity corresponding to a resistivity of 100 Ω·m. Fig. 8 presents the electric potential distribution in the vertical plane containing the conductor axis at the peak magnitude (10 kA) of the lightning impulse current.

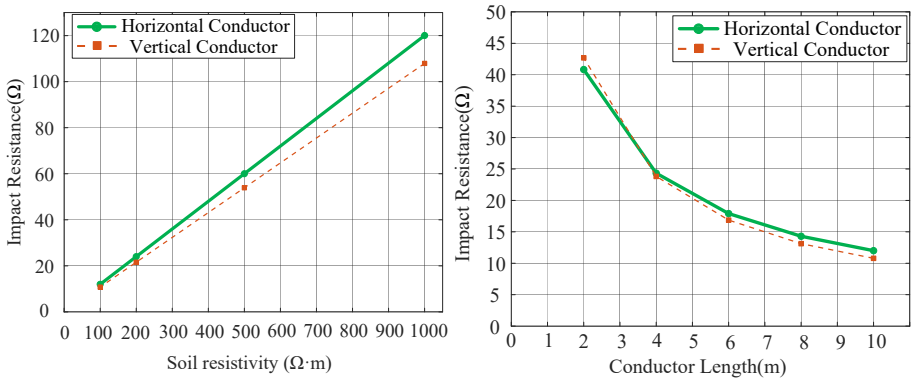
10



(a) (b)

Fig. 8. Potential distribution near the grounded conductor (unit: V). (a) Vertical Conductor, (b)Horizontal Conductor

The impulse resistance of the grounding conductor is determined by calculating the peak electric potential developed during lightning current injection. A parameter variation study was conducted with soil resistivities of 1000 Ω·m, 500 Ω·m, 200 Ω·m, and 100 Ω·m. The computed impulse resistance values are summarized in Fig. 9 (a).



(a) (b)

Fig. 9. Results of finite element model. (a) Different soil resistivities, (b) Different conductor lengths

It can be seen that under the linear model, the larger the soil conductivity, the smaller the impulse resistance value, and the two are linearly related.

Setting the soil resistivity as 100 Ω·m and changing the length of the conductor, the impulse resistance is calculated as Fig. 9 (b). From the results, the longer the conductor length, the lower the impulse resistance.

4.3 Impulse characterization of a single conductor

For the representative case of 100 Ω·m soil resistivity, the structural layout of the square grounding grid and the equipotential distribution in its axial plane are shown in Fig. 10.

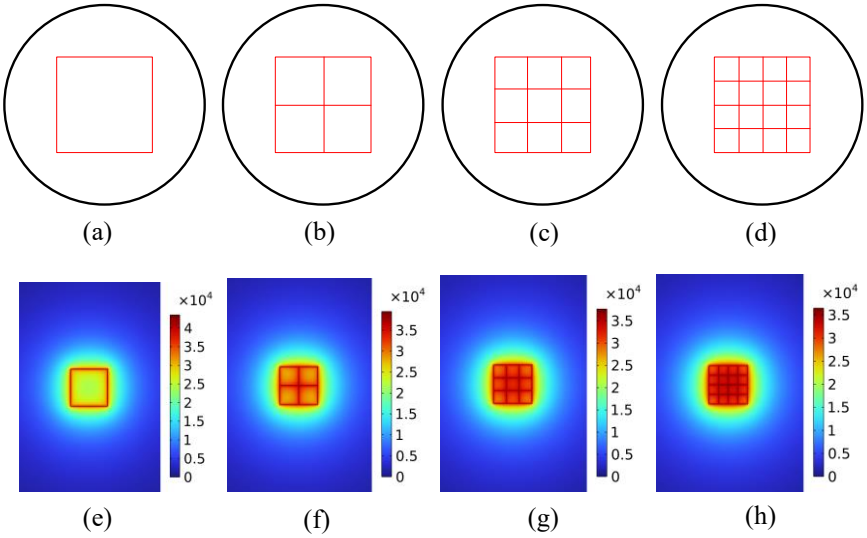


Fig. 10. Schematic diagram of the grounding network and potential distribution. (unit: V) (a) 1×1, (b) 2×2, (c) 3×3, (d) 4×4; (e) 1×1, (f) 2×2, (g) 3×3, (h) 4×4.

The spatial distributions of electric potential surrounding the grounding conductors under each considered scenario are quantitatively summarized in Table 2:

Table 2. Table captions should be placed above the tables.

Grounding network form	Impulse resistance(Ω)
1×1	4.3560
2×2	3.9454
3×3	3.7647
4×4	3.6468

Numerical analysis demonstrates that incorporating grid topology into the grounding system significantly reduces impulse resistance. Furthermore, grounding resistance exhibits a monotonic decrease with increasing grid discretization density. Beyond critical density thresholds, however, the resistance reduction progressively attenuates, indicating diminishing returns on meshing refinement.

12

5 Conclusions

Based on the fundamental principles of the convolution method and the finite element method , this paper establishes a computational model for analyzing the impulse characteristics of grounding devices and achieves the simulation of impulse grounding resistance. The specific research procedure is as follows:

According to circuit theory, a lightning discharge circuit and a convolution-based computational circuit model were constructed and tested. The tests indicate that the model exhibits high computational accuracy. Subsequently, the model was applied to simulate grounding systems with significant inductive and capacitive characteristics.

Based on electromagnetic field theory, a finite element analysis model was developed to simulate working conditions under different types of conductors or grounding grids and varying soil resistivity values. Detailed simulation analyses were subsequently conducted.

The study yields the following conclusions:

The convolution method enables rapid and accurate calculation of impulse grounding resistance. Further analysis reveals that for grounding systems with notable capacitive characteristics, the convolution method offers higher accuracy in impulse resistance calculations.

Finite element simulations demonstrate that technical measures such as increasing conductor length, reducing local soil resistivity, and adopting grounding grids with appropriate mesh density can effectively enlarge the current dissipation area in the soil, thereby significantly reducing the resistance value of the grounding system.

Acknowledgement: This work is supported by the Science and Technology Project of State Grid Jilin Electric Power Co. Ltd.

References

1. Zhang Liuchun.: Lightning protection of ±1100kV UHVDC transmission lines[J]. Transactions of China Electrotechnical Society, 33(19): 197-203 (2018).
2. Shang Zhiwei. Study on Experiments and Simulation on the Current Dispersing and Impulse Grounding Resistance Law of Tower Grounding Devices [D]. Huazhong University of Science & Technology (2016).
3. Mousa A M. The Soil Ionization Gradient Associated with Discharge of High Currents into Concentrated Electrodes[J]. IEEE Transactions on Power Delivery, 9(3): 1669-1677 (1994).
4. Grcev L. Impulse efficiency of ground electrodes[J]. IEEE Transactions on Power Delivery, 24(1): 441-451(2009).
5. Visacro S, Alipio R. Frequency dependence of soil parameters: experimental results, predicting formula and influence on the lightning response of grounding electrodes[J]. IEEE Transactions on Power Delivery, 27(2): 927-935 (2012).
6. Jinliang He，et.al. Characteristics and fitting formula of impulse coefficient of grounding device of transmission line[J]. Journal of Tsinghua University(Science and Technology),(05):10-13 (1999).

7. Sekioka S.Lorentzou M I, Philippakou M P, et al. Current-dependent grounding resistance modelbased on energy balance of soil ionization[J]. lEEE Transactions on Power Delivery, 21(1):194-201 (2006).
8. Nor N M, Haddad A, Griffiths H. Determination of threshold electric field EC of soil under highimpulse currents[J]. IEEE Transactions on Power Delivery, 20(3): 2108-2113 (2005).
9. Nor N M, Haddad A, Grifiths H, Characterization of ionization phenomena in soils under fastimpulses[J]. lEEE Transactions on Power Delivery, 21(1): 353-361 (2006).
10. SIMA Wenxia,et.al. Measurement and Analysis of Impulse Characteristics of Grounding Grids in Different Soil Structures[J] High Voltage Engineering, (07):1342-1346 (2008).
11. Yuan Tao et.al. Simulation Analysis of the Impact Characteristic of Grounding Electrode Based on the Current Shielding Effect[J]. Transaction of China Electrotechnical Society, 30(01):177-185 (2015)
12. WEI Jian,QU Lu,LU Hai-liang, et al. Design and Development of Portable Impulse Grounding Resistance Measurement Equipment Based on Convolution Principle[J]. Instrument Technique and Sensor, 2(2): 21-23+26 (2016).
13. A. Habjanic and M. Trlep, The simulation of the soil ionization phenomenon around the grounding system by the finite element method. IEEE Transactions on Magnetics, vol. 42, no. 4, pp. 867-870 (2006)

003 PV Output Forecasting Based on the Combinations of Scene-Adaptive Decomposition and SENet-reweighted Informer

Ruilin Liu, Lin Zhu, and Dechang Yang (✉)

College of Information and Electrical Engineering, China Agricultural University, Beijing 100091, China
yangdechang@cau.edu.cn

Abstract. Photovoltaic (PV) output forecasting is vital for grid stability. To improve the accuracy of PV output forecasting, many deep learning models have been adopted. However, traditional forecasting models often struggle to adapt to diverse weather conditions and neglect local feature details. To cope with these limitations, this paper proposes a feature-reweighted, scene-adaptive framework. This framework integrates Whale Migration Algorithm (WMA)-optimized Variational Mode Decomposition (VMD) and SENet-reweighted Informer. In the first stage, features are filtered by correlation analysis and clustered into distinct weather scenes. Next, WMA adaptively optimizes the VMD parameters for each specific scene. This optimization produces intrinsic mode functions (IMFs), which effectively separate multi-scale temporal components. Moreover, the Informer-SENet model incorporates the Squeeze-and-Excitation (SE) block after the self-attention distillation procedure. This approach reweights critical local features while preserving long-sequence processing ability. Finally, the framework was evaluated by using real data from a Ningxia PV power plant. Experimental results demonstrate that the proposed framework achieves a maximum error reduction of 96.8% in MSE over the baseline models.

Keywords: Photovoltaic Power Forecasting, Whale Migrating Algorithm, Variational Mode Decomposition, Informer, Squeeze-and-Excitation Networks.

1 Introduction

Accurate PV output forecasting can enhance grid reliability and scheduling efficiency, promoting the transition to clean energy [1]. To improve forecasting accuracy, various forecasting models have been developed. PV output forecasting models can be divided into statistical, physical, machine learning, and hybrid models [2]. Physical models include total sky imagery, numerical weather forecasts, and satellite imagery models [3]. However, the accuracy of physical models heavily depends on accurate meteorological information and geographic details [4]. Statistical models use historical data and mathematical methods to construct the forecasting framework [5]. However, these models cannot effectively handle nonlinear problems [6]. Therefore, machine learning models

have become pivotal in PV forecasting. Recurrent Neural Networks (RNN) distribute parameters between layers for sequential data processing. Using RNN as a preprocessing step to capture spatial information enables PV output forecasting to consider both spatial and temporal information [7]. However, RNNs struggle with long-term dependencies [8]. One-dimensional convolutional neural networks (1D CNNs) can automatically extract features based on the characteristics of sequential data, which enables them to capture more meaningful information without manual feature engineering. However, 1D CNNs may overlook the relationships between sequential elements when processing long sequences [9]. In addition, Long Short-Term Memory Network (LSTM) and its variants are applied to PV output forecasting. Ait Mansour et al. [10] applied bidirectional long short-term memory networks (Bi-LSTMs) with 1D-CNNs and Gated Recurrent Units (GRUs) to forecast PV output. Although these models capture local and long-term features to some extent, their ability to catch long-term dependencies is limited by the gradient vanishing problem. Besides, the serial structure of LSTM reduces computational efficiency. Unlike RNN and LSTM, Transformer relies on a self-attentive mechanism to process sequence data, enabling it to capture long-range dependencies effectively. By eliminating the need for loop connections, it achieves parallelization, which significantly reduces training time and improves accuracy. Wang and Ma [11] proposed a robust hybrid deep learning model for PV output forecasting using a context-embedded causal convolutional Transformer (CCTrans) structure, which combines dynamic contextual information and single target variable forecasting (CDCTF). However, this model did not consider the unique features of individual components and the use of adaptive weight assignment during reconstruction. Informer combines sparse global attention with an efficient encoding-decoding architecture, which enables effective capture of global features. However, its tendency to overlook local features persists. Cao et al. [12] combined LSTM-Informer with an improved Stacking algorithm (ISt-LSTM-Informer). However, its performance in short-term forecasting was inferior to classical models.

As analyzed above, the common problems of PV output forecasting are as follows: in terms of extracting long-term dependencies, traditional models suffer from issues such as gradient vanishing and gradient explosion. Besides, the sequential nature of sequence processing limits computational efficiency. Meanwhile, long-sequence-optimized models often neglect local features. To deal with these challenges, this study proposes a PV output forecasting model that integrates scene-optimized decomposition (WMA-VMD) and feature-enhanced Informer (Informer-SENet) to improve accuracy in PV output forecasting. The main contributions of this study are as follows:

- In this study, WMA optimization, which is believed to achieve fast convergence, is utilized to enhance the scene-optimized decomposition.
- This study demonstrates an Informer-SENet deep learning model specifically designed for long sequence forecasting tasks, which is specialized in capturing both local features and long-term dependencies to perform PV output forecasting.

The structure of this paper can be summarized as follows: Section II introduces the scene-adaptive decomposition framework formed by WMA-based VMD parameter optimization and the methodology of the Informer-SENet architecture. Section III

presents the case study and analysis of forecast results. Section IV summarizes the conclusion of this research.

2 Methodology

2.1 WMA-VMD

Dragomiretskiy and Zosso [13] proposed Variational Mode Decomposition (VMD), which is an adaptive, quasi-orthogonal signal processing method based on variational optimization. By minimizing the total bandwidth of all modes, VMD decomposes signals into intrinsic mode functions (IMFs) with finite bandwidths and distinct center frequencies. This iterative approach extracts both dominant and noise modes, enabling multi-scale analysis. When VMD is applied to PV output data, it converts nonlinear random sequences into stable IMFs that isolate periodic features at different time scales. By forecasting and aggregating these IMFs, this method enables targeted learning of temporal variations and improves the accuracy of forecasts. However, VMD cannot realize parameter self-optimization; therefore, an optimization algorithm is required.

Ghasemi et al. [14] proposed an optimization method based on the cooperative migration behavior of humpback whales, which is called the Whale Migrating Algorithm (WMA). WMA combines the dynamics of leaders and followers with adaptive migration strategies to balance exploitation and exploration, thereby enhancing its ability to converge efficiently and avoid local optima when searching for global optimization. The optimization process of WMA is as follows:

Initialization. An initial group of migrant whales ($\boldsymbol{W}_i$) is created randomly between the upper bound U and lower bound L by Eq.(1), where the function rand(1, D) generates random numbers from the interval [0, 1] of the dimension D. "$\odot$" signifies the Hadamard product of two vectors and N_{pop} is the number of population members.

$$W_i = L + \text{rand}(1, D) \odot (U - L), i = 1, 2, \ldots, N_{pop} \tag{1}$$

Calculate the current position of whales. The leader whales who demonstrate superior knowledge guide the group. Therefore, the algorithm describes the entire group's actual position by calculating the leaders' average position and obtaining a single point. Through calculation, $\boldsymbol{W}_{Mean}$ represents the average of the present leaders' positions. The optimal position and current optimal parameters are updated based on the fitness of the current iteration.

Calves are influenced by their nearest neighbor. All whales are sorted in descending order according to their fitness value, and the best member is denoted by $\boldsymbol{W}_{Best}$. In the sequence, the nearest member influences every less experienced member (calf).

Leaders guide the calves. The position of the whole group of whales is equal to $\boldsymbol{W}_{Mean}$. The distance between points $\boldsymbol{W}_{Mean}$ and $\boldsymbol{W}_{Best}$ decreases as the entire group of experienced whales moves closer to $\boldsymbol{W}_{Best}$. Then, the calves must also start moving in the direction given by the vector rand $(1, D) \odot (\boldsymbol{W}_{Best} - \boldsymbol{W}_{Mean})$. Finally, the equation describing the new position of the less experienced member i is:

$$W_i^{new} = W_{Mean} + \text{rand}(1, D) \odot \left(W_{i-1} - W_i\right) + \text{rand}(1, D) \odot \left(W_{Best} - W_{Mean}\right) \tag{2}$$

2.2 Informer-SENet

Long sequence time-series forecasting (LSTF) predicts outcomes over extended future periods rather than for single time steps. Therefore, LSTF models must effectively handle long-range dependencies. Based on Transformer, Zhou et al. [15] proposed Informer, an efficient Transformer variant optimized for LSTF. The model follows an encoder-decoder architecture, where the encoder extracts features from historical data. As shown in Fig. 1, the encoder input consists of an original input vector (dark-colored) and a stamp containing positional encoding and global timing information (light-colored). To enhance computational efficiency, Informer introduces self-attention distilling in the encoder, which reduces memory usage and processing time by progressively condensing feature maps through convolutional and pooling layers. This mechanism prioritizes the most prominent features for forecasting and reduces the computational complexity from $O(L^2)$to $O(L\ \ln(L))$ [16]. The decoder is then used to forecast future target values. Informer uses a generative style decoder to get all the forecasts in one step, which is faster than the Transformer model using step-by-step decoding.

$ProbSparse$ Self-attention mechanism is used to learn the correlation between each element and other elements in a sequence. It filters out important queries to reduce computational complexity. The mechanism works as Eq.(3), where Q, K, and V respectively denote the Query, Key, and Value matrices obtained by linear mapping, d_k is the dimension of the hidden layer, and $\frac{\bar{Q}K^T}{\sqrt{d_k}}$ denotes the similarity of the query to the key. The $Softmax$ function allows the mechanism to get the attentional weights of each position concerning other positions, which are then used to weight and sum the values. Compared to Transformer, Informer calculates attention scores only for selected key query vectors $\bar{Q}$, thereby reducing computational complexity.

$$Attention(Q, K, V) = Softmax\left(\frac{\bar{Q}K^T}{\sqrt{d_k}}\right)V \tag{3}$$

Hu et al. [17] proposed the Squeeze-and-Excitation Network (SENet). It is an attention mechanism based on the Convolutional Neural Network (CNN). SENet can learn the features of different channels and enhance the feature extraction capability through the adaptive feature recalibration mechanism of its "$Squeeze\text{-}and\text{-}Excitation$ (SE)" block, which is used to learn the relationship between the channels of the CNN convolutional kernels. The structure of the SE block is $squeeze$, $excitation$ and $scale$. The $squeeze$ operation compresses the data dimensions of the input channels and converts

the multidimensional data into single values. The $excitation$ operation generates individual feature weights for each feature channel. The $scale$ operation calculates weighted output features by multiplying the weights of each channel with the features in the original channel. The relevant formulas are as follows:

$$z_c = \frac{1}{h \times w} \sum_{\substack{1 \leqslant i \leqslant h \\ 1 \leqslant j \leqslant w}} u_c(i, j) \tag{4}$$

$$s = \sigma\left(w_2 \delta\left(w_1 z\right)\right) \tag{5}$$

$$\tilde{x}_c = s_c \cdot u_c \tag{6}$$

where z_c is the squeezed output, u_c is the eigenvalue of the feature map on channel c, and $h \times w$ denotes spatial dimensions. w_1 and w_2 are fully connected layer operations, and δ denotes the ReLU function. The output undergoes the Sigmoid function σ to get s, which denotes the weight of the feature map in the matrix u_c. s_c is the weight, reflecting the importance of each feature channel. The weight coefficients of each channel can be learned through $s_c \cdot u_c$.

The structure of the Informer-SENet model is shown in Fig.1. In this hybrid model, the long-sequence processing capability of Informer ensures effective capture of long-term dependencies. Meanwhile, the SE block explicitly models inter-channel relationships within feature maps generated by the self-attention mechanism of Informer, enabling fuller utilization of multivariate dependencies. In the architecture, SENet integration is implemented by inserting the SE block after the down-sampling layer in the encoder, where feature channels are dynamically reweighted through these phases:

1. Squeeze Phase: Compressing the spatial information of each channel into channel descriptors by global average pooling.
2. Excitation Phase: Learning channel weights through two fully-connected layers with ReLU activation.
3. Feature Recalibration: Multiplying original features with the Sigmoid-activated weights.

The optimized representations are delivered to the decoder for sequence forecast, allowing simultaneous sequence length reduction and targeted feature improvement. This adaptive mechanism enhances critical feature channels while suppressing non-essential ones, which is particularly advantageous for multivariate PV output forecasting.

6

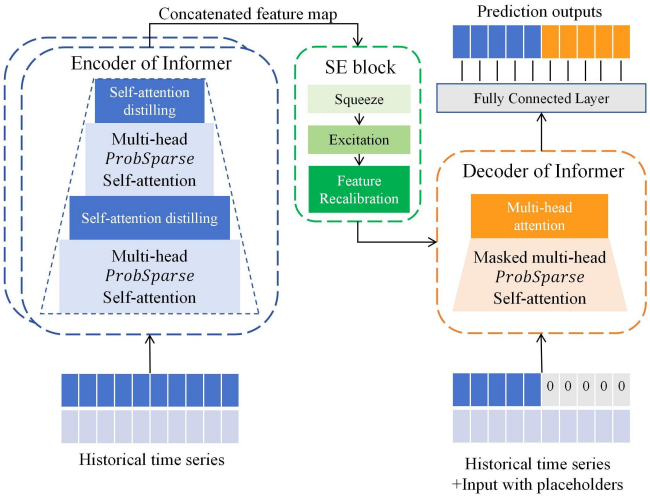


Fig. 1. The schematic diagram of the Informer-SENet model

2.3 Forecasting Framework

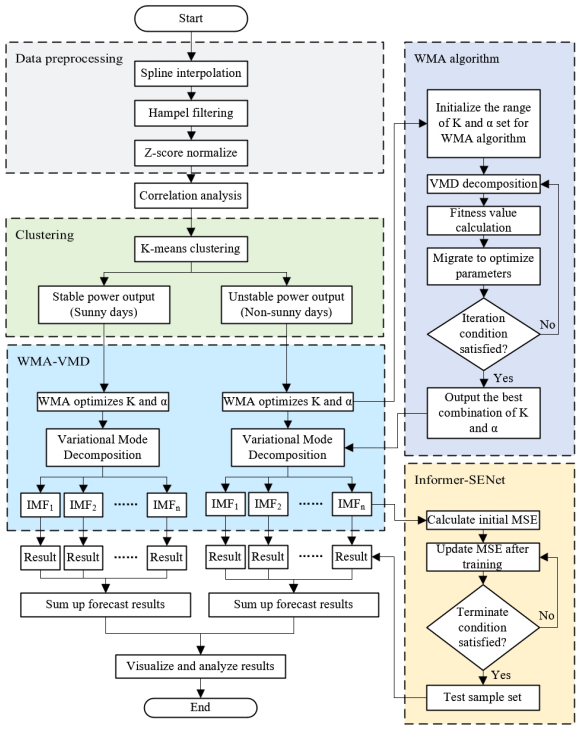


Fig. 2. The flowchart of the forecasting framework

Fig. 2 illustrates the entire PV output forecasting framework. It cleans and standardizes the data, removes redundant features through correlation coefficient analysis, and classifies the power data based on weather scenes. After optimizing the parameters with WMA, VMD decomposes PV power data under various weather scenes. Finally, the Informer-SENet model forecasts each IMF component to get the forecast results.

Each IMF component and the selected meteorological features are concatenated to form the input for the Informer-SENet model. Explicit weighting is not applied prior to input because the Informer-SENet subsequently recalibrates feature importance.

3 Experiments

3.1 Data preprocessing

The dataset used in this study comes from the 2019 annual data of a 100kW PV power plant in Ningxia, with a recording accuracy of 15 minutes. To improve prediction accuracy, the records of zero power output during nighttime are removed, resulting in a total of 22,995 entries that contains 15 features: temperature, azimuth, cloud opacity, dew point temperature, DNI (Direct Normal Irradiance), DHI (Diffuse Horizontal Irradiance), GTI (Global Tilted Irradiance), GHI (Global Horizontal Irradiance), atmospheric precipitation, relative humidity, ground air pressure, wind direction, wind speed, zenith angle and actual power. To deal with the missing values, outliers, and noise interference in the data, the data quality is optimized through preprocessing, which is carried out as follows:

Spline interpolation. Reconstructing missing points through the relationship of neighboring data. It avoids local distortion caused by simple filling while ensuring a continuous time series.

Hampel Filtering. Based on the sliding window, the anomalies that obviously deviate from the normal range are dynamically recognized and corrected. To better adapt to the PV output forecasting scene by retaining the effect of sudden weather, the width of the Hampel filter window is set to 6 hours, and the threshold is set to 3σ.

Z-Score Normalization. To ensure comparability of features with different scales, all data are scaled to a standard deviation of 1 and a mean of 0 to eliminate scale differences and facilitate model calculations.

3.2 Feature selection

Different weather-related factors affect PV output to different degrees. To improve the efficiency of the model, feature selection is required. Therefore, Pearson's correlation coefficient [18] is used to calculate the correlation between 14 features and PV power, and the redundant features are eliminated. The formula is as follows:

8

$$r_{xy} = \frac{\sum_{i=1}^{n}(x_i - \bar{x})}{\sqrt{\sum_{i=1}^{n}(x_i - \bar{x})^2 \sum_{i=1}^{n}(y_i - \bar{y})^2}} \tag{7}$$

where x_i and y_i denote the feature variables and PV power data, $\bar{x}$ and $\bar{y}$ denote their mean values, and n is the number of samples. The calculated Pearson correlation coefficients are used to plot the heat map shown in Fig. 3. The features with the highest correlation coefficients: DHI, DNI, GHI, GTI, zenith angle, and relative humidity are selected as features for PV output forecasting.

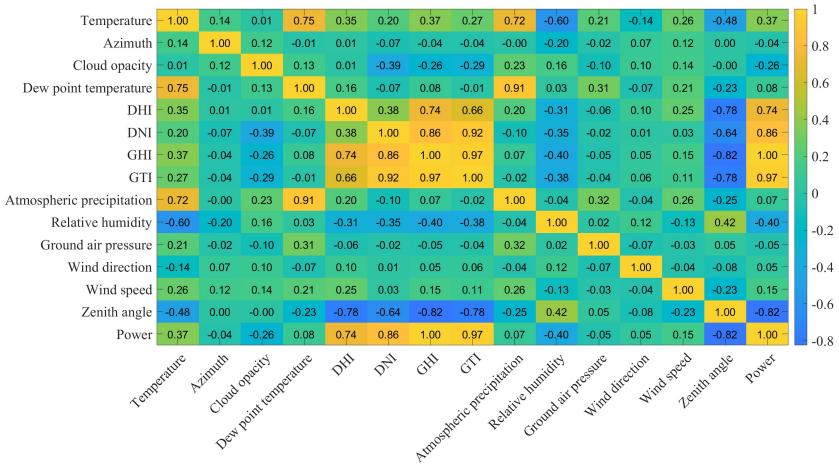


Fig. 3. Pearson correlation coefficient heat map

3.3 Clustering

PV output is highly weather-dependent, which is smooth on sunny days and irregular on cloudy days. Therefore, PV power data on cloudy days requires more modes to capture sudden changes. Classifying different weather scenes by clustering enables optimization of the modal decomposition parameters for different scenes to improve forecasting accuracy.

The K-means clustering method is often used for large-scale data clustering [19]. In this study, the normalized GHI data, which is the most relevant feature to PV power, is selected as the clustering object. To obtain the best clustering results, the Calinski-Harabasz index (CH), the Davies-Bouldin index (DBI), and the silhouette coefficient (SC) are used as the evaluation functions of the clustering results. Fig. 4 shows the comparison of the evaluation indexes under different numbers of clusters.

The general choice is to cluster the dataset into three scenes: sunny, rainy, and cloudy scenes. However, after the comprehensive analysis of the evaluation indexes, the

optimal clustering of the dataset in this research is the two categories shown in Fig. 5. Considering that this study uses data from the dry climate region of Ningxia, the irradiance fluctuation patterns of cloudy and rainy days are similar, which causes the clustering algorithm to merge these two categories of weather conditions automatically. Meanwhile, sunny days are clearly distinguished from the other categories. Therefore, the two categories of sunny and non-sunny days are finally obtained.

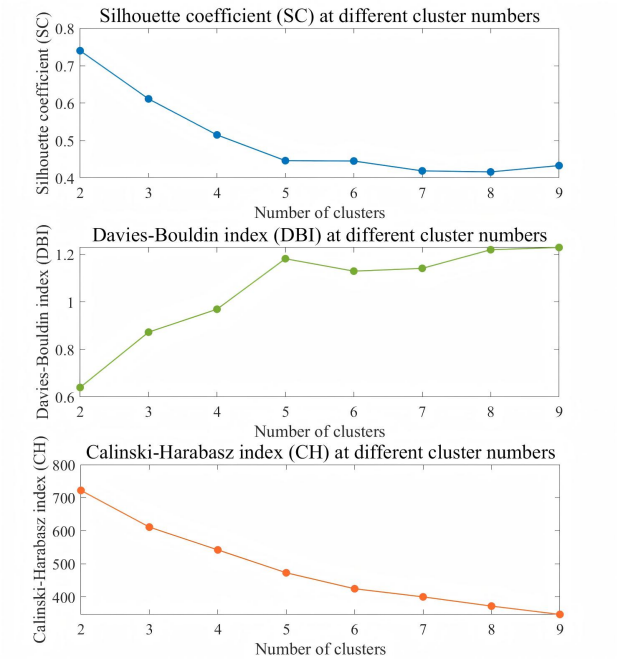


Fig. 4. The comparison of the evaluation indexes

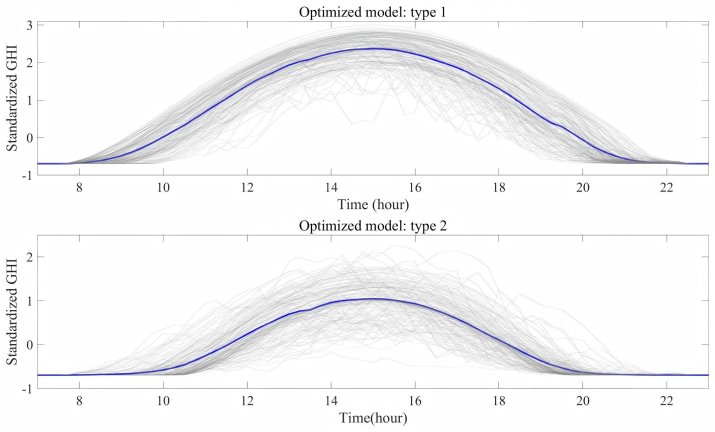


Fig. 5. Optimal clustering results

3.4 Data decomposition

The decomposition effect of VMD is critically influenced by two key parameters: the number of modes (K) and the penalty factor (α). A too large K value can lead to modal aliasing or additional noise, while an insufficient K value can lead to incomplete mode decomposition. Similarly, an overly large α value can cause excessive modal smoothing, and an α value that is too small can lead to modal band aliasing. Therefore, WMA is employed to determine the optimal parameter combination of K and α. Then, the data in the above two scenes are respectively decomposed by VMD under the optimal parameters. In the implementation of WMA, the parameter search spaces are defined as $K \in [2,10]$ and $\alpha \in [20,200]$. The population size is set to 15, and the maximum number of iterations is set to 20. These parameters are determined through literature review and preliminary experiments. The optimization process uses envelope entropy as the fitness function, which is mathematically expressed in Eq.(8), where p_i is the probability of each energy distribution after signal envelopment and N is the number of components. A smaller entropy value indicates more concentrated signal feature information. WMA can effectively identify optimal VMD parameters that yield the most physically meaningful IMFs by minimizing envelope entropy. This approach can avoid the loss of features caused by over-decomposition or under-decomposition while reducing noise interference on the decomposed signal components.

$$E = -\sum_{i=1}^{N} p_i \log_2 p_i \tag{8}$$

Fig. 6 shows the convergence of the WMA algorithm during the iteration process. In the first five iterations or fewer of the optimization process, the fitness function decreases significantly, which indicates that WMA can swiftly converge to find the optimal solution in the initial stage. The fitness value tends to be stable after five iterations, suggesting that after reaching the optimal solution, the algorithm can effectively avoid overfitting caused by excessive searching. This shows the effectiveness of WMA in optimizing the VMD parameters.

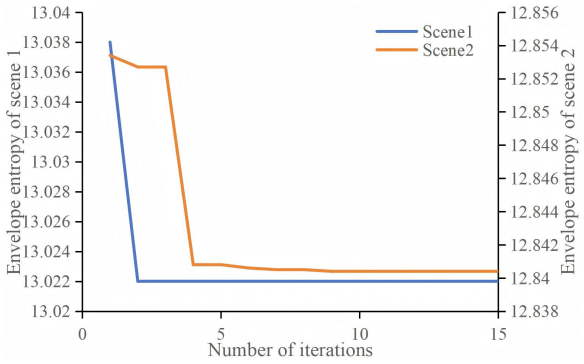


Fig. 6. Convergence curve of the WMA algorithm

After the iteration of WMA is completed, the optimization results for scene 1 are: optimal number of modes K is 7, optimal penalty factor α is 65.68, and minimum envelope entropy is 13.0220. The optimization results for scene 2 are: optimal number of modes K is 9, optimal penalty factor α is 56.66, and minimum envelope entropy is 12.8404. The decomposition results are shown in Fig. 7, where the first sequence signifies the original signal, and the rest of the sequences denote the intrinsic modes obtained after the signal is decomposed by VMD.

The modes with different fluctuations have different meanings. The IMFs that change slowly and fluctuate roughly reflect the basic trend in a time period. The IMFs with more extreme changes and higher frequencies reflect the random essence of PV output to a certain extent.

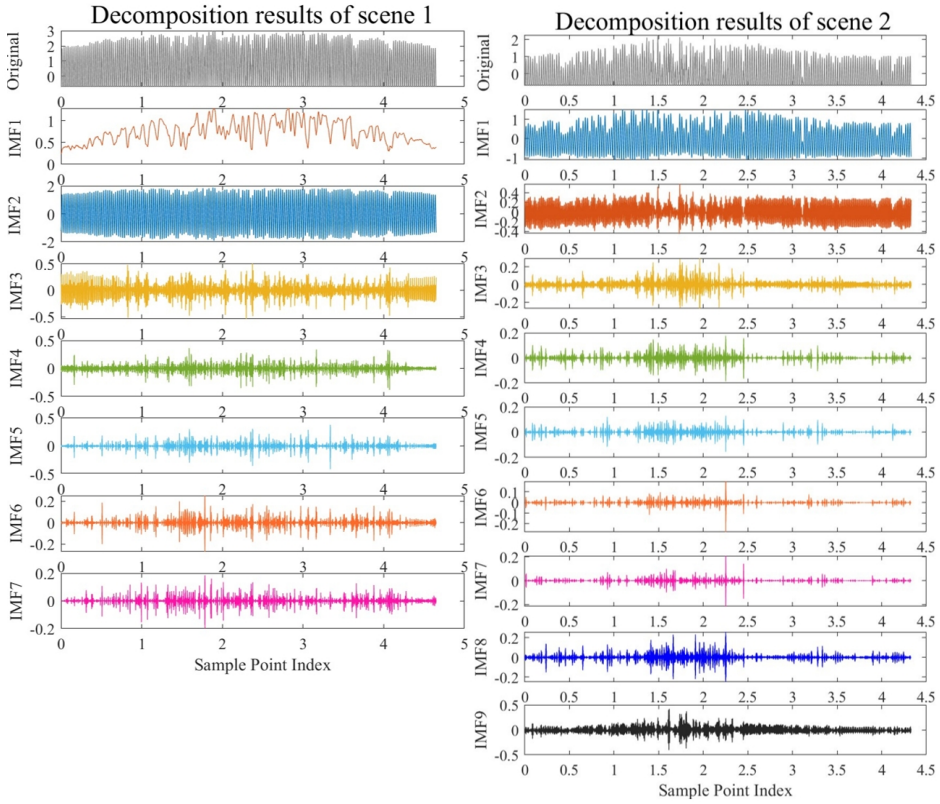


Fig. 7. The comparative diagram of the decomposition results. Non-sunny scene (Scene 2) has more modes because its larger fluctuations require more modes to capture.

3.5 Forecasting

To evaluate the proposed model's performance, we selected seven test days in the test set across two weather scenes and ran six models, including baseline models and developed combined models. Their parameter settings are outlined in Table 1.

Table 1. Parameter settings.

Parameter	Value setting
Training set	80%
Test set	20%
Window length	24
Decoder length	12
Batch size	32
Learning rate	0.0003
Dropout	0.1

The evaluation metrics used for comparison are Mean Squared Error (MSE), Root Mean Squared Error (RMSE), and Mean Absolute Error (MAE) [20]. These metrics are calculated as follows:

$$MSE = \frac{1}{n}\sum_{i=1}^{n}\left(\hat{y}_i - y_i\right)^2 \tag{9}$$

$$RMSE = \sqrt{\frac{1}{n}\sum_{i=1}^{n}\left(y_i - \hat{y}_i\right)^2} \tag{10}$$

$$MAE = \frac{1}{n}\sum_{i=1}^{n}\left|\hat{y}_i - y_i\right| \tag{11}$$

where n denotes the number of forecasted samples, $\hat{y}_i$ denotes the forecasted value of PV power, y_i denotes the actual monitored value of PV power, and $\bar{y}$ denotes the average value of actual PV power.

The comparison of forecast results (Fig. 8 and Fig. 9) shows that the proposed model's forecast best aligns with the actual value. Besides, forecasting performances are different in different phases. In the stable output phase, the forecast values of all models are more consistent with the exact values than in the unstable output phase. This is because PV power output shows a regular fluctuation pattern, which enables all models to effectively fit the relationship between PV power output and weather factors.

As shown in Table 2, experimental results show the outstanding performance of the proposed WMA-VMD-Informer-SENet model across both weather scenes. Model accuracy also varies significantly with weather patterns. For the proposed model, compared to non-sunny conditions, MSE, RMSE, and MAE values during sunny conditions are reduced by 60.32%, 36.90% and 35.16% respectively, reflecting solar irradiance's impact on forecasting stability.

Comparative analysis with deep learning benchmarks reveals substantial improvements. In the sunny condition, compared to Transformer, our model reduces MSE, RMSE, and MAE by 96.82%, 82.14% and 82.88% respectively; compared to LSTM, it reduces MSE and RMSE by 19.67% and 10.31% despite a marginal 0.37% MAE increase attributable to LSTM's inherent robustness. For the non-sunny scene with higher power fluctuations, the proposed model shows more pronounced advantages:

compared with LSTM, MSE, RMSE, and MAE decrease by 57.92%, 35.15% and 36.19% respectively; compared with Transformer, reductions reach 79.45%, 54.67% and 52.93%. Notably, although the Transformer model fits the curve better on sunny days, the mismatch of peaks and valleys leads to a larger error.

Ablation experiments confirm each component's contribution. Compared with the Informer model, the Informer-SENet model decreases MSE, RMSE, and MAE by up to 47.90%, 23.73% and 31.38%. Further enhancement is achieved by integrating WMA: the WMA-VMD-Informer-SENet model outperforms the unoptimized VMD-Informer-SENet that uses default parameters (K=5, α=20) in error reduction, with MSE, RMSE, and MAE decreasing by up to 70.48%, 45.61% and 43.83% respectively.

The comprehensive evaluation establishes that our framework achieves maximum error reduction of 96.8% in MSE relative to the poorest-performing baseline, demonstrating that scene-adaptive decomposition combined with the optimized architecture substantially boosts forecasting accuracy.

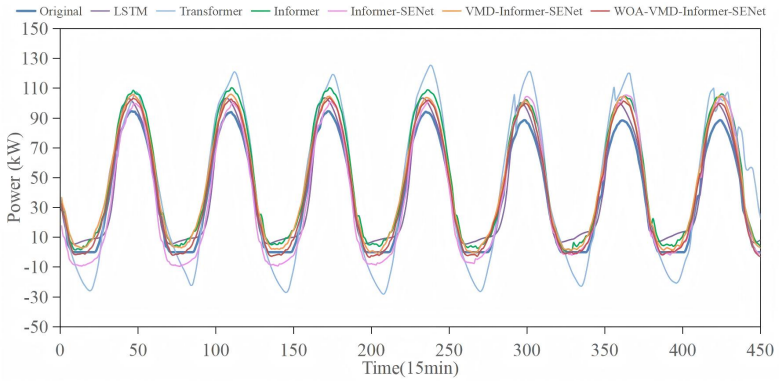


Fig. 8. The comparative diagram of forecasts for scene 1

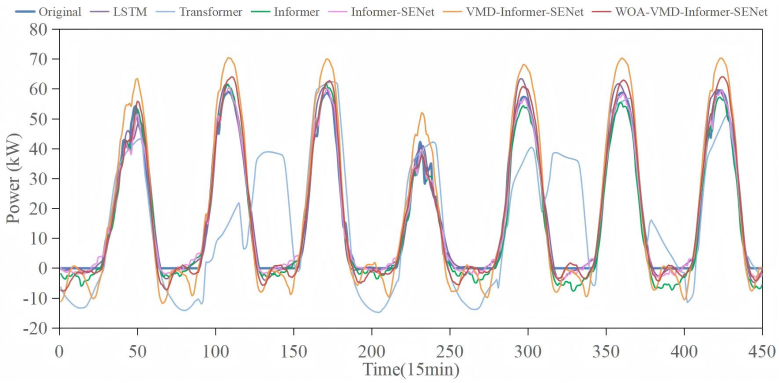


Fig. 9. The comparative diagram of forecasts for scene 2

14

Table 2. Comparison of prediction errors.

Scene	Model	MSE(kW²)	RMSE(kW)	MAE(kW)
Scene 1 (Sunny scene)	LSTM	14.5928	3.8251	2.7772
	Transformer	368.8862	19.2051	16.2792
	Informer	85.4036	8.8607	7.8577
	Informer-SENet	44.4960	6.7579	5.3918
	VMD-Informer-SENet	39.7115	6.3083	4.9630
	WMA-VMD-Informer-SENet	11.7221	3.4308	2.7876
Scene 2 (Non-sunny scene)	LSTM	70.2128	8.3834	6.7372
	Transformer	143.7747	11.9941	9.1339
	Informer	86.0017	9.2169	7.9338
	Informer-SENet	51.5532	7.1799	5.5613
	VMD-Informer-SENet	67.3421	8.2036	7.0242
	WMA-VMD-Informer-SENet	29.5444	5.4368	4.2989

4 Conclusions

This paper proposes a novel PV output forecasting method integrating Whale Migrating Algorithm (WMA)-optimized Variational Mode Decomposition (VMD) with an Informer-SENet hybrid model. The methodology demonstrates superior performance through these approaches: First, the WMA-optimized VMD decomposes PV power data effectively, and WMA shows excellent convergence performance. Besides, the Informer model enhances computational efficiency through its self-attention mechanism, while the incorporated SE block improves feature extraction through the recalibration mechanism. Moreover, the K-means-based scenario clustering enables adaptive VMD parameter optimization for different conditions. Comprehensive experiments confirm that the proposed method outperforms baseline models in forecasting accuracy.

Acknowledgement: This work is supported by the National Natural Science Foundation of China under grant number (U2166208).

References

1. Zheng, J., Du, J., Wang, B., et al.: A hybrid framework for forecasting power generation of multiple renewable energy sources [J]. Renewable and Sustainable Energy Reviews 172, 113046 (2023).
2. Gupta, A.K., Singh, R.K.: A review of the state of the art in solar photovoltaic output power forecasting using data-driven models [J]. Electrical Engineering 107(4), 4727–4770 (2025).
3. Mayer, M.J.: Benefits of physical and machine learning hybridization for photovoltaic power forecasting [J]. Renewable and Sustainable Energy Reviews. 168, 112772 (2022).

4. Zhang, M., Zhen, Z., Liu, N., et al.: Optimal graph structure based short-term solar PV power forecasting method considering surrounding spatio-temporal correlations [J]. IEEE Transactions on Industry Applications 59(1), 345–357 (2023).
5. Ramadhan, R.A.A., Heatubun, Y.R.J., Tan, S.F., et al.: Comparison of physical and machine learning models for estimating solar irradiance and photovoltaic power [J]. Renewable Energy 178, 1006–1019 (2021).
6. Gupta, P., Singh, R.: PV power forecasting based on data-driven models: A review [J]. International Journal of Sustainable Engineering 14(6), 1733–1755 (2021).
7. Babalhavaeji, A., Radmanesh, M., Jalili, M., et al.: Photovoltaic generation forecasting using convolutional and recurrent neural networks [J]. Energy Reports 9, 119–123 (2023).
8. Pacella, M., Papa, A., Papadia, G.: On integrating time-series modeling with long short-term memory and bayesian optimization: A comparative analysis for photovoltaic power forecasting [J]. Applied Sciences 14(8), 3217 (2024).
9. Agga, A., Abbou, A., Labbadi, M., et al.: Convolutional neural network (CNN) extended architectures for photovoltaic power production forecasting. [C] // 2021 9th International Conference on Smart Grid and Clean Energy Technologies (ICSGCE). pp. 104–108. IEEE, Sarawak, Malaysia (2021).
10. Ait Mansour, A., Tilioua, A., Touzani, M.: Bi-LSTM, GRU and 1D-CNN models for short-term photovoltaic panel efficiency forecasting case amorphous silicon grid-connected PV system [J]. Results in Engineering 21, 101886 (2024).
11. Wang, X., Ma, W.: A hybrid deep learning model with an optimal strategy based on improved VMD and transformer for short-term photovoltaic power forecasting [J]. Energy 295, 131071 (2024).
12. Cao, Y., Liu, G., Luo, D., et al.: Multi-timescale photovoltaic power forecasting using an improved stacking ensemble algorithm based LSTM-informer model [J]. Energy 283, 128669 (2023).
13. Dragomiretskiy, K., Zosso, D.: Variational mode decomposition [J]. IEEE Transactions on Signal Processing 62(3), 531–544 (2014).
14. Ghasemi, M., Deriche, M., Trojovský, P., et al.: An efficient bio-inspired algorithm based on humpback whale migration for constrained engineering optimization [J]. Results in Engineering 25, 104215 (2025).
15. Zhou, H., Zhang, S., Peng, J., et al.: Informer: Beyond efficient transformer for long sequence time-series forecasting [J]. Proceedings of the AAAI Conference on Artificial Intelligence 35(12), 11106–11115 (2021).
16. Li, Q., Ren, X., Zhang, F., et al.: A novel ultra-short-term wind power forecasting method based on TCN and informer models [J]. Computers and Electrical Engineering 120, 109632 (2024).
17. Hu, J., Shen, L., Sun, G.: Squeeze-and-excitation networks. [C] // 2018 IEEE/CVF Conference on Computer Vision and Pattern Recognition. pp. 7132–7141. IEEE, Salt Lake City, UT, USA (2018).
18. Lin, P., Peng, Z., Lai, Y., et al.: Short-term power prediction for photovoltaic power plants using a hybrid improved kmeans-GRA-elman model based on multivariate meteorological factors and historical power datasets [J]. Energy Conversion and Management. 177, 704–717 (2018).
19. Bian, H., Zhong, Y., Sun, J., et al.: Study on power consumption load forecast based on K-means clustering and FCM–BP model [J]. Energy Reports 6, 693–700 (2020).
20. Zhang, R., Wu, Y., Zhang, L., et al.: A multiscale network with mixed features and extended regional weather forecasts for predicting short-term photovoltaic power [J]. Energy 318, 134792 (2025).

004 基于灰狼优化算法的同步调相机 PID 参数优化

汪家晗，石开明，孔繁泽，彭腾辉，党　泉，于　淼

（内蒙古工业大学电力学院，呼和浩特，010080）

PID parameter optimization of synchronous condenser based on grey wolf optimization algorithm

WANG Jiahan,SHI Kaiming,KONG Fanze,PENG Tenghui,DANG Quan,YU Miao

(School of Electric Power,Inner Mongolia University of Technology, Hohhot 010080)

ABSTRACT: When the transient overvoltage occurs in the wind farm due to the fault, the dynamic voltage stability of the system faces severe challenges.Through the systematic analysis of the dynamic reactive power characteristics of the synchronous condenser, it can be seen that optimizing the PID control parameters of the excitation system can suppress the transient overvoltage of the wind farm and improve the dynamic voltage performance of the system. Therefore, an optimization method of PID control parameters of excitation system based on grey wolf optimization algorithm is proposed. This method realizes the accurate configuration of PID parameters through the intelligent optimization ability of the algorithm, which can speed up the response and adjustment speed of the condenser to the wind farm voltage, improve the control accuracy, effectively suppress the transient overvoltage problem of the wind farm, and finally effectively improve the dynamic voltage stability of the wind farm system.

KEY WORDS: synchronous condenser;transient overvoltage; PID parameter optimization;grey wolf optimization algorithm

摘要：当风电场因故障出现暂态过电压时，系统动态电压稳定性面临严峻挑战。通过对同步调相机动态无功特性的系统分析可知，优化其励磁系统 PID 控制参数可抑制风电场暂态过电压、改善系统动态电压性能。为此，提出了基于灰狼优化算法的励磁系统 PID 控制参数优化方法。该方法通过算法的智能寻优能力，实现对 PID 参数的精准配置，能加快调相机对风电场电压的响应调节速度、提高控制精度，有效抑制风电场暂态过电压问题，最终切实提升风电场系统的动态电压稳定性。

关键词：同步调相机；暂态过电压；PID 参数优化；灰狼优化算法

DOI：10.13335/j.1000-3673.pst.2014.01.论文序号（小五号 Times New Roman 字体加黑）

0　引言

全球能源转型推动风电、光伏等新能源迅猛发展，但其间歇性与波动性导致电力系统面临电压波动、无功不平衡等稳定挑战[1-2]。同步调相机因能提供动态无功支撑、增强电压稳定性，在新能源场站广泛应用[3-4]。

同步调相机励磁系统通过调节励磁电流控制端电压与无功输出，PID 控制器因结构简单、易实现，成为其励磁系统常用装置。但传统 PID 参数依赖经验设定，难适应复杂电网工况，参数优化遂成研究热点。文献[5]以分布式调相机为对象，基于“无功-电压”双闭环模型，以有效无功电流增益为评价指标，经频域灵敏度分析确定关键励磁参数，再用改进蜂群算法建立优化模型，仿真验证其可降低电压波动、提升动态无功输出。文献[6]同理以有效无功电流增益为指标，通过频域灵敏度分析揭示励磁参数优化规律，仿真证实优化可改善调相机动态特性。文献[7]提出 PSVR 参数优化方法，能提升调相机无功出力、改善电压稳定性；文献[8]提出励磁系统与升压变参数联合优化法，基于 Park 模型提升动态无功分析精度，结合人工鱼群算法优化，验证该方法可替代仅优化电磁参数，降低制造成本。文献[9]以提升电压安全裕度、减小网损为目标，设计风电场稳态无功优化策略，进一步提出稳态-暂态协同优化策略，用改进算法求解并验证有效性。文献[10]通过频域灵敏度分析确定励磁参数优化方向，用改进粒子群算法优化，提升调相机动态响应与电压支撑能力。文献[11]在“无功-电压”双闭环基础上引入电网电压参考，结合模糊 PID 优化励磁策略，增强故障时无功支撑、减小过电压冲击。文献[12]分析调相机降速并网励磁控制特性，提出带 PID 的顺序混合控制方案，提升启动可靠性；文献[13]设计模糊 PID 励磁系统，解决无功调节超调与波动问题，

加快系统恢复。文献[14]引入并网母线电压环作为前馈量，用灰狼算法优化前馈 PID 参数，对比粒子群算法，提升电压调节速度与准确性。文献[15-16]用粒子群算法优化双轴励磁调相机 PID 参数，结合模糊控制应对参数时变非线性，仿真证实优化励磁系统可改善电压稳定性。

综上，现有研究围绕新能源并网点电压稳定，聚焦调相机励磁系统优化，涵盖评价指标与关键参数确定、多算法参数优化、多控制策略探索。鉴于 PID 参数对励磁系统响应速度、稳定性、调节精度影响显著，本文采用收敛快、适复杂问题的灰狼算法，对 PID 参数进行优化求解。

1 调相机励磁系统数学模型

同步调相机的动态无功特性，本质是当电力系统遭遇扰动导致电压突发变化时，调相机通过输出动态无功功率对系统电压进行调控的核心性能。具体而言，在系统发生故障的场景下，同步调相机依托励磁系统的快速响应能力调整自身无功功率输出，这一调节过程可细分为次暂态过程与暂态过程两个阶段：其中，次暂态过程持续时间极短，仅集中在故障发生后的十几个周波内，此阶段励磁调节器基本未参与作用；而暂态过程则对应故障发生后的 2~3 秒时间段，该阶段励磁调节器会启动并全程参与无功功率调节，以实现对系统电压的稳定控制。

按照发电机参考方向的惯例，且不考虑定子绕组电阻的影响，同步调相机各电气量的相量关系如图 1 所示。图中，U 为升压变高压侧电压，Ut 为机端电压，E_q、E_q'、E_q'' 为 q 轴电动势、暂态电动势及次暂态电动势。

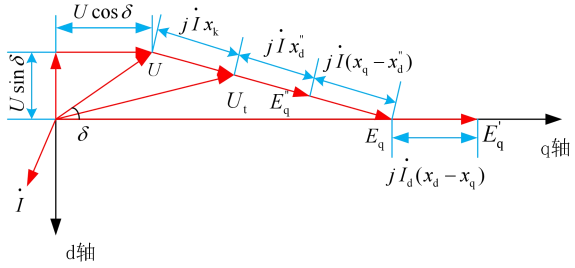


图 1 调相机动态电气向量图

Fig. 1 Dynamic electrical vector diagram of condenser

同步调相机向系统提供的无功功率为：

$$Q = U_q I_d - U_d I_q \tag{1}$$

在调相机正常运行时：

$$U_d = U\sin\delta \approx 0 \tag{2}$$

$$U_q = U\cos\delta \approx U \tag{3}$$

则调相机产生的无功功率为：

$$Q = U\cos\delta I_d - U\sin\delta I_q \approx UI_d \tag{4}$$

当电力系统出现故障时，母线电压会产生突发变化，此时同步调相机为维持自身机端电压的稳定而启动调节动作，其输出的无功功率变化量可表示为：

$$\begin{aligned}\Delta Q &= Q - Q_0 = UI_d - U_0 I_{d0} \\ &= (U_0 + \Delta U)(I_{d0} + \Delta I_d) - U_0 I_{d0} \\ &= U\Delta I_d + \Delta U I_{d0}\end{aligned} \tag{5}$$

式中各符号对应的物理意义具体如下:Q 代表系统发生故障时，同步调相机实际输出的无功功率;Q_0 指同步调相机处于稳态运行工况下的无功功率;ΔQ 为故障工况与稳态工况下，调相机输出无功功率的变化量;U 表示系统故障发生瞬间，高压侧母线的实际电压;U_0 为系统稳态运行时，高压侧母线的电压;Δ U 为故障发生时与稳态工况下，高压侧母线电压的变化量;I_d 代表系统故障期间，同步调相机 d 轴的电流;I_{d0} 指系统稳态运行时，同步调相机 d 轴的电流;ΔI_d 为故障期间与稳态工况下，调相机 d 轴电流的变化量。其中 U 与系统参数和网架结构有关，Δ U 取决于机端和故障点的电气距离与故障类型，I_{d0} 取决于故障前调相机的初始状态，调相机故障后无功响应性能优劣主要取决于 ΔI_d 快速跟随系统暂态无功需求变化的能力。

调相机定子端电压变化值 ΔU_t 与励磁电压变化量 ΔE_f 的关系为：

$$\Delta E_f = -\frac{k_A\left(k_P + \frac{k_I}{s} + \frac{k_D}{sT_D + 1}\right)}{(sT_m + 1)(sT_Z + 1)}\Delta U_t = -F(s)\Delta U_t \tag{6}$$

$$\Delta I_d = \left(\frac{as + b - F(s)X_d''}{As^2 + Bs + C + F(s)X_k} - 1\right)\frac{\Delta U}{X_d'' + X_k} \tag{7}$$

即得调相机励磁系统 PID 参数与励磁电压之间的关系，通过调整调相机励磁系统的 PID 参数，可以改变励磁电压的大小，从而改善调相机的动态无功特性。

比例环节能够快速响应电压偏差，当系统电压出现波动时，比例项会立即根据偏差的大小产生相应的控制信号，调整励磁电流，从而增加调相机的无功输出。比例系数越大，对电压偏差的响应越灵敏，无功输出的调整速度越快，能够在短时间内提供更多的无功功率，增强系统的无功支撑能力。积分环节主要用于消除电压偏差的稳态误差。在系统

电压存在长期的、持续的偏差时，积分项会不断累积偏差值，逐渐增加控制信号，使励磁电流持续调整，直到电压偏差完全消除。这有助于在系统受到扰动后，使调相机的无功输出能够持续作用，直到系统电压恢复到稳定状态，从而提高无功输出的精度和稳定性。微分环节可以预测电压偏差的变化趋势，提前调整励磁电流。当系统电压出现快速变化时，微分项能够根据电压变化率产生相应的控制信号，使调相机提前增加或减少无功输出，以抑制电压的进一步变化，提高系统的动态响应能力，增强无功输出的及时性和有效性。

合理的PID参数可以使调相机励磁系统具有较快的动态响应速度，能够及时跟踪系统电压的变化，并快速调整励磁电流，使调相机的无功输出与系统需求相匹配。这样可以有效减小系统电压的波动幅度，缩短电压恢复时间，提高风电场系统的动态电压稳定性，因此通过智能算法优化 PID 参数非常重要。

2 基于灰狼优化算法的 PID 参数优化模型

同步调相机励磁系统中，PID 控制模块的参数选取对励磁系统的响应速度、运行稳定性及调节精度具有直接且关键的影响。但在风电高占比的电力系统中，对母线电压的精确控制要求不断提升，传统上依赖经验整定 PID 参数的方法，已逐渐无法满足这一需求。故而，亟需引入智能算法对 PID 控制参数开展优化工作，从而助力同步调相机励磁系统达成更为精准、精细的控制目标。

为有效抑制风电场暂态过电压，基于灰狼优化算法在参数寻优方面具有简单易实现、收敛速度快、求解精度高等优点，据此，本文提出调相机励磁系统的 GWO-PID 算法控制策略，该策略可实现对励磁系统 PID 控制参数的寻优，最终获得最优参数，其控制框图如图 2 所示。

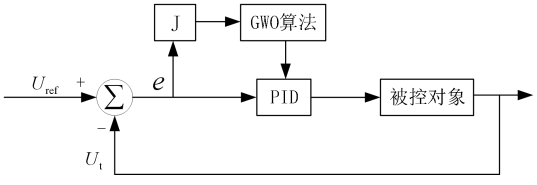


图 2 GWO-PID 算法优化控制器结构图

Fig. 2 GWO-PID algorithm to optimize the controller structure diagram

如上图所示，对灰狼种群进行初始化，将初始化种群依次赋值给 PID 控制器中的 Kp、Ki、Kd，PID 控制器输出作用于被控对象。将调相机机端电压参考值与实际机端电压的误差 e 的目标函数 J 返回到 GWO 算法中，通过 GWO 算法以误差 e 的绝对值对时间的对数作为计算适应函数，完成对灰狼种群的更新。重复上述过程直至满足迭代次数达到最大，得到 PID 参数的优化值，此优化过程中适应度值越小，对应的 PID 控制参数越好。

3 算法实现

对同步调相机励磁系统PID控制器参数进行优化时，第一步需将控制器关键参数 Kp、Ki、Kd，映射为灰狼优化算法中个体灰狼的位置向量。在预先划定的参数搜索空间内，通过定义专属适应度函数，可计算出每组 PID 参数对应的适应度值；接着从所有参数组中挑选出适应度最优的三组，分别作为 α 狼、β 狼、δ 狼的位置数据，再根据这三只狼的位置变化，对 PID 控制器参数进行动态更新。该寻优机制能够持续改进调相机励磁系统的控制性能，有效抑制风电场暂态过电压问题，进而提升电网的电压支撑水平。此算法优化的具体流程如图 3 所示：

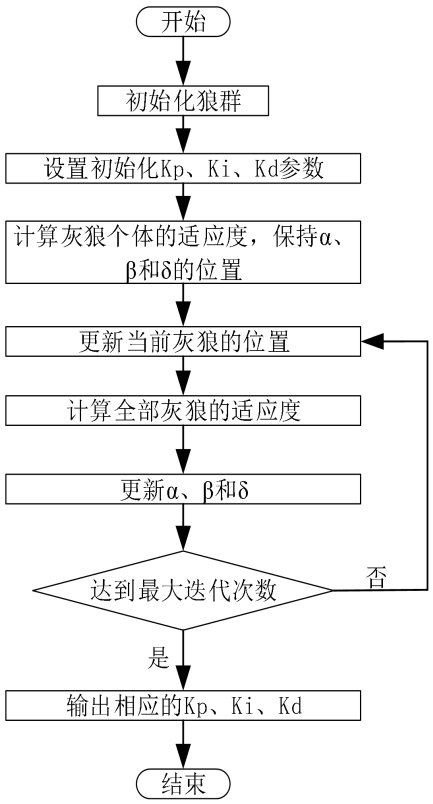


图 3 GWO-PID 算法流程图

Fig. 3 GWO-PID algorithm flow chart

4 算例分析

以风电总装机容量为 300MW 并网为例，在 MATLAB/Simulink 构建如图 4 所示的仿真模型。风

电经 0.69/35kV 箱变、35/220kV 升压站后通过集电线路送入 220kV 电网，35kV 母线装设 2 台 50Mvar 分布式调相机作为无功补偿装置。

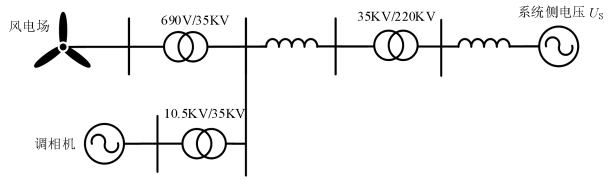


图 4 系统结构图

Fig. 4 structure chart of system

在 MATLAB 语言环境下编写灰狼优化算法，优化 Simulink 所搭建的待优化仿真模型，由于系统运行状态不同，GWO 算法优化 PID 参数所获得的结果也不同。本文针对系统发生三相短路故障时，经 GWO 算法优化的 PID 参数对系统暂态过电压的抑制效果进行 GWO 算法优化，优化完成后得到的适应度曲线如图 5 所示。

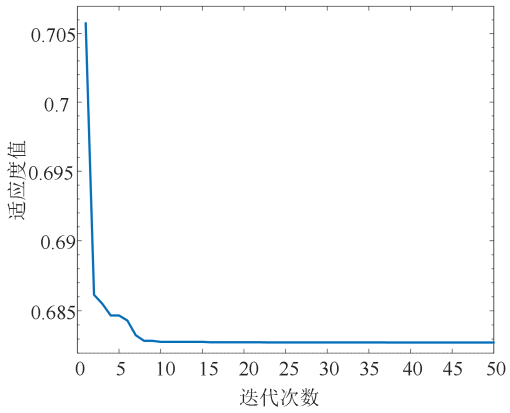


图 5 算法迭代曲线

Fig. 5 Algorithm iterative curve

经 GWO 算法优化的结果如表 1 所示。

表 1 参数优化结果

Tab.1 Parameter optimization results

	K_p	K_i	K_d
无算法	2	0.9	0.024
GWO 算法	4.4019	0.0038	0.0005

设置系统运行 2s 时 35kV 母线发生三相短路故障，经 0.4s 后消除故障，仿真结果见图 6 所示。

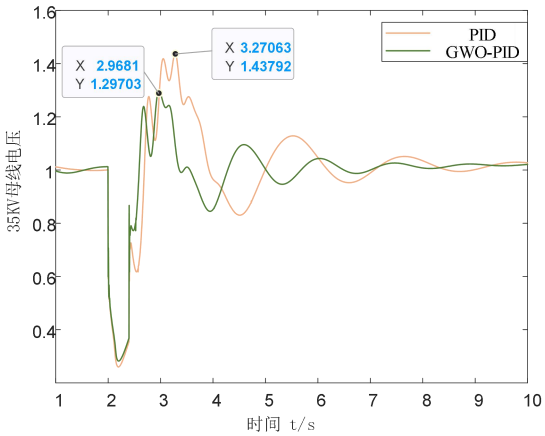


图 6 35KV 母线电压

Fig. 6 35KV bus voltage

由图 6 的仿真实验结果可知，经灰狼优化算法优化后，风电场 35kV 母线的暂态过电压得到显著抑制：其暂态过电压峰值从优化前的 1.43792pu 降至优化后的 1.29703pu，降低幅度达 0.14089pu。该数据明确证明，通过 GWO 算法优化得到的 PID 控制参数，对风电场母线暂态过电压具有显著的抑制效果。此外，采用该优化算法所得的 PID 控制参数，还能有效缩短风电场母线电压的暂态过程时长，促使电压以更快的响应速度过渡至稳定运行状态。这一“暂态过电压幅值降低”与“暂态调节时间缩短”的双重优化效果形成协同作用，进一步强化了风电场系统在故障工况下的暂态电压稳定性能，为系统安全运行提供了更可靠的保障。

5 结论

针对风电场暂态故障引发的母线电压暂态过电压问题，为进一步提升同步调相机对该类暂态过电压的抑制效能，本文提出一种基于灰狼优化算法的调相机励磁系统 PID 参数优化方法。通过灰狼优化算法对励磁系统 PID 参数进行寻优配置，优化后的参数可显著增强同步调相机对暂态过电压的抑制能力，切实降低故障对风电并网系统的影响，有力保障整个系统的安全稳定运行。

参考文献

[1] 肖先勇,郑子萱.“双碳”目标下新能源为主体的新型电力系统：贡献、关键技术与挑战[J].工程科学与技术,2022,54(01):47-59.

[2] 李萌,姚增慧,包博,等.“双高”电力系统暂态电压稳定新问题综述与展望[J/OL].中国电机工程学报,1-18.

[3] 周莹坤,孙华东,徐式蕴,等.提升电网电压支撑强度的调相机优化配置方法[J].电网技术,2022,46(10):3848-3856.

[4] 王雅婷,张一驰,周勤勇,等.新一代大容量调相机在电网中的应用研究[J].电网技术,2017,41(01):22-28.

[5] 付敏,崔灿灿,王璐瑶,等.分布式调相机励磁系统参数优化模型研究[J].电机与控制学报,2022,26(02):102-110.

[6] Fu M, Cui C, Wang L, et al. Influence of Excitation Parameters on the Dynamic Characteristics of the Distributed Synchronous Condenser[C]//2021 13th International Symposium on Linear Drives for Industry Applications (LDIA). IEEE, 2021: 1-6.
[7] 李志远.调相机附加电压调节器参数优化研究[D].郑州大学,2021.
[8] 潘学萍,许一,赵天骐,等.考虑系统稳定边界的同步调相机励磁与升压变参数联合优化[J].电力系统保护与控制,2024,52(08):45-54.
[9] 赵天骐,郭金鹏,张海燕,等.考虑调相机的风电场稳态-暂态无功协同优化控制[J].电力系统自动化,2024,48(24):54-65.
[10] 张显忠.大容量调相机对系统电压稳定影响及其无功支撑优化研究[D].沈阳工业大学,2023.
[11] 刘旭东,王宏华,王成亮.高压直流系统中调相机模糊控制研究[J].机械制造与自动化,2019,48(03):207-210.
[12] Wang P, Yuan T, Mou Q, et al. Reliability analysis of excitation control modes of a synchronous condenser during grid-integration at the speed-falling stage[J]. Microelectronics Reliability, 2020, 114: 113886.
[13] 印钊阳.新一代同步调相机在高压直流输电系统中动态性能研究[D].哈尔滨理工大学,2020.
[14] 周莹坤,孙华东,徐式蕴,等.提升电网电压支撑强度的调相机优化配置方法[J].电网技术,2022,46(10):3848-3856.
[15] 陈尚鹏.调相机励磁控制及其容量配置研究[D].兰州理工大学,2023.
[16] 刘振华.双轴励磁调相机的励磁控制及电压稳定性研究[D].哈尔滨理工大学,2023



汪家晗

收稿日期：2025-08-24。

作者简介：
汪家晗(2001)，男，硕士研究生，研究方向为电力系统规划运行与新能源发电研究，E-mail：2921473765@qq.com；
石开明(1970)，男，副教授，硕士生导师，研究方向为电力系统规划运行与新能源发电研究，E-mail：skming2006@126.com。

005 基于等式残差抗差总体最小二乘法的谐波状态估计与定位

孔繁泽，石开明，汪家晗，彭腾辉，党　泉，于　淼

（内蒙古工业大学电力学院，呼和浩特，010080）

Harmonic state estimation and localization based on the overall least squares method of residual resistance to equation

KONG Fanze,SHI Kaiming,WANG Jiahan,PENG Tenghui,DANG Quan,YU Miao

(School of Electric Power,Inner Mongolia University of Technology, Hohhot 010080)

ABSTRACT: The harmonic state estimation model is introduced, and on the basis of comprehensively considering the measurement data error and parameter error, the overall least squares anti-gross error resistance is insufficient, and the overall least squares method based on equation residuals is proposed for harmonic state estimation. The IEEE-13 node system model is built for testing, and the gross error and normal distribution error of different sizes are added to the measured data and parameter matrix, and the estimation results of least squares method, population least squares method and the proposed method are compared and analyzed. The simulation results show that the overall least squares method of resistive difference based on equation residuals has higher accuracy in harmonic state estimation. Finally, according to the harmonic state estimation results, the harmonic active power injected by the node is analyzed to achieve accurate positioning of the multi-harmonic source.

KEY WORDS: harmonic state estimation;parameter error; equation residuals;Immunity to the total least squares

摘要：介绍了谐波状态估计的模型，在综合考虑量测数据误差和参数误差的基础上，针对总体最小二乘抗粗差能力不足的问题，提出了基于等式残差的抗差总体最小二乘法进行谐波状态估计。搭建 IEEE-13 结点系统模型进行测试，分别向量测数据和参数矩阵添加不同大小的粗差和正态分布误差，对比分析了最小二乘法、总体最小二乘法与所提方法的估计结果。仿真结果表明利用基于等式残差的抗差总体最小二乘法进行谐波状态估计具有更高的精度。最后，根据谐波状态估计结果分析了结点注入的谐波有功功率实现了多谐波源准确定位。

关键词：谐波状态估计；参数误差；等式残差；抗差总体最小二乘法

DOI：10.13335/j.1000-3673.pst.2014.01.论文序号（小五号 Times New Roman 字体加黑）

0　引言

随着电力电子设备的广泛应用，在增强电网可控性和灵活性的同时，非线性负载的增加导致电网谐波污染日益严重，进而引起电能质量恶化、能量损耗增加、电气设备的加速老化等一些列问题[1]。了保证电力系统的安全运行，减少谐波产生的污染，进行准确有效的谐波状态估计实现谐波源局域化对开展谐波源治理有重要的意义[3]。电力系统谐波状态估计是根据少量的量测数据估计出整个系统的谐波状态，该问题由 Heydt 首次提出[4]。随后得到迅速发展。文献[5]在系统不完全可观的情况下提出使用奇异值分解法来进行谐波状态估计，可以准确估计电网的谐波状态。文献[6]在参数矩阵含有参数误差和测量数据存在粗差的情况下提出使用抗差总体最小二乘法进行谐波状态估计能得到更精确的估计结果。文献[7]使用套索回归，通过引入 L1 范数，压缩非谐波源节点对谐波状态估计方程的影响，以残差平方和最小为目标对谐波电流进行估计，克服了因测量装置少而导致量测方程欠定问题。要准确划分谐波责任，解决谐波污染问题，对系统中谐波源定位至关重要。目前谐波源定位方法主要可以分为两类，一类是基于等效电路模型的方法，通过在公共耦合点构建系统侧与用户侧等效模型，依据阻抗比或功率方向原理[8]判定主导谐波源，该类方法具有单节点辨识特性[9]，一般适用于单一谐波源系统；另一类是基于谐波状态估计的方法，该类方法通过量测数据建立谐波状态方程，依托于谐波状态估计的结果，对整体电网的多个谐波源辨识[10]，文献[11]提出基于最大后验估计的参数辨识算法来估计系统谐波电流实现谐波源的定位。文献

[12]将非谐波源等效为电阻－电感串联电路模型，谐波源等效为非线性电路模型基础上，利用两类模型的明显差异，可以有效地区分谐波源与非谐波源，但该方法需要每条负载供电线路的电能质量监测数据，实际应用难以获得。

在设计抗差总体最小二乘法时，由于总体最小二乘估计不适用于残差预测，根据单个随机量残差进行重定权存在理论缺陷，为了更精准估计系统的谐波分布，本文提出基于等式残差的抗差总体最小二乘法[错误!未找到引用源。]进行谐波状态估计。最后根据谐波状态估计结果，计算各节点注入的谐波有功功率来辨识谐波源。

1 谐波状态估计模型

本文以谐波电压为状态量，节点谐波电压和支路谐波电流作为量测量。

谐波状态估计数学模型为

$$z = Hx \tag{1}$$

式中，z 为 $n\times 1$ 维测量值；H 为 $n\times m$ 维参数矩阵；x 为 $m\times 1$ 维状态量。

实际系统中，受限于仪器精度不足、方法缺陷及随机噪声干扰，实际量测值存在误差，考虑了量测量含有误差后式(1)变为

$$z+\varepsilon = Hx \tag{2}$$

式中，ε 为 $n\times 1$ 维量测误差向量。

由于实际网络参数的准确值难以获得，当综合考虑量测误差和参数误差后式(2)变为

$$z+\varepsilon = \left(H+E_H\right)x \tag{3}$$

式中，E_H 为 $n\times m$ 维参数随机误差。

2 谐波源辨识

谐波源辨识是通过谐波状态估计的状态量，计算系统各节点注入到系统的谐波有功功率。当节点注入的有功为正时，则判为谐波源，反之则认为是吸收源。本文以谐波电压作为状态量，得到各个节点的谐波电压后，计算各节点谐波注入电流，即

$$\dot{I}_i^h = \sum_{j=1}^{n} Y_{ij}^h \dot{U}_j^h \tag{4}$$

式中，$\dot{I}_i^h$ 为 h 次谐波电流，$\dot{U}_j^h$ 为各节点谐波电压，Y_{ij}^h 表示为 h 次谐波导纳。

通过上述步骤获得所需谐波电流、谐波电压数据，可确定各节点各次的谐波有功功率，如下式所示

$$P_i^h = \mathrm{Re}\left(\dot{U}_i^h \cdot \dot{I}_i^{h*}\right) \tag{5}$$

通过式(5)来判断各节点谐波有功功率的正负，以此来判断是否为谐波源。

3 谐波状态估计数学模型的求解

3.1 最小二乘法

最小二乘观测方程为

$$z+\varepsilon = Hx \tag{6}$$

相应残差方程为

$$v = Hx - z \tag{7}$$

式中，x 为 x 的估计值，v 为余差向量。估计准则为

$$\sum_{i=1}^{n} v_i^2 = \min \tag{8}$$

求解式(8)得到

$$x = \left(H^T H\right)^{-1} H^T z \tag{9}$$

由于最小二乘没有综合考虑误差，导致最小二乘派生出来的算法均不能准确反应实际误差对谐波状态估计的影响。

3.2 基于等式残差的抗差总体最小二乘法

与最小二乘法不同的是总体最小二估计不适用于残差预测，对于单个观测方程的系数还是观测值来说无论是谁被污染，都会影响观测方程的其他随机量，因此对单个随机量残差进行重定权存在理论缺陷。基于等式残差进行重定权设计相应的抗差总体最小二乘法，说明了等式残差具有最小二乘估计残差的性质，具有更好的抗差性。

考虑参数矩阵中含有误差的 EIV 模型

$$\begin{cases} z+\varepsilon = \left(H+E_H\right)\cdot x \\ e = \begin{bmatrix} \varepsilon \\ \varepsilon_H \end{bmatrix} = \begin{bmatrix} \varepsilon \\ vecE_H \end{bmatrix} \sim N\left(0,\sigma_0^2 Q\right) \end{cases} \tag{10}$$

式中，σ_0^2 为单位权方差，$vec(\bullet)$ 表示为矩阵拉直变换算子，Q 为 H 和 z 对应的 $n(m+1)\times n(m+1)$ 阶的协因数矩阵，与权阵互为逆矩阵。

相应的总体最小二乘问题可以转变为如下非线性约束问题

$$e^T Q^- e = \min \ s.t.\ f\left(Y-e,x\right)=0 \tag{11}$$

式中，$Y = \begin{bmatrix} vec(H) \\ z \end{bmatrix}$ 是由 H 和 z 中元素组成的列向量，Q^- 为 Q 的广义逆矩阵。通过泰勒展开，保留一次项，最后可得参数增量公式[错误!未找到引用源。]

$$\delta\hat{x}^{j+1}=\left[H^{j^T}\left(Q_l^j\right)^{-1}H^j\right]^{-1}H^j\left(Q_l^j\right)^{-1}\left(z-Hx^j\right) \quad (12)$$

由增量公式可得

$$\hat{x}^{j+1}=\hat{x}^j+\delta\hat{x}^{j+1} \quad (13)$$

残差预测值 $\tilde{e}^{j+1}$：

$$\tilde{e}^{j+1}=QB^{j^T}\left(Q_l^j\right)^{-1}\left(l^j-H^j\delta\hat{x}^{j+1}\right) \quad (14)$$

式中，$l^j=z-Hx^j$，$B^j=\left[x^{j^T}\otimes I_n-I_n\right]$，“$\otimes$”表示为矩阵之间的直积，$Q_l^j=B^jQB^{j^T}$。闭合差 l^j 的残差预测值 $\tilde{e}_l^{\,j+1}$：

$$\tilde{e}_l^{\,j+1}=z-H\hat{x}^{j+1} \quad (15)$$

$\tilde{e}_l^{\,j+1}$ 由观测向量和系数矩阵线性构成，表现为最小二乘法预测残差的形式，被称为“等式残差”。

等价权函数选取 IGGIII权函数，其协因数因子函数为

$$R_i=\begin{cases}1, \left|\tilde{v}_{li}\right|\le k_0\\ \dfrac{\left|\tilde{v}_{li}\right|}{k_0}\left(\dfrac{k_1-k_0}{k_1-\left|\tilde{v}_{li}\right|}\right)^2, k_0\langle\left|\tilde{v}_{li}\right|\le k_1\\ 10^{10}, \left|\tilde{v}_{li}\right|\rangle k_1\end{cases} \quad (16)$$

式中，R_i 是 R 的第 i 个对角线元素；$\tilde{v}_{li}=\dfrac{\tilde{e}_{li}^{\,j+1}}{\hat{\sigma}_0Q_{\tilde{e}_{li}}^{j+1}}$ 是第 i 个“等式残差”，$\tilde{e}_{li}^{\,j+1}$ 和 $Q_{\tilde{e}_{li}}^{j+1}$ 分别为等式残差的第 i 个分量和协因数矩阵的第 i 个对角线元素。进一步得到协因数矩阵如下

$$\bar{Q}_l^{j+1}=\sqrt{R}Q_l^{j+1}\sqrt{R} \quad (17)$$

式中，R 中的元素由式(17)给出，非对角元素为零，$\sqrt{R}$ 为 R 中对角元素取平方根。为了避免单位权中误差畸变，采用中位数计算得

$$\hat{\sigma}_0=1.4826\cdot\underset{i=1}{\overset{m}{med}}\left(\left|\frac{\tilde{e}_{li}^{\,j+1}}{\sqrt{Q_{\tilde{e}_{li}}^{j+1}}}\right|\right) \quad (18)$$

式中，$\underset{i=1}{\overset{m}{med}}(\cdot)$ 为求取 m 个元素得中位数。

采用迭代算法进行计算，流程如下：

（1）设置迭代收敛阈值 δ；

（2）通常采用最小二乘作为初值：

$\hat{x}^0=\left(H^TQ_y^{-1}H\right)^{-1}H^TQ_y^{-1}z, R=I_m$；

（3）$B^1=\left[\hat{x}^{1^T}\otimes I_n-I_n\right], Q_l^1=\left(B^1QB^{1^T}\right)$；

（4）置 $j=1$,进入循环；

（5）$\bar{Q}_l^j=\sqrt{R}Q_l^j\sqrt{R}, l^j=z-H\hat{x}^j$；

（6）$\delta\hat{x}^{j+1}=\left[H^{j^T}\left(\bar{Q}_l^j\right)^{-1}H^j\right]^{-1}H^j\left(\bar{Q}_l^j\right)^{-1}\left(z-Hx^j\right)$，$\hat{x}^{j+1}=\hat{x}^j+\delta\hat{x}^{j+1}$；

（7）计算 $\tilde{e}_l^{\,j+1}=z-H\hat{x}^{j+1}$；

（8）$B^{j+1}=\left[\hat{x}^{j+1^T}\otimes I_n-I_n\right]$，$Q_l^{j+1}=B^{j+1}QB^{j+1^T}$；

（9）$Q_{\tilde{e}_l}^{j+1}=Q_l^{j+1}-A^{j+1}\left[A^{j+1^T}\left(Q_l^{j+1}\right)^{-1}A^{j+1}\right]^{-1}A^{j+1^T}$；

（10）计算 $\hat{\sigma}_0=1.4826\cdot\underset{i=1}{\overset{m}{med}}\left(\left|\dfrac{\tilde{e}_{li}^{\,j+1}}{\sqrt{Q_{\tilde{e}_{li}}^{j+1}}}\right|\right)$，

$\tilde{v}_{li}=\dfrac{\tilde{e}_{li}^{\,j+1}}{\hat{\sigma}_0Q_{\tilde{e}_{li}}^{j+1}}$，计算 R；

（11）迭代前后两次误差小于 σ，即 $\left\|\hat{x}^{j+1}-\hat{x}^j\right\|\langle\sigma$。

4 仿真算例

本文的算例在 IEEE13 结点系统上进行测试，采用MATLAB2016b仿真软件搭建模型进行仿真分析。IEEE13 节点系统拓扑和 PMU 配置如图 1 所示，在节点 9，11 和 12 接入谐波源，本文采用 0-1 整数规划算法确定系统所需要的PMU数量和安装位置，在保证系统完全可观的条件下使量测装置数量最小化[14]。配置优化模型为

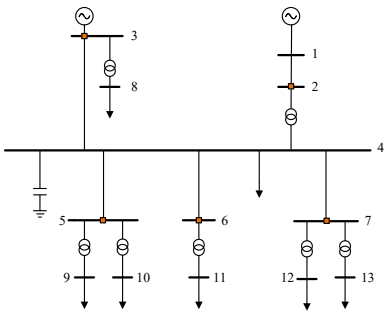


图 1 IEEE13 结点系统及量测配置

Fig.1IEEE13 node system and measurement configuration

$$\begin{cases}\min\sum_{i=1}^{n}x_i\\ s.t.\quad L(i)=YX\ge B\end{cases} \quad (19)$$

式中，n 代表节点总个数，x_i =1 代表在 i 点安装了 PMU 装置，x_i =0 则表示未安装，Y 为节点关联矩阵，$Y(i,j)=\begin{cases}1 & i=j\text{或}i、j\text{相接}\\ 0 & \text{其他}\end{cases}$，$X$ 为 x_i 的列向量，B 为单位列向量。通过求解式(19)可得

IEEE13 节点至少需要 5 个 PMU 才能满足系统可观性，即在 2、3、5、6 和 7 节点安装。

本文所用算法：1.基于等式残差的抗差总体最小二乘法，即本文所用算法；2.总体最小二乘法；3.最小二乘法。

以 5 次谐波电压幅值、相角为例，谐波源采用谐波电流源代替，根据谐波电流典型频谱来计算各次谐波大小。图 2 是无误差节点电压幅值估计结果和相角绝对误差，由于没有误差，三种算法估计结果一致，都可得到较为准确的结果。

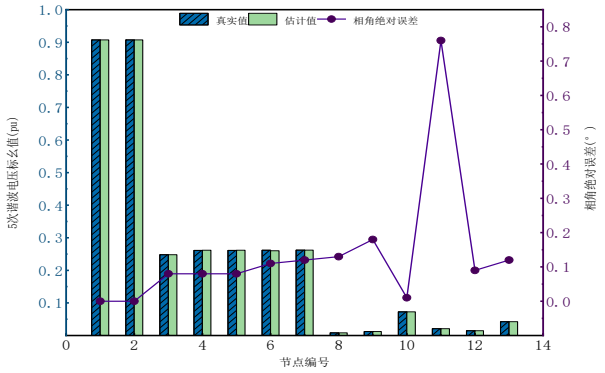


图 2 无误差电压估计值与相角绝对误差

Fig. 2 Error-free voltage estimate and phase angle absolute error

下面分别在参数矩阵加 1%的正态分布误差，在测量值中加 1%的正态分布误差，使 5%的数据添加标准差为 3%的粗差，分别用上述算法进行谐波状态估计，由于相角相对误差很小，仅讨论幅值相对误差。

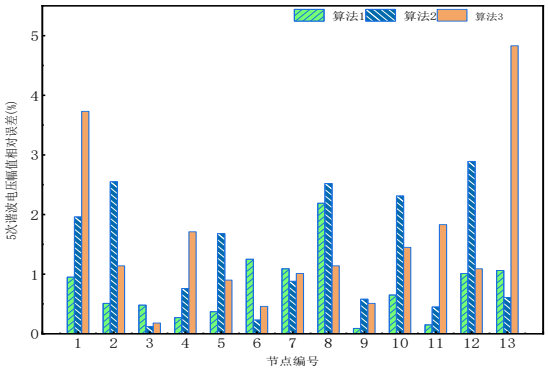


图 3 节点 5 次谐波电压相对误差

Fig.3 Relative error of the 5th harmonic voltage of the node

如图 3 所示，算法 2 和 3 整体误差都偏大，由于没有抗粗差能力，在 1、12 和 13 节点相比算法 1 偏差较大，对于算法 1 大部分节点误差都能保持在 1%内，相较于算法 2 和 3 整体估计结果较优。

保持参数矩阵和测量值的误差不变，改变测量值中添加的粗差，比例不变，分别取标准差为 3%、6%和 9%，形成不同粗差的量测数据集，为避免偶然性，每个粗差下取进行 50 次估计，共进行 150 组。通过对比算法 1 至 3 的平均相对误差，验证所取算法在多误差水平下的有效性，结果如图 4 所示。

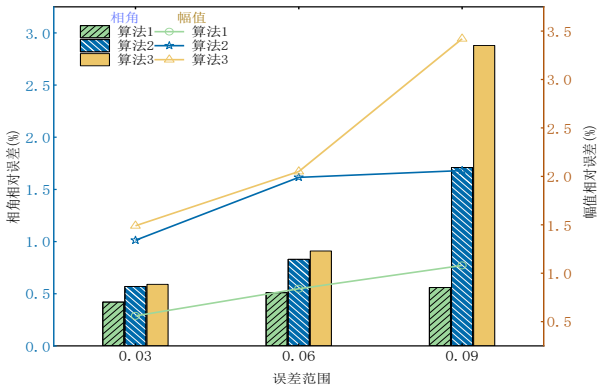


图 4 不同粗查下算法估计误差对比

Fig. 4 Comparison of algorithm estimation errors under different rough checks

根据图 4，虽然误差在随着粗差的增大而增大，但是算法 1 无论是幅值相对误差还是相角相对误差较其余两种算法都很小，验证了所用算法的有效性。

根据算法 1 进行谐波状态估计得出的结果，通过式(4)、(5)得到各节点 5 次谐波有功功率如表 1 所示

表 1 各节点 5 次谐波功率计算结果

Table 1 Calculation results of 5th harmonic power of each node

节点	谐波功率/W
1	-121.12
2	-283.11
3	-434.5
4	-160.24
5	-16.9
6	-133.4
7	-136.26
8	-2.34
9	**3085.89**
10	-24.96
11	**493.03**
12	**232.23**
13	-11.68

根据表 1 计算的结果，可知 9、11 和 12 节点功率为正，识别为谐波源，与仿真设置的谐波源位置一致。因此，所采用的根据谐波状态估计的结果来定位系统中的谐波源是准确有效的。

5 结论

总体最小二乘法虽同时考虑了两种误差，但不具备抗粗差能力；并且在设计抗差总体最小二乘法时，由于总体最小二乘估计不适用于残差预

测，根据单个随机量残差进行重定权存在理论缺陷，针对这些不足，本文提出了将基于等式残差设计相应的抗差总体最小二乘法用于谐波状态估计。仿真结果表明，在参数误差、量测误差与粗差同时存在情况下，本文所取方法估计精度显著优于最小二乘与总体最小二乘。最后计算了系统中各节点注入的有功功率，通过判断各节点向系统注入有功功率正负实现了谐波源的精准定位。

本文所加粗差非杠杆观测粗差，当存在杠杆粗差时，所选取的抗差方法不能得到准确的估计结果，如何在存在杠杆粗差的情况下设计有效的抗差估计算法，进行更准确的谐波源定位，有待进一步研究。

参考文献

[1] Wu W，Zeng D，Li J，et al. Harmonic state estimation and localization based on broad-band measurement[J]. Frontiers in Energy Research，2023，11：1320433.

[2] Wang Y，Dong Z，Li H，et al. A novel iterative observer approach for real‐time harmonic estimation in power distribution networks[J]. IET Generation，Transmission & Distribution，2021，15(2)：226-236.

[3] 冯函宇，王红，齐林海，等. 基于时空图卷积网络的谐波状态估计方法研究 [J]. 电网技术， 2023，47 (11)：4488-4501.

[4] Heydt G T. Identification of harmonic sources by a state estimation technique[J]. IEEE Transactions on Power Delivery，1989，4(1)：569-576.

[5] 徐志向，侯世英，周林，等. 基于奇异值分解的电力系统谐波状态估计[J]. 电力自动化设备，2006，(11)：28-31.

[6] 牛胜锁，张达，梁志瑞，等. 基于抗差总体最小二乘法的电力系统谐波状态估计[J]. 电力系统保护与控制，2014，42 (11)：106-111.

[7] 程宏波，万紫彤，李宗伟，等. 套索回归在配电网谐波源定位的应用[J]. 电力系统及其自动化学报，2024(6).

[8] 白志轩，肖先勇，张逸，等. 计及谐波视在功率的谐波源识别方法[J]. 电力系统自动化，2017，41 (08)：11-15.

[9] 孟姗姗. 电力系统谐波源辨识方法的研究[D]. 辽宁工业大学，2017.

[10] 丁同，陈红坤，吴斌，等. 多谐波源定位及谐波责任量化区分方法综述[J]. 电力自动化设备，2020，40 (01)：19-30.

[11] 陈少伟，邵振国. 基于最大后验估计的谐波源定位[J]. 电力系统及其自动化学报，2019，31 (12)：64-69.

[12] 张晨浩，李洋，宋国兵，等. 基于模型识别的配电网谐波源定位方法[J]. 中国电机工程学报，2021，41 (17)： 5803-5813.

[13] 吕志鹏. 基于等式残差的抗差总体最小二乘估计算法[J]. 大地测量与地球动力学，2025，45 (07)：732-737.

[14] 韩茂岳，尹忠东，沈子伦，等. 基于相量测量单元优化配置的配电网谐波状态估计研究[J]. 科学技术与工程，2024，24 (08)：3243-3250.

[15] 曹鹏，刘敏. 基于改进的整数规划法结合零注入节点的 PMU 优化配置方法[J]. 电力系统保护与控制，2021，49 (16)：143-150.



孔繁泽

收稿日期：2025-08-16。

作者简介：

孔繁泽(2000)，男，硕士研究生，研究方向为电能质量，E-mail：1203071762@qq.com；

石开明(1970)，男，副教授，硕士生导师，研究方向为电力系统规划运行与新能源发电研究，E-mail：skming2006@126.com。

（编辑　五号楷体，居右，段前空 6pt）

006 基于多变量模态分解与 BiLSTM 的超短期光伏功率概率预测

马　硕[1]，李佳丽[1]，王德林[1]，王世山[2]

（1. 西南交通大学电气工程学院，四川 成都 611756；2. 南京航空航天大学 自动化学院，江苏 南京 210016）

Ultra-short term photovoltaic power probability prediction based on multivariate mode decomposition and BiLSTM

MA Shuo[1], LI Jiali[1], WANG Delin[1], WANG ShiShan[2]

(1. School of Electrical Engineering Southwest Jiaotong University, Chengdu 611756, China; 2. School of Automation, Nanjing University of Aeronautics and Astronautics, Nanjing 210016, China)

ABSTRACT: In view of the poor performance of current photovoltaic power prediction methods in ultra-short-term predictions and other issues, this paper proposes an ultra-short-term photovoltaic power probability prediction method based on multivariate modal decomposition and BiLSTM. Firstly, the historical photovoltaic power data and irradiance data are decomposed into two sets of sub-modes through snake optimization variational mode decomposition. Then, the sub-modes along with some meteorological factors are reduced in dimension by using the maximum correlation and minimum redundancy algorithm to lower the complexity of the data. Then, the concise and clear data is used as the input feature to obtain the point prediction results of each sub-mode through the BiLSTM model and superposition them. Subsequently, the point prediction results are subjected to quantile regression to obtain the probability prediction results. Finally, a case study was conducted based on the historical data of two sets of photovoltaic power stations. The experimental results verified the excellent performance of the method proposed in this paper in the probability prediction of ultra-short-term photovoltaic power.

KEY WORDS: Photovoltaic power generation; Modal decomposition; Probabilistic prediction; Quantile regression

摘要：针对目前光伏功率预测方法在超短期预测下表现较差等问题，本文提出一种基于多变量模态分解与 BiLSTM 的超短期光伏功率概率预测方法。首先，将历史光伏功率数据和辐照度数据通过蛇优化变分模态分解分解成两组子模态。然后，将子模态连同部分气象因素利用最大相关最小冗余算法降维，降低数据复杂性；接着，将简洁清晰的数据作为输入特征通过 BiLSTM 模型中得到各个子模态的点预测结果并叠加；之后，将点预测结果经分位数回归得到概率预测结果。最后，基于两组光伏电站历史数据进行算例分析，实验结果验证了本文所提方法在超短期光伏功率概率预测上的优良性能。

关键词：光伏发电；模态分解；概率预测；分位数回归

DOI：10.13335/j.1000-3673.pst.2014.01.

0　引言

随着传统电力系统向新型电力系统的过渡，以光伏发电为代表的新能源发电逐步占据主导地位[1-2]。由于新能源发电功率具有很强的随机性、间歇性和波动性，研究高精度的超短期新能源功率预测是保障电力系统安全稳定的有效手段[3-4]。

现有研究以确定性的点预测为主，文献[5]通过建立风功率的季节性自回归综合移动平均模型，并结合重采样、插值方法处理原始数据，实现了海上风电的复杂时间序列获取。文献[6]结合遗传算法与双向长短期记忆网络，将目标光伏变电站的历史发电数据输入，得到未来光伏功率的短期预测数据。文献[7-9]利用模糊聚类和分类等方法，将天气类型分为晴天、雨天和少云等，较好的结合了各个气象因子，提升了风光功率预测精度。但是天气类型的划分没有统一标准，当空间位置改变后可能出现预测精度的急剧下降。上述点预测方法提供的信息较为单一，难以全面满足电力系统实时调度的需求[10-11]。概率预测通过提供功率的概率信息弥补其不

基金项目：国家自然科学基金项目(52207117)，四川省成都市科技局揭榜挂帅项目(2023-JB00-00002- SN)。

Project supported by National Natural Science Foundation of China（52207117）。

足，但现有方法存在精度低、时序特征提取不充分、灵活性差等问题。

综上所述，本文提出一种多变量模态分解和BiLSTM的超短期光伏概率预测方法。首先，本文同时将历史光伏功率数据和辐照度数据经VMD分解，充分提取时序信息，降低信号非平稳性；接着，将处理后的特征数据同部分气象数据通过mRMR降维；接着，分别将上述的输入特征输入BiLSTM中获得各个子模态的点预测结果；最后，将得到的点预测结果通过分位数回归方法得到区间概率预测结果。由于VMD和BiLSTM对初始的超参数敏感，本文分别引入蛇优化算法和贝叶斯优化算法对初始的超参数进行寻优。采用我国宁夏某地区集中式光伏电站和欧洲某地区分布式光伏电站数据进行实验评估，验证本文方法的有效性。

1 研究方法

1.1 蛇优化算法

蛇优化算法(Snake Optimization Algorithm, SOA)是一种2022年提出的基于生物行为的优化算法，灵感来源于蛇的交配和觅食习性。该算法主要用于解决复杂的优化问题，尤其在连续函数优化和组合优化领域表现出色。蛇优化算法的计算步骤详见文献[12]。

1.2 变分模态分解

变分模态分解（Variational Mode Decomposition, VMD）是一种技术理论成熟完备的信号处理方法，有效避免了EEMD和EMD等信号分解方法产生的端点效应和模态混叠等情况，降低了原始数据的波动性。VMD信号分解变分约束条件：

$$\begin{cases}\min\limits_{\{u_k\},\{\omega_k\}}\left\{\sum\limits_{k=1}^{K}\left\|\partial_t\left[\left(\delta(t)+\dfrac{j}{\pi t}\right)u_k(t)\right]e^{-j\omega_k t}\right\|_2^2\right\} \\ s.t.\sum\limits_{k=1}^{K}u_k=f(t)\end{cases} \tag{1}$$

式中，$\{u_k\}$为分解后第k个模态表达式；$\{\omega_k\}$为分解后第k个模态中心频率；K为模态分解个数；$\delta(t)$为狄克拉函数。

1.3 最大相关最小冗余算法

最大相关最小冗余算法（Max-Relevance and Min-Redundancy, mRMR）算法是一种特征选择的过滤方法，它结合了搜索策略。该算法通过增量搜索的方式，从原始特征集中快速找到与类别相关性最大的，同时特征之间相关性最小的特征子集。最优特征可表示为：

$$mRMR=\max_{x_j\in F_m-J_{n-1}}\left[I(x_j,y)-\frac{1}{n-1}\sum_{x_i\in J_{n-1}}I(x_j,x_i)\right] \tag{2}$$

式中，n为特征个数；x,y为随机变量；I为互信息。

1.4 双向长短期记忆神经网络

双向长短期记忆网络（Bidirectional Long Short-Term Memory, BiLSTM）由2个相反方向的LSTM构成，通过双向信息流提升了模型对上下文的理解能力。双向长短期记忆网络对应网络结构图如图 **1** 所示。

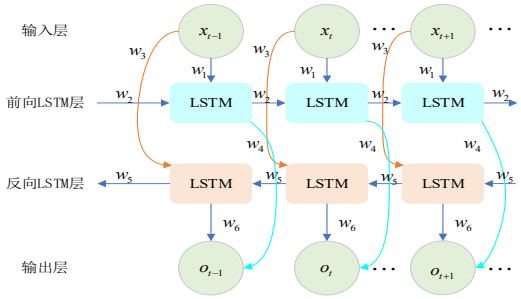


图 1 BiLSTM 结构

Fig 1 BiLSTM structure

1.5 贝叶斯理论

贝叶斯优化（Bayesian Optimization, BO）算法是一种用于寻求优化问题最优解的策略，本文用于设定双向长短期记忆神经网络的超参数，避免手动设置超参数带来的一系列问题。贝叶斯优化通常使用高斯过程作为先验函数，通过高斯过程建立概率模型，求解后验概率。高斯模型可表示为：

$$\{f(n)\}\sim N\left[m(n),k\left(n,n^{'}\right)\right] \tag{3}$$

式中，m为均值；k为协方差；n为超参数矩阵。

1.6 分位数回归

分位数回归（Quantile Regression, QR）是一种非参数概率预测方法，该方法无需先验假设。相比参数化概率预测模型，分位数回归很好的建立了因变量与自变量之间的关系，表现出较好的抗干扰能力。非线性QR的表达式为：

$$Q_{yi}(\lambda|x_i)=f\left[x_i,\omega(\lambda),\nu(\lambda)\right]\ i=[1,2,\cdots n] \tag{4}$$

式中，x为解释变量；y为响应变量；λ为分位数，取值范围是[0,1]；f为非线性函数。

通过计算权重向量，分位数从0到1连续取值，得到最终的区间预测结果。

2 光伏功率超短期预测组合模型

2.1 优化变分模态分解

利用VMD进行信号分解时需要预先设置惩罚因子和分解个数，而这些参数的选择会直接影响分解的效果，不同样本数据需要不同的参数。因此，

为了提高预测模型的灵活性，本文提出蛇优化算法对 VMD 的惩罚因子和分解个数进行寻优，流程图如图 2 所示。

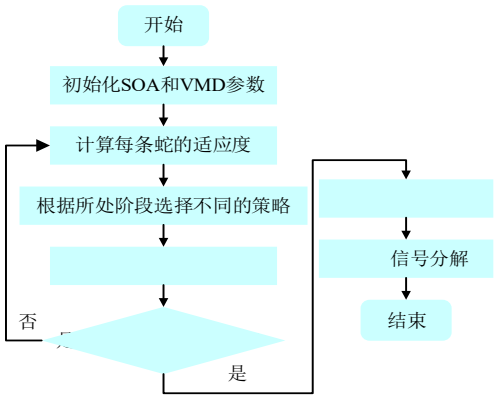


图 2　SOA 优化 VMD 流程

Fig 2　VMD optimization process of SOA

2.2 基于多变量模态分解与 BiLSTM 的预测流程

由于大气系统的混沌特性，光伏功率具有极强的随机性、非线性和非平稳性。为了提升光伏功率预测的精度和预测模型的灵活性，尤其是在多转折天气下的预测精度，提出了多变量模态分解与 BiLSTM 结合的超短期概率预测方法。预测流程框架如图 3 所示，分述如下：

（1）采集包含历史光伏功率数据、太阳辐照度和温度等历史数据。之后对这些数据剔除空值和无效值，并划分训练集和测试集。

（2）利用 SOA 优化的 VMD 方法对原始光伏功率序列和太阳辐照度序列进行分解，分别得到一系列不同尺度的子序列。

（3）使用最大相关最小冗余算法降低输入特征的维度，从原始光伏功率数据以及天气因素中提取出最优的输入特征。

（4）根据 VMD 的分解结果，输入 BiLSTM 神经网络中进行训练，神经网络模型的超参数使用贝叶斯算法优化，进一步提升模型精度。

（5）针对每一个光伏功率子序列预测分量，使用对应的最优特征集作为输入，经过预测模型，得到各个子序列的预测值。

（6）将得到的子序列叠加并进行反归一化处理，得到最终的光伏功率点预测值。基于点预测结果，利用分位数回归拟合得到概率预测结果。

（7）最后分析评估预测模型效果，分别采用点预测与概率预测指标，对比不同光伏电站场景和不同预测模型下的预测效果分析。

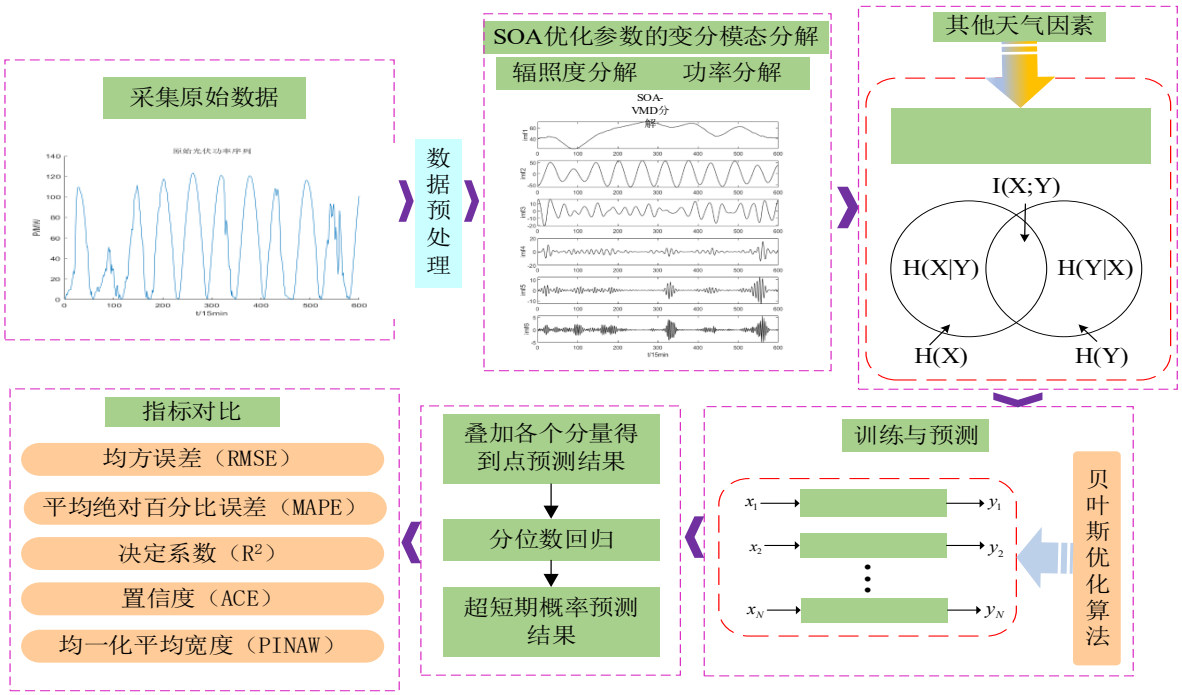


图 3　基于多变量模态分解与 BiLSTM 超短期光伏概率预测框架

Fig 3　Based on multivariable mode decomposition and BiLSTM ultra short term PV probabilistic prediction framework

2.3 评估指标

点预测评估指标选用均方误差（RMSE）、平均绝对百分比误差（MAPE）与决定系数（R^2）。

置信度是概率区间预测的重要评估指标。置信度由预测区间覆盖概率（Prediction Interval Coverage Probability, PICP）计算而来，给定 1-α为置信水平，置信度可表示为：

$$x_{ACE} = x_{PICP} - (1-\alpha) \qquad (5)$$

预测区间覆盖率可表示为：

$$x_{PICP}=\frac{1}{n}\sum_{i=1}^{n}c_i \tag{6}$$

式中，n 为样本总数；ci 可表示为：

$$c_i=\begin{cases}1 & c_i\in[L_i^{\alpha},U_i^{\alpha}]\\ 0 & c_i\notin[L_i^{\alpha},U_i^{\alpha}]\end{cases} \tag{7}$$

式中，[Liα,Uiα]为给定置信度下的区间。

概率预测结果的集中情况可用预测区间归一化平均宽度（Prediction Interval Normalized Average Width, PINAW）描述，计算公式为：

$$x_{PINAW}=\frac{1}{n\left(Y_{\max}-Y_{\min}\right)}\sum_{i=1}^{n}\left(U_i^{\alpha}-L_i^{\alpha}\right) \tag{8}$$

式中，Y 为实际值。

3 算例

3.1 数据来源

本文光伏所用数据分别来自我国宁夏地区某集中式光伏电站和欧洲地区某分布式光伏电站，选取 2022 年数据段，采样频率是 15min，分别包含 35040 个数据组。考虑到夜间光伏电站出力为 0，截取每天 7：00-21：00 时间段的数据进行训练和测试。为验证所提方法的灵活性，分别在不同季节、多转折天气以及不同类型光伏电站下进行预测，预测时间尺度为 15min，最后对点预测和概率预测结果进行分析。

3.2 算例 1 实验分析

为验证本文方法在超短期光伏概率预测中的灵活性和有效性，分别随机选取四种季节中的一天和多转折天气一天，选取宁夏地区某集中式光伏电站 2022 年数据为例验证。分别展示出 2022 年 1 月 15 日、4 月 29 日、7 月 11 日、9 月 18 日和转折天气预测结果。

在测试集中添加多种方法对比，分别与单变量分解、LSTM 模型和 VMD-SVM 模型对比，所得结果如图 4 所示。从图 4 中可以看出，本文方法相比于仅仅分解历史光伏功率的预测方法在转折天气下有更好的精度，充分说明了本文方法能够通过辐照度分解提取出云层的运动信息，达到精准预测光伏功率的目的。而其他两种对比方法的精度均呈现出不同程度的下降，这是因为这两种方法对历史时序信息提取的不够充分。

为了避免呈现结果的偶然性和更好的评估模型性能，计算点预测评估指标，所得结果如表 1 所示。从表 1 可以看出，本文方法相比其他三种方法，在不同季节和转折天气下均表现出了良好的效果。相较于单变量分解预测，采用本文方法的 RMSE、MAPE 两个指标分别平均下降 45.8%和 51.8%，R^2 更加贴近于 1。由于 LSTM 模型在波动剧烈的天气下不能够充分提取时序信息，导致用该模型预测结果表现最差。

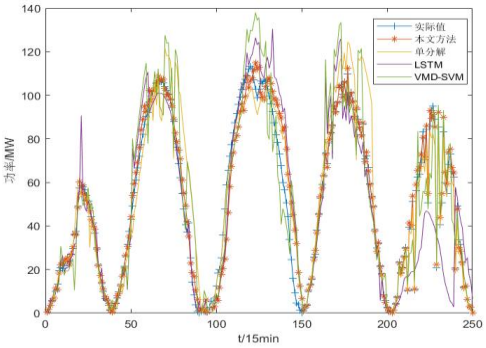


图 4 宁夏集中式电站点预测结果

Fig 4 Forecast results of centralized power stations in Ningxia

表 1 宁夏集中式电站点预测评估指标

Table 1 Ningxia centralized power station forecast evaluation index

		RMSE	*MAPE/%*	R^2
春	本文方法	24.5	3.35	0.992
	单分解	77.2	4.57	0.961
	LSTM	87.4	11.74	0.904
	VMD-SVM	82.6	5.89	0.955
夏	本文方法	14.9	6.88	0.997
	单分解	23.2	9.85	0.995
	LSTM	125.8	50.93	0.237
	VMD-SVM	16.1	7.38	0.370
秋	本文方法	25.8	5.63	0.998
	单分解	50.7	11.30	0.995
	LSTM	227.2	44.31	0.754
	VMD-SVM	34.1	6.77	0.587
冬	本文方法	35.5	6.20	0.994
	单分解	62.5	35.54	0.965
	LSTM	57.3	32.55	0.570
	VMD-SVM	64.2	90.45	0.591
转折	本文方法	40.6	10.50	0.967
	单分解	60.5	34.60	0.750
	LSTM	80.4	75.84	0.286
	VMD-SVM	103.5	53.59	0.343

3.3 算例 2 实验分析

为进一步评估本文方法在不同环境下的适应度，将欧洲某地区分布式光伏电站 2020 年一年的数据作为实验对象，采用本文方法和对比模型进行预测分析。由于在算例 1 中分析了我国地区集中式光伏电站在不同季节下的预测性能，在此考虑不同天气类型下的预测效果，选取晴天、多云和阴天天气作为具体天气类型。同时，从算例 1 的结果分析来看，采用 LSTM 模型表现最差，因此算例 2 拟采用 VMD-TCN-Attention、CEEMDAN-BiLSTM 和 CNN-GRU 作为对比模型。

为进一步检验本文方法效果，在算例 2 点预测

的基础上，将此三天的概率预测结果展示，如图 5 所示。从图 5 中可以看出置信区间在 90%和 80%时的区间预测情况，80%区间能够覆盖绝大部分实际功率。本文方法区间预测精度较高，在实际应用中置信水平可取 90%~80%。

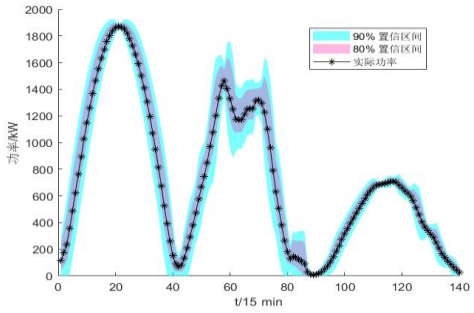


图 5　欧洲分布式电站概率预测结果

Fig 5　Probabilistic prediction results for distributed power stations in Europe

计算此算例概率预测评价指标结果，如表 2 所示。从表 2 中可以看出本文方法在晴天且置信区间取 90%时，置信度的值为 0.8909，均高于 VMD-TCN-Attention 和 CEEMDAN-BiLSTM；预测区间均一化平均宽度的值为 0.1019，均低于 VMD-TCN-Attention 和 CEEMDAN-BiLSTM，表明本文方法具有较高的置信度和较紧凑的预测区间。尽管 CNN-GRU 的 PINAW 低于本文方法，但是其 ACE 值为 0.7694，区间预测效果仍不理想。当置信区间取 80%时，本文方法在多云天气下置信度的值为0.7942，预测区间均一化平均宽度的值为0.0909，展示出较好的预测效果。同时，可以看出本文方法在其余天气类型下的预测效果，相比对比模型有不同程度优势。

表 2　欧洲分布式电站概率预测评估指标

Table 2　European distributed power station probability prediction evaluation index

		ACE		*PINAW*	
		90%	80%	90%	80%
晴天	本文方法	0.89	0.78	0.10	0.10
	VMD-TCN-Attention	0.83	0.67	0.12	0.11
	CEEMDAN-BiLSTM	0.85	0.71	0.15	0.12
	CNN-GRU	0.76	0.62	0.08	0.01
多云	本文方法	0.89	0.79	0.09	0.09
	VMD-TCN-Attention	0.83	0.72	0.31	0.13
	CEEMDAN-BiLSTM	0.80	0.65	0.13	0.11
	CNN-GRU	0.63	0.75	0.76	0.66
阴天	本文方法	0.87	0.77	0.12	0.12
	VMD-TCN-Attention	0.80	0.65	0.15	0.14
	CEEMDAN-BiLSTM	0.78	0.63	0.19	0.17
	CNN-GRU	0.72	0.69	0.11	0.10

4　结论

本文提出了一种基于多变量模态分解和 BiLSTM 的超短期光伏功率概率预测方法，主要结论如下：

（1）针对 VMD 和 BiLSTM 对初始超参数敏感的问题，分别引入蛇优化算法和贝叶斯优化算法对初始超参数进行寻优，避免了人工确定超参数的问题，实现了对不同数据的最优子模态数；

（2）本文同时将光伏功率数据和辐照度数据利用 VMD 分解，充分提取历史功率和辐照度的时序信息，数据可获得性高。在给定置信区间为 90%和 80%下，预测区间均一化平均宽度相比单变量分解分别平均降低了 18.04%和 10.65%；

（3）本文模型能够最大限度利用已有数据，得到概率预测结果。经过两个光伏电站算例验证了本文方法在点预测与概率预测上的优势。相比对比模型，本文所采用方法提高了光伏功率概率预测的精度，五个评估指标均有不同程度提升。

参考文献

[1] 国家能源局.新型电力系统发展蓝皮书[R]．北京，2023.6.

[2] 国家发改委，国家能源局，国家数据局．加快构建新型电力系统行动方案（2024—2027 年）[R]．北京，2024.7.

[3] 万灿,宋永华.新能源电力系统概率预测理论与方法及其应用[J]．电力系统自动化,2021,45(01):2-16.

[4] WAN C，LIN J，WANG J，et al. Direct quantile regression for nonparametric probabilistic forecasting of wind power generation［J］. IEEE Transactions on Power Systems，2016，32（4）：2767-2778.

[5] HUANG B, WANG J H. Applications of physics-informed neural networks in power systems—a review [J]. IEEE Transactions on Power Systems, 2023, 38(1): 572 - 588.

[6] ZHEN H，NIU D X，WANG K K，et al. Photovoltaic power forecasting based on GA improved Bi-LSTM in microgrid with-out meteorological information［J］. Energy，2021，231：120908.

[7] 杨茂,韩超,张薇.基于深度图聚类和特征重构的风电集群功率短期预测方法[J]．电力自动化设备， 2025-01-16:1-26.

[8] Jimenez-Perez P, Mora-Lopez L, et al. Modeling and forecasting hourly global solar radiation using clustering and classification techniques[J]. Solar Energy， 2016,135:682-691.

[9] 师浩琪,郭力,刘一欣,等.基于多源气象预报总辐照度修正的光伏功率短期预测[J]．电力自动化设备，2022,42(03):104-112.

[10] Haupt S E, Branko Kosovic Variable generation power fore-casting as a big data problem[J]. IEEE Transactions on Sustainable Energy，2017,8(2):725-732.

[11] 张金良,刘子毅.基于混合模型的超短期风速区间预测[J]．电力系统保护与控制，2022,50(22):49-58.

[12] Hashim. F. A.,& Hussien, A. G. Snake Optimizer: A novel meta-heuristic optimization algorithm. Knowledge-Based Systems，2022:10830.



马硕

收稿日期：2025-09-23

作者简介：

马硕(2001)，男，硕士研究生，研究方向为新能源功率预测，E-mail：shuoma@my.swjtu.edu.cn；

王德林(1970)，男，教授，博士生导师，研究方向为电力系统机电动态、扰动传播、频率稳定与控制、连续体建模等，E-mail：dlwang@swjtu.cn。

007 Comprehensive assessment of normal operational benefit and extreme event responsiveness for distribution systems

Longteng Wu[1], Ruijin Huang[1], Sibo Wang[2], Di Zhang[2], Yiheng Bian[2], Gengfeng Li[2]

[1] Guangdong Power Grid Corporation, Guangzhou, China

[2] State Key Laboratory of Electrical Insulation and Power Equipment, Xi'an Jiaotong University, Xi'an, China

*gengfengli@xjtu.edu.cn

Abstract. In order to conduct a quantitative study on the economic benefits of the new power system under normal operation and its recovery capacity after extreme disasters, this paper proposes a comprehensive assessment method that simultaneously considers normal operational benefit and extreme event responsiveness. On the one hand, this paper starts from the perspective of economic benefits: Firstly, it proposes economic indicator *E* that simultaneously consider costs, benefits and discount rates; Secondly, it considers the multi-market coupling mechanism of carbon-electricity-green certificates to construct a cost-benefit model with the goals of minimizing costs and maximizing benefit; Thirdly, the ADMM algorithm is used to reconstruct the model; Finally, the cost-benefit double-layer iterative model solved by the ADMM algorithm was obtained, which can be used to solve the economic indicators. On the other hand, in the resilience assessment for extreme scenarios, firstly, the uncertainty of distribution network faults and recovery time is considered, the time series Monte Carlo simulation method is used to deduce the evolution process of distribution network component faults and generate a dynamic scene set of extreme events; Secondly, establish a distribution network restoration model under extreme events to simulate the entire process of the distribution network responding to disasters; Finally, calculate the elasticity index based on the simulation

results. Ultimately, the numerical examples prove the feasibility of this comprehensive assessment method. Therefore, the application of this comprehensive assessment method can guide the construction of the unit from multiple objective perspectives including economy and post-disaster recovery.

Keywords: Comprehensive Assessment, Economy, Resilience, Distribution Network.

1 Introduction

Today, energy shortages, climate change and environmental pollution have posed severe challenges to the energy system and human society. There is an urgent need to accelerate the energy transition process and promote the transformation of the power system to a new paradigm of low-carbonization [1-2]. In the context of global warming, extreme natural disasters such as typhoons, rainstorms and cold waves are showing a trend of "frequent, frequent, strong and concurrent", posing serious challenges to the new power system. What's more, the flexibility of the power system will be enhanced by increasing energy storage and demand-side response resources such as incentives through electricity price mechanisms[3]. Therefore, it is a matter of great concern for investors to develop corresponding models and set indicators for the normal operation and the extreme scenarios of the distribution network, which is helpful to guide the construction of units.

For the establishment of flexible regulation resource models, numerous literatures have been modeled and applied simulations of flexible regulation source-storage resources and new energy modeling studies such as deeply retrofitted thermal power units[4], thermal power units equipped with carbon capture devices[5-6], hydroelectric units[7], and energy storage systems[8-9], but no studies have conducted unified scheduling studies of multiple types of flexible regulation resources in the carbon-electricity-green certificate markets. For the carbon-electricity-green market research section, early studies at home and abroad mainly focus on the coupling optimization problem of a single carbon trading[10-12] or green certificate trading mechanism[13] with the electricity market. After 2020, with the gradual establishment and improvement of the green certificate trading market, research on the carbon-electricity-green certificate market have gradually increased[14]. However, such studies only examine the feasibility of the model and did not further concretize the economic indicators of the system.

Meanwhile, strengthening the defense against extreme events and reducing power outage losses are of great practical significance for safeguarding the national economy and people's livelihood. In terms of disaster modeling, reference [15] established the vulnerability curve of the power system under storm by analyzing historical storm data and using the method of data fitting; In terms of resilience assessment， reference [16] set the recovery capacity indicator as the ratio of the part

of the system performance recovered at time *t* after disturbance to the part of the system initially damaged. Some studies have considered flexible resources such as distributed power sources, energy storage, intelligent switches, as well as rapid recovery after disasters. Reference [17] established an optimal configuration model of intelligent telecontrol switches for distribution networks, achieving distribution fault isolation in disaster situations; However, none of these studies took into account the dynamic fault evolution of distribution networks in disaster situations and the uncertainty of emergency repairs.

Therefore, this paper presents an assessment method that takes into account both normal operation efficiency and recovery capabilities of disaster prevention, which could not only evaluate the economic benefits of the system under normal operation, but also evaluate the capacity of defensing against extreme events of the system after disaster. In this paper, an improved IEEE 37-node system is used as the test system, and the result of an example analysis shows the feasibility of the method. The main contributions of this paper are as follows.

1) This paper adopts a comprehensive assessment method for the distribution network system, considering both normal operational benefit and extreme event responsiveness. This comprehensive assessment method can guide the multi-objective construction of the new distribution system in terms of economy and resilience.

2) In the resilience assessment for extreme scenarios, the uncertainty of distribution network faults and recovery time is considered, the time series Monte Carlo simulation method is used to deduce the evolution process of distribution network component faults and generate a dynamic scene set of extreme events, establish a distribution network recovery model under extreme events, simulate the entire process of distribution network response to disasters, and achieve system resilience assessment.

3) In the economy assessment for normal scenarios, it proposes a new kind of economic indicator *E* and a normal operation simulation method for solving this indicator. Simultaneously considering the multi-market coupling mechanism of carbon-electricity-green certificates and the goals of minimizing total costs and maximizing total benefits, this method uses the ADMM algorithm to reconstruct the model to obtain the cost-benefit double-layer iterative model, which can be used to solve the economic indicator *E* of any distribution network system.

2 An Assessment Method Considering Both normal operational Benefit And Post-Disaster Recovery Capability

2.1 Index Construction

Normal Operational Benefit Indicator. Based on the CBR and NPV indicators, this paper proposes a normal operational benefit indicator for distribution networks as shown below. A smaller value of this indicator means a lower power generation cost and a higher benefit of the distribution network system, both of which further mean a better economic benefit.

$$E = \frac{C_{all}}{F_{all}}(1+r)^{y} \tag{1}$$

Where C_{all} mean the cost of power generation for all generating units in the distribution network within 24 hours on a typical day; F_{all} mean the net benefit generated by all generating units in the distribution network within 24 hours on a typical day; r mean the discount rate; y mean the years the device have been in use.

extreme event responsiveness Indicator. In extreme disaster scenarios, component failures in the distribution network can lead to system load loss. Capacity loss load and capacity loss load proportion can reflect the loss situation of the distribution network. Monte Carlo simulation can obtain a large number of load loss indicators for various scenarios. Average capacity loss load and average capacity loss load proportion can respectively represent the average value and average proportion of system load loss.

$$F_{CLL} = \sum_{t\in T}\sum_{j\in \mathcal{V}} \varpi_j^e \cdot P_{shed,j,t} \cdot \Delta t \tag{2}$$

$$F_{CLLP} = \frac{\sum_{t\in T}\sum_{j\in \mathcal{V}} \varpi_j^e \cdot P_{shed,j,t} \cdot \Delta t}{\sum_{t\in T}\sum_{j\in \mathcal{V}} \varpi_j^e \cdot P_{L,j,t} \cdot \Delta t} \tag{3}$$

$$F_{ACLL} = \frac{\sum_{i=1}^{N_s} F_{CLL,i}}{N_s} \tag{4}$$

$$F_{ACLLP} = \frac{\sum_{i=1}^{N_s} F_{CLLP,i}}{N_s} \tag{5}$$

In the formula: $\mathcal{N}$ is the power system bus set; T is the recovery time set; ϖ_j^e is the weight of node j; $P_{shed,j,t}$ is the excised active load of node *j* at time *t*. Δt is the time step; $F_{CLL,i}$ is the capacity loss load in the *i*-th simulation; $F_{CLLP,i}$ is the capacity loss load proportion in the *i*-th simulation; F_{ACLL} is the average capacity loss load ; F_{ACLLP} is the average capacity loss load proportion; N_s is the number of simulations.

2.2 Normal Operational Benefit Simulation Method

In order to simulate the transactions of each unit in the distribution network during normal operation, it is necessary to consider both the cost minimization objective that is more suitable for the overall interest and the net benefit maximization objective that is more suitable for the individual interest. Therefore, the objective function of this simulation method is:

$$\max \quad U_{all} = -C_{all} + \sum_{i}^{I} F_i \tag{6}$$

Where C_{all} mean the total cost of the carbon-electricity-green certificate market for all power generation subjects in the distribution network within 24 hours; F_i mean the net benefit of power generation subject *i* of the distribution network in the carbon-electricity-green certificate market within 24 hours.

The total cost of the carbon-electricity-green certificate market for all power generation subjects in the distribution network within 24 hours can be expressed as:

$$C_{all} = \sum_{i}^{I}\sum_{t}^{T} C_i^t = \sum_{i}^{I}\sum_{t}^{T} (C_{i,ele}^t + C_{i,car}^t + C_{i,tgc}^t) \tag{7}$$

Where *t* is used to mark the current time period; C_i^t mean the three-market operating cost of the power generation subject *i* in time period t; $C_{i,ele}^t$ mean the power generation cost of the power generation subject *i* in time period t; $C_{i,car}^t$ mean the carbon market transaction cost of the power generation subject *i* in time period t. If the subject is a buyer, this value will be positive representing cost. Inversely, if the subject is a seller, this value will be negative representing profit; $C_{i,tgc}^d$ mean the green certificate market transaction cost of the power generation subject *i* in time period t. If the subject is a buyer, this value will be positive representing cost. Inversely, if the subject is a seller, this value will be negative representing profit.

1）Power generation cost:

$$C_{i,ele}^t = a_i P_i^{t2} + b_i P_i^t + c_i \tag{8}$$

Where P_i^t mean the power generated by the generating subject *i* in period t; a_i, b_i, c_i mean the fuel cost coefficient of the generating subject *i* .

2）Carbon market transaction costs:

$$C_{i,car}^{t} = \alpha_{car}^{d}(\chi_i - \chi_{set})P_i^t \tag{9}$$

Where χ_{set} mean the proportion of free carbon quotas allocated to thermal power units by the relevant authorities; χ_i mean the proportion of actual carbon emissions of the power generation subject i. For the seller subject, the relationship between the two satisfies: $0 < \chi_i < \chi_{set}$, which guarantee that its carbon market transaction cost is negative, indicating the obtainable benefit; For the buyer, the relationship satisfies: $\chi_{set} < \chi_i < 1$,which guarantee that its carbon market transaction cost is positive, indicating the cost to be paid; α_{car}^{d} mean the carbon market clearing price for the day, simply referred to as the carbon price.

3）Green certificate market transaction costs:

$$C_{i,tgc}^{t} = \alpha_{tgc}^{d}\eta_i P_i^t \tag{10}$$

Where η_i mean the proportion of the demand for green certificates by the power generation subject i. For the seller subject, it satisfies: $-1 < \eta_i < 0$,which guarantee that its green certificate market transaction cost is negative, indicating the obtainable profit; For the buyer, it satisfies: $0 < \eta_i < 1$,which guarantee that its green certificate market transaction cost is positive, indicating the cost to be paid; α_{tgc}^{d} is the clearing price of the green certificate market for the day, simply referred to as the green certificate price.

The net income of distribution network power generation subject *i* in the carbon-electricity-green certificate market within 24 hours can be expressed as:

$$F_i = \sum_{t}^{T} \alpha_{deal}^{t} P_i^t - \sum_{t}^{T} C_i^t \tag{11}$$

Where α_{deal}^{t} mean the electricity market clearing price at period *t* after the electricity market clearing; C_i^t mean the carbon-electricity-green certificate market operating cost of the power generation subject *i* during the period t; P_i^t mean the power generated by the power generation subject *i* in period t.

For the electricity market trading mechanism, each power generation enterprise adopts the centralized bidding trading method and is uniformly cleared at the system marginal electricity price.

Specifically, the quotations of the power generation subject i $\alpha_{i,bid}^{t}$ are calculated based on marginal cost:

$$\alpha_{i,bid}^{t}=\frac{\partial C_i^t}{\partial P_i^t} \tag{12}$$

The electricity market clearing price obtained by generating subject i α_{deal}^{t} is based on the quotations of all generating subjects, using the marginal pricing mechanism. The clearing price is the highest quotation of all generating subjects:

$$\alpha_{deal}^{t}=\max\{\alpha_{1,bid}^{t},...,\alpha_{I,bid}^{t}\} \tag{13}$$

This model needs to set constraint conditions based on the system balance and the operation of the unit:

1）System power balance conditions

$$\sum_{n}^{N}L_n^t=\sum_{i}^{I}P_i^t \tag{14}$$

2）Upper and lower limit constraints on unit output

$$P_{i,\min}\le P_i^t\le P_{i,\max} \tag{15}$$

Where $P_{i,\max}$ and $P_{i,\min}$ are respectively the upper and lower limits of the output of the power generation subject *i*.

3）Ramping/sliding capacity

$$\Delta P_{i,\min}\le P_i^t-P_i^{t-1}\le\Delta P_{i,\max} \tag{16}$$

Where $\Delta P_{i,\max}$ and $\Delta P_{i,\min}$ are respectively the upper limits of the ramping and sliding capacity of the power generation subject *i*.

4）Capacity constraints for energy storage devices

$$E_{i,\min}\le\sum_{\tau=1}^{t}P_i^{\tau}\Delta\tau\le E_{i,\max} \tag{17}$$

Where $E_{i,\max}$ and $E_{i,\min}$ are respectively the upper and lower limits of the capacity of energy storage device i; This study is based on 1-hour intervals, so $\Delta\tau = 1$.

In fact, in order to solve the optimization problem more intuitively and conveniently, this paper uses the ADMM method to decompose the optimization problem into a two-layer model for iterative solution, as shown in the figure.

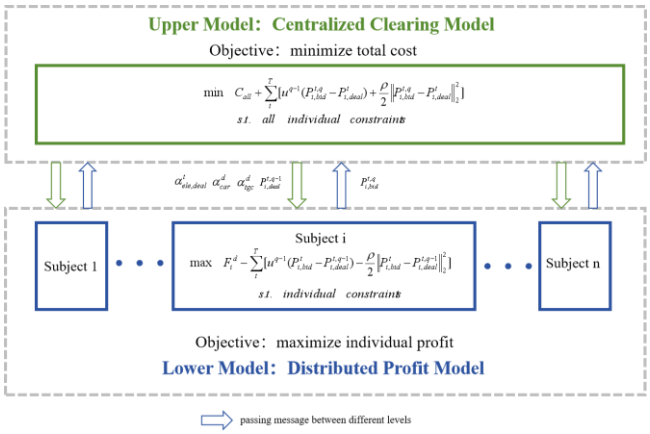


Fig. 1. Schematic diagram of the two-layer model

The upper layer of the two-layer model is the centralized clearing model, whose objective is to minimize the overall cost. After being modified by the ADMM algorithm, its objective function is:

$$\min \quad C_{all} + \sum_{t}^{T}[u^{q-1}(P_{i,bid}^{t,q} - P_{i,deal}^{t}) + \frac{\rho}{2}\left\|P_{i,bid}^{t,q} - P_{i,deal}^{t}\right\|_2^2] \tag{18}$$

The lower layer of the two-layer model is the distributed profit model, whose objective is to maximize individual profit. After being modified by the ADMM algorithm, its objective function is:

$$\max \quad F_i^d - \sum_{t}^{T}[u^{q-1}(P_{i,bid}^{t} - P_{i,deal}^{t,q-1}) - \frac{\rho}{2}\left\|P_{i,bid}^{t} - P_{i,deal}^{t,q-1}\right\|_2^2] \tag{19}$$

Where $P_{i,bid}^{t}$ mean the power reported by the generating subject *i* in period t, which is the optimization result of the lower model; $P_{i,deal}^{t}$ mean the power cleared by the power generation subject *i* in period t, which is the optimization result of the upper model; u^{q-1} mean the ADMM multiplier in the q-1 iteration; ρ mean the penalty factor.

The information flow mode is as follows: The dispatching center obtains the optimization results based on the centralized clearing model and calculates the

clearing electricity prices for each period in the current power market, then transmits the clearing electricity prices and clearing power to each subject. Then, each subject uses the distributed profit model based on the above information to optimize and obtain the reported power of each subject, which is then passed back to the dispatch center. The above two steps are repeated continuously, until the difference between the reported power and the cleared power is less than the upper limit of the ADMM residuals.

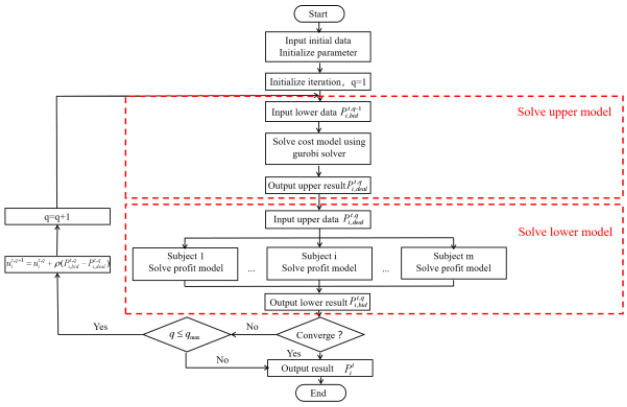


Fig. 2. algorithm flow chart of normal operation simulation method

2.3 Extreme Event Responsiveness Simulation Method

Dynamic Scene Generation of Extreme Events. In the case of storm disasters, the failure rate of distribution network lines is related to the maximum average wind speed of the storm. This paper refers to reference [21] using the bats model to generate time-series wind speeds for calculating fault rates, and the failure rate of the lines can be obtained from an exponential function model:

$$\lambda_k = \left(\gamma_1 e^{\gamma_2 w(t_k)} - \gamma_3\right)\lambda_{\text{norm}} \tag{20}$$

Where $w(t_k)$ is the wind speed at the *k* hour; λ_k is the component failure rate at the *k*-th hour; λ_{norm} is the failure rate of the component under normal circumstances; The first γ_1、γ_2、γ_3 is the fitting coefficient, γ_1=0.21, γ_2=0.49, γ_3=9.83.

Through time-series Monte Carlo simulation, generate the time when lines are out of service and the time when they are repaired and restored in a storm disaster. The line shutdown time is generated as follows: a random number *u* is drawn, which is uniformly distributed in the [0,1] space. According to the forced shutdown rate function of the distribution line during the passage of the typhoon, the time t_{down} corresponding to the fulfillment is determined as the random shutdown time of the distribution line $u = F(t_{\text{down}})$. If the shutdown time is greater than the departure time

of the storm, the line will not fail and shut down in that scenario. The forced outage rate function $F(t)$ can be derived from an exponential function model:

$$F(t)=1-C_k e^{-\lambda_k(t-t_k)}\ ,\ \ t_k \le t < t_{k+1} \tag{21}$$

In the formula: C_k is the integral constant, $C_k=1-F(t_k)$;where $F(t_0)=0$; t_k is the *k*-th hour.

The same sampling method is used to extract the repair time of damaged lines T_{ij}^R in the storm disaster, and the repair time of each damaged line follows an independent and identically distributed Weibull probability density function:

$$f_{T_{ij}^R}(t)=\begin{cases}\dfrac{\beta_T}{\alpha_T}\left(\dfrac{t}{\alpha_T}\right)^{\beta_T-1}\exp\left[-\left(\dfrac{t}{\alpha_T}\right)^{\beta_T}\right] & t\ge 0\\ 0 & t<0\end{cases} \tag{22}$$

In the formula: α_T、β_T is the parameter of the Weibull distribution.

Distribution Network Recovery Model. This section presents the distribution network recovery model under extreme disasters with the objective function of minimizing the power cut-off load, expressed as:

$$\sum_{t\in T}\sum_{j\in N}\varpi_j^e\cdot P_{shed,j,t}\cdot\Delta t \tag{23}$$

This paper constructs running constraints using a linearized Dist Flow model.

$$\begin{cases}\sum\limits_{i\in\delta(j)}P_{ji,t}-\sum\limits_{i\in\lambda(j)}P_{ij,t}=P_{DG,j,t}+P_{j,t}^E-\left(P_{L,j,t}-P_{shed,j,t}\right)\\ \sum\limits_{i\in\delta(j)}Q_{ji,t}-\sum\limits_{i\in\lambda(j)}Q_{ij,t}=Q_{DG,j,t}-\left(Q_{L,j,t}-Q_{shed,j,t}\right)\end{cases},\forall j\in N,\forall t \tag{24}$$

$$\begin{cases}U_{i,t}-U_{j,t}-\dfrac{r_{ij}P_{ij,t}+x_{ij}Q_{ij,t}}{U_0}\le \mathrm{M}\cdot\left(1-c_{ij,t}\right)\\ U_{i,t}-U_{j,t}-\dfrac{r_{ij}P_{ij,t}+x_{ij}Q_{ij,t}}{U_0}\ge -\mathrm{M}\cdot\left(1-c_{ij,t}\right)\end{cases},\forall(i,j)\in L,\forall t \tag{25}$$

$$\begin{cases}-S_{ij}^{\max}c_{ij,t}\le P_{ij,t}\le S_{ij}^{\max}c_{ij,t}\\ -S_{ij}^{\max}c_{ij,t}\le Q_{ij,t}\le S_{ij}^{\max}c_{ij,t}\end{cases},\forall(i,j)\in L,\forall t \tag{26}$$

$$U_j^{\min} \le U_{j,t} \le U_j^{\max}, \forall j \in N \setminus N_{\mathrm{DG}}, \forall t \tag{27}$$

$$\begin{cases} P_{DG,j}^{\min} \le P_{DG,j,t} \le (1 - x_{j,t}^{\mathrm{Isolate}}) P_{DG,j}^{\max} \\ Q_{DG,j}^{\min} \le Q_{DG,j,t} \le (1 - x_{j,t}^{\mathrm{Isolate}}) Q_{DG,j}^{\max} \end{cases}, \forall j \in N_{\mathrm{DG}}, \forall t \tag{28}$$

$$\begin{cases} 0 \leqslant P_{shed,j,t} \leqslant P_{\mathrm{L},j,t} \\ 0 \leqslant Q_{shed,j,t} \leqslant Q_{\mathrm{L},j,t} \end{cases}, \forall j \in N, \forall t \tag{29}$$

In the formula: N_{DG} is a set of distributed generator nodes. $P_{ij,t}$ and $Q_{ij,t}$ are respectively the active power and reactive power flowing through the line $i-j$ at time t; $P_{\mathrm{L},j,t}$, $Q_{\mathrm{L},j,t}$ are the active load and reactive load of node j in the power system at time t; $P_{\mathrm{DG},j,t}$, $Q_{\mathrm{DG},j,t}$ are the DG output active power and reactive power of node j at time t, respectively; $P_{\min,\mathrm{DG},j}$ and $P_{\max,\mathrm{DG},j}$ are the minimum and maximum active power limits of DG at node j, respectively; $Q_{\min,\mathrm{DG},j}$ and $Q_{\max,\mathrm{DG},j}$ are respectively the minimum and maximum active power limits of DG at node j; $P_{\mathrm{shed},j,t}$, $Q_{\mathrm{shed},j,t}$ are the active and reactive loads removed from node j at time t, respectively; $U_{j,t}$ is the voltage at node j at time t; $U_{\max,j}$ and $U_{\min,j}$ are respectively the maximum and minimum voltage limits at node j; U_0 is voltage rating; r_{ij} and x_{ij} are respectively the resistance and reactance of the line $i-j$; $S_{\max,ij}$ is the maximum capacity of the line $i-j$; $c_{ij,t}$ is a 0-1 variable for the state of the line $i-j$ at time t, where 0 is open and 1 is closed; $x_{j,t}^{\mathrm{Isolate}}$ is the 0-1 variable of whether node j is affected by the fault at time t, take $x_{j,t}^{\mathrm{Isolate}}$ 1 if the node is affected by the fault, and 0 otherwise; M is a larger positive number.

Distribution networks typically need to operate under a radial network structure, and the necessary and sufficient condition for maintaining the radial topology is: ① the number of closed lines is equal to the difference between the number of nodes and the number of subgraphs in the topology; ② The connectivity of each subgraph is satisfied. During the network reconfiguration and recovery process after a failure, subgraphs may include subgraphs connecting substations, subgraphs powered only by DG, and passive island subgraphs. The radial topology constraints of the distribution network are as follows:

$$\sum_{(i,j)\in \mathbf{L}} c_{ij,t} = |N| - |N_{\mathrm{sub}}| - \sum_{j \in \mathbf{N}} \gamma_{j,t}, \forall t \tag{30}$$

$$\gamma_{j,t} \le \sum_{i\in\delta(j)\cup\lambda(j)} \left(1-c_{ij,t}\right), \forall j \in \mathbf{N}, \forall t \tag{31}$$

$$\begin{cases} \sum_{i\in\delta(j)} V_{ij,t} - \sum_{i\in\lambda(j)} V_{ji,t} = W_{j,t}\gamma_{j,t} - 1, \forall j \in N \setminus N_{\text{sub}}, \forall t \\ \sum_{i\in\delta(j)} V_{ij,t} - \sum_{i\in\lambda(j)} V_{ji,t} = W_{j,t}, \forall j \in N_{\text{sub}}, \forall t \end{cases} \tag{32}$$

$$-\mathrm{M}c_{ij,t}^{s} \le V_{ij,t}^{s} \le \mathrm{M}c_{ij,t}^{s}, \forall (i,j) \in \mathbf{L}, \forall t \tag{33}$$

Where: $|N|$ is the number of nodes in the power system; $|N_{\text{sub}}|$ is the number of substations; N_{sub} is a set of substation nodes; $\lambda(j)$, $\delta(j)$ are respectively the sets of parent nodes and child nodes of node *j* respectively. $c_{ij,t}$ is a 0-1 variable for the state of the line $i-j$ at time *t*, where 0 is open and 1 is closed; $\gamma_{j,t}$ is the 0-1 variable for whether node *j* is the source node at time t; $V_{ij,t}$ is the virtual power of the line $i-j$ at time t ; $W_{j,t}$ is output the virtual power supply at node *j* at time *t*, as an unrestricted real number. In the virtual network, substation nodes and nodes $\gamma_{j,t}$ = 1 are regarded as source nodes, with unrestricted virtual power output set, and other nodes set virtual loads with a load value of 1.

When a distribution network line fails, the power supply to the area connected to the fault point should be cut off. The effect of the fault spreads along the line centered on the fault point until the nearest switch is disconnected. The task of fault isolation is to limit the impact of the fault to as small an area as possible by disconnecting some switches. The fault impact transmission constraints under distribution network $N-k$ faults are as follows:

$$-y_{ij,\kappa}^{\text{RCS}} \cdot u_{ij\kappa,t}^{\text{SW}} \cdot M \le y_{ij\kappa,t} - y_{ij\kappa,t-1} \le y_{ij,\kappa}^{\text{RCS}} \cdot u_{ij\kappa,t}^{\text{SW}} \cdot M, \forall (i,j) \in L, \forall t, \kappa = 1,2 \tag{34}$$

$$\varepsilon\left(2-y_{ij1,t}-y_{ij2,t}\right) \le 1-c_{ij,t} \le M\left(2-y_{ij1,t}-y_{ij2,t}\right), \quad \forall (i,j) \in L, \forall t \tag{35}$$

$$\begin{cases} Mx_{j,t}^{\text{Isolate}} \ge \sum_{i\in\pi(j)} y_{ij2t} \cdot \left(1-u_{ij,t}^{\text{Line}}\right) + \sum_{s\in\delta(j)} y_{js1,t} \cdot \left(1-u_{ij,t}^{\text{Line}}\right) \\ Mx_{j,t}^{\text{Isolate}} \ge \sum_{i\in\pi(j)} y_{ij1,t} \cdot y_{ij2,t} \cdot x_{i,t}^{\text{Isolate}} + \sum_{s\in\delta(j)} y_{js1,t} \cdot y_{js2,t} \cdot x_{s,t}^{\text{Isolate}} \end{cases}, \quad \forall j \in \mathbf{N}, \forall t \tag{36}$$

In the formula: ε , M are respectively close to 0 and larger positive numbers; $u_{ij\kappa,t}^{\mathrm{SW}}$ is a binary parameter, taking 1 if the *i*-side ($\kappa=1$) or *j*-side ($\kappa=2$) switch of the line $i-j$ is faulty, otherwise taking 0; $u_{ij,t}^{\mathrm{Line}}$ is a binary parameter, take 1 if the line $i-j$ is functioning properly, or 0 otherwise; $y_{ij1,t}$, $y_{ij2,t}$ are binary variables of the switch status on the *i*-side and *j*-side of the line $i-j$ at time *t*, taking 1 if no switch is configured or the switch is closed, otherwise taking 0; $y_{\mathrm{RCS},ij,\kappa}$ is a binary parameter, take 1 if the *i* side ($\kappa=1$) or *j* side ($\kappa=2$) of the line $i-j$ is equipped with a remote-controlled *j* switch *j*, and 0 otherwise.

The energy storage operation constraints are as follows:

$$E_j^{\min}\leqslant E_{j,t}\leqslant E_j^{\max},\forall j,\forall t \tag{37}$$

$$E_{j,t}=(1-\sigma_j)E_{j,t-1}-\frac{P_{j,t}^{E}\Delta t}{\eta_j},\forall j,\forall t,\forall s \tag{38}$$

$$\begin{cases} P_j^{E,\min}\leqslant P_{j,t}^{E}\leqslant P_j^{E,\max},\forall j,\forall t \\ Q_j^{E,\min}\leqslant Q_{j,t}^{E}\leqslant Q_j^{E,\max},\forall j,\forall t \end{cases} \tag{39}$$

In the formula: $E_j^{\max}$ 、 $E_j^{\min}$ are respectively the upper and lower limits of the charge capacity of the energy storage power station at node *j*; $E_{j,t}$ is the state of charge of the energy storage station at node *j* at time *t*; σ_j 、 η_j are the self-discharge rate and charge-discharge efficiency of the energy storage station at node *j*, respectively; $P_{j,t}^{E}$ and $Q_{j,t}^{E}$ are respectively the active and reactive outputs of the energy storage power station at node *j* at time *t*; $P_j^{E,\min}$ 、 $P_j^{E,\max}$ are respectively the upper limit of active power output of the energy storage power station at node *j*; $Q_j^{E,\min}$ 、 $Q_j^{E,\max}$ are respectively the upper limits of reactive power output of the energy storage station at node *j*.

3 Case Studies

3.1 The Modified IEEE 37-Bus System

To verify the validity of the proposed model, this paper conducts an example tes on an improved IEEE 37-node system[17], with the system topology shown in Figure 1. There are five connection lines in the system that are disconnected during normal operation, and the connection lines have been configured with RCS. The distribution system consists of 37 nodes and 41 lines. The system is equipped with one circuit

breaker, 20 RCS, two DGs at nodes 709 and 734 respectively for photovoltaic units and gas turbines, and one energy storage power station at node 744. Node 701 is connected to the substation, and circuit breakers are configured on the connection lines. The RCS configuration position and load data are set in reference [18], the normalized data of the available output power of the distributed units and the load curve of the system are shown in Figure 4, and the energy storage power station parameters are set in reference [19-20]. It is worth noting that 60kW is selected as the standard power for the load and photovoltaic power station under the normal operation of the distribution network.

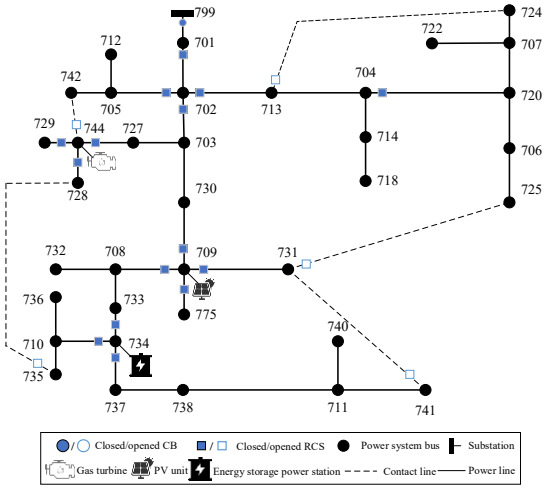


Fig.3. Modified IEEE 37-bus system

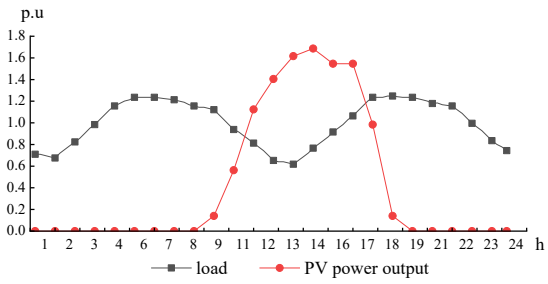


Fig.4. Normalized data curve of available output power and load for distributed units

In the distribution network area, there is one gas-fired power plant, one energy storage power station and one photovoltaic power station involved in the transaction. The parameters of each unit are shown in the table, among which the initial capacity of the energy storage power station is 500kWh.

Table 1. The parameters of each unit

	Gas-fired power plant	photovoltaic power station	energy storage power station
a (yuan/(kW)^2）	1	0	0
b (yuan/kW）	235	200	5
c (yuan/kW）	57	100	0
the upper limits of the output（kW）	500	x	300
The lower limits of the output（kW）	30	x	-300
the upper limits of the climb ability（kW/h）	8	x	x
the upper limits of the landslide ability（kW/h）	6	x	x
the upper limits of the capacity（kWh）	x	x	5000
the lower limits of the capacity（kWh）	x	x	0

From the perspective of the carbon market and the green certificate market, there are fewer participants in the distribution network. Therefore, this example uses a constant value of 77 yuan /t for the carbon price and a constant value of 180 yuan/certificate for the green certificate price. The remaining market-related values areas shown in the table below.

Table 2. The parameter in the market part

physical quantity	value
Carbon price α_{car}	77 yuan/t
green certificate price α_{tgc}	180yuan/certificate
Carbon emission standard ratio χ_{set}	0.67t/kW
Carbon emission ratio of gas-fired power stations χ_f	0.7t/kW
The green certificate demand proportion of gas-fired power stations η_f	0.35certificate/kW

For parameters in the ADMM algorithm, set the residual cap $\zeta = 1$,the penalty factor $\rho = 5$ .In the metric, the discount rate is temporarily disregarded, that is $r = 0$, and the device usage year is one year, that is $y = 1$.

3.2 Simulation And Calculation Of Normal Operational Benefit Indicators

Interpretation Of Simulation Result. Based on the above examples, simulations were conducted using the distribution network normal operation simulation method, and the output of the photovoltaic power station, gas turbine, energy storage power station and the total load on the user side were obtained as shown in the following figure.

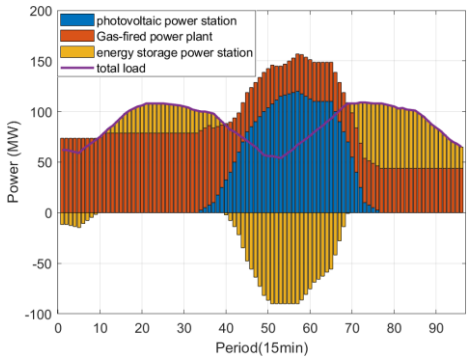


Fig. 5. Comparison chart of output of each unit and user load curves

It can be seen from the figure that the distribution network system mainly bears the base load by the gas turbine and the photovoltaic power station, and bears the peak load by the energy storage power station. Then, the energy storage power station will be mainly analyzed: Comparing the peak and trough periods of the load from a cost perspective, since the cost of gas turbine power generation shows a secondary growth trend with the power generation capacity, the dispatch center will choose to have the energy storage power station absorb power appropriately during the trough period of the load in order to replace gas turbine power generation during the peak period of the load reducing the power generation cost of the distribution network; From the perspective of profit, since the clearing electricity price is lower at the bottom of the load and higher at the peak of the load, the energy storage power station itself will choose to purchase electricity at the bottom of the load and sell it at the peak of the load to maximize profits. Therefore, it can be seen that the distribution network normal operation simulation method proposed in this paper can simulate the situation that takes into account both profit maximization and cost minimization while maintaining normal power balance, and can be used to further solve for total cost, total benefit and economic indicators.

Calculation Of normal operational Indicator. The cost, benefit and economic indicators of each subject are shown in the table below. When considering the coupling of the carbon-electricity-green certificate multi-market, energy storage power stations have the best economic benefits when the distribution network is operating normally, followed by photovoltaic power stations and then gas turbines. It can be seen that this economic indicator can be used to compare the economic benefits of each unit in the distribution network for guiding unit construction, and at the same time, the overall economic benefits of the distribution network can be calculated for assessing the economic level of the distribution network system.

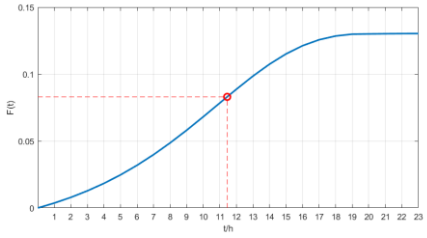
Table 3. Cost-profit-economic indicator table

	photovoltaic	Gas-fired power	energy storage	Total

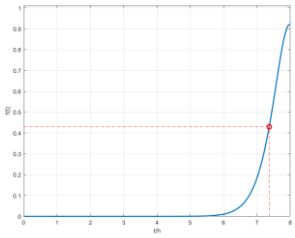
	power station	plant	power station	
Cost C/yuan	918100	2253989.2	18486.3	3190575.5
Profit F/yuan	238360.3	326588.8	40016.1	604965.2
economic indicator E	3.85	6.90	0.46	5.27

3.3 Simulation And Calculation Of Extreme Event Responsiveness Indicators

Metric Results. In this paper, 1000 scenarios were randomly selected for simulation of distribution network response recovery under extreme disasters. The number of distribution network line outages was set at 1 to 6. The distribution network line outage scenario set was generated based on Monte Carlo simulation using the method in section 2. The forced outage rate curve of distribution lines during storm passage is shown in Figure 6a, and the repair time distribution curve of damaged lines is shown in Figure 6b. Based on the load loss in each simulation result, calculate the average load loss of the resilience index as 3081.55kWh, the average load loss ratio was 13.01%. Figure 8 shows the distribution network's load loss under extreme disasters, including the average load loss and the average proportion of load loss at each moment for 1000 scenarios. As shown in Figure 8, the average proportion of load loss increases as the storm approaches the distribution area and decreases as the storm's impact weakens, and the load loss curve is consistent with the load curve.



a)The forced outage rate curve of distribution lines



b)The repair time distribution curve of damaged lines

Fig.6. Forced outage rate curve of distribution lines and the repair time distribution curve of damaged lines during the passage of the storm

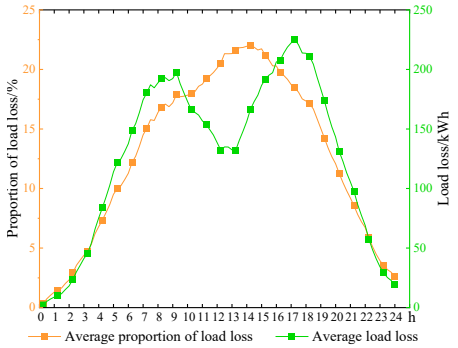


Fig.7. The average amount and proportion of load loss at each time point for 1000 scenarios

4 Conclusions

This paper proposes a comprehensive assessment method that simultaneously considers normal-operational benefit and extreme event responsiveness recovery capacity. In normal scenarios, this paper proposes a cost-benefit double-layer iterative model considering the multi-market coupling mechanism of carbon-electricity-green certificates to achieve the normal operation benefit simulation method, which can be used to obtain the normal-operational benefit indicator of a typical daily distribution network . The economic indicator E presented in this paper can guide the construction of units within the distribution network and assess the overall economic benefits of the distribution network under normal operation. In extreme scenarios, this paper proposes a distribution network resilience assessment method considering power grid reconfiguration and emergency repair of faulty lines. It uses the time-series Monte Carlo simulation method to characterize the uncertainty of distribution network faults and recovery time, deduces the evolution process of distribution network faults, generates a dynamic scene set of extreme events, establishes a distribution network recovery model under extreme events, and calculates resilience indicators, and verify it through numerical examples. The resiliency index proposed in this paper can assess the ability of distribution networks to cope with extreme disasters and provide suggestions for rapid recovery decisions after disasters. In the future, more optimization goals should be added to this comprehensive assessment method to achieve all-round and multi-objective construction of the unit.

Acknowledgement: this work is supported by Research Project of China Southern Power Grid Corporation. (Project No. 036000KK52222036(GDKJXM20222392)).

References

1. Fragkos, P., Laura van Soest, H., Schaeffer, R., Reedman, L., Koberle, AC., Macaluso, N., Evangelopoulou, S., De Vita, A., Sha, F., Qimin, C., Kejun, J., Mathur, R., Shekhar, S., Dewi, RG., Diego, SH., Oshiro, K., Fujimori, S., Park, C., Safonov, G., Iyer, G. (2021). Energy system transitions and low-carbon pathways in Australia, Brazil, Canada, China, eu-28, India, Indonesia, Japan, Republic of Korea, Russia and the United States. Energy, 216:119385.
2. Bie, Z., Lin, Y., Li, G., and Li, F., (2017), Battling the Extreme: A Study on the Power System Resilience. Proceedings of the IEEE, 105: 1253-1266.
3. H.Li, Z.Lu, Y.Qiao, J.Qi. Wind power consumption assessment method based on non-sequential production simulation[J].electric power construction,2015,36(10):129-137.
4. YANG Yinping, ZENG Yuan, QIN Chao, et al. Planning Model for Flexibility Reformation of Thermal Power Units for Deep Peak Regulation[J]. Automation of Electric Power Systems,2021,45(17):79-88.
5. HUANG Linsheng, YANG Bingfang, LI Xiaqiong. Economic Analysis of Deep Peak Shaving Renovation of Thermal Power in High Proportion Renewable Energy Power System[J] Power & Energy,2024,45(01):15-19+64.
6. YU Haibin, GAO Yiling, LU Zengjie. Low-carbon economic scheduling of deep peak regulating market with the participation of wind power,thermal power,storage and carbon capture units considering demand response[J]. Integrated Intelligent Energy,2023,45(08):80-89.
7. LIU Jiangwei, CHEN Yiping, XIAO Yunpeng, et al. Research Overview of Hydropower Participation in Electricity Market[J]. Electric Power,1-15[2025-05-26].http://kns.cnki.net/kcms/detail/11.3265.TM.20240929.1800.002.html.
8. KONG Piaohong, JIANG Zhengwei, YANG Liqiang, et al. Mechanism and Risk Quantification Model Design of Hydrogen Storage System Participation in Power Market[J]. Distribution & Utilization,2022,39(01):31-39.
9. CAI Xinlei, WANG Qin ,CHEN Yefu, et al. Economic Dispatch and Real-time Control of Wind-solar-storage Industrial Park Considering Demand-side Response[J]. Electric Drive,1-11[2025-02-04].
10. LI Jialong, CHEN Yuguo, LIU Sijie, et al. Electricity Market Equilibrium Analysis Considering Carbon Emission Cost[J].Power System Technology,2016,40(5):1558-1563.

11. Duan Shengzhi, Chen Haoyong, Zheng Xiaodong, et al. Bidding strategy of electricity generation and electricity market equilibrium analysis under the background of carbon market[J]. Electrical Measurement & Instrumentation,2022,59(5):33-41.
12. WANG Leilei, GAO Hongjun, LIU Chang, et al. Electricity Carbon Coupling Sharing Among Intelligent Buildings Considering Time-of-use Carbon Emission Measurement[J]. Power System Technology, 2022,46(6):2054-2063.
13. AN Xuena, ZHANG Shaohua, LI Xue. Equilibrium Analysis of Oligopolistic Electricity Markets Considering Tradable Green Certificates[J].Automation of Electric Power Systems，2017，41(9)：84-89.
14. CHEN Wei, JIANG Yuewen. Interactive Optimization of Day-ahead Market Trading Considering Coupling of Carbongreen Certificate-renewable Electricity Consumption Market[J]. Power System Technology,2024,48(05):1967-1979.
15. W. P. Zarakas, S. Sergici, H. Bishop, et al. Utility investments in resiliency: balancing benefits with cost in an uncertain environment[J]. The Electricity Journal, 2014, 27(5): 31-41.
16. M. Shinozuka, S. E. Chang, T. Cheng, et al. Resilience of integrated power and water systems[M].Multidisciplinary Center for Earthquake Engineering Research, 2003
17. BIAN Yiheng, BIE Zhaohong. Resilience-Enhanced Optimal Placement Model of Remote-controlled Switch for Smart Distribution Network[J]. Automation of Electric Power Systems, 2021, 45(03): 33-39.
18. WU Xue1, ZHANG Dahai1, ZHENG Xinxin, et al. Collaborative resilience planning model of flexible resources considering frequency security under typhoon disaster[J/OL]. Electric Power Automation Equipment,1-20[2025-08-17].https://doi.org/10.16081/j.epae.202507031.
19. Barker K, Ramirez-Marquez JE, Rocco C M. Resilience-based network component importance measures[J]. Reliability Engineering & System Safety, 2013, 117(2):89-97
20. LIU Ziyu, LIU Dafu, YANG Qiming, et al. Pre-disaster deployment and post-disaster dispatching method of distribution network restoration resources under typhoon and waterlogging compound disaster[J/OL]. Automation of Electric Power Systems,1-22[2025-08-15].https://link.cnki.net/urlid/32.1180.TP.20240730.1616.006.
21. SUN Shaohua, LI Gengfeng, ZOU Wenqiu, et al. Multi-type Energy Storage Equipment Configuration Strategy Balancing Economy in Conventional Scenarios and Resilience in Extreme Scenarios[J/OL]. High Voltage Engineering,1-14[2025-08-15]. https://doi.org/10.13336/j.1003-6520.hve.20250023.

008 课堂、科创、实习基地融合的电力系统专业建设

王世山[1]，王麒轩[1]，刘军[2]，张安红[2]，沈湛[3]

（1. 南京航空航天大学，南京 211106； 2. 杭州钱江电气集团股份有限公司，杭州 311200；
3. 东南大学，南京 211189）

The Construction of Power System Specialty with the Integration of Classroom, Scientific Innovation and Internship Base

WANG Shishan[1], WANG Qixuan[1], LIU Jun[2], ZHANG Anhong[2], SEHN Zhan[3]

(1. Nanjing University of Aeronautics and Astronautics，Nanjing 211106；
2. Hangzhou Qianjiang Electric Group Co., Ltd.， Hangzhou, 311200；
3. Southeast University, Nanjing, 211189)

ABSTRACT: As a core engineering major, Electrical Power System and its Automation plays a crucial role in national economic development and talent cultivation. Cultivating professionals with relevant expertise is of great significance to social development. This paper, taking the electrical engineering major of our university as an example, elaborates on the implementation paths of classroom teaching, extracurricular scientific and technological activities for college students, and internship bases by analyzing their respective characteristics. It focuses on exploring the integration mode of the three from freshman to senior year: integrating scientific and technological innovation elements into classroom teaching, combining theory and practice in scientific and technological innovation, and taking project-based practice in internship bases as the sublimation of classroom theories and the expansion of scientific and technological innovation. After nearly 20 years of integrated practice, this mode has been recognized by students and employers. Its experience is worthy of promotion in the major of Electrical Engineering and Automation and even in the engineering field, hoping to communicate with peers.

KEY WORDS: Power system specialty, scientific innovation, internship base, integration.

摘要[1]：电力系统及其自动化专业作为工科核心专业，在国民经济建设与人才培养中作用关键，培养具备专业素养的相关人才对社会发展意义重大。本文围绕课堂教学、大学生课外科技活动及实习基地的特点，以本校电气工程专业为例，阐述三者的实施路径。重点探索三者从大一至大四的融合模式：课堂融入科创元素，科创结合理论与实践，实习基地的项目式实践则是课堂理论的升华与科创的拓展。经过近 20 年的融合实践，该模式获学生与用人单位认可，其经验值得在电气工程及自动化专业乃至工科领域推广，以期与同行交流。

关键词：电力系统专业，科创，实习基地，融合。

0 前言

在电气工程学科体系中，电力系统专业作为核心支柱，承担着培养电力能源领域创新人才的关键使命。作为连接电能生产、传输、分配与应用的枢纽，电力系统的高效运行直接关系到国家能源安全与社会经济发展，其专业建设水平不仅决定着电气工程学科的实践深度，更是推动智能电网、新能源并网等前沿技术突破的重要基础。与此同时，科创活动能够激发学生的创新思维与科研能力，实习基地则为理论知识向工程实践的转化提供了真实场景，二者与课堂教学协同发展，是提升电力系统专业人才培养质量、满足行业动态需求的核心路径。

然而，传统电力系统专业建设中，课堂教学、科创实践与实习基地建设往往呈现“割裂”状态[1][2]。部分高校将课堂教学局限于理论知识灌输，忽视与实际工程场景的结合；科创活动仅作为少数学生的“第二课堂”，缺乏系统性课程衔接；实习基地建设则多以短期参观为主，难以实现长期深度参与。如文献[3]对江西省地方院校电气学生的调研显示，大部分学生缺乏将电力系统专业课程与科创项目联动设计的能力，难以将理论知识应用于实践创新，创新能力不强，企业接收学生实习因此不再那么积极了。这种“单枪匹马”的建设模式，不仅造成教学资源的重复投入，更使学生在知识整合与工程实践能力培养上存在明显断层。

[1] **项目资助**：南京航空航天大学项目式实习基地建设；国家自然科学青年基金资助(52207191)。
Project Supported by the Construction of Project-based Internship Base of Nanjing University of Aeronautics and Astronautic；Natural Science Foundation of China for Young Scientists(52207191).

为此，我校电力系统专业团队基于“一体化贯通培养”理念，探索课堂教学、科创活动与实习基地建设深度融合的新路径。通过构建从大一至大四的递进式培养体系，打破时间与空间壁垒，让学生在理论学习的同时参与科创项目，并将课堂知识及时应用于实习基地实践，形成“学、研、用”一体化的闭环模式。本文将从融合背景、实施路径与实践成效等方面，系统阐述该创新培养模式的具体策略与阶段性成果。

1 课堂教学

课堂教学是师生开展教与学活动的核心场域，其核心在于通过教学互动实现知识传递与能力培养，而非传统模式中教师“独角戏”式的单向灌输。随着新工科建设推进及工程教育专业认证对“以学生为中心”“强化学习主动性”的要求，传统教学模式亟待革新。

针对电气工程及其自动化(含电力系统自动化方向)专业本科四个年级的教学实践，课堂教学改革可从以下维度展开：

(1) 案例驱动的互动式教学：结合电力系统典型事故案例(如大面积停电、变压器烧毁、线路短路、设备爆炸等)，构建“问题导向—小组研讨—深度探究”的教学闭环。此类案例如同“电力系统的病理分析”，教师不直接给出结论，而是通过提问引导学生自主思考(如“配电网崩溃时潮流异常如何触发继电保护动作？”“变压器短路坍塌是温度过高还是电磁力过大导致？”)，并可设置课后思考题，预留研讨空间，以调动学生主动探究的积极性，实现“思考式学习”的有效性。

(2) 信息化工具的深度融合：借助雨课堂、学习通等平台，结合移动终端实现教学过程的实时互动。授课中嵌入选择题、填空题等即时测试内容，学生需当堂作答，既减少课堂分心现象，又能通过答题数据反馈学情；平台自动记录的答题正确率可纳入平时成绩，形成过程性评价体系，强化学习过程管理。

以具体教学场景为例：在“电力系统分析”课程中，选取美国大电网崩溃、区域性配电网故障等案例，剥离复杂系统中的关键环节(如潮流计算模块)设计定性选择题，引导学生理解潮流异常的影响机制；在“电机学”课程中，针对变压器短路事故设置“短路力与温度对设备破坏的主次关系”等辨析题，兼顾专业深度与课堂互动效率。此类设计避免了本科阶段难以完成的定量计算(通常留待课程设计或后续研究中结合专业软件实现)，更侧重培养学生的问题分析与定性判断能力。

通过案例驱动与信息化工具的结合，课堂教学可实现从“教师主导”向“学生主体”的转变，既契合工程教育认证理念，也为学生后续参与科创活动与实践应用奠定认知基础。

2 大学生课外科技活动

大学生课外科技活动作为课堂教学的重要延伸与补充，对电气工程及其自动化专业学生的成长具有不可替代的意义。它不仅搭建起理论知识与工程实践之间的桥梁，推动学生将课本上的电路原理、电子技术、计算机编程等抽象概念转化为具象的创新成果，更能在探索过程中激发自主学习动力——面对未学过的专业内容时，学生需主动查阅资料、拆解问题、寻求解决方案，这种自学能力的培养，正是工科人才核心素养的重要组成部分。同时，活动中涉及的项目规划、团队协作、成果展示等环节，能全方位提升学生的工程思维、沟通表达与抗压能力，为后续应对复杂工程问题、适应职场挑战奠定坚实基础[4]。

结合南京航空航天大学电气工程及其自动化专业的特点，课外科技活动的开展形式紧密依托专业课程体系，呈现出阶段性与递进性特征。大一阶段以“代入式”参与为主，通过简单的电路设计、编程入门等基础项目，帮助学生初步建立科技探索的兴趣与认知，熟悉实验室基本操作规范；大二阶段成为活动主力，凭借已掌握的高等数学、电路理论、电子技术及计算机高级语言等核心知识，可独立或组队承担具有一定复杂度的课题，如小型控制系统开发、电气设备性能优化等；大三学生虽仍可参与，但因专业方向深化、科研任务增加等原因，逐渐从核心主导角色过渡为辅助指导；大四则不再重点支持，以便学生专注于毕业设计、课程设计及升学就业等关键任务，确保学业与发展的有序衔接。

表 1 近年课外科技活动典型题目举例

序号	题　目
1	中频条件下变换器分布参数模型的建立
2	Visual C++开发的静电场模拟电荷法可视化软件与应用
3	干式空心电抗器的优化设计
4	平面滤波器的开发研究
5	母线型 EMI 滤波器原理的探索与研制
6	基于“磁—热—流体”耦合场特性的永磁同步电机设计及软件开发
7	一种高容量密度电容器的开发及其在功率变换系统中的应用

8	高频电缆线束内电磁串扰模型的建立及其测试
9	小功率 DC/DC 变换器系统内 PCB 导线远场辐射电磁干扰特性研究
10	基于高频电磁噪声预测的变换器分立元器件模型
11	频线缆屏蔽性能的仿真和测试技术
12	电子对抗无人机系统内电磁干扰的评估
13	无人机电缆抗电磁干扰能力及故障分析
14	基于抑制电磁干扰的无人机系统性能提升
15	基于非整数匝技术的平面型变压器设计及其在 LLC 谐振变换器中的应用
16	基于多物理场耦合特性的平面型变压器设计及实现
17	平面磁性元件中容性效应的探索及其对性能的影响
18	应用于新能源领域超高压电力变压器优化设计
19	电力传输线集中参数模型建立的 MATLAB 工具箱开发

通过对参与学生的座谈调研可知，这些课外科技活动真正实现了“课外”的价值——既是对课程知识的提炼与升华，也是对专业体系的深度整合。学生在解决实际问题时，需综合运用电路、控制、编程等多领域知识，逐步掌握从问题定义到方案设计、从实验调试到成果总结的完整工程流程。同时，在项目申请时与导师沟通选题方向、向职能部门提交材料，结题时准备汇报答辩等过程，不仅锻炼了书面与口头表达能力，更培养了严谨的科研态度、责任意识与协作精神，使思想品质与专业能力得到同步提升，为成长为高素质电气工程师积累了宝贵经验。

3 实习基地

3.1 核心功能

实习是高等教育体系中连接理论教学与工程实践的关键纽带，在大学生知识内化、能力培养与职业认知中具有不可替代的地位。它通过将课堂所学转化为解决实际问题的能力，帮助学生完成从“知”到“行”的跨越，是培养应用型、创新型人才的重要环节。实习基地作为高校与用人单位(企业、科研机构等)长期合作建立的实践场所，既是保障实习环节有序开展的物质载体，也是深化产学研融合的核心平台。其核心功能在于为学生提供真实的工程环境、行业前沿的技术场景与符合产业需求的实践任务，同时推动高校与企业在人才培养、技术研发等方面的协同创新，实现教育链、人才链与产业链的有机衔接[5]。

3.2 实践模式及特点

基于电力系统专业的培养目标与实习基地的运行机制，目前主要形成三种实习模式，各具优势与局限：

3.2.1 分散性实习

分散性实习是指学生自主联系实习单位，或由学校推荐至不同企业、不同岗位进行的个体化实践。

优点：灵活性强，可结合学生个人职业规划选择实习单位与岗位，满足个性化发展需求；能接触多样化的行业场景，拓宽职业视野；减轻学校集中组织的管理压力。

缺点：实习质量难以统一把控，部分单位可能将学生视为“劳动力”，安排重复性工作，与专业培养目标脱节；学校对实习过程的监督与指导较弱，易出现“放羊式”管理；学生分散各地，难以形成团队协作与知识共享的氛围。

3.2.2 集中式实习

集中式实习是指学校统一组织学生在固定实习基地进行的集体实践，由校内教师带队，按统一计划完成规定实习内容。

优点：实习内容与专业培养方案高度契合，目标明确，便于学校统筹管理与质量监控；学生集中参与，可通过集体讨论、协作强化专业认知；校内教师全程跟进，能及时解决理论与实践衔接问题。

缺点：同质化程度高，难以兼顾学生个体差异与职业需求；实习岗位多为企业常规流程性工作，创新性、挑战性不足；大规模集中实习对基地承载能力要求高，易受企业生产计划限制。

3.2.3 项目式实习(新工科背景下的创新模式)

项目式实习是新工科建设背景下，基于企业真实技术需求或科研课题，以项目为载体组织的团队化实践[6]。电力系统专业通过与企业共建实习基地，将学生按项目分组(每组 2-5 人)，在企业导师与校内导师共同指导下完成针对性任务。

项目式实习以真实项目为驱动，任务来源于企业实际工程问题(如电力系统稳定性优化、智能电网调度方案设计等)；强调理论与实践的深度融合，学生在企业设计中心、技术中心参与方案论证、仿真分析、现场调试等环节，而非单纯的操作性工作；实行“双导师制”，企业导师(需具备中级及以上职称的资深工程师)负责工程实践指导，校内导师负责理论支撑与方法引导。

优点：紧密对接产业需求，学生直接参与解决企业实际问题，实践能力与创新思维同步提升；双导师协同指导机制实现“理论—实践”无缝衔接，既避免纯仿真的脱离实际，又突破单纯操作的技能

局限；团队化运作培养学生的协作能力、沟通能力与项目管理能力，符合现代工程对复合型人才的要求；为企业输送具备实践经验的潜在人才，同时为高校提供行业前沿的教学案例，实现校企双赢。

缺点：对实习基地的合作深度要求高，需企业投入大量人力(资深导师)与资源(技术平台、项目课题)；项目周期较长(通常为 2 个月左右)，需充足经费支持学生差旅、住宿及导师补贴，对经费不足的院校构成挑战；项目难度与学生能力的匹配度需精准把控，否则易因任务过难或过简影响实习效果。

实施策略：项目式实习的有效推进依赖于“校企协同、项目驱动、双师护航”的机制设计，课题基于企业提出的实际技术需求(如“配电网分布式电源接入对电压稳定性的影响分析”“电力系统故障诊断算法的工程化应用”等)，校企共同论证形成实习课题库。

团队组建：以课题为单位组建学生团队，每组 2-5 人，明确分工(如方案设计、数据采集、仿真验证等)；

过程管理：分阶段推进——校内开题阶段(1 周)，学生结合理论知识完成项目方案设计；企业实践阶段(1 个多月)，在双导师指导下开展现场调研、方案优化与成果验证；校内总结阶段，通过答辩梳理实践成果，形成实习报告。

结合电力系统专业特点，我们的项目式实习课题可以选择如表 2 的一些题目。

表 2 项目式实习题目选择

序号	项目式实习题目
1	基于数字孪生的变电站设备状态监测系统设计
2	微电网储能系统优化配置与调度策略研究
3	电力市场改革背景下用户侧电价响应模型的实践分析
4	新能源电站并网对区域电网继电保护的影响及改进方案
5	人工智能在变压器设计中的应用
6	超低噪声高压电力变压器的开发
7	基于多物理场的高压自耦式电力变压器的优化设计
8	集装箱式光伏储能变电站的设计
9	油浸式配电变压器的数字化制造工艺
10	220kV 天然酯绝缘液电力变压器的设计与工艺
11	电力变压器油箱的优化设计
12	层压木夹件变压器的结构设计
13	Deepseek+RAG+变压器技术本地知识库搭建及深化应用
14	电力变压器部件设计的自动化绘图
15	高压真空断路器优化设计与性能分析
16	断路器状态监测与寿命预测的智能算法研究
17	适用于智能微网的光伏-储能-负载能量管理策略研究
18	500W 双向 Buck/Boost 变换器在光伏储能中的应用研究
19	1200V IGBT 逆变器驱动保护电路优化设计
20	高频软开关 LLC 谐振变换器的优化设计

发展挑战与应对：随着新工科建设与产业升级的推进，项目式实习成为电力系统专业深化产教融合的核心方向，但需应对如下挑战：

经费保障：通过校企共建专项基金、申报教育改革项目、争取企业赞助等方式，解决学生实践成本与导师补贴问题。

基地建设：建立长期稳定的校企合作机制，明确双方权责(如企业提供课题与导师，高校负责学生选拔与理论支撑)，避免短期化、形式化合作。

质量评估：构建“过程+成果”双维度评价体系，结合企业导师对实践能力的评分、校内导师对理论应用的评估及项目成果的实际价值，确保实习质量。

项目式实习通过将企业真实需求转化为教学资源，既提升了学生的工程素养与创新能力，又为电力行业输送了“上手快、能创新”的高素质人才，是推动电力系统专业建设与产业需求同频共振的关键路径。

4 融合的专业建设

要实现符合工程需求的复合型人才培养，关键在于打破课堂教学、大学科创与实习基地项目式实习之间的壁垒，构建三者深度融合、互促共生的闭环体系。

课堂教学需从大一开始便埋下科创与实践的种子，将工科核心理论(如微积分、电路分析、潮流计算等)与产业实际问题相勾连，让学生初步感知知识的应用场景。进入大二，在掌握基础研究方法后，应鼓励学生利用假期、休息日走进实习基地开展短期认知实践——不必局限于学分要求，即便是一两天的参观交流，也能促使他们带着专业问题与企业导师探讨。这种互动既能让学生了解产业工艺与发展现状，学会提出有价值的问题(而非脱离实际的空想)，也能反向激活课堂学习动力，当学生恍然大悟“原来节点电压法是解决工厂配电问题的工具”时，理论学习的主动性便会显著提升。

大学科创则可衔接这一过程：大二学生作为主力军参与项目研发，大一学生随队观摩学习，大三、大四学生以“顾问”身份将实习中接触的产业需求转化为科创课题，形成“认知—实践—创新”的递进链条。企业导师与校内导师协同指导，让科创项目既扎根理论又对接产业，实习基地则成为检验科创成果、发现新问题的“试验场”。

三者如同环状电路，课堂教学为科创与实践提供理论支撑，科创活动将理论转化为解决问题的能

力，实习基地则输入真实产业需求并反哺课堂教学内容更新。如此循环往复，学生在毕业时便能对专业领域形成系统性认知，毕业设计也能真正触及产业痛点，实现从“知识学习者”到“工程实践者”的蜕变。

5 结论

本文以电气工程及其自动化专业本科生的成长为研究对象，以课堂教学、大学生课外科技活动及实习基地建设三方面的教学活动及其融合为整体研究脉络，经实践探索得出如下结论：

第一，需打破课堂教学、大学生课外科技活动与实习基地实践活动之间的时间与空间壁垒，使学生的专业知识学习与能力成长贯穿大一至大四全学段，覆盖从校园到社会、从理论场景到实践场地的全空间维度，实现时间上的连续衔接与空间上的贯通融合，避免各环节的割裂。

第二，要实现三种教学方式在时间与空间维度的深度融合，需构建多方协同支持体系：校内导师与产业导师形成指导合力，学校院系及各级主管部门在人力、财力等资源上给予充分保障，通过全方位的支持与统筹协调，确保融合举措落到实处，最终助力学生全面成长，满足产业界对高素质人才的需求。

参考文献

[1] 姚志树,蒋冬梅,施敏敏.电气教学示范中心“一体化、三层次”递进式实验教学新模式构建及实践[J].科技视界,2022,(26):139-141.

[2] 马威.电气教学中学生实践能力的培养研究[J].新课程研究,2019,(14):58-60.

[3] 肖根福,刘欢,旷虚波,等.大数据时代地方院校电气专业产教融合的问题与对策[J].信息记录材料,2018,19(12):154-155.

[4] 向贤兵.基于成果导向教育的专本贯通一体化人才培养模式探索与实践[J].重庆电力高等专科学校学报,2023,28(03):70-73.

[5] 贺达江,姚美雄,黄利军,等.工科人才校企一体化培养的实践教学体系探索与实践——以电气信息类专业为例[J].怀化学院学报,2022,41(05):105-108.

[6] 周丽萍,赵勇成,蒙明明.产教融合背景下电气自动化专业创新教学方法研究[J].家电维修,2025,(07):43-45.

009 Active Fault Location Method for Interphase Short Circuit of Distribution Network with Distributed Generation

Huamin Liang[1], Lidong Lin[1], Chaohong Man[1], Haifeng Li[1]

[1] School of Electric Power Engineering, South China University of Technology, Guangzhou 510641, China

Abstract. With the large-scale integration of distributed generation (DG) into the distribution network, the multi-source and bidirectional fault current characteristics of DG seriously undermine the assumptions of radial operation and unidirectional fault current relied upon by traditional fault location methods, resulting in a significant decline in the accuracy of fault analysis methods based on power frequency electrical quantities and traveling wave methods, and even their failure. Aiming at the problem that the large-scale access of distributed power to the distribution network leads to the failure of traditional fault location methods, this paper proposes a new phase-to-phase short-circuit fault location method. The method uses the single-ended power frequency and characteristic frequency electrical quantities to construct the ranging equation at the same time, which effectively overcomes the influence of the load current on the end. The simulation results show that the proposed method can achieve accurate positioning under different fault conditions, and significantly improve the reliability and accuracy of fault location of distribution network with high permeability distributed generation.

Keywords: Distributed Generation, Distribution Network, Short-circuit Fault, Fault Location, Single-ended Method.

1 Introduction

With the increasing penetration of distributed generation (DG) in the distribution network, its bidirectional and random power flow characteristics have profoundly changed the unidirectional radial operation mode of the traditional distribution network [1-3]. This change not only injects vitality into the system, but also brings severe challenges to the traditional fault detection and location technology. Especially for fault location, the traditional method depends on the deterministic system parameters and one-way fault current characteristics [4][5]. However, the access of distributed power supply introduces fault current with multi-source, variable amplitude and complex phase, which causes fundamental distortion of electrical characteristics after fault and destroys the application premise of traditional ranging algorithm [6][7].

The traditional fault location method of AC distribution network is usually based on the passive measurement of the electrical quantity generated when the fault occurs. According to its principle, it can be divided into two categories: fault analysis method and traveling wave method [8]. The fault analysis method establishes a fault loop equation to calculate the fault distance by collecting voltage and current data. If the fault analysis method based on single-terminal electrical quantity is adopted, when a non-metallic short-circuit fault occurs, the ranging accuracy will be significantly reduced due to the co-increasing effect of the opposite-end system on the fault current [9]. Based on the necessary conditions of single-ended fault location and the equivalent circuit structure of fault component network, a new fault location method is studied in [10], but this method is only suitable for single-phase grounding short circuit. In [11], an accurate single-ended fault location method based on fault current angle is proposed. However, this method is affected by the phase of the opposite current.

The use of double-ended electrical quantities for fault analysis can effectively avoid the influence of the auxiliary current, but it depends on the strict time synchronization of the sampled data at both ends [12]. Reference [13] proposed a new idea of using double-ended synchronous zero-sequence waveforms to achieve accurate cable fault location. However, this method requires synchronous acquisition of zero-sequence voltage and current signals at both ends, which requires high communication time synchronization.

By capturing the characteristics of the transient traveling wave generated by the fault point along the transmission line, the traveling wave ranging method measures the time difference or wave head time that it reaches the measuring device at both ends of the line, and then calculates the fault location [14]. However, due to the extremely fast propagation speed of the traveling wave, in order to achieve accurate detection of the wave head, both the single-ended method and the double-ended method require extremely high sampling frequency. In addition, the ranging accuracy of the traveling wave method is easily affected by the fault resistance and the initial angle of the fault, which has certain limitations in practical applications. Reference [15] estimated the potential fault area by measuring the arrival time of multiple reflected waves and searching the possible traveling wave propagation path according to the structure of the distribution network. This method does not rely on synchronous communication, but requires high sampling frequency of the acquisition equipment.

Aiming at the problem of insufficient accuracy of traditional fault location method in distribution network with distributed generation, this paper makes use of the high controllability of power electronic equipment in DG, and makes DG actively output characteristic signal when short circuit occurs in the line through additional control strategy. Based on the electrical quantity generated by the characteristic signal, a new fault location principle is constructed to improve the accuracy of fault location.

2 Control Strategy of DG

In order to ensure the safe, stable and reliable access of DG to the grid and meet the requirements of grid-connected regulations, the system adopts a multi-level and col-

laborative advanced control strategy. The core control architecture includes outer-loop power control and inner-loop current control, and on this basis, a variety of special working condition control modes are integrated, as follows:

1) Constant power control strategy

Constant power control is the basic operation mode of the system under normal operating conditions of the power grid, which aims to accurately manage the active and reactive power transmitted by DG to the power grid. By collecting the voltage and current signals of the point of common coupling (PCC), the instantaneous active power P and reactive power Q are calculated. The measured values P and Q are compared with the given reference values P_{ref} and Q_{ref}. The error is adjusted by the PI controller to generate the reference command signals I_{dref} and I_{qref} of the inner loop current control, so as to realize the closed-loop control.

2) Low voltage ride through control strategy

By monitoring the voltage amplitude of PCC point in real time, once it is lower than the set threshold and the duration meets the requirements of LVRT curve, the LVRT control mode is triggered immediately. According to the depth of voltage drop, the reference value of reactive current required is calculated according to the grid-connected standard, so as to prevent large-scale off-grid of DG and aggravate system instability.

3) Maximum current limiting control strategy

This function is the core guarantee to protect the safety of the inverter itself. It has the highest priority in all operating modes to ensure that the amplitude of the output current of the inverter does not exceed the maximum safety limit I_{max} allowed by its power device and heat dissipation system. Among them, I_{max} can be set to 1.2 ~ 1.5 times the current rating according to the safety requirements of the actual system.

4) Eliminating negative sequence control strategy

When there is an asymmetric fault (such as two-phase short circuit) or unbalanced load in the power grid, the grid-connected point voltage will generate a negative sequence component, resulting in unbalanced grid-connected current, power oscillation, equipment overheating and other problems. In order to ensure that the grid-connected current maintains three-phase symmetry, reduce the power quality pollution to the power grid, and reduce the loss and stress of the inverter itself, it is necessary to use the dual synchronous coordinate system decoupling to independently control the positive-sequence and negative-sequence current components. The reference value of the negative-sequence current component is set to zero to eliminate the negative-sequence current injected into the power grid.

5) Characteristic signal injection control strategy

The fault location method proposed in this paper is realized by injecting characteristic signals. In order to ensure high-precision ranging, the appropriate characteristic signal amplitude, frequency and injection time should be selected. The amplitude selection of the characteristic signal should take into account the tolerance of the detection device, the performance of the power electronic device, and the requirements of the system for the influence of the signal. The larger the amplitude, the more conducive to the detection. However, the overcurrent capacity of the power electronic device is weak, and the secondary impact caused by the injected signal should be

avoided. The frequency of the injected signal must strictly avoid the power frequency (50Hz) and its main integer harmonic frequency band (such as 100Hz, 150Hz, etc.) to prevent confusion with the background harmonics and interfere with the detection accuracy. The duration of the characteristic signal injection needs to be long enough to achieve a steady-state response, but it cannot be too long to avoid a continuous impact on power quality. Considering the above factors, this paper selects a current signal with an amplitude of 0.1 times the rated current and a frequency of 10 times the power frequency, and injects it with a duration of 200 ms.

3 The Principle of Fault Location

In the following, the fault location equation under different fault types is analyzed by taking the 10 kV low resistance grounding system of Fig. 1 as an example. The neutral point of the system adopts a small resistance grounding method, the grounding resistance is 10 Ω, the main transformer ratio is 110 kV/10 kV, the main transformer capacity is 20 MVA, the length of the MN section of line 1 is 20 km, and the M-terminal is connected with a DG with a capacity of 2 MVA.

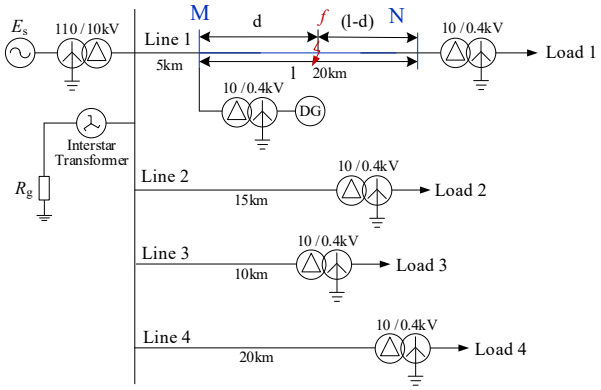


Fig. 1. A 10 kV low resistance grounding distribution network with distributed generation connected.

3.1 Three-phase Short Circuit Ranging Equation

When three-phase short circuit occurs in the MN section of line 1, due to the symmetry of each phase, it can be analyzed by single-phase circuit. The power frequency equivalent circuit of three-phase short circuit is shown in Fig. 2 and Fig. 3.

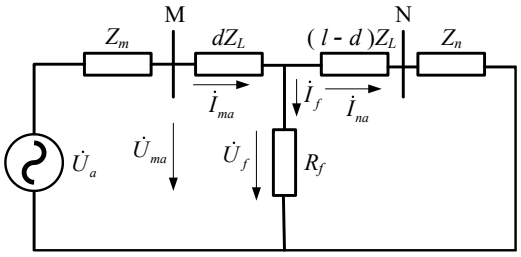


Fig. 2. Three-phase short-circuit power frequency equivalent circuit.

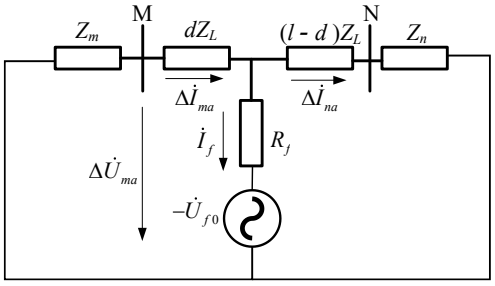


Fig. 3. Three-phase short-circuit fault additional network.

The fault location equation is constructed by using the power frequency voltage and current of any phase at the first end of the fault section:

$$\dot{U}_{\mathrm{ma}} = \dot{I}_{\mathrm{ma}} dZ_{\mathrm{L}} + \frac{\Delta\dot{I}_{\mathrm{ma}}\left(lZ_{\mathrm{L}} + Z_{\mathrm{n}}\right)R_{\mathrm{f}}}{\left[(l-d)Z_{\mathrm{L}} + Z_{\mathrm{n}}\right]} - \frac{\Delta\dot{U}_{\mathrm{ma}} R_{\mathrm{f}}}{\left[(l-d)Z_{\mathrm{L}} + Z_{\mathrm{n}}\right]} \tag{1}$$

In Eq. (1), $\dot{U}_{\mathrm{ma}}$ is the M-terminal phase A voltage. $\dot{I}_{\mathrm{ma}}$ is the M-terminal phase A current. d is the distance from M-terminal to the fault point. Z_{L} is the unit impedance of the line in the MN section. $\Delta\dot{I}_{\mathrm{ma}}$ is the M-terminal phase A fault component current. l is the line length in MN section. Z_{n} is the equivalent impedance downstream of the N-terminal, $Z_{\mathrm{n}} = R_{\mathrm{n}} + \mathrm{j}X_{\mathrm{n}}$, R_{n} and X_{n} are the equivalent resistance and reactance downstream of the N-terminal, respectively. R_{f} is the fault resistance. $\Delta\dot{U}_{\mathrm{ma}}$ is the phase A fault component voltage at the M terminal. Two equations can be obtained by solving the real part and the imaginary part of the equation.

However, according to the above two equations, the four unknowns d, R_{f}, R_{n} and X_{n} cannot be solved. It is necessary to use the 10 high-frequency current detection signals injected by DG to the line to construct the ranging equation under the high-frequency equivalent circuit. The three-phase short-circuit 10 times frequency equivalent circuit is shown in Figure 4.

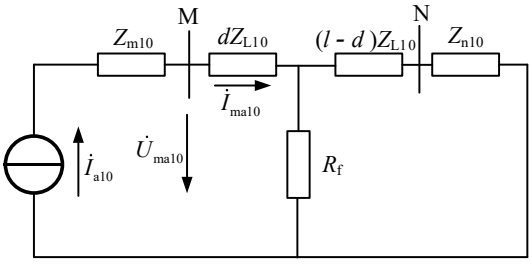


Fig. 4. Three-phase short circuit 10 times frequency equivalent circuit.

According to the equivalent circuit of three-phase short-circuit 10 times frequency, it can be obtained:

$$\dot{U}_{ma10} = \dot{I}_{ma10} dZ_{L10} + \dot{I}_{ma10} \frac{R_f \left\lfloor (l-d) Z_{L10} + Z_{n10} \right\rfloor}{R_f + (l-d) Z_{L10} + Z_{n10}} \tag{2}$$

In Eq. (2), $\dot{U}_{ma10}$ is the 10th harmonic voltage of the phase A at the M terminal. $\dot{I}_{ma10}$ is the 10th harmonic current of phase A at M terminal. Z_{L10} is the 10 times frequency unit impedance of the line in MN section. Z_{n10} is the equivalent impedance of 10 times downstream of the N-terminal, $Z_{n10} = R_n + j10X_n$. Two equations can be obtained by solving the real and imaginary parts of the equation, and the fault distance d can be solved by combining the two equations obtained by the power frequency current.

3.2 Two-phase Short Circuit Ranging Equation

When a two-phase short-circuit occurs in the MN section of line 1 (taking phases B and C as an example), the two-phase short-circuit power frequency equivalent circuit is shown in Fig. 5 and Fig. 6.

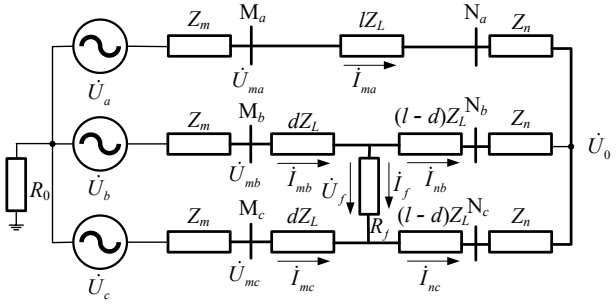


Fig. 5. Two-phase short-circuit power frequency equivalent circuit.

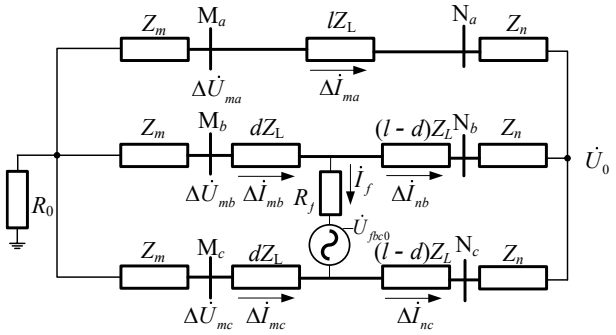


Fig. 6. Two-phase short-circuit fault additional network.

The fault location equation is constructed by using the power frequency voltage and current of the fault phase at the first end of the fault section:

$$\dot{U}_{\mathrm{mbc}} = \dot{I}_{\mathrm{mbc}} dZ_{\mathrm{L}} + \frac{\Delta\dot{I}_{\mathrm{mbc}}\left(lZ_{\mathrm{L}} + Z_{\mathrm{n}}\right)R_{\mathrm{f}}}{2\left[\left(l-d\right)Z_{\mathrm{L}} + Z_{\mathrm{n}}\right]} - \frac{\Delta\dot{U}_{\mathrm{mbc}} R_{\mathrm{f}}}{2\left[\left(l-d\right)Z_{\mathrm{L}} + Z_{\mathrm{n}}\right]} \tag{3}$$

In Eq. (3), $\dot{U}_{\mathrm{mbc}}$ is the power frequency voltage difference between phase B and phase C at the M terminal. $\dot{I}_{\mathrm{mbc}}$ is the power frequency current difference between phase B and phase C at the M terminal. $\Delta\dot{I}_{\mathrm{mbc}}$ is the difference between the power frequency fault component currents of phase B and phase C at the M terminal. $\Delta\dot{U}_{\mathrm{mbc}}$ is the difference between the power frequency component voltage of phase B and phase C at the M terminal. Similarly, it is also necessary to use the 10 high-frequency current detection signals injected by DG to the line to construct the ranging equation under the high-frequency equivalent circuit. The two-phase short-circuit 10 times frequency equivalent circuit is shown in Fig. 7.

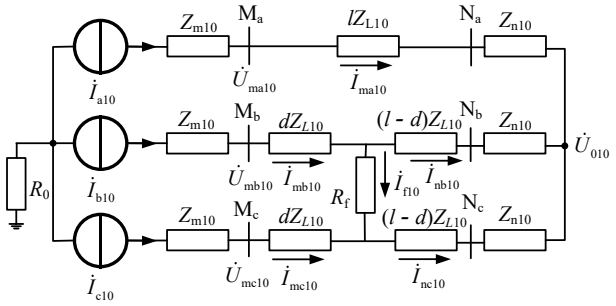


Fig. 7. Two-phase short circuit 10 times frequency equivalent circuit.

According to the two-phase short-circuit 10 times frequency equivalent circuit, it can be obtained:

$$\dot{U}_{\mathrm{mbc10}} = \dot{I}_{\mathrm{mbc10}} d Z_{\mathrm{L10}} + \dot{I}_{\mathrm{mbc10}} \frac{R_{\mathrm{f}} \left\lfloor (l-d) Z_{\mathrm{L10}} + Z_{\mathrm{n10}} \right\rfloor}{R_{\mathrm{f}} + 2\left[(l-d) Z_{\mathrm{L10}} + Z_{\mathrm{n10}} \right]} \tag{4}$$

In Eq. (4), $\dot{U}_{\mathrm{mbc10}}$ is the difference between the 10th harmonic voltage of phase B and phase C at the M terminal. $\dot{I}_{\mathrm{mbc10}}$ is the difference of the 10th harmonic current between phase B and phase C at the M terminal.

By separating the real and imaginary parts of Eq. (3) and Eq. (4), the distance d between the fault point and the first end of the ranging section can be obtained by solving the equations.

4 Fault Location Process

Fig. 8 is the flowchart of the interphase fault location method proposed in this paper. The specific process is as follows:

1) Taking the power frequency cycle as the time window length, the voltage of each phase at the head end of the fault section is sampled. When the start-up criterion is satisfied, the fault location method is started, and the DG injects 10 high-frequency currents into the line. Among them, the starting criterion is that the phase voltage of the first end of the fault section is lower than the setting value of the starting voltage:

$$\min\left(\frac{\left|\dot{U}_{\mathrm{ma}}\right|}{U_{\mathrm{n}}}, \frac{\left|\dot{U}_{\mathrm{mb}}\right|}{U_{\mathrm{n}}}, \frac{\left|\dot{U}_{\mathrm{mc}}\right|}{U_{\mathrm{n}}}\right) < U_{\mathrm{set}} \tag{5}$$

In Eq. (5), $\dot{U}_{\mathrm{ma}}$, $\dot{U}_{\mathrm{mb}}$ and $\dot{U}_{\mathrm{mc}}$ are the phase voltage of fault section of the first end. U_{n} is the rated value of phase voltage. U_{set} is the starting voltage setting value, which can be taken as 0.9.

2) The three-phase voltage and current of each power frequency cycle before and after the fault at the first end of the fault section are sampled.

3) The fast Fourier algorithm is used to extract the power frequency component and high-order harmonic component of each phase voltage and current, and the power frequency fault component is calculated.

4) The fault type and fault phase are determined by the difference between the fault components of the power frequency current between each two phases.

The fault type and fault phase are judged by the difference between the fault components of the power frequency current. Among them, the criterion of three-phase short circuit is:

$$\begin{cases} \left| \left|\Delta\dot{I}_{\mathrm{mab}}\right| - \left|\Delta\dot{I}_{\mathrm{mbc}}\right| \right| \le k_{\mathrm{set1}} \\ \left| \left|\Delta\dot{I}_{\mathrm{mbc}}\right| - \left|\Delta\dot{I}_{\mathrm{mca}}\right| \right| \le k_{\mathrm{set1}} \\ \left| \left|\Delta\dot{I}_{\mathrm{mca}}\right| - \left|\Delta\dot{I}_{\mathrm{mab}}\right| \right| \le k_{\mathrm{set1}} \end{cases} \tag{6}$$

In Eq. (6), $\Delta\dot{I}_{\text{mab}}$ is the difference between phase A and B power frequency current fault components. $\Delta\dot{I}_{\text{mbc}}$ is the difference between the fault components of power frequency current between phase B and C. $\Delta\dot{I}_{\text{mca}}$ is the difference between the fault components of power frequency current between phase C and A. k_{set1} is the three-phase short-circuit margin coefficient, which can be selected according to the line imbalance and measurement error, and 0.01 is taken in this paper. When the above equation is satisfied, it is judged that the line has a three-phase short circuit.

Taking the phase B and C fault as an example, the criterion of two-phase short circuit is:

$$\begin{cases} \max\left(\left|\Delta\dot{I}_{\text{mab}}\right|,\left|\Delta\dot{I}_{\text{mca}}\right|,\left|\Delta\dot{I}_{\text{mbc}}\right|\right)=\left|\Delta\dot{I}_{\text{mbc}}\right| \\ \left|\left|\Delta\dot{I}_{\text{mbc}}\right|-2\left|\Delta\dot{I}_{\text{mab}}\right|\right|\le k_{\text{set2}} \\ \left|\left|\Delta\dot{I}_{\text{mbc}}\right|-2\left|\Delta\dot{I}_{\text{mca}}\right|\right|\le k_{\text{set2}} \end{cases} \tag{7}$$

In Eq. (7), k_{set2} is the two-phase short-circuit margin coefficient, and the appropriate value can be selected according to the line unbalance degree and measurement error, and 0.01 is taken in this paper. When the above equation is satisfied, it is judged that the line has a two-phase short circuit.

5) According to the fault type, the fault location equation is written and the fault location equation is solved by LM algorithm. The fault distance is obtained and the fault location process is completed.

10

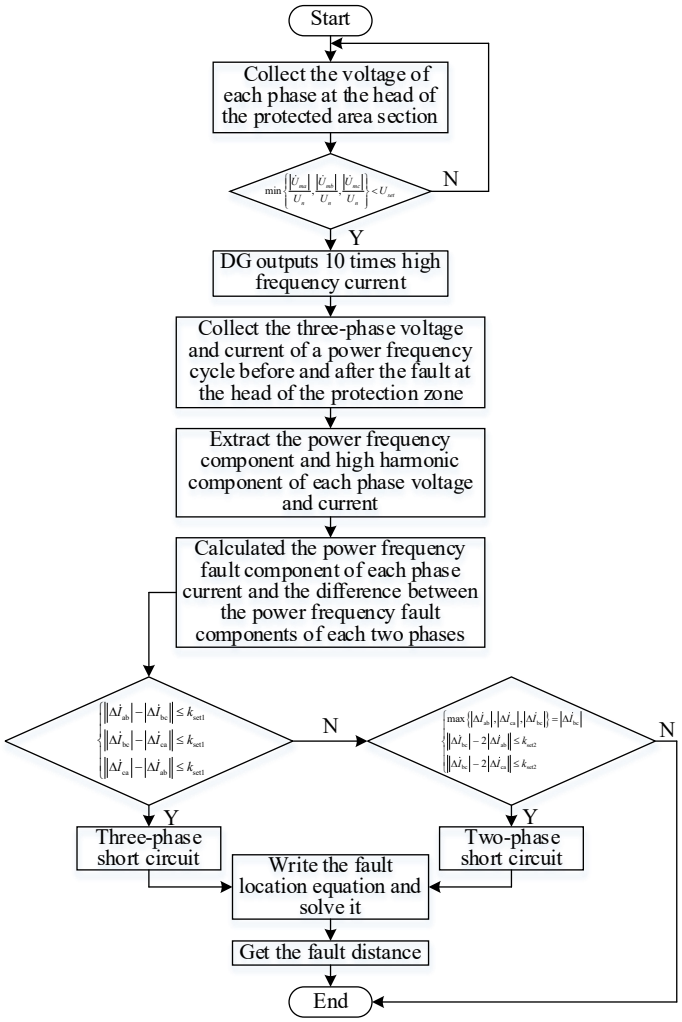


Fig. 8. Flowchart of active fault location method for interphase short circuit of distribution network with distributed generation.

5 Simulation

In PSCAD, a 10 kV low-resistance grounding distribution network model with distributed generation connected is built as shown in Fig. 1 for simulation test. The specific model parameters are shown in Table 1.

Table 1. Main parameters of distribution network.

Parameter	Value

System voltage (kV)	10
Systematic impedance (Ω)	1j
Neutral point grounding resistance (Ω)	10
Line MN length (km)	20
Line unit positive-sequence resistance (Ω/km)	0.125
Line unit positive-sequence inductance (mH/km)	1.299
Line unit positive-sequence capacitance (μF/km)	0.0096
Line unit zero-sequence resistance (Ω/km)	0.275
Line unit zero-sequence inductance (mH/km)	4.595
Line unit zero-sequence capacitance (μF/km)	0.0054
Load capacity (MVA)	1.5

When the setting time is 0.3 s, three-phase short circuit occurs in the line, and the fault resistances are recorded as 0, 10, 20 and 50 Ω, respectively. The simulation results are shown in table 2 when the fault point is 10%, 50% and 90% of the total length of the line.

Table 2. Three-phase short circuit simulation results.

Fault resistance (Ω)	Fault distance (km)	Calculated distance (km)	Error (%)
0	2	1.603	1.985
	10	9.207	3.965
	18	16.323	8.385
10	2	1.997	0.015
	10	8.569	7.155
	18	16.789	6.055
20	2	1.997	0.015
	10	9.299	3.505
	18	16.539	7.305
50	2	1.632	1.84
	10	10.295	1.475
	18	16.361	8.195

Similarly, a two-phase short circuit occurs when the setting time is 0.3 s, and the fault resistances are recorded as 0, 10, 20 and 50Ω, respectively. The simulation results are shown in Table 3 when the fault point is 10%, 50% and 90% of the total length from the line head.

Table 3. Two-phase short circuit simulation results.

Fault resistance (Ω)	Fault distance (km)	Calculated distance (km)	Error (%)
0	2	1.615	1.925
	10	9.72	1.4

12			
	18	18.35	1.75
	2	1.976	0.12
10	10	9.822	0.89
	18	17.666	1.67
	2	1.963	0.185
20	10	10.21	1.05
	18	17.78	1.1
	2	2.377	1.885
50	10	9.595	2.025
	18	19.771	8.855

In order to verify the effectiveness of the proposed method under different line lengths, the line length of MN in line 1 is changed to 10 km, and the three-phase short circuit occurs when the setting time is 0.3 s. The fault resistance is recorded as 0, 10, 20 and 50 Ω, respectively. The simulation results when the fault point is 10%, 50% and 90% of the total length from the head end of the line are shown in Table 4.

Table 4. Three-phase short-circuit simulation results when the line MN is 10 km.

Fault resistance (Ω)	Fault distance (km)	Calculated distance (km)	Error (%)
	1	0.807	1.93
0	5	4.541	4.59
	9	8.756	2.44
	1	1.043	0.43
10	5	4.605	3.95
	9	8.124	8.76
	1	0.832	1.68
20	5	4.563	4.37
	9	8.791	2.09
	1	0.995	0.05
50	5	4.751	2.49
	9	8.812	1.88

It can be seen from the above simulation results that the proposed method can accurately calculate the fault location when the interphase short circuit of different sizes of fault resistance occurs at different positions in the 10 kV low-resistance grounding system with distributed generation, and the calculation error is less than 10%.

6 Conclusion

Aiming at the problem of insufficient accuracy of traditional fault location method in distribution network with distributed generation, this paper proposes a fault location method suitable for interphase short circuit. The main conclusions are as follows:

1) The interphase short circuit fault location method proposed in this paper does not need to install an additional high-frequency signal injection device. It can be realized by adding a high-frequency current injection control strategy based on the original DG control mode in the distribution network, and the control accuracy is high.

2) This method can adjust the amplitude and frequency of the injected signal according to the actual needs to adapt to different line conditions, and has strong flexibility and adaptability.

3) The proposed method is not affected by the location of the fault point and the fault phase. No matter the fault point is located at the head, midpoint or end of the line, the error between the calculation distance result and the actual distance is low.

Acknowledgement: This work is supported by Guangdong Basic and Applied Basic Research Foundation (No. 2024A1515012289).

References

1. Li, H., Liang, H., Wang, Z., Zhang, Z., Liang, Y.: Active protection scheme based on high-frequency current for distribution networks with inverter-interfaced distributed generators. IET Renew. Power Gener. 1–14 (2024).
2. Han B, Li H, Wang G, et al. A Virtual Multi-Terminal Current Differential Protection Scheme for Distribution Networks With Inverter-Interfaced Distributed Generators[J]. IEEE Transactions on Smart Grid, 2017:1-1.
3. Mirshekali H, Dashti R, Keshavarz A, et al. A novel fault location methodology for smart distribution networks[J]. IEEE Transactions on smart grid, 2020, 12(2): 1277-1288.
4. Stefanidou-Voziki P, Sapountzoglou N, Raison B, et al. A review of fault location and classification methods in distribution grids[J]. Electric Power Systems Research, 2022, 209: 108031.
5. Khalid H, Shobole A. Existing developments in adaptive smart grid protection: A review[J]. Electric Power Systems Research, 2021, 191: 106901.
6. Buzo R F, Barradas H M, Leao F B. A new method for fault location in distribution networks based on voltage sag measurements[J]. IEEE Transactions on Power Delivery, 2020, 36(2): 651-662.
7. Galvez C, Abur A. Fault location in active distribution networks containing distributed energy resources (DERs)[J]. IEEE Transactions on Power Delivery, 2020, 36(5): 3128-3139.
8. Zheng T, Wang Y, Lv W, et al. Fault identification scheme for UPFC compensated transmission line based on characteristic voltage active injection[J]. International journal of electrical power and energy systems, 2022(May):137.
9. Huai Q, Liu K, Hooshyar A, et al. Single-ended line fault location method for multi-terminal HVDC system based on optimized variational mode decomposition[J]. Electric Power Systems Research, 2021, 194: 107054.

10. Li B, Shi L, Wen W, et al. Research on a New Single-End Fault Location Method for Single-Phase Grounding Faults of Transmission Lines Through Transition Resistance[J]. Frontiers in Energy Research, 2021, 9: 772345.
11. Muli V, Perli S B. Single Ended Fault Locator Using Fault Current Phase Angle[C]//2024 IEEE 3rd International Conference on Electrical Power and Energy Systems (ICEPES). IEEE, 2024: 1-6.
12. Zhang M, Zhao W, Li P. Two-terminal fault combination location method on MMC-HVDC transmission lines based on ensemble empirical mode decomposition[J]. Energy Reports, 2023, 9: 987-995.
13. Qu K, Zhang W, Zhang S, et al. Model-free underground cable incipient fault location using two-terminal zero-sequence measurements[J]. International Journal of Electrical Power & Energy Systems, 2022, 140: 108057.
14. Shu H, Liu X, Tian X. Single-ended fault location for hybrid feeders based on characteristic distribution of traveling wave along a line[J]. IEEE Transactions on Power Delivery, 2020, 36(1): 339-350.
15. Shi Y, Zheng T, Yang C. Reflected traveling wave based single-ended fault location in distribution networks[J]. Energies, 2020, 13(15): 3917.

010 Transient Fault-Current Characteristics and Second-Order Equivalent Modeling of Grid-Following Converters under Low-Voltage Ride-Through

Gan Wang, Haifeng Li, Huamin Liang, Chaohong Man, Xiangyu Yang

School of Electric Power Engineering, South China University of Technology, Guangzhou 510641, China

Abstract. This paper investigates the transient fault-current behavior of grid-following converters in distribution networks during low-voltage ride-through (LVRT) under an inner-current and outer-power control architecture. A second-order equivalent model is derived by coupling the inner-loop PI controller with the converter circuit dynamics, clearly showing how the natural frequency and damping ratio depend on the proportional (K_p) and integral (K_i) gains. To incorporate engineering practices, reactive-power priority with a 1.2 pu current limit is considered, and we propose an amplitude-slope unified reachability constraint for reference generation and feasibility assessment. Comparative studies on a 10-kV system demonstrate strong agreement between PSCAD simulations under overdamped conditions and the proposed model, establishing applicability boundaries across underdamped, critically damped, and overdamped regimes. Based on these findings, practical tuning guidelines are provided for LVRT, aiding relay protection settings and grid-connection control parameterization.

Keywords: Transient fault current, Current inner loop, Second-order equivalent model, Damping ratio, Current limiting.

1 Introduction

As converter-based resources increasingly penetrate distribution networks, the transient fault-current behavior of power-electronic generators during faults significantly influences short-circuit level estimation, relay-protection coordination, and overall system stability. Grid-following (GFL) converters usually utilize an inner-current and outer-power control architecture with a phase-locked loop (PLL). During low-voltage ride-through (LVRT), the power control loop is bypassed. In contrast, the current loop enforces grid-code requirements that emphasize reactive-power support and include current-magnitude limits (e.g., 1.2 pu). As a result, the transient dynamics and the handling of constraints by the current loop are critical in shaping the fault-current response [1], [2].

Electromagnetic-transient (EMT) modeling in PSCAD is often used to study the fault behavior of grid-connected converters; however, such simulation is computa-

tionally intensive and does not easily reveal the underlying analytical structure [3]. This encourages the development of analytical models for transient fault-current analysis.

Unlike synchronous generators, the converter fault current is mainly determined by inverter control. References [4], [5] obtain current responses by solving second-order differential equations but assume step-input excitation and overlook amplitude and slew-rate limits. Reference [6] develops an EMT model for photovoltaic units with LVRT from a "full-process ride-through" perspective and derives closed-form short-circuit current expressions during the fault interval; however, a unified quantitative framework for nonlinear control interactions is lacking, and robustness and applicability still need validation. Reference [7] examines the short-circuit current contribution of VSC-HVDC in AC/DC hybrid networks. It proposes a three-sequence calculation model based on topology and control features. Still, it does not fully account for the nonlinear LVRT control dynamics of grid-connected inverters, limiting its direct use for distribution-level units. Reference [8] improves PLL dynamic modeling by proposing an accurate dynamic PLL model that does not require pre-fault phase angles and linearizes it for faster computation. Reference [9] introduces an analytical approach for inverter-based fault transients that includes PLL dynamics; through complex-domain decoupling and time-interval segmentation, it characterizes d-q coupling transients and the decay of underdamped oscillations. Its limitations include dependence on segmentation and parameter matching, and the unified handling of constraints such as current limiting, reactive-power priority, and amplitude bounds remains incomplete.

Related Work and Motivation. Existing studies either focus on sequence-component modeling and network-layer coupling [7], emphasize analytical short-circuit current solutions during the LVRT process [10-12], or examine nonlinearities caused by PI saturation and PLL dynamics [8], [9]. Engineering evidence also shows the negative impact of transient fault-current spikes on protective-relay performance [13]. However, a unified constraint–reachability framework that combines reference allocation (reactive-power priority and current-magnitude limit) with the dynamic feasibility of the DC-link voltage remains underdeveloped. In particular, there is a lack of analytical design criteria that address both amplitude constraints and slew-rate (rate-limiting) constraints at the same time. Additionally, the boundaries of applicability and the quantitative error bounds for using second-order equivalent models as substitutes for PSCAD waveforms across underdamped, critically damped, and overdamped regimes are not sufficiently explored.

Contributions. This paper focuses on the PI-regulated current inner loop. It derives a second-order equivalent model consistent with the circuit equations, thereby characterizing how the proportional (K_p) and integral (K_i) gains influence the natural frequency, damping ratio, and settling time. Under the engineering practice of reactive-power priority with a 1.2 pu current limit, we formulate a unified dynamic-reachability condition that simultaneously enforces amplitude and slew-rate constraints, upon which a reference-shaping strategy is built. We conduct comparative validation in three damping regimes-underdamped, critically damped, and overdamped- by aligning the PSCAD system model with the equivalent model, delin-

eating applicability boundaries, and identifying error sources in each regime. For practical deployment, we summarize clear guidelines for parameter selection and model substitution tailored to relay protection calculations and grid connection control settings. The proposed approach offers a reusable methodology and technical support for transient modeling, control design, and protection coordination in distribution systems with GFL renewable resources.

2 Typical GFL Converter Control and Implementation

Fig. 1 depicts the control architecture of a typical GFL converter. The inner loop regulates the converter current, whereas the outer loop regulates active and reactive power [14]. The converter is connected to the point of common coupling (PCC) through an LC filter. The three-phase voltages and currents are measured at the PCC, where a PLL estimates the voltage phase angle. The measured signals are then transformed from the abc frame to the synchronous dq frame and supplied to the inner control loop, which also provides inputs for power calculation in the outer loop. The inner loop tracks the current reference from the outer loop and outputs the dq-axis reference voltage. This reference voltage is then converted back to the abc frame through the dq-abc inverse transformation to obtain the three-phase reference voltage e_abc. Finally, the reference voltage is modulated using pulse width modulation (PWM) to generate the gating signals.

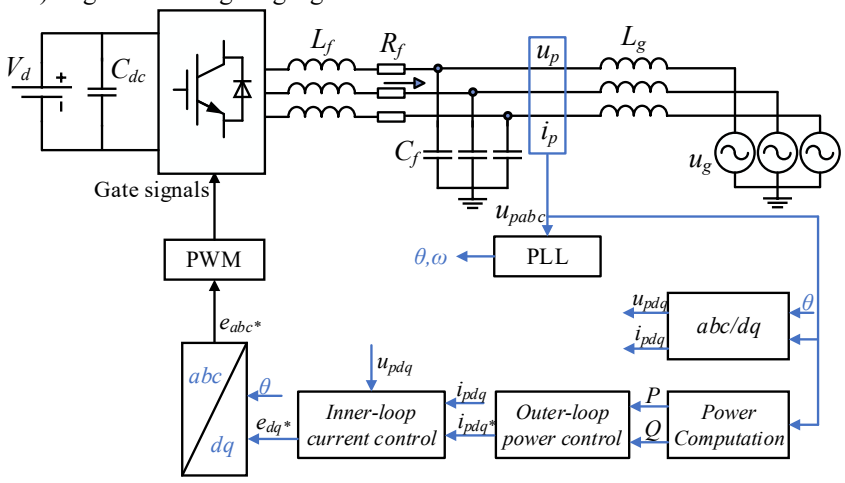


Fig. 1. Control architecture of a typical GFL converter.

2.1 Steady-State Control Strategy

Ignoring switching harmonics, the voltage drop across the series filter impedance in phase i∈{a,b,c} is given by.

$$e_i^* = u_{pi} + L_f \frac{di_{pi}}{dt} + R_f i_{pi} \tag{1}$$

Assuming the PLL accurately tracks the PCC voltage angle, the series R_f-L_f branch in (1) expressed in the PCC referenced synchronous dq frame is

$$\begin{cases} e_d^* = u_{pd} + (R_f + sL_f)i_{pd} - \omega_s L_f i_{pq} \\ e_q^* = u_{pq} + (R_f + sL_f)i_{pq} + \omega_s L_f i_{pd} \end{cases} \tag{2}$$

Where subscripts d and q denote the axis components of the corresponding variables, s denotes the differential operator, and ω_s is the synchronous angular frequency, with $\omega_s=2*\pi f$, where f=50Hz.

To simplify control, a grid-voltage-oriented vector control is used by aligning the d-axis with the PCC voltage vector.

$$\begin{cases} u_{pd} = U_p \\ u_{pq} = 0 \end{cases} \tag{3}$$

where U_P is the magnitude of the PCC voltage vector.

Building upon this foundation, Fig. 2 illustrates the control block diagram of the GFL converter, which consists of an outer power loop and an inner current loop.

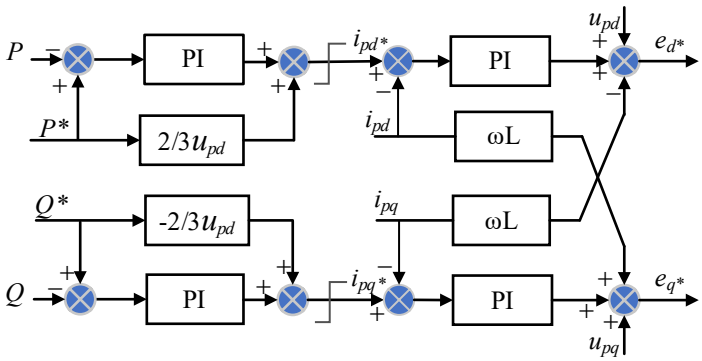


Fig. 2. Control Block Diagram of the GFL Converter.

2.2 Steady-State Control Strategy

When a grid fault reduces the PCC voltage, the converter switches to LVRT mode according to [15] and relevant grid codes. The outer power loop is bypassed, and a dedicated allocator generates current references with reactive-power priority while enforcing current-magnitude and slew-rate limits. The objectives are: (i) provide reactive support at the PCC; (ii) protect the converter by respecting the maximum current envelope Imax (e.g., 1.2 pu); and (iii) maintain the DC-link energy balance by derating active current as needed.

A concise rule for reference allocation is:

$$I_{q_ref.f}=\begin{cases}0 & ,U_{p.f}>0.9p.u.\\ K_1(0.9-U_{p.f})I_N & ,0.2\le U_{p.f}\le 0.9p.u.\\ K_2I_N & ,U_{p.f}<0.2p.u.\end{cases} \tag{4}$$

Where $I_{q_ref.f}$ denotes the reactive current reference, I_N is the DG's rated output current, $U_{p.f}$ is the per-unit PCC voltage magnitude after the fault, K_1 is the voltage-support coefficient (reflecting the requested reactive support versus sag depth), and K_2 is the maximum per-unit reactive current the DG is permitted to inject under low-voltage conditions.

To prevent over-stress of the power devices, the DG output current is limited according to GB50797-2012, which specifies an overload capacity of $1.2I_N$ for PV stations. Meanwhile, during LVRT, the DG should fulfill the reactive-power requirement first and then maximize active-power delivery within the allowable current envelope.

Accordingly, the LVRT reference allocation is specified as:

$$\begin{cases}I_{DG.q}=I_{q_ref.f}\ ,\ (I_{q_ref.f}\le K_{\max}I_N)\\ I_{DG.d}=\min\left\{I_{d_ref.f}=\dfrac{2P^*}{3U_{p.f}},\sqrt{(K_{\max}I_N)^2-I_{q_ref.f}^2}\right\}\end{cases} \tag{5}$$

Where $I_{DG.d}$ and $I_{DG.q}$ represent the active and reactive currents injected by the DG, respectively; $I_{d_ref.f}$ indicates the reference value of the active current during LVRT operation; and K_{max} denotes the maximum allowable current coefficient.

2.3 Controller Parameter Design

During a voltage sag, the outer power loop is bypassed, and the current references are supplied directly by the LVRT allocator; therefore, the fault transient analysis focuses only on the inner current loop. The equivalent control block diagram-PI regulator plus converter or filter dynamics-is shown in Fig. 3.

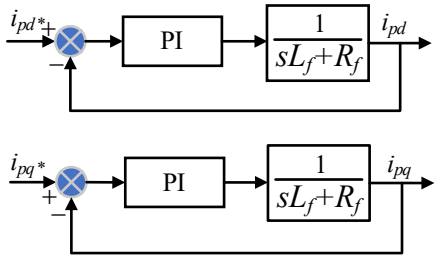


Fig. 3. Equivalent inner-loop control and converter circuit model.

The inner-loop PI controller is:

$$C(s)=K_p+\frac{K_i}{s} \tag{6}$$

With unity feedback, the closed-loop transfer from the reference current to the measured current is:

$$T(s) = \frac{K_p s + K_i}{L_f s^2 + (K_p + R_f)s + K_i} \tag{7}$$

Equation (7) has the canonical second-order characteristic polynomial. In practical DG systems, to enhance the disturbance rejection capability of the current inner loop, the current inner loop controller is typically designed as a standard second-order system. Based on (7), the natural frequency and damping ratio related to the characteristic equation can be derived as:

$$\omega_n = \sqrt{\frac{K_i}{L_f}}, \zeta = \frac{R_f + K_p}{2\sqrt{K_i L_f}} \tag{8}$$

The closed-loop pole locations are： $s_{1,2} = -\zeta\omega_n \pm j\omega_n\sqrt{1-\zeta^2}$.

As shown in the above equation, the real part of the pole is:

$$\mathrm{Re}\left(s_{1,2}\right) = -\zeta\omega_n = -\frac{R_f + K_p}{2L_f} \tag{9}$$

This depends only on R_f, L_f, and K_p and is independent of K_i. Because R_f is typically much smaller than K_p, the proportional component effectively improves the system's damping, which directly increases the real part of the pole and speeds up the response envelope's decay. In contrast, the integral component affects the closed-loop natural frequency and steady-state error but does not influence the envelope decay rate. As a result, when sufficient damping is present, changes in K_i have little effect on the settling time.

3 Transient Characteristics

When a grid fault triggers LVRT, the external power loop is bypassed, leaving only the current inner loop and the PLL active, the sudden PCC voltage dip, the associated phase disturbance, and the activation or deactivation of current-limiting logic produce a response across multiple time scales, which can be summarized as fast current regulation and slow synchronization (since the inner loop bandwidth is much smaller than the PLL bandwidth). This section examines the transient behavior within the specified operating ranges and constraints.

3.1 Transient Response Characteristics in the Linear Region

In the linear region—that is, when the PCC voltage remains within the acceptable modulation range and the current's magnitude and rate of change do not reach their limits-the current inner loop can be modeled as a second-order LTI system. Standard

responses, including underdamped, critically damped, and overdamped, then describe how it tracks reference variations.

To analyze the inner-loop dynamics, we make the following assumptions:

(1) The modulation remains unsaturated， $u_{pwm} \le U_{\max} = \frac{m_{\max}}{2} U_{DC}$;

(2) The PLL maintains a small angle error;

(3) The equivalent grid-side voltage can be approximated as a short-term constant.

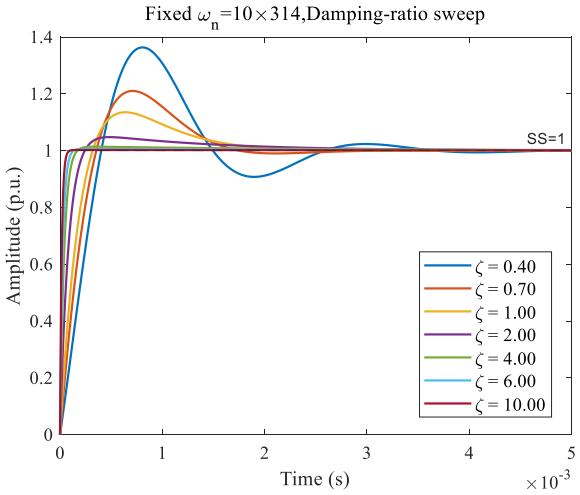
Under these conditions, the following formula holds:

$$L_f \frac{di_p}{dt} = u_{pwm} - u_p - R_f i_p - \omega L_f i_p \tag{10}$$

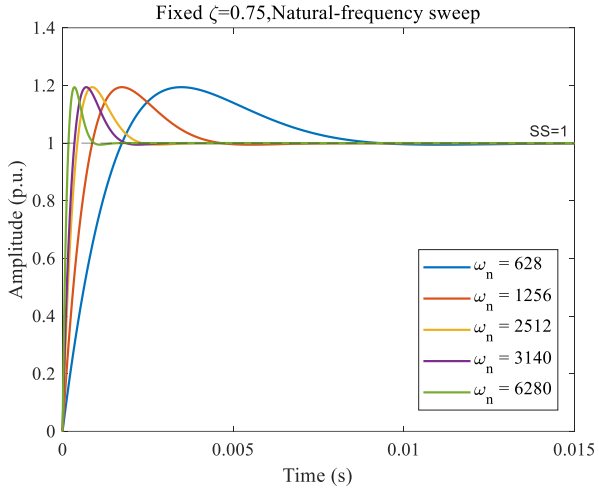
Where $\omega = \begin{bmatrix} 0 & -1 \\ 1 & 0 \end{bmatrix} \omega_s$, when SPWM control is employed, the $m_{\max}$ value is set to 1; whereas, when SVPWM control is applied, the $m_{\max}$ value is set to $2/\sqrt{3}$.

When integrated with PI control, the current inner loop can be simplified to a second-order linear time-invariant system with the current reference as the input. In the case of a step reference, the system's rise time, overshoot, and settling time are completely determined by the natural frequency and damping ratio.

As shown in Figure 4(a), when ω_n is held constant, both the overshoot and settling time of the converter's current inner loop unit step response increase gradually as ζ decreases. Under over-damped conditions, the settling time stays below 1 ms. As shown in Figure 4(b), with ζ held steady, the overshoot of the current inner loop unit step response remains the same as ω_n decreases, while the settling time gradually increases.



(a) under different ζ values



(b) under different ω_n values

Fig. 4. Unit step responses of grid-connected converters.

3.2 Transient Response Under Slew-Rate Limitation

Under faulted-voltage conditions, the current reference usually hits its amplitude limit first. In practical engineering, reactive-power prioritization and vector-based amplitude limiting are often used to meet grid-integration standards and ensure compliance with requirements. However, amplitude limiting only affects the final state; it does not ensure that the dynamic trajectory is feasible under the combined constraints of limited modulation voltage and the DC-link voltage.

Many existing studies approximate the current reference variation as a step input and analyze the resulting second-order closed-loop response. However, in LVRT scenarios, this approximation often fails: the inverter output voltage needed to reach a specified current slope is limited by the available modulation-voltage margin. Therefore, it is more accurate to model the current reference as a ramp signal with a limited slope (i.e., under a slew-rate constraint).

Let $i_p^*(t)$ denote the reference trajectory. Based on the electromagnetic equations, the following relationship can be derived:

$$L_f \frac{di_p}{dt} \le U_{\max} - u_p - R_f i_p - \omega L_f i_p \tag{11}$$

Available voltage margin.

$$u_{sat}(t) = U_{\max} - \left\| u_p + R_f i_p^* + \omega L_f i_p^* \right\| \tag{12}$$

To prevent saturation and maintain linear second-order behavior, the reference amplitude and slope must jointly meet a unified constraint.

$$i_p^*(t) \le K_{\max} I_N, \left|\frac{di_p^*(t)}{dt}\right| \le \min\left\{\frac{u_{sat}(t)}{L_f}, \frac{\varepsilon K_i}{R_f}\right\} \tag{13}$$

Specifically, $u_{sat}(t)/L_f$ denotes the constraints on dynamic reachability and the upper voltage limit, while $\varepsilon K_i/R_f$ represents the requirement for linear trackability, characterized by an allowable maximum steady-state ramp error ε.

4 Simulation Analysis

As discussed earlier, when the damping ratio ζ is sufficiently large, the converter's current inner loop displays a non-overshooting transient. As a result, the three-phase fault current of the distributed power source has no peak, and the time to reach steady state is very short. Therefore, within the permissible error margins of relay protection design and setting calculations, the transient component of the fault current from the distributed source during a grid short circuit can be ignored. In distribution network fault studies involving distributed power sources, these sources can thus be represented by steady-state fault-current models.

However, as ζ decreases, the inner-loop current control enters a region where nonlinearities become significant, resulting in more complex fault-transient behavior. In such cases, modeling the distributed power source only with a steady-state fault-current representation can cause substantial inaccuracies. It may not meet the requirements for relay-protection principle studies and setting calculations.

To study the fault-current characteristics of the converter's inner-loop current controller, a 10-kV distribution network model with a T-connected inverter-interfaced distributed generator (IIDG) is developed in PSCAD, as shown in Fig. 5.

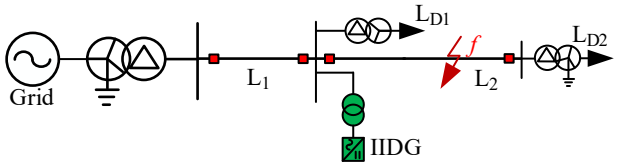


Fig. 5. 10-kV distribution network with a T-connected IIDG.

The system parameters are as follows: the IIDG has a rated capacity of 2 MVA and a rated line-to-line voltage of 10 kV. The AC filter includes an inductor of 50 mH with an internal resistance of 0.01 Ω and a capacitor of 0.01 μF. The line impedance per unit length is Z=0.27+j0.347 Ω/km. The parameter $K_{\max}$ is set to 1.2, and the parameter K_2 is set to 1.05.

In the simulation cases below, the IIDG operates at unity power factor before the fault. At t = 0.5s, a three-phase symmetrical fault occurs at point f with a fault resistance of 0.01 Ω, causing the PCC voltage at the IIDG connection point to drop from 1.0 pu to 0.1 pu. Under the LVRT control strategy, the reactive and active current references for the inner loop are denoted as $I_{DG.q} = 1.05$ and $I_{DG.d} = 0.58$, respectively. The control parameters of the current inner loop are summarized in Table

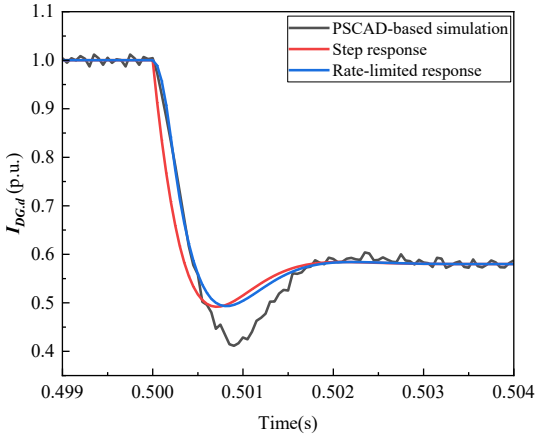
10

1.

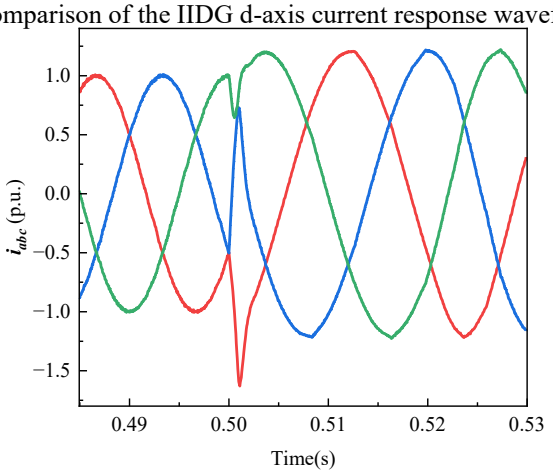
Table 1. Control parameters of the current inner loop.

Cases	K_p	K_i	ω_n	ζ	$\left\|di_{pd}^{*}(t)/dt\right\|$
Underdamped	4.396	9859	10ωs	0.7	0.0002
Critically damped	6.28	9859	10ωs	1	0.0002
Overdamped	62.8	9859	10ωs	10	0.0005

The fault-current characteristics of the IIDG under underdamped, critically damped, and overdamped conditions are shown in Figs. 6-8, respectively. In each figure, panel (a) presents the fault-response waveforms, comparing the second-order equivalent model under step and rate-limited inputs with the measured PSCAD results; panel (b) shows the three-phase currents at the PCC.

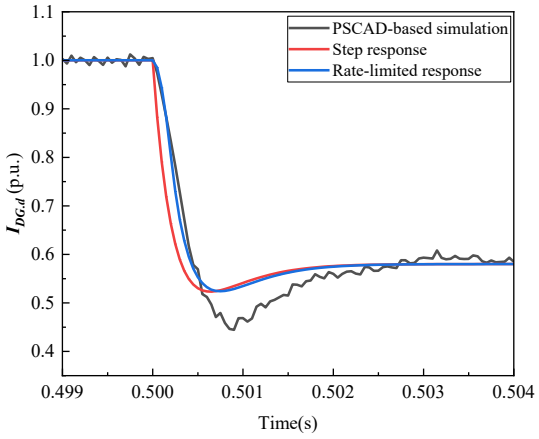


(a) Comparison of the IIDG d-axis current response waveforms

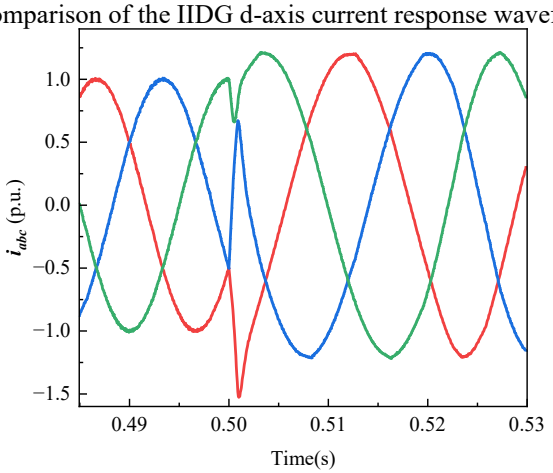


(b) Three-phase current waveforms of the IIDG at the PCC.

Fig. 6. Fault-current characteristics of the IIDG under the underdamped condition.

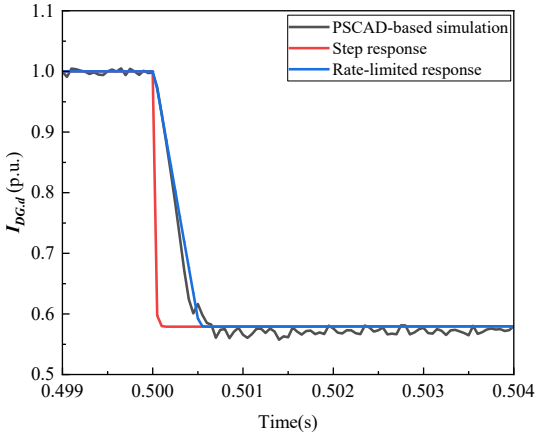


(a) Comparison of the IIDG d-axis current response waveforms



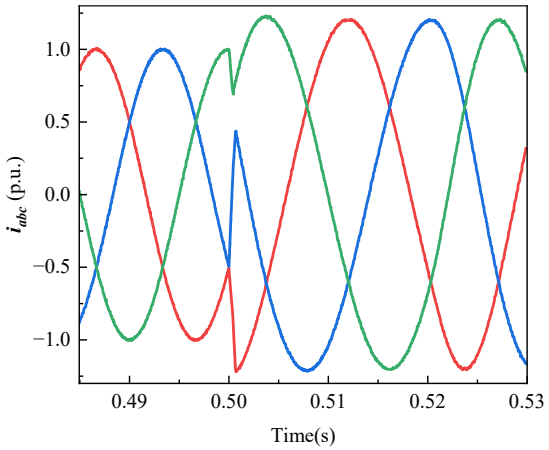
(b) Three-phase current waveforms of the IIDG at the PCC.

Fig. 7. Fault-current characteristics of the IIDG under the critically damped condition.



(a) Comparison of the IIDG d-axis current response waveforms

12



(b) Three-phase current waveforms of the IIDG at the PCC.

Fig. 8. Fault-current characteristics of the IIDG under the overdamped condition.

Examining Figs. 6-8 reveals the following observations:

(1) The rate-limited-input-based equivalent model accurately reproduces both the rising and settling segments of the measured response. Under the overdamped condition, the simulated rate-limited-input response is nearly identical to the PSCAD waveform.

(2) The measured waveforms show deeper troughs and more noticeable jitter, indicating the presence of nonlinear and high-frequency components during the fault transient that the second-order linear model does not capture.

(3) As the damping ratio ζ rises, the amplitude of the transient peak in the IIDG three-phase fault current diminishes, and the current stabilizes more quickly.

(4) Regardless of whether the input is a step, a rate-limited ramp, or the damping transitions from underdamped to overdamped conditions, the occurrence time of the first trough relative to the fault moment t_0 remains approximately within a fixed time window, with its position nearly invariant to input shaping. In contrast, the depth of the trough and the subsequent attenuation rate exhibit significant variation. This observation suggests that the system's inherent oscillation frequency primarily governs the timing of the first trough, while the damping level and the degree of saturation influence the trough depth. Consequently, a "measurement-inference" approach can be established: the equivalent oscillation frequency can be estimated based on the first trough time, thereby determining the order of magnitude of the control bandwidth, and the damping coefficient can then be inferred from the amplitude attenuation ratio between adjacent extrema, enabling robust parameter identification for the second-order equivalent model.

The simulation analysis above shows that when the equivalent transfer function is underdamped, a significant peak current may occur in the IIDG three-phase fault current during grid short-circuit events, lasting for a relatively long time. In such cases, modeling the IIDG only by a steady-state fault current in distribution-network fault studies can cause major inaccuracies. Conversely, under overdamped conditions, the rate-limited-input-based equivalent response aligns closely with the PSCAD wave-

form; therefore, the second-order equivalent model with ramp input can effectively serve as a substitute for the IIDG fault model in these scenarios.

5 Conclusions

This paper examines the transient behaviors of IIDG fault currents during grid short-circuit conditions and analyzes their influencing factors, leading to the following conclusions:

(1) Parameter effects and damping-interval criteria: In the second-order model, which is equivalent to the inner loop and circuit equations, increasing the proportional gain enhances damping and shifts the real part of the poles approximately linearly, thereby determining the envelope decay rate. The integral gain mainly influences the natural frequency and steady-state error, with little effect on the envelope decay. Based on this distinction, inner-loop parameter settings can be categorized into underdamped, critically damped, and overdamped intervals, allowing prediction of fault-current overshoot and settling behavior.

(2) Unified amplitude and slope constraint and trajectory reachability: Under a reactive-power priority and 1.2 pu current-amplitude limit control strategy, constraining only the final value is insufficient to guarantee trajectory reachability. By deriving a unified constraint among the available modulation-voltage margin, reference slope, and allowable error from the electromagnetic equations, the reference input is transitioned from a step to a slope-limited ramp, thus avoiding deep saturation and the onset of strong nonlinear effects under modulation constraints.

(3) Model applicability and engineering equivalence: Under overdamped conditions, the second-order equivalent model with ramp input closely aligns with PSCAD results in both the rising and settling phases, making it suitable as a substitute for relay-protection calculations. In contrast, under underdamped conditions, significant peak fault-current transients with extended duration are observed, heavily influenced by saturation and nonlinear effects; in such cases, steady-state models or linear second-order equivalents are not recommended. Critical damping falls between these extremes and should be applied with careful consideration of voltage-margin and current-limiting strategies.

Acknowledgement: This work was supported by the Guangdong Basic and Applied Basic Research Foundation (No. 2024A1515012289).

References

1. Zhe Yang, Hongyi Wang, Wenlong Liao, et al., "Protection Challenges and Solutions for AC Systems with Renewable Energy Sources: A Review", *Protection and Control of Modern Power Systems*, vol.10, no.1, pp.18-39, 2025.
2. Q. Liu, K. Jia, B. Yang, et al., "Analytical Model of Inverter-Interfaced Renewable Energy Sources for Power System Protection," in IEEE Transactions on Power Delivery, vol. 38, no. 2, pp. 1064-1073, April 2023, doi: 10.1109/TPWRD.2022.3204825.

3. Y. Chang, J. Hu, W. Tang, et al., “Fault current analysis of type-3 WTs considering sequential switching of internal control and protection circuits in multi time scales during LVRT,” IEEE Trans. Power Syst., vol. 33, no. 6, pp. 6894–6903, Nov. 2018.
4. Z. Shuai, C. Shen, X. Yin, et al., “Fault analysis of inverter-interfaced distributed generators with different control schemes,” IEEE Trans. Power Del., vol. 33, no. 3, pp. 1223–1235, Jun. 2018.
5. K. Jia, Z. Yang, L. Zheng, et al., “Spearman correlation-based pilot protection for transmission line connected to PMSGs and DFIGs,” IEEE Trans. Ind. Informat., vol. 17, no. 7, pp. 4532–4544, Jul. 2021.
6. LIU Yuyan, ZHU Yihua, ZHOU Xin, et al., "Analytical Method for Short-Circuit Current During the Entire Fault Ride-Through Process of Photovoltaic Generation Units", Southern Power System Technology, 1-12[2025-08-21]. https://link.cnki.net/urlid/44.1643.TK.20250623.0851.002.
7. YI Yang, SHEN Yu, LIN Zhangsui. "Characteristics and Analysis Methods of AC Short-circuit Current Contributed by VSC-HVDC", High Voltage Engineering, 2018,44(07): 2150-2158. DOI: 10.13336/j.1003-6520.hve.20180628006.
8. B. Li, R. Mu, J. He, et al., "Transient Fault Current Calculation Method for the PV Grid-Connected System Considering Dynamic Response of PLL," in IEEE Transactions on Industry Applications, vol. 60, no. 5, pp. 7537-7547, Sept.-Oct. 2024, doi: 10.1109/TIA.2024.3403955.
9. JIA Ke, LIU Qian, YANG Bin, et al., "Transient Fault Current Analysis of the Inverter-interfaced Renewable Energy Sources Considering the Dynamic Characteristics of the Phase-locked Loop", Power System Technology,2021,45(11): 4242-4251. DOI: 10.13335/j.1000-3673.pst.2021.0508.
10. Yafang Tang, Guojuan Luo, Yi Pu, “Short-circuit calculation approach of grids with high proportion of inverter-interfaced generator stations”, Electric Power Systems Research, Volume 241,2025,111407, ISSN 0378-7796, https://doi.org/10.1016/j.epsr.2024.111407.
11. S. Shi, Z. Huang and Y. Zhang, "Improvement of Short-circuit Calculation for distribution network with distributed generation," *2021 IEEE 4th Advanced Information Management, Communicates, Electronic and Automation Control Conference (IMCEC)*, Chongqing, China, 2021, pp. 21-24, doi: 10.1109/IMCEC51613.2021.9482104.
12. X. Shi, H. Zhang, C. Wei, et al., "Fault Modeling of IIDG Considering Inverter’s Detailed Characteristics," in *IEEE Access*, vol. 8, pp. 183401-183410, 2020, doi: 10.1109/ACCESS.2020.3027323.
13. KONG Xiangping, YUAN Yubo, HUANG Haosheng, et al., "Fault Current Transient Features and Its Related Impact Factors of PV Generator", Power System Technology,2015,39(09): 2444-2449. DOI: 10.13335/j.1000-3673.pst.2015.09.011.
14. Chenqi Wu, Ning Li, Jieyu Yao, et al., "A Virtual Converter Control Scheme Achieving Fast Fault Current Injection With Minimal Impact on Stability in Grid-Following Converters", IET Generation, Transmission & Distribution, vol.19, no.1, 2025.
15. K. Jia, Q. Liu, B. Yang, et al., "Transient Fault Current Analysis of IIRESs Considering Controller Saturation," in IEEE Transactions on Smart Grid, vol. 13, no. 1, pp. 496-504, Jan. 2022, doi: 10.1109/TSG.2021.3118680.

011 High voltage overhead line insulator breakage detection technology based on lightweight DETR

WANG Wuwei[1,2], WANG Feng[1,2], WANG Jingqi[1,3],
WANG Bin[1,3], WANG Shuohe[1,3]
[1] Hebei Province Wind and Solar Power Generation, Transmission and Distribution Integrated

Innovation Center, Shijiazhuang 050000, Hebei Province, China
[2] Guoshun Technology Group Co., Ltd., Shijiazhuang 050000, Hebei Province, China
[3] School of Electrical and Electronic Engineering, Shijiazhuang Tiedao University, Shijiazhuang 050043, Hebei Province, China

Abstract. Aiming at the task of insulator breakage detection in the inspection of high-voltage overhead lines under complex background, a lightweight DETR based insulator breakage detection technology for overhead lines is proposed. Aiming at the problem of insufficient feature capture of tiny insulator damage under complex background, this paper replaced the backbone network of the object detection model DETR with the lightweight MobileViTv3, and through its innovative CNN-ViT hybrid architecture and jump enhanced attention SEA module. Under the lightweight design, the core problem that it is difficult to capture the tiny damage characteristics of insulators in complex backgrounds is perfectly solved. Compared with the original model, the accuracy of the improved DETR network is improved by 3.9 percentage points to 91.3%, and the parameter number is only 39.5% of the original model. The improved DETR network reduces the model parameter amount and improves the insulator damage detection ability of the model in complex environments.

Keywords: High voltage overhead line; Object detection algorithm; Insulator breakage; Uav inspection

1 Introduction

With the rapid expansion of the scale of new energy grid connection, the importance of intelligent inspection of high voltage overhead line as a key channel of wind power transmission has become increasingly prominent. As the core components of high voltage overhead lines, once the insulator is damaged, it may cause line flashover, power failure and other accidents, which will not only affect the stable operation of the grid, but also restrict the efficient consumption and delivery of new energy. At present, the inspection work mainly relies on the combination of UAV visible light shooting and manual map judgment, which has prominent problems of low efficiency and high missed detection rate, and is difficult to meet the higher requirements for the safety and reliability of high-voltage transmission channels under the high proportion of new energy access.

In recent years, the field of high-voltage overhead line insulator inspection has achieved rapid development [1]. Compared with traditional manual inspection, target detection technology has significantly reduced labor costs. Yong Jiang et al. [2] proposed an optimized lightweight insulator defect detection model, DBB-YOLOv8N, which adopts a new lightweight module in its backbone architecture, replacing traditional bottlenecks with RepViTBlocks and replacing SE modules with EMA attention mechanism. Zhendong He et al. [3] proposed an insulator defect detection algorithm based on adaptive feature fusion and lightweight YOLOv5s model, and integrated the ASFF module to replace the backbone of YOLOv5s with lightweight convolutional neural network EfficientNet. Shoutian Dong et al. [4] proposed an enhanced insulator defect detection technology method YOL011n-SSA, and introduced the StarNet network in the backbone part of the model, and used the SOPN feature pyramid network in the neck part of the model. And the ADown module is used to improve the trunk and neck parts of the model. Yin Yingying et al. [5] proposed an advanced intelligent insulator detection model YOLOv5s-TC, which replaced the C3 module with a bottleneck converter, introduced a CBAM convolutional block attention module, and adopted an improved loss function OSIoU. Qiang Chen et al. [6] proposed an improved lightweight DGNCA-Net insulator defect detection algorithm based on YOLOv11 framework, designed a lightweight Ghost-backbone network, replaced the original C2PSA module with the CSPCA module of flash attention fusion, and constructed a DC-PUFPN neck network.

However, the existing target detection algorithms generally have the problem of insufficient ability to capture small damaged features in complex backgrounds. Such small target features are easy to be submerged by background noise, resulting in reduced accuracy of the detection model and increased miss detection rate. In view of the above problems, this paper proposes a detection method of high voltage overhead line insulator breakage based on lightweight DETR. This method takes DETR model as the baseline model, replaces its backbone network with lightweight network MobileViTv3, deeply integrates the local representation advantages of lightweight convolution and the global modeling ability of multi-head self-attention MHSA of ViT Transformer, and combines the efficient inverted residual channel attention IRCA module. The background interference is effectively suppressed and the local salient features of the insulator region are highlighted. Its MHSA module is mainly responsible for global modeling, and the background interference is suppressed by long-distance dependence, and the insulator area is distinguished from the complex background. The IRCA module is mainly responsible for the enhancement and inhibition of feature channels, which improves the sensitivity to local salient features, and acts on the preliminary filtered feature map to make the damaged features become more prominent. The detection technology of insulator breakage of high voltage overhead line based on lightweight DETR can be widely used in the detection operation of key components of high voltage overhead line under complex background.

2 Principle and improvement of DETR model

2.1 Improved DETR high voltage overhead line insulator breakage detection model

DETR is an object detection model based on Transformer architecture, which directly predicts object bounding boxes and categories in an end-to-end manner, avoiding complex anchor design and post-processing steps in traditional methods. However, the ResNet backbone network used by the traditional DETR model has the problems of high computational complexity and slow inference speed when identifying damaged insulators under complex backgrounds. Therefore, in this paper, DETR is used as the benchmark model, and the backbone network is replaced by the lightweight MobileViTv3 to enhance the detection ability of the model for small damage features of insulators in complex backgrounds. The network structure diagram of the improved DETR model is shown in Fig. 1, and the improved part has been marked with a red dashed box.

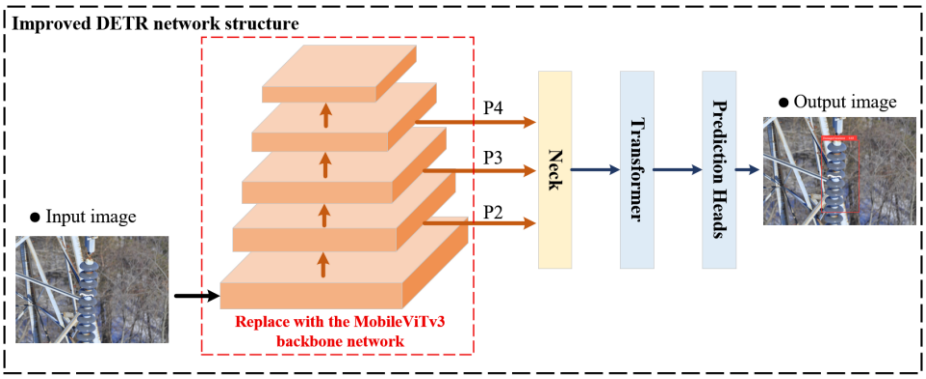


Fig. 1. Improved DETR model network structure diagram

2.2 Lightweight backbone Network based on MobileViTv3

The original backbone network of DETR is ResNet series, which has experienced multiple downsampling in the feature extraction process, resulting in a significant loss of spatial resolution. It makes the tiny and low-contrast damaged details difficult to be retained in the deep feature map, and the feature map gradually becomes blurred, and the ability to accurately locate small targets and capture fine features is insufficient.

To solve the above problems, in order to improve the detection ability of the model for damaged insulator under complex background and improve the inference speed of the model, this paper introduces the lightweight backbone network MobileViTv3, fuses the global modeling ability of lightweight convolution and Vision Transformer, and extracts local low-level features efficiently through lightweight convolution. Capture the contour and local deformation of the insulator body; Through the self-attention mechanism, the ViT module dynamically models the global dependencies

between all regions in the image on the basis of retaining sufficient spatial resolution, and accurately "focuses" on the tiny pixel changes at abnormal textures or fractures in complex backgrounds, which greatly enhances the model's resistance to background interference and the perception ability to weak damaged features. Fig 2 shows the network structure diagram of MobileViTv3.

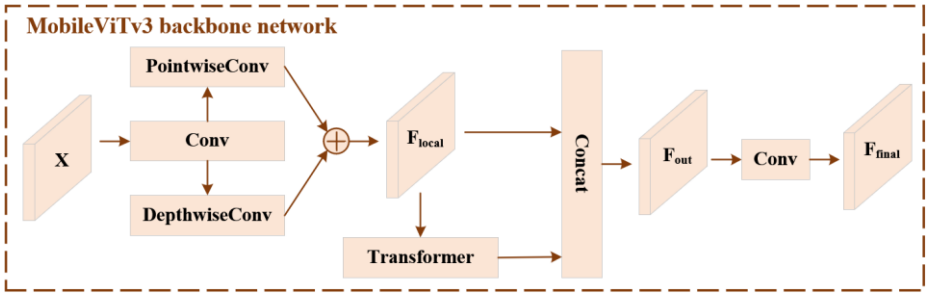


Fig. 2. MobileViTv3 network structure diagram

In A complex background, the background noise of the insulator image will interfere with the extraction of small damage features. MobileViTv3 firstly extracts the preliminary features of the input image X through a lightweight convolution layer, and retains the local structure information of the insulator image through convolution operation:

$$F_0 = \mathrm{Conv}\left(X;\ W_{\mathrm{conv}}\right) \tag{1}$$

Where $F_0 \in \mathbb{R}^{H' \times W' \times C'}$ is the preliminary extracted feature map and W_{conv} is the convolution kernel parameter.

Tiny damage of insulators is usually manifested as local texture or shape changes, so the lightweight depthwise separable convolution is used to further extract local features and enhance the sensitivity of the model to local details:

$$F_{\mathrm{depth}} = \mathrm{DepthwiseConv}\left(F_0;\ W_{\mathrm{depthwise}}\right) \tag{2}$$

$$F_{\mathrm{point}} = \mathrm{PointwiseConv}\left(F_0;\ W_{\mathrm{pointwise}}\right) \tag{3}$$

$$F_{\mathrm{local}} = F_{\mathrm{depth}} + F_{\mathrm{point}} \tag{4}$$

Where $W_{\mathrm{depthwise}}$ and $W_{\mathrm{pointwise}}$ are the weights of depth convolution and pointwise convolution, respectively.

Because the insulator image usually contains A lot of interference information under complex background, it is difficult to accurately identify small damage by only relying on local features. Therefore, MobileViTv3 introduces the Transformer module to model the global context information and divide the local feature F_{local} into N patches:

$$P = \mathrm{Patchify}(F_{\mathrm{local}}), P \in \mathbb{R}^{N \times d} \tag{5}$$

Patches are globally modeled by multi-head self-attention mechanism:

$$Q = PW_Q, K = PW_K, V = PW_V \tag{6}$$

$$\text{Attention}(Q, K, V) = \text{Softmax}(\frac{QK^T}{\sqrt{d}})V \tag{7}$$

Where W_Q, W_K, W_V is the learnable weight matrix. To combine local details and global context information, the output of the Transformer module is fused with local features:

$$F_{\text{out}} = \text{Concat}\left(F_{\text{local}}, \text{Transformer}\left(P\right)\right) \tag{8}$$

Finally, a lightweight convolution layer is used to reduce the dimension and adjust the fused features:

$$F_{\text{final}} = \text{Conv}\left(F_{\text{out}}; W_{\text{final}}\right) \tag{9}$$

Where W_{final} is the convolution kernel parameter.

By combining the local feature extraction ability of CNN and the global modeling ability of Transformer, MobileViTv3 significantly improves the ability of the model to capture small damaged features in complex backgrounds. Its lightweight design makes the model still run efficiently in scenarios with limited computing resources.

3 Experiments

3.1 Preparation of the data set

The data set in this paper is obtained by photographing high-voltage overhead lines by UAV, with a total of 4159 insulator images, including 2911 in the training set and validation set, and 1248 in the test set. Some damaged insulator images are shown in Fig 3.

6



Fig. 3. Part of the damaged insulator image

3.2 Experiment environment configuration and evaluation index

The experiment running system is Windows11 64-bit operating system, the running environment is Pycharm, and the Pytorch deep learning framework is used to build, train and test the model. The model evaluation index selected in this study is as follows: accuracy P, which measures the proportion of samples predicted as positive by the model that are really positive; Recall, R, is a measure of the proportion of all true positives that are correctly detected by the model. The average precision mean mAP was used to evaluate the overall performance of target detection and recognition. The number of parameters, Para, measures the size and complexity of the model.

3.3 Analysis of detection results

In order to show the change degree of lightweighting and accuracy of DETR model in the improvement process, Table 1 shows the results of ablation experiment. It can be seen from Table 1 that the accuracy of the original DETR model is 87.4%, and the accuracy of the model after introducing the MobileViTv3 backbone network reaches 91.3%, which is 3.9 percentage points higher than that of the original model. The number of parameters of the model is only 39.5% of the original model, which greatly reduces the complexity of the model and enhances the detection ability of the model for small damage characteristics of insulators under complex background.

Table 1. Results of ablation experiments.

Model	P/%	R/%	mAP/%	Para/M
DETR	87.4	83.7	82.2	59.47
DETR+MobileViTv3	91.3	91.1	89.4	23.49

In Table 2, different models such as YoloV5 [7] and YoloV8 [8] are selected to compare the performance data with this model for the detection task of damaged insulators under complex backgrounds. It can be seen from Table 2 that the improved DETR model in this paper has the highest accuracy of 91.3%, and the least number of model parameters.

Table 2. Comparing experimental results.

Model	P/%	R/%	mAP/%	Para/M
YoloV5	90.4	87.8	87.3	96.63
YoloV8	84.1	82.2	82.9	35.85
DETR	87.4	83.7	82.2	59.47
Improved DETR	91.3	91.1	89.4	23.49

Based on the traditional DETR model, this paper replaces its backbone network with MobileViTv3, and constructs a lightweight improved DETR model to realize fast and accurate detection of insulator breakage characteristics under complex backgrounds. The detection diagram is shown in Fig. 4.

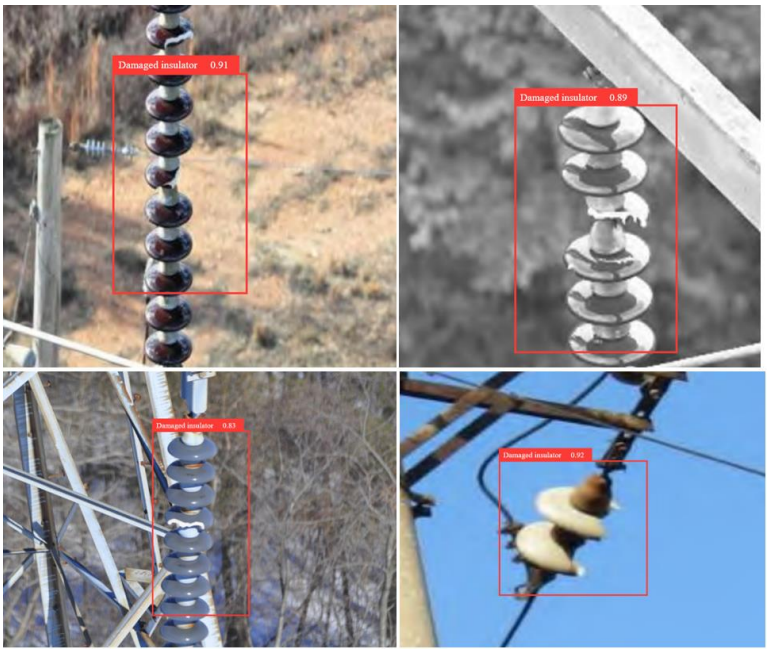


Fig. 4. Damaged insulator inspection diagram

8

4 Conclusion

Aiming at the problem that the features of insulator breakage are small and difficult to detect under complex background, this paper replaces the backbone network of DETR with lightweight MobileViTv3, introduces efficient inverted residual structure to reduce computational overhead, and uses lightweight ViT module to replace part of the convolution operation, while maintaining the local feature extraction ability and introducing the global receptive field. The accuracy of the improved DETR model reaches 91.3%, and the number of parameters is only 39.5% of the original model. The improved DETR model proposed in this paper has obvious advantages in the detection task of damaged insulators under complex backgrounds. In the future, we will try to further improve the accuracy of model detection without increasing the complexity of the model.

Acknowledgement: This work is supported by Hebei Provincial Technology Innovation Center for Integrated Application of Wind Power Generation, Transportation and Distribution (FGFSP-2025-4).

References

1. Zhang D ,Cao K ,Han K , et al. PAL-YOLOv8: A Lightweight Algorithm for Insulator Defect Detection [J]. Electronics, 13(17): 3500-3500 (2024).
2. Jiang Y ,Wang S ,Cao W , et al. RDB-YOLOv8n: Insulator defect detection based on improved lightweight YOLOv8n model [J]. Journal of Real-Time Image Processing, 21(5): 178-178 (2024).
3. He Z ,Wang Y ,Zheng A , et al. Insulator defect detection algorithm based on adaptive feature fusion and lightweight YOLOv5s [J]. Journal of Real-Time Image Processing, 22(1): 12-12 (2024).
4. Dong S ,Qin Y ,Li B , et al. Insulator Defect Detection Based on Improved YOLO11n Algorithm Under Complex Environmental Conditions [J]. Electronics, 14(14): 2898-2898 (2025).
5. Yin Y ,Duan Y ,Wang X , et al. YOLOv5s-TC: An Improved Intelligent Model for Insulator Fault Detection Based on YOLOv5s [J]. Sensors, 25(16): 4893-4893 (2025).
6. Chen Q ,Luo Y ,Yuan W , et al. DGNCA-Net: A Lightweight and Efficient Insulator Defect Detection Model [J]. Algorithms, 18(8): 528-528 (2025).
7. Yanli Y ,Xinlin W . Insulator detection using small samples based on YOLOv5 in natural background [J]. Multimedia Tools and Applications, 82(29): 44841-44857 (2023).
8. Su J ,Yuan Y ,Przystupa K , et al. Insulator defect detection algorithm based on improved YOLOv8 for electric power [J]. Signal, Image and Video Processing, 18(8-9): 6197-6209 (2024).

012 Multi-Time Scale Optimal Scheduling of Hydrogen Integrated Energy Systems Considering Seasonal Fluctuations in Wind-Solar Power

Liang Yumei[1],Tang Yifan[1],Yang Zhen[1],Sun Hexu[1,2],Zhao Yuyang[1,2]（✉）

[1] School of Electrical Engineering, Hebei University of Science and Technology, Shijiazhuang, Hebei 050018, China

E-mail: zhaoyuyang@hebust.edu.cn

[2] Hebei Engineering Laboratory of Wind Power and Photovoltaic Coupling Hydrogen Production and Comprehensive Utilization, Shijiazhuang, Hebei 050018, China

E-mail: shx_prof@163.com

Abstract. Due to worsening environmental pollution and severe energy shortages, the optimal operation of low-carbon park integrated energy systems has become a research hotspot. This paper constructs a park integrated energy system including wind-solar power generation, electrolytic hydrogen production, combined heat and power generation, and other equipment. A VMD-BOA-LSTM combined prediction model based on Variational Mode Decomposition (VMD), Butterfly Optimization Algorithm (BOA), and Long Short-Term Memory network (LSTM) is proposed to achieve high-precision prediction of wind and solar power. On this basis, a multi-time-scale optimization model for different seasons, including day-ahead, intraday, and real-time scales, is established, aiming at minimizing the economic cost and environmental cost and maximizing wind-solar energy consumption rate. Three schemes are proposed based on the impact of seasonal differences on the system. Finally, taking the Zhangjiakou Chongli wind-solar coupled hydrogen production demonstration project as a case study, it effectively proves that the proposed optimization scheme has economic efficiency and environmental friendliness. Through energy integration, resource waste has been significantly reduced.

Keywords: hydrogen-containing integrated energy system; multi-time-scale optimization; wind and solar power prediction.

1 Introduction

Driven by the "dual-carbon" goal 1, Hydrogen-containing Integrated Energy Systems (HIES) have emerged as core for low-carbon energy transformation, leveraging its advantages in multi-energy coupling and synergy 234. However, HIES involves multiple energy forms such as electricity, heat, natural gas, and hydrogen, resulting in complex energy flows, which pose significant challenges to operational optimization [56]. In existing research, Reference 7 propose the energy hub structure, with subsequent studies focusing on system modeling and scheduling. References 89 explored

the design of multi-energy coupling structures, emphasizing the conversion mechanisms among electricity, heat, and hydrogen. Reference 10 highlighted that the seasonal characteristics of equipment output are key factors affecting system stability, while Reference 11 proposed a season-specific multi-time-scale optimization strategy: day-ahead, intra-day, and real-time. This strategy enables real-time responses to energy supply-demand changes through spatiotemporal local model optimization, serving as a core approach to address the complex characteristics of such systems. To tackle energy fluctuations, References 1213 combined scheduling models with multi-time-scale strategies to mitigate the seasonal impact on equipment performance over time. In terms of low-carbon economic operation, Reference 14 constructed an HIES operational framework with objectives of cost and carbon emissions. To achieve carbon emission reduction, References 1516 propose an optimized quota method for carbon trading and electricity-carbon sharing under different seasons A review of the literature reveals limitations in existing studies: affected by seasonal changes, time-scale scheduling strategies lack accuracy and adaptability in addressing seasonal energy fluctuations, and the synergistic potential of multi-energy complementarity and low-carbon economy is underexplored. To address these, this study constructs a unified system model that accurately characterizes multi-energy flow and interaction in HIES. The model enables real-time seasonal adjustments of multi-time scale scheduling for energy changes and facilitates coordinated achievement of HIES' economic and low-carbon goals via multi-element collaborative optimization.

2 HIES Operational Framework

The constructed off-grid integrated energy system enables electricity-gas-heat energy complementarity via three core links: energy supply, energy hub, and demand sides as shown in Fig.1. The energy supply side is composed of regional wind-solar resources and natural gas input. The energy hub equipment includes gas turbine (GT), gas boilers (GB), waste heat boiler (WHB), methane reactors (MR), electrolyzers (EL), hydrogen fuel cells (HFC), and hydrogen refueling stations (HRS); energy storage devices include hydrogen storage tank (HST) and heat storage tanks (HS); the demand side includes electrical loads, thermal loads, and hydrogen loads.

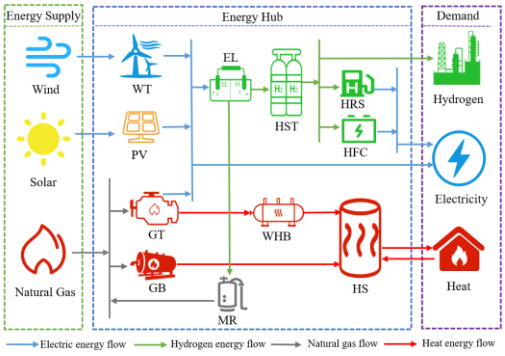


Fig. 1. Operation framework of HIES

3 Power Prediction Model

3.1 VMD-BOA-LSTM Prediction

In HIES, wind and solar clean energies are critical but exhibit strong output randomness, which cause fluctuations in system operation. Insufficient accuracy in power prediction may lead to energy supply-demand imbalances. Therefore, accurate prediction of renewable energy output is a precondition for realizing optimal system scheduling. This paper proposes a wind-solar power output prediction method based on VMD-BOA-LSTM: firstly, Variational Mode Decomposition (VMD) preprocesses original data to simplify signal features; then, the Butterfly Optimization Algorithm (BOA) optimizes Long Short-Term Memory (LSTM) network parameters to enhance convergence speed and generalization; finally, a multi-time-scale optimization model is built with energy source output characteristics and load demands to provide reliable prediction support for system scheduling.

3.2 Wind Power Prediction

To verify the accuracy and applicability of the VMD-BOA-LSTM combined prediction model, 1000 normal power data samples at10-minute interval from a 1.5MW wind turbine in Zhangjiakou Chongli wind-solar-hydrogen coupling demonstration project were selected: the first 700 for model training and the remaining 300 for prediction testing. At the first, VMD is used to comprehensively screen and finely decompose wind farm historical data into multiple pure modal components by frequency characteristics, extracting data with significant patterns and features. After preprocessing, the BOA-LSTM prediction model is applied to predict these modal components, with refined reconstruction of predicted values to obtain final wind power prediction results. To demonstrate the superiority of the VMD-BOA-LSTM model, comparative predictions on the same data are conducted using BOA-LSTM, BOA-BP, and VMD-PSO-BP models for typical seasonal wind power, with results shown in Fig.2.

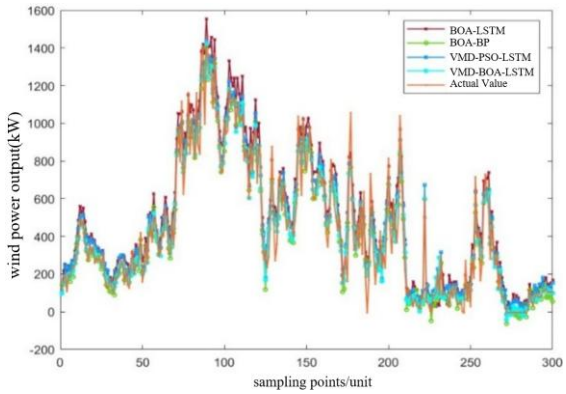


Fig.2.-a Comparison of wind power prediction in transition seasons

4

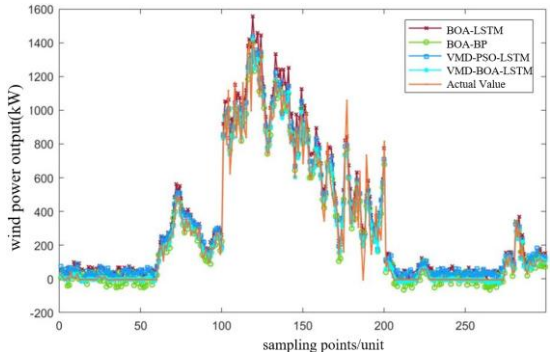


Fig.2.-b Comparison of wind power prediction in summer

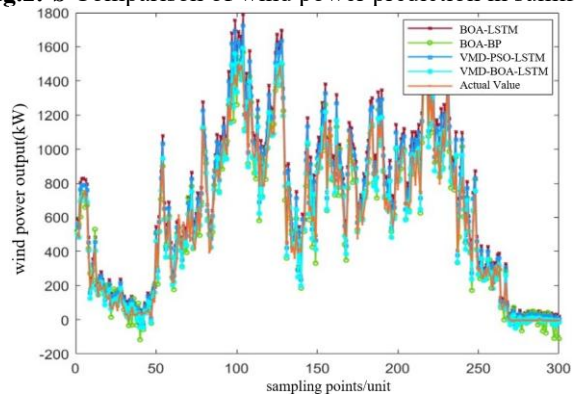


Fig.2.-c Comparison of wind power prediction in winter

To demonstrate the performance of the four prediction models, their Mean Absolute Error (MAE), Root Mean Square Error (RMSE), and Mean Absolute Percentage Error (MAPE) are calculated and compared in a table. Which can be shown in Table 1.

Table 1 Prediction indicators of four prediction models in different seasons

Typical seasons	Prediction Model	MAE (kW)	RMSE (kW)	MAPE (%)
Transitional seasons	BOA-BP	45.2758	82.5958	10.8734
	BOA-LSTM	43.9032	74.5451	8.1951
	VMD-PSO-LSTM	22.6673	38.2037	6.8241
	VMD-BOA-LSTM	14.2132	24.9710	5.1123
Summer	BOA-BP	41.7754	80.9855	10.6779
	BOA-LSTM	40.2597	69.7354	8.5236
	VMD-PSO-LSTM	20.9483	39.2559	6.8037
	VMD-BOA-LSTM	12.7250	22.6940	4.9420
Winter	BOA-BP	48.1418	91.1208	12.2892
	BOA-LSTM	43.7094	79.9250	9.6137
	VMD-PSO-LSTM	28.4198	42.5961	8.3996
	VMD-BOA-LSTM	16.7676	28.1246	5.4592

As shown in Table 1, the VMD-BOA-LSTM model achieves optimal performance across all seasons with consistent error indicator trends, with the transitional season analyzed as an example: Compared to BOA-BP, BOA-LSTM reduces MAE, RMSE, and MAPE by 1.3546 kW, 8.0507 kW, and 2.6783% respectively, demonstrating LSTM's capability for higher-precision wind power prediction. Relative to BOA-LSTM, VMD-BOA-LSTM further lowers these indicators by 29.69 kW, 49.5741 kW, and 3.0828%, verifying the significant error-reducing effect of VMD preprocessing. Compared to VMD-PSO-LSTM, VMD-BOA-LSTM decreases errors by 8.4541 kW, 13.2327 kW, and 1.7118%, indicating BOA's stronger LSTM parameter optimization ability and superior model prediction performance.

3.3 Photovoltaic Power Output Prediction

To verify the BOA-LSTM model's accuracy in predicting photovoltaic output, 30-minute interval data from a 1000kW PV system are used, and summer's complex weather data is selected as the test set. The prediction results shown in the Fig.3.

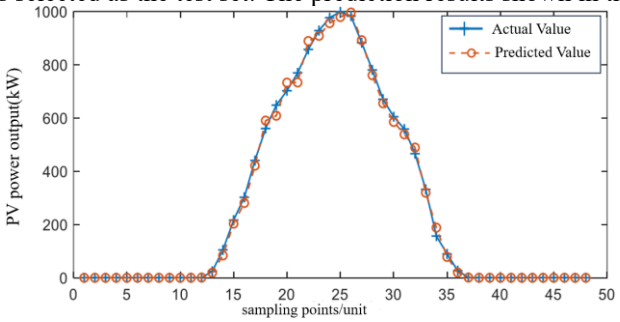


Fig. 3. Prediction results of photovoltaic output power in summer

As shown in Fig.3, the periodic characteristics of photovoltaic power facilitate prediction, and the BOA-LSTM model performs well: it tracks the 07:00–11:00 power rise, accurately locates the 12:00–14:00 peak, and reflects the 15:00–18:00 decline, with small deviations from actual values. The errors are MAE of 4.6613 kW, RMSE of 7.8821 kW, and MAPE of 5.82%, which indicate excellent prediction performance.

4 Multi-Time-Scale Optimal Scheduling Model

To address power fluctuations and dynamic load changes under large-scale wind-solar integration, a season-specific multi-time-scale optimal scheduling strategy is proposed, with its control principle shown in Fig.4, which includes three links: day-ahead, intraday rolling, and real-time adjustment. The three-level scheduling works in coordination to ensure efficient and reliable operation of the system and meet the needs of wind and solar output as well as user energy supply, as follows:

(1) Based on day-ahead wind-solar predictions, an objective function covering energy purchase, operation and maintenance, environmental, and curtailment costs is constructed. Calculations determine device output, renewable energy absorption, carbon emissions, and generate plans for power generation, energy supply, and equipment operation.

(2) According to the day-ahead plan, a model predictive control rolling optimization strategy is adopted, with a control horizon of 4 hours and a time scale of 15 minutes. The load and wind power within the control domain are predicted; initial optimization based on the day-ahead plan yields optimal device output and low-carbon economic benefits, retaining only the first 4 points. Subsequent control domains repeat optimization with new predictions for rolling updates to correct deviations.
(3) The system status is monitored at high frequency with a time scale of 5 minutes.which enables real-time minor adjustments to energy equipment per intraday plans, with output adjusted via feedback to quickly respond to abnormalities. This collaborates with the first two links to ensure system stability.

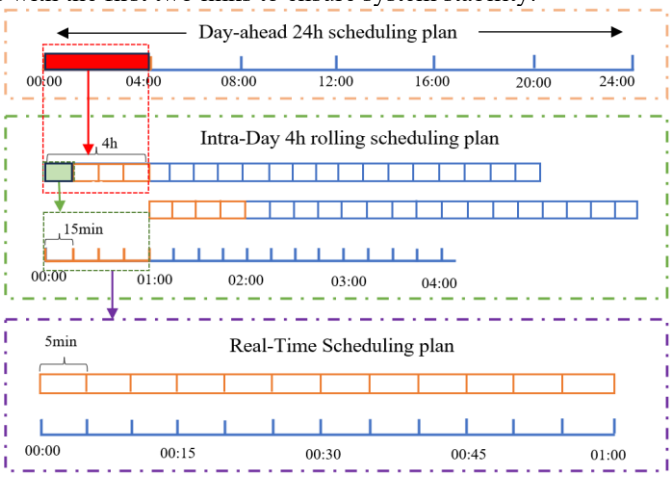


Fig. 4. Multi-Time-Scale optimal scheduling control

4.1 Day-Ahead Scheduling Optimization

Objective Function: Since the off-grid park IES cannot interact with the external grid, its capacity configuration must balance equipment scale optimization, energy demand satisfaction across all operating conditions, and improved renewable energy utilization efficiency. Based on the above analysis, the day-ahead scheduling model sets four objectives: minimum economic cost, minimum carbon emissions, minimum load shortage rate, and maximum renewable energy absorption rate.

Minimum System Economic Cost: F_1 consists of investment cost C_{cst}, operation and maintenance cost C_{om}, and gas purchase cost C_g.

$$\begin{cases} F_1 = C_{\text{cst}} + C_{\text{om}} + C_{\text{g}} \\ C_{\text{cst}} = \sum_{\text{N}} [k_{\text{ic}}^{\text{N}} R^{\text{N}} \dfrac{\eta^{\text{N}}(1+\eta^{\text{N}})^{L_{\text{sf}}^{\text{N}}}}{(1+\eta^{\text{N}})^{L_{\text{sf}}^{\text{N}}} - 1}] \\ C_{\text{om}} = \sum_{\text{N}} [k_{\text{oc,FIX}}^{\text{N}} R^{\text{N}} + k_{\text{oc,VAR}}^{\text{N}} \sum_{t=1}^{T} P_t^{\text{N}}] \\ C_{\text{g}} = \sum_{t=1}^{T} c_{\text{g}} V_t^{\text{in}} \Delta t \end{cases} \tag{1}$$

Where k_{ic}^{N} is the unit investment cost; R^{N} is the equipment capacity; N is the type of equipment; η^{N} is the equipment discount rate, set at 5%; L_{sf}^{N} is the equipment lifespan; $k_{\text{oc,FIX}}^{\text{N}}$ and $k_{\text{oc,VAR}}^{\text{N}}$ are the fixed and variable cost coefficient of the equipment,; P_t^{N} is the power of the equipment at time t; c_{g} is the natural gas price; V_t^{in} is the gas purchase volume at t.

Minimum Carbon Emission Penalty Cost:

$$F_2 = c_{\text{CO}_2} \varepsilon_{\text{g}} (V_t^{\text{GT}} + V_t^{\text{GB}}) - V_t^{\text{MR}_{\text{CO}_2}} \tag{2}$$

Where c_{CO_2} is the unit price of emission penalty; ε_{g} is the carbon emission coefficient of natural gas production; V_t^{GT} and V_t^{GB} are the gas consumption of GT and GB, respectively; $V_t^{\text{MR}_{\text{CO}_2}}$ is the carbon dioxide absorption capacity of MR.

Minimum Penalty Cost for Insufficient Load Supply:

$$F_3 = \sum_{i=1}^{T} [\beta_{\text{e}}(t) P_t^{\text{loss,e}} + \beta_{\text{h}}(t) H_t^{\text{loss,h}} + \beta_{\text{cut}} P_t^{\text{cut}}] \Delta t \tag{3}$$

Where $P_t^{\text{loss,e}}$ is the power loss; $H_t^{\text{loss,h}}$ is the heat loss; $\beta_{\text{e}}(t), \beta_{\text{h}}(t)$ are the penalty costs per unit of power loss and heat loss, β_{cut} is the penalty cost per unit of curtailed wind and solar energy, set at 0.2 ; P_t^{cut} is the amount of curtailed wind and solar energy.

Maximum Wind and Solar Energy Absorption Rate:

$$F_4 = \sum_{s=1}^{Ns} \omega_{\text{s}} \frac{1}{T} \sum_{t=1}^{T} \left(\frac{P_t^{\text{load}} + P_t^{\text{EL}} + P_t^{\text{MR}} + P_t^{\text{HFC, char}}}{P_t^{\text{WT}} + P_t^{\text{PV}}} \right) \tag{4}$$

Where P_t^{load} is the electrical load; P_t^{EL} is the power consumption of EL; P_t^{MR} is the power consumption of MR; $P_t^{\text{HFC,char}}$ is the charging power of HFC; P_t^{WT} is the wind power output; P_t^{PV} is the photovoltaic power output.

Day-Ahead Constraints: System energy supply-demand balance is the core constraint for operation, it requires the supply of various energy sources and loads be dynamically matched at all times It is necessary to optimize equipment capacity planning and operation strategies to adapt to the time-series fluctuations of wind-solar output and load while meeting economy, reliability, and energy efficiency requirements. The constraints are as follows:

Energy Balance Constraints:

$$\begin{cases} P_t^{\mathrm{WT}} + P_t^{\mathrm{PV}} + P_t^{\mathrm{GT}} + P_t^{\mathrm{HFC,dis}} + P_t^{\mathrm{HRS}} = P_t^{\mathrm{load}} + P_t^{\mathrm{EL}} + P_t^{\mathrm{MR}} + P_t^{\mathrm{HFC,char}} \\ H_t^{\mathrm{GB}} + H_t^{\mathrm{WHB}} + H_t^{\mathrm{HS,dis}} = H_t^{\mathrm{load}} + H_t^{\mathrm{HS,char}} \\ V_t^{\mathrm{in}} + V_t^{\mathrm{MR}} = V_t^{\mathrm{GT}} + V_t^{\mathrm{GB}} \\ m_t^{\mathrm{EL}} + m_t^{\mathrm{HST,dis}} = m_t^{\mathrm{H_load}} + m_t^{\mathrm{HFC}} + m_t^{\mathrm{HRS}} + m_t^{\mathrm{MR}} + m_t^{\mathrm{HST,char}} \end{cases} \tag{5}$$

Where P_t^{GT} is the output power of GT; $P_t^{\mathrm{HFC,dis}}$ is the discharge power of HFC; P_t^{HRS} is the electric power reflux of HRS; H_t^{GB} and H_t^{WHB} are the heat output power of GB and WHB, H_t^{load} is the heat load; $H_t^{\mathrm{HS,char}}$ is the heat storage capacity of HS; $H_t^{\mathrm{HS,dis}}$ is the heat release capacity of HS; V_t^{MR} is the natural gas volume generated by the methanation reactor; m_t^{EL} is the hydrogen production of EL; $m_t^{\mathrm{HST,dis}}$ is the hydrogen release of HST; $m_t^{\mathrm{H_load}}$ is the hydrogen load; m_t^{HFC} is the hydrogen consumption of HFC; m_t^{HRS} is the hydrogen consumption of HRS; m_t^{MR} is the hydrogen consumption of MR; $m_t^{\mathrm{HST,char}}$ is the hydrogen storage capacity of HST.

GT Constraints:

$$\begin{cases} P_t^{\mathrm{GT}} = \eta^{\mathrm{GT,e}} \delta_{\mathrm{g}} V_t^{\mathrm{GT}} \\ H_t^{\mathrm{GT}} = \eta^{\mathrm{GT,h}} \delta_{\mathrm{g}} V_t^{\mathrm{GT}} \\ P_t^{\mathrm{GT,min}} \le P_t^{\mathrm{GT}} \le P_t^{\mathrm{GT,max}} \\ H_t^{\mathrm{GT,min}} \le H_t^{\mathrm{GT}} \le H_t^{\mathrm{GT,max}} \end{cases} \tag{6}$$

Where $\eta^{\mathrm{GT,e}}$ is the power generation efficiency of GT; δ_{g} is the calorific value of natural gas; $\eta^{\mathrm{GT,h}}$ is the heat production efficiency of GT; $P_t^{\mathrm{GT,max}}$ and $P_t^{\mathrm{GT,min}}$ are the upper and lower limits of GT's power generation; $H_t^{\mathrm{GT,max}}$ and $H_t^{\mathrm{GT,min}}$ are the upper and lower limits of GT's heat output.

GB Constraints:

$$\begin{cases} H_t^{\mathrm{GB}} = \eta^{\mathrm{GB}} \delta_{\mathrm{g}} V_t^{\mathrm{GB}} \\ H_t^{\mathrm{GB,min}} \le H_t^{\mathrm{GB}} \le H_t^{\mathrm{GB,max}} \end{cases} \tag{7}$$

Where η^{GB} is the heat production efficiency of GB; $H_t^{GB,max}$ and $H_t^{GB,min}$ are the upper and lower limits of GB's heat output power.

WHB Constraints:

$$\begin{cases} H_t^{WHB} = \eta^{WHB} H_t^{GT} \\ H_t^{WHB,min} \le H_t^{WHB} \le H_t^{WHB,max} \end{cases} \tag{8}$$

Where η^{WHB} is the waste heat recovery coefficient of WHB; $H_t^{WHB,max}$ and $H_t^{WHB,min}$ represent the upper and lower limits of WHB's heat output power.

EL Constraints:

$$\begin{cases} m_t^{EL} = \dfrac{\eta_t^{H_2} M_{H_2} P_t^{EL}}{UzF} \\ P_t^{EL,min} \le P_t^{EL} \le P_t^{EL,max} \end{cases} \tag{9}$$

Where $\eta_t^{H_2}$ is the total efficiency of electrolytic hydrogen production; M_{H_2} is the molar mass of hydrogen; U is the voltage of EL; z is the number of charges transferred in the electrolysis reaction; F is the Faraday constant; $P_t^{EL,max}$ and $P_t^{EL,min}$ are the upper and lower limits of the hydrogen production power of EL.

HFC Constraints:

$$\begin{cases} P_t^{HFC,dis} = \dfrac{\eta^{HFC} m_t^{HFC} \delta_{H_2}}{\rho_0} \\ P_t^{HFC,dis,min} \le P_t^{HFC,dis} \le P_t^{HFC,dis,max} \end{cases} \tag{10}$$

Where η^{HFC} is the energy conversion efficiency of HFC; m_t^{HFC} is the mass of hydrogen input at time *t*; δ_{H_2} is the calorific value of hydrogen; ρ_0 is the density of hydrogen under standard conditions; $P_t^{HFC,dis,max}$ and $P_t^{HFC,dis,min}$ are the upper and lower limits of HFC's power generation.

MR Constraints:

$$\begin{cases} V_t^{MR} = \dfrac{v_1 V^{MR,H_2} \delta_{H_2}}{\delta_g} \\ V_t^{MR,min} \le V_t^{MR} \le V_t^{MR,max} \end{cases} \tag{11}$$

Where v_1 is the reaction coefficient of MR; V^{MR,H_2} is the hydrogen consumption of MR; $V_t^{MR,max}$ and $V_t^{MR,min}$ are the upper and lower limits of MR's gas production.

Energy Storage Equipment Constraints:

$$\begin{cases} m_t^{HST,min} \le m_t^{HST} \le m_t^{HST,max} \\ H_t^{HS,min} \le H_t^{HS} \le H_t^{HS,max} \end{cases} \tag{12}$$

Where m_t^{HST} is the hydrogen storage capacity of HST at time t; $m_t^{\mathrm{HST,max}}$ and $m_t^{\mathrm{HST,min}}$ are the upper and lower limits of HST's hydrogen storage capacity; H_t^{HS} is the heat storage capacity of HS at time t; $H_t^{\mathrm{HS,max}}$ and $H_t^{\mathrm{HS,min}}$ are the upper and lower limits of HS's heat storage capacity.

Operation Penalty Constraints:

$$\begin{cases} 0 \le P_t^{\mathrm{loss,e}} \le \lambda_{\mathrm{e}} P_t^{\mathrm{load}} \\ 0 \le H_t^{\mathrm{loss,e}} \le \lambda_{\mathrm{h}} H_t^{\mathrm{load}} \\ 0 \le P_t^{\mathrm{EL}} \le \lambda_{\mathrm{cut}} P_t^{\mathrm{WT_PV}} \end{cases} \tag{13}$$

Where λ_{e}, λ_{h}, λ_{cut} are the penalty ratios for power loss, heat loss, and curtailed wind-solar energy, respectively. In actual operation, these three types of operational penalty scenarios should be controlled within a certain range; otherwise, the normal operation of the system will be affected.

4.2 Intra-day Rolling Scheduling Optimization

In conjunction with the day-ahead model, intra-day scheduling adopts rolling horizon optimization, updating supply-demand forecasts and equipment status at a 4-hour cycle and 15-minute time step, with the optimization results applied in real time. Compared with the one-time day-ahead scheduling, it is more reliable and adaptable in coping with operational errors and wind-solar uncertainties, which can effectively reduce adverse impacts and improve system efficiency.

Objective Function： Affected by the system coupling characteristics and energy output uncertainties caused by weather conditions, errors exist in the long-cycle day-ahead optimization. To avoid such errors, intra-day plans need to be adjusted based on the latest real-time forecast data. To ensure system stability and the coherence of day-ahead scheduling, intra-day rolling scheduling aims to minimize the sum of adjustment penalties, ensuring the smallest deviation from the day-ahead plan. The objective function is as follows:

$$F_5 = (C_{\mathrm{punish_p}} + C_{\mathrm{punish_h}}) \tag{14}$$

Where $C_{\mathrm{punish_p}}$ and $C_{\mathrm{punish_h}}$ are the penalty costs for electricity-related equipment and heat-related equipment, which are expressed as follows:

$$\begin{cases} C_{\text{punish_p}} = \lfloor \lambda_{\text{GT}}\Delta P^{\text{GT}} + \lambda_{\text{HFC}}\Delta P^{\text{HFC}} + \lambda_{\text{EL}}\Delta P^{\text{EL}} + \lambda_{\text{CCS}}\Delta P^{\text{MR}} + \lambda_{\text{HRS}}\Delta P^{\text{HRS}} \rfloor \\ \Delta P^{\text{GT}} = \sum_{t=1}^{T} \left| P_t^{\text{GT}} - P_t^{\text{GT_0}} \right| \\ \Delta P^{\text{HFC}} = \sum_{t=1}^{T} \left| P_t^{\text{HFC}} - P_t^{\text{HFC_0}} \right| \\ \Delta P^{\text{EL}} = \sum_{t=1}^{T} \left| P_t^{\text{EL}} - P_t^{\text{EL_0}} \right| \\ \Delta P^{\text{MR}} = \sum_{t=1}^{T} \left| P_t^{\text{MR}} - P_t^{\text{MR_0}} \right| \\ \Delta P^{\text{HRS}} = \sum_{t=1}^{T} \left| P_t^{\text{HRS}} - P_t^{\text{HRS_0}} \right| \end{cases} \tag{15}$$

Where ΔP^{GT}, ΔP^{HFC}, ΔP^{EL}, ΔP^{MR} and ΔP^{HRS} are the adjustment amounts of each electrical energy conversion device in the intra-day scheduling plan compared to the day-ahead plan. λ_{GT}, λ_{HFC}, λ_{EL}, λ_{MR} and λ_{HRS} are the penalty coefficients for each electrical energy conversion device.

$P_t^{\text{GT_0}}$, $P_t^{\text{HFC_0}}$, $P_t^{\text{EL_0}}$, $P_t^{\text{MR_0}}$ and $P_t^{\text{HRS_0}}$ are the power of each electrical energy conversion device in the day-ahead scheduling period.

$$\begin{cases} C_{\text{punish_h}} = \min \lfloor \lambda_{\text{GB}}\Delta H^{\text{GB}} + \lambda_{\text{WHB}}\Delta H^{\text{WHB}} + \lambda_{\text{HS}}\Delta H^{\text{HS}} \rfloor \\ \Delta H^{\text{GB}} = \sum_{t=1}^{T} \left| H_t^{\text{GB}} - H_t^{\text{GB_0}} \right| \\ \Delta H^{\text{WHB}} = \sum_{t=1}^{T} \left| H_t^{\text{WHB}} - H_t^{\text{WHB_0}} \right| \\ \Delta H^{\text{HS}} = \sum_{t=1}^{T} \left| H_t^{\text{HS}} - H_t^{\text{HS_0}} \right| \end{cases} \tag{16}$$

Where ΔH^{GB}, ΔH^{WHB} and ΔH^{HS} are the adjustment amounts of each thermal energy conversion device in the intra-day stage compared to the day-ahead scheduling plan, and λ_{GB}, λ_{WHB} and λ_{HS} are the penalty coefficients for each thermal energy conversion device; $H_t^{\text{GB_0}}$, $H_t^{\text{WHB_0}}$ and $H_t^{\text{HS_0}}$ are the power of each thermal energy conversion device in the day-ahead scheduling period.

Intra-Day Constraints: The constraints of the intra-day rolling horizon plan are basically consistent with those of the day-ahead plan, and will not be repeated here. However, due to the slow response of heating equipment, it is difficult to adjust quickly in a short period of time. The small time span between adjacent time periods

may cause output plan overlap, which affects the execution of intra-day plans and system stability. Thus, the following constraints are introduced to ensure reasonable adjustment of heating equipment output.

$$\begin{cases} \left| H_{t_\mathrm{a}}^{\mathrm{GB}} - H_{t_b}^{\mathrm{GB}} \right| \le \lambda_{RS} H^{\mathrm{GB,n}} \\ \left| H_{t_\mathrm{a}}^{\mathrm{WHB}} - H_{t_b}^{\mathrm{WHB}} \right| \le \lambda_{RS} H^{\mathrm{WHB,n}} \end{cases} \tag{17}$$

Where $H_{t_\mathrm{a}}^{\mathrm{GB}}$ and $H_{t_\mathrm{a}}^{\mathrm{WHB}}$ are the heat power of GB and WHB in the previous time t; $H_{t_\mathrm{b}}^{\mathrm{GB}}$ and $H_{t_\mathrm{b}}^{\mathrm{WHB}}$ are the heating power of GB and WHB in the next time t; λ_{RS} is the adjustment constraint factor of the rolling horizon plan; $H^{\mathrm{GB,n}}$ and $H^{\mathrm{WHB,n}}$ are the rated power of GB and WHB.

Frequent charging and discharging of HFC can shorten its service life. Thus, daily constraints must be added to limit its charge-discharge cycles, ensuring battery protection while meeting day-ahead and intra-day plan requirements. The newly added constraint is as follow:

$$n_{\mathrm{HFC,char}} + n_{\mathrm{HFC,dis}} \le n_{\mathrm{HFC,allow}} \tag{18}$$

Where $n_{\mathrm{HFC,char}}$ and $n_{\mathrm{HFC,dis}}$ are the number of charging and discharging cycles of HFC, $n_{\mathrm{HFC,allow}}$ is the allowable number of charging and discharging cycles for the HFC device.

4.3 Real-Time Scheduling Optimization

Real-time scheduling operates on a 5-minute time scale, taking as input the equipment output and energy storage charging and discharging power determined by intra-day scheduling. It uses the rapid response capability of hydrogen energy storage to mitigate power fluctuations and improve wind power absorption. At this stage, only hydrogen energy storage regulation costs are considered, with the objective function as follows:

$$\begin{cases} F_6 = \lambda_{\mathrm{HFC}} \Delta P^{\mathrm{HFC}} + \lambda_{\mathrm{HS}} \Delta H^{\mathrm{HS}} + \lambda_{\mathrm{HST}} \Delta m^{\mathrm{HST}} \\ \Delta m^{\mathrm{HS}} = \sum_{t=1}^{T} \left| m_t^{\mathrm{HS}} - m_t^{\mathrm{HS_0}} \right| \end{cases} \tag{19}$$

Where Δm^{HST} is the adjustment amount of HST in the intra-day stage compared to the day-ahead scheduling plan; λ_{HST} is the penalty coefficient of HST; $m_t^{\mathrm{HS_0}}$ is the hydrogen production volume of HST in the day-ahead scheduling period. Similar to intra-day scheduling, the real-time stage involves the variation costs of HFC, HST, and HS, which will not be elaborated on here. The constraint conditions include the adjustment constraints of these three types of equipment and the number of repeated power generation cycles of fuel cells.

5 Verification of Multi-Time-Scale Optimization Results

5.1 Actual Park Case Study

For grid-remote industrial parks with high transmission costs and abundant wind-solar resources, the multi-time-scale optimization model is by using the Zhangjiakou Chongli Wind-Solar Coupled Hydrogen Production Demonstration Project with 1500 kW wind turbine and 1000 kW photovoltaic array. Based on the park's annual wind-solar output , electrical and thermal load data, three season-specific typical days (transition season, summer, winter) are defined to address seasonal uncertainties. Wind-solar resource data and load demands for these typical days, reflecting actual operational characteristics, are analyzed and shown in Fig.5

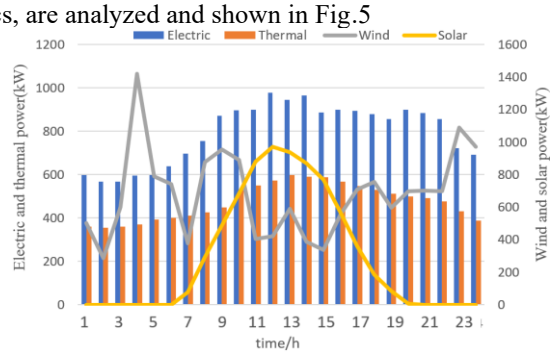


Fig. 5.-a Transition season power data

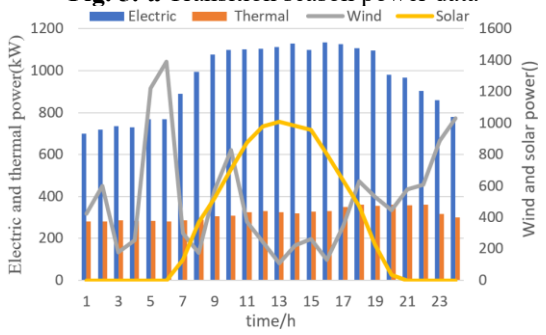


Fig. 5.-b Summer power data

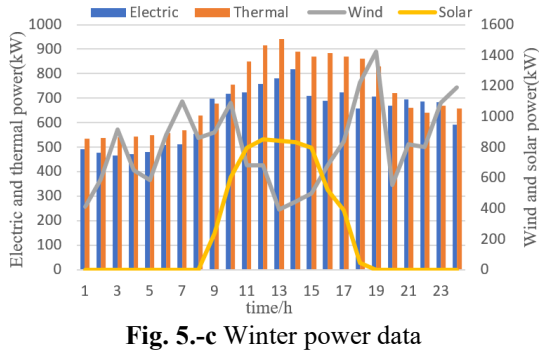


Fig. 5.-c Winter power data

From Fig 5, it can be seen that this low-carbon park mainly has the following three characteristics:
(1) The wind power fluctuates significantly, with an instantaneous peak value of up to 1500 kW, while it can stabilize at 900 kW during regular operation;
(2) Photovoltaic output is strongly correlated with seasonal sunlight intensity, with a summer peak of 1000 kW and a winter peak of about 800 kW;
(3) Load demands show obvious seasonal differentiation: thermal load dominates in winter, with a peak value of around 900 kW, while daytime electrical load dominates in summer, with a stable peak of 1100 kW.
Based on the characteristic analysis of the above park, using the three typical day scenarios as input data and combining with the characteristics of the multi-time-scale optimization framework, the three planning schemes are as followed:
Scheme 1: Considering the diversified utilization of hydrogen energy, only day-ahead single-time-scale optimization is performed for the system.
Scheme 2: Without considering the diversified utilization of hydrogen energy, day-ahead, intra-day, and real-time multi-time-scale optimization is performed for the system.
Scheme 3: Considering the diversified utilization of hydrogen energy, day-ahead, intra-day, and real-time multi-time-scale optimization is performed for the system.

5.2 Analysis of Multi-Time-Scale Optimization Configuration Results

To analyze the three schemes' typical daily performance, transition season condi-tions are tested, with Scheme 1's day-ahead single-time-scale optimization electrical and thermal results shown in Figures 6-a and 6-b:
From 22:00–6:00 is low load period, WT dominate supply as PV output is negligible. CHP units and HFC supplement deficits. Reduced hydrogen refueling demand allows surplus energy reconversion to grid electricity.7:00–18:00 is high renewables period, which rises PV peaking at 14:00, creating excess power used for electrolytic hydrogen production. Stored hydrogen is utilized industrially via MR.19:00–21:00 is load re-covery period, which requires GT and auxiliary equipment to offset declining PV output and meet evening peak electrical demand. Thermal balance is maintained by waste heat recovery from GT via WHB, with GB covering residual thermal loads.

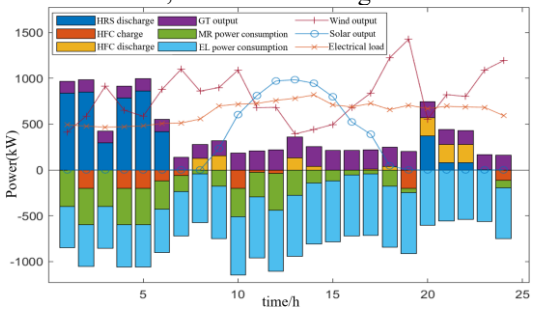


Fig. 6.-a Scheme 1's transition season electrical load supply-demand curve

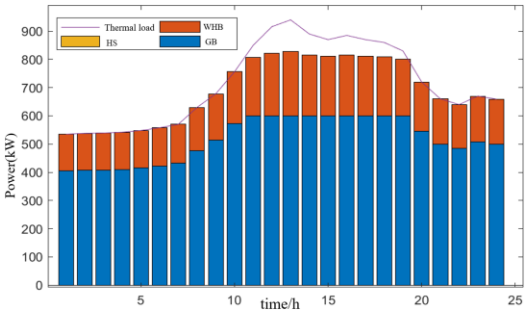


Fig. 6.-b Scheme 1's transition season thermal load supply-demand curve

Scheme 2's transition season capacity optimization results shown in Figures 7-a and 7-b apply multi-time-scale optimization without diversified hydrogen use. Sharing similar basic conditions with Scheme 1, the key differences are highlighted:

22:00–6:00 is low load period: Without HRS energy feedback, HFC and GT must increase output. Multi-time-scale optimization refines their power allocation to balance supply-demand economically.7:00–18:00 is high renewables period: Absent methanation hydrogen consumption, surplus electricity is stored in HST and HFC, with HFC output rising in other periods.19:00–21:00 is load recovery period: HFC becomes the primary supply-demand balancer as evening loads increase.

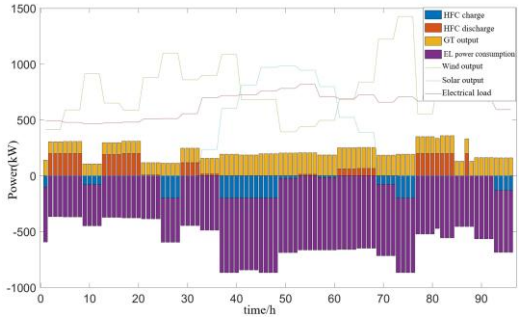


Fig. 7.-a Scheme 2's transition season electrical load supply-demand curve

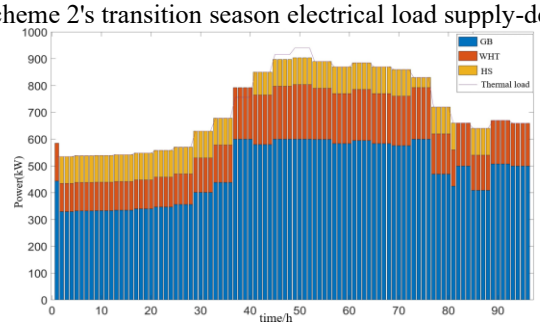


Fig. 7.-b Scheme 2's transition season thermal load supply-demand curve

The electrical and thermal operation optimization results of Scheme 3 are shown in Figures 8-a and 8-b. This scheme implements full-time-scale optimization for system equipment capacity under the premise of incorporating diversified hydrogen energy utilization. The basic environmental conditions of the three time periods in this

scheme are similar to those in Schemes 1 and 2, so the repeated parts in the analysis of Scheme 3 will not be elaborated. The focus will be on analyzing the differences: During the low-load period from 22:00 to 6:00, with the addition of HRS backflow electricity and MR power consumption, the output of GT can be reduced, the output details of equipment can be refined, and energy loss can be decreased. In the high renewable energy period from 7:00 to 18:00, there is more electricity consumption by EL during this period, and the MR is also in continuous use, which can reduce the impact of equipment start-up and shut down. During the load recovery period from 19:00 to 21:00, the electricity consumption by EL decreases, and the use of HFC begins to increase.

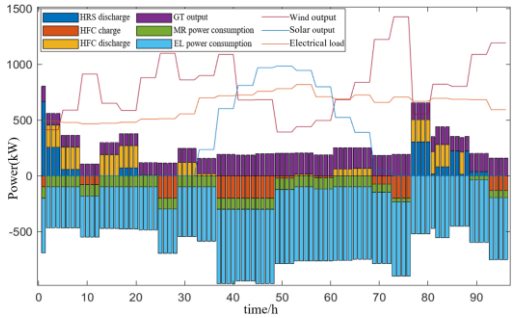


Fig. 8.-a Scheme 3's transition season electrical load supply-demand curve

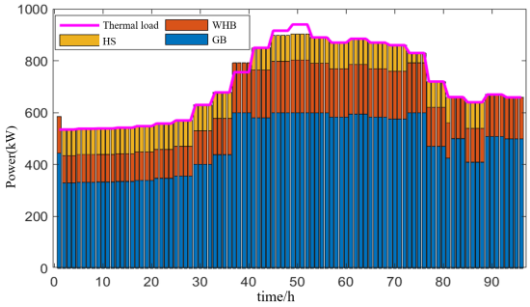


Fig. 8.-b Scheme 3's transition season thermal load supply-demand curve

Comparison of the three schemes' electrical and thermal load scheduling shows GT and HFC compensate for renewable energy deficits when WT and PV capacity are insufficient. Waste heat from GT and EL operations is recovered via WHB to meet thermal demands. Multi-time-scale optimization refines time-period energy schemes, using fast-response, low start-stop cost equipment to offset deficits. This ensures stable operation of high start-stop cost equipment such as EL, MR units, reducing costs and boosting benefits. So scheme 3 can not only cuts gas purchases and penalty costs, but also enhances economic performance.

Since the system's environmental costs mainly come from carbon emissions generated by natural gas combustion, Scheme 3 proactively reduces the share of GT in electricity supply compensation, and increases the output proportion of HFC and other devices. It also expands hydrogen utilization methods through HRS and reduces carbon emissions with equipment such as MR. These measures not only lower the system's energy procurement costs but also reduce wind and solar curtailment, decrease

the system's electrical and thermal load shortages, and improve the reliability of energy supply. To verify the universality of Scheme 3, optimal operation simulations were conducted for typical summer and winter day scenarios within the system, with the results shown in Figures 9-a to 9-d

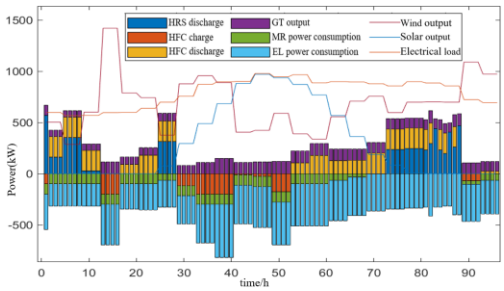


Fig. 9.-a Scheme 3's summer electrical load supply-demand curve

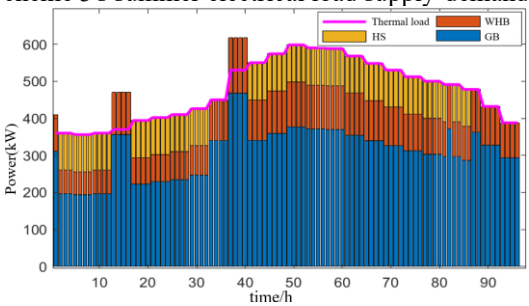


Fig. 9.-b Scheme 3's summer thermal load supply-demand curve

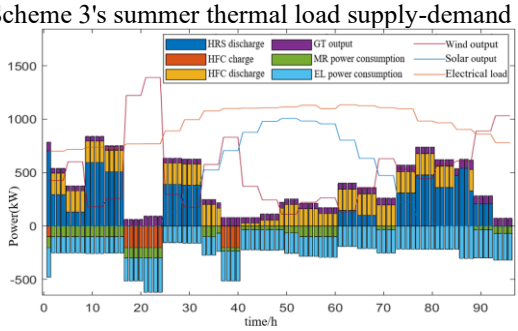


Fig. 9.-c Scheme 3's winter electrical load supply-demand curve

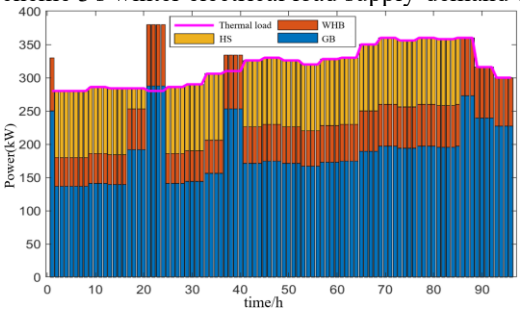


Fig. 9.-d Scheme 3's winter thermal load supply-demand curve

In summer, electrical loads are relatively high while wind energy output is low, resulting in a decrease in electricity consumption of EL and a increase in electrical energy feedback from HRS. However in summer, when sunlight is abundant, PV output is significantly higher than in other seasons. At this time, the system increases electricity consumption of EL and charging of HFC to provide electrical energy output for periods with high electrical load demand. In winter, due to low temperatures, thermal loads within the system are relatively high, while wind and solar renewable energy resources are abundant. When renewable energy generation exceeds the system's electrical power demand, to fully accommodate renewable energy generation, EL is used for hydrogen production, with hydrogen stored and utilized. Meanwhile, the system recovers waste heat from EL devices to supply the heating system, maintaining the stability of the system.

To compare the advantages and disadvantages of the capacity configuration results of the above three schemes, test operations were conducted under three scenarios: typical day in the transition season, typical day in summer, and typical day in winter. Through calculations, the objective function values are obtained, which are shown in Table 3, Table 4, and Table 5 respectively.

Table 3: Objective functions of the three schemes for the typical day

Scheme	F1(10 thousand CNY)	F2(10 thousand CNY)	F3(10 thousand CNY)	F4（%）
1	31.58	4.56	0.13	88.13
2	31.76	4.16	0.08	98.07
3	32.11	3.94	0	99.92

Table 4: Objective functions of the three schemes for the summer day

Scheme	F1(10 thousand CNY)	F2(10 thousand CNY)	F3(10 thousand CNY)	F4（%）
1	40.57	5.31	0.33	89.52
2	41.43	4.86	0.21	97.73
3	40.21	4.33	0	99.91

Table 5: Objective functions of the three schemes for the winter day

Scheme	F1(10 thousand CNY)	F2(10 thousand CNY)	F3(10 thousand CNY)	F4（%）
1	29.45	3.89	0.11	86.22
2	32.79	3.22	0.04	98.81
3	32.81	3.01	0	99.95

From the results of the aforementioned objective functions, Scheme 1’s environmental cost F2 and operational penalty F3 are the highest. Although Scheme 3 has a slightly higher economic cost F1, its environmental cost F2 and operational penalty F3 are relatively lower. After adopting the multi-time-scale optimization configuration method that considers diversified hydrogen energy utilization, it demonstrates more excellent performance in reducing the system's energy procurement cost and mitigating environmental pollution, along with better functional reliability. Specifically, Scheme 3 effectively increases the renewable energy accommodation rate to over 99%. Therefore, the optimal scheduling result of Scheme 3 is more reliable.

6 Conclusions

This paper proposes a multi-time-scale optimal scheduling method for the integrated energy system of low-carbon parks based on a wind-solar-hydrogen-storage system. By analyzing its experimental results across different seasons at multi-time scales such as day-ahead and intra-day, the key conclusions are as follows: A framework for the integrated energy system of low-carbon parks is constructed, and mathematical models for key equipment including WT, PV, CHP units, and EL are established. Combined with the analysis of equipment response time, the multi-scale allocation of scheduling time is completed. To address the uncertainty of wind and solar power generation, a VMD-BOA-LSTM combined power prediction model is constructed. Verified by actual data, this model exhibits higher prediction accuracy than other algorithms, providing data support for intra-day and real-time scale optimal scheduling. The multi-time-scale scheduling optimization of the HIES is completed. In the day-ahead stage, optimization is performed with the objectives of minimizing economic and environmental costs, and maximizing energy supply reliability and energy utilization efficiency; in the intra-day stage, short-term rolling adjustments are made according to seasons; in the real-time stage, the final optimization results are determined. Comparisons show that this method can meet complex load demands and optimize multiple performance aspects of the system. Furthermore, by considering diversified hydrogen energy utilization, the renewable energy accommodation rate is effectively increased to over 99%.

Acknowledgement: This work is supported by the National Natural Science Foundation of China Project under Grant U20A20198, the S&T Program of Hebei under Grant 23284502Z and Grant 242Q4502Z, and the University Foundation of Hebei University of Science and Technology under Grant KFJ202409.

References

1. Yuan Yue, Miao Ankang, Wu Han ,et al. Review of the research framework and key issues for low-carbon integrated energy system[J]. Proceedings of the High Volt. Eng50(09):4019-4036, (2024).
2. Shi Mengge, Wang Han, Xie Peng ,et al. Distributed energy scheduling for integrated energy system clusters with peer-to-peer energy transaction[J]. IEEE Transactions on Smart Grid14(1):142–156, (2023).
3. Liu Jiejie, Li Yao, Ma Yanan,et al. Two-layer multiple scenario optimization framework for integrated energy system based on optimal energy contribution ratio strategy[J]. Energy285: 128673, (2023).
4. Wang Xiaopeng, Deng Yeheng, Mei Linghao ,et al. Integrated energy system scheduling model based on non-complete interval multi-objective fuzzy optimization[J]. Renewable Energy218:119289, (2023).
5. Dong Zhaoyang, Yang Jiajia, Yu Li ,et al. A green hydrogen credit framework for international green hydrogen trading towards a carbon neutral future[J]. International Journal of Hydrogen Energy47(2):728-734, (2022).

6. Li Jingyu, Wang Mushui, Wu Zhaoyuan ,et al. Optimal Operation Strategy of Electricity-Hydrogen Regional Energy System under Carbon-Electricity Market Trading[J]. Energy Engineering121(3): 619-641, (2024).
7. Wang Hui, Zhou Kerui, Wu Zuohui ,et al. Multi-time scale optimal scheduling of integrated energy system coupling power-to-gas and carbon capture system[J]. Proceedings of the Electr. Power57(08):214-226, (2024).
8. Wu Yong, Lv Lin, Xu Lixiong ,et al. Optimized allocation of various energy storage capacities in a multi-energy micro-grid considering electrical/thermal/gas coupling demand response[J]. Proceedings of the PSPC48(16):1-10, (2020).
9. Ma Yiming, Wang Haixin, Hong Feng ,et al. Modeling and optimization of combined heat and power with power - to - gas and carbon capture system in integrated energy system[J]. Energy236:121392, (2021).
10. Wang Zhi, Tao Hongjun, Cai Wenkui ,et al. Study on the multitime scale rolling optimization operation of a near-zero energy building energy supply system[J]. Energy Conversion and Management270: 116255, (2022).
11. Li Peng, Wang Zixuan, Wang Jiahao ,et al. Two-stage optimal operation of integrated energy system considering multiple uncertainties and integrated demand response[J]. Energy225:120256, (2021).
12. Wang Zhewei, Du Banghua, Li Yang ,et al. Multi-time scale scheduling optimization of integrated energy systems considering seasonal hydrogen utilization and multiple demand responses[J]. International Journal of Hydrogen Energy67: 728-749, (2024).
13. Yan Ning, Zhao Zhenjie, Li Xiangjun ,et al. Multi-time scales low-carbon economic dispatch of integrated energy system considering hydrogen and electricity complementary energy storage[J]. Journal of Energy Storage104:114514, (2024).
14. Zhao Yuyang, Wei Yifan, Tang Yifan ,et al. Multi-objective robust dynamic pricing and operation strategy optimization for integrated energy system based on stackelberg game[J]. International Journal of Hydrogen Energy83:826-841, (2024).
15. Li Yunzhi, Liu Jizhen, Hu Yang ,et al. Multi-time-scale Source-Load Interaction Optimal Scheduling for Integrated Energy Systems Considering Low-Carbon Response[J]. Proceedings of the Acta Energ. Sol. Sin45 (11): 84-98, (2024).
16. Huo Shasha, Li Qi, Pu Yuchen ,et al. Low carbon dispatch method for hydrogen-containing integrated energy system considering seasonal carbon trading and energy sharing mechanism[J]. Energy308:132794, (2024).

013 电力系统混合振荡源定位的模态耗散能量流方法

李震宇[1]，王炜宇[1]，陈春[1]

（1. 长沙理工大学电气与信息工程学院（电网防灾减灾全国重点实验室），湖南省 长沙市 410114）

Hybrid Oscillation Source Location in Power Systems Using Modal Dissipating Energy Flow

LI Zhenyu[1]，WANG Weiyu[1]，Chen Chun[1]

(1. School of Electrical and Information Engineering, Changsha University of Science and Technology, Changsha 410000, Hunan Province, China)

ABSTRACT: With the widespread integration of renewable energy and power electronic devices, complex interactions between devices with different dynamic characteristics often lead to wideband oscillations caused by multiple frequency bands and oscillation sources. Timely identification and elimination of the oscillation sources is key to preventing the expansion of oscillation incidents. To address this, this paper proposes a hybrid oscillation source localization method based on Modal Dissipating Energy Flow (MDEF). First, Koopman operator theory is introduced to identify the equivalent linear model of the power system from measurement data. Based on this, key oscillation modes are selected, and spectral decomposition of the measurement data is performed based on the modal information of the system. The data components corresponding to the key oscillation modes are extracted, and the modal dissipating energy flow is calculated to quantify the influence of each device on the system's oscillations, thereby achieving hybrid oscillation source localization. The proposed method is validated through simulations on a DIgSILENT/PowerFactory platform using an IEEE 39-bus system with Grid-Forming Converters (GFM). The results show that the method can accurately locate the oscillation sources and determine their dominant oscillation frequencies in scenarios with multiple frequency bands and oscillation sources.

KEY WORDS: Oscillation source location; Koopman operator; Model identification; Dissipating energy flow; Modal analysis; Wideband oscillations

摘要：随着新能源与电力电子设备的广泛接入，具有不同动态特性的设备之间存在复杂的交互作用，易引发多频段、多振荡源的宽频振荡，及时确定并切除振荡源是抑制振荡事故扩大的关键。为此本文提出一种基于模态耗散能量流(Modal dissipating energy flow，MDEF)的混合振荡源定位方法。首先，引入 Koopman 算子技术，通过量测数据辨识电力系统的等效线性模型；在此基础上，筛选关键振荡模态，并基于系统的模态信息对量测数据进行谱分解，提取关键振荡模态对应的数据分量，进而计算模态耗散能量流，量化各设备对电力系统振荡的影响，实现混合振荡源定位。本文在 DIgSLENT/PowerFactory 平台上搭建了含构网型变流器(Grid-forming converter，GFM)的 IEEE 39 母线系统，对所提方法进行仿真验证。结果表明，该方法能够在多频段、多振荡源的场景下准确定位振荡源以及确定其主导振荡频率。

关键词：振荡源定位；Koopman 算子；模型辨识；耗散能量流；模态分析；宽频振荡

DOI：

0 引言

在我国的双碳(“碳达峰·碳中和”)目标下，电力系统逐渐向风电、光伏等新能源为主导的新型电力系统转型[1-3]。新型电力系统呈现出“双高”(高比例新能源与高比例电力电子)的特性，与传统电力系统相比，具有多时间尺度(宽频带)动态响应特性、惯量低等特点[4,5]。由于新型电力系统中具有不同时间尺度动态特性的设备之间存在复杂交互作用，“双高”系统中易引起几 Hz 到几 kHz 的宽频振荡[6]，严重影响电力系统的安全稳定运行，因此，在振荡发生时需要快速、准确定位振荡源并切除，从而抑制振荡扩散，引发连锁故障[7,8]。因此，如何迅速准确地识别振荡源位置，是电力系统宽频振荡抑制的首要任务[9]。

目前，随着广域测量系统(Wide area measurement system，WAMS)与同步测量单元(Synchrophasor measurement unit，PMU)的发展，基

于在线量测数据的振荡源定位技术得到了快速发展[10-13]，主要的振荡源定位方法有耗散能量流法、阻尼转矩法与行波法等[14-17]。阻尼转矩法通过分析各机组的阻尼特性，计算各机组的阻尼转矩系数，将阻尼转矩系数为负的机组判定为振荡源，但阻尼转矩法的准确性依赖详细的系统模型，模型结构、参数误差会对分析结果造成较大影响。行波法利用机电波传播原理来定位振荡源，但是需要 PMU 高精度的行波到达时间，由于网络中非恒定波速的影响以及实际应用中不同网络拓扑的独立性，导致振荡源识别误差较大。

近年来，耗散能量流法凭借数据驱动模式、对系统模型依赖度低、物理意义明确及高定位精度，已成为电力系统振荡源定位的主流方式。传统的时域耗散能量流法通过在时域计算各设备的振荡能量流实现振荡源定位，但是不具备频谱分辨能力，无法判定振荡所处的主导频率[18]。文献[19]提出一种基于频域信息的振荡源定位方法，该方法利用快速傅立叶变换计算电压幅值和相位与有功功率和无功功率信号的交叉功率谱密度(Cross-power spectral density，CPSD)，以 CPSD 的最大正虚部为判据定位振荡源，实现了在频率上的振荡源定位。文献[20]提出了一种基于小波耗散能量谱(Wavelet dissipation energy spectrum，WDES)的电力系统强迫振荡源频域定位方法，将电力系统广域测量信息进行连续小波变换(Continous wavelet transform，CWT)，计算小波耗散能量谱，根据小波耗散能量谱定位振荡源，并由小波耗散能量谱的跃变特性确定系统的强迫振荡频率。上述方法虽然能实现多频段、多振荡源的振荡源定位，但当系统中同时存在多个振荡源且其主导振荡频率接近时，可能导致能量谱出现混叠现象，影响振荡源定位的准确性。

综上，如何实现振荡源的精准分频段定位并同步识别其主导频率，是当前亟待解决的核心问题。为此，本文提出一种基于模态耗散能量流(Modal dissipating energy flow，MDEF)的混合振荡源定位方法。首先，引入 Koopman 算子技术辨识电力系统的等效线性模型；然后，对等效线性模型进行模态分析，得到各模态特征值与阻尼比，并筛选出关键振荡模态；进一步，对各个振荡模态的量测数据进行谱分解获得模态分量，并根据得到的模态分量计算该振荡模态下的模态耗散能量流，定量分析各设备对电力系统振荡的影响，从而定位该振荡模态下的振荡源。本文在 DIgSILENT 中构建了含构网型变流器(Grid-forming converter，GFM)的 IEEE 39 母线系统模型，并对所提方法的有效性与准确性进行验证。

1 耗散能量流振荡源定位原理

在电力系统发生振荡期间设备之间伴随着能量交互，振荡源向电力系统注入振荡能量，非振荡源耗散电力系统的振荡能量。可以计算设备的耗散振荡能量流来定位振荡源，由节点 i 流向节点 j 的耗散能量流可以用 P、Q、V、f 量测数据进行计算，即

$$E_{ij}=\int\left(\Delta P_{ij}2\pi\Delta f_j\,dt+\Delta Q_{ij}\,d(\Delta\ln V_i)\right) \tag{1}$$

式中，ΔP_{ij} 和 ΔQ_{ij} 分别是由节点 i 流向节点 j 上有功和无功功率的变化量；$\Delta\ln V_i$ 和 Δf_i 表示节点 i 处的电压幅值对数和频率与稳态值的偏差。

以功率输出的方向作为参考方向，当节点 i 流向节点 j 的耗散能量流 E_{ij} 为正，该节点发出振荡能量，在该节点下的设备判定为振荡源；当节点 i 流向节点 j 的耗散能量流 E_{ij} 为负，该节点吸收振荡能量，在该节点下的设备判定为非振荡源。

2 基于 Koopman 算子的等效线性模型构建

本节将介绍基于电力系统量测数据的 Koopman 等效线性模型辨识方法。Koopman 算子是一种无限维线性算子，它可以将非线性动力学问题转到无限维线性空间，借助强大的线性系统分析工具分析复杂的非线性动力学问题。根据式(1)，计算耗散能量流需要电压幅值的对数 $\ln V$，而实际测量数据为电压幅值 V，对实测电压幅值 V 对数处理，处理后的量测数据为

$$\mathbf{x}_k=\left[P_1,Q_1,\ln V_1,f_1,\ldots,P_n,Q_n,\ln V_n,f_n\right]^T \tag{2}$$

式中，x_k 是电力系统中的测量数据。

则电力系统演化可表达为

$$\mathbf{x}_{k+1}=\mathbf{F}(\mathbf{x}_k) \tag{3}$$

式中，$\mathbf{F}(\mathrm{x}_k)$为非线性离散函数。

对非线性系统 $\mathbf{F}(\mathrm{x}_k)$通过一组可观测函数 $\mathbf{g}(\mathbf{x}_k)$提升到高维可观测空间，基于 Koopman 算子系统演化如图 1。在这个空间中，系统的演化由 Koopman 线性算子 $\mathbf{K}$ 控制，即

$$\mathbf{K}\mathbf{g}(\mathbf{x}_k)=\mathbf{g}(\mathbf{F}(\mathbf{x}_k))=\mathbf{g}(\mathbf{x}_{k+1}) \tag{4}$$

Koopman 算子需要在无穷维线性空间对系统进行分析，但是实际中无法构建无穷维观测函数。在实际应用中 Koopman 算子可以近似为一个有限维线性算子，通过一组有限的可观测函数 $\mathbf{g}(\mathrm{x})$，将原始测量值提升到更高维的空间，形成一个新的增广数据集 $L(\mathrm{x})$

$$L(\mathbf{x})=[\mathbf{x}^T\quad\mathbf{g}(\mathbf{x})^T]^T \tag{5}$$

式中，**g**(x)为包括多项式函数、三角函数、Thinplate径向函数等构成的观测函数。

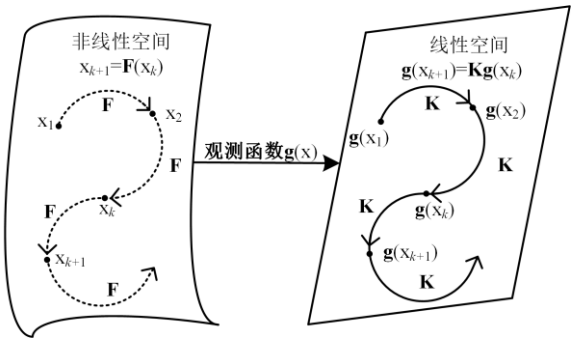


图 1　基于 Koopman 算子系统演化过程

Fig. 1　System evolution under the Koopman operator framework

为反映电力系统在高维线性空间的演进动态，构建出两个子矩阵，即

$$L(\mathrm{x})=\begin{bmatrix}\vdots & \vdots & & \vdots\\ L_1(\mathrm{x}) & L_2(\mathrm{x}) & \cdots & L_{b-1}(\mathrm{x})\\ \vdots & \vdots & & \vdots\end{bmatrix}$$
$$L'(\mathrm{x})=\begin{bmatrix}\vdots & \vdots & & \vdots\\ L_2(\mathrm{x}) & L_3(\mathrm{x}) & \cdots & L_b(\mathrm{x})\\ \vdots & \vdots & & \vdots\end{bmatrix} \tag{6}$$

为了获得 Koopman 算子 **K**，对 L 应用奇异值分解以降低维度

$$L\approx\mathbf{U}\mathbf{\Sigma}\mathbf{V}^{*} \tag{7}$$

式中，‘*’表示共轭转置，奇异值对角矩阵，**U**，**V** 分别是左、右奇异向量酉矩阵。

保留前 n 个奇异值较大分量，构造对应截断后的奇异值矩阵，有限维 Koopman 近似算子可以构造为

$$\tilde{\mathbf{K}}=\mathbf{U}_n^{*}L'\mathbf{V}_n\mathbf{\Sigma}_n^{-1} \tag{8}$$

式中，$\tilde{\mathbf{K}}$ 代表有限维 Koopman 近似算子。

3　等效线性电力系统模态分析

在得到有限维等效线性模型后，可对 Koopman 等效线性系统进行模态分析，找出少量真正关键的振荡模态，为后续不同频率的振荡源定位奠定基础。

由于有限维 Koopman 近似算子 $\tilde{\mathbf{K}}$ 为线性模型，因此满足

$$\tilde{\mathbf{K}}\mathbf{\Phi}_i=\lambda_i\mathbf{\Phi}_i \tag{9}$$

式中，λ_i 和 $\mathbf{\Phi}_k$ 分别为第 i 个特征值和特征向量。

根据特征值和特征向量，在 k 时刻，反映系统演进动态的可观测函数 **g**(x)可表示为

$$\mathbf{g}_k(\mathrm{x})=\sum_{i=1}^{n}\lambda_i^k\mathbf{\Phi}_i p_i \tag{10}$$

式中，p_i 是第 i 个 Koopman 模态的激发情况，由系统的初始条件确定。

设 **g**(x)是原始测量值 x，在 k 时刻，第 j 个测量值 $x_{j,\,k}$ 可以表示为

$$x_{j,k}=\lambda_1^k\mathbf{\Phi}_{j1}p_1+\lambda_2^k\mathbf{\Phi}_{j2}p_2+\cdots\lambda_i^k\mathbf{\Phi}_{ji}p_i+\cdots+\lambda_n^k\mathbf{\Phi}_{jn}p_n \tag{11}$$

式中，$\mathbf{\Phi}_{ji}$ 表示第 j 个测量值中 Koopman 近似算子第 i 个特征向量。

设电力系统有 b 个设备，将特征向量分为 b 块，即

$$\mathbf{\Phi}=\left[\mathbf{\Phi}_1,\mathbf{\Phi}_2,\ldots,\mathbf{\Phi}_{\mathrm{a}},\ldots,\mathbf{\Phi}_b\right]^{\top} \tag{12}$$

式中，b 为电力系统设备的个数；$\mathbf{\Phi}_a$ 为设备 a 的特征向量。

通过式(11)得到每个测量轨迹的模态分量，这些模态分量可用于计算每个设备的耗散能量流。在第 i 个模态下、k 时刻、设备 a 测量值的模态分量可表示为

$$\begin{cases}P_{ai,k}=\lambda_i^k\mathbf{\Phi}_{a1,i}p_i\\ Q_{ai,k}=\lambda_i^k\mathbf{\Phi}_{a2,i}p_i\\ \ln V_{ai,k}=\lambda_i^k\mathbf{\Phi}_{a3,i}p_i\\ f_{ai,k}=\lambda_i^k\mathbf{\Phi}_{a4,i}p_i\end{cases} \tag{13}$$

式中，P、Q、$\ln V$、f 分别为设备 a 的有功功率、无功功率、电压幅值的对数与频率。角标 a_1、a_2、a_3、a_4 分别为在特征向量矩阵中设备 a 的 P、Q、$\ln V$ 和 f 对应的行。

为了筛选关键模态，将 Koopman 有限维线性近似算子 $\tilde{\mathbf{K}}$ 的离散特征值 λ_i 转换为连续的特征值 μ_i，即

$$\mu_i=\frac{\ln(\lambda_i)}{\Delta t} \tag{14}$$

式中，Δt 是采样间隔。

将阻尼比小于某一阈值的振荡模态定为振荡模态，即

$$S_\omega=\{\mu_i\in C:\xi_i<\xi_t,i=1,2,\ldots,n\} \tag{15}$$

式中，S_ω 是振荡模态的集合；ξ_i 是阻尼比；ξ_t 是阻尼比阈值，本文取 0.01。

4　混合振荡源定位

在振荡模态集合上，进行设备级别的振荡源的定位。基于式(12)得到的模态分量(P、Q、$\ln V$ 和 f)，第 i 个模态下的设备 a 的耗散能量流可以表示为

$$E_{ai}=\int\left(\Delta P_{ai}\cdot 2\pi\Delta f_{ai}dt+\Delta Q_{ai}d(\Delta\ln V_{ai})\right) \tag{16}$$

式中，ΔP_{ai} 和 ΔQ_{ai} 分别是模态 i 下设备 a 有功功率和无功功率与稳态值的偏差；$\Delta\ln V_{ai}$ 和 Δf_{ai} 表示模态

i 下设备 a 电压幅值的对数和频率与稳态值的偏差。E_{ai} 表示模态 i 下设备 a 的耗散能流。

为定量分析各设备对系统振荡的影响，以设备功率输出的方向作为参考方向，计算振荡时间内各设备耗散能量流的积分，即

$$\begin{cases} I_{a,i}=\int_{t_0}^{t_1}E_{a,i}(t)dt\approx\sum_{k=1}^{N}E_{a,i}(k)\Delta t \\ I_{a,i}^{+}=\max\left(I_{a,i},0\right), \end{cases} \tag{17}$$

式中，$I_{a,i}$ 为 a 设备耗散能量流的积分；$I_{a,i}^{+}$ 为设备正向耗散能量流的积分；Δt 是采样间隔。

取设备正向耗散能量流的积分，计算所有设备在振荡模态 i 下的相对贡献度，即

$$s_{a,i}=I_{a,i}^{+}\left(\sum_{k=1}^{b}I_{k,i}^{+}\right)^{-1} \tag{18}$$

式中，$s_{a,i}$ 表示模态 i 下设备 a 在电力系统正向耗散能量流的占比。

正向耗散能量流的占比超过振荡模态 i 下全部正向耗散能量流的 15%的设备为振荡源，即满足

$$s_{a,i}\geq 0.15 \tag{19}$$

综上，本文所提的基于模态耗散能量流的混合振荡源定位方法的流程如图 2。

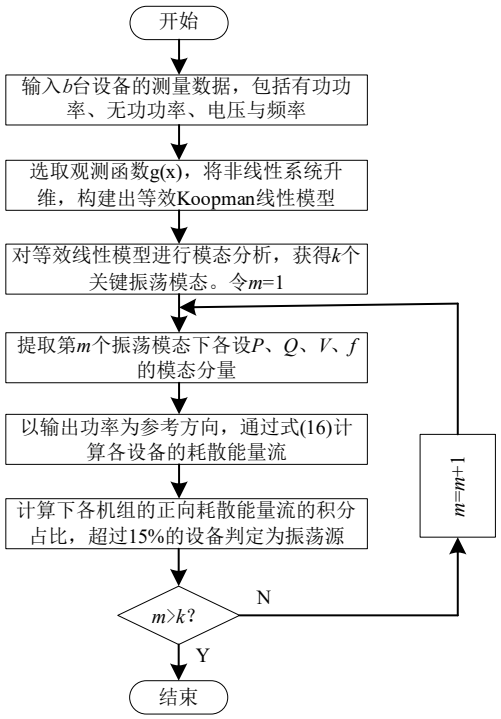


图 2　模态耗散能量流的混合振荡源定位方法流程图

Fig. 2　Flow chart of the hybrid oscillation-source localization method based on MDEF

5　仿真分析

本文以 IEEE39 母线系统为基础，在 10 号母线和 29 号母线接入大容量构网型储能系统 GFM3 和 GFM9，代替发电机组 G3、G9，系统拓扑如图 3 所示，采用 DIgSLENT/ PowerFactory 进行仿真验证。

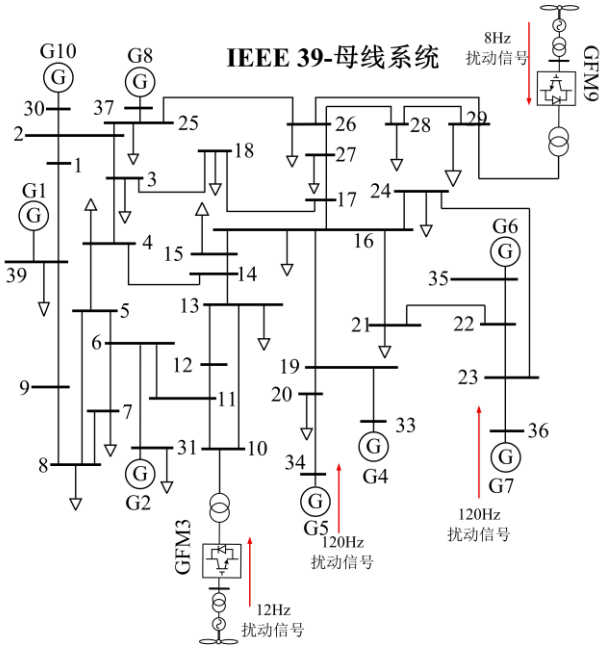


图 3　含构网型储能的 IEEE39 母线系统

Fig. 3　IEEE 39-Bus New England System With Grid-Forming Energy Storage

为验证所提方法对多频强迫振荡源定位的有效性，对该系统注入四个扰动信号，分别为：(1)构网型储能 GFM3 的 12Hz 扰动信号；(2)GFM9 的 8Hz 扰动信号；(3)发电机组 G5 的 120Hz 扰动信号；(4)G7 的 120Hz 扰动信号。仿真步长为 0.001 s，仿真时长为 20 s。

在本次仿真中，阻尼比低于 0.01 的模态(式(14)中的 $\xi=0.01$)被选为振荡模态，可以观察到 3 个振荡模态，分别为 119.99Hz，12.00Hz，8.00Hz 的振荡模态，作为为 GFM3，GFM9，G5 和 G7 的振荡模态，如表 1 所示。

表 1　振荡模态

Table 1　Oscillatory Mode

模态	特征值	阻尼比	频率（Hz）
1	-0.064+753.89i	$8.447e^{-5}$	119.99
2	-0.00015+75.39i	$1.992e^{-6}$	12.00
3	-0.0022+50.26i	$4.379e^{-5}$	8.00

为验证 Koopman 线性模型的准确性，以 GFM3 为例，给出了 GFM3 在 5-8s 时间段内原始轨迹与 Koopman 预测轨迹做出对比，如图 4 所示。

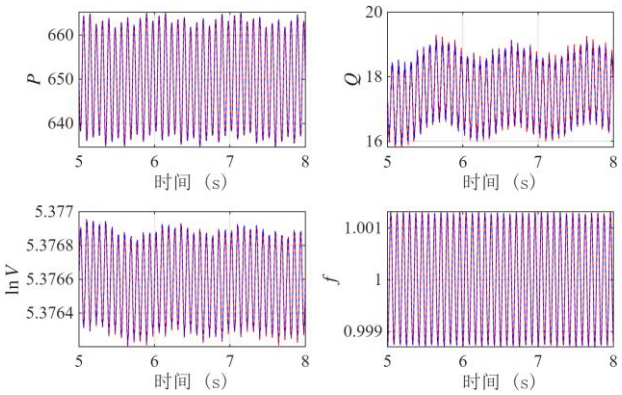
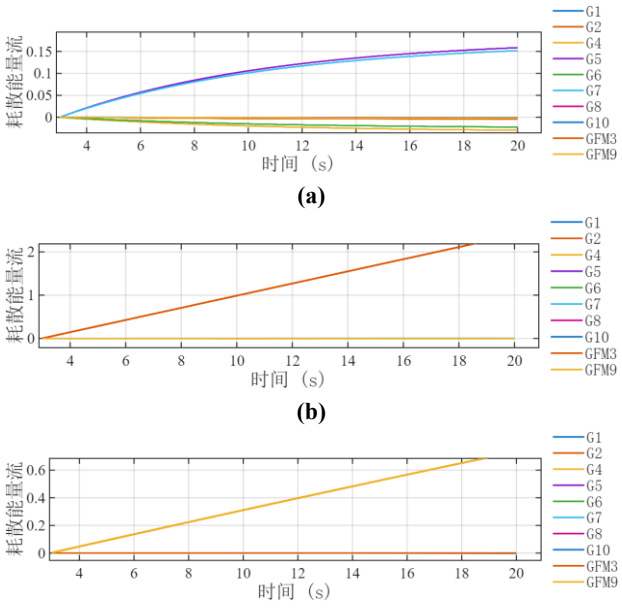


图 4　测量轨迹与 Koopman 预测轨迹对比

Fig. 4　Comparison Between Measured and Koopman Prediction Trajectory

根据式(12)，可以从量测数据中提取出各个设备在振荡模态下的有功功率、无功功率、电压幅值的对数以及频率，从而通过式(15)计算每个设备在每个振荡模态下的耗散能量流。各设备在每个振荡模态下的耗散能量流如图 5 所示，各设备在每个振荡模态下正向耗散能量流的积分占比如表 2 所示。



(a)

(b)

(c)

图 5　振荡模态下的各设备的振荡能量流

Fig. 5　Oscillatory Energy Flow Across Devices for the Oscillatory Mode

表 2　各设备正向耗散能量流的积分占比

Table 2　Proportional Integral of Positive Dissipating Energy Flow for Each Device

设备	各设备正向耗散能量流积分的占比		
	模态 1	模态 2	模态 3
G1	0	0	0
G2	0	0	0
G4	0	0.065%	0.038%
G5	51.09%	0	0
G6	0	0	0.051%
G7	49.91%	0.059%	0
G8	0	0	0
G10	0	0.044%	0
GFM3	0	99.87%	0
GFM9	0	0	99.91%

在图 5(a)中，在振荡模态 1 中 G5 与 G7 将振荡能量注入到系统中，且 G5 与 G7 的正向耗散能量流积分占比分别为 51.09%与 49.91%，均超过式(19)的阈值 15%，而其他设备消耗或不注入振荡能量，因此可以得到 G5 与 G7 为振荡模态 1 的 120Hz 振荡源。类似地，在图 5(b)中，GFM3 为振荡模态 2 的 12Hz 振荡源；在图 5(c)中，GFM9 为振荡模态 3 的 8Hz 振荡源。

因此，所提出的方法成功为将 GFM3 识别为振荡模态 2 的 15Hz 振荡源；GFM9 识别为振荡模态 3 的 8Hz 振荡源；G5 与 G7 识别为振荡模态 1 的 120Hz 振荡源，这与扰动信号注入的位置一致。

6　结论

本文提出一种基于模态耗散能量流的混合振荡源定位方法，引入 Koopman 算子技术辨识电力系统等效线性模型，随后对等效的线性模态分析得到关键振荡模态，从而在振荡模态下计算各设备的耗散能量流，量化各设备对系统振荡的影响，直观地展示定位振荡源的结果。最后，在含构网型储能的 IEEE39 母线系统上搭建多频率、多振荡源的仿真场景，仿真结果表明，所提的方法能够准确识别各振荡源以及确定其主导振荡频率。

本文所提方法与量测数据紧密相关，后续工作将重点在含噪声环境及实际 PMU/WAMS 测量条件下开展研究。

参考文献

[1] 韩肖清,李廷钧,张东霞,等. 双碳目标下的新型电力系统规划新问题及关键技术[J]. 高电压技术,2021,47(9): 3036-3046.

[2] 胡博,谢开贵,邵常政,等. 双碳目标下新型电力系统风险评述：特征、指标及评估方法[J]. 电力系统自动化,2023,47(5): 1-15.

[3] 任大伟,肖晋宇,侯金鸣,等. 双碳目标下我国新型电力系统的构建与演变研究[J]. 电网技术,2022,46(10): 3831-3839.

[4] 谢小荣,贺静波,毛航银,等. “双高”电力系统稳定性的新问题及分类探讨[J]. 中国电机工程学报,2021,41: 461-475.

[5] 张子扬,张宁,杜尔顺,等. 双高电力系统频率安全问题评述及其应对措施[J]. 中国电机工程学报,2022,42(1): 1-25. 杨浩,冯双,孙健萍,等. 基于电磁波理论的电力系统宽频振荡传播特性分析方法[J]. 电网与清洁能源,2025,41(6): 20-30.

[6] 马宁宁,谢小荣,贺静波,等. 高比例新能源和电力电子设备电力系统的宽频振荡研究综述[J]. 中国电机工程学报,2020,40: 4720-4732.

[7] 衣立东,马宁宁,丁茂生,等. 新型电力系统宽频振荡防控体系架构[J]. 电网技术,2023,47(10): 4092-4102.

[8] 杨浩,冯双,孙健萍,等. 基于电磁波理论的电力系统宽频振荡传播特性分析方法[J]. 电网与清洁能源,2025,41(6): 20-30.

[9] Xu, Yanhui,Cheng,et al. A Criterion for Oscillation Source

Localization with IBRs Based on Sub-synchronous Frequency Component of Instantaneous Power[J]. IEEE Transactions on Power Systems,2024,Vol.39(6): 1-13.

[10] Wilsun Xu,Jing Yong,Horacio J. Marquez,et al. Interharmonic Power – A New Concept for Power System Oscillation Source Location[J]. IEEE Transactions on Power Systems,2025: 1-13.

[11] Maslennikov, Slava. Enhancing the Efficiency of Locating the Oscillation Source[J]. IEEE Transactions on Power Systems,2024,Vol.39(6): 1-9.

[12] Yufan He,Wenjuan DuCA1,Qiang Fu,et al. A model-free method to detect the risk and locate the sources of sub-synchronous oscillations in a large-scale renewable power system[J]. International Journal of Electrical Power & Energy Systems,2025,Vol.165: 110460.

[12] Guowei Cai,Lei Xuan,Zhenglong SunCA1,et al. Ambient data-based online identification and location of frequency oscillations[J]. International Journal of Electrical Power & Energy Systems,2024,Vol.157: 109843

[14] Yunfei Chen,Ziyu Fan,David Gregory,et al. A Survey of Oscillation Localization Techniques in Power Systems[J]. IEEE Access,2025,Vol.13: 28836-28860.

[15] 刘芳,彭宇恒,刘乾易,等. 基于振荡模态辨识的负阻尼振荡故障源定位方法[J]. 电力系统保护与控制,2025,53(9): 60-69.

[16] 李阳海,黄莹,刘巨,等.基于阻尼转矩分析的电力系统低频振荡源定位[J].电力系统保护与控制,2015,43(14):84-91.

[17] Samreen Javaid,Dongyu LiCA1,Abhisek Ukil. High pass filter based traveling wave method for fault location in VSC-Interfaced HVDC system[J]. Electric Power Systems Research,2024,Vol.228: 110004.

[18] Jing Ma,Yongxin Zhang,Yaqi Shen,et al. Equipment-Level Locating of Low Frequency Oscillating Source in Power System With DFIG Integration Based on Dynamic Energy Flow[J]. IEEE Transactions on Power Systems,2020,Vol.35(5): 3433-3447.

[19] Denis Osipov,Stavros Konstantinopoulos,Joe H. Chow. A Cross-Power Spectral Density Method for Locating Oscillation Sources Using Synchrophasor Measurements[J]. IEEE Transactions on Power Systems,2023,Vol.38(6): 5526-5534.

[20] 姜涛,高淦,李筱静,等. 基于小波耗散能量谱的电力系统强迫振荡源定位[J]. 电工技术学报,2023,38(7): 1737-1750.

014 一种微电网分层能量协调控制策略研究

（上海科梁信息科技股份有限公司， 上海市 200233）

魏明洋，赵玉伟

Research on a Hierarchical Energy Coordination Control Strategy for Microgrids

WEI Mingyang, ZHAO Yuwei

(Shanghai KeLiang Information Technology Co., Ltd, Shanghai, 200233, China)

ABSTRACT: For microgrid systems with a high proportion of photovoltaic (PV) integration, this paper proposes a hierarchical multi-mode energy management control strategy. The system consists of diesel generators, PV arrays, battery storage, and loads, adopting a two-layer architecture of the main grid and sub-microgrids. Three operation modes adapted to different operating states and their smooth switching logic are designed, and a hierarchical PV consumption control logic is established. Simulation results demonstrate that the proposed control strategy significantly improves the PV consumption rate and enables smooth transitions between various control modes, ensuring stable system operation.

KEY WORDS: Microgrid; Energy Management; Photovoltaic Consumption; Mode Switching; Hierarchical Control

摘要：针对高比例光伏接入的微电网系统，本文提出一种分层多模式能量管理控制策略。系统由柴油发电机、光伏阵列、储能电池及负荷构成，采用主网与子微网双层架构。设计了适应不同运行状态的三种运行模式及其平滑切换逻辑，并建立了分层光伏消纳控制逻辑。仿真结果表明，所提控制策略显著提升了光伏消纳率，并能够对各种控制方式进行平滑切换，保证了系统稳定运行。

关键词：微电网；能量管理；光伏消纳率；模式切换；分层控制

DOI：10.13335/j.1000-3673.pst.2014.01.论文序号

0 引言

随着电网发展向更加安全、智能、高效、可靠、绿色方向转变，包含光伏、风机、柴油发电机、储能的微电网正在快速发展，研究开发绿色清洁的可再生能源已成为世界各国的能源发展战略和技术方向。高比例光伏接入微电网在多时间尺度能量管理以及灵活应对运行状态变化方面面临挑战，从世界可再生能源的利用与发展趋势看，光伏发电是目前应用最为广泛的可再生能源发电技术并得到了飞速发展和广泛应用。然而，光伏间歇性电源固有的随机性和间歇性特点，导致其规模化接入对电网发电调度、调峰调频和备用容量规划等方面带来很大挑战，同时还会对电网的安全稳定运行和电能质量带来不利影响。

为了有效解决上述微电网存在的问题，对微电网能量分配的研究已成为当前电力行业的研究热点和发展趋势[1-4]。本文提出一种基于状态判据的多模式运行策略及其切换逻辑，旨在无缝衔接不同运行需求，提升系统灵活性。针对消纳优化目标，设计了主-子微网层级间的光伏消纳率协同计算与跟踪机制，以协调局部与全局消纳目标。探索在提升光伏就地消纳能力的同时，兼顾系统稳定运行的协调控制方法。

1 系统结构

1.1 主回路拓扑

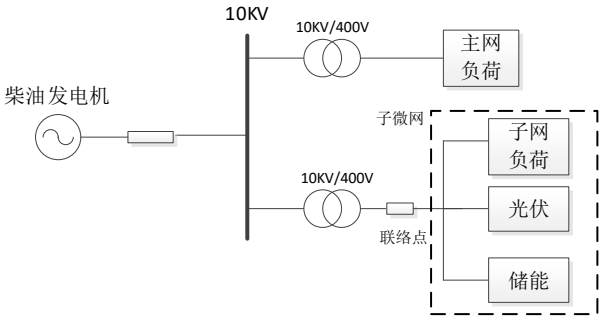


图 1 微电网系统结构图

微电网系统包括主网架，柴油发电机、变压器、负荷、光伏发电系统、储能系统组成。主网架分为两个电压等级：400V 母线和 10kV 母线。其中柴油发电机通过传输线接入 10kV 交流母线，子微网内部包含光伏发电系统、储能系统、本地负荷等组成的微电网，子微网既可以与外部电网并列运行，也可以孤岛运行，单独为本地负荷供电。

各设备的额定功率如下表 1 所示。

表 1 设备额定功率

设备	额定功率
柴油发电机	300kW
光伏发电单元	300kW
储能	100kW
主网负荷	350 kW
子微网负荷	250kW

1.2 柴油发电机单元

柴油发电机包括励磁系统，柴油发电机动力部分及调节器、同步机和自动准同期装置组成，柴油发电机模型如图 2 所示，柴油发电机参数界面如图 3 所示。

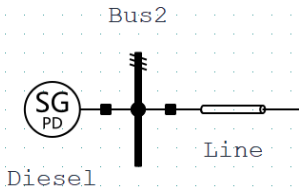


图 2 柴油发电机模型

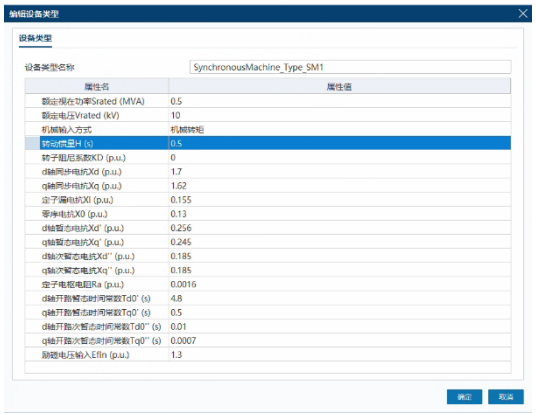


图 3 柴油发电机参数界面

1.3 光伏发电单元

光伏发电的主电路采用双级式结构，即光伏阵列的输出端通过电容器连接到逆变器的直流侧，逆变器再通过滤波器接到母线上，如下图 4 所示：

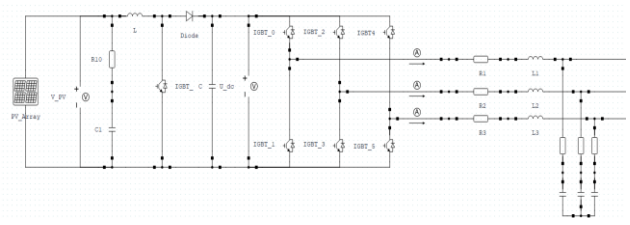


图 4 光伏发电主电路模型

1.3.1 光伏阵列建模

根据光伏电池板的输出特性搭建光伏阵列模型，光伏电池板参数如表 2 所示。

表 2 光伏板参数

技术参数	数值	单位
开路电压	37.5	V
短路电流	15	A
最大功率点电压	29.6	V
最大功率点电流	8.28	A
光伏电池串联数	28	/
光伏电池并联数	44	/
光照强度	1000	W/h
环境温度	35	℃

1.3.2 光伏并网控制建模

两极式非隔离型光伏并网系统分前后两极控制。对光伏组件的最大功率跟踪控制（MPPT）在前级 Boost 升压部分实现，对并网电流的控制在后级 DC-AC 逆变部分实现。MPPT 控制策略从本质上来讲是一种通过调节外部负载阻抗，使其能与光伏组件所输出阻抗相匹配，从而实现光伏组件最大功率输出的自寻优控制策略[5-6]。

本文采用基于电导增量法的最大功率跟踪控制，对光伏电池 P-U 特性曲线进行一阶求导，一阶求导为零的点即为光伏电池的最大功率点。

1.4 储能单元

1.4.1 电池单元建模

电池模型采用 SimuNPS 软件中自带电池模块，电池类型为锂离子电池，电池主要参数如下表 3 所示。

表 3 电池参数

名称	取值	单位
标称电压 Vnom	810	V
截止电压 Voff	750	V
充满电压	850	V
额定容量	100	Ah
额定电压下容量	90	Ah
电池内阻	0.0133	Ω

1.4.2 储能换流器建模

储能换流器采用三相二电平拓扑，直流侧为电池，离网运行时，换流器可通过 VSG 控制对负载提供交流电压支撑，并网运行时，通过设置 VSG 控制功率参考值的正负，可实现电流充电或放电。

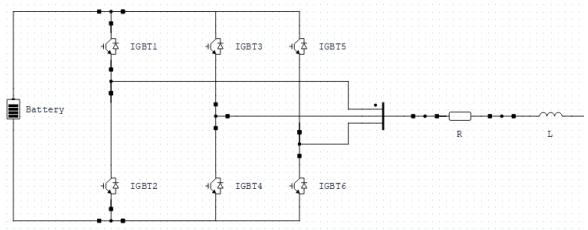


图 5 储能双向换流器

表 4 储能换流器关键器件参数

名称	数值
交流额定电压	400V
额定功率	100kVA
直流侧电压	800V
滤波电感	2mH
滤波电容	10uF

1.4.3 储能换流器控制策略设计

目前 VSG 控制研究以同步发电机经典的 2 阶模型为主，主要包括电磁部分与机械运动部分[7-10]。机械运动方程反映了虚拟同步机的转子惯性以及阻尼特征，目前针对机械部分的建模较为统一，主要利用转子运动方程来实现，通过引入转动惯量 J 和阻尼系数 D，使 VSG 控制在功率和频率动态变化过程中具有惯性和阻尼功率振荡的能力。总体控制框图如图 6 所示。

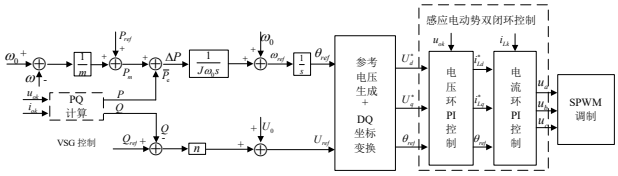


图 6 整体控制框图

1.4.3.1 并网预同步控制策略

并网预同步控制旨在实现逆变器输出与电网电压幅值、频率和相位的精确同步，从而降低并网时的冲击，提高系统稳定性。考虑在并网前换流器输出电压与电网电压幅值大小基本一致，因此，本设计只进行相位同步控制。根据电网电压相位与换流器输出电压相位的差，进行闭环 PI 控制，通过不断调整换流器输出电压相位，使并网前换流器输出电压相位与电网电压相位一致，从而实现相位同步并网。

通过锁相环（PLL）计算电网相位，根据电网电压相位与换流器输出电压相位差值进行 PI 闭环控制，使换流器输出电压相位与电网电压相位一致，相位差可通过以下公式计算：

$$\Delta\theta = \theta_{grid} - \theta_{vsg} \qquad (1)$$

1.4.3.2 换流器控制策略

换流器 VSG 控制输出的有功功率 Pe 和无功功率 Qe 可通过瞬时功率理论计算得到：

$$P_e = e_\alpha i_\alpha + e_\beta i_\beta \qquad (2)$$

$$Q_e = e_\beta i_\alpha - e_\alpha i_\beta \qquad (3)$$

其中，e_α 和 e_β 为逆变器桥臂中点电压的基波在 αβ 坐标系下的表达式，iα 和 iβ 为电感 L 中的电流在 αβ 坐标系下的表达式。

根据发电机的机械运动方程可以得到换流器运动方程表示为：

$$P_{ref} + D_p(\omega_n - \omega) - P_e \approx J\omega_n \frac{d\omega}{dt} = J\omega_n \frac{d^2\theta}{dt^2} \qquad (4)$$

式中：J 为 VSG 的转动惯量；w，w_n 分别为机械角速度和额定角速度，D_p 阻尼系数。J 使得功率和频率的动态过程中具有了惯性，阻尼系数 D_p 使换流器具有阻尼系统功率振荡的能力。

由 VSG 有功-频率控制框图，可以看出，VSG 的有功具有了同步发电机的惯性和一次调频特性。

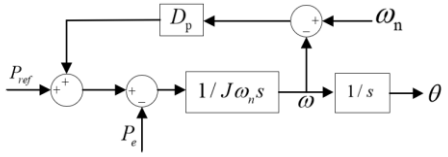


图 7 VSG 的有功-频率控制

电力系统中的电压与系统中的无功功率密切相关，根据无功功率与电压之间的关系，当励磁电势 E 数值一定时，输出的无功功率也一定，为保证系统的电压水平，系统中应有充足的无功电源。

同步发电机是电力系统中的主要无功电源，通过励磁控制器调节器无功输出，实现系统无功功率在并联运行的发电机组之间合理分配，从而维持系统无功平衡。VSG 控制中，励磁调节器设计的目的就是使虚拟同步发电机能够实现合理分配无功功率，从而维持系统电压的稳定。

根据同步发电机励磁控制器电压方程：

$$E_m = \frac{1}{K_s}\left[D_q(V_n - V_o) + (Q_{\text{ref}} - Q_e)\right] \qquad (5)$$

对于 VSG 控制来说，无功环只需要模拟同步发电机一次调压特性即可，因此，可以将励磁调节器的输出作为调制波电压的幅值。根据上式（5）可以画出 VSG 控制无功环的控制框图如图 8 所示。

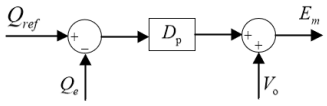


图 8 VSG 的无功环控制

1.4.3.3 双闭环控制

通过分析可知，VSG 的有功环和无功环模拟了同步发电机的特性，VSG 有功环的输出作为逆变器调制波的频率和相位，无功环的输出作为逆变器调制波的幅值，三相励磁电压参考值 e_{am}、e_{bm}、e_{cm}的表达式为：

$$\begin{cases} e_{am} = E_m \sin\theta \\ e_{bm} = E_m \sin(\theta - 120^0) \\ e_{cm} = E_m \sin(\theta + 120^0) \end{cases} \quad (6)$$

VSG 控制策略的目的就是通过控制使储能变换器输出电压与上述三相励磁电压一致。此过程后部分的控制为电压、电流双闭环控制，与跟网控制下的双闭环控制部分基本相似。

对上述式（6）的电压方程，在旋转坐标系下进行变换，得到旋转坐标系下电压方程为：

$$\begin{cases} U_d = (K_P + \dfrac{K_I}{s})(i_d^* - i_d) - \omega_0 L i_q + E_d \\ U_q = (K_P + \dfrac{K_I}{s})(i_q^* - i_q) + \omega_0 L i_d + E_q \end{cases} \quad (7)$$

进一步可得出u_d和u_q的控制方程为：

$$\begin{cases} u_{dref} = K_p(i_{dref} - i_d) + \dfrac{K_i}{S}(i_{dref} - i_d) - \omega L i_q + i_d R \\ u_{qref} = K_p(i_{qref} - i_q) + \dfrac{K_i}{S}(i_{qref} - i_q) + \omega L i_d + i_q R \end{cases} \quad (8)$$

通过上述公式可以构建出 VSG 控制的电压、电流双闭环解耦控制框图如下图 9 所示：

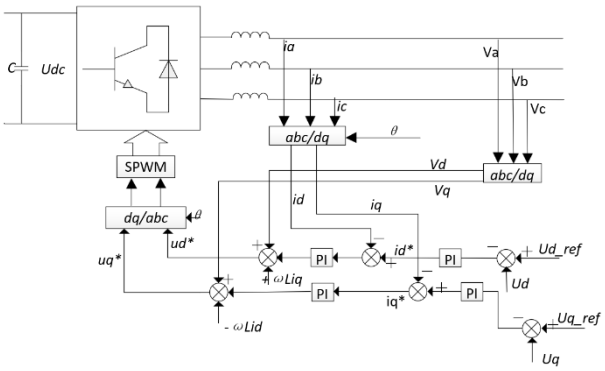


图 9 电压电流双闭环控制

2 微电网系统运行策略

微网能量管理策略分为上层微网能量管理策略（即主网能量管理策略）与子微网能量管理策略，上层微网能量管理仅接受调度指令并下发给下层子微网能量管理。

主网柴油发电机输出功率满足：

$$P_{DG} = P_{main_load} + P_{exchange} \quad (9)$$

式中，P_{DG}为柴油发电机功率，P_{main_load}为主网负荷功率，$P_{exchange}$为主子网交互功率。

子微网光伏与储能输出功率满足：

$$P_{PV} + P_{bat} = P_{sub_load} + P_{exchange} \quad (10)$$

式中，P_{PV}为光伏发电功率，P_{bat}为储能功率，P_{sub_load}为子微网本地负荷功率，$P_{exchange}$为主子网交互功率。

2.1 子微网能量管理策略

子微网接受上层微网控制指令，上层微网根据预测每隔固定时间给子微网发送功率指令，下层微网能量管理系统根据指令及当前光伏发电量、储能电池容量、负荷情况进行能量管理，合理对储能电池的 PCS 控制器分配充放电指令，然后 PCS 控制所属的储能电池逆变器进行充放电，当电池容量不足或已满，则不根据下发指令运行，需要投切发电机来调节储能电池的充放电，以达到最小弃光率。

（1）模式 1 功率服从模式

在功率服从模式下，子微网能量管理器的目标为：通过控制储能模块的功率，在满足本地负载的前提下，根据上层能量管理器下发的 P,Q 指令满足上层管理器的需求。储能充放电功率满足指令：

$$P_{bat} = P_{ref} - (P_{PV} - P_{sub_load}) \quad (11)$$

式中，P_{bat}为储能功率，P_{ref}为上层能量管理器下发的有功功率指令，P_{PV}为光伏发电功率，P_{sub_load}为子微网本地负荷功率。

该模式下需要满足的约束条件：储能 SOC≥30%且并网运行。

（2）模式 2 消纳服从模式

在消纳服从模式下，子微网能量管理器根据上层控制器的下发命令，改变光储系统的输出功率，从而改变用于本地负载与提供给上层电网的功率比例。满足“子微网光伏消纳率”与“主网光伏消纳率”。

定义主网消纳率指令α_{grid}，子微网本地消纳率β_{local}，储能功率补偿量P_{bat_ref}。

控制逻辑流程为：

1）主网下发消纳率指令 α_{grid}，子微网接收到指令后，根据当前子微网本地消纳率 β_{local} 计算出需要储能功率补偿量 P_{bat_ref}；

2）根据储能功率补充量指令，控制储能充放电，使得外送到主网上的功率满足主网消纳指令。

该模式下需要满足的约束条件：储能 30%≤SOC≤ 90%且并网运行。

（3）模式 3 子微网内部平衡模式

在内部平衡模式下，子微网能量管理器的目标为：通过控制储能模块的功率，不考虑上层能量管理器的需求，使子微网内部的发电与用电量达到平衡，从而减少能量交换。

该模式下需要满足的约束条件：储能 SOC< 30%或离网运行。子微网内部功率满足：

$$P_{PV} = P_{sub_load} + \Delta P_{bat} \quad (12)$$

式中，P_{PV} 为光伏发电功率，P_{sub_load} 为子微网本地负荷功率，ΔP_{bat} 为储能功率变化量。

2.2 分层消纳控制逻辑

在并网情况下，子微网运行在功率服务和消纳服从模式，在功率服从模式下光伏发电在满足本地负荷用电后，将根据主网调度指令外送功率，多余电量则给储能充电，储能 SOC 充电范围[30% 90%]。当接收到主网下发的消纳率指令时，子微网控制模式切换为消纳服从模式，通过调整光储功率，计算出储能功率补充量，使得经过联络点外送到主网的功率满足消纳率要求，控制逻辑如下图 10 所示。

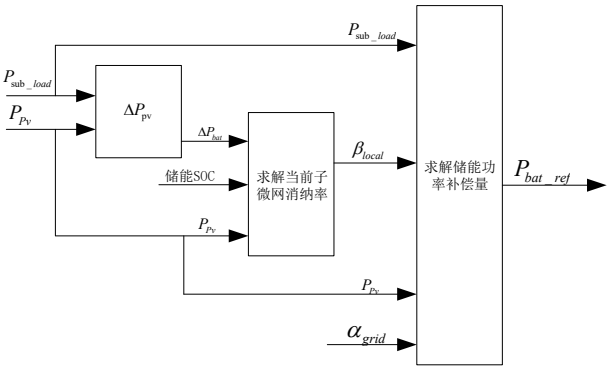


图 10 分层消纳控制逻辑

3 仿真分析

按照图 1 拓扑，在 SimuNPS 软件中搭建完整的微电网仿真模型和能量协调控制策略。开展以下仿真测试：

（1）子微网功率服从测试

子微网并网运行，控制方式接收上层微网控制器调度，在 0-1s 时，主网负荷功率 200kW，柴油发电机发电功率 200kW,柴油电机功率能够满足主网负荷需求，此时主网功率调度指令为 0。子微网光伏发电功率 200kW,本地负荷功率 150kW,光伏发电在满足本地负荷后将多余功率给储能充电，储能充电功率 50kW。在 1-2s 时，主网负荷由 200 kW 变为 350 kW，由于柴油发电机额定功率为 300kW，不满足主网负荷要求，综合考虑柴油发电机经济运行成本和负荷要求，柴油发电机将发电功率提升到 250kW，同时向子微网下发调度指令 100kW，其中光伏发电外送功率 50kW，储能由充电变为放电，储能放电功率 50kW，合计 100kW 满足主网功率指令。仿真结果如下图所示：

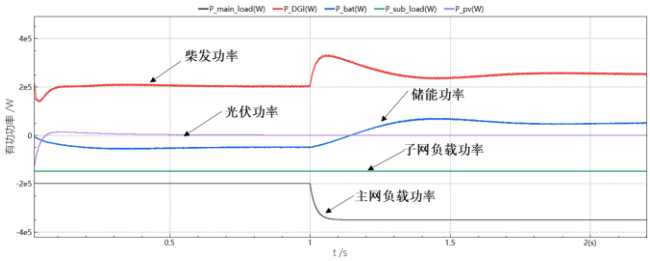


图 11 各单元有功功率波形

储能初始 SOC 为 50%，在 0-1s 期间光伏持续给储能充电 SOC 逐步增大，在 1-1.1s 期间储能从充电状态转变为放电状态，SOC 达到最大值，此后持续放电，SOC 逐渐降低，如图 12 所示。

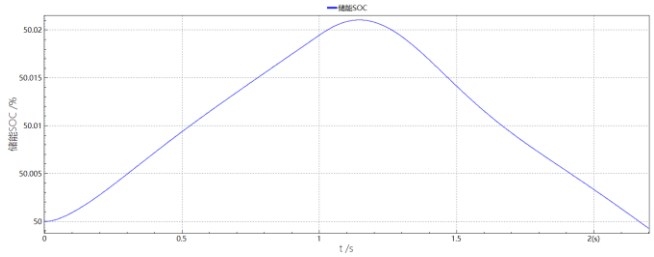


图 12 储能 SOC 的波形

（2）子微网孤岛运行测试

子微网初始时刻并网运行，子微网工作在功率服从模式。主网负荷功率 200kW，子微网负荷功率 250kW，光伏发电功率 300kW，柴油发电机发电功率 150kW，主网给子微网下发调度指令 50kW，全部由光伏提供，储能不发功率；在 0.8s 时，子微网由并网转为孤岛运行，储能由并网控制切换为离网构网运行，支撑子微网 400V 母线电压，子微网控制器切换为内部平衡模式，此时光伏发电大于负荷用电，多余的 50kW 功率给储能充电，主网柴油发电机功率增加到 200kW 给主网负荷供电。在 1.6s 时，模拟光照强度减弱，光伏发电功率降低为 200kW，负荷缺额功率 50kW 由储能来提供，仿真结果如图 13、图 14 和图 15 所示。

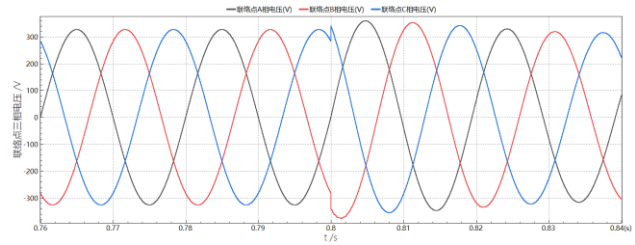


图 13 并网转离网联络点三相电压波形

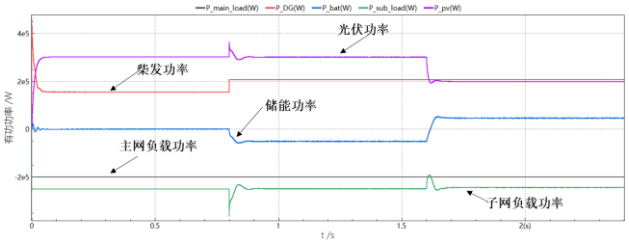


图 14 各单元有功功率波形

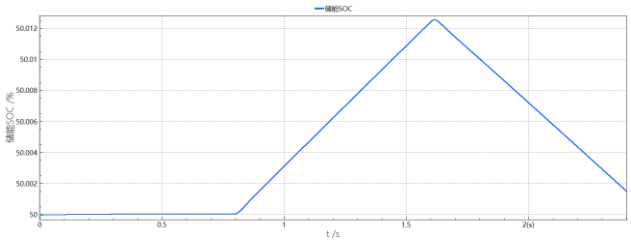


图 15 储能 SOC 的波形

（3）子微网运行模式切换测试

初始时刻子微网并网运行，工作在功率服从模式，在满足子微网本地负载的同时，根据上层微网调度指令进行响应，此时主网负荷功率 300kW，子微网负荷功率 250kW，光伏发电功率 300kW，柴油发电功率 250kW，主网给子微网下发调度指令 50kW，全部由光伏提供，储能不发功率。在 1s 时刻，主网控制模式由功率控制转换为消纳控制，主网给子微网下发消纳率指令 0.3，子微网控制方式同步由功率服从改为消纳服从模式，根据主网消纳率指令调节光伏、储能输出功率，其中光伏输出功率 50kW，储能输出功率 40kW，合计外送主网功率 90kW，使子微网光伏消纳率由 0.83 变为设置的 0.7 目标值，主网光伏消纳率由 0.17 变为目标值 0.3。仿真结果如图 16、图 17 和图 18 所示。

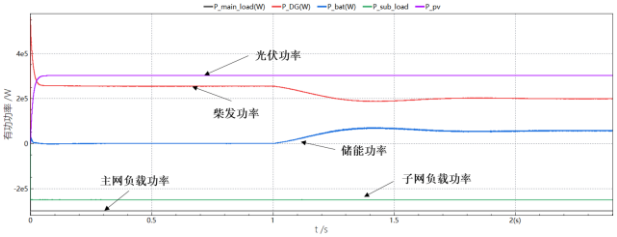


图 16 各单元有功功率波形

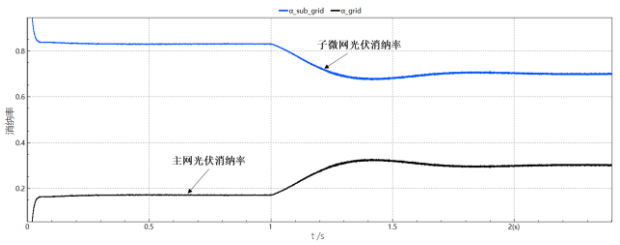


图 17 主网、子微网光伏消纳率变化波形

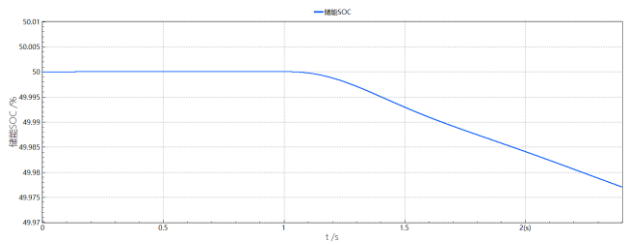


图 18 储能 SOC 变化波形

4 结论

针对微电网结构特点，本文构建了一套包含柴油发电机、光伏发电单元、储能及负荷组成的微电网系统，首先对各个发电单元进行了单体建模，其中储能采用构网控制策略，在离网状态下能够实现子微网平稳运行，最后在 SimuNPS 仿真软件搭建了微电网系统模型，开展了微电网并/离网工况下，三种能量管理策略的仿真验证，结果显示所提策略有效提升了新能源的消纳水平，并能够对各种控制方式进行平滑切换，保证了系统稳定运行。

参考文献

[1] 吴鸣，张楠春，梁英，等．新型电力系统背景下微电网技术研究与发展[J]．新型电力系统，2024，2(3)：251-271．

[2] 桑博，张涛，刘亚杰，等．多微电网能量管理系统研究综述[J]．中国电机工程学报，2020,40(10)：3077-3092．

[3] 陈奕斌，林基明，刘迪迪．微电网小区间的能量协作调度策略研究[J]．电力系统保护与控制，2017，45(22)：55-62．

[4] 朱晓荣，杜雯菲．基于能量管理的直流微电网集群协同控制策略[J]．电力自动化设备，2025,45(1)：123-130．

[5] 张明冉，常治国，吴昊，等．一种新型光伏控制器 MPPT 控制策略[J]．电力电子技术，2021,55(9)：75-77．

[6] 吴伯彪，郭禧斌。基于功率预测的自适应变步长 MPPT 算法研究[J].电测与仪表，2024,61(5)：60-64.

[7] 刘辉，于思奇，孙大卫，等．构网型变流器控制技术及原理综述[J]．中国电机工程学报，2025，45(1):277-296.

[8] Zhong Q C, Nguyen P L, Ma Z Y, et al. Self- synchronized synchronverters: Inverters without a dedicated synchronization unit[J]. IEEE Transactions on Power Electronics, 2014, 29(2): 617-630.

[9] Jouini T , Arghir C , F Dörfler. Grid-Friendly Matching of Synchronous Machines by Tapping into the DC Storage[J]. IFACPapersOnLine, 2016.

[10] Catalin A , Taouba J , Florian D . Grid-forming Control for Power Converters based on Matching of Synchronous Machines[J]. Automatica, 2017, 95:273-282.

作者简介：。

魏明洋(1986)，男，硕士，工程师，主要从事电力系统建模与实时仿真研究，mingyang.wei@keliangtek.com；

赵玉伟(1989)，男，本科，工程师，主要从事电力系统建模与实时仿真研究，yuwei.zhao@keliangtek.com；

015 Research on Frequency Stability of a New Power System Considering Inertia Constraints

Xinyue Zhang[1], Yanling Lv[1*] and Shiqiang Hou[1]

[1] Harbin University of Science and Technology, Harbin Heilongjiang 150080, China
1744307478@qq.com

Abstract. This paper conducts an in-depth study on the frequency stability of the new power system considering inertia constraints, analyzes the inertia demand of the power system, builds a model that comprehensively considers the inertia characteristics of conventional units and wind turbines, and derives a minimum inertia calculation method based on the constraints of the rate of change of frequency and the lowest frequency point. Furthermore, a new power system optimization operation model was created with the goal of minimizing operating costs. By taking multiple constraints into comprehensive consideration and systematic integration, the IEEE-30 node power system is used as a typical example to verify the rationality and practicability of the proposed model. The comprehensive analysis shows that in the new power system, incorporating frequency safety constraints is an important means to improve system frequency stability; relying on the coordinated dispatch of efficient thermal power units and wind turbines can effectively alleviate the pressure of operation cost while ensuring frequency stability.

Keywords: Inertia constraints, rate of change of frequency, lowest frequency point, frequency safety constraints, operation costs.

1 Introduction

Against the backdrop of China's steadfast pursuit of its "carbon peaking and carbon neutrality" goals, the development of a new-type power system with renewable energy at its core has become a strategic focal point of the national energy agenda. According to the State Council's Opinions on Fully and Accurately Implementing the New Development Philosophy to Achieve Carbon Peaking and Carbon Neutrality [1], the total installed capacity of wind and solar power is projected to exceed 1.2 TW by 2030, with non-fossil energy accounting for more than 80% of total energy consumption by 2060. These policy mandates signal an imminent transition of China's power sector into a new era dominated by renewable energy sources. From the perspective of installed capacity expansion, renewables are exhibiting a rapid and sustained increase in their share of the national energy mix. Official statistics show that by the end of 2023, China's total installed power generation capacity reached 2.92 TW, including 440 GW of wind power—a year-on-year increase of 13.9%—and 610 GW of

solar power, which grew at a striking rate of 55.2% over the same period [2]. According to standardized international unit conversions, China's installed wind power capacity stands at approximately 370 GW, while solar photovoltaic capacity has reached around 390 GW. Projections suggest that by 2050, renewables could account for over 60% of the nation's total installed power generation capacity [3].

Despite the numerous advantages of renewable energy generation, its inherently weak coupling with the grid—primarily via power electronic converters—introduces new challenges to the secure and stable operation of power systems. In particular, the declining system inertia observed in recent years has emerged as a critical concern, directly impacting the frequency stability and dynamic performance of modern power grids. The concept of minimum inertia assessment has opened a new paradigm for optimizing system operation strategies. This method quantitatively evaluates the system's resilience to disturbances by analyzing constraints on the rate of change of frequency (RoCoF) and frequency deviation under predefined contingencies, thereby determining the minimum inertia threshold required to maintain frequency stability. Conducting in-depth studies on the frequency stability of renewable-rich power systems is essential not only for ensuring operational security and stability but also for enabling the efficient integration of renewables, driving technological innovation within the power sector, and informing science-based policymaking. As the installed capacity of renewable energy continues to expand, achieving its reliable and efficient operation within the grid has become a central focus in the ongoing transformation of the electricity sector.

The rapid expansion of renewable energy generation presents unprecedented challenges to the operational security of modern power systems. In this study, inertia constraints are incorporated into the system optimization framework, and the dynamic frequency response mechanisms are investigated to determine the inertia requirements under high renewable penetration. By jointly considering the safety limits of two critical indicators—the rate of change of frequency (RoCoF) and the frequency nadir—this work aims to identify the minimum inertia level necessary to ensure frequency stability, while simultaneously achieving the lowest possible operational cost.

2 Inertia requirements in emerging power systems with high renewable penetration

System inertia reflects the power grid's intrinsic ability to sustain its current operating state and serves as a fundamental attribute characterizing its resilience to power fluctuations. As such, inertia plays a pivotal role in safeguarding the stable operation of the electrical grid [4]. In the event of an active power disturbance, the power system's inertia provides the initial defense, arresting the rate of frequency decline and mitigating the risk of cascading failures. The active power–frequency regulation characteristics of the system can be described by the classic swing equation of the synchronous generator rotor motion, given as:

$$2H_{\text{sys}}\frac{df_t}{f_N dt} = P_{\text{m}} - P_{\text{e}} - D_{\text{sys}}\Delta f_t \tag{1}$$

where H_{sys} denotes the system inertia constant, f_t is the system frequency, P_m represents the total mechanical power input, P_e is the total electromagnetic power output, D_{sys} is the damping coefficient, and Δf_t is the frequency deviation.

The system's inertia requirement originates from its fundamental need to maintain frequency stability and represents a foundational physical property for the secure operation of power systems. A reduction in inertia leads to steeper frequency excursions following disturbances; in severe cases, this can cause distributed energy resources to disconnect and jeopardize the safe operation of synchronous units. Lower inertia levels also exacerbate the frequency nadir, increasing the likelihood of triggering last-resort protection schemes [5]. With the large-scale integration of renewable energy into the grid, system inertia has undergone profound changes. Therefore, a thorough investigation of inertia requirements and their necessity is of critical importance for ensuring the secure operation of future power systems.

In conventional power systems, thermal power units constitute the primary source of rotational inertia, and their operational characteristics critically determine the overall inertia level. Owing to the mechanical inertia of their rotating components, these units provide natural frequency support. Large turbo-generators generally exhibit high inertia constants and can buffer frequency deviations during power imbalances by releasing or absorbing kinetic energy from the rotor mass. The inertia contribution of thermal units is inherently tied to their physical structure. Retaining a certain number of thermal generators as inertia-supporting units can help mitigate the decline in frequency stability caused by insufficient inertia. However, as the proportion of renewable energy increases, the share of synchronous generators in the system decreases, thereby reducing the equivalent system inertia. This dilution effect makes the power system more sensitive to disturbances, aggravating frequency-stability concerns, and resulting in insufficient inertia under high renewable penetration. With the maturing of virtual synchronous generator (VSG) technology, renewable units are transitioning from inertia consumers to potential inertia providers. By emulating the electromechanical transient behavior of synchronous machines, VSG-controlled power electronic converters can mimic inertia, damping, and frequency-regulation characteristics, thereby actively participating in grid operation and control. Through control algorithms that emulate the swing equation, VSGs shape the inverter output to resemble that of a synchronous generator, enabling proactive participation in frequency regulation. When a frequency decline is detected, a VSG-controlled inverter can increase its power output to emulate the inertia response of conventional synchronous machines.

3 Dynamic frequency stability constraints for modern power grids

3.1 System Frequency Response and Inertia Support

The frequency response of a power system reflects the imbalance between active power supply and demand. When sudden load variations or unexpected generator outages occur, the system frequency dynamically adjusts over time in an effort to re-establish equilibrium. This process embodies the power system's capability to maintain stable operation and lies at the heart of frequency stability analysis.

The initial stage of a power system's frequency disturbance process is the inertia response, during which the kinetic energy stored in synchronous generator rotors provides immediate support. When a power deficit occurs in the system, the generator rotor immediately releases its stored kinetic energy, compensating for the power imbalance through a transient change in rotational speed—reflected as a variation in system frequency [6].This inertia response is rapid and short-lived, typically lasting only a few seconds. Primary frequency control occurs in the second stage, following the inertial response, and is executed automatically by the generator's governor system. When the frequency deviation exceeds a predefined threshold, the governor adjusts the prime mover's output to restore the power balance. With a typical response time ranging from a few seconds to several tens of seconds, primary control effectively suppresses further frequency decline; however, its regulation capability is inherently limited, generally compensating only a portion of the power shortfall. The secondary frequency control stage, which relies on automatic generation control (AGC), restores area power balance with higher precision; its response time usually ranges from 30 seconds to 15 minutes and results in zero steady-state error. The tertiary frequency control, also known as economic dispatch, represents the final stage of frequency response and aims to coordinate energy balance with economic optimization.

The inertia response and primary frequency control stages jointly determine the key dynamic frequency indicators and correspond to the period of highest risk for frequency instability. Accordingly, this paper focuses primarily on the inertia response and primary frequency control.

3.2 Power System Dynamic Frequency Indices

Dynamic frequency indicators are critical parameters for quantifying power system frequency stability, particularly during the initial post-disturbance period [7]. The rate of change of frequency (RoCoF) measures the speed at which the system frequency varies immediately following a disturbance (in Hz/s), and serves as a key indicator of the system's dynamic frequency response. Its magnitude dictates whether RoCoF protection schemes are triggered; thus, to avoid undesirable relay operations, the RoCoF must remain within acceptable limits, as it directly reflects the speed of frequency deviation under disturbances and determines whether the dynamic security boundary is breached [8]. The nadir frequency (NF), defined as the lowest frequency reached after a disturbance (in Hz), typically occurs within 5–15 seconds and represents the combined effect of the inertia response and primary frequency control. It is

another vital metric for assessing frequency stability. From the disturbance onset (t = 0) to the nadir point, electrical power exceeds mechanical power, creating a persistent power imbalance and a downward trend in system frequency. Together, RoCoF and NF constitute two critical indicators for determining the frequency stability of a power system [9].

3.3 Frequency Security Constraints

Minimum Inertia Requirement Based on RoCoF Constraint. Based on the frequency response model of the new-type power system, the corresponding system transfer function can be derived as follows:

$$G_{1}(s)=\frac{m_0+m_1 s}{n_0+n_1 s+n_2 s^2} \tag{2}$$

$$\begin{cases} m_0 = R_{Gi} \\ m_1 = R_{Gi} T_{Gi} \end{cases}$$

$$\begin{cases} n_0 = i + R_{Gi} D_{\text{sys}} + R_{Gi} \dfrac{1}{R_W} \\ n_1 = 2R_{Gi} H_{\text{sys}} + R_{Gi} T_{Gi} D_{\text{sys}} + iF_{\text{H}} T_{Ri} + R_{Gi} K_V + R_{Gi} T_{Ri} \dfrac{1}{R_W} \\ n_2 = 2R_{Gi} H_{\text{sys}} T_{Ri} + R_{Gi} T_{Ri} K_V \end{cases}$$

Based on the SFR model, the system frequency response is transformed into the time domain through inverse Laplace transformation, yielding the differential expression of the frequency response. When the frequency reaches its nadir, the derivative of the frequency response becomes zero. Applying the initial value theorem of the Laplace transform, the RoCoF can be obtained as:

$$\left.\frac{\mathrm{d}f}{\mathrm{d}t}\right|_{\max} = \left.\frac{\mathrm{d}\Delta f}{\mathrm{d}t}\right|_{t=0} = \lim_{s\to\infty} s^2 \Delta f(s) = \lim_{s\to\infty} s^2 \frac{\Delta P_L}{s} G_1(s) = \Delta P_L \frac{1}{2H_{sys}+K_V} \tag{3}$$

Minimum Inertia Requirement Based on NF Constraint. Based on the frequency response model of the new power system shown in Fig. 4-1, the additional power provided by the generator during the frequency response process is expressed as:

$$\Delta P_{\text{G}} = \frac{\Delta P_{\text{L}}}{1+D_{\text{sys}} R_G}(1+A_{\text{m}}\,\mathrm{e}^{-at}\sin(\omega t+\varphi)) \tag{4}$$

Since the generator power surge curve can be approximated as a straight line during the period from time 0 to the lowest frequency point, the formula can be linearized. By performing a Taylor series expansion about the operating point $t=0$, $\exp(-at)\approx(1-at)$, $\sin(\omega t+\varphi)=\sin\varphi$, and since $A_{\text{m}}\sin\varphi=-1$,we obtain:

$$\Delta P_{\mathrm{G}}=\frac{\Delta P_{\mathrm{L}}}{1+D_{\mathrm{sys}}R_G}at=Kt=\frac{\Delta P_{\mathrm{L}}}{2}(\frac{1}{T_{\mathrm{R}}}+\frac{F_{\mathrm{H}}}{2HR_G})t \tag{5}$$

In the expression,K represents the generator's power increment coefficient, and H denotes its inertia time constant.Let R' denote the equivalent droop coefficient.

$$R'=R_G/(1+D_{\mathrm{sys}}R_G) \tag{6}$$

Accordingly, the frequency expression can be derived as:

$$\Delta f=(\frac{1}{2}Kt^2-\Delta P_{\mathrm{L}}t)/(2H_{\mathrm{sys}}) \tag{7}$$

By evaluating t_{nadir} at the frequency nadir, the corresponding expression for $\Delta f_{\mathrm{nadir}}$ is derived.

$$\Delta f_{\mathrm{nadir}}=-\frac{\Delta P_L}{2H_{\mathrm{sys}}(\frac{1}{T_{\mathrm{R}}}+\frac{F_H}{2HR_G})} \tag{8}$$

The linearized expression for the nadir frequency can thus be written as:

$$f_{\mathrm{nadir}}=f_{\mathrm{N}}-\frac{\Delta P_L}{2H_{\mathrm{sys}}(\frac{1}{T_{\mathrm{R}}}+\frac{F_{\mathrm{H}}}{2HR_G})} \tag{9}$$

4 Optimal Dispatch Model for Power Systems under Minimum Inertia Constraints

A frequency response model of the new-type power system is constructed, as shown in Fig.1. When wind turbine generators (WTGs) participate in primary frequency control, their contribution consists of two superimposed components: droop control and inertial response control. In this model, R_W denotes the droop coefficient of the WTG, which determines the proportional relationship between primary frequency regulation power and frequency deviation; K_V represents the virtual inertia constant of the WTG, used to emulate the inertial response of a synchronous generator; The differential operator reflects the RoCoF-based response within the virtual inertia controller. For the thermal power unit section, R_{Gi} denotes the regulation coefficient of thermal unit i, F_{Hi} is the inertia time constant of thermal unit i, reflecting its capability to provide inertial support to frequency changes, and T_{Ri} refers to the governor time constant of the thermal unit, characterizing the response speed of the governor.

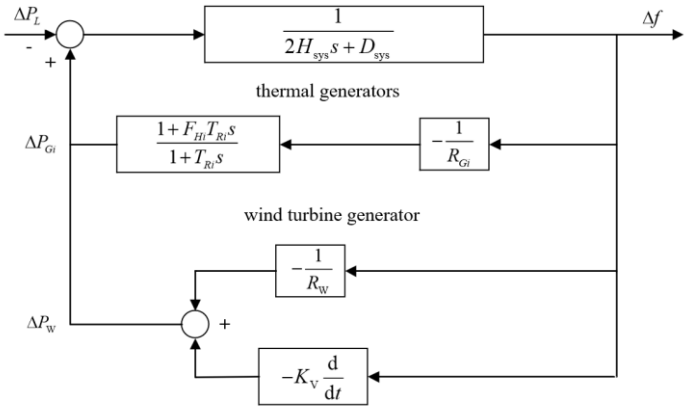


Fig.1 Frequency response model of the new power system

The system operation process under inertia constraints adopted in this study is illustrated in Fig. 2.

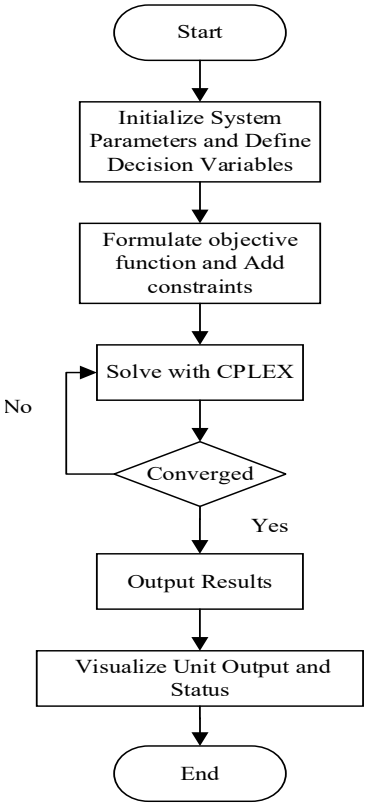


Fig.2 Program flowchart

4.1 Optimization of Emerging Power Systems with Minimum Inertia Requirements

Objective Function. This study aims to minimize the total operating cost, comprising the generation cost and start-up/shutdown cost of conventional units. As wind turbines consume no primary fuel, their operating costs are excluded. The objective function is formulated as follows:

$$minF = \sum_{t=1}^{T}\sum_{i=1}^{N}\left(a_i P_{Gi.t}^2 + b_i P_{Gi.t} + c_i\right) + \sum_{t=1}^{T}\sum_{i=1}^{N}\left(S_i U_{i.t}1\text{-}U_{i.t\text{-}1}\right) \tag{10}$$

where F denotes the total operating cost; a_i, b_i, c_i is the generation cost coefficient of the i-th conventional unit (thermal unit in this study); S_i is the start-up cost of the i-th thermal unit; $U_{\mathrm{i.t}}$ is the binary variable representing the on/off status of the i-th unit at time period t ($U_{\mathrm{i.t}}$=1 if the unit is online, and $U_{\mathrm{i.t}}$=0 otherwise); N is the total number of thermal units, with i indexing each unit; and T denotes the scheduling horizon for thermal power units, $t = 1,2,...,24$ indexes the hourly time intervals within the scheduling horizon.

Constraints.

(1) Power Balance Constraints

$$\sum_{i=1}^{N} P_{i.t} + \sum_{j=1}^{M} P_{m.j.t} = L_t \tag{11}$$

where M is the total number of wind turbines, and L_t is the total system load at time t.

(2) Thermal Unit Output Constraints

$$U_{i.t}P_{i.\min} \le P_{i.t} \le U_{i.t}P_{i.\max} \tag{12}$$

(3) Unit Ramp Rate Constraints

$$\begin{cases} P_{it} - P_{it\text{-}1} \le L_{p\max} \\ P_{it} - P_{it\text{-}1} \ge L_{p\min} \end{cases} \tag{13}$$

$L_{p\max}, L_{p\mathrm{mim}}$ are the upper and lower limits of the power increase and decrease of the unit, respectively.

(4) Rotational Backup Constraints

$$\sum_{i=1}^{n} U_{i.t}(P_{i.\max} - P_{i.t}) \ge R_t \tag{14}$$

$P_{i.\max}$ is the maximum output of the unit, and R_t is the standby capacity of the system at that moment.

(5) Minimum Up/Down Time Constraints for Units

$$\begin{cases} \sum_{k=t}^{t+T_{on.i}-1} U_{i.k} \geq T_{on.i}\left(U_{i.t} - U_{i.t\text{-}1}\right) \\ \sum_{k=t}^{t+T_{off.i}-1} \left(1 - U_{i.k}\right) \geq T_{off.i}\left(U_{i.t\text{-}1} - U_{i.t}\right) \end{cases} \tag{15}$$

$T_{on.i}$ is the minimum startup time for the unit, and $T_{off.i}$ is the minimum shutdown time for the unit.

5 Case Study

The IEEE-30 bus test system is employed in this study, configured with six thermal generating units, one wind turbine generator, and one 800 MW HVDC link. The network topology is shown in Fig. 3. The thermal units are connected at buses 1, 2, 5, 8, 11, and 13, while both the wind farm and the 800 MW HVDC link are connected at bus 23. The frequency security constraints are specified as $f_{\text{nadir.min}}$ =49.5Hz, $RoCoF_{\max}$ =0.5Hz/s. The system has a rated frequency of 50 Hz and a rated capacity of 1000 MVA. Each thermal generator has an inertia time constant of 0.3 s and a governor time constant of 6 s. The frequency response coefficient of the wind turbine generator is set to 5, and the scheduling horizon covers a 24-hour period.

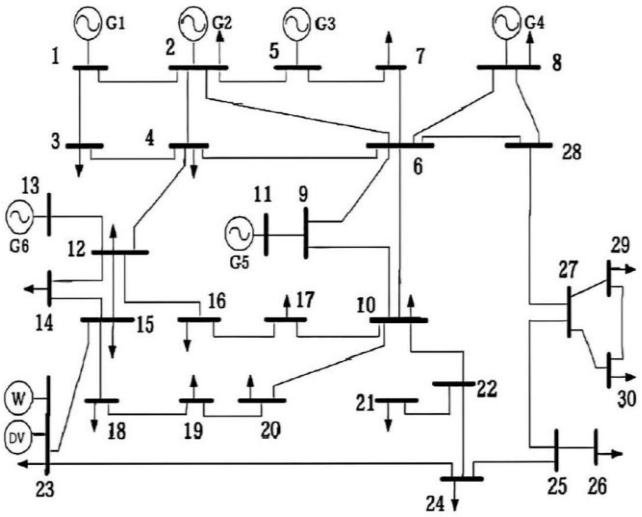


Fig.3 IEEE-30 node system configuration diagram

A multi-scenario approach is adopted to analyze the system's operational performance. Units 1–6 are conventional thermal generators, unit 7 is the wind turbine generator, and unit 8 represents the 800 MW HVDC link. The following four scenarios are investigated:

Scenario 1: No frequency stability constraints; only conventional units provide inertia response and primary frequency control.

Scenario 2: No frequency stability constraints; both conventional units and the wind turbine generator provide inertia response and primary frequency control.

Scenario 3: Frequency stability constraints are enforced; only conventional units provide inertia response and primary frequency control.

Scenario 4: Frequency stability constraints are enforced; both conventional units and the wind turbine generator provide inertia response and primary frequency control.

The unit commitment status, maximum frequency deviation, operational cost, and analysis under each scenario are presented as follows:

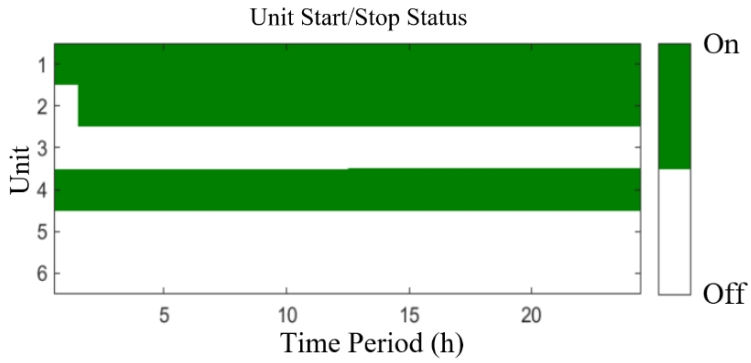


Fig.4 Unit Commitment Status under Scenarios 1 and 2

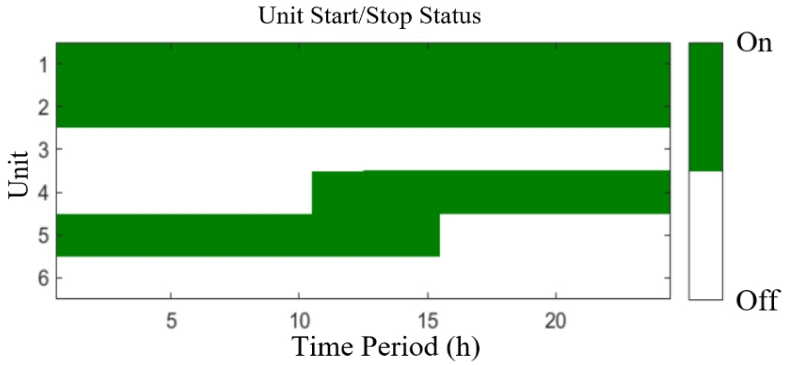


Fig.5 Unit Commitment Status under Scenarios 3

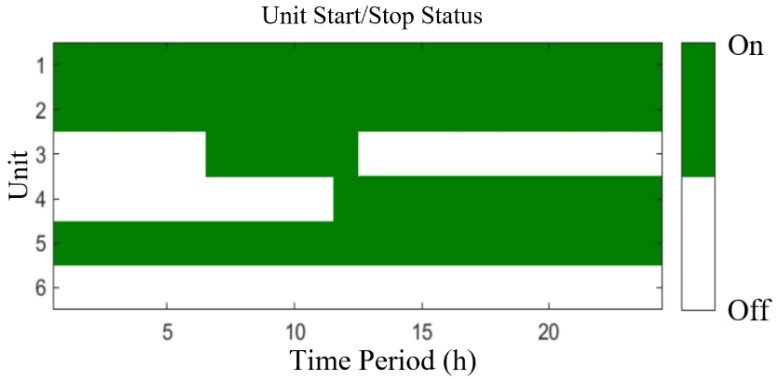


Fig.6 Unit Commitment Status under Scenarios 4

In both Scenario 1 and Scenario 2, the commitment status of the generating units remains identical, with a total of 71 unit start-ups over the 24-hour period. In Scenario 1, system inertia is supplied solely by units 1, 2, and 4. In Scenario 2, in addition to the inertia contributed by thermal units, virtual inertia is provided by the wind turbine generator. Under Scenario 3, the number of online generators is the highest, with a total of 91 start-ups in 24 hours; system inertia is supplied by units 1, 2, 3, 4, and 5, resulting in a more sufficient inertia margin than in Scenarios 1 and 2. In Scenario 4, the total number of unit start-ups is 77, and inertia support originates from thermal units 1, 2, 4, and 5, supplemented by the wind turbine generator.

Table 1. Maximum Frequency Deviation under Scenario 1

Time period/h	Frequency/Hz	Time period/h	Frequency/Hz	Time period/h	Frequency/Hz
1	49.772	9	49.807	17	49.805
2	49.844	10	49.794	18	49.814
3	49.842	11	49.783	19	49.818
4	49.840	12	49.777	20	49.825
5	49.837	13	49.788	21	49.829
6	49.833	14	49.796	22	49.827
7	49.827	15	49.794	23	49.835
8	49.818	16	49.801	24	49.838

Table 2. Maximum Frequency Deviation under Scenario 2

Time period/h	Frequency/Hz	Time period/h	Frequency/Hz	Time period/h	Frequency/Hz
1	49.777	9	49.810	17	49.808

12

Table 2 (continued). Maximum Frequency Deviation under Scenario 2

Time period/h	Frequency/Hz	Time period/h	Frequency/Hz	Time period/h	Frequency/Hz
2	49.847	10	49.798	18	49.817
3	49.845	11	49.787	19	49.821
4	49.842	12	49.781	20	49.828
5	49.840	13	49.791	21	49.832
6	49.836	14	49.800	22	49.830
7	49.830	15	49.798	23	49.838
8	49.821	16	49.804	24	49.840

Table 3. Maximum Frequency Deviation under Scenario 3

Time period/h	Frequency/Hz	Time period/h	Frequency/Hz	Time period/h	Frequency/Hz
1	49.849	9	49.856	17	49.854
2	49.845	10	49.846	18	49.860
3	49.842	11	49.838	19	49.864
4	49.840	12	49.866	20	49.868
5	49.838	13	49.841	21	49.872
6	49.935	14	49.847	22	49.870
7	49.870	15	49.846	23	49.877
8	49.864	16	49.851	24	49.878

Table 4. Maximum Frequency Deviation under Scenario 4

Time period/h	Frequency/Hz	Time period/h	Frequency/Hz	Time period/h	Frequency/Hz
1	49.852	9	49.811	17	49.808
2	49.847	10	49.799	18	49.817
3	49.844	11	49.840	19	49.821
4	49.843	12	49.835	20	49.828
5	49.841	13	49.843	21	49.832
6	49.937	14	49.849	22	49.830
7	49.830	15	49.848	23	49.838
8	49.822	16	49.804	24	49.840

Since Scenario 1 does not include frequency security constraints, it exhibits the largest frequency deviation, fluctuating between 49.772 Hz and 49.844 Hz, with the

nadir occurring in time period 1 at 49.772 Hz. Compared with Scenario 1, Scenario 2 incorporates frequency support from the wind turbine generator, resulting in a significant improvement in frequency deviation, which ranges from 49.777 Hz to 49.847 Hz; the lowest frequency recorded is 49.777 Hz. In Scenario 3, after imposing frequency security constraints, the frequency fluctuation range is narrowed to 49.838 Hz–49.935 Hz, indicating a marked enhancement in frequency stability. The nadir occurs in period 5 at 49.838 Hz. Scenario 4 adds wind turbine frequency support on the basis of Scenario 3, yielding a fluctuation range of 49.799 Hz–49.937 Hz. The lowest frequency appears in period 10 at 49.799 Hz; overall, the system frequency in this scenario is closer to the rated frequency than in Scenario 2, which lacks frequency security constraints.

Table 5. Comparison of Operating Costs across Scenarios

Scenario	1	2	3	4
Cost/$	587269.618	587269.618	623290.002	601793.72

The operational cost in Scenarios 1 and 2 is identical, as the participation of the wind turbine generator in frequency regulation in Scenario 2 does not introduce any additional cost. In Scenario 3, the total cost increases by 5.78% compared with Scenarios 1 and 2 due to the enforcement of frequency security constraints. Although the wind turbine generator similarly incurs no extra cost for frequency regulation in Scenario 4, changes in unit commitment lead to different generation and start-up/shutdown costs. As a result, the operational cost of thermal units in Scenario 4 decreases by 3.57% relative to Scenario 3.

6 Conclusions and Outlook

This study addresses the critical challenge of frequency stability in power systems with high penetration of renewable energy, focusing on the optimal operation framework incorporating inertia constraints. As the share of wind and photovoltaic generation increases, the proportion of conventional synchronous generators declines, leading to insufficient equivalent system inertia and a heightened risk of frequency instability. To address this challenge, we develop a novel frequency response model for modern power systems, integrated into a multi-constraint optimization framework aimed at minimizing operating costs. The key findings are as follows:

Coordinated optimization of thermal and wind power units: Comparing Scenarios 1–2 with Scenarios 3–4, the addition of wind turbine participation in frequency regulation noticeably improves the nadir frequency, bringing it closer to the nominal frequency. Furthermore, relative to Scenario 3, Scenario 4 yields a 3.57% reduction in thermal generation cost due to changes in unit commitment and optimal dispatch following the introduction of wind-based frequency support. Under the premise of frequency stability, economic benefits can be achieved through coordinated scheduling of thermal and wind units.

Effectiveness of the minimum inertia requirement assessment: By incorporating RoCoF and NF-based frequency security constraints in Scenarios 3 and 4, the nadir

frequency can be significantly enhanced (e.g., from 49.833 Hz to 49.935 Hz under the same time period), leading to a marked improvement in frequency stability. Although the introduction of frequency security constraints increases operational cost, this can be mitigated by the use of wind turbine frequency support and optimized scheduling. Rational allocation of frequency regulation resources is therefore the key to balancing system security and economic efficiency.

Practical value of the proposed optimization model: The inertia-constrained optimization model developed herein integrates conventional constraints such as power balance and ramp rate with RoCoF and NF-based dynamic security constraints, thus providing useful guidance for real-world operation and scheduling. Multi-scenario comparative analysis demonstrates the effectiveness of the proposed model. Considering inertia, frequency response, and operational cost in an integrated framework, Scenario 4—where frequency security constraints are enforced and wind turbines participate in frequency regulation—emerges as the optimal option for the new-type power system.

Although this study offers valuable insights into frequency stability optimization, several open issues merit further investigation, such as refined quantification of virtual inertia contributions, dynamic adjustment of inertia constraints in large-scale systems, and the design of market mechanisms to incentivize renewable participation in inertia support. With further increases in renewable penetration, optimal operational strategies that account for inertia constraints will become crucial to ensuring secure and stable power system operation.

References

1. The Central Committee of the Communist Party of China, The State Council: Opinions on Fully, Accurately and Comprehensively Implementing the New Development Concept to Achieve Carbon Peaking and Carbon Neutrality [N]. People's Daily, 2021-10-25(001).
2. Wang, M., Guo, J., Ma, S., et al.: Review on transient frequency stability analysis and frequency regulation control methods of new energy power systems [J]. Proceedings of the CSEE, 2023, 43(05): 1672–1694.
3. Wu, Z., Zhou, M., Zhang, Z., et al.: An incentive profit-sharing mechanism for welfare transfer in balancing market integration [J]. Renewable and Sustainable Energy Reviews, 2022, 168: 112762.
4. Chen, Y., Yao, Y., Li, J., et al.: Impact of DC frequency limiter on frequency stability of low-inertia systems [J]. Electric Power Science and Engineering, 2022, 38(12): 18–26.
5. Guo, H., Xiao, Y., Wan, H., et al.: Inertia analysis methods for new-type power systems [J]. Yunnan Electric Power Technology, 2023, 51(4): 54–59.
6. Li, Z.: Optimal operation of new energy power systems considering inertia demand [D]. Beijing: North China Electric Power University, 2023.
7. Xie, Y.: Frequency stability mechanism and coordinated control of power systems under large-scale frequency deviation scenarios [D]. Jinan: Shandong University, 2021.
8. Liu, F., Qing, M., Tang, F., et al.: Calculation of the limit value of wind power penetration considering wind power primary frequency regulation and frequency constraints [J]. Power System Technology, 2021, 45(03): 863–870.

9. Sun, L., Wang, W., Wang, Y., et al.: Optimal scheduling of wind–solar–thermal–storage hybrid systems considering minimum inertia constraints [J]. Journal of Power System and Automation, 2024, 36(08): 30–38.

016 灵活检修策略下的矿山柔性资源运行优化研究

刘海龙[1,2]，黄建锋[3]，牟英新[3]，梁睿[1]，张紫皓[1]

（1.中国矿业大学 电气工程学院，江苏 徐州 221116；
2.中煤集团新疆能源有限公司，新疆维吾尔自治区 乌鲁木齐市 830011
3. 国投哈密能源开发有限责任公司，新疆维吾尔自治区 哈密市 839099）

Study on Operation Optimization of Mine Flexible Resources under the Flexible Maintenance Strategy

Liu Hailong[1,2], Huang Jianfeng[3], Mou Yingxin[3], Liang Rui[1], Zhang Zihao[1]

(1.School of Electrical Engineering, China University of Mining and Technology, Xuzhou 221116, China;
2. China National Coal Group Xinjiang Energy Co., Ltd., Urumqi 830011, China;
3. SDIC Hami Energy Development Co., Ltd., Hami 839099, China)

Abstract: Under the background of "double carbon", mining enterprises are facing multiple challenges, such as high energy costs, insufficient new energy absorption capacity, significant load peak valley difference and limited regulation means. In view of this, the scheduling potential of flexible resources such as mine transportation, drainage, compressed air and heating in the safe operation range was deeply explored, and the Mies architecture containing flexible resources was constructed. At the same time, considering the maintenance needs of high energy consuming production units, the maintenance time of 6 hours per day is shifted according to different working conditions of each link to form a flexible maintenance strategy, and Mies operation model is established with the goal of minimizing the daily energy cost of the system and maximizing the photovoltaic absorption rate. Taking a mine in Western China as an example, the seasonal simulation is carried out. The results show that the flexible resource scheduling mechanism and flexible maintenance strategy constructed in this paper can effectively optimize the mine energy cost, improve the energy efficiency, and provide a feasible technical path for the energy efficiency optimization of high energy consumption mine scenarios.

Keywords: mining area integrated energy system; photovoltaic absorption; flexible resources; maintenance strategies; operation optimization

摘要：在“双碳”背景下，矿山企业面临能源成本过高、新能源消纳能力不足、负荷峰谷差显著及调节手段有限等多重挑战。鉴于此，深入挖掘矿山运输、排水、压风、供热等柔性资源在安全运行区间内的调度潜力，构建了包含柔性资源的 MIES 架构。同时，考虑高耗能生产机组检修需求，根据各环节不同工况，将每日 6 小时检修时间进行平移，形成灵活检修策略，并以系统日用能成本最小化和光伏消纳率最大化为目标建立 MIES 运行模型。以我国西部某矿山为实例进行分季节仿真模拟，结果表明，本文所构建的柔性资源调度机制及灵活检修策略，能够有效优化矿山用能成本，提升能源利用效率，为高耗能矿山场景的能效优化提供了可行的技术路径。

关键词：矿山综合能源；光伏消纳；柔性资源；灵活检修；运行优化

0 引言

随着“碳达峰、碳中和”战略目标的推进，矿山企业面临多重挑战。一方面，矿山的生产负荷具有刚性强、波动大的特点，用电需求在不同时间段差异明显；另一方面，分布式可再生能源的出力与矿山负荷需求在时空维度上不匹配。这种供需矛盾导致矿山综合能源系统在运行过程中存在可再生能源的浪费、用能成本过高等诸多问题[1][2]。因此，如何充分挖掘矿山各环节的调节潜力[3]，实现能源的高效利用和经济运行，成为了矿山企业亟待解决的关键问题。

柔性资源作为一种具备灵活调节能力的可调度单元，通过弹性调控其能量输入输出特性，成为提升系统灵活性、可靠性与经济性的关键手段[4]。文献[5]针对可平移、可转移及可削减三类柔性负荷，探究了柔性负荷参与系统调节对优化运行的影响机制。文献[8]聚焦热能源系统，利用建筑物热惯性实现热能存储，挖掘电热系统协同调度的调节潜力；文献[10]推导了配电网边界交互功率与新能源出力的映

基金项目：国家自然科学基金重点资助项目(62133015)
Project Supported by the Key Program of the National Natural Science Foundation of China(62133015)

射关系，并引入高斯混合模型对交互功率的概率分布进行非参数化刻画。文献[11]考虑空调负荷与柔性热负荷的动态调节特性，构建了电热混合储能鲁棒优化配置模型。文献[12]提出一种考虑电动汽车渗透率、用户停车行为模式及电网基础设施约束的随机优化模型，显著提升了电网对可再生能源的消纳能力与运行稳定性。然而，在矿山场景中，物料传输容量限制、设备运行临界阈值、设备检修约束等非电安全约束构成更为严苛的运行边界。因此，在挖掘负荷侧资源调节潜力的同时，需考虑多维度安全约束，实现调节效能与安全裕度的协同优化。

针对矿山场景的运行优化，文献[13]从乏风、涌水等矿山伴生能源余热回收利用的角度出发，构建包含多能耦合设备的矿山综合能源系统（Mining area Integrated Energy System, MIES）模型。文献[15]提出光-储-气-废弃矿井抽蓄多能耦合的 MIES 模型，通过配置混合电储能系统平抑光伏出力波动。文献[16]则从矿山生产工艺流程入手，构建运煤、排水等多环节运行模型，实现了多环节协同运行下的系统经济低碳优化。然而上述研究未考虑设备检修期对 MIES 运行的影响，在可再生能源与工业负荷的协同优化方面存在改进空间。

为解决矿山新能源消纳与能源效率提升问题，本文提出包含柔性资源调度环节的 MIES 系统架构；构建运输、排水、压风、供热环节的柔性资源模型；并融入设备检修约束、生产安全约束等约束条件构建 MIES 运行优化模型，以系统用能成本最小化与光伏消纳率最大化为目标，生成最优调度方案；最后以西部某实际煤矿为算例，仿真验证所提模型在提升可再生能源消纳能力、降低系统运行成本方面的有效性。

1 含柔性资源的 MIES 系统架构设计

我国西部矿山普遍存在煤电一体化运营特征，依托本地煤炭资源形成火电厂直供和市政电网结合的能源供给模式，保障了矿山高强度生产的能源需求。但随着分布式光伏的规模化接入，其发电峰值与矿山负荷峰值存在时序上的不匹配，导致大量弃光现象产生，也影响了供电系统的经济性与稳定性。同时，矿山生产负荷刚性强，传统固定运行模式难以适配新能源出力特性，进一步加剧了供电波动风险。

针对上述问题，本文以西部某实际运营矿山为研究对象，构建了包含柔性资源调度环节的 MIES 系统架构，如图 1 所示。该架构整合火电厂直供电、分布式光伏及市电三种电源，并根据光伏出力波动与分时电价，实时调整运输、排水、压风、供热环节的设备运行功率，实现负荷的弹性适配。在此基础上，提出基于用能情况与电价波动的灵活检修机制，通过优化高耗能生产设备的检修时段，提高系统对低谷电价电能的利用效率，实现负荷调控与检修计划的协同调度，有效提升 MIES 在高比例光伏接入场景下的综合运行效能。

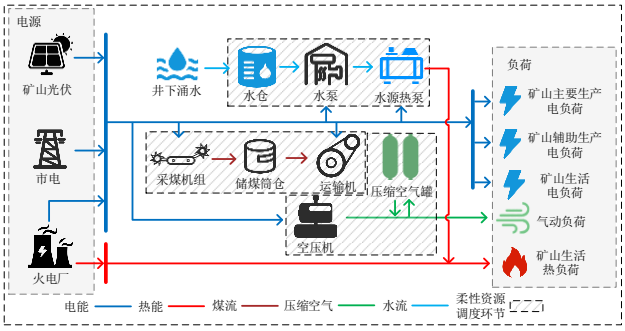


图 1 包含柔性资源调度环节的 MIES 系统架构

Fig.1 MIES System Architecture Including the Flexible Resource Scheduling Component

2 考虑柔性资源与灵活检修的 MIES 运行模型

针对运输、排水、压风、供热各环节的柔性资源模型，其构建均遵循行业通用方法[17]。

2.1 运行目标

矿山供电系统目标函数涵盖用能成本 F_1 与弃光惩罚成本 F_2，以经济性最优和光伏消纳率最大为核心目标。

$$\min F = F_1 + F_2 \tag{1}$$

$$F_1 = \sum_{t=1}^{T}(P_{mains}^{t}\lambda_{mains}^{t} + P_{straight}^{t}\lambda_{straight}^{t}) + \max(P_{mains}^{t})\lambda_{demand} + \sum_{t=1}^{T} H_{pp}^{t}\tau_{pp}^{t} \tag{2}$$

$$F_2 = \sum_{t=1}^{T}\sum_{i=1}^{npv}\alpha P_{i,t}^{ab} \tag{3}$$

式中，F_1, F_2 分别为矿山的用能成本及弃光惩罚。P_{mains}^{t} 为市电供电量；λ_{mains}^{t} 为市电电价；$P_{straight}^{t}$ 为火电厂直供电供电量；$\lambda_{straight}^{t}$ 为直供电电价；λ_{demand} 为需量电价；H_{pp}^{t} 为火电厂的热功率；τ_{pp}^{t} 为火电厂供热单价；npv 为分布式光伏数量；α 为弃光惩罚因子，$P_{i,t}^{ab}$ 为第 i 个分布式光伏在 t 时刻的弃光量。

2.2 约束条件

2.2.1Distflow 支路潮流约束

包含二阶锥松弛的最优潮流模型见文献[20]。针对二阶锥松弛变换的有效性及松弛精度问题，文献[21]、文献[22]进行了充分研究，并表明在宽松的条件下，二阶锥松弛产生的误差很小，模型仍然是准确的。

2.2.2 功率平衡约束

包括电功率、热功率及压缩空气平衡约束：

$$P_{load}^{t}+P_{s}^{t}+P_{b}^{t}+\sum P_{p,i}^{t}+P_{com}^{t}+P_{wshp}^{t}=P_{pv}^{t}+P_{mains}^{t}+P_{straight}^{t} \tag{4}$$

$$H_{pp}^{t}+H_{wshp}^{t}=H_{load}^{t} \tag{5}$$

$$A_{com}^{t}+A_{ch}^{t}=A_{dis}^{t}+A_{load}^{t} \tag{6}$$

式中，P_{load}^{t} 为矿山配电网各节点的基础电负荷；$P_{s}^{t},P_{b}^{t},P_{p,i}^{t},P_{com}^{t},P_{wshp}^{t}$ 分别为采煤机、运输机、水泵、空压机、水源热泵的电功率；H_{load}^{t} 为矿山所需的热负荷；A_{load}^{t} 为井下气动设备的气负荷，随采煤量波动及检修计划动态调整；A_{ch}^{t},A_{dis}^{t} 分别为压缩空气罐充放气功率。

2.2.3 电源上下限约束

除常规电源上下限约束外，基于煤电一体化的运营特征，煤矿与火电厂签订的合作合同中，明确约定一个周期内从火电厂的购能需满足最低额度。

$$\sum_{t=1}^{T}P_{straight}^{t}\geq P_{straight,\min} \tag{7}$$

$$\sum_{t=1}^{T}H_{pp}^{t}\geq H_{pp,\min} \tag{8}$$

$P_{straight,\min}$ 为直供电系统供电量下限；$H_{pp,\min}$ 为火电厂热出力下限。

2.2.4 灵活检修约束

在矿山生产过程中，主要生产设备与辅助设备需每日进行连续 6 小时的固定时段检修，保障设备长期安全稳定运行、规避突发故障风险。然而，固定检修时段可能与电价低谷期、光伏出力高峰期等场景重叠，不仅会错失低价电能利用窗口而增加运行成本，还可能挤占光伏消纳空间，导致能源利用效率下降。

灵活检修策略则允许突破传统固定时段限制，将各高耗能机组原本固定的 6 小时连续检修时间，灵活调整至调度周期内的合适时段。其核心在于综合权衡日内电价波动、光伏出力时段特征及矿山生产流程的连续性要求，结合各环节特性与实际用能状况动态优化检修安排，在时间维度上实现生产负荷的均衡分配，同时精准控制运行成本。

$$0\leq P_{j}^{t}\leq P_{j,\max}\left(1-m_{j}^{t}\right) \tag{9}$$

$$m_{j}^{t}=\begin{cases}0, & t\in[t_1,t_2]\\ 1, & \end{cases} \tag{10}$$

$$\sum_{t=1}^{T}m_{j}^{t}=T_{j} \tag{11}$$

$$\sum_{t=1}^{T-1}\left|m_{j}^{t+1}-m_{j}^{t}\right|=2 \tag{12}$$

式中，P_{j}^{t} 为矿山生产各环节设备 t 时刻的平均功率，$j\in\{s,b,p,com\}$；$P_{j,\max}$ 为各个用能设备的最大功率；m_{j}^{t} 为检修变量，取值为 1 代表该设备处于检修期，设备停工，取值为 0 代表该设备正常运行，t_1,t_2 分别为检修开始和结束时间；T_{j} 表示各设备的检修时长；式(12)表示一个调度周期仅进行一次检修，因此状态变量在一个调度周期内变化 2 次。

2.2.5 矿山生产安全约束

生产安全约束包括电约束和非电约束，电约束为式(9)用能设备最大功率限制约束和配电网电压电流上下限约束；非电约束则包括储煤筒仓内煤料限制约束、井下水仓空仓率限制约束、压缩空气罐气量限制约束以及采煤机组与运输机物料匹配约束：

$$0.1E_{silo}^{\max}\leq E_{silo}^{t}\leq 0.9E_{silo}^{\max} \tag{13}$$

$$0\leq V^{t}\leq 0.5V_{\max} \tag{14}$$

$$0.1E_{c}^{\max}\leq E_{c}^{t}\leq 0.9E_{c}^{\max} \tag{15}$$

$$Q_{s}^{t}=Q_{b}^{t} \tag{16}$$

式中，E_{silo}^{t} 为煤仓在 t 时刻的储煤量；$E_{silo}^{\max}$ 为煤仓容量最大值；V^{t} 为 t 时刻水仓储水量；$V_{\max}$ 为水仓最大容量；E_{c}^{t} 为压缩空气罐的储气量；$E_{c}^{\max}$ 为压缩空气罐容量；Q_{s}^{t},Q_{b}^{t} 分别为采煤机和运输机在 t 时刻处理的煤量。

3 案例分析

本文选取的矿山案例中，市电为峰平谷电价，直供电为单一电价，矿山配电网简化拓扑结构如图 2 所示，配电网中的四个地面 10kV 节点（4、6、11、12）分别配置了额定功率 6MW 的分布式光伏，其日前发电功率预测结果如图 3 所示。仿真模型以 24 小时为调度周期，时间间隔为 1h，各变量均取 1h 均值。仿真基于 MATLAB_R2020b 平台，通过 YALMIP 工具箱构建数学模型，并调用 Gurobi 12.0.1 进行求解。

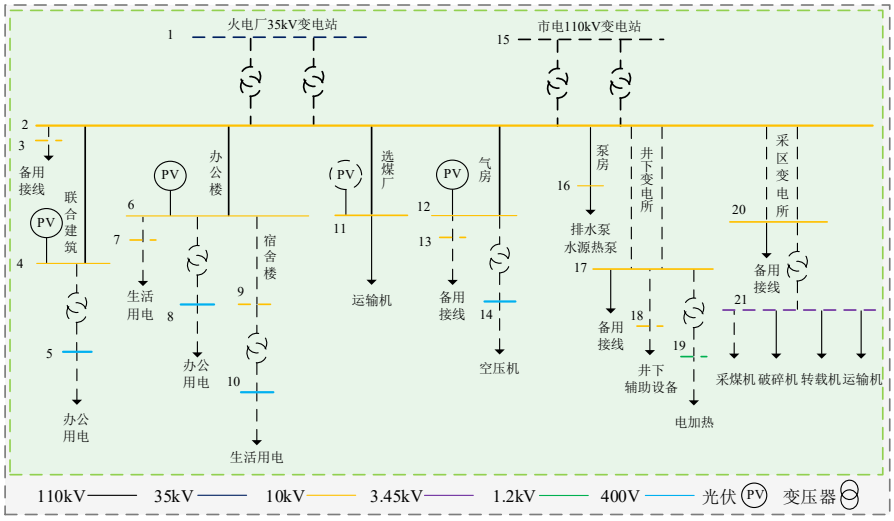


图 2 矿山供电系统拓扑图

Fig.2 Topological Diagram of Mine Power Supply System

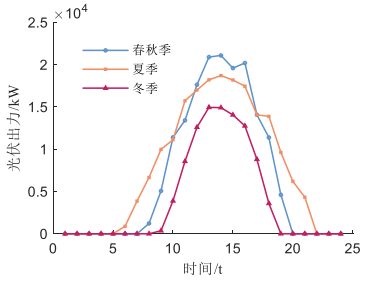


图 3 不同季节分布式光伏出力曲线

Fig.2 Output Curves of Distributed PVs in Different Seasons

为避免检修时段因短期波动而频繁调整，结合矿山生产与用能的季节性特征，将全年划分为春秋季、夏季和冬季三个场景，每个场景选取一个典型日，凡生产任务、用能需求及光伏出力规律与典型日相似的时段，均采用统一的检修期安排。

3.1 对比分析

初始场景对应矿山现行基础运行方案，仅遵循固定的采煤作业计划与设备检修周期对系统运行进行安排，所有高耗能生产机组的检修时段严格固定，每日统一执行 11:00-16:00 的 6 小时连续检修，不结合季节工况、电价峰谷变化调整检修时段；煤仓、井下水仓、压缩空气罐等缓冲装置仅作为保障矿山基本生产生活需求的附属设施运行，未能发挥能源跨时段调度或可再生能源消纳的调节作用；整体运行无任何针对经济性与新能源消纳的优化设计。

表 1 不同季节检修时段调整

Table 1 Adjustments of Maintenance Time Periods in Different Seasons

	初始情况	调整后
春秋季	11:00-16:00	18:00-23:00
夏季	11:00-16:00	21:00-次日 02:00
冬季	11:00-16:00	18:00-23:00

初始检修时段与低电价时段及光伏高发期部分重叠，导致检修作业占用低价电能或挤占光伏消纳空间。结合表 1 数据可知，经调整后，检修时段被置于电价相对较高的峰段或平段，增加了对低价电能的利用，从而控制用能成本；且通过合理规划避开光伏出力高峰，为光伏电量的高效利用预留了空间。

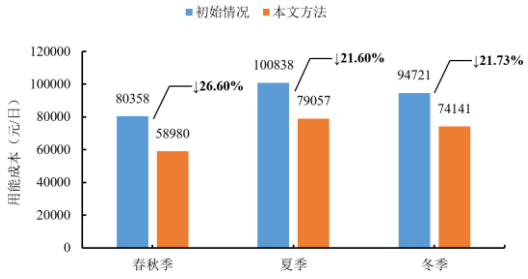


图 4 用能成本对比

Fig.4 Energy Cost Comparison

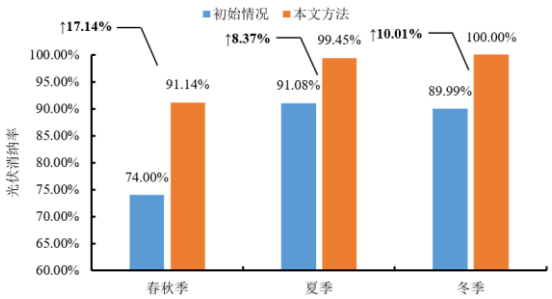


图 5 光伏消纳率对比

Fig.5 PV Absorption Rate Comparison

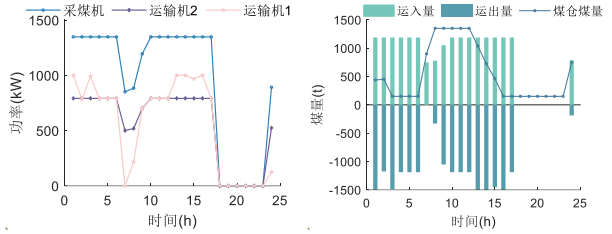
$$\beta=\frac{\sum_{t=1}^{T}\sum_{i=1}^{npv}P_{i,t}-P_{i,t}^{ab}}{\sum_{t=1}^{T}\sum_{i=1}^{npv}P_{i,t}}\times 100\% \tag{17}$$

光伏消纳率定义为全天实际消纳量/全天光伏预测出力总量。式中，β 为光伏消纳率；$P_{i,t}$ 为第 i 个分布式光伏在第 t 时刻的预测功率。如图 4、图 5 所示，三个季节的用能成本均实现不同程度的降低，

同时，光伏出力消纳率提升至 90%以上，其中冬季工况下实现光伏全额消纳，充分体现了所提方法在高比例可再生能源消纳方面的有效性。

3.2 调度结果分析

三个季节的柔性资源调度机制机制本质相同，差异主要体现在参数适配层面，而非调度逻辑的根本性改变。鉴于春秋季光伏出力处于全年峰值水平，该工况最能凸显本文所建模型在柔性资源调节能力上的优势，因此，本节选取春秋季工况作为典型案例展开详细分析。



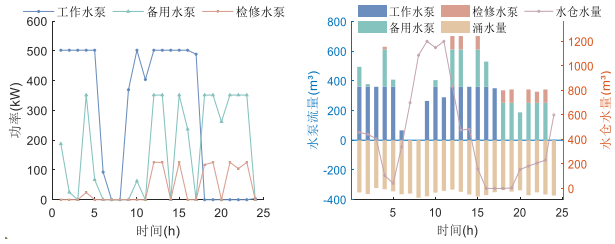
(a)采煤、运输机功率曲线　(b)煤仓煤量变化情况

(a) Power curves of shearer and conveyors　(b) Variation of coal quantity in coal silo

图 6 运输环节调度情况

Fig.6 Transportation Link Scheduling Situation

运输机 2 将采煤机开采的煤料转运至煤仓，其功率需与采煤机协同匹配，运输机 1 因煤仓缓冲作用，其调度具备更高灵活性。由图 6(a)可知，8:00-10:00 为市电电价峰段，此期间采煤设备与运输设备功率呈下降趋势。由于此时段之前煤仓煤料存量趋近下限，为保障后续生产流程的连续性，需在此期间积累煤料储备，以便于在光伏高发期实现运输策略优化；18:00-23:00 涵盖电价平段与峰段，将设备检修计划调整至该时段，可有效规避高电价时段运行成本。煤仓煤量变化情况如图 6 (b)所示，除去设备检修期外，储煤量呈现出较大波动。



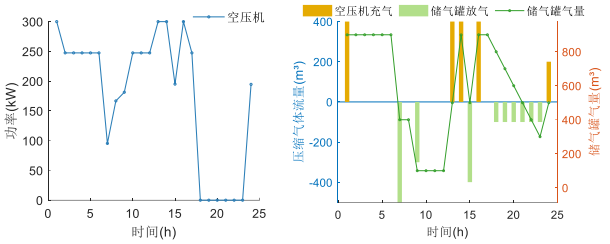
(a)水泵功率曲线　(b)水仓水量变化情况

(a) Power curve of water pumps　(b) Variation of water volume in sump

图 7 排水环节调度情况

Fig.7 Drainage Link Scheduling Situation

在传统水泵调度模式中，工作水泵运行优先级最高，而备用水泵与检修水泵长期处于低负荷状态，导致机组整体运行效率受限。本文提出的优化方案将三台水泵统一调度，实现水泵机组运行效率提升。调度结果如图 7(a)所示，当进入光伏出力高发期时，三台水泵同步进行满功率排水作业。水仓水量变化情况如图 7 (b)所示，与运输环节的特性类似，水仓内水量在调度周期内同样波动较大。



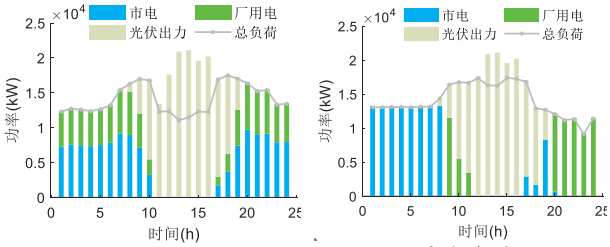
(a)空压机功率曲线　(b)压缩空气罐气量变化

(a) Power curve of air compressor　(b) Variation of air volume in compressed air tank

图 8 空压环节调度情况

Fig.8 Air Compression Link Scheduling Situation

从图 8(a)可以看出，空压机功率曲线和图 6(a)采煤机功率曲线存在相似性。在采煤机正常作业时段，井下气动设备处于正常运行状态，压风需求量较大；而当采煤机停机检修时，井下仅有极少部分气动负荷，压风需求显著降低。进一步结合图 8 (b)分析，在 14:00-15:00 光伏功率峰值时段，空压机提高运行功率，在满足井下用气的同时将光伏盈余电能转换为压缩空气能。当采煤机组检修时，只有小部分气动负荷，此时空压机停机检修，仅用压缩空气罐进行供气。



(a)初始情况　(b)本文方法

(a) Initial situation　(b) Method in this paper

图 9 春秋季电能成分与负荷调整情况

Fig.9 Electric energy composition and load adjustment in spring and Autumn

从图 9 可以看出，本文方法基于市电与直供电的分时价格差异，通过对能源供应结构的动态调整，在提升光伏消纳率的同时有效改善负荷曲线形态，达成削峰填谷的需求响应效果。

4 结论

针对矿山光伏消纳能力不足、能源成本高、现有设备利用率不足等一系列问题，本研究构建了矿山各环节柔性资源动态调度模型，进一步提出考虑灵活检修的矿山柔性资源运行优化方法。通过选取真实矿山企业案例进行仿真分析，得出以下结论：

（1）通过建立运输、排水、压风、供热环节的柔性资源模型，实现了各环节设备功率的动态调控，充分释放了矿山生产环节的柔性潜力，为新能源消纳与成本优化提供了核心支撑。

（2）灵活检修策略显著提升了系统经济性与光

伏消纳能力。将传统固定检修时段动态调整至电价峰段或光伏出力低谷期，有效规避了检修对低价电能时段的占用，为光伏消纳留出空间。

（3）柔性资源与灵活检修的协同优化实现了系统综合效能的提升，矿山负荷曲线得到重构；同时，能源供应结构更贴合电价与光伏出力特征，既降低了用能成本，又提升了新能源利用水平。

参考文献

[1] 朱汉雄,耿笑颖,肖宇,等.新时代西北地区推进能源革命的战略路径研究[J].中国工程科学,2021,23(01):92-100.

[2] 葛世荣,刘洪涛,刘金龙,等.我国煤矿生产能耗现状分析及节能思路[J].中国矿业大学学报,2018,47(01):9-14.

[3] 梁睿,李嘉翔,巩敦卫,等.全清洁能源下的高品质矿区能源系统配置优化方法[J].煤炭学报,2024,49(03):1669-1679.

[4] 齐宁,程林,田立亭,等.考虑柔性负荷接入的配电网规划研究综述与展望[J].电力系统自动化,2020,44(10):193-207.

[5] 颜湘武,王庆澳,卢俊达,等.计及电动汽车和柔性负荷的微电网能量调度[J].电力系统保护与控制,2023,51(17):69-79.

[6] 邓杰,姜飞,王文烨,等.考虑电热柔性负荷与氢能精细化建模的综合能源系统低碳运行[J].电网技术,2022,46(05):1692-1704.

[7] 许周,孙永辉,谢东亮,等.计及电/热柔性负荷的区域综合能源系统储能优化配置[J].电力系统自动化,2020,44(02):53-59.

[8] 束娜,江山,刘春伶,等.计及灵活性资源多时间尺度协调互济的电-气-热综合能源系统优化调度[J].电力建设,2024,45(12):3-15.

[9] 韩丽,喻洪波,王冲,等.考虑建筑物热惯性的综合能源系统主从博弈协调优化策略[J].太阳能学报,2024,45(09):197-209.

[10] 梅府贤,李昀熠,万灿,等.计及交互功率不确定性和柔性负荷的输配协同优化调度[J].高电压技术,2024,50(08):3521-3535.

[11] 张宏业,吴杰康,蔡锦健,等.考虑空调负荷和柔性热负荷响应的综合能源系统储能鲁棒优化配置[J].电网技术,2022,46(07):2733-2744.

[12] Yang, C. Y., et al. Electric vehicles, load response, and renewable energy synergy: A new stochastic model for innovation strategies in green energy systems [J]. Renewable Energy, 2025, 238: 121890.

[13] Hu, H. J., et al. Enhanced evolutionary multi-objective optimization-based dispatch of coal mine integrated energy system with flexible load [J]. Applied Energy, 2022, 307: 118130.

[14] Huang, H. X., et al. Two-stage robust stochastic scheduling for energy recovery in coal mine integrated energy system [J]. Applied Energy, 2021, 290: 116759.

[15] 梁喆,李梅,周孟然.含 P2G 和混合电储能的矿山综合能源系统多目标优化调度[J].电力自动化设备,2021,41(10):122-129.

[16] 吕超贤,罗刚,孙文,等.产-需全链条耦合的矿山综合能源电-热-煤协同低碳调度[J].电力自动化设备,2025,45(02):61-68.

[17] 陈迪蕾,郑征,黄涛,等.基于采煤机和刮板输送机能耗模型的速度协同优化控制[J].煤炭学报,2022,47(06):2483-2498.

[18] Zhang S, Xia X. Modeling and energy efficiency optimization of belt conveyors[J]. Applied energy, 2011, 88(9): 3061-3071.

[19] 吴晨.矿山综合能源系统协同运行与能量交易策略[D].华北电力大学(北京),2024.

[20] 周丹,孙可,张全明,等.含多个综合能源联供型微网的配电网日前鲁棒优化调度[J].中国电机工程学报,2020,40(14):4473-4485+4727.

[21] 林哲,胡泽春,宋永华.最优潮流问题的凸松弛技术综述[J].中国电机工程学报,2019,39(13):3717-3728.

[22] 陈伟,陈龙康,魏占宏,等.基于净能力及二阶锥规划的分布式光储多场景协同优化策略[J].电力自动化设备,2024,44(06):26-34.

017 Oscillation Sppression of Permanent Magnet Synchronous Motor Based on RTDS Hardware-in-the-Loop

Xiangnan Zhang[1],Yanling Lv[1*] and Yuchen Zhang[1]

[1] Harbin University of Science and Technology, Harbin Heilongjiang 150080, China
2671953028@qq.com

Abstract. In actual operation, the phenomenon of oscillation in permanent magnet synchronous motors is quite common, and the occurrence of oscillation accidents may have a serious impact on the stability and reliability of the system. This article proposes a fractional-order PI$^{\lambda}$ control suppression strategy. On the basis of the eigenvalue analysis method to analyse the oscillation mechanism of the permanent magnet synchronous motor, the intrinsic oscillation frequency of the motor is calculated, and a perturbation source with the same frequency as the intrinsic oscillation frequency is introduced to excite the resonance. On the basis of traditional PI control, a fractional-order PI$^{\lambda}$ control strategy is introduced. Through tuning, the integral order of fractional-order PI$^{\lambda}$ that achieves the optimal suppression effect is obtained. The control performance of fractional-order PI$^{\lambda}$ is compared with that of traditional PI control to highlight the advantages of the fractional-order PI$^{\lambda}$ control strategy. The rationality and effectiveness of the fractional-order PI$^{\lambda}$ control strategy are verified through the RTDS hardware-in-the-loop experimental platform.

Keywords: Permanent magnet synchronous motors, Oscillation, Eigenvalue analysis, PI control, RTDS.

1 Introduction

Under the goal of the “dual-carbon” strategy, wind power technology has been developed rapidly, and has become one of the most mature and fastest growing clean energy technologies in the world. Among them, Permanent Magnet Synchronous Motor (PMSM), because its rotor is directly connected to the wind turbine, makes the energy transmission process simplified and the energy conversion efficiency improved. The absence of gears, slip rings and brush structures reduces the frequency of failures and reduces the maintenance workload and money at a later stage[1], so it is widely used.

2

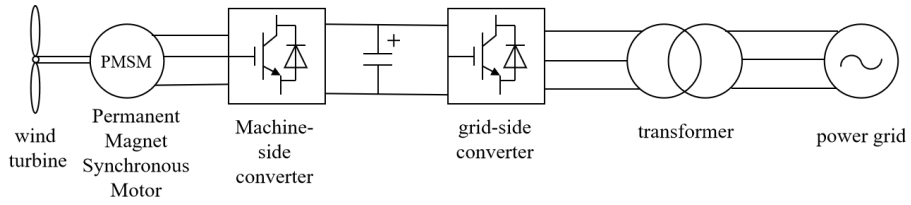


Fig. 1. Structure of PMSM wind power system.

However, the parameters of PMSMs are designed based on ideal grid conditions when they leave the factory. When disturbed by external factors, the initial parameters of wind turbine units cannot guarantee their stable operation, thus causing oscillations. Therefore, it is of vital importance to analyze and suppress the oscillation of PMSM.

At present, the research on oscillations mainly focuses on the analysis of the oscillation mechanism and the strategies for suppressing oscillations. The eigenvalue analysis method is one of the main approaches for analyzing oscillation mechanisms. Reference [2], the eigenvalue analysis method was employed to establish a linearized mathematical model for the grid-connected system of direct-drive wind power generation. Study the impact of changes in grid strength and adjustments to static var generator control parameters on system operational stability. References [3-4] address the issue of significant differences in oscillation frequencies between different regions, with 4 Hz oscillations occurring in Texas and 30 Hz oscillations occurring in western China. Using eigenvalue analysis, it was determined that these differences were caused by differences in phase-locked loop parameters. Reference [5] constructed a linearized state-space representation suitable for grid-connected wind farms through system modeling and parameter optimization. It used eigenvalue analysis to analyze the specific effects of these factors on the system's oscillation characteristics when there were differences in the operating conditions of each direct-drive wind turbine and the control parameters were not completely identical.

PI control strategy is one of the main methods for oscillation suppression. Reference [6] addresses issues such as large overshoot of PMSM speed and low rotor position detection accuracy, and proposes a BP neural network-intelligent PID sliding mode observer control strategy. Reference [7] proposed a multi-objective optimization control strategy for water-wind pumped storage interconnected microgrids and designed a fractional-order PID control speed regulation system for pumped storage units to improve the power supply quality and stability of their grid-connected systems. Reference [8] addresses the issue of motor control performance degradation due to the coupling of multiple factors during vector control of PMSM speed control systems, and proposes a dual-loop control strategy based on self-coupled PI control optimization.

Based on the traditional PI control, this paper introduces the fractional-order PI^{λ} control to further enhance the overall suppression effect of oscillations. Reference [9] applied the fractional-order control theory in the design of conventional controllers, extending the traditional PID control to fractional-order PID control. Reference [10] added two new parameters, namely the integral order λ and the derivative order μ,

to the traditional PID controller, thereby obtaining the fractional-order PID controller. Reference [11] based on the fractional-order control theory, proposed the fractional-order PID control for servo systems. Reference [12] introduced a fractional-order PID controller to analyze the nonlinear problems of various parameters in the rocket launcher AC servo system under different disturbances.

Use the RTDS hardware-in-the-loop experimental platform to verify the rationality and effectiveness of the fractional-order PI^{λ} control strategy for suppressing oscillations.

2 Mathematical model of Permanent Magnet Synchronous Motors

This paper selects a surface-type PMSM with equal direct and cross-axis inductances ($L_d = L_q$) as the research object. Due to the overly complex internal structure of PMSM, the following assumptions are made: (1) Without considering the rotor magnetic resistance, and ignoring the influence of eddy currents and hysteresis losses; (2) It is believed that both the excitation magnetic field and the armature reaction magnetic field exhibit a sinusoidal distribution pattern in the air gap region; (3) Assuming that the permanent magnet does not have conductive properties, its internal magnetic permeability is the same as that of the air medium. To simplify the analysis and solution process, the mathematical equations of PMSM in the d-q coordinate system are adopted[13]:

Voltage equation:

$$\begin{cases} u_d = R_s i_d + L_d \dfrac{di_d}{dt} - \omega_e L_q i_q \\ u_q = R_s i_q + L_q \dfrac{di_q}{dt} + \omega_e L_d i_d + \omega_e \psi_f \end{cases} \tag{1}$$

motion equation:

$$\frac{d\omega_e}{dt} = \frac{N_p}{J}(T_e - T_L) - \frac{B}{J}\omega_m \tag{2}$$

Torque equation:

$$T_e = 1.5 N_p i_q \left[\psi_f + (L_d - L_q) i_d \right] \tag{3}$$

Where, u_d and u_q represent the components of the stator voltage in the d and q axes. i_d and i_q represent the components of the stator current in the d and q axes; ω_e represent the electrical angular velocity of the rotor; ψ_d and ψ_q represent the d and q axis magnetic fluxes of the generator; L_d and L_q represent the inductance of the d and q axes; N_p represent the number of pole pairs of the motor.

3 Analysis of the oscillation mechanism of Permanent Magnet Synchronous Motors

3.1 Eigenvalue analysis method

The eigenvalue analysis method is a commonly used approach for analyzing oscillation mechanisms. It transforms the complex data into a set of independent feature vectors and corresponding eigenvalues by performing operations on the matrix and decomposing the eigenvalues[14].

(1) State space representation: Describing a dynamic system as a set of n first-order nonlinear ordinary differential equations:

$$\dot{\boldsymbol{x}} = \boldsymbol{f}(\boldsymbol{x}, \boldsymbol{u}) \tag{4}$$

Where, $\boldsymbol{x} = \begin{bmatrix} x_1 & x_2 & \cdots & x_n \end{bmatrix}^{\mathrm{T}}$; $\boldsymbol{u} = \begin{bmatrix} u_1 & u_2 & \cdots & u_n \end{bmatrix}^{\mathrm{T}}$; $\boldsymbol{f} = \begin{bmatrix} f_1 & f_2 & \cdots & f_n \end{bmatrix}^{\mathrm{T}}$; The column vector x represents the state vector; The single value x_i represents a state variable; The column vector $\boldsymbol{u}$ represents the input vector of the system; $\dot{\boldsymbol{x}}$ represents the derivative of the state variable with respect to time.

(2) Linearization representation: Now, the steps for the linearization formula (4) are described. Equilibrium points x_0 and u_0 represent the initial state vector and the initial input vector respectively. When all the differential terms are simultaneously equal to 0, the equilibrium point is obtained:

$$\dot{\boldsymbol{x}} = \boldsymbol{f}(\boldsymbol{x}_0, \boldsymbol{u}_0) = 0 \tag{5}$$

The nonlinear function $\boldsymbol{f}(\boldsymbol{x}_0, \boldsymbol{u}_0)$ can be expressed using the Taylor expansion formula. When the second and higher-order terms of $\boldsymbol{x}_0$ and $\boldsymbol{u}_0$ are ignored, the result is:

$$\begin{aligned} \dot{\boldsymbol{x}}_i = f_i(\boldsymbol{x}_0, \boldsymbol{u}_0) = \frac{\partial f_i}{\partial x_1} x_1 + \cdots + \frac{\partial f_i}{\partial x_n} x_n \\ + \frac{\partial f_i}{\partial u_1} u_1 + \cdots + \frac{\partial f_i}{\partial u_r} u_r \end{aligned} \tag{6}$$

Where, $i = 1, 2, \cdots n$. Therefore, the linearized form of Equation (6) is:

$$\Delta \dot{\boldsymbol{x}} = \mathbf{A} \Delta \boldsymbol{x} + \mathbf{B} \Delta \boldsymbol{u} \tag{7}$$

Where, $\mathbf{A} = \begin{pmatrix} \frac{\partial f_1}{\partial x_1} & \cdots & \frac{\partial f_1}{\partial x_n} \\ \vdots & \ddots & \vdots \\ \frac{\partial f_n}{\partial x_1} & \cdots & \frac{\partial f_n}{\partial x_n} \end{pmatrix}$ represents the state matrix; $\mathbf{B} = \begin{pmatrix} \frac{\partial f_1}{\partial u_1} & \cdots & \frac{\partial f_1}{\partial u_r} \\ \vdots & \ddots & \vdots \\ \frac{\partial f_n}{\partial u_1} & \cdots & \frac{\partial f_n}{\partial u_r} \end{pmatrix}$ represents the input matrix; $\boldsymbol{x}$ represents an n-dimensional state vector; $\boldsymbol{u}$ represents an n-dimensional input vector.

(3) Eigenvalue: The eigenvalues of the matrix are the parameters λ when the equation $\boldsymbol{\phi} \neq 0$ is satisfied.

$$\mathbf{A}\boldsymbol{\phi} = \lambda\boldsymbol{\phi} \tag{8}$$

Where, $\mathbf{A}$ is an $n \times n$ matrix; $\boldsymbol{\phi}$ is an $n \times 1$ vector.

To obtain the eigenvalues, Equation (8) is transformed into:

$$(\mathbf{A} - \lambda\mathbf{I})\boldsymbol{\phi} = 0 \tag{9}$$

The characteristic values are obtained by solving the following characteristic equation:

$$|\boldsymbol{A} - \lambda\boldsymbol{I}| = 0 \tag{10}$$

Where, λ is the sought eigenvalue; $\mathbf{I}$ is identity matrix. The sought eigenvalues is either real numbers or complex numbers.

(4) stability analysis: The eigenvalue is $\lambda = \sigma + j\omega$. When the eigenvalues are different, the stability of the system also varies. Specifically, there are two scenarios as follows:

a. When the eigenvalue is a real number ($\omega = 0$), the system exhibits a non-oscillatory mode.

b. When the eigenvalue is a complex number ($\omega \neq 0$), the system exhibits an oscillatory mode.

The real part of the eigenvalue indicates the damping, whereas the imaginary part indicates the rate of oscillations. Therefore, the oscillation frequency expressed in Hz is:

$$f = \frac{\sqrt{\sigma^2 + \omega^2}}{2\pi} \tag{11}$$

damping ratio:

$$\xi = \frac{-\sigma}{\sqrt{\sigma^2 + \omega^2}} \tag{12}$$

3.2 computational analysis of examples

Using the mathematical equations of PMSM in the d-q coordinate system as described in the previous chapter, the oscillation of the PMSM is theoretically analyzed through the eigenvalue analysis method. The parameters of the PMSM are shown in Table 1.

Table 1. Model parameters of permanent magnet synchronous motor.

Symbol	Parameters	Units	Numerical value
N_P	number of pole-pairs	-	4
R_s	stator resistance	Ω	2.5
L_d	d-axis inductor	mH	8.5
L_q	q-axis inductor	mH	8.5
ψ_f	rotor flux	Wb	0.175
J	rotational inertia	Kg • m^2	0.02
B	damping coefficient	Nm/s	0.008
T_L	load torque	N • m	3

The state variables are:

$$\dot{\boldsymbol{x}} = \boldsymbol{f}(i_{\mathrm{d}}, i_{\mathrm{q}}, \omega_{\mathrm{e}}) \tag{13}$$

The equation of state in space can be expressed as:

$$\begin{cases} \dot{i}_{\mathrm{d}} = -\dfrac{R_s}{L_{\mathrm{d}}} i_{\mathrm{d}} + \dfrac{u_{\mathrm{d}}}{L_{\mathrm{d}}} + \omega_{\mathrm{e}} \dfrac{L_{\mathrm{q}}}{L_{\mathrm{d}}} i_q \\ \dot{i}_{\mathrm{q}} = -\dfrac{R_s}{L_{\mathrm{q}}} i_{\mathrm{q}} + \dfrac{u_{\mathrm{q}}}{L_{\mathrm{q}}} - \omega_{\mathrm{e}} \dfrac{L_{\mathrm{d}}}{L_{\mathrm{q}}} i_{\mathrm{d}} - \omega_{\mathrm{e}} \dfrac{1}{L_{\mathrm{q}}} \psi_{\mathrm{f}} \\ \dot{\omega}_{\mathrm{e}} = \dfrac{N_{\mathrm{p}}}{J}(T_{\mathrm{e}} - T_L) - \dfrac{B}{J} \omega_{\mathrm{e}} \end{cases} \tag{14}$$

Using equation (14) to solve for the equilibrium point, the equilibrium point refers to the point where all the differential terms $\dot{\boldsymbol{i}}_{\mathrm{d}}$、$\dot{\boldsymbol{i}}_{\mathrm{q}}$、$\dot{\boldsymbol{\omega}}_{\mathrm{e}}$ are simultaneously zero. At this point, all the variables have a constant value and do not change with time.Using the MATLAB program, we calculated the equilibrium points of the PMSM itself:

$$i_{\mathrm{d}} = -0.3825、\ i_{\mathrm{q}} = 2.7801、\ \omega_{\mathrm{e}} = -40.467 \tag{15}$$

Linearize equation (14) at the equilibrium point, and its matrix form is:

$$\begin{bmatrix} \dot{i}_{\mathrm{d}} \\ \dot{i}_{\mathrm{q}} \\ \dot{\omega}_{\mathrm{e}} \end{bmatrix} = \begin{bmatrix} -\dfrac{R_s}{L_{\mathrm{d}}} & \omega_{\mathrm{e}} \dfrac{L_{\mathrm{q}}}{L_{\mathrm{d}}} & \dfrac{L_{\mathrm{q}}}{L_{\mathrm{d}}} i_{\mathrm{q}} \\ -\omega_{\mathrm{e}} \dfrac{L_{\mathrm{d}}}{L_{\mathrm{q}}} & -\dfrac{R_s}{L_{\mathrm{q}}} & -\dfrac{\psi_{\mathrm{f}}}{L_{\mathrm{q}}} - \dfrac{L_{\mathrm{d}}}{L_{\mathrm{q}}} i_{\mathrm{d}} \\ \dfrac{1.5 i_{\mathrm{q}} (L_{\mathrm{d}} - L_{\mathrm{q}})}{J} & \dfrac{1.5 i_{\mathrm{d}} (L_{\mathrm{d}} - L_{\mathrm{q}})}{J} + \dfrac{1.5 \psi_{\mathrm{f}}}{J} & -\dfrac{B}{J} \end{bmatrix} \begin{bmatrix} i_{\mathrm{d}} \\ i_{\mathrm{q}} \\ \omega_{\mathrm{e}} \end{bmatrix} + \begin{bmatrix} \dfrac{1}{L_{\mathrm{d}}} & 0 \\ 0 & \dfrac{1}{L_{\mathrm{q}}} \end{bmatrix} \begin{bmatrix} u_{\mathrm{d}} \\ u_{\mathrm{q}} \end{bmatrix} \tag{16}$$

Where:

$$\mathbf{A} = \begin{bmatrix} -\dfrac{R_s}{L_{\mathrm{d}}} & \omega_{\mathrm{e}} \dfrac{L_{\mathrm{q}}}{L_{\mathrm{d}}} & \dfrac{L_{\mathrm{q}}}{L_{\mathrm{d}}} i_{\mathrm{q}} \\ -\omega_{\mathrm{e}} \dfrac{L_{\mathrm{d}}}{L_{\mathrm{q}}} & -\dfrac{R_s}{L_{\mathrm{q}}} & -\dfrac{\psi_{\mathrm{f}}}{L_{\mathrm{q}}} - \dfrac{L_{\mathrm{d}}}{L_{\mathrm{q}}} i_{\mathrm{d}} \\ \dfrac{1.5 i_{\mathrm{q}} (L_{\mathrm{d}} - L_{\mathrm{q}})}{J} & \dfrac{1.5 i_{\mathrm{d}} (L_{\mathrm{d}} - L_{\mathrm{q}})}{J} + \dfrac{1.5 \psi_{\mathrm{f}}}{J} & -\dfrac{B}{J} \end{bmatrix} \quad \mathbf{B} = \begin{bmatrix} \dfrac{1}{L_{\mathrm{d}}} & 0 \\ 0 & \dfrac{1}{L_{\mathrm{q}}} \end{bmatrix} \tag{17}$$

Where, A is state matrix, which is also Jacobian matrix; B is input matrix.

Use the calculated equilibrium point as the initial value of state variable. Together with parameters of motor, substitute it into the state matrix **A** to solve for the

eigenvalues. Substitute the state matrix **A** into $|\mathbf{A}-\lambda\mathbf{I}|=0$ to obtain the characteristic equation, and then calculate the eigenvalues of matrix **A** using the MATLAB program.

Tab 2. Characteristic values of permanent magnet synchronous motor.

Modal	Eigenvalue	Oscillation frequency/Hz	Damping ratio
$\lambda_{1,2}$	-2.9368+j0.4059	0.4718	0.9906
λ_3	-0.0127	0	1

As can be seen from Table 2, the PMSM has one oscillatory mode and one non-oscillatory mode. Using formulas (11) and (12), the oscillation frequency of mode $\lambda_{1,2}$ was calculated to be 0.4718 Hz, and the corresponding damping ratio was 0.9906. This falls within the low-frequency oscillation frequency range.

This frequency $f=$ 0.4718 Hz can be regarded as the resonance frequency of the system. By introducing a disturbance source with the same natural frequency as the system, the oscillation mode of the system can be effectively excited, thereby enabling a further analysis of the suppression strategy for the oscillation.

4 Permanent magnet synchronous motor oscillation suppression strategy

Taking the oscillation model of PMSM obtained in the previous chapter as the research object, the oscillation suppression strategies for the PMSM are studied. Based on the traditional PI control, a fractional-order PI^{λ} control strategy was designed; and in MATLAB/Simulink environment, simulation models of both were established. By adjusting different integration orders, the fractional-order PI^{λ} control with the best suppression effect was determined. Compared with the traditional PI, the suppression effect of the fractional-order PI^{λ} is highlighted. That is, in this study, the fractional-order PI^{λ} control strategy is selected for the oscillation suppression.

4.1 Traditional PI control

The time-domain mathematical expression of the traditional PI:

$$u(t)=K_{\mathrm{p}}e(t)+K_{\mathrm{i}}\int e(t)dt \tag{18}$$

Where, K_{p} represents coefficient of proportional link; K_{i} represents coefficient of integral link.

Transfer function of traditional PI is:

$$G_c(s)=K_{\mathrm{p}}+\frac{K_{\mathrm{i}}}{s} \tag{19}$$

4.2 Fractional-order PI^{λ} control

When the differential order $\mu=0$, the $PI^{\lambda}D^{\mu}$ control is equivalent to the fractional-order PI^{λ} control. When fractional order $\lambda=1$, it is equivalent to the traditional PI

control. Compared with the traditional PI controller, it adds an additional parameter λ , which can take any real value within the range of 0 to 2. This expansion of the controller's value range enhances the precision and flexibility of the control system.

The time-domain mathematical expression of the fractional-order PI$^{\lambda}$:

$$u(t) = K_p e(t) + K_i s^{-\lambda} e(t) \tag{20}$$

Transfer function of fractional-order PI$^{\lambda}$ is:

$$G_c(s) = K_p + \frac{K_i}{s^{\lambda}} \tag{21}$$

Where, λ represents the fractional order of the integration section, $\lambda > 0$.

Figure 2 is block diagram of fractional-order PI$^{\lambda}$ control system.

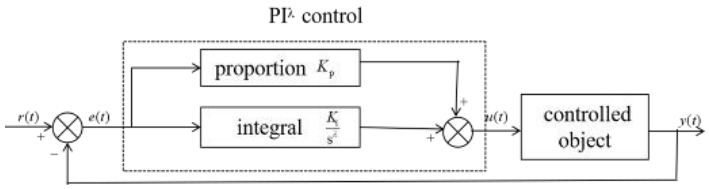


Fig. 2. Structural diagram of fractional-order PI$^{\lambda}$ control system.

In the figure, $r(t)$ represents the desired input of the control system, $y(t)$ represents the output of the control system, and $e(t)$ represents error between desired input and actual output.

Figure 3 shows fractional-order PI$^{\lambda}$ control structure diagram of PMSM:

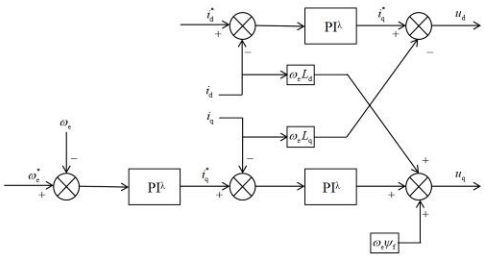


Fig. 3. Fractional-order PI$^{\lambda}$ control structure diagram of PMSM.

4.3 Comparison of control effects

In MATLAB/Simulink, traditional PI and fractional-order PI$^{\lambda}$ control strategy were respectively established. By adjusting different integration orders, the optimal integration order for the fractional-order PI$^{\lambda}$ to achieve the best suppression effect was obtained. Then, the suppression effect of this order of fractional-order PIλ was compared with that of the traditional PI.

The integral order λ of the fractional-order PI$^{\lambda}$ control was compared when it was 0.5, 0.4, and 0.3. It was concluded that when the integral order of the fractional-order

PI$^{\lambda}$ for suppressing ω_e was 0.4, the overshoot of the controlled quantity was the smallest, closest to the target value, and the suppression effect was the best.

The integral order λ of the fractional-order PI$^{\lambda}$ control was compared when it was 0.4, 0.3, and 0.2. It was concluded that when the integral order of the fractional-order PI$^{\lambda}$ for suppressing i_d was 0.3, the overshoot of the controlled quantity was the smallest, closest to the target value, and the suppression effect was the best.

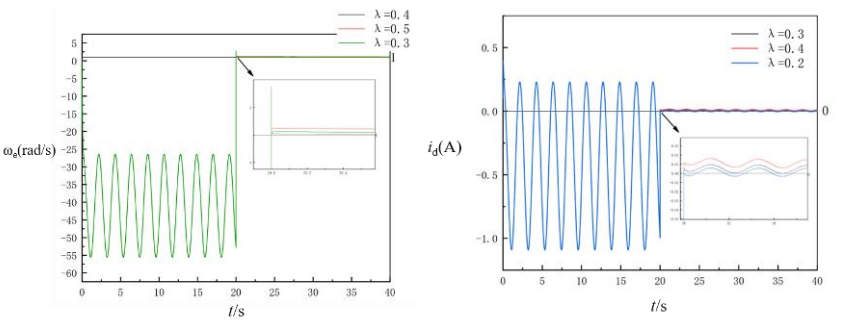


Fig. 4. The inhibitory effect of ω_e and i_d at different integral orders.

To verify superiority of fractional-order PI$^{\lambda}$ control performance, while keeping proportional coefficient K_p and the integral coefficient K_i the same, oscillation suppression was carried out at 20 seconds. The suppression effect was compared through waveform diagrams.

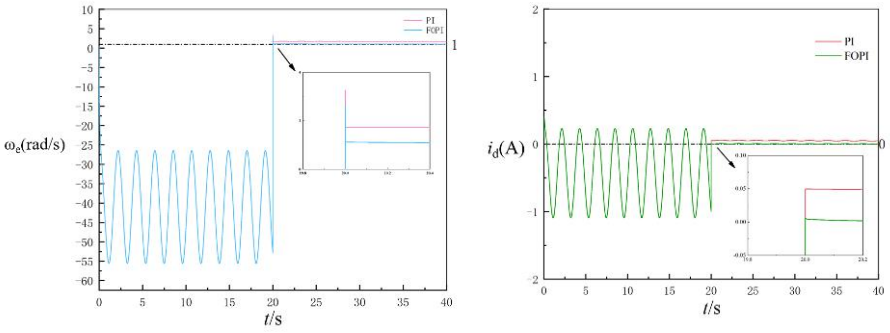


Fig. 5. Comparison of oscillation suppression effects of ω_e and i_d.

In the simulation experiment, the output target value of ω_e and i_d was set to the nominal value $\omega_e^* = 1$ and $i_d^* = 0$. At 20 seconds, the control strategy began to suppress the oscillation. In Figure 5, compared with traditional PI control, fractional-order PI$^{\lambda}$ control strategy only changes the integration order λ, which enables output value to stably remain near the target value. This result indicates that fractional-order PI$^{\lambda}$ control has superior performance in suppressing ω_e and i_d oscillations.

5 RTDS hardware-in-the-loop experimental verification

This chapter builds a mathematical model that is exactly the same as the oscillation model of PMSM in MATLAB/Simulink using corresponding software platform RSCAD. Real-time simulation analysis is conducted using RTDS. After discretizing the fractional-order PI$^{\lambda}$ control strategy, it is embedded into the DSP controller. Using RTDS as the input signal source and connecting it to the DSP controller, the output signal of the DSP is fed back to RTDS through a differential amplifier, thereby achieving the oscillation suppression of PMSM. Figure 6 shows the overall experimental scheme. Figure 7 presents closed-loop control experimental platform, which is used to verify the rationality and effectiveness of the oscillation control strategy for the permanent magnet synchronous motor.

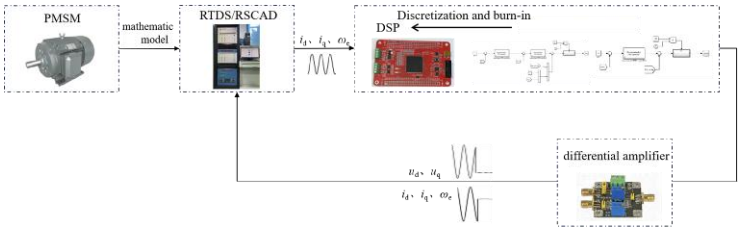


Fig. 6. Overall experimental plan diagram.



Fig. 7. RTDS hardware in the loop closed-loop system.

5.1 Implemented based on the DSP control program

Discretization of Fractional-order PI$^{\lambda}$ Control: The previous chapter's simulation experiment has verified that the fractional-order PI$^{\lambda}$ control is selected for the oscillation suppression of PMSM. To make the DSP function as a controller, the debugged fractional-order PI$^{\lambda}$ control program needs to be burned into the DSP. Since the DSP controller cannot directly process continuous signals, the continuous signals must be converted into discrete form signals. Therefore, the fractional-order PI$^{\lambda}$ control discrete processing is realized through MATLAB's M-function. And a simulation model of the discretized fractional-order PI$^{\lambda}$ control strategy is established.
Simulink program burning: This paper employs the TMS320F28379D model of DSP developed by TI Company as the oscillation suppression controller. Installing

the hardware support package Embedded Coder Support Package for Texas Instruments C2000 Processors in MATLAB, ensure that the three files, TI controlSUITE, TI Code Composer Studio and TI C2000Ware, are already present on the computer, and set up the corresponding paths to enable MATLAB to complete the code generation process[15].



Fig. 8. Simulink program burning.

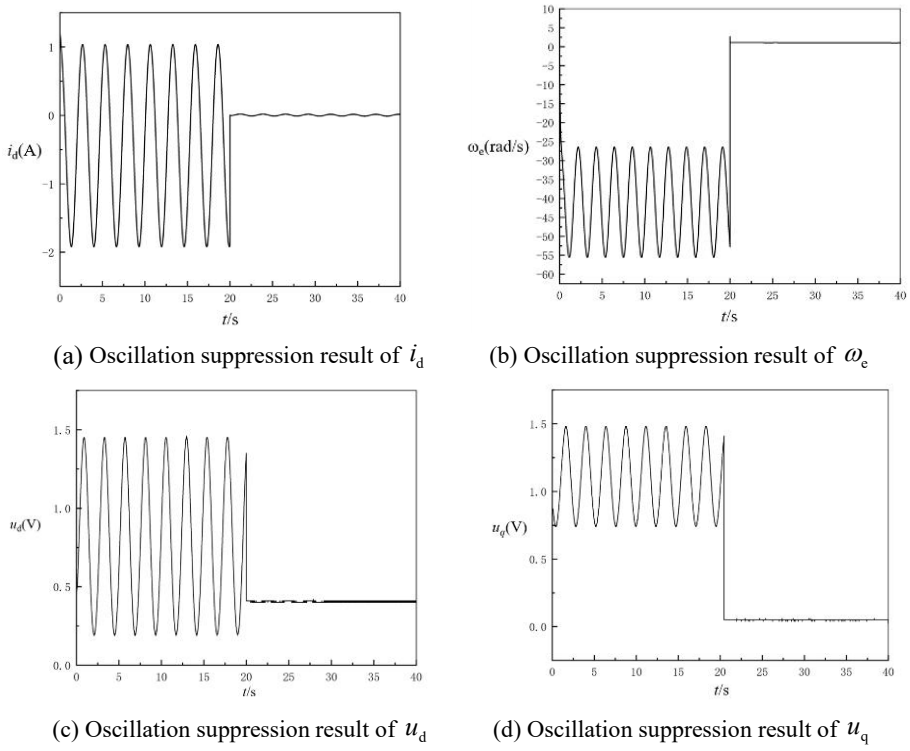
5.2 RTDS simulation model

To verify effectiveness and feasibility of fractional-order PI $^{\lambda}$ control strategy, simulation model of PMSM oscillation and suppression, which is consistent with that in MATLAB/Simulink, was established in the RTDS supporting software RSCAD. That is, PMSM oscillation suppression model was run in RTDS for real-time simulation analysis.

5.3 experimental result

The mathematical model of PMSM is run in RTDS. i_d , i_q ,and ω_e are input quantities that enter the DSP which contains fractional-order PI $^{\lambda}$ control strategy. The output u_d and u_q are sent through a differential amplifier back to RTDS. The input and output quantities are fed back to the RTDS through the DSP controller. The oscillation suppression effect of i_d、 ω_e is shown in the waveform diagram in RSCAD. The oscillation suppression results of u_d and u_q are depicted as the waveforms collected by the oscilloscope, as shown in Figure 9.

According to Figure 9, it can be concluded that before 20 seconds, the fractional-order PI$^{\lambda}$ control in the DSP did not suppress the oscillation. At 20 seconds, the oscillation characteristics of i_d , ω_e , u_d and u_q were significantly suppressed. Among them, the overshoot of i_d was only 0.008, that of ω_e was 0.075, that of u_d was 0.08, and that of u_q was 0.07; and all of them were able to precisely stabilize at the target value.



(a) Oscillation suppression result of i_d (b) Oscillation suppression result of ω_e

(c) Oscillation suppression result of u_d (d) Oscillation suppression result of u_q

Fig. 9. Oscillation suppression result.

The experimental verification results conducted using the RTDS hardware-in-the-loop system indicate that the fractional-order PI$^{\lambda}$ control strategy has a significant effect in suppressing the oscillations of PMSM, thereby validating effectiveness of this oscillation suppression strategy.

6 conclusion

This paper analyzes oscillation suppression problem of PMSM. It uses the eigenvalue analysis method to analyze the oscillation mechanism of the motors. The oscillation suppression of the motors is achieved through the fractional-order PI$^{\lambda}$ control strategy. Combined with the case study analysis and the RTDS hardware-in-the-loop experiment verification, the following conclusions are drawn:

(1) The oscillation mechanism of PMSM was studied by using the eigenvalue analysis method. Firstly, the theoretical basis of the eigenvalue analysis method was expounded. Then, it was used to analyze the oscillation mechanism of PMSM, and stable equilibrium point of motor was solved. Subsequently, the natural oscillation frequency of the motor was determined to be f=0.4718 Hz and the damping ratio was 0.9906. Finally, the oscillation frequency of the disturbance source is determined

based on the inherent oscillation frequency. A cos disturbance source with an oscillation frequency of f=0.4718 Hz is introduced to excite resonance, which is used as the basis for building the oscillation model of PMSM.

(2) To suppress oscillation of PMSM, a fractional-order PI$^{\lambda}$ control strategy was proposed. This method was an improvement based on traditional PI control, and the mathematical model of fractional-order PI$^{\lambda}$ control strategy was established, and its control principle was analyzed. A MATLAB/Simulink simulation model of the traditional PI and fractional-order PI$^{\lambda}$ control system was established. By adjusting different fractional-order PI$^{\lambda}$ integration orders, it was determined that when the integration order of the fractional-order PI$^{\lambda}$ for suppressing ω_e was 0.4 and the integration order for suppressing i_d was 0.3, the overshoot of the fractional-order PI$^{\lambda}$ control output was much smaller than that of the traditional PI, and it could better stabilize around the target value. The overall oscillation suppression performance was more superior.

(3) Using the RTDS hardware-in-the-loop experimental platform, the effectiveness of the fractional-order PI$^{\lambda}$ control suppression strategy was verified. A fractional-order PI$^{\lambda}$ control system with DSP as the controller was built. The permanent magnet synchronous motor system model was established in the RTDS simulation system to realize a hardware-in-the-loop semi-physical closed-loop system. The experimental results show that the overshoot of i_d is only 0.008, that of ω_e is 0.075, that of u_d is 0.08, and that of u_q is 0.07. Therefore, the analysis method and suppression strategy for the oscillation of PMSM proposed in this paper are feasible and effective.

References

1. Hong Faping. Analysis and control of wind power grid integration based on a permanent magnet synchronous generator [D].Tianjin University of Technology, Tianjin (2020).
2. Wang Dazhong, Wang Yupeng. Influence Analysis of SVG on Subsynchronous Oscillation Characteristics of Direct drive Wind Farm [J]. Jilin Electric Power 51(06), 21-26 (2023).
3. Fan L， Miao Z． Wind in Weak Grids： 4Hz or 30Hz Oscillations? [J]. IEEE Transactions on Power Systems 33(5), 5803-5804 (2018).
4. Li Y, Fan L, Miao Z． Wind in Weak Grids： Low-Frequency Oscillations, Subsynchronous Oscillations, and Torsional Interactions [J]. IEEE Transactions on Power Systems 35(1), 109-118 (2020).
5. Dong Wenkai, Du Wenjuan, Wang Haifeng. Dynamic Equivalent Model of a Grid-connected Wind Farm for Oscillation Stability Analysis [J]. Proceedings of the CSEE 41(01), 75-87+399 (2021).
6. Zheng Rui, Zhang Jixiang, Dong Xuesong,et al. BP Neural Network-intelligent PID Synovial Observation Vector Control Algorithm for Permanent Magnet Synchronous Motor [J]. Journal of Detection & Control 46(05), 124-131 (2024).
7. Multi-objective Fractional-order PID-based Optimal Control of Hydro-Wind Pumped Storage Grid-Connected System, http//kns．cnki．net/kcms/detail/42, 2025/03/05．

8. Guan Wenqing, Cheng Yi, Dou Manfeng,et al. Speed Control System Based on Proportional Resonance Autocoupling PI Control [J]. Journal of Northwestern Polytechnical University 42(04), 673-682 (2024).
9. Xue Dingyu, Chen Yangquan. Solving Control Mathematical Problems with MATLAB [M]. 1th ed. Tsinghua University Press, Beijing (2004).
10. Odlubny,I． Fractional-order systems and $PI^{\lambda}D^{\mu}$-controllers [J]. IEEE Transactions on Automatic Control 44(1), 208-214 (1999).
11. Shao Junpeng, Zhang Ling, Jin Zhaohui. Fractional Order PID Control for an Electro-hydraulic Position Servo System Based on Repetitive Control Compensation [J]. Journal of Beijing University of Technology 41(04), 519-525 (2025).
12. Yin Jinsong, Wang Ronglin, Gao Qiang,et al. Fractional Order PID of AC Servo System Based on Neural Network Active Disturbance Rejection Control [J]． Electronics Optics & Control 26(05), 20-25 (2019)．
13. Li Yang, Yang Fangyan, Li Qingdu,et al. Global Integral Terminal Sliding Mode Vector Control of Permanent Magnet Global Integral Terminal Sliding Mode Vector Control of Permanent Magnet [J]. Automation of Electric Power Systems, 1-12 (2024).
14. Hu Shousong. Principles of Automatic Control [M]. 6th ed. Science Press, Beijing (2004).
15. Wang Yuanlin, Wu Xuan, Zhao Dongdong, et al. Permanent Magnet Motor Control Based on Simulink + DSP Code Generation [M]. 1th ed. China Machine Press, Beijing (2024).

018 基于滑模自抗扰控制的光伏并网次同步振荡抑制方法研究

杨旭东，张心怡，王德林

（西南交通大学电气工程学院，四川 成都 611756）

Research on Sub-synchronous Resonance Suppression Method Based on Sliding Mode-active Disturbance Rejection Control for Power Grid Connected with PV

Yang Xudong，Zhang Xinyi，Wang Delin

(Southwest Jiaotong University, Sichuan 611756, China)

ABSTRACT: When distributed PV is connected to a weak AC power grid, the converter control interacts with the power grid, resulting in sub-synchronous oscillation of the system. In order to solve this problem, this paper proposes a photovoltaic grid-connected sub-synchronous oscillation suppression strategy based on Sliding Mode Active Disturbance Rejection Control (SMC-ADRC), which suppresses the oscillation by compensating the oscillation component in real time by expanding the state observer, which has strong robustness. Firstly, a mathematical model of distributed photovoltaic grid connection was established. An active disturbance rejection controller based on linear expansion state observer and sliding mode state feedback law is designed to replace the current inner loop PI control of inverter. The distributed photovoltaic grid-connected model is established in PSCAD/EMTDC, and the effectiveness of the proposed sub-synchronous oscillation suppression strategy is verified by simulation analysis, and the simulation results show that the SMC-ADRC control has a good suppression effect on the oscillation under different working conditions and grid strengths.

KEY WORDS: PV inverter system; sub-synchronous oscillation; active disturbance rejection control; sliding mode control; oscillation suppression

摘要：分布式光伏接入弱交流电网时，换流器控制与电网形成交互作用，导致系统发生次同步振荡(sub-synchronous oscillation，SSO)。针对这一问题，首先，建立了分布式光伏并网数学模型。然后根据 SSO 产生机理提出一种基于滑模自抗扰控制(SMC-ADRC)的光伏并网次同步振荡抑制方法，在传统 ADRC 的基础上，通过改进线性扩张状态观测器实时补偿振荡分量抑制振荡，使用滑模反馈律增强控制稳定性，参数容易整定且具有较强的鲁棒性，用其替代换流器电流内环 PI 控制。最后，在 PSCAD/EMTDC 中建立了分布式光伏并网模型，通过仿真分析验证所提次同步振荡抑制方法的有效性。仿真结果显示，SMC-ADRC 在不同工况和电网强度下对振荡有良好的抑制效果。

关键词：光伏发电；次同步振荡；自抗扰控制；滑模控制；振荡抑制

DOI：10.13335/j.1000-3673.pst.2014.01

0 引言

由于全球经济快速发展而导致的能源短缺以及环境污染等问题，使可再生能源技术的开发和应用受到人们的广泛关注。太阳能作为一种清洁能源，具有资源充足、不受地区限制的优势，在众多可再生能源中占据重要地位。截至 2023 年，中国光伏发电累计装机容量达 609.5GW，同比增长 55.2%，占全球光伏发电累计装机容量的 40%左右，成为中国仅次于火电的第二大能源。随着新能源发电的占比提高，电力系统电力电子化趋势越发明显，由新能源发电控制与弱电网交互引起的次同步振荡成为影响电力系统稳定的重要问题。

为了抑制次同步振荡，国内外学者进行了大量研究。文献[2]根据电网阻抗调整 PV 系统控制参数以增强系统稳定性，但改变 VSC 控制参数可能对系统其他性能造成影响。附加阻尼控制是最常用的振荡抑制方法，该方法通过在并网换流器或 FACTS 装置上附加控制补偿次同步电流/电压，达到增大阻尼，抑制振荡的效果。例如文献[3]设计了双通道附加阻尼控制器，并通过阻抗模型分析论证了其抑

基金项目：国家自然科学基金项目(52207117)。

Project supported by National Natural Science Foundation of China（52207117）。

制作用。文献[4][5]通过在静止无功发生器(SVG)和静止同步补偿器(SSC)中加入附加阻尼控制器抑制振荡。但附加阻尼控制对预设频率外的振荡抑制效果不佳，额外添加设备需要的改造工程量大也会加重维护检修负担。

自抗扰控制无需系统有精确的模型，是以扩张状态观测器为核心的非线性控制方法，它通过估计内外部总扰动并加以补偿以提升系统的控制精度，在电力系统领域应用广泛。

本文以分布式光伏并网系统作为研究对象，首先建立光伏发电数学模型，阐述了 SSO 产生机理。然后，设计一种滑模自抗扰控制的次同步振荡抑制方法。采取线性扩张状态观测器(LESO)，用带宽法获取观测器增益，减少了参数整定难度，并且采用新的集总误差变量，增强对状态变量的跟踪精度，使用滑模控制作为状态反馈律，采用 fal 函数替代符号函数，抑制抖振，进一步增大系统的鲁棒性和抗干扰能力。最后，在 PSCAD/EMTDC 搭建光伏接入弱交流电网模型，对比 SSDC 与所提方法的振荡抑制效果，验证了 SMC-ADRC 可以在不同工况下对光伏并网 SSO 进行抑制。

1 光伏并网系统建模及 SSO 机理

1.1 光伏并网系统建模

光伏并网系统由光伏阵列、DC/AC 换流器及其控制系统，滤波器构成。其拓扑结构如图 1 所示。图中 u_{dc} 为直流电压，i_{dc} 为换流器直流输入电流，L 为滤波电感，L_1 为输电线路等效电感。

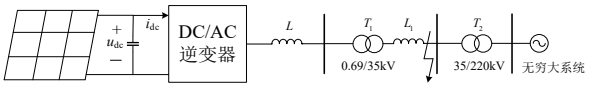


图1 光伏发电并网系统拓扑结构

Fig.1 Topology of grid-connected PV inverter system

光伏并网换流器在 dq 坐标系下的数学模型为

$$\begin{cases} L\dfrac{\mathrm{d}i_d}{\mathrm{d}t} = u_d + \omega L i_q - u_{gd} \\ L\dfrac{\mathrm{d}i_q}{\mathrm{d}t} = u_q - \omega L i_d - u_{gq} \\ C\dfrac{\mathrm{d}u_{dc}}{\mathrm{d}t} = i_{dc} - \dfrac{3}{2}\left(m_d i_d + m_q i_q\right) \end{cases} \tag{1}$$

式中，i_d、i_q、u_d、u_q 为换流器交流侧电流和电压的 dq 轴分量，u_{gd}、u_{gq} 为并网点电压的 dq 轴分量，ω 为系统角频率。

并网换流器采用三相两电平的电压源型换流器，使用 dq 坐标系下双闭环解耦控制策略。m_d、m_q 为换流器调制信号，有：

$$\begin{cases} m_d = \dfrac{2}{u_{dc}}\left[\left(k_{pi} + \dfrac{k_{ii}}{s}\right)\left(i_{dref} - i_d\right) - \omega L i_q + u_{gd}\right] \\ m_q = \dfrac{2}{u_{dc}}\left[\left(k_{pi} + \dfrac{k_{ii}}{s}\right)\left(i_{qref} - i_q\right) + \omega L i_d + u_{gq}\right] \end{cases} \tag{2}$$

式中，k_{pi}、k_{ii} 为电流内环 PI 控制器比例、积分系数。i_{dref}、i_{qref} 为 dq 轴电流参考值。

1.2 次同步振荡产生机理

光伏发电设备接入弱交流电网后，在并网点处受到干扰，产生次同步振荡电流Δi_{g_sso}，从而衍生出次同步电压分量Δu_{g_sso}，受其影响，锁相环输出含扰动相角 θ_s，其表达式为

$$\theta_s = \int[\omega_0 + \left(k_{ppll} + \frac{k_{ipll}}{s}\right)\Delta u_{gq_sso}]\mathrm{d}t \tag{3}$$

电压电流从三相坐标系转换为两相旋转坐标系的表达式为

$$\begin{bmatrix} u_d \\ u_q \end{bmatrix} = T(\theta_s)\begin{bmatrix} u_a \\ u_b \\ u_c \end{bmatrix}, \begin{bmatrix} i_d \\ i_q \end{bmatrix} = T(\theta_s)\begin{bmatrix} i_a \\ i_b \\ i_c \end{bmatrix} \tag{4}$$

式中，$T(\theta_s)$为含扰动相角的派克变换矩阵。

在干扰相角 θ_s 的影响下，并网点电压、电流 i_{gabc}、u_{gabc} 经过 abc/dq 变换，产生扰动电流Δi_{gdq_sso}、Δu_{gdq_sso}，扰动电流信号输入到 VSC 电流内环 PI 控制器，经过比例和积分环节被进一步放大，生成调制信号Δm_{d_sso} 和Δm_{q_sso} 为

$$\begin{cases} \Delta m_{d_sso} = \dfrac{2}{u_{dc}}\left[\left(k_{pi} + \dfrac{k_{ii}}{s}\right)\Delta i_{d_sso} - \omega L\Delta i_{q_sso} + \Delta u_{gd_sso}\right] \\ \Delta m_{q_sso} = \dfrac{2}{u_{dc}}\left[\left(k_{pi} + \dfrac{k_{ii}}{s}\right)\Delta i_{q_sso} + \omega L\Delta i_{d_sso} + \Delta u_{gq_sso}\right] \end{cases} \tag{5}$$

调制信号通过 dq/abc 变换形成新的次同步电压 Δu_{g_sso2}，接着通过外部电路产生新的次同步电流分量 Δi_{g_sso2}，该分量无法通过滤波电感彻底滤除，新的次同步电流与原有次同步电流相互叠加，导致正反馈效应使得振荡增强，进而使系统发生 SSO。从阻抗角度分析则表现为，光伏发电系统与弱电网交互作用，产生的电气谐振点在次同步频率点的相位裕度不足，导致振荡发生。

利用自抗扰控制抑制次同步振荡的原理为：在 SSO 发生后，ADRC 对扰动进行实时估计、补偿，维持换流器输出电流不变，阻断了 SSO 的产生，达到抑制振荡的目的。

2 基于 SMC-ADRC 的振荡抑制方法

线性自抗扰控制(LADRC)由线性跟踪微分器(Linear Tracking Differentiator，LTD)、线性扩张

状态观测器(Linear Extended State Observer，LESO)、线性误差反馈率(Linear State Error Feedback，LSEF)三部分组成。n 阶 LADRC 结构如图 2 所示，r 表示被控量参考值，y 为系统输出量，u 为控制量，b_0 为动态补偿因子，z_1，…，z_{n-1} 为状态变量观测值，z_n 为总扰动观测值。

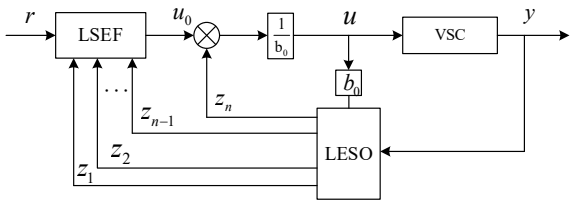


图 2　LADRC 控制框图

Fig.2　Control diagram of LADRC

2.1 改进扩张状态观测器设计

LESO 的作用是根据输入、输出数据实时估计系统的总扰动并进行补偿，是自抗扰控制的核心部分。式(1)的 d 轴电流方程可写为自抗扰控制的标准形式：

$$\frac{\mathrm{d}i_d}{\mathrm{d}t}=bu_d+f \tag{6}$$

式中，f 为包括耦合项的系统内外总扰动，b 为反馈系数。

将 f 扩展为新的状态变量，可得到 LESO 的数学模型：

$$\begin{cases}\dot{z}_1=z_2-\beta_1(z_1-x_1)+b_0u\\ \dot{z}_2=-\beta_2(z_1-x_1)\end{cases} \tag{7}$$

式中，z_1 表示状态变量的观测值。z_2 为 LESO 对系统内外扰动的观测值。β_1、β_2 为增益系数，b_0 为补偿因子。

为了更好的描述状态变量估计值与系统实际值间的误差，对 LESO 做出改进。根据式(7)可得

$$\begin{cases}z_1=e_1+x_1\\ z_2=\dot{z}_1+\beta_1e_1-b_0u\end{cases} \tag{8}$$

可写为：

$$\begin{cases}z_1=x_1+e_1\\ z_2=x_2+\dot{e}_1+\beta_1e_1\end{cases} \tag{9}$$

使用 $e_2=\dot{e}_1+\beta_1e_1$ 作为新的集总扰动观测误差，得到改进扩张状态观测器如下：

$$\begin{cases}e_1=z_1-x_1\\ \dot{z}_1=z_2-\beta_1e_1+b_0u\\ \dot{z}_2=-\beta_2(\dot{e}_1+\beta_1e_1)\end{cases} \tag{10}$$

采用带宽法设计改进 LESO 参数为

$$\begin{cases}\beta_1=2\omega_0\\ \beta_2=\omega_0^2\end{cases} \tag{11}$$

式中，ω_0 为观测器带宽。

2.2 基于 SMC 的状态误差反馈律设计

LADRC 控制采用比例控制作为状态误差反馈律，在系统动态响应较快的情况下，当偏差过大时会降低系统鲁棒性。本文使用滑模控制(SMC)来增强自抗扰控制的稳定性。

以 d 轴电流为例，定义滑模面为

$$e_d=i_{dref}-z_1 \tag{12}$$

改进滑模控制结构：

$$\begin{cases}h=k_1|e_d|^r\,sign(e_d)+v\\ \dot{v}=k_2sign(e_d)\end{cases} \tag{13}$$

式中，h、v 为状态变量。k_1、k_2、r 为待设计参数，r 通常取 0.5。

符号函数容易产生抖振。使用新型幂次函数 fal 替代符号函数 sgn 可减少系统抖振，表达式如下：

$$fal(e_d,\alpha,\delta)=\begin{cases}|e_d|^{\alpha}\,sign(e_d) & |e_d|\ge\delta\\ \dfrac{e_d}{\delta^{\alpha-1}} & |e_d|\le\delta\end{cases} \tag{14}$$

式中，$0<\delta<1,\alpha>0$。$|e_d|\ge\delta$ 时对应的 $|e_d|^{\alpha}$ 的值偏小；$|e_d|<\delta$ 时，对应的 $e_d/\delta^{\alpha-1}$ 的值偏大。通过这种设计可以有效抑制抖振现象。

结合式(10)、式(11)得到 SMC-SEF 表达式为

$$u_0=-k_1\int_0^t fal(e_d)\mathrm{d}t-k_2|e_d|^r\,fal(e_d) \tag{15}$$

$$u=\frac{u_0-z_2}{b_0} \tag{16}$$

综上所述，得到最终的控制结构如图 3 所示，这里以 d 轴自抗扰控制器设计为例，q 轴控制器设计也是同样的原理，不再赘述。用 SMC-ADRC 替代换流器内环 PI 控制，即可实现对次同步分量的实时估计和补偿，抑制振荡。

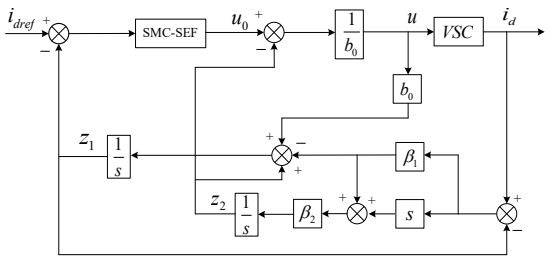


图 3　SMC-ADRC 控制框图

Fig.3　Control diagram of SMC-ADRC

3　算例

为验证所提方法抑制 SSO 的有效性，在 PSCAD/E-MTDC 搭建图 1 所示光伏并网模型，其具体参数如表 1 所示。用调整 PCC 点短路比 SCR 的方式

模拟电网强度变化。在各种工况下对比换流器在不同控制方式下的振荡抑制效果，验证本文所提振荡抑制方法的有效性。

表 1 光伏并网系统参数

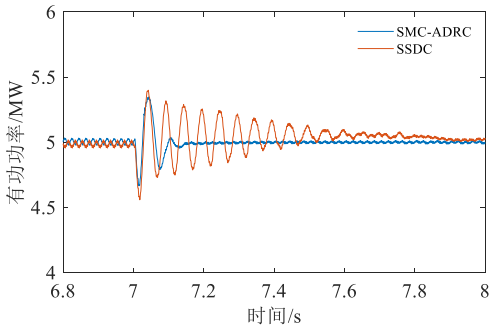
Table 1　Parameters of photovoltaic grid-connected system

参数	数值
直流电容 C	10000μF
滤波电感 L	0.0001H
ESF 增益参数	k_1=0.2，k_2=0.08
VSC 内环 PI 参数	k_{pi}=0.6，k_{ii}=0.1
VSC 外环 PI 参数	k_{pdc}=0.5，k_{idc}=0.01
LESO 的增益参数	b_0=500

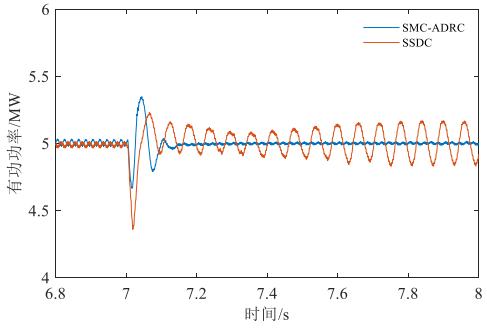
3.1 不同电网强度下的振荡抑制效果

附加次同步阻尼控制(SSDC)是常用的振荡抑制方法，其基本原理是，用滤波器筛选出换流器交流测电流 i_d、i_q 中的次同步分量 i_{sub}，经过移相、限幅后向 VSC 输入电压参考信号，使 VSC 输出与 i_{sub} 同相位的次同步电压 u_{sub}，补偿次同步分量的影响，等效为增加了 VSC 在次同步频率下的正阻尼，起到抑制振荡的作用。对比 SSDC 和 SMC-ADRC 的振荡抑制性能。

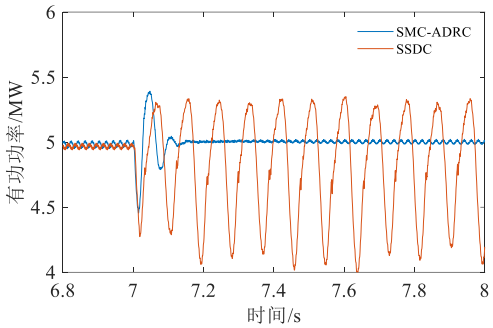
保持光伏输出 P=5MW，在 7 s 时投入电感，改变系统 SCR，激发振荡。SMC-ADRC 与 SSDC 在不同短路比下的振荡抑制效果对比如图 4 所示。



(a)SCR=3 时的输出功率



(b)SCR=2.8 时的输出功率



(c)SCR=2.5 时的输出功率

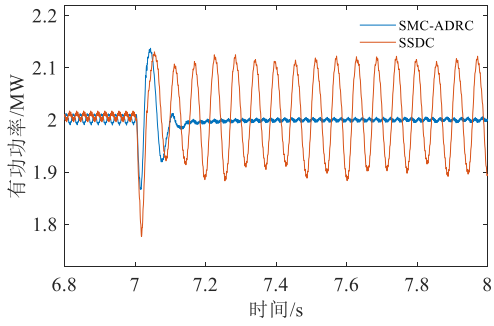
图 4　不同电网强度下 SMC-ADRC 与 SSDC 抑制效果对比

Fig.4　Comparison of suppression effect between SMC-ADRC and SSDC under different SCR

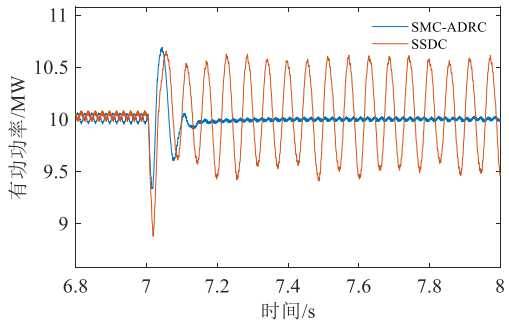
由图 4 可知，当 SCR=3 时，采用 SMC-ADRC 和 SSDC 均能抑制振荡，SMC-ADRC 只需 0.2 s 即可抑制振荡，而 SSDC 则需要 1s 才能抑制次同步分量，作用缓慢，效果欠佳。当 SCR=2.8、2.5 时，SSDC 先前整定的参数难以适用，无法提供阻尼效果，光伏系统开始振荡，输出功率波形发生畸变，而 SMC-ADRC 仍有着良好的抑制效果。

3.2 不同光伏输出下的振荡抑制效果

光伏出力具有较大的波动性、间歇性。保持系统 SCR=2.8 不变，改变光伏输出容量为 2MW、10MW，其他条件不变。SMC-ADRC 与 SSDC 的抑制效果对比如图 5 所示。



(a)P=2MW



(b)P=10MW

图 5　不同光伏容量下 SMC-ADRC 与 SSDC 抑制效果对比

Fig.5　Comparison of suppression effect between SMC-ADRC and SSDC under different PV rated power

根据图 5 可以看出，随着光伏输出功率发生改变，SSDC 不再能抑制振荡，而 SMC-ADRC 由于其优良的抗扰特性，保持了振荡抑制效果。

4 结论

本文针对光伏并网次同步振荡问题，根据 SSO 发生机理，利用自抗扰控制特性，提出了基于滑模自抗扰控制的振荡抑制方法。在 PSCAD/EMTDC 中搭建光伏并网模型，通过仿真验证该抑制措施的有效性。得出以下结论：

(1)当电网强度发生变化时，次同步振荡频率会发生改变，所设计的 SMC-ADRC 控制的性能优于附加次同步阻尼控制，对于不同频率的振荡都有着良好的抑制效果；

(2) 光伏出力具有波动性，SSDC 在光伏出力变化较大时抑制效果下降，而 SMC-ADRC 凭借其良好的自适应能力和抗干扰性能，确保了不同工况下的稳定性。

参考文献

[1] 孙东阳，申文强，周凯，等．电网次同步振荡对光伏发电系统的影响分析及抑制策略研究[J]．中国电机工程学报，2024，44(23)：9262-9275．

[1] SUN Dongyang，SHEN Wenqiang，ZHOU Kai．Influence analysis and suppression stategy research of sub-synchronous oscillation on photovoltaic power generation system[J]．Proceeding of the CSEE，2024，44(23)：9262-9275．

[2] 严干贵，李龙，黄亚峰，等．弱电网下联网光伏逆变系统稳定性分析及控制参数整定[J]．太阳能学报，2013，34 (11)：1853-1859．

[2] YAN Gangui，LI Long，HUANG Yafeng．Stability analysis and control parameter setting of networked photovoltaic inverter system under weak power grid[J]．Acta Energi-ae Solaris Sinica，2013，34 (11)：1853-1859．

[3] 李博浩，郭昆丽，吕家君，等.次同步电流双通道附加阻尼抑制次同步振荡策略及阻抗模型分析[J]．分布式能源，2023，8(06):1-10.

[3] LI Bohao，GUO Kunli，LU Jiajun. Subsynchronous current dual additional damping suppression subsynchronous oscillation strategy and impedance model analysis[J]．Distributed Energy，2023，8(06)：1-10．

[4] 张帆，高本锋，李铁成．基于 SVG 的光伏并网 SSO 附加阻尼抑制策略[J]．中国电力，2021，54(12):11-19+44．

[4] ZHANG Fan，GAO Benfeng，LI Tiecheng．SVG based supplementary damping mitigation strategy for sub-synchronous oscillation in grid-connected photovoltaic plants．Electric Power，2021，54(12)：11-19+44．

[5] 高本锋，王飞跃，于弘洋，等．应用静止同步串联补偿器抑制风电次同步振荡的方法[J]．电工技术学报，2020，35(06)：1346-1356．

[5] GAO Benfeng，WANG Feiyue，YU Hongyang et al．The suppression method of wind power sub-synchronous oscillation using static synchronous series compensator[J]．Transactions of China electrotechnical society，2020，35(06):1346-1356.

[6] D. Yang，X. Wang，F. Liu，K. Xin，Y. Liu and F．Blaabjerg. Symmetrical PLL for SISO Impedance Modeling and Enhanced Stability in Weak Grids [J]．IEEE Transactions on Power Electronics，vol. 35，no. 2，pp. 1473-1483，Feb．2020．

[7] G. He，W. Wang and H. Wang. Coordination Control Method for Preventing Sub/Super Synchronous Oscillations of Multi-wind Farm Systems[J]．in CSEE Journal of Power and Energy Systems，vol. 9，no. 5，pp．1655-1665，September 2023．

[8] Pang，B. and Nian，H．(2020)，Active damping technique based on H∞ controller for VSC under parallel compensation grid[J]. IET Electronics Letters，2019，56(3)：2682-2691．

[9] 王刚，高本锋，王晓，等．基于滑模控制的直驱风电场次同步振荡抑制策略[J]．太阳能学报，2023，44(04)：163-172．

[9] WANG Gang，GAO Benfeng，et al. Subsynchronousoscillation suppression strategy for direct drive windfarm based on sliding mode control[J]．Acta Energi-ae Solaris Sinica，2023，44(04)：163-172．

[10] Zhiqiang Ga．Scaling and bandwidth-parameterization based controller tuning．Proceedings of the 2003 American Control Conference，2003. Denver，CO，USA，2003，pp. 4989-4996.12．

[11] 马宁宁，谢小荣，贺静波，等．高比例新能源和电力电子设备电力系统的宽频振荡研究综述[J]．中国电机工程学报，2020，40(15):4720-4732．

[11] MA Ningning，XIE Xiaorong，HE Jingbo. Review of wide-band oscillation in renewable and power electronics highiy integrated power system[J]. Proceedings of the CSEE，2020，40(15)：4720-4732．

[12] 陈实，李兴源，李宽．光伏并网附加控制抑制交流串补引起的次同步谐振[J]．电力自动化设备，2016，36(01)：24-29．

[12] CHEN Shi，LI Xingyuan，LI Kuan．Supplementary photovoltaic grid-connection control for damping SSR induced by series capacitive compensation[J]．Electric Power Automation Equipment，2016，36(01)：24-29．

[13] 李宽，李兴源，陈实，等．光伏并网抑制由直流输电引起的次同步振荡的可行性分析[J]．电力自动化设备，2015，35(03)：41-46．

[13] LI Kuan，LI Xingyuan，CHEN Shi．Analysis on feasibility of damping HVDC-induced subsynchronous oscillation by photovoltaic grid-connection[J]．Electric Power Automation Equipment，2015，35(03)：41-46．

[14] 杨明，杜少通，郑征，等．大规模光伏并网系统谐振机理及稳定性分析[J]．电源学报，2019，17(01)：53-61．

[14] YANG Ming，DU Shaotong，ZHENG Zheng．Resonance Mechanism and Stability Analysis of Large-scale Grid-connected Photovoltaic System[J]．Journal of Power Supply，2019，17(01)：53-61．

[15] 张兴，余畅舟，刘芳，等．光伏并网多逆变器并联建模及谐振分析[J]．中国电机工程学报，2014，34(03)：336-345．

[15] ZHANG Xing，YU Changzhou，LIU Fang．Modeling and resonance analysis of multi-paralleled grid-tied inverters in PV systems[J]. Proceedings of the CSEE，2014，34(03)：336-345．

收稿日期：2025-08-15。



杨旭东

作者简介：

杨旭东(2001—)，男，硕士研究生，研究方向为电力系统稳定与控制，E-mail：3361791253@qq.com；

王德林(1970—)，男，教授，博士生导师，研究方向为电力系统分析、稳定和控制等，E-mail：wdl@swjtu.edu.cn。

019 Evaluation System and Assessment Method for Distributed New Energy Hosting Capacity of Multi-Dimensional Observable Distribution Networks

Tong Wei[1], Yuhang Wang[1], Gongjin Ma[1], Pingliang Zeng[1,*], Cheng Xie[2], and Chao Chen[2]

[1] School of Automation, Hangzhou Dianzi University, Hangzhou 310018, China
[2] State Grid Zhejiang Electric Power Co., Ltd. Electric Power Science Research Institute, Hangzhou 310014, China
plz@hdu.edu.cn

Abstract. Against the backdrop of large-scale grid integration of new energy, the operation of distribution networks involves various aspects such as power grid security, reliable power supply, and green economy. Their hosting capacity is a comprehensive reflection of multiple dimensions, including planning, operation modes, and the characteristics of distributed new energy. Thus, proposing a systematic, multi-linkage-covered, and intuitive evaluation indicator system for hosting capacity has become a primary issue to be urgently addressed. This study explores an evaluation framework for the distributed new energy hosting capacity of observable distribution networks, constructs a multi-dimensional evaluation indicator system for distribution network hosting capacity, and establishes a comprehensive scoring model based on combined weighting via the projection pursuit method—enabling the rapid acquisition of information on the current hosting capacity of distribution networks. Finally, scenarios with different new energy penetration rates are designed for hosting capacity assessment. Simulation results from the modified IEEE-33 bus test system show that the proposed hosting capacity assessment method can more accurately identify the potential new energy hosting capacity of distribution networks, and it does not require excessive reliance on subjective experience or feature extraction of data.

Keywords: Distribution Network, Hosting Capacity, Projection Pursuit Method, Evaluation Framework.

1 Introduction

The new energy hosting capacity of the distribution network refers to the maximum capacity of distributed new energy that the distribution network can accommodate and absorb on the premise of ensuring the safe and stable operation of the power grid and meeting the requirements of power quality [1]. This indicator characterizes the inherent capability and potential of the distribution network to adapt to and host the integration of distributed new energy, and serves as a key basis for evaluating the

development prospects of renewable energy in the context of energy transition [2]. This paper focuses on the construction of an evaluation system and framework for the new energy hosting capacity of the distribution network, conducts in-depth research, and proposes corresponding optimization methods and technical paths for hosting capacity.

Based on the reliability indicators of traditional distribution networks, In [3] constructs reliability evaluation indicators for distribution networks with distributed generation (DG), and systematically establishes reliability evaluation indicators from the perspectives of DG reliability, power supply reliability, and user satisfaction. In [4] develops a reliability evaluation system that includes indicators such as distribution system failure/repair probability, DG output adequacy assessment indicators, and DG mechanical failure/repair probability. Taking into account the large installed capacity of new energy and the high volatility of its output, In [5] proposes an improved voltage stability evaluation indicator for DG. In [6] establishes a comprehensive power quality evaluation indicator system suitable for low-voltage DC distribution systems. In [7] first puts forward risk evaluation indicators including overload risk, system splitting risk, and secondary risks to realize risk assessment. In [8] conducts a hierarchical assessment of power quality based on the cross-data envelopment analysis method. In [9] proposes the "comprehensive deviation degree of power quality" indicator to measure the deviation degree of power quality. The determination of indicator weights is a crucial link in realizing the observability of hosting capacity. At the current stage, the main weighting methods include subjective analysis and objective analysis. Among them, subjective weighting methods include the Analytic Hierarchy Process (AHP) and the Delphi method, while objective weighting methods include the entropy weight method and the grey relational analysis method. Subjective weighting methods generally rely on the expert experience in the industry; they are simple in operation but are excessively influenced by human factors [10]. Objective weighting methods calculate weights based on sample data, yet they are overly dependent on theories and may deviate from practical scenarios [11]. Comprehensive weighting analysis takes into account the respective advantages and disadvantages of subjective and objective weighting analyses, integrates the two methods to offset weaknesses with strengths, and aims to scientifically and objectively measure the importance of evaluation indicators. The core issue of comprehensive weighting analysis lies in determining the weight allocation between the two weighting methods. Currently, in relevant research, the mathematical derivation of most methods is overly cumbersome, resulting in poor applicability and low operability.

In summary, although the existing evaluation indicator systems take the integration of distributed new energy into account, with the increasing enrichment of distribution network resources and equipment types, the original evaluation indicator systems are unable to comprehensively and accurately measure the distributed new energy hosting capacity of distribution networks. Meanwhile, in view of the problems and shortcomings existing in the current weighting methods, the systematic and scientific methods for indicator quantification and weight determination still need further research.

2 New Energy Hosting Capacity Evaluation System

2.1 New Energy Hosting Capacity Assessment Framework

To address the issue of evaluating the distributed energy hosting capacity of distribution networks, a multi-level evaluation framework named "Distribution Network Layer - Node Layer - User Layer" is proposed, as shown in Fig. 1. Meanwhile, a multi-dimensional indicator assessment is conducted on this framework, and finally, the comprehensive score of the distributed new energy hosting capacity of the distribution network is obtained through weighted summation.

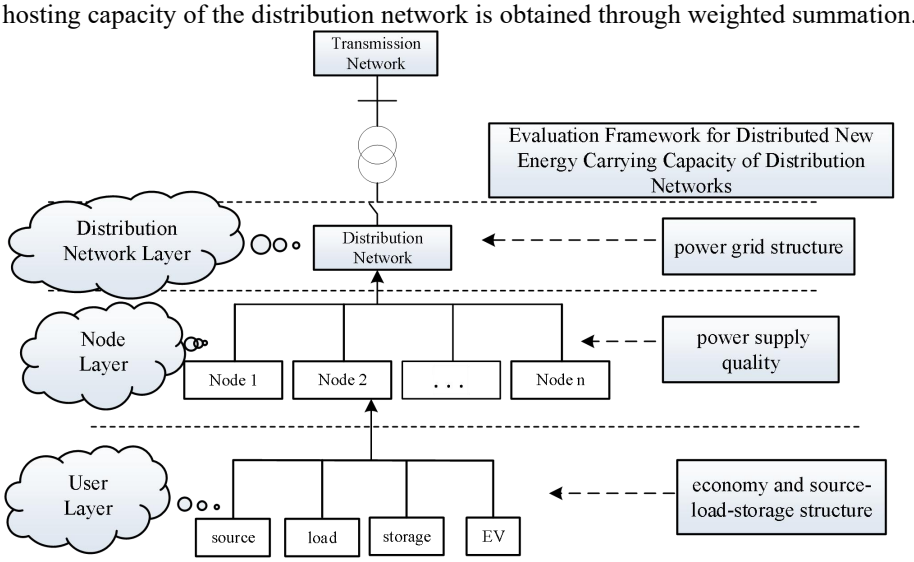


Fig. 1. Multi-Level Evaluation Framework of "Distribution Network Layer - Node Layer - User Layer"

Among them, the Distribution Network Layer, as the level directly connected to the transmission network, its core function is to evaluate the overall impact of distributed new energy integration on the main system of the distribution network. Insufficient hosting capacity at this layer will directly lead to the blockage or collapse of the entire network. The evaluation of the Distribution Network Layer must focus on the power grid structure dimension. This is because this layer undertakes the interaction function between the transmission and distribution networks and is directly related to the safety boundary of the entire network: the power grid structure dimension prevents systemic collapse caused by the overload of main equipment.

The Node Layer is located below the Distribution Network Layer and is used to accurately identify the weak links of key nodes within the distribution network. The volatility of distributed new energy is prone to cause local voltage violations or faults, and this layer is the core for diagnosing "bottleneck" issues. Therefore, the Node Layer should emphasize the power supply quality dimension. Due to its positioning as

a tool to diagnose the physical bottlenecks of key nodes (such as the end of feeders), the integration of new energy is most likely to induce power supply quality problems such as voltage fluctuations and harmonic pollution at this layer. It is essential to accurately quantify fault risks and the degree of power quality degradation through an independent dimension.

Meanwhile, the User Layer, as the bottom layer, includes equipment such as distributed generation, loads, and energy storage systems. Its core value lies in exploring the potential of flexible improvement in hosting capacity through the collaboration of end-user resources. Traditional evaluations overlook user-side flexibility, while this layer transforms distributed resources into regulatory variables similar to a "virtual power plant". The User Layer must integrate the economic dimension and the distributed generation-load-storage structure dimension. This layer integrates various types of resources: the economic dimension drives user-side investment and willingness to regulate, while the distributed generation-load-storage structure dimension analyzes the efficiency of resource collaboration. These two dimensions jointly support the quantitative exploration of "flexible hosting capacity".

For the multi-level evaluation framework, the next step is to collect the basic data of the distribution network to be evaluated. First, the Distribution Network Layer represents the system-level backbone network data. In terms of the time scale for data collection, an "annual planning and mid-term analysis" approach is adopted, while the spatial scale is selected to cover the entire distribution network area. This is because system-level congestion (such as main transformer overload) must be managed in a holistic manner.The Node Layer serves as the data source for local bottleneck diagnosis. On the time scale, it focuses on minute-level monitoring and fault transient data, as high-precision capture is required for voltage sags and harmonic pollution. The spatial scale is limited to key feeder zones, such as areas with a new energy penetration rate > 30%, to avoid redundancy in full-volume data.Finally, the User Layer acts as the data source for resource collaboration. For the time scale, a hierarchical design (second-level - minute-level - day-ahead) is adopted to match the response characteristics of resources. The spatial scale is clustered by user type, as industrial and commercial clusters (with a large number of adjustable loads) and residential areas (with high PV penetration) require differentiated modeling.

To scientifically evaluate the hosting capacity of distribution networks for distributed new energy, it is necessary to establish an index system with a clear hierarchy and comprehensive dimensions. For this purpose, this paper, integrating the analytic hierarchy process theory, constructs a target layer with "evaluation of distributed new energy hosting capacity of distribution networks" as the ultimate goal. Below the target layer, four key criterion layer dimensions are established: economy, distributed generation-load-storage structure, power grid structure, and power supply quality. These dimensions are not set arbitrarily; instead, each of them profoundly influences the scale and safety of distributed new energy accommodation in distribution networks from different yet interrelated core fields.

2.2 Hosting Capacity Evaluation Indicator System

The economic dimension is directly related to the market feasibility and investment attractiveness of technical applications. The distributed generation-load-storage structure dimension reflects the optimization level of the coordination among distributed generation, loads, and energy storage, which is crucial for expanding the accommodation space. The power grid structure dimension measures the robustness and regulation capability of the grid's own physical framework, serving as the infrastructure guarantee for hosting capacity. The power supply quality dimension is the ultimate manifestation of the effectiveness of hosting capacity, which is related to users' actual experience. By integrating these four dimensions, this system strives to scientifically characterize the distributed energy accommodation potential of distribution networks from multiple perspectives and levels.

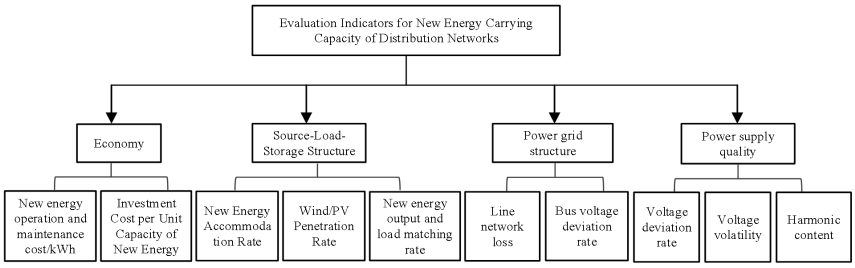


Fig. 2. Evaluation Dimensions and Indicators for New Energy Hosting Capacity of Distribution Networks

To provide a clear and quantitative systematic demonstration of the distribution network's hosting capacity, this paper selects a total of 10 specific evaluation indicators based on the aforementioned dimensions.

In the economic dimension, the primary focus is on input-output efficiency and resource utilization efficiency, encompassing the unit capacity investment costs of wind power, photovoltaic (PV) power, and energy storage (related to initial investment), as well as the curtailment rates of wind power and PV power (reflecting energy loss).

The distributed generation-load-storage structure dimension focuses on the configuration coordination among power sources, loads, and energy storage in the system, along with their fluctuation impacts. The specific indicators include: the installed penetration rates of wind power, PV power, and energy storage (quantifying their status in the system); the output volatility of wind power and PV power (reflecting intermittent characteristics); the proportion of adjustable loads (measuring demand-side flexibility); the load peak-valley difference rate (reflecting the amplitude of load fluctuations); the new energy accommodation rate (directly evaluating the system's effectiveness in utilizing new energy for power generation); and the normalized shape matching rate between new energy output and load (examining the temporal alignment between power sources and loads).

The power grid structure dimension assesses the withstand capacity and operational efficiency of grid equipment, covering the transformer capacity-load ratio (reflecting transformer load margin), transformer voltage regulation margin (indicating voltage control capability), active-reactive current ratio (characterizing line reactive power conditions and potential impacts), system reverse load rate (evaluating the impact of reverse power flow intensity on equipment), and line power loss (measuring energy transmission efficiency).

Finally, the power supply quality dimension focuses on the actual quality of electrical energy on the user side, including the voltage deviation rate (describing the degree of voltage deviation from the rated value), voltage fluctuation rate (reflecting the short-term voltage variation amplitude), and harmonic content (assessing the degree of waveform distortion).

3 Evaluation Method

To address the issues of over-reliance on subjective experience and insufficient data feature extraction in existing weighting methods for new energy hosting capacity evaluation, a multi-dimensional dynamic weighting system integrating subjective and objective weights is proposed. First, a multi-dimensional evaluation index system covering economy, distributed generation-load-storage structure, and power grid structure is constructed. Subsequently, the grey relational analysis method (for objective weighting) and the analytic hierarchy process (for subjective weighting) are adopted to obtain the basic weight set. Innovatively, the projection pursuit technique is introduced: by establishing an optimal projection objective function in the high-dimensional data space, the optimal projection direction is dynamically solved to realize weight optimization. This method breaks through the limitations of traditional static weighting, and while ensuring the accuracy of economic evaluation, it significantly improves the system topology adaptability.

3.1 Objective Analysis Method

The Grey Relational Analysis (GRA) is a multi-factor statistical analysis method used to evaluate the correlation degree between various factors in a system. Its basic idea is to judge the tightness of the connection between different sequences by comparing the geometric shapes of sequence curves, with the specific steps as follows:

(1) Indicator Correlation Coefficient:

$$\gamma_{ij} = \frac{\min\limits_{i}\min\limits_{j}|x_{0j}^{*}-x_{ij}^{*}|+\rho\max\limits_{i}\max\limits_{j}|x_{0j}^{*}-x_{ij}^{*}|}{|x_{0j}^{*}-x_{ij}^{*}|+\rho\max\limits_{i}\max\limits_{j}|x_{0j}^{*}-x_{ij}^{*}|} \tag{1}$$

Where: x_{0j}^{*} is the reference sequence, i.e., the ideal value of each indicator; x_{ij}^{*} is the standardized value of the j indicator for the i sample; ρ is the distinguishing coefficient.

(2) Grey Relational Grade:

$$\gamma_j = \frac{1}{m}\sum_{i=1}^{m}\gamma_{ij} \tag{2}$$

Where: γ_j represents the average correlation coefficient of the j indicator across all samples; m is the number of samples.

(3) Generation of Objective Weight Vector

$$\omega_j^O = \frac{\gamma_j}{\sum_{k=1}^{n}\gamma_k} \tag{3}$$

Where: n is the number of indicators.

3.2 Subjective Analysis Method

The Analytic Hierarchy Process (AHP) is a decision-making analysis method that combines qualitative and quantitative approaches to solve complex multi-objective problems. This method integrates quantitative analysis with qualitative analysis: it uses decision-makers' experience to judge the relative importance between the criteria for achieving various evaluation objectives, reasonably assigns weights to each criterion of each decision-making scheme, and uses these weights to determine the priority ranking of different schemes. It is effectively applied to projects that are difficult to solve with purely quantitative methods, with the specific steps as follows:

(1) Constructing the Judgment Matrix

$$A = \begin{bmatrix} 1 & a_{12} & a_{13} & \cdots & a_{1n} \\ \frac{1}{a_{12}} & 1 & a_{23} & \cdots & a_{2n} \\ \frac{1}{a_{13}} & \frac{1}{a_{23}} & 1 & \cdots & a_{3n} \\ \vdots & \vdots & \vdots & \ddots & \vdots \\ \frac{1}{a_{1n}} & \frac{1}{a_{2n}} & \frac{1}{a_{3n}} & \cdots & 1 \end{bmatrix} \tag{4}$$

Where: a_{ij} denotes the relative importance of the i indicator with respect to the j indicator.

Among these, the importance assignment between different indicators is determined using the 1-9 scaling method proposed in [12].

The consistency check formula for the judgment matrix is as follows:

$$CI = \frac{\lambda_{\max} - n}{n-1} \tag{5}$$

Where: $\lambda_{\max}$ is the maximum eigenvalue of the judgment matrix . If the CI value is less than 0.1, the matrix passes the consistency check; if it is greater than 0.1, the comparison values in the judgment matrix need to be revised.

(2) Generation of Subjective Weight Vector

The weights of each indicator are obtained by solving the eigenvector of the judgment matrix, as specified in the following formula:

$$\omega_j^S = \frac{v_j}{\sum_{j=1}^{n} v_j} \tag{6}$$

Where: v_i is an element in the eigenvector; ω_i is the weight of the i indicator.

3.3 Solution Based on the Improved Genetic Algorithm (GA)

Basic Combined Weight. The combined weight calculation formula based on the multiplicative synthesis method is as follows:

$$\omega_j^M = \frac{\sqrt{\omega_j^O \omega_j^S}}{\sum_{j=1}^{n} \sqrt{\omega_j^O \omega_j^S}} \tag{7}$$

By taking the square root of the product of subjective and objective weights, the weights of indicators with consistency between the two (subjective and objective weights) can be amplified, while indicators with conflicts—such as those overestimated by experts but deemed unimportant by data—can be suppressed.

Optimization of Basic Combined Weight. The projection pursuit method is a dimensionality reduction and optimization approach for feature extraction and structural analysis of high-dimensional data. Its core idea is to map multi-dimensional indicator data to a low-dimensional subspace through nonlinear projection, and maximize the reflection of the inherent characteristics or classification information of the data in the projection direction. This method constructs a projection index function (such as inter-class distance, information entropy, or density function) as the optimization objective, and combines intelligent algorithms to find the optimal projection direction, thereby overcoming the defect that traditional weighting methods have insufficient adaptability to high-dimensional nonlinear data. First is the calculation of projection values:

$$\begin{cases} z_i = \sum_{j=1}^{n} a_j x_{ij}^* \quad (i = 1, 2, \cdots, m) \\ a_j^{(0)} = \dfrac{\sqrt{\omega_j^O \omega_j^S}}{\sum_{j=1}^{n} \sqrt{\omega_j^O \omega_j^S}} \end{cases} \tag{8}$$

Where: z_i is the projection value of the i sample in the one-dimensional space; x_{ij}^* is the standardized indicator data of n indicators among m samples; $a_j^{(0)}$ is the projection direction at the 0-th iteration.

Projection Value Function:

$$Q(a) = S_z D_z \tag{9}$$

Where: S_z is the standard deviation; D_z is the local density.

Among them, the standard deviation reflects the dispersion of the projections:

$$S_z = \sqrt{\frac{1}{m-1}\sum_{i=1}^{m}(z_i - \bar{z})^2} \tag{10}$$

Where: $\bar{z}$ is the average projection value of all samples.

The local density reflects the aggregation of the projections:

$$\begin{cases} D_z = \sum_{i=1}^{m}\sum_{k=1}^{m}(R - r_{ik}) f(R - r_{ik}) \\ r_{ik} = \mid z_i - z_k \mid \end{cases} \tag{11}$$

Where: r_{ik} is the projection distance between samples; R is the adaptive density window radius, which is set to $0.1S_z$ in this study, $f(x)$ is the unit step function, which is specified as follows:

$$f(x) = \begin{cases} 1, & x \geq 0 \\ 0, & x < 0 \end{cases} \tag{12}$$

Improved GA. This algorithm is based on the traditional Genetic Algorithm (GA). During the population initialization process, the combination of basic weights ω_j^M is incorporated as the initial guiding direction, whereas the traditional GA randomly generates the initial population during its population initialization process. The specific steps are as follows:

(1) Population initialization

$$a_j^{(0)} = \frac{\omega_j^M + \delta_i}{\| \omega_j^M + \delta_i \|}, \quad \delta_i \in (-\varepsilon, \varepsilon) \tag{13}$$

Where: δ_i is the random disturbance term; ε is the disturbance value.

(2) Crossover operation

$$\begin{cases} a^c = \lambda a^{p1} + (1-\lambda)\lambda a^{p2}, \quad \lambda \in (0.3, 0.7) \\ P_c(t) = 0.8 - 0.2\dfrac{t}{T} \end{cases} \tag{14}$$

Where: a^{p1} and a^{p2} are the projection direction weight vectors of different parent individuals; λ is the linear interpolation coefficient, which controls the proportion of offspring inheriting parental weights; $P_c(t)$ is the dynamic crossover probability; t is the current number of iterations; T is the total number of iterations.

(3) Mutation operation

$$\begin{cases} a_{kj}^{'} = a_{kj} + N(0,\sigma^2) \\ \sigma(t) = 0.1(1-\dfrac{t}{T}) \end{cases} \tag{15}$$

Where: $N(0,\sigma^2)$ is a Gaussian distribution disturbance with a mean of 0 and a standard deviation of σ; σ is the dynamically decaying disturbance intensity.

(4) Termination condition

$$\Delta Q(a) = | Q^{best}(t) - Q^{best}(t-10) | \tag{16}$$

$$\begin{cases} \Delta Q(a) < 1\times10^{-5} \\ t \geq T \end{cases} \tag{17}$$

Where: $\Delta Q(a)$ is the fitness change threshold.

The algorithm terminates when the change in the optimal solution is less than 10^{-5} for 10 consecutive iterations or the maximum number of iterations is reached, and then outputs the optimized weight combination.

(5) Comprehensive Score of New Energy Hosting Capacity

The specific calculation formula is as follows:

$$O = \sum_{i=1}^{n} x_i a_i \tag{18}$$

Where: x_i is the processed i indicator data; a_i is the optimized i indicator weight.

3.4 Evaluation Model

Take maximizing the projection value of the basic combination weighting as the objective function, and the specific formula is as follows:

$$F = \max Q(a) \tag{19}$$

Where: $Q(a)$ is the projection value function of basic combination weighting.

Take the unit length of the projection direction and the non-negativity of weights as constraints:

(1) Unit Length Constraint of the Projection Direction: It ensures that the projection direction vector a is a standardized direction.

$$\sum_{j=1}^{n} a_j = 1 \tag{20}$$

Where: a_j is the weight of the j indicator.

(2) Non-Negativity Constraint of Weights: All indicators make positive superposition contributions to the projection value, facilitating analysis.

$$a_j \geq 0 \quad (\forall j = 1,2,\cdots,n) \tag{21}$$

The specific solution process:

1) First, collect the basic operation data of the distribution network to be evaluated, and calculate the indicator values under different dimensions in accordance with the distribution network new energy hosting capacity evaluation indicator system presented in this paper.

2) The calculated indicators are subjected to numerical positive transformation and standardization, which are as follows respectively:
   a) Positive Transformation: The range method is used to perform positive transformation on indicators such as the new energy operation and maintenance cost per kilowatt-hour, new energy investment cost per unit capacity, line network loss, bus voltage deviation rate, voltage deviation rate, voltage fluctuation rate, and harmonic content in the indicators. The formula is as follows:

$$x' = \frac{x_{\max} - x}{x_{\max} - x_{\min}} \tag{22}$$

   Where: $x_{\max}$ and $x_{\min}$ are the maximum value and minimum value of the data, respectively.
   b) Standardization: To preserve the original direction of the data, the Min-Max standardization method is used for processing. The formula is as follows:

$$x^* = \frac{x - x_{\min}}{x_{\max} - x_{\min}} \tag{23}$$

3) Subjective weighting and objective weighting are performed respectively for the indicator weights; the specific calculation process is as follows:
   a) Calculation of Objective Weights: First, calculate the correlation coefficients of all indicators based on [relevant data/information, note: the original text omits the basis for calculation, so a placeholder is added for clarity]; then calculate the grey correlation degree of the indicators; finally, calculate the objective weight of each indicator.
   b) Calculation of Subjective Weights: First, construct the judgment matrix based on the comparison values of relative importance between different indicators provided by experts. Next, test the consistency CI of the judgment matrix . If the value of CI is less than 0.1, the consistency test is passed and the judgment matrix is valid. If the value of CI is greater than 0.1, the element values in the judgment matrix need to be adjusted and recalculated. Finally, calculate the subjective weight vector.
4) Combine the subjective weight values and objective weight values of the indicators using the multiplicative synthesis method to obtain the basic weight combination
5) Take the basic weight combination calculated in Step (4) as input, and use the projection pursuit method for further optimization.
6) Incorporate the weights optimized by the projection pursuit method into different indicators, and calculate according to Formula (18) to obtain the comprehensive score of the new energy hosting capacity of the distribution network.

12

4 Case Study

In this invention, the threshold score for the new energy hosting capacity of the distribution network is set to 0.5, and the modified IEEE-33 bus test case is used for simulation analysis. To simulate scenarios with high new energy penetration, distributed photovoltaics (PV) are taken as the representative of new energy and connected to Bus 18, Bus 22, and Bus 33. Three penetration rates (10%, 30%, 60%) are set. Meanwhile, energy storage devices are connected to Bus 13. as illustrated in Fig. 3.

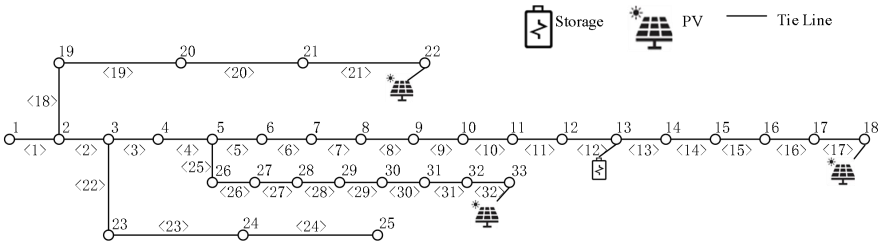


Fig. 3. Modified IEEE-33 Bus System

The above system is simulated and analyzed using Python. Data results under different scenarios are recorded, input into the established evaluation system, and optimized using the indicator weighting method proposed in this paper. The specific comparison results of the three scenarios are shown in the Fig. below.

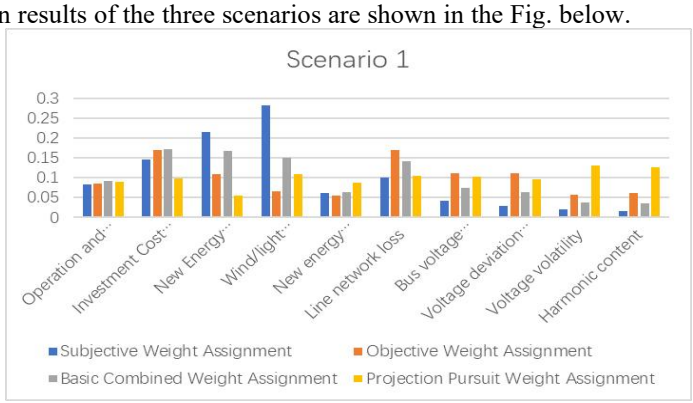


Fig. 4. Weight Assignment Results of Different Indicators Under Scenario 1

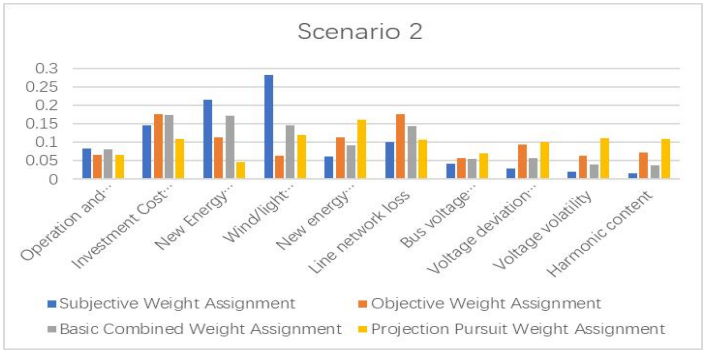


Fig. 5. Weight Assignment Results of Different Indicators Under Scenario 2

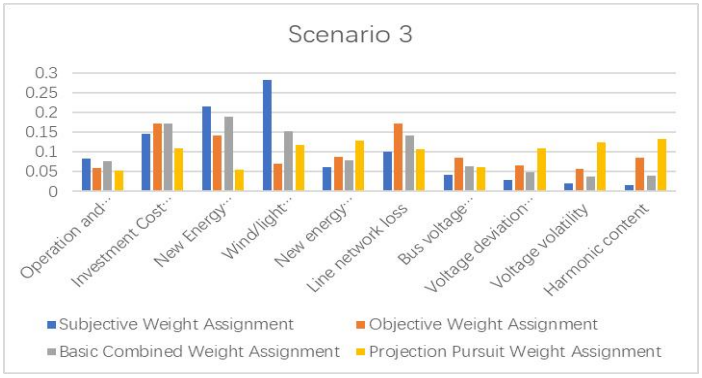


Fig. 6. Weight Assignment Results of Different Indicators Under Scenario 3

As shown in Fig. 6, the weight distribution of the subjective weighting method (Analytic Hierarchy Process, AHP) exhibits a significant polarization characteristic: indicators related to the source-load-storage structure dominate, while the weights of power supply quality indicators are severely low. This bias stems from the excessive emphasis on the "source-grid-load-storage" synergy capability by expert experience in the Analytic Hierarchy Process, leading to a systematic underestimation of economic indicators and power grid structure indicators. The objective weighting method (Grey Relational Analysis, GRA) reconstructs the weight system driven by data, significantly increasing the weights of indicators that reflect actual operational bottlenecks, such as line network loss and voltage deviation rate. However, it has a drawback of insufficient capture of the implicit correlation between the temporal characteristics of new energy output.

The optimization method proposed in this paper effectively mitigates the defects of subjective and objective weighting: first, it integrates subjective and objective weighting based on the multiplicative synthesis method. While retaining experts' core considerations regarding the system's regulatory capacity, it dynamically corrects empirical cognitive biases through data correlation analysis, effectively alleviating the problem of extreme weight polarization in traditional methods. Furthermore, it

introduces projection pursuit technology to break through the limitations of linear weighting dimensions, construct a non-linear mapping channel from the high-dimensional indicator space to key features, intelligently identify implicit core indicators such as power supply quality and adaptively enhance their weights, and accurately reveal the non-linear evolution law of system vulnerability near the new energy penetration rate critical point.

It can be seen from Table 1 (Comparison of Weighting Scores Under Various Scenarios) that the subjective weighting scores fluctuate slightly across the three scenarios (ranging from 0.3831 to 0.4006), with the highest score being only 0.4006. This reflects the insufficient sensitivity of expert experience in AHP to changes in penetration rate—especially in the high-penetration scenario, the system is still misjudged as being in a "safe state" (with a score of 0.3831). Although the objective weighting scores show a linear increase with the rise in penetration rate, the increment is moderate (5.5%), failing to capture the abrupt change effect of voltage stability after the increase in penetration rate. The basic combined weighting method improves the score stability through the integration of subjectivity and objectivity (with a standard deviation of 0.0028), but falls into the trap of "static equilibrium"—the scores of the three scenarios remain in the range of 0.4268 to 0.4321, concealing the early warning value of power supply quality indicators. In contrast, the projection pursuit optimization scores show an accelerated upward trend (with an increase of 5.7%), accurately mapping the non-linear attenuation law of the system from "safety margin" to "critical state, " which demonstrates the superiority of the method proposed in this paper.

Table 1. Comprehensive Scoring Results After Weight Assignment for Each Scenario.

Weight Assignment Method	Scenario 1	Scenario 2	Scenario 3
Score of Subjective Weight Assignment	0.3954	0.4006	0.3831
Score of Objective Weight Assignment	0.4407	0.4490	0.4651
Score of Basic Combined Weight Assignment	0.4321	0.4268	0.4271
Score of Projection Pursuit Optimization	0.4662	0.4871	0.4927

Meanwhile, as shown in Fig.7, the improved genetic algorithm (GA) outperforms traditional methods in both convergence speed and optimization quality: In Scenario 3, the improved GA reaches the optimal fitness in only 80 generations. In Scenario 2, the improved GA shows a steep upward phase at the 50th generation and reaches the convergence value 130 generations earlier than the traditional method. In Scenario 1, the improved GA grows more rapidly than the traditional GA in the first 30 generations, which verifies the effectiveness of the initial population guidance strategy. Moreover, the number of convergence iterations for the three curves of the improved GA is reduced to more than half of that of the traditional GA, confirming the advantage of projection direction guidance.

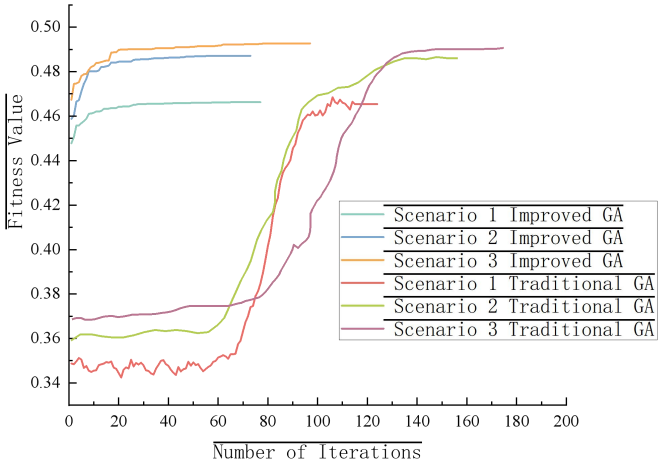


Fig. 7. Iterative Processes of Different Algorithms for Solution

5 Conclusion

At the beginning of this paper, the latest research trends and practical progress in the field of distribution network evaluation systems and assessment methods both domestically and internationally are systematically reviewed, and the advantages and limitations of existing achievements are in-depth analyzed. On this basis, the paper innovatively proposes a multi-dimensional and observable evaluation framework for the distributed energy hosting capacity of distribution networks. This framework not only focuses on the traditional power grid analysis perspective, but also incorporates the dynamic interaction between energy, load and energy storage into core considerations, aiming to provide a more comprehensive insight into hosting capacity that is more in line with the actual operating status. To promote the effective implementation of this framework, the paper subsequently constructs a set of highly adaptive multi-dimensional evaluation indicator system for the distributed energy hosting capacity of distribution networks. This system deeply integrates four key dimensions: economy, source-load-storage structure, power grid structure and power supply quality. Each dimension concisely includes the most representative core indicators (such as investment cost, absorption rate, capacity-load ratio, voltage deviation, etc.), which together form a scientific benchmark for describing the potential of distribution networks to accommodate and support the development of distributed energy.

The economic dimension can reflect the cost control and economic benefits of distribution networks in aspects such as investment, construction, operation and maintenance. It helps decision-makers achieve optimal resource allocation and cost minimization on the premise of meeting power supply demand and reliability requirements. The source-load-storage structure dimension reflects the balance relationship between power sources and loads. It can evaluate the access effect of

distributed power sources and the rationality of energy storage system configuration, so as to ensure the rational utilization of distributed power sources and the safe operation of the power grid. The power grid structure dimension is related to power quality and operational flexibility, and is crucial to the safe, stable and efficient operation of distribution networks. The power supply quality dimension is directly related to users' electricity consumption experience and satisfaction, and reflects the performance of distribution networks in meeting users' electricity demand, reducing power outage time and improving power quality.

To overcome the shortcomings of single weighting methods and realize the reasonable integration of objectivity in weight allocation and subjective cognition, the paper innovatively proposes a comprehensive scoring model for subjective and objective weighting based on the projection pursuit method. Through mathematical optimization means, this model intelligently explores the optimal weight combination that best balances the intrinsic value of indicators in various dimensions and decision-makers' preferences. This ensures that the assessment results can more accurately and convincingly reflect the actual distributed energy hosting capacity of distribution networks, providing strong theoretical support and tool guarantee for scientific planning and intelligent decision-making.

Acknowledgement: This research was supported by the State Grid Zhejiang Electric Power Company Science and Technology Project “Research on New Distribution System State and Hosting Capacity Assessment Technology for Large-Scale Distributed Renewable Energy Integration” (Project No. B311DS240017).

References

1. K. Lee, P. Zhao, A. Bhattacharya, B. K. Mallick and L. Xie, "An Active Learning-Based Approach for Hosting Capacity Analysis in Distribution Systems," in *IEEE Transactions on Smart Grid*, vol. 15, no. 1, pp. 617-626, Jan. 2024, doi: 10.1109/TSG.2023.3290414.
2. C. A. P. Chitacapa, S. P. Z. Asanza, E. M. L. Guamán, B. D. J. León, J. B. Leite and J. F. F. Baquero, "Rooftop Solar PV Hosting Capacity Analysis in MV-LV Distribution Networks Using Quasi-Static Time-Series Simulation," *2023 IEEE PES Innovative Smart Grid Technologies Latin America (ISGT-LA)*, San Juan, PR, USA, 2023, pp. 80-84, doi: 10.1109/ISGT-LA56058.2023.10328352.
3. Y. Chen *et al*., "Many-Criteria Evaluation of Infrastructure Investment Priorities for Distribution Network Planning," in *IEEE Access*, vol. 8, pp. 221111-221118, 2020, doi: 10.1109/ACCESS.2020.3043248.
4. X. Li and Q. Han, "An EV Charging Station Load Prediction Method Considering Distribution Network Upgrade," in *IEEE Transactions on Power Systems*, vol. 39, no. 2, pp. 4360-4371, March 2024, doi: 10.1109/TPWRS.2023.3311795.
5. X. Li and Q. Han, "An EV Charging Station Load Prediction Method Considering Distribution Network Upgrade," in *IEEE Transactions on Power Systems*, vol. 39, no. 2, pp. 4360-4371, March 2024, doi: 10.1109/TPWRS.2023.3311795.
6. N. Liu, H. Wang, C. Zhao and Q. Duan, "Standard System of Medium and Low Voltage DC Distribution System in Regional Energy Internet," *2023 IEEE 7th Conference on*

Energy Internet and Energy System Integration (EI2), Hangzhou, China, 2023, pp. 576-580, doi: 10.1109/EI259745.2023.10513197.

7. A. M. Leite da Silva and A. M. de Castro, "Risk Assessment in Probabilistic Load Flow via Monte Carlo Simulation and Cross-Entropy Method," in *IEEE Transactions on Power Systems*, vol. 34, no. 2, pp. 1193-1202, March 2019, doi: 10.1109/TPWRS.2018.2869769.
8. R. Bakhshi-Jafarabadi, R. Ghazi and J. Sadeh, "Power Quality Assessment of Voltage Positive Feedback Based Islanding Detection Algorithm," in *Journal of Modern Power Systems and Clean Energy*, vol. 8, no. 4, pp. 787-795, July 2020, doi: 10.35833/MPCE.2018.000509.
9. H. Li *et al*., "Power Supply Reliability Enhancement for Low-Voltage Distribution Area With Power Quality Improvement Function," in *IEEE Access*, vol. 10, pp. 130619-130631, 2022, doi: 10.1109/ACCESS.2022.3229424.
10. L. He, K. Shang, Y. Nan, H. Ishibuchi and D. Srinivasan, "Relation Between Objective Space Normalization and Weight Vector Scaling in Decomposition-Based Multiobjective Evolutionary Algorithms," in *IEEE Transactions on Evolutionary Computation*, vol. 27, no. 5, pp. 1177-1191, Oct. 2023, doi: 10.1109/TEVC.2022.3192100.
11. C. Cai, J. Chen, M. Xi, Y. Tao and Z. Deng, "Multi-Objective Planning of Distributed Photovoltaic Power Generation Based on Multi-Attribute Decision Making Theory," in *IEEE Access*, vol. 8, pp. 223021-223029, 2020, doi: 10.1109/ACCESS.2020.3042010.
12. B. Zhang, C. -C. Li, Y. Dong and W. Pedrycz, "A Comparative Study Between Analytic Hierarchy Process and Its Fuzzy Variants: A Perspective Based on Two Linguistic Models," in *IEEE Transactions on Fuzzy Systems*, vol. 29, no. 11, pp. 3270-3279, Nov. 2021, doi: 10.1109/TFUZZ.2020.3018110.

020 基于 KJ-Kano-模糊综合评价模型的新一代集控站智能运维功能提升策略

康君召[1]，朱轶伦[1]，宁福军[1]，姚 高[1]，许 杰[1]，杨薇薇[1]

（1. 浙江华云信息科技有限公司，杭州 310027）

Promotion Strategy of Intelligent Operation and Maintenance Function of New Generation Centralized Control Station based on KJ-Kano-Fuzzy Comprehensive Evaluation Model

KANG Junzhao[1],ZHU Yilun[1],NING Fujun[1],YAO Gao[1],XU Jie[1],YANG Weiwei[1]

(1.Zhejiang Huayun Information Technology Co., Ltd, Hangzhou,310027, China)

Abstract: Power grid enterprises are currently undergoing digital transformation.Considering the operational reliability requirements of next-generation centralized control station equipment, this paper conducts an in-depth study on the functional enhancement of intelligent operation and maintenance platforms.Firstly, affinity clustering was applied to 46 requirements using the KJ method.Secondly, the Kano model and Better-Worse analysis were employed to categorise 11 types of requirement elements. Concurrently, validation through a fuzzy comprehensive evaluation model revealed that four requirements, including panoramic display, fall under delight-type requirements.Two requirements such as data acquisition, constitute necessity-type requirements.Three requirements including system monitoring, represent expectation-type requirements.The other two requirements, such as channel surveillance, belong to indifference-type requirements. Finally, a comparative analysis with mainstream products like dispatch automation revealed that the intelligent operations platform remains underdeveloped in four functional modules. The findings indicate that proposing functional enhancement strategies for intelligent operations based on different requirement element types can effectively support the standardisation and intelligentisation of operations at next-generation centralised control stations.

Key words: new generation centralized control station; intelligent operation and maintenance; KJ affinity map method; kano model; fuzzy comprehensive evaluation;demand elements; function improvement;

摘要：当前电网企业正经历数字化改革，考虑新一代集控站设备可靠运行需求，本文对集控站智能运维平台展开功能深化研究。首先，基于 KJ 法对 46 条需求进行亲和聚类；其次，基于卡诺（Kano）模型及 Better-Worse 分析法开展 11 类需求要素归类，同时通过模糊综合评价模型展开验证，发现全景展示等 4 类需求属于魅力型需求，数据采集等 2 类需求属于必要型需求，系统监控等 3 类需求属于期待型需求，通道监视等 2 类需求属于无差别型需求；最后对比调度自动化等主流产品展开差异化分析，发现智能运维平台 4 个模块功能仍不完善。研究结果表明，根据不同需求要素类型提出智能运维功能提升策略，能够有效支持新一代集控站运维工作标准化与智能化。

关键词：新一代集控站；智能运维；KJ 亲和图法；Kano 模型；模糊综合评价；需求要素；功能提升；

DOI：

0 引言

当前电网数字化水平正飞快发展，“主辅监视”、“一键顺控”、“穿透调阅”及“远程智能巡视”等关键技术已融入到新一代集控站设备管理工作当中[1]。然而集控站系统运行时常常伴随监控对象复杂、设备分区隔离、告警信号分散等问题[2]，导致集控站设备维护任务量及相应费用不断攀升，加之常态化维护工作缺乏显著的即时成就感，相关运维工作质量存在较大可靠性隐患，结合当前背景现状研究，新一代集控站智能运维系统作为集控站自动化运维工具应运而生[3]。

新一代集控站智能运维系统是通过实时采集集控系统各类运行指标，通过一体化监控仪表板实现对集控站设备的全面运维管控，目前业内自动化

类运维系统大多从监控手段与产品功能2个角度展开：监控手段方面，文献[4]探索了动态阈值设定的规则框架，提升设备监控规则适应性；文献[5]提出基于大数据分析的电力系统故障诊断方法；文献[6]提出分层分布式监控规则，支持变电站设备实时状态评估与预警；文献[7]利用机器学习算法优化监控规则，实现设备健康状态的预测性维护；文献[8]基于监控规则提升一次设备实时预警能力及再生能源的接入适应性；文献[9]提出了基于深度强化学习的自适应电力系统紧急控制方法；文献[10]用图像识别技术开展变电站辅助装置运维；文献[11]通过数字孪生技术构建高压设备的状态分析；据《2025-2031 年智能电网运维监测产品行业市场调研及发展趋势预测报告》介绍，北美学者通过强化学习规则融合电网拓扑变化以提升系统鲁棒性，日韩技术则通过边缘计算技术优化监控规则减少数据传输延迟[12]。产品功能方面，文献[13]设计了换流站三维数字化智能巡检系统，文献[14-16]通过UWB 等定位技术对智能变电站系统进行优化，实现远程智能巡检功能；文献[17]优化了产品功能以提高调度效率；在国外，美国采用的 5G 通信技术巡检机器人已覆盖复杂地形下电网设备检测与维护，德国西门子开发的变电站数字孪生平台已实现设备虚拟仿真与运维策略预验证，欧美广泛应用的集中监控系统（SCADA）已集成 AI 模块，支持预测性维护与资源调度优化[18-19]。

尽管电力行业标准与技术创新同步更新，但是部分研究在复杂运维场景中适应性不足，现有自动化运维系统缺乏实时辅助决策能力，人机交互界面存在瓶颈。鉴此本文聚焦运维业务实战化场景，对新一代集控站智能运维功能需求展开研究，运用KJ-Kano-模糊综合评价模型提出新一代集控站智能运维功能提升策略。

1　KJ-Kano-模糊综合评价模型

本文通过集成 KJ-KANO-模糊综合评价模型，旨在将不同需求分析阶段与各类研究方法相结合，克服单一方法造成局限性，整体新一代集控站智能运维功能提升策略研究思路如图 1 所示，主要按照 4 个阶段展开：（1）通过 KJ 法确定原始需求；（2）基于 KANO 模型确定需求要素具体归类，并与主流产品功能进行关联对比；（3）对所分析需求要素分析结果的可靠性进行验证；（4）提出针对性策略。

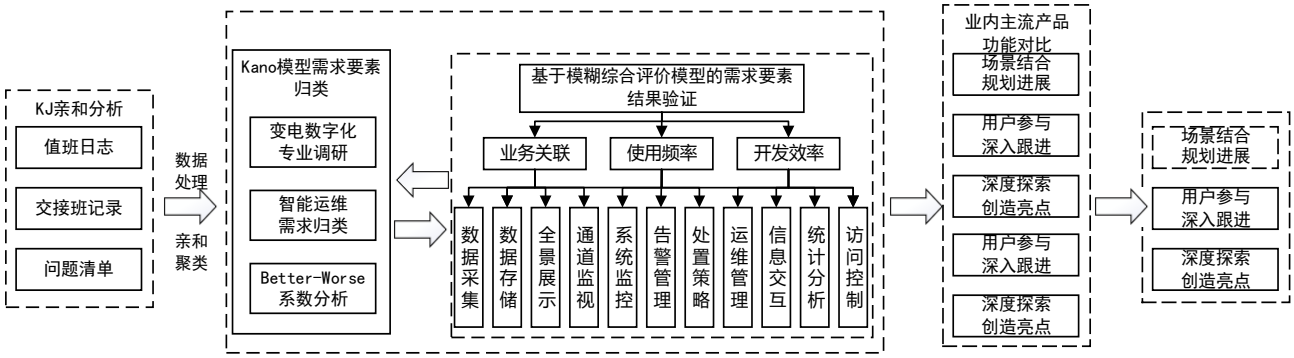


图 1 新一代集控站智能运维功能提升策略研究思路

Fig.1　Research ideas on improving the intelligent operation and maintenance functions of the new generation of centralized control stations

1.1 KJ 亲和图法

KJ 亲和图法(Affinity Diagram)由日本 Jiro Kawakita 教授提出[20]，旨在利用混乱的信息内在相互关联对其进行归纳，自下而上聚合成有序的主题，本文将使用 KJ 亲和图法对新一代集控站智能运维需求要素进行归纳整理，应用 KJ 亲和图法的主要流程包括需求要素调研、需求信息去重简化、功能卡片聚类需求要素 3 个步骤。

1.2 Kano 模型

卡诺（Kano）模型是日本 Noriaki Nano 教授提出一种产品质量管理模型[21]，目的在于识别主次需求，引用双因素理论对使用者主观感受与产品或服务进行分析如图 2 所示，该方法主要分为模型评价、混合类型分析及 Better-Worse 分析三个阶段。

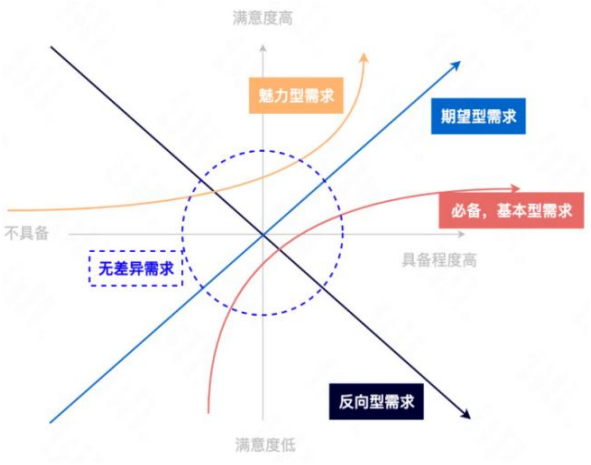


图 2 Kano 双因素理论
Fig.2 Kano's Two-Factor theory

1.2.1 Kano 模型评价

以被调研专业人员需求期望值作为标准，将产品功能分为 5 个类型：A 型需求（魅力型）；M 型需求（必要型）；O 型需求（期望型）；I 型需求（无差异型）；R 型需求（消极型）。

当某两个需求类型统计数值较为接近时，则无法准确进行分类。参照谭春辉等[22]经验，在 Kano 模型分类方法基础上，综合运用混合归类分析法和 Better-Worse 系数分析法对需求归类作进一步深入分析。

1.2.2 混合类型分析

混合归类分析方法如式（1）和式（2）所示。

$$S_T = \frac{(N_A+N_M+N_O)}{N} \tag{1}$$

$$S_C = \frac{(Max\{N_A,\ N_M,\ N_O,\ N_I\}-Second\ Max\{N_A,\ N_M,\ N_O,\ N_I\})}{N} \tag{2}$$

其中 N 表示有效样本数量，NM、NO、NA、NI 表示对应归类选择数量；ST 表示总的需求强度；SC 表示需求的归类强度，即用户认为需求属于某一类的程度。当 SC＞0.06 时，可以肯定需求划分到某归类；当 SC≤0.06 并且 ST＞0.6 时，应当划分为用字母 H 表示的混合归类需求，例如魅力型需求、期望型需求的混合归类表示为 H（A+M）。

1.2.3 Better-Worse 系数分析

Better -Worse 系数分析法是由学者 Berge 提出，分别通过 Better 和 Worse 系数来分析需求要素与用户满意度之间、需求要素与用户不满意度之间关联。这计算方法如式（3）和式（4）所示。

$$C_{Better} = \frac{(N_A+N_O)}{(N_A+N_M+N_O+N_I)} \tag{3}$$

$$C_{Worse} = -\frac{(N_M+N_O)}{(N_A+N_M+N_O+N_I)} \tag{4}$$

1.3 模糊综合评价模型

模糊综合评价法是一种模糊数学的多准则综合性评价方法，基于模糊变换和最大隶属度原则，将具有模糊性和不易量化性的因素（指标）定量化进行模糊集成[23]。本文采用该方法对新一代集控站智能运维需求要素分析结果进行验证，具体步骤包含：（1）评估指标竞争程度评价集合梳理；（2）建立 n 个评估指标的权重分配向量 W；（3）通过单指标模糊评价获得模糊关系矩阵 R。（4）进行模糊集成。（5）进行归一化并开展对比分析。

2 基于 KJ 法的需求亲和分析

收集近 3 年运维人员值班日志、交接班记录、问题清单等资料，梳理与新一代集控站智能运维相关的关键词，采用微词云作为工具对关键词进行频率分析，对前排名 100 词汇进行修正，总结出“数据采集”、“数据关联”、“系统规模展示”、“网安管理”、“处置策略”等 46 条需求场景。结合 KJ 亲和图理论，通过专家组群策群力方式进行需求聚类，得到“数据采集”、“数据存储”、“全景展示”等 11 个需求要素详见表 1 所示。

表 1 需求要素聚类结果
Table 1 Clustering results of demand elements

序号	需求要素	需求场景
1	数据采集	数据采集、数据合并、数据转发
2	数据存储	数据关联、数据存储、历史数据管理
3	全景展示	系统规模展示、数字孪生机房
4	通道监视	VLAN 管理、网安管理、流量监控
5	系统监控	动环监控、故障定位、接口监测、进程监视、信号告警窗、异常检测、应用状态监视、硬件设备监视
6	告警管理	告警封锁、故障规则
7	处置策略	处置策略、处置流程维护、专家库维护

8	运维管理	风险管理、工单处理、计划管理、门禁授权、软件升级、视频管理、台账维护、文件监视、业务监控、值班交接、值班考勤、值班日志、智能巡视
9	信息交互	短信告警、语音交互、问答机器人
10	统计分析	报表统计、模块化报表
11	访问控制	角色管理、白名单管理、权限管理

3 基于 Kano-模糊综合评价模型的需求要素归类

3.1 变电数字化专业调研

以问卷星作为工具设计出正反向问题，面向电力公司相关专业人员开展两轮调研。第一轮主要是介绍问卷的原因和目的，并且了解被调研对象的基础信息，包含所在性别、学位、工作年限、部门、职称等信息，用以判断本次所收集问卷质量；第二轮问卷面向用户需求，试卷中对相同问题分别通过以正反向两个角度发问，题目以选择题形式对各个需求强度进行 5 级量化（很低、较低、一般、较高、很高）测度，不同题目之间顺序随机处理。运用 Kano 模型划分需求归类时，根据正反两个问题的回答将数量值最大的选项作为判定需求归类的依据。若同一需求正反问题答案的数量值相同且非“无所谓”，则定义该需求归类不可靠并过滤结果。本轮调查时间为 2024 年 8 月 10 日-12 月 20 日，共发放问卷 96 份，经回收及无效结果过滤后得到问卷回馈 84 份，有效回收率为 87.5%。样本中受访人员具有丰富的理论和实践经验，基本信息如表 2 所示。

表 2 受访人员基本情况

Table 2 Basic information of interviewees

基本信息	结果	人数	占比（%）
性别	男	79	94.05%
	女	5	5.95%
最高学位	博士	3	3.57%
	硕士	12	14.29%
	本科	57	67.86%
	专科	7	8.33%
从事相关工作年限（年）	1-5 年	33	39.29%
	5-10 年	29	34.52%
	10-20 年	17	20.24%
	20 年及以上	5	5.95%
专业部门	运维检修部	6	7.14%
	变电运维中心	13	15.48%
	生产指挥专业	9	10.85%
	超高压中心	6	7.14%
	调度自动化	11	13.10%
	产业部门	39	46.43%
最高职称	教授级高级工程师	2	2.38%
	高级工程师	13	15.48%
	中级工程师	27	32.14%
	助理工程师	31	36.90%
	其他	11	13.10%

采用 SPSS 工具进行 Cronbach’s α 和 KMO（Kaiser-Meyer-Olkin）分析，发现 CR=0.8125＞0.7，效度 KMO 系数=0.785>0.5，表明样本具备良好信度和效度，可以继续开展数据分析。

3.2 智能运维需求归类

依据 Kano 模型规则，对整理后的需求问卷数据进行需求分类，根据需求分类结果发现，全景展示（N_A=36，N_I =33）、通道监视（N_M=31，N_I=34）、访问控制（N_M =40，N_O =35）3 个需求要素中各自存在 1 处与 Kano 模型归类数量接近的需求归类，按照 1.2 节中 Kano 模型关于相近数量的选项值处理办法，通过式（1）~式（2）分别对上述 3 个需求要素展开混合分析得出混合归类如表 3 所示。

依据混合归类归类思路，S_T＞0.6 且 S_C≤0.06，说明全景展示、通道监视、访问控制需求要素为混合归类需求：全景展示由由魅力型需求变成魅力型需求和无差别型需求的混合归类，通道监视由无差别型需求变成必要型需求和无差别型需求的混合归类，访问控制由由必要型需求变成必要型需求和期望需求的混合归类。

表 3 新一代集控站智能运维需求归类结果

Table 3 Classification results of intelligent operation and maintenance requirements for the new generation of centralized control stations

需求要素	数量统计（人）					Kano 归类	S_T	S_C	混合归类
	A	M	O	I	R				
数据采集	5	67	4	8	0	M	0.905	0.702	M
数据存储	4	74	5	1	0	M	0.988	0.821	M
全景展示	36	5	10	33	0	A	0.607	0.036	H（A+I）
通道监视	8	32	11	33	0	I	0.607	0.012	H（M+I）
系统监控	2	1	80	1	0	O	0.988	0.929	O
告警管理	71	4	3	6	0	A	0.929	0.774	A
处置策略	5	3	75	1	0	O	0.988	0.833	O

运维管理	8	3	69	4	0	O	0.952	0.726	O
信息交互	75	1	3	5	0	A	0.940	0.833	A
统计分析	2	3	10	69	0	I	0.179	0.702	I
访问控制	40	7	35	2	0	M	0.976	0.060	H（M+O）

3.3 Better-Worse 系数分析

使用 Better-Worse 系数分析方法对智能运维需求要素展开分析，通过式（3）~式（4）对进行 Better 与 Worse 系数计算，结果如表 4 所示。

表 4 新一代集控站智能运维需求求 Better-Worse 系数分析

Table 4 Analysis of Better-Worse coefficient for intelligent operation and maintenance requirements of new-generation centralized control stations

需求要素	Better 系数	Worse 系数	Better-Worse 归类
数据采集	0.107	-0.845	M
数据存储	0.107	-0.940	M
全景展示	0.548	-0.179	A
通道监视	0.226	-0.512	I
系统监控	0.976	-0.964	O
告警管理	0.881	-0.083	A
处置策略	0.952	-0.929	O
运维管理	0.917	-0.857	O
信息交互	0.929	-0.048	A
统计分析	0.143	-0.155	I
访问控制	0.893	-0.500	A

将信息需求要素划分至 4 个象限以确定功能优化的优先级。将 Better 与 Worse 系数平均值的绝对值（0.607，0.547）作为原点，以 Better 系数作为横坐标、以 Worse 系数绝对值作为纵坐标作出分析散点图如图 3 所示。

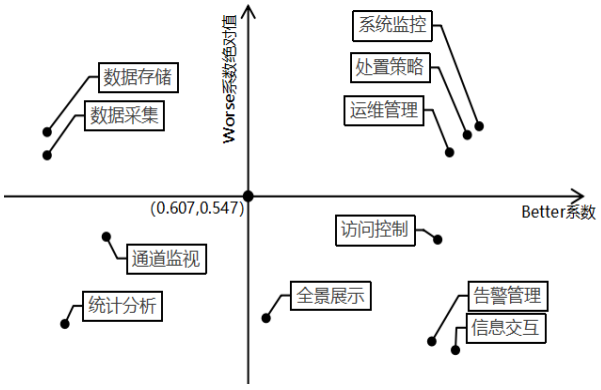


图 3 智能运维需求要素 Better-Worse 系数分析散点图

Figure 3 Scatter Plot of Better-Worse Coefficient Analysis for Intelligent Operation and Maintenance Requirement Elements

由图 3 散点图得知，新一代集控站智能运维需求要素被划分到 4 个象限。第一象限内 Better 系数与 Worse 系数绝对值都大于平均值，说明该类型需求要素能够显著提升集控系统运维单位工作能力，可定义为期望型需求，通常作为基础功能首要实现；同理第二象限到第四象限分别定义为必要型、无差别型、魅力型需求。

3.4 基于模糊综合评价模型的需求要素结果验证

为保证新一代集控站智能运维 Kano 模型分析结果的可靠性，采用模糊综合评价法对其进行验证。将业务关联、使用频率、开发效率 3 项因子整理评价集合为 U=[u1,u2,u3]，同时将要求性评价指标设置为很低、较低、一般、较高及很高 5 个等级，按照确定指标确定评价集合，由上述调研 84 名对象依次进行评价并归一化如表 5 所示。

表 5 新一代集控站智能运维需求要素评价结果

Table 5 Evaluation results of intelligent operation and maintenance requirement elements for the new generation of centralized control stations

需求要素	权重	占比统计				
		很低	较低	一般	较高	很高
数据采集	0.4	0.000	0.012	0.095	0.048	0.845
	0.3	0.071	0.083	0.774	0.012	0.060
	0.3	0.036	0.345	0.476	0.107	0.036
数据存储	0.4	0.024	0.119	0.036	0.000	0.821
	0.3	0.083	0.060	0.560	0.238	0.060
	0.3	0.000	0.036	0.643	0.238	0.083
全景展示	0.4	0.345	0.476	0.083	0.024	0.071
	0.3	0.060	0.107	0.786	0.036	0.012
	0.3	0.036	0.071	0.036	0.024	0.833
通道监视	0.4	0.119	0.607	0.119	0.083	0.071
	0.3	0.821	0.095	0.048	0.012	0.024
	0.3	0.119	0.131	0.036	0.643	0.071
系统监控	0.4	0.095	0.036	0.000	0.000	0.869
	0.3	0.119	0.036	0.048	0.036	0.762
	0.3	0.119	0.083	0.024	0.238	0.536
告警管理	0.4	0.083	0.095	0.071	0.726	0.024
	0.3	0.048	0.083	0.798	0.036	0.036
	0.3	0.798	0.071	0.024	0.036	0.071
处置策略	0.4	0.071	0.048	0.024	0.036	0.821
	0.3	0.000	0.012	0.000	0.000	0.988
	0.3	0.000	0.917	0.012	0.071	0.000
运维管理	0.4	0.000	0.000	0.000	0.024	0.976
	0.3	0.012	0.024	0.048	0.000	0.917
	0.3	0.000	0.202	0.179	0.238	0.524
信息交互	0.4	0.024	0.595	0.298	0.083	0.000
	0.3	0.405	0.512	0.071	0.012	0.000
	0.3	0.036	0.060	0.095	0.750	0.060
统计分析	0.4	0.048	0.071	0.119	0.655	0.107

	0.3	0.048	0.679	0.024	0.107	0.143
	0.3	0.369	0.095	0.345	0.107	0.083
访问控制	0.4	0.500	0.393	0.036	0.012	0.060
	0.3	0.131	0.714	0.024	0.083	0.048
	0.3	0.119	0.012	0.762	0.060	0.048

定义因子权重 W=[w1，w2，w3]=[0.4，0.3，0.3]，并根据打分结果形成相应的关系矩阵 R={R1，R2，R3，……，R11}。以数据 R1 为例见式（8）。

$$R_1=\begin{bmatrix} r_{11} & r_{12} & r_{13} & r_{14} & r_{15} \\ r_{21} & r_{22} & r_{23} & r_{24} & r_{25} \\ r_{31} & r_{32} & r_{33} & r_{34} & r_{35} \end{bmatrix}=\begin{bmatrix} 0.000 & 0.012 & 0.095 & 0.048 & 0.845 \\ 0.071 & 0.083 & 0.774 & 0.012 & 0.060 \\ 0.036 & 0.345 & 0.476 & 0.107 & 0.036 \end{bmatrix} \tag{8}$$

采用模糊数学定义两数相加取大、两数相乘取小，计算模糊综合评价结果向量 b1=W1*R1=[0.107，0.395，0.695，0.167，0.495]，归一化结果 b1=[0.058，0.213，0.374，0.09，0.266]，结合最大隶属度法则可知，综合评价结果为一般，同理计算其余评价结果如式（9）所示。

$$B=\begin{bmatrix} b_1 \\ b_2 \\ b_3 \\ b_4 \\ b_5 \\ b_6 \\ b_7 \\ b_8 \\ b_9 \\ b_{10} \\ b_{11} \end{bmatrix}=\begin{bmatrix} 0.058 & 0.213 & 0.374 & 0.090 & 0.266 \\ 0.054 & 0.108 & 0.322 & 0.241 & 0.275 \\ 0.231 & 0.304 & 0.220 & 0.044 & 0.201 \\ 0.279 & 0.325 & 0.105 & 0.205 & 0.086 \\ 0.182 & 0.084 & 0.039 & 0.149 & 0.545 \\ 0.257 & 0.149 & 0.235 & 0.281 & 0.078 \\ 0.056 & 0.282 & 0.028 & 0.084 & 0.550 \\ 0.007 & 0.122 & 0.124 & 0.141 & 0.606 \\ 0.176 & 0.373 & 0.228 & 0.194 & 0.029 \\ 0.175 & 0.207 & 0.197 & 0.273 & 0.148 \\ 0.321 & 0.348 & 0.178 & 0.076 & 0.076 \end{bmatrix} \tag{9}$$

最终得出专家组在智能运维需求要素的综合模糊评价排序为运维管理、处置策略、系统监控、告警管理、统计分析、数据采集、数据存储、信息交互、访问控制、通道监视、全景监视，其中运维管理、处置策略、系统监控等评分较高，由此验证上述 Kano 模型分析结果具备有效性。

4　智能运维 Kano 需求与业内主流产品功能匹配情况

对比前文 Kano 需求要素分类结果，分析当前业内主流自动化运维平台产品功能与新一代集控站运维需求的差异与关联。课题总结相关主流自动化运维平台共 10 余例，考虑篇幅原因，此处选择调度自动化运行监测平台、配网自动化监控系统等 5 例产品作为调研目标，其对比结果如表 6 所示。

表 6　智能运维 Kano 需求与业内主流自动化运维平台产品功能匹配情况

Table 6　Matching between Kano requirements for intelligent operation and maintenance and the functionalities of mainstream automated operation and maintenance platform products in the industry

需求要素	需求归类	对应功能				
		调度自动化运行监测平台	配网自动化监控平台	电力监控网络安全监测主站平台	自动化机房动环监控平台	蓝鲸机房管理平台
数据采集	M	数据采集	数据采集	网安集成	数据采集	数据集成服务
数据存储	M	数据存储	数据存储	数据存储	数据存储	容器数据库
全景展示	A	运维首页、3D 孪生机房	项目概况、大屏显示	网络拓扑图	电子地图	运维大屏
通道监视	I	网管模块	系统拓扑图	实时监视	综合布线	网络监控
系统监控	O	实时监控台	配电监测、重点设备监控	网安监控	远程管理	应用监控
告警管理	A	运行监测	事件记录	预警告警	实时告警	告警中心
处置策略	O	/	/	/	/	/
运维管理	O	作业监视与审计	能源管理、设备台账、运行报告	/	日志管理、动态编辑	工单自动化
信息交互	A	/	/	/	/	/
统计分析	I	数据分析	实时集抄、电能报表	审计分析	辅助分析	/
访问控制	A	系统管理	中心控制	人员管理	权限管理	运维门户

由表 6 得知，当下业内主流产品功能相对比较完善，但也存在个别功能点未涵盖到位：调度自动化运行监测平台、配网自动化监控平台及自动化机房动环监控平台各缺少需求点 2 类，电力监控网络安全监测主站平台及蓝鲸机房管理平台各缺少需求点 3 类。从单个需求要素维度上看，数据采集、数据存储、系统监控等核心要素在各类平台均已实现，而处置策略、运维管理、信息交互及统计分析这 4 个需求要素在各类主流产品中存在缺失情况。梳理前文 Kano 需求要素，与对比业内主流产品及智能运维平台已有功能进行

匹配分析生成映射关联图，待提升功能通过高亮颜色标注如图 4 所示，结果发现新一代集控站智能运维平台在处置策略、统计分析、运维管理、信息交互 4 个方面功能仍不完善，存在较大提升空间较大方向。

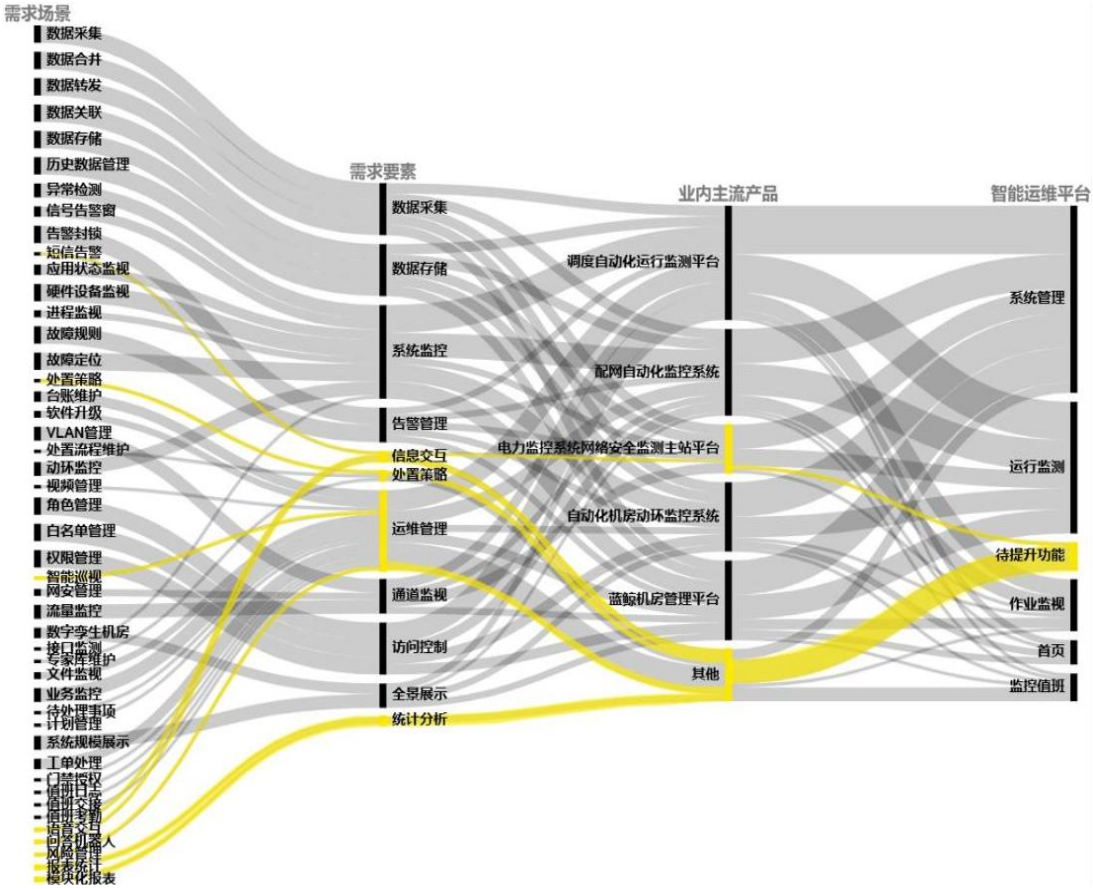


图 4 需求要素-业内产品-智能运维平台已有功能情况分析

Figure 4 Demand Factors - Industry Products - Analysis of Existing Features in Intelligent Operation and Maintenance Platforms

5 新一代集控站智能运维功能提升策略

5.1 场景结合，规划进展

根据 Better-Worse 系数分析结果规划功能提升计划，通过任务 WBS 分解、单位工作时间评估及优先级标记等手段将不同模块分为多个阶段实施。对于“数据采集”、“系统监控”等期望型需求和必要型需求，优先投入资源团队，确保可交付成果按时完成。

5.2 主业参与，持续跟进

定期组织座谈会、问卷调查及现场调研，将现场运维作业人员反馈痛点需求纳入功能迭代计划，同时围绕告警管理、处置策略等功能建立专家库并实现动态更新，形成“需求采集-功能设计-开发实施-效果评估”的闭环管理流程。此外定期组织运维人员进行操作培训和应急演练，提升其数字化应用能力及对新功能的满意度。

5.3 深度探索，创造亮点

结合魅力型需求特点，进一步提升功能的多元性和实用性。结合自然语言处理、聚类分析算法、三维数字孪生机房等技术对运维数据深度挖掘，打造具备智能化辅助决策、语音交互、全景展示等高级应用，为运维人员的决策及处置辅助提供科学方法。

6 结语

本研究旨在深入了解新一代集控站智能运维主要需求要素，通过应用 KJ-Kano-模糊综合评价模型模型对上述需求展开归类及验证，将分析结果与自身实际情况以及业内主流自动化运维平台产品进行对比分析，并为改善新一代集控站智能运维功能、提升集控系统班组人员业务能力与数字化综合素养，激发变电运维专业创新生命力提供了建设性指导。

参考文献

[1] 孙琛,陈宁.新一代集控系统一键顺控防误操作技术研究[J].电力与能源,2024,45(05):594-598.

[2] 魏勇军,黎炼,张弛,等.电力系统自动化运行状态监控云平台研究[J].现代电子技术,2017,40(15):153-158.

[3] 刘旭,汤玮,龙姣,等.电力调度平台全景化管控的实现方式研究[J].粘接,2020,44(12):149-152.

[4] 李挺,王萍,胡聪.电网信息系统运维管理自动化探索与研究[J].科技与创新,2017,(23):77-78.

[5] 朱兴东，何小伟，等.基于大数据分析的电力系统故障诊断方法研究[J].电力系统保护与控制,2018,46(11):59-65.

[6] 黄伟，王鑫，等.基于物联网技术的电力系统智能监控系统设计与应用[J].电力信息与自动化设备,2019,39.

[7] 刘洋，赵丽，等.基于机器学习的电力系统故障诊断与预测方法研究[J].电力系统保护与控制， 2021，49(5)

[8] Nitasha K ,Zeeshan S ,Mansoor M A , et al.Energy Management Systems Using Smart Grids: An Exhaustive Parametric Comprehensive Analysis of Existing Trends, Significance, Opportunities, and Challenges[J].International Transactions on Electrical Energy Systems,2022

[9] Joseph A , Balachandra P .Smart Grid to Energy Internet: A Systematic Review of Transitioning Electricity Systems[J].IEEE Access, 2020, 8:215787-215805.

[10] 乐弘习,陆昱,黄维华,等.图像识别技术在室内变电站智能运维辅助装置的应用研究[J].电力设备管理,2021,(01):35-37.

[11] 王伟杰,雍明超,黄金魁,等.高压设备数字孪生体构建及状态分析技术研究[J].高压电器,2023,59(11):119-128.

[12] 普华有策.2025-2031 年智能电网运维监测产品行业市场调研及发展趋势预测报告[EB/OL].https://www.163.com/dy/article/JKRF0GVE0518WMF4.html,2025.01.

[13] 简思亮,张浩,张珏,等.换流站三维数字化及智能巡检系统设计与应用[J].南方能源建设,2023,10(05):41-49.

[14] 方涛,钱少锋,王祯,等.UWB 定位技术在数字孪生变电站中的应用[J].电工技术,2022,(12):49-52.

[15] 许飞,唐曙光,刘文涛,等.变电站远程智能巡检系统研究与应用[J].自动化仪表,2022,43(04):81-85.

[16] 金鹰.室内变电站智能运维辅助装置中图像识别技术应用[J].上海轻工业,2023,(05):156-158.

[17] Liu W ,Chi M ,Liu Z , et al.Distributed optimal active power dispatch with energy storage units and power flow limits in smart grids[J].International Journal of Electrical Power and Energy Systems,2019,105420-428.

[18] 原创力文档.2025 年电网运维检修市场分析报告[EB/OL].https://max.book118.com/html/2024/1229/8046027114007013.shtm,2024.12.

[19] 原创力文档.2025 年国内外变电站自动化技术发展现状及发展趋势(精) [EB/OL].https://max.book118.com/html/2025/0110/8014130005007020.shtm,2025.01.



康君召

收稿日期：2025-08-24。

作者简介：

康君召（1993-），男，通信作者，硕士，工程师，主要从事电力系统自动化等领域研究工作，KJZ1993@foxmail.com，杭州市西湖区文一西路 83 号文华楼 411，310027；

朱轶伦（1989-），男，硕士，高级工程师，主要从事电力系统自动化等领域研究工作；

宁福军（1989-），男，硕士，助理工程师，主要从事人工智能与自动控制领域研究工作；

姚高（1990-），男，本科，主要研究方向：电力系统分析与控制；

许杰（1994-），男，助理工程师，主要研究方向：电力系统分析与控制；

杨薇薇(1988)，女，硕士，助理工程师，主要从事电力系统自动化等领域研究工作。

（编辑）

021 风光氢储系统综述

李　响，韩如月，陈　建，锁　连

（内蒙古工业大学电力学院、呼和浩特 010000）

A Comprehensive Review of Integrated Wind-Solar-Hydrogen-Storage Systems

LI Xiang,HAN Ruyue,CHEN Jian,SUO Lian

(School of Electric Power,Inner Mongolia University of Technology,Huhhot 010000,China)

ABSTRACT: Driven by the national "carbon peaking and carbon neutrality goals", the National Development and Reform Commission and the National Energy Administration have explicitly proposed the objective of constructing a "Wind-Power-Hydrogen-Storage integrated system". This aims to promote the green transformation of the energy sector through diversified application scenarios utilizing wind power, photovoltaics, hydrogen energy, and others. This paper systematically reviews the research progress in the integrated system concerning capacity configuration, operation optimization, economic analysis, hydrogen production technology, and market mechanisms: Key approaches include intelligent algorithms for capacity optimization, operational frameworks combining prediction and decision-making, and economic models integrating lifecycle costs with green hydrogen market mechanisms.

KEY WORDS: Wind-Power-Hydrogen-Storage;capacity configuration;operation optimization;hydrogen production technology;market mechanism

摘要：在国家“双碳”目标驱动下，国家发展改革委和国家能源局明确提出构建“风光氢储一体化系统”的目标，旨在通过风能、光伏、氢能等多元化应用场景，推动能源绿色转型。本文系统梳理了风光氢储一体化系统在在容量配置、运行优化、经济性、制氢技术及市场机制中的研究进展：通过改进优化算法求解系统容量配置模型，构建“预测－决策”协同运行框架提升调控效率，融合全生命周期成本模型与绿氢市场机制设计分析经济性等。结论表明，风光氢储系统通过技术－经济－市场多维度协同，有效实现可再生能源高效利用。

关键词：风光氢储；容量配置；运行优化；制氢技术；市场机制

基金项目：中国工程院战略研究与咨询项目“内蒙古构建新型能源体系战略研究”（项目编号：2024-DFZD-56）

Project Supported by Strategic Research and Consulting Project of the Chinese Academy of Engineering (CAE)"Research on the Strategy of Building a New Energy System in Inner Mongolia" (2024-DFZD-56).

0　引言

随着全球温室效应等环境问题日益恶化与化石能源储量减少，全球能源结构逐渐向低碳化转型。为实现绿色低碳发展，我国于 2021 年率先提出了“碳达峰”和“碳中和”的目标。电力行业积极响应这一战略目标，使可再生能源接入电网的比例逐渐提高。

据国家能源局报告显示，2024 年，风光发展迅猛，装机容量和发电量均实现大幅增长，体现了中国能源转型的加速：风光累计发电装机容量达 14.07 亿千瓦，同比增长 33.9%，其中，新增装机容量为 3.58 亿千瓦；同时，风光发电量达到 1.83 万亿千瓦时，占总新增发电量的 58.1%，同比增长显著[1]，凸显了其在电力结构中的主导地位。这些数据说明风光已成为中国新增电力的主力军，支撑了清洁能源目标的实现。然而，以风电、光伏为代表的可再生能源以其显著的不确定性和间歇性特征给电网的安全稳定运行带来了挑战。风光氢储一体化系统整合风电、光伏、制氢与储能装置，利用电解水制氢等环节所具备的强大灵活调节能力，能够有效消纳新能源，减少弃风弃光率，提高风能和太阳能的利用率。

1　风光氢储系统简介

风光氢储系统是一种集成可再生能源与氢能技术的清洁能源解决方案，旨在克服风能和太阳能固有的间歇性与波动性挑战，实现电力的稳定供给与跨周期存储。风力发电机组与光伏阵列负责生产“绿电”；电解水制氢装置利用富余或波动的可再生能源电力将水分解为高纯度的“绿氢”和氧气；氢气进行安全存储后，通过燃料电池发电反送电网或在工业、交通等领域直接利用。其价值在于将难

以直接并网消纳的风光电力转化为高能量密度的氢气进行大规模、跨季节储存，并通过氢气灵活利用的特性平抑可再生能源出力波动，提升电力系统的可靠性与灵活性。

2 风光氢储系统容量配置优化

风光氢储系统容量配置优化是一个关键的规划设计环节，达到为特定区域或应用场景确定风能、太阳能与氢储能系统最佳容量组合的目标。其优化流程包含：收集分析数据，如当地的风速、太阳辐照度、天气等；对各单元建立相应的模型，选择设备；确定目标函数和约束条件；采用优化算法进行求解，得到最优解并验证解的有效性。

风光氢储容量配置是风光氢储系统研究的基础，其中，优化算法创新是其核心方向。目前，容量配置模型的构建广泛采纳了多目标改进优化算法的理论框架。围绕优化算法的改进、适应性问题以及多约束目标模型的构建，国内外研究者已开展了大量卓有成效的研究。国内研究多采用遗传算法、粒子群优化、猫群算法等优化算法。朱赵晴等人[2]构建了基于猫群算法的风光储微电网容量优化模型，以系统综合运行成本最小化为目标，优化风、光、储单元容量配比，有效规避了局部最优陷阱；洪毅[3]针对并网型微电网的混合储能配置，提出包含罚函数的粒子群算法优化铅酸电池与液态金属电池容量，显著降低了全生命周期成本；仲恒等人[4]利用改进灰狼算法处理氢－蓄电池混合系统容量优化，引入步长欧氏距离权重策略强化了全局搜索能力。欧洲国家注重风光氢储在电网、工业场景的协同运行。例如，德国“能源村”项目通过氢储能实现风光电力自给自足，并利用混合整数线性规划有效优化了储氢罐与燃料电池容量配比[5]。

综上所述，风光氢储系统容量配置研究在全球范围内均高度依赖高效、适应性强的优化算法作为支撑。其主要研究方向为：如何通过算法的创新与优化模型的构建，解决多能源耦合、多约束条件下的复杂容量配置问题，并满足不同应用场景的核心需求。

3 风光氢储系统运行优化

运行控制的核心在于构建多时间尺度能量管理框架，在可再生能源集成系统的能量管理研究中，多方面优化策略的进展显著提升了系统性能。徐甜甜等人[6]针对综合能源系统的效益分配问题，系统地纳入了经济性、环境性及稳定性三方面。构建了包含多方面因素的分层效益均衡模型。该模型通过量化不同因素的贡献权重，实现了资源分配的精细化平衡，为后续研究提供了基准框架。王涛[7]在并网与独立运行状态下，建立了功率平衡控制策略与系统切换机制。这些策略结合实时监控与反馈调整，确保能量流能够稳定传输和高效管理，尤其在频繁工况变化场景中显著增强了系统的适应性和鲁棒性。杨丽君等人[8]则通过强化柔性负荷的协同作用，将负荷细分为可激励型和可中断型两类，设计了“源－网－储－荷”融合的优化能量管理方案。此方案不仅提升了负荷侧响应的灵活性，还通过动态调节机制促进了多源协同效率。姜杰等人[9]在园区风光储系统中提出了一套结构化运行调控框架，将模型分解为预测模块和决策模块两个模块，在预测模块中,运用机器学习或统计学方法，精确预测风光发电输出与负荷需求波动；在优化决策模块中，集成混合整数规划算法，依据预测结果实时制定最优调控策略。这套运行框架提升了策略的可扩展性，同时为复杂系统的智能调度奠定了理论基础。在国际层面，美国 Wind2H2 计划通过动态规划算法协调制氢单元与风电机组的运行策略，提升风能消纳与制氢效率[10]。

上述研究共同推动了能量管理系统从单维优化向多维协同的演进，强调了智能化、优化算法和柔性负载在“双碳”目标下运行优化的作用。

4 风光氢储系统经济性与商业运营模式

为突破当前绿氢制备与建设规模扩张的瓶颈，即投资回报周期长、制氢成本高企等关键经济性制约，研究重点已从单一的成本核算维度，逐步向“政策－市场－技术”深度融合的三重耦合分析拓展。围绕经济效益优化的目标，近期研究从多维度提出了解决方案，形成了优化策略框架。从波动平抑与排放协同方向，钱宇等人[11]引入频谱分析和滤波分析方法，揭示了风光互补平抑波动特点对电力波动量化的影响，并结合生命周期评价方法，定量解析了风光耦合制氢系统的全生命周期碳排放性能。从调度优化与运行成本控制方向，袁铁江等人[12]针对大规模间歇性制氢系统实际运行中电解槽频繁启停导致成本陡增的问题，建立了考虑电解槽启停特性的制氢储氢系统日前出力特性模型，同时针对交通用氢、燃气掺氢等差异化应用场景，构建了风光制氢出力优化模型，有效改善了购置高额峰段电量与电解槽设备损耗加剧两大瓶颈问题。从多源协同与综合收益最大化方向，姚芳等人[13]为优化风光氢

储能源系统的整体经济性，为解决系统弃风弃光造成的可再生能源浪费以及负荷中断导致的用户经济损失的问题，构建了一个以系统全生命周期总收益最大化为目标的优化模型。该模型综合考虑了系统投资、售氢售氧与售购电能的成本和利润、运维成本、中断负荷的惩罚费用及附加弃风弃光。从经济评价体系与投资决策支撑方向，陈昱杉等人[14]为有效电解制氢成本高的主要限制，通过构建系统化、定量化的投资回报评估方法，以总投资收益率、项目投资回收期、财务内部收益率、财务净现值和项目资本金净利润率等为主要经济评价指标，构建了一套层次分明的经济评价体系。

上述研究从平抑波动、精准调度、协同收益、量化评价等方向发力，构建了覆盖风光氢储系统“源－储－荷”全链条的经济性优化策略体系，为提升项目经济效益、加速绿氢产业规模化发展开辟了多方向的科学路径。

5 制氢技术与适应性优化

风光氢储系统的技术挑战在于电解水制氢环节与风光波动性之间的协同匹配。当前碱性、质子交换膜、固体氧化物等电解槽技术路线并存，其动态响应特性、效率衰减机制及成本差异，直接影响系统制氢效率与经济性。黄启帆等人[15]针对碱性电解槽低成本优势和质子交换膜电解槽快速响应特性，提出了一种复合电解槽协同制氢系统架构，通过多类型电解槽的协同运行，实现对风光出力波动的灵活调节，在功率平稳时段优先运行碱性电解槽以降低单位制氢成本，在功率骤变阶段则切换至质子交换膜电解槽以保障响应速度。降低了单位氢气生产成本，为高效消纳波动性风光资源提供了设备层解决方案。袁铁江等人[16]综合考虑了环境兼容性、技术可行性及经济成本效益三大指标，构建了基于层次分析法的氢储单元选型模糊综合评价模型。该模型通过量化评估不同储能技术在平抑风光波动、支撑电解制氢的综合表现，为高波动场景下风光氢储协同系统的优化配置提供了决策依据。林佳亮等人[17]通过博弈论构建主客观组合赋权法，采用了连续区间有序加权平均算子改进层次分析法以缓解主观判断偏差，结合熵权法优化改进标准间冲突性相关性算法量化指标间冲突性关联，得到主客观权重，最后基于直觉模糊多属性决策实现技术方案的优选评估。康忠健等人[18]则致力于混合电解槽的容量优化，提出基于决策试验与模糊层次分析法的混合优化模型。通过分析 9 个灵活性指标指标间的相互作用修正层次权重，构建双层评估模型。提升了高比例风光场景下混合电解槽容量配置方案的动态适应性与经济性。

为破解风光制氢的动态适配瓶颈，上述研究从硬件协同架构、多维度评价体系及决策算法等多方面，解决风光波动与制氢系统的适配性矛盾，推动了高波动场景下制氢系统经济性与稳定性的跃升。这些协同路径为规模化绿氢系统的工程落地提供了关键技术支撑。未来研究可进一步探索跨区域多能流协同优化机制，以期在更复杂的波动场景及多类型负荷需求下实现绿氢生产稳定性与经济性的更精细化平衡。

6 参与市场的策略及机制

随着电力市场化改革深化，风光氢储系统如何通过策略参与电力交易实现收益最大化成为关键议题。当前研究关注于构建差异化市场场景下竞价决策模型、优化交易策略和量化外部政策的影响。刘佳楠等人[19]以风光储联合体整体收益最大化为目标函数，构建多能源协同参与电力市场的优化决策模型，证明了联合体运行模式下收益增长的可行性，为风光氢储发电企业制定交易策略提供了量化基准。德格吉日夫等人[20]为提高风储混合电站参与电力现货竞价优势，制定了风储电站参与电力现货市场的精细化决策，建立了两阶段优化框架：第一阶段考虑风电出力与现货价格的不确定性，构建包含发电收益、运维成本及不平衡功率惩罚函数的优化模型；第二阶段结合现货市场中标信息动态修正运行计划。该模型有效解决了高波动性场景下风储电站的竞价风险控制与收益保障问题。孙波等人[21]通过对比分析风光储混合发电商作为价格接受者与价格影响者参与电力市场竞争对均衡博弈行为，展现了其参与对市场结构的重塑效应。研究发现：风光储发电商可显著抑制传统发电商的市场垄断力，并通过灵活性资源优化发电路径产生的电价均衡效应；当其作为价格影响者主动调整投标出力时，虽会弱化电价调控强度，但可通过策略性报价实现自身收益提升。这一结论为市场主体角色定位提供了战略指导。王凯等人[22]突破纯电量交易局限，提出碳交易－电力现货市场耦合作用下的风光储场站报价决策机制。其研究引入碳配额成本与绿电溢价双重政策变量，构建基于氢－储耦合灵活性的场站报量报价双层模型。该机制在绿电消纳与碳减排约束下，实现了系统总收益的提升。

上述研究通过竞价决策模型优化、市场角色博

弈分析及政策－市场协同机制创新，系统构建了风光氢储系统参与电力市场的收益优化路径。未来需进一步探索高比例可再生能源渗透下，电力辅助服务市场、绿证交易与碳金融工具的政策联动机制，并开发适应多时间尺度的交易－调度协同决策模型，以全面提升系统在复杂市场环境中的风险抵御能力与综合盈利水平。

7 结语

风光氢储系统通过电氢转换与跨周期储能，有效化解了可再生能源的间歇性难题。本文系统梳理了各环节的关键进展：在容量配置中，优化算法驱动了经济可靠的最优解生成；运行优化通过“预测－决策”闭环框架提升了动态响应能力；经济性层面构建了多维度评价体系与绿氢溢价模型；制氢技术通过复合架构与适应性优化突破波动场景瓶颈；参与市场机制则耦合碳电交易策略，为商业化铺路。未来，可进一步开发秒级－季节多尺度耦合的调控模型，强化极端天气下的鲁棒性；探索固体氧化物电解槽高温制氢与风光波动的动态匹配机制。建立氢能管网与电网、热网的协同调度模型，实现“西氢东输”与负荷中心的精准匹配；设计绿证－碳配额－辅助服务的复合交易机制，量化氢储的调频容量价值，激发市场主体积极性；通过碱性与质子交换膜电解槽混合运行、废弃风电制氢等模式进一步压缩绿氢成本，推动产业规模化拐点到来。

参考文献

[1] 国家能源局．2024 年度中国电力市场发展报告[EB/OL]． (2025-07-17)[2025-07-20]． https：//www．nea．gov．cn/20250717/54ae0fdb11f04b39a5b670999c04ef81/c．html．

[2] 朱赵晴，方芩璐，夏焰坤，等．基于改进沙猫群算法的微电网日前优化调度[J]．四川电力技术，2024，47(05)：14-20+43．

[3] 洪毅．基于粒子群算法的含光伏微电网并网功率控制系统[J]．电子设计工程，2023，31(23)：127-130+135．

[4] 仲恒，魏立明，王楷硕，等．基于风光储微电网优化调度模型研究[J]．节能与环保，2025，(02)：36-43．

[5] Timalsina S，Zhang Chengyi，Kumar D，et al．Optimizing hydrogen transportation infrastructure and supply chain under uncertainty： An integrated mixed integer linear programming and real options analysis[J]．International Journal of Hydrogen Energy，2025，111：635-647．

[6] 徐甜甜，杜易达，周晓彤，等．计及风险偏好的风光氢储醇耦合系统多目标运行优化及效益均衡模型[J/OL]．太阳能学报，1-12[2025-08-03]．https：//doi．org/10．19912／j．0254-0096．tynxb．2024-2344．

[7] 王涛．离网型风光储互补系统能量管理研究[J]．电力设备管理，2024，(16)：129-131．

[8] 杨丽君，黄凯婷，孔晓磊，等．考虑柔性负荷的并网型微电网系统容量优化配置[J]．太阳能学报，2021，42(02)：309-316．

[9] 姜杰，付申杰，漆晓凤，等．园区风光储系统的储能容量优化及运行调控策略研究[J]．电气技术与经济，2023，(10)：110-112．

[10] Pourrahmani H，Zahedi R，Daneshgar S，et al．Lab-Scale Investigation of the Integrated Backup／Storage System for Wind Turbines Using Alkaline Electrolyzer[J]．Energies，2023，16(9)：1．

[11] 钱宇，陈耀熙，史晓斐，等．太阳能波动特性大数据分析与风光互补耦合制氢系统集成[J]．化工学报，2022，73(05)：2101-2110+2290．

[12] 袁铁江，万志，王进君，等．考虑电解槽启停特性的制氢系统日前出力计划[J]．中国电力，2022，55(01)：101-109．

[13] 姚芳，杨晓娜，葛磊蛟，等．风-光-氢能源系统容量优化配置研究[J]．综合智慧能源，2022，44(05)：56-63．

[14] 陈昱杉，李琦，郑博，等．基于风光氢储一体化系统的容量配置优化及经济评价[J]．油气储运，2023，42(07)：763-773．

[15] 黄启帆，陈洁，曹喜民，等．基于碱性电解槽和质子交换膜电解槽协同制氢的风光互补制氢系统优化[J]．电力自动化设备，2023，43(12)：168-174．

[16] 袁铁江，张昱，栗磊，等．计及功率密度约束含氢储能的预装式多元储能电站容量优化配置研究[J]．电工技术学报，2021，36(03)：496-506．

[17] 林佳亮，李暖群，黄焯辉，等．智慧配电网关键技术示范应用优选评估方法[J]．电力需求侧管理，2024，26(04)：16-22．

[18] 康忠健，范佳瑄，陈光，等．基于 AHP-DEMATEL 的风光储氢系统中混合电解槽容量配置优化方法[J]．电力需求侧管理，2025，27(04)：35-43．

[19] 刘佳楠，熊宁，朱文广，等．电力市场环境下风光储联合运行优化策略[J]．电力科学与技术学报，2017，32(01)：11-15．

[20] 德格吉日夫，谭忠富，李梦露，等．考虑不确定性的风储电站参与电力现货市场竞价策略[J]．电网技术，2019，43(08)：2799-2807．

[21] 孙波，樊亚南，李志恒，等．偏差电量考核下风光储混合发电商的市场均衡博弈研究[J]．水电能源科学，2020，38(02)：202-205．

[22] 王凯，延肖何，蒋凯，等．考虑碳交易的风光储场站参与电力现货市场报价策略与调控方法[J]．中国电机工程学报，2023，43(18)：7091-7103．



收稿日期：

作者简介：

李响（1997-），男，硕士研究生，研究方向为电力系统规划，E-mail:lix1325@163.com

韩如月（1979-），通讯作者，女，副教授，硕士生导师，研究方向为电力系统规划、电力市场，E-mail:hanry1979@163.com

陈建（1987-），男，副教授，硕士生导师，研究方向为新能源并网与电能质量控制、风光制氢一体化，E-mail:chenjian19870612@163.com

锁连（1979-），男，副教授，硕士生导师，研究方向为直流配电网、微电网、电能质量、继电保护，E-mail:suolian@imut.edu.cn

（编辑 ）

022 Research and practice of LLM agent for human resource business of large enterprises

Jianfeng Zhang [1]，Xuxin Dai [2]，Yingying Li [3]，Siyi Wang [4]，Shan wan [5]

Foshan Electrical and Lighting Co. Ltd, China

Abstract. With the transformation of human resource management in large enterprises to digital and intelligent, traditional HR systems have gradually shown limitations in dealing with complex business scenarios, ensuring data security and improving service personalization. Based on domestic LLMs such as DeepSeek and Qwen, this paper proposes a LLM agent solution for human resource business in large enterprises. Using LangGraph as the main process engine, it is responsible for orchestrate complex business processes across systems and roles, and integrates LangChain, LlamaIndex, LangSmith and other agent tools. Focusing on the four core technologies of privatized deployment architecture, generative LLM capability integration, agent business adaptation and prompt word engineering optimization, an intelligent system covering the whole process of recruitment, training, salary and performance and employee service is constructed by using intelligent collaboration of multiple technical means. The practice of a large power grid enterprise and a manufacturing enterprise shows that the agent can improve the efficiency of the recruitment process by 52%, and the staff service response speed by 3.8 times, and the data compliance is guaranteed through the privatization deployment. This study provides a reusable technical framework and practical path for the intelligent upgrading of human resource business in large enterprises.

Keywords: Human resource management; AI; LLM; Agent; Generative AI; Prompt word engineering; Agent platform

1 Introduction

1.1 Research background and problem formulation

Human resource management in large enterprises has the characteristics of complex business scenarios (covering recruitment, training, compensation, employee relations, etc.), high data sensitivity (involving employee privacy and organizational strategic data), multiple service objects (employees, managers, HR teams), and the coexistence of standardization and personalization of processes. Traditional HR systems rely on rule engines and modular design, resulting in three core pain points:

Lack of flexibility in response: limited ability to deal with unstructured requirements (such as complex employee consultation and personalized training programs);

Data security and compliance risks: the invocation of the general cloud service LLM may lead to the leakage of sensitive enterprise data, which violates the Data Security Law and industry compliance requirements;

Low efficiency of business collaboration: data isolation of HR modules and lack of cross-scenario intelligent collaboration capabilities (such as the connection between recruitment and training, and the linkage between performance and compensation).

The development of large language Model (LLM) and agent technology, represented by GPT-4 and DeepSeek, provides a new paradigm for solving the above problems. However, existing research mainly focuses on a single business scenario (such as recruitment screening) or a general agent framework, and lacks a privatized, full-process, and landing agent solution for the human resource business of large enterprises.

2 Related work

2.1 Application research of LLMs in the field of human resources

Existing research mainly focuses on local scene optimization:

Recruitment scenario: BERT, GPT model implementation CV screening[1](Sun et al., 2023), and based on the modal analytical technology, to resume document semantic deconstruction, output three-dimensional evaluation matrix (base map qualities/skills/career trajectory), automatic generation of post competency radar map and risk early warning report, Effectively improve the efficiency and accuracy of resume screening[2] (Zhang Y, et al. 2024), but more to rely on public cloud API, not solve the problem of data security;

Employee service: an intelligent question answering system is developed based on the dialogue model [3] (Zhao et al., 2022), but it lacks deep adaptation to enterprise organizational architecture and business rules.

Content generation: automatically generate job descriptions [4], performance reviews, etc. [5] (Li et al., 2024 /sun) et al 2023), but the generated content is insufficient to fit the industry characteristics and culture of the enterprise.

2.2 Technology progress of privatization and deployment of LLMs

Privatized deployment is the core requirement for large enterprises to apply LLMs. There are two types of challenges in existing schemes:

High technical threshold: problems such as model compression, computing power adaptation, and internal network environment compatibility need to be solved[6] (Chen et al., 2023).

Balance difficult: cost and performance of the whole quantity deployed billions of parameter model needs huge calculate power input, and lightweight model can lead to performance loss.

3 The overall architecture design of LLM agent

3.1 Overview of the overall architecture

The LLM agent for the human resource business of large enterprises adopts a four-dimensional technical framework (see the following figure) of "privatized deployment - generative capability - agent cooperation - prompt optimization" to realize the full link closed loop from the underlying technical support to the implementation of the upper business (see 错误!未找到引用源。).:

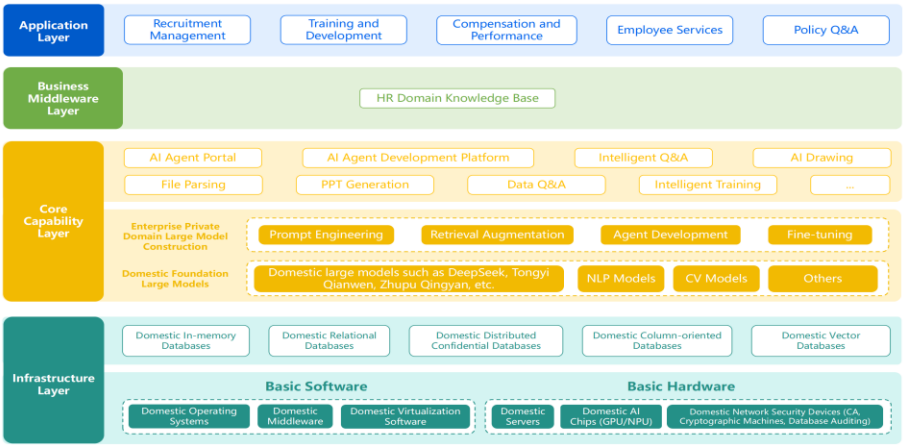


Fig. 1.Architecture Diagram

Infrastructure layer: provide privatized deployment of hardware resources, data security and model management capabilities;

Core competence layer: integrated and generative LLM, prompt word engine and agent collaboration framework, which is the "brain" of the agent; The open source DeepSeek R17B /8B/14B, Qwen2.5-7B/14B or GLM-4-9B models were selected, and LangGraph was used as the main process engine to be responsible for the orchestration of complex business processes across systems and roles. LangChain was integrated to realize LLM call and tool integration. -Construct enterprise knowledge retrieval layer by using LlamaIndex; The whole process observability and continuous optimization are realized by LangSmith.

Business middle layer: through the encapsulation of HR business knowledge, standardization of process rules, and precipitation of historical experience, the HR domain knowledge base was formed, which provided scenarized support for the core competence layer, solved the problem of "disconnection between technical capabilities and business requirements", and provided scenarized support for agents.

4

Application layer: covering five core business scenarios: recruitment management, training and development, salary and performance, employee service, and policy Q&A.

3.2 Agent development framework

At present, agent development frameworks represented by LangChain, LlamaIndex, AutoGPT, BabyAGI are constantly evolving and gradually forming a multi-level technology ecosystem.

LangChain is one of the most widely used LLM application development frameworks. Its core advantages lie in its modular design and high composability. The framework provides chain calls (Chains), the proxy mechanism (Agents), Memory management (Memory) and external tool integration and other core components, support to quickly build agent system based on natural language interaction. In enterprise human resources scenarios, LangChain can be used to implement functions such as employee self-service question answering, policy interpretation, and form filling assistance, especially for single-step, low-complexity interaction tasks.

LlamaIndex: knowledge retrieval engine, RAG architecture core support

LlamaIndex focuses on the structured organization and semantic Retrieval of private knowledge, and is a key tool for retrieval Augmented Generation (RAG). The framework supports extracting information from PDF, Word, database and other sources and constructing vector indexes, which can efficiently respond to high-frequency query needs of employees about compensation and benefits, vacation systems, compliance policies and so on.

In the human resource business, LlamaIndex can be used as the underlying knowledge engine of "intelligent policy assistant", which significantly improves the accuracy and authority of answers. However, it should be pointed out that LlamaIndex itself does not provide process control capabilities to support end-to-end task execution independently. Llamaindex is more suitable as the knowledge retrieval module of LangChain or LangGraph to serve higher level agent systems.

LangSmith: An Agent Observability and Operations Platform

As an important part of the LangChain ecosystem, LangSmith provides debugging, evaluation and monitoring capabilities for the full life cycle of agents.

Comprehensive, each frame in the process of building the intelligent body positioning:

- LangGraph is used as the main process engine to orchestrate complex business processes across systems and roles;
- Integrate LangChain to implement LLM call and tool integration;
-Construct enterprise knowledge retrieval layer using LlamaIndex;
-Achieve full process observability and continuous optimization by LangSmith.

4 Realization of key technologies

4.1 Deployment plan for privatization of large enterprises

4.1.1 Deployment architecture design

For the core requirement of "data not going out of the domain" in large enterprises, the "hybrid deployment + hierarchical isolation" architecture is adopted:

Model selection: Based on open source LLMs (such as DeepSeek, Qwen, etc.), enterprise-level fine-tuning was carried out to retain core parameters while removing general Internet data to reduce security risks.

Computing power configuration: deployed in the enterprise private cloud, using the "GPU cluster + edge computing" mode: the core model (such as 13B parameter model) runs on the GPU cluster, and lightweight tasks (such as employee question and answer) are processed by the edge nodes.

Data security mechanism:

Physical isolation: the model is completely disconnected from the Internet and only connects to the HR system through the internal network interface;

Permission control: Based on RBAC (role-based access control) model, the access scope of agents to sensitive data (such as salary and performance) is limited.

Operational audit: record all model calls and data access behaviors to support compliance traceability.

4.1.2 Model optimization strategy

In order to balance performance and deployment cost, a combination scheme of "domain fine-tuning + lightweight optimization" is adopted:

Domain fine-tuning: use internal enterprise data (recruitment data, training materials, employee manuals, etc., about 5 million texts in the past three years) to fine-tune the basic model and enhance the understanding of enterprise terms (such as "group management trainee" and "OKR assessment cycle").

Model compression: through quantization (INT8/INT4) and knowledge distillation technology, the volume of the model is compressed by 60%, the inference speed is increased by 2 times, and the loss of accuracy is controlled within 5%.

Dynamic reasoning: selected automatically according to the task complexity model scale (such as a simple question and answer with 7 b model, complex copywriter with 13 b model).

4.2 Business adaptation mechanism for large generative models

Generative capability is the core of agents to deal with unstructured tasks, and its application mechanisms include:

4.2.1 Enterprise knowledge base fusion

The "dynamic knowledge graph + Prompt injection" mode is constructed to ensure that the generated content conforms to the actual situation of the enterprise:

The knowledge graph covers the organizational structure of the enterprise (departments, positions, reporting relationships), business rules (such as recruitment process,

training credit requirements), and historical cases (such as excellent employee reviews, high conversion rate recruitment copy).

When the task is triggered, the agent automatically retrives the knowledge graph and injects the relevant information into the Prompt (example: "Based on Chapter 5 of the Group's 2024 Training Management Measures, generate a training plan containing 3 required courses for new employees in the R&D department").

4.2.2 Application of multiple scenarios generation

- **Recruitment scenario**

Automatic generation of recruitment information: automatically generate recruitment information, analyze job files to refine core requirements, and help efficient release.

- Training scenario

Automated content creation: Quickly generate multilingual training content on demand to meet globalization needs.

- Employee service scenario

Employee satisfaction survey: regularly investigate employee satisfaction and analyze the results to provide reference for management improvement.

Employee self-service Q&A: intelligently answers employees' questions about policies and processes to improve efficiency and satisfaction.

Certificate automatic generation: automatic generation of compliance personnel certificate, embedded in the official seal template and approval process.

- Intelligent Question and Answer scenario

Hr policy Q&A: Integrate HR policy documents, accurately analyze questions and answer them in a popular way.

Hr data Q&A: understand natural language data questions, retrieve data warehouse to extract information, and present it in visual form.

4.3 Autonomous collaboration and task management of agents

Agents realize autonomous processing of complex business processes through "task disassembling, resource scheduling and resultaggregation" :

4.4 Agent portals

It supports agent management, realizes the convenient use and efficient integration of agents through recommendation, creation, collection, embedding and removal management, and provides a unified

entrance for various agent applications.

(1) Recommendations

(2) Creating features

- Form Creation mode
- Choreography creates patterns
- Develop Create Mode

(3) Bookmark function

- Personal favorites management

- Bookmark Agent quick call

(4) Embed function

It supports embedding agents into various existing business systems of enterprises, such as OA systems, ERP (enterprise resource planning) systems, etc. Through the open standard API interface, developers can integrate the agent function into the corresponding business process of the enterprise system.

(5) Takedown management function

5 Practical cases and effect analysis

5.1 Application enterprise profile

Application Enterprise 1: A large manufacturing group with 23,000 employees and 8 business divisions. Its HR business pain points include long recruitment cycle (average 45 days), slow employee consultation response (average 24 hours), and serious homogenization of training programs.

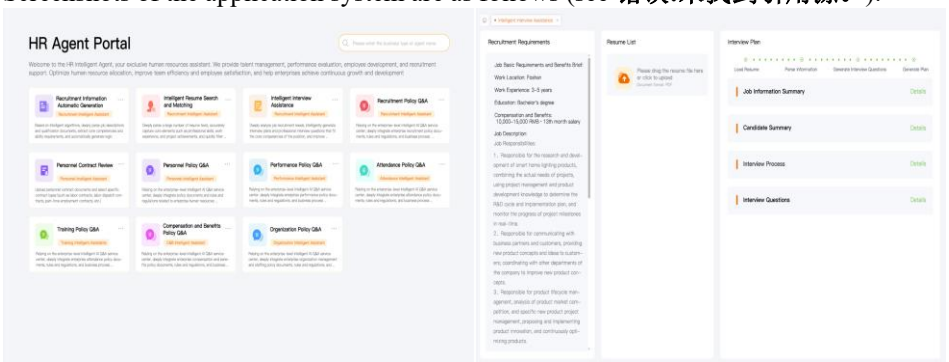
Application Enterprise 2: a large electric power enterprise with 31,000 employees and 36 secondary units, its HR business pain points include long recruitment cycle (average 60 days), slow employee consultation response (average 28 hours), outdated training test question bank or low efficiency (average 1 day /1 set), etc.

5.2 agent deployment and application

Deployment environment: Based on the enterprise private cloud, the fine-tuned LLaMA-2-13B model (recruitment/training scenario) and Qwen-7B model (employee service scenario) were deployed to connect the SAP HR system and OA platform of the group.

Core functions: covering the whole recruitment process (copy generation, resume screening, interview arrangement), personalized training (program generation, course recommendation, training test generation), employee self-service (intelligent question answering, certificate issuance).

Screenshots of the application system are as follows (see **错误!未找到引用源。**):



8

Fig.2. Intelligent portal and recruitment assistant

6 Discussion

6.1 Summary of innovation points

Architecture innovation: A "four-layer collaboration" architecture was proposed to realize the deep integration of privatized deployment, generative capabilities, intelligent agent collaboration and business scenarios.

Technical innovation: through the combination of domain fine-tuning and prompt word engineering, the adaptation problem of LLMs in specific scenarios of enterprises was solved.

Practical innovation: the practicability of the agent is verified in the complex HR scene of a large enterprise, and a reusable landing path is provided.

6.2 Limitations and Future Directions

Limitations: The privatized deployment cost is high (the initial hardware investment is about 5 million yuan), and the threshold for small and medium-sized enterprises is high; Complex business scenarios (such as executive compensation negotiation) still need to be led by humans;

Future Directions:

Explore the "federated learning + LLM" model to reduce the deployment cost of privatization of smes;

Introducing multimodal capabilities (e.g., analyzing employee behavior data, video interview analysis);

And augmenting agents with ethical decision-making capabilities (e.g., avoiding implicit bias in hiring).

7 References

1. Sun, Y., et al. (2023). Large language models for resume screening: A comparative study. Journal of Business Analytics, 6(2), 89-105.
2. Zhang Y, et al. JD-GPT: Job Description Generation with Large Language Models [J]. arXiv:2309.12345, 2024.
3. Zhao, J., et al. (2022). Intelligent employee service chatbot based on pre-trained language models. IEEE Access, 10, 112345-112356.
4. Li et al. (2024) proposed a dynamic knowledge graph-augmented framework for job description generation, achieving a 35% improvement in industry-specific term accuracy .
5. Sun et al. (2023) introduced a multi-dimensional behavioral evidence fusion mechanism to address the disconnection between performance reviews and actual contributions .
6. Chen, M., et al. (2023). Private deployment of large language models in enterprise: Challenges and solutions. arXiv preprint arXiv:2308.12456.

023 Deep Reinforcement Learning based Emergency Control of Cyber-Physical Power System

Zhenqian Wang [1], Dongliang Jiang [1], Yuchen Zeng [1], Min Gao [1], Xiang Xu [1], Kai-shun Xiahou [1*], Huijuan Tan [2]

[1] South China University of Technology, Guangzhou 510640, China
[2] Power Dispatching Control Center, Guangdong Power Grid Co., Ltd., Guangzhou 510000, China

Abstract. The growing power system scale and increasing distributed renewable energy sources have amplified operational uncertainty, raising the difficulty of real-time transient stability control. Concurrently, the evolution of cyber-physical power systems (CPPS) which are characterized by deep coupling between information and physical domains introduces cross-domain attack risks. Traditional emergency control methods are limited by computational complexity and model dependency and struggle to generate timely strategies under these uncertainties. To address this, this paper proposes an intelligent emergency control framework for CPPS using the proximal policy optimization (PPO) algorithm, which balances training efficiency and computational simplicity. Two cross-domain attack scenarios are considered: false data injection attacks (FDIA) on state information collection and control signal delay attacks (CSDA) on command execution. The emergency control problem is formulated as a Markov decision process (MDP), with a reward function integrating control cost efficiency and generator operational safety. Case studies are simulated on the IEEE 39-bus system, and the results demonstrate that the proposed method achieves optimal control strategies under load fluctuations and exhibits superior generalization performance and robustness against cross-domain attacks.

Keywords: Generator tripping and load shedding, Deep reinforcement learning, Emergency control, Cross-domain attack.

1 Introduction

The growing proportion of distributed renewable energy and the expansion of system scale in modern power systems are gradually pushing grid operating states toward the limit of stable operation, significantly increasing the difficulty of stability control [1][2][3]. In recent years, multiple large-scale blackouts caused by transient instability have occurred globally[4][5]. Additionally, with a substantial increase in advanced communication, sensing, and control components, power systems have gradually evolved into cyber-physical power systems (CPPS) with deep integration of the physical and information sides[6]. This implies that cross-domain attacks launched through the CPPS information side have the potential to bypass the three lines of defense in

power systems, thereby threatening power security[7]. Under this context, studying emergency control schemes with "real-time decision-making and real-time control" capabilities and stronger robustness against cross-domain attacks is of significant importance.

Existing transient stability analysis methods for power systems are categorized into three types: dynamic optimization-based approaches, energy function-based approaches and emerging data-driven approaches:

Optimization-based approaches require detailed modeling and simulation of power systems, ultimately solving post-disturbance differential equations of motion to obtain generator power angles for transient stability assessment. Reference [8] improves AlexNet to capture generator power angle trajectories under disturbances and conducts sensitivity analysis on emergency control actions to identify effective actions. Reference [9] enhances the stability rule expression based on support vector machine methods, enabling real-time transient stability evaluation. However, establishing physical models that accurately describe increasingly complex power system characteristics is becoming more challenging, while model complexity often reduces computational accuracy and may even lead to control strategy mismatch.

Energy function-based approaches which is grounded in Lyapunov stability theory require constructing a scalar function analogous to "energy"[10]. By comparing the post-disturbance function value with the critical stable value, these methods are able to qualitatively assess transient stability with low computational complexity. Reference [11] designs a solution for critical generator tripping amount in emergency control based on system acceleration energy, combining dynamic monitoring after tripping actions to achieve real-time emergency control. Reference [12] establishes a mapping between generator electrical features and stability margins using a random forest model, then selects control actions beneficial to system stability to form an emergency control set. However, energy function-based approaches for deriving emergency control strategies require significant simplifications, which often lose partial details of dynamic models, leading to low computational accuracy and conservative solutions [13].

Data-driven approaches use machine learning techniques to establish mappings between power system features and stability margins, enabling trained agents to predict and assess transient stability. Reinforcement learning (RL) is a subset of machine learning, which requires neither precise physical models for power system nor large amounts of labeled training data when learning emergency control strategies. RL models the emergency control problem as a markov decision process (MDP), acquiring effective control strategies through trial-and-error interactions between the agent and the environment. However, Q-value mapping approach of traditional RL struggles with high-dimensional or continuous state spaces. To address this, Google proposed deep reinforcement learning (DRL) that uses deep neural networks (DNN) to replace Q-value tables for mapping. In recent years, DRL has been gradually applied to develop novel emergency control methods. Reference [14] employs the DQN algorithm to solve generator tripping and load shedding problems considering stochastic time delays, incorporating transient energy functions into the reward function to enhance agent training efficiency. Reference [15] uses the DDPG algorithm to train agents for optimal generator tripping strategies, integrating CNN into the policy network with weight-shared

convolution operations to shorten training time and improve generalization. Reference [16] develops a load shedding control strategy combining meta-policy optimization and the PARS algorithm, achieving high control returns. Reference [17] applies the DSAC method to obtain underfrequency load shedding control strategies, demonstrating superior convergence and robustness under load fluctuations and communication delays.

In summary, methods based on dynamic optimization and energy functions struggle to meet the real-time performance and effectiveness requirements of emergency control due to their reliance on models or conservative results. In contrast, DRL is more suitable for developing "real-time decision-making and real-time control" strategies, owing to its strong mapping capability and extremely low response latency. However, current DRL-based emergency control research generally lacks consideration of cross-domain attacks encountered during emergency control processes in CPPS.

To address the research gap in DRL-based emergency control considering cross-domain attacks, this paper proposes an intelligent emergency control framework for CPPS based on the Proximal Policy Optimization (PPO) algorithm. Invalid action reward and generator failure reward are incorporated into the reward function of the MDP model to mitigate agent's inefficient exploration and generator over-generation risks. Meanwhile, case studies examine the impact of false data injection attacks (FDIA) and control signal delay attacks (CSDA) on the performance of DRL-based emergency control strategies, and investigate the robustness of different DRL methods under cross-domain attacks.

The remainder of this paper is structured as follows: Section 2 introduces the optimization model for emergency control in power systems. Section 3 establishes the MDP model for emergency control problems. Section 4 presents the PPO algorithm and training process used in this study, and elaborates on the implementation of two cross-domain attacks. Case studies are conducted in Section 5, and Section 6 concludes the entire paper.

2 OPTIMIZATION MODEL FOR EMERGENCY CONTROL

The transient stability of a power system refers to its ability to withstand faults or large disturbances. Emergency control, implemented when disturbances threaten to destabilize the system, serves as a critical intervention to prevent more severe transient instability issues. Its dual objectives are to maintain system stability while minimizing the cost of control actions. This paper focuses on the control method of generator tripping and load shedding for in-depth research.

2.1 Objective Function

In this paper, emergency control optimization is a decision optimization problem minimizing the total cost of generator tripping and load shedding actions during emergency control. Its objective function is presented below:

$$minF = \sum_{t=T_0}^{T_f} \left(\sum_{i=1}^{n_G} \left(\rho_{Gi} \cdot \boldsymbol{A}_{Gi.t} \right) + \sum_{i=1}^{n_L} \left(\rho_{Li} \cdot \boldsymbol{A}_{Lj.t} \right) \right) \quad (1)$$

where T_0 and T_f denote the start and end times of emergency control, respectively; $\boldsymbol{A}_{\mathrm{G}i.t}$ and $\boldsymbol{A}_{\mathrm{L}j.t}$ are binary variables indicating emergency control actions (generator tripping or load shedding) for the $i-th$ generator or $j-th$ load at time step t; n_G and n_L are the total numbers of generators and loads available for emergency control; ρ represents the cost coefficient for different control actions.

2.2 Dynamic Constraints

The dynamic constraints of emergency control are composed of the differential equations of all dynamic devices in the power grid. Here, the classical second-order generator model is taken as an example:

$$\begin{cases} \dot{\delta}_i = \omega_i - 1 \\ M_{\mathrm{start}i}\dot{\omega}_i = P_{\mathrm{m},i} - P_{\mathrm{e},i} - D_{\mathrm{coef}i}(\omega_i - 1) \end{cases} \tag{2}$$

where δ_i and ω_i denote the rotor angle and speed of the $i-th$ generator; $P_{\mathrm{m},i}$ and $P_{\mathrm{e},i}$ are the mechanical power input and electromagnetic power output of the $i-th$ generator; $D_{\mathrm{coef}i}$ and $M_{\mathrm{start}i}$ the damping coefficient and mechanical starting time.

2.3 Static Constraints

The static constraints of emergency control include AC power flow (3), dynamic devices algebraic (4), and interface (5). The AC power flow equations are presented as follows:

$$\begin{cases} P_{\mathrm{g}i} - P_{\mathrm{l}i} = U_i \sum_{j=1}^{n} U_j (G_{ij} cos\ \theta_{ij} + B_{ij} sin\ \theta_{ij}) \\ Q_{\mathrm{g}i} - Q_{\mathrm{l}i} = U_i \sum_{j=1}^{n} U_j (G_{ij} sin\ \theta_{ij} - B_{ij} cos\ \theta_{ij}) \end{cases} \tag{3}$$

where $i, j \in 1,2,\cdots,n$ denote bus indices; P_g and Q_g are the active and reactive power injected by generators at buses; P_l and Q_l are the active and reactive load demands at buses; U represents the bus voltage magnitude; θ_{ij} is the phase angle difference between bus i and bus j; G_{ij} and B_{ij} are the real and imaginary parts of mutual admittance between bus i and bus j.

Taking generators as an example, the internal algebraic equations of such dynamic devices govern the evolution trends of their electrical parameters during emergency control. The algebraic equations for generators are given as:

$$\begin{cases} P_{\mathrm{e},i} = \left(u_{\mathrm{q},i} + r_{\mathrm{a},i} i_{\mathrm{q},i}\right) i_{\mathrm{q},i} + \left(u_{\mathrm{d},i} + r_{\mathrm{a},i} i_{\mathrm{d},i}\right) i_{\mathrm{d},i} \\ u_{\mathrm{q},i} = E'_{\mathrm{q},i} - X'_{\mathrm{d},i} i_{\mathrm{d},i} - r_{\mathrm{a},i} i_{\mathrm{q},i} \\ u_{\mathrm{d},i} = X'_{\mathrm{d},i} i_{\mathrm{q},i} - r_{\mathrm{a},i} i_{\mathrm{d},i} \end{cases} \tag{4}$$

where u_d and u_q are the direct-axis and quadrature-axis voltage components of the generator; i_d and i_q are the direct-axis and quadrature-axis current components; r_a is the armature resistance; X'_d is the direct-axis transient reactance; E'_q is the quadrature-axis transient voltage.

In addition to the internal algebraic equations mentioned above, dynamic devices (e.g., generators) require interface equations to interact with the power grid. The interface equations for generator-grid connection are presented as follows:

$$\begin{cases} 0 = U_k \, sin(\delta_i - \theta_k) - u_{\mathrm{d},i} \\ 0 = U_k \, cos(\delta_i - \theta_k) - u_{\mathrm{q},i} \\ 0 = P_{gk} - \sum_{i \in \mathcal{G}_k} \left(u_{\mathrm{d},i} i_{\mathrm{d},i} + u_{\mathrm{q},i} i_{\mathrm{q},i}\right) \\ 0 = Q_{gk} - \sum_{i \in \mathcal{G}_k} \left(u_{\mathrm{q},i} i_{\mathrm{d},i} + u_{\mathrm{d},i} i_{\mathrm{q},i}\right) \end{cases} \tag{5}$$

where k denotes the bus connected to the $i-th$ generator; $\mathcal{G}_k$ is the set of generator units connected to bus k.

2.4 Transient Constraint

This paper takes the maximum power angle difference between any two generators in the power system after a large disturbance as the basis for judging transient stability. When this value is less than π, the system satisfy the transient constraint:

$$max\left|\delta_{\mathrm{G}i} - \delta_{\mathrm{G}j}\right| < \pi, \forall i, j \in \mathcal{I} \tag{6}$$

where δ_{G} is the power angle of generator, $\mathcal{I}$ contains all the generators in the power system

3 DRL BASED EMERGENCY CONTROL MODEL

To address the emergency control optimization problem in Section 2 using deep reinforcement learning, it is necessary to transform the problem into an MDP model. This section will introduce the fundamentals of MDP and the composition of the emergency control MDP model proposed in this paper.

3.1 Markov Decision Process

Markov Decision Process (MDP), a key concept in RL, is formalized as a 5-tuple $\langle S, A, P, r, \gamma \rangle$. Here, S denotes the state space and A the action space for the agent. The state transition function $P(s_{t+1}|s, a)$ is defined such that, as MDP states inherently encapsulate historical context, its value depends neither on past states nor their sequence. The reward $r(s, a)$ jointly relies on the executed action and the current state. The discount factor γ within $[0,1)$ determines the agent's prioritization of long-term rewards over immediate gains.

3.2 MDP Model for Emergency Control

In the context of emergency control problems, the power system is modeled as an interactive environment. The control center acts as an agent that continuously acquires electrical features from sensing components as states during system operation and executes emergency control actions. The state space, action space, and reward of agent are defined as follows.

State Space. The state space information should accurately reflect the transient characteristics of the power grid. Considering that this paper uses the power angle difference between generators as the criterion for transient stability, the electrical variables of generators hold significant observational value. Additionally, the variation magnitudes of

bus voltage amplitudes and angles can also reflect the system's transient stability. Therefore, this paper selects six electrical variables to form the agent's state space: generator power angles, rotor speeds, active power, reactive power, bus voltage amplitudes and phase angles.

$$S = \{\delta_{\mathrm{G}i}, \omega_{\mathrm{G}i}, P_{\mathrm{G}i}, Q_{\mathrm{G}i}, V_{\mathrm{N}j}, \theta_{\mathrm{N}j}\} \tag{7}$$

where $i = 1,2,\cdots,m$ denotes generator indices; δ_{G} and ω_{G} represent the power angle and rotor speed of generator, respectively; P_{G} and Q_{G} are the active and reactive power outputs of generator. Similarly, $j = 1,2\cdots n$ denotes bus indices in the system; V_{N} and θ_{N} are the voltage amplitude and phase angle of bus.

Action Space. In the power system environment, the agent can issue control instructions to curtail generator output or shed partial load. Considering that actual power generation nodes typically contain multiple generators and load shedding actions are also discrete, each generator and load is simplified into two identical independent devices. The action space A of agent is defined as follows:

$$A = \{a_{\mathrm{G}1}, \dots, a_{\mathrm{G}m}, a_{\mathrm{L}1}, \dots, a_{\mathrm{L}l}, None\} \tag{8}$$

where a_{G} and a_{L} are Boolean variables for generator tripping and load shedding actions, respectively. When $a_{\mathrm{G}} = 1$, the corresponding generator reduces its active power output by half; similarly, when $a_{\mathrm{L}} = 1$, the corresponding load is shed by half. Additionally, the action space includes a "$None$" action, indicating the agent performs no control at this time step.

Reward. The goal of emergency control is to restore stability as quickly as possible with minimal control cost. To properly guide the agent during training, this paper divides the reward at each time step into four components:

$$R_t = r_{\mathrm{act}} + r_{\mathrm{Gcut}} + r_{\mathrm{inv}} + r_{\mathrm{ins}} \tag{9}$$

Control Cost Reward. The control cost reward reflects the cost of emergency control actions taken by the agent at this time step:

$$r_{\mathrm{act}} = \sum_{i=1}^{m} K_{\mathrm{G}i} a_{\mathrm{G}i} + \sum_{j=1}^{l} K_{\mathrm{L}j} a_{\mathrm{L}j} \tag{10}$$

$$K_{\mathrm{G}i} = -\frac{P_{\mathrm{G}i}}{max(P_{\mathrm{G}1}, P_{\mathrm{G}2}\cdots P_{\mathrm{G}m})} \tag{11}$$

$$K_{\mathrm{L}j} = -\frac{P_{\mathrm{L}j}}{max(P_{\mathrm{L}1}, P_{\mathrm{L}2}\cdots P_{\mathrm{L}l})} \tag{12}$$

where $K_{\mathrm{G}i}$ and $K_{\mathrm{L}j}$ denote the action cost coefficients of the Boolean variables $a_{\mathrm{G}i}$ and $a_{\mathrm{L}j}$ for emergency control actions, respectively; $P_{\mathrm{G}i}$ is the pre-fault active power output of the $i-th$ generator, and $P_{\mathrm{L}j}$ is the active power load of the $j-th$ load.

Generator Failure Reward. When a generator is fully curtailed, other generators may face over-generation risks to meet the active power demand of power system. Therefore, in addition to the control cost reward, this paper sets a generator failure reward to quantify such risks:

$$r_{\mathrm{Gcut}} = \begin{cases} K_{\mathrm{Gcut}}, & \text{generator failure} \\ 0, & \text{else} \end{cases} \tag{13}$$

where K_{Gcut} is the generator failure coefficient. When set to -2, the agent becomes more cautious when executing the control action of fully cutting off generators, effectively avoiding the agent from always choosing a conservative control strategy to address load fluctuations.

Invalid Action Reward. During training, the agent inevitably makes invalid decisions, such as issuing control commands to generators or loads that have already been fully curtailed. These invalid actions not only have no control effect but also delay the implementation of effective control actions. Therefore, to better guide the training of agent, an invalid action penalty will be imposed once the agent takes an invalid action:

$$r_{\mathrm{inv}} = \begin{cases} K_{\mathrm{inv}}, & \text{invalid action} \\ 0, & \text{else} \end{cases} \tag{14}$$

where K_{inv} is the invalid action coefficient. Through comparative training results, it is found that setting it to -3 effectively prevent the agent from taking invalid actions.

Transient Stability Reward. After the agent takes a control action, if the power system still does not meet the transient constraint (6) after a time step, the environment will provide a transient stability reward:

$$r_{\mathrm{ins}} = \begin{cases} K_{\mathrm{ins}}, & \text{not satisfy transient constraint} \\ 0, & \text{else} \end{cases} \tag{15}$$

where K_{ins} is the transient stability coefficient, which is set to -10 in this paper.

4 PPO-BASED EMERGENCY CONTROL METHOD

4.1 PPO Algorithm

The PPO algorithm is an online policy learning algorithm under the Actor-Critic framework[18]. Other policy gradient-based algorithms, due to the lack of restriction on the update step size of policy network parameters θ, are prone to sudden significant deterioration of the policy when updating network parameters. In contrast, the clipping mechanism of the PPO algorithm directly restricts the distance between parameters θ and θ_{old} in the objective function to maintain training stability:

$$\max_{\theta} L_{\theta_{\text{old}}}(\theta) = \mathbb{E}_{s,a}\left[min\left(\rho(\theta)A^{\theta_{\text{old}}}(s,a), clip(\theta)A^{\theta_{\text{old}}}(s,a)\right)\right] \tag{16}$$

$$\rho(\theta) = \frac{\pi_\theta(a|s)}{\pi_{\theta_{\text{old}}}(a|s)} \tag{17}$$

where $\rho(\theta)$ is the importance sampling weight, reflecting how the probability of the same action under the new policy compares to that under the old policy; ϵ is the clipping range, and $clip(\theta)$ restricts $\rho(\theta)$ to the range $[1-\epsilon, 1+\epsilon]$ to prevent excessive policy changes within a single time step.

The PPO algorithm with clipping mechanism maintains high training stability while keeping computational complexity low compared to other algorithms.

4.2 Training Process

The PPO algorithm requires simultaneous training of the actor network (policy network) and the critic network (value network). In this paper, both actor network and critic network are composed of fully connected layers. The structure of the actor network is shown in Fig. 1:

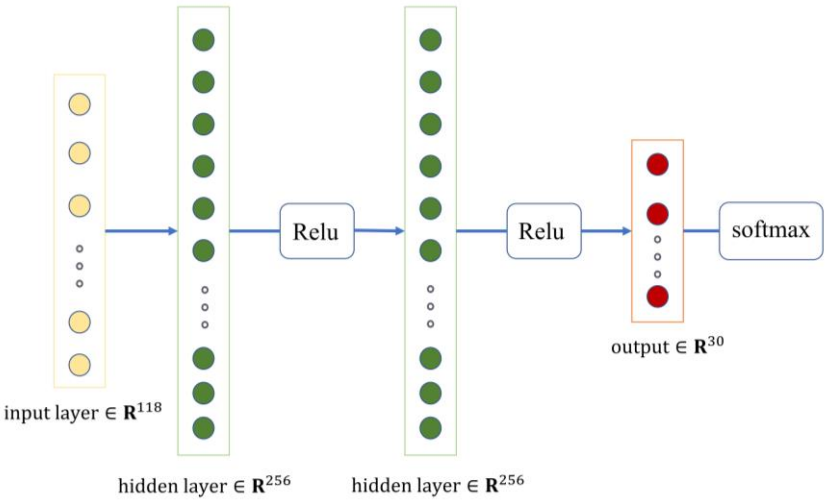


Fig. 1. Policy network structure

Policy network and value network follow the following update steps ①-⑤ during the agent training process of the PPO algorithm:

①Initialization. Initialize the parameters θ and ω of the policy network $\pi_\theta(a|s)$ and value network $V_\omega(s)$, and determine hyperparameters.

②Create a Copy for Old Policy Network. Copy the current policy network's parameters θ to θ_{old}. At this point, the two policy networks $\pi_\theta(a|s)$ and $\pi_{\theta_{\text{old}}}(a|s)$ are identical, but $\pi_{\theta_{\text{old}}}(a|s)$ will not update its parameters in subsequent update operations.

③Data Collection. Use the old policy network $\pi_{\theta_{\text{old}}}(a|s)$ to interact with the environment, collect a sequence of quintuple $\langle s, a, s', r, done \rangle$ data containing all time steps, and store it in the sequence buffer D.

④Compute Returns and Advantage Estimates. Use the value network to evaluate the state sequence $s_1, s_2, \ldots, s_{T-1}$, then compute the advantage $\mathrm{A}(s_t, a_t)$, and obtain the target value $V_{\text{target}}(s_t) = \mathrm{A}(s_t, a_t) + V_\omega(s_t)$.

⑤Multi-Round Policy Update. Extract all data of the current episode sequence from buffer D, compute the policy network's objective function and update its parameters θ; then calculate the value network's loss function using the target value from step ④ and the current state value, and update its parameters ω. This step requires repeating the network update operation N_{k} times. If the number of trained episodes has not reached the preset N_{e}, return to step ②.

The above training steps are visualized as shown in Fig. 2:

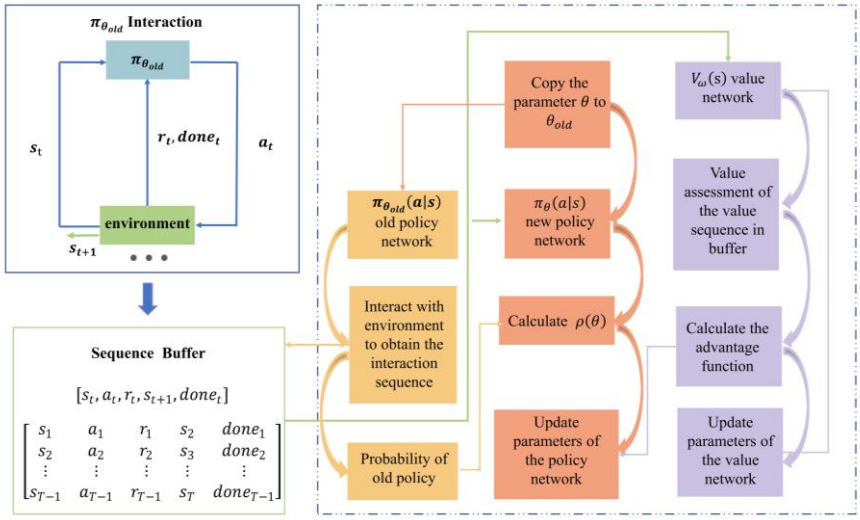


Fig. 2. Training flowchart of PPO algorithm

4.3 Cross-domain Attack

Cross-domain attack refer to attack means where attackers use cyber attacks to induce failures in the information domain of CPPS, such as monitoring devices or communication networks. Leveraging the tight cyber-physical coupling of CPPS, these failures are then propagated to the physical domain. Such attacks span both cyber and physical domains, potentially compromising system stability control capabilities.

This paper focuses on intelligent emergency control methods for CPPS, with particular emphasis on analyzing the impacts of FDIA and CSDA on emergency control processes. Based on their generalized modeling approaches and the proposed emergency control MDP model, this chapter designs the attack forms for both cross-domain attacks.

FDIA. FDIA refers to a cross-domain attack targeting the power system state estimation (PSSE) process, primarily characterized by disrupting the accuracy and consistency of data [19]. In a successful FDIA, attackers construct attack vectors that evade the bad data detection (BDD) mechanism in PSSE to tamper with sensor state measurements. In emergency control scenarios, this compromises the control center's perception of system states, leading to maloperation or non-operation of control center. If each bus in the power system is treated as a information node in the communication network, information nodes can be classified into two categories based on the dimension of measurement vectors:

$$z_i(t) = \begin{cases} \{\delta_{\mathrm{G}i.t}, \omega_{\mathrm{G}i.t}, P_{\mathrm{G}i.t}, Q_{\mathrm{G}i.t}, V_{\mathrm{N}i.t}, \theta_{\mathrm{N}i.t}\}, i \in \text{א} \\ \{V_{\mathrm{N}i.t}, \theta_{\mathrm{N}i.t}\}, i \in \text{ב} \end{cases} \tag{18}$$

where $z_i(t)$ denotes the measurement vector of information node i; $i = 1,2,\cdots,n$ represents the information node index; א denotes the set of information nodes with 6-dimensional measurement vectors (buses connected to generators), and ב denotes the set of information nodes with 2-dimensional measurement vectors.

When a short-circuit fault occurs on a bus, the voltage magnitude of the fault bus or its adjacent buses drops significantly. Therefore, this paper implements FDIA by superimposing an attack vector $a_i(t)$ on information nodes with excessively low voltage:

$$a_i(t) = \begin{cases} \{0,0,0,0, V_{\mathrm{N}j.t} \cdot G_{\mathrm{M}}, 0\}, when\ i \in \text{א}, j = choice(\text{א}') \\ \{V_{\mathrm{N}j.t} \cdot G_{\mathrm{M}}, 0\}, when\ i \in \text{ב}, j = choice(\text{ב}') \end{cases} \tag{19}$$

where $choice(\ )$ denotes selecting an information node from the set; א′ and ב′ represent the sets א and ב with information node i removed, respectively. G_{M} is sampled from a Gaussian random variable with mean 1 and standard deviation 0.05.

The measurement vector $z_{\mathrm{a},i}(t)$ that the agent can obtain from the attacked information node i after FDIA is:

$$z_{\mathrm{a},i}(t) = z_i(t) + a_i(t) \tag{20}$$

CSDA. CSDA targets control commands issued by the control center, acting as a cross-domain attack that extends the arrival time of control signals to execution terminals by blocking the communication network. CSDA poses significant threats to emergency control scenarios requiring real-time response. Control signals affected by CSDA are as follows:

$$u_{\mathrm{a}}(t) = u(t - \tau) \tag{21}$$

where u denotes the emergency control action vector; τ represents the delay imposed on control signals.

5 CASE STUDIES

5.1 Experimental Setting

This paper adopts the classical IEEE 39-bus system which is widely applied in transient stability studies as the test case. Its topology is shown in Fig. 3, where generators adopt the classical sub-transient model and loads use the constant impedance model.

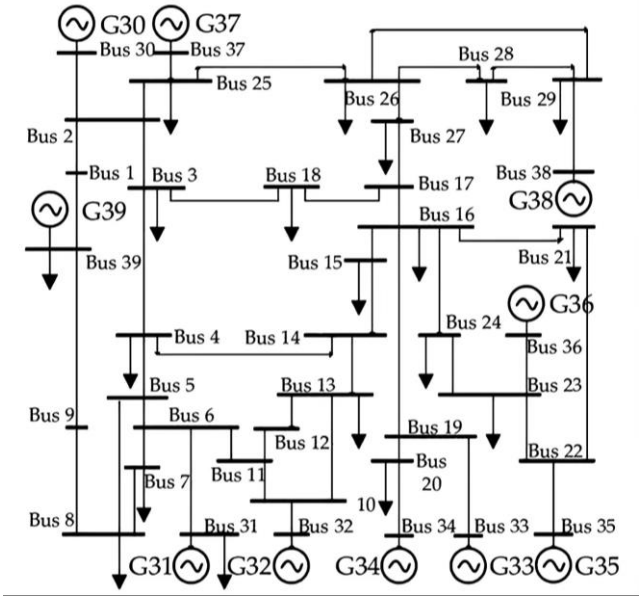


Fig. 3. Topology of IEEE 39-bus system

The preset fault scenarios in the training set of this paper include: ① a three-phase short-circuit fault on bus 17, with duration of 0.22s; ② a three-phase short-circuit fault on bus 26, with duration of 0.25s. Considering load fluctuations in actual power system operation, the system load level is randomly initialized within 0.95-1.05. During the initialization phase before each episode of agent learning, the system randomly selects one of the two fault scenarios, and the load level is also randomly chosen within the range. Such random combinations may cause transient instability in the power system under certain conditions, requiring agent intervention for emergency control. Additionally, Gaussian white noise with a mean of 0 and a standard deviation of 0.005 is added to all measurement signals to simulate sampling errors. The simulation step size T_s of the Simulink power system model is 0.01s, and the emergency control interaction step size T_c between the agent and the environment is set to 0.2s. The hyperparameter settings for agent training are shown in Table 1.

12

Table 1. Hyperparameters for PPO training.

Hyperparameter	Value
Training episodes N_{e}	1000
Episode update frequency N_{k}	10
Maximum interaction steps N_{s}	10
Clipping range ϵ	0.2
Discount factor γ	0.98
Advantage estimation coefficient λ	0.95
Learning rate of actor η_{actor}	0.001
Learning rate of critic η_{critic}	0.01

5.2 Case Tests

Under the parameter settings described earlier, the reward per episode during PPO algorithm training reflects the convergence trend of the policy network, as shown in Fig. 4.

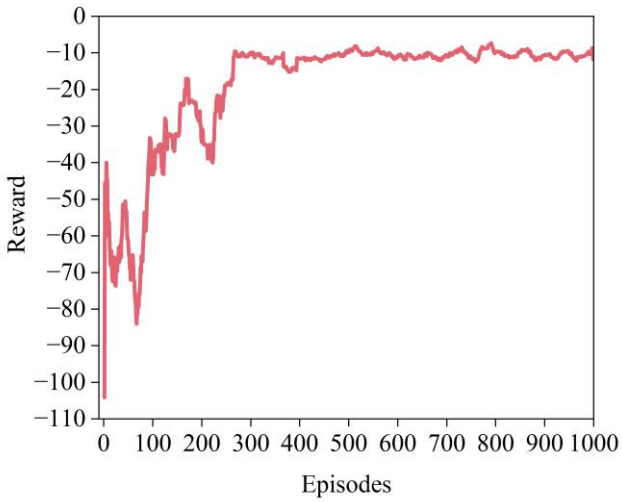


Fig. 4. Training curves of PPO

When the episode count is less than 300, the agent is in the exploration stage, with low and highly fluctuating rewards. During this stage, the emergency control commands taken by the agent cannot effectively ensure the transient stability of power system. As the episode count increases, the agent gradually identifies optimal emergency control strategies for various fault scenarios. After 500 episodes, the agent is essentially fully trained.

Control Test in Training Set. Using the trained agent based on PPO for emergency control effect testing, the fault scenario is set as follows: load level is 1, a three-phase short-circuit fault occurs at bus 17 at 1s and lasts for 0.22s. The agent detects power angle instability at 1.65s and intervenes for emergency control. The emergency control commands given by the agent in this scenario are shown in Table 2.

Table 2. Emergency control commands for a three-phase short-circuit fault on bus 17.

Control step	Control command	Excision volume (MW)	Stability	Reward
step1	Trip 50% output of G34	254	Unstable	-10.508
step2	Shed 50% load of L29	141.75	Unstable	-0.257
control result	—	—	Stable	-10.765

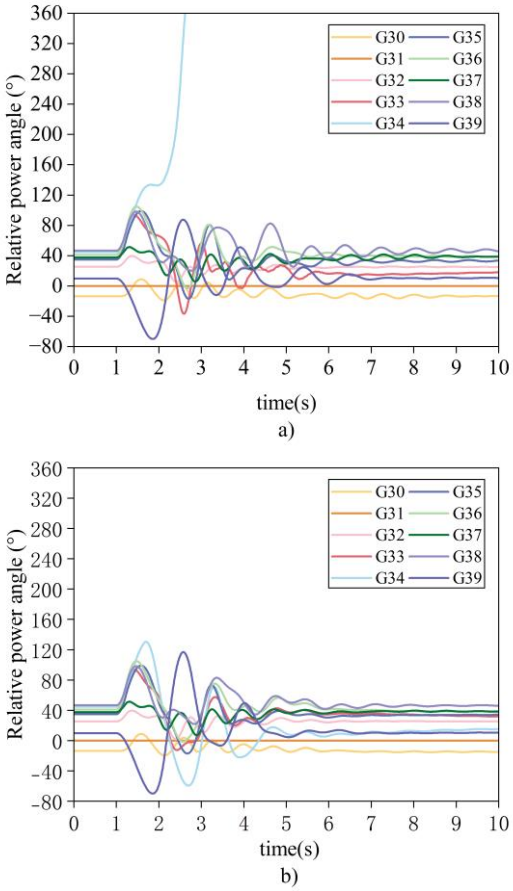


Fig. 5. Power angle curves before and after Intelligent agent control in the case of bus 17 fault: a) without emergency control; b) after emergency control

Fig. 5 illustrates the changes in relative rotor angles of power system generators before and after emergency control by the trained agent. The agent trips 50% active power output of G34 at 1.65s and sheds 50% load of L29 at 1.85s. As shown by comparing Fig. 5(a) and (b), the generators remain synchronized after control, and the power system gradually recovers transient stability.

Generalization Ability Analysis of Agents. Another advantage of DRL lies in the generalization capability from DNNs. To test the generalization ability of the trained agent based on PPO, this subsection introduces several fault scenarios outside the training set into the test set: ① a two phase short-circuit fault lasting 0.44s on bus 17; ② a two-phase-to-ground short-circuit fault lasting 0.36s on bus 17; ③ a two phase short-circuit fault lasting 0.35s on bus 26; ④ a two-phase-to-ground short-circuit fault lasting 0.35s on bus 26. Before each test round, the system randomly selects one of the 6 fault scenarios, while the system load level remains initialized within 0.95-1.05. To highlight the advantages of the PPO algorithm, this subsection introduces Double DQN as a control group, which is also trained for 1000 episodes on the aforementioned training set. Both trained agents undergo 1000 rounds of control effect testing in the test set, and the reward distribution during testing is shown in Fig. 6.

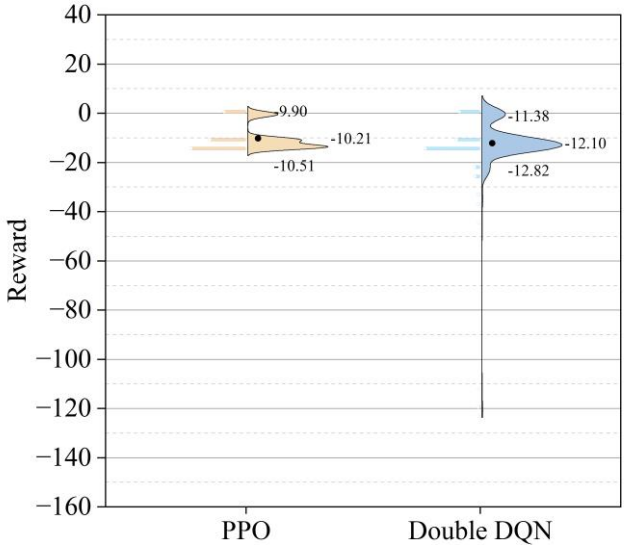


Fig. 6. Comparison of agent generalization ability between PPO and Double DQN

As shown in Fig. 6, the PPO agent achieves a reward mean of -10.21, with a 95% confidence interval whisker range of -9.90 (upper) to -10.51 (lower). The data exhibits minimal outliers and concentrates within $[-20,0]$. In contrast, the Double DQN agent has a reward mean of -12.10, with a 95% confidence interval whisker range of -11.38 (upper) to -12.82 (lower), accompanied by multiple outliers below -30. In certain fault scenarios, the reward even drops below -100 for the Double DQN agent, indicating

complete failure of its emergency control strategy. Overall, the trained agent based on PPO demonstrates significantly stronger generalization in this test set, maintaining stable performance when facing untrained fault scenarios.

Robustness Analysis against Cross-domain Attacks. To analyze the robustness of trained agents using different algorithms under cross-domain attacks, this subsection incorporates the two cross-domain attacks designed in Section 4.3 into the training set, forming a test set which accounts for cross-domain attacks. The Double DQN-trained agent undergoes 1000 emergency control tests in both the training set and this test set, with their reward differences shown in Fig. 7.

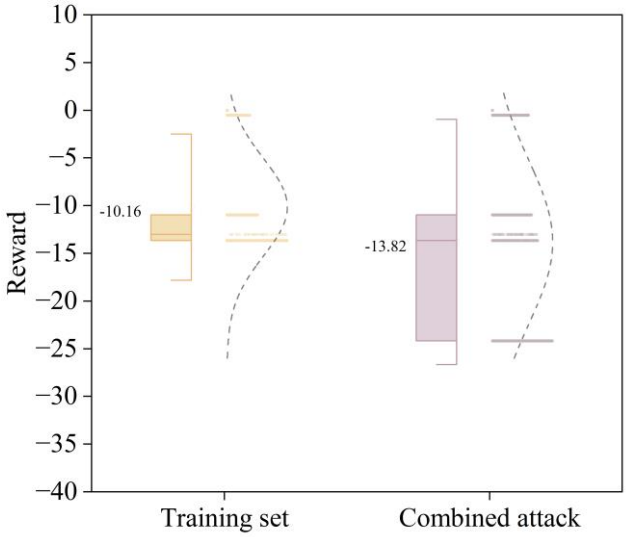


Fig. 7. The influence of combined attacks on the reward obtained by Double DQN agent

The test results indicate that cross-domain attacks significantly reduce the reward obtained by the Double DQN agent, with the average reward in this test set dropping from -10.16 in the training set to -13.82. This implies that the agent requires longer control time and higher control costs in this test set.

To compare with the Double DQN algorithm, four test scenarios are further established: (a) Training set, (b) CSDA, (c) FDIA, and (d) Combined attack. The trained agent using PPO undergoes 1000 emergency control tests in each of the four test scenarios, with the reward distribution in each group as shown in Fig. 8.

16

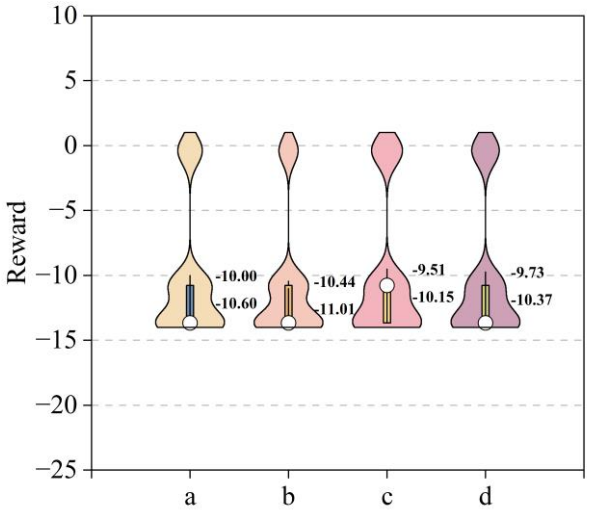


Fig. 8. The influence of cross-domain attacks on the reward obtained by PPO agent The test results show no significant difference in reward distribution between the three test sets and the training set. The PPO agent maintains a high consistency in emergency control performance before and after cross-domain attacks, demonstrating significantly stronger resilience compared to the Double DQN agent under the two cross-domain attacks designed in this paper.

6 CONCLUSION

With the aim of achieving real-time and reliable emergency control for CPPS, this paper models the emergency control problem as an MDP and proposes an intelligent emergency control method. For the reinforcement learning algorithm, this paper adopts the efficient and low-complexity PPO algorithm for agent training. Its online learning characteristic enables easier capture of key factors affecting transient stability and identification of optimal control strategies. Regarding MDP model design, this paper introduces generator failure reward and invalid action reward into the reward function, aiming to reduce the risk of generator over-generation and minimize invalid actions during the exploration stage. Case studies on the IEEE 39-bus system demonstrates that trained agent based on the proposed method effectively ensures transient stability under load fluctuations. Compared to the Double DQN algorithm, the proposed method exhibits significant advantages in agent generalization performance and robustness against cross-domain attacks.

Acknowledgement： This work is supported in part by the National Natural Science Foundation of China under Grant 52207106 (Corresponding author: Kaishun Xiahou, e-mail: xiahouks@scut.edu.cn).

References

[1] Jiang C X, Liu C X, Lin Z, et al. A review of transient stability control strategies for power systems based on deep reinforcement learning. High Voltage Engineering, 2023, 49(12): 5171-5186.

[2] Wu Q H, Lin Y, Hong C, et al. Transient stability analysis of large-scale power systems: A survey[J]. CSEE Journal of Power and Energy Systems, 2023, 9(4): 1284-1300.

[3] Zhou Y Q, Li J Y, Chen G, et al. Distributionally robust optimization modeling and evaluation of power system operational reliability with high wind power penetration[J]. Power System Protection and Control, 2025, 53(11): 116-124

[4] Yuan P, Zhang Q, Zhang T, et al. Analysis and enlightenment of the blackouts in Argentina and New York[C]//2019 Chinese Automation Congress (CAC). IEEE, 2019: 5879-5884.

[5] Wang W S, Lin W F, He G Q, et al. Insights from the 2021 major blackout in Texas, USA for China's new energy development. Proceedings of the CSEE, 2021, 41(12): 4033-4043.

[6] Xiahou K S, Du W, Xu X Y, et al. Resilience assessment for hybrid AC/DC cyber-physical power systems under cascading failures [J]. IEEE Transactions on Reliability, 2025（Early Access）

[7] Zhang T, Fei J X, Wang Q, et al. Research on cross-domain attack collaborative defense architecture and mechanism for cyber-physical power systems. Acta Electronica Sinica, 2024, 52(04): 1205-1218.

[8] Qiang Z Y, Wu J Y, Li B Q, et al. Emergency control strategy for transient angle instability of power systems based on improved AlexNet. High Voltage Engineering, 2022, 48(07): 2794-2804.

[9] Hu W, Zhang W L, Min Y, et al. Real-time decision-making method for emergency control of power systems based on support vector machine. Proceedings of the CSEE, 2017, 37(16): 4567-4576+4881.

[10] Zheng Z, Wei M Y, Li S L, et al. MMC control strategy based on a direct Lyapunov method[J]. Power System Protection and Control, 2024, 52(19): 35-46

[11] Wu W, Tang Y, Sun H D, et al. Quantitative research on generator tripping control measures based on system acceleration energy. Proceedings of the CSEE, 2014, 34(34): 6134-6140.

[12] Wang T, Liu J L, Zhu S X, et al. Transient stability assessment and emergency control strategy for power systems based on random forest. Power System Technology, 2020, 44(12): 4694-4701.

[13] Chen Y, Zhu J, Liu Y, et al. Distributed hierarchical deep reinforcement learning for large-scale grid emergency control[J]. IEEE Transactions on Power Systems, 2023. 39(02). 4446-4458

[14] Li H H, Zhang P, Liu Z, et al. Decision-making method for transient stability emergency control based on deep reinforcement learning. Automation of Electric Power Systems, 2023, 47(05): 144-152.

[15] Lin B, Wang H, Zhang Y, et al. Real-time power system generator tripping control based on deep reinforcement learning[J]. International Journal of Electrical Power & Energy Systems, 2022, 141: 108127.
[16] Huang R, Chen Y, Yin T, et al. Learning and fast adaptation for grid emergency control via deep meta reinforcement learning[J]. IEEE Transactions on Power Systems, 2022, 37(6): 4168-4178.
[17] Xie J, Sun W. Distributional deep reinforcement learning-based emergency frequency control[J]. IEEE Transactions on Power Systems, 2021, 37(4): 2720-2730.
[18] Schulman J, Filip W, Dhariwal P, et al. Proximal policy optimization algorithms [J]. Machine Learning, 2017.
[19] Liu Y, Reiter M K, Ning P. False Data Injection Attacks Against State Estimation in Electric Power Grids[A]. In: Proceedings of the 2009 ACM Conference on Computer and Communications Security, CCS 2009, Chicago, Illinois, USA, November 9-13, 2009[C], 2009.

024 Low-Carbon Economic Scheduling of CCHP Microgrids Based on Two-stage Scenario Generation and Stepwise Carbon Trading

Kewen Wang, Jian Chen, Wen Zhang

Key Laboratory of Power System Intelligent Dispatch and Control of Ministry of Education, Shandong University, Jinan, 250061, China
202514758@mail.sdu.edu.cn

Abstract. To enhance the low-carbon economic operation of combined cooling, heating, and power (CCHP) microgrids with high penetration of wind and solar energy, this paper proposes a two-stage approach that integrates scenario generation and stochastic optimization, incorporating renewable energy uncertainty and a stepwise carbon trading mechanism. First, a two-stage scenario generation method based on Latin hypercube sampling(LHS) and improved K-means clustering is developed to produce representative wind-solar scenarios. Second, a stepwise carbon trading mechanism is embedded into a mixed-integer linear programming (MILP) model aimed at minimizing total operating cost. Case studies demonstrate that the proposed strategy significantly improves both economic and environmental performance compared to conventional dispatch methods, with the stepwise carbon trading mechanism effectively balancing cost efficiency and emission reduction.

Keywords: Microgrid, Wind-solar Uncertainty, Combined Cooling, Heating and Power; Two-stage Scenario Generation; Stepwise Carbon Trading; Optimal Operation.

1 Introduction

Against the backdrop of global environmental pollution, climate deterioration and rising energy demand, developing efficient and clean renewable energy has become inevitable [1]. Combined cooling, heating and power (CCHP) microgrids significantly enhances overall energy efficiency by integrating electricity, heat, gas and other energy sources. However, the high uncertainty of new energy is a key challenge for its optimal operation, with the core lying in how to achieve low-carbon and efficient operation through multi-energy complementarity and conversion [2].

The uncertainty of output from renewable energy sources such as wind and photovoltaic power poses challenges to the optimal scheduling of systems. Three commonly used uncertainty handling methods in current research include robust optimization, scenario analysis, and chance-constrained programming. Reference [3] proposes a multi-energy coordinated scheduling method based on robust optimization,

which characterizes load randomness by constructing an uncertainty set. Reference [4] uses a typical probability density function to represent renewable energy prediction errors and generates a set of representative scenarios through the Monte Carlo method. Reference [5] combines Monte Carlo sampling with the fast forward elimination method to generate typical wind power output scenarios and realize the optimal scheduling of wind-storage systems. Reference [6] defines wind speed as a random fuzzy variable, extracts the membership function of Weibull distribution parameters using the maximum likelihood method, and establishes a stochastic fuzzy chance-constrained model for the economic optimization of day-ahead scheduling. However, the above optimal scheduling methods considering the uncertainty of wind and photovoltaic power do not take carbon emission factors into account in their models. Therefore, incorporating carbon emission factors into the optimal operation model considering wind and photovoltaic uncertainty can further promote the efficient utilization of distributed energy and reduce carbon emissions.

In the field of microgrids, the application of carbon trading mechanisms has demonstrated their potential in promoting energy transition and improving energy utilization efficiency [7]. Carbon trading mechanisms achieve emission control by establishing legal carbon emission rights and allowing their trading [8]. Reference [9] addresses the problem of uncertainty in renewable energy output by introducing a stepwise carbon trading mechanism and constructing a low-carbon economic dispatch model for microgrids based on robust optimization, which effectively reduces system carbon emissions. Reference [10] proposes a bi-level game optimization strategy considering wind and photovoltaic uncertainty, which reduces carbon emissions while improving system economy. Reference [11] introduces a stepwise carbon trading mechanism and effectively reduces carbon emissions in integrated energy systems by incorporating stepwise carbon costs into the objective function. However, existing research on carbon trading markets still has the problem of overly simplistic construction of carbon emission models. Most studies only calculate equipment carbon emissions using a linear relationship [12], thus requiring the establishment of more refined low-carbon optimal operation models.

To this end, this paper proposes a low-carbon economic operation optimization scheduling model suitable for CCHP microgrids under the analysis of wind and photovoltaic uncertainty. First, a stepwise carbon trading mechanism is introduced based on the original CCHP microgrids architecture to further constrain carbon emissions, and the impact of the stepwise carbon trading mechanism and different carbon trading base prices on low-carbon operation is studied. Second, aiming at wind and photovoltaic uncertainty, scenario analysis is used to obtain typical scenarios and their corresponding scenario probabilities. Finally, a low-carbon optimal operation model with the goal of minimizing the comprehensive operation cost is constructed. The model is solved in Matlab using the Yalmip toolbox and Cplex solver. Through case analysis, the rationality and effectiveness of the proposed model are verified by comparing the operation results under different typical scenarios.

2 Stepwise Carbon Trading Mechanism

2.1 CCHP Microgrids Structure

The CCHP is an integrated energy system combining power generation, heating, and cooling supply. Its structure involves multiple energy sources, including natural gas, cooling energy, electricity, and heat, with complex conversion relationships between them as shown in Figure 1. Key equipment within the microgrid includes energy storage batteries, wind turbines (WT), photovoltaic cells (PV), micro gas turbines (MT), heat recovery boilers (RB), heat exchangers (HE), gas boilers (GB), absorption coolers (AC), and electric coolers (EC).

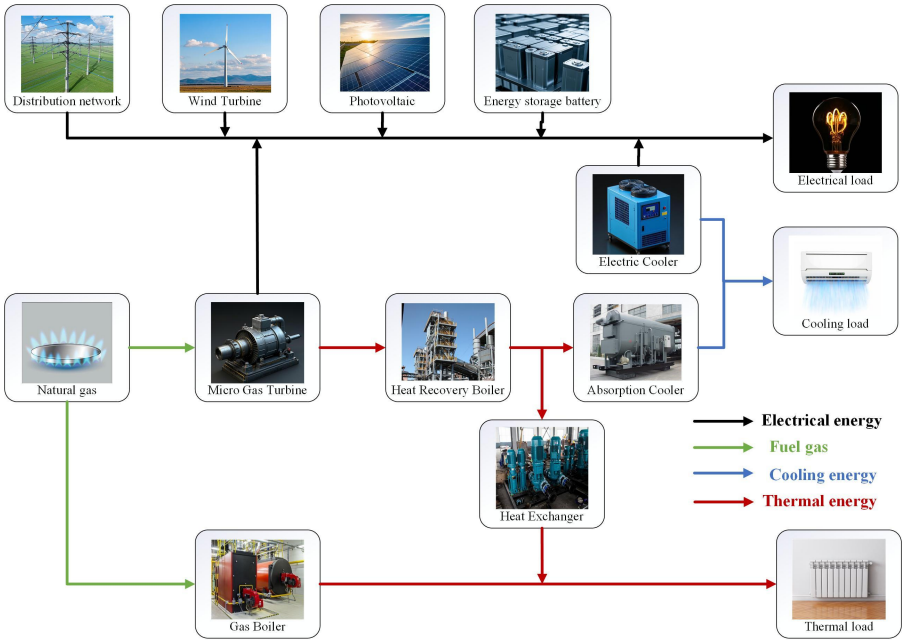


Fig. 1. Internal Structure of CCHP microgrids.

2.2 Carbon Emission Model

The actual carbon emissions of the microgrid at time *t* originate from equipment such as micro gas turbines and electricity purchased from the grid. Based on the emission factor method, this paper approximates that the actual carbon emissions of units are proportional to their output. Thus, the actual carbon emissions of the microgrid at time *t* are:

$$E_{ac} = \kappa_{MT} P_{MT}(t) + \kappa_{GB} P_{GB}(t) + \kappa_{net} P_{buy}(t) \tag{1}$$

Where κ_{MT}, κ_{GB}, and κ_{net} are the carbon emission coefficients of the micro gas

turbine, gas boiler, and microgrid system, respectively.

2.3 Stepwise Carbon Trading Model

With the improvement of carbon trading markets, traditional constant carbon trading prices, which are ineffective in incentivizing enterprises to reduce emissions, are gradually replaced by stepwise pricing principles.

The stepwise carbon trading mechanism combines stepwise pricing with carbon emission rights trading, promoting emission reduction through differentiated quota allocation and pricing rules. Its core is to set multi-level thresholds for enterprise emissions: free or low-price within basic emissions, with incremental prices for excess quotas purchased in steps. The stepwise carbon trading cost is:

$$C_{CO_2}=\begin{cases}\rho(1+\tau)(E_{diff}+\Delta d), E_{diff}\le -\Delta d\\ \rho E_{diff}, -\Delta d\le E_{diff}\le 0\\ \rho E_{diff}, 0\le E_{diff}\le \Delta d\\ \rho(1+\tau)(E_{diff}-\Delta d), \Delta d\le E_{diff}\le 2\Delta d\\ \rho(1+2\tau)(E_{diff}-\Delta d), 2\Delta d\le E_{diff}\end{cases} \tag{2}$$

where C_{CO_2} is the carbon trading cost of the microgrid system; ρ is the base price of stepwise carbon trading; τ is the growth rate of stepwise carbon trading; Δd is the price interval length of stepwise carbon trading; $E_{diff}=\sum E_r - E_{cap}$ is the difference between actual carbon emissions and the carbon quota.

3 Two-stage Scenario Generation

3.1 Modeling of Wind-Solar Uncertainty

Establishing reliable probability models is crucial for accurately characterizing wind speed statistics and ensuring microgrid operational stability. The Weibull distribution, a two-parameter probability model with scale and shape parameters [15], effectively describes the asymmetric distribution characteristics of wind speed and demonstrates superior fitting accuracy for wind speed probability density functions. The wind speed probability density function constructed by defining scale parameter *c* and shape parameter *k* is as follows:

$$f_{wt}(v)=\frac{k}{c}\left(\frac{v}{c}\right)^{k-1}\exp\left[-\left(\frac{v}{c}\right)^{k}\right] \tag{3}$$

where *v* represents the actual wind speed.

The Beta distribution effectively characterizes the probability distribution of solar irradiance, with its probability density function expressed as:

$$f_{PV}(I)=\frac{\Gamma(\alpha+\beta)}{\Gamma(\alpha)+\Gamma(\beta)}\left(\frac{I}{I_{max}}\right)^{\alpha-1}(1-\frac{I}{I_{max}})^{\beta-1} \tag{4}$$

where I and I_{max} are the actual and maximum solar irradiance, respectively.

3.2 Scenario Generation

Scenario analysis, an effective method for handling uncertainty, consists of two key steps: scenario generation and scenario reduction. It characterizes the statistical features of uncertain factors through representative typical scenario sets, transforming complex stochastic optimization problems into deterministic multi-scenario optimization problems to reduce solution difficulty.

LHS adopts a stratified orthogonal sampling strategy, dividing the probability distribution interval of each random variable into equal-probability subintervals, sampling independently within each subinterval, and finally achieving orthogonal combination of multi-dimensional variables through random permutation.

Assuming a sampling size of N the specific sampling steps are:

(1) Probability interval division: Divide the cumulative distribution curve of each random variable X_k (Equation 5) into N equal parts over the interval [0,1].

$$Y_k=F_k(X_k) \tag{5}$$

(2) Random sampling: Randomly select a value within each interval as the sampling value y_{kn} of Y_k, where $n\in[1,N]$.

(3) Inverse transformation mapping: Obtain the sample value x_{kn} of variable X_k through the inverse function F_k^{-1} of the cumulative distribution function.

$$y_{kn}=\frac{n-rand}{N},n=1,2,\ldots,N \tag{6}$$

$$x_{kn}=F_k^{-1}(y_{kn})F_k^{-1}\left(\frac{n-rand}{N}\right) \tag{7}$$

(4) Sample matrix construction: Generate an $\mathrm{M}\times N$ sample matrix S_0 after completing sampling for all variables.

After sampling, if there is correlation between sample data points, sorting is required. This paper uses the Cholesky decomposition method to sort the sample matrix:

(1) Random sorting and correlation coefficient calculation: Randomly sort the sample matrix S_0 and calculate its rank correlation coefficient matrix ρ_L.

$$\rho_L = DD^T \tag{8}$$

(2) Cholesky decomposition: Decompose to obtain the lower triangular matrix D using the square root method and calculate the new order matrix L.

$$G = D^{-1}L \tag{9}$$

(3) Re-sorting: Re-sort the sample matrix S_0 according to matrix L to obtain the new sample matrix S.

3.3 Scenario Reduction

In Section 3.2, LHS is used to discretize the probability distribution of wind and PV output, generating many wind-solar output scenarios with equal probability characteristics. However, an excessive number of scenarios significantly increases computational complexity, necessitating reduction of the original scenario set to retain representative typical scenarios with corresponding probability weights. Based on the traditional K-means algorithm, this paper improves the determination of cluster number and initial center selection to enhance adaptability and accuracy in clustering uncertain scenarios[14].

First, the Silhouette Coefficient (SC) is introduced to objectively determine the optimal cluster number k. This coefficient evaluates clustering performance by measuring intra-cluster compactness and inter-cluster separation, with values closer to 1 indicating more reasonable classification. The formula for the silhouette coefficient is:

$$SC(i) = \frac{b_i - a_i}{\max(b_i - a_i)} \tag{10}$$

where a_i is the average distance between sample i and other samples in the same cluster; b_i is the average distance between sample i and samples in the nearest neighboring cluster.

The specific steps are:

(1) Calculate the intra-cluster similarity a_i and inter-cluster difference b_i for each sample;

(2) Calculate the silhouette coefficient for each sample using the formula;

(3) Calculate the average silhouette coefficient for all samples;

(4) Plot the line graph of average silhouette coefficients for different k values and select the k corresponding to the maximum average silhouette coefficient as the optimal number of clusters.

Second, initial cluster centers are selected based on density to mitigate algorithm sensitivity to initial values. The specific steps are:

(1) Construct the original scenario set S;

(2) Calculate the Euclidean distance between sub-scenarios in the scenario set as in Equation (10);
(3) Generate the distance matrix $D_{n\times n}$ after calculating all sub-scenario distances;

$$D_{n\times n}=\left\{d(s_i,s_j)|1\le i,j\le n\right\} \tag{11}$$

(4) Sort the row vectors in the distance matrix to obtain the distance parameter $d\left(s_{im}\right)$;

$$d\left(s_{im}\right)=sort\left\{d(s_i,s_j),1\le j\le n|m\right\} \tag{12}$$

Select the scenario corresponding to the minimum value in the distance array D_m as the initial cluster center.
Subsequently, the remaining initial centers are selected based on the max-min distance principle:
(1) Input the optimal number of clusters k and initial cluster center V_1;
(2) Select the scenario farthest from V_1 as the second cluster center V_2;
(3) Calculate the minimum distance between remaining scenarios and existing cluster centers, and select the scenario corresponding to the maximum minimum distance as a new cluster center;
(4) Repeat the above steps until all cluster centers are selected;
(5) Calculate the mean of each cluster as the new cluster center and iteratively optimize until the termination condition is met:

$$\max\left(d\left(V_i^{k+1},V_i^k\right)\right)<\epsilon_e \tag{13}$$

where ϵ_e is the cluster center distance threshold, typically set to 0.1.

4 Low-Carbon Optimal Operation Model of CCHP Microgrids

4.1 Objective Function

The objective function is to minimize the comprehensive cost, considering the stepwise carbon trading model, including electricity purchase cost C_{net}, gas purchase cost C_{ng}, equipment operation and maintenance cost C_{CO_2}, and carbon trading cost C_{op}. The corresponding expression is:

$$\min C=\sum_{e\in\varepsilon}\mu_e\sum(C_{net}+C_{ng}+C_{CO_2}+C_{op}) \tag{14}$$

Electricity Purchase Cost.

$$C_{net} = \sum_{t=1}^{T} (C_{buy}(t) + P_{buy}(t) - C_{sell}(t) P_{sell}(t)) \tag{15}$$

where $C_{buy}(t)$ and $C_{sell}(t)$ are the electricity purchase and sale prices at time t, respectively; $P_{sell}(t)$ and $P_{buy}(t)$ are the electricity sale and purchase powers at time t, respectively.

Gas Purchase Cost.

In the CCHP microgrids, natural gas is mainly consumed by MT and GB. The total gas purchase cost is:

$$C_{ng} = \sum_{t=1}^{T} (C_{MT}(t) + C_{GB}(t)) \tag{16}$$

where the gas purchase cost for the micro gas turbine is:

$$C_{mt}(t) = \frac{C_{ngu}}{LHVng \times \eta_{MT}} P_{MT}(t) \tag{17}$$

and the gas purchase cost for the gas boiler is:

$$C_{GB}(t) = \frac{C_{ngu}}{LHVng \times \eta_{GB}} Q_{GB}(t) \tag{18}$$

where C_{ngu} is the unit price of natural gas; $LHVng$ is the gas calorific value; $P_{MT}(t)$ is the output power of MT at time t; $Q_{GB}(t)$ is the heat output of GB at time t.

Equipment Operation and Maintenance Cost.

$$\begin{aligned} C_{op}(t) = {} & \alpha_{PV} P_{PV}(t) + \alpha_{WT} P_{WT}(t) + \alpha_{MT} P_{MT}(t) + \alpha_{GB} P_{GB}(t) + \alpha_{RB} P_{RB}(t) \\ & + \alpha_{HE} P_{HE}(t) + \alpha_{AC} P_{AC}(t) + \alpha_{EC} P_{EC}(t) \end{aligned} \tag{19}$$

where α_{PV}、α_{WT}、α_{MT}、α_{GB}、α_{RB}、α_{HE}、α_{AC}、α_{EC} are the operation and maintenance cost coefficients of PV, WT, MT, GB, RB, HE, AC and EC equipment respectively.

Carbon Trading Cost.

The carbon trading cost C_{CO_2} is calculated using Equation (2).

4.2 Constraints

Electrical Power Balance Constraint

$$\begin{aligned} &P_{buy}(t)+P_{WT}(t)+P_{PV}(t)+P_{MT}(t)+P_{cha}(t) \\ &=P_{eLoad}(t)+P_{sell}(t)+P_{EC}(t)+P_{dis}(t) \end{aligned} \tag{20}$$

where $P_{cha}(t)$ and $P_{dis}(t)$ the charging and discharging powers of the battery at time t, respectively; $P_{eLoad}(t)$ is the electric load power at time t; $P_{EC}(t)$ is the electric power consumed by EC at time t.

Thermal Balance Constraint.

$$Q_{HE}(t)+Q_{GB}(t)=Q_{hLoad}(t) \tag{21}$$

where $Q_{HE}(t)$ is the heat output of HE at time t; $Q_{hLoad}(t)$ is the heat load power at time t.

Cooling Balance Constraint.

$$Q_{AC}(t)+Q_{EC}(t)=Q_{cLoad}(t) \tag{22}$$

where Q_{AC} is the cooling output of AC at time t; Q_{cLoad} is the cooling load power at time t.

Grid Interaction Power Constraint.

$$\begin{cases} 0 \le P_{buy}(t) \le U_{buy}(t) P_{net}^{\max} \\ 0 \le P_{sell}(t) \le U_{sell}(t) P_{net}^{\max} \\ 0 \le U_{buy}(t)+U_{buy}(t) \le 1 \\ U_{buy}(t) \in \{0,1\}; U_{buy}(t) \in \{0,1\} \end{cases} \tag{23}$$

where $P_{net}^{\max}$ is the maximum electricity purchase/sale power; $U_{buy}(t)$ and $U_{sell}(t)$ are the electricity purchase and sale states in time period t, respectively.

Battery Constraints.

$$\begin{cases} 0 \le P_{cha}(t) \le U_{ess,c}(t) P_{cs\max} \\ 0 \le P_{dis}(t) \le U_{ess,d}(t) P_{cs\max} \\ SOC(t+1) = SOC(t) + \dfrac{\eta_{cha} P_{cha}(t) - \eta_{dis} P_{dis}(t)}{E_{\max}} \\ SOC_{\min} \le SOC \le SOC_{\max} \\ 0 \le U_{ess,c}(t) + U_{ess,d}(t) \le 1 \\ U_{ess,c}(t) \in \{0,1\}; U_{ess,d}(t) \in \{0,1\} \end{cases} \tag{24}$$

where P_{csmax} is the maximum charging/discharging power of the battery; E_{max} is the maximum capacity of the battery; $SOC(t)$ is the state of charge of the battery in time period t; $U_{ess,c}$ and $U_{ess,d}$ are the charging and discharging states of the battery in time period t, η_{cha} and η_{dis} are the charging and discharging efficiency of the battery in time period t, respectively.

Output Upper and Lower Limits of Internal Microgrid Equipment.

$$\begin{cases} 0.2P_{mt}^{max} \le P_{mt}(t) \le P_{mt}^{max} \\ 0.45P_{ec}^{max} \le P_{ec}(t) \le P_{ec}^{max} \\ 0.4Q_{ac}^{max} \le Q_{ac}(t) \le Q_{ac}^{max} \\ 0.4Q_{he}^{max} \le Q_{he}(t) \le Q_{he}^{max} \\ 0.35Q_{gb}^{max} \le Q_{gb}(t) \le Q_{gb}^{max} \end{cases} \tag{25}$$

wher P_{mt}^{max} and P_{ec}^{max} are the maximum output powers of MT and EC, respectively; Q_{ac}^{max} , Q_{he}^{max} and Q_{gb}^{max} are the maximum heat/cooling outputs of AC, HE, and GB, respectively.

4.3 Model Solution Workflows

The energy purchase cost, equipment operation and maintenance cost, etc., within the system are calculated using Equations (14)–(19). The stepwise carbon trading mechanism is introduced, and the objective function and constraints for low-carbon economic optimization scheduling are set. Under the constraints of alternative demand response, energy constraints of each equipment, and energy balance, the model is solved using the Yalmip toolbox and CPLEX solver in Matlab. The detailed solution process of the model is shown in Figure 2.

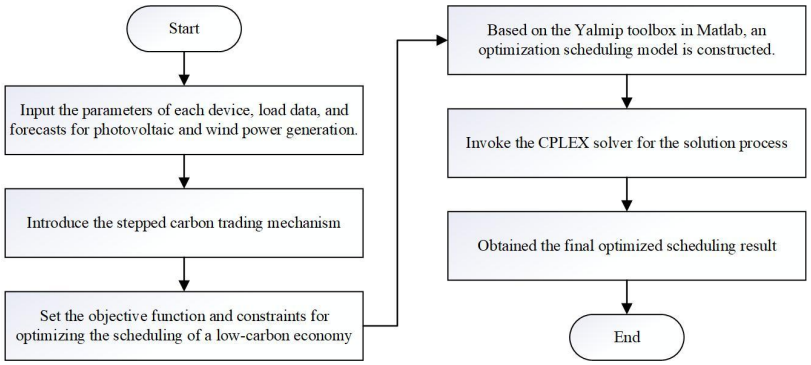


Fig. 2. The model solution workflow.

5 Case Study

To verify the effectiveness of the microgrid optimal operation method, this paper conducts simulation research on the established model using the CPLEX solver called by the Matlab platform. Typical scenario data obtained via scenario analysis are used as input, with a 24-hour period as the optimization cycle. Under the premise of ensuring the overall operational stability of the microgrid and meeting daily load demands, the mixed-integer linear programming problem is solved using the objective function and relevant constraints of the microgrid low-carbon optimization model, fully considering the impact of carbon emissions. Optimal operation methods are explored through comparative analysis of different scenarios to reduce the total operation cost of the microgrid. The microgrid system studied in this paper mainly includes wind turbines, photovoltaic cells, microturbines, gas-fired boilers, waste heat boilers, heat exchange devices, absorption chillers, electric chillers, user loads, and energy storage devices. The relevant parameters of the main equipment in the microgrid are shown in Table 1-2.

Table 1. Main Equipment Parameters of Microgrid.

Parameter	Value	Parameter	Value
Power efficiency of MT	0.4	COP of EC	4
Waste heat coefficient of MT	0.85	Maximum power of EC	400
Maximum power of GT /kW	500	Efficiency of HE	0.8
Efficiency of RB	0.85	Maximum power of	400
COP of AC	1.2	Efficiency of GB	0.9
Maximum power of AC /kW	400	Maximum power of GB/kW	500
Carbon emission factor of MT	0.68	Carbon emission factor of GB	0.635
Maximum capacity /kWh	300	SOC	0.1-0.9
Charge-discharge efficiency	0.9	Maximum charge-discharge power /kW	40

Table 2. Time-of-Use Pricing in Microgrids.

	Time period		Power purchase / CNY·kWh^{-1}	Power sale / CNY·kWh^{-1}
Peak	08:00-12:00	17:00-21:00	0.82	0.68
Flat	12:00-17:00	21:00-24:00	0.53	0.42
Valley	00:00-08:00		0.25	0.22

5.1 Scenario Generation Results

Based on historical wind and solar power generation data from a northern region in China, the probability distribution of wind and solar output at any time is derived using probability models. 1000 load and PV output scenarios are generated using LHS, and scenario reduction is performed using the improved K-means clustering algorithm to calculate the probability corresponding to each scenario. Figures 3 and 4 show the distribution of original wind and solar output scenarios.

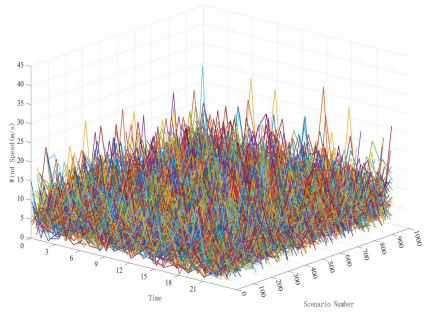


Fig. 3. Original scenario of wind speed irradiance

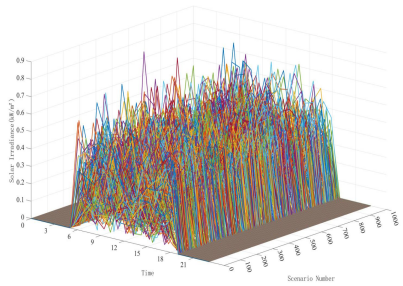


Fig. 4. Original scenario of solar

Figures 5 and 6 present the wind and solar output curves under typical scenarios, and Table 6 lists the probability distribution of typical wind and solar scenarios.

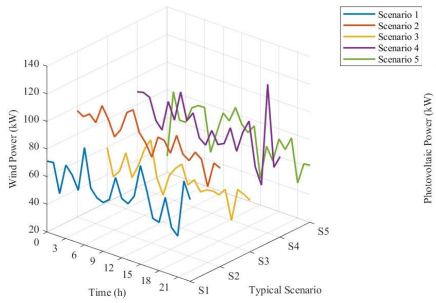


Fig. 5. Typical scenario of WT output

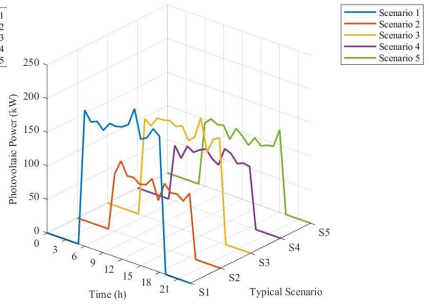


Fig. 6. Typical scenario of PV output

Table 3. Probability value of typical scenarios.

number	1	2	3	4	5
probability	25.40%	18.50%	21.60%	17.70%	16.80%

5.2 Case Scenario Settings

To specifically analyze the impact of wind-solar output uncertainty and the feasibility of low-carbon economic operation of the microgrid under carbon trading mechanisms, the following scenarios are set for comparative analysis:
Case 1: Traditional carbon trading mechanism is adopted, with the objective function considering both economic cost and carbon trading cost;
Case 2: Stepwise carbon trading mechanism is adopted, with the objective function considering only economic cost;
Case 3: Stepwise carbon trading mechanism is adopted, with the objective function considering both economic cost and carbon trading cost.

5.3 Economic Cost Analysis

Taking typical Case 1 as an example, the optimization results of various costs under different cases are shown in Table 7. As indicated in Table 7, the participation of the carbon trading mechanism affects the system's energy purchase cost, operation and maintenance cost, and carbon trading cost. Comparing Case 1, which uses the baseline method, with Case 3, which uses the stepwise carbon trading mechanism, the total cost of Case 3 is lower, with a reduction of 475.73 yuan, approximately 37.94%. Further analysis of cases under the stepwise carbon trading mechanism shows that compared with Case 2, which considers only the single economic cost objective, Case 3, which considers the comprehensive objective of both economic cost and carbon trading cost, reduces carbon trading cost by lowering microgrid carbon emissions, thereby reducing the total cost by 508.76 yuan, approximately 39.53%.
The significant cost disparity between Case 3 and Case 1 stems from the mechanistic differences in their carbon pricing schemes. The traditional fixed-price mechanism imposes a constant penalty of base carbon price on excess emissions, which often fails to sufficiently incentivize aggressive emission reductions. This leads to greater reliance on fossil-based equipment and grid purchases. Conversely, the stepwise mechanism applies progressively higher prices to larger emission excesses, using a base price of 0.25 CNY/kg CO2 plus an incremental growth rate for each interval. This approach strongly encourages prioritizing renewable energy integration, efficient multi-energy conversion, and storage utilization. As a result, Case 3 achieves lower overall energy purchase costs, despite potential short-term adjustments, and reduces carbon trading penalties, yielding a net total cost savings of 37.94%. This highlights the stepwise approach’s superior ability to balance economic optimization with.

Table 4. Optimization operation results.

Case	Total cost / CNY	Energy purchase cost / CNY	Carbon trading cost / CNY	Equipment O&M cost / CNY
1	1253.98	54.28	199.24	386.75
2	1287.01	160.39	922.24	204.38
3	778.25	240.94	110.95	168.43

5.4 Carbon Reduction Analysis

Figure 7 presents a comparison of total carbon emissions and carbon trading costs across different scenarios. As illustrated, integrating the carbon trading mechanism into the objective optimization function exerts a significant impact on carbon trading costs. Under the stepwise carbon trading mechanism, Case 3 reduces total carbon emissions by 815.92 kg, corresponding to a 43.16% decrease, and lowers carbon trading costs by 811.29 yuan, marking an 87.97% reduction compared to Case 2. A further analysis of Case 1 and Case 3, which adopt different carbon trading mechanisms, shows that Case 3 outperforms Case 1 by cutting total carbon emissions by 214.54 kg, a 16.64% reduction, and reducing carbon trading costs by approximately 88.29 yuan, representing a 44.31% decrease. In terms of balancing economic and low-carbon requirements for microgrid optimization, Case 3 demonstrates effective carbon reduction performance. It achieves a 43.16% reduction in total carbon emissions compared to the single economic optimization objective and a 16.64% reduction relative to the traditional baseline carbon quota allocation mechanism.

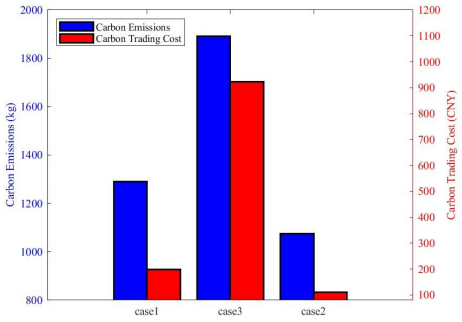


Fig. 7. Situation of total carbon emissions and carbon trading costs in each case.

Results show that the stepwise carbon trading mechanism outperforms traditional mechanisms in economic benefits and emission reduction, with a 39.53% reduction in total cost and 43.16% reduction in carbon emissions, demonstrating excellent economic and environmental coordination. In grid-connected mode, the system's daily average comprehensive cost is approximately 778.25 yuan through energy storage scheduling and time-of-use electricity price strategies. Moreover, wind-solar

complementarity effectively improves renewable energy utilization and reduces curtailment, verifying the effectiveness and practicality of the proposed method in promoting low-carbon, economic, and stable operation of microgrids.

6 Conclusion

To address renewable energy uncertainty and carbon constraints in microgrid operation, this paper proposes a two-stage stochastic optimization strategy for CCHP microgrids that integrates a tiered carbon trading mechanism. A refined system model is developed, clarifying the coupling between waste heat and multi-energy loads, along with a renewable priority strategy. The proposed two-stage framework employs probabilistic uncertainty modeling through LHS and an enhanced K-means clustering method to generate and reduce scenarios effectively. Simulation results demonstrate that the proposed approach reduces operating costs by 39.5% and carbon emissions by 43.2%, achieving synergistic improvement in both economic and environmental performance.

References

1. Liu, C., Chen, H.N., Han, Z.J., et al.: AC-AC Type Active Power Spring for Distributed Voltage Regulation. Proceedings of the CSEE 42(02), 737–747 (2022).
2. Pan, C., Fan, G.B., Wang, J.P., et al.: Low-Carbon Optimization of Electric-Heat Integrated Energy System with Flexible Resources Participation. Transactions of China Electrotechnical Society 38(06), 1633–1647 (2023).
3. Zhu, L., Niu, P.Y., Tang, L.J., et al.: Robust Optimal Operation of Micro-Energy Grid Considering Uncertainty of Direct Load Control. Power System Technology 44(04), 1400–1413 (2020).
4. Ahmed, H.M.A., Eltantawy, A.B., Salama, M.M.A.: A planning approach for the network configuration of AC-DC hybrid distribution systems. IEEE Transactions on Smart Grid 9(3), 2203–2213 (2016).
5. Wu, X., Wang, X.L., Li, J., et al.: Joint Scheduling Model and Solution for Wind Power-Storage Hybrid System. Proceedings of the CSEE 33(13), 10–17 (2013).
6. Li, P., Cai, Y.Q., Han, X.Q., et al.: Optimal Operation of AC-DC Hybrid Microgrid Considering Stochastic-Fuzzy Dual Uncertainties. High Voltage Engineering 46(07), 2269–2279 (2020).
7. Ma, Y.: Research on Low-Carbon Economic Dispatch of Microgrid Based on Robust Optimization. Taiyuan University of Technology (2023).
8. Sun, P.R., Hao, X.J., Wang, J., et al.: Low-carbon economic operation for integrated energy system considering carbon trading mechanism. Energy Science & Engineering 9(11), 2064–2078 (2021).
9. Ma, Y., Meng, R.Q., Wei, B., et al.: Two-Stage Robust Optimal Dispatch of Microgrid Considering Stepwise Carbon Trading Mechanism. Power System Protection and Control 51(10), 22–33 (2023).
10. Mi, Y., Zhao, H.H., Fu, Q.X., et al.: Bi-Level Game Optimal Operation of Regional Integrated Energy System Considering Wind-Solar Uncertainties and Carbon Trading. Power System Technology 47(06), 2174–2188 (2023).

11. Zhou, J.H., Liang, C.Y., Shi, L.J., et al.: Optimal Dispatch of Integrated Energy System Considering Stepwise Carbon Trading Mechanism. Electric Power 58(02), 77–87 (2025).
12. Houyou, H., Zhao, L., Qian, W., et al.: Joint Operation Mechanism of Distributed Photovoltaic Power Generation Market and Carbon Market Based on Cross-Chain Trading Technology. IEEE Access 08(01), 66116–66130 (2020).
13. Galarza, J., Condezo, D., Camayo, B., et al.: Assessment of wind power density based on Weibull distribution in region of Junin, Peru. Energy and Power Engineering 12(1), 16–27 (2020).
14. Yu, R.J.: Research on Optimal Dispatch of Microgrid Considering Wind-Solar Uncertainties. Northeast Petroleum University, DOI:10.26995/d.cnki.gdqsc.2024.000418 (2024).

025 Research on Co-optimization Strategies Based on Cooperative Game in the Electricity Supply Chain

Shangyuan Zhang, Yanbo Che, Yaling Sun and Yingshu Liu

School of Electrical and Information Engineering, Tianjin University, Tianjin, 300072, China

Abstract. With the deepening of electricity market reforms and the integration of renewable energy, the competition and coordination conflicts between traditional thermal power plants (TPPs) and renewable energy plants (REPs) have intensified. Addressing the challenge of profit distribution and achieving electricity supply chain (ESC) synergy has become a critical issue. To overcome the limitations of conventional game models in reflecting interactions and ensuring fairness, a cooperative game strategy for the ESC is proposed. First, an ESC model comprising TPPs, REPs, retail electricity companies (RECs), and end-users is established to analyze multi-dimensional interaction mechanisms. Second, based on varying levels of ESC collaboration, three game modes—non-cooperation, semi-cooperation, and full cooperation—are defined. The Nash equilibrium is solved via backward induction to reveal the impacts on individual profits and overall efficiency. Furthermore, the Shapley value method is used to quantify the contributions of participants. The result demonstrates that the total ESC profit in full cooperation mode increases by 170% and 141% compared to non-cooperation and semi-cooperation modes, respectively. The Shapley value method can fairly allocate benefits among all parties.

Keywords: Electricity Supply Chain, Cooperative Game, Shapley Value, Profit Distribution.

1 Introduction

With the profound transformation of the global energy structure and the rapid deployment of renewable energy, the power system is transitioning from a traditional centralized, single-energy-dominated model to a distributed, diversified energy collaboration model [1]. In this context, the deepening reform of the electricity market has introduced complex interactions among power generators, retailers, and consumers, where the operational efficiency of the ESC critically determines market stability and end-user satisfaction [2]. Particularly, the inherent competition-coordination dilemma between TPPs and REPs poses significant challenges to equitable profit allocation and collaborative optimization. Therefore, there is an urgent need for a game model comprehensively considers the interests of multiple parties and dynamically adjust profit distribution strategies to optimize the operational efficiency of the ESC [3].

2

Supply chain management is crucial in modern enterprise operations, especially in the energy sector. With the development of renewable energy and the increasing complexity of the electricity market, research on the ESC has attracted significant attention. Existing studies have proposed various innovative methods in optimizing structures, improving energy efficiency, and enhancing system resilience. From the perspective of structural optimization, Ref. [4] proposed a hybrid method combining recursive neural networks and optimization models for designing resilient ESCs based on wind and solar energy. Ref. [5] proposed a multi-objective mixed-integer programming model to construct a sustainable closed-loop renewable energy supply chain by considering the forward and reverse flow through solar, biogas, and incineration power plants (PPs). Ref. [6] proposed a model based on the quality function deployment method to evaluate the innovative strategies of green supply chain management in energy companies. Ref. [7] proposed a green supply chain framework based on non-cooperative games, recording the trust value of sensors in the blockchain, significantly improving system transparency and trust. Ref. [8] proposed a greenness evaluation method for the supply chain based on a multi-regional input-output model and data envelopment analysis, calculating the consumption of renewable and non-renewable energy in the global supply chain and measuring the greenness of the supply chain. Regarding energy security and storage, Ref. [9] evaluated the advantages of fuel power generation by optimizing the design of a power-to-fuel supply chain for seasonal energy storage in large geographical areas. Ref. [10] comprehensively assessed the security level of China's coal, oil, and natural gas supply systems from the perspective of the energy supply chain, considering network structure, sustainability, and network utility. Despite existing research on the ESC has achieved significant results in optimization and sustainability, most focus on single-objective optimization, making it difficult to balance economic, environmental, and social benefits. More critically, there is a lack of research on cooperation mechanisms, which is essential for reconciling competition-coordination conflicts in evolving electricity markets.

Cooperative game theory, as a tool for solving multi-agent transaction problems, has been increasingly applied in the energy supply chain field in recent years. Existing studies have explored cooperation mechanisms between different entities and their impact on supply chain efficiency by constructing game models. Ref. [11] studied the coordination game between TPP and REP supply chains, comparing the differences in decision-making under centralized and decentralized scenarios. Ref. [12] used game theory to study the impact of government support strategies on competing bioenergy and traditional energy supply chains under cap-and-trade regulations. Ref. [13] applied an evolutionary game model to a two-level green supply chain composed of green suppliers and green manufacturers, analyzing various internal and external factors that influenced the behavior of both parties in the game. Ref. [14] designed a two-stage profit distribution model, applying cooperative games with externalities to model the market behavior of networked microgrids, and distributed the profits of the grand coalition to participating microgrids. Ref. [15] constructed a cooperative game model among multiple microgrids, coordinating profit distribution among microgrids through Nash bargaining and analyzing the optimal trading capacity and tariff be-

tween microgrids. Ref. [16] proposed a three-layer risk-averse game theory-based strategy to coordinate smart buildings and electric vehicle fleets with microgrid scheduling. Ref. [17] proposed a day-ahead scheduling model for local integrated energy systems based on cooperative games, which can be transformed into a continuous two-step optimization problem to reduce computational complexity. Ref. [18] established an optimal operation model for distribution network operators and community energy prosumer alliances based on a hybrid game, promoting coordination among cooperative alliances by integrating Stackelberg and cooperative games. Ref. [19] proposed a cooperative game theory framework to address the instability of community energy transactions caused by the unpredictability and intermittency of distributed energy. Ref. [20] studied the environmental impact of the behavior of green manufacturers, retailers, and managers in a single-level green closed-loop supply chain, using cooperative games to resolve the interest relationships among parties. Although cooperative game theory has made some progress in the application of energy supply chains, existing research mostly focuses on static game models, failing to fully reflect the changes and uncertainties of the electricity market. Existing cooperative game models are still deficient in the design of fairness and stability of the benefit distribution mechanism. Therefore, it is urgent to further explore cooperative game models in combination with the characteristics of the ESC to improve the overall efficiency and sustainability.

This paper summarizes the shortcomings of the above research and proposes a co-optimization and profit distribution strategy based on cooperative game in the ESC. The main contributions are as follows:

(1) A novel ESC model integrating REPs, TPPs, RECs and consumers is established, explicitly characterizing multi-dimensional interactions among energy flow, financial flow, and information flow. This model quantifies the interdependencies between traditional and renewable energy suppliers under REC-mediated market mechanisms.

(2) Three cooperation modes—non-cooperative, semi-cooperative and full-cooperative—are formulated to reflect ESC collaboration scenarios. By solving Nash equilibria via backward induction, the analysis reveals that the necessity of co-optimizing TPP-REP-REC interactions in power systems, enabling holistic optimization of the generation-retail-consumption chain.

(3) The Shapley value method is used to achieve fair and adaptive profit distribution. This method is provided for optimizing the ESC under the background of power system reform, promoting the efficient and sustainable development of the power system.

The structure of this paper is as follows: The ESC model is established in Section 2. The cooperative game model and solution method of the ESC are proposed in Section 3. The case analysis is presented in Section 4. Finally, the conclusions are provided in Section 5.

2 Electricity Supply Chain Model

This paper studies the co-optimization and profit distribution problems of the ESC under different cooperation modes. The ESC process can be described as follows: the TPP generates conventional energy power, the REP generates renewable energy power, and the REC, which does not have power generation capacity, acts as an intermediary to sell electricity to end consumers who consume electricity. There are interactions of energy flow, capital flow and information flow among all parties in the supply chain. The ESC structure is shown in Fig. 1.

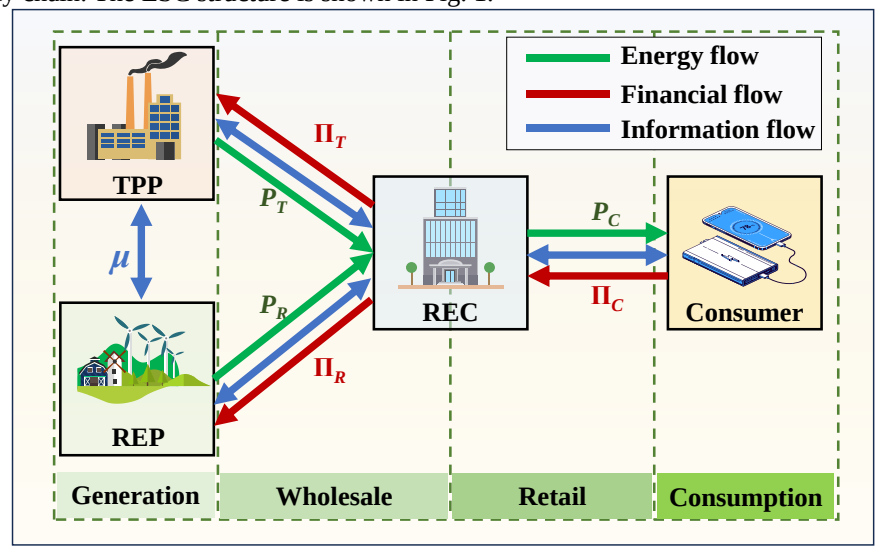


Fig. 1. Structure of the ESC.

2.1 Profit Model of the REC

This paper focuses on the game between PPs and the REC. Both types of PPs invest in their own R&D optimization and upgrading, while cooperation and communication between enterprises can promote mutual optimization, achieving cost reduction and efficiency improvement. The REC, which obtains lower-cost electricity, is willing to subsidize PPs to encourage their optimization behavior, such as providing more accurate load demand forecasts, intelligent scheduling suggestions, or financial support. Ultimately, lower-tariff electricity is delivered to consumers, benefiting the entire ESC. In this process, the profit of the REC is:

$$\Pi_C = (q_t - MC_C)P_C - wP_T - vP_R - (E_T + E_R)\eta \tag{1}$$

$$P_C = P_T + P_R = \gamma P_C + (1-\gamma)P_C \tag{2}$$

where Π_C is the profit of the REC; q_t is the selling tariff; MC_C is the marginal cost of the REC; P_C, P_T, P_R are the electricity transaction volumes by the REC with consumers, the TPP and REP, respectively; E_T, E_R are the optimization costs of the

TPP and REP, respectively; w and v are the transaction prices by the REC with the TPP and REP, respectively; η is the optimization subsidy rate of the REC to PPs; γ is the share of the thermal power generation.

The REC, with its extensive customer base and big data analysis capabilities, can more accurately predict power demand in different regions, industries and time periods. By analyzing historical sales data, economic trends, seasonal changes, weather conditions and other multi-dimensional factors, the REC provides PPs with demand forecast reports which are accurate to the hour or even minute level, helping them optimize operations, schedule power generation more efficiently, and avoid over- or under-production. Thereby, the utilization rate of power generation equipment will be improved and the effective output will be increased. In this process, the AJ model proposed by Aspremont is adopted. The optimization cost of PPs is:

$$E_T = \frac{1}{2}\lambda_T e_T^{\ 2} \tag{3}$$

$$E_R = \frac{1}{2}\lambda_R e_R^{\ 2} \tag{4}$$

where λ_T, λ_R are the optimization efficiency coefficients of the TPP and REP, respectively; e_T, e_R are the optimization benefits of the TPP and REP, respectively.

2.2 Profit Model of the TPP

The production cost of the TPP includes fuel costs, operation and maintenance costs, emission costs, etc. A quadratic function is used for fitting. The optimization of PPs reduce their respective marginal production costs. Through mutual cooperation, the marginal production costs of each other are also reduced. The profit of the TPP is:

$$\Pi_T = (w + e_T + \mu e_R - MC_T)P_T + E_T(\eta - 1) \tag{5}$$

$$C_T = r_{T1}P_T^2 + r_{T2}P_T + r_{T3} \tag{6}$$

$$MC_T = \frac{dC_T}{dP_T} = 2r_{T1}P_T + r_{T2} \tag{7}$$

where Π_T is the profit of the TPP; μ is the cooperation coefficient between the TPP and REP and $0 \le \mu \le 1$; MC_T is the marginal cost of the TPP; C_T is the cost of thermal power generation; r_{T1}, r_{T2}, r_{T3} are the cost coefficients of thermal power generations.

2.3 Profit Model of the REP

The production cost of the REP usually includes fixed costs, variable costs, operation and maintenance costs, etc. A linear function is used for fitting. The profit of the REP is:

$$\Pi_R = (v + e_R + \mu e_T - MC_R)P_R + E_R(\eta - 1) \tag{8}$$

$$C_R = r_{R1}P_R + r_{R2} \tag{9}$$

$$MC_R = \frac{dC_R}{dP_R} = r_{R1} \tag{10}$$

where Π_R is the profit of the REP; MC_R is the marginal cost of the REP; C_R is the cost of renewable energy power generation; r_{R1}, r_{R2} are the cost coefficients of renewable energy power generations.

2.4 Demand Model Based on Tariff Elasticity

With the deepening of the electricity market reform, the implementation scope of time-of-use tariff policy is increasingly widespread. At the same time, electricity is a special commodity with timeliness. Changing the tariff in a certain period will not only affect the load in that period but also affect the load in other periods. Therefore, dividing a day into N periods, the load tariff elasticity coefficient is established:

$$\varepsilon_{tt} = \frac{\Delta P_t / P_{t0}}{\Delta q_t / q_{t0}} \tag{11}$$

$$\varepsilon_{tu} = \frac{\Delta P_u / P_{u0}}{\Delta q_t / q_{t0}} \tag{12}$$

where ε_{tt} is the self-elasticity coefficient, reflecting the impact of tariff changes in period t on the load in period t; ε_{tu} is the cross-elasticity coefficient, reflecting the impact of tariff changes in period t on the load in period u; ΔP_t is the load change after tariff adjustment in period t; P_{t0} is the original load in period t; Δq_t is the tariff change in period t; q_{t0} is the original tariff in period t.

After receiving the tariff change signal, consumers will adjust their electricity consumption behavior. It is approximately considered that the tariff and load satisfy a linear relationship. Price elasticity model based on the demand response is expressed as:

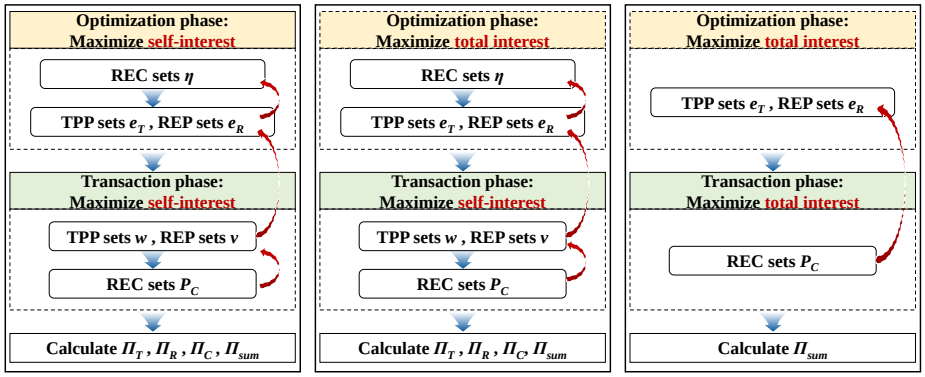
$$q_t = a - bP_C \tag{13}$$

$$\begin{bmatrix} P_{C1} \\ P_{C2} \\ \vdots \\ P_{CN} \end{bmatrix} = \begin{bmatrix} P_{C10} \\ P_{C20} \\ \vdots \\ P_{CN0} \end{bmatrix} + \begin{bmatrix} P_{C10} & 0 & \cdots & 0 \\ 0 & P_{C20} & \cdots & 0 \\ \vdots & \vdots & \ddots & \vdots \\ 0 & 0 & \cdots & P_{CN0} \end{bmatrix} \cdot \begin{bmatrix} \varepsilon_{11} & \varepsilon_{12} & \cdots & \varepsilon_{1N} \\ \varepsilon_{21} & \varepsilon_{22} & \cdots & \varepsilon_{2N} \\ \vdots & \vdots & \ddots & \vdots \\ \varepsilon_{N1} & \varepsilon_{N2} & \cdots & \varepsilon_{NN} \end{bmatrix} \cdot \begin{bmatrix} \Delta q_1 / q_{10} \\ \Delta q_2 / q_{20} \\ \vdots \\ \Delta q_N / q_{N0} \end{bmatrix} \tag{14}$$

where a, b are constants greater than 0 and $P_C \le \frac{a}{b}$.

3 Establishment and Solution of Cooperative Models

Considering different cooperation scenarios in the ESC, three modes including non-cooperation, semi-cooperation and full cooperation are selected to describe different scenarios. Corresponding game models which are divided into optimization phase and transaction phase are established, and the Nash equilibrium is solved using backward induction to analyze the impact of different cooperation modes on the profits of all parties in the ESC. Differences between each mode are shown in Fig. 2.



(a) Mode1: non-cooperation (b) Mode2: semi-cooperation (c) Mode3: full cooperation

Fig. 2. Flowchart of cooperative game of the ESC.

3.1 Mode 1: Non-Cooperation

In this mode, three enterprises in the ESC do not cooperate in either optimization phase or transaction phase, pursuing their own maximum profit.

Electricity Transaction Phase

In this phase, the REC determines the transaction volume based on market demand to maximize its own profit, while the TPP and REP determine the transaction price to maximize their own profits.

The REC determines the transaction volume to maximize its own profit:

$$\frac{\partial \Pi_C}{\partial P_C} = a - 2bP_C - \gamma w - (1-\gamma)v - MC_C = 0 \tag{15}$$

$$\bar{P}_C(w,v) = \frac{a - \gamma w - (1-\gamma)v - MC_C}{2b} \tag{16}$$

where $\bar{P}_C$ is the transaction volume that maximizes profit of the REC in Mode 1.

The TPP and REP determine the transaction price to maximize their own profits:

$$\left.\frac{\partial \Pi_T}{\partial w}\right|_{P_T=\gamma \bar{P}_C} = \frac{\gamma^3 r_{T1}[a - MC_C - \gamma w - v(1-\gamma)]}{b^2} + \frac{\gamma^2 r_{T2} - \gamma^2(w + e_T + \mu e_R) + \gamma[a - MC_C - \gamma w - v(1-\gamma)]}{2b} = 0 \tag{17}$$

$$\left.\frac{\partial \Pi_R}{\partial v}\right|_{P_R=(1-\gamma)\bar{P}_C} = \frac{(\gamma-1)^2(r_{R1} - 2v - e_R - \mu e_T)}{2b} - \frac{(\gamma-1)(a - MC_C - \gamma w)}{2b} = 0 \tag{18}$$

By solving the above equations, the transaction price $\bar{w}(e_T, e_R)$ of the TPP and the transaction price $\bar{v}(e_T, e_R)$ of the REP can be obtained.

Optimization Phase

In this phase, the REC determines the optimization subsidy for the TPP and REP to maximize its own profit, while the TPP and REP determine their respective optimization benefit to maximize their own profits.

The TPP and REP determine the optimization benefit to maximize their own profits:

$$\left.\frac{\partial \Pi_T}{\partial e_T}\right|_{P_T=\gamma \bar{P}_C, w=\bar{w}} = 0 \tag{19}$$

$$\left.\frac{\partial \Pi_R}{\partial e_R}\right|_{P_R=(1-\gamma)\bar{P}_C, v=\bar{v}} = 0 \tag{20}$$

By solving above equations, the optimization benefit $\overline{e_T}(\eta)$ of the TPP and the optimization benefit $\overline{e_R}(\eta)$ of the REP can be obtained.

The REC determines the subsidy rate for the TPP and REP:

$$\left.\frac{\partial \Pi_C}{\partial \eta}\right|_{P_T=\gamma \bar{P}_C, P_R=(1-\gamma)\bar{P}_C, e_R=\overline{e_R}, e_T=\overline{e_T}, w=\bar{w}, v=\bar{v}} = 0 \tag{21}$$

By solving (21), the optimal subsidy rate $\bar{\eta}$ of the REC for PPs can be obtained. The subsidy rate, optimization benefit, transaction price and transaction volume in Mode 1 can be determined using backward induction to solve the Nash equilibrium. Then, the profits of all parties in Mode 1 can be calculated.

3.2 Mode 2: Semi-Cooperation

In this mode, three enterprises in the ESC cooperate in the optimization phase but do not cooperate in the transaction phase.

Electricity Transaction Phase

In this phase, the TPP and REP determine the transaction price to maximize their own profits, and the REC determines the transaction volume to maximize its own profit. The transaction volume and transaction price are the same as that in Mode 1:

$$P_C = \bar{P}_C \tag{22}$$

$$w = \bar{w} \tag{23}$$

$$\hat{v} = \bar{v} \tag{24}$$

where P_C is the transaction volume; w, $\hat{v}$ are the transaction prices by the REC with the TPP and REP in Mode 2, respectively.

Optimization Phase

In this phase, the REC determines the optimization subsidy for the TPP and REP, and the TPP and REP determine their respective optimization benefit to maximize the total profits of the ESC.

The total profit of the ESC is:

$$\Pi_{sum} = \Pi_T + \Pi_R + \Pi_C \tag{25}$$

where Π_{sum} is the total profit of the ESC.

The TPP and REP determine the optimization benefits to maximize the total profit of the ESC:

$$\left.\frac{\partial \Pi_{sum}}{\partial e_T}\right|_{P_T=\gamma P_S, w=w, v=\hat{v}} = 0 \tag{26}$$

$$\left.\frac{\partial \Pi_{sum}}{\partial e_R}\right|_{P_R=\gamma P_S, w=w, v=\hat{v}} = 0 \tag{27}$$

It is necessary to ensure that the total profit of Mode 2 is greater than that of Mode 1, otherwise cooperation is difficult to maintain:

$$\Delta\Pi_{sum} = \Pi_{sum} - \overline{\Pi}_{sum} \geq 0 \tag{28}$$

where $\Delta\Pi_{sum}$ is the cooperative surplus profit; Π_{sum} is the total profit of Mode 2; $\overline{\Pi}_{sum}$ is the total profit of Mode 1.

To reflect the principle of fairness, the cooperative surplus profit is distributed according to the investment ratio:

$$\Delta\Pi_C = \Pi_C - \overline{\Pi}_C = \eta\Delta\Pi_{sum} \tag{29}$$

By solving (29), the subsidy rate η in Mode 2 can be determined. Using backward induction to solve the Nash equilibrium, the optimization benefit, transaction price, and transaction volume of the enterprise can be obtained. Then, the profits of all parties in Mode 2 can be calculated.

3.3 Mode 3: Full Cooperation

In this mode, the three enterprises cooperate in both the optimization phase and the transaction phase.

Electricity Transaction Phase

The REC determines the transaction volume to maximize the total profit of the ESC:

$$\frac{\partial \Pi_{sum}}{\partial P_C} = 0 \tag{30}$$

Optimization Phase

The TPP and REP determine the optimization benefit to maximize the total profit of the ESC:

$$\left.\frac{\partial \Pi_{sum}}{\partial e_T}\right|_{P_T=\gamma \tilde{P}_C} = 0 \tag{31}$$

$$\left.\frac{\partial \Pi_{sum}}{\partial e_R}\right|_{P_R=(1-\gamma)\tilde{P}_C} = 0 \tag{32}$$

where P_S is the transaction volume that maximizes the total profit in Mode 3.

3.4 Distribution Method Based on Shapley Value

For the cooperative alliance of PPs and the REC, the profits of full cooperation should be shared by all members. Reasonable distribution of cooperative profits is crucial for maintaining long-term cooperation in the alliance.

The Shapley value method can calculate the marginal contribution of each member in the cooperative alliance, ensuring that profit of each member equals the expected value of their marginal contribution to achieve fair distribution.

The expression for calculating the contribution degree and profit of member i in the cooperation is:

$$x_i = \sum \frac{[(S-1)!(n-S)!]}{n!} \times [I_S - I_{S-\{i\}}] \tag{33}$$

$$\Phi_i = \frac{x_i}{\sum_{j=1}^{n} x_j} \Pi_{sum} \tag{34}$$

where x_i is the contribution degree of member i; n is the total number of members participating in the cooperative game; S is the number of members in the alliance; I_S is the performance evaluation value of the alliance; $I_{S-\{i\}}$ is the performance evaluation value of the alliance with member i removed; Φ_i is the profit of member i.

4 Case Study

To verify the effectiveness of co-optimization and profit distribution strategies based on cooperative game in the ESC proposed in this paper, a case study of a distributed ESC in a certain region is selected, which implements the policy of time-of-use tariff. The tariff and demand response are shown in Fig. 3. The relevant parameters of each enterprise are shown in Table 1.

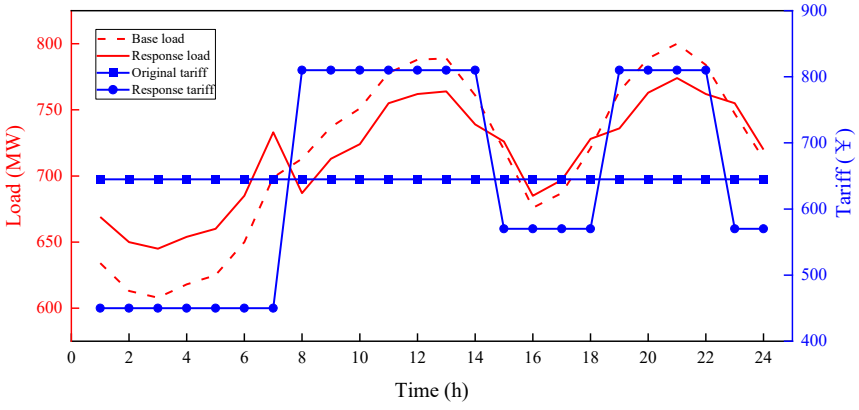


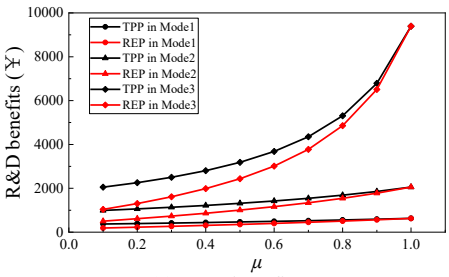
Fig. 3. Typical load tariff curve.

Table 1. Parameters of supply chain model.

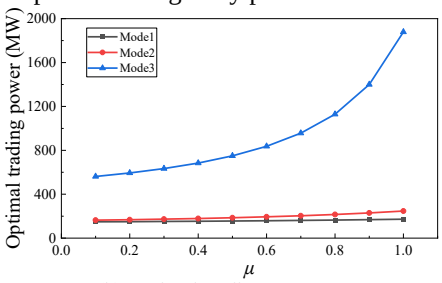
Parameter	Value
r_{R1} /￥·MW^{-2}	0.15
r_{R2} /￥·MW^{-1}	310
r_{T1} /￥·MW^{-1}	50
MC_C /￥·MW^{-1}	80
λ	0.2
γ	0.7

4.1 Analysis of Price Change and Optimal Transaction Volume

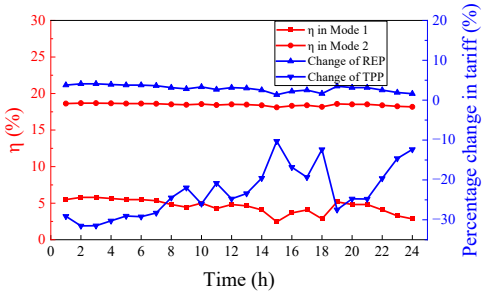
In order to analyze the effects of different modes on optimization benefits of PPs and trading power of the REC, the change curves taking t = 12 as an example are shown in Fig. 4(a) and Fig. 4(b). The results indicates that the optimization benefit and optimal trading power are improved with the increase of technology exchange between PPs. The optimization benefit and optimal trading power in Mode 2 are approximately double those in Mode 1; the results of Mode 3 are two to five times higher than those of Mode 1 and Mode 2. It shows that with the deepening of the cooperation, the optimization of the production process of each enterprise can be greatly promoted.



(a) R&D benefits at t = 12



(b) Optimal trading power at t = 12



(c) Changes of R&D subsidy rates and transaction prices when μ = 0.5

Fig. 4. Price change and optimal transaction volume.

To analyze the impact of different modes on the transaction prices of parties in the ESC, taking μ = 0.5 as an example. The optimization subsidy rate curve and the tariff reduction curve are shown in Fig. 4(c). Since the internal transactions between buyers

and sellers are not considered in Mode 3, there is no optimization subsidy rate and price change curve for it. Compared with Mode 1, it is observed that the transaction price with the REP in Mode 2 increases by less than 5%, but the transaction price with the TPP decreases by more than 20%. Overall, the REC obtains electricity at a lower price. The R&D subsidy rate is around 5% in Mode 1, while it rises to nearly 20% in Mode 2, indicating that the REC, which obtains electricity at a lower price, is willing to provide more R&D subsidies to promote R&D of PPs. PPs are encouraged to participate in cooperation and reduce electricity purchase costs. Meanwhile, the overall efficiency of the ESC is improved.

In Mode 1, each entity's pursuit of individual profit maximization establishes a critical, albeit inefficient, baseline for comparison. The resulting Nash equilibrium is inherently suboptimal due to classic supply chain inefficiencies, primarily double marginalization and a phenomenon related to information asymmetry known as moral hazard.

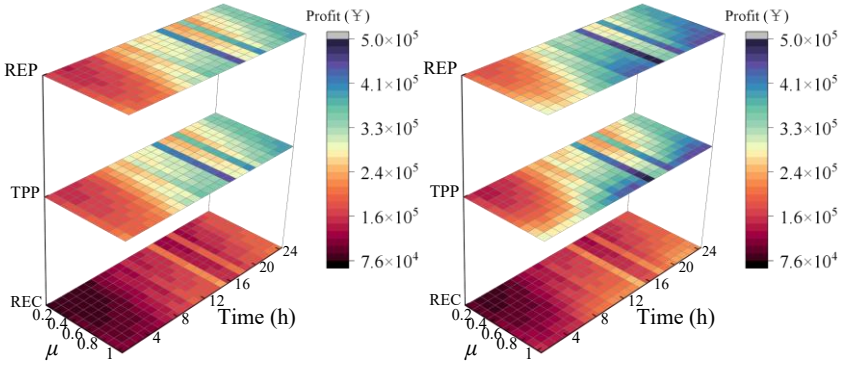
Double marginalization occurs because both levels of the supply chain—the PPs and the REC—independently add their own profit margins. The power plants determine a transaction price to maximize their profit, and the REC, in turn, sets its selling tariff to maximize its own. This sequential markup results in a higher final price for consumers and lower transaction volumes than would be optimal for the supply chain as a whole.

More critically, the decisions surrounding optimization investments create a low-level, mutually hindering equilibrium. Firstly, while a higher subsidy would encourage power plants to optimize and lower their production costs, the REC bears 100% of the subsidy cost while only capturing a fraction of the total benefit. To maximize its own profit, it under-invests in this incentive mechanism. Secondly, The optimization costs rise quadratically with the benefits, making significant investment unattractive without sufficient external support. Low optimization levels will be chosen, knowing that much of the value created would be passed on to the REC or dissipated through market competition rather than being retained as profit.

In this mode, a vicious cycle is created: the REC's low subsidy discourages optimization, and the power plants' resulting low optimization effort validates the REC's decision not to offer a higher subsidy. Consequently, this non-cooperative equilibrium results in excessively high operational costs for the entire supply chain, as neither party is incentivized to make the investments necessary for collective improvement.

4.2 Analysis of profits in Different Modes

In different time and levels of technical sharing, the profits of each enterprise in Mode 1 and Mode 2 are shown in Fig. 5. Taking t = 12 as an example, the profit data of each enterprise is shown in Table 2. Compared with Mode 1, the profits of all enterprises in Mode 2 generally increase. As the technical sharing between the TPP and REP increases, the profits also increase. The growth rate of profits gradually rise from 5.8% to 24.2% for the REP and from 18.7% to 26.2% for the REC. The profit slightly decreases when μ<0.5 but it gradually increases when μ≥0.5, indicating that the development of enterprises can be promoted by strengthening cooperation.



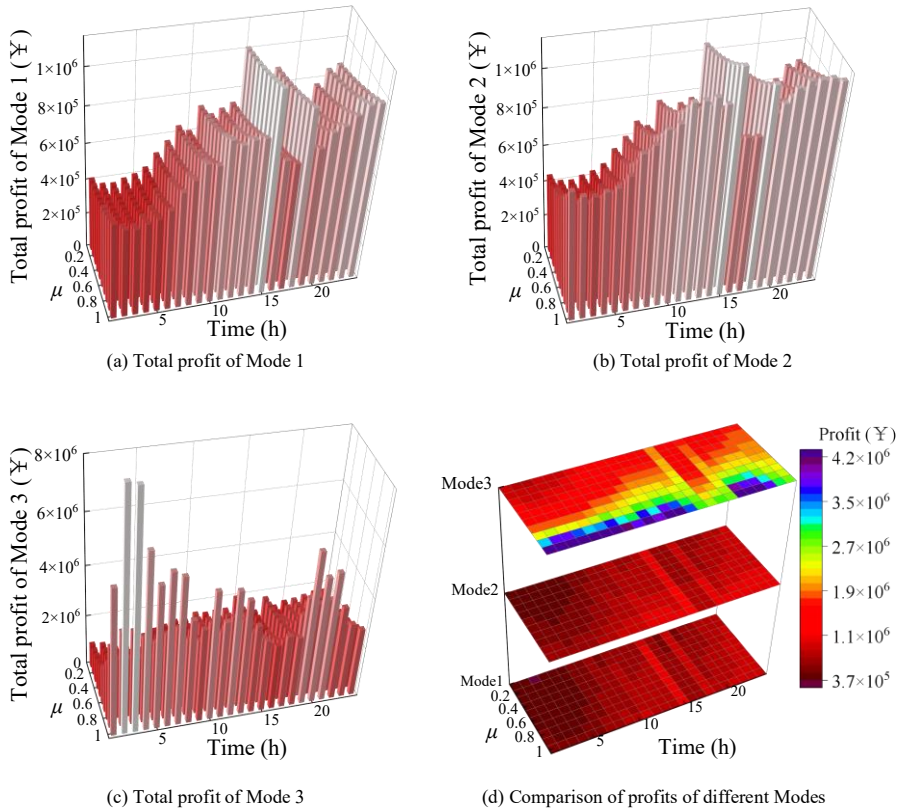
(a) Profits for all parties in Mode 1 (b) Profits for all parties in Mode 2

Fig. 5. Profits of supply chain parties in Mode 1 and Mode 2.

Table 2. Comparison of profits in Modes 1 and 2.

μ	REP			TPP			REC		
	Mode1 /×10^5 ￥	Mode2 /×10^5 ￥	Rate /%	Mode1 /×10^5 ￥	Mode2 /×10^5 ￥	Rate /%	Mode1 /×10^5 ￥	Mode2 /×10^5 ￥	Rate /%
0.1	1.39	1.47	5.8	2.76	2.60	-5.8	2.68	3.18	18.7
0.2	1.42	1.51	6.3	2.80	2.67	-4.6	2.72	3.26	19.9
0.3	1.45	1.56	7.6	2.85	2.76	-3.2	2.77	3.35	20.9
0.4	1.49	1.62	8.7	2.91	2.87	-1.4	2.83	3.45	21.9
0.5	1.53	1.69	10.5	2.97	3.00	1.0	2.90	3.56	22.8
0.6	1.57	1.76	12.1	3.03	3.17	4.6	2.97	3.68	23.9
0.7	1.62	1.86	14.8	3.11	3.38	8.7	3.07	3.82	24.4
0.8	1.68	1.97	17.3	3.20	3.63	13.4	3.17	3.98	25.6
0.9	1.74	2.10	20.7	3.30	3.96	20.0	3.29	4.15	26.1
1	1.82	2.26	24.2	3.41	4.38	28.4	3.43	4.33	26.2

The total profits in each mode are demonstrated in Fig. 6. It can be seen that the total profit is the lowest in Mode 1, increases in Mode 2, and reaches its highest in Mode 3, with Mode 3 achieving approximately 141% and 170% greater returns compared to Mode 2 and Mode 1, respectively. This suggests that the full cooperation model can maximize the overall return of the ESC and enhance the synergistic efficiency.



(a) Total profit of Mode 1

(b) Total profit of Mode 2

(c) Total profit of Mode 3

(d) Comparison of profits of different Modes

Fig. 6. Total profits of different modes.

4.3 Effectiveness Analysis of Shapley Value

The effectiveness of the Shapley value method is critical for translating the theoretical gains of full cooperation into a stable and practical alliance. A deeper analysis of the profit allocation under Mode 3, taking the case of μ=0.5, confirms its ability to distribute benefits fairly and incentivize participation. The results of this allocation are shown in Fig. 7.

The Shapley value method allocates the cooperative surplus in a manner that reflects each participant's actual contribution to the total profit. The distribution is not equal; rather, it is weighted by the marginal value each entity adds. In this case, the TPP receives the largest absolute profit, which reflects its central role in power generation within the supply chain model. The REC, as the crucial intermediary that optimizes transaction volumes for the entire system in Mode 3, also receives a significant share.

Crucially, while the REP receives the smallest absolute profit, it experiences the largest relative gain. This highlights that the Shapley value properly rewards the REP for its cooperation, which is essential for maximizing system efficiency, even if its individual generation capacity is smaller than the TPP's. By systematically quantify-

ing each member's contribution and distributing profits accordingly, the Shapley value method proves to be an effective tool for achieving a fair, stable, and highly profitable cooperative electricity supply chain.

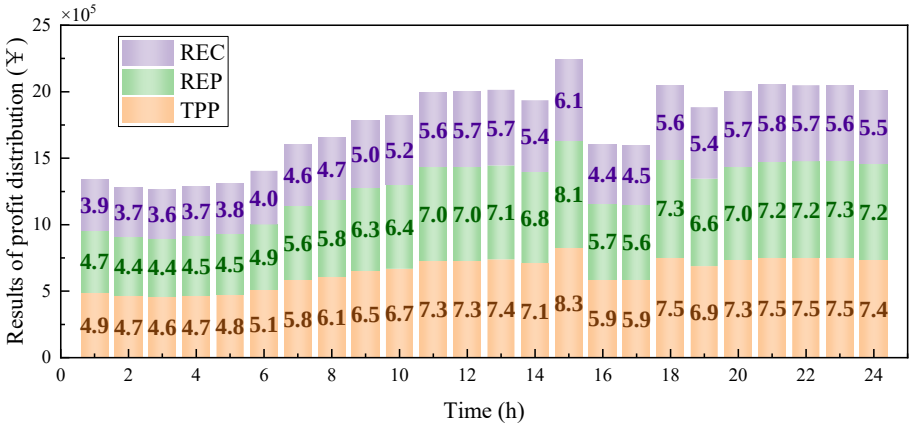


Fig. 7. Distribution result based on the Shapley value in Mode 3 when μ = 0.5.

5 Conclusions

Based on the cooperative game theory, this paper constructs an ESC model composed of the TPP, REP, REC, and consumers, exploring the impact of different cooperation modes on the profits of all parties in the ESC.

Cooperation modes significantly influence supply chain profitability. Full cooperation maximizes overall profit, while non-cooperation results in low profits and poor synergy. Semi-cooperation increases total profit marginally but fails to significantly benefit individual parties. In contrast, full cooperation substantially enhances profits for all parties, with total ESC profit increasing by 170% and 141% compared to non-cooperation and semi-cooperation, respectively. These findings demonstrate that deeper cooperation improves supply chain efficiency, sustainability, and cost reduction, ultimately benefiting end consumers through optimized resource allocation. The Shapley value method achieves fair and adaptive profit distribution, which promotes the efficient and sustainable development of the power system.

As power system reforms progress, improving collaborative efficiency and equitable profit distribution in the ESC has gained significant importance. This study proposes co-optimization and profit distribution strategies based on cooperative game, offering both a theoretical framework for collaboration and an innovative approach to profit distribution in the electricity market. By encouraging deeper supply chain cooperation, the research provides new insights and methods for optimizing electricity supply strategies amid ongoing reforms, supporting the efficient and sustainable development. Looking ahead, as new energy technologies emerge and additional PPs and RECs enter the electricity market, the competitive landscape will grow increas-

ingly complex. The proposed framework can better facilitate electricity market development and foster positive interactions among enterprises.

Acknowledgement： This work is supported by the Science and Technology Research Project of the Inner Mongolia Power (Group) Co., Ltd. (No. 2023-5-36).

References

1. Li, L.L., Zhang, Z.Y., Sethanan, K., Tseng, M.L.: Multi-energy synergistic planning of distributed energy supply system: Wind-solar-hydrogen coupling energy supply [J]. Renewable Energy 237, (2024).
2. Bahmani, P., Sadrabadi, M.H.D., Makui, A., Jafari-Nodoushan, A.: An optimization-based design methodology to manage the sustainable biomass-to-biodiesel supply chain under disruptions: A case study [J]. Renewable Energy 229, (2024).
3. Shen, J.J., Cheng, C.T., Jia, Z.B., Zhang, Y., Lv, Q., Cai, H.X., Wang, B.C., Xie, M.F.: Impacts, challenges and suggestions of the electricity market for hydro-dominated power systems in China [J]. Renewable Energy 187, 743-759 (2022).
4. Panahi, H., Sabouhi, F., Bozorgi-Amiri, A., Ghaderi, S.F.: A data-driven optimization model for renewable electricity supply chain design [J]. Renewable Sustainable Energy Rev. 202, (2024).
5. Giri, B.K., Roy, S.K.: Fuzzy-random robust flexible programming on sustainable closed-loop renewable energy supply chain [J]. Appl. Energy 363, (2024).
6. Haiyun, C., Zhixiong, H., Yüksel, S., Dinçer, H.: Analysis of the innovation strategies for green supply chain management in the energy industry using the QFD-based hybrid interval valued intuitionistic fuzzy decision approach [J]. Renewable Sustainable Energy Rev. 143, (2021).
7. Bai, Y., Fan, K., Zhang, K., Cheng, X., Li, H., Yang, Y.: Blockchain-based trust management for agricultural green supply: A game theoretic approach [J]. J. Cleaner Prod. 310, (2021).
8. Wang, Q., Jiang, F., Li, R.: Assessing supply chain greenness from the perspective of embodied renewable energy – A data envelopment analysis using multi-regional input-output analysis [J]. Renewable Energy 189, 1292-1305 (2022).
9. Sánchez, A., Martín, M., Zhang, Q.: Optimal design of sustainable power-to-fuels supply chains for seasonal energy storage [J]. Energy 234, (2021).
10. Wang, S., Li, B., Zhao, X., Hu, Q., Liu, D.: Assessing fossil energy supply security in China using ecological network analysis from a supply chain perspective [J]. Energy 288, (2024).
11. Bangjun, W., Yue, W., Linyu, C., Kejia, X.: Supply chain coordination mechanisms of coal power enterprises under renewable energy quota system: A perspective of game analysis [J]. J. Cleaner Prod. 426, (2023).
12. Amiri-Pebdani, S., Alinaghian, M., Khosroshahi, H.: Pricing in competitive energy supply chains considering government interventions to support CCS under cap-and-trade regulations: A game-theoretic approach [J]. Energy Policy 179, (2023).
13. Liu, Z., Qian, Q., Hu, B., Shang, W.-L., Li, L., Zhao, Y., Zhao, Z., Han, C.: Government regulation to promote coordinated emission reduction among enterprises in the green supply chain based on evolutionary game analysis [J]. Resour. Conserv. Recycl. 182, (2022).

14. Yan, M., Shahidehpour, M., Alabdulwahab, A., Abusorrah, A., Gurung, N., Zheng, H., Ogunnubi, O., Vukojevic, A., Paaso, E.A.: Blockchain for Transacting Energy and Carbon Allowance in Networked Microgrids [J]. IEEE Trans. Smart Grid 12, 4702-4714 (2021).
15. Chen, W., Wang, J., Yu, G., Chen, J., Hu, Y.: Research on day-ahead transactions between multi-microgrid based on cooperative game model [J]. Appl. Energy 316, (2022).
16. Mansouri, S.A., Paredes, Á., González, J.M., Aguado, J.A.: A three-layer game theoretic-based strategy for optimal scheduling of microgrids by leveraging a dynamic demand response program designer to unlock the potential of smart buildings and electric vehicle fleets [J]. Appl. Energy 347, (2023).
17. Chen, C., Li, Y., Qiu, W., Liu, C., Zhang, Q., Li, Z., Lin, Z., Yang, L.: Cooperative-Game-Based Day-Ahead Scheduling of Local Integrated Energy Systems With Shared Energy Storage [J]. IEEE Trans. Sustainable Energy 13, 1994-2011 (2022).
18. Zhao, B., Duan, P., Fen, M., Xue, Q., Hua, J., Yang, Z.: Optimal operation of distribution networks and multiple community energy prosumers based on mixed game theory [J]. Energy 278, (2023).
19. Malik, S., Duffy, M., Thakur, S., Hayes, B., Breslin, J.: A priority-based approach for peer-to-peer energy trading using cooperative game theory in local energy community [J]. Int. J. Electr. Power Energy Syst. 137, (2022).
20. Asghari, T., Taleizadeh, A.A., Jolai, F., Moshtagh, M.S.: Cooperative game for coordination of a green closed-loop supply chain [J]. J. Cleaner Prod. 363, (2022).

026 A Reactive Power Optimization Method for Substations Based on PSO-Genetic Fusion Algorithm

Fengqiang Deng[1], Jiazheng Ding[1], Xiaoyang Xu[1],

Zhidong Wang[1] and Bingzhen Meng[1]

[1] South China University of Technology, Guangzhou Guangdong 510000, China
epfqdeng@scut.edu.cn

Abstract. The optimization of reactive power flow distribution in the power grid, the reduction of active power loss and voltage loss, and the improvement of voltage quality are all closely linked to the optimization of reactive power in substations. However, achieving optimal reactive power performance in substations has consistently been a challenging area of re-search. To address this, we propose a substation reactive power optimization method based on a Particle Swarm Optimization-Genetic Fusion Algorithm. This method inte-grates Particle Swarm Optimization (PSO) and Genetic Algorithm (GA), constructing a multi-objective function that targets power loss and voltage quality. It also introduces con-straints on the number of device operations and adjusts the inertia weight during the iter-ation process. By combining PSO with GA and incorporating selection, crossover, and other GA operations into PSO,we enhance the optimization process. Additionally, a new calculation method for the inertia weight in PSO is proposed. The method was applied to the substation network topology for verification, and the results demonstrated that the fu-sion algorithm achieved better reactive power optimization effect than traditional algo-rithms.

Keywords: Reactive power control, Substations, Particle Swarm Optimization, Genetic Algorithm, multi-objective Optimization.

1 Introduction

According to reference [1], voltage quality is a crucial measure of power quality in power sys-tems. Among various power quality issues, excessive voltage fluctuations not only directly impact the performance of electrical equipment and increase network losses but also complicate the stable and safe operation of the system.

By optimizing the reactive power in substations, the reactive power flow distribution in the power grid can be improved, reducing both active power loss and voltage loss to ideal levels. This, in turn, enhances voltage quality, ensures the safe and reliable operation of electrical equipment, and boosts efficiency.

References [2, 3, 4] discuss control strategies for reactive power optimization in sub-stations, including nine-zone voltage and reactive power control strategies, voltage

and reactive power control strategies based on load prediction, and strategies based on expert systems.

Currently, mainstream methods for calculating voltage and reactive power control strategies in substations based on load forecasting include the Genetic Algorithm (GA), Simulated Annealing Algorithm (SA), Taboo Search Algorithm (TS), and Particle Swarm Optimization (PSO). References [5, 6] introduced the Genetic Algorithm, highlighting its advantages, such as no initial value requirements, strong generality, and robust global search ability. However, its local search ability is weak, accuracy is poor, and convergence is slow. Reference [5] also introduced the Taboo Search Algorithm, which excels in local search ability and optimization speed but has weak global search ability and cannot search the entire optimization space simultaneously. The initial value quality directly af-fects the algorithm's convergence speed and quality. References [6, 7] introduced the Sim-ulated Annealing Algorithm, which is simple, easy to understand, and suitable for solv-ing multiple synchronous optimal problems. Its drawbacks include sensitivity to initial parameter settings and a slow, time-consuming calculation process. Reference [8] pro-posed an improved Particle Swarm Optimization algorithm based on the ε-Greedy strat-egy and Pareto archive algorithm. It dynamically adjusts the ratio of global and local searches based on iteration count, enhancing global search ability and balancing multiple objective functions. This algorithm performs better in multiple objective values and can restore node voltage to normal ranges but is highly dependent on initial values and prone to local optima. Reference [9] introduced an improved Genetic Algorithm, combining i-NSGA-II (elitist non-dominated sorting genetic algorithm with inheritance) and the wheel selection algorithm to improve convergence speed while maintaining accuracy. It performs well in comprehensive objective optimization, considering multiple control var-iables, but tends to fall into local optima in complex multi-objective problems. Reference [10] proposed an improved Particle Swarm Optimization algorithm that introduces chaos theory to update inertia weight in each iteration and uses dynamic learning factors to form the overall objective function with constraints. This algorithm shows an 11% im-provement over the standard Particle Swarm Optimization algorithm, though further im-provements are needed.

These methods are convenient, fast, and accurate for solving voltage and reactive power control problems, but each has its shortcomings when used independently.

In reactive power optimization, substation equipment must consider dynamic load changes and the daily allowable operation limits of control variables, resulting in dynam-ic reactive power optimization scheduling. This process involves multiple objectives, var-ious constraints, non-linear objective functions, and constraints, making it difficult to solve with conventional methods.

To address these issues, this paper proposes a substation reactive power optimiza-tion method based on the Particle Swarm Optimization-Genetic Fusion Algorithm. This method combines Particle Swarm Optimization with the Genetic Algorithm, integrating selection, crossover, and other operations from the Genetic Algorithm into Particle Swarm Optimization. Additionally, a new calculation method for inertia weight in Particle Swarm Optimization is utilized. Experimental verification shows that this method achieves fast convergence while maintaining population diversity, leading to better reac-tive power optimization results.

2 Mathematical Model For Reactive Power Optimization In Substations

2.1 Objection function

From an economic perspective, this paper adopts the objective function of minimizing active power loss while considering the voltage offset of the substation, while ensuring that various voltages and reactive power outputs are not exceeded on stage any restrictions on the availability of materials or information. New methods and protocols should be described in detail while well-established methods can be briefly described and appropriately cited.

$$F = min(\omega_1 f_1 + \omega_2 f_2 + \omega_3 f_3) \tag{1}$$

Where, $f_1, f_2\ and\ f_3$ is optimization results of sub objective functions, $\omega_1, \omega_2\ and\ \omega_3$ are the weights of the optimization functions for active power loss and voltage quality respectively; moreover, $\omega_1 + \omega_2 + \omega_3 = 1$， $\omega_1 > \omega_2$.

$$f_1 = \sum_{r=1}^{N_r} G_{a,b} \cdot [U_a^2 + U_b^2 - 2U_a U_b \cos(\theta_a - \theta_b)] \tag{2}$$

Where, *Nr* is the total number of branches in the topology structure of the substation network that need to be optimized, $G_{a,b}$ is the conductivity of branch r between nodes a and b， *Ua*, *Ub* are the voltages of nodes a and b respectively, θ_a, θ_b are the phase angles of nodes a and b respectively.

$$f_2 = \sum_{g=1}^{N_1} (U_g - U_{g,set}) \tag{3}$$

Where, U_g and $U_{g,set}$ are respectively represented the voltage on the low-voltage side of the transformer bus-bar and its expected value, N_1 is the total number of transformers. Reference [11] proposed that the target can be normalized by subtracting the minimum value from the current value and dividing it by the range.

$$\mathrm{f_3} = \sum_{\mathrm{t=1}}^{\mathrm{T}} (\mathrm{KQ_t} + \mathrm{KC_t}) \tag{4}$$

Where, KC_{t-1} and KQ_{t-1} are indicates the number of times the capacitor and reactor bank is switched and the number of times the transformer is shifted at t hour, T is total time.

The corresponding constraints for the above goals include the power flow equation constraints, as well as inequality constraints such as reactive power compensation capacity, generator reactive power output, transformer tap, and voltage amplitude constraints.

2.2 Constraint condition

Equality constraint. Consider the constraint of the power flow balance equation for the substation system as:

$$P_{Gi} - P_{Bi} = U_i \sum_{j \in i} (G_{ij} \cos\theta_{ij} + B_{ij} \sin\theta_{ij}) \tag{5}$$

$$Q_{Gi} - Q_{Bi} + Q_{Ci} = U_i \sum_{j \in i} U_j \left(G_{ij} \sin \theta_{ij} + B_{ij} \cos \theta_{ij} \right) \quad (6)$$

Where, P_{Gi}, Q_{Gi} are inject active and reactive power into the generator node, P_{Bi}, Q_{Bi} are the active and reactive power of the load node, Q_{Ci} is compensated reactive power, U_i, U_i are the voltage amplitudes of nodes *i* and *j* respectively, G_{ij}, B_{ij} are the conductivity and admittance between nodes *i* and *j*, δ_{ij} is the voltage phase difference between node *i* and *j*, $j \in i$ represents all nodes connected to node *i*.

Inequality constraint. Inequality constraints can be divided into two categories: control variable constraints and state variable constraints.

Control variable constraints:

$$U_{i,min} \le U_i \le U_{i,max} \quad (7)$$

$$Q_{g,j,min} \le Q_{g,j} \le Q_{g,j,max} \quad (8)$$

$$Q_{c,j,min} \le Q_{c,j} \le Q_{c,j,max} \quad (9)$$

$$T_{qmin} \le T_q \le T_{qmax} \quad (10)$$

$$Q_{kmin} \le Q_{kt} \le Q_{kmax} \quad (11)$$

Where, i=1,2,⋯,N_B, q=1,2,⋯,Ng, k=1,2,⋯,Nc, j=1,2,⋯,N_G, N_G is the number of reactive power sources, N_C is the number of parallel capacitors and reactors, $Q_{g,\,j,min}$, $Q_{g,\,j,max}$ are the upper and lower limits of reactive power output for reactive power source j, respectively, $Q_{c,\,j,min}$, $Q_{c,\,j,max}$ are the upper and lower limits of reactive power compensation values for capacitor reactance j respectively, $U_{i,min}$, $U_{i,max}$ are the upper and lower limits of voltage for node i, N_B is the number of nodes, T_{qmin}, T_{qmax} are the minimum and maximum values of the transformer gear respectively, $Q_{kmin,}$ Q_{kmax} are the minimum and maximum values of reactive power compensation capacity for parallel capacitors respectively, T_q is the current tap position of the transformer q, and Q_k is the reactive power compensation capacity of the parallel capacitor or reactor k.

State variable constraints:

$$\sum_{t=1}^{T} |\mathrm{KC_t} - \mathrm{KC_{t\text{-}1}}| \le \mathrm{M_c} \quad (12)$$

$$\sum_{t=1}^{T} |\mathrm{KQ_t} - \mathrm{KQ_{t\text{-}1}}| \le \mathrm{M_q} \quad (13)$$

Where, Mc is the maximum allowable number of switching times for capacitor banks within a day, M_q is the maximum allowable number of gear shifts for the transformer group within a day.

3 Particle Swarm Optimization-Genetic Fusion Algorithm

Particle Swarm Optimization is a heuristic search algorithm based on swarm intelligence. The basic idea is to simulate the foraging behavior of bird flocks, treating each particle created in the algorithm as an individual, i.e., the initial solution. Through communication and iteration between the entire particle population, the entire population can find an optimal solution. The iteration and evolution operations of Particle Swarm Optimization algorithm can be described as:

$$\begin{cases} v_i = w \cdot v_i + c_1 \cdot rand \cdot (pb - x_i) + c_2 \cdot rand \cdot (gb - x_i) \\ x_i = x_i + v_i \end{cases} \tag{14}$$

Where, v_i, x_i is the velocity and position of the particle i, c_1, c_2 are the learning factors, pb is the optimal particle in the current population, gb is the global optimal particle in the population, *rand* represents a uniform random number distributed between (0,1).

The Genetic Algorithm is a heuristic search algorithm. According to [5], it leverages Darwin's theory of natural selection and the mechanism of genetic variation, using computer-generated initial populations as initial solutions to simulate natural selection, inheritance, crossover, and mutation in the process of biological evolution to search for the optimal solution.

The Particle Swarm Optimization-Genetic Fusion Algorithm can avoid the issue of get-ting stuck in local extreme within a multi-modal search space, thus offering superior global search capabilities.

3.1 Particle grouping operation

According to reference [12], to prevent highly fit particles generated early in the evolution process from adversely affecting the global optimization performance of the algorithm and resulting in local or sub-optimal solutions, this method divides the particle swarm into two subgroups based on particle fitness: the base population and the pioneering population.

Particles are sorted in ascending order based on their fitness. In this paper, the top 20%of particles are defined as the pioneering population, while the remaining 80% constitute the base population. The base population is the standard population under default parameters, and particles with higher fitness are selected to be substituted into the updated population.

The pioneering population is more active compared to the base population and can seek optimal solutions in a wider space.

However, due to the high fitness of particles in the pioneering population, it is necessary to reduce their selection probability, give them a higher speed, and then substitute them for updates. This approach addresses the issue of incorrect orientation of highly fit particles in the initial stage of the algorithm and the tendency for particles to cluster in the middle and later stages.

3.2 Calculate inertia weight

The calculation method of inertia weight used in this paper is as follows. The calculation formula is:

$$w = \delta_e \left(\frac{\delta_s}{\delta_e}\right)^{\frac{1}{1+20\times iter/maxiter}} \tag{15}$$

Where, δe, δs is the first and second constants given in advance for calculating the inertia weight *w*, *iter* is the iterations of the current iteration, *maxiter* is the given number maximum number of iterations.

Reference [13,14] indicate that inertia weight reflects the ability of particles to retain their previous velocities during updates. A larger inertia weight favors global search, while a smaller inertia weight favors local search. As the number of iterations increases, the solution to the velocity update formula changes, and fixed inertia weights can be inconvenient.

In this paper, the inertia weight *w* is set to dynamically balance global and local search in combination with Particle Swarm Optimization. This adaptive approach to inertia weight allows the particles to achieve better optimization results.

3.3 Selection, crossover, and variation

This paper adopts the "last elimination" selection method for selection operations. In this method, each particle is binary-coded, and the top A of particles with the highest fitness are selected as elite particles. For the next level B%, the tournament selection method is used to select the winning particles for the next generation population, while the remaining C% of particles are randomly updated, with A+B+C=100%. This selection method helps maintain population diversity.

The proposed method involves crossover operations between the base population and the pioneering population, as well as within the pioneering population. Crossover is performed using the random number method described in reference [13]. The process involves selecting a random number a between (0,1). During crossover, the first two particles are multiplied by a and (1-a) respectively, summed, and assigned to the first particle. Then, the first two particles are multiplied by (1-a) and a respectively, summed, and assigned to the second particle.

Additionally, the method introduces random perturbations while updating the position of each particle to mimic the mutation operation in Genetic Algorithms.

The selection, crossover, and mutation operations are characteristic of Genetic Algorithms. The new population generated through these operations can significantly improve the convergence speed of the algorithm, compensating for the slow convergence speed of Particle Swarm Optimization. Conversely, combining with Particle Swarm Optimization prevents Genetic Algorithms from falling into local optima during the iteration process, avoiding the "dead cycle" phenomenon.

3.4 Punish out of bounds particles

The formula for calculating the penalty intensity of the method used in this paper for punishing out of bounds particles is:

$$Y = \sum_{n}^{N} L_n \cdot \lambda_n \tag{16}$$

By setting the penalty intensity Y, the constrained problem is transformed into an unconstrained optimization problem. The solution to the original constrained problem is obtained by solving a series of these unconstrained optimization problems. During the iteration process, the constraints act like boundary fences. If the current solution is far from the constraints, meaning it has not crossed the boundary, the penalty intensity is very small; otherwise, the penalty intensity approaches infinity. The penalty intensity *Y* penalizes in-feasible points, forcing iteration points to approach the feasible domain.

3.5 Reactive power optimization method for substations based on particle swarm optimization- genetic fusion algorithm

The process flow of a substation reactive power optimization method based on Particle Swarm Optimization-Genetic Fusion Algorithm proposed in this article is shown in Fig. 1.

The specific plan is as follows:

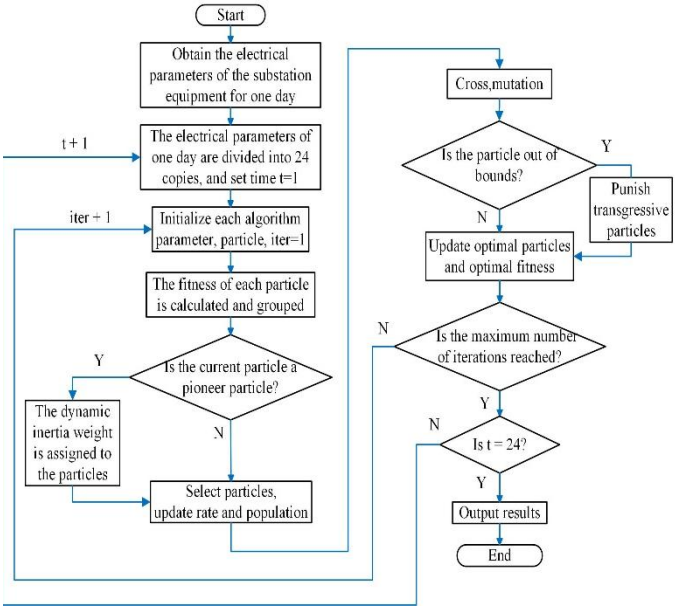


Fig. 1. Algorithmic flow

Step 1. Obtain the electrical parameters of the sub-station equipment and the load data for the next 24 hours.

Step 2. Initialize the population.

Step 3. Calculate the initial fitness of particles and cluster them.

Step 4. Update inertia weights.

Step 5. Update particle velocity and population.

Step 6. Select, cross, and mutate particles.

Step7. Determine if the particle is out of bounds. If it crosses the boundary, punishment will be imposed on the particles that have crossed the boundary; If the boundary is not exceeded, proceed to the next step.

Step 8. Update the optimal particles and fitness within the population.

Step9. Determine whether the termination criteria are met. If they are met, terminate the program and out-put the optimization results; If not met, go back to Step 2.

4 Example analysis

The topology structure of the substation network in this example is shown in 0.

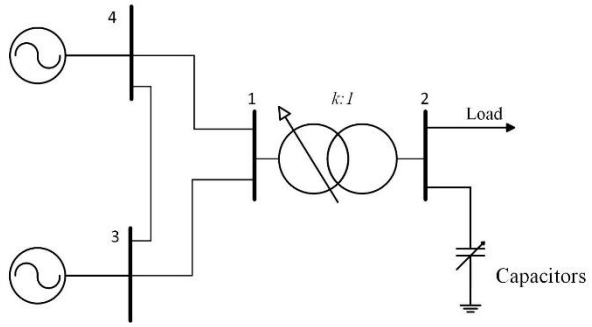


Fig. 2. The topology of the substation network

For this example, the weights of the two optimization functions in the objective function are set as $\omega_1 = 0.40$, $\omega_2 = 0.10$ and $\omega_3 = 0.5$ with a population size of 50.

The electrical parameters (partial) of the substation equipment are as follows: the rated voltage of the transformer is 110kV/38.5kV, the short-circuit voltage percentage is *Uk*%=10.5, the rated capacity is 63MVA, and the tap position of the transformer is 110 ± 4×2.5% /38.5kV. The maximum daily action times for the transformer (*Mq*) and the capacitor bank (*Mc*) are both 24. The per-unit value of the initial transformer ratio is 1.1282, the initial input number of capacitor banks is 0, each capacitor bank has a capacity of 5Mvar, and the maximum input number of capacitor banks is 5.

The load data of the substation equipment in this example for the next 24 hours is shown in 0.

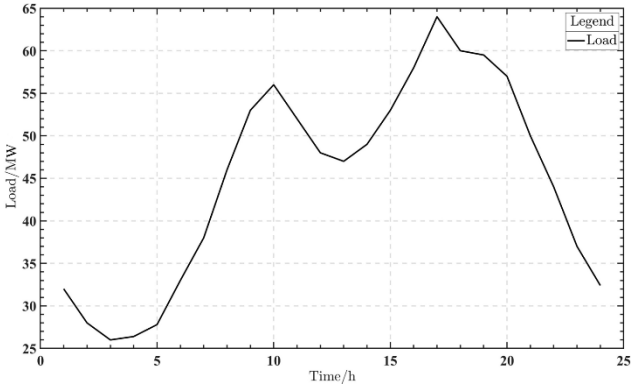


Fig. 3. The load data of the substation equipment for the next 24 hours

In this example, the reference voltage on the high voltage side of the transformer is set to 110kV, and on the low voltage side, it is set to 35kV. The voltage of two power sources, transformer ratio, and number of capacitor banks in Fig 2 are controlled.

The inertia weight of the basic group is set to 0.783, with the first and second constants used to calculate the inertia weight w set to 0.2 and 0.9, respectively. The penalty factor Ln for out-of-bounds particles considers that exceeding the number of switching times per day causes less harm than voltage and reactive power output exceeding the limit. Therefore, when the number of transformer adjustments and capacitor group switching times exceed the limit, the corresponding penalty factor Ln is set to 30, while for voltage and reactive power output exceeding the limit, it is set to 50.

The top 10% of particles are selected as elite particles, the next 60% as participants in the tournament selection method, and the remaining 30% for random updates.

Table 1. Optimization results table for different algorithms

Algorithm type	Transformer adjustment times	Number of switching times for capacitor banks	total times of actions
Fusion algorithm	8	16	24
PSO	2	25	27
GA	22	5	27

Table 2. The optimized value of the objective function

Algorithm type	Network loss/Mw	Voltage offset /p.u.	24-hour average offset /p.u.
Fusion algorithm	46.8486	0.0502	0.0021
PSO	44.7029	0.0779	0.0032
GA	54.6780	0.2054	0.0086

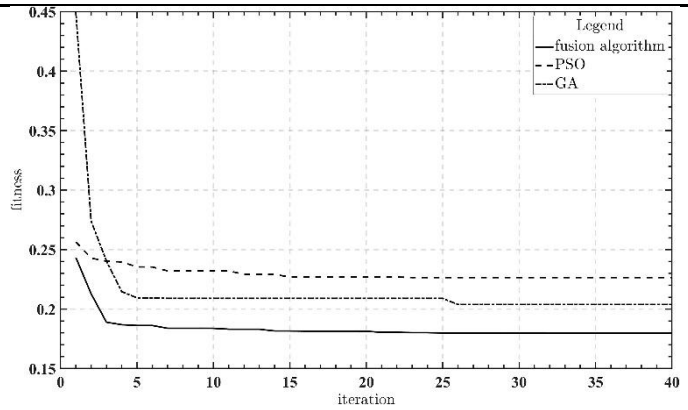


Fig. 4. Fitness curve

Table I shows the number of transformer ratio adjustments and capacitor bank switching times at 40 iterations. Table II presents the optimization results of the objective functions for three algorithms. Fig.4 presents the optimization results for different iterations.

The results in the table and figure show that with 40 iterations, the total number of transformer adjustment times and capacitor bank switch adjustments is 24 under the fusion algorithm, 27 under PSO, and 27 under GA. The fusion algorithm demonstrates superiority over PSO and GA in optimizing transformer adjustment times and capacitor bank switching times. Additionally, the fusion algorithm has a more uniform distribution of regulation times, while the PSO favors with more adjustments of the transformer, and the GA prefers to adjust the capacitor bank. In terms of the objective function optimization, the fusion algorithm is slightly inferior to the PSO in terms of

active power loss reduction, but it shows clear advantages over PSO and GA, particularly in reducing voltage offset, indicating better convergence accuracy.

In Fig. 4, the fusion algorithm converged at about 20 iterations, exceeding the convergence rate of about 26 iterations for GA and inferior to the convergence rate of about 16 iterations for PSO. However, the value of the fitness function under the optimization of the fusion algorithm is smaller, implying that the convergence accuracy of the fusion algorithm is higher than that of the above two algorithms, and these results indicate that the fusion algorithm has a better optimization effect than PSO and GA, which confirms the advantage of the previous advantages of the fusion algorithm to optimize with less number of operations.

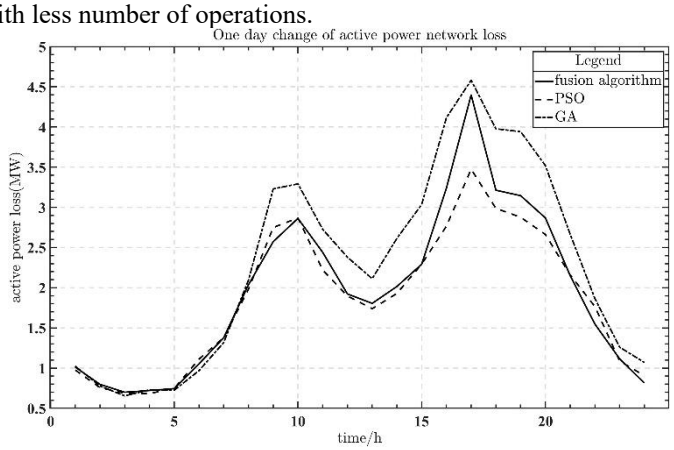


Fig. 5. Power loss

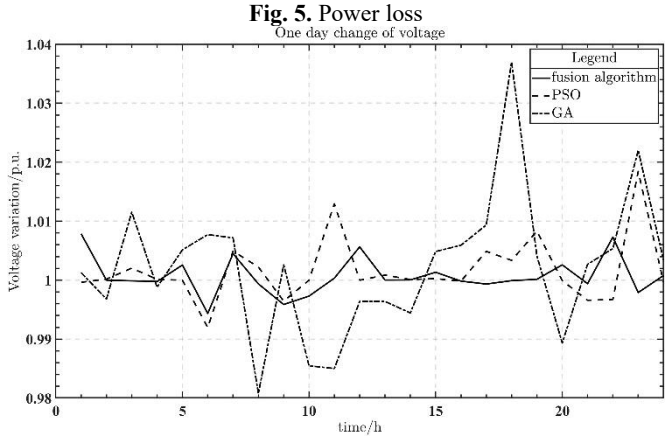


Fig. 6. Voltage variation

Further, Fig. 5 and Fig. 6 show the hourly active power loss and voltage offset data in one day after optimization by three different algorithms. It could be seen that the reduction of active power loss at each moment of time by the fusion algorithm and PSO is significantly better than the GA when the time is subdivided into each hour, while the difference be-tween the fusion algorithm and PSO is not very large; and in terms of the voltage offset, the voltage offset under the optimization of the fusion algorithm is at a smaller value at each hour, and is more uniform overall, which is more effective than the other two algorithms.

Therefore, combining the above figures and tables, we can consider the transformer adjustment and capacitor bank switching strategies given by the fusion algorithm are reasonable and satisfactory.

5 Conclusion

To reduce the number of adjustments for adjustable transformers and reactive power compensation capacitor banks in substations, as well as active power grid losses, this paper proposes a substation reactive power optimization method based on the Particle Swarm Optimization-Genetic Fusion Algorithm. The method uses voltage offset as the objective function to reduce active power losses, improve voltage quality, and decrease the total number of adjustments for transformers and parallel capacitor banks. It integrates GA's selection and crossover operations into PSO and improves PSO by adding particle clustering operations. This approach effectively combines the convergence speed and accuracy of PSO and GA, yielding superior optimization results. This method is a scientifically sound and feasible multi-objective reactive power optimization approach for power systems, widely applicable to substation equipment, with significantly engineering practical value and broad application prospects.

Future improvements to this method could focus on enhancing the robustness and adapt-ability of the optimization algorithm under varying grid conditions and loads. Implementing real-time data analytic and machine learning techniques could further refine the optimization process, allowing for more precise and dynamic adjustments. Additionally, expanding the algorithm to include a broader range of power quality indices and incorporating renewable energy sources into the optimization framework would increase its relevance and applicability in modern power systems. These advancements would not only improve operational efficiency but also contribute to the sustainable development of power grids.

Acknowledgement： This work is supported by Higher Education Teaching Reform Project of Guangdong Province (C9233013), Collaborative Education Project for Industry-University Cooperation (E9250090 & E9250110), Teaching and Research Reform Project of South China University of Technology(C9254600).

References

1. Li Bangfeng, Zhang Yongjun, Ren Zhen.: A review of reactive power optimization scheduling in power system. Power System Technology, (02):50–56, 2005.
2. Hu Jingwei et al Chen Zhihua, Ke Qiang.: Research on reactive voltage control strategy of active distribution network with distributed photovoltaic. Power Capacitor and Reactive Power Compensation, 43(02):16–24, 2022.
3. Jin Lu.: Research on voltage reactive power control of substation based on fuzzy control. Master's thesis, Harbin Institute of Technology, 2015.
4. Yifei Guo, Houlei Gao, Qiuwei Wu, Jacob Østergaard, Dachuan Yu, and Mohammad Shahidehpour.: Distributed coordinated active and reactive power control of wind farms

based on model predictive control. International Journal of Electrical Power and Energy Systems, 104:78–88, 2019.

5. Li Zhaohan Li Xiaotong.: Reactive power optimization of distribution network based on genetic taboo mixing algorithm. Electrical Engineering and Electrical, (04):13–18, 2019.
6. Wang Haiqian et al Huang Junhui, Wang Weiyuan.: Research on reactive power optimization and voltage control of ac/dc system based on simulated annealing genetic algorithm. Protection and Control of Electric Power System, 44(10):37–43, 2016.
7. Yao Chao et al. Wang Jiehong, Li Kunhua. Research on reactive power optimization of distribution network based on improved genetic algorithm.: Electronic Devices, 43(04):767–770, 2020.
8. Xiaofei Liu, Pei Zhang, Hui Fang, and Yinglu Zhou.: Multi-objective reactive power optimization based on improved particle swarm optimization with ε-greedy strategy and pareto archive algorithm. IEEE Access, 9:65650–65659, 2021.
9. Yichen Liu, Dragan Ćetenović, Haiyu Li, Elena Gryazina, and Vladimir Terzija.: An optimized multi-objective reactive power dispatch strategy based on improved genetic algorithm for wind power integrated systems. International Journal of Electrical Power and Energy Systems, 136:107764, 2022.
10. Wang B ,Zhang C ,Chen X , et al.: Price-based Demand Response Supported Three-stage Hierarchically Coordinated Voltage Control for Microgrids[J].Journal of Modern Power Systems and Clean Energy,2025,13(01):338-350.
11. Wang Y ,Zhou X ,Tang J , et al.: Adaptive Harmonic Virtual Impedance Control for Improving Voltage Quality of Microgrids[J].Journal of Modern Power Systems and Clean Energy,2024,12(05):1548-1558.
12. Haghighat M ,Niroomand M ,Tafti D H , et al.: A Review of State-of-the-art Flexible Power Point Tracking Algorithms in Photovoltaic Systems for Grid Support:Classification and Application[J].Journal of Modern Power Systems and Clean Energy,2024,12(01):1-21.
13. Wang Y ,Qi D ,Zhang J , et al.: Novel Optimal Load Control for Power System Frequency and Voltage Regulation[J].Journal of Modern Power Systems and Clean Energy,2023,11(06):1746-1755.
14. Ji Jin et al Li Ang, Dong Xiaoyang.: Research on reactive power optimization of power system based on improved particle swarm algorithm. Electrotechnical Studies, (03):11–13+17, 2022.
15. Liu, Z., Guo, G., Gong, D., Xuan, L., He, F., Wan, X., Zhou, D.: Cluster Partitioning Method for High-PV-Penetration Distribution Network Based on mGA-PSO Algorithm. Energies 2025, 18, 1197.
16. Chen, T., Dai, Z., Shan, X., Li, Z., Hu, C., Xue, Y., Xu, K.: Reactive Power Optimization Method of Power Network Based on Deep Reinforcement Learning Considering Topology Characteristics. Energies 2024, 17, 6454.
17. Tao, Z., Wang, T., Cai, D., Chen, R.: Research on Reactive Power Optimization of Synchronous Condensers in HVDC Transmission Based on Reactive Power Conversion Factor. Energies 2024, 17, 4294.
18. Li, Z., Xiong, J.: Reactive Power Optimization in Distribution Networks of New Power Systems Based on Multi-Objective Particle Swarm Optimization. Energies 2024, 17, 2316.

027 Risk Assessment of Power System Restoration Considering the Uncertain State of Lines to Be Restored

Chenyang Song, Hao Zhang, Runjia Sun

Shandong University,
Jinan, China
202534793@mail.sdu.edu.cn
202534810@mail.sdu.edu.cn
sunrunjia@sdu.edu.cn

Abstract. For the power system restoration with potential faulty lines, the closing of faulty lines brings the risk of a prolonged restoration process. This paper develops a fast risk assessment method for power system restoration considering the uncertain fault state of lines to be restored. Firstly, the development process of accidents after restoring faulty lines is analyzed, which mainly considers the trip-off of wind farms due to low voltage and load restoration delay. Then, to rapidly judge the trip-off of restored wind farms, a linearized bus voltage calculation method is proposed based on the restoration topology adjoint network. Finally, a system restoration risk assessment index considering load loss caused by line fault is proposed. A power system restoration model considering the influence of wind farm trip-off and line outage is constructed to calculate the load loss. The New England 39-bus system is adopted to demonstrate the effectiveness of the proposed power system restoration risk assessment method.

Keywords: Power System Restoration Risks, Wind Power, Fault, Uncertainty, Risk Assessment

1 Introduction

Frequent extreme natural disasters cause highly random damage to transmission lines exposed to external environment. The damage of lines may cause cascading failure and even large-scale blackouts, leading to large economic loss. Struck by Hurricane Fiona, severe damage to transmission lines and infrastructure occurred in Puerto Rico on September 18, 2022, which triggered generator tripping and system instability and caused 100% outage rate[1]. The stochastic damage of natural disasters engenders uncertainty in the fault states of transmission lines. To restore the power system after blackouts, transmission lines need to be energized one by one. Energizing a faulty line may lead to wind turbines trip-off. Hence, uncertainty in line fault conditions during power system restoration exacerbates the risk of load shedding and secondary system collapse. In view of the uncertainty of the state of lines to be restored after the disaster,

rapid risk assessment of system restoration is valuable to guide the restoration decision-making of dispatchers.

In order to improve the restoration speed of the new power system, existing studies adopt various methods—such as mathematical optimization and reinforcement learning—to formulate power grid restoration schemes. In [2], a weighted undirected complex network model of transmission lines is constructed. Meanwhile, a parallel restoration partition method for power systems is proposed. This method is based on an improved local expansion algorithm and aims to realize rapid system restoration during the power grid black-start process. In [3], the uncertainty in line fault probability is considered, and a distributed robust optimization model is proposed. This model aims to maximize load restoration under the worst-case emergency scenarios. In [4], a post-disaster restoration decision-making method for distribution systems based on reinforcement learning embedded with expert knowledge is proposed. This method effectively improves the efficiency of the optimization space and significantly reduces the restoration time of the power system. Reference [5] proposes a flexible air conditioning control method based on maximum load pickup to reduce load pickup while considering the impact on customers, thereby rapidly restoring power supply to customers. As evidenced by the aforementioned literature, most existing studies focus on the restoration speed and capability of power systems while overlooking the quantitative assessment of the risks arising from the uncertain state of lines to be restored.

To support reliable post-disaster restoration of power systems, a risk assessment method for new power system restoration is proposed, considering the uncertainty of faults in lines to be restored. Firstly, the restoration risk caused by the operation of lines with fault uncertainty is analyzed. It mainly encompasses two kinds of risks: wind farm trip-off due to voltage drop and load restoration delay caused by line outage. Subsequently, the impedance matrix of the topology is linearly computed to calculate the bus voltages rapidly. The voltage helps determine whether restored wind farms fail low-voltage ride-through and thus trip-off. Finally, a power system restoration optimization model considering the impacts of wind farm trip-off and line outage is constructed to calculate the load restoration amount. A system restoration risk index incorporating line fault uncertainty is proposed based on the load restoration amount to quantify the restoration risk. The test results of the New England 39-bus system demonstrate that the voltage of each bus can be accurately calculated with the proposed method to judge the trip-off of wind farms. Additionally, the proposed method can calculate the risk for the next hour within 0.306 seconds.

2 Fault scenario description and system restoration risk analysis

Uncertainty in the fault states of power systems caused by extreme weather and natural disasters stems from two main aspects. Firstly, extreme weather events have stochastic destructive effects. For instance, strong winds and cold waves can cause unpredictable physical damage to transmission lines. This damage significantly increases the probability of faults such as short circuits and line breaks. Secondly, after large-scale

power outages, the monitoring and dispatching functions of power systems may be restricted. It becomes difficult to perceive the specific location and extent of line faults in real time. This lack of fault information introduces unknown risks to network reconfiguration during system restoration[6]. The fault scenario and restoration risk analysis are shown in Fig. 1.

The first type of risk for lines with uncertain restoration states is the risk of load loss caused by wind farm trip-off. Specifically, during outage restoration, a short-circuited line may be mistakenly energized. If this line is in close electrical distance to a wind farm, it will cause a sudden voltage drop and frequency decline in the system. When the bus voltage drops to the low-voltage ride-through (LVRT) threshold of the wind farm, the wind farm will trip off the power grid[7]. The load originally supported by these wind farm will be forced to shed, leading to system load loss during the restoration process. In severe cases, it may even cause another system outage or collapse.

The second type of risk is load restoration delay. During the restoration process, line faults are often permanent. Once a faulty line is disconnected and taken out of service, its restoration time must be considered. This causes the restoration of some system loads in subsequent periods to be delayed. According to the system load restoration curve, if a line with uncertain fault status is restored when the power system has low robustness, the risk of load restoration delay will be high. In contrast, restoring such a line when the power system has high robustness results in a lower risk. Therefore, it is necessary to develop a risk assessment method for power system restoration. The proposed method, which needs to account for the uncertainty in the fault status of lines to be restored, can guide the timing of energizing potentially faulty lines. By doing so, the risk of load restoration delay caused by energizing faulty lines can be minimized.

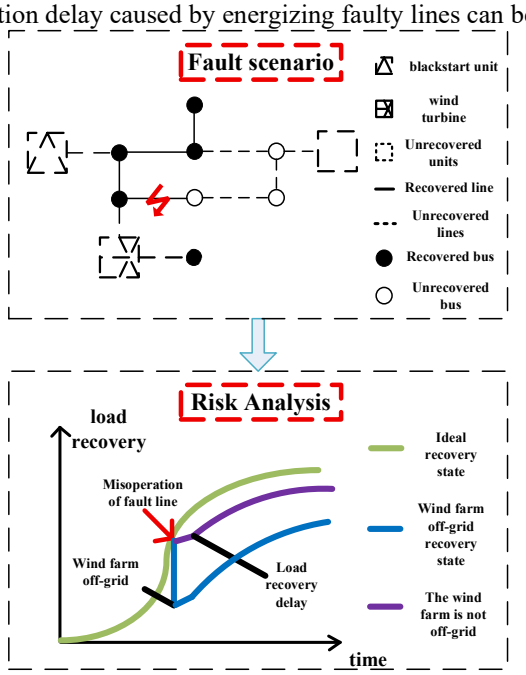


Fig. 1. Failure Scenarios and Risk Analysis

4

3 Rapid judgment of wind farm trip-off based on restoration topology adjoint network

To rapidly determine whether wind farms trip-off the grid, this section takes the restoration topology adjoint network as an example. It explains the linearized calculation method for the impedance of the restoration topology and the rapid calculation of each bus voltage. On this basis, it further constructs a model for judging wind farm trip-off. The example topology of the power grid during the restoration process is shown in Fig. 2. Solid lines represent restored lines, while dashed lines represent unrestored lines.

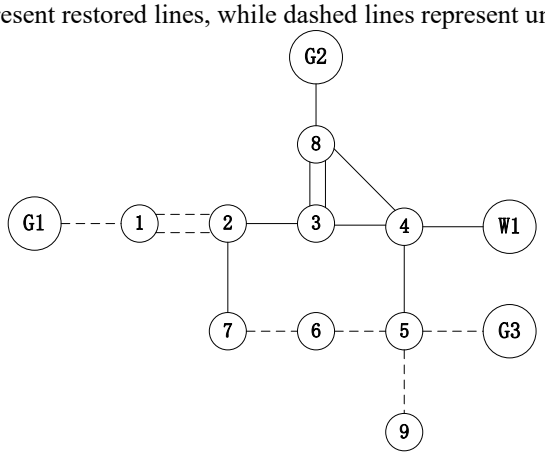


Fig. 2. Power grid sample topology diagram in the restoration process

Taking G2 as the black-start unit, assume a short-circuit fault occurs at the 50% point of line 4-5. Generator sets, lines, and transformers are modeled as branches. Specifically, reactance approximation is used to characterize the branch impedance of lines or transformers. Generator sets are represented by the grounding branch with transient reactance values[8]. The adjoint network of the restoration topology is constructed, as shown in Fig. 3. Unrestored generators and lines are not included in the adjoint network.

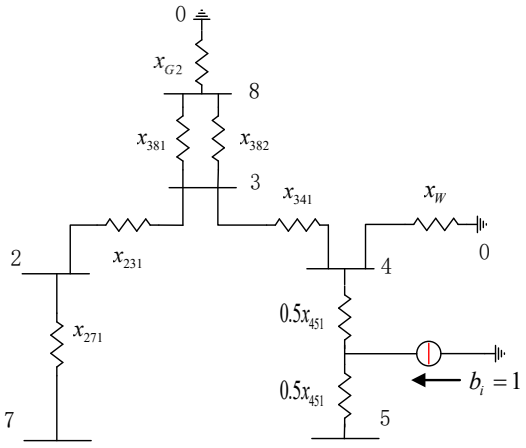


Fig. 3. Adjoint network of the restoration topology example

The adjoint network constraints based on the restoration topology are as follows:

$$\sum_{j:(j,i,c)\in L} I_{jic} - \sum_{j:(i,j,c)\in L} I_{ijc} = b_i, \forall i \in N \tag{1}$$

$$b_i = 1 \quad i = f \tag{2}$$

$$b_i = 0 \quad \forall i \in N \quad i \neq f \tag{3}$$

$$I_{ijc} = \frac{1}{x_{ijc}}(V_{if} - V_{jf}) \quad \forall (i,j,c) \in L^0 \tag{4}$$

$$V_i \geq 0 \quad \forall i \in N \tag{5}$$

where I_{ijc} is the current on the restoration topology adjoint network line *i-j-c*; V_{if} is the voltage of the restoration topology adjoint network bus *i* under the fault scenario; b_i is the injection current restoration topology adjoint network bus *i*; x_{ijc} is the reactance value on the line *i-j-c*; *L* is the set of system lines; L^0 is the set of extended lines, which includes grounding branches.

According to the physical meaning of the impedance matrix: when the unit current (b_i=1) is injected at the fault bus in the network and the current of the remaining buses is set to zero. The voltage value of the bus *i* is the mutual impedance Z_{if} between the bus and the short-circuit bus. The voltage value of the node *f* is the self-impedance Z_{ff} of the short-circuit bus; thus, the impedance matrix of the original network can be linearly generated.

The short-circuit voltage of each bus can be obtained by the impedance matrix of the topology. According to the superposition theorem, the fault network can be divided into two parts: normal condition and fault additional network[9]. The following formulas of fault voltage component and short circuit current are obtained:

$$\dot{V}_i = \dot{V}_i^{(0)} + \Delta\dot{V}_i = \dot{V}_i^{(0)} - Z_{if}\dot{I}_f \tag{6}$$

$$\dot{I}_f = \frac{\dot{V}_f^{(0)}}{Z_{ff} + z_f} \tag{7}$$

where, $\dot{I}_f$ is the injected current of the fault node *f*; $\dot{V}_i^{(0)}$ is the normal voltage of bus *i* before short circuit; z_f is the grounding impedance of the short-circuit node *f*.

Considering that the per-unit value of the system bus voltage before the fault is close to 1, z_f is negligible. Based on the impedance matrix generated by the adjoint network, combined with Eq. (6) and Eq. (7), the mathematical expression of the short-circuit voltage of each bus can be derived as follows:

$$\dot{V}_i = 1 - \frac{Z_{if}}{Z_{ff}} = 1 - \frac{V_{if}}{V_{ff}} \geq V_{i,\min} \tag{8}$$

The variable F_i is introduced to establish the wind farm off-grid judgment mode[10]

$$\begin{cases} (1 - V_{i,\min})V_{ff} - V_{if} \geq V_{\max}(F_i - 1) \\ (1 - V_{i,\min})V_{ff} - V_{if} \leq V_{\max}F_i \end{cases} \quad \forall i \in W \tag{9}$$

When F_i=1, the wind farm does not trip off the grid, and when F_i = 0, the wind farm trips off the grid. *W* is the set of wind farm bus; $V_{i,min}$ is threshold voltage for wind farm low-voltage ride-through (LVRT) failure. The model utilizes the adjoint network

to calculate the short-circuit voltage of each bus in the actual network; then, by comparing each bus voltage with $V_{i,min}$, it determines whether the wind farm trips off the grid.

4 Risk assessment of new power system restoration scheme

4.1 Restoration risk assessment indicators

The risk of power system restoration is defined as a comprehensive measure of the probability and severity of the uncertain factors faced by the power system[11]. During the power system restoration process, the risk assessment of the power system restoration scheme involves two key factors: the fault probability of lines and the impact of line faults on system load loss. Therefore, this paper defines the line restoration risk as the product of the line's fault probability and the system load loss caused by the line's restoration failure.

The impact of a fault on line *i-j-c* on the system's restoration load loss is calculated using a specific difference. This difference refers to the gap between the system's load restoration amount after the fault occurs on line *i-j-c* and the load restoration amount under ideal conditions. The definition of this calculation method is given by the following equation:

$$J_{i-j-c} = p_{i-j-c} \bullet \left(l_B^f - l_B^0 \right) \tag{10}$$

$J_{i\text{-}j\text{-}c}$ is the risk index of line *i-j-c* failure; $p_{i\text{-}j\text{-}c}$ is the fault probability of line *i-j-c*; l_B^0 is the load restoration amount during the system restoration process under ideal conditions; l_B^f is the load restoration amount during the system restoration process under the fault scenario *f* state.

4.2 Load restoration amount calculation considering the influence of wind farm off-grid and line outage

According to the system restoration risk index proposed in section 4.1, it is necessary to construct a model to quantitatively calculate the system load restoration under ideal conditions and fault scenario *f* state. Therefore, based on the wind farm off-grid judgment model, this section establishes a load restoration model considering the impact of wind farm off-grid and line outage.

(1) Maximize the amount of system load restoration during the restoration process:

$$\max f_r = l_B^f \tag{11}$$

(2) Topological constraints

$$\begin{cases} z_{ijc}^k = 1 \Rightarrow e_{i,k-1} + e_{j,k-1} \geq 1 \\ z_{ijc}^k = 1 \Rightarrow e_{i,k} = 1, e_{j,k} = 1 \end{cases} \tag{12}$$
$$\forall i \in N, \forall (i,j,c) \in L, \forall k \in K$$

$$\begin{cases} e_{i,k} \geq e_{i,k-1}, \quad \forall i \in N, \forall k \in K_F \\ z_{ijc}^{k} \geq z_{ijc}^{k-1}, \forall i \in N, \forall (i,j,c) \in L, \forall k \in K_F \end{cases} \tag{13}$$

$$u_{i,k}^{\text{start}} \leq e_{i,k}, \quad \forall i \in N_G, k \in K_F \tag{14}$$

where z_{ijc}^{k} is a 0-1 variable denoting the commissioning state of line *i-j-c* in time period *k*: when z_{ijc}^{k}= 1, the line is commissioned; when z_{ijc}^{k}= 0, the line is not commissioned ; K_F is the system restoration period; N_G is the set of unit nodes; $e_{i,k}$ is the energized state of bus *i* in period *k*, $e_{i,k}$=1 means energized, and $e_{i,k}$=0 means not energized. $u_{i,k}^{start}$ is the 0-1 variable ($u_{i,k}^{start}$ = 1 starts, $u_{i,k}^{start}$ = 0 does not start) whether the unit of bus *i* has started in period *k*.

(3) Security constraints

$$\begin{cases} U_i^{\min} \leq U_i^{k} \leq U_i^{\max} \\ P_{ijc}^{\min} \leq P_{ijc}^{k} \leq P_{ijc}^{\max} \\ \theta_{ij}^{\min} = \theta_{ij}^{k} \leq \theta_{ij}^{\max} \\ 0 \leq P_g \leq P_g^{\max} \end{cases} \tag{15}$$

where U_i^k is the voltage amplitude of bus *i* in period *k*, P_{ijc}^k is the active power flow on line *i-j-c* in period *k*, θ_{ij}^{max} is the maximum allowable value of phase angle difference, and P_g^{max} is the maximum output of conventional units.

(4) Restoration model considering the impact of wind farm off-grid and line outage

$$\begin{cases} P_{ijc}^{k} \geq \dfrac{\theta_{ij}^{k}}{x_{ijc}} - M(1-w_{ijc}) \\ P_{ijc}^{k} \leq \dfrac{\theta_{ij}^{k}}{x_{ijc}} + M(1-w_{ijc}) \\ -w_{ijc}P_{ijc}^{\max} \leq P_{ijc}^{k} \leq w_{ijc}P_{ijc}^{\max} \end{cases} \tag{16}$$

$$\forall (i,j,c) \in L, k \in K_F$$

$$\sum_{g \in G_i} P_g + \sum_{w \in W_i} P_w + \sum_{jc(j,i,c) \in L} P_{jic} - \sum_{jc(i,j,c) \in L} P_{ijc} = P_{i,r}^{k} + P_i^{cr} u_{i,k}^{start} \tag{17}$$

$$\forall i \in N, k \in K_F$$

$$\begin{cases} P_w \leq F_i P_{i,k}^{wp} \\ P_w \leq u_{i,k}^{w} P_{i,k}^{wp} \end{cases}, \forall i \in W, k \in K_F \tag{18}$$

$$l_B^f = \sum_{i \in N} P_{i,r}^{k}, \quad k \in K_F \tag{19}$$

w_{ijc} is a 0-1 variable indicating the disconnection state of line *i-j-c*: when w_{ijc}= 1, the line is not disconnected, and when w_{ijc}= 0, the line is disconnected. G_i is the set of units on bus *i*, and P_w is the active power output of wind farm; $P_{i,r}^k$ is the restored load of bus *i* in *k* period ; P_i^{cr} is the starting power of bus *i* unit; $u_{i,k}^w$ is whether the wind farm bus *i* unit is connected to the grid in the period *k* ($u_{i,k}^w$ = 1 is closed, $u_{i,k}^w$ = 0 is not closed).

The development of wind farm modeling is mature[12], and this paper does not repeat the relevant expression.

5 Case studies

5.1 Case introduction

The IEEE 39-bus system as shown in Fig. 4 is used to analyze the power system restoration risk. The conventional units at bus 32 and 33 are replaced with wind farms with rated capacities of 500MW and 800MW. Two fault scenarios (Scenario 1 and Scenario 2) are established to verify the effectiveness of the proposed method.

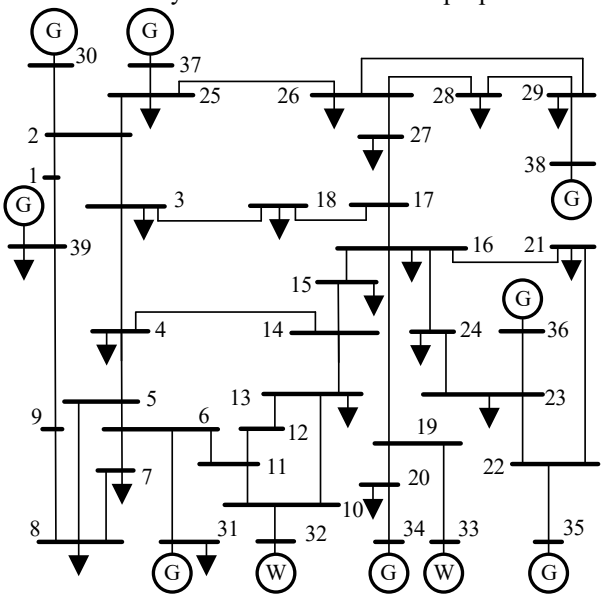


Fig. 4. IEEE 39-bus system with wind farm

The restoration sequence of lines and generators in the given restoration scheme is shown in Table 1. The generator at bus 36 is used as the black-start generator, and the whole system is restored in seven periods. The relevant parameters are set as follows: the system power reference value is 100 MVA, and the single-period length is 1h. Set the limit voltage $V_{i,min}$ = 0.2 p.u. when the wind farm trips off.

Table 1. Input sequence of each line and generator under the restoration scheme

period	generator	line
1	36	-
2	35	23-36,22-23,22-35,23-24,24-16,15-16
3	32	22-21,16-21,16-17,17-27,27-26,15-14,14-13,13-10,10-32
4	30,33	16-19,19-33,26-28,17-18,18-3,3-2,2-30,13-12,12-11
5	31,34,39	28-29,2-1,1-39,3-4,4-14,11-6,6-31,10-11,19-20,20-34
6	37,38	2-25,25-26,26-29, 29-38,25-37,39-9,9-8,4-5,5-8
7	-	8-7,5-6,6-7

5.2 Fault scenario 1

A three-phase short-circuit fault is set at the midpoint of line 19-20. The grounding impedance is 0, and the fault probability $p_{19\text{-}20}$ is 50%. When Line 19-20 is restored, the voltage of bus 32 in the adjoint network—calculated based on the current restoration topology—drops to 0.658523 p.u. In this case, no large-scale wind farm trip-off. Meanwhile, the voltage of bus 33 in the same adjoint network drops to 0.178319 p.u. This value is lower than the wind farm's voltage limit of 0.2 p.u. As a result, wind farms experience low-voltage ride-through failure, leading to wind farm trip-off.

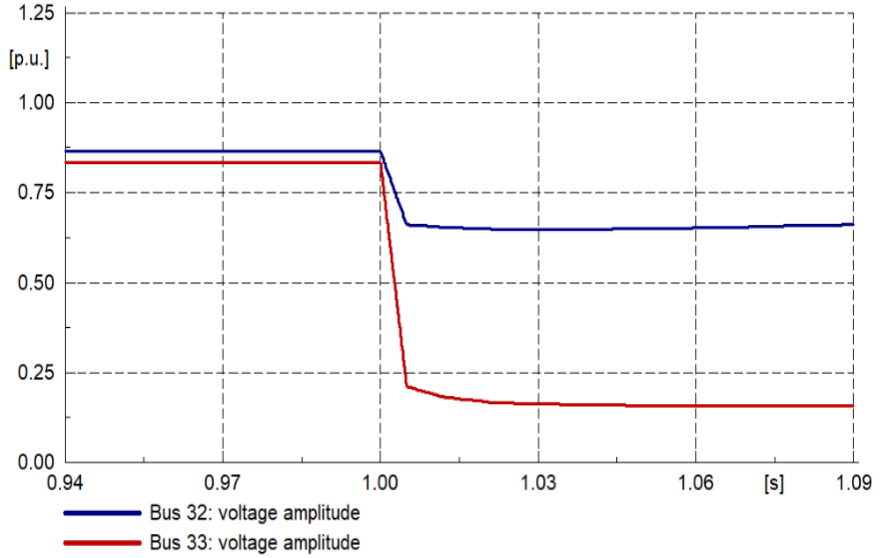


Fig. 5. Bus32 and bus33 voltage curves of line 19-20 short circuit fault

In order to illustrate the effectiveness of the proposed method—evaluates wind farm trip-off based on the restoration topology impedance element adjoint network— relevant verification is carried out. Electromagnetic transient simulation is conducted on the *DIgSILENT/PowerFactory* platform under the same fault scenario. The simulation results are then compared with those obtained from the proposed method, and the comparison results are shown in Fig. 5. During the fault period, the minimum voltage amplitudes of bus 32 and bus 33 drop to 0.647 p.u and 0.162 p.u, respectively. This simulation result is basically consistent with the bus voltages calculated based on the adjoint network, which indicates that the adjoint network calculation method has good calculation accuracy and applicability in the transient analysis of power system short-circuit faults.

10

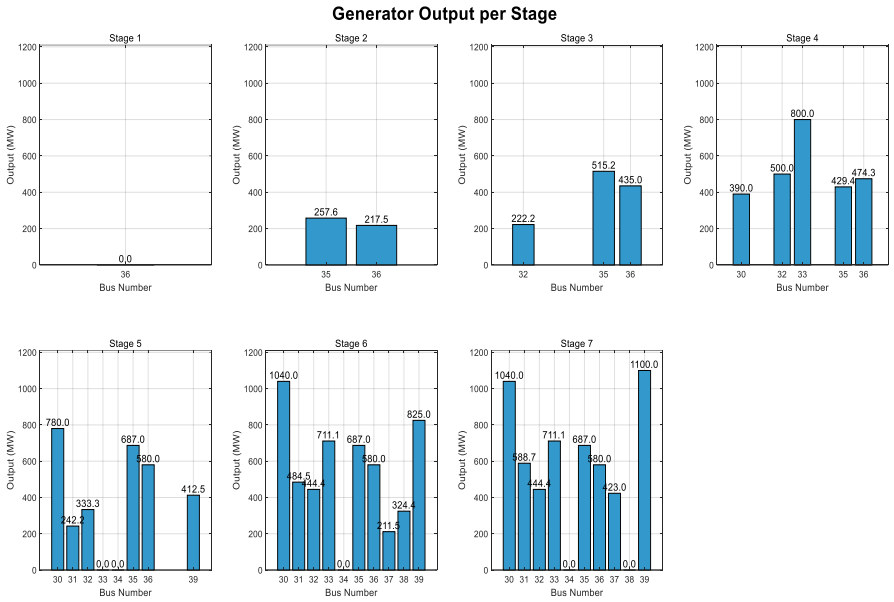


Fig. 6. Fault scenario 1 generator output in each period

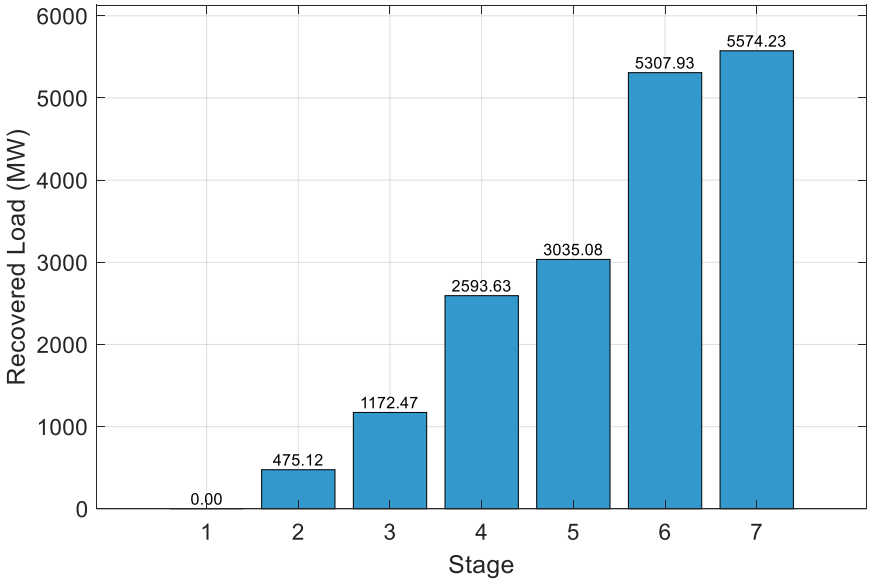


Fig. 7. Fault scenario 1 system load restoration

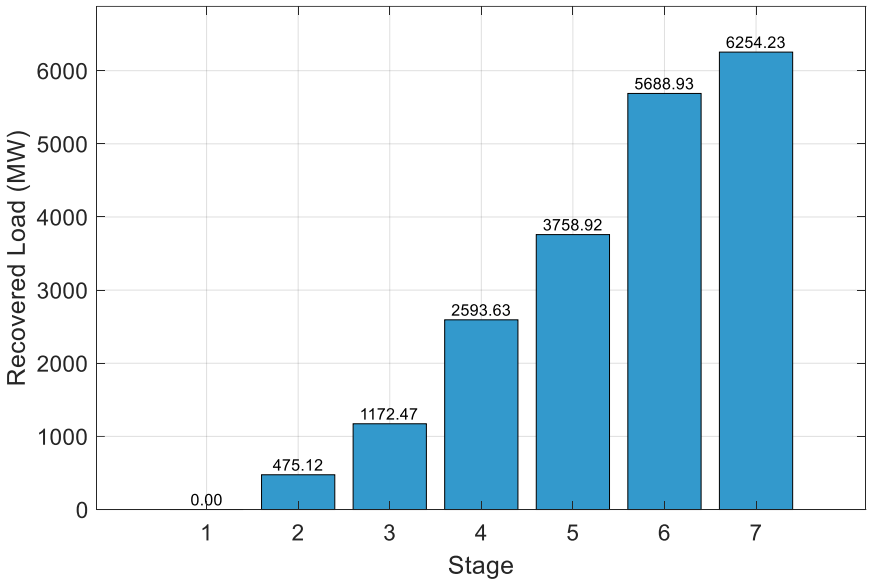


Fig. 8. System load restoration under ideal conditions

It can be seen from Fig. 6 that when the faulty line 19-20 is put into operation in the fifth period, the wind farm at bus 33 trips off rapidly, and its active power output drops sharply to 0. As shown in Fig. 7, the system load restoration in the fifth period is 3035.08 MW. As shown in Fig. 8, under ideal conditions, the system load restoration at this time is 3758.92 MW. The reason for the increased load loss lies in two key factors. First, the wind farm connected to bus 33 trips off the power grid on a large scale. Second, although the restoration line 19-20 is in the restoration process, it cannot be put into operation. This also delays the load restoration process during this period.

The risk index $J_{19\text{-}20}$ under Fault Scenario 1 is 361.92 MW. The calculation time of the case is 0.306 seconds. It should be clarified that this index does not represent a specific equivalence relationship. Specifically, it does not mean the system load loss caused by the uncertainty of the short-circuit fault on Line 19-20 is equal to 361.92 MW. The function of this index is to serve as a core quantitative indicator. It provides key quantitative support for subsequent research on optimization decision-making regarding the coordination of risk perception and restoration efficiency, where multiple uncertainties are taken into account.

5.3 Fault scenario 2

A three-phase short-circuit fault is set at the midpoint of line 16-19 the grounding impedance is 0, and the fault probability $p_{16\text{-}19}$ is 50%. When Line 16-19 is restored, the voltage of bus 36 is calculated to 0.545025 p.u. based on the topological adjoint network. There is no large-scale trip-off of the wind farm here. The wind farm at bus 33 has not been restored. The calculated restoration risk index $J_{16\text{-}19}$ is 218.315 MW.

The reason why this index is lower than that in Fault Scenario 1 is as follows. Specifically, the electrical distance between the faulty line and the restored wind farm is

relatively long, which ensures that the voltage at the wind farm's grid-connected point does not drop below the trip-off threshold. During the restoration process, the wind farm does not trip off the power grid, thus avoiding serious load loss. In addition, the value of the risk index is derived from a specific factor: the load restoration delay in the fourth period relative to the ideal restoration scenario. In the current period, the system connectivity is low and the grid structural robustness is weak. Under such conditions, the system restoration also faces a high risk of load restoration delay.

6 Conclusion

A rapid risk assessment method for power system restoration considering the uncertainty of the line state to be restored is proposed. This method can support the power system restoration decision-making, coordinating the restoration risk and efficiency under multiple uncertainties. Considering the load loss risk caused by wind farm trip-off and the load restoration delay risk caused by line faults in the current period, a wind farm trip-off judgment model based on the restoration topology adjoint network is constructed. This model can quickly and accurately calculate the voltage of each bus in the restoration topology and determine whether the wind farm experiences trip-off. Furthermore, a system restoration risk index is proposed as the basis of restoration decision-making, which considers the line fault probability and load loss due to line fault. Based on the index, the proposed risk assessment method can quickly quantify the system restoration risk in different line fault scenarios.

Acknowledgement: This work is supported by National Natural Science Foundation of China (52307111)

References

[1] Xu, L., Lin, N., Poor, H.V., et al.: Quantifying cascading power outages during climate extremes considering renewable energy integration [J]. Nature Communications 16(1), 2582 (2025).

[2] Wei, Z., Guan, X., Gao, H., et al.: Power system parallel restoration partitioning method based on improved local expansion algorithm [J]. Proceedings of the CSU-EPSA 32(5), 62–68 (2020).

[3] Cai, S., Xie, Y., Wu, Q., et al.: Distributionally robust microgrid formation approach for service restoration under random contingency [J]. IEEE Transactions on Smart Grid 12(6), 4926–4937 (2021).

[4] Xiao, W., Chen, J., Yu, T., et al.: Distribution system post-disaster recovery decision-making method based on expert knowledge embedded reinforcement learning [J]. Automation of Electric Power Systems 49(12), 91–100 (2025).

[5] Fan, R., Sun, R., Liu, Y., et al.: Adaptive power load restoration considering flexible control of air conditioners for resilience enhancement [J]. International Journal of Electrical Power & Energy Systems 148, 108959 (2023).

[6] Sun, R., Liu, Y.: Online decision-making for unit restoration based on deep learning and Monte Carlo tree search [J]. Automation of Electric Power Systems 42(14), 40–47 (2018).
[7] State Grid Corporation of China. Technical Regulations for Wind Farm Grid Connection [S]. Beijing: State Grid Corporation of China, 2009.
[8] Li, S., Ren, Y., Gu, X., et al.: Optimization of transmission network structure based on explicit linear modeling of short circuit current constraints [J]. Transactions of China Electrotechnical Society 35(15), 3292–3302 (2020).
[9] Lu, R., Lu, A.: Applications of the superposition theorem to nonlinear resistive circuits [C] // APCCAS 2006 - 2006 IEEE Asia Pacific Conference on Circuits and Systems. pp. 1333–1336. IEEE, Singapore (2006).
[10] Li, S., Zhang, Y., Gu, X.: Optimization method for power system restoration decision-making considering the impact of short-circuit faults and wind power [J]. Proceedings of the CSEE 43(20), 7827–7841 (2023).
[11] Ni, M., McCalley, J.D., Vittal, V., et al.: Online risk-based security assessment [J]. IEEE Transactions on Power Systems 18(1), 258–265 (2003).
[12] Wang, Y., Feng, Y., Ma, H.: Study on the calculation method of representative annual wind speed based on Copula function [J]. Acta Energiae Solaris Sinica 46(1), 151–157 (2025).

028 A two-layer optimal scheduling method for active power regulation of electric vehicle cluster power system

Haomin Li[1]、Yue Li[2]、Chunhua Lin[2]、Wanli Sun[2]、
Jiangning Wu[2]、Qun Yang[2]、Chen Zhou[2] and Mingze Zhang[1*]

[1] Harbin University of Science and Technology, Harbin, China
hmli2002@163.com
mzzhang1997@163.com
[2] State Grid Dalian Electric Power Supply Company Dalian, China
A798375381@126.com
38854223@qq.com
sunwanli96@126.com
wujiangning@sohu.com
881013yq@sina.com
3212718978@qq.com

Abstract. Based on the challenges faced by EV clusters participating in full-band frequency control auxiliary services (FCAS) under high wind power penetration, this paper proposes a-ahead scheduling double-layer optimization framework. The upper layer main grid dispatching aims to minimize the system's daily operation cost, designing a heterogeneous resource collaborative participation operation mechanism the whole time FCAS, to achieve global optimization allocation; the lower layer EV aggregator (EVA) aims to maximize their own benefits, and the control decision of multi- EV responding to the system command is re-optimized, to achieve complementary synergy. To address the dynamic change problem of cluster adjustable capacity caused by EV access/disconnection and electricity, an innovative generalized equivalent energy storage aggregation model for multi-type EVs is constructed based on Minkowski and method, which accurately quantifies its dynamic adjustable power range and energy feasible. The simulation results of the modified IEEE-39 node system show that the strategy can significantly enhance the system frequency security and stability margin and wind power consumption capacity while guaranteeing economicity of EVA, and optimally coordinate the safety, quality, and economic operation objectives of the high proportion new energy power system.

Keywords: Electric vehicle cluster, Active power regulation, Day-ahead scheduling, Double-layer planning, Multi-resource coordination.

1 Introduction

With the gradual integration of high-proportion renewable energy into power grids, higher demands are placed on grid frequency regulation capabilities. Frequency Control Auxiliary Services (FCAS), as a means to ensure frequency safety, face declining

regulation capacity due to the gradual replacement of main regulation units—thermal power plants—with renewable energy units. To maintain stable frequency security, there is an urgent need to introduce new flexible regulation resources to enhance system regulation capabilities. EVs, as novel flexible resources existing on the load side, still possess substantial dispatch potential when source-side and grid-side regulation resources are exhausted. With the continuous expansion of EV market scale and advancements in V2G technology, EVs are becoming high-quality resources contributing to power system operations. However, scheduling only single-type EVs fails to fully utilize their dispatch potential. EV participation in grid regulation can be categorized into three types: large centralized management EVs, small centralized management EVs, and non-centralized management EVs. Their dispatch potential can be maximized by coordinating multi-source EVs for active power regulation across all time scales. This study focuses on three aspects:

1) Quantifying dispatchable capacities of multiple EV types. Existing research primarily focuses on single-type EVs without considering multi-category EVs. For example, [1] proposed a GES model parameter prediction method based on bidirectional long-term-short-term memory networks to quantify individual EV dispatch capacity, while [2] modeled EV dispatch capacity using historical data. These studies all quantified single EVs.

2) Exploring how EVs can participate in grid regulation services across all time scales. Current research primarily focuses on specific types of grid regulation services without considering the full time scale. For instance, EVs participate in secondary frequency regulation (SFR) and peak shaving (PR) adjustments[1] or engage in rapid frequency response (FFR) and primary frequency regulation (PFR)[1].

3) How to balance the interests of multiple stakeholders including the grid and EV aggregators (EVA). Existing studies either focus solely on EVA itself or on direct grid dispatching, lacking multi-level coordination mechanisms that balance both grid operations and EVA interests. For example, strategies for coordinating EVs with conventional units are developed from a grid perspective[4], while clearing plans for EV participation in grid services are proposed from an EVA standpoint[3]. Through this analysis, there exists a lack of coordinated mechanisms for EV participation in FCAS:

1) Coordination between EVs and conventional units;

2) Coordination among different EV types within EV clusters;

3) Coordination among various dispatching entities.

Based on these findings, this paper proposes a day-ahead optimal scheduling method for multiple EV cluster coordination involving grid-EVA stakeholders, enabling regular unit participation in FCAS across the full time scale.

2 Quantification method of dispatchable capacity of EV cluster

Given the operational challenges in managing individual EVs, this study employs Minkowski addition to aggregate them into energy storage units for dispatch participation[5]. The implementation requires maintaining consistency across variable space

domains. Considering the inherent time lag between EV grid connection and disconnection, the system extends EV scheduling to include dispatch days, as follows:

$$b_{i,t}=\begin{cases}0,\forall t\notin[\mathrm{t}_{i,\mathrm{in}},\mathrm{t}_{i,\mathrm{out}}]\\1,\forall t\in[\mathrm{t}_{i,\mathrm{in}},\mathrm{t}_{i,\mathrm{out}}]\end{cases} \tag{1}$$

In the formula, $b_{i,t}$ is a Boolean variable, where 1 indicates that EV is online and 0 indicates that EV is offline. Thus, the expression $\Delta E_{\mathrm{ev},t}$ for the stepwise change of EV cluster power caused by EV's online/offline is obtained:

$$\Delta E_{\mathrm{ev},t}^{\mathrm{out}}=\sum_{i\in N}\mathrm{SoC}_{i,\mathrm{target}}\mathrm{E}_{i,\max}b_{i,t-1}\left(b_{i,t-1}-b_{i,t}\right) \tag{2}$$

$$\Delta E_{\mathrm{ev},t}^{\mathrm{in}}=\sum_{i\in N}\mathrm{SoC}_{i,\mathrm{in}}\mathrm{E}_{i,\max}b_{i,t}\left(b_{i,t}-b_{i,t-1}\right) \tag{3}$$

$$\Delta E_{\mathrm{ev},t}=\Delta E_{\mathrm{ev},t}^{\mathrm{out}}+\Delta E_{\mathrm{ev},t}^{\mathrm{in}} \tag{4}$$

Among which, N is the number of EVs in the network during the period, $\mathrm{SoC}_{i,\mathrm{in}}$ is the SoC of EV users when they enter the network, $\mathrm{SoC}_{i,\mathrm{target}}$ is the expected SoC of EV users when they leave the network, t_{in} and $\mathrm{t}_{\mathrm{out}}$ respectively represent the on/off periods of EVs.

The generalized energy storage model and constraints of the EV cluster are shown as follows:

$$\begin{cases}P_{\mathrm{ev},t}^{\mathrm{dis},\max}=\sum_{i\in N}P_{i,\mathrm{dis}}^{\max}v_t\\P_{\mathrm{ev},t}^{\mathrm{ch},\max}=\sum_{i\in N}P_{i,\mathrm{chg}}^{\max}\left(1-v_t\right)\end{cases} \tag{5a}$$

$$\begin{cases}P_{\mathrm{ev},t}^{\mathrm{dis},\max}=\sum_{i\in N}P_{i,\mathrm{dis}}^{\max}v_t\\P_{\mathrm{ev},t}^{\mathrm{ch},\max}=\sum_{i\in N}P_{i,\mathrm{chg}}^{\max}\left(1-v_t\right)\end{cases} \tag{5b}$$

$$\begin{cases}0\le P_{\mathrm{ev},t}^{\mathrm{dis}}\le P_{\mathrm{ev},t}^{\mathrm{dis},\max}\\0\le P_{\mathrm{ev},t}^{\mathrm{ch}}\le P_{\mathrm{ev},t}^{\mathrm{ch},\max}\end{cases} \tag{5c}$$

$$E_{\mathrm{ev},t}=E_{\mathrm{ev},t-1}+\left(\eta_{\mathrm{c}}P_{\mathrm{ev},t}^{\mathrm{ch}}-P_{\mathrm{ev},t}^{\mathrm{dis}}/\eta_{\mathrm{d}}\right)\Delta t+\Delta E_{\mathrm{ev},t} \tag{5d}$$

$$E_{\mathrm{ev},t}^{\min}\le E_{\mathrm{ev},t}\le E_{\mathrm{ev},t}^{\max} \tag{5e}$$

Here, the v_t is a Boolean variable indicating the charging and discharging state of the EVs (1 for discharging, 0 for charging); $P_{\mathrm{ev},t}^{\mathrm{dis},\max}$ and $P_{\mathrm{ev},t}^{\mathrm{ch},\max}$ are the maximum dis/charge power limits of the EV cluster in time t; $E_{\mathrm{ev},t}^{\max}$ and $E_{\mathrm{ev},t}^{\min}$ are the maximum/minimum allowable energy of the EV in time t; $\mathrm{SoC}_{i,\min}$ and $\mathrm{SoC}_{i,\max}$ are the minimum/maximum SoC to ensure the safe operation of the EV batteries; $P_{\mathrm{ev},t}^{\mathrm{ch}}$, $P_{\mathrm{ev},t}^{\mathrm{dis}}$, and e are the charging and discharging output and energy of the EV cluster in time t, respectively; η_{c} and η_{d} are the charging and discharging efficiency of the EVs.

Based on the energy storage model established for EV clusters in the previous article, the up and down reserve capacity that EV clusters can provide by participating in FCAS during the daily scheduling phase can be obtained. The expression is as follows:

$$P_{\mathrm{ev},t}^{\mathrm{up}} = P_{\mathrm{ev},t}^{\max} + P_{\mathrm{ev},t}^{\mathrm{ch}} - P_{\mathrm{ev},t}^{\mathrm{dis}} \tag{6}$$

$$P_{\mathrm{ev},t}^{\mathrm{down}} = P_{\mathrm{ev},t}^{\max} - P_{\mathrm{ev},t}^{\mathrm{ch}} + P_{\mathrm{ev},t}^{\mathrm{dis}} \tag{7}$$

In this formula, $P_{\mathrm{ev},t}^{\mathrm{up}}$ and $P_{\mathrm{ev},t}^{\mathrm{down}}$ are the up/down reserve capacity that can be provided by the EV cluster in time t, respectively. $P_{\mathrm{ev},t}^{\max}$ is the maximum power limit of the EV cluster at this time. In addition, the LSTM can be used to predict the uncertainty of EV parameters, and the prediction of each parameter of EV in the day is based on historical data.

3 EV clusters participate in the full time scale FCAS mechanism

There are three types of disturbances: step disturbance (s), non-step disturbance (min), and net load fluctuation (h), corresponding to four active power regulation methods: FFR, PFR, SFR, and PR. This section will construct a full-time-scale FCAS mechanism for EV clusters by focusing on these four regulation approaches.

3.1 IFR & PFR

The specific principle and process of IFR and PFR and two indexes to evaluate the operation stability of the system, the initial frequency change rate $RoCoF^{0^+}$ and the lowest point f^{nadir}. For details, refer to the literature [7] This paper judges whether EV participates in IFR and PFR through judging $RoCoF^{0^+}$ and the lowest frequency point f^{nadir}.

When the system is disturbed, RoCoF is[7]:

$$d\Delta f_t / dt = RoCoF_t^{0^+} = \Delta P_{\mathrm{L},t} f^{\mathrm{N}} / 2H_{\mathrm{sys},t} P_{\mathrm{B}} \tag{11}$$

where Δf_t is the amount of frequency change, $\Delta P_{\mathrm{L},t}$ is the amount of power disturbance, f^{N} is the rated frequency of the system before the disturbance occurs, P_{B} is rated capacity of the system, and is the sum of the capacity of the regulating components that can participate in the IFR and PFR regulation in the current time period in the system e is the total inertia time constant of the system, and its expression is:

$$H_{\mathrm{sys},t} = \left(\sum_{i=g}^{\mathrm{G}} \left(H_g u_{g,t} P_g^{\mathrm{N}} \right) + H_{\mathrm{ev},t} P_{\mathrm{ev},t}^{\max} \right) \Big/ P_{\mathrm{B}} \tag{15}$$

In the formula: G is the number of conventional units that can participate in IFR and PSR in the system within this period, H_g is the inertia time constant of power unit g, $u_{g,t}$ is a Boolean variable indicating the startup and shutdown state of unit g (1 for startup and 0 for shutdown), P_g^{N} is the rated installed capacity of g, $H_{\mathrm{ev},t}$ is the virtual inertia time constant of the EV cluster, and $P_{\mathrm{ev},t}^{\max}$ is the maximum discharge power of the EV cluster in the current period.

Combining Equation (13) and Equation (15), we get the RoCoF constraint of the system:

$$H_{\mathrm{sys},t} \geq \Delta P_{\mathrm{L},t}^{\max} f^{\mathrm{N}} / 2RoCoF^{\max} P_{\mathrm{B}} \tag{16}$$

When the IFR backup provided by the conventional units is sufficient, $H_{\mathrm{ev},t} = 0$ otherwise, the virtual inertia expression provided by EV through FFR is:

$$H_{\mathrm{ev},t} = K_{\mathrm{ev},t}^{\mathrm{FFR}} f^{\mathrm{N}} / 2P_{\mathrm{ev},t}^{\max} \tag{17}$$

where $K_{\mathrm{ev},t}^{\mathrm{FFR}}$ is the virtual inertia response coefficient of EV cluster storage, which is related to the reserve capacity $P_{\mathrm{ev},t}^{\mathrm{FFR}}$ of EV cluster storage participating in FFR.and its expression is:

$$P_{\mathrm{ev},t}^{\mathrm{FFR}} = K_{\mathrm{ev},t}^{\mathrm{FFR}} RoCoF^{\max} \tag{18}$$

Thus, the backup capacity constraint for EV clusters to participate in FFR is obtained:

$$P_{\mathrm{ev},t}^{\mathrm{FFR}} \geq \Delta P_{\mathrm{L},t}^{\max} - 2\sum_{i=1}^{\mathrm{G}} \left(H_i u_{i,t} P_{g,i}^{\mathrm{N}} \right) RoCoF^{\max} \Big/ f^{\mathrm{N}} \tag{19}$$

When disturbed, f_t^{nadir} expression is:

$$f_t^{\mathrm{nadir}} = f^{\mathrm{N}} - \Delta P_{L,t} / 2\mathrm{P_B} \left(\sum_{g=1}^{\mathrm{G}} X_g u_{g,t} + K_{\mathrm{ev},t}^{\mathrm{PFR}} / \mathrm{P_B} \right) \tag{20}$$

In this formula, X_g , is the gain coefficient of conventional thermal power unit[5], and $K_{\mathrm{ev},t}^{\mathrm{PFR}}$ is the virtual sag control coefficient of EV cluster energy storage. The response frequency of EV energy storage changes rapidly, so its gain coefficient can be approximated as the virtual sag control coefficient.

The PFR regulation capability of the thermal power unit is:

$$P_{g,t}^{\mathrm{PFR}} = K_{g,t}^{\mathrm{PFR}} \left(\Delta f^{\max} - f^{\mathrm{db}} \right) \tag{21}$$

In this formula, $K_{g,t}^{\mathrm{PFR}}$ is the sag control coefficient of each conventional thermal power unit, $\Delta f^{\max}$ is the maximum linear operating frequency of the unit, and f^{db} is the action dead zone of the unit PFR.

If the constraints f^{nadir} in literature [7] are satisfied, the EV cluster will not participate; otherwise, the EV cluster needs to participate in PFR, and the reserved amount $P_{\mathrm{ev},t}^{\mathrm{PFR}}$ of EV required is:

$$P_{\mathrm{ev},t}^{\mathrm{PFR}} = K_{\mathrm{ev},t}^{\mathrm{PFR}} \left(f^{\mathrm{N}} - f^{\min} - \Delta f^{\max} \right) \tag{22}$$

3.2 SFR

The collaborative SFR reserve strategy for conventional units and EV clusters is expressed as follows:

$$\sum_{g=1}^{\mathrm{G}} P_{g,t}^{\mathrm{SFR_up}} + P_{\mathrm{ev},t}^{\mathrm{SFR_up}} = R_t^{\mathrm{SFR_up}} \tag{23}$$

$$\sum_{g=1}^{\mathrm{G}} P_{g,t}^{\mathrm{SFR_down}} + P_{\mathrm{ev},t}^{\mathrm{SFR_down}} = R_t^{\mathrm{SFR_down}} \tag{24}$$

Here, $P_{g,t}^{\mathrm{SFR_up}}$ and $P_{g,t}^{\mathrm{SFR_down}}$ represents the upper and lower reserve capacities of each thermal power unit under the SFR during the specified period. $P_{\mathrm{ev},t}^{\mathrm{SFR_up}}$ and $P_{\mathrm{ev},t}^{\mathrm{SFR_down}}$ denote the current-period upper and lower reserve capacities of EV cluster energy storage, while $R_t^{\mathrm{SFR_up}}$ and $R_t^{\mathrm{SFR_down}}$ denotes the required upper and lower reserve capacities for the system during the current period. In this study, the system's required upper and lower reserve capacities are determined by applying 5% of load forecasting values and 10% of wind power forecasting values[8].

3.3 PR

For the same reason, the correlation principle of PR is detailed in literature [8].

Therefore, PR backup should be reserved.

$$\sum_{g=1}^{G} P_{g,t}^{\mathrm{PR_up}} + P_{\mathrm{ev},t}^{\mathrm{PR_up}} = R_t^{\mathrm{PR_up}} \tag{25}$$

$$\sum_{g=1}^{G} P_{g,t}^{\mathrm{PR_down}} + P_{\mathrm{ev},t}^{\mathrm{PR_down}} = R_t^{\mathrm{PR_down}} \tag{26}$$

Where: $P_{g,t}^{\mathrm{PR_up}}$ and $P_{g,t}^{\mathrm{PR_down}}$ are the PR up/down reserve capacity of each thermal power unit in the current period, $P_{\mathrm{ev},t}^{\mathrm{PR_up}}$ and $P_{\mathrm{ev},t}^{\mathrm{PR_down}}$ are the PR up/down reserve capacity of EV cluster energy storage in the current period, $R_t^{\mathrm{PR_up}}$ and $R_t^{\mathrm{PR_down}}$ is the PR reserve required for each period.

This paper introduces the risk value theory (VaR) [8] and gives the probability density function of wind power prediction deviation value:

$$\mathrm{PDF}\left(\Delta P_{\mathrm{w},t}\right) = \frac{1}{\sigma_t\sqrt{2\pi}} \exp\left(-\frac{\left(\Delta P_{\mathrm{w},t}\right)^2}{2\sigma_t^2}\right) \tag{29}$$

In the formula, σ_t is the standard deviation of $\Delta P_{\mathrm{w},t}$. It is mentioned in [8] that the prediction error of wind power in current day-ahead data can be as as 10–21%, and in this paper, according to the 3σ principle of normal distribution,this paper takes:

$$\sigma_t = 21\% P_{\mathrm{w},t}^{\mathrm{pre}} / 3 \tag{30}$$

4 A dual-layer optimization model for power grid-EVA scheduling is proposed recently

This section will construct a two-layer optimization day-ahead scheduling model with the power grid as the upper layer and EVA as the lower layer. The purpose is to formulate resource coordination scheduling strategies that can minimize the total daily operation cost of the main network while taking into account the daily operation revenue of EVA.

4.1 Upper power grid mathematical model

4.1.1 objective function

In this paper, the whole day dispatching time is divided into 96 periods, each of which is 15min. The upper-level model aims at minimizing the daily operation cost of the power grid, which includes the operation cost of thermal power units, the wind abandon cost of wind power units and the compensation cost when EV participates in FCAS.

$$\min C_{\text{grid}}^{\text{da}} = \sum_{t=1}^{\text{T}} \left(C_{\text{G},t} + C_{\text{EVA},t} + C_{\text{w},t} \right) \tag{31}$$

Where: $C_{\text{G},t}$ is the operating cost of thermal power units in the period t ; $C_{\text{EVA},t}$ is the cost of grid compensation to EVA participating in FCAS; and $C_{\text{w},t}$ is the wind curtailment cost.

1) $C_{\text{G},t}$:includes the start-up $C_{\text{G},t}^{\text{on}}$ and shutdown $C_{G,t}^{\text{off}}$ costs of the unit, the generation cost of the unit $C_{\text{G},t}^{\text{ge}}$, the cost of the unit participating in SFR $C_{\text{G},t}^{\text{SFR}}$ and the cost of the unit entering DPR $C_{\text{G},t}^{\text{DPR}}$. The participation of the unit in IFR and PFR is compulsory regulation and therefore not included in the cost:

$$C_{\text{G},t} = C_{\text{G},t}^{\text{on}} + C_{\text{G},t}^{\text{off}} + C_{\text{G},t}^{\text{ge}} + C_{\text{G},t}^{\text{SFR}} + C_{\text{G},t}^{\text{DPR}} \tag{32}$$

Due to the limited space, the specific expressions are referenced in references [9]. In this paper, we take. $P_g^{\text{DPR1}} = 50\% P_g^{\max}$ $P_g^{\text{DPR2}} = 40\% P_g^{\max}$.

2) $C_{\text{EVA},t}$:The EVA compensated by the power grid to EVA respectively participates in the standby costs($C_{\text{EVA},t}^{\text{FFR}}$ 、 $C_{\text{EVA},t}^{\text{PFR}}$ 、 $C_{\text{EVA},t}^{\text{SFR}}$ 、 $C_{\text{EVA},t}^{\text{PR}}$) of FFR, PFR, SFR and PR.

$$C_{\text{EVA},t} = C_{\text{EVA},t}^{\text{FFR}} + C_{\text{EVA},t}^{\text{PFR}} + C_{\text{EVA},t}^{\text{SFR}} + C_{\text{EVA},t}^{\text{PR}} \tag{34a}$$

$$C_{\text{EVA},t}^{\text{FFR}} = c_{\text{EVA}}^{\text{FFR}} P_{\text{ev},t}^{\text{FFR}} \Delta t \tag{34b}$$

$$C_{\text{EVA},t}^{\text{PFR}} = c_{\text{EVA}}^{\text{PFR}} P_{\text{ev},t}^{\text{PFR}} \Delta t \tag{34c}$$

$$C_{\text{EVA},t}^{\text{SFR}} = c_{\text{EVA}}^{\text{SFR}} \left(P_{\text{ev},t}^{\text{SFR_up}} + P_{\text{ev},t}^{\text{SFR_down}} \right) \Delta t \tag{34d}$$

$$C_{\text{EVA},t}^{\text{PR}} = c_{\text{EVA}}^{\text{PR}} \left(P_{\text{ev},t}^{\text{PR_up}} + P_{\text{ev},t}^{\text{PR_down}} \right) \Delta t \tag{34e}$$

Among $c_{\text{EVA}}^{\text{FFR}}$ $c_{\text{EVA}}^{\text{PFR}}$ $c_{\text{EVA}}^{\text{SFR}}$, $c_{\text{EVA}}^{\text{PR}}$ are the compensation unit prices (\$/MWh) provided by the grid for EVA's participation in corresponding regulation t services, $P_{\text{ev},t}^{\text{FFR}}$ and $P_{\text{ev},t}^{\text{PFR}}$ represent the FFR and PFR reserve capacities reserved by EVA during the time period; $P_{\text{ev},t}^{\text{SFR_up}}$ and $P_{\text{ev},t}^{\text{SFR_down}}$ are the upper/lower SFR reserve capacities reserved by EVA; $P_{\text{ev},t}^{\text{PR_up}}$ and $P_{\text{ev},t}^{\text{PR_down}}$ are the upper/lower PR reserve capacities reserved by EVA.

3) $C_{\text{w},t}$: Wind curtailment cost during daily operation of the system:

$$C_{\text{w},t} = c_{\text{w}} \left(P_{\text{w},t}^{\text{pre}} - P_{\text{w},t} \right) \Delta t \tag{35}$$

In the formula, c_{w} is the unit wind curtailment cost (\$/MWh); $P_{\text{w},t}^{\text{pre}}$ is the forecast value of wind power in the day-ahead period t ;and $P_{\text{w},t}$ is the planned output of wind turbines in the period t .

4.1.2 Constraints

The constraints of the system and various units in the operation of the power grid are as follows:

1) Power balance constraint:

$$\sum_{g=1}^{G} P_{g,t} + P_{w,t} + P_{ev,t}^{dis} - P_{ev,t}^{chg} = P_{L,t} \tag{36}$$

In this formula, $P_{L,t}$ is the typical daily load of the period t.

2) System rotation backup constraint:

$$\sum_{g=1}^{G} \left(u_{g,t} P_g^{max} - P_{g,t} \right) + P_{ev,t}^{up} \geq \gamma P_{L,t} \tag{37}$$

In the formula, P_g^{max} is the upper limit of the unit g output; $P_{ev,t}^{up}$ is the increased reserve capacity of EV cluster in the period t; γ is the minimum rotating reserve coefficient required by the system, which is 8%[9] in this paper.

3) Reference literature [9] for thermal power unit constraints, which will not be described here.

4) EVA constraints: The detailed power and energy constraints of EVA are shown in Equation (6) in Section 2 EV Cluster Modeling. Here, the overall constraints of EVA as an energy storage element participating in FCAS are given as follows:

$$0 \leq P_{ev,t}^{FFR} + P_{ev,t}^{PFR} + P_{ev,t}^{SFR_up} + P_{ev,t}^{PR_up} \leq P_{ev,t}^{up} \tag{39a}$$

$$0 \leq P_{ev,t}^{SFR_down} + P_{ev,t}^{PR_down} \leq P_{ev,t}^{down} \tag{39b}$$

In Equation (39a) and Equation (39b), the upper and lower reserve capacity constraints regulated by EVA are respectively shown. The specific constraints of EVA participating in each type of FCAS are detailed in Section 3.

5) Wind turbine constraint: During operation, the actual wind power output absorbed by the system is not greater than the power generation output of wind power, that is:

$$0 \leq P_{w,t} \leq P_{w,t}^{pre} \tag{40}$$

4.2 Lower EVA mathematical model

4.2.1 objective function

The lower-level model focuses on Energy Value (EVA), which maximizes daily operational benefits by coordinating dispatchable resources from various EV types to respond to grid dispatch plans. The revenue $R_{ev,t}$ includes compensation for participating in grid regulation services, while costs $C_{ev,t}$ cover both the expenses incurred by EVA when EVs discharge energy for regulation and those associated with providing reserve capacity.

$$\max C_{EVA}^{da} = \sum_{t=1}^{T} \left(R_{ev,t} - C_{ev,t} \right) \tag{41}$$

$$C_{ev,t} = C_{ev,t}^{dis} + C_{ev,t}^{FFR} + C_{ev,t}^{PFR} + C_{ev,t}^{SFR} + C_{ev,t}^{PR} \tag{42}$$

among ,

$$C_{\mathrm{ev},t}^{\mathrm{dis}}=\sum_{j=1}^{\mathrm{type}}c_{\mathrm{ev},j}^{\mathrm{dis}}P_{\mathrm{ev},j,t}^{\mathrm{dis}}\Delta t \tag{43a}$$

$$C_{\mathrm{ev},t}^{\mathrm{FFR}}=\sum_{j=1}^{\mathrm{type}}c_{\mathrm{ev},j}^{\mathrm{FFR}}P_{\mathrm{ev},j,t}^{\mathrm{FFR}}\Delta t \tag{43b}$$

$$C_{\mathrm{ev},t}^{\mathrm{PFR}}=\sum_{j=1}^{\mathrm{type}}c_{\mathrm{ev},j}^{\mathrm{PFR}}P_{\mathrm{ev},j,t}^{\mathrm{PFR}}\Delta t \tag{43c}$$

$$C_{\mathrm{ev}}^{\mathrm{SFR}}=\sum_{j=1}^{\mathrm{type}}c_{\mathrm{ev},j}^{\mathrm{SFR}}\left(P_{\mathrm{ev},j,t}^{\mathrm{SFR_up}}+P_{\mathrm{ev},j,t}^{\mathrm{SFR_down}}\right)\Delta t \tag{43d}$$

$$C_{\mathrm{ev},t}^{\mathrm{PR}}=\sum_{j=1}^{\mathrm{type}}c_{\mathrm{ev},j}^{\mathrm{PR}}\left(P_{\mathrm{ev},j,t}^{\mathrm{PR_up}}+P_{\mathrm{ev},j,t}^{\mathrm{PR_down}}\right)\Delta t \tag{43e}$$

among which , $R_{\mathrm{ev},t}$ is equal to $C_{\mathrm{EVA},t}$ in the upper-level power grid model; type is the EV type, In this paper, EVs are divided into three categories based on the uncertainty of EV travel and battery capacity. Since the goal of EV grid connection is to meet charging demand, EVA will not provide compensation during charging, while discharge operation contradicts the goal of EVs, so EVA needs to provide discharge compensation. $C_{\mathrm{ev},t}^{\mathrm{dis}}$ is the compensation cost paid by EVA for various EVs through discharge response FCAS, and $c_{\mathrm{ev},j}^{\mathrm{dis}}$ is the unit price of discharge compensation required by type j EV ($/MWh), $P_{ev,j,t}^{\mathrm{dis}}$ is the discharge power of EV of type j at time t; Similarly, $C_{\mathrm{ev},t}^{\mathrm{FFR}}$、$C_{\mathrm{ev},t}^{\mathrm{PFR}}$、$C_{\mathrm{ev},t}^{\mathrm{SFR}}$、$C_{\mathrm{ev},t}^{\mathrm{PR}}$ represent the compensation electricity prices paid by EVA to EV users when EVs of different types participate in various FCAS systems, which constitute operational costs of EVA. $c_{\mathrm{ev},j}^{\mathrm{FFR}}$、$c_{\mathrm{ev},j}^{\mathrm{PFR}}$、$c_{\mathrm{ev},j}^{\mathrm{SFR}}$、$c_{\mathrm{ev},j}^{\mathrm{PR}}$ denote the EVA compensation unit prices ($/MWh) required for EVs of type to participate in various regulation services. $P_{\mathrm{ev},j,t}^{\mathrm{FFR}}$、$P_{\mathrm{ev},j,t}^{\mathrm{PFR}}$、$P_{\mathrm{ev},j,t}^{\mathrm{SFR_up}}$、$P_{\mathrm{ev},j,t}^{\mathrm{SFR_down}}$、$P_{\mathrm{ev},j,t}^{\mathrm{PR_up}}$、$P_{\mathrm{ev},j,t}^{\mathrm{PR_down}}$ respectively indicate the reserve capacities provided by EVs of type during the specified time periods when participating in FCAS through EVA.

4.2.2 Constraints

When scheduling multiple EV resources to participate in FCAS, EVA needs to meet the power, energy constraints and related reserve capacity constraints of each EV category. For each EV category, the above constraints are shown in Equation (6) and Equation (38), which will not be detailed here.

For the lower EVA, it is necessary to coordinate the scheduling of each EV category to respond to the total output plan and reserve plan of EV cluster issued by the power grid. The constraint set is shown in the following table:

$$\sum_{j=1}^{\mathrm{type}}P_{\mathrm{ev},j,t}^{\mathrm{chg}}+P_{\mathrm{ev},j,t}^{\mathrm{dis}}=P_{\mathrm{ev},t}^{\mathrm{dis}}+P_{\mathrm{ev},t}^{\mathrm{chg}} \tag{44a}$$

$$\sum_{j=1}^{\mathrm{type}}P_{\mathrm{ev},j,t}^{\mathrm{FFR}}=P_{\mathrm{ev},t}^{\mathrm{FFR}} \tag{44b}$$

$$\sum_{j=1}^{\mathrm{type}}P_{\mathrm{ev},j,t}^{\mathrm{PFR}}=P_{\mathrm{ev},t}^{\mathrm{PFR}} \tag{44c}$$

$$\begin{cases} \sum_{j=1}^{\text{type}} P_{\text{ev},j,t}^{\text{SFR_up}} = P_{\text{ev},t}^{\text{SFR_up}} \\ \sum_{j=1}^{\text{type}} P_{\text{ev},j,t}^{\text{SFR_down}} = P_{\text{ev},t}^{\text{SFR_down}} \end{cases} \tag{44d}$$

$$\begin{cases} \sum_{j=1}^{\text{type}} P_{\text{ev},j,t}^{\text{PR_up}} = P_{\text{ev},t}^{\text{PR_up}} \\ \sum_{j=1}^{\text{type}} P_{\text{ev},j,t}^{\text{PR_down}} = P_{\text{ev},t}^{\text{PR_down}} \end{cases} \tag{44e}$$

Among them, Equation (44a) is the constraint of the total EV charging and discharging plan formulated by the upper power grid for the lower EV to meet; Equation (44b) --Equation (44e) is the reserve capacity balance constraint that each type of EV needs to participate in various FCAS during each period of EVA scheduling.

5 Case analysis

This section takes the case system of 10 machines bus [10] of IEEE-39 nodes as the basis for simulation research, and sets up calculation examples to analyze and prove the effectiveness and superiority of the model established in this paper.

5.1 Case data

In order to effectively demonstrate the day-ahead optimization model established in this paper, the case system is modified as follows: Replace G1 and G2 units with wind turbines with an installed capacity of 600MW, introduce an EVA virtual energy storage station composed of 4,000 V2G charging piles, and replace G3, G4, G5 and G6 with frequency modulation units.

In this study, the $\text{RoCoF}^{\max}$ parameter $f^{\min}$ $f^{\min}$ setting is defined as follows: The maximum power deficit disturbance during daily system operation f^{db} f^{db} $\Delta f^{\max}$ is $\Delta f^{\max}$ set c_g^{DPR1} at 15 c_g^{DPR2} c_g^{DPR1} % of the system's c_g^{DPR2} η_{c} baseline η_{d} capacity. η_{c} The η_{d} unit's operational $E_{\text{ev},t}^{\min}$ $E_{\text{ev},t}^{\max}$ dead t zone is defined $E_{\text{ev},t}^{\max}$ $c_{\text{ev}}^{\text{FFR}}$ as $E_{\text{ev},t}^{\min}$ $c_{\text{ev}}^{\text{PFR}}$ 0.033Hz t ,=0.2Hz, with values of \$40/MWh $c_{\text{ev}}^{\text{FFR}}$ $c_{\text{ev}}^{\text{PFR}}$ and \$80/MWh respectively. Both EV charging c_{W} /discharging efficiency $\beta = 95\%$ and energy storage capacity are c_{W} maintained at 90 $\beta = 95\%$ %. The safety thresholds for EV energy storage are set at 20% and 80% of the total energy during EV cluster periods, respectively, with corresponding upper/lower limits of \$60/MWh. The unit price for regulating components participating in SFR is \$30/MWh, while the unit price for EVA involved in PR is \$20/MWh. The wind curtailment unit price is \$70/MWh. Confidence levels are specified in the table below. Detailed parameters for conventional units and various EV types are presented in Tables 1 and 2, respectively. Daily load curves and wind power forecast outputs are illustrated in Figures 2 and 3.

In this paper, $\mathrm{RoCoF}^{\max}$ =0.5Hz/s, $f^{\min}$ =49.5Hz, and the most serious power shortfall disturbance quantity that may in the daily operation stage of the system is taken as 15% of the system's benchmark capacity. The action deadband of the unit f^{db} =0.033Hz, $\Delta f^{\max}$ =0.2Hz, c_g^{DPR1} =40$/MWh, c_g^{DPR2} =80$/MWh,the charging and discharging efficiency of the EV η_{c} and η_{d} both 90%, and the upper and lower limits of the safe threshold of the EV electricity $E_{\mathrm{ev},t}^{\min}$ and $E_{\mathrm{ev},t}^{\max}$ are 20% and 80% of the total under the time period of the EV cluster t, $c_{\mathrm{ev}}^{\mathrm{FFR}}$ and $c_{\mathrm{ev}}^{\mathrm{PFR}}$ are 60$/MWh, the regulation element participating in the SFR unit price is 30$/M, EVA participating in the PR unit price is 20$/MWh, the system curtailment wind price is 70$/MWh, and the confidence level $\beta=95\%$. In this paper, the relevant parameters of each conventional unit and various EVs are detailed in the following Table 1 and Table 2, and the daily load curve and wind prediction output are shown in Figure 1 and Figure 2, respectively.
Table 1 Unit parameters.

Table 1. Parameters of generators.

Generators	$C_{\mathrm{g}}^{\mathrm{on}}$, $C_{\mathrm{g}}^{\mathrm{off}}$ ($)	$\mathrm{T}_g^{\mathrm{on}}$, $\mathrm{T}_g^{\mathrm{off}}$ (15min)	a, b, c ($/MW²h, $/MWh, $)	$P_g^{\max}$ (MW)	$P_g^{\min}$ (MW)	R_g^+, R_g^- (MW)	H_g (s)	K_g^{PFR} (p.u.)
G3	550	20	0.00200, 16.60, 700	130	20	20	8.1	20
G4	560	20	0.00211, 16.50, 680	130	20	20	8.1	20
G5	900	24	0.004, 19.7,450	162	25	25	8.1	21
G6	170	12	0.0071, 22.26, 370	80	20	18	5.8	17
G7	260	12	0.00079, 27.74, 480	85	25	20	5.8	17
G8	30	4	0.00413, 25.92, 660	55	10	15	5.8	17

12

G9	30	4	0.00222, 27.27, 665	55	10	15	5.8	17
G10	30	4	0.00173, 27.79, 670	55	10	15	5.8	17

Table 2. Three types of EV battery parameters and compensation prices.

Type	$P_{ev,j}^{max}$ (MW)	$E_{ev,j}^{max}$ (MWh)	$c_{ev,j}^{dis}$ ($/MWh)	$c_{ev,j}^{FFR}$ ($/MWh)	$c_{ev,j}^{PFR}$ ($/MWh)	$c_{ev,j}^{SFR}$ ($/MWh)	$c_{ev,j}^{PR}$ ($/MWh)
Private	0.08	0.08	7	7	7	14	14
Bus	0.1	0.24	8.5	8.5	8.5	16	16
Office	0.08	0.08	5.5	5.5	5.5	12	12

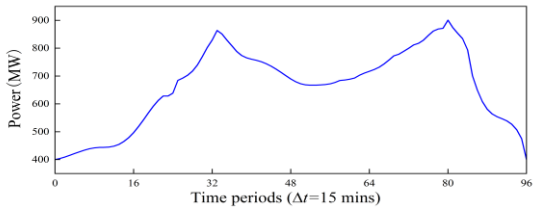


Fig. 1. Daily load data.

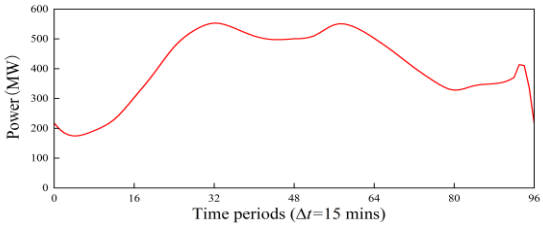


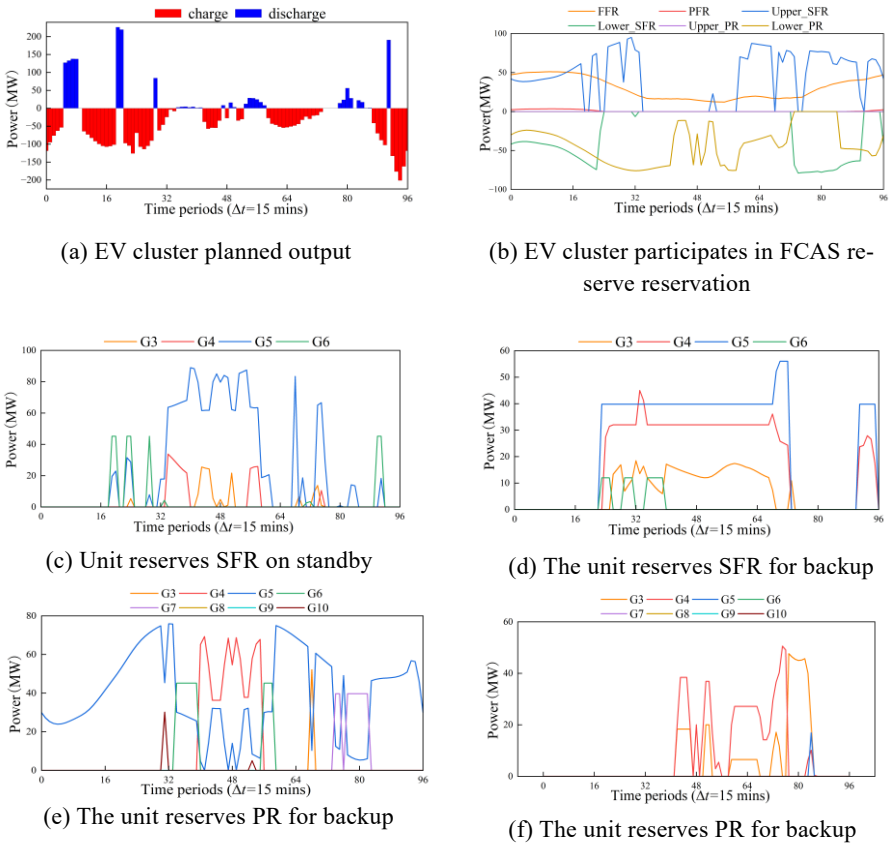
Fig. 2. Wind power generation forecast.

5.2 Optimization result analysis

5.2.1 Optimization results

The model simulation in this paper was executed on an Intel® Core™ i7-10870H CPU (2.20GHz) processor. Using MATLAB2023a and the CPLEX solver, the optimal solution was obtained after 270 seconds of computation. The daily operational cost for the upper-level power grid reached $612,875, while the daily EVA (Energy

Value Added) benefit for the lower-level grid stood at $78,143. The detailed scheduling strategy is illustrated in Figure 3.



(a) EV cluster planned output

(b) EV cluster participates in FCAS reserve reservation

(c) Unit reserves SFR on standby

(d) The unit reserves SFR for backup

(e) The unit reserves PR for backup

(f) The unit reserves PR for backup

Fig. 3. Day-ahead dispatch strategy for the modified IEEE 39-bus 10-unit system.

Figure 3(a) shows the EV cluster in the daily scheduling stage: discharging to balance the power grid during peak load (36-42,78-87 periods), and charging to absorb wind power during low load, showing flexible regulation characteristics.

Figure 3(b) illustrates the FCAS backup strategy for EV clusters: During periods when the thermal power ratio decreases, leading to insufficient inertia and PFR capacity (periods 0-23 and 87-96), PFR and FFR reserves are reserved to ensure that the frequency dynamic characteristics under step disturbance (15%) meet the specifications. This approach satisfies RoCoF constraints, prevents frequency drop triggering UFLS, and enhances system safety.

Figure 3 (b) -3 (d) shows that EV clusters can effectively cope with net load fluctuations by undertaking a large amount of SFR reserve (accounting for 45.8% of the total). During periods 0-18, SFR upward reserve for thermal power units is exempted

to maintain high load rate; during periods 0-22 and 74-90, SFR downward reserve is exempted to enhance wind power absorption capacity.

Figure 3 (b), 3 (e)- 3 (f) show the peak regulation reserve (PR) allocation: The PR up-regulated reserve is borne by thermal power obligations; the higher cost PR down-regulated reserve is mainly provided by EV clusters at a cost, which avoids thermal power units entering the high-cost deep peak regulation (DPR) state and reduces economic and equipment losses.

6 Conclusions

This study employs a Minikowski addition and deep learning integration approach to quantify the dynamic dispatch potential of various electric vehicle (EV) resources during daily operations. By constructing an optimization model to coordinate their dispatch capabilities, it provides a basis for grid operators and EV aggregators (EVA) to formulate day-ahead dispatch plans involving multiple EV types. The proposed solution achieves coordination between EV clusters and conventional units in Frequency Control Assistance Services (FCAS) across all time scales, fully leveraging the flexible frequency regulation characteristics of distributed energy storage resources to assist conventional units in reserve provisioning. Simulation validation demonstrates that this scheme can withstand 15% stepwise disturbances to the system's maximum base capacity, significantly enhancing frequency security. Notably, load-side applications beyond EVs include air conditioning and electric water heaters, which also possess dispatch potential. Additionally, EV users' responsiveness to FCAS participation is a critical factor influencing cluster dispatch capacity – aspects not yet addressed in current frameworks, representing key research priorities for future development.

Acknowledgement： This work is supported by the Postdoctoral Science Foundation Funded Project of Heilongjiang Province under Grant LBH-Z24197; Key Research and Development Program Project of Heilongjiang Province under Grant 2024ZXDXC32; and Fundamental Research Foundation for Universities of Heilongjiang Province under Grant 2024-KYYWF-0948. (Corresponding author: Mingze Zhang).

References

1. Wang Huabiao, LI Xiaoyong. Prediction of electric vehicle charging load based on improved BiLSTM with hybrid attention mechanism[J]. Power System and Clean Energy, 2022, 38(6): 104-112
2. Hou Linan, Zhang Xiao, Luo Xiaofei, et al. Data-driven modeling and optimization for electric vehicle charging scheduling: A review[J]. Electrical Engineering, 2024(21): 39-43, 49.

3. WEI Yanyan. Research on control strategy of electric vehicles participating in primary frequency regulation of power grid[D]. Jiangsu: Jiangsu University, 2015.
4. Zhang Ruiqi, Yang Hui, Wang Zirui, et al. Construction and analysis of multi-time-period schedulable domain for electric vehicles in vehicle-garage-network hierarchical coordination control system[J]. Transactions of China Electrotechnical Society, 250425.
5. Zhan Liu, Yue Zhou, Lin Yufeng F, et al. Mechanism and implementation method of electric vehicle-grid interaction considering interests of different stakeholders[J]. Electric Power Automation Equipment, 2024, 44(11).
6. Zhan Xiangpeng, Yang Jun, Han Sining, et al. Two-stage market bidding strategy for charging stations considering schedulable potential of electric vehicles[J]. Automation of Electric Power Systems, 2021, 45(10): 86-96.
7. Zhang Mingze, Li Weidong, Yu Samson, et al. Optimal day-ahead large-scale battery dispatch model for multi-regulation participation considering full timescale uncertainties[J]. Renewable and Sustainable Energy Reviews, 2024, 189: 113963.
8. Zhang Mingze, Li Weidong, Yu Samson, et al. Day-ahead optimization dispatch strategy for large-scale battery energy storage considering multiple regulation and prediction failures[J]. Energy, 2023, 270: 126945.
9. WANG L, YU Z W, WEN F S. Optimal spinning reserve capacity determination based on chance-constrained programming[D]. 2006.
10. Subcommittee P M. IEEE reliability test system[J]. IEEE Transactions on power apparatus and systems, 1979 (6): 2047-2054.

029 Coordinated Optimal Planning of Stations and Networks in Hydrogen-Integrated Energy Systems

Zihan Qi[1], Peng Zhang[1], Xingtang He[1], Jie Wu[1], Xinhao Zhao[1]

[1] State key laboratory of Smart Power Distribution Equipment and System, Tianjin University
Tianjin:300072.China
zhqi@tju.edu.cn

Abstract. The rapid growth of global energy demand and the urgency of carbon emission reduction underscore the importance of integrated energy systems(IES). This study proposes a model for the coordinated optimal planning of stations and networks in hydrogen-integrated energy systems, which simultaneously optimizes the siting and capacity of multiple energy stations, the dispatch operation of equipment, and collaboratively plans the energy supply network between stations. The upper-level employs an improved *p*-median model, considering scenarios where energy stations cannot meet load demands, to determine the optimal number and locations of energy stations as well as their energy supply relationships with various load centers, aiming to minimize annual investment and operational costs. The lower-level employs mixed-integer linear programming to jointly optimize equipment capacities, inter-station energy pipeline capacities, and the operation of related equipment. The optimization model is formulated in MATLAB via the YALMIP modeling toolbox and solved using the commercial solver CPLEX. Case study results demonstrate that the model effectively avoids unreasonable site selection and load distribution imbalances. By introducing hydrogen energy and multi-energy coupling technologies, it enhances both the economic efficiency and environmental friendliness of the system while achieving efficient spatiotemporal transfer of energy.

Keywords: Hydrogen-integrated energy systems, Improved *p*-median model, Hydrogen energy, Coordinated optimal planning.

1 Introduction

The rapid growth in global energy demand and overdependence on fossil fuels are exacerbating resource depletion and environmental degradation. Developing integrated energy systems (IES) with multi-energy complementarity has become an inevitable pathway to improve energy efficiency [1-2]. Through multi-energy coupling, IES enables coordinated utilization of electricity, heat, cooling, and hydrogen, while supporting energy complementarity across stations via interconnected networks, thereby enhancing overall energy utilization efficiency.

Current research on the planning and operation of integrated energy systems primarily focuses on the capacity allocation and dispatch of equipment within energy stations. However, regarding the integrated optimization of sources and networks, literature [3] considers a gas-electricity interconnected integrated energy system and employs a multi-objective planning method to plan both the equipment inside energy stations and the pipelines and transmission lines. Literature [4] studies an integrated energy system composed of electricity, gas, heat, and cooling, constructing a two-level planning model where the upper level performs expansion planning for the energy networks, and the lower level plans the equipment capacity within the energy stations. Literature [5] investigates electricity-gas hybrid integrated energy systems, considers the coupling relationships among various energy forms, and optimizes the siting and capacity determination of units within energy stations, as well as transmission lines and natural gas pipelines. In contrast, literature [6] utilizes the Dijkstra algorithm to determine the supply relationships between energy stations and load points, and plans the equipment within the stations and the energy supply network between stations. However, simply using the shortest path algorithm to assign load points to energy stations and constructing inter-station supply pipelines accordingly can easily lead to the overloading of energy stations. Furthermore, research on the role of hydrogen energy in multi-energy systems is insufficient, particularly regarding the capacity configuration of electrolyzers, hydrogen storage tanks, and fuel cells. Moreover, there is scarce research on the initial planning of station-network systems for hydrogen-integrated energy systems.

To address these limitations, this paper proposes a collaborative station-network planning framework for hydrogen-integrated energy systems. The upper-level model, based on the classical *p*-median model, introduces the integrated energy distance and standardized load quantity to optimize the number and siting of energy stations, as well as the energy supply relationships with load centers, while considering the reassignment of load points in case of energy station overload. The lower-level model further conducts joint optimization of equipment capacities within stations and pipeline capacities between stations, considering multi-energy coupling and the integration of hydrogen energy technologies. Through this bi-level optimization framework, this study aims to reduce the annual investment and operational costs of the system, address issues such as unreasonable station siting and imbalanced load distribution, and achieve efficient spatiotemporal transfer of energy.

2 Basic Architecture of Hydrogen-Integrated Energy Station-Network

This paper models the equipment and energy supply network within the energy station based on the energy hub theory.

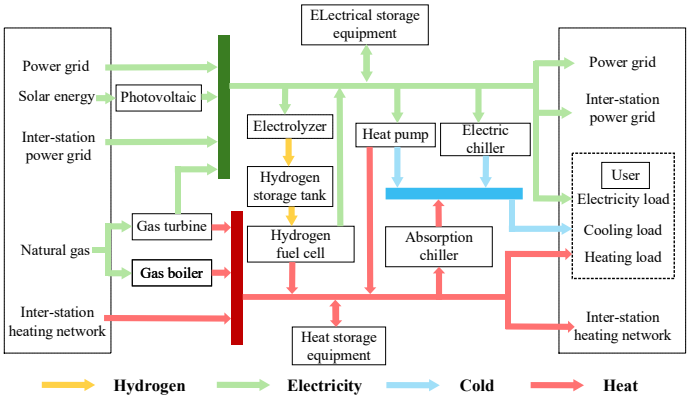


Fig. 1. Internal structure of the energy station

The internal structure of the energy station is shown in Fig. 1, and the mathematical model of the electrolyzer is as follows:

$$P_{t,j,H_2} = \eta_{EL} P_{t,j,EL} \tag{1}$$

Where P_{t,j,H_2} represents the hydrogen production output power of the electrolyzer (EL) at energy station j and time t; η_{EL} is the hydrogen production conversion efficiency of the electrolyzer; $P_{t,j,EL}$ corresponds to the electrical input power during hydrogen production.

The mathematical model of the hydrogen fuel cell is as follows:

$$\begin{cases} P_{t,j,HFC} = \eta_{HFC,e} P^{\mathrm{H_2}}_{t,j,HFC} \\ H_{t,j,HFC} = \eta_{HFC,h} P^{\mathrm{H_2}}_{t,j,HFC} \end{cases} \tag{2}$$

Where $P_{t,j,HFC}$ describes the power generation output of the hydrogen fuel cell (HFC) at energy station j and time t; $P^{\mathrm{H_2}}_{t,j,HFC}$ is the input power of the hydrogen fuel cell, and $\eta_{HFC,e}$ characterizes the power generation efficiency; $H_{t,j,HFC}$ is the heat generation power of the hydrogen fuel cell in energy station j at time t; $\eta_{HFC,e}$ and $\eta_{HFC,h}$ represent the conversion efficiency for electricity generation and heat generation of the hydrogen fuel cell, respectively.

The mathematical model of the hydrogen storage tank is analogous to that of electrical storage equipment and heat storage equipment:

$$W_{t_0,j,H_2} = W_{t,j,H_2} = W^0_{j,H_2} = \varepsilon_{H_2} W_{j,hes} \tag{3}$$

$$W^{ch}_{t,j,H_2} = \frac{P_{t,j,H_2}}{d_{H_2}} \tag{4}$$

$$W^{disc}_{t,j,H_2} = \frac{P^{H_2}_{t,j,HFC}}{d_{H_2}} \tag{5}$$

$$W_{t=1,j,H_2} = (1-\sigma_{H_2}) W_{j,H_2,0} + W^{ch}_{t,j,H_2} \eta^{ch}_{H_2} - W^{dis}_{t,j,H_2} / \eta^{dis}_{H_2} \tag{6}$$

$$W_{t,j,H_2} = (1-\sigma_{H_2}) W_{t-1,j,H_2} + W^{ch}_{t,j,H_2} \eta^{ch}_{H_2} - W^{dis}_{t,j,H_2} / \eta^{dis}_{H_2} \tag{7}$$

Where W_{t,j,H_2} defines the amount of hydrogen stored in the hydrogen storage tank (HES); W_{t_0,j,H_2} is the initial hydrogen storage amount at the start of the day; $\varepsilon_{H_2} j$ represents the initial capacity to construction capacity ratio; $W_{j,hes}$ is the construction capacity of the hydrogen storage tank in energy station *j*; σ_{H_2} refers to the self-discharge rate; W^{ch}_{t,j,H_2} and W^{disc}_{t,j,H_2} are the amounts of hydrogen charged into and released from the hydrogen storage tank at time *t*, respectively; d_{H_2} is the unit conversion coefficient for converting electrical energy into hydrogen energy of the same energy content, taken as 39.65 kW·h/Kg in this paper; $\eta^{ch}_{H_2}$ and $\eta^{dis}_{H_2}$ are the charging and discharging efficiencies of hydrogen in the hydrogen storage tank, respectively. The models of other equipment within the energy station can be found in reference [7].

3 Collaborative Initial Planning Model for Hydrogen-Integrated Energy Systems Considering Station-Network Layout

3.1 Improved P-Median Station-Network Collaborative Configuration Model

The *p*-median model is a classical location optimization model widely used to solve facility siting problems. This paper addresses the initial planning of a regional integrated energy system, where the quantity of energy stations is not fixed but a decision variable. Therefore, modifications are made to the standard p-median model. The standardized load at each center serves as a weighting factor, guiding the siting of *p* energy stations with the objective of minimizing the aggregate weighted integrated energy distance to the load centers, thus yielding an improved model. Furthermore, the investment and construction costs of the energy stations and the inter-station energy pipelines are also considered. The mathematical expressions for the objective function and constraints of the improved p-median model are as follows:

Objective Function:

$$\min C_{up} = \sum_{i,j} L_i d_i^{\min}(R_{i,j}) y_{i,j} + C_{low} \tag{8}$$

Constraints:

$$\sum_j y_{i,j} = 1 \tag{9}$$

$$\sum_j x_{i,j} = p \tag{10}$$

$$y_{i,j} \le x_j \tag{11}$$

$$p_{\min} \le p \le p_{\max} \tag{12}$$

In Equation (8), the objective function of the upper-level model is represented by C_{up}, which consists of two main components. $\sum_{i,j} L_i d_i^{\min}(R_{i,j}) y_{i,j}$ calculates the total weighted integrated energy distance, where L_i denotes the standardized load at load point i, $d_i^{\min}(R_{i,j})$ represents the lowest integrated energy distance from load point i to energy station j, and $y_{i,j}$ is a binary decision variable indicating whether load point ii is supplied by energy station j. C_{low} corresponds to the objective function of the lower-level model, which is detailed in the following section.

Integrated energy distance Model. In the improved p-median model, this study applies the concept of integrated energy distance to represent the cost between the selected energy stations and the load points. The integrated energy distance $R_{i,j}$ is defined as the cost of laying energy supply pipelines between energy station j and load point i, which consists of the investment cost $C_{i,j}^{inv}$ and the maintenance cost $C_{i,j}^{m}$ of the energy supply pipelines. The expression is as follows:

$$R_{i,j} = C_{i,j}^{inv} + C_{i,j}^{m} \tag{13}$$

$$\begin{cases} C_{i,j}^{inv} = \sum_{i,j} \phi_r D_{i,j} (\alpha_e s_{e,i,j} + \beta_e y_{e,i,j} + \alpha_h s_{h,i,j} + \beta_h y_{h,i,j} + \alpha_c s_{c,i,j} + \beta_c y_{c,i,j}) \\ \phi_r = \dfrac{m(1+m)^N}{(1+m)^N - 1} \\ C_{i,j}^{m} = z_1 C_{i,j}^{inv} \end{cases} \tag{14}$$

Standardized Comprehensive Load Model. Typically, the demand of load points is known. In the improved p-median model, it is necessary to calculate the weighted integrated energy distance based on the weight of each load point. Therefore, this paper introduces a weighting coefficient to represent the standardized comprehensive load of load point i over the course of a year L_i [8]. The specific expression is as follows:

$$L_i = \mu_i^e l_i^e + \mu_i^h l_i^h + \mu_i^c l_i^c \tag{15}$$

$$l_i^e = \frac{L_i^e}{L_{\max}^e} \tag{16}$$

$$L_i^e = \sum_t L_{t,i}^e \tag{17}$$

$$\mu_i^e = \frac{\dfrac{T_{i,\max}^e}{\kappa^e}}{\dfrac{T_{i,\max}^e}{\kappa^e} + \dfrac{T_{i,\max}^h}{\kappa^h} + \dfrac{T_{i,\max}^c}{\kappa^c}} \tag{18}$$

3.2 Integrated Optimization Model for Multi-Energy Station Planning and Operation

Objective Function. The optimization objective of the lower-level model is to minimize the total economic cost, including the investment and operational costs of equipment and networks, as well as the environmental protection cost.

$$\min C_{low} = C_{inv} + C_{om} + C_{grid} + C_{gas} + C_{env} \tag{19}$$

The objective function consists of five components: Equation (20) represents the annual investment cost, Equation (21) the annual operation and maintenance cost, Equation (22) the electricity purchase and sale cost, Equation (23) the fuel cost, and Equation (24) the environmental protection cost. The specific expressions are as follows:

$$C_{inv} = \sum_{j}(\sum_{s}\phi_s H_{j,s} c_{inv}) + \sum_{r}\sum_{j,k}\phi_r D_{j,k}(\alpha_r s_{r,j,k} + \beta_r y_{r,j,k}) \tag{20}$$

$$C_{om} = \sum_{t,j,s} P_{t,j,s} c_{j,s}^{om} \tag{21}$$

$$C_{grid} = \sum_{t,j}(P_{t,j}^{buy} c_t^{buy} - P_{t,j}^{sell} c_t^{sell}) \tag{22}$$

$$C_{gas} = c_F \frac{1}{G_{\mathrm{CH_4}}} \sum_{t,j,s} g_{t,j,s}^{GAS} \tag{23}$$

$$C_{env} = c^{Ctax}(E_f \sum_{t,j,s} g_{t,j,s}^{GAS} + \frac{E_{grid}}{\eta_{grid}} \sum_{t,j} P_{t,j}) \tag{24}$$

Constraints.

Equipment Capacity Constraints. The capacities of equipments are planning variables in the lower-level model, subject to the following constraints:

$$y_{j,s} S_{j,s}^{\min} \le S_{j,s} \le y_{j,s} S_{j,s}^{\max} \tag{25}$$

$$y_{r,j,k} s_{r,j,k}^{\min} \le s_{r,j,k} \le y_{r,j,k} s_{r,j,k}^{\max} \tag{26}$$

Equipment Operation Constraints. For equipment within energy stations, the operating power must be constrained within a certain range, as defined by the following general constraint:

$$x_{t,j,s} S_{j,s} \rho_{j,s,\min} \le P_{t,j,s} \le x_{t,j,s} S_{j,s} \rho_{j,s,\max} \tag{27}$$

Energy Storage Operation Constraints. The energy storage devices studied in this paper include electrical storage, thermal storage, and hydrogen storage tanks. The operational constraints for hydrogen storage tanks are provided here, with analogous constraints applying to electrical storage devices and thermal storage devices.

$$\rho_{H_2,\min} W_{j,hes} \le W_{t,j,hes} \le \rho_{H_2,\max} W_{j,hes} \tag{28}$$

$$0 \le W_{t,j,H_2}^{ch} \le x_{t,j,H_2}^{ch} \rho_{j,\max}^{ch,hes} W_{j,ees} \tag{29}$$

$$0 \le W_{t,j,H_2}^{dis} \le x_{t,j,H_2}^{dis} \rho_{j,\max}^{dis,hes} W_{j,ees} \tag{30}$$

$$x_{t,j,H_2}^{ch} + x_{t,j,H_2}^{disc} \le 1 \tag{31}$$

Energy Pipeline Constraints. The energy pipelines between stations studied in this paper include electrical and thermal pipelines. The operational constraints for these pipelines are as follows:

$$x_{t,r,jk}\rho_{r,j,k,\min}s_{r,j,k} \le q_{t,r,jk} \le x_{t,r,jk}\rho_{r,j,k,\max}s_{r,j,k} \tag{32}$$

$$x_{t,r,jk} + x_{t,r,kj} \le 1 \tag{33}$$

System Energy Balance Constraints.

$$\begin{aligned} L^{e}_{t,j} = {} & P_{t,j,GT} + P_{t,j,PV} + P_{t,j,HFC} - P_{t,j,EC} - P_{t,j,HP} - P_{t,j,EL} + \\ & (P^{dis}_{t,j,e} - P^{ch}_{t,j,e}) + (P^{sell}_{t,j} - P^{buy}_{t,j}) + \sum_{k}(q^{end}_{t,e,kj} - q^{start}_{t,e,jk}) \end{aligned} \tag{34}$$

$$\begin{aligned} L^{h}_{t,j} = {} & H_{t,j,GT} + H_{t,j,GB} + H_{t,j,HFC} - H_{t,j,AC} - H_{t,j,HP} + \\ & (P^{dis}_{t,j,h} - P^{ch}_{t,j,h}) + \sum_{k}(q^{end}_{t,h,kj} - q^{start}_{t,h,jk}) \end{aligned} \tag{35}$$

$$L^{c}_{t,j} = c_{t,j,AC} + c_{t,j,HP} + c_{t,j,EC} \tag{36}$$

Construction and Operation Constraints.

$$x \le y \tag{37}$$

Constraint (37) ensures that equipment can only operate after construction is completed.

3.3 Two-layer Model Optimization Process

Upper-Level Solution Strategy. In this paper, an exhaustive search method is adopted, traversing different combinations of stations to find the optimal solution. The specific algorithm procedure is as follows:

For the regional integrated energy system under study, it can be regarded as a graph $G = (V, E, W)$, where N is the set of candidate energy stations, M is the set of load points, and Q is the set of road network nodes, including both to-be-constructed and existing road network nodes. Let $\chi(N)$ denote the power set of N, and let $\chi_k(N)$ be the subset of $\chi(N)$ with cardinality k. The upper-level model imposes a constraint on the number of energy stations: $p_{\min} \le p \le p_{\max}$, where p is the number of energy stations. Let P be the set of selected energy stations, with $|P| = p$. Let C_{up} denote the objective function of the upper-level model, and $X = \{x_n \mid n = 1, 2, 3, \cdots p\}$ the set of supply relationships between energy stations and load points, where x_n represents the set of load points supplied by energy station n.

Step 1: Calculate the comprehensive load of each load point by inputting its electricity, heat, and cooling load demands, and input the coordinates of all nodes in the system graph G. Initialize the upper-level objective function $C_{up} = +\infty$, and let sets P and X be empty.

Step 2: Based on the connectivity of nodes in graph G, compute the adjacency matrix E. The elements of E are defined as $e(i, j)$. $e(i, j) = 0$ if nodes i and j are adjacent, otherwise $e(i, j) = 1$. Its expression is as follows:

$$e(i,j)=\begin{cases}1 & \text{If } i \text{ and } j \text{ are adjacent nodes}\\ 0 & \text{If } i \text{ and } j \text{ are non-adjacent nodes}\\ 0 & \text{If } i \text{ and } j \text{ are the same node}\end{cases} \tag{38}$$

$$\forall i,j \in N \cup M \cup Q \tag{39}$$

For each load point $m \in M$, calculate the integrated energy distance matrix R_m using the adjacency matrix E and the node coordinates in graph G. The element of matrix R_m is $r(i,j)$, defined as:

$$r(i,j)=\begin{cases}R_{i,j} & \text{If } i \text{ and } j \text{ are adjacent nodes}\\ \infty & \text{If } i \text{ and } j \text{ are non-adjacent nodes}\\ 0 & \text{If } i \text{ and } j \text{ are the same node}\end{cases} \tag{40}$$

Modify each load point's comprehensive distance matrix by setting elements corresponding to other load points (other than itself) to infinity.

Step 3: Initialize the number of energy stations as $p = p_{\min}$. If $p \le p_{\max}$, then set $\lambda = 1$; otherwise, go to Step 10.

Step 4: When $\lambda \le |\chi_k(N)|$ and k=p, let $\chi_k(N)$ be the λ -*th* element in $\chi_k^{\lambda}(N)$, which is the current set of selected energy stations. For each energy station in $\chi_k^{\lambda}(N)$, modify the comprehensive distance matrix by setting rows and columns corresponding to non-selected energy stations to infinity, yielding a modified distance matrix.

Step 5: Use the Dijkstra algorithm to compute the minimum comprehensive distance between each load point m and energy station n, denoted as $R_{m.n}$, and record the shortest path. For each load point j, assign it to the energy station i with the minimum integrated energy distance. Add load point j to the set x_i. Repeat until all load points are assigned, and calculate the total electricity, heat, and cooling loads each station must supply. The main procedure of the Dijkstra algorithm can be seen in Figure. 2.

Step 6: Check the loads supplied by each energy station. If any station exceeds its capacity, reassign the nearest load point (in terms of comprehensive distance) to another energy station with available capacity. Update set X and repeat Step 5 until all energy stations meet their capacity constraints.

Step 7: Check the supply relationship set X between energy stations and load points. When there exists $x_i = 0$, it means that energy station i does not supply any load point, that is, in the current set of energy stations $\chi_k^{\lambda}(N)$, there always exists an energy station γ such that $d_{m,\gamma} < d_{m,i}$. If at this time $p = p_{\min}$, then the current energy station combination does not satisfy the condition; If at this time $p > p_{\min}$, then the current energy station combination degenerates and coincides with one of the combinations when the number of energy stations is p−1. In this case, let $\lambda = \lambda + 1$, and return to Step 3. If all $x_i \ne 0$, then it indicates that each energy station supplies the required load points and proceeds to Step 7.

Step 8: Calculate the upper-level objective function C_{up}, in which the annual investment cost is returned from the lower-level model. If $C_{up} < C_{up,\min}$ (where $C_{up,\min}$ is the current minimum objective function value), then update the objective function, let $C_{up} = C_{up,\min}$, $P = \chi_k^{\lambda}(N)$, save X; let $\lambda = \lambda + 1$, and return to Step 4.

Step 9: Let $p = p + 1$, and return to Step 3.

Step 10: Output the value of the upper-level objective function C_{up}, the number of selected energy stations p, the selected combination of energy stations P, the supply relationship set $\chi_k^{\lambda}(N)$ between energy stations and load points, and the optimal routing of energy supply pipelines.

Lower-Level Solution Strategy. The lower-level model, which optimizes equipment and pipeline capacities along with hourly operational power, is formulated as a 0-1 mixed-integer nonlinear program and linearized using standard techniques; it is solved via YALMIP/MATLAB with CPLEX to minimize the total cost C_{low}, and the resulting value of C_{low} is then returned to the upper-level model.

4 Case Study

This study takes a regional integrated energy system in a northern area of China [7] as a case to validate the effectiveness and practicality of the proposed two-layer collaborative initial planning model. The system includes 62 existing road network nodes, 58 additional nodes planned for construction, 6 potential energy station nodes identified based on regional needs and conditions, and 14 distinct load nodes. Among these, nodes 127–129 represent three electrical load centers, nodes 130–133 are integrated electrical and thermal load centers, and nodes 134–140 comprise seven electrical, thermal, and cooling load centers.

10

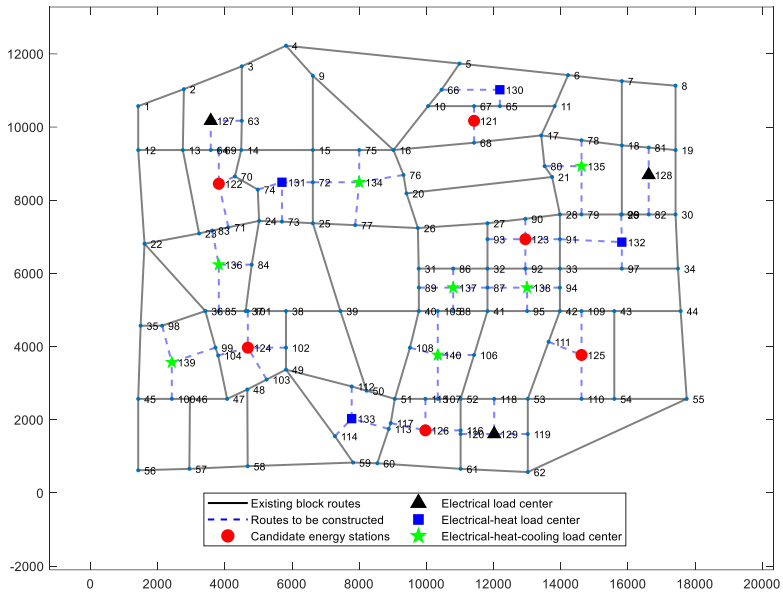


Fig. 2. Schematic Diagram of the Regional Integrated Energy System Structure

The planning results for different energy station combinations with varying quantities and locations are shown in fig. 2. The horizontal axis represents the index of valid planning solutions, while the vertical axis indicates the station-network collaborative construction cost in yuan.

4.1 Optimal Selection of the Number and Locations of Energy Stations

As shown in fig. 3, when p=2, the combination {123, 124}is a local optimal solution, designated as Scenario 1. When p=3, the combination {123, 124, 126} is a local optimal solution, designated as Scenario 2. When p=4, the combination{121, 123, 124, 126}is a local optimal solution, designated as Scenario 3.

Comparing the local optimal solutions under the three energy station quantities (Scenario 1, 2, and 3), it can be observed that when p=4 with the combination {121, 123, 124, 126}, the total cost of the station-network collaborative configuration obtained by the upper-level model is minimized. Therefore, Scenario 3 is identified as the global optimal solution. A comparison of costs under different scenarios is shown in Table 1.

Table 1. Cost Comparison in Scenarios 1-3

Scenario	C_{up} /(10^4 yuan)	$R_{i,j}$ /(10^4 yuan)	C_{low} /(10^4 yuan)	C_{inv} /(10^4 yuan)	C_{om} /(10^4 yuan)	C_{grid} /(10^4 yuan)	C_{fuel} /(10^4 yuan)	C_{Env} /(10^4 yuan)

1	9556.79	724.79	8831.99	1075.42	138.37	2253.62	3884.42	1480.16
2	9072.46	625.19	8447.27	1244.89	144.63	1635.04	3997.68	1425.02
3	8753.67	550.34	8203.32	1442.13	149.76	1185.43	4059.18	1366.83

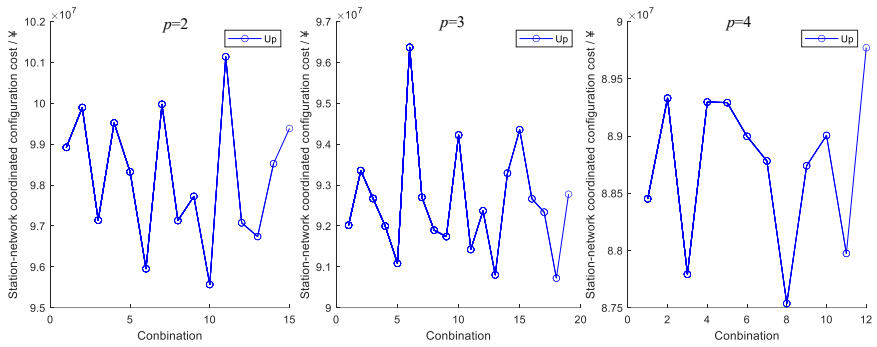


Fig. 3. Schematic Diagram of the Regional Integrated Energy System Structure

Since the load demand at each load point is fixed, an increase in the number of energy stations leads to a corresponding reduction in the electricity, heating, and cooling loads that each station needs to supply. As a result, the amount of electricity and natural gas purchased by each energy station from the upper-level grid and the natural gas network is significantly reduced, ultimately lowering the electricity procurement cost, environmental cost, and the total operational cost at the lower level for each energy station. Conversely, if the number of energy stations decreases, each station must supply a larger load, leading to an increase in costs.

Figure 2 shows that energy station 125 is considerably distant from the other load points, which leads to a larger integrated energy distance. Therefore, during the optimization process, when p=2 and the energy station combination is {123,125}, if only the Dijkstra shortest path algorithm is used to assign load points with the smallest integrated energy distance to the energy stations, only load points 129 and 133 are supplied by energy station 135, while the remaining load points are all supplied by energy station 123. This ultimately results in an overload at energy station 123, specifically in terms of thermal load, making it unable to meet the load demands of all load points. In contrast, the algorithm proposed in this paper adjusts the loads supplied by energy station 123, which exceeds its supply capacity. Among them, load point 128 is the load point with the smallest integrated energy distance to energy station 125. However, load point 128 is an electrical load center and has no thermal load demand. Transferring it to energy station 125 provides little help in alleviating the thermal load pressure on energy station 123. Load point 138, as the load point with the second-smallest integrated energy distance to energy station 125, is subsequently assigned to energy station 125 for supply. However, after algorithmic verification, energy station 123 still cannot meet the load demand. Therefore, load point 132, as the load point with the third-smallest integrated energy distance to energy station 125,

is assigned to energy station 125. After another verification, energy station 123 is finally able to meet the load demand. However, this solution incurs higher costs and is ultimately discarded.

4.2 Equipment Capacity and Inter-station Energy Pipeline Capacity Configuration Plan

The equipment capacity within energy stations and the capacity of inter-station energy supply pipelines obtained from the planning of Scenario 3 are shown in the tables below:

Table 2. Equipment Capacity Planning Results

Energy Station	GT /kW	GB /kW	PV /kW	AC /kW	EC /kW	HP /kW	EL /kW	HFC /kW	EES /(kW·h)	TES /(kW·h)	HES /Kg
121	1198.09	240.41	2000	565.4	52.88	769.13	0	0	3000	3000	0
123	2781.04	430.41	2000	1780	498.77	1404.9	0	0	3000	3000	0
124	2342.77	96.23	2000	1755	400	1125.33	0	0	3000	3000	0
126	1430.54	173	2000	870	190	699.05	38.59	49.46	3000	3000	7.34

Table 3. Inter-station Energy Pipeline Planning Results

Power transmission pipeline capacity between stations /kW						Heat supply pipeline capacity between stations /kW					
121-123	121-124	121-126	123-124	123-126	124-126	121-123	121-124	121-126	123-124	123-126	124-126
371.68	0	0	0	0	0	0	0	0	0	0	0

From the planning results of Scenario 3, it can be observed that the planned capacity of photovoltaic equipment in each energy station has reached the upper limit of installation capacity. Additionally, the planned capacities of electrical and thermal storage equipment have also reached their upper limits, indicating that energy storage devices play a crucial role in reducing total costs, integrating clean energy, and peak shaving.

As another key energy storage component in the hydrogen-integrated energy system, the hydrogen storage tank also plays a significant role. Under the optimized configuration, Energy Station 126 is planned to be equipped with an electrolyzer, a hydrogen storage tank, and a hydrogen fuel cell. The combination of electrolyzer, hydrogen storage tank, and hydrogen fuel cell can strengthen the coupling among electricity, heat, and hydrogen. However, due to the relatively low energy conversion efficiency of the electrolyzer and the hydrogen fuel cell, this setup leads to considerable energy loss under the conditions defined in this case. Therefore, although the hydrogen stor-

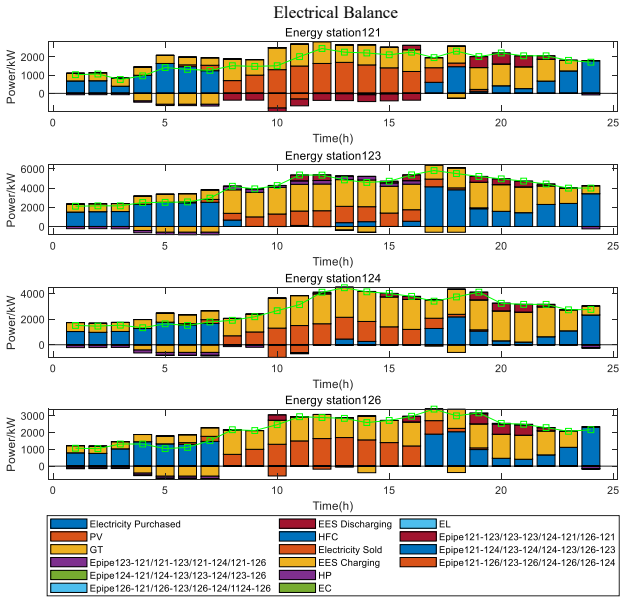
age tank exhibits low self-loss, it is not selected as the preferred energy storage option in the optimal planning results.

In Scenario 3, the installed capacity of inter-station power supply pipelines is 371.68 kW. These pipelines enable energy transfer between different energy stations, improving economic efficiency and reliability of system operation.

4.3 Typical Daily Operation Strategy of Energy Stations

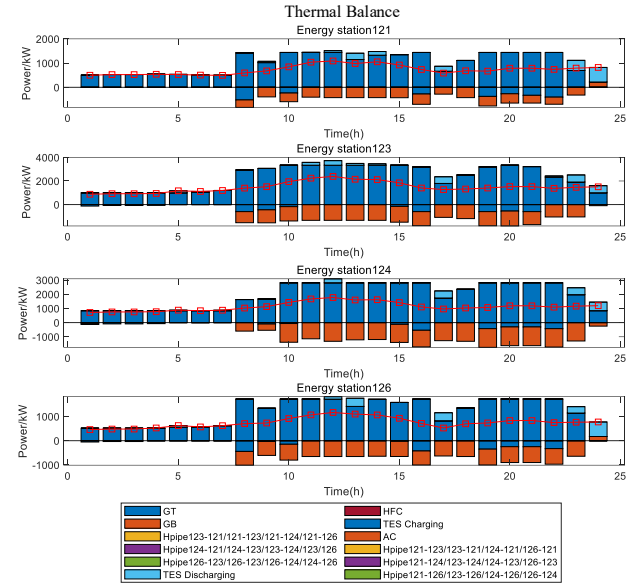
Taking summer as an example, daily load balance is analyzed from the perspectives of equipment operation status and output:

Summer Operation Results.

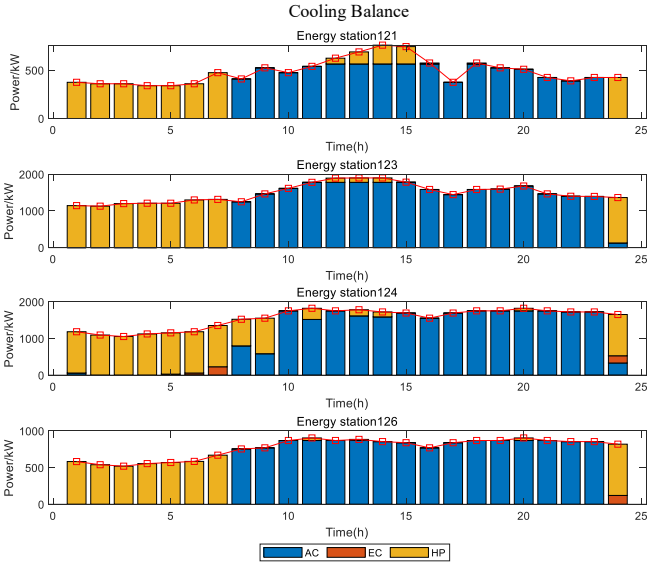


(a) Electrical Balance

14



(b) Thermal Balance



(c) Cooling Balance

Fig. 4. Typical Summer Day Operation Results

Summer residential electricity demand exhibits a "double peak" characteristic. In the early morning, energy stations primarily rely on purchasing electricity from the grid and gas turbine generation. At night, cooling demand is almost entirely met by heat pumps.

During daytime (8:00–18:00), with sufficient sunlight, user electricity demand is mainly supplied by photovoltaic (PV) systems and gas turbines. Shortfalls are supplemented by energy storage equipment discharge and grid purchases. Excess electricity can be sold to the grid, transferred to other stations via inter-station power pipelines, stored in batteries, or used by electrolyzers to produce hydrogen for storage.
For daytime cooling demand, in addition to electric chillers, heat pumps supply the remaining cooling load. Evening electricity demand is mainly met by gas turbines, battery discharge, and grid purchases. Summer daily heat demand is low and largely satisfied by gas turbine waste heat, with surplus heat stored in thermal storage systems.
Due to its lower load, energy station 121 transfers excess electricity to energy station 123 via inter-station pipelines, alleviating the supply pressure on energy station 123.

5 Conclusion

This study proposes a collaborative planning framework for hydrogen-integrated energy station-networks to address these challenges. The framework simultaneously determines the optimal locations, capacities, and operational strategies of multiple energy stations, while coordinating the configuration of the inter-station energy supply network. By incorporating hydrogen energy production, storage, and conversion, alongside multi-energy coupling technologies, the proposed method achieves a significant reduction in overall system costs while enhancing the utilization rate of renewable energy. Furthermore, it effectively mitigates issues such as irrational facility siting, imbalanced load distribution among stations, and excessive energy transmission costs. However, it should be noted that the model developed in this study does not account for the delay effects in electricity and heat supply, and all time steps are calculated on an hourly basis. Future work could enhance the model's sophistication by incorporating factors such as power flow calculation.

References

1. WANG Dan, MENG Zhengji, JIA Hongjie, et al. Research and prospect of key technologies for energy interconnection system planning for new-type towns[J]. Automation of Electric Power Systems, 2019, 43(14):16-28.
2. WANG D, WANG C, LEI Y, et al. Prospects for key technologies of new-type urban integrated energy system[J]. Global Energy Interconnection, 2019, 2(5):403-413.
3. LÜ Zhenhua, LI Qiang, HAN Huachun. Research on planning of integrated gas-electricity energy system based on multi- objective[J]. Power Capacitor & Reactive Power Compensation, 2021, 42(5):214-220.
4. HUANG Wujing, ZHANG Ning, DONG Ruibiao, et al. Coordinated planning of multiple energy networks and energy hubs[J]. Proceedings of the CSEE, 2018, 38(18):5425-5437
5. HUANG Guori, LIU Weijia, WEN Fushuan, et al. Collaborative planning of integrated electricity and natural gas energy systems with power-to-gas stations[J]. Electric Power Construction, 2016, 37(9):1-13.

16

6. HUANG Wei, LIU Wenbin. Multi-energy complementary based coordinated optimal planning of park integrated energy station-network[J]. Automation of Electric Power Systems,2020, 44(23): 20-28
7. ZHANG Ying, HUANG Wei, LIU Wenbin, et al. Energy Station-network Collaborative Planning with Flexible Load [J]. Journal of Electrical Engineering, 2022, 17(02):176-186.
8. SHEN Xinwei, ZHU Shouzhen, ZHENG Jinghong, et al. Active distribution network planning-operation co-optimization considering the coordination of ESS and DG [J]. Power System Technology, 2015, 39(7):1913-1920.

030 面向量子通信设备部署的电力系统信息安全强化策略

何宇昊[1]，钱雨琦[1]，谢海鹏[1]

(1.西安交通大学，陕西 西安 710049)

A Strategy for Enhancing Power System Information Security Oriented Towards Quantum Communication Equipment Deployment

HE Yuhao[1], QIAN Yuqi[1],XIE Haipeng[1]

(1. Xi'an Jiaotong University, 710049, China)

ABSTRACT: With the significant improvement in the degree of information-physical coupling in new power systems, cyber attacks represented by false data injection attacks pose a threat to power business security and dispatching decisions. This study first established a state estimation system based on the linearized DistFlow model using the weighted least squares method, and introduced the Dijkstra algorithm to analyze the communication routing characteristics to optimize the weight distribution of measurement data. Secondly, a quantum communication equipment deployment strategy based on the "defense-attack-defense" model was proposed. The column constraint generation algorithm was used to solve the constructed two-stage robust optimization model, and an IEEE33 node example was selected for evaluation. Simulation analysis shows that this strategy can effectively reduce the system state estimation error caused by FDIA. Compared with traditional methods, it is more effective and adaptable under different attack scales, effectively improving the network attack defense capability of the distribution network and providing a theoretical reference for the targeted deployment of quantum communication equipment in the distribution network.

KEY WORDS: quantum communication; state estimation; false data injection attack; robust optimization; column and constraint generation algorithm

摘要：随着新型电力系统中信息物理耦合程度的显著提升，以虚假数据注入攻击为代表的网络攻击对电力业务安全和调度决策构成威胁。本研究首先基于线性化的 DistFlow 模型，采用加权最小二乘法建立了状态估计体系，并引入 Dijkstra 算法分析通信路由特征以优化量测数据的权重分配。其次，提出了基于“防御-攻击-防御”模型的量子通信设备部署策略，采用列约束生成算法求解所构建的两阶段鲁棒优化模型，同时选取了 IEEE33 节点算例进行评估。仿真分析表明，本策略能有效降低 FDIA 造成的的系统状态估计误差，与传统方法相比，在不同攻击规模下效果均更好且更具适应性，有效提升了配电网的网络攻击防御能力，对量子通信设备在配电网中的定向部署提供了理论参考。

关键词：量子通信；状态估计；虚假数据注入攻击；鲁棒优化；列约束生成算法

DOI：

0 引言

为实现“双碳”目标，习近平总书记指出要构建以新能源为主体的新型电力系统。随着大规模分布式新能源和海量智能终端的接入，新型电力系统的信息物理耦合程度显著提升[1-3]，直接与用户相连的配电网中设备数量激增、网络攻击风险增大，且通信网络的故障极易引发物理层的连锁性故障，电力系统的信息安全需求愈加迫切[4]。

虽然中国实行“安全分区、网络专用、横向隔离、纵向认证”原则[5]的电力通信体系在网络架构上具备较高安全性，但在信息物理电力系统(Cyber Physical Power System,CPPS)的环境下，以虚假数据注入攻击(False Data Injection Attack，FDIA)为代表的电力系统网络攻击对电力业务安全和调度决策构成威胁[6]，攻击者可以通过注入虚假的新能源预测信息、电力市场信息等方式实施攻击[7]。乌克兰大停电事故就是二次系统遭遇网络攻击后引发一次系统故障的典型案例[8]。

量子密钥分发(Quantum key distribution，QKD)作为当前最成熟的量子通信技术，能够在物理层面实现无条件安全通信，为解决电力系统中的信息安全隐患提供了富有潜力的手段[9-10]。然而，传统的 QKD 网络局限于小规模网络，难以满足大规模电力系统的通信需求[11]。因此，亟需开展基于 QKD

的电力系统通信安全强化研究，构建适用于电力系统的 QKD 网络架构，并针对不同攻击场景制定通信网络安全强化策略，从而实现关键电力应用的安全通信。

电力系统状态估计作为电网实时监测与安全运行的关键技术，其目标是为调度决策与设备保护提供精确信息[12]。面对新型电力系统信息物理深度耦合带来的安全挑战，本文围绕配电网状态估计的信息安全展开研究，提出针对 FDIA 的配电网状态估计信息安全防御策略，构建三层博弈模型，通过量子加密通信设备的部署，为复杂攻防场景下的关键节点防护提供系统性解决方案。

1 配电网抵御信息攻击的基础理论与方法

1.1 配电网状态估计模型的建立

1.1.1 状态估计的参数定义

对于一个系统，量测量 z 与待估计的状态变量 x 的关系见式(1)，假设量测噪声服从正态分布且各量测数据之间相互独立。

$$z = h(x) + e \tag{1}$$

式中：$h(x)$为关于状态变量 x 的非线性函数；e 为量测误差向量。

定义状态变量 x 为支路的有功功率 P_l 和无功功率 Q_l，即 $x=[P_1,Q_1,P_2,Q_2,...,P_m,Q_m]^{\mathrm{T}}$。定义量测量 $z=[z_{voltage},z_{load}]^{\mathrm{T}}$，其中 $z_{voltage}$ 是根节点与非根节点之间电压差的集合；而 z_{load} 是非根节点的有功负荷 $P_{l,k}$ 和无功负荷 $Q_{l,k}$。

采用 Distflow 模型来刻画辐射状配电网[13]。定义配电网 $G=(V,E)$，如图 1 所示，其中 V 和 E 分别是系统 G 中节点和线路的集合。

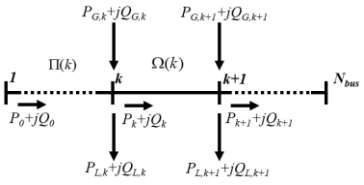


图 **1** DistFlow 模型示意图

Fig.1 Schematic diagram of the DistFlow model

在忽略线路网损后，可以得到线性化的 DistFlow 模型，如公式(2)至公式(4)所示[14]。如此，可以使系统状态估计的量测方程线性化。

$$\sum_{l\in\Omega(j)} P_l - \sum_{l\in\Pi(j)} P_l = P_{G,j} - P_{L,j}, \forall j \in V \tag{2}$$

$$\sum_{l\in\Omega(j)} Q_l - \sum_{l\in\Pi(j)} Q_l = Q_{G,j} - Q_{L,j}, \forall j \in V \tag{3}$$

$$u_i - u_j = (r_l P_l + x_l Q_l), \forall l = (i,j) \in E \tag{4}$$

式中：对于某线路 l，P_l 与 Q_l 是线路 l 首端流过的有功和无功功率；对于某节点 j，u_j 是电压幅值，$P_{L,j}$ 是有功负荷，$Q_{L,j}$ 是无功负荷，$P_{G,j}$ 是电源的有功出力，$Q_{G,j}$ 是电源的无功出力；$\Pi(j)$是以节点 j 为末节点的线路集合，$\Omega(j)$是节点 j 为始节点的线路集合。

1.1.2 构造量测矩阵

（1）电压量测矩阵 $H_{voltage}$

对于非根节点 k，其电压与支路功率的关系式为：

$$z_{voltage,k} = U_{root} - U_k = \sum_{(i,j)\in Path(k)} (r_{ij}P_{ij} + x_{ij}Q_{ij}) + e_{voltage,k} \tag{5}$$

式中：$z_{voltage,k}$ 是根节点与节点 k 的电压差；根节点电压 U_{root}=1.0*p.u.*；*Path(k)*指从根节点到节点 k 的路径；电阻 r 和电抗 x 是已知的支路参数；$e_{voltage,k}$ 指电压数据量测误差向量。

从而得到电压差与支路功率关系的矩阵形式：$z_{voltage,k}=H_{voltage}\,x+e_{voltage,k}$，其中 $H_{voltage}$ 是电压量测矩阵，$e_{voltage,k}$ 是电压量测量的误差向量。$H_{voltage}$ 为系统量测矩阵 H 的一部分，其每一行对应一个非根节点的电压方程，若支路(i,j)不在路径 *Path(k)*上，则对应元素为 0。

（2）负荷伪量测矩阵 H_{load}

本研究不涉及分布式发电，令 $P_{G,j}=Q_{G,j}=0$，对于非根节点 k，功率平衡方程为：

$$\begin{cases} \sum_{l\in\Pi(j)} P - \sum_{l\in\Omega(j)} P_l = P_{L,k} \\ \sum_{l\in\Pi(j)} Q_l - \sum_{l\in\Omega(j)} Q_l = Q_{L,k} \end{cases} \tag{6}$$

从而得到功率平衡方程的矩阵形式：$z_{load,k}=H_{load}\,x+e_{load,k}$，其中 H_{load} 是负荷伪量测矩阵，$e_{load,k}$ 是负荷伪量测量的误差向量。H_{load} 为量测矩阵 H 的一部分，其每一行对应节点流入/流出支路的系数，流入是+1，流出是-1。

在获得 $H_{voltage}$ 和 H_{load} 之后，可以构造系统量测矩阵 $H=[H_{voltage}, H_{load}]^{\mathrm{T}}$。

1.1.3 基于加权最小二乘法的状态估计

给定量测量 z 后，基于加权最小二乘法的目标函数为[15]：

$$\min J(x) = (z - Hx)^{\mathrm{T}} W (z - Hx) \tag{7}$$

式中：W 是权重矩阵，反映量测的可靠性。

在本研究中，采用基于 Dijkstra 算法的通信路由分析方法[16]确定各节点量测数据的置信程度，以此得到状态估计中各量测数据的权重。具体而言，即获取各节点到调控中心的最短通信路由，并通过统计所有路由中各通信节点的被经过频次，定量评估节点在网络中的重要性。在进行置信程度分级来确定各量测数据的方差后，可以得到权重矩阵，进而计算状态变量 x 的估计值，即令 *J(x)*对 x 的导数为 0，可得到状态变量估计值 $\hat{x}=(H^{\mathrm{T}}WH)^{-1}H^{\mathrm{T}}Wz$。

1.2 虚假数据注入攻击对状态估计的影响

为了电网安全运行，调度控制中心会对电网量测数据进行不良数据检测，传统检测方法是残差检验[17]，而隐蔽性强的 FDIA 能够绕过检测，将虚假

数据注入 SCADA 系统的量测数据集。被篡改的数据经通信网络传递到调控中心干扰状态估计。系统被注入虚假数据后，调控中心实际接收到的量测量 $z_{att}=z+\delta$，其中 z 是实际量测量；δ 是虚假数据。

本文研究的网络攻击聚焦于成功绕过检测的 FDIA，其机制如下。

假设攻击者成功获得矩阵 H，则可以构造攻击向量$\delta=Hc$，其中 c 是一个常向量。该构造方式使δ存在于 H 的列空间中。在调控中心进行的状态估计过程为：

$$\begin{aligned}\hat{x}_{att}&=\left(H^{\mathrm{T}}WH\right)^{-1}H^{\mathrm{T}}Wz_{att}\\&=\left(H^{\mathrm{T}}WH\right)^{-1}H^{\mathrm{T}}W(z+\delta)\\&=\left(H^{\mathrm{T}}WH\right)^{-1}H^{\mathrm{T}}W(z+Hc)=\hat{x}+c\end{aligned}\tag{8}$$

由式(8)知，攻击之后得到的状态变量相比于攻击前只多了一个常向量 c，则残差保持不变，如式(9)所示，则δ将无法被残差检测发现。

$$\begin{aligned}r_{att}&=z_{att}-H\hat{x}_{att}\\&=(z+\delta)-H(\hat{x}+c)\\&=(z-H\hat{x})+(\delta-Hc)\\&=z-H\hat{x}\\&=r\end{aligned}\tag{9}$$

攻击者通过掩盖真实的网络状态信息，诱导调度人员做出错误决策。例如，当系统处于安全运行状态时，可能诱使调度员执行不必要的切负荷操作；而在系统面临紧急情况时，又可能导致调度员未能及时采取必要的控制措施[8]。本文研究的信息攻击影响仅讨论 FDIA 对状态估计造成的直接误差影响，不讨论状态估计误差导致的潜在误操作造成的后续影响。下一章针对配网级的通信网络设计了节点防御策略，并采用列约束生成(Column and Constraint Generation,C&CG)算法求解构建的两阶段鲁棒优化问题[18]。由于通信节点是 FDIA 的主要目标，故不确定性攻击场景集可构造为[19]：

$$\mathcal{D}:=\{\sum_{i\in V}v_i\le B_{att}\}\tag{10}$$

式中：B_{att} 为被攻击节点的上限；v_i 是攻击者的 0/1 决策变量。

2 针对量子通信设备部署的安全强化策略

2.1 基于 DAD 架构的量子设备部署模型

2.1.1 量子设备部署模型的目标函数

本节建立了 CPPS 配置量子通信装置防御 FDIA 的三层优化模型，反映了防御者与攻击者之间的博弈。目标函数为：

$$\min_{q\in C}\ \max_{v\in C}\ \min_{\boldsymbol{y}}(\boldsymbol{\omega}\left\|\boldsymbol{x}_{att}-\boldsymbol{x}_{true}\right\|)\tag{11}$$

式中：$\left\|\hat{x}_{att}-x_{true}\right\|$代表系统遭受 FDIA 后状态变量的误差；$q$ 是防御者的 0/1 决策变量；v 是攻击者的 0/1 决策变量；$\boldsymbol{\omega}$ 是状态变量误差的权重，表示某状态变量的误差对系统运行的重要程度；$\boldsymbol{y}$ 是连续变量的集合，表示为 $\boldsymbol{y}=[b, c, att, att_v, att_{load}, x_{est}, x_{diff}, z_{att}]^{\mathrm{T}}$。

此处对于优化变量 $\boldsymbol{y}$ 统一做出解释：b 是引入的辅助变量，使目标函数线性化；c 是攻击者构造攻击向量时引入的常向量；att 是攻击者构造的虚假数据，它分为两部分，分别是针对电压量测数据的 att_v 和针对负荷伪量测数据的 att_{load}；x_{est} 是系统遭受网络攻击后得到的状态估计结果；x_{diff} 是 x_{est} 与系统实际状态变量值 x_{true} 之差；z_{att} 是被掺杂虚假数据后的量测数据。

三层问题均针对系统状态变量误差，目标分别是最小化、最大化、最小化状态变量误差。为了将原问题转化为线性规划问题，引入辅助变量 b_i，通过设定 b_i 和$\left\|\hat{x}_{att}(i)-x_{true}(i)\right\|$的相关约束，将目标函数转化为：

$$\min_{q\in C}\ \max_{v\in C}\ \min_{\boldsymbol{y}}\sum_{i=2}^{n}\omega_i b_i\tag{12}$$

第一层 min 指防御者配置量子通信加密装置，目标是在有限的防御预算内，通过选择性地配置量子加密装置，尽量降低 FDIA 引起的状态估计误差。根据量子通信的无条件安全性，我们认为某节点在部署设备后，量测数据将不会受到攻击者的干扰。决策变量是 0/1 变量 q_i，当 q_i=1 时，表示节点 i 配置了量子通信加密设备；当 q_i=0 时，表示节点 i 未配置设备。

第二层 max 指攻击者依据其预算选择目标节点进行攻击，其目标是使系统的状态估计误差最大化。决策变量是 0/1 整数变量 v_i，当 v_i=1 时，表示节点 i 遭到了 FDIA 攻击；当 v_i=0 时，表示节点 i 未遭到攻击。

引入 0/1 变量 $F_i=1-v_i(1-q_i)$来表示通信节点 i 的最终状态，F_i=1 表示通信节点 i 未受到网络攻击影响，即未被攻击者选中或配置了量子通信加密设备；F_i=0 表示节点 i 受到虚假数据注入。对于 F_i，需要进行线性化操作。引入辅助变量 $s_i=v_i(1-q_i)$，线性化后如下所示：

$$\begin{cases}s_i\le v_i\\ s_i\le 1-q_i\\ s_i\ge v_i+(1-q_i)-1\\ F_i=1-s_i\end{cases}\tag{13}$$

第三层 min 是状态估计误差最小化问题，指系统在获得 z_{att} 后进行最优状态估计，在给定的虚假数据注入下，尽可能将状态估计误差降到最低。

2.1.2 约束条件

（1）预算约束

$$\begin{cases}\sum_{i\in V}q_i\le B_{def}\\ \sum_{i\in V}v_i\le B_{att}\end{cases}\tag{14}$$

在 DAD 模型中，防御预算 B_{def} 与攻击预算 B_{att} 指防御或攻击通信节点的数量。该约束确保防御策

略在经济可行范围内进行量子加密设备部署。

（2）辅助变量 b_i 的上下界约束

b_i 的下界约束为：

$$\begin{cases} b_i - x_{diff,i} \geq 0 \\ b_i + x_{diff,i} \geq 0 \end{cases} \tag{15}$$

式中：对于状态分量 i，$x_{diff,i}$ 指 $x_{est,i}$ 与真实状态变量值 $x_{true,i}$ 之差。

状态分量 i 可能引起的最大状态变量误差分量存储在矩阵 M_b 中，对于节点 j，只有当 s_j=1 时，才允许对应部分贡献误差，则 b_i 的上界约束为：

$$b_i - \sum_{j=2}^{n} M_b(i,j)s_j \leq 0 \tag{16}$$

（3）决策变量线性化约束

该约束同式(13)。

（4）虚假数据注入约束：

$$-(F_i - 1)att_{\max} \leq att \leq (F_i - 1)att_{\max} \tag{17}$$

式中：att_{max} 表示合理的最大虚假数据注入量，并对电压量测量注入和负荷伪量测量注入分别进行讨论。

（5）状态估计约束

$$\begin{cases} x_{est} - (H^{\mathrm{T}}WH)^{-1}H^{\mathrm{T}}Wz_{att} = 0 \\ x_{est} - x_{diff} = x_{true} \end{cases} \tag{18}$$

此约束基于加权最小二乘法构建的状态估计方程，表示了状态估计过程。

（6）列空间约束

$$att = Hc \tag{19}$$

该约束刻画了 FDIA 绕过传统残差检测的隐蔽性机制。

2.2 使用 C&CG 求解 DAD 模型

本节采用 C&CG 算法对三层优化模型求解，引入辅助变量，并采用大 M 法对非线性项进行线性化。将三层优化模型的上层模型作为第一阶段主问题，采用强对偶理论将下层问题与中层问题转换成单层问题，以此作为第二阶段子问题。

2.2.1 优化问题紧凑化

紧凑化后的两阶段鲁棒优化模型如下。

$$\min_{q}\{\max_{\boldsymbol{m}} \min_{y\in\Omega(q,\boldsymbol{m})} \boldsymbol{c}^{\mathrm{T}}\boldsymbol{y}\}$$
$$\Omega(q,\boldsymbol{m}) = \begin{cases} \boldsymbol{D}_{\boldsymbol{m}}\boldsymbol{m} \leq \boldsymbol{d} \\ \boldsymbol{E}_{\boldsymbol{y}}\boldsymbol{y} \geq \boldsymbol{0} \\ \boldsymbol{P}_{\boldsymbol{m}}\boldsymbol{m} + \boldsymbol{P}_{\boldsymbol{y}}\boldsymbol{y} \leq \boldsymbol{n} \\ \boldsymbol{A}\boldsymbol{y} = \boldsymbol{h} \end{cases} \tag{20}$$

式中：$\boldsymbol{c}$ 为目标函数对应的系数列向量；$\boldsymbol{D}_{\boldsymbol{m}}$、$\boldsymbol{E}_{\boldsymbol{y}}$、$\boldsymbol{P}_{\boldsymbol{m}}$、$\boldsymbol{P}_{\boldsymbol{y}}$、$\boldsymbol{A}$ 为对应约束中变量的系数矩阵；$\boldsymbol{d}$、$\boldsymbol{n}$、$\boldsymbol{h}$ 为常数列向量；不确定变量 $\boldsymbol{m}$ 是变量 v、s、F 的集合；$\Omega(q,\boldsymbol{m})$表示在给定一组$(q,\boldsymbol{m})$时，优化变量 $\boldsymbol{y}$ 的可行域。

紧凑化过程为：约束 $\boldsymbol{D}_{\boldsymbol{m}}\boldsymbol{m}\leq\boldsymbol{d}$ 对应预算约束和决策变量线性化约束；约束 $\boldsymbol{E}_{\boldsymbol{y}}\boldsymbol{y}\geq\boldsymbol{0}$ 对应辅助变量 b 的下界约束，该约束对应的对偶变量设为λ_1；约束 $\boldsymbol{P}_{\boldsymbol{m}}\boldsymbol{m}+\boldsymbol{P}_{\boldsymbol{y}}\boldsymbol{y}\leq\boldsymbol{n}$ 对应辅助变量 b 的上界约束、虚假数据注入约束，该约束对应的对偶变量设为λ_2；约束 $\boldsymbol{A}\boldsymbol{y}=\boldsymbol{h}$ 对应状态估计约束、列空间注入约束、量测量构造约束，该约束对应的对偶变量设为λ_3。

2.2.2 列写主问题和子问题

（1）主问题

$$\min_{q} \alpha$$
$$\text{s.t.}\begin{cases} \alpha \geq \boldsymbol{c}^{\mathrm{T}}\boldsymbol{y}_l \\ \boldsymbol{D}_{\boldsymbol{m}}\boldsymbol{m}_l^* \leq \boldsymbol{d} \\ \boldsymbol{E}_{\boldsymbol{y}}\boldsymbol{y}_l \geq \boldsymbol{0} \\ \boldsymbol{P}_{\boldsymbol{m}}\boldsymbol{m}_l^* + \boldsymbol{P}_{\boldsymbol{y}}\boldsymbol{y}_l \leq \boldsymbol{n} \\ \boldsymbol{A}\boldsymbol{y}_l = \boldsymbol{h} \\ \forall l \leq k \end{cases} \tag{21}$$

式中：k 为当前的迭代次数；y_l 为第 l 次迭代后子问题的解；$\boldsymbol{m}_l^*$为第 l 次迭代后得到的最恶劣场景下不确定变量 $\boldsymbol{m}$ 的取值。

（2）对偶子问题

$$\max_{\boldsymbol{m},\lambda_1,\lambda_2,\lambda_3} [(\boldsymbol{n} - \boldsymbol{P}_{\boldsymbol{m}}\boldsymbol{m})^{\mathrm{T}}\lambda_2 + \boldsymbol{h}^{\mathrm{T}}\lambda_3]$$
$$\text{s.t.}\begin{cases} \boldsymbol{E}_{\boldsymbol{y}}{}^{\mathrm{T}}\lambda_1 + \boldsymbol{P}_{\boldsymbol{y}}{}^{\mathrm{T}}\lambda_2 + \boldsymbol{A}_{\boldsymbol{y}}{}^{\mathrm{T}}\lambda_1 \leq \boldsymbol{c} \\ \boldsymbol{D}_{\boldsymbol{m}}\boldsymbol{m} \leq \boldsymbol{d} \\ \lambda_1 \geq 0, \lambda_2 \geq 0, \lambda_3 \in \mathbb{R} \end{cases} \tag{22}$$

在给定$(q,\boldsymbol{m})$时，原子问题的第三层最小化是一个线性问题，通过强对偶将其转化为最大化，并与第二层的最大化合并，得到对偶子问题。

（3）对偶子问题的线性化

引入中间变量 $\boldsymbol{temp}=\boldsymbol{P}_{\boldsymbol{m}}{}^{\mathrm{T}}\lambda_2$，引入辅助变量 $\boldsymbol{u}=\boldsymbol{m}^{\mathrm{T}}\boldsymbol{temp}$，得到线性化对偶子问题。

$$\max_{\boldsymbol{m},\lambda_1,\lambda_2,\lambda_3} (\boldsymbol{n}^{\mathrm{T}}\lambda_2 + \boldsymbol{h}^{\mathrm{T}}\lambda_3 - \boldsymbol{u})$$
$$\text{s.t.}\begin{cases} \boldsymbol{E}_{\boldsymbol{y}}{}^{\mathrm{T}}\lambda_1 + \boldsymbol{P}_{\boldsymbol{y}}{}^{\mathrm{T}}\lambda_2 + \boldsymbol{A}_{\boldsymbol{y}}{}^{\mathrm{T}}\lambda_1 \leq \boldsymbol{c} \\ \boldsymbol{D}_{\boldsymbol{m}}\boldsymbol{m} \leq \boldsymbol{d} \\ 0 \leq u_j \leq M \cdot m_j \\ temp_j - M(1-m_j) \leq u_j \leq temp_j \\ \lambda_1 \geq 0, \lambda_2 \geq 0, \lambda_3 \in \mathbb{R} \end{cases} \tag{23}$$

至此，原问题被分解为主问题和线性化的对偶子问题，可使用 C&CG 算法求解。

2.2.3 求解步骤

首先，设置初始场景，初始化上下界，设置迭代次数 k=1；然后，根据给定的场景 $\boldsymbol{m}_1{}^*$求解主问题得到最优解，取主问题的目标函数值作为新的下界；再将求得的主问题解代入子问题，得到子问题的目标函数值和相应 $\boldsymbol{m}$ 的取值 $\boldsymbol{m}_{k+1}{}^*$，然后更新上界；最后进行判敛，若收敛则停止迭代，返回解，否则增加变量 $\boldsymbol{y}^{k+1}$ 以及如式(24)的约束，回到第三步，令 $k=k+1$，直到收敛。

$$\text{s.t.}\begin{cases} \alpha \geq \boldsymbol{c}^{\mathrm{T}}\boldsymbol{y}^{k+1} \\ \boldsymbol{D}_{\boldsymbol{m}}\boldsymbol{m}_{k+1}^* \leq \boldsymbol{d} \\ \boldsymbol{E}_{\boldsymbol{y}}\boldsymbol{y}^{k+1} \geq \boldsymbol{0} \\ \boldsymbol{P}_{\boldsymbol{m}}\boldsymbol{m}_{k+1}^* + \boldsymbol{P}_{\boldsymbol{y}}\boldsymbol{y}^{k+1} \leq \boldsymbol{n} \\ \boldsymbol{A}\boldsymbol{y}^{k+1} = \boldsymbol{h} \end{cases} \tag{24}$$

求解流程如图 2 所示。

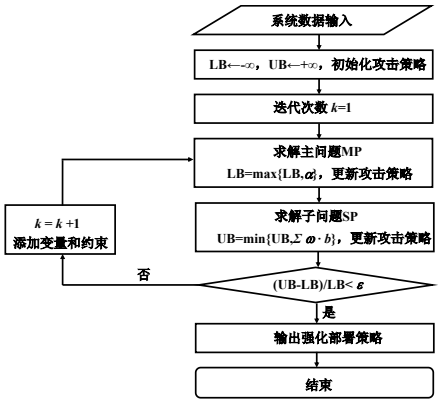


图 2　C&CG 算法求解流程图

Fig.2　Solution flow chart of C&CG algorithm

3　算例仿真

3.1 算例参数

本研究选取 IEEE33 节点配电网系统作为算例，该系统额定电压为 12.66kV，总负荷为 3.715MW+2.3MVar，详细数据见 MATPOWER7.1 工具箱。关于参数设置，电压量测虚假数据注入最大值设置为 0.02p.u.，负荷伪量测虚假数据注入最大值设置为 0.001p.u.。

本研究的对象是 CPPS，为模拟信息物理耦合特性，将节点 6 设定为电网调度中心，负责全网量测数据的接收与状态估计，并在原辐射状一次拓扑基础上引入冗余链路。改进后的 IEEE33 节点信息系统拓扑网络见图 3，认为调度中心不会受到网络攻击。

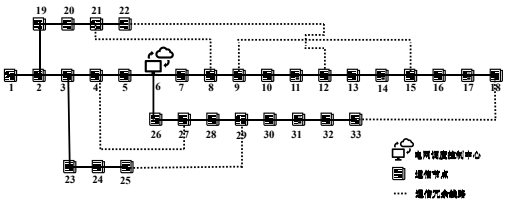


图 3　改进后的 IEEE33 节点信息系统拓扑图

Fig.3　Improved IEEE33 node information system topology diagram

采用列约束生成算法求解三层 DAD 模型，迭代收敛阈值设为 10^{-3}。编程环境为 YALMIP 工具箱，调用 GUROBI11.0.1 商业求解器处理混合整数线性规划问题。攻击预算 B_{att} 设定为 1~4，防御预算 B_{def} 设定为 1~4，覆盖不同攻防强度场景，其中典型场景 B_{att}=3、B_{def}=3 用于重点分析。

以通信时延作为边权，通过 Dijkstra 算法获得各量测节点到调度中心的最短通信路由，例如，节点 2 的通信路由为：2→3→4→27→26→6。节点 27 被 15 条路由经过，占全网通信路由的 46.86%，表明其在通信网络中的关键性。基于此，将节点按中继频次分为三级：高频节点、中频节点、低频节点，对应量测数据的置信水平，标准差依次设置为 0.005、0.0075、0.0085，最终得到差异化的量测权重矩阵。

3.2 状态估计误差分析

3.2.1 不同防御预算结果分析

首先研究在不同防御预算 B_{def} 和攻击预算 B_{att} 下得到的信息安全强化策略，目标函数值如图 4 所示。目标函数的物理意义是加权支路状态估计误差和，用来衡量 FDIA 对配电网状态估计的影响，其值越大，表示网络攻击的负面影响越大。

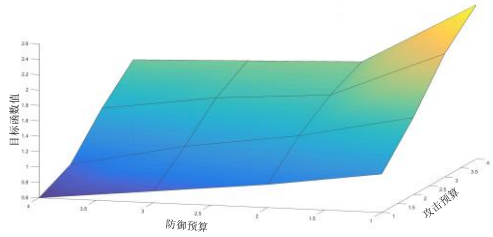


图 4　不同攻防预算的目标函数值统计图

Fig.4　Statistics of objective function values for different attack and defense budgets

从图 4 可以看出，随着攻击预算的提高，目标函数值递增，说明更高的攻击预算总是可以造成更大的状态估计误差；随着 B_{def} 的增加，目标函数值是递减的，这说明更高的强化预算总能够提升系统抵御 FDIA 的能力。

3.2.2 典型场景的状态估计误差对比分析

本节分析典型场景(B_{att}=3、B_{def}=3)下的系统状态估计结果。C&CG 算法求解的收敛过程如图 5 所示，迭代到第 10 次时收敛，效率较高。在该场景下的优化结果是：量子保护装置最佳配置位置为节点 5、节点 7、节点 8；攻击者选中的的攻击位置为节点 4、节点 9、节点 28。接下来针对支路有功功率的状态估计结果进行分析。

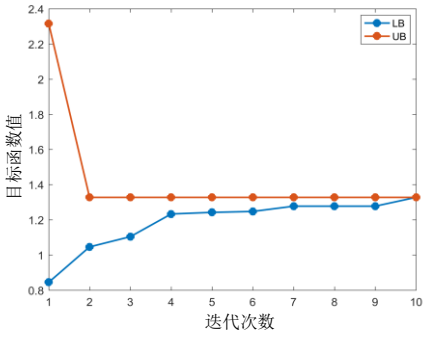


图 5　C&CG 算法收敛图

Fig.5　Convergence diagram of C&CG algorithm

各支路有功功率估计值在有无量子防御的情况下的对比见图 6 所示。在设置有限预算的量子防御的情况下，多条支路的状态估计值更贴近真实值，是由于量子设备部署形成节点防护屏障，阻断了虚假数据向主干网络的扩散。

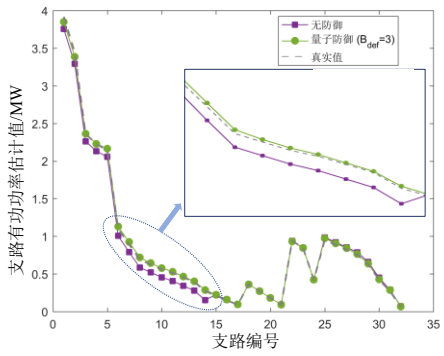


图 6　各支路有功功率估计值误差比较图

Fig.6　Comparison of errors in active power estimation of each branch

各条支路在有无量子防御的情况下的有功功率估计值偏差数值对比见图 7 所示。支路 6 至支路 14 在无量子防御的情况下的偏差远远超过在有量子防御的情况下的偏差，其中支路 14 有量子防御的情况下的偏差为 6.02%，无量子防御的情况下的偏差达到了 43.65%。

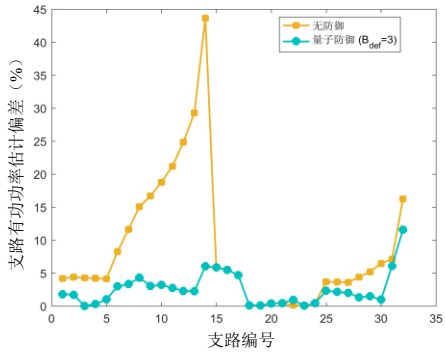


图 7　特定支路的有功功率估计偏差比例比较图

Fig.7　Comparison of the deviation ratio of active power estimation values from certain branches

支路 6 至支路 14 位于网络主干，其上游包含了多个潜在的优先攻击/防御节点，一旦攻击者在这些节点上注入虚假数据，而防御者未选择对其进行量子保护，就会导致对应支路的状态估计误差在量测矩阵 H 对应行中的非零条目的作用下迅速放大，这说明了在有限的量子加密设备的部署预算下，可以对整个通信网络起到明显的状态估计误差抑制作用。

3.3 模型有效性验证

为了验证提出的基于 DAD 模型的信息安全强化策略的有效性，本节构建一种新的强化方案制定策略来进行对比。该新策略基于复杂网络理论，通过计算各通信节点的介数，选取介数最高的通信节点进行防御。这里给出节点 k 的介数 g(k)的计算公式：

$$g(k)=\sum_{i\neq j\in V}\frac{n_{ij}(k)}{n_{ij}} \tag{25}$$

式中：n_{ij} 表示从节点 i 到节点 j 的所有最短路径数，$n_{ij}(k)$表示 n_{ij} 中经过节点 k 的路径数。

图 8 给出各节点的介数，其中介数最高的前四个节点分别为节点 8、节点 9、节点 15、节点 21。

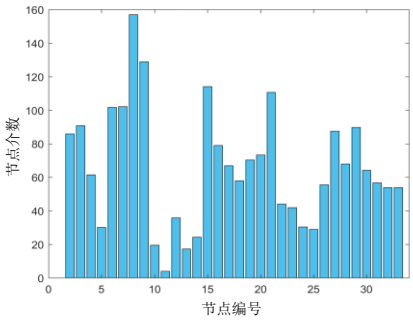


图 8　各节点介数统计图

Fig.8　Statistics of betweenness of each node

基于 DAD 模型的防御策略和基于复杂网络理论的防御策略的优化结果如表 1 所示。可以看出，当 B_{att}≤2 时，利用复杂网络理论进行节点保护不能抑制网络攻击造成的状态估计误差，在 B_{att} 等于 3 和 4 时，复杂网络理论防御策略对状态估计误差起了一定抑制作用，但效果不如基于 DAD 模型的防御策略。这说明节点 9、节点 15、节点 21 在拓扑结构上虽然比较重要，但当系统遭受网络攻击时，这些节点并不一定是优先保护的，而 DAD 模型能结合网络参数和量测权重，综合考量攻击者、防御者之间的博弈关系，这证明了基于 DAD 模型制定信息安全强化策略的有效性。

表 1　策略保护效果比较表

Table 1　Comparison table of policy protection effects

B_{att}	无保护时的目标值	复杂网络策略		DAD 策略	
		保护节点	目标值	保护节点	目标值
1	1.29	8	1.29	5	1.13
2	1.58	8;9	1.58	5;7	1.36
3	1.79	8;9;15	1.63	5;7;8	1.51
4	1.90	8;9;15;21	1.81	5;7;8;26	1.74

4　结论

本文针对 FDIA 对配电网状态估计的安全威胁，研究了基于量子密钥分发的通信安全强化策略。通过建立 DAD 三层优化模型，采用 C&CG 算法求解量子加密通信设备的最优部署方案。仿真结果表明：

（1）所提策略能有效降低 FDIA 导致的状态估计误差，对主干线路的误差抑制效果尤为明显；

（2）与基于复杂网络理论的传统方法相比，所提策略防御效果更好，更具适应性。

后续研究可考虑在模型中引入通信时延与带宽约束，拓展多类型攻击协同场景，并结合配电网运行状态动态优化量子设备部署策略，以提升防御机制的实时性和适应性。

参 考 文 献

[1] 樊强，刘东，王宇飞，等．电力信息物理系统形态演进关键技术及其进展[J]．中国电机工程学报，2024，44(21)：8341－8353．
FAN Qiang, LIU Dong, WANG Yufei, et al. Key technologies and progress in morphological evolution of cyber-physical power systems[J]. Proceedings of the CSEE, 2024, 44(21): 8341-8353.

[2] 何瑞文，龙隆，张宝仁，等．电力信息物理系统中信息系统物理化的建模及分析方法[J]．中国电机工程学报，2024，44(01)：72－85．
HE Ruiwen, LONG Long, ZHANG Baoren, et al. Modeling and analysis method for physicalization of information systems in cyber-physical power systems[J]. Proceedings of the CSEE, 2024, 44(01): 72-85.

[3] Ilić M D, Xie L, Khan U A, et al. Modeling of future cyber–physical energy systems for distributed sensing and control[J]. IEEE Transactions on Systems, Man, and Cybernetics-Part A: Systems and Humans, 2010, 40(4): 825-838.

[4] 叶飞，钟晓静，关前锋．电力信息物理系统的网络攻击建模、演化规律及应对成本研究[J]．综合智慧能源，2024，46(5)：58－64．
YE Fei, ZHONG Xiaojing, GUAN Qianfeng. Research on cyber attack modeling, evolution law and response cost in cyber-physical power systems[J]. Integrated Intelligent Energy, 2024, 46(5): 58-64.

[5] 汤奕，陈倩，李梦雅，等．电力信息物理融合系统环境中的网络攻击研究综述[J]．电力系统自动化，2016，40(17)：59-69.
TANG Yi, CHEN Qian, LI Mengya, et al. A review on cyber attacks in cyber-physical power systems[J]. Automation of Electric Power Systems, 2016, 40(17): 59-69.

[6] 阮振，吕林，刘友波，等．考虑负荷数据虚假注入的电力信息物理系统协同攻击模型[J]．电力自动化设备，2019，39(02)：181－187．
RUAN Zhen, LYU Lin, LIU Youbo, et al. A coordinated attack model for cyber-physical power system considering false data injection of load data[J]. Electric Power Automation Equipment, 2019, 39(02): 181-187.

[7] 陈沛,吕腾,王美刚.切换网络攻击下异构多区域电力系统的负荷频率控制[J].电力系统及其自动化学报,2024,36(12):140-148.DOI:10.19635/j.cnki.csu-epsa.001417.
CHEN Pei, LYU Teng, WANG Meigang. Load frequency control of heterogeneous multi-area power systems under switching network attacks[J]. Proceedings of the CSU-EPSA, 2024, 36(12): 140-148. DOI:10.19635/j.cnki.csu-epsa.001417.

[8] 赵俊华，梁高琪，文福拴，等．乌克兰事件的启示：防范针对电网的虚假数据注入攻击[J]．电力系统自动化，2016，40(07)：149－151．
ZHAO Junhua, LIANG Gaoqi, WEN Fushuan, et al. Lessons from Ukraine's blackout: Preventing false data injection attacks

[9] 项俊栋，方赟朋，姚海燕，等．量子通信技术在电力信息系统保密传输中的应用研究[J]．数字通信世界，2024，(06)：149－151．
XIANG Jundong, FANG Yunpeng, YAO Haiyan, et al. Research on the application of quantum communication technology in secure transmission of electric power information systems[J]. Digital Communication World, 2024(06): 149-151.

[10] 谢海鹏，钱雨琦，付炜，等．电力系统中量子信息学的应用现状及展望[J]．中国电机工程学报，2023，43(12)：4485－4508．
XIE Haipeng, QIAN Yuqi, FU Wei, et al. Application status and prospects of quantum information science in power systems[J]. Proceedings of the CSEE, 2023, 43(12): 4485-4508.

[11] Z. Tang, P. Zhang, W. O. Krawec and L. Wang. Quantum Networks for Resilient Power Grids: Theory and Simulated Evaluation. IEEE Transactions on Power Systems, 2023, 38(2): 1189-1204.

[12] 张静，毕天姝，刘灏．电力系统状态估计精度综合评价与分析体系[J]．电力系统保护与控制，2024，52(20)：12－24．
ZHANG Jing, BI Tianshu, LIU Hao. A comprehensive evaluation and analysis system for power system state estimation accuracy[J]. Power System Protection and Control, 2024, 52(20): 12-24.

[13] Baran M E, Wu F F. Optimal capacitor placement on radial distribution systems[J]. IEEE Transactions on Power Delivery. 1989, 4(1):725–734.

[14] Farivar M, Low S S H. Branch flow model: Relaxations and convexification[J]. IEEE Transactions on Power Systems. 2013, 28(3):2554–2564.

[15] 薛辉，贾清泉，王宁，等．基于 PMU 量测数据和 SCADA 数据融合的电力系统状态估计方法[J]．电网技术，2008，(14)：44－49．
XUE Hui, JIA Qingquan, WANG Ning, et al. A power system state estimation method based on PMU and SCADA measurement data fusion[J]. Power System Technology, 2008(14): 44-49.

[16] 王树西，李安渝．Dijkstra 算法中的多邻接点与多条最短路径问题[J]．计算机科学，2014，41(06)：217－224．
WANG Shuxi, LI Anyu. Multi-adjacent vertices and multiple shortest paths problem in Dijkstra algorithm[J]. Computer Science, 2014, 41(06): 217-224.

[17] 杨玉泽，刘文霞，李承泽，等．面向电力 SCADA 系统的 FDIA 检测方法综述[J]．中国电机工程学报，2023，43(22)：8602－8622．
YANG Yuze, LIU Wenxia, LI Chengze, et al. A review of FDIA detection methods for power SCADA systems[J]. Proceedings of the CSEE, 2023, 43(22): 8602-8622.

[18] Zeng B, Zhao L. Solving two-stage robust optimization problems using a column-and-constraint generation method[J]. Operations Research Letters. 2013, 41(5):457–461

[19] Yuan W, Zhao L, Zeng B. Optimal power grid protection through a defender-attacker-defender model[J]. Reliability Engineering and System Safety. 2014, 121:83–89.

作者简介：

何宇昊，男，，硕士研究生，主要研究方向为电力系统信息安全。E-mail：heyuhao1777@stu.xjtu.edu.cn

钱雨琦，女，博士研究生，主要研究方向为量子信息学在电力系统中的应用。E-mail：qianyuqi77@stu.xjtu.edu.cn

谢海鹏，男，通信作者，副教授，博士生导师，主要研究方向为电力系统可靠性、配电网优化运行和量子信息学应用。E-mail：haipengxie@xjtu.edu.cn

031 A Coordinated Robust Volt/VAR Optimization for Distribution Systems with High Renewable Penetration

Yifei Tang[1], Gongjin Ma[1], Pingliang Zeng[1,*], Cheng Xie[2], and Chao Chen[2]

[1] School of Automation, Hangzhou Dianzi University, Hangzhou 310018, China
[2] State Grid Zhejiang Electric Power Co., Ltd. Electric Power Science Research Institute, Hangzhou 310014, China
plz@hdu.edu.cn

Abstract. With the high-penetration integration of intermittent renewable energy sources such as wind and solar power into distribution networks, the uncertainty of their output poses significant challenges to system voltage stability, security, and economic operation. To address this challenge, this paper proposes a coordinated robust optimization dispatch model for distribution networks. The model first employs a data-driven method based on the Multivariate Gaussian Mixture Model (MGMM) to accurately characterize the joint uncertainty and spatio-temporal correlations of wind and solar power, and subsequently constructs a polyhedral uncertainty set. Furthermore, a robust optimization model is established with the objective of minimizing network losses and voltage margin deviations. This model coordinately dispatches multiple classes of heterogeneous distributed resources, including on-load tap changers, microturbines, energy storage systems, and RES. Case studies conducted on a 27-node distribution network demonstrate that the proposed model can strictly maintain all nodal voltages within the desired range (0.97 p.u. to 1.03 p.u.). across various typical scenarios, exhibiting excellent voltage control capability and robustness. By deeply leveraging and coordinating the control potential of various resources, the model achieves significant effects in optimizing network-wide power flow distribution, promoting the local consumption of renewable energy, and reducing network losses. The results prove that the proposed model provides an effective solution for the uncertain operational control problems in distribution networks with high penetration of renewable energy.

Keywords: Robust Optimization, Voltage Control, Uncertainty, Multivariate Gaussian Mixture Model, Coordinated Dispatch.

1 Introduction

As modern power systems evolve,the high-penetration integration of renewable energy sources,primarily wind and solar,into distribution networks is profoundly altering the traditional operational paradigm and control requirements.The inherent intermittency and volatility of wind and solar generation present severe challenges to voltage stability.Furthermore, wind and solar outputs are not mutually independent stochastic

processes;their complex spatio-temporal correlations make it difficult for traditional single-variable uncertainty modeling methods to accurately characterize the associated risks.Without effective coordinated strategies, dispersed generation resources cannot achieve synergistic complementarity and may even lead to control conflicts,failing to fully leverage their potential for voltage support in an uncertain environment.Therefore, there is an urgent need to develop a robust dispatch method that can simultaneously and accurately characterize multi-source uncertainties while coordinately optimizing multiple classes of heterogeneous resources, thereby ensuring the secure operation of distribution networks with high penetrations of RES 1.

In the field of reactive power optimization for distribution networks with high penetration of renewable energy, while existing research has made notable progress, limitations persist in two main areas: the comprehensiveness of uncertainty characterization and the breadth of coordinated control resources.

Regarding uncertainty modeling, some studies focus on a single renewable source. For instance, the coordinated algorithm proposed by Maataoui et al. only considers uncertainty from distributed photovoltaics, without accounting for wind power disturbances, which limits its applicability in complex scenarios with coexisting wind and solar generation 2. The robust dispatch model by Li et al., while addressing the spatio-temporal uncertainty of wind power, does not incorporate multi-source randomness from PV and loads 3. Furthermore, while You et al. applied Gaussian Mixture Models to handle wind uncertainty, their model is oriented towards transmission grids and lacks a detailed characterization of distributed PV and the corresponding voltage constraints at the distribution network level 4.

Existing strategies also exhibit limitations in the breadth of coordinated control resources. In the aforementioned model by Li et al., controllable assets are limited to energy storage and grid interaction, making the control dimension relatively narrow. Similarly, the two-layer Volt/Var strategy proposed by Muthukaruppan et al. only coordinates on-load tap changers and inverters, lacking the integration of fast power regulation units such as energy storage systems and microturbines. This renders the approach insufficient for the demands of large-scale coordinated optimization of heterogeneous, multi-source devices 5.

To address the aforementioned research gaps, this paper proposes a robust reactive power optimization model for distribution networks capable of coordinately optimizing multi-source, heterogeneous resources. First, the model employs a data-driven method based on the Multivariate Gaussian Mixture Model to learn the joint probability distribution and spatio-temporal correlations of wind and solar output from historical data, constructing a polyhedral uncertainty set that accurately characterizes their uncertainty. Second, a coordinated robust optimization framework is established, which incorporates slow mechanical devices like on-load tap changer with fast electronic devices such as energy storage systems, microturbines, and renewable energy inverters into a unified dispatch to handle uncertainty impacts 6. With the objective of minimizing system network losses and voltage margin deviations, the model's effectiveness and robustness in guaranteeing voltage quality and enhancing operational economy are verified through case study analysis.

2 Modeling Wind and Solar Power Output Uncertainty with a Multidimensional Gaussian Mixture Model

To accurately characterize the joint uncertainty of wind and photovoltaic (PV) power generation, it is essential to move beyond traditional deterministic forecasting methods. These conventional approaches only provide a single expected value (i.e., a point forecast) and thus fail to capture the stochastic fluctuations inherent in renewable energy output. This limitation is inadequate for models aiming to enhance system operational resilience. Furthermore, wind and solar power generation are not mutually independent stochastic processes; they are jointly influenced by regional and seasonal meteorological systems and, consequently, exhibit significant inter-source correlations.

To address this issue, this section introduces a data-driven method based on the Multivariate Gaussian Mixture Model (MGMM). The objective is to learn the joint probabilistic characteristics of wind and solar generation from historical data. Based on this, an uncertainty set is constructed that reflects the correlations between these sources, providing a well-founded input for the subsequent robust optimization model.

In order to capture complex joint scenarios, such as "high solar irradiance–high wind speed" or "high solar irradiance–low wind speed," it is insufficient to perform clustering on wind and solar outputs separately. Instead, they must be treated as a single multivariate random vector and analyzed holistically, i.e.,

$$P_t = \left[P_{j_1,t}^{PV}, \ldots, P_{j_2,t}^{WT}, \ldots \right]^T \tag{1}$$

The joint probability density function (PDF) of the renewable energy output vect P_t or can be represented as a linear combination of K multivariate Gaussian distributions:

$$f_{MGMM}\left(P_t\right) = \sum_{k=1}^{K} \omega_{k,t} \mathcal{N}\left(P_t \mid \mu_{k,t}, \Sigma_{k,t}\right) \tag{2}$$

Where:K is the optimal number of joint scenarios. $\omega_{k,t}$ is the probability of the k-th joint scenario occurring at time t. $\mu_{k,t}$ is the mean vector of the k-th scenario at time t, which contains components for both WT and PV outputs. $\Sigma_{k,t}$ is the covariance matrix of the k-th scenario at time t.

The MGMM can identify typical joint operational patterns, such as "high solar irradiance–high wind speed" and "high solar irradiance–low wind speed." It outputs explicit mean vectors and covariance matrices for each pattern, providing the data foundation for the construction of the uncertainty set.

2.1 Construction of the Joint Uncertainty Set

After obtaining the mean vectors and covariance matrices for each joint scenario, a polyhedral uncertainty set is constructed to capture the inter-source correlations 7.

First, the actual active power output of a renewable energy source at node j and time t is decomposed into the sum of its forecasted mean value and an uncertain deviation term. That is:

$$P_{j,t}^{PV} = P_{j,t}^{PV,DA} + \Delta P_{j,t}^{PV} \tag{3}$$

$$P_{j,t}^{WT} = P_{j,t}^{WT,DA} + \Delta P_{j,t}^{WT} \tag{4}$$

Here， $P_{j,t}^{PV,DA}$ and $P_{j,t}^{WT,DA}$ are determined by the mean vector of the joint scenario at time t,which is obtained from the MGMM clustering analysis.The bounds for the deviation terms, $\Delta P_{j,t}^{PV}$ and $\Delta P_{j,t}^{WT}$ are dictated by the covariance matrix of the corresponding scenario, $\sum_{k,t}$. The deviation bounds are defined by taking the square root of the diagonal elements of the covariance matrix:

$$\begin{cases} \Delta P_{j,t}^{PV} = 3\xi_{j,t}^{PV} \cdot \sigma_{j,t}^{pv} \\ -1 \le \xi_{j,t}^{PV} \le 1 \end{cases} \tag{5}$$

$$\begin{cases} \Delta P_{j,t}^{WT} = 3\xi_{j,t}^{WT} \cdot \sigma_{j,t}^{WT} \\ -1 \le \xi_{j,t}^{WT} \le 1 \end{cases} \tag{6}$$

Among them, $\xi_{j,t}^{PV}$ and $\xi_{j,t}^{WT}$ are normalized uncertain variables.

An "uncertainty budget" parameter,Γ, is introduced to construct the joint uncertainty set, U 8.

$$U = \left\{ \xi_{j,t}^{PV}, \xi_{j,t}^{WT} \left| \begin{array}{l} -1 \le \xi_{j,t}^{PV} \le 1, \quad \forall t \in T, j \in N_{PV} \\ -1 \le \xi_{j,t}^{WT} \le 1, \quad \forall t \in T, j \in N_{WT} \\ \sum_{t \in T} \left(\sum_{j \in N_{pv}} \left| \xi_{j,t}^{PV} \right| + \sum_{j \in N_{wt}} \left| \xi_{j,t}^{WT} \right| \right) \le \Gamma \end{array} \right. \right\} \tag{7}$$

Here, N_{PV} and N_{WT} represent the sets of nodes where PV systems andWT are installed, respectively. The parameter Γ is a decision variable that controls the model's level of conservatism by adjusting the system's operational margin. A lower value for Γ results in a more conservative model, whereas a higher value allows the model to accommodate greater fluctuations, thus exhibiting enhanced robustness.

To distinctly address the unique uncertainty characteristics of wind and solar energy, this paper constructs a partitioned-budget uncertainty set. This method assigns independent budget parameters to the two classes of uncertain sources—PV and wind. This forces the model, when constructing the worst-case scenario, to simultaneously consider the joint fluctuations of both power source types within their respective budgets.

This uncertainty set, U, is jointly defined by the following two sets of constraints:

$$\begin{cases} \sum_{j\in\mathcal{N}_{PV}} |\xi_{j,t}^{PV}| \le \Gamma_{PV} \\ \sum_{j\in\mathcal{N}_{WT}} |\xi_{j,t}^{WT}| \le \Gamma_{WT} \end{cases} \tag{8}$$

Among them, Γ_{PV} and Γ_{WT} are the uncertainty budget parameters independently set for PV and WT, respectively.

2.2 Transformation of Uncertainty Constraints

The partitioned-budget uncertainty set constructed in the preceding section includes absolute value constraints that are dependent on the uncertain variable ξ, rendering the model intractable in its direct form. To resolve this issue, these uncertain constraints must be transformed into an equivalent deterministic formulation.

First, by introducing a set of non-negative auxiliary variables, $z_{j,t}$, each absolute value term, $|\xi_{j,t}|$, can be replaced by a set of linear constraints:

$$\begin{cases} \xi_{j,t} \le z_{j,t} \\ -\xi_{j,t} \le z_{j,t} \end{cases} \tag{9}$$

This allows the partitioned-budget constraint to be expressed as the following linear formulation:

$$\begin{cases} \sum_{j\in\mathcal{N}_{PV}} z_{j,t}^{PV}{}_{j,t} \le \Gamma_{PV} \\ \sum_{j\in\mathcal{N}_{WT}} z_{j,t}^{WT} \le \Gamma_{WT} \end{cases} \tag{10}$$

For other model constraints that are a function of the uncertain variable ξ, a transformation based on duality theory is utilized. The conversion of these constraints into their dual form results in a set of purely deterministic, linear conditions.

2.3 Cooperative Reactive Power Optimization Strategy

Voltage control resources in distribution networks can be divided into two major categories. On-load tap changer is regarded as a type of slow, discrete mechanical reactive power regulating equipment. Their adjustment actions will cause mechanical losses and are not suitable for frequent operation. Micro gas turbines, energy storage systems, wind turbines, photovoltaics and their inverters can be continuously adjusted to provide dynamic support for voltage.

(A) Constraints of on-load tap changing transformers

$$\sum_{d=K_{min}}^{K_{max}} \lambda_{d,t} = 1 \tag{11}$$

$$u_{0,t}=\left(\sum_{d=K_{min}}^{K_{max}}\lambda_{d,t}\cdot\left(1+d\cdot\Delta U^{tap}\right)\right)^2 \tag{12}$$

A binary variable, $\lambda_{d,t}$, is introduced to ensure that only one tap position is selected at each time step t. This establishes the relationship between the tap selection and the transformer's secondary side voltage, $u_{0,t}$.In this formulation, ΔU^{tap} is the parameter representing the voltage regulation step size per tap position. K_{min} and K_{max} denote the minimum and maximum available tap positions of the OLTC, respectively.

$$|\sum_{d} d\cdot\lambda_{d,t}-\sum_{d} d\cdot\lambda_{d,t-1}|\le(K_{max}-K_{min})\cdot\delta_t^{OLTC} \tag{13}$$

$$\sum_{t\in T}\delta_t^{OLTC}\le N_{max}^{OLTC} \tag{14}$$

By introducing a binary auxiliary variable δ_t^{OLTC} to identify whether the tap changer position changes, the total number of daily operations is limited to no more than the parameter N_{max}^{OLTC}.

(B) MT constraints

Constraints on start-stop status:

$$\begin{cases} z_{j,t}^{MT}-z_{j,t-1}^{MT}=y_{j,t}^{start}-y_{j,t}^{shut} \\ y_{j,t}^{start}+y_{j,t}^{shut}\le 1 \end{cases} \tag{15}$$

In the formula, $z_{j,t}^{MT}$, $y_{j,t}^{start}$, and $y_{j,t}^{shut}$ respectively denote the start-stop state and the start action, shut-down action of the MT at node j at time t.

Constraints on minimum start-stop time

$$\begin{cases} \sum_{k=t-T_{j,up}^{MT}+1}^{t} y_{j,k}^{start}\le z_{j,t}^{MT},\forall t\ge T_{j,up}^{MT} \\ \sum_{k=t-T_{j,down}^{MT}+1}^{t} y_{j,k}^{shut}\le 1-z_{j,t}^{MT}\forall t\ge T_{j,down}^{MT} \end{cases} \tag{16}$$

In the formula, $T_{j,up}^{MT}$ and $T_{j,down}^{MT}$ denote the minimum operation time and minimum shutdown time, respectively,which constrain that only one start or stop action can be executed at most during this period.

Constraints on MT output

$$\begin{cases} z_{j,t}^{MT}\cdot P_{j,min}^{MT}\le P_{j,t}^{MT}\le z_{j,t}^{MT}\cdot P_{j,max}^{MT} \\ \left(P_{j,t}^{MT}\right)^2+\left(Q_{j,t}^{MT}\right)^2\le\left(z_{j,t}^{MT}\cdot S_{j,max}^{MT}\right)^2 \end{cases} \tag{17}$$

In the formula, $P_{j,t}^{MT}$, $P_{j,max}^{MT}$, and $P_{j,min}^{MT}$ are respectively the time - varying value and upper and lower limits of the active power output of the MT at node j; $S_{j,max}^{MT}$ is the maximum apparent power of the MT.

Constraints on climbing rate

$$\begin{cases} P_{j,t}^{MT} - P_{j,t-1}^{MT} \le \beta_{j,up}^{MT} \\ P_{j,t-1}^{MT} - P_{j,t}^{MT} \le \beta_{j,down}^{MT} \end{cases} \tag{18}$$

In the formula, $\beta_{j,up}^{MT}$ and $\beta_{j,down}^{MT}$ are the upper limits of the upward and downward ramping power of the MT, respectively.

(C) Constraints of energy storage systems

Constraints on charge and discharge power

$$\begin{cases} \left(P_{j,t}^{dis} - P_{j,t}^{ch}\right)^2 + \left(Q_{j,t}^{BESS}\right)^2 \le \left(S_{j,max}^{BESS}\right)^2 \\ 0 \le P_{j,t}^{ch} \le b_{j,t}^{ch} \cdot P_{j,max}^{BESS} \\ 0 \le P_{j,t}^{dis} \le b_{j,t}^{dis} \cdot P_{j,max}^{BESS} \\ b_{j,t}^{ch} + b_{j,t}^{dis} \le 1 \end{cases} \tag{19}$$

In the formula, $P_{j,t}^{dis}$ and $P_{j,t}^{ch}$ are the discharge power and charging power of the energy storage device at node j at timet; $P_{j,max}^{BESS}$ is the upper limit of discharge and charging power of the energy storage device at node j; $Q_{j,t}^{BESS}$ is the reactive power output of the energy storage at node j at time t; $S_{j,max}^{BESS}$ is the maximum apparent power of the energy storage at node j; $b_{j,t}^{ch}$ and $b_{j,t}^{dis}$ are 0-1 auxiliary variables describing the charging and discharging states of the energy storage.

Constraints on the state of charge

$$\begin{cases} E_{j,t}^{BESS} = E_{j,t-1}^{BESS} + \left(P_{j,t}^{ch} \cdot \eta^{ch} - P_{j,t}^{dis} / \eta^{dis}\right) \cdot \Delta t \\ E_{j,min}^{BESS} \le E_{j,t}^{BESS} \le E_{j,max}^{BESS} \\ E_{j,T}^{BESS} = E_{j,0}^{BESS} \end{cases} \tag{20}$$

In the formula, $E_{j,t}^{BESS}$、$E_{j,min}^{BESS}$ and $E_{j,max}^{BESS}$ are the energy storage devices at node j 9.

(D) Reactive power output constraints of renewable energy

$$\begin{cases} \left(P_{j,t}^{PV}\right)^2 + \left(Q_{j,t}^{PV}\right)^2 \le \left(S_{j,max}^{PV}\right)^2 \\ \left(P_{j,t}^{WT}\right)^2 + \left(Q_{j,t}^{WT}\right)^2 \le \left(S_{j,max}^{WT}\right)^2 \end{cases} \tag{21}$$

Here, $P_{j,t}^{PV}$ and $P_{j,t}^{WT}$ are the actual active power outputs after robust correction; $S_{j,max}^{PV}$ and $S_{j,max}^{WT}$ are the maximum apparent powers corresponding to WT and PV, respectively.

3 NetworkCollaborative Robust Optimization Model

3.1 Objective function

The objective function is constructed as the linearly weighted sum of the number of discrete device adjustments and the voltage over-limit amount.

$$min\ f_1 = \sum_{t\in T}\left(P_t^{loss} + \omega^{volt} \sum_{j\in \mathcal{N}} \left(\varepsilon_{j,t}^{up} + \varepsilon_{j,t}^{low} \right) \right) \tag{22}$$

In the formula,T is the set of scheduling periods, and N is the set of nodes in the power grid. The first term P_t^{loss} in the objective function represents the total network loss of the system at time t, which is calculated as follows:

$$P_t^{loss} = \sum_{(i,j)\in L} r_{ij} l_{ij,t} \tag{23}$$

where L is the set of branches in the distribution network, r_{ij} is the resistance parameter of branch (i,j), and $l_{ij,t}$ is the square of the current amplitude of this branch at time t. The second term of the objective function is a voltage margin deviation penalty term constructed by introducing the weight ω^{volt} .This term is used to optimize the voltage quality and operational flexibility of the distribution network, where $\varepsilon_{j,t}^{up}$ and $\varepsilon_{j,t}^{low}$ are non-negative slack variables, representing the deviations of the voltage at node j at time t beyond its preset ideal upper and lower margin boundaries, respectively.

3.2 Constraints

In addition to the constraints on generator sets and mechanical equipment mentioned above, the constraints for the safe operation of the distribution network must also be satisfied.

This model adopts the DistFlow branch power flow model and converts it into convex constraints 10 through second-order cone relaxation technology to ensure solution efficiency and optimality 11.

(A) Constraints on power balance

$$\sum_{i:(i,j)\in L} \left(P_{ij,t} - r_{ij} l_{ij,t} \right) + P_{j,t}^{g} + P_{j,t}^{BESS} = \sum_{k:(j,k)\in L} P_{jk,t} + P_{j,t}^{L} \tag{24}$$

$$\sum_{i:(i,j)\in L}\left(Q_{ij,t}-x_{ij}l_{ij,t}\right)+Q_{j,t}^{g}+Q_{j,t}^{BESS}=\sum_{k:(j,k)\in L}Q_{jk,t}+Q_{j,t}^{L} \tag{25}$$

where, $P_{ij,t}$ and $Q_{ij,t}$ are the active power and reactive power variables flowing through the branch; x_{ij} is the reactance parameter of the branch; $P_{j,t}^{g}$ and $Q_{j,t}^{g}$ are the active and reactive injection powers including the MT; $P_{j,t}^{BESS}$ and $Q_{j,t}^{BESS}$ are the active and reactive injection powers of the energy storage system; $P_{j,t}^{L}$ and $Q_{j,t}^{L}$ are the given active and reactive load parameters at the node.

(B) Voltage drop constraint

$$u_{j,t}=u_{i,t}-2(P_{ij,t}r_{ij}+Q_{ij,t}x_{ij})+(r_{ij}^{2}+x_{ij}^{2})l_{ij,t} \tag{26}$$

(C) Second-order cone relaxation constraint

Relax the original non-convex power flow constraints into standard second-order cone constraints

$$\left\|\begin{bmatrix}2P_{ij,t}\\2Q_{ij,t}\\l_{ij,t}-u_{i,t}\end{bmatrix}\right\|_{2}\le l_{ij,t}+u_{i,t} \tag{27}$$

The formula(24)-formula(27) is a distflow power flow constraint based on the second-order cone.

(D) Line capacity constraint

$$0\le l_{ij,t}\le l_{ij}^{max} \tag{28}$$

Where l_{ij}^{max} is the upper limit of line capacity

(E) Voltage Constraints

$$U_{min}^{2}\le u_{j,t}\le U_{max}^{2} \tag{29}$$

$$\left(U_{mag,min}\right)^{2}-\varepsilon_{j,t}^{low}\le u_{j,t}\le\left(U_{mag,max}\right)^{2}+\varepsilon_{j,t}^{up} \tag{30}$$

The combination of voltage hard constraints and voltage soft constraints ensures that the voltage, while satisfying the safe hard constraints, has as small a voltage deviation as possible, thereby enhancing the robustness of the model.

4 Case Study

To verify that this model, as a single-stage regulation mode with a 1-hour time interval when considering the uncertainty of wind and solar output, has higher robustness compared to deterministic models. Considering the equipment contained in the multi-source heterogeneous distribution network, optimization simulations will be conducted based on the 27-node distribution network constructed in a certain location in Zhejiang Province. The system consists of main power generation resources such as wind turbines, photovoltaics, micro gas turbines, and energy storage, as well as OLTC

as slow mechanical regulation equipment. Within a 24-hour test cycle, with an interval of 1 hour, collaborative optimization and regulation of the equipment will be carried out to utilize the regulation characteristics of different equipment. The collaborative regulation strategies of each equipment under different scenarios will be verified respectively.

4.1 MGMM - based PV and wind power uncertainty set

Based on the analysis results from the MGMM, a polyhedral uncertainty set is constructed for the subsequent robust optimization. Within this framework, the actual output of each renewable energy node is decomposed into a deterministic forecasted mean and a bounded uncertain deviation. The bounds of this deviation are determined by the covariance matrix of the corresponding scenario, thereby transforming probabilistic information into tractable boundary constraints for the optimization model.

For the case study, we utilize active power output data from wind turbines and PV systems at a location in Zhejiang Province, China, from 2019 to 2020, with a 1-hour sampling interval. Following data preprocessing, a complete dataset of 8,760 hourly samples was obtained. Through clustering analysis, four distinct types of operational scenarios were identified. The data on wind and solar power generation under these scenarios is shown in Fig. 1.

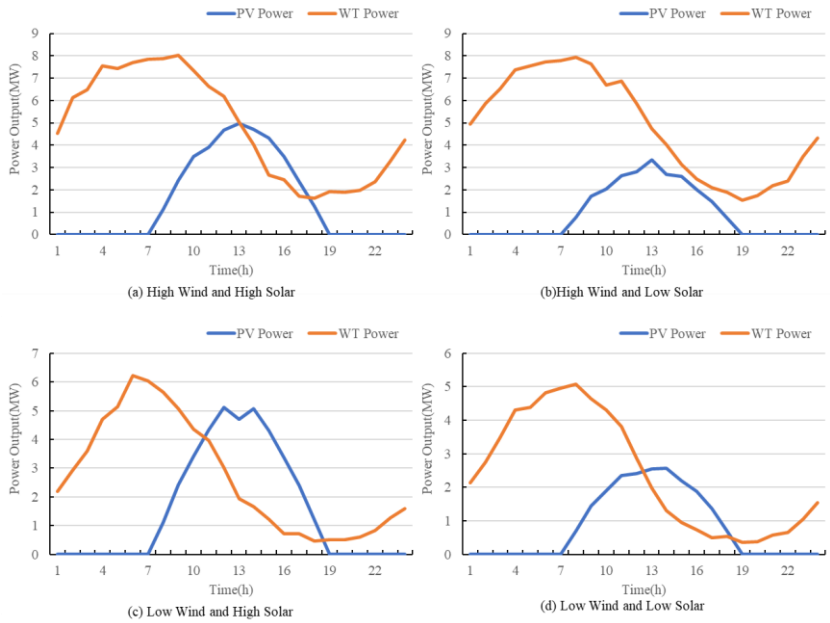


Fig. 1. Mean distribution of active power output fromWT and PV

In all four scenarios depicted, wind farms serve as the primary source of intra-day renewable generation. Their output exhibits a complementary, off-peak pattern rela-

tive to solar PV generation, which indicates a significant potential for coordinated control.

In the "high wind–high Solar" output scenario, renewable generation between 00:00 and 07:00 is primarily supplied by wind turbines. Subsequently, from 07:00 to 14:00, PV output steadily increases with solar irradiance, reaching its peak. During this midday period, the combined mean power from PV and wind approaches 10 MW. This high level of renewable generation is also characterized by significant volatility and uncertainty, posing risks of voltage limit violations and reverse power flow.

In scenarios with lower renewable energy penetration, the trend of the wind and solar output curves is similar to that of the "high-high" scenario. However, due to the reduced overall generation, coordinated control that integrates distributed microturbines and energy storage systems becomes necessary to meet load demands and decrease reliance on the main grid.

4.2 Result Analysis

As shown by the voltage optimization results in Fig. 2， the proposed coordinated control strategy successfully maintains the voltage of all network nodes within the desired range across the four different wind and solar output scenarios. The light blue shaded area indicates that all nodal voltages are kept between 0.97 p.u. and 1.03 p.u. throughout the entire dispatch period. The system operates well clear of the hard safety constraint boundaries, which confirms the robustness of the model.

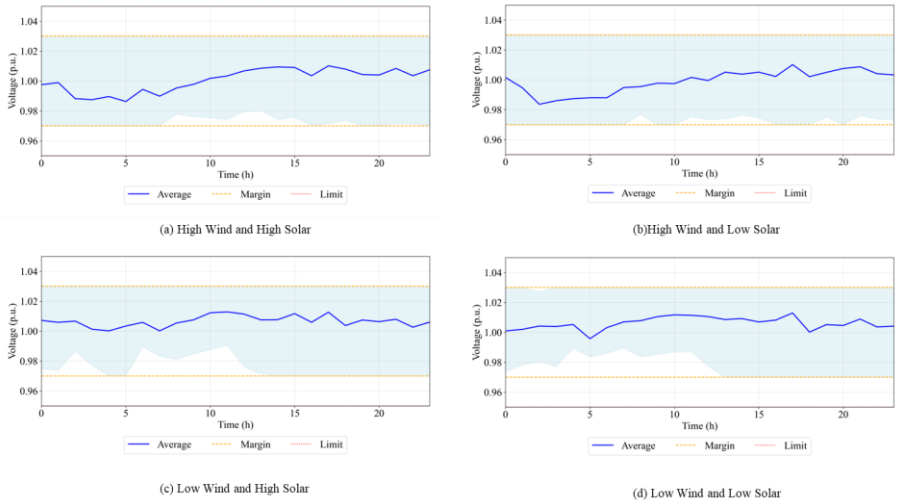


Fig. 2. Voltage deviation analysis

During the 00:00–07:00 period, the system load is low, and uncertainty is dominated by wind power. In the "high wind speed" scenarios (Fig. 2., top-left and top-right), the sustained high-power injection from wind turbines poses a significant overvoltage risk. However, the model's dispatch results show a small fluctuation range for the

system's average voltage. This indicates that coordinated actions, such as charging energy storage and regulating microturbines, effectively counteract the voltage rise caused by high wind generation during the night. In contrast, under "low wind speed" conditions, the integration of wind power is observed to raise the lower voltage bound. With regulation, the system operates stably in this period, exhibiting an average voltage profile that is flatter and closer to 1.0 p.u.

The 10:00–16:00 period corresponds to peak PV generation. In the "high wind–high solar" scenario (Fig. 2, top-left), the combined renewable output peaks, causing the most severe impact on the system. The light blue shaded area shows that the voltage fluctuation in this scenario is the widest of the four, reflecting significant power flow variations and high control pressure. Even so, the model strictly constrains the maximum voltage below the 1.03 p.u. margin, mitigating the risk of violations from reverse power flow. Conversely, in the "low wind–low solar" scenario, the shaded area is the narrowest. This indicates that due to lower renewable penetration, the voltage profile is the most stable, and the control burden is minimized.

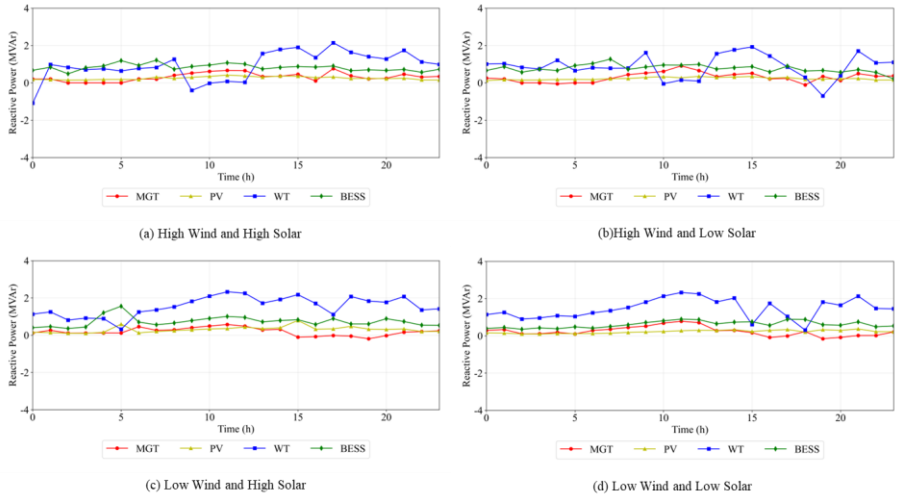


Fig 3 Reactive power output curve

From the perspective of the overall reactive power strategy in Fig 3, wind turbines serve as the primary source of dynamic reactive power support in all scenarios. As depicted by the blue curves, the reactive power output from the wind turbines is the largest in magnitude and fluctuates most frequently, indicating that their control actions are closely tied to the system state. This is particularly evident during periods of high renewable generation, such as the "high wind–high solar" scenario (approx. 10:00–17:00), when the system faces overvoltage risks. In response, the wind turbines are dispatched to absorb significant reactive power (up to 2–3 MVAr), thereby effectively suppressing the local voltage rise caused by high active power injection. This proactive reactive power management is key to the model's ability to strictly constrain the maximum network voltage below the 1.03 p.u. margin.

Energy storage systems (ESS) and photovoltaics (PV) participate in voltage regulation as flexible, ancillary reactive power sources. Their reactive power output (green and yellow curves) is consistently positive, providing stable, foundational support to the system, though the depth and frequency of their regulation are lower than that of the wind turbines. The contribution from BESS and PV is especially critical in scenarios like "low wind–low solar," where the overall system voltage is low and requires support. In contrast, the participation of microturbines in reactive power regulation is minimal (red curve near zero). This suggests that, driven by economic efficiency, the model prioritizes zero-marginal-cost resources (renewables and storage) for reactive power services, reserving the microturbines primarily for active power backup and thereby achieving an optimal resource allocation.

A comparison across the four scenarios reveals the highly adaptive nature of the model's reactive power dispatch strategy. The more extreme the scenario, the greater the need for reactive power regulation. In the "high wind–high solar" scenario (top-left), the total reactive power output is at its maximum to counteract the most severe voltage pressure. Conversely, in the "low wind–low solar" scenario (bottom-right), where power flows are lower and the voltage is more stable, reactive power outputs are kept at minimal levels to avoid unnecessary network losses. This coordinated, on-demand reactive power optimization strategy is what ultimately ensures the excellent voltage quality observed under all operating conditions, as discussed previously.

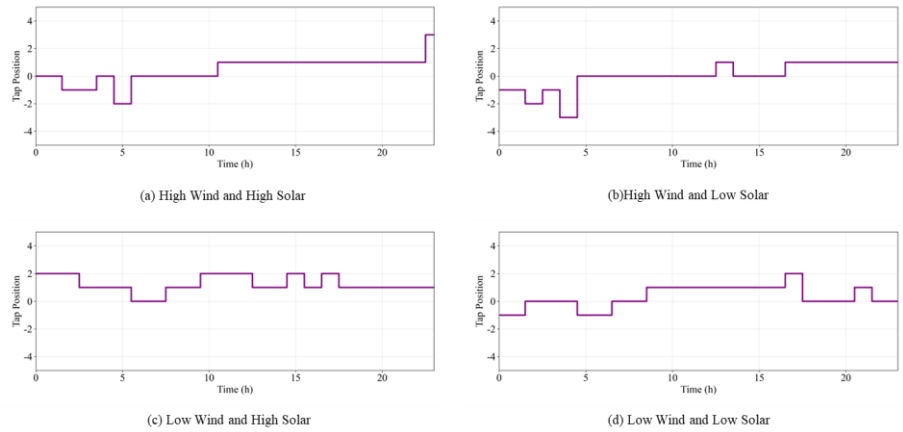


Fig 4 Scheduling Strategy for On-Load Tap Changer

The dispatch strategy for the On-Load Tap Changer (OLTC) is directly correlated with the dynamic characteristics of each scenario. In the "low wind–high solar" scenario (In the bottom-left subgraph in Fig 4), the OLTC's operational sequence is the most complex and frequent. Here, the daytime system voltage relies heavily on PV support, and the rapid decline of PV generation in the evening causes a sharp voltage drop. To adapt to this significant intra-day shift in operating conditions, the model performs multiple tap adjustments throughout the day. In contrast, for scenarios with

more stable source-load characteristics, such as "low wind–low solar," the OLTC's control actions are simpler, involving only a few key adjustments.

The timing and direction of the OLTC's actions reflect an anticipatory control logic. In all scenarios, tap adjustments are concentrated around key time points: the early morning load ramp-up (05:00–07:00), the midday power flow transition, and the evening ramp period (after 17:00). The model executes a tap-down (voltage reduction) operation around 04:00 to mitigate the overvoltage risk posed by high wind speeds and low loads during the night. In the "high wind–high solar" scenario, a notable tap change occurs near the end of the day, likely as a preemptive measure to provide voltage support against the persistent overnight load and potential wind power fluctuations.

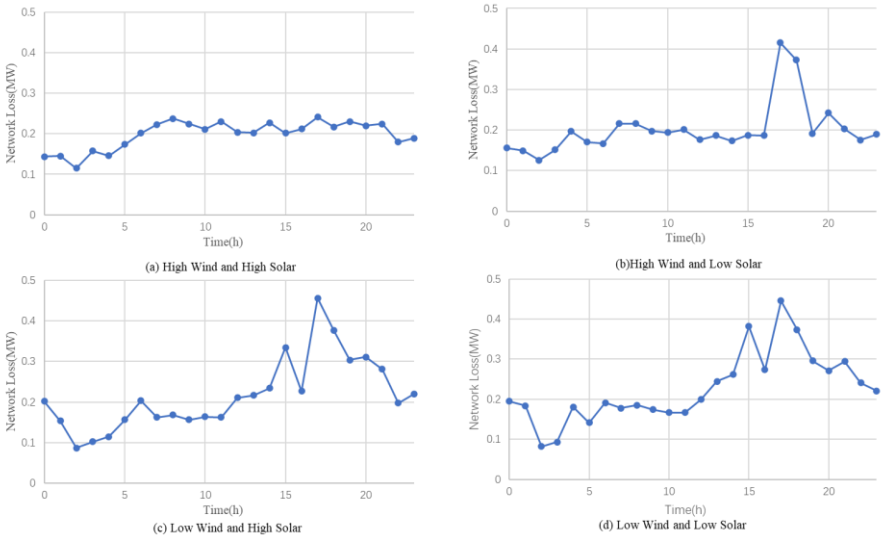


Fig 5 Network loss curves under four types of scenarios

By observing the overall trend and peak values of network loss in Fig 5, it can be found that in most cases, the system will have the most significant loss peak during the evening electricity consumption peak period (17:00–19:00). This phenomenon is particularly pronounced in cases with insufficient wind and solar generation. This highlights an operational challenge: after the rapid decline of high-penetration PV power, the system must rely heavily on dispatchable microturbines for long-distance power support to meet the evening peak load. This leads to a sharp increase in line currents and, consequently, substantial network losses. In contrast, the loss curve for the "high wind–high solar" scenario is the flattest and lacks a distinct evening peak. This is because ample distributed generation is still available, which avoids centralized, long-distance transmission and optimizes the network-wide power flow distribution.

The management of network losses during the daytime period (08:00–16:00) highlights the economic benefits of distributed renewable energy. Losses are consistently kept at a low level, around 0.2 MW. This is attributable to the model's strategy of

maximizing the local consumption of wind and solar resources, where distributed generation serves local loads. This approach significantly shortens power transmission distances, thereby reducing line losses. These results quantitatively demonstrate the value of the coordinated optimization model in promoting the efficient utilization of renewables and enhancing the overall economic efficiency of system operation.

5 Conclusion

The coordinated robust optimization model proposed in this paper effectively addresses the challenges posed by the uncertainty of wind and solar power generation in day-ahead scheduling. By coordinating multiple classes of distributed resources with diverse response characteristics, the model successfully formulates a highly robust operational strategy.

By deeply leveraging and coordinating the reactive power potential of resources including OLTCs, wind turbines, and energy storage, the model strictly maintains system voltages within desired margins across all typical scenarios. This demonstrates the model's excellent voltage control capabilities and overall robustness.

With network loss minimization as a key objective, the model significantly reduces system losses by maximizing the local consumption of renewable energy and optimizing the network-wide power flow distribution. The analysis shows that the model's performance is closely correlated with the characteristics of the renewable generation, particularly in managing critical periods such as the evening ramp.

Ultimately, the case study analysis clearly demonstrates that the proposed model can achieve the secure dispatch of distribution networks with high penetrations of renewable energy. It provides an effective solution for the operational control challenges posed by the uncertainty inherent in renewable generation.

Acknowledgement: This research was supported by the State Grid Zhejiang Electric Power Company Science and Technology Project “Research on New Distribution System State and Hosting Capacity Assessment Technology for Large-Scale Distributed Renewable Energy Integration” (Project No. B311DS240017).

References

1. T. Tewari, A. Mohapatra, and S. Anand, “Coordinated control of OLTC and energy storage for voltage regulation in distribution network with high PV penetration,” IEEE Trans. Sustain. Energy, vol. 12, no. 1, pp. 262–272, Jan. 2021, doi: 10.1109/TSTE.2020.2991017.
2. C. Li et al., “A two-stage adaptive-robust optimization model for active distribution network with high penetration wind power generation,” IET Renewable Power Gener., vol. 18, no. 7, pp. 1204–1217, 2024, doi: 10.1049/rpg2.12836.
3. L. You, H. Ma, T. K. Saha, and G. Liu, “Gaussian mixture model based distributionally robust optimal power flow with CVaR constraints,” Oct. 26, 2021, arXiv: arXiv:2110.13336. doi: 10.48550/arXiv.2110.13336.

4. V. Muthukaruppan, Y. Shi, and M. Baran, “A supervisory Volt/Var control scheme for coordinating voltage regulators with smart inverters on a distribution system,” Front. Smart Grids, vol. 3, Apr. 2024, doi: 10.3389/frsgr.2024.1356074.
5. T. Tewari, A. Mohapatra, and S. Anand, “Coordinated control of OLTC and energy storage for voltage regulation in distribution network with high PV penetration,” IEEE Trans. Sustain. Energy, vol. 12, no. 1, pp. 262–272, Jan. 2021, doi: 10.1109/TSTE.2020.2991017.
6. M. Cheramin, R. L.-Y. Chen, J. Cheng, and A. Pinar, “Data-driven robust optimization using scenario-induced uncertainty sets,” July 11, 2021, arXiv: arXiv:2107.04977. doi: 10.48550/arXiv.2107.04977.
7. D. Bertsimas and M. Sim, “The price of robustness,” Oper. Res., vol. 52, no. 1, pp. 35–53, Feb. 2004, doi: 10.1287/opre.1030.0065.
8. T. A. Nguyen and M. L. Crow, “Stochastic optimization of renewable-based microgrid operation incorporating battery operating cost,” IEEE Trans. Power Syst., vol. 31, no. 3, pp. 2289–2296, May 2016, doi: 10.1109/TPWRS.2015.2455491.
9. M. E. Baran and F. F. Wu, “Optimal capacitor placement on radial distribution systems,” IEEE Trans. Power Del., vol. 4, no. 1, pp. 725–734, Jan. 1989, doi: 10.1109/61.19265.
10. R. A. Jabr, “Radial distribution load flow using conic programming,” IEEE Trans. Power Syst., vol. 21, no. 3, pp. 1458–1459, Aug. 2006, doi: 10.1109/TPWRS.2006.879234.
11. J. Barr and R. Majumder, “Integration of distributed generation in the volt/VAR management system for active distribution networks,” IEEE Trans. Smart Grid, vol. 6, no. 2, pp. 576–586, Mar. 2015, doi: 10.1109/TSG.2014.2363051.

032 平抑风电波动的电氢储能容量优化配置

孙天贺[1]，翟晨[1]

（1. 辽宁省电网节能与控制重点实验室，沈阳工程学院，沈阳，110136）

Optimal allocation of electric hydrogen energy storage capacity to smooth out wind power fluctuations

SUN Tianhe[1], ZHAI Chen[1]

(1.Key Laboratory of Energy Saving and Controlling in Power System of Liaoning Province, Shenyang Institute of Engineering, Shenyang, 110136)

ABSTRACT: Wind energy itself has the characteristics of intermittence and uncertainty, which poses a great challenge to the stable operation of power grid system. This paper analyzes the essential characteristics of wind power fluctuation, and proposes to use energy storage system to buffer short-term fluctuation. In this paper, based on the fluctuation characteristics of wind power, the method based on empirical mode decomposition (EMD) is introduced to implement multi-scale decomposition of power signal, so as to achieve reasonable load distribution between units of energy storage equipment. In the simulation analysis stage, an optimization model is developed to simulate and test the charging and discharging characteristics, SOC change performance and the response ability of the whole system to wind power fluctuation of the super capacitor and the electric hydrogen production system. The results show that the hybrid energy storage system has good performance in stabilizing wind power fluctuations and improving power supply stability, and presents high economic feasibility.

KEY WORDS: wind power, electro-hydrogen hybrid energy storage, wind power fluctuation smoothing, electrolyzer, fuel cell

摘要：风能本身存在间歇性和不确定性的特质，对电网系统稳定运行构成了不小挑战，本文剖析了风电功率波动的本质特征，提出借助储能系统缓冲短期起伏。本文就风电功率的波动特性而言，引入基于经验模态分解(EMD)的办法对功率信号实施多尺度分解，做到储能设备各单元间的合理负载分配。在仿真分析阶段，制订了优化模型，对超级电容和电制氢系统的充放电特性、SOC 变化表现以及整个系统对风电波动的响应能力开展模拟测试。 结果说明，该混合储能系统在平抑风电功率波动、提高供电稳定性方面呈现良好性能，同时呈现较高的经济可行性。

关键词：风力发电，电-氢混合储能，风电波动平抑，电解槽，燃料电池

DOI：

基金项目：

Project Supported by National Natural Science Foundation of China(NSFC)(51037003).

0 引言

在“碳达峰、碳中和”目标推动下，风力发电作为清洁可再生能源，其装机容量与并网规模持续扩大。然而，风电所具有的波动性和间歇性对电网的稳定运行构成了严峻挑战。为提升电网对风电的接纳能力，引入储能系统成为关键解决方案。

目前就风电与储能系统联合调控问题而言，有研究制定了一种融合递推平均和加权指数平滑机制的波动抑制对策[1]。文献[2]就风电场输出的不确定性问题展开研究，构建了一种具备自适应能力的小波包分解方案，其目的是对输出功率的时频特征做深入刻画。在实际应用这一方面，文献[3]继续探索了小波包技术在风电功率平滑中的作用。

本文规划了一个针对风电系统的电氢混合储能运行结构，如何分配风电功率流向到超级电容、锂电池和氢系统之间，以及怎样对系统容量开展经济性优化，均有系统的阐述呈现。

1 风电发电原理及数学模型

1.1 风力发电基本原理

风力发电是风能到机械能再到电能的转化。

风力发电工作工程中的输出功率为：

$$P = \frac{1}{2} C_p \pi R^2 \rho V^3 \tag{1.1}$$

式中，P 为风力发电的输出功率；C_p 为风力发电过程中的风能利用系数；R 为风机叶片的半径；ρ 为空气密度；V 为风速。

由上述模型可得，风力发电因风速的不确定性会造成风力发电功率输出的波动性和不确定性。

1.2 风力发电数学模型

1.2.1 风力发电功率输出特性

地区的风速变化情况一般常用风速概率密度模型来描述和测定其中包括：Weibull 分布、Rayleigh 分布和 Gaussian 分布，其中 Weibull 分布为最常用的风速概率密度模型，它可有效地捕捉风速变化情况，其概率密度方程数学表达式如式(1.2)所示[4]。

$$F(v)=\frac{k}{v}\cdot\left(\frac{v}{c}\right)^{k-1}e^{-\left(\frac{v}{c}\right)^{k}} \tag{1.2}$$

式中，c 和 k 分别为韦布尔分布的尺度系数和形状系数。

风机的输出功率特性由式(1.3)所示。

$$P=\begin{cases}0 & v<v_{in},v>v_{out}\\ \dfrac{v^3-v_{in}}{v_N^3-v_{in}}\cdot P_N & v_{in}\le v<v_N\\ P_N & v_N\le v<v_{out}\end{cases} \tag{1.3}$$

式中，P_N 为风机的额定功率；v 为当前的实际风速；v_{in} 为切入风速；v_{out} 为切出风速；v_N 为额定风速。

1.2.2 风力发电功率波动特性

风功率波动量通常定义为在特定时间间隔内风电输出功率最大值与最小值之间的风功率波动量,受采样时间和时间窗口长度的影响[5]。风功率波动量如式(1.4)所示。

$$\Delta P_{\max}(t_0)=\max[P_{wind}(t)]-\min[P_{wind}(t)] \tag{1.4}$$

式中，$\max[P_{wind}(t)]$和$\min[P_{wind}(t)]$分别为 T 时段内风电的最大功率值和最小功率值；$\Delta P_{\max}(t_0)$为 T 时段内风功率的最大值与最小值之差。

2 储能系统原理及数学模型

2.1 电-氢系统的原理及数学模型

电氢系统主要是指通过电解槽以电解水的方式产生氢气和氧气，利用储氢罐将产生的 氢气进行储存，最后通过燃料电池的形式产生电能供负荷使用。

2.1.1 电解槽

通过电解槽对电流的响应，感知风力发电机组的出力变化，根据调度需求和功率变化 情况灵活制氢，电解槽的制氢效率如下式(2.1)所示，产氢功率如下式(2.2) 所示，电解槽的电解效率如下式(2.3)所示。

$$\eta_{H_2}(t)=\frac{\eta_{el}(t)P_{el}(t)}{R_{H_2}} \tag{2.1}$$

$$P_{H_2}(t)=\eta_{H_2}P_{el}(t) \tag{2.2}$$

$$\eta_{el}=1-\frac{\gamma_{H_2}}{\rho_{H_2}}-2\frac{\gamma_{O_2}}{\rho_{O_2}} \tag{2.3}$$

式中，$\eta_{H_2}(t)$—电解槽的制氢效率；$\eta_{el}(t)$—电解槽的电解效率；$P_{el}(t)$—t 时刻电解装置的耗电功率；R_{H_2}—氢气的燃烧热值；$P_{H_2}(t)$—产氢功率(理想情况下为 1)；ρ_{H_2}—产氢密度；γ_{H_2}—氢气渗透通量密度；γ_{O_2}—氧气渗透通量密度。

2.1.2 储氢系统

氢气储存过程的能量约束如式(2.4)所示，储氢罐的功率方程如式(2.5)所示。

$$\begin{cases}E_{\tan kin}^{\min}e_{in}(t)\le E_{\tan kin}(t)\le E_{\tan kin}^{\max}e_{in}(t)\\ E_{\tan kin}^{\min}e_{out}(t)\le E_{\tan kout}(t)\le E_{\tan kin}^{\max}e_{out}(t)\\ e_{in}(t)+e_{out}(t)\le 1\\ e_{in}(t)\in\{0,1\}\\ e_{out}(t)\in\{0,1\}\end{cases} \tag{2.4}$$

$$P_S(t)=P_o(t)+\alpha\frac{\Delta n_{H_2}WT_s}{M_{H_2}V_s} \tag{2.5}$$

式中，$E_{\tan kin}(t)$—t 时刻储氢罐储存的能量；$E_{\tan kout}(t)$—t 时刻储氢罐释放的能量；$e_{in}(t)$、$e_{out}(t)$—储氢罐充放能量的标志位；$P_s(t)$—储氢罐的功率；$P_O(t)$—储氢罐内的初始压强；α—氢气的压缩因子；W—气体常数；Δn_{H_2}—储氢的变化量；T_s—储氢罐的温度；V_s—储氢罐的体积；M_{H_2}—氢气的摩尔质量。

2.1.3 燃料电池

燃料电池利用电解水反应将所储存的氢气通过与氧气发生化学反应从而产生电能。

燃料电池的输出功率如式(2.6)所示。

$$P_f=P_{el}\eta_{el}\eta_f \tag{2.6}$$

式中，P_f—燃料电池的输出功率；η_f—燃料电池的工作效率。

3 平抑风电波动的电-氢混合储能配置

3.1 电-氢混合储能协调运行框架

3.1.1 电-氢混合储能系统架构

为应对风电大规模并网引起的功率波动，本文构建了一种电-氢混合储能系统(HESS)协同运行机制[6]，整体框架如图 1 所示。

在原有将氢储能整体用于调峰的基础上，进一步提出氢储能的模块化配置策略：将其中一部分功率和容量划分为波动平抑模块，利用氢储能循环寿命长的特点，与响应迅速但循环寿命有限的电化学储能形成互补，共同抑制风电的分钟级波动。

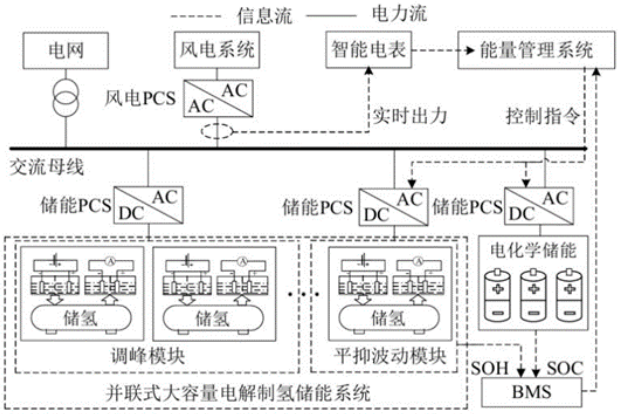


图 1 HESS 协调运行框架

Figure 1 HESS Coordinated Operation Framework

其模块化的数学模型如式(3.1)所示：

$$\begin{cases} P_{EL}^{rated} = P_{EL}^{stabrated} + P_{EL}^{pshrated} \\ P_{FC}^{rated} = P_{FC}^{stabrated} + P_{FC}^{pshrated} \\ V_{STO}^{rated} = V_{STO}^{stabrated} + V_{STO}^{pshrated} \end{cases} \tag{3.1}$$

式中，rated 代表氢储能各子系统的总规模，stabrated 为平抑波动模块各子系统的规模，pshrated 分别为调峰模块各子系统的规模。

3.1.2 基于 EMD 的风电功率分配策略

采用EMD方法对原始风电信号进行分析，可得到一系列固有模态函数(IMF)。若对每个IMF分量分别进行处理，将增加额外的计算负担。结合风电并网对波动幅度的限制要求，可将经EMD分解后的风电信号重新整合为低频和高频两个部分。其中，低频分量直接并入电网，而高频分量则交由混合储能系统(HESS)处理。IMF重构的依据是设定相应指标，通过叠加不同频段内的各分量，分别合成低频和高频信号。重构方式包括高频重构(fine to coarse, f2c)和低频重构(coarse to fine, c2f)：高频重构是从高频到低频依次累加IMF，如式(3.2)所示；而低频重构则是从低频到高频依次累加IMF，具体形式见式(3.3)[7]。

$$\begin{cases} f2_c(1) = IMF1 \\ f2_c(2) = IMF1 + IMF2 \\ \vdots \\ f2_c(p+1) = IMF1 + IMF2 + \cdots + IMFP + res \end{cases} \tag{3.2}$$

$$\begin{cases} c2f(1) = res \\ c2f(2) = res + IMF_p \\ \vdots \\ c2f(p+1) = res + IMF_P + \cdots + IMF_1 \end{cases} \tag{3.3}$$

在上述信号分解和信号重构基础上，通过风电功率分配策略流程，完成功率分配，如图 2 所示。

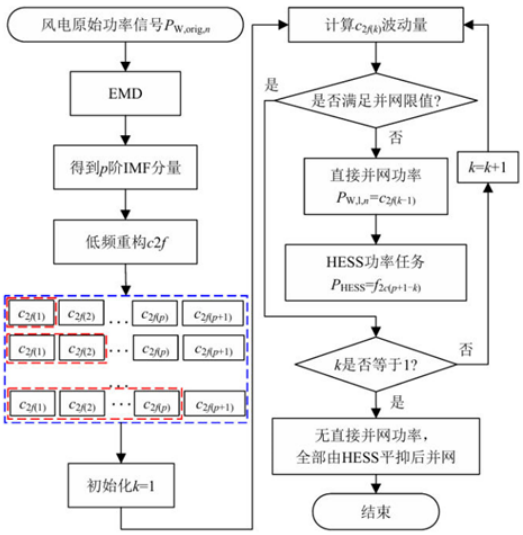


图 2 基于 EMD 的风电功率分配策略流程

Figure 2 Wind Power Distribution Strategy Process based on EMD

3.1.3 电-氢 HESS 能量管理策略

本文推出了一种融合碱性电解槽运行特性的电-氢 HESS 能量协调策略，具体而言：

以电化学储能作为辅助单元，优先把其 *SOC* 维持在中值区间，以此保留充放电的调整空间。

以氢储能系统作为主力单元，借助引入两个 *SOC* 阈值(SOC_{EL} 与 SOC_{FC})确定不同储能设备的调度边界，以此防止电化学储能的过度运用，且保证电解槽的运行安全性。在传统运行模式的基础上该策略增加了以下几种特殊运行模式：

（1）工作模式 1：当系统满足以下条件时:

$$\begin{cases} 0 < P_{HESS} \\ SOC_{\max} \le SOC \\ SOH \le 0.9 \end{cases} \tag{3.4}$$

电化学储能放电为电解槽运行提供差额功率，避免电解槽停机，使其以最低功率运行。

（2）工作模式 2：当系统满足以下条件时:

$$\begin{cases} 0 < P_{HESS} \\ SOC_{EL} \le SOC \le SOC_{\max} \end{cases} \tag{3.5}$$

此时位于电解槽的启停缓冲带，该运行模式有两种作用：拓宽电解槽的运行区间；维持 *SOC* 状态处于中间水平。

（3）工作模式 3：当系统满足以下条件时:

$$\begin{cases} P_{HESS} \le 0 \\ SOC \le SOC_{\min} \\ 0.1 \le SOH \end{cases} \tag{3.6}$$

储能系统当前正处于放电阶段，电解槽可能开

启运行，主要用于吸收风电的过剩部分；燃料电池处于待命状态。

（4）工作模式4：当系统满足以下条件时:

$$\begin{cases} P_{HESS} \le 0 \\ SOC_{\min} \le SOC \le SOC_{FC} \end{cases} \tag{3.7}$$

此时燃料电池处于启停缓冲带内。如果 n-1 时刻燃料电池为启动状态，则继续保持运行；若 n-1 时刻为停机状态，则维持停机状态。该运行模式的主要目的是：避免储能 SOC 在接近 $SOC_{\min}$ 时波动，防止燃料电池频繁为其充电。

3.2 混合储能系统容量配置模型

3.2.1 目标函数

设置目标函数为：

$$\min C = C_{BAT} + C_{HES} + C_W^{comp} \tag{3.8}$$

式中，C 为年综合成本；C_{BAT} 为电化学储能成本；C_{HES} 为氢储能成本；C_W^{comp} 为风电功率波动机会补偿成本。

$$\begin{aligned} C_{BAT} &= C_{BAT}^{inv} + C_{BAT}^{oper} \\ C_{HES} &= C_{HES}^{inv} + C_{HES}^{oper} \end{aligned} \tag{3.9}$$

式中，C_{BAT}^{inv} 和 C_{BAT}^{oper} 分别为电化学储能的投资成本和运行维护成本；C_{HES}^{inv} 和 C_{HES}^{oper} 分别为氢储能的投资成本和运行维护成本。

3.2.2 约束条件

氢储能需要预留部分功率和容量用于平抑风电功率波动，因此该模块的功率和容量应控制在氢储能总功率和容量范围内，如式(3.10)。

$$\begin{aligned} 0 \le P_{EL}^{stabrated} &\le P_{EL}^{rated} \\ 0 \le P_{FC}^{stabrated} &\le P_{FC}^{rated} \\ 0 \le V_{STO}^{stabrated} &\le V_{STO}^{rated} \end{aligned} \tag{3.10}$$

功率平衡约束：混合储能功率任务 P_{HESS} 分为正向波动和负向波动。当 $P_{HESS,n} \ge 0$ 时为正向波动，此时需要电化学储能充电或电解槽启动以吸收波动；当 $P_{HESS,n} \le 0$ 时为负向波动，此时则需要电化学储能放电或燃料电池启动对波动进行补偿。

$$\begin{aligned} P_{HESS,n} = {} & P_{EL,n}^{stab} + P_{BAT,n}^{ch} + P_{P-uncomp,n} \\ & - P_{N-uncomp,n} - P_{FC,n}^{stab} - P_{BAT,n}^{disch} \end{aligned} \tag{3.11}$$

充放电功率约束分为电化学储能(3.12)和氢储能(3.13)：

$$\begin{cases} 0 \le P_{BAT,n}^{ch} \le P_{BAT}^{rated} \\ -P_{BAT}^{rated} \le P_{BAT,n}^{disch} \le 0 \\ P_{BAT,n}^{ch} P_{BAT,n}^{disch} = 0 \end{cases} \tag{3.12}$$

$$\begin{cases} P_{EL}^{stab\,\min} \le P_{EL,n}^{stab} \le 1.2 P_{EL}^{stabrated} \\ P_{FC}^{stab\,\min} \le P_{FC,n}^{stab} \le P_{FC}^{stabrated} \\ P_{EL,n}^{stab} P_{FC,n}^{stab} \le 0 \end{cases} \tag{3.13}$$

式中，$P_{EL}^{stab\,\min}$ 为电解槽最低运行功率；$P_{FC}^{stab\,\min}$ 为燃料电池放电功率下限。储能状态约束分为电化学储能(3.14)和氢储能(3.15)：

$$\begin{cases} SOC_n - SOC_{n-1} = \left(\dfrac{P_{BAT,n}^{ch} \eta_{BAT}}{E_{BAT}^{rated}} - \dfrac{P_{BAT,n}^{disch}}{E_{BAT}^{rated} \eta_{BAT}} \right) \Delta t \\ SOC_{\min} \le SOC_n \le SOC_{\max} \end{cases} \tag{3.14}$$

$$\begin{cases} v_{STO,t}^{stabin} = v_{EL}^{stab} \\ v_{STO}^{stabout} = v_{FC,t}^{stab} \\ SOH_n^{stab} - SOH_{n-1}^{stab} = \left(\dfrac{v_{STO,n}^{stabin}}{m_{STO}^{stabrated}} - \dfrac{v_{STO,n}^{stabout}}{m_{STO}^{stabrated}} \right) \Delta t \\ SOH_{\min}^{stab} \le SOH_n^{stab} \le SOH_{\max}^{stab} \end{cases} \tag{3.15}$$

4 仿真分析

4.1 仿真设置与模型描述

仿真过程中，首先导入典型的日数据，定义了超级电容和电制氢系统的相关参数，并设置了优化问题。通过使用 YALMIP 框架，采用 CPLEX 作为求解器来优化混合储能系统的配置。

4.2 仿真结果与图形分析

超级电容充放电功率曲线如图3所示：该图反映了超级电容在系统中的作用，展示了其如何通过实时调节电力负荷来平抑波动，确保系统稳定运行。

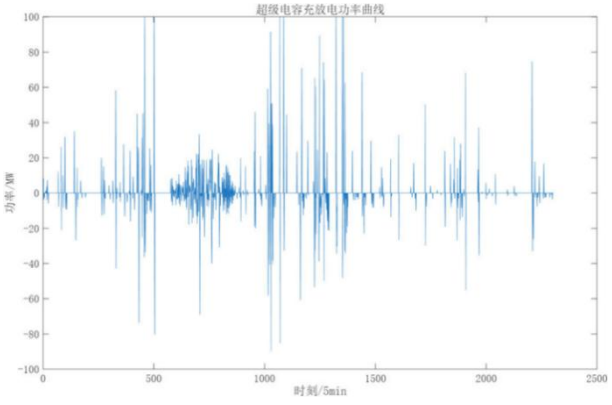


图 3 超级电容充放电功率曲线

Figure 3 Charging and discharging power curve of super capacitor

图 4 展示了超级电容的荷电状态随时间的变化趋势，曲线的上升与下降分别对应超级电容的充电

与放电过程，直观呈现了储能系统在优化过程中的充放电周期。通过观察曲线的波动幅度与频率，可分析超级电容的容量利用效率。

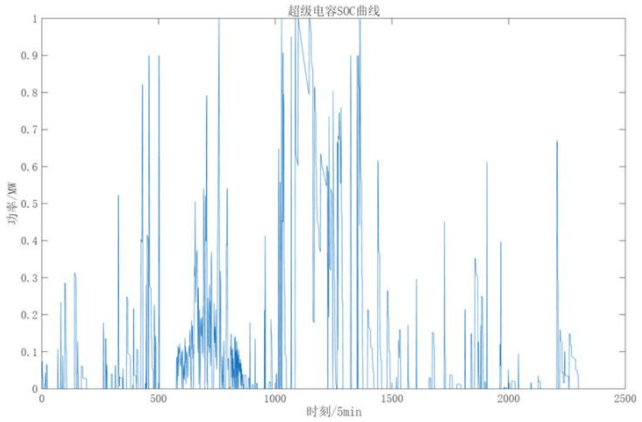


图 4 超级电容 SOC 曲线

Figure 4 Supercapacitor SOC Curve

图 5 对比了风电高频功率在平抑前、平抑后及平抑后丢弃正向波动量后的变化情况，三组曲线的对比清晰显示了混合储能系统对风电高频波动的抑制效果，为提升电网稳定性提供了直观依据。

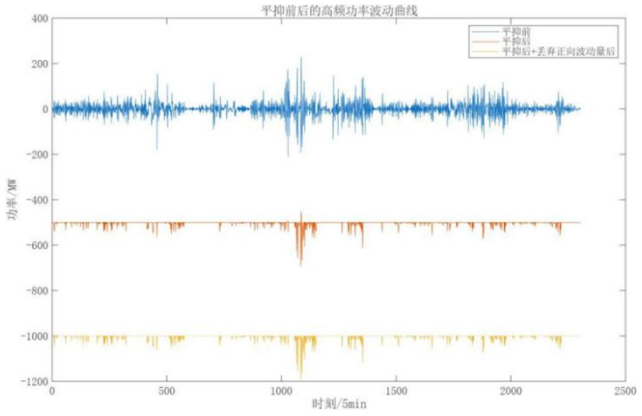


图 5 平抑前后的风电高功率波动曲线

Figure 5 High Power Fluctuation Curve of Wind Power before and after Stabilization

图 6 和 7 展示了风电并网功率波动平抑后的曲线和平抑前后的曲线。通过将风电功率与储能系统的平抑波动结果进行比较，进一步展示了系统如何调整并网功率以减少波动。图 6 验证了混合储能系统在平抑风电波动、降低并网功率偏差方面的实际效果， 符合电网对功率输出稳定性的技术要求。图 7 表明储能系 统通过“削峰填谷”操作有效缓冲了功率波动，既避免了过高的尖峰负荷，又维持了基本 功率输出下限。两组曲线的差异量化了混合储能系统对风电并网功率的平滑效果，为评估系统的实际调控能力提供了数据支撑。

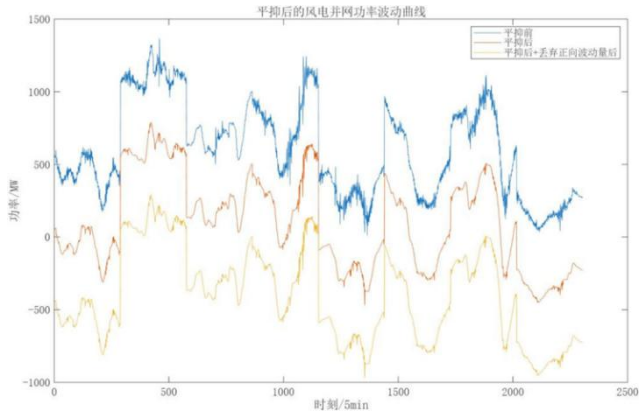


图 6 平抑后的风电并网功率波动曲线

Figure 6 The Stabilized Wind Power Grid-connected Power Fluctuation Curve

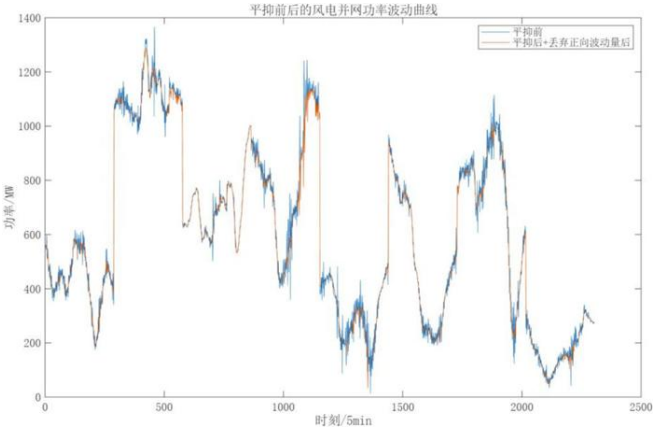


图 7 平抑前后的风电并网功率波动曲线

Figure 7 Wind Power Grid-connected Power Fluctuation Curve before and after Stabilization

图8展示了初始并网功率的低频分量与平抑后的功率曲线。这一图表反映了风电功率低频分量的变化及平抑后并网功率的稳定性。

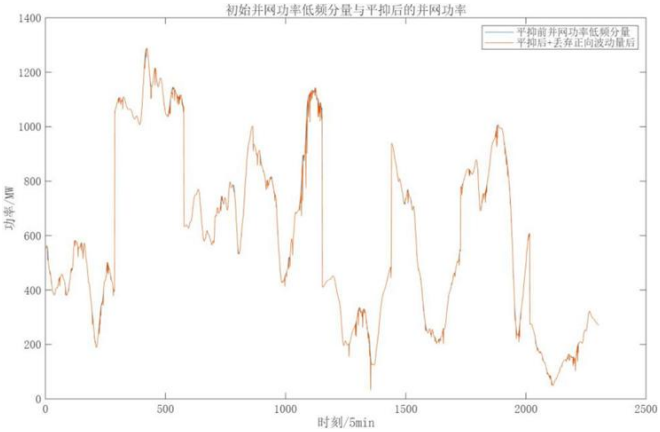


图 8 初始并网功率低频分量与平抑后的并网功率

Figure 8 The Low-frequency Component of the Initial Grid-connected Power and the Stabilized Grid-connected Power

图 9 展示了电制氢的充放电功率曲线。该图反映了电制氢系统如何利用充电和放电来满足风电波动平抑的需求。

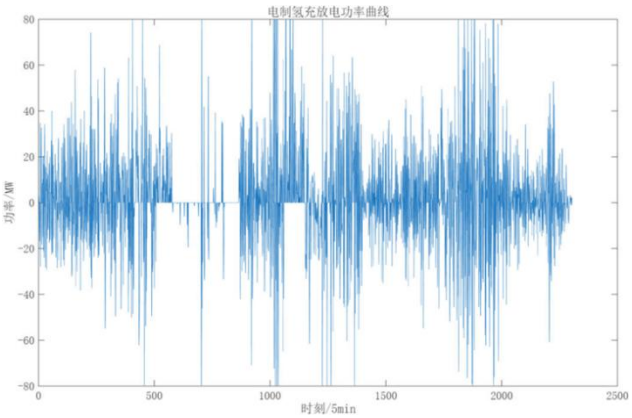


图 9 电制氢充放电功率曲线

Figure 9 Charging and Discharging Power Curve of Electric Hydrogen Production

4.3 最优容量配置结果

如表 1 所示，混合储能系统的最优配置容量为：超级电容的容量配置为 8.34 MW，电制氢的容量配置为 79.74 MW。在成本方面，超级电容的投资和运行成本为 21,571,123.22 元 ，电制氢的投资和运行成本为 13,542,726.41 元，平抑风电波动的费用为 24,949,914.64 元，最终的综合成本为 60,063,764.27 元。

Table 1 Optimal Capacity

表 1 最优配置容量

	项目	数值
容量配置	超级电容	8.34MW
	电制氢	79.74MW
成本	超级电容	21,571,123.22 元
	电制氢	13,542,726.41 元
	平抑风电波动	24,949,914.64 元
	综合成本	60,063,764.27 元

5 结论

本文聚焦风电系统输出波动对电网运行产生的挑战，围绕怎样运用储能途径实现波动调节，得出以下结论：

（1）采用基于 EMD 分解的风电功率分配办法，以及结合电解槽运行特性所构建的能量管理策略，达成了储能系统对风功率波动的自适应跟进。

（2）在模型仿真的阶段里，采用实际数据进行验证，结果表明该系统在提升电网接入质量、稳固运行稳定性等方面优势十分明显，且给出了可实际应用的容量配置建议。

参考文献

[1] 张萍，李永强，杏华良．基于变分模态分解的平抑风电波动混合储能容量优化配置[J/OL]．发电技术，2025，1-10．

[2] 吴杰．平抑风电波动的混合储能系统控制策略及容量优化配置研究[D]．合肥工业大学，2019．

[3] 吕慧香．平抑风电波动的混合储能系统容量优化配置及功率协调策略研究[D]．湘潭大学，2023．

[4] 魏鹏，侯林虎．基于风力发电的配电网储能系统优化配置方法[J]．自动化应用，2025，66(03)：153-155.

[5] 谢金勇，张逸，张亚超，等．提升新能源消纳的混合电解槽协同运行的园区级氢能系统优化配置方法[J/OL]．电网技术，2025，1-15.

[6] 李子晨，夏杨红，孙勇，等．考虑氢能长短周期储能特性的电氢综合能源系统容 量配置方法[J]．电网技术，2025，49(01)：12-21.

[7] 郭建华．含电—氢混合储能的电力系统优化运行[D]．大连理工大学，2022.



翟晨

收稿日期：

作者简介：

翟晨(2002)，男，硕士研究生，研究方向为电力系统分析、运行与控制，E-mail：2412447975@qq.com；

孙天贺(1991)，男，副教授，研究方向为电力系统分析与控制，E-mail：sunth@sie.edu.cn。

033 超声辅助固化对抑制环氧树脂/金属嵌件界面残余应力的作用

杜世杰，李　进，高宇昂，王禹淮，任　帅

（天津大学电气自动化与信息工程学院 天津 300072）

The Role of Ultrasonic-Assisted Curing in Suppressing Residual Stress at the Epoxy Resin/Metal Insert Interface

Du Shijie, Li Jin, Gao Yuang, Wang Yuhuai, Ren Shuai

(School of Electrical and Information Engineering, Tianjin University, Tianjin 300072, China)

ABSTRACT: Epoxy resin composite materials are widely used in GIS and GIL equipment, and in the actual manufacture of insulating parts, metal inserts are often placed in the epoxy resin. During the pouring process, residual stresses are generated around the metal inserts, which can affect the strength, hardness, fatigue performance, etc. of the epoxy resin composite material and pose a threat to the electrical system. In this paper, by changing the metal inserts, the epoxy resin system components, and the curing process flow, different insulating parts in actual production are simulated. A platform for ultrasonic assisted curing and two different platforms for residual stress detection were set up. The experimental results show that the ultrasonic vibration assisted curing process can have an effect on the residual stress of the epoxy resin system insulating parts, providing reference for selecting ideal ultrasonic assisted curing process parameters.

KEY WORDS: epoxy resin; residual stress; ultrasonic vibration; photoelasticity; acoustic elasticity effect.

摘要：环氧树脂复合材料在 GIS 和 GIL 设备中广泛应用，在实际的绝缘件制造时往往需要在环氧树脂中预置金属嵌件，而在浇注固化过程中金属嵌件周围会产生残余应力，对环氧树脂绝缘件的强度、硬度、疲劳等性能产生影响，对电力装备产生威胁。本文通过改变金属嵌件结构、环氧树脂体系成分以及固化工艺流程来模拟实际中绝缘件的不同情况，并搭建了超声辅助固化平台以及两种不同的残余应力检测平台。实验结果表明超声振动辅助固化可以对环氧树脂体系绝缘件的残余应力起到抑制效果，为选择理想的超声辅助固化工艺的参数提供了参考。

关键词：环氧树脂；残余应力；超声振动；光弹性法；声弹效应

0　引言

环氧树脂复合材料，凭借高电气强度、设计灵活和低成本优势，广泛应用于高压开关、变压器、电缆终端等设备核心绝缘构件的制造[1]。环氧树脂在固化成型过程中受嵌件和固化物热膨胀系数差异、固化收缩效应以及温度梯度等因素的影响会在金属嵌件的周围产生残余应力[2]。在严苛运行工况环境，如高温、低温、强电场和侵水环境下，环氧绝缘构件必须承受各种机械载荷，如拉伸、压缩、弯曲和振动，这可能导致机械损伤和绝缘故障，甚至危及电力设备的正常运行[3]。

在无外力或外力矩作用下，构件或材料内部存在的自身保持平衡的宏观应力一般被定义为残余应力[4]。残余应力会降低环氧树脂体系的绝缘子的机械性能和电气性能，是绝缘子在运行过程中遭受损坏从而导致绝缘失效的重要因素之一[5]。因绝缘裕度要求，绝缘件设计尺寸往往较大，这会进一步加剧残余应力集中程度，造成绝缘子局部损伤，引发沿面放电等电气事故，严重情况下可能导致绝缘子炸裂，威胁电力系统的安全稳定运行。因此需要掌握环氧树脂绝缘件残余应力的分布规律，并提出行之有效的抑制或调控手段。

在实际中广泛使用的残余应力检测方法主要分为有损检测方法和无损检测方法。有损检测方法主要为去层技术和钻孔法：去层技术是一种用于分离复合材料层压板中的层间界面或层内微观结构的方法[6]；钻孔法原则上是一种柔度技术，这种方法通过在材料表面钻取一个小孔，从而释放材料内部的残余应力，经过测量计算后可以测量出残余应力[7]。无损检测方法中有代表性的方法有光弹性和声弹性检测方法：光弹性法基于聚合物链的光学偏振性是各向异性的特点，可通过双折射测量来确认

基金项目：国家自然科学基金项目（52377153）
Project Supported by National Natural Science Foundation of China (52377153）

残余应力大小[8]，作为一种无损检测方法，具有操作方便，设备需求简单的优点；超声波检测技术基于超声纵波在材料中传播声速与材料所承受应力呈线性关系，具有高精度，可以捕捉微小应力变化的特点[9]。因此本文测量透明的无填料环氧树脂绝缘件的残余应力使用光弹性法，对于掺杂氧化铝的环氧树脂残余应力的检测采用超声波检测法。

在实际应用中常用的削弱残余应力的方法主要有时效消除法、机械拉伸法、冷压缩法、超声辅助固化法等[10]。

时效法消除残余应力的基本原理是利用材料在一定温度下随时间发生的塑性变形来释放内部应力，这种方法消除残留压力的效果非常有限。机械拉伸方法是一种在特定时间内对构件施加一定永久拉伸塑性变形量的方法。通过弹性变形向塑性变形的转变来松弛应力、消除应力，只适用于板材和其他截面简单的构件。冷压缩法针对经过淬火处理的合金材料，在规定时间内选择一个或多个面施加压力，并在常温下进行，以使坯料发生永久压缩塑性变形，从而使应力得到松弛，抑制残余应力。

超声辅助固化法通过激振器使构件产生振动，在振动作用下，材料的原有残余应力与产生的应力相叠加，当应力幅值超过材料的屈服强度时，材料将发生塑性变形，达成降低残余应力的工艺目的。相较于传统固化方法，超声辅助固化技术展现出显著优势。该技术通过高频低振幅的能量传递机制[11]，在保证工件微观结构优化的同时，最大限度地减少了宏观形变，从而实现了更高的尺寸精度和更低的疲劳损伤风险[12]。超声振动可以在不改变树脂体系的固化反应机制条件下，减少反应活化能，加速固化过程[13]。检测表征超声振动后的固化胶形态和结构，表明环氧树脂胶混合更加均匀，环氧树脂胶的交联密度变大，胶体组织结构有序性提高[14]。

基于其广阔的应用前景，本文重点研究超声辅助固化流程抑制残余应力的效果。本文建立了超声辅助固化平台，以及光弹性和声弹性残余应力检测平台，通过控制超声辅助固化过程的时间和温度条件开展了残余应力抑制效果的检测验证。

1 检测方法及试样制备

1.1 光弹性效应

本文中基于光弹性原理的残余应力检测平台如图 1 所示。在实验中光源采用自然光（白光），将试样放在光源与偏振片形成的偏振光场中，可以通过观测到光弹性条纹来反映试样内部残余应力的大小和分布情况。入射光在穿过试样后被分解为振动方向正交的两束偏振光，因两个主应力平面方向电磁波的传播速度不同，那么光波通过后会产生一定的光程差，通过测量光程差可以计算出平面模型内各点的主应力差[15]

$$\sigma_1-\sigma_2=\frac{n\lambda}{Ch} \tag{1}$$

$$\sigma_1-\sigma_2=\frac{nf}{C} \tag{2}$$

$$f=\frac{\lambda}{C} \tag{3}$$

式中：主应力差为$\sigma_1-\sigma_2$，n 为条纹阶数，λ为入射光波波长，C 为材料光学灵敏度系数，h 为样品厚度，f 为材料的条纹值。本文所选环氧树脂的条纹值f=11 MPa*mm，入射光波波长λ= 490 nm[16]。

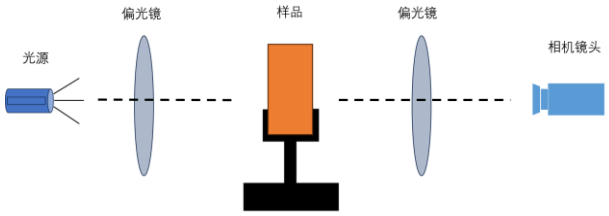


图 1 光弹性法测量残余应力平台

Fig. 1 A platform for measuring residual stresses by photoelasticity method.

1.2 声弹性效应

超声波应力检测的原理是利用超声波声速随应力而变化的声弹性效应。在超声临界折射纵波（LCR 波）单轴应力检测中，这一原理体现在固定传播距离内超声波传播时间与应力之间呈线性关系。通过测量超声波的传播时间，可以对试样内部的残余应力大小进行检测。

假设 LCR 波在被测试样中传播的固定声程为 L，所用传播时间为 T，传播时间与应力变化的关系可以用式（4）来表示。Auteliano 等人基于这个关系式，研究了应力与超声波传播时间之间的关系。

$$d\sigma=\frac{E}{K_tT_0}dT \tag{4}$$

式中：dσ为应力变化量，表示加载应力下应力 σ 与初始应力σ_0之差，单位 MPa；T_0为初始应力下试样中超声临界折射纵波传播时间，单位 μs；dT 为试样中超声临界折射纵波传播时间的变化量，表示加载应力下传播时间 T 与初始应力下传播时间T_0差值，单位 μs；E 为弹性模量，单位 GPa；K_t为表示为超声传播时间与应力变化关系的声弹性系

数，与弹性常数、超声波波形和超声频率有关。

由式（4）可推出声弹性系数 K_t 的计算式:

$$\sigma_c = \frac{E}{K_t T_0}(T - T_0) + \sigma_0 \tag{5}$$

$$K_t = \frac{E(T - T_0)}{T_0(\sigma_c - \sigma_0)} \tag{6}$$

在实验测试当中，残余应力可以通过测量材料中超声纵波反射回波的时间差和波程来计算超声声速。如图 2 所示，在材料中发生第一次底面反射时，部分反射波被记录为波 M1。接着，其余部分在试样表面上发生反射，随后反射波经底部发生第二次反射，第二次反射波穿过被测试样品并被探头接收，标记为波 M2，两波峰之间的时间差 T 即为超声传播时间。声弹性方程为：

$$\frac{V - V_0}{V_0} = K(\sigma - \sigma_0) \tag{7}$$

式中，V_0为初始应力下超声纵波声速，σ_0为初始应力，V 为变化后应力对应的超声纵波声速，σ 为变化后的应力，K 为声弹性系数。材料的声弹性系数 K 是一个常数，体现了超声声速与应力变化之间的关系，和被测材料及超声的性质相关，可以通过测量得到[17]。

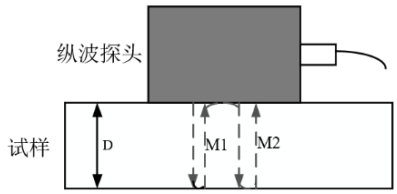


图 2　超声测量示意图

Fig. 2 Ultrasonic measurement diagram

1.3 超声辅助固化平台

本文使用的超声辅助固化平台采用春霖超声波清洗机，型号为 CR-020S，频率为 40KHz，超声波功率为 120W，可以对水浴温度以及振动时间进行调整。能满足材料在超声辅助固化过程中，对外加动应力的需求。在构件完成二阶段固化过程后立即放入超声水浴平台中，通过改变水浴温度以及超声振动辅助固化时间来研究不同条件下超声辅助固化过程对残余应力的抑制效果。

1.4 试样制备

本实验制备试样过程中所使用的原材料主要包括环氧树脂、环氧树脂固化剂、促进剂以及氧化铝颗粒。环氧树脂体系绝缘件中，环氧树脂/固化剂/促进剂的最佳混合比例为 100：85：0.2。将直径为 5mm、高度为 8cm 的金属圆柱体和长为 8cm、宽为 1cm、厚度为 1mm 的金属薄片安置于模具内，然后在 100℃的条件下进行 45 分钟的预热。最后，将其倒入硅橡胶模具中进行两步固化过程。在环氧树脂绝缘子中掺杂氧化铝颗粒能够显著提升其综合性能。

氧化铝颗粒的加入增强了环氧树脂的机械强度，包括硬度、抗压和抗拉强度，使其更加耐用。同时，氧化铝的高导热性和耐高温性提高了绝缘子的热稳定性，延缓了高温环境下的老化过程。此外，氧化铝还能改善绝缘子的电气性能，提升介电强度和耐电弧性，减少局部放电和击穿的风险。其高硬度还增加了绝缘子的耐磨性，延长了在恶劣环境中的使用寿命，因此本文也对氧化铝/环氧树脂复合材料体系绝缘件进行研究。氧化铝/环氧树脂复合材料体系绝缘件制备过程与环氧树脂构件制备过程一致，将氧化铝颗粒、环氧树脂、固化剂、促进剂按照 300 ：100：85：0.2 的比例混合，使用玻璃棒单向、缓慢、匀速搅拌。随后进行 10min 抽真空处理并进行预热处理。将长 8cm、宽 5.3cm、厚度 1mm 的金属片固定在模具一边并进行预热。最后倒入硅橡胶模具中，进行两阶段固化过程。模具嵌件相对位置如下图 4 所示。

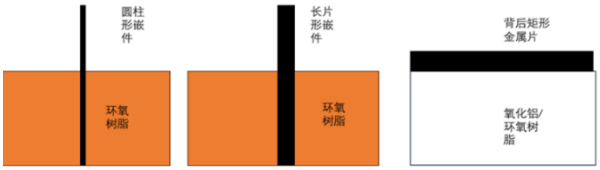


图 3　试样中金属嵌件位置示意图

Fig. 3 Diagram of the location of metal inserts in the sample

共制备 21 个试样，其中 A1～A7 试样的中心嵌件为圆柱形金属导体，B1～B7 试样的中心嵌件为长条形金属导体，C1～C7 试样为金属片固定于模具一侧，再将氧化铝/环氧树脂体系注入固化。试样制备和超声辅助固化流程参数如图所示。固化工艺参数为 “100℃ 4 h， 120℃ 4 h”的试样的固化流程为：第一次固化将温度升高至 100℃保持 4 h，第二次固化将温度升高至 120℃保持 4 h。固化工艺参数为“100℃ 4 h， 120℃ 3 h，80℃ 1 h”的试样的固化流程为：第一次固化将温度升高至 100℃保持 4 h，第二次固化将温度升高至 120℃保持 3h，第三次固化将温度降低至 80℃保持 1h。超声辅助固化参数为“60℃，0.5 h”的流程为在完成固化流程后在 60℃条件下保持 0.5 h 后在 60℃的水温下超声振动 0.5h，以此类推。超声辅助固化参数

为“无”的即为在完成固化流程后冷却至室温即可。试样固化流程和超声振动流程工艺参数如表 1 所示。

表 1 试样固化流程和超声振动流程工艺参数

Table 1 Process parameters of sample curing process and ultrasonic vibration process

样品编号	固化	超声辅助
A1 B1 C1	100℃ 4 h， 120℃ 4 h	无
A2 B2 C2	100℃ 4 h， 120℃ 4 h	60℃，0.5 h
A3 B3 C3	100℃ 4 h， 120℃ 4 h	60℃，1 h
A4 B4 C4	100℃ 4 h， 120℃ 4 h	60℃，1.5 h
A5 B5 C5	100℃ 4 h， 120℃ 4 h	40℃，1 h
A6 B6 C6	100℃ 4 h， 120℃ 4 h	80℃，1 h
A7 B7 C7	100℃ 4 h， 120℃ 3 h 80℃ 1 h	无

2 金属嵌件/环氧树脂界面残余应力抑制效果

2.1 光弹性效应检测简述

据光弹性的原理，可以通过条纹级次来表征残余应力的大小和分布。条纹越密集，主应力差越大，残余应力越大。远离金属嵌件部分的固化过程可以视为自由收缩过程，处于无应力状态，贴近金属嵌件的部分收缩过程受到影响，从而产生残余应力。在实际测试中，靠近金属嵌件的部分条纹分布相对边缘位置更为密集，与理论相符。经对比固化完成后直接冷却的试样和经过超声振动处理的试样，条纹分布明显变得均匀，可以得出超声振动时效法对残余应力有抑制和均化的效果。

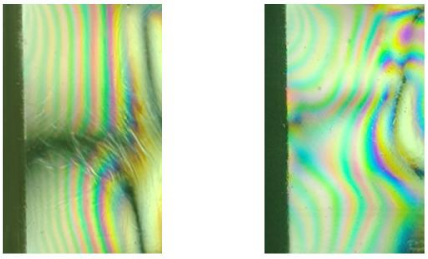
2.2 界面处残余应力计算

由于平面模型自由边界上的任意一点都是单向应力状态，每个点两个主应力当中有一个为零，另一个主应力与边界相切，所以界面处残余应力与主应力差数值相等，方向与边界相切。利用公式（1）进行计算，具体计算结果如表 2，表 3 所示。

表 2 圆柱形嵌件/环氧树脂界面处残余应力

Table 2 Residual stress at cylindrical insert/epoxy resin interface

试样编号	试样厚度/mm	残余应力/MPa
A1	19.644	8.959
A2	19.885	9.404
A3	19.813	8.327
A4	19.995	8.802
A5	19.485	9.597
A6	19.602	7.856
A7	19.714	8.340



(a) 未经处理　　(b) 超声辅助固化后

图 4 A 组超声振动处理试样光弹性条纹对比样例

Fig. 4 Comparison of photoelastic fringes of A group of ultrasonic vibration treated samples

对比 A1~A7 试样的光弹条纹图，如图五所示可以观察到超声辅助固化流程使试样中残余应力分布发生变化，总体上残余应力分布变均匀，不过效果不明显。对比 A1~A4，在 60℃情况下，超声处理的时间过短或过长都会导致处理效果较差，在 1h 的恰当时间时，超声处理后的残余应力明显减小。

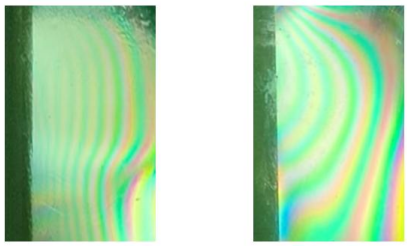
比较 A3、A5 和 A6，在超声处理 1h 的情况下，80℃的环境温度具有最好的效果。

而通过 A1 与 A7 的对比，可以得出在进行处理时，先将试样降温到 80℃再冷却至室温也具有抑制残余应力的效果。

表 3 长片形嵌件/环氧树脂界面处残余应力

Table 3 Residual stress at the long sheet insert/epoxy resin interface

试样编号	试样厚度/mm	残余应力/MPa
B1	19.715	7.253
B2	19.983	6.606
B3	19.924	4.969
B4	19.548	4.502
B5	19.745	5.571
B6	19.771	5.563
B7	19.856	7.756



(a) 未经处理　　(b) 超声辅助固化后

图 5　B 组超声振动处理试样光弹性条纹对比样例

Fig. 5 Comparison of photoelastic fringes of B group of ultrasonic vibration treated samples

对比 B1 与 B2～B7 试样的结果，可以观察到超声辅助固化流程可以不同程度使试样中的残余应力分布变得均匀。对比 B1~ B4 试样界面处的残余应力，超声辅助固化的时间会影响界面处残余应力的大小，时间越长，残余应力的抑制效果越好。对比 B3、B5 与 B6 试样界面处的残余应力，在 60 度条件下残余应力抑制效果最好。

在浇注过程中，环氧树脂复合材料由于局部温度不均匀，会导致不同部位的环氧树脂与酸酐的交联反应程度出现差异性。这种差异性会造成环氧树脂复合材料固化度的不均匀分布，进而产生不均匀的固化收缩应变[18]。Guo 等人采用有限元法对环氧树脂与金属材料体系的应力分布进行了分析，结果表明在环氧树脂与金属材料界面处存在应力集中。二阶段固化过程温度的大小会影响复合材料构件内部的温度和固化度，随着温度的升高和固化反应的进行，树脂的化学收缩反应逐渐释放热量，造成温度和固化度的差异增大，与此同时内部嵌件的回弹程度也会随温度变化[19]，最终表现为残余应力大小的变化。

3　环氧树脂/氧化铝复合材料残余应力抑制效果

3.1 声弹性系数计算

本文环氧树脂/氧化铝复合材料试样的声弹性系数是通过实验测得，即使用液压机对试块施加不同大小的垂直压应力，检测试块在不同压应力下的超声波形，通过上文公式计算超声声速。液压机表盘显示的压强值为 0、0.5、1、1.5、2、2.5、3、3.5、4 MPa，通过公式(8)进行换算，得到试样所受的压应力大小。

$$p_1 = \frac{p_0 S_0}{S_1} \tag{8}$$

式中，p_0为液压机表示数，S_0为油缸面积，p_1为试样承受的压应力，S_1为试样受压面积。

如图 7 所示，在实验的过程中可以观察到试样在压力的作用下会发生形变，而且随着压力的增加形变程度也在线性增加，因此在计算超声声速的时候应考虑压应力对超声声程的影响。

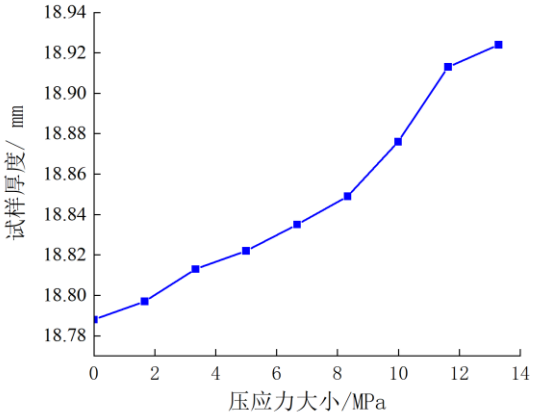


图 6　试样厚度与压应力关系

Fig.6 Relation between specimen thickness and compressive stress

如图 8 所示，通过对超声纵波声速-应力直线进行拟合，可以得到的线性相关系数 R^2 和斜率 k。

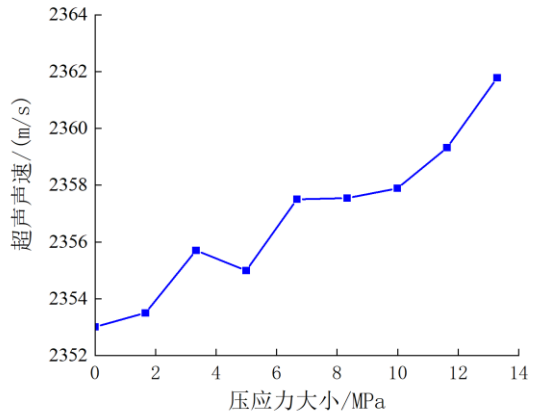


图 7　超声声速-应力关系

Fig.7 Acousto-stress relation

试样标块中的超声纵波声速和垂直压应力的变化趋势相同，声速随着应力的增大而增大，线性相关系数 R^2 值接近 1，也证明了环氧树脂体系中声弹性效应的存在。声弹性系数为声速-应力拟合直线的斜率 k 与 V_0之比，计算得到环氧试样标块的声弹性系数，如表 4 所示。

表 4 参数计算结果

Table 4　Parameter calculation results

	线性相关系数R^2	斜率 k	声弹性系数 K/MPa^{-1}
计算参数	0.9313	0.6608	2.808×10^{-4}

在得到环氧树脂试样中传播的超声声速以及对应环氧树脂浇注配方的声弹性系数后，可以通过公式计算试样中的残余应力。如表 5 所示。

表 5 超声波检测法检测结果

Table 5 Ultrasonic test results

试样编号	超声声速/ (m/s)	残余应力/ MPa
C1	2368.203	23.01
C2	2367.438	21.85
C3	2363.681	16.17
C4	2360.378	11.17
C5	2362.655	14.61
C6	2361.152	12.34
C7	2368.152	23.041

可以看出超声振动时效法过程和固化过程参数对试样的残余应力的大小产生了影响。通过 C1 与 C2～C6 试样的残余应力对比，经过超声振动时效法处理的环氧树脂试样的残余应力均出现不同程度的下降，可得超声振动时效法处理可以对环氧树脂体系构件的残余应力起到抑制作用。

通过 C2～C4 试样的残余应力比较，可以看出残余应力的大小与超声辅助固化流程的时间有关，超声振动的时间越长，对残余应力的抑制效果就越明显。通过 C3、C5、C6 试样的残余应力比较，超声振动时效法处理的水浴温度对残余应力也存在影响，温度的提高对残余应力的抑制效果有促进效果。对比 C1 与 C7，固化流程的改变对残余应力的大小有影响，在降低二阶段固化流程的温度后，残余应力有了小幅增大。

3.2 超声辅助固化机理讨论

Luban 等人发现，当受到的交变作用力介于某个范围时，材料中残余应力将会发生变化[20]，图 8 为交变作用下应力和应变的关系曲线图。

在超声辅助固化过程中，材料因受超声波震动，不断进行微小的拉伸与收缩。

据包申格效应，当材料先受到拉伸塑性形变后再受到压缩塑性形变时，其压缩屈服强度会低于仅受到拉伸塑性形变时的屈服强度，在超声波处理的过程中，交变循环持续进行。最终，在特性曲线稳定后，受处理的材料内部残余应力从σ_A降至σ_B。

由交变应力下的应力和应变关系可知，振动时效过程中若要减小或消除构件中的残余应力，必须满足以下条件，即：

$$\sigma_{残}+\sigma_{动}>\sigma_s \tag{9}$$

其中：$\sigma_{残}$为材料内部残余应力，$\sigma_{动}$为外加动应力，σ_s为材料屈服极限。

所以超声辅助固化过程中，超声波施加的外加动应力应大于材料的屈服极限，让材料在处理过程中，能产生拉伸与收缩的塑性形变。

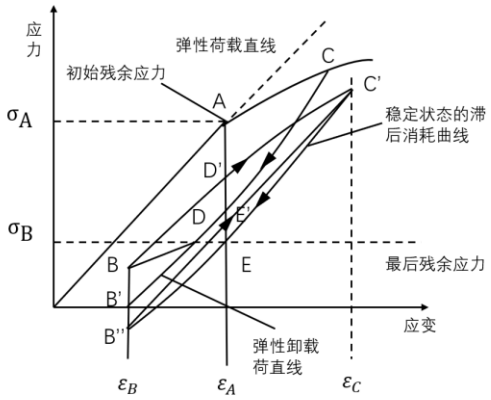


图 8　交变应力下应力-应变关系示意图

Fig. 8 Schematic diagram of stress-strain relationship under alternating stress

4　结论

本文建立了在各种环氧树脂体系下研究不同形状金属嵌件的残余应力模型，且搭建了光弹性法和超声波检测法的残余应力检测平台。主要结论如下：

（1）总结 A、B、C 三组实验结果，超声辅助固化过程可以减小界面处的残余应力大小，并优化残余应力分布，减少应力集中现象。

（2）在 A 组圆柱形金属嵌件试样实验结果中，在 80℃条件下超声振动一个小时的工艺抑制残余应力效果最好。

（3）在 B 组片状金属嵌件试样实验结果中，60℃条件下，残余应力抑制效果最好。

（4）在 C 组环氧树脂/氧化铝复合材料试样实验结果中，在实验范围内温度越高，超声辅助固化过程的作用时间越长，对残余应力的抑制效果越好。

综上，环氧树脂体系的配方和金属嵌件的形状尺寸会影响试样的固化过程，改变残余应力的分布和大小导致超声辅助固化流程对残余应力的抑制效果各不相同。总体上使用超声辅助固化过程，可以对环氧树脂体系绝缘件的残余应力起到抑制效果，但在不同条件的固化过程中，要达到最佳的结果需要对超声辅助固化工艺的参数进行调整。之后

将会继续深入完善实验，扩大温度与处理时间的范围，同时探究超声振动的频率以及振动幅度大小对于超声辅助固化效果的影响。

参考文献

[1] DL/T 617-2010. 气体绝缘金属封闭开关设备技术条件[S]. 北京: 国家能源局, 2010.

[2] Jung W K, Chu W S, Ahn S H, et al. Measurement and compensation of spring-back of a hybrid composite beam[J]. Journal of Composite Materials, 2007, 41(7): 851-864.

[3] 苑维琦. 特高压盆式绝缘子裂纹缺陷放电研究[D]. 北京: 华北电力大学, 2014.

[4] 赵卫军. 深冷处理工艺对材料残余应力影响的研究[D]. 太原科技大学, 2018.

[5] 孙青. 电力设备中导体与绝缘界面处固化残余应力的机理研究[D]. 西安理工大学, 2021.

[6] Hindle C S, White J R, Dawson D and Thomas K. Internal stress molecular orientation and distortion in injection moldings, polypropylene and glass-fibre filled polypropylene[J]. Polymer Engineering and Science, 1992, 32: 157-171.

[7] 苏耕, 伍维健, 周峻，等. 残余应力测试方法在 GIS 盆式绝缘子中的应用前景[J]. 绝缘材料, 2017, 50(03): 1-5.

[8] ASTM D4093-2005, 透明或半透明塑性材料中双折射及残余应变的光弹性量度的标准试验方法[S].

[9] 李进, 薛润东, 赵仁勇, 等. 基于声弹效应的芳纶增强环氧复合材料残余应力检测技术研究[J]. 电工技术学报，2023，38(09): 2519-2527.

[10] 荣亚鹏, 陈允, 王亚祥,等.环氧树脂复合材料残余应力检测技术研究进展[J].复合材料科学与工,2024,(08):110-118.

[11] 芦亚萍等. 振动时效机理研究. 机械科学与技术，2001，20(4): 587---589.

[12] Aoki, Nishimura T. Reduction of residual stress for welded joints using vibrational load[J]. Pressure Vessel and Piping, 1998, 216(4): 168-173.

[13] 杨旭静, 张良胜, 李茂君, 等. 超声振动对快速固化环氧树脂体系固化动力学特性的影响[J]. 复合材料学报, 2022, 39(5): 2470-2481.

[14] 王辉, 季炜, 陈璟, 等. 超声振动对环氧胶黏剂结构组织影响及胶层裂纹改善分析[J]. 塑料工业, 2020, 48(10): 170-174.

[15] 计欣华, 邓宗白, 鲁阳. 工程实验力学[M]. 北京: 机械工业出版, 2005.

[16] 李蕊, 乔梦嫣, 杨佳, 等. 环氧树脂基体中圆柱夹杂引起的界面残余应力研究[J]. 工程塑料应用, 2019, 47(08): 101-104.

[17] Dos Santos A A, Ambiel L B, Garcia R H, et al. Stress analysis in carbon/epoxy composites using LCR waves[J]. Journal of Composite Materials, 2013, 48(27):3425-3434.

[18] Guo Z, Wu Z, Wang H, et al. Experimental and numerical study on formation of interface separation and interfacial dielectric strength of GIL insulator[J]. IEEE Transactions on Dielectrics and Electrical Insulation, 2019, 26(6): 1738-1746.

[19] 周洪, 李宁, 李阔, 等. 固化工艺影响 L 形复合材料制件固化变形研究[J]. 航空精密制造技术, 2021, 57(01): 17-22.

[20] Luban D J, Felger R P. Residual stress change of metal specimens under alternating stress[J]. Plasticity and Greep of Metals, 1961, 59(3): 86-89.

李 进 男，1988 年生，博士，副教授，研究方向为高压电力设备绝缘设计与缺陷检测。

034 基于产教融合培养适应新型电力系统发展的新质生产力人才

沈 娜，马永良， 郭长兴， 杨向宇，张尧， 李杰辉

（广州城市理工学院电气工程学院， 广东广州 510800）

摘要：在“双碳”目标引领下，以新能源为主体的新型电力系统正加速重构能源格局，对高素质复合型人才提出迫切需求。然而，当前高校人才培养存在知识滞后、实践薄弱、跨学科整合不足等问题，导致人才供给与产业需求之间存在显著结构性矛盾。本文基于产教融合视角，探讨如何通过体制机制创新、课程体系重构、“双师型”队伍建设和实践平台共建，培养适应新型电力系统发展的新质生产力人才。结合国家与广东省政策导向，分析国内外产教融合的实践模式与经验，并以广州城市理工学院“新能源与新型配电网现代产业学院”为例，阐述其在校企协同育人、项目化课程开发、资源整合与成果转化等方面的具体实践与成效。研究表明，深化产教融合是破解人才供需瓶颈、支撑能源转型与产业升级的有效路径，对推动教育供给侧改革、提升国家新质生产力具有重要战略意义。

关键词：产教融合；新型电力系统；新质生产力人才

中图分类号：G642　　文献标志码：A

Cultivating New-Quality Productive Forces Talent Adapted to the Development of New Power Systems Through Industry-Education Integration

SHEN Na，MA Yongliang，GUO Changxing，YANG Xiangyu，Zhang Yao，LI Jiehui

（School of Electrical Engineering，Guangzhou City University of Technology， Guangzhou 510800，China ）

Abstract: Guided by the dual carbon goals, the new power system centered on renewable energy is accelerating the restructuring of the energy landscape, creating an urgent demand for high-caliber, multidisciplinary talent. However, current university talent cultivation faces challenges such as knowledge lag, weak practical training, and insufficient interdisciplinary integration, resulting in a significant structural mismatch between talent supply and industrial demand. This paper explores, from an industry-education integration perspective, how to cultivate new productive forces talent suited for the development of the new power system through institutional innovation, curriculum restructuring, building a “dual-qualified” faculty, and co-constructing practical platforms. Aligning with national and Guangdong provincial policy directions, it analyzes domestic and international models and experiences in industry-education integration. Using Guangzhou City University of Science and Technology's “Modern Industry College for New Energy and New Distribution Grid” as a case study, it details its concrete practices and achievements in collaborative education between enterprises and universities, project-based curriculum development, resource integration, and achievement transformation. Research indicates that deepening industry-education integration represents an effective pathway to address talent supply-demand bottlenecks and support energy transition and industrial upgrading. This approach holds significant strategic importance for advancing education supply-side reform and enhancing the nation's new quality productive forces.

Key words:industry-education integration; new electric power system; new quality productivity talent

0　引言

当前，以新能源为主体的新型电力系统建设正在全球范围内加速推进，成为实现“碳达峰、碳中和”目标的核心支撑[1]。新型电力系统深度融合高比例可再生能源、先进电力电子设备、智能化调控技术与大容量储能系统，其结构复杂性、运行互动性和技术综合性远超传统电网[2]。这一

收稿日期：2025.10.2

依托项目：广东省现代产业学院建设项目“新能源与新型配电网现代产业学院”（52108021）

Project Supported by Guangdong Provincial Modern Industry College Construction Project: “Modern Industry College for New Energy and New

变革不仅推动能源技术的迭代升级，更对人才素质提出全新要求：亟需具备多学科交叉知识、复杂工程实践能力、创新思维与绿色发展理念的高素质复合型人才[3]。

然而，当前高等教育人才培养体系仍存在诸多不适应之处：专业设置滞后于技术发展、课程内容脱离工程实际、实践教学资源匮乏、跨学科整合机制缺失，导致人才供给质量与产业需求之间存在显著差距。特别是在新型电力系统的规划设计、智能运维、市场运营、网络安全等核心领域，“人才荒”现象日益凸显，已成为制约行业安全高效发展和新质生产力提升的关键瓶颈。

在此背景下，深化产教融合，构建教育链、人才链与产业链、创新链有机衔接的协同育人机制，具有重大的现实意义与战略价值：

一是赋能能源产业升级与国家能源安全。 通过紧密对接新型电力系统建设中的关键技术领域和“卡脖子”难题，产教融合可培养具备前沿技术掌握能力和复杂问题解决能力的专业人才，为构建清洁低碳、安全高效的现代能源体系提供核心智力支持，助力国家能源转型战略落地。

二是推动高等教育内涵发展与生态重塑。 产教融合推动高校打破学科壁垒，动态优化专业结构与课程体系，引入企业真实项目与先进技术，共建高水平实训基地与双师型教学团队，是实现工程教育提质增效、响应新工科建设的重要路径。

三是锻造国家新质生产力的战略支撑。 新型电力系统是能源领域新质生产力的核心载体。产教融合所培养的，正是能够驾驭颠覆性技术、推动产业变革、契合新质生产力内涵的创新型、应用型、复合型人才。他们是实现能源科技自立自强、参与全球能源科技竞争的关键力量。

因此，本研究聚焦产教融合视域下新型电力系统领域人才培养模式的创新与实践，旨在破解人才供需结构性矛盾，为加速能源绿色低碳转型、筑牢国家能源安全基石、实现经济高质量发展提供坚实的人才保障与智力支持。

1 我国促进产教融合的政策体系

国家层面通过系统性、多层次的政策设计，构建了产教融合发展的“四梁八柱”。2017 年国务院办公厅印发《关于深化产教融合的若干意见》，首次从国家层面确立产教融合的制度框架，核心是打破教育界与产业界之间的体制壁垒，通过探索多元化办学体制强化企业重要主体作用，推动企业深度参与人才培养全过程[4]。2022 年教育部办公厅发布《示范性特色学院建设管理办法》，进一步聚焦载体建设，将现代产业学院明确为实现“四链”（产业链、创新链、教育链、人才链）衔接的重要实体平台，要求其承担人才培养、技术创新、社会服务等复合功能[5]。

2023 年，《行业产教融合共同体建设指南》出台，创新性地提出以“龙头企业+高水平高校”双牵头模式，整合跨区域、跨行业资源，破解产教融合中的区域发展不平衡问题[6]。同年发布的《教育强国建设规划纲要（2024—2035 年）》标志着战略进一步升级，首次明确提出构建“人才供需适配机制”，依托国家大数据平台实现分行业、分领域的人才需求精准预测与供给对接，推动高等教育从供给导向转向需求导向，全面提升教育服务产业转型升级的能力[7]。

广东省作为国家产教融合改革试点省，积极探索“赋权实体+精准适配”的特色路径。2020 年推出《产教融合建设试点实施方案》，率先构建省级试点网络，鼓励各地市开展差异化探索。2023 年《深化本科高校现代产业学院内涵建设的意见》提出突破性举措：明确产业学院作为独立实体应具备“独立的人、财、物管理权限”，通过专项招生计划、理事会共同治理（企业席位占比不低于 40%）等机制增强其办学自主权，有效破解了传统校企合作中“虚实脱节”的困境[8]。2024 年《加快培育未来产业行动方案》进一步将产教融合嵌入未来产业发展布局，要求高校动态设置人工智能、量子科技、新型储能等前沿专业，直接服务广东“制造业当家”战略[9]。

总体来看，中央与地方政策呈现“国家顶层设计—地方深度试验”的协同演进格局：国家政策重在构建制度框架与指明方向，广东则聚焦于操作层面的突破创新，如其产业学院实体化改革为国家政策提供了可复制、可推广的经验；未来产业—教育绑定机制将“人才供需适配”从理念转化为区域实践；粤港澳大湾区跨区域产教融合共同体建设更是走在全国前列。当前深化产教融合仍面临企业参与动力不足、数据平台行业壁垒待破除、跨区域利益协调机制缺失等挑战。但毋庸置疑，政策演进已形成“制度破冰—载体创新—数字赋能—实体化改革”的完整链条，推动产教融合从松散型合作走向机制化、实体化、深度融合的新阶段，为教育供给侧结构性改革提供了坚实支撑。

2 国内外产教融合的探索实践

2.1 国内实践：政策驱动与多层次融合创新

国内产教融合实践具有明显的政策驱动特征，目前已形成以现代产业学院、产教融合共同体等为代表的多层次融合体系。国家层面通过示范性特色学院推动“四链衔接”，涌现出一批典型案例。例如，东莞理工学院与西门子合作共建的智能制造学院，由企业捐赠全套生产线、派驻工程师驻校授课，实施“2 年在校学习+2 年企业实践”的培养模式，毕业生对口就业率高达 92%。华为公司牵头组建的集成电路产教融合共同体，整合 76 所高校和 12 家产业链重点企业，共建共享实训基地与课程资源，成功将人才培养周期缩短 50%。

广东省在体制机制改革上率先突破。深圳技术大学微电子学院由深圳大学、香港科技大学与中芯国际联合共建，依托理事会赋予的招生自主与资源调配权，开展本硕博一体化人才培养。佛山机器人产业学院通过政府提供场地支持、企业捐赠生产线等方式，实现年技术服务收入超 3000 万元，有效破解了合作“虚化”问题，成为产教融合自我造血的成功范例。

2.2 国际经验：多元模式与机制创新

发达国家在产教融合方面积累了丰富经验，呈现出多元化、创新化的发展路径。德国“双元制”教育体系持续升级，引入数字孪生技术用于模拟实训、开发 AR（增强现实）维修教学模块，并新增绿色能源与低碳技术课程，保持技能供给与产业需求的同步[10]。美国注重高校与企业的联合研发与人才共育，如 MIT-IBM Watson AI 实验室投入 1.5 亿美元共同培养人工智能高端人才；社区学院与亚马逊合作建设“智慧供应链”微证书项目，实现学习与就业无缝衔接。新加坡实施“技能创前程”计划，以微证书堆叠体系为核心，并配套企业培训补贴，激励劳动者持续提升技能。日本则通过立法明确企业职业教育责任，如《职业能力开发促进法》规定企业须将营业收入的 0.5%投入职工培训，否则缴纳同等金额的职业教育税，从而强化企业参与产教融合的刚性约束。

3 新能源与新型配电网产业学院的创新实践

在国家“双碳”战略和能源转型目标的驱动下，构建以新能源为主体的新型电力系统已成为我国能源发展的核心方向。2024 年 8 月发布的《中国的能源转型》白皮书明确提出，要加快推进能源技术、产业模式和商业机制创新，推动新能源及其关联产业成为新的经济增长点，培育新质生产力。新能源产业也被广东省列入“双十”战略性产业集群。面对行业高速发展带来的巨大人才缺口，广州城市理工学院作为一所应用型本科院校，紧扣区域经济发展需求，开设电气工程及其自动化、新能源科学与工程等专业，与广州发展新能源股份有限公司、广州智光储能科技有限公司等行业龙头企业合作，于 2023 年共同组建“新能源与新型配电网现代产业学院”，2025 年 1 月被认定为广东省现代产业学院。该学院通过校企共管共建、联合培养，积极探索产教深度融合的新路径，致力于培养具备实践能力、创新精神的高素质应用型人才。

3.1 完善“校行企”协同育人机制，整合教育资源

学院立足能源革命与产业升级需要，通过构建学校、行业、企业三方协同育人机制，实现资源深度整合与优化配置。其中，学校是人才培养的主体和知识创新的源泉，企业提供需求导向、技术前沿与实战平台，行业协会发挥桥梁纽带和标准引领作用。三方共同组成联合管理委员会，在课程开发、师资建设、实践基地管理、质量评估等环节实现共同决策、共同投入、共同负责。如图 1 所示。

这一机制有效解决了传统教育中“学用脱节”问题，建立了人才供给与产业需求之间的动态调整机制。行业协会发布人才需求预测和能力标准图谱，学校据此灵活调整专业方向和培养方案，企业通过“产教融合班”“冠名班”等形式提前锁定目标人才，从而实现人才供应链的高效衔接。

学院致力于实现育人资源的“深度整合”与“价值倍增”，体现为“三个贯通”：一是空间贯通，打破课堂、校内实训与企业现场的物理界限，构建“立体化学习场域”；二是知识贯通，推动基础理论、专业技能与工程实践、行业前沿深度融合；三是主体贯通，促进高校教师、企业专家、技术骨干共同参与教学设计、项目实施与评价反馈，塑造学生的综合能力图谱。最终目标是培养学生面对真实产业环境的能力，使其成为既具备扎实理论根基，又拥有出色工程实践与创新能力的高素质应用型人才。

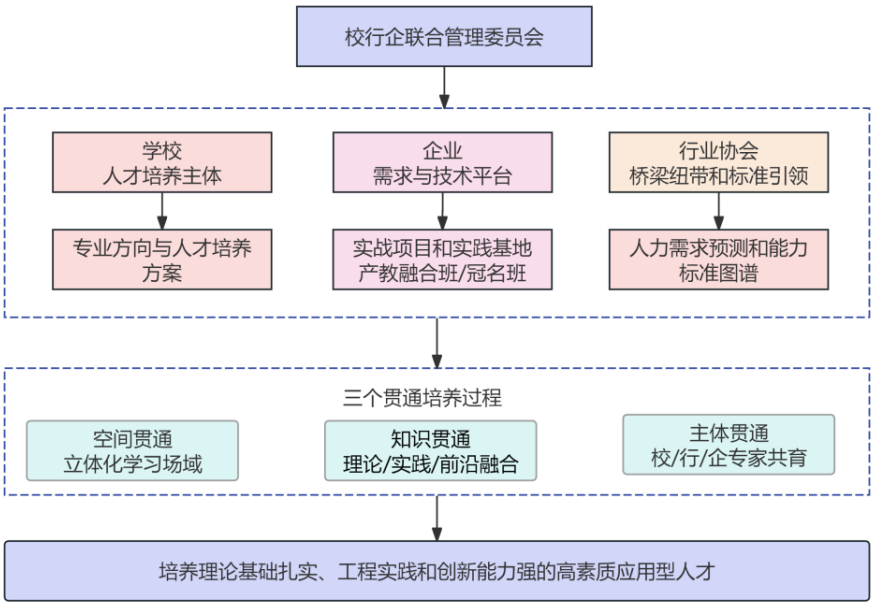


图 1 校行企协同育人思路

Fig.1 School-Enterprise-Industry collaborative education approach

3.2 构建“项目化专创融通”课程体系，创新育人范式

产业学院建设思路图以“项目化专创融通”课程体系为核心，通过阶梯式项目链、多课堂融合教学、价值引领式思政融入及四维支撑机制，构建了产教深度融合的育人新范式，如图 2 所示。

纵向贯通“四级项目链”驱动能力进阶：自学期 2 至学期 8 分设激发创新意识与工程认知的“兴趣项目”、训练创新方法与工程分析的“基石项目”、强化跨学科设计与应用的“综合项目”、聚焦产品制造与成果转化的“顶点项目”，每阶段≥2 学分，项目学分占比超 25%，形成“认知→分析→设计→制造”能力跃迁路径。

横向融合四类课程模块：通识核心课奠基人文素养，专业基础课支撑学科理论，专业课深化领域知识，校企行业课植入企业真实案例与技术前沿，实现“课堂即工程、教师即工程师”。

教学模式创新“多课堂动态循环”：采用理论精讲+技能实训+企业现场教学/跨学科协作的多层次教学模式，打破教室边界；推行“三阶段六环节”教学法，每阶段嵌入“教师导学-企业点评-学生迭代”双反馈机制。思政教育全程渗透：在课程设计层挖掘“卡脖子技术攻坚精神”等专业思政元素，案例教学层凝练“双碳使命”等产业实践，项目层植入社会责任议题，实现价值引领与能力培养同频共振。

该课程体系以真实产业问题为起点，以多场景切换拓宽教学边界，以专创融通提升学生的技术硬实力与创新软实力，最终形成“产业需求驱动—项目任务承载—双师协同教学—价值全程融入”的人才培养生态。

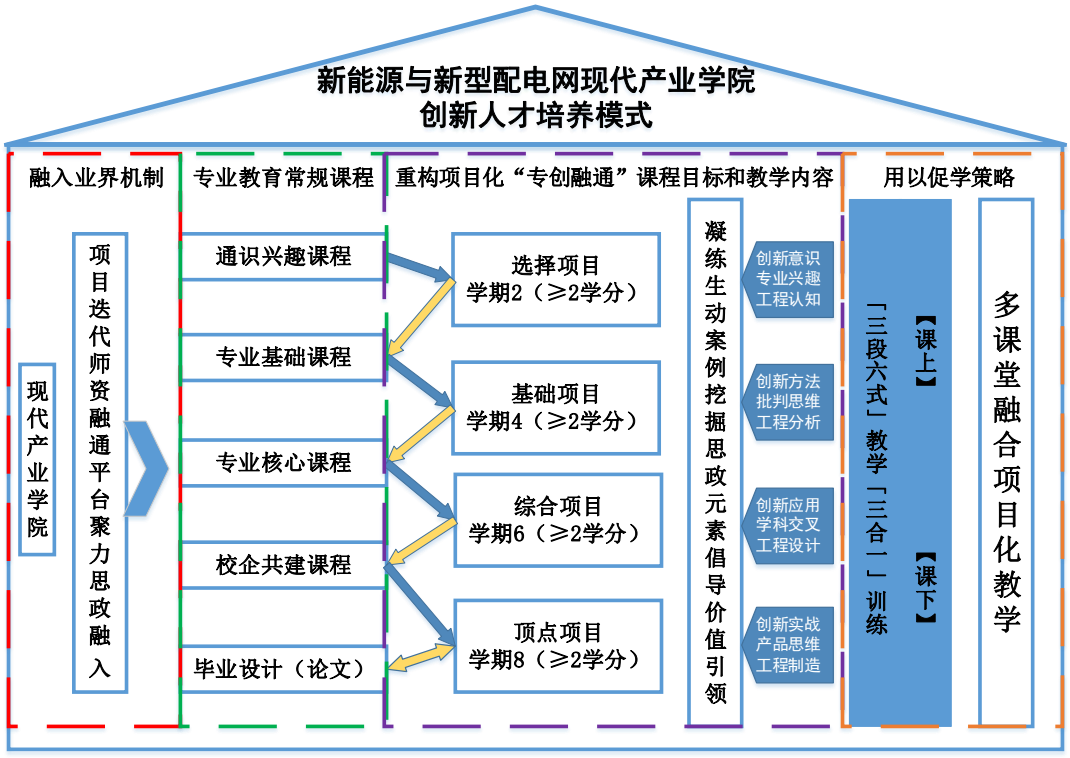


图 2 产业学院创新人才培养模式

Fig.2 Innovates talent development models of industry-academia collaboration

3.3 校企共建课程，推动教学内涵创新

校企共建课程的本质是构建“教育链与产业链共生体”，利用校企双方资源，共建课程从优化教学大纲、建立特色课程资源库和构建双师型教学团队三维度进行课程创新改革，打造理论+实践一体化的教学创新模式。三维度课程创新重构教学内核：一是动态优化教学大纲，企业直接参与课程标准制定，每学年按技术迭代更新 30%内容，并将岗位技能图谱拆解为课程知识单元；二是共建特色资源库，企业提供项目工单模板、工程案例等实战素材，学校开发活页教材与微课，实现工艺专利与教学资源的双向流通；三是打造双师型团队，实施“工程师入校授课+教师企业挂职”双向赋能机制，企业将授课纳入 KPI 考核，学校认定产业导师职称，实现人力资本融合。通过学校和企业双主体对课程进行共建、共管、共享，并通过校内和企业的评价进行持续改进，提升课堂教学效果，打破教育和企业的脱钩，实现共赢。校企共建课程创新思路如图 3 所示。

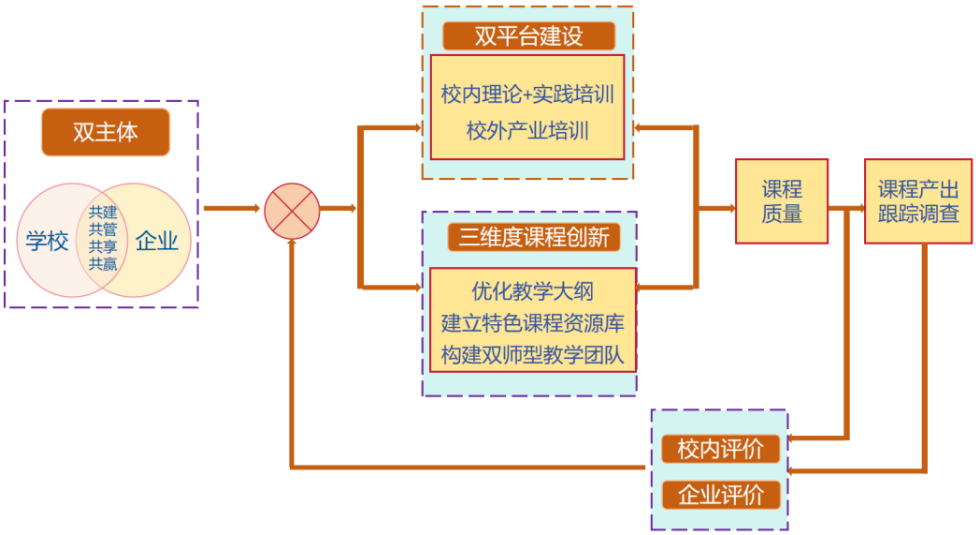


图 3 校企共建课程思路

Fig.3 Approach to jointly developing courses between schools and enterprises

根据新能源和新型电力系统发展对人才的新要求，重构了人才培养课程体系。课程体系严格遵循“成果导向”（OBE）教育理念，实施“反向设计、正向施工”的原则。其核心路径是：首先，深入粤港澳大湾区新能源与新型电力系统产业链，与行业领军企业共同开展人才需求调研，精准分析新型配电网、新能源、储能等真实岗位（群）所需的技术技能、工程素养与创新能力，据此锚定人才培养的具体目标和毕业要求。然后，以此目标为逻辑终点，反向推导并系统设计与之完全匹配的课程模块与实践体系。以此构建起一个目标清晰、逻辑严密、动态优化、支撑产业发展的应用型课程新体系。企业全程参与人才培养，深度进行课程共建，提升人才培养质量。产业学院人才培养课程体系如图 4 所示。



图 4 产业学院人才培养课程体系

Fig.4 Talent development curriculum system of industry-academia collaboration

3.4 打造“双师双能型”师资队伍，强化教学支撑

学院大力推动企业技术专家与学校教师的双向流动与融合发展，打造既能胜任理论教学又具备工程实践能力的“双师型”教学团队。具体措施包括：定期选派教师至合作企业参与实际工程项目，接受新技术培训，提升实践能力与技术开发水平；选聘 5 年以上经验的企业技术骨干担任兼职教师，承担 30%以上的专业核心课程教学，并开设技术讲座、工作坊，传递行业最新动态；结合新能源与新型配电网领域的前沿技术，联合开发教学案例和横向课题，推动科研反哺教学。

通过这些机制，学院不仅优化了师资结构，也提升了整体教学、科研与社会服务能力。

3.5 科教融汇，促进学生创新能力提升

科教融汇是提升学生创新能力的核心途径，通过构建深度产学研协同平台、开展项目驱动与竞赛牵引的实践教学、打造校企互通的双师团队，形成“平台—项目—师资”三位一体的育人生态。具体而言，首先以校企共建的产学研实践基地、联合实验室和工程技术中心为载体，将新能源并网、储能技术、智能调度等新型电力系统领域的真实工程场景和前沿技术难题引入校园，为学生提供贴近产业的实践环境与先进设备支撑。在此基础上，教师带领学生承接企业横向课题、参与纵向科研项目及成果转化任务，使学生经历从需求分析、技术论证、方案设计、仿真验证到系统开发的完整创新链条，同时在“互联网+”、“挑战杯”等高水平竞赛中锤炼其跨学科整合能力、快速迭代与团队协作精神。此外，通过聘请企业专家担任产业导师、选派青年教师赴企业挂职，构建“双师型”教学团队，确保教学内容与工程实践同步更新，有效引导学生将理论知识与复杂工程问题相结合，最终系统性地培养其批判性思维、技术攻坚与创新实践能力，为能源电力行业输送具备解决复杂工程问题的高素质应用型人才。

结语

新能源与新型配电网现代产业学院的建设，是响应国家能源转型战略、服务粤港澳大湾区高质量发展的重要举措。其根本意义在于构建了一个深度融合“产、学、研、用”的创新教育生态，实现了教育链、人才链与产业链、创新链的精准对接与协同发展。

学院通过颠覆传统工科人才培养模式，将产业前沿需求融入人才培养全过程，有效整合了高校的教育资源、企业的技术平台与行业的组织优势，实现了资源优化配置与效能提升。它已成为支撑大湾区能源结构优化与智能电网建设的人才摇篮，也是推动产学研用一体化的区域枢纽。

经过持续探索，学院在校企协同、人才培养、师资建设、成果转化等方面取得显著成效：通过灵活的人事机制成功打造了“双师双能型”教学团队；依托共建实训基地和虚拟仿真平台大幅提升学生工程实践能力；通过技术研发与成果转化服务企业转型升级，催生新业态、新模式。学院培养的大批高素质应用型人才，有效缓解了区域产业发展中的人才瓶颈，成为助推新能源与新型电力系统发展的生力军。

综上所述，新能源与新型配电网现代产业学院通过体制机制创新与资源深度整合，探索出了一条产教融合、协同育人的有效路径，不仅重塑了应用型人才培养模式，也为区域经济发展和国家能源战略提供了坚实支撑，实现了教育提升、产业升级与社会发展的多方共赢。

参考文献

[1] 中共中央国务院.《2030 年前碳达峰行动方案》. 北京：2021.
The Central Committee of the Communist Party of China and the State Council. Action Plan for Carbon Peaking Before 2030. Beijing: 2021.

[2] 刘吉臻，王庆华，胡阳等. 新型电力系统的内涵、特征及关键技术[J]. 新型电力系统，2023，1（01）：49-65.
Liu Jizhen, Wang Qinghua, Hu Yang et al. The Essence, Characteristics, and Key Technologies of New Power Systems [J]. New Power Systems, 2023, 1(01): 49-65.

[3] 毕天舒. 如何打造新型电力系统产学研用“强引擎”——访华北电力大学副校长毕天舒. 中国能源报，2023 年 2 月 6 日 第 13 版.
Bi Tianshu. How to Build a Powerful Engine for Industry-Academia-Research Collaboration in New Power Systems — An Interview with Bi Tianshu, Vice President of North China Electric Power University. China Energy News, February 6, 2023, Page 13.

[4] 国家办公室.《关于深化产教融合的若干意见》. 北京：2017.
State Council General Office. Several Opinions on Deepening the Integration of Industry and Education. Beijing: 2017.

[5] 教育部办公厅.《示范性特色学院建设管理办法》. 北京：2022.
Ministry of Education General Office. Administrative Measures for the Development of Exemplary Characteristic Colleges. Beijing: 2022.

[6] 教育部.《行业产教融合共同体建设指南》. 北京：2023. Ministry of Education. Guidelines for Building Industry-Education Integration Communities. Beijing: 2023.

[7] 中共中央国务院.《教育强国建设规划纲要（2024—2035年）》. 北京：2023. The Central Committee of the Communist Party of China and the State Council. Outline of the Plan for Building China into an Education Powerhouse (2024–2035). Beijing: 2023.

[8] 广东省教育厅.《深化本科高校现代产业学院内涵建设的意见》. 广州：2023. Department of Education of Guangdong Province. Opinions on Deepening the Development of Modern Industry Colleges in Undergraduate Institutions. Guangzhou: 2023.

[9] 广东省人民政府.《加快培育未来产业行动方案》. 广州：2024. People's Government of Guangdong Province. Action Plan for Accelerating the Cultivation of Future Industries. Guangzhou: 2024.

[10] 燕峰. 德国双元制职业教育中学习模块设计与启示[J]. 现代职业教育，2018,（21）:156-157. Yan Feng. Design of Learning Modules and Implications in Germany's Dual Vocational Education System [J]. Modern Vocational Education, 2018, (21): 156-157.

作者简介：

沈娜（1984—），女，博士研究生，研究方向为新能源发电技术，shenna@gcu.edu.cn；

马永良（1982—），男，硕士研究生，研究方向为电力系统稳定与控制，mayl@gcu.edu.cn；

郭长兴（1988—），男，硕士研究生，研究方向为新能源发电技术，guocx@gcu.edu.cn；

035 基于 MATLAB 构建传输线集中参数模型

王麒轩[1]，李仲春[1]，刘方舟[1]，王世山[1]，沈湛[2]

（1.南京航空航天大学自动化学院，江苏省 南京市 211106；

2.东南大学电气工程学院，江苏省 南京市 211189）

Construction of Lumped Parameter Model for Transmission Lines Based on MATLAB

Wang Qixuan[1], Li Zhongchun[1],Liu Fangzhou[1], Wang Shishan[1], Shen Zhan[2]

(1.College of Automation Engineering, Nanjing University of Aeronautics and Astronautics, Nanjing 211106;

2.School of Electrical Engineering, Southeast University, Nanjing 211189)

ABSTRACT: With the increasing complexity of power transmission lines, the demand for their precise modeling has become increasingly urgent. This paper presents a method for constructing a lumped parameter model of transmission lines based on MATLAB, aiming to achieve highly accurate and efficient integrated modeling and expand the MATLAB toolbox. The conversion between distributed parameters and lumped parameters is analyzed, and the characteristics of π-type and T-type equivalent two-port network models are discussed, with their different application scopes and corresponding precise modeling methods expounded. A hierarchical framework for MATLAB-based modeling is proposed, and case studies are conducted for verification. This method addresses the issues of low efficiency and inaccuracy in traditional modeling, providing an efficient tool for power system analysis.

KEY WORDS: Transmission line, lumped parameters, MATLAB

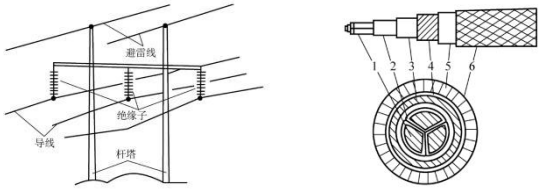
摘要：随着电力传输线的复杂化，对其精确建模的需求日益迫切。本文提出基于 MATLAB 构建传输线集中参数模型的方法，旨在实现高精确性、高效率的集成化建模，并扩展 MATLAB 工具箱。论文分析了分布参数与集中参数的转换及π、T 型等效二端口网络特性，阐述其不同的适用范围，及所使用的建模方式，给出了基于 MATLAB 建模的分层框架，并进行了算例验证：论文所提方法解决了传统建模的低效率、不精准的问题，为电力系统分析提供了高效工具。

关键词：传输线，集中参数，MATLAB

DOI：

0[1] 引言

随着电力系统的不断发展和复杂化，对电力传输线的精确建模和仿真需求日益增加。电力传输线的集中参数模型在电力系统分析、设计和优化中扮演着至关重要的角色。根据电力线路的结构，传输线可以分为架空线路和电缆线路两大类别(图 1)。



(a)架空传输线　　(b)电力电缆

图 1 传输线

对于传输线能量传输的研究，核心方法分为场（Field）方法与路（Circuit）方法，实际分别对应“微分”法与“积分”法。场方法基于电磁场物理本质与麦克斯韦方程组，能精确描述电磁波在传输线周围的传播行为，具有精度高、通用性强的优势，尤其适用于高频或复杂电磁环境下的分析，但该方法计算复杂且耗时较长，对计算资源要求高，工程推广难度大。路方法则将传输线等效为集中参数电路(如 R、C、L、G)，通过电路理论分析，特别适配位移电流可忽略的低频或工频电力系统。不过，传统路方法建模需手动计算与复杂数学推导，既增加工程师工作负担，也易引入人为误差。

然而，随着电力系统规模扩大、结构复杂化，无论是计算繁琐的场方法，还是依赖手动推导的路方法，其传统建模模式都难以满足现代电力系统对高精度与高效率的双重需求。近年来相关研究虽呈现场路融合趋势，如用场方法解析耦合规律[1]、以路方法构建等效模型[2]、通过场路互补开展研究[3]，但传统方法的固有局限仍需进一步突破。

MATLAB 作为全球知名软件包，不同的专业学科在不断扩展其工具箱 ToolBox。因此，扩展 MATLAB 工具箱也是提升自主知识产权的重要途径。

因此，本文旨在通过基于 MATLAB 构建集成

[1] 本文受国家重点研发计划“政府间国际科技创新合作”重点专项 2022YFE0196300 ，国家自然科学基金 52207191 和南京航空航天大学大学生创新实践工程创新训练资助。

化、自动化的建模平台，进行高准确性、高效率的传输线集中参数建模。

1 传输线从“分布”到“集中”参数的等效

1.1 单位长度电磁参数

对于有色金属导线(铝线、铜芯铝线和铜线)，它们每相单位长度的电阻：

$$r_1=\frac{\rho}{S} \tag{1}$$

式中，ρ为导线材料电阻率(Ω·mm^2/km)；S为导线的横截面积(mm^2)。

而在实际应用中，线路的实际运行温度异于产品目录或手册中20℃的电阻值[4,5]，因此在必要时可修正为：

$$r_t=r_{1(20)}\left[1+\alpha\left(t-20\right)\right] \tag{2}$$

式中，$r_{1(20)}$是20℃时的单位长度(km)电阻；α是电阻温度系数(1/℃)。

每相具有n根的分裂导线线路电抗：

$$r_{\mathrm{eq}}=\sqrt[n]{r\left(d_{12}d_{13}\cdots d_{1n}\right)}=\sqrt[n]{rd_{\mathrm{m}}^{(n-1)}} \tag{3}$$

$$x_1=\omega\left(4.6\lg\frac{D_{\mathrm{m}}}{r_{\mathrm{eq}}}+\frac{0.5\mu_{\mathrm{r}}}{n}\right)\times10^{-4} \tag{4}$$

式中，r为每根导体的半径(mm)；d_{12}、d_{13}、…、d_{1n}为每根导体与其余(n-1)根导体间的距离；d_{m}为各根导体之间的几何均距；n为每相具有的分裂导线根数；ω为角频率($\omega=2\pi f$，f为交流电的频率,单位:Hz)；μ_{r}为导线材料的相对磁导率；D_{m}为几何均距(单位应与r的单位相同)。

单位长度正序电容：

$$C_1=\frac{0.0241}{\lg\frac{D_{\mathrm{m}}}{r_{\mathrm{eq}}}}\times10^{-6} \tag{5}$$

对应的电纳：

$$b_1=\omega C_1 \tag{6}$$

每相对等值对地电导可按式(7)计算：

$$g_1=\frac{\Delta P_{\mathrm{g}}}{U^2}\times10^{-3} \tag{7}$$

式中，ΔP_{g}为三相线路泄漏损耗功率和电晕损耗功率(kW/km)，可借助专用的电力监测设备得到；U为线路线电压(kV)。

又由于实际泄漏通常很小，在设计线路中，就已检验了所选导线的半径能否满足晴朗天气不发生电晕的要求，在一般情况下可设g_1=0。

1.2 等效二端口网络模型

1.2.1 等效二端口网络

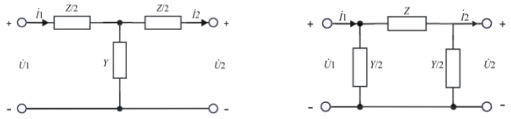
基于传输线基本参数与电路特性，可由此建立等效二端口网路模型[6,7](图2)。



图2 传输线等效二端口网络模型

常见的等效二端口网路分为T型二端口网络与π型二端口网络(图3)。其中，T型二端口在音频电路、低频放大器等低频应用中较为常见；阻抗特性相对较为稳定，适用于对阻抗变化要求不高的场合。而π型二端口在射频电路、微波电路等高频领域应用广泛；具有较强的阻抗变换能力，能够在较宽的频率范围内实现不同阻抗之间的匹配；且可以减少电力系统的节点总数，能够简化线路的电气模型，便于进行潮流计算、短路分析。

正由于π型网络具有减少节点总数，简化模型的优点，因此在本次模型建立中优选π型二端口网络模型(图3b)。



(a)T 型二端口　　(b)π型二端口

图3 常见等效二端口网络

等效二端口网络均可使用$\boldsymbol{T}$参数传输矩阵进行表示：

$$\begin{pmatrix}U_1\\I_1\end{pmatrix}=\boldsymbol{T}\begin{pmatrix}U_2\\I_2\end{pmatrix} \tag{8}$$

其中，$\boldsymbol{T}$参数矩阵可表达为：

$$\boldsymbol{T}=\begin{pmatrix}\cosh(\gamma l) & Z_{\mathrm{c}}\sinh(\gamma l)\\ \dfrac{\sinh(\gamma l)}{Z_c} & \cosh(\gamma l)\end{pmatrix} \tag{9}$$

式中，Z_{c}、γl：

$$\begin{cases} z_1 = r_1 + jx_1 \\ y_1 = g_1 + jb_1 \\ Z_c = \sqrt{z_1 / y_1} \\ \gamma l = \sqrt{z_1 y_1} l \end{cases} \tag{10}$$

对于图 3(a)，其等效电路参数值：

$$\begin{cases} Z/2 = Z_c \dfrac{\cosh \gamma l - 1}{\sinh \gamma l} \\ Y = \dfrac{1}{Z_c} \sinh \gamma l \end{cases} \tag{11}$$

相似地，对于图 3(b)，其等效电路参数值为：

$$\begin{cases} Z = Z_c \sinh \gamma l \\ Y/2 = \dfrac{1}{Z_c} \dfrac{\cosh \gamma l - 1}{\sinh \gamma l} \end{cases} \tag{12}$$

1.2.2 简易计算与精确计算

在计算机技术尚未普及的时期，为保证计算的高精度与人工计算的简易性，往往会使用简易计算，即引入修正系数对等效电路进行系数修正[8]，又由于电导往往很小，可忽略。因此，等效电路参数值修正为：

$$\begin{cases} Z = k_r r_1 l + \mathrm{j} k_x x_1 l \\ Y = \mathrm{j} k_b b_1 l \end{cases} \tag{13}$$

其中，修正系数为：

$$\begin{cases} k_r = 1 - x_1 b_1 \dfrac{l^2}{3} \\ k_x = 1 - (x_1 b_1 - \dfrac{r_1^2 b_1}{x_1}) \dfrac{l^2}{6} \\ k_b = 1 + x_1 b_1 \dfrac{l^2}{12} \end{cases} \tag{14}$$

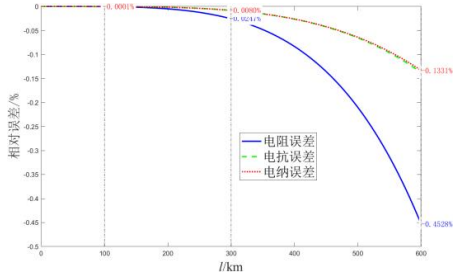
代入可得：

$$\begin{cases} Z = r_1 l (1 - x_1 b_1 \dfrac{l^2}{3}) + \mathrm{j} x_1 [1 - (x_1 b_1 - \dfrac{r_1^2 b_1}{x_1}) \dfrac{l^2}{6}] \\ Y = \mathrm{j} b_1 l (1 + x_1 b_1 \dfrac{l^2}{12}) \end{cases} \tag{15}$$

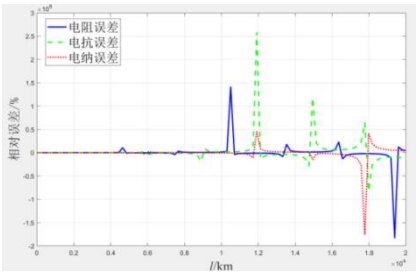
对于一般导线，即长度在(100~300)km 之间的架空线路和不超过 100km 的电缆线路，修正系数均接近于 1.0(其中 k_r 与 k_x 均小于 1，k_b 大于 1)，此时，采用简易计算引入的误差相对较小，可以不考虑其分布参数特性；然而对于长线路，即长度超过 300km 的架空线路和超过 100km 的电缆线路，随着传输线路的增长，采用简易计算引入的误差也会随之变大，不能不考虑其分布参数特性。

图 4 中以“4×LGJ-300/50 分裂导线，直径：24.26mm，分裂间距 450mm，三相水平排列，相间距离 13m”为案例[4]，通过以精确计算得到的阻抗与导纳实虚部为基准，计算与使用修正系数计算所得到的相应部分的相对误差，显示随着传输线的增长各部分误差的变化情况，表明：

随着线路明显增长，电阻、电抗与电纳三参数的相对误差均呈现出明显的变化趋势，并在特定长度区间内出现多个峰值。其根本原因在于：依据式(11)、(12)，精确计算涉及双曲函数，其可展开为关于长度 l 的不同幂次的级数之和，导致各等效参数值成为 l 的复杂函数组合，且各参数函数中 l 的幂次系数不同，致使误差峰值位置各异。当线路长度在 600km 之下时，参数误差较小；而当线路过长时，采用修正系数进行计算会引入较大误差，不利于后续对于传输线的分析。此时必须采用精确计算模型以保证分析准确性。



(a)0-600km 误差曲线



(b)长导线下的误差曲线

图 4 简易与精确计算误差曲线图

2 MATLAB 建模及 ToolBox 开发

2.1 开发流程

在使用 MATLAB 进行复杂系统建模时，随着模型规模的扩大和功能复杂度的提升，M 文件中的代码量会显著增加，各功能模块间的逻辑关系也愈发复杂[9]。为了提高代码的可读性、可维护性和可

扩展性，同时降低模块间的耦合度，一种有效的方法是采用主函数与子函数相结合的分层架构进行建模[10](图 5)。

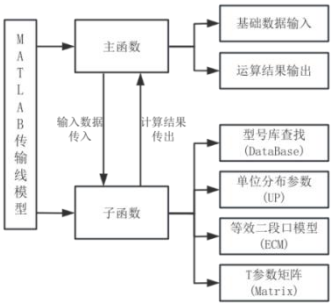


图 5 代码流程图

分层架构以“功能解耦”为核心，将整个建模系统划分为主函数层与子函数层，各层职责边界清晰，具体实现逻辑如下：

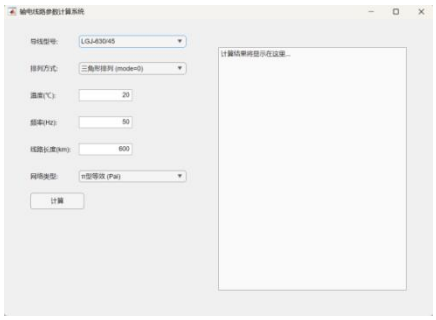
主函数作为整个模型的核心调度器，不参与具体数据计算，仅负责全局参数配置、模块间数据流向的控制以及最终结果的整合与输出。

子函数依据不同的功能，进行模块化处理，每个子函数专注于完成单一的任务，严格遵循软件工程中的“单一职责原则”，使得每个函数的功能明确、代码简洁。例如，“型号库查找”子函数仅负责导线参数的匹配与调用，“分布参数计算”子函数仅负责对给定的诗句进行相应参数计算。

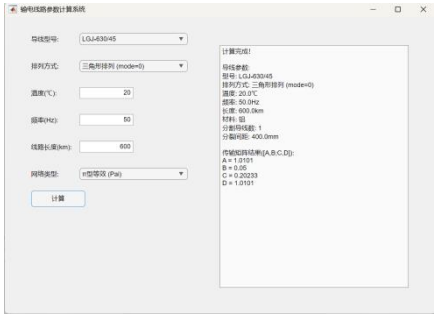
在实际实现时，子函数根据功能将其分离为独立的 M 文件，形成模块化的文件组织形式。各子函数之间无直接数据交互，均通过主函数实现间接协作。该设计可以有效降低主界面的复杂度，同时又降低了代码维护难度(即当某一部分出现问题时，便可快速定位到对应子函数进行维护)，也提升了系统的可展开性，便于后续增加其他功能的子函数。

2.2 主函数设计

在主函数设计中，设置一个人机交互界面(图 6)，便于用户选择使用或退出。通过人机交互界面引导用户输入导线排列方式、温度、频率及导线型号等信息，依托型号库进行查找，并给出相应的基础参数值。继续调用后续子函数，计算分布参数值，并基于长传输线理论构建所需等效电路的集中参数模型，最终输出传输矩阵参数，进行界面化显示，便于用户进行读取，为电力系统分析提供基础数据。



(a)用户输入



(b)结果反馈

图 6 菜单界面

2.3 子函数设计

依据不同功能，将子函数进行模块化处理，每个子函数仅执行单一的功能，并于主函数进行对接，返回子函数。单一功能子函数，有利于分析其逻辑与各部分的联系，且易于进行故障排查。以下为各子函数的设计：

(1) “型号库”的建立与查找(DataBase)：根据传输线的国家标准建立一个传输线型号库，依据不同型号提供式(1)-(7)计算所需的基础参数。与主函数中用户输入的导线型号进行识别与参数匹配。系统采用双分支处理：当输入型号存在于库中时，自动输出完整参数集；若型号不存在，则触发手动录入流程，确保系统的灵活性与扩展性。数据库结构设计支持后续参数更新与模型迭代，为电力系统计算提供可靠的数据支撑。

(2) 单位分布参数计算(UP)：基于“型号库”的建立与查找模块(DataBase)得到的基础参数，用户提供的导线排列方式、运行温度及系统频率等工况条件，依托于式(1)-(7)得到精确的单位分布参数(r_t、x_1、C_1、b_1、g_1)的相关数据。

(3) 分布参数与集中参数等效模型转换(ECM)：基于单位分布参数计算模块(UP)计算出的单位分布参数，用户提供的传输线长度及目标等效模型类型(π型、T 型)，依托于式(10)、(12)、(14)，对等效二端口网络模型中的集中参数进行精确化计算。

(4) 等效二端口 T 参数矩阵(Matrix)：基于分

布参数与集中参数等效模型转换模块(ECM)得出的二端口网络集中参数模型，通过式(11)、(13)，得到对应型别等效二端口 T 参数矩阵。

2.4 实例验证

为验证本文所建 MATLAB 传输线集中参数模型的准确性及计算效率，以某 220kV 架空输电线路为例进行分析。

表 1 案例信息

输入 / 序号	传输线型号	排列方式	T/℃	f/Hz	l/km	等效类型
①	LGJ-630/45	三角形	20	50	600	π型
②	4×LGJ-300/50	水平	20	50	450	T 型

当型号存在于数据库(如①)时，用户无需输入其它参数，程序便可给出准确结果(表 2)。

表 2 案例①结果

Z	Y/2	$\boldsymbol{T}$ 参数矩阵
26.025+j225.66	3.9116×10^{-6}+j8.7842×10^{-4}	$\begin{pmatrix} 0.80+j0.02 & 26.03+j225.66 \\ -0.00+j0.00 & 0.80+j0.02 \end{pmatrix}$

当型号不存在与数据库(如②)时，用户需输入其它参数数据，以便得到集中参数计算结果。

表 3 案例②输入参数

n	S/mm²	D_m/mm	r/mm	d_m/mm	导线材料
4	300	13000	12.13	450	铝

当参数数据完备，程序同案例①进行相应计算过程，并反馈出结果(表 4)。

表 4 案例②结果

Z/2	Y	$\boldsymbol{T}$ 参数矩阵
5.4713+j60.8509	0.0000+j0.0018	$\begin{pmatrix} 0.89+j0.01 & 9.72+j115.05 \\ 0.00+j0.00 & 0.89+j0.01 \end{pmatrix}$

借助该程序开展传输线集中参数模型的计算工作，能够有效简化参数查询、参数计算等一系列繁琐环节，显著缩短整体计算耗时，提升工作效率。程序运行过程中会自动调用内置参数库，并通过优化算法完成运算，减少人工干预可能产生的误差。将程序运算结果与权威参考数据进行系统性对比分析，可验证计算数据的高度准确性，且与人工计算相对比，相对误差可控制在 0.2%之内，进一步验证了该计算工具具备高精度的显著优势，为相关工程应用提供了可靠的技术支持。

3 结论

本文提出的基于 MATLAB 构建传输线集中参数模型的方法，通过理论与实例的验证，证明了其有效性与实用性，具有以下意义：

(1) 通过进行计算机程序编写，用户仅需要输入一定的数据，后续便可通过代码内部进行相应计算，得到结果。该过程不仅简化了用户对于数据的查找与计算过程，同时也可以进行更为精确的计算，避免人工计误差带来的影响。

(2) 通过使用 MATLAB 这一全球知名软件进行编程，有利于扩展其自身软件的适用性，可将构建传输线集中参数模型这一实际工程计算融入到 MATLAB 之中，形成固定函数或公式，便于今后对传输线这一工程问题进行分析与研究。

(3) 构建传输线集中参数模型，为后续传输线及电力系统分析，如丰富型号库内容、优化模型算法、进行潮流计算等内容，提供了一定的基础。为电力系统的设计、运行、分析提供了更加便捷，更加有力的工具支持。

参考文献

[1] 曹杰. 发动机电控系统大电流注入电磁耦合特性与试验研究[D]. 南京航空航天大学, 2022.

[2] 王贤超. 输电线缆耦合强电磁脉冲的特性及其防护措施的研究[D]. 南京：南京信息工程大学, 2023.

[3] 冯纪航. 面向微波无线输能系统的高效率整流电路小型化研究[D]. 成都：电子科技大学, 2024.

[4] 陈珩.电力系统稳态分析[M]. 北京：中国电力出版社，1985.

[5] Abedin Tarek, Lipu M. Shahadat Hossain, Hannan Mahammad A., Ker Pin Jern, Rahman Safwan A., Yaw Chong Tak, Tiong Sieh K., Muttaqi Kashem M.. Dynamic Modeling of HVDC for Power System Stability Assessment: A Review, Issues, and Recommendations[J]. Energies, 2021, 14 (16): 4829-4829.

[6] 黄怡凌. 提高距离保护耐受过渡电阻及过负荷能力的方法研究[D]. 北京：华北电力大学, 2021.

[7] 唐旻,吴林晟,毛军发.关于传输线等效集总电路模型的拓展教学[J]. 电气电子教学学报, 2020, 42 (06): 75-78.

[8] 谷中鑫,尹小龙,张前平,等.感应电动机等效电路参数获取方法及应用[J].电气应用,2024,43(10):110-116.

[9] Yu Haocheng, Wu Zhengtian, Jiang Baoping, Karimi Hamid Reza. Fault section location for distribution network based on linear integer

programming[J]. International Journal of Systems Science, 2023, 54 (2): 391-404.

[10] 刘宗鑫. 基于电力电子变压器的交直流混合微电网协调控制策略[D].秦皇岛：燕山大学, 2024.

036 A Distributionally Robust Optimization Method for Operational Risk Analysis and Power Outage Warning in Unbalanced Distribution Networks

Zhongliang Xin[1], Yuehao Yan[1], Xiaohui Liu[1], Huidong Jia[1] and Qilong Chen[1]
[1] State Grid Zhengzhou Power Supply Company, Zhengzhou, 450000, China
15938915312@163.com

Abstract: The extensive integration of distributed resources such as distributed photovoltaics and electric vehicles into three-phase unbalanced distribution networks has led to a significant increase in bidirectional violations of voltage and power limits. These violations may damage power equipment and elevate the risk of power outages, thereby threatening the safe and reliable power supply of distribution networks. This paper proposes a grid operational risk index and its identification method based on Wasserstein distributionally robust optimization. This index not only reflects the likelihood of safety boundary violations but also captures their nonlinearly increasing severity. Furthermore, based on the grid operational risk, the probability of power outages in distribution networks is analyzed and warned. Case studies on the IEEE 33-node system demonstrate that the proposed method can more accurately reflect grid operational risks under uncertainties. The hierarchical power outage warning mechanism provides effective decision support for operators, reducing the risk of power outages in distribution networks.

Keywords: Distribution network, operational risk, power outage warning, distributionally robust optimization.

1 Introduction

The extensive integration of renewable energy generation (REG) and re-electrification represent pivotal approaches for decarbonizing distribution systems (DSs) [1]. Nevertheless, the inherent intermittency in REG output introduces substantial operational difficulties for these networks.

Operational risk in power systems typically includes both reliability risk and security risk. The work concentrates on security risks, specifically addressing voltage limit breaches and branch overloads within DSs. Fluctuating bidirectional power flows, driven by the variability of REG, can induce significant bus voltage deviations [2] and cause lines to exceed their capacity limits. Such overloading conditions cause critical assets like transmission lines and transformers to overheat, which may result in insulation deterioration or complete equipment breakdown. These operational anomalies consequently elevate the probability of electrical service interruptions, presenting considerable threats to system integrity and underscoring the need for proactive risk alerts.

Concerning operational risk evaluation metrics, the most fundamental indicator is the probability of constraint violation [2]. However, risk measures based solely on likelihood may overlook tail risks. Conditional Value at Risk serves as an adopted metric [3], capturing the expected loss from

low-probability risk events by accounting for their long-tail properties. Despite this, CVaR-oriented metrics may not capture fluctuations in risk probability under varying operational conditions.

Incorporating risks linked to the overloading of power system components is essential [4]. This necessity arises because equipment impairment escalates nonlinearly with the extent of overvoltage. Moreover, given that the thermal energy produced in electrical equipment is proportional to the current squared, the seriousness of an overload is likewise expressed through a nonlinear relationship with the relevant state variable, such as branch power.

Regarding uncertainty management, prevailing methodologies for risk index assessment often rely on stochastic optimization techniques [4], [5], wherein data-driven empirical distributions are commonly employed for modeling uncertainties. A limitation of stochastic approaches, however, is their potential inadequacy under limited data samples, which can result in underestimated risk levels and thereby introduce security vulnerabilities to system operation. In this context, distributionally robust optimization methods offer notable benefits [6].

Yet, current distributionally robust frameworks are seldom capable of evaluating operational risk indices in the comprehensive manner outlined—i.e., simultaneously quantifying both the probability of security violations and their nonlinearly escalating severity. Motivated by this research gap, the present paper develops a day-ahead distributionally robust operational assessment framework for asymmetric distribution networks and, based on this foundation, formulates a mechanism for outage risk alert.

2 Treatment of Uncertainties

This study addresses multiple day-ahead uncertainties, which primarily encompass forecasting inaccuracies associated with renewable energy generation (REG) outputs and load demand. These uncertainties are assumed to follow certain probability distributions ($\mathbb{P}_{\mathrm{REG}}$, $\mathbb{P}_{\mathrm{load}}$). The random variables ξ_{REG} , ξ_{load} constructed within ambiguity sets defined by the Wasserstein distance, are expressed as follows:

$$\xi_{\mathrm{REG}} \sim \mathbb{P}_{\mathrm{REG}}, \quad \xi_{\mathrm{load}} \sim \mathbb{P}_{\mathrm{load}} \tag{1}$$

To account for potential inaccuracies in the estimated probability distributions, they are belonged to the ambiguity sets as follows:

$$\mathbb{P}_{\mathrm{REG}} \in \mathcal{P}_{\mathrm{REG}}, \quad \mathbb{P}_{\mathrm{load}} \in \mathcal{P}_{\mathrm{load}} \tag{2}$$

The uncertain REG outputs and load demands at bus i and time t are mathematically represented as follows:

$$\begin{cases} \tilde{P}^{\phi}_{\mathrm{REG},i,t} = P^{\mathrm{pre},\phi}_{\mathrm{REG},i,t}\left(1+\xi_{\mathrm{REG},t}\right) \\ \tilde{P}^{\phi}_{\mathrm{load},i,t} = P^{\mathrm{pre},\phi}_{\mathrm{load},i,t}\left(1+\xi_{\mathrm{load},t}\right) \end{cases} \quad \forall \phi, \forall i, \forall t \tag{3}$$

Given that the proposed risk management framework is designed for day-ahead operational planning, the datasets are formulated as follows:

$$\begin{cases} \hat{\boldsymbol{\xi}}^{s_{\mathrm{REG}}}_{\mathrm{REG}} = \left[\hat{\xi}^{s_{\mathrm{REG}}}_{\mathrm{REG},1},\ldots,\hat{\xi}^{s_{\mathrm{REG}}}_{\mathrm{REG},T}\right], s_{\mathrm{REG}} = 1,\ldots,S_{\mathrm{REG}} \\ \hat{\boldsymbol{\xi}}^{s_{\mathrm{load}}}_{\mathrm{load}} = \left[\hat{\xi}^{s_{\mathrm{load}}}_{\mathrm{load},1},\ldots,\hat{\xi}^{s_{\mathrm{load}}}_{\mathrm{load},T}\right], s_{\mathrm{load}} = 1,\ldots,S_{\mathrm{load}} \end{cases} \tag{4}$$

Accordingly, empirical distributions $\hat{\mathbb{P}}_{\mathrm{REG}}$, $\hat{\mathbb{P}}_{\mathrm{load}}$ can be derived from the dataset in (4). The actual distributions of the random variables ξ_{REG} , ξ_{load} are considered to reside within the corresponding Wasserstein ambiguity sets constructed above.

3 Operational Security Risk Index

This paper introduces the following risk severity functions for bus voltages, denoted as υ^{over} and υ^{under}.These functions are designed to grow exponentially as voltage deviations exceed operational limits [5]:

$$\begin{cases}\upsilon^{\text{over}}(\theta)=\left(\exp(\theta-V_{\max})-1\right)/\left(\mathrm{e}-1\right)\\ \upsilon^{\text{under}}(\theta)=\left(\exp(V_{\min}-\theta)-1\right)/\left(\mathrm{e}-1\right)\end{cases} \tag{5}$$

Similarly, to assess the severity of overloading incidents in branch power flows, the following functions ρ^{over} and ρ^{under} are proposed. These increase quadratically with the extent to which power flow limits are exceeded. For simplicity, this article will only consider the effects of merit.

$$\begin{cases}\rho^{\text{over}}(P)=(P-P_{\max})^2\\ \rho^{\text{under}}(P)=(P_{\min}-P)^2\end{cases} \tag{6}$$

To jointly capture both the likelihood and the nonlinearly escalating severity of operational security violations, an index Λ^{risk} formulated as a conditional expectation of the above-mentioned functions is adopted. The formulation accounts for the fact that risk materializes only when voltage or power flow exceeds security constraints:

$$\Lambda^{\text{risk}}=\Lambda^{\text{volt}}+\Lambda^{\text{load}},\ \Lambda^{\text{volt}}=\frac{1}{3}\sum_{t}\sum_{i}\sum_{\phi}\Lambda_{i,t}^{\text{volt},\phi},\ \Lambda^{\text{load}}=\frac{1}{3}\sum_{t}\sum_{ij}\sum_{\phi}\Lambda_{ij,t}^{\text{load},\phi} \tag{7}$$

The index Λ^{risk} is for the whole network in a day. In unbalanced distribution systems, the overall risk index is aggregated from phase-specific risk indices, as security violations in each phase can simultaneously cause damage to corresponding electrical equipment. The voltage risk are defined as:

$$\begin{aligned}\Lambda_{i,t}^{\text{volt},\phi}&=\mathrm{E}_{\mathrm{P}}\left(\upsilon^{\text{over}}(\tilde{V}_{i,t}^{\phi})\middle|\tilde{V}_{i,t}^{\phi}-V_{\max}\geq 0\right)+\mathrm{E}_{\mathrm{P}}\left(\upsilon^{\text{under}}(\tilde{V}_{i,t}^{\phi})\middle|V_{\min}-\tilde{V}_{i,t}^{\phi}\geq 0\right),\ \forall\phi,\forall i,\forall t\\ \Lambda_{ij,t}^{\text{load},\phi}&=\mathrm{E}_{\mathrm{P}}\left(\rho^{\text{over}}(\tilde{P}_{ij,t}^{\phi})\middle|\tilde{P}_{ij,t}^{\phi}-P_{\max}\geq 0\right)+\mathrm{E}_{\mathrm{P}}\left(\rho^{\text{uder}}(\tilde{P}_{ij,t}^{\phi})\middle|P_{\min}-\tilde{P}_{ij,t}^{\phi}\geq 0\right),\ \forall\phi,\forall ij,\forall t\end{aligned} \tag{8}$$

This paper develops a novel distributionally robust operational risk assessment model for unbalanced distribution systems, built upon data-driven ambiguity sets for REG outputs and load demands. Therefore, the worst-case index in the set is evaluated as follows:

$$\Lambda_{\text{DR}}^{\text{risk}}=\max_{\mathbb{P}_{\text{REG}}\in\mathcal{P}_{\text{REG}},\,\mathbb{P}_{\text{load}}\in\mathcal{P}_{\text{load}}}\left(\Lambda^{\text{risk}}\right) \tag{9}$$

4 Solution Methodology for the Power System Operational Risk Assessment Model

To enhance model performance, both the 1-norm and ∞-norm Wasserstein metrics are adopted for characterizing uncertainties in REG outputs and load demands [7]. Accordingly, the risk assessment problem is restructured into the following formulation (10):

$$\Lambda_{\text{DR}}^{\text{risk}}=\max_{\Delta\xi_{\text{REG}},\,\Delta\xi_{\text{load}}}\left\{\Lambda^{\text{volt}}+\Lambda^{\text{load}}\right\} \tag{10a}$$

$$\text{s.}t.\begin{cases}\mathrm{E}_{\mathrm{P}}\left(\tilde{P}_{\text{REG},i,t}^{\phi}\right)=P_{\text{REG},i,t}^{\text{pre},\phi}\left(1+\dfrac{1}{S_{\text{REG}}}\displaystyle\sum_{s_{\text{REG}}=1}^{S_{\text{REG}}}\left(\hat{\xi}_{\text{REG},t}^{s_{\text{REG}}}-\Delta\xi_{\text{REG},t}^{s_{\text{REG}}}\right)\right)\\ \mathrm{E}_{\mathrm{P}}\left(\tilde{P}_{\text{load},i,t}^{\phi}\right)=P_{\text{load},i,t}^{\text{pre},\phi}\left(1+\dfrac{1}{S_{\text{load}}}\displaystyle\sum_{s_{\text{load}}=1}^{S_{\text{load}}}\left(\hat{\xi}_{\text{load},t}^{s_{\text{load}}}-\Delta\xi_{\text{load},t}^{s_{\text{load}}}\right)\right)\end{cases}\quad\forall\phi,\forall i,\forall t \tag{10b}$$

$$\begin{cases} \dfrac{1}{S_{\mathrm{REG}}}\displaystyle\sum_{s_{\mathrm{REG}}=1}^{S_{\mathrm{REG}}}\left\|\Delta\boldsymbol{\xi}_{\mathrm{REG}}^{s_{\mathrm{REG}}}\right\|_1 \le r_{\mathrm{REG}}^1, \quad \dfrac{1}{S_{\mathrm{REG}}}\displaystyle\sum_{s_{\mathrm{REG}}=1}^{S_{\mathrm{REG}}}\left\|\Delta\boldsymbol{\xi}_{\mathrm{REG}}^{s_{\mathrm{REG}}}\right\|_\infty \le r_{\mathrm{REG}}^\infty \\ \dfrac{1}{S_{\mathrm{load}}}\displaystyle\sum_{s_{\mathrm{load}}=1}^{S_{\mathrm{load}}}\left\|\Delta\boldsymbol{\xi}_{\mathrm{load}}^{s_{\mathrm{load}}}\right\|_1 \le r_{\mathrm{load}}^1, \quad \dfrac{1}{S_{\mathrm{load}}}\displaystyle\sum_{s_{\mathrm{load}}=1}^{S_{\mathrm{load}}}\left\|\Delta\boldsymbol{\xi}_{\mathrm{load}}^{s_{\mathrm{load}}}\right\|_\infty \le r_{\mathrm{load}}^\infty \end{cases} \tag{10c}$$

Power flowequations and other constraints (10d)

In this reformulated model, the followed probability distribution can be represented as:

$$\begin{aligned} &\Pr\left\{\boldsymbol{\xi}_{\mathrm{REG}} = \hat{\boldsymbol{\xi}}_{\mathrm{REG}}^{s_{\mathrm{REG}}} - \Delta\boldsymbol{\xi}_{\mathrm{REG}}^{s_{\mathrm{REG}}}\right\} = \frac{1}{S_{\mathrm{REG}}}, \forall s_{\mathrm{REG}} \\ &\Pr\left\{\boldsymbol{\xi}_{\mathrm{load}} = \hat{\boldsymbol{\xi}}_{\mathrm{load}}^{s_{\mathrm{load}}} - \Delta\boldsymbol{\xi}_{\mathrm{load}}^{s_{\mathrm{load}}}\right\} = \frac{1}{S_{\mathrm{load}}}, \forall s_{\mathrm{load}} \end{aligned} \tag{11}$$

As a result, the objective of risk minimization under the worst-case distribution is transformed into identifying the most adverse realizations of the deviation variables $\Delta\boldsymbol{\xi}_{\mathrm{REG}}$, $\Delta\boldsymbol{\xi}_{\mathrm{load}}$ rather than directly searching for the worst-case outcomes of the original uncertainties $\mathbb{P}_{\mathrm{REG}} \in \mathcal{P}_{\mathrm{REG}}$, $\mathbb{P}_{\mathrm{load}} \in \mathcal{P}_{\mathrm{load}}$ in this Wasserstein-based distributionally robust optimization (DRO) framework, historical samples are treated as discrete scenarios within the optimization model, and each random variable is considered to follow the discrete distribution given in (11). Through this mathematical reformulation, the computation of distributionally robust grid operational risk indices becomes tractable and can be effectively solved using conventional optimization techniques.

5 Outage Risk Warning Under Risk Propagation

This research examines outage incidents in distribution networks triggered by excessive voltage at individual nodes (including distribution transformers) or branch overloading conditions. The implementation workflow consists of the following steps:

Step 1: Acquire the risk indices, denoted as $\Lambda_{i,t}^{\mathrm{volt},\phi}*, \Lambda_{ij,t}^{\mathrm{load},\phi}*$ for node voltages and branch power flows, respectively, after solving the previously described assessment model.

Step 2: Establish a mapping relationship between the probability of an outage event occurring at each node or branch and its corresponding risk index value:

$$\begin{aligned} q_{i,t}^{\mathrm{volt},\phi} &= 1-\exp(-\gamma_{\mathrm{volt}} \bullet \Lambda_{i,t}^{\mathrm{volt},\phi}*) \\ q_{ij,t}^{\mathrm{load},\phi} &= 1-\exp(-\gamma_{\mathrm{load}} \bullet \Lambda_{ij,t}^{\mathrm{load},\phi}*) \end{aligned} \tag{12}$$

Here, $\gamma>0$ represents a sensitivity coefficient, calibrated using historical data records linking limit violations to actual outages. Equation (13) is derived from the standard "intensity → event probability" expression used in reliability and survival analysis. By interpreting the "security violation risk" as the event intensity over an interval, the probability of at least one outage occurring within a time window ΔT naturally takes this form—a well-established result originating from Poisson process theory and exponential lifetime distributions.

Step 3: Under this framework, the system-wide probability of experiencing at least one outage during the entire day, from a day-ahead perspective, is computed as:

$$Q_{\mathrm{day}} = 1-\prod_{i,t,\phi}(1-q_{i,t}^{\mathrm{volt},\phi}) - \prod_{ij,t,\phi}(1-q_{ij,t}^{\mathrm{load},\phi}) \approx \prod_{i,t,\phi} q_{i,t}^{\mathrm{volt},\phi} + \prod_{ij,t,\phi} q_{ij,t}^{\mathrm{load},\phi} \tag{13}$$

This resulting probability metric can be directly utilized for issuing day-ahead outage risk alerts, enabling proactive grid management.

6 Case study

6.1 Parameter Settings

This section employs an unbalanced IEEE 33-bus system, as shown in Figure 3, to verify the proposed method. To make the results more pronounced, the load is set to 1.2 times its original value. The permissible voltage range is from 0.95 to 1.05 p.u., and the maximum allowable value for line power flow is 7 MW.

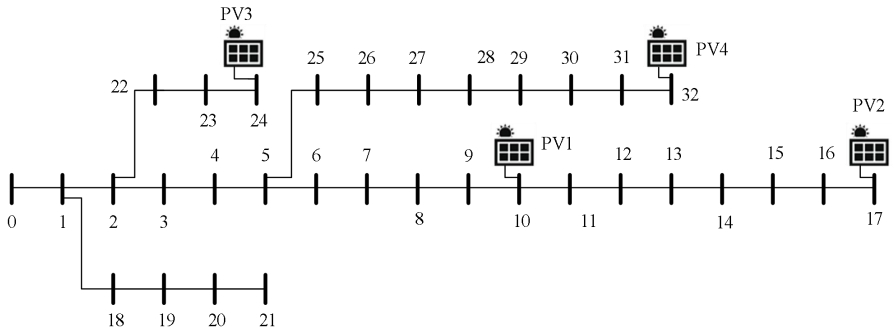


Fig. 1. Unbalanced IEEE 33-bus system

Photovoltaic (PV) panels are selected in this study as a representative form of renewable energy generation (REG). The load and PV profiles are adopted from Reference [8]. The distribution system operator (DSO) manages four PV stations, each with an installed capacity of 800 kW.

To address uncertainties in PV output and load demand, a Wasserstein ambiguity set is employed. A total of 50 samples for each uncertain parameter are generated by sampling from a normal distribution [9]. The means are set as the predictions and the standard deviations are 10% of them. This sampling strategy ensures reproducibility and comparability, though it can be substituted with alternative techniques or actual historical datasets. The confidence level for the Wasserstein metric constraint is 90% [10].

The numerical experiments are implemented on the YALMIP platform, utilizing a commercial solver for optimization.

6.2 Power Grid Risk Assessment

In this sub-section, we compare two methods to validate the proposed method.

Method 1: stochastic method with REG outputs and load demands following the Gaussian distributions $N\left(\hat{\xi}_{\mathrm{REG}}^{s_{\mathrm{REG}}},(10\%\cdot\hat{\xi}_{\mathrm{REG}}^{s_{\mathrm{REG}}})^2\right)$ and $N\left(\hat{\xi}_{\mathrm{load}}^{s_{\mathrm{load}}},(10\%\cdot\hat{\xi}_{\mathrm{load}}^{s_{\mathrm{load}}})^2\right)$.

$$\begin{aligned}
&\Lambda_1^{\mathrm{risk}} = \Lambda_1^{\mathrm{volt}} + \Lambda_1^{\mathrm{load}} \\
&\Lambda_1^{\mathrm{volt}} = \frac{1}{3}\sum_t\sum_i\sum_\phi\left[\mathrm{E_P}\left(\tilde{V}_{i,t}^{\phi}\left|\tilde{V}_{i,t}^{\phi}-V_{\max}\geq 0\right.\right)+\mathrm{E_P}\left(\tilde{V}_{i,t}^{\phi}\left|V_{\min}-\tilde{V}_{i,t}^{\phi}\geq 0\right.\right)\right] \\
&\Lambda_1^{\mathrm{load}} = \frac{1}{3}\sum_t\sum_{ij}\sum_\phi\left[\mathrm{E_P}\left(\tilde{P}_{ij,t}^{\phi}\left|\tilde{P}_{ij,t}^{\phi}-P_{\max}\geq 0\right.\right)+\mathrm{E_P}\left(\tilde{P}_{ij,t}^{\phi}\left|P_{\min}-\tilde{P}_{ij,t}^{\phi}\geq 0\right.\right)\right]
\end{aligned} \tag{14}$$

Method 2 (the proposed approach) defines system risk by integrating two key components: exponential voltage violations and quadratic branch power flow violations. This composite risk metric is mathematically formulated as a distributionally robust conditional expectation. The underlying uncertainties from REG outputs and load demands are modeled within a data-driven Wasserstein ambiguity set.

Under the tested configuration, **Method 2** yields a risk index of 0.081, which is lower than the 0.118 computed by **Method 1**. Furthermore, Figure 2 illustrates the distinct probability distributions for the

power flow on Branch 1-2 at 19:00, as derived from the two methods.

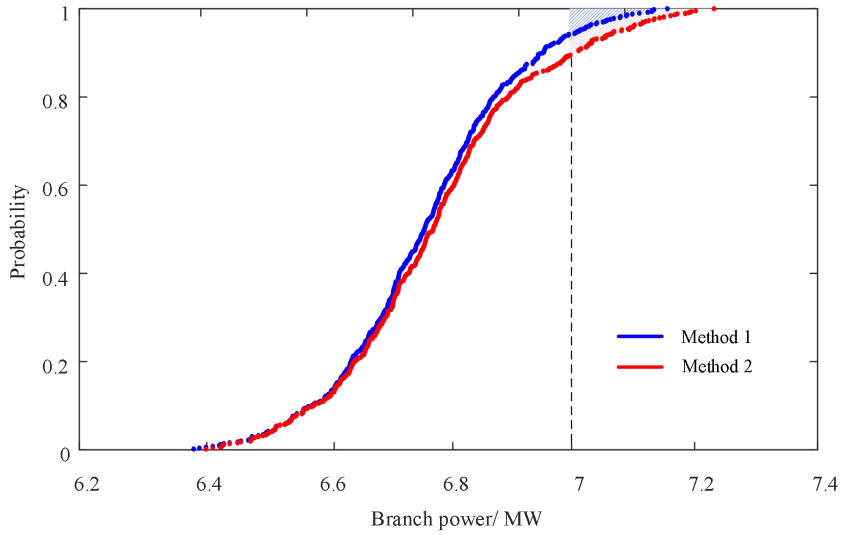


Fig. 2. Distributions of branch flow in different risk assessment

A probabilistic overload occurs during evening periods as a result of heavy loading conditions. Here, Method 1 is defined as the approach calculated using predefined PDFs, while Method 2 identifies the worst-case realization from a data-driven ambiguity set. The red curve (**Method 2**) shows a more pronounced tail extending beyond the operational threshold compared to the blue one (**Method 1**), indicating enhanced robustness by circumventing reliance on empirical distributions.

To validate the benefits of considering nonlinear characteristics, the risk indices are computed under increased sample standard deviations, which are 15% and 20% of the mean in Table 1. Additionally, to further compare methodological traits, the growth rates of the risk index were derived and summarized in Table 1. The calculation of growth rate from A to B is (B – A) / A.

Table 1. Analysis of the proposed risk assessment method

Sample Standard Deviation Coefficient	**10%**	**15%**	**20%**
Method 1			
Value	0.118	0.163	0.215
Growth rate	-	38.1%	31.9%
Method 2			
Value	0.081	0.134	0.219
Growth rate	-	65.4%	63.4%

Premised on the exponential increase in risk severity with voltage non-compliance, Method 2 is designed to deliver assessments of greater fidelity. Its superior performance, evidenced by a steeper response to growing uncertainty in Table 1, confirms this advantage over Method.

6.3 Power Outage Risk Warning

The focus of this section is on assessing distribution network outage risk induced by operational security challenges, leveraging parameter analysis, all-day outage probability computation, and warning classification.

Leveraging the approach from Section V, the requisite risk indices for node voltages and branch power flows are first acquired. Key parameters are subsequently determined, either by sensitivity scanning or through MLE based on historical "limit violation-outage" data. The assumption of

independence for system-wide intraday "at least one outage" events allows the all-day outage probabilities to be aggregated, as shown in the table below. As a specific case, the outage risks corresponding to varying standard deviations are presented for the parameters γ_{volt} =1.5 and γ_{load} =1.

Table 2. Power outage risk under different standard deviations

Standard Deviation Coefficient	10%	15%	20%
Power Outage Risk	7.8%	12.5%	19.7%

Power outage risk is critically influenced by the uncertainty associated with modern loads and generation sources. An all-day warning framework is established, categorized into four levels based on the computed Q_{day} value:

• **Blue (Q_{day} < 2.5%)**: Mandates routine inspection.

• **Yellow (2.5% ≤ Q_{day} < 7.5%)**: Requires intensified monitoring during critical intervals and pre-positioning of switching/reactive power resources.

• **Orange (7.5% ≤ Q_{day} < 15%)**: Initiates trial operations for load transfer, reactive power optimization, and peak shaving.

• **Red (Q_{day} ≥ 15%)**: Triggers official warnings and potential activation of load shedding or network reconfiguration to address overloads and voltage issues.

The computed results reveal that the warning level remains at Orange or higher, independent of uncertainty variations. This consistently indicates an unacceptable day-ahead risk profile for the current network configuration, necessitating proactive control strategies like reconfiguration to achieve meaningful risk improvement.

7 Conclusion

1) This paper introduces a novel operational risk assessment framework for distribution networks experiencing high penetration levels of distributed photovoltaics and electric vehicles. The methodology is founded on Wasserstein distributionally robust optimization and incorporates a hybrid risk metric that captures both the likelihood and the nonlinearly escalating severity of limit violations. This enables a quantitative evaluation of risks associated with voltage deviations and branch overloads.

2) By adopting a data-driven distributionally robust model, the approach addresses key shortcomings of conventional stochastic optimization—specifically, its susceptibility to inaccurate pre-defined distributions and its frequent underestimation of actual risks. This significantly improves the assessment's practical applicability and robustness. A mapping between operational risk indices and outage probability is further formulated, facilitating day-ahead outage risk classification and early warning.

3) Case studies confirm that the proposed technique more accurately characterizes the rapid escalation of risk under growing uncertainties. The resulting warning system offers actionable decision-making support for grid operators, aiding in the proactive mitigation of outage risks.

While this study does not yet incorporate the effects of operational tactics like network reconfiguration or active control on risk propagation pathways, future work will prioritize the development of integrated assessment and warning optimization methods that explicitly account for these strategic couplings.

Acknowledgements: This work is supported by Technology Project of State Grid Henan Electric Power Company (521710230007).

References

1. DE LIMA T D, TABARES A, BAÑOL ARIAS N, et al. Investment & generation costs vs CO2 emissions in the distribution system expansion planning: A multi-objective stochastic programming approach[J]. *International Journal of Electrical Power & Energy Systems*, 2021, 131: 106925.
2. PUKHREM S, BASU M, CONLON M F. Probabilistic risk assessment of power quality variations and events under temporal and spatial characteristic of increased PV integration in low-voltage distribution networks[J]. *IEEE Transactions on Power Systems*, 2018, 33(3): 3246-3254.
3. HUILING T, JIEKANG W, LINGMIN C, et al. A control optimization model for CVaR risk of distribution systems with PVs/DSs/EVs using Q-learning powered adaptive differential evolution algorithm[J]. *International Journal of Electrical Power & Energy Systems*, 2021, 132: 107209.
4. WAN T, TAO Y, QIU J, et al. Data-driven hierarchical optimal allocation of battery energy storage system[J]. *IEEE Transactions on Sustainable Energy*, 2021, 12(4): 2097-2109.
5. YIN Y, LIU T, WU L, et al. Day-ahead risk-constrained stochastic scheduling of multi-energy system[J]. *Journal of Modern Power Systems and Clean Energy*, 2021, 9(4): 720-733.
6. WANG C, GAO R, WEI W, et al. Risk-based distributionally robust optimal gas-power flow with Wasserstein distance[J]. *IEEE Transactions on Power Systems*, 2019, 34(3): 2190-2204.
7. LI J, XU Z, LIU H, et al. A Wasserstein distributionally robust planning model for renewable sources and energy storage systems under multiple uncertainties[J]. *IEEE Transactions on Sustainable Energy*. 2023, 14(3): 1346-1356.
8. ZHANG S, GE S, LIU H, et al. A multi-objective chance-constrained information-gap decision model for active management to accommodate multiple uncertainties in distribution networks[J]. *Journal of Modern Power Systems and Clean Energy*. 2023, 11(1): 17-34.
9. ZHANG S, GE S, LIU H, et al. Distributionally robust hierarchical multi-objective voltage risk management for unbalanced distribution systems[J]. *International Journal of Electrical Power & Energy Systems*, 2023, 154: 109446.
10. ZHANG S, GE S, LIU H, et al. An analytical method for delineating feasible region for PV integration capacities in net-zero distribution systems considering battery energy storage system flexibility[J]. *Journal of Modern Power Systems and Clean Energy*. 2024, 12(2): 475-487.

037 GIS/GIL 支柱绝缘子界面缺陷的超声频谱特征

任帅，王禹淮，孙一涵，陈思源，杜世杰，李进

（天津大学电气自动化与信息工程学院，天津，300072）

ABSTRACT: GIS/GIL are critical equipment in ultra/extra-high voltage power grids, and the internal defect detection of their core component—epoxy resin insulators—is essential for ensuring safe and stable operation. Addressing the lack of attention in traditional ultrasonic testing to defects at the interface bonding area between metal inserts and epoxy resin, this paper proposes an interface defect detection method based on the ultrasonic reflection method, which can effectively identify and distinguish typical defects in the interface region. Specifically, the ultrasonic spectral characteristics of bubble defects show significant energy enhancement in both the low-frequency band and the frequency band near the probe's central frequency, while metal particle defects exhibit a frequency extension of the reflected signal into higher frequency bands and an increase in duration. This detection approach provides an efficient and non-destructive testing means for quality assessment of GIS/GIL insulators.

KEY WORDS: Ultrasonic testing; Post insulator; Interfacial defects; Frequency spectrum characteristics

摘要：GIS/GIL 是超/特高压电网的关键装备，其核心部件环氧树脂绝缘子的内部缺陷检测对设备安全稳定运行至关重要。针对传统超声检测少有关注金属嵌件与环氧树脂界面粘合区域缺陷的问题，本文提出了一种基于超声反射法的界面缺陷检测方法，可有效识别和区分界面区域的典型缺陷，其中气泡缺陷的超声频谱特征表现为低频段与探头中心频率附近频段的能量显著增强，而金属颗粒缺陷则表现为反射信号频率向高频段延展且持续时间增加。此检测为 GIS/GIL 绝缘子的质量评估提供了一种高效、无损的检测手段。

关键词：超声检测；支柱绝缘子；界面缺陷；频谱特征

0 引言

气体绝缘金属封闭开关设备(gas-insulated switches, GIS)将变电站的电气元件集成于填充绝缘气体的压力金属密闭容器内，具有体积小、免维护、高可靠的优点，适用于空间受限或环境恶劣的场所，是特高压电网的必备设备[1-2]。而气体绝缘封闭输电线路(rigid gas-insulated transmission line，GIL)因传输容量大、传输损失小、环境友好的优点，适于超/特高压输电线路跨越复杂地理环境，而被广泛使用[3]。环氧树脂绝缘子具有优良的电气特性、机械支撑、耐腐蚀性能，是 GIS/GIL 设备的核心部件。GIS/GIL 设备的稳定运行与环氧树脂绝缘子密切相关，随着 GIS/GIL 设备电压等级与通流量不断提高，对环氧树脂绝缘子的制造水平与缺陷检测技术提出了更高要求[4]。现有检测手段如局部放电、工业 CT 等步骤繁琐、价格昂贵，具有一定的局限性，而超声波检测法具有检测速度快、对人体无辐射伤害、成本低、设备简单灵活的优势，其可识别制造过程或因环境造成的残余应力和热应力，对应力集中提前告警，避免机械结构损坏[5]。此外，超声检测法亦可识别环氧树脂绝缘子因制造工艺和长期运行中可能出现的气泡、气缝、脱壳等内部集中缺陷[6]。

但针对集中缺陷的超声检测多关注单一的环氧树脂复合材料，且受限于超声检测的自身特点，研究多集中于易于耦合的大曲率区域和表层缺陷[7-8]，少有针对金属嵌件与环氧树脂复合材料界面粘合区域内缺陷的超声信号特征。本文基于超声反射法提出了用于环氧树脂绝缘子界面缺陷的检测方法，并给出气泡与金属颗粒两种典型缺陷的超声频谱特征。通过对超声探头进行优化增强其曲面耦合能力并结合傅里叶变换与小波分析，使用数个人为制造缺陷的支柱环氧树脂绝缘子样品进行实验验证，可实现缺陷信号的有效分析识别。

1 超声检测原理

1.1 超声缺陷检测原理

环氧树脂复合材料的缺陷检测使用超声纵波反射法，当超声纵波从一种介质传播到另一种介质时，由于声阻抗差异超声波会发生反射。如图 1 所示，当超声波在环氧树脂复合材料中传播时，若遇到气泡、金属杂质、裂隙等缺陷，将发生反射，不同空间位置的缺陷因声程各异，其反射回波再次抵达探头的时间不同，如图中右侧折线所示的接收信号，缺陷信号将在始波 F 和底面回波 B 之间产生，因此呈现不同的时域特性；同时，由于各类缺陷的声学特性，如声阻抗、几何形态不同，它们的反射超声幅度与频率响应特性也存在差异，从而在频域

上表现出可区分的特征，因此，通过分析回波的时域与频域特征参数，可实现缺陷定位与类型识别[9]。

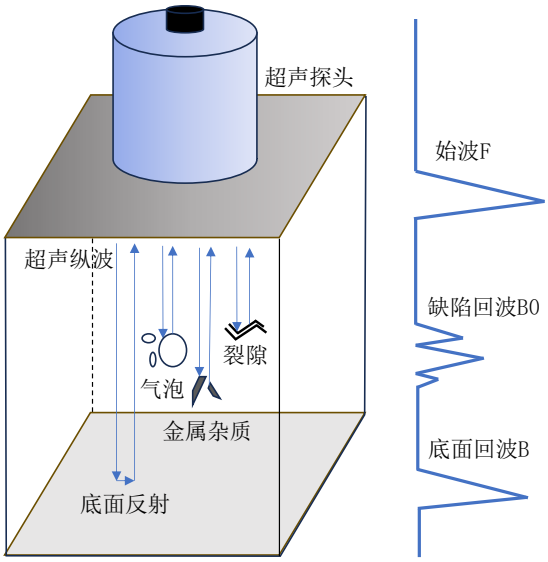


图 1 超声检测反射法示意图

1.2 信号处理方法

本文采用快速傅里叶变换(Fast Fourier Transform, FFT)和小波变换(Wavelet Transform)对超声回波信号进行处理以分析其频率特性。

FFT 是一种高效的计算算法，用于将信号从时域变换到频域，可提取超声反射信号包含的频率成分及其强度[10]。它是计算离散傅里叶变换（Discrete Fourier Transform, DFT）的一种快速算法，能将计算复杂度显著降低，从而实现了速度的极大提升，由于是对有限长度信号进行变换，会不可避免地产生频谱泄漏和栅栏效应。

小波变换与傅立叶变换类似，也能将信号分解成不同频率的成分，其优点在于可以同时提供时间和频率的信息，并且可以通过选择不同的小波基函数来适应不同类型的信号。此外，小波变换还具有良好的局部性质，可以有效地处理非平稳信号和非平稳噪声，通过选择不同的时间窗和频率窗，小波变换可以调节频域的分辨率，非常适合用于提取信号的局部特征[11]。上述特性使得小波变换可有效处理多层非连续声阻抗介质的超声反射信号。连续小波变换可表示为：

$$W_{\psi}=\frac{1}{\sqrt{a}}\int_{-\infty}^{+\infty}f(t)\overline{\psi}(\frac{t-b}{a})dt \qquad (1)$$

其中，ψ 为一母小波，a 为伸缩因子，b 为平移因子，则函数 $f(t)$ 可以重构为：

$$f(t)=\frac{1}{a^2C_{\Psi}}\iint_{R^2}W_{\psi}f(a,b)\psi_{a,b}(t)dadb \qquad (2)$$

其中，C_{Ψ} 为归一化因子，通过改变伸缩因子 a 的取值，可以调整母小波在时域上的支撑宽度，从而实现对信号中不同频带成分的分析[12]。

此外，基于小波变换生成的时频图可明确频率随时间的变化，如图 2 所示，其特点为在低频段使用较长时间窗，频域分辨率好，时域分辨率差；而在高频段，使用较短时间窗，时域分辨率好，频域分辨率差。其处理非平稳信号的优势在于能够根据信号频率成分自动调节分析窗的时长，实现了对信号时频局部化分析的自适应性，从而既能有效地捕捉短时的高频瞬态突变[13]。

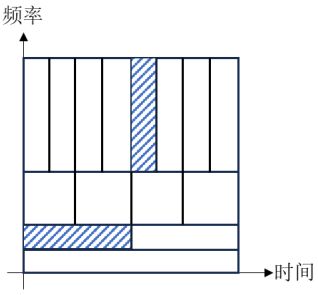


图 2 时频图示意图

2 平台搭建及试样制备

2.1 超声检测系统搭建

实验中的超声检测系统如图 3 所示。超声检测系统包括超声脉冲发生器、超声波探头、示波器、上位机和电缆线。探头为双晶探头，为了增强超声波探头与待测样品界面间的耦合，探头上装有与试样金属嵌件内曲面贴合良好的延时楔块。

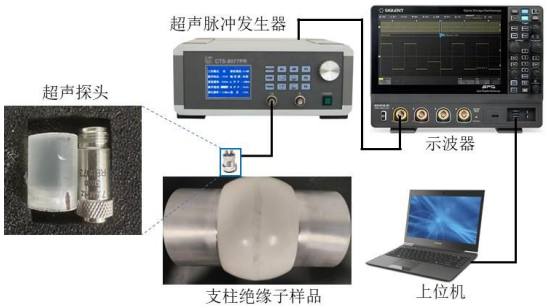
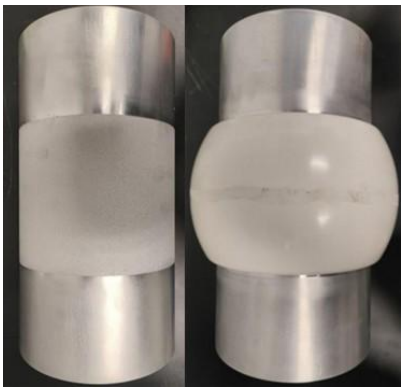


图 3 超声检测系统示意图

2.2 试样制备



(a) 金属嵌件与支柱绝缘子样品



(b) 气泡缺陷与金属颗粒缺陷制备

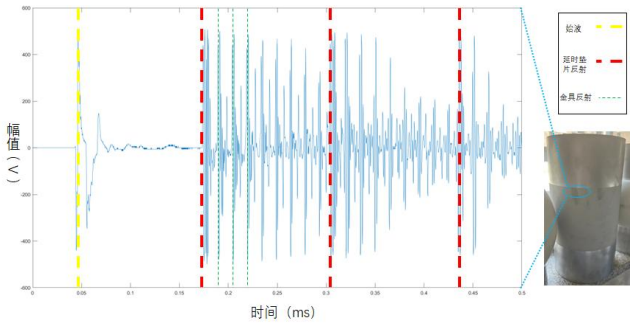
图 4 用于检测的样品实物图

所制备的样品如图 4(a)所示，样品分为金属嵌件和支柱绝缘子样品，其中支柱绝缘子样品在制造过程中，通过放置空腔薄膜泡和金属微粒，人为制造气隙缺陷和金属颗粒缺陷，如图 4(b)所示。支柱绝缘子样品采用真空铸造工艺制备，金属嵌件形状规则，不同区域厚度相同，支柱绝缘子样品中环氧树脂复合材料的厚度变化较大，缺陷位置与测试点均位于端部环氧树脂复合材料小厚度区域。

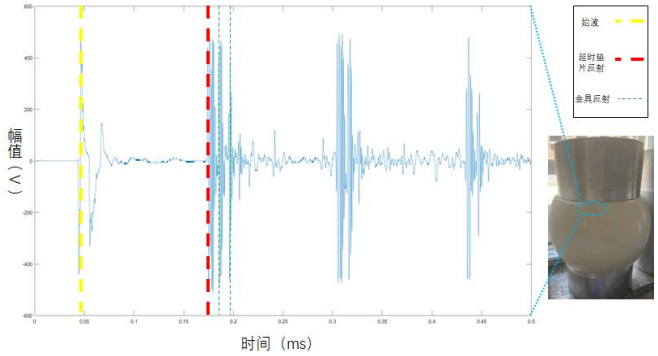
真空铸造工艺中使用的环氧、氧化铝、酸酐固化剂的种类和质量见表 1。将固体环氧树脂、固化剂、氧化铝填料和模具、嵌件放在真空干燥室中进行预热。预热温度和时间分别设定为 100℃和 60 min，预热完成后，将金属嵌件固定在模具内，放入铸造腔内。按照表 1 中的比例，将环氧树脂、固化剂、氧化铝加入搅拌槽中搅拌除泡。然后将混合液缓慢注入模具。固化结束后，用砂纸对试样表面进行处理，并用无纺布蘸取酒精进行清洗。

3 检测结果分析

3.1 超声波形分析



(a) 单金属嵌件



(b) 支柱绝缘子样品

图 5 超声反射信号时域波形

与以往研究的绝缘子超声缺陷检测相比，受绝缘子曲面结构限制，超声探头布置于金属嵌件内测，故超声波需经多层介质，其反射信号需要匹配的不同类型区域多。声学结构上，上层金属嵌件为高波阻抗低衰减、下层环氧树脂复合材料为低波阻抗高衰减特性，运用反射法检测时声波会产生严重的混叠，时域上各类型特征区别变小且相互掩盖[14]。如图 5 所示，超声传播的第一层介质为延时垫块，其可保证超声的有效耦合，第二层为金具，超声信号在此层衰减弱并在介质界面间发生多次反射，故会接收到有周期性规律的多次尖峰信号，如图中绿色虚线所示；第三层为环氧树脂复合材料，但其信号被金具的高频反射信号混叠以致淹没，无法在时域中有效分析。

3.2 超声频谱特征研究

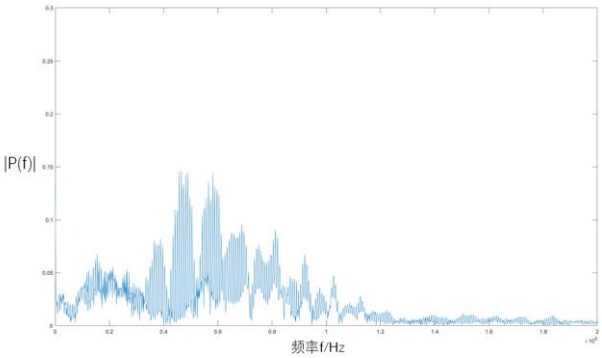
超声脉冲发生器设置为 7.5MHz，与探头频率相匹配，接收增益设置为 30dB，此参数设置可以较好地平衡噪声与回波信号幅值大小。

3.2.1 气泡缺陷的超声频谱特征

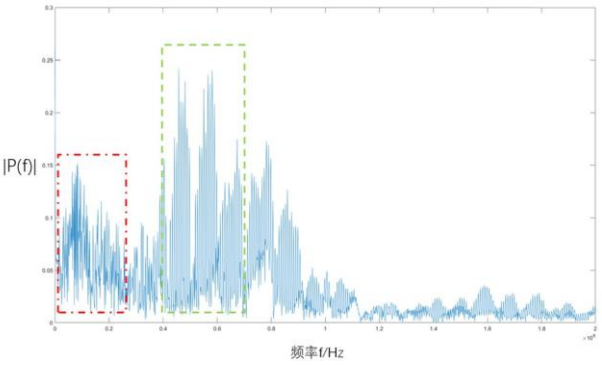
超声探头向绝缘子内部发射一个中心频率为 7.5MHz 的脉冲，并接收反射回来的时域信号，对获取的时域超声信号通过 FFT 处理后，如图 6 所示，气泡缺陷的回波信号低频段能量显著增强(红框)，且超声信号在始波频率(7.5MHz)附近的频段能量显著增强(绿框)。

产生上述显著特点的原因是气隙中的气体介

质对超声波具有强烈衰减作用，导致低频分量在反射回波中被相对保留，表现为低频能量显著增强；同时，气泡与固体材料间巨大的声阻抗差异造成超声波在界面发生强烈的全反射，该反射能量主要集中于发射探头的中心频率（7.5MHz）附近窄带，使其能量显著集中；此外，气泡内部复杂的多重反射、散射效应与时域混叠干扰了清晰的金具反射信号路径，使得能量在各个频段上均有出现。



(a) 无缺陷



(b) 含气泡缺陷

图 6 超声反射信号频谱图

3.2.2 金属颗粒缺陷的超声频谱特征

如图 7 所示，测量同一截面上的无缺陷区域与含金属颗粒区域并进行 FFT 处理，可见金具与环氧树脂正常接触与含有金属微粒的频谱图不具有显著差异，不能识别缺陷。FFT 常用于观察信号的整体频率成分，可有效识别缺陷在整体频率上的“指纹特征”，但针对金属颗粒缺陷需通过 Morlet 小波对信号进行分解构建时频图。

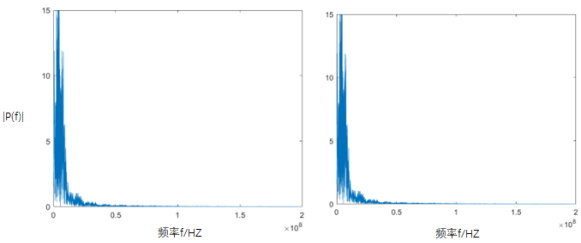


图 7 无缺陷(左)与金属颗粒缺陷(右)的频谱图

为识别缺陷，通过 Morlet 小波对超声回波信号进行分解构建时频图，如图 8 所示，以反映其频率随时间的动态变化。含金属颗粒时金属嵌件的首次超声反射信号在向高频段显著延展，且信号持续时间增加，如红框所示。这是因为高频分量波长较短，更易穿透颗粒间隙或绕射，而低频分量受散射影响大，易发生大角度散射，大量低频声波的能量被散射到了各个不同的方向，而不是沿着原始路径返回接收探头导致信号高频成分显著；此外，金属微粒使超声波在传播中经历多次反射、折射，形成多重散射路径，声波传播路径长短不一，导致信号持续时间增加。

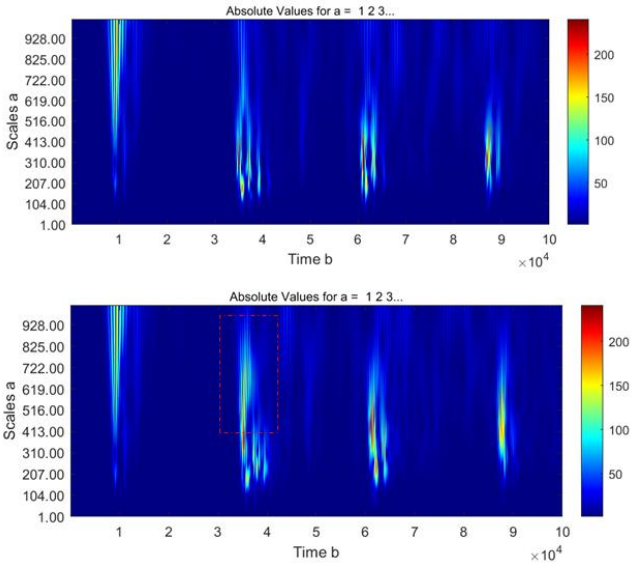


图 8 无缺陷（上）与含金属微粒（下）区域的时频图

4 结论

本研究基于超声反射法对人工制备的界面间存有气泡、金属颗粒缺陷的支柱绝缘子样品进行了检测与频谱分析：

（1）多层声阻抗不同的介质中界面产生多次反射回波，这些回波会与缺陷回波在时域上发生混叠，严重干扰对缺陷的识别，易造成误检或漏检，通过引入小波分析可以识别缺陷。

（2）不同缺陷的频谱及时频特征存在根本差异。研究发现了具有判别意义的特征模式：气泡缺陷因强烈反射与声阻抗差异造成频率选择，表现为低频与中心频段能量显著增强；而金属颗粒缺陷因高频散射效应，其反射信号呈现回波频率高频延展、持续时间增加的典型特征。

参考文献

[1] 韩先才，孙昕，陈海波，等.中国特高压交流输电工程技术发展综述[J].中国电机工程学报，2020，40(14)：4371-4386.

[2] 黄冬梅，王桂芳，胡安铎，等.GIS 在电网规划中的应用研究综述[J].

智能处理与应用，2021，11(03)：70-73.
[3] 张长虹，张博雅，李明洋，等.高压直流 GIL 设备绝缘关键技术研究综述[J].高电压技术，2023，49(03)：920-936.
[4] 陈刚，郭冲，李平，等.超/特高压 GIS 绝缘可靠性提升研究综述[J].高压电器，2025，61(06)：1-15.
[5] 韩帅，高飞，廖思卓，等. GIS 盆式绝缘子表面缺陷及其诊断方法研究综述[J].绝缘材料，2022，55(02)：12-22.
[6] 郝艳捧，梁学致，黄盛龙，等.GIS/GIL 绝缘子超声检测研究进展与展望[J].高电压技术，2023，49(09)：3596-3606.
[7] 郑尧.GIS/GIL 绝缘子的应力与缺陷超声检测和机械失效机理研究[D].广州: 华南理工大学，2022.
[8] 梁学致.GIS 盆式绝缘子残余应力超声波测量方法研究[D].广州华南理工大学,2023.
[9] TIAN F Y, HAO Y P, ZOU Z Y, et al. An ultrasonic pulse-echo method to detect internal defects in epoxy composite insulation[J].Energies, 2019, 12(24)：4804.
[10] 吕立翔，杨卓然，刘剑，等.基于超声反射法的环氧树脂复合材料内部缺陷检测与频谱分析研究[J].绝缘材料，2024，57(09)：131-139.
[11] 李阳，刘君伟，徐兴龙，等.GIS 盆式绝缘子检测用超声导波信号降噪方法研究[J].电磁避雷器，2025(03)：120-127.
[12] 朱建峰，郭伟剑，刘俊邦,等.小波变换在多层复合材料的超声波检测中的应用[J].四川兵工学报，2014 ,35 (07)：
[13] 崔治. 小波分析在超声检测信号处理中的应用研究[D]，湖南：湖南大学，2013.
[14] 陈祎婷，陆铭慧，朱颖，等.多层包铁结构超声反射频谱数值仿真[J].压电与声光，2022,44(06)：98-1006.

-04。



任帅

硕士研究生，研究方向为高
：18822061679@163.com；
研究方向为超/特高压
、
超/
等。

038 Parameters Design of Controller for DFIG Grid-connected System and Analysis of Oscillation Influencing Factors

Yue Pan[1,2] and Zeyin Zheng[1,2] and Moufa Guo[1,2] and Wei Gao[1,2]

[1] College of Electrical Engineering and Automation, Fuzhou University, Fuzhou 350108, China
[2] Engineering Research Center of Smart Distribution Grid Equipment, Fujian Province University, Fuzhou 350108, China
240127016@fzu.edu.cn

Abstract. With the increasing popularity of renewable energy, doubly-fed induction generator (DFIG) connected to weak power grids are susceptible to grid interaction, leading to broadband oscillations. The stability of wind power grid-connected systems is currently receiving widespread attention, and their impedance characteristics are of great significance for the stability analysis of new power systems. This paper establishes a sequence impedance model for a DFIG grid-connected system and designs the parameters of the grid-connected controller to ensure stable operation when connected to an ideal grid. Furthermore, based on frequency-domain impedance sensitivity, the main parameters influencing the impedance characteristics of the grid-connected system are analyzed, and a parameter optimization method for improving system stability is proposed. Finally, a 1.5 MW DFIG grid-connected simulation model is constructed to verify the correctness of the proposed impedance model and analysis.

Keywords: doubly-fed induction generator (DFIG), controller design, sequence impedance modeling, frequency domain sensitivity

1 Introduction

In recent years, with the increasing integration of renewable energy sources such as wind power into the grid, the weakening of grid characteristics has led to heightened risks of wideband oscillations in power systems [1]. Impedance modeling of grid-connected systems containing wind turbines and deep research the broadband oscillation mechanism caused by grid-connected wind turbines have important engineering significance for improving power systems stability and power supply reliability.

Impedance analysis and state-space analysis are two main methods used to analyze this problem. The state-space modeling method can accurately determine the stability of the system and identify the dominant oscillation factor through participation factors [2]. The modeling method based on the state-space model can comprehensively

consider a variety of key factors affecting system stability [3] and is suitable for modeling and analysis of complex wind farms [4,5]. In addition, this method can deeply reveal the dynamic interaction mechanism between the power grid and wind turbines, providing a theoretical basis for system stability analysis [6]. However, for highly nonlinear, multi-harmonic coupled oscillation systems, the harmonic linearization method is more applicable.

Impedance analysis evaluates system stability through frequency domain modeling [8]. This modular approach simplifies the impedance characterization of each component [9] and is more efficient than the state-space method. It has been widely used in renewable energy grid integration research. The impedance model constructed based on harmonic linearization theory can not only effectively explain the system oscillation mechanism [10], but also accurately reflect the internal dynamic characteristics of power electronic equipment and its control characteristics [11]. However, existing impedance modeling methods require approximation or simplification of the frequency domain matrix [12], which reduces accuracy and introduces stability analysis errors.

In summary, current stability analyses for wind turbine grid integration remain incomplete. A comprehensive approach considering multiple factors is needed to establish accurate models reflecting grid-connected system characteristics, deeply investigate oscillation mechanisms, and achieve holistic stability assessment for wind power integration.

This paper investigates the sequence impedance modeling of a doubly-fed induction generator (DFIG) and the stability of its grid-connected system. First, based on harmonic linearization theory, a complete sequence impedance model of the DFIG grid-connected system is established, taking into account the dynamic characteristics of the current control loop and phase-locked loop (PLL). Second, based on the established impedance model, the Alternating Current (AC) current loop and PLL controller parameters are designed. Impedance frequency-sweep verification is performed to verify the accuracy of the model and the rationality of the parameter design. Based on the above analysis, frequency-domain impedance sensitivity analysis is performed to identify the key parameters affecting the impedance characteristics of the DFIG, and a parameter optimization method was proposed to enhance the stability of the system.Finally, a grid-connected system simulation model was constructed in MATLAB/Simulink to verify the correctness of the analysis presented in this paper.

2 Sequence Impedance Modeling of DFIG Grid-Connected System

2.1 Principle of DFIG Grid-connected System

The structure of the grid-connected system of the DFIG is shown in Fig.1. Due to the large capacitance of the DC bus capacitor, the voltage across it exhibits only minor fluctuations when the DFIG grid-connected system operates stably. Therefore, when

conducting impedance modeling, the interaction between the grid-side converter (GSC)and the rotor-side converter (RSC) can be ignored. In this paper, the GSC and the RSC are modeled independently, and finally they are connected in parallel to obtain the total output impedance of the DFIG.

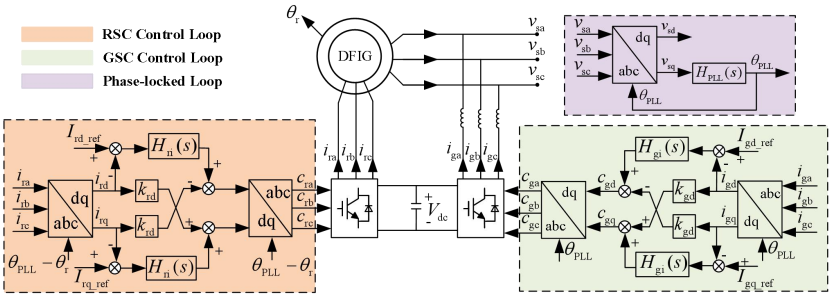


Fig. 1. The grid-connected system structure of DFIG

In Fig.1, i_{ga}、i_{gb}、i_{gc} are the three-phase output currents of the GSC; i_{gd}、i_{gq} represent the d-axis and q-axis components of the GSC three-phase output currents, respectively; I_{gd_ref}、I_{gq_ref} are the reference values for i_{gd}、i_{gq} ; c_{ga}、c_{gb}、c_{gc} are the three-phase modulation signals of the GSC; c_{gd}、c_{gq} are the d-axis and q-axis components of the GSC modulation signals, respectively; $H_{gi}(s)$ is the current PI controller of the GSC; v_{sa}、v_{sb}、v_{sc} are the three-phase stator output voltages; v_{sd}、v_{sq} are the d-axis and q-axis components of the stator three-phase voltages, respectively; i_{ra}、i_{rb}、i_{rc} are the three-phase output currents of the RSC; i_{rd}、i_{rq} are the d-axis and q-axis components of the RSC three-phase output currents, respectively; I_{rd_ref}、I_{rq_ref} are the reference values for i_{rd}、i_{rq} ; c_{ra}、c_{rb}、c_{rc} are the three-phase modulation signals of the RSC; c_{rd}、c_{rq} are the d-axis and q-axis components of the RSC modulation signals, respectively; $H_{ri}(s)$ is the current PI controller of the RSC. Additionally, θ_{PLL} is the grid voltage phase angle; θ_r is the rotor position angle; $H_{PLL}(s)$ is the transfer function of the PLL; V_{dc} is the DC-link voltage of the grid-connected converter.

2.2 Sequential Impedance Modeling of GSC

The GSC adopts a closed-loop control strategy of output current based on the voltage direction. The voltage outer loop control of the GSC is omitted in this paper, and the current control instructions I_{gd_ref} and I_{gq_ref} of the GSC are regarded as fixed parameters. According to the system structure shown in Fig. 1, the positive sequence impedances of the GSC can be expressed as Eq.1.

2.3 Sequential Impedance Modeling of RSC

The RSC adopts a closed-loop control strategy for the rotor current based on stator voltage orientation. In the modeling process of this paper, the role of the power outer

loop is ignored, and the RSC current control instructions $I_{\mathrm{rd_ref}}$ and $I_{\mathrm{rq_ref}}$ are regarded as fixed parameters. Based on Fig. 1, the positive sequence impedance of the RSC can be expressed as Eq.2.

$$Z_{\mathrm{gi_p}}(s)=\frac{sL+\frac{V_{\mathrm{dc}}}{2}\left[H_{\mathrm{gi}}(s-\mathrm{j}2\pi f_1)-\mathrm{j}k_{\mathrm{gd}}\right]}{1-\frac{V_{\mathrm{dc}}}{4}H_{\mathrm{gi}}(s-\mathrm{j}2\pi f_1)T_{\mathrm{PLL}}(s-\mathrm{j}2\pi f_1)(I_{\mathrm{gd_ref}}+\mathrm{j}I_{\mathrm{gq_ref}})} \tag{1}$$

$$Z_{\mathrm{ri_p}}(s)=\frac{sL_{\mathrm{sr}}+R_{\mathrm{s}}+\frac{R_{\mathrm{r}}'}{\rho_{\mathrm{p}}(s)}+\frac{V_{\mathrm{dc}}N_{\mathrm{s}}^2\left[H_{\mathrm{ri}}(s-\mathrm{j}2\pi f_1)-\mathrm{j}k_{\mathrm{rd}}\right]}{2N_{\mathrm{r}}^2\rho_{\mathrm{p}}(s)}}{1+\frac{V_{\mathrm{dc}}N_{\mathrm{s}}H_{\mathrm{ri}}(s-\mathrm{j}2\pi f_1)T_{\mathrm{PLL}}(s-\mathrm{j}2\pi f_1)(-I_{\mathrm{rd_ref}}-\mathrm{j}I_{\mathrm{rq_ref}})}{4N_{\mathrm{r}}\rho_{\mathrm{p}}(s)}} \tag{2}$$

3 Grid-Connected Inverter Controller Design and Simulation Verification

3.1 AC Current Loop

According to the grid-connected system structure of DFIG in Fig.1, the AC current control loop can be derived as $T_{\mathrm{i}}(s)=(H_{\mathrm{i}}(s)/sL)/(1+H_{\mathrm{i}}(s)/sL)$ .To reduce the steady-state error of the system, it is necessary to increase the gain of the system transfer function in the fundamental frequency range. To improve the dynamic response speed, the cutoff frequency of the system transfer function should be increased. However, an excessively high cutoff frequency will weaken the system's attenuation capability for high-frequency harmonics. Therefore, based on a comprehensive consideration of the current loop's rapidity and steady-state performance, this paper sets the parameters of the AC current loop controller as $k_{\mathrm{P_ri}}=0.0008$, $k_{\mathrm{I_ri}}=1.5$, $k_{\mathrm{P_gi}}=0.035$, $k_{\mathrm{I_gi}}=45$.

3.2 Phase-Locked Loop

Since the grid environment is relatively complex, voltage amplitude and frequency fluctuations inevitably exist during actual operation. Therefore, the PLL must be employed to track the grid's real-time dynamic information. The closed-loop transfer function of the PLL can be expressed as $T_{\mathrm{PLL}}(s)=(2\xi\omega_{\mathrm{n}}s+\omega_{\mathrm{n}}^2)/(s^2+2\xi\omega_{\mathrm{n}}s+\omega_{\mathrm{n}}^2)$ .To rapidly track the grid and acquire the fundamental phase information of grid voltage, it is necessary to increase the control bandwidth of the PLL. Meanwhile, to ensure the quality of grid-connected current and achieve high-quality power transmission, the PLL control bandwidth should not be set excessively high. In this paper, the damping ratio (ξ) is set to 0.707, and the PLL bandwidth (BW_{PLL}) is set to 20 Hz. Based on these, the controller parameters are set as $k_{\mathrm{P_PLL}}=0.1469$, $k_{\mathrm{I_PLL}}=6.0767$.

3.3 Simulation Verification

Based on the aforementioned sequencing impedance modeling and controller parameter design, a comprehensive 1.5MW DFIG system simulation model was

constructed in Matlab/Simulink. Simulation scans are performed under both ideal grid conditions and non-ideal operating conditions (voltage sag).The results are shown in Fig. 2. It can be seen that the simulation scanning results are show close agreement with the theoretical curve, which proves the accuracy of the established DFIG sequence impedance model and the rationality of the parameter design.

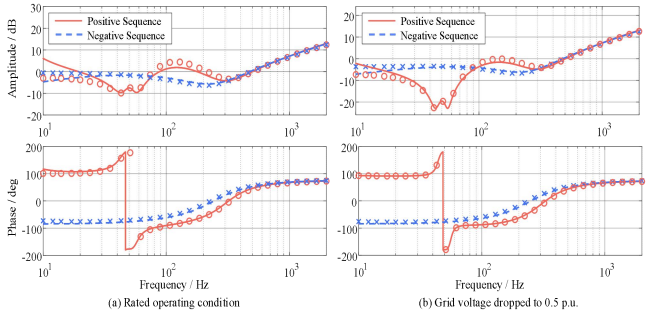


Fig. 2. Simulation verification results

4 Parameter optimization method based on frequency-domain impedance sensitivity

4.1 Frequency-domain impedance sensitivity

The DFIG positive sequence impedance expression is regarded as a transfer function in the complex number domain, and its frequency domain characteristics are represented by the real part sensitivity and the imaginary part sensitivity. The positive or negative of impedance sensitivity reflects the direction in which the system impedance changes with parameters. The absolute value of impedance sensitivity reflects the degree to which parameter changes affect the system impedance. The expression of frequency domain sensitivity is as follows

$$H_i(i,s)=\lim_{\Delta i\to 0}\frac{H(i+\Delta i,s)-H(i,s)}{\Delta i},\ H_{i_\mathrm{Re}}(i,s)=\mathrm{Re}(H_i(i,s)),\ H_{i_\mathrm{Im}}(i,s)=\mathrm{Im}(H_i(i,s)) \tag{3}$$

4.2 Calculation of impedance sensitivity

To analyze the influence of DFIG control parameters on system impedance characteristics, it is necessary to calculate the impedance sensitivity of each parameter and plot the corresponding sensitivity curves. The real and imaginary parts of impedance sensitivity curves for each parameter are shown in Fig. 3. By comparing the sensitivity calculation results, the dominant control parameters affecting the system impedance characteristics can be identified.

As shown in Fig. 3, the PLL proportional coefficient and the RSC current controller parameters exhibit significantly more pronounced impacts on the system impedance characteristics than GSC parameters. Specifically, with increasing

frequency: (1) the impedance real part initially decreases then increases with higher k_{P_PLL} values while the imaginary part shows a convex trajectory; (2) the real part demonstrates concave variation versus k_{P_ri} changes whereas the imaginary part follows convex behavior; (3) both the real and imaginary parts of the impedance first decrease and then increase with the increase of k_{I_ri}. Therefore, when considering suppressing the oscillation of the grid-connected system by adjusting the control parameters, the RSC control parameters and the PLL proportional coefficient should be adjusted first.

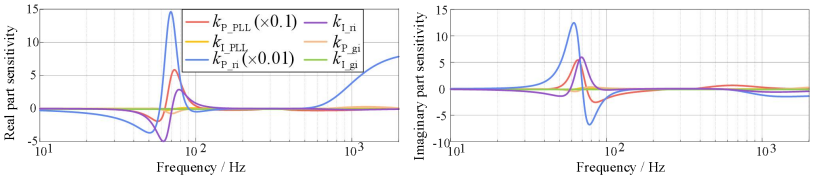


Fig. 3. Frequency-domain impedance sensitivity curve

4.3 Parameter optimization method

Fig. 4 shows the real part-frequency and imaginary part-frequency curves of the system equivalent sequence impedance model, obtained by varying k_{P_PLL} and k_{I_PLL} respectively while keeping other control parameters constant. As shown in the left figure, reducing k_{P_PLL} will increase the real part of the impedance, and at the same time, the virtual part of the impedance in the medium and low frequency bands will show a trend of first increasing and then decreasing, while in the high frequency band, the imaginary part curves under different k_{P_PLL} tend to coincide. By reducing the k_{P_PLL} value, the real part of impedance at the imaginary-part zero-crossing frequency can be maintained above zero, thereby preventing system instability at these frequencies. In contrast, as shown in the right figure, the variation of k_{I_PLL} has a relatively small impact on the real and imaginary parts of the impedance. Therefore, its value should be selected through comprehensive consideration of dynamic performance indices such as phase margin while ensuring system stability.

Fig. 5 shows the real part-frequency and imaginary part-frequency curves of the system equivalent sequence impedance model, obtained by varying k_{P_ri} and k_{I_ri} respectively while keeping other control parameters constant. As shown in the left figure, the influence of k_{P_ri} values on the real part of impedance is mainly reflected in the medium and high frequency bands, while the influence in the low frequency band is relatively small. The real part curves of impedance under different k_{P_ri} conditions tend to be consistent. In contrast, the change in k_{P_ri} has little impact on the imaginary part of impedance. In the medium and high frequency bands, the real part of the impedance is always positive, and as the k_{P_ri} decreases, the amplitude of the impedance drops. Therefore, if the system has insufficient damping or slight

oscillation problems in the medium and high frequency bands, the k_{P_ri} can be appropriately increased to improve the stability of the system. As shown in the right figure, the influence of the change in k_{I_ri} on the real part of the impedance shows a trend of first decreasing and then increasing, and the real part curves of the impedance under different k_{I_ri} in the high-frequency band gradually overlap. In addition, k_{I_ri} has a relatively small influence on the imaginary part of the impedance. It should be noted that increasing k_{I_ri} can ensure the real part of impedance remains positive at the imaginary part zero-crossing frequency, thereby preventing system instability at this specific frequency.

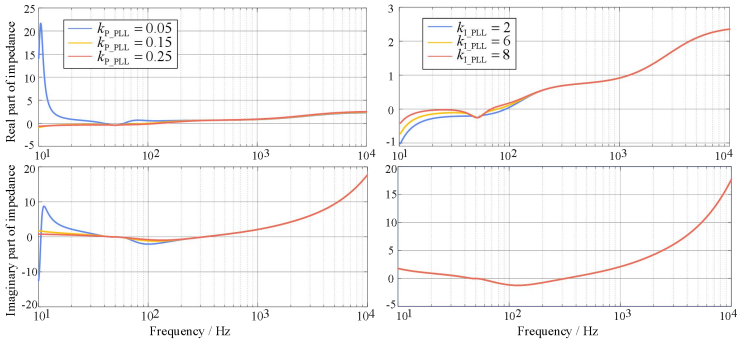


Fig. 4. The influence of the proportion and integration coefficient of PLL

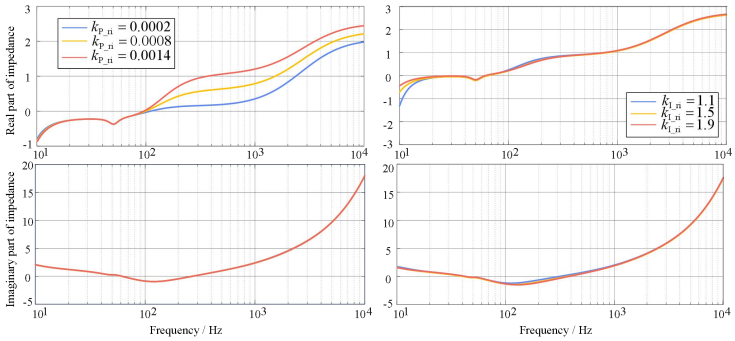


Fig. 5. The influence of the proportion and integration coefficient of RSC

5 Conclusion

This paper establishes a grid-connected system sequence-impedance model that comprehensively considers the influences of current loops and PLL based on the harmonic linearization method. The simulation model was constructed on the MATLAB/Simulink platform to verify the correctness of the constructed model.

Frequency-domain impedance sensitivity analysis was used to identify the main parameters affecting the impedance characteristics of the doubly-fed generator, and their influence on system stability was revealed using impedance characteristic curves. Furthermore, a parameter optimization method was proposed to improve system stability, providing a theoretical basis for stability analysis and parameter design of DFIG grid-connected system.

Acknowledgement: This work is supported in part by the National Natural Science Foundation of China under Award 51677030, in part by the Natural Science Foundation of Fujian Province, China under Award 2023J05106.

References

1. Yuan S, Hao Z, Zhang T, et al. Impedance modeling based method for sub/supsynchronous oscillation analysis of D-PMSG wind farm[J]. Applied Sciences, 2019, 9(14): 2831.
2. Velpula S, Thirumalaivasan R, Janaki M. A review on SubSynchronous Resonance and its mitigation techniques in DFIG based wind farms[J]. International Journal of Renewable Energy Research, 2018, 8(4): 2275-2288.
3. Wang Y, Long C, Xie F, et al. Robustness Enhanced control for Grid-Forming PMSG wind farm[J]. International Journal of Electrical Power & Energy Systems, 2025, 168: 110679.
4. Gao L, Lyu J, Cai X. Analysis of wideband interactions in multiple offshore wind farms interconnected with AC grids[J]. Electric Power Systems Research, 2025, 243: 111489.
5. Li Y, Wen T, Cao Y, et al. Virtual Series Impedance Damping Control for SSR Suppression of MMC-HVDC Interconnected With PMSG-Based Wind Farm[J]. Power Delivery, IEEE Transactions on, 2025, 40(1):532-547.
6. Fang X, Yao J, Liu R, et al. Small-signal stability analysis and current control reference optimization algorithm of DFIG-based WT during asymmetric grid faults[J]. IEEE Transactions on Power Electronics, 2020, 36(7): 7750-7768.
7. Zong H, Zhang C, Lyu J, et al. Generalized MIMO sequence impedance modeling and stability analysis of MMC-HVDC with wind farm considering frequency couplings[J]. IEEE Access, 2020, 8: 55602-55618.
8. Sun J. Impedance-based stability criterion for grid-connected inverters[J]. IEEE transactions on power electronics, 2011, 26(11): 3075-3078.
9. Chen Y, Wu F, Shi L, et al. Analysis and Suppression Strategies of Sub-Synchronous Oscillations in DFIG Wind Farm Integrated with Synchronous Pumped Storage System[J]. Sustainability, 2025, 17(10): 4588.
10. Du W, Ma Z, Wang Y, et al. Harmonic Oscillations in a Grid-Connected PV Generation Farm Caused by an Increased Number of Parallel-Connected PV Generating Units and Damping Controllers[J]. CSEE Journal of Power and Energy Systems, 2020, 10(6): 2350-2359.
11. Ji K, Tang G, Yang J, et al. Harmonic stability analysis of MMC-based DC system using DC impedance model[J]. IEEE Journal of Emerging and Selected Topics in Power Electronics, 2019, 8(2): 1152-1163.
12. Zhang Y, Chen X, Sun J. Sequence impedance modeling and analysis of MMC in single-star configuration[J]. IEEE Transactions on Power Electronics, 2019, 35(1): 334-346.

039 基于 RF 特征优选的 DGA 电力变压器故障诊断

周国华[1]，黄乐鉴[1]，周阅宁[2]，沈宇炫[3]

（1.杭州和达能源有限公司，杭州 310008;
2.杭州职业技术大学，杭州 310008;
3.杭州市临空资产经营管理有限公司，杭州 311200）

Fault diagnosis of DGA power transformers based on RF feature optimization

ZHOU Guohua[1]，HUANG Lejian[1]，ZHOU Yuening[2]，SHEN Yuxuan[3]

（[1] Hangzhou Heda Energy Co., Ltd., Hangzhou 310008 China，
[2] Hangzhou Polytechnic University, Hangzhou 310008 China，
[3] Hangzhou Airport Asset Management Co., Ltd., Hangzhou 311200 China）

ABSTRACT: To improve the accuracy of fault diagnosis for power transformers and detect early faults of transformers in a timely manner, a DGA power transformer fault diagnosis method based on RF feature optimization is proposed. Data equalization processing is carried out using the synthetic minority oversampling technique (SMOTE) algorithm, and the no-code ratio method is employed to expand the fault diagnosis capabilities. Secondly, the importance ranking of the feature vector set is carried out using RF, and the results are then input into the extreme learning machine (ELM), SVM, and LSTM neural networks to obtain the optimal basic model and the combination of the number of features. Then, the relevant hyperparameters in the best basic model are optimized using the HBA optimization algorithm to address the hyperparameter setting problem in the best basic model. Finally, through relevant comparative experiments, the effectiveness of the proposed model in diagnosing faults in DGA power transformers was verified. The results show that the expansion of fault data samples through the SMOTE algorithm and the feature expansion of fault data by the no-code ratio method can effectively address the issues of unbalanced fault data samples and overly scattered DGA data with significant differences in data volume, providing a data basis for subsequent model analysis. Feature optimization and the determination of the best basic prediction model are carried out using RF, which avoids the interference of redundant features on the prediction model and reduces the model's complexity. The best basic prediction model obtained is LSTM. Compared with inputting all the features, it effectively improves the fault diagnosis accuracy of the model.

KEY WORDS: SMOTE algorithm, RF neural network, power transformer, fault diagnosis

摘要：为提高电力变压器的故障诊断准确率，及时发现变压器的早期故障，提出了一种基于 RF 特征优选和的 DGA 电力变压器故障诊断方法，通过合成少数类过采样技术(synthetic minority oversampling technique, SMOTE)算法进行数据均衡处理，采无编码比值法对故障诊断进行扩充；其次，通过 RF 对特征向量集合进行重要度排序，分别输入极限学习机(extreme learning machine, ELM)、SVM 和 LSTM 神经网络，得到最佳基础模型和特征个数组合；然后，通过 HBA 优化算法对最佳基础模型中相关超参数进行寻优，解决最佳基础模型中超参数的设置问题；最后，经过相关对比实验，验证了所提模型在 DGA 电力变压器故障诊断上的有效性。结果表明，通过 SMOTE 算法进行故障数据样本扩充和无编码比值法进行故障数据特征扩充，可有效解决所用故障数据样本不均衡和 DGA 数据过于分散且数据量差异较大的问题，为后续模型分析提供了数据基础；通过 RF 进行特征优选和最佳基础预测模型判断，避免了冗余特征对预测模型的干扰，降低了模型复杂度，得到最佳基础预测模型为 LSTM。相比于输入全部特征，有效提高了模型故障诊断精度。

关键词：SMOTE 算法，RF 神经网络，电力变压器,故障诊断

1 引言

近年来,中国经济持续发展得快速增长，各个领域对电力的需求显著增加了，在输变电系统里,变电站是电力传输的重要环节，电力变压器作为变电站的主要设备,它的运行运行状态直接影响着整体电网的可靠性，及时检测并精确诊断变压器的故障很重要，这能辅助确立适当的维护方案，确保电网安全运行[1-3]，常见的变压器诊断方法包含若干，局部放电检测是一种，绝缘电阻测定也

是一种，还有油中溶解气体分析，缩写叫 DGA[4-6]，DGA 技术操作便捷，获取的数据完整且便于处理，它不受外部电磁干扰，这些优越性让它在电力变压器的状态监控和故障预测工作中广泛应用于。

目前，DGA 电力变压器故障诊断方法主要包括两种，传统比值法[8]简便高效，但在识别某些故障时界限过于绝对，不能完全反映电力变压器故障状态，人工智能法[9]随着技术的发展而发展，文献[10]将粒子群优化算法与支持向量机(support vector machine, SVM)融合，提高了故障诊断精度，文献[11]采用贝叶斯分类器进行故障诊断，保留了贝叶斯网络处理不确定性问题的优点，还提升了收敛速度。文献[12]使用核主成分分析法和随机森林(random forest, RF)进行故障诊断，增强了算法抗干扰能力，提高了诊断正确率，这个方法极为简便也较为便捷操作，不过需要大量数据来优化模型，在应对失衡的数据集时，模型很较易倾向于主类别数据实例，次类别样本通常未受重视，因而电力变压器故障分类就容易产生误差。DGA 电力变压器数据属于代表性的不平衡数据，需用抽样技术来均衡调整，这些模型都没有充分利用长短期记忆神经网络(LSTM)这类深度学习方法来实现故障诊断，人工调整模型参数效率较低，难以确保模型性能，它们还忽视了冗余特征对整个模型的影响。

基于这一问题，研究提出了一种基于 RF 特征优选的 DGA 电力变压器故障诊断方法，第一步，采用 SMOTE 算法处理数据均衡问题，使用无编码比值法扩充故障诊断样本[13]，第二步，利用 RF 对特征向量进行重要性排序，将结果分别输入 ELM、SVM 和 LSTM 神经网络，确定最佳基础模型和特征数量组合，第三步，通过 HBA 优化算法调整最佳基础模型的超参数设置。综上所述，通过对比实验验证了该方法在 DGA 电力变压器故障诊断中的有效性。

2 数据扩充

2.1 SMOTE 样本扩充

SMOTE 算法优化了随机过采样的方式，它不再简单复制粘贴样本，这种方法运用非均衡数据集中的少数类样本，通过线性随机插值生成新样本，这样处理后，原始数据集转为均衡，深度学习分类模型的精度和泛化能力故而得到增强，应用 SMOTE 算法扩展样本的流程如下。

（1）在一个不平衡数据集中，从少数类样本中选择一个样本 x_i，这个样本作为根样本，用于新样本的扩展。

（2）根据公式(1)计算每种少数类故障类型中选为根样本的数据到相应少数类样本集中所有样本的距离 d，得到每个根样本 k 个邻近的同类别样本。

$$d=\sqrt{\sum_{i=1}^{m}\left(x_i-y_i\right)^2} \tag{1}$$

式中：x_i 代表各个少数类样本集中的基准样本，y_i 代表每个少数类样本集中除根样本以外的样本，m 代表少数类样本集中除根样本以外的样本数目。

（3）计算 DGA 电力变压器故障数据集中多数类与少数类间的不平衡程度，根据计算结果，按照公式(2)选取向上采样倍率 n，即从 x_i 的 k 个邻近样本中随机选取 n 个样本作为辅助样本记为 $y_1,y_2,\cdots,y_n$；

$$n=f\left(I_L\right) \tag{2}$$

式中：$f(\bullet)$ 表示四舍五入运算函数；I_L 表示不平衡程度；

（4）在 DGA 变压器少数类故障类型的根样本 x_i 和随机选择的辅助样本 y_i 之间进行随机插值，详细如公式(3)所示，分别合成 n 个对应少数类故障样本 p_i，实现了对故障类型少数类样本的扩充，进行的是多维扩充，对每一少数故障类型的 5 种特征气体数据都进行了扩充，达到了数据平衡的目的。

$$p_i=x_i+r\left(y_i-x_i\right) \tag{3}$$

式中：r 表示 $(0,1)$ 之间的随机数。

SMOTE 算法的采样过程很简明，它在少数类数据样本点和其最邻近样本的连线上进行随机插值，这种直线插值的方式具有明确目标性，它遵循既定的数学规则来构造数据，这样做的好处是避免了随机性，也克服了固有缺陷，最终能够能改善随机过采样带来的过拟合问题。

2.2 特征扩充

工程现场通常会选择 H_2、CO、CO_2、CH_4、C_2H_4、C_2H_6、C_2H_2 这 7 种气体作为 DGA 电力变压器故障诊断的依据，没有经过特征参量选取的 DGA 数据通常比较分散，数据量的差异程度也很大，因此采用无编码比值法来进行特征扩充，扩

充后的特征具体信息均列在表 1 里。

表 1　DGA 特征扩充

编号	特征信息	编号	特征信息
1	H_2	10	C_2H_2/C_2H_4
2	CO	11	C_2H_4/C_2H_6
3	CO_2	12	CH_4/A
4	CH_4	13	C_2H_4/A
5	C_2H_4	14	C_2H_6/A
6	C_2H_6	15	C_2H_2/A
7	C_2H_2	16	B
8	A	17	CO/B
9	CH_4/H_2	18	CO_2/B

表 1 中，A 是 CH_4、C_2H_4、C_2H_6、C_2H_2 这四种气体总和的量，B 是 CO 和 CO_2 两种气体加在一起的量。

3　算法原理

3.1 随机森林算法

RF 是一种分类器，它用多棵决策树来训练样本并集成预测，它采用 Bagging 方法，从原始样本中随机重复抽样，每个重抽样样本会生成一棵决策树，综上所述，这些树组合在一起，通过投票得出预测结果，抽取过程中存在大约 1/3 的样本不会被抽取，这些就是袋外数据(out of bag, OOB)，我们可以用袋外数据来评估每个特征的重要性指标，也就是平均精度下降。这个指标能表明我们特征的重要重要性，用它就能筛选重要的特征。

3.2 蜜獾优化算法

蜜獾优化算法(honey badger algorithm, HBA)是 Fatma A 等人提出的，该算法来源于蜜獾寻找食物的过程，蜜獾具备两种关键活动：挖掘行为和采蜜行为。

3.2.1　种群初始化

在设定的范围内随机初始化蜜獾的数量和位置，如公式(4)所示：

$$x_i = lb_i + r_1 \times \left(ub_i + lb_i\right) \tag{4}$$

式中：r_1 表示（0，1）相互间的随机数，x_i 表示 N 个候选个体的第 i 个个体的位置，lb_i 和 ub_i 分别表示搜索空间的上限及下限。

3.2.2　定义强度

蜜獾的嗅觉敏锐程度取决于两个因素，一是猎物散发的气味有强度，二是猎物离蜜獾距离，当猎物的气味更为强烈时，蜜獾就行动更为迅速，气味减弱，蜜獾的速度就趋于缓慢，这个关系在公式(5)里明确表述。

$$\begin{cases} I_i = r_2 \times \dfrac{s}{4\pi d_i^2} \\ s = \left(x_i - x_{i+1}\right)^2 \\ d_i = x_{prey} - x_i \end{cases} \tag{5}$$

表达式：I_i 表示目标对象的气味强度，r_2 表示 (0,1) 之间的随机数，s 表示源强度或目标对象的集中强度，d_i 表示猎物与当前搜索主体个体相互间的距离。

3.2.3　更新密度因子

密度因子 a 促使蜜獾从勘探转向开采的过程更平稳，它用公式(6)的方法更新，这样能减少蜜獾搜寻资源时随时间变化带来的变数。

$$a = C \times \exp\left(\frac{-t}{t_{\max}}\right) \tag{6}$$

式中：$t_{\max}$ 表示最大迭代次数；$C \geq 1$（一般默认取 2）。

3.2.4　挖掘阶段

探寻阶段的蜂蜜獾，动态如同心形曲线，心形的运动轨迹，采用公式(7)模拟。

$$x_{new} = x_{prey} + F \times b \times I \times x_{prey} + F \times r_3 \times a \times d_i \times \left|\cos\left(2\pi r_4\right) \times \left[1 - \cos\left(2\pi r_5\right)\right]\right| \tag{7}$$

式中 x_{prey} 表示当前状态下蜜獾的全局最优位置，$b \geq 1$ 通常预设取 6 表示蜜獾捕获食物的能力，r_3、r_4、r_5 表示 (0,1) 之间的 3 个随机数值，F 表示调整搜索方向的标志，具体即公式(8)所示。

$$F = \begin{cases} 1, r_6 \leq 0.5 \\ -1, else \end{cases} \tag{8}$$

式中：r_6 表示 (0,1) 之间的随机数。

3.2.5　采蜜阶段

在采蜜阶段，蜜獾跟随导蜜鸟找到蜂巢的行为可通过公式(9)进行模拟：

$$x_{new} = x_{prey} + F \times r_7 \times a \times d_i \tag{9}$$

其中，x_{new} 表示更新后蜜獾的全局最优位置；F、a 和 d_i 分别通过公式(5)、公式(3)和公式(2)计算；r_7 表示 (0,1) 之间的随机数。

4　DGA 电力变压器故障诊断模型

为了提升 DGA 电力变压器故障诊断的准确率，本研究提出一种方法，该方法立足于 RF 特征优选，DGA 电力变压器故障诊断的整体流程在图 1 中予以展示。

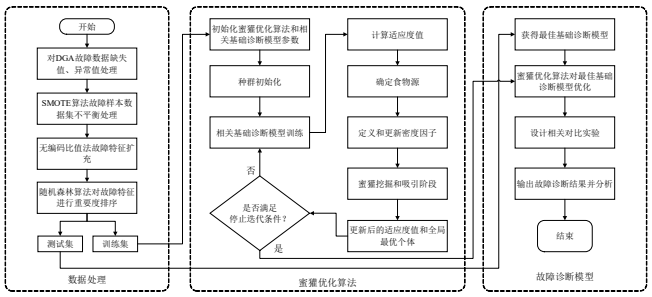


图 1　故障诊断流程图

5　算例分析

5.1 数据来源及预处理

这篇文章使用的数据来自一家公司的电力变压器实测数据，总共有 708 个样本，这些样本涵盖了低温过热（低于 150℃）、电弧放电、电弧放电兼过热、高温过热（高于 700℃）、局部放电和变压器正常老化六种故障类型，DGA 电力变压器样本的具体分布情况可以参考表 2。

表 2　DGA 样本数据分布

编号	运行状态	样本个数
1	低温过热(低于 150℃)	28
2	电弧放电	80
3	电弧放电兼过热	37
4	高温过热(高于 700℃)	52
5	局部放电	379
6	变压器正常老化	132

数据在传输时可能遇到通信故障等情况，需要对数据进行预处理，该处理方式可以避免缺失数据和异常数据影响模型，样本数据之间不存在时间上的逻辑关联，传统的均值填充各类填充方法不适用，书写此文选择直接剔除缺失数据和异常数据。

5.2 评价指标

书写此文采纳普遍的准确率作为评估标准，它能全面评估分类预测模型的性能，详细计算方式见公式(10)。

$$L_{accuracy}=\frac{TP+TN}{TP+FN+FP+TN} \tag{10}$$

式中：$L_{accuracy}$ 表示分类预测模型的准确率；

TP 表示将正样本预测为正样本的个数；TN 表示将正样本预测为负样本的个数；FN 表示将负样本预测为正样本的个数；FP 表示将负样本预测为负样本的个数。

5.3 样本平衡及特征扩充

从表 2 表明，不同故障类别的数据样本数量差别显著，采用人工智能算法分类模型分析这种正负样本不平衡的数据集时，故障诊断结果会偏向多数类，少数类样本的故障诊断准确率就比较低，所以用 SMOTE 算法对故障数据集实施了样本扩充，扩充前后的 DGA 电力变压器故障数据集分布情况在图 2 中呈现，详细的数据大小和占比列出在下表 3。

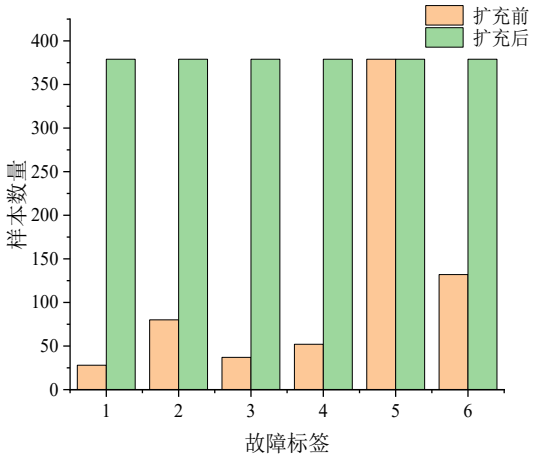


图 2　SMOTE 扩充前后数据对比

表 3　SMOTE 扩充前后数据大小及占比

编号	SMOTE 扩充前		SMOTE 扩充后	
	数量	占比	数量	占比
1	28	3.95%	379	16.67%
2	80	11.30%	379	16.67%
3	37	5.23%	379	16.67%
4	52	7.34%	379	16.67%
5	379	53.53%	379	16.67%
6	132	18.64%	379	16.67%

从图 2 和表 3 可以观察，经过 SMOTE 样本扩充后的数据集中，各类故障样本的数据占比变得相同，这有效解决了故障样本数据不平衡的问题，采用无编码比值法对每个故障样本的特征进行了扩充，具体的特征和编号在表 1 中呈现。

5.4 RF 特征优选及最佳基础模型确定

目标是降低冗余特征对故障诊断模型的影响，我们对 DGA 电力变压器故障样本数据实施了 RF 特征筛选，为了避免偶然性导致的影响，采用了多次运行取平均值的方法来确定最终结果，具体的结果展示在图 4 中。

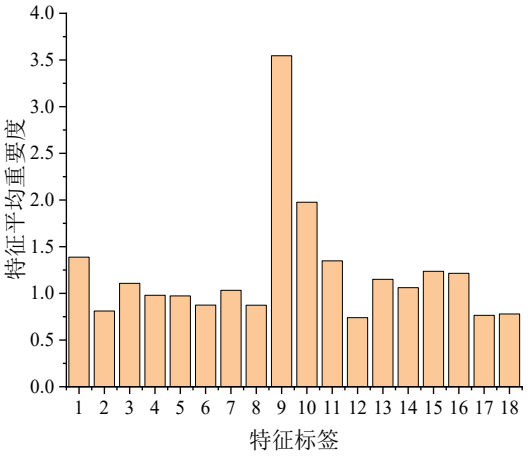
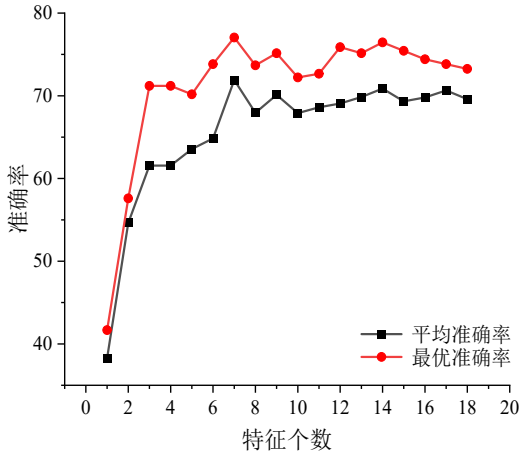
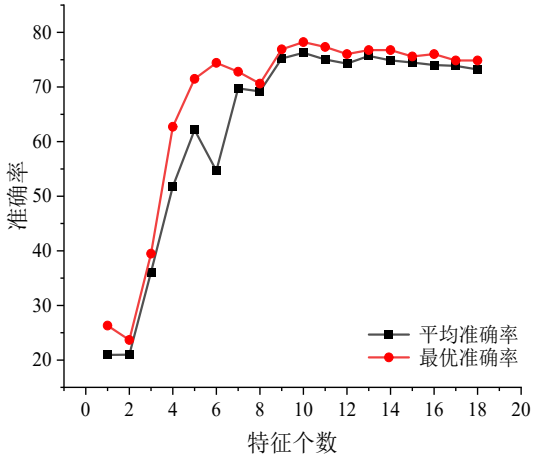


图 4　特征重要性程度

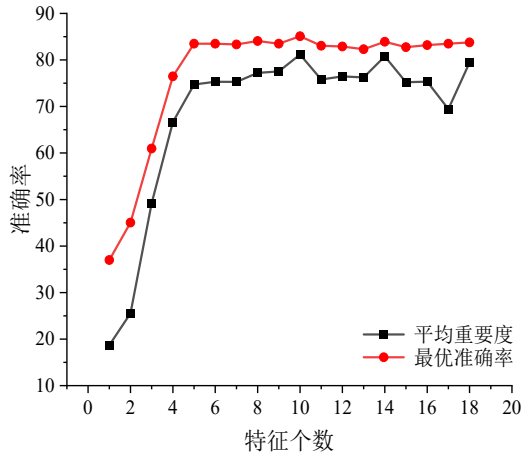
这些故障特征按照特征平均重要度排列后，依次输入到 SVM、ELM 和 LSTM 中，目的是消除基础预测模型的波动，每个特征都运行了 10 次，准确率作为评价指标，要求到了平均准确率和最佳准确率，三个基础模型的准确率结果呈现在图 5 中。



(a) ELM



(b) SVM



(c) LSTM

图 5　基础模型的准确率曲线

从图 5 可以观察，基础预测模型 ELM 的峰值特征个数是 7，SVM 的最佳特征个数是 10，LSTM 的最佳特征个数同样为 10，ELM 的最佳平均准确率实现 71.90%，最优准确率为 77.05%，SVM 的最佳平均准确率为 76.27%，最优准确率为 78.22%，LSTM 的最佳平均准确率为 81.15%，最优准确率为 85.09%。LSTM 是最优的基础预测模型，前十个特征效果最优，特征编号是 9、10、1、11、15、16、13、3、14 以及 7。

5.5 故障诊断结果分析

目标是验证 IHBA 在优化 LSTM 神经网络上的效果，我们将其与 DBO、HBA 和 WOA 进行对比，迭代曲线展示在图 6 中。

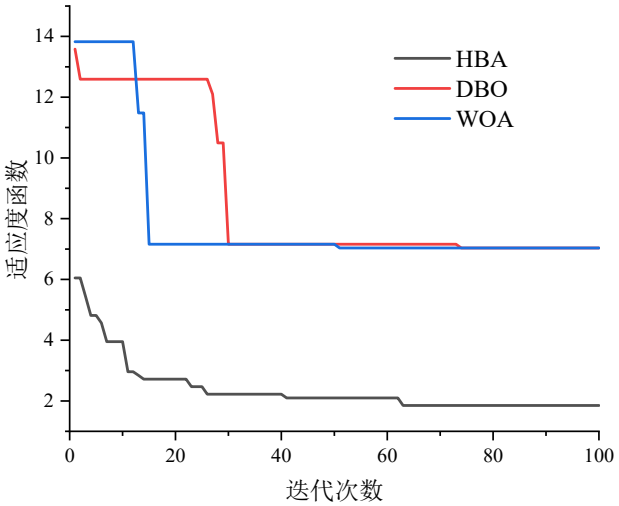
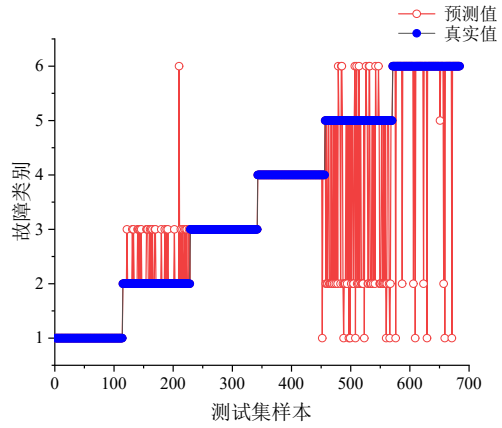


图 6　优化 LSTM 迭代曲线

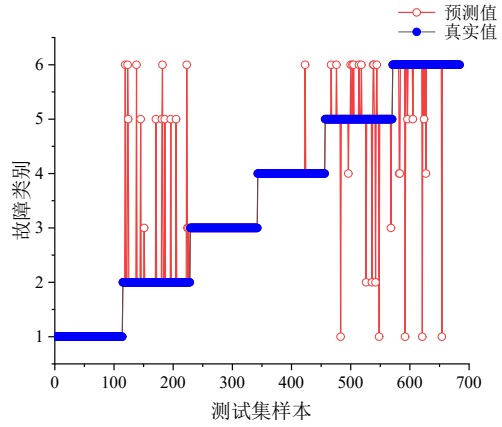
图 6 呈现，在优化 LSTM 神经网络时，HBA 比其他算法更为迅速地更为精确地地确定最小值，它能够摆脱局部最优解，这验证了改进策略的有效性。

为了检验故障诊断模型的有效性，分别将训

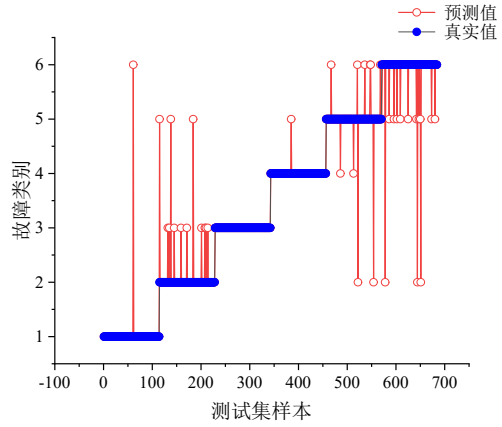
练样本输入 WOA-LSTM、DBO-LSTM 和 HBA-LSTM 进行分析对比，诊断结果如图 7 所示，具体结果如表 4 所示。



(a) WOA-LSTM



(b) DBO-LSTM



(c) HBA-LSTM

图 7　诊断结果

表 4　准确率结果

故障诊断模型	准确率
WOA-LSTM	85.23%
DBO-LSTM	93.86%
HBA-LSTM	94.44%

从图 7 和表 4 数据显示，HBA-LSTM 的准确率比 WOA-LSTM 提高了 0.6%，比 DBO-LSTM 提高了 10.8%，选择合适的模型参数能够优化性能，HBA-LSTM 故障诊断模型可以识别编号为 2、5、6 的故障类别。

6　结论

文章阐述了一种技术，采用 RF 特征优选来进行 DGA 电力变压器故障诊断，它可精确辨识电力变压器的各种故障状态，我们获得了以下结论。

（1）使用 SMOTE 算法扩充故障数据样本，采用无编码比值法扩展故障数据特征，这解决了故障数据样本不均衡的问题，也解决了 DGA 数据十分分散且量差较大的情况，为后续模型分析奠定了数据基础。

（2）采用 RF 方法筛选特征并选定最佳基础预测模型，这样做可以减少冗余特征的影响，降低模型的复杂度，最终确定 LSTM 是最佳基础预测模型，与使用全部特征相比，这种方法明显提高了故障诊断的准确性。

随后的工作将研究实际情境不同故障程度的诊断方法，需要设计更精准的诊断模型，以此能够处理更复杂的故障情况。

参考文献

[1] Bashir T, Wang H, Tahir M, et al. Wind and solar power forecasting based on hybrid CNN-ABiLSTM, CNN-transformer-MLP models[J]. Renewable Energy, 2025, 239122055-122055.

[2] 赵剑，张哲，李召端，等. 三端口 CLLC 固态变压器的设计与优化[J]. 电工技术学报, 2024, 39(23):7542-7553.

[3] Zhang X, Feng Z, Mu W. Reformer: Re-parameterized kernel lightweight transformer for grape disease segmentation[J]. Expert Systems with Applications, 2025, 265125757-125757.

[4] 李清泉，李斯盟，司雯，等. 基于局部放电的电力变压器油纸绝缘状态评估关键问题分析[J]. 高电压技术, 2017, 43(08):2558-2565.

[5] 国家能源局. 电力设备预防性试验规程：DL/T 596—2021[S]. 北京：中国电力出版社, 2021.

[6] 亓秋波，于乃海，齐国栋，等. 二次取气法在油中溶解气体分析中的应用研究[J]. 山东电力技术, 2021, 48(03):42-46.

[7] 侯赛，成润坤，刘达. 基于二次采样和集成学习方法的变压器故障预测[J]. 智慧电力, 2024, 52(07):40-47.

[8] 唐建伟，武建卫，林生红，等. 油中溶解气体分析的变压器故障诊断方法探讨[J]. 无线互联科技, 2022, 19(12):121-124.

[9] Amin Z, Kassymzhomart K, Akhavan S B, et al. Transformer Fault Prognosis Using Deep Recurrent Neural Network Over Vibration Signals[J]. IEEE TRANSACTIONS ON INSTRUMENTATION AND MEASUREMENT, 2021, 70.

[10] 董明, 屈彦明, 周孟戈, 等. 基于组合决策树的油浸式电力变压器故障诊断[J]. 中国电机工程学报, 2005, (16):35-41.

[11] 赵文清. 基于选择性贝叶斯分类器的变压器故障诊断[J]. 电力自动化设备, 2011, 31(02):44-47.

[12] 胡青, 孙才新, 杜林, 等. 核主成分分析与随机森林相结合的变压器故障诊断方法[J]. 高电压技术, 2010, 36(07):1725-1729.

[13] 相晨萌, 闫鹏, 赵海涛, 等. 基于无编码比值法的天然酯绝缘油变压器故障诊断方法研究[J]. 河北电力技术, 2022, 41(02):62-66.

[14] Xie H, Xiao D, Mao Z. Exploration of grade distribution in iron mines based on rough set extreme learning machine and multispectral[J]. Expert Systems with Applications, 2025, 265125938-125938.

[15] Zhao Y, Yang Z, Hou Z, et al. Deep learning based on image analysis for refrigerant charging and leakage detection in building heat pump[J]. Energy & Buildings, 2025, 328115157-115157.

[16] 王妍, 王新发, 王延峰, 等. 基于改进天鹰优化算法优化LSTM的滚动轴承故障诊断方法[J]. 振动与冲击, 2024, 43(23):144-154.

收稿日期：2025-09-24。



作者简介：

周国华(1978 年-)，男，工程师，研究方向为电力系统稳定与控制，E-mail：zhouguohua@hedagroup.com.cn；

039 Fault Diagnosis of DGA Power Transformers Based on RF Feature Optimization

ZHOU Guohua[1], HUANG Lejian[1], ZHOU Yuening[2] and SHEN Yuxuan[3]

[1] Hangzhou Heda Energy Co., Ltd., Hangzhou 310008, China
[2] Hangzhou Polytechnic University, Hangzhou 310008, China
[3] Hangzhou Airport Asset Management Co., Ltd., Hangzhou 311200, China

Abstract: To improve the accuracy of fault diagnosis for power transformers and detect early faults of transformers in a timely manner, a DGA power transformer fault diagnosis method based on RF feature optimization is proposed. Data equalization processing is carried out using the synthetic minority oversampling technique (SMOTE) algorithm, and the no-code ratio method is employed to expand the fault diagnosis capabilities. Secondly, the importance ranking of the feature vector set is carried out using RF, and the results are then input into the extreme learning machine (ELM), SVM, and LSTM neural networks to obtain the optimal basic model and the combination of the number of features. Then, the relevant hyperparameters in the best basic model are optimized using the HBA optimization algorithm to address the hyperparameter setting problem in the best basic model. Finally, through relevant comparative experiments, the effectiveness of the proposed model in diagnosing faults in DGA power transformers was verified. The results show that the expansion of fault data samples through the SMOTE algorithm and the feature expansion of fault data by the no-code ratio method can effectively address the issues of unbalanced fault data samples and overly scattered DGA data with significant differences in data volume, providing a data basis for subsequent model analysis. Feature optimization and the determination of the best basic prediction model are carried out using RF, which avoids the interference of redundant features on the prediction model and reduces the model's complexity. The best basic prediction model obtained is LSTM.

Compared with inputting all the features, it effectively improves the fault diagnosis accuracy of the model.

Keywords: SMOTE Algorithm, RF Neural Network, Power Transformer, Fault Diagnosis.

1 Introduction

In recent years, China's economy has sustained rapid growth, leading to a significant increase in electricity demand across various sectors. In power transmission and transformation systems, substations serve as critical nodes for electricity transmission. Power transformers, being the primary equipment in substations, have operational conditions that directly impact the overall reliability of the power grid. Timely detection and accurate diagnosis of transformer faults are crucial, as they help establish appropriate maintenance plans and ensure the safe operation of the grid[1-3]. Common transformer diagnostic methods include several approaches, one of which is partial discharge detection. Insulation resistance measurement is another method, in addition to dissolved gas analysis (DGA)[4-6]. DGA is easy to operate. It provides complete and easily processed data and is unaffected by external electromagnetic interference. These advantages make it widely applicable in the condition monitoring and fault prediction of power transformers.

Currently, DGA-based power transformer fault diagnosis methods primarily consist of two approaches. The traditional ratio method[8] is simple and efficient but tends to be overly rigid in identifying faults, failing to fully reflect the fault conditions of power transformers. Artificial intelligence methods[9] have evolved with technological advancements. A previous study[10] combines the particle swarm optimization algorithm with support vector machines (SVM) to improve fault diagnosis accuracy. Another study[11] utilizes Bayesian classifiers for fault diagnosis, leveraging the advantages of Bayesian networks in handling uncertainty while also improving convergence speed. A researcher[12] utilizes kernel principal component analysis and random forests (RF) for fault diagnosis, thereby enhancing the algorithm's anti-interference capability and diagnostic accuracy. This method is highly straightforward and convenient to operate. However, it requires large amounts of data to optimize the model. When dealing with imbalanced datasets, the model

tends to favor majority-class data instances, often neglecting minority-class samples, which can lead to errors in power transformer fault classification. DGA power transformer data is a typical example of imbalanced data, requiring sampling techniques for balanced adjustment. These models do not fully leverage deep learning methods like long short-term memory (LSTM) neural networks for fault diagnosis. Manual adjustment of model parameters is inefficient and struggles to ensure model performance. They also overlook the impact of redundant features on the overall model.

To address this issue, this paper proposes an RF feature optimization-based method for DGA power transformer fault diagnosis. First, the SMOTE algorithm is employed to address data imbalance by expanding fault diagnosis samples using the non-coding ratio method[13]. Second, RF is employed to rank the importance of feature vectors, with the results fed into ELM, SVM, and LSTM neural networks to determine the optimal base model and feature quantity combination. Third, the HBA optimization algorithm adjusts the hyperparameters of the optimal base model. In conclusion, comparative experiments have verified the effectiveness of this method in diagnosing DGA power transformer faults.

2 Data Augmentation

2.1 SMOTE Sample Augmentation

The SMOTE algorithm improves upon random oversampling by avoiding simple sample duplication. It utilizes minority class samples from imbalanced datasets to generate new samples via linear random interpolation. This transforms the original dataset into a balanced one, thereby enhancing the accuracy and generalization capability of deep learning classification models. The SMOTE sample expansion process is as follows.

(1) In an imbalanced dataset, select a minority class sample x_i as the root sample for new sample expansion.

(2) Calculate the distance d between each root sample of minority fault types and all other samples in its corresponding minority class set using Formula (1). Identify k neighboring samples of the same class for each root sample.

$$d = \sqrt{\sum_{i=1}^{m} \left(x_i - y_i \right)^2} \tag{1}$$

In the formula, x_i represents the reference sample in each minority class set; y_i denotes samples other than the root sample in each minority class set; m indicates the number of samples in the minority class set excluding the root sample.

(3) Compute the imbalance degree between majority and minority classes in the DGA power transformer fault dataset. Based on the result, select an upsampling ratio using Formula (2). Randomly choose auxiliary samples from neighboring samples, denoted as $y_1, y_2, \cdots, y_n$.

$$n = f\left(I_L \right) \tag{2}$$

Where: $f(\bullet)$ represents the rounding function; I_L denotes the imbalance degree;

(4) Perform random interpolation between the root sample x_i of DGA transformer minority fault types and randomly selected auxiliary samples y_i , as detailed in Formula (3). This synthesizes n minority fault samples p_i , achieving multidimensional expansion. All five characteristic gas data types for each minority fault type are expanded, accomplishing data balance.

$$p_i = x_i + r\left(y_i - x_i \right) \tag{3}$$

Where: r represents a random number between (0, 1).

The sampling process of the SMOTE algorithm is straightforward. It performs random interpolation on the line connecting minority class data sample points and their nearest neighbors. This linear interpolation method has a clear objective, as it follows established mathematical rules to construct data. The advantage of this approach is that it avoids randomness and overcomes inherent defects, ultimately improving the overfitting problem caused by random oversampling.

2.2 Feature Expansion

In engineering practice, seven gases: H_2, CO, CO_2, CH_4, C_2H_4, C_2H_6, and C_2H_2 are selected as the basis for DGA-based power transformer fault diagnosis. DGA data without feature parameter selection are usually scattered, with significant variations in

data volume. Therefore, the non-coding ratio method is used for feature expansion. The specific information of the expanded features is listed in Table 1.

Table 1. DGA Feature Expansion

No.	Feature Information	No.	Feature Information
1	H_2	10	C_2H_2/C_2H_4
2	CO	11	C_2H_4/C_2H_6
3	CO_2	12	CH_4/A
4	CH_4	13	C_2H_4/A
5	C_2H_4	14	C_2H_6/A
6	C_2H_6	15	C_2H_2/A
7	C_2H_2	16	B
8	A	17	CO/B
9	CH_4/H_2	18	CO_2/B

In Table 1, A represents the total quantity of CH_4, C_2H_4, C_2H_6, and C_2H_2, while B represents the total quantity of CO and CO_2.

3 Algorithm Principle

3.1 Random Forest Algorithm

RF is a classifier that uses multiple decision trees to train samples and integrate predictions. It employs the Bagging method by randomly resampling from the original dataset. Each resampled dataset generates a decision tree. These trees are then combined, and the prediction result is determined through voting. Approximately one-third of the samples are not selected during the resampling process, forming the out-of-bag (OOB) data. The OOB data can be used to evaluate the importance of each feature, specifically the mean decrease in accuracy. This metric indicates the importance of our features, allowing us to screen for significant features.

3.2 Honey Badger Algorithm

The Honey Badger Algorithm (HBA) was proposed by Fatma A. et al. This algorithm is inspired by the honey badger's food-searching process, which involves two key activities: digging behavior and honey harvesting behavior.

Population Initialization Randomly initialize the quantity and positions of honey badgers within the defined range, as shown in Equation (4):

$$x_i = lb_i + r_1 \times \left(ub_i + lb_i\right) \tag{4}$$

Where: r_1 represents the random number between (0, 1), x_i denotes the position of the i-th individual among N candidate individuals, lb_i and ub_i represent the upper and lower bounds of the search space, respectively.

Definition Intensity The olfactory acuity of honey badgers depends on two factors: the intensity of the scent emitted by the prey and the distance between the prey and the honey badger. When the prey's scent is stronger, the honey badger moves more swiftly. As the scent weakens, the honey badger's speed slows down. This relationship is explicitly expressed in Equation (5).

$$\begin{cases} I_i = r_2 \times \dfrac{s}{4\pi d_i^2} \\ s = \left(x_i - x_{i+1}\right)^2 \\ d_i = x_{prey} - x_i \end{cases} \tag{5}$$

Expression: I_i represents the scent intensity of the target object, r_2 denotes the random number between (0, 1), s indicates the source intensity or concentration intensity of the target object, and d_i represents the distance between the prey and the current search agent individual.

Renewal Density Factor The density factor a facilitates a smoother transition for honey badgers from exploration to exploitation. It is updated using the method in

Equation (6), which reduces the variability over time during the honey badger's resource search.

$$a = C \times \exp\left(\frac{-t}{t_{\max}}\right) \tag{6}$$

Where: $t_{\max}$ denotes the maximum number of iterations; $C \geq 1$ (generally defaulted to 2).

Digging Phase During the exploration phase, the honey badger exhibits a cardioid curve-like movement, with its heart-shaped trajectory being represented in Equation (7).

$$\begin{aligned} x_{new} &= x_{prey} + F \times b \times I \times x_{prey} + F \times r_3 \times \\ &\quad a \times d_i \times \left|\cos\left(2\pi r_4\right) \times \left[1 - \cos\left(2\pi r_5\right)\right]\right| \end{aligned} \tag{7}$$

Where: x_{prey} represents the global optimal position of the honey badger in the current state, $b \geq 1$ (generally defaulted to 6) denotes the honey badger's ability to capture food. r_3, r_4, and r_5 represent three random numbers between (0, 1), and F denotes the flag for adjusting the search direction, as specifically shown in Equation (8).

$$F = \begin{cases} 1, r_6 \leq 0.5 \\ -1, else \end{cases} \tag{8}$$

Where: r_6 represents a random number between (0, 1).

Honey Harvesting Phase In the honey harvesting phase, the behavior of honey badgers following honeyguide birds to locate beehives can be simulated using Equation (9):

$$x_{new} = x_{prey} + F \times r_7 \times a \times d_i \tag{9}$$

Where: the updated global optimal position of the honey badger is defined as x_{new}. F, a, and d_i are derived from Equation (5), Equation (3), and Equation (2), respectively; r_7 represents a random number between (0, 1).

4 DGA Power Transformer Fault Diagnosis Model

To improve the accuracy of DGA power transformer fault diagnosis, this study proposes a method based on RF feature selection. The overall process of DGA power transformer fault diagnosis is illustrated in Figure 1.

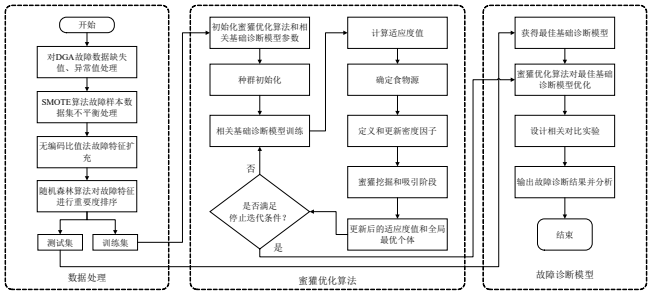


Fig. 1. Fault Diagnosis Flowchart

5 Case Study Analysis

5.1 Data Sources and Preprocessing

The data used in this article comes from actual measurements of power transformers from a certain company, totaling 708 samples. These samples cover six fault types: low-temperature overheating (below 150°C), arc discharge, arc discharge with overheating, high-temperature overheating (above 700°C), partial discharge, and normal aging. The specific distribution of DGA power transformer samples can be referred to in Table 2.

Table 2. Distribution of DGA Sample Data

No.	Operating Status	Number of Samples
1	Low-temperature overheating (below 150°C)	28
2	Arc discharge	80
3	Arc discharge with overheating	37
4	High-temperature	52

	overheating (above 700°C)	
5	Partial discharge	379
6	Normal aging	132

During data transmission, communication failures and other issues may occur, necessitating data preprocessing. This approach avoids the impact of missing or abnormal data on the model. Since there is no temporal logical relationship between sample data, traditional methods like mean filling are not applicable. This paper chooses to directly remove missing and abnormal data.

5.2 Evaluation Metrics

This paper adopts the commonly used accuracy rate as the evaluation criterion, which comprehensively assesses the performance of the classification prediction model. The detailed calculation method is shown in Formula (10).

$$L_{accuracy} = \frac{TP + TN}{TP + FN + FP + TN} \tag{10}$$

Where: $L_{accuracy}$ defines the accuracy rate of the classification prediction model. TP denotes the number of positive samples correctly predicted as positive, FN represents the number of positive samples incorrectly predicted as negative, FP indicates the number of negative samples incorrectly predicted as positive, and TN signifies the number of negative samples correctly predicted as negative.

5.3 Sample Balancing and Feature Expansion

As shown in Table 2, the number of data samples for different fault categories varies significantly. When using AI algorithm classification models to analyze such imbalanced datasets, fault diagnosis results tend to favor the majority class, leading to lower accuracy for minority class samples. Therefore, the SMOTE algorithm was applied to expand the fault dataset. The distribution of the DGA power transformer fault dataset before and after expansion is presented in Figure 2, with detailed data sizes and proportions listed in Table 3 below.

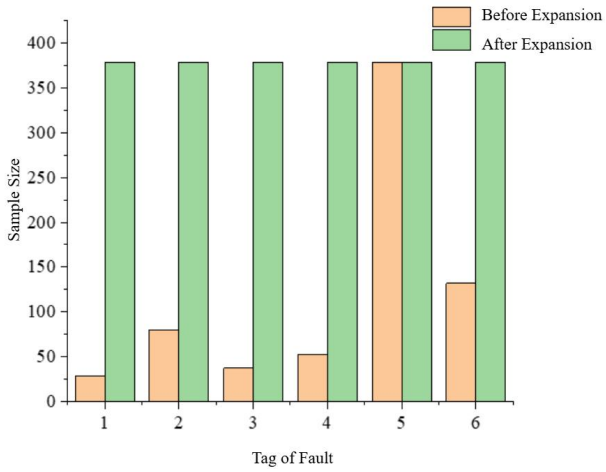


Fig. 2. Comparison of data before and after SMOTE augmentation

Table 3. Data size and proportion before and after SMOTE augmentation

No.	Before SMOTE augmentation		After SMOTE augmentation	
	Quantity	Proportion	Quantity	Proportion
1	28	3.95%	379	16.67%
2	80	11.30%	379	16.67%
3	37	5.23%	379	16.67%
4	52	7.34%	379	16.67%
5	379	53.53%	379	16.67%
6	132	18.64%	379	16.67%

From Figure 2 and Table 3, it can be observed that in the dataset after SMOTE sample augmentation, the data proportions of various fault samples become equal. This effectively addresses the issue of imbalanced fault sample data. The non-coding ratio method is used to expand the features of each fault sample, with specific features and numbers presented in Table 1.

5.4 RF Feature Selection and Determination of the Optimal Base Model

To reduce the impact of redundant features on the fault diagnosis model, RF feature screening was performed on DGA power transformer fault sample data. To avoid

randomness, the average of multiple runs was used to determine the final results, as shown in Figure 4.

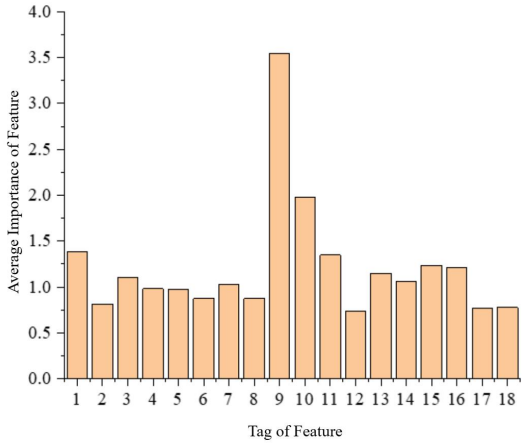
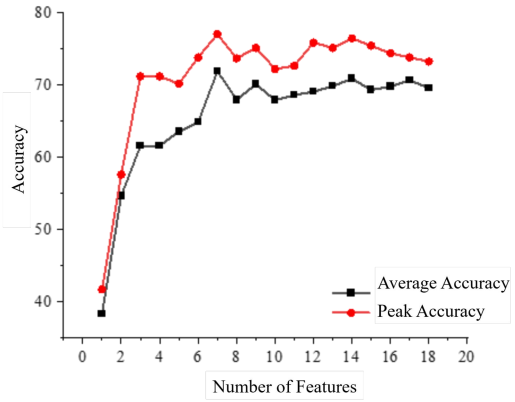
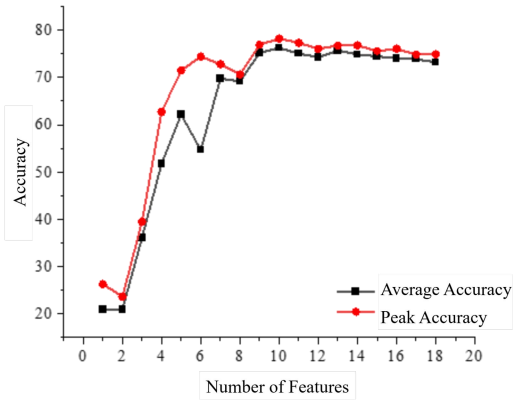


Fig. 4. Feature importance ranking

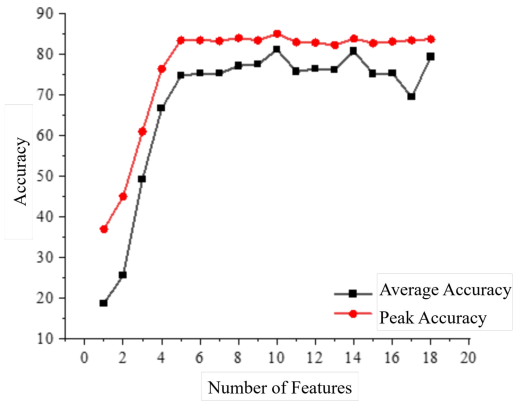
After ranking these fault features by their average importance, they were sequentially input into SVM, ELM, and LSTM to eliminate fluctuations in the base prediction models. Each feature is run 10 times, with accuracy as the evaluation metric. The average accuracy and best accuracy were obtained, and the accuracy results of the three base models are presented in Figure 5.



(a) ELM



(b) SVM



(c) LSTM

Fig. 5. Accuracy curves of the base models

From Figure 5, it can be observed that the peak number of features for the base prediction model ELM is 7, while SVM and LSTM both have an optimal feature count of 10. ELM achieved a best average accuracy of 71.90% and a peak accuracy of 77.05%. SVM's best average accuracy was 76.27%, with a peak accuracy of 78.22%. LSTM achieved a best average accuracy of 81.15% and a peak accuracy of 85.09%. LSTM is the optimal base prediction model, with the top 10 features performing best. The feature numbers are 9, 10, 1, 11, 15, 16, 13, 3, 14, and 7.

5.5 Analysis of Fault Diagnosis Results

To verify the effectiveness of IHBA in optimizing the LSTM neural network, we compared it with DBO, HBA, and WOA. The iteration curves are shown in Figure 6.

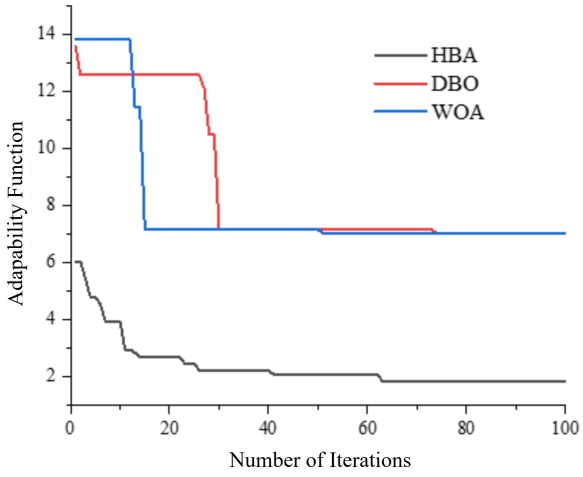
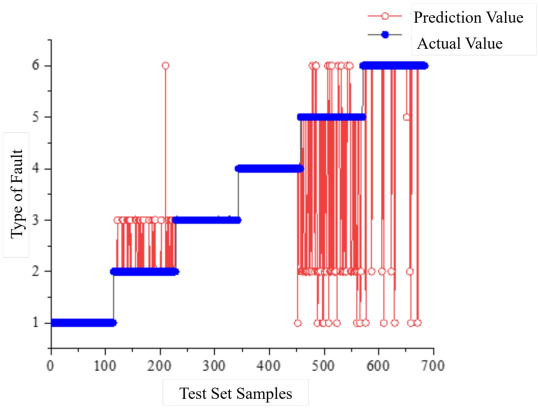


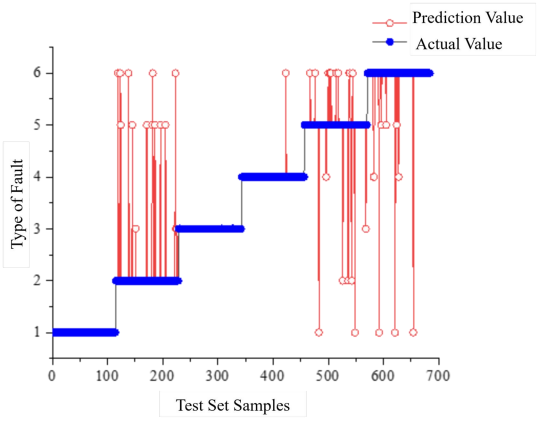
Fig. 6. Iteration curves for optimizing LSTM

Figure 6 shows that when optimizing the LSTM neural network, HBA identifies the minimum value more quickly and accurately than other algorithms. It can escape local optima, demonstrating the effectiveness of the improvement strategy.

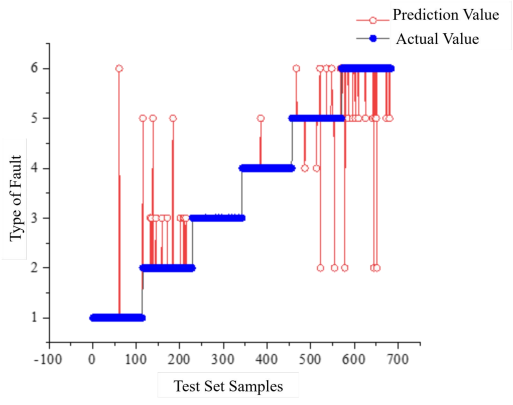
To exam the effectiveness of the fault diagnosis model, training samples were input into WOA-LSTM, DBO-LSTM, and HBA-LSTM for comparison and analysis. Results of the diagnosis are shown in Figure 7. Details can be found in Table 4.



(a) WOA-LSTM



(b) DBO-LSTM



(c) HBA-LSTM

Fig. 7. Diagnostic results

Table 4. Accuracy Results

Fault Diagnosis Model	Accuracy
WOA-LSTM	85.23%
DBO-LSTM	93.86%
HBA-LSTM	94.44%

The data from Figure 7 and Table 4 show that the accuracy of HBA-LSTM is 0.6% higher than WOA-LSTM and 10.8% higher than DBO-LSTM. Selecting appropriate model parameters can optimize performance. The HBA-LSTM fault diagnosis model can identify fault categories numbered 2, 5, and 6.

6 Conclusion

This paper presents a technique that uses RF feature selection for DGA-based power transformer fault diagnosis, which can accurately identify various fault states of power transformers. We have drawn the following conclusions.

(1) The SMOTE algorithm is used to expand fault data samples, and the non-coding ratio method is employed to extend fault data features. This addresses the issue of imbalanced fault data samples and the highly dispersed and large-variation DGA data, laying a data foundation for subsequent model analysis.

(2) The RF method is used to screen features and select the best base prediction model. This reduces the impact of redundant features and lowers model complexity. Ultimately, LSTM is determined to be the best base prediction model. Compared to using all features, this method significantly improves fault diagnosis accuracy.

Future work will focus on diagnosing faults of varying severity in real-world scenarios. More precise diagnostic models need to be designed to handle more complex fault conditions.

References

1. Bashir T, Wang H, Tahir M, et al., Wind and solar power forecasting based on hybrid CNN-ABiLSTM, CNN-transformer-MLP models, Renewable Energy, 239122055-122055 (2025).
2. Zhao J, Zhang Z, Li Z.D., et al., Design and Optimization of a Three-Port CLLC Solid-State Transformer, Transactions of China Electrotechnical Society, 39(23):7542-7553 (2024).
3. Zhang X, Feng Z, Mu W., Reformer: Re-Parameterized Kernel Lightweight Transformer for Grape Disease Segmentation, Expert Systems with Applications, 265125757-125757 (2025).
4. Li Q.Q., Li S.M., Si W, et al., Analysis of Key Issues in Evaluating Oil-Paper Insulation Conditions of Power Transformers Based on Partial Discharge, High Voltage Engineering, 43(08): 2558-2565 (2017).
5. Preventive Test Code for Power Equipment, numbered DL/T 596—2021 issued by the National Energy Administration[S]. Beijing: China Electric Power Press (2021).
6. Qi Q.B., Yu N.H., Qi G.D., et al., Research on the Application of Secondary Gas Extraction Method in Dissolved Gas Analysis in Oil, Shandong Electric Power Technology, 48(03): 42-46 (2021).
7. Hou S, Cheng R.K., Liu D., Transformer Fault Prediction Based on Secondary Sampling and Ensemble Learning Method, Smart Power, 52(07): 40-47 (2024).
8. Tang J.W., Wu J.W., Lin S.H., et al., Discussion on Transformer Fault Diagnosis Method Based on Dissolved Gas Analysis in Oil, Wireless Internet Technology, 19(12): 121-124 (2022).
9. Amin Z, Kassymzhomart K, Akhavan S B, et al., Transformer Fault Prognosis Using Deep Recurrent Neural Network Over Vibration Signals, IEEE Transactions on Instrumentation and Measurement, 70 (2021).
10. Dong M, Qu Y.M., Zhou M.G., et al., Fault Diagnosis of Oil-Immersed Power Transformers Based on Combined Decision Trees, Proceedings of the CSEE, (16): 35-41.
11. Zhao W.Q., 2011, Transformer Fault Diagnosis Based on Selective Bayesian Classifier, Electric Power Automation Equipment, 31(02): 44-47 (2005).
12. Hu Q, Sun C.X., Du L, et al., A Transformer Fault Diagnosis Method Combining Kernel Principal Component Analysis and Random Forest, High Voltage Engineering, 36(07): 1725-1729 (2010).
13. Xiang C.M., Yan P, Zhao H.T., et al., A Study of a Transformer Fault Diagnosis Method Based on the Non-Coding Ratio Method for Natural Ester Insulating Oil, Hebei Electric Power Technology, 41(02): 62-66 (2022).
14. Xie H, Xiao D, Mao Z., Exploration of Grade Distribution in Iron Mines Based on Rough Set Extreme Learning Machine and Multispectral, Expert Systems with Applications,

265125938-125938 (2025).

15. Zhao Y, Yang Z, Hou Z, et al., Deep Learning Based on Image Analysis for Refrigerant Charging and Leakage Detection in Building Heat Pump, Energy & Buildings, 328115157-115157 (2025).
16. Wang Y, Wang X.F., Wang Y.F., et al., Rolling Bearing Fault Diagnosis Method Based on Improved Aquila Optimizer Optimized LSTM, Journal of Vibration and Shock, 43(23): 144-154 (2024).

Paper received on: September 24, 2025



Author's Information:
ZHOU Guohua, male, born in 1978, engineer; Direction of research: stability and control of electric power systems, Email: zhouguohua@hegroup.cn

040 基于深度强化学习的综合能源系统优化运行研究

孙天贺[1]， 莫庆军[1]

（1. 辽宁省电网节能与控制重点实验室，沈阳工程学院，沈阳，110136）

Research on Optimal Operation of Integrated Energy Systems Based on Deep Reinforcement Learning

Tianhe Sun[1], Qingjun Mo[1]

(1.Key Laboratory of Energy Saving and Controlling in Power System of Liaoning Province, Shenyang Institute of Engineering, Shenyang, 110136)

ABSTRACT: Renewable energy sources are difficult to predict and control due to their fluctuating, intermittent and uncertain output. To address this challenge, the Integrated Energy System (IES) has emerged. In this paper, the Proximal Policy Optimization (PPO) algorithm is adopted, with the goal of minimizing the economic operation cost. Through the coupling and coordination of multiple energy sources such as electricity and heat, efficient and low-carbon energy utilization is achieved. As the system scale expands and the number of internal devices increases, the complexity of the system also rises. Against this backdrop, the core objective of the IES's optimal operation is to reduce the operation cost while ensuring the load demand, especially under the condition of meeting the integrated demand response, how to coordinate the output of various devices has become a key research topic.

KEY WORDS: integrated energy system; Proximal Policy Optimization; Minimization of economic operation cost

摘要：可再生能源因其出力的波动性、间歇性和不确定性而难以预测与控制，为应对这一挑战，综合能源系统（IES）应运而生，本文选用近端策略优化（PPO）算法，以经济运行成本最小化为目标，通过电、热、等多能源的耦合与协同，实现高效低碳的能源利用。随着系统规模扩大，内部设备不断增多，系统复杂性日益提升。在此背景下，综合能源系统优化运行是为了保障负荷需求的同时降低运行成本，特别在满足综合需求响应的情况下，如何协调各类设备出力已成为关键研究课题。

关键词：综合能源系统；近端策略优化；经济运行成本最小化

DOI：

基金项目：六号宋体，中英文对照。

Project Supported by National Natural Science Foundation of China(NSFC)(51037003)

0 引言

在综合能源系统优化运行研究中，对于氢能利用单一以及储氢系统建模精度较低问题，文献[1]提出了一种区域 IES 中长期优化方法，通过融入储氢装置的热力学特性与多模式应用场景，提升了系统规划的合理性。文献[2]构建了基于合作博弈理论的优化框架，设计利益分配机制以激励多主体协同调度，在降低供能成本的同时控制碳排放，为跨主体协调提供了新思路。文献[3]则建立了热电联产调度模型，计及电转气变效率特性，以购能成本、运维费用及能量损耗最小化为目标，通过多能流耦合约束下的变量优化，提升了系统能效与经济性。然而，可再生能源出力的波动性与间歇性导致预测精度有限，严重影响系统运行稳定性。为处理此类不确定性问题，现有研究通常借助鲁棒优化、随机规划及区间优化等方法建立适应性分析模型。文献[4]提出一种结合预测概率分布与滚动优化的集成框架，采用鲁棒模型预测控制（RMPC）处理源-荷双侧不确定性。文献[5] 通过引入模糊集描述概率分布的波动，提出了分布鲁棒优化方法；文献[6] 则基于风电出力的不确定性区间构建模型，并利用区间序关系将其转化为确定性优化问题。

本文聚焦于综合能源系统（IES）的经济性优化问题，基于近端策略优化（PPO）算法构建了多能源耦合环境下的经济优化模型。

1 综合能源系统结构

与传统能源系统的运行方式有所不同的是，综合能源系统（IES）通过电力、燃气、热力等多类型能源的有机融合为可再生能源的规模化接入提供关键支撑，实现了能源生产、传输、转换、消费及存储的贯通。并且作为现代能源体系的核心载体，综合能源系统通过强化电-热-气多能流的协同

互动机制，显著提升了可再生能源消纳能力，并促进不同能源形式的优势互补与协调优化，也实现了能量的梯级利用与高效转化。

本文所研究的综合能源系统架构核心组件包括能量转换装置（CHP 机组、电锅炉 EB、燃气锅炉 GB、风电机组 PW）及电/热负荷。该系统支持与上级电网、天然气网络建立能量交互，并且构建起基于多时间尺度优化调度框架的协同控制体系。此外，该系统通过灵活调节各设备出力，可以实现多能流协同优化，所以该架构设计既保留了传统能源转换设备的灵活性，又展现出可再生能源接入与储能系统的协同价值，为后续经济性优化研究奠定物理模型基础。

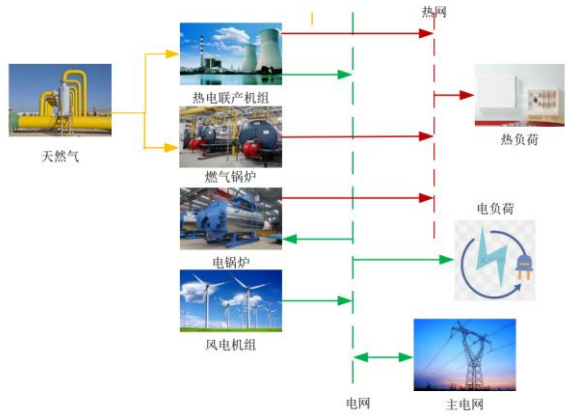


图 1 综合能源系统结构图

Figure 1 Comprehensive Energy System Structure Diagram

（1）热电联产机组模型

热电联产机组（CHP）是综合能源系统的关键设备，通过能源梯级利用机制，将燃料中的化学转化为电能和热能，实现电、热、冷等多种能源的协同供应。在实际运行中，CHP 与电网、热网及储能装置协同工作，可根据负荷需求动态调整电、热输出比例。

CHP 运行中热、电功率间的耦合关系被表征为“电热特性”，其主要运行模式可分为定热电比与变热电比两种。其中，定热电比模式在实际应用中更为常见，其物理意义可表示为：

$$b=\frac{H_{\mathrm{chp}}(t)}{P_{\mathrm{chp}}(t)} \tag{1}$$

式中，$H_{\mathrm{chp}}(t)$ 是 t 时刻热电联产机组输出的热功率，$P_{\mathrm{chp}}(t)$ 为 t 时刻热电联产机组输出的电功率。

在 t 时刻，以天然气为燃料的热电联产机组同步产生电、热能量，其在数学模型中的电功率输出定义如下：

$$P_{\mathrm{chp}}(t)=M_{\mathrm{chp}}(t)H_{\mathrm{ng}}\eta_{\mathrm{chp}} \tag{2}$$

式中，$P_{\mathrm{chp}}(t)$ 和 $M_{\mathrm{chp}}(t)$ 分别表示 t 为时刻热电联产机组输出电功率和天然气消耗量，H_{ng} 和 η_{chp} 分别表示为天然气热值和热电联产机组能源转换效率。

（2）电锅炉模型

电锅炉作为通过电能直接转化为热能的设备，本文选用电阻式电锅炉进行削峰填谷与多能协同，该设备在 t 时刻电锅炉输出的热功率为：

$$H_{\mathrm{eb}}(t)=P_{\mathrm{eg}}(t)\eta_{\mathrm{eb}} \tag{3}$$

式中，$H_{\mathrm{eb}}(t)$ 和 $P_{\mathrm{eg}}(t)$ 分别为 t 时刻电锅炉输出的热功率以及电锅炉消耗的电功率，η_{eb} 为电锅炉能量转化效率。

（3）燃气锅炉模型

燃气锅炉在 t 时刻输出的热功率为：

$$H_{\mathrm{gb}}(t)=M_{\mathrm{gb}}(t)H_{\mathrm{ng}}\eta_{\mathrm{gb}} \tag{4}$$

式中，$H_{\mathrm{gb}}(t)$ 和 $M_{\mathrm{gb}}(t)$ 分别表示为 t 时刻燃气锅炉输出热功率和天然气消耗量，H_{ng} 和 η_{gb} 分别表示为天然气热值和燃气锅炉转化效率。

1.1 经济目标函数

系统运行总成本 F 为：

$$F=\min\left(C_{\mathrm{e}}+C_{\mathrm{r}}\right) \tag{5}$$

式中，F 为系统运行总成本，C_{e} 为系统运行常规运行成本，C_{r} 为系统弃风惩罚成本。

IES 运行成本为：

$$\begin{aligned}C_{\mathrm{e}}=&\sum_{t=1}^{T}\varepsilon_{\mathrm{e}}(t)P_{\mathrm{grid}}(t)\Delta t\\&+\sum_{t=1}^{T}\varepsilon_{\mathrm{ng}}(t)M_{\mathrm{ng}}(t)\Delta t\\&+\sum_{t=1}^{T}\rho_{\mathrm{chp}}(t)P_{\mathrm{chp}}(t)\Delta t\end{aligned} \tag{6}$$

$$M_{\mathrm{ng}}(t)=M_{\mathrm{chp}}(t)+M_{\mathrm{gb}}(t) \tag{7}$$

式中，C_{e} 为系统运行常规运行成本，$P_{\mathrm{grid}}(t)$ 为 t 时刻系统与主电网交互的电功率，$P_{\mathrm{grid}}(t)$ 为正时表示从主电网购电，负时则表示从主电网售电，$\varepsilon_{\mathrm{e}}(t)$ 为 t 时刻电价，$P_{\mathrm{grid}}(t)$ 为正时电价取购电电价，负时为取售电电价，$M_{\mathrm{ng}}(t)$ 为 t 时刻系统购买天然气总量，$\rho_{\mathrm{chp}}(t)$ 为热电运行成本系数。

风电机组弃风惩罚成本为：

$$C_{\mathrm{r}}=\lambda P_{\mathrm{i.}}(t) \tag{8}$$

式中，C_{r} 为系统弃风惩罚成本，λ 为弃风成本系数，$P_{\mathrm{i.}}(t)$ 为 t 时刻系统弃风功率。

1.2 约束条件

（1）功率约束条件：

电功率平衡约束：

$$\begin{aligned}P_{\mathrm{load}}(t)=&P_{\mathrm{chp}}(t)+P_{\mathrm{grid}}(t)\\&+P_{\mathrm{pw}}(t)-P_{\mathrm{eb}}(t)\end{aligned} \tag{9}$$

式中，$P_{\text{chp}}(t)$为t时刻热电联产机组输出电功率，$P_{\text{grid}}(t)$为t时刻系统与主电网交互的电功率，$P_{\text{pw}}(t)$为t时刻风电机组输出电功率，$P_{\text{eb}}(t)$为电锅炉消耗的电功率，$P_{\text{load}}(t)$为t时刻的电负荷。

能源交互约束：

考虑到电网侧和系统稳定性，IES 与电交互功率以及系统天然购买总量须满足在一定范围内。

$$P_{\text{grid}}^{\min} \le P_{\text{grid}}(t) \le P_{\text{grid}}^{\max} \tag{10}$$

$$M_{\text{ng}}^{\min} \le M_{\text{ng}}(t) \le M_{\text{ng}}^{\max} \tag{11}$$

式中，$P_{\text{grid}}^{\min}$和$P_{\text{grid}}^{\max}$分别表示为系统以及主电网交互电功率的最小值和最大值，$M_{\text{ng}}^{\min}$和$M_{\text{ng}}^{\max}$分别表示为系统天然气购买总量的最小值和最大值。

热功率平衡约束：

$$H_{\text{chp}}(t)+H_{\text{gb}}(t)+H_{\text{eb}}(t)=H_{\text{load}}(t) \tag{12}$$

式中，$H_{\text{chp}}(t)$表示为t时刻热电联产机组输出热功率，$H_{\text{gb}}(t)$表示为t时刻燃气锅炉输出热功率，$H_{\text{eb}}(t)$表示为t时刻电锅炉输出热功率，$H_{\text{load}}(t)$表示为t时刻热负荷。

（2）设备运行约束条件：

热电联产机组运行约束：

$$P_{\text{chp}}^{\min} \le P_{\text{chp}}(t) \le P_{\text{chp}}^{\max} \tag{13}$$

式中，$P_{\text{chp}}^{\min}$和$P_{\text{chp}}^{\max}$分别为热电联产机组输出功率最小值和最大值。

电锅炉运行约束：

$$H_{\text{eb}}^{\min} \le H_{\text{eb}}(t) \le H_{\text{eb}}^{\max} \tag{14}$$

式中，$H_{\text{eb}}^{\min}$和$H_{\text{eb}}^{\max}$分别表示为电锅炉输出热功率下限和上限。

燃气锅炉约束条件：

$$H_{\text{gb}}^{\min} \le H_{\text{gb}}(t) \le H_{\text{gb}}^{\max} \tag{15}$$

式中，$H_{\text{gb}}^{\min}$和$H_{\text{gb}}^{\max}$分别表示为燃气锅炉输出热功率下限和上限。

2 基于策略的深度强化学习下各算法对比

同深度确定性策略梯度（Deep Deterministic Policy Gradient，DDPG）算法比较，PPO 有效避免了因确定性策略和 Q 值估计偏差带来的训练不稳定问题。DDPG 虽借助经验回放和双网络结构提升了一定性能，但实现较为复杂；PPO 则无需目标网络，支持单批样本多次更新，在保证样本效率的同时显著降低了实现难度。

对比于异步优势 Actor-Critic（Asynchronous Advantage Actor-Critic，A3C）算法，PPO 也具备明显优势。A3C 采用并行探索，训练速度快但对策略更新步长敏感，易出现策略崩溃或收敛缓慢；PPO 通过裁剪新旧策略差异，增强了对超参数的鲁棒性，更适用于高维复杂环境下的稳定训练。

在综合能源系统调度中，信任域策略优化（TRPO）通过 KL 散度约束确保训练稳定，但依赖复杂的高维二阶优化；PPO 则以策略裁剪机制柔性限制策略更新幅度，在保持稳定性的同时避免了高阶运算。

综上所述，PPO 在训练效率、稳定性和实现复杂度之间取得了良好平衡，已成为强化学习中广泛应用的基准算法之一。

2.1 PPO 算法原理

近端策略优化（PPO）算法采用 Actor-Critic 双网络架构，两网络分别具有独立的损失函数与更新机制。其训练过程主要包括三个阶段：首先，Actor 网络与环境交互采集数据并存入经验回放缓冲区；随后，Critic 网络估计状态价值，计算累积奖励与优势函数，并通过梯度下降提升估值准确性；最后，使用一个结构相同但参数延迟的采样网络计算重要性权重，以更新 Actor 策略梯度，在保证稳定性的同时提高数据利用效率。该架构将策略评估与策略生成分离，Actor 负责探索，Critic 专注价值估计，而滞后更新机制有效平衡了探索与稳定性，避免训练震荡，为连续动作控制提供了高效稳健的解决方案。这一框架适用于综合能源系统等复杂决策环境，能够通过端到端策略学习实现设备参数的动态优化。

（1）Critic 网络训练

对于 Critic 网络，利用优化损失函数$L(\omega)$来更新网络权重。

$$L(\omega)=E\left[y_t-V(s_t;\omega)\right]^2 \tag{16}$$

$$y_t=R_t+\gamma V(s_{t+1};\omega) \tag{17}$$

式中，$L(\omega)$为 Critic 网络的损失函数，y_t为$t+1$时刻对$V(s_t;\omega)$做出的估计值，$V(s_t;\omega)$为t时刻 Critic 网络输出值，R_t为t时刻即时奖励，ω为 Critic 网络权重。

以梯度下降算法更新 Critic 网络权重：

$$\omega \leftarrow \omega-\alpha\nabla_{\omega}L(\omega) \tag{18}$$

式中，∇是梯度计算函数，α是 Critic 网络学习率。

（2）Actor 网络训练

在 Actor 网络中，利用优化损失函数$J(\theta)$来更新网络权重。

$$J(\theta)=E_{(s_t,a_t)\sim\pi(\cdot;\theta')}\Big[\min\big(r_t(\theta)A(s_t,at),\ \text{clip}\big(r_t(\theta),1-\varepsilon,1+\varepsilon\big)A(s_t,a_t)\big)\Big] \tag{19}$$

$$r_t(\theta)=\frac{\pi\left(a_t|s_t;\theta\right)}{\pi\left(a_t|s_t;\theta'\right)} \tag{20}$$

$$\mathrm{clip}\left(x,x^{\min},x^{\max}\right)=\begin{cases}x,x\min\le x\le\max\\x^{\min},x<x^{\min}\\x^{\max},x>x^{\max}\end{cases} \tag{21}$$

式中，$J(\theta)$为 Actor 网络损失函数，$\pi\left(a_t|s_t;\theta\right)$为$t$时刻 Actor 网络输出值，$A(s_t,a_t)$为优势函数，$r_t(\theta)$为$t$时刻重要性采样比，$\theta$为 Actor 网络权重，$\varepsilon$为一个超参数用来限制$r_t(\theta)$的变化范围。

以梯度上升算法更新 Actor 网络权重方法如下：

$$\theta\leftarrow\theta+\beta\nabla_\theta J(\theta) \tag{22}$$

式中，β为 Actor 网络学习率。

3 算例分析

3.1 数据输入

以国内某重点园区为例，将系统运行成本最小化作为目标函数，调度周期设为 24 小时，系统内各设备运行参数如表 1 所示。电、热负荷需求曲线，风电预测实际出力和弃风情况分别示于图 2 与图 3 中。

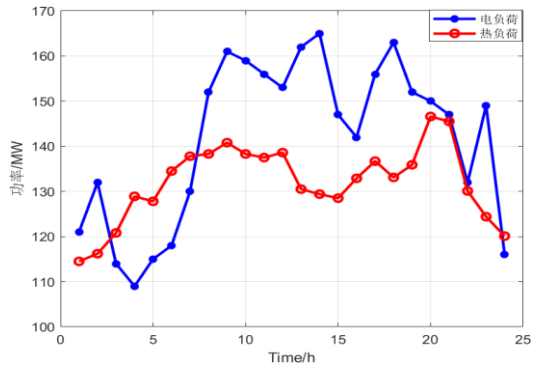


图 2 电负荷、热负荷需求曲线图

Figure 2 Curve of electrical and thermal load demand

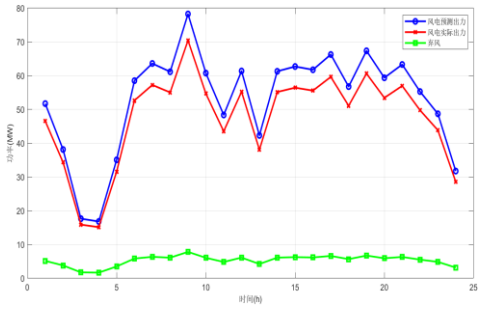


图 3 风电预测、实际出力及弃风曲线图

Figure 3 Wind power forecast, actual output and curtailment curve

表 1 机组设备容量

Table 1 Unit Equipment Capacity

设备	参数	数值	设备	参数	数值
热电机组	P^{min}_{chp}/MW	50	风电机组	P^{min}_{pw}/MW	0
	P^{max}_{chp}/MW	150		P^{max}_{pw}/MW	200
	Q^{min}_{chp}/MW	50	燃气锅炉	P^{min}_{gb}/MW	0
	Q^{max}_{chp}/MW	100		P^{max}_{gb}/MW	60
电锅炉	P^{min}_{eb}/MW	0			
	P^{max}_{eb}/MW	40			

3.2 场景设置对比分析

本研究设置两个对比场景：场景一仅考虑基本能量供需平衡，不含灵活性调节机制；场景二在能量平衡基础上引入需求响应等灵活性调节机制以提升系统灵活性。

在场景一中，系统运行以基础能量平衡为核心。如图 4 与 5 所示，电力供应主要由热电联产（CHP）与风电机组（PW）协同提供，以满足电负荷需求。热力供应则依靠 CHP 和燃气锅炉，两者共同承担基本供热任务；当热负荷需求超出其额定供热能力时，电锅炉将投入运行，将电能转换为热能进行补足，保障热负荷需求。

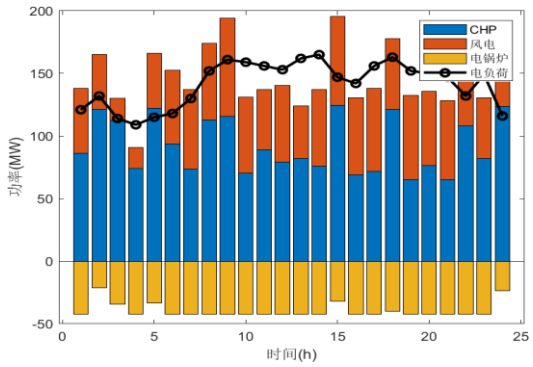


图 4 电功率平衡

Figure 4 Power Balance

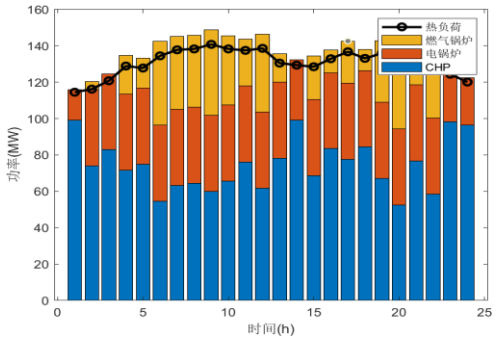


图 5 热功率平衡

Figure 5 Thermal Power Balance

场景二引入了完善的灵活性调节机制。由图 6 与 7 可见，热电联产机组（CHP）在电、热供应中适应性更强，能够根据负荷变化灵活调整电出力与热出力。

在电力系统中，为应对风电出力的波动，电锅炉和储能设备起到关键调节作用，通过灵活调节出力以满足电负荷实时变化。在热力供应中，各设备

协同配合，及时响应负荷需求，保障供热稳定，体现出灵活性机制对提升系统运行稳定性和可靠性的重要作用。

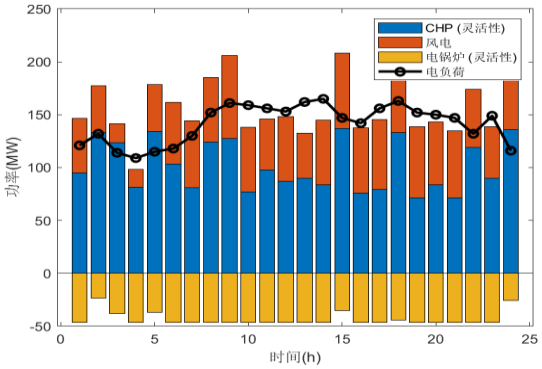


图 6 电功率平衡

Figure 6 Power Balance

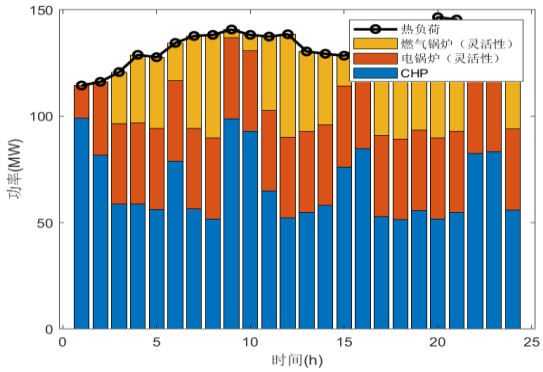


图 7 热功率平衡

Figure 7 Thermal Power Balance

通过对比两个场景下的设备出力调度可知，在保证能量供需平衡的基础上，引入灵活性调节机制的场景二优势明显。该模式下，系统通过对热电、燃气锅炉、储能及电锅炉等关键设备进行动态、精细化的出力调节，实现了多设备协同优化运行。

这一灵活调控策略显著提高了风电消纳能力，有效缓解了弃风问题。结果表明，引入灵活性调节机制显著改善了综合能源系统的运行经济性，也为实现系统经济高效运行提供了可靠的技术路径与方法支持。

4 结论

本文研究进一步构建了基于近端策略优化（PPO）算法的经济优化模型，依托典型 IES 结构，建立多时间尺度调度框架，实现与上级电网和气网的灵活交互。该系统通过协调设备出力、整合可再生能源与储能，在保持传统设备运行灵活性的同时，为后续经济性优化奠定了模型基础。IES 通过多能协同与优化调度在提升能源利用效率和促进低碳运行方面展现出显著潜力，具有重要的理论意义和工程应用价值。

参考文献

[1] 任洲洋，罗潇，覃惠玲，等．考虑储氢物理特性的含氢区域综合能源系统中长期优化运行[J]．电网技术，2022，46(09)：3324-3333.

[2] Yongli W, Zhen L, Chengcong C, et al. Research on the optimization method of integrated energy system operation with multi-subject game[J]. Energy, 2022, 245.

[3] 崔杨，闫石，仲悟之，等．含电转气的区域综合能源系统热电优化调度[J]．电网技术，2020，44(11)：4254-4264.

[4] Xing D, Chenghui Z, Bo S. Optimization strategy based on robust model predictive control for RES-CCHP system under multiple uncertainties[J]. Applied Energy, 2022, 325.

[5] Qiu H, You F. Decentralized-distributed robust electric power scheduling for multi-microgrid systems[J]. Applied Energy, 2020, 269.

[6] 苏永新，聂伟棋，谭貌．考虑风电接入和气电转换的综合能源系统日前区间优化[J]．电力系统自动化，2019，43(17)：63-71.



收稿日期：2025-09-27

作者简介：

莫庆军(2002)，男，硕士研究生，研究方向为电力系统运行，E-mail：MoqingJ@163.com；

孙天贺(1991)，男，副教授，研究方向为电力系统分析与控制，E-mail：sunth@sie.edu.cn。

莫庆军

041 Reliability Planning of High-penetration Renewable Power Systems Considering Extreme Stagnant Meteorological Scenarios

Shiyu Long[1], Xiaojun Wang[1], Fangyuan Si[1,*], Jinming Hou[2], Xunyan Lv[2], Haiyang Jiang[3]

[1] School of Electrical Engineering, Beijing Jiaotong University, Beijing 100044, China
[2] Global Energy Interconnection Group Co., Ltd Economic & Technology Research Institute, Beijing 100031, China
[3] State Key Laboratory of Power System Operation and Control, Department of Electrical Engineering, Tsinghua University, Beijing 100084, China
fysi@bjtu.edu.cn, 241213@bjtu.edu.cn

Abstract. In the context of climate change and high penetration of renewable energy integration, the reliability of power systems is significantly affected by multi-timescale meteorological fluctuations. Particularly, prolonged "low-wind and low-insolation" stagnant weather weakens wind and solar output, exacerbating supply-demand imbalances. To address the issues of scarce samples of extreme stagnant events, empirical criteria, and distorted scenario weights in existing studies, this paper proposes a reliability planning method for high-renewable power systems based on meteorological data reconstruction. First, using 20 years of wind speed and insolation data from a province, multi-scale decomposition is performed to extract climatic, seasonal, and diurnal components. Random disturbances are introduced via the Itô process to reconstruct numerous wind and solar time series that meet statistical characteristics and cover tail risk. Second, a joint criterion for quantile thresholds and duration of "low-wind and low-insolation" events is calibrated, with event frequency mapped to load-shedding cost weights, forming a risk-sensitive scenario weighting system for planning optimization. This enhances system adaptability and robustness under extreme stagnant weather. Case studies show that the proposed method preserves temporal correlations of extreme scenarios, reduces load shedding during prolonged stagnant conditions compared to traditional methods, and avoids redundant investment.

Keywords: Itô process, extreme scenario generation, wind–solar output decomposition, power system planning, low-wind–low-solar.

1 Introduction

In the context of global climate change and the deep coupling with new power systems, the correlation between power system reliability and meteorological conditions exhibits multidimensional spatiotemporal heterogeneity. Although extreme stagnant

weather does not directly damage power equipment or significantly affect load demand, it severely weakens the sustained and stable output of renewable energy generation, directly threatening the supply-demand balance of power systems [1]. For instance, during the winter of 2020, in the Northwest Grid of the State Grid Corporation of China, low wind power output (less than 10% of installed capacity) was evident during periods of cold air intermittency, with the longest duration reaching nearly 120 hours. Similarly, in Hunan and Jiangxi regions, sustained widespread overcast and rainy weather led to low photovoltaic output, with the longest duration exceeding 10 days [2,3]. Unlike the impacts of specific meteorological disasters on power systems, the occurrence of prolonged stagnant weather in power systems typically does not result in equipment damage or destruction. However, prolonged mismatches between generation and load can jeopardize the secure supply of electricity.

Currently, relevant studies have conducted in-depth analyses of multi-day consecutive "low-wind and low-insolation" stagnant weather events [1,4–9]. However, the selection and calibration of joint criteria for extreme stagnant events often rely on empirical assumptions, lacking a specific selection process. Meanwhile, existing research predominantly focuses on adequacy assessment [10–14], with little consideration of the multi-timescale fluctuation characteristics of meteorological factors. Additionally, the limited samples of extreme scenarios may lead to an underestimation of their impact on power systems.

To address the issues of underestimation of the frequency of compound "low-wind and low-insolation" events due to small sample sizes, distortion of scenario weights, and deficiencies in calibration methods for extreme stagnant event criteria, this paper proposes a reliability planning method for high-penetration renewable energy power systems based on meteorological data reconstruction. The core concept is as follows: perform multi-scale decomposition and reconstruction of long-term wind speed and irradiance sequences, identify compound low-wind and low-insolation events using joint criteria of quantile thresholds and duration, and statistically analyze their frequency. This frequency is then coupled with the corresponding marginal cost of load shedding to form a risk-sensitive scenario weighting system. This system drives the coordinated configuration of wind power, photovoltaic systems, energy storage, and adjustable loads, thereby enhancing adaptability and reliability in response to extreme stagnant weather events.

2 Extreme Scenario Sample Generation Method

2.1 Time Series Decomposition Method

MSTL (Multiple Seasonal-Trend decomposition using Loess) is an extension of the classical STL (Seasonal-Trend decomposition using Loess) method. It is designed to simultaneously extract multiple seasonal components from a single time series, making it particularly suitable for decomposing renewable energy data (such as wind and solar power) with composite rhythms like "annual cycle + diurnal cycle" (and even "weekly cycle"). While retaining the robustness, interpretability, and non-parametric smoothing advantages of STL, MSTL achieves the separation of components at dif-

ferent scales through iterative or sequential Loess smoothing of multiple seasonal cycles and cyclic updates of residuals [15].
In this paper, the MSTL decomposition algorithm is employed to decompose the historical wind and solar sequence data of a certain province in China over the past 20 years into climatic, seasonal, and diurnal components.

2.2 Massive Scenario Generation Method

The Itô process is a continuous-time stochastic process driven by standard Brownian motion. It characterizes the random evolution of a state over time using a stochastic differential equation, capable of expressing the state's mean trend and volatility intensity, both of which may depend on the state itself. Its fundamental integral form is given by:

$$\xi_t = \xi_0 + \int_0^t \mu(t,\xi_t)dt + \int_0^t \sigma(t,\xi_t)dW_t \tag{1}$$

Where ξ_t is the original input time series vector. $\mu(t,x)$ is the drift function, which characterizes the average change in the variable's value, and $\sigma(t,x)$ is the diffusion function, which controls the magnitude of local uncertainty. W_t is the standard Brownian motion, possessing independent, stationary normal increments and almost everywhere non-differentiable paths. The corresponding fundamental differential equation is expressed as:

$$d\xi_t = \mu(t,\xi_t)dt + \sigma(t,\xi_t)dW_t \tag{2}$$

To facilitate the application in modeling and analyzing stochastic processes of renewable energy, Equation (2) is further discretized to obtain the difference equation:

$$\xi_t = \xi_{t-1} + \mu(t,\xi_{t-1})\Delta t + \sigma(t,\xi_{t-1})\Delta W_t \tag{3}$$

This paper adopts a Gaussian Mixture Model to fit the probability density function of the time series, thereby characterizing the uncertainty of components at different time scales, as shown in Equation (3):

$$\begin{aligned} f(\xi_t) &\sim \sum_{i=1}^{\mathrm{K}} a_i e^{-(\xi_t - b_i)^2/2c_i^2} \\ \mathbf{a} &= [a_1,\cdots,a_i,\cdots,a_{\mathrm{K}}] \\ \mathbf{b} &= [b_1,\cdots,b_i,\cdots,b_{\mathrm{K}}] \\ \mathbf{c} &= [c_1,\cdots,c_i,\cdots,c_{\mathrm{K}}] \end{aligned} \tag{4}$$

Where K represents the number of different individual Gaussian models included in the Gaussian Mixture Model, and $\mathbf{a}$, $\mathbf{b}$, $\mathbf{c}$ are coefficient vectors.

Typically, the drift function $\mu(t,x)$, the diffusion function $\sigma(t,x)$, and the probability density function of load shedding must satisfy the Fokker–Planck equation relationship, as shown in Equation (5):

$$\frac{\partial}{\partial t} f(\xi_t) = -\frac{\partial}{\partial t}\left(f(\xi_t)\mu(t,\xi_t)\right) + \frac{\partial^2}{\partial x^2}\left(f(\xi_t)\sigma(t,\xi_t)\right) \tag{5}$$

By further integrating Equation (6), the relationship between the drift function A and the diffusion function B can be obtained as follows:

$$\sigma^2(t,\xi_t) = 2\frac{\int_{-\infty}^{\xi_t} \mu\left(t,\xi'\right) f\left(\xi'\right) \mathrm{d}\xi'}{f(\xi_t)} \tag{6}$$

From equations (1) to (6), it can be seen that the time series components obtained through MSTL decomposition can be used for uncertainty fitting via a Gaussian mixture model. The probability density function obtained from the fitting, along with the calculated drift term $\mu(\bullet)$, can then be used to derive the diffusion term $\sigma(\bullet)$, thereby completing the construction of the Itô process formula.

This paper employs the Itô process to model the climate and diurnal components of renewable energy time series, defining the drift function as follows:

$$\mu(t,\xi_{\mathrm{t}}) = -\theta\left(\xi_t - \overline{\xi}_t\right) \tag{7}$$

Where θ is the temporal autocorrelation coefficient, and $\overline{\xi}_t$ is the mean value of the time series.

Since the seasonal component exhibits repetitive fluctuations, it can be determined by calculating the average of historical data for one year across the four seasons, while data for other years remain unchanged.

Using the above method, different components of the historical renewable energy time series are modeled. Based on the Itô process, a large volume of time series data is simulated, preserving the temporal correlations of extreme static stability scenarios.

3 Identification Method for Extreme Stagnant Weather Events

Based on the massive time-series data obtained in the previous section, extreme stagnant weather events are identified. To fully account for the impact of such events on the power system, the identification method should be defined from the perspectives of value range and duration [1]:

$$\begin{cases} \overline{\xi}_t \Big|_{d_1 \le t \le d_2} \le \alpha \overline{\xi}_t^{\max} \\ d_2 - d_1 \ge \delta \end{cases} \tag{8}$$

Where $\bar{\xi}_t$ and $\bar{\xi}_t^{\max}$ represent the daily average and maximum value of renewable energy meteorological data, respectively, and d_1, d_2 denote the start and end times of the extreme stagnant weather event. α is the threshold ratio for determining the occurrence of "low wind" and "low solar radiation" conditions, and δ is the minimum duration of the extreme stagnant weather event.

The specific selection of criterion values will be detailed in Section 4.2.2. Based on the identification results of long-term low-output events for wind speed and solar radiation, events where both conditions occur simultaneously are defined as "low wind and low solar radiation" events, i.e., extreme stagnant weather events. Using the above method, the frequency of "low wind and low solar radiation" events across a large number of simulated years is calculated. This frequency is then incorporated as an additional weight into the subsequent planning model, with the specific calculation method as follows:

$$\eta_d = num_d / N^{year} \tag{9}$$

Where d is the date, N^{year} is the number of simulated years, and num_d is the total number of times an extreme stagnant weather event occurs on date d across the N^{year} simulated years.

$$\eta_t = [\eta_{d=0101}, \eta_{d=0102}, \eta_{d=0103}, \cdots, \eta_{d=1231}] \tag{10}$$

4 Planning Model with Extreme Scenario Generation

4.1 Renewable Energy Modeling

Wind Turbines (WT)

The operational constraints of WT are defined by the upper and lower power limits, as shown in Equation (11):

$$0 \le P_{wt,t}^{i} \le p_{wt_\max} \cdot V_{wt} \tag{11}$$

Where $p_{wt_\max}$ is the power output limit of WT as a percentage of maximum capacity.

The power output of WT is determined by wind speed through the piecewise function given in Equation (12):

$$P_{wt,t} = \begin{cases} 0 & 0 \leqslant V_t \leqslant V_{ci} \\ g_1 V_t + g_2 & V_{ci} \leqslant V_t \leqslant V_r \\ P_{wt_rated,t} & V_r \leqslant V_t \leqslant V_{\text{co}} \\ 0 & V_{co} \leqslant V_t \end{cases} \tag{12}$$

In this formulation, $P_{wt,t}$ represents the output power of the WT at time t, and V_t is the wind speed at time t. The parameters V_{ci}, V_r and V_{co} denote the cut-in, rated, and cut-out wind speeds, respectively, while $P_{wt_rated,t}$ is the rated power of the wind turbine at time t. The coefficients g_1 and g_2, which are calculated using Equation (13), complete the model.

$$\begin{cases} g_1 = \dfrac{P_{wt_rated,t}}{V_r - V_{ci}} \\ g_2 = -g_1 V_{ci} \end{cases} \tag{13}$$

Photovoltaic (PV)

The operational constraints of a PV generator are defined by its upper and lower power limits, as expressed in Equation (14):

$$0 \le P_{pv,t}^{i} \le p_{pv_\max} \cdot V_{pv} \tag{14}$$

Where $p_{pv_\max}$ represents the maximum output power limit of the PV generator as a percentage of its capacity.

The output power of the PV generator is related to solar irradiance, as given by Equation (15):

$$P_{pv,t} = \gamma \cdot A \cdot \eta \tag{15}$$

Where $P_{pv,t}$ is the output power of the PV generator at time t, γ is the actual solar irradiance, A is the total area of the PV panel array, and η denotes the overall photoelectric conversion efficiency.

4.2 Objective Function

Investment Cost

The total system investment cost is the sum of the investment costs for all types of generation units, as shown in Equation (16):

$$C_{inv} = C_{g_inv} + C_{es_inv} + C_{wt_inv} + C_{pv_inv} + C_{hd_inv} \tag{16}$$

Where C_{g_inv}, C_{es_inv}, C_{wt_inv}, C_{pv_inv} and C_{hd_inv} represent the investment costs of thermal power units, electrochemical energy storage, wind power, photovoltaic power, and pumped hydro storage, respectively.

Operational Cost

The operational cost consists of the sum of maintenance costs for all types of units, demand response costs, and renewable energy curtailment costs, as expressed in Equation (17):

$$C_{ope} = C_{g_ope} + C_{es_ope} + C_{wt_ope} + C_{pv_ope} + C_{hd_ope} + C_{dr} + C_{load} \tag{17}$$

Where C_{g_ope}, C_{es_ope}, C_{wt_ope}, C_{pv_ope} and C_{hd_ope} denote the maintenance costs for thermal power units, electrochemical energy storage, wind power, photovoltaic power, and pumped hydro storage, respectively. C_{dr} is the demand response cost; and C_{load} is the load shedding cost.

Considering the impact of extreme stagnant weather events on system load shedding, the formula for C_{load} is given as follows:

$$C_{load} = \sum_{t=1}^{T}((1/\eta_t)\cdot\max(P_{load} - P_{wt} - P_{pv} - P_{es} - P_{hd} - P_G, 0)) \tag{18}$$

Where $P_{dg_rated,t}$ is represents the rated power of DG (including WT and PV) at time t, $P_{wt,t}$ and $P_{pv,t}$ denote the actual transmission power of WT and PV power at time t, respectively, and $T = 365$.

4.2.3 Overall objective function

The objective function is to minimize the total system cost, as shown in Equation (19):

$$\min f = (C_{inv} + C_{ope}) \tag{19}$$

5 Case Study

5.1 Case Setup

This study utilizes 20 years of actual meteorological data for wind and solar resources from a provincial location in China as raw input. The planning constraint parameters are set according to the "Research on China's Energy and Power Development Plan for 2030 and Outlook for 2060." As the study focuses on provincial-level planning, the corresponding magnitudes are appropriately scaled down. The maximum installed capacities are set as follows: thermal power at 1.05×10^5 MW, wind and solar power at 8×10^4 MW and 1.03×10^5 MW, respectively, electrochemical energy storage at 3.58×10^4 MW, and pumped hydro storage at 1.2×10^4 MW. Additionally, the minimum renewable energy penetration rate is set at 0.48.

5.2 Planning Results

This section uses wind speed as an example, with the analytical method for solar irradiance being identical and thus not elaborated here.

Decomposition of Raw Data

To meet the analytical requirements, this study focuses on time scales of diurnal and above. The daily average time series is decomposed into climatic, seasonal, and diurnal components. The climatic component reflects interannual variations, the seasonal component captures seasonal periodic fluctuations, and the diurnal component represents daily fluctuations.

Fig. 1 illustrates the decomposition results of wind speed data from 1980 to 2000 for a specific location in the province. The climatic component indicates a general slow decline in wind speed from 1980 to 2000, stabilizing by the late 1990s. The seasonal component shows stable periodic patterns (higher in winter and spring, lower in summer).

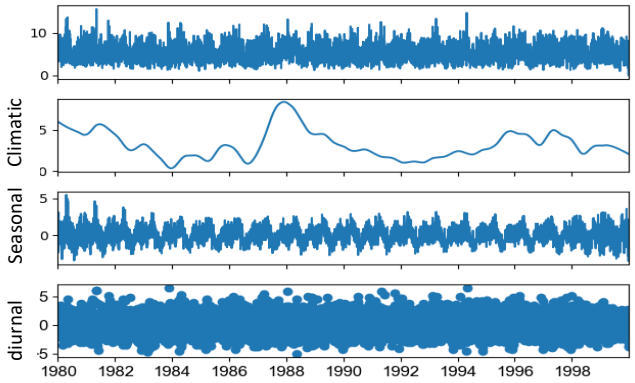


Fig. 1. Decomposition of Historical Wind Speed Data

Reconstructed Data Analysis

Given that the random fluctuations of the diurnal component directly influence the distribution patterns of extreme stagnant scenarios, this study primarily examines the distribution fitting characteristics of the diurnal component. As shown in Figs. 2 and 3, the Itô process largely preserves the distribution properties of the diurnal data, demonstrating the effectiveness of this method for generating extreme scenario samples.

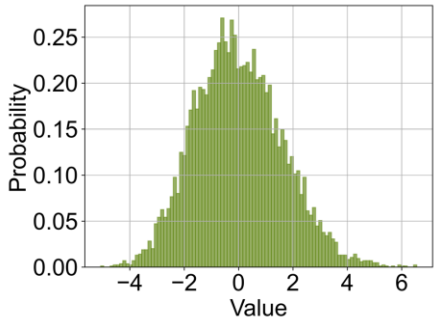


Fig. 2. Simulated distribution of historical wind speed diurnal data

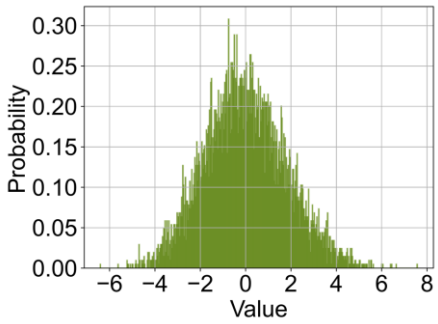


Fig. 3. Simulated distribution of reconstructed wind speed diurnal data

Assuming the year with the smallest fluctuation in the diurnal component of wind speed in the historical data is defined as the typical wind speed year, and by analogy with the CVaR confidence level set at 20%, the reconstructed century-long data is quantized in a stepwise manner to form a calendar heatmap with five distinct levels. Based on this heatmap, the year with the longest continuous duration of the lowest output level is identified as the most extreme scenario year. As shown in Figs. 4 and 5, in terms of seasonal distribution, the maximum continuous low-wind-speed scenario occurs in August for both the baseline year and the extreme year, corresponding to the month with a relatively low seasonal component in the wind speed series. The longest duration of "low-wind" events in the typical wind speed year is 4 days, whereas in the extreme scenario year, it extends to 8 days. Based on this result, the assumption can be made for subsequent analysis.

10

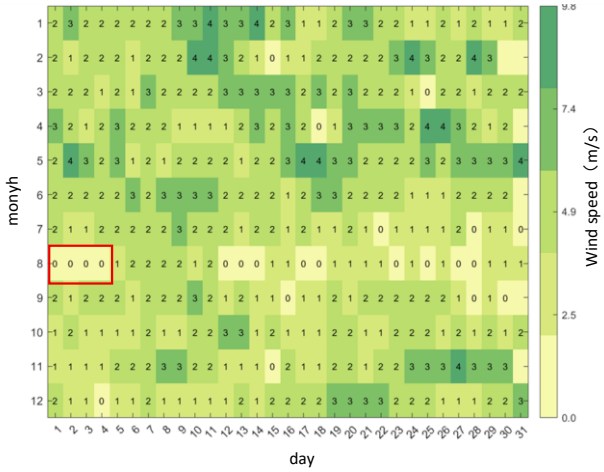


Fig. 4. Schematic diagram of "low-wind" events in the typical wind speed year

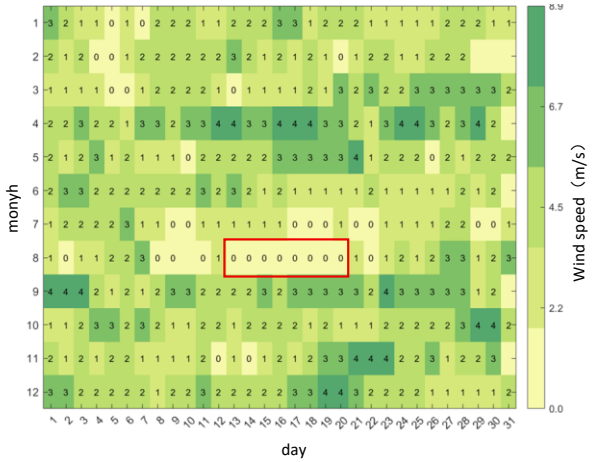


Fig. 5. Schematic diagram of "low-wind" events in the extreme scenario year

Using the above method, two criteria for "low-wind" events are obtained, namely α = 20% and δ = 4. Applying the same method to solar radiation data yields two criteria for "low-solar-radiation" events, namely α = 20% and δ = 7. Dates on which both conditions occur simultaneously are defined as "low wind and low solar radiation" event days, and their frequency is statistically analyzed as shown in Fig. 6.

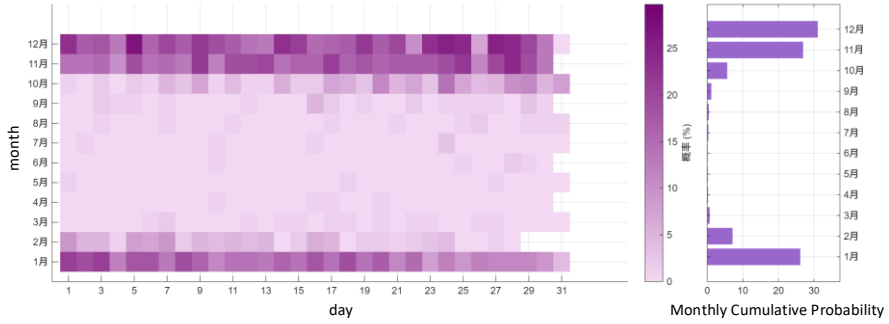


Fig. 6. Frequency spectrum of "low-wind" events

As illustrated in the figure, extreme stagnant events in this region are predominantly concentrated in January, February, November, and December, indicating distinct seasonal characteristics, primarily occurring in winter (November to February of the following year). This pattern may be attributed to meteorological conditions such as stable atmospheric stratification, lower wind speeds, and frequent temperature inversion events during winter.

Comparison of Planning Results

This study employs classical reliability indicators—EENS (Expected Energy Not Supplied), LOLP (Loss of Load Probability), and LOLE (Loss of Load Expectation)—to evaluate the effectiveness of the proposed method. Two planning scenarios are compared: Scenario 1 does not consider extreme stagnant weather events, while Scenario 2 accounts for them. The comparative results of the two planning schemes are presented in Table 1.

Tab.1 Comparison of planning schemes

		Scenario 1	Scenario 2
Equipment Capacity (MW)	G	66251	66250
	PV	47491	47488
	WT	56984	56985
	HD	12000	12000
	ES	24566	24565
Cost Items	Investment Cost（10^8 $）	116.1916	116.1902
	Operating Cost（10^8 $）	865.9560	866.2780
	Total Cost（10^8 $）	982.1420	982.4640
Reliability Indicators	EENS（MWh）	2.0993e+07	5.0763e+06
	LOLP（%）	0.4313	0.4015
	LOLE(annual days)	157.4167	146.5417

12

As can be seen from the above table, after considering extreme stagnant weather events, the reliability indicators are significantly optimized while the total cost increases by only 0.03%.

6 Conclusion and Perspectives

To address the supply risk issue of high-penetration renewable energy power systems under extreme stagnant weather conditions, this paper proposes a reliability planning method for such systems that accounts for extreme stagnant scenarios. Based on 20 years of wind speed and solar irradiance data from a province, multi-scale decomposition is applied to extract climatic, seasonal, and diurnal components. The Itô process is introduced to inject stochastic perturbations, generating a large number of simulated sequences that conform to statistical characteristics and cover tail risk. Subsequently, criteria for continuous "low wind and low solar radiation" events are identified and analyzed. Heat maps are used to visualize their annual calendar distribution, and by comparing event frequencies, these are mapped as weighting factors for load-shedding costs and integrated into the optimization model to achieve the allocation of flexibility resources. This method effectively enhances the robustness of the planning and the system's adaptability to extreme weather.

Case study results demonstrate that the proposed method can preserve the temporal correlations of extreme stagnant scenarios while reducing load shedding under continuous "low wind and low solar radiation" conditions compared to traditional methods, and simultaneously avoiding redundant investment.

Future research could further extend the method to multi-factor joint modeling (e.g., temperature, load, electricity price), calibrate long-term trends and tail probabilities in combination with climate change scenarios, and attempt to characterize more complex extreme events. Additionally, the applicability and scalability of the method could be validated under conditions involving larger regions, longer time frames, and the interaction of cross-regional interconnection and market mechanisms.

Acknowledgement: This work is supported by Global Energy Interconnection Group Co., Ltd. Science and Technology Project (SGGE0000JYJIS2400036)

References

1. Jiang Haiyang, Jiang Minghua, Ding Kun, et al. Risk Assessment and Management for Power Systems under Extreme Stagnant Weather Events [J]. Automation of Electric Power Systems, 2025, 49(4): 42-52.
2. Li Hongmei. 2021 Green Book on Climate Change Released: Chinese Cities Becoming Greener and More Low-Carbon [EB/OL]. http://yn.people.com.cn/n2/2021/1228/c378440-35070755.html, 2021.
3. Sun Jingbo, Wang Yang, Yang Xiaofan, et al. Analysis of Spatiotemporal Variation Characteristics of Climate Risks for Wind and Solar Resources in China [J]. Electric Power, 2023, 56(5): 1-10.

4. PAN G, HU Q, GU W, et al. Assessment of plum rain's impact on power system emissions in Yangtze-Huaihe River basin of China[J]. Nature Communications, 2021, 12(1): 6156.
5. ZHENG D, TONG D, DAVIS S J, et al. Climate change impacts on the extreme power shortage events of wind-solar supply systems worldwide during 1980–2022[J]. Nature Communications, 2024, 15(1): 5225.
6. Lv Xunyan, Xiao Jinyu, Hou Jinming, et al. A Preliminary Study on the Spatio-temporal Distribution Characteristics of Consecutive Multi-Day Low Wind Speed Events and Their Impact on Power Supply [J]. Automation of Electric Power Systems, 2025, 49(4): 79-89.
7. VAN DER WIEL K, STOOP L P, VAN ZUIJLEN B R H, et al. Meteorological conditions leading to extreme low variable renewable energy production and extreme high energy shortfall[J]. Renewable and Sustainable Energy Reviews, 2019, 111: 261-275.
8. WANG L, LIU Y, ZHAO L, et al. Unraveling climate change-induced compound low-solar-low-wind extremes in China[J]. National Science Review, 2024, 12(1).
9. MCKENNA R, LILLIESTAM J, HEINRICHS H U, et al. System impacts of wind energy developments: Key research challenges and opportunities[J]. Joule, 2025, 9(1): 101799.
10. Shuai Xiaohan, Miu Shuwei. A Time-Step-Varying Wind Speed Simulation Model Incorporating Quarterly Trends and Its Application [J]. Proceedings of the CSU-EPSA, 2024, 36(3): 132-141.
11. YANG L, TEH J, LAI C M. Assessing power grid vulnerability to extreme weather: The impact of electric vehicles and energy storage systems[J]. Journal of Energy Storage, 2025, 112: 115534.
12. PANTELI M, MANCARELLA P. Influence of extreme weather and climate change on the resilience of power systems: Impacts and possible mitigation strategies[J]. Electric Power Systems Research, 2015, 127: 259-270.
13. LIU S, SHU J, QIAO M. Assessment of the Impact of Extreme Weather on Power System Reliability[C]//2024 9th Asia Conference on Power and Electrical Engineering (ACPEE). Shanghai, China, 2024: 2475-2480.
14. MUJJUNI F, BETTS T R, BLANCHARD R E. Evaluation of Power Systems Resilience to Extreme Weather Events: A Review of Methods and Assumptions[J]. IEEE Access, 2023, 11: 87279-87296.
15. KRECHIEM A, KHADIR M T. Algerian Electricity Consumption Forecasting with Artificial Neural Networks Using a Multiple Seasonal-Trend Decomposition Using LOESS[C]//2023 International Conference on Decision Aid Sciences and Applications (DASA). Annaba, Algeria, 2023: 586-591.

042 Analysis and Modeling of Grounding Characteristics of Transmission Tower Based on Method of Moments

Wei Xu[1], Xingyu Meng[1], Wenyuan Zhang[1,2], Gang Li[1]

[1] Jilin University, Changchun 130061, China
[2] Northeast Electric Power Design Institute Co.,Ltd Of China Power Engineering Consulting Group, Changchun 130022, China
ligang2013@jlu.edu.cn

Abstract. To investigate the grounding performance of transmission towers, this study develops a grounding electrode model based on Method of Moments (MoM) and conducts simulations using the CDEGS software package. The impacts of grounding configuration, soil resistivity, and high-frequency excitation on grounding behavior are systematically examined. The results show that the length of horizontal radial conductors, soil resistivity, and excitation frequency significantly influence grounding resistance. Extending the length of radial conductors reduces grounding resistance, although the effect diminishes with further extension. A positive correlation is observed between soil resistivity and grounding resistance, exhibiting nonlinear characteristics in stratified soils. In addition, grounding impedance increases markedly under high-frequency conditions. The application of resistance-reducing agents effectively improves grounding performance in high-resistivity regions. These findings provide theoretical support and practical guidance for the design of transmission tower grounding systems, lightning protection, and surface potential distribution analysis.

Keywords: Transmission tower, Method of Moments (MoM), Electromagnetic field simulation, Grounding resistance.

1 Introduction

The continuous development of power networks toward higher voltage levels, greater transmission capacity, and longer transmission distances has significantly increased the requirements for operational security, dynamic stability, and economic efficiency of modern power systems[1,2]. As a core component of the grid, transmission towers, due to their wide spatial distribution and direct exposure to natural environments, frequently serve as primary units subjected to high-frequency surges. In Jilin Province, there are approximately 130,000 transmission towers of 66 kV and above, located in diverse and complex geological conditions, including mountainous and hilly terrain, cultivated plains, grasslands, and water areas, as well as special geomorphologies such as secondary salinization and marshlands. Consequently, soil resistivity varies significantly across different locations and depths. Moreover, due to

differences in construction periods and continuous technological upgrades, the grounding configurations of transmission towers currently in operation also exhibit substantial variations. However, existing literature remains insufficient in addressing the variation patterns of grounding resistance arising from these conditions.

At present, numerical calculation methods based on electromagnetic field theory mainly include the method of moments (MoM) [9,10], the equivalent charge method (ECM) [3], the boundary element method (BEM) [4,5], the finite element method (FEM) [6,7], and the finite-difference method (FDM) [8]. The ECM simplifies calculations by discretizing point charges, with clear principles and relatively high efficiency, but it neglects the non-uniformity of surface charge distribution on conductors, limiting accuracy. The BEM requires discretization only on boundaries, reducing the problem dimension and showing strong adaptability to complex boundaries, yet it lacks flexibility when dealing with non-uniform media or complex geometries. The FEM and FDM both require meshing of the computational domain; FEM, derived from the variational principle, is well-suited for complex geometries and nonlinear materials, while FDM directly discretizes differential equations, offering simplicity but poor mesh adaptability. Both methods require artificial boundary conditions to address open-domain problems, leading to a significant increase in computational complexity.

By contrast, the MoM, based on integral equations, enables accurate layered modeling of soils with different resistivities. By discretizing excitation sources, the integral equations are transformed into matrix equations, which can both accurately reflect field source distributions and efficiently handle open-domain problems without artificial boundaries. This method achieves high accuracy while conserving computational resources. Particularly for large-scale electromagnetic radiation problems, the MoM, when combined with acceleration techniques such as the fast multipole method, demonstrates remarkable advantages and has become one of the most important approaches in electromagnetic field numerical analysis.

SES Inc. of Canada has developed the large-scale electromagnetic field simulation software CDEGS by integrating electromagnetic field theory with the MoM . This software is capable of accurately simulating grounding system characteristics, current distribution, electromagnetic field responses, and electromagnetic interference issues under complex soil structures, and is widely applied in the design and verification phases of power system engineering. Among its modules, the MALZ module further solidifies processes of the method of moments—such as basis function selection and impedance matrix construction—into algorithms, and is commonly used to calculate the grounding resistance and potential distribution of subsurface grounding systems under frequency-domain current excitation.

On this basis, this paper adopts the MoM as the mathematical foundation and employs the MALZ module of the CDEGS software to conduct systematic analyses of transmission tower grounding systems. The study investigates grounding configurations, conductor length, soil resistivity conditions, the application of grounding enhancement materials, and grounding characteristics under high-frequency conditions, with the aim of providing both practical guidance and theoretical support for the design of transmission tower grounding systems.

2 Transmission Tower Grounding and Discretization Models

2.1 Fundamental Structure of Transmission Tower

The grounding body of a transmission line tower consists of a horizontal grounding device and a vertical tower foundation. The horizontal grounding device can be classified into different types, while the vertical tower foundations are generally divided into two categories: cylindrical and stepped. At present, 220 kV transmission towers mostly adopt a single-pile cylindrical concrete foundation, which is usually designed by the empirical coefficient method. The design requirements specify that the pile diameter should be greater than 0.8 m, with a burial depth generally exceeding 6 m [11,12].

Since a large number of reinforcing bars are embedded in the concrete foundation, a more accurate evaluation of the overall grounding performance requires detailed modeling of the reinforcement. In this study, a WJK1-15 manually excavated pile foundation was adopted, and the reinforcement structure was modeled in detail in CDEGS. The main reinforcement configuration is illustrated in Fig. 1, with the resistivity of the steel bars set to 1.1×10^{-7} Ω·m. Other specific parameters are listed in Table 1 [11].

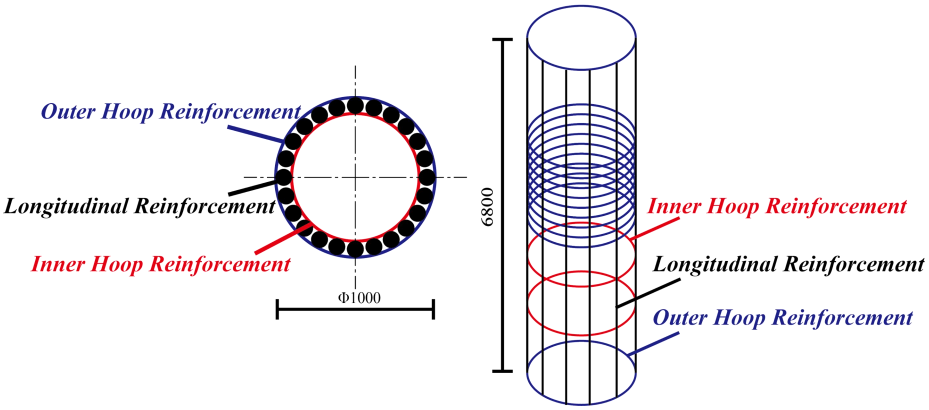


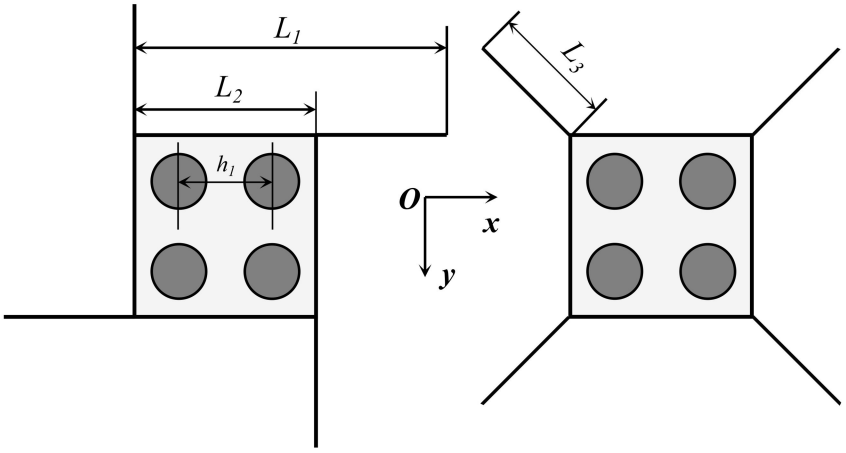
Fig. 1. WJK1-15 Manually Excavated Pile Foundation Model

Table 1. Parameters of the WJK1-15 Manually Excavated Pile Foundation Mode

Column Length /m	Concrete Grade	Name	Specification/mm	Quantity
6.8	C25	Longitudinal Reinforcement	Φ20	24 bars
		Outer Hoop Reinforcement	Φ8	35 hoops
		Inner Hoop Reinforcement	Φ16	6 hoops

2.2 Grounding Grid of Transmission Tower

The grounding grid of a 220 kV transmission tower is generally arranged in a horizontal configuration, consisting of a square conductor mesh combined with radial conductors. According to the layout of the radial conductors, there are typically two types: linear and oblique, as shown in Fig. 2. In Fig. 2, h_1 denotes the root-opening length of the tower foundation, L_1 the grounding electrode length, L_2 the side length of the square conductor mesh, and L_3 the length of the radial conductor. The grounding grid of the tower is connected to the tower body through grounding down conductors. In this study, the model parameters were set as h_1 = 11 m and L_2 = 16 m.



(a) Linear Configuration (b) Oblique Configuration

Fig. 2. Two Types of Grounding Configurations

2.3 Design of Different Grounding Schemes

In order to conduct a detailed analysis of the grounding characteristics of a 220 kV transmission tower and to compare the advantages and disadvantages of different grounding configurations, two grounding schemes were designed in this study.

Scheme I. Conventional grounding configuration, namely the simulation of the currently used tower grounding model. The model is illustrated in Fig. 3.

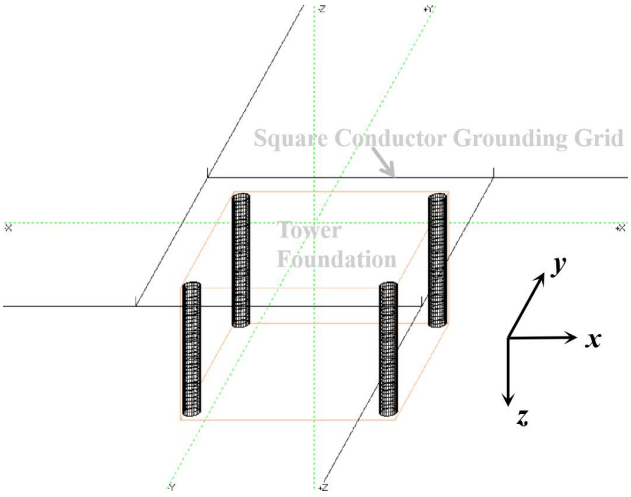


Fig. 3. Scheme I (Conventional Grounding Configuration)

Scheme II. In this scheme, electrical continuity is achieved by connecting the square mesh grounding device with the reinforced concrete structure inside the tower foundation through laid conductors. Since the foundation contains a densely distributed conductive steel reinforcement framework, the variation characteristics of the grounding resistance after its connection to the external grounding grid require further investigation.

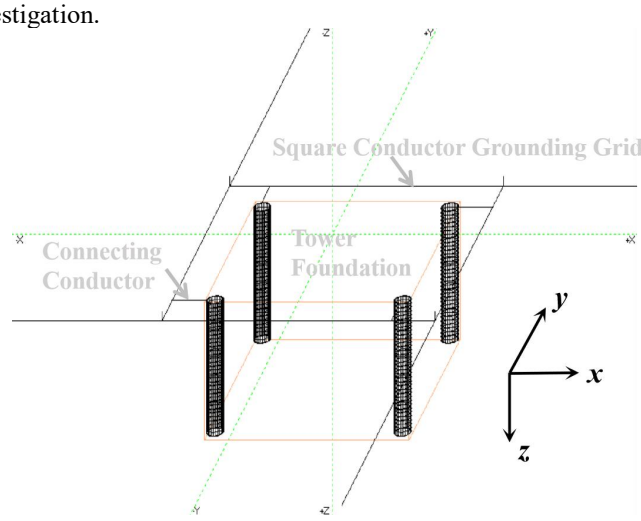


Fig. 4. Scheme II (Connection of Grounding Grid with Reinforcement in Tower Foundation)

3 Fundamental Principles of MoM

Due to the non-uniform distribution of axial currents and leakage currents in the grounding grid, as well as the complex layered soil conditions at the actual location of the transmission tower, MoM was adopted for the analysis of the specific problem [13-15].

Let the charge density of each small segment dl' on the grounding electrode be $\tau(r')$. Then, the potential $\varphi(\boldsymbol{r})$ at a field point $\boldsymbol{r}$ satisfies the following integral equation:

$$\varphi(\boldsymbol{r}) = \frac{1}{4\pi\varepsilon}\int L\frac{\tau(\boldsymbol{r'})}{\left|\boldsymbol{r'}-\boldsymbol{r}\right|}dl' \tag{1}$$

where ε denotes the permittivity of the medium, τ the linear charge density, $\boldsymbol{r}$ the vector of the field point, $\boldsymbol{r'}$ the vector of the source point, and L the path along which the charge distribution is located.

For practical transmission lines, the grounding electrode usually consists of multiple parts, and the potential at a field point requires correction. Assuming that there are two grounding electrodes, Eq. (1) should be modified according to the method of images as follows:

$$\varphi(\boldsymbol{r}) = \frac{1}{4\pi\varepsilon}\left[\int_{L_1}\frac{\tau(\boldsymbol{r'})}{\left|\boldsymbol{r'}-\boldsymbol{r}_1\right|}dl' - \int_{L_2}\frac{\tau(\boldsymbol{r'})}{\left|\boldsymbol{r'}-\boldsymbol{r}_2\right|}dl'\right] \tag{2}$$

Where $\boldsymbol{r_1}$ and $\boldsymbol{r_2}$ are the reference point vectors of the two grounding electrodes, and L_1 and L_2 are the corresponding electrode paths.

The grounding electrode is divided into several small segments, and the charge density of each segment is assumed to be approximately constant. Let the electrode length l' be divided into N segments, with each segment having a charge density τ_i. The current distribution can then be expressed using basis functions:

$$\tau(\boldsymbol{r}) = \sum_{i=1}^{N} f_i(\boldsymbol{r})\tau_i \tag{3}$$

By substituting Eq. (3) into the potential equation (2), the overall potential distribution of the grounding electrode can be obtained:

$$\varphi(\boldsymbol{r}) = \frac{1}{4\pi\varepsilon}\left[\sum_{i=1}^{N}\tau_i\int_{L_1}\frac{f_i(\boldsymbol{r'})}{\left|\boldsymbol{r'}-\boldsymbol{r_1}\right|}dl' - \sum_{i=1}^{N}\tau_i\int_{L_2}\frac{f_i(\boldsymbol{r'})}{\left|\boldsymbol{r'}-\boldsymbol{r_2}\right|}dl'\right] \tag{4}$$

By choosing the Dirac delta function δ as the weighting function ω_j, the discretized form of the potential equation can be obtained.

$$\omega_j = \delta_j(\boldsymbol{r}-\boldsymbol{r_j'}), j = 1,2,\cdots,N \tag{5}$$

By taking the inner product of Eq. (4) with each ω_j over the integration region l' and simplifying, the system matrix can be constructed to represent the relationship between the grounding current density and the potential, namely:

$$[L_{ji}][\tau_i] = [\varphi_j] \tag{6}$$

Thus, the matrix form of the linear charge density τ_{i} for each conductor segment can be obtained as

$$[\tau_i] = [L_{ji}]^{-1}[\varphi_j] \tag{7}$$

By applying the Gauss–Seidel iterative method, the matrix of Eq. (7) can be solved, and the electric field strength can thus be calculated:

$$E(\boldsymbol{r}) = \frac{1}{4\pi\varepsilon}\sum_{i=1}^{N}\tau_i \left| \int_{\Delta l_{1i}'} \frac{\boldsymbol{r'} - \boldsymbol{r}_1}{\left|\boldsymbol{r'} - \boldsymbol{r}_1\right|^3} dl' - \int_{\Delta l_{2i}'} \frac{\boldsymbol{r'} - \boldsymbol{r}_2}{\left|\boldsymbol{r'} - \boldsymbol{r}_2\right|^3} dl' \right| \tag{8}$$

The magnetic flux density $\boldsymbol{B}(\boldsymbol{r})$ can be obtained, where μ_0 is the permeability of free space and $\boldsymbol{i}$ is the current.

$$\boldsymbol{B}(\boldsymbol{r}) = \frac{\mu_0}{4\pi}\int L \frac{\left|\boldsymbol{i}\right|}{\left|\boldsymbol{r} - \boldsymbol{r}'\right|} d\vec{l} \times (\boldsymbol{r} - \boldsymbol{r}') \tag{9}$$

The relationship between the grounding current $\boldsymbol{J}(\boldsymbol{r}')$ and the potential gradient $\nabla\varphi(\boldsymbol{r}')$ is given by Ohm's law, as shown in Eq. (10). The total current I_{ground} through the grounding electrode can be obtained by integrating the current density along the electrode path.

$$\boldsymbol{J}(\boldsymbol{r}') = -\sigma\nabla\varphi(\boldsymbol{r}') \tag{10}$$

$$I_{\mathrm{ground}} = L \quad \boldsymbol{J}(\boldsymbol{r}) \cdot dl' = -L \quad \sigma\nabla\varphi(\boldsymbol{r}) \cdot dl' \tag{11}$$

The grounding resistance R_{g} is defined as the ratio of the grounding potential difference V_{ground} to the grounding current I_{ground}.

$$R_{\mathrm{g}} = \frac{V_{\mathrm{ground}}}{I_{\mathrm{ground}}} \tag{12}$$

In summary, the fundamental principles and computational methods of grounding resistance for transmission towers have been derived in detail using the method of moments. By considering the variations in layered soil resistivity, the geometrical characteristics of the grounding device, and the coupling relationship between the electric field and current density, the spatial distributions of the electric and magnetic fields can be deduced, and the grounding resistance can subsequently be calculated. This provides a systematic computational approach and theoretical support for engineering practice.

4 Analysis of Grounding Characteristics of Transmission Tower

On this basis, the present study employs the method of moments as the mathematical foundation and utilizes the MALZ module of the CDEGS software to carry out the analysis. A systematic investigation is conducted on the grounding configuration of transmission towers, grounding electrode length, different soil resistivity conditions, the application of ground resistance reducing agents, and the grounding characteristics under high-frequency operating conditions, with the aim of providing practical guidance and theoretical support for the grounding design of transmission towers.

4.1 Influence of Grounding Grid Configurations

To investigate the influence of grounding grid configuration on the grounding resistance of transmission towers, the square conductor mesh side length in Fig. 2(a) and (b) is set to 16 m, and the radial conductor length is set to 59 m, giving a total grounding electrode length of 75 m with a root opening of 11 m. The power-frequency current is specified as 4 A, with 1 A injected at each of the four vertices of the square mesh through grounding down conductors. The soil resistivity is set to 500 Ω·m, while the resistivity of the tower foundation concrete remains constant at 2000 Ω·m [16]. The grounding resistances of Scheme I and Scheme II are shown in Table 2.

Table 2. Grounding Resistance under Different Grounding Grid Configurations

Grounding Scheme	Grounding Resistance / Ω	
	Linear Configuration	Oblique Configuration
I	4.71	4.61
II	4.63	4.55

As shown in Table 2, for Scheme I, the deviation between the linear and oblique configurations is 2.12%, while for Scheme II, the deviation is 1.49%. Within the allowable engineering error range, the power-frequency impedance characteristics of the tower grounding system do not exhibit significant differences. It can therefore be concluded that the grounding conductors arranged in linear and oblique layouts are equivalent in meeting current technical standards. Considering computational efficiency and modeling simplicity, the subsequent numerical simulations will preferentially adopt the linear topology as the reference model.

4.2 Influence of Soil Resistivity

Soil resistivity is an important factor affecting the grounding resistance of transmission towers. To investigate its effect, the resistivity of the tower foundation concrete is kept constant at 2000 Ω·m, the total grounding electrode length is set to 75 m, and the power-frequency current is specified as 4 A. With increasing depth, the soil moisture content decreases, porosity is reduced, and the concentration of

conductive ions decreases; therefore, the overall resistivity shows an upward trend [17]. To better simulate the complex soil resistivity conditions in Jilin Province, it is necessary to consider both single-layer and two-layer cases. In the two-layer case, the boundary between the upper and lower soil layers is taken at a depth of 0.5 m below the surface. The grounding resistances under different soil resistivity conditions are shown in Fig. 5 and Fig. 6.

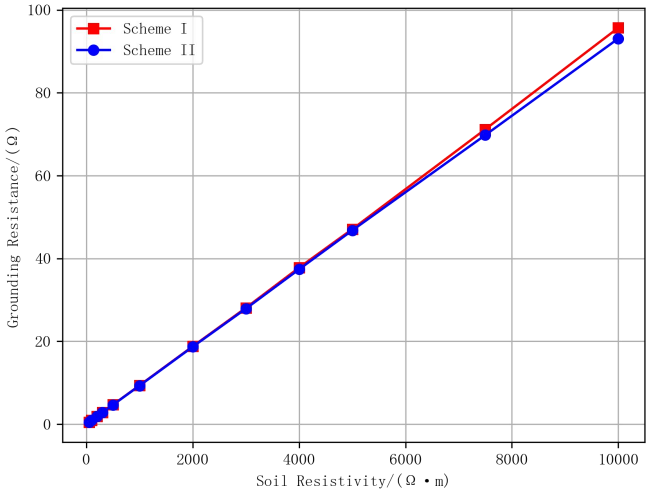


Fig. 5. Variation of Grounding Resistance under Single-Layer Soil Resistivity

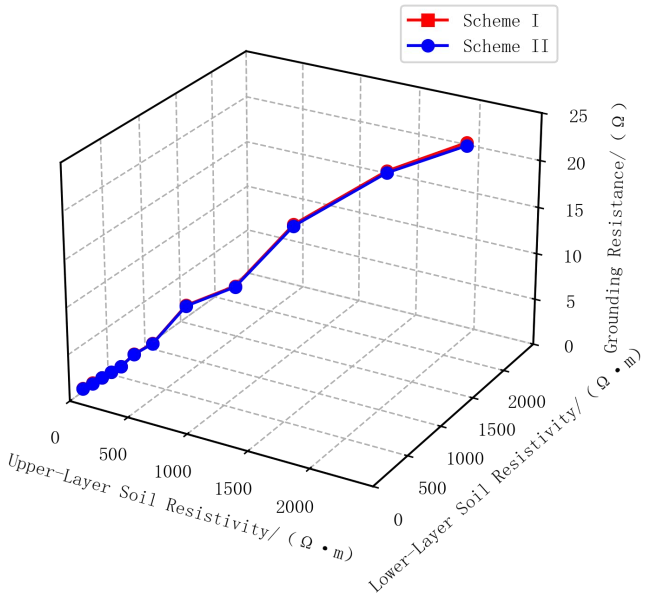


Fig. 6. Variation of Grounding Resistance under Two-Layer Soil Resistivity

10

As shown in Fig. 5 and Fig. 6, the grounding resistance of transmission towers increases with increasing soil resistivity. In the case of homogeneous single-layer soil, the grounding resistance is approximately proportional to the soil resistivity; whereas in the case of heterogeneous two-layer soil, the influence of the upper and lower soil resistivities on the grounding resistance is coupled, and the relationship between grounding resistance and soil resistivity becomes nonlinear but remains positively correlated. Moreover, the grounding resistance obtained from Scheme II is always lower than that of Scheme I, indicating a better current-dissipation capability and stronger grounding reliability.

4.3 Influence of Grounding Electrode Length

To investigate the influence of grounding electrode length on the grounding resistance of transmission towers, different electrode lengths were set in the CDEGS modeling, and the effects on the grounding resistance of Scheme I and Scheme II were observed. The soil resistivity was specified as 500 Ω · m, while the resistivity of the tower foundation concrete remained constant at 2000 Ω·m. The grounding resistances under different electrode lengths are shown in Fig. 7.

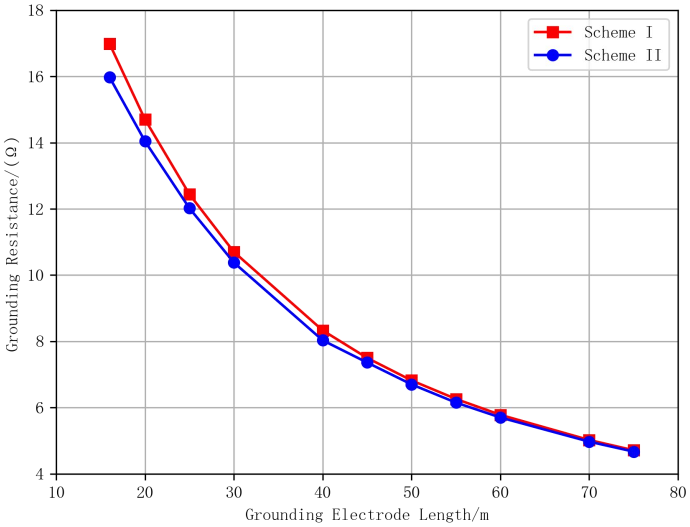


Fig. 7. Influence of Grounding Electrode Length on Grounding Resistance

As shown in Fig. 7, the grounding electrode length has a significant impact on the grounding resistance. A longer electrode provides stronger current-dissipation capability, resulting in lower grounding resistance and higher safety of transmission towers. Moreover, as the electrode length increases, the power-frequency grounding impedance values obtained from the two design schemes gradually converge (relative deviation < 5%), indicating that the influence of the electrical interconnection between the foundation reinforcement and the grounding device on the overall current-dispersion characteristics of the system decreases with increasing electrode

scale. In contrast, when the grounding electrode length is relatively short (L < 25 m), the connection mode leads to significant variations in the impedance values.

4.4 Influence of Grounding Resistance Reduction Agent

Ground resistance reducing agents (GRRAs) are typically composed of highly conductive substances, such as metal oxides, carbon-based materials, or natural minerals. These substances exhibit excellent conductivity and can effectively improve the electrical conductivity of the soil. When applied to the soil of the grounding system, GRRAs undergo chemical reactions or physical adsorption with soil particles, thereby reducing soil resistivity and enhancing soil conductivity. By lowering the soil resistivity, this process enables current to flow more uniformly around the grounding electrode, significantly reducing the grounding resistance. GRRAs are particularly effective in dry or high-resistivity soils, where they can markedly improve soil conductivity and thereby enhance grounding performance.

In both Scheme I and Scheme II, GRRAs are placed along the radial conductors of the grounding grid and buried underground together with the grid during construction, as illustrated in Fig. 8. The cross-section of the GRRA is set to 1 m × 1 m, with its length equal to that of the radial conductors. The resistivity of the GRRA is specified as 1 Ω·m, the soil resistivity as 500 Ω·m, and the concrete resistivity as 2000 Ω·m, consistent with the previous settings. The root opening is kept constant at 11 m. The study investigates the variation in electrode length required for Schemes I and II to achieve the same grounding resistance before and after the application of GRRAs. The results are presented in Table 3.

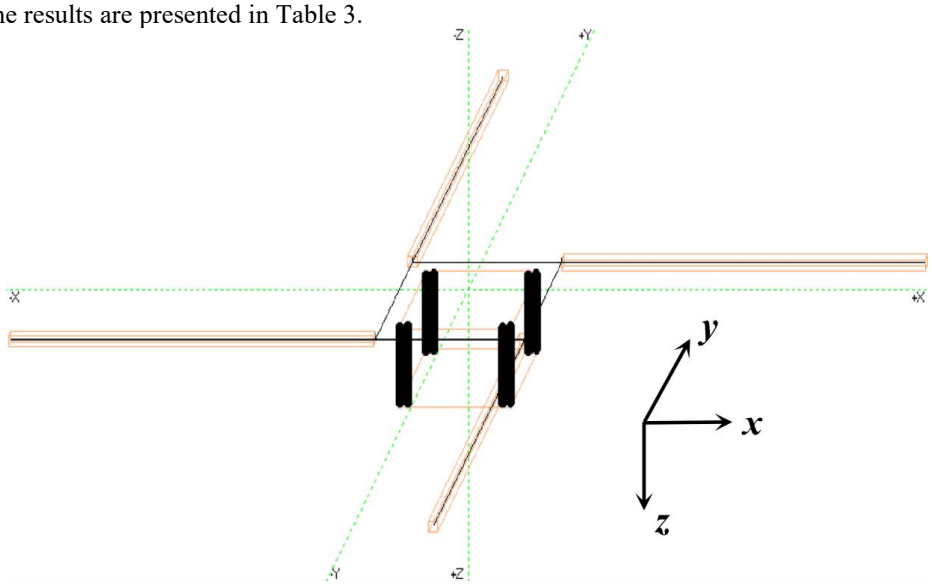


Fig. 8. Injection of Ground Resistance Reducing Agent around Radial Conductors

12

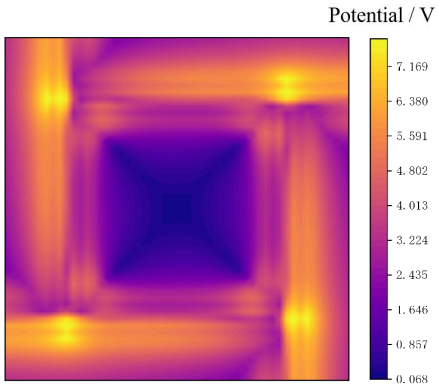
Table 3. Effect of Ground Resistance Reducing Agent on Grounding Performance

Grounding Scheme	Without GRRA		With GRRA	
	Grounding Electrode Length/m	Grounding Resistance/Ω	Grounding Electrode Length/m	Grounding Resistance/Ω
I	75.0	4.71	45.8	4.71
II	75.0	4.63	44.9	4.62

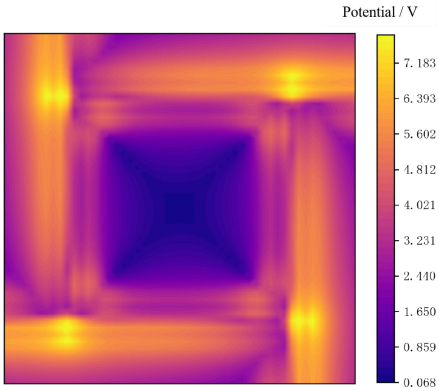
As shown in Table 3, the application of GRRAs exhibits a significant effect in reducing grounding resistance for both Scheme I and Scheme II. With the addition of GRRAs, the current-dissipation capability of the conductors is enhanced, which to some extent offsets the increase in grounding resistance caused by shorter electrode lengths, thereby maintaining a relatively low resistance value. Therefore, in regions with high soil resistivity and complex geological conditions, the reasonable use of GRRAs can reduce engineering difficulty and save grounding conductor materials.

4.5 Influence of High-Frequency Current

To provide a more intuitive investigation of the grounding characteristics of transmission tower grounding devices under high-frequency conditions, a total excitation current of 100 A is specified, with 25 A injected through the grounding down conductors at each of the four vertices of the square conductor mesh. The total grounding electrode length is set to 75 m, the soil resistivity to 500 Ω·m, and the distribution and grounding impedance are calculated for six cases: 50 Hz, 1 kHz, 100 kHz, 1 MHz, 10 MHz, and 25 MHz. The results are shown in Fig. 9 and Table 4.



(a) 50Hz



(b) 1kHz

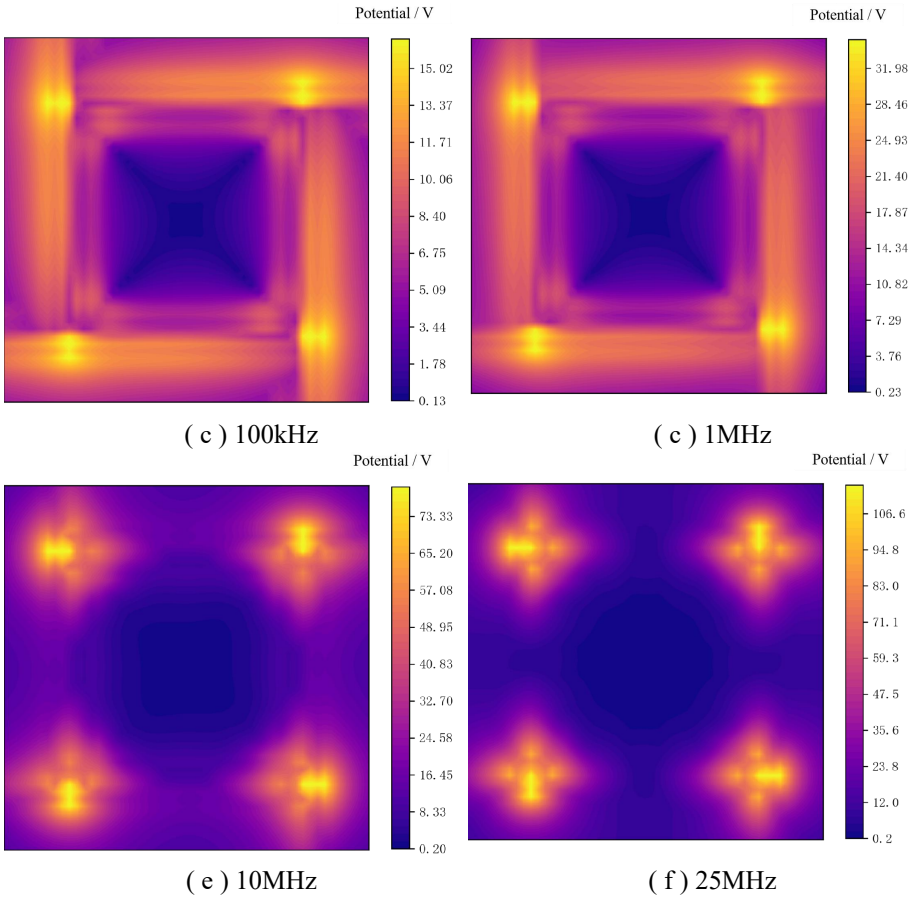


Fig. 9. Surface Potential Distribution under Different Frequencies

Table 4. Influence of Frequency on the Grounding Resistance of Transmission Towers

Current Frequency /Hz	Grounding Resistance/Ω	
	Scheme I	Scheme II
50	4.71	4.67
1k	4.72	4.64
100k	7.49	7.40
1M	13.78	13.37
10M	32.94	32.12
25M	55.44	54.67

From the comparative analysis of Fig. 9, it can be observed that the surface potential of the transmission tower grounding device exhibits a centrosymmetric distribution. At low current frequencies, both the magnitude and distribution of the

surface potential are nearly identical. As the frequency increases, the surface potential also rises. When the injected current frequency reaches the order of 10 MHz, as shown in Fig. 9(e) and (f), the potential distribution displays a pronounced spatial concentration effect, mainly focused in the vicinity of the injection points. This leads to a significant increase in potential magnitude and a rapid rise in conductor impedance. Under such high-frequency conditions, current conduction along the grounding electrode over long distances becomes difficult, and current diffusion is mainly confined to the surrounding soil medium near the injection points.

5 Conclusion

Based on the CDEGS software and the method of moments principle, this study conducts simulation analysis on the grounding resistance of transmission towers under different operating conditions. The findings show that the grounding resistance is significantly affected by grounding grid type, soil resistivity, grounding electrode length, and excitation current frequency: linear and diagonal grounding grids exhibit approximately equal resistance, so the linearly structured one—with lower construction difficulty—is preferred in practical engineering; soil resistivity has a significant positive correlation with grounding resistance (linear in single-layer soil, nonlinear in double-layer soil), requiring on-site measurements at different depths to guide construction material selection; while increasing grounding electrode length reduces resistance, the reduction effect diminishes gradually, so its length should be determined by combining resistance requirements and site spatial constraints.

In engineering practice, resistance-reducing agents can be applied around the radial conductors of the grounding grid under high soil resistivity or complex geological conditions, as this measure effectively lowers overall system resistance and reduces excavation workload. Additionally, high-frequency current excitation weakens the conductor's current dispersion capacity, causing current to concentrate near the injection point and significantly increasing grounding resistance—thus targeted resistance reduction measures for this area are necessary in design. In conclusion, optimizing grounding system design requires comprehensive consideration of technical feasibility, economic viability, and environmental requirements to enhance the operational safety and construction efficiency of transmission towers.

Acknowledgement: This work is supported by the Science and Technology Project of State Grid Jilin Electric Power Co. Ltd.

References

1. Wang, L., Liu, Z., Song, M., et al.: Impact of Newly Built Grounding Grid on the Original Grounding Grid Based on the Method of Moments [J]. Power System and Clean Energy, 39(9), 32–39, 46 (2023).
2. National Energy Administration: Implementation Plan for High-Quality Development of Distribution Networks (2024–2027) [J]. Rural Power Management, 2024(9), 5 (2024).
3. Yang, F., Yao, D., Peng, H., et al.: Measurement and Analysis of Shielding Effectiveness for Power Frequency Electromagnetic Field in HV Substation [J]. High Voltage Apparatus, 46(1), 85–88 (2010).
4. Wang, Z., Fan, L., Xia, T., et al.: Numerical Calculation of Bundle Conductor Surface Electric Field on Transmission Tower Based on Boundary Element Method [J]. High Voltage Engineering, 43(12), 3835–3842 (2017).
5. Wang, Z., Shi, Y.: Fast Multipole Curved Boundary Element Method for 3D Electrostatic Field [J]. Transactions of China Electrotechnical Society, 33(24), 5797–5804 (2018).
6. Zhu, G., Hao, F., Shen, N., et al.: Three-Dimensional Ion Flow Field Calculation and Characteristic Analysis Considering the Influence of Dielectric Charge [J]. Power System Technology, 48(11), 4638–4647 (2024).
7. Wei, W., Dan, S.: Evaluation of Ultimate Capacity of Cable Transmission New Energy Based on Finite Element and Neural Network [J]. Journal of Electric Power Science and Technology, 38(1), 191–200 (2023).
8. Zhan, J., Yang, T., Guo, J.: Experimental Analysis of Shielding Characteristics of Overhead Transmission Lines Based on Lightning Fractal Model [J]. Smart Power, 44(1), 126–135 (2025).
9. Bruns, H.D., Schuster, C., Singer, H.: Numerical Electromagnetic Field Analysis for EMC Problems [J]. IEEE Transactions on Electromagnetic Compatibility, 49(2), 253 – 262 (2007).
10. Wang, L., Zhang, Z., Wu, Y., et al.: High Efficiency Method of Estimating Broadband Scattering Response for HV Transmission Lines [J]. Smart Power, 51(2), 111–117 (2023).
11. Tong, J., Tian, J., Guo, Y., et al.: Grounding Resistance Characteristics Analysis of Transmission Line Towers in Mountainous Regions [J]. Smart Power, 46(1), 71 – 76 (2018).
12. Zheng, D., Chen, L.: Grounding Characteristics Analysis of Transmission Line Towers in Mountainous Regions Based on Finite Element Method [J]. Electrical Engineering, 25(8), 47–52 (2024).
13. Tang, B., Wang, F., Zhang, J., et al.: Solution and Analysis of Scattering Field of Power Transmission Lines Based on Characteristic Mode Theory [J]. IEEE Access, 12, 50613–50622 (2024).
14. Harrington, R.F.: Field Computation by Moment Methods [M]. IEEE Press, Piscataway, NJ, New York (2000).
15. Maddah-Ali, M., Sadeghi, S.H.H., Dehmollaian, M.: A Method of Moments for Analysis of Electromagnetic Scattering from Inhomogeneous Anisotropic Bodies of Revolution [J]. IEEE Transactions on Antennas and Propagation, 66(6), 2976–2986 (2018).
16. Xia, J., Zheng, Y., Wang, Y.: Study on Effective Resistivity and Representative Volume Element of Concrete Based on Multi-Scale Model [J]. Materials Reports, 39(4), 91 – 97 (2025).
17. Yao, J., Zheng, X.: Issues in Field Testing of Shallow Soil Resistivity in Inner Mongolia [J]. Urban Construction Theory Research (Electronic Edition), 2025(14), 7–9 (2025).

043 Research on Pre-Synchronization Control Strategy of VSG-Based Energy Storage Converter Without Phase-Locked Loop

Xingchi Hou, Yuehui Hu, Weilin Liu
School of Electrical Engineering, Shandong University
Jinan, Shandong, China
15552309486@163.com

Abstract. Modern power electronics-dominated power systems face urgent challenges related to the integration of renewable resources. The increased penetration of emerging inertial-less renewable sources, such as solar and wind, has led to reduced grid inertia, posing a risk to frequency regulation stability. Additionally, the inherent characteristics of intermittent resources and the dynamics of power converters exacerbate the risks associated with voltage and frequency stability. Furthermore, stringent requirements regarding harmonic distortion levels have diminished the synchronization accuracy of critical devices, such as energy storage converters that rely on conventional phase-locked loops (PLLs). To address these challenges, a phase-locked loop free control strategy based on the virtual synchronous generator is proposed. This strategy utilizes phase synchronization within the dq coordinate system and incorporates virtual impedance compensation. The research entails the formulation of equations and models, the design of a double-closed-loop control architecture, and the correction of deviations through the integration of virtual impedance with voltage feed-forward compensation. Simulation results validate the efficacy of the proposed strategy in adapting to the complex operational conditions of the grid. This approach provides an effective solution for improving the performance of energy storage converters and enhancing the resilience (or robustness) of microgrids.

Keywords: Energy Storage Converter, Phase-Locked Loop Free, Virtual Impedance, Virtual Synchronous Generator (VSG).

1 Introduction

The penetration of renewable energy sources heavily depending on the grid-following control strategy demands accurate Phase-locked loops (PLLs) aiming at synchronizing with the grid. Yet, it also means reduced grid inertia and stability with less rotating mass because traditional generators are being replaced [1]. This reduced inertia is a big challenge for conventional PLLs because they are more sensitive to harmonics prevailing in the modern grid where the distortion levels are increased [2]. The reduced inertia leads to larger and faster frequency/phase oscillations that are difficult for PLLs to properly follow, resulting in failure of Synchronous level such as the power converter working in storage elements. While Virtual Synchronous Generator (VSG) technology offers high potential by emulating synchronous generator characteristics to provide virtual inertia [3], there is still a big drawback: VSG pre-synchronization methods are mainly based on the PLLs. This dependence results in a constrained resilience of low inertia power systems in imperfect grids with harmonics, asymmetries and the highly dynamic variation amplified by low inertia.

Conventional pre-synchronization controls utilize the phase-locked loops (PLLs) in order to extract amplitude and phase information from outputs of a VSG and a grid voltage. The voltage deviation and phase deviation are taken as input to Q-U controller and P-*f* controller through PI controllers, which facilitates smooth transition from off-grid operation to grid-connected mode [4] . However, PLLs are also sensitive to grid voltage unbalance, frequency error and waveform distortion itself, this sensitivity decreases the detection accuracy, produces deviations and even lead to loss of lock [2]. The application of similar positive modifications could lead to a prolongation of the PLL working time and, hence, to a decrease in the global system response speed.

To address this, Reference [5] investigated a virtual synchronous generator control method independent of phase-locked loops (PLLs), utilizing voltage phase direct detection technology to achieve smooth transitions between multi-mode operations. While this strategy eliminates PLL dependency, its poor adaptability to three-phase voltage asymmetry conditions makes stable switching challenging under unbalanced conditions. Reference [6] proposed a phase-locked loop-free virtual synchronous generator synchronization control method for doubly-fed wind turbines. This approach integrates frequency/phase regulation and amplitude synchronization modules into the VSG outer-loop control structure, ensuring stator-side electrical parameter alignment with grid requirements prior to grid connection. By introducing equivalent impedance compensation through Q-U control loops, it significantly enhances grid-connected process stability. Reference [7] developed a synchronization control module employing virtual power and secondary voltage/frequency regulation. This PLL-free, simplified design effectively improves the system's ability to track active and reactive power. Reference [8] designed an optimized control architecture capable of predicting operational mode transitions and configuring required output parameters for regulators, enabling disturbance-free transitions between grid-connected and off-grid states. Specifically addressing microgrid characteristics, they developed a digital algorithm-based phase synchronization technique to establish precise phase references for energy storage converters, ensuring stable bus voltage phase transitions and continuity during mode-switching. Reference [9] Based on the

secondary frequency and voltage regulation mechanism of virtual synchronous generators, a pre-synchronous control strategy for microgrids has been designed. This approach optimizes the secondary regulation process of system frequency and voltage, effectively reducing current surges during grid connection operations. It ensures stable switching between off-grid operation and grid-connected operation modes in microgrid systems.

There are several methods for the PLL-free control of inverters the proposed method is based on grid state voltage measurement methodology by exploiting the virtual synchronization mechanism of VSG. This method is realized by integrating the internal virtual rotor speed implemented in the VSG inside its controller to obtain the phase angle needed for synchronizing. This integration automatically makes the system synchronized to the rotational dynamics of the grid since it removes the requirement of a regular PLL for dq-transformation. Further a re-configurable virtual impedance is introduced in the control loop for the purpose of harmonic suppression by counterbalancing voltage distortion due to load. This compensation is also important in a pre-synchronized mode and grid-connected modes, which use feedforward action. Finally, to enable the successful connection of the inverter output voltage to the grid, three main criteria are strictly tested and enforced by the controller: average voltage deviation ($\Delta V<5\%$), frequency deviation ($\Delta f<0.2$Hz) and phase angle error ($\Delta\theta<10°$) [10]. The controller commits to closing switch only after all of these conditions are satisfied concurrently for some fixed period of time.

2 Proposed Control Strategy

2.1 VSG Modeling and Dual-Loop Control

The VSG rotor dynamics and droop characteristics are modeled as[10]:

$$J\frac{d\omega}{dt} = P_{set} - P_e - D_p\left(\omega - \omega_N\right) \tag{1}$$

$$E_m = U_n + K_q\int\left(Q_{set} - Q_e\right)dt \tag{2}$$

where J=0.5kg·m^2 , D_p=10 , and K_q=3.11e^{-3} . As shown in Fig. 1, active-frequency and reactive-voltage loops form the dual-control architecture. The output phase angle θ=∫ωdt replaces PLL for coordinate transformation.

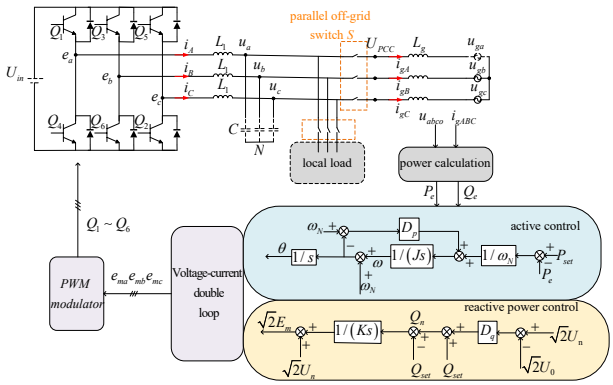


Fig. 1. The main circuit topology and control structure of the virtual synchronous machine

2.2 PLL-Free Synchronization

Grid voltage features are extracted via orthogonal decomposition [11]:

$$\Delta\theta = \theta_g - \theta \approx \sin^{-1}\left(u_{gq}/u_{gd}\right) \tag{3}$$

Phase/frequency synchronization uses PI regulators Fig. 2:

$$\Delta\omega = K_p\Delta\theta + K_i\int\Delta\theta dt \tag{4}$$

Amplitude matching employs voltage feedforward[12]:

$$u_{ref} = u_N + K_{p,u}\left(u_g - u\right) + K_{i,u}\int\left(u_g - u\right)dt \tag{5}$$

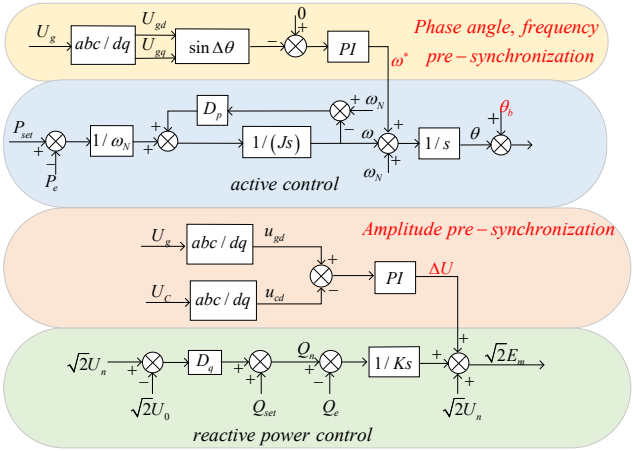


Fig. 2. Optimized control chart based on coordinate transformation pre-synchronization.

2.3 Virtual Impedance Compensation

To mitigate grid-tie current surges, a programmable virtual impedance $Z_v=R_v+j\omega L_v$(0.27Ω/0.3mH) is embedded,where R_v = 0.27Ω and L_v = 0.3mH provide 1.2× line impedance matching. The compensation operates in two modes[7]:

1） Pre-synchronization Mode:

$$V_{\text{comp}} = i_{abc} \otimes Z_v \tag{6}$$

(⊗ denotes convolution).

2） Grid-Connected Mode:

$$\Delta V_d = -i_q X_v, \Delta V_q = i_d X_v \tag{7}$$

decoupling dq-axis cross-coupling.

The virtual power P_{syn} validates synchronization [8]:

$$P_{syn} = \frac{3}{2}\left(v_d i_d + v_q i_q\right) \to 0$$
$$\Delta\theta \to 0 \tag{8}$$

When the absolute value of the virtual synchronizing power $|P_{syn}|$ is less than 0.05 p.u. for 100 ms, the system triggers grid connection.

3 Simulation Validation

3.1 Simulation Setup

A comprehensive simulation study using MATLAB/Simulink was carried out to assess the suggested pre-synchronization strategy without phase-locked loop (PLL) for voltage-source-grid-based energy storage converters. The simulation scenario replicates a low-voltage microgrid and includes the essential components listed below:

The Power Stage employs a two-level Voltage Source Converter (VSC) as the primary converter topology. The Grid Interface incorporates an LCL filter (L_f=3mH, C_f=20μF) connected to the Point of Common Coupling (PCC) for harmonic mitigation. The DC Link comprises an ideal DC source that sustains V_{dc}=800V [12].

1) Control Implementation

The VSG Core integrates virtual inertia (J=0.5kg·m²), damping (D_p=10), and reactive droop (K_q=3.11×10⁻³) to regulate power. The Inner Loop utilizes a PR current controller with a bandwidth of GBW=800 Hz. PLL-Free Synchronization is accomplished through phase/frequency estimation using orthogonal decomposition and amplitude matching with feedforward. Virtual impedance is included as a programmable impedance $Z_v=R_v+j\omega L_v$ for current limitation and stability, with R_v=0.27Ω and L_v=0.3mH.

2) Simulation Parameters

The nominal system power is P_n=20 kW, the AC voltage is V_n=220V line-to-line root mean square (RMS), the grid frequency is 50 Hz, switching/sampling operates at a frequency of f_{sw}=10 kHz with synchronized control, and a variable-step solver is employed for precision.

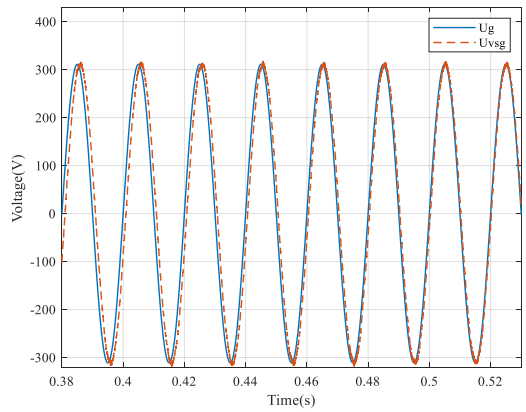
3.2 Results

1) Ideal Grid: The voltage/frequency/phase error converges within less than 1 second, as shown in Fig 3 (a)-Fig 3 (c). Phase mismatch less than 5° meets grid connection standards [10].

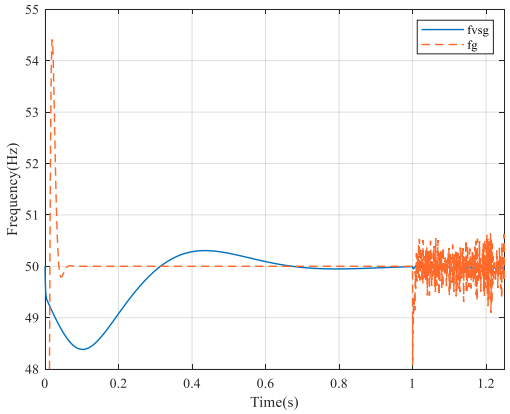
2) Voltage Distortion (THD=5%): By using the i_p-i_q method, the THD of the VSG output is reduced to 1.5%, as shown in Fig 3 (d) [11]. Virtual impedance suppressed 2nd-harmonic oscillation by 85%.

3) Frequency Fluctuation (±0.5 Hz): VSG tracks the grid frequency within 0.8 seconds as shown in Fig 3 (e). Power overshoot less than 10%[10].

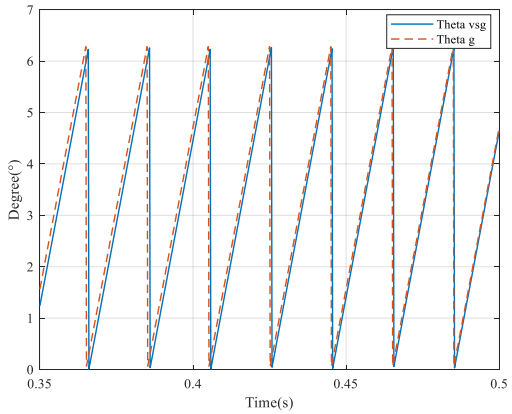
4) Grid-Tie Current: At the synchronization threshold of $\Delta U<5\% U_N$, $\Delta f<0.2$Hz and $\Delta\theta<10°$, the inrush current is limited to 8% of the rated value, as shown in Fig 3 (f).



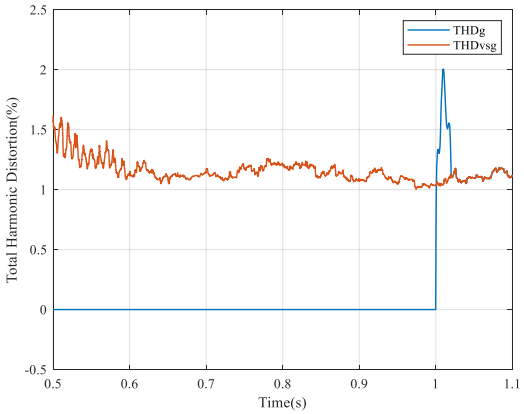
(a) Power grid voltage and VSG output voltage waveform.



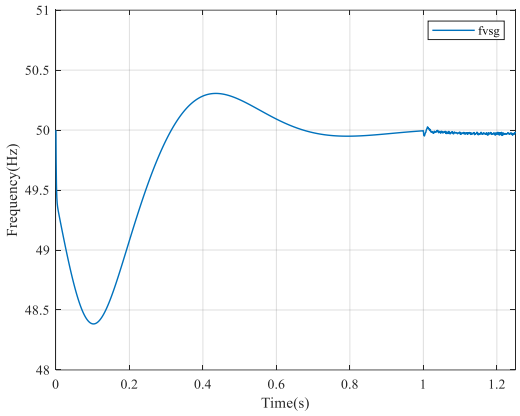
(b) Power grid frequency and VSG output frequency waveform.



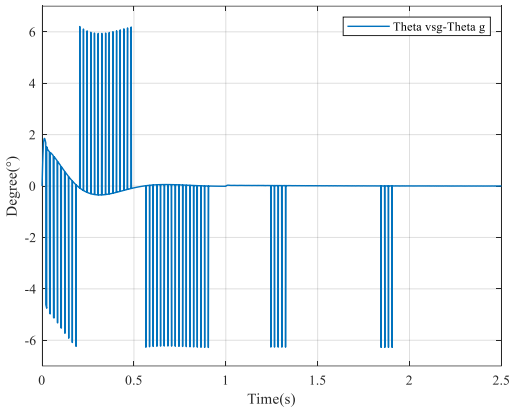
(c) Power grid voltage phase and VSG output phase waveform.



(d) THD waveform of output voltage and grid voltage after pre-synchronous regulation.



(e) The tracking waveform of the VSG output frequency.



(f) Waveform of phase difference.

Fig. 3. Simulation result diagram.

Key simulation parameters are summarized in Table 1.

Table 1. Key simulation parameters.

Parameter	Value
AC Voltage	220 V
Power	20 kW
DC-Link Voltage	800 V
Grid Frequency	50 Hz
Switching Frequency	10 kHz
LCL Filter(L_f,C_f)	3 mH,20 μF
Inner Loop Bandwidth	800Hz
VSG: J / D_p / K_q	0.5 kg·m²/10/ 3.11e^{-3}
Virtual Impedance	0.27 Ω+jω(0.3 mH)
Synchronization Hold Time	10 ms

4 Conclusion

This paper proposes a PLL-free pre-synchronization strategy for VSG-based energy storage converters, addressing harmonic susceptibility in traditional PLLs and enhancing microgrid robustness. The core innovations include:

1) dq-coordinate phase synchronization using VSG's inherent rotor dynamics ($\theta=\int\omega dt$) for grid phase estimation, eliminating PLL dependency[10].

2) Virtual impedance compensation (Z_v = 0.27Ω + jω·0.3mH) combined with voltage feedforward to suppress harmonic interference and correct amplitude deviations. This reduced THD from 5% to 1.5% under voltage distortion[7, 11].

3) Triple grid-tie criteria ($|\Delta V| < 5\%Un$,$|\Delta f|<0.2$Hz,$|\Delta\theta| < 10°$) with 50–100ms delay, limiting inrush current to ≤8% of rated value[10, 12].

Simulations under complex grid conditions validated the strategy's adaptability:

1) Frequency fluctuations (±0.5Hz) were tracked within 0.8s with <0.05Hz steady-state error and <10% power overshoot[10].

2) Virtual inertia (J=0.5kg·m^2) and damping (D_p=10) ensured smooth power transitions during synchronization[12].

This method improves microgrid resilience by utilizing virtual synchronization of virtual synchronous generators (VSGs) for direct grid sensing. Subsequent research will concentrate on hardware validation to tackle nonlinearities such as dead-time effects, as well as coordinating multiple VSGs for power distribution in decentralized systems [3, 13].

Acknowledgment

I am deeply grateful to my mentor, Professor Zhao Tao. With his guidance, I was introduced to the field of power electronics and acquired valuable knowledge that laid a solid foundation for my postgraduate entrance exam preparation and future academic journey. He has been my guiding light in this path.

This work is supported by the Science and Technology Project of State Grid Corporation of China (4000-202318099A-1-1-ZN)).

References

[1] F. Blaabjerg, R. Teodorescu, M. Liserre, and A. V. Timbus, "Overview of control and grid synchronization for distributed power generation systems," *IEEE Transactions on industrial electronics,* vol. 53, no. 5, pp. 1398-1409, 2006.
[2] Y. Yang, B. Liao, L. Zhou, Y. Chao, and C. Si, "An approach to obtain reference sinusoidal signal for grid-connected inverter without phase-locked loop," *Power System Technology,* vol. 37, no. 7, pp. 2000-2005, 2013.
[3] Zhong *et al.*, "Self-Synchronized Synchronverters: Inverters Without a Dedicated Synchronization Unit," *IEEE Transactions on Power Electronics,* vol. 29, no. 2, pp. 617-630, 2014.
[4] R. Shi, X. Zhang, H. Xu, F. Liu, C. Hu, and Y. Yu, "Seamless Switching Control Strategy for Microgrid Operation Modes Based on Virtual Synchronous Generator," *Automation of Electric Power Systems,* vol. 40, no. 10, pp. 16-23, 2016.
[5] M. Li, X. Ma, S. Wei, H. Shi, and Y. Zhang, "Research on Narrow Pulse Suppression of Three-Level Virtual Space Vector Pulse Width Modulation Algorithm," *Transactions of China Electrotechnical Society,* vol. 33, no. 14, 2018.
[6] P. Zhou, X. Zhang, Q. Di, J. Yue, and C. Xing, "Pre-synchronous Grid-connection Strategy of DFIG-based Wind Turbine with Virtual Synchronous Generator Control," *Automation of Electric Power Systems,* vol. 44, no. 14, pp. 71-78, 2020.
[7] Y. Wei, H. Zhang, K. Sun, Q. Song, and Z. Guo, "Pre-synchronization Method of Virtual Synchronous Generator Using Virtual Power," *Automation of Electric Power Systems,* vol. 40, no. 12, pp. 124-129+178, 2016.
[8] C. Jie, C. Xin, F. Zhi-yang, G. Chun-ying, and Y. Yang-guang, "A control strategy of seamless transfer between grid-connected and islanding operation for microgrid," *Proceedings of the CSEE,* vol. 34, no. 19, pp. 3089-3097, 2014.
[9] Y. Shi, J. Lai, J. Su, X. Yang, W. Wu, and Y. Du, "ControlStrategyofSeamlessTransferforMicrogridOperationMode," *Automation of Electric Power Systems,* vol. 40, no. 08, pp. 85-91, 2016.
[10] Z. Lü *et al.*, "Virtual Synchronous Generator and Its Applications in Microgrid," *Proceedings of the CSEE,* vol. 34, no. 16, pp. 2591-2603, 2014.
[11] W. Zhaoan, L. Min, and Z. Fang, "A study on the theory of instantaneous reactive power of three-phase circuits," *Transactions of China electrotechnical society,* vol. 3, pp. 55-59, 1992.
[12] Y. Zhang, L. Zhang, and W. Ma, "Pre-Synchronization Grid-Connected Control Strategy Without PLL Based on Virtual Synchronous Generator," *Electric Machines & Control Application,* vol. 47, no. 11, pp. 82-90+103, 2020.
[13] Y. Hirase, K. Sugimoto, K. Sakimoto, and T. Ise, "Analysis of Resonance in Microgrids and Effects of System Frequency Stabilization Using a Virtual Synchronous Generator," *IEEE journal of emerging and selected topics in power electronics,* vol. 4, no. 4, pp. 1287-1298, 2016.

044 柔性接地装置注入信号的配电网单相接地故障测距方法

叶家男[1]，常仲学[1]，刘晓润[1]

（1．西安交通大学电气工程学院，陕西省西安市）

A Single-phase Grounding Fault Location Method For Distribution Networks Based On The Signal Injection Of Flexible Grounding Devices

YE Jianan[1], CHANG Zhongxue[1], LIU Xiaorun[1]

(1.School of Electrical Engineering, Xi'an Jiaotong University, Xi'an, Shanxi Province, China)

ABSTRACT: Accurate and reliable single-phase grounding fault location methods in distribution networks are critical for reducing fault localization time and enabling rapid service restoration. To address the issue of low location accuracy in conventional methods caused by indistinct fault characteristics, this paper proposes a single-ended fault location method that employs non-power-frequency signal injection through flexible grounding devices. First, the distribution patterns of characteristic signals injected into the neutral point during single-phase grounding faults are analyzed. Equivalent models of three-phase and zero-sequence networks at characteristic frequencies are established, and fault boundary conditions are applied to eliminate unknown load currents downstream of the fault point in the equations, deriving a single-ended fault location equation. Subsequently, power-frequency quantities are utilized to estimate the transition resistance, determining the feasible ranges for both transition resistance and fault distance. A traversal algorithm is employed to determine the precise fault distance. Finally, the selection criteria for characteristic signals injected by flexible grounding devices and the location scheme are presented. Simulation results demonstrate that the method achieves high location accuracy while exhibiting immunity to transition resistance and load variations.

KEY WORDS: Distribution Networks, Single-phase Grounding Fault, Fault Location, Flexible Grounding Devices, Signal Injection

摘要：准确可靠的配电网单相接地故障测距方法对于缩短故障查找时间、快速恢复供电具有重要意义。针对传统方法因故障特征不明显导致测距精度低的问题，本文提出了一种利用柔性接地装置注入非工频信号的单端故障测距方法。首先，分析了单相接地故障时中性点注入特征信号的分布规律，采用特征频率下的三相网络与零序网络等效模型以及故障边界条件，消去方程中故障点下游未知的负荷电流，得到单端测距方程。然后，采用工频量估算过渡电阻，给出过渡电阻和故障位置的取值范围，采用遍历法求解故障精确距离，最后给出了柔性接地装置注入特征信号选取原则以及测距方案。仿真结果表明：该方法具有测距精度高、不受过渡电阻及负荷影响的优点。

关键词：配电网；单相接地故障；故障测距；柔性接地装置；注入法

DOI：10.13335/j.1000-3673.pst.2014.01.论文序号（小五号 Times New Roman 字体加黑）

0 引言

配电网作为电力系统的末端环节，直接面向用户供电，其安全稳定运行对保障电能质量和社会经济活动至关重要。统计数据表明，在电力系统故障中，80%以上是单相接地故障[1]。因此，当配电网发生单相接地故障时，迅速检测并精确定位故障有利于及时消除故障、恢复供电，提升供电可靠性。

目前，配电网单相接地故障测距方法主要可分为以下三类：故障分析法[2-5]、行波法[6-9]以及人工智能算法[10-13]。故障分析法一般基于故障特征构建测距方程，通常采用工频稳态电气量实现测距。文献[5]基于零序电压分布特征，在已有配网自动化节点采集数据并拟合零序电压函数，通过联立方程求解故障点。但高阻接地故障时，故障特征微弱，故障分析法的测距精度将会大大降低。行波法主要基于故障暂态行波的折反射特性，利用其从故障点传播至母线的时延差，计算故障距离。文献[6]针行波波头难识别的问题，提出一种结合广义 S 变换与 Teager 能量算子的双端行波定位方法，通过提升时间分辨率与能量特征提取实现精准故障定位。文献[9]利用投入小电阻后产生的幅值显著、特征清晰的电流行波及其零模/线模分量，通过单端反射波检测

实现单相接地故障测距。但行波法存在故障波头识别难、采样率高等问题。人工智能算法适用于电气量与故障距离存在约束的场景，通过比较与推理，寻找满足测距方程的最优解。文献[13]提出一种融合图论拓扑分解与广义回归神经网络（GDL）的配电网故障定位方法，实现高精度的快速故障定位，但对故障特征数据的训练要求较高，前期工作所需时间较长，灵活性较低。

随着配电网中接入的新能源种类日渐增多，为了克服传统无源消弧装置难以完全补偿接地故障电流等的缺陷，柔性消弧技术在国内外得到了广泛的研究与应用[14-16]。因此，针对上述提出的配电网单相接地故障测距的问题，可以结合已有的柔性接地装置的高可控性，向配电网中性点注入幅值相位可调、时长可控的非工频信号，利用探测信号进行故障测距，从而提高单相接地故障测距的灵敏度和可靠性。

本文提出了一种利用柔性接地装置注入非工频电流的配电网单相接地故障单端测距算法。通过分析单相接地故障的相网络与零序网络故障特征，建立了探测信号频率下的单端测距方程，采用遍历法求解测距方程。该方法无需采集负荷侧量测数据，拓宽了柔性接地装置的功能，降低了故障测距成本，能够兼顾经济性和定位精度两方面的要求。

1　测距模型的分析

1.1 相网络模型

假设线路参数与负荷三相对称，特征频率尺度下的等效相网络模型如图 1 所示，线路采用集中参数 Π 型等值电路。由于相网络部分的测距方程仅涉及故障点上游线路的电气量，图中仅给出故障点上游模型。仅考虑线路相间电容耦合，图中 r_1、l_1 为故障线路单位长度正序电阻和正序电感；c_g、c_m 分别为线路单位长度相间电容及对地电容；p 为故障点到母线的距离。开关 K 闭合，代表消弧线圈接地运行方式；开关 K 打开，代表不接地运行方式。$\dot{I}_{in}$ 为柔性接地装置注入的探测信号。$\dot{U}_{nA}$、$\dot{U}_{nB}$、$\dot{U}_{nC}$、$\dot{I}_{nA}$、$\dot{I}_{nB}$、$\dot{I}_{nC}$ 为故障线路 l_n 首端三相电压、电流。$\dot{U}_{fA}$ 为故障点电压；$\dot{I}_{fA}$ 为流经过渡电阻 R_f 的电流。$\dot{I}_{nAB}$、$\dot{I}_{nAC}$、$\dot{I}_{nAg}$ 分别为 M 侧 A 相流向 B、C 相的相间电容电流和 M 侧 A 相对地电容电流。$\dot{I}_{ZA}$ 为 M 侧流经 A 相线路串联阻抗的电流。

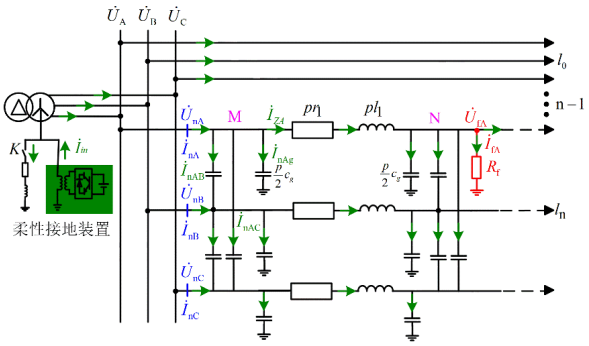


图 1 特征频率尺度下的等效相网络模型

Fig. 1. The equivalent phase network model at characteristic frequency scales

M 侧 A 相线路电容电流之和 $\dot{I}_{Ac\Sigma}$ 为：

$$\begin{cases} \dot{I}_{Ac\Sigma} = \dot{I}_{nAB} + \dot{I}_{nAC} + \dot{I}_{nAg} \\ \dot{I}_{nAB} = \dfrac{p}{2} j\omega c_m (\dot{U}_{nA} - \dot{U}_{nB}) \\ \dot{I}_{nAC} = \dfrac{p}{2} j\omega c_m (\dot{U}_{nA} - \dot{U}_{nC}) \\ \dot{I}_{nAg} = \dfrac{p}{2} j\omega c_g \dot{U}_{nA} \end{cases} \tag{1}$$

定义零序电压补偿系数 K_c：

$$K_c = \frac{c_g}{c_g + 3c_m} - 1 = \frac{c_0}{c_1} - 1 \tag{2}$$

式中，c_0、c_1 分别为线路单位长度零序电容及正序电容，$c_0=c_g$，$c_1=c_g+3c_m$。将式(2)代入式(1)，可得：

$$\dot{I}_{Ac\Sigma} = \frac{p}{2} j\omega c_1 (\dot{U}_{nA} + K_c \dot{U}_0) \tag{3}$$

M 侧流经 A 相线路串联阻抗的电流 $\dot{I}_{ZA}$ 为：

$$\dot{I}_{ZA} = \dot{I}_{nA} - \dot{I}_{Ac\Sigma} = \dot{I}_{nA} - \frac{p}{2} j\omega c_1 (\dot{U}_{nA} + K_c \dot{U}_0) \tag{4}$$

$\dot{I}_{ZA}$ 对应的零序电流 $\dot{I}_{Z0}$ 为：

$$\dot{I}_{Z0} = \dot{I}_0 - \dot{I}_{c0\Sigma} = \dot{I}_0 - \frac{p}{2} j\omega c_0 \dot{U}_0 \tag{5}$$

式中，$\dot{I}_0$ 和 $\dot{U}_0$ 分别为故障线路首端零序电流、电压；$\dot{I}_{c0\Sigma}$ 为故障线路 M 侧对地电容电流。

A 相故障点电压可表示为：

$$\dot{U}_{fA} = \dot{U}_{nA} - pr_1 \left(\dot{I}_{ZA} + 3K_R \dot{I}_{Z0} \right) - j\omega p l_1 (\dot{I}_{ZA} + 3K_L \dot{I}_{Z0}) \tag{6}$$

1.2 零序网络模型

建立与图 1 对应的零序网络模型如图 2 所示。图中，r_0、l_0、c_0 为故障线路单位长度零序电阻和零序电感、零序电容；$\dot{U}_{f0}$ 为故障点零序电压；$\dot{I}_{f0}$ 为流经 Z_f 的零序电流，Z_f 为正序网络、负序网络与 $3R_f$ 的串联等效阻抗；$\dot{U}_{b0}$ 为故障线路末端零序电压。

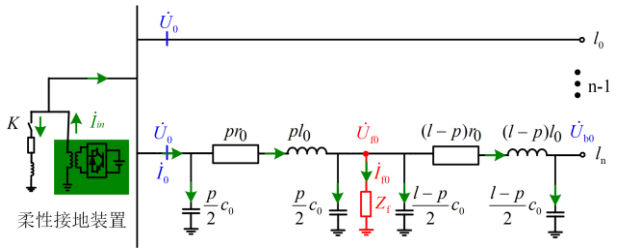


图 2 特征频率尺度下的等效零序网络模型

Fig. 2. The equivalent zero-sequence network model at characteristic frequency scales

$\dot{I}_{f0}$ 可表示为：

$$\begin{cases} \dot{I}_{f0}=\dot{I}_0-\dfrac{p}{2}\mathrm{j}\omega c_0\dot{U}_0-\dfrac{p}{2}\mathrm{j}\omega c_0\dot{U}_{f0}-\dfrac{l-p}{2}\mathrm{j}\omega c_0\dot{U}_{f0} \\ \qquad -\dfrac{l-p}{2}\mathrm{j}\omega c_0\dot{U}_{b0} \\ \dot{U}_{f0}=\dot{U}_0-(\dot{I}_0-\dfrac{p}{2}\mathrm{j}\omega c_0\dot{U}_0)p(r_0+\mathrm{j}\omega l_0) \\ \dot{U}_{b0}=\dot{U}_{f0}-\dfrac{l-p}{2}\mathrm{j}\omega c_0\dot{U}_{b0}\times(l-p)(r_0+\mathrm{j}\omega l_0) \end{cases} \tag{7}$$

式中，l 表示故障线路全长。

1.3 测距方程的构建

引入单相接地故障边界条件，可将故障相电流 $\dot{I}_{fA}$ 代换到零序网络，将其用零序网络中线路参数及零序电气量表示，使未知量可以求解。

$$\dot{I}_{fA}=3\dot{I}_{f0} \tag{8}$$

联立式(4)至(8)，即可得测距方程：

$$\begin{aligned} f(p,R_f)=&\dot{U}_{nA}-pr_l\left(\dot{I}_{ZA}+3K_R\dot{I}_{Z0}\right)-\mathrm{j}\omega pl_l(\dot{I}_{ZA}+3K_L\dot{I}_{Z0}) \\ &-3R_f(\dot{I}_{Z0}-\frac{l}{2}\mathrm{j}\omega c_0\dot{U}_{f0}-\frac{l-p}{2}\mathrm{j}\omega c_0\dot{U}_{b0}) \\ =&0 \end{aligned} \tag{9}$$

2 测距方程的求解

2.1 过渡电阻及故障距离的取值范围

发生单相接地故障后，配电网基频零序不平衡电流 $\dot{I}_{0E}$ 为：

$$\dot{I}_{0E}=-(\dot{E}_AY_A+\dot{E}_AG_E+\dot{E}_BY_B+\dot{E}_CY_C) \tag{10}$$

式中：$Y_A=\mathrm{j}\omega C_A$、$Y_B=\mathrm{j}\omega C_B$、$Y_C=\mathrm{j}\omega C_C$，C_A、C_B、C_C 为 A、B、C 三相线路对地分布总电容；Y_0 为中性点对地导纳，对于不接地系统 Y_0=0。

根据零序电压产生机理，故障后基频零序电压在零序阻抗上产生的电流与基频零序不平衡电流 $\dot{I}_{0E}$ 相等，则有：

$$\begin{aligned} &\dot{U}_{0_50Hz}(Y_A+Y_B+Y_C+Y_0+G_E) \\ &=-(\dot{E}_AY_A+\dot{E}_AG_E+\dot{E}_BY_B+\dot{E}_CY_C) \end{aligned} \tag{11}$$

基频故障相电压 $\dot{U}_{A_50Hz}$ 可表示为：

$$\dot{U}_{A_50Hz}=\dot{E}_A+\dot{U}_{0_50Hz} \tag{12}$$

式中，$\dot{E}_A$ 为电源电压。

将(12)代入式(11)，可得过渡电阻初值 $R_{f_initial}$：

$$R_{f_initial}=real(\frac{\dot{U}_{A_50Hz}}{-\dot{U}_{0_50Hz}(Y_A+Y_B+Y_C+Y_0)}) \tag{13}$$

严格意义上，$R_{f_initial}$ 为故障点过渡电阻和故障区间线路阻抗之和，因此过渡电阻 R_f 取值范围为：

$$0\le R_f\le R_{f_initial} \tag{14}$$

故障距离 p 的取值范围为：

$$0<p<l \tag{15}$$

2.2 遍历法求解测距方程

求解测距方程 $f(p,R_f)=0$ 时，代入线路首端测得的特征频率故障相电压、故障相相电流、零序电压、零序电流，遍历过渡电阻 R_f 的取值范围，求解对应的 p。当 p 的虚部为 0 时，p 的实部即为故障距离，对应的 R_f 即为过渡电阻真实值。如下式所示：

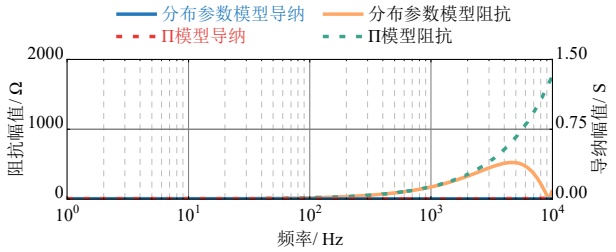
$$\begin{cases} f(p,R_f)=0 \\ S=\{p_1,p_2,\cdots,p_n\} \\ p=\min_{p_i\in S}(|\mathrm{Im}(p_i)|) \\ \text{s.t. } \mathrm{Re}(p)\in[0,l] \end{cases} \tag{16}$$

若满足式(16)的 p 存在多个，可利用基频电气量排除伪根。

3 探测信号的选取及测距方案

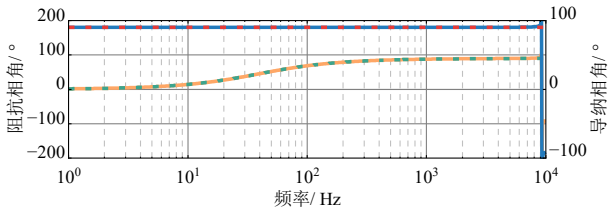
3.1 频率选取

本文提出的故障测距算法所采用的配电网线路模型为集中参数 Π 型等值电路模型，而实际线路为分布参数模型，故注入频率需考虑该线路模型的适用频带。选取 10 kV 配电线路的典型参数，可以得到分布参数与集中参数 Π 型电路的线路阻抗和导纳的幅频特性和相频特性如图 3 所示。



(a) 幅频特性

(a) Magnitude-Frequency Characteristics



(b) 相频特性

(b) Phase-Frequency Characteristics

图 3 配电线路两种模型的幅频特性与相频特性

Fig. 3. Magnitude-Frequency and Phase-Frequency Characteristics of Distribution Lines for Both Modeling Approaches

由图 3 可知，两种模型的频率特性差异随频率升高而增大，可确定截止频率为 1590Hz。为减小工频谐波对检测和提取探测信号的影响，应选择间谐波作为探测信号。此外，探测信号的频率应限制在柔性接地装置载波频率的 10%（500Hz）以下，以确保探测信号能被柔性接地装置精确调制。

3.2 幅值选取

探测电流幅值过低时信号采集较为困难，幅值过高又会导致中性点过电压问题。因此，探测电流幅值不应超过最大负荷电流(600 A)的 3%，并限制探测电压不高于额定电压的 12.5%。

综上所述，本文选择采用 225 Hz、5 A 的恒流注入方案，以兼顾测距精度、设备能力与系统安全。

3.3 故障测距方案

如图 4 所示，系统持续监测中性点零序电压，当连续三次采样数据大于 10%额定相电压时，输入选相结果，若为单相接地故障，柔性接地装置随即启动，向配电网中性点注入特征频率探测信号。持续注入 400 ms，确保信号稳定并满足测距算法数据窗时长需求，将采集得到的故障线路首端基频、特征频率电气量代入计算故障距离及过渡电阻。

4 仿真验证

4.1 仿真模型

为验证上文方法的可行性，本文利用电磁暂态仿真软件 PSCAD/EMTDC 建立如图 5 所示 10 kV 配电网单相接地故障模型进行分析。配电网仿真模型由多条馈线组成，其中，l_1 和 l_2 为电缆线路，l_3 为架空线路，各条线路长度如图 5 所示，l_1 和 l_3 线路负荷均设置为 1.5 MW，l_2 线路负荷 0.9 MW。消弧线圈电感取 0.45 H，阻尼电阻 14 Ω，过补偿度 10%。电缆与架空线的参数如表 1 所示。

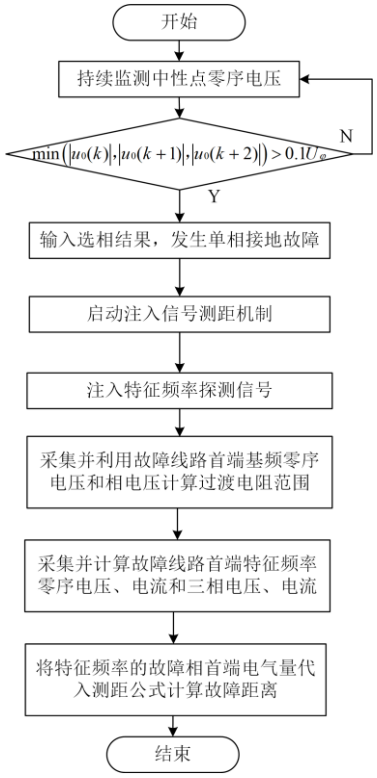


图 4 故障测距流程图

Fig. 4. Fault Location Flowchart

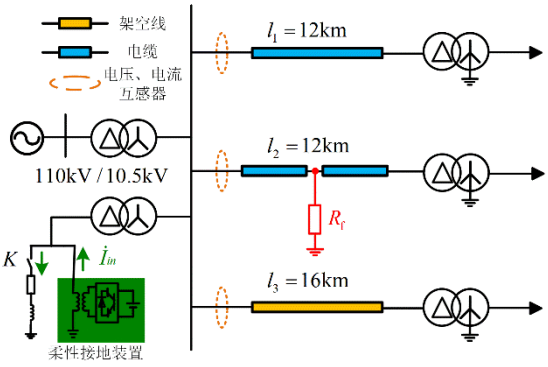


图 5 仿真模型

Fig. 5. Simulation Model

表 1 电缆及架空线参数

Table 1. Parameters for Cable and Overhead Lines

线路类型	相序	电阻 /(Ω/km)	电感 /(mH/km)	电容 /(μF/km)
架空线	正序	0.279	1.13	0.0055
	零序	0.387	1.148	0.0042
电缆	正序	0.27	0.255	0.339
	零序	2.7	1.019	0.280

设故障发生时刻为 0.985 s，柔性接地装置注入

频率 225 Hz 的电流，注入电流幅值 5 A，电流开始注入时刻为 1s，持续注入至 1.4 s，选取 1.2 s 至 1.4 s 的数据执行故障测距算法。

4.2 中性点不接地系统仿真结果

设线路 l_2 发生 A 相单相接地故障，故障距离 1 km，过渡电阻为 500 Ω，获取故障后线路 l_2 首端的电压和电流数据，计算过渡电阻初值 $R_{f_initial}$ 为 502.18Ω，递减地遍历 $R_{f_initial}$-0Ω，步长为 1Ω，将特征频率电气量与 R_f 代入测距方程，计算相应的 p。计算得到，当 R_f=500.18Ω 时，p 的虚部绝对值 $|\mathrm{Im}(p)|$ 最小，此时故障距离为 1013.50 m。该算法不仅可以计算出单相接地故障距离，还可以准确识别过渡电阻大小。

为了比较不同故障条件下的测距结果和误差，分别将故障点设置在线路 l_2 距离首端 1、6、11 km 处；为了验证过渡电阻的影响，分别将接地电阻设置为 10 Ω、500 Ω、1000 Ω、2000 Ω；为了验证负荷的影响，分别将线路 l_2 负荷设置为 0.9 MW、4.5 MW。定义相对误差=｜测距结果-实际故障距离｜/线路总长，仿真结果如表 2 所示。

表 2 中性点不接地系统故障仿真结果

Table 2. Fault Simulation Results for Ungrounded Systems

负荷 MW	故障距离/m	R_f/Ω	测距结果/m	相对误差/%	R_f 计算值/Ω
0.90	1000	10	976.62	0.19	10.05
		500	1013.50	0.11	500.18
		1000	991.00	0.08	999.57
		2000	1024.70	0.21	2005.78
	6000	10	5993.90	0.05	10.01
		500	5989.70	0.09	499.82
		1000	5981.70	0.15	999.39
		2000	5974.00	0.22	2001.11
	11000	10	11025.90	0.22	9.96
		500	10993.00	0.06	499.97
		1000	10988.40	0.10	1000.06
		2000	10992.40	0.06	2002.18
4.50	1000	10	1010.00	0.08	9.98
		500	988.13	0.10	499.71
		1000	1005.00	0.04	1000.25
		2000	1024.00	0.20	2005.86
	6000	10	5985.60	0.12	10.03
		500	5997.70	0.02	500.04
		1000	5979.70	0.17	999.33
		2000	5972.00	0.23	2001.20
	11000	10	11031.70	0.26	9.95
		500	10997.00	0.03	499.90
		1000	10982.00	0.15	1000.48
		2000	10992.60	0.06	2002.53

通过对比表 2 中测距结果可知，最大相对误差为 0.26%，最大绝对误差为 31.7m，测距精度高，且不受过渡电阻和负荷的影响。

4.3 消弧线圈接地系统仿真结果

为进一步验证方法不受中性点接地方式影响，中性点经消弧线圈接地系统故障测距结果如表 3 所示。

表 3 消弧线圈接地系统故障仿真结果

Table 3. Simulation Results for the Arc-Suppression-Coil Grounded System

负荷 MW	故障距离/m	R_f/Ω	测距结果/m	相对误差/%	R_f 计算值/Ω
0.90	1000	10	990.59	0.08	10.02
		500	1002.80	0.02	499.97
		1000	997.00	0.03	999.63
		2000	972.65	0.23	1960.56
	6000	10	5999.70	0.00	10.00
		500	5985.00	0.13	499.69
		1000	5975.70	0.20	999.06
		2000	5951.00	0.41	1968.96
	11000	10	11024.50	0.20	9.96
		500	10996.10	0.03	499.91
		1000	10985.50	0.12	1000.05
		2000	10969.90	0.25	1975.83
4.50	1000	10	998.92	0.01	10.00
		500	968.29	0.26	499.39
		1000	991.00	0.08	999.34
		2000	974.39	0.21	1961.38
	6000	10	6011.70	0.10	9.98
		500	5982.30	0.15	499.66
		1000	5982.40	0.15	999.34
		2000	5958.00	0.35	1970.34
	11000	10	11016.70	0.14	9.97
		500	10982.80	0.14	500.13
		1000	10989.20	0.09	999.91
		2000	10971.70	0.24	1977.47

通过对比表 3 中测距结果可知，最大相对误差为 0.41%，最大绝对误差为 49m，测距精度高，且不受过渡电阻和负荷的影响。综合分析表 2、表 3 可知，该测距方法不受中性点接地方式影响。

以上仿真结果证明，本文所提出的利用柔性接地装置注入信号的配电网单相接地故障测距方法准确有效。

5 结论

针对现有单相接地故障测距方法在高阻接地故障时故障特征微弱，测距精度不足的问题，本文通过分析特征频率下单相接地故障的三相网络与零序网络故障特征，提出一种基于柔性接地装置信号注入的配电网单相接地故障测距方法。理论分析与仿真证明：

（1）通过分析单相接地故障时注入特征信号的分布规律，建立特征频率下的三相网络与零序网络等效模型，可以得到不受负荷电流影响的单端测

距方程。

（2）特征信号的选取需综合考虑线路模型的适用频带、装置的性能约束、中性点电压阈值以及信号动态调节时间等关键因素。

（3）利用柔性接地装置的可控性注入非工频信号，可显著提升测距精度，且不受过渡电阻和负荷影响。

本文的方法仅适用于无分支线场景，后续还需进一步研究含分支线场景下的测距方法。

参考文献

[1] 梁睿，孟祥震，周鲁天，等．配电网故障定位技术发展现状及展望[J]．电力工程技术，2018，37(06)：20-27

[2] 索南加乐，康小宁，宋国兵，等．基于参数识别的继电保护原理初探[J]．电力系统及其自动化学报，2007，(01)：14-20+27．

[3] Dashti R，Sadeh J．Fault section estimation in power distribution network using impedance-based fault distance calculation and frequency spectrum analysis[J]．IET Gener. Transm. Distrib.，2014，8：1406-1417．

[4] Fang J，et al．Analysis of Multi-point Synchronous Measurement Data for Fault Location of Distribution Network[C]．2020 10th International Conference on Power and Energy Systems (ICPES)．Chengdu，China，2020：384-387．

[5] 刘江东，董礼清，薛晨，等．基于零序电压分布特征的小电流接地故障测距初探[J]．电力系统保护与控制，2022，50(03)：59-67．

[6] 刘文杰，舒勤，韩晓言．基于广义 S 变换和 TEO 的配电网故障定位方法[J]．电力系统及其自动化学报，2019，31(01)：12-18

[7] Wang C，Wu N，Fan S．Fault Location In Multi-Branch Distribution Network Based On The First Traveling Wave Time Difference Of Arrival Relationship[C]．2019 Chinese Automation Congress (CAC)．Hangzhou，China，2019：4443-4450．

[8] Hongchun S，Xu W，Qi X，et al．A fault location method of traveling wave for distribution network with only two-phase current transformer using artificial neutral network[C]．2010 3rd International Congress on Image and Signal Processing．Yantai，China，2010：2942-2945．

[9] 齐郑，杭天琦，李悦悦．消弧线圈并联小电阻接地方式下的行波故障测距[J]．电力系统自动化，2020，44(01)：175-182．

[10] 贾科，李论，杨哲，等．基于贝叶斯压缩感知理论的配网故障定位研究[J]．中国电机工程学报，2019，39(12)：3475-3486．

[11] 王宇杉，王晨，王淑侠，等．基于 IWOA 的配电网故障定位方法[J]．智慧电力，2024，52(11)：98-105．

[12] 熊芮，赵林军，张宇航．基于灰狼-粒子群算法的有源配电网故障定位[J]．电力系统及其自动化学报，2025，37(05)：141-148+158．

[13] Zhou S，Xue Z，Ai L，et al．Distribution Network Fault Location Method Based on Graph Theory and Deep Learning under Charging Load Access[C]．2021 IEEE 5th Conference on Energy Internet and Energy System Integration (EI2)．Taiyuan，China，2021：1237-1241．

[14] 卫晓辉，邵文权，程远，等．配电网单相接地故障有源消弧技术综述[J]．电力工程技术，2020，39(06)：58-65．

[15] 郭谋发，游建章，郑泽胤．配电网单相接地故障柔性消弧技术综述[J]．高电压技术，2023，49(10)：4232-4246．

[16] 喻泉，曾祥君，喻锟，等．基于对地参数双端测量及闭环控制的配电网柔性接地有源消弧方法[J]．高电压技术，2022，48(03)：1011-1021．



叶家男

收稿日期：2013-07-04。

作者简介：

叶家男(2002)，女，硕士研究生，研究方向为配电网故障处理，E-mail：gianna_ye@163.com；

常仲学(1991)，男，副教授，博士生导师，研究方向为电力系统继电保护，E-mail：changzhx@xjtu.edu.cn。

（编辑　五号楷体，居右，段前空 6pt）

045 Analysis on Equivalent Impedance Characteristics for VSG-Controlled Wind Farms

Xinyao Li, Zhongxue Chang

Xi'an Jiaotong University, Xi'an 710049, China
lxy3124304264@stu.xjtu.edu.cn

Abstract. The control strategy shapes the equivalent impedance characteristics of wind farms. VSG employs self-synchronization mechanisms to eliminate grid dependency and is widely used in wind farms. Currently, research on fault characteristics is mostly focused on grid-following controlled wind farms, while studies on VSG-controlled wind farms are still insufficient. This paper proposes a method for calculating steady-state fault voltages/currents based on the simultaneous solution of node voltage equations, fault boundary conditions, and VSG control equations. On this basis, the equivalent impedance of VSG-controlled wind farms is calculated and its characteristics are analyzed. A simulation model is built in PSCAD/EMTDC. Different fault types and location cases are simulated and results show that the proposed method is feasible.

Keywords: VSG control, adaptive virtual impedance, equivalent impedance, wind farm.

1 INTRODUCTION

In recent years, wind power has emerged as one of the most rapidly expanding renewable energy sources [1]. Currently, grid-following (GFL) control is widely adopted in the grid-side converters (GSCs) of wind power generation systems, as it relies on PLL to synchronize with the power grid. This architecture may lead to frequency instability [2] and undesirable interactions between converters [3] under weak grid conditions. In contrast, VSG control employs a self-synchronization mechanism, eliminating the grid dependency, and provides active support to grid voltage and frequency by emulating the regulation characteristics of synchronous generators (SGs).[4] Despite its numerous advantages, the voltage-source behavior of VSG control is characterized by a potential for severe overcurrent during grid faults. To address this, two schemes have been proposed: direct current limiting [5] and indirect current limiting [6]. As an indirect current limiting strategy, virtual impedance control has been extensively researched and adopted due to its capability to limit overcurrent while preserving the voltage source behavior of the converter. It is classified into fixed virtual impedance and adaptive virtual impedance. The former offers straightforward parameter tuning but poor adaptability to complex conditions; the latter, despite its structural complexity, enables active adjustment of virtual

impedance based on fault severity, thereby exhibiting greater practical applicability [7].

Research on VSG fault characteristics has made progress, but limitations remain. Reference [8] applied transfer functions to derive the steady-state current expression under symmetrical fault conditions; however, it needs the post-fault terminal voltage for calculation. To overcome this shortcoming, Reference [9] obtained the steady-state voltages and currents that account for the interaction effect by solving the equations based on the composite sequence network. Additionally, References [10-11] extended the research scope to transient processes and proposed an iterative algorithm for calculating transient fault current; however, a significant drawback of this algorithm is its neglect of time delays in the control system, which leads to substantial errors. Through the findings from the fault characteristics analysis, the equivalent impedance characteristics of wind farms have been studied. Reference [12] focused on the transient behavior of the DFIG's equivalent impedance phase angle, noting a wide variation range in the positive-sequence component. Reference [13] analyzed the equivalent impedance characteristics of wind farms by means of theoretical derivation, simulation verification, and recorded waveform data analysis. It concluded that equivalent impedance is unstable and that the positive-sequence and negative-sequence impedances are not equal. Building on this, Reference [14-15] utilized control equations and network topology to derive the possible range of equivalent impedance for converters, further quantifying the characteristics of the equivalent impedance. However, the studies mentioned above were all conducted on GFL-controlled wind farms. Due to their unique control characteristics, VSG-controlled wind farms show distinct equivalent impedance characteristics compared to traditional plants, which renders existing research findings difficult to apply directly.

This paper analyzes the equivalent impedance characteristics of VSG-controlled wind farms. First, the control method and fault ride-through (FRT) strategy of the VSG are introduced. Then, a novel calculation method for steady-state fault voltages/currents is proposed and employed to calculate and analyze the wind farms' equivalent impedance. A simulation model was ultimately developed using PSCAD/EMTDC, and the simulation results show that the proposed method has high accuracy.

2 VSG CONTROL METHOD AND FAULT RIDE-THROUGH STRATEGY

The fault characteristics of wind farms are mainly governed by the control strategies of their generation units. Consequently, this section focuses on the control method of the VSG and its fault ride-through (FRT) strategy.

2.1 Topology of the VSG-controlled Wind Farm Transmission System

The VSG-controlled wind farm transmission system consists of a wind farm (which includes PMSG-based wind turbines and a medium-voltage collection system), high-voltage transmission lines, and a receiving grid. Considering that geographical distribution of wind turbines has little impact on the fault characteristics of wind farms [16], a single-machine equivalent aggregation model is adopted. Fig. **1** shows the

topological structure of the wind power transmission system.

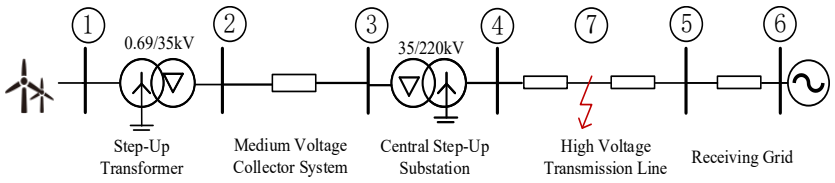


Fig. 1 The topological structure of the VSG-controlled wind farm transmission system

2.2 VSG Control Method

PMSG-based wind turbine interfaces with the grid via full-power converters. The machine-side converter aims to maintain constant DC-link voltage. It is replaced by an ideal DC voltage source when DC voltage fluctuations can be ignored. The grid-side converter (GSC) is responsible for output power regulation and employs a VSG control strategy that includes power synchronization, virtual impedance, and voltage-current closed-loop control.

Power synchronization control comprises P-f control and Q-U control. The P-f control emulates the second-order rotor swing equation of SGs to generate the phase angle of the reference voltage, and the Q-U control emulates the excitation and voltage regulation characteristics to generate a reference voltage magnitude. The equations for power synchronization control are as follows.

$$\begin{cases} J\dfrac{\mathrm{d}\omega}{\mathrm{d}t}=\dfrac{k_{\mathrm{p}}(\omega_0-\omega)+P_{\mathrm{ref}}-P_{\mathrm{e}}}{\omega_0}-D(\omega-\omega_0) \\ E=E_{\mathrm{ref}}+k_{\mathrm{q}}\left(Q_{\mathrm{ref}}-Q_{\mathrm{e}}\right) \end{cases} \tag{1}$$

Where: P_{ref} , Q_{ref} , P_{e} , Q_{e} are the reference value and actual value of active and reactive power; J , D are virtual inertia and virtual damping; ω is virtual angular velocity, ω_0 is rated angular velocity; k_{p} , k_q are active and reactive power droop coefficients; E_{ref} is VSG rated voltage value, E is voltage reference amplitude.

Virtual impedance control is proposed to mimic the stator winding characteristics of SGs, which can limit the short-circuit current and provide reactive power support to the grid during faults. The virtual impedance control equation is as follows.

$$\begin{cases} e_{\mathrm{d}}=E_{\mathrm{d}}-R_{\mathrm{v}}i_{\mathrm{Ld}}+\omega L_{\mathrm{v}}i_{\mathrm{Lq}} \\ e_{\mathrm{q}}=E_{\mathrm{q}}-R_{\mathrm{v}}i_{\mathrm{Lq}}-\omega L_{\mathrm{v}}i_{\mathrm{Ld}} \end{cases} \tag{2}$$

Where: E_{d} , E_{q} are the voltage reference value generated by the power outer loop; I_{Ld} , I_{Lq} are the current of filter inductor; R_{v} , X_{v} are virtual resistance and virtual reactance; e_{d} , e_{q} are the voltage reference value of the voltage outer loop.

The voltage and current closed-loop control typically employ PI controllers with the introduction of feedforward and decoupling terms. The voltage loop, with a lower bandwidth, ensures precise steady-state regulation of the output voltage, while the

current loop, featuring a higher bandwidth, enables rapid dynamic response under external disturbances. This differentiated bandwidth design not only ensures the steady-state control accuracy of the system but also guarantees the stability of dynamic processes. The topology and control block diagram of VSG is shown in Fig. 2. u_{abc} is the three-phase voltage across the filter capacitors; i_{abc} is the three-phase current flowing through the filter inductor; i_{Labc} is the three-phase current injected from the converter into the grid.

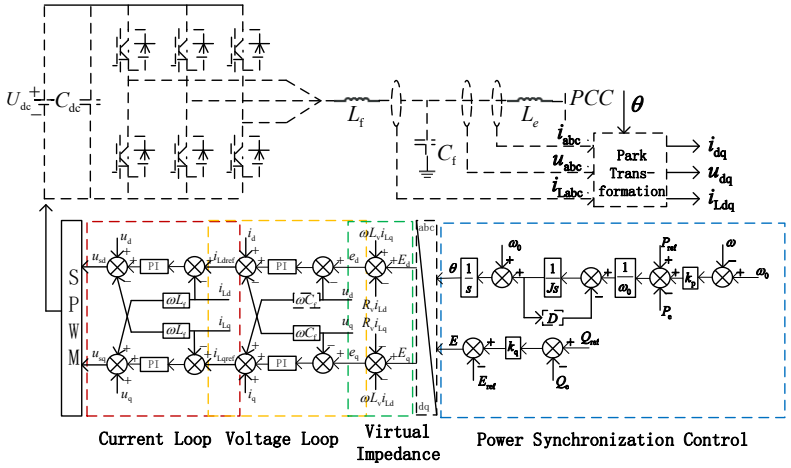


Fig. 2. Topology and control block diagram of VSG

2.3 Fault Ride-Through (FRT) Control Strategy for VSG

The fault ride-through control strategy adopted in this paper is as follows.

1) Freezing power synchronization control [17]. The P-f control is frozen to prevent the converter from losing power angle stability. Similarly, the Q-U control is frozen in order to maintain a constant internal electromotive force (EMF). This approach is implemented by forcibly setting the active and reactive power discrepancies in the control equations to zero.

2) Employing adaptive virtual impedance. Building upon current-proportional adaptive virtual impedance, a PI controller is introduced to achieve both smooth impedance engagement and steady-state fault current regulation with zero error. A purely inductive virtual impedance is adopted here for two reasons: it maximizes the converter's reactive power capacity during faults, enhancing voltage support, and provides effective current limiting with low impedance value, reducing adverse system impacts. The calculation formula of virtual impedance is as follows.

$$\begin{cases} X_{\mathrm{v}} = \left(K_{\mathrm{pv}} + \dfrac{K_{\mathrm{iv}}}{s} \right) \left(I_{\mathrm{fault}} - I_{\max} \right) \\ R_{\mathrm{v}} = kX_{\mathrm{v}} \end{cases} \tag{3}$$

Where: I_{fault} is the amplitude of the short-circuit fault current at the filter inductor; is the maximum allowable positive sequence current; k is The ratio of virtual reactance

to virtual resistance.

3) Introducing negative-sequence control. Asymmetric faults introduce negative- and zero-sequence components into the system. Considering the vector group of the converter transformer, zero-sequence components can't flow into the wind turbine side. For negative-sequence components, negative-sequence reactive current should be absorbed to reduce the voltage asymmetry [18]. The reference value of negative-sequence current is as follows.

$$\begin{cases} I_{\mathrm{Ldref}} = 0 \\ I_{\mathrm{Lqref}} = -K_2^- I_{\mathrm{N}} U_*^- \end{cases} \tag{4}$$

Where, k_2^- is the proportional coefficient of negative-sequence reactive current; I_{N} is the system rated current value; U_*^- is per-unit value of negative-sequence voltage at the PCC of the wind turbine grid-side converter.

3 ANALYSIS ON EQUIVALENT IMPEDANCE CHARACTERISTICS FOR WIND FARMS

Building on the VSG fault ride-through strategy detailed in Section 2, this section computes the equivalent impedance of wind farms by means of a novel method for calculating steady-state fault voltages and currents and analyzes its characteristics.

3.1 Steady-state Fault Voltages and Currents Calculation Method

The value of adaptive virtual impedance is affected by various factors, such as fault type, fault distance, transition resistance, and system parameters. Qualitative analysis is insufficient to provide accurate numerical results. Therefore, a quantitative calculation method is necessary and is proposed in this section.

The idea of the calculation method is to solve the node voltage equations, fault boundary conditions, and VSG control equations simultaneously. The node voltage equations are as follows.

$$\begin{cases} I_+ = Y_+ U_+ \\ I_- = Y_- U_- \\ I_0 = Y_0 U_0 \end{cases} \tag{5}$$

For the fundamental types of faults, fault boundary conditions at the fault node (node 7) can be established from the construction of the composite sequence network.

$$\begin{cases} \dot{U}_{7.+} + \dot{U}_{7.-} + \dot{U}_{7.0} + \left(\dot{I}_{7.+} + \dot{I}_{7.-} + \dot{I}_{7.0}\right) R_{\mathrm{f}} = 0 \\ \dot{I}_{7.+} - \dot{I}_{7.-} = 0 \\ \dot{I}_{7.+} - \dot{I}_{7.0} = 0 \end{cases} \quad (\mathrm{AG}) \tag{6}$$

$$\begin{cases} \dot{U}_{7.+} - \dot{U}_{7.-} = 0 \\ \dot{U}_{7.-} - \dot{U}_{7.0} - 3\dot{I}_{7.0}R_{\mathrm{f}} = 0 \\ \dot{I}_{7.+} + \dot{I}_{7.-} + \dot{I}_{7.0} = 0 \end{cases} \quad (\mathrm{BCG}) \tag{7}$$

$$\begin{cases} \dot{I}_{7.0} = 0 \\ \dot{I}_{7.+} + \dot{I}_{7.-} = 0 \\ \dot{U}_{7.+} - \dot{U}_{7.-} + \dot{I}_{7.+}R_{\mathrm{f}} = 0 \end{cases} \quad (\mathrm{BC}) \tag{8}$$

$$\dot{U}_{7.+} + \dot{I}_{7.+}R_{\mathrm{f}} = 0 \quad (\mathrm{ABC}) \tag{9}$$

Where: $U_+ = \left[\dot{U}_{1.+} \cdots \dot{U}_{7.+}\right]$, $U_- = \left[\dot{U}_{1.-} \cdots \dot{U}_{7.-}\right]$, $U_0 = \left[\dot{U}_{3.0} \cdots \dot{U}_{7.0}\right]$ are the voltage vectors of each node in the positive, negative and zero sequence network; $I_+ = \left[\dot{I}_{1.+} \cdots \dot{I}_{7.+}\right]$, $I_- = \left[\dot{I}_{1.-} \cdots \dot{I}_{7.-}\right]$, $I_0 = \left[\dot{I}_{3.0} \cdots \dot{I}_{7.0}\right]$ are current injection vectors of each node in the positive, negative and zero sequence network; Y_+ , Y_- , Y_0 are positive, negative and zero sequence node admittance matrices.

To facilitate the solution, this complex equation system is transformed into a real-number form. Since the currents injected at the wind turbine node (node 1) are unknown, the resulting equation system is underdetermined and cannot be solved for all unknowns. Therefore, additional equations derived from the VSG control strategy must be introduced.

The positive-sequence additional equations can be derived from equation (2) and the first fault ride-through strategy.

$$\begin{cases} I_{1\mathrm{x}.+} = \dfrac{E_{1\mathrm{y}} - U_{1\mathrm{y}.+}}{X_{\mathrm{v}}} \\ I_{1\mathrm{y}.+} = -\dfrac{E_{1\mathrm{x}} - U_{1\mathrm{x}.+}}{X_{\mathrm{v}}} \end{cases} \tag{10}$$

Where: $E_{1\mathrm{x}}$, $E_{1\mathrm{y}}$ are the value of pre-fault internal electromotive force; $U_{1\mathrm{x}.+}$, $U_{1\mathrm{y}.+}$ are the post-fault wind turbine node positive-sequence voltage value; $I_{1\mathrm{x}.+}$, $I_{1\mathrm{y}.+}$ are the post-fault wind turbine node positive-sequence injection current.

The negative-sequence equation can be derived from equation (4). It is evident that in the negative-sequence network, the wind turbine can be modeled as a constant impedance Z_{s}^- .This impedance is determined by the rated impedance Z_{N} and the negative-sequence reactive current proportional coefficient K_2^- . The negative-sequence additional equation and the expression for Z_{s}^- are given as follows.

$$\begin{cases} I_{1\mathrm{x}.-} = -\dfrac{K_2^- U_{1\mathrm{y}.-}}{Z_{\mathrm{N}}} \\ I_{1\mathrm{y}.-} = \dfrac{K_2^- U_{1\mathrm{x}.-}}{Z_{\mathrm{N}}} \end{cases} \tag{11}$$

$$Z_{\mathrm{s}}^- = \frac{Z_{\mathrm{N}}}{K_2^-} e^{j90^\circ} \tag{12}$$

Where: $U_{1x.-}$, $U_{1y.-}$ are the post-fault wind turbine node negative-sequence voltage value; $I_{1x.-}$, $I_{1y.-}$ are the post-fault wind turbine node positive-sequence injection current.

By combining equations (5), (10), and (11) with the fault boundary conditions, it is found that the virtual impedance term appears in the admittance matrix. For each input virtual impedance value, the node voltage equations can be solved once to obtain the corresponding voltage and current vectors.

From equation (5), it is known that the amplitude of the positive-sequence short-circuit current after the fault is limited to I_{max}. If the value of the virtual impedance is known, then the amplitude of the short-circuit current obtained by solving the corresponding node voltage equations must satisfy $|\dot{I}_{fault}| = I_{max}$. Therefore, after a given initial value, the adjustment direction of the virtual impedance can be determined according to the current residual $|I_{fault} - I_{max}|$. Based on this idea, a method for calculating fault voltages and currents is proposed, and the calculation flow chart is as follows.

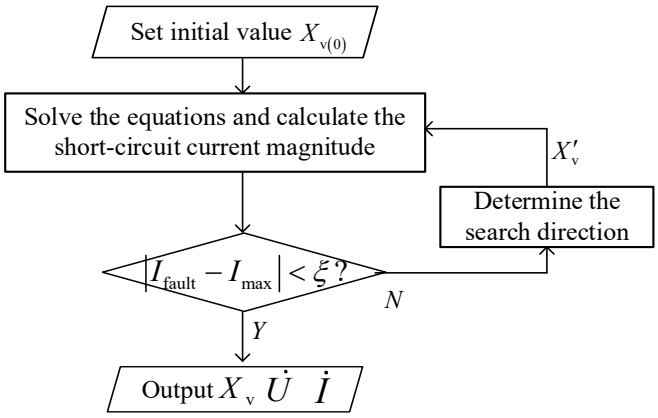


Fig. 3. Flowchart for fault voltages/currents calculation

3.2 Analysis on Equivalent Impedance Characteristics for Wind Farms

Using the proposed method, the equivalent impedance characteristics of wind farms are analyzed. The expression for the positive-sequence equivalent impedance is as follows.

$$Z_m^+ = -\frac{\dot{U}_{(0)} - \dot{U}}{\dot{I}_{(0)} - \dot{I}} \tag{13}$$

Where: $\dot{U}_{(0)}$, $\dot{U}$ are the voltage at Node 4 before and after the fault; $\dot{I}_{(0)}$, $\dot{I}$ are the current flowing through the line between Node 4 and Node 7 before and after the fault; Z_m^+ is the positive-sequence equivalent impedance of wind farms.

Different types of faults are set on the transmission line, and all combinations of fault distance (1–99 km, step size 1 km) and transition resistance (0–220 Ω, step size 1 Ω) are traversed. The results are substituted into equation (13) to calculate the positive-sequence equivalent impedance of wind farms. The impedance distribution characteristics under different fault conditions are as follows.

$U_{(\ )}$ U

$I_{(\ )}$

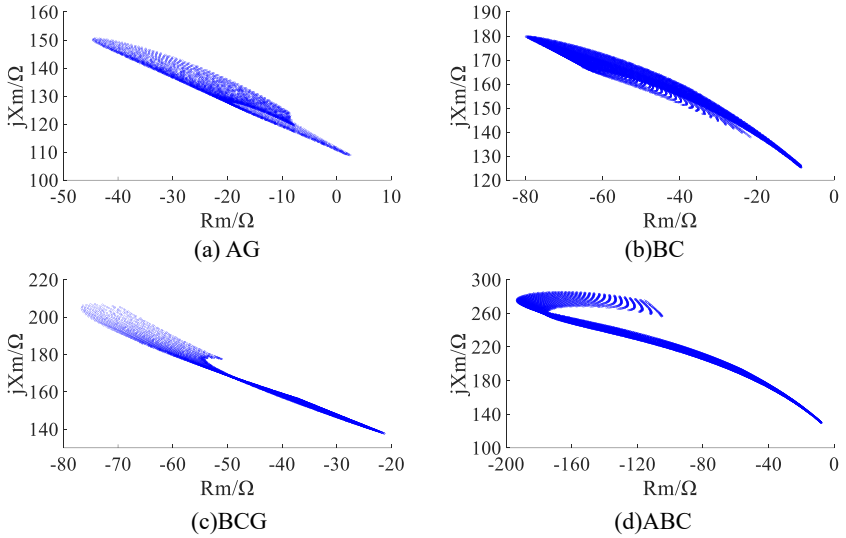


Fig. 4. Positive-sequence equivalent impedance of the wind farm

It should be noted that only the equivalent impedance of the converter entering the LVRT state is depicted in the figure. This is because, as the fault distance increases and the transition resistance grows, the voltage sag and current increase perceived by the converter may no longer satisfy the LVRT criteria. Under such conditions, the post-fault electrical relationships do not conform to the equations mentioned above. Given the complexity of the equivalent impedance characteristics in this scenario, further discussion is omitted in this paper.

The characteristics of the negative-sequence equivalent impedance of wind farms are also analyzed. The negative-sequence impedance of the wind turbine was mentioned earlier as a fixed value. The negative-sequence impedance of wind farms is obtained by adding this constant impedance and the line impedance. Therefore, the negative-sequence impedance of wind farms will also be a fixed value.

$$Z_{\mathrm{m}}^{-} = Z_{\mathrm{S}}^{-} + Z_{\mathrm{T}} \tag{14}$$

Where: Z_{m}^{-} is the negative-sequence equivalent impedance of wind farms; Z_{T} is the impedance between the PCC of converter and the step-up substation.

4 SIMULATION VERIFICATION

To validate the accuracy of the proposed calculation method and the equivalent impedance characteristic analysis for wind farms, a VSG-controlled wind farm model was developed in PSCAD/EMTDC. The parameters of each system component are listed in Table 1. V is the operating voltage level of the individual components; k is the transformer turns ratio; L is the length of the line; R , X , B are the resistance, reactance, and susceptance of each component, referred to the 220 kV level.

Table 1. Parameters of the wind farm

Component name	V(kV)	k	L(km)	$R(\Omega)$	$X(\Omega)$	$B(S)$
Step-up Transformer	\	0.69/35	\	0.00	42.35	0.00
Collection System	35	\	5	10.87	12.71	0.00
Step-up Substation	\	35/220	\	0.00	42.35	0.00
Transmission System	220	\	100	4.96	30.89	3.68e-4
Receiving-End Grid	220	\	\	1.97	19.89	0.00

4.1 Validation of the Accuracy of Calculation Method

To validate the accuracy of the proposed method, different fault types and location cases were simulated, and the relative errors between the theoretical and simulated values of voltage and current at Node 4 were calculated. Relative errors for different fault distances and transition resistances are shown in Table 2 and Table 3, respectively. Distance is the distance from the fault point to Node 4; Rf is the transition resistance.

Table 2 Relative errors of voltage and current under different fault distances（Rf=10Ω）

Fault Type	Distance/km	$\dot{U}_A$	$\dot{U}_B$	$\dot{U}_C$	$\dot{I}_A$	$\dot{I}_B$	$\dot{I}_C$
ABCG	10	0.0021	0.0007	0.0016	0.0141	0.0058	0.0115
	50	0.0042	0.0016	0.0027	0.0183	0.0064	0.0126
	90	0.0050	0.0015	0.0035	0.0211	0.0059	0.0154
AG	10	0.0021	0.0040	0.0021	0.0061	0.0124	0.0188
	50	0.0028	0.0042	0.0019	0.0077	0.0169	0.0383
	90	0.0032	0.0041	0.0019	0.0076	0.0230	0.0568
BC	10	0.0041	0.0035	0.0050	0.0479	0.0088	0.0160
	50	0.0041	0.0034	0.0051	0.0493	0.0093	0.0173
	90	0.0040	0.0031	0.0055	0.0458	0.0097	0.0165
BCG	10	0.0033	0.0030	0.0032	0.0155	0.0033	0.0121
	50	0.0038	0.0036	0.0044	0.0395	0.0050	0.0141
	90	0.0041	0.0035	0.0048	0.0485	0.0061	0.0178

Table 3 Relative errors of voltage and current under different fault transition resistances(50km)

Fault Type	Rf/Ω	$\dot{U}_A$	$\dot{U}_B$	$\dot{U}_C$	$\dot{I}_A$	$\dot{I}_B$	$\dot{I}_C$
ABCG	0	0.0215	0.0141	0.0219	0.0228	0.0128	0.0227
	50	0.0042	0.0001	0.0039	0.0285	0.0059	0.0260
	100	0.0034	0.0016	0.0028	0.0241	0.0109	0.0197
AG	0	0.0074	0.0049	0.0018	0.0112	0.0187	0.0295
	30	0.0001	0.0033	0.0021	0.0036	0.0162	0.0346
	60	0.0016	0.0025	0.0032	0.0058	0.0149	0.0492

Table 4(continued)

Fault Type	Rf/Ω	$\dot{U}_A$	$\dot{U}_B$	$\dot{U}_C$	$\dot{I}_A$	$\dot{I}_B$	$\dot{I}_C$
BC	0	0.0045	0.0040	0.0049	0.0535	0.0081	0.0223
	50	0.0032	0.0029	0.0017	0.0345	0.0151	0.074
	100	0.0020	0.0028	0.0015	0.0194	0.0183	0.0095
BCG	0	0.0039	0.0040	0.0047	0.0219	0.0072	0.0095
	50	0.0042	0.0037	0.0048	0.0421	0.0051	0.0277
	100	0.0042	0.0038	0.0047	0.0482	0.0062	0.0253

The data in the tables show that the relative errors of both voltage and current remain within 5% under all tested conditions, demonstrating the high computational accuracy of the proposed method.

4.2 Validation of the Accuracy of the Equivalent Impedance Characteristic Analysis for Wind Farms

Different fault types and location cases were simulated to measure the positive-sequence impedance of the wind farm. The results are presented in Table 5. Z_m^+ is the positive-sequence equivalent impedance of the wind farm.

Table 5 Positive-sequence equivalent impedance of wind farms

Fault Type	Distance/km	Rf/Ω	Z_m^+	$\arg(Z_m^+)$/deg
ABC	10	0	-112.01+271.47i	112.4213
		50	-188.92+279.84i	124.0233
		100	-146.16+260.52i	119.2938
	50	0	-106.08+263.84i	111.9032
		50	-171.32+267.62i	122.6258
		100	-103.28+236.35i	113.6043
	90	0	-100.40+255.50i	111.4526
		50	-132.29+247.71i	118.1045
		100	-43.92+189.41i	103.0549
AG	10	0	-7.35+120.61i	93.4873
		30	-39.60+149.73i	104.8142
		60	-25.06+145.75i	99.7559
	50	0	3.05+109.46i	88.4039
		30	-23.22+136.67i	99.6524
		60	-1.51+120.58i	90.7275
	90	0	8.40+104.17i	85.3898
		20	-19.38+132.82i	98.3015
		40	0.96+116.97i	89.5298
BC	10	0	-34.07+153.59i	102.5071
		50	-72.41+179.30i	111.9912
		100	-74.57+184.30i	112.0288
	50	0	-28.74+146.97i	101.0646
		50	-69.56+175.94i	111.5720
		100	-57.94+174.94i	108.3248

Table 6(continued)

Fault Type	Distance/km	Rf/Ω	Z_m^+	arg(Z_m^+)/deg
	90	0	-23.34+140.46i	99.4345
		50	-62.51+172.77i	109.8907
		100	-26.63+153.52i	99.8408
BCG	10	0	-67.86+200.93i	108.6613
		50	-52.15+170.36i	107.0202
		100	-43.30+161.34i	105.0229
	50	0	-57.80+186.48i	107.2210
		50	-41.50+159.80i	104.5581
		100	-35.07+153.20i	102.8938
	90	0	-52.09+179.28i	106.2013
		50	-31.72+148.79i	102.0345
		100	-27.38+144.42i	100.7351

The simulated equivalent impedance is plotted alongside the theoretical values. In the figure, blue points denote the theoretically derived fluctuation region of the wind farm's impedance, while red points represent the values obtained from simulation. It can be observed that all simulated (red) points fall within the theoretical (blue) region, verifying the accuracy of the derivation.

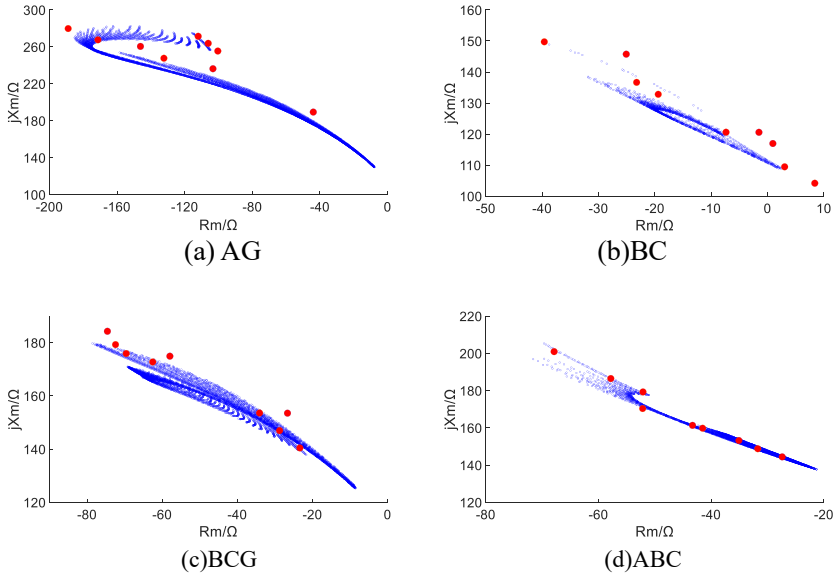


Fig. 5 Verification of the positive-sequence equivalent impedance of the wind farm

From the figure above, we can know that the positive-sequence equivalent impedance has the following characteristics: 1. The imaginary part of the equivalent impedance is greater than its real part, with the phase angle ranging between 45 and 135 degrees. 2.Its magnitude is relatively large, typically on the order of several hundred ohms.

With the theoretical derivation of the positive-sequence equivalent impedance validated, the focus now shifts to verifying its negative-sequence counterpart. The system parameters are set as follows: the rated voltage is 220 kV, the rated capacity is 100 MVA, the negative-sequence reactive current coefficient is 2.0, and the line impedance is (10.8653 + 97.4104i) Ω. Using these parameters, the negative-sequence equivalent impedance of the wind farm Z_m^- can be calculated as (10.8653 + 339.4104i) Ω. The fault distance is set to 90 km, and the negative-sequence equivalent impedances measured under different transition resistance conditions are systematically presented in Table 7. error is the relative error between the simulated impedance and the theoretical impedance.

Table 7 Negative-sequence equivalent impedance of the wind farm

Fault Type	R_f/Ω	Z_m^-	$\arg(Z_m^-)$/deg	error
AG	0	-5.23+342.02i	90.8761	0.0480
	20	-2.33+345.51i	90.3864	0.0428
	40	-9.27+342.88i	91.5487	0.0602
BC	0	11.05+347.26i	88.1774	0.0231
	50	17.05+348.93i	87.2025	0.0334
	100	24.38+348.01i	85.9927	0.0472
BCG	0	10.29+343.92i	88.2862	0.0134
	50	10.37+346.80i	88.2873	0.0218
	100	10.14+347.02i	88.3263	0.0225

As shown in the table, the simulation results are distributed around the theoretical results with all errors within the acceptable range, confirming the accuracy of the theoretical analysis.

5 CONCLUSION

This paper proposes a steady-state fault voltages and currents calculation method based on the simultaneous solution of node voltage equations, fault boundary conditions, and VSG control equations. Using this method, we analyze the equivalent impedance characteristics of VSG-controlled wind farms and obtain the following key conclusions:

1) The proposed calculation method demonstrates high accuracy, and the relative errors of both voltage and current remain within 5%;
2) The positive-sequence equivalent impedance is located in the first and second quadrants of the complex plane, with its phase angle ranging between 45° and 135°;
3) The negative-sequence equivalent impedance remains constant, with a value determined by the rated impedance Z_N and the negative-sequence reactive current proportional coefficient K_2^-.

Acknowledgement: This work is supported by National Key Research and Development Program of China(2023YFB2407404)'High Power Density Flexible Interconnection Technology and Equipment for Distribution Grid'.

References

1. Renewables 2014 Global Status Report, *REN21*, Paris, France, 2014.[Online]. Available: http://www.ren21.ne
2. M. Fatima and O. Beik, "A Wind Turbine Conversion System Featuring Grid Forming Control," 2023 IEEE Energy Conversion Congress and Exposition (ECCE), Nashville, TN, USA, 2023, pp. 1386-1390.
3. R. Rosso, M. Andresen, S. Engelken and M. Liserre, "Analysis of the Interaction Among Power Converters Through Their Synchronization Mechanism," *IEEE Transactions on Power Electronics*, vol. 34, no. 12, pp. 12321–12332, Dec. 2019.
4. H. Xu, Y. Cai, Y. Chen and G. Li, "A Review of Control Technologies and Principles for Grid-Forming Converters," *2025 10th Asia Conference on Power and Electrical Engineering (ACPEE)*, Beijing, China, 2025, pp. 1496-1500.
5. I. Sadeghkhani, M. E. Hamedani Golshan, J. M. Guerrero and A. Mehrizi-Sani, "A Current Limiting Strategy to Improve Fault Ride-Through of Inverter Interfaced Autonomous Microgrids," in *IEEE Transactions on Smart Grid*, vol. 8, no. 5, pp. 2138-2148, Sept. 2017.
6. X. N. Lu, J. H. Wang, J. M. Guerrero, and D. B. Zhao, "Virtual-impedance-based fault current limiters for Inverter dominated AC microgrids," *in IEEE Transactions on Smart Grid*, vol. 9, no. 3, pp. 1599–1612, 2018.
7. H. Wu and X. Wang, "Small-Signal Modeling and Controller Parameters Tuning of Grid-Forming VSCs With Adaptive Virtual Impedance-Based Current Limitation," in *IEEE Transactions on Power Electronics*, vol. 37, no. 6, pp. 7185 - 7199, June 2022.
8. D. Wei, J. He, M. Li, X. Du and Y. Wei, "Fault Current Calculation of Virtual Synchronous Generator Based on Adaptive Virtual Impedance," 2025 8th International Conference on Energy, Electrical and Power Engineering (CEEPE), Wuxi, China, 2025, pp. 946-950.
9. D. Song and B. Wang, "Research on Calculation of Short-circuit Current of Distribution Network with Inverter-Distributed Generation with VSG," *2025 8th International Conference on Energy, Electrical and Power Engineering (CEEPE)*, Wuxi, China, 2025, pp. 353-358.
10. M. E. Baran and I. El-Markaby, "Fault analysis on distribution feeders with distributed generators," *IEEE Trans. Power Syst.*, vol. 20, no. 4, pp. 1757 - 1764, Nov. 2005.
11. H. Zhao， J. Ge， Z. Shuai， Y. Cheng， J. Lei and J. Shen， "An Asymmetrical Fault Current Iterative Algorithm of Droop-controlled Inverter，" *2019 IEEE Energy Conversion Congress and Exposition （ECCE）*， Baltimore， MD， USA， 2019， pp. 2219-2223.
12. T. Huang, Y. Lu, and C. Cai, "Analysis of phase angle characteristics of DFIG equivalent sequence superimposed impedances and its impact on fault components based direction relay," *Proceedings of the CSEE*, 36(14): pp. 3929–3940, 2016.
13. Wang, C. Q., Song, G. B., Liu, K., et al. Adaptability Analysis of Incremental Quantity Protection in Wind Power Integration Systems [J]. Proceedings of the CSEE, 2014, 34 (31): 5485–5492.
14. Song, G.; Chang, P.; Hou, J.; Zhang, C.; Lyu, J. Adaptability Analysis of Fault Component Directional Component in AC/DC Multi-terminal Infeed System. *Autom. Electr. Power Syst.* 2021, 45, 136–145.

15. Chang, P.; Song, G.; Song, G.; Li, W.; Zhang, C. Adaptability analysis of traditional AC line protection in inverter-interfaced system. *Electric Power Automation Equipment* .2024, 44, 57-66.
16. Song G., Li D., Chang Z., Wang C., Guo R. Analysis of Impact of Wind Speed and Wind Turbine Location Distribution Characteristics on PMSG Wind Farm Fault Characteristics. *Power System Technology*, 2016, 40, 1689–1695.
17. Jia K., Liu Y., Bi T., et al. Asymmetric fault ride through of grid-forming control of renewable energy based on adaptive virtual impedance[J/OL]. Proceedings of the CSEE, 1-11[2025-04-07].
18. Technical requirements for connecting photovoltaic power system to distribution network （GB/T 29319-2024），Standardization Administration of China (SAC)，2024.

046 考虑不确定性的新型电力系统优化调度研究

孙天贺[1]，孙晓优[1]

（1. 辽宁省电网节能与控制重点实验室，沈阳工程学院，沈阳，110136）

Research on optimal dispatch of new-type power systems considering uncertainties

Sun Tianhe[1],SUN Xiaoyou[1]

(1.Key Laboratory of Energy Saving and Controlling in Power System of Liaoning Province, Shenyang Institute of Engineering, Shenyang, 110136)

ABSTRACT: Amid over-exploitation of fossil energy, clean energy such as wind and photovoltaic power has become a solution to the energy crisis due to its high efficiency and environmental friendliness, and is widely used in power systems. To address uncertainties like renewable energy output fluctuations, load changes and equipment failures, an optimal scheduling model with multi-source uncertainties is needed to enhance system risk resistance. However, traditional scheduling methods have large errors in handling wind and photovoltaic volatility and uncertainty.Firstly, this paper proposes a robust optimal scheduling model for power systems with energy storage: aiming to minimize comprehensive operation costs, it achieves multi-time-scale optimal scheduling by combining wind power's robust uncertainty set. Meanwhile, considering that wind-storage scheduling is affected by the accuracy of wind power and load forecasting, a joint scheduling strategy including wind, thermal, energy storage and pumped storage is established. Based on differences in energy response speeds, a three-stage power generation plan is formulated: 24 hours (day-ahead), 4 hours (intra-day) and 5 minutes (real-time).Secondly, stage-specific schemes are refined: the day-ahead stage formulates start-stop and output plans for thermal and pumped storage units (considering dynamic frequency constraints); the intra-day stage optimizes battery energy storage charging/discharging plans and adjusts the output of thermal and pumped storage to promote wind power consumption.Finally, through case analysis on the improved IEEE-30 bus system, simulations show that the proposed strategy can improve demand response enthusiasm, reduce carbon emissions, and balance low-carbon performance and economy. It is evident that this robust optimal scheduling method has significant advantages, as it balances system economy and low-carbon performance with excellent performance.

KEY WORDS: new power system, uncertainty, multiple time scales, optimized scheduling

摘要：化石能源过度开采下，风电、光伏等清洁能源因高效环保成能源危机解决方案，广泛应用于电力系统。为应对可再生能源出力波动、负荷变化及设备故障等不确定性，需建多源不确定性优化调度模型以提升系统抗风险能力，而传统调度方法处理风光波动与不确定性误差大。本文首先针对含储能电力系统提鲁棒优化调度模型：以综合运行成本最小为目标，结合风电鲁棒不确定性集实现多时间尺度优化调度；同时考虑风储调度受风电与负荷预测准确性影响，建含风电、火电、储能及抽水蓄能的联合调度策略，并按能源响应速度差异，定 24 小时（日前）、4 小时（日内）、5 分钟（实时）三阶段发电计划。其次细化阶段方案：日前阶段定火电机组与抽水蓄能机组启停及出力计划（考虑动态频率约束）；日内阶段优化电池储能充放电计划、调整火电与抽水蓄能出力，促风电消纳。最后经改进 IEEE-30 节点系统算例分析，仿真显示所提策略可提高需求响应积极性、降碳排放、平衡低碳性与经济性。可见，该鲁棒优化调度方法优势显著，能兼顾系统经济性与低碳性，性能优异。

关键词：新型电力系统，不确定性，多时间尺度，优化调度

DOI：

0 引言

在全球能源危机、环境污染加剧及我国 “双碳” 目标背景下，风电、光伏等可再生能源快速发展，但因其出力受天气影响具有强随机性与波动性，叠加多元负荷复杂性，传统确定性调度方法难以适配，导致弃风弃光、供需失衡等问题，影响经济与环境。同时，大规模互联电网成型后，“跨区联络功率-系统内清洁能源-传统火电”动态关联及应对新能源消纳波动、跨区域输电难题，成为推动清洁能源消纳与实现碳达峰的关键[1]。

当前已有研究提出多种优化策略，人工智能也助力电能调度向 “数据-知识混合驱动” 转变。文献[2]提出计及分类需求响应的电力系统多目标鲁棒优化调度。文献[3]提出了一种新型电力系统多

时间尺度自动调度方法。文献[4]提出一种计及需求响应的风储集群电力系统多时间尺度优化调度策略。文献[5]含间歇式电源的电力系统鲁棒优化调度方法。文献[6]含间歇式电源的电力系统鲁棒优化调度方法并提出一种基于源荷预测的日前日内优化调度方法。

对此，本文基于电力系统动态频率响应模型，结合风电、火电、抽蓄和电池储能的互补特性，构建含系统频率与惯量约束的“日前-日内”多时间尺度协调优化调度模型：日前阶段制定风、火、抽蓄机组启停计划，日内阶段规划电池储能充放电计划，以维持功率平衡、提升风电消纳率，并在含相关能源的 IEEE-30 节点系统仿真验证方案可行性。

1 新型电力系统优化调度价格需求模型

需求响应机制是指用户根据供电企业的奖励信号或实时电价自主调整用电行为以优化资源调配。电价上升时，用户减少非必要用电（如推迟大功率电器使用、调低空调温度）；电价下降时，则可能增加用电（如低价时段使用电热水器）。

价格需求特性即 DR 特性可以用价格需求弹性矩阵来描述，弹性矩阵 E(m,n)中的第 m 行第 n 列的原素表示 m 时刻度 n 时刻的电价弹性系数，数学模型为：

$$e_{m,n}=\frac{\Delta P_{\mathrm{L},m_\mathrm{e}}/P_{\mathrm{L},m_\mathrm{e}0}}{\Delta\rho_n/\rho_{n_0}} \tag{1}$$

式中：$\Delta P_{L,m_e}$为m时刻响应前后负荷变化量；$\Delta P_{L,m_e0}$为负荷原始量；$\Delta\rho_n$为需求响应前后n时刻电价变化量；ρ_{n_0}为n时刻原电价；需求响应后可中断负荷的变化量$\Delta P_{CL,m_e}$为：

$$\Delta P_{\mathrm{CL},m_\mathrm{e}}=P_{\mathrm{CL},m_\mathrm{e}0}\left[\sum_{n=1}^{24}S\,E_{\mathrm{CL}}(m,n)\frac{\rho_n-\rho_{n_0}}{\rho_{n_0}}\right] \tag{2}$$

式中：P_{CL,m_e0}为m时刻原来可中断负荷量；$E_{CL}(m,n)$可中断负荷价格需求弹性矩阵；ρ_n为n时刻电价。

根据可转移负荷理论，用户可以根据自己的需求和实时电价信息，灵活地改变自己能源使用的时间分布，把高电价时段的负荷转移到低电价或者平价时段。在这种情况下，DR 后的可转移负荷变化量可以建立如下的数学模型：

$$\Delta P_{\mathrm{SL},m_e}=P_{\mathrm{SL},m_e0}\left[\sum_{n=1}^{24}S\,E_{\mathrm{SL}}(m,n)\frac{\rho_n-\rho_{n_0}}{\rho_{n_0}}\right] \tag{3}$$

式中：P_{SL,m_e0}为m时刻原来可转移负荷量；$E_{SL}(m,n)$为可转移负荷价格需求弹性矩阵。

2 考虑新型电力系统多时间尺度优化调度

2.1 新型电力系统日前优化调度模型

日前最优调度是综合负荷、电源、电网等信息，通过最优算法与模型安排发电计划、调整电网潮流，以保障系统经济、安全、可靠运行，有效融合源荷资源，支撑电网平稳经济运行及电力市场发展。其依据风电和负荷短期预测，每 24 小时执行一次机组组合，制定启停计划，提前 24 小时调度，最小时长 1 小时，分 24 个时段，每日调度 1 次。

以新型电力系统运行费用最小化建立目标函数：

$$minF=\sum_{t=1}^{N}(f_1+f_2+f_3+f_4) \tag{4}$$

式中，F 表示模型的目标函数，表示电力系统的运行费用；f_1、f_2、f_3、f_4分别代表常规燃煤机组、储能系统、风电机组和用户负荷的成本函数；N 为优化调度的周期。

约束条件：

（1）系统平衡约束：

$$\begin{aligned}&\sum_{g}^{N_{\mathrm{G}}}P_{g,t,s}+\sum_{w}^{N_{\mathrm{W}}}P_{w,t,s}+\sum_{ec}^{N_{\mathrm{EC}}}P_{ec,t,s}\\&+\sum_{h}^{N_{\mathrm{H}}}P_{h,t,s}=D^{\mathrm{fixed}}+\Delta P_{t,s}^{\mathrm{IDRA}}-P_{t,s}^{\mathrm{loss}}\end{aligned} \tag{5}$$

式中，N_G代表系统中燃煤机组的数量，$P_{g,t,s}$代表燃煤机组 g 在第 s 个可能性场景下时刻 t 的输出功率；N_W表示风电的机组数量，$P_{w,t,s}$表示风机 w 在第 s 个可能的场景下时刻 t 的输出功率；N_{EC}表示电化学储能电站的数量，$P_{ec,t,s}$表示电化学储能 ec 在第 s 个可能的场景下时刻 t 的输出功率；N_H表示抽水蓄能电站的数量，$P_{h,t,s}$表示抽水蓄能电站 h 在第 s 个可能的场景下时刻 t 的输出功率；D^{fixed}表示预测负荷；$\Delta P_{t,s}^{\mathrm{IDRA}}$表示在第$s$个可能的场景$t$时间点$A$类$IDR$载荷的变化量，$P_{t,s}^{\mathrm{loss}}$表示载荷的失电量。

（2）火电机组处理约束：

$$u_{g,t,s}P_{g,min}\le P_{g,t,s}\le u_{g,t,s}P_{g,max} \tag{6}$$

式中，$P_{g,\min}$和$P_{g,\max}$为分别为机组i的最小、最

大出力限制，$u_{g,t,s}$ 代表燃煤机组 g 在第 s 个可能性场景下时刻 t 的启动和停止状态。

（3）火电机组爬坡约束：

$$\begin{cases} P_{g,t,s}-P_{g,t-1,s}\le u_{g,t,s}R_u \\ P_{g,t-1,s}-P_{g,t,s}\le u_{g,t-1,s}R_d \end{cases} \tag{7}$$

式中，R_u 和 R_d 分别为机组的上下爬坡速率。

（4）机组启停时间约束：

$$\begin{cases} \sum_{k=t}^{t+TO-1} u_{g,k,s}\ge TO\left(u_{g,t,s}-u_{g,t-1,s}\right) \\ \sum_{k=t}^{t+TS-1}\left(1-u_{g,k,s}\right)\ge TS\left(u_{g,t-1,s}-u_{g,t,s}\right) \end{cases} \tag{8}$$

式中，TO 和 TS 分别为最小开机和关停时间。

（5）风电出力约束：

$$0\le P_{w,t,s}\le P_{w,t,s}^{\mathrm{pre}} \tag{9}$$

式中，$P_{w,t,s}^{\mathrm{pre}}$ 表示风电机组 w 在第 s 个可能的场景下时刻 t 的预测输出功率。

（6）光伏出力约束：

$$0\le P_{pv,t,s}\le P_{pv,t,s}^{\mathrm{pre}} \tag{10}$$

式中，$P_{pv,t,s}$ 代表光伏机组在第 s 个可能性场景下时刻 t 的输出功率，$P_{pv,t,s}^{\mathrm{pre}}$ 表示光伏机组 w 在第 s 个可能的场景下时刻 t 的预测输出功率。

（7）抽水蓄能储能电站约束：

$$P_{h,s}^{min}\le P_{h,t,s}\le P_{h,s}^{max} \tag{11}$$

式中，$P_{h,s}^{\max}$ 和 $P_{h,s}^{\min}$ 分别表示出力的上下限。

（8）传输线的输电功率约束：

$$-P_{ij}^{max}\le B_{ij}\left(\theta_{i,t,s}-\theta_{j,t,s}\right)\le P_{ij}^{\max} \tag{12}$$

式中，$P_{ij}^{\max}$ 表示负荷节点 i 和负荷节点 j 之间联络线上的最大输送功率；B_{ij} 表示负荷节点 i 和负荷节点 j 之间的电纳；$\theta_{i,t,s}$ 表示节点 i 的相角。

2.2 日内优化调度模型

将改良成果融入日内调度，用滚动技术更新日前模型。日内以运行成本最小为目标，不考虑机组启停，需基于日前数据用正态分布重新预测风电和负荷，且将预测提前时间缩至 4 小时、间隔 1 分钟，以减小误差、提高准确度。

滚动时域优化通过滑动时间窗口持续优化，周期性更新系统状态和预测数据，每个决策时段闭环执行：获取最新信息、刷新数据、求解模型、实施指令，动态调整以确保策略最优。其效果优于单次静态优化，可靠性和适应性更强，能减少不确定因素影响，提升调度稳定性。

日内短时间尺度调度阶段的优化目标为最小化电力系统总运行成本：

$$\min F=\sum_{t=1}^{N_{\mathrm{T}}}\left(f_{\mathrm{G},t}+f_{\mathrm{E},t}+f_{\mathrm{W},t}+f_{\mathrm{L},t}\right) \tag{13}$$

式中，$f_{G,t}$ 表示燃煤机组的运行成本；$f_{E,t}$ 储能系统的运行成本；$f_{W,t}$ 表示风电机组的运行成本；$f_{L,t}$ 表示用户负荷的运行成本。

约束条件：

（1）功率平衡约束：

$$\begin{aligned} &\sum_{g}^{N_G}P_{g,t,s}+\sum_{w}^{N_W}P_{w,t,s}+\sum_{ec}^{N_{EC}}P_{ec,t,s}+\sum_{h}^{N_H}P_{h,t,s} \\ &=D^{fixed}+\Delta P_{t,s}^{IDRA}+\Delta P_{t,s}^{IDRB}-P_{t,s}^{loss} \end{aligned} \tag{14}$$

$$\begin{cases} 0\le P_{t,s}^{\mathrm{IDRB+}}\le P_{\max}^{\mathrm{IDRB+}} \\ 0\le P_{t,s}^{\mathrm{IDRB-}}\le P_{\max}^{\mathrm{IDRB-}} \end{cases} \tag{15}$$

式中，$P_{t,s}^{\mathrm{IDRB+}}$ 和 $P_{t,s}^{\mathrm{IDRB-}}$ 分别表示 B 类 IDR 负荷的增加量和减少量。

（2）火电机组爬坡约束：

$$\begin{cases} P_{\mathrm{G},i}(t)-P_{\mathrm{G},i}(t-1)\leqslant\dfrac{R_{\mathrm{G},i}^{\mathrm{U}}}{4} \\ P_{\mathrm{G},i}(t-1)-P_{\mathrm{G},i}(t)\leqslant\dfrac{R_{\mathrm{G},i}^{\mathrm{D}}}{4} \end{cases} \tag{16}$$

（3）旋转备用约束：

$$\sum_{i=1}^{N}\left(P_{\mathrm{G},i}^{\max}-P_{\mathrm{G},i}(t)\right)+\sum_{j=1}^{M}P_{\mathrm{b},j}^{\mathrm{dis}}(t)\geqslant r_{\mathrm{sys}}^{\mathrm{up}}(t) \tag{17}$$

$$r_{\mathrm{sys}}^{\mathrm{up}}(t)=\mu_1\left[P_{\mathrm{load}}^{\mathrm{PDR}}(t)+P_{\mathrm{IDR}}(t)\right]+\mu_2\sum_{j=1}^{M}P_{\mathrm{w},j}(t) \tag{18}$$

$$\sum_{i=1}^{N}\left(P_{\mathrm{G},i}(t)-P_{\mathrm{G},i}^{\min}\right)+\sum_{j=1}^{M}P_{\mathrm{b},j}^{\mathrm{ch}}(t)\geqslant r_{\mathrm{sys}}^{\mathrm{down}}(t) \tag{19}$$

$$\begin{aligned} r_{\mathrm{sys}}^{\mathrm{down}}(t)&=\mu_1\left[P_{\mathrm{load}}^{\mathrm{PDR}}(t)\right. \\ &\left.+P_{\mathrm{IDR}}(t)\right]+\mu_2\sum_{j=1}^{M}P_{\mathrm{w},j}(t) \end{aligned} \tag{20}$$

式中：$r_{\mathrm{sys}}^{\mathrm{up}}(t)$、$r_{\mathrm{sys}}^{\mathrm{down}}(t)$ ——系统向上、向下旋转

备用容量，MW；μ_1、μ_2——负荷和风电的旋转备用容量系数。

2.3 实时调度模型

实时调度依据系统实时状态和监测数据做短期决策，保障安全稳定运行并最大化资源效益，采用 5 分钟时间尺度、15 分钟提前调度的方案。

经日前和日内调度，系统整体运行成本已尽可能降低，实时调度主要进一步精确调度所有机组出力，通过细化时间颗粒实现更贴近实际的预调度，为实际调度提供精确参考。

目标函数：

$$f_{\text{load},t}=\sum_{s=1}^{N_S}\sum_{t=1}^{N_T}p_s\left[k_{\text{c}}^{\text{IDRC}}\Delta\left|P_{t,s}^{\text{IDRC}}\right|+k_{\text{c}}^{\text{IDRD}}\Delta\left|P_{t,s}^{\text{IDRD}}\right|+k_{\text{c}}^{\text{loss}}P_{t,s}^{\text{loss}}\right] \tag{21}$$

式中，$k_{\text{c}}^{\text{IDRC}}$、$k_{\text{c}}^{\text{IDRD}}$表示费用系数；$\Delta\left|P_{t,s}^{\text{IDRC}}\right|$、$\Delta\left|P_{t,s}^{\text{IDRD}}\right|$分别表示 C 类和 D 类 IDR 载荷的调用量。

约束条件：

$$\begin{cases}0\le P_{t,s}^{\text{IDRC+}}\le P_{\max}^{\text{IDRC+}}\\0\le P_{t,s}^{\text{IDRC-}}\le P_{\max}^{\text{IDRC-}}\end{cases} \tag{22}$$

$$\begin{cases}0\le P_{t,s}^{\text{IDRC+}}\le P_{\max}^{\text{IDRC+}}\\0\le P_{t,s}^{\text{IDRC-}}\le P_{\max}^{\text{IDRC-}}\end{cases} \tag{23}$$

式中，$P_{t,s}^{\text{IDRC+}}$、$P_{t,s}^{\text{IDRD+}}$分别为 C 类和 D 类 IDR 增加正荷量；$P_{t,s}^{\text{IDRC-}}$、$P_{t,s}^{\text{IDRD-}}$为 C 类和 D 类 IDR 减少负荷量。

3 新型电力系统结构

本文以一个 IEEE6 机 30 节点系统进行仿真分析，该系统有 6 台火电机组，分别位于节点 1、2、5、8、11、13 处，模型在 MATLAB 平台的 YALMIP 工具包调用 CPLEX 软件进行求解。具体系统结构如图 1 所示：

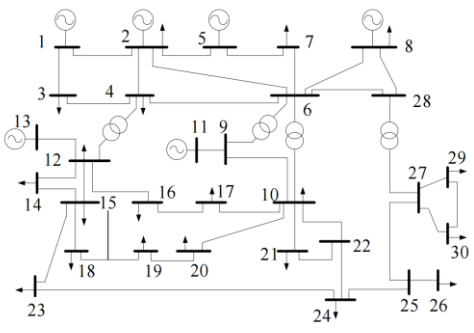


图 1 IEEE6 机 30 节点系统图

Figure 1 IEEE 6-Machine 30-Bus System Diagram

4 算例分析

4.1 输入数据

风电数据如图 2 所示。

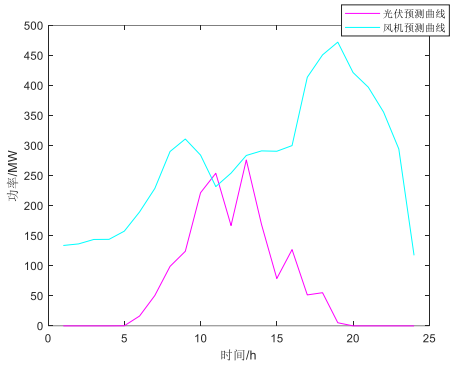


图 2 风电光伏预测图

Figure 2 Wind Power and Photovoltaic Power Forecast Chart

火电机组数据如表 1 所示。

表 1 火电厂机组数据

Table 1 Thermal Power Plant Unit Data

机组 j	$P_{G,j}^{\min}$	$P_{G,j}^{\max}$	$r_{u,j}$、$r_{d,j}$	$a_j/10^{-5}$	b_j	c_j
1	50	150	± 240	1.02	0.277	9.2
2	30	60	± 210	1.21	0.288	8.8
3	20	60	± 150	2.17	0.29	7.2
4	15	50	± 120	3.42	0.292	5.2
5	10	40	± 70	6.63	0.306	3.5
6	10	45	± 70	5.32	0.287	4.2

4.2 需求响应前后用户负荷曲线

考虑需求响应前后电负荷需求曲线如图 3 所示。

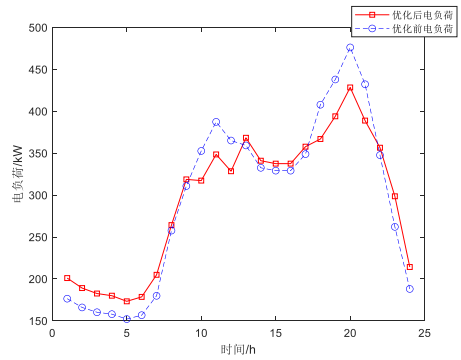


图 3 需求响应前后用户电负荷曲线

Figure 3 User Electricity Load Curves Before and After Demand Response

考虑需求响应前后用户热负荷曲线如图 4 所示。

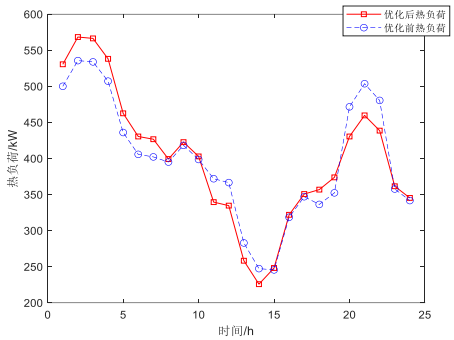


图 4 需求响应前后用户热负荷曲线

Figure 4 User Heat Load Curves Before and After Demand Response

分时电价如图 5 所示。

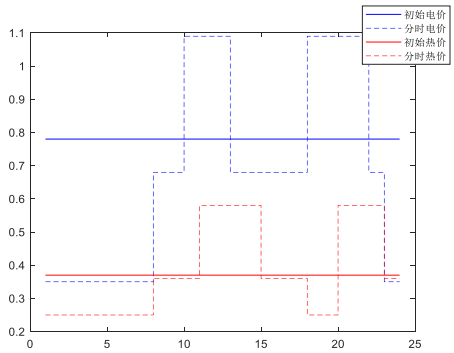


图 5 价格曲线

Figure 5 Price Curve

图表数据显示，执行需求响应策略后，负荷曲线峰谷差距缩小，表明其在改善用户用电行为上作用显著，成效主要有两方面：一是分时电价改变用户用能习惯，促使调整用电时间；二是对负荷转移和中断用户给予补贴，鼓励更多用户参与调整。以电负荷为例，10:00-12:00 和 18:00-21:00 为负荷高峰且电价处于峰时段，在电价引导和补偿激励下，部分负荷被中断，可转移负荷转至 1:00-9:00、13:00-17:00 和 22:00-24:00 时段。

4.3 场景优化调度图

正调峰时风电出力与负荷趋势一致，利于消纳；反调峰则相反。为此构建多时间尺度优化调度模型，结合储能、需求侧响应等灵活资源动态调整出力计划。

针对综合能源系统电源多元、变量与约束复杂的问题，设计分层优化调度策略：上层以平抑净负荷波动、提升储能收益为目标，缩小峰谷差异以增强可再生能源接纳能力；下层聚焦最小化火电运行成本和弃电，实现传统机组与新能源协调优化。为解决新能源消纳问题，选取含 5 台火电机组、200MW 储电设备的 IEEE6 机 30 节点系统仿真，下图为多场景机组优化调度图。

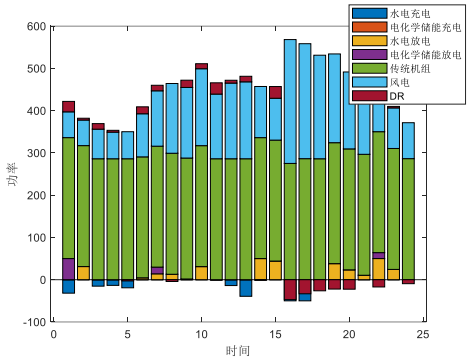


图 6 风电正调峰调度图

Figure 6 Wind Power Positive Peak Regulation Dispatch Chart

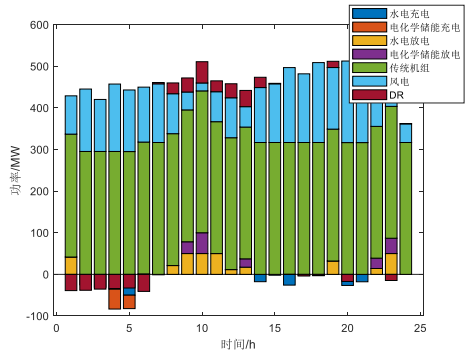


图 7 风电反调峰图

Figure 7 Wind Power Negative Peak Regulation Chart

风电正调峰高发于日中及午后，此时需求响应负荷大、IDR 资源调用少，储能调用量也更少；反调峰高发于凌晨及傍晚，此时白天出力小、夜晚大且易弃风，需求响应负荷小，需通过 IDR 资源调用与储能充电提升风电消纳，反调峰还会增加系统调峰成本与投资。

4.4 多时间尺度优化调度

4.4.1 各机组日前优化调度

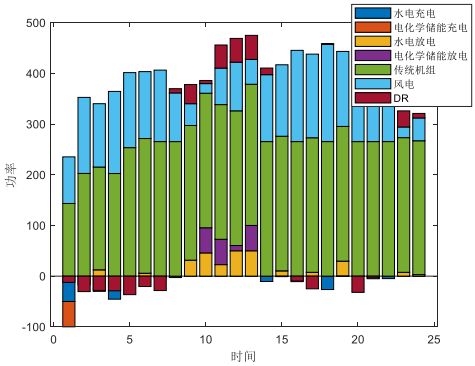


图 8 各机组日前调度优化

Figure 8 Day-Ahead Dispatching Optimization of Each Unit

由图可知，风能高频发电时段在 16~18h，此时段内系统可以利用 DR 负荷的正调用来提升此时段内的风电消纳水平。此外，通过 DR 调节负荷，在低谷时段吸收多余的水电出力，在高峰时段优化火电机组运行方式，提高新型电力系统消纳。日前 24 小时调度计划因为充分发挥了两种储能的双向调节能力，所以它具有很好的削峰填谷性能，能够有效地降低火电机组的功率上下调整功率。

4.4.2 各机组日内优化调度

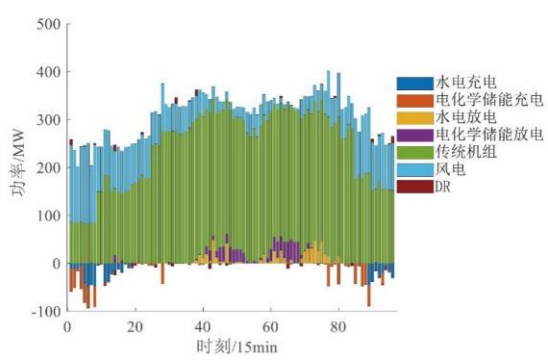


图 9 各机组日内调度优化

Figure 9 Intra-Day Dispatching Optimization of Each Unit

由上图，日内调度中，风电功率受天气影响波动大且不稳定。风电和负荷突变时，电化学储能可快速充放电（风电高时充电、不足时放电）以削峰填谷；抽水蓄能能快速调节，平衡日前与日内出力偏差；传统机组出力稳定，可在风电低时提供基础负荷支撑。日内滚动调度中，利用抽水蓄能与 B 类 IDR 负荷的快速响应能力，应对短时间尺度的风电和负荷波动，减轻火电机组功率调节压力。

4.4.3 实时调度

各机组实时调度如图 10 所示。

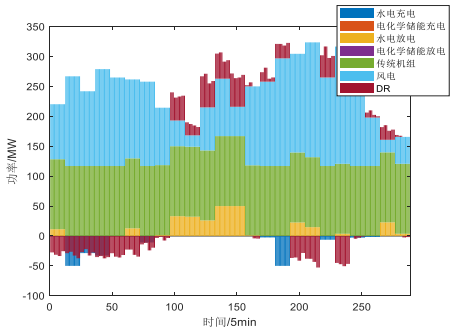


图 10 各机组实时调度图

Figure 10 Real-Time Dispatching Chart of Each Unit

在实时调度中通过细化时间颗粒可以实现更为接近于实际调度的预调度，其为实际调度提供了更为精确的参考依据在实时调度中可以通过快速调整抽水蓄能机组、电化学储能机组的输出功率缓解实时尺度内火电机组的功率调整压力。对于急剧变化的风电和负荷波动，可以通过调节速度更快的 DR 负荷来进行调节。

5 总结

本项目基于风、水、电等多时间尺度，开展新能源系统优化调度研究，构建能满足负荷需求且效益最大的风电-水电组合发电系统。为减小风电波动对电网的负面影响，以准确源荷预报为基础，开展基于储能的风力发电系统调频辅助服务优化，发挥抽蓄机大容量存储与蓄电池快速响应优势，解决弃风问题，提升电网接纳能力，为“源网荷储”协同运行提供借鉴。以某地区风电场、光热电站及水电站预测出力数据为对象，通过 MATLAB 仿真显示：水电承担负荷、光热调节风电波动，可显著提升系统出力稳定性，增加整体经济效益。

研究还考虑风电正、反调峰特性，提出计及机组主动调峰能力的多能互补优化调度策略；针对可再生能源波动性，按响应速度差异，提出日前 24h、日内 4h 和实时 15min 的机组调度策略。仿真表明，电化学与抽水蓄能储能互补，为风、火电力高峰提供更优存储空间。

参考文献

[1] 葛晓琳．水火风发电系统多周期联合优化调度模型及方法[D]．北京：华北电力大学，2013.

[2] 刘兵．计及分类需求响应的电力系统多目标鲁棒优化调度研究[D]．江西：华东交通大学，2019.

[3] 刘胜波．新型电力系统多时间尺度自动调度方法[J]．自动化应用，2023，64(17):160162.

[4] 彭伟鹏，邵振国，陈飞雄，等．计及需求响应的风储集群电力系统多时间尺度优化调度[J]．太阳能学报，2025，46(02):282292.

[5] 谢鹏．含间歇式电源的电力系统鲁棒优化调度研究[D]．江西：华东交通大学，2015.

[6] 李若琼，司宇杰，杨承辰，等．考虑柔性负荷的新型电力系统源荷日前日内低碳优化调度[J]．南方电网技术，2025，19(03):116129.



收稿日期：2025-09-30。

作者简介：

孙晓优(2003)，女，硕士研究生，研究方向为电力系统运行，E-mail：12025101306@stu.sie.edu.cn；

孙天贺(1991)，男，副教授，研究方向为电力系统分析与控制，E-mail：sunth@sie.edu.cn

047 防止输电断面连锁过载的新能源电力系统鲁棒性控制方法

黄 思[1]，杨松浩[1]，郝治国[1]

（1．西安交通大学电气工程学院，陕西省西安市 710049）

Robust Control Approach for Preventing Cascading Overloads of Transmission Sections in Renewable Energy Integrated Power Systems

Huang Si[1], YANG Songhao[1], HAO Zhiguo[1]

(1.School of Electrical Engineering, Xi'an Jiaotong University, Xi'an 710049, China)

ABSTRACT: Removing overloaded lines can cause power flow to shift to other lines within the relevant transmission section, leading to cascading tripping incidents. Rapidly developing a reasonable and effective power flow control strategy to eliminate line overloading is key to preventing cascading tripping. Addressing the issue of insufficient robustness in existing methods under scenarios with uncertain renewable energy output, this paper proposes a robust rapid control method to prevent cascading overloading in transmission sections based on comprehensive sensitivity. First, an improved comprehensive sensitivity is adopted; Then, a composite priority index coupling comprehensive sensitivity with renewable energy fluctuation risks is proposed to address the issue that traditional node ranking methods overlook the uncertainty of renewable energy output. The adjustment quantity constraint conditions are improved based on the principle of reverse equal-quantity pairing. Finally, the proposed method's rapidity and accuracy are verified through simulation analysis of the IEEE 39-bus system.

KEY WORDS: transmission section safety, cascading failure, comprehensive sensitivity, renewable energy uncertainty, robust control

摘要：切除过载线路会导致潮流转移至相关输电断面内的其他线路上，造成连锁跳闸事故，快速制定合理有效的潮流控制策略，消除线路过载，是阻止连锁跳闸发生的关键。针对现有方法在新能源出力不确定性场景下面临鲁棒性不足的问题，本文基于综合灵敏度，提出一种防止输电断面连锁过载的鲁棒性快速控制方法。首先采用改进后的综合灵敏度；然后优化调整节点的排序策略，提出耦合综合灵敏度与新能源波动风险的复合优先级指标，解决传统节点排序方法忽视新能源出力不确定性的问题；在调整节点对的选择与调整量的确定上，基于反向等量配对原则，完善调整量约束条件。最后利用 IEEE 39 节点系统的仿真分析验证了所提方法的快速性和准确性。

关键词：输电断面安全，连锁过载，综合灵敏度，新能源不确定性，鲁棒控制

0 引言

高比例接入电网的风电、光伏等新能源出力具有不确定性，使得电网传输功率波动频繁。输电断面是构成电网的基础，当线路出现潮流越限并故障跳闸后，将导致关联输电断面发生潮流大范围转移，造成输电断面内新的潮流过载，最终导致电网发生大规模连锁跳闸事故，这严重威胁着电力系统的安全稳定运行[1]-[2]。因此，当切除过载线路会导致关联输电断面面临连锁过载风险时，需快速制定潮流紧急控制策略以消除过载，阻止过载保护延时动作切除线路，从而阻断连锁故障的蔓延[3]-[4]。

现有文献对于过载支路潮流紧急控制的方法可分为灵敏度分析[5]-[9]和优化控制两大类：优化控制类方法所得的控制方案经济性和安全性较好，但其计算求解时间过长，难以满足潮流控制的快速性要求。而基于灵敏度的分析方法不存在判断是否收敛的问题，计算时间更短，便于实际快速执行操作。

文献[5]提出一种结合重要性权重的主成分分析法，用以评价节点消除断面过载的综合能力并获得控制节点操作序列，但该方法在调整序列的确定中未考虑每轮调整后系统运行状态变化给节点排序造成的影响。文献[6]针对传统灵敏度算法在消除输电断面过载时的缺陷，提出了基于综合灵敏度分析的快速控制算法，以综合灵敏度的大小确定调整节点的排序，但该方法中的综合灵敏度，未考虑到调整给断面内正常支路带来的潮流越限风险。文献[7]提出了一种改进的综合灵敏度概念，认为节点对断面的综合灵敏度是断面内过载支路与正常支路

灵敏度的加权和，并考虑了各条支路运行状态的权重差异，在一定程度上确保了调整过程中断面内的正常支路潮流不会越限，但其在调整节点的排序过程中并未考虑到系统参数不确定性的影响，排序指标较为单一。文献[8]提出了基于综合灵敏度的潮流越限切负荷调整方案，通过改变节点负荷大小实现线路过载的消除，但在实际中机组出力调整应优先于削减负荷操作，其在实际系统中应用的合理性有待验证。文献[9]提出一个基于正负综合灵敏度的输电断面双层优化潮流控制策略，通过考虑节点对过载和重载线路的整体调节作用，能够更准确地识别对输电断面潮流控制效果显著的节点，但该方法并未考虑不同类型的发电机节点对潮流影响的不同。

考虑到潮流控制的快速性要求，应在过载保护动作前完成整个方案的输出和执行。因此针对现有灵敏度控制方法未考虑新能源不确定性的问题，本文提出一种计及新能源出力不确定性的输电断面鲁棒性控制策略。首先在调整节点的分类与排序上，改进传统综合灵敏度算法，提出耦合综合灵敏度与新能源波动风险的复合优先级指标，解决传统节点排序方法忽视新能源出力不确定性的问题。在调整节点对的选择与调整量的确定上，完善调整量约束条件，把新能源波动对支路潮流的最坏影响量化为裕度阈值，嵌入调整量的计算中，通过裕度预留确保调整方案的鲁棒性。最后在 IEEE 39 节点系统中进行了仿真验证，结果表明本文方法可消除断面过载，并确保在极端波动场景下断面的安全性。

1 耦合综合灵敏度与新能源波动风险的复合优先级指标

1.1 节点对断面的综合灵敏度

节点注入的有功变化对支路有功潮流变化的影响，即节点对支路的有功灵敏度：

$$S_{l,i}=\frac{\Delta P_l}{\Delta P_i} \tag{1}$$

式(1)中 $S_{l,i}$ 为节点 i 对支路 l 的有功潮流灵敏度，其物理意义为系统中节点 i 的有功功率增加一个单位值引起的支路 l 有功潮流的变化量。

以输电断面整体为保护对象，假设断面 T 内有 L 条过载支路以及 M 条负载率大于设定值 β（本文中取值为 0.8）的正常支路，根据断面内过载支路的过载程度及正常支路的冗余程度，加权传统灵敏度得到综合灵敏度。节点 k 对断面 T 综合灵敏度 $S_{T,k}$ 的计算公式为：

$$S_{T,k}=\sum_{l=1}^{L}\alpha_l\cdot S_{l,k}+\sum_{m=1}^{M}\alpha_m\cdot S_{m,k} \tag{2}$$

式(2)中 α_l 和 α_m 分别为过载支路和正常支路对应的权重，过载支路过载量越大、正常支路冗余量越小，其对应权重越大。其计算公式为：

$$\alpha_l=\frac{\lambda}{H}\cdot\frac{\Delta P_l}{\max(\Delta P_l)} \tag{3}$$

$$\alpha_m=\frac{1}{H}\cdot\frac{\min\left(\Delta P_m\right)}{\Delta P_m} \tag{4}$$

式(3)-(4)中 λ 为过载支路的整体指标权重 $(\lambda>1)$，本文中统一取值为 2；ΔP_l 为过载支路 l 的过载量；ΔP_m 为正常支路 m 的冗余量。

1.2 考虑新能源出力不确定性的复合优先级指标

综合灵敏度 $S_{T,k}$ 的符号与大小包含丰富的信息，对快速消除当前系统过载的确定性优化调整有着重要的意义，但在考虑新能源出力的不确定性时，其作为优先级指标过于单一。因此，在节点优先级排序的过程中，需综合考虑节点出力调整对消除断面过载的效率高低以及新能源节点出力不确定性给断面带来的风险大小，通过适当提高新能源节点的优先级，实现对其波动风险的主动控制，确保调整方案的鲁棒性。节点 i 对输电断面 T 的复合优先级指标 $R_{T,i}$ 的计算公式为：

$$R_{T,i}=\alpha\cdot\frac{\left|S_{T,i}\right|}{\max\left(\left|S_{T,i}\right|\right)}+(1-\alpha)\cdot\frac{B_{T,i}}{\max\left(B_{T,i}\right)} \tag{5}$$

式(5)中 $\alpha\in[0,1]$ 为风险抑制系数，用于调节综合灵敏度与波动风险在复合优先级计算中的占比；$B_{T,i}$ 为节点 i 对断面 T 的波动风险，用于表明节点出力波动对断面潮流的最坏影响，其表达式如下：

$$B_{T,i}=\delta_i\cdot P_i^{\text{forecast}}\cdot S_{T,i}^{'} \tag{6}$$

式(6)中 δ_i 为调整后发电机节点出力的最大波动范围，传统机组取值为 0；P_i^{forecast} 为发电机节点 i 调整后的预测出力；$S_{T,i}^{'}=\sum_{l\in T}S_{l,i}$ 为节点 i 对断面 T 内所有支路的灵敏度之和，用于表示该节点出力变化对断面总体潮流的影响。

综合灵敏度 $S_{T,i}$ 用于系统当前的过载调节，优先调整对关键支路影响显著的节点出力，对调整方案的快速性有着重要作用；波动风险 $B_{T,i}$ 用于系统未来的风险抑制，优先限制给断面带来高波动风险的节点出力，对调整方案的鲁棒性有着重要意义。按照复合优先级指标 $R_{T,i}$ 的大小进行节点优先级排序，可综合当前过载与未来波动，平衡系统在新能源出力波动下调整方案的快速性与鲁棒性。$R_{T,i}$ 越大，节点对系统稳定性和抗波动能力的综合贡献就越大，越应优先调整。

2 计及新能源出力不确定性的调整量确定

2.1 反向等量配对调整原则

在消除断面过载的过程中，为了确保系统的总发电量不变，避免因功率失衡而导致频率波动或平衡节点越限，需采用反向等量配对调整原则对节点调整量进行约束[10]。反向等量配对调整原则的含义是：为每一加出力发电机节点找到一个与之配对的减出力发电机节点，反之亦然。每一对配对节点的出力调整量大小相等，调整方向相反，用以保证系统总的功率平衡，避免出现频率偏差或平衡节点的大幅度调整，尽可能的避免平衡机越限。

2.2 计及新能源出力不确定性的调整量动态裕度约束

对于断面内任一支路 m，在新能源机组出力最大波动场景下，其有功潮流变化量可表示为：

$$\Delta P_m^{\mathrm{bd}} = \sum_{i\in G} \delta_i \cdot P_i^{\mathrm{forecast}} \cdot \left| S_{m,i} \right| \tag{7}$$

式(7)中 G 为系统中所有发电机节点的集合；δ_i 为调整后发电机节点出力的最大波动范围；P_i^{forecast} 为发电机节点调整后的预测出力。

一对调整节点 a,b 的调整量由下式确定：

$$\Delta P = \min\{\Delta P_{\mathrm{xtl}}, \Delta P_a^{\max}, \Delta P_b^{\max}, \Delta P_{\mathrm{ys}}^{\min}, \Delta P_{\mathrm{fxys}}^{\min}\} \tag{8}$$

式(8)中 ΔP_{xtl} 为消除当前过载且留有一定裕度所需要的调整量；$\Delta P_a^{\max}$ 是上调出力节点 a 的最大可上调量；$\Delta P_b^{\max}$ 是下调出力节点 b 的最大可下调量；$\Delta P_{\mathrm{ys}}^{\min}$ 为防止原有的正常支路潮流越限的约束量；$\Delta P_{\mathrm{fxys}}^{\min}$ 为保证断面内所有的支路潮流方向不发生改变的约束量。各个量的详细计算如下：

（1）约束 1：过载支路的过载量约束。对断面内的某一过载支路 l，设其过载量为 ΔP_l，当 $S_{l,ab} < 0$ 时，表明调整节点对出力将减小支路潮流。为消除过载且确保调整后支路在新能源波动的极端场景下仍不过载，调整节点对所需要的调整量应当为：

$$\Delta P_{\mathrm{xtl}}{}' = -\left(\frac{\Delta P_l + \Delta P_l^{\mathrm{bd}}}{S_{l,ab}} \right) \tag{9}$$

当断面内存在多条过载支路时，需求调整量应当取最大值：

$$\Delta P_{\mathrm{xtl}} = \max\{\Delta P_{\mathrm{xtl1}}{}', \Delta P_{\mathrm{xtl2}}{}', \cdots\} \tag{10}$$

（2）约束 2：正常支路的潮流越限约束。针对断面内的某一正常支路 n，设其冗余量为 ΔP_n，当 $S_{n,ab} > 0$ 时，表明调整节点对出力将增大该正常支路的潮流，这与预期结果相背，该风险在新能源出力波动场景下被进一步放大。为了避免调整后正常支路潮流越限，并防止其在新能源波动场景下过载，需对调整节点对的调整量进行约束，约束量为：

$$\Delta P_{\mathrm{ys}} = \frac{\Delta P_n - \Delta P_n^{\mathrm{bd}}}{S_{n,ab}} \tag{11}$$

为保证断面内所有的正常支路潮流都不越限，应取所有支路约束量的最小值：

$$\Delta P_{\mathrm{ys}}^{\min} = \min\{\Delta P_{\mathrm{ys1}}, \Delta P_{\mathrm{ys2}}, \cdots\} \tag{12}$$

（3）约束 3：任一支路的潮流反向约束。对断面内任一支路 m，当 $S_{m,ab} < 0$ 时，调整节点对出力将使得支路的潮流下降，这是预期的结果。但如果调整量过大，则可能导致该支路的潮流大幅下降，甚至出现潮流反向的风险。为避免基本潮流方向改变而带来新的问题，需要在调整量的确定过程中增加考虑了新能源出力不确定性的支路潮流反向增长约束。定义裕度系数 $K_l > 1$，设支路当前的有功潮流为 P_0，则调整节点对的最大可调整量为：

$$\Delta P_{\mathrm{fxys}} = -K_l \left(\frac{P_0 + \Delta P_m^{\mathrm{bd}}}{S_{m,ab}} \right) \tag{13}$$

为确保断面内任何支路均不出现潮流反向增长的情况，取所有支路最大可调整量中的最小值作为约束量：

$$\Delta P_{\mathrm{fxys}}^{\min} = \min\{\Delta P_{\mathrm{fxys1}}, \Delta P_{\mathrm{fxys2}}, \cdots\} \tag{14}$$

在完成每一轮配对调整计算后，需及时更新输电断面内各支路的运行状态及各节点的出力情况。若一轮调整结束后仍存在支路过载现象，表明该调整对中至少存在一个节点出力已达到限值，需重新进行配对调整及后续计算。

3 算例分析

本文在改造后的 IEEE 39 节点系统中验证了所提控制算法的有效性与适用性。过载支路 3 所在的输电断面共包含 4 条支路。若直接切除支路 3，会导致系统面临连锁过载跳闸的风险，须立即采取紧急措施消除支路过载，阻断连锁反应的发生。此时系统如图 1 所示。

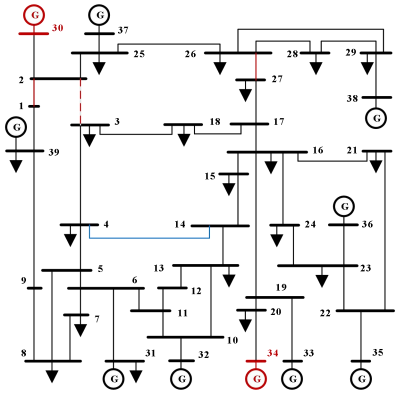


图 1 改造后的 IEEE 39 节点系统示意图

Fig 1 Schematic diagram of the modified IEEE 39 bus system

在图 1 中，红色虚线表示因过载而切除的支路 3，红色实线表示断开支路 3 后出现过载的支路 1 和 42，蓝色实线表示负载率大幅上升的支路 9。

3.1 调整方案的计算及快速性验证

在第一轮配对调整过程中，各发电机节点对断面的综合灵敏度 $S_{T,i}$、波动风险 $B_{T,i}$ 及复合优先级指标 $R_{T,i}$ 的计算结果如表 1 所示。

表 1 第一轮配对调整计算结果

Table 1 First round of pairing adjustment calculation results

	发电机节点							
	30	32	33	34	35	36	37	38
$S_{T,i}$	+0.17	-0.04	-0.07	+0.08	-0.07	-0.07	+0.24	+0.16
$B_{T,i}$	40.99	0	0	46.14	0	0	0	0
$R_{T,i}$	0.79	0.09	0.14	0.59	0.15	0.15	0.54	0.35

根据表 1 中综合灵敏度的符号对节点进行分类，根据波动风险的大小对节点进行排序，在第一轮配对调整计算中，得到上调出力节点序列为 35、36、33、32，下调出力节点序列为 30、34、37、38。分别选取两个序列中的第一个节点组成调整节点对，计算调整量并进行调整。当节点 35 达到其出力上限时，本次调整结束。在本轮调整中，新能源节点 30 对断面的综合灵敏度小于节点 37，但考虑到其出力不确定性给断面潮流带来的风险，其复合优先级更高，优先下调其出力来主动抑制波动风险；而节点 34 虽具有更高的波动风险，但由于其综合灵敏度最小、调整效率最低，综合考虑之下并未赋予其靠前的节点排序。

值得注意的是，在每一轮调整计算中，并不是沿用第一次配对调整计算的结果，而是需要重新对节点进行分类和排序。与第一轮配对调整计算的流程相同，在二轮调整中，节点 30 的波动风险较上一次调整已有所降低，但由于其较高的综合灵敏度仍在复合优先级计算中贡献了较大数值，使其仍排在调整序列首位。当节点 30 达到其出力下限时，本轮调整结束，重复进行相同计算直至满足终止条件，最终控制调整方案如表 2 所示。

表 2 最终控制调整方案

Table 2 Final control scheme

节点编号	机组类型	初始出力 (MW)	调整方向	调整量 (MW)	最终出力 (MW)
35	传统机组	650	上调	71.4	721.4
30	新能源机组	250	下调	75.0	175.0
32	传统机组	650	上调	88.7	738.7
37	传统机组	540	下调	85.1	454.9

由表 2 知，最终调整方案共调整 4 个节点，进行了 3 轮调整，其中新能源节点 30 参与了前两轮调整，通过下调自身出力实现了对波动风险的主动抑制；新能源节点 34 并未参与调整，完全通过调整方案预留的裕度来实现对波动风险的被动防御。

调整前后断面内各支路的负载率变化如图 2 所示。

本案例通过 93 毫秒完成了最终调整方案的生成，计算速度较快，可以满足输电断面保护对于快速性的要求，具有一定的参考价值。

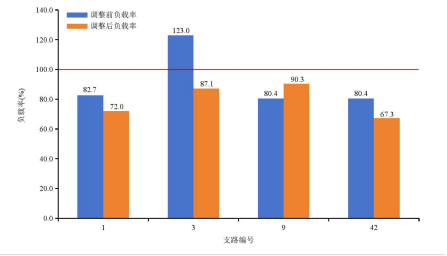


图 2 调整前后断面内各支路负载率变化图

Fig 2 Comparison of load rates before and after adjustment

3.2 鲁棒性调整与确定性调整的对比分析

若仅将综合灵敏度的符号和数值大小作为节点排序依据，且在调整量的计算中不考虑新能源出力的不确定性，则可得到确定性调整控制方案，此种方案调整前后断面内各支路负载率变化如图 3。

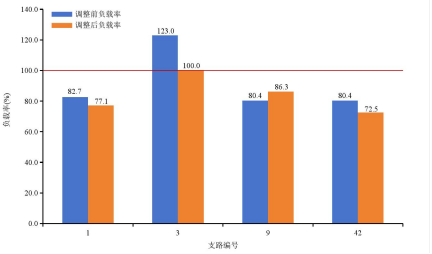


图 3 确定性调整前后断面内各支路负载率变化图

Fig 3 Comparison of load rates before and after deterministic adjustments

由图 3 可知，确定性优化调整可恰好消除支路 3 的过载，但若计及新能源出力的不确定性，则支路的过载无法消除。而与确定性调整方法相比，鲁棒性调整策略更注重方案的稳健性，通过在调整节点的排序与调整量的计算两个方面考虑新能源出力的不确定性，确保调整结果在所有可能的参数波动范围内仍能满足约束条件，可减少不确定性对系统的影响，更适用于新能源接入的电力系统。图 4 所示为调整后在极端波动场景下断面内各支路的负载率变化图。

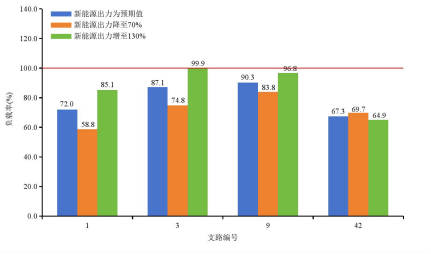


图 4 极端波动场景验证

Fig 4 Extreme scenario validation

由图 4 可以看出，当新能源机组调整后出力突

增或骤降至预测出力的 130%或 70%时，本文采用的鲁棒性调整策略仍能通过调整方案中事先预留的裕度，确保断面内所有支路不会过载。

3.3 不同风险抑制系数取值下的对比分析

表 3 为不同α取值下调整方案的对比分析。

表 3 不同α取值下调整方案的对比分析

Table 3 Comparison analysis of schemes under different α values

α 取值	新能源机组参与调整的顺序	新能源机组总调整量(MW)	传统机组总调整量(MW)	调整节点个数	断面内支路的最大负载率(%)
0.1	34、30	227.4	341.0	7	92.8
0.5	30、34	227.4	341.0	7	92.8
0.6	30	75.0	245.2	4	90.3
0.7	30	71.4	253.0	4	90.5
0.9	无	0	365.2	4	91.6

在调整节点的排序过程中提出了一种耦合综合灵敏度与新能源波动风险的优先级指标，通过调节风险抑制系数α的大小，可以在当前过载消除的要求和未来波动防御的需要之间找出平衡。

（1）α越小，越优先限制波动风险高的新能源节点出力。α取值为 0.1 时，尽管第 34 号新能源节点对输电断面的综合灵敏度数值很小，但由于其较高出力水平所带来的较大波动风险，其优先级高于中等灵敏度中等波动风险的第 30 号新能源节点，调整过程中优先下调其出力以实现对风险的主动抑制；随着α增大，波动风险在复合优先级计算中所占的比重降低，34 号节点优先级逐渐下降，当α取值为 0.5 时，30 号节点在第一轮调整中反超节点 34 而被首先调整，但因其仍参与了后续的调整配对，且其对输电断面的调节效率很低，这两种取值情况都需要其余传统机组贡献更多调整量才能消除断面过载，导致调整方案偏保守，调整量偏大。

（2）α越大，越优先调整综合灵敏度$S_{T,i}$大的节点出力。当α增大至 0.6 时，34 号节点因优先级太低而彻底不参与调整，但 30 号节点仍保有较高的优先级，此时通过主动下调 30 号节点出力来实现对波动风险的主动控制，通过预留裕度来实现对波动风险的被动防御，并以最小的总调整量、最少的调整节点个数以及最低的断面内支路负载率实现了对输电断面的安全控制，调整方案既不保守也不激进，在两者之间取得了很好的平衡；而随着α继续增大，调整方案过于注重当前过载的快速消除，调整偏激进，对于波动风险的主动控制力度渐弱，当α取值为 0.7 时，30 号节点因优先级降低而只参与最后一轮配对调整，当增大至 0.9 时，已无新能源节点参与配对调整，此时完全依靠传统火电机组预留裕度来覆盖未被主动降低的波动风险，调整量偏大。

4 结论

本文以输电断面整体为保护对象，针对新能源接入的电力系统，提出一种防止输电断面连锁过载的新能源电力系统鲁棒性快速控制方法。首先考虑调整节点对断面内过载支路与正常支路的整体调整效果，采用改进后的综合灵敏度；然后优化调整节点的排序策略，提出耦合综合灵敏度与新能源波动风险的复合优先级指标，解决传统节点排序方法忽视新能源出力不确定性的问题；在调整节点对的选择与调整量的确定上，基于反向等量配对原则选择调整节点对，完善调整量约束条件，把新能源波动对支路潮流的最坏影响量化为裕度阈值，嵌入调整量的计算中，通过裕度预留确保调整方案的鲁棒性。最后利用 IEEE 39 节点系统的仿真分析验证了所提方法的快速性和准确性。

参考文献

[1] 钟海旺，张广伦，程通，等．美国得州 2021 年极寒天气停电事故分析及启示[J]．电力系统自动化，2022，46(06)：1-9.

[2] 王国春，董昱，许涛，等．巴西“8．15”大停电事故分析及启示[J]．中国电机工程学报，2023，43(24)：9461-9470.

[3] Qi J，Ju W，Sun K．Estimating the Propagation of Interdependent Cascading Outages with Multi-Type Branching Processes[J]．IEEE Transactions on Power Systems，2017，32(2)：1212-1223.

[4] 顾雪平，张尚，王涛，等．安全域视角下的有功安全校正优化控制方法[J]．电力系统自动化，2017，41(18)：17-24.

[5] 姚峰，张保会，周德才，等．输电断面有功安全性保护及其快速算法[J]．中国电机工程学报，2006，(13)：31-36.

[6] 程临燕，张保会，郝治国，等．基于综合灵敏度分析的快速控制算法研究[J]．电力自动化设备，2009，29(04)：46-49.

[7] 牟颖，张保会，薄志谦．防止输电断面连锁过载的快速控制算法[J]．电力系统自动化，2017，41(03)：39-45.

[8] 徐伟，李群，杨君军，等．基于综合贡献度指标的紧急减负荷控制多目标优化方法[J]．电力自动化设备，2018，38(08)：189-194.

[9] 谢大为，王博欣，王京景，等．基于正负综合灵敏度的输电断面双层优化潮流控制策略[J]．电力工程技术，2023，42(01)：107-115.

[10] 邓佑满，黎辉，张伯明，等．电力系统有功安全校正策略的反向等量配对调整法[J]．电力系统自动化，1999，(18)：5-8.

收稿日期：2025-mm-dd



黄思

作者简介：

黄思(2003)，女，硕士研究生，研究方向为为电网稳定性控制，15773750886@163.com；

杨松浩(1989)，男，博士生导师，研究方向为电网稳定性控制；

郝治国(1976)，男，博士生导师，研究方向为电力系统继电保护。

（编辑　）

048 两相旋转坐标系下的可调度虚拟振荡器虚拟惯性控制

文嘉俊，颜景斌

（哈尔滨理工大学电气与电子工程学院，哈尔滨 150080）

摘要：在高比例新能源接入的背景下，虚拟振荡器控制是一种新兴的构网型控制。针对虚拟振荡器控制具有惯性水平低,在负载变化时频率不稳的问题。本文提出了一种在两相旋转坐标系虚拟惯性增强的三相逆变器可调度虚拟振荡器控制策略，该策略将一种的虚拟惯性增强技术与两相旋转坐标系下的可调度虚拟振荡器控制相结合，为微电网提供所需的惯性响应并减轻负载变化下对频率稳定性的不利影响。在仿真中，验证了该控制策略能够为微电网提供对应的虚拟惯性，减少了负载阶跃变化下频率的过冲，有效的提升了电力系统的稳定性。

关键词：三相逆变器控制；可调度虚拟振荡器；虚拟惯性；频率变化

DOI：10.13335/j.1000-3673.pst.2014.01

Virtual inertia control and Simulation of schedulable virtual oscillator in two phase rotating coordinate system

WEN jiajun,YAN jingbin

(School of electrical and electronic engineering, Harbin University of Technology, Harbin150080)

ABSTRACT: In the context of high proportion of new energy access, virtual oscillator control is a new type of network control. The virtual oscillator control has the problems of low inertia level and unstable frequency when the load changes. This paper proposes a three-phase inverter schedulable virtual oscillator control strategy based on virtual inertia enhancement in two-phase rotating coordinate system. The strategy combines a virtual inertia enhancement technology with schedulable virtual oscillator control in two-phase rotating coordinate system to provide the required inertia response for microgrid and reduce the adverse impact on frequency stability under load changes. In the simulation, it is verified that the control strategy can provide the corresponding virtual inertia for the microgrid, reduce the frequency overshoot under the load step change, and effectively improve the stability of the power system.

KEY WORDS: Three phase inverter control; Schedulable virtual oscillator; Virtual inertia; Frequency variation

.

0 引言

目前，我国大部分电能来源于以化石能源为主的火力发电厂。随着绿色低碳战略的实施，国家逐步建立起以高比例新能源和高比例电力电子为送端，电动汽车等灵活性负载为受端的新型电力系统。与此同时，由于国内经济水平的提升。电能消耗正快速增长。因此，有必要推动电力能源由化石能源转向清洁能源,由高碳转向低碳[1]。但在实际运行中，新型电力系统中大量的电力电子器件和开关器件的接入,提高了响应速度的同时也导致系统惯性进一步下降。这一趋势，导致了当系统的输出功率或负载波动时，都会对系统的安全稳定运行造成影响。根据研究表明系统惯性受系统内电容容量的影响，但是在实际应用中，通过增加电容器容量来提高系统惯性，将增大电力系统的设备成本。单一增加电容器容量，也会减少电力系统动态调节的速度。所以，如何通过增加系统惯性来增强微电网稳定运行的研究，具有实际意义[2]。

针对上述问题，研究人员类比发电机的惯性，引入了虚拟惯性这一概念。在不增加系统电容器容量的前提下，通过在并网逆变器的控制策略中加入惯性控制环节,可有效增加系统惯性。从而提高系统的暂态稳定和电能质量。

目前，构网型控制已成为提高电网稳定性和可靠性的重要逆变器控制策略。与传统的跟网型控制相比，构网型逆变器作为电压源运行，通常不需要

锁相环，并且可以用于独立运行[3]。构网型控制的常见控制策略包括下垂控制[4]，虚拟同步发电机控制[5]、虚拟同步器控制[6]、功率同步控制[7]。除了上述方法之外，虚拟振荡器控制是构网型控制方法的新兴方法。在设定对应的功率额定值下，模仿弱非线性极限环振荡器的动态特性，生成对应的电压波形[8]。

而最近提出的可调度虚拟振荡器控制方案（dVOC），相比于其他的构网型控制方案，具有更强的电压动态调节性能，以及在电压接近稳态时所表现得的嵌入式下垂控制规律的特点[9]。这意味着相比其他的下垂控制方案，可调度虚拟振荡器在保持各个负载的额定功率的同时，其有更优越的电压调节性能[10]。

尽管可调度虚拟振荡器具有上述的优点，但由于在其方程中没有明确建模的时间常数，它不具有对应的虚拟惯性。最近，在文献[11]，[12]中在虚拟振荡器中引入了虚拟惯性。然而，这些控制器使用导数项来提供虚拟惯性，这会降低系统的抗噪性。在文献[14]、[15]中，作者证明了低通滤波器（LPF）能够在提供虚拟惯性的前提下，提升系统的稳定性。

针对上述问题，本文在两相旋转坐标系下建立了具有虚拟惯性的可调度虚拟振荡器模型。该模型通过引入 LPF，为系统提供对应的虚拟惯性。此外为了提升系统的稳定性，模型引入了静止坐标系下的比例谐振控制器的电压电流双闭环控制结构。最后在 Matlab/Simulink 的平台搭建了对应的系统仿真模型，通过对比改进前后的可调度虚拟振荡器的仿真结果，验证所提控制方案的有效性与优越性。

1 可调度虚拟振荡器模型

可调度虚拟振荡器控制是一种适用于分布式控制的构网型逆变器控制策略。其优势在于，在实现逆变器控制与电网同步的同时，能够保证系统对每个逆变器的功率注入和电压幅值与相位的精确控制。本章节从两相静止坐标系出发，通过不同参考系之间的关系推出两相旋转坐标系下的dVOC的数学模型，再通过虚拟惯性计算模块为 dVOC 提供虚拟惯性，并进行对应的数学建模。其控制框图如图 1 所示：

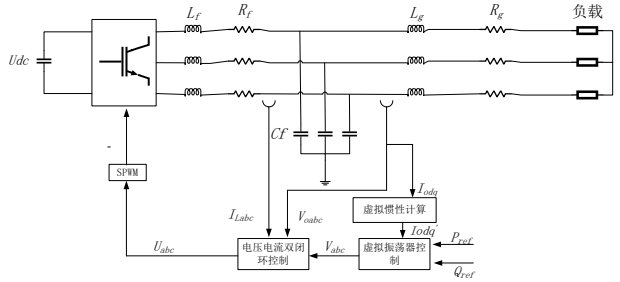


图 1 虚拟振荡器控制框图

Figure 1 control block diagram of virtual oscillator

在应用可调度虚拟振荡器时,每个逆变器监测其输出电流i，反馈至控制器后输出对应的电压波形，并同时采用 PWM 策略输出其端电压矢量v。可调度虚拟振荡器控制的基本表达式如下所示：

$$\frac{d}{dt}(\mathbf{v}) = j\omega_{\mathrm{r}}\mathbf{v} + \mu\left(V_{\mathrm{r}}^2 - V^2\right)\mathbf{v} + \eta\left(\mathbf{i}_{\mathbf{r}} - \mathbf{i}\right)e^{j\phi} \quad (1)$$

式中，ω_{r}和V_{r} 分别表示角频率参考和电压幅度参考。μ和η是两个控制参数，而ϕ是面对线路参数阻感比对应的设计参数。

其中电流参考矢量为$i_{\mathrm{r}} = i_{\alpha\mathrm{r}} + ji_{\beta\mathrm{r}}$和实际电流矢量$i = i_{\alpha} + ji_{\beta}$计算如下：

$$\begin{bmatrix} i_{\alpha\mathrm{r}} \\ i_{\beta\mathrm{r}} \end{bmatrix} = \frac{2}{3}\frac{1}{V^2}\begin{bmatrix} v_{\alpha} & v_{\beta} \\ v_{\beta} & -v_{\alpha} \end{bmatrix}\begin{bmatrix} P_{\mathrm{r}} \\ Q_{\mathrm{r}} \end{bmatrix} \quad (2)$$

$$\begin{bmatrix} i_{\alpha} \\ i_{\beta} \end{bmatrix} = \frac{2}{3}\frac{1}{V^2}\begin{bmatrix} v_{\alpha} & v_{\beta} \\ v_{\beta} & -v_{\alpha} \end{bmatrix}\begin{bmatrix} P \\ Q \end{bmatrix} \quad (3)$$

其中$v = v_{\alpha} + jv_{\beta}$。$P_{\mathrm{r}}$和$Q_{\mathrm{r}}$分别是有功和无功功率的设定值，而$P$和$Q$是逆变器的实际有功和无功功率输出。根据对应的数学关系式可调度虚拟振荡器的工作原理可以说明如下：谐振子项$j\omega_{\mathrm{r}}\mathbf{v}$被施加到 q 轴，并且以$\omega_{\mathrm{r}}$ rad/s 的速度进行旋转。幅度校正项沿着 d 轴径向施加到电压矢量上，使矢量幅度保持为V_{r}，而不考虑初始条件。可调度虚拟振荡器控制器在两相静止坐标系中的经典实现如图 2 所示，

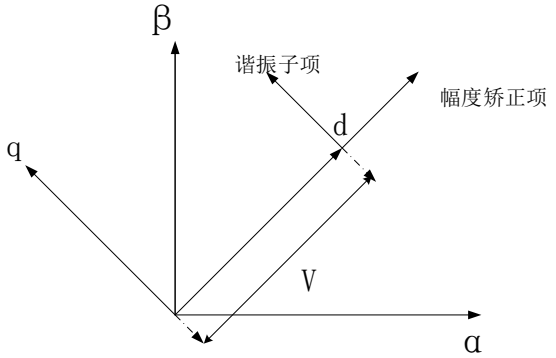


图 2 可调度虚拟振荡器经典实现图

Figure 2 classic implementation diagram of schedulable virtual oscillator

对虚拟振荡器的数学关系式可进行更进一步的分析。根据式（3），电流误差矢量Δi由式（4）给出：

$$\begin{aligned} \Delta i &= (i_{\alpha\mathrm{r}} - i_{\alpha}) + j(i_{\beta\mathrm{r}} - i_{\beta}) \\ &= \left[\frac{2}{3}\frac{1}{V^2}\left(P_{\mathrm{r}} - P\right)\right]\mathbf{v} + j\left[-\frac{2}{3}\frac{1}{V^2}\left(Q_{\mathrm{r}} - Q\right)\right]\mathbf{v} \\ &= \left(e_{\mathrm{iP}} + je_{\mathrm{iQ}}\right)\mathbf{v}. \end{aligned} \quad (4)$$

在实际电路应用中，一般取线路为感性进行分析。故此处相位角ϕ 取 90 度，并将式（4）代入式（2）中，可得到电压的一阶导数为

$$\frac{d}{dt}(\mathbf{v})=[j(\omega_r+\eta e_{iP})+(\mu e_v-\eta e_{iQ})]\mathbf{v}. \quad (5)$$

比较（5）和（1），可以推导出虚拟振荡器下垂特性公式如下所示：

$$\frac{d}{dt}(V)=\mu V\left(V_r^2-V^2\right)-\eta V e_{iQ} \quad (6)$$

$$\omega=\omega_r+\eta e_{ip} \quad (7)$$

在两相旋转坐标系中，电压矢量 v 也可以通过派克变换从两相静止坐标系转化为两相旋转坐标系。将 Park 变换应用于（3）中等式的两侧，可得到电流的两相旋转坐标系表达式：

$$\begin{bmatrix} i_{dr} \\ i_{qr} \end{bmatrix}=\frac{2}{3}\frac{1}{V^2}\begin{bmatrix} V & \\ & -V \end{bmatrix}\begin{bmatrix} P_r \\ Q_r \end{bmatrix} \quad (8)$$

$$\begin{bmatrix} i_d \\ i_q \end{bmatrix}=\frac{2}{3}\frac{1}{V^2}\begin{bmatrix} V & \\ & -V \end{bmatrix}\begin{bmatrix} P \\ Q \end{bmatrix} \quad (9)$$

其中，$i_r=i_{dr}+ji_{qr}$　$i=i_d+ji_q$

将式（8）和式（9）代入式（6）中，可以获得虚拟振荡器在两相旋转坐标系下的下垂关系为：

$$\frac{d}{dt}(V)=\mu V\left(V_r^2-V^2\right)-\eta\left(-\frac{2}{3}\frac{Q_r}{V}-i_q\right) \quad (10)$$

$$\omega=\omega_r+\eta\left(\frac{2}{3}\frac{P_r}{V}-i_d\right)\frac{1}{V}. \quad (11)$$

式（1）和（2）的虚拟振荡器表达式可以得出，传统可调度虚拟振荡器无法模拟惯性，因为在这些非线性方程中无法识别时间常数，此外，当负载波动时，容易造系统失稳。为了解决这些问题，可调度虚拟振荡器需要注入一定的虚拟惯性以提高稳定性。本文通过对有功功率和无功功率使用 LPF，将惯性效应引入到逆变器的动态方程中，其数学动态模型如下式所示：

$$\frac{d}{dt}(V)=\mu V\left(V_r^2-V^2\right)-\eta\left(-\frac{2}{3}\frac{Q_r}{V}-\frac{1}{T_f s+1}i_q\right) \quad (12)$$

$$\omega=\omega_r+\eta\left(\frac{2}{3}\frac{P_r}{V}-\frac{1}{T_f s+1}i_d\right)\frac{1}{V}. \quad (13)$$

其中 T_f 指的是惯性时间常数，其取值的大小取决于设定的频率变化率。其取值如表 1 所示。

根据增加了虚拟惯性的下垂特性 dVOC 数学模型，从而可以建立对应的数学模型。

2　电压电流双闭环模型

在电力系统中，电网出现负载的扰动是频繁的，而本文采用的 LCL 型滤波器存在在弱电网下稳定性不足的问题[16]。为了确保电压幅值与频率在负载波动时的稳定性，本文采用基于静止坐标系下的电压外环与电感电流内环相结合的双闭环控制结构。

在电流内环上，本文采用比例控制器。比例控制器具有结构简单，响应速度快的优势。在电压外环上，本文采用比例谐振(QPR)控制器。该控制器基于谐振控制器改良而来。其能够在谐振频率处放大增益。此外，该控制器还可根据逆变器的需求，设定谐振频率处带宽。通过合理设计控制器参数，该闭环结构能够在实现对交流量的无差控制。从而在降低系统复杂度的同时，进一步提升系统稳定性。

本文采用的 LCL 滤波器下的电压电流双闭环回路控制框图如图 3 所示。电流内环与电压外环的传递函数分别表示为：

$$\begin{cases} G_i(s)=k_{pi} \\ G_v(s)=k_p+\dfrac{2k_r\omega_c s}{s^2+2\omega_c s+\omega_n^2} \end{cases} \quad (14)$$

式中：*Kpi* 表示电流环的比例系数。k_p 表示电压环的比例系数，k_r 表示电压环的谐振系数和 ω_c 表示谐振角频率。

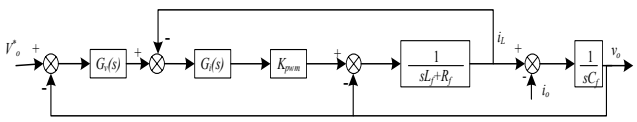


图 3 电压电流双闭环结构框图

Figure 3 voltage and current double closed loop structure block diagram

为确定 QPR 控制器参数。可以通过给 k_p，k_r 和 ω_c 赋值的方式得到传递函数 $G_v(s)$ 的 Bode 图。对其进一步的分析，分析参数对于带宽与增益的影响再确定具体的取值。不同取值下传递函数 $G_v(s)$ 的 Bode 图如图 4，图 5 所示。

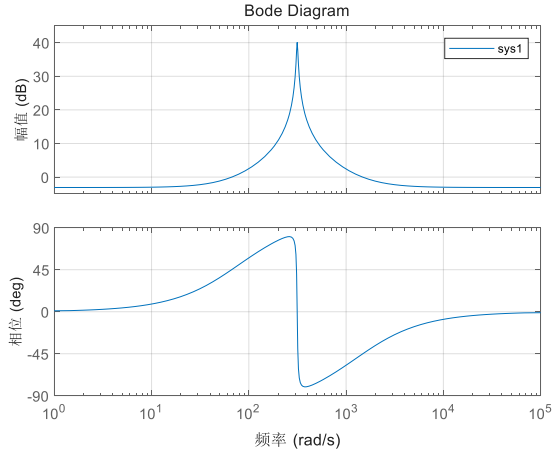


图 4 k_p =0.7，k_r =100 和 ω_c =5 时，QPR 控制器的 Bode 图

Figure 4 Bode diagram of QPR controller when k_p =0.7, k_r =100 and ω_c =5

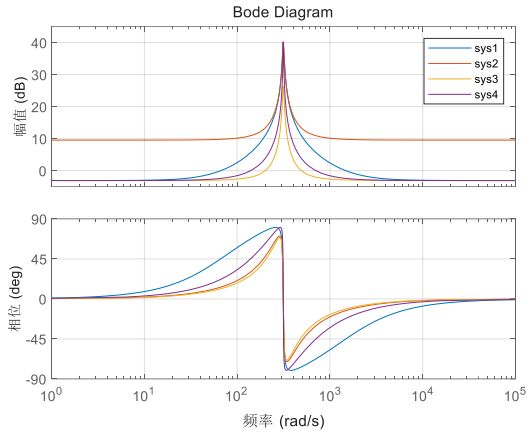


图 5 k_p，k_r 和 ω_c 取不同值时，QPR 控制器的 Bode 图

Figure 5. Bode diagram of QPR controller with different values of k_p，k_r and ω_c

其中图 4 为 k_p=0.7，k_r=100 和 ω_c=5 时，传递函数的 Bode 图，图 5 是 k_p，k_r 和 ω_c 分别取不同值时，传递函数的 Bode 图。其中 sys1 代表 k_p=0.7，k_r=100 和 ω_c=5 时，sys2 代表 k_p=3，k_r=100 和 ω_c=5 时，sys3 代表 k_p=0.7，k_r=20 和 ω_c=5 时，sys4 代表 k_p=0.7，k_r=100 和 ω_c=2 时。

图 5 中可以看出，谐振角频率 ω_c 主要影响控制器带宽，随着 ω_c 增大，控制器的带宽也随之增大。本文设计的电网频率允许波动范围为±0.2Hz，依据此选择对应的 ω_c 的取值。而比例系数 k_p 与控制器增益大小成正比，随着 k_p 增大，控制器增益变大。此外，稳态误差和谐振系数 k_r 成反比，k_r 越大，稳态误差越小。但 k_r 过大将造成系统的谐波分量增大，从而降低系统电流质量。故 k_p 与 k_r 的取值应该同步进行分析。根据上述分析，电压电流双闭环模型的参数取值如表 1 所示

3 仿真验证

表 1 控制系统仿真参数

Table 1 control system simulation parameters

参数	取值	参数	取值
L_g	3.2mH	L_f	9mH
C_f	6.5 μ F	P_r	1kW
Q_r	0	F_0	50hZ
T_f	0.05	W_r	100 π
K_{pi}	50	K_r	100
K_p	0.7	W_c	1.26
负载 1	1kW	负载 2	2kW

在 Matlab/Simulink 平台上，分别搭建了如图 1 所示的改进前后基于可调度虚拟振荡器的逆变器系统仿真模型。系统的仿真参数见表 1。为了验证改进后的仿真模型能够应对负载阶跃的变化，并为系统提供足够的功率。仿真开始运行时接入负载 1，0.35s 后加入负载 2，0.7s 时负载 2 切除。所得的频率，有功功率的波动图如图 6，图 7 所示。

从图 6，图 7 中可以看出，在 0.35s 负载阶跃变化时，控制器输出的频率迅速下降 0.1Hz，并迅速维持稳定。输出的有功功率从 1kW 阶跃到 3kW。在 0.7s 负载 2 切除后，系统频率回到 50Hz，系统输出功率回到 1kW。从图 6 与图 7 中可以得到结论改进后的控制策略能够为系统提供对应的虚拟惯性，并且能够快速适应负载的阶跃变化，迅速为负载提供对应的功率。

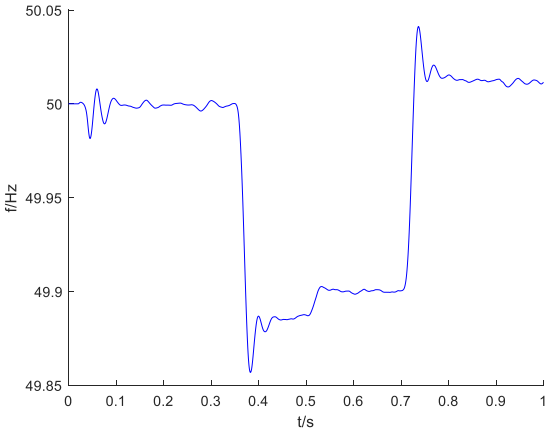


图 6 频率波动图

Figure 6 frequency fluctuation diagram

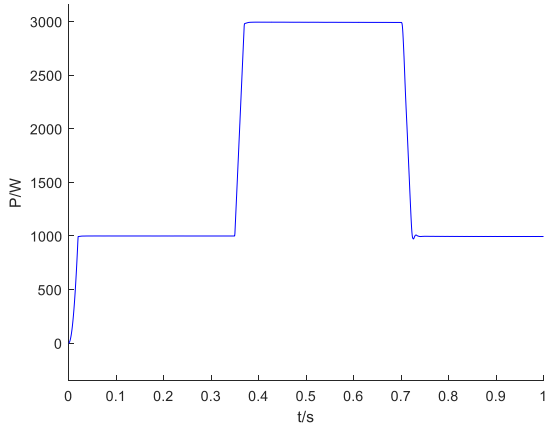


图 7 有功功率波动图

Figure 7 active power fluctuation diagram

为进一步验证改进后的控制策略相比于改进前的优越性，本文设置相同的负载阶跃变化场景，将二者进行比较。在仿真开始时设置接入负载 1，0.5s 后加入负载 2，改进前后的频率变化对比如图 8 所示。从该图可以得出结论，当使用改进的控制策略提供虚拟惯性时应对负载的阶跃变化时，能够减小频率的变化。此外，从二者前后频率下降的速度可以看出，改进后的控制策略能有效减小频率瞬变的过冲的作用。

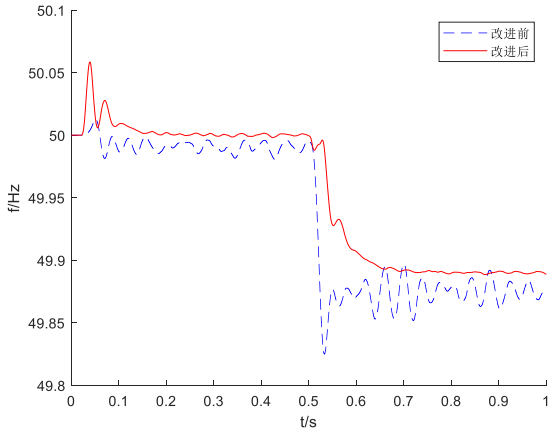


图 8 改进前后的频率波动对比图

Fig. 8 Comparison of frequency fluctuation before and after improvement

4 结论

针对现代高比例新能源接入电网后所带来的电力系统惯性下降，进一步对系统频率稳定性带来的挑战。本文提出了一种基于两相旋转坐标系下的可调度虚拟振荡器模型.该方法将低通滤波器集成到可调度虚拟振荡器的动态特性中，从而为虚拟振荡器提供了相应的惯性响应。此外，本文采用比例谐振控制器，在三相静止坐标系下建立了具有电压电流双闭环结构的可调度虚拟振荡器模型，通过合理地设计控制器的参数，实现了系统的稳定性的进一步提升。在 Matlab/Simulink 中的仿真结果表明，所提出的改进后的可调度虚拟振荡器模型，能够为系统提供虚拟惯性，在负载变化的情况下在减小系统频率变化的同时，可减少频率瞬变的过冲。

参考文献

[1] 谭显东,刘俊,徐志成,等.“双碳”目标下“十四五” 电力供需形势[J].中国电力,2021,54(5):1-6.

[2] 谢小荣,贺静波,毛航银,等.“双高”电力系统稳定性的新问题及分类探讨[J].中国电机工程学报,2021,41 (2):461-475.

[3] B. Muftau and M. Fazeli, “The Role of Virtual Synchronous Machines in Future Power Systems: A Review and Future Trends,” Electr. Power Syst. Res., vol. 206, no. October 2021, p. 107775, May 2022,

[4] K. De Brabandere, B. Bolsens, J. Van Den Keybus, A. Woyte, J. Driesen, and R. Belmans, “A voltage and frequency droop control method for parallel inverters,” PESC Rec. - IEEE Annu. Power Electron. Spec. Conf., vol. 4, no. 4, pp. 2501–2507, 2004,

[5] J. Driesen and K. Visscher, “Virtual synchronous generators,” IEEE Power Energy Soc. 2008 Gen. Meet. Convers. Deliv. Electr. Energy 21st Century, PES, pp. 26–28, 2008,

[6] Qing-Chang Zhong, Phi-Long Nguyen, Zhenyu Ma, and Wanxing Sheng, “Self-Synchronized Synchronverters: Inverters Without a Dedicated Synchronization Unit,” IEEE Trans. Power Electron., vol. 9, no. 2, pp. 617–630, Feb. 2014,

[7] W. Zhang, A. M. Cantarellas, J. Rocabert, A. Luna, and P. Rodriguez, “Synchronous Power Controller With Flexible Droop Characteristics for Renewable Power Generation Systems,” IEEE Trans. Sustain. Energy, vol. 7, no. 4, pp. 1572–1582, Oct. 2016,

[8] W. Zhang, A. M. Cantarellas, J. Rocabert, A. Luna, and P. Rodriguez, “Synchronous Power Controller With Flexible Droop Characteristics for Renewable Power Generation Systems,” IEEE Trans. Sustain. Energy, vol. 7, no. 4, pp. 1572–1582, Oct. 2016,

[9] M. Lu, S. Dhople, and B. Johnson, “Benchmarking Nonlinear Oscillators for Grid-Forming Inverter Control,” IEEE Trans. Power Electron., vol. 37, no. 9, pp. 10250–10266, Sep. 2022,

[10] S. D’Arco and J. A. Suul, “Improving the power reference tracking of virtual synchronous machines by feed-forward control,” in Proc. IEEE 19th Int. Power Electron. Motion Control Conf., 2021, pp. 102–107.

[11] S. D’Arco and J. A. Suul, “Phase angle feed-forward control for improving the power reference tracking of virtual synchronous machines,” IEEE Trans. Ind. Appl., vol. 60, no. 1, pp. 851–864, Jan./Feb. 2024.

[12] S. A. Aghdam and M. Agamy, “Adaptive Virtual Inertia Synthesis via Enhanced Dispatchable Virtual Oscillator Controlled Grid-Tied Inverters,” in IECON 2021 – 47th Annual Conference of the IEEE Industrial Electronics Society, IEEE, Oct. 2021, pp. 1–6.

[13] J. Li, J. E. Fletcher, D. G. Holmes, and B. P. McGrath, “Developing a machine equivalent inertial response for a Virtual Oscillator Controlled Inverter in a machine-inverter based microgrid,” in 2020 IEEE Energy Conversion Congress and Exposition (ECCE), IEEE, Oct. 2020, pp. 4314–4321.

[14] S. D’Arco and J. A. Suul, “Equivalence of virtual synchronous machines and frequency-droops for converter-based Microgrids,” IEEE Trans. Smart Grid, vol. 5, no. 1, pp. 394–395, 2014,

[15] J. Liu, Y. Miura, and T. Ise, “Comparison of Dynamic Characteristics between Virtual Synchronous Generator and Droop Control in Inverter-Based Distributed Generators,” IEEE Trans. Power Electron., vol. 31, no. 5, pp. 3600–3611, 2016,

[16] 刘展宁,刁瑞盛,阿敏夫,等.提升跟网型逆变器稳定性的滤波器参数优化方法[J].电力系统及其自动化学报,2025,37(06):1-12.

收稿日期：2025-08-25。

作者简介：

文嘉俊(2001-)，男，硕士研究生，研究方向为新能源发电与控制，E-mail:；1445073708@qq.com



文嘉俊

049 虚拟同步发电机的改进自适应控制策略

杨璐嘉，颜景斌

（哈尔滨理工大学电气与电子工程学院，哈尔滨 150080）

Improved adaptive control strategy for virtual synchronous generator

YANG Lujia,YAN Jingbin

(School of electrical and electronic engineering, Harbin University of Science and Technology，Harbin 150080，China)

Abstract: Virtual synchronous generator (VSG) technology provides an effective way to enhance the stability of the system by simulating the operation characteristics of synchronous generators. This paper proposes an optimization scheme for self-adaptive control based on virtual synchronous generator. In the single VSG control system, the inertia and damping adaptive control method is introduced. The virtual inertia and damping parameters of VSG are dynamically adjusted to improve the frequency stability. According to the output power and line parameters of each VSG, the virtual impedance can be adjusted adaptively to improve the reliability and stability of parallel system. Simulation results show that the proposed control strategy can effectively improve the dynamic performance of VSG under the condition of system load fluctuation and multiple parallel machines, which provides theoretical and technical support for the wide application of VSG in new energy power system and promotes the stable operation of power system.

Keywords: virtual synchronous generator; rotational inertia; damping coefficient; virtual impedance

摘　要：虚拟同步发电机技术通过模拟同步发电机的运行特性，为提升系统的稳定性提供了一种有效的办法。本文提出基于虚拟同步发电机自适应控制的优化方案。在单台控制中，引入惯量和阻尼自适应控制方法，通过实时监测系统的频率变化率和频率偏差，动态调整虚拟同步发电机的虚拟惯量和阻尼参数，提升系统频率的稳定性。在针对多台并联运行场景中，提出了虚拟阻抗自适应控制策略，依据各发电机的输出功率和线路参数，自适应调节虚拟阻抗，优化功率分配精度，提高并联系统的运行可靠性和稳定性。通过仿真实验验证，所提的控制策略在系统负荷波动及多机并联的工况下，能够有效地改善动态性能，为虚拟同步发电机在新能源电力系统中的广泛应用提供了理论和技术支持，促进了电力系统的稳定运行。

关键词：虚拟同步发电机；转动惯量；阻尼系数；虚拟阻抗

DOI：10.13335/j.1000-3673.pst.2014.01.

基金项目：国网黑龙江公司科技项目(522243718000T)。

Project Supported by National Natural Science Foundation of China(NSFC)(51037003): State Grid Heilongjiang Company Science and Technology Project (522243718000T)

0 引　言

在微电网中，传统的同步发电机长期以来承担着维持电力系统稳定运行的核心作用[1]。但是在电网高比例接入新能源后，新能源机组多通过电力电子设备并网，缺乏常规机组的频率和电压支撑能力，削弱电网频率调节能力，加剧电网稳定运行的风险。

一次能源因为间歇性及不稳定性加剧电网的运行风险[2]。电力电子设备通过 VSG(虚拟同步发电机)技术模拟同步发电机的惯量、阻尼等输出特性，让新能源发电设备像传统同步发电机一样提供频率和电压支撑，提升电力电子化电网的稳定性。但在面对快速变化的功率指令或系统扰动时，响应速度依然不如传统同步发电机。目前，国内外学者聚焦 VSG 模型的优化、参数设计等环节，并推动相关成果在工程实践中落地应用。文献[3][3]以提升孤岛直流微网的惯性和新能源消纳能力为目标，研究含有氢储能直流微网的虚拟同步机协同控制方法。在此基础上，通过建立该复合储能系统的状态方程，实现了复合储能系统的调节。针对光伏发电的随机性和无法给系统提供惯性支持的问题，文献[4]研究了基于 VSG 的光伏混合储能的控制策略，成功抑制系统功率的波动。文献[5]研究的具体内容是从单个到整体，对虚拟振子控制下的带阻感负载的性能进行分析。上述研究从不同角度分析了新能源接入对电网稳定性的影响以及调控思路。但在面对高比例新能源微电网的动态稳定机制，尤其是电力电子装备交互引发的特定风险方面，仍需更针对性的研究。

基于此，本文首先针对以下问题展开研究：新能源如风电、光伏等发电受自然条件存在较大波动。当电网的负荷突变或故障时，固定的惯量和阻尼参数容易导致频率波动剧烈，难以兼顾不同工况下的震荡抑制效果[6]。为此，本文提出惯量阻尼自适应控制方法，其核心机制如下：能根据新能源出力波

动幅度、电网频率变化率等参数，动态调整虚拟惯量数值和阻尼系数；扰动初期能自动增大阻尼以促进系统稳定，在系统趋于稳定后，又能减小阻尼以提升调节的灵活性。最后，通过仿真实验验证了文中分析方法及影响规律的正确性[7]。

本文针对的第二个问题[8-14]是：多机并联时，各机组到公共连接点的线路阻抗不同，若沿用固定虚拟阻抗控制，会导致无功功率分配不均，进而引发电压不平衡或某台机组过载。为此，本文采用虚拟阻抗自适用控制：通过实时监测电网电压与频率的偏差，动态调整虚拟阻抗的大小以及性质，使 VSG 能更加精确地补偿电压的跌落，从而提升电网的稳定性。

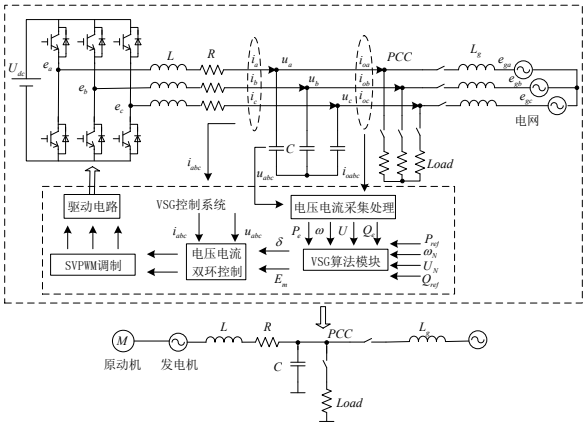


图 1　VSG 型的拓扑结构及控制框图

Fig. 1　Block diagram of basic topology and control structure of VSG type

在分布式电源并网逆变器的控制算法体系内，创新融入虚拟惯量与阻尼环节[15]。这个设计的本质是使逆变器具备类似同步发电机(SG)的运行特性，因此可以借助 SG 的经典理论框架对 VSG 进行建模分析[16]。其功率传输与功角关系可通过如下方程精确描述：

$$\begin{cases} J\dfrac{dw}{dt}=\dfrac{P_{ref}}{w}-\dfrac{P_e}{w}-D_p(w-w_0) \\ \delta=\int(w-w_0)\,dt \end{cases} \quad (1)$$

式中：δ 为 VSG 的攻角，反映了电动势与电网电压之间的相位差，是功率传输的关键相位参数；J 代表了虚拟转动惯量，它模拟了同步发电机转子的惯性特性，决定系统应对功率突变时的动态响应“惯性”；w 和 w_0 分别对应输出的角频率与电网额定角频率，二者的差别体现了系统的频率偏移程度；D_p 作为阻尼系数，作用是抑制系统频率振荡，加速了动态过程的稳态收敛。

在虚拟同步发电机的控制体系中，无功电压控制模块承担着类似虚拟同步发电机励磁调节的功能。其核心逻辑基于下垂控制原理展开：首先依据无功功率的变化情况推导出参考电压；再借助特定控制算法确定并输出电动势的幅值，以此实现对无功功率和电压的动态调整。该模块涉及的无功电压控制关系满足如下表达式：

$$E=E_0+K_u(U_{ref}-U)+K_q(Q_{ref}-Q) \quad (2)$$

式中：E_0 代表空载电动势；K_u 与 K_q 分别是电压下垂系数和无功下垂系数；U 为 VSG 的输出电压；Q_{ref} 和 Q 则依次对应无功功率的参考值与实际输出值。

前述已说明虚拟同步发电机的拓扑与建模。鉴于固定的惯量和阻尼参数在应对新能源波动及电网扰动时存在局限，下文阐述基于上述模型的惯量阻尼自适应控制方案。

1 惯量和阻尼自适应控制

1.1 转动惯量和阻尼系数对系统的影响

根据经典控制理论，可以得出 VSG 的角频率和阻尼比分别为：

$$\begin{cases} w_0=\sqrt{\dfrac{mK_p}{\lambda}} \\ \zeta=\dfrac{1}{2\sqrt{m\lambda K_p}} \end{cases} \quad (3)$$

式中：

$$\begin{cases} m=\dfrac{1}{D+K_p} \\ \lambda=\dfrac{J}{D+K_p} \end{cases} \quad (4)$$

式中：通过以上的公式可以得出虚拟转动惯量 J 和阻尼系数 D 对系统的影响。虚拟转动惯量直接影响 VSG 的惯性响应能力。J 越大，系统抵抗角速度变化的能力越强，频率变化率越小。当系统出现有功功率扰动时，较大的 J 可以延缓下降速度，为了二次调频争取时间。然而，过大的 J 会延长频率恢复时间，导致系统响应迟缓；J 过小则无法提供足够惯性支撑，频率波动剧烈。

阻尼系数 D 主要作用于抑制系统振荡。当系统频率波动时，D 产生与转速偏差成正比的阻尼转矩，快速消耗系统的过剩能量，加快频率恢复速度。适当增大阻尼系数可以有效抑制频率振荡，但是过高时，会让系统响应过于“刚性”，削弱 VSG 的惯性响应能力，甚至导致系统出现过阻尼现象，延长频率调节时间。

基于公式分析可知，虚拟惯量和阻尼系数均影响系统的稳定性。因此，VSG 应对负载有功突变时，需实时二者调整以改善稳定性。

1.2 惯量和阻尼自适应控制原理

前述分析已经明确，虚拟惯量和阻尼系数均直接影响 VSG 输出的超调量和稳定时间，参数如果不适合会导致系统性能恶化。

针对这一参数配置，本文提出了一种惯量和阻尼自适应调控方法：通过角频率偏移量和角频率变化率的动态反馈，实时调整 J 和 D。通过对角频率

偏移量和角频率变化率的变化曲线的分析，可以得到如表 1 所示的 J 和 D 在不同状态区间的自适应原则：

表 1　转动惯量 J 和阻尼系数 D 的调整规律

Table 1　Adjustment rule of J and D

时段	$\Delta\omega$	$d\Delta\omega/dt$	J取值	D取值
t_1-t_2	>0	>0	较大	恒定
t_2-t_3	>0	<0	较小	较大
t_3-t_4	<0	<0	较大	恒定
t_4-t_5	<0	>0	较小	较大

基于表 1 所示阻尼系数和转动惯量的参数整定规律设计自适应控制策略如下：

$$D_p=\begin{cases}D_0,|\Delta w|\le T_d\\ D_0+K_D e^{|\Delta w|},|\Delta w|>T_d\end{cases}\tag{5}$$

$$J=\begin{cases}J_0,\left|\dfrac{dw}{dt}\right|\le T_j\\ J_0+K_{J1}\left|\Delta w\dfrac{dw}{dt}\right|,\left|\dfrac{dw}{dt}\right|>T_j\cap\Delta w\dfrac{dw}{dt}>0\\ J_0-K_{J2}\left|\Delta w\dfrac{dw}{dt}\right|,\left|\dfrac{dw}{dt}\right|>T_j\cap\Delta w\dfrac{dw}{dt}\le 0\end{cases}\tag{6}$$

式中：D_0 和 J_0 分别是虚拟同步发电机稳态运行时 D 和 J 的基础数值；K_{J1}、K_{J2} 和 K_D 分别是虚拟惯量和阻尼系数自适应控制的调节系数；T_j 和 T_d 分别是虚拟惯量和阻尼系数的稳态区间阈值。

基于转子角频率的偏差及其变化率构建双物理量的反馈机制；以角频率的偏差表征系统频率波动的幅值，以转子角频率的变化率来刻画频率波动的协同特征。通过实时采集这两个核心物理量，控制可以精准识别稳态、小扰动和大扰动的工况。

1.3 仿真分析

为验证前文理论分析以及所提控制策略的有效性，借助 Simulink 软件在前文搭建的 VSG 的仿真模型的基础上加入虚拟惯量和阻尼自适应控制，关键参数配置详见表 2：

表 2　仿真模型的参数

Table 2　Parameters of simulation model

仿真模型的参数	数值
系统额定电压	10kV
系统额定频率	50Hz
交流侧额定电压	220V
直流侧额定电压	750V
负载额定有功功率	10000W
并联侧滤波电容	20μF
并联侧滤波电感	3.2mH
转动惯量	0.2
阻尼系数	10

本文首先在传统非自适应控制的 VSG 中进行仿真，设置初始的有功功率为 20000W,在 0.5s 时，有功功率下降至 10000W，1s 时有功功率再次增至 20000W。具体仿真结果如图 2 和图 3 所示：

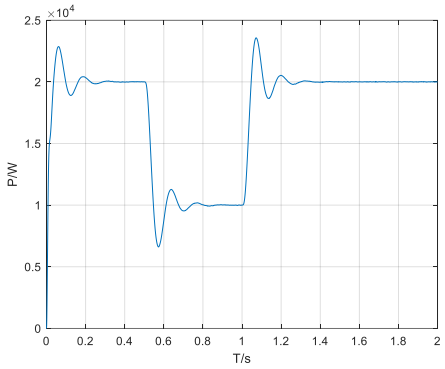


图 2　传统 VSG 输出的有功功率曲线

Fig. 2　Traditional VSG active power curve

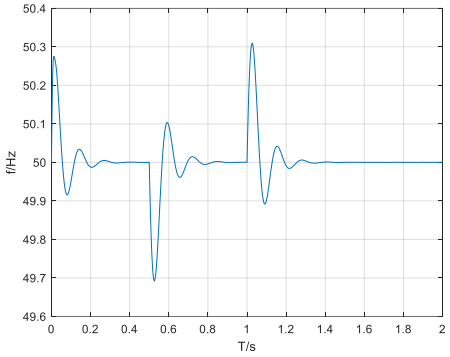


图 3　传统 VSG 输出的频率曲线

Fig. 3　Frequency curve of traditional VSG output

在 VSG 中增加了惯量阻尼自适应控制，输出的有功功率和输出的频率曲线如图 4 和图 5 所示：

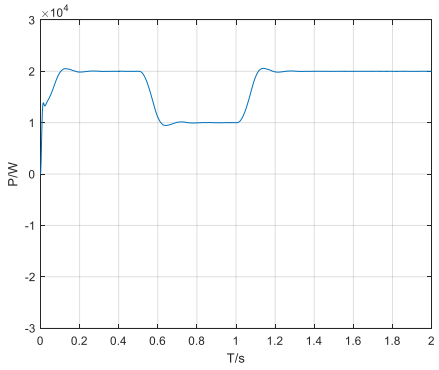


图 4　改良后的 VSG 输出的有功功率曲线

Fig. 4　The modified VSG output active power curve

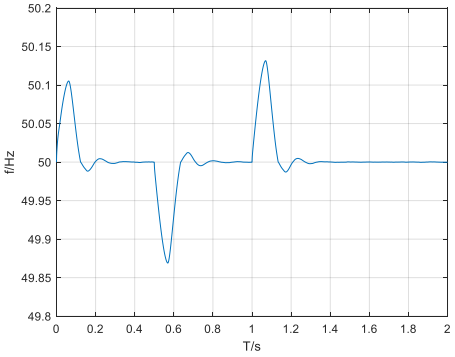


图 5　改良后的 VSG 输出的频率曲线

Fig.5 The frequency curve of the modified VSG output

通过上述曲线图的前后对比，在传统非自适应控制的 VSG 中，在 0.5s 时，因为有功功率突变，受到惯量的影响，有功功率的超调量较大，峰值达到了 23kW 左右，采用控制策略后，有功功率的超调量得到了进一步的控制，同时峰值也有明显的下降，达到了 21kW 左右。

通过上述曲线图前后的对比，在传统非自适应控制的 VSG 中，因为功率突变导致 VSG 的输出频率迅速偏离额定数值，幅值达到 50.27Hz，最终恢复到额定值的时间约为 0.3s。在 0.5s 时，有功功率出现突变，输出的频率在 49.7Hz 到 50.1Hz 之间振荡。采用文献惯量阻尼自适应控制策略后，频率的振荡有明显的降低。在刚开始的运行过程中，频率的幅值达到了 50.1Hz，最终恢复时间约为 0.2s。在 0.5s 时，有功功率出现瞬时突变，输出的频率在 49.8Hz 到 50.01Hz 之间振荡。

经过仿真验证，在发电功率突增或者突降的工况下，应用本文提出的控制策略，VSG 可以稳定在 50Hz。可见，该策略能有效削弱虚拟同步发电机的输出有功功率的超调量，降低频率偏移程度，还可以同时加快系统的动态响应，提升了稳定性，有力地验证了其在功率突变场景下的调节效能。

2 自适应虚拟阻抗控制

2.1 自适应虚拟阻抗控制原理

在微电网中，由于并联运行的各个分布式电源与公共耦合点(PCC)之间的线路阻抗不同，常规的下垂控制方法实际上难以达到准确的功率分布，会导致无功功率不均衡，影响微电网的运行稳定性。此外，微电网中还存在着大量的非线性负载，会产生谐波电流，进一步恶化电能质量。早期为了解决这一问题，通过在逆变器控制中，引入固定的虚拟电阻和虚拟电感，来改变逆变器的输出阻抗特性。然而，固定虚拟阻抗在面对复杂多变的电网中存在着明显的缺陷，难以满足系统对限流和稳定性的要求。

为量化分析固定虚拟阻抗的缺陷，需对线路阻抗与电压跌落的关系进行建模。设实际电路中：R和X为相同大小的电路阻抗；ΔR和ΔX是两线路的阻抗之差；ΔU_1和ΔU_2分别表示两个并网变流器输出电压到耦合点处的电压下降的数值，U_0为 PCC 并网处的电压幅值，假设ΔR和ΔX均大于 0，分析得出公式 7：

$$\begin{cases} \Delta U_1 \approx \dfrac{XQ_1 + RP_1}{U_0} \\ \Delta U_2 \approx \dfrac{XQ_2 + RP_2}{U_0} + \dfrac{\Delta XQ_2 + \Delta RP_2}{U_0} \end{cases} \quad (7)$$

通过公式 7 量化分析可知，由于线路阻抗差异，两个变流器的电压跌落呈现显著的偏差，直接导致系统的无功功率分配失衡。为抵消这种因线路固有差异而产生的电压降落不一致性，本文拟通过引入自适应虚拟阻抗来动态弥补压降差。设并网变流器输出功率在虚拟阻抗上产生的电压降为ΔU_v，R_v为虚拟电阻，$X4_v$为虚拟电抗，令虚拟电阻与虚拟电抗相等，即$M_v = X_v = R_v$，克服因为阻抗不同而产生的电压降落损失，则有：

$$\Delta U_v + \Delta U_2 = 0 \quad (8)$$

结合以上两个公式和虚拟电阻与虚拟电抗的等式关系，可以得到公式 9：

$$M_v = -\frac{\Delta X + \Delta R cot\varphi}{1 + cot\varphi} \quad (9)$$

式中：$cot\varphi = P_2/Q_2$。为实现无功功率的精确分配，虚拟阻抗需按公式 9 进行设计。但是直接设定虚拟阻抗需要预先掌握线路阻抗参数，为了规避这一前题条件，研究中采用负荷功率作为虚拟阻抗的调节依据。通过该方式生成的虚拟阻抗电压降，可以抵消分布式电源由于线路阻抗不一致导致的电压降偏差，最终达成功率的优化。由于$cot\varphi$的数值与功率因数直接相关联，结合公式 9 可以得出，为实现精确控制，虚拟阻抗值应能依据负荷功率因数的波动而实现动态自调整。图 6 展示了自适应虚拟阻抗的控制结构。将分布式电源（DG）的无功功率偏差输入至积分控制器，其输出即为自适应虚拟阻抗。该阻抗随后作用于下垂控制产生的电压参考值并与之合成。当无功功率的实际值与参考值相等时，虚拟阻抗保持恒定。其数值的改变仅由负荷功率的波动触发。如图 6 所示为虚拟阻抗自适应控制结构:

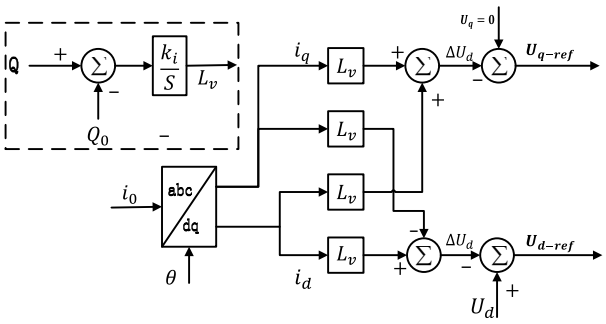


图 6 自适应虚拟阻抗控制拓扑

Fig.6 Topology of adaptive virtual impedance controller

图 6 中，L_V 表示自适应虚拟阻抗，U_d、U_q 和 θ 均由下垂控制器得出，Q_0 为逆变器输出无功功率设定值；K_i 为积分系数。通过积分器可以在无功补偿的基础上对电网的阻抗进行动态调节，不仅能有效地抑制电网的不一致性，还能调节电网的运行状况，从而达到最优的无功分配。该自适应虚拟阻抗的表达式为：

$$L_V = \frac{K_i}{S}(Q - Q_0) \quad (10)$$

针对并联逆变器的无功功率分配的问题，本文拟提出一种自适应虚拟阻抗方法。中央控制器根据总无功负荷和各逆变器容量计算其参考值Q_0，实现

按容量比例分配。改进后的下垂控制通过引入虚拟阻抗 L_s 调整输出电压参考的数值，表达式为：

$$\begin{cases} U_{id_ref} = U_{id} - L_V I_{id} + L_V I_{iq} \\ U_{iq_ref} = U_{iq} - L_V I_{iq} - L_V I_{id} \end{cases} \tag{11}$$

上述是自适应虚拟阻抗控制拓扑，为验证其实际效果，通过 Simulink 搭建仿真模型，开展无功功率分配特性探究。

2.2 自适应虚拟阻抗控制仿真

在 Simulink 软件的仿真环境下，搭建了两台虚拟同步发电机并联运行的仿真模型，用于探究无功功率的分配特性。

仿真设置了两组对比实验：第一组是未采用虚拟阻抗自适应控制策略，系统的母线电压设定为 800V，配置的电感电容滤波器，其中滤波电感值为 0.0006H，滤波电容的数值为 0.0015F。设置的两台 VSG 连接至公共母线的线路阻抗数值存在差异，线路 1 的电阻为 0.04Ω，电感数值为 0.0004H，线路 2 的电阻为 0.024Ω，电感数值为 0.000306H。仿真运行时间设置为 3 秒，在 0-1 秒时，系统投入有功功率 20kW，无功功率 20kvar 的恒定负荷；在 1-2 秒时刻，新增投入 10kW 的有功负荷、无功功率 20kvar，模拟系统负荷突变工况。第一组仿真情况如图 7 所示：

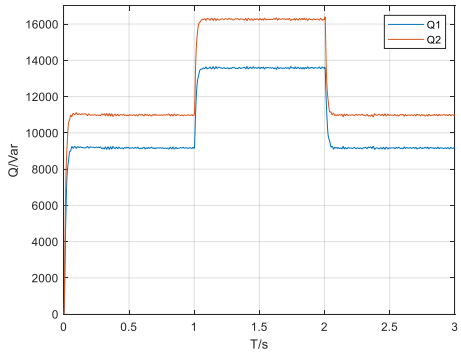


图 7 两个并联 VSG 非自适应控制策略的无功功率

Fig. 7 The Reactive Power of Two Parallel VSG Non-Adaptive Control Strategies

第二组是在 VSG 的基础上采用虚拟阻抗自适应控制策略，仿真如图 8 所示：

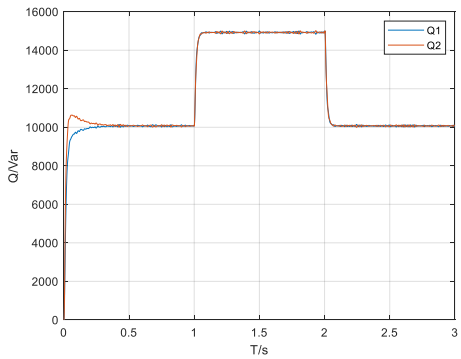


图 8 两个并联 VSG 虚拟阻抗自适应控制策略的无功功率

Fig. 8 The Reactive Power of Two Parallel VSG Virtual Impedance Adaptive Control Strategies

从仿真结果图 7 和图 8 可以看出，在未投入自适应虚拟阻抗控制时，受到线路阻抗不一致的影响，两台 VSG 的无功功率输出存在着显著的差异；而在自适应虚拟阻抗控制模块装设完成后，0 到 1 秒之间，系统承载了 20kvar 的无功负荷，1 到 2 秒增加 10kvar 的无功负荷的工况下，两台 VSG 的无功功率分配精度大幅提升。在负荷动态变化的过程中，无功功率均分误差始终控制在极小的范围，实现了无功功率的精准平分。该结果验证了自适应阻尼阻抗控制策略可以有效克服线路差异带来的影响，显著提多台 VSG 并联系统的功率分配的均衡性与运行稳定性。

3 结论

本文针对虚拟同步发电机在电力系统中的应用，围绕提升系统稳定性与多机并联运行性能展开研究，提出并且验证了单台 VSG 的阻尼惯量自适应控制策略以及多台 VSG 的虚拟阻抗自适应控制方法。在单台控制层面，通过动态调节虚拟惯量与阻尼系数，实现了对系统频率波动的快速响应，有效增强频率稳定性；在多机并联的场景中，基于实时功率与线路参数的虚拟阻抗自适应控制策略，显著提升了无功功率分配的均衡性。

参考文献：

[1] 洪灏灏，顾伟，黄强，等. 微电网中多虚拟同步机并联运行有功振荡阻尼控制 [J]. 中国电机工程学报，2019，39 (21)：6247-6255.

[2] 赵辉，王涛，胡平，等. 改进 VSG 和下垂控制双驱动的孤岛微电网稳定运行控制策略 [J]. 电力系统及其自动化学报，2024，36 (10)：117-126.

[3] 姚钢，石片超，周荔丹，等. 含氢储直流微电网的 VSG 协同控制策略[J].电力系统及其自动化学报，2025，37(02)：151-158.

[4] 杨萍，陈卓，罗婷，等.基于 VSG 的光伏发电与混合储能的控制方法[J].电网与清洁能源，2023，39(02)：83-91+113.

[5] 李立，宋蕙慧.基于虚拟振子的并联逆变器调压与预同步策略研究[D].哈尔滨工业大学，2023.

[6] 王振雄，易皓，卓放，等. 应用于光伏微网的一种虚拟同步发电机结构及其动态性能分析 [J]. 中国电机工程学报，2017，37 (02)：444-454.

[7] 吕志鹏，盛万兴，钟庆昌，等. 虚拟同步发电机及其在微电网中的应用 [J]. 中国电机工程学报，2014，34 (16)：2591-2603.

[8] 尚磊，胡家兵，袁小明，等. 电网对称故障下虚拟同步发电机建模与改进控制[J].中国电机工程学报，2017，37(02)：403-412.

[9] 吕志鹏，盛万兴，刘海涛，等. 虚拟同步机技术在电力系统中的应用与挑战[J].中国电机工程学报，2017，37(02)：349-360.

[10] 万晓凤，詹子录，丁小华，等. 基于虚拟同步发电机的多逆变器并联改进控制策略[J].电机与控制学报，2020，24(02)：118-127.

[11] 任大江，魏亚斌，席志峰，等. 基于 VSG 的逆变器功率均分控制策略[J].电力电子技术，2020，54(02)：28-31.

[12] 张萍，李扬. 孤岛模式下基于 VSG 的光储发电系统多机并联运行策略[J].全球能源互联网，2025，8(01)：98-109.

[13] 章伟明，赵巧娥，刘毓梅等.孤岛模式自适应转动惯量 VSG 逆变电源控制策略[J].电力系统及其自动化学报，2019，31(02)：95-100.

[14] 张常友，朱作滨，孙树敏，等. 微电网并联 VSG 环流抑制与功率精确分配控制策略研究[J].电气工程学报，2023，18(03)：369-376.

[15] 陈晓龙，郑杰颖，杜钰珑. 基于参数灵敏度及虚拟阻抗的 VSG 并网系统稳定性提升策略 [J/OL]. 高电压技术， 1-16[2025-08-04].
[16] 涂春鸣，谢伟杰，肖凡，等. 多虚拟同步发电机并联系统控制参数对稳定性的影响分析[J].电力系统自动化，2020，44(15)：77-86.

收稿日期：2025-10-02。

作者简介：


杨璐嘉

杨璐嘉（2000—），女，硕士研究生，研究方向为新能源发电与控制，E-mail：3179125489@qq.com

颜景斌（1972—），男，博士，教授，硕士生导师，研究方向为新能源发电技术、微网环境变换器协调控制，E-mail：565510645@qq.com

050 含分布式电源的油田井场综合负荷建模方法研究

陈治锟[1]，仉志华[1*]，孙 东[2]，李 炜[2]，吴 越[1]，魏淑静[1]

（1.中国石油大学（华东）新能源学院，山东 青岛 266580；2.中国石油化工股份有限公司胜利油田能源低碳监测中心,山东 东营 257000）

Research on Load Modeling Method for Oilfield Distribution Network with Distributed Power Sources

CHEN Zhikun[1], ZHANG Zhihua[1*], SUN Dong[2], LI Wei[2], WU Yue[1], WEI Shujing[1]

(1. College of New Energy，China University of Petroleum，Qingdao 266580，China;2. Shengli Oilfield Energy Low Carbon Monitoring Center, China Petroleum and Chemical Corporation, Dongying 257000, China)

ABSTRACT: Comprehensive load modeling is essential for accurately analyzing the operational characteristics of power grids and ensuring safe, stable, and economical operation. However, with a high proportion of renewable energy access, oilfield power grids lack load modeling methods that accurately reflect the impact of renewable energy and the requirements for coordinated control. This paper investigates a load modeling method for oilfield wellsites containing distributed power sources (DGs) within a common DC bus power supply system. First, the topology and operational characteristics of the DGs and lifting systems in the oilfield are analyzed to construct a comprehensive load model for the oilfield wellsite. Next, the comprehensive load model is reduced in dimension based on parameter trajectory sensitivity analysis, and a hybrid optimization algorithm for parameter identification is proposed. Finally, a case study is conducted using engineering examples to verify the effectiveness, generalization capability, and performance of the proposed load modeling method and optimization algorithm.

KEY WORDS: load modeling; distributed photovoltaic; distributed energy storage; parameter identification

摘要：综合负荷建模是准确分析电网运行特性、保障系统安全稳定经济运行的基础。在高比例新能源接入条件下，油田电网缺少能准确反映新能源影响和协同控制要求的负荷建模方法。本文针对油田井场共直流母线供电系统，研究了含分布式电源的油田井场负荷建模方法。首先，分析油田中分布式电源和举升系统的拓扑结构和运行特性，构建油田井场综合负荷模型；之后，基于参数轨迹灵敏度分析对综合负荷模型进行降维，再提出一种用于参数辨识的混合优化算法；最后，结合工程实例进行算例分析，验证了本文所提负荷建模方法的有效性、泛化能力和优化算法的性能。

关键词：负荷建模；分布式光伏；分布式储能；参数辨识

DOI：10.13335/j.1000-3673.pst.2014.01.论文序号

基金项目：新型油气勘探开发国家科技重大专项项目（SQ2025AAA120047）National Science and Technology Major Project for Advanced Oil and Gas Exploration and Development (SQ2025AAA120047).

0 引言

近年来，分布式新能源接入电网已成为大势所趋，是构建清洁、安全、稳定电力系统的重要环节[1]。随着油田电网中分布式电源渗透率的提高，油田井场微电网的动态特性发生了显著变化。为了准确描述负荷动态特性，为油田电网的规划设计、运行调度及安全稳定运行提供数据支撑，应建立含分布式电源的油田井场综合负荷模型。

目前的负荷模型[2-3]不能反映分布式电源的多时间尺度动态行为，对此，文献[4]基于光伏并网系统仿真，引入多项式等值模型替代传统光伏发电模型。文献[5]通过对电池暂态运行特性的仿真分析,提出了一种面向负荷的电池储能系统等效模型。文献[6]将光伏发电系统接于综合负荷模型的虚拟母线上，增强了传统负荷模型的适应性。

对于综合负荷模型降维与参数辨识方面的研究，文献[7]通过灵敏度分析，对负荷模型进行降维。文献[8]利用 PMU 小扰动数据与时变参数辨识器，实现了对负荷模型的时变参数辨识。文献[9]通过 Circle 混沌映射改进算法以提高初始解的质量，并通过改进觅食阶段提高全局搜索能力。

本文针对油田井场共直流母线供电系统，研究了含分布式电源的油田井场综合负荷建模方法。首先，分析油田中各广义负荷的运行特性，得到油田井场综合负荷模型；之后，对综合负荷模型进行降维，并提出一种用于参数辨识的混合

优化算法；最后，进行算例分析，验证了本文所提负荷建模方法的有效性和优化算法的性能。

1 共直流母线系统的油田井场综合负荷建模分析

油田井场典型的共直流母线供电系统的结构如图 1 所示。

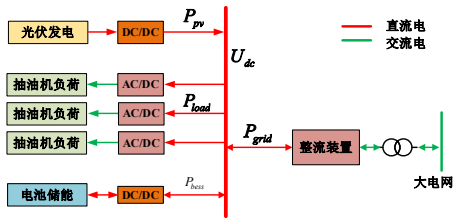


图 1 油田共直流母线供电系统结构

Fig.1 Structure of oilfield common DC bus power supply system

由于负荷建模母线为交流母线，而上述供电结构下设备均接于共直流母线，因此要建立交流母线与直流母线之间的电压关系，再研究直流母线侧各设备的负荷模型。交流侧与直流侧之间的电压关系如下所示。

$$u_{dc}=\frac{3\sqrt{3}}{\pi}u_m=1.35u_{LL} \tag{1}$$

在共直流母线供电结构下，油田井场举升系统因其核心变频器采用闭环恒压频比控制策略，其从直流母线吸收的功率呈现出典型的恒功率负载特性。

1.1 光伏发电系统的等值模型

采用最大功率追踪策略控制光伏模块的 DC/DC 变换器，由于光伏发电系统的输出功率不受直流母线电压的影响，且在机电暂态尺度（秒级）下，可近似认为光照与温度不变，因此光伏发电系统可用恒功率源等效。

1.2 电池储能系统的等值模型

储能电池由蓄电池和双向 DC/DC 变换器组成，其等效电路如图 3 所示[10]。按图中参考方向，输出电压和电流的关系如式（2）所示。

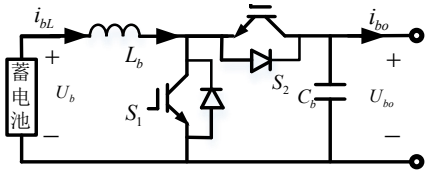


图 3 电池储能系统等效电路

Fig.3 Equivalent circuit of battery energy storage system

$$\begin{cases}\dfrac{di_{bL}}{dt}=-\dfrac{1-d_{bess}}{L_b}\cdot U_{bo}+\dfrac{U_b}{L_b}\\[2ex]\dfrac{dU_{dc}}{dt}=\dfrac{1-d_{bess}}{C}\cdot i_{bL}-\dfrac{i_{bL}}{C}\end{cases} \tag{2}$$

其中，U_b 为储能装置端电压，i_{bL} 为储能输出电流，L_b 为双向 DC/DC 滤波电感，C 为直流母线电容，i_{bo}、U_{bo} 为储能注入直流母线侧的电流值和电压值；d_{bess} 为储能控制器控制占空比。采用稳定直流母线电压的双闭环控制策略来控制双向 DC/DC 变换器，控制策略表达式如下所示。

$$\begin{cases}i_{bL-ref}=k_p(u_{dc-ref}-u_{dc})+k_i\int(u_{dc-ref}-u_{dc})\\d_{bess}=k_{pb}(i_{bL-ref}-i_{bL})+k_{ib}\int(i_{bL-ref}-i_{bL})\end{cases} \tag{3}$$

其中，k_p 为电压控制环节系数，k_i 为电压控制时间常数，k_{pb} 为电流控制环节系数，k_{ib} 为电流控制环节常数。

上述双闭环控制表达式完整表征了储能电池系统在暂态过程中的动态响应特性，将控制策略表达式与上文式（2）所示的储能系统的输出电压电流关系表达式联立，就得到了储能系统的完整负荷模型。

1.3 共直流母线系统的油田井场综合负荷模型

将上述提出的光伏发电系统、电池储能系统和举升系统的等值模型并联在直流母线上，再通过式（1）与交流侧建立电压的联系，就得到了含分布式电源的油田井场综合负荷模型等值电路如图 4 所示，表达式如式（4）所示。

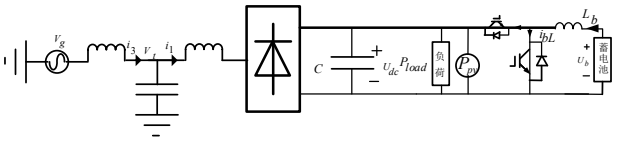


图 4 油田井场综合负荷模型等值电路

Fig.4 Equivalent circuit of comprehensive load model for oilfield distribution network

$$\begin{cases}u_{dc}=\dfrac{3\sqrt{3}}{\pi}u_m=1.35u_{LL}\\P=P_b+P_{pv}+P_{load}\\P_b=u_{dc}\cdot(1-d_{bess})i_{bL}\\i_{bL-ref}=k_p(u_{dc-ref}-u_{dc})+k_i\int(u_{dc-ref}-u_{dc})\\d_{bess}=k_{pb}(i_{bL-ref}-i_{bL})+k_{ib}\int(i_{bL-ref}-i_{bL})\\\dfrac{du_{dc}}{dt}=\dfrac{1-d_{bess}}{C}i_{bL}\\\dfrac{di_{bL}}{dt}=\dfrac{U_b-r_bi_{bL}}{L_b}-\dfrac{1-d_{bess}}{L_b}u_{dc}\end{cases} \tag{4}$$

2 基于参数轨迹灵敏度分析的综合负荷模型降维方法

上述建立的油田井场综合负荷模型共有五个待辨识参数，分别是储能滤波电感 L_b，电压环节系数 k_p，电压环节时间常数 k_i，电流环节系数 k_{pb}，电流环节时间常数 k_{ib}。采用轨迹灵敏度分析的方法进行降维，灵敏度反映了某参数扰动对系统输出动态特性的影响程度。若灵敏度较大，说明该参数对系统行为影响显著，可优先进行辨识；反之，若灵敏度较低，该参数在系统辨识中贡献较小，应采用统计综合法获得的典型值代替。

为定量分析各参数对储能系统动态行为的影响程度，本文采用中心差分法对模型参数进行轨迹灵敏度分析。在保持其他参数不变的前提下，对某一待辨识参数施加微小扰动，分别计算系统在参数偏移下的输出响应，并据此求解相应的灵敏度系数。构造如下形式的相对灵敏度表达式。

$$S_{\theta_i}(t)=\frac{\theta_i}{y_0}\cdot\frac{y(t,\theta_i+\Delta\theta)-y(t,\theta_i-\Delta\theta)}{2\Delta\theta} \tag{5}$$

其中，$S_{\theta_i}(t)$ 表示参数 θ_i 在时刻 t 的相对灵敏度，y_0 为标称输出值，$\Delta\theta$ 为相对于标称值的小幅扰动，$y(t,\cdot)$ 为系统在不同参数取值下的响应。

通过上述公式计算各待辨识参数的轨迹灵敏度，得到灵敏度曲线如图 5 所示。由图可知，油田井场综合负荷模型的待辨识参数中较灵敏的参数是 L_b、k_p、k_{pb}、k_{ib}，对于灵敏度较低的参数根据工程经验选择典型值。

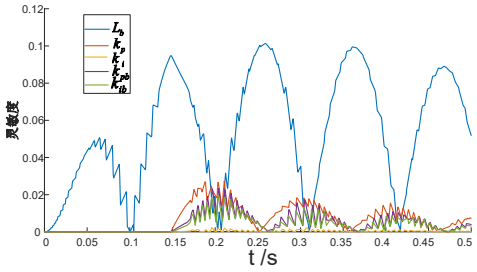


图 5 待辨识参数灵敏度曲线

Fig.5 Sensitivity curve of parameters to be identified

3 油田井场综合负荷模型参数辨识方法

为了实现对油田井场综合负荷模型关键参数的高精度辨识，本文提出了一种混沌鲸雀优化算法（CW-SHOA）。

3.1 混沌映射初始化策略

为增强种群初始分布的遍历性和多样性，CW-SHOA 采用 Logistic 混沌映射代替传统随机初始化方式。其表达式为：

$$x_{i+1}=\mu x_i(1-x_i),\quad x_i\in(0,1),\quad \mu=4 \tag{6}$$

$$X_{i,j}^{(0)}=l_j+x_{i,j}\cdot(u_j-l_j) \tag{7}$$

其中，$X_{i,j}^{(0)}$ 表示第 i 个个体在第 j 个参数维度上的初始值，l_j，u_j 分别为该参数的上下界。该策略可有效防止早期搜索陷入局部最优区域。

3.2 鲸鱼优化算法（WOA）原理

鲸鱼优化算法模拟座头鲸捕食猎物的行为，其搜索行为主要分为两种：

（1）包围猎物阶段：

$$\vec{X}_i^{(t+1)}=\vec{X}^*(t)-\vec{A}\cdot\left|\vec{C}\cdot\vec{X}^*(t)-\vec{X}_i^{(t)}\right| \tag{8}$$

（2）螺旋猎食阶段：

$$\vec{X}_i^{(t+1)}=D\cdot e^{bl}\cdot\cos(2\pi l)+\vec{X}^* \tag{9}$$

其中，$D=\left|\vec{X}^*-\vec{X}_i^{(t)}\right|$ 为当前位置与最优位置的距离，b 为螺旋形状常数，螺旋推进对参数细节的调整更平滑，尤其适用于模型中非线性响应较强的 L_b，可以抑制误差震荡。

WOA 每次随机选择一种行为进行更新，从而在搜索初期具备良好的全局探索能力。

3.3 麻雀搜索算法（SSA）原理

麻雀搜索算法模拟麻雀群体觅食和防御行为，在油田井场综合负荷模型参数辨识中，SSA 用于对 WOA 已获得的较优解进行进一步微调，尤其是缓慢响应区域。有以下两种更新机制。

（1）发现者更新机制：

对于前 $a\cdot N$ 个适应度最好的个体，执行如下更新：

$$\theta_i^{(t+1)}=\theta_i^{(t)}\cdot\exp\left(-\frac{i}{\alpha T}\right) \tag{10}$$

该机制适用于精度调节阶段，以控制系统响应的速度和平滑性。

（2）加入者更新机制：

其余个体围绕当前最优与最差个体之间进行搜索，更新如下：

$$\theta_i^{(t+1)}=\theta_i^{(t)}+\beta\cdot\frac{\theta_i^{(t)}-\theta_{\text{worst}}^{(t)}}{i^2} \tag{11}$$

该机制可修正一些由于扰动造成的非稳态拟合区域，特别有效于电压突变后的拟合恢复段。

3.4 混沌鲸雀优化算法

本文提出的混沌鲸雀优化算法集成了混沌映射的初始种群多样性，鲸鱼优化算法的全局寻优能力，以及麻雀搜索算法的局部搜索精度调节机制，实现了对全局与局部搜索的有效协调。

CW-SHOA 的思路是：首先通过 Logistic 混沌映射生成初始种群，提高搜索空间的遍历性，避免初期种群集中于局部区域；在主搜索阶段，算法采用鲸鱼优化行为，实现对粗粒度参数的快速定位；当算法检测到连续 M 代目标函数无显著下降，则认为当前种群可能陷入局部最优区域，

自动切换为麻雀搜索策略。这种机制使CW-SHOA在拟合过程中能够有效克服模型非线性强、误差多峰、参数耦合等问题，从而获得高拟合精度与良好鲁棒性。综上，综合负荷模型参数辨识的步骤如图6所示。

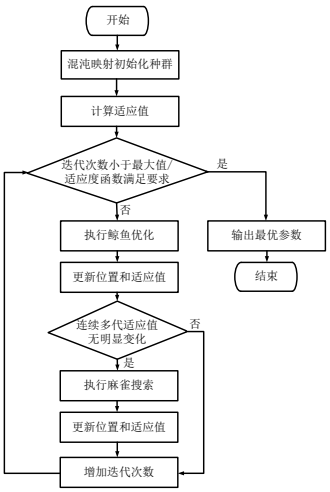


图6 参数辨识流程图

Fig.6 Parameter identification flow chart

4 算例分析

4.1 综合负荷模型的自描述能力验证

在MATLAB/Simulink仿真平台中，搭建基于图1所示结构的某油田井场共直流母线供电系统模型。该系统包括交流电网、变压器、整流单元、光伏发电装置、电池储能系统等关键组成部分。设置在仿真时间t=1s时系统发生三相短路故障，致使在建模母线处（即变压器低压侧）发生20%的电压跌落，并记录为样本1，在t=1.1s时设置故障消失，系统恢复正常运行。由于光照和温度变化的时间尺度一般为5min，所以认为在这段时间内光照和温度保持不变，测得流经变压器低压侧的功率响应曲线如图7所示。

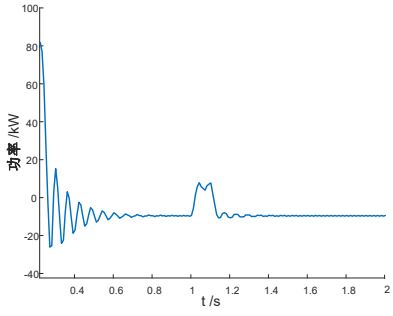


图7 建模母线处功率响应曲线

Fig.7 Modeling the power response curve at the busbar

如前述，对于油田井场综合负荷模型中灵敏度较低的次要参数，采用统计综合法确定，对于灵敏度较高的重点待辨识参数，采用本文所提的CW-SHOA算法进行参数辨识，验证本文所提综合负荷模型的自描述能力。

在建模母线处拟合实际线路与综合负荷模型的功率响应，得到样本1的拟合曲线如图8所示。

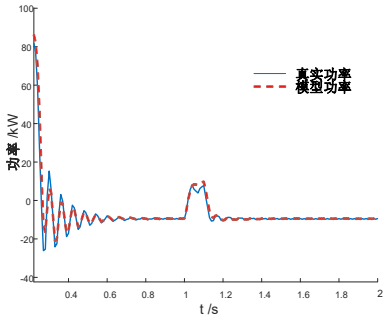


图8 建模母线处功率拟合曲线

Fig.8 Modeling the power fitting curve at the busbar

通过观察图8可知，样本1中建模母线处的实测功率与综合负荷模型功率响应曲线拟合程度较好，可以明显看出本文所构建的综合负荷模型具有良好的自描述能力，能够并且较为准确地反映综合负荷在建模母线处的动态特性。

4.2 综合负荷模型的泛化能力验证

综合负荷模型的泛化能力体现其在不同电压跌落下的适应能力，是衡量模型鲁棒性和实用性的关键指标。本文采用如下表所示的三种建模母线电压跌落作为数据样本来验证综合负荷模型的泛化能力。

表1 数据样本

Table 1 Data sample

数据样本	样本1	样本2	样本3
电压跌落幅度/%	20	15	25

将4.1节中对样本1进行参数辨识得到的模型参数值用于拟合样本2和3，以此验证综合负荷模型的泛化能力，其中对2号样本的拟合用于衡量模型的内插性能，对3号样本的拟合用于衡量模型的外推性能，对外推内插性能的拟合曲线如图9和图10所示。相应的拟合误差如表2所示。

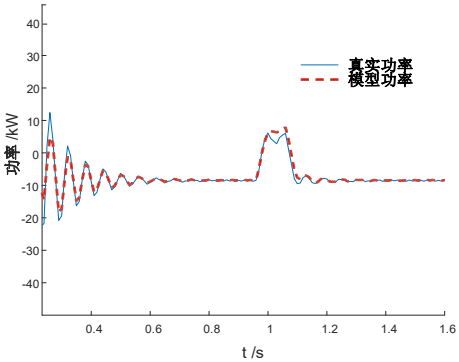


图 9 内插拟合曲线

Fig.9 Interpolation fitting curve

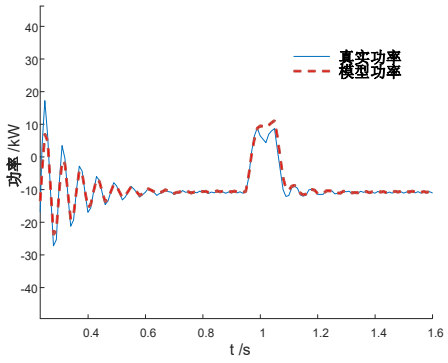


图 10 外推拟合曲线

Fig.10 Extrapolation fitting curve

表 2 模型拟合误差

Table 2 Model fitting error

数据样本	样本 2	样本 3
拟合误差	0.069	0.091

由图 9 和图 10 可知，电压跌落幅度为 20%时得到的参数值，可以较好地拟合电压跌落幅度为 15%和 25%时负荷模型的功率响应情况，由此可以证明综合负荷模型具有较好的泛化能力。

4.3 CW-SHOA 算法性能验证

为验证本文所提优化算法的性能，选择传统鲸鱼算法 WOA 与 CW-SHOA 进行比较，分别采用这两种优化算法进行参数辨识，得到的模型拟合误差如表 3 所示，为了直观地衡量两种优化算法在计算精度和收敛速度两方面的性能，选取典型参数绘制收敛曲线如图 11 所示。

表 3 不同算法拟合误差

Table 3 Fitting errors of different algorithms

算法	CW-SHOA	WOA
拟合误差	0.045	0.103

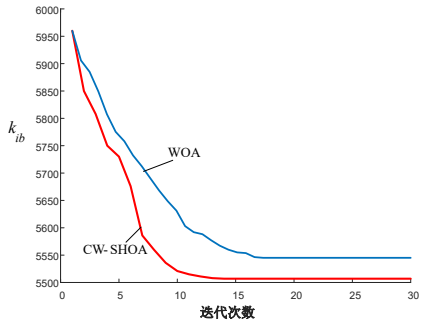


图 11 不同算法的收敛曲线

Fig.11 Convergence curves of different algorithms

由上可知，CW-SHOA 相比 WOA 有更小的拟合误差，通过观察收敛曲线可以得到 CW-SHOA 拟合误差小的原因是融合了混沌初始化和麻雀搜索机制，不仅增强了种群的初始多样性，还显著提升了局部搜索能力，收敛速度快，拟合精度高，具有良好的性能。

5 结论

本文研究了含分布式电源的油田井场综合负荷建模方法，主要成果如下：

（1）研究了油田井场共直流母线供电系统与典型分布式电源的运行特性，构建了含分布式电源的油田井场综合负荷模型。

（2）根据参数的灵敏度进行分析，筛选出了待辨识的重点参数，并在混沌映射与鲸鱼优化算法和麻雀搜索算法的基础上，提出一种混沌鲸雀优化算法，将其应用于综合负荷模型的参数辨识。

（3）结合工程实例进行算例分析，并与传统算法相对比，验证了本文所提综合负荷模型的有效性和优化算法的先进性。

参考文献

[1] 陶劲宇,秦川,金宇清,等.面向新型电力系统的负荷模型研究综述[J].电力系统保护与控制,2025,53(05):168-187.

[2] Park R, Song K, Lee K .The Load Model Com-position Method in Power Systems Using Artificial Neural Network[J].Journal of Electrical Engineering Technology, 2020, 15(8):519-526.

[3] Abhinav K, Kumar S M .Measurement-based ZIP load model ling using opposition based differential evolution optimization [J].Engineering Research Ex-press, 2023, 5(3):035024-035037.

[4] 屈星,李欣然,盛义发,等.面向广义负荷的光伏发电系统等效建模研究[J].电网技术,2020,44(06):2143-2150.

[5] 屈星,李欣然,盛义发,等.考虑电池储能系统的配电网广义综合负荷建模[J].高电压技术,2020,46(02):490-501.

[6] 盛四清,关皓闻,雷业涛等.基于混沌海鸥优化算法的含光伏发电系统负荷模型参数辨识[J].太阳能学报,2022,43(07):64-72.

[7] 李培强,李慧,李欣然.基于灵敏度与相关性的综合负荷模型参数优化辨识策略[J].电工技术学报,2016,31(16):181-188.

[8] 刁涵彬,李培强,郭思源,等.PMU 小扰动信号下的综合负荷模型参数辨识方法[J].电力系统保护与控制,2023,51(13):37-49.

[9] 谭舜,范必双.基于改进海象优化算法的永磁同步电机参数辨识[J/OL].制造技术与机床,1-13[2025-07-20].

[10] 屈星,李欣然,盛义发,等.考虑电池储能系统的配电网广义综合负荷建模[J].高电压技术,2020,46(02):490-501.

收稿日期：

作者简介：



陈治锟

陈治锟(2000)，男，硕士研究生，研究方向为电力系统负荷建模，E-mail：1326996288@qq.com；

仉志华(1977)，通讯作者，男，教授，博士生导师，研究方向为多能互补系统优化调控、电力系统保护与控制等，E-mail：zzh-upc@163.com。

051 基于广义 S 变换-FIR 的油田井场混合储能容量配置方法

吴 越[1]，仉志华[1*]，李 炜[2]，孙 东[2]，魏淑静[1]，陈治锟[1]

（1.中国石油大学（华东）新能源学院，山东 青岛 266580；2.中国石油化工股份有限公司 胜利油田能源低碳监测中心,山东 东营 257000）

Hybrid Energy Storage Capacity Configuration for Oilfield Well Sites Using Generalized S-Transform and FIR Filtering

WU Yue[1], ZHANG Zhihua[1*], LI Wei[2], SUN Dong[2], WEI Shujing[1],CHEN Zhikun[1]

(1. College of New Energy，China University of Petroleum，Qingdao 266580，China;2. Shengli Oilfield Energy Low Carbon Monitoring Center, China Petroleum and Chemical Corporation, Dongying 257000, China)

ABSTRACT: To enhance power system stability against challenges from new energy integration and load fluctuations in oilfields, this paper studies a combined optical storage network and pumping unit group system. It proposes a photovoltaic-oilfield hybrid energy storage capacity configuration method. First, the load with PV is analyzed using generalized S-transform, obtaining an energy spectrum linking power change frequency to energy distribution. FIR filtering removes spikes, separating load into low and high-frequency components for lithium battery and supercapacitor capacity allocation respectively. Then, an optimization model configures their capacities, considering lifecycle factors like system economy, renewable consumption, and grid power fluctuation. Finally, a case study in a typical PV-oilfield scenario validates the method's effectiveness.

KEY WORDS: generalized s-transform; hybrid energy storage; capacity configuration; genetic algorithm

摘要：为应对油田井场新能源接入和抽油机群负荷波动对电力系统稳定运行带来的挑战，本文以光储网联合发电系统与抽油机群为研究对象，提出了一种含光伏的油田井场混合储能容量配置方法。首先，基于广义 S 变换对抽油机群负荷进行时频分析，得到对应能量谱，采用 FIR(Finite Impulse Response)滤波器分析方法滤除尖峰，形成用于混合储能容量配置的负荷低频分量与高频分量，分别用于锂电池与超级电容的容量配置；然后，计及储能全生命周期的系统运行经济性、新能源消纳能力、网侧供电功率波动性等指标，构建了油田井场锂电池与超级电容的容量优化配置模型，形成了油田井场混合储能容量配置方法。最后，以含光伏的典型油田井场场景为案例，对比分析结果证明了该方法的有效性。

关键词：广义 S 变换；混合储能；容量配置；遗传算法

DOI：

0 引言

随着“双碳”战略推进[1-2]，油田井场接入分布式光伏[3]。然而，光伏出力的随机性、波动性[4]与抽油机群负荷的剧烈波动及倒发电现象，导致光伏与负荷[5]时序不匹配，新能源消纳困难。为此，油田井场需配置混合储能以平抑功率波动。其中，能量型的锂电池适合调节低频波动[6]；功率型的超级电容则应对高频波动需求[7]。两者功能互补，使混合储能系统能够稳定、高效地协同优化新能源消纳与负荷平抑。

针对混合储能平抑功率波动的优化调度，现有方法存在局限：文献[8]采用变分模态分解（variational mode decomposition，VMD）进行功率分配，但易导致模态混淆，使高低频信号边界模糊；文献[9]基于光伏混合储能系统采用小波包分频，需人工选择基函数，分解效果不稳定；文献[10]提出的联合优化方法频率分辨率有限，难以精确处理多尺度波动，易致储能冗余；文献[11]结合 FIR 与 EMD（empirical mode decomposition）自适应重构分量，但 EMD 存在模态混叠与参数敏感问题，在剧烈波动工况下稳定性不足。现有混合储能容量配置研究仍存在一定不足，部分研究仍面临如参数选择依赖较强、分解精度尚有提升空间，难以在油田井场中实现功率分配的准确性。

基金项目：新型油气勘探开发国家科技重大专项课题(2025ZD1406905);

National Science and Technology Major Project of New Oil and Gas Exploration and Developmen(2025ZD1406905)

针对上述问题，本文提出一种含光伏的油田井场混合储能容量配置方法。首先，基于广义 S 变换方法对负荷进行时频分析，并采用 FIR 方法滤除尖峰，形成用于混合储能容量配置的低频分量与高频分量，进行锂电池与超级电容的容量配置；然后，计及储能全生命周期的系统运行经济性等指标，形成油田井场混合储能容量配置方法，降低储能运行成本，提高新能源消纳和减小短时网侧供电功率。

1 含光伏的油田井场交流微电网系统

含光伏的油田井场中，为了确保油田井场的稳定运行，在其低压侧集中配置储能，以此来平抑多时间尺度下分布式光伏与负荷的波动，油田井场交流微电网拓扑结构，如图 1 所示。包括光伏发电系统，混合储能系统以及负载单元等。

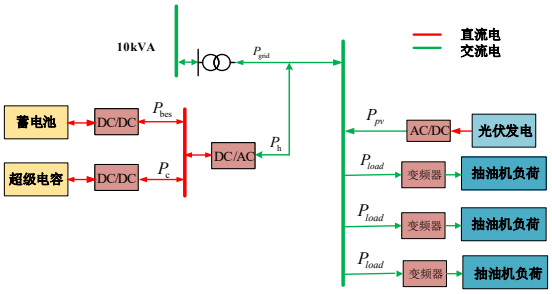


图 1　交流微电网拓扑结构图

Fig.1 Topology of the AC microgrid

图 1 中，P_{grid} 为电网功率，P_{pv} 为光伏出力，P_{h} 为混合储能的参考功率，P_{load} 为抽油机的功率。

功率平衡关系可表示为：

$$P_{\text{grid}} + P_{pv} + P_{\text{h}} = P_{load} \tag{1}$$

$$P_{\text{h}} = P_{\text{bes}} + P_{\text{cs}} \tag{2}$$

式中：P_{bes}、P_{cs} 分别为锂电池、超级电容参考功率。

2 基于广义 S 变换-FIR 滤波的油田井场负荷能量谱分解方法

2.1 广义 S 变换原理及其离散形式

本文采用广义 S 变换[12]对负荷进行时频分析。对于抽油机群功率信号 $p[i]$，其离散化形式为：

$$S(n,f) = \sum_{i=0}^{N-1} p[i]\omega(n-i,f)e^{-\frac{j2\pi fi}{N}} \tag{3}$$

式中，$\omega(n-i,f)$ 为随频率变化的高斯窗函数；f 为频率变量；n 为时间变量；N 为信号总长度。

设定能量阈值划分高低频功率，计算出频率分界点 f_c，可将其分解为高低频分量，具体表示为：

$$\begin{cases} p_l(n) = \sum_{f=0}^{f_c} \text{Re}\left[S(n,f)e^{-\frac{j2\pi fi}{N}} \right] \\ p_h(n) = \sum_{f=0}^{f_c} \text{Re}\left[S(n,f)e^{-\frac{j2\pi fi}{N}} \right] \end{cases} \tag{4}$$

式中，$p_l(n)$ 为低频分量；$p_h(n)$ 为高频分量；$\text{Re}[\bullet]$ 表示取实部，用于还原实信号。

2.2 基于 FIR 滤波器的高频功率处理方法

为平滑高频功率的大量瞬态尖峰，引入 FIR 滤波器[13]平滑处理。FIR 滤波器在不引入显著相位畸变的情况下削弱高频尖峰功率，其数学模型为：

$$y(n) = h(n) * p_h(n) = \sum_{i=0}^{N} h(i)p_h(n-1) \tag{5}$$

式中：$y(n)$ 为滤波输出；$h(n)$ 为 FIR 滤波的冲击响应；i 为采样时刻；N 为滤波器阶数；$h(i)$ 为滤波器第 i 级冲激响应。

同时，以滤波前后无偏估计方差百分比作为滤波性能评价指标，无偏估计方差如式（6）所示。

$$\sigma^2 = \frac{1}{N-1}\sum_{i=1}^{N}(p_h - \overline{p})^2 \tag{6}$$

式中：$\overline{p}$ 为高频功率的均值；N 为数据点的总和。

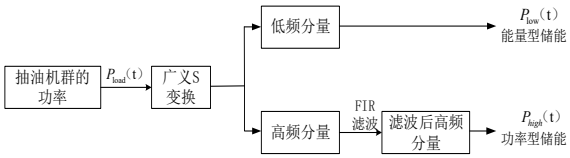


图 2　功率分配方法

Fig.2 Power allocation method

3 油田井场混合储能容量优化配置方法

3.1 混合储能容量配置原则

在混合储能系统中，为保证锂电池较长的使用寿命，将低频功率与光伏功率差值记为 P_{cp}。选取每 15min 内 P_{cp} 的最小值作为该时间段的锂电池充放电参考功率，对应时间为 t_1，共计 96 个时间段，剩余功率记为 P_{grid3}。超级电容用于实时响应高频功率变化，对应时间为 t_2，共计 86400s。在容量配置优化中，各时刻总购电功率 P_{gridz} 需要考虑优化调度下各时刻的储能配置时购电功率与 P_{grid3} 的总和，且网侧供电功率波动由 96 个时间段的 P_{gridz} 波动方差的平均值来表征。基于储能容量和 SOC 限值计算混合储能额定容量配置 $E_{i,rate}$，为统一表示，用下标 i 表示储能类型，其中当 $i=1$ 时，表示锂电池，当 $i=2$ 时，表示超级电容，如式（7）所示。

$$E_{i,rate} = \frac{E_{i,\max} - E_{i,\min}}{SOC_{i,\max} - SOC_{i,\min}} \tag{7}$$

式中，$E_{i,rate}$ 分别为锂电池和超级电容的额定容量；$E_{i,\max}$、$E_{i,\min}$ 分别为锂电池和超级电容累计电量的最大值与最小值；$SOC_{i,\max}$、$SOC_{i,\min}$ 分别为锂电池和超级电容荷电状态的最大值与最小值。

3.2 混合储能容量优化配置模型

3.2.1 混合储能目标函数

为验证本文策略在经济方面的优越性，将混合储能的年值法[14]的年综合成本 C_{h} 作为目标函数，

如式（8）所示。

$$C_{\mathrm{h}}=\sum_{i=1}^{2}C_i+C_{grid3}+C_{pv} \tag{8}$$

式中：C_i 分别为混合储能容量规划成本；C_{grid3} 为锂电池容量配置时遗漏的电网购电功率成本；C_{cf} 为光伏未完全消纳的惩罚成本。

1)混合储能年值成本 C_i：

$$C_i=C_{i-\mathrm{ini}}+C_{iM}-C_{i-res} \tag{9}$$

式中，$C_{i-\mathrm{ini}}$ 分别为混合储能的安装成本年值；C_{iM} 为混合储能的年运维成本；C_{i-res} 为混合储能的回收成本年值。

$$C_{i-\mathrm{ini}}=(C_{iPI}P_{iN}+C_{iEI}E_{iN})\frac{r(1+r)^{T_i}}{r(1+r)^{T_i}-1} \tag{10}$$

式中，C_{iPI} 和 C_{iEI} 分别表示为混合储能的单位功率成本和单位容量成本；P_{iN} 和 E_{iN} 分别表示为混合储能的额定功率和额定容量；T_i 为混合储能的工作寿命，单位为年。

$$C_{iM}=C_{if}+C_{igrid} \tag{11}$$

$$C_{if}=(C_{i1}^{*}E_{iN}+C_{i2}^{*}P_{iN}) \tag{12}$$

式中，C_{if} 为混合储能的年维护成本；C_{i1}^{*} 为混合储能的单位容量维护成本；C_{i2}^{*} 为混合储能单位功率维护成本；C_{igrid} 为混合储能的购电成本。

$$C_{ir-res}=\alpha C_{i-\mathrm{ini}} \tag{13}$$

式中，α 为回收系数。

2）遗漏的电网供电功率成本 C_{grid3}：

$$C_{grid3}=T_{\mathrm{n}}\int_{1}^{86400}\frac{P_{\mathrm{grid3},t}c_t}{3600}dt \tag{14}$$

式中：T_{n} 为 365 天，c_t 为对应时刻的网电价格。

3）在油田井场中存在部分新能源未能被完全消纳，此时的总惩罚成本为 C_{pv}：

$$C_{pv}=E_{\mathrm{pvw}}*2.32*T_{\mathrm{n}} \tag{15}$$

式中：E_{pvw} 为一天中未被消纳的新能源总能量。

3.2.2 混合储能约束条件

为保证混合储能系统运行的安全性与稳定性，容量配置过程需满足以下约束条件：

1）锂电池约束条件

$$\begin{cases}SOC_{i,o}=SOC_{i,end}\\ SOC_{i,t+1}=SOC_{i,t}+\dfrac{P_{ic,t}\eta_{ic,t}-P_{id,t}/\eta_{id,t}}{uE_{i,rate}}\\ SOC_{i,\min}\le SOC_i(t)\le SOC_{i,\max}\\ P_{ic,t}P_{id,t}=0\\ 0\le P_{ic,t}\le P_{ic,\max}\\ 0\le P_{id,t}\le P_{id,\max}\end{cases} \tag{16}$$

式中：$SOC_{i,o}$、$SOC_{i,end}$ 为混合储能起始与末尾的荷电状态；$SOC_{i,t}$、$SOC_{i,t+1}$ 分别为 t_1、t_{1+1} 时刻混合储能的荷电状态；η_{ic}、η_{id} 分别为混合储能的充放电效率系数；P_{ic}、P_{id} 分别为混合储能的充放电功率；当 $i=1$ 时，$u=4$，当 $i=2$ 时，$u=3600$。

2）电网约束条件

$$0\le P_{grid,t}\le P_{grid,\max}^{buy} \tag{17}$$

式中：$P_{grid,t}$ 为混合储能容量规划下的实时网电购电传输功率（不能余电上网）。

4 算例分析

4.1 研究场景与参数设定

以某油田井场为研究对象，选取 2024 年典型日的光伏出力与抽油机群负荷数据。光伏装机容量为 28 kW，负荷数据采样间隔 1s，时长 1 天，峰值为 27.3 kW，谷值-6.2 kW，其光伏出力曲线与负荷曲线如图 3 所示。

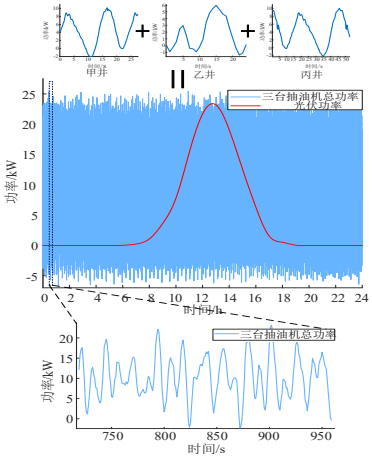


图 3 抽油机群负荷与光伏功率

Fig. 3 Pumping unit group load and photovoltaic power

广义 S 变换分析表明，能量主要集中在频率为 0 Hz 的部分。为便于工程应用，本文选取 90%的累计能量作为划分阈值，将其分解为高、低频功率，如图 4 所示。

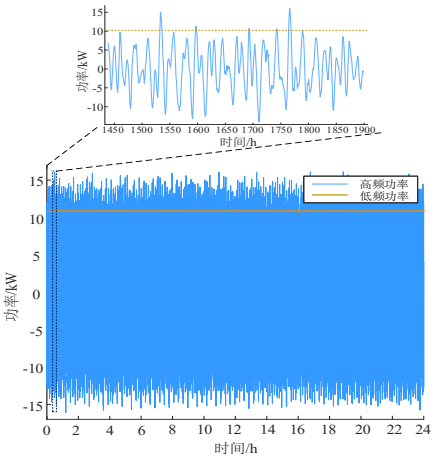


图 4 高频功率与低频功率

Fig.4 High-Frequency Power and Low-Frequency Power

当采用 FIR 滤波进行平滑处理时，滤波后高频

功率的无偏估计方差降至原始值的 95%以内，可在尖峰功率的同时保持整体变化趋势，能够降低对超级电容的冲击并优化其容量配置，如图 5 所示。

综上，低频功率全天波动平缓，峰谷差值仅 1.5 kW，适合由锂电池承担。滤波后的高频功率，主频率集中于 0.04 Hz-0.08 Hz，幅值范围由±16.3 kW 降至±15.2 kW，易于减小超级电容容量配置。

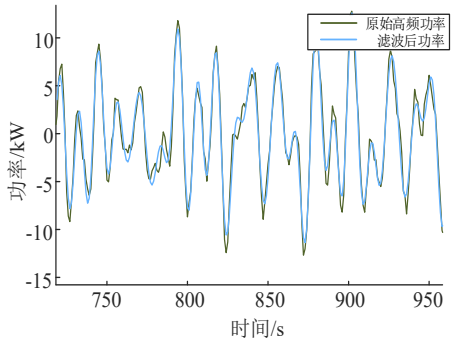


图 5　FIR 滤波前后高频功率曲线

Fig.5 High frequency power curve before and after FIR filtering

混合储能的经济模型各项参数如表 1 所示[15]。

表 1　混合储能的相关参数

Table 1 Related parameters of hybrid energy storage

参数类型	超级电容	锂电池
SOC 范围	[0.1-0.9]	[0.1-0.9]
充放电效率（%）	95	90
使用寿命（年）	15	10
单位容量成本（元/kWh）	12400	1600
单位功率成本（元/ kW）	1860	1000
单位功率运维成本（元/kW）	80.6	3
单位容量运维成本	0.134	0.5
单位功率报废处理成本元（元/kW）	93	50
单位容量报废处理成本（元/kWh）	620	80

4.2 混合储能优化配置结果

采用遗传算法[16]（GA）求解混合储能系统最优容量配置，如表 2 所示。相应的混合储能的充放电功率变化分别如图 6 和图 7 所示。由图 6 可得，在 10:00-16:00 光伏出力大且低频功率波动小，因此

表 2　超级电容与锂电池的最优容量配置结果

Table 2 Optimal Capacity Configuration Results of Supercapacitor and Lithium Battery

配置参数	超级电容	锂电池
容量配置/kWh	1. 65	54. 42
最大功率配置/kW	17. 11	19. 02
年投资成本/元	6114. 87	15813. 69
年运维成本/元	1379. 33	5305. 56
年回收成本/元	68. 97	5305. 56
年购电成本/元	1331. 36	27901. 51
总年成本/元	8894. 53	43715. 21

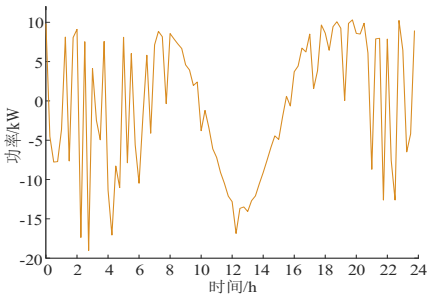


图 6　锂电池充放电功率

Fig.6 Lithium battery charge and discharge power

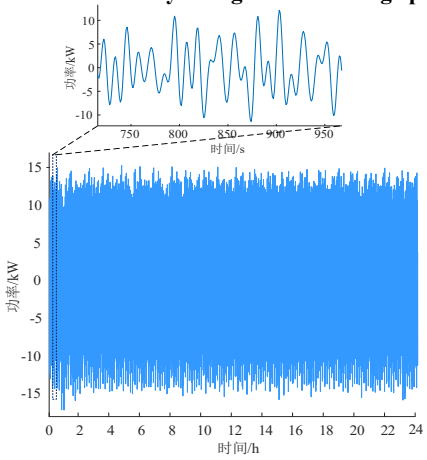


图 7　超级电容充放电功率

Fig.7 Charge and Discharge Power of the Supercapacitor

网侧供电功率较小且锂电池主要处于充电状态；在 18:00-21:00 光伏出力较小或无且电价处于峰值，锂电池以放电为主。由图 7 可得，超级电容主要承担高频功率实时调节。购电总成本为 32,427 元，年综合费用为 59,852 元。电网各时刻调度功率如图 8 所示，在 2:00-5:00 电价低，此时网侧功率同时向负荷和混合储能供电。

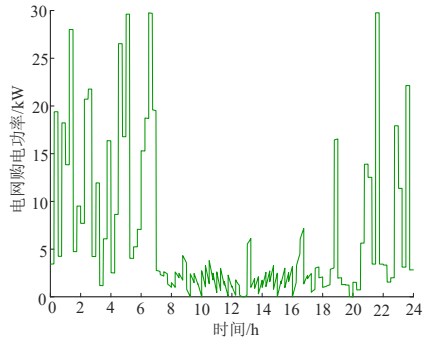


图 8　电网各时刻调度功率

Fig.8 Grid Scheduling Power at Different Time Instants

为验证基于广义 S 变换-FIR 的功率分配策略在混合储能优化配置中的优势，本文分别采用只对负荷进行广义 S 变换、在本文方法基础上仅配置锂电池和对负荷进行 FIR-EMD 双层平抑功率分配策略进行对比分析。对不同功率分配方法的总年成本、新能源消纳能力及短时网侧供电功率波动等指标，其优化后的储能容量配置结果见表 3。

表 3　不同优化调度策略的混合储能配置结果

Table 3 Hybrid Energy Storage Configuration Results With Different Optimal Scheduling Strategies

配置参数	无储能	只配置锂电池	只采用 S 变换	FIR-EMD 双层平抑	本文方法
级电容容量/kWh	0	0	1. 81	1. 72	1. 65
超级电容最大功率/kW	0	0	17. 67	17. 32	17. 11
锂电池容量/kWh	0	56. 34	54. 42	59. 6	54. 42
锂电池最大功率/kW	0	20. 01	19. 02	19. 5	19. 02
新能源消纳率/%	60. 1	83. 8	96. 3	90. 3	95. 8
网侧供电功率波动性/kW^2	23. 51	10. 77	0. 23	0. 20	0. 05
总年成本/元	87317. 5	69863. 16	61522. 97	67509. 95	59852. 46

本文提出的广义 S 变换-FIR 策略在混合储能容量配置中展现出明显优势。相比无储能系统，年总成本降低 45.8%，新能源消纳率提升 35.7%；相比单锂电池方案，年成本减少 16.7%，新能源消纳率提高 12%，网侧功率波动性显著降低。其原因在于单锂电池系统仍需承担部分高频功率，导致其容量规划偏大且部分光伏无法消纳，增加了配置与惩罚成本；而引入超级电容协同平抑高频波动，即减轻了锂电池的负担，也优化了经济性。

与 FIR-EMD 双层平抑算法相比，年成本降低 12.8%，新能源消纳率增加 5.5%，并减小网侧供电功率波动性。这得益于功率分配精度上的提升，有效解决 EMD 模态混叠问题，提高了高低频功率分配准确性,从而使混合储能的容量配置更加合理。

5 结论

本文提出了基于广义 S 变换-FIR 的含光伏的油田井场混合储能容量配置方法，得到如下结论：

1）提出了一种“广义 S 变换-FIR 滤波器”功率分配策略，可精确分离抽油机群负荷中的高频与低频功率。并采用 FIR 滤波分析方法滤除高频尖峰，优化了锂电池与超级电容的功率分配。

2）构建了混合储能年值成本优化模型，兼顾储能全生命周期的系统运行经济性、新能源消纳能力、网侧供电功率波动性等多目标，构建了油田井场混合储能容量配置方法。

3）在典型油田井场开展算例分析，验证了本文方法的优越性。结果表明，本文策略相较单一 S 变换与 FIR-EMD 算法等多种策略，在多个方面均具有优越性。

参考文献

[1] 发展改革委. 能源局关于推进电力源网荷储一体化和多能互补发展的指导意见[EB/OL].（2021-02-25）[2025-07-20]. https://www.gov.cn/zhengce/zhengceku/2021-03/06/content_5590895.htm.

[2] 李晖,刘栋,姚丹阳.面向碳达峰碳中和目标的我国电力系统发展研判[J].中国电机工程学报,2021,41(18):6245-6259.

[3] 张沈习,程浩忠,邢海军,等.配电网中考虑不确定性的分布式电源规划研究综述[J].电力自动化设备,2016,36(08):1-9.

[4] 徐潇源,王晗,严正,等.能源转型背景下电力系统不确定性及应对方法综述[J].电力系统自动化,2021,45(16):2-13.

[5] 王博,赵海森,李和明,等.用于模拟游梁式抽油机电动机动态负荷的测试系统设计及应用[J].中国电机工程学报,2014,34(21):3488-3495.

[6] 刘畅,卓建坤,赵东明,等.利用储能系统实现可再生能源微电网灵活安全运行的研究综述[J].中国电机工程学报,2020,40(01):1-18+369.

[7] 李相俊,马会萌,李焓宁.电力市场环境下新型储能规划与控制方法综述及展望[J].供用电,2024,41(08):54-64.

[8] 陈浈斐,马程,葛磊蛟,等.分布式光伏接入下智能配电网的集中式混合储能选址定容优化方法[J/OL].电网技术,1-16. https://doi.org/10.13335/j.1000-3673.pst.2024.1409.

[9] 程龙,张方华.用于混合储能系统平抑功率波动的小波变换方法[J].电力自动化设备,2021,41(03):100-104+128.

[10] 段晓磊,王宇飞,魏云峰,等.考虑新能源消纳的配电网中分布式光伏及储能联合优化配置[J/OL].现代电力,1-14. https://doi.org/10.19725/j.cnki.1007-2322.2023.0441.

[11] 李培强,刘抒睿,郭榕.基于 FIR 滤波器降幅平抑波动的混合储能优化调度[J].南方电网技术,2025,19(03):39-50.

[12] 刘宇舜,周文俊,李鹏飞,等.基于广义 S 变换模时频矩阵的局部放电特高频信号去噪方法[J].电工技术学报,2017,32(09):211-220.

[13] 李泽森,李冰洁,刘国静,等.基于自适应特征模态分解的新能源配网负荷波动指标提取与平抑研究[J].能源与环保,2025,47(04):209-216+224.

[14] 罗鑫,何宇,张靖,等.基于 VMD-ISSA 的新能源场站混合储能容量优化配置[J/OL].电子科技,1-11

[15] 吕慧香.平抑风电波动的混合储能系统容量优化配置及功率协调策略研究[D].湖南：湘潭大学,2023.

[16] 马速良,马会萌,蒋小平,等.基于 Bloch 球面的量子遗传算法的混合储能系统容量配置[J].中国电机工程学报,2015,35(03):592-599.

收稿日期：



吴越

作者简介：

吴越(2001)，男，硕士研究生，研究方向为油田微电网的多时间尺度混合储能容量优化，E-mail：1218483788@qq.com；

仉志华(1977)，男，教授，博士生导师，研究方向为多能互补综合能源系统结构设计与优化调控技术等，E-mail：zzh-upc@163.com。

052 面向新能源消纳能力提升的油田井场源荷动态匹配策略研究

魏淑静[1]，仉志华[1*]，李炜[2]，孙东[2]，陈治锟[1]，吴越[1]

（1. 中国石油大学(华东) 石大山能新能源学院，山东 青岛 266580；
2.胜利油田能源低碳监测中心，山东 东营 257000）

A Dynamic Source-Load Matching Strategy for Enhanced Renewable Energy Accommodation in Oilfield Wellsites

WEI Shujing[1], ZHANG Zhihua[1], LI Wei[2], SUN Dong[2], CHEN Zhikun[1], WU Yue[1]

(1. College of New Energy, China University of Petroleum, Qingdao 266580, China; 2.Technical Detection Center, Shengli Oil Field of SINOPEC, Dongying 25700, China)

ABSTRACT： Amidst the low-carbon energy transition, oilfield enterprises balance stable hydrocarbon production with renewable energy development. However, spatiotemporal mismatches between volatile renewable output and production loads hinder renewable energy accommodation and efficiency. This paper proposes a dynamic source-load matching strategy for oilfield wellsites to enhance accommodation capacity. We first establish two key metrics: the Source-Load Mismatch Degree (SLMD) for short-term spatiotemporal coordination and the Source-Load Dispersion Degree (SLDD) for spatial distribution. Then, incorporating load flexible regulation capabilities, we develop a multi-objective optimization model. The solution set is derived using the GA-Pareto method, with the CRITIC-TOPSIS model selecting the optimal compromise solution from the Pareto front, enabling dynamic strategy updates based on operational conditions and time. Case studies using actual oilfield data show significant improvement in renewable energy accommodation while maintaining energy efficiency.

KEY WORDS: Oilfield wellsite; Renewable energy accommodation; Source-load matching; Multi-objective optimization

摘要：在能源低碳转型背景下，油田企业推行稳定油气生产与发展新能源的双轮驱动战略，但新能源出力的波动性与油气生产负荷存在时空错配，导致新能源消纳能力及能源利用效率不足。本文提出面向新能源消纳能力提升的油田井场源荷动态匹配策略：首先，结合源荷匹配程度与相对分散程度，构建考虑短时间尺度时空变化的源荷不匹配度指标及反映空间分布特征的源荷分散度指标；其次，计及负荷柔性调节能力，建立源荷匹配多目标优化模型；最后，采用 GA-Pareto 最优法求解方案集，并通过 CRITIC-TOPSIS 决策模型从 Pareto 前沿筛选最优均衡解，形成随工况与时序动态更新的策略。某油田实际算例分析表明，该方法可在保障能效的同时有效提升新能源消纳能力。

关键词：油田井场；新能源消纳；源荷匹配；多目标优化

DOI：10.13335/j.1000-3673.pst.2014.01.论文序号

0 引言

在全球能源转型加速推进的背景下，提升新能源消纳能力已成为能源系统的核心挑战[1]。油田场景中，源-荷时空错配引发的局部弃光严重制约新能源消纳水平。作为高能耗工业场景，油田核心电力负荷（如抽油机、注水站）具备显著柔性调控潜力[2]，而光伏发电的强间歇性加剧了源荷时空失配问题，导致局部弃光与过量购电[3]，引发电网隐性传输损耗及调节压力[4]。现有固定式源荷匹配策略难以适应动态生产任务下对光伏就地消纳、传输路径优化及运行成本控制的需求[5]，亟需探索面向短时尺度的动态匹配机制。

在能源系统中长期规划层面，文献[6]提出基于多断面源荷特征匹配的配电网集群划分方法，但依赖历史数据构建典型场景；文献[7]、[8]分别建立虚拟电厂分区重组与动态重构模型，聚焦跨区域功率互济与经济性优化。上述方法均属日级及以上时间尺度的规划层优化，难以适应油田安全生产任务的日变特性与不可预测工况波动，无法保障高比例新能源实时消纳需求。

基金项目：新型油气勘探开发国家科技重大专项项目（SQ2025AAA120047）
National Science and Technology Major Project for Advanced Oil and Gas Exploration and Development (SQ2025AAA120047).

在动态协同优化层面，文献[9]开发园区微电网群动态组网模型，但未量化网间传输损耗；文献[10]、[11]分别采用需求响应技术与源储荷协同控制提升系统灵活性，其目标函数集中于经济性优化或全网功率平滑。此类方法虽释放可调潜力，但依赖高比例柔性负荷，且缺乏对油田场景新能源消纳能力与能效协同机制的针对性设计。

本文提出一种面向油田井场的源荷动态匹配策略。首先，构建双维度评价指标：源荷不匹配度（Source-Load Mismatch Degree, SLMD）量化短时尺度下光伏出力与负荷需求的时空协调特性，源荷分散度（Source-Load Dispersion Degree, SLDD）表征空间分布紧凑性。其次，纳入负荷柔性调节裕度约束，建立 SLMD 与 SLDD 协同优化的多目标模型。最终，采用 Pareto 与遗传算法（GA-Pareto）生成随工况动态更新的匹配方案集，并基于 CRITIC-TOPSIS 决策模型筛选最优均衡解，实现新能源消纳能力与系统能效的协同提升。

1 油田井场供配电系统结构

油田井场总体供配电结构如图 1 所示，其电能供给体系以油田企业电网为根基，分布式光伏与集中式光伏作为重要补充，三者通过交流母线互联，协同满足油田井场交流与直流电负荷供能需求。

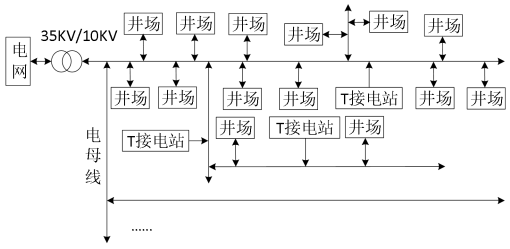


图 1　油田井场总体供配电结构图

Fig.1 Power Supply and Distribution Architecture of the Oilfield Wellsite

油田井场的主要电负荷为抽油机，生产任务明确，井场由分布式光伏、集中式光伏及油田电网联合供电。抽油机等柔性负荷的实际可调节能力（即柔性调节裕度）随运行工况动态变化。目前，油田企业已实现在保障安全生产的前提下，以 30 分钟为周期对柔性调节裕度的预测。

基于上述运行特性，本文确立以下核心问题。首先，更新周期同步化，将柔性调节裕度预测的更新周期直接映射为源荷匹配方案的动态更新周期，$T=30$；其次，将本文所求解的具有内部电力互济能力与协同运行特性的单元，称为“源荷匹配区域”。

2 油田井场源荷匹配评价指标

2.1 源荷不匹配度

将井场与光伏电站用 gm 统一表示，假定源荷匹配区域 G_i 内，T_x 时段 t 时刻的总负荷 $P_{load}^{G_i,t}$、光伏总出力 $P_{source}^{G_i,t}$、总净负荷 $P_{netload}^{G_i,t}$ 分别为：

$$\begin{cases} P_{load}^{G_i,t}=\sum\limits_{gm\in G_i}P_{load}^{gm,t} \\ P_{source}^{G_i,t}=\sum\limits_{gm\in G_i}P_{source}^{gm,t} \\ P_{netload}^{G_i,t}=\sum\limits_{gm\in G_i}P_{netload}^{gm,t} \end{cases} \tag{1}$$

其中，$P_{load}^{gm,t}$、$P_{source}^{gm,t}$、$P_{netload}^{gm,t}$ 分别为 G_i 区域内第 gm 个井场或光伏电站的负荷、光伏出力、净负荷的预测值。

源荷匹配区域 G_i 内的不平衡功率 $P_{unb}^{G_i,t}$ 为：

$$P_{unb}^{G_i,t}=\left|P_{netload}^{G_i,t}\right| \tag{2}$$

源荷匹配区域 G_i 内 T_x 时段 t 时刻的源荷相对不匹配程度 $K_{unbalance}^{G_i,T_x}$ 表示为：

$$K_{unbalance}^{G_i,T_x}=\frac{\sum\limits_{t=1}^{T}P_{unb}^{G_i,t}}{\sum\limits_{t=1}^{T}P_{load}^{G_i,t}} \tag{3}$$

总净负荷波动性越小，内部功率平衡效果越好，源荷匹配程度越好；但由于现场源荷均存在一定随机或周期波动性，需消除在 T_x 时段内 $P_{netload}^{G_i,t}$ 波动性对于源荷匹配策略的影响，引入变异修正系数，如下所示。

$$\begin{cases} C_{netload}^{G_i,T}=\dfrac{\sqrt{\dfrac{1}{T-1}\sum\limits_{t=1}^{T}\left(P_{netload}^{G_i,t}-\overline{P_{netload}^{G_i,\tau}}\right)^2}}{\left|\overline{P_{netload}^{G_i,\tau}}\right|}, & \overline{P_{netload}^{G_i,\tau}}\neq 0 \\ C_{netload}^{G_i,T}=\dfrac{\sqrt{\dfrac{1}{T-1}\sum\limits_{t=1}^{T}\left(P_{netload}^{G_i,t}-\overline{P_{netload}^{G_i,\tau}}\right)^2}}{\max\left\{\left|\overline{P_{netload}^{G_i,\tau}}\right|,\left|\overline{P_{netload}^{G_i,t}}\right|\right\}}, & \overline{P_{netload}^{G_i,\tau}}=0,\overline{P_{netload}^{G_i,t}}\neq 0 \\ C_{netload}^{G_i,T}=10^{-6}, & \overline{P_{netload}^{G_i,t}}=0,\overline{P_{netload}^{G_i,\tau}}=0 \end{cases} \tag{4}$$

式中：$C_{netload}^{G_i,T}$ 表示 T_x 时段源荷匹配区域 G_i 的总净负荷 $P_{netload}^{G_i,t}$ 的变异修正系数。

综合考虑源荷匹配区域 G_i 内功率相对平衡及其波动程度，建立表征 SLMD 的指标 $M_{SLMD}\left(G_i,T_x\right)$，如公式（5）所示。

$$M_{SLMD}\left(G_i,T_x\right)=C_{netload}^{G_i,T}*K_{unbalance}^{G_i,T} \tag{5}$$

$M_{SLDD}\left(G_i,T_x\right)$ 值越低，表明 G_i 区域内源荷时空匹配度越高，光伏出力消纳的程度越高。

2.2 源荷分散度

根据光伏电站、井场净负荷的正负，对其进行划分，当净负荷 $P_{netload}^{gm,t}>0$ 时，用 gmj 表示；净负荷 $P_{netload}^{gm,t}<0$ 时，用 gmi 表示。

源 gmi 与荷 gmj 进行电能交互时，电气距离计算公式 $D_{gmi,gmj}$ 如下所示：

$$D_{gmi,gmj}=\sum_{lm\in M} d_{gmi,gmj}^{main,lm} r^{main}+\sum_{\in} d_{gmi,gmj}^{branch,lb} r^{branch} \tag{6}$$

式中：LM 、LB 分别表示线路主干线段、分支线段集合；$d_{gmi,gmj}^{main,lm}$ 、$d_{gmi,gmj}^{branch,lb}$ 分别表示系统成员 gmi 、gmj 之间的第 lm 段主干线、lb 段分支线的长度；r^{main} 、r^{branch} 分别表示主干线、分支线的单位长度电阻。

电气距离局限于交互双方，无法体现匹配区域内部的空间特征，且单一时间断面的电气距离无法指导周期内的源荷匹配区域划分。为衡量当前时段源荷匹配区域内的源荷空间分布的紧凑性，建立 SLDD 指标，用 $M_{SLDD}\left(G_i,T_x\right)$ 表示，公式如下。

$$M_{SLDD}\left(G_i,T_x\right)=\frac{1}{T}\sum_{t=1}^{T}\frac{\sum_{gmi\in G_{i,sou}^{t}}\sum_{gmj\in G_{i,lo}^{t}} D_{gmi,gmj}}{\left|G_{i,sou}^{t}\right|*\left|G_{i,lo}^{t}\right|} \tag{7}$$

式中：$G_{i,sou}^{t}$、$G_{i,lo}^{t}$ 分别为 T_x 时段 t 时刻的源、荷集合，$\left|G_{i,sou}^{t}\right|$、$\left|G_{i,lo}^{t}\right|$ 分别集合元素个数。

SLDD 反映匹配区域内源荷空间分布的紧凑性。SLDD 越低则传输损耗越小，能效越高。

3 源荷匹配优化模型构建

SLMD 最小化要求扩大源荷匹配区域规模以增强互补性，但可能导致 SLDD 增加。二者存在时空维度上的内在冲突。为实现协同优化，建立多优化协同目标函数，如下所示。

$$\begin{cases}\min\sum_{G_i\in G} D\left(G_i,T_x\right)\\ \min\sum_{G_i\in G} M\left(G_i,T_x\right)\end{cases} \tag{9}$$

式中：G 为所有源荷匹配区域集合；$\sum_{G_i\in G} M\left(G_i,T_x\right)$、$\sum_{G_i\in G} D\left(G_i,T_x\right)$ 分别为 T_x 时段为源荷匹配区域划分方案（简称源荷匹配方案）的 SLMD、SLDD，两者共同构成对方案的综合度量。

油田柔性负荷的调节能力是平抑光伏波动的关键。为保障系统运行稳定性，要求源荷匹配区域区域具备足够的实时调节裕度。

$$s.t.\ k_{soft}^{\min}\le\min\left\{\frac{P_{loadup}^{G_i,t}-P_{loaddown}^{G_i,t}}{P_{source}^{G_i,t}}\right\}\le k_{soft}^{\max} \tag{10}$$

式（8）中：$P_{loadup}^{G_i,t}$ 、$P_{loaddown}^{G_i,t}$ 是源荷匹配区域 G_i 总柔性负荷运行的上、下边界；$k_{soft}^{\min}$ 、$k_{soft}^{\max}$ 表示匹配区域的最小、最大调节能力。

本文“源荷匹配区域划分”与“系统运行控制”为递进阶段，约束需分阶段落地，说明如下。

1）阶段目标差异。本研究聚焦“划分阶段”，核心是确定“井场与光伏的协同拓扑边界”，通过 SLMD 与 SLDD 协同优化新能源消纳潜力；“潮流、电压、热稳定等约束”属于后续“运行阶段”任务，二者构成“结构优化-运行保障”链条。

2）合理性。划分阶段纳入运行约束会导致变量维度与计算复杂度剧增，偏离“找最优匹配拓扑”的核心目标；且符合工程中先定协同边界，再细化运行规则的实际优化逻辑。

3）可行性。通过 SLDD 优先选择紧凑区域，已间接规避传输损耗、热稳定等风险，为后续运行约束校验提供良好基础。

4 基于 GA-Pareto 的源荷匹配求解方法及决策机制

本章提出融合 CRITIC-TOPSIS 决策的 GA-Pareto 多目标优化框架，基于 SLMD 与 SLDD 指标，求解动态更新的源荷匹配方案，实现新能源消纳与能效的协同优化。

4.1 Pareto 最优理论框架

定义源荷匹配方案支配关系：已知方案 $S_1=\{G_1,G_2,...G_a\}$， $S_2=\{G_1,G_2,...G_b\}$。

$$\begin{cases}M\left(S_1,T_x\right)\ge M\left(S_2,T_x\right)\\ D\left(S_1,T_x\right)\ge D\left(S_2,T_x\right)\\ \exists i\in\{1,2\},f_i(S_1)>f_i(S_2)\end{cases} \tag{11}$$

当且仅当满足同时满足以上三个条件时，方案 S_2 是 S_1 的支配解。

在优化过程中，若存在某个方案能在不增加 SLDD 的前提下降低 SLMD，或反之，则当前方案未达到 Pareto 最优。通过调整方案内的源荷匹配区域划分，最终可以获得一组非支配方案，即 Pareto 最优方案集。

4.2 遗传算法

采用遗传算法求解源荷动态匹配方案，在染色体编译部分，如图 2 所示，采用整数编码，基因值表示该成员所属的源荷匹配区域编号。

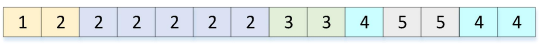


图 2　染色体整数编码示意图

Fig.2 Schematic Diagram of Chromosome Integer Encoding

在初始化方面，融合油田地理信息与源荷预测信息，设计初始化策略。

（1）连分布策略：空间相邻成员划入同一匹配区域，降低方案的 SLDD；

（2）源荷混合策略：源/荷性成员强制同组，降低方案的 SLMD；

（3）混合策略：随机交叉上述两种策略的染色体，生成 SLDD 与 SLMD 均衡的个体；

（4）随机策略：生成随机匹配方案，提高种群多样性。

在交叉操作中时，采用部分匹配交叉的方法，保留父代优良分组片段；在变异操作中，以低概率随机调整成员所属匹配区域编号。此外，在油田源荷匹配区域划分方案优化求解过程中，对于单节点匹配区域，迭代前期保留，后期强制其并入邻近块，避免无效解。

4.3 CRITIC-TOPSIS 最优决策模型

Pareto 最优非支配方案集无法直接支撑工程决策。建立 CRITIC-TOPSIS 筛选机制，通过客观赋权与贴近度量化，将多维 Pareto 解映射为可排的单维决策序列，求解 Pareto 最优解。

基于改进遗传算法与 Pareto 最优理论，设计多目标优化框架，通过多策略初始化加速收敛、自适应惩罚机制、工程约束校验保障方案可行性，并通过 CRITIC-TOPSIS 最优决策模型选取最优解。

5. 算例分析

某油田实际场景拓扑结构如图 3 所示，导线类型 LJ-120/20，含井场、T 接光伏电站。选取 12:00-12:30 时段的负荷、光伏及柔性调节裕度预测数据，进行算例分析。

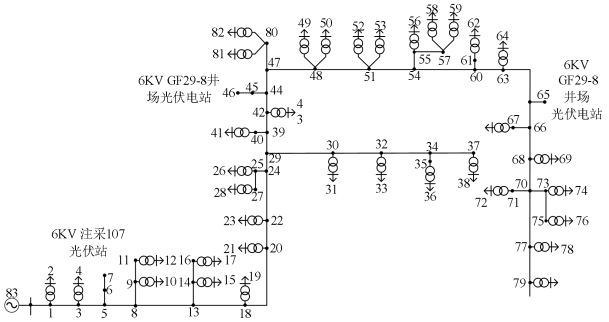


图 3　线路拓扑结构图

Fig.3 Topology Structure of the Distribution Network

光伏装机容量如表 1 所示。

表 1 光伏电站的装机容量

Table 1 Installed Capacity Configuration of PV Stations

节点	7	46	65
装机容量/kWp	400	630	630
案例 1	运行	未运行	运行
案例 2	运行	运行	运行

案例 1、2 中，12:00-12:30 的井场负荷预测如图 4 所示，呈差异化波动特性。

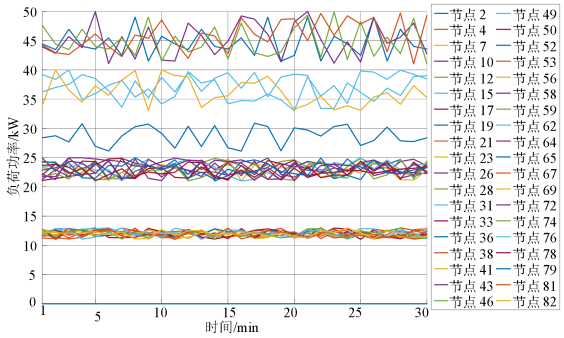


图 4　负荷预测

Fig.4 Forecasted Load Power of the Microgrid

基于光伏发电、负荷及柔性调节裕度预测信息，通过基于 GA-Pareto 的源荷匹配求解方法对源荷匹配划分方案进行多目标优化求解，得到案例 1、2 的 Pareto 最优解集。

以双优化目标为 Y 轴，对最优解集中的进行展开，如图 5、图 6 所示。

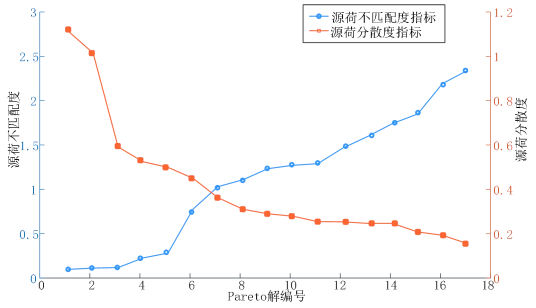


图 5　案例 1-Pareto 最优解集展开图

Fig.5 Case Study I: Expansion of the Pareto Optimal Solution Set

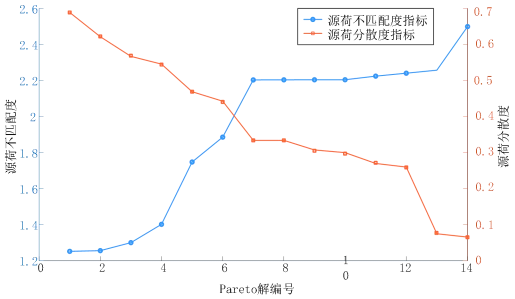


图 6　案例 2-Pareto 最优解集展开图

Fig.6 Case Study II: Expansion of the Pareto Optimal Solution Set

基于 CRITIC-TOPSIS 最优决策模型，对案例 1、2 的 SLMD、SLDD 赋权，求解 Pareto 最优方案集中具有综合优势的源荷匹配最优方案。

基于 12:00-12:30 时案例 1、2 的预测信息，分别令所有系统成员形成一个源荷匹配区域，进行 SLMD、SLDD 的计算，作为两案例的对照组。

案例 1、2 的源荷匹配区域划分最优方案分别如图 7、图 8 所示。

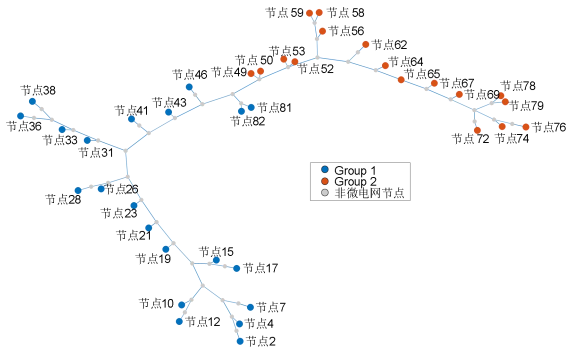


图 7 案例 1-源荷匹配结果

Fig.7 Case Study I: Source-Load Matching Results

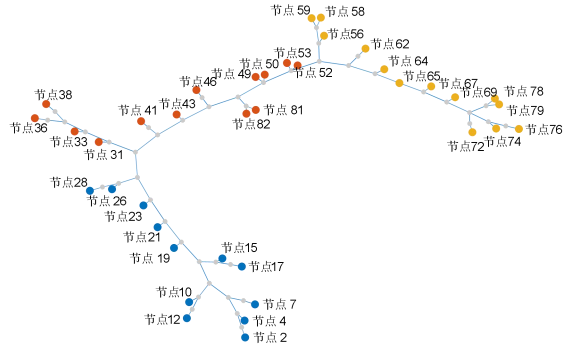


图 8 案例 2-源荷匹配结果

Fig.8 Case Study II: Source-Load Matching Results

案例 1、2 中对照组与源荷匹配区域划分最优方案的 SLMD、SLDD 如表 2 所示。

表 2 源荷匹配最优方案

Table 2 The Pareto Optimal Solution

案例	源荷匹配区域	SLMD	SLMD 相对优化率	SLDD	SLDD 相对优化率
案例 1	G1	0.1067	70.12%	0.664	47.76%
	G2	0.0126	96.47%	0.597	53.03%
	对照组	0.3571	0%	1.271	0%
案例 2	G1	0.6775	28.89%	0.432	54.67%
	G2	0.7284	23.54%	0.419	56.03%
	G3	0.6517	31.59%	0.330	65.37%
	对照组	0.9527	0%	0.953	0%

以对照组为基准，计算 SLMD 相对优化率、SLDD 相对优化率。案例 1 中包含两个源荷匹配区域 G1、G2，投入运行的光伏装机容量为 1030kWp，实现了 SLMD 最小 70.12%的降低，对应 SLDD 降低 47.76%；SLMD 最大降低达到了 96.47%，对应 SLDD 降低 53.03%。案例 2 中包含三个源荷匹配区域 G1、G2、G3，实现了分组自动调整，此时投入运行的光伏装机容量为 1660kWp，实现了 SLMD 最小 23.54%的降低，对应 SLDD 降低 56.03%；SLMD 最大降低达到了 31.59%，对应 SLDD 降低 65.37%，仍实现了 SLMD 与 SLDD 的显著优化。

案例 1、2 结果表明，在不同运行工况与多源预测信息输入下，本文所提策略通过驱动源荷时空互补，均显著提升新能源消纳能力，同时保障系统能效性，验证了策略对油田复杂场景的适应性及多目标协同优化机制的有效性，为高比例光伏接入的油田企业场景提供了系统解决方案。

6 结束语

本文针对油田井场新能源消纳能力受限的关键问题，提出了一种面向新能源消纳能力提升的油田井场源荷动态匹配策略。通过构建量化时空匹配度与空间分散度的双维度评价指标，并融合负荷柔性调节裕度约束，建立了以提升新能源就地消纳能力为核心、兼顾系统能效的多目标优化模型。算例分析表明，该策略能显著降低源荷不匹配度（优化率最高达 96.47%）和源荷分散度（优化率最高达 65.37%），有效提升了光伏发电的消纳水平，为油田场景下提升新能源消纳能力与系统整体能效提供了系统化的解决方案，具有明确工程应用价值。

后续研究将基于本阶段划分结果，融入运行约束，构建 “划分-运行”一体化方案。

参考文献

[1] 肖峻, 潘安鹏, 贺国伟, 等. 配电网 DG 消纳与源荷匹配的定量分析[J]. 电力自动化设备, 2025.

[2] 李阳，张启亮，李开灿，等.计及主动需求响应的配电网有功无功鲁棒优化调度[J].山东电力技术，2024，51(1) ：35-44.

[3] Majzoobi A, Khodaei A. Application of Microgrids in Supporting Distribution Grid Flexibility[J]. IEEE Transactions on Power Systems, 2017, 32(5): 3660-3669.

[4] Li Q, Zhou F, Guo F, et al. Optimized Energy Storage System Configuration for Voltage Regulation of Distribution Network With PV Access[J]. Frontiers in Energy Research, 2021, 9.

[5] 陶继升.微电网群两阶段源储荷协调优化方法研究[D].安徽大学，2019.

[6] 彭琦, 欧阳森, 张晋铭, 等. 考虑多断面源荷特征匹配的高比例分布式光伏接入配电网的集群划分方法[J]. 南方电网技术, 2025, 19(4): 161-172, 184.

[7] 丁长新，王翔，赵波，等. 基于动态组网的园区微电网群运行优化[J]. 电网与清洁能源，2024，40(5) ：1-9.

[8] 张叶青，陈文彬，徐律军，等. 面向多虚拟电厂的分层分区多层互补动态聚合调控策略[J]. 发电技术，2024，45(1) ：162-169.

[9] 孙玲玲，李海滨，贾清泉，等.基于动态重构的虚拟电厂资源聚合规划方法[J].电力系统自动化,2024，48(18) ：115-128.

[10] 蒋光梓，彭杨，纪昌明，等. 计及价格型需求响应的水风光互补短期调度[J]. 水力发电学报, 2023, 42(10): 1-12.

[11] 胡静，李娜娜，闫湖，等. 考虑新能源消纳能力的配电网源储荷协同控制[J]. 电力信息与通信技术, 2025.

收稿日期：

作者简介：



魏淑静

魏淑静(2000)，女，硕士研究生，研究方向为油田井场多微电网动态成群及优化运行，E-mail:wsj1815583659@163.com；

仉志华(1977)，男，通信作者，博士，教授，研究方向为多能互补综合能源系统结构设计与优化调控技术等;E-mail:zzh-upc@163.com。

053 Method for Two-Point Ground Fault Location with Different Phases on the Same Line Based on Load-Side Phase Voltage

ZHANG Xiangdong, ZHANG Zhihua*, XING Yuxiao, SHI Haojie

(College of New Energy, China University of Petroleum, Qingdao 266580, China)

Abstract. The detection methods for single-phase ground faults in ungrounded systems have matured considerably. However, research on two-point ground fault remains insufficient. With the continuous advancement of intelligent distribution station areas, the increasing availability of monitoring data from the low-voltage side offers new insights for fault location on the medium-voltage side. This paper proposes a method for locating double ground faults on the same line but in different phases in ungrounded systems, based on phase voltages observed from the load side. First, a mapping relationship between the low-voltage side phase voltages and the voltage fault components on the medium-voltage side is established to achieve accurate voltage inversion. Second, the positive-sequence current fault component is calculated using the positive-sequence voltage fault component and line parameters. The distribution characteristics of this component are then utilized to derive criteria for fault line selection and section positioning. Finally, simulations verify the accuracy of the inversion results and the effectiveness of the proposed method. The analysis also examines the impact of various factors, including load magnitude, load power factor, transition resistance, and distributed generation, on the accuracy of the method.

Keywords: Ungrounded system, Two-point ground fault, Low-voltage side phase voltage, Fault section location

1 Introduction

In China, most 10kV distribution networks operate with an ungrounded neutral. Among various fault types, the single-phase ground fault is the most frequent. When such a fault occurs, the voltage of the faulty phase decreases, while the voltages of the non-faulty phases increase. Due to the low fault current, the system is typically allowed to continue operating with the fault for 1 to 2 hours. However, during this period, the sustained overvoltage on the non-faulty phases may break down weak insulation points, leading to a two-point ground fault [1]. As the structure of distribution networks becomes more complex and their scale continues to expand, the likelihood of cross-phase two-point ground faults is increasing. Consequently, research on locating these faults is gaining significant importance.

Currently, extensive research has been conducted on single-phase ground faults in ungrounded systems [2-4], and the corresponding detection technologies have matured considerably. In contrast, studies on two-point ground faults remain relatively limited. As most single-phase fault detection methods are ineffective for all types of two-point ground faults, these faults often persist for extended periods. Therefore, there is an urgent need for in-depth research on detection methods for two-point ground faults to meet the demands of power supply reliability.

Several studies have addressed aspects of two-point ground faults. For instance, Reference [5] summarized the evolution mechanism, fault pattern representation, and scenario screening criteria for successive faults. Reference [6] established a transient equivalent circuit for such faults, identified differences in transient power direction between healthy and faulty lines, and proposed a multi-level protection scheme. Reference [7] analyzed the variation characteristics of zero-sequence admittance in faulty and sound paths before and after a two-point ground fault, leading to a section location method. Reference [8] examined the zero-sequence current and reactive power characteristics during same-phase two-point ground faults and introduced a two-stage line selection method based on reactive power differences. By analyzing sequence networks during different-phase two-point ground faults at various locations, Reference [9] proposed a fault location algorithm using multi-measurement unit data. However, the implementation of these methods relies heavily on numerous feeder terminals to provide measurement data.

The widespread deployment of smart station-area integration terminals (TD-SFT) has significantly enhanced the acquisition of low-voltage side parameters, such as voltage, thereby providing data support for fault location in medium-voltage distribution networks. Several methods utilizing this data have been developed: Reference [10] located single-phase ground faults by exploiting the characteristic that the negative-sequence voltage on the low-voltage side peaks at the fault point. Reference [11] analyzed the distribution of low-voltage side negative-sequence current during such faults, using it for line selection and performing location based on the ratio of negative-sequence to positive-sequence voltage amplitudes. Reference [12] classified low-voltage side measurement node voltages using the k-nearest neighbor algorithm to identify fault sections and applied an iterative search to pinpoint the exact location. Reference [13] inversely calculated medium-voltage side fault components from low-voltage side voltage data to achieve section location. While the aforementioned methods successfully locate simple medium-voltage side faults using low-voltage side data, they neither analyze the low-voltage side characteristics during different-phase two-point ground faults nor propose corresponding detection methods for such complex scenarios.

This paper proposes a fault location method for successive different-phase two-point ground faults on the same line in ungrounded systems, based on low-voltage side phase voltage information. By establishing a mapping relationship between the low-voltage side phase voltages and the medium-voltage side voltage fault components, accurate inversion of the voltage information is achieved. Using the obtained positive-sequence voltage fault components from the inversion calculation, together with the network topology and line impedance, the positive-sequence current fault

components for each section are calculated. Based on their distribution characteristics, criteria for fault line selection and section location are proposed. Verification on the MATLAB simulation platform demonstrates that the proposed method can accurately locate the fault section under various conditions, including different fault locations, transition resistances, load levels, and scenarios with distributed generation integration.

2 Phasor mapping relationship between medium- and low-voltage sides

The structure of the ungrounded system is illustrated in Figure 1. Each distribution transformer is equipped with a smart station-area integration terminal on its low-voltage side. These terminals measure the low-voltage side voltages in real time and transmit the data to the master station. The most common wiring configuration for these transformers is Dyn-11. Due to the electrical isolation characteristic for zero-sequence components between the medium-voltage and low-voltage sides of this transformer type, only the positive- and negative-sequence components from the medium-voltage side can be derived from the low-voltage side voltages.

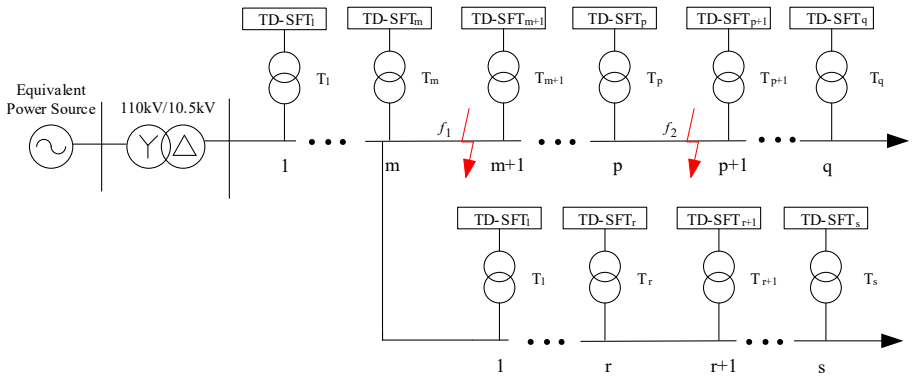
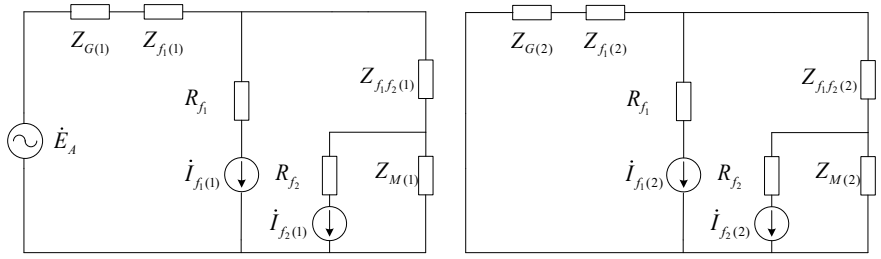


Fig.1 Typical topology of neutral-point ungrounded distribution system

The three-phase systems on the medium-voltage side and the low-voltage side are denoted as A~C and a~c. The fault point closer to the bus is defined as the first fault point, while the one farther from the bus is the second fault point. In Figure 1, a B-phase-to-ground fault and a C-phase-to-ground fault occur at points f_1 and f_2, with transition resistances of R_{f_1} and R_{f_2}. When only considering that fault points are located on the main line and not considering the influence of branch linesthe positive- and negative-sequence networks for the successive different-phase two-point ground fault on the same line can be derived, as shown in Figure 2.

4



(a) Positive-sequence equivalent network (b) Negative-sequence equivalent network

Fig.2 Equivalent network of positive-negative sequence for two-point ground fault

In Figure 2, $\dot{E}_A$ represents the A-phase source voltage of the system; $Z_{G(1)}$ and $Z_{G(2)}$ denote the system's positive-sequence and negative-sequence impedances. $Z_{f_1(1)}$ and $Z_{f_1(2)}$ are the positive-sequence and negative-sequence impedances of the line section between the busbar and fault point f_1 ,while $Z_{f_1f_2(1)}$ and $Z_{f_1f_2(2)}$ represent those between fault points f_1 and f_2. $Z_{M(1)}$ and $Z_{M(2)}$ are the total positive-sequence and negative-sequence impedances, respectively, representing the sum of the downstream line and load impedances beyond fault point f_2 , $\dot{I}_{f_1(1)}$, $\dot{I}_{f_1(2)}$, $\dot{I}_{f_2(1)}$ and $\dot{I}_{f_2(2)}$ correspond to the positive-sequence and negative-sequence fault additional current sources at fault points f_1 and f_2.

As shown in Figure 2, the positive-sequence voltage fault component $\dot{U}_{i\mathrm{F}(1)}$ and the negative-sequence voltage fault component $\dot{U}_{i\mathrm{F}(2)}$ at any arbitrary node k located upstream of fault point *i* can be expressed as:

$$\begin{cases}\dot{U}_{i\mathrm{F}(1)} = -(\dot{I}_{f_1(1)} + \dot{I}_{f_2(1)})(Z_{\mathrm{G}(1)} + Z_{f_1(1)} - Z_{if_1(1)}) \\ \dot{U}_{i\mathrm{F}(2)} = -(\dot{I}_{f_1(2)} + \dot{I}_{f_2(2)})(Z_{\mathrm{G}(2)} + Z_{f_1(2)} - Z_{if_1(2)})\end{cases} \tag{1}$$

When all transformers are configured with the Dyn-11 connection and have a turns ratio of *k*, the three-phase voltages on the low-voltage side at any node can be expressed as:

$$\begin{cases}\dot{U}_{ia} = \dot{U}_{ia|0|} + \dfrac{1}{k}e^{j30^\circ}\dot{U}_{i\mathrm{F1}} + \dfrac{1}{k}e^{-j30^\circ}\dot{U}_{i\mathrm{F2}} \\ \dot{U}_{ib} = e^{-j120}\dot{U}_{ia|0|} + \dfrac{1}{k}e^{-j90^\circ}\dot{U}_{i\mathrm{F1}} + \dfrac{1}{k}e^{j90^\circ}\dot{U}_{i\mathrm{F2}} \\ \dot{U}_{ic} = e^{j120^\circ}\dot{U}_{ia|0|} + \dfrac{1}{k}e^{j150^\circ}\dot{U}_{i\mathrm{F1}} + \dfrac{1}{k}e^{-j150^\circ}\dot{U}_{i\mathrm{F2}}\end{cases} \tag{2}$$

Where $\dot{U}_{ia|0|}$ is the pre-fault phase A voltage. Given the low-voltage side phase voltages at a node, the positive-sequence and negative-sequence voltage fault components on the medium-voltage side can be obtained. By incorporating the boundary conditions at the fault points, the expressions for the three-phase voltages after the fault $\dot{U}_{ia}$, $\dot{U}_{ib}$, $\dot{U}_{ic}$ are derived as follows:

$$\begin{cases} \dot{U}_{ia} = e^{j30^\circ}\dot{U}_{ia|0|} - \dfrac{1}{k}e^{j60^\circ}X - e^{j30^\circ}Y - e^{-j30^\circ}P \\ \dot{U}_{ib} = e^{-j90^\circ}\dot{U}_{ia|0|} - \sqrt{3}e^{-j120}X - \sqrt{3}e^{-j60^\circ}Q - e^{-j90^\circ}Y - e^{j90^\circ}P \\ \dot{U}_{ic} = \dfrac{1}{k}e^{j150^\circ}\dot{U}_{ia|0|} - \sqrt{3}e^{j120^\circ}Q - e^{j150^\circ}X - e^{-j150^\circ}Y \end{cases} \tag{3}$$

Equation (3) indicates that the three-phase voltage variations are distinct for each node located upstream of the first fault point.

Regarding any node *j* located between the two fault points:

$$\begin{cases} \dot{U}_{ja} = e^{j30^\circ}\dot{U}_{ja|0|} - \sqrt{3}e^{j60^\circ}M - e^{j30^\circ}Y - e^{-j30^\circ}P \\ \dot{U}_{jb} = e^{-j90^\circ}\dot{U}_{ja|0|} - \sqrt{3}e^{-j120}M - \sqrt{3}e^{-j60^\circ}N - e^{-j90^\circ}Y - e^{j90^\circ}P \\ \dot{U}_{jc} = e^{j150^\circ}\dot{U}_{ja|0|} - \sqrt{3}e^{j120^\circ}N - \dfrac{1}{k}e^{j150^\circ}Y - \dfrac{1}{k}e^{-j150^\circ}P \end{cases} \tag{4}$$

Equation (4) shows that the variation in Phase-A voltage is the same for all nodes located between the two fault points, while the variations in the other two phases are different.

$$\begin{cases} X = \dfrac{1}{k}\dot{I}_{f_1(1)}(Z_{f_1(1)} - Z_{if_1(1)}) \\ Y = \dfrac{1}{k}(\dot{I}_{f_1(1)} + \dot{I}_{f_2(1)})Z_{G(1)} \\ P = \dfrac{1}{k}(\dot{I}_{f_1(2)} + \dot{I}_{f_2(2)})Z_{G(2)} \\ Q = \dfrac{1}{k}\dot{I}_{f_2(1)}(Z_{f_1(1)} - Z_{if_1(1)}) \\ M = \dfrac{1}{k}\dot{I}_{f_1(1)}Z_{f_1(1)} \\ N = \dfrac{1}{k}\dot{I}_{f_2(1)}(Z_{f_1(1)} + Z_{f_1f_2(1)} - Z_{jf_2(1)}) \end{cases} \tag{5}$$

Based on the above analysis, when a successive two-point ground fault occurs on the same line, the variation patterns of the low-voltage side three-phase voltages at nodes along the main feeder can be categorized into three distinct cases: exhibiting entirely different variations from the adjacent upstream node, sharing an identical variation in one phase, or having identical variations in all three phases.

3 Fault characteristic analysis and location method

3.1 Activating criterion

When the zero-sequence voltage of the busbar exceeds the threshold, the TD-SFTs use the moment of this initial exceedance as the reference time point. It saves the data prior to this moment as the pre-fault phase voltage data. The terminal continuously monitors the system's zero-sequence voltage. If a sudden change occurs again while the voltage remains above the threshold, it uses the time of this second change as a

new benchmark and saves the subsequent data as the post-fault phase voltage data. Finally, the saved pre-fault and post-fault phase voltage information is uploaded to the master station.

3.2 Criteria for Faulty Line Selection and Section Location

After the positive-sequence voltage fault component on the medium-voltage side is derived from the low-voltage side phase voltage inversion calculation, the positive-sequence current fault component $\dot{I}_{(i,i+1)\mathrm{F}(1)}$ for any section (i, i+1) can be obtained by incorporating the line parameters. Since the fault current on the faulty line is significantly larger than that on non-faulty lines, the faulty line can be identified as the one with the maximum magnitude of the positive-sequence current fault component at the line's first section.

Regarding any non-faulty section (i, i+1) located between the first fault point and the busbar, the following relationship holds:

$$I_{(i,i+1)\mathrm{F}(1)} = \left| \frac{\Delta \dot{U}_{(i,i+1)\mathrm{F}(1)}}{Z_{i+1(1)} - Z_{i(1)}} \right| \approx \left| \dot{I}_{f_1(1)} + \dot{I}_{f_2(1)} \right| \tag{6}$$

Assuming that the first fault point is located in section (m, m+1), the following relationship holds for this faulty section:

$$I_{(m,m+1)\mathrm{F}(1)} = \left| \frac{\Delta \dot{U}_{(m,m+1)\mathrm{F}(1)}}{Z_{m+1(1)} - Z_{m(1)}} \right| < \left| \dot{I}_{f_1(1)} + \dot{I}_{f_2(1)} \right| \tag{7}$$

Regarding any section (j, j+1) located between the two fault points, the following relationship holds:

$$I_{(j,j+1)\mathrm{F}(1)} = \left| \frac{\Delta \dot{U}_{(j,j+1)\mathrm{F}(1)}}{Z_{j+1(1)} - Z_{j(1)}} \right| \approx \left| \dot{I}_{f_2(1)} \right| \tag{8}$$

Assuming that the second fault point is located in section (n, n+1), the following applies to this faulty section:

$$I_{(n,n+1)\mathrm{F}(1)} = \left| \frac{\Delta \dot{U}_{(n,n+1)\mathrm{F}(1)}}{Z_{n+1(1)} - Z_{n(1)}} \right| < \left| \dot{I}_{(j,j+1)\mathrm{F}(1)} \right| \tag{9}$$

For the downstream section (n+1, n+2) of the faulty section:

$$\dot{I}_{(n+1,n+2)\mathrm{F}(1)} = \left| \frac{\Delta \dot{U}_{(n+1,n+2)F(1)}}{Z_{n+2(1)} - Z_{n+1(1)}} \right| \approx 0 \tag{10}$$

Based on the above analysis, the positive-sequence current fault components between the busbar and the first fault point are approximately equal. Similarly, the current between the two fault points is approximately equal but differs from that in the section preceding the first fault point. Downstream of the second fault point, the current is significantly smaller, approximating zero. Based on the distribution pattern of the positive-sequence current fault components along the faulty line, the section location method is derived as follows:

Calculate the positive-sequence current fault component for each section and add an auxiliary section with a value of zero at the end of each line. Perform the analysis

sequentially from the end of the line back to the busbar. Identify the first section whose calculated value differs significantly from that of its immediate downstream section as fault section N. If the components in the upstream sections of fault section N exhibit no significant difference, then both fault points are located within section N. If a significant difference exists, then the section that differs from the others is identified as the fault section closer to the busbar.

4 Simulation Verification

This paper employs MATLAB to build a simulation model of a medium-voltage distribution network to validate the accuracy of the proposed method. The model topology is presented in Figure 3.

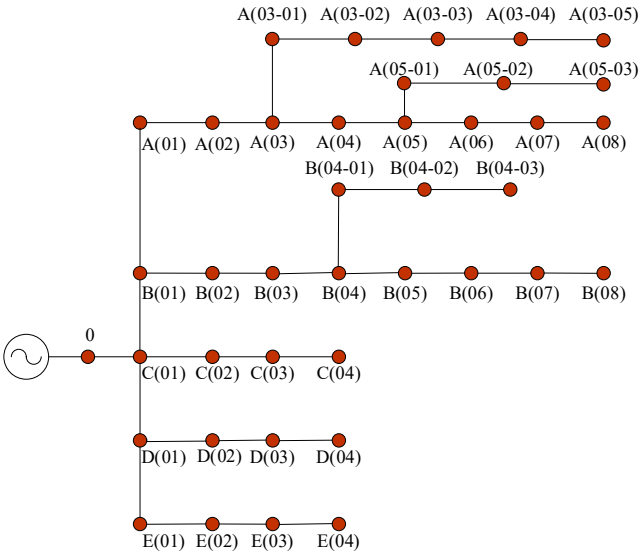


Fig.3 Simulation model topology diagram

4.1 Verification of voltage mapping relationship

Set metallic ground faults of phase B and phase C to occur in sections A(03)-A(04) and A(06)-A(07) of Line 1, respectively. The medium-voltage side positive-sequence voltage fault components of each node in Line 1 are obtained through the inversion calculation of low-voltage side voltage, and the comparison between the calculated results and the actual simulation results is shown in Fig. 4.

8

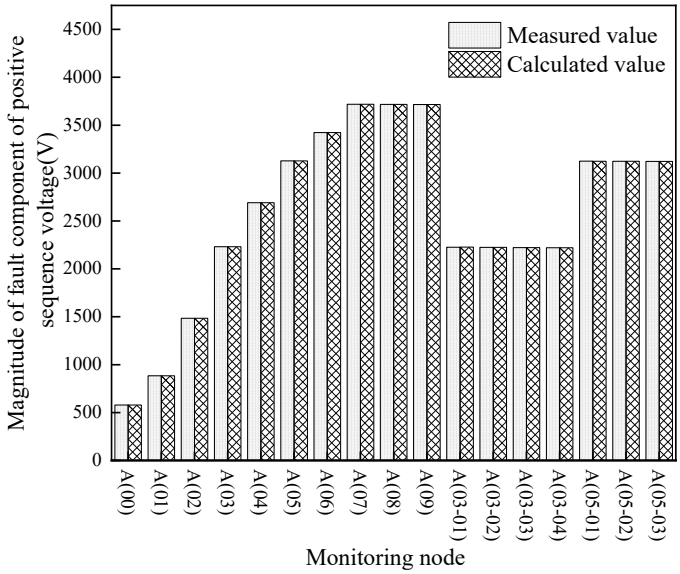


Fig.4 Comparison between calculated results and simulation results

As shown in Figure 4, the error between the inverted calculation values and the simulated measurements is minimal, demonstrating that the medium-voltage side fault components can be accurately inverted from the low-voltage side phase voltages.

4.2 Verification of the faulty line selection method

Under the aforementioned fault conditions, after obtaining the positive-sequence voltage fault components at each node, the positive-sequence current fault components at the starting point of each line were calculated using the line parameters. The line with the maximum current magnitude was selected as the faulty line. The calculated positive-sequence current fault components at the starting point of each line are presented in Table 1.

Table.1 Positive-sequence current fault component at each line head

Line	Amplitude of positive-sequence current fault component
Line1	1731.16
Line2	7.53
Line3	4.27
Line4	2.55
Line5	1.98

As shown in Table 1, the positive-sequence current fault components at the head ends of Line is significantly greater than those of the other lines, confirming the correct identification of the faulty line.

4.3 Verification of the section location method

When metallic ground faults occur on phase B and phase C at the 50% points of sections A(03)-A(04) and A(06)-A(07) in Line 1, respectively, the amplitudes of the positive-sequence current fault components in each section of the main trunk are shown in Figure 5.

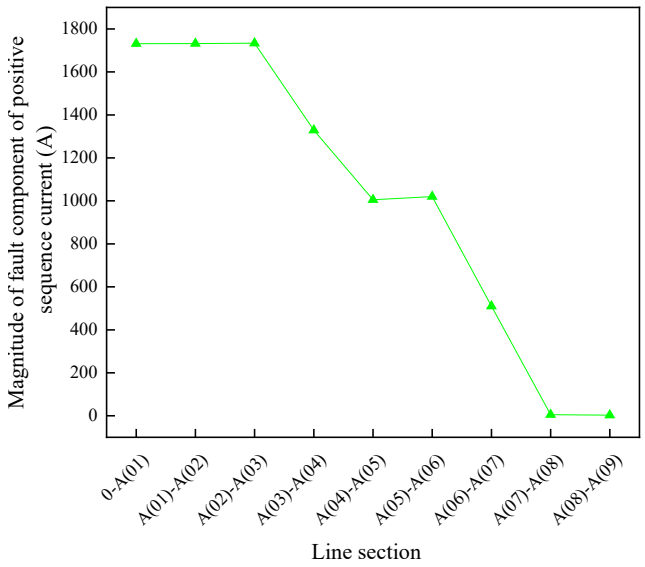


Fig.5 Section location results

As shown in Figure 5, when analyzing the sections from the end of the main trunk toward the busbar, the first section whose positive-sequence current fault component amplitude differs significantly from its downstream section is A(06)-A(07). Since no branch line is connected within or downstream of this section, it is identified as a fault section. Moving upstream, another section whose amplitude distinctly differs from its adjacent downstream section is identified as A(03)-A(04). Similarly, with no branch line connected within or downstream of section A(03)-A(04), it is also confirmed as a fault section.

4.4 Analysis of influencing factors

Influence of load level Metallic ground faults were set at the midpoints of sections A(03)-A(04) and A(06)-A(07), with load levels set to 100%, 50%, and 20% of the reference load, respectively. The amplitudes of the positive-sequence current fault components in each section of the main trunk of Line 1 under these conditions are shown in Figure 6.

10

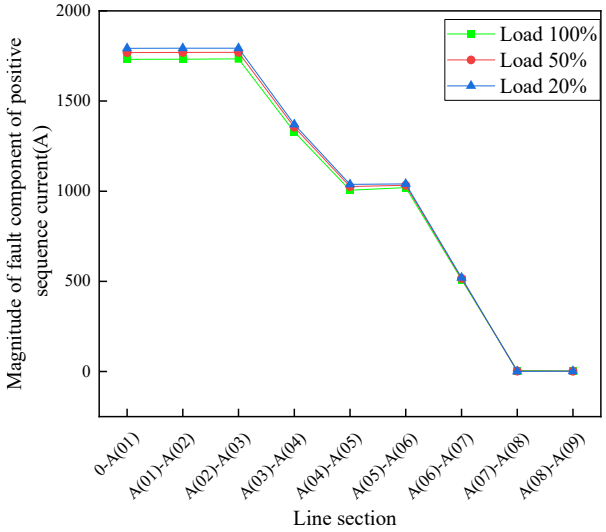


Fig.6 Localization results under different load size

As shown in Figure 6, under the reference load conditions of 100%, 50%, and 20%, the fault sections are correctly located as A(03)-A(04) and A(06)-A(07), demonstrating the accuracy of the section location results across varying load levels.

Influence of load power factor As shown in Figure 7, under power factor conditions of 0.8, 0.875, and 0.95, the fault sections are correctly identified as A(03)-A(04) and A(06)-A(07) in all cases, demonstrating the consistency and accuracy of the section location method.

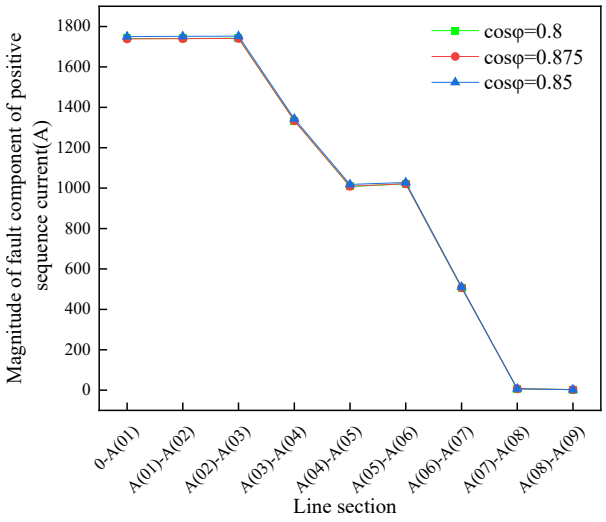


Fig.7 Location results under different load power factors

Figure 7 demonstrates that under power factors of 0.8, 0.875, and 0.95, the fault sections are consistently and correctly identified as A(03)-A(04) and A(06)-A(07), confirming the robustness of the section location method against variations in power factor.

Influence of transition resistance Metallic ground faults were set at the midpoints of sections A(03)-A(04) and A(06)-A(07). The transition resistance was configured under three scenarios: 500 Ω at both fault points, 250 Ω at both fault points, and 0 Ω and 1000 Ω at the two points respectively. The amplitudes of the positive-sequence current fault components for each section of the main trunk of Line 1 under these configurations are shown in Figure 8.

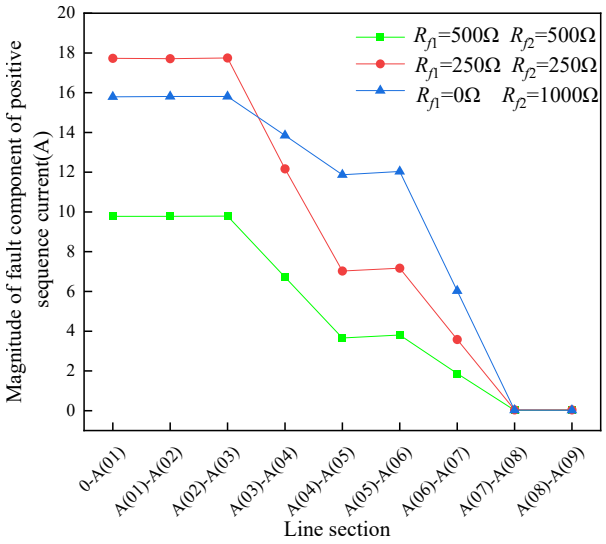


Fig.8 Localization results under different transition resistances

Figure 8 shows that the fault sections are correctly identified as A(03)-A(04) and A(06)-A(07) under all the specified transition resistance conditions (500 Ω at both points, 250 Ω at both points, and 0 Ω and 1000 Ω, respectively), confirming the accuracy of the section location method.

Influence of DG integration Metallic ground faults were set at the midpoints of sections A(03)-A(04) and A(06)-A(07). DG was connected at three different locations: upstream of the fault points at A(01) and A(02); on both sides of the fault points at A(02) and A(08); and downstream of the fault points at A(07) and A(08). The amplitudes of the positive-sequence current fault components for each section of the main trunk of Line 1 under these DG integration scenarios are shown in Figure 9.

12

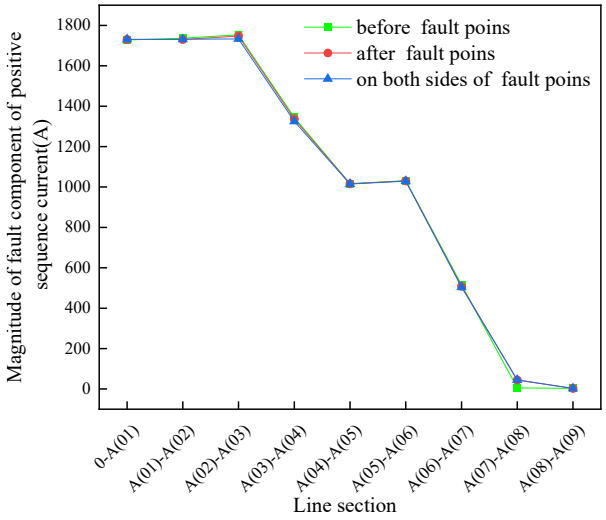


Fig.9 Location results under different DG access locations

Figure 9 demonstrates that the fault sections are correctly identified as A(03)-A(04) and A(06)-A(07) under different DG integration scenarios, including DG connected upstream of the fault points, on both sides of the fault points, and downstream of the fault points. The simulation results confirm that the proposed section location method achieves accurate fault identification under various conditions—including load levels, power factors, transition resistances, and DG integration scenarios—demonstrating strong robustness.

5 Conclusion

This paper proposes a fault location method for successive different-phase two-point ground faults on the same line in ungrounded systems, utilizing low-voltage side phase voltage information. The following conclusions are drawn from theoretical analysis and simulation verification:

1. Based on the established voltage mapping relationship between the medium-voltage and low-voltage sides, the positive-sequence voltage fault components on the medium-voltage side can be accurately calculated from the low-voltage side phase voltages, enabling analysis of the low-voltage side voltage variation patterns.

2. The positive-sequence current fault components on the faulty line exhibit a distinct stepped distribution characteristic, which can be utilized to achieve precise section location.

3. The proposed method achieves accurate fault location under various conditions, including different load levels, power factors, transition resistances, and distributed generation integration scenarios. Furthermore, it requires no additional measurement devices, demonstrating economic efficiency.

References

1. LIU Yingtong, HUANG Chun, YUAN Jingbo, et al. Transient characteristics and fault line selection of two-point same-phase grounding fault in resonant grounding system[J]. Electric Power, 2022, 55(10): 62-70.
2. WANG Wenxuan, CHENG Lihan, FAN Yi, et al. Grounding fault identification method for distribution stations without relying on zero-sequence voltage [J]. Automation of Electric Power Systems, 2021, 45(9): 122-129.
3. LIU Jian, ZHANG Zhihua, LI Yunge, et al. Automatic processing of single-phase grounding fault in distribution network based on fault phase grounding [J]. Automation of Electric Power Systems, 2020, 44(12): 169-177.
4. ZHANG Li, YANG Peng, SI Dongmei, et al. Online fault location in neutral ungrounded system based on zero-sequence power direction [J]. Automation of Electric Power Systems, 2008, 32(17): 79-82.
5. XUE Yusheng, XIE Yunyun, WEN Fushuan, et al. Review on research of successive failures in power systems [J]. Automation of Electric Power Systems, 2013, 37(19): 1-9+40.
6. LIU Yong, LIU Dapeng, MU Yong, et al. Multi-level protection technology for cross-line successive two-point grounding fault in ungrounded system[J]. Distribution & Utilization, 2024, 41(05): 56-63.
7. XUE Yongduan, QI Zhibin, CAI Zhuoyuan, et al. Detection of cross-line successive two-point grounding fault with different phases based on zero-sequence admittance variation[J]. Automation of Electric Power Systems, 2023, 47(7): 174-183.
8. ZHANG Zongxi, XUE Yongduan, DONG Liming, et al. Power frequency characteristics and line selection of two-point grounding fault with same phase in ungrounded system[J]. Proceedings of the CSU-EPSA, 2022, 34(9): 9-16.
9. HE Qian, LI Qujia, DENG Yan, et al. Fault location algorithm for cross-phase double-ground faults in active distribution networks[J]. Electric Power Automation Equipment, 2025, 45(6): 64-71.
10. Zhang D, Zhang W, Wang C, et al. Fault Segment Location for MV Distribution System Based on the Characteristic Voltage of LV Side[J]. Electronics, 2023, 12(7): 1734.
11. Zhang M, Ai X. A New Approach for Single-Phase-to-Ground Fault Detection in Mid-Voltage Systems Using Low-Voltage Sensors[J]. Symmetry, 2024, 16(4): 410.
12. Zhang S, Chen H, Tang J, et al. Fault Location Based on Voltage Measurement at Secondary Side of Low-Voltage Transformer in Distribution Network[J]. IEEE Transactions on Instrumentation and Measurement, 2022, 71: 1-12.
13. Zhang Z, Xing Y, Xu B, et al. Voltage mapping relationship based single-phase-to-ground fault sector location method for low resistance neutral grounded system[J]. International Journal of Electrical Power & Energy Systems, 2025, 170: 110913.

054 Research of Full Sequence Impedance Equivalent Modeling of Wind Farm

Yirui Wang[1], Zhijie Zeng[2], Ye Tian[2], Chen Qi[3], Jin Liu[1]

[1] School of Electric and Electronic Engineering, North China Electric Power University. Beijing, China
wangyirui77@163.com
[2] Fujian Electric Power Research Institute, Fuzhou 350007, China
[3] National Key Laboratory of Renewable Energy Grid-Integration (China Electric Power Research Institute), Haidian District, Beijing 100192, China

Abstract. The accuracy of wind farm equivalent models forms the basis for investigating the dynamic characteristics of their grid-connected systems. Traditional aggregation models often oversimplify the collection network, a limitation that compromises the precision of simulating wind farm electrical characteristics. To address this, this paper introduces a refined equivalent modelling approach incorporating the impedance of all sequences (positive, negative, and zero sequence) of the collection lines. This method first establishes a full-sequence equivalent impedance model for the collection system. Concurrently, the wind turbines and their step-up transformers are equivalenced using a weighted capacitance approach, thereby constructing an equivalent model for the entire wind farm. The validity of the proposed method is verified through comparative simulations with a detailed model under typical operational scenarios. Results demonstrate that the equivalent model effectively captures the dynamic response of the detailed reference model, providing a reliable framework for assessing the stability of large-scale wind power integration systems.

Keywords: Equivalent Modeling, Wind Farm Station, Collector network.

1 Introduction

Since wind farms consist of tens or hundreds of wind turbines and a complex energy collection network, the use of a detailed model for simulation analysis involves problems of high computational complexity and low simulation efficiency. The equivalent accuracy of the collector line directly affects the simulation accuracy of the electrical characteristics of the wind farm port[1]-[2], especially when the analysis involves asymmetric faults and other scenarios, the equivalent method considering the full sequence (positive sequence, negative sequence, zero sequence) impedance of the collector line is particularly important.

With regard to the principle of equivalence, scientists generally agree that, in order to achieve equality before and after equivalence, the same amount of electricity

This work was supported by Science and Technology Program of SGCC （Testbench-based test technologies of offshore wind turbine transmitted by VSC-HVDC system, 4000-202321074A-1-1-ZN).

should be available in the grid[3]-[7]. However, there are different views on the specific implementation methods: on the one hand, most studies ignore the influence of negative sequence and zero sequence impedance in asymmetric operation, focusing on the equivalence of positive sequence impedance. On the other hand, although some literary sources have put forward the idea of zero sequence equivalence, their specific modelling methods, the basis for calculating parameters, and applicability to various types of faults have not yet been formed into a unified paradigm. For example, the reference [4] points out that the existing research mostly ignores the influence of zero sequence mutual inductance and grounding mode of collector line, resulting in large error of equivalent model in grounding fault simulation.

In summary, within the framework of ongoing research, a relatively mature system of methods has been developed in the field of positive sequence equivalence of collection lines. However, there are still obvious shortcomings in the field of complete impedance sequence equivalence, particularly in the area of precise modelling of zero sequence circuits. Therefore, this paper intends to carry out in-depth research on the wind farm equivalent method considering the positive, negative and zero sequence impedance of the collector line, in order to improve the simulation accuracy of the equivalent model under asymmetric operation and fault conditions.

2 Structure of Wind Farm Transmission Systems

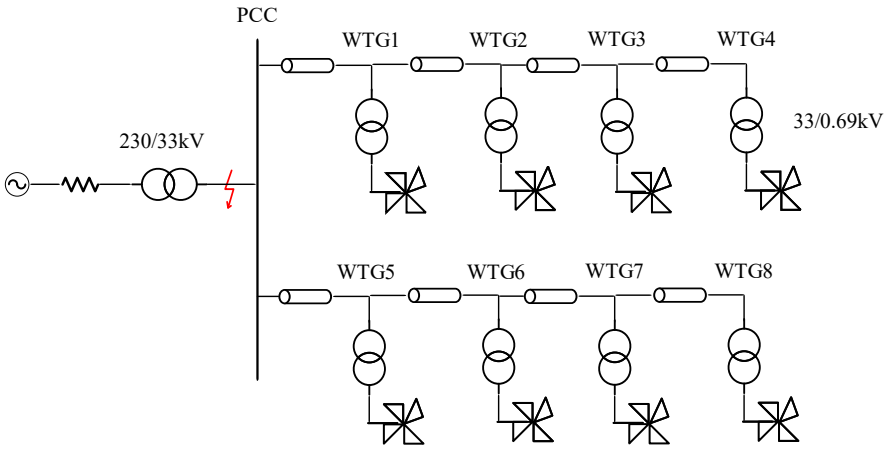


Fig. 1. Detailed model of wind farm transmission system

In this paper, the permanent magnet direct drive wind turbine is analyzed as an example. The wiring diagram of the detailed model of the wind farm is shown in **Fig. 1**. The wind farm is connected to the 33kV collecting bus PCC through 690V/33kV terminal transformer and cable, and then sent to the grid through the wind farm outlet

transformer (33kV/230kV) and overhead line. The collecting line and cable adopt Π - type equivalent circuit[8].

The basic design of a direct drive wind turbine includes a wind turbine, a synchronous generator with permanent magnets, a full-power converter and a terminal transformer. The mechanical power of wind turbine and the energy generated by wind energy can be calculated according to the following formula:

$$P = \frac{\rho}{2} \times A_r \times V_W{}^3 \times C_p(\lambda, \theta) \tag{1}$$

Where, P is the mechanical power extracted from the wind turbine, ρ is the air density in kg/(m3), A_r is the swept area of the rotor blade in m^2, V_W is the wind speed in m/sec, λ is the tip speed ratio, θ is the pitch angle, C_p is the power factor and is a function of λ and θ. C_p is one of the characteristics of wind turbines, and manufacturers usually provide a series of parameter curves related to C_p.

The electrical control system mainly comprises the control of the generator-side inverter, the grid-side inverter and the pitch angle, and must be able to operate at low voltage[9]-[10]. Compared with mechanical control, the dynamic response speed of electrical control is faster and the time constant is smaller.

3 Equivalent modeling of wind farm

3.1 Equivalent modeling of wind farm collector line

To create a simplified model suitable for system-level analysis, it is usually necessary to convert a complex data collection network into one or more equivalent networks. Traditional equivalence methods (such as equal voltage loss method and equal power loss method) focus on the equivalence of positive sequence impedance to ensure the consistency of electrical characteristics of the system under normal three-phase balance conditions, but generally ignore the accurate equivalence of negative sequence impedance, especially zero sequence impedance. This simplification will lead to significant errors in the analysis of key scenarios involving zero sequences, such as asymmetric operation or ground faults.

To fill this research gap, this article focuses on an innovative modeling method for the zero-series equivalent impedance of power collection lines based on positive-sequence impedance equivalence using the equal voltage drop method. A specific equivalent diagram[11] is shown in **Fig. 2**. In the diagram, I_i denotes the output current of the i^{th} fan, Z_i represents the collector circuit impedance of fan i. Equivalence simplification commences from the terminal fan and progresses step-by-step towards the PCC point.

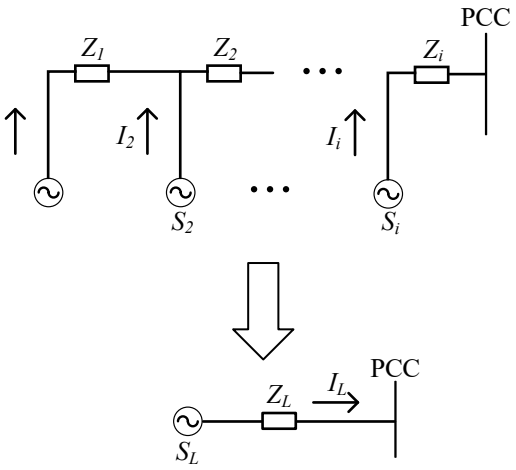


Fig. 2. Schematic diagram of equivalent model

The refined equivalent model mainly includes three core parts:

A. Positive sequence equivalent impedance model

Calculate the voltage difference between each wind turbine terminal in the wind farm and the grid connection access point PCC of the offshore wind power flexible direct transmission system, as shown in the following formula:

$$\Delta U_k = \frac{\sum_{i=1}^{k}(Z_{ip} * \sum_{j=k}^{K} P_{jp})}{\sqrt{3} * U_{PCC}} \tag{2}$$

Where, ΔU_k represents the voltage difference between the k^{th} terminal point of a wind turbine in a wind farm and the grid connection point of a flexible system for direct transmission of energy from an offshore wind farm, Z_{ip} is the positive sequence impedance value of the corresponding line at the end of the i^{th} wind turbine in the wind farm, K is the total number of wind turbines in the wind farm, P_{jp} is the positive sequence active power of the j^{th} wind turbine in the wind farm, U_{PCC} represents the voltage value of the grid connected access point of the offshore wind power flexible direct transmission system.

The weight coefficient is determined based on the ratio of the output power of each unit to the total power of the paralleling point, and the total voltage loss of the wind farm before equivalent can be obtained by weighted summation of the voltage loss of each section of the collector line, as shown in the following formula:

$$\Delta U_{origin} = \sum_{k=1}^{K} \frac{P_{kp}}{\sum_{k=1}^{K} P_{kp}} \Delta U_k \tag{3}$$

Where, ΔU_{origin} is the total voltage loss of the wind farm, and P_{kp} is the active power of the positive sequence of the k^{th} wind turbine of the wind farm.

Based on the principle of equal voltage loss before and after equivalence[12]-[13], the expression for the equivalent impedance of the positive sequence of the collector line is as follows:

$$Z_{eq(\mathrm{p})} = \frac{\sqrt{3} * U_{pcc}}{\sum_{k=1}^{K} P_k} \Delta U_{origin} \tag{4}$$

Where, $Z_{eq(\mathrm{p})}$ is the positive sequence equivalent impedance of the power collection line of the wind farm.

In the above equivalent calculation, only resistive and inductive parameters are considered, and capacitive parameters are calculated separately. Assuming that the voltage distribution in a given wind farm is uniform, the capacitive parameter is the sum of all the capacitive resistances of the lines as concentrated capacitance[14].

B. Negative sequence equivalent impedance model

Since the collector line is a static component, its positive and negative sequence impedance parameters are the same. However, in case of fault, due to the negative sequence current suppression strategy of the grid side converter, the negative sequence current at the AC side is zero, so the negative sequence equivalent impedance of the collector line is infinite.

C. Zero sequence equivalent impedance model

Calculate the zero-sequence component of the voltage phasor and current phasor at each wind turbine terminal of the wind farm and calculate the active power of the zero-sequence component based on the zero-sequence component of the voltage phasor and current phasor according to the following formula:

$$P_{(k)0} = 3(U_{(k)0,\mathrm{Re}} I_{(k)0,\mathrm{Re}} + U_{(k)0,\mathrm{Im}} I_{(k)0,\mathrm{Im}}) \tag{5}$$

Where, $P_{(k)0}$ represents the active power of the zero sequence component of the fundamental wave at the turbine end of the k^{th} wind turbine generator, $U_{(k)0}$.Re is the impedance real part of the fundamental zero sequence component of the voltage phasor at the turbine end of the k^{th} wind turbine generator, $I_{(k)0.\mathrm{Re}}$ represents the real impedance part of the fundamental zero sequence component of the current phasor at the turbine end of the k^{th} wind turbine generator, $U_{(k)0.\mathrm{Im}}$ represents the imaginary part of the impedance of the zero sequence component of the fundamental wave of the voltage phasor at the turbine end of the k^{th} wind turbine generator, $I_{(k)0.\mathrm{Im}}$ represents the imaginary part of the impedance of the fundamental zero sequence component of the current phasor at the turbine end of the k^{th} wind turbine generator.

As shown in the following formula, the effective value of the phase voltage of the fundamental zero component of the series must be calculated from the fundamental zero component of the voltage series:

$$U_{(k)0} = \sqrt{U_{(k)0,\mathrm{Re}}^2 + U_{(k)0,\mathrm{Im}}^2} \tag{6}$$

Where, $U_{(k)0}$ represents the effective value of phase voltage of zero sequence component of fundamental wave at the end of the k^{th} wind turbine generator.

The equivalent impedance of the zero sequence of the wind turbine's busbar is calculated using the active power and the effective value of the phase voltage of the zero sequence component of the fundamental wave at the end of each wind turbine. The specific derivation process is analogous to that of equations $\Delta U_k = \frac{\sum_{i=1}^{k}(Z_{ip} * \sum_{j=k}^{K} P_{jp})}{\sqrt{3} * U_{PCC}}$ (2)- $Z_{eq(\mathrm{p})} = \frac{\sqrt{3} * U_{pcc}}{\sum_{k=1}^{K} P_k} \Delta U_{origin}$ (4), here, only the expression is provided:

$$Z_{eq0} = \frac{\sqrt{3} * U_{PCC0}}{\sum_{k=1}^{K} P_{(k)0}} \left(\sum_{n=2}^{K} \left(\frac{P_{(n)0}}{\sum_{k=1}^{K} P_{(k)0}} \Delta U_{(n)0}\right)\right) \tag{7}$$

Where, Z_{eq0} is the zero sequence equivalent impedance of the wind farm collector line, U_{PCC0} represents the fundamental zero sequence component of the voltage phasor at the grid connection access point of the offshore wind power flexible direct transmission system, $P_{(n)0}$ represents the active power of the zero sequence component of the fundamental wave at the end of the n^{th} wind turbine in the wind farm, $\Delta U_{(n)0}$ represents the voltage difference between the effective value of the phase voltage of the zero sequence component of the fundamental wave at the end of the n^{th} wind turbine in the wind farm and U_{PCC0}.

To sum up, the full sequence (positive sequence, negative sequence, zero sequence) equivalent impedance model constructed in this paper, especially the zero sequence equivalent part, breaks through the limitations of traditional methods, and lays a reliable model foundation for comprehensive and accurate stability analysis of wind farm grid connected system.

3.2 Equivalent modeling of wind farm system

Equivalent modelling of a wind farm typically involves three main components: the wind turbine, the terminal transformer and the Collector network. In this article, after simplifying full impedances of the energy collection network designed to collect wind turbines, a power-based weighted average method is used[15]. This method is suitable for wind farms composed of wind turbines with the same type and similar capacity and control parameters. In principle, an entire wind farm corresponds to a single wind turbine with the same power, and the parameters of the corresponding unit are determined by calculating the weighted average of the parameters of each wind turbine using its rated power as a weighting factor. This combined method preserves the gen-

eral external characteristics of the wind farm, but also effectively reduces the complexity of the model and the computational load.

For the equivalent treatment of wind turbine terminal transformer, the capacity expansion equivalent method is usually used, that is, all unit transformers are equivalent to one transformer after capacity expansion, and its parameters are uniformly converted to the equivalent fan side. This method mainly involves the equivalent calculation of two key parameters of transformer capacity and impedance. The specific formula is as follows:

$$\begin{cases} S_{T_eq} = \sum_{i=1}^{N} S_{T_i} \\ Z_{T_eq} = \dfrac{Z_{T_i}}{N} \end{cases} \tag{8}$$

Where, S_{T_eq} and Z_{T_eq} are the capacity and impedance of equivalent transformer respectively, S_{T_i} and Z_{T_i} are the capacity and impedance of the i^{th} typhoon generator set in the original wind farm respectively.

4 Model validation

PSCAD/EMTDC is used to build the full topology detailed model of the wind farm as shown in **Fig. 1**. Based on the above method for modelling the equivalent of the wind farm with regard to the positive, negative and zero impedance of the collection line, an equivalent model of the wind power system was obtained, as shown in **Fig. 3**, in which the three wind turbines near the PCC in the first feeder are equivalent to a 15MW wind turbine, and the four wind turbines in the second feeder are equivalent to a 20MW wind turbine.

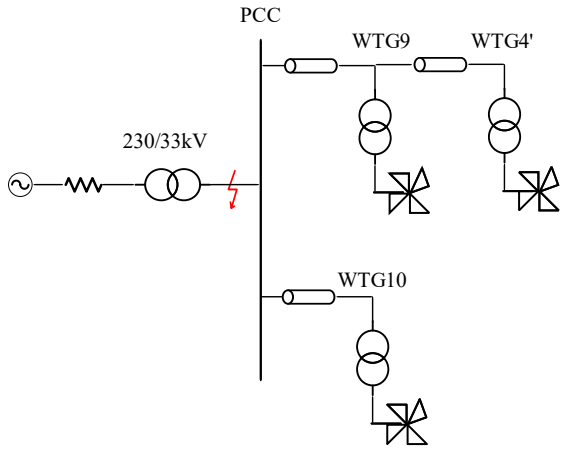


Fig. 3. Equivalent model of wind power generation system

Set faults at PCC of detailed model and equivalent model respectively, and compare the consistency of power and voltage operation characteristics at PCC of wind farm collection bus and WTG4. See **Table 1** for specific simulation parameter settings, **Table 2** and **Table 3** for parameters before and after equivalence of collection line.

Fig. 4 and **Fig. 5** respectively show the comparison of electrical quantities at PCC and WTG4 port of the wind turbine at the end of the first feeder. The results indicate that, the simulation results of both the system level PCC point and the unit terminal under steady-state and fault transient conditions are highly consistent with the detailed model, and the error is kept in a small range.

Table 1. Simulation parameter setting.

Parameter	Value
Total simulation time	5s
Simulation step size	250μs
Fault occurrence time	2s
Fault Type	Two-phase grounding fault
Fault duration	0.625s

Table 2. Parameters before equivalence of collector line.

cable	Length/ km	*R*/(ohm/m)		*X*$_L$/(ohm/m)		*X*$_C$/(Mohm*m)	
		+	0	+	0	+	0
PCC-WTG1	3.32	4.7E-6	616.6314E-6	120E-6	283.2306E-6	13.9610	13.9610
WTG1-WTG2	0.802	75.4E-6	701.5903E-6	130E-6	332.3300E-6	16.4927	16.4927
WTG2-WTG3	0.759	153E-6	861.3076E-6	140E-6	403.9151E-6	20.4045	20.4045
WTG3-WTG4	1.598	193E-6	929.0586E-6	150E-6	426.2567E-6	21.8020	21.8020
PCC-WTG5	4.116	47E-6	616.6314E-6	120E-6	283.2306E-6	13.9610	13.9610
WTG5-WTG6	0.803	75.4E-6	701.5903E-6	130E-6	332.3300E-6	16.4927	16.4927
WTG6-WTG7	0.801	153E-6	861.3076E-6	140E-6	403.9151E-6	20.4045	20.4045
WTG7-WTG8	0.801	193E-6	929.0586E-6	150E-6	426.2567E-6	21.8020	21.8020

Table 3. Parameters after equivalence of collector line.

cable	Length/km	R/(ohm/m)		X$_L$/(ohm/m)		X$_C$/(Mohm*m)	
		+	0	+	0	+	0
PCC-WTG9	1	15.42E-5	1.828E-3	3.512E-4	0.8436E-3	51.6530	51.6530
WTG9-WTG4’	1.589	193E-6	929.0586E-6	150E-6	426.2567E-6	21.8020	21.8020
PCC-WTG10	1	26.78E-5	3.074E-3	5.882E-4	1.418E-3	76.6231	76.6231

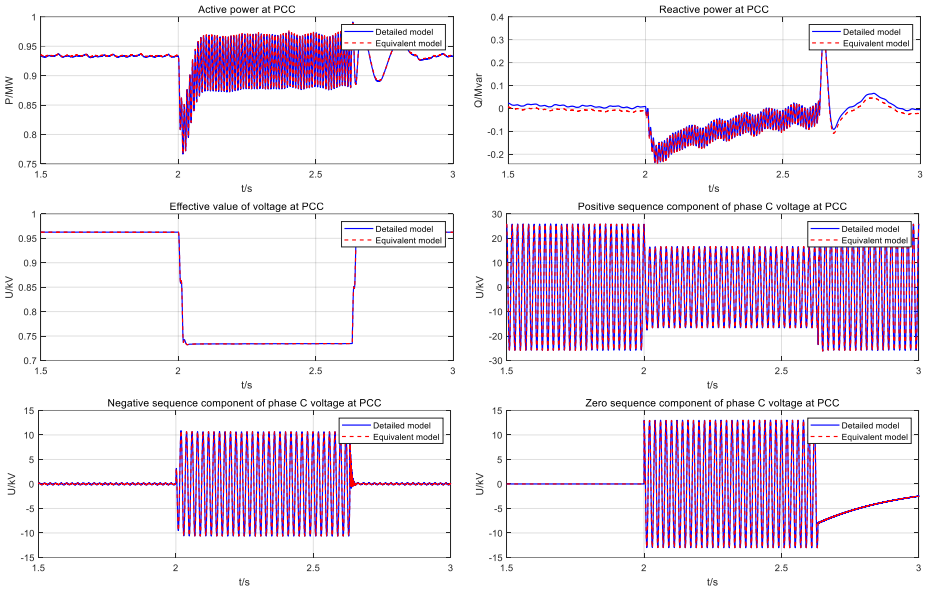


Fig. 4. Waveforms of electrical quantities at PCC

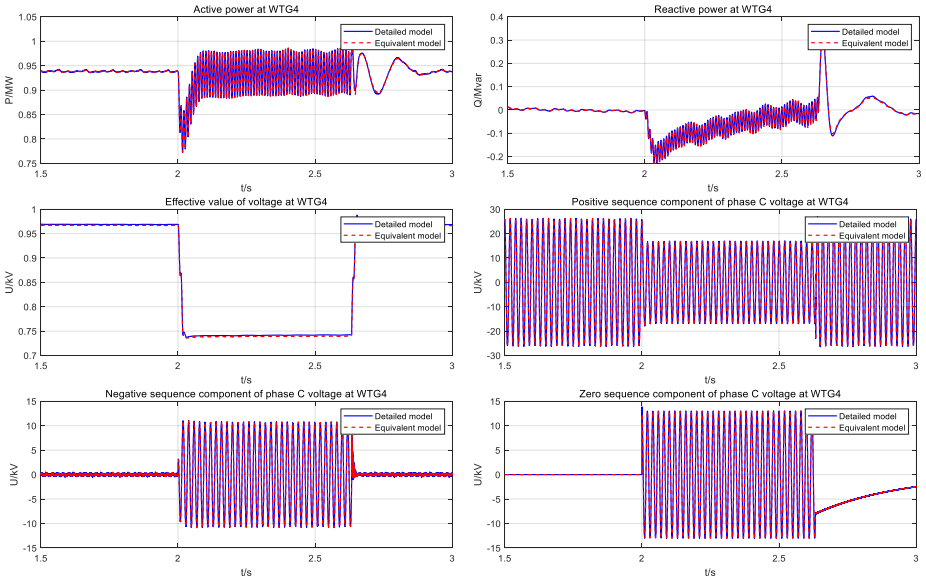


Fig. 5. Waveforms of electrical quantities at WTG4

5 Conclusion

This article discusses the accuracy of wind turbine modelling with a focus on accurate modelling of the complete impedance sequence of the collector line. The existing methods often oversimplify the collector network, which is difficult to accurately reflect the dynamic characteristics involving asymmetric operation. Therefore, this paper proposes and verifies a refined equivalent modeling method for wind farms considering the full sequence impedance of power collection lines.

The main work and conclusions of this study are as follows:

The refined full sequence equivalent model is established: firstly, the full topology detailed model of the wind farm is constructed as the verification benchmark. On this basis, the equivalent model which can accurately reflect the positive sequence, negative sequence and zero sequence impedance characteristics of the power collection line is established.

The efficiency and advantages of the model have been verified: Comparing the dynamic responses of the proposed equivalent model and detailed model under typical operating conditions, the modelling results demonstrate that the equivalent model constructed in this study can reproduce the dynamic characteristics of the original detailed system. Furthermore, the errors in key electrical quantities remain within the acceptable range for the project.

References

[1] CHAO Pupu, LI Weixing, JIN Xiaoming. Views and discussions on dynamic equivalent of DFIG wind farms[J]. Automation of Electric Power Systems,2016,40(12):194-199.

[2] LU Fei, LIU Qihui, ZHAO Yanan, et al. Equivalent modeling method for wind farm inner fault based on demagnetizing control of low voltage ride through[J]. Automation of Electric Power Systems,2016,40(10):24-30,37.

[3] Lin Hong, Chao Qin. Application of Equivalent Loss Power Method in Equivalent Calculation of Wind Farm[J]. Electrical Measurement and Instrumentation,2011,48(08):5-9.

[4] Gao Feng, Zhao Donglai, Zhou Xiaoxin, et al. Dynamic equivalence of direct drive wind turbine wind farm[J]. Grid Technology,2012,36(12):222-227.

[5] Gao Yongqiang, Mei Yong, Wang Hanyue, et al. Optimization of wind farm equivalence based on unit aggregation and line equivalence influencing factors[J]. Guangdong Electric Power,2023,36(06):11-22.

[6] Gupta A P, Mohapatra A, Singh S N. Apparent Power Loss Based Equivalent Model of Wind Farm Collector System[C] // 2018 IEEE Power & Energy Society General Meeting. IEEE, 2018.

[7] Zou J, Peng C, Xu H, et al. A Fuzzy Clustering Algorithm-Based Dynamic Equivalent Modeling Method for Wind Farm With DFIG[J]. IEEE Transactions on Energy Conversion, 2015, 30(4): 1329–1337.

[8] Xue Yicheng, Zhang Zheren, Xu Zheng. A dynamic equivalent modeling method for wind farms applicable to short-circuit fault analysis[J]. Journal of Solar Energy,2022,43(05):327-335.

[9] Yang Yangcai, Yu Jianfeng, Ouyang Jinxin, et al. Equivalent modeling method for the en-

tire process of electromechanical transient of permanent magnet direct drive wind turbines under power grid faults[J]. New Technology of Electrical Energy,2021,40(05):22-33.

[10] Zuo Jiaxin, Yang Xiu, Zhao Xiaoli, et al. Equivalent modeling method for multi machine aggregation identification of direct drive permanent magnet wind farms considering LVRT power characteristics[J]. Power System Protection and Control,2025,53(02):14-26.

[11] Wang Jian'an, Zhu Wenjun, Xu Maoning, et al. Real time digital simulation equivalent modeling research on wind farm direct drive units[J]. Electric Power Science and Engineering,2023,39(11):45-52.

[12] Chen Zhao, Xia Anjun, Wang Ningbo, et al. An Equivalent Method for Collection Lines in Wind Farms Suitable for Low Voltage Ride-Through Simulation[J]. Automation of Electric Power Systems, 2016, 40(08): 51-56.

[13] ZHU Lin, GE Jun, WU Xueguang, et al. Power system equivalence for practical engineering[J]. Electric Power Automation Equipment,2017,37(9):178-184.

[14] Sun Chaoqiang, Pan Xueping, Pan Shengyun, et al. Structural analysis and parameter identification of equivalent model for wind farm collection network[J]. Electric Power Automation Equipment,2020,40(10):85-91.

[15] Fu Zhaoyuan, Xu Zhiyuan, Wang Wanbao, et al. Application of Weighted Capacity Method in Multi Unit Equivalent Wind Farm[J]. Shandong Electric Power Technology,2014,(02):21-24.

055 规模化新能源接入的电力现货市场出清模型及仿真

罗佳谊，雷霞

（西华大学电气与电子信息学院，四川省 成都市 610039）

Clearing Model and Simulation of Electricity Spot Market for Large-scale New Energy Access LUO Jiayi, LEI Xia

(School of Electrical Engineering and Electronic Information , Xihua University, Chengdu 610039, Sichuan province, China)

ABSTRACT: Electricity is the core carrier of modern energy system, and building a clean and low-carbon energy system with new energy as the main body is an effective way for economic and ecological civilization to progress together. However, the large-scale integration of new energy will lead to weakened stability of the power system and insufficient market regulation capabilities. The traditional spot electricity market cannot quantify the impact of its randomness and volatility, thus exhibiting certain limitations. To this end, this article is based on the concept of "equal power load" and constructs a scenario for new energy without volatility and randomness. The scenario simulation comparison method is used to calculate the equilibrium cost; Then, based on its randomness and volatility, establish accuracy and correlation indices, and use the minimum cross entropy method to weight and form a quality index; Then, by combining the quality index with output allocation to balance costs, a quality price is formed and added to the quotation to participate in the market; Finally, the feasibility of the method was verified through IEEE 30 node system simulation.

KEY WORDS: balancing costs; electricity spot market; new energy quality; clear the model

摘要：电能是现代能源体系的核心载体，构建以新能源为主体的清洁低碳能源体系，是经济与生态文明共进的有效途径。但规模化新能源接入会导致电力系统稳定性减弱、市场调节能力不足，传统电力现货市场无法量化其随机性与波动性的影响，存在一定局限性。为此，本文基于“等电量—顺负荷”，构建新能源无波动性与无随机性场景，利用场景模拟比较法计算平衡成本；再根据其随机性与波动性构建准确性、相关性指数，以最小叉熵法赋权形成品质指数；后结合品质指数与出力分摊平衡成本形成品质价格，将其附加在报价中参与市场；最后通过 IEEE30 节点系统仿真验证了方法可行性。

关键词：平衡成本；电力现货市场；新能源品质；出清模型

DOI：10.13335/j.1000-3673.pst.2014.01.

0 引言

2025 年 2 月 9 日，国家发展和改革委员会发布《关于深化新能源上网电价市场化改革，促进新能源高质量发展的通知》，明确要求自 2025 年 6 月 1 日起新能源全部进入电力市场，标志着我国新能源电价全面迈入市场化阶段[1]。然而，新能源发电具有显著的随机性与波动性[2]，其规模化接入对电力系统的稳定性和市场调节能力构成双重挑战。原来的政府指导性定价，将难以形成有效价格信号引导，导致辅助服务激励不足，进而影响系统安全稳定运行[3]。因此，设计科学合理的电力现货市场交易机制，通过市场手段有效引导新能源减少其对系统的负面影响，已成为亟待解决的关键问题。

保障实时电力电量平衡是电力系统运行的基本要求。新能源出力的不确定性使其消纳严重依赖于灵活性调节资源，由此系统将产生的额外成本，即新能源平衡成本。该成本受系统负荷、电源结构、新能源渗透率、常规机组调节能力等多重因素影响，难以精确计算。文献[4]指出新能源电源价值与其引发的平衡成本应分别对待；文献[5]提出新能源随机性将增加系统备用需求，波动性将增加常规机组启停成本，但未深入研究；文献[6]将平衡成本归纳为常规机组额外运行成本与电网阻塞等新增成本，但未提出具体计算方法。

为准确计算新能源对系统运行成本的影响，学者们开展了多项研究。文献[7]通过将风电出力曲线等效为无波动的恒值曲线以剥离其波动性影响；文献[8]提出“等电量–顺负荷”方法，通过构建无风电

波动场景，对比系统总运行成本变化以测算波动成本，并初步提出风电品质分段概念；文献[9]系统阐述了该方法原理与流程，基于安全机组组合约束(SCUC)模型对比得出风电平衡成本。在此基础上，文献[10]–[12]进一步探讨了平衡成本分摊机制，例如按平衡成本对风电分段并给予火电调峰补偿[10]、从净负荷波动角度建立调峰成本计算与责任认定模型[11]、采用改进 Shapley 值法分摊风电波动成本[12]等。然而，上述研究大多未考虑新能源随机性对平衡成本的影响，且多采用事后分摊方式，未在市场出清中以价格体现新能源对系统的影响，无法通过市场激励新能源厂商改善自身品质。

在新能源参与电力市场的机制设计与出清建模方面，文献[13]构建了高比例新能源接入的市场体系并提出了配电网控制策略；文献[14]将可再生能源保障性消纳要求嵌入市场机制，设计了弃能触发的二次出清流程；文献[15]基于电量约束型机组特性差异构建了申报电量-价格曲线的出清模型；文献[16]提出了两阶段分层边际定价机制，适用于省间-省内两级市场；文献[17]优化了现货市场出清流程，建立新能源与火电共同参与的预出清与双边调峰交易机制；文献[18]运用系统动力学构建新能源消纳分析模型，提出双层市场优化框架。这些研究为新能源参与市场提供了重要借鉴，但普遍未能体现新能源品质差异，也未能通过报价机制有效反映其引发的系统平衡成本，在激励相容与公平竞争方面仍存在不足。

综上，传统电力现货市场机制难以适应规模化新能源接入的新形态，亟需建立能够量化其随机性与波动性影响的市场新模式。本文基于“等电量—顺负荷”方法，构建无波动性与无随机性新能源出力场景，采用场景对比法测算系统平衡成本；引入准确性指数与相关性指数，通过最小叉熵法确定权重构建品质指数；进而分摊平衡成本形成品质价格并附加在新能源报价中，以价格反应其对电力系统的影响。最后，基于 IEEE 30 节点系统的仿真验证所提方法的可行性与有效性，为完善规模化新能源接入的电力现货市场体系提供参考。

1 现货市场新能源平衡成本的计算

由于新能源出力具有显著的不确定性，由此系统为应对新能源发电与电力系统负荷之间的功率不平衡，维持电力系统安全稳定运行将额外调用常规能源付出额外的费用，该费用即系统的平衡成本，主要包括备用成本、启停成本和电能量成本。

由于负荷也具有不确定性，所以为计算出新能源引起的平衡成本必须剥离负荷导致的平衡成本。本文采用“等电量-顺负荷”的方法，其计算公式如(1)与(2)所示，构建两种场景，实际场景与虚拟场景。实际场景下各个新能源机组的出力遵循真实的出力情况，具有随机性和波动性，所以为了维持电力系统的稳定性，系统需要额外调度常规机组增减出力，预留更多的备用容量。虚拟场景新能源的出力曲线经过“等电量—顺负荷”变换后再参与电力现货市场，此时新能源机组出力无随机性与波动性，日前市场和实时市场新能源出力曲线相同，顺应负荷变化，系统将不再为其产生额外的成本。

$$\sum_{t=1}^{T} P_{w,t}^{1} = \sum_{t=1}^{T} P_{w,t}^{2} \tag{1}$$

$$\frac{P_{w,t}^{1} - P_{w,t-1}^{1}}{P_{w,t-1}^{1}} = \frac{P_{d,t} - P_{d,t-1}}{P_{d,t-1}} \tag{2}$$

其中 $P_{w,t}^{2}$ 为真实场景下新能源出力曲线，$P_{w,t}^{1}$ 为“等电量—顺负荷”变换后的曲线，$P_{d,t}$ 为负荷曲线。

1.1 实际场景各项成本计算

实时场景下各项成本计算采用主能量和备用联合优化方式。日前根据新能源出力曲线与负荷的预测曲线，在满足负荷需求及系统安全运行约束的前提下，同时优化常规机组启停、各机组出力及正负备用，使调度周期内的系统总运行成本最小。

(1)日前市场目标函数为：

$$\min C^{pr} = \min(C_g^{pr} + C_w^{pr} + C_g^{R} + C_g^{OC}) \tag{3}$$

其中 C^{pr} 为系统日前市场运行的总成本，包括各个常规机组日前市场的发电成本 C_g^{pr}，常规机组提供的上、下备用成本 C_g^{R}，常规机组的启停成本 C_g^{OC}，以及各个新能源机组的发电成本 C_w^{pr}。

(2)各项成本计算公式如下：

1)常规机组发电成本。

$$C_g^{pr} = \sum_{t=1}^{T} \sum_{g=1}^{N^G} u_{g,t} C_{g,t}(P_{g,t}^{pr}) \tag{4}$$

$$C_{g,t}\left(p_{g,t}^{pr}\right) = a_g \left(p_{g,t}^{pr}\right)^2 + b_g p_{g,t}^{pr} + c_g \tag{5}$$

$$u_{g,t} \in \{0,1\} \tag{6}$$

其中 T 表示一个调度周期，N^G 为常规机组集合，$u_{g,t}$ 为 g 机组在 t 时刻的启停状态，1 表示运行状态，0 表示停机状态，$p_{g,t}^{pr}$ 为 t 时刻常规机组 g 的出力，$C_{g,t}\left(p_{g,t}^{pr}\right)$ 为 t 时刻常规机组 g 的发电成本，a_g、b_g 和 c_g 为常规机组 g 的发电成本。

2)新能源发电成本。

$$C_w^{pr} = \sum_{t=1}^{T} \sum_{w=1}^{N^W} C_{w,t}\left(P_{w,t}^{pr}\right) \tag{7}$$

其中 N^W 为新能源机组的集合，$P_{w,t}^{pr}$ 为 t 时刻新能源

w 的出力，$C_{w,t}\left(P_{w,t}^{pr}\right)$ 为新能源 w 的报价函数。

3)常规机组上、下备用成本。

$$C_g^R=\sum_{t=1}^{T}\sum_{g=1}^{N^G}\left(u_{g,t}C_{g,t}^{ru}R_{g,t}^{ru}+u_{g,t}C_{g,t}^{rd}R_{g,t}^{rd}\right) \tag{8}$$

其中 $R_{g,t}^{ru}$、$R_{g,t}^{rd}$、$C_{g,t}^{ru}$ 和 $C_{g,t}^{rd}$ 分别为常规机组 g 在 t 时刻的上、下备用容量与报价。

4)常规机组的启停成本。

$$C_g^{OS}=\sum_{t=1}^{T}\sum_{g=1}^{N^G}\left(C_{g,t}^{O}+C_{g,t}^{S}\right) \tag{9}$$

其中 $C_{g,t}^{O}$、$C_{g,t}^{S}$ 分别为常规机组 g 在 t 时刻启停成本。

(3)各项约束条件如下：

1)系统功率平衡约束。

$$\sum_{g=1}^{N^G}P_{g,t}^{pr}+\sum_{w=1}^{N^W}P_{w,t}^{pr}=\sum_{d=1}^{N^D}P_{d,t}^{pr} \tag{10}$$

其中 N^D 为负荷数量，$P_{d,t}^{pr}$ 为 t 时刻第 d 个负荷功率。

2)常规机组的出力约束。

$$u_{g,t}P_g^{\min}\le P_{g,t}^{pr}\le u_{g,t}P_g^{\max} \tag{11}$$

其中 $P_g^{\min}$、$P_g^{\max}$ 为常规机组 g 的最大、最小出力。

3)新能源机组的出力约束。

$$0\le P_{w,t}^{pr}\le P_{w,t}^{f} \tag{12}$$

其中 $P_{w,t}^{f}$ 为新能源 w 在 t 时刻出力预测值。

4)常规机组爬坡约束。

$$P_{g,t-1}^{pr}-P_{g,t}^{pr}\le P_g^{D}u_{g,t-1} \tag{13}$$

$$P_{g,t}^{pr}-P_{g,t-1}^{pr}\le P_g^{U}u_{g,t} \tag{14}$$

其中 P_g^{U}、P_g^{D} 分别为常规机组 g 的上、下爬坡限值。

5)常规机组最小启停时间约束。

$$\sum_{k=t}^{t+T_g^O-1}u_{g,k}\ge T_g^O\left(u_{g,t}-u_{g,t-1}\right) \tag{15}$$

$$\sum_{k=t}^{t+T_g^S-1}(1-u_{g,k})\ge T_g^S(u_{g,t-1}-u_{g,t}) \tag{16}$$

其中 T_g^O、T_g^S 为常规机组 g 的最大、最小关停时间。

6)常规机组启停成本约束。

$$C_{g,t}^{O}\ge\max\left\{H_g(u_{g,t}-u_{g,t-1}),0\right\} \tag{17}$$

$$C_{g,t}^{S}\ge\max\left\{J_g(u_{g,t-1}-u_{g,t}),0\right\} \tag{18}$$

其中 H_g、J_g 为常规机组 g 单次启动、关停成本。

7)常规机组的备用约束。

$$u_{g,t}P_g^{\max}\ge P_{g,t}^{pr}+R_{g,t}^{ru} \tag{19}$$

$$u_{g,t}P_g^{\min}\le P_{g,t}^{pr}-R_{g,t}^{rd} \tag{20}$$

$$\sum_{g=1}^{N^G}R_{g,t}^{ru}\ge R_d\sum_{d=1}^{N^D}P_{d,t}^{pr}+R_w\sum_{w=1}^{N^W}P_{w,t}^{pr} \tag{21}$$

$$\sum_{g=1}^{N^G}R_{g,t}^{rd}\ge R_d\sum_{d=1}^{N^D}P_{d,t}^{pr}+R_w\sum_{w=1}^{N^W}P_{w,t}^{pr} \tag{22}$$

其中 R_d、R_w 分别为负荷与新能源的备用需求系数。

8)线路潮流约束。

$$-P_l^{\max}\le\sum_{g=1}^{N^G}G_{g,l}P_{g,t}^{pr}+\sum_{w=1}^{N^W}G_{w,l}P_{w,t}^{pr}-\sum_{d=1}^{N^D}G_{d,l}P_{d,t}^{pr}\le P_l^{\max} \tag{23}$$

其中 $P_l^{\max}$ 为支路 l 有功功率限值，$G_{g,l}$、$G_{w,l}$ 与 $G_{d,l}$ 分别为常规机组 g，新能源 w 与负荷 d 所在节点对支路 l 的功率转移因子。

实时市场是在日前市场确定的机组启停状态基础上，根据超短期预测进行逐时刻出清。

实时市场的目标函数为：

$$\min C^{re}=\min(C_g^{re}+C_w^{re}+C_g^{R,re} \tag{24}$$

其中 C^{re}、C_g^{re}、$C_g^{R,re}$ 和 C_w^{re} 分别为实时市场总成本、常规机组发电成本、备用成本和新能源发电成本。成本计算公式与日前市场相同。

实时市场约束条件包括系统功率平衡约束、常规机组出力约束、新能源机组出力约束、常规机组爬坡约束、常规机组备用约束和线路潮流约束，其各自计算公式与日前市场相似，将对应的日前市场的参数值替换为实时市场的参数值即可。

根据上述日前市场与实时市场模型的出清结果进行实际场景下各成本分项的计算，公式如下：

$$C_{e,T^C}^{1}=\sum_{t=1}^{T^C}\sum_{g=1}^{N^G}(\lambda_t^{e}P_{g,t}+u_{g,t}(1-u_{g,t-1})C_{g,t}^{O}+u_{g,t-1}(1-u_{g,t})C_{g,t}^{S}) \tag{25}$$

$$C_{r,T^C}^{1}=\sum_{t=1}^{T^C}\sum_{g=1}^{N^G}(\lambda_t^{ru}R_{g,t}^{ru}+\lambda_t^{rd}R_{g,t}^{rd}) \tag{26}$$

其中 C_{e,T^C}^{1}、C_{r,T^C}^{1}、λ_t^{e}、λ_t^{ru} 和 λ_t^{rd} 分别为实际场景下电量和启停成本、备用成本、电量出清价、上备用和下备用出清价

1.2 虚拟场景各项成本计算

通过公式(1)与(2)进行“等电量—顺负荷”得到变换后的新能源出力曲线。虚拟场景日前与实时市场各自目标函数、约束条件与 1.1 节中相同，只需替换新能源出力曲线，其常规机组电量和启停成本 C_{e,T^C}^{2}，备用成本 C_{r,T^C}^{2} 计算与实际场景同理。

1.3 平衡成本计算

将两种场景计算得到的常规机组的各项成本对应相减得到系统的平衡成本 C_{T^C}，计算公式如下：

$$C_{T^C}=(C_{e,T^C}^{1}-C_{e,T^C}^{2})+(C_{r,T^C}^{1}-C_{r,T^C}^{2}) \tag{27}$$

2 新能源品质指数及其品质价格计算

2.1 新能源品质量化

新能源与气象密切相关，因而具有随机性，其出力预测必然存在误差。为消除预测误差的影响，电力系统需平衡偏差并产生相应成本，故预测误差是平衡成本的影响因素。同样，新能源出力随气象变化波动性强，将加大系统峰谷差，电力系统也需

调用更多资源进行平衡，产生额外成本，因此波动性作为平衡成本的另一影响因素。

随机性用随机性指数 $E^{ac}_{w,T^C,d}$ 表示，计算如下：

$$K^{ac}_{w,T^C,Di}=\sqrt{\sum_{t=1}^{T^C}(P^{re}_t-P^{pr}_t)^2/T^C} \tag{28}$$

$$E^{ac}_{w,T^C,d}=\frac{K^{ac'}_{w,T^C,D1}+K^{ac'}_{w,T^C,D2}+K^{ac'}_{w,T^C,D3}+\cdots+K^{ac'}_{w,T^C,Dd}}{d} \tag{29}$$

其中 $K^{ac}_{w,T^C,Di}$ 为新能源 w 在 T^C 时段下第 D_i 天的均方根误差，$K^{ac'}_{w,T^C,Dd}$ 为其归一化后的结果，越小越好。

波动性用相关性指数 $E^{vd}_{w,T^C,d}$ 表示，计算如下：

$$K^{vd}_{w,T^C,Di}=\sum_{t=1}^{T^C-1}b_{w,t}b_{d,t}\Big/\Big(\sqrt{\sum_{t=1}^{T^C-1}b^2_{w,t}}\sqrt{\sum_{t=1}^{T^C-1}(b_{d,t})^2}\Big) \tag{30}$$

$$E^{vd}_{w,T^C,d}=\frac{K^{vd'}_{w,T^C,D1}+K^{vd'}_{w,T^C,D2}+K^{vd'}_{w,T^C,D3}+\cdots+K^{vd'}_{w,T^C,Dd}}{d} \tag{31}$$

其中 $K^{vd}_{w,T^C,Di}$ 为新能源 w 在 T^C 时段下第 D_i 天的相关性大小，$b_{w,t}=P^e_{w,t+1}-P^e_{w,t}$，$b_{d,t}=P_{d,t+1}-P_{d,t}$，$K^{vd'}_{w,T^C,Dd}$ 为其归一化后的结果，越小越好。

在计算出新能源的预测准确性指数和负荷相关性指数后，通过构建每个中标日无相关性场景和无预测误差场景，构建方法与虚拟场景相似，计算两种场景平衡成本，将其作为输入采用最小叉熵法计算两种指数权重形成新能源品质指数 $S_{w,T^C,d}$。

2.2 新能源品质价格计算

对新能源平衡成本进行分摊得到品质价格。考虑到平衡成本还与上网电量大小有关，因此本文在分摊之前计算出了按传统市场出清时各新能源厂商上网电量占比，将其作为权重因子，结合品质指数，形成分摊因子分摊平衡成本。具体计算公式如(32)-(35)所示。

$$W_{w,T^C,d}=\sum_{t=1}^{T^C}P_{w,t}\Big/\sum_{w=1}^{N^W}\sum_{t=1}^{T^C}P_{w,t} \tag{32}$$

$$R_{w,T^C,d}=W_{w,T^C,d}S_{w,T^C,d} \tag{33}$$

$$\begin{cases}C_{w,T^C}=R_{w,T^C,d}\Big/\sum_{w=1}^{N^W}R_{w,T^C,d},R_{w,T^C,d}\ge 0\\ C_{w,T^C}=(1/R_{w,T^C,d})\Big/(\sum_{w=1}^{N^W}1/R_{w,T^C,d}),R_{w,T^C,d}<0\end{cases} \tag{34}$$

$$\lambda_{w,t}=C_{w,T^C}\Big/\sum_{t=1}^{T^C}P_{w,t} \tag{35}$$

其中 $W_{w,T^C,d}$、$R_{w,T^C,d}$、C_{w,T^C} 和 $\lambda_{w,t}$ 分别为新能源 w 在 T^C 时段下的权重因子、分摊系数、分摊到的平衡成本和品质价格。

3 新能源参与的电力现货市场模式

为使在现货市场中反映新能源接入对电力系统的影响，本文将新能源的品质价格附加在其报价之中，作为最终参与电力现货市场的报价，进行市场竞争与出清。由于附加品质价格后的报价并不是新能源提供的电力价值，所以在电费结算的环节，新能源机组在日前与实时交易中的最终结算价格需根据市场出清电价进行二次调整，即扣除对应的品质价格，以此来确保各市场主体的收益合理。

4 算例分析

如图 1 所示，采用改进的 IEEE30 节点系统进行仿真验证。系统内共包含 8 台常规机组，两台新能源机组，其中新能源占比为 36%，且两台新能源机组一天总发电量相近。由于系统在负荷各时段下的裕度不同，因此本文将一天分为峰、平、谷三个时段进行计算分析，其中，峰时段为 08:00-11:00 与 17:00-23:00，平时段为 12:00-16:00，谷时段为 24:00-7:00。

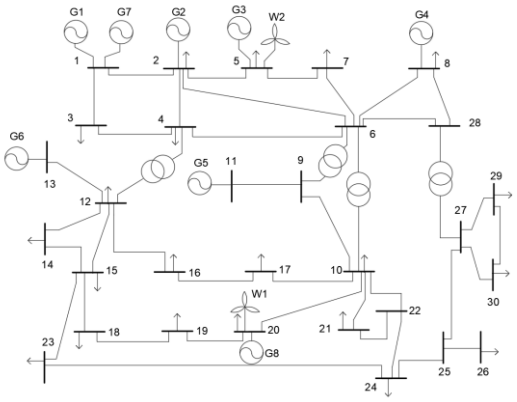


图 1　改进的 IEEE30 节点拓扑图

Fig 1　Improved IEEE30 node topology

通过历史数据按照本文所提方法计算可得到新能源 W1 与 W2 的品质指数，如表 1 所示。其中 W2 在各时段的品质明显优于 W1。

表 1 新能源品质指数

Tab 1　New energy quality index

新能源厂商	峰时段	平时段	谷时段
W1	0.4933	0.7207	0.8568
W2	0.2702	0.1386	0.1966

结合新能源的上网电量，分摊其平衡成本，形成品质价格。将品质价格附加在其原始报价中，形成其最终报价，如表 2 所示。

表 2 新能源最终报价

Tab 2　Final quotation for new energy

新能源厂商	附加品质价格后的报价			各时段未附加品质价格时的报价（元/（MW·h））
	峰时段（元/MW）	平时段（元/MW）	谷时段（元/MW）	
W1	291.86	384.63	141.07	140
W2	233.18	195.11	75.89	150

可以明显看出，附加品质价格后使得原本报价更高的 W2 反而获得了价格优势，最后两者中标电量如图 2 所示，W2 的总中标电量明显更多。

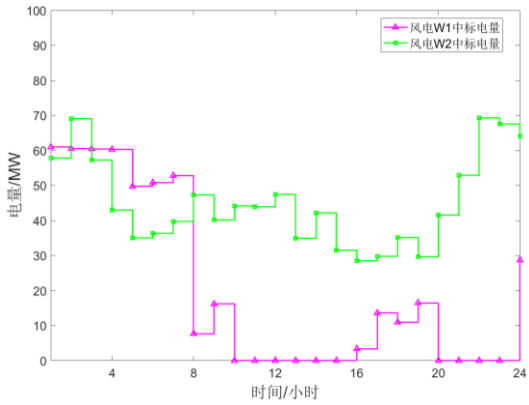


图 2　新能源中标电量

Fig 2　New energy winning bid quantity

结合新能源所在节点的出清电价，计算出其最终收益。由于结算电价需剥离新能源的品质价格，所以 W2 获得更多中标电量的同时结算价格也相对更高，其最终收益如表 3 所示，明显多于 W1。

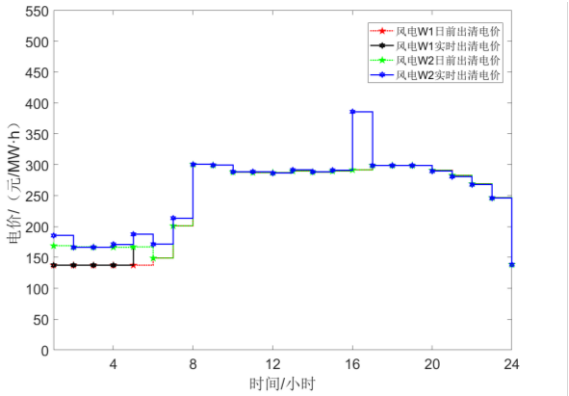


图 2　新能源出清电价

Fig 2　New energy clearing electricity price

表 3 新能源机组结算收益表

Tab 5　Settlement income of new energy units

新能源厂商	总收益（元）
W1	79387
W2	258289

5　结论

本文通过计算新能源的平衡成本，并量化其品质指数形成品质价格，并附加在其报价中，使得新能源中标容量不再单纯依靠厂商报价，品质更优的新能源即便初始报价更高也能获得较高收益。新能源厂商为获得更高收益必须进行技术升级或配置储能等方式，降低新能源的不确定性与波动性，以提升品质，减少其对电网安全的影响。

同时，品质价格的引入缩小了新能源与常规火电机组的价差，减少了零电价、负电价现象。这保障了火电收益，有助于新能源的消纳。

参考文献

[1] 廖睿灵.深化新能源上网电价市场化改革[N].人民日报海外版，2025-02-11(003).

[2] 张浩楠，崔丽敏. 新型电力系统的气候风险适应性分析及展望[J]. 电力建设，2025，46(03)：16-33.

[3] 李凌春子. 考虑低碳减排政策的电力市场定价策略研究[D]. 华中科技大学，2023.

[4] MACGILL I F. Impacts and best practices of large-scale wind power integration into electricity markets—some Australian perspectives[C] // 2012 IEEE Power and Energy Society General Meeting，July 22-26，2012，San Diego，USA：1-6.

[5] DU C，WANG X F，WANG X L， et al. Comprehensive value assessment of wind power by layer[J]. IEEE Transactions on Power Systems，2016，31(2)：1238-1247.

[6] HIRTH L，UECKERDT F，EDENHOFER O. Integration costs revisited-an economic framework for wind and solar variability[J]. Renewable Energy，2015，74：925-939.

[7] MILLIGAN M，ELA E，HODGE B，et al. Cost-causation and integration cost analysis for variable generation [R]. Golden，Colorado：National Renewable Energy Laboratory，2011.

[8] 李璐，郑亚先，陈长升，等. 风电的波动成本计算及应用研究[J]. 中国电机工程学报，2016，36(19)：5155-5163.

[9] 耿建，程海花，张凯锋，等. 风电调度接纳成本的等电量顺负荷计算方法及分析[J]. 电力系统自动化，2017，41(20)：32-37+132.

[10] 吴迪，程海花，赵晋泉，等. 基于平衡成本的风电分段及火电调峰补偿方法[J]. 电力系统自动化，2019，43(03)：116-122.

[11] 叶伦，姚建刚，杨胜杰，等. 含高比例可再生能源电力系统的调峰成本量化与分摊模型[J]. 电力系统自动化，2022，46(15)：20-28.

[12] 郑晨昕，江岳文. 基于改进 Shapley 值的风电波动成本分摊策略[J]. 电网技术，2021，45(11)：4387-4394.

[13] Wang H，Huang Y，Luo J，et al. Study on Power Market System Architecture and Clearance Pricing Adapted to Large Scale Access of New Energy Resources[J]. Applied Mathematics and Nonlinear Sciences，2024，9(1)：

[14] 陈启鑫，刘学，房曦晨，等. 考虑可再生能源保障性消纳的电力市场出清机制[J]. 电力系统自动化，2021，45(06)：26-33.

[15] 孟繁林，钟海旺，夏清. 基于非凸报价的高比例新能源现货市场机制[J]. 电网技术，2023，47(01)：120-128.

[16] 尚静怡，姜欣，肖东亮，等. 基于边际成本比较型竞价模式的电力现货市场机制设计[J]. 电力系统自动化，2024，48(09)：67-74.

[17] 赵书强，宋金历，王傲儿，等.考虑新能源-火电双边调峰交易分时竞价博弈的电力现货市场运行优化[J]. 太阳能学报，2024，45(10)：153-161.

[18] Xu X，Guan L，Wang Z，et al. A double-layer forecasting model for PV power forecasting based on GRU-Informer-SVR and Blending ensemble learning framework[J]. Applied Soft Computing，2025，172112768-112768.



罗佳谊

收稿日期：。

作者简介：

罗佳谊(2002)，男，硕士研究生，研究方向为电力市场，E-mail：2914354523@qq.com；

雷霞(1973)，女，通信作者，教授，工学博士，硕士生导师，研究方向为电网弹性、电力市场、电网规划和调度，E-mail：Snow_lei@mail.xhu.edu.cn；

056 Optimization Method for Energy Storage Operation of New Energy Station Accessories Considering Multiple Benefits

Yanhao Wang[1], Bing Sun[2], Nana Li[3], Jing Hu[4], Zihan Meng[5] and Lun Ye[6]

[1] State Key Laboratory of Smart Power Distribution Equipment and System, Tianjin University [2] State Grid Energy Research Institute Co., Ltd., Beijing 102209, China
[3] State Grid Hunan Electric Power Company Limited Economic & Technical Research Institute, Changsha 410004, China, yelun92@126.com

Abstract. This paper proposes a multi-benefit-oriented optimization method for energy storage systems co-located with new energy stations, addressing challenges in renewable energy integration such as intermittency and volatility. By constructing a comprehensive optimization framework, the study aims to enhance economic returns, operational reliability, and system flexibility. Key contributions include: (1) a model prioritizing renewable energy consumption benefits to maximize grid-connection revenue and reduce curtailment; (2) an operational profit-maximization model focusing on minimizing penalties from generation forecast deviations; and (3) an analytical framework evaluating energy storage's value in providing frequency regulation and ramping services. Through case studies in a regional power system with high wind and solar penetration, the method demonstrates significant cost savings and improved grid stability. Results show that incorporating ramping services reduces thermal power generation by 14.34 GWh and saves 7 million CNY in costs, highlighting the critical role of energy storage in ancillary services.
The study validates the economic and technical feasibility of coordinated energy storage operation, providing insights for policy-making and sustainable business models.

Keywords: Energy Storage Optimization, Renewable Energy Integration, Multiple Benefits, Frequency Regulation, Ramping Capability, Ancillary Services

1 Introduction

Against the backdrop of the accelerated global transition of energy structures towards cleanliness and low carbon, China is actively advancing the "carbon peaking and carbon neutrality" strategy, with the installed capacity of renewable energy such as wind power and photovoltaic power continuing to grow rapidly. However, the grid connection of high-proportion renewable energy, due to its inherent intermittency and volatility[1], poses severe challenges to the real-time balance, safe and stable operation of the power system. The problem of insufficient system flexibility regulation capacity has become increasingly prominent, and it has become a key bottleneck restricting

the efficient consumption of new energy and the improvement of power grid carrying capacity.

Energy storage systems, especially the new-type electrochemical energy storage represented by lithium-ion batteries, are gradually becoming a core means to enhance the grid-connection performance of new energy stations and system flexibility, relying on their characteristics of rapid response and flexible regulation[2]. The collocated energy storage systems can not only effectively smooth out the output fluctuations of new energy[3] and reduce power curtailment caused by prediction deviations[4], but also provide a variety of key technical functions, including improving short-circuit current levels, supporting voltage stability[5], providing virtual inertia[6], participating in black starts[7], and suppressing wide-frequency oscillations[8]. These functions significantly enhance the support capacity of new energy stations for the power grid, transforming them from simple "power generation units" into "friendly smart units" that stabilize the power grid.

Despite the rapid development, the current energy storage collocation with new energy stations still faces many challenges. On the one hand, there is a significant imbalance in regional development. The collocation ratio is highly dependent on local policies and resource endowments, and the progress in some regions is still relatively lagging. On the other hand, the application models and value realization of energy storage are not sufficient. The current collocation mostly focuses on meeting local single demands (such as meeting the mandatory collocation ratio), and lacks collaborative planning and refined operation for its multiple benefits[9]. In addition, different energy storage technology routes have significant differences[10] in applicable scenarios and economy, and the levelized cost of electricity throughout the whole life cycle is still relatively high. How to scientifically select technical routes and design sustainable business models has become an urgent problem to be solved.

This paper aims to study the operation optimization method of energy storage collocated with new energy stations considering multiple benefits, so as to achieve the multiple improvement of economy, reliability and flexibility. The main contributions of this paper are as follows: (1) Construct a target model centered on improving the consumption benefit of new energy, aiming to maximize grid-connection revenue and reduce power curtailment; (2) Establish an optimization model targeting the maximization of station operation profit, focusing on reducing the assessment cost caused by power generation prediction deviations; (3) Build an analysis model for system frequency regulation and ramping capability, and quantitatively evaluate the value and cost of energy storage in participating in system auxiliary services.

2 Optimization Model for New Energy Consumption Benefits

To address the need for increasing the grid-connected electricity volume and grid-connected revenue of new energy sources, an energy storage utility analysis model is established. With maximizing the new energy consumption rate and reducing curtailment of wind and solar power as its core objectives, this model focuses on optimizing the configuration of energy storage capacity and consumption efficiency.

The objective function is designed to maximize the new energy consumption benefits:

$$\max \sum_{t=1}^{T}\left[\lambda_t \cdot P_t^{grid} + \mu \cdot (P_t^{RE,pred} - P_t^{eurtail}) - C_t^{storage}\right] \tag{1}$$

Where λ_t and P_t^{grid} denote the grid-connected electricity price at time t and total power fed into the power grid by the new energy station at time t, respectively; μ is the benefit coefficient for reducing curtailment of electricity; $P_t^{RE,pred}$ and $P_t^{eurtail}$ represent the new energy predicted power at time t and the curtailed wind/solar power at time t, respectively; $C_t^{storage}$ denote the operating cost of the energy storage system at time t.

The core constraint conditions are as follows:

$$P_t^{grid} = P_t^{RE,actual} - P_t^{curtail} + P_t^{dch} - P_t^{ch} \tag{2}$$

$$0 \le P_t^{RE,actual} \le P_t^{RE,pred} \tag{3}$$

$$0 \le P_t^{curtail} \le P_t^{RE,actual} \tag{4}$$

$$0 \le P_t^{ch} \le \delta_{ch} \cdot E_G^{BESS} / \Delta t \tag{5}$$

$$0 \le P_t^{dch} \le \delta_{dch} \cdot E_G^{BESS} / \Delta t \tag{6}$$

$$SOC_{\min} \le SOC_t \le SOC_{\max} \tag{7}$$

$$SOC_{t+1} = SOC_t + \Delta t \cdot \left(\eta_{ch} \cdot P_t^{ch} - \frac{P_t^{dch}}{\eta_{dch}}\right) / E_G^{BESS} \tag{8}$$

$$P_t^{grid} \le P_{\max}^{grid} \tag{9}$$

Where $P_t^{RE,actual}$ denotes the actual power generation of new energy station at time t; P_t^{dch} and P_t^{ch} represent the discharging and charging power of the energy storage system at time t, respectively; E_G^{BESS} denote the rated capacity of the energy storage system; δ_{ch} and δ_{dch} represent the maximum charging and discharging rates of energy storage, respectively; SOC_t is the state of charge of the energy storage system at time t; $SOC_{\min}$ and $SOC_{\max}$ represent the minimum and maximum state of charge allowed for the energy storage system, respectively; η_{ch} and η_{dch} represent the charging and discharging efficiency of energy storage, respectively; $P_{\max}^{grid}$ is the the maximum allowable transmission power at the grid connection point of the power station.

3 Optimization Model for Station Operation Profit

To address the needs of mitigating forecasting errors and optimizing the day-ahead power generation curve declaration of new energy stations, an operational optimization model is established with the goal of maximizing station profits. This model guides new energy stations in optimizing the execution of intraday power generation curves and enhances operational economy.

The objective function is as follows:

$$\max C_t^R(P_t^{ch},P_t^{dch})=(\lambda_t P_t^{grid}-c_{t,s}^{m,(+)}\Delta P_t^{(+)}-c_{t,s}^{m,(-)}\Delta P_t^{(-)})\Delta t-C_t^{storage} \tag{10}$$

$$C_t^{storage}=\left|SOC_{t+1}-SOC_t\right|c_{BESS}E_G^{BESS} \tag{11}$$

Where C_t^R is the total profit gained by the power station at time *t*; $c_{t,s}^{m,(+)}$ and $c_{t,\mathrm{s}}^{\mathrm{m},(-)}$ are the unit penalty price for positive and negative power deviations at time *t*, respectively; $\Delta P_t^{(+)}$ and $\Delta P_t^{(-)}$ represent the positive and negative power deviation amounts at time *t*, respectively; and c_{BESS} is the unit cycle cost coefficient of the battery energy storage system.

The physical and safety constraints on the operation of energy storage systems and power stations are as follows:

$$\begin{cases} 0\le P_t^{ch}\le \delta_{ch}E_G^{BESS}/\Delta t & \forall t \\ 0\le P_t^{dch}\le \delta_{dch}E_G^{BESS}/\Delta t & \forall t \\ SOC_{\min}\le SOC_t\le SOC_{max} & \forall t \\ 0\le P_t^{grid}\le P_{\max}^{grid} & \forall t \end{cases} \tag{12}$$

4 System Frequency Regulation and Ramping Capability Analysis Model

To evaluate the role of energy storage in maintaining system frequency stability, a system frequency regulation capability analysis model is established. With the goals of minimizing frequency deviation and frequency regulation costs, this model integrates the system's dynamic frequency response, AGC (Automatic Generation Control) mechanism, and the rapid frequency regulation characteristics of energy storage.

The objective function is as follows:

$$\min\sum_{t=1}^{T}\left[w_1\cdot(\Delta f_t)^2+w_2\cdot C_t^{ACC}+w_3\cdot C_t^{BESS,freq}\right] \tag{13}$$

Where w_1, w_2, w_3 denote the weight coefficients of frequency stability, traditional frequency regulation cost, and energy storage frequency regulation cost, respectively; Δf_t is the system frequency deviation at time *t*; C_t^{ACC} is the cost of AGC frequency regulation services provided by traditional generators at time *t*; $C_t^{BESS,freq}$ is the cost of frequency regulation services provided by the battery energy storage system at time *t*.

The frequency regulation demand analysis is as follows:

$$\begin{cases} \Delta P_t^{AGC}=K_I\int_0^t\Delta f(\tau)d\tau+K_P\cdot\Delta f_t \\ \sigma_{AGC}^2=\sigma_{load}^2+\sigma_{RE}^2+2\rho_{load,RE}\sigma_{load}\sigma_{RE} \\ R_t^{AGC,up}=3\sigma_{AGC}+\Delta P_t^{schedule} \\ R_t^{AGC,down}=3\sigma_{AGC}-\Delta P_t^{schedule} \end{cases} \tag{14}$$

Where ΔP_t^{AGC} is the total regulation power required by the AGC system at time t; K_I and K_P are the integral and proportional control gains, respectively; σ_{AGC}^2, σ_{load}^2, σ_{RE}^2 are the variance of AGC regulation power demand, load fluctuation power, and renewable energy output fluctuation, respectively; $\rho_{load,RE}$ is the correlation coefficient between load fluctuation and renewable energy output fluctuation; $R_t^{AGC,up}$ and $R_t^{AGC,down}$ are the upward and downward frequency regulation reserve capacities at time t, respectively; $\Delta P_t^{schedule}$ is the deviation between scheduled power generation and scheduled load at time t.

The system frequency dynamic model is as follows:

$$\begin{cases} 2H\dfrac{d\Delta f}{dt} = \Delta P_{mech} - \Delta P_{load} - D\cdot\Delta f \\ \Delta f_{t+1} = \Delta f_t + \dfrac{\Delta t}{2H}\left[\Delta P_t^{mech} - \Delta P_t^{loal} - D\cdot\Delta f_t\right] \end{cases} \tag{15}$$

Where H is the equivalent inertia time constant of the system; ΔP_{mech} and ΔP_{load} are the variation of generator mechanical power and load power, respectively; D is the equivalent damping coefficient of the system.

The energy storage frequency regulation constraints are as follows:

$$|P_t^{BESS,freq}| \le P_{rated}^{BESS}\cdot\alpha_{freq} \tag{16}$$

$$SOC_{\min} \le SOC_t \le SOC_{\max} \tag{17}$$

$$\left|\frac{dP^{BESS}}{dt}\right| \le r_{BESS}^{ramp} \tag{18}$$

Where $P_t^{BESS,freq}$ is the power command value of the energy storage system for frequency regulation at time t; P_{rated}^{BESS} is the rated power of the energy storage system; α_{freq} is the frequency regulation power coefficient; P^{BESS} is the energy storage system output power; r_{BESS}^{ramp} is the maximum allowable power ramping rate of the energy storage system.

To address the issue of increased system ramping demand caused by the integration of new energy sources, a ramping capability analysis model for energy storage systems is established. With the goal of minimizing the system's ramping deficit cost, this model quantifies the ramping response capability of energy storage systems and evaluates the contribution of energy storage to enhancing system flexibility.

The objective function is as follows:

$$\min\sum_{t=1}^{T}\left[C_t^{ramp,shartage}\cdot P_t^{ramp,shartage} + C_t^{BESS,ramp}\cdot(P_t^{BESS,up} + P_t^{BESS,down})\right] \tag{19}$$

Where $C_t^{ramp,shartage}$ is the penalty cost for unit ramping power shortage at time t; $P_t^{ramp,shartage}$ is the ramping power shortage at time t; $C_t^{BESS,ramp}$ is the cost coefficient for unit ramping services provided by the energy storage system at time t; $P_t^{BESS,up}$

and $P_t^{BESS,down}$ are the upward and downward ramping power provided by the energy storage system at time *t*, respectively.

The ramping constraint conditions are as follows:

$$P_t^{BESS,up} + P_t^{BESS,down} \le R_t^{BESS,available} \tag{20}$$

$$SOC_t + \frac{P_t^{BESS,up} \cdot \eta_{ch} \cdot \Delta t}{E_G^{BESS}} \le SOC_{\max} \tag{21}$$

$$SOC_t - \frac{P_t^{BESS,down} \cdot \Delta t}{\eta_{dch} \cdot E_G^{BESS}} \ge SOC_{\min} \tag{22}$$

Where $R_t^{BESS,available}$ is the maximum total ramping capacity available in the energy storage system at time *t*.

The evaluation of flexible ramping potential on the storage side is as follows:

$$RU_{sto}(t) = \min\left(\frac{P_{dis}^{\max} - P_{dis}(t)}{\Delta t}, \frac{SOC(t) - SOC_{\max}}{\eta_{dis} \cdot \Delta t} \cdot E_G^{BESS} \right) \tag{23}$$

$$RD_{sto}(t) = \min\left(\frac{P_{ch}^{\max} - P_{ch}(t)}{\Delta t}, \frac{SOC_{\max} - SOC(t)}{\Delta t} \cdot \frac{1}{\eta_{ch}} \cdot E_G^{BESS} \right) \tag{24}$$

Where $RU_{sto}(t)$ and $RD_{sto}(t)$ are the upward and downward ramping potential of the energy storage system at time *t*, respectively; $P_{dis}^{\max}$ and $P_{ch}^{\max}$ are the maximum discharging and charging power of the energy storage system, respectively; $P_{dis}(t)$ and $P_{ch}(t)$ are the actual discharging and charging power of the energy storage system, respectively.

5 Case Study

The power source structure of a certain region is as follows: the installed capacity of wind power is 12.18 million kW, that of photovoltaic power is 13.56 million kW, that of thermal power is 26.15 million kW, and that of other power sources is approximately 200,000 kW. In terms of load characteristics, the maximum load in this region is 11 million kW, the minimum load is about 7.5 million kW, and the daily load rate is roughly 0.82. Under the condition that all parameters remain unchanged and ramping services are not considered, the day-ahead economic dispatch for the Shanbei region is simplified from a detailed 96-interval operation simulation to a rough 24-interval one. The resulting energy storage device dispatch results are shown in Fig. 1. Flexible resources support the system's peak shaving, and there is also a small amount of their deployment.

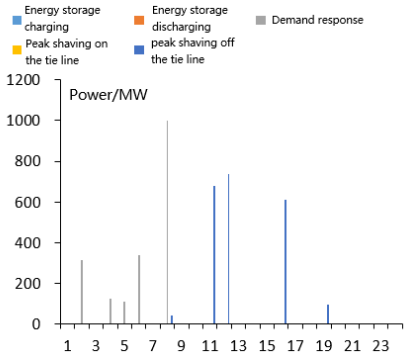


Fig. 1. Three types of flexible resources supporting system peak shaving

It is not difficult to find that, as the unit start-stop schedule does not take ramping requirements into account, the system still has a large-capacity ramping demand even after making full use of the ramping capacity of thermal power units. The output of the system's thermal power units is 119.91 million kWh, which is an increase of 14.34 million kWh compared with the optimized result of 105.57 million kWh when ramping services are considered, leading to a 7 million yuan increase in thermal power costs. The total power generation cost of the system is 30.59 million yuan, among which the additional cost for ramping services is 2.1 million yuan.

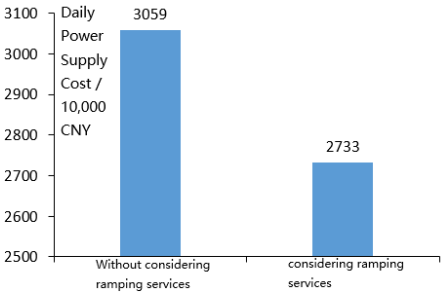


Fig. 2. Comparison of power supply costs

With the economy of system power supply as the optimization objective, and considering the fuel costs of thermal power units and the deployment costs of various ramping resources, the day-ahead dispatch plan for thermal power units and various ramping resources is obtained. Under this dispatch result, the daily dispatch cost of the Shanbei region is 27.33 million yuan in total, among which the deployment cost of ramping resources is 8.93 million yuan. This includes 530,000 yuan for energy storage devices, 910,000 yuan for demand response, and 7.49 million yuan for inter-provincial tie lines.

8

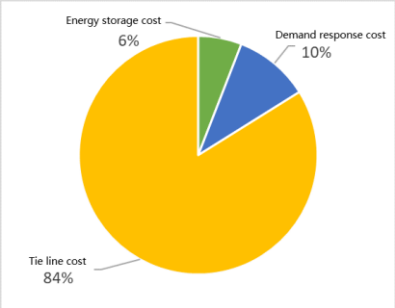


Fig. 3. Composition of ramping service deployment costs

6 Conclusion

This study presents a comprehensive optimization method for energy storage systems co-located with renewable energy stations, emphasizing multiple benefits including economic efficiency, operational reliability, and enhanced grid flexibility. By integrating models for renewable energy consumption, operational profit maximization, and ancillary service provision such as frequency regulation and ramping support, the approach effectively addresses challenges related to intermittency and volatility in high-penetration renewable systems.

Case studies in a regional power system demonstrate significant cost savings and improved stability. The results validate the economic and technical feasibility of multi-benefit-oriented energy storage operation, providing a practical foundation for policy formulation and sustainable business models in support of carbon neutrality goals.

Acknowledgement: This paper is supported by the State Grid scientific and technological projects of China (Research on new energy storage operation optimization and monitoring analysis technology under market environment, 5419-202357783A-3-8-KJ).

References

1. Zhang Yuhua, Li Qingsong, Wang Cong, et al: Grid-connected Method of Regional Wind-solar Low-frequency Correlation Complementation and High-frequency Hybrid Energy Storage Stabilization [J]. Proceedings of the Chinese Society of Electrical Engineering 43(4), 1492–1503 (2023).
2. Chen, Tianmei, Jin, Yi, Lv, Hanyu, et al.: Applications of Lithium-Ion Batteries in Grid-Scale Energy Storage Systems [J]. Transactions of Tianjin University 26(3), 208-217 (2020).
3. Zhang Ping, Hu Long, Di Hongliang, et al: Adaptive frequency regulation control and low-frequency pump-shedding strategy for pumped-storage in high-proportion new energy power systems [J]. Power System Protection and Control 53(2), 1-13 (2025).

4. Wu Yin, Dou Fei, Cheng Jinmin, et al: Optimal Operation Strategy of Energy Storage Systems for Suppressing Wind Power Fluctuations [J]. Power System and Clean Energy 41(5), 110-115 (2025).
5. Zhu Guannan, Chen Min, Wang Pengcheng, et al: Stability Enhancement Control Strategy for Grid-Forming Transformerless Energy Storage System under Low Grid Impedance Conditions [J]. Transactions of China Electrotechnical Society 40(9), 2697-2711 (2025).
6. Shi Rongliang, Zhang Lieping, Wang Wencheng, et al: Research on Virtual Inertia Control Strategy for Energy Storage Converters Based on a Frequency Derivative Scheme [J]. Proceedings of the Chinese Society of Electrical Engineering 41(6), 2088-2100 (2021).
7. Zhang Yingmin, Wu Jinyi, Jiang Qin, et al: Receiving-end Power Grid Black Start Technology and Coordinated Restoration Strategy Based on Wind-storage Combined System [J]. Advanced Engineering Sciences 55(2), 72-83 (2023).
8. Kumar R, Mohanty SR, Verma MK: Enhancing damping of low-frequency oscillations in power networks through energy storage system-based controller [J]. International Journal of Circuit Theory and Applications 53(4), 2292-2317 (2024).
9. Zhang Cheng, Jiang Weilong, Luo Yujin, et al: Collaborative optimal operation of multiple data center microgrids and shared energy storage considering wind power and photovoltaic uncertainty [J]. Power System Protection and Control 53(4), 72-84 (2025).
10. Comodi G, Carducci F, Sze JY, et al: Storing energy for cooling demand management in tropical climates: A techno-economic comparison between different energy storage technologies [J]. Energy 121, 676-694 (2017).

057 Study on Return Current Distribution Mechanism and Abnormal Return Mitigation in Heavy Haul Railway Traction Systems Considering Train Operation

Xing Wang, Ke Wang, Sai Chen, Jiawei Lu, Haitao Hu

School of Electrical Engineering, Southwest Jiaotong University, Chengdu, Sichuan, China

wx@my.swjtu.edu.cn

Abstract. As a critical component of the traction power supply system, the operational status of the traction return system has a direct impact on the safety and efficiency of railway transportation. With the increasing service life of existing traction power supply systems, the issue of poor return flow at traction substations has become increasingly prominent, leading to frequent safety incidents that cannot be ignored and require urgent resolution. To address this, this paper develops a dynamic train load model that accounts for variations in train traction power, speed fluctuations, and position changes based on actual train operations. By integrating the impedance of the traction network, impedance of various return paths, leakage impedance, and cross-connection lines, an equivalent model of the traction-return system is established. Power flow analysis is then employed to reveal how operational parameters influence return current distribution patterns. Building on this foundation, a comprehensive mitigation scheme for abnormal return current was proposed, incorporating the reconstruction of the substation grounding grid, optimization of N-return conductors, and the installation of a continuous earth return conductor. The scheme was validated through on-site engineering tests. Results demonstrate that the proposed model can accurately and effectively reflect real operating conditions, clearly revealing the impact of system parameter variations on the distribution of traction return current. Furthermore, the proposed optimization scheme significantly improves the distribution among return paths, effectively enhances the safety and stability of the traction power supply system. The research findings provide theoretical support and engineering reference for the design optimization, operation, and maintenance management of similar electrified railway systems.

Keywords: Heavy Haul Railway; Traction Return System; Train Operation; Dynamic Power Flow Calculation; Return Current Distribution Mechanism; Abnormal Return Optimization.

1 Introduction

The traction return system is a crucial component of the electrified railway traction power supply system, serving to safely and reliably return the traction current ob-

tained by the train from the overhead contact line to the traction substation [1]. The operating condition of the return system not only affects the safety of power supply equipment, power supply reliability, and the electromagnetic environment of facilities along the railway line, but is also directly related to the personal safety of train crew members and trackside maintenance personnel [2,3].

In recent years, with the growth in rail transport volume, the increase in locomotive power, and the aging of existing traction power supply systems, the distribution of traction return current among multiple paths—such as rails, return conductors, and grounding grids—has exhibited increasingly complex characteristics [4, 5]. In particular, within traction power supply systems of heavy-haul railways that adopt the direct supply mode (including configurations with return conductors), abnormal traction return conditions may arise due to factors such as irregular impedance distribution, differences in grounding conditions, and line aging. The main manifestations include abnormally elevated rail potential, resulting in step voltage and touch voltage exceeding safety limits, which poses personal safety risks to trackside workers and train crew members [6,7]. In addition, such conditions may cause electromagnetic interference with track circuits and signaling systems, as well as accelerate electrochemical corrosion of metallic facilities along the line [8-11]. Meanwhile, an increase in substation grounding grid return current can lead to a rise in grounding grid potential, thereby increasing the risk of electric shock during maintenance and operation, and potentially causing overheating or insulation damage to traction transformers, thus threatening the long-term safe and stable operation of the power supply system [12-14].

Existing traction return modeling methods primarily represent the traction return system as a static equivalent circuit, which can clearly and intuitively reflect return characteristics [15-19]. However, such models are built on static assumptions and lack integration of dynamic variations in train traction power, speed, and load position into the multi-path return system modeling. As a result, they are unable to accurately reflect the return characteristics under actual operating conditions, thereby limiting their application value in engineering design and condition assessment. At the same time, load flow calculations of existing traction power supply systems, based on simplified models that approximate the traction return system as a single rail, typically neglect rail leakage impedance and multi-path coupling, and fail to consider the various components of the traction return system and their interrelationships [20]. This makes it challenging to analyze the mechanism of traction return and to identify key influencing factors. Additionally, the operation and maintenance of the traction return system primarily rely on personnel experience and regular inspections. Due to the unclear distribution mechanism, hidden hazards in the traction return system are challenging to detect in a timely and accurate manner, and targeted solutions based on mechanistic analysis are lacking [21].

Based on the above issues, this study focuses on investigating the traction return distribution mechanism under actual train operation to develop a traction–return system model that comprehensively reflects the coupled effects of multiple factors, including line impedance, grounding impedance, and load position. The model systematically reveals the influence of each factor on return current distribution, and propos-

es an optimized governance scheme for abnormal return conditions at traction substations.

2 Traction Return Mechanism and System Composition

In the direct supply mode with return conductors, the topology of the traction return system is illustrated in Fig. 1. The traction current originates from the traction substation, flows through the overhead contact line into the locomotive, and returns to the traction substation via the rails, N-return conductors, and the earth. In the vicinity of the substation, the current passes through the N-return conductors and the grounding grid to the traction grounding box, and ultimately flows back into the traction substation, thereby completing the closed-loop circuit.

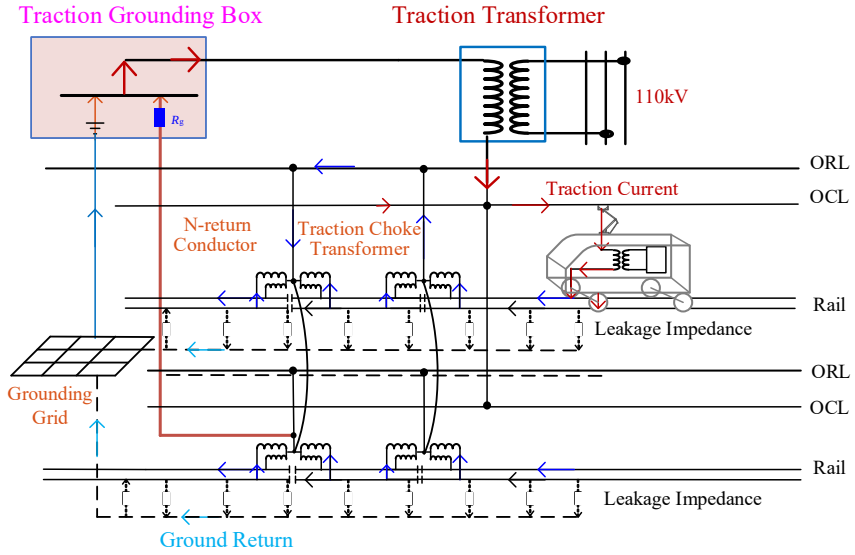


Fig. 1. Schematic Diagram of Traction–Return System

In the traction return current path, the flow is influenced by multiple factors, including the distribution of line impedance, leakage impedance, and ground conditions, resulting in branching and dispersion characteristics along the line, as well as a converging characteristic near the substation.

The branching characteristic refers to the parallel network formed between the locomotive and the substation, composed of the up-line and down-line running rails, return conductors, and combined earth wires (in the AT power supply system). The return current is distributed among these multiple paths in proportion to their impedance, which is affected by factors such as conductor material, structural configuration, location of cross-bonds, and grounding conditions.

The dispersion characteristic arises due to the presence of leakage impedance between the running rails and the earth, causing part of the return current to flow into

the ground toward the substation. This may lead to corrosion of buried equipment along the line or cause an increase in ground potential.

The converging characteristic describes how, when the ground current approaches the substation, it is partially re-injected into the running rails due to the leakage impedance between the grounding grid and the rails. This portion of the current combines with the existing rail current, and finally, through the grounding grid and the N-return conductor, is concentrated in the traction grounding box, returning to the negative terminal of the power supply system to complete the circuit.

3 Modeling and Power Flow Analysis of the Traction–Return System Considering Train Operation

3.1 Dynamic Load Modeling of the Train

During train operation, the traction power, speed, and position vary non-constantly over time. Different operating conditions correspond to significant variations in the traction current and traction return current. Therefore, it is necessary to perform dynamic modeling of the train.

Train traction calculation. During operation, the train is subjected to forces as illustrated in Fig. 2. The primary forces acting on the train are the traction force (F_T) and the impedance force (F_Z).

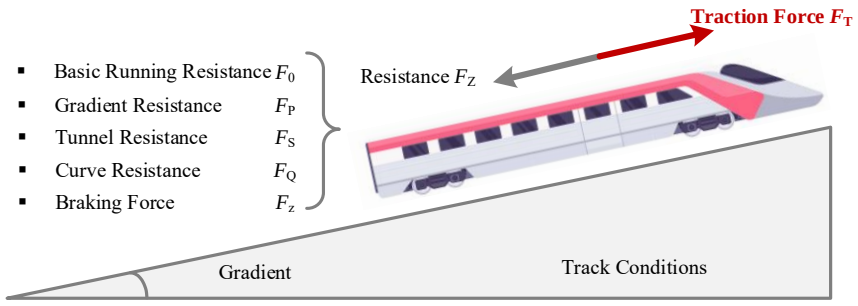


Fig. 2. Schematic Diagram of Train Forces

From Fig. 2, the net force in the direction of train motion per unit mass can be expressed as:

$$F_H = \frac{F_T - F_Z}{m \cdot g} \tag{1}$$

Where m is the train mass, in tonnes(t); g is the gravitational acceleration, equal to 9.8m·s^{-2} F_Z represents the total impedance, including basic running impedance(F_0), gradient impedance(F_p), tunnel impedance(F_S), curve impedance(F_Q), and braking force(F_z), The detailed calculation of these components can be found in Ref. [22].

Based on the kinetic energy theorem, the relationship between acceleration a, velocity v, and displacement s can be expressed as:

$$\begin{cases} a_i = \dfrac{F_H}{108} & \left(km/(h\cdot s)\right) \\ v_{i+1} = v_i + 3.6 a_i \Delta t & (km/h) \\ s_{i+1} = s_i + \dfrac{v_j \Delta t}{3.6} + \dfrac{a_j \Delta t^2}{2} & (m) \end{cases} \tag{2}$$

During train operation, the traction force and braking force are influenced by the control strategy. According to the relative magnitude of traction and braking forces, the operating state can be classified into three modes: traction, coasting, and braking. Under complex track conditions, to ensure safe, smooth, and efficient locomotive operation, the traction control strategy must be adapted to the relationship among the actual speed, target speed, and regenerative braking speed, thereby enabling seamless transitions between the three operating modes [20]. A commonly used approach is the constant-speed control strategy, in which automatic switching among traction, coasting, and braking is achieved by controlling the speed deviation. Detailed calculation procedures for this strategy can be found in Ref. [23].

Dynamic load modeling. By analyzing the time-varying characteristics of the train's active power and reactive power during operation within a section, a dynamic load model can be established. The required power for the train is supplied by the traction substation (TS) through the overhead contact line (OCL) to the pantograph (PT), then passes through the onboard traction transformer (TT), rectifier (RC), inverter (INV), and traction motor (TM) via the gearbox (GB), before being finally converted into the output power required by the train's wheels, as illustrated in Fig. 3, where TS denotes the traction substation, OCL the overhead contact line, PT the pantograph, TT the traction transformer, RC the rectifier, INV the inverter, TM the traction motor, and GB the gearbox.

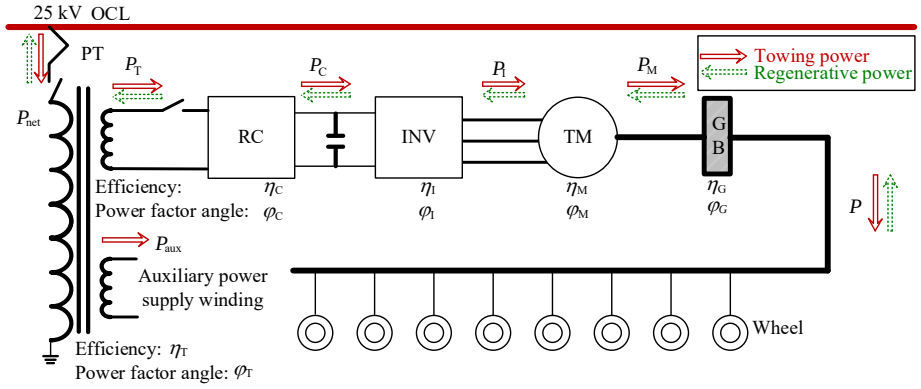


Fig. 3. Power Flow Diagram of the Traction Drive System

Based on Fig. 3, the grid-side active power under different operating conditions can be expressed as:

$$P_{net}(t)=\begin{cases}\dfrac{P(t)}{\eta_G\eta_M\eta_C\eta_I\eta_T}+P_{aux} & P(t)<0\\ P_{aux} & P(t)=0\\ P(t)\eta_G\eta_M\eta_C\eta_I\eta_T+P_{aux} & P(t)>0\end{cases} \tag{3}$$

In the formula, $P(t)<0$ represents traction operation, $P(t)>0$ represents regenerative braking operation, and represents coasting operation. Here, P_{aux} denotes the rated capacity of the auxiliary winding, η represents transmission efficiency, and subscripts indicate the respective transmission sections in the diagram, derived from the train's rated parameters. Among these $P(t)=1000F_D(t)v(t)/3.6$, the train's traction power is represented, obtained from the aforementioned traction calculation results, with units in watts (W).

Based on the dynamic active power model of the electric multiple unit (EMU), the corresponding reactive power model can be expressed as:

$$Q_{net}(t)=P_{net}(t)/\tan(\varphi_T) \tag{4}$$

Finally, by combining equations (1)-(4), the dynamic power model of the train as a function of speed and position can be obtained.

3.2 Traction–Return System Modeling

Calculation of impedance and capacitance parameters for the traction–return network. The impedance of the traction–return network consists of the conductor self-impedance (comprising the internal impedance and the external impedance) and the mutual impedance. The internal impedance of the conductor is determined using the formula for the internal impedance of a circular conductor. In ordinary track sections, the conductor external impedance and mutual impedance are calculated using the classical Carson formula. For tunnel sections, the model proposed by Tylavsky, which assumes an infinitely long circular tunnel surrounding the conductor, is adopted [24]. The unit of impedance is *Ω/km*. The calculation formulas are as follows:

$$Z_{i,\mathrm{Self}}=Z_{i,\mathrm{in}}\times10^3+Z_e+j\omega\frac{\mu_0}{2\pi}\ln\frac{D_g}{r_i} \tag{5}$$

$$Z_{ij}=Z_e+j\omega\frac{\mu_0}{2\pi}\ln\frac{D_g}{d_{ij}} \tag{6}$$

$$D_g=\frac{0.2085}{\sqrt{f\sigma\times10^{-9}}} \tag{7}$$

Where Z_e is the earth's AC impedance (Ω/km), $Z_{i,in}$ is the internal impedance of the conductor (Ω/km), D_g is the equivalent earth-return depth (cm), and d_{ij} is the distance between conductors (km).

The capacitance of the traction–return network mainly depends on the conductor radius and position, and can be obtained using the electrostatic image method as:

$$\begin{cases} P_{ii} = \dfrac{1}{2\pi\varepsilon_0} \ln \dfrac{2h_i}{r_c}, \text{ km/F} \\ P_{ij} = \dfrac{1}{2\pi\varepsilon_0} \ln \dfrac{D_{ij}}{d_{ij}}, \text{ km/F} \end{cases} \tag{8}$$

Where is the vacuum permittivity (8.854×10-9F/km); h_i is the conductor height (km); r_c is the conductor radius (km); D_{ij} is the image conductor distance (km).

Grounding network model and leakage impedance. Because the rails are in contact with the earth, part of the return current flows along the rails, while the other part dissipates through the rail–sleeper–ballast–earth path. Therefore, in addition to their longitudinal impedance, the rails also have a leakage impedance to earth. This leakage path determines the magnitude of the leakage impedance, whose value is typically taken in the range of 1~20Ω·km for calculation purposes.

Soil conditions and the size of the grounding network area primarily influence the impedance of the grounding network. According to [7], its calculation formula can be expressed as:

$$R_e = 0.443\frac{\rho}{\sqrt{S}} + 0.159\frac{\rho}{L}\ln\frac{0.635L^2}{h \cdot d \times 10^4} \tag{9}$$

Where ρ is the soil resistivity of the grounding network (Ω·m); S is the area (m^2); L is the length of the grounding electrode (m); h is the grounding depth (m); d is the diameter of the grounding electrode (m).

Chain-network model. The traction–return network consists of multiple parallel conductors. Based on the multi-conductor transmission line theory, the traction–return network is divided into transverse and longitudinal elements, and a chain-network model is constructed as shown in Fig. 5 [25–27].

In Fig. 4, Z_n represents the line impedance between adjacent cells, equivalent to an $m \times m$ π-type circuit. I_n denotes the current injected at the nth cross-section, and Y_n represents the admittance matrix of the nth cross-section. For Figure 5, the node voltage equation can be expressed as:

$$\begin{bmatrix} Y_1+Z_1^{-1} & -Z_1^{-1} & 0 & \cdots & 0 & 0 \\ -Z_1^{-1} & Z_1^{-1}+Y_2+Z_2^{-1} & -Z_2^{-1} & \cdots & 0 & 0 \\ 0 & -Z_2^{-1} & Z_2^{-1}+Y_3+Z_3^{-1} & \cdots & 0 & 0 \\ \vdots & \vdots & \vdots & \ddots & \vdots & \vdots \\ 0 & 0 & 0 & \cdots & Z_{N-2}^{-1}+Y_{N-1}+Z_{N-1}^{-1} & -Z_{N-1}^{-1} \\ 0 & 0 & 0 & \cdots & -Z_{N-1}^{-1} & Z_{N-1}^{-1}+Y_N \end{bmatrix} \begin{bmatrix} V_1 \\ V_2 \\ V_3 \\ \vdots \\ V_{N-1} \\ V_N \end{bmatrix} = \begin{bmatrix} I_1 \\ I_2 \\ I_3 \\ \vdots \\ I_{N-1} \\ I_N \end{bmatrix} \quad (10)$$

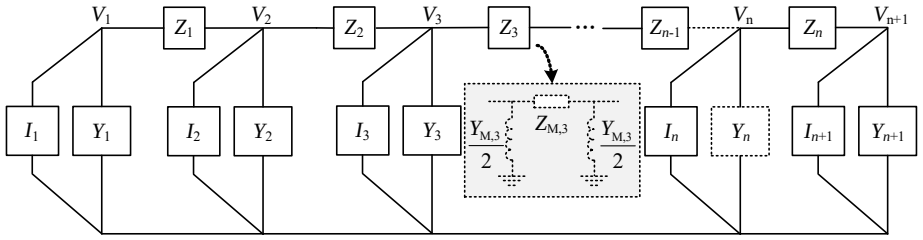


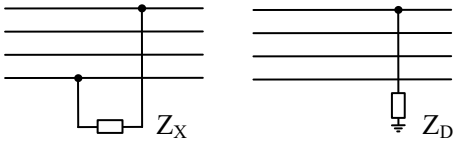
Fig. 4. Chain-network model of the traction power supply network

Equation (10) simplifies to:

$$YV = I \quad (11)$$

In the equation, Y represents the node admittance matrix of the traction-reflux network.

Considering the parallel connections and grounding between the return lines, as shown in Fig. 5:



a) Between two conductors b) Leakage impedance

Fig. 5. Parallel impedance element model

The admittance matrix at the parallel junction of two lines is:

$$Y = \frac{1}{Z_X} = \begin{bmatrix} 1 & 0 & 0 & -1 \\ 0 & 0 & 0 & 0 \\ 0 & 0 & 0 & 0 \\ -1 & 0 & 0 & 1 \end{bmatrix} \quad (12)$$

When leakage impedance exists, the node admittance matrix is:

$$Y = \frac{1}{Z_D} = \begin{bmatrix} 1 & 0 & 0 & 0 \\ 0 & 0 & 0 & 0 \\ 0 & 0 & 0 & 0 \\ 0 & 0 & 0 & 0 \end{bmatrix} \quad (13)$$

3.3 Dynamic power-flow calculation

Dynamic power-flow calculation involves continuously solving the power-flow distribution at each moment in the time domain, enabling the simulation and analysis of the entire operating process. The basic approach is as follows: based on the locomotive position and load variations at any given time, a model of the traction–return system is established. By updating the currents through the voltage between the catenary and the rails, the initial nodal voltages of the traction–return system are obtained; through iterative convergence, the final nodal voltages and current distribution are determined. The detailed procedure is illustrated in Fig. 6. The detailed calculation steps are as follows.

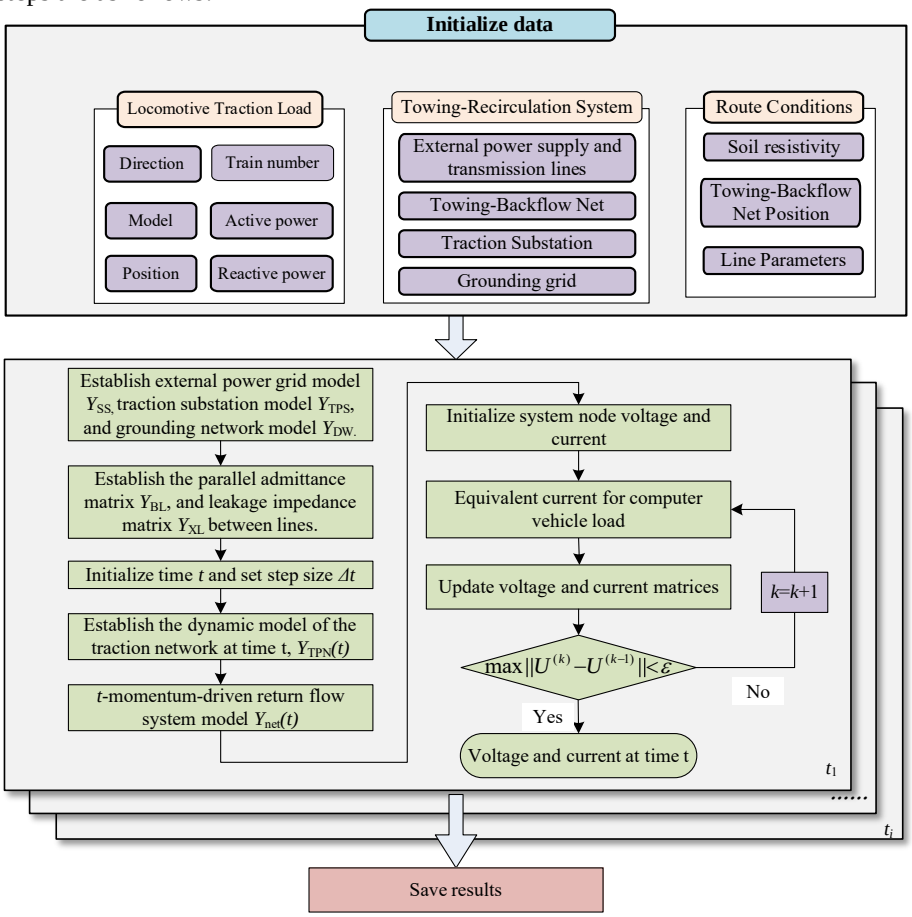


Fig. 6. Traction–return system power-flow calculation flowchart

Step 1: Input the initial data required for the model, including locomotive traction load parameters (obtained from train traction calculation and dynamic load modelling), traction power supply system parameters (line impedance, mutual impedance,

leakage impedance, etc.), and line structural conditions. These data can be obtained from Section 3.1.

Step 2: Based on the train's position at time t, the traction power, and the initialization parameters, generate the equivalent circuit model of the traction–return system at that time, retaining all loops, including catenary, rails, return conductors, and earth. Form the impedance matrix Z and admittance matrix Y of the multi-conductor network.

Step 3: Initialize the traction–return network voltages: set the catenary voltage to the rated value U_T^i , and set the initial rail voltage to $U_R^i=0$.

Step 4: Based on the locomotive traction load parameters combined with the initial voltages of the catenary and rails, calculate the locomotive injected current:

$$I_e^{Tr,i}=(P^{Tr,i}-jQ^{Tr,i})/\left(U_T^{Tr,i}-U_R^{Tr,i}\right) \tag{14}$$

Step 5: Update the current matrix of the traction–return system, and compute the voltages using the Gauss–Seidel iterative method, as expressed by:

$$U^{(k)}=Y^{(k)}I^{(k)} \tag{15}$$

Step 6: Check the convergence criterion. If the condition is satisfied, terminate the iteration and obtain the voltage and current values at time t, then proceed to the next time step calculation. Otherwise, return to Step 4.

Through the above procedure, the power-flow distribution of the train operation over the entire continuous power-supply section can be obtained, including the return currents and voltages of each path. This provides an accurate scenario for analyzing the factors affecting the return current.

4 Key influencing factors analysis

4.1 Simulation Parameters

The left-arm power-supply section of a traction substation has a total length of 23.8 *km* and adopts a direct-feed configuration with return conductors(RL). The rail leakage impedance is 5 Ω ·km, and the Grounding grid impedance is 0.2 Ω. Every 4 km, the up-track and down-track return conductors and rails are transversely interconnected via a feeder line. The spatial layout of the line is shown in Fig. 7.

Based on the parameters specified by the conductor type and the suspension position, the impedance and capacitance parameters of each conductor are calculated, as shown in Tables 1 and 2.

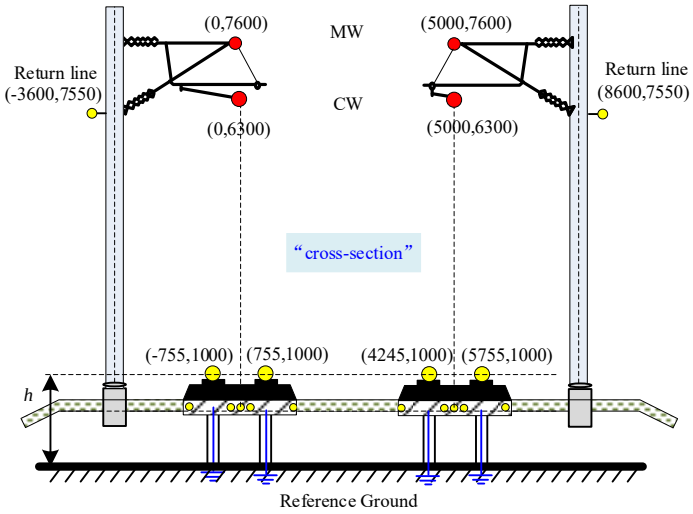


Fig. 7 Spatial Position of the Line

Table 1. Traction network impedance

	T1	R1	RL1	T2	R2	RL2
T1	0.079+0.597j	0.049+0.324j	0.049+0.353j	0.049+0.333j	0.049+0.307j	0.049+0.300j
R1	0.049+0.324j	0.064+0.580j	0.049+0.308j	0.049+0.307j	0.049+0.335j	0.049+0.285j
RL1	0.049+0.353j	0.049+0.308j	0.094+0.739j	0.049+0.300j	0.049+0.285j	0.049+0.278j
T2	0.049+0.333j	0.049+0.307j	0.049+0.300j	0.079+0.597j	0.049+0.324j	0.049+0.353j
R2	0.049+0.307j	0.049+0.335j	0.049+0.285j	0.049+0.324j	0.064+0.580j	0.049+0.308j
RL2	0.049+0.300j	0.049+0.285j	0.049+0.278j	0.049+0.353j	0.049+0.308j	0.094+0.739j

Table2. Traction Network Capacitor

	T1	R1	RL1	T2	R2	RL2
T1	1.179e-08	-7.622e-10	-1.923e-09	-1.955e-09	-3.738e-10	-5.278e-10
R1	-7.622e-10	0.25	-2.863e-10	-3.738e-10	-3.095e-10	-9.049e-11
RL1	-1.923e-09	-2.863e-10	7.794e-09	-5.278e-10	-9.049e-11	-2.082e-10
T2	-1.955e-09	-3.738e-10	-5.278e-10	1.179e-08	-7.622e-10	-1.923e-09
R2	-3.738e-10	-3.095e-10	-9.049e-11	-7.622e-10	0.25	-2.863e-10
RL2	-5.278e-10	-9.049e-11	-2.082e-10	-1.923e-09	-2.863e-10	7.794e-09

4.2 Model Validation

As shown in Fig. 8, the comparison results between the measured values and simulated calculations for the N-line return current and ground grid return current are presented.

From the figure, it can be seen that the simulation results and the measured data are consistent both in terms of variation trend and magnitude, with the discrepancy falling within the allowable range. This demonstrates that the full traction–return system model established in this study, together with the proposed dynamic power-flow calculation method, can effectively represent actual operating conditions, thereby verifying the correctness and feasibility of both the model and the calculation method.

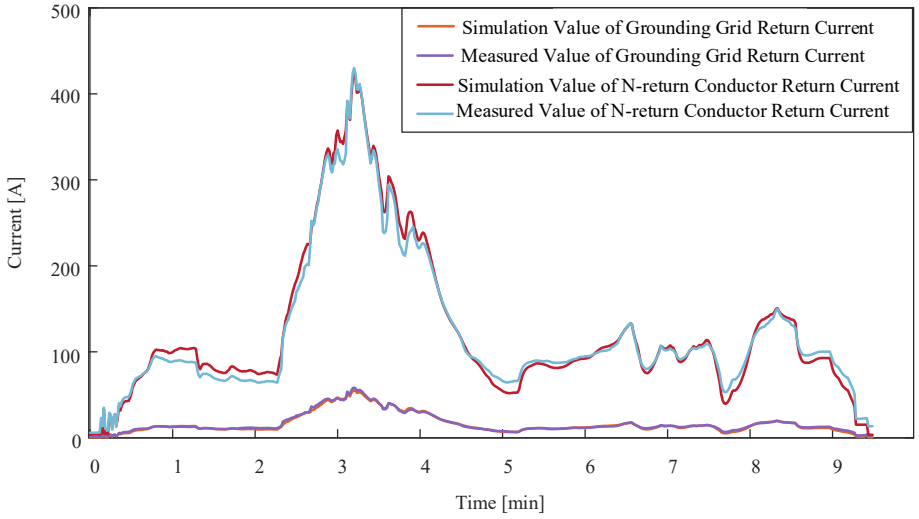


Fig. 8 Actual and Simulated Return Current Values

4.3 Influencing factors analysis

Since poor return flow in traction substations is primarily caused by excessive return current through the grounding grid, this paper mainly analyzes the factors affecting the return current through the grounding grid.

Return network impedance. For double-track railways (DX), the return current structure typically adopts a parallel configuration with up-track and down-track lines. Compared with single-track railways (ST), the total return-path impedance of the line is smaller.

From Fig. 9, it can be observed that, for both single-track and double-track railways, due to the presence of feeder connections, the proportions of the different return paths remain almost unchanged at locations far from the traction substation, maintaining a constant value. However, in the areas close to the substation, these proportions

change: the shares of grounding-grid return and return-conductor return decrease, while the share of rail return increases. Moreover, compared with single-track railways, double-track railways show higher proportions of rail return current (RR%) and return-conductor return current (RCR%), and a lower proportion of grounding-grid return, which can effectively reduce the amount of ground-borne return current (GGR%).

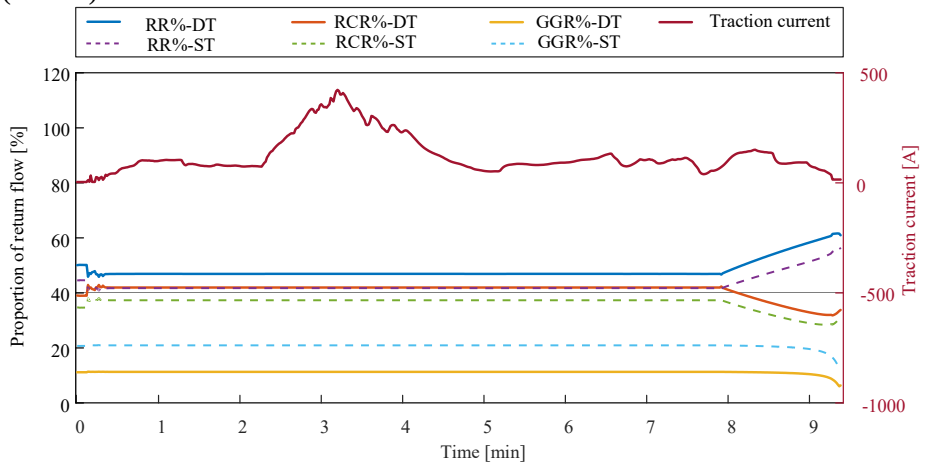


Fig. 9 Single-line vs. Multi-line Return Flow Proportion Comparison

Grounding-grid impedance. Using a double-track traction power supply network as an example, and keeping all other conditions unchanged, the grounding grid impedance is varied. Measurement points are selected along the line within a distance of 0–24 km from the traction substation. The relationship between the proportion of each return path and the grounding-grid impedance is shown in Fig. 10.

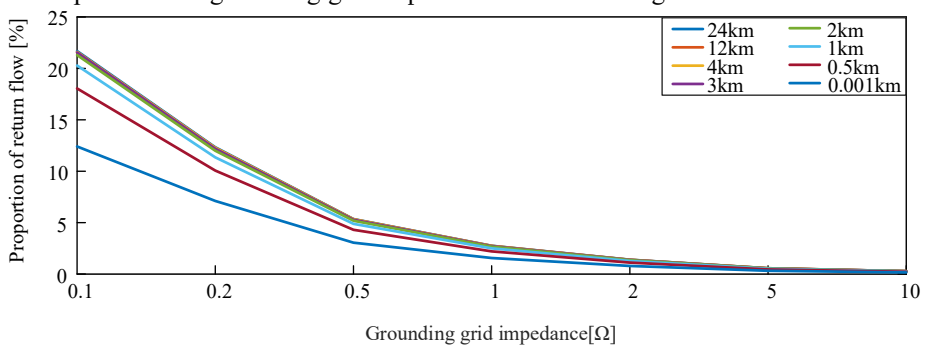


Fig. 10 Effect of Substation Grounding-Grid on Return Current Proportion

From the figure, it can be seen that the grounding-grid impedance has a significant effect on the proportion of grounding-grid return. As the grounding-grid impedance increases, the proportion of grounding-grid return decreases. This influence becomes more pronounced at locations farther from the traction substation. When the ground-

ing-grid impedance increases within the range of 0–10 Ω, the proportion of grounding-grid return can decrease by more than 20%.

Rail Leakage Impedance. Keeping all other conditions unchanged, the rail leakage impedance is varied. The relationship between the proportion of each return path and the rail leakage impedance is shown in Fig. 11.

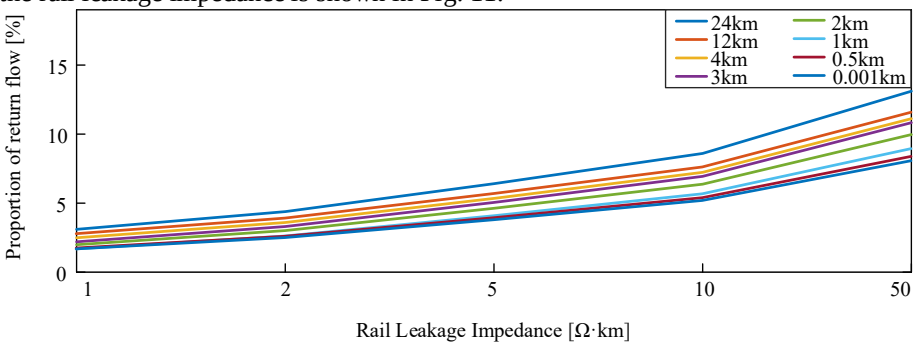


Fig. 11 Effect of Rail Leakage Impedance on Return Current Proportion

From the figure, it can be seen that as the rail leakage impedance increases, the proportion of return current through the grounding grid also increases. This is because the smaller the rail impedance between the rails and the ground, the more the current near the traction substation tends to flow back to the rails. This effect is particularly pronounced when the leakage impedance varies within the range of 5–50Ω·km.

Soil Resistivity. Keeping all other conditions unchanged, the soil resistivity is varied. The relationship between the proportion of each return path and the soil resistivity is shown in Fig. 12.

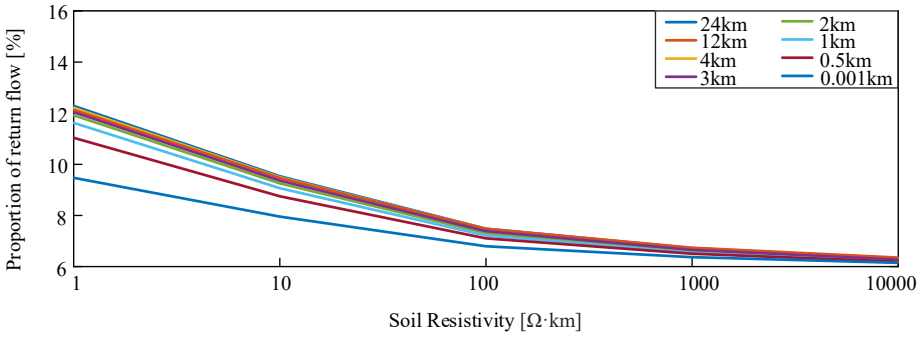


Fig. 12 Effect of Soil Resistivity on Return Current Proportion

From Fig. 12, it can be observed that as the soil resistivity increases, the proportion of grounding-grid return decreases. When the soil resistivity is in the range of 1–1000Ω·km, its influence on the grounding-grid return proportion is particularly significant.

N-Return-Conductor Impedance. Keeping all other conditions unchanged, the impedance of the N-return conductor is varied. The relationship between the N-return-conductor impedance and the proportion of each return path is shown in Fig. 13.

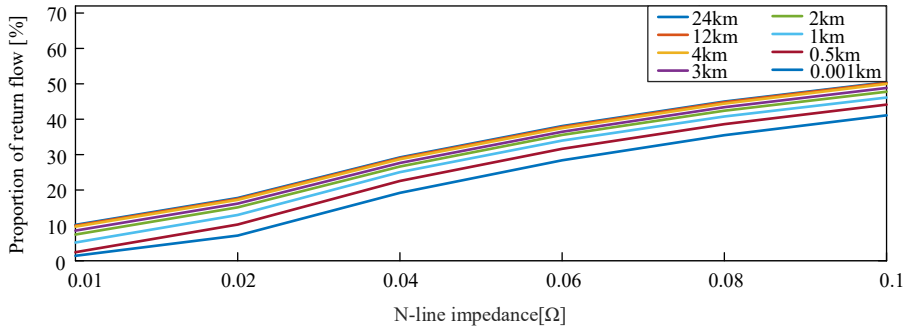


Fig. 13 Effect of N-Return-Conductor Impedance on Return Current Proportion

From Fig. 13, it can be observed that as the N-return-conductor impedance increases, the proportion of grounding-grid return rises significantly, indicating a considerable influence.

Continuous Grounding Wire. In existing heavy-haul traction substations adopting the direct-supply mode with N-return conductors, the return-current paths do not include a constant grounding wire (GW). In contrast, newly constructed railways, whether using the autotransformer (AT) feeding mode or the direct-supply mode with N-return conductors, are equipped with a continuous grounding wire. Therefore, one modification approach for existing heavy-haul railways is to install an additional continuous grounding wire. Keeping all other conditions unchanged, a constant grounding wire is added, and the resulting proportion of each return path is shown in Fig. 14.

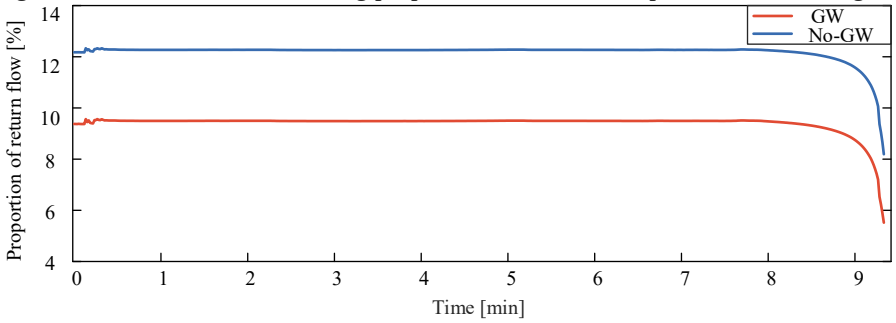


Fig. 14 Effect of Continuous-Grounding-Wire on Return Current Proportion

From Fig. 14, it can be observed that adding a continuous grounding wire reduces the impedance of the return network, effectively decreasing the proportion of ground-

ing-grid return. Furthermore, after the final transverse connection, the closer the location is to the traction substation, the smaller the influence of the continuous grounding wire on the grounding-grid return proportion becomes.

5 Optimization Scheme Design

Based on the on-site testing results, and to optimize the return-current proportion, reduce the impedance of the traction power-supply system return paths, and enhance operational reliability, the following integrated optimization measures are proposed:

1）Optimization of incoming-return cables: Increase the cross-sectional area of the wires leading into the substation, or re-lay the incoming-return cables in newly excavated trenches to shorten the cable length, thereby reducing their impedance.

2) Grounding-grid reconstruction: Optimize the geometry and layout of the grounding grid, and reasonably configure the number and distribution of horizontal grounding conductors and vertical grounding electrodes to increase the grounding-grid impedance, ensuring that it does not exceed the standard value.

3) Improvement of the return system: Install an additional continuous grounding wire and connect it directly back to the traction substation, thereby reducing the impedance of the return network.

4) Conversion to a double-track parallel return network: Where conditions permit, transform a single-track return network into a double-track parallel structure of up and down lines. Given the large scale of such modification, phased implementation should be considered based on technical and economic assessments.

The above measures should be implemented in phases, in accordance with on-site operating conditions and budget constraints:

1) Short-term measures: Optimization of incoming-return cables, grounding-grid reconstruction;

2) Medium- to long-term measures: addition of continuous grounding wire, and conversion of the single-track network to a parallel double-track structure.

6 Optimization Effect Evaluation

In this study, the short-term measures of the proposed governance scheme were implemented. The return-current proportions before and after implementation were obtained through simulation, and the results are shown in Fig. 15.

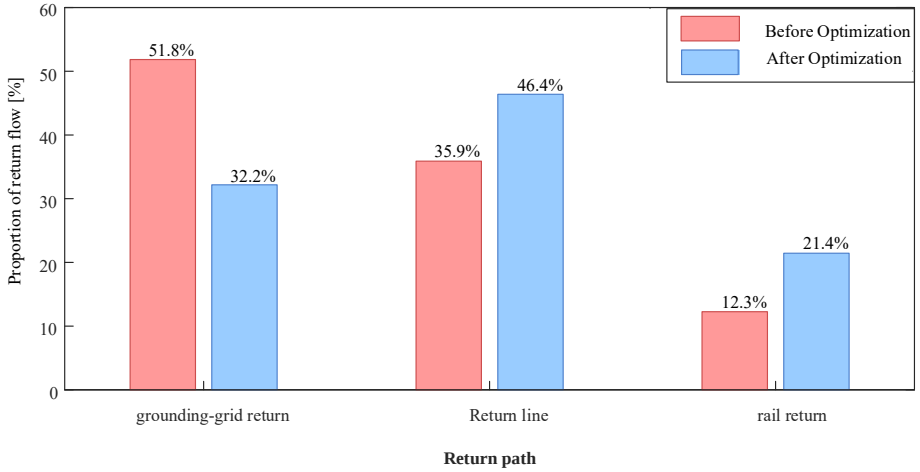


Fig. 15 Comparison of Return-Current Proportions Before and After Governance

From the figure, it can be observed that after governance, the proportion of grounding-grid return decreased from 51.8% to 32.2%, while the proportion of N-return-conductor return increased from 12.3% to 21.4%, and rail return increased from 35.9% to 46.4%. This indicates that the overall return-current distribution was effectively optimized.

7 Conclusion

This study focuses on the mechanism of traction-return current distribution and the mitigation of abnormal return phenomena in heavy-haul railway traction power-supply systems. In response to issues such as the aging of return systems due to long-term service, excessive grounding-grid return currents, and elevated rail potentials, an optimization scheme was proposed, taking into account both theoretical analysis and engineering feasibility. The main conclusions are as follows:

1) A dynamic train-load model was developed, considering traction-power variations, speed fluctuations, and operating position. By including traction-network impedance, return-path impedance, leakage impedance, and transverse connections, a global equivalent traction–return model was formed. Combined with dynamic power-flow calculations, it reflects return-current distribution.

accurately, with results closely matching field measurements, validating the model.

2) On this basis, an in-depth analysis of key factors influencing traction-return distribution was conducted. It was clarified that parameters such as grounding-grid impedance, rail leakage impedance, N-return-conductor impedance, and the presence of continuous grounding wires significantly affect the proportion of current carried by each return path, providing a theoretical foundation for the design of abnormal-return mitigation schemes.

3) A phased optimization scheme was proposed, including the optimization of incoming-return cables, reconstruction of the grounding grid, enhancement of rail insulation, addition of continuous grounding wires, and conversion of single-track networks into parallel double-track configurations. Short-term measures were verified through an on-site application. Simulation and test results indicate that, after governance, the proportion of grounding-grid return decreased from 51.8% to 32.2%, substantially reducing grounding-grid current, improving return-path distribution, and effectively enhancing the safety and stability of system operation.

4) The research results not only provide direct engineering guidance for the safe operation of heavy-haul railway traction power-supply systems, but also offer theoretical support and reference for the design optimization and operation-maintenance management of other types of electrified railway traction-return systems.

Acknowledgement: This work is supported by China Railway Taiyuan Bureau Group Co., Ltd. Science and Technology Research and Development Project "Research on Online Monitoring Device and Backflow Parameter Evaluation Technology for Traction Substation" (A2023GD01).

References

[1] Qunzhan Li, Jianmin He, Traction Power Supply System Analysis, 3rd ed. Chengdu (China): Southwest Jiaotong University Press, 2012.

[2] Wenxun Huang, Analysis of abnormal return circuit in typical high-speed railway traction substation and study on suppression scheme, Railway Standard Design, 2021, 65(03): 143–148.

[3] Xiaobin Cao, Manxiang Wang, Chuanlin Zhu, et al., Distribution and influencing factors of traction return current under direct power supply mode in heavy-haul railways, China Railway Science, 2021, 42(04): 137–144.

[4] Shiwu Yang, Chang Liu. Discrete modeling and calculation of traction return-current network for 400 km/h high-speed railway [J]. Proceedings of the Institution of Mechanical Engineers, Part F: Journal of Rail and Rapid Transit, 2023, 237: 445-457.

[5] Shuzeng Qin, Yixuan Yang, Shiwu Yang, Study on dynamic distribution and harmonic characteristics of traction return current based on CR450 EMU, China Railway, 2025, (02): 64–70.

[6] Youpeng Zhang, Yao Zhang, Xiaokai Fan, et al., Scheme for limiting rail potential of electrified railways in arid regions, Power Grid Technology, 2013, (02): 533–538.

[7] Kewen Wang, Weilan Li, Hui Wang, Analysis on influencing factors and suppression measures of rail potential under bilateral power supply, Journal of Railway Science and Engineering, 2024, (06): 2465–2475.

[8] Wangqun Sheng, Study on electromagnetic interference of AC electrified railway on oil and gas pipelines along the line based on CDEGS, Journal of Railway Science and Engineering, 2020, 17(08): 2101–2108.

[9] Hong Li, Chongmo Zhang, Zuoxing Wang, et al., Review on formation mechanism and suppression methods of electromagnetic interference in high-speed train power supply systems, Proceedings of the CSEE, 2023, 43(08): 3137–3154.

[10] Minwu Chen, Jiuguo Zhu, Shaofeng Xie, et al., Modeling and simulation of resistive coupling AC interference of buried pipelines caused by traction power supply systems, China Railway Science, 2018, 39(02): 80–86.
[11] Qing Tong, Xu Dong, Ruining Peng, et al., Assessment and mitigation measures of AC interference on buried pipelines from newly built AC electrified railways, Corrosion and Protection, 2025, 46(06): 75–82.
[12] Guowang Yu, Junqi Zhang, Mingli Wu, Simulation analysis of influencing factors of ground return in traction substations, Journal of Railway Engineering, 2015, (07): 73–76+93.
[13] Xiufang Jia, Yifeng Ma, Jun Huang, et al., Study on ground return current and grounding grid potential rise in traction substations, Power System Protection and Control, 2012, 40(10): 116–119, 126.
[14] Qiulong Xiong, Analysis of abnormal return current in high-speed railway substations, Railway Construction Technology, 2021, (09): 84–87+106.
[15] Wei Wei, Wei Liu, Xiaowen Ye, Modeling and analysis of high-speed railway traction return systems, Journal of Railway Science and Engineering, 2018, 15(01): 31–38.
[16] Wu G, Gao G, Dong A, et al. Study on the Performance of Integrated Grounding Line in High-Speed Railway[J]. IEEE Transactions on Power Delivery, 2011, 26: 1803-1810.
[17] Botong Li, Chunbo Li, Bin Li, et al. Study on the distributed-parameter impedance earth model and potential distribution of the monopole-ground-return HVDC[J]. Electric Power Systems Research, 2020, 187: 106478.
[18] Bosko Milesevic,Bozidar Filipovic-Grcic,Ivo Uglesic, et al. Estimation of current distribution in the electric railway system in the EMTP-RV[J]. Electric Power Systems Research, 2018, 162: 83-88.
[19] Guinan Zhang, Zhigang Liu, Xiaoxu Guo, et al., Modeling and analysis of traction network in high-speed railway tunnel and viaduct sections, Journal of the China Railway Society, 2015, 37(11): 16–24.
[20] Ke Wang, Haitao Hu, Wenjing Wei, et al., Dynamic traction load modeling method for high-speed railways based on train timetable, China Railway Science, 2017, 38(01): 102–110.
[21] Xiaosi Yu, Xueping Xu, Analysis of causes and countermeasures for poor traction return in substations of the Han–Yi Railway, Electrified Railway, 2019, (03): 30–34.
[22] Ke Wang, Dynamic modeling and power quality analysis of high-speed railway traction power supply system [D]. Southwest Jiaotong University, 2015.
[23] Guanjun Li, Xiaoyun Feng, Lijun Wang, et al., Research and simulation on constant speed control strategy of high-speed EMU, Electric Drive for Locomotives, 2007, (05): 12–14.
[24] Huang K, Liu Z, Su D, et al. A traction network chain-circuit model with detailed consideration of integrated grounding system in tunnel path[J]. IEEE Transactions on Transportation Electrification, 2019, 5(2): 535-551.
[25] Zhengyou He, Haitao Hu, Lei Fang, et al., Research on harmonics and their transmission characteristics in high-speed railway traction power supply systems, Proceedings of the CSEE, 2011, 31(16): 55–62.
[26] Haitao Hu, Zhengyou He, Jiangfeng Wang, et al., Power flow calculation of high-speed railway traction network based on vehicle–network coupling, Proceedings of the CSEE, 2012, 32(19): 101–108+192.
[27] Mingli Wu, Unified chain circuit model of electrified railway traction network, Proceedings of the CSEE, 2010, 30(28): 52–58.

058 基于云边协同的多微网分布式优化调度策略

刘迎澍*，李承泽，戴雨竹，马骁野，李 鹏，于 浩

（天津大学电气自动化与信息工程学院）

A Distributed Optimization Scheduling Strategy for Multi-microgrids Based on Cloud-edge Collaboration

Yingshu Liu*, Chengze Li, Yuzhu Dai, Xiaoye Ma, Peng Li, Hao Yu

(School of Electrical and Information Engineering, Tianjin University)

ABSTRACT: To address the centralized control bottleneck and multi-agent coordination challenges faced by the optimal dispatch of multi-microgrid systems with high proportions of renewable energy integration, this paper proposes a distributed optimization dispatch strategy based on cloud-edge collaboration. Firstly, a two-layer control architecture of cloud-edge collaboration is designed, and a closed-loop dispatch mechanism of prediction-optimization-feedback is constructed from the aspects of collaborative planning layer and distributed autonomous layer. Then, a high-precision and high-reliability edge measurement and control hardware and experimental platform design centered on the "State Grid Core" SCM630 is proposed. Finally, the experimental results and analysis of the system are presented, demonstrating that this strategy can effectively improve the operational economy, stability and renewable energy consumption level of multi-microgrid systems, providing an effective solution for the collaborative re gulation of distributed resources in new distribution systems.

KEY WORDS: Cloud-edge collaboration; distributed optimization; edge computing; microgrid

摘要：为应对高比例新能源接入下多微网系统优化调度所面临的集中式控制瓶颈与多主体协同难题，本文提出一种基于云边协同的分布式优化调度策略。本文首先设计了云边协同的双层控制架构，并从协同规划层和分布式自治层两个方面构建“预测-优化-反馈”的闭环调度机制。然后，本文提出了一种以“国网芯”SCM630 为核心的高精度、高可靠性边缘测控硬件及实验平台设计；最后，本文展示了系统的实验结果与分析，证明了本策略可以有效提升了多微网系统的运行经济性、稳定性与可再生能源消纳水平，为新型配电系统分布式资源的协同调控提供了有效解决方案。

关键词：云边协同；微电网；分布式优化；边缘计算

0 引言

随着以高比例可再生能源为特征的新型电力系统加速建设，配电网中接入了海量的分布式电源、微电网、多元化负荷与分散式储能[1]。在运行过程中，这些“源-网-荷-储”单元持续生成高频实时数据，同时虚拟电厂、负荷聚合商和独立储能电站等新型市场主体逐步参与灵活电力交易，对系统的感知、计算与协同控制能力提出了更高要求。传统集中式优化依赖全局信息汇集与中心决策，在面对广域分布、多主体博弈和高动态响应的新型配电网调控需求时，不仅存在单点故障风险、通信带宽瓶颈与决策延迟等问题，也难以满足本地自治需求[2-5]。

在此背景下，分布式优化与云边协同的测控架构成为实现新型配电网高效调控的关键路径。该架构通过将决策权下放至边缘节点，形成“局部感知、就地决策、全局协同”的运行模式，显著提升系统对局部扰动和不确定性的响应能力[6]。边缘计算节点依托分布式算法，仅通过相邻单元间的有限信息交互即可逼近全局最优，实现多主体协同优化[7]。此外，该架构为柔性资源的即插即用与聚合调控提供了基础，支持前文所述的新型主体参与系统调节，构建起“源-网-荷-储”灵活互动的配电网生态[8-9]。

基于上述需求与问题，本文提出一种面向多微网系统的云边协同分布式优化调度框架，重点研究上下双层协同优化算法，设计并实现基于“国网芯”SCM630 的边缘测控硬件平台，最终通过实验验证此方法在提升系统经济性、稳定性与新能源消纳能力方面的有效性。

1 云边协同与优化调度框架

* 通讯作者
E-mail address: liu_ysh@tju.edu.cn (Y. Liu).

资助项目：北京智芯微电子科技有限公司实验室科研专项项目(SGSCDT00XPQT2400763)。

Project Supported by the Laboratory Scientific Research Special Project of Beijing Zhixin Microelectronics Technology Co., Ltd. (SGSCDT00XPQT2400763).

1.1 云边协同框架概述

本研究构建了一种面向多微网系统的云边协同计算框架，其核心在于将复杂的全局优化问题分解，并依托云端的宏观规划能力、边缘层的分布式实时计算能力与终端层的本地执行能力进行协同求解。该框架以背靠背电压源变流器（VSC）与混合储能系统构成的交直流柔性互联网络为物理基础，形成“能量传输-缓冲-调节”一体化体系，为微网间的功率互济提供底层支撑。

在控制架构上，系统采用“全局优化-本地执行”的双层协同模式。协同规划层（上层、云端）依托全局信息生成 VSC 功率指令及储能调度策略；分布式自治层（下层、边缘端）则作为分布式计算核心，基于本地实时数据执行高频优化计算，实现功率的跟踪与动态调整，并将运行实时数据反馈至云端。通过将计算任务下沉至边缘节点，系统在避免集中式单点故障的同时，显著降低通信延迟，并依托本地化数据处理保障各微电网的数据隐私与自治，整体架构具备良好的可扩展性与实时性[10]。

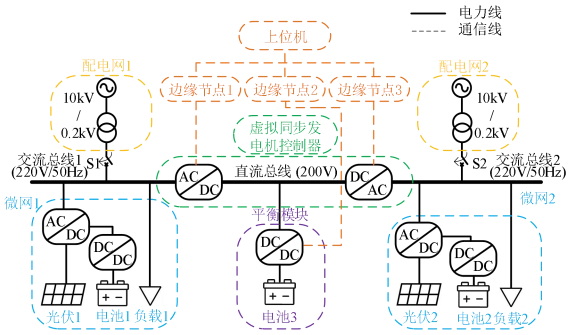


图 1.1 云边协同架构

1.2 优化调度框架设计

在上述云边协同架构的基础上，本文以“预测-执行-反馈”为闭环逻辑进一步设计了与之配套的双层优化调度机制。

协同规划层系统作为调度决策中心，融合短期预测与全局约束，在固定时间尺度内滚动生成未来时段功率计划，并将其下发至各边缘节点；分布式自治层系统则依托边缘计算能力，基于接收到的计划指令与实时采集的本地信息，采用分布式算法进行在线优化，实现对 VSC 功率、储能充放电等关键变量的实时控制。与此同时，分布式自治层将本地执行数据持续上传，用于协同规划层模型的动态修正，形成持续优化的闭环调度流程。该机制有效协调了不同时间尺度的优化目标，在保证系统整体运行经济性的同时，也提升了其对不确定性的适应能力与动态响应能力[11]。

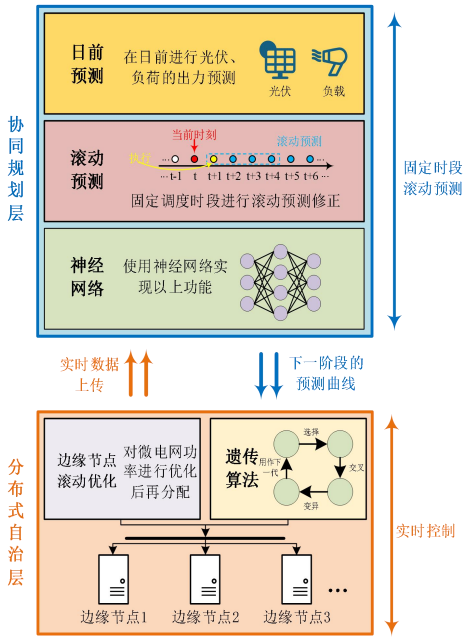


图 1.2 双层协同控制策略

2 多微网系统分布式双层优化算法

2.1 协同规划层模型

2.1.1 协同规划层算法模型

本文的协同规划层控制架构采用兼顾时空特征的 CNN-BiLSTM 混合神经网络算法进行日前规划与日内滚动预测，核心任务是制定一个经济最优的日前调度计划，并随着实时数据的更新进行滚动修正，使整个多微网系统的总运行成本最小化。

首先对协同规划层控制器进行离线训练：基于历史气象、负荷及时间特征数据训练神经网络模型，通过前向传播与误差反向传播算法不断优化网络参数[12]，使其具备高精度预测能力。本文使用长短期记忆网络 LSTM 对时序数据进行特征分析与建模[13]。对于给定数列 X=$\{x_1, x_2, \cdots, x_T\}$，LSTM 自适应捕捉时间序列在长短期的依赖关系，并不断更新隐藏状态h_t，其前向传播过程可简要表示为：

$$h_t = f(U_{ih}x_t + U_{oh}h_{t-1} + b_h) \quad (1)$$

式(1)中，U_{ih}、U_{oh}和b_h分别是输入权重、输出权重与偏置项。通过这种方法，模型可以实现较高精度的预测。

离线训练后，即可进入在线应用阶段。协同规划层控制系统于每日固定时刻(如每日 0 时)启动日前规划，将最新气象预报等信息输入训练好的网络，预测未来 24 小时负荷及可再生能源出力，并求解优化模型生成日前调度计划下发给分布式自治层边缘节点。进入日内运行后，协同规划层以固定周期(如每 15 分钟)触发滚动预测修正，首先融合分布

式自治层上传的实时运行数据与最新超短期气象预报，滚动更新未来固定时间尺度的预测结果；随后以此数据为输入重新求解优化模型，生成更精确的预测曲线并下发，从而形成“预测-优化-执行-反馈-修正”的闭环控制机制。

该流程通过神经网络强大的非线性拟合能力与滚动优化策略，有效提升了系统应对不确定性的能力，确保了调度计划的经济性与可靠性。

2.1.2 协同规划层条件约束

协同规划层规划和预测的功率约束条件如下所示：

$$P_{MGx,t}^{pr,Load}+P_{MGx,t}^{Bat}=P_{MGx,t}^{pr,PV}+P_{MGx,t}^{Bal}+P_{MGx,t}^{Grid},x=1,2\cdots \quad (2)$$

$$P_{Bal,t}^{Bat}+\sum_{x=1}^{n}P_{MGx,t}^{Bal}=0 \quad (3)$$

式(2)、(3)中，$P_{MGx,t}^{pr,Load}$代表微网 x 的负荷在 t 时刻的预测功率,$P_{MGx,t}^{Bat}$代表微网 x 的储能在 t 时刻的功率,$P_{MGx,t}^{pr,PV}$代表微网 x 的光伏在 t 时刻的预测功率，$P_{MGx,t}^{Bal}$代表平衡单元在 t 时刻给微网 x 输送的功率，$P_{MGx,t}^{Grid}$代表电网在 t 时刻给微网 x 输送的功率，$P_{Bal,t}^{Bat}$代表平衡单元的储能在 t 时刻的功率。

除了满足功率平衡约束，联络线功率以及内部储能功率也必须满足出力范围约束：

$$P_{MGx}^{Grid,max}\geq P_{MGx,t}^{Grid}\geq P_{MGx}^{Grid,min},x=1,2,\cdots \quad (4)$$

$$P_{MGx}^{Bal,max}\geq P_{MGx,t}^{Bal}\geq P_{MGx}^{Bal,min},\quad x=1,2,\cdots \quad (5)$$

$$P_{MGx}^{Bat,max}\geq P_{MGx,t}^{Bat}\geq P_{MGx}^{Bat,min},\quad x=1,2,\cdots \quad (6)$$

$$P_{Bal}^{Bat,max}\geq P_{Bal,t}^{Bat}\geq P_{Bal}^{Bat,min},\quad x=1,2,\cdots \quad (7)$$

式(4)-式(7)中，$P_{MGx}^{Grid,max}$和$P_{MGx}^{Grid,min}$分别代表微电网 x 与电网传输功率的上限与下限，$P_{MGx}^{Bal,max}$和$P_{MGx}^{Bal,min}$分别代表微电网 x 与平衡单元传输功率的上限与下限，$P_{MGx}^{Bat,max}$和$P_{MGx}^{Bat,min}$分别代表微电网 x 内部储能出力的上限与下限，$P_{Bal}^{Bat,max}$和$P_{Bal}^{Bat,min}$分别代表平衡单元储能出力的上限与下限。

此外，储能必须满足容量约束：

$$E_{MGx}^{Bat,max}\geq\sum_{t=1}^{k}P_{MGx,t}^{Bat}\Delta T+E_{MGx,0}^{Bat}\geq E_{MGx}^{Bat,min},\quad x=1,2\cdots \quad (8)$$

$$E_{Bal}^{Bat,max}\geq\sum_{t=1}^{k}P_{Bal,t}^{Bat}\Delta T+E_{Bal,0}^{Bat}\geq E_{Bal}^{Bat,min} \quad (9)$$

式(8)、(9)中，$E_{MGx}^{Bat,max}$和$E_{MGx}^{Bat,min}$分别代表微电网 x 储能容量的上限和下限，ΔT代表滚动预测选取的时间尺度，$E_{MGx,0}^{Bat}$代表微电网 x 储能初始容量，$E_{Bal}^{Bat,max}$和$E_{Bal}^{Bat,min}$分别代表平衡单元储能容量的上限和下限，$E_{Bal,0}^{Bat}$代表平衡单元储能初始容量。

2.2 分布式自治层模型

2.2.1 分布式自治层算法模型

本文的分布式自治层控制架构采用遗传算法进行边缘节点的滚动优化，分布式自治层边缘节点接收协同规划层下发的日前预测曲线后，立即启动以遗传算法为核心的实时滚动优化过程，其核心任务是在短时间尺度内，根据下发的计划指令控制本地系统实际运行状态并进行优化，同时确保电压、频率等安全指标不越限。

该算法以降本增效并提高可再生能源消纳为目标，具体目标函数如下：

$$F_k=\sum_{x=1}^{n}\sum_{t=k}^{k+m}(P_{MGx,t}^{Grid}-P_{MGx,t}^{pr,Grid})^2+(P_{MGx,t}^{Bal}-P_{MGx,t}^{pr,Bal})^2 \quad (10)$$

式中，F_k代表 k 时刻对下一个滚动周期进行优化的目标函数，m 代表滚动周期内包含 m 个滚动时间尺度，$P_{MGx,t}^{pr,Grid}$代表微网 x 与电网在 t 时刻的基于内部电价的规划交易功率，$P_{MGx,t}^{pr,Bal}$代表微网 x 与平衡单元在 t 时刻的基于内部电价规划交易功率。

其工作流程始于初始化阶段，基于协同规划层指令与实时采集的本地状态（如负荷实际值、光伏/风电瞬时出力、储能 SOC）随机生成一组表征可能调度策略的初始种群；随后在每一滚动周期内，算法通过选择、交叉与变异算子迭代演化种群，其中适应度函数负责评估每条染色体所对应策略的优劣，引导搜索逼近最优解；为避免早熟收敛，本算法引入了精英保留与动态调整交叉/变异概率的机制[14]。

本文采用的适应度函数采用了加权求和法，其具体为：

$$F=\omega_1\cdot f_1+\omega_2\cdot f_2+\cdots+\omega_n\cdot f_n \quad (11)$$

式中，F 为适应度，ω_i为第 i 个目标的权重系数，f_i为第 i 个目标的权重系数。其中，权重系数之和为 1。

经若干代进化后，算法输出当前最优解，即下一时段各可控单元(如 VSC 传输功率、储能充放电指令)的最优设定值，交由本地执行单元快速实施；同时，本层的实际运行数据(如测量到的电压、功率、SOC 状态)被实时打包上传至协同规划层，为下一轮的滚动预测与优化提供数据反馈，从而构成一个闭环优化系统。

该设计有效发挥了遗传算法处理非线性、高维约束问题的优势，赋予边缘层显著的自主决策与实时响应能力。

2.2.2 分布式自治层条件约束

分布式自治层滚动优化的功率约束条件与协同规划层基本一致，但在实际运行中要考虑到系统安全约束，其中包括电压偏差约束与频率波动约束：

$$|V_i(t)-V_{nom}|\leq\Delta V_{max} \quad (12)$$

$$|f(t)-f_{nom}|\leq\Delta f_{max} \quad (13)$$

式(12)为电压偏差约束函数，其中$V_i(t)$代表在 t 时刻下 i 节点的实时电压测量值，V_{nom}代表该节点的额定电压，ΔV_{max}代表允许的最大电压偏差绝对值；式(13)为频率波动约束函数，其中$f(t)$代表在 t

时刻下系统的实时频率测量值，f_{nom}代表系统的额定频率(通常为 50Hz)，Δf_{max}代表允许的最大频率偏差绝对值。

在遗传算法求解中，这些约束通过罚函数法处理，即构造以下函数附加到目标函数中：

$$\Phi(\dot{x}) = \sum_{i=1}^{n} \lambda_i [g_i(\dot{x})^2] \quad (14)$$

其中，$\dot{x}$代表决策变量向量，包含边缘节点可调度的控制变量，Φ代表罚函数，g_i代表 i 节点的约束违反程度，λ_i代表 i 节点的罚因子[15]。

利用罚函数对原目标函数的修正，可以将原约束优化问题转化为无约束优化问题，进而引导种群向可行域收敛。

3 实验系统的设计与构建

3.1 边缘节点硬件设计

在边缘节点设计中，本文构建了以国产“国网芯”SCM630 为核心的硬件平台，具备实时数据采集、边缘计算与闭环控制功能，显著提升了节点的本地计算能力和响应速度。

此节点采用多核异构处理器、双模冗余电源与高精度信号调理电路，集成多模通信接口，并采用四层 PCB 布局和“模拟-数字-电源”三区隔离策略确保信号完整性与热稳定性。该硬件平台具备宽温工作、紧凑型结构与高度国产化特征，为微电网边缘计算提供了坚实的底层硬件支撑。



图 3.1 边缘节点实物图

3.2 实验平台搭建

在本实验平台中，使用了设计的“国网芯”测控单元作为柔性互联变流器和基于虚拟同步机的混合储能的边缘节点，并将其应用于交直流柔性互联及平衡系统。平台实物如下图所示：

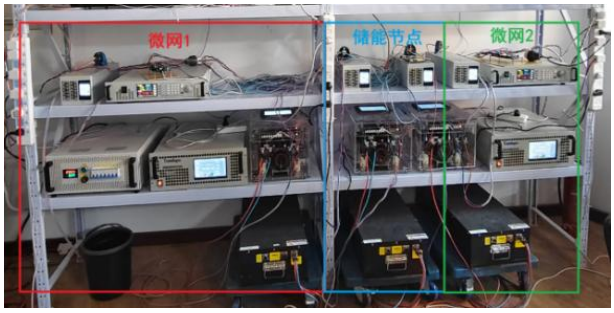


图 3.2 实验平台实物图

微网 1 和微网 2 均由光伏模拟电源、负荷模拟器、DC/DC 变流器和 AC/DC 变流器组成。其中，DC/DC 变流器的型号为 YXPHM-DCCxb-I，AC/DC 变流器的型号为 DZ-IdAC6k。

微网 1 和微网 2 通过背靠背的电压源变流器实现两个交流系统之间的能量交互，并由连接 VSC 的直流母线及连接在直流母线上的混合储能系统构成能量池。

在联接两个交流微电网系统的柔性互联及平衡单元中，两台背靠背的 VSC 变流器、以及储能变流器均配备“国网芯”测控单元。其中，VSC 变流器型号也为 DZ-IdAC6k。如前文所述，整个系统采用双层协同控制策略，上层是各控制器之间根据柔性互联系统的运行要求进行协同调度，下层通过国网芯高性能嵌入式控制器与各自变流器构成闭环控制系统，VSC 变流器的嵌入式控制器负责根据调度信号进行功率传输，基于 VSG 的储能控制器负责直流母线的功率平衡[16]。

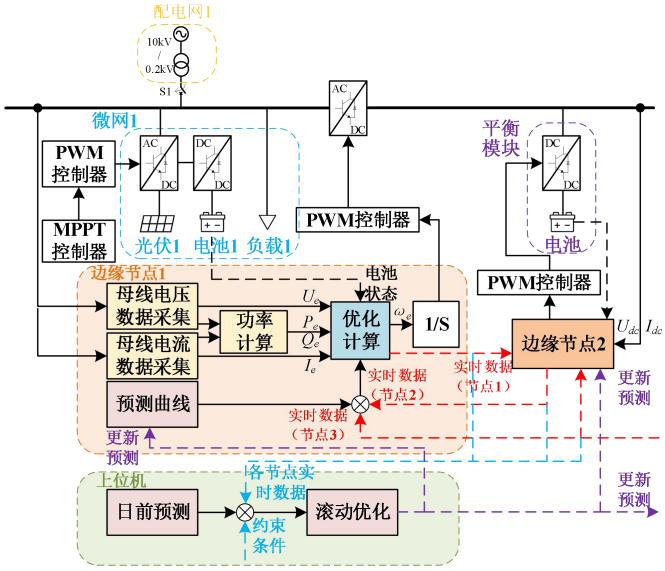


图 3.3 实验平台控制系统框架图

4 实验结果

本研究使用上述平台进行了 96 时段的实验。实验中，光伏和负荷设置的曲线设置为每 15 分钟变化一次，因此滚动优化的周期、实际运行功率的变化周期也是 15 分钟。

在实验参数设置中，微网 1 模拟光伏充沛的发电侧，微网 2 模拟负荷密集的用电侧，平衡节点模拟储能电站。微网 1、微网 2 的光伏与负荷的变化如下所示：

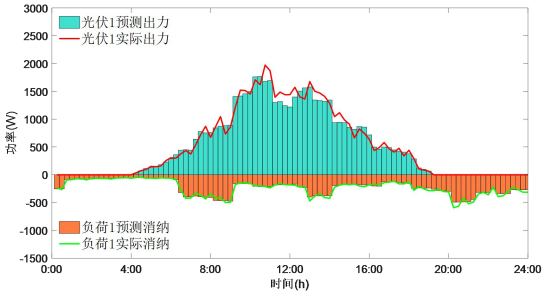


图 4.1 微网 1 光伏/负荷变化图

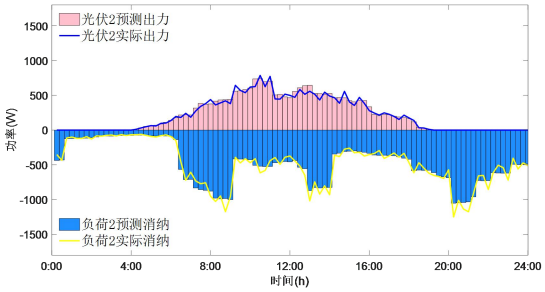


图 4.2 微网 2 光伏/负荷变化图

控制的结果是在光伏和负荷出力存在偏差,且考虑电网能量交互的情况下，基本达到要求的调度计划的目标，最后日内实际双层协同控制的运行趋势与调度计划基本一致，具体结果如下所示：

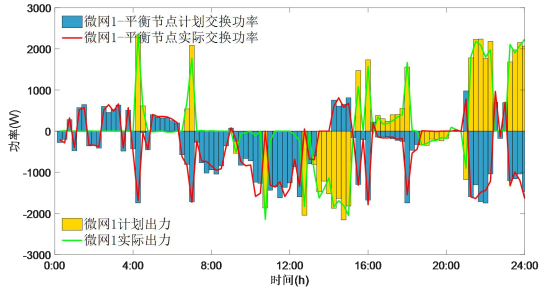


图 4.3 微网 1 的计划/实际交换功率与出力

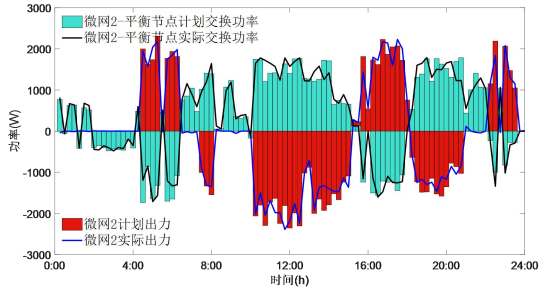


图 4.4 微网 2 的计划/实际交换功率与出力

值得说明的是，在实验结果中观察到，即便在光伏出力和负荷需求均无明显波动的情况下，微网与边缘节点之间的交互功率仍会出现阶跃性调整。该现象源于边缘节点依据预测计划所执行的主动优化策略：通过优化计算，边缘节点在系统扰动发生前发出功率指令，动态调整微网间的能量交互，从而在全局层面实现可再生能源消纳的最大化，并有效抑制直流母线电压波动，提升系统运行稳定性。

5 结论

综上所述，本文针对高比例新能源接入下多微网系统的优化调度问题，提出并实践了一种基于云边协同的多微网分布式优化调度策略。通过构建云边协同的双层控制架构、设计自主可控的高性能边缘硬件平台、并分别在协同规划层采用 CNN-BiLSTM 混合神经网络进行预测规划、分布式自治层采用遗传算法进行实时滚动优化，形成了一套完整的“感知-决策-控制”闭环解决方案。

理论分析与实验验证表明，本文所提方法较传统方法有很多优势。首先，所设计的云边协同框架将计算密集型任务下沉至边缘，显著降低了系统延迟，实现了快速功率扰动响应。其次，以国产“国网芯”为核心的边缘节点硬件设计，兼具高精度、高可靠性与高国产化率，为算法的稳定运行提供了坚实的物理基础。最后，通过“预测-优化-执行-反馈”的闭环机制，系统能够动态适应新能源出力与负荷的波动，在 96 时段的实验运行中，实际出力与计划曲线吻合较为良好，证明了该方法在提升系统运行经济性、稳定性与可再生能源消纳能力方面的有效性。

然而，本研究仍存在可进一步深入探讨之处。例如，未来可将更复杂的不性规划理论融入上层模型，以进一步增强对风光不确定性的鲁棒性；同时，边缘节点间的通信拓扑优化与安全防护机制亦是重要的研究方向。总体而言，本文的研究为构建高效、可靠、自主可控的多微网系统提供了有价值的理论参考与工程实践路径。

参考文献

[1] 袁铁江,张文达.新型电力系统源-储-荷协同规划研究综述[J].中国电机工程学报,2025,45(17):6664-6683.

[2] Y. Yang et al., "A New Virtual Inductance Control Method for Frequency Stabilization of Grid-Forming Virtual Synchronous Generators," in IEEE Transactions on Industrial Electronics, vol. 70, no. 1, pp. 441-451, Jan. 2023.

[3] 赵琮皓,周俊,李健,等.计及源-网-荷-储灵活调节资源的新能源合理利用率评估方法[J/OL].电网技术,1-12[2025-10-04].

[4] 蒋建波,惠学智,刘飞,等.一种光-储整合系统拓扑及协同控制策略设计[J].太阳能学报,2025,46(08):359-368.

[5] Z. Zhang, Y. Zhang, D. Yue, C. Dou, L. Ding and D. Tan, "Voltage Regulation With High Penetration of Low-Carbon Energy in Distribution Networks: A Source – Grid – Load-Collaboration-Based Perspective," in IEEE Transactions on Industrial Informatics, vol. 18, no. 6, pp. 3987-3999, June 2022.

[6] H. Gao, R. Wang, S. He, L. Wang, J. Liu and Z. Chen, "A Cloud-Edge Collaboration Solution for Distribution Network Reconfiguration Using Multi-Agent Deep Reinforcement Learning," in IEEE Transactions on Power Systems, vol. 39, no. 2, pp. 3867-3879, March

2024.

[7] Z. Xu, W. Jiang, J. Xu, Y. Deng, S. Cheng and J. Zhao, "A Power-Grid-Mapping Edge Computing Structure for Digital Distributed Distribution Networks," in IEEE Transactions on Smart Grid, vol. 15, no. 4, pp. 3432-3445, July 2024.

[8] 刘展鹏,虞颖,范帅,等.配电网源荷承载力协同评估及提升方法[J/OL].电力系统自动化,1-18[2025-09-26].

[9] R. S. Tulabing, B. C. Mitchell, G. A. Covic, "Localized management of distributed flexible energy resources," International Journal of Electrical Power & Energy Systems, vol. 157, no. 109790, June 2024.

[10] J. Liu, S. S. Yu, H. Hu, J. Zhao and H. M. Trinh, "Demand-Side Regulation Provision of Virtual Power Plants Consisting of Interconnected Microgrids Through Double-Stage Double-Layer Optimization," in IEEE Transactions on Smart Grid, vol. 14, no. 3, pp. 1946-1957, May 2023.

[11] L. Djilali, C. J. Vega, E. N. Sanchez and J. A. Ruz-Hernandez, "Distributed Cooperative Neural Inverse Optimal Control of Microgrids for Island and Grid-Connected Operations," in IEEE Transactions on Smart Grid, vol. 13, no. 2, pp. 928-940, March 2022.

[12] V. Pentsos, S. Tragoudas, J. Wibbenmeyer and N. Khdeer, "A Hybrid LSTM-Transformer Model for Power Load Forecasting," in IEEE Transactions on Smart Grid, vol. 16, no. 3, pp. 2624-2634, May 2025.

[13] C. Zhao and X. Li, "Microgrid Optimal Energy Scheduling Considering Neural Network Based Battery Degradation," in IEEE Transactions on Power Systems, vol. 39, no. 1, pp. 1594-1606, Jan. 2024.

[14] A. G. Maklewa, C. K. Kim, H.-G. Kim, R. Nyenge, and N. Musila, "Modelling and optimization of microgrid with combined genetic algorithm and model predictive control of PV/Wind/FC/battery energy systems," Energy Reports, vol. 13, pp. 238-255, 2025.

[15] F. N. Budiman, M. A. M. Ramli, H. R. E. H. Bouchekara, A. H. Milyani, "Optimal scheduling of a microgrid with power quality constraints based on demand side management under grid-connected and islanding operations," International Journal of Electrical Power & Energy Systems, vol. 155, Part B, no. 109650, Jan. 2024.

[16] 兰征,刁伟业,曾进辉,等.含异构微源孤岛微电网内虚拟同步发电机预同步控制策略[J].电力系统自动化,2022,46(19):154-161.

059 A Robust Regression-Based Approach for Node Inertia Index Estimation in Power Systems

Yalun Wang[1], Zhou Li[1], Yurong Wang[1] and Qi Wang[1*]

[1] School of Electrical Engineering, Southeast University, Nanjing, China
wangqi@seu.edu.cn

Abstract. The integration of large-scale inverter-based resources into power systems has led to reduced system inertia levels and increased spatial heterogeneity in inertia distribution. Conventional system-level inertia estimation methods are inadequate for assessing inertia with spatial distribution characteristics. This paper proposes a node-level inertia index evaluation method based on robust regression. First, a node-level inertia index is introduced and its dynamic properties are analyzed. Then, a robust regression-based estimation approach is developed to effectively evaluate the spatial distribution of inertia while mitigating the influence of outliers. Finally, the effectiveness and robustness of the proposed method are validated through tests on the IEEE 39-bus system and a provincial-level interconnected grid.

Keywords: Node Inertia Index, Spatial Distribution of Frequency, Robust Regression.

1 Introduction

With the increasing integration of renewable energy and other converter-interfaced resources into power grids, system inertia has been continuously declining, thereby weakening the inertia support capability of the system [1]. To characterize frequency response behavior and ensure frequency stability, accurate assessment of system inertia is essential [2]. Meanwhile, the spatial distribution of inertia has become increasingly heterogeneous, and frequency exhibits more pronounced spatial characteristics. Conventional inertia estimation approaches can no longer meet the requirements of practical inertia assessment, as system-wide inertia results fail to guarantee frequency security in local low-inertia regions [3].

To assess the spatial distribution of inertia, estimation methods have been extended to regional and nodal levels. Region inertia estimation, based on predefined partitions, evaluates inertia within regions and effectively reveals heterogeneity in inertia distribution [4]. Node inertia estimation, in contrast, provides an indicator tied to node frequency, reflecting the capability of inertia to resist changes in node frequency [5]. The definition, characteristics, and estimation methods of node inertia indicators remain at a preliminary stage of investigation.

The concept of inertia distribution was introduced in [6] to describe the spatial characteristics of system inertia. The notion of node inertia and its associated characterization matrix were proposed in [7]. The concept of calculated node inertia and related computational methods were presented in [8]. Furthermore, [9] introduced the nodal equivalent inertia index, analyzing its properties and providing analytical expressions. However, existing node inertia estimation approaches do not account for the presence of measurement noise in practical engineering applications, resulting in insufficient robustness.

Motivated by this limitation, this paper proposes a robust regression-based method for node inertia estimation. First, a node inertia indicator is defined, and its dynamic characteristics are analyzed in both spatial and temporal dimensions. Then, a robust regression-based approach for estimating node inertia is developed. Finally, the effectiveness and robustness of the proposed method are validated using the IEEE 39-bus test system and a provincial interconnected power system.

2 Node Inertia Index

2.1 Definition of Node Inertia Index

Under a disturbance at node d, the node inertia index $H_{\mathrm{B},k}^{d}$ of node k is defined as

$$H_{\mathrm{B},k}^{d}(t) = -\frac{\Delta P_{\mathrm{D}}^{d} f_{\mathrm{N}}}{2S_{\mathrm{B}} \dfrac{\mathrm{d}f_{\mathrm{B},k}(t)}{\mathrm{d}t}} \tag{1}$$

where $f_{\mathrm{B},k}$ is the frequency at node k; f_{N} is the rated frequency; S_{B} is the system base power.

It should be noted that the node inertia index differs from the actual system inertia or generator inertia. Instead, it serves as an evaluation metric associated with nodal frequency, representing the manifestation of system inertia at a given node. The index reflects the capability of system inertia to resist frequency deviations at that node, and its magnitude characterizes the initial frequency response behavior of the node.

2.2 Dynamic Characteristics of Node Inertia Index

In low-inertia power systems, the spatial distribution of frequency becomes more pronounced following a disturbance, leading to significant differences in the dynamic frequency responses among nodes. Accordingly, the node inertia index also exhibits spatial-temporal dynamic characteristics.

From a spatial perspective, for the same disturbance, the node inertia indices differ significantly across nodes. Conversely, for different disturbances, the node inertia index of a given node also varies markedly. From a temporal perspective, the node inertia index depends on the system operating condition, and under a fixed disturbance, the index changes over time.

In summary, the node inertia index dynamically varies with the location of the assessed node, the disturbance event, the operating condition, and the evaluation time. In low-inertia power systems, such dynamic characteristics of the node inertia index become increasingly evident.

3 Estimation Method of Node Inertia Index

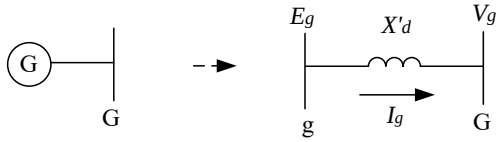


Fig. 1. Schematic diagram of internal node expansion of generator.

Considering the generator internal reactance, the extended dynamic power flow equation can be expressed as [10]:

$$\begin{bmatrix} \Delta \boldsymbol{P}_{\mathrm{g}} \\ \Delta \boldsymbol{P}_{\mathrm{G}} \\ \Delta \boldsymbol{P}_{\mathrm{L}} \end{bmatrix} = \begin{bmatrix} \boldsymbol{H}_{\mathrm{gg}} & \boldsymbol{H}_{\mathrm{gG}} & 0 \\ \boldsymbol{H}_{\mathrm{Gg}} & \boldsymbol{H}_{\mathrm{GG}} & \boldsymbol{H}_{\mathrm{GL}} \\ 0 & \boldsymbol{H}_{\mathrm{LG}} & \boldsymbol{H}_{\mathrm{LL}} \end{bmatrix} \begin{bmatrix} \Delta \boldsymbol{\delta}_{\mathrm{g}} \\ \Delta \boldsymbol{\theta}_{\mathrm{G}} \\ \Delta \boldsymbol{\theta}_{\mathrm{L}} \end{bmatrix} \tag{2}$$

where $\boldsymbol{P}_{\mathrm{g}}$ is the active power vector at the generator internal nodes; $\boldsymbol{P}_{\mathrm{L}}$ is the load vector; $\boldsymbol{P}_{\mathrm{G}}$ is the active power at the generator terminal buses; $\boldsymbol{H}$ is the Jacobian matrix of active power with respect to voltage phase angles; The subscripts g, G, and L correspond to generator internal nodes, generator terminal nodes, and load nodes, respectively; $\boldsymbol{\delta}$ and $\boldsymbol{\theta}$ are the phase angles of generator internal nodes and other nodes.

By extracting the nodal phase angles, the above equation can be reformulated as:

$$\begin{bmatrix} \Delta \boldsymbol{\theta}_{\mathrm{G}} \\ \Delta \boldsymbol{\theta}_{\mathrm{L}} \end{bmatrix} = -\begin{bmatrix} \boldsymbol{H}_{\mathrm{GG}} & \boldsymbol{H}_{\mathrm{GL}} \\ \boldsymbol{H}_{\mathrm{LG}} & \boldsymbol{H}_{\mathrm{LL}} \end{bmatrix}^{-1} \begin{bmatrix} \boldsymbol{H}_{\mathrm{Gg}} \\ 0 \end{bmatrix} \Delta \boldsymbol{\delta}_{\mathrm{g}} + \begin{bmatrix} \boldsymbol{H}_{\mathrm{GG}} & \boldsymbol{H}_{\mathrm{GL}} \\ \boldsymbol{H}_{\mathrm{LG}} & \boldsymbol{H}_{\mathrm{LL}} \end{bmatrix}^{-1} \begin{bmatrix} \Delta \boldsymbol{P}_{\mathrm{G}} \\ \Delta \boldsymbol{P}_{\mathrm{L}} \end{bmatrix} \tag{3}$$

After a disturbance occurs, the disturbance power remains constant. Taking the first derivative, the relationship between nodal frequencies and generator frequencies is given by:

$$\boldsymbol{f}_{\mathrm{B}} = \begin{bmatrix} \Delta \dot{\boldsymbol{\theta}}_{\mathrm{G}} \\ \Delta \dot{\boldsymbol{\theta}}_{\mathrm{L}} \end{bmatrix} = -\begin{bmatrix} \boldsymbol{H}_{\mathrm{GG}} & \boldsymbol{H}_{\mathrm{GL}} \\ \boldsymbol{H}_{\mathrm{LG}} & \boldsymbol{H}_{\mathrm{LL}} \end{bmatrix}^{-1} \begin{bmatrix} \boldsymbol{H}_{\mathrm{Gg}} \\ 0 \end{bmatrix} \Delta \dot{\boldsymbol{\delta}}_{\mathrm{g}} = \boldsymbol{D}_{f} \Delta \dot{\boldsymbol{\delta}}_{\mathrm{g}} \tag{4}$$

where $\boldsymbol{f}_{\mathrm{B}}$ is the nodal frequency vector; $\boldsymbol{D}_{f}$ is the influence of internal frequency of the generator on nodal frequency of gird, referred to as the frequency correlation matrix.

By further differentiation, one obtains:

$$\dot{\boldsymbol{f}}_{\mathrm{B}} = \boldsymbol{D}_f \dot{\boldsymbol{f}}_{\mathrm{g}} \tag{5}$$

The vector of node inertia index is then expressed as:

$$\boldsymbol{H}_{\mathrm{B}}^{d} = -(f_{\mathrm{N}} \Delta \boldsymbol{P}_{\mathrm{D}}^{d}) ./ (2S_{\mathrm{N}} \dot{\boldsymbol{f}}_{\mathrm{B}}) \tag{6}$$

where $\Delta \boldsymbol{P}_{\mathrm{D}}^{d}$ is the disturbance power matrix, extended over multiple time instants; $\dot{\boldsymbol{f}}_{\mathrm{B}}$ is the matrix of nodal frequency deviations over multiple time instants.

Combining (5) and (6) yields:

$$\boldsymbol{H}_{\mathrm{B}}^{d} = -(f_{\mathrm{N}} \Delta \boldsymbol{P}_{\mathrm{D}}^{d}) ./ (2S_{\mathrm{N}} \boldsymbol{D}_f \dot{\boldsymbol{f}}_{\mathrm{g}}) \tag{7}$$

From the swing equation of generators:

$$\dot{\boldsymbol{f}}_{\mathrm{g}} = -f_{\mathrm{N}} (2S_{\mathrm{N}} \boldsymbol{H}_{\mathrm{g}})^{-1} \Delta \boldsymbol{P}_{\mathrm{g}} \tag{8}$$

where $\boldsymbol{H}_{\mathrm{g}}$ is the diagonal matrix of generator inertia constants, $\boldsymbol{H}_{\mathrm{g}} = diag(H_{g1}, H_{g2}, \cdots)$

By combining (7) and (8), one obtains:

$$\boldsymbol{H}_{\mathrm{B}}^{d} = \Delta \boldsymbol{P}_{\mathrm{D}}^{d} ./ (\boldsymbol{D}_f (H_{\mathrm{g}})^{-1} \Delta \boldsymbol{P}_{\mathrm{g}}) \tag{9}$$

This expression indicates that the node inertia index vector is composed of the disturbance vector, the frequency correlation matrix, generator inertia, and the disturbance power undertaken by generators.

Rearranging (9) gives:

$$\boldsymbol{H}_{\mathrm{B}}^{d} .* (\boldsymbol{D}_f (H_{\mathrm{g}})^{-1} \Delta \boldsymbol{P}_{\mathrm{g}}) = \Delta \boldsymbol{P}_{\mathrm{D}}^{d} \tag{10}$$

Let $\boldsymbol{Q}_{\mathrm{g}} = \boldsymbol{D}_f (H_{\mathrm{g}})^{-1} \Delta \boldsymbol{P}_{\mathrm{g}}$,then:

$$\boldsymbol{H}_{\mathrm{B}}^{d} .* \boldsymbol{Q}_{\mathrm{g}} = \Delta \boldsymbol{P}_{\mathrm{D}}^{d} \tag{11}$$

By taking $\boldsymbol{Q}_{\mathrm{g}}$ as the input and $\Delta \boldsymbol{P}_{\mathrm{g}}$ as the output of the parameter identification model, the input–output pairs are extracted for each node. For each node *k*, the node inertia index is independently identified using robust regression. The k-th row of $\boldsymbol{Q}_{\mathrm{g}}$ and $\Delta \boldsymbol{P}_{\mathrm{g}}$ is extracted, $\boldsymbol{Q}_{\mathrm{g},k} = [Q_{\mathrm{g}}(k,1), Q_{\mathrm{g}}(k,2), \cdots Q_{\mathrm{g}}(k,n)]^{\mathrm{T}}$, $\Delta \boldsymbol{P}_{\mathrm{g},k} = [P_{\mathrm{g}}(k,1), P_{\mathrm{g}}(k,2), \cdots P_{\mathrm{g}}(k,n)]^{\mathrm{T}}$.

The parameter identification model of the node inertia index at node k is expressed as:

$$\Delta \boldsymbol{P}_{\mathrm{D},k}^{d} = H_{\mathrm{B},k}^{d} \boldsymbol{Q}_{\mathrm{g},k} + \boldsymbol{\varepsilon}_k \tag{12}$$

where $\boldsymbol{\varepsilon}_i$ is the error or noise term, $\boldsymbol{\varepsilon}_i = [\varepsilon(i,1), \varepsilon(i,2), \cdots \varepsilon(i,n)]^{\mathrm{T}}$.

To enhance robustness, the Huber loss function is adopted in place of the conventional squared loss used in least squares regression. The optimization objective and the Huber loss function are defined as:

$$\min_{H_{\mathrm{B},k}^{d}} \sum_{t=1}^{n} \rho(\Delta P_{\mathrm{g},k}(t) - H_{\mathrm{B},k}^{d} Q_{\mathrm{g},k}(t)) \tag{13}$$

$$\rho(r)=\begin{cases}0.5r^2 & ,|r|\le\beta\\ \beta(|r|-0.5\beta) & ,|r|>\beta\end{cases} \tag{14}$$

The node inertia indices are obtained by minimizing the loss function through gradient descent. The Huber loss function preserves the efficiency of squared loss for small residuals close to the true relationship, while switching to linear loss for large residuals likely caused by outliers. This reduces the influence of potential outliers, mitigates sensitivity to noise, and lowers dependence on data quality. Consequently, the approach improves the robustness of parameter identification, implicitly achieves a regularization effect, and is particularly suitable for practical engineering scenarios where measurement data may contain noise or outliers.

4 Case Study

4.1 Case 1

The proposed method is validated on the IEEE 39-bus system. The system topology is shown in Fig. 2, where Generator 1 represents the equivalent external grid and Generator 2 serves as the slack generator. The disturbance is modeled as a change in load active power, with system deviations kept within the governor deadband. The system nominal frequency is 60 Hz, and the base power is 1000 MVA. The simulation step size is set to 20 ms. At $t=5$ s , a sudden load increase of 20 MW is applied at bus 20.

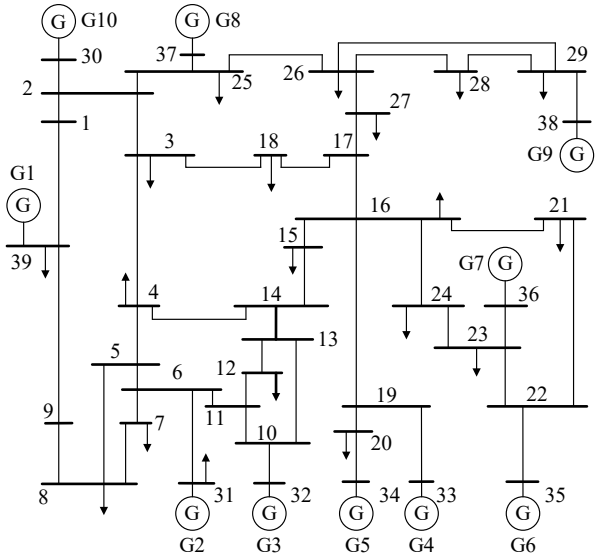


Fig. 2. IEEE 39-bus system.

Using the robust regression method, the node inertia indices are identified, and their distribution across nodes is shown in Fig. 3.

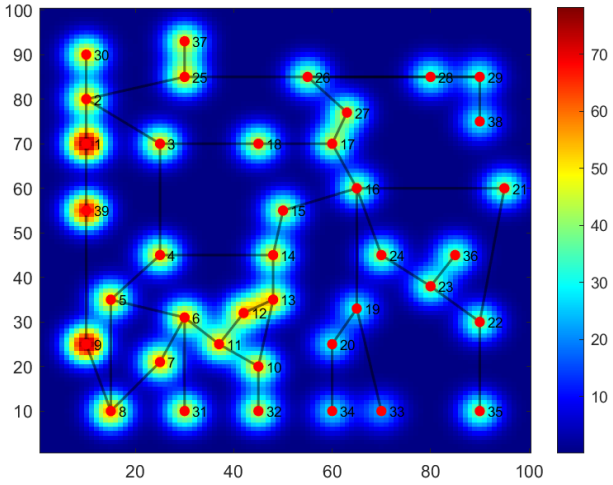
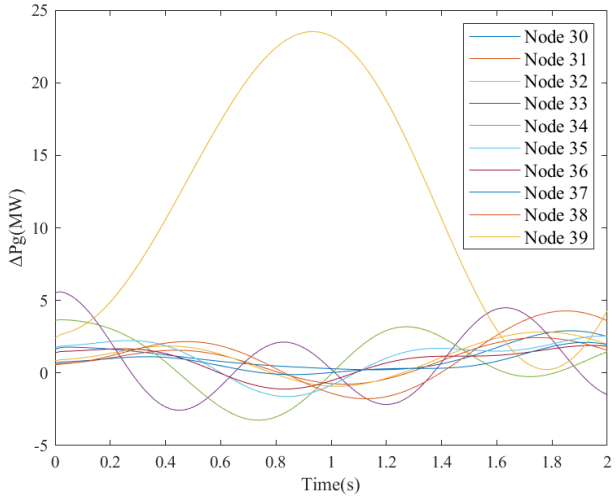


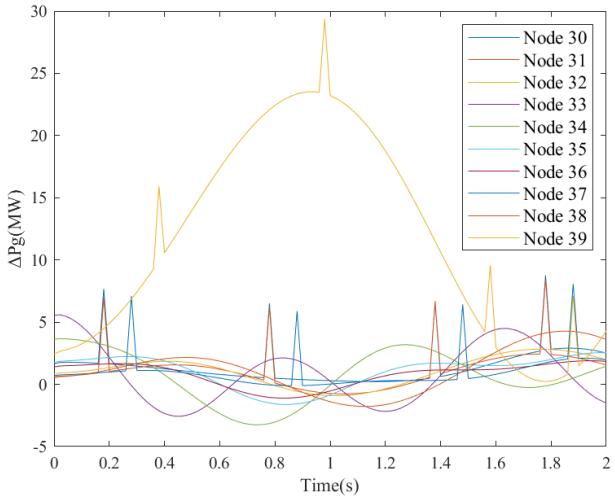
Fig. 3. Node inertia index results for IEEE 39-bus system.

The results clearly demonstrate differences among the node inertia indices. Under this disturbance, the nodes in the left part of the system exhibit larger node inertia indices, with smaller fluctuations in frequency deviation rates, indicating stronger capability to resist frequency changes.

To test noise robustness, outliers are injected into the output power data of G1, G2, G8, and G10. The data before and after outlier injection are shown in Fig. 4.



(a)



(b)

Fig. 4. Comparison of data before and after adding noise.

The proposed robust regression method is compared with the conventional least squares method. The comparative results of node inertia index estimation obtained by both approaches are presented in Fig. 5.

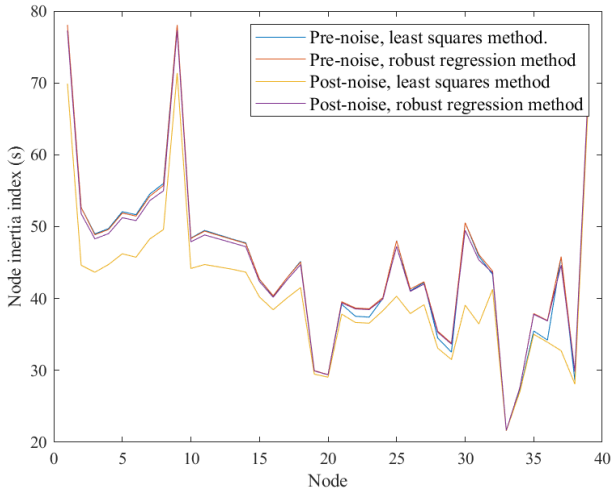


Fig. 5. Comparison of node inertia index results.

As shown in Fig. 5, the proposed robust regression–based method for node inertia index estimation can effectively suppress the influence of outliers, ensuring the validity of the identified indices and making the approach suitable for practical engineering applications.

4.2 Case 2

The proposed method is further validated on a provincial interconnected power system under the typical operating condition of the summer peak in 2030. The distribution of the node inertia indices is illustrated in Fig. 6.

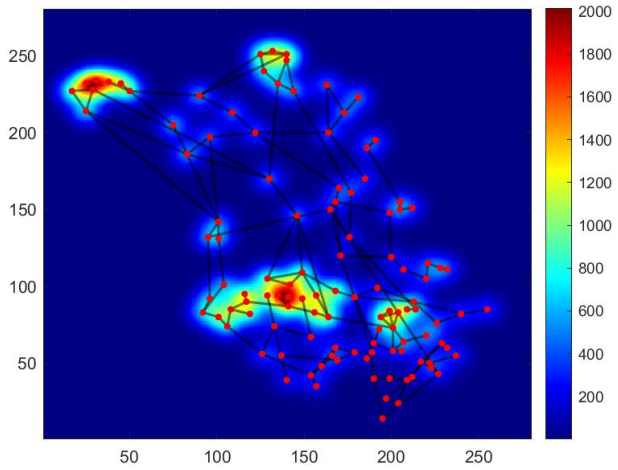


Fig. 6. Node inertia index results for a provincial interconnected system.

The results indicate that, under this operating condition, the node inertia distribution of the system is markedly non-uniform. The node equivalent inertia index provides an effective means of identifying weak regions, thereby offering valuable guidance for subsequent inertia optimization.

5 Conclusion

This paper proposes a robust regression–based method for node inertia index estimation, which enables effective assessment of inertia distribution. Moreover, the method mitigates the impact of outliers, ensures the reliability of the assessment results, and is well-suited for practical engineering scenarios.

Acknowledgement: This work was supported by the National Key Research and Development Program of China under Grant 2024YFB2408900 and the Science and Technology Project of the State Grid Corporation of China under Grant SGTYHT/24-JS-001.

References

1. Tan, B. and Zhao, J.: Data-driven adaptive unscented Kalman filter for time-varying inertia and damping estimation of utility-scale IBRs considering current limiter[J]. IEEE Transactions on Power Systems, 39, (6), 7331-7345 (2024).
2. Wang Y., Wang Q., Tang Y., Xu Y., and Hu J.: Online estimation of region inertia based on dynamic division with spatial-temporal perception[J]. IEEE Transactions on Power Systems,1-14 (2025).
3. Bi T., Liu J., and Wang C.: Online estimation of area-level inertia considering inter-area equivalent frequency dynamics[J]. IEEE Transactions on Power Systems, 40, (1), 57-72 (2025).
4. Wang Y., Shi L., Jiang Y., and Wang Q.: Real-time dynamic division based online estimation of region inertia in power systems[C] // 2024 IEEE Power & Energy Society General Meeting (PESGM). pp. 1-5, Seattle, WA (2024).
5. Li W., Ding L.: A preliminary research on the representation form of spatial-temporal distribution characteristics of power system inertia under large disturbances[J]. Proceedings of the CSEE, 44 (12), 4601-4615 (2024)
6. Zeng F., Zhang J., Zhou Y., et al: Online identification of inertia distribution in normal operating power system[J]. IEEE Transactions on Power Systems, 35(4), 3301-3304 (2020).
7. Zeng F., Zhang J.: Temporal and spatial characteristics of power system inertia and its analysis method[J]. Proceedings of the CSEE, 40 (01), 50-58+373 (2020).
8. Liu F., Xu G., Liu J., et al: Inertia distribution characteristics of power system considering structure and parameters of power grid[J]. Automation of Electric Power Systems, 45 (23), 60-67 (2021).
9. Liu J., Wang C., and Bi T.: Node equivalent inertia index for temporal-spatial frequency dynamics of renewable energy power system and its applications[J]. Proceedings of the CSEE, 43 (20), 7773-7789 (2023).
10. Sun H., Li Q., Zhang M., et al: Continuation power flow method based on dynamic power flow equation[J]. Proceedings of the CSEE, 31 (07), 77-82 (2011).

060 Research Impact on Electrolytic Water Hydrogen Production on SSO in Wind-PV Complementary System

Xing Jiabao and Xu Tao

College of Electric Power, Inner Mongolia University of Technology, Hohhot 010080, China
xjbwork@126.com

Abstract. Using abandoned wind and photovoltaic (PV) to produce hydrogen from electrolytic water is helpful to promote the coordinated development of electricity and hydrogen, ensure national energy security, and achieve "carbon peak and carbon neutralization". The power characteristics of PV and wind power are complementary in the wind-PV complementary electrolytic water hydrogen production system. The interaction between power electronic equipment and series compensation system leads to the unique evolution law of subsynchronous oscillation (SSO). To this end, this paper constructs a dynamic model of the complementary wind-PV coupling electrolytic water hydrogen production system. The eigenvalue analysis method is used to calculate the frequency, participation factor and damping ratio of each oscillation mode, and the key state variables affecting SSO are identified. The nonlinear relationship between the capacity of the hydrogen production device and the stability of the system is deeply explored, and the internal correlation between the coupling effect of wind, PV and hydrogen production device and SSO is proposed.

Keywords: Coupling Wind-Photovoltaic (PV), Series Compensation Capacitor System, Electrolytic Water Hydrogen Production, Subsynchronous Oscillation (SSO).

1 Introduction

With the increasingly serious problem of climate change, it is an important part of China 's construction of new power system to promote the transformation of energy system to clean and low-carbon direction by actively promoting carbon peak carbon neutralization and accelerating the planning and construction of new energy system [1-3].

As core components of renewable energy, wind and PV power have become key drivers of the energy transition due to their abundant availability, wide geographical distribution, and clean, pollution-free characteristics [4-6]. At present, the technology of hydrogen production by electrolytic water has made breakthrough progress. With the

wide application of high-efficiency equipment such as proton exchange membrane (PEM) electrolyzer, the efficiency and stability of hydrogen production have been continuously improved [7]. The wind-PV complementary power generation system, which leverages complementary temporal and spatial distributions of these energy sources, has become a widely adopted solution for creating more stable, reliable, and efficient power generation system [8]. However, the unique interaction patterns between wind-PV complementary power characteristics and power electronic equipment coupled with series compensation systems in hybrid electrolysis systems, which makes the SSO problem of the system more complicated [9]. Therefore, it is necessary to conduct in-depth research on the problem of the wind-PV complementary coupling electrolytic water hydrogen production system.

Based on the aforementioned background, this paper studies the key factors affecting the SSO of the wind-PV complementary hydrogen production system. The research process comprises three main stages: First, a dynamic model was established for the wind-PV hybrid system coupled with electrolytic water hydrogen production system. Second, eigenvalue analysis was employed to calculate the frequencies, participation factors, and damping ratios of oscillation modes, identifying critical state variables affecting SSO. Finally, through in-depth exploration of the nonlinear relationship between hydrogen production capacity and system stability, the intrinsic correlation between the coupling effect of wind, PV, and hydrogen and SSO is elucidated.

2 Modeling of Complementary Wind-PV Coupling Hydrogen Production System

2.1 Modeling the Overall Structure of the System

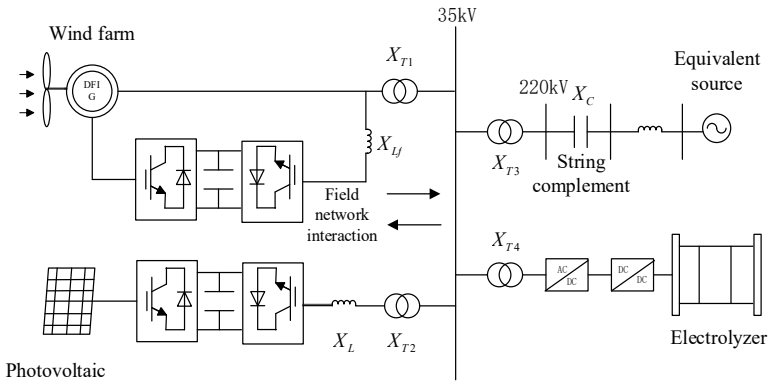


Fig. 1. System-wide grid-connected structure diagram.

The complementary wind-PV coupling electrolytic water hydrogen production system is composed of a doubly-fed induction generator, PV grid-connected power generation unit, series compensation transmission device, and electrolytic water hydrogen production unit. In the topology of the wind-PV-hydrogen coordinated grid-connected system shown in Fig.1, the electrolytic water hydrogen production device uses the wind-PV hybrid electric field as the energy input source.

2.2 System-Wide Small Signal Model

The state space equations of doubly-fed induction generator, photovoltaic module and electrolytic water hydrogen production device are linearized, and the mathematical expression of small signal dynamic model of complementary wind-PV coupling hydrogen production system is established:

$$\frac{d\Delta X}{dt} = A\Delta X \tag{1}$$

$$\begin{cases} \Delta X_{\text{shaft}} = \begin{bmatrix} \Delta\omega_{\text{t}} & \Delta\omega_{\text{r}} & \Delta\theta \end{bmatrix} \\ \Delta X_{\text{dc}} = \begin{bmatrix} \Delta U_{\text{dc}} \end{bmatrix} \\ \Delta X_{\text{Gen}} = \begin{bmatrix} \Delta i_{\text{qs}} & \Delta i_{\text{ds}} & \Delta i_{\text{qr}} & \Delta i_{\text{dr}} \end{bmatrix} \\ \Delta X_{\text{RSC}} = \begin{bmatrix} \Delta z_1 & \Delta z_2 & \Delta z_3 & \Delta z_4 \end{bmatrix} \\ \Delta X_{\text{GSC}} = \begin{bmatrix} \Delta z_5 & \Delta z_6 & \Delta z_7 \end{bmatrix} \\ \Delta X_{\text{dc1}} = \begin{bmatrix} \Delta u_{\text{dc1}} \end{bmatrix} \end{cases} \begin{cases} \Delta X_{\text{K}} = \begin{bmatrix} \Delta x_1 & \Delta x_2 & \Delta x_3 & \Delta u_{\text{dcref}} & \Delta i_{\text{cqref}} \end{bmatrix} \\ \Delta X_{\text{PLL}} = \begin{bmatrix} \Delta\omega & \Delta\theta_1 \end{bmatrix} \\ \Delta X_{\text{LCL}} = \begin{bmatrix} \Delta i_{\text{cd}} & \Delta i_{\text{cq}} & \Delta u_{\text{td}} & \Delta u_{\text{tq}} \end{bmatrix} \\ \Delta X_{\text{SCL}} = \begin{bmatrix} \Delta u_{\text{sq}} & \Delta u_{\text{sd}} & \Delta i_{\text{Rq}} & \Delta i_{\text{Rd}} \end{bmatrix} \\ \Delta X_{\text{BH}} = \begin{bmatrix} \Delta V_{\text{DC}} & \Delta i_{\text{d}} & \Delta i_{\text{q}} \end{bmatrix} \\ \Delta X_{\text{HD}} = \begin{bmatrix} \Delta v_{\text{EL}} & \Delta i_{\text{Lf2}} & \Delta i_{\text{Lf1}} \end{bmatrix} \end{cases} \tag{2}$$

Through Matlab programming, the system's state matrix eigenvalues were calculated. After the non-oscillating modes are removed by modal screening, the calculation results of the retained effective eigenvalues are listed in Table 1.

The oscillation frequencies of mode $\lambda_{7,8}$ and $\lambda_{9,10}$ are in the range of supersynchronous frequency and subsynchronous frequency. The damping ratio of the pair of eigenvalues of $\lambda_{9,10}$ is negative, which is a pair of oscillating divergent oscillation modes and is the focus of this paper. The characteristic frequency of $\lambda_{9,10}$ is 37.83 Hz, and its negative damping characteristic indicates that the mode originates from the subsynchronous control interaction between the wind-PV-hydrogen multi-energy coupling system and the series compensation line. The oscillation frequency of $\lambda_{7,8}$ is 61.53 Hz, which is close to 100 Hz with the oscillation frequency of $\lambda_{9,10}$, which conforms to the mechanism of subsynchronous and supersynchronous oscillation.

4

Table 1. Eigenvalue calculation results.

Oscillation mode	Eigenvalue	Oscillation frequency	Damping ratio
$\lambda_{1,2}$	$-37.23 \pm j1689.73$	269.06Hz	0.022
$\lambda_{3,4}$	$-38.69 \pm j1781.67$	283.71Hz	0.021
$\lambda_{5,6}$	$-68.97 \pm j711.62$	113.32Hz	0.096
$\lambda_{7,8}$	$-18.98 \pm j386.42$	61.53Hz	0.049
$\lambda_{9,10}$	$0.86 \pm j237.58$	**37.83Hz**	-0.0036
$\lambda_{15,16}$	$-6.92 \pm j92.31$	14.69Hz	0.075
$\lambda_{21,22}$	$-1.634 \pm j11.72$	1.86Hz	0.138

3 The Impact Factors of Hydrogen Production System on SSO

3.1 The Impact of Control Parameters

The control strategy of the electrolytic water hydrogen production system with PEM adopts the voltage-current dual-loop proportional-integral regulation architecture. The topology of the control system is shown in Fig. 2.

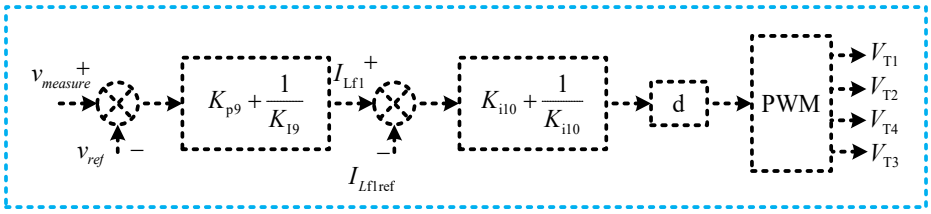


Fig. 2. Control block diagram of phase-shifting full bridge converter.

When the control parameters of the electrolytic water hydrogen production device change, it is necessary to study the impact of its dynamic response characteristics on the oscillation mode of the whole system. Under the reference condition, when the gain parameter configuration of the voltage outer-loop control module is set to K_{p9}=0.5, the system responds to negative damping ratio. In order to thoroughly analyze the coupling relationships between parameters, adjust individual parameters and calculate damping ratios under different system states. The parameter $K_{i9}=1/T_{i9}$ changes continuously in the interval [20~100]. According to eigenvalue analysis, the evolution path of the

damping ratio and frequency response of the system oscillation mode with K_{i9} can be obtained, as shown in Fig. 3.

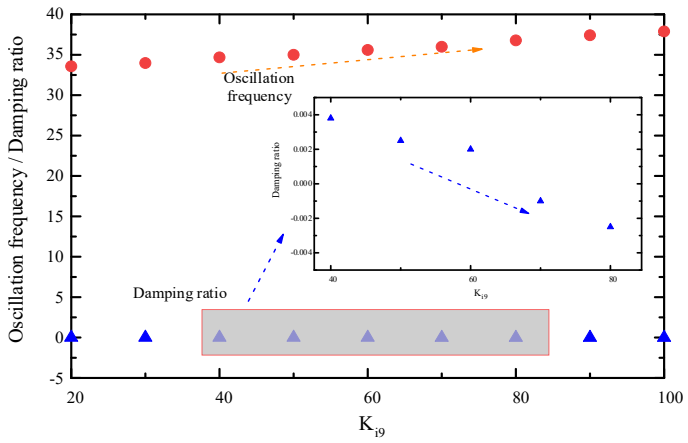


Fig. 3. The impact of SSO on oscillation mode when Ki9 changes.

As K_{i9} increases, the system's damping ratio exhibits a monotonically decreasing trend, gradually becoming negative damping and ultimately losing stability. When the control parameter K_{i9} shows an increasing trend, its inherent oscillation characteristics gradually approach the oscillation component of the output power of the wind-PV hybrid electric field.

When the control parameters of the electrolytic water hydrogen production device are set to (K_{p9}=5, K_{i9}=80), the waveform and spectral characteristics of the DC side current are analyzed as shown in Fig. 4. The results show that there is a frequency component with an amplitude of 39 Hz in the working current of the electrolytic water hydrogen production device, which is consistent with the theoretical analysis results.

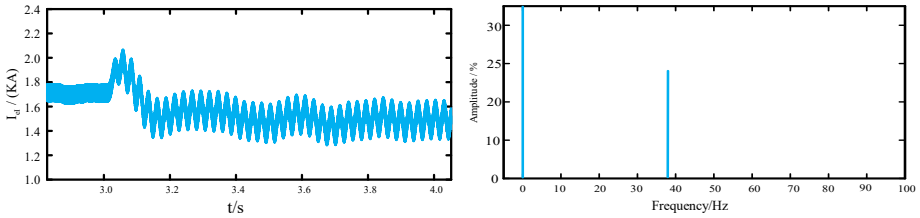


Fig. 4. DC current waveform of electrolytic water hydrogen production device.

3.2 The Impact of Capacity of Electrolytic Cell

The capacity of the hydrogen production system is gradually expanded from 10 MW to 120 MW by using 10 MW fixed step size to adjust the capacity of the hydrogen

production system step by step. The impact of the capacity change of the electrolytic water hydrogen production device on the SSO damping ratio and oscillation frequency is shown in Fig. 5.

In the initial stage of capacity expansion (10 MW to 70 MW), the system's oscillation mode damping ratio initially followed a monotonically increasing trend but the damping ratio is still negative and the system stability is improved with the increase of capacity. When the capacity exceeds the critical value of 70 MW, the damping ratio changed to a gradual decline pattern. When hydrogen production power is below 70 MW, capacity expansion effectively enhances local stability by optimizing damping distribution. However, beyond this critical point, intensified negative impedance interactions between hydrogen production units and the grid leads to reduced damping ratios, resulting in a contraction of the small signal stability boundary of the system.

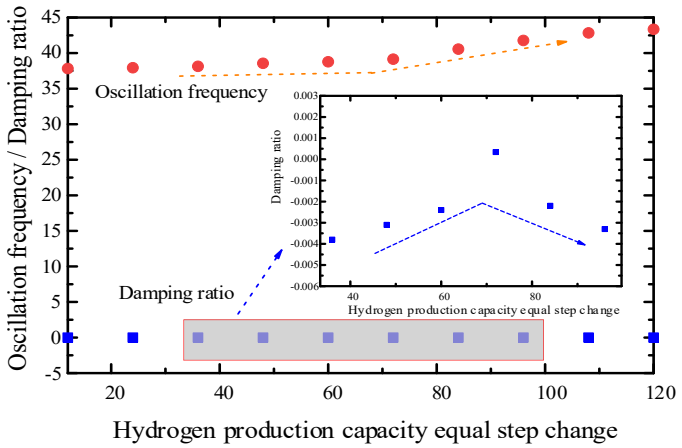


Fig. 5. The impact of hydrogen production capacity change on oscillation mode.

According to the above analysis, there are several scenarios for capacity configuration of electrolytic water hydrogen production device:

Scenario 1: Under the set grid operation boundary, the maximum power capacity of the wind-PV hybrid system is limited to 470 MW. Based on an idealized assumption (ignoring the transmission and distribution losses and the power generation unit is in full power operation state), 30MW of unutilized wind-PV surplus power is selected to drive the electrolytic water hydrogen production unit. In this operation mode, the active power output of the wind-PV hybrid electric field is shown in the time domain waveform in Fig. 6.

Scenario 2: Under the set grid operation boundary, the maximum power that the wind-PV hybrid power generation system can be accepted by the grid is limited to 430MW. The remaining wind-PV 70MW power that has not been absorbed by the grid is selected as the driving energy for the electrolytic water hydrogen production device. In this operation mode, the active power output of the wind-PV hybrid electric field is shown in the time domain waveform in Fig. 7.

Scenario 3: Under the condition of the limited grid acceptance capacity, the maximum grid-connected power of the wind-PV hybrid system is set to 380 MW. To address renewable energy integration bottlenecks, 120 MW of excess wind-PV power not absorbed by the grid serves as input energy for the electrolytic water hydrogen production system. The active power output of the wind-PV hybrid electric field under this operational mode is illustrated in the time-domain waveform shown in Fig. 8.

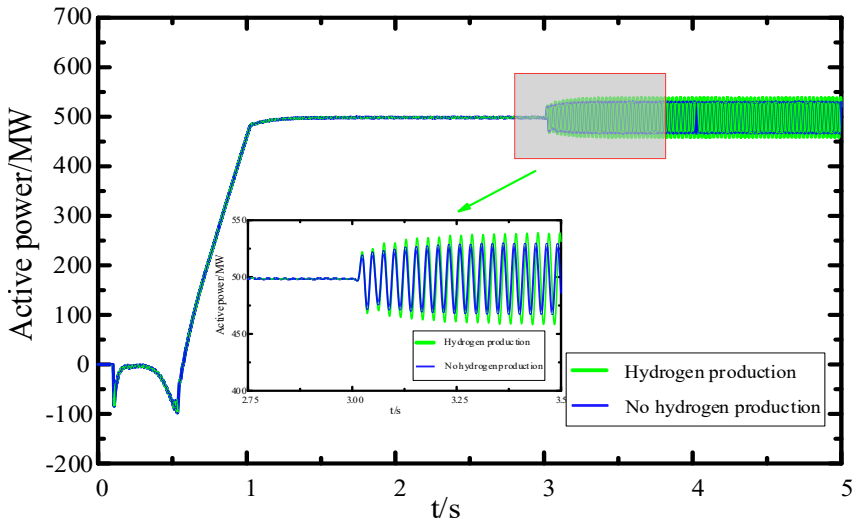


Fig. 6. The impact of 30MW on active power of electrolytic water hydrogen production device.

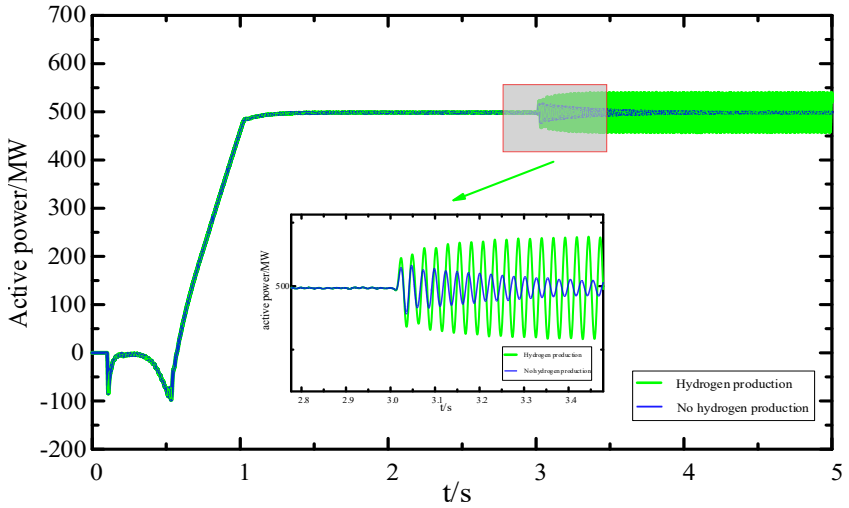


Fig. 7. The impact of 70 MW on active power of electrolytic water hydrogen production device.

8

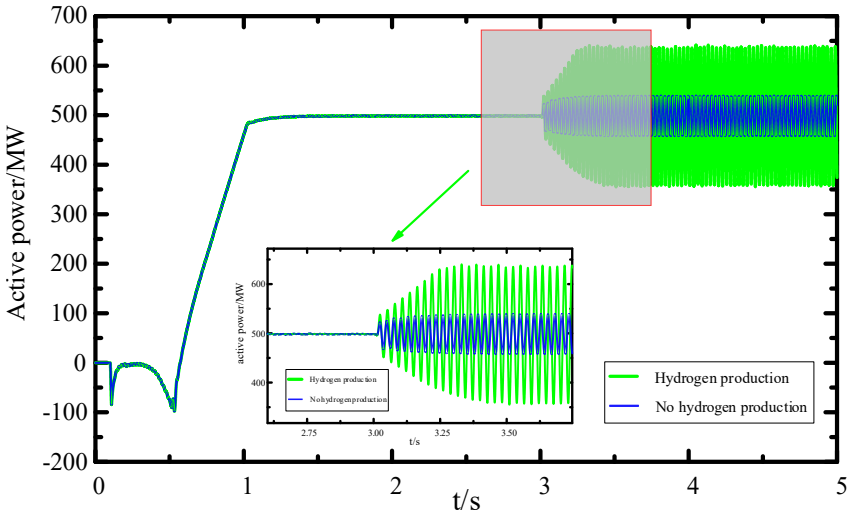


Fig. 8. The impact of 120 MW on active power of electrolytic water hydrogen production device.

The dynamic simulation results show that when t=0 s, the electrolytic water hydrogen production device is connected to the grid at capacities of 30 MW, 70 MW and 120 MW, the wind-PV hybrid power generation cluster has power fluctuations. After the series compensation device is put into operation at t=3 s, compared with the system condition without hydrogen production unit, the grid connection of 30 MW and 70 MW hydrogen production units can attenuate the amplitude of SSO, and the attenuation effect is more significant under 70 MW condition. However, after the 120 MW hydrogen production unit is connected, the SSO amplitude of the system is enhanced, resulting in a significant decrease in operating stability, indicating that there is a critical value for the hydrogen production capacity, which will aggravate the system oscillation.

In conclusion, there is an inherent correlation between electrolytic cell capacity and SSO. Within a specific range, increasing electrolytic cell capacity significantly increases the damping ratio of SSO modes, which leading a marked attenuation trend in oscillation energy amplitude. When exceeding the critical threshold of electrolytic cell capacity, continued increases in capacity will lead to the aggravation of the negative damping effect of oscillation modes, which will increase the divergence rate of SSO in the system.

4 Conclusion

This paper analyzes the internal correlation between the coupling effect of wind, PV and hydrogen and SSO. The main work is summarized as follows:

(1) When the controller parameters in the hydrogen production system are not properly set, the hydrogen production device will affect the SSO characteristics of the system.

(2) There is an inherent correlation between the capacity configuration of hydrogen production device and the SSO of the system. Within the critical capacity value range, the system stability increases with the increase of hydrogen production device capacity; however, when the hydrogen production capacity exceeds the critical value, the SSO of the system will show a divergent trend.

Acknowledgement: This work is supported by Natural Science Foundation Inner Mongolia Autonomous Region (2023LHMS05049) and by Fundamental Research Funds for Universities Directly under the Autonomous Region (JY20240014).

References

1. Chen Guoping, Dong Yu, Liang Zhifeng.: Analysis and thinking on high-quality development of new energy with Chinese characteristics in energy transformation [J]. Chinese Journal of Electrical Engineering40(17), 5493-5506 (2020).
2. People's Daily, https://www.gov.cn/lianbo/bumen/202408/content_6966370.htm, last accessed 2025/07/04.
3. Guo Xinyang, Chen Xinyu, Chen Xia, et al.: Grid Integration Feasibility and Investment Planning of Offshore Wind Power under Carbon-neutral Transition in China[J]. Nature Communications14(1), 24-47 (2023).
4. Wen Xuan, Sun Bo, Gu Bing, et al.: Multi-Time Scale Optimal Scheduling Model of Wind and Hydrogen Integrated Energy System Based on Carbon Trading[J]. PROCESSES11(2), 337-321 (2023).
5. Ding Jian, Fang Xiaosong, Song Yunting, et al.: Conception of electricity-hydrogen integrated energy network for new energy transmission in western China under the background of carbon neutrality [J]. Power system automation45(24), 1-9 (2021).
6. Gao Jie, Song Jie, Wang Jianxiao, et al.: Morphology and key technologies of electro-hydrogen coupling system supporting China 's energy security [J]. Power system automation47(19), 1-15 (2023).
7. Jiang Qirong, Wang Yuzhi.: Analysis and suppression of electromagnetic oscillation in power system with high proportion of power electronic equipment [J]. Chinese Journal of Electrical Engineering40(22), 7185-7201 (2020).
8. Farshid Salehi, Igor Brandão Machado Matsuo, Azade Brahman, et al.: Sub-Synchronous Control Interaction Detection: A Real-Time Application [J]. IEEE Transactions on Power Delivery35(1), 106-116 (2020).
9. Hui Li, Mohamed Abdeen, Zhaosen Chai, et al.: An Improved Fast Detection Method on Subsynchronous Resonance in a Wind Power System with a Series Compensated Transmission Line[J]. IEEE Access7(2), 61512-61522 (2019).

061 Control Parameter Identification Method for Grid-Following Converters Based on Multi-Disturbance Response

Jianzhi Song [1], Weilin Zhong[1], Chenchen Ge[1],Junru Chen[1], Baoyu Zhai[2], Dongliang Nan[2]

[1] School of Electrical Engineering Xinjiang University
[2] State Grid Xinjiang Electric Power Co., Ltd. Electric Power Research Institute

Abstract. Accurate identification of converter control parameters is fundamental to transient analysis of renewable energy power systems. However, the overall identification accuracy is often limited due to the low sensitivity of certain control parameters to system external characteristics. To address this issue, this paper proposes a multi-disturbance-response-based identification method for control parameters of grid-following converters. First, by analyzing the correlation between system external characteristics and controller dynamics, multiple small disturbance signals are injected into the system to achieve dynamic decoupling of different controllers under system external characteristics. Second, a quantitative identifiability analysis of control parameters is performed based on the sensitivity method, and appropriate disturbance types and observation variables are designed for parameter identification. Third, leveraging the sensitivity differences of control parameters under different disturbance responses, a stepwise identification strategy is developed to resolve the difficulty of simultaneously identifying low-sensitivity control parameters. Finally, a grid-following converter test system is built on the MATLAB/Simulink platform, and the effectiveness of the proposed method is validated using simulation data.

Keywords: Grid-following converter, Parameter identification, Disturbance response, Sensitivity analysis.

1 Introduction

With the increasing penetration of renewable energy generation units interfaced through converters, the dynamic characteristics of power systems are undergoing significant changes[1]. In renewable energy grid-connected systems, the accuracy of controller parameters in the model plays a critical role in system dynamic analysis and fault protection design. However, due to confidentiality of testing techniques or intellectual property protection, most manufacturers do not disclose accurate models and parameters. Without the correct controller parameters of renewable energy grid-connected systems, it is difficult for the constructed model to accurately reproduce the real system's dynamic behavior[2]. Therefore, identifying controller parameters from

measured signals such as current and voltage in renewable energy grid-connected systems is essential.

At present, converters in renewable energy power systems typically adopt a grid-following control strategy. The control system mainly consists of a phase-locked loop (PLL) PI controller and a dual-loop vector PI controller. As a key device for renewable energy integration, the converter's control system greatly influences the operating state of the generation system. The mechanism models of renewable energy grid-connected systems are well established, and current research focuses on parameter identification of these models, particularly on both physical parameters and control parameters.

Parameter identification methods can be broadly classified into integrated identification and stepwise identification approaches. In integrated identification methods, numerous novel optimization algorithms, such as particle swarm optimization and dung beetle optimization[3-4], have been applied. However, in the context of control parameter identification for renewable energy grid-connected systems, dynamic coupling among multiple controllers often results in highly nonlinear fault response behavior[5]. Moreover, the number of parameters within multiple controllers can exceed the order of the identification model, leading to a rank-deficiency problem. Significant differences in parameter sensitivities further hinder accurate convergence of multi-parameter identification using integrated methods.

In stepwise identification methods, some studies simplify the control model of renewable energy grid-connected systems by using external characteristics, thereby reducing model order and the number of parameters to be identified[6]. However, such simplified models are unsuitable for dynamic system analysis. To address multi-parameter model identification challenges, some literature introduces trajectory sensitivity methods that classify parameters into highly sensitive and ill-conditioned low-sensitivity groups. The low-sensitivity parameters are fixed to empirical or default values, while only high-sensitivity parameters are identified independently. Nevertheless, under different operating conditions, low-sensitivity parameters may lead to incorrect fault analysis results. For example, the parameter probability pre-evaluation method in[7] examines the influence of low-sensitivity parameters on high-sensitivity parameter identification, showing that inaccurate low-sensitivity parameters can prevent accurate optimization. Other studies have focused on identification of control parameters in different time scales or frequency bands[8]. For instance,[9] establishes a dynamic fault response differential identification model for PLLs, using post-fault time-window short-circuit current measurements to identify PLL control parameters, but this method imposes restrictions on fault types.

In summary, the main challenge in identifying control parameters of grid-following converters lies in the fact that traditional simultaneous identification methods cannot effectively identify low-sensitivity control parameters using system external characteristics. Stepwise identification strategies can reduce the number of parameters identified simultaneously, but existing methods often require internal converter measurement signals, which are difficult to obtain in practice. To address these issues, this paper investigates the coupling characteristics among controllers such as PLL, outer voltage loop, and inner current loop, and proposes a control parameter identification

method for grid-following converters based on multi-disturbance responses. The proposed method injects appropriate disturbances into a grid-following renewable energy system to decouple the actions of different controllers, enabling the parameters of multiple controllers to exhibit significant sensitivity differences in voltage and current measurements at the point of common coupling (PCC), without relying on internal converter measurements. Then, the sensitivity differences of control parameters under multi-disturbance responses are utilized to perform stepwise identification, solving the difficulty of identifying low-sensitivity parameters simultaneously and improving the overall identification accuracy. Finally, simulation test system data are used to validate the effectiveness of the proposed method.

2 Modeling of Grid-Following Converter Systems

The grid-following converter control system adopts a PLL-synchronized vector control scheme consisting of an outer voltage loop and an inner current loop. The structure of the grid-following converter is shown in Fig. 1.

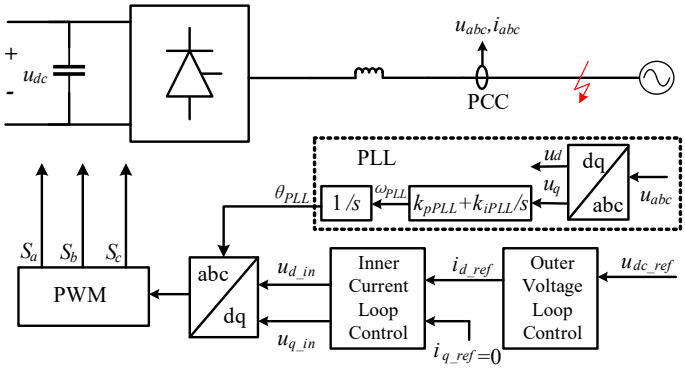


Fig. 1. Structure of a grid-following converter

In the figure, u_{dc} denotes the DC-link capacitor voltage; u_{abc} and i_{abc} represent the three-phase voltage and current at the point of common coupling (PCC), respectively; u_d, u_q, id, and i_q are the dq-axis components of the PCC three-phase voltage and current obtained through the Park transformation. u_{d_in} and u_{q_in} denote the dq-axis components of the converter input voltage.

Since the filter adopts an L-type structure and mainly serves to suppress high-frequency components, its influence on the fundamental-frequency current can be neglected. Thus, in the dq-axis reference frame, the relationship between the converter output terminal and the PCC can be expressed as:

$$\begin{cases} u_{d_out} = L\dfrac{di_d}{dt} - \omega_{PLL} L i_q + u_d \\ u_{q_out} = L\dfrac{di_q}{dt} + \omega_{PLL} L i_q + u_q \end{cases} \tag{1}$$

where L is the filter inductor between the converter output and the PCC, ω_{PLL} is the angular frequency output of the PLL, and u_{d_out} and u_{q_out} are the dq-axis components of the converter output voltage.

The phase-locked loop (PLL) adopts a classical synchronous reference frame PLL model. The input to the PLL is the three-phase measured voltage at the PCC (u_{abc}). The PLL PI controller dynamically adjusts the output phase angle to synchronize with the actual system phase. At steady state, the u_q component becomes zero. The control model of the PLL can be expressed as:

$$\frac{d\theta_{PLL}}{dt} = u_q (k_{pPLL} + \int k_{iPLL}) \tag{2}$$

where θ_{PLL} is the system phase angle output of the PLL, and k_{pPLL} and k_{iPLL} are the proportional and integral gains of the PLL controller, respectively.

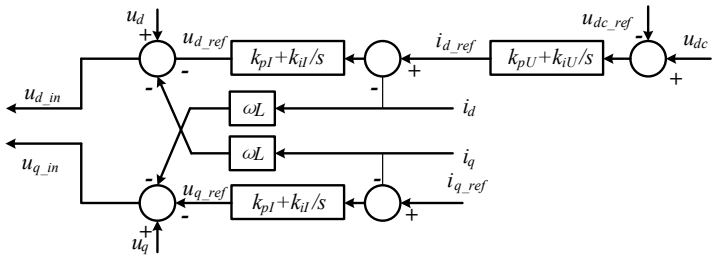


Fig.2 Double closed loop vector control structure diagram

The converter adopts a dual-loop vector control structure, as shown in Fig. 2. The input to the outer voltage control loop is the DC-link capacitor voltage (u_{dc}) and its reference (u_{dc_ref}), which serves to stabilize the DC-side voltage while regulating the active power output of the system. The output of the voltage control loop is the d-axis reference current (i_{d_ref}) for the inner current control loop. The control model of the outer voltage loop can be expressed as:

$$i_{d_ref} = k_{pU} \Delta u_{dc} + k_{iU} \int \Delta u_{dc} \tag{3}$$

where $\Delta u_{dc} = u_{dc} - u_{dc_ref}$, k_{pU} and k_{iU} are the proportional and integral gains of the PI controller in the outer voltage control loop, respectively.

The inner current control loop has another input, the q-axis reference current (i_{q_ref}), which is typically set to zero to maintain the system power factor close to unity. The u_{d_in} and u_{q_in} signals are transformed back to three-phase voltages via the inverse Park transformation to generate the PWM control signals (S_{abc}). The control model of the inner current loop can be expressed as:

$$\begin{cases} u_{d_in} = u_d - \omega_0 L i_q + k_{pI}\Delta i_d + k_{iI}\int \Delta i_d \\ u_{q_in} = u_q + \omega_0 L i_d + k_{pI}\Delta i_q + k_{iI}\int \Delta i_q \end{cases} \tag{4}$$

where $\Delta i_d = i_d - i_{d_ref}$, $\Delta i_q = i_q - i_{q_ref}$, ω_0 is the synchronous angular frequency of the system, and k_{pI} and k_{iI} are the proportional and integral gains of the PI controller in the inner current control loop, respectively.

In practice, since the carrier frequency of the pulse-width modulation (PWM) is very high, typically in the range of several kilohertz, the converter input voltage in the dq frame (u_{dq_in}) can be assumed equal to the output voltage (u_{dq_out}). Therefore, by combining (1) and (4), one can obtain:

$$\begin{cases} L\dfrac{di_d}{dt} + \Delta\omega L i_q = k_{pI}\Delta i_d + k_{iI}\int \Delta i_d dt \\ L\dfrac{di_q}{dt} + \Delta\omega L i_d = k_{pI}\Delta i_q + k_{iI}\int \Delta i_q dt \end{cases} \tag{5}$$

where $\Delta\omega = \omega_0 - \omega_{PLL}$.

From (5), it can be seen that if a system fault occurs, the PLL angular frequency (ω_{PLL}) no longer remains synchronized with the nominal system frequency. Consequently, there exists a frequency deviation between the control system and the actual transmission line, and the dq-axis currents cannot be completely decoupled, exhibiting nonlinear characteristics due to the PLL dynamics. Moreover, the dynamic behavior of the PLL also affects the Park and inverse Park transformations, influencing the conversion of the three-phase measured currents at the PCC into the dq reference frame. Therefore, during a fault, a significant coupling exists between the PLL and the dual-loop control path of the converter.

3 Control Parameter Sensitivity Analysis of Grid-Following Converters

Although the stepwise identification strategies commonly adopted for grid-following converter parameter identification can address the issue of inaccurate estimation of multiple control parameters by reducing the model order, they typically rely on internal measurements of the converter. To enable identification of converter control parameters solely from external system characteristics, this study introduces small dis-

turbances into secondary-side signals of the system to excite the dynamic responses of different controllers. Furthermore, a quantitative identifiability analysis of control parameters under multiple disturbance responses is carried out based on parameter sensitivity.

3.1 Method for Calculating Parameter Sensitivity

In this study, the trajectory sensitivity method is employed to quantitatively analyze the identifiability of each control parameter under different types of disturbances and observed variables. The calculation steps for the trajectory sensitivity and sensitivity values of a control parameter θ_j under a given disturbance and observation variable are as follows[10]:

1) Increase the value of the parameter θ_j by $\Delta\theta_j$ and compute the resulting trajectory of the observed variable $y(t, \theta_j+\Delta\theta_j)$.
2) Decrease the value of the parameter θ_j by $\Delta\theta$ and compute the resulting trajectory of the observed variable $y(t, \theta_j-\Delta\theta_j)$.
3) Calculate the trajectory sensitivity curve of the parameter θ_j according to (6):

$$L = y(t,\theta_j + \Delta\theta_j) - y(t,\theta_j - \Delta\theta_j), t = 1,...K \tag{6}$$

4) Calculate the average sensitivity of the parameter θ_j according to Equation (7).

$$S_j = \frac{1}{K}\sum_{t=1}^{K} \frac{[y(t,\theta_j + \Delta\theta_j) - y(t,\theta_j - \Delta\theta_j)]/\, y_0}{2\Delta\theta_j / \theta_{j0}} \tag{7}$$

In the equation, S_j denotes the sensitivity value of the parameter θ_j; y represents the model output of the observed variable, and y_0 is taken as the maximum value of y. In this study, $\Delta\theta_j$ is set to 10% of the actual value of the parameter. Sensitivity provides the basis for analyzing the identifiability of parameters under different disturbances and observed variables. First, the theoretical identifiability of a parameter can be assessed by examining whether its trajectory sensitivity curve crosses zero simultaneously with those of other parameters. Second, by comparing the differences in sensitivity values among parameters, the relative difficulty of identifying each parameter under various disturbances and observed variables can be quantitatively analyzed.

Currently, there is no clear standard for judging the identifiability of parameters and the magnitude of sensitivity values. Therefore, this study adopts the following criteria:

1) Under the same disturbance excitation and observed variable, parameters whose sensitivity S_j is more than ten times lower than the highest sensitivity are considered difficult-to-identify parameters. These low-sensitivity parameters are easily affected by the simultaneous identification of other parameters and should not be identified at the same time.
2) Under different disturbances and observed variables, without considering the influence of other parameters being simultaneously identified, the larger the

sensitivity S_j of a parameter θ_j, the more favorable the corresponding disturbance type is for the accurate identification of that parameter.

3.2 Multi-Type Disturbance Settings

Suitable disturbances and observed variables form the basis for parameter identification. Considering that the three controllers of the converter all have voltage or current signals as their inputs, this study applies disturbances directly or indirectly at the input ports of different controllers to excite the dynamic characteristics of each controller.

Disturbance 1: As shown in Fig. 1, the input of the phase-locked loop (PLL) is the PCC measured voltage. Therefore, a fault can be applied on the primary side of the system to induce a voltage drop and excite the dynamic response of the PLL controller. Specifically, a single-phase-to-ground fault lasting 50ms is introduced, causing a small voltage drop of approximately 5% at the PCC. This disturbance sufficiently excites the dynamic characteristics of the PLL without triggering nonlinear system behaviors.

Disturbance 2: For cascaded PI controllers consisting of the voltage outer loop and the current inner loop, applying a disturbance at the input of the voltage outer loop will inevitably activate the current inner loop simultaneously. However, analysis of the dual-loop vector control structure of the converter (Fig. 2) shows that the output of the voltage outer loop mainly controls the d-axis reference current of the current inner loop and has limited influence on the q-axis reference current. Therefore, to independently excite the dynamics of the current inner loop, a disturbance is applied to the q-axis component of the PCC measured current at the converter input, effectively decoupling the actions of the inner and outer loops. As illustrated in Fig. 3, before the disturbance occurs, the digital signal processor (DSP) acquires the steady-state three-phase PCC current via the PMU, converts it to dq-axis components using the Park transformation, and applies a brief step disturbance on the q-axis component. The perturbed dq-axis currents are then transformed back to three-phase signals using the inverse Park transformation. During the disturbance, the DSP switches the analog input to inject the disturbed three-phase current i^*_{abc} into the converter. The disturbance amplitude is set to 0.01p.u. and lasts for 50ms.

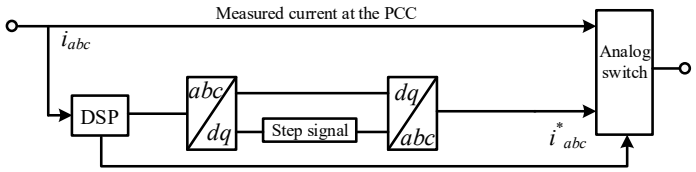


Fig.3 The structure diagram of PCC measurement current disturbance generator

Disturbance 3: The q-axis input signal of the current inner loop is not only related to the PCC measured current i_q but also to the system reference value i_{q_ref}. Therefore, an additional step disturbance is applied to the converter's q-axis reference current. The disturbance amplitude is set to 0.05p.u., with a duration of 50ms.

Disturbance 4: Similarly, the input signal of the voltage outer loop is affected not only by the measured DC-link voltage u_{dc} but also by the system reference value u_{dc_ref}. Thus, a step disturbance is applied to the converter's DC voltage reference, with an amplitude of 5% and a duration of 50ms.

To avoid triggering nonlinear elements in the control system, such as saturation limits or low-voltage ride-through mechanisms, all disturbances are designed as small-signal perturbations.

To accurately identify the six control parameters k_{pPLL}、k_{iPLL}、k_{pI}、k_{iI}、k_{pI}, and k_{iI}, the choice of observed variables is crucial. Considering that the converter control system uses dq-axis decoupled vector control and that the PLL output angle θ_{PLL} can be obtained from a PMU device, the dq-axis voltage and current components (u_d、u_q、i_d、i_q) can be indirectly derived via Park transformation from system external measurements. This approach enhances the identification accuracy and success rate of the control parameters.

3.3 Sensitivity Analysis of PLL Control Parameters

Under Disturbance 1, the sensitivity values of the PLL control parameters with respect to different observed variables are calculated using Equation (7), and the results are summarized in Table 1.

When u_q is chosen as the observed variable, the PLL control parameters k_{pPLL} and k_{iPLL} exhibit relatively large sensitivity values of 0.1704 and 0.0666, respectively. In contrast, the sensitivities of the voltage outer-loop and current inner-loop control parameters are much smaller, differing by up to two orders of magnitude.According to the parameter sensitivity analysis method, the influence of the outer- and inner-loop control parameters on the PLL parameters is negligible. Therefore, the PLL control parameters can be prioritized for identification with minimal interference from the other loops.

Tab.1 Control parameter sensitivity under disturbance 1

parameter	sensitivity value			
	u_d	u_q	i_d	i_q
k_{pPLL}	0.0011	**0.1704**	**0.0039**	0.1744
k_{iPLL}	1.69e-4	**0.0666**	8.53e-4	0.0592
k_{pI}	2.03e-5	1.28e-4	0.0014	0.1554
k_{iI}	1.89e-5	1.27e-4	0.0017	0.1720
k_{pU}	3.35e-5	3.32e-4	**0.0206**	0.1630
k_{iU}	1.47e-5	1.38e-4	**0.0057**	0.0907

3.4 Current Inner-Loop Control Parameter Sensitivity Analysis

Under Disturbance 2 and Disturbance 3, the sensitivity values of the current inner-loop control parameters were calculated for different observed variables, as shown in Tables 2 and 3. The similarity is that the current inner-loop parameters only exhibit

relatively high sensitivity values for the u_q and i_q observed variables under both disturbances.

The difference is that when i_q is used as the observed variable, under Disturbance 3, the current inner-loop control parameters have sensitivity values close to those of the voltage outer-loop parameters, whereas under Disturbance 2, the current inner-loop parameters exhibit absolutely higher sensitivity values compared with the other four parameters.

Therefore, according to the parameter sensitivity analysis method, under Disturbance 2 and using i_q as the observed variable, the settings of the PLL and voltage outer-loop control parameters have little effect on the waveform of i_q, enabling decoupled identification of the cascaded current inner-loop and voltage outer-loop parameters.

Tab.2 Control parameter sensitivity under disturbance 2

parameter	sensitivity value			
	u_d	u_q	i_d	i_q
k_{pPLL}	2.33e-9	**0.0011**	4.59e-9	7.09e-5
k_{iPLL}	3.08e-10	1.56e-4	5.43e-10	4.67e-8
k_{pI}	1.44e-7	**0.0010**	1.22e-5	**0.3986**
k_{iI}	2.034e-8	2.49e-5	9.84e-6	**0.1509**
k_{pU}	2.07e-8	1.46e-5	7.00e-5	6.24e-4
k_{iU}	5.08e-9	7.06e-6	8.22e-5	4.38e-5

Tab.3 Control parameter sensitivity under disturbance 3

parameter	sensitivity value			
	u_d	u_q	i_d	i_q
k_{pPLL}	1.53e-6	**0.2086**	9.58e-5	0.0030
k_{iPLL}	2.44e-6	**0.1137**	1.74e-4	0.0027
k_{pI}	4.40e-6	**0.1831**	2.38e-4	0.0068
k_{iI}	1.65e-6	**0.0497**	1.65e-4	0.0051
k_{pU}	3.91e-6	**0.1626**	3.06e-4	0.0060
k_{iU}	2.83e-6	**0.1189**	2.15e-4	0.0031

3.5 Voltage Outer-Loop Control Parameter Sensitivity Analysis

Under Disturbance 4, the sensitivity values of the voltage outer-loop control parameters under different observed variables were calculated, as shown in Table 4. The voltage outer-loop parameters exhibit relatively large sensitivity only in the observed variables u_q、i_d, and i_q, with the highest sensitivity appearing in i_q.

Although the voltage outer-loop control parameters have the maximum sensitivity in i_q, the current inner-loop control parameters also show relatively high sensitivity in i_q. This is because the disturbance is applied at the input of the outer loop, which inevitably excites the dynamics of the current inner loop, resulting in increased sensitivity of the inner-loop parameters. If the current inner-loop parameters are unknown, all

four parameters of the inner and outer loops would need to be identified simultaneously.Therefore, based on the sensitivity analysis, i_d is selected as the observed variable for the identification of the voltage outer-loop parameters.

Tab.4 Control parameter sensitivity under disturbance 4

parameter	sensitivity value			
	u_d	u_q	i_d	i_q
k_{pPLL}	1.28e-7	0.0847	5.26e-7	3.98e-4
k_{iPLL}	2.31e-8	0.0158	7.17e-8	1.44e-5
k_{pI}	7.50e-6	0.0089	0.0019	**0.2741**
k_{iI}	6.11e-6	0.0075	0.0018	**0.1228**
k_{pU}	6.44e-5	0.0671	**0.0240**	**0.4520**
k_{iU}	2.14e-6	0.0046	**0.0024**	**0.0136**

4 Stepwise Identification Method for Control Parameters of Grid-Following Converters

Based on the sensitivity analysis approach presented in Section 3, under the same disturbance and observation variable, parameters with sensitivity values more than one order of magnitude (i.e., at least ten times) lower than the maximum sensitivity are discarded, while the remaining parameters are retained for simultaneous identification. Table 6 summarizes the control parameters that need to be identified simultaneously under different disturbances and observation variables.

Tab.5 Sensitivity analysis conclusion of parameters

Disturbance Type	Identifiable Parameters		
	u_q	i_d	i_q
1	k_{pPLL} ,k_{iPLL}	k_{pPLL},k_{pU},k_{iU}	$k_{pPLL},k_{iPLL},k_{pI},k_{iI},$ k_{pU},k_{iU}
2	k_{pPLL} ,k_{pI}	$k_{pI},k_{iI},k_{pU},k_{iU}$	k_{pI},k_{iI}
3	k_{pPLL} ,k_{iPLL},k_{pI} ,$k_{iI},$ k_{pU},k_{iU}	$k_{pPLL},k_{iPLL},k_{pI},k_{iI},k_{pU},k_{iU}$	$k_{pPLL},k_{iPLL},k_{pI},k_{iI},$ k_{pU},k_{iU}
4	$k_{pI},k_{iI},k_{pU},k_{iU}$	k_{pU},k_{iU}	$k_{pI},k_{iI},k_{pU},k_{iU}$

As previously discussed, simultaneously identifying an excessive number of parameters may lead to difficulties in achieving accurate and stable estimation of the control parameters. Therefore, based on the analysis results presented in Tables 1–4 and the sensitivity analysis conclusions summarized in Table 5, this paper proposes a step-

wise identification strategy for control parameters. Specifically, in Disturbance 1, the parameter identification is carried out using u_q as the observation variable, where the two parameters of the PLL PI controller are identified first, while the other four unknown parameters are assigned random values. Subsequently, in Disturbance 2, i_q is selected as the observation variable to independently identify the current inner-loop parameters with relatively higher sensitivity, while the unknown voltage outer-loop parameters are assigned random values. Finally, in Disturbance 3, i_d is used as the observation variable to identify the voltage outer-loop control parameters.

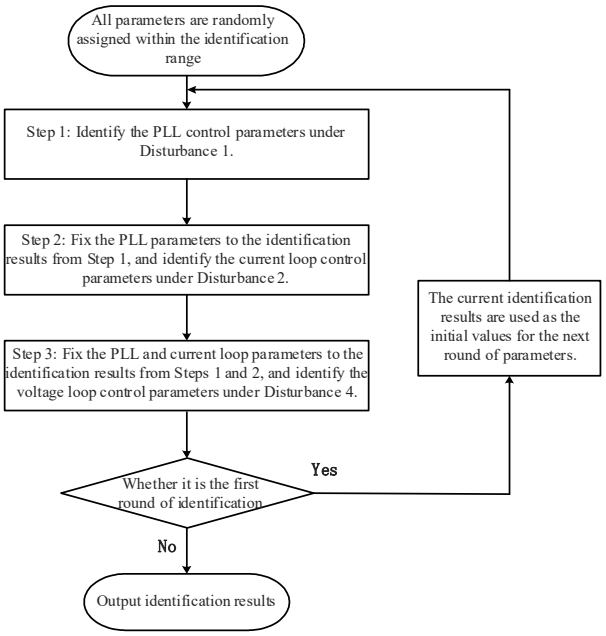


Fig.4 Step identification process of control parameters

The stepwise identification strategy proposed in this paper fully exploits the sensitivity differences of the grid-following converter control parameters under different disturbances and observation variables. In the first step, the two PLL controller parameters exhibit relatively higher sensitivity, ensuring their independent identification. Similarly, in the second step, sensitivity analysis indicates that the current inner-loop parameters hold a distinct advantage over the voltage outer-loop parameters, thereby enabling decoupled identification of the two cascaded controllers. Finally, the voltage outer-loop parameters, which have the lowest sensitivity and are thus the most difficult to identify, are estimated. Since the parameters of each controller are identified sequentially, the identified results can be used as known quantities in the subsequent steps, gradually reducing the influence of unidentified parameter accuracy on the identification outcome. In the first iteration, all parameters are initialized randomly

within their search ranges; however, the randomness of unidentified parameters may affect waveform fitting and reduce accuracy. To address this, the results obtained from the first iteration are employed as the known values of the unidentified parameters in subsequent iterations, thereby improving identification accuracy. The overall flowchart of the proposed stepwise identification method is shown in Fig. 4.

The identification of control parameters in grid-connected converters is achieved by minimizing the fitting error between the outputs of the simulation model and the actual measured outputs, thereby optimizing the model parameters toward their true values. Accordingly, this study adopts equation (8) as the objective function for control parameter identification:

$$J(\theta)=\sqrt{\sum_{t=1}^{K}\left(y(t,\theta)-y_m(t,\theta)\right)^2} \tag{8}$$

where $J(\theta)$ denotes the objective function for control parameter identification, θ represents the set of control parameters to be identified, K is the number of discrete sampling points, $y(t,\theta)$ is the model output of the observed variable, and $y_m(t,\theta)$ denotes the actual measurement data of the observed variable.Ideally, an online parameter identification method should be able to obtain the optimal parameter solution directly from (8) based on the measured outputs. However, as can be seen from (1)–(5), the converter control system composed of multiple controllers exhibits complex nonlinear dynamic characteristics. Therefore, this study employs the particle swarm optimization (PSO) algorithm as the identification method.

5 Simulation Validation

To verify the accuracy of the proposed parameter identification method, a simulation model of a grid-connected renewable energy generation system was built in MATLAB/Simulink. The true values and search ranges of the converter control parameters to be identified are listed in Table 6.

Tab.6 The value of the control parameters

parameter	true parameter value	parameter search range
k_{pPLL}	0.55	[0.01, 5]
k_{iPLL}	9.80	[0.1, 20]
k_{pI}	100	[10, 500]
k_{iI}	10000	[5000, 50000]
k_{pU}	2	[0.1, 15]
k_{iU}	20	[5, 100]

The parameter identification algorithm in this study employs the Particle Swarm Optimization (PSO) method, with a swarm size of 20 particles and a maximum of 50 iterations. The inertia weight decreases from 0.9 to 0.45 over the iterations, and the learning factors are set as C1=C2=2. During the stepwise identification of control

parameters, the unknown parameters are randomly initialized within their respective search ranges. Based on the proposed identification method, simulations were conducted on the constructed system, and the identification results of the grid-connected converter control parameters are presented in Table 7.

Tab.7 Identification results of control parameters

parameter	Identification results	Identification error
k_{pPLL}	0.53	0.03%
k_{iPLL}	9.801	0.01%
k_{pI}	99.7584	0.24%
k_{iI}	10021.1542	0.21%
k_{pU}	2.0508	0.02%
k_{iU}	19.9856	0.07%

As shown in Table 7, the proposed stepwise identification method yields overall small parameter errors. This can be attributed to the stepwise identification of control parameters based on multiple disturbance responses: (1) it reduces the number of parameters identified simultaneously, avoiding the "many-to-one" problem caused by an underdetermined identification model, which facilitates stable convergence of the identification results; (2) it mitigates the mutual influence of multiple dynamically changing parameters during the optimization process, thereby improving the success rate of accurate parameter identification; and (3) it employs small disturbance types that are rarely used in traditional methods, which helps accurately identify low-sensitivity parameters that are difficult to identify simultaneously, thus enhancing the overall accuracy of control parameter identification.

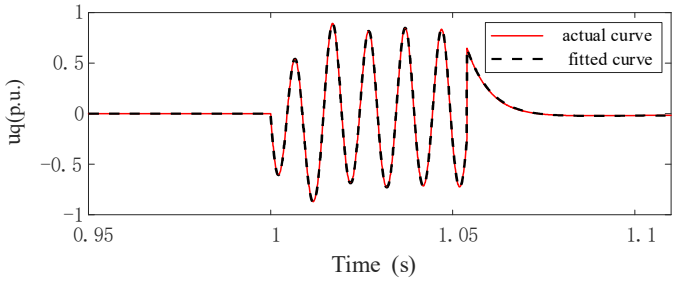


Figure 5. Disturbance 1

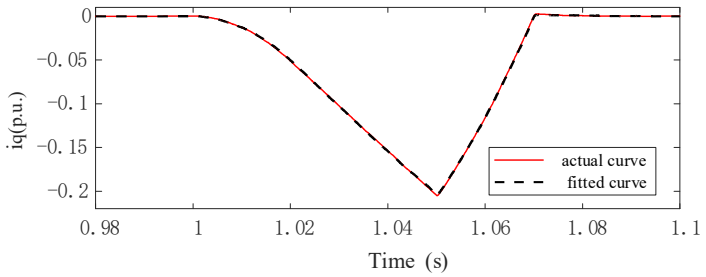


Figure 6. Disturbance 2

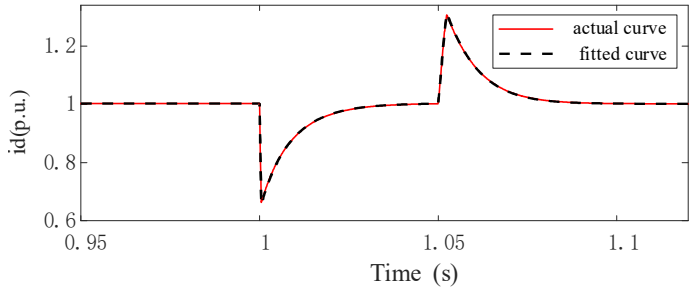


Figure 7. Disturbance 4

From the identification results shown in Figures 5–7, it can be observed that by applying multiple disturbance signals, the PLL, current-loop, and voltage-loop control parameters of the grid-following converter can be decoupled and identified in the time domain. The mean errors between the identified parameters and the true values set in the experimental model are relatively small, indicating that the proposed method can accurately identify the control parameters of grid-following converters.

6 Conclusion

To address the low accuracy, poor multi-scenario adaptability, and difficulty in simultaneously identifying low-sensitivity parameters in conventional grid-following inverter control parameter identification methods, this paper proposes a multi-disturbance-response-based identification approach. The method can accurately and stably identify the control parameters of grid-following inverters. The main conclusions are as follows:

1）Independent identification of PLL parameters: By exploiting the sensitivity advantage of PLL control parameters with respect to the *q*-axis component of the PCC-measured voltage, the PLL parameters can be identified independently even when other control parameters are unknown.

2）Decoupled identification of inner and outer loops: By applying independent disturbances to the *dq*-axis components of the measured current on the system's secondary side, the actions of the inner- and outer-loop controllers are decoupled, ena-

bling separate identification of the current inner-loop and voltage outer-loop control parameters.

3）Stepwise identification method: Leveraging the sensitivity differences of control parameters under different types of disturbances, a stepwise identification strategy is proposed. This greatly reduces the number of parameters identified simultaneously and significantly improves the identification accuracy of low-sensitivity parameters.

References

[1] Fang C，Mu L，Wang Z，et al．Analysis of grid forming IIDG transient and steady-state fault model[J]．IEEE Transactions on Smart Grid，2022，13(2)：1187–1199．

[2] Jia K, Liu Q, Yang B, et al．Transient fault current analysis of IIRESs considering controller saturation[J]．IEEE Transactions on Smart Grid，2022，13(1)：496–504．

[3] Liu Z，Wei H，Li X，et al．Global identification of electrical and mechanical parameters in PMSM drive based on dynamic self-learning PSO[J]．IEEE Transactions on Power Electronics，2018，33(12)：10858-10871．

[4] Wang Huaizhi, Li Gangqiang, Wang Guibin, et al. Deep learning based ensemble approach for probabilistic wind power forecasting[J]. Applied Energy, 2017, 188: 56-70.

[5] Chang Y，Hu J，Zhang E，et al．Impact of nonlinearity on type-3WT fault current[C]// IEEE 4th Southern Power Electronics Conference，2018：1-7．

[6] Moshksar E，Ghanbari T．Adaptive estimation approach for parameter identification of photovoltaic modules[J]．IEEE Journal of Photovoltaics，2017，7(2)：614–623．

[7] Jin Y，Lu C，Ju P，et al．Probabilistic Preassessment Method of Parameter Identification Accuracy With an Application to Identify the Drive Train Parameters of DFIG．IEEE Transactions on Power Systems，2020，35(3)：1769-1782．

[8] Reddy S，Loganathan U．Offline recursive identification of electrical parameters of electrical parameters of VSI-fed induction motor drives[J]．IEEE Transactions on Power Electronics，2020，35(10)：10711–10719．

[9] Jia K，Jiang X，Zhang Y， et al．Fault Dynamic Response Difference-Based PLL Controller Parameter Identification of IIRESs[J]．IEEE Transactions on Smart Grid，2024，15(2)：1725-1734．

[10] Acilan E，Gol M．Novel parameter error identification method for power plant dynamic models[J]．IEEE Transactions on Power Systems，2024，39(1)：957-966．

062 Low-Frequency Oscillation Analysis and Active Damping Suppression Strategy for Multi-Machine Parallel Grid-Forming Energy Storage Systems

Chaobo Ying [1], muyang Liu[1], Chenchen Ge[1],Junru Chen[1], Fan sun[2]

[1] School of Electrical Engineering Xinjiang University
[2] State Grid Xinjiang Electric Power Co., Ltd.

Abstract. Grid-forming energy storage has attracted significant attention as an effective solution for emerging power systems. However, when multiple grid-forming units operate in parallel, low-frequency oscillations may occur, threatening system stability. Most existing studies focus on single-unit scenarios, while research on multi-unit grid-connected systems is limited. This paper develops a state-space small-signal model of a multi-inverter grid-forming system and investigates the effects of virtual inertia and damping coefficients on stability through eigenvalue analysis. An active damping strategy, combining self-damping and mutual-damping controllers, is proposed to suppress transient power oscillations. Simulation results of a three-unit parallel system in Matlab/Simulink verify the effectiveness of the proposed method in enhancing damping and improving stability.

Keywords: Grid-forming energy storage ; low-frequency oscillation ; small-signal modeling ; virtual inertia ;

1 INTRODUCTION

With the large-scale integration of renewable generation and energy storage systems [1], grid-forming (GFM) converters based on power electronics are increasingly replacing conventional synchronous generators, assuming essential roles in frequency support and voltage regulation [2]. In multi-machine parallel GFM energy storage systems, however, strong dynamic coupling effects make them susceptible to low-frequency power oscillations under disturbances such as active power steps, frequency fluctuations, or voltage perturbations. These oscillations not only disrupt balanced power sharing but can also undermine the system's dynamic stability [3–5]. Existing studies have primarily focused on single-machine GFM modeling and control or stability analysis under islanded conditions [6–8], leaving the mechanisms and targeted suppression of low-frequency oscillations in multi-machine configurations insufficiently addressed.

In recent years, grid-forming control methods such as the Virtual Synchronous Generator (VSG) and droop control have been widely studied for the grid-connected operation of distributed generation and energy storage systems. Reference [9]

compares the dynamic differences between VSG and droop control, establishes small-signal and state-space models, and points out that the swing equation endows VSG with virtual inertia, thereby affecting the system's dynamic response and stability. References [13] and [14] develop small-signal models for multi-machine parallel systems, and through eigenvalue and participation factor analysis, reveal the influence patterns of line impedance, output power, and active power loop parameters on low-frequency modes. To mitigate power oscillations caused by insufficient damping, Reference [10] proposes a virtual dynamic inter-damping control method, which suppresses transient power oscillations by adding an inter-damping torque to reduce torque and frequency differences among multiple machines. Reference [11], starting from the lack of inertia and damping in microgrids, reviews the development of inertia and damping emulation technologies, pointing out that low inertia and weak damping are prominent issues for current microgrid stability. In addition to frequency stability, Reference [12] investigates the transient voltage stability of VSG-based parallel systems with asynchronous motor loads and proposes enhancement measures considering fault current limitation. Overall, existing research has achieved substantial results in the modeling and analysis of frequency and voltage stability for both single-machine and multi-machine VSG systems. However, effective and low-parameter-dependent control methods for the coordinated suppression of self-excited oscillations and mutual power oscillations in multi-machine systems remain lacking.

To address this, the present study investigates the low-frequency oscillation mechanisms of multi-machine parallel GFM energy storage systems and develops a comprehensive small-signal state-space model incorporating active/reactive power control, dual voltage-current control loops, filters, and transmission lines. This model identifies dominant oscillation factors and quantifies the influence of key parameters. Building on these insights, an improved active power control strategy integrating self-damping and mutual-damping functionalities is proposed. The self-damping controller employs a band-pass filter to provide targeted damping within specific oscillation frequency ranges, effectively suppressing self-excited oscillations. The mutual-damping controller, leveraging an upper-layer communication link and weighted frequency deviation compensation, actively decouples inter-unit frequency disturbances to mitigate mutual power oscillations. Eigenvalue analysis and time-domain simulations confirm that the proposed strategy effectively suppresses low-frequency oscillations, significantly enhances damping and stability, and offers a practical solution for the reliable operation of multi-machine parallel GFM energy storage systems.

2 Modular Modeling of Multi-Machine Parallel Grid-Forming Energy Storage Systems

The grid-forming energy storage system consists of storage batteries, a DC-side capacitor, a DC bus, a grid-forming grid-connected converter, an LC filter, and a control system. Its multi-machine parallel topology is shown in Fig. 1.Here, L_{fn} and C_{fn} represent the output filter inductance and capacitance of the n=1 、 2 、

3、……、N grid-forming units, respectively. R_{ln} and L_{ln} denote the equivalent resistance and inductance between the filter and the Point of Common Coupling (PCC). Considering that the investigation of oscillation-inducing factors primarily focuses on the converter side, the external grid is simplified as a grid-side resistance R_g and grid-side inductance L_g . P_n and Q_n denote the active and reactive power outputs of the n-th grid-forming energy storage converter. i_{fn} is the filter inductor current, u_{fn} is the filter capacitor voltage, i_{ln} is the transmission line current, and u_{pcc} is the PCC voltage.

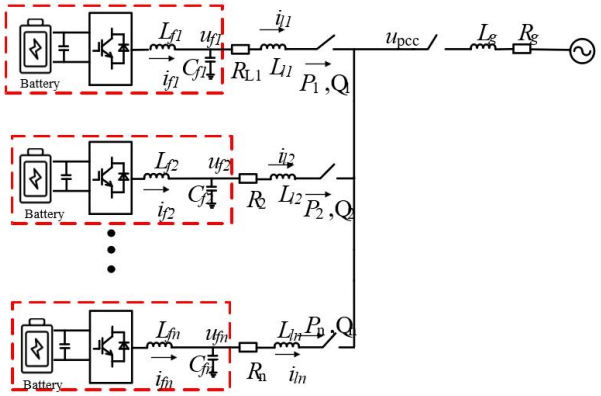


Fig. 1. Topology of a Multi-Machine Parallel Grid-Forming Energy Storage System

The electromagnetic power—namely, the inverter's active power P_n and reactive power Q_n—is then calculated from these quantities. Next, the reactive power is processed through the Automatic Voltage Control (AVC) to generate the reference voltage magnitude E, while the active power is fed into the outer-loop virtual synchronous generator (VSG) control to obtain the phase angle θ_n .Through voltage synthesis and coordinate transformation, the reference voltage in the dq rotating frame is generated. Finally, the dual-loop voltage–current controller, combined with coordinate transformation, produces the modulation signals, which are processed via Space vector pulse width modulation (SVPWM) to generate the switching commands. These commands control the turn-on and turn-off of the inverter's power switches, thereby achieving the inversion process.

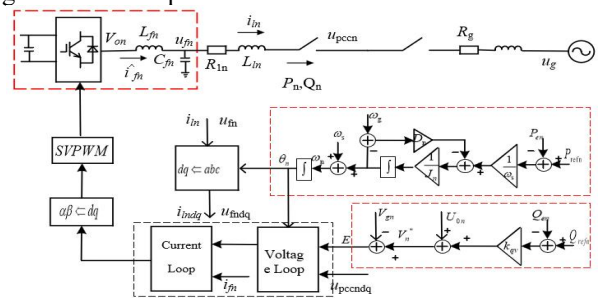


Figure 2. Control Structure of a Single Grid-Forming Energy Storage Unit

2.1 Modeling of the Grid-Forming Energy Storage Control Module

Each grid-forming energy storage converter mainly consists of active power control (APC), reactive power control (RPC), and a dual-loop voltage–current control. The overall control scheme is shown in Fig. 2. The instantaneous power of the *n*-th grid-forming energy storage converter is expressed in (1).

$$\begin{cases} P_{\mathrm{n}} = \dfrac{3}{2}(u_{\mathrm{fnd}} i_{\mathrm{lnd}} + u_{\mathrm{fnq}} i_{\mathrm{lnq}}) \\ Q_{\mathrm{n}} = \dfrac{3}{2}(u_{\mathrm{fnq}} i_{\mathrm{lnd}} - u_{\mathrm{fnd}} i_{\mathrm{lnq}}) \end{cases} \tag{1}$$

The grid-forming active power control simulates the rotor motion equation of a synchronous generator, enabling the converter to possess the inertial and damping characteristics of a synchronous generator. The mathematical model is shown in equation (2).

$$\begin{cases} \dfrac{P_{refn}}{\omega} - \dfrac{P_{\mathrm{n}}}{\omega} - D(\omega_n - \omega) = J\dfrac{\mathrm{d}\omega_n}{\mathrm{dt}} \\ \theta_n = \int \omega_n \mathrm{dt} \end{cases} \tag{2}$$

Here, P_{ref} is the active power reference value, J is the grid-forming control moment of inertia, D is the damping coefficient, ω is the rated rotor angular frequency, ω_n is the synchronous generator's rotor angular frequency, and θ_n is the synchronous generator's internal voltage angle.

The reactive power control loop employs AVC (Automatic Voltage Control), which simulates the excitation system of synchronous generators to achieve reactive power-voltage droop characteristics. The mathematical model is shown in equation (3).

$$E = U_{nref} + K_{qv}(Q_{\mathrm{nref}} - Q_{\mathrm{n}}) \tag{3}$$

Here, U_{nref} is the voltage reference value, K_{qv} is the droop coefficient of the reactive power-voltage characteristic, and Q_{nref} is the reactive power reference value.

The mathematical model of the voltage-current dual-loop control is shown in equations (4) and (5).

$$\begin{cases} i_{\mathrm{dnref}} = K_{\mathrm{pvn}} \dfrac{\mathrm{d}\chi_{\mathrm{dn}}}{\mathrm{d}t} + K_{\mathrm{ivn}}\chi_{\mathrm{dn}} - \omega_n C_{\mathrm{fn}} u_{\mathrm{fnq}} \\ i_{\mathrm{qnref}} = K_{\mathrm{pvn}} \dfrac{\mathrm{d}\chi_{\mathrm{qn}}}{\mathrm{d}t} + K_{\mathrm{ivn}}\chi_{\mathrm{qn}} + \omega_n C_{\mathrm{fn}} u_{\mathrm{fnd}} \end{cases} \tag{4}$$

$$\begin{cases} v_{ond} = K_{\mathrm{pin}} \dfrac{\mathrm{d}\gamma_{\mathrm{dn}}}{\mathrm{d}t} + K_{\mathrm{iin}}\gamma_{\mathrm{dn}} + u_{\mathrm{fnd}} - \omega_n L_{\mathrm{fn}} i_{\mathrm{fnq}} \\ v_{onq} = K_{\mathrm{pin}} \dfrac{\mathrm{d}\gamma_{\mathrm{qn}}}{\mathrm{d}t} + K_{\mathrm{iin}}\gamma_{\mathrm{qn}} + u_{\mathrm{fnq}} + \omega_n L_{\mathrm{fn}} i_{\mathrm{fnd}} \end{cases} \tag{5}$$

Here, i_{dqnref} is the reference value output from the voltage control loop to the current control loop, K_{pvn} and K_{ivn} are the proportional and integral coefficients of the outer voltage loop respectively, v_{ondq} is the inverter output voltage, K_{pin} and K_{ivn} are the

proportional and integral coefficients of the inner current loop respectively, and χ_{dqn} , γ_{dqn} are two intermediate variables whose derivatives are defined as:

$$\begin{cases} \dfrac{\mathrm{d}\chi_{\mathrm{dqn}}}{\mathrm{d}t} = u_{\mathrm{dqref}} - u_{\mathrm{fndq}} \\ \dfrac{\mathrm{d}\gamma_{\mathrm{dqn}}}{\mathrm{d}t} = i_{\mathrm{dqnref}} - i_{\mathrm{fndq}} \end{cases} \tag{5}$$

2.2 The modeling of filters and transmission lines

The grid-forming energy storage converter connects its output voltage and current to the AC point of common coupling (PCC) via an LC filter and transmission line, with its state equation shown in equation (6).

$$\begin{cases} \dfrac{di_{fndq}}{dt} = \dfrac{1}{L_{fn}}(v_{ondq} - u_{fndq} - R_{fn}i_{fndq} \mp w_n L_{fn} i_{fnqd}) \\ \dfrac{du_{fndq}}{dt} = \dfrac{1}{C_{fn}}(i_{fndq} - i_{\mathrm{ln}dq} \mp w_n C_{fn} u_{fnqd}) \\ \dfrac{di_{\mathrm{ln}dq}}{dt} = \dfrac{1}{L_{ln}}(u_{fndq} - u_{pccndq} - R_{ln} i_{\mathrm{ln}dq} \mp w_n L_{ln} i_{\mathrm{ln}qd}) \end{cases} \tag{6}$$

For analytical convenience, the small-signal models of multiple inverters in the multi-machine parallel system are transformed into a unified common rotating reference frame. This paper selects the grid dq-frame as the common coordinate system, whose angular frequency ω_g is assumed constant. Let δ_n be the angular difference between the n-th grid-forming energy storage converter and the grid coordinate system.

$$\delta_n = \int (\omega_{\mathrm{n}} - \omega_g) dt \tag{7}$$

The coordinate transformation between the nth grid-forming energy storage converter and the grid dq-frame can be defined as:

$$\begin{cases} u_{\mathrm{pccn}} = \left(\cos\delta_n - j\sin\delta_n\right) u_{\mathrm{pcc}} \\ i_{ln} = \left(\cos\delta_n + j\sin\delta_n\right) i_{\mathrm{pcc}} \end{cases} \tag{8}$$

The dynamic characteristics of the grid-side transmission lines are modeled in the dq-frame as shown in Fig. 1.

$$\frac{\mathrm{d}i_{\mathrm{gdq}}}{\mathrm{d}t} = \frac{1}{L_{\mathrm{g}}}(u_{\mathrm{pccdq}} - R_{\mathrm{g}} i_{\mathrm{gdq}} - \omega_g L_{\mathrm{g}} i_{\mathrm{gqd}} - u_{\mathrm{gqd}}) \tag{9}$$

Table 1. Circuit Parameters

Symbol	Values	Symbol	Values
S_{en}/MW	3	R_{fn}/Ω	0.0025
V_{en}/V	690	R_{ln}/Ω	0.0004
P_{ref}/MW	1	L_{ln}/Ω	0.264
Q_{ref}/Var	0	R_g/Ω	0.005
L_{fn}/mH	0.08	L_g/ mH	0.5
C_{fn}/μF	1300		

Table 2. Control Parameters

Symbol	Values	Symbol	Values
J_n/（kg/m^2）	90	K_{ivn}	1570.8
D_n/(Nms/rad)	300	K_{pin}	4985.7
K_{qv}	0.0005	K_{iin}	3132.6
K_{pvn}	1.6046		

3 The stability analysis of multi-converter parallel systems based on state-space small-signal models

3.1 Oscillation Mode Identification and Damping Ratio Assessment

By consolidating and linearizing the mathematical models of the above subsystems, the system-wide small-signal model for the nth converter can be derived as shown in equation (10).

$$\frac{\mathrm{d}}{\mathrm{d}t}\begin{bmatrix}\Delta X_{vsgn}\\ \Delta X_{cirn}\\ \Delta X_{lgdq}\end{bmatrix}=A_{sysn}\begin{bmatrix}\Delta X_{vsgn}\\ \Delta X_{cirn}\\ \Delta X_{lgdq}\end{bmatrix}+B_{sysn}u_{sysn} \quad (10)$$

In the system, Δi_{gd}、Δi_{gq}、Δi_{fnd}、Δi_{fnq}、Δu_{fnd}、Δu_{fnq}、Δi_{lnd}、$\Delta i_{\ln q}$、$\Delta\omega_n$、$\Delta\delta_n$、$\Delta\chi_{nd}$、$\Delta\chi_{nq}$、$\Delta\gamma_{nd}$、$\Delta\gamma_{nq}$ is the state variable, where $\Delta X_{lg}=\begin{bmatrix}\Delta i_{gd} & \Delta i_{gq}\end{bmatrix}$，$\Delta X_{cirn}=\begin{bmatrix}\Delta i_{fnd} & \Delta i_{fnq} & \Delta u_{fnd} & \Delta u_{fnq} & \Delta i_{lnd} & \Delta i_{\ln q}\end{bmatrix}$，$\Delta X_{\mathrm{GFMn}}=\begin{bmatrix}\Delta\omega_n & \Delta\delta_n & \Delta\chi_{nd} & \Delta\chi_{nq} & \Delta\gamma_{nd} & \Delta\gamma_{nq}\end{bmatrix}$.

Based on equation (10), the small-signal model of the grid-forming energy storage multi-converter parallel system can be expressed as a set of differential equations:

$$\dot{X}=A_{sys}\begin{bmatrix}\Delta X_{\mathrm{GFM1}} & \Delta X_{cir1} & \Delta X_{\mathrm{GFM2}} & \Delta X_{cir2} & \cdots & \Delta X_{\mathrm{GFMN}} & \Delta X_{cirN} & \Delta X_{lgdq}\end{bmatrix}^T\triangleq\begin{bmatrix}\Delta X_1 & \Delta X_2 & \cdots & \Delta X_m\end{bmatrix}^T \quad (11)$$

Where ΔX_1 to ΔX_m are state variables (m being the total number of states, $m=12N+2$，$i=1、2、3\cdots$m), and matrix A_{sys} is the state matrix of the multi-converter parallel system.

Substituting the circuit parameters from Table 1 and control parameters from Table 2 into matrix A_{sys} yields the system eigenvalues λ_i. As the primary objective of this work is to propose an oscillation suppression method for improving dynamic performance – rather than maximizing the number of parallel grid-forming energy storage units – the system is configured with three parallel grid-forming converters as a generalized case. Subsequently, eigenvalue variations are analyzed under different inertia and damping parameters of each grid-forming unit. Damping ratios are evaluated and oscillation modes identified, wherein eigenvalues with real parts greater than -20 are considered dominant. The remaining eigenvalues, located farther from the imaginary axis, have negligible influence. By examining the impact of dominant

participation factors on state variables, the evolution of system stability characteristics is established.

Table 3. Dominant Characteristic Roots of Grid-Forming Multi-Converter Parallel Systems

	Characteristic Root	Oscillation Frequency	damping ratio	Dominant Participation Factor
$\lambda_{9,10}$	-16.1681±44.3958i	47.2482	0.3421	$\Delta\omega_1$, $\Delta\delta_1$, $\Delta\chi_{1d}$, $\Delta\chi_{1q}$
$\lambda_{11,12}$	-0.6258±0.0683i	0.0063	0.9942	$\Delta\gamma_{3d}$, $\Delta\gamma_{3q}$
$\lambda_{21,22}$	-22.8132 + 40.5969i	40.5969	0.4899	$\Delta\omega_3$, $\Delta\delta_3$, $\Delta\chi_{2d}$, $\Delta\chi_{2q}$
$\lambda_{23,24}$	-0.6258±0.0068i	0.0068	0.99994	$\Delta\gamma_{3d}$, $\Delta\gamma_{3q}$
$\lambda_{33,34}$	-16.1681±44.3958i	47.2482	0.3421	$\Delta\omega_3$, $\Delta\delta_3$, $\Delta\chi_{3d}$, $\Delta\chi_{3q}$
$\lambda_{35,36}$	-0.6224 ± 0.0085i	0.0085	0.9999	$\Delta\gamma_{3d}$, $\Delta\gamma_{3q}$
$\lambda_{37,38}$	-4.9857±3.1416e+2i	314.1996	0.0159	Δi_{gd} , Δi_{gq}

The three-unit grid-forming parallel system is initialized with the parameters listed in Tables 1 and 2. To compare interactions under identical versus mismatched parameters, the rotational inertias J_n of the three grid-forming units are set to 60 (kg/m^2), 60 (kg/m^2), and 90 (kg/m^2), respectively, and the line impedance of the second unit is increased to 1.5 times its original value. The dominant eigenvalues obtained under these settings are summarized in Table 3; all eigenvalues lie in the left half-plane, indicating that the system is stable under the initial conditions. An analysis of the low-frequency oscillation modes shows—based on the participation factor table—that $\lambda_{9,10}$ 、 $\lambda_{21,22}$ 、 $\lambda_{33,34}$ is most strongly correlated with the active power loop output angle ($\Delta\delta_n$) and angular frequency ($\Delta\omega_n$), followed by the dynamic response of the voltage loop ($\Delta\chi_{nd}$, $\Delta\chi_{nq}$). Mode $\lambda_{9,10}$ 、 $\lambda_{11,12}$ is more significantly influenced by the parameters of the first unit, $\lambda_{21,22}$ 、 $\lambda_{23,24}$ by the second unit, and $\lambda_{33,34}$ 、 $\lambda_{35,36}$ by the third unit. Based on the above participation factor analysis, it can be concluded that the system's low-frequency oscillation modes are mainly affected by the active power control loop. Therefore, the influence of active power loop parameters on system stability is analyzed first.

3.2 Impact of Active Power Control Loop Parameters on System Stability

Based on the stability analysis of the multi-machine parallel system in Section 2.1, the dynamic characteristics of grid-forming control are jointly determined by the moment of inertia J, damping coefficient D , and active power droop coefficient K_{qv}. Since the influence mechanisms of the active power droop coefficient K_{qv} and the damping coefficient D on the system's dynamic characteristics are similar, this paper focuses on investigating the impact of variations in J and D on system stability. The parameters of the three-grid-forming-unit parallel system are set as shown in Tables 1 and 2.As illustrated in Fig. 3(a), when the damping coefficient is set to 300, the dominant eigenvalue root locus is plotted for J_n varying from 8 to 200.Fig. 3(b) shows the dominant eigenvalue root locus when J_n=10 and D_n varies from 10 to 1000.In the figures, the arrows indicate the direction of increasing J_n. Fig. 3(c) presents a three-dimensional plot of the damping ratio variation when J_n varies from 8 to 200 and D_n varies from 10 to 1000.

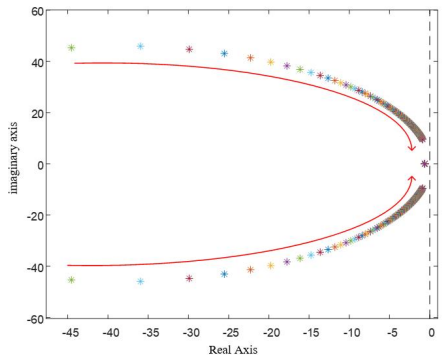


Figure 3（a）. Locus of Dominant Characteristic Roots for J_n∈（8，100）

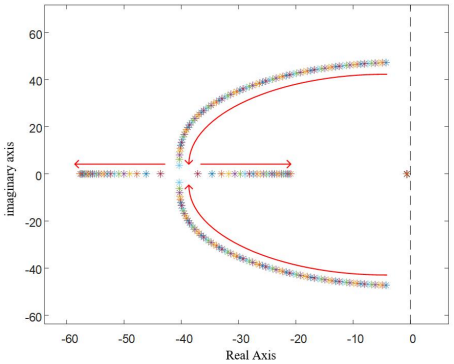


Figure 3（b）. Locus of Dominant Characteristic Roots for D_n∈（8，100）

From Fig. 3(a), it can be observed that as the system inertia coefficient increases, the eigenvalues move to the right, approaching the imaginary axis but without crossing it. This indicates that the system stability deteriorates but remains in a stable state, and the larger the inertia value, the smaller its impact on the stability of the low-frequency oscillation modes. From Fig. 3(b), it can be seen that as the damping coefficient increases, the negative real part of the system eigenvalues increases, and the system

stability is gradually enhanced. At the same time, the overshoot of the GFM output power continuously decreases with the increase of D_n. When D_n increases further, the eigenvalues coincide on the real axis, with one eigenvalue's negative real part decreasing (i.e., gradually approaching the imaginary axis) and the other's negative real part increasing (i.e., gradually moving away from the imaginary axis).In this case, the eigenvalue closer to the imaginary axis will dominate the system's dynamic response, leading to a reduced damping rate of the dominant mode and a decline in overall stability.

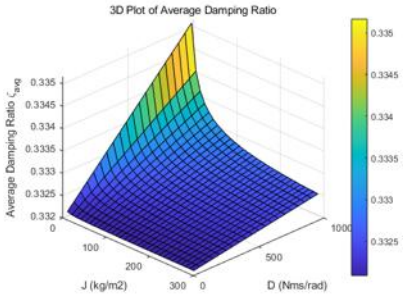


Figure 4 Damping ratio variation for $J_n \in (8,100)$ and $D_n \in (8,100)$

Within the range $J_n \in (8,100)$ and $D_n \in (8,100)$, the average damping ratio is calculated as:

$$\zeta = \sum_{n=1}^{N} \frac{-\mathrm{Re}\,al(\lambda_n)}{N\sqrt{\mathrm{Re}\,al(\lambda_n)^2 + \mathrm{Im}\,ag(\lambda_n)}} \tag{12}$$

The distribution of the damping ratio under different parameters is shown in Fig. 4.In the J_n–D_n parameter plane, the average damping ratio remains between 0 and 1, indicating that the system is in an underdamped state. Only when J_n is relatively small and D_n is sufficiently large does the average damping ratio show a slight increase, reaching a maximum of 0.3352.Based on the above analysis, it can be seen that even when J_n and D_n vary over a wide range, the damping of the multi–grid-forming energy storage unit parallel system remains significantly insufficient. Therefore, when the system encounters external disturbances such as active power steps, frequency fluctuations, or voltage perturbations, the output power is prone to oscillations. In general, as shown in Fig. 4, increasing the damping coefficient D_n and decreasing the system inertia J_n can enhance the system's damping performance. However, smaller inertia results in a higher RoCoF (Rate of Change of Frequency) and larger initial frequency deviation, which can trigger high-frequency oscillations and weaken the grid inertia support capability of the grid-forming energy storage system. While larger damping can suppress oscillations quickly, it excessively dissipates kinetic energy, reducing the power angle stability. The combination of these effects makes the system response "fast but fragile": after a disturbance, the frequency changes abruptly and recovers rapidly, but the ability to withstand large disturbances declines, and the risk of instability in weak grids increases significantly. On this basis, the following suppression strategy is proposed in this paper.

4 Active Damping Suppression Strategy

Based on the preceding analysis, this paper proposes a low-frequency oscillation suppression strategy that enhances system stability without altering the inherent moment of inertia J_n or damping coefficient D_n in grid-forming multi-converter parallel systems, as illustrated in Figure 5.

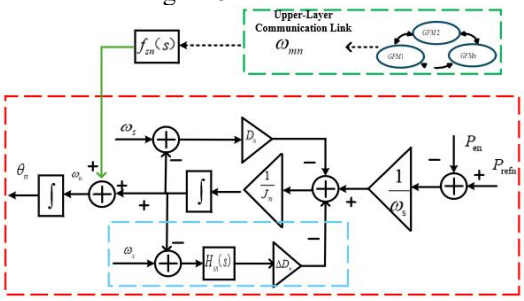


Figure 5 Control Block Diagram of the Active Damping Suppression Strategy

As shown in Fig. 5, the low-frequency oscillation suppression strategy proposed in this paper consists of a self-damping controller (blue dashed box) and a mutual-damping controller (green dashed box).The self-damping controller provides additional damping related to the oscillation frequency, enhancing the system's ability to suppress its own oscillations and improving small-signal stability, while preserving the inertia response characteristics. The mutual-damping controller detects and compensates for frequency disturbances from other grid-forming units via an upper-layer communication link, thereby achieving "active decoupling" of frequencies among units, suppressing low-frequency power oscillations mutually excited between multiple units, and improving the dynamic stability of the entire parallel system. The improved grid-forming active power control loop is thus obtained as follows:

$$\begin{cases} \dfrac{P_{refn}}{\omega}-\dfrac{P_{\mathrm{en}}}{\omega}-\left[D+\Delta \mathrm{D}^{*}H_{sn}(s)\right](\omega-\omega_n)=J\dfrac{\mathrm{d}\omega_n}{\mathrm{dt}} \\ \theta_n=\int(\omega_n+\omega_{\mathrm{mn}}(t)f_{sn}(s))\mathrm{dt} \end{cases} \tag{13}$$

4.1 Self-Damping Control Unit

Since grid-forming (GFM) controlled units explicitly imitate the swing equation of synchronous machines, their inherent low-damping characteristics can easily lead to self-excited low-frequency power oscillations under disturbances, especially when the inertia is large and the damping coefficient is small, in which case the oscillations become more pronounced. Although directly increasing the conventional damping coefficient D_n can enhance stability, it would weaken the inertia response, which is detrimental to the frequency support capability.

As shown in the equation (13), $\Delta \mathrm{D}^{*}H_{sn}(s)$ represents the self-damping controller, $\Delta \mathrm{D}\approx(0.5-2)D_n$ is the self-damping coefficient with

$\Delta D \approx (0.5-2)D_n$, and $H_{sn}(s)$ denotes the second-order bandpass filter transfer function, whose expression is given by equation (14).

$$H_{sn}(s) = \frac{k\omega_n^2 s}{s^2 + 2\xi\omega_n s + \omega_n^2} \tag{14}$$

Within this context, k represents the gain at the center frequency, ξ denotes the bandwidth coefficient, and ω_n is the low-frequency center oscillation angular frequency ($\omega_n = 2\pi f_c$). By introducing center oscillation frequency f_c feedback and applying additional frequency-dependent damping, this strategy enhances suppression capability within the oscillation band, effectively mitigates self-excited oscillations, and increases the system's average damping ratio.

4.2 Mutual-Damping Controller

Mutual power oscillations arise from interactions between parallel virtual synchronous generators (VSGs). Due to grid impedance, active power changes in one grid-forming device introduce phase angle deviations in the grid voltage observed within the dq-frame of other VSGs. This subsequently excites mutual power oscillations at distinct frequencies ω_n . To compensate for these phase angle deviations, the mutual damping controller f_{sn} is implemented as follows:

$$\begin{cases} f_{sn} = \dfrac{\omega_{on} s}{T_m s^2 + \omega_{on} s + T_m \omega_{on}^2} \\ \omega_{mn}(t) = k_{mn}^{base}\left(1 + \alpha \dfrac{1}{N-1}\sum_{i=1, i\neq n}^{N} \left|\omega_i(t) - \omega_0\right| / \omega_{ref}\right) \end{cases} \tag{15}$$

Where ω_{on} denotes the center frequency, T_m represents the maximum gain coefficient at this frequency, k_{mn}^{base} is the base gain for mutual-oscillation frequency compensation, $\omega_i(t)$ indicates the instantaneous angular frequency of the i-th grid-forming device, ω_0 is the reference angular frequency, ω_{ref} signifies the reference frequency deviation, and α denotes the amplification coefficient.

By introducing a frequency-deviation weighted-average gain adjustment mechanism, the controller is endowed with stronger oscillation suppression capability during severe system disturbances, while automatically reducing its effect in steady-state operation to avoid interfering with the primary frequency control. With the introduction of the frequency-deviation weighted average, the instantaneous frequency deviations of all units in the system are aggregated via a communication link and weighted according to unit capacity, control weight, or operating status, resulting in a unified weighted-average frequency deviation used as the input for mutual damping control. This approach enables each unit to compensate for mutual power oscillations on the same dynamic reference, thereby fundamentally reducing damping imbalance problems caused by differences in local responses and improving the coordinated oscillation suppression capability among multiple units.

4.3 Effectiveness Analysis of the Active Damping Suppression Strategy

To validate the effectiveness of the proposed suppression strategy, Eq. (13) was substituted for Eq. (2), and Eqs. (14) and (15) were incorporated. Using the parameters specified in Tables I and II, the eigenvalues before and after implementing the self-damping and mutual-damping controllers are illustrated in the figure.

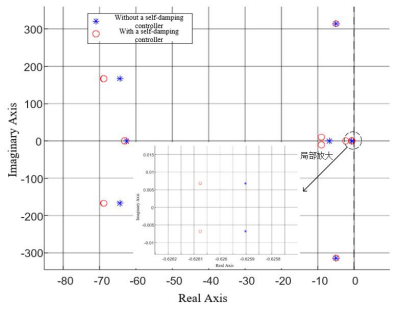


Figure 6(a) With only self-damping implemented

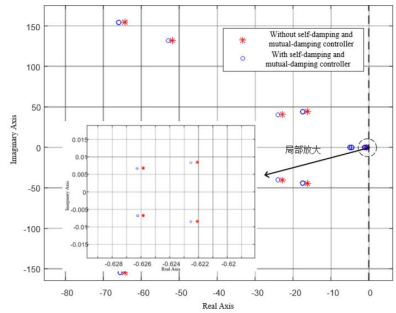


Figure 6(b) With both self-damping and mutual-damping implemented

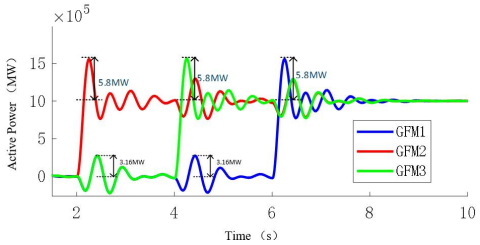
Figs. 6(a) and 6(b) compare the eigenvalue distributions of the multi–grid-forming parallel system before and after applying the proposed oscillation suppression strategy. Results show that introducing self- and mutual-damping controllers shifts several low-damping modes leftward in the complex plane, increases damping ratios, and effectively suppresses oscillations. Moreover, this improvement is consistently observed under different parameter settings, confirming the robustness and effectiveness of the proposed strategy in enhancing system stability.

5 Simulation Verification

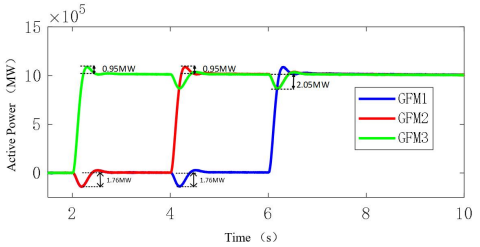
To validate the correctness and effectiveness of the proposed oscillation suppression strategy, a simulation model of three grid-forming units operating in parallel was developed in MATLAB/Simulink for comprehensive verification.

5.1 Oscillation Suppression Verification Under Identical Parameters

To verify the effectiveness of the proposed suppression strategy for three parallel units with identical parameters, an active power step event was designed in the MATLAB/Simulink model. Step changes of 1 MW were applied to each grid-forming unit at t = 2 s, 4 s, and 6 s respectively. Active power variations were compared before and after implementing the oscillation suppression controller.



（a） Conventional grid-forming control



(b) Integration of Self-Damping Control into Grid-Forming Control

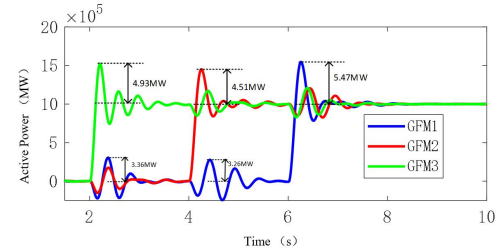
Figure 7 Comparison of Active Power Step Responses in Multi-Machine Parallel Systems with Identical Parameters

As shown in Figure 7(a), under conventional grid-forming control, the power responses of each unit exhibit significant low-frequency oscillations, with large overshoot and long settling time. The maximum overshoot reaches 5.8 MW, and when a step change occurs in the power of one unit, it induces power oscillations in the other units, indicating low system damping and strong power coupling. In Figure 7(b), after introducing the self-damping control, the oscillations are significantly reduced, the step responses become smoother, and the power quickly stabilizes at the target value, demonstrating good local stability and system decoupling capability. These results verify the effectiveness of the proposed self-damping control strategy in suppressing resonance and low-frequency oscillations caused by frequency disturbances in multi-machine parallel systems, significantly improving the dynamic performance and stability of grid-forming multi-machine systems.

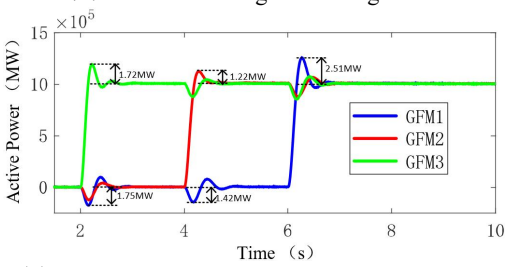
5.2 Oscillation Suppression Verification Under Varied Parameters

To verify the effectiveness of the proposed damping strategy under different parameters for three parallel units, a Matlab-Simulink model was used. The rotational inertias J_n of the three grid-forming units were set to 60 kg·m², 60 kg·m², and 90 kg·m², respectively, to compare the influence of different inertias on low-

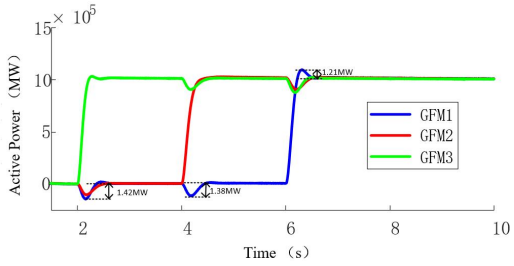
frequency oscillations. The line impedance of the second unit was set to 1.5 times its original value to examine the impact of different line impedances on low-frequency oscillations. A step change in active power was designed, with 1 MW active power steps applied to the three grid-forming units at 2 s, 4 s, and 6 s, respectively, to compare the active power responses with and without the oscillation damping controller.



（a） Conventional grid-forming control



(b) With only the self-damping controller added



(c) With both the self-damping and mutual-damping controllers added

Figure 8 Comparison of Active Power Steps in Multi-Machine Parallel Systems with Different Parameters

When parameter differences exist among the three units, the traditional grid-forming control (Fig. 8a) exhibits significant power oscillations following active power steps at 2 s/4 s/6 s: the three machines mutually affect each other, with frequent overshoots, peak deviations in the range of 4.5–5.5 MW, and slow oscillation damping. This indicates that inter-machine coupling modes are strongly excited, with GFM2 experiencing the heaviest oscillations due to its larger line impedance. With only self-damping added (Fig. 8b), local self-excitation is effectively suppressed, and the first overshoot of the three machines is reduced to about 1.2–2.5 MW, approximately 60–75% lower than under the traditional scheme. The oscillation period shortens and damping increases; however, since each unit still regulates based on its local

frequency deviation, inter-machine coupling modes persist, and noticeable follower oscillations can still be observed when a neighboring unit experiences a step change. With both self- and mutual-damping applied simultaneously (Fig. 8c), where the mutual-damping gain is driven by the weighted average frequency deviation, the three machines respond cooperatively under a unified dynamic reference: during step events, non-stepped machines show almost no significant power overshoot, the first overshoot is nearly eliminated, short-term fluctuations vanish rapidly, and steady-state power sharing returns to the expected level. This demonstrates that the proposed strategy significantly enhances system damping characteristics and effectively improves the dynamic performance and stability margin of the multi-machine parallel system.

6 CONCLUSION

This study focuses on the low-frequency oscillation problem in grid-forming energy storage multi-machine parallel systems. A complete small-signal state-space model was established, the oscillation mechanisms and key influencing factors were clarified, and an improved active power control strategy with both self-damping and inter-damping functions was proposed. Through eigenvalue analysis and simulation verification, it is demonstrated that this strategy can effectively suppress low-frequency power oscillations and enhance system stability in grid-forming energy storage multi-machine parallel systems. The main conclusions are as follows:

1) Through a multi-machine small-signal model incorporating active/reactive power control, dual-loop voltage–current regulation, filters, and line dynamics, combined with eigenvalue and participation factor analysis, it is concluded that low-frequency power oscillations are primarily dominated by the active power control loop, while the rotational inertia and damping coefficients have a significant impact on system stability.

2) The self-damping controller provides additional damping within the target oscillation frequency band via a band-pass filter, thereby enhancing system state stability. The mutual-damping controller leverages higher-level communication links to compensate for inter-unit frequency disturbances, achieving active decoupling and suppressing mutual power oscillations.

3) This strategy effectively enhances the system damping ratio, shifting low-damping modes toward the stable region. Consequently, power responses become smoother, oscillations are significantly attenuated, and the system's dynamic performance is substantially improved.

References

1. National Energy Administration. China's Installed Wind and Solar Power Capacity Surpasses Coal Power. [EB/OL].[2024-08-02]. https://www.nea.gov.cn

16

2. XU Jieyi,LIU Wei,LIU Shu,et al.Current stateand development trends of power system convertergrid-forming control technology[J].Power SystemTechnology,202 2,46(9):3 5 8 6-3 5 94.
3. QIN Benshuang, XU Yonghai. Modal Analysis of Mul ti-virtual Synchronous Machine Grid-connected Pow er-frequency Oscillation[J]. Proceedings of the CSEE, 41(19): 6570-658 1.
4. LIN Jican, LIU Shenquan, WANG Gang, HUANG Min. Coordinated power oscillation suppression of multi-VSG based on consensus algorithm[J]. Power System Technol-ogy: 1-14[2023-11-01]
5. Jian Sun. Impedance-based stability criterion for grid-connected inverters[J]. IEEE transactions on power electronics, 2011, 26(11): 3075–3078.
6. YANG Yuheng, YAO Jun, GONG Sheng,et WANG Zhihui. et Analysis of Sub-synchronous Oscillation Mechanism Induced by the Interaction betweenHigh Inertia Energy Storage Synchronous Condenser and Direct-drive Wind Farm [J/OL]. Power System Technology,1-13[2025-08-11].
7. Shi Peng;Zhou Jinghao;Gan Deqiang;Wang Zhen.A Rational Fractional Representation Method for Wind Power Integrated Power System Parametric Stability Analysis[J].IEEE Transactions on Power Systems,2018,33(6).
8. XU Hao,GAN Deqiang,HUANG Run. et Parameter Tuning Method for Power System Stabilizer Based on Minimum Characteristic Locus [J]. Automation of Electric Power Systems,2023,v.47;No.747(05).
9. Jia Liu, Y. Miura and T. Ise, "Dynamic characteristics and stability comparisons between virtual synchronous generator and droop control in inverter-based distributed generators," 2014 International Power Electronics Conference (IPEC-Hiroshima 2014 - ECCE ASIA), Hiroshima, 2014, pp. 1536-1543,
10. LI Zhenyao,GAN Deqiang,LUAN Moude;. Frequency Stability Analysis Based on Full State Model in Autonomous-Synchronization Voltage Source Interfaced Power System [J]. Electric Power,2023,v.56;No.654(05).
11. XI Xinze1,HUANG Yingbo,XING Chao A Virtual Dynamic Mutual Damping Control Method for Multi-VSGs Parallel System [J]. Power System Technology,2025,49(05):1941-1950.DOI:10.13335/j.1000-3673.pst.2024.0080.
12. ZHAO En’sheng, HAN Yang, ZHOU Siyu, LIU Yuxiang. et al Review and Prospect of Inertia and Damping Simulation Technologies of Microgrids [J]. Proceedings of the CSEE,2022,42(04):1413-1428.DOI:10.13334/j.0258-8013.pcsee.210543.
13. CHENG Huijie, SHUAI Zhikang, PENG Yelun, et al Study on Transient Voltage Stability and Improvement Measures ofParalleled Virtual Synchronous Generators System With Induction Motors [J]. Proceedings of the CSEE,2021,41(14):4787-4798.
14. ZENG Deyin, YAO Jun, ZHANG Tian. Research on Frequency Small-signal Stability Analysis of Multi-parallel Virtual Synchronous Generator-based System [J]. Proceedings of the CSEE,2020,40(07):2048-2061+2385.
15. WEI Zheng,SHEN Qian, Jl Qiu-hua. Research on Small Signal odeling and Stability Analysis ofVirtual Synchronous Generator Parallel System [J]. Power Electionics,2019,53(08):11-15.

063 电动飞机对机场电力系统的挑战

周师琦[1]，赖俊升[1]，贾宏杰[1]，袁毓杰[2]

(1． 电气自动化与信息工程学院，天津大学，天津，300072)

(2． 空中交通管理学院，中国民航大学，天津，300300)

The Challenges of Airport Power System: Electric Aircraft

Zhou Shiqi[1], Chun Sing Lai[1], Hongjie Jia[1], Yujie Yuan[2]

(1. School of Electrical Automation and Information Engineering, Tianjin University, Tianjin, 300072)

(2. School of Air Traffic Management, Civil Aviation University of China, Tianjin, 300300)

ABSTRACT: As transportation emissions reduction and green aviation goals continue to advance, electric aircraft are gaining widespread attention and are being developed towards a more sustainable model. However, the large-scale adoption of electric aircraft poses significant challenges to airport power systems. This paper first categorize electric aircraft and analyze their charging requirements. It will then systematically examine the specific challenges they pose to airport charging systems, power supply systems, and management systems. A review of currently proposed countermeasures and technical solutions will follow. Finally, the paper will discuss key scientific questions and technical bottlenecks that currently exist, and outline future research directions.

KEY WORDS: Electric aircraft, electrification of air traffic, power systems, power systems optimization

摘要：随着交通运输业减排、绿色航空目标持续推进，电动飞机受到广泛关注，并朝着更可持续的模式发展。然而电动飞机的大规模接入对机场的电力系统带来了重大挑战。本文将首先分类阐述电动飞机并分析其充电需求特性；再系统分析其对机场充电系统、供电系统、管理系统等方面带来的具体挑战；并综述当前提出的各类应对策略与技术解决方案，最后，将讨论当前存在的关键科学问题与技术瓶颈，并对未来研究方向提出展望。

关键词：电动飞机，航空交通电气化，电力系统，电力系统优化

DOI：10.13335/j.1000-3673.pst.2014.01.论文序号

0 引言

随着全球气候变化问题日益严峻和"双碳"目标的深入推进，交通运输业的脱碳已成为世界各国的共识与迫切任务。根据国际能源署的数据，航空业贡献了全球约 2.5%二氧化碳排放量，且在持续增长中[1]。航空业作为碳排放的重要来源之一，其绿色转型势在必行。2023 年，国家在绿色航空制造业发展纲要指出加快推广绿色低碳技术，推动绿色航空发展[2]。在欧洲，航迹 2050《欧洲航空愿景》提出的航空脱碳目标要求机场在 2050 年前实现无碳排放[3]。在此背景下，电动飞机凭借其零排放、低噪音、高能效等优势，受到广泛关注，引领着全球航空业的一场深刻革命。

然而，这场航空动力系统的变革不仅限于飞行器本身，其成功需要高度依赖于地面基础设施的同步发展，尤其是机场的能源供给系统。传统机场的电力系统主要服务于航站楼、助航灯光、地勤设备等辅助设施，容量和架构相对固定。电动飞机的普及将彻底改变机场的能源需求格局，使其从传统的“燃油枢纽”转变为“高功率电能枢纽”。大功率、快节奏、高能耗的充电需求将对机场电网的容量、稳定性、可靠性及智能化水平提出高要求。电动飞机的大规模接入预计将从负载特性、电能质量、电网扩容几个层面影响机场电力系统。

目前，国内外研究多集中于电动飞机本体技术（如电池、电机、电控）的突破，或对其市场前景、运营模式的分析。而对于其地面基础设施，特别是对机场电力系统带来的系统性、连锁性影响的综合性研究尚处于起步阶段。相关研究成果分散在电力工程、航空航天、交通运输等多个交叉领域，缺乏全面、结构化的梳理与总结。

本综述旨在填补这一研究空白，全面审视电动

基金项目：天津市科技局科技计划项目-自然基金-多元基金项目-青年项目 24JCQNJC00280

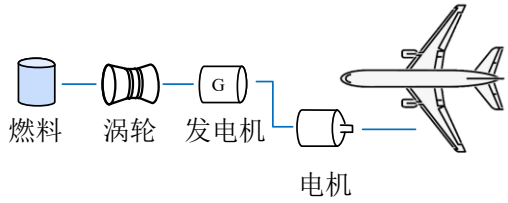
Tianjin Science and Technology Bureau Science and Technology Plan Project - Natural Science Foundation - Multi-Fund Project - Youth Project 24JCQNJC00280

飞机发展对机场电力系统产生的影响。本文在第 1 节中首先分类阐述电动飞机，再以敦煌机场为例，分析其充电需求特性。在 2 节中系统分析其对机场充电系统、供电系统、管理系统等方面带来的具体挑战，并综述当前提出的各类应对策略与技术解决方案。最后，对文章进行总结，并将讨论当前存在的技术瓶颈，并对未来研究方向提出展望。

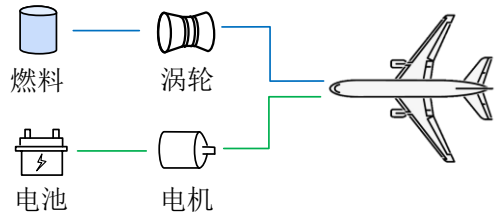
1 电动飞机的电力需求分析

1.1 电动飞机的发展

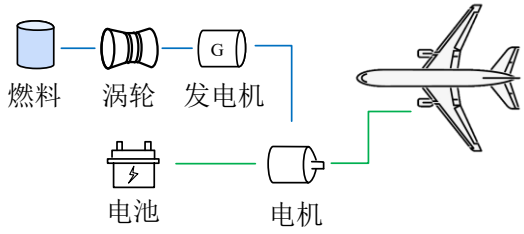
航空电气化发展，从多电飞机起步，过渡到混电飞机，再向最终目标全电飞机迈进。三种电动飞机的主要区别在于推进动力的来源不同[4]，图 1 展示了其飞机推进系统的技术原理图。



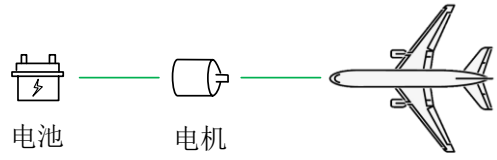
（a）多电飞机



（b）并联混电飞机



（c）串联混电飞机



（d）全电飞机

图 1 各类电动飞机的推进系统

Figure 1 The Propulsion Systems for Various Types of Electric Aircraft

多电飞机如图 1(a)所示，其电气化部分在机载系统，而推进系统仍然是航空燃油。混电飞机如图 1(b)(c)所示，推进动力来源为航空燃料与电能的混合。主要包含串联混合电力推进系统和并联混合电力推进系统两种。全电飞机如图 1(d)所示，其动力均来源于电能。其中，全电飞机是航空工业中唯一能够实现净零排放的潜在技术，但是其所需要的电能耗是远高于多电飞机与混电飞机，对机场电力系统的影响最强烈。

Eviation Alice 是世界上第一架 9 座级别的全电通勤客机，设计可容纳 2 名机组人员和 9 名乘客，电池功率为 900kWh，如图 2-3 所示。该原型已于 2022 年 9 月 27 日进行了首次飞行[5]。目前，已经完成首飞的全电飞机设计的关键进展如表 1 所示。近些年来，许多公司正朝着各种方向努力，以实现全电动飞行的概念和克服重大障碍，包括增加电池的能量容量和提出新的电力推进系统，实现未来飞机的进一步电气化。

表 1 全电飞机设计的关键进展

Table 2 The Key Advances in All-Electric Aircraft Design

名称	相关信息
Airbus E-Fan[6]	2 座；最大飞行速度 220 公里/小时；2014 首飞
Magnus eFusion[7]	2 座；最大飞行速度 266 公里/小时；2016 首飞
Siemens Extra 330 LE[8]	2 座；最大飞行速度 337.50 公里/小时；2016 首飞；
Rolls Royce/YASA ACCEL[9]	1 座；最大飞行速度 483 公里/小时；2020 首飞
Eviation Alice [5]	9 座；最大飞行速度 463 公里/小时；2022 首飞

1.2 不同充电模式下的负荷特性

电动飞机充电系统主要包含插电式和换电式。插电式：电动飞机通过专用充电器直接连接到母线，从而实现电力传输实现电池充电。换电式：电动飞机在电池交换站将耗尽的电池与充满电的电池进行交换，交换站则通过充电器连接到母线进行充电。

以某日的敦煌机场为例，假设 Alice 在最理想的状态下，可执飞 800 公里左右的航班。据统计，敦煌机场某日起落航班总计 42 次，其中 Alice 可执飞航班为 10 次（到达与出发各 5 次），且有 3 次航班在抵达后仍有飞行任务，即需要进行立即充电或更换电池设备以免影响后续航班飞行计划。在插电式充电方案中，三架飞机需在半小时内完成充电，其余两架飞机安排在夜间低峰时间段完成。在换电式方案中，将五驾飞机的电池均安排在夜间低峰时间段完成。以第一架电动飞机 Alice 为例，分析不同充电模式下的负荷特性。其各项参数如表 2 所示[5]。

表 2 Alice 各项参数

Table 2 The Configuration of Alice

参数	数值	参数	数值
最大速度	463 公里/小时	最大航程	815 公里
巡航速度	407 公里/小时	峰值推进功率	900 千瓦
巡航高度	3048 公里	最大有效载荷	1134 公斤

经计算，机场内一天的负荷曲线如图 2 所示，包含原始负荷曲线，插电式充电负荷曲线以及换电式负荷曲线。从图中可以观察到，机场的电力负荷主要由航站楼、拖车、乘客所产生，其负荷峰值出现在 9：00 和 17：00 航班较为集中的时刻，且最高峰值在 500kW 以内。在插电式方案中，三架飞机的落地时间集中在 10：00-14：00，且由于后续的飞行任务需要立即充电，使机场的电力负荷峰值急剧升高，最高峰值突破 2000kW，给机场的电力系统带来了巨大的压力。换电式方案在很大程度上能够缓解电动飞机的峰值情况，但电动飞机的巨大能耗，仅五个电池的充电能耗已完全覆盖机场一日的能耗。给机场的电力系统带来了不小的压力，其夜间负荷仍高出白天机场的基础负荷的峰值。

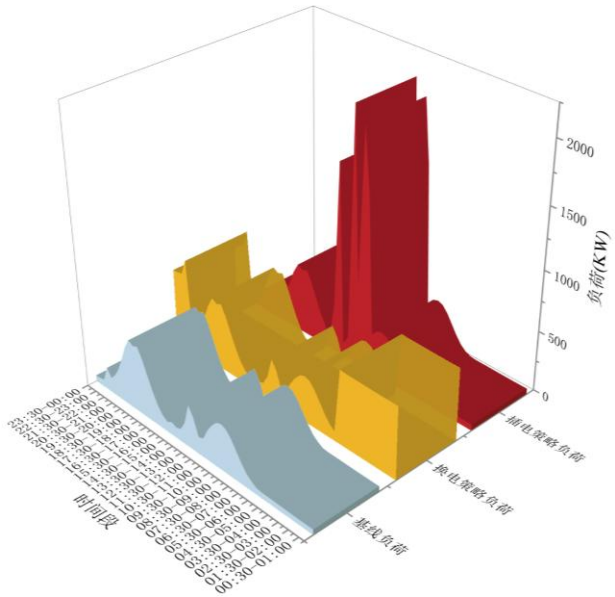


图 2 不同充电策略下的敦煌机场一日内电力负荷曲线
Figure 2 The load curve of Dunhuang Mogao international airport within a day under different charging strategies

电动飞机接入机场电网后，对电力负荷特性主要呈现在三个方面：

（1）瞬时峰值极高。机场需为瞬时峰值功率与累积能量同时做规划，不再以传统航站楼/设备耗电为主。飞机充电功率极高（兆瓦级），充电行为集中，在短时间内形成一个极其陡峭的负荷尖峰。

（2）能源需求量增加。与传统机场相对平稳的负荷曲线不同，电动飞机充电负荷呈现高频、间歇、高功率的尖峰特性。这两种负荷叠加后，将在特定时段（如航班集中到港、快速补电期间）产生巨大的峰值功率需求，这种峰值可能远超现有市政电网接入容量和机场内部配电系统的设计极限。

（3）电能质量下降。兆瓦级充电桩本质上是大规模电力电子装置，采用大功率整流器将交流电转换为直流电为电池充电。其频繁的启停和功率调节会对电网的电能质量产生严重干扰，引入谐波、闪变和瞬时电压跌落，对机场内其他精密敏感设备的正常运行构成威胁。

2 带来的挑战与发展趋势

电动飞机具有大功率、快节奏、高能耗的充电需求，对机场的电力系统带来了巨大的影响。总结在电池充电系统、供电系统和管理系统三个方面。

2.1 电池充电系统

电动飞机电池容量为 900kWh 的全电动支线飞机，其峰值充电需求可能达到 2MW，超过了目前的轻型地面电动汽车充电技术和标准。电动飞机的高功率需求与重型电动卡车更为接近，文献[10]总结了目前的电动卡车充电器的技术规范，为实现电动飞机的地面充电提供参考。

大功率电动飞机充电系统，同时也带来了额外的高能耗需求。实现智能充电是减少峰值影响，缓解电网冲击关键方法。智能充电技术在电动汽车中已经得到了广泛的应用[11-13]，且在航空交通电气化中，有部分智能充电的研究集中于机场内电动汽车的优化[14,15]。但由于电动飞机充电特性与电动汽车差异较大，这类方法可为电动飞机智能充电提供参考而无法直接应用。基于此，在电动飞机的背景下，智能充电技术可以两个方面进行研究。

（1）基于航班时间表，有效地管理充电负荷，从而减少与电动飞机充电相关的电网影响。文献[16]对混电飞机的航班安排进行优化，有效管理机场拥堵和峰值电力需求。通过细微调整大幅降低峰值电力需求，减少电网基础设施升级的需求。

（2）从电池性能出发，根据电池 SOC、电池化学性质、热管理系统和环境条件对充电功率进行智能控制，可以显著减少充电次数，延长电池寿命。文献[17]利用锂离子电池的电路模型，推导出恒流-恒压充电策略下电动飞机的充电功率曲线，为管理充电功率的探究提供基础。

换电概念使智能充电技术的应用具有更大的灵活性，文献[18]提出了针对电动飞机电池更换和充电的功率优化和功率投资优化策略，该策略使峰

值电力消耗降低了 61%，电力成本降低了 25%。然而，在实际换电过程中会遇到许多技术难题。首先，所需的可移动电池组设计难，需在易于更换和飞行安全可靠性之间找到平衡。第二，充电接口标准化门槛高。第三，初始成本大，需投入昂贵的自动化换电机器人和大量备用电池组。

2.2 供电系统

传统机场的电力需求主要集中在航站楼照明、暖通空调、地勤设备及辅助设施上，其电力需求平稳。而随着电动飞机的引入，机场将面临全新的高能量负荷挑战。为满足这类新型电力需求，机场需对内部配电系统进行全面升级。此外，现有机场接入市政电网的容量往往不足以支撑如此大幅的增长，因此可能需新建高压变电站甚至专用输电线路。这类改造不仅投资巨大，还涉及复杂的电网规划和多方协调。

为了满足电动飞机高耗能的充电需求，同时规避对机场现有电网进行昂贵且复杂的升级改造，可以将本地储能系统和现场可再生能源发电源集成到充电站中，以供应较大的脉动负载。该策略在电网负荷低谷或光伏发电高峰时储存电能，当多架电动飞机同时充电导致负荷激增时，再由储能系统释放电能，从而大幅平滑对上级电网的功率需求，并保障电网的稳定运行。本地储能系统和现场可再生能源发电源集成在家庭和居民区得到研究和应用。文献[19]讨论了各种可再生能源，储能，对电网和电网系统的的可行性，并通过实例分析建模安装太阳能电池板，实现了家用储能和使用电动汽车的能源和节省。文献[20]提出“可再生能源社区”的概念，通过在一个光伏发电渗透率较高的真实住宅区利用不同能源网络之间的协同作用，探讨了储能系统和多联产在可再生能源自我消费中的潜在作用。近年来在机场电力系统中，也受到关注。文献[21]评估了太阳能光伏发电和蓄电池储能在维斯比机场支持电动航空和车辆基础设施中的作用，结果表明太阳能光伏发电和蓄电池储能能够较好的帮助机场实现电气化。此外，根据生命周期循环对第一代电动飞机进行评估，如果为电动飞机提供电能的来源仍来着煤炭等传统发电，带来的排放要高于传统飞机的排放[22]。发展新能源作为分布式电源，有助于更进一步的交通行业脱碳。

2.3 管理系统

随着大功率电动飞机充电系统建设，额外的高能耗需求增加，电能质量下降、系统的不稳定性加剧。因此，需要对对机场区域内的能源流动进行监测、协同优化与实时决策，从而确保供电的安全、稳定与经济性。

通过优化调度、需求响应协同调度光伏、储能、飞机电池、传统电网等多类能源，实现削峰填谷和优化运行，建设智能能源管理系统。文献[23]提出了一个机场微电网双目标基础设施规划框架，用于容纳停车场电动汽车和电动飞机，对机场充电系统进行优化调度。文献[24]提出提出了一种通过车辆到电网（V2G）和航空到电网（A2G）实现机场微电网的灵活频率控制方法，能够保持有效的频率控制结果。文献[25]提出一种考虑电动飞机储能和需求响应的鲁棒自适应模糊控制器，在控制器信号和系统不确定性取得了良好的效果。

大功率充电器是严重的谐波源和电压扰动源，其快速启停会造成电压骤升骤降。电能质量恶化会严重影响机场其他精密设备的正常运行甚至波及所在区域的市政电网，威胁整个电力系统的安全稳定运行。实时监测电网的电压、频率和谐波含量。需要采用先进的电力电子设备（如 APF 有源电力滤波器、智能变压器）来补偿无功功率、抑制谐波。文献[26]探究了智能变压器如何升级现有的机场电源系统，从而为可再生能源，电动汽车和未来的混合动力和电动飞机提供了有效的界面。文献[27]通过基于支持向量机。实现智能滤波器控制，优化了电压和电源质量。且电动飞机引入了兆瓦级充电设备和大容量高能量密度电池，为机场电力系统带来巨大的电气火灾与爆炸风险。需要对故障情况、热管理系统等进行实时监控与防护。

此外，在航空电气化转型的过程中，需要确保电力系统确保经济性和可持续性。与电网公司、能源供应商进行协同规划，制定新的电价机制和电力市场交易策略[27-30]。通过市场手段优化充电行为，提升机场以及其邻近区域的能源使用效率。今后机场将不再只是一个被动的电网消费者，而是将其升级为一个集生产、存储、消费和智能管理于一体的主动能源节点。并建立安全保障系统，维护机场电力系统的稳定运行，实现经济、可靠的电力系统。

3 总结与展望

本文探讨了电动飞机发展对机场电力系统产生的影响。介绍了电动飞机的发展过程，并以敦煌机场为例，分析电动飞机所带来的负荷特特性变化。从充电系统、供电系统、管理系统三个方面探讨了机场电力系统在电动飞机发展背景下的挑战和发展方向。

最核心的瓶颈仍集中于高功率、高频率充电需求与现有电网承载力及稳定性之间的矛盾。目前对充电需求与电网之间的技术研究，仍停留在电动汽车，而在电动飞机高功率、高频率充电的需求下，这些技术无法适用。在电动飞机背景下的机场电力系统研究仍处于初步阶段，还有一个主要的原因是电动飞机受高密度电池技术的限制，电动飞机的续航能力不足。目前的电动飞机只能实现区域飞行，还无法满足机场的飞行需求。因此目前的研究仍以仿真模拟为主，缺乏真实数据集。依据电池发展历史，在未来实现拥有高密度电池的电动飞机将不再处于构想，机场电力系统的研究也将在航空电气化中发挥关键作用。

参考文献

[1] IEA. Tracking viation [EB/OL]. (2025-1-16) https://www.iea.org/energy-system/transport/aviation.

[2] 中国政府网. 工业和信息化部等四部门关于印发绿色航空制造业发展纲要（2023-2035 年）的通知[EB/OL]. (2023-10-1) https://www.gov.cn/zhengce/zhengceku/202310/content_6908243.htm

[3] Eisenhut D, Moebs N, Windels E, et al. Aircraft requirements for sustainable regional aviation[J]. Aerospace, 2021, 8(3): 61.

[4] Cano T C, Castro I, Rodríguez A, et al. Future of electrical aircraft energy power systems: An architecture review[J]. IEEE Transactions on Transportation Electrification, 2021, 7(3): 1915-1929.

[5] “Alice – Eviation. [EB/OL]. ” https://www.eviation.co/alice/ (2021-3-16).

[6] “Airbus E-Fan.” [EB/OL] https://en.wikipedia.org/wiki/Airbus_E-Fan#Design_and_development. (2025-9-13).

[7] “Magnus-Efusion” [EB/OL] https://www.aircraft.com/aircraft/33495005/magnus-efusion (2025-9-13).

[8] “Extra 330LE Electric Aircraft” [EB/OL] https://www.airport-technology.com/projects/extra-330le-electric-aircraft/?cf-view. (2025-9-13).

[9] “Rolls-Royce All-Electric Aircraft”. [EB/OL] https://www.airport-technology.com/projects/rolls-royce-all-electric-aircraft/(2025-9-13).

[10] Liang Y, Mouli G R C, Bauer P. Charging technology for electric aircraft: State of the art, trends, and challenges[J]. IEEE Transactions on Transportation Electrification, 2023, 10(3): 6761-6788.

[11] Wang Q, Liu X, Du J, et al. Smart charging for electric vehicles: A survey from the algorithmic perspective[J]. IEEE Communications Surveys & Tutorials, 2016, 18(2): 1500-1517.

[12] Sachan S, Deb S, Singh S N. Different charging infrastructures along with smart charging strategies for electric vehicles[J]. Sustainable Cities and Society, 2020, 60: 102238.

[13] Moghaddam Z, Ahmad I, Habibi D, et al. Smart charging strategy for electric vehicle charging stations[J]. IEEE Transactions on transportation electrification, 2017, 4(1): 76-88.

[14] Hasan S, Zeyad M, Ahmed S M M, et al. Techno-economic feasibility analysis of an electric vehicle charging station for an International Airport in Chattogram, Bangladesh[J]. Energy Conversion and Management, 2023, 293: 117501.

[15] Liu X, Li M, Liu X, et al. Quantifying energy flexibility potential of ground electric vehicles in an airport with real behavior data[J]. Sustainable Cities and Society, 2024, 105: 105331.

[16] Hou B, Bose S, Marla L, et al. Impact of aviation electrification on airports: Flight scheduling and charging[J]. IEEE Transactions on Intelligent Transportation Systems, 2023, 25(3): 2342-2354.

[17] Liang Y, Bodnár D, Mouli G R C, et al. Charging Demand Prediction: Small All-Electric Aircraft and Electric Vertical Takeoff and Landing Aircraft[J]. IEEE Transactions on Transportation Electrification, 2024.

[18] Justin C Y, Payan A P, Briceno S I, et al. Power optimized battery swap and recharge strategies for electric aircraft operations[J]. Transportation Research Part C: Emerging Technologies, 2020, 115: 102605.

[19] Speidel S, Bräunl T. Leaving the grid—The effect of combining home energy storage with renewable energy generation[J]. Renewable and Sustainable Energy Reviews, 2016, 60: 1213-1224.

[20] Bartolini A, Carducci F, Muñoz C B, et al. Energy storage and multi energy systems in local energy communities with high renewable energy penetration[J]. Renewable Energy, 2020, 159: 595-609.

[21] Ollas P, Sigarchian S G, Alfredsson H, et al. Evaluating the role of solar photovoltaic and battery storage in supporting electric aviation and vehicle infrastructure at Visby Airport[J]. Applied Energy, 2023, 352: 121946.

[22] Schäfer A W, Barrett S R H, Doyme K, et al. Technological, economic and environmental prospects of all-electric aircraft[J]. Nature Energy, 2019, 4(2): 160-166.

[23] Guo Z, Li B, Taylor G, et al. Infrastructure planning for airport microgrid integrated with electric aircraft and parking lot electric vehicles[J]. Etransportation, 2023, 17: 100257.

[24] Liu X, Fan P, Yang J, et al. A flexible frequency control strategy for airport-microgrid through vehicle-to-grid and aviation-to-grid[J]. Journal of Energy Storage, 2025, 125: 116980.

[25] Shayeghi H, Davoudkhani I F, Bizon N. Robust self-adaptive fuzzy controller for load-frequency control of islanded airport microgrids considering electric aircraft energy storage and demand response[J]. IET Renewable Power Generation, 2024, 18(4): 616-653.

[26] Buticchi G, Pereira T, De Carne G, et al. A smart transformer for the electrical power system of green airports: Smart power management[J]. IEEE Industrial Electronics Magazine, 2023, 18(3): 6-16.

[27] Akbarimajd A, Heiran A M. Implementation of a power supply with optimized voltage and power quality control by a smart filter[J]. Majlesi Journal of Electrical Engineering, 2024, 18(4): 1-9.

[28] Xiang Y, Cai H, Liu J, et al. Techno-economic design of energy systems for airport electrification: A hydrogen-solar-storage integrated microgrid solution[J]. Applied energy, 2021, 283: 116374.

[29] Bahman N. Airport sustainability through life cycle assessments: A systematic literature review[J]. Sustainable Development, 2023, 31(3): 1268-1277.

[30] Ajayi A. Future grid for a sustainable green airport: meeting the new loads of electric taxiing and electric aircraft[J]. 2023.

收稿日期：2025-xx-xx。

作者简介：

作者照片



作者姓名
周师琦

周师琦(1999)，女，硕士，研究方向为电力系统分析、负荷预测，E-mail：shiqizhou@hdu.edu.cn；

赖俊升(1991)，男，教授，博士生导师，研究方向为微电网、低空经济等，E-mail：Cslai@tju.edu.cn；

贾宏杰(1973)，男，教授，博士生导师，研究方向为电力系统分析、稳定和控制等,E-mail: hjjia@tju.edu.cn；

袁毓杰(1993)，女，博士，讲师，研究方向为低空经济、城市空中交通调度等,E-mail:yjyuan@cauc.edu.cn。

（编辑　五号楷体，居右，段前空 6pt）A

064 An MILP framework for Demand Response Incentive Design with NILM-based Potential Estimation

Feiyu Chen[1], Rui Yang[1], Xi Ming [1]and Kai Zhou[1,*]

[1] Soochow University, Suzhou 215006, China
*kzhou@suda.edu.cn

Abstract. Demand response (DR) programs pay electricity customers to reduce or shift their electricity consumption during peak demand periods or system stress, improving reliability and stability while reducing costs and emissions. Most DR programs rely on aggregated demand elasticity or pre-specified willing-to-accept (WTA) curves derived from surveys or stylized assumptions, which can only estimate DR potential with limited granularity. Therefore, we propose a DR framework that estimates appliance-level DR potential based on non-intrusive load monitoring (NILM) and optimizes retailer incentives through a mixed-integer linear programming model. First, the NILM decomposes advanced metering infrastructure (AMI) data and derives flexible loads from the appliance-level consumption. Then, the framework optimizes incentive levels to maximize the retailer's profit informed by the NILM-based potential. Case study shows that the proposed method can better estimate the DR potential and enables more targeted, effective incentives, yielding greater peak-load reduction and higher retailer profit compared with aggregated elasticity-based baselines. The framework is practical with standard AMI data and scalable to large customer portfolios.

Keywords: Demand response, incentive design, non-intrusive load monitoring, linear programming.

1 Introduction

Electric power systems face tightening operating margins as electrification and variable renewable generation increase net-load volatility and raise the cost of serving peaks. Demand response (DR) is a proven tool that enhances reliability, lowers energy costs, shifts peak loads, and reduce emissions by shifting or curtailing load during stressed periods [1,2]. DR programs are usually implemented by utilities or electricity retailers, who are self-interested entities with objective of maximizing their own profits. One main type of DR programs is based on price. Retailers design price or incentive strategies to influence the electricity consumption behavior so that loads can be reduced or shifted.

The foundation of price-based DR is accurately reflecting the demand elasticity, which is a measure of how sensitive electricity consumption is to changes in its price. This is often built from power consumption data under various tariffs using experimental or survey methods. For example, [3] designs and implements an incentive-based

demand response system for load serving entities. It introduces coupons aiming to shift loads from high price hours to low-price hours and exposits real-life experiments. [4] conducts a choice experiment in Germany to analyze consumers' acceptance of TOU tariffs. These methods are weakly tied to how individual devices actually operate because electricity consumption is constrained by device physics. The result is uncertainty such that programs may over- or under-estimate flexible capacity, incentives can be mistargeted and realized load reduction may be less than expected.

It is not possible to monitor every customer's appliance. Non-intrusive load monitoring (NILM) techniques address this by extracting appliances' states from aggregated electricity features. Since first introduced by Hart [5], NILM research develops rapidly. Regarding data resolution, [6] reviews NILM algorithms that base on low-frequency data, while [7] reviews NILM based on high-frequency data. In terms of the mathematical model, it can be mainly divided into three categories: optimization, random process, and neural networks. Most of the studies of NILM focus on the accuracy and robustness of disaggregation algorithms, such as [8], which introduces a method based on transfer knowledge between domains.

NILM studies mainly focus on disaggregating the total loads to appliance levels; however, the connection between NILM results to DR programs is underexplored. Existing studies of DR often target a single class of major load, such as thermostatically controlled loads (TCLs) and electric vehicles (EVs). [9] proposes a NILM-based approach to estimate the DR potential of the TCLs, and then assist retailers in formulating the price strategy. [10] proposes a contrastive sequence-to-point learning method for substation-level flexible load disaggregation. Moreover, [11] designs a building-level system with hardware and software for the application of NILM in DR but without incentive design. A general framework that converts NILM results into incentive strategies for retailers is still missing.

To address this gap, we propose a mixed-integer linear programming (MILP) framework for demand response incentive design with NILM-based potential estimation. First, NILM is applied to smart meter data to reveal appliance-level consumptions and identify feasible load flexibility. Second, we develop a method to translate these NILM outputs into DR potentials. Finally, an MILP model is introduced to maximize retailer's profit by optimizing DR incentives.

2 DR incentive strategy framework

The retailer collects smart meter data and disaggregates the total electricity consumption into appliance-level profiles using the NILM module. Then, it groups different appliances and assigns the willingness-to-accept (WTA, the minimum compensation that is worth of a customer's flexible energy use that can be modified to provide grid services, such as reducing peak demand, providing reserves, or adjusting for renewable energy fluctuations.) to infer each customer's flexibility and aggregate DR potential across the portfolio. Finally, an MILP is applied to maximize the retailer's profit, incorporating the NILM-based DR potential. The proposed framework is illustrated in Figure 2.

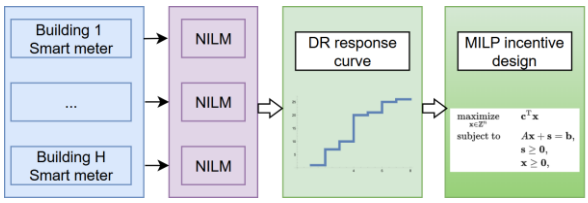


Fig. 1. The framework of the retailer's incentive design using NILM-based potential.

2.1 NILM algorithm

Smart meter data are typically low sampling rate (≤1 Hz), so we use a coupled factorial hidden Markow Model (CFHMM) to disaggregate aggregate household power [12]. We rely on steady-state features that require no extra sensors; examples include time of day, day of week, and outdoor temperature.

Each appliance $e \in \{1,\ldots,E\}$ in household $b \in B$ has a binary state $q_{e,t}^{(b)} \in \{0,1\}$ (off/on) evolving as a Markov chain. Let $\mathbf{c}_t = (c_{1,t},\ldots,c_{K,t})$ denote exogenous features. The observed aggregate real power at time t is $p_t^{(b)}$.

Initial state probabilities:

$$\pi_{e,s}^{(b)} = P(q_{e,1}^{(b)} = s) \tag{1}$$

The observed real power consumption follows an additive normal distribution:

$$p_t^{(b)} |\ \mathbf{q}_t^{(b)} \sim \mathcal{N}\Big(\mu_0 + \sum_{e=1}^{E} \mu_e q_{e,t}^{(b)}, \sigma^2\Big) \tag{2}$$

Transitions with exogenous features and optional cross-appliance coupling is:

$$P(q_{e,t+1}^{(b)} |\ \mathbf{q}_t^{(b)}, \mathbf{c}_t) \propto A_e^{(q_{e,t}^{(b)}, q_{e,t+1}^{(b)})}(\mathbf{c}_t) \prod_{m \neq e} M_{e,m}^{(q_{e,t+1}^{(b)}, q_{m,t}^{(b)})} \tag{3}$$

where $A_e^{(\cdot,\cdot)}(\mathbf{c}_t)$ are feature-conditioned transition factors and $M_{e,m}^{(\cdot,\cdot)}$ are cross-appliance factors; the proportionality constant ensures normalization.

Then, the joint probability distribution is:

$$P(p_{1:T}^{(b)}, \mathbf{q}_{1:T}^{(b)} |\ \lambda) = \prod_{e=1}^{E} \pi_{e,q_{e,1}}^{(b)} \prod_{t=1}^{T-1} \prod_{e=1}^{E} P(q_{e,t+1}^{(b)} |\ \mathbf{q}_t^{(b)}, \mathbf{c}_t) \prod_{t=1}^{T} P(p_t^{(b)} |\ \mathbf{q}_t^{(b)}) \tag{4}$$

where $\lambda = \{\pi_e, A_e(\cdot), M_{e,m}, \mu_0, \mu_e, \sigma^2\}$ are parameters.

Given training data, we learn λ by Expectation–Maximization [12,13] using an approximate E-step.

Given λ, we estimate the hidden sequence by

$$\mathbf{q}^{(b)*} = \arg\max_{\mathbf{q}} P(\mathbf{q}^{(b)} |\ p_{1:T}^{(b)}, \lambda) \tag{5}$$

It is solved approximately by methods such as simulated annealing algorithm. Posterior appliance power is estimated by the posterior mean:

$$\hat{p}_{e,t}^{(b)} = \mu_e P(q_{e,t}^{(b)} = 1 |\ p_{1:T}^{(b)}, \lambda) \tag{6}$$

2.2 Extract DR potential from NILM result

After having the NILM results, we aggregate these appliance-level power consumption profiles to determine flexible loads.

From B buildings/households, NILM gives appliance time series $p_{e,t}^{(b)}$ for appliance e. We aggregate the real powers to the retailer's portfolio:

$$p_{e,t} = \sum_{b=1}^{B} \hat{p}_{e,t}^{(b)} \tag{7}$$

End-use appliances are heterogeneous: some are curtailable, some shiftable; some draw substantial power, others are negligible. For DR, the retailer does not need to know exact power for each appliance. Instead, we group appliances according to the typical DR actions and WTAs into six categories, as shown in Table 1. The base consumption is also listed as "others" in the bottom row and assigned a WTA value v_6. We make v_6 a large number so that the optimization treats it as nonsheddable.

Table 1. Appliance categories with WTA for DR programs

ID	Appliance category	Typical DR action	WTA
1	Lighting & misc. plug loads	turn off /dim	v_1
2	EV charging	Shift or throttle	v_2
3	Dishwasher	Delay start	v_3
4	Washer/Dryer	Delay cycle	v_4
5	HVAC/air conditioner/electric furnace	Thermostat setback	v_5
6	Others	Not changeable	v_6

At each time period t, each type of flexible load category $h_{m,t}(m \in \{1,...,6\})$ is associated with it WTA v_m. The set $\{(h_{m,t}, v_t)\}$ defines a stepwise DR response curve. This lays the foundation of retailers' incentive strategies.

2.3 MILP for DR incentive strategy

We formulate the DR incentive strategy as an MILP optimization problem. The NILM-based DR potential is introduced as a constraint to represent the DR response:

$$0 \le x_{n,m,t} \le h_{n,m,t} z_{n,m,t} \quad m \in M \tag{8}$$

$$\sigma_t \ge v_m + (\bar{\sigma} - v_m)(1 - z_{m,t}) \quad m \in M \tag{9}$$

$$z_{m,t} \in \{0,1\} \quad m \in M \tag{10}$$

$$z_{m,t} \le z_{m-1,t} \quad m \ge 2 \tag{11}$$

where $x_{n,m,t}$ is the power consumption in segment m of the DR response curve at load bus n, M is the set of DR appliance categories, $z_{n,m,t}$ is the corresponding auxiliary binary variable, σ_t is the DR incentive at time period t. If $\sigma_t \ge v_{m,t}$, then $z_{m,t}$ can be 1 and $x_{m,t} \le h_{m,t}$; if $\sigma_t < v_{m,t}$ then $z_{m,t}$ must be 0 so that $x_{m,t} = 0$, representing that the load is not shed.

Other constraints include demand aggregation and bounds:

$$r_{n,t} = \sum_{m=1}^{M} x_{n,m,t} \tag{12}$$

$$d_{n,t} = p_{n,t} - r_{n,t} \tag{13}$$

$$0 \le \sigma_t \le \bar{\sigma} \quad t \in T, n \in \mathcal{N}^{\mathrm{DR}} \tag{14}$$

where $d_{n,t}$ is the total load at bus n, $r_{n,t}$ is reduced/shifted load, and $\bar{\sigma}$ is the upper bound of the incentive.

The objective function is to maximize the retailer's profit during the planning periods and avoid losing during the high locational marginal price (LMP).

$$\max S \sum_{t \in \mathcal{T}} \sum_{n \in \mathcal{N}^{\mathrm{DR}}} (\tau_t - \lambda_{n,t}) d_{n,t} - \sigma_t r_{n,t} \tag{15}$$

where S is the base apparent power (MVA), $\mathcal{T}$ is the set of time periods, $\mathcal{N}^{\mathrm{DR}}$ is the set of DR buses located within the retailer's footprint, τ_t is the retail price, $\lambda_{n,t}$ is the LMP in the wholesale market at bus n. Profft consists of two parts: profit by selling electricity and the incentive cost of reducing load.

The objective function has a bilinear term $\sigma_t r_{n,t}$. It makes the problem nonconvex and nonlinear and hence hard to solve. Therefore, we linearize the bilinear term with the McCormick envelope. We introduce a new decision variable w and use bounds $0 \le r_{n,t} \le \bar{r}, n$ and $0 \le \sigma_t \le \bar{\sigma}$. Then we replace the bilinear term in the objective function by w and add the four linear inequalities:

$$w_t \ge 0 \tag{16}$$

$$w_t \ge \bar{r}_n \sigma_t + \bar{\sigma} r - \bar{r}_n \bar{\sigma} \tag{17}$$

$$w_t \le \bar{\sigma} r_{n,t} \tag{18}$$

$$w_t \le \bar{r}_n \sigma_t \tag{19}$$

Then, the linearized objective function is:

$$\max S \sum_{t \in \mathcal{T}} \sum_{n \in \mathcal{N}^{\mathrm{DR}}} (\tau_t - \lambda_{n,t}) d_{n,t} - w_t \tag{20}$$

In short, the problem is a mixed integer linear programming that can be solved by off-the-shelf solvers. It is summarized as follows:

Table 2. MILP for retailer profit maximization

Retailer profit maximization problem	
variables:	$q_{n,t}, \sigma_t, w_t, z_{m,t}, x_{n,m,t}$
maximize:	(20)
subject to:	(8)–(14) and (16)–(19)

3 Case study

We test the proposed method on public datasets. The smart meter data and LMP are collected from Pecan street dataset[14]. Specifically, we use smart meter readings from California research region (1-minute resolution) and 1-week average LMP from CAISO. The simulations have been conducted on an Intel Core i7-13850HX (with 2.10

GHz CPU, 64 GB of RAM, and 64-bit Windows system). The MILP is solved by Pyomo with glpk solver.

We train a CFHMM on 297 days of smart meter data, and test on the last week. We compare the result in terms of six appliance categories. Figure 2 shows the hourly true EV consumption and the disaggregated result on the test dataset. We use root mean square error (RMSE) to evaluate the performance. RMSE quantifies the deviation between the predicted and the actual power consumption. The overall RMSE is 3.31MWh.

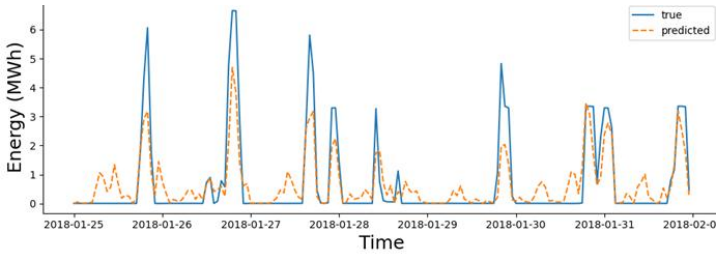


Fig. 2. Disaggregation results of the EV charger hourly consumption.

Based on the NILM results, we built the DR response curve. We estimate the WTA value as $v=[v_1,...,v_6]=[5,10,15,20,25,100]$ in \$/MWh. $v_6=100$ because the upper bound of incentive $\bar{\sigma}$ is 30 . Note that these WTAs are a rough approximation used for this case study. Figure 3 shows the aggregated DR curve.

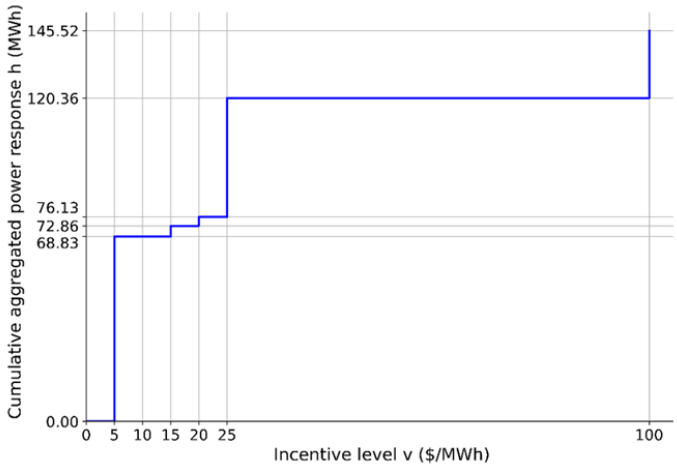


Fig. 3. Aggregated DR response curve for the retailer at a random hour.

Next, we incorporate the DR response curve into the MILP retailer profit maximization problem. Three scenarios are considered: (1) scenario 1: baseline with no DR, (2) scenario 2: uniform elasticity, (3) scenario 3: the proposed framework. In scenario 2, a uniform elasticity model is used. Specifically, the WTA use the average $v = 15$, the DR potential is approximated as one-fourth of the total power consumption, and the DR response curve is modeled as $\{(v,h)\} = \{(15, p_t / 4)\}$. The power consumption of the three scenarios is shown in Figure 4. It shows that the introduction of DR leads to a noticeable reduction in electricity consumption compared with the baseline, and the proposed framework (scenario 3) achieves a more significant load reduction than the uniform elasticity model.

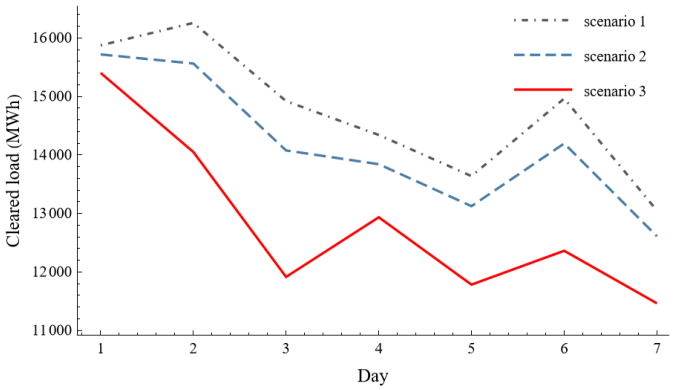


Fig. 4. The daily cleared load of the three scenarios using different DR frameworks.

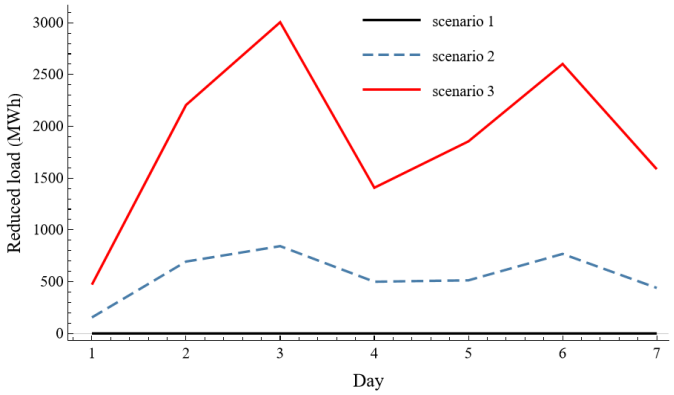


Fig. 5. The daily electricity reduction of the three scenarios using different DR frameworks.

Moreover, the daily electricity reductions and profits are shown in Figure 5 and 6, respectively. They show that DR contributes to substantial daily electricity savings and a remarkable increase in retailer profits, with the proposed framework outperforming the uniform elasticity model in terms of both reduction efficiency and profitability. Day 3 has a large negative profit without DR because the system load is extremely high, and the LMP is large, while the retail price is fixed. The DR successfully reduce/move the load as shown in scenario 3, and the retailer avoids a significant loss.

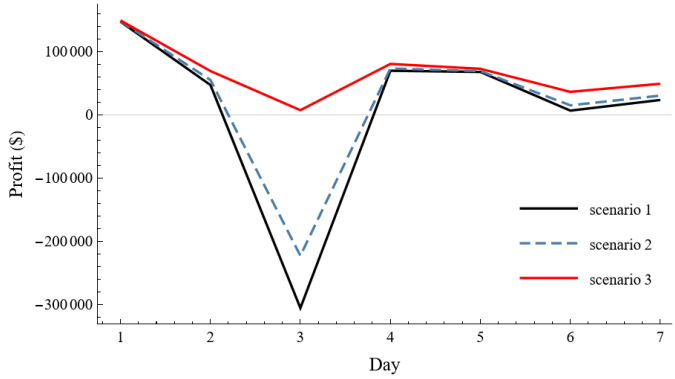


Fig. 6. The daily profits of the three scenarios.

4 Conclusion

This study has proposed an MILP framework that leverages NILM DR potential estimation for optimizing retailer incentive design. The NILM DR potential estimation allows for appliance-level load flexibilities, which provides finer granularity than conventional aggregated elasticity or single-resource DR such as TCLs or EVs. Then, the resulting stepwise DR response curve is incorporated into a retailer profit maximization problem. The bilinear term is linearized by McCormick envelopes; thus, the problem is an MILP that can be solved easily and guaranteed optimality. Case studies show the effectiveness of the proposed method. The proposed framework connects advanced NILM techniques with practical DR program design.

Acknowledgement: This work is supported by the National Natural Science Foundation of China under Grant 52407132, and the China Postdoctoral Science Foundation under 2025M770509.

References

1. Dupont, B.; Dietrich, K.; De Jonghe, C.; et al. Impact of residential demand response on power system operation: A Belgian case study. Applied Energy 2014, 122, 1–10.
2. Lau, E.; Yang, Q.; Stokes, L.; et al. Carbon savings in the UK demand side response programmes. Applied Energy 2015, 159, 478–489.
3. Xia, B.; Ming, H.; Lee, K.Y.; et al. EnergyCoupon: A Case Study on Incentive-based Demand Response in Smart Grid. In Proceedings of the Proceedings of the Eighth International Conference on Future Energy Systems, Shatin Hong Kong, May 2017; pp. 80–90.
4. Sundt, S.; Rehdanz, K.; Meyerhoff, J. Consumers' willingness to accept time-of-use tariffs for shifting electricity demand. Energies 2020, 13, 1895.
5. Hart, G. Nonintrusive Appliance Load Monitoring. Proceedings of the IEEE 1992, 80, 1870–1891.
6. Huber, P.; Calatroni, A.; Rumsch, A.; et al. Review on Deep Neural Networks Applied to Low-Frequency NILM. Energies 2021, 14, 2390.
7. Papageorgiou, P.G.; Christoforidis, G.C.; Bouhouras, A.S. NILM in High Frequency Domain: A Critical Review on Recent Trends and Practical Challenges. Renewable and Sustainable Energy Reviews 2025, 213, 115497.
8. Lin, J.; Ma, J.; Zhu, J.; et al. Deep Domain Adaptation for Non-Intrusive Load Monitoring Based on a Knowledge Transfer Learning Network. IEEE Transactions on Smart Grid 2022, 13, 280–292.
9. Tao, Y.; Qiu, J.; Lai, S.; et al. Customer-Centered Pricing Strategy Based on Privacy-Preserving Load Disaggregation. IEEE Transactions on Smart Grid 2023, 14, 3401–3412.
10. Gao, A.; Zheng, J.; Mei, F.; et al. Toward Intelligent Demand-Side Energy Management via Substation-Level Flexible Load Disaggregation. Applied Energy 2024, 367, 123361.
11. He, D.; Lin, W.; Liu, N.; et al. Incorporating Non-Intrusive Load Monitoring Into Building Level Demand Response. IEEE Transactions on Smart Grid 2013, 4, 1870–1877.
12. Kim, H.; Marwah, M.; Arlitt, M.; et al. Unsupervised disaggregation of low frequency power measurements. In Proceedings of the Proceedings of the 2011 SIAM international conference on data mining. SIAM, 2011, pp. 747–758.
13. Moon, T.K. The expectation-maximization algorithm. IEEE Signal processing magazine 1996, 13, 47–60.
14. Smith, C.A. The Pecan Street Project: developing the electric utility system of the future 2009.

065 Parameter Identification of Photovoltaic Cells Based on Cardinal Curves and Improved AHO

Yanling Lv[1*], Fanyu Kong[1]

[1] School of Electrical and Electronic Engineering, Harbin University of Science and Technology, Harbin, Heilongjiang Province, China

Abstract. To enhance the accuracy of photovoltaic (PV) cell parameter identification, this study introduces a hybrid approach that integrates the Cardinal interpolation curve with an improved Hippo Optimization Algorithm (AHO).The interpolation capability of the Cardinal curve enables precise fitting of PV I–V characteristics, while algorithmic enhancements to AHO—namely chaotic opposition-based initialization and dynamic parameter weighting—substantially improve its global search efficiency.Within this framework, the unknown parameters of the single-diode model are effectively extracted from the fitted data points, yielding more accurate identification results.Experimental evaluations confirm that the proposed method markedly reduces parameter estimation errors under both standard and non-standard test conditions, thereby achieving superior identification accuracy. These results highlight its potential as a reliable tool for PV system performance analysis and fault diagnosis.

Keywords: Photovoltaic (PV) Cell; Single Diode Model; Parameter Identification; Cardinal Fitting Curve; Improved Hippo Optimization Algorithm.

1. Introduction

As a critical component of solar power generation, accurately establishing the circuit model of photovoltaic (PV) cells is of great significance for studying their performance. Among these, the single diode model, as an essential tool for describing the I-V characteristics of PV cells, is widely applied in the modeling and optimization of PV systems. Developing an accurate topological model of PV cells

serves as a necessary foundation for investigating battery aging and fault assessment [1,2]. However, the multiple unknown parameters in the model (e.g., photocurrent, saturation current, series resistance, etc.) are difficult to measure directly. These parameters typically need to be obtained through parameter identification based on experimental data. The precision of parameter identification not only affects the accuracy of the model but also directly impacts the reliability of efficiency optimization and fault detection in PV systems[3].

Currently, various methods have been employed for photovoltaic (PV) cell parameter identification, including traditional analytical methods, numerical optimization techniques (e.g., least squares method), and modern intelligent optimization algorithms (e.g., particle swarm optimization, genetic algorithms, etc.).

The output characteristics of the photovoltaic (PV) cell single diode model constitute an implicit transcendental model, exhibiting strong nonlinear features. Addressing this characteristic, reference [4] employs an analytical method utilizing the Lambert W function, which facilitates integration and differentiation, to provide fully analytical solutions for all parameters in the five-parameter model. However, this approach heavily relies on the given initial values, and poor initial values can easily lead to convergence at local optima. Additionally, such methods impose strict requirements on the optimization objective, such as differentiability and convexity, which the PV model parameter identification problem often fails to meet. Alternatively, some researchers start from the equation itself, converting the transcendental equation into an algebraic one by assigning series and parallel resistance values [5] or neglecting them [6,7] to solve for unknown parameters. However, these prior approximations introduce certain errors [8]. Numerical optimization methods (e.g., the least squares method) are suitable for short-term iterations, small datasets, and linearly related parameter identification,

offering advantages such as fast computation and minimal data requirements. However, they are significantly affected by outliers, assume linear relationships by default, and have considerable limitations in application. Metaheuristic algorithms represent the current mainstream approach to PV parameter identification, with researchers employing traditional algorithms such as particle swarm optimization and neural networks [9]. Additionally, newer optimization algorithms, such as the grey wolf optimization algorithm [10], salp swarm algorithm , and manta ray foraging optimization algorithm , have been used for PV cell parameter identification, achieving promising results.

However, the methods proposed in the aforementioned literature, when addressing multi-parameter and highly nonlinear problems, often encounter issues such as slow convergence and entrapment in local optima. This is particularly evident under complex environmental conditions, where identification accuracy exhibits significant limitations. Consequently, improving the efficiency and accuracy of parameter identification has become a critical challenge in the field of photovoltaic (PV) research. To address these issues, most researchers adopt strategies involving the improvement or combination of metaheuristic algorithms. Reference [11] enhances the quantum particle swarm optimization algorithm through an elite learning strategy, addressing the issue of the global optimal particle lacking a basis for tracking and struggling with self-updating. Reference [12] proposes a novel radial movement optimization method and validates its effectiveness in improving solar parameter identification. Reference [13] introduces an enhanced adaptive genetic algorithm based on multi-objective optimization metrics, incorporating both minimum mean square error and Pearson residual optimization as objective functions to fit the I-V characteristic curve. This approach mitigates local minima and convergence issues, eliminates the likelihood of underfitting/overfitting, and achieves optimal PV design parameters. Reference [14] improves the cuckoo search optimization algorithm, enhancing the overall performance

of parameter identification.

Meanwhile, considering that the quantity and precision of measured data affect the error in results, and that obtaining such data is relatively cumbersome, it is a direction for improvement to explore how to maintain identification accuracy while reducing the workload associated with data measurement. To this end, reference [15] proposes a method using two quadratic Bézier curves to fit the photovoltaic (PV) output curve, addressing the complexity of acquiring measured data. Similarly, reference [16] suggests employing three cubic Bézier curves for more precise fitting of the PV output curve and compares the model using the least squares fitting method, validating the accuracy of using cubic Bézier curves to represent the I-V curves of a wide range of PV cells and arrays. However, when using Bézier curves for fitting, the selection of control points directly impacts the accuracy of the fitted curve, with their calculation being relatively complex and the fitting precision still requiring improvement.

To address the aforementioned issues, this paper proposes a photovoltaic (PV) cell parameter identification method based on Cardinal curves and an improved Hippo Optimization Algorithm (AHO). This method leverages the flexibility and smoothness of Cardinal curves to fit the I-V characteristic curve of PV cells, thereby reducing fitting errors. Simultaneously, by enhancing the search mechanism of the AHO algorithm, the global optimization capability is improved, enabling high-precision identification of unknown parameters in the PV cell model. The effectiveness of the proposed method is validated through simulations and experiments, with its performance evaluated under various test conditions, ensuring that it not only enhances parameter identification accuracy but also provides significant support for the performance optimization and fault diagnosis of PV systems.

2. Materials and Methods

2.1 Establishment of the mathematical model of photovoltaic cells

Photovoltaic (PV) cell models can be classified into single diode and double diode models, corresponding to the 5-parameter model and the 7-parameter model, respectively. The single diode model, due to its simple structure and fewer parameters to be identified, is currently the most widely used PV cell model in research and applications. Figure 1 illustrates the equivalent circuit of the PV cell single diode model.

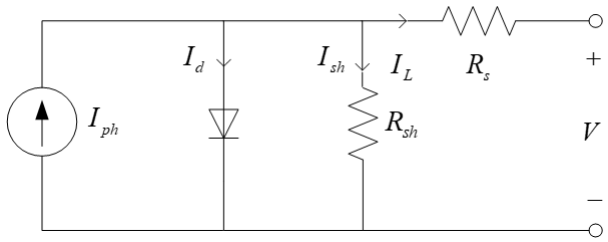


Fig.1 Single diode model of the equivalent circuit of a photovoltaic cell

As shown in Figure 1, the photovoltaic (PV) cell single diode model primarily consists of a series resistance R_s, a shunt resistance R_{sh}, a photovoltaic diode, and a current source. Here, the current source simulates the photocurrent I_{ph} generated by the PV cell upon receiving solar irradiation, while the diode represents the P-N junction. The mathematical model is expressed as follows:

$$I_L = I_{ph} - I_o\left(\exp\left(\frac{V + R_s I_L}{V_T a} - 1\right)\right) - \frac{V + I_L R_s}{R_{sh}} \tag{1}$$

In the equation, I_o represents the reverse saturation current of the diode, and V denotes the output voltage of the photovoltaic (PV) cell. $V_T = (k \times T)/q$ is the thermal voltage of the PV cell, k is the Boltzmann constant (1.38065×10^{-23} J/K), T is the operating temperature of the PV cell, a is the diode ideality factor, and q is the electron charge (1.6022×10^{-19} C). Here,

$$I_d = I_o\left(\exp\left(\frac{V + R_s I_L}{V_T a} - 1\right)\right) \tag{2}$$

$$I_{sh} = \frac{V + I_L R_s}{R_{sh}} \tag{3}$$

I_d is the diode current, and I_{sh} is the current flowing through R_{sh}.

In order to obtain the desired voltage, the cells are typically connected in series or parallel to form a module. The output current I_L of the photovoltaic (PV) module is given by:

$$I_L = I_{ph}N_p - I_o N_p \left(\exp\left(\left(V + R_s \left(\frac{N_s}{N_p} \right) I_L \right) / N_s V_T a - 1 \right) \right) - \frac{V + I_L \left(N_s / N_p \right) R_s}{R_{sh} \left(N_s / N_p \right)} \tag{4}$$

In the equation, N_s and N_p represent the number of cells connected in series and parallel, respectively.

Photovoltaic (PV) cell manufacturers typically provide only limited data in their datasheets, such as the number of series and parallel-connected cells, short-circuit current, maximum power, and open-circuit voltage. However, the five unknown parameters involved in the topology of Equation (1.4) are not specified. Due to the nonlinear nature of the transcendental equation, accurately solving these unknown parameters is not only beneficial for analyzing the aging of PV cells but also provides a critical foundation for fault diagnosis in photovoltaic power systems.

2.2 Cardinal interpolation is used to fit the output characteristic curve.

Cardinal splines can be fully determined by four consecutive control points. The middle two control points serve as the endpoints of the curve segment, while the other two points are used to compute the slope at the curve segment's endpoints. Let the four consecutive control points be P_{k-1}, P_k, P_{k+1}, P_{k+2}. Let $P(u)$ be the cubic parametric function between control points P_k and P_{k+1}, where the parameter t represents the tension coefficient. The parameter t controls the tightness of the Cardinal spline relative to the control points, with u∈[0,1]. The boundary conditions for the Cardinal spline, determined by the four points P_{k-1}, P_k, P_{k+1}, P_{k+2}, are given by:

$$\begin{cases} P(0) = P_k \\ P(1) = P_{k+1} \\ P'(0) = \dfrac{1}{2}(1-t)\cdot(P_{k+1} - P_{k-1}) \\ P'(1) = \dfrac{1}{2}(1-t)\cdot(P_{k+2} - P_k) \end{cases} \tag{5}$$

$$P(u)=\begin{bmatrix}u^3 & u^2 & u & 1\end{bmatrix}\cdot\begin{bmatrix}2 & -2 & 1 & -2\\ -3 & 3 & -2 & -1\\ 0 & 0 & 1 & 0\\ 1 & 0 & 0 & 0\end{bmatrix}\cdot\begin{bmatrix}P_{k-1}\\ P_k\\ s\cdot(P_{k+1}-P_{k-1})\\ s\cdot(P_{k+2}-P_k)\end{bmatrix}$$
$$=\begin{bmatrix}u^3 & u^2 & u & 1\end{bmatrix}\cdot M_c\cdot\begin{bmatrix}P_{k-1}\\ P_k\\ P_{k+1}\\ P_{k+2}\end{bmatrix} \tag{6}$$

Among them, $s=\frac{1}{2}(1-t)$ is the shaping parameter that adjusts the curve's shape.

Several characteristics of the curve can be observed from the cubic Cardinal spline curve:

Shape Adjustability

From Equations 1.5 and 1.6, it can be seen that, with the same control points, varying the value of *s* produces curves of different shapes. As shown in the figure below, by selecting (0,0), (10,5), (10,5), and (20,0) as control points and plotting the image, changing the parameter sss alters both the curvature and smoothness of the curve.

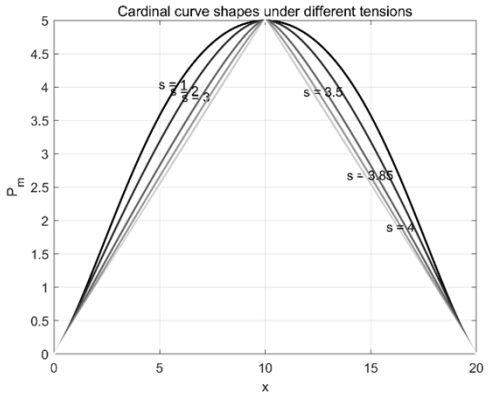


Fig.2 The shapes of Cardinal curves under different tension coefficients

Locality

The cubic Cardinal spline curve exhibits the characteristic of locality, which arises from its definition: the shape of each segment of the curve depends entirely on the corresponding four control points, and is independent of the control points of other segments. Therefore, when a control point is

modified, only the curve segment directly controlled by that point undergoes a shape change, while the rest of the overall curve remains unchanged. In other words, the influence of adjusting a control point is localized; it does not affect the entire curve, and there will be no drastic adjustment of the entire curve system due to changes at a particular point. This property gives the cubic Cardinal spline curve strong stability in applications, preventing the issue of "a change in one part causing the entire system to adjust."

Flexibility of Shape

By modifying the four control points and the shape parameter sss, the cubic Cardinal spline curve can describe both freeform curves and be represented as straight lines and circular arcs.

Based on the properties of the Cardinal spline curve mentioned above, this paper proposes a method for fitting the photovoltaic output characteristic curve using the Cardinal spline. The specific approach is as follows:

The control points are selected using the open-circuit voltage point, short-circuit current point, maximum power point, and two auxiliary points generated through calculations, as the five control points for the curve. Define the open-circuit voltage point, short-circuit current point, and maximum power point provided by the photovoltaic panel manufacturer as P1,P2,P3, respectively. Two auxiliary points, P0 and P4, are generated such that P0 = P1+ (P1-P2), assuming P0 is in the opposite direction of P1 and symmetric with respect to P2; and P4 =P3+(P3-P2), assuming P4 is in the opposite direction of P3 and symmetric with respect to P2.After defining the control points, cubic Cardinal interpolation is performed. The curve tension coefficient is varied in steps to obtain different fitted curves. After determining the optimal fitted curve, the curve plotting procedure is used to compare the manufacturer's data with the output characteristic curve fitted using two quadratic Bézier curves, as proposed in reference [20], as shown in Figure 3.

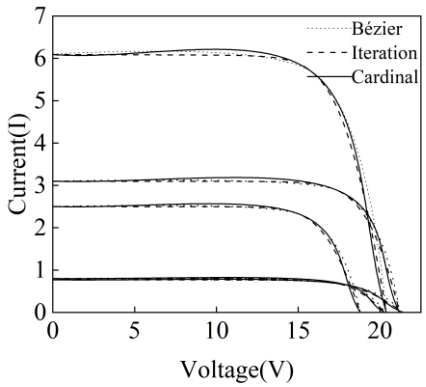


Figure 3 Comparison of the fitting results of the optimal fitting curves for different types of batteries

To obtain a more intuitive understanding of the error in the cubic Cardinal spline curve fitting, the error is calculated using Equation (7), with the results shown in Table 1.

$$E_r = \frac{\sum |I - I_{real}|}{\sum I_{real}} \tag{7}$$

Where: I is the current value obtained from the curve fitted using the function; I_{real} is the current value obtained from the manufacturer's provided data.

Table1 Manufacturer data of five types of batteries

Battery type	$E_{r.\text{Cardinal}}$	$E_{r.\text{Bézier}}$	$E_{r.iteration}$	$T_{Cardinal}$	$T_{\text{Bézier}}$	$T_{iteration}$
SunWare12/1	0.005321892	0.005695062	0.0070646	0.1334	0.1352	2.9905
Pll-36 GET AK Laminat	0.005469264	0.005763848	0.0065974	0.1387	0.1424	2.8645
KC35	0.005692463	0.00598209	0.0071002	0.1385	0.1408	2.4827
PSP 90000/12+	0.005315924	0.005561511	0.0087317	0.1384	0.1353	2.7911
Terra-Piatta®-Solar	0.005366198	0.005544226	0.0065058	0.1338	0.1349	2.5517

As shown in Figure 3 and Table 1, the curve fitting performs well, with the fitting errors for the output characteristic curves of the five different battery models all being below 0.6%, within the acceptable error range. Additionally, compared to traditional iterative methods and the use of quadratic Bézier functions to fit photovoltaic output characteristic curves, the proposed method achieves smaller errors

and faster fitting speeds. Therefore, the Cardinal interpolation method proposed in this paper provides more accurate results and faster fitting speeds for the output characteristic curves.

2.3 Parameter Identification Based on the Hippo Optimization Algorithm

The Hippopotamus Optimization Algorithm (HO), proposed by MH Amiri et al. in 2024, is a heuristic optimization algorithm inspired by the behavior patterns of hippos in the wild. This algorithm simulates the position updates of hippos in rivers or ponds, their defense strategies against predators, and their escape strategies, including the behaviors of dominant hippos, female hippos, and male hippos. The basic rules of the algorithm are as follows:

Initialization Phase

The initial population is generated randomly, with the dimension of each individual matching the optimization problem (in this case, 5 dimensions). Each individual represents a candidate solution, with its parameter values within the lower and upper bounds. The initial solution generation formulas are as follows:

$$x_{i,j} = lb_j + (ub_j - lb_j) \cdot rand(), i = 1,2,\ldots; j = 1,2,\ldots; \tag{8}$$

$$x_{i,j} = lb_j + (ub_j - lb_j) \cdot rand(), i = 1,2,\ldots; j = 1,2,\ldots; \tag{9}$$

Where: $x_{i,j}$ is the j-th parameter value of the i-th individual, lb_j and ub_j are the lower and upper bounds of the j-th parameter, and rand() generates a random number in the range [0,1].

Exploration Phase

The hippopotamus group has a complex structure, consisting of several adult females, juveniles, multiple adult males, and a dominant male (the leader of the group). The dominant male in the group is responsible for protecting the group and its territory from external threats. In the social structure of hippos, females are typically placed under the protection of males. As adult male hippos mature, they are often driven

out of their original group by the dominant male. These males must then establish their own leadership by attracting females or competing with other mature males.

The dominant hippo is responsible for guiding other individuals toward the current global optimum solution. The position of each individual is updated by considering both the global optimum solution and the average position of the population, conducting a global search according to the following formula:

$$x_i^{new} = x_i + \alpha \cdot r_i \cdot \left(x_{best} - x_i\right) + \omega \cdot r_2 \cdot \left(x_{mean} - x_i\right) \tag{10}$$

In the formula, x_i represents the current position of the individual; x_{best} is the position of the current optimum solution (dominant hippo); x_{mean} is the average position of the population; r_1 and r_2 are random numbers in the range [0, 1]; α is the position update coefficient, which controls the step size of the search; ω is the inertia weight, used to balance exploration and exploitation (which decreases with the number of iterations). The inertia weight is expressed as:

$$\omega = 1 - \frac{iter}{\max gen} \tag{11}$$

Female hippos fine-tune their positions near the dominant hippo (global optimum solution) to refine the solution, conducting a local search according to the following formula:

$$x_i^{new} = x_i + \alpha \cdot r_2 \cdot \left(x_{best} - x_i\right) \tag{12}$$

Male hippos attempt to explore new search areas by updating their positions based on randomly selected individuals' locations. This enhances the algorithm's global search capability, helping to avoid getting trapped in local optima.

$$x_i^{new} = x_i + MR \cdot r_3 \cdot \left(x_{rand} - x_i\right) \tag{13}$$

x_{rand} denotes the position of a randomly selected individual from the population; MR is the migration rate, which controls the extent of exploration; r_3 is a random number in the range [0, 1], used to introduce stochasticity.

Defense Strategy

The primary defense strategy adopted by hippos is to swiftly turn toward predators and emit loud vocalizations to deter them from approaching. At this stage, hippos may exhibit approach behavior toward predators to induce their retreat, thereby effectively countering potential threats. If an individual fails to improve over an extended period, it is considered to be trapped in a local optimum. To escape, it updates its position by referring to both the population's average location and the global optimum solution.

$$x_i^{new} = x_i + \beta \cdot (x_{mean} - x_i) + \gamma \cdot \left(x_{best} - x_i\right) \tag{14}$$

The parameters β and γ represent the influence factors of the population's average position and the global optimum solution, respectively.

Escape Strategy

Another behavior exhibited by hippos when facing predators occurs when they encounter a group of predators or are unable to drive them away through defensive actions. In such cases, the hippo attempts to leave the area. That is, if the defense strategy fails (i.e., there is no improvement in fitness), the escape strategy is triggered, whereby the individual randomly jumps to a new location to restart the search:

$$x_i^{new} = lb + \left(ub - lb\right) \cdot rand\left(1, D\right) \tag{15}$$

Here, *lb* and *ub* represent the lower and upper bounds of the parameters, respectively; rand(1,D) denotes a newly generated random position.

2.4 Improved Hippo Optimization Algorithm

Based on the basic rules of the algorithm outlined above, the following improvements are made to achieve efficient and accurate solutions for nonlinear problems:

1)During the initialization phase, a chaotic opposition-based initialization mechanism is introduced, generating positions that are opposite to the current solution through the Logistic map, and incorporating

chaotic perturbations to enhance population diversity. Simultaneously, invalid solutions generated during the initialization phase are handled by random reinitialization, thereby enhancing the robustness of the population.

2) Several key parameters are dynamically adjusted, such as the inertia weight w, which varies according to the iteration count:

$$w = w_{\max} - (w_{\max} - w_{\min}) \cdot \left(\frac{iter}{\max gen} \right)^2 \tag{16}$$

In the equation, w_{max} and w_{min} represent the upper and lower limits for weight updates, *iter* denotes the current iteration count, and *maxgen* is the maximum number of iterations.

The mutation probability $P_{mutation}$ and the local search radius r_{local} are also adjusted according to the following formulas:

$$p_{mutation} = p_{mutation,init} \cdot \left(1 - \frac{iter}{\max gen} \right)^{0.5} \tag{17}$$

$$r_{local} = r_{local,init} \cdot \left(1 - \frac{iter}{\max gen} \right)^{0.3} \tag{18}$$

These dynamically adjusted parameters enable the algorithm to explore the global solution space in the early stages, while focusing on local optimization in the later stages, thereby balancing the algorithm's global search and local exploitation capabilities.

3) During the exploration phase, a step size adjustment mechanism based on success rate is introduced, which adaptively adjusts the search step size by statistically analyzing each individual's historical success rate. In addition, a golden ratio search strategy is incorporated, which performs a refined search near the optimal solution using the golden ratio to further optimize individual solutions.

4) During the defense phase, Levy flight is used to simulate long-distance jumping behavior, with the step size distribution following the Levy distribution, thereby enhancing global search capabilities.

The update formula for the new position introduces a dynamic adjustment based on the distance to the predator, as described by the following equation:

$$X_{new} = Levy \cdot predator + \frac{b}{c - d\cos(l)} \cdot \frac{1}{dis\tan ce2Leader} \tag{19}$$

Here, *b, c, d,* and *l* are random factors, and *distance2Leader* represents the distance between the current individual and the predator.

5) During the escape phase, the local search range is dynamically reduced, and diverse search behaviors are generated by combining a normal distribution with various random factors, making the predator-escaping strategy more adaptive, thereby enabling finer exploitation.

2.5 AHO for determining photovoltaic cell parameters

To more intuitively reflect the deviation between the identification results and the true values, the Root Mean Square Error (RMSE) is calculated using Equation 2.13 as the objective function for the algorithm.

$$RMSE = \sqrt{\frac{1}{N}\sum_{i=1}^{N}\left(I_{i,BASE} - I_{i,IDEN}\right)^2} \tag{20}$$

Here, $I_{i,BASE}$ is the reference value, and $I_{i,IDEN}$ is the identified value.

In summary, the photovoltaic cell parameter identification steps based on the Cardinal curve and AHO are as follows, with the flowchart shown in Figure 4:

Step 1: Use the method proposed in Section 1.2 to fit the photovoltaic cell output characteristic curve, providing the model required for the algorithm.

Step 2: Initialize the AHO algorithm, determining the population size, problem dimensions (requiring the identification of 5 parameters), search space bounds (the defined range for the 5 parameters), and strategy selection parameters.

Step 3: Check the iteration termination conditions. If satisfied, the iteration ends; otherwise, repeat Step 3.

Step 4: Upon iteration completion, output the fitness and the identified parameter values.

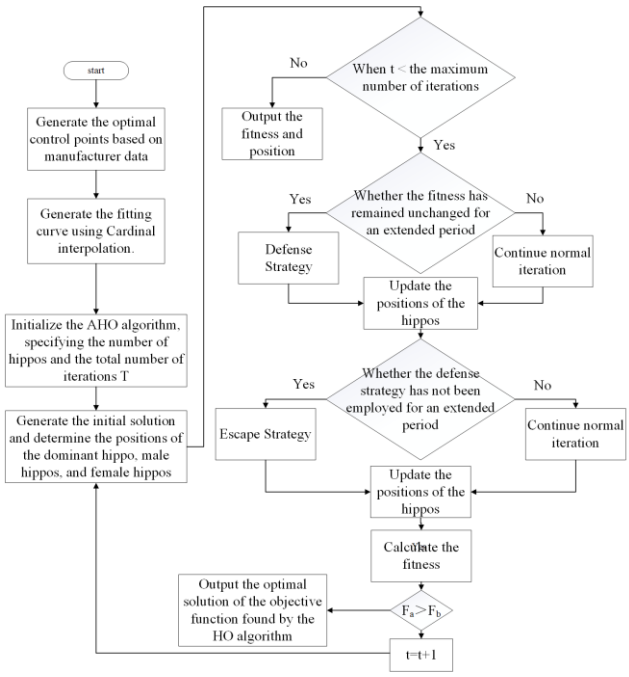


Fig. 4 Flow chart of parameter identification

3. Results and Discussion

3.1 Case study analysis under standard conditions

To validate the proposed Cardinal curve and AHO for photovoltaic cell parameter identification, six commercially available batteries were randomly selected, with the battery data shown in Table 2. Under standard conditions, the widely used Particle Swarm Optimization (PSO) algorithm and the improved Hippo Algorithm (AHO) were selected for comparison. The convergence curves were calculated for each, as shown in Figure 5, and the identification results and corresponding Root Mean Square Error (RMSE) for all six batteries used in the experiment are presented in Table 3.

Table 2: Selected Battery Data

battery model	Uoc	Isc	Um	Im
SOL 50K	20.70	3.20	17.20	2.94
PWX 500T	21.60	3.30	17.30	3.00
RSM 50 Photowatt	21.70	3.10	17.00	2.80
IBC-80 Megaline 1998	21.00	5.08	17.00	4.71
SRT 35	10.70	4.50	8.05	4.15
PL 8/65	21.00	4.40	16.90	4.00

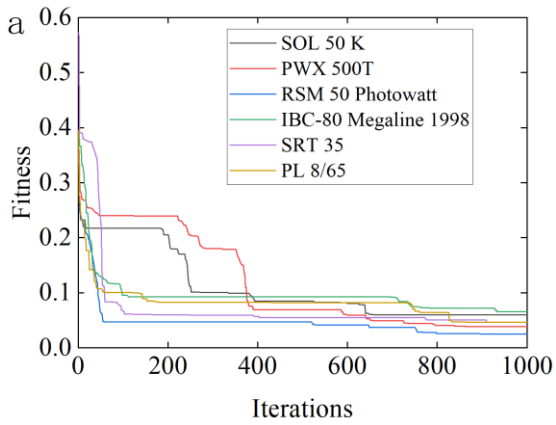


Fig.5(a) PSO algorithm adaptation

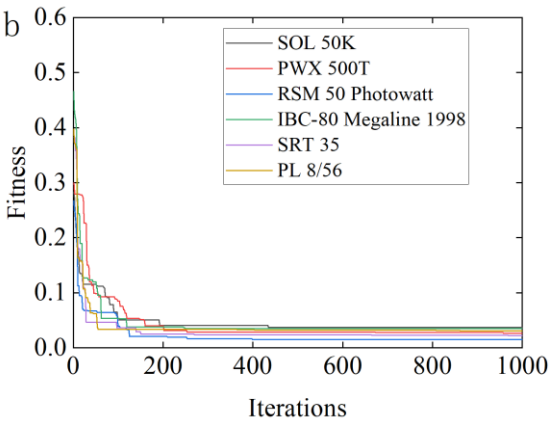


Fig.5(b) AHO algorithm adaptation

Fig. 5 Algorithm fitness comparison graph

Table 3 Parameters identified and errors under the standardized conditions

battery model	algorithm	I_{ph}	I_o	a	R_s	R_{sh}	*RMES*
SOL 50 K	PSO	3.1679	8.2801E-7	1.4850	0.0020	2211.93	0.0601
	AHO	3.2104	8.7188E-7	1.4941	0.0056	3474.42	0.0368
PWX 500T	PSO	3.2618	79.1206E-7	1.8067	0.0753	240.7934	0.0385
	AHO	3.3860	51.2237E-7	1.7410	0.0435	169.6980	0.0266
RSM50 Photowatt	PSO	3.1055	96.1934E-7	1.8535	0.1803	243.0698	0.0248
	AHO	3.0993	28.2202E-7	1.9968	0.0042	111.5478	0.0152
IBC-80 Megaline	PSO	5.2974	84.2587E-7	1.7681	0.0124	5915.4981	0.0656
	AHO	5.1678	56.0431E-7	1.6459	0.0071	7371.0344	0.0351
SRT 35	PSO	4.6591	42.9514E-7	1.9357	0.0188	398.5429	0.0464
	AHO	4.5735	19.6546E-7	1.8544	0.0105	243.1053	0.0220
PL8/65	PSO	4.6312	83.5146E-7	1.9245	0.0071	756.9812	0.0462
	AHO	4.4211	99.8681E-7	1.7438	0.0031	523.8822	0.0306

As shown in Figure 5, the fitness curve of the AHO algorithm decreases at a significantly faster rate than that of the PSO algorithm. AHO converges in fewer iterations (approximately 200 iterations), while PSO requires more iterations (over 400) to reach a similar level. AHO demonstrates faster convergence in photovoltaic parameter identification, enabling more efficient identification of the optimal solution and reducing computation time. Moreover, as seen in Table 3, the RMSE values for the AHO algorithm are lower than those of the PSO algorithm for all test models. On average, it reduces the error by 2%-3%, exhibiting strong adaptability to different types of photovoltaic cells and maintaining high precision and low error across various batteries. This results in parameter identification outcomes that are closer to the

true values, using fewer iterations and computational resources.

Figure 6 shows the simulated values and manufacturer data curves calculated using the photovoltaic formula, with data identified using the method proposed in this paper, for batteries such as SOL50, PWX500T, and RSM 50 Photowatt. As seen in Figure 6, the curve fitted by the proposed AHO algorithm closely coincides with the manufacturer's curve. The fitting results meet practical engineering requirements, verifying the reliability of the AHO algorithm in photovoltaic parameter identification.

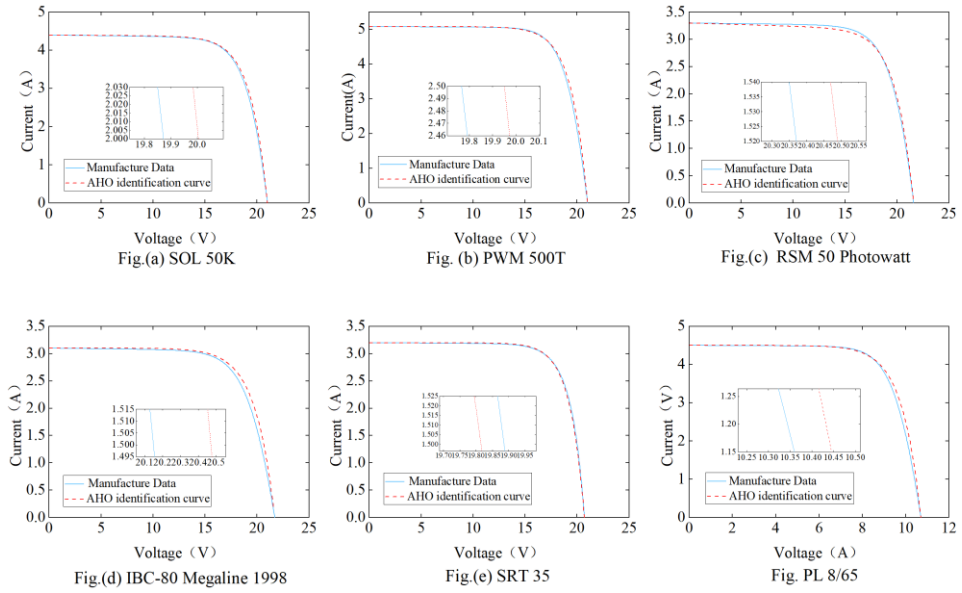


Fig.6 Comparison of iterative fitting and identification curves for different models (a)-(f) of batterie

3.2 Case study analysis under non-standard conditions

To further discuss the applicability of the proposed method in engineering practice, the photovoltaic parameter identification problem under non-standard conditions, considering variations in irradiance and temperature, is addressed. Three different operating conditions are defined as follows:

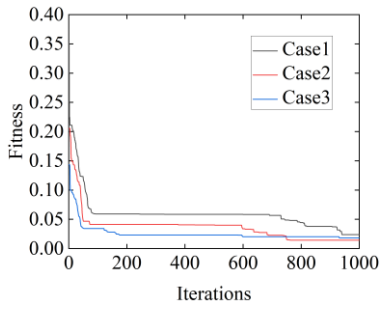
Condition 1: irradiance of 1000 W/m² and cell temperature of 15°C; Condition 2: irradiance of 800 W/m² and cell temperature of 25°C; Condition 3: irradiance of 600 W/m² and cell temperature of 5°C.

First, the relevant data of the photovoltaic cell output characteristics under non-standard conditions are obtained. To achieve this, the conclusions from references [17-19] are applied, and the open-circuit

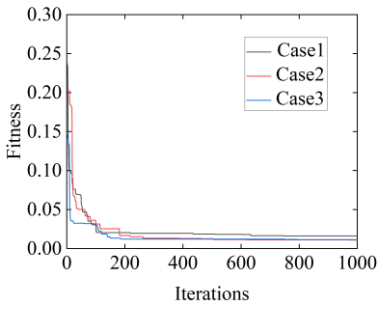
voltage U_{oc}, maximum power point voltage U_{mp}, short-circuit current I_{sc}, and maximum power point current I_{mp} for six photovoltaic cells under varying operating conditions can be calculated using the formulas.

Next, the four obtained parameters are used with the method mentioned earlier to construct the characteristic curve at this point, which is then used as the objective function model for optimization. Taking the SOL 50K battery as an example, the convergence curve under non-standard conditions is shown in Figure 7. Similarly, the curve fitting results for the SOL 50K battery under varying operating conditions are displayed in Figure 8.

As shown in Figure 7, under non-standard conditions, the average number of iterations for the proposed algorithm to reach the optimal solution remains around 200, which is similar to the results under standard conditions. The obtained identification results also exhibit good accuracy. This verifies the feasibility and accuracy of the proposed parameter identification method.



(a) Fitness under non-standard conditions for PSO



(b) Fitness under non-standard conditions for AHO

Fig. 7 SOL 50K off-specification adaptability

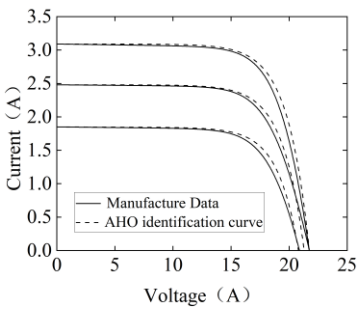


Fig.8 Output characteristic curves of SOL 50K under non-standard condition

4. Conclusions

This paper primarily investigates the photovoltaic cell parameter identification problem and presents the following conclusions:

(1) The Cardinal interpolation curve fitting method for photovoltaic cell output characteristics is introduced into parameter identification. By utilizing the properties of the Cardinal interpolation curve and manufacturer data, appropriate control points are selected for curve fitting. A method is proposed for fitting the photovoltaic cell output characteristic curve using only manufacturer-provided data, without the need for experimental testing. The fitting errors for the output characteristic curves of five different battery models are all below 0.6%, which is within the allowable error range.

(2) The Hippopotamus optimization algorithm is adjusted by employing improvements such as population initialization optimization and dynamic adjustment of key parameters. An improved Hippopotamus optimization algorithm is designed for photovoltaic cell parameter identification, which, compared to the traditional PSO, enhances the optimization ability and improves the accuracy of photovoltaic cell parameter identification.

(3) A parameter identification model combining the Cardinal interpolation curve fitting method for photovoltaic cell output characteristics with the AHO algorithm is proposed. Through verification, the model demonstrates a reduction in error by 0.5%-1% and an average error reduction of 0.6% compared to the traditional PSO-based model. This provides a valuable reference for fault diagnosis research and battery performance assessment.

References

[1] Singla, M.K., Nijhawan, P. Triple diode parameter estimation of solar PV cell using hybrid algorithm. Int. J. Environ. Sci. Technol. 19, 4265–4288 (2022). https://doi.org/10.1007/s13762-021-03286-2

[2] Changmai, P.; Deka, S.; Kumar, S.; Babu, T.S.; Aljafari, B.; Nastasi, B. A Critical Review on the Estimation Techniques of the Solar PV Cell's Unknown Parameters. Energies 2022, 15, 7212. https://doi.org/10.3390/en15197212

[3] Cheng, Z., Lili, Q., & Yongsheng, Q. (2025). Fault Diagnosis of Photovoltaic Array under Deep Generation Digital Twin Framework. In *Proceedings of the CSU-EPSA* .

[4] PENG, L., & MENG, Z. (2014). Parameters extraction and optimization for PV module based on Lambert W function. *Acta Energiae Solaris Sinica*, *35*(8), 1429-1434.

[5] Celik AN, Acikgoz N. Modelling and experimental verification of the operating current of mono-crystalline photovoltaic modules using four- and fiveparameter models. Appl Energy 2007;84:1–15.

[6] Yu, F., Huang, G., & Xu, C. (2020). An explicit method to extract fitting parameters in lumped-parameter equivalent circuit model of industrial solar cells. *Renewable Energy*, *146*, 2188-2198.

[7] E. Moshksar and T. Ghanbari, "Constrained optimisation approach for parameter estimation of PV modules with single-diode equivalent model," in IET Renewable Power Generation, 2018, 12, no. 12, pp. 1398-1404.

[8] BATZELIS E I，PAPATHANASSIOU S A. A method for the analytical extraction of the single- diode PV model parameters［J］. IEEE transactions on sustainable energy， 2016，7（2）：504-512.

[9] Ye M, Wang X , Xu Y . Parameter identification for proton exchange membrane fuel cell model using particle swarm optimization[J]. International Journal of Hydrogen Energy, 2009, 34(2):981-989.

[10] Robandi, I. Photovoltaic parameter estimation using grey wolf optimization. In 2017 3rd International Conference on Control, Automation and Robotics (ICCAR); 2017, April; IEEE; pp. 593-597.

[11] Zhihua, L., Haoqiang, M., & Chunhua, W. (2022). Diagnosing the aging degree of photovoltaic modules based on three parameters. *Proceedings of the CSEE*, *42*(9), 3327-3338.

[12] Radial movement optimization based parameter extraction of double diode model of solar photovoltaic cell B.S.S. Ganesh Pardhu a , Venkata Reddy Kota

[13] Adaptive Genetic Algorithm Based Multi-Objective Optimization for Photovoltaic Cell Design Parameter Extraction Ashwini Kumari. Pa, P. Geethanjali

[14] Gude, S., Jana, K.C., 2020. Parameter extraction of photovoltaic cell using an improved cuckoo search optimization. Sol. Energy 204, 280–293.

[15] Shi, N., Lv, Y., Zhang, Y., & Zhu, X. (2023). Linear fitting Rule of I–V characteristics of thin-film cells based on Bezier function. *Energy*, *278*, 127997.

[16] Szabo, R., & Gontean, A. (2018). Photovoltaic cell and module IV characteristic approximation using Bézier curves. *Applied Sciences*, *8*(5), 655.

[17] Nhan Thanh Tong, Wanchalerm Pora,A parameter extraction technique exploiting intrinsic properties of solar cells,Applied Energy,Volume 176,2016,Pages 104-115,ISSN 0306-2619,https://doi.org/10.1016/j.apenergy.2016.05.064.

[18] N. Rajasekar, Neeraja Krishna Kumar, Rini Venugopalan,Bacterial Foraging Algorithm based solar PV parameter estimation,Solar Energy,Volume 97,2013,Pages 255-265,ISSN 0038-092X,https://doi.org/10.1016/j.solener.2013.08.019.

[19] J. J. Soon and K. -S. Low, "Photovoltaic Model Identification Using Particle Swarm Optimization With Inverse Barrier Constraint," in IEEE Transactions on Power Electronics, vol. 27, no. 9, pp. 3975-3983, Sept. 2012, doi: 10.1109/TPEL.2012.2188818

066 An Adaptive Adjustment Method of Reclosing Time Based on Estimation of the Off-grid Time

Zhengtong Wang[1], Houlei Gao[1], Fang Peng[1] and Haoran Song[1]

[1] Shandong University, Jinan 250061, China
houleig@sdu.edu.cn

Abstract. To address the failure of conventional reclosing caused by inverter-based distributed generators (IBDGs) continuously supplying power to fault points during low-voltage ride-through in active distribution networks, this paper proposes an adaptive reclosing time adjustment method based on IBDG off-grid time estimation. By analyzing the coupling relationship between IBDG output current and the voltage of point of common coupling (PCC) in islanded systems, a set of nonlinear equations is established to characterize system behavior. The Levenberg-Marquardt algorithm is employed to iteratively solve for PCC voltage, enabling precise estimation of IBDG off-grid time. Building upon this, the method adaptively sets reclosing time to reduce outage duration. Simulation results demonstrate that this approach has low communication requirements, adapts to various fault types, locations, and typical fault resistances. While ensuring successful reclosing, it shortens reclosing time by approximately 1-2 seconds compared to conventional fixed-delay methods, enhancing power supply reliability.

Keywords: IBDG, Reclosing, Active distribution network, LVRT.

1 Introduction

In traditional passive distribution networks, statistical data indicates that approximately 70% to 90% of faults are transient faults [1]. After protection tripping, the fault point loses power supply, and system insulation often self-recover. Based on this characteristic, engineering practice commonly deploys instant accelerated protection trip at feeder outlets. Reclosing after a transient fault can restore power supply, significantly enhancing distribution network reliability.

However, with large-scale integration of IBDGs, traditional passive networks have evolved into active distribution networks. The Chinese national standard requires that IBDGs in 10-35kV power grids must have low-voltage ride-through (LVRT) capability, and LVRT priority is higher than anti-islanding protection. This technical requirement means that after the circuit breaker trips, the distributed power source continues to operate through LVRT control, providing continuous power to the isolated system with fault [2]. After the IBDG meets the LVRT time, anti-islanding protection disconnects the IBDG from the grid, the fault point loses its power supply, and the transient fault disappears.

These protection sequences reveal that the ideal reclosing time in active distribution networks is critically linked to IBDG off-grid time. If the traditional passive distribution network reclosing strategy is still used, it will reclose to the fault and cause another trip. This will not only further increase power outage losses, but also cause multiple impacts on the IBDG, reducing the life of power electronic equipment. Thus, a new reclosing time adjustment method are urgently needed for active distribution networks.

The simplest and most reliable method is to extend the reclosing time to 3 to 3.5 seconds to avoid the longest disconnection time of the IBDG [3-5]. However, this prolongs load restoration, increasing user outage losses [6]. By installing communication equipment, information from each IBDG can be transmitted back to the reclosing device installation site [7-8]. This method can achieve rapid and reliable reclosing, but for most distribution grids, it is difficult to achieve real-time communication between all IBDGs and the reclosing device. References [9-11] utilize auto-reclosure with voltage check to avoid the low voltage ride-through time of IBDG. This method will reclose when the voltage of the isolated system is detected to be 0. However, in the event of a three-phase fault, the island voltage remains close to zero, and voltage detection reclosing may malfunction, resulting in reclosing failure. Reference [12] uses voltage rise information to set the reclosing time. This method only considers self-extinguishing arc scenarios and ignores scenarios where the fault persists. Reference [13] investigates both scenarios, leveraging the characteristic that the voltage at the feeder outlet circuit breaker is typically higher than the PCC voltage. It uses the feeder outlet circuit breaker voltage to replace the PCC voltage in calculations. The advantage of this approach is that it does not require additional equipment. However, due to differences between the voltage measurement point and the actual voltage at the PCC, there is still room for improvement in reclosing time.

In response to the above issues, this paper proposes an adaptive adjustment method of reclosing time based on estimation of the off-grid time. This method analyzes the fault characteristics of the isolated island system formed after the circuit breaker at the feeder outlet trips, estimates the voltage magnitude at the PCC, and further combines the low-voltage ride-through curve of the distributed power source to obtain the off-grid time, ultimately adaptively adjusting the reclosing time. The correctness of the theory was verified through PSCAD/EMTDC simulation results.

2 Analysis of Recloser Operation Time

2.1 Analysis of Pre-accelerated Reclosing

Traditional passive distribution networks often employ directional reclosing. Figure 1 illustrates a rural 10 kV distribution system. Feeders utilize directional reclosing at their source circuit breakers (CB1, CB4). Feeder 2 lacks distributed generation, feeder 1 contains DG.

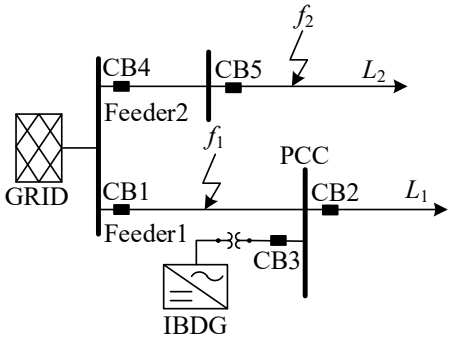


Fig. 1. Schematic diagram of distribution network with IBDG

1) If a fault occurs at f_2, the current at CB4 exceeds the protection threshold, triggering an immediate non-selective trip. After waiting for the fault to extinguish, CB4 recloses. If the current returns to normal levels after reclosing, it indicates a temporary fault, and the reclosing operation is successful, restoring power supply to the system; if the current remains above the protection threshold after reclosing, CB4 will not trip immediately but will instead trigger a selective trip at CB5. The pre-accelerated reclosing timing sequence coordinates with the overcurrent protection at each location, enabling rapid clearance of transient faults while selectively clearing permanent faults.

2) However, IBDG integration alters timing dynamics. The tripping behavior of CB3 at the PCC depends on islanding protection and LVRT strategies. This disrupts coordination with reclosing of CB1.

If a fault occurs at point f_1, the reclosing of CB1 still follows the traditional passive distribution network's arc extinction time before reclosing. At this point, the distributed power source is undergoing LVRT. On one hand, the fault point is still supplied by IBDG, and the arc generally does not extinguish, leading to reclosing failure; on the other hand, IBDG will undergo three voltage surges due to the fault, reclosing, and subsequent tripping, which can damage the operational lifespan of IBDG.

2.2 Analysis of Reclosing in Active Distribution Network

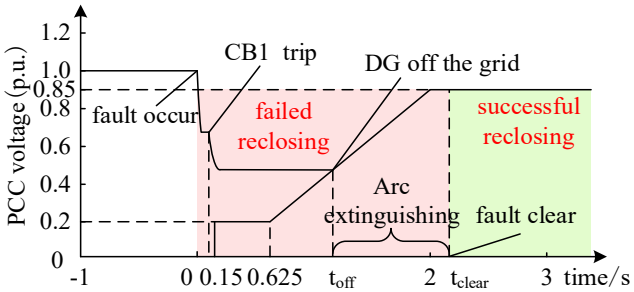


Fig. 2. Reclosure sequence diagram of active distribution network

If a transient fault occurs at f_1, the IBDG enters LVRT mode. The protection at CB1 operates after the current increases, and the IBDG continues to supply power to the fault and load, forming an isolated island with the fault. The power supplied by the

IBDG in an isolated island system often fails to meet the load demand, resulting in the island system voltage being below the rated value. The voltage curve at the PCC and the LVRT curve are plotted in Figure 2.

After the fault occurs, the voltage of the entire active distribution grid system drops rapidly. Before the first disconnection of CB1, the grid remains connected to the distribution system. This is the first steady state after the fault, referred as State 1; after CB1 disconnects, an isolated island system powered only by DG is formed, and the voltage at the PCC is generated only by the ohmic response of the system's equivalent impedance. This is the second steady state after the fault, referred as state 2. At the intersection of the voltage at the PCC and the LVRT curve, the DG goes off-grid and waits for the arc to extinguish before clearing the fault. When the recloser operates before t_{clear}, the arc has not yet extinguished, and the fault still exists. After reclosing, the system side will still supply a large fault current, leading to reclosing failure or even causing the original transient fault to develop into a permanent fault; when the recloser operates after t_{clear}, the arc has been extinguished for transient faults, and the feeder power supply can be restored after reclosing.

Through the above timing analysis, it can be seen that the key to setting the reclosing time is to obtain the voltage at the PCC in state 2 and then obtain the DG off-grid time.

3 Estimation of IBDG Off-grid Time

3.1 LVRT Control Strategy for IBDG

Most IBDGs utilize a dual-loop control structure comprising outer power control and inner current control. During asymmetric grid faults, a negative-sequence current suppression strategy maintains balanced three-phase current output. Under normal operation, the reference values for the dq-axis currents from an IBDG are:

$$\begin{cases} i_{\text{dref}} = \dfrac{2}{3}\dfrac{P}{U^{+}_{\text{PCC}}} \\ i_{\text{qref}} = \dfrac{2}{3}\dfrac{Q}{U^{+}_{\text{PCC}}} \end{cases} \tag{1}$$

In the formula: i_{dref} is the reference value of the d-axis current output by IBDG, P is the rated active power of IBDG, U^{+}_{PCC} is the effective value of the positive sequence voltage at PCC, i_{qref} is the reference value of the q-axis current output by IBDG, and Q is the rated reactive power of IBDG.

When the system experiences a fault or disturbance that causes a voltage drop at the PCC, the system switches to a LVRT control strategy. Relevant standards [2] require IBDGs to have a certain fault ride-through capability when the voltage at the PCC falls below a predetermined value. The dynamic reactive current output should be able to track changes in the voltage at the PCC in real time and satisfy equation (2).

$$i_{\text{qref}} = K \times (0.85 - \frac{U_{\text{PCC}}^{+}}{U_{\text{N}}}) \times I_{\text{N}} \tag{2}$$

In the formula: K is the ratio of the dynamic reactive current to voltage change at the inverter output, with a value range of 1.5 to 2.5; U_{N} is the system rated voltage; I_{N} is the rated current of the distributed power source.

In addition, to avoid damage to power electronic devices caused by faults or overloads, the maximum output current of IBDG is often limited. Assuming that the maximum output current does not exceed 1.5 times the rated current, the active current output of IBDG should be taken as the smaller value between the normal control strategy and the current limiting strategy:

$$i_{\text{dref}} = \min\left\{\frac{2}{3}\frac{P}{U_{\text{PCC}}^{+}}, \sqrt{(1.5I_{\text{N}})^2 - i_{\text{qref}}^{\ 2}}\right\} \tag{3}$$

The three-phase current output of IBDG is

$$\begin{cases} \boldsymbol{I}_a = \sqrt{i_{\text{dref}}^2 + i_{\text{qref}}^2}\cos(\theta + \omega t - \arctan\dfrac{i_{\text{qref}}}{i_{\text{dref}}}) \\ \boldsymbol{I}_b = \sqrt{i_{\text{dref}}^2 + i_{\text{qref}}^2}\cos(\theta + \omega t - \dfrac{2}{3}\pi - \arctan\dfrac{i_{\text{qref}}}{i_{\text{dref}}}) \\ \boldsymbol{I}_c = \sqrt{i_{\text{dref}}^2 + i_{\text{qref}}^2}\cos(\theta + \omega t + \dfrac{2}{3}\pi - \arctan\dfrac{i_{\text{qref}}}{i_{\text{dref}}}) \end{cases} \tag{4}$$

In the formula: $\boldsymbol{I}_a, \boldsymbol{I}_b, \boldsymbol{I}_c$ are the abc-phase currents output by IBDG respectively, and θ is the voltage phase angle at PCC.

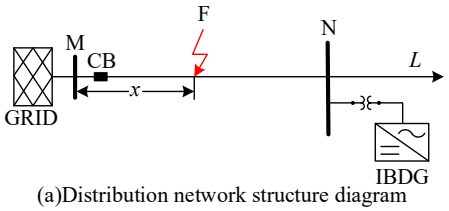
After extracting the positive sequence component, the positive sequence current component of DG output is obtained:

$$\boldsymbol{I}_{\text{DG}}^{+} = \sqrt{i_{\text{dref}}^2 + i_{\text{qref}}^2}\angle(\theta - \arctan\frac{i_{\text{qref}}}{i_{\text{dref}}}) \tag{5}$$

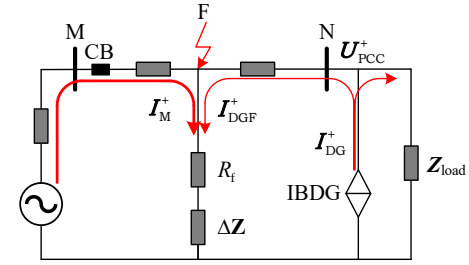
In the formula, $\boldsymbol{I}_{\text{DG}}^{+}$ is the positive sequence current output by IBDG.

3.2 Estimated off-grid time for a single IBDG system

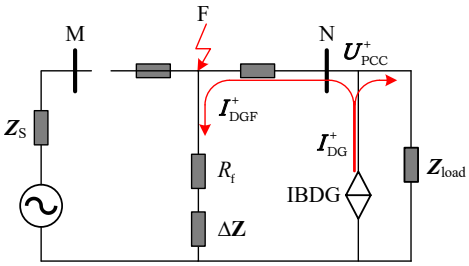
From analysis 2.2, we can see that after a fault, the active distribution network will experience state 1, in which it remains connected to the main grid, and state 2, in which it is disconnected from the main grid. The off-grid time of the IBDG depends on the positive sequence voltage amplitude at the PCC in state 2. When the system is in state 2, the IBDG can be equivalent to a current source model controlled by the positive sequence voltage at the PCC. At this point, the positive sequence voltage at the PCC is no longer constrained by the grid voltage but is instead determined by the Ohm law. To briefly illustrate the methodological approach, we first analyze a simple islanded system, as shown in Figure 3.



(a)Distribution network structure diagram



(b)State 1 Positive Sequence Composite Network



(c)State 2 Positive Sequence Composite Network

Fig. 3. Single DG system structure diagram

The load in this paper uses the equivalent impedance model shown in the following equation.

$$\boldsymbol{Z}_{\text{load}} = \left(\frac{\boldsymbol{U}_{\text{N}}^2}{P_{\text{load}} + jQ_{\text{load}}} \right)^* = \frac{\boldsymbol{U}_{\text{N}}^2}{P_{\text{load}} - jQ_{\text{load}}} \tag{6}$$

Quantify the load power using the measured power at point M before the fault, and obtain the following from the law of conservation of energy.

$$P_{\text{load}} + jQ_{\text{load}} = P_{\text{M}} + jQ_{\text{M}} - (P_{\text{DG}} + jQ_{\text{DG}}) \tag{7}$$

In the equation: P_{load} and Q_{load} are the active power and reactive power absorbed by the load, respectively; P_{M} and Q_{M} are the active power and reactive power measured at point M, respectively; P_{DG} and Q_{DG} are the rated active power and reactive power of DG, respectively.

In state 2, the positive sequence voltage at PCC is:

$$\boldsymbol{U}^+_{\text{PCC}} = \boldsymbol{I}^+_{\text{DG}} \times \left[(\boldsymbol{Z} \times (D_{\text{MN}} - x) + \Delta\boldsymbol{Z} + R_{\text{f}}) \,||\, \boldsymbol{Z}_{\text{load}} \right] \tag{8}$$

In the formula: $\boldsymbol{Z}$ is the line impedance per unit length, D_{MN} is the line length between MN, x is the distance from the fault point to the M end, R_{f} is the transition resistance, and is the positive sequence equivalent impedance.

Combining (5), we can see that $\boldsymbol{I}_{\mathrm{DG}}^{+}$ and $\boldsymbol{U}_{\mathrm{PCC}}^{+}$ are mutually coupled. To obtain the electrical quantities when the system is stable, it is necessary to iteratively solve the system of equations formed by the two. After obtaining the expressions for the intermediate variables and from equations (2) and (3), we obtain the system of equations (9):

$$\begin{cases} \boldsymbol{U}_{\mathrm{PCC}}^{+}=\boldsymbol{I}_{\mathrm{DG}}^{+}\times\left[(\boldsymbol{Z}\times(D_{\mathrm{MN}}-x)+\Delta\boldsymbol{Z}+R_{\mathrm{f}})\,\|\,\boldsymbol{Z}_{\mathrm{load}}\right] \\ \boldsymbol{I}_{\mathrm{DG}}^{+}=\sqrt{i_{\mathrm{dref}}^{2}+i_{\mathrm{qref}}^{2}}\angle(\theta-\arctan\dfrac{i_{\mathrm{qref}}}{i_{\mathrm{dref}}}) \\ i_{\mathrm{dref}}=\min\left\{\dfrac{2}{3}\dfrac{P}{U_{\mathrm{PCC}}^{+}},\sqrt{(1.5I_{\mathrm{N}})^{2}-i_{\mathrm{qref}}^{2}}\right\} \\ i_{\mathrm{qref}}=K\times(0.85-\dfrac{U_{\mathrm{PCC}}^{+}}{U_{\mathrm{N}}})\times I_{\mathrm{N}} \end{cases} \tag{9}$$

Treat a complex equation as two equations, and a complex unknown as two unknowns. Then, equation system (9) contains six equations with eight unknowns, including i_{dref} , i_{qref} , $\boldsymbol{U}_{\mathrm{PCC}}^{+}$, $\boldsymbol{I}_{\mathrm{DG}}^{+}$, x ,and R_{f} . If the fault location x and transition resistance R_{f} can be determined, the equation system can be used to find the solution for state 2.

To determine the fault location x and the transition resistance R_{f} , two new equations must be introduced without introducing additional unknowns. Write KVL equations for the system in state 1.

$$\boldsymbol{U}_{\mathrm{M}}^{+}=\boldsymbol{I}_{\mathrm{M}}^{+}\boldsymbol{Z}x+(\boldsymbol{I}_{\mathrm{DGF}}^{+}+\boldsymbol{I}_{\mathrm{M}}^{+})(\Delta\boldsymbol{Z}+R_{\mathrm{f}}) \tag{10}$$

In the equation: $\boldsymbol{U}_{\mathrm{M}}^{+}$ is the measured positive-sequence voltage at the M terminal, $\boldsymbol{I}_{\mathrm{M}}^{+}$ is the current at the M terminal, and $\boldsymbol{I}_{\mathrm{DGF}}^{+}$ is the shunt current to the fault point.

This equation is a complex equation and can be decomposed into two equations for the real and imaginary parts, corresponding to the two unknowns x and R_{f} .

Thus, the system connected to the main grid after the fault can be obtained from the system of equations (11):

$$\begin{cases} \dot{\boldsymbol{U}}_{\mathrm{PCC}}^{+}=\alpha(x,R_{\mathrm{f}})\dot{\boldsymbol{U}}_{\mathrm{M}}^{+}+\beta(x,R_{\mathrm{f}})\dot{\boldsymbol{I}}_{\mathrm{DG}}^{+} \\ \boldsymbol{U}_{\mathrm{M}}^{+}=\boldsymbol{I}_{\mathrm{M}}^{+}\boldsymbol{Z}x+(\boldsymbol{I}_{\mathrm{DGF}}^{+}+\boldsymbol{I}_{\mathrm{M}}^{+})(\Delta\boldsymbol{Z}+R_{\mathrm{f}}) \\ \boldsymbol{I}_{\mathrm{DG}}^{+}=\sqrt{i_{\mathrm{dref}}^{2}+i_{\mathrm{qref}}^{2}}\angle(\theta-\arctan\dfrac{i_{\mathrm{qref}}}{i_{\mathrm{dref}}}) \\ i_{\mathrm{dref}}=\min\left\{\dfrac{2}{3}\dfrac{P}{U_{\mathrm{PCC}}^{+}},\sqrt{(1.5I_{\mathrm{N}})^{2}-i_{\mathrm{qref}}^{2}}\right\} \\ i_{\mathrm{qref}}=K\times(0.85-\dfrac{U_{\mathrm{PCC}}^{+}}{U_{\mathrm{N}}})\times I_{\mathrm{N}} \end{cases} \tag{11}$$

In the formula:

$$\alpha(x,R_{\mathrm{f}})=\frac{[R_{\mathrm{f}}+\Delta\boldsymbol{Z}]\,\|\,[(D_{\mathrm{MN}}-x)\boldsymbol{Z}+\boldsymbol{Z}_{\mathrm{load}}]}{x\boldsymbol{Z}+[R_{\mathrm{f}}+\Delta\boldsymbol{Z}]\,\|\,[(D_{\mathrm{MN}}-x)\boldsymbol{Z}+\boldsymbol{Z}_{\mathrm{load}}]}\times\frac{\boldsymbol{Z}_{\mathrm{load}}}{(D_{\mathrm{MN}}-x)\boldsymbol{Z}+\boldsymbol{Z}_{\mathrm{load}}}$$ and

$$\beta(x,R_{\mathrm{f}})=\boldsymbol{Z}_{\mathrm{load}}\,\|\,[(D_{\mathrm{MN}}-x)\boldsymbol{Z}+(R_{\mathrm{f}}+\Delta\boldsymbol{Z})\,\|\,(x\boldsymbol{Z}+\boldsymbol{Z}_{s})].$$

Equation (11) consists of 8 equations and 8 unknowns, which can be used to solve for the fault distance and transition resistance. Substituting these known values into equation (9) allows us to solve for the positive-sequence voltage amplitude at the PCC of the distributed power source in a single-source, single-load system. Substitute the amplitude into the low penetration curve shown in Figure 2, and the x-coordinate of the intersection point is the IBDG off-grid time.

The IBDG off-grid time determined based on the voltage drop should satisfy the LVRT curve shown in Figure 2. From Figure 2, we can see that the IBDG off-grid time is

$$t_{\mathrm{off}}=\begin{cases}0.15 & U_{p.u.}<0.2\\ 2.115(U_{p.u.}-0.2)+0.625 & 0.2\leqslant U_{p.u.}\leqslant 0.85\\ \infty & U_{p.u.}>0.85\end{cases}\tag{12}$$

In the formula: t_{off} is the off-grid time of IBDG, and $U_{p.u.}$ is the standard value of U^{+}_{PCC}. After IBDG goes off-grid, reclosing still needs to wait for the arc to extinguish and the ionization time to pass, plus a certain margin. The reclosing action time is

$$t_{\mathrm{reclose}}=t_{\mathrm{off}}+t_{\mathrm{y}}\tag{13}$$

In the formula: t_{y} is the time required for the arc at the fault point to extinguish and for the surrounding medium to restore its insulation strength. Based on the operating experience of some power systems, t_{y} is often taken as 1 s in engineering applications.

4 Simulation Verification

To validate the accuracy of the active distribution network fault distance and transition resistance estimation method, as well as the effectiveness of the proposed adaptive reclosing time setting method, a distribution line simulation model was established based on the PSCAD/EMTDC platform, as shown in Figure 1. The total length of the line between the busbar and the PCC is 10.5 km. The DG capacity was set to 2 MW, the load capacity to 2 MVA, and the power factor to 0.95. The control strategy introduced in Section 3.1 was adopted.

To validate the effectiveness of the proposed method, two fault cases were constructed:

Case1: a B-C phase to phase short-circuit fault with 0 Ω transition resistance at 4.5km from the busbar;

Case2: a three-phase short-circuit fault with 10 Ω transition resistance at 4.5km from the busbar.

The voltage change curves of the PCC are shown in Figure 4. After the 0s fault occurs, the system becomes state 1, which maintains connection with the main network. In case1, the $\boldsymbol{U}_{\mathrm{PCC}}^{+}$ drops to 0.550 p.u.; After detecting the fault current, CB1 disconnected at 0.1 s, and the system became state 2 isolated from the main network, with the $\boldsymbol{U}_{\mathrm{PCC}}^{+}$ changing to 0.690 p.u. From equation (12), we can see that the off-grid time of each IBDG is 1.662 s. The voltage at PCC calculated by equation (9) is 0.691 p.u., and the estimated off-grid times of each IBDG are 1.663 s, which is about 0.001 s different from the simulated off-grid time, and the error meets the engineering requirements. Based on the estimated off-grid time, add 1 s of engineering margin, and set the reclosing time to 2.663 s.

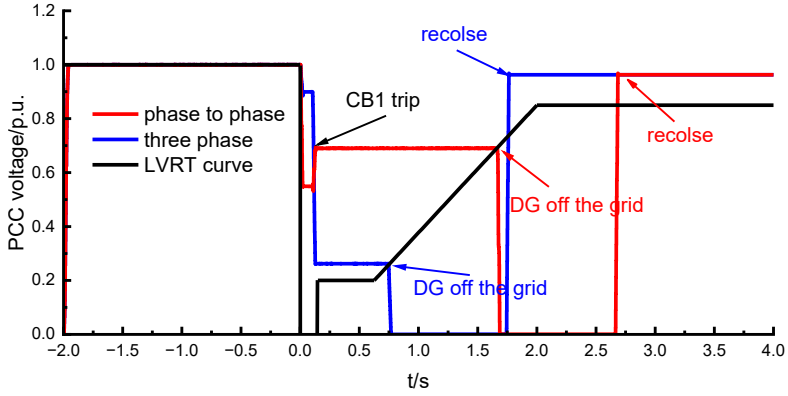


Fig. 4. Short circuit voltage curve

In case2, the $\boldsymbol{U}_{\mathrm{PCC}}^{+}$ drops to 0.899 p.u. ; After detecting the fault current, CB1 disconnected at 0.1 s, and the system became state 2 isolated from the main network, with the $\boldsymbol{U}_{\mathrm{PCC}}^{+}$ changing to 0.262 p.u. From equation (12), we can see that the off-grid time of each IBDG is 0.792 s. The voltage at PCC calculated by equation (9) is 0.240 p.u., and the estimated off-grid times of each IBDG are 0.742 s, which is about 0.050 s different from the simulated off-grid time, and the error meets the engineering requirements. Based on the estimated off-grid time, add 1 s of engineering margin, and set the reclosing time to 1.742 s.

Table 1. Results of different fault conditions of phase to phase short circuit

fault distance /km	transition resistance /Ω	PCC voltage /p.u.		fault clearance time /s		reclosing time /s
		simulation value	estimated value	simulation value	estimated value	
1.5	0	0.694	0.695	1.669	1.672	2.676
	2.5	0.701	0.702	1.684	1.686	2.688
	5	0.707	0.708	1.698	1.698	2.698
4.5	0	0.690	0.691	1.662	1.663	2.663
	2.5	0.698	0.698	1.678	1.679	2.679
	5	0.705	0.705	1.693	1.693	2.693
9	0	0.685	0.685	1.652	1.651	2.651
	2.5	0.693	0.694	1.668	1.669	2.669

10

	5	0.700	0.701	1.682	1.685	2.685

Faults with transition resistances of 0-5 Ω were simulated at distances of 0 km,1.5km, 4.5 km, and 9 km from the busbar. The test results are shown in Table 1 and Table 2 respectively. According to the method proposed in this paper, the estimation error of the fault clearance time was less than 0.1 s under different fault conditions, and the reclosing operation was reliable.

Table 2. Results of different fault conditions of three phase short circuit

fault distance /km	transition resistance /Ω	PCC voltage /p.u.		fault clearance time /s		reclosing time /s
		simulation value	estimated value	simulation value	estimated value	
1.5	0	0.093	0.093	0.15	0.15	1.15
	2.5	0.133	0.131	0.15	0.15	1.15
	5	0.182	0.175	0.15	0.15	1.15
4.5	0	0.063	0.072	0.15	0.15	1.15
	2.5	0.108	0.106	0.15	0.15	1.15
	5	0.162	0.154	0.15	0.15	1.15
9	0	0.016	0.034	0.15	0.15	1.15
	2.5	0.076	0.072	0.15	0.15	1.15
	5	0.136	0.129	0.15	0.15	1.15

5 Conclusion

In response to the issue that traditional reclosing is no longer applicable in active distribution networks, this paper analyzes the timing logic of reclosing when the fault persists. And we reach the conclusion that the key to determining the reclosing time is to obtain the IBDG off-grid time through the positive sequence voltage at the PCC. Based on the coupling relationship between the positive-sequence voltage at the PCC and the positive-sequence current output of the IBDG, nonlinear equation systems are formulated for the two steady-state. Through iterative solution, the positive-sequence voltage at the PCC is obtained, enabling the setting of the reclosing time. The performance of the proposed adaptive reclosing method was verified through theoretical analysis and PSCAD simulation data, demonstrating its ability to adaptively adjust reclosing time for faults of different types, locations, and transition resistances. The proposed method only requires electrical quantities at the reclosing installation site, without the need for communication equipment or voltage detection devices, making it economically advantageous. In cases of metallic faults or small transition resistances, the proposed method estimates fault distances with minimal error, serving as a reference for fault location. It improves reclosing success rates under transient faults, accelerates reclosing speed, reduces user losses, and enhances the reliability of active distribution grid power supply.

Some recommended standards already stipulate that IBDG should use negative sequence current control in the event of an asymmetric fault. Under this control strategy, the impact of the negative sequence network on the off-grid time needs to be taken into consideration. Further research on IBDG for this control strategy can be conducted in the future.

Acknowledgement： This work is supported by National Natural Science Foundation of China (No. 52277109)； Science and Technology Project of Shandong Electric Power Company(520612230001).

References

1. Xu, B., Li, T., Xue, Y.: Relaying Protection and Automation of Distribution Networks[M]. China Electric Power Press, Beingjing (2017).
2. Yan, X., Chen, W., He, Z.: Experimental research on self-extinction behavior of arc caused by single-phase earth fault in 10kV distribution network [J]. Power System Technology **32**(8), 25-28 (2008).
3. Liu, J., Lin, T., Li, L.: Adaptability of distribution automation systems to photovoltaic installation [J]. Power System Protection and Control **42**(20), 7-12 (2014).
4. Zhao, Y., Fang, Y., Wang, N.: Research on the impacts on feeder automation by inverter-based distribution generation connected to the distribution network [J]. Power System Protection and Control **41**(24), 117-122 (2013).
5. E.baran, M., Hooshyar, H., Shen, Z.: Accommodating high PV penetration on distribution feeders [J]. IEEE Transactions on Smart Grid **3**(2), 1039-1046 (2012).
6. Li, T., Zhao, H., Ou, D.: Short interruption and its cost appraisal [J]. Automation of Electric Power Systems **36**(20), 59-62 (2012).
7. Wang, Z., Wu, Z., Gao H.: A fault recovery scheme cooperating with reclosing and LVRT for active distribution network [J]. Power System Protection and Control **47**(3), 81-87 (2019).
8. Ishchenko, D., Oudalov, A., Stoupis, J.: Adaptive auto-reclosing based on DER connectivity data with IEC 61850. [C] // 2014 IEEE PES General Meeting. pp. 1–5. IEEE, MD, USA (2014).
9. Li, Y., Wang, Z., Wang, W.: Influence of PV with LVRT capability access to distribution network on automatic reclosing and its countermeasures [J]. Power System Protection and Control **44**(15), 61-67 (2016).
10. Liu K., Xia, M.: Impacts of DG on automatic reclosing of distribution networks. [C] // 2011 International Conference on Advanced Power System Automation and Protection. IEEE, Beijing, China (2011).
11. Seo, H., Kim, C..: An Adaptive Reclosing Algorithm Considering Distributed Generation [J]. International Journal of Control Automation and Systems **6**(5), 651-659 (2008).
12. Yang, B., Jia K.,Li, J.: Adaptive reclosing of distribution network with renewable energy based on voltage rise time limit detection [J]. Automation of Electric Power Systems **47**(22), 66-74 (2023).
13. WU Yue, FAN Kaijun, XU Bingyin, et al. “Time-limited adaptive reclosing method for distribution networks in coordination with anti-islanding protection,” Automation of Electric Power Systems, vol.48, no.3, pp.122-132 , Feb. 2024.

067 一种融合已知类识别和未知类诊断的配电变压器故障诊断方法

李奕锋，李晓芳，高伟

（ 福州大学电气工程与自动化学院 福建省 福州市）

A Transformer Fault Diagnosis Method Integrating Known Type Identification and Unknown Type Diagnosis

LI Yifeng，LI Xiaofang，GAO Wei

(College of Electrical Engineering and Automation, Fuzhou University, Fuzhou , Fujian Province, China)

ABSTRACT: Benefiting from significant advances in machine learning, considerable progress has been made in the identification of known operating conditions for distribution transformers. However, diagnostic methods for unknown fault types remain underdeveloped. To address this issue, this paper proposes an integrated fault diagnosis method capable of simultaneously identifying known types and detecting unknown types in distribution transformers. The method leverages a temporal convolutional network (TCN) as its backbone and incorporates a Hausdorff distance-based center loss (HDCL) function to enhance intra-class compactness and maximize inter-class separation within the feature space. Furthermore, a density-aware hierarchical density-based spatial clustering (HDBSCAN) algorithm is employed to cluster the features extracted by the TCN. Since samples from unknown categories form new clusters in the feature space, this approach can effectively identify unknown types. Experimental results demonstrate that the proposed HDCL significantly enhances intra-class constraints and increases inter-class distances. By integrating the HDBSCAN algorithm, the method achieves high accuracy in diagnosing unknown fault types.

KEY WORDS: distribution transformer; fault diagnosis; vibration signal; temporal convolutional network; unknown type diagnosis

摘要：得益于机器学习技术的显著进步，配电变压器在已知类工况识别方面已取得显著成果，然而针对未知类的诊断上仍存在明显不足。针对这一问题，本文提出一种融合已知类识别与未知类诊断的配电变压器故障诊断新方法。该方法以时间卷积网络(temporal convolutional network, TCN)为骨干网络，引入豪斯多夫距离中心损失函数(Hausdorff distance-based center loss，HDCL)，在增强特征空间中类内特征聚合度的同时，进一步扩大类间分离程度。在此基础上，采用 HDBSCAN 算法(hierarchical density-based spatial clustering, HDBSCAN)对 TCN 所提取的特征进行聚类分析。由于未知类的样本会在特征空间中形成新的聚类簇，该方法可据此有效识别出该类型。实验结果表明，所提出的 HDCL 能够显著加强类内约束并提高类间距离。在此基础上，结合 HDBSCAN 算法对未知类进行诊断，具有良好的准确性。

关键词：配电变压器；故障诊断；振动信号；时间卷积网络；未知类诊断

DOI：10.13335/j.1000-3673.pst.2014.01.论文序号（小五号 Times New Roman 字体加黑）

0 引言

变压器作为电力系统中的关键组成部分，承担着电能电压转换的任务[1]。由于运行规模大、持续工作于复杂工况下，配电变压器在长期服役过程中易出现诸如绕组螺丝松动、绕组变形、铁芯多点接地等渐进性故障。此类缺陷若未能被及时检测，可能进一步演变为严重故障，甚至导致停电事故。然而，早期故障往往缺乏明显的电气特征，使得基于传统继电保护的诊断方法难以及时预警。因此，为实现低压配电系统的高可靠性运行，发展基于新机理的实时状态监测与诊断方法显得尤为重要。

振动信号分析技术[2]作为一种有效的监测方法，可用于感知变压器内部运行状态。该技术通过采集并分析变压器在运行过程中因磁致伸缩和电磁力激励所产生的振动信号，从而实现对变压器机械状态的评估与诊断。文献[3]提出一种将振动信号、自适应噪声完备集合经验模态分解(complete ensemble empirical mode decomposition with adaptive noise, CEEMDAN)与图卷积神经网络(graph convolutional network, GCN)三者有机结合的故障诊断方法，用以解决配电变压器故障特征提

取困难、故障识别难度大的问题。文献[4]则采用了改进自适应噪声完备经验模态分解和卷积神经网络-双向门控循环单元分类网络以实现故障诊断，用以解决当前电力变压器机械故障实时诊断准确率较低的问题。针对变压器的多模态数据中存在差异性和样本缺失的问题，邢致恺团队[5]提出了一种基于振动信号和红外图像数据的多模态信息融合方法,分析多模态数据对电力变压器故障状态进行有效、快速的评估。文献[6]为进一步提高变压器故障诊断精度，提出一种基于同步压缩小波变换（synchrosqueezed wavelet transform, SSWT）-灰度共生矩阵（gray-level co-occurrence matrix, GLCM）的时频诊断方法。

尽管现有研究在构建的数据集上已展现出卓越的性能与诊断效果，然而在实际工程应用中，由于变压器运行环境的复杂性与不确定性，研究者所采用的数据集往往难以涵盖全部可能的振动信号类型。当实际中出现数据集中未包含的未知类别振动信号时，现有方法的泛化能力面临严峻挑战，其识别性能可能出现显著下降。因此，近年来学者开始致力于解决未知类别识别的问题。卢思佳等人[7]提出了一种两阶段诊断模型，第一阶段区分变压器正常/异常状态；第二阶段对异常样本，使用多个改进 ELM 二分类器进行细分类，识别失败则标记为未知类别。但是未知类诊断效果严重依赖于二分类器的数量，计算成本较大。Zhang 等人[8]通过将分数阶布朗运动(fractional brownian motion, FBM)融入一维卷积神经网络，构建概率阈值决策机制：当测试样本的 Softmax 层输出最大概率低于预设阈值时，将其归类为未知类别。然而，上述方法在实施过程中均高度依赖于人工预设的阈值，而阈值的合理选取本身是一项关键挑战。阈值设定不当易导致系统误判，具体表现为误报率或漏检率的升高，从而严重影响诊断方法的可靠性与实用性。

为了进一步研究未知类诊断问题，避免使用人工预设的阈值，本研究提出了一种以时间卷积网络(temporal convolutional network, TCN)为主体，引入引入豪斯多夫距离中心损失函数(Hausdorff distance-based center loss，HDCL)，并结合 HDBSCAN 算法(hierarchical density-based spatial clustering, HDBSCAN)同时实现配电变压器故障的已知类识别和未知类诊断。

1 算法介绍

1.1 时间卷积网络

TCN 的核心架构主要由两个关键组件构成：因果卷积和膨胀卷积。该网络凭借其并行计算的优势、多尺度特征融合能力以及长程时序依赖建模机制，在处理时间序列数据方面展现出显著优势[9]。TCN 的详细结构示意图如图 1 所示。

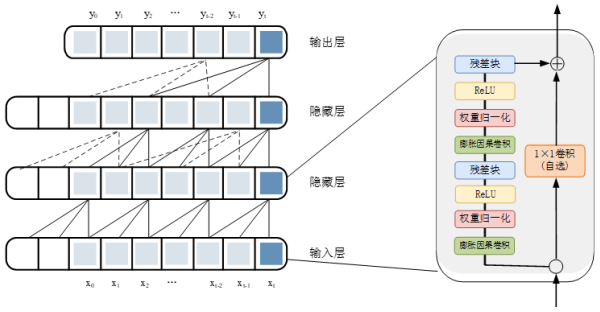


图 1 TCN 网络结构

Fig.1 TCN network structure

1.1.1 因果卷积

因果卷积是 TCN 中的关键机制，其目的是确保时间顺序一致性，避免使用未来信息。具体而言，在预测输出 y_t 时，该结构仅允许利用当前及历史输入 x_1，x_2，…，x_t，而禁止使用任何未来时刻的输入 x_{t+1}，x_{t+2}，…，从而确保建模过程符合物理系统的时间因果关系。此外，随着网络深度的增加，每一层的输出节点所能覆盖的历史信息范围也逐渐扩展。例如，位于第二层的输出可能仅依赖于 x_{t-2}，x_{t-1}，x_t；而在更深的层级中，感受野可进一步扩展至更早时刻的输入 x_{t-3}，x_{t-2}，x_{t-1}，x_t。其感受野会随着层数的加深而扩大。因此，因果卷积通过层级叠加机制逐步增大有效感受野，在保证因果约束的前提下，实现对长程依赖关系的有效建模。总而言之，因果卷积凭借其严格的时间约束和逐步扩大的时序感知能力，成为一种适用于序列建模的高效且理论严密的卷积结构。

1.1.2 膨胀卷积

膨胀卷积是一种通过引入间隔以扩展感受野的特殊卷积操作。该结构通过设置膨胀率这一超参数，控制卷积核中元素之间的间隔距离。在不同膨胀率下，卷积表现出不同的行为：当膨胀率为 1 时，该操作退化为标准卷积；随着膨胀率增大，卷积核的感知范围随之扩大，但实际用于计算的有效权重的数量保持不变，从而在不显著增加参数数量或计算复杂度的前提下，扩展了感受野。该机制实现了感受野的扩展与计算效率之间的平衡，适用于需捕获长程依赖关系的任务。

一维时间序列的膨胀卷积运算定义如下：

$$F(s)=\sum_{i=0}^{k-1} f(i)x_{s-d*i} \tag{1}$$

其中，$F(s)$表示一维时间序列元素 x_s 的膨胀卷积；$x \in R^D$ 表示一维时间序列；k 表示卷积核大小；i 表示网络层数；d 表示膨胀因子，用于控制膨胀卷积的采样步幅。

1.2 豪斯多夫距离中心损失函数

需要注意的是本文只针对已知类型进行训练，这会出现一个问题。在封闭集训练范式下，Softmax 函数的归一化特性迫使模型将所有输入样本强制分配到已知类别，导致高维特征空间被已知类别的特征表示过度占据。这种情况使得未知类样本在特征空间中缺乏明确的容留区域，其嵌入向量往往落入已知类簇的邻近区域。当 HDBSCAN 基于此类混淆特征进行特征聚类时，未知类样本的特征与最近邻已知类的特征在特征空间上趋于接近，最终导致后续方法无法有效区分已知与未知类别。

针对上述特征空间侵占问题，本研究从分类损失函数入手，在原有交叉熵损失函数的基础上，提出双重优化策略：

(1) 增强类内约束。为实现已知类别的特征空间高效利用，本文采用中心损失建立类内特征聚合度约束。

(2) 扩大类间距离。在中心损失函数的基础上，为了进一步增强类间可分性，本文提出一种豪斯多夫距离损失(Hausdorff distance loss, HDL)。

1.2.1 中心损失函数

中心损失函数是一种有效提高潜在特征区分能力的损失函数，能够在保持不同类别特征可分离的同时最小化类内变化[10]。其定义为：

$$Lc=\frac{1}{2n}\sum_{i=1}^{n}\left\|q_i-c_{p_i}\right\|_2^2 \tag{2}$$

其中 $c_{pi} \in R$ 是第 p_i 类的潜在特征 q_i 的中心，n 则代表已知类别数量。

这个简单的公式通过惩罚潜在特征与其中心之间的距离来有效地表征类内变化。但是，q_i 和 c_{yi} 在深度学习当中是未知的。具体来说，q_i 由深度学习中的可学习参数得出，c_{yi} 则是由属于第 p_i 类的潜在特征平均值给出。这意味着，在理想情况下，c_{yi} 应该随着训练过程中潜在特征 q_i 的变化而更新。这要求我们必须要考虑整个训练集，并在每次迭代中平均每个类的深度特征，这是不切实际的。因此公式(2)不能直接使用。

为了解决这个问题，文献[11]做了两个必要的修改。首先，不是根据整个训练集更新中心，而是基于每批次的样本进行更新。在每次迭代中，通过对每批次中相同类别的特征进行平均来更新中心。值得注意的是，如果每批次中不包括相应类别的特征，则某些类别中心可能不会更新。其次，为了避免少数错误标记的样本对中心造成大的扰动，使用移动平均策略来控制中心的学习。在这个过程中，中心损失函数 Lc 和潜在特征 q_i、类别中心 c_{yi} 的梯度关系为：

$$\frac{\partial Lc}{\partial q_i}=\frac{1}{n}(q_i-c_{p_i}) \tag{3}$$

$$\Delta c_j=\frac{\sum_{i=1}^{n}\delta(p_i=j)\bullet(c_j-q_i)}{\varepsilon+\sum_{i=1}^{n}\delta(p_i=j)} \tag{4}$$

其中，c_j 是类别 j 的中心，q_i 是属于类别 j 的第 i 个样本，$\delta(p_i=j)$是指示函数，当 q_i 的标签 p_i 等于类别 j 时取值为 1，否则为 0。ε 是一个很小的正数，用来避免分母为 0 的情况出现，通常 $\varepsilon=1e^{-5}$。

式(4)是中心损失的更新公式，它用于计算每个类别的中心，并在训练过程中更新这些中心，以减少类内变化并提高模型的判别能力。

需要注意的是，中心损失不能单独使用，否则深度学习的特征和中心将会退化为 0。本文将交叉熵损失函数与中心损失结合起来，共同监督模型的学习，增强类内紧致性。公式如下：

$$L=Lc+Lcross \tag{5}$$

其中 L 指的是中心损失函数与交叉熵损失函数求和后的损失函数。$Lcross$ 指的是交叉熵损失函数，由于交叉熵损失函数是广泛使用的标准损失函数，其具体定义和推导可参考相关文献[12]。

1.2.2 中心损失函数

为了进一步增强模型的类间可分性，本研究提出 HDL，作为对经典中心损失的扩展改进。

豪斯多夫距离(Hausdorff distance)是在度量空间中任意两个集合之间定义的一种距离[13]。如图 2 所示，对于两个点集 A 和 B，从 A 到 B 的单侧豪斯多夫距离定义为:

$$h(A,B)=\max_{a\in A}\min_{b\in B}\left\|a-b\right\|_2 \tag{6}$$

同样的，从 B 到 A 的单侧豪斯多夫距离为：

$$h(B,A)=\max_{b\in B}\min_{a\in A}\left\|a-b\right\|_2 \tag{7}$$

所以，这两组之间的豪斯多夫距离为：

$$HD(A,B)=\max(h(A,B),h(B,A)) \tag{8}$$

在上面的定义中，我们使用了欧几里得距离，但也可以使用其他度量。直观地说，$HD(A,B)$是从两个集合之一的一个点到另一个集合中最近点的最长距离。相较于传统欧氏距离，豪斯多夫距离有两个独特的优势，一是豪斯多夫距离不要求两个点集的数量要保持一致，这在模型训练中尤为关键，因为实际训练时，各批次中不同类别的样本数量往往难以做到完全均衡；二是其最大最小距离准则天然有助于分类任务的决策边界划分。

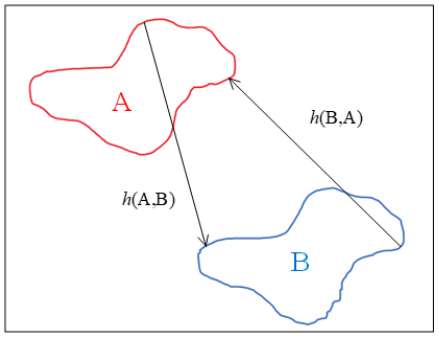


图 2 豪斯多夫距离原理图

Fig.2 Schematic diagram of the Hausdorff distance

但与传统应用中通过最小化豪斯多夫距离实现集合匹配不同，在类间可分性优化场景下，我们需要最大化类间豪斯多夫距离以增强决策边界隔离。为实现这一目标，本文设计如下豪斯多夫间隔函数：

$$Lh=k\bullet\exp(-\sum_{i=1}^{n}HD(A_i,B_i)) \tag{9}$$

其中，k 是缩放系数，通常取 1~10^4。

综上所示，可以形成本研究的完整损失函数，即 HDCL，如下所示：

$$Lhdcl=Lh+L \tag{10}$$

本文所设计的损失函数旨在优化已知类别特征的表达，防止其过度占据特征空间，从而为未知类别预留必要的空间。这有助于避免已知类别特征与未知类别特征在特征空间中发生混淆，为后续的未知类别识别提供了坚实基础。

1.3 HDBSCAN 算法

HDBSCAN[14]是由 Campello 等开发的一种基于密度的聚类算法，它是 DBSCAN 聚类算法的一种变体，具有自动选取最优聚类数、发现不同密度簇和处理噪声点的能力。

在聚类的过程中，HDBSCAN 首先根据密度对数据空间进行相应的变换，求出所有样本点的最小生成树，然后对变换后的空间进行单连锁聚类。HDBSCAN 不以单个半径值作为树状图的分割线，而是在不同高度对树进行切割，根据集群的稳定性选择不同密度的集群[15]。

综上所述，HDBSCAN 作为一种基于密度的层次聚类算法，其核心优势在于能够有效识别密度各异的簇结构，并同时检测离群点。并且，最为关键的是，该算法无需预设聚类数目，可依据数据分布特性自主推断最优聚类划分，这一特性使其特别适用于未知类别的识别任务。在实际应用中，由于未知故障类型的数量往往无法预先确定，HDBSCAN 能够以数据驱动的方式自适应地发现潜在类别结构，从而显著提升了对未知类别样本的辨识能力与诊断系统的泛化性能。

1.4 算法流程

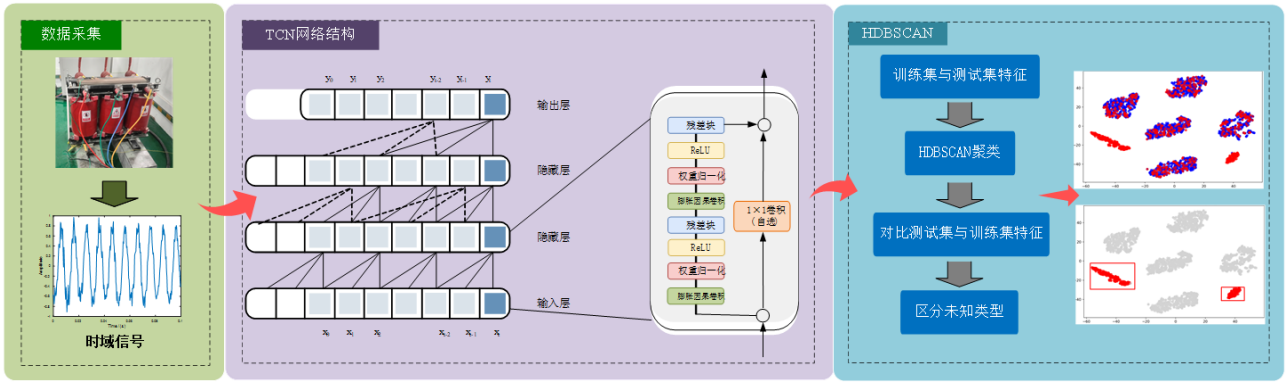


图 3 算法流程

Fig.3 Algorithm process

综上所述，融合已知类识别和未知类诊断的配电变压器故障诊断的流程如图 3 所示。

具体如下：

1）对实验采集到的时域振动数据，划分出训练集和测试集，其中训练集只包含已知类数据，测试集包含了已知类数据和未知类数据(未知类数据

的构造详见本文 2.1 节)；

2）将训练集输入到 TCN 模型中进行训练，得到训练集的特征集，以及一个已完成训练的分类模型用以进行已知类识别；

3）使用训练好的模型对测试集进行分类和特征提取。模型输出初步分类结果，值得注意的是，在这次分类中，所有样本均被归类为已知类，包括实际未知类的样本；

4）将测试集和训练集的所提特征作为 HDBSCAN 算法的输入。基于已知类与未知类样本在特征空间中的分布差异，该算法能够将二者聚类至不同的簇中。由于已知类样本在特征空间中具有较高的内在相似性与分布一致性，HDBSCAN 能够有效识别并分离出测试集中的未知类样本，从而实现未知类的二次识别与分类。

2 算例分析

2.1 数据集与实验设置

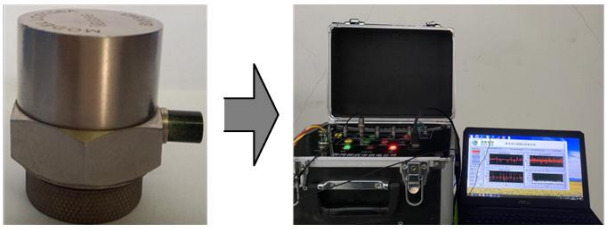


图 4 数据采集系统

Fig.4 Data acquisition system

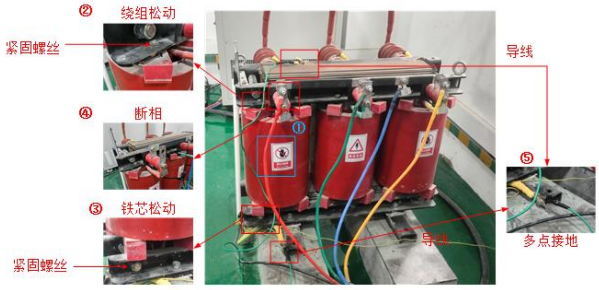


图 5 故障模拟实验

Fig.5 Fault simulation experiment

本研究采用一套便携式数据采集装置，对一台 SC12-30/10 型、额定容量为 30kVA 的 10kV/380V 干式变压器进行了振动信号采集。振动信号以 3kHz 的采样频率进行采集，单次采样时长为 0.1 秒。该变压器接入 10kV 中压实验系统并网运行，其低压侧配置有可调 RLC 负载（容量范围 0–30kVA），用于模拟实际负载工况。数据采集系统主要包括三个部分：压电式加速度传感器（型号 LC0156A）、信号采集设备（NI USB-6218 模块）以及基于 LabVIEW 平台开发的上位机控制与记录软件，整体结构如图 4 所示。

实验装置的安装布局及模拟实验的示意图如图 5 所示。实验中模拟了配电变压器中常见的四类故障，包括：绕组螺栓松动、铁芯螺栓松动、铁芯多点接地以及低压侧 C 相断线。上述故障类型与正常运行状态共同构成本研究所定义的“已知类”，用于后续故障诊断模型的训练与验证。

为扩展故障类型的覆盖范围并评估模型对未见状态的识别能力，本研究在四类主要故障的基础上，额外引入两种未知故障场景：其一为接地不良故障，定义为未知类Ⅰ；其二选自凯斯西储大学轴承振动开放数据集中的典型样本，作为未知类Ⅱ。通过纳入上述两类未知状态，构建了更具挑战性和泛化需求的数据集，其详细组成如表 1 所示。

表 1 振动信号数据集

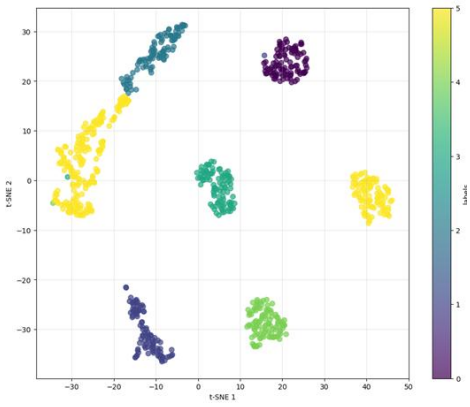
Table 1 Vibration signal dataset

工况类别	训练集数量	测试集数量	样本尺寸	标签
正常工况	300	100	300	0
绕组松动	300	100	300	1
铁芯松动	300	100	300	2
铁芯多点接地	300	100	300	3
断相	300	100	300	4
未知类Ⅰ	\	100	300	5
未知类Ⅱ	\	100	300	5

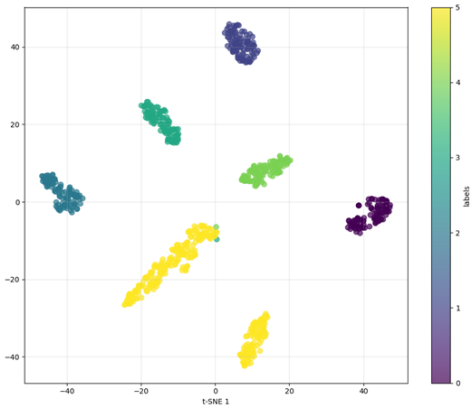
2.2 豪斯多夫距离中心损失函数效果验证

为了解决高维特征空间被已知类的特征表示过度占据的问题，本研究在交叉熵损失函数的基础上引入了中心损失函数和 HDL，共同构成了 HDCL。为验证所提出损失函数的有效性，我们进行了对比实验。实验分别对比了仅使用交叉熵损失函数和 HDCL 所训练模型的性能差异。通过应用 t-SNE 技术可视化训练集样本在特征空间中的分布，直观评估了不同损失函数对特征空间结构的影响。该可视化结果如图 6 所示。

从图中可以看出，相较于仅使用交叉熵损失函数的模型，经由了 HDCL 训练的模型所提取的特征在特征空间中展现出更优的结构特性，特别是类间可分性显著增强。为定量评估本研究所提方法在优化特征空间结构方面的效果，引入以下三个聚类有效性指标作为评价标准：



（a）仅使用交叉熵损失函数 t-SNE 可视化



（b）使用 HDCL 的 t-SNE 可视化

图 6 特征空间 t-SNE 可视化

Fig.6 Feature space visualization using t-SNE

(1) 轮廓系数：衡量单个样本与其自身类别的紧密度相对于其他类别的分离度，反映聚类结构的整体清晰度。值越高，表示类内约束越紧凑、类间分离越好。

(2) Calinski-Harabasz 指数：通过计算类间离散度与类内离散度的比率来评估聚类的有效性。值越高，表示类间离散度大、类内离散度小，即聚类结构更优。

(3) 归一化类内距离：计算每个类别内所有样本到其类中心的平均距离并进行归一化处理。值越低，表示类内样本越聚集，特征表示越紧致。

这些指标共同提供了对特征空间类内约束和类间可分性的多角度量化评估。上述三个聚类有效性指标在不同损失函数的模型上的定量结果如表 2 所示。

表 2 聚类有效性指标

Table 2 Clustering validation metrics

损失函数	轮廓系数	Calinski-Harabasz 指数	归一化类内距离
交叉熵损失函数	0.6643	2506.9537	0.1169
HDCL	0.9297	39616.2181	0.0545

从表中可以看出，在三个指标上，使用本文所提出的 HDCL 训练后的模型均取得最优结果。这表明损失函数的改进，即引入 HDCL 后，显著优化了特征空间结构。其中，在轮廓系数的表现上，使用 HDCL 的模型达到了 0.9297 的高分，远优于交叉熵损失的 0.6643，这表明其聚类结果的簇结构更加清晰，样本归属的确定性更高。在 Calinski-Harabasz 指数上，HDCL 取得了极为显著的提升，指数值高达 39616.2，有力地验证了该损失函数在增强类间分离度方面的卓越效果。而在归一化类内距离上，HDCL 将距离从 0.1169 大幅压缩至 0.0545，直观体现了其强化类内紧致性、压缩特征分布的能力。

综上所述，所有指标从不同的维度一致表明：HDCL 损失函数能同时优化聚类结果的多个方面，不仅使类内特征更加聚合，也使得类间边界更为分明，从而在特征空间中构建出判别性更强、容错性更高的表示。

2.3 基于 HDBSCAN 聚类的未知类诊断验证

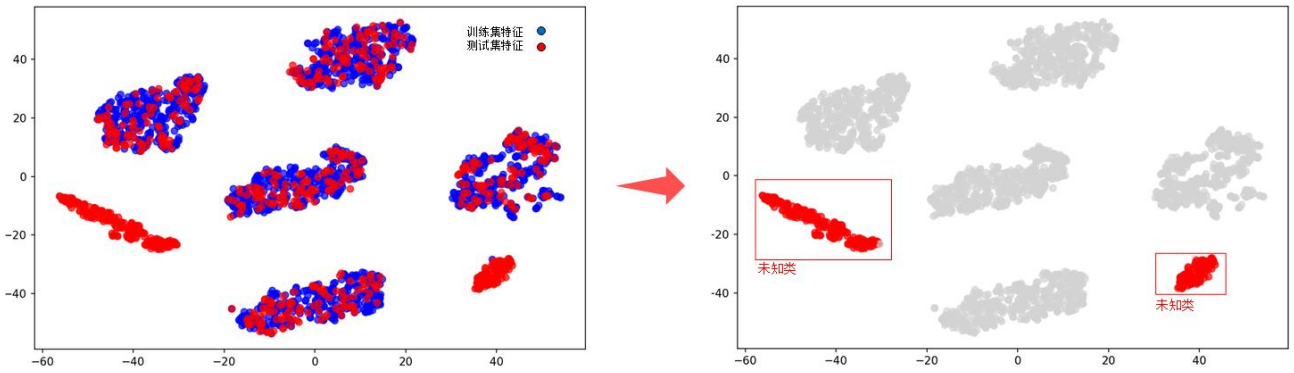


图 7 HDBSCAN 聚类结果

Fig.7 HDBSCAN clustering results

如前所述，本研究引入了 HDCL，以增强特征空间中的类内聚合度并扩大类间分离度。结果表明，HDCL 能够有效约束同类样本的分布，同时确保不同类别之间保持显著间距，从而显著提升了特征的可区分性。这种特性为后续使用 HDBSCAN 聚类算法奠定了基础。本研究采用 HDBSCAN 的核心目的在于：因为已经通过 HDCL 对特征进行了一次预处理，使特征空间中的样本已呈现出显著的类内聚合与类间分离特性。在此基础上，HDBSCAN 能够更有效地将已知类样本凝聚为高密度簇，同时将未知类样本判别为离群点或独立形成的低密度簇，从而避免未知类样本被误判为已知类，实现已知类与未知类的有效分离。HDBSCAN 聚类效果如图 7 所示。

从图中可以观察到，测试集中与训练集特征分布存在显著差异的样本，能够被清晰地分离并聚合为独立的簇。这种明显的聚类特征，可作为判别未知类样本的重要依据：若测试样本在特征空间中形成与已知类显著分离的簇结构，则其被判定为未知类。

图 8 展示了用混淆矩阵表示的所提方法的测试结果。模型在已知类上达到 99.4%平均准确率，类间混淆极低。关键的是，98%的未知类被正确拒绝，这证明所提方法能有效分离已知类数据和未知类数据。

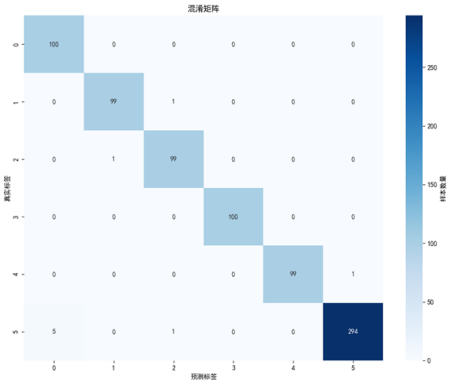


图 8 分类结果

Fig.8 HDBSCAN clustering results

3 结论

本文提出一种基于 TCN 的干式变压器故障诊断框架，同步处理已知类分类和特征提取，并利用所提取的特征，经过 HDBSCAN 聚类算法诊断未知类，在 TCN 分类的基础上完成二次分类。经实验验证，所提模型对于干式变压器的准确率达到 99%，其中对未知类识别的准确率高达 98%，在所构建的测试集上取得较好的分类结果。鉴于不同型号变压器的振动信号特性可能会有差异，下一阶段将重点研究其信号表征差异，以提升所提方法的泛化能力。

参考文献

[1] Tightiz L, Nasab M A, Yang H, et al. An intelligent system based on optimized ANFIS and association rules for power transformer fault diagnosis[J]. ISA transactions, 2020, 103: 63-74.

[2] Cao C, Xu B, Li X. Monitoring method on loosened state and deformational fault of transformer winding based on vibration and reactance information[J]. IEEE Access, 2020, 8: 215479-215492.

[3] 洪翠, 邱仕达, 高伟. CEEMDAN 与 GCN 结合的配电变压器故障诊断[J]. 电子测量与仪器学报, 2023, 36(12): 86-96.

[4] 李浩,魏繁荣,王浩,等.基于振动信号与深度学习的电力变压器故障诊断方法[J].电工电能新技术,2024,43(10):1-12.

[5] 邢致恺,何怡刚,姚其新.基于多模态信息融合的变压器在线故障诊断方法[J].电子测量与仪器学报,2024,38(09):95-103.

[6] 杨义,李晓华,李俊聪,等.基于 SSWT-GLCM 与改进 WOA-SVM 的变压器机械故障时频诊断[J]. 振动．测试与诊断,2024,44(06):1135-1143+1247.

[7] Lu S, Gao W, Hong C, et al. A newly-designed fault diagnostic method for transformers via improved empirical wavelet transform and kernel extreme learning machine[J]. Advanced Engineering Informatics, 2021, 49: 101320.

[8] Zhang Y, Qin N, Huang D, et al. Precise diagnosis of unknown fault of high-speed train bogie using novel FBM-Net[J]. IEEE Transactions on Instrumentation and Measurement, 2022, 71: 1-11.

[9] 宋建材,刘健蓉,张鑫洋.基于蜣螂优化时间卷积网络的太阳辐照度预测算法[J].太阳能学报,2025,46(06):494-500.

[10] 王军杰,王泉,蒋平,等.一种孤立中心损失方法及其在人脸表情识别中的应用[J].西安交通大学学报,2022,56(04):119-126.

[11] Wen Y, Zhang K, Li Z, et al. A comprehensive study on center loss for deep face recognition[J]. International Journal of Computer Vision, 2019, 127(6): 668-683.

[12] Connor R, Dearle A, Claydon B, et al. Correlations of cross-entropy loss in machine learning[J]. Entropy, 2024, 26(6): 491.

[13] Karimi D, Salcudean S E. Reducing the hausdorff distance in medical image segmentation with convolutional neural networks[J]. IEEE Transactions on medical imaging, 2019, 39(2): 499-513.

[14] Campello R J G B, Moulavi D, Sander J. Density-based clustering based on hierarchical density estimates[C]//Pacific-Asia conference on knowledge discovery and data mining. Berlin, Heidelberg: Springer Berlin Heidelberg, 2013: 160-172.

[15] 董宏成,赵学华,赵成,等.基于 HDBACAN 聚类的自适应过采样技术[J].计算机工程与设计,2020,41(05):1295-1300.

收稿日期：2013-07-04。

作者简介：

李奕锋（2000 年），男，硕士研究生，研究方向为配电变压器故障诊断，E-mail：2119028943@qq.com。



李奕锋

（编辑　五号楷体，居右，段前空 6pt）

068 小电流接地系统单相接地故障暂态零序特征分析及应用

王　岩，高厚磊，沈　澳

（山东大学电气工程学院，山东省　济南市　250061）

Analysis and application of transient zero-sequence characteristics of single-phase grounding fault in low-current grounding system

WANG Yan, GAO Houlei, SHEN Ao

（School of Electrical Engineering, Shandong University, Jinan 250061, Shandong Province, China）

ABSTRACT: Among the faults occurring in current power supply systems, single-phase grounding faults account for the highest proportion and often lead to serious incidents. Therefore, fault line selection and localization after such faults are particularly critical. This paper first analyzes the transient zero-sequence characteristics following single-phase grounding faults in small-current grounding systems and defines the generalized transient zero-sequence power. It demonstrates that during the initial fault stage (approximately 0~5 ms), both arc suppression coil grounded systems and ungrounded neutral systems exhibit identical generalized transient zero-sequence power characteristics, which can effectively distinguish among upstream sections, downstream sections of the fault point, and non-faulted lines. Based on this, a fault section localization method using the algebraic sum of generalized transient zero-sequence power is proposed. Validation through RTDS simulations confirms that this method is sensitive, reliable, and capable of rapidly locating single-phase grounding faults in small-current grounding systems.

KEY WORDS: Single-phase ground fault; Transient zero-sequence features; Generalized transient zero-sequence power; Segment positioning

摘要： 在目前供电系统所发生的故障中，单相接地故障占比最高，常引发严重事故，故障发生后的选线和定位显得尤为重要。本文首先分析了小电流接地系统发生单相接地故障后的暂态零序特征，定义了广义暂态零序功率；论证了在故障初期（约 0~5ms），经消弧线圈接地和中性点不接地系统具有相似的广义暂态零序功率特征，并能有效区分故障点上游区段、下游区段以及非故障线路。据此提出基于广义暂态零序功率代数和的区段定位方法，经 RTDS 仿真验证，该方法灵敏可靠，能快速定位小电流接地系统发生的单相接地故障。

关键词：单相接地故障；暂态零序特征；广义暂态零序功率；区段定位

DOI：10.13335/j.1000-3673.pst.2014.01.

1　引言

在现代电力系统中，中性点接地方式的选择直接影响到系统的安全稳定运行。小电流接地方式因其独特的运行特性，被广泛应用于中低压配电网络。随着供电系统复杂化及智能化程度的不断提高，对供电的可靠性及保护的快速性提出了更高要求，尽管采用小电流接地方式的配电网可带故障持续运行一段时间，但若故障长时间存在，可能引发相间短路等众多更加严重的故障，严重威胁电力系统的正常运行。统计数据显示，单相接地故障在小电流接地系统电网故障中的占比高达 80%。因此，充分了解小电流接地系统在单相接地故障时的特征，能够正确、快速地进行故障选线及区段定位显得尤为重要。

对小电流接地系统发生单相故障时的稳态特征的研究目前已较为成熟，且以此为理论支撑开发了多种故障选线方法，例如基波比幅比相法、有功分量故障选线方法等等。但由于故障后稳态分量的数值往往较小，难以快速、正确地选出故障线路。经过多年研究及现场录波可知，在接地故障初期，系统会经历一个暂态过程，并且暂态时期的电气量较稳态时更加显著，这对于小电流接地系统的故障识别、故障选线及区段定位等具有重要意义。

为此，本文提出一种暂态零序功率算法进行故障区段定位，且通过 RTDS 仿真，得到录波数据进行验证。

2　单相接地故障暂态零序特征分析

为实现小电流接地系统在单相接地故障时快

速且准确的故障选线及区段定位，必须充分了解系统在发生单相接地故障时各条线路及各个区段的故障特征，为研究不同接地方式下系统的暂态故障特征，特建立如图 1 所示的电路模型。

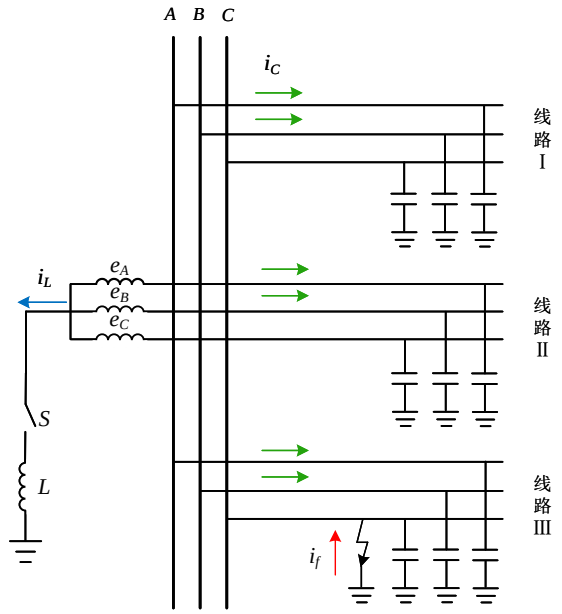


图 1　发生单相接地故障的小电流接地系统供电网络

Fig. 1 Neutral non-effective grounding system with single-phase to ground fault

当图 **1** 所示系统中的 *S* 开关闭合时，即为中性点经消弧线圈接地系统，在分析电容电流及电感电流在故障初期暂态过程中的特征时，可将其用图 **2** 所示的等效网络来近似[1]。

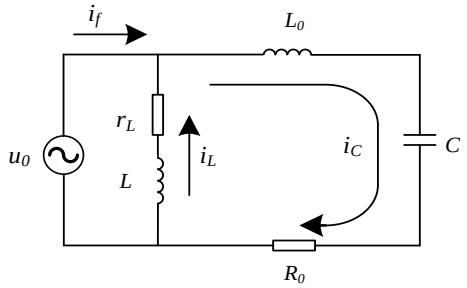


图 2 消弧线圈接地系统单相接地故障等效零序网络图

Fig. 2 Zero-sequence network diagram of the equivalent zero-sequence network of single-phase grounding fault of arc suppression coil grounding system

图 2 中 *C* 为系统的三相对地电容总和；L_0 表示系统各元件在零序回路中的等值电感；R_0 表示零序回路中的等值电阻；*L* 和 r_L 和分别表示消弧线圈的电感和损耗电阻；u_0 为零序电压。i_f 为故障点的零序电流；i_C 为非故障相的对地电容电流；i_L 为消弧线圈的补偿电流。

在分析暂态电容电流时，由于 *L* 一般远大于 L_0，可将 *L* 所在回路作开路处理，由剩余串联回路并结合 KVL 可得微分方程：

$$R_0 i_C + L_0 \frac{di_C}{dt} + \frac{1}{C}\int_0 i_C dt = U_{\phi m}\sin(\omega t + \varphi) \quad (1)$$

根据式（1）对应的齐次方程的特征方程判别式 $\Delta = R_0^2 - 4L_0/C$ 不同，暂态电容电流会经历不同的振荡及衰减过程。

对于架空线路，由于电感较大而电容较小，其暂态过程中故障电流会迅速衰减，自由振荡频率通常处于 300~1500Hz 的范围内。相反，电缆线路因电感极小但电容极大，其自由振荡频率较高，一般大于 1500Hz。

可利用初始条件 $i_C(0)=0$ 和 $I_{Cm}=U_{\phi m}C\omega$ 并经拉式变换等运算解式(1)得:

$$\begin{aligned} i_C &= i_{C.os} + i_{C.st} \\ &= I_{Cm}\left[\begin{array}{l}(\dfrac{\omega_f}{\omega}\sin\varphi\sin\omega_f t - \cos\varphi\cos\omega_f t)e^{-\delta_C t} \\ +\cos(\omega t+\varphi)\end{array}\right] \end{aligned} \quad (2)$$

其中

$$\omega_f = \sqrt{\frac{1}{L_0 C} - \left(\frac{R_0}{2L_0}\right)^2} \quad (3)$$

$$\delta_C = \frac{1}{\tau_C} = \frac{R_0}{2L_0} \quad (4)$$

$i_{C.os}$ 为电容电流中的暂态振荡分量；$i_{C.st}$ 为稳态工频分量；ω_f 为暂态自由振荡分量的角频率；δ_C 为自由振荡分量的衰减系数，φ 为初相角。

在分析暂态电感电流时，可将图 2 中的 L_0、*C*、R_0 所在支路视为开路，根据剩余串联回路，可运用 KVL 出暂态电感电流的方程：

$$U_{\phi m}\sin(\omega t+\varphi) = r_L i_L + W\frac{d\phi_L}{dt} \quad (5)$$

其中 *W* 为消弧线圈的匝数；ϕ_L 为消弧线圈的磁通。

由于 r_L 的值很小，可视为零，可得消弧线圈自身阻抗约为 ωL，电路相角约为零，并且在 *t*=0 时，线圈中还未流过感性电流，即没有磁通，则有 ϕ_L=0。根据以上条件可解得暂态电感电流为：

$$i_L = I_{Lm}[\cos\varphi e^{-\delta_L t} - \cos(\omega t+\varphi)] \quad (6)$$

$$\delta_L = \frac{1}{\tau_L} = \frac{r_L}{2L} \quad (7)$$

I_{Lm} 为暂态电感电流的幅值；δ_L 为其自由振荡分量的衰减系数。

故障点的暂态零序电流为两者叠加，即：

$$i_f = i_C + i_L$$
$$= I_{Cm}\left[\left(\frac{\omega_f}{\omega}\sin\varphi\sin\omega_f t - \cos\varphi\cos\omega_f t\right)e^{-\delta_C t}\right]$$
$$+ I_{Lm}\cos\varphi e^{-\delta_L t} + (I_{Cm} - I_{Lm})\cos(\omega t + \varphi) \quad (8)$$

由式（8）及前述分析并参考相关文献可知，故障初期（约 0~5ms）[5]内暂态零序电流频率较高，容抗与频率成反比，感抗与频率成正比，流过线路的容性电流较大，感性电流较小，且电容电流的自由振荡频率远大于电感电流，两者在频率和幅值上都相差较大，所以消弧线圈在此时段内还未发挥补偿作用或补偿作用不明显。

中性点不接地系统发生单相接地故障时，故障点仅存在暂态电容电流，与中性点经消弧线圈接地系统相比，其故障等效零序网络中无 L 所在支路，可知其暂态电容电流的分析过程和上述过程类似，在此不再赘述。

3 广义暂态零序功率算法原理

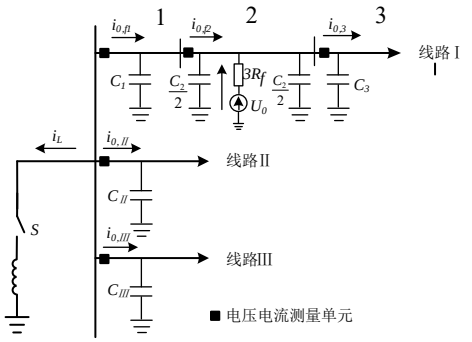


图 3 小电流接地系统单相接地故障零序等效网络
Fig. 3 Zero-sequence equivalent network for single-phase-to-ground fault in non-effectively grounded system

如图 3 所示网络，各区段上游均有电压电流测量单元。假设线路 I 上的区段 2 中部发生单相接地故障，则区段 2 为故障区段，区段 1 为故障点上游区段，区段 3 为故障点下游区段，线路 I 为故障线路，线路 II、III为非故障线路。

当 S 断开时，系统为中性点不接地系统，故障点下游区段 3 的零序电流为：

$$i_{0,3} = C_3\frac{du_{0,3}}{dt} \quad (9)$$

C_3 为区段 3 测量单元到线路末端的等效对地电容，$u_{0,3}$ 为测量单元采集的零序电压，非故障线路零序电流 $i_{0,\mathrm{II}}$、$i_{0,\mathrm{III}}$ 同理可表示为：

$$i_{0,\mathrm{II}} = C_{\mathrm{II}}\frac{du_{0,\mathrm{II}}}{dt} \quad (10)$$

$$i_{0,\mathrm{III}} = C_{\mathrm{III}}\frac{du_{0,\mathrm{III}}}{dt} \quad (11)$$

则非故障线路及故障点下游区段零序电流可统一表示为：

$$i_{0,i} = C_i\frac{du_{0,i}}{dt} \quad (12)$$

故障点上游区段 1 的零序电流为：

$$i_{0f,1} = -(i_{0,\mathrm{II}} + i_{0,\mathrm{III}})$$
$$= -C_{f,1}\frac{du_{0,1}}{dt} \quad (13)$$

故障点区段 2 上游的零序电流为：

$$i_{0f,2} = i_{0f,1} - C_1\frac{du_{0,1}}{dt}$$
$$= -C_{f,2}\frac{du_{0,1}}{dt} \quad (14)$$
$$= -C_{f,2}\frac{du_{0,2}}{dt}$$

$C_{f,1}$、$C_{f,2}$ 为区段 1、2 测量单元到线路 II、III末端的等效对地电容之和，C_1 为区段 1 的对地电容，$u_{0,1}$、$u_{0,2}$ 为区段 1、2 测量单元采集到的零序电压。

则故障点上游区段及故障点区段上游零序电流可表示为：

$$i_{0f,i} = -C_{f,i}\frac{du_{0,i}}{dt} \quad (15)$$

S 闭合之后，由于消弧线圈的存在，故障点会流过与电容电流方向相反的电感补偿电流，其故障点上游区段及故障区段上游的零序电流为：

$$i_{0f,i} = i_L - C_{f,i}\frac{du_{0,i}}{dt} \quad (16)$$

由前述分析可知在故障初期（约 0~5ms），消弧线圈几乎不发生补偿作用，流过消弧线圈的电感电流可近似为零，则式（16）中的 i_L 可忽略，可将其等效为式（15）。

定义“广义暂态零序功率”为零序电压的导数与零序电流的乘积，其在不同测量点对应的表达式如下：

非故障线路及故障点下游区段为：

$$p_{0,i} = \frac{du_{0,i}}{dt}\cdot i_{0,i} = C_i\cdot\left(\frac{du_{0,i}}{dt}\right)^2 \quad (17)$$

故障区段及故障点上游区段为：

$$p_{0f,i} = \frac{du_{0,i}}{dt}\cdot i_{0f,i} = -C_{f,i}\cdot\left(\frac{du_{0,i}}{dt}\right)^2 \quad (18)$$

由式（17）和式（18）可知，在故障发生后的约前 1/4 周波内，非故障线路及故障点下游区段广义暂态零序功率为正值，故障区段上游及故障点上游区段为负值，利用此特性可进行中性点不接地系统及消弧线圈接地系统发生单相接地故障的故障选线及区段定位。

实际线路保护单元采集离散信号，可利用采样

值的中间差分代替导数进行计算，即：

$$\frac{du_{0,i}}{dt} \approx \frac{u_{0,i}[n+1]-u_{0,i}[n-1]}{2\Delta t} \tag{19}$$

在实际供电系统中，受电磁噪声、线路绝缘不平衡以及消弧线圈匹配偏差等因素影响，零序电压和电流的波形往往存在随机波动。若仅依据个别点位暂态零序功率的正负进行选线判断，容易导致误判。为此，对相应线路发生故障后的前 1/4 周波的暂态零序功率进行累加得到 $\sum p_{0,i}$，利用其正负进行区段定位，可大大降低误判情况。

4 算法仿真验证

为验证所提区段定位方法的有效性，以图 4 所示的某矿井供电系统为目标，利用实时数字仿真系统（RTDS）的 RSCAD 软件进行建模与仿真。对中压 10kV 线路，即虚线框所示部分线路设置单相接地故障进行暂态零序功率选线算法验证。

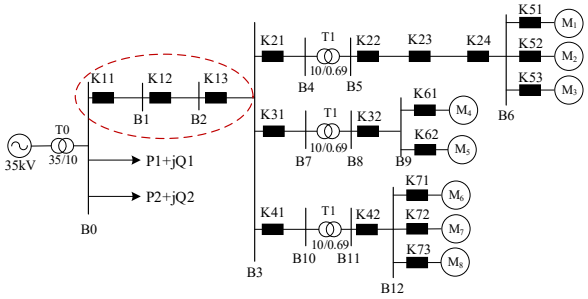


图 4 矿井供电系统模型

Fig. 4 The power supply system model for mine

该矿井供电系统电压等级为 10 kV，系统电源为 35 kV，等值阻抗为 0.122+1.22j Ω，主变为 35/10 kV。

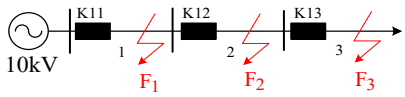


图 5 供电系统中压线路简化拓扑结构

Fig. 5 The medium voltage line of the power supply system simplifies the topology

中压线路三区段均采用电缆，零序参数如表 1 所示：

表 1 中压线路零序参数

Table 1 Zero-sequence parameters of medium-voltage lines

区段	长度/m	R(Ω/m)	X（H/m）	C(μF/m)
1	1280	1.81E-3	2.72E-7	5.13E-4
2	100	1.81E-3	2.72E-7	5.13E-4
3	50	1.81E-3	2.72E-7	5.13E-4

如图 K11、K12、K13 分别为区段 1、2、3 的测量单元，均位于相应区段首端。

在不同过渡电阻条件下，分别在 F_1、F_2、F_3 三个故障点位置进行单相接地故障实验，利用 RSCAD 得到测量单元零序电压和零序电流采样值数据，绘制典型接地故障下各测量单元的广义暂态零序功率，并计算各个测量单元处的前 1/4 周波内的 $\sum p_{0,i}$，验证算法是否能正确进行区段定位。

（1）中性点不接地系统广义暂态零序功率计算

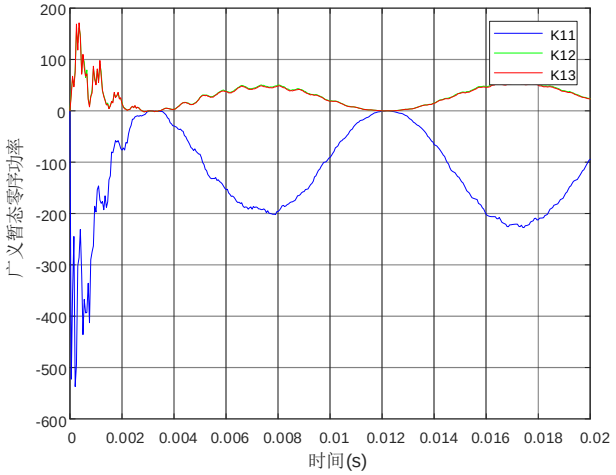


图 6 F_1 处经 100Ω过渡电阻单相接地故障广义暂态零序功率对比图

Fig. 6 Comparison diagram of generalized transient zero-sequence power through 100Ω transition resistance single-phase ground fault at F1

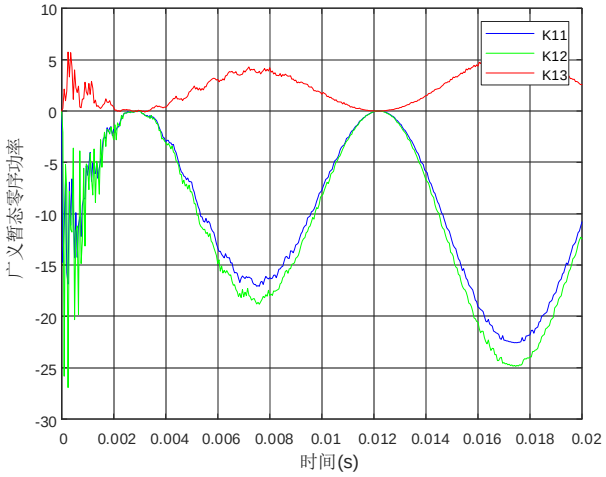


图 7 F2 处经 1000Ω过渡电阻单相接地故障广义暂态零序功率对比图

Fig. 7 Comparison diagram of generalized transient zero-sequence power through 1000Ω transition resistance single-phase ground fault at F2

由图 6 及图 7 可知，中性点不接地系统发生经过渡电阻单相接地故障后，故障点上游区段及故障区段上游广义暂态零序功率始终为负值，下游区段始终为正值，符合前述特性。

表 2 经 100Ω 过渡电阻接地故障广义暂态零序功率求和

Table.2 The sum of the generalized transient zero-sequence power of the ground fault through the 0Ω transition resistor

故障位置	区段 1	区段 2	区段 3
F_1	-11008	2578	2525

F_2	-10892	-11905	2522
F_3	-6753	-7426	-7475

表 3 经 1000Ω 过渡电阻接地故障广义暂态零序功率求和

Table.3 The sum of the generalized transient zero-sequence power of the ground fault through the 100Ω transition resistor

故障位置	区段 1	区段 2	区段 3
F_1	-672	157	154
F_2	-412	-451	93
F_3	-525	-573	-574

（2）中性点经消弧线圈接地系统广义暂态零序功率计算

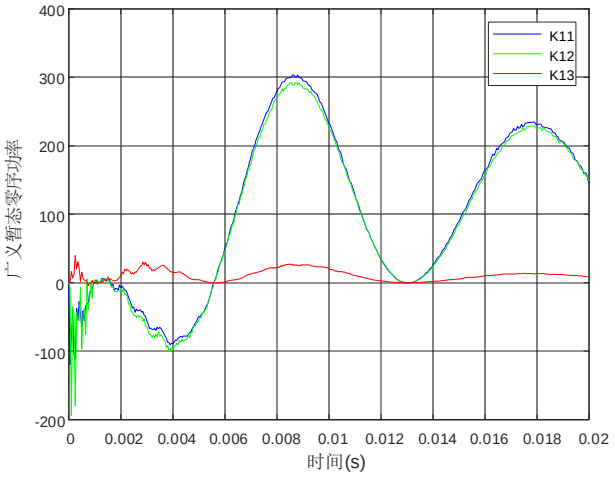


图 8 F2 处经 100Ω过渡电阻单相接地故障广义暂态零序功率对比图

Fig. 8 Comparison diagram of generalized transient zero-sequence power through 100Ω transition resistance single-phase ground fault at F2

由图 8 可知，消弧线圈接地系统发生单相接地故障后，广义暂态零序功率只在接地故障初期符合前述特性，约 5ms 后，故障点上、下游区段广义暂态零序功率均为正值，印证了前述分析：消弧线圈在基地故障初期（约 0~5ms）几乎不发挥补偿作用。

表 4 经 100Ω过渡电阻接地故障广义暂态零序功率求和

Table 4 The sum of the generalized transient zero-sequence power of the ground fault through the 100Ω transition resistor

故障位置	区段 1	区段 2	区段 3
F_1	-3146	522	505
F_2	-4468	-4987	1238
F_3	1202	153	-206

由上述三表数据可知，对于两种系统，在不同位置设置相应接地故障后，在前 1/4 周波，均有故障点上游区段及故障区段广义暂态零序功率求和为负值，故障点下游线路区段广义暂态零序功率求和为正值，与理论推导相符，利用其正负可确定故障区段，而后由相应保护单元切除故障。

5 结论

理论分析表明，中性点不接地系统与经消弧线圈接地系统在单相接地故障初期（约 1/4 周波）具有相似的暂态特征。

通过对定义的广义暂态零序功率在故障后 1/4 周波时段内进行代数求和，可依据其正、负值实现故障选线和故障区段定位。

基于 RTDS 的仿真验证表明，该方法能够正确辨认出小电流接地系统故障区段，检测灵敏，可靠性高，具有较大允许过渡电阻能力。

6 参考文献

[1] 张保会，尹项根．电力系统继电保护[M].北京：中国电力出版社 2005.

[2] 薛永端，徐丙垠，冯祖仁，等．小电流接地故障暂态方向保护原理研究[J]．中国电机工程学报，2003，(07)：51-56.

[3] Wenjun G，Heng W，Ying Z．Fault Line Selection of Small Current Grounding System Research Based on Zero Sequence Circuit Current Phase[J]．Journal of Physics：Conference Series，2024，2872(1)：012049-012049.

[4] 续达．配电网小电流接地系统单相接地故障选线方法研究[D]．电子科技大学，2025.

[5] 罗建，夏豪，钟加勇，等．基于消弧线圈补偿特性的单相接地故障选线方法[J]．电力系统保护与控制，2025，53(11)：158-169.

[6] 陈正.利用暂态无功功率的配电网单相接地故障选线研究[D].山东理工大学,2013.

[7] Han Z, Pinghao Y, Hongbo C, et al. Research on single-phase to ground fault simulation base on a new type neutral point flexible grounding mode[J]. IEEE Access, 2019, 8: 782563-82570.

[8] 冯光，管廷龙，王磊，等．利用电流－电压导数线性度关系的小电流接地系统接地故障选线[J]．电网技术，2021，45(1)：302-311.

[9] 王雪文，石访，张恒旭，等.基于暂态能量的小电流接地系统单相接地故障区段定位方法[J]．电网技术，2019，43(3)：818－825.

[10] Liu B, Ma H, Xu H, et al. Single-phase-to-ground fault detection with distributed parameters analysis in non-direct grounded systems[J]. CSEE Journal of Power and Energy Systems, 2019, 5(1): 139-147.

[11] 高伟,郑子杰,李育凤,等.基于暂态零序功率特性的配电网单相接地故障选段实验设计[J].实验技术与管理,2025,42(07):34-42.

[12] 石勇,魏巍,王栎涛,等.配网单终端的暂态功率方向接地选线方法[C 2024 年水电智能与智慧化关键技术研讨会暨中国水力发电工程学会智能与智慧化专业委员会年会论文集.南京南瑞继保电气有限公司;,2024:247-251.

[13] 董富德.10kV 配电线路单相接地故障智能选线方法研究[D].广东工业大学,2015.



王岩

收稿日期：2013-07-04。

作者简介：

王岩(2002)，男，硕士研究生，研究方向为电力系统继电保护，E-mail：202434757@mail.sdu.edu.cn;

高厚磊(1963)，男，教授，博士生导师，通信作者，研究方向为电力系统继电保护等，E-mail：houleig@sdu.edu.cn。

（编辑　五号楷体，居右，段前空 6pt）

069 Research on a PI-LADRC Hybrid Control Strategy for Grid-Forming Inverters in Strongly Series-Compensated Power Grids

Tao Zhang[1], Xin shan[23], Feng zhao[1],Kai Hou[23], Liang Guo[23], Sujuan Sun[23]
1.North China Branch of State Grid Corporation of China, Beijing 100053, China
2.NARI Technology Co., Ltd., Nanjing 211106, China
3.NARI Nanjing Control System Co., Ltd., Nanjing 211106, China

Abstract—The grid-forming inverter plays a pivotal role in integrating renewable energy into the power grid, where its stable operation is crucial for maintaining the safety and reliability of the entire system. Nevertheless, when interfaced with long-distance transmission lines incorporating series compensation, the conventional voltage current dual-loop control based on proportional-integral (PI) regulators can exhibit a lack of adequate phase in the output impedance at sub-synchronous frequencies, which in turn may induce oscillatory behavior at those frequencies. To address this issue, a hybrid control strategy combining PI regulation for the voltage loop together with Linear Active Disturbance Rejection Control (LADRC) applied to the current loop, functioning as an alternative to the conventional dual-PI structure is proposed. By employing harmonic linearization, sequence-domain impedance representations of the grid-forming inverter are developed for both the traditional dual-PI and the proposed PI-LADRC schemes. The Nyquist stability criterion is then applied to evaluate inverter stability under varying series-compensated grid conditions. Findings reveal that the proposed method substantially increases the stability phase margin of the output impedance across the sub-synchronous region, thus efficiently curbing oscillatory phenomena. Experimental validations confirm the feasibility and robustness of the strategy, especially in strongly series-compensated grids, where it significantly improves the grid-connection stability of grid-forming inverters and supports the reliable integration of high-penetration renewable resources.

Index Terms—Grid-forming inverter, grid connection stability, sub-synchronous oscillations.

1. Introduction

Owing to the increasing penetration of renewable energy, grid-connected converters based on power electronics have emerged as essential components for facilitating the integration of these energy sources into power systems. At present, the majority of these converters utilize grid-following (GFL) control schemes that rely on phase-locked loops (PLLs), functioning essentially as controlled current sources [1]. However, the asymmetric structure of PLLs causes their stability to degrade markedly as renewable penetration rises and grid strength declines [2]. In contrast, grid-forming (GFM) converters operate with voltage-source characteristics, enabling autonomous regulation of voltage and frequency without the need for PLLs. Owing to their superior performance in weak grid scenarios, GFMs have gained significant attention and become an active area of research over the past few years [3,4].

The control of grid-forming converters is generally composed of an outer loop for power regulation and an inner loop for voltage and current control. The outer power loop replaces the PLL used in grid-following converters and provides reference signals for the inner voltage-current inner loop[5]. Currently, grid-forming converters frequently employ a dual-loop voltage and current control framework regulated by dual PI controllers, favored for its simplicity and engineering maturity. Within power systems integrating renewable energy, a range of devices for reactive power compensation are extensively utilized to boost the efficiency of electricity transmission while lowering both voltage and power losses, among which the use of series capacitor compensation is particularly widespread. As power grids expand, the share of series-compensated transmission lines has shown a consistent upward trend. however, Nevertheless, in scenarios where a series-compensated grid is interfaced with a dual PI control-based grid-forming inverter, the inverter’s output impedance at low frequencies may couple with that of the network, which can readily induce sub-synchronous oscillations, thus compromising system stability and, in extreme situations, leading to equipment failures or generator trips [6,7]. Numerous cases of oscillations associated with series compensation have been documented in power systems worldwide[8,9,10]. To mitigate this problem, a commonly used approach involves introducing virtual impedance, through which the inverter’s output impedance is adjusted to increase the phase margin at the gain crossover frequency. [11,12]. Nonetheless, adding a virtual impedance component can induce coupling effects between the voltage control loop, the current control loop, and the virtual impedance itself, which increases the complexity of control system design and parameter tuning [13], and may additionally reduce the DC bus voltage [14].

To fundamentally resolve the instability problem of grid-forming inverters connected to series-compensated power networks, It is necessary to implement advanced control methods based on the instability mechanism rather than relying on conventional dual PI regulation. By modifying the output impedance characteristics, such methods can improve the phase margin and consequently enhance overall system stability. In recent years, numerous advanced techniques have been introduced for managing grid-connected converters. The sliding-mode control approach outlined in [15] is capable of enhancing the robustness against frequency disturbances, although its inherent chattering limits practical deployment. The low-sampling-rate distributed model predictive control strategy presented in [16] enables the restoration of frequency and voltage in microgrids operating under islanded conditions, but its strong reliance on model precision and high computational burden remain challenges. The

adaptive output voltage regulation method in [17] addresses the issue of DC bus undervoltage in grid-forming inverters; however, it is prone to delays under large parameter variations and depends heavily on system data. In contrast, LADRC does not rely on precise modeling, has a simple design, inherent decoupling capability, and strong disturbance rejection, and has shown notable control performance in grid-connected converter scenarios. For instance, [18] applies LADRC to manage the voltage regulation of grid-connected inverters to improve voltage stability under weak grid conditions. The method in [19] tackles potential resonance and uncertainty issues in LCL-based inverters by introducing a segmented-capacitance LADRC approach, which enhances grid current quality and system stability via reduced-order modeling and parameter refinement. Additionally, [20] proposes an LADRC-phase-locked loop (LADRC-PLL) strategy that significantly improves oscillation suppression in grid-connected inverters under weak grid conditions. Although LADRC has demonstrated excellent results in controlling grid-connected converters, systematic and in-depth investigation into its stability in grid-forming inverter applications, particularly in series-compensated grid conditions, remains insufficient.

The present study introduces a hybrid dual-loop control framework in which the voltage outer loop is regulated by a PI controller, while the current inner loop is governed by an LADRC controller. This configuration replaces the conventional dual PI control, aiming to mitigate sub-synchronous oscillations that frequently arise when grid-forming inverters operate within series-compensated power systems. To establish sequence impedance models for the grid-forming inverter under both the proposed and conventional control schemes, the harmonic linearization method is employed, taking into account the effects of phase angle disturbances and the influence of the outer power loop. The Nyquist stability criterion is subsequently applied to evaluate the stability performance across various series-compensated grid scenarios. By means of comparative analysis, it is verified that the proposed scheme considerably improves the phase characteristic of the inverter output impedance close to the fundamental frequency. This enhancement leads to a larger phase margin at the intersection between the inverter and grid impedance magnitude curves, thereby facilitating stable operation under series-compensated grid conditions. The experimental findings offer further confirmation of the accuracy and dependability of the theoretical forecasts.

2. Sequence Impedance Modeling and Grid-Connected Stability Analysis of Grid-Forming Inverters Based on Conventional Dual-PI Control

Fig. 1 illustrates the control architecture of the grid-forming inverter system implementing the proposed strategy. In the model, decentralized energy resources, including storage batteries and PV modules, are equivalently modeled as a DC source, symbolized by U_{dc}. The parameters L_f, R_L, and C_f denote, in turn, the filter inductance on the inverter side, its corresponding equivalent series resistance, and the associated filter capacitor. Here, L_w is assigned to the grid-side filter inductance, while Z_g corresponds to the equivalent impedance of the grid connection. The current variables $i_{Lx}(x=a,b,c)$ indicate the three-phase inductor currents, $i_{ox}(x=a,b,c)$ describe the inverter output currents, $u_x(x=a,b,c)$ specify the phase voltages on the inverter side, and $u_{ox}(x=a,b,c)$ represent the corresponding phase voltages delivered at the inverter output.

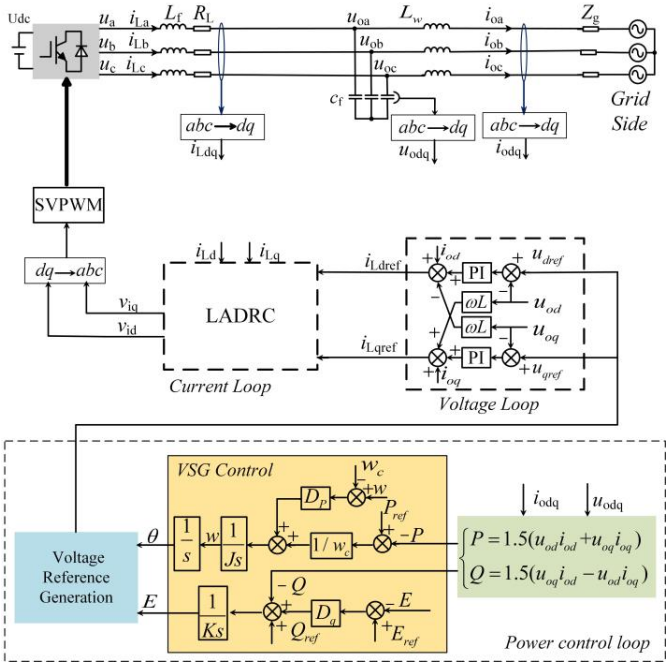


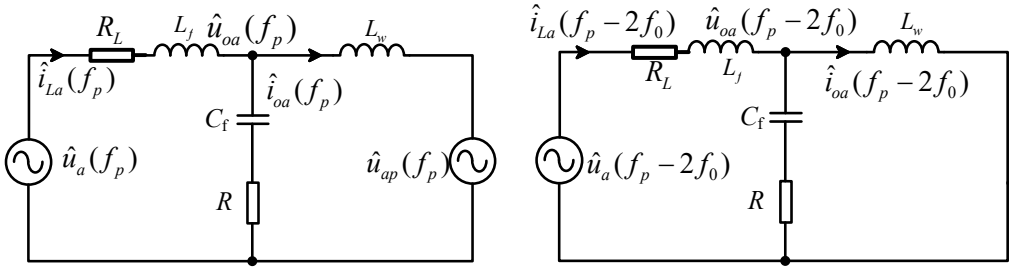
Fig. 1 Control structure for the grid-forming inverter system employing the proposed control strategy

2.1 Sequence Impedance Modeling

The formulation representing the standard dual-loop PI control can be expressed as：

$$\begin{aligned} i_{Ldref} &= (u_{odref} - u_{od})G_u(s) - w_c C_f u_{oq} \\ i_{Lqref} &= (u_{oqref} - u_{oq})G_u(s) + w_c C_f u_{od} \\ v_{id} &= (i_{Ldref} - i_{Ld})G_i(s) - w_c L_f i_{Lq} + u_{od} \\ v_{iq} &= (i_{Lqref} - i_{Lq})G_i(s) + w_c L_f i_{Ld} + u_{oq} \end{aligned} \tag{1}$$

When modeling the sequence impedance of grid-forming inverters, it is essential to take into account the twofold mirror-frequency coupling phenomenon [21]. A disturbance in the positive sequence occurring at frequency f_p results not only in a corresponding positive-sequence response at f_p but also in a negative-sequence component at f_p-2f_0. For phase A, Fig. 2 presents the small-signal equivalent representation of the primary circuit under the condition that a harmonic perturbation in the positive sequence at frequency fp is applied on the grid side.



(a) The small-signal equivalent circuit at the frequency f_p (b) The small-signal equivalent circuit at the frequency f_p-2f_0

Fig. 2 The small-signal equivalent circuit diagram corresponding to phase A

Fig. 2, illustrates that e $\hat{u}_a(f)$, $\hat{u}_{oa}(f)$, $\hat{i}_{La}(f)$ and $\hat{i}_{oa}(f)$ correspond to the positive and negative sequence responses associated with the small signal quantities u_a, u_{oa}, i_{La}, i_{oa}. The symbol $\hat{u}_{ap}(f_p)$ denotes a harmonic disturbance in the positive sequence voltage at frequency fp applied to the grid side. When such a disturbance is introduced, as depicted in Fig. 2, the mirror frequency coupling phenomenon gives rise to time domain formulations for the small signal components of the phase A output voltage, the current injected into the grid, and the inverter output current, expressed as follows:

$$\begin{cases} \hat{u}_{oa} = U_{p1}\cos(\omega_p t + \delta_{p1}) + U_{p2}\cos(\omega_{p2} t + \delta_{p2}) \\ \hat{i}_{oa} = I_{p1}\cos(\omega_p t + \alpha_{p1}) + I_{p2}\cos(\omega_{p2} t + \alpha_{p2}) \\ \hat{i}_{La} = I_{Lp1}\cos(\omega_p t + \alpha_{Lp1}) + I_{Lp2}\cos(\omega_{p2} t + \alpha_{Lp2}) \end{cases} \tag{2}$$

Where $\omega_{p2} = \omega_p - 2\omega_c$, ω_p representing the disturbance angular frequency and ω_{p2} referring to the angular frequency linked to negative-sequence coupling. U_{p1}, U_{p2}; I_{p1}, I_{p2} and I_{Lp1}, I_{Lp2} present the amplitudes of u_{oa}、i_{oa} and i_{La}; δ_{p1}, δ_{p2}; α_{p1}, α_{p2} and α_{Lp}, α_{Lp2} are the corresponding initial phase angles.

Through the Park transformation, the inverter output voltage, inverter output current, and current fed into the grid are expressed in the dq reference frame, yielding constant-state values u_{od}, u_{oq} together with perturbation terms $\hat{u}_{od}$, $\hat{u}_{oq}$ for the output voltage, constant operating values i_{Ld}, i_{Lq} in conjunction with fluctuation terms $\hat{i}_{Ld}$, $\hat{i}_{Lq}$ for the output current, as well as fixed-state quantities i_{od}, i_{oq} along with their perturbative counterparts $\hat{i}_{od}$, $\hat{i}_{oq}$ for the grid-connected current.

$$\begin{bmatrix} \hat{u}_{od} = \hat{u}_{d0} + u_q\hat{\theta}_p \\ \hat{u}_{oq} = \hat{u}_{q0} - u_d\hat{\theta}_p \end{bmatrix}$$

$$\begin{aligned} \hat{u}_{d0} &= U_{P1}\frac{e^{j[(w_p - w)t + \delta_{p1} - \beta]} + e^{-j[(w_p - w)t + \delta_{p1} - \beta]}}{2} + U_{P2}\frac{e^{j[(w_p - w)t + \delta_{p2} + \beta]} + e^{-j[(w_p - w)t + \delta_{p2} + \beta]}}{2} \\ \hat{u}_{q0} &= U_{P1}\frac{e^{j[(w_p - w)t + \delta_{p1} - \beta]} - e^{-j[(w_p - w)t + \delta_{p1} - \beta]}}{2j} - U_{P2}\frac{e^{j[(w_p - w)t + \delta_{p2} + \beta]} - e^{-j[(w_p - w)t + \delta_{p2} + \beta]}}{2j} \end{aligned} \tag{3}$$

$$\begin{bmatrix} \hat{i}_{od} = \hat{i}_{d0} + i_q\hat{\theta}_p \\ \hat{i}_{oq} = \hat{i}_{q0} - i_d\hat{\theta}_p \end{bmatrix}$$

$$\begin{aligned} \hat{i}_{d0} &= I_{P1}\frac{e^{j[(w_p-w)t+\alpha_{p1}-\beta]}+e^{-j[(w_p-w)t+\alpha_{p1}-\beta]}}{2} + I_{P2}\frac{e^{j[(w_p-w)t+\alpha_{p2}+\beta]}+e^{-j[(w_p-w)t+\alpha_{p2}+\beta]}}{2} \\ \hat{i}_{q0} &= I_{P1}\frac{e^{j[(w_p-w)t+\alpha_{p1}-\beta]}-e^{-j[(w_p-w)t+\alpha_{p1}-\beta]}}{2j} - I_{P2}\frac{e^{j[(w_p-w)t+\alpha_{p2}+\beta]}-e^{-j[(w_p-w)t+\alpha_{p2}+\beta]}}{2j} \end{aligned} \tag{4}$$

$$\begin{bmatrix} \hat{i}_{Ld} = \hat{i}_{Ld0} + i_{Lq}\hat{\theta}_p \\ \hat{i}_{Lq} = \hat{i}_{Lq0} - i_{Ld}\hat{\theta}_p \end{bmatrix}$$

$$\begin{aligned} \hat{i}_{Ld0} &= I_{LP1}\frac{e^{j[(w_p-w)t+\alpha_{Lp1}-\beta]}+e^{-j[(w_p-w)t+\alpha_{Lp1}-\beta]}}{2} + I_{LP2}\frac{e^{j[(w_p-w)t+\alpha_{Lp2}+\beta]}+e^{-j[(w_p-w)t+\alpha L_{p2}+\beta]}}{2} \\ \hat{i}_{Lq0} &= I_{LP1}\frac{e^{j[(w_p-w)t+\alpha_{Lp1}-\beta]}-e^{-j[(w_p-w)t+\alpha_{Lp1}-\beta]}}{2j} - I_{LP2}\frac{e^{j[(w_p-w)t+\alpha_{Lp2}+\beta]}-e^{-j[(w_p-w)t+\alpha_{Lp2}+\beta]}}{2j} \end{aligned} \tag{5}$$

Here, β denotes the initial phase angle, while $\hat{\theta}_p$ represents the minor-signal deviation in the phase angle.

Formulations describing the minor-signal characteristics of both active and reactive power associated with the grid-forming inverter are provided in (6).

$$\begin{cases} \hat{P} = \frac{3}{2}G_F(s)\cdot(\hat{u}_{od}i_{od} + u_{od}i_{od} + \hat{u}_{oq}i_{oq} + u_{oq}\hat{i}_{oq}) \\ \hat{Q} = \frac{3}{2}G_F(s)\cdot(\hat{u}_{oq}i_{od} + u_{oq}\hat{i}_{od} - \hat{u}_{od}i_{oq} - u_{od}\hat{i}_{oq}) \end{cases} \tag{6}$$

The low-pass filter’s transfer function can be expressed as $G_F(s) = \omega_f/(s+\omega_f)$, where ω_f denotes the filter's cutoff frequency.

The core of active power–frequency control in a VSG grid-connected inverter lies in employing droop control to emulate the frequency response characteristics of a synchronous generator, while incorporating the rotor motion equation to replicate the inertia and damping properties of the synchronous generator rotor. Reactive power-voltage control is achieved through reactive power droop control. The specific formulation is given in Equation (7).

$$\begin{cases} \hat{f} = -\frac{1}{2\pi(J\omega s + D_p\omega)}\hat{P} \\ \hat{u}_{dref} = -\frac{1}{7.1s + D_q}\hat{Q} \\ \hat{u}_{qref} = 0 \\ \hat{\theta}_p = 2\pi\hat{f}\frac{1}{s} \end{cases} \tag{7}$$

As presented in Equation (7), J denotes the moment of inertia, D_P the damping coefficient, D_q the reactive power-voltage droop coefficient, w the angular frequency generated by the VSG. $\hat{u}_{dref}$ and $\hat{u}_{qref}$ represent the reference values associated with the small-signal components of the output voltage in the dq coordinate system. Voltage and current perturbations cause phase shifts within the system, leading the active power control loop to exhibit an output phase angle represented as $\theta = \theta_0 + \hat{\theta}_p$, where $\hat{\theta}_p$ and θ_0 denote the steady-state and small-signal perturbation components of the fundamental waveform phase angle, respectively.

The small-signal output after dual PI loop control is given by:

$$\begin{aligned} \hat{i}_{Ldref} &= G_u(s)(\hat{u}_{dref} - \hat{u}_{od}) - w_c C_f \hat{u}_{oq} \\ \hat{i}_{Lqref} &= G_u(s)(\hat{u}_{qref} - \hat{u}_{oq}) + w_c C_f \hat{u}_{od} \\ \hat{v}_{id} &= G_i(s)(\hat{i}_{Ldref} - \hat{i}_{Ld}) - w_c L_f \hat{i}_{Lq} \\ \hat{v}_{iq} &= G_i(s)(\hat{i}_{Lqref} - \hat{i}_{Lq}) + w_c L_f \hat{i}_{Ld} \end{aligned} \tag{8}$$

$G_i(s)$ and $G_u(s)$ represent the transfer functions of the PI regulators utilized in the current and voltage control loops, respectively. The quantities $\hat{v}_{id}$ and $\hat{v}_{iq}$ denote the small-signal components of the output voltage regulated by the dual-loop PI control scheme in the *dq* synchronous reference frame.

The small-signal output of phase-A in the control loop is given by:

$$\hat{u}_a = (\hat{v}_{id} - v_{iq}\hat{\theta}_p)\cos\theta + (-\hat{v}_{iq} - v_{id}\hat{\theta}_p)\sin\theta \tag{9}$$

$\hat{u}_a$ comprises small-signal components at two distinct frequencies. By combining Equations (3)-(9), the expressions for $\hat{u}_a(f_p)$ 和 and $\hat{u}_a(f_p)$ are obtained as follows:：

$$\begin{aligned}
\hat{u}_a(f_p) &= \left(\frac{-jX_1(s)+X_3(s)-X_5(s)-jX_7(s)}{2}\right)\frac{U_{p1}}{\sqrt{2}}e^{j\delta_{p1}} + \left(\frac{X_2(s)-jX_4(s)-jX_6(s)-X_8(s)}{2}\right)\frac{I_{p1}}{\sqrt{2}}e^{j\alpha_{p1}} \\
&+(-G_i(s)+jw_cL_f)\frac{I_{Lp1}}{\sqrt{2}}e^{j\alpha_{Lp1}} + [j(w_p-2w_c)L_w\left(\frac{jX_1(s)+X_3(s)+X_5(s)-jX_7(s)}{2}\right) \\
&+\frac{X_2(s)+jX_4(s)-jX_6(s)+X_8(s)}{2}]\frac{I_{p2}}{\sqrt{2}}e^{j(\alpha_{p2}+2\beta)} \\
\hat{u}_a(f_p-2f_0) &= \left(\frac{-jX_1(s)+X_3(s)+X_5(s)+jX_7(s)}{2}\right)\frac{U_{p1}}{\sqrt{2}}e^{j(\delta_{p1}-2\beta)} + \left(\frac{X_2(s)-jX_4(s)+jX_6(s)+X_8(s)}{2}\right)\frac{I_{p1}}{\sqrt{2}}e^{j(\alpha_{p1}-2\beta)} \\
&+[j(w_p-2w_c)L_w\frac{jX_1(s)+X_3(s)-X_5(s)+jX_7(s)}{2} + \frac{X_2(s)+jX_4(s)+jX_6(s)-X_8(s)}{2}]\frac{I_{p2}}{\sqrt{2}}e^{j\alpha_{p2}} \\
&+(-G_i(s)-jw_cL_f)\frac{I_{Lp2}}{\sqrt{2}}e^{j\alpha_{Lp2}}
\end{aligned} \tag{10}$$

The expressions for X1(s)-X8(s) are provided in the Appendix1.

The mirror-coupled current, obtained from Fig. 2(b) in conjunction with Equation (10), is expressed as in Equation (11).

$$\frac{I_{P2}}{\sqrt{2}}e^{j\alpha_{p2}} = \frac{M_{p1}(s)U_{p1}e^{j(\delta_{p1}-2\beta)} + N_{p1}(s)I_{P1}e^{j(\alpha_{p1}-2\beta)}}{L_{P1}(s)} \tag{11}$$

The expressions for $M_{p1}(s)$， $N_{p1}(s)$ and $L_{p1}(s)$ are provided in the Appendix1.

Substituting the mirror-frequency current from Equation (11) into Equation (10), and incorporating the results presented in Fig. 3(a), lead to the determination of the inverter’s positive-sequence impedance, which is formulated in Equation (12).

$$Z_{imvp} = \frac{(N_p(s)+L_p(s)\frac{N_{p1}(s)}{L_{p1}(s)}) + \left[(-G_i(s)+jw_cL_f)-(jw_pL_f+R_L)\right]}{(M_p(s)+L_p(s)\cdot\frac{M_{p1}(s)}{L_{p1}(s)}-1) + \frac{\left[(-G_i(s)+jw_cL_f)-(jw_pL_f+R_L)\right]}{\frac{1}{jw_pC_f}+R}} + jw_pL_w \tag{12}$$

The expressions for $M_p(s)$， $N_p(s)$ and $L_p(s)$ are given in Appendix1.

According to the transformation correlation linking the inverter’s positive- and negative-sequence impedances allows the derivation with respect to the negative-sequence output impedance, formulated as: $Z_{invn} = Z^*_{invp}(-s)$.

2.2 Grid-connected stability analysis

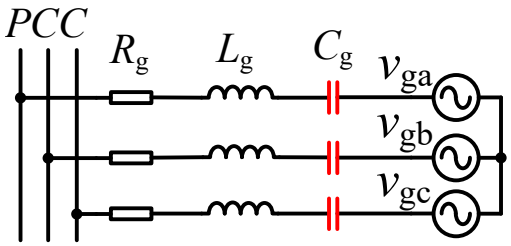


Fig.3 Equivalent circuit diagram of series-compensated grids

As shown in Fig. 3, the power grid under series compensation is represented by its equivalent circuit and the related impedance model.

$$Z_g(s) = R_g + sL_g + 1/(sC_g) \tag{13}$$

For a series-compensated grid, the compensation capability is commonly evaluated through the series compensation level (SCL), which in practical scenarios usually falls within the range of 50% to 60%. The SCL is formulated as：

$$SCL = \frac{1}{\omega_c^2 L_g C_g} \tag{14}$$

In a power grid, the short-circuit ratio (SCR) changes according to operating states and transmission characteristics, thereby necessitating adjustments in the series compensation level. Consequently, evaluating the stability of grid interconnection under

various SCR scenarios, considering the presence of series compensation capacitors, becomes crucial. The SCR can be calculated using the following expression:

$$SCR = \frac{S_{AC}}{P_N} = \frac{U_N^2}{P_N Z} \tag{15}$$

Where S_{AC} denotes the short-circuit capacity of the grid, P_N represents the rated power, U_N corresponds to the RMS value of the rated phase voltage, and Z signifies the equivalent impedance of the grid.

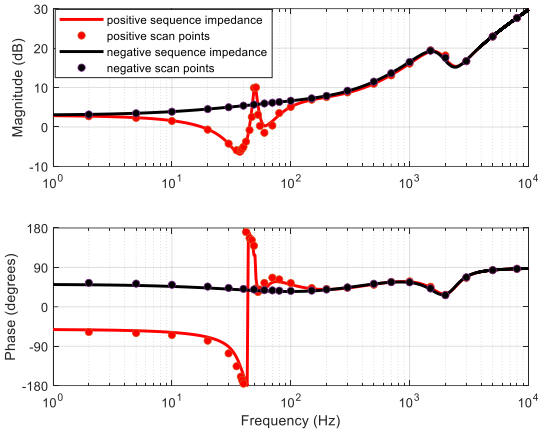


Fig.4 Models of positive- and negative-sequence impedances along with their associated scanning curves

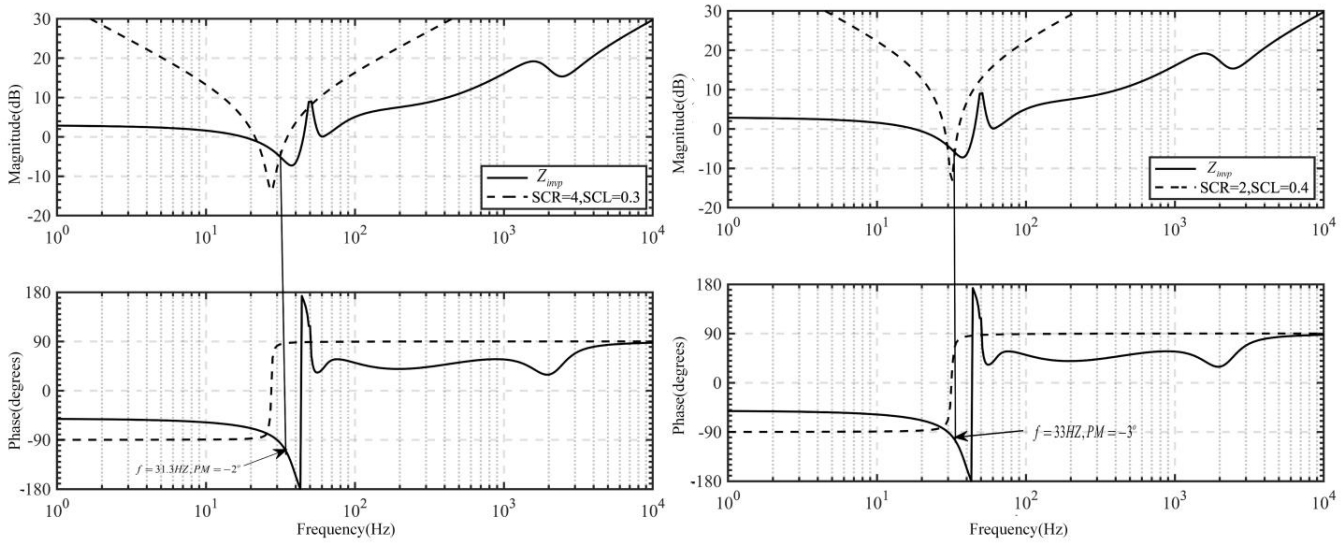
The theoretical values of the positive- and negative-sequence output impedances are depicted by the solid lines in Fig. 4. To validate the accuracy of the impedance modeling, the sweep frequency method is employed to measure the output impedance. As shown in Fig. 4, the theoretical results closely match the sweep frequency measurement points, thereby confirming the validity of the impedance model.

In weak power grids characterized by a low short-circuit ratio (SCR), series compensation devices are commonly utilized. Accordingly, this research centers on weak grids whose SCR values are less than 5. As shown in Fig. 4, an inverter configured with a dual-PI loop control scheme presents a capacitive response in the output impedance corresponding to the positive sequence, while the impedance characteristic associated with the negative sequence exhibits inductive behavior in the frequency region lower than the fundamental, belonging to the sub-synchronous band. The capacitive nature of the inverter's positive-sequence impedance may couple with the grid's inductive characteristics.

Based on system robustness criteria, the phase-angle safety margin at which the output impedance characteristic of the inverter intersects with the grid impedance must remain greater than 0°. The mathematical expression used to evaluate this phase-angle margin can be written as:

$$PM(f) = 180 - |Z_g(f) - Z_{inv}(f)| \tag{16}$$

If the safety margin in phase angle at the crossing point where the output-side impedance of the inverter intersects with the grid impedance is inadequate, the system is likely to experience oscillatory instability. As illustrated in Fig. 5, considering grid scenarios characterized by distinct series compensation levels-specifically, SCR = 4, SCL = 0.3 and SCR = 2, SCL = 0.4-the grid impedance interacts with the inverter impedance controlled by a dual-loop PI scheme in the sub-synchronous frequency range. The magnitude characteristic curves intersect at 31.3 Hz and 33 Hz, respectively, and according to Eq. (16), the phase margins at these intersections are −2° and −3°, both of which are negative, indicating that the robust stability criterion is not satisfied.



(a)Positive-sequence output impedance of the inverter and grid impedance under the condition of SCR = 4 and SCL = 0.3.(b)Positive-sequence output impedance of the inverter and grid impedance under the condition of SCR = 2 and SCL = 0.4.

Fig 5. Sequence impedance analysis of an inverter with conventional dual-PI control.

3. Sequence impedance modeling and grid-connected stability analysis of grid-forming inverters based on PI-LADRC control

3.1 Design of PI-LADRC

The mathematical model of a VSG-based inverter is given as:

$$\begin{aligned}\begin{bmatrix}\frac{di_{La}}{dt}\\ \frac{di_{Lb}}{dt}\\ \frac{di_{Lc}}{dt}\end{bmatrix}&=\frac{1}{L_f}\begin{bmatrix}u_a\\u_b\\u_c\end{bmatrix}-\frac{1}{L_f}\begin{bmatrix}u_{oa}\\u_{ob}\\u_{oc}\end{bmatrix}-\frac{R_L}{L_f}\begin{bmatrix}i_{La}\\i_{Lb}\\i_{Lc}\end{bmatrix}\\ C_f\begin{bmatrix}\frac{du_{oa}}{dt}\\ \frac{du_{ob}}{dt}\\ \frac{du_{oc}}{dt}\end{bmatrix}&=\begin{bmatrix}i_{La}\\i_{Lb}\\i_{Lc}\end{bmatrix}-\begin{bmatrix}i_{oa}\\i_{ob}\\i_{oc}\end{bmatrix}\end{aligned} \tag{17}$$

Left-multiplying Equation (17) by the Park transformation matrix yields.

$$\begin{aligned}\begin{bmatrix}\frac{di_{Ld}}{dt}\\ \frac{di_{Lq}}{dt}\end{bmatrix}&=\frac{1}{L_f}\begin{bmatrix}u_d\\u_q\end{bmatrix}-\frac{1}{L_f}\begin{bmatrix}u_{od}\\u_{oq}\end{bmatrix}-\frac{R_L}{L_f}\begin{bmatrix}i_{Ld}\\i_{Lq}\end{bmatrix}+\begin{bmatrix}wi_{Ld}\\wi_{Lq}\end{bmatrix}\\ \frac{1}{C_f}\begin{bmatrix}i_{Ld}\\i_{Lq}\end{bmatrix}&=\begin{bmatrix}\frac{du_{od}}{dt}\\ \frac{du_{oq}}{dt}\end{bmatrix}+\frac{1}{C_f}\begin{bmatrix}i_{od}\\i_{oq}\end{bmatrix}-\begin{bmatrix}wu_{oq}\\-wu_{od}\end{bmatrix}\end{aligned} \tag{18}$$

Rearranging (18) yields

$$\begin{cases}\frac{di_{Ld}}{dt}=\frac{1}{L_f}u_d-\frac{1}{L_f}u_{od}-\frac{R_LC_f}{L_f}\frac{du_{od}}{dt}-\frac{R_L}{L_f}i_{od}+\frac{R_LC_f}{L_f}wu_{oq}+wi_{Ld}\\ \frac{di_{Lq}}{dt}=\frac{1}{L_f}u_q-\frac{1}{L_f}u_{od}-\frac{R_LC_f}{L_f}\frac{du_{od}}{dt}-\frac{R_L}{L_f}i_{od}-\frac{R_LC_f}{L_f}wu_{od}+wi_{Lq}\end{cases} \tag{19}$$

The d-axis component in (19) represents a first-order mathematical model in the time domain; therefore, a first-order LADRC controller is required. The control equation for a first-order plant is given as:

$$\dot{y} = b_0 u + f \tag{20}$$

In this formulation, u represents the control signal, b_0 represents the gain of the controller corresponding to the input of the system, y corresponds to the plant output, and f indicates the overall disturbance acting on the system. By defining the state variables as $x_1 = y, x_2 = f$, the corresponding extended state-space representation can be expressed as follows:

$$\begin{cases} \begin{bmatrix} \dot{x}_1 \\ \dot{x}_2 \end{bmatrix} = \begin{bmatrix} 0 & 1 \\ 0 & 0 \end{bmatrix} \begin{bmatrix} x_1 \\ x_2 \end{bmatrix} + \begin{bmatrix} b_0 & 0 \\ 0 & 1 \end{bmatrix} \begin{bmatrix} u \\ h \end{bmatrix} \\ y = x_1 \end{cases} \tag{21}$$

Where $h = df / dt$ 。

The formulation of the first-order LESO is given by:

$$\begin{cases} \begin{bmatrix} \dot{z}_1 \\ \dot{z}_2 \end{bmatrix} = \begin{bmatrix} -\beta_1 & 1 \\ -\beta_2 & 0 \end{bmatrix} \begin{bmatrix} z_1 \\ z_2 \end{bmatrix} + \begin{bmatrix} b_0 & \beta_1 \\ 0 & \beta_2 \end{bmatrix} \begin{bmatrix} u \\ y \end{bmatrix} \end{cases} \tag{22}$$

Where β_1, β_2 denote the gains of the LESO， z_1, z_2 represent the estimated state variables. By appropriately selecting β_1, β_2 is capable of achieving real-time tracking of z_1, z_2 to x_1, x_2 with minimal steady-state error.

When the estimation error is neglected, system (9) can be reformulated into an equivalent structure consisting of two integrators in series, as presented below.

$$\dot{y} = x_2 + b_0 u = x_2 + b_0 \frac{u_0 - z_2}{b_0} \approx u_0 \tag{23}$$

From Equation (10), the characteristic equation corresponding to the LESO is obtained through further derivation, as presented below.

$$\lambda(s) = s^2 + \beta_1 s + \beta_2 \tag{24}$$

Where $\beta_1 = 2w_0, \beta_2 = w_0^2$， w_0 denotes the bandwidth of the LESO.

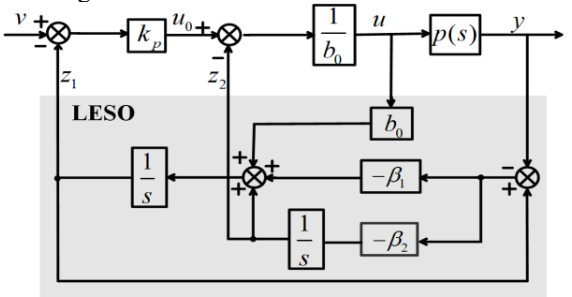
The PD controller is designed as：

$$u_0 = k_p (v - z_1) \tag{25}$$

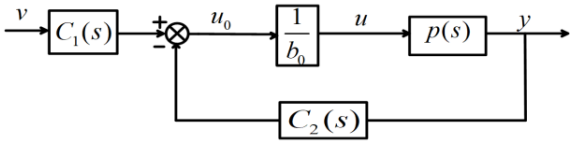
Where v denote the reference signal, $k_p = w_n$ represents the proportional gain of the controller, and w_n indicates the controller bandwidth. Based on Equations (23) and (15), the system's closed-loop transfer function can be expressed as follows:

$$G_{c1}(s) = \frac{k_p}{s + k_p} \tag{26}$$

As shown in Fig. 6 and derived from Equations (23)-(25), the block diagram representing the first-order LADRC is presented, in which *P*(s) signifies the plant being controlled.



(a)Control block diagram



(b)Equivalent form

Fig. 6 First-order LADRC

From Eqs(22)-(25), the first-order LADRC can be reformulated into its equivalent representation as follows:

$$u = C_1(s)v - C_2(s)y \tag{27}$$

Where $C_1(s) = \frac{1}{b_0}\frac{(s+w_0)^2 w_n}{(s^2+2w_0 s+w_n s)}$, $C_2(s) = \frac{1}{b_0}\frac{(w_0{}^2 s+2w_n w_0 s+w_n w_0{}^2)}{(s^2+2w_0 s+w_n s)}$.

3.2 Sequence impedance modeling

For the PI-LADRC control, the small-signal components of u_d and u_q are expressed as follows:

$$\begin{aligned}
\hat{i}_{Ldref} &= G(s)(\hat{u}_{dref} - \hat{u}_{od}) - w_c C_f \hat{u}_{oq} \\
\hat{i}_{Lqref} &= G(s)(\hat{u}_{qref} - \hat{u}_{oq}) + w_c C_f \hat{u}_{od} \\
\hat{v}_{id} &= C_1(s)\hat{i}_{Ldref} - C_2(s)\hat{i}_{Ld} \\
\hat{v}_{iq} &= C_1(s)\hat{i}_{Lqref} - C_2(s)\hat{i}_{Lq}
\end{aligned} \tag{28}$$

When PI-LADRC is applied, the formulation of the positive-sequence output impedance is described below:

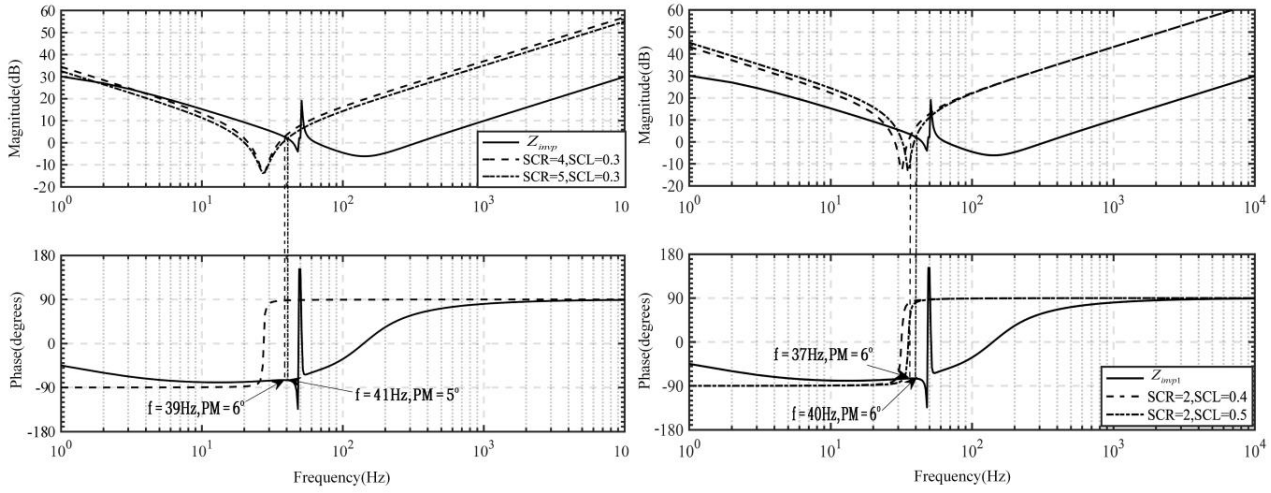
$$Z_{invp1} = \frac{(N_{p2}(s) + L_{p2}(s)\frac{N_{p3}(s)}{L_{p3}(s)}) - (C_2(s) + jw_p L_f + R_L)}{(M_{p2}(s) + L_{p2}(s)\cdot\frac{M_{p3}(s)}{L_{p3}(s)} - 1) + \frac{\left[-C_2(s) - (jw_p L_f + R_L)\right]}{\frac{1}{jw_p C_f} + R}} + jw_p L_w \tag{29}$$

The detailed expressions for $M_{p2}(s)$, $N_{p2}(s)$, $L_{p2}(s)$, $M_{p3}(s)$, $N_{p3}(s)$, $L_{p3}(s)$ and their associated variables are provided in Appendix 2.

The negative-sequence impedance is obtained : $Z_{invn1} = Z^*_{invp1}(-s)$.

3.3 Grid-connected stability analysis

Under various series-compensated grid conditions, the analytical curves of the positive-sequence impedance of the PI-LADRC-controlled inverter and the grid impedance are presented in Fig. 7.



(a)Positive-sequence output impedance of the inverter and grid impedance of SCL = 0.3,SCR=4,5.(b)Positive-sequence output impedance of the inverter and grid impedance of SCR = 2 and SCL = 0.4,05.

Fig 7. Sequence impedance analysis of an inverter with conventional PI-LADRC control.

By comparing Figures 7 and 5, it can be observed that PI-LADRC, in contrast to traditional dual-loop PI regulation, significantly improves the phase characteristics of the inverter's positive-sequence impedance in the vicinity of the fundamental frequency. From Fig. 7(a), when SCL = 0.3 and SCR = 4, and 5, the magnitude characteristic curves intersect at 39 Hz and 41 Hz, and according to Equation (16), the phase margins at the intersection points are 6° and 5°, both greater than zero, indicating system stability. From Fig. 7(b), when SCR = 2, SCL = 0.4, and 0.5, the magnitude characteristic curves intersect at 37 Hz and 40 Hz, with phase margins of 6° at both intersections, again exceeding zero, thereby ensuring system stability. In summary, PI-LADRC control can effectively improve the grid-connected stability of inverters in strongly series-compensated networks.

4. Experimental Validation

To validate the advantages of the PI-LADRC-controlled grid-forming inverter under heavily series-compensated grid conditions, comparative experiments were conducted between the conventional dual-PI control strategy and the proposed PI-LADRC approach. The key experimental parameters are listed in Table 1. The comparison tests were performed on an OPAL-RT hardware-in-the-loop (HIL) simulation platform.

PARAMETERS OF THE EXPERIMENTAL SETUP

Parameter	Value
Input voltage U_{dc}	700V
Rated power P_N	10KW
Grid Frequency f_0	50HZ
Filter inductance L_f	3mH
Buffer resistance R_L	0.1Ω
Filter capacitor C_f	20μF
Capacitive impedance L_w	0.5mH
inertia coefficient K	7.1
Moment of inertia J	0.057
Damping coefficient D_p	17.80
Reactive-voltage regulation coefficient D_q	321
Scale factor K_{pu}	0.5
Scale factor K_{iu}	150
Scale factor K_{pi}	15
Scale factor K_{ii}	300
Scale factor K_p	55
Scale factor K_i	0.03
Controller bandwidth w_0	6500
Obeserver bandwidth w_n	1500

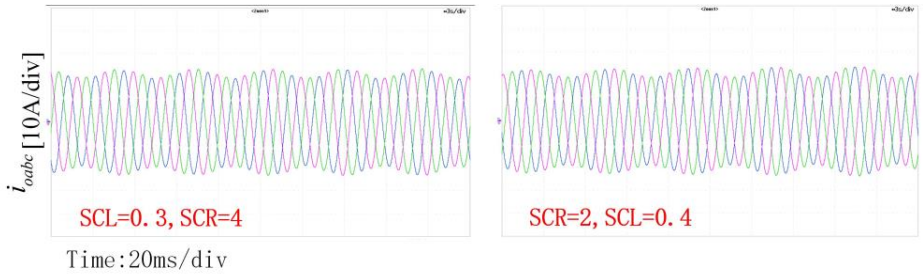
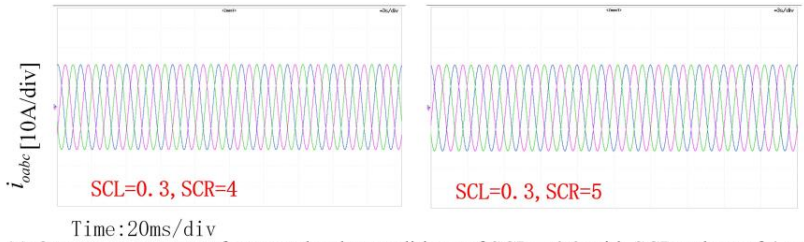
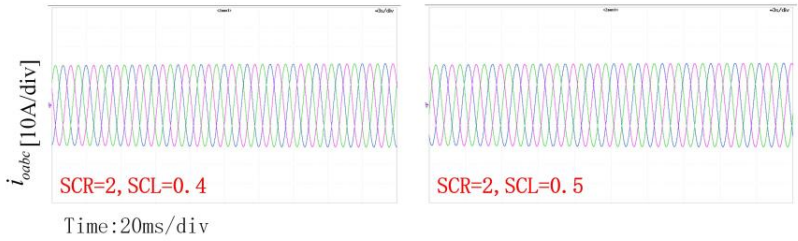


Fig.8 Experimental waveforms of the inverter with conventional dual-PI control under conditions of SCL = 0.3, SCR = 4 and SCL = 0.4, SCR = 2.



(a) Output current waveforms under the conditions of SCL = 0.3 with SCR values of 4 and 5



(b) Output current waveforms under the conditions of SCR = 2 with SCL values of 0.4 and 0.5

Fig.9 Experimental waveforms of the inverter with PI-LADRC control

Fig. 8 presents the experimental waveforms of the grid current for an inverter with conventional dual-PI control of SCL = 0.3, SCR = 4 and SCL = 0.4, SCR = 2. As shown, significant oscillations occur in the grid current under these strong series-compensation conditions. The experimental results are highly consistent with the theoretical analysis in Section 2.2, confirming the accuracy of the analytical findings, and further demonstrating that the conventional dual-PI control exhibits poor grid-connection stability in heavily series-compensated networks.

Fig. 9 illustrates the grid current waveforms of the inverter with PI-LADRC control under SCL = 0.3, SCR = 4 and SCL = 0.4, SCR = 2, as well as under enhanced compensation levels of SCL = 0.3, SCR = 5 and SCL = 0.4, SCR = 2. The results show that in the first two cases, the grid current remains stable, in agreement with the analysis in Section 3.3. Even when the series-compensation level is further increased to the latter two conditions, the grid current stability is maintained, thereby validating the superior stability of the proposed control strategy under strong series-compensation scenarios.

5. Conclusion

When a grid-forming inverter operates in a series-compensated power network, the standard dual-PI control strategy often fails to maintain sufficient phase margin at the point where the inverter’s output impedance curve intersects with the grid impedance in the magnitude-frequency profile. This deficiency, when occurring in the sub-synchronous band, often results in oscillatory instability. To overcome this problem, this study proposes an upgraded PI-LADRC dual-loop configuration as a replacement for the conventional dual-PI design. The PI-LADRC approach merges the simple adjustability and practical implementation benefits of PI regulation with LADRC’s strong ability to reject disturbances and achieve dynamic decoupling. Experimental results together with theoretical analysis verify that the proposed method substantially improves the inverter’s output impedance phase margin in the sub-synchronous domain, which serves to suppress sub-synchronous oscillations and markedly reinforce the stability and reliability of grid-forming inverters under varying series-compensation conditions.

Acknowledgement： This work is supported byscience and technology projects of State Grid Corporation of China （Project number：529923230001）

Appendix 1:

$$G_u(s)=(k_{pu}+\frac{k_{iu}}{j(w_p-w_c)})\ G_i(s)=(k_{pi}+\frac{k_{ii}}{j(w_p-w_c)})\ k_p(s)=\frac{1}{2\pi(Jw(w_p-w_c)+D_pw_c)}\ k_q(s)=\frac{1}{7.1(w_p-w_c)+D_q}$$

$$G_q(s)=-\frac{3}{2}k_q(s)\frac{w_f}{j(w_p-w_c)+w_f}\ G_P(s)=-2\pi\frac{1}{s}k_p(s)\frac{3}{2}\frac{w_f}{j(w_p-w_c)+w_f}$$

$$E(s)=G_i(s)(-G_u(s)u_{oq}+w_cC_fu_{od}-i_{Lq})+w_cL_fi_{Ld}-v_{iq}\ F(s)=G_i(s)(G_u(s)u_{od}+w_cC_fu_{oq}+i_{Ld})+w_cL_fi_{Lq}-v_{id}$$

$$\begin{cases} X_1(s) = G_i(s)(G_u(s)G_q(s)i_{od} - w_c C_f) + E(s)G_p(s)i_{oq} \\ X_2(s) = G_i(s)G_u(s)G_q(s)u_{oq} + E(s)G_p(s)u_{od} \\ X_3(s) = G_i(s)G_u(s)(-G_q(s)i_{oq} - 1) + E(s)G_p(s)i_{od} \\ X_4(s) = -G_i(s)G_u(s)G_q(s)u_{od} + E(s)G_p(s)u_{oq} \\ X_5(s) = -[-G_i(s)G_u(s) + F(s)G_p(s)i_{oq}) \\ X_6(s) = -F(s)G_p(s)u_{od} \\ X_7(s) = -(G_i(s)w_c C_f + F(s)G_p(s)i_{od}) \\ X_8(s) = -F(s)G_p(s)u_{oq} \end{cases}$$

$$\begin{cases} M_{p1}(s) = \dfrac{-jX_1(s) + X_3(s) + X_5(s) + jX_7(s)}{2} \\ N_{p1}(s) = \dfrac{X_2(s) - jX_4(s) + jX_6(s) + X_8(s)}{2} \\ L_{p1}(s) = j(w_p - 2w_c)L_w + \left\{[j(w_p - 2w_c)L_f + R_L] - (-G_i(s) - jw_c L_f)\right\}[\dfrac{j(w_p - 2w_c)L_w}{\dfrac{1}{j(w_p - 2w_c)C_f} + R} + 1] \\ \qquad -[j(w_p - 2w_c)L_w \dfrac{jX_1(s) + X_3(s) - X_5(s) + jX_7(s)}{2} + \dfrac{X_2(s) + jX_4(s) + jX_6(s) - X_8(s)}{2}] \end{cases}$$

$$\begin{cases} M_p(s) = \dfrac{-jX_1(s) + X_3(s) - X_5(s) - jX_7(s)}{2} \\ N_p(s) = \dfrac{X_2(s) - jX_4(s) - jX_6(s) - X_8(s)}{2} \\ L_p(s) = j(w_p - 2w_c)L_w(\dfrac{jX_1(s) + X_3(s) + X_5(s) - jX_7(s)}{2}) + (\dfrac{X_2(s) + jX_4(s) - jX_6(s) + X_8(s)}{2}) \end{cases}$$

Appendix 2:

$$G(s) = (k_p + \frac{k_i}{j(w_p - w_c)})$$

$$C_1(s) = \frac{1}{b_0}\frac{[j(w_p - w_c) + w_0]^2 w_n}{\{[j(w_p - w_c)]^2 + 2w_0 j(w_p - w_c) + w_n j(w_p - w_c)\}}$$

$$C_2(s) = \frac{1}{b_0}\frac{({w_0}^2 j(w_p - w_c) + 2w_n w_0 j(w_p - w_c) + w_n {w_0}^2)}{\{[j(w_p - w_c)]^2 + 2w_0 j(w_p - w_c) + w_n j(w_p - w_c)\}}$$

$$
\begin{cases}
M_{p2}(s)=\dfrac{-jY_1(s)+Y_3(s)-Y_5(s)-jY_7(s)}{2} \\
N_{p2}(s)=\dfrac{Y_2(s)-jY_4(s)-jY_6(s)-Y_8(s)}{2} \\
L_{p2}(s)=j(w_p-2w_c)L_w(\dfrac{jY_1(s)+Y_3(s)+Y_5(s)-jY_7(s)}{2}) \\
+(\dfrac{Y_2(s)+jY_4(s)-jY_6(s)+Y_8(s)}{2}) \\
M_{p3}(s)=\dfrac{-jY_1(s)+Y_3(s)+Y_5(s)+jY_7(s)}{2} \\
N_{p3}(s)=\dfrac{Y_2(s)-jY_4(s)+jY_6(s)+Y_8(s)}{2} \\
L_{p3}(s)=j(w_p-2w_c)L_w-[j(w_p-2w_c)L_w\dfrac{jY_1(s)+Y_3(s)-Y_5(s)+jY_7(s)}{2}+\dfrac{Y_2(s)+jY_4(s)+jY_6(s)-Y_8(s)}{2}] \\
+[j(w_p-2w_c)L_f+R_L+C_2(s)][\dfrac{j(w_p-2w_c)L_w}{\dfrac{1}{j(w_p-2w_c)C_f}+R}+1]
\end{cases}
$$

$$
\begin{cases}
Y_1(s)=(C_1(s)\cdot(G(s)\cdot(G_q(s)\cdot i_{od}-G_p(s)\cdot i_{oq}\cdot u_{oq})+C_f\cdot w_c\cdot(G_p(s)\cdot i_{oq}\cdot u_{od}-1))-G_p(s)\cdot i_{oq}\cdot u_q \\
\quad -C_2(s)\cdot G_p(s)\cdot i_{Lq}\cdot i_{oq}) \\
Y_2(s)=(C_1(s)\cdot(G(s)\cdot(G_q(s)\cdot u_{oq}-G_p(s)\cdot u_{od}\cdot u_{oq})+C_f\cdot G_p(s)\cdot u_{od}^2\cdot w_c)-G_p(s)\cdot u_{od}\cdot u_q \\
\quad -C_2(s)\cdot G_p(s)\cdot i_{Lq}\cdot u_{od}) \\
Y_3(s)=-(-C_1(s)\cdot(G(s)\cdot(G_q(s)\cdot i_{oq}+G_p(s)\cdot i_{od}\cdot u_{oq}+1)-C_f\cdot G_p(s)\cdot i_{od}\cdot u_{od}\cdot w_c)-G_p(s)\cdot i_{od}\cdot u_q \\
\quad -C_2(s)\cdot G_p(s)\cdot i_{od}\cdot i_{Lq}) \\
Y_4(s)=(-C_1(s)\cdot(G(s)\cdot(G_p(s)\cdot u_{oq}^2+G_q(s)\cdot u_{od})-C_f\cdot G_p(s)\cdot u_{od}\cdot u_{oq}\cdot w_c)-G_p(s)\cdot u_{oq}\cdot u_q \\
\quad -C_2(s)\cdot G_p(s)\cdot i_{Lq}\cdot u_{oq}) \\
Y_5(s)=(-C_1(s)\cdot(G(s)\cdot(G_p(s)\cdot i_{oq}\cdot u_{od}-1)+C_f\cdot G_p(s)\cdot i_{oq}\cdot u_{oq}\cdot w_c)-G_p(s)\cdot i_{oq}\cdot u_d \\
\quad -C_2(s)\cdot G_p(s)\cdot i_{Ld}\cdot i_{oq}) \\
Y_6(s)=(-C_1(s)\cdot(G_p(s)\cdot G(s)\cdot u_{od}^2+C_f(s)\cdot G_p(s)\cdot u_{oq}\cdot w_c\cdot u_{od})-G_p(s)\cdot u_{od}\cdot u_d \\
\quad -C_2(s)\cdot G_p(s)\cdot i_{Ld}\cdot u_{od}) \\
Y_7(s)=(-C_1(s)\cdot(C_f\cdot w_c\cdot(G_p(s)\cdot i_{od}\cdot u_{oq}+1)+G_p(s)\cdot G(s)\cdot i_{od}\cdot u_{od})-G_p(s)\cdot i_{od}\cdot u_d \\
\quad -C_2(s)\cdot G_p(s)\cdot i_{od}\cdot_{Ld}) \\
Y_8(s)=(-C_1(s)\cdot(C_f\cdot G_p(s)\cdot w_c\cdot u_{oq}^2+G_p(s)\cdot G(s)\cdot u_{od}\cdot u_{oq})-G_p(s)\cdot u_{oq}\cdot u_d \\
\quad -C_2(s)\cdot G_p(s)\cdot i_{Ld}\cdot u_{oq})
\end{cases}
$$

References

[1] Z. Xu, “Physical mechanism and research approach of generalized synchronous stability for power systems,” vol. 40, no. 9, pp. 3-9. Oct .2020.

[2] X. Wang, M. G. Taul, H. Wu, Y. Liao, F. Blaabjerg, and L. Harnefors, “Grid-synchronization stability of converter-based resources—An overview,” vol. 1, pp. 115-134. Aug. 2020.

[3] R. Rosso, X. Wang, M. Liserre, X. Lu, and S. Engelken, "Grid-forming converters: An overview of control approaches and future trends." pp. 4292-4299. Oct. 2020.

[4] Dingrui Li, Yu Su, Fred Wang, Mohammed Olama, Ben Ollis, and Maximiliano Ferrari. Power flow models of grid-forming inverters in unbalanced distribution grids. IEEE Transactions on Power Systems,39(2):4311–4322, 2024.

[5] Yun Wei Li. Control and resonance damping of voltage-source andcurrent-source converters with lc filters(article). IEEE Transactions on Industrial Electronics, pages 1511–1521, 2009.

[6] Wang Liang, Xie Xiaorong, Jiang Qirong, Liu Hui, Li Yu, Liu Huakun. Investigation of SSR in practical DFIG-based wind farms connected to a seriescompensated power system. IEEE Trans Power Syst Sep.2014;30(5):2772–9.

[7] Xie Xiaorong, Wang Liang, Guo Xijiu, Jiang Qirong, Liu Quan, Zhao Yonglin. Development and field experiments of a generator terminal subsynchronous damper. IEEE Trans Power Electron Jun,2014;29(4):1693–701. http://dx.doi.org/10.1109/TPEL.2013.2267550.
[8] Gross Lawrence C, et al. Sub-synchronous grid conditions: New event new problem and new solutions. In: Proc. western protective relay conf.. Vol. 2010, Sep.2010, p. 1–19.
[9] Adams John, Pappu Venkata Ajay, Dixit Anuj. ERCOT experience screening for sub-synchronous control interaction in the vicinity of series capacitor banks. In: Proc. 2012 IEEE power energy soc. general meeting. IEEE; Jul.2012, p. 1–5.
[10] Wang Weisheng, Zhang Chong, He Guoqing, Li Guanghui, Zhang Jianyun, Wang Haijiao. Overview of research on subsynchronous oscillations in large-scale wind farm integrated system. Power Syst Technol Jul.2017;41(4):1050–60.
[11] K. Shi, Y. Wang, Y. Sun, P. Xu, and F. Gao, “Frequency-coupled impedance modeling of virtual synchronous generators,” vol. 36, no. 4, pp. 3692-3700. Jan. 2021.
[12] X. Wang, Y. W. Li, F. Blaabjerg, and P. Loh, “Virtual-impedance-based control for voltage-source and current-source converters,” vol. 30, no. 12, pp. 7019-7037. Dec. 2014.
[13] M. Eskandari, and L. Li, “Microgrid operation improvement by adaptive virtual impedance,” vol. 13, no. 2, pp. 296-307. Nov. 2019.
[14] J. M. Guerrero, J. Matas, L. G. de Vicuna, M. Castilla, and J. Miret, “Decentralized control for parallel operation of distributed generation inverters using resistive output impedance,” vol. 54, no. 2, pp. 994-1004. Mar. 2007.
[15] S. Huang et al., "Predefined-time Observer-based Sliding Mode Control for Fast Frequency Support in Heterogeneous Power System Through Grid-Forming Converter," in IEEE Transactions on Power Systems, doi: 10.1109/TPWRS.2025.3578804.
[16] S. Huang et al., "Predefined-time Observer-based Sliding Mode Control for Fast Frequency Support in Heterogeneous Power System Through Grid-Forming Converter," in IEEE Transactions on Power Systems, doi: 10.1109/TPWRS.2025.3578804.
[17] C. Luo, X. Ma, T. Liu and X. Wang, "Adaptive-Output-Voltage-Regulation-Based Solution for the DC-Link Undervoltage of Grid- Forming Inverters," in IEEE Transactions on Power Electronics, vol. 38, no. 10, pp. 12559-12569, Oct. 2023.
[18] He G, Chen G, Dong Y, Li G, Zhang W. Research on LADRC of Grid-Connected Inverter Based on LCCL. Energies 2022; 15(13): 4686.
[19] He G, Chen G, Dong Y, Li G, Zhang W. Research on LADRC of Grid-Connected Inverter Based on LCCL. Energies 2022; 15(13): 4686.
[20] Xie Z , Chen Y , Wu W ,et al.Admittance Modeling and Stability Analysis of Grid-Connected Inverter With LADRC-PLL[J].IEEE Transactions on Industrial Electronics, 2021(68-12).DOI:10.1109/TIE.2020.3044789.
[21] Gao, Z. Scaling and bandwidth-parameterization based controller tuning. In Proceedings of the American Control Conference, Denver, CO, USA, 4 – 6 June 2003; pp. 4989 – 4996.

070 Control Technology Based on Integration of Grid-Forming Flywheel Energy Storage and New Energy Power Stations

Guangyu Sun[1], Yangyang Ge [1], Bing Xie [1], Xiaotong Zhang[1], Yuchen Wang[2], Xingyu Jiang[2]

[1] State Grid Liaoning Electric Power Co., Ltd. Electric Power Science Research Institute,Shenyang110006,China

[2] Shenyang Institute of Engineering,Shenyang110136,China

jiangxingyu0711@163.com

Abstract: This paper focuses on microgrid scenarios and studies the integrated control technology of grid-forming flywheel energy storage and new energy stations/facilities. By establishing models of permanent magnet direct-drive wind turbines, photovoltaic cells, and flywheel energy storage, an adaptive parameter virtual synchronous generator (VSG) control strategy is adopted, and simulations are conducted using Matlab/Simulink. With wind speed, solar irradiance, and load step as disturbance conditions, the effectiveness and superiority of this strategy in improving the frequency stability, voltage quality of the microgrid, and anti-interference capability of the DC bus are verified.

Keywords: Microgrid, Flywheel Energy Storage, Virtual Synchronous Generator (VSG), Adaptive Control

1 Introduction

New energy power generation features strong intermittency and randomness. Its large-scale

Fund Project: Science and Technology Project of Liaoning Electric Power Company of State Grid（2024YF-102）

Corresponding author:Xingyu Jiang, female, lecturer, Doctor of Engineering. Her main research field is the stability of power systems. Email：jiangxingyu0711@163.com

grid connection tends to reduce the stability of power grid frequency and voltage, restricting the absorption capacity[1]. The "new energy + energy storage" coordinated mode is a key means to solve this problem, among which flywheel energy storage has become an ideal choice for supporting the stable operation of new energy due to its long cycle life, fast response and high efficiency[2]. The grid-side converters of traditional flywheel energy storage mostly adopt grid-following control, whose operation relies heavily on phase-locked loops to achieve grid synchronization. They can only passively respond to commands to provide specific active and reactive power, and lack inertia support capability. To make up for this deficiency, this paper proposes applying grid-forming control to the flywheel energy storage system, which enhances the system's anti-disturbance capability by simulating the inertia characteristics and voltage/frequency support capability of synchronous generators.

However, existing research in this field still has limitations. Literature [3] adopts the traditional fixed-parameter control method for virtual synchronous generators, but when there are step changes in wind speed, light intensity, or load, fixed parameters tend to cause problems such as large frequency/voltage overshoot and long adjustment time in the system. Literature [4] employs a rule-based adaptive strategy, yet the formulation of its rules relies on experience, making it difficult to cope with complex real-world scenarios. The interleaved control strategy proposed in Literature [5] adjusts the moment of inertia and damping coefficient separately in different time intervals, but it does not clearly provide specific selection criteria for relevant parameters. Literature [6] uses reinforcement learning algorithms to optimize the control strategy, however, it suffers from long training time, high hardware requirements, and difficulty in ensuring convergence to the global optimal solution.

To address the above issues, this paper focuses on microgrid scenarios and proposes a grid-forming flywheel energy storage control technology based on the adaptive-parameter virtual synchronous generator (VSG). By dynamically adjusting the virtual moment of inertia and damping coefficient of the flywheel energy storage system, the energy storage system can not only provide sufficient inertia support but also quickly suppress oscillations under disturbances such as fluctuations in new energy output and load steps, thereby providing technical support for the efficient coordinated operation of "new energy + energy storage".

2 Integrated Control Strategy for Flywheel Energy Storage and New Energy Stations

2.1 Grid-Forming Control Principle

The grid-forming operation control of flywheel energy storage is mainly realized by the grid-side converter [7]. The grid-forming control adopted in this paper is virtual synchronous generator (VSG) control.

The active power control equation of the virtual synchronous generator is as follows:

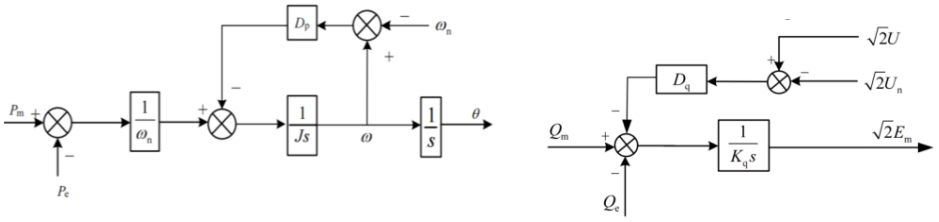
$$\begin{cases} J\dfrac{d\omega}{dt} = \dfrac{P_{\mathrm{m}}}{\omega_{\mathrm{n}}} - \dfrac{P_{\mathrm{e}}}{\omega_{\mathrm{n}}} - D_{\mathrm{p}}(\omega - \omega_{\mathrm{n}}) \\ \theta = \int \omega dt \end{cases} \tag{1}$$

In the formula:： J is the moment of inertia of the synchronous generator, D_{p} D is the damping coefficient of the synchronous generator, P_{m} and P_{e} are the mechanical power and electromagnetic power of the synchronous generator, ω and ω_{n} are the electrical angular velocity and rated electrical angular velocity, respectively, θ is the reference phase.The reactive power control equation of the virtual synchronous generator is：

$$\sqrt{2}K_{\mathrm{q}}\frac{dE_{\mathrm{m}}}{dt} = Q_{\mathrm{m}} - Q_{\mathrm{e}} - D_{\mathrm{q}}\left(\sqrt{2}U - \sqrt{2}U_{\mathrm{n}}\right) \tag{2}$$

In the formula： K_{q} is the integral coefficient, E_{m} is the voltage reference value derived from the reactive power loop, Q_{m} is the reference value for reactive power, Q_{e} is the output value of reactive power, D_{q} is the droop coefficient between reactive power and voltage difference, U signifies the output voltage, U_{n} stands for the rated voltage.

Based on Equations (1) and (2), the control block diagrams for Links $P-\theta$ and $Q-E$ of the Virtual Synchronous Generator (VSG) can be derived, as shown in **Fig. 1**.



(a) Control Block Diagram of the P-θ Link (b) Control Block Diagram of the Q-E Link

Fig. 1. Control Block Diagram of the Virtual Synchronous Generator (VSG)

2.2 Adaptive VSG Control

Using the small-signal model analysis method of generators, the transfer function of input-output active power for the virtual synchronous generator is shown in Equation (3), which is a typical second-order transfer function.

$$G(s)=\frac{P(s)}{P_{\text{ref}}(s)}=\frac{\dfrac{1}{J\omega_{\text{n}}}\dfrac{EU}{Z}}{s^2+\left(\dfrac{D}{J}+\dfrac{K_{\omega}}{J\omega_{\text{n}}}\right)s+\dfrac{1}{J\omega_{\text{n}}}\dfrac{EU}{Z}} \tag{3}$$

In the formula： K_{ω} is the droop coefficient, Z is the impedance of the virtual synchronous generator filter circuit.

According to Equation (4), the natural angular frequency ω_{n} and damping ratio ξ of the corresponding second-order model are derived as follows：

$$\begin{cases} \omega_{\text{s}}=\sqrt{\dfrac{EU}{J\omega_{\text{n}}Z}} \\ \xi=D\sqrt{\dfrac{\omega_{\text{n}}Z}{4JEU}}+K_{\omega}\sqrt{\dfrac{Z}{4J\omega_{\text{n}}EU}} \end{cases} \tag{4}$$

If parameter $0<\xi<1$ is selected and the error band is set to ±5%, the corresponding overshoot $\sigma\%$ and settling time ts of the second-order system are $\sigma\%=\mathrm{e}^{-\pi\xi/\sqrt{1-\xi^2}}\times 100\%$ and $t_{\text{s}}=\dfrac{3.5}{\xi\omega_{\text{n}}}=3.5/\left(\dfrac{D}{2J}+\dfrac{K_{\omega}}{2J\omega_0}\right)$ respectively.

Under the condition that the active power command and reactive power command are given, the dynamic performance of the second - order system is determined by the moment of inertia J , damping coefficient D , and droop coefficient K_{ω} . The moment of inertia J of the virtual synchronous generator determines the oscillation frequency in the output active power response process, while the damping coefficient D determines the attenuation rate of active power response oscillation [7].To analyze the influence of parameters J and D on the output frequency, transforming Equation (1) yields：

$$\Delta\omega=\frac{T_{\text{m}}-T_{\text{e}}-J\mathrm{d}\omega/\mathrm{d}t}{D} \tag{5}$$

$$\frac{T_{\text{m}}-T_{\text{e}}-T_{\text{D}}}{J}=\frac{\mathrm{d}\omega}{\mathrm{d}t} \tag{6}$$

It can be seen from Equations (5) and (6) that when other conditions remain unchanged, the damping coefficient D is inversely proportional to the frequency deviation $\Delta\omega$, and the

inertia coefficient J is inversely proportional to the angular velocity change rate $\mathrm{d}\omega/\mathrm{d}t$. To ensure frequency stability, the changes in $\mathrm{d}\omega/\mathrm{d}t$ and $\Delta\omega$ can be suppressed by appropriately adjusting the parameters J and D. The selection principles of the moment of inertia and damping coefficient under different conditions are shown in **Table 1**.

Table 1. Selection Principles of J and D under Different Conditions

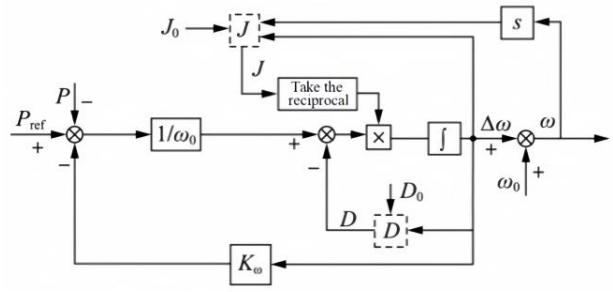
Interval	$\Delta\omega$	$\mathrm{d}\omega/\mathrm{d}t$	$\Delta\omega(\mathrm{d}\omega/\mathrm{d}t)$	J	D
①	>0	>0	>0	Increase	Increase
②	>0	<0	<0	Decrease	Increase
③	<0	<0	>0	Increase	Increase
④	<0	>0	<0	Decrease	Decrease

According to the selection principles in Table 1, the adaptive control strategy is as follows：

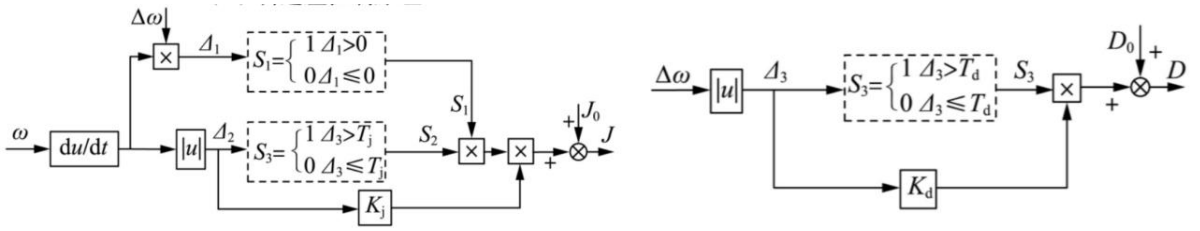
$$J=\begin{cases} J_0 & \Delta\omega\left(\mathrm{d}\omega/\mathrm{d}t\right)\leqslant 0 \\ J_0 & \left|\mathrm{d}\omega/\mathrm{d}t\right| \leqslant T_\mathrm{j} \\ J_0+K_\mathrm{j}\left|\mathrm{d}\omega/\mathrm{d}t\right| & \Delta\omega\left(\mathrm{d}\omega/\mathrm{d}t\right)>0\cap\left|\mathrm{d}\omega/\mathrm{d}t\right|>T_\mathrm{j} \end{cases} \tag{7}$$

$$D=\begin{cases} D_0 & \left|\Delta\omega\right|\leqslant T_\mathrm{d} \\ D_0+K_\mathrm{d}\left|\Delta\omega\right| & \left|\Delta\omega\right|>T_\mathrm{d} \end{cases} \tag{8}$$

Where J_0 and D_0 represent the moment of inertia and damping coefficient of the virtual synchronous generator during stable operation, respectively; K_j and K_d are the adjustment coefficients for the moment of inertia and damping coefficient, respectively; T_j and T_d are the variation thresholds. The schematic diagram of the collaborative adaptive control for the moment of inertia and damping coefficient is shown in **Fig. 2**.



(a) Adaptive Control Principle



(b)The Adaptive Control Principle of Moment of Inertia (c)The Adaptive Control Principle of Damping Coefficient

Fig. 2. Schematic Diagram of Collaborative Adaptive Control for Moment of Inertia and Damping Coefficient

3 Simulation Operation and Result Analysis

A microgrid model consisting of a permanent magnet direct-drive wind turbine, a two-stage photovoltaic cell, and a flywheel energy storage system was established using the simulation software Matlab/Simulink.The specific design as follows:The wind speed is 7 m/s from 0 to 0.5 s, 8 m/s from 0.5 to 1 s, and 7 m/s from 1 to 2 s.The light intensity is 1,000 W/m² from 0 to 0.4 s, 1,200 W/m² from 0.4 to 0.9 s, and 900 W/m² from 0.9 to 2 s.Loads of 10 kW and 2 kVar are connected to the inverter output side at 1.3 s and 1.5 s, respectively.

It can be seen from **Fig. 3** that in terms of frequency fluctuation magnitude: at 0.5s, the frequency increased by 0.003Hz under fixed-parameter control, while it increased by 0.002Hz under adaptive-parameter control, a reduction of 33% in comparison; at 1.3s, the frequency decreased by 0.005Hz under fixed-parameter control, whereas it decreased by 0.003Hz under adaptive-parameter control, representing a 40% reduction. It is evident that the microgrid has stronger frequency stability during grid-connected operation under adaptive-parameter VSG control. In terms of voltage fluctuation magnitude: at 15s, the voltage decreased by 1.3V and 0.9V respectively under the two control strategies, and the fluctuation under adaptive-parameter control was reduced by 30%. It is thus clear that the microgrid also exhibits stronger voltage stability during grid-connected operation under adaptive-parameterVSG control.

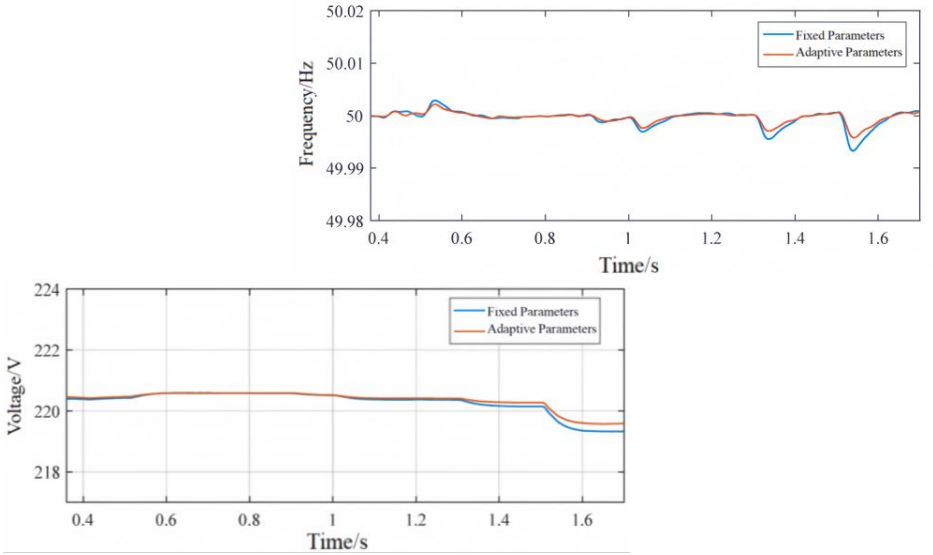


Fig. 3. The frequency and voltage output by the inverter under different control strategies

It can be seen from **Fig. 4** that in terms of the magnitude of DC bus voltage fluctuation, at 0.5s, the voltage increased by 16V under fixed-parameter control while it increased by 7V under adaptive-parameter control, representing a reduction of 56.25% in comparison; at 1.3s, the voltage decreased by 25V under fixed-parameter control whereas it decreased by 10V under adaptive-parameter control, showing a 60% reduction, and it is evident that the DC bus has stronger anti-disturbance capability under the adaptive-parameter VSG control.

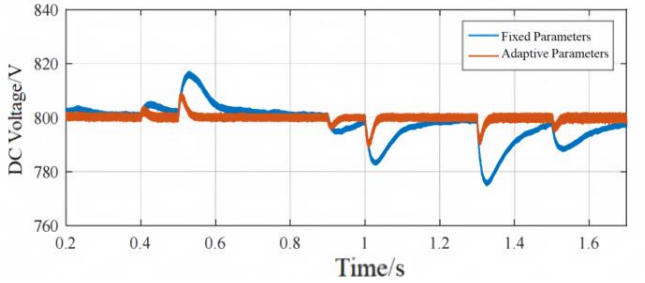


Fig. 4.DC Voltage Variations under Different Control Strategies

4 Conclusion

This paper takes the microgrid as the research object and focuses on the research of a grid-forming adaptive-parameter VSG control strategy based on a flywheel energy storage system. Models of the permanent magnet direct-drive wind turbine, two-stage photovoltaic cell, and flywheel energy storage system are established respectively. On this basis, a simple microgrid is built for simulation. Disturbances in the actual system are simulated by step changes in wind speed, solar irradiance, and load. The fluctuation ranges of the microgrid's DC bus voltage, the output frequency of the grid-connected inverter, and the output voltage are used as evaluation indicators to verify the effectiveness and superiority of the adaptive-parameter VSG control strategy.

References

1. Huang Sen, Yao Jun, Zhong Qinmin, et al. Transient Synchronous Stability Analysis of Hybrid Power System with Sliding-Grid and Grid-Forming New Energy Generation Units [J]. Proceedings of the CSEE, 2024, 44(21): 8378-8392.
2. Song Juan. Application of Flywheel Energy Storage Control Technology in New Energy Wind Power Generation System [J]. Energy Storage Science and Technology, 2025, 14(09): 3431-3433.
3. Liu J, Miura Y, Ise T. Fixed-parameter damping methods of virtual synchronous generator control using state feedback[J]. IEEE Access, 2019, 7: 99177-99190.
4. Li X, Wang Y, Zhang L. Adaptive Virtual Synchronous Generator Control for Microgrid Stability Enhancement[J]. IEEE Transactions on Sustainable Energy, 2020, 11(3): 2102-2111.
5. Song, Q., Zhang, H., Sun, K., et al. (2017). Improved adaptive control of moment of inertia for virtual synchronous generators in an isolated microgrid with multiple micro-sources. Proceedings of the CSEE, 37(2), 412-423.
6. Chen J, Liu H, Zhao W. Reinforcement Learning-Based Optimal Control for Virtual Synchronous Generators in Renewable Energy Systems[J]. Applied Energy, 2021, 285: 116452.
7. Tang Xisheng. An Introduction to the Development of Grid-Forming Flywheel Energy Storage [J]. Advanced Technology of Electrical Engineering and Energy, 2025, 44 (08): 1-8.

071 Research on Photovoltaic Power Ultra-Short Term Prediction Model Optimized by IQPSO for LSTM

Xiaoming Zhang[1], Yuhang Sun[1], Wenbin Cao[1]

[1] Chaoyang Power Supply Company, Chaoyang 122000, China
13940547201@163.com

Abstract: To address the challenge of improving power prediction accuracy in large-scale photovoltaic power grid integration, this study proposes an ultra-short-term photovoltaic power forecasting method based on an improved quantum particle swarm optimization algorithm (IQPSO) for LSTM network. The proposed approach first employs Pearson correlation coefficient to identify key factors influencing photovoltaic power as input variables, followed by cosine similarity analysis for clustering similar days to simplify model complexity and construct training datasets. Subsequently, the IQPSO-LSTM model is optimized through the enhanced quantum particle swarm algorithm to establish a high-performance forecasting framework. Simulation analysis using operational data from photovoltaic power stations in a specific region validates the effectiveness and practicality of the proposed methodology.

Keywords: Pearson method; cosine similarity; quantum particle swarm algorithm; LSTM network

Foreword

The grid integration of large-scale solar photovoltaic (PV) systems has become an inevitable trend under China's "dual carbon" goals [1]. With its clean, pollution-free, and easily implementable characteristics, PV technology offers unique advantages unmatched by other renewable energy sources. However, When both large-scale PV plants and small distributed rooftop PV systems are uncontrolled integrated into power transmission and distribution networks, they pose significant threats to grid stability and operational safety [2-4]. As documented in [5], the uncertainties in PV grid integration significantly impact stable grid operations. Therefore, developing accurate

Fund Project: Science and Technology Project of Liaoning Electric Power Company of State Grid (2024YF-33)

PV power prediction methods proves crucial for optimizing dispatch planning, ensuring grid adaptability, and enhancing emergency response capabilities.

Domestic scholars have conducted extensive research on photovoltaic power generation forecasting. Literature [6] proposed a novel short-term prediction method for PV power generation using an improved particle swarm optimization algorithm to optimize the parameters of a BP neural network, though BP networks are prone to getting trapped in local optima during training. Literature [7] introduced the Sparrow Search algorithm to enhance support vector machine (SVM) performance for PV power prediction, but SVM requires substantial data scale. Compared with both BP networks and SVM, the deep learning algorithm Long Short-Term Memory (LSTM) has gained increasing adoption in photovoltaic applications due to its superior learning capabilities. Literature [8] proposed establishing a PV power prediction model using LSTM networks, yet failed to address hyperparameter optimization for the network.

To reduce the complexity of the prediction model and fully account for environmental factors' impact on photovoltaic power generation predictions, this study first employs Pearson correlation coefficient analysis to screen meteorological characteristic data, selecting key factors with strong correlations to photovoltaic power generation as input parameters. Subsequently, cosine similarity analysis is applied for clustering of similar days. To enhance the learning performance of the LSTM network, we optimize the traditional quantum particle swarm optimization algorithm to improve convergence efficiency. Finally, through hyperparameter tuning of t he LSTM network, we establish an optimal photovoltaic power generation prediction model based on IQPSO-LSTM.

1 Preprocessing of Photovoltaic Power Prediction Data

1.1 Screening of Meteorological Characteristic Factors

This study conducts experimental simulation analysis using operational data from a regional photovoltaic power station. The meteorological parameters analyzed include historical photovoltaic power generation data, solar irradiance, ambient relative humidity, real-time wind speed, and ambient temperature [9]. By calculating correlation coefficients between each meteorological parameter and photovoltaic power output, we retain those with higher correlation values. The Pearson correlation coefficient is calculated using the formula :

$$r = \frac{\sum_{i=1}^{m}(x_i - \bar{x})}{\sqrt{\sum_{i=1}^{m}(x_i - \bar{x})^2 \sum_{i=1}^{m}(t_i - \bar{t})}} \tag{1}$$

Where: m-the number of meteorological characteristic data groups; x_i —the i-th meteorological feature in the real environment; t—actual photovoltaic power generation; $\bar{x}$ —the mean of the two data points.

The absolute value of the Pearson correlation coefficient quantifies the correlation between meteorological characteristics and photovoltaic power generation. A higher

absolute value indicates stronger correlations. Therefore, this study retains four meteorological features with larger Pearson correlation coefficients: solar altitude (x2), solar irradiance (x3), cloud opacity (x5), and relative humidity (x10). These data points provide essential samples for constructing model training datasets and classifying weather patterns in subsequent research.

1.2 Similarity Clustering Analysis

This study classifies daily weather types into three categories: sunny, cloudy and rainy. For the four characteristic variables identified through Pearson correlation analysis in Section 1.1, cosine similarity analysis is conducted. By comparing cosine similarity values between current-day predictions and historical data, we screen out similar days within the same weather type [11]. The cosine similarity analysis formula is as follows:

$$K_{cvs} = \frac{\sum_{n=1}^{N} y_t(n) y_0(n)}{\sqrt{\sum_{n=1}^{N} y_t^2(n) \sum_{n=1}^{N} y_0^2(n)}} \tag{2}$$

Where: Kcos—cosine similarity value;n— time nodes ； N—Sampling time series length; y0(n)—predicts the feature vector at the time node n of the day; yi(n)—the feature vector at time node n of t he i-th forecast day.

2 Construction of Photovoltaic Power Generation Prediction Model

2.1 Long and Short Term Memory Networks

Since the evolution of photovoltaic power generation is closely tied to meteorological factors like solar radiation intensity, and these factors exhibit temporal correlations forming causally robust time series, the deep learning capabilities of Long Short-Term Memory (LSTM) networks can effectively uncover hidden correlations between influencing factors and historical photovoltaic power generation data, thereby improving the accuracy of photovoltaic power prediction. The structural framework of the LSTM is shown in **Fig. 1**.

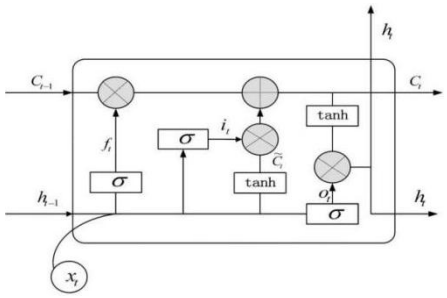


Fig. 1. Structure of LSTM Network Unit

The working principle of LSTM network is as follows:

$$ft=\sigma\left(Wf\left[ht-1, xt\right] + bf\right) \tag{3}$$

$$it=\sigma\left(Wi\left[ht\text{ -1, }xt\right]+bi\right) \tag{4}$$

$$ot=\sigma\left(Wo\left[ht\text{ -1, }xt\right]+bo\right) \tag{5}$$

$$\tilde{C}_t=\tanh(Wc\ [ht\text{ - 1,}xt\ ]+bc \tag{6}$$

$$C_t=ft*C_t\text{-1}+It*\tilde{C}_t \tag{7}$$

$$ht=ot*\tanh(C_t) \tag{8}$$

Where: ft, it, ot —output value of the forgetting gate, input gate and output gate;Wf 、Wi、 Wo、 Wc、—weight linear transformation matrix;σ(), tanh() —activation function, hyperbolic tangent function;b—deviation vector;

2.2 Improved quantum particle swarm algorithm

The computational formula for the original quantum particle swarm algorithm is:

$$x_{i\sigma}^{t+1}=a_{i\sigma}^{t}\pm\frac{1}{2}L_{rt}^{t}\ln(\frac{1}{u_{i\sigma}^{t+1}}) \tag{9}$$

$$ai(t)d=\varphi pi(t)d+\left(1\text{-}\varphi\right)pg(t)d \tag{10}$$

$$\varphi=\frac{c_1r_1}{c_1r_1+c_2r_2} \tag{11}$$

$$I_{ii}^{t}-2CE\left|\overline{P}_d^t-x_{ii}^{t}\right| \tag{12}$$

$$\overline{P_d}^{'}=\frac{1}{N}\sum_{i=1}^{N}p_{id}^{'}=\sum_{i=1}^{N}(\omega_i^{'}p_{id}^{'}) \tag{13}$$

Where:x_{id}^{t} --the position of particle i at time t; a_{id}^{t}—the local potential of the algorithm; L_{id}^{i} —search feature length, determines the search range of particles; ω_i^d—particle position update weight $\omega_i^d=1/N$; u_{id}^{t+1}—any number evenly distributed in the interval [0,1]; $\overline{P_d^t}$—the average best position of all particles in the population;ω_i^t —the weight of the weight of the i-th particle at the r-th iteration. CE is the contraction and expansion factor, and its value affects the final convergence speed of the algorithm , it can be concluded that the algorithm can obtain optimal performance when CE =0.75.

The improvement measures are to introduce the Gaussian distribution to determine the value of a_{id}^{t}, enhance the local convergence ability of the algorithm and its ability to jump out of the local optimal solution in time. The expression is as follows:

$$ga_i^t=[ga_{i1}^t,\cdots,ga_{id}^t,\cdots,ga_{iD}^t]=\text{Normal}(a_i^t,\overline{P}^t-p_i^t) \tag{14}$$

Therefore, the position update strategy of particles is as follows:

$$x_{id}^{t+1}=ga_{id}^{t}\pm CE\left|\overline{P}_d^t-x_{id}^{t}\right|\ln(\frac{1}{u_{id}^{t+1}}) \tag{15}$$

In this paper, the improved quantum particle swarm algorithm is used to optimize the parameters of LSTM, and the photovoltaic power generation prediction algorithm IQPSO-LSTM is obtained.

3 Short-Term Prediction Model of Photovoltaic Power Generation Based on IQPSO-LSTM

3.1 Model Building

The establishment steps of IQPSO-LSTM prediction model are as follows:

Step1: Sampling data preprocessing. The training set and test set constructed by cosine similarity analysis method will be normalized, expressed as:

$$X^{'} = \frac{X - X_{min}}{X_{max}} - X_{min} \tag{16}$$

Where: X--original time series data; X_{max} and X_{min} are the original data maximum and minimum values.

Step 2: Initialize the quantum particle swarm parameters. Take the hyperparameters of t he LSTM network as the target values for the optimal positions of particles, update and adjust the particle positions according to the improvement strategy in Section 2.2, and finally obtain the optimal hyperparameter combination for the photovoltaic power generation prediction model.

Step3: Set the model loss function. The root mean square error of the predicted model output is taken as the value of the model loss function, and its expression is:

$$Loss = \sqrt{\frac{1}{N}\sum_{k=1}^{N}[e(X)]^2}, e(X) = Y_{\hat{k}}(X) - \hat{Y}_{\hat{k}}(X) \tag{17}$$

Where: N--number of training samples;$Y_k(X)$ —expected output value of photovoltaic power generation; $\widehat{Y}_k(X)$ — actual output value of photovoltaic power generation.

Step 4: Model Training. Determine whether the output results of the prediction model meet the accuracy requirements or whether the quantum particle swarm optimization algorithm has reached the maximum iteration count. If the conditions are met, apply these parameters to establish a prediction model for short-term photovoltaic power generation forecasting; if not, repeat the process.

The modeling process is shown in **Fig. 2**:

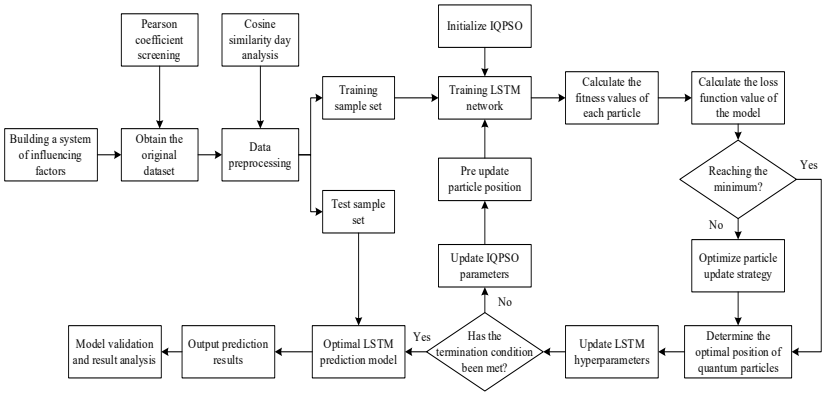


Fig. 2. Schematic Diagram of Photovoltaic Power Generation Prediction Model

3.2 Evaluation Index of Prediction Accuracy of Model

In order to comprehensively and accurately evaluate the prediction accuracy of the model, relative root mean square error (RRMSE), fitting goodness coefficient of determination (R 2) and mean absolute percentage error (MAPE) were selected as the evaluation indexes of the prediction model.

The smaller the value of the relative root mean square error and the average absolute percentage error, the higher the accuracy of the soft measurement model; R2 → 1, the effect of the soft measurement model is better.

4 Experimental Simulation Analysis

This study analyzes operational data from a photovoltaic power station in a specific region, with solar power generation measurements collected between August and October 2023. Daily sampling periods were set from 9:30 AM to 7:30 PM at 15-minute intervals, yielding 41 daily datasets. Three representative dates—August 12 (sunny), September 23 (cloudy), and October 13 (rainy)—were selected for prediction. Using cosine similarity analysis, the top 10 most similar days were identified as training sets based on their power generation data, with the final selection results detailed in Table 1-3.

Table 1. Cosine Similarity of Similar Days on Sunny Days

order number	1	2	3	4	5	6	7	8	9	10
cosine similarity	0.083	0.092	0.102	0.111	0.127	0.128	0.131	0.137	0.167	0.215

Table 2. Cosine similarity of cloudy days similar to sunny days

order number	1	2	3	4	5	6	7	8	9	10
cosine similarity	0.063	0.085	0.096	0.105	0.137	0.214	0.219	0.368	0.421	0.452

Table 3. Cosine similarity of cloudy days similar to rainy days

order number	1	2	3	4	5	6	7	8	9	10
cosine similarity	0.054	0.087	0.251	0.262	0.295	0.369	0.425	0.521	0.538	0.650

The parameters of the improved quantum particle swarm algorithm were set as dimension D =30, population size N =400, particle acceleration coefficients c1=c2=2, and iteration count 1000. The convergence performance was compared with the particle swarm algorithm and quantum particle swarm algorithm using training error as the vertical coordinate. The convergence results of each algorithm are shown in **Fig. 3**.

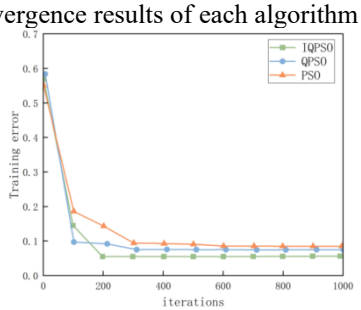
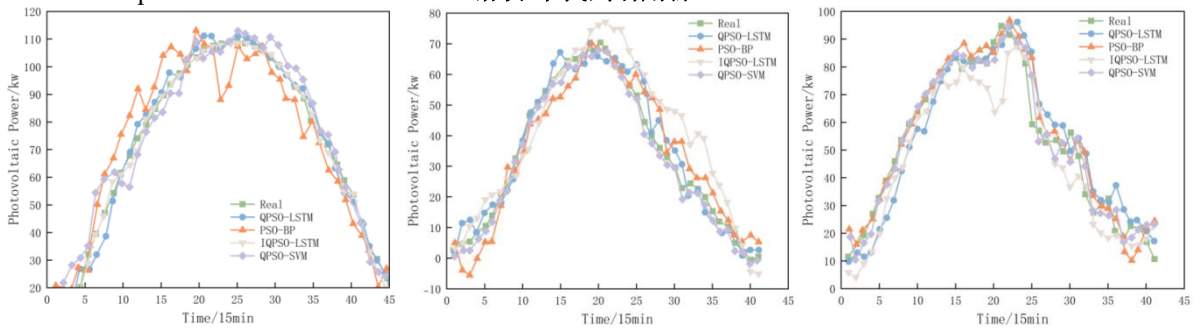


Fig. 3. Comparison of Convergence of Three Algorithms

The IQPSO algorithm converges to a global optimum after 200 iterations with minimized training errors, demonstrating faster convergence speed and higher accuracy compared to QPSO and PSO algorithms. This proves the superiority of the improved quantum particle swarm optimization (QPSO) algorithm proposed in this study. The final output of the IQPSO algorithm yields the following hyperparameters for the LSTM: 86 hidden layers, a network learning rate of 1.62× 10^-3, and a regularization coefficient of 1.18× 10^-4.

The trained IQPSO-LSTM prediction model was used to forecast the daily photovoltaic power generation under sunny, cloudy and rainy conditions. In order to compare the advantages of t he proposed model, PSO-BP network model, QPSO-SVM prediction model and QPSOLSTM prediction model were selected for comparison. The prediction results are shown in **错误!未找到引用源。**.



(a)Sunny Days (b)Cloudy Days (c)Rainy Days

Fig. 4. Comparison of Photovoltaic Power Generation Prediction Results under Different Weather Conditions

As can be seen from the comparison of the prediction results of the four models under severe weather types in Fig.4, the prediction results of IQPSO-LSTM model have better fitting effect with the actual values. **Table 1** shows the comparison results of the prediction errors of each model.

Table 1. Comparison of Evaluation Indexes of Various Prediction Models

Weather type	prediction model	RRMSE	MAPE/%	R2
Sunny 8.12	PSO-BP	0.2698	7.21	0.85
	PSO-SVM	0.2354	5. 12	0.89
	QPSO-LSTM	0.2109	2.36	0.91
	IQPSO-LSTM	0. 1140	1.51	0.96
Cloudy 9.23	PSO-BP	0.3890	10.61	0.72
	PSO-SVM	0.3178	7.95	0.81
	QPSO-LSTM	0.2912	4.36	0.82
	IQPSO-LSTM	0. 1720	1.88	0.94
Rainy 10.13	PSO-BP	0.3998	12.69	0.77
	PSO-SVM	0.3354	9. 12	0.79
	QPSO-LSTM	0.3209	4.75	0.88
	IQPSO-LSTM	0. 1940	2.39	0.92

As shown in Table 5, the proposed model demonstrates superior prediction performance under clear weather conditions, with a goodness-of-fit coefficient (R^2)

approaching 1 and a Mean Absolute Percentage Error (MAPE) of merely 1.51%. Although the evaluation metrics for rainy and cloudy conditions show minor fluctuations, the model still outperforms other methods in these scenarios, validating its inherent advantage in achieving higher prediction accuracy.

5 Conclusion

Accurate prediction of photovoltaic power generation can enhance real-time grid absorption capacity and minimize grid impact during solar integration. By applying Pearson correlation coefficient method to pre-screen key meteorological factors affecting PV power output, this study utilizes cosine similarity analysis to cluster similar days as training datasets, thereby simplifying model architecture. The optimized quantum particle swarm optimization algorithm was employed to fine-tune LSTM network parameters, establishing an optimal short-term forecasting model. Simulation comparisons with other models demonstrate that the IQPSO-LSTM model exhibits superior prediction accuracy across three weather conditions, outperforming alternatives in both prediction error and precision metrics.

6 Reference

1. Zhou C ,Zhang F ,Gu S , et al.A short-term power prediction method based on the transformation of multi-source spatiotemporal feature for photovoltaic cluster[J].International Journal of Green Energy,2025,22(12):2663-2679.
2. Wan H ,Qiu Z ,Wang J , et al.Optimizing renewable energy forecasting: a hybrid approach integrating MSADBO, BiGRU, and TCN for PV/wind power generation prediction[J].The Journal of Supercomputing,2025,81(13):1269-1269.
3. Xu Y ,Ji X ,Zhu Z .A photovoltaic power forecasting method based on the LSTM-XGBoost-EEDA-SO model[J].Scientific Reports,2025,15(1):30177-30177.
4. Ahmad R M ,Zakaria F N ,Jadin S M, et al. Optimization-driven extreme learning machine for floating photovoltaic power prediction: a teaching-learning-based approach[J].Engineering Research Express,2025,7(3):035341-035341.
5. Liu S ,Qi Y ,Li D , et al. Adversarial multi-source domain generalization approach for power prediction in unknown photovoltaic systems[J].Applied Soft Computing,2025,181113495-113495.
6. Zhang P ,Yao H ,Chen T , et al. Research on photovoltaic power generation prediction based on EPSO-ELM model[J].Journal of Physics: Conference Series,2024,2896(1):012047-012047.
7. FanY ,WuH ,LinJ , et al. A distributed photovoltaic short-term power forecasting model based on lightweight AI for edge computing in low-voltage distribution network[J].IET Renewable Power Generation,2024,18(16):3955-3966.
8. Sulaiman H M ,Jadin S M ,Mustaffa Z , et al. Short-Term forecasting of floating photovoltaic power generation using machine learning models[J].Cleaner Energy Systems,2024,9100137-100137.
9. Liu M ,Rao S ,Huang M , et al. Short-term photovoltaic power forecasting based on improved transformer with feature enhancement[J].Sustainable Energy, Grids and Networks,2025,43101759-101759.

10. Xiong X ,Hu H ,Jia Q , et al. Research on dynamic prediction and optimization of high altitude photovoltaic power generation efficiency using GVSAO-CNN Model under 8-climate modes[J].Discover Applied Sciences,2025,7(7):668-668.
11. Xu Y ,Lu Z .Enhanced PV power prediction using LSTM-integrated soft actor–critic model based on long short-term memory[J].Journal of Computational Methods in Sciences and Engineering,2025,25(5):4774-4786.

072 Distributed Economic Dispatch of Integrated Transmission and Distribution Systems towards Reserve Sharing

Lanxing Qin, Hengwei Yu, and Zhigang Wu*

South China University of Technology, Guangzhou, Guangdong, 510641, China

Abstract. To fully coordinate generation resources in transmission and distribution networks under large-scale renewable energy source integration, enhancing power system flexibility and addressing multiple uncertainties, a distributed economic optimal scheduling method for transmission and distribution systems oriented toward reserve sharing is proposed in this paper. While coordinating the base-point boundary power during the pre-dispatch coordination phase, a reserve sharing mechanism to handle uncertainties is established in this model. By setting bidirectional reserve support capabilities between transmission and distribution systems, the reliability and economy of the system are improved. To address privacy protection requirements and the challenge of decoupling boundary power consistency constraints in transmission-distribution coordinated computing, the parallelized alternating direction method of multipliers(ADMM) is adopted for distributed solving of the model, with an adaptive penalty factor strategy introduced to enhance algorithm convergence. Case studies on a modified T39D2 system demonstrate the effectiveness of the proposed model and method.

Keywords: Transmission-distribution coordination, Reserve sharing, Distributed optimization, Distributionally robust chance constraints, Economic dispatch

1 Introduction

Driven by the "Dual Carbon" strategy, the penetration of renewable energy sources(RES) such as wind power and photovoltaics in transmission and distribution networks has rapidly increased. The inherent intermittency and stochasticity of RES pose new challenges to the traditional independent scheduling paradigm, which operates in a hierarchical and voltage-level-segregated manner. On the one hand, despite the rapid regulation potential of distributed generation(DG) and energy storage(ES) within active distribution networks(ADNs), information barriers prevent transmission power systems(TPS) from effectively utilizing these resources. This results in insufficient coordination of adjustable resources between transmission and distribution networks. On the other hand, the propagation and accumulation of RES prediction errors across hierarchical levels may exacerbate boundary power fluctuations, increase real-

time operational risks, and lead to redundant reserve capacity allocation under independent scheduling modes, thereby elevating overall system operating costs. Consequently, it is urgent to advance research on modeling and distributed optimization methods of integrated transmission-distribution(ITD) system with high penetration of RES access.

To address the challenges posed by high-penetration RES integration into power systems, it is essential to collaboratively optimize the reserve capacity required by the system when formulating dispatch plans. Reference[1] adopts a deterministic reserve allocation method that ensures the total operating reserve remains above a certain threshold, while Reference[2] employs a probabilistic reserve allocation approach to configure reserve resources for a transmission-distribution coupled power system incorporating wind power. However, these methods only allocate reserves from the perspective of power system operational adequacy and are not suitable for meeting the flexibility requirements of systems with widespread distributed resource integration. In recent years, the problem of reserve allocation for regulating resources under RES uncertainty has been extensively studied. Reference**错误!未找到引用源。** uses a scenario-based method to sample wind power output scenarios and allocate reserve resources. Reference[3] establishes a two-stage adaptive robust optimization model for dynamic economic dispatch in transmission-distribution systems, considering wind power uncertainty. Reference**错误!未找到引用源。** constructs a distributionally robust optimal scheduling model for transmission-distribution systems based on distributionally robust chance constraint(DRCC) optimization. Nevertheless, these studies focus solely on optimizing reserve allocation within individual subsystems and do not consider reserve sharing between transmission and distribution systems.

The privacy protection requirements and independent operational management modes of transmission and distribution networks pose challenges to distributed optimization computing for ITD scheduling. Scholars worldwide have conducted extensive research on this issue. Reference[5] proposed a distributed coordination method based on feasible region projection theory, while Reference**错误!未找到引用源。** introduced a distributed optimization approach utilizing improved multiple agents and target cascading method. However, these algorithms may incur significant communication burdens when addressing large-scale RES uncertainties. To overcome these limitations, the alternating direction method of multipliers(ADMM) has demonstrated superior performance[7]. At present, further research is needed to explore how to apply the ADMM algorithm in a reserve-sharing-oriented ITD model to achieve a scheduling strategy that balances both robustness and economic efficiency.

To address the aforementioned gaps and requirements, this paper proposes a distributed economic optimal scheduling method for transmission-distribution systems oriented toward reserve sharing, which mainly focuses on the following points:

A transmission-distribution coordinated scheduling model based on a reserve sharing mechanism is constructed, enhancing bidirectional reserve support capabilities and reducing system costs.

By coupling local affine policies with power curtailment strategy, collaborative optimization with adjustable resources is achieved, enabling more accurate affining of RES uncertainty and alleviating system reserve pressure.

DRCC based on the Wasserstein distance are adopted to characterize RES uncertainty, and a parallelized ADMM algorithm is employed for distributed solution, incorporating an adaptive penalty factor strategy to improve convergence.

2 Distributionally Robust Optimization Model for Transmission and Distribution Systems

2.1 Structure of the Transmission and Distribution System

The operational structure of the ITD model is illustrated in

Fig. 1. The schedulable resources in the TPS include traditional synchronous generator(SG) and centralized grid-connected wind farms, while those in the ADN comprise distributed generation units, distributed photovoltaics, and energy storage. The model accounts for the uncertainty of RES output, network security constraints, and the need for reserve sharing between transmission and distribution levels. It achieves global optimality for coordinated ITD operation through joint optimization.

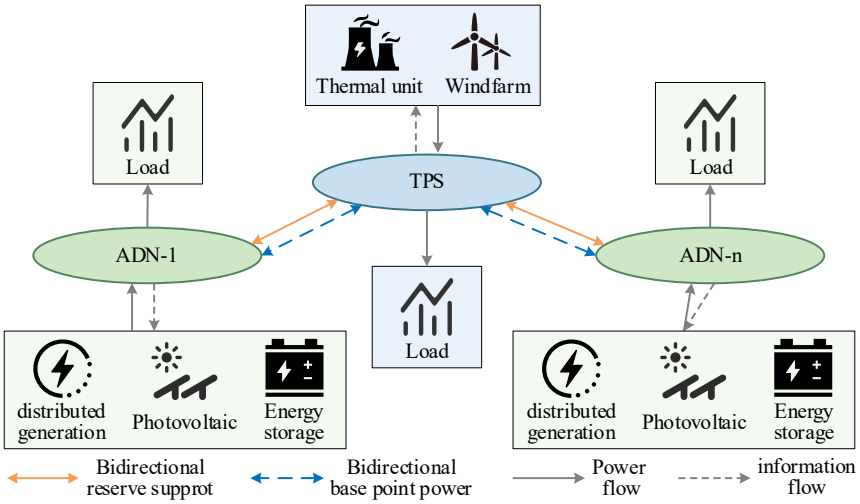


Fig. 1. The operational architecture of the ITD

2.2 RES Uncertainty Modeling

In actual operation, the available active power output of RES is a random variable composed of a forecasted value and a forecast error. To mitigate the supply-demand contradiction between RES output volatility and limited power system absorption capacity under extreme scenarios, the active power curtailment strategy is considered to be introduced on demand:

$$\tilde{P}^{\mathrm{R}}_{r,t} = P^{\mathrm{R}}_{r,t} - \xi_{r,t}, \forall r \in \mathcal{R}, t \in \mathcal{T} \tag{1}$$

$$\xi_t = [\xi_{1,t}, \xi_{2,t}, \cdots, \xi_{|\mathcal{R}|,t}]^{\mathrm{T}}, t \in \mathcal{T} \tag{2}$$

$$\tilde{P}_{r,t}^{\mathrm{R,C}} = (1-\delta_{r,t})\tilde{P}_{r,t}^{\mathrm{R}}, \forall r \in \mathcal{R}, t \in \mathcal{T} \tag{3}$$

In the formula: r and $\mathcal{R}$, along with t and $\mathcal{T}$, are the indices and sets for RES and scheduling periods, respectively; $\tilde{P}_{r,t}^{\mathrm{R}}$ represents the available active power output of RES; $P_{r,t}^{\mathrm{R}}$ denotes the forecasted value; $\xi_{r,t}$ stands for the stochastic forecast error; $\boldsymbol{\xi}_t$ is the vector form of the RES forecast errors in the system; $\tilde{P}_{r,t}^{\mathrm{R,C}}$ indicates the actual active power output of RES; $\delta_{r,t}$ represents the power curtailment rate. This paper assumes that the RES operates in the mode of the constant power factor $\cos\phi$, and that $\varphi = \sqrt{(1-\cos^2\phi)/(\cos^2\phi)}$. Based on this, the actual reactive power of the RES can be modeled[9].

2.3 Objective Function

The transmission system costs include the generation cost and regulation reserve cost of SG, the RES curtailment cost, and the load shedding cost. The distribution system costs comprise the generation and regulation reserve cost of DG, the charging/discharging and regulation reserve cost of ES, the RES curtailment cost, as well as the load shedding cost. Based on this, the optimized objective function is proposed as follows:

$$\min \sum_{t\in\mathcal{T}} C_t^{\mathrm{Tran}} + \sum_{k\in\mathcal{K}} \sum_{t\in\mathcal{T}} C_{k,t}^{\mathrm{Dist}} \tag{4}$$

$$\begin{aligned} C_t^{\mathrm{Tran}} = & \sum_{g\in\mathcal{G}_{\mathrm{T}}} \left[\mathrm{c}_g^{\mathrm{p}} P_{g,t}^{\mathrm{G}} + \mathrm{c}_g^{\mathrm{r}} \left(r_{g,t}^{+} + r_{g,t}^{-} \right) \right] \\ & + \sum_{r\in\mathcal{R}_{\mathrm{T}}} \mathrm{c}_r^{\mathrm{cur}} \delta_{r,t} P_{r,t}^{\mathrm{R}} + \sum_{d\in\mathcal{D}_{\mathrm{T}}} \mathrm{c}_d^{\mathrm{cut}} P_{d,t}^{\mathrm{cut}} \end{aligned} \tag{5}$$

$$\begin{aligned} C_{k,t}^{\mathrm{Dist}} = & \sum_{g\in\mathcal{G}_{\mathrm{D}}} \left[\mathrm{c}_g^{\mathrm{p}} P_{g,t}^{\mathrm{G}} + \mathrm{c}_g^{\mathrm{r}} \left(r_{g,t}^{\mathrm{P},+} + r_{g,t}^{\mathrm{P},-} \right) \right] \\ & + \sum_{e\in\mathcal{E}_{\mathrm{D}}} \left[\mathrm{c}_e^{\mathrm{ch}} \chi_{ch} P_{e,t}^{\mathrm{E}} + \mathrm{c}_e^{\mathrm{dch}} \chi_{dch} P_{e,t}^{\mathrm{E}} + \mathrm{c}_e^{\mathrm{r}} (r_{e,t}^{+} + r_{e,t}^{-}) \right] \\ & + \sum_{r\in\mathcal{R}_{\mathrm{D}}} c_r^{\mathrm{cur}} \delta_{r,t} P_{r,t}^{\mathrm{R}} + \sum_{d\in\mathcal{D}_{\mathrm{D}}} c_r^{\mathrm{cut}} P_{d,t}^{\mathrm{cut}} \end{aligned} \tag{6}$$

In the formula: g and $\mathcal{G}$ are the index and set of generators, respectively; e and $\mathcal{E}$ are the index and set of ES, respectively; d and $\mathcal{D}$ are the index and set of loads, respectively. C_t^{Tran} and $C_{k,t}^{\mathrm{Dist}}$ represent the costs of the transmission system and the k-th distribution system during time period t, respectively. $\mathrm{c}_g^{\mathrm{p}}$ and $\mathrm{c}_g^{\mathrm{r}}$ denote the generation and reserve cost coefficients of generators; $P_{g,t}^{\mathrm{G}}$, $r_{g,t}^{+}$, and $r_{g,t}^{-}$ represent the generation power and upward/downward regulation reserves of generators. $\mathrm{c}_e^{\mathrm{ch}}$, $\mathrm{c}_e^{\mathrm{dch}}$, and $\mathrm{c}_e^{\mathrm{r}}$ are the charging/discharging and reserve cost coefficients of ES; $P_{e,t}^{\mathrm{E,ch}}$, $P_{e,t}^{\mathrm{E,dch}}$

and $r_{e,t}^{+}$, $r_{e,t}^{-}$ represent the active charging/discharging power and upward/downward regulation reserves of ES, respectively. c_r^{cur} is the cost coefficient of RES power curtailment. $P_{d,t}^{\mathrm{cut}}$ is the cost coefficient of load shedding, and $P_{d,t}^{\mathrm{cut}}$ is the magnitude of load shedding.

2.4 Regulation Resource Response Modeling

Building upon the traditional localized affine policy [10], this paper incorporates a reserve sharing mechanism between transmission and distribution systems. The adjustable resources within each system can respond not only to the RES forecast errors of their own system but also to the uncertainties of interconnected systems.

For $\forall t \in \mathcal{T}$, the actual output of the SG in the transmission system is:

$$\tilde{P}_{g,t}^{G} = P_{g,t}^{G} + (\alpha_{g,t}^{G})^{\mathrm{T}} \xi_t^{\mathrm{T}} + \sum_{k \in \mathcal{K}} (\beta_{k,g,t}^{G})^{\mathrm{T}} \xi_{k,t}^{\mathrm{D}}, \forall g \in \mathcal{G}_{\mathrm{T}} \tag{7}$$

In the formula: $\tilde{P}_{g,t}^{\mathrm{G}}$ represents the generation power of the SG after responding to uncertainties; $\boldsymbol{\xi}_t^{\mathrm{T}}$ and $\boldsymbol{\xi}_{k,t}^{\mathrm{D}}$ represent the RES forecast errors of the transmission network and the k-th distribution network; $\boldsymbol{\alpha}_{g,t}^{\mathrm{G}}$ and $\boldsymbol{\beta}_{k,g,t}^{\mathrm{G}}$ denote the affine participation factors of the SG to the transmission and distribution networks, respectively.

Substations can provide bidirectional reserve capacity support to the interconnected transmission and distribution networks by adjusting the power at the outlet bus. For $\forall t \in \mathcal{T}, k \in \mathcal{K}$, the boundary power is modeled as:

$$\tilde{P}_{k,t} = P_{k,t} - (\boldsymbol{\mu}_{k,t})^{\mathrm{T}} \boldsymbol{\xi}_t^{\mathrm{T}} + (\boldsymbol{\gamma}_{k,t})^{\mathrm{T}} \boldsymbol{\xi}_{k,t}^{\mathrm{D}} \tag{8}$$

In the formula: $P_{k,t}$ and $\tilde{P}_{k,t}$ represent the boundary power during the pre-dispatch phase and after responding to uncertainties, respectively, with the direction defined from the transmission grid to the distribution grid; $\boldsymbol{\mu}_{k,t}$ and $\boldsymbol{\gamma}_{k,t}$ denote the affine participation factors of the boundary power to the transmission and distribution networks, respectively.

Since the boundary power can only respond to the forecast errors of RES in one specific grid side, the following constraint should be imposed:

$$\left\| \boldsymbol{\mu}_{k,t} \right\| \bullet \left\| \boldsymbol{\gamma}_{k,t} \right\| = 0 \tag{9}$$

2.5 Transmission System Constraints

Due to its low line impedance ratio characteristic, the transmission network is modeled using an active DC power flow model, with all voltage magnitudes assumed to be at rated values and reactive power neglected. For readability, conditional term $\forall t \in \mathcal{T}$ is omitted in the following formulas:

$$\sum_{g \in \mathcal{G}_{\mathrm{T}}} P_{g,t}^{\mathrm{G}} + \sum_{r \in \mathcal{R}_{\mathrm{T}}} (1 - \delta_{r,t}) P_{r,t}^{\mathrm{R}} - \sum_{k \in \mathcal{K}} P_{k,t}^{\mathrm{T}} = \sum_{d \in \mathcal{D}_{\mathrm{T}}} (P_{d,t}^{\mathrm{D}} - P_{d,t}^{\mathrm{cut}}) \tag{10}$$

$$1-\delta_{r,t}=\sum_{g\in\mathcal{G}_{\mathrm{T}}}\alpha_{g,r,t}^{\mathrm{G}}+\sum_{k\in\mathcal{K}}\mu_{k,r,t}^{\mathrm{T}},\forall r\in\mathcal{R}_{\mathrm{T}} \tag{11}$$

$$\sum_{g\in\mathcal{G}_{\mathrm{T}}}\beta_{g,r,t}^{\mathrm{G}}=\sum_{k\in\mathcal{K}}\gamma_{k,r,t}^{\mathrm{T}},\forall r\in\mathcal{R}_{\mathrm{D}}^{k} \tag{12}$$

$$\begin{aligned}\tilde{f}_{l,t}=&\sum_{g\in\mathcal{G}_{\mathrm{T}}}\mathrm{G}_{l-g}\tilde{P}_{g,t}^{\mathrm{G}}+\sum_{r\in\mathcal{R}_{\mathrm{T}}}\mathrm{G}_{l-r}(1-\delta_{r,t})\tilde{P}_{r,t}^{\mathrm{R}}-\\&\sum_{k\in\mathcal{K}}\mathrm{G}_{l-k}\tilde{P}_{k,t}-\sum_{d\in\mathcal{D}_{\mathrm{T}}}\mathrm{G}_{l-d}(P_{d,t}^{\mathrm{D}}-P_{d,t}^{\mathrm{cut}}),\forall l\in\mathcal{L}_{\mathrm{T}}\end{aligned} \tag{13}$$

$$\inf_{\mathbb{P}\in\mathcal{P}_t}\mathbb{P}\left\{\tilde{f}_{l,t}\le F_l^{\max}\right\}\ge 1-\varepsilon,\forall l\in\mathcal{L}_{\mathrm{T}} \tag{14}$$

$$\inf_{\mathbb{P}\in\mathcal{P}_t}\mathbb{P}\left\{-F_l^{\max}\le\tilde{f}_{l,t}\right\}\ge 1-\varepsilon,\forall l\in\mathcal{L}_{\mathrm{T}} \tag{15}$$

$$P_{g,t}^{\mathrm{G}}+r_{g,t}^{+}\le P_g^{\max},\forall g\in\mathcal{G}_{\mathrm{T}} \tag{16}$$

$$P_{g,t}^{\mathrm{G}}-r_{g,t}^{-}\ge P_g^{\min},\forall g\in\mathcal{G}_{\mathrm{T}} \tag{17}$$

$$(P_{g,t}^{\mathrm{G}}+r_{g,t}^{+})-(P_{g,t-1}^{\mathrm{G}}-r_{g,t-1}^{-})\le R_g^{\mathrm{u}},\forall g\in\mathcal{G}_{\mathrm{T}} \tag{18}$$

$$(P_{g,t-1}^{\mathrm{G}}+r_{g,t-1}^{+})-(P_{g,t}^{\mathrm{G}}-r_{g,t}^{-})\le R_g^{\mathrm{d}},\forall g\in\mathcal{G}_{\mathrm{T}} \tag{19}$$

$$\inf_{\mathbb{P}\in\mathcal{P}_t}\mathbb{P}\left\{(\boldsymbol{\alpha}_{g,t}^{\mathrm{G}})^{\mathrm{T}}\boldsymbol{\xi}_t^{\mathrm{T}}+\sum_{k\in\mathcal{K}}(\boldsymbol{\beta}_{k,g,t}^{\mathrm{G}})^{\mathrm{T}}\boldsymbol{\xi}_{k,t}^{\mathrm{D}}\le r_{g,t}^{+}\right\}\ge 1-\varepsilon,\forall g\in\mathcal{G}_{\mathrm{T}} \tag{20}$$

$$\inf_{\mathbb{P}\in\mathcal{P}_t}\mathbb{P}\left\{(\boldsymbol{\alpha}_{g,t}^{\mathrm{G}})^{\mathrm{T}}\boldsymbol{\xi}_t^{\mathrm{T}}+\sum_{k\in\mathcal{K}}(\boldsymbol{\beta}_{k,g,t}^{\mathrm{G}})^{\mathrm{T}}\boldsymbol{\xi}_{k,t}^{\mathrm{D}}\ge -r_{g,t}^{-}\right\}\ge 1-\varepsilon,\forall g\in\mathcal{G}_{\mathrm{T}} \tag{21}$$

$$0\le\delta_{r,t}\le 1,\forall r\in\mathcal{R}_{\mathrm{T}} \tag{22}$$

$$0\le P_{d,t}^{cut}\le P_{d,t}^{\mathrm{c,max}},\forall d\in\mathcal{D}_{\mathrm{T}} \tag{23}$$

Formulas (10)–(11) represent the base-point power balance constraints of the system; formula (12) defines the affine participation factor balance constraint for the uncertain components; formulas (13)–(15) describe the line transmission power constraints; formulas (16)–(17) impose the maximum and minimum output constraints of the SG; formulas (18)–(19) specify the ramp-up and ramp-down constraints of the SG. formulas (20)–(21) set the upward and downward reserve constraints of the SG; formula (22) reflects the RES power curtailment rate constraint; formula (23) represents the maximum load shedding constraint.

In the formula: l and $\mathcal{L}_{\mathrm{T}}$ are the index and set of transmission lines in the transmission network, respectively; $\tilde{f}_{l,t}$ represents the actual line transmission power; G_{l-g}, G_{l-r}, G_{l-k} and G_{l-d} denote the power transfer distribution factors of generator g, renewable energy source r, distribution network k, and load d to line l, respectively; $F_l^{\max}$ is the maximum transmission capacity of the line. $P_g^{\max}$ and $P_g^{\min}$ represent the maximum and minimum power output of generator g, respectively; R_g^{u} and R_g^{d} are the ramp-up and ramp-down rates of generator g, respectively; $P_{d,t}^{\mathrm{c,max}}$ is the maximum allowable load shedding amount.

2.6 Distribution System Constraints

Under high penetration of distributed generation, the ADN faces high risks of voltage limit violations. This paper employs a linearized Distflow model[11] to characterize the voltage-reactive power coupling characteristic. This model ensures that the optimization model remains convex while maintaining high accuracy, and is compatible with node voltage dynamic regulation mechanisms. The constraints for DG, RES power curtailment rate, and load shedding are similar to those in the transmission network and will not be reiterated. For readability, conditional term $\forall t \in \mathcal{T}$ is omitted in the following formulas:

For the boundary node $i \in \mathcal{N}_{\text{D-root}}$, the network power flow constraint is formulated as:

$$P_{k,t}^{\text{D}} = \sum_{ij \in \mathcal{L}_{\text{D}}} f_{ij,t}^{\text{P}} \tag{24}$$

$$Q_{k,t}^{\text{D}} = \sum_{ij \in \mathcal{L}_{\text{D}}} f_{ij,t}^{\text{Q}} \tag{25}$$

$$-\mu_{k,r,t}^{\text{D}} = \sum_{ij \in \mathcal{L}_{\text{D}}} \alpha_{ij,r,t}^{\text{P,L}}, \forall r \in \mathcal{R}_{\text{T}} \tag{26}$$

$$-\varphi\mu_{k,r,t}^{\text{D}} = \sum_{ij \in \mathcal{L}_{\text{D}}} \alpha_{ij,r,t}^{\text{Q,L}}, \forall r \in \mathcal{R}_{\text{T}} \tag{27}$$

$$\gamma_{k,r,t}^{\text{D}} = \sum_{ij \in \mathcal{L}_{\text{D}}} \beta_{ij,r,t}^{\text{P,L}}, \forall r \in \mathcal{R}_{\text{D}} \tag{28}$$

$$\varphi\gamma_{k,r,t}^{\text{D}} = \sum_{ij \in \mathcal{L}_{\text{D}}} \beta_{ij,r,t}^{\text{Q,L}}, \forall r \in \mathcal{R}_{\text{D}} \tag{29}$$

For internal nodes $\forall i \in \mathcal{N}_{\text{D}}$, the network power flow constraint is formulated as:

$$P_{i,t}^{\text{G}} + P_{i,t}^{\text{E}} + (1-\delta_{i,t})P_{i,t}^{\text{R}} - P_{i,t}^{\text{D}} + P_{i,t}^{\text{cut}} = \sum_{ij \in \mathcal{L}_{\text{D}}} f_{ij,t}^{\text{P}} \tag{30}$$

$$\alpha_{i,r,t}^{\text{G,P}} + \alpha_{i,r,t}^{\text{E}} - (1-\delta_{i,t}) = \sum_{ij \in \mathcal{L}_{\text{D}}} \alpha_{ij,r,t}^{\text{P,L}}, \forall r \in \mathcal{R}_{\text{T}} \tag{31}$$

$$\beta_{i,r,t}^{\text{G,P}} + \beta_{i,r,t}^{\text{E}} - (1-\delta_{i,t}) = \sum_{ij \in \mathcal{L}_{\text{D}}} \beta_{ij,r,t}^{\text{P,L}}, \forall r \in \mathcal{R}_{\text{D}} \tag{32}$$

$$Q_{i,t}^{\text{G}} + (1-\delta_{i,t})Q_{i,t}^{\text{R}} - Q_{i,t}^{\text{D}} + Q_{i,t}^{\text{cut}} = \sum_{ij \in \mathcal{L}_{\text{D}}} f_{ij,t}^{\text{Q}} \tag{33}$$

$$\alpha_{i,r,t}^{\text{G,Q}} - \varphi(1-\delta_{i,t}) = \sum_{ij \in \mathcal{L}_{\text{D}}} \alpha_{ij,r,t}^{\text{Q,L}}, \forall r \in \mathcal{R}_{\text{T}} \tag{34}$$

$$\beta_{i,r,t}^{\text{G,P}} - \varphi(1-\delta_{i,t}) = \sum_{ij \in \mathcal{L}_{\text{D}}} \beta_{ij,r,t}^{\text{P,L}}, \forall r \in \mathcal{R}_{\text{D}} \tag{35}$$

$$V_{i,t}^2 = V_{j,t}^2 - 2(\text{r}_{ij} f_{ij,t}^{\text{P}} + \text{x}_{ij} f_{ij,t}^{\text{Q}}) \tag{36}$$

$$\alpha_{i,t}^{\text{V}} = \alpha_{j,t}^{\text{V}} - 2(\text{r}_{ij}\alpha_{ij,r,t}^{\text{P,L}} + \text{x}_{ij}\alpha_{ij,r,t}^{\text{Q,L}}), \forall r \in \mathcal{R}_{\text{T}} \tag{37}$$

$$\beta_{i,t}^{\text{V}} = \beta_{j,t}^{\text{V}} - 2(\text{r}_{ij}\beta_{ij,r,t}^{\text{P,L}} + \text{x}_{ij}\beta_{ij,r,t}^{\text{Q,L}}), \forall r \in \mathcal{R}_{\text{D}} \tag{38}$$

For $\forall e \in \mathcal{E}_{\text{D}}$, the constraints for ES in the distribution network are formulated as:

$$E_{e,0} = E_{e,|\text{T}|} \tag{39}$$

$$E_{e,t+1} = E_{e,t} - \chi_{dch}\eta_e^{\mathrm{dch}} P_{e,t}^{\mathrm{E}} \Delta t - \chi_{ch} P_{e,t}^{\mathrm{E}} \Delta t / \eta_e^{\mathrm{ch}} \tag{40}$$

$$E_e^{\min} \le E_{e,t} \le E_e^{\max} \tag{41}$$

$$\chi_{ch} P_{e,t}^{\mathrm{E,ch,max}} \le P_{e,t}^{\mathrm{E}} \le \chi_{dch} P_{e,t}^{\mathrm{E,dch,max}} \tag{42}$$

$$\chi_{ch} + \chi_{dch} \le 1 \tag{43}$$

$$P_{e,t}^{\mathrm{E}} + r_{e,t}^{+} \le P_{e,t}^{\mathrm{E,dch,max}} \tag{44}$$

$$P_{e,t}^{\mathrm{E}} - r_{e,t}^{-} \ge -P_{e,t}^{\mathrm{E,ch,max}} \tag{45}$$

$$\inf_{\mathbb{P}\in\mathcal{P}_i} \mathbb{P}\left\{(\boldsymbol{\alpha}_{e,t}^{\mathrm{E}})^{\mathrm{T}} \boldsymbol{\xi}_t^{\mathrm{T}} + (\boldsymbol{\beta}_{e,t}^{\mathrm{E}})^{\mathrm{T}} \boldsymbol{\xi}_t^{\mathrm{D}} \le r_{e,t}^{+}\right\} \ge 1-\varepsilon \tag{46}$$

$$\inf_{\mathbb{P}\in\mathcal{P}_i} \mathbb{P}\left\{(\boldsymbol{\alpha}_{e,t}^{\mathrm{E}})^{\mathrm{T}} \boldsymbol{\xi}_t^{\mathrm{T}} + (\boldsymbol{\beta}_{e,t}^{\mathrm{E}})^{\mathrm{T}} \boldsymbol{\xi}_t^{\mathrm{D}} \ge -r_{e,t}^{-}\right\} \ge 1-\varepsilon \tag{47}$$

In the formula: $E_{e,0}$ and $E_{e,|\mathrm{T}|}$ represent the initial energy level and the energy level at the end of the scheduling period for the ES, respectively; $E_e^{\max}$ and $E_e^{\min}$ denote the maximum and minimum energy capacity, respectively; η_e^{ch} and η_e^{dch} are the charging and discharging efficiencies, respectively; Δt is the scheduling time duration; $P_{e,t}^{\mathrm{E,ch,max}}$ and $P_{e,t}^{\mathrm{E,dch,max}}$ represent the maximum charging and discharging power, respectively; χ_{dch} and χ_{ch} are binary variables indicating the charging and discharging states.

The constraints for maximum line transmission capacity and node voltage are formulated as follows:

$$\inf_{\mathbb{P}\in\mathcal{P}_i} \mathbb{P}\left\{(\tilde{f}_{ij,t}^{\mathrm{P}})^2 + (\tilde{f}_{ij,t}^{\mathrm{Q}})^2 \le (S_{ij}^{\max})^2\right\} \ge 1-\varepsilon, \forall l \in \mathcal{L}_{\mathrm{D}} \tag{48}$$

$$\inf_{\mathbb{P}\in\mathcal{P}_i} \mathbb{P}\left\{\tilde{V}_{i,t}^2 \le \mathrm{V}_{\max}^2\right\} \ge 1-\varepsilon, \forall i \in \mathcal{N}_{\mathrm{D}} \tag{49}$$

$$\inf_{\mathbb{P}\in\mathcal{P}_i} \mathbb{P}\left\{\tilde{V}_{i,t}^2 \ge \mathrm{V}_{\min}^2\right\} \ge 1-\varepsilon, \forall i \in \mathcal{N}_{\mathrm{D}} \tag{50}$$

In the formula: $S_{ij}^{\max}$ represents the maximum transmission capacity of the line; $\mathrm{V}_{\max}$ and $\mathrm{V}_{\min}$ denote the maximum and minimum voltage magnitudes, respectively. In this paper, the maximum allowable voltage deviation is set to 5 %.

2.7 Consistency Constraints

In the distributed coordinated scheduling of transmission and distribution systems, the transmission grid treats the distribution grid as an uncertain load, while the distribution grid treats the transmission grid as an adjustable generator. The boundary power must satisfy the following consistency constraints:

$$\begin{cases} P_{k,t}^{\mathrm{T}} = P_{k,t}^{\mathrm{D}}, r_{k,t}^{\mathrm{T},+} = r_{k,t}^{\mathrm{D},+}, r_{k,t}^{\mathrm{T},-} = r_{k,t}^{\mathrm{D},-} \\ \mu_{k,r,t}^{\mathrm{T}} = \mu_{k,r,t}^{\mathrm{D}}, \gamma_{k,r,t}^{\mathrm{T}} = \gamma_{k,r,t}^{\mathrm{D}} \end{cases} \tag{51}$$

In the formula: $P_{k,t}$ represents the base-point boundary power; $r_{k,t}^{+}$ and $r_{k,t}^{-}$ denote the upward and downward shared reserve of the boundary power, respectively.

Meanwhile, the boundary power must satisfy the following constraints:

$$P_{k,t} + r_{k,t}^{+} \le P_k^{\max} \tag{52}$$

$$P_{k,t} - r_{k,t}^{-} \ge -P_k^{\max} \tag{53}$$

$$\inf_{\mathbb{P}\in\mathcal{P}_i} \mathbb{P}\left\{-(\boldsymbol{\mu}_{k,t})^{\mathrm{T}}\boldsymbol{\xi}_t^{\mathrm{T}} + (\boldsymbol{\gamma}_{k,t})^{\mathrm{T}}\boldsymbol{\xi}_{k,t}^{\mathrm{D}} \le r_{k,t}^{+}\right\} \ge 1-\varepsilon \tag{54}$$

$$\inf_{\mathbb{P}\in\mathcal{P}_i} \mathbb{P}\left\{-(\boldsymbol{\mu}_{k,t})^{\mathrm{T}}\boldsymbol{\xi}_t^{\mathrm{T}} + (\boldsymbol{\gamma}_{k,t})^{\mathrm{T}}\boldsymbol{\xi}_{k,t}^{\mathrm{D}} \ge -r_{k,t}^{-}\right\} \ge 1-\varepsilon \tag{55}$$

In the formula: $P_k^{\max}$ represents the maximum transmission power of the interconnection line between the transmission and distribution grids.

3 Solution Methodology

3.1 Non-Convex Constraint Reformulation

The centralized transmission-distribution system distributionally robust optimization model established in Section 2 can be expressed in the following compact form:

$$\begin{aligned} &\min_{\Theta} \text{formula(4)} \\ &\text{s.t. formula(9)} \sim \text{formula(55)} \end{aligned} \tag{56}$$

For formula(9), it can be convexified by introducing binary variables into the following constraints:

$$\begin{cases} \mu_{k,r,t} \le p_{k,t}^{1}, \forall r \in \mathcal{R}_{\mathrm{T}} \\ \gamma_{k,r,t} \le p_{k,t}^{2}, \forall r \in \mathcal{R}_{\mathrm{D}} \\ p_{k,t}^{1} + p_{k,t}^{2} \le 1, \forall p_{k,t}^{1}, p_{k,t}^{2} \{0,1\} \end{cases} \tag{57}$$

For the DRCC in the form of formula (14), it can be expressed as follows:

$$\inf_{\mathbb{P}\in\mathcal{P}} \mathbb{P}\left\{a^{\mathrm{T}}(x)\xi + b(x) \le 0\right\} \ge 1-\varepsilon \tag{58}$$

The construction of the ambiguity set based on the Wasserstein distance can be found in Reference[12]. By approximating the formula(58), it can be transformed into the following series of linear constraints:

$$\begin{cases} \lambda\theta - \beta\varepsilon + \dfrac{1}{N}\sum_{n=1}^{N} z_n \le 0 \\ \boldsymbol{a}^{\mathrm{T}}(\boldsymbol{x})\hat{\xi}_n + b(\boldsymbol{x}) + \beta \le z_n, n = 1,2,...,N \\ -\lambda \le a_n(x) \le \lambda, n = 1,2,...,N \\ \lambda, \beta, z_n \ge 0,, n = 1,2,...,N \end{cases} \tag{59}$$

In the formula: λ, β and z_n are all auxiliary variables; N represents the number of data points in the ambiguity set $\mathcal{P}$; $\left\{\hat{\xi}_1, \hat{\xi}_2, \cdots \hat{\xi}_{\mathrm{N}}\right\}$ are the historical data that used to construct the ambiguity set $\mathcal{P}$.

3.2 Parallelized ADMM Distributed Coordination Algorithm

To solve the transmission-distribution system distributionally robust optimization model in a distributed manner, a parallelized computational framework based on the ADMM is established in this paper. The TPS and each ADN can simultaneously and independently solve their respective regional optimization problems, then exchange boundary information and update their local models. When all coupling variables are sufficiently close, the optimal scheduling scheme for the ITD can be obtained.

The augmented lagrangian function for the centralized transmission-distribution system distributionally robust optimization model is formulated as follows:

$$F(\boldsymbol{x}^{\mathrm{T}})+\sum_{k\in\mathcal{K}}\left\lfloor F_k(\boldsymbol{x}_k^{\mathrm{D}})+L_k(\boldsymbol{x}_k^{\mathrm{T}},\boldsymbol{x}_k^{\mathrm{D}},\boldsymbol{\lambda}_k)\right\rfloor \tag{60}$$

$$L_k(\boldsymbol{x}_k^{\mathrm{T}},\boldsymbol{x}_k^{\mathrm{D}},\boldsymbol{\lambda}_k)=\boldsymbol{\lambda}_k^{\mathrm{T}}(\boldsymbol{x}_k^{\mathrm{T}}-\boldsymbol{x}_k^{\mathrm{D}})+0.5\rho\left\|\boldsymbol{x}_k^{\mathrm{T}}-\boldsymbol{x}_k^{\mathrm{D}}\right\|_2^2 \tag{61}$$

To enable parallel computation for the transmission and distribution networks, a third-party variable $\bar{\boldsymbol{x}}$ is introduced. Each variable can be updated through the following parallelizable process:

$$\boldsymbol{x}_k^{\mathrm{D},+}=\arg\min_{\boldsymbol{x}_k^{\mathrm{D}}}F_k(\boldsymbol{x}_k^{\mathrm{D}})+L_k(\bar{\boldsymbol{x}},\boldsymbol{x}_k^{\mathrm{D}},\boldsymbol{\lambda}_k^{\mathrm{D}}),\forall k\in\mathcal{K} \tag{62}$$

$$\boldsymbol{x}^{\mathrm{T},+}=\arg\min_{\boldsymbol{x}^{\mathrm{T}}}F(\boldsymbol{x}^{\mathrm{T}})+\sum_{k\in\mathcal{K}}L_k(\boldsymbol{x}_k^{\mathrm{T}},\bar{\boldsymbol{x}},\boldsymbol{\lambda}_k^{\mathrm{T}}) \tag{63}$$

$$\bar{\boldsymbol{x}}^{+}=(\boldsymbol{x}^{\mathrm{T},+}+\boldsymbol{x}^{\mathrm{D},+})/2 \tag{64}$$

$$\boldsymbol{\lambda}_k^{\mathrm{T}+}=\boldsymbol{\lambda}_k^{\mathrm{T}}+\rho(\boldsymbol{x}_k^{\mathrm{T},+}-\bar{\boldsymbol{x}}_k^{+}),\forall k\in\mathcal{K} \tag{65}$$

$$\boldsymbol{\lambda}_k^{\mathrm{D},+}=\boldsymbol{\lambda}_k^{\mathrm{D}}+\rho(\boldsymbol{x}_k^{\mathrm{D},+}-\bar{\boldsymbol{x}}_k^{+}),\forall k\in\mathcal{K} \tag{66}$$

3.3 Varying Penalty Factor Strategy

In the classical ADMM algorithm, the penalty factor ρ is typically set as a constant, known as the constant penalty factor(CPF) strategy. However, since the convergence properties of ADMM are highly sensitive to the value of the penalty factor, it is often difficult to determine its optimal value. To address this issue, the varying penalty factor strategy(VPF), is introduced during the ADMM iterative process[13].

$$\rho^{n+1}=\begin{cases}\omega^{up}\rho^{n}, gap^{P}>\vartheta gap^{D}\\ \rho^{n}/\omega^{dn}, gap^{D}>\vartheta gap^{P}\\ \rho^{n}, others\end{cases} \tag{67}$$

In the formula: gap^P and gap^D represent the primal residual and dual residual, respectively.

During the iterative process, the penalty factor can be adjusted based on the relative values of the primal and dual residuals. When the primal residual is ϑ times the dual residual, the VPS increases ρ by a factor of ω^{up}; conversely, it decreases ρ by a factor of ω^{dn}. By dynamically updating the value of the penalty factor according to

the iterative results in the ADMM process, the convergence properties of the algorithm are enhanced, and the parameter selection issue is mitigated.

3.4 Solution Procedure

The computational procedure of the parallelized ADMM distributed algorithm incorporating the VPF is as follows:

Algorithm: Parallelized ADMM Distributed Algorithm

Initialization:

Initialize the penalty factor with value ρ^0, the Lagrange multipliers with values [illegible] and [illegible], and the boundary power with value $\bar{\boldsymbol{x}}^0$.

Set the iteration count to $n=0$, the maximum iteration count to *M*, the primal residual tolerance, the dual residual tolerance, and the parameters ω^{up}, ω^{dn}, and ϑ.

Repeat:

Step1: Send $\bar{\boldsymbol{x}}_{n}$ [illegible] and $\bar{\boldsymbol{x}}_{n}$ [illegible] to the TPS and each ADN respectively, and solve each optimization subproblem in parallel.

Step2: Determine whether the convergence tolerance is satisfied. If yes, output the results; otherwise, proceed to *Step 3*.

Step3: Check if the maximum iteration count *M* has been reached. If reached, terminate the program; otherwise, proceed to *Step 4*.

Step4: Update $\boldsymbol{x}_{n+1}^{\mathrm{T}}$, $\boldsymbol{x}_{k,n+1}^{\mathrm{D}}$, $\bar{\boldsymbol{x}}_{n+1}$, [illegible], [illegible], and [illegible] according to formulas(62)–(67), and return to *Step 1*.

4 Case Study

In this section, the proposed ITD distributionally robust distributed optimal scheduling(ITD-DRDOS) model is simulated and analyzed on the T39-D2 system to validate the effectiveness of the proposed methodology. The T39-D2 system consists of one modified IEEE39-bus TPS connected to two modified IEEE33-bus ADNs. The ADNs are connected to bus 16 and bus 20 of the TPS, respectively. Unit data, RES data, ES data, load curve and other example data are provided in Appendix A.

This paper sets the number of scheduling time periods to $|\mathrm{T}|=24$ with a scheduling step size of 1 hour. Using the Monte Carlo method, 1000 forecast error scenarios are generated following a Gaussian distribution with a mean of 0 and a standard deviation equal to 5% of the RES forecast value. Among these, 100 scenarios are selected to construct the DRCC, while the remaining 900 scenarios are used to validate the maximum empirical violation probability(MEVP) of each chance constraint. The confidence level for each chance constraint is set to 0.95. In this system, the initial value of the penalty factor is set to 1, and parameters ω^{up}, ω^{dn}, and ϑ are set to 2, 2,

and 10, respectively. To facilitate subsequent analysis, the following three scheduling methods are defined for comparison:

M1. ITD distributionally robust centralized optimal scheduling method.

M2. ITD distributionally robust distributed optimal scheduling method without reserve sharing.

M3. TDC-DRDOS method proposed in this paper.

All models were solved on a computer equipped with a 2.5 GHz Intel Core i5-12400H CPU and 16 GB of RAM. The optimization software used was Gurobi 11.0.3, implemented in Python 3.12.0, with the solver convergence gap set to 0.0015.

4.1 Comparison of Economic Costs Between Centralized and Distributed Scheduling Methods

The economic costs of the three scheduling methods are summarized in Table 1. No load shedding occurred in any method, and thus related results are omitted. Compared to the centralized scheduling method M1, the distributed scheduling method M3 exhibits negligible differences in all economic cost categories, with a total cost error of only 0.088%, fully validating the computational accuracy of the M3 method under a distributed computing architecture. In contrast, due to the lack of a reserve sharing mechanism, the M2 method requires each subsystem to independently balance the RES forecast errors within its own system, leading to a significant increase in total cost. Specifically, the reserve cost of M2 increased by 1.02% compared to M3, and the power curtailment cost also rose. In terms of computational performance, the M2 and M3 methods converged after 46 and 62 iterations, respectively. The solution time increased approximately linearly compared to M1, demonstrating the favorable convergence and computational efficiency of the proposed model.

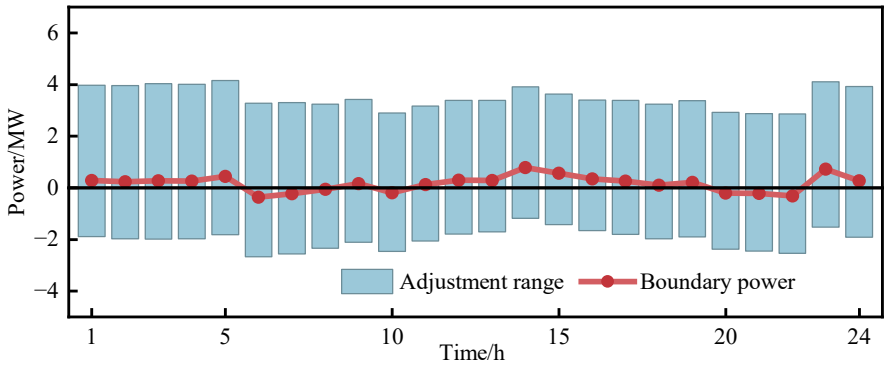
Table 1. Comparison of economic costs among the three methods/CNY

Method	Total cost	TPS cost	AND-1 cost	AND-2 cost
M1	282045.49	279657.99	1197.64	1189.87
M2	283181.52	280718.53	1243.40	1219.59
M3	282292.74	279835.10	1244.52	1213.11
Method	Reserve cost	Curtailment cost	Iteration count	Solution time/s
M1	10286.82	12049.73	1	3.63
M2	10556.71	12100.57	46	156.29
M3	10450.55	12067.91	62	242.75

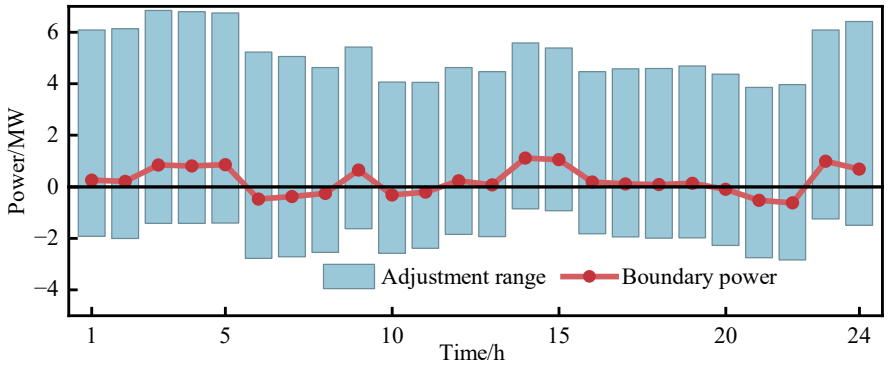
4.2 Comparison of Reserve Sharing and Non-Sharing

Fig. 2 illustrates the base-point boundary power and the allocation of shared reserves across time periods under the M3 method. After the realization of RES uncertainties, the boundary power can be adjusted within the reserve range, remaining feasible even during reverse power flow periods at hours 6–8 and 20–22, demonstrating the bidirec-

tional reserve support capability between the TPS and ADN. Meanwhile, the relatively smooth variation curve of the boundary power indicates that the shared reserves effectively mitigate power impacts at the transmission-distribution interface. Fig. 3 further compares the total system reserve capacity per time period between the M2 and M3 methods. Compared to the independent reserve configuration in each system under the M2 method, the M3 method significantly reduces the total reserve requirement of the system through the sharing mechanism, thereby improving overall resource utilization efficiency.



(a) TPS-AND1



(b) TPS-AND2

Fig. 2. Base-point boundary power and shared reserve range in transmission-distribution network under M3 method

14

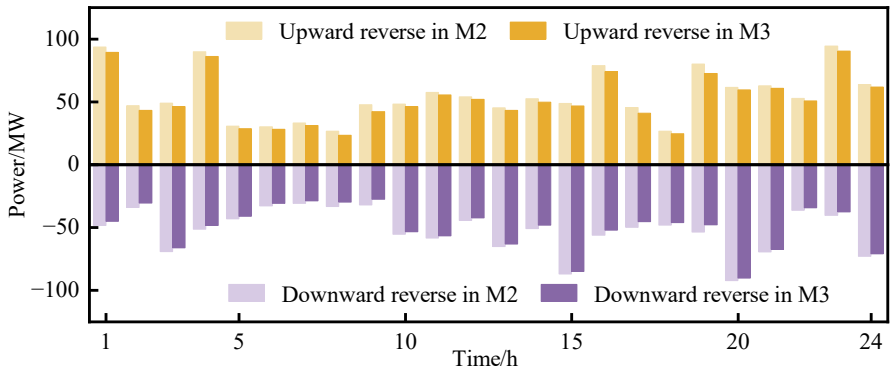
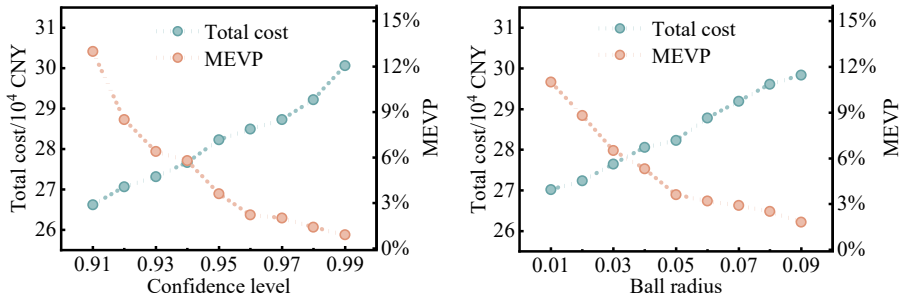


Fig. 3. Comparison of total system reserve capacity between M2 and M3 methods

4.3 Sensitivity Analysis of the DRCC Method

Fig. 4(a) and Fig. 4(b) illustrate the impacts of varying confidence levels and different Wasserstein ball radius on the MEVP, respectively. In Fig. 4(a), the total cost shows an increasing trend as the confidence level rises, while the MEVP decreases. This indicates that although higher confidence levels enhance system robustness, they come at the expense of increased operational costs. In Fig. 4(b), as the Wasserstein ball radius expands, a broader set of potential probability distributions of RES uncertainty scenarios are taken into account. This improves system robustness under the most extreme distributions, leading to a corresponding reduction in MEVP and a gradual increase in total cost.



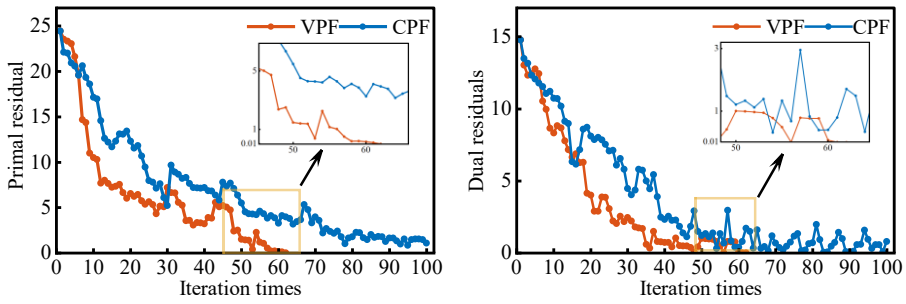
(a) Confidence level sensitivity (b) Ball radius sensitivity

Fig. 4. Parameter sensitivity analysis of the DRCC method

4.4 ADMM Convergence Analysis

Fig. 5 compares the variations of the primal and dual residuals with iterations in the ADMM algorithm under the VPF and CPF strategies. The primal residual reflects the inconsistency among the solutions of the subproblems. In

Fig. 5(a), the primal residual under the VPF strategy decreases rapidly in the early iterations and converges at the 62-th iteration. In contrast, the CPF strategy exhibits slower overall convergence speed. The dual residual indicates the satisfaction degree of the dual optimality conditions. In
Fig. 5(b), the VPF strategy demonstrates better performance in reducing the dual residual, meeting the convergence accuracy for the first time at the 56th iteration. Due to the fixed penalty factor's inability to adapt to dynamic changes in the problem, the CPF strategy shows significant oscillations in the later iterations. The VPF strategy converges after 62 iterations, whereas the CPF strategy fails to meet the convergence accuracy even after 100 iterations, validating the effectiveness and superiority of the VPF strategy in handling complex coupled optimization problems.



(a) Primal residual (b) Dual residual

Fig. 5. Comparison of residual variation in ADMM between CPF and VPF strategies

5 Conclusion

This paper proposes a distributed economic optimal scheduling method for transmission-distribution systems oriented to reserve sharing, which fully coordinates the adjustable resources within the integrated system to alleviate reserve pressure under high-penetration RES integration. The main conclusions are as follows:

DRCC optimization model based on bidirectional reserve sharing is proposed, incorporating a local affine-power curtailment coupling strategy. This approach achieves coordinated optimization of adjustable resources across transmission and distribution systems, significantly reducing system reserve redundancy and economic costs.

To address the coupling challenges caused by boundary power consistency constraints, a parallelized ADMM solution architecture is constructed, and a VPF update strategy based on the primal-dual residual ratio is further proposed. This framework simultaneously solves all subproblems while effectively enhancing the convergence speed of the algorithm.

References

[1] Zhang Z, Du E, Teng F, et al. Modeling frequency dynamics in unit commitment with a high share of renewable energy[J]. IEEE Transations on Power Systems, 2020, 35(6): 4383-4395.

[2] Yu J, Li Z, Guo Y, et al. Decentralized chance-constrained economic dispatch for integrated transmission-district energy systems[J]. IEEE Transactions on Smart Grid, 2019, 10(6): 6724-6734.

[3] ZHANG Xu, WANG Hongtao. Optimal dispatch method of transmission and distribution coordination for power systems with high proportion of renewable energy[J]. Automation of Electric Power Systems, 2019, 43(3):67-75.

[4] Chen Z, Li Z, Guo C, et al. Fully distributed robust reserve scheduling for coupled transmission and distribution systems[J]. IEEE Transactions on Power Systems, 2021, 36(1): 169-182.

[5] SHA Licheng, XU Kai, LI Li, et al. Distributed distributionally robust optimization of integrated transmission and distribution system considering unimodality-skewness information about uncertainty[J]. Proceedings of the CSU-EPSA, 2025, 37(04): 118-128+138.

[6] Tan Z, Yan Z, Zhong H, et al. Non-iterative solution for coordinated optimal dispatch via equivalent projection-part I: theory[J]. IEEE Transactions on Power Systems, 2024, 39(1): 890-898.

[7] JI Xingquan, SUN Chenhao, ZHANG Yumin, et al. Coordinated optimal scheduling of transmission and distribution networks based on multiple agents and improved target cascading method[J]. Automation of Electric Power Systems, 2025, 49(2): 165-174.

[8] Wang Q, Wu W, Lin C, et al. A spatio-temporal decomposition method for the coordinated economic dispatch of integrated transmission and distribution grids[J]. IEEE Transactions on Power Systems, 2024, 39(3): 4835-4851.

[9] Yang L, Yang H, Cao X, et al. Distributionally robust frequency-constrained microgrid scheduling towards seamless islanding[A]. arXiv, 2024.

[10] Roald L, Krause T, Andersson G. Integrated balancing and congestion management under forecast uncertainty[C]//2016 IEEE International Energy Conference (ENERGYCON), 2016: 1-6.

[11] Zhai J, Jiang Y, Shi Y, et al. Distributionally robust joint chance-constrained dispatch for integrated transmission-distribution systems via distributed optimization[J]. IEEE Transactions on Smart Grid, 2022, 13(3): 2132-2147.

[12] Xu D, Wu Z. Enhanced frequency aware microgrid scheduling towards seamless islanding under frequency support of heterogeneous resources: A distributionally robust chance constrained approach[J]. International Journal of Electrical Power & Energy Systems, 2024, 162: 110310.

[13] Chen Z, Guo C, Dong S, et al. Distributed robust dynamic economic dispatch of integrated transmission and distribution systems[J]. IEEE Transactions on Industry Applications, 2021, 57(5): 4500-4512.

073 Multi-Time-Scale Economic Dispatch Model and Method for Active Distribution Networks Driven by Complex Network Algorithms

Liu Yihua[1], Wang Zhirui[1], Sun Zhiheng[1], Hao Jiawei[1], Sun Lilin[1], Jiao Jiacheng[2], Li Gang[2], Wang Zhiyuan[2]

[1] State Grid Shanghai Electric Power Company Shinan Power Supply Company, Shanghai, China
[2] Nanjing Normal University, Nanjing, China

Abstract. Complex network theory still faces challenges in the economic dispatch of active distribution networks (ADNs), such as insufficient multi-time-scale coordination and inaccurate handling of distributed energy resource uncertainties. To address these challenges, this paper proposes a multi-time-scale economic dispatch model and method for active distribution networks driven by complex network algorithms. First, a distribution network topology model is constructed with node importance as the core, incorporating factors such as node power load and access to distributed energy resources into the multi-time-scale dispatch framework. Secondly, a hierarchical complex network clustering algorithm is used to cluster various resources, improving the accuracy of load and power generation forecasts and the efficiency of coordinated dispatch. A Monte Carlo method is introduced to model and simulate the uncertainty of renewable energy output. Economic dispatch is solved using a mixed-integer quadratic programming algorithm, and a rolling optimization technique is used to dynamically update dispatch decisions across different time scales. Simulation results demonstrate that the proposed method effectively reduces the overall system operating cost to 7,077 yuan, increases the renewable energy absorption rate to 95.8%, and reduces dispatch response speed to 2.35% in a case study of an IEEE 33-node active distribution network, demonstrating strong adaptability and cost-effectiveness. This paper provides theoretical and technical support for the multi-timescale economic operation and optimization of active distribution networks.

Keywords: Complex Network, Active Distribution Network, Multi-Timescale, Economic Dispatch, Mixed-Integer Quadratic Programming.

1 Introduction

Due to the high penetration of distributed energy resources and the dual uncertainty of sources and loads, active distribution networks face complex network structures, difficulties in multi-source coordination, and significant challenges in economical and efficient operation. Traditional dispatch strategies often rely on simple, single-layer

optimization models, making them incapable of addressing the complex internal logic of distribution networks characterized by node diversity, renewable energy volatility, and spatiotemporal load variations. In actual operation, the interplay of multiple factors, such as uneven resource distribution among nodes, dynamic changes in network topology, and meteorological and load forecasting errors, significantly limits the coordination and robustness of economic dispatch in distribution networks. Complex network theory provides a powerful tool for understanding and modeling the structure and dynamic evolution of active distribution networks, helping to reveal the profound impact of factors such as node importance and network community structure on dispatch efficiency and fault tolerance.

Combining complex network analysis with multi-timescale economic dispatch is expected to overcome the bottlenecks of traditional dispatch models in resource coordination and uncertainty management. By clustering and segmenting network structures, key nodes and local load/generation patterns can be more accurately identified, providing a model foundation with higher spatial resolution for the forecasting and dispatch of distributed energy and loads. Furthermore, multi-scenario generation and rolling optimization based on uncertainty modeling can dynamically adapt to real-time fluctuations in renewable energy and load, enhancing the flexibility of economic dispatch and the safety margin of decision-making.

This paper integrates complex network theory, hierarchical clustering algorithms, Monte Carlo uncertainty modeling, and a rolling optimization dispatch framework to construct a new multi-timescale economic dispatch model for active distribution networks. This innovative approach uses network node importance as a key indicator for resource clustering and dispatch weighting, breaking through the limitations of traditional static partitioning and taking into account both network structure evolution and the dynamic response of sources and loads. Through cluster-driven multi-timescale scheduling and uncertainty scenario simulation, the paper achieved system collaborative optimization and high-confidence risk control, providing theoretical innovation and technical paths for the economic operation of active distribution networks.

2 Related Works

With the continuous increase in the penetration of distributed energy resources, multi-timescale scheduling and optimization have become a hot topic in active distribution network operation research. Researchers have conducted extensive research on issues such as flexible resource coordination and multi-energy complementarity. Zeng et al. [1] took the minimization of the total operating cost of AC and DC distribution networks as the objective function and established a distribution network equipment model, a second-order cone power flow model and a distribution network reconstruction model. Based on the different flexibility of the equipment, a multi-time scale collaborative scheduling method of intraday, day-ahead and real-time was proposed to meet different control requirements. Wang et al. [2] proposed a multi-time scale distributed optimization operation strategy for AC and DC distribution

networks considering flexibility in response to the problem of increased demand for flexibility resources due to the high proportion of renewable energy access to the distribution network and the increased complexity of multi-flexibility resource control. Yuan et al. [3] proposed a two-stage multi-time-scale optimization scheduling method for medium and low voltage distribution networks with a high proportion of photovoltaic power, and verified the effectiveness of the proposed method based on the improved IEEE 33-bus medium voltage system and 21-bus low voltage system. Li et al. [4] considered the power prediction accuracy characteristics of source and load and the equipment operation and control characteristics, and proposed a multi-time-scale intelligent optimization and control method for active distribution networks based on deep reinforcement learning algorithm. Teng et al. [5] took into account the spatial distribution characteristics and time series characteristics of the distribution network, and proposed a multi-time-scale distribution network reconstruction and reactive power collaborative optimization method based on adaptive graph attention network. Li et al. [6] explored a continuous-time distributed algorithm for the economic dispatch problem of power and water grids. Wen et al. [7] systematically reviewed the latest achievements in grid dispatch and divided them into distributed discrete-time economic dispatch and continuous-time economic dispatch for smart grids in the presence of multiple generators. Chen and Li [8] proposed a distributed economic dispatch algorithm in which each intelligent control unit iterates the estimated electricity price of the distribution system and the average power mismatch estimate of the entire microgrid through a leader-following algorithm and an average consensus algorithm, respectively. Chen et al. [9] proposed a coordinated robust dynamic economic dispatch model to improve cost-effectiveness and reliability from a system perspective. Li et al. [10] proposed a global centralized dispatch model that applies battery energy storage system technology to distribution networks containing renewable energy. Scholars around the world have proposed a variety of innovative modeling and optimization methods for multi-time scale economic dispatch, providing a solid theoretical foundation and technical support for improving the flexibility and economy of distribution network operation.

3 Methods

3.1 Distribution Network Topology and Node Importance Modeling

The active distribution network is abstracted as a complex network, where each node represents a substation, distribution transformer, or important load access point, and the edge represents a distribution line. The structural importance of the node in the topology is characterized by indicators such as node degree and betweenness centrality [11-12]. The weight of the node not only considers its topological position in the network, but also introduces electrical attributes such as node power load (P_i) and distributed energy resources (DERs) access capacity (Q_i). The comprehensive importance of the node is defined as:

$$I_i=\alpha\cdot\frac{k_i}{k_{max}}+\beta\cdot\frac{P_i}{P_{max}}+\gamma\cdot\frac{Q_i}{Q_{max}} \quad (1)$$

k_i is the degree of node i, P_i is the node load, Q_i is the DERs access capacity, and the edge weight is defined as follows based on the line impedance, power flow capacity, and reliability index:

$$w_{ij}=\frac{1}{Z_{ij}}\cdot\frac{C_{ij}}{C_{max}} \quad (2)$$

Z_{ij} is the line impedance between nodes i and j, and C_{ij} is the line capacity. Based on this modeling, a multi-timescale scheduling framework is constructed, combining node load characteristics with DER output forecast data. Node and edge weight parameters are dynamically adjusted at three timescales: day-ahead, intraday, and real-time. This allows for a refined description of the distribution network's structural characteristics and resource distribution. This process lays the topological and physical foundation for subsequent complex network clustering, clustered scheduling, and global optimization, effectively improving the modeling accuracy and adaptability of multi-timescale economic scheduling.

3.2 Hierarchical Complex Network Clustering and Resource Clustering

A hierarchical complex network clustering method is used to cluster nodes in the active distribution network. A weighted adjacency matrix A is constructed based on the comprehensive node importance and edge weights. A spectral clustering algorithm is used to extract the network's main characteristic subspaces and divide the nodes into several functional subregions. The weighted Laplace matrix L is calculated and defined as:

$$L=D-A \quad (3)$$

D is the node degree matrix. L is subjected to eigendecomposition to obtain the eigenvectors corresponding to the first k smallest eigenvalues to form the characteristic matrix U. K-means clustering is then applied to U to obtain the cluster label of each node [13]. During the clustering process, the load correlation, DER output characteristics, and geographical proximity are comprehensively considered, and the clustering effect is optimized using the following distance metric formula:

$$d_{ij}=\lambda_1|P_i-P_j|+\lambda_2|Q_i-Q_j|+\lambda_3 D_{geo}(i,j) \quad (4)$$

$D_{geo}(i,j)$ is the geographic distance between nodes i and j, and λ is the weighting coefficient. The clustering results directly serve multi-timescale coordinated scheduling, achieving a high degree of matching and flexible allocation of renewable energy output and load within each sub-region. Table 1 shows the typical node clustering and characteristic parameter statistics:

Table 1. Typical node clustering and characteristic parameter statistics.

Cluster ID	Number of Nodes	Average Load (MW)	DERs Installed Capacity (MW)

1	7	1.52	2.01
2	6	1.37	1.65
3	8	1.60	2.23
4	5	1.44	1.77
5	7	1.50	2.18

3.3 Distributed Energy Uncertainty Modeling

To address the volatility and uncertainty of the output of distributed renewable energy sources (such as photovoltaic and wind power) in active distribution networks, Monte Carlo (MC) methods are used to perform probabilistic modeling and simulation. Historical meteorological and output data are used to fit probability distributions. Assuming that photovoltaic output follows a Beta distribution and wind power output follows a Weibull distribution, the probability distributions are expressed as follows:

$$f_{PV}(x)=\frac{x^{\alpha-1}(1-x)^{\beta-1}}{B(\alpha,\beta)},0<x<1 \tag{5}$$

$$f_{W}(x)=\frac{k}{\lambda}\left(\frac{x}{\lambda}\right)^{k-1}e^{-(x/\lambda)^{k}},x\geq 0 \tag{6}$$

$B(\alpha,\beta)$ is the Beta function, and α,β are the shape parameters. Based on the above distribution, a large number of random scenarios of photovoltaic and wind power output are generated using the Monte Carlo method. Assuming the renewable energy output of node i in the s-th simulation, the scenario probability p_s is weighted in the scheduling optimization to form the expected cost target and constraint:

$$min\sum_{s=1}^{S} p_s \cdot C_s \tag{7}$$

C_s is the system operating cost under the sth scenario, and S is the total number of simulation scenarios. Through large-sample simulation, the system can cover output changes under various meteorological and load conditions, and realize quantitative analysis of uncertainty risks in the distribution network [14].

3.4 Multi-Time-Scale Economic Dispatch Optimization

Multi-time-scale economic dispatch optimization is carried out on three nested time scales: day-ahead, intraday, and real-time. The dispatch model adopts a mixed integer quadratic programming framework to integrate source-load balance, switch status, unit constraints, and renewable energy uncertainty scenarios. The scheduling goal is to minimize the expected operating cost of the system. The decision variables include the conventional unit power generation power $P_{i,t}$, the distributed power generation output $P_{DER,i,t}$ and the switch status. The rolling optimization mechanism realizes the dynamic correction of the decision within the rolling window of each time scale. The objective function form is:

$$min\sum_{t=1}^{T}\sum_{i=1}^{N}(a_iP_{i,t}^2+b_iP_{i,t}+c_i)+\sum_{s=1}^{S}p_sC_s \tag{8}$$

a_i , b_i , c_i are unit cost coefficients, and C_s is the additional cost under uncertainty scenario s. Constraints include node source-load balance:

$$\sum_{i\in G} P_{i,t} + \sum_{i\in DER} P_{DER,i,t} = \sum_{j\in L} D_{j,t} \tag{9}$$

After each scheduling window ends, the input data and scenario probabilities are updated in real time, and the decision-making for the next period is dynamically optimized to improve the adaptability and timeliness of scheduling [15]. Figure 1 shows the main scheduling performance indicators after optimization at different time scales:

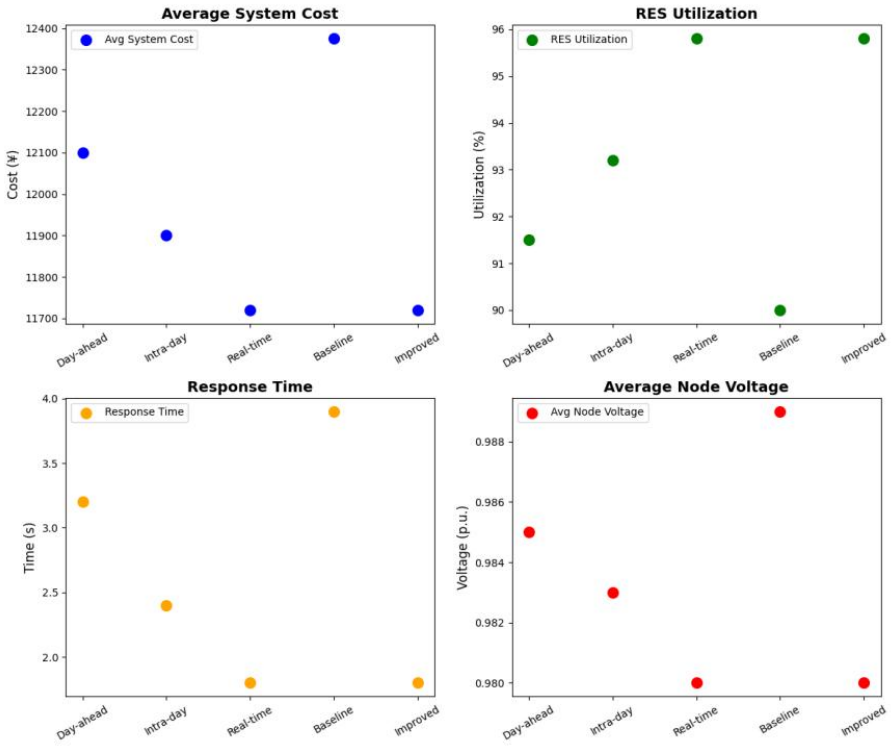


Fig. 1. Key Dispatch Performance Indicators.

4 Results and Discussion

4.1 Simulation Platform and Example Setup

This study's simulations are based on a proprietary active distribution network dispatch analysis platform. The underlying platform utilizes a deep integration of MATLAB and the Gurobi optimizer, implementing an integrated, automated iterative

process for complex network modeling, clustering, Monte Carlo randomized scenario generation, and mixed-integer quadratic programming. The example uses a typical IEEE 33-node active distribution network. The node physical parameters and topology were refined based on a survey of an actual distribution network in southern China, fully reflecting the operational characteristics of regions in China with high distributed energy penetration. Each node is assigned historical load curves and local DER output characteristics (including photovoltaic and wind power), with data granularity down to 15 minutes, effectively reproducing source-load fluctuations across multiple timescales. A weather data interface connects to the National Meteorological Administration's public API, dynamically driving renewable energy output scenarios. To enhance the rigor of simulation comparisons, all cases are run in parallel with traditional single-layer scheduling and non-clustering scenarios, outputting key metrics such as scheduling performance, economic efficiency, and absorption rate. The platform's visualization module displays node load, DER output, and power flow distribution in a dynamic graphical format, providing intuitive support for subsequent algorithm iteration and results analysis.

4.2 Economic Efficiency and Renewable Energy Absorption

After the introduction of the multi-time-scale economic dispatch model, the system operating cost dropped from 7507 to 7077 yuan, and the overall economic efficiency was significantly improved. Under the traditional non-dispatch mechanism, some renewable energy sources were abandoned due to the mismatch between output fluctuations and loads, and the average absorption rate was only 89.8%. The introduction of the dispatch model fully utilized the temporal and spatial complementarity of resources between nodes, and the absorption rate was increased to 95.8%. The dispatch model achieves dynamic response and flexible optimization to load fluctuations and distributed energy uncertainties, improves the local absorption of renewable energy within each sub-area and the economic allocation capacity of the entire network trend, and significantly reduces the overall operating cost and dependence on external power purchases. Figure 2 shows the specific analysis results. Operating costs at all nodes decreased to varying degrees, with an average savings rate of approximately 5.7%. The overall renewable energy absorption rate increased, with some nodes exceeding 6%. This improvement is primarily due to the synergy between hierarchical clustering and multi-timescale scheduling, which fully exploits the spatial complementarity between loads and renewable energy output within each sub-interval, reducing wind and solar curtailment. The scheduling model accurately simulates and dynamically optimizes the uncertainty of distributed energy output, adjusting power allocation at each node and line in real time. This makes the system more adaptable to fluctuating and sudden loads, ultimately achieving simultaneous improvements in both economic efficiency and green absorption capacity.

8

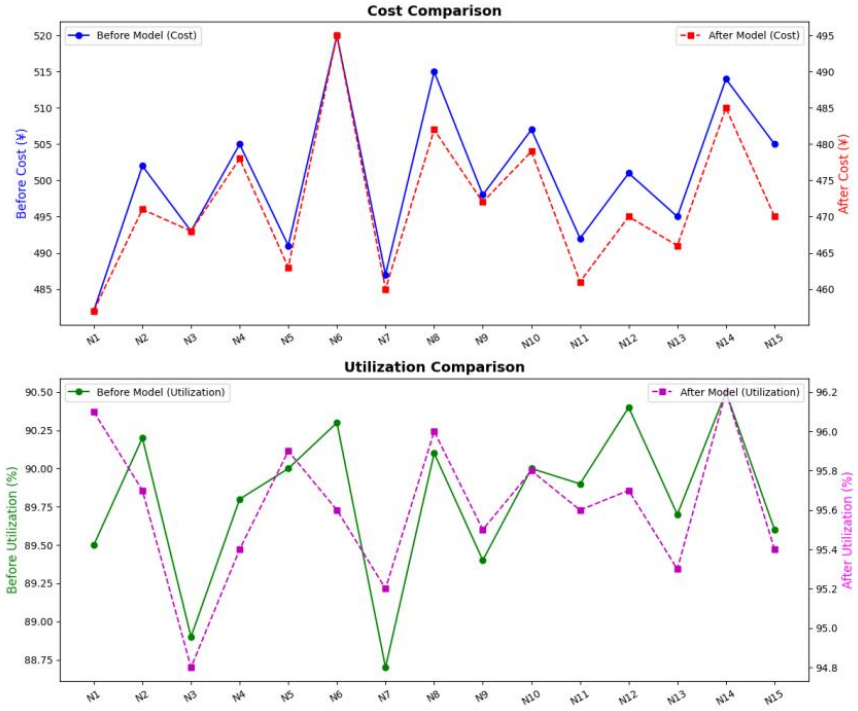


Fig. 2. Operating Costs and Absorption Rate.

4.3 Dispatching Response Speed and Adaptability

In terms of dispatch response speed, the test work was carried out in a high-performance computing environment, uniformly using 64-thread multi-core servers, pre-loading all node loads, DERs output and meteorological scenario data to ensure that the input delay is negligible. Each dispatch simulation is strictly timed, from the receipt of the latest load and output data to the optimization decision and the issuance of control instructions, and the response time of the entire process is recorded. To ensure the comprehensiveness of the test, 15 typical time periods throughout the day were selected, covering load peaks, troughs and violent fluctuations, and compared and evaluated under two situations: no dispatch model and the introduction of a multi-time scale dispatch algorithm. Figure 3 shows the dispatch response speed test results:

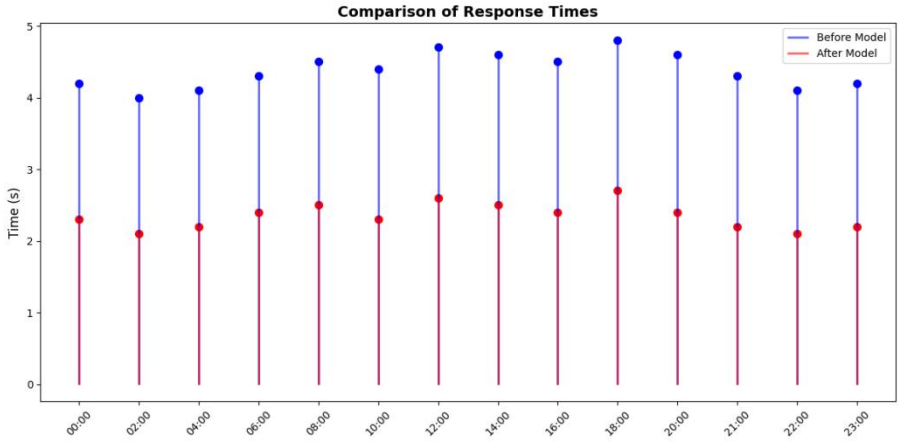


Fig. 3. Dispatch Response Speed.

Dispatch response speed has generally improved since the introduction of the multi-timescale scheduling model, with the average response time significantly reduced from 4.38 seconds to 2.35 seconds. This reduction represents a 45% to 50% improvement across typical daily hours. This is particularly true during periods of significant load fluctuation, such as 12:00 PM and 6:00 PM. The model's efficient data parallel processing and rolling optimization mechanism significantly shortens the decision-making process, effectively improving the system's adaptability to dynamic changes. This improved response speed not only expedites the issuance of dispatch instructions and reduces system lag, but also provides more timely control support for real-time load and distributed energy fluctuations, fully leveraging the flexible dispatch advantages of the active distribution network.

4.4 Sensitivity Analysis

The sensitivity analysis focuses on the impact of key parameters on dispatch optimization. Four parameters are selected: distributed energy installed capacity, renewable energy output fluctuations, load forecast error, and number of scenarios. Multiple simulation conditions are designed, and individual variables are gradually adjusted to observe changes in core indicators such as system operating costs, renewable energy absorption rate, and dispatch response time. Each data set is based on a fixed network structure and load curve to ensure comparability of results. During the analysis, the installed capacity increase was set at 10%, the renewable energy output fluctuation ranges were set at 5%, 10%, and 15%, and the load forecast error was set at 2%, 5%, and 8%, respectively. The number of scenarios was increased from 50 to 150, and each scenario was simulated and optimized statistically to quantify the sensitivity of each parameter to system economics and dispatch performance. Table 2 shows the results of the sensitivity analysis:

Table 2. Sensitivity Analysis Results.

Heading level	DER Capacity	RES Fluctuation	Forecast Error (%)	Scenario Num	System Cost (¥)	RES Utilization	Response Time (s)

10

	(MW)	(%)				(%)	
1	1.0	5	2	50	12,120	94.0	2.31
2	1.1	5	2	50	11,970	95.3	2.34
3	1.0	10	2	50	12,350	92.5	2.37
4	1.0	5	5	50	12,210	93.1	2.39
5	1.0	5	2	100	12,080	94.7	2.45
6	1.1	10	5	150	11,960	94.2	2.54

A 10% increase in distributed energy installed capacity (from 1.0 MW to 1.1 MW) can reduce system operating costs by approximately 1.2% and increase renewable energy utilization by 1.3 percentage points, demonstrating a certain degree of economic and green resilience. Increased volatility in renewable energy output (5% to 10%), increased system costs, and decreased absorption rates indicate that volatility has a negative impact on economic operations and requires further strengthening of dispatch flexibility. The number of negative scenarios increased, and response time slightly increased, indicating that scenario richness improves risk coverage but increases computational burden.

5 Conclusions

Based on complex network theory, this paper innovatively integrates node importance, hierarchical clustering, and multi-timescale rolling scheduling to systematically construct a new optimization paradigm for multi-timescale economic dispatch of active distribution networks. Through resource clustering driven by complex network algorithms, the potential value of network structure and source-load spatial distribution is fully explored, and the flexible mutual assistance capability between nodes is enhanced. The introduction of uncertainty modeling and Monte Carlo simulation mechanisms enables high-confidence quantification of distributed energy output fluctuations, providing a solid data foundation for scheduling decisions. The scheduling model, based on mixed-integer quadratic programming and coupled with rolling optimization, effectively addresses dynamic variations in load and renewable energy output over different timescales, demonstrating excellent economic efficiency and dispatch responsiveness. Case studies validate the method's comprehensive advantages in multi-source coordination, risk prevention and control, and network-wide economic operation. It should be pointed out that the model still has room for further improvement in aspects such as scenario generation, parameter selection and actual communication delay. In the future, it can be combined with artificial intelligence algorithms, actual distribution network operation data and communication physical layer optimization to continuously improve the economic dispatch theory system and engineering application capabilities of active distribution networks.

Acknowledgments: This work was supported by the Science and Technology Project of State Grid Shanghai Electric Power Company (Grant No. 520933250004).

References

1. Zeng Fei, Su Wei, Xu Guangkai, Ni Hanyi, Shi Mingming, Wei Zhinong. Multi-time-scale economic dispatch of low-voltage DC interconnected distribution networks with fast charging loads [J]. Power Grid and Clean Energy, 2022, 38(1): 14-23
2. Wang Luyang, Zhao Qianyu, Wang Shouxiang. Multi-time-scale distributed optimization operation and dispatch strategy for AC/DC distribution networks considering flexibility [J]. Journal of Electric Power Systems and Automation, 2025, 37(4): 57-68
3. Yuan Tianmeng, Yang Yining, Hu Zechun. Multi-time-scale optimization scheduling strategy for medium and low voltage distribution networks considering distributed photovoltaic and energy storage integration[J]. Journal of Electric Power Science and Technology, 2025, 40(1): 101-112
4. Li Peng, Zhong Hanming, Ma Hongwei, Li Jianfeng, Liu Yang, Wang Jiahao. Multi-time-scale source-load-storage collaborative optimization control of active distribution network based on deep reinforcement learning[J]. Transactions of the Chinese Society of Electrical Engineering, 2025, 40(5):1487-1502
5. Teng Jie, Liu Huijia, Xiao Dong. Multi-time-scale distribution network reconstruction and reactive power collaborative optimization based on adaptive graph attention network[J]. China Southern Power Grid Technology,2025,19(5):49-60
6. Li P, Hu J, Qiu L, et al. A distributed economic dispatch strategy for power–water networks[J]. IEEE Transactions on Control of Network Systems, 2021, 9(1): 356-366.
7. Wen G, Yu X, Liu Z. Recent progress on the study of distributed economic dispatch in smart grid: an overview[J]. Frontiers of Information Technology & Electronic Engineering, 2021, 22(1): 25-39.
8. Chen W, Li T. Distributed economic dispatch for energy internet based on multiagent consensus control[J]. IEEE Transactions on automatic control, 2020, 66(1): 137-152.
9. Chen Z, Guo C, Dong S, et al. Distributed robust dynamic economic dispatch of integrated transmission and distribution systems[J]. IEEE Transactions on Industry Applications, 2021, 57(5): 4500-4512.
10. Li X, Wang L, Yan N, et al. Cooperative dispatch of distributed energy storage in distribution network with PV generation systems[J]. IEEE Transactions on Applied Superconductivity, 2021, 31(8): 1-4.
11. Agrawal S, Patel A. Clustering algorithm for community detection in complex network: a comprehensive review[J]. Recent Advances in Computer Science and Communications (Formerly: Recent Patents on Computer Science), 2020, 13(4): 542-549.
12. Artime O, Grassia M, De Domenico M, et al. Robustness and resilience of complex networks[J]. Nature Reviews Physics, 2024, 6(2): 114-131.
13. Lee C Y, Hasegawa H, Gao S. Complex-valued neural networks: A comprehensive survey[J]. IEEE/CAA Journal of Automatica Sinica, 2022, 9(8): 1406-1426.
14. Wang K, Wang C, Zhang Z, et al. Multi-timescale active distribution network optimal dispatching based on SMPC[J]. IEEE Transactions on Industry Applications, 2022, 58(2): 1644-1653.

12

15. Yu P, Wan C, Sun M, et al. Distributed voltage control of active distribution networks with global sensitivity[J]. IEEE Transactions on Power Systems, 2022, 37(6): 4214-4228.

074 Research on Optimal Scheduling of Photovoltaic-Hydrogen-Storage-Electric Vehicle Microgrids Based on the NGO-MOGWO Algorithm

Xin Yin and Wenyi Li*

Inner Mongolia University of Technology, Hohhot, China
lwyyyll@vip.sina.com

Abstract. For a microgrid system incorporating photovoltaic, hydrogen, energy storage, and electric vehicle components, this paper proposes a novel multi-objective optimal scheduling method based on a hybrid NGO-MOGWO algorithm that integrates the Northern Goshawk Optimizer and the Multi-Objective Grey Wolf Optimizer. First, a comprehensive optimization model is formulated through the coordinated dispatch of multiple components including photovoltaics, electrolyzers, hydrogen fuel cells, hydrogen storage tanks, battery energy storage systems, and electric vehicles. The model simultaneously addresses three critical objectives: minimizing system operating costs, mitigating tie-line power fluctuations, and reducing the photovoltaic curtailment rate. To effectively solve this complex multi-objective optimization problem, the hybrid NGO-MOGWO algorithm incorporates advanced mechanisms for adaptive parameter adjustment and sophisticated constraint handling. This integration enhances the algorithm's capability to navigate the high-dimensional solution space while maintaining feasible solutions. Simulation results demonstrate that the proposed method significantly enhances photovoltaic utilization efficiency, substantially reduces operating costs and carbon emissions, and effectively suppresses tie-line power fluctuations. Furthermore, comprehensive comparative analysis confirms that the proposed approach outperforms several established algorithms including NGO, MOGWO, NSGA-II, SPEA2, and MOEAD in terms of convergence speed, solution distribution uniformity, and population diversity of the obtained Pareto solution set.

Keywords: Photovoltaic-Hydrogen-Storage-Electric Vehicle Microgrid; Multi-objective Optimal Scheduling; NGO-MOGWO Algorithm

1 Introduction

In the field of microgrid optimal scheduling, researchers worldwide have conducted extensive investigations, primarily focusing on three key aspects: scheduling models, optimization algorithms, and multi-energy coordination. Regarding scheduling models, research has predominantly concentrated on economic efficiency and environmental sustainability. For instance, reference [1] establishes its objective function based on operational maintenance and environmental management costs; however, it

fails to account for power supply reliability during microgrid operation. Reference [2] proposed a multi-objective optimal scheduling model for grid-connected microgrids, simultaneously considering operational costs and environmental protection costs; however, it overlooked grid stability. In contrast, reference [3] developed an economic operation and optimal scheduling model aiming to minimize daily operational costs and environmental pollution penalty costs, adopting the Pareto-optimal solution set method. Although this approach addresses islanded microgrid operation, it neglects the interactive power exchange between the microgrid and the main grid. While reference [4] has made progress in reducing operational costs and environmental pollution while concurrently considering grid stability, its algorithm demonstrates limited performance when handling the three-objective optimization problem.

Regarding multi-energy coordination, the integration of hydrogen and EVs has introduced innovative approaches to microgrid scheduling. However, existing research has yet to fully exploit their synergistic potential. Reference [5] proposed a multi-strategy improved Northern Goshawk Optimization algorithm and applied it to microgrid optimization, effectively guiding user electricity consumption patterns to align with renewable energy output, thereby enhancing renewable utilization and economic benefits. Nevertheless, this approach may lead to power imbalance within the microgrid system, whose fluctuations could adversely impact main grid stability. Reference [6] developed an improved Bald Eagle Search algorithm for addressing economic aspects in EV-integrated microgrids, achieving satisfactory economic dispatch solutions. While effectively resolving economic concerns, this study solely focused on economic factors while neglecting other crucial considerations. Although reference [7] incorporated a hydrogen energy system, it failed to adequately address the coordination mechanism between hydrogen and flexible loads such as EVs.

In terms of optimization algorithms, traditional approaches such as NSGA-II and MOPSO tend to converge to local optima when handling complex Pareto fronts [8], while emerging metaheuristic algorithms still require improvements in balancing convergence speed and population diversity [4]. Hybrid models, capable of integrating advantages from different algorithms, have become a research focus among scholars [9]. Recent years have witnessed various enhancement strategies—including fuzzy rough operators [7], multi-objective hare algorithm [10], and adaptive inertia weight [11]—which have significantly improved the distribution uniformity and convergence speed of Pareto solution sets. Nevertheless, these methods still struggle to effectively address complex scheduling problems characterized by high dimensionality and multiple constraints.

In summary, to address the limitations in existing research, this study focuses on the following aspects: In terms of scheduling strategy, electrolyzers, hydrogen storage tanks, and hydrogen fuel cells are systematically incorporated to establish a coordinated operational framework for the PV-hydrogen-storage-EV microgrid model. Regarding optimization objectives, a multi-objective optimization model is developed that systematically considers operational costs, tie-line power fluctuations, and the photovoltaic curtailment rate. For the solution algorithm, a hybrid NGO-MOGWO algorithm integrating the NGO-MOGWO is proposed, which enhances solving per-

formance and convergence efficiency for complex high-dimensional problems through mechanism fusion and adaptive constraint handling.

2 Microgrid System Model

The microgrid system primarily comprises a photovoltaic (PV) array, an electrolyzer for hydrogen production, a hydrogen storage tank, a hydrogen fuel cell (HFC), a battery energy storage system (BESS), electric vehicles (EVs), and other loads. The system structure is depicted in Figure 1.

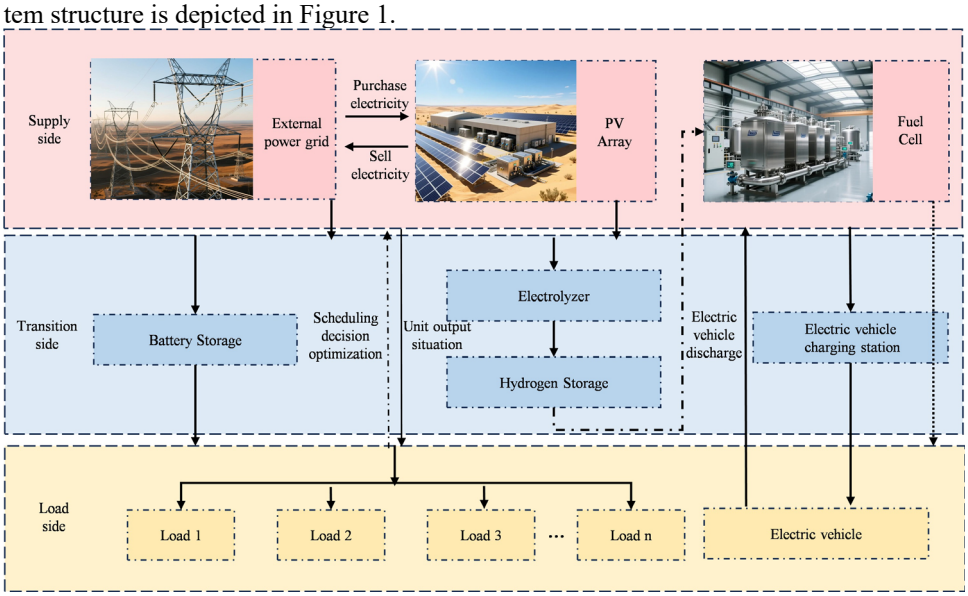


Fig. 1. Architecture of the Integrated Photovoltaic-Hydrogen-Storage-Electric Vehicle Microgrid System.

2.1 Objective Function

A multi-objective optimization model is formulated with the objectives of minimizing comprehensive operational cost, tie-line power fluctuation, and photovoltaic curtailment rate. Specifically, the operational cost comprises electricity purchase cost from the grid, operation and maintenance cost, carbon emission cost, and hydrogen energy revenue. The tie-line power fluctuation is characterized by a weighted combination of the tie-line power variation rate and peak power. The photovoltaic curtailment rate is defined as the ratio of curtailed PV power to the total available PV power output.

Operational Costs The objective function for operational costs is formulated to minimize the total system operational cost, expressed as follows:

$$\min F_{cost} = \sum_{t=1}^{T} \begin{bmatrix} C_{grid}(t) + C_{device}(t) + C_{carbon}(t) \\ -R_{sell}(t) - R_{H_2}(t) \end{bmatrix} + P_{soc} + P_{coord} \tag{1}$$

where $C_{\text{grid}}(t)$ denotes the cost of purchasing electricity from the main grid at time t, $C_{\text{device}}(t)$ signifies the total operation and maintenance cost of all devices (electrolyzer, fuel cell, battery, etc.) at time t, $C_{\text{carbon}}(t)$ refers to the cost associated with carbon emissions from grid power consumption at time t, $R_{\text{sell}}(t)$ stands for the revenue generated from selling surplus electricity to the main grid at time t, $R_{\text{H}_2}(t)$ indicates the revenue from hydrogen production and utilization at time t, P_{soc} represents the penalty term for State of Charge (SOC) limit violations of energy storage systems, P_{coord} denotes the penalty term for coordination constraint violations among multiple energy sources or loads.

Tie-Line Power Fluctuation To ensure grid-friendly operation, the tie-line power fluctuation objective minimizes the variation of interactive power, formulated as follows:

$$F_{\text{grid}} = \sum_{t=1}^{T} |P_{\text{grid}}(t)| \cdot \Delta t + \lambda_1 \cdot \sum_{t=2}^{T} |P_{\text{grid}}(t) - P_{\text{grid}}(t-1)| + \lambda_2 \cdot \sum_{t=3}^{T} |\Delta^2 P_{\text{grid}}(t)| \tag{2}$$

where the first term represents the energy purchased from the grid, the second term denotes the first-order fluctuation, and the third term signifies the second-order fluctuation.

with the following definitions:

$$\Delta^2 P_{\text{grid}}(t) = P_{\text{grid}}(t) - 2P_{\text{grid}}(t-1) + P_{\text{grid}}(t-2) \tag{3}$$

PV Curtailment Rate PV curtailment rate objective enhances renewable energy utilization by minimizing the proportion of unused photovoltaic power, formulated as follows:

$$F_{\text{curtail}} = \frac{\sum_{t=1}^{T} \max(0, P_{\text{pv}}(t) - P_{\text{pv,used}}(t)) \cdot \Delta t}{\sum_{t=1}^{T} P_{\text{pv}}(t) \cdot \Delta t + \epsilon} \tag{4}$$

where ϵ is a small positive constant to prevent division by zero.

2.2 Objective Function

Microgrid Power Balance Constraint This constraint ensures real-time matching between generation and load within the system, formulated as follows:

$$\begin{aligned} &P_{\text{load}}(t) + P_{\text{batt,ch}}(t) + P_{\text{ely}}(t) + P_{\text{ev,ch}}(t) = \\ &P_{\text{pv}}(t) + P_{\text{batt,dis}}(t) + \eta_{\text{fc}} \cdot P_{\text{fc}}(t) + P_{\text{ev,dis}}(t) + P_{\text{grid}}(t) \end{aligned} \tag{5}$$

where P_{load} is the load power, P_{ely} is the electrolyzer hydrogen production power, , P_{pv} is the PV power generation, $P_{\text{batt,dis}}$ is the battery discharge/charge power, P_{fc} is

the fuel cell output power, η_{fc} is the power generation efficiency, $P_{\text{ev,dis}}$ is the EV discharge/charge power, and $P_{\text{grid}}(t)$ is the grid power purchase at time t.

Equipment Operational Constraints To prevent device overloading and ensure secure operation, the operational constraints for each component are formulated as follows:

$$\begin{cases} 0 \le P_{\text{batt,ch}}(t) \le P_{\text{batt,max}} \\ 0 \le P_{\text{batt,dis}}(t) \le P_{\text{batt,max}} \\ 0 \le P_{\text{ely}}(t) \le P_{\text{ely,max}} \\ 0 \le P_{\text{fc}}(t) \le P_{\text{fc,max}} \\ 0 \le P_{\text{ev,ch}}(t) \le P_{\text{ev,max}} \\ 0 \le P_{\text{ev,dis}}(t) \le P_{\text{ev,max}} \end{cases} \tag{6}$$

SOC Constraints The state of charge (SOC) dynamics for hydrogen storage, batteries, and electric vehicles are expressed as follows:

$$\begin{cases} \text{SOC}_{\text{H}_2}(t+1) = \text{SOC}_{\text{H}_2}(t) + \eta_{\text{PEM}} P_{\text{ely}}(t)\Delta t - P_{\text{fc}}(t)\Delta t \\ \text{SOC}_{\text{batt}}(t+1) = \text{SOC}_{\text{batt}}(t) + \eta_{\text{ch}} P_{\text{batt,ch}}(t)\Delta t - \dfrac{P_{\text{batt,dis}}(t)}{\eta_{\text{dis}}}\Delta t \\ \text{SOC}_{\text{ev}}(t+1) = \text{SOC}_{\text{ev}}(t) + \eta_{\text{ev,ch}} P_{\text{ev,ch}}(t)\Delta t - \dfrac{P_{\text{ev,dis}}(t)}{\eta_{\text{ev,dis}}}\Delta t \end{cases} \tag{7}$$

where η_{PEM} is the electrolyzer efficiency, η_{ch} is the charging efficiency, η_{dis} is the discharging efficiency, $\eta_{\text{ev,ch}}$ is the EV charging efficiency, and $\eta_{\text{ev,dis}}$ is the EV discharging efficiency.

EV SOC Boundary Constraints SOC at the time of departure must satisfy:

$$\text{SOC}^k_{\min} \le \text{SOC}^k(t) \le \text{SOC}^k_{\max}, \quad k \in \{\text{batt}, \text{H}_2, \text{ev}\} \tag{8}$$

EV Departure SOC Requirement EV battery SOC at the time of departure must satisfy:

$$\text{SOC}_{\text{ev}}(t_d) \ge \text{SOC}_{\text{req}}, \quad \forall t_d \in \mathcal{T}_{\text{depart}} \tag{9}$$

where SOC_{req} is the user-expected minimum travel energy requirement, and $\mathcal{T}_{\text{depart}}$ is the set of departure times.

3 NGO-MOGWO Algorithm

The proposed NGO-MOGWO algorithm employs a dual-phase strategy: it frequently adopts the linear pursuit mechanism of NGO to rapidly refine the solution set, while periodically invoking MOGWO's dynamic encircling operator to expand the search radius—thereby balancing exploration and exploitation. Enhanced by subpopulation migration, niching clustering, and vectorized constraint repair, the method systematically coordinates global exploration and local refinement, efficiently obtaining a well-distributed Pareto-optimal solution set.

3.1 Objective Function

To mitigate the limitations of random initialization in complex search spaces, four heuristic rules with distinct priorities—cost minimization, PV utilization maximization, fluctuation suppression, and hydrogen optimization—were designed based on Latin Hypercube Sampling (LHS) to generate four groups of "seed" individuals. This approach ensures the initial population not only achieves broad coverage of the solution space but also directly anchors multiple promising regions where the Pareto front is likely to distribute, thereby establishing a high-quality foundation for subsequent optimization.

3.2 Adaptive Hybrid Search Strategy and Elite Guidance

An adaptive selector based on population diversity is designed to dynamically integrate the search capabilities of the MOGWO and the NGO. In the early stages, when population diversity is high, the "linear-guided search" strategy of NGO is employed to leverage its strong global exploration capability for rapidly scanning the feasible region. During later stages, as the population converges, the "wolf pack hunting" strategy of MOGWO is activated, utilizing the social hierarchy of α, β, and δ wolves for refined local exploitation. To guide the search process toward the genuine Pareto-optimal front, leaders are selected from an elite archive maintained through non-dominated sorting and niching-based clustering. The niching technique preserves solutions in sparse regions by evaluating Euclidean distances, which maintains a uniformly distributed solution set and prevents premature convergence to local optima.

3.3 Parallel Subpopulation Evolution

To further enhance the optimization capability, a parallel subpopulation evolution mechanism is implemented. The population is divided into several independently evolving subpopulations, with elite individuals periodically selected based on crowding distance for migration. This strategy not only accelerates the search process through parallel computation but also effectively prevents premature convergence, thereby facilitating a more robust and stable global search.

Through the coordinated operation of these components, the proposed algorithm effectively balances exploration and exploitation while maintaining an optimal trade-off between convergence speed and solution diversity.

4 Case Study Analysis

4.1 Case Study

To validate the effectiveness of the proposed NGO-MOGWO algorithm in solving multi-objective optimization problems, a case study is conducted on a grid-connected microgrid system integrating 50 MW of photovoltaics, a 120 MW alkaline electrolyzer with 75% hydrogen production efficiency, a 100 MW hydrogen fuel cell with 60% power generation efficiency, a 200 MWh lithium iron phosphate battery storage system with ±2 MW charge/discharge power and an SOC operating range of 0.1–0.9, and a fleet of 200 electric vehicles. The economic model incorporates hydrogen production cost at 0.20 ¥/kWh-H_2, fuel cell generation cost at 0.15 ¥/kWh, battery degradation cost at 0.05 ¥/kWh, and start-stop cost at 50 ¥/cycle. Carbon emissions are priced at 0.5 ¥/kg based on a grid emission factor of 0.8 kg CO_2/kWh. The system operates under time-of-use electricity tariffs with peak hours (8:00-11:00, 18:00-23:00) at 0.83 ¥/kWh for purchase and 0.65 ¥/kWh for sale, flat hours (7:00-8:00, 11:00-18:00) at 0.49 ¥/kWh for purchase and 0.38 ¥/kWh for sale, and valley hours (0:00-7:00, 23:00-24:00) at a unified rate of 0.17 ¥/kWh for both purchase and sale. Additional penalty costs of 500 ¥/MWh for energy surplus and 5400 ¥/MWh for energy deficit are implemented to ensure system reliability.

Experiments are conducted on a Python-based simulation platform. To validate the effectiveness of the proposed NGO-MOGWO model, a multi-objective optimization comparison is performed against the following six algorithms: Model 1: NGO, Model 2: MOGWO, Model 3: NSGA-II, Model 4: SPEA2, Model 5: MOEAD, and Model 6: NGO-MOGWO.

4.2 Analysis of Results

To evaluate the performance of the proposed NGO-MOGWO algorithm, the Pareto-optimal solutions obtained by NGO, MOGWO, NSGA-II, SPEA2, MOEAD, and NGO-MOGWO are compared, with their corresponding non-dominated fronts illustrated in Figure 2.

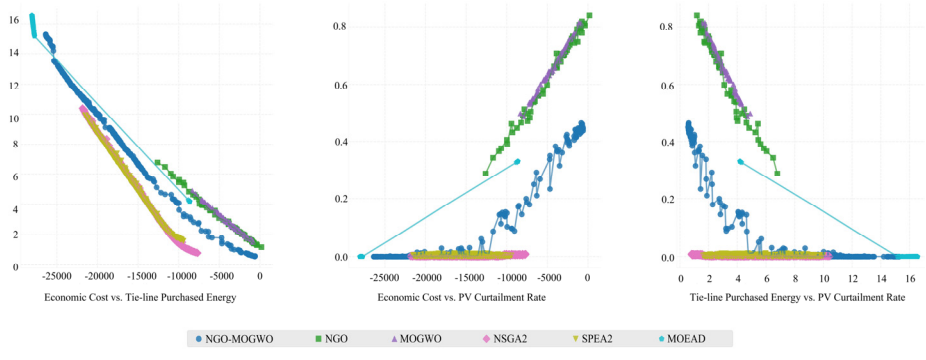


Fig. 2. Comparison of Pareto Fronts for Different Algorithms.

In the "Economic Cost vs. Tie-line Purchased Energy" plot, the solutions of NGO-MOGWO form a non-dominated front located in the lower-left region, indicating lower economic costs and reduced purchased energy. In contrast, the solutions obtained by NSGA-II, SPEA2, and MOEAD are distributed in regions characterized by higher costs and greater purchased energy.

Regarding the "Economic Cost vs. PV Curtailment Rate," the NGO-MOGWO solutions consistently reside in areas with lower curtailment rates and reduced economic costs, demonstrating superior dispatch performance compared to both NGO and MOGWO. Specifically, MOGWO's solutions are confined to medium and high curtailment regions within NGO's solution range.

In the " Tie-line Purchased Energy vs. PV Curtailment Rate" analysis, NGO-MOGWO achieves solutions with both lower purchased energy and lower curtailment rates, outperforming other algorithms whose solutions are predominantly located in high purchased energy and high curtailment regions. Therefore, NGO-MOGWO exhibits superior dispatch performance and enhanced multi-objective optimization capability in balancing the three objectives.

Figure 3 illustrates the relationship between tie-line purchased power and time-of-use electricity price.

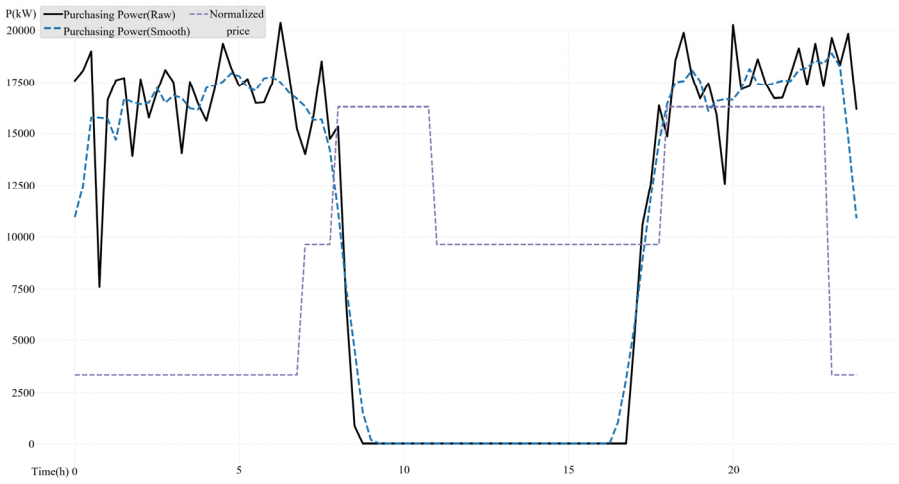


Fig. 3. Tie-line Power Fluctuation Curve.

The proposed method increases power purchase during off-peak hours with lower electricity prices and significantly reduces purchased power during peak hours, even feeding power back to the main grid. This "peak shaving and valley filling" strategy effectively flattens the tie-line power curve, resulting in a notable reduction in power fluctuations. These findings demonstrate the capability of the proposed method to effectively mitigate tie-line power volatility.

Based on the 24-hour power balance results of the microgrid system (as shown in Figure 4), the system exhibits a typical coordinated operational mode of photovoltaic-hydrogen-storage.

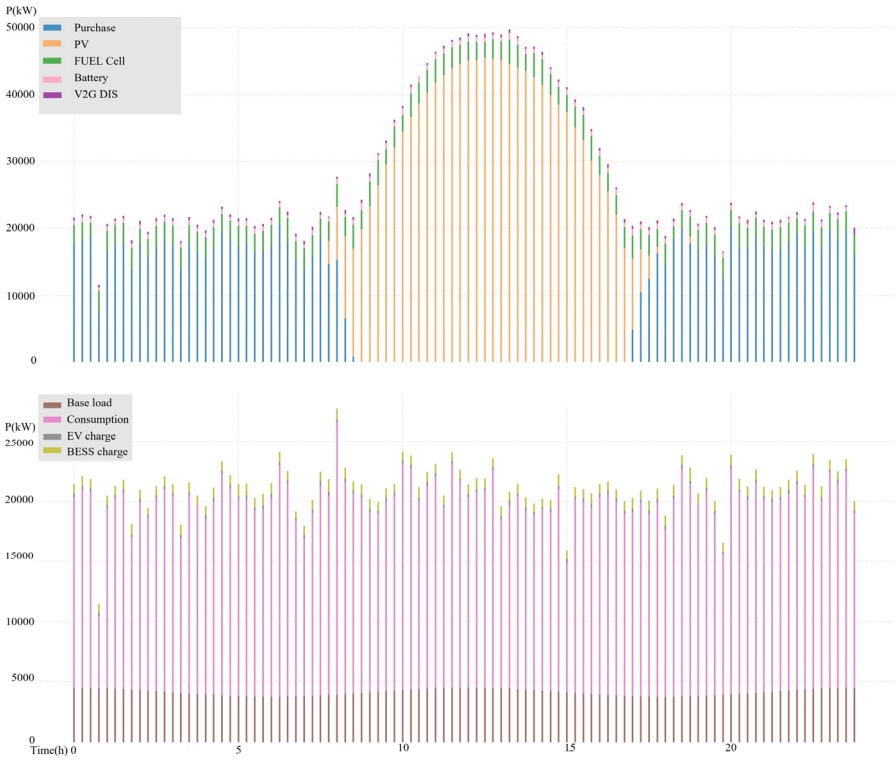


Fig. 4. 24-Hour Power Balance Results of the Microgrid System.

The dispatch process can be categorized into the following three scenarios according to operational patterns:

High PV Generation Period (09:00–15:00): During peak PV output hours, the electrolyzer load increases significantly, converting surplus electricity into hydrogen for storage. This coordinated operation reduces grid power purchase, demonstrating effective "hydrogen-based energy storage" utilization.

Peak Load Period (Morning and Evening): During these high-demand periods, the electrolyzer load decreases rapidly while hydrogen fuel cells and storage tanks activate simultaneously, providing 0.5-2 MW of smooth compensation power to help alleviate peak grid demand.

Hydrogen Production Coordination Scenario Hydrogen production load strictly follows PV output patterns, operating at full capacity during peak PV hours and nearly shutting down at night. This operational strategy reflects efficient bidirectional "electricity-hydrogen" conversion and cross-temporal energy management.

These scenarios collectively demonstrate the system's capability to dynamically coordinate multiple energy resources through intelligent dispatch strategies.

Figure 5 illustrates the detailed operational strategy of the hydrogen energy chain.

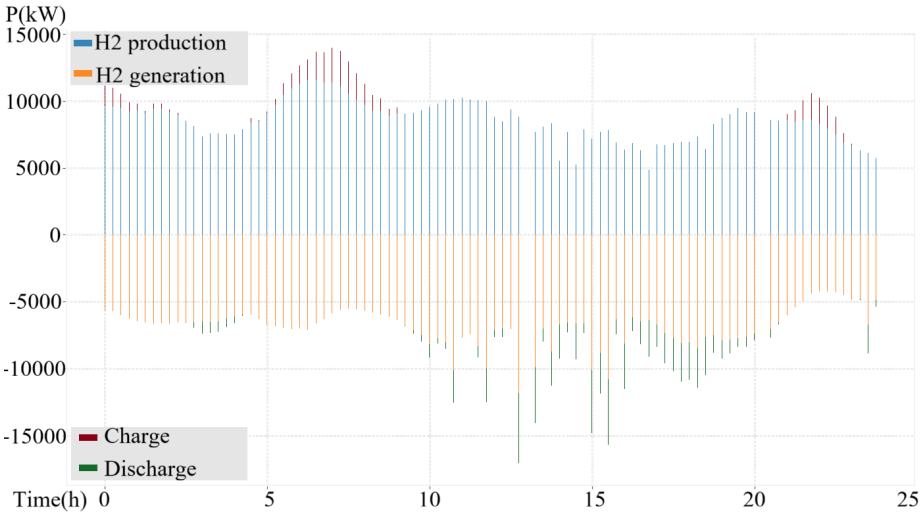
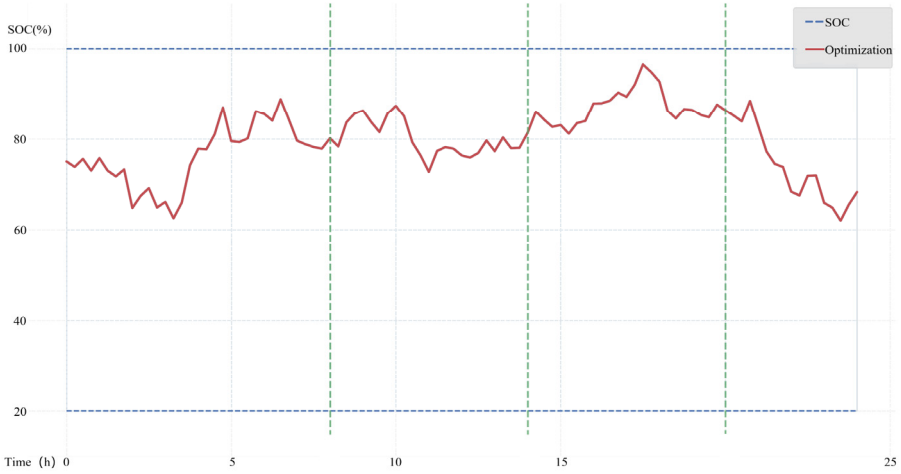


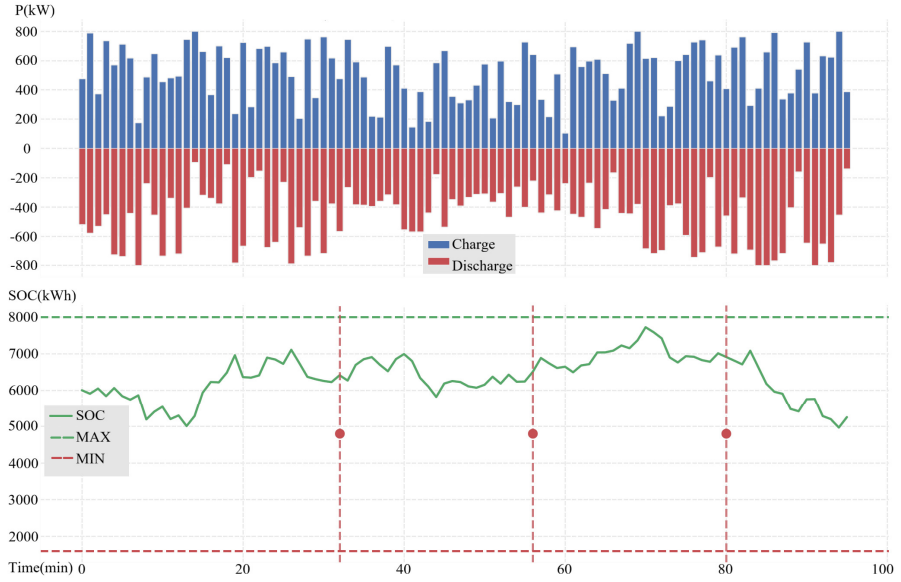
Fig. 5. H_2 System (ELZ, H_2 Tank, FC) Operating Power.

During midday periods of PV power surplus, the electrolyzer operates at full capacity for hydrogen production. During evening and afternoon peak load periods, the fuel cell and hydrogen storage tank engage in coordinated "slow-fast" peak shaving, with a maximum peak-shaving capacity of 16 MW. Throughout the day, hydrogen production by the electrolyzer and hydrogen consumption by the fuel cell remain approximately balanced, achieving a closed-loop hydrogen flow.

Figure 6 presents the time-of-use charging/discharging strategy and SOC status of the EV cluster. Under rational charging/discharging control, the fleet not only meets the total energy required for three designated departure periods but also effectively implements peak shaving and valley filling. Throughout this process, the SOC remains consistently maintained within a reasonable operating range.



a) EV cluster power constraints



b) EV cluster SOC change

Fig. 6. EV Cluster Charging/Discharging Power and SOC Status.

Figure 7 demonstrates the system's operational performance through three key aspects.

12

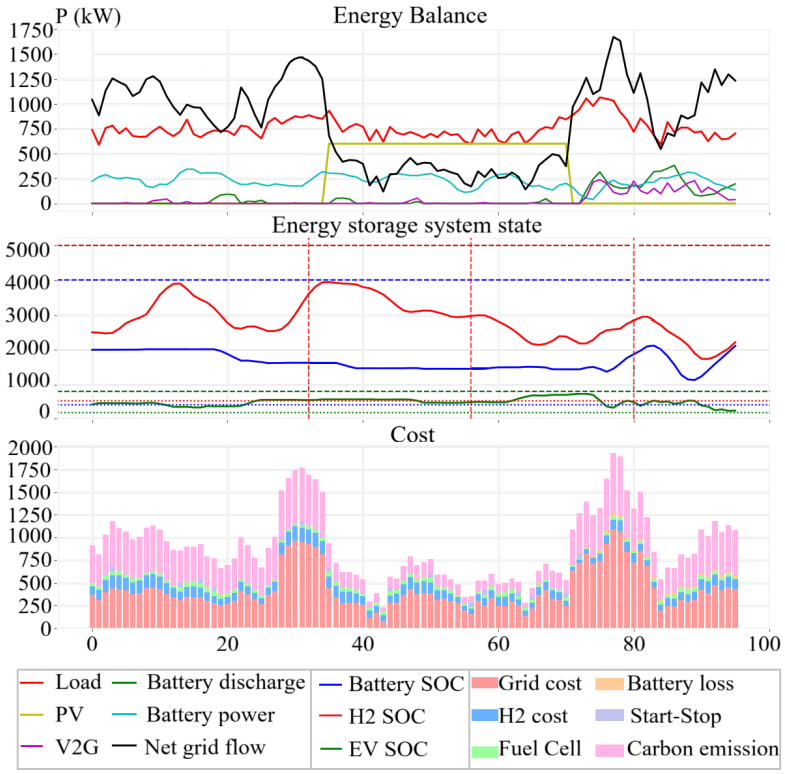


Fig. 7. Comprehensive Overview of Microgrid Optimal Dispatch

The power balance diagram shows that load demand and PV output effectively offset each other, with tie-line power fluctuations confined within a ±1.5 MW range. Battery storage, fuel cells, and V2G collectively provide short-duration, high-power pulse compensation to achieve power smoothing. In the energy storage status diagram, the battery SOC operates within the 30-40 MWh range while hydrogen storage SOC gradually decreases from 60,000 kWh to 35,000 kWh, both maintaining safe operating limits. The cost analysis reveals a significant reduction in grid electricity purchase expenses, with fuel and degradation costs collectively accounting for less than 10% of total costs. In summary, the proposed optimization strategy simultaneously improves PV utilization, effectively reduces the grid peak-valley difference, and maintains energy storage lifespan.

5 Conclusion

The main conclusions are as follows:

The proposed NGO-MOGWO hybrid algorithm successfully overcomes the common limitations of traditional algorithms—premature convergence and uneven solu-

tion distribution—when solving high-dimensional complex problems through mechanism fusion and adaptive search.

By leveraging the coordinated operation of photovoltaic-hydrogen-storage-EV systems and utilizing the hydrogen energy chain for "daytime charging and nighttime discharging" combined with flexible EV scheduling, the approach effectively achieves peak shaving and valley filling, mitigates tie-line power fluctuations, and enhances economic performance.

This study integrates carbon emission costs into the economic objective without imposing separate carbon constraints; thus, emission reduction effectiveness is influenced by the preset carbon price level. Future work will introduce robust optimization methods to address uncertainties in carbon emission factors, further improving the economic efficiency and low-carbon reliability of microgrid dispatch strategies.

Acknowledgement: This work is supported by the Inner Mongolia Science and Technology Plan under Grant 2022JBGS0043

References

1. Bai Long, Yu Bin, Gao Feng, et al.: Optimal scheduling of microgrids based on improved multi-objective grey wolf algorithm [J]. Information Technology4(4), 89–96 (2025).
2. Li Xing Xin, Zhang Jing, He Zi, et al.: Multi-objective optimal scheduling of microgrids based on improved particle swarm optimization algorithm [J]. Electric Power Science and Engineering37(3), 1–7 (2021).
3. Li Xing Chen, Yuan Xu Feng, Li Pei Ran, et al.: Multi-objective optimal operation strategy of microgrids based on improved OPSO algorithm [J]. Electric Power Science and Engineering 36(12), 22–29 (2020).
4. Zhou Meng Chen, Zhou Meng Ran, Hu Feng, et al.: Multi-objective scheduling optimization of microgrids based on improved multi-objective Walking Optimization Algorithm [J]. Journal of Chongqing Technology and Business University (Natural Science Edition), 1-16 (2025).
5. Chen Jiang Hong, Wang Xi Mu, Li Wei Liang, et al.: Research on optimal scheduling of microgrids using improved northern goshawk algorithm [J]. Journal of Chongqing University of Technology (Natural Science)38(1), 281–289 (2024).
6. Wu Jun Yue, Zhao Er Gang, Guo Zeng Liang, et al.: Ultra-short-term multi-step prediction of photovoltaic output based on Spearman coefficient and TCN [J]. Acta Energiae Solaris Sinica44(9), 180–186 (2023).
7. Hao Xue Li, Zhao Mei Xuan, Pei Li Li, et al.: Optimal scheduling decision of wind/photovoltaic/hydrogen storage highway microgrids based on improved Pareto algorithm [J]. Journal of Traffic and Transportation Engineerin24(4), 71–82 (2024).
8. Zhong Deng Yuan, Wang Xi Huai.: Optimal scheduling of island microgrids based on a multi-strategy enhanced non-dominated sorting gravitational search algorithm. [C] 2025 IEEE 3rd International Conference on Power Science and Technology (ICPST). pp. 1114–1121 IEEE, Kunming, China, (2025).
9. Li Qing, Zhang Xin Yuan, Ma Tian Jiao, et al.: A multi-step ahead photovoltaic power prediction model based on similar day, enhanced colliding bodies optimization, variational mode decomposition, and deep extreme learning machine [J]. Energy 224, 120094 (2021).

10. Zhang Zhi Yu, Wei Lan Xin.: Optimal scheduling study of microgrid based on multi-objective hare algorithm. [C] 2025 4th International Conference on New Energy System and Power Engineering (NESP). pp. 330–335 IEEE, Fuzhou, China, (2025).
11. Dai Xiao Hong, Hu Xu Bo, Zhang Lei, et al.: Multi-objective optimal scheduling of distribution networks based on multi-objective particle swarm optimization algorithm. [C] 2025 2nd International Symposium on New Energy Technologies and Power Systems (NETPS). pp. 422–428 IEEE, Hangzhou, China, (2025).

075 Physics-Constrained Neural network Co-Design for Integrated Modeling and Control of DC/DC Power Converters

Peifeng Hui[1], Chenggang Cui[1], Pengfeng Lin[2], Xitong Niu[1] and Chuanlin Zhang[1]

[1] Intelligent Autonoumous Systems Lab, Shanghai University of Electric Power, Shanghai, China 200090.
[2] School of Electrical Engineering, Shanghai Jiaotong University, Shanghai, China 200240.
huipeifeng@mail.shiep.edu.cn

Abstract. Considering the inherent trade-offs between modeling fidelity and data dependency in conventional control paradigms, this paper proposes a physics-embedded neural control framework that unifies artificial intelligence with governing partial differential equations of power electronic systems. The proposed framework leverages a physics-informed neural network (PINN) to extract spatiotemporal features, embed physical constraints, generate adaptive control policies, and propagate losses across multiple domains. The concurrent enforcement of PDE-constrained gradients and data-derived regularizations achieves real-time decoupling of time-varying parameter drift and exogenous disturbance signatures. By co-optimizing physics-constrained gradients and data-driven adaptation, the framework achieves real-time identification and compensation of parameter variations and external disturbances. Through differential reinforcement learning, the framework enhances transient response and steady-state performance under uncertain operating conditions. Simulation studies on DC power supply systems validate the framework's effectiveness in practical applications.

Keywords: Physics informed neural network, DC power supply, Fusion control framework, Intelligent control.

1 First Section

Power electronic converters serve as critical interfaces between renewable energy sources, loads, and power grids. These systems facilitate renewable energy integration through bidirectional power flow regulation and dynamic power quality improvement, particularly harmonic suppression and transient mitigation[1]. Power electronic systems maintain operational stability under variable loading conditions via adaptive voltage regulation and optimized energy dispatch, while advancing decentralized grid architectures through intelligent control capabilities. The proliferation of distributed generation and microgrid installations underscores their critical role in modern power infrastructure[2].

Large-scale deployment of power electronic systems faces inherent control challenges as physics-based strategies struggle to address nonlinear dynamics, time-varying parameters, and stochastic load interactions exacerbated by switching parasitic inductance and sensor bandwidth limitations. Manual tuning methodologies dependent on switching pattern analysis not only prolong commissioning but escalate protection coordination risks and thermal management complexity, driving interest in model-free control (MFC) approaches[3]. MFC implementations in DC/DC converters demonstrated enhanced stability under source-load disturbances, with subsequent extensions to voltage-source inverters and motor drives improving parametric robustness and transient recovery[4]. While machine learning techniques show potential in overcoming these constraints, practical adoption remains challenged by training data acquisition burdens and real-time computational resource requirements inherent in power electronic applications[5].

This paper introduces a physics-guided neural network architecture co-designed with model predictive control, integrating temporal feature extraction through recurrent networks, physics-regularized learning via circuit-theoretic constraints, and embedded control law optimization. The trained network operates as a self-contained controller, demonstrating enhanced dynamic performance over conventional methods in numerical simulations under concurrent parameter variations and multi-domain disturbances. Simulation results validation under constant power loads fluctuations confirms operational robustness, indicating practical viability for renewable energy systems with stochastic operating conditions.

2 Preliminaries

2.1 A.Power Electronic Systems with Uncertainties

When handling systems with parametric uncertainties and nonlinear couplings, conventional modeling approaches often adopt oversimplified representations categorized as "black-box" or "gray-box" models. These methodologies approximate system dynamics through input–output mappings while neglecting internal dynamic interactions, as mathematically expressed by:

$$x_{k+1} = f(x_k, u_k, \theta_k, d_k) \tag{1}$$

where x_k denotes the state vector at discrete time k, u_k represents the control input vector. θ_k encapsulates intrinsic system parameters, and d_k accounts for unmodeled dynamics. The state transition function $f(\cdot)$ attempts to map current states and control actions to subsequent states through empirical approximation. Such simplifications prove particularly problematic in power electronic conversion systems, where small-signal modeling techniques struggle to capture nonlinear phenomena induced by parameter variations and exogenous disturbances.

The limitations become more pronounced in power electronics applications characterized by strong nonlinearities, where parametric sensitivity and operational

uncertainty significantly influence dynamic behavior. This underscores the necessity for physics-integrated data-driven modeling frameworks capable of simultaneously resolving two fundamental challenges: (1) accurate characterization of instantaneous parameter states and disturbance conditions, and (2) reliable prediction of state evolution considering both intrinsic parameters and external perturbations. Effective modeling strategies must maintain consistency with first-principle physical laws while assimilating operational data to address the dual requirements of parametric transparency and predictive fidelity.

2.2 Physics-Informed Machine Learning

Consider a dynamic system described by (1), it could be convert as $Y = f(X)$. X and Y represent the system's state and output, respectively. The PINN fitting process is shown in Fig. 1:

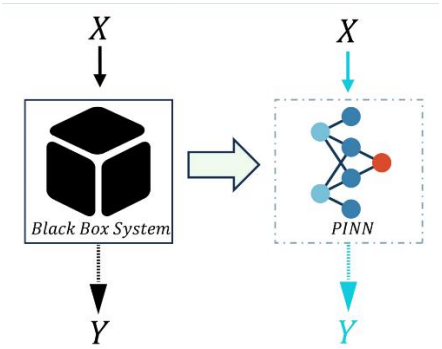


Fig. 1. The process of fitting a black-box converter model using PINN.

1) Constructing Hybrid-Physics-Data Models: In the construction of Hybrid-Physics-Data Models, a fusion of physics-based numerical models with neural network techniques is employed to enhance the precision and reliability of predictive models.

Initially, a physics-based numerical model $f_{phy}: X \to Y$ is established, leveraging input variables X (which are physically related to the target variable Y) to simulate the value of Y. Subsequently, a neural network model $f_{nn}: X \to Y$ is developed, designed to predict by discerning the relationship between the inputs X and the target Y.

2) Hybrid Physics and Data-driven Loss Function: The core design of this loss function is to ensure that the neural network's predictions are consistent with the training data and conform to known physical laws. Such a loss function can be formalized as:

$$\arg\min_f \mathrm{Loss}\left(\hat{Y}, Y\right) + \lambda_{phy}\mathrm{Loss}_{phy}\left(\tilde{Y}, Y\right) \tag{2}$$

where $\mathrm{Loss}\left(\hat{Y},Y\right)$ represents the discrepancy between model predictions and actual data, $\mathrm{Loss}_{phy}\left(\tilde{Y}\right)$ represents the physical consistency error, and the hyper parameter λ_{phy} controls the weight of physical consistency in training.

3 PINN Co-Optimizing Frame Design

The proposed framework implements a co-design architecture integrating physics-constrained components, data-driven learning modules, and control synthesis mechanisms through functionally complementary subsystems. Multi-objective loss functions coordinate these components by enforcing measurement consistency, physical law compliance, and control performance objectives. This architecture achieves unified system modeling through concurrent training of neural networks and physics-based governing equations, where first-principle inductive biases regularize data-driven representations. A distinctive embedded control generation mechanism employs differentiable optimization layers to autonomously synthesize control policies from neural network predictions, seamlessly bridging system identification and control execution within a single computational structure, as illustrated in Fig. 2.

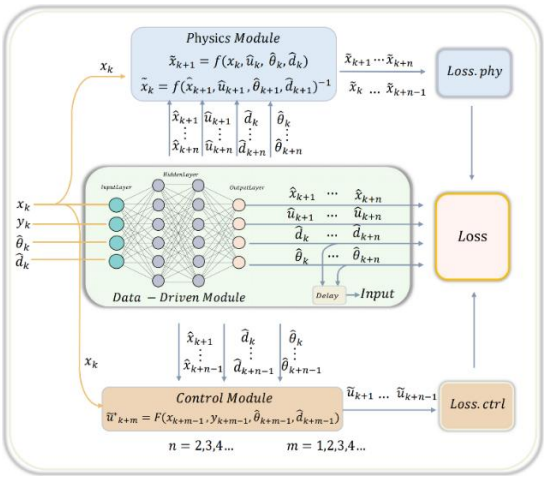


Fig. 2. The framework of proposed method.

3.1 Physics Module Design

Physics module systematically incorporates fundamental electromagnetic laws into the neural network training paradigm, enabling co-optimization of data-driven learning and physical principle compliance. A parameter-varying discrete state-space formulation, derived through switched-mode power converter modeling principles, ensures prediction consistency with both measurement data and physical conservation laws. Assuming the state variables of the converter are $x=[x_1,x_2,x_3,...,x_n]^T$ and the control inputs are $u=[u_1,u_2,u_3,...,u_m]^T$, the state-space representation for

power electronic systems considers circuit topology characteristics through system matrices:

$$\frac{dx}{dt} = A(\theta)x + B(\theta)u + E(\theta)d \tag{3}$$

where $A(\theta)$, $B(\theta)$ and $E(\theta)$ respectively denote the state-transition, control-input, and disturbance matrices parameterized by θ. These time-variant matrices capture the nonlinear dynamics of power converters through physics-embedded computations. The computational graph simultaneously executes neural network-based parameter estimation alongside physical equation solving with implicit time integration, while performing constrained state prediction through nonlinear algebraic loop resolution. The physics-informed loss term quantifies the deviation between predicted states x_{k+1} and actual measurements $\hat{x}_{k+1}$, enforcing first-principle compliance throughout the learning process.

3.2 Control Module Design

Control module employs neural networks to internalize dynamical characteristics governed by advanced control architectures, enabling autonomous strategy synthesis through parameterized policy learning. This module generates control variables by synthesizing data-driven predictions with physical constraints, optimizing the system cost function to enhance operational adaptability and tracking precision. The quadratic cost formulation integrates multi-step predictive control requirements:

$$J(u) = \sum_{i=1}^{n} (Q(y_{k+i} - y_{ref})^2 + R(u_{k+i} - \hat{u}_{k+i})^2) \tag{4}$$

where Q and R represent positive-definite weighting matrices for tracking error and control effort respectively, with n defining the prediction horizon. The optimal control input $\tilde{u}^*$ is derived through constrained optimization:

$$\tilde{u}^* = F\left(x_k, y_k, \hat{\theta}_k, \hat{d}_k\right) \tag{5}$$

where $F(\cdot)$ denotes the parameterized control law mapping. The parameterized control law mapping governs system behavior, with its corresponding cost function integrated into a global loss formulation for unified parameter optimization. Such integration facilitates adaptive control policy generation under operational uncertainty, contrasting conventional data-driven methods that require extensive empirical datasets.

3.3 Data-driven Module Design

Accurate identification of parametric variations and external disturbances proves essential for implementing high-performance control strategies in power electronic systems. A neural network-based predictive framework is developed to simultaneously estimate future system states $\hat{x}_{k+n}$, control law projections $\hat{u}_{k+n}$,

parameter variations θ_{k+n}, and disturbance patterns d_{k+n} across multiple prediction horizons $n \in N^+$. The integrated estimation model enhances closed-loop control robustness through coupled temporal relationships:

$$\begin{bmatrix} \hat{\boldsymbol{x}}_{k+n} \\ \hat{\boldsymbol{u}}_{k+n} \\ \hat{\boldsymbol{\theta}}_{k+n} \\ \hat{\boldsymbol{d}}_{k+n} \end{bmatrix} = f_{\mathrm{NN}}\left(\boldsymbol{x}_{[k-m:k]}, e_{[k-m:k]}, \theta_{[k-m:k]}, d_{[k-m:k]}\right) \tag{6}$$

where $f_{NN}(\cdot)$ represents the neural mapping function with m historical samples as temporal context. The multi-output architecture employs parameter-shared hidden layers for cross-feature correlation learning while maintaining dedicated output heads to preserve domain-specific physical units.

The data-driven framework integrates dual-timescale feature extraction through partitioned neural architectures to address coupled electro-thermal dynamics in power electronic systems. The macroscopic-scale processing constructs multi-cycle operational datasets through continuous acquisition of historical state variables, including load transients and parameter perturbations. The time window duration D_{macro} aligns with dominant slow dynamics, defined as:

$$D_{macro} = \{x(kT_s), \theta(kT_s), d(kT_s)\},\ T_s = \tau_{thermal},\ k = 1, 2, 3 \ldots N \tag{7}$$

where T_s represents the characteristic response time of thermal parameter variations. Parameter uncertainty bounds are rigorously incorporated through constrained learning layers.

$$\mathcal{D}_{micro} = \{x(t), d(t)\}_{nT_{sw}}^{(n+1)T_{sw}},\quad T_{sw} = \frac{1}{f_{sw}} \tag{8}$$

The microscopic phase resolves switching-cycle transients via state-space equation reformulation, with window length synchronized to switching frequency . Boundary conditions explicitly encode switching device transitions, enabling precise modeling of current ripple dynamics and voltage oscillation patterns.

3.4 Physics-based and Control-based Loss Functions Design

To ensure alignment with physical knowledge, physics-informed and control-constrained loss functions are implemented for training data-driven models. These functions maintain consistency with fundamental physical principles and control system laws while enhancing predictive accuracy through structural regularization. The composite loss function of the data-driven model integrates domain knowledge as follows:

$$Loss = \lambda_1 \cdot Loss_{\mathrm{data}} + \lambda_2 \cdot Loss_{\mathrm{phy}} + Loss_{control} \tag{9}$$

where $\lambda_1, \lambda_2, \lambda_3$ are weighting coefficients. The data fidelity term quantifies prediction deviations through weighted mean square error (MSE) between neural network outputs and measured values:

$$Loss_{\text{data}} = \frac{1}{N}\sum_{k=1}^{N}\left\| x_{k+1} - \hat{x}_{k+1} \right\|^2 \tag{10}$$

The physics-constrained term evaluates physical plausibility through residual analysis of governing equations:

$$Loss_{\text{phy}} = \frac{1}{N}\sum_{k=1}^{N}\left\| \frac{dx_k}{dt} - A(\theta)x_k - B(\theta)u_k - E(\theta)d_k \right\|^2 \tag{11}$$

The control-oriented term $Loss_{control}$ imitation learning reference control strategies through imitation learning:

$$Loss_{control} = \frac{1}{N}\sum\nolimits_{i=1}^{N} l(||(u_{k+i}, \tilde{u}_{k+i})||^2 + ||(\tilde{u}_{k+i}, \hat{u}_{k+i})||^2) + J(u). \tag{12}$$

The composite loss function implements adaptive balancing via trainable coefficients $\lambda_1, \lambda_2, \lambda_3$, enabling simultaneous optimization of prediction accuracy, physical consistency, and control compatibility during backpropagation.

4 Performance verification

This section evaluates the performance of the proposed control strategy through a DC/DC Buck converter. The parameters of the Buck converter are summarized in Table I:

Table 1. Simulation and Traing Parameter Setting

Parameters	Description	Value
V_{ref}	Load Bus Reference Voltage	25V
f_{ref}	Switching Frequency	20k Hz
E	Input Voltage	50V
L	Inductance	2 mH
C	Capacitance	1.5 mF

Considering the fact that the system stability is most challenged when feeding pure CPL, this study employs CPL connected to the load bus for simulation comparisons. Three distinct sets of parameters and two operational conditions are defined, enabling a comprehensive comparison against nonlinear disturbance observartion GPC, dual PI controller, and the offset free GPC, the simulation results is shown in Fig.3. Initially, a 60W CPL is connected to the bus. Subsequently, the CPL escalates to 120W and 200W at 0.03s, before reverting to 60W at 0.07s. Observations indicate that the

proposed method adeptly acquires control behaviors from the target controller, ensuring voltage stability during load fluctuations, and either matches or exceeds the performance of alternative controllers. The proposed methodology autonomously identifies system parameter variations without relying on observer-based frameworks typical of conventional parameter uncertainty mitigation approaches, enabling accelerated parameter convergence through real-time identification while eliminating observer design iterations and demonstrating superior dynamic response characteristics compared to PI-controlled implementations.

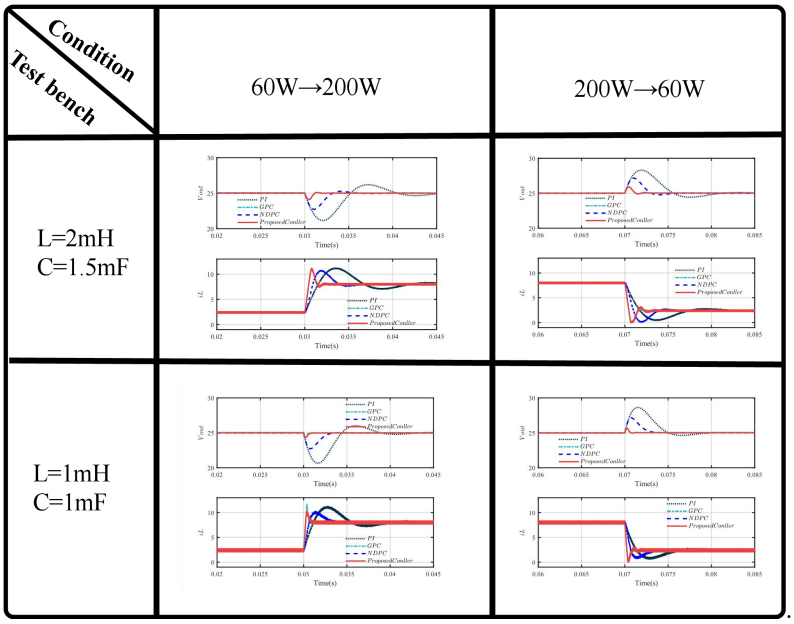


Fig. 1. Validation of the proposed control method through adaptability testing and comparison with alternative methods.

5 Conclusions

This paper proposes a physics-constrained neural framework that systematically integrates model-driven uncertainty quantification and data-driven control synthesis through PINNs, embedding circuit-theoretic principles via constrained optimization. Experimental validation confirms enhanced voltage regulation and generalization capabilities over conventional methods in DC/DC buck converters. The modular architecture enables direct applicability to diverse power converter topologies with parametric uncertainties, while future investigations will explore real-time embedded implementations and multi-domain control coordination under stochastic operating conditions.

References

[1] Q. Hou, E. Du, N. Zhang, and C. Kang, "Impact of High Renewable Penetration on the Power System Operation Mode: A Data-Driven Approach," *IEEE Transactions on Power Systems,* vol. 35, no. 1, pp. 731-741, 2020, doi: 10.1109/TPWRS.2019.2929276.

[2] H. Pishbahar, F. Blaabjerg, and H. Saboori, "Emerging grid-forming power converters for renewable energy and storage resources integration - A review," *Sustainable Energy Technologies and Assessments,* Review vol. 60, Dec 2023, Art no. 103538, doi: 10.1016/j.seta.2023.103538.

[3] W. Li, H. Yuan, S. Li, and J. Zhu, "A Revisit to Model-Free Control," *IEEE Transactions on Power Electronics,* vol. 37, no. 12, pp. 14408-14421, 2022, doi: 10.1109/TPEL.2022.3197692.

[4] W. Li, S. Li, H. Yuan, Y. Zhang, and J. Zhu, "Controller Design Automation for Power Electronics: A Model-Free Approach," *IEEE Transactions on Power Electronics,* vol. 39, no. 2, pp. 2155-2168, 2024, doi: 10.1109/TPEL.2023.3334861.

[5] P. Henderson, R. Islam, P. Bachman, J. Pineau, D. Precup, and D. Meger, "Deep reinforcement learning that matters," in *Proceedings of the AAAI conference on artificial intelligence*, 2018, vol. 32, no. 1.

076 Optimal Capacity Configuration of Large-Scale Wind–Solar Hydrogen Production Systems with Dynamic Hydrogen Production Efficiency

Ran Li[1] and Wenyi Li[2]

[1] Inner Mongolia University of Technology, Hohhot, China
[2] Inner Mongolia University of Technology, Hohhot, China
lwyyyll@vip.sina.com

Abstract. Traditional capacity configuration models for hydrogen production systems often neglect the dynamic efficiency characteristics of electrolyzers, making it difficult to balance both the economic performance and supply stability of large-scale hydrogen production. To address this issue, a dynamic electrolyzer model is established using data-fitting methods by considering the effects of input power and operating temperature on hydrogen production efficiency. An optimization model is then formulated for large-scale wind–solar hydrogen production systems, aiming to minimize operating costs and maximize the average daily hydrogen supply, while incorporating constraints such as power balance, hydrogen supply–demand balance, and grid interaction. Based on typical wind and solar output scenarios, the model is solved using the Proximal Policy Optimization (PPO) algorithm. Finally, case studies compare the capacity configurations obtained from the proposed model and conventional models under six representative scenarios. The results demonstrate that the proposed model can effectively adjust hydrogen production, storage, and dispatch according to renewable energy output characteristics, thereby enhancing both the economic efficiency and reliability of system operation.

Keywords: Large-scale wind–solar hydrogen production system, Dynamic hydrogen production efficiency, Capacity optimization configuration.

1 Introduction

The output of wind and solar is characterized by randomness and volatility, which poses new challenges to the secure operation of power systems and the integration of renewable energy. The development of hydrogen energy storage technology provides solutions for the consumption of new energy and friendly grid connection.

Recent studies have investigated the dynamic efficiency of power-to-hydrogen conversion. Reference [1] developed an electrolyzer efficiency model incorporating temperature coefficients and analyzed its impact on system operation under different power levels. Reference [2] established an energy management model for industrial parks considering hydrogen production efficiency, exploring the relationship between

equipment efficiency and cost under hydrogen demand constraints. Reference [3] proposed a simplified model of electrolyzer input power versus efficiency, significantly reducing model complexity. Reference [4] further incorporated the effects of operating temperature and start–stop cycles, enhancing the accuracy of electrolyzer efficiency modeling and improving system economy. These studies highlight the critical role of dynamic efficiency in hydrogen system stability and economic performance.

Optimizing system capacity is another approach to reducing construction costs. Reference [5] proposed a multi-scenario wind–solar–hydrogen capacity configuration model constrained by power balance. Reference [6] developed a wind–solar–hydrogen scheduling model and analyzed the optimal electrolyzer capacity under gigawatt-scale power generation. Reference [7] constructed a configuration model based on the wide power adaptation range of alkaline electrolyzers, extending the input power flexibility. Reference [8] presented a capacity optimization framework for off-grid wind–solar–hydrogen systems. Reference [9] proposed an off-grid wind–solar complementary hydrogen production strategy, researching the capacity optimization models at different scales; however, they overlooked the dynamic efficiency of electrolyzers. Reference [10] developed a grid-connected hydrogen storage configuration model for industrial parks that considered hydrogen efficiency, enhancing system economic performance. Nevertheless, existing models mostly focus on small- to medium-scale systems, with limited attention to large-scale hydrogen production plants exceeding hundreds of megawatts.

In summary, current research on large-scale wind–solar hydrogen production systems faces three major challenges: (i) balancing the trade-off between electrolyzer dynamic efficiency and system economic performance; (ii) coordinating storage devices with electrolyzers to achieve high renewable energy utilization while meeting hydrogen demand; and (iii) establishing energy interaction constraints between the grid and hydrogen systems to ensure grid-friendly operation.

To address these challenges, a capacity optimization model for large-scale wind–solar hydrogen production systems considering dynamic hydrogen production efficiency was first developed. Subsequently, six representative scenarios were generated using the density peaks clustering self-organizing feature map (DPC-SOFM) method. The model was then solved through the proximal policy optimization (PPO) algorithm. Finally, based on one year of wind and solar power data from a hybrid power plant in western Inner Mongolia, a comparative analysis was conducted between fixed-efficiency and dynamic-efficiency operating conditions.

2 Large-Scale Wind–Solar Hydrogen Production System Model

2.1 System Structure

The structure of the large-scale wind–solar hydrogen production system is illustrated in Fig. 1. The system consists of a wind farm, a photovoltaic (PV) plant, a water electrolysis hydrogen production system (including an electrolyzer cluster, electrochemical energy storage, and hydrogen storage tanks), and hydrogen loads.

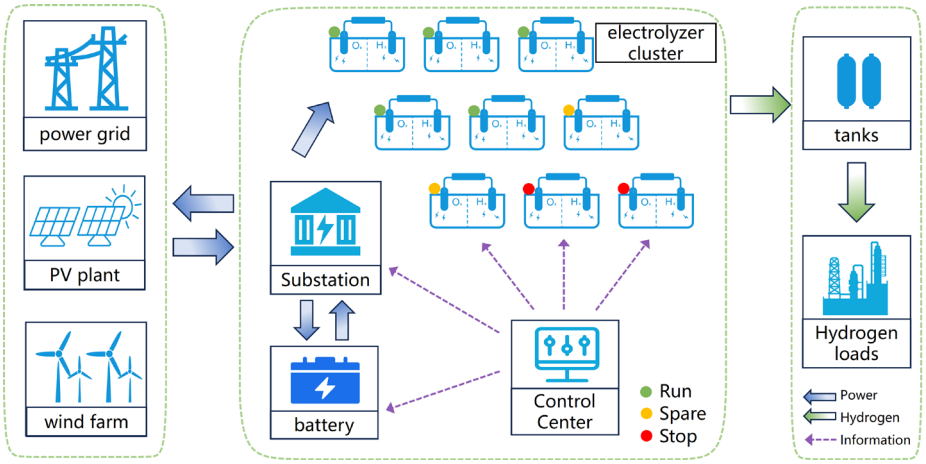


Fig. 1. Large-scale wind and solar hydrogen production system diagram.

2.2 Proton Exchange Membrane Electrolyzer Model

Based on the experimental data reported in [4], a dynamic hydrogen production efficiency model for the Proton Exchange Membrane Electrolyzer (PEM) is developed. The relationship between the input electrical power and its rated capacity is expressed in Eq.(1).

$$P_t^{pu} = \frac{P_t^{in}}{P_N} \tag{1}$$

where P_t^{in} is the input electrical power of the PEM at time t and P_N is rated capacity.

To capture the dependence of dynamic hydrogen production efficiency on input power, rated capacity, and operating temperature, the efficiency model of the electrolyzer is formulated as shown in Eqs.(2)–(3).

When $P_{\mathrm{t}}^{pu} \in [0, 0.15\,pu]$

$$\eta = a_1^{T_{el}} P_{\mathrm{t}}^{pu3} + b_1^{T_{el}} P_{\mathrm{t}}^{pu2} + c_1^{T_{el}} P_{\mathrm{t}}^{pu} + d_1^{T_{el}} \tag{2}$$

When $P_{\mathrm{t}}^{pu} \in [0.15\,pu, 1]$

$$\eta = a_2^{T_{el}} P_{\mathrm{t}}^{pu3} + b_2^{T_{el}} P_{\mathrm{t}}^{pu2} + c_2^{T_{el}} P_{\mathrm{t}}^{pu} + d_2^{T_{el}} \tag{3}$$

where P_t^{pu} and η respectively denote the per-unit input power and hydrogen production efficiency at time t; $a_m^{Tel}, b_m^{Tel}, c_m^{Tel}, d_m^{Tel}$ are parameters which obtained from experimental fitting as illustrated in Fig. 2.

4

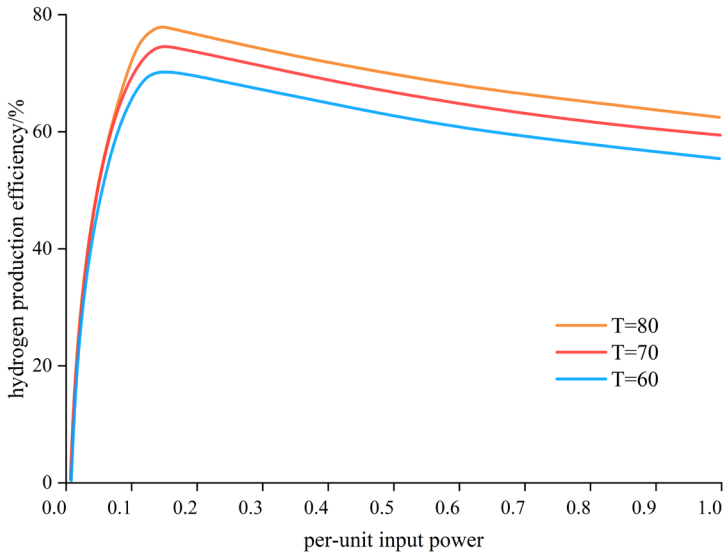


Fig. 2. Curve of the relationship between electrolyzer hydrogen production efficiency and per-unit input power.

As shown in Fig. 2, the hydrogen production efficiency of the electrolyzer is correlated with both input power and temperature. According to its operating state, the system can be divided into three regions: shutdown, buffer, and operation. Specifically, the per-unit input power is within [0, 0.05] in the shutdown region, [0.05, 0.1] in the buffer region, and [0.1, 1] in the operation region. Within the operation region, the efficiency is defined as high when exceeding 65%, which corresponds to a per-unit input power range of [0.1, 0.8].

The relationship between the input power and the hydrogen production power of the electrolyzer is given in Eq.(4).

$$P_{\mathrm{t}}^{out} = \varepsilon_t \eta P_{\mathrm{t}}^{in} \tag{4}$$

where P_t^{out} denotes the hydrogen production power of the PEM at time t, and ε_t represents the operating state of the PEM; $\varepsilon_t = 1$ indicates operation and $\varepsilon_t = 0$ indicates shutdown.

3 Capacity Configuration Model of Large-Scale Wind–Solar Hydrogen Production System Considering Dynamic Efficiency

3.1 Objective Function

The objective function is formulated to minimize the total system cost, which includes the investment and operation costs of the wind, PV plants and the hydrogen production system, and the penalty cost of curtailed renewable power. The investment costs are annualized and converted into daily costs. The objective function is formulated as shown in Eqs.(5)-(6).

$$\min C = \sum_{t=1}^{T}\left(C_t^{w.s} + C_t^{pbs} + C_t^{cut}\right) \tag{5}$$

$$\begin{cases} \mathrm{C}_{\mathrm{t}}^{w.s} = \mathrm{C}_{\mathrm{w\&s.b}} + \mathrm{C}_{\mathrm{w\&s.m}} - \mathrm{C}_{\mathrm{ws2g}} \\ \mathrm{C}_{t}^{\mathrm{pbs}} = \mathrm{C}_{\mathrm{pbs.b}} + \mathrm{C}_{\mathrm{pbs.m}} + \mathrm{C}_{\mathrm{g2pbs}} - \mathrm{C}_{\mathrm{pbs2H}} \\ C_t^{cut} = c_{cut} P_t^{cut} \end{cases} \tag{6}$$

where $\mathrm{C}_t^{w.s}$ and C_t^{pbs} denote the construction and operation cost of the wind–PV plant and the hydrogen production system at time t; C_t^{cut} represents the penalty cost due to renewable curtailment at time t. The curtailment penalty coefficient (c_{cut}) is specified as 0.8 CNY/kWh in this study.

Expressions for the investment and operation costs follows Ref.[11]。

3.2 Constraints

Power Balance Constraint. The large-scale wind-solar hydrogen production system operate in grid-connected mode, with power balance constraints mainly including generation power, grid interaction power, lithium battery charge and discharge power, electrolyzer operating power, and curtailed power.

$$P_t^w + P_t^s + \varsigma_m P_{g2pbs} = P_t^{in} + P_{bat} + P_t^{cut} \tag{7}$$

In the equations, P_t^w and P_t^s respectively denote the wind and PV outputs power at time t; P_{g2pbs} represents the grid interaction power at time t; P_{bat} denotes the charging/discharging power of the lithiumion battery at time t; and ς_m is the interaction state of the hydrogen production system with the grid, where a value of 1 indicates electricity purchase and −1 indicates electricity sale.

Hydrogen Supply Stability. The average daily hydrogen supply rate (PR_1) is defined as the ratio of the average daily hydrogen output to the average daily hydrogen demand. The calculation is given by Eq.(8).

$$PR_1 = \frac{\sum_{t=1}^{T} V_{\mathrm{fh}H_2}(t)}{W_{H_2}} \times 100\% \tag{8}$$

where T is the daily operating time of the hydrogen production system (set to 24h), $V_{\mathrm{fhH}_2}(t)$ is the hydrogen output at time t, and W_{H_2} is the daily hydrogen loads demand which sets to 30,000 kg/day, the constraint range of PR_1 is [0.95, 1.15].

Other Constraints. The renewable energy consumption constraint is defined according to Ref.[12], the electrolyzer operational characteristics constraint follows Ref.[4], the hydrogen storage tank capacity constraint is given in Ref.[11], and the interaction with power grid is formulated in Ref.[13].

3.3 Typical Days Generation Based on DPC-SOFM

The Self-Organizing Feature Map (SOFM) is an unsupervised neural network method that learns high-dimensional input data to extract key features and achieve low-dimensional mapping. Compared with traditional clustering algorithms (e.g., k-means), SOFM does not require predefined cluster centers or the number of clusters. Instead, it relies on a competitive learning mechanism among neurons to adaptively adjust weights and gradually optimize the network structure. However, the clustering results obtained by SOFM often suffer from uncertainty in cluster numbers, making it difficult to fully capture the stochasticity and variability of regional renewable energy outputs.

To address this limitation, the Density Peaks Clustering (DPC) algorithm is incorporated into the SOFM framework. The DPC algorithm identifies density centers based on local density and relative distance of sample points, thereby refining the clustering results of SOFM. This integration ensures that the generated typical-day samples more accurately reflect the stochastic and temporal characteristics of renewable energy outputs.

3.4 Model Solution Based on Proximal Policy Optimization Algorithm

The Proximal Policy Optimization (PPO) algorithm is a reinforcement learning method that ensures training stability by constraining the extent of policy updates. Owing to its robustness and efficiency, PPO is well-suited for the joint optimization of capacity configuration and operational strategies in large-scale wind–solar hydrogen production systems. The detailed algorithmic process can be found in [14].

4 Example Analysis

The Inner Mongolia region possesses abundant wind and solar resources, offering significant potential for renewable energy integration. In this study, real-world wind and solar power data with a temporal resolution of 1 h, together with a time-of-use electricity price scheme, are adopted for the western Inner Mongolia region. Effects of fixed efficiency and dynamic efficiency hydrogen production systems on hydrogen supply stationarity and operating economy under different typical days.

4.1 Renewable Power Scenario Classification

A total of six representative days are derived using the DPC-SOFM clustering method, as shown in Fig.3. These representative days adequately capture the regional climatic characteristics of low precipitation, abundant sunlight, and high wind availability. Based on the representative day profiles, two system configuration schemes are designed:

Scheme 1: A fixed-efficiency hydrogen production model is employed, and the system capacity is optimized using the PPO algorithm.

Scheme 2: The proposed dynamic-efficiency hydrogen production model is applied, and the system capacity is optimized using the PPO algorithm.

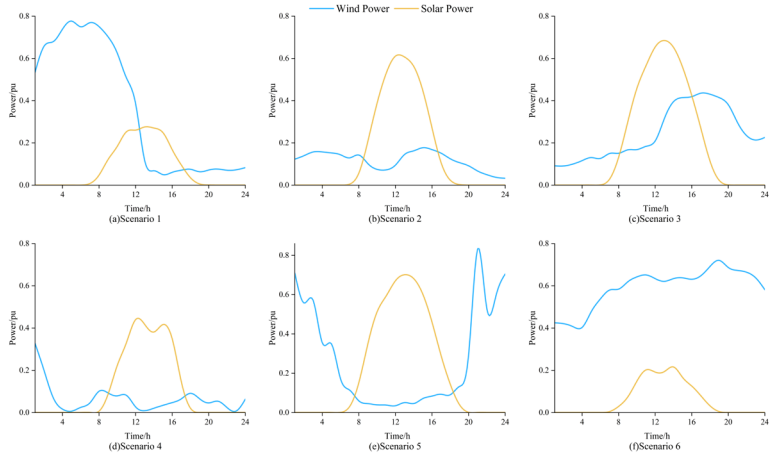


Fig. 3. 6 typical scenarios of wind-solar power generation

4.2 Capacity Configuration

The optimal capacity allocation results for the hydrogen production system under the two schemes are presented in Table 1, while the corresponding performance indicators are summarized in Table 2.

Table 1. Capacity Configuration Result

Device	Scheme 1	Scheme 2
PEM capacity	150 MW	200 MW
Lithium Battery capacity	257 MW·h	184 MW·h
Tank capacity	8000 kg	15000 kg

Compared with Scheme 1, the PEM capacity in Scheme 2 increases by 33.33%, and the hydrogen storage tank capacity increases by 87.5%, while the lithium battery capacity decreases by 28.4%. Incorporating dynamic hydrogen production efficiency

leads to an increase in PEM capacity, which improves renewable energy utilization and hydrogen production. Meanwhile, the reduced battery capacity indicates that part of the short-term energy balancing function is replaced by direct hydrogen production. The increased storage tank capacity enables large-scale hydrogen storage and flexible dispatch. From the perspective of cost, Scheme 2 incurs an additional daily equipment investment of 173,145.84 CNY and an additional daily operation and maintenance (O&M) cost of 55,753.42 CNY compared with Scheme 1.

Table 2. Evaluation Index

Scheme	Index	Font size					
		Scenario 1	Scenario 2	Scenario 3	Scenario 4	Scenario 5	Scenario 6
1	Hydrogen supply rate	92.2%	47.3%	69.9%	34.9%	80.7%	101%
	Renewable energy Consumption rate	98.24%	99.67%	99.65%	99.94%	98.94%	97.82%
	Cost of operation (10,000 yuan)	-34.233	42.815	2.152	64.653	-5.659	-68.303
2	Hydrogen supply rate	115%	77.06%	103%	51.5%	113%	115%
	Renewable energy Consumption rate	99.26%	99.89%	99.98%	99.97%	99.69%	97.14%
	Cost of operation (10,000 yuan)	-32.005	22.414	-14.817	62.091	-31.307	-57.108

As shown in Table 2, there are five scenarios in Scheme 1 that fail to meet the minimum hydrogen supply requirements. In particular, Scenarios 2 and 5 achieve hydrogen supply rates below 50%, which severely hinders the normal operation of hydrogen loads. Only Scenario 6 fulfills the daily hydrogen supply target. In contrast, under Scheme 2, only two scenarios fail to meet the hydrogen supply requirement, demonstrating significantly improved supply stability.

Based on the performance metrics in Table 2, the six scenarios are further classified into high-output, medium-output, and low-output types according to hydrogen production and supply capability. The correspondence between representative scenarios and output types is summarized in Table 3.

Table 3. Typical scenario number and output type

Scenarios	Amount	Probability	Type
1	100	27.4%	medium
2	38	10.41%	low
3	71	19.45%	medium
4	7	1.92%	low
5	36	9.86%	high
6	113	30.96%	high

As shown in Table 3, Scenarios 1 and 6 exhibit the highest occurrence probabilities, together accounting for 58.36% of the total days in a year. The proportions of high-output, medium-output, and low-output days are 40.82%, 46.85%, and 12.33%, respectively.

From the perspective of hydrogen supply stability, under Scheme 1 with a fixed-efficiency capacity configuration model, only Scenario 6 is able to meet the daily hydrogen supply requirement. In contrast, the hydrogen supply requirement cannot be satisfied only in low-output scenarios of Scheme 2, which account for 12.33% of the total days in a year. Regarding the renewable energy consumption rate, Scheme 2 achieves an average improvement of 0.21% compared with Scheme 1. From the perspective of operational cost, Scheme 2 incurs an average increase of 19.79%, mainly due to the higher capital investment associated with PEM. However, in terms of operational revenue, Scheme 2 shows an average increase of 15.72%. The dynamic-efficiency model enhances the power-to-hydrogen conversion rate, thereby increasing hydrogen sales revenue and reducing the investment cost. From the perspective of operational strategy, Scheme 2 demonstrates significant improvements in hydrogen supply stability. Nevertheless, in low-output scenarios, the hydrogen supply rate falls below 95% due to two main reasons:

(i) Insufficient renewable generation on low-output days, combined with the constraints on grid interaction, results in inadequate electricity available for hydrogen production;

(ii) In the simulation, the initial daily state of charge of the hydrogen storage tank is fixed, preventing inter-day hydrogen scheduling.

To further investigate this issue, a detailed hydrogen production scheduling analysis was conducted for representative scenarios. Specifically, one medium-output scenario with a relatively high occurrence probability (Scenario 1) and one low-output scenario where the daily hydrogen supply target was not achieved (Scenario 2) were selected. The corresponding hydrogen production scheduling results are shown in Figure 4.

10

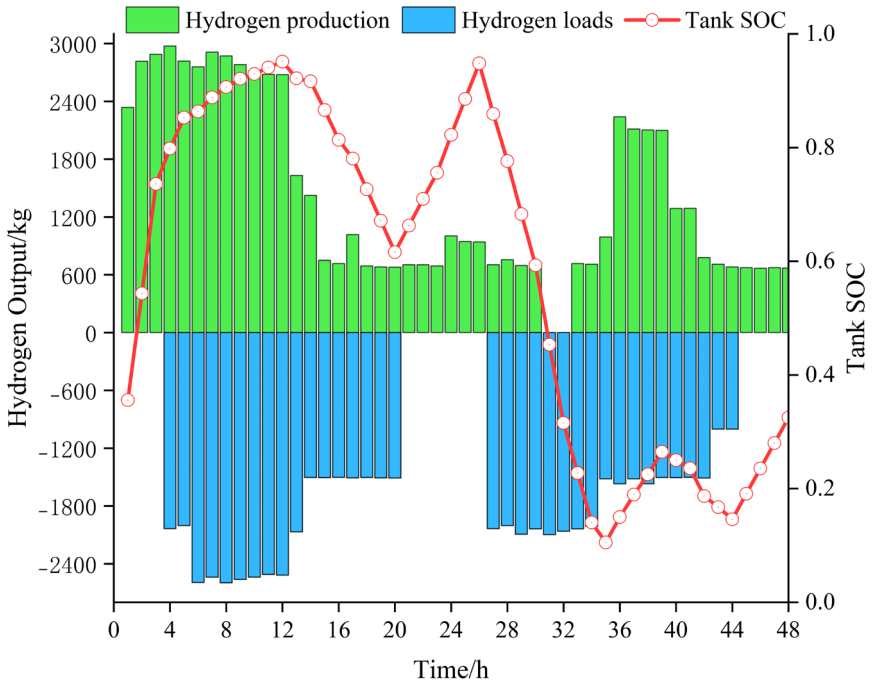


Fig. 4. Hydrogen production scheduling in typical scenarios

As illustrated in **Figure 4**, during the period from 1h to 3h, the PEM produced hydrogen and stored it, resulting in a rapid decrease in the storage tank volume. Starting from 4h, hydrogen was delivered to the load, and the storage rate began to slow down. To ensure that the storage capacity of the hydrogen tank met the requirements of intraday scheduling, additional hydrogen was supplied to the load between 6h and 12h, thereby alleviating the storage pressure of the hydrogen system. From 14h to 20h, the PEM operated at a stable power level, entering a steady intraday hydrogen supply stage. By 20h, the hydrogen system had already achieved 115% of the daily hydrogen supply upper limit. Beginning at 21h, all the hydrogen produced was stored in the tank. By 26h, the state of charge (SOC) of the hydrogen tank reached 94.8%, and to ensure the safe operation of the system, hydrogen was subsequently delivered externally. Due to insufficient renewable energy output, the PEM could not meet real-time hydrogen demand, and the SOC of the hydrogen tank declined from 0.948 to 0.105 within 9 hours. By 44h, the daily hydrogen supply rate reached 101.95%, which represents an improvement of 32.3% compared with Scenario 2, thereby meeting the scheduled hydrogen supply target.

In summary, the proposed model enhances hydrogen production capacity, leading to an average improvement of 23.5% in the daily hydrogen supply rate. By leveraging rational storage and dispatching strategies for the hydrogen tank, the system can reliably fulfill hydrogen demand even under low-output renewable energy conditions.

5 Conclusion

To address the limitation of fixed-efficiency models in ensuring hydrogen supply stability for large-scale hydrogen production systems, this study developed a capacity optimization model that incorporates dynamic hydrogen production efficiency. The results demonstrate that, compared with the fixed-efficiency model, the proposed dynamic efficiency model not only improves renewable energy utilization and hydrogen yield, but also enhances supply stability through the rational use of hydrogen storage tanks, thereby increasing the overall operational profitability of the system. Furthermore, by employing the DPC-SOFM method to generate typical days, the model effectively preserves the statistical characteristics of renewable energy data while reducing the computational complexity of problem solving.

Acknowledgement: This work is supported by the Analysis of Hybrid Energy Storage Operation Characteristics under Grant SSJS2025-NM-DK-070.

References

1. Niu, M., Hong, Z., Li, B., et al.: Optimal control strategy of wind power to hydrogen system considering electrolyzer efficiency improvement [J]. Acta Energiae Solaris Sinica 44(9), 366–376 (2023).
2. Abomazid, A.M., El-Taweel, N.A., Farag, H.E.Z.: Optimal energy management of hydrogen energy facility using integrated battery energy storage and solar photovoltaic systems [J].IEEE Transactions on Sustainable Energy 13(3), 1457–1468 (2022).
3. Jiang, Y., Yang, G., Chen, Y., et al.: Optimal operation for hydrogen network under consideration of the dynamic hydrogen production efficiency of electrolyzers [J]. Proceedings of the CSEE 43(8), 3014–3027 (2023).
4. Duan, L., Jia, Y., Huang, L., et al.: Optimization strategy for an integrated electric-hydrogen-thermal energy system with multiple types of electrolyser modules [J/OL]. Journal of Shanghai Jiaotong University, 1–17 (2025).
5. Wang, H., Chen, X., Yang, Q., et al.: Optimization of renewable energy hydrogen production systems using volatility improved multi-objective particle swarm algorithm [J]. Energies 17(10), 2384 (2024).
6. Tian, C., Tan, Q., Fang, G., et al.: Hydrogen production to combat power surpluses in hybrid hydro–wind–photovoltaic power systems [J]. Applied Energy 371, 123627 (2024).
7. Liu, Y., Fan, Y., Hao, J., et al.: Capacity configuration and optimal scheduling of a wind-photovoltaic-hydrogen-thermal virtual power plant based on a wide range power adaptation strategy for an alkaline electrolyzer [J]. Power System Protection and Control 50(10), 48–60 (2022).
8. Li, Q., Han, Y., Bai, Z., et al.: Coordination operation strategy and capacity optimization of off-grid wind-solar hydrogen production system [J]. Proceedings of the CSEE 44(20), 8136–8146 (2024).
9. Wang, H., Zhang, R., Zhou, J., et al.: Optimal capacity configuration of off-grid wind-solar hydrogen production and green ammonia synthesis system [J]. Integrated Intelligent Energy 46(11), 73–82 (2024).

10. Chen, Y., Ai, X., Wang, Z., et al.: Optimal allocation of hydrogen storage capacity in industrial parks considering dynamic efficiency characteristics of electro-hydrogen conversion [J]. Acta Energiae Solaris Sinica 46(6), 184–195 (2025).
11. Deng, Z., Zhou, J., Xu, G., et al.: Capacity scheduling optimization analysis of on/off grid wind-solar hybrid hydrogen synthesis ammonia system [J]. Thermal Power Generation 53(9), 136–146 (2024).
12. Xu, Y., Li, G.: Capacity configuration optimization of off-grid wind-solar coupling hydrogen production system based on alkaline–proton exchange membrane hybrid electrolyzers [J]. Electric Power Automation Equipment 45(4), 1–9 (2025).
13. Kong, L., Jia, Z., Shi, Z., et al.: Capacity optimization configuration of wind-solar-hydrogen-ammonia coupling system considering on/off grid electricity constraints [J]. Smart Power 53(1), 75–81+97 (2025).
14. Liang, T., Sun, B., Tan, J., et al.: Scheduling scheme of wind-solar complementary renewable energy hydrogen production system based on deep reinforcement learning [J]. High Voltage Engineering 49(6), 2264–2275 (2023).

077 配电系统的可用供电能力

焦 衡[1]，肖 峻[2]

（1. 河北工程大学 信息与电气工程学院，河北省 邯郸市 056038;

2. 天津大学 智能配用电装备与系统全国重点实验室，天津市 南开区 300072）

Available Supply Capability for Distribution Systems

JIAO Heng[1], XIAO Jun[2]

（1. School of Information and Electrical Engineering, Hebei University of Engineering, Handan 056038, China;

2. State key laboratory of Intelligent Power Distribution Equipment and System, Tianjin University, Tianjin 300072, China)

ABSTRACT: This paper proposes the definition, model, and calculation method of available supply capability (ASC) for distribution systems. Firstly, the definition of ASC is proposed. ASC is defined as the set of all the allowed load increments from the present operating point to the security boundary of a distribution system. Secondly, the mathematical model and calculation method of ASC are established. The results of the proposed method can describe the available supply capability of a distribution system completely, including not only the ASC values, but also some other important data, such as all load growth paths and cross-boundary points when the system reaches its security boundary. Finally, an IEEE RBTS case with DGs is used to demonstrate the proposed concepts and methods. The proposed ASC is an important index for operators, similar to the ATC of the transmission system.

KEY WORDS: distribution system, available supply capability (ASC), security boundary

摘要：本文提出了配电系统可用供电能力的定义、模型和计算方法。首先，提出了 ASC 的定义。ASC 定义为从当前运行点到配电系统安全边界的所有允许负载增量的集合。其次，建立了 ASC 的数学模型和计算方法。所提出的方法的结果可完整描述配电系统的可用供电能力，不仅包括 ASC 值，还包括其他一些重要数据，例如系统达到安全边界时的所有负荷增长路径和越界点。最后，采用 IEEE RBTS 有源网算例验证了所提概念及方法。所提 ASC 是配电运行的重要指标，类似于输电系统的 ATC。

关键词：配电系统；可用供电能力；安全边界

基金项目：国家自然科学基金面上项目(52177105)。

Project Supported by National Natural Science Foundation of China (NSFC) (52177105).

DOI：10.13335/j.1000-3673.pst.2019.05. XX

1 引言

能力是一个系统完成其主要功能的重要指标。对于输电系统，最大输电能力[1]（TTC）描述了其能力极限。可用输电能力[2]（ATC）是仅次于 TTC 的重要概念，反映了系统能力裕度。对于配电系统，最大供电能力[3]（TSC）描述了其能力极限，与 TTC 对应，但长期以来没有出现与 ATC 对应的概念。

2011 年，文[3]首次提出了 TSC 的概念，定义为配电网在满足 N-1 安全准则下的最大负荷供应能力。在 TSC 指标族[3]中，第一次出现了可用供电能力（ASC）的概念，定义为 N-1 安全准则下配电网在当前负荷基础上可增加的供电能力。文[3]借鉴输电系统 ATC 的计算思路[2]，给出了 ASC 的计算方法，即用 TSC 减去当前总负荷。该方法计算简单，但未考虑已有负荷不易削减的实际情况，其结果往往无法直接指导实际运行。

目前，TSC 已形成较完整的理论体系，但 ASC 相关研究仍然较少。文[4,5]提出了一系列可用供电能力（ALSC）的概率评估指标。ALSC 与 ASC 名称相似，但区别较大：1）计算 ASC 需先得到最大值 TSC，ALSC 不需要；2）现有负荷按 ASC 增长后，会达到 TSC，ALSC 不一定；3）ASC 不限制负荷增长路径，ALSC 限制；4）求解 ASC 考虑 N-1 安全约束，ALSC 不考虑。文[6]建立了考虑移动储能系统接入的 Open capacity 模型，将 ASC 求解转化为线性规划问题。该模型同时计及了主变 N-1 和馈线出口 N-1 约束，提高了精确性。

综上，ASC 的研究非常缺乏，很多基础性问题尚未解决。首先，ASC 术语未统一，易混淆，如

ALSC、Open capacity。ASC 与输电系统的 ATC 相对应，规范性更好，因此本文沿用该名称。同时，现有 ASC 计算结果并不全面，不能满足运行的要求。现有方法[3,6]所得 ASC 仅是一个值，即配电网满足安全性和可操作性条件下可增加供电能力的最大值，反映了当前运行点下允许负荷增长最多的理想路径。本文发现还存在大量其他运行点发展路径。实际中很难保证当前运行点按照理想路径发展，现有研究尚未刻画这些路径。其实，TSC 的研究历程中也有类似问题。2018 年，文[7]提出了 TSC 曲线，能完整刻画配电网在各种不同负荷分布下的最大供电能力，TSC 仅是该曲线上的最大值点。

TSC 曲线的研究[7,8]表明，配电系统的供电能力不仅是 TSC 一个值，而是一个区间。受此启发，本文提出了 ASC 的新定义，相对现有 ASC 的定义更加完整和准确。新的 ASC 定义和模型能考虑当前点所有可能的负荷增长路径，所得结果同样是一个区间，现有方法所得 ASC 是该区间的一个值。

2 ASC 的定义与模型

2.1 ASC 的定义

ASC 最早出现于 TSC 指标族[3]，计算方法如下

$$\mathrm{ASC}=\mathrm{TSC}-\mathrm{CTL} \tag{1}$$

式中，CTL 为系统当前总负荷。

式(1)计算简单，物理意义清晰，但未考虑已有负荷不可减的实际情况，所得结果往往无法直接指导运行。文[6]模型考虑了这个实际情况，所得结果是一个略小于式(6)结果的最大值。

现有研究聚焦于计算 ASC 的最大值[3]或特定前提下的极大值[6]，这不足以完整刻画系统的供电潜力。本文重新定义了 ASC，如下：

ASC 定义为满足 N-1 安全准则下，配电系统当前运行点在各馈线/馈线段已有负荷不减小条件下的负荷可增长量集合。

2.2 ASC 的数学模型

基于新定义，本文建立 ASC 数学模型如下：

$$\mathrm{ASC}=\{\mathrm{ASC}_i\},\ i=1,2,...,N_{\mathrm{ASC}} \tag{2}$$

$$\begin{cases} \mathrm{ASC}_i=\mathrm{Val}(\boldsymbol{W}_{\mathrm{ASC}}^{\beta,i})-\mathrm{Val}(\boldsymbol{W}^{c}) & (3\text{-}1)\\ s.t.\ \ S_{L,k}^{\beta,i}\ge S_{L,k}^{c},\ \forall k\in[1,2,...,n] & (3\text{-}2)\\ \boldsymbol{W}_{\mathrm{ASC}}^{\beta,i}\in\partial\boldsymbol{\Omega}_{\mathrm{st}} & (3\text{-}3)\\ \partial\boldsymbol{\Omega}_{\mathrm{st}}=\left\{\beta_j\mid j=1,2,3,\ldots\right\} & (3\text{-}4)\\ \beta_j=\left\{\mid\mathbf{K}_{L,eq}\boldsymbol{S}_L+\mathbf{K}_{G,eq}\boldsymbol{S}_{DG}\mid=\boldsymbol{c}_{eq}\right\} & (3\text{-}5)\\ \qquad\left\{\mid\mathbf{K}_{L,ie}\boldsymbol{S}_L+\mathbf{K}_{G,ie}\boldsymbol{S}_{DG}\mid\le\boldsymbol{c}_{ie}\right\} & (3\text{-}6) \end{cases} \tag{3}$$

式(2)表示 ASC 是一系列 ASC_i 值的集合。ASC_i 为当前运行点到第 i 个安全边界点的负荷增长量，N_{ASC} 为可到达的边界点数，每个边界点对应了一种可能的负荷增长路径。

式(3-1)为 ASC_i 值的表达式。$\boldsymbol{W}_{\mathrm{ASC}}^{\beta,i}$ 为 ASC_i 对应的边界点，$\boldsymbol{W}^{c}$ 为当前运行点。

式(3-2)表示已有负荷不减小。$S_{L,k}^{\beta,i}$ 和 $S_{L,k}^{c}$ 分别为 $\boldsymbol{W}_{\mathrm{ASC}}^{\beta,i}$ 和 $\boldsymbol{W}^{c}$ 的第 k 回馈线/馈线段负荷。

式(3-3)表示 $\boldsymbol{W}_{\mathrm{ASC}}^{\beta,i}$ 位于安全边界$\partial\boldsymbol{\Omega}_{\mathrm{st}}$上，确保任一馈线/馈线段负荷不能再增加。

式(3-4)至式(3-6)为安全边界约束：

式(3-4)表示完整的安全边界$\partial\boldsymbol{\Omega}_{\mathrm{st}}$一般由多个边界组成。$\beta_j$为$\partial\boldsymbol{\Omega}_{\mathrm{st}}$的第$j$个边界。

式(3-5)是β_j的等式约束，共r行。$\mathbf{K}_{L,eq}$和$\mathbf{K}_{G,eq}$分别为等式约束的负荷系数矩阵和DG系数矩阵。其中，$\mathbf{K}_{L,eq}$不含有纯零列，表明所有的负荷变量都受到等式约束，即运行点任一负荷都不能再增加，保证了临界性。$\boldsymbol{c}_{eq}$为r维的常向量，元素为对应的主变或馈线容量。

式(3-6)是β_j的不等式约束，共s行。其中，$\mathbf{K}_{L,ie}$和$\mathbf{K}_{G,ie}$分别为不等式约束的负荷系数矩阵和DG系数矩阵，$\boldsymbol{c}_{ie}$为s维的常向量。

2.3 ASC 指标和相关概念

2.3.1 ASC 指标

1）最大 ASC：所有 ASC_i 中的最大值，记作 $\mathrm{ASC}_{\max}$。$\mathrm{ASC}_{\max}$ 对应了裕度最大的负荷增长路径。

$$\mathrm{ASC}_{\max}=\max\{\mathrm{ASC}_i\},\ i=1,2,...,N_{\mathrm{ASC}} \tag{4}$$

2）最小 ASC：所有 ASC_i 中的最小值，记作 $\mathrm{ASC}_{\min}$。$\mathrm{ASC}_{\min}$ 对应了裕度最小的负荷增长路径。

$$\mathrm{ASC}_{\min}=\min\{\mathrm{ASC}_i\},\ i=1,2,...,N_{\mathrm{ASC}} \tag{5}$$

$\mathrm{ASC}_{\max}$ 就是文[6]计算的 ASC；$\mathrm{ASC}_{\min}$ 是一个新指标，反映了系统供电能力裕度的下限，在系统运行评估中应关注。

2.3.2 ASC 相关概念

1）ASC 越界点：在各馈线/馈线段负荷不减小的条件下，当前点 $\boldsymbol{W}^{c}$ 负荷增长后可到达的安全边界点，用符号 $\boldsymbol{W}_{\mathrm{ASC}}^{\beta,i}$ 表示。

$$\boldsymbol{W}_{\mathrm{ASC}}^{\beta,i}=\{\boldsymbol{W}\in\partial\boldsymbol{\Omega}_{\mathrm{st}}\mid S_{L,k}^{\beta,i}\ge S_{L,k}^{c},\ \forall k\in[1,2,...,n]\} \tag{6}$$

2）ASC 越界点数：ASC 越界点的个数，取决于当前负荷分布和采样精度，用符号 N_{ASC} 表示。

3）ASC 越界点集：所有 ASC 越界点的集合，用符号 $\boldsymbol{W}_{\mathrm{ASC}}^{\beta}$ 表示。

$$\boldsymbol{W}_{\mathrm{ASC}}^{\beta}=\{\boldsymbol{W}_{\mathrm{ASC}}^{\beta,i}\},\ i=1,2,...,N_{\mathrm{ASC}} \tag{7}$$

4）$\mathrm{ASC}_{\min}$ 越界点：$\boldsymbol{W}_{\mathrm{ASC}}^{\beta}$ 中负荷总量最小的运

行点，$\boldsymbol{W}^c$ 到达这些点后，负荷增长量为 $\mathrm{ASC}_{\min}$，用符号 $\boldsymbol{W}^{\beta}_{\mathrm{ASC}\,\min}$ 表示。

$$\boldsymbol{W}^{\beta}_{\mathrm{ASC}\,\min}=\{\boldsymbol{W}\in\boldsymbol{W}^{\beta}_{\mathrm{ASC}}\,|\,\mathrm{Val}(\boldsymbol{W})-\mathrm{Val}(\boldsymbol{W}^c)=\mathrm{ASC}_{\min}\}\quad(8)$$

5）$\mathrm{ASC}_{\max}$ 越界点：$\boldsymbol{W}^{\beta}_{\mathrm{ASC}}$ 中负荷总量最大的运行点，$\boldsymbol{W}^c$ 到达这些点后，负荷增长量为 $\mathrm{ASC}_{\max}$，用符号 $\boldsymbol{W}^{\beta}_{\mathrm{ASC}\max}$ 表示。

$$\boldsymbol{W}^{\beta}_{\mathrm{ASC}\,\max}=\{\boldsymbol{W}\in\boldsymbol{W}^{\beta}_{\mathrm{ASC}}\,|\,\mathrm{Val}(\boldsymbol{W})-\mathrm{Val}(\boldsymbol{W}^c)=\mathrm{ASC}_{\max}\}\quad(9)$$

越界点蕴含了丰富信息。每个越界点对应了当前点达到安全边界的一个负荷增长路径，也对应了一个 ASC_i 值。

2.4 优化 ASC 的定义和模型

ASC是在已有负荷不减条件下得到的，若计算所得ASC不够大，还想进一步扩大ASC，可以放宽条件进一步挖掘系统的供电潜力。为此，本文提出了优化ASC（OASC）的概念。

OASC是部分馈线/馈线段负荷减小条件下，优化后值大于$\mathrm{ASC}_{\max}$的ASC。OASC的数学模型如下

$$\mathrm{OASC}=\{\mathrm{OASC}_i\},\quad i=1,2,...,N_{\mathrm{OASC}}\qquad(10)$$

$$\begin{cases}\mathrm{OASC}_i=\mathrm{Val}(\boldsymbol{W}^{\beta,i}_{\mathrm{OASC}})-\mathrm{Val}(\boldsymbol{W}^c) & (11\text{-}1)\\ s.t.\ \ \mathrm{OASC}_i>\mathrm{ASC}_{\max} & (11\text{-}2)\\ S^{\beta,i}_{L,k}<S^c_{L,k},\ \exists k\in[1,2,...,n] & (11\text{-}3)\\ \boldsymbol{W}^{\beta,i}_{\mathrm{OASC}}\in\partial\boldsymbol{\Omega}_{\mathrm{st}} & (11\text{-}4)\\ \partial\boldsymbol{\Omega}_{\mathrm{st}}=\{\beta_j\,|\,j=1,2,3,\ldots\} & (11\text{-}5)\\ \beta_j=\begin{Bmatrix}|\mathbf{K}_{L,eq}\boldsymbol{S}_L+\mathbf{K}_{G,eq}\boldsymbol{S}_{DG}|=\boldsymbol{c}_{eq}\end{Bmatrix} & (11\text{-}6)\\ \quad\ \begin{Bmatrix}|\mathbf{K}_{L,ie}\boldsymbol{S}_L+\mathbf{K}_{G,ie}\boldsymbol{S}_{DG}|\le\boldsymbol{c}_{ie}\end{Bmatrix} & (11\text{-}7)\end{cases}\qquad(11)$$

OASC的数学模型与ASC的整体相似，有两处不同：式(11-2)表示OASC_i只保留大于$\mathrm{ASC}_{\max}$的部分；式(11-3)表示允许已有负荷减小。

与ASC类似，OASC也具有指标和相关概念，它们的含义、符号及计算方法与ASC的相同。

OASC是ASC的补充。ASC和OASC共同完整反映了系统的可用供电能力。

3 ASC 的计算方法

对于一定供电区域内配电网，其 ASC 计算的具体步骤如下：

步骤 1：读取电网结构和参数，列写 DSSR 表达式，并化简为最简式。根据最简式求解安全边界表达式。

步骤 2：根据馈线/馈线段容量，确定状态空间。按一定步长对状态空间进行等间隔采样，生成采样点集。进一步，从该采样点集中筛选出满足安全边界表达式的采样点，得到安全边界点。

步骤 3：根据式(3-2)，从边界点中筛选出当前运行点对应的 ASC 越界点。进而，根据式(3-1)计算各越界点的 ASC_i。

步骤 4：根据式(4)、(5)计算 ASC 指标。

步骤 1、2 是离线预先执行的，只要电网结构和参数不变就无须重新计算；步骤 3、4 是当前运行点变化后反复执行的。

OASC 的计算流程与 ASC 的整体相似，在步骤 3 中有所不同：根据式(11-2)、(11-3)，从 $\boldsymbol{W}^{\beta}$ 中筛选出当前运行点对应的 OASC 越界点。进而，根据式(11-1)计算各越界点的 OASC_i。

4 算例验证

4.1 算例概况

采用含源 IEEE RBTS-Bus4 算例验证。算例的电网结构见图 1，含 3 座变电站，7 回馈线，43 个节点（38 个负荷节点，5 个 DG 节点）。单回馈线的负荷功率范围为[0.0, 8.0] MVA，单个 DG 的功率范围为[-2.0, 0.0] MVA。年最大负荷为 42.0 MVA，DG 总容量为 10.0 MVA，容量渗透率为 23.8%。算例的其它参数见表 1。

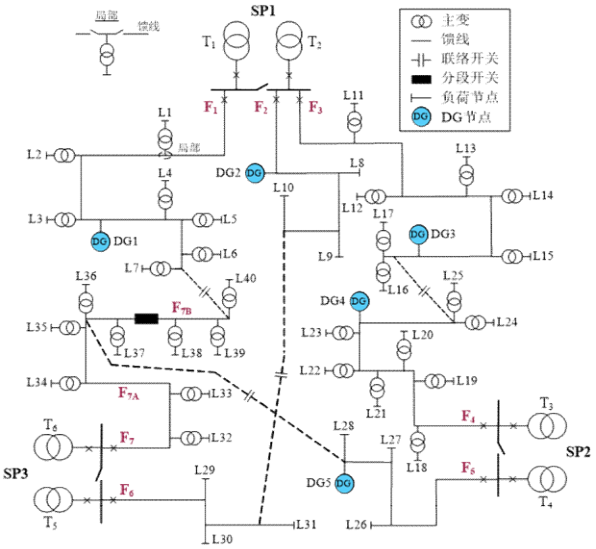


图 1　IEEE RBTS-Bus4 有源配电网

表1　变电站数据

变电站	主变压器	变比 /kV/kV	主变容量 /MVA	馈线总容量 /MVA
S1	T1	35/10	10.0	6.0
	T2	35/10	10.0	12.0
S2	T3	35/10	8.0	6.0
	T4	35/10	8.0	6.0
S3	T5	35/10	8.0	6.0
	T6	35/10	10.0	6.0

4.2 ASC 计算

设 DG 总出力为-6.5 MVA，其中，$S_{DG,1}$=$S_{DG,4}$=-1.0 MVA、$S_{DG,2}$=$S_{DG,3}$=$S_{DG,5}$=-1.5 MVA。考虑

不同的负荷总量及分布，取 12 个典型运行点计算 ASC，结果见表 2。

表 2 典型运行点的 ASC 计算结果

序号	运行点名称	$\boldsymbol{W}^c$/MVA	Val($\boldsymbol{W}^c$)/MVA	N_{ASC}	$\boldsymbol{W}^{\beta}_{ASC\,min}$/MVA	$\boldsymbol{W}^{\beta}_{ASC\,max}$/MVA	ASC/MVA
1	零负荷点 W_0	(0.0,0.0,0.0,0.0,0.0,0.0,0.0,0.0,0.0,0.0)	0.0	16107	(1.0,0.0,7.5,1.0,1.5,5.5,0.0,6.0)等 351 个	(7.0,5.5,3.5,5.0,7.5,2.0,0.0,0.0)等 81 个	[22.5, 30.5]
2	不均轻载点 W_1	(6.0,1.2,0.0,0.0,0.0,0.0,0.0,0.0,0.0,0.0)	7.2	1008	(6.0,1.5,7.5,1.0,6.5,4.0,0.0,1.0)等 72 个	(7.0,5.5,3.0,5.5,7.5,2.0,0.0,0.0)等 81 个	[20.3, 23.3]
3	较均轻载点 W_2	(1.6,1.4,1.2,1.0,0.8,0.6,0.4,0.2)	7.2	5985	(2.0,1.5,7.5,1.0,2.5,4.0,0.5,4.5)等 63 个	(6.0,5.5,3.0,5.5,6.5,2.0,0.5,0.5)等 81 个	[16.3,22.3]
4	均匀轻载点 W_3	(0.9,0.9,0.9,0.9,0.9,0.9,0.9,0.9,0.9,0.9)	7.2	6255	(1.0,1.0,7.5,1.0,1.5,4.5,1.0,5.0)等 72 个	(5.0,5.5,3.0,5.5,5.5,2.0,1.0,1.0)等 81 个	[15.3,21.3]
5	不均中载点 W_4	(6.0,5.2,0.0,0.0,0.0,0.0,0.0,0.0,0.0,0.0)	11.2	384	(6.0,5.5,7.5,1.0,6.5,0.0,0.0,1.0)等 48 个	(7.0,5.5,1.5,7.0,7.5,2.0,0.0,0.0)等 9 个	[16.3, 19.3]
6	较均中载点 W_5	(2.1,1.9,1.7,1.5,1.3,1.1,0.9,0.7)	11.2	1953	(2.5,2.0,7.0,1.5,3.0,4.0,1.0,3.5)等 36 个	(5.0,2.0,2.0,6.5,5.5,5.5,1.0,1.0)等 64 个	[13.3, 17.3]
7	均匀中载点 W_6	(1.4,1.4,1.4,1.4,1.4,1.4,1.4,1.4)	11.2	2394	(1.5,1.5,7.0,1.5,2.0,4.5,1.5,4.0)等 42 个	(4.0,1.5,1.5,7.0,4.5,6.0,1.5,1.5)等 81 个	[12.3, 16.3]
8	不均重载点 W_7	(6.0,6.5,3.5,0.0,0.0,0.0,0.0,0.0,0.0,0.0)	16.0	108	(6.0,6.5,6.5,1.0,6.5,0.0,0.0,1.0)等 21 个	(7.0,6.5,3.5,4.0,7.5,1.0,0.0,0.0)等 5 个	[11.5, 13.5]
9	较均重载点 W_8	(2.7,2.5,2.3,2.1,1.9,1.7,1.5,1.3)	16.0	330	(3.0,2.5,6.0,2.5,3.5,4.5,1.5,2.5)等 18 个	(4.0,2.5,2.5,6.0,4.5,5.0,1.5,1.5)等 49 个	[10.0, 11.5]
10	均匀重载点 W_9	(2.0,2.0,2.0,2.0,2.0,2.0,2.0,2.0,2.0,2.0)	16.0	462	(2.0,2.0,6.5,2.0,2.5,4.5,2.0,3.0)等 18 个	(3.0,2.0,2.0,6.5,3.5,5.5,2.0,2.0)等 64 个	[8.5, 10.5]

注：第 3 列只显示运行点元素的负荷部分，即($S_{L,1}$, $S_{L,2}$, $S_{L,3}$, $S_{L,4}$, $S_{L,5}$, $S_{L,6}$, $S_{L,71}$, $S_{L,72}$)。

表 2 含有配电系统运行非常关心的数据，以第 8 行为例介绍：

1）当前运行点 W_7 的总负荷是 16.0 MVA，ASC 等于 11.5~13.5 MVA，表示保证配电网 N-1 安全前提下还允许总负荷增长 11.5~13.5 MVA。

2）共有 108 个 ASC 越界点，对应了当前运行点到安全边界共有 108 个负荷增长路径。其中：5 个 ASC_{max} 越界点对应了增长量最大的路径（13.5 MVA）；21 个 ASC_{min} 越界点对应了增长量最小的路径（11.5 MVA）。

在表 2 基础上放宽条件，允许部分馈线/馈线段负荷减少，ASC 还能得到进一步优化得到 OASC。放宽条件后，OASC 比 ASC 稍许增大；存在部分运行点所得 ASC 已没有优化的空间，OASC 得不到大于 ASC_{max} 的结果。

4.3 与现有方法对比

以表 2 运行点为例，本文方法与现有方法[3,6]的 ASC 计算结果如表 3 所示。

表 3 本文方法与现有方法所求 ASC 的对比

序号	运行点名称	$\boldsymbol{W}^c$/MVA	Val($\boldsymbol{W}^c$)/MVA	ASC/MVA			
				文献[3]	文献[6]	本文	
						ASC	OASC
1	零负荷点 W_0	(0.0,0.0,0.0,0.0,0.0,0.0,0.0,0.0,0.0,0.0)	0.0	30.5	30.5	[22.5, 30.5]	---
2	不均轻载点 W_1	(6.0,1.2,0.0,0.0,0.0,0.0,0.0,0.0,0.0,0.0)	7.2	23.3	23.3	[20.3, 23.3]	---
3	较均轻载点 W_2	(1.6,1.4,1.2,1.0,0.8,0.6,0.4,0.2)	7.2	23.3	22.3	[16.3,22.3]	(22.3,23.3]
4	均匀轻载点 W_3	(0.9,0.9,0.9,0.9,0.9,0.9,0.9,0.9,0.9,0.9)	7.2	23.3	21.3	[15.3,21.3]	(21.3,23.3]
5	不均中载点 W_4	(6.0,5.2,0.0,0.0,0.0,0.0,0.0,0.0,0.0,0.0)	11.2	19.3	19.3	[16.3, 19.3]	---
6	较均中载点 W_5	(2.1,1.9,1.7,1.5,1.3,1.1,0.9,0.7)	11.2	19.3	17.3	[13.3, 17.3]	(17.3,19.3]
7	均匀中载点 W_6	(1.4,1.4,1.4,1.4,1.4,1.4,1.4,1.4)	11.2	19.3	16.3	[12.3, 16.3]	(16.3,19.3]
8	不均重载点 W_7	(6.0,6.5,3.5,0.0,0.0,0.0,0.0,0.0,0.0,0.0)	16.0	14.5	13.5	[11.5, 13.5]	(13.5,14.5]
9	较均重载点 W_8	(2.7,2.5,2.3,2.1,1.9,1.7,1.5,1.3)	16.0	14.5	11.5	[10.0, 11.5]	(11.5,14.5]
10	均匀重载点 W_9	(2.0,2.0,2.0,2.0,2.0,2.0,2.0,2.0,2.0,2.0)	16.0	14.5	10.5	[8.5, 10.5]	(10.5,14.5]

由表 3 可知，

1）现有方法[3,6]计算得到的 ASC 均是单一数值，而本文方法计算得到的 ASC 是一个区间。

2）本文结果含有现有文献的结果：文[6]结果是本文 ASC 的区间上界；文[3]结果是本文 OASC 的区间上界。

3）文[3]方法较为粗糙，无法区分负荷总量相同运行点的 ASC，如运行点 W_1、W_2 和 W_3。文[6]方法和本文方法能区分。

与现有方法相比，本文方法还能得到更多有价值的数据。以运行点 W_7 为例，本文得到 108 个 ASC 越界点。而现有方法只得到了一个 ASC 值，并没有给出对应的越界点。

本文按现有方法的 ASC 值计算对应的越界点，进而汇总不同方法的负荷增长路径数及负荷变化，如表 4 所示。

表 4　不同方法的负荷增长路径数及负荷变化

文献	路径数	负荷变化							
		$S_{L,1}$	$S_{L,2}$	$S_{L,3}$	$S_{L,4}$	$S_{L,5}$	$S_{L,6}$	$S_{L,71}$	$S_{L,72}$
文献[6]	5	↑	-	↑/-	↑	↑	↑	-	-
文献[3]	81	↑	↓	↑/↓/-	↑	↑	↑	-	-
本文(ASC)	108	↑/-	↑/-	↑/-	↑	↑	↑/-	↑/-	↑/-
本文(OASC)	263	↑	↓	↑/↓/-	↑	↑	↑	↑/-	↑/-

注：“↑”表示 $S_{L,i}$ 上升，“↓”表示 $S_{L,i}$ 下降，“-”表示 $S_{L,i}$ 不变。

由表 4 可知，

1）文[6]ASC 和本文 ASC 都是在馈线/馈线段已有负荷不减条件下得到的：文[6]考虑了 5 个负荷增长路径；本文计算 ASC 考虑了 108 个路径。

2）文[3]ASC 和本文 OASC 都是在已有负荷减小前提下得到的：文[3]考虑了 81 个负荷增长路径；本文计算 OASC 考虑了 263 个路径。

现有方法仅考虑了 ASC 最大时的负荷增长路径，本文方法则考虑了当前点到安全边界的所有可能路径，所得结果全面。

在 DSSR 中可视化不同方法所得 ASC 及 OASC 的越界点和负荷增长路径，如图 4 所示。

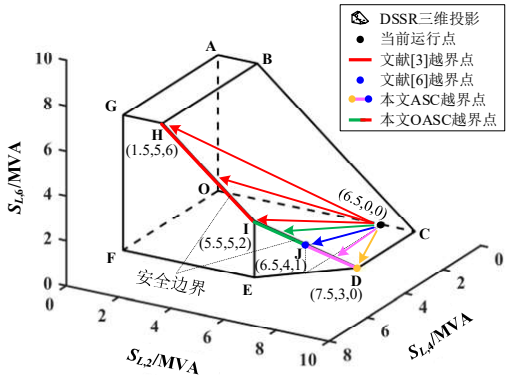


图 2　不同方法的越界点在 DSSR 边界上可视化

由图 2 可知，

1）文[6]ASC 对应的越界点是蓝点。当前点沿蓝色路径到达该点，此时在负荷不减条件下的总负荷增长最多。但文[6]结果有时会失效，例如 F_2 负荷增长，则无法到达蓝点。

2）文[3]ASC 对应越界点位于红线上。当前运行点沿红色路径到达这些点，此时总负荷增长最多。但文[3]结果有时会失效，例如 F_2 负荷减小量达不到 1.0 MVA（即 $S_{L,2}$ 无法从 6.5 MVA 减小到 5.5 MVA 及以下），则无法到达文[3]ASC 的红线点。

3）本文的 ASC 越界点是一系列点（黄、粉、蓝），涵盖了负荷不减条件下所有可能的增长路径；本文的 OASC 越界点也是一系列点（绿、红），涵盖了负荷允许减小条件下所有可能的增长路径。

5 结语

可用输电能力（ATC）是输网运行的关键指标。对于配网，与 ATC 对应的可用供电能力（ASC）的研究刚刚开始。本文主要贡献如下：

1）提出了 ASC 的新定义及指标，考虑了当前运行点到安全边界的所有可能增长路径，能完整反映配电系统的可用供电能力。

2）提出了 ASC 的数学模型及其计算方法。

3）提出了优化 ASC（OASC）的定义和数学模型，能在部分负荷降低条件下进一步挖掘 ASC。

采用 IEEE RBTS 算例验证了本文工作。与现有方法对比表明本文方法具有如下优势：（1）结果完整，包含了现有方法的结果；（2）数据丰富，除 ASC 外还能得到增长路径和越界点数据。

参考文献

[1] NERC, Transmission Transfer Capability: A reference document for calculating and reporting the electric power transfer capability of interconnected electric systems. North American Electric Reliability Council, 1995.

[2] NERC. Available transfer capability definitions and determination. North American Electric Reliability Council. June, 1996.

[3] Xiao J, et al. Total supply capability and its extended indices for distribution systems: definition, model calculation and applications[J]. IET Generation, Transmission & Distribution, 2011, 5(8), 869-876.

[4] Zhang S, et al. Probabilistic evaluation of available load supply capability for distribution system[J]. IEEE Transactions on Power Systems, 2013, 28(3), 3215-3225.

[5] Arabi A, et al. Probabilistic evaluation of available load supply capability of distribution networks as an index for wind turbines allocation[J]. IET Renewable Power Generation, 2016, 10(10), 1631-1637.

[6] Huang D, et al. Open capacity enhancement model of medium voltage distribution network with mobile energy storage system[J]. IEEE Access, 2020, 8, 205061-205070.

[7] 肖峻，张苗苗，司超然，等. 配电网的供电能力分布[J].电网技术，2017，41(10)：3326-3335.

[8] 肖峻，王传奇，鲍震宇，等. 有源配电网的供电能力曲线和消纳能力曲线[J]. 高电压技术，2023，49(02)：672-681.



收稿日期：2025-09-30。

作者简介：

焦衡(1995)，男，讲师，硕士生导师，研究方向为智能配电系统规划与运行，E-mail：jiaoheng@tju.edu.cn；

肖峻(1971)，男，教授，博士生导师，研究方向为智能配电系统规划与运行，E-mail：xiaojun@tju.edu.cn

焦衡

078 构网型储能联合风光火打捆低电压穿越控制

张博，杨炳元，李浪

（内蒙古工业大学电力学院，呼和浩特，010080）

Network-type energy storage combined with wind, solar, and thermal bundling for low voltage ride through control

Zhang Bo, Yang Bingyuan, Li Lang

(School of Electric Power,Inner Mongolia University of Technology, Hohhot 010080)

ABSTRACT: In a new type of power system where wind, solar, thermal, and storage sources are jointly transmitted through flexible DC transmission, although network-type energy storage converters have active support capabilities and can effectively reduce the risks faced by the new power system, they are prone to instability and overcurrent issues when the system experiences disturbances that cause varying degrees of voltage dips, thereby threatening the safe and stable operation of the power system. This paper first describes the control strategies of typical network-type energy storage converters and grid-following converters. To address voltage dips caused by short-circuit faults in wind-solar-thermal-storage joint transmission lines, a comparative analysis of the low-voltage ride-through (LVRT) capabilities of network-type and conventional wind-solar generation systems was conducted. A control strategy based on network-type energy storage was designed, which can effectively suppress fault currents while supporting system voltage stability. Using the RTDS simulation platform, low-voltage ride-through control experiments were conducted on the established network-type energy storage LVRT coordinated control mechanism, and the results confirmed its effectiveness in suppressing fault currents during voltage transients.

KEY WORDS: photovoltaic energy storage; grid-type; following grid type; low voltage ride through

摘要：在风光火储多源联合经柔性直流输电外送的新型电力系统中，构网型储能变流器虽具备主动支撑能力、可有效降低新型电力系统所面临的风险，但当电力系统受到扰动导致电压呈现不同程度的跌落时，易出现失稳及过电流问题，威胁电力系统运行的安全稳定性。该文首先对典型构网型储能变流器和跟网型变流器的控制策略进行描述。为应对风光火储联合输电线路短路故障导致的电网电压跌落，对比分析了构网型与常规风光发电系统的低电压穿越（LVRT）能力，设计了一种基于构网型储能的控制策略，该策略在支撑系统电压稳定的前提下，可实现对故障电流的有效抑制。基于 RTDS 仿真平台，对所构建的构网型储能 LVRT 协调控制机制进行低电压穿越控制实验，结果证实其在电压暂态过程中能对故障电流抑制。

关键词：风光火储；构网型；跟网型；低电压穿越

0 引言

随着可再生能源渗透率提高，风光火储多源联合系统经柔性直流输电（VSC-HVDC）外送成为新型电力系统的重要模式。在安全风险攀升的新型电力系统中，构网型储能变流器因其主动抗扰与支撑能力备受关注[1]。该变流器通过功率外环控制输出电压幅值和相位，呈现电压源特性，尤其适用于弱电网[2]。其具备的电压、频率支撑能力，有效解决了传统跟网型控制（依赖锁相环）在弱电网中易脱网、失稳的问题[3]。然而，当并网点发生网侧电压降落时，由于传统电压源型变流器瞬时电压不能突变，将导致并网变流器不可避免地出现过流现象[4]。同时，相关规定要求当网侧电压发生跌落时，并网变流器应在一定电压范围内保持持续运行，分布式电源不得随意脱网，即低电压穿越(Low Voltage Ride Through，LVRT)[5][6]。因此，在电网发生故障时，保证并网变流器半导体器件不发生损坏，同时对电网电压进行支持，实现低电压穿越，具有十分重要的意义。

1 系统拓扑及并网变流器控制策略

图 1 所示为风光火储联合系统经柔性直流输电外送的结构。其中，储能变流器采用构网型（grid-forming）控制以提供自主同步能力；本研究中的新能源变流器与柔直换流器，其控制架构均配置为依托于锁相环的跟网型（grid-following）模式。

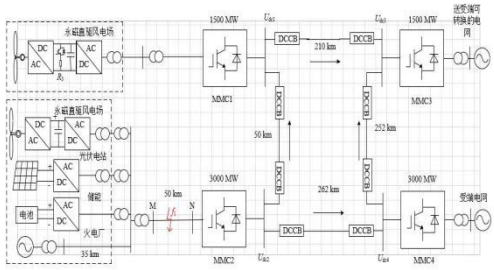


图 1 风光火储打捆经联络线接入柔直系统拓扑图

Figure 1: Topology diagram of wind solar thermal storage bundling connected to flexible straight system via connecting line.

1.1 构网型变流器控制策略

当前典型的构网型控制技术包括下垂控制（Droop）、虚拟同步发电机（VSG）、功率同步控制（PSC）和虚拟振荡器控制（VOC）。本文采用虚拟同发电机控制策略。

图 2 所示 VSG 控制的构网型变流器中，采集的滤波电容电压与电感电流信号经 abc/dq 变换后，分别输入内环控制与功率计算外环。外环生成参考电压幅值/相位反馈至内环；内环包含电压电流双反馈回路，其输出的参考电压 dq 分量经 dq/abc 逆变换为三相电压，最终由 PWM 模块生成变流器驱动信号。该结构通过构网控制自主产生相角，无需锁相环（PLL）。

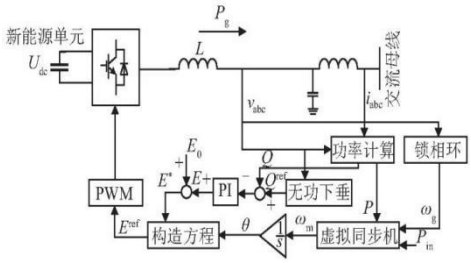


图 2 构网型变流器 VSG 控制框图

Figure 2 VSG Control Block Diagram of Network-Forming Converter.

典型的 VSG 控制下，有功与频率的关系方程以及无功与电压的关系方程如下：

$$\begin{cases} J\dfrac{d\omega}{dt}=\dfrac{P_{ref}-P_e}{\omega_0}-D\left(\omega-\omega_0\right) \\ V_{set}-V=M_Q\left(Q_{\text{set}}-Q_e\right) \end{cases} \tag{1}$$

式中：f_{set} 和 P_{set} 分别表示频率和有功的设定值；f 是 VSG 控制输出的频率,W 代表转动惯量；D 表示阻尼系数；对应的控制框图见图 3。

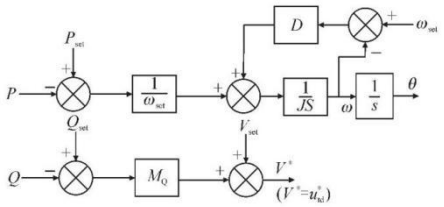


图 3 VSG 控制框图

Figure 3 VSG Control Block Diagram.

1.2 跟网型变流器的控制策略

图 4 所示跟网型变流器采用双闭环控制结构。系统首先采集滤波电容电压与网侧电感电流信号，锁相环（PLL）利用滤波电容电压实时跟踪电网电压相位，输出同步旋转角（θ）用于坐标变换。采集的滤波电容电压和网侧电感电流经 abc/dq 变换得到同步旋转坐标系下的直轴/交轴分量 Vdq 和 Idq。外环（功率控制环）利用变换后的 Vdq 和 Idq I_{dq} 计算实时功率，并通过功率控制器（如 PQ 控制）生成电流参考值。内环（电流控制环）接收电流参考值和实际电流参考值，结合电压前馈，通过电流控制器（通常为 PI 控制）输出参考电压。该参考电压经 dq/abc 反变换得到三相调制波，最终由 PWM 调制器生成驱动变流器功率开关器件的信号。

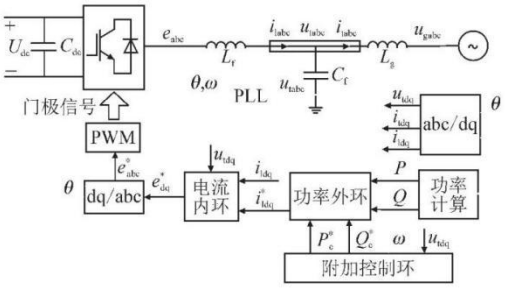


图 4 跟网型变流器控制

Figure 4 shows the control of the grid-type converter.

2 故障穿越控制策略

2.1 风光火低电压穿越控制

风光火储系统交流线路短路故障时，短路电流具有多源协同供给特性：交流侧电流源于新能源变流器（风电/光伏逆变器）与火电同步机组的共同作用，而柔性直流换流站（VSC-HVDC）则主导直流侧电流，其幅值受闭锁策略与直流断路器特性约束。尽管各换流器控制切换存在微秒级响应差异（<100 μs），但因其对机电暂态过程（毫秒级）影响可忽略。本文故障特性分析忽略此响应差异的影响，故障特征由故障穿越控制启动时刻决定。

交流侧故障导致电压骤降时，鉴于柔直换流站的无功调节能力优于逆变型电源，应充分利用其提供无功支撑。因此，当并网点电压大于 0.2pu 以及小于 0.9pu 时，增大无功电流，通过注入容性无功电流（按电压偏差动态调节）支撑电压至 1.0~1.05 p.u.，同时执行电流限幅保护（交流侧≤1.5 倍额定电流，直流侧≤1.2 倍）。在柔性直流换流站采用限幅控制时，其 dq 轴电流参考值可表示为：

$$\begin{cases} I_q = 1.5(0.9 - U_{AC})I_N \ \ (0.2 \le U_{AC} < 0.9) \\ I_{\mathrm{d}} = \sqrt{I_{\max}^2 - I_q^2} \\ I_{d\min} \le I_{d\max} \\ I_{q\min} \le I_{q\max} \end{cases} \tag{2}$$

式中：U_{AC} 为电压标幺值，I_{dmax}，I_{qmax} 分别为 d、q 轴电流限幅值，数值大小为 1.5。发生短路故障时，风光储作采取换流器实现功率控制，需具备良好的低电压穿越能力。依据各系统并网技术规范[7-9]，图 5 明确风光储的穿越能力标准：

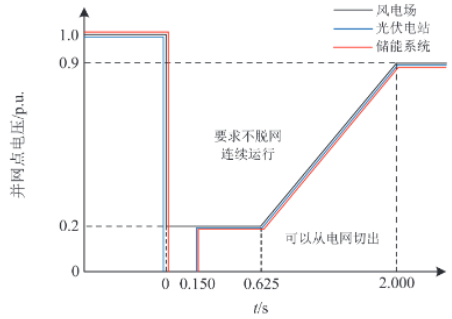


图 5 风光火低电压穿越要求

Figure 5 Requirements for low voltage ride through of wind, solar and fire.

电压跌落至阈值时，逆变电源需按式(3)向电网注入动态无功电流以满足支撑需求。

$$\begin{cases} I_{\mathrm{u}} = K_1(0.9 - U_1)I_{N1} \\ I_v = K_2(0.9 - U_1)I_{N2} \end{cases} \tag{3}$$

式中：I_W 和 I_{PV} 分别表示风能和光能各自注入电网的无功电流，U_t 为场站并网点电压标幺值，K_1 和 K_2 为风能和光能各自的动态无功电流比例系数，I_{N1} 和 I_{N2} 风能和光能各自的额定输出电流。

故障穿越期间，逆变器内环给定 dq 轴电流参考值并实施限幅，q 轴参考值见式(4)，d 轴参考值及限幅策略如下：

$$\begin{cases} I_{\mathrm{d}} = \sqrt{I_{\max}^2 - I_q^2} \\ I_{\mathrm{d}} \le I_{d\max} \\ I_q \le I_{q\max} \end{cases} \tag{4}$$

式中：i_{dmax} 和 i_{qmax} 分别表示逆变电源 d 轴和 q 轴电流的限幅值。i_{max} 代表逆变电源限幅环节的上限值，本文取 1.1p.u.

非对称故障下，逆变电源采用抑制负序电流策略，即设负序 dq 电流参考值为零，故障电流只有正序分量。然而，若线路两端电力电子设备均采用此策略，可能导致交流侧过电压或系统不利影响[10-12]。因此，柔直侧不能抑制负序电流，限幅即可。

发生故障时，同步发电机通过次暂态电抗释放 3-8 倍额定电流的衰减性工频电流；当机端电压跌落至 0.85 p.u.以下时，励磁系统在 100ms 内触发强励动作（1.6-2.0 倍额定励磁电压）支撑电压，同时配合转子过流保护（反时限特性）与失磁保护；故障清除后，发电机通过转动惯量维持暂态稳定，与新能源变流器协同实现短路电流支撑与动态无功补偿的互补，保障电力系统故障穿越可靠性。下图 6 为励磁调节原理图

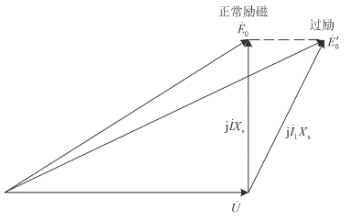
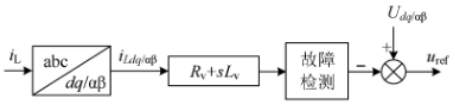


图 6 励磁调节原理图

Figure 6 Excitation Regulation Schematic

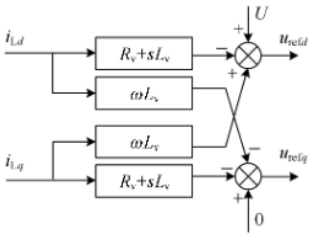
2.2 构网型储能低电压穿越控制

虚拟阻抗控制可无电流内环[13]或有电流内环[14-16]实现（图 7），图中 R_V R_v、L_V 虚拟阻感，外部故障时投入该控制。



(a) 不带电流内环的虚拟阻抗控制

(b) Virtual impedance control without current inner loop



(b)带电流内环的虚拟阻抗控制

(b) Virtual impedance control with a current-carrying inner loop

图 7 虚拟阻抗控制

Fig. 7 Virtual impedance control

双环控制可快速实现电流限制，配合虚拟阻抗技术可有效地限制电流，虚拟阻抗表达式如下：

$$\begin{cases} e_d = u_d + \left(R_v + sL_v\right) i_d - \omega L_v i_q \\ 0 = u_q + \left(R_v + sL_v\right) i_q - \omega L_v i_q \end{cases} \tag{5}$$

其中虚拟电抗 $X_v=\omega L_v=\sigma R_v$，虚拟阻抗基于电流越限情况启用。本文采用的自适应阻抗方法，故障电流越大，其虚拟阻抗值越大，限流效果越好。

$$R_v = \begin{cases} 0, I \le I_{th} \\ K_v(I - I_{th}), I > I_{th} \end{cases} \tag{6}$$

3 仿真验证

为验证构网型储能变流器在风电、光伏和火电中控制策略的效果，基于 RTDS 仿真平台搭建图 1 所示风光火储经柔直外送系统。仿真参数见表 1。

表 1 仿真参数表

Table 1 Simulation Parameters Table

模型名称	参数名称	数值
风电场		900MW
光伏电站	额定有功出力	450WM
灵活性火电机组		300WM
构网型蓄电池储能系统		450WM

故障设于输电端交流线路中点，0.2 秒时，仿真模型故障启动。

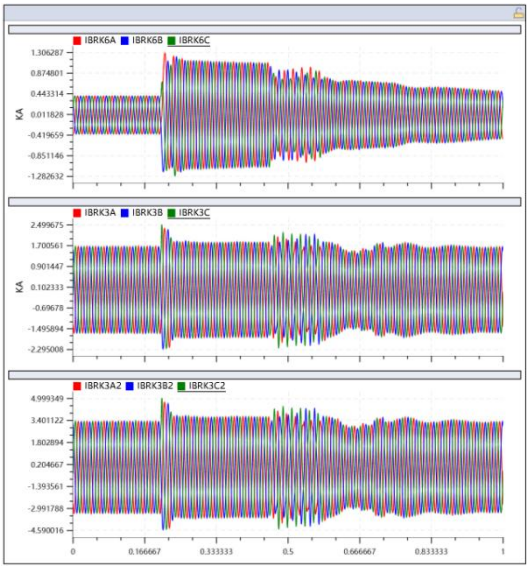


图 8 无低电压穿越控制策略电流图

Figure 8 current diagram without low voltage ride-through control strategy

图 8 为构网型储能变流器和风、光无低电压穿越控制仿真结果，从上到下依次为构网型储能、光伏电站、永磁直驱风场。在 0.2s 系统发生扰动，0.25s 扰动切除。根据实验结果表明，构网型储能扰动电流增加至 2.5（pu），光伏电站扰动电流增加至 1.3（pu），永磁直驱风场扰动电流增加至 1.4（pu）出现明显过电流现象。

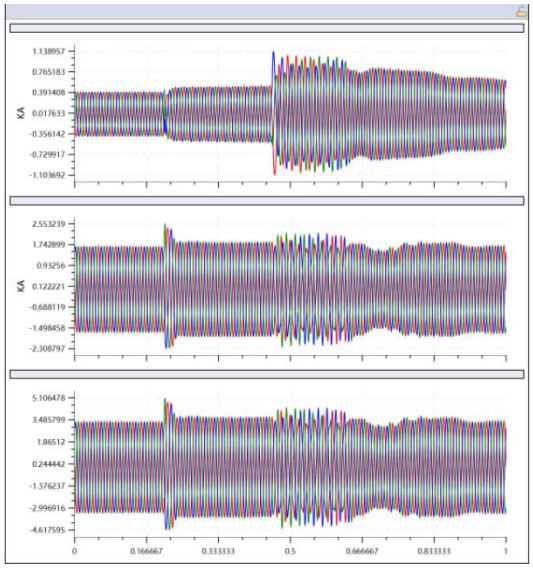


图 9 含低电压穿越控制策略电流图

Figure 9 shows the current diagram of the low voltage ride-through control strategy.

图 9 为加入低电压穿越控制仿真波形图，与图 8 相比，扰动期间构网型储能变流器扰动电流从 2.5(pu)降为 1.2(pu)，永磁直驱风场扰动电流从 1.4

（pu）降为 1.06（pu）,光伏电站扰动电流从 1.3（pu）降为 1.05(pu)。验证了所提控制策略可以实现低电压穿越。

4 结论

本文新能源采用了跟网及构网控制换流器，针对故障时换流器因过流而造成换流器损坏问题，提出了定电流技术及自适应虚拟阻抗技术限制换流器幅值，对于跟网型换流器，有效地将电流幅值限制在 1.1 以内；对于构网型换流器，限制在 1.3 以内，实现了低电压故障穿越。

参考文献

[1] 郝艺,周瑀涵,刘晨曦,等.含跟网型储能的新能源多馈入系统小扰动电压支撑强度分析[J].电工技术学报，2024，39(11):3569-3580.Hao Yi, Zhou Yuhan, Liu Chenxi, et al. Smalldisturbance voltage support strength analysis for renewable multi-infeed system with grid-following energy storage[J]. Transactions of China Electrotechnical Society, 2024, 39(11):3569-3580.

[2] 徐政.新型电力系统背景下电网强度的合理定义及其计算方法[J].高电压技术，2022，48(10):3805-3819.Xu Zheng. Reasonable definition and calculation method of power grid strength under the background of new type power systems[J]. High Voltage Engineering, 2022, 48(10):3805-3819.

[3] 罗家林,陈超,黄梅,等.弱电网矿区下构网型储能控制技术研究[J].高压电器, 2023, 59(7):95-103.Luo Jialin, Chen Chao, Huang Mei, et al. research on grid-forming energy storage control technology in weak network mining area[J]. High Voltage Apparatus,2023, 59(7):95-103.

[4] 李琦.基于 VSG 的构网型变流器低电压穿越控制策略研究[D].西安理工大学,2024.DOI:10.27398/d.cnki.gxalu.2024.000276.

[5] Deng H, Qi Y, Fang J, et al. A low-voltage-ride-through strategy for grid-forming convertersbased on reactive power synchronization[C]. 2022 IEEE Energy Conversion Congress and Exposition (ECCE). IEEE, 2022: 1-6.

[6] 孙艺鹤. 电网对称故障下构网型并网逆变器低电压穿越控制技术研究[D]. 中国矿业大学, 2023

[7] 风电场接入电力系统技术规定 第 1 部分：陆上风电:GB/T 19963.1—2021[S].

[8] 光伏发电站接入电力系统技术规定: GB/T 19964—2024[S].

[9] 电化学储能系统接入电网技术规定: GB/T 36547—2024[S].

[10] 郑黎明, 贾科, 毕天姝, 等. 海上风电接入柔直系统交流侧故障特征及对保护的影响分析[J]. 电力系统保护与控制，2021，49(20):20-32.

[11] 郑涛, 庄心怡, 吕文轩. 海上风电柔直换流站负序电流参考值选取及保护适应性分析[J]. 电力系统自动化,2023, 47(3): 133-141.

[12] SHI Lei, ADAM G P, LI Rui, et al. Control of offshoreMMC asymmetric offshore AC faults for wind powertransmission[J]. IEEE Journal of Emerging and SelectedTopics in Power Electronics, 2020, 8(2): 1074-1083.

[13] VILATHGAMUWA D M，LOH P C，LI Y．Protection of microgrids during utility voltage sags[J] ．IEEE Transactions on Industrial Electronics，2006，53(5)：1427-1436．

[14] HE Jinwei，LI Yunwei．Analysis，design，and implementation of virtual impedance for power electronics interfaced distributed generation[J]．IEEE Transactions on industry Applications，2011，47(6)：2525-2538．

[15] LI Yumwei ， KAO C N ． An accurate power control strategy for power-electronics-interfaced distributed generation units operating in a low-voltage multibus microgrid[J]． IEEE Transactions on Power Electronics，2009，24(12)：2977-2988．

[16] LU Xiaonan ， WANG Jianhui ， GUERRERO J M ， et al ． Virtual-impedance-based fault current limiters for inverter dominated AC microgrids[J]．IEEE Transactions on Smart Grid，2018，9(3)：1599-1612．

收稿日期：2025-09-26。



作者简介：

张博(2000)，男，硕士研究生，研究方向为电力系统继电保护，E-mail：501316390@qq.com；

杨炳元(1967)，男，教授，硕士生导师，研究方向为电力系统规划运行分析，E-mail：yangbingyuan@imut.edu.cn

张博

079 Post-disaster Recovery Strategy of Distribution Network Considering Uncertainty of V2G Response Potential

Xinhui Chen[1], Zhenshan Zhu[1,2], Junlin Liu[3], Qile Chen[1]
(1. College of Electrical Engineering and Automation, Fuzhou University, Fuzhou 350108, Fujian, China; 2. Fujian Provincial University Engineering Research Center of Intelligent Distribution Network Equipment, Fuzhou 350108, Fujian, China; 3. State Grid Fuzhou Electric Power Company, Fuzhou 350004, Fujian, China)

Abstract: To address the issues of uncertainty in the vehicle-to-grid (V2G) response potential of electric vehicle (EV) clusters and the fluctuation of renewable energy outputs during power supply recovery in distribution networks under extreme disasters, this paper proposes a collaborative optimization model integrating fuzzy logic and information gap decision theory (IGDT). First, a quantitative model of EV response potential considering incentive electricity prices, state of charge (SOC), and disaster severity is established to estimate available energy resources. Second, IGDT is employed to handle photovoltaic (PV) power output uncertainty, while fuzzy numbers are introduced to characterize deviations in EV response willingness. Fuzzy chance constraints are converted into deterministic forms to achieve robust decision-making. Finally, evaluation indicators are designed, and simulations on an improved IEEE 33-bus system verify the proposed model's effectiveness in quantifying response fluctuation impacts on incentive costs, achieving a co-optimization of economic efficiency and robustness in post-disaster distribution network recovery.
Keywords: Post-disaster recovery; V2G; Fuzzy model; Uncertainty; IGDT

0 Introduction

According to the Provisional State of the Global Climate 2023 report released by the World Meteorological Organization (WMO) [1], global warming has become increasingly prominent along with industrialization. In recent years, the frequency of extreme weather events—such as cold waves, heatwaves, wildfires, heavy rainfalls, and floods—has increased significantly compared with historical averages [2], severely threatening human life and property safety. When large-scale blackouts are triggered by extreme disasters, Ref. [3] and Ref. [4] proposed emergency restoration strategies for distribution networks, considering the controllability of conventional energy sources and the uncertainty of renewable energy output, respectively.

On the other hand, with the continuous promotion of the "dual-carbon" policy and the rapid development of the electric vehicle (EV) industry, large-scale EV clusters have gradually become one of the largest distributed flexible resources in modern power systems [5]. Compared with other standalone energy storage systems, if properly scheduled, EVs can fully utilize their onboard energy storage capacity to support the grid, which presents a tremendous opportunity for power system resilience. Refs. [6] and [7] proposed charging and discharging scheduling strategies for electric buses that take into account traffic routes to support short-term power supply restoration in distribution networks under extreme weather conditions. Ref. [8] developed a coordinated active–reactive power optimization method for distribution networks considering EV load uncertainty and reactive power compensation. Ref. [9] constructed a two-stage distributionally robust planning model minimizing both distribution network operation costs and transportation network investment costs, jointly considering traffic flow, renewable energy output, and load uncertainty. However, these studies generally overlook variations in environmental conditions and differences in user information processing capabilities. Therefore, building a mathematical model that can accurately describe EV users' V2G response willingness is crucial for quantifying the response potential of EV clusters and improving control precision.

Information Gap Decision Theory (IGDT) [20] is a non-probabilistic interval-based optimization approach that does not rely on any assumptions regarding probability distributions of uncertain variables. By adopting a risk-averse strategy, IGDT ensures that optimization results never fall below a minimum

desired performance level, achieving a balance between robustness and economy. Scholars have applied IGDT in various fields such as post-disaster distribution network restoration [21], integrated energy system optimization [22], multi-energy market hierarchical trading [23], and optimal energy storage allocation [24]. However, research integrating both V2G response willingness uncertainty and renewable energy output uncertainty remains limited.

In summary, this paper proposes a post-disaster restoration model that accounts for the uncertainty of V2G user response willingness, and its main contributions are as follows:

Under post-disaster conditions, a V2G response willingness assessment method integrating a TSK fuzzy model is developed. It systematically quantifies the impacts of incentive price, SOC, and disaster severity on EV user behavior, improving the expressiveness and adaptability of demand response modeling.

Fuzzy numbers are introduced to model deviations in response willingness. Their fluctuation ranges are represented using membership functions, which are then transformed into deterministic constraints through uncertainty programming theory. This flexible representation of user uncertainty enhances the credibility of response potential estimation.

IGDT is employed to handle renewable energy output uncertainty, constructing a robust scheduling model that improves the resilience of post-disaster restoration strategies while maintaining economic efficiency.

1 Estimation of Post-disaster V2G Response Willingness Based on the TSK Fuzzy Model

1.1 Fuzzy Model for Quantifying the Response Potential of EV Clusters

As highly distributed and flexible resources, electric vehicles (EVs) have enormous potential in post-disaster power supply restoration. However, their V2G response potential is influenced by multiple factors simultaneously. Accurately evaluating this potential is critical for formulating appropriate incentive pricing strategies during post-disaster restoration, thereby maximizing overall system benefits. Considering that EV owners are likely to park their vehicles at safer locations during disasters, this study focuses primarily on EVs parked at charging stations.

Objective Constraints on EV Cluster Response: The rated power of charging piles imposes an upper bound on the reverse power output during V2G discharging. Moreover, the number of available charging piles is limited by station size and infrastructure capacity. Therefore, the following constraint is introduced:

$$P_n^{\mathrm{V2G,max}} = \min\left\{P_n^{\mathrm{EV,max}},\ P_n^{\mathrm{CP,max}}\right\} \tag{1}$$

$$0 \le P_{n,t}^{\mathrm{EV}} \le N_n^{\mathrm{z}} \cdot P_n^{\mathrm{V2G,max}} \tag{2}$$

Where $P_n^{\mathrm{EV,max}}$ denotes Indicates the upper limit of the single electric vehicle discharge power in the electric vehicle cluster under the jurisdiction of the nth electric vehicle charging station; $P_n^{\mathrm{CP,max}}$ denotes the upper limit of the reverse charging power for the charging pile in the nth electric vehicle charging station. $P_n^{\mathrm{V2G,max}}$ represents the reverse charging power limit of a single charging pile at station *i*; $P_{n,t}^{\mathrm{EV}}$ is the maximum discharge power per EV; N_n^{z} is the number of charging piles at station *i*.

EV Battery Safety Operation Constraint: Safe battery operation is a prerequisite for EV participation in power restoration. The SOC must remain within safe bounds:

$$S_{n,t+1}^{\mathrm{SOC,EV}} = S_{n,t}^{\mathrm{SOC,EV}} - \frac{1}{\eta_n} \cdot P_{n,t}^{\mathrm{EV}} \cdot \frac{\Delta T}{N_n^{\mathrm{re}} \cdot E^{\mathrm{EV}}} \tag{3}$$

$$S_{\min}^{\mathrm{SOC,EV}} \le S_{n,t}^{\mathrm{SOC,EV}} \le S_{\max}^{\mathrm{SOC,EV}} \tag{4}$$

where ΔT is the time step length; $S_{n,t}^{\mathrm{SOC,EV}}$ denotes the average SOC of the EV cluster *i* at time *t*; E^{EV} is the battery capacity of a single EV; η_n is the discharging efficiency; $S_{\max}^{\mathrm{SOC,EV}}$ and $S_{\min}^{\mathrm{SOC,EV}}$ are the lower and upper limits of SOC, respectively.

1.2 Fuzzy Model for Evaluating the Subjective Willingness of EV Cluster Response

To quantify the demand response potential of electric vehicle clusters for post-disaster power supply restoration, this study constructs a TSK fuzzy model. By analyzing key factors influencing V2G response willingness, fuzzy semantic rules are established to characterize user response behavior. The study identifies three core influencing factors: additional incentive electricity price, battery state of charge, and disaster severity level—where disaster severity is measured by the estimated main grid reconnection time at the vehicle owner's node.The electric vehicle aggregator (EVA) collects information such as questionnaires and historical behavior data to define the boundaries of three fuzzy subsets "Low," "Medium," "High" for each factor, using trapezoidal membership functions to compute membership degrees. After quantifying the influencing factors, each combination of fuzzy subsets for the input parameters is defined as an independent scenario. Based on TSK fuzzy rules, the mapping relationship between the membership relations of input parameters and the dispatch tendency of electric vehicle clusters is solved for each scenario. Finally, a comprehensive response willingness value is obtained through weighted average calculation.The fuzzy inference function for the *k*-th scenario is formulated as:

$$\begin{aligned} &\mathrm{rule}(k):\mathrm{IF}\ x_1\ \text{is}\ A_1^k\ \text{and}\ x_2\ \text{is}\ A_2^k\ \text{and}\ x_3\ \text{is}\ A_3^k \\ &\mathrm{THEN}\ f^k(x) = a_0^k + a_1^k x_1 + a_2^k x_2 + a_3^k x_3, k = 1,2,...,K \end{aligned} \tag{5}$$

Where *K* is the total number of scenarios;x_1, x_2, x_3 denote the input variables (incentive price, SOC, and estimated recovery time, respectively); A_1^k, A_2^k, A_3^k are under the k-th rule, the fuzzy subsets corresponding to input variables x1, x2, and x3.a_0, a_1, a_2, a_3 are model parameters;

The overall response willingness δ' for each EV cluster affiliated with a charging station is derived as the weighted sum of all scenario outputs:

$$\delta' = \frac{\sum_{k=1}^{K} \theta_1^k(x_1)\theta_2^k(x_2)\theta_3^k(x_3) f^k(x)}{\sum_{k=1}^{K} \theta_1^k(x_1)\theta_2^k(x_2)\theta_3^k(x_3)} \tag{6}$$

After obtaining the response willingness of each station's EV cluster, the fuzzy number of responsive vehicles in each cluster can be derived as:

$$N_n^{\mathrm{re}} = k_{n,t_0} \cdot \delta_n^{'} \cdot N_n^{\mathrm{EV}} \tag{7}$$

where: k_{n,t_0} is the idle probability of the EV cluster under the *n*-th charging station when the response request is issued; N_n^{EV} is the number of electric vehicles in the *n*-th charging station. The V2G response capability of the *n*-th EV cluster is then subject to the following response scale constraint:

$$0 \le P_{n,t}^{\mathrm{EV}} \le N_n^{\mathrm{re}} \cdot P_n^{\mathrm{V2G,max}} \tag{8}$$

The fuzzy membership degrees of specific electric vehicles for each indicator and the fuzzy rule parameter table are shown in the following table.

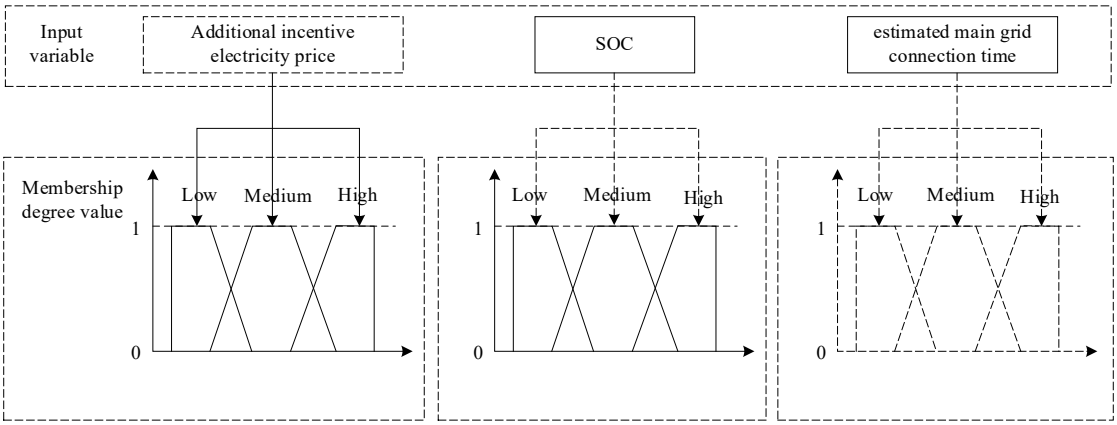


Fig.1 Factor Influence Input Processing Framework

Table 1 Fuzzy Rules

Additional Incentive Electricity Price	Average Initial SOC	Estimated Reconnection Time with Main Grid	$f^k(\cdot)$
L	L	L	0.4
M	L	L	0.6
H	L	L	0.7
L	M	L	0.5
M	M	L	0.6
H	M	L	0.8
L	H	L	0.7
M	H	L	0.8
H	H	L	0.9
L	L	M	0.3
M	L	M	0.4
H	L	M	0.6
L	M	M	0.4
M	M	M	0.5
H	M	M	0.7
L	H	M	0.6
M	H	M	0.7
H	H	M	0.8
L	L	H	0.1
M	L	H	0.2
H	L	H	0.4
L	M	H	0.2
M	M	H	0.3

H	M	H	0.5
L	H	H	0.4
M	H	H	0.5
H	H	H	0.7

3. A Post-Disaster Power Supply Restoration Framework Based on V2G and MES

The Electric Vehicle Aggregator can formulate incentive and scheduling plans for electric vehicle clusters based on the obtained coupling information between charging stations and the power grid, as well as user-reported vehicle status. This study proposes a collaborative optimization framework for distribution network power supply restoration. By integrating the assessment of V2G response potential from electric vehicles with the dynamic scheduling of Mobile Energy Storage systems, a three-level coordination mechanism—"distribution network - electric vehicle aggregator - end user"—is established. This framework enhances distribution network resilience and reduces the economic losses experienced by users during the post-disaster recovery period.

3.1 Overall Objective

Following a distribution network fault, an optimization model for post-disaster power supply restoration is established, with the objective function set to maximize the benefits of both the power grid and electric vehicle users. The objective function in this study can be expressed as follows:

$$F = \max(-F_1 + F_2) \tag{9}$$

In the equation, F_1 represents the losses incurred by the distribution network side due to power outages, primarily consisting of two components. The first term in F_1 denotes the outage costs imposed on various industrial and residential users due to load curtailment. Users are categorized into residential users and primary, secondary, and tertiary industrial users. The unit outage cost for each user category is determined using the indirect analysis method [15]. Specifically, F_1can be expressed in functional form as:

$$\begin{aligned} F_1 = \sum_{1}^{t=T} (& \sum_{z \in S_{\text{ind}}} \sum_{j \in S_z} l_z \cdot (1-\alpha_{j,t}) \cdot P_{j,t}^{\text{D}} + \sum_{n \in S_{\text{EV}}} C_{\text{ac}} \cdot P_{n,t}^{\text{EV}} + \sum_{w \in S_{\text{g}}} C_{\text{g}} \cdot P_{w,t}^{\text{GT}} + \sum_{f \in S_{\text{PV}}} C_{\text{PV}} \cdot P_{f,t}^{\text{PV}} + \\ & \sum_{m \in S_{\text{MES}}} (C_m \cdot \sum_{r' \to r \in \Omega_R} \lambda_{r' \to r,t}^{m} + \sum_{r \in R} C_{\text{p}} \cdot P_{m,r,t}^{\text{cha}})) \cdot \Delta T + \sum_{m \in S_{\text{MES}}} C_{\text{p}} \cdot E_m^{\text{MES}} \end{aligned} \tag{10}$$

Where: t=1,2,…,$T$with T being the duration of the post-disaster load restoration process; $z \in S_{\text{ind}}$, where S_{ind} is the set of users at different levels; $j \in S_{\text{N}}$, where S_{N} is the set of distribution network nodes; S_z is the set of nodes belonging to the z-th user category; l_z is the unit outage cost for the z-th user category; $\alpha_{j,t}$ indicates the load restoration status at node j during time period t; $P_{j,t}^{\text{D}}$ is the load demand at node j during time period t; $n \in S_{\text{EV}}$, where $S_{\text{EV}}$is the set of charging stations; C_{ac} represents the subsidy electricity price paid by the grid to the EVA; $w \in S_{\text{g}}$ where S_{g} is the set of micro-gas turbines; C_{g} represents the output cost of micro-gas turbines; $f \in S_{\text{PV}}$, where S_{PV} is the set of distributed energy resources; C_{PV} is the output cost of distributed energy resources; $P_{f,t}^{\text{PV}}$ is the output of the f-th renewable energy unit during time period t; $m \in S_{\text{MES}}$, where S_{MES} is the set of Mobile Energy Storage systems; C_{m} is the travel cost per unit time for the MES; C_{p} represents the charging cost per unit for the MES; E_m^{MES} is the battery capacity of the m-th MES.In Equation (9), F_2 represents the difference between the grid-side electricity revenue and the

compensation electricity price provided to EV users. Considering the efficiency loss during the charging and discharging process of electric vehicles, it can be specifically expressed as:

$$F_2 = \sum_{1}^{t=T} \sum_{n \in S_{\mathrm{EV}}} \left[C_{\mathrm{ac}} - \left(\frac{C_{\mathrm{EV}}}{\eta_n^{\,2}} + x_{1,n} \right) \right] \cdot P_{n,t}^{\mathrm{EV}} \cdot \Delta T \tag{11}$$

Where: C_{EV} represents the unit charging cost of EVs; $\frac{C_{\mathrm{EV}}}{\eta_n^{\,2}}$ denotes the base electricity price paid by the aggregator to EV users, considering both the charging behavior before response and the efficiency of discharging behavior during response; $x_{1,n}$ represents the additional incentive unit electricity price paid by the EVA.

3.2 Evaluation Metrics

To evaluate the effectiveness of the strategy, this paper proposes a multi-dimensional comprehensive evaluation system for restoration effects. The system assesses power supply reliability using the Power Loss Rate η_z^{s}, evaluates economic performance using the Economic Loss Due to Power Outage E^{s}, and quantifies the utilization efficiency of demand response resources using the E^{DR} and η^{DR} indicators. This evaluation framework integrates technical performance and economic value, providing a quantitative analysis basis for post-disaster power supply restoration.

Power Loss Rate:

$$\eta_z^{\mathrm{s}} = \frac{\sum_{1}^{t=T} \sum_{j \in S_z} (1 - \alpha_{j,t}) P_{j,t}^{\mathrm{D}}}{\sum_{1}^{t=T} \sum_{j \in S_z} P_{j,t}^{\mathrm{D}}} \tag{12}$$

Economic Loss Due to Power Outage:

$$E^{\mathrm{s}} = \sum_{1}^{t=T} \sum_{z \in S_{\mathrm{ind}}} \sum_{j \in S_z} l_z \cdot (1 - \alpha_{j,t}) \cdot P_{j,t}^{\mathrm{D}} \cdot \Delta T \tag{13}$$

Response Potential and Its Utilization Rate:

$$E^{\mathrm{DR}} = \sum_{n \in S_{\mathrm{EV}}} k_{n,t_0} \cdot \delta_n \cdot N_n^{\mathrm{EV}} \cdot E^{\mathrm{EV}} \cdot (S_{n,0}^{\mathrm{SOC,EV}} - S_{\min}^{\mathrm{SOC,EV}}) \cdot \eta_n \tag{14}$$

$$\eta^{\mathrm{DR}} = \frac{\sum_{1}^{t=T} \sum_{n \in S_{\mathrm{EV}}} P_{n,t}^{\mathrm{EV}} \cdot \Delta T}{E^{\mathrm{DR}}} \times 100\% \tag{15}$$

Where: η_z^{s} represents the average power loss rate across all sectors and the entire time horizon. E^{s} represents the total economic loss due to power outage for all users. E^{DR} denotes the achievable response potential under the strategy. $SOC_{n,0}^{\mathrm{EV}}$ indicates the average state of charge of the n-th EV cluster in the initial state. η^{DR}represents the utilization rate of response energy.

4. A Distribution Network Post-Disaster Restoration Method Based on Information Gap Decision Theory

By leveraging the TSK fuzzy model to construct a distribution network restoration strategy that considers V2G response potential, and through global energy management optimization techniques, the load restoration effectiveness has been significantly improved. However, during the actual implementation of the strategy, the response level of electric vehicle clusters may deviate to some extent from the fuzzy assessment results. Meanwhile, due to insufficient prediction accuracy of photovoltaic power generation, the generated scheduling strategy may lead to new supply-demand imbalances, resulting in suboptimal or even failed decision outcomes.

4.1 Handling Uncertainties in V2G Response Scale

To accurately characterize the uncertainties in the actual V2G response process of electric vehicle clusters, fuzzy numbers are adopted to represent their fluctuation degree. This section selects triangular membership functions as the tool to describe the deviation range of actual V2G response willingness, as illustrated in Figure 2:

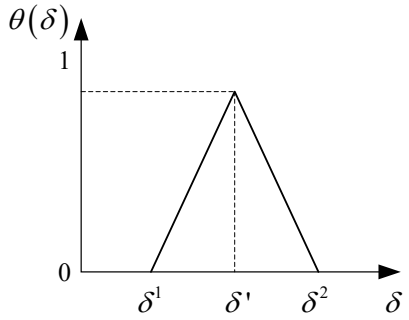


Fig.2 The expression of the triangular membership function for actual willingness

It can be observed that the relationship between the fuzzy representation of the deviation coefficient in EV user response willingness assessment and the membership function parameters is as follows:

$$\begin{aligned} &\delta \in \left(\delta^1, \delta^2\right) \\ &\begin{cases} \delta^1 = r_1 \delta' \\ \delta^2 = r_2 \delta' \end{cases} \end{aligned} \tag{16}$$

Where: δ^1 is the fuzzy representation of the response degree of the EV cluster; r_1 , r_2 are parameters of the triangular membership function, with $0<r_1\leq 1$, $r_2 \geq 1$;The scaling coefficient is typically determined based on historical data of EV cluster responses or obtained from professional data systems to ensure accuracy and reliability; δ^1 、 δ^2 represent the lower and upper bounds of the fluctuation range, respectively.

The fuzzy number of responsive vehicles in each EV cluster, considering the deviation range of response willingness, can then be expressed as:

$$N_n^{\mathrm{re}} = k_{n,t_0} \cdot \delta_n \cdot N_n^{\mathrm{EV}} \tag{17}$$

Where: N_n^{re} *resp*represents the fuzzy number of responsive electric vehicles; δ_n is the fuzzy response degree of the electric vehicle cluster under the *n*-th charging station.

In the model, the discharge power of the dispatched electric vehicle clusters must satisfy the confidence level requirement:

$$\mathrm{Cr}\left\{P_{n,t}^{\mathrm{EV}} \le N_n^{\mathrm{re}} \cdot P_n^{\mathrm{V2G,max}}\right\} > \varphi \tag{18}$$

Where: φ represents the confidence level, typically set to 0.95.Following the theory of uncertain programming, this study transforms the deterministic EV cluster response assessment model as follows. This transformation converts the fuzzy chance constraint in Equation (18) above into a deterministic constraint by setting a confidence level:

$$P_{n,t}^{\mathrm{EV}} \le \left\lfloor (2-2\varphi)\delta_n' + (2\varphi-1)\delta_n^1 \right\rfloor \cdot k_n \cdot N_n^{\mathrm{EV}} \cdot P_n^{\mathrm{V2G,max}} \tag{19}$$

At this point, the treatment of uncertainties in the electric vehicle cluster's response willingness is completed. The deterministically transformed response degree δ_n can be expressed as:

$$\delta_n = (2-2\varphi)\delta_n' + (2\varphi-1)\delta_n^1 \tag{20}$$

4.2 IGDT-Based Optimization Scheduling Model for Post-Disaster Restoration

The IGDT model comprises an objective function, equality constraints, and inequality constraints. When the optimization model is deterministic—that is, when uncertain parameters are calculated using predicted values—it can be expressed in the following form:

$$\text{objective: } \max\ F_0(o,v) \tag{21}$$

$$\text{s.t.} \begin{cases} B(o,v) = 0 \\ \Gamma(o,v) \le 0 \end{cases} \tag{22}$$

Where:F_0represents the objective function;$o$denotes the decision variables;$v$represents the uncertain variables. In the deterministic model, the parameter value of $v$equals v_0, which is the predicted value of the uncertain variables;Brepresents the equality constraints; Γ represents the inequality constraints.

In practical scenarios, the variable v fluctuates within a certain range around the predicted value v_0. Such uncertainty can be described by the following model:

$$\begin{cases} v \in U(\alpha_{\mathrm{u}}, v_0) \\ U(\alpha_{\mathrm{u}}, v_0) = \left\{v : |v - v_0| \le \alpha_{\mathrm{u}}\right\}, \alpha_{\mathrm{u}} \ge 0 \end{cases} \tag{23}$$

Where:α_{u} indicates the degree of deviation of the actual variable from its predicted value;$U(\alpha_{\mathrm{u}},v_0)$is the set representing the fluctuation range of the variable.

Based on this, the uncertain variable $\mathbf{v}$is expressed as a function of the deviation degree α_{u}:

$$U(\alpha_{\mathrm{u}}, v_0) = \left\{v : v = (1 \pm \alpha_{\mathrm{u}})v_0\right\} \tag{24}$$

If the optimal value obtained from the deterministic model in Equations (21) and (22) is f_0, and the decision-maker's acceptable performance deviation threshold for risk aversion is set as β_{u}, then according to the model requirements, for any input of uncertain variables, the resulting objective value should satisfy:

$$F_0(o,v) \ge (1-\beta_{\mathrm{u}})f_0 \tag{25}$$

$$0 \le \beta_{\mathrm{u}} \le 1 \tag{26}$$

To obtain the maximum fluctuation range of the uncertain variables for which the objective value is not lower than the decision-maker's expectation, the corresponding IGDT optimization model can be formulated as follows:

$$\text{objective}: \max\ \alpha_{\mathrm{u}}$$
$$\text{s.t.}\begin{cases} F_0(o,v) \geq (1-\beta_{\mathrm{u}})f_0 \\ B(o,v)=0 \\ \Gamma(o,v) \leq 0 \\ v=(1\pm\alpha_{\mathrm{u}})v_0 \end{cases} \tag{27}$$

In severe weather conditions, the initially acquired data may lack accuracy, leading to deviations between predicted values and actual power output. Therefore, during the modeling process, the actual maximum output of photovoltaic units is treated as an uncertain variable. This uncertainty is characterized using a box uncertainty set $U(\tau, P_{f,t}^{\mathrm{PV}*})$ based on the existing predicted values:

$$U(\tau, P_{f,t}^{\mathrm{PV}*}) = \left\{ P_{f,t}^{\mathrm{PV}} : (1-\tau) P_{f,t}^{\mathrm{PV}*} \leq P_{f,t}^{\mathrm{PV}} \leq (1+\tau) P_{f,t}^{\mathrm{PV}*} \right\} \tag{28}$$

$$0 \leq \tau \leq 1 \tag{29}$$

Where: $P_{f,t}^{\mathrm{PV}}$ represents the actual maximum output limit of the PV unit;τ indicates the deviation degree of the actual output relative to the predicted value, i.e., the scaling factor of the uncertainty set.When τ=1, the actual output of the PV unit is 0, representing the maximum volatility scenario;When τ=0, the actual output equals the predicted value.

To mitigate operational risks in the distribution network caused by potential shortfalls in actual PV power generation, the case where the actual maximum PV output is lower than predicted is described using the parameter $\tau$from Equation (28):

$$P_{f,t}^{\mathrm{PV}} = (1-\tau) P_{f,t}^{\mathrm{PV}*} \tag{30}$$

This approach aims to avoid potential risks to grid operation arising from instability in PV unit output power during the decision-making process. Therefore, distribution system dispatchers typically incorporate risk aversion into their considerations. To quantify this decision process, the performance deviation symbol β_{u} from Equation (25) is adopted. Let the solution of the deterministic model yield f_0 with distribution-side economic loss denoted as f_1 and electric vehicle aggregator-side economic revenue as f_2. The additional funding the distribution side is willing to allocate is $\beta_{\mathrm{u}} f_1$. Consequently, the IGDT optimization model requires an additional minimum revenue constraint compared to the deterministic model:

$$F \geq -(1+\beta_{\mathrm{u}})f_1 + f_2 = f_0 - \beta_{\mathrm{u}} f_1 \tag{31}$$

Where**:** F represents the overall benefit for both the distribution network and the electric vehicle aggregator.

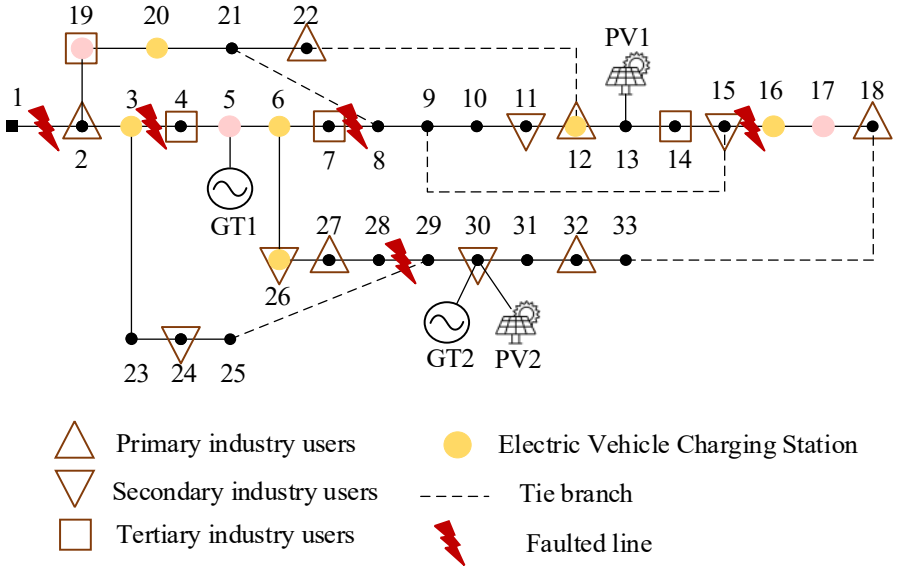
5 Case Study

To validate the effectiveness of the proposed post-disaster restoration optimization strategy with uncertainty handling, a mixed-integer linear programming model is established and solved using the Gurobi solver.

5.1 Parameters and Case Setup

The case study is based on a modified IEEE 33-node system, which comprises 33 nodes and 37 branches (including 5 tie lines). After the fault occurrence, the connection line between the main grid substation and the distribution network is disconnected, with additional branch faults present. The initial

fault locations, positions of distributed generation units (including micro-gas turbines and PV systems), MES access nodes, electric vehicle charging station locations, user types, and their respective locations are shown in Figure 3.



*Except for the nodes where primary, secondary, and tertiary industry users are located, the remaining nodes are residential users.

Fig.3 Improved IEEE 33-Node Distribution Network Schematic Diagram

5.2 Optimization Result Analysis

Analysis of V2G Response Willingness Uncertainty: To reasonably evaluate the impact of variations in the V2G response willingness error range on the proposed strategy, three fluctuation scenarios are assumed:

Scenario A: Willingness error range of 10%, where parameters r_1 and r_2 are set to 0.9 and 1.1, respectively.Scenario B: Willingness error range of 20%, where r_1 and r_2 are set to 0.8 and 1.2, respectively.Scenario C: No error range considered.

The confidence level for V2G response uncertainty is set at 95% to complete the deterministic transformation of the model. For comparative analysis, the strategy optimization results of the deterministic models under the aforementioned three scenarios are presented in Tables 2 and 3.

Table 2 Evaluation Metrics for Post-Disaster Power Restoration

Scenario	η_1^s/%	η_2^s/%	η_3^s/%	η_4^s/%	E^s/yuan	E^{DR}/kWh	η^{DR}/%
A	0	0	0	12.59	1951	2128	49.97
B	0	0	0	14.42	2235	1941	50.43
C	0	0	0	10.30	1596	2343	54.55

Table 3 economic benefits of all parties

Scenario	F_1/ yuan	F_2/ yuan	F/元
A	9225	2623	-6602
B	9128	2352	-6776
C	9747	3287	-6460

Table 4 Electric vehicle additional incentive electricity price

Scenario	EVs-1	EVs-2	EVs-3	EVs-4	EVs-5	EVs-6
A	0.8944	1.7353	1.0000	0.5000	0.9882	1.6743
B	0.9386	1.8171	0.9677	0.5000	0.9246	1.9233
C	0.8935	0.9935	0.9698	0.9822	0.9698	1.9991

A comparison of the optimization scheduling results across different scenarios reveals that when fluctuations in response willingness are not considered, the achievable energy response potentials in Scenarios A and B—calculated based on the additional incentive electricity prices in Table 4, Equation (6), and Equation (14)—are 2,339 kWh and 2,367 kWh, respectively, which are largely consistent with the values obtained without considering response fluctuations. However, when the lower bound of the response willingness fluctuation range is incorporated as a constraint and the response potential is calculated according to the confidence level requirement, the evaluated energy response potentials in Scenarios A and B decrease compared to Scenario C. This implies that for the electric vehicle cluster to provide the same amount of energy support to the distribution network, the EVA would need to pay higher incentive costs. Due to the profit-seeking nature of the EVA, both the scheduling cost paid by the distribution side for emergency restoration resources and the economic revenue of the EVA are reduced, leading to a decrease in the supportive energy provided by V2G to the distribution network. Consequently, the load restoration levels in Scenarios A and B are lower than that in Scenario C, with the economic losses due to power outages increasing by 355 CNY and 639 CNY, respectively. Based on the comprehensive calculation results, it can be concluded that considering the fluctuation characteristics of V2G response willingness leads to more conservative strategy optimization outcomes, and the conservatism intensifies as the fluctuation range of response willingness widens.Furthermore, since the focus of this paper is on addressing uncertainties in V2G response willingness and renewable energy output, MES—as a resource that can be fully dispatched by the grid—is only used to supplement the energy provided by V2G and is not analyzed in detail.

Reliability Analysis: Based on the above analysis, the scheduling scheme for flexible resources and the economic benefits for all parties have been obtained for the case with a V2G response willingness fluctuation range of 10%. Using Equation (9), the overall benefit F for the distribution side and the EVA is calculated to be -6,602 CNY. Building on the optimization results of the deterministic model, the IGDT optimization model is further employed to handle the uncertainty in the output of photovoltaic units. To avoid operational risks, the allowable performance deviation set by the distribution-side decision-maker is specified as 5%.

To validate the feasibility of the optimization strategy results, the actual maximum output of the PV units during the post-disaster restoration period is assumed to be a random variable within the interval, which can be expressed as , where is a scaling coefficient and . Based on the calculation results above, 10 simulation tests were conducted by randomly sampling different values of τ_0 from the output fluctuation interval to simulate the actual power generation of the PV units. These tests were used to evaluate the load

restoration effectiveness of the IGDT-based optimization strategy and the deterministic restoration strategy under PV output fluctuations. The corresponding optimization results are shown in Tables 5 and 6, respectively.

Table 5 Recovery results under photovoltaic output fluctuation test based on IGDT strategy

number of trials	τ_0	Load Restoration Effectiveness /MWh	Load Shedding /MWh
1-10	Refer to Table 5.	8.1736	0

Table 6 Recovery results of photovoltaic output fluctuation test under deterministic model

number of trials	τ_0	Load Restoration Effectiveness /MWh	Load Shedding /MWh
1	0.9448	8.2311	0.1352
2	0.4446	8.0633	0.3031
3	0.6414	8.1315	0.2348
4	0.7968	8.2039	0.1624
5	0.8941	8.2311	0.1352
6	0.9826	8.2496	0.1167
7	0.5318	8.1043	0.262
8	0.6049	8.1136	0.2527
9	0.8319	8.2114	0.1549
10	0.7208	8.1767	0.1897

6. Conclusion

To address the uncertainties in post-disaster distribution network V2G response assessment errors and renewable energy output, this paper proposes a model and draws the following conclusions:

When assessing the response potential of EVs, it is necessary to incorporate the lower bound of the response willingness fluctuation range. Research indicates a positive correlation between the magnitude of response willingness fluctuation and incentive costs: a larger fluctuation range requires higher incentive costs for the EVA to provide the same capacity of energy support. Given the profit-seeking nature of EVAs, this cost increase leads to a reduction in V2G response energy, thereby weakening load restoration effectiveness. Consequently, an expanded response willingness fluctuation range reflects an increase in the conservatism of the scheduling strategy.

Simulation results demonstrate that the IGDT-based optimal scheduling strategy can ensure the safe and stable operation of the distribution network within the maximum fluctuation range of PV output. In contrast, deterministic scheduling schemes face supply-demand imbalances when PV output decreases, necessitating load shedding measures. It is noteworthy that as the fluctuation amplitude of PV output continues to increase, the amount of load shedding shows a monotonically increasing trend. Beyond a certain critical point, the restoration effectiveness of deterministic schemes becomes inferior to that of the IGDT-based optimization approach. The proposed post-disaster restoration optimization model enhances the risk resilience of the distribution network while achieving an optimal balance between economy and robustness.

Acknowledgement: This work is supported by Research on Cooperative Defense Strategies Against Extreme Meteorological Disasters Considering the Coupling Characteristics of Road Traffic and Power Supply，No.72401069.

References

1. World Meteorological Organization. Provisional state of the global climate 2023[M]. Dubai: WMO, 2023.
2. ZHAO Zongci, LUO Yong, HUANG Jianbin. 2015-2022 the warmest years globally[J]. Climate Change Research, 2023, 19(03): 400-402.
3. XU Yin, WANG Ying, HE Jinghan, et al. Multi-source coordinated optimization decision method for multi-period load restoration in distribution network[J]. Automation of Electric Power Systems, 2020, 44(02): 123-131.
4. LIU Jiayu, ZHANG Qigi, WANG Ying, et al. Emergency power supply restoration strategy for distribution network considering distributed renewable energy generation[J]. Journal of Global Energy Interconnection, 2020, 3(06): 600-606.
5. HUANG Xueliang, LIU Yongdong, SHEN Fei, et al. Electric vehicle-grid interaction: Review and prospects[J/OL]. Automation of Electric Power Systems: 1-21 [2024-03-26].
6. SU Su, WEI Cunhao, CHEN Qifang, et al. Hierarchical scheduling strategy for electric vehicles considering road repair and load restoration[J]. Automation of Electric Power Systems, 2022, 46(12): 140-150.
7. LI B D, CHEN Y, WEI W, et al. Routing and scheduling of electric buses for resilient restoration of distribution system[J]. IEEE Transactions on Transportation Electrification, 2021, 7(4): 2414-2428.
8. CHEN Haipeng, TANG Junmin, WU Hao, et al. Coordinated active-reactive power optimization in distribution network with EV considering reactive compensation and uncertainty[J/OL]. Power System Technology 2025.
9. ZHENG Huhu, YE Jianhua, LUO Fengzhang. Distributionally robust planning method for coupled active distribution network and transportation network[J]. Acta Energiae Solaris Sinica, 2025, 46(4): 200-209.
10. AHMADIGORJI M, AMJADY N, DEHGHAN S, et al. A robust model for multiyear distribution network reinforcement planning based on information-gap decision theory[J]. IEEE Transactions on Power Systems, 2018, 33(2): 1339-1351.
11. CHEN Kening, WU Wenchuan, ZHANG Boming, et al. Robust restoration decision-making method for active distribution network based on IGDT[J]. Proceedings of the CSEE, 2014, 34(19): 3057-3062.
12. KONG Dezheng, ZHANG Jing, HE Yu, et al. Bi-level energy optimal scheduling for regional integrated energy system based on IGDT-MPC[J]. Power System Technology, 2022, 46(10): 3970-3979.
13. JIANG Yuewen, ZHAO Wanting. Hierarchical iterative trading in regional electricity-heat-gas market based on IGDT[J]. Power System Technology, 2022, 46(03): 956-973.
14. PENG Chunhua, CHEN Lu, ZHANG Jinke, et al. Multi-objective optimal allocation of energy storage in distribution network based on classified probability chance-constrained IGDT[J]. Proceedings of the CSEE, 2020, 40(09): 2809-2819.
15. YAN Han, WANG Jianhua, FAN Xulu, et al. Post-disaster power supply restoration model for active distribution network based on customer outage cost assessment[J]. Automation of Electric Power Systems, 2022, 46(05): 31-42.

080 Flexible Arc Suppression Method Based on Voltage-Current Mutual Compensation Using Fuzzy PI Control for Distribution Networks

Bin-Long Zhang[1,2], Mou-Fa Guo[1,2,*], Ze-Yin Zheng[1,2], and Wei Gao[1,2]

[1] College of Electrical Engineering and Automation, Fuzhou University, Fuzhou 350108, China
[2] Engineering Research Center of Smart Distribution Grid Equipment, Fujian Province University, Fuzhou 350108, China

Abstract. Single phase-to-ground (SPG) faults in distribution networks usually pose significant safety and operational risks, such as fire hazards, electric shock incidents, and widespread service interruptions. A common mitigation approach involves connecting a power electronic converter to the neutral point of the distribution network to suppress the fault current and voltage until the arc is extinguished. However, conventional suppression schemes, whether current-based or voltage-based, employing proportional–integral control (PIC) often exhibit limited adaptability to varying and uncertain fault resistances and the insulation parameters and line impedance of the distribution networks. This limitation results in extended transient response durations and substantial residual fault currents and voltages. To address these shortcomings, this paper proposes a flexible arc suppression method based on voltage-current mutual compensation using fuzzy PIC for distribution networks. In this method, voltage-based and current-based control can be run in parallel and serve as a compensation for each other. Based on fuzzy PIC, voltage-based and current-based suppression methods can play a leading role in the ground fault resistance conditions where their respective advantages are. The simulation validation demonstrate that the proposed method achieves simultaneous suppression of fault current and voltage with a shorter transient response time and reduced residual values under different fault resistance conditions.

Keywords: Distribution Networks, Flexible Arc Suppression, Voltage-Current Mutual Compensation, Fuzzy PI Control, Single Phase-to-Ground Faults.

1 Introduction

1.1 Research Background

Single phase-to-ground (SPG) faults represent the predominant type of fault encountered in medium-voltage distribution networks, accounting for more than 70% of all recorded incidents [1]. When such a SPG fault occurs, a substantial current

passes through the corresponding fault branch, frequently initiating fault arcs that may result in fires and large-scale service interruptions [2]. Furthermore, the high fault voltage induces a step potential in the vicinity of the fault location, therefore increasing the likelihood of electric shock hazards for pedestrians [3]. Moreover, transient overvoltage may arise, which can, in turn, evolve into more critical disturbances such as inter-phase short circuits [4].

1.2 Method Overview

The use of power electronic converters offers an effective means to suppress fault current and voltage in distribution networks [5]. In common practice, the converter is coupled to the neutral point of a Z-type transformer within the bus and operates using either current-based or voltage-based suppression strategies until the fault arc is extinguished [6]. The voltage-based suppression strategy takes the neutral point voltage as the control target. Its advantage is that it does not require the measurement of the distribution network insulation parameters and is more effective under high-resistance grounding faults. However, the fault current and voltage have an AC transient component attenuation process, and is greatly affected by the impedance of the distribution network line [7]. The current-based suppression strategy takes the output current of the power electronic converter as the control target. Its advantage is that it is less affected by the impedance of the distribution network line and works well in the case of low-resistance grounding faults. However, the fault current and voltage have a DC transient component attenuation process, and accurate insulation parameter measurement is required [8].

These arc suppression techniques often rely on proportional–integral control (PIC) schemes [9]. Nevertheless, their performance is still limited when dealing with uncertain or varying fault resistances. This limitation leads to prolonged transient response times and considerable residual fault current and voltage, which in turn hinder reliable arc suppression [10]. As a result, an arc-induced overvoltage may arise in distribution networks, heightening the risk of cross-line faults due to insulation failure [11].

1.3 Contributions of This Study

In this paper, a novel flexible arc suppression method based on voltage-current mutual compensation using fuzzy PIC is proposed for distribution networks with an SPG fault. The voltage-based and current-based control strategies can operate in parallel, providing mutual compensation. By employing the fuzzy-PIC framework, each suppression method can assume the dominant role under different ground fault resistance conditions where its respective advantages are most pronounced. Therefore, the transient component attenuation process of fault current and voltage can be reduced, and the residual fault current and voltage are decreased. Moreover, the influence of insulation parameter measurement errors and line impedance of the distribution network can also be reduced. The simulation study is conducted, which verifies the feasibility and effectiveness of the proposed method.

2 Principle of Flexible Arc Suppression in Distribution Networks

In this section, the reference values of control targets of voltage-based and current-based fault arc suppression methods are derived, and the control equations using PI controllers are presented.

2.1 Derivation of Reference Values of Control Targets

Fig. 1 presents a distribution network with n feeder lines. An SPG fault occurs in phase-A of the distribution network. u_{A} , u_{B} , and u_{C} are three phase-to-ground voltages, respectively. The three total phase-to-ground impedances (PGI) are distributed on the feeder lines, including the phase-to-ground capacitance $C_0/3$ and the phase-to-ground resistance $3R_0$. A power electronic converter is connected to the bus through a Z-type transformer (Z-T) constructing a neutral point.

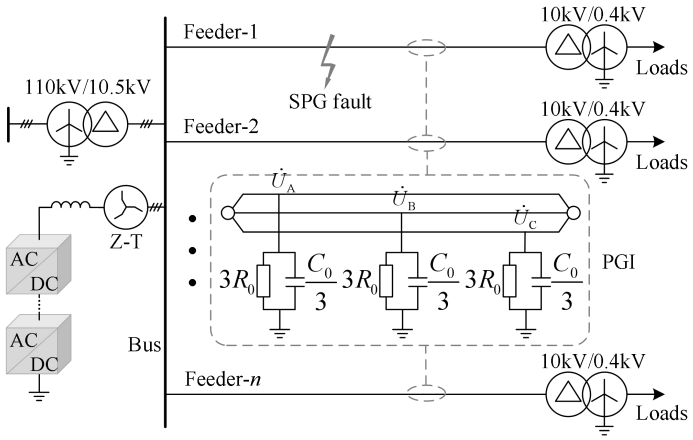


Fig. 1. A distribution network with n feeder lines and a power electronic converter for flexible arc suppression of an SPG fault.

Following Fig. 1 with the current law of Kirchhoff, the SPG fault current can be presented as

$$\begin{aligned}\dot{I}_{\mathrm{f}} &= \frac{\dot{U}_{\mathrm{A}}}{R_{\mathrm{f}}} = \frac{\dot{E}_{\mathrm{A}}+\dot{U}_0}{R_{\mathrm{f}}} = \dot{I}_{\mathrm{P}} - \dot{U}_{\mathrm{A}}\left(\frac{1}{3R_0}+\frac{\mathrm{j}\omega C_0}{3}\right) - \dot{U}_{\mathrm{B}}\left(\frac{1}{3R_0}+\frac{\mathrm{j}\omega C_0}{3}\right) - \dot{U}_{\mathrm{C}}\left(\frac{1}{3R_0}+\frac{\mathrm{j}\omega C_0}{3}\right) \\ &= \dot{I}_{\mathrm{P}} - \left(\dot{U}_{\mathrm{A}}+\dot{U}_{\mathrm{B}}+\dot{U}_{\mathrm{C}}\right)\left(\frac{1}{3R_0}+\frac{\mathrm{j}\omega C_0}{3}\right) \\ &= \dot{I}_{\mathrm{P}} - 3\dot{U}_0\left(\frac{1}{3R_0}+\frac{\mathrm{j}\omega C_0}{3}\right) = \dot{I}_{\mathrm{P}} - \dot{U}_0\left(\frac{1}{R_0}+\mathrm{j}\omega C_0\right)\end{aligned} \tag{1}$$

where $\dot{I}_{\mathrm{P}}$ is the output current of power electronic converter; $\dot{E}_{\mathrm{A}}$ is the fault phase supply voltage; $\dot{U}_0$ is the neutral point voltage of the distribution network; R_{f} is fault resistance.

From (1), it can be observed that appropriate reference voltage and current values exist which are capable of reducing both the fault current and fault voltage to zero, thereby enabling effective fault arc suppression, as expressed by

$$\begin{cases} \dot{U}_{0\mathrm{ref}} = -\dot{E}_{\mathrm{A}} \\ \dot{I}_{\mathrm{Pref}} = \dot{U}_0\left(\dfrac{1}{R_0} + \mathrm{j}\omega C_0\right) \end{cases} \tag{2}$$

2.2 Control Equations Based on PI controllers

Therefore, the neutral point voltage $\dot{U}_0$ of the distribution network and the output current $\dot{I}_{\mathrm{P}}$ of the power electronic converter can be taken as control targets, and their control equations using PI controllers are

$$\begin{cases} \Delta\dot{U}_{\mathrm{VM}} + \dot{U}_0 = K_{\mathrm{VP}}\left(-\dot{E}_{\mathrm{A}} - \dot{U}_0\right) + K_{\mathrm{VI}}\int\left(-\dot{E}_{\mathrm{A}} - \dot{U}_0\right)dt + \dot{U}_0 \\ \Delta\dot{U}_{\mathrm{IM}} + \dot{U}_0 = K_{\mathrm{IP}}\left(\dot{I}_{\mathrm{Pref}} - \dot{I}_{\mathrm{P}}\right) + K_{\mathrm{II}}\int\left(\dot{I}_{\mathrm{Pref}} - \dot{I}_{\mathrm{P}}\right)dt + \dot{U}_0 \end{cases} \tag{3}$$

where K_{VP} is the proportional coefficient of PIC for the neutral point voltage $\dot{U}_0$ of the distribution network; K_{VI} is the integral coefficient of PIC for the neutral point voltage $\dot{U}_0$ of the distribution network; $\dot{U}_{\mathrm{VM}}$ is the control component output by the PI controller for the neutral point voltage $\dot{U}_0$ of the distribution network. Likewise, K_{IP} is the proportional coefficient of PIC for the output current $\dot{I}_{\mathrm{P}}$ of the power electronic converter; K_{II} is the integral coefficient of PIC for the output current $\dot{I}_{\mathrm{P}}$ of the power electronic converter; $\dot{U}_{\mathrm{IM}}$ is the control component output by the PI controller for the output current $\dot{I}_{\mathrm{P}}$ of the power electronic converter.

3 Voltage-Current Mutual Compensation using Fuzzy PI Control

In this section, a voltage-current mutual compensation-based fault arc suppression method is presented, and a fuzzy system is designed for PI controllers to jointly regulate the PIC parameters.

3.1 Voltage-Current Mutual Compensation Method

Typically, only one of the neutral point voltage $\dot{U}_0$ of the distribution network and the output current $\dot{I}_{\mathrm{P}}$ of the power electronic converter can be selected as the independent control target using PIC. When the neutral point voltage $\dot{U}_0$ of the distribution network is selected as the control target, it is called voltage-based fault arc suppression method. If the output current $\dot{I}_{\mathrm{P}}$ of the power electronic converter is selected as the control target, it is called current-based fault arc suppression method.

For the voltage-based fault arc suppression method, its advantage is that it does not require the measurement of the distribution network insulation parameters and is more effective under high-resistance grounding faults. However, the fault current and voltage have an AC transient component attenuation process and is greatly affected by the impedance of the distribution network line. For the current-based suppression method, its advantage is that it is less affected by the impedance of the distribution network line and works well in the case of low-resistance grounding faults. However, the fault current and voltage have a DC transient component attenuation process, and accurate insulation parameter measurement is required.

Considering the complementary advantages of the voltage-based and current-based fault arc suppression methods, a voltage-current mutual compensation-based fault arc suppression method is presented here. The control schematic diagram can be shown in Fig. 2. The controls of neutral point voltage $\dot{U}_0$ of the distribution network and the output current $\dot{I}_P$ of the power electronic converter have their own PI parameters. It is hoped that the voltage-based fault arc suppression method will be dominant, i.e., the control of neutral point voltage $\dot{U}_0$ of the distribution network is the main control and the control of output current $\dot{I}_P$ of the power electronic converter is used as compensation in the case of high-resistance grounding faults. On the contrary, it is hoped that the current-based fault arc suppression method will be dominant, i.e., the control of output current $\dot{I}_P$ of the power electronic converter is the main control and the control of neutral point voltage $\dot{U}_0$ of the distribution network is used as compensation in the case of low-resistance grounding faults. Therefore, PIC with fuzzy system is required to regulate the respective PI parameters of voltage-based and current-based fault arc suppression methods. The errors of two control targets can be expressed as

$$\begin{cases} e_V = -\dot{E}_A - \dot{U}_0 \\ e_I = \dot{I}_{Pref} - \dot{I}_P \end{cases} \tag{4}$$

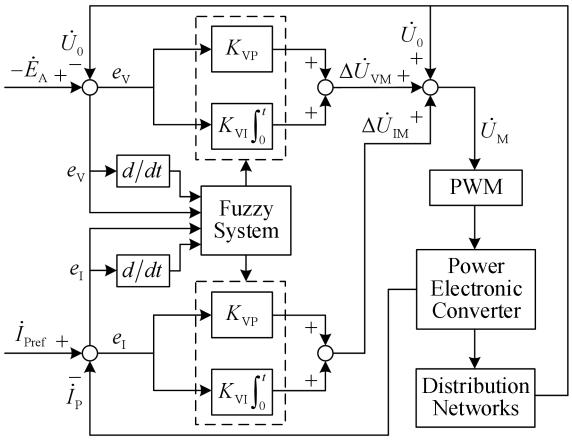


Fig. 2. Control schematic diagram.

3.2 Design of Fuzzy System for PI Control

According to Fig. 2, the errors e_{V} and e_{I}, and their respective derivatives e_{Vc} and e_{Ic} are used as the input of fuzzy system for fuzzification. Fuzzification maps continuous error values onto discrete fuzzy sets. The four parameters K_{VP}, K_{VI}, K_{IP}, and K_{II} of the PI controllers are modified online to meet different requirements of control parameters for different fault conditions, so that the controlled targets have good dynamic and static performance.

The output of the fuzzy system is ΔK_{VP}, ΔK_{VI}, ΔK_{IP}, and ΔK_{II}. They can change dynamically with the e_{V}, e_{I}, e_{Vc} and e_{Ic}. K_{VP0}, K_{VI0}, K_{IP0}, and K_{II0} are the initial parameters of the PIC. The final values of the PI controllers include the initial value and the dynamic value, and they can be presented as

$$\begin{cases} K_{\mathrm{VP}} = K_{\mathrm{VP0}} + \Delta K_{\mathrm{VP}} \\ K_{\mathrm{VI}} = K_{\mathrm{VI0}} + \Delta K_{\mathrm{VI}} \\ K_{\mathrm{IP}} = K_{\mathrm{IP0}} + \Delta K_{\mathrm{IP}} \\ K_{\mathrm{II}} = K_{\mathrm{II0}} + \Delta K_{\mathrm{II}} \end{cases} \tag{5}$$

The fuzzy control is designed by fuzzy logic designer in MATLAB, as shown in Fig. 3. The input variables e_{V}, e_{I}, e_{Vc} and e_{Ic}, and the output variables ΔK_{VP}, ΔK_{VI}, ΔK_{IP}, and ΔK_{II} are normalized to [-1, 1]. For the input variables e_{V}, e_{I}, e_{Vc} and e_{Ic}, Gaussian2-type membership functions shown in Fig. 4 are applied, and for the output variables ΔK_{VP}, ΔK_{VI}, ΔK_{IP}, and ΔK_{II}, trapezoidal-type membership functions are adopted, as shown in Fig. 5.

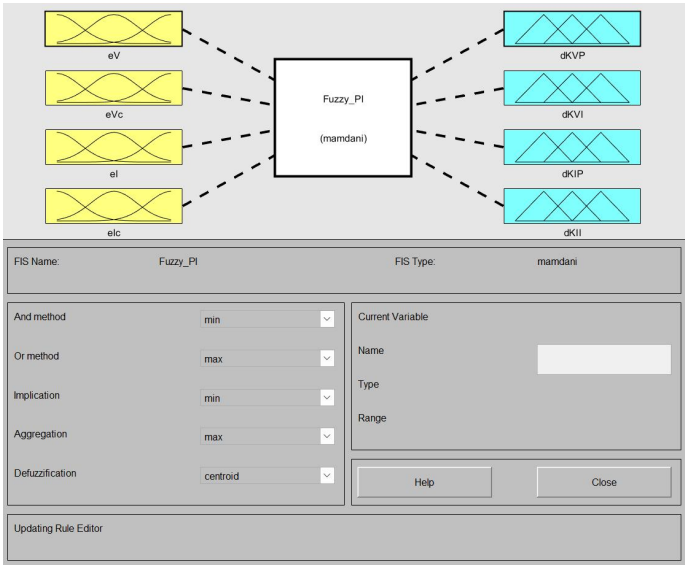


Fig. 3. Fuzzy PI control module in MATLAB.

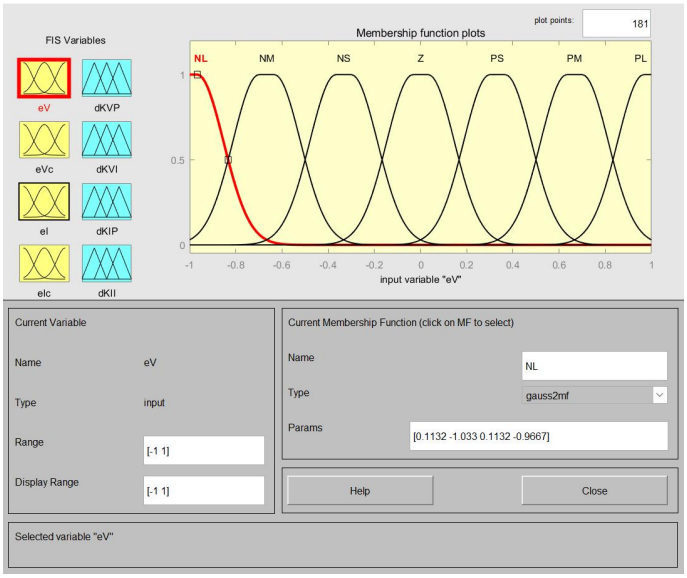


Fig. 4. Fuzzy PI control input membership function.

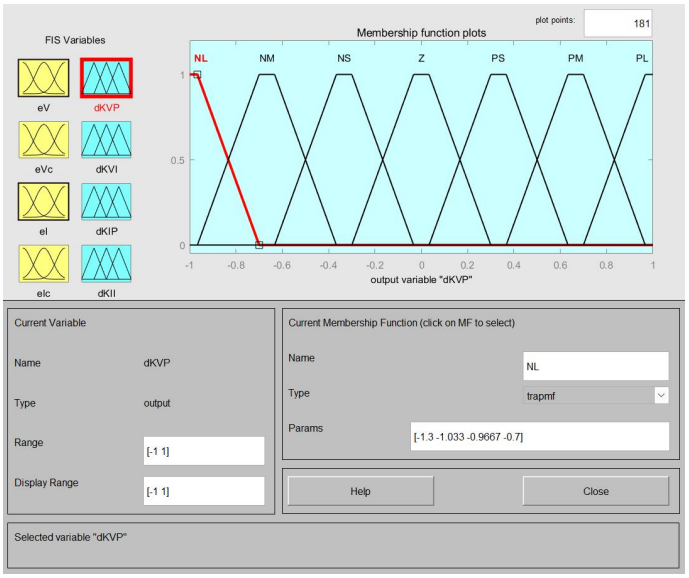


Fig. 5. Fuzzy PI control output membership function.

The four inputs are divided into seven fuzzy sets: Negative Large (NL), Negative Medium (NM), Negative Small (NS), Zero (Z), Positive Small (PS), Positive Medium (PM), Positive Large (PL). The outputs are the compensation of the proportional coefficient and the integral coefficient. For example, PML means a positive medium

proportional coefficient and large integral coefficient. The fuzzy rule table is provided in Table 1.

Table 1. Fuzzy rule table.

e_V / e_I e_{Vc} / e_{Ic}	NL	NM	NS	Z	PS	PM	PL
NL	PML	PMM	PSS	PZS	PSS	PMM	PML
NM	PLL	PMM	PSS	PZS	PSS	PMM	PLL
NS	PLL	PLM	PMS	PZZ	PMS	PLM	PLL
Z	PLL	PLL	PLM	PZZ	PLM	PLL	PLL
PS	PLL	PLM	PMS	PZZ	PMS	PLM	PLL
PM	PLL	PMM	PSS	PZS	PSS	PMM	PLL
PL	PML	PMM	PSS	PZS	PSS	PMM	PML

4 Simulation Validation

In this section, the proposed method is verified through simulation in MATLAB under low and high fault resistance conditions, and the transient and steady-state results of fault current and voltage suppression are analyzed and evaluated.

4.1 Simulation Results under Low Fault Resistance Conditions

Fig. 6 shows the current-voltage mutual compensation-based fault arc suppression results based on the fuzzy PIC in the case of $R_f = 100\Omega$. The proposed method still maintains good transient response results. Moreover, the proposed method maintains a good fault current and voltage steady-state suppression results.

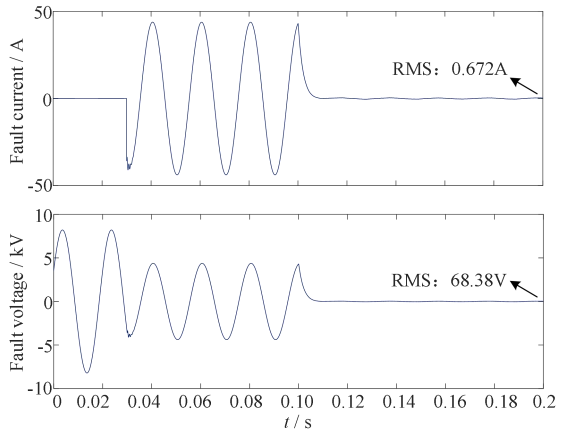


Fig. 6. Simulation results under fault resistance of 100 ohm.

4.2 Simulation Results under High Fault Resistance Conditions

Fig. 7 shows the current-voltage mutual compensation-based fault arc suppression results based on the fuzzy PIC in the case of $R_f = 1\text{k}\Omega$. The proposed method maintains a good transient response result so that the fault current and voltage can be suppressed in a short time. Furthermore, the proposed method still maintains a better fault current and voltage steady-state fusion suppression results.

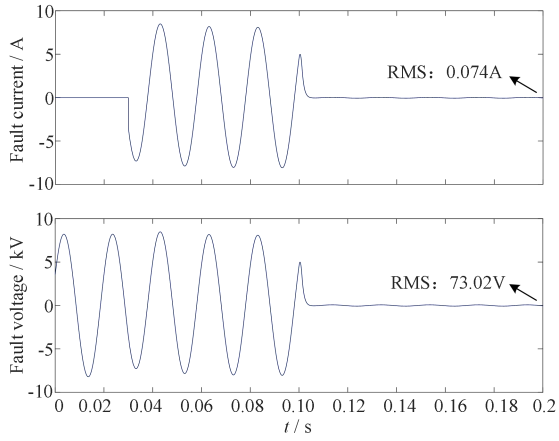


Fig. 7. Simulation results under fault resistance of 1k ohm.

5 Conclusion

This paper proposes the flexible arc suppression method based on voltage-current mutual compensation using fuzzy PIC for distribution networks. In this method, voltage-based and current-based control can be run in parallel and serve as a compensation for each other. Based on fuzzy PIC, voltage-based and current-based suppression methods can play a leading role in the ground fault resistance conditions where their respective advantages are. Simulation validation demonstrate that the proposed method achieves simultaneous suppression of fault current and voltage with a shorter transient response time and reduced residual values under low and high fault resistance conditions.

References

1. X. Wei, X. Wang, J. Gao, D. Yang, K. Wei, and L. Guo: Faulty feeder detection for single-phase-to-ground fault in distribution networks based on transient energy and cosine similarity [J]. *IEEE Trans. Power Del.*, 37(5), 3968-3979 (2022).
2. B. -L. Zhang, M. -F. Guo, M. Lak, C. -M. Lin, and Q. Hong: Improved fault arc suppression capability and minimized required power of Y-type cascaded H-bridge

converters without DC sources in active distribution networks [J]. *IEEE J. Emerg. Sel. Topics in Power Electron.*, early access (2025), doi: 10.1109/JESTPE.2025.3572045.

3. A. Nikander: Development and testing of new equipment for faulty phase earthing by applying RTDS [J]. *IEEE Trans. Power Del.*, 32(3), 1295-1302 (2017).
4. A. Cerretti, F. M. Gatta, A. Geri, S. Lauria, M. Maccioni, and G. Valtorta: Ground fault temporary overvoltages in MV networks: evaluation and experimental tests [J]. *IEEE Trans. Power Del.*, 27(3), 1592-1600 (2012).
5. S. Ouyang, J. Liu, Y. Yang, X. Chen, S. Song, and H. Wu: Control strategy for arc-suppression-coil-grounded star-connected power electronic transformers [J]. *IEEE Trans. Power Electron.*, 34(6), 5294-5311 (2019).
6. B. -L. Zhang, M. -F. Guo, M. Lak, C. -M. Lin, and Q. Hong: Minimizing required DC sources of cascaded H-bridge multilevel converter for fault suppression in active distribution networks [J]. *IEEE Trans. Ind. Electron.*, 72(6), 5761-5770 (2025).
7. Y. Hou, Q. Guo, C. Tu, F. Jiang, L. Wang, X. Wang, and F. Xiao: Adaptive active voltage-type arc suppression strategy considering the influence of line parameters in active distribution network [J]. *IEEE Trans. Ind. Electron.*, 70(5), 4799-4808 (2023).
8. W. Wang, X. Zeng, L. Yan, X. Xu, and J. M. Guerrero: Principle and control design of active ground-fault arc suppression device for full compensation of ground current [J]. *IEEE Trans. Ind. Electron.*, 64(6), 4561-4570 (2017).
9. B. Fan, G. Yao, W. Wang, X. Zeng, Josep M. Guerrero, K. Yu, and C. Zhuo: Principle and control design of a novel hybrid arc suppression device in distribution networks [J]. *IEEE Trans. Ind. Electron*., 69(1), 41-51 (2022).
10. M. Barzegar-Kalashani, and M. A. Mahmud: A linear hybrid active disturbance rejection controller design to extenuate powerline bushfires in resonant grounded distribution power systems [J]. *Int. J. Electr. Power Energy Syst.*, 142, 108192 (2022).
11. B. -L. Zhang, M. -F. Guo, Z. -Y. Zheng, and Q. Hong: Fault current limitation with energy recovery based on power electronics in hybrid ac–dc active distribution networks [J]. *IEEE Trans. Power Electron.*, 38(10), 12593-12606 (2023).

081 Analysis of Fault Suppression Performance of Flexible Arc Suppression Methods in Distribution Networks

Guo-Jun Zhao, Mou-Fa Guo*, Bin-Long Zhang, and Ze-Yin Zheng

College of Electrical Engineering and Automation,
Fuzhou University, Fuzhou 350108, China

Abstract—Single-line-to-ground (SLG) faults are the most common type of faults in distribution networks and may result in severe consequences such as electric shock and forest fires. Due to the uncertainties in fault location and transition resistance, the arc suppression performance of traditional flexible arc suppression methods is significantly affected. To address this issue, this paper systematically analyzes the suppression performance of current-type and voltage-type flexible arc suppression methods under varying fault locations and transition resistance conditions, revealing the relationships among residual current, residual voltage, zero-sequence voltage, and fault parameters under multi-variable fault scenarios. The findings provide a theoretical basis for the improvement and optimization of flexible arc suppression methods. Finally, PSCAD/EMTDC simulations are conducted to validate the analysis results.

Keywords: distribution network, SLG, flexible arc suppression method.

1 Introduction

The distribution network exhibits a complex structure and operates in a dynamic environment, making it highly vulnerable to SLG faults [1]. These faults are frequently accompanied by arc discharges which, if not promptly extinguished, may lead to insulation breakdown of power equipment, electric shock incidents, or catastrophic events such as forest fires [2].

The extinction of AC arcs depends on the interplay between the recovery rate of dielectric strength and the voltage recovery rate. When the arc current crosses zero, the ground arc can be extinguished without reignition if the dielectric strength at the fault point recovers faster than the voltage [3]. Consequently, suppressing the fault current reduces both its thermal effect and air ionization, thereby facilitating arc extinction. Based on this principle, distribution networks commonly employ the arc-suppression coil grounding method to mitigate the hazards of SLG arcs [4]. However, with the expansion of distribution networks, the growing proportion of cables, and the large-scale integration of nonlinear loads, the active and harmonic components of fault currents have increased significantly [5]. Due to device limitations, arc-suppression coils cannot compensate for these components, and under certain operating conditions, the arc may persist.

With the development of power electronics, flexible arc suppression devices based on power converters have been developed, offering controllable current and voltage outputs. These devices enable full compensation of grounding fault currents, thereby ensuring reliable arc extinction [6]. This approach is referred to as the flexible arc suppression method. Depending on the reference values applied to the converter, it can be classified into the current-type flexible arc suppression (C-FAS)method and the voltage-type flexible arc suppression(V-FAS) method [7]. In the C-FAS method, the control objective is the fault current, and the reference is calculated as the ratio of the fault-phase source voltage to the network-to-ground impedance [8]. Although this method achieves complete compensation of the fault current, its effectiveness is affected by measurement errors in ground parameters. To address this issue, several enhancements to the C-FAS method have been proposed [9], [10], thereby improving its fault suppression performance. In contrast, the V-FAS method eliminates the need for ground parameter measurement by adopting voltage as the control objective and suppresses the ground arc by forcing the fault-phase bus voltage to zero [11]. In this method, the controller reference can be set either to zero or to the negative of the fault-phase source voltage [12]. However, due to uncertainties in fault location and large variations in transition resistance, this method is affected by line impedance voltage drops under low-resistance fault conditions, which hinders effective fault current suppression and limits arc extinction performance.

Existing studies have demonstrated that both C-FAS and V-FAS methods can suppress SLG arcs effectively to a certain extent. However, their performance is strongly influenced by multiple coupled factors, including fault location, transition resistance, and system-to-ground capacitance. This gap constrains both the optimal design and the practical application of flexible arc suppression methods in real distribution networks.

To address this issue, this paper systematically investigates the suppression characteristics of C-FAS and V-FAS methods under varying fault locations and transition resistances, revealing the transient and steady-state behaviors of zero-sequence voltage and their correspondence with fault parameters. Moreover, the interrelationships among residual current, residual voltage, zero-sequence voltage, and fault parameters are clarified, providing a theoretical foundation for the improvement and optimization of the flexible arc suppression method.

2 Principle of flexible arc suppression for SLG fault

The arc suppression schematic of a cascaded H-bridge flexible arc suppression device(FASD) connected to the neutral point of the distribution network is shown in Fig. 1.

After a SLG fault occurs in the distribution network, the FASD injects current through the neutral point to control the fault-point voltage and current to zero, thereby achieving arc suppression.

In Fig. 1, $\dot{E}_{\mathrm{A}}$, $\dot{E}_{\mathrm{B}}$, and $\dot{E}_{\mathrm{C}}$ represent the phase voltages of the distribution network; $\dot{U}_{\mathrm{A}}$, $\dot{U}_{\mathrm{B}}$, and $\dot{U}_{\mathrm{C}}$ denote the bus voltages of each phase; $\dot{U}_{0}$ represents the

zero-sequence voltage of the distribution network after the fault; $\dot{I}_{\mathrm{f}}$ is the fault point current; $R_{1\mathrm{A}}$, $R_{1\mathrm{B}}$, and $R_{1\mathrm{C}}$ represent the phase-to-ground leakage resistances; $C_{1\mathrm{A}}$, $C_{1\mathrm{B}}$, and $C_{1\mathrm{C}}$ are the phase-to-ground capacitances; R_{f} is the transition resistance; $\dot{I}_{\mathrm{Z}}$ is the output current of the cascaded H-bridge FASD. In addition, phase C is the ground-faulted phase.

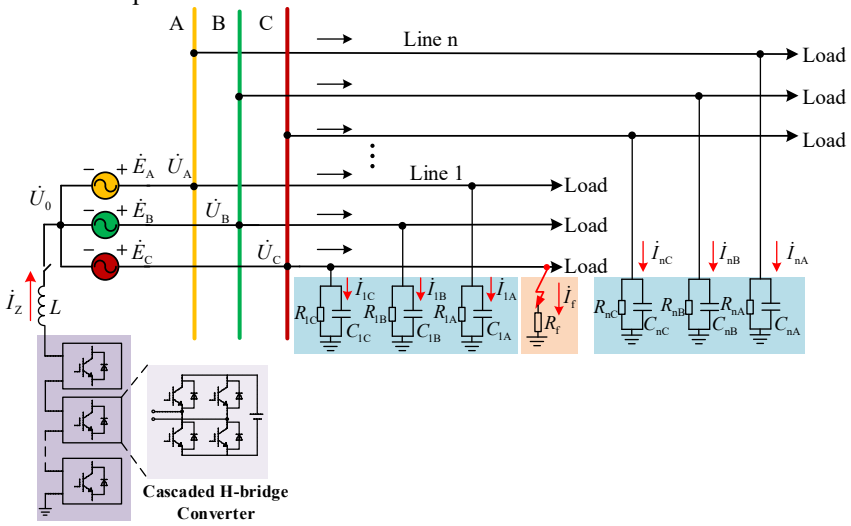


Fig. 1. Schematic diagram of flexible arc suppression.

Applying Kirchhoff's current law (KCL) to $\dot{I}_{\mathrm{Z}}$ yields

$$\dot{I}_{\mathrm{Z}} = \dot{I}_{1\mathrm{A}} + \dot{I}_{1\mathrm{B}} + \dot{I}_{1\mathrm{C}} + \cdots + \dot{I}_{\mathrm{nA}} + \dot{I}_{\mathrm{nB}} + \dot{I}_{\mathrm{nC}} + \dot{I}_{\mathrm{f}} \tag{1}$$

Eq. (1) can be further derived as

$$\dot{I}_{\mathrm{Z}} = \dot{U}_{\mathrm{A}} Y_{\Sigma\mathrm{A}} + \dot{U}_{\mathrm{B}} Y_{\Sigma\mathrm{B}} + \dot{U}_{\mathrm{C}} Y_{\Sigma\mathrm{C}} + (\dot{U}_0 + \dot{E}_{\mathrm{C}})/R_{\mathrm{f}} \tag{2}$$

In (2), $Y_{\Sigma\mathrm{A}}$, $Y_{\Sigma\mathrm{B}}$, and $Y_{\Sigma\mathrm{C}}$ represent the phase-to-ground admittances of the distribution network. In the equation, $Y_{\Sigma\mathrm{A}} = 1/R_{\Sigma\mathrm{A}} + \mathrm{j}\omega C_{\Sigma\mathrm{A}}$, $Y_{\Sigma\mathrm{B}} = 1/R_{\Sigma\mathrm{B}} + \mathrm{j}\omega C_{\Sigma\mathrm{B}}$, $Y_{\Sigma\mathrm{C}} = 1/R_{\Sigma\mathrm{C}} + \mathrm{j}\omega C_{\Sigma\mathrm{C}}$.

When the three-phase source and phase-to-ground parameters are symmetrical, Eq. (2) can be further simplified as

$$\dot{I}_{\mathrm{Z}} = \dot{U}_0 Y_0 + (\dot{U}_0 + \dot{E}_{\mathrm{C}})/R_{\mathrm{f}} \tag{3}$$

In (3), $Y_0 = 3Y_{\Sigma\mathrm{A}} = 3Y_{\Sigma\mathrm{B}} = 3Y_{\Sigma\mathrm{C}} = 1/Z_0$. By setting $\dot{U}_0 = -\dot{E}_{\mathrm{C}}$, we obtain $\dot{U}_{\mathrm{f}} = 0$, and $\dot{I}_{\mathrm{f}} = 0$. Under this condition, the injected current $\dot{I}_{\mathrm{Z}}$ can be expressed as

$$\dot{I}_{\mathrm{Z}} = -\dot{E}_{\mathrm{C}} Y_0 = -\dot{E}_{\mathrm{C}}/Z_0 \tag{4}$$

Therefore, the FASD can use (4) as the reference value for the controller and adjust the neutral-point voltage of the distribution network to $\dot{U}_0 = -\dot{E}_{\mathrm{C}}$ by injecting current, thereby achieving $\dot{U}_{\mathrm{f}} = 0$, and $\dot{I}_{\mathrm{f}} = 0$. This constitutes the fundamental operating principle of the C-FAS method.

In addition, the FASD can directly control the voltage to $\dot{U}_0 = -\dot{E}_{\mathrm{C}}$, i.e., using

$-\dot{E}_C$ as the controller reference, or control the fault-phase voltage at the bus to $\dot{U}_C = 0$, i.e., using 0 as the controller reference. This constitutes the fundamental operating principle of the V-FAS method.

3 Performance Analysis of SLG Fault Suppression by the Flexible Arc Suppression Method

3.1 Theoretical Analysis

Both types of flexible arc suppression methods mentioned above have not taken into account the effect of fault line impedance voltage drop caused by load current. To address this issue, this paper further investigates the grounding fault suppression performance of the V-FAS and C-FAS methods under the combined influence of line impedance voltage drop and transition resistance.

As illustrated in Fig. 1, when a SLG fault occurs in phase C of the distribution network, and both the line impedance voltage drop and the transition resistance are considered, the analytical expressions of the zero-sequence voltage, bus fault-phase voltage, fault-point voltage, and fault-point current for the V-FAS method are given in (5)–(8).

$$\dot{U}_{01} = -\dot{E}_C \tag{5}$$

$$\dot{U}_{C1} = 0 \tag{6}$$

$$\dot{U}_{f1} = -\dot{U}_L \tag{7}$$

$$\dot{I}_{f1} = -\dot{U}_L / R_f \tag{8}$$

In (7)–(8), $\dot{U}_L$ denotes the line impedance voltage drop, and the meanings of other parameters are consistent with those defined earlier.

It can be seen that, during the fault suppression process of the V-FAS method, the zero-sequence voltage is controlled to the negative value of the fault-phase source voltage, the bus fault-phase voltage is regulated to zero, the residual voltage at the fault point equals the line impedance voltage drop, and the residual current at the fault point depends on the ratio of the line impedance voltage drop to the transition resistance. In the case of low-resistance grounding faults, the residual current at the fault point may even exceed the fault current prior to suppression.

Correspondingly, the C-FAS method needs to account for the influence of grounding parameter measurement errors.

In this paper, the relative error of grounding capacitance measurement is adopted as a reference, and its calculation is given in (9). On this basis, by further considering the combined effects of line impedance voltage drop and transition resistance, the analytical expressions of the zero-sequence voltage, bus fault-phase voltage, fault-point voltage, and fault-point current for the C-FAS method during fault suppression are derived, as shown in (10)–(13).

$$\lambda = (C_{0_MV} - C_{0_TV}) / C_{0_TV} \tag{9}$$

$$\dot{U}_{02} = -\dot{E}_{\mathrm{C}}\left(1+\frac{\lambda}{1+R_{\mathrm{f}}/Z_0}\right)+\frac{\dot{U}_{\mathrm{L}}}{1+R_{\mathrm{f}}/Z_0} \tag{10}$$

$$\dot{U}_{\mathrm{C2}} = \frac{-\lambda\dot{E}_{\mathrm{C}}}{1+R_{\mathrm{f}}/Z_0}+\frac{\dot{U}_{\mathrm{L}}}{1+R_{\mathrm{f}}/Z_0} \tag{11}$$

$$\dot{U}_{\mathrm{f2}} = -\frac{\lambda\dot{E}_{\mathrm{C}}+\dot{U}_{\mathrm{L}}}{1+Z_0/R_{\mathrm{f}}} \tag{12}$$

$$\dot{I}_{\mathrm{f2}} = -(\lambda\dot{E}_{\mathrm{C}}+\dot{U}_{\mathrm{L}})/(R_{\mathrm{f}}+Z_0) \tag{13}$$

In (9), λ a denotes the relative error of the system grounding capacitance measurement, C_{0_MV} is the measured grounding capacitance, and C_{0_TV} is the actual grounding capacitance. In addition, the meanings of other parameters in (10)–(13) are the same as those defined earlier and are not repeated here.

Compared with (5)–(8), the values of $\dot{U}_{02}$, $\dot{U}_{\mathrm{C2}}$, $\dot{U}_{\mathrm{f2}}$, and $\dot{I}_{\mathrm{f2}}$ in (10)–(13) vary with R_{f} and Z_0. The specific variation characteristics are as follows:

When $|R_{\mathrm{f}}| \ll |Z_0|$, $\dot{U}_{02}$, $\dot{U}_{\mathrm{C2}}$, $\dot{U}_{\mathrm{f2}}$, and $\dot{I}_{\mathrm{f2}}$ can be further expressed as

$$\begin{cases} \dot{U}_{02} \approx -\dot{E}_{\mathrm{C}}(1+\lambda)+\dot{U}_{\mathrm{L}}; \\ \dot{U}_{\mathrm{C2}} \approx -\lambda\dot{E}_{\mathrm{C}}+\dot{U}_{\mathrm{L}}; \\ \dot{U}_{\mathrm{f2}} \approx 0; \\ \dot{I}_{\mathrm{f2}} \approx -(\lambda\dot{E}_{\mathrm{C}}+\dot{U}_{\mathrm{L}})/Z_0. \end{cases} \tag{14}$$

When $|R_{\mathrm{f}}| \gg |Z_0|$, $\dot{U}_{02}$, $\dot{U}_{\mathrm{C2}}$, $\dot{U}_{\mathrm{f2}}$, and $\dot{I}_{\mathrm{f2}}$ can be further expressed as

$$\begin{cases} \dot{U}_{02} \approx -\dot{E}_{\mathrm{C}}(1+\lambda); \\ \dot{U}_{\mathrm{C2}} \approx 0; \\ \dot{U}_{\mathrm{f2}} \approx -(\lambda\dot{E}_{\mathrm{C}}+\dot{U}_{\mathrm{L}}); \\ \dot{I}_{\mathrm{f2}} \approx 0. \end{cases} \tag{15}$$

During the fault suppression process of the C-FAS method, the analytical expressions of the zero-sequence voltage, bus fault-phase voltage, fault-point voltage, and fault-point current are influenced by the transition resistance, grounding impedance, and grounding parameter measurement errors, which makes them different from those of the V-FAS method. As the transition resistance increases, these electrical quantities gradually converge to the corresponding values of the V-FAS method during fault suppression.

Compared with the V-FAS method, the fault-point residual current of the current-type method is constrained by the grounding impedance and therefore does not exceed the fault current under small transition resistance conditions. The residual voltage at the fault point is affected by grounding parameter measurement errors: when the relative error is negative, the residual voltage is lower than that of the V-FAS method, whereas when the relative error is positive, the residual voltage is higher.

3.2 Simulation Analysis

To validate the theoretical analysis of the fault suppression performance of the C-FAS and V-FAS methods, a 10 kV distribution network SLG fault simulation model was built using PSCAD/EMTDC in this study.

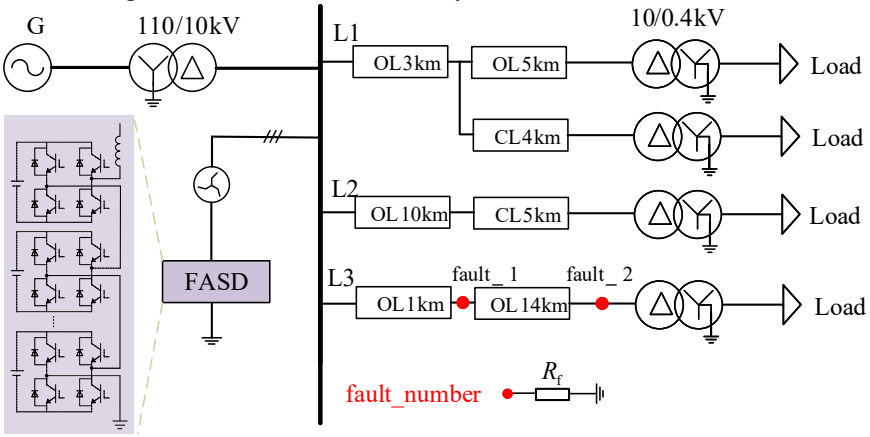


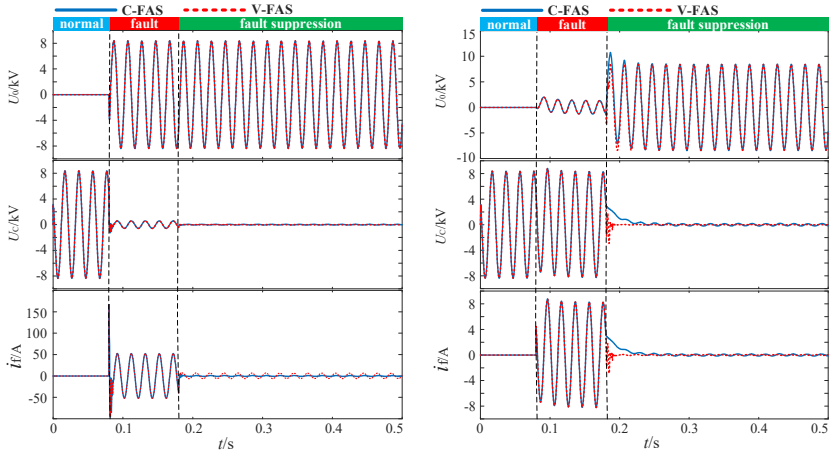
Fig. 2. Schematic diagram of distribution network simulation model.

Assuming a SLG fault occurs on phase C in Fig. 2, the fault locations are set at fault_1 and fault_2 to evaluate the arc suppression performance of the C-FAS and V-FAS methods under different fault positions. In addition, the transition resistance at the fault point is set to 10Ω and 1kΩ to represent low-resistance and high-resistance fault conditions, respectively.

Fig. 3 and 4 illustrate the waveforms when the fault occurs at fault_1 and fault_2, respectively. The waveforms include the zero-sequence voltage, the fault-phase voltage at the bus, and the fault-point current. In the simulation, the SLG fault occurs at 0.08 s, and the cascaded H-bridge based flexible arc suppression device is activated at 0.18 s. The numerical results of fault-point suppression corresponding to Figs. 3 and 4 are summarized in Table I.

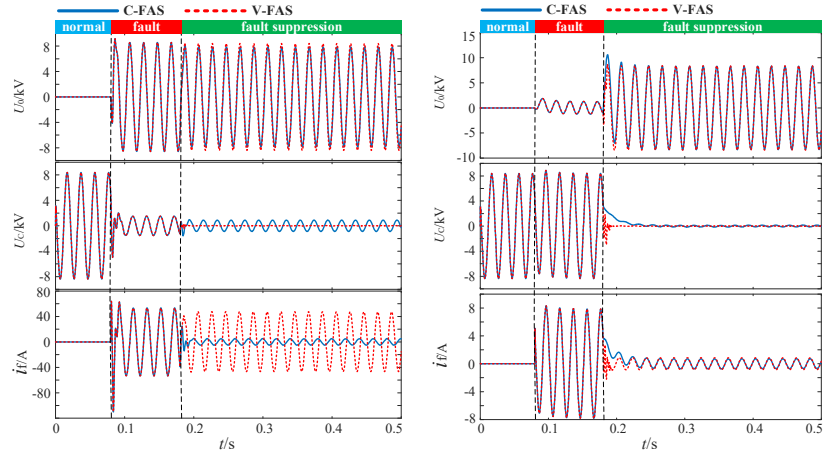
As shown in Figs. 3 and 4 and Table I, the V-FAS method is not affected by transition resistance or grounding impedance, and can directly regulate the neutral-point zero-sequence voltage and the bus fault-phase voltage. In contrast, the C-FAS method is influenced by both transition resistance and grounding impedance: under low-resistance conditions, the neutral-point zero-sequence voltage and bus fault-phase voltage reflect the variation of the line voltage drop, whereas under high-resistance conditions, these voltage quantities are essentially consistent with those of the V-FAS method.

Furthermore, Figs. 3, 4, and Table I indicate that the C-FAS method is also affected by grounding parameter measurement errors and its intrinsic fault suppression characteristics. Under high-resistance conditions, its arc suppression performance is inferior to that of the V-FAS method, whereas under low-resistance conditions, it outperforms the V-FAS method.



(a) (b)

Fig. 3. SLG occurs at fault_1. (a) $R_f = 10\Omega$. (b) $R_f = 1\text{k}\,\Omega$.



(a) (b)

Fig. 4. SLG occurs at fault_2. (a) $R_f = 10\Omega$. (b) $R_f = 1\text{k}\,\Omega$.

Table 1. SLG Fault Suppression Results Corresponding to Figs. 3 and 4

fault conditions		fault occurs			V-FAS			C-FAS		
fault location	R_f (Ω)	U_0^{RMS} (kV)	U_C^{RMS} (kV)	I_f^{RMS} (A)	U_{01}^{RMS} (kV)	U_{C1}^{RMS} (kV)	I_{f1}^{RMS} (A)	U_{02}^{RMS} (kV)	U_{C2}^{RMS} (kV)	I_{f2}^{RMS} (A)
fault_1	10	5.932	0.412	36.91	5.942	0.014	4.66	5.912	0.035	0.67
	1k	0.884	5.866	5.81	5.945	0.018	0	5.889	0.122	0.1
fault_2	10	6.068	1.073	33.75	5.942	0.021	33.26	5.565	0.629	3.46
	1k	0.885	5.938	5.53	5.947	0.019	0.61	5.912	0.095	0.49

4 Conclusion

The C-FAS method is affected by transition resistance, grounding impedance, and grounding parameter measurement errors. Under low-resistance conditions, the residual current of the C-FAS method reflects the line voltage drop variation, and its arc suppression performance is superior to that of the V-FAS method; under high-resistance conditions, its zero-sequence voltage and bus fault-phase voltage are essentially consistent with those of the V-FAS method, but the arc suppression performance is slightly inferior due to parameter measurement errors.

In summary, both C-FAS and V-FAS methods have their respective advantages, and an optimized combination of the two can effectively enhance the adaptability and reliability of distribution networks under different SLG fault conditions.

References

[1] J. H. Lin, M. F. Guo, Q. T. Hong, and R. Jiang, "An Earth Fault Diagnosis Method Based on Online Dynamically Calculated Thresholds for Resonant Ground Systems," *IEEE Trans. Smart Grid*, vol. 15, no. 4, pp. 3459-3473, Jul. 2024.

[2] K. L. Liu, S. Zhang, B. R. Li, C. Zhang, B. Y. Liu, H. Jin, and J. F. Zhao, "Flexible Grounding System for Single-Phase to Ground Faults in Distribution Networks: A Sys-tematic Review of Developments," *IEEE Trans. Power Del*., vol. 37, no. 3, pp. 1640-1649, Jun. 2022.

[3] K. Y. Chen, W. H. Zhang, and X. Y. Xiao, "Faulted terminal open circuit voltage controller for arc suppression in distribution network," *IET Gener.Trans. Distrib*., Vol. 14, no. 14, pp. 2763-2770, Sep. 2020.

[4] M. Mitolo, R. Musca, M. Tartaglia, and G. Zizzo, "Electrical Safety Analysis in the Presence of Resonant Grounding Neutral," *IEEE Trans. on Ind. Applicat*., 2019, 55(5): 4483-4489. vol. 55, no. 5 pp. 4483-4489, Oct. 2019.

[5] B. S. Fan, G. Z. Yao, W. Wen, J. M. Guerrero, K. Yu, and C. Zhuo "Principle and Con-trol Design of a Novel Hybrid Arc Suppression Device in Distribution Networks, " *IEEE Trans. Ind Electron*., Vol. 69, no. 1, pp. 41-51, Jan. 2022.

[6] Y. C. Hou, Q. Guo, C. M. Tu, F. Xiao, L. Wang, F. Jiang, K. Yu, and X, Wang, "A review of single-phase-to-ground fault regulation devices for distribution networks," *Renew. Sustain. Energy Rev*., vol. 200, Aug. 2024, Art. no. 114602.

[7] G.-J. Zhao, M.-F. Guo, B -L. Zhang, Z.-Y. Zheng, and Q. T. Hong, "Cascaded H-Bridge Converter-Based Flexible Arc Suppression Method Adapting to Line Parameter Variations," *IEEE Trans. Power Electron,* vol. 40, no. 8, pp. 11809-11819, Aug. 2025.

[8] B. L. Zhang, M. F. Guo, M. Lak, C. M. Lin, and Q. T. Hong, "Minimizing Required DC Sources of Cascaded H-Bridge Multilevel Converter for Fault Suppression in Active Distribution Networks," *IEEE Trans. Ind Electron*., vol. 72, no. 6, pp. 5761-5770, June 2025.

[9] M. F. Guo, Y. H. Jiao, Z. Y. Zheng, J. H. Lin, and Q. T. Hong, "Online Split-phase Identification of Asymmetric Parameters Between Distribution Lines and Ground for Unbalanced Voltage Compensation Based on Power Electronics," *IEEE Trans. Power Electron*., vol. 39, no. 8, pp. 1-12, Aug. 2024.

[10] Z. Y. Zheng, J. F. Xu, M. F. Guo, "Online Identification Method of Distribution Line-to-ground Parameters and Grounding Online Identification Method of Distribution Line-to-Ground Parameters and Grounding Transition Conductance During Arc Suppression," *Prot. Control Mod. Power Syst.*, vol. 10, no. 4, pp. 103-115, July 2025.

[11] W. Wang, X. J. Zeng, L. J. Yan, X. Y. Xu, and J. M. Guerrero, "Principle and Control Design of Active Ground-Fault Arc Suppression Device for Full Compensation of Ground Current," *IEEE Trans. Ind Electron*., Vol. 64, no. 6, pp. 4561-4570, Jun. 2017.

[12] X. M. Luan, X. P. Li, S. Y. Wu, C. J. Jia, H. K. Mei, and L. X. Gao, "Arc Suppression Control with Adaptive Parameters of Active Grounding Device Considering Ground Fault Resistance Uncertainty," *IEEE Trans. Power Del*., vol. 39, no. 1, pp. 426-435, Feb. 2024.

082 基于藤蔓优化算法并考虑需求侧响应的直流电网最优潮流计算

李强生[1]，刘锋[1]，张馨元[1]，李镕皓[1]，谭亲跃*[1]，丁月明[2]，王松[1]，宋莹[1]

（1.西北农林科技大学，陕西省 咸阳市 712100;2 国网山东省电力公司日照供电公司，山东省 日照市 276800，山东省 日照市 276800）

Optimal Power Flow Calculation in DC Power Grid Based on Vine Optimization Algorithm Considering Demand Side Response

LI Qiangsheng[1], LIU Feng[1], ZHANG Xinyuan[1], TAN Qinyue[1], DING Yueming[2], WANG Song[1], SONG Ying[1]

(1. Northwest A&F University, Xianyang 712100, China; 2. Rizhao Power Supply Company, State Grid Shandong Electric Power Company，Rizhao 276800, China)

ABSTRACT: The randomness and intermittency of new energy generation pose new challenges to the safe, stable, and economic operation of power systems. In particular, optimizing the OPF of DC systems and improving overall energy efficiency have become prominent issues that require urgent research and resolution. Based on this, an OPF solution framework integrating the VOA and DC grid is proposed. Firstly, an objective function aiming at minimizing system power loss is established using variables such as voltage and power. Secondly, a demand response mechanism is implemented, with load changes incorporated into the model as variables. Thirdly, the constrained objective function is transformed into an unconstrained one. Finally, the effectiveness and stability of the proposed algorithm are verified using the Cigre B4 test system. Results show that when the demand response mechanism is introduced, the proposed algorithm achieves a power loss at the order of 10^{-4} ,demonstrating high calculation accuracy and robustness.

KEY WORDS: DC grid; demand-side response; vine optimization algorithm; optimal power flow; source-load interaction

摘要：针对新能源发电随机性、间歇性的特点对系统安全、稳定和经济运行带来新的挑战，特别是如何优化直流系统的潮流分布，提高整体能效，成为一个亟待研究和解决的突出问题。基于此提出一种融合藤蔓优化算法(Vine Optimization Algorithm, VOA)与直流电网潮流的最优潮流求解框架。首先，通过电压和功率等变量建立以系统网损最小为目标函数。其次，设置需求侧响应机制，将负荷变化作为变量加入到模型中。然后，将带约束的目标函数改造成无约束的目标函数。最后，通过 Cigre B4 测试系统验证所提算法的有效性与稳定性。结果表明，所提算法在引入需求侧响应机制时，算法损失为 10^{-4} 数量级，计算准确且鲁棒性高。

关键词：直流电网；需求侧响应；藤蔓优化算法；最优潮流；源荷互动

1 引言

随着“双碳”目标的推进和新型电力系统建设的深入，直流电网因其输电效率高、可控性强、易于可再生能源接入等优势，逐渐成为能源转型的重要载体[1]。然而，高比例风光可再生能源的并网引入了显著的不确定性[2]，使得电力系统最优潮流(Optimal Power Flow, OPF)问题从传统的确定性优化向不确定性建模转变[3]。在此背景下，如何在满足系统安全约束的前提下，实现潮流优化，已成为当前研究的核心挑战[4,5]。

OPF 求解方法主要分为两类：一是基于数学规划的确定性算法，比如简化梯度法[6]、内点法[7]、二次规划法[8]；二是智能群体优化算法，常见的有粒子群算法 [9]、飞蛾扑火算法 [10]、灰狼算法 [11]等。

近年研究表明，融合新型智能算法突破上述瓶颈的有效路径 [12]。；文献[13]基于改进差分进化算法，有效提升了计算 OPF 的收敛精度；文献[14]提出基于聚类的两阶段差分进化策略，获取更高质量的全局最优解。文献[15]通过求解重构的凸包约束下的优化问题，获得互联多微网系统在最优成本下各子微网的运行成本及耦合变量的值；文献[16]基于袋獾优化算法求解含电压源换流器(Voltage Source Converter ,VSC)的交直流系统多目标 OPF；文献[17]通过反向变异与非线性收敛因子改进海鸥

优化算法，以平衡全局探索与局部开发能力。然而，上述研究均未能充分考虑算法框架的鲁棒性约束，亦未提供可验证的理论或数值依据以论证其稳定性和收敛条件。

综上所述，尽管大量研究将智能优化算法[18]引入 OPF 计算领域，但普遍存在三方面局限：一是未能充分考虑风光等新能源功率波动引发的不确定性影响；其二，尚未提供可验证的理论分析或实验数据以支撑算法的鲁棒性边界及稳定性条件；三是多数研究未涉及负荷时变特性等动态场景的建模，或仅单一考量其中某一方面。基于此，本文提出一种基于 VOA 并考虑需求侧响应的直流电网 OPF 计算，保证求解准确性的前提下，又有很强的鲁棒性。

2 OPF 数学模型

电力系统 OPF 计算是在电力系统网络拓扑结构、电气元件参数及系统负荷情况给定时，找到满足所有约束条件的最优控制变量。其主要构成包括变量集合、约束条件和目标函数，控制变量是可控制的自变量。如下式（1）~（4）所示。

$$Min \quad F(x,u) \tag{1}$$

$$s.t. \quad g(x,u) \le 0 \tag{2}$$

$$h(x,u) = 0 \tag{3}$$

$$u \in U \tag{4}$$

式中：F 是待优化的目标函数；g 是不等式约束；h 是等式约束；x 和 u 分别是控制变量和状态变量，U 是状态变量集合。

2.1 直流电力系统模型及元件参数

本文研究的直流电力系统为包含风电机组和光伏电站的新型电力系统，该系统的结构拓扑见下图 1 所示。图中共有 11 条直流母线、两个电源、三个光伏电站、三个风电机组和 14 条直流线路。1 号母线所连接的换流器采用恒电压控制，其余换流器均采用恒功率控制。系统额定电压 400kV，线路电阻为 0.016Ω/km 。

由于风电和光伏所提供的功率具有不确定性，因此构建不确定性模型[19]，并对采样的功率点附加正态扰动。如下式(5)~(6)所示。

$$P_W^r = P_w^r + P_{w,err}^r \quad r = 1,2,3 \tag{5}$$

$$P_{PV}^s = P_{pv}^s + P_{pv,err}^s \quad s = 1,2,3 \tag{6}$$

式中：P_W^r 和 P_{PV}^s 是风光的参考输出功率；P_w^r 和 P_{pv}^s 是模拟的风光输出功率；$P_{w,err}^r$ 和 $P_{pv,err}^s$ 是考虑正态分布误差的附加风光功率。

此外，对于每个母线所连接的负荷同样具有不确定性构建负荷的不确定性模型，如下式(7)所示。

$$P_{ld}^i = P_N^i + P_{add}^i \quad i = 1,2,3,\ldots,11 \tag{7}$$

式中，P_{ld}^i 是第 i 个母线的实际负荷功率；P_N^i 是第 i 个母线的额定负荷功率；P_{add}^i 是考虑波动的第 i 个母线的附加负荷功率。

为适应新型电力系统的不确定性，本文考虑负荷参与到电力系统的调度中来，针对每条线路，在保证基础功率的前提下，给出不同的需求侧响应的功率。因此，负荷功率被改造为下式(8)所描述。

$$P_{LD}^i = \begin{cases} P_{ld}^i + P_{adjust}^i & \sum P_{LD}^i \le \sum P_w^r + P_{PV}^s \\ P_{ld}^i - P_{adjust}^i & \sum P_{LD}^i > \sum P_w^r + P_{PV}^s \end{cases} \tag{8}$$

其中，P_{adjust}^i 是第 i 个母线参与到系统调度中的需求侧响应功率；P_{LD}^i 是考虑需求侧响应的所有负荷功率。

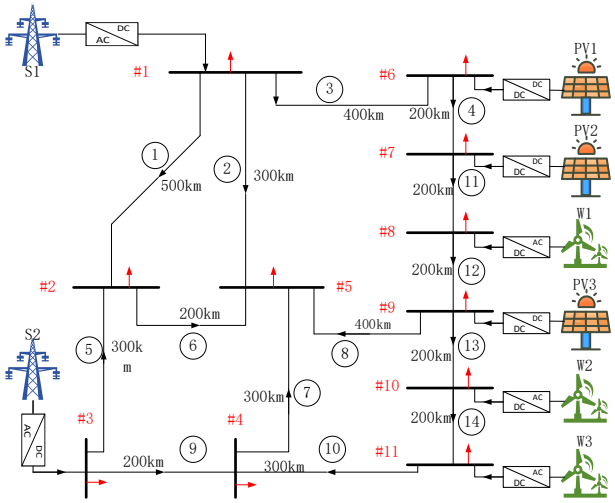


图 1 CIGRE B4 直流电网的拓扑图

Fig.1 Topology diagram of CIGRE B4 DC grid

2.2 OPF 的目标函数

本文主要讨论含分布式电源的新型直流电力系统的网损情况，因此构建以网损总和最小的目标函数，目标函数的表达式为式(9)所示。

$$P_{loss} = \frac{1}{2} \times tr\left[-\boldsymbol{Y}_1(\boldsymbol{U}_i - \boldsymbol{U}_j)^2\right] \tag{9}$$

其中，P_{loss} 是网损的总和；$\boldsymbol{Y}_1$ 是改造的节点导纳矩阵；$(\boldsymbol{U}_i - \boldsymbol{U}_j)^2$ 是线路电压矩阵的平方。

2.3 OPF 的约束条件

OPF 考虑的系统约束条件如下，共分为不等式约束和等式约束两类，具体如下。

1)各母线电压幅值最大值/最小值约束：

$$-0.9U_N \le U_i \le 1.1U_N \tag{10}$$

其中，U_i 是第 i 个母线的电压；U_N 是额定电压。

2)各母线功率守恒约束：

$$tr(P_{\Sigma} - \boldsymbol{Y}_2(\boldsymbol{U}_i - \boldsymbol{U}_j)) = 0 \tag{11}$$

其中，P_{Σ} 是该条线路的输入功率和负荷功率的代数和；$\boldsymbol{Y}_2$ 是改造的功率节点导纳矩阵。

3)各外部电源出力最大值/最小值约束：

$$P_{\min} \le P_{S1} \le P_{\max} \tag{12}$$

$$P_{\min} \le P_{S2} \le P_{\max} \tag{13}$$

其中，P_{S1} 和 P_{S2} 是外部电源注入功率；$P_{\min}$ 和 $P_{\max}$ 是线路传输功率的上下限。

3 VOA

3.1 主藤蔓的数学模型

主藤蔓在向原位置移动的策略我们总结为下面三个方式，

第一，以正弦的形式移动。

第二，以余弦的形式移动。

第三，以正切的形式移动。

图 2 形象地展示了主藤蔓的移动策略。这种主藤蔓的移动策略保证主藤蔓可以感知周围环境以及与其他主藤蔓进行交流，同时又可以避免所有主藤蔓集中于一个位置，增加了种群的多样性。

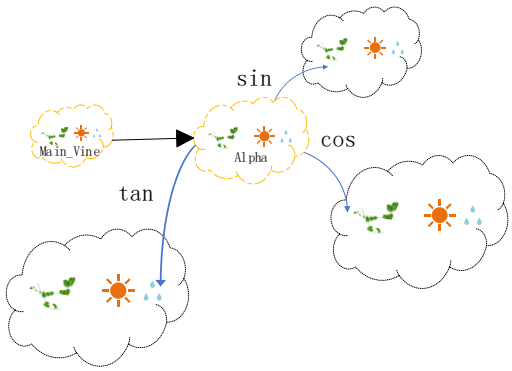


图 2 主藤蔓更新策略

Fig.2 Main vine update strategy

3.2 侧藤蔓的数学模型

侧藤蔓是主藤蔓在生长的过程中长出的嫩芽形成的枝条。在 VOA 算法中，设定每个生长周期主藤蔓固定产生 6 个侧藤蔓。形象化的移动策略如图 3 所示。

3.3 存活法则

通过与其所在的主藤蔓和其他侧藤蔓对比后，结合优胜劣汰机制的制约，若主藤蔓所在位置营养物质最多，则所有侧藤蔓均死亡，否则最优侧藤蔓存活且转化为主藤蔓。具体更新公式如式(14)所示。

$$\boldsymbol{X}_i^{t+1} = \begin{cases} \boldsymbol{X}_i^t & F(\boldsymbol{X}_i^t) < F(\boldsymbol{X}_{i(vine)}^t) \\ \boldsymbol{X}_{i(vinek)}^t & \min(F(\boldsymbol{X}_{i(vine)}^t)) \end{cases} \tag{14}$$

其中，$\boldsymbol{X}_i^{t+1}$ 表示迭代次数为 $t+1$ 时主藤蔓 i 所在的位置；$F(\bullet)$ 表示求取适应度值；$\boldsymbol{X}_{i(vinek)}^t$ 表示侧藤蔓中适应度值最低的位置；k 为 1~6 中任一个整数。

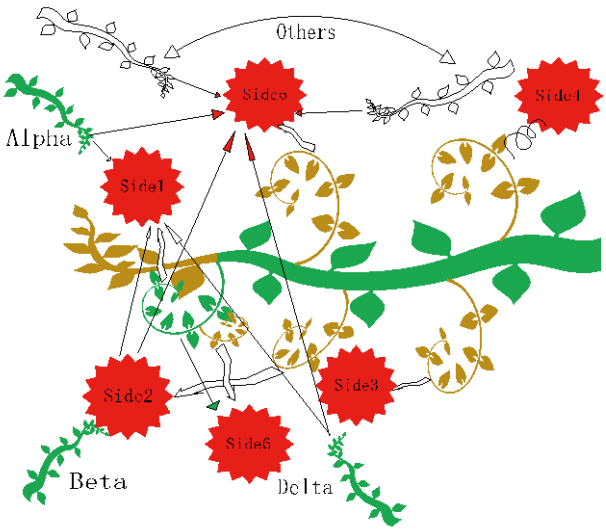


图 3 侧藤蔓更新策略

Fig.3 Side vine update strategy

4 算例分析

4.1 适应 VOA 算法的潮流计算公式

VOA 在处理含约束条件的优化问题时，无法直接进行求解，需要利用惩罚项将约束条件改造成目标函数的一部分，改造后的目标函数如下所示。

$$F = tr\left[-\boldsymbol{Y}_I(\boldsymbol{U}_i - \boldsymbol{U}_j)^2\right] + \lambda \bullet \left|tr(P_{\Sigma} - \boldsymbol{Y}_2(\boldsymbol{U}_i - \boldsymbol{U}_j))\right|^2 \tag{15}$$

其中，λ 是惩罚因子，因视所有约束条件同等地位，因此采用相同的固定的惩罚因子，数值为 10000。

4.2 三种算法性能比较

分别对 PSO，GWO 和 VOA 进行了运行时间和收敛性测试。将引入需求侧响应机制的案例称为 CS1,未引入需求侧响应机制的案例称为 CS2。设置循环次数为 10。在上述描述的基础上统计程序运行时间和收敛率如表 1 所示。在 CS1 和 CS2 情况下，PSO 收敛率最高只有 29.17%，运行时间最少为 17.05s，GWO 均未能收敛，然而 VOA 的收敛率最低为 79.17%，运行时间最长为 14.84s。三种算法比较之下，VOA 的性能更佳。

表 1 三种算法性能对比分析

Tab.1 Optimization value comparison analysis

案例	算法	时间/s	收敛率/%
CS1	PSO	17.05	20.83
	GWO	39.87	0
	VOA	14.63	83.33
CS2	PSO	17.28	29.17
	GWO	40.13	0
	VOA	14.84	79.17

4.3 VOA 案例结果

采用本文所提 VOA 算法框架求解一天内的 OPF 问题，在此本文选择其中四个时间节点作为展示，将得到最优的目标值、决策变量和控制变量结果展示在表 2~3 所示。

表 2 中初始值对应的区域所展示的是算法初始设置的值，优化值对应的区域所展示的是经过 VOA 计算之后的优化值。首先，两两对比电网输电功率变化，出现了传输功率减少以及反向传输的情况。其次，对比每个节点的电压分布情况，可以发现，由于 VOA 算法不依赖于初始值，在电压限制范围内随机分配节点电压，明显可以发现初始情况下电压分布比较离散。但是经过 VOA 计算之后，各节点的电压基本稳定在额定电压附近，且分布较为均匀。同时也能够很明显的发现，在 10h 这个时间节点，电网接收到了馈入功率，这是因为此时光伏功率逐渐增加，超过了负荷的需要，将多余电能传递至电网。

表 3 中所展示的是功率损耗和算法损失情况以及需求侧响应的调节量。对于 CS1 而言，可以发现，在 0 时，由于风电 1 的功率较大，算法调节正的可调负荷，以便消纳清洁能源；在 6 时，由于光伏发电的功率较大，并且风电 3 的功率也很大，算法调节正的可调负荷，以便消纳清洁能源；在 10 时，由于风电和光伏发电的功率都很大，实际上超过负荷此时刻可能得最大需求功率，在进行不确定性调节之后，剩余功率便向电网反馈。而在 22 时，风电和光伏发电均不够明显，此时刻需要外部电网支撑区域内的所有负荷，以维持电网的稳定。P_{loss} 行所展示的便是系统网损情况，0 时和 6 时因为有分布式电源的支撑，电网负担减小，所以流经线路的功率损耗也减小，10 时和 22 时，因为分布式电源很大或者很小，需要向电网反馈功率或者依赖电网支撑，线路的损耗激增，且反馈功率时损耗更大。P_{error} 行所展示的是算法的违反程度，其是通过计算式(35)的违反项计算出来的，从图 4 和表 3 中结果可以看到，P_{error} 均小于 10^{-2}，计算结果准确。CS2 与 CS1 情况类似，趋势一致，可以发现其线路损耗总体相比较而言更低一些且 P_{error} 更小，均小于 10^{-4}。

表 2　不同变量初始值和优化值的比较分析

Tab.2　Comparison analysis of initial and optimized values of different variables

变量		初始值				优化值			
时间/h		0	6	10	22	0	6	10	22
CS1	P_{S1} / MW	1000	1000	1000	1000.00	353.24	0.00	-475.38	1000.00
	P_{S2} / MW	1000	1000	1000	1000.00	172.58	683.98	0.00	905.80
	U_2 / kV	423.15	391.63	403.57	413.60	419.08	420.65	417.76	417.09
	U_3 / kV	417.19	398.71	407.49	405.02	420.03	423.79	417.08	419.26
	U_4 / kV	396.55	378.47	405.67	404.51	420.12	422.43	418.31	416.03
	U_5 / kV	413.98	397.78	400.51	411.98	419.37	420.74	419.74	416.21
	U_6 / kV	399.81	437.88	407.57	384.56	418.07	421.20	433.29	416.33
	U_7 / kV	407.70	423.68	388.52	382.34	418.26	421.94	434.92	416.06
	U_8 / kV	406.57	408.90	386.50	389.36	418.48	422.10	434.91	413.83
	U_9 / kV	417.12	406.59	397.43	392.61	419.91	422.23	430.12	414.07
	U_{10} / kV	408.21	394.60	413.88	373.88	422.71	423.05	425.50	415.18
	U_{11} / kV	405.64	382.68	414.95	366.49	422.30	424.56	421.71	414.09
CS2	P_{S1} / MW	1000	1000	1000	1000	1000	466.81	-437.56	1000
	P_{S2} / MW	1000	1000	1000	1000	335.94	697.69	-4.62	1000
	U_2 / kV	424.52	417.68	405.66	417.61	415.32	419.72	418.71	418.41
	U_3 / kV	424.37	418.77	390.56	426.36	415.72	422.63	417.99	422.21
	U_4 / kV	434.22	426.90	376.28	416.43	414.85	420.65	419.26	417.98
	U_5 / kV	414.40	425.47	397.15	415.73	416.01	419.52	420.74	417.01
	U_6 / kV	398.37	379.78	414.40	383.34	419.29	417.55	432.99	413.63
	U_7 / kV	395.80	380.51	389.58	397.80	421.36	417.74	436.24	412.73
	U_8 / kV	370.41	403.40	371.36	402.35	417.78	419.25	436.95	411.60
	U_9 / kV	381.05	415.42	383.33	398.35	415.55	420.12	432.25	412.44
	U_{10} / kV	385.06	417.55	379.77	396.72	413.81	420.67	427.75	413.13
	U_{11} / kV	418.86	439.99	373.22	415.85	414.23	421.96	423.17	416.23

表 3　负荷侧及线路损耗优化值对比分析

Tab.3　Load side and line loss optimization value comparison analysis

变量		数值			
	时间/h	0	6	10	22
CS1	$P_{adjust1}$ / MW	199.25	0.00	165.64	0.00
	$P_{adjust2}$ / MW	200.00	0.00	2.32	0
	$P_{adjust3}$ / MW	21.12	0.00	0.45	-200
	$P_{adjust4}$ / MW	0.00	55.29	0.00	0
	$P_{adjust5}$ / MW	19.60	0.00	0.28	-0.00
	$P_{adjust6}$ / MW	197.82	200.00	199.57	0
	$P_{adjust7}$ / MW	200.00	0.00	199.25	-152.21
	$P_{adjust8}$ / MW	51.37	0.00	0.00	0
	$P_{adjust9}$ / MW	0.00	0.00	0.06	0
	$P_{adjust10}$ / MW	200.00	0.00	182.64	-0.02
	$P_{adjust11}$ / MW	28.65	162.25	22.32	-200
	P_{loss} / MW	14.85	6.29	76.25	25.83
	P_{error} / MW^2	-7.71E-03	-4.96E-06	1.82E-06	-1.31E-07
CS2	P_{loss} / MW	5.29	6.04	68.86	14.50
	P_{error} / MW^2	6.18E-06	-4.50E-06	1.13E-05	-8.12E-06

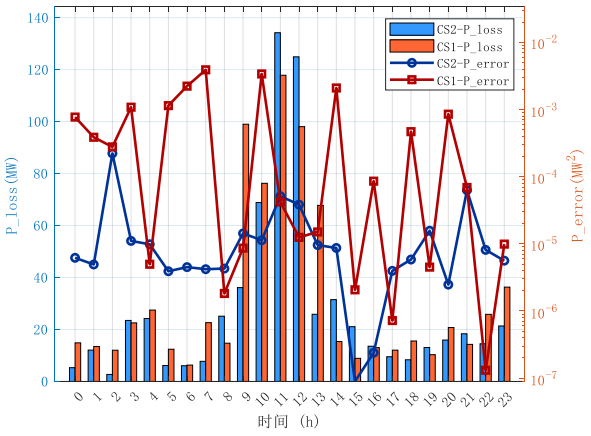


图 4　系统一天内线损及算法损失

Fig.4　System daily line loss and algorithm loss

4.4 算法稳定性分析

设置算法搜索个体为 1000，迭代次数为 5000 代，分别独立计算 50 次。算法稳定的条件是不违反约束或者违反约束的程度在可接受范围。计算的结果绘制在图 5。

通过观察图 5 可知，VOA 算法求解 CS1 的结果中 P_{error} 基本在 10^{-4} 数量级附近，精度足够。具体而言，小于 10^{-1} 的总和为 1126，计算的准确度为 93.83%；小于 10^{-2} 的总和为 1121，计算的准确度为 93.42%；小于 10^{-3} 的总和为 844，计算的准确度为 70.33%；小于 10^{-4} 的总和为 571，计算的准确度为 47.58%。由此可见，算法的精度足够，并且算法的一致性较高，算法的稳健性比较好。

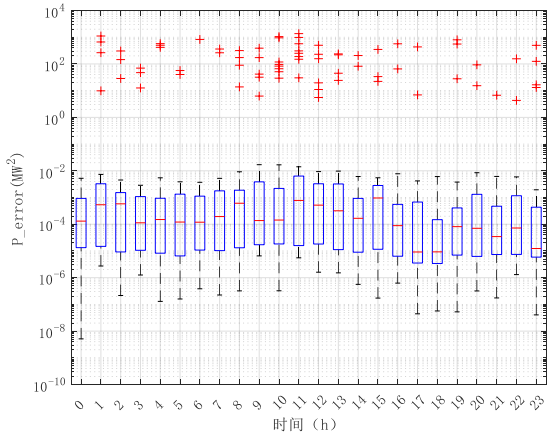


图 5　CS1 独立计算箱型图

Fig.5　Box plot under CS1

5　结论

（1）VOA 算法能处理复杂等式和不等式约束优化问题，可用于高维度、非线性、非凸优化问题求解。

（2）VOA 算法是一种切实有效的求解 OPF 问题的算法，能够保持约束算法损失在 10^{-4} 数量级，并且搜索到高质量的最优潮流解。

（3）VOA 算法在处理负荷参与到直流电网 OPF 计算中的鲁棒性较好，计算的准确度也比较高。

参考文献

[1] 张智刚，康重庆. 碳中和目标下构建新型电力系统的挑战与展望[J]. 中国电机工程学报，2022，42(08)：2806-2819.

[2] 李夫刚，李夫海，琚承乾，等. 新能源不确定性表征方法及关键技术问题研究现状、挑战及展望[J]. 电力系统保护与控制，2025，53(15)：172-187.

[3] 尚文强，李广磊，丁月明，等. 考虑源荷不确定性和新能源消纳的综合能源系统协同调度方法[J]. 电网技术，2024，48 (02)：517-532.

[4] 夏晓荣，杨宇，刘勇，等. 电-气综合能源系统的分布式最优调度方法[J]. 电网与清洁能源，2025，41(02)：60-66+74.

[5] 汤明润，李若昜，程晓钰，等. 基于博弈论-改进云模型的新能源电力系统适应性评估[J]. 电力系统保护与控制，2025，53(07)：40-51.

[6] 王鲁，相年德，王世缨. 应用简化梯度法研究分布式并行最优潮流计算[J]. 中国电机工程学报，1991，(S1)：128-133.

[7] 袁越，久保川淳司，佐佐木博司，等. 基于内点法的含暂态稳定约束的最优潮流计算[J]. 电力系统自动化，2002，(13)：14-19.

[8] Burchett R C，Happ H H and Vierath D R. Quadratically convergent optimal power flow[J]. IEEE Transactions on Power Apparatus and Systems，2007，11：3267-3275.

[9] Kennedy J，Eberhart R. Particle swarm optimization[C]. Proceedings of ICNN'95-international conference on neural networks，Perth，Australia，Nov 27，1995：1942-1948.

[10] Mirjalili S. Moth-flame optimization algorithm：A novel nature-inspired heuristic paradigm[J]. Knowledge-Based Systems，2015，89： 228－249.

[11] Mirjalili S，Mirjalili S M，Lewis，A. Grey Wolf Optimizer[J]. Advances in Engineering Software，2014，69，46－61.

[12] Ebeed M，Kamel S，Jurado F. Optimal power flow using recent optimization techniques[J]. Classical and recent aspects of power system optimization. Academic Press，2018，157-183.

[13] 孙江，任家智. 改进差分进化算法在电力系统最优潮流计算中的应用[J]. 电工技术，2023，(21)：1-4.

[14] 田玮，江晓东. 基于聚类的差分进化算法的两阶段最优潮流方法[J]. 电力系统及其自动化学报，2021，33(11)：50-55.

[15] 沈祎淳，彭弘毅，晏鸣宇. 基于投影的非迭代互联多微网系统分布式最优潮流计算方法[J/OL]. 电网技术，2025，1-12.

[16] 束洪春，廖孟黎，安娜，等. 基于多目标袋獾算法的含 VSC 换流器交直流系统最优潮流[J]. 电网技术，2023，47(11)：4679-4695.

[17] 陈将宏，李伟亮，王羲沐. 基于反向变异海鸥优化算法的最优潮流计算[J]. 燕山大学学报，2024，48(05)：396-407.

[18] Bhattacharya A，Chattopadhyay P K. Application of biogeography-based optimization to solve different optimal power flow problems[J]. IET Generation，Transmission and Distribution，2011，5(1)：70-80.

[19] 陈艳波，王德帅，田昊欣，等. 基于源荷储协调运行的电网可用输电能力优化方法[J]. 电力系统保护与控制，2024，52(23)：119-134.

收稿日期：2025-09-30。

作者照片



作者简介：

李强生(1997)，男，硕士研究生，研究方向为智能优化算法在电力系统中的应用，E-mail：liqiangsheng@nwafu.edu.cn；

通讯作者：谭亲跃(1975)，男，副教授，硕士生导师，研究方向电能质量、新能源发电与智能微电网等，E-mail：qinyuetan@nwsuaf.edu.cn。

083 覆冰灾害下考虑多手段协同的柔性互联配电网增韧策略

过亮[1]，黄勇[1]，林岚清[2]，汤雨[3*]，贾艺菲[3]，
（1．国电南瑞科技股份有限公司，江苏省 南京市 211106；
2.清华大学电机工程与应用电子技术系，北京市 海淀区 100084
3． 河北工业大学，天津市 北辰区 300000）

摘要：当前冰灾频发，而现有的韧性增强措施难以有效保障配电网的安全运行。因此本文结合网络重构、柔性互联装置与移动储能融冰系统的应用优势，提出兼顾电力-交通耦合的多时段配网韧性改善策略。首先确定基于线路负荷损失度的韧性保障目标。然后，计算冰雪天气对行程速度的影响，以及 MESIMS 时空动态演化机制，建立起交通路径调度和配网增韧调度协同的双层优化模型，并通过增加关联约束，将双层模型转化为单层模型，从而求解，建立交通路径调度和配网增韧调度协同的双层优化模型，计算冰雪天气对行程速度的影响，以及 MESIMS 时空动态演化机制。最终，融冰计算实例模拟采用 IEEE-33，结果表明该策略在增强配网韧性的决策，降低了总负荷损失风险，降低了约 24.7%，进一步平衡线路融冰效率与电网运行稳定性。

关键词：覆冰场景；多手段协同；电力－交通耦合；移动储能融冰系统；柔性互联配电网
中图分类号：TM7 **文献标志码：**A
DOI：10.19635/j.cnki.csu-epsa.00081

Research on Toughening Strategy of Flexible Interconnected Distribution Network Considering Multi Means Collaboration Under Ice Cover Disaster

GUO Liang[1], HUANG Yong[1], LIN Lanqing[2], TANG Yu[3*], JIA Yifei[3]
（1.Guodian Nanrui Technology Co. Ltd. Nanjing，211106, Jiangsu Province China；
2.Department of Electrical Engineering and Applied Electronic Technology，Tsinghua University, Haidian District, Beijing 100084, China
3. Hebei University of Technology, Beichen District, Tianjin 300000, China）

Abstract: The current frequent occurrence of ice disasters makes it difficult for existing resilience enhancement measures to effectively ensure the safe operation of the distribution network. Therefore, this article combines the application advantages of network reconstruction, flexible interconnection devices, and mobile energy storage ice melting systems to propose a multi period distribution network resilience improvement strategy that takes into account power transportation coupling. Firstly, determine the resilience guarantee target based on the degree of line load loss. Then, the impact of ice and snow weather on travel speed, as well as the spatiotemporal dynamic evolution mechanism of MESIMS, were calculated to establish a dual layer optimization model for the coordination of traffic path scheduling and distribution network toughening scheduling. By adding correlation constraints, the dual layer model was transformed into a single layer model to solve and establish a dual layer optimization model for the coordination of traffic path scheduling and distribution network toughening scheduling. The impact of ice and snow weather on travel speed and the spatiotemporal dynamic evolution mechanism of MESIMS were calculated. Finally, the simulation of the ice melting calculation example was conducted using IEEE-33, and the results showed that this strategy enhanced the resilience of the distribution network, reduced the risk of total load loss by about 24.7%, and further balanced the efficiency of line ice melting and the stability of power grid operation.

Keywords: Ice covering scenario; multi-means coordination; power-traffic coupling; mobile energy storage ice melting

基金项目：国家自然科学基金（52307199）
通信作者:汤雨（1980—），男，博士，教授，主要研究方向为电力电子电能变换，zgsjit@163.com。

system; flexible interconnected distribution network; and toughness improvement

0 引言

电网韧性是指电力系统能充分反应，并在系统遭受极端事件时恢复到正常状态的能力[1]。近年来，全球气候异常导致冰雪风暴频发，同时配电网最贴近用户。因此，配电网在应对覆冰灾害时所表现出的韧性受到越来越多的关注和重视。

随着新型配电网的建设与发展，多种源网荷侧灵活资源为配电网的安全稳定运行提供了更全面的设备支撑，有效增强了配电网的抗灾能力[2-6]。

文献[7]提出了一种防御者-攻击者-防御者的模型，在最坏情况下实现最小负荷削减。需求响应计划（DRP）通过激励和管理策略维持电网的电力平衡[9]。文献[8]设计了一个面向韧性的电力系统供应市场，以刺激资源投资。

需求响应通过激励与管理控制策略调整负荷侧资源的灵活性，从而优化配电网的运行状态。分布式电源(DG)具有为电力系统提供电能的优势，可以在一定程度上使系统在遭遇“小概率-高破坏的极端天气影响时，恢复失去电力的供电负荷[9]。柔性互联装置（Flexible interconnection device,FID）是代替传统的联络开关，灵活地实现有功率交换、无功率补偿和电压调节。文献[10]建立柔性互连配网故障恢复模型，在失去联系的边子网和连接网络的边子网上加入失电供电负荷恢复模型。

当前的研究大多集中于冰雪灾害后的负荷恢复[11-15]，但从灾中增强配电网韧性角度开展的研究仍较为稀缺。因此，科学探索配电线路的融冰方法至关重要，以减轻覆冰灾害带来的损失，并确保配电网在灾害中的高效稳定运行。

配电网除冰方法主要包括传统机械方法和一些更有效的技术，如过载融冰和短路电流法[16]。过载融冰技术通过重新分配潮流来增加受冰线路的电流，从而迅速加热线路以融化冰。由于这一过程不会影响配电网的正常运行且易于实施，因此在允许电力流动传输的配电网中具有广阔的应用前景。基于 FID 优化调度的柔性互联配电网除冰和防冰措施逐渐受到关注[9]]。然而，配电网在一个复杂多样的环境中运行，包含许多分支线路。由于 FID 位置的限制和配电网络的拓扑结构，单靠 FID 在实现分支线路除冰方面存在局限。移动储能融冰系统（mobile energy storage ice melting system，MESIMS），其通过在车辆上配置直流电源，实现线路融冰功能[19]。相较于固定式融冰装置，MESIMS 在调配方面展现出更高的灵活性。

综合来看，各种融冰手段互为补充，在时空的合理协调配合下，可以明显提高融冰效果。为实现更科学的韧性提升，本文以含 FID 的柔性互联配网为研究对象，在兼顾增强配网韧性和防范潮流越限风险的基础上，提出了一种交通路径与电力潮流协同调度的双层优化模型，结合 FID、MESIMS 和网络重构的增韧策略，通过算例验证了该模型的有效性。

1 覆冰下线路风险分析和决策指标

在进行配电网韧性提升前，须对线路覆冰增长特性进行研究并确定韧性保障目标，以保证增韧方案的合理性。

1.1 覆冰增长模型

冰风暴天气通常覆冰增速较快，因此应分析覆冰增长量对融冰优化决策的影响有多大，以下式表示单位时间覆冰增长量

$$\Delta R=\frac{1}{\rho_i\cdot\pi}\sum_{j=1}^{\tau_1}\sqrt{(\rho_o S_j)^2(3600V_j\cdot 0.067S_j^{0.846}\alpha_d)^2} \tag{1}$$

式中：ρ_i，ρ_o 分别是增厚覆冰量，增厚冻雨量；S_j，V_j，τ_1 表示降水强度的大小，风速的大小，以及冻雨的持续时间；α_d 为在不同的地理条件下冰层覆盖的修正因子。

$$\alpha_d=\begin{cases}1.0, & \text{平原}\\ 1.0\sim1.2, & \text{郊区}\\ 0.9\sim1.0, & \text{市区}\end{cases} \tag{2}$$

1.2 韧性保障目标的建立

本文提到的韧性主动提升策略属于抵御时期，这一阶段的内涵是指通过弹性资源，在灾难中配置电网，有能力对事件做出快速的应急反应，有效减少其冲击与干扰。围绕如下图 1 所示韧性指标构建体系，结合线路故障条数期望值、电力不足期望值、平均失电负荷比例三方面建立韧性增强目标。

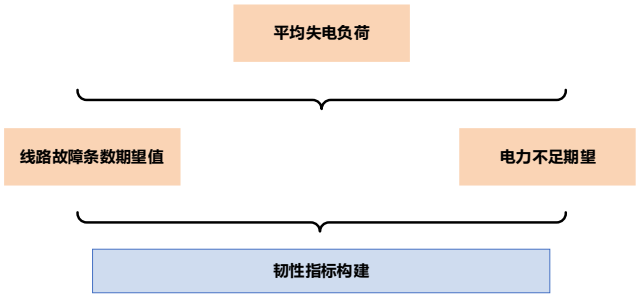


图 1 韧性指标构建

Fig.1 Resilience index construction

配电网覆冰线路 l 在第 T 个时段的覆冰厚度为 $H_l(T)$ 下的故障概率 $P[H_l(T)]$ 为：

$$P[H_l(T)] = p_0 + (1-p_0)\frac{H_l(T)}{H_{l,n}} \tag{3}$$

式中：p_0 为 l 的初始故障概率；$H_l(T)$，$H_{l,n}$ 分别为线路 l 的当前时刻覆冰厚度和最大允许覆冰厚度。

配电网线路负荷损失度 $S_{ev,l,T}$ 计算如下：

$$S_{ev,l,T} = \sum_{T\in T_m}\sum_{i\in l}\omega_{i,T}P_i \tag{4}$$

式中：T_m 为配电网融冰时间，ω_i，P_i 分别为节点 i 处负荷重要度的权重和出力。

配电网线路 l 的断线风险 C_{melt} 可量化为：

$$C_{melt} = P[H_l(T)]S_{ev,l,T} \tag{5}$$

融冰线路负荷损失度 $S_{ev,l,t}$ 计算如下：

$$S_{ev,l,t} = \sum_{t\in t_m}\sum_{i\in l}\omega_{i,t}P_i \tag{6}$$

式中：t_m 为直流融冰时停电时间。

综上，增韧目标 R 确定为：

$$R = \frac{1}{T}\sum_{T=1}^{N}P[H_l(T)]S_{ev,l,T} + S_{ev,l,t} \tag{7}$$

2 多手段韧性主动提升技术

本文提出的配电网韧性主动提升手段包括网络重构、FID 与 MESIMS 三种调控资源。

2.1 MESIMS增韧调控模型

MESIMS 是由移动式储能车经过融冰功能模块改造而成的设备。改造完成后，MESIMS 兼具线路融冰和保供电双重功能。其工作原理是通过向车辆安装换流器、移动电源和变压器等设备，实现线路融冰作业，其原理是基于直流融冰技术。通常认为，经过一定时间的 MESIMS 融冰处理后，覆冰厚度可降至零。流程涵盖了很多步骤，比如断电，融冰，复电。

线路覆冰厚度的变化可以公式（8）描述，基于 MESIMS 的线路融冰时，其具体数值受到覆冰程度、现场条件和环境因素的影响。另外，MESIMS 到达目标线路所需要的交通运行时间也需考虑。冰雪天气下 MESIMS 需要在交通道路上运行，为保证融冰作业的高效率，断路、拥堵、通行距离等因素都需要特别关注。

$$H_l(T) = \begin{cases} H_0 + \Delta HT - c_{melt}T', & t = 1 \\ H_{l,t-1} + \Delta HT - c_{melt}T', & t \neq 1 \end{cases} \tag{8}$$

式中：C_{melt} 为 MESIMS 的融冰速度，与设置的短路电流有关；T'为融冰持续时间。

2.2 基于FID及网络重构的潮流调控模型

FID 可通过转移功率以产生热量，从而达到融冰需求。在特定的融冰周期内，假定温度和风速等外部环境因素保持恒定，以热平衡方程为基础，对覆冰厚度的减少量直接融冰电流进行控制。配网线路呈辐射状分布，各分支线路在电流上存在一定的差异，因此配网线路的配网和配网线路选用最小电流包含 FID 分支线路作为线路的融冰电流 I，使融冰效果得到最大程度的保证。

$$I = \left[\frac{\Delta t}{r_0(r_{T0}+r_{T1})} + \frac{1}{r_{T0}T_r}\left(10_{g_0}db + \frac{0.045g_0D^2}{r_{T0}+r_{T1}}\left(r_{T1} + 0.22\frac{r_{T0}}{\lg\frac{D}{d}}\right)\Delta t\right)\right]^{\frac{1}{2}} \tag{9}$$

式中：r_0 为 0℃时导线的电阻；T_r 为融冰时间；Δt 为导体温度与外界气温之差；g_0 为冰的比重；b 为冰层厚度；D 为导体覆冰后的外径；r_{T0} 为等效冰层传导热阻；r_{T1} 为对流及辐射等效热阻[11]。[11]

为全面评估 FID 的容量限制及整体产热效能，充分利用其四象限运行特性，通过调节有功功率与无功功率，以实现产热效率的最大化。以融冰线路为例，FID 转移功率对产热值 Q_1 的影响可表

示为：

$$Q_1=\frac{S_1 r}{|Z|}=\sqrt{(P_0+P_{VSC})^2+(Q_0+Q_{VSC})^2}\frac{r}{|Z|} \quad (10)$$

式中：S_1为线路的视在功率；$|Z|$为线路阻抗的模值；P_0和Q_0分别为线路中原有的有功功率和无功功率。

类似地，某一融冰周期t启动后，在第T个时段内，线路l的覆冰厚度$H(T)$如下式：

$$H_l(T)=\begin{cases}H_0+\Delta HT-H_{\text{melt}}(I), & t=1\\ H_{l,t-1}+\Delta HT-H_{\text{melt}}(I), & t\neq 1\end{cases} \quad (11)$$

式中H_0为l的初始覆冰厚度；$H_{\text{melt}}(I)$为融冰电流函数。

FID调节过程中需满足自身运行约束

$$S_{ee,i,T}=\begin{cases}P_{VSC1}+P_{VSC2}+P_{SOP,loss}=0\\ P_{FID,loss}=A_{FID}\left(\sqrt{P_{VSC1}^2+Q_{VSC1}^2}+\sqrt{P_{VSC2}^2+Q_{VSC2}^2}\right)\\ \sqrt{P_{VSC}^2+Q_{VSC}^2}\le S_{VSC}\end{cases} \quad (12)$$

式中：A_{FID}为FID的损耗系数P_{VSC1}和P_{VSC2}分别为FID中换流器1和2的有功功率；Q_{VSC1}和Q_{VSC2}分别为FID中换流器1和2的无功功率。S_{VSC}为换流器的容量。

在进行融冰操作时，必须注意可能产生的风险，结合网络重构技术，不仅可以实现分支线路的融冰，还能有效减少配电网中的电压波动，从而提升电网的整体性能和供电质量。

在配电网重构过程中，采用虚拟潮流约束保证配电网的连通性和辐射性：

$$\begin{cases}f_{di}+\sum_{j\in C(i)}\alpha_{ij}f_{ij,t}=0\\ N_b=N_n-N_s\end{cases} \quad (13)$$

式中：f_{di}为节点i的虚拟负荷；$f_{ij,t}$为时段支路立处流过的虚拟流量；N_b为支路数；N_n为节点数；N_s为电源数。

综上，本文通过网络重构划分改变网络拓扑并基于FID灵活转供潮流实现增韧调度。

3 基于多手段协调的柔性互联配电网主动增韧调控策略

结合网络重构、FID与MESIMS三种调控资源的互补性，不仅能够提高融冰的效率，还能够降低因融冰操作而可能引起的潮流越限风险。在融冰决策实施过程中，电力调节与MESIMS相互影响。MESIMS的破冰会改变趋势分布。同时，动力调校也会因MESIMS的融冰路线而改变覆冰状态。因此，本文采用电力-交通协调增韧调度模型，如图2所示，这种调度方式实现了交通网络与配电网之间的双向耦合。通网络与配电网之间的双向耦合。

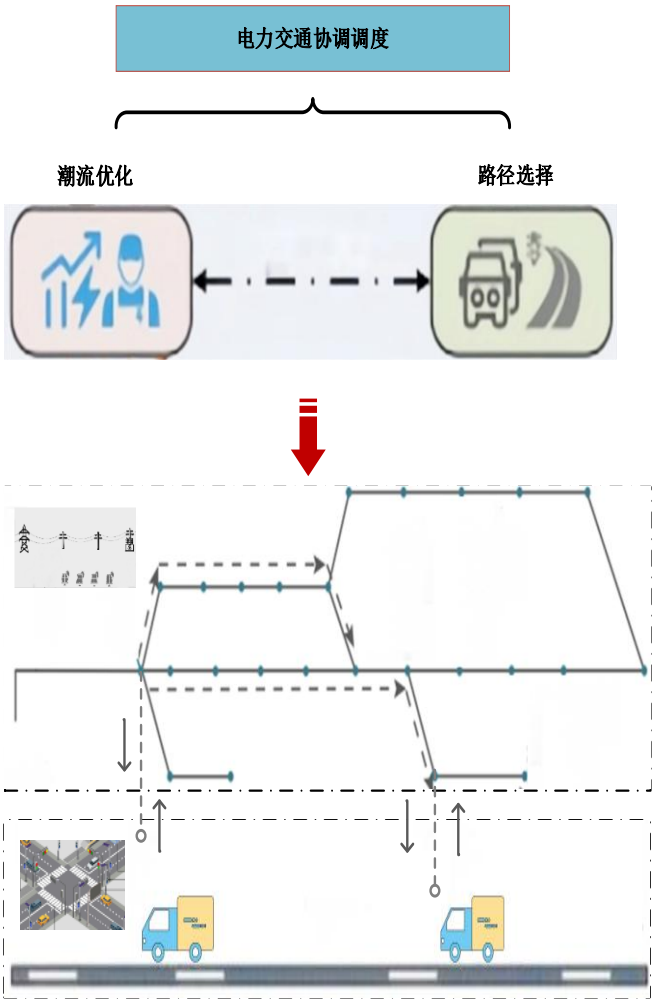


图2 电力-交通协调增韧调度框图

Fig.2 Block diagram of power-transportation coordination and toughness scheduling

3.1 交通路径模型

3.1.1 目标函数

最大限度地降低因覆冰导致的线路断线风险，优化 MESIMS 的位置及路线。

$$\mathrm{F}=C_{melt}=P\left[H_l(T)\right]S_{ev,l,T} \tag{14}$$

3.1.2 约束条件

1） 交通网约束

由于极端天气的影响，交通路况会呈现湿滑的情况，赶往目的地的时间 $T_{i,j,m}^{\mathrm{ME}}$ 为

$$\begin{cases} v_m^{\mathrm{ME}}=\dfrac{\mu g}{Q}\left[(3600-1.7Q)^2-\dfrac{2Q^2L_m}{\mu g}\right]^{0.5} \\ T_{i,j,m,0}^{\mathrm{ME}}=\dfrac{D_{i,j}}{v_m^{\mathrm{ME}}} \\ T_{i,j,m}^{\mathrm{ME}}=T_{i,j,m,0}^{\mathrm{ME}}\left[1+\alpha_{\mathrm{TP}}\left(\dfrac{Q}{C_{\mathrm{TP}}}\right)^{\xi}\right] \end{cases} \tag{15}$$

2） MESIMS 操作约束

当线路的覆冰厚度未超过融冰预警值 0.4 cm 时，不执行直流融冰操作，以避免因融冰操作导致线路供电中断。

$$H_{\mathrm{melt}}(I)=\begin{cases} H_{\mathrm{melt}}(I), & H_l(T)\geq 0.4\ \mathrm{cm} \\ 0, & H_l(T)<0.4\ \mathrm{cm} \end{cases} \tag{16}$$

3.2 潮流调度模型

3.2.1 目标函数

在融冰过程中，为了有效提高配电网络的产热效果，FID 需要大幅度提高电流。但在实际操作中，融冰过程本身的波动性和不确定性，以及负荷和分布式电源都有可能造成配网支路电流和节点电压超出安全限制的风险。这种越限风险不仅威胁电网的稳定运行，还可能引发安全事故。因此，在确保线路能够顺利完成融冰任务的前提下，如何有效降低线路潮流的越限风险，成为了保障电网安全稳定运行的关键问题。具体的目标函数表达式如下：

$$\begin{cases} \mathrm{f}=\min\left\{R+f_1\right\} \\ f_1=\sum_{i=1}^{N_{bus}}\sum_{j=1}^{T}\left|V_{ij}-\bar{V}_i\right| \end{cases} \tag{17}$$

3.2.2 约束条件

1) 潮流约束

$$\begin{cases} \sum_{k,i=1}^{N}\left(P_{ki,T}-r_{ki}I_{ki,T}^2\right)+P_{i,T}=\sum_{i,j=1}^{N}P_{ij,T} \\ \sum_{k,i=1}^{N}\left(Q_{ki,T}-x_{ki}I_{ki,T}^2\right)+Q_{i,T}=\sum_{i,j=1}^{N}Q_{ij,T} \end{cases} \tag{18}$$

$$U_{i,T}^2-U_{j,T}^2+\left(r_{ij}^2+x_{ij}^2\right)I_{ij,T}^2+2\left(r_{ij}P_{ij,T}+x_{ij}Q_{ij,T}\right)=0 \tag{19}$$

式中：$P_{ij,T}$、$Q_{ij,T}$ 和 $I_{ij,T}$ 分别为第 T 个时段从节点 i 流向节点 j 的有功功率、无功功率和电流；r_{ij}、x_{ij} 分别为节点 i 至节点 j 间的电阻和电抗。

2) 电压、电流运行约束

$$U_{i,\min}\leq U_{i,T}\leq U_{i,\max} \tag{20}$$

$$I_{l,T}\leq\begin{cases} I_{\mathrm{melt},l,T}, & R_{\mathrm{melt}}(I)>0 \\ I_{\max,l,T}, & R_{\mathrm{melt}}(I)=0 \end{cases} \tag{21}$$

3) 设备约束

该部分约束包括 FID、MESIMS 与 DG 的运行约束。

3.3 求解流程

电力-交通耦合系统复杂性高，不易直接求解。结合 Dijkstra 算法求出在交通网中的最短行驶路径。应用 KKT 互补松弛条件将其转化为单层模型，将单层非线性模型转化为混合整数线性模型。利用 CPLEX 求解。如图 3 所示的解题过程。

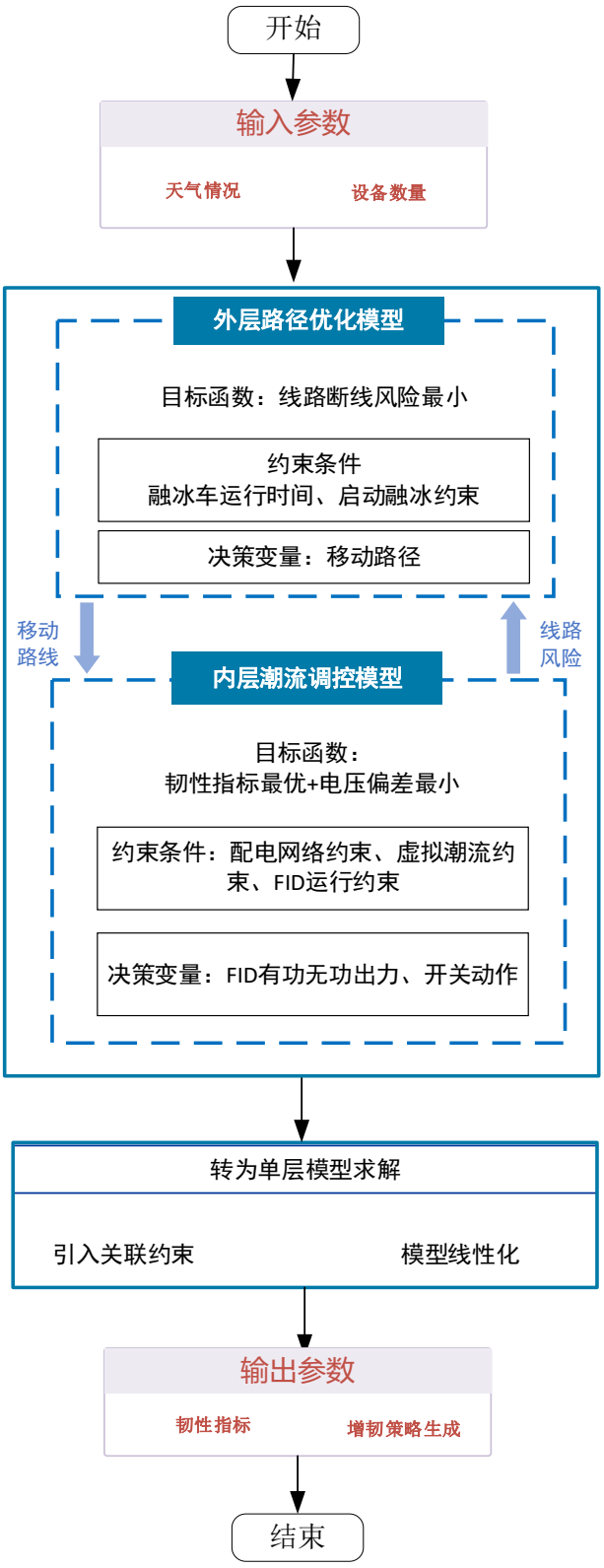


图 3 电力-交通协调增韧决策求解流程图

Fig.3 Flow chart of power and transportation coordination and toughness decision solving

4 算例分析

本研究基于改进的 IEEE 33 节点配电网络和 12 节点交通网络测试系统，如图 4 所示。改进后的 IEEE 33 节点配电网络中，FID1 和 FID2 分别取代了连接节点 12-22 和 18-33 的联络开关。光伏系统集成在节点 5、15、23 和 28，而风力发电装置安装在节点 14 和 29。其他详细参数请参考文献[19]。12 节点运输网络的参数基于文献[20]，相邻节点之间的道路距离设定为 3 km 或 6 km。

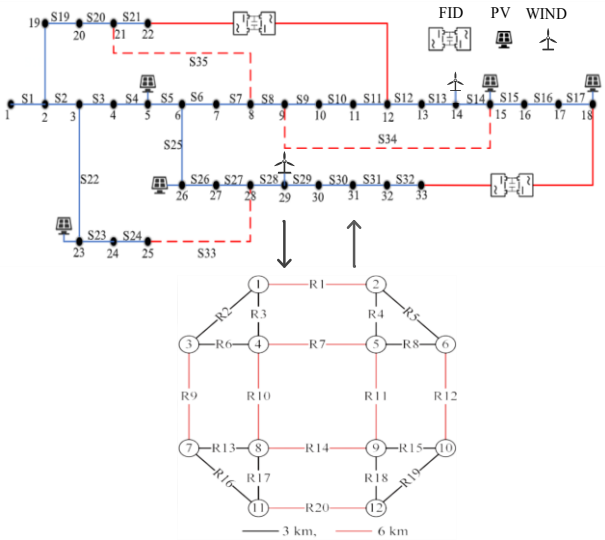
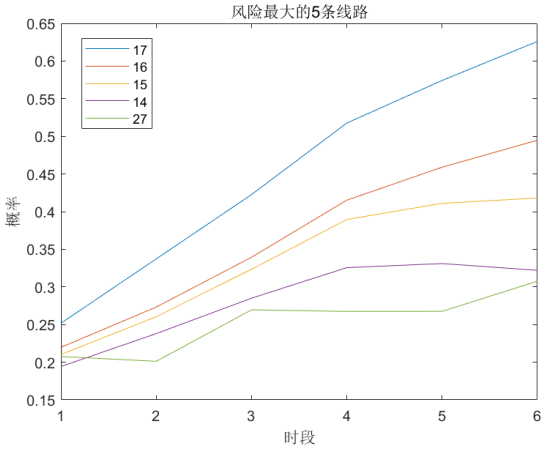


图 4 改进的 33 节点配电网络和 12 节点交通网络结构

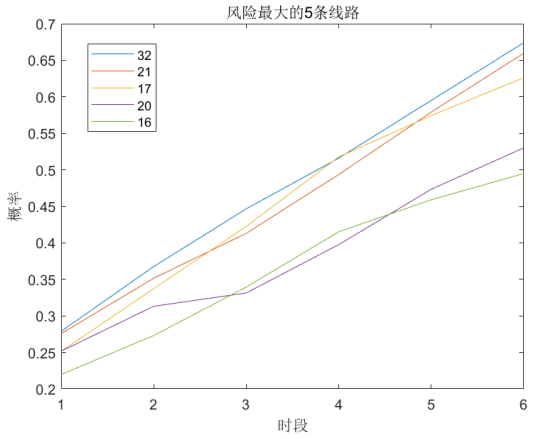
Fig.4 Structure of modified IEEE 33-bus distribution network and 12-bus transportation network.

考虑了不同时间段内的负荷波动和气象参数变化，假设同一时间段内的负荷和气象参数基本保持不变。过载条件下的冰融化时间通常为 2 到 4 小时。因此，整个周期被分为五个时段，每个时段持续 4 小时。为对比不同增韧手段对柔性互联配电网韧性的提升效果，设置了 4 组方案，具体如下：方案 1 为无主动增韧措施的基准方案；方案 2 为仅采用 MESIMS 的单一增韧方案；方案 3 为 FID 与网络重构协同增韧方案，不引入 MESIMS；方案 4 为本文提出的网络重构、FID 与 MESIMS 多手段协同增韧方案。

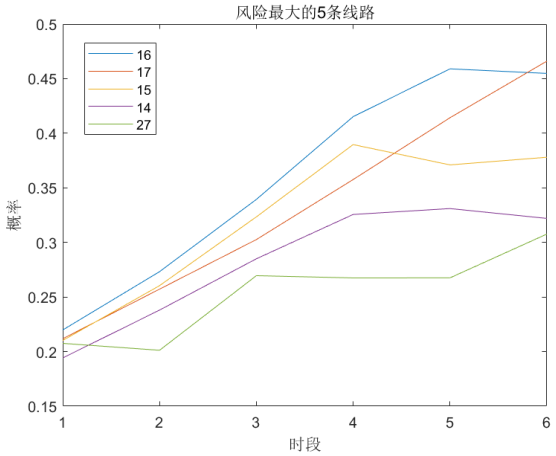
所提出的方案 4 的韧性增强效果与其他方案进行了比较。计算方案对应的负荷损失期望分别是 2088.82kWh、2711.32kWh、1651.48kWh、791.04 kWh。



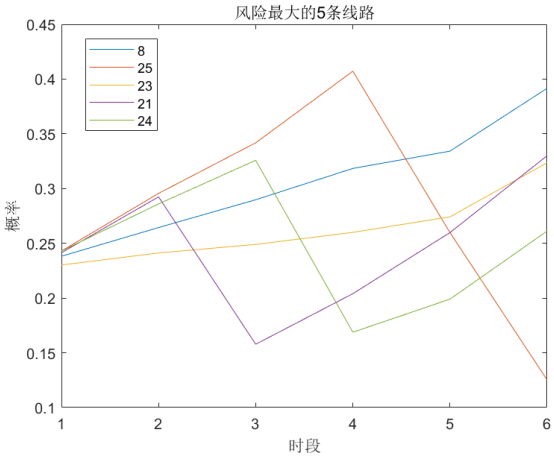
（a）方案 1 线路风险情况变化



（b）方案 2 线路风险情况变化



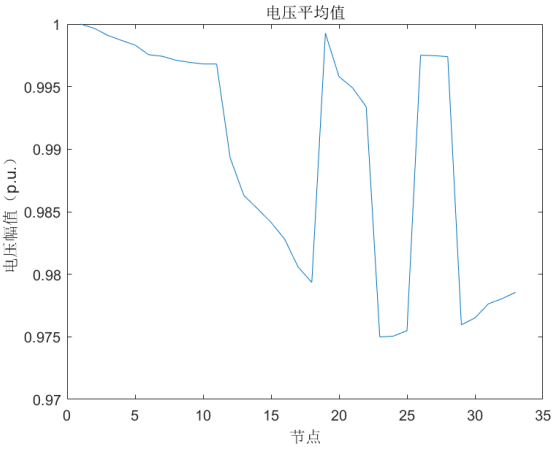
（c）方案 3 线路风险情况变化



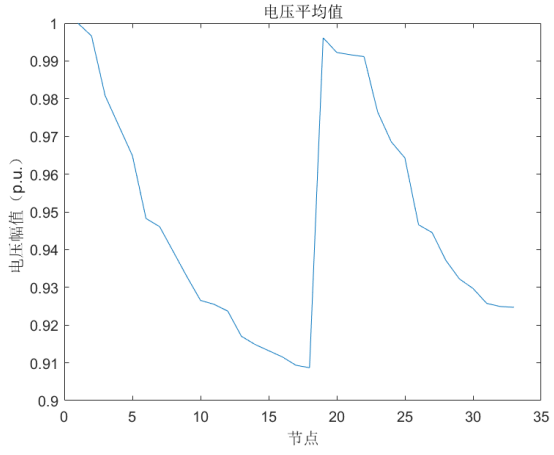
（d）方案 4 线路风险情况变化

图 4 不同方案线路风险情况变化

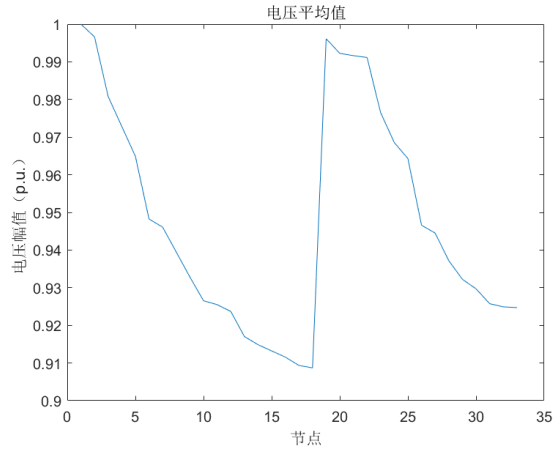
Fig.4 Line risk situation of different schemes changes



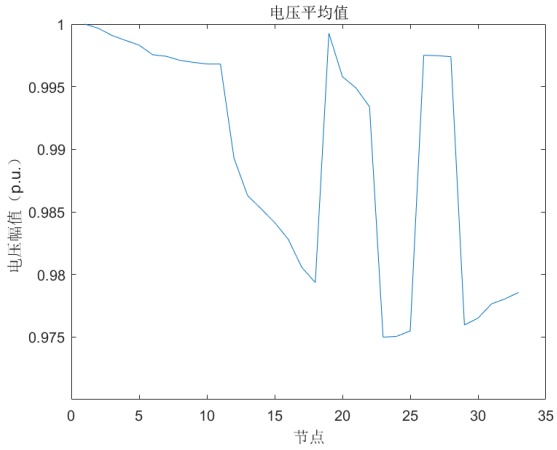
（a）方案 1 节点电压偏移情况



（b）方案 2 节点电压偏移情况



（c）方案 3 节点电压偏移情况



（d）方案 4 节点电压偏移情况

图 5 不同方案下节点电压偏移情况

Fig.5 Node voltage offset case of different schemes

图 4 和图 5 分别给出了风险最大的 5 条线路变化情况和不同方案节点电压偏移情况。分析得出如下：

1）MESIMS 作为一种移动式设备，可以在需要融冰的线路上实施停电融冰，这种方法虽然需要暂时中断供电，但可以确保融冰的有效性。对于含 MESIMS 增韧策略，负荷损失风险降低，但电压质量需要优化。

2）通过 FID 互联的配电线路可以在不中断供电的情况下进行融冰，保证了供电的连续性，但电压质量也需要优化。

3）结合网络重构技术，不仅可以实现分支线路的融冰，还能有效减少主动配电网中的电压波动，从而提升电网的整体性能和供电质量。

5 结论

综上，本文所提结合网络重构、柔性互联装置（FID）和移动储能融冰系统（MESIMS）的应用优势，提出一种考虑电力-交通耦合的多时段配电网韧性提升策略。

（1）与单一手段相比，多手段策略协调显著提高了配电网的韧性。整个期间，所有线路的断线风险概率都较低，断线风险降低超过 50%。

（2）所提增韧调度优化模型线路同时考虑断开风险和潮流违规问题，从而降低了总负荷损失风险，降低了约 24.7%，兼顾线路融冰效率与电网的安稳运行。

考虑到覆冰灾害时变性强、灾中大规模新能源出力大幅下降、用户负荷持续增加。后续研究可从涵盖灾前预防、灾中应对以及灾后恢复的全阶段及计及源-荷失配风险的韧性增强策略两方面展开。

参考文献

[1] 别朝红，林超凡，李更丰等. 能源转型下弹性电力系统的发展与展望[J]. 中国电机工程学报, 2020, 40(9): 2735-2745.
BIE Zhaohong, LIN Chaofan, LI Gengfeng, etc Development and prospect of elastic power system under energy transition [J]. Chinese Journal of Electrical Engineering, 2020, 40 (9): 2735-2745(in Chinese).

[2] 许寅，王颖，和敬涵，等. 多源协同的配电网多时段负荷恢复优化决策方法[J]. 电力系统自动化，2020，44(2)：123-131.
XU Yin, WANG Ying, and JING Han, et al. Optimization decision method for multi time load recovery in multi source collaborative distribution networks [J]. Power System Automation, 2020, 44 (2): 123-131(in Chinese).

[3] CAO Yan，MU Yunfei，JIA Hongjie，et al. A multi-objective stochastic optimization approach for planning a multi-energy microgrid considering unscheduled islanded operation[J]. IEEE Transactions on Sustainable Energy，2024，15(2)：1300-1314.

[4] 穆云飞，金尚婷，赵康宁，等. “人-车-桩-路-网”深度耦合下的配电网协同规划与运行优化[J]. 电力系统自动化，2024，48(7)：24-37.
MU Yunfei, JIN Shangting, ZHAO Kangning, et al. Collaborative planning and operation optimization of

distribution network under deep coupling of "human vehicle pile road network" [J]. Power System Automation, 2024, 48 (7): 24-37(in Chinese).

[5] HOU Kai，JIA Hiandong，YU Xongjie，et al．A reliability assessment approach for integrated transportation and electrical power systems incorporating electric vehicles[J]．IEEE Transactions on Smart Grid， 2018，9(1)：88-100．

[6] 张巍，罗浩．考虑电力–信息–交通网络耦合的配电网韧性提升策略分析[J]．电网技术，2024，48(1)：361-372．
ZHANG Wei, LUO Hao. Analysis of resilience enhancement strategies for distribution networks considering power information transportation network coupling [J]. Grid Technology, 2024, 48 (1): 361-372(in Chinese).

[7] Zhang H, Ma S, Ding T, Lin Y, Shahidehpour M. Multi-stage multi-zone defender-attacker-defender model for optimal resilience strategy with distribution line hardening and energy storage system deployment[J], IEEE Trans Smart Grid 2021;12(2):1194-205.

[8] Xiao Y, Zhu Y, Qu Y, et al. A market for power system resilience provision[J]. Appl Energy 2025;382:125335.

[9] JAFARISHIADEH F ， MOHAMMADI F ， SAHRAEIARDAKANI M. Preventive dispatch for transmission de-icing［J］. IEEE Transactions on Power Systems，2020，35（5）：4104-4107.

[10] 娄铖伟,张筱慧,丛鹏伟等.含柔性软开关的有源配电网故障恢复策略[J].电力系统自动化,2018.42(1):23-31.
LOU Chengwei, ZHANG Xiaohui, CONG Pengwei, etc Fault recovery strategy for active distribution networks with flexible soft switches [J]. Power System Automation, 2018.42 (1): 23-31(in Chinese).

[11] 张璐,李晨语,蔡永翔,等.考虑潮流越限风险的柔性交流配电网融冰优化策略[J].电力系统自动化,2022,46(16):160-169.
ZHANG Lu, LI Chenyu, CAI Yongxiang, etc Optimization strategy for melting ice in flexible AC distribution networks considering the risk of exceeding current limits [J]. Power System Automation, 2022, 46 (16): 160-169(in Chinese).

[12] 王成山，季节，冀浩然，等 ．配电系统智能软开关技术及应用［J］．电力系统自动化，2022，46（4）：1-14.
WANG Chengshan, JI Jie, JI Haoran, etc Intelligent soft switching technology and application in power distribution system [J] Power System Automation, 2022, 46 (4): 1-14(in Chinese).

[13] YUAN Yubo， ZHANG Chenyu， YUAN Xiaodong，et al. Energy management strategy and control method of hybrid distribution network based on soft open point［J］. Automation of Electric Power Systems，2021，45（8）：60-67.

[14] 班国邦，谈竹奎，郝正航，等 ．多能互补柔性互联配电网在线融冰方法［J］.南方电网技术，2019，13（9）：43-48.
BAN Guobang, TAN Zhukui, HAO Zhenghang, etc Multi energy complementary flexible interconnected distribution network online ice melting method [J] Southern Power Grid Technology, 2019, 13 (9): 43-48(in Chinese).

[15] 孙守晶，丛伟，邱吉福，等 ．含智能软开关的智能配电网分布式 供电恢复方法[J].电力系统自动化，2022，46（8）：79-85.
SUN Shoujing, CONG Wei, QIU Jifu, etc Distributed power supply restoration method for intelligent distribution network with intelligent soft switch [J] Power System Automation, 2022, 46 (8): 79-85(in Chinese)

[16] Sinha D, Bharadwaj S, Kumar V. A review paper on icing and methods to de-ice the transmission line［J］. Int. J. Eng. Res. Rev., 2015, 3(2): 5-9.

[17] Yan M, Ai X, Shahidehpour M, et al.Enhancing the transmission grid resilience in ice storms by optimal coordination of power system schedule with pre-positioning and routing of mobile DC de-icing devices［J］. IEEE Transactions on Power Systems, 2019, 34(4): 2663-2674.

[18] Zhang L, Li C, Wu M, et al. Optimal anti-icing and de-icing coordination scheme for resilience enhancement in distribution networks against ice storms［J］. IEEE Transactions on Smart Grid, 2024.

[19] LAVORATO M， FRANCO J F， RIDER M J， et al. Imposing radiality constraints in distribution system optimization problems［J］. IEEE Transactions on Power Systems，2012，27（1）：172-180.

[20] Li P, Ji H, Wang C, et al. Coordinated control method of voltage and reactive power for active distribution networks based on soft open point［J］. IEEE Transactions on Sustainable Energy, 2017, 8(4): 1430-1442.

[21] Xu Y, Wang Y, He J, et al. Resilience-oriented distribution system restoration considering mobile emergency resource dispatch in transportation system［J］. IEEE Access, 2019, 7: 73899-73912.

作者简介：

过亮（1982），男，硕士，高级工程师，研究方向为配电网、风电变流器控制及并网，gliangVIP@163.com

黄勇（1986），男，硕士，高级工程师，研究方向为配网电力电子及新能源并网控制装备，278897413@qq.com

林岚清（2001），女，硕士，研究方向为电机工程与应用电子技术，linlq23@mails.tsinghua.edu.cn

084 Wave-Velocity-Free Single-Phase Grounding Fault Location in Distribution Networks Using Modal Traveling Waves and Tower Distances

Zheng Yulin[1,2], Guo Moufa[1,2]*, Chen Fangxu[1,2], Zeng Xiankai[1,2] and Lin Jiahao[1,2]

[1] College of Electrical Engineering and Automation, Fuzhou University, Fuzhou 350108, China
[2] Fujian Province University Engineering Research Center of Smart Distribution Grid Equipment (Fuzhou University), Fuzhou 350108, China
gmf@fzu.edu.cn

Abstract. Accurate and rapid location of single-phase grounding faults in distribution networks is critical for enhancing power supply reliability. However, existing traveling-wave-based fault location methods face several challenges, including dependence on time synchronization, difficulties in identifying fault-induced reflected waves, and errors caused by wave velocity estimation and line length variations. To address these problems, an improved double-ended fault location method based on initial modal traveling waves and tower distances is proposed in this study. First, the time differences of local modal traveling waves are mathematically analyzed to derive a wave-velocity-free analytical expression for the fault distance proportion. Then, the wavefront calibration is optimized using particle swarm optimization (PSO)-enhanced variational mode decomposition (VMD) combined with a novel Teager energy operator (NTEO), ensuring both adaptability and precision. Finally, the effectiveness of the proposed method is validated through PSCAD/EMTDC simulations and experimental cases, demonstrating higher accuracy compared to traditional double-ended methods.

Keywords: Distribution networks, Single-phase grounding fault, Modal traveling wave, PSO-VMD.

1 Abstract

Distribution networks, positioned at the terminal end of power systems, experience frequent faults, with single-phase grounding faults accounting for over 80% of all cases [1]. To reduce the burden of manual line inspection and enable rapid fault recovery in distribution networks, the precise fault location of single-phase grounding faults has long been a key research focus. Current studies primarily adopt a progressive technical approach of “fault detection-feeder selection-section selection-fault location” [2-4]. With advancements in distribution network automation technologies, the precise location of fault sections has gradually become feasible [5]. In the fault lo-

cation stage, traveling-wave-based fault location methods stand out due to their high accuracy and independence from system operating conditions.

Traveling wave methods can be classified into two main categories based on principles: double-ended and single-ended methods. Double-ended methods offer higher accuracy but require microsecond-level time synchronization, posing strict requirements for the numerous terminals in distribution networks. Single-ended methods feature lower implementation costs and easier deployment, yet the complex wave propagation paths formed by multi-branch network structures make it difficult to accurately identify fault-induced reflected waves. To overcome these limitations in traditional methods, reference [6] proposed a single-ended location method based on modal wave velocity differences, which achieves fault location by only detecting the time difference between initial aerial- and zero-modal traveling waves, but suffers from significant errors due to severe attenuation of zero-modal wave velocity.

To address the challenge of accurately determining zero-modal wave velocity, recent studies have proposed methods such as adding measurement points [7] or detecting multiple reflected waves [8] to derive fault location formulas that eliminate the zero-modal wave velocity variable. However, these methods increase both the cost of measurement devices and the difficulty of identifying multiple reflected waves. References [9-11] have attempted to fit zero-modal wave velocity curves using characteristic quantities such as the wavefront Lee index, fault distance, and the arrival time difference of zero-modal traveling waves at both ends. Nevertheless, these methods require establishing models for different line types and operating conditions, leading to considerable workload and challenges in ensuring fitting accuracy.

Furthermore, line length varies with temperature, with studies reporting variations of up to 10% [12], which can introduce significant errors in fault location. To address this issue, reference [13] proposed a fault location method based on tower distance, employing time-frequency composite analysis through the natural frequency method. This method eliminates the need to calculate traveling wave velocity and remains unaffected by line length variations. However, in distribution networks, frequent wave reflections and refractions cause frequency aliasing, making it challenging to accurately extract the natural frequencies.

To address the aforementioned challenges, this paper proposes a novel fault location method based on tower distance and double-ended modal traveling wave time differences, which eliminates the need for double-ended time synchronization, reflection wave detection, and wave velocity estimation, while also being immune to variations in line length. First, by integrating the single-ended and double-ended modal wave velocity difference-based algorithms, the wave velocity variable is eliminated. Through mathematical computation of local modal time differences, an analytical expression for the fault proportion is derived, which is then converted into a tower-distance-based fault location method. Second, particle swarm optimization (PSO) is employed to adaptively optimize the parameters of variational mode decomposition (VMD), combined with the novel Teager energy operator (NTEO) to precisely calibrate the initial arrival times of modal traveling waves. Finally, comprehensive validation through PSCAD/EMTDC simulations and experimental cases demonstrate the effectiveness of the proposed method across various fault scenarios.

2 Fault location method

2.1 Tower location method

Without loss of generality, consider a distribution line of length L with a single-phase grounding fault occurring at point F, as shown in Fig. 1. In the figure, t_F represents the fault inception time, while t_{Am} and t_{Bm} denote the arrival times of the initial modal traveling waves at measurement points A and B, respectively. The variable v_m indicates the modal traveling wave velocity. The subscript m denotes the mode type, where m=1, 2 correspond to aerial modes and m=0 represents the zero mode.

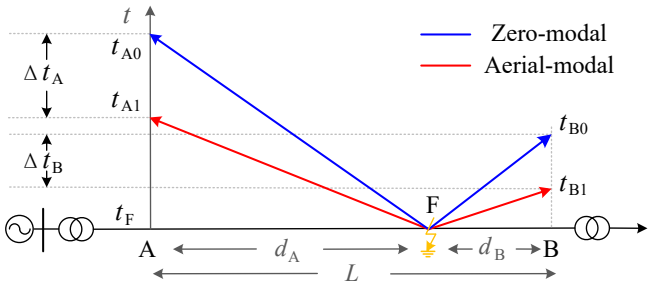


Fig. 1. Modal traveling waves

The distances from the fault point to terminals A and B are denoted by d_A and d_B, respectively. Their expressions are:

$$\begin{cases} d_A = v_1(t_{A1} - t_F) = v_0(t_{A0} - t_F) \\ d_B = v_1(t_{B1} - t_F) = v_0(t_{B0} - t_F) \end{cases} \tag{1}$$

By eliminating t_F, the single-ended fault location algorithm based on modal wave velocity difference can be derived:

$$\begin{cases} d_A = \dfrac{v_0 v_1}{\Delta v} \Delta t_A \\ d_B = \dfrac{v_0 v_1}{\Delta v} \Delta t_B \end{cases} \tag{2}$$

where $\Delta t_A = t_{A0} - t_{A1}$, $\Delta t_B = t_{B0} - t_{B1}$, $\Delta v = v_1 - v_0$. The distance difference Δd_{AB} between the fault point and the two terminals is:

$$\Delta d_{AB} = d_A - d_B = \frac{v_0 v_1}{\Delta v}(\Delta t_A - \Delta t_B) \tag{3}$$

Given that $d_A + d_B = L$, the double-ended fault location algorithm based on modal wave velocity difference is obtained:

$$\begin{cases} d_{\mathrm{A}} = \dfrac{L}{2} + \dfrac{v_0 v_1}{2\Delta v}(\Delta t_{\mathrm{A}} - \Delta t_{\mathrm{B}}) \\ d_{\mathrm{B}} = \dfrac{L}{2} - \dfrac{v_0 v_1}{2\Delta v}(\Delta t_{\mathrm{A}} - \Delta t_{\mathrm{B}}) \end{cases} \tag{4}$$

By combining equations (2) and (4), an improved double-ended fault location algorithm based on modal time difference is derived:

$$\begin{cases} d_{\mathrm{A}} = \dfrac{L(t_{\mathrm{A0}} - t_{\mathrm{A1}})}{t_{\mathrm{A0}} - t_{\mathrm{A1}} + t_{\mathrm{B0}} - t_{\mathrm{B1}}} = \dfrac{L\Delta t_{\mathrm{A}}}{\Delta t_{\mathrm{A}} + \Delta t_{\mathrm{B}}} \\ d_{\mathrm{B}} = \dfrac{L(t_{\mathrm{B0}} - t_{\mathrm{B1}})}{t_{\mathrm{A0}} - t_{\mathrm{A1}} + t_{\mathrm{B0}} - t_{\mathrm{B1}}} = \dfrac{L\Delta t_{\mathrm{B}}}{\Delta t_{\mathrm{A}} + \Delta t_{\mathrm{B}}} \end{cases} \tag{5}$$

Compared to single-ended and double-ended modal wave velocity difference-based algorithms, this algorithm eliminates the v_0 variable (which exhibits attenuation characteristics), avoids the need to estimate the zero-modal wave velocity, and does not require time synchronization between terminals.

Furthermore, to mitigate the impact of sag variations on fault location accuracy, the towers can be approximated as a set of parallel lines perpendicular to the ground with equal heights. The horizontal distance between towers and the corresponding line length maintain a proportional relationship. The percentage position of the fault point along the total line length approximately equals its percentage position relative to the total horizontal distance between towers [14].

Therefore, based on Equation (5), the fault location along the line can be converted into a proportional locating method based on tower distances. The fault distance proportion K can be expressed as:

$$K = \frac{d_{\mathrm{A}}}{L} = \frac{\Delta t_{\mathrm{A}}}{\Delta t_{\mathrm{A}} + \Delta t_{\mathrm{B}}} = \frac{d_{\mathrm{A}}^*}{L^*} \tag{6}$$

where d_{A}^* is the horizontal distance from the fault point to the measurement point, and L^* is the total horizontal distance between towers, as shown in Fig. 2. After fault occurrence, the fault proportion can be obtained by Equation (6). Combined with the distribution of tower locations along the line, the relative location of the fault point between towers can be precisely identified.

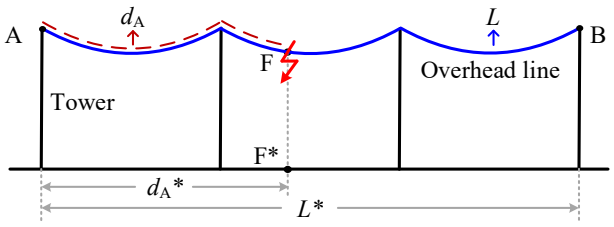


Fig. 2. Tower-distance-based fault location method

This method eliminates the need to measure the actual line length, which varies with temperature, and instead relies only on the fixed horizontal straight-line distance between towers to achieve fault location. As a result, the influence of line length fluctuations is removed, improving fault location accuracy.

2.2 Wavefront calibration method

As multi-frequency composite signals, traveling waves can effectively isolate high-frequency components through decomposition methods, significantly improving wavefront calibration accuracy. To address the challenge of manually presetting key VMD parameters (the penalty factor α and the number of modes k), PSO is introduced for adaptive parameter optimization. Through iterative global search, PSO identifies the optimal parameter combination that achieves the best signal decomposition performance, thereby eliminating reliance on empirical parameter settings.

To further improve the accuracy of wavefront identification, it is essential to select modal components that exhibit minimal noise interference and distinct mutation features. For this purpose, this study develops a fitness function based on fuzzy entropy and kurtosis. The fuzzy entropy metric evaluates signal regularity by constructing a phase space through the embedding dimension m. A smaller fuzzy entropy value $\mathrm{En}_{\mathrm{Fuzzy}}$ indicates stronger signal regularity, as defined by:

$$\mathrm{En}_{\mathrm{Fuzzy}}(s_k) = -\ln\left(\frac{\Phi^{m+1}(r)}{\Phi^{m}(r)}\right) \tag{7}$$

where s_k represents the k-th modal component, $\phi^m(r)$ denotes the average fuzzy similarity, and r is the similarity tolerance.

Kurtosis serves as a key indicator for quantifying the steepness and peak characteristics of signal distributions. An increasing kurtosis value f_i corresponds to a sharper signal distribution profile, as given by:

$$q_k = \frac{E(s_k - \mu)^4}{\sigma^4} \tag{8}$$

where E represents the mathematical expectation, μ is the mean of the modal component, and σ denotes its standard deviation. For Gaussian signals, the expected kurtosis is around 3. To ensure the VMD results simultaneously achieve low entropy values and high kurtosis values, the fitness function is:

$$f_i = \min_k \frac{\mathrm{En}_{\mathrm{Fuzzy}}(s_k)}{|q_k - 3|} \tag{9}$$

The PSO algorithm [15] is employed to iteratively search for the optimal combination of parameters α and k that minimizes the fitness function f_i. With these optimized parameters, VMD is performed on the traveling wave signals [16]. The core principle of VMD is to minimize the sum of the estimated bandwidths of all intrinsic mode function (IMF) components, subject to the constraint that their sum reconstructs the original signal.

To overcome the computational inefficiency and noise sensitivity limitations of traditional signal processing methods, this study employs the NTEO, which introduces a configurable resolution parameter i that determines the sampling interval for energy calculation, where signal energy is derived from three data points separated by i sampling intervals, significantly improving both transient feature extraction accuracy and interference resistance. The NTEO is expressed as:

$$\psi\lfloor s(n)\rfloor = s^2(n) - s(n+i)s(n-i) \tag{10}$$

where $\Psi[s(n)]$ represents the energy operator and $s(n)$ denotes the signal under analysis. Since the first IMF component (IMF1) obtained through VMD exhibits the most distinct mutation characteristics, the traveling wave arrival time is identified as the first peak in the energy spectrum of IMF1.

2.3 Fault location procedure

The key steps of the proposed method are illustrated in Fig. 3, with the specific procedure as follows:

(1) Signal acquisition: Three-phase voltage traveling waves are captured at both terminals, which are then converted into zero-modal and aerial-modal waves using Karenbauer phase-mode transformation.

(2) Wavefront identification: The PSO-optimized VMD combined with NTEO processing is applied to both aerial-modal and zero-modal traveling waves respectively to calibrate the initial wavefront arrival.

(3) Fault location: The modal time differences at both ends are substituted into Equation (6) to calculate the fault proportion, which is then combined with tower distances for precise fault location.

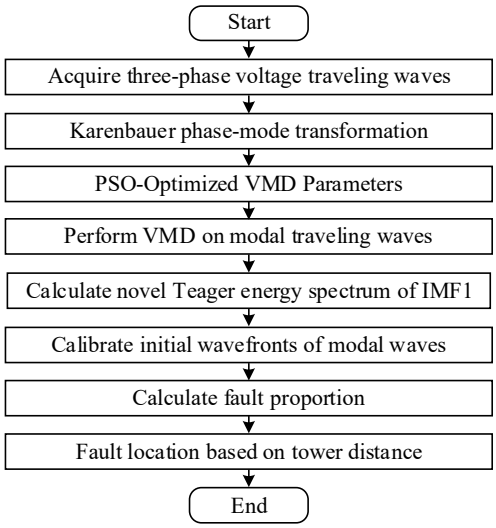


Fig. 3. Flowchart of the proposed method

3 Case studies

A 10 kV distribution network, modeled in PSCAD/EMTDC, is shown in Fig. 4. The main transformer adopts a Yg/D11 connection with a voltage ratio of 110 kV/10.5 kV, and the line terminal load is modeled as constant power. The overhead line uses LGJ-120 conductors with frequency-dependent parameters, having an impedance of Z=0.263+j0.348 Ω/km. The three-phase line inductance and capacitance parameters at 50 Hz are provided in Table 1. Traveling wave measurement devices with a sampling frequency of 10 MHz are installed at the head-end busbar of the distribution network and the terminals of all branch lines.

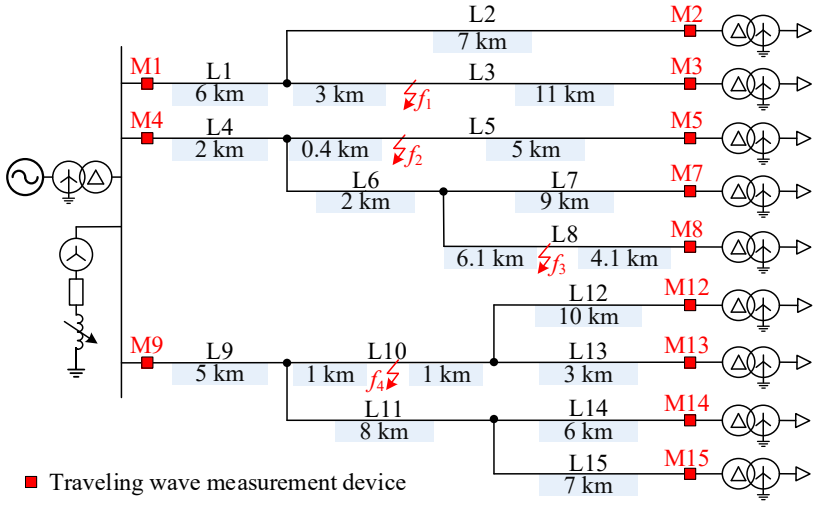


Fig. 4. Structure chart of the distribution network

Table 1. Line parameter

Phase sequence	Capacitance (10^{-6} μF/km)	Inductance (10^{-3} mH/km)
Positive	10.678	1.058
Zero	2.871	5.018

When a single-phase grounding fault occurs, the fault section is first determined [5]. Subsequently, the traveling wave measurement devices adjacent to the fault point are then selected to extract the fault voltage traveling waves. For quantitative assessment of the method's performance, the fault proportion error Δk is defined as:

$$\Delta k = \left| K - K_{\mathrm{R}} \right| \times 100\% \tag{11}$$

where K and K_{R} represent the measured fault location proportion and the actual fault location proportion, respectively.

3.1 Performance assessment

In the simulation system shown in Fig. 4, a single-phase grounding fault occurs at point f_1, located at 45% of the line length from the power supply side, with a 10 Ω fault resistance and 10° fault inception angle. After fault occurrence, the faulted section is identified as Line 1. The three-phase voltage traveling waves captured by measurement devices M1 and M2 are then decoupled using Karenbauer phase-mode transformation, yielding modal traveling waves at both the supply side and load side within 100 μs post-fault, as presented in Fig. 5.

Table 2. PSO optimization ranges and results

	Optimization range	Supply-side aerial mode	Supply-side zero mode	Load-side aerial mode	Load-side aerial mode
Penalty factor (α)	80~2500	80	2295	100	1000
Decomposition level (k)	3~5	5	5	3	4

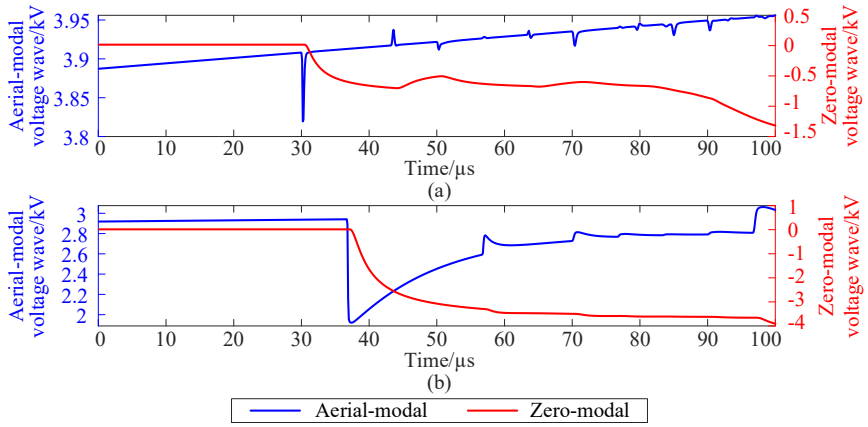


Fig. 5. Modal traveling waves: (a) supply-side; (b)load-side

The aerial- and zero-modal traveling waves are processed separately using PSO-optimized VMD, with the PSO search ranges and optimization results presented in Table 2. The IMF1 components obtained from decomposition are then analyzed through NTEO, and the wavefront calibration results are shown in Fig. 6 (only shows the 50 μs window surrounding the initial wavefront). The time differences between modal wave arrivals are measured as 0.5 μs at the supply side and 0.6 μs at the load side. Substituting these values into Equation (6) produces a calculated fault location proportion K=45.45%, corresponding to a proportion error Δk=0.45%.

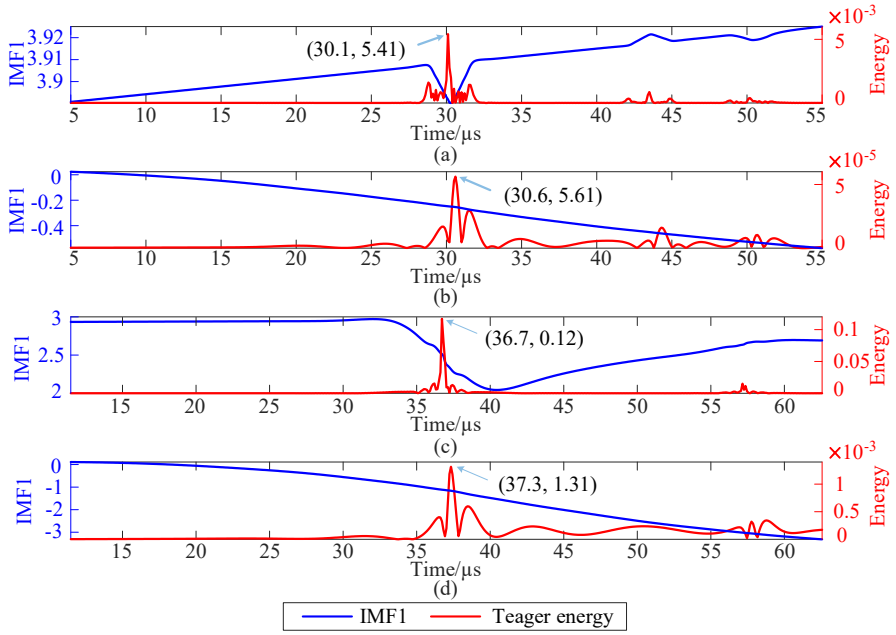


Fig. 6. IMF1 components and Teager energy values: (a) Supply-side aerial mode; (b) Supply-side zero mode; (c) Load-side aerial mode; (d) Load-side zero mode

3.2 Adaptability Verification

To verify the effectiveness of the proposed method for arcing ground faults, the classical Emanuel arc model is adopted to simulate the fault resistance in high-impedance arcing faults. As illustrated in Fig. 7, this model consists of two diodes (D_p, D_n), two voltage sources (V_p, V_n), and two resistors (R_p, R_n). For parameter settings, V_p is randomly varied within 1.3~2.3 kV, while V_n is set to fluctuate between 0.4~1.2 kV. The resistances R_p and R_n are assigned random values ranging from 700~1000 Ω and 300~600 Ω, respectively.

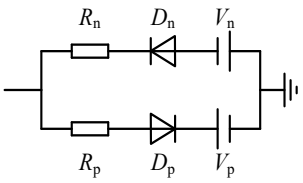


Fig. 7 Emanuel arc model

A single-phase arcing ground fault is simulated at location f_1 with an initial fault inception angle of 10°. The resulting modal traveling waves, shown in Fig. 8, exhibit significant oscillations characteristic of arcing faults. After processing with the PSO-VMD-NTEO algorithm for wavefront calibration, the results presented in Fig. 9

demonstrate consistent performance with the non-arcing ground fault scenario shown in Fig. 6. This confirms the applicability of the proposed method to arcing ground faults.

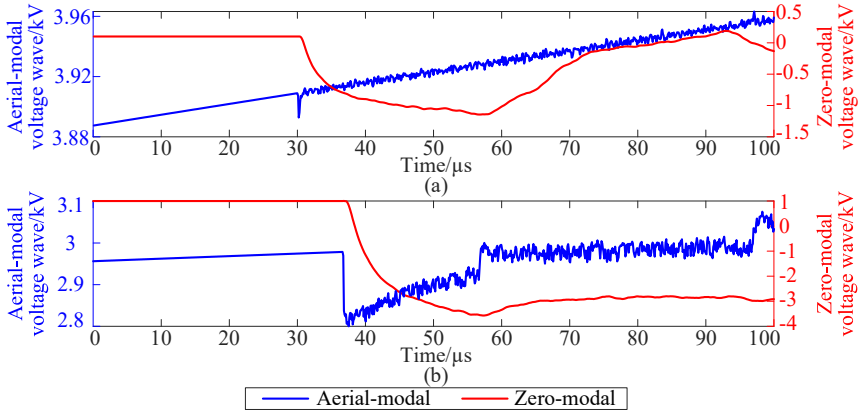


Fig. 8. Modal traveling waves: (a) supply-side; (b)load-side

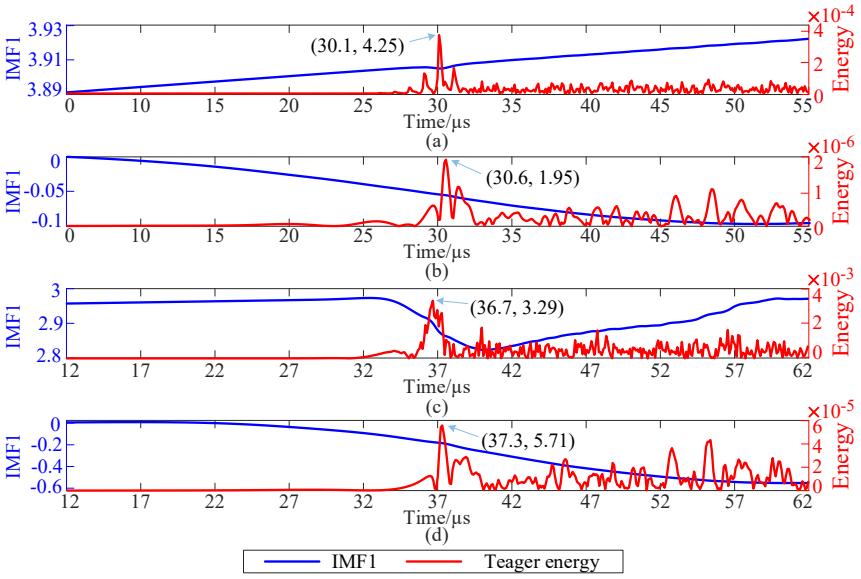


Fig. 9. IMF1 components and Teager energy values: (a) Supply-side aerial mode; (b) Supply-side zero mode; (c) Load-side aerial mode; (d) Load-side zero mode

To further validate the applicability of the proposed method, the fault location results under varying fault resistances, inception angles, and faulted phases are shown in Table 3. The results demonstrate that neither fault resistances nor faulted phase affect the fault location accuracy. Furthermore, the proposed method maintains the fault

proportion error below 1% (corresponding to an absolute error <100 m) across all fault locations.

Table 3. Fault location results under different scenarios

Fault point	Actual proportion (K_R)/%	Fault resistance/Ω	Fault inception angle/(°)	Faulted phase	Fault proportion (K)/%	Fault proportion error (Δk)/%
		10	15	A	33.33	0.90
f_2	32.43	100	45	B	33.33	0.90
		1000	90	C	33.33	0.90
		100	15	A	71.43	0.30
f_3	71.13	1000	45	B	71.43	0.30
		10	90	C	71.43	0.30
		1000	15	A	60.00	0
f_4	60.00	10	45	B	60.00	0
		100	90	C	60.00	0

3.3 Comparative Analysis

A comparative analysis is performed between the proposed method, the traditional double-ended method (Method 1) and the modal wave velocity difference-based double-ended method (Method 2). The fault location proportion calculations for Methods 1 and 2 are given by Equations (12) and (13) respectively.

$$K = [\frac{1}{2} + \frac{v_1(t_{B1} - t_{A1})}{2L}] \times 100\% \tag{12}$$

$$K = [\frac{1}{2} + \frac{v_0 v_1}{2L\Delta v}(\Delta t_A - \Delta t_B)] \times 100\% \tag{13}$$

The modal wave velocities are derived from the line parameters listed in Table 1, yielding calculated values of v_1=2.975×10^8 m/s and v_0=2.635×10^8 m/s. In the simulation system shown in Fig. 4, the PSO-VMD-NTEO algorithm is employed to calibrate wavefronts for faults occurring at locations f_1~f_4. The fault location accuracy of Method 1, Method 2, and the proposed method is evaluated under both fixed line length conditions and scenarios with maximum sag variation (up to 10% of the total line length [12]). The resulting fault location errors are summarized in Table 4.

Under conditions neglecting sag variation, the traditional double-ended method (without synchronization error) demonstrates the highest accuracy. However, according to the electric power industry standard DL/T 357-2019 “Technical Specifications for Traveling Wave Fault Location Devices on Transmission Lines,” when utilizing the device’s built-in time synchronization function, the error relative to the standard time system must remain below 1 μs. In engineering applications, an error of ±1 μs

can introduce absolute errors of approximately ±300 m. Under such conditions, as shown in Table 4, the double-ended method exhibits proportion errors of 1.52%, 4.13%, 2.18%, and 3.03% respectively, significantly higher than those of the proposed method.

Table 4. Comparison of different fault location method

Fault point	Fault location method	Fault proportion error (Δk)/%	
		Fixed line length	Variable line length (10% variation)
	Method 1 (without synchronization error)	0.02	0.06
f_1	Method 2	4.42	4.86
	Proposed method	0.45	0.45
	Method 1 (without synchronization error)	0.08	0.12
f_2	Method 2	>10	>10
	Proposed method	0.90	0.90
	Method 1 (without synchronization error)	0.07	0.11
f_3	Method 2	>10	>10
	Proposed method	0.30	0.30
	Method 1 (without synchronization error)	0.03	0.07
f_4	Method 2	8.84	9.77
	Proposed method	0	0

Furthermore, the modal wave velocity difference-based double-ended method exhibits the most significant errors due to its reliance on zero-modal wave velocity, which suffers severe attenuation. When considering sag variations, both traditional methods show progressively deteriorating performance. By contrast, the proposed method maintains superior accuracy, as it unaffected by time synchronization errors, wave velocity inaccuracies, or sag variation impacts.

4 Experimental verification

To validate the practicality of the proposed method, verification tests are conducted using the experimental system. The distribution cabinet, measurement devices and lines are shown in Fig. 10. The line-to-line voltage of the system is 380 V, and the lines are connected to the feeder cabinet and a controllable fault generator to establish a dynamic experimental platform for traveling-wave-based fault location.

As illustrated in Fig. 10(b), voltage signals are captured at both ends using differential probes with a 100:1 ratio, while oscilloscopes are used to monitor phase voltage variations. The length of the connected cable is measured as 1.3 km.

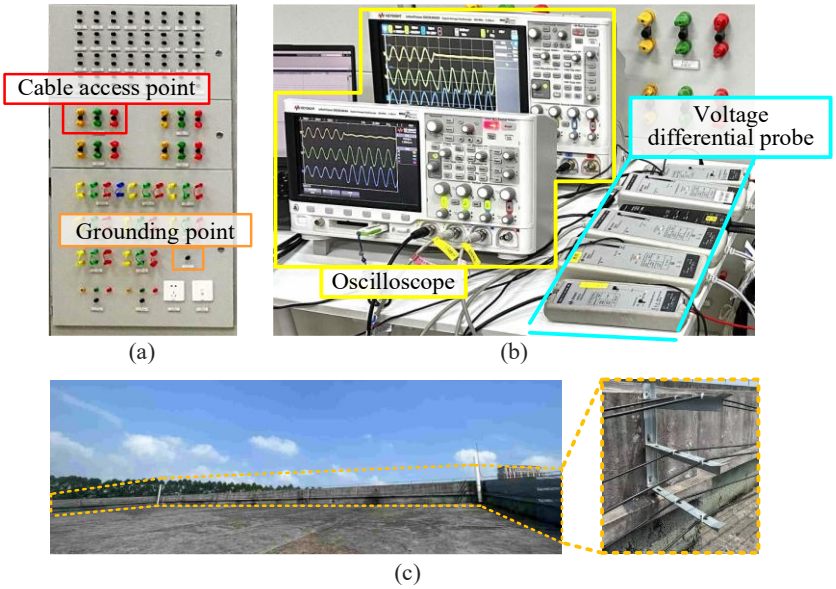


Fig. 10. Experimental system: (a) feeder cabinet; (b) measurement device; (c) line

An A-phase-to-ground fault with a fault resistance of 10 Ω is applied at 61.54% of the line length from the supply side. Edge-triggered fault recording captures 100-ms waveforms at a sampling frequency of 10 MHz. Using the 500-μs pre-wavefront period as baseline, a subsequent 1-ms segment of the three-phase voltage waveforms is extracted, as shown in Fig. 11.

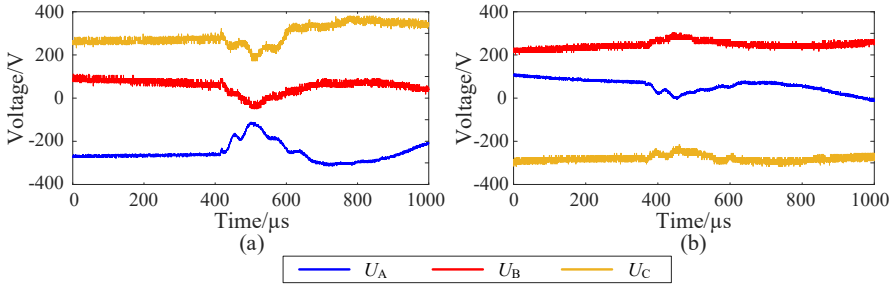


Fig. 11. Three phase voltage traveling waves: (a) supply-side; (b) load-side

The voltage waveforms shown in Fig. 11 contain significant white noise interference and noticeable impulse noise near the wavefront onset, which poses a challenge for accurate wavefront calibration. To address this, multiple moving-average filtering [17] (with a window size of 10 ms and applied twice) is used to reduce white noise, while median filtering (with a window length of 70 ms) is applied to suppress impulse noise. The resulting denoised modal waves are shown in Fig. 12.

14

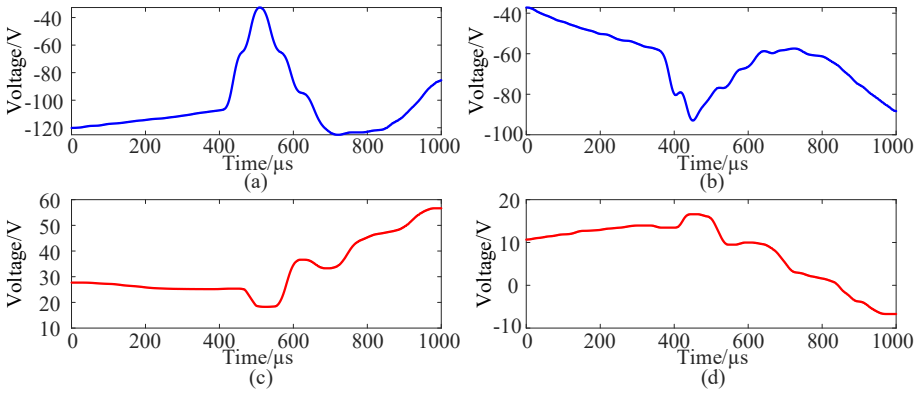


Fig. 12 Denoised modal traveling waves: (a) Supply-side aerial mode; (b) Load-side aerial mode; (c) Supply-side zero mode; (d) Load-side zero mode

The aerial- and zero-modal traveling waves are processed using the PSO-VMD-NTEO algorithm. The resulting IMF1 components show Teager energy spectra that provide precise wavefront calibration, as shown in Fig. 13. The measured arrival time differences between aerial- and zero-modal waves are 37.3 μs on the supply side and 21.6 μs on the load side, resulting in a calculated fault location proportion of 63.33%, with a proportion error of 1.79%. The results confirm the method's accuracy under strong noise interference.

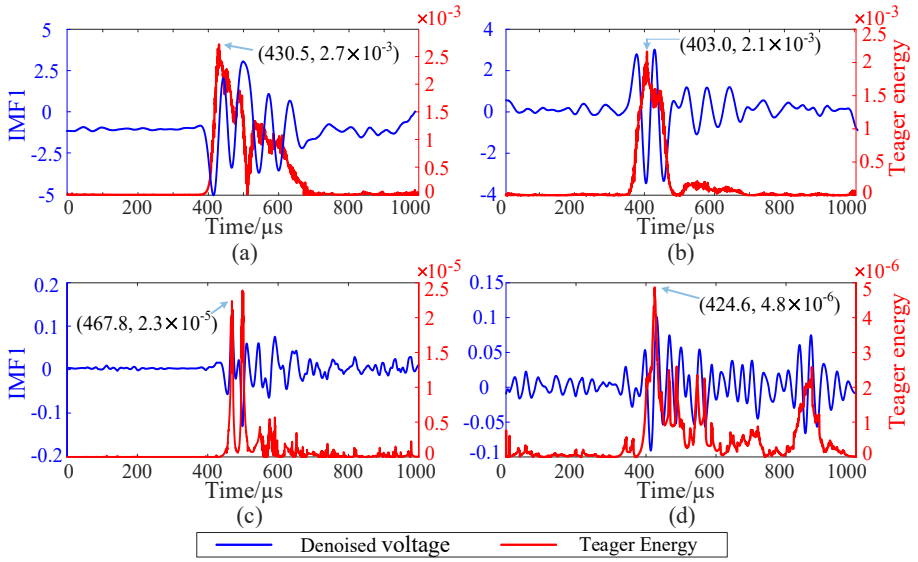


Fig. 13. IMF1 components and Teager energy values: (a) Supply-side aerial mode; (b) Load-side aerial mode; (c) Supply-side zero mode; (d) Load-side zero mode

5 Conclusion

This paper proposes a tower-distance-based fault location method utilizing modal traveling wave time differences, which effectively eliminates the influences of time synchronization, wave velocity selection, and line length variations. The principal conclusions are as follows:

(1) Through mathematical derivation, the wave velocity variable is eliminated, establishing an analytical fault location proportion formula requiring only modal traveling wave time differences. The tower-distance-based location method removes line length dependencies while avoiding the time synchronization requirements and reflected wave identification challenges inherent in traditional methods.

(2) PSCAD/EMTDC simulation results under various fault scenarios demonstrate that the proposed method achieves rapid and reliable single-phase grounding fault location in distribution networks, with performance remaining robust against arcing ground faults, fault resistance, and fault inception angle. Experimental tests further verify that the method maintains high accuracy under strong noise conditions, achieving a location error of only 1.79%.

(3) Comparative analysis across multiple fault scenarios shows the proposed method's superior accuracy over both traditional double-ended method and modal velocity difference-based double-ended method. By completely eliminating synchronization dependencies while overcoming wave velocity inaccuracies and line length variations, the method demonstrates significant precision advantages.

Acknowledgement: This work is supported by National Natural Science Foundation of China in 51677030 and the Natural Science Foundation of Fujian Province, China in 2023J05106.

References

1. Gholami M, Abbaspour A, Moeini-Aghtaie M, et al. Detecting the Location of Short-Circuit Faults in Active Distribution Network Using PMU-Based State Estimation[J]. IEEE Transactiions on Smart Grid, 2020,11(2):1396-1406.
2. Tong N, Zeng X J, Sun K Q, et al. A Fast Protection Relay for MMC-Based DC Grids Robust to Cyber-Physical Anomalies[J]. IEEE Transactions on Smart Grid, 2023,14(4):3085-3101.
3. Lin J H, Guo M F, Hong Q T, et al. An earth fault diagnosis method based on online dynamically calculated thresholds for resonant ground systems[J]. IEEE Transactions on Smart Grid, 2024, 15(4): 3459-3473.
4. Wu Y Q, Li Z T, Lin X N, et al. A novel single-ended transient-based boundary protection scheme for 35 kV active distribution networks based on capacitive voltage transformers[J]. IEEE Transactions on Smart Grid, 2024, 15(5): 4492-4510.
5. Gao J H, Guo M F, Lin S Y, et al. Advancing high impedance fault localization via adaptive transient process calibration and multiscale correlation analysis in active distribution networks[J]. Measurement, 2024,229.

6. Mardiana R, Al Motairy H, Su C Q. Ground Fault Location on a Transmission Line Using High-Frequency Transient Voltages[J]. IEEE Transactions on Power Delivery, 2011,26(2):1298-1299.
7. Ding J L, Wang X, Zheng Y H, et al. Distributed Traveling-Wave-Based Fault-Location Algorithm Embedded in Multiterminal Transmission Lines[J]. IEEE Transactions on Power Delivery, 2018,33(6):3045-3054.
8. Xie L W, Li Y, Luo L F, et al. Fault Location Method for Multi-branch Lines Based on Extreme-point Symmetric Mode Decomposition[J]. Proceedings of the Chinese Society of Electrical Engineering, 2021,41(21):7326-7338.
9. Zhang F, Pan Z C, Zhang H F, et al. New Algorithm Based on Traveling Wave for Location of Single Phase to Ground Fault in Tree Type Distribution Network[J]. Proceedings of the Chinese Society of Electrical Engineering, 2007,27(28):46-52.
10. Zhang Y N, Xu M, Liu Y H, et al. A Novel Travelling Wave Fault Location Algorithm for HVDC Transmission Lines Considering Variation Characteristics of Wave Speed[J]. Power System Technology, 2011,35(7):227-232.
11. Wang W, Wang Q J, Yin L, et al. Two-terminal fault location method for high-voltage transmission line based on zero-mode traveling wave velocity quantization[J]. Electric Power Automation Equipment, 2022, 42(12):165-170.
12. Liang J, Ma C H, Yun Z H. A fault location algorithm for high voltage overhead power transmission line based on line parameter estimation[J]. Power System Technology, 2004, 28(4): 60-63, 68.
13. Li X, Huang R H, Yao S J, et al. A novel fault location method by tower based on traveling wave time-frequency analysis[J]. Power System Protection and Control, 2015, 43(20): 130-136.
14. Lin S, Mei J H, Chen S, et al. Fault Detection and Faulty Phase Determination of Transmission Lines Based on Time-Frequency Characteristics of Transient Travelling Waves[J]. Power System Technology, 2012, 36(7): 48-53.
15. Shami T M, El-Saleh A A, Alswaitti M, et al. Particle Swarm Optimization: A Comprehensive Survey[J]. IEEE Access, 2022,10:10031-10061.
16. Yu D C, Zhou N C, Liao J Q, et al. Modified VMD Algorithm-Based Fault Location Method for Overhead-Cable Hybrid Transmission Line in MTDC System[J]. IEEE Transactions on Instrumentation and Measurement, 2024,73.
17. Robles E, Ceballos S, Pou J, et al. Variable-Frequency Grid-Sequence Detector Based on a Quasi-Ideal Low-Pass Filter Stage and a Phase-Locked Loop[J]. IEEE Transactions on Power Electronics, 2010,25(10):2552-2563.

085 A Day-Ahead Optimization Control Method Considering the Ramping Capability of Energy Storage Systems

Zhiwei Wan[1], Kai Yuan[1], Chongbo Sun[1], Yudi Ding[1], Ming Nie[1] and Yang Zhao[1]

[1] State Grid Economic and Technological Research Institute Co. Ltd, Beijing, China
376347704@qq.com

Abstract. Conventional day-ahead scheduling methods often overlook the impact of renewable generation uncertainty on system ramping capability and lack effective economic incentives for flexibility resources such as energy storage. This study proposes a coordinated optimization scheduling approach for multiple categories of flexibility resources that explicitly accounts for the ramping capability of energy storage systems. A refined mathematical model is developed to characterize the ramping characteristics of storage devices, incorporating state-of-charge (SOC) constraints, charging/discharging power limits, and cycling degradation costs. A coordinated scheduling framework is constructed, integrating storage, demand response, virtual power plants, gas-fired units, coal-fired units, and interconnection support. A case study based on the power grid in northern Shaanxi demonstrates that the proposed method significantly enhances system ramping adequacy.

Keywords: Flexibility Resources, Energy Storage Systems, Ramping Capability, Coordinated Scheduling, Day-ahead Optimization.

1 Introduction

With the profound transformation of China's energy structure and the continuous advancement of the "dual-carbon" targets, the development of a new power system dominated by a high share of renewable energy has become an inevitable trend[1]. In 2022, China added 125 GW of new wind and solar capacity, bringing the total installed renewable capacity to over 1.2 TW, accounting for about half of the nation's total generation capacity[2]. However, the inherent intermittency, variability, and uncertainty of renewable energy pose unprecedented challenges to power system operation. Net load curves increasingly exhibit "duck curve" and even "valley" shapes, with widening peak–valley differences, thereby placing higher demands on system flexibility[3]. During the 14th Five-Year Plan period, the peak–valley load gap is expected to increase annually. The current generation mix and adjustment speed of existing flexibility resources are insufficient to accommodate the high penetration of renewables, highlighting the urgent need to establish a diversified flexibility resource portfolio to ensure supply–demand balance[4].

Energy storage, as a crucial component of the new power system, offers unique advantages in enhancing system ramping capability. Compared with the typical ramp-

ing rate of 1–2%/min for conventional coal-fired units, storage systems provide response times ranging from seconds to milliseconds, with fast bidirectional regulation capability[5]. They can effectively mitigate the rapid fluctuations of renewable generation. Acting both as a source and as a load, storage systems exhibit wider adjustment ranges under the same rated power, along with superior start–stop capability, thereby supplying valuable flexibility to the system. With rapid technological progress and continuous cost reduction, the role of energy storage in improving system flexibility has become increasingly prominent, positioning it as a key enabler for renewable energy integration and the secure and stable operation of power systems[6].

Nonetheless, existing day-ahead optimization methods face significant limitations under high renewable penetration[7]. Traditional scheduling models mainly rely on load forecasts for unit commitment optimization, often neglecting the impact of renewable generation uncertainty on ramping adequacy[8]. This may lead to "tight-fit" clearing results that barely meet the forecasted demand. In current spot markets, clearing is performed based only on forecasted net load variations, without reserving sufficient ramping margins to accommodate forecast errors in subsequent intervals. When large deviations occur, the system lacks adequate ramping capacity to address rapid net load changes, resulting in renewable curtailment or even load shedding[9]. Furthermore, current mechanisms fail to provide effective economic incentives or fair compensation for ramping services offered by flexibility resources such as energy storage, and lack transparent price signals for ramping supply and demand.

This paper aims to develop a day-ahead optimization control framework that incorporates the ramping capability of energy storage systems, thereby improving the flexibility and economic efficiency of power systems with high renewable penetration. The main contributions of this work are as follows: (1) a refined mathematical model of storage ramping characteristics is established, considering SOC constraints, charging/discharging limits, and cycling degradation costs; (2) a case study based on a real-world grid verifies the effectiveness of the proposed method, demonstrating that it significantly improves ramping adequacy, reduces renewable curtailment, and lowers system operating costs.

2 Modelling of Energy Storage Ramping Capability

Compared with conventional regulating resources, energy storage systems (ESS) play an irreplaceable and unique role in providing ramping services. Functioning as both a source and a load, storage systems offer a wider output adjustment range than conventional generating units of the same rated power, thereby enabling simultaneous upward and downward ramping services. Their fast response allows them to effectively mitigate second-to-minute level fluctuations of renewable generation, compensating for the limited ramping rates of conventional coal-fired units (typically 1–2%/min).

On a given time scale, the flexible adjustment range of ESS can be described as follows:

$$P_{\mathrm{ES},t+\tau} \in \left\lfloor \max\left\{-P_{\mathrm{c,max}}, \frac{E_t - E_{\max}}{\eta_{\mathrm{c}}\tau}\right\}, \min\left\{P_{\mathrm{d,max}}, \frac{\left(E_t - E_{\min}\right)\eta_{\mathrm{d}}}{\tau}\right\}\right\rfloor \tag{1}$$

Where $P_{\mathrm{c,max}}$ and $P_{\mathrm{d,max}}$ denote the maximum charging and discharging limits per unit time, respectively; E_t is the storage level of the device at time t; $E_{\max}$ and $E_{\min}$ represent the upper and lower bounds of the storage capacity; η_{c} and η_{d} denote charging and discharging efficiencies, respectively.

The power boundary of storage (electrical or thermal) devices is defined as:

$$0 \le P_t^{\mathrm{ES,store}} \le z_t^{\mathrm{ES,s}} P_{\mathrm{ES,s}} \tag{2}$$

$$0 \le P_t^{\mathrm{ES,release}} \le z_t^{\mathrm{ES,r}} P_{\mathrm{ES,r}} \tag{3}$$

SOC constraint:

$$SOC_{\min} \le SOC_0 \le SOC_{\max} \tag{4}$$

$$SOC_{\min} \le SOC_t \le SOC_{\max} \tag{5}$$

$$\sum_{t=1}^{T}\left(\eta_{ES,s} P_t^{ES,store} - \frac{P_t^{ES,release}}{\eta_{ES,r}}\right) = 0 \tag{6}$$

The storage operation model includes ramping limits, energy capacity constraints, and efficiency considerations:

$$b_i = b_{i-1} + x_i, \quad b_i \in [b_{\min}, b_{\max}], \forall i \tag{7}$$

$$f(x_i) = \frac{[x_i]^+}{h\eta_{\mathrm{ch}}} - \frac{\eta_{\mathrm{dis}}[x_i]^-}{h} = \frac{\max(0, x_i)}{h\eta_{\mathrm{ch}}} - \frac{\eta_{\mathrm{dis}}\max(0, -x_i)}{h} \tag{8}$$

$$x_i \in [X_{\min}, X_{\max}] \tag{9}$$

$$\eta_{\mathrm{ch}}^* = \eta_{\mathrm{ch}}\eta_{\mathrm{conv}}, \eta_{\mathrm{dis}}^* = \eta_{\mathrm{dis}}\eta_{\mathrm{conv}} \tag{10}$$

$$x_i - x_{i-1} \in [\tau_{\min}, \tau_{\max}] \tag{11}$$

The operational constraints are designed based on representative daily and ramping scenarios, ensuring that investment decisions satisfy power balance requirements under different operating conditions. The system power balance for each scenario is formulated as:

$$\begin{cases} \sum\limits_{i\in\Omega_{\mathrm{g}}\cup\Omega_{\mathrm{nes}}\cup\Omega_{\mathrm{ng}}} p_{i,s,t} + \sum\limits_{i\in\Omega_{\mathrm{w}}} w_{i,s,t} - w_{s,t}^{\mathrm{c}} = \sum\limits_{i\in\Omega_{\mathrm{d}}} d_{i,s,t} - d_{s,t}^{\mathrm{c}} \quad \forall s,t \\ 0 \le w_{s,t}^{\mathrm{c}} \le \varphi^{\mathrm{w}} \sum\limits_{i\in\Omega_{\mathrm{w}}} w_{i,s,t} \quad \forall s,t \\ 0 \le d_{s,t}^{\mathrm{c}} \le \varphi^{\mathrm{d}} \sum\limits_{i\in\Omega_{\mathrm{d}}} d_{i,s,t} \quad \forall s,t \end{cases} \tag{12}$$

The upward ramping (discharge power increase) calculation for the energy storage ramping capability model is as follows:

$$RU_{sto}(t)=\min\left(\frac{P_{dis}^{max}-P_{dis}(t)}{\Delta t},\frac{SOC(t)-SOC^{min}}{\eta_{dis}\cdot\Delta t}\cdot E_{rated}\right) \tag{13}$$

The downward ramping (charging power increase) calculation is as follows:

$$RD_{sto}(t)=\min\left(\frac{P_{ch}^{max}-P_{ch}(t)}{\Delta t},\frac{SOC^{max}-SOC(t)}{\Delta t}\cdot\frac{1}{\eta_{ch}}\cdot E_{rated}\right) \tag{14}$$

Where $P_{dis}(t)$ and $P_{ch}(t)$ denote the actual discharging and charging power at time t (MW), respectively; $SOC(t)$ represents the state of charge (%); η_{dis} and η_{ch} denote charging and discharging efficiencies; and E_{rated} is the rated capacity (MWh).

3 Day-Ahead Optimization Model Considering Energy Storage Ramping Capability

The proposed day-ahead optimization scheduling model aims to minimize system operating costs, while explicitly incorporating the ramping service value of energy storage devices into the conventional unit commitment framework. The model is formulated as a mixed-integer linear programming (MILP) problem, optimizing the on/off status, output schedule, and ramping service allocation of various resources. The objective function consists of generation cost, start-up and shut-down costs, ramping service costs, and penalty costs for curtailed wind and solar generation.

$$\min F=\sum_{t=1}^{T}\left[\begin{array}{l}\sum_{i\in G}(C_i^{gen}P_{i,t}+C_i^{su}u_{i,t}+C_i^{sd}v_{i,t})+\sum_{j\in S}C_j^{\mathrm{cyc}}\mid P_{j,t}\mid\\+\sum_{k\in R}(C_k^{ru}R_{k,t}^{up}+C_k^{rd}R_{k,t}^{\mathrm{dn}})+\sum_{w\in W}C^{curt}P_{w,t}^{curt}\end{array}\right] \tag{15}$$

where G,S,R,W denote the sets of conventional units, energy storage devices, ramping resources, and renewable energy resources, respectively; C_i^{gen} is the generation cost; $P_{i,t}$ is the unit output; $u_{i,t}$ and $v_{i,t}$ are start-up and shut-down status variables; C_j^{cyc} is the storage cycling cost; C_k^{ru} and C_k^{rd} are ramping service costs; $R_{k,t}^{up}$ and $R_{k,t}^{\mathrm{dn}}$ represent ramping capacities; and C^{curt} is the penalty cost for wind and solar curtailment.

Main constraints include:

(1) System power balance constraint:

$$\sum_{i\in G}P_{i,t}+\sum_{j\in S}P_{j,t}^{dis}-\sum_{j\in S}P_{j,t}^{ch}+\sum_{w\in W}(P_{w,t}^{fore}-P_{w,t}^{curt})=P_t^{load} \tag{16}$$

(2) Conventional unit operation constraints:

$$I_{i,t}P_i^{min}\le P_{i,t}\le I_{i,t}P_i^{max} \tag{17}$$

$$-RD_i\le P_{i,t}-P_{i,t-1}\le RU_i \tag{18}$$

(3) Correlation between available ramping capacity of energy storage and SOC status:

$$R_{j,t}^{up} \le \min\left\{P_j^{max} - P_{j,t}^{dis}, \frac{(SOC_{j,t} - SOC_j^{min}) \cdot E_j}{\Delta t \cdot \eta_j^{dis}}\right\} \tag{19}$$

$$R_{j,t}^{dn} \le \min\left\{P_j^{max} - P_{j,t}^{ch}, \frac{(SOC_j^{max} - SOC_{j,t}) \cdot E_j \cdot \eta_j^{ch}}{\Delta t}\right\} \tag{20}$$

Where E_j is the rated capacity of storage; η_j^{dis} and η_j^{ch} are charging and discharging efficiencies.

(4) Ramping adequacy constraint to address renewable generation uncertainty:

$$\sum_{i \in G} R_{i,t}^{up} + \sum_{j \in S} R_{j,t}^{up} + \sum_{k \in R} R_{k,t}^{up} \ge R_t^{up,req} + \alpha \cdot \sigma_t^{net} \tag{21}$$

$$\sum_{i \in G} R_{i,t}^{dn} + \sum_{j \in S} R_{j,t}^{dn} + \sum_{k \in FR} R_{k,t}^{dn} \ge R_t^{dn,req} + \alpha \cdot \sigma_t^{net} \tag{22}$$

Where FR denotes the set of other flexibility resources; $R_t^{up,req}$ and $R_t^{dn,req}$ represent ramping requirements based on net load forecasts; σ_t^{net} is the standard deviation of the net load forecast; and α is the confidence coefficient.

The value of energy storage ramping services is quantified through opportunity cost as follows:

$$C_{j,t}^{ramp} = \lambda_t^{ramp} \cdot (R_{j,t}^{up} + R_{j,t}^{dn}) + C_j^{deg} \cdot \Delta DOD_{j,t} \tag{23}$$

Where λ_t^{ramp} is the shadow price of ramping service; C_j^{deg} is the degradation cost coefficient of storage; and $\Delta DOD_{j,t}$ is the variation in depth of discharge.

Considering transmission network constraints, the DC power flow constraint is adopted:

$$P_{l,t} = \sum_{n \in N} GSF_{l,n} \cdot (P_{n,t}^{gen} - P_{n,t}^{load}) \tag{24}$$

$$-P_l^{max} \le P_{l,t} \le P_l^{max} \tag{25}$$

4 Case Study

The Shaanbei region is rich in wind and solar resources and serves as an important renewable energy base, supplying electricity to the Guanzhong region and other provinces. The installed capacities include 12.18 GW of wind power, 13.56 GW of photovoltaic (PV) power, and 26.15 GW of thermal power, with a maximum load of 11.0 GW and 12.0 GW of electricity delivered to other provinces. According to historical records, the net load curve in the Shaanbei region exhibits significant volatility, leading to ramping requirements. Based on available resources and development plans, the ramping services of the system are mainly provided by thermal power units, energy storage systems (planned), demand response, and inter-provincial tie-lines. After flexibility retrofits, the minimum output of thermal units is approximately 40% of the rated capacity, and the ramping rate is 1.5%/min. The capacity of energy storage systems is considered as 10% of the total installed capacity of wind and PV generation;

the capacity of demand response is set as 5% of the maximum load; and the power of inter-provincial tie-lines cannot exceed their rated capacities. As shown in Fig. 1, the price of each ramping resource is modeled in the form of dynamic pricing.

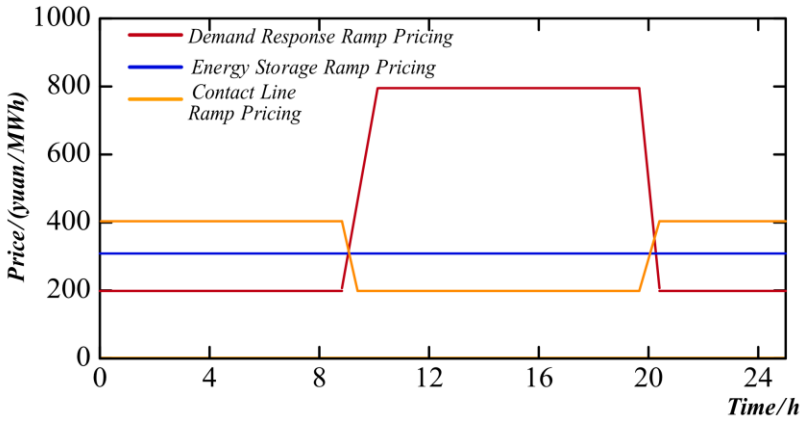


Fig. 1. Dynamic Pricing for Multiple Hill-climbing Services.

With the system's economic operation as the optimization objective, considering the fuel costs of thermal units and the activation costs of ramping resources, the day-ahead scheduling scheme of thermal units and various ramping resources is obtained. As shown in Fig. 2, under this scheduling result, the daily scheduling cost of the Shaanbei region amounts to 27.33 million CNY, of which the activation cost of ramping resources totals 8.93 million CNY, including 0.53 million CNY for energy storage systems, 0.91 million CNY for demand response, and 7.49 million CNY for inter-provincial tie-lines.

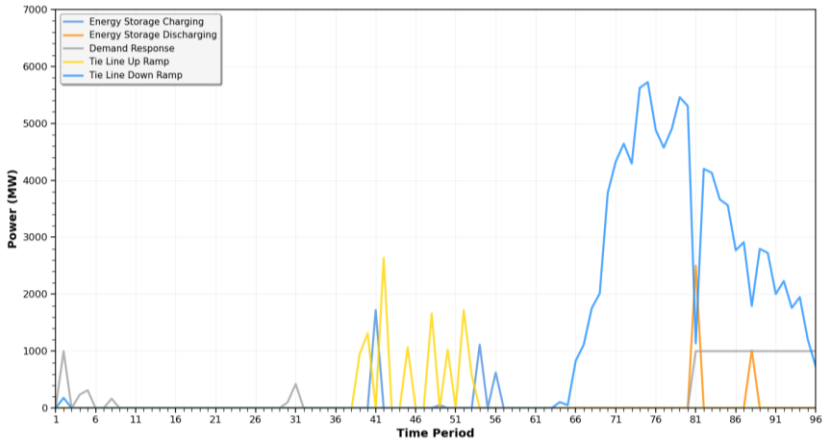


Fig. 2. Call Results for Climbing Resources.

During the optimization process, the curtailment ratios of wind and PV generation can be set according to practical requirements. The ramping resource utilization results are presented for wind and PV curtailment ratios of 0%, 2%, and 5%. It can be observed that the higher the utilization rate of wind and PV generation, the more ramping services are required. Even when the curtailment ratio is relaxed to 5%, the activation cost of ramping resources does not decrease significantly. The main reason is that ramping services in this optimization process also include peak shaving, without further detailed disaggregation.

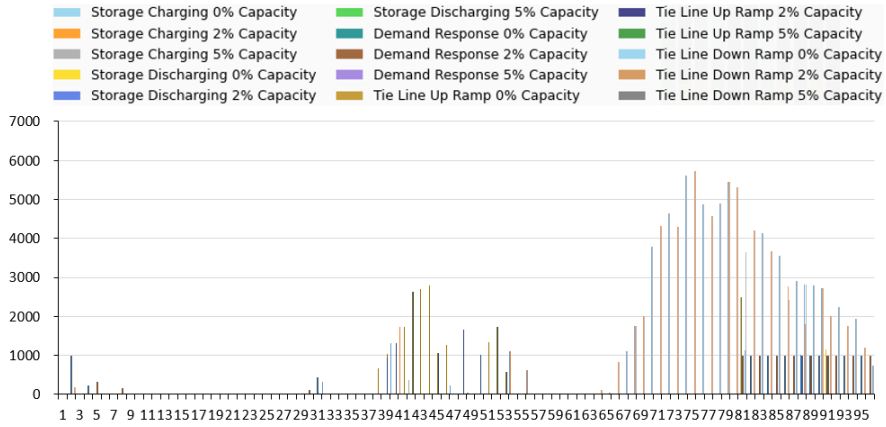


Fig. 3. Sensitivity Analysis of Climbing Service Call Costs on New Energy Utilization Rate.

5 Conclusion

In response to the problem of insufficient power system flexibility under high penetration of renewable energy, this paper proposes a coordinated optimization scheduling method for multiple types of flexibility resources, taking into account the ramping capability of energy storage devices. By comprehensively considering the SOC state constraints, charging and discharging power limits, and cycling loss costs, a refined mathematical model of the ramping characteristics of energy storage devices and a coordinated scheduling model of multiple flexibility resources are established.

The case study results show that, under the condition of configuring energy storage with 10% of the total installed capacity of wind and photovoltaic generation and demand response with 5% of the maximum load, the system's daily scheduling cost is 27.33 million yuan, of which the ramping resource invocation cost is 8.93 million yuan. Energy storage, by virtue of its fast response advantage, is preferentially dispatched, effectively alleviating the ramping pressure caused by the net load "duck curve."

Acknowledgement: Project supported by Science and Technology Project of State Grid Corporation of China. (5419-202356782A-3-8-KJ).

8

References

1. Jian Q, Liu X, Yang J, et al. Optimal allocation of power system flexibility resources considering demand response[J]. Modern Electric Power38(3): 11 (2021).
2. Tang X, Hu Y, Zheng D, et al. Optimization method of microgrid energy storage configuration considering power grid flexibility[J]. Power Supply and Use37(12): 54-60 (2020).
3. Makhdoomi H, Moshtagh J.: Optimal Scheduling of Electrical Storage System and Flexible Loads to Participate in Energy and Flexible Ram** Product Markets[J]. Journal of Operation and Automation in Power Engineering11(3): 203-212 (2023).
4. Lu D, Peng Y, Sun J. Dual-Stage optimization scheduling model for a Grid-Connected renewable energy system with hybrid energy storage[J]. Energies17(3): 737 (2024).
5. Memarzadeh G, Noori H, Memarzadeh R, et al. Optimal energy storage system management in an uncertain smartgrid[J]. Journal of Energy Storage117: 116125 (2025).
6. Sun Y, Hui H, Qi T, et al. Multitime scale optimization of urban micro-grids considering high penetration of PVs and heterogeneous energy storage systems[J]. IEEE Internet of Things Journal11(14): 24428-24438 (2024).
7. Rawa M, Al-Turki Y, Sedraoui K, et al. Optimal operation and stochastic scheduling of renewable energy of a microgrid with optimal sizing of battery energy storage considering cost reduction[J]. Journal of Energy Storage59: 106475 (2023).
8. Mu Y, Zhang Y, Jia H, et al. Day-ahead optimal scheduling of building energy microgrids based on time-varying virtual energy storage[J]. IET Renewable Power Generation17(2): 376-388 (2023).
9. Pan Y, Ju L, Yang S, et al. A multi-objective robust optimal dispatch and cost allocation model for microgrids-shared hybrid energy storage system considering flexible ram** capacity[J]. Applied Energy369: 123565 (2024).

086 Research on Efficiency Optimization Control of Off-grid Photovoltaic Electrolysis System Considering Multi-energy Coupling

Jing Fangjie[1], Wang Xiaolei[2], Man Ji[1], Yang Wenhao[1], and Fan Dongdong[1]

[1] Henan Source Grid Load Storage Electrical Research Institute Co., Ltd, Xuchang Henan 461000, China
[2] XJ Electric Co., Ltd, Xuchang Henan 461000, China
jing_fangjie@126.com

Abstract. Addressing the issues of neglected multi-energy flow coupling among photovoltaic, electrolytic cell and auxiliary equipment in off-grid photovoltaic electrolysis systems, as well as the sharp increase in auxiliary power consumption proportion with system scale. This paper constructs a multi-energy coupling dynamic model encompassing main components such as photovoltaic arrays, PEM electrolytic cells, heat exchangers, dryers, compressors, pumps, and water purifiers. Based on the electrochemical-thermal-mass transfer coupling mechanism, the effects of operating pressure, temperature, and current density on the polarization of the electrolytic cell, waste heat, and transmembrane water migration are quantified. Additionally, the variable power consumption of auxiliary equipment is incorporated into the system efficiency evaluation system. Furthermore, with the goal of maximizing hydrogen production efficiency, a nonlinear constrained optimization model is established to simultaneously optimize current density, operating pressure, and ambient temperature. A particle swarm optimization algorithm is adopted to achieve rapid solution. Results of the case study show that under typical daily photovoltaic fluctuation conditions, multi-parameter collaborative optimization increases the 24-hour cumulative hydrogen production more than 7% compared to the traditional strategy of only adjusting the current density. This verifies the effectiveness of the proposed model and strategy in improving the efficiency and economy of off-grid photovoltaic electrolysis systems.

Keywords: Optimization, Photovoltaic, Electrolysis, Multi-energy.

1 First Section

1.1 A Subsection Sample

Hydrogen energy is becoming a core carrier for achieving deep utilization of renewable energy due to its advantages of zero carbon emissions, high energy density, and easy long-term storage. Compared with grid-connected hydrogen production, off-

grid photovoltaic electrolysis systems break free from the temporal and spatial constraints of the power grid, and can directly achieve on-site conversion of "green electricity and green hydrogen" in resource-rich areas. This significantly reduces transmission investment, avoids grid peak regulation pressure, and achieves cross seasonal and regional energy transmission through hydrogen.

The International Renewable Energy Agency predicts that by 2030, off-grid hydrogen production will account for over 25% of global green hydrogen production capacity. And the system cost of photovoltaic electrolysis cell combination is expected to drop below $1.5/kg, indicating an increasingly economic turning point. China has already entered the feasibility stage for several GW level off-grid hydrogen production demonstration projects in super-large photovoltaic and wind power bases planned in deserts, gobi, and other areas. The technological roadmap needs to be upgraded from "hydrogen production capability" to "efficient hydrogen production".

At present, the research on improving the efficiency of the PV electrolysis system mainly focuses on three aspects:

1) By coordinating the operation and scheduling of the source-load-storage system to achieve economic control. Reference [1] proposes a method based on fuzzy logic control to realize short-term power compensation for battery/supercapacitor hybrid energy storage. Reference [2] improves the economic performance by optimizing the capacity configuration of multiple energy sources. References [3-4] presents a multi-time-scale optimization operation scheduling strategy considering the supply-demand balance of the source-load-storage system, aiming to enhance the economic performance of the off-grid hydrogen production system.

2) By coordinating and optimizing the multi electrolytic cells system, the hydrogen production efficiency is enhanced. In reference [5], an equal force distribution strategy and rotation strategy are proposed based on a multi electrolytic cells hybrid wind-hydrogen system. Reference [6] establishes a model of the multi-machine cluster system for optimizing the operation of hydrogen production plants and proposes a unified solution framework. Reference [7] presents an optimization strategy for power distribution in a multi-stack PEM system, considering degradation conditions.

3) According to the polarization characteristics of the electrolytic cell, the efficiency is improved by dynamically adjusting the current density, temperature, and pressure. Reference [8] investigates the impact of temperature and pressure changes on the electrolytic efficiency, and achieves the optimal operating efficiency through the optimization of temperature and pressure. Reference [9] analyzes the influence of temperature on the electrolysis rate, and implements the adaptive temperature control strategy, enabling the cell to operate at the optimal temperature point. Reference [10] expands the schedulable space of the system by taking into account the dynamic thermal process and the hydrogen-to-oxygen impurity crossover processes of electrolyzers. Reference [11] investigates the effects of pressure, temperature and liquid flow rate on hydrogen-to-oxygen and voltage. By analyzing the pressure and liquid flow rate, the optimal pressure-current density variation trend is obtained. Through pressure optimization control, the number of start-stop cycles is reduced, and the energy utilization rate of the off-grid hydrogen production system is improved.

The above research focuses on the efficiency characteristics of the electrolytic cell, but does not take into account the energy consumption characteristics of the auxiliary equipment, and ignores the potential for collaborative optimization brought about by the coupling of multiple energy within the system. For instance, under the conventional MPPT strategy, the excess power of the PV array is directly limited. The auxiliary processes such as hydrogen storage, compression, purification, and circulating cooling introduce multiple types of loads such as compressors, pumps, and fans. The power demands fluctuate asynchronously with the photovoltaic power, resulting in the distortion of the overall efficiency evaluation of the system. And the multi-energy coupling characteristics have become a key bottleneck restricting the further improvement of hydrogen production efficiency in off-grid's system.

With the expansion of the system scale, the power consumption of auxiliary equipment continues to increase, and its multi-energy coupling characteristics have become the bottleneck restricting the further improvement of the efficiency of off-grid hydrogen production. Considering the multi-energy coupling of auxiliary equipment, the hydrogen production efficiency can be refined. It is necessary to establish a multi energy coupling dynamic model covering photovoltaic cells auxiliary equipment, and propose an optimal control strategy aiming at the hydrogen production efficiency. Aiming at the above problems, this paper carries out the research on the efficiency optimization control of off-grid photovoltaic electrolysis system considering multi-energy coupling, is in order to provide theoretical methods and technical support for the efficient, reliable and economic off-grid green hydrogen system.

2 Modeling of the Off-grid Photovoltaic Electrolysis System

The structure of the off-grid photovoltaic electrolysis system is shown in Fig.1. Solar cells form a stable DC bus voltage through DC/DC converters. Electrolytic cells are connected to the DC bus through DC/DC converters, and the production of hydrogen is controlled by the current density. Auxiliary equipment such as compressors, coolers, dryers, and pumps are connected to the DC bus through AC/DC converters.

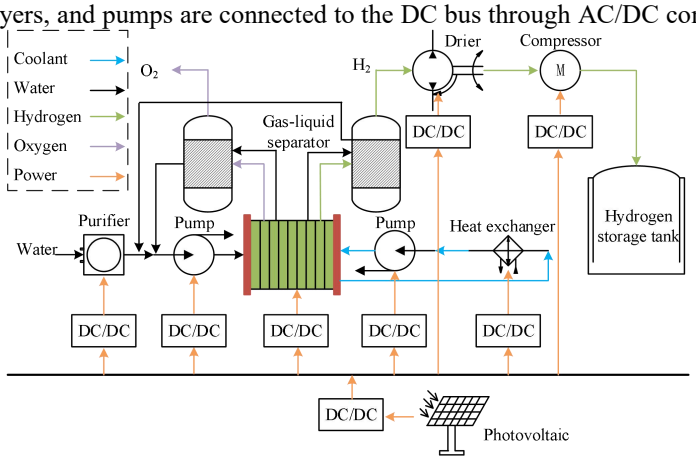


Fig.1 Topology of off-grid photovoltaic electrolysis system.

The coupling of electric energy, thermal energy and hydrogen energy exists among various equipment in the off-grid photovoltaic electrolysis system, and the energy flow relationship is shown in Fig.2. It can be seen that the multi-energy coupling of the system is complex, and a detailed analysis model needs to be established to realize the in-depth analysis of the hydrogen production efficiency.

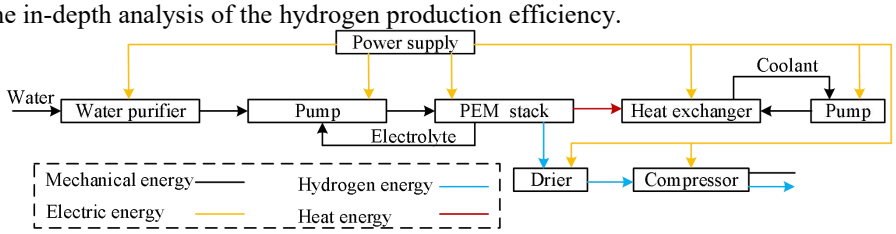


Fig.2 Multi-energy coupling relationship of off-grid photovoltaic electrolysis system.

2.1 Modeling of PEM Electrolytic Cell

PEM electrolytic cell is composed of electrode plate, gas channel, diffusion layer and membrane electrode. The electrolyte enters the anode and generates oxygen and H^+ through electrolytic reaction. The oxygen is brought out with the circulation of electrolyte, and H^+ passes through the PEM to the cathode, and reacts with electrons to generate hydrogen. The expression of the electrochemical model of electrolytic cell is

$$U_{\text{cell}} = U_{\text{act}} + U_{\text{rev}} + U_{\text{ohm}} \tag{1}$$

Where U_{cell} is the terminal voltage of the electrolytic cell; U_{rev}, U_{act}, and U_{ohm} are the reversible voltage, activation over-potential, and ohmic over-potential respectively.

The activation over-potential can be calculated by Butler-Volmer equation[12]:

$$U_{\text{act}} = \frac{2RT}{zF}\sinh^{-1}\frac{j}{2j_{0,\text{a}}} + \frac{2RT}{zF}\sinh^{-1}\frac{j}{2j_{0,\text{c}}} \tag{2}$$

Where j is the electrolysis current; $j_{0,\text{a}}$ and $j_{0,\text{c}}$ are the exchange current densities of the positive and negative electrodes, respectively.

The reversible voltage can be calculated by Nernst equation[12]:

$$U_{\text{rev}} = U_{\text{rev}}^{0} + \frac{RT}{zF}\ln\frac{p_{\text{H}_2}p_{\text{O}_2}^{0.5}}{p_{\text{H}_2\text{O}}} \tag{3}$$

Where U_{rev}^{0} is the reversible voltage under standard conditions; R is the gas constant; z is the amount of electrons transferred in the 1 mol water electrolysis reaction; T is the temperature during electrolysis; F is Faraday constant; And p_{H_2} and p_{O_2} are respectively the pressures of hydrogen and oxygen.

The ohmic over-potential can be divided into two parts, namely, the ohmic over-potential of the membrane electrode and the total ohmic over-potential of the electrode plate and the gas diffusion layer, which can be calculated by equation (4).

$$U_{\text{ohm}} = Aj\left(R_{\text{mem}} + R_{\text{pla}}\right) \tag{4}$$

Where A is the effective electrolytic area; R_{mem} is the membrane electrode ohmic resistance, whose value can be obtained according to the empirical formulas, as

shown in equation (5); R_{pla} is the total ohmic resistance of the cell's electrodes and other components, which can be regarded as a constant within the range of electrolytic cell operating parameters.

$$R_{mem} = \frac{\delta_m}{a(T,p)\sigma_m} \tag{5}$$

Where δ_m is the thickness of membrane electrode; $a(T, p)$ is the conductivity correction coefficient of membrane electrode under certain operating parameters which can be calculated by equation (6)[13], and p is the operating pressure of membrane electrode; σ_m is the conductivity of membrane electrode in standard state; d_{ij} is the empirical parameter in the correction coefficient.

$$a(T,p) = d_{00} + d_{01}p + d_{10}T + d_{02}p^2 + d_{20}T^2 + d_{11}Tp + d_{03}p^3 + d_{12}Tp^2 + d_{21}T^2p \tag{6}$$

During operation, the electrolyte enters the electrolytic cell from the anode. While the electrolyte circulates to take away the oxygen generated by the anode, part of the electrolyte will penetrate into the cathode across the membrane. The transmembrane permeation mainly includes diffusion permeation, differential pressure permeation and electric resistance permeation. Diffusion infiltration is mainly caused by the difference of electrolyte content between the positive and negative electrodes, which is manifested by diffusion from the side with higher electrolyte content to the lower side. The diffusion amount can be calculated by Fick's law, that is:

$$N_{H_2O_diff} = \frac{AD_w}{\delta_m}\left(C_{H_2O_an} - C_{H_2O_cat}\right) \tag{7}$$

Where D_w is the electrolyte diffusion coefficient; $C_{H_2O_an}$ and $C_{H_2O_cat}$ are the electrolyte contents at the cathode and anode, respectively.

The electrolyte at the cathode side is mainly obtained by the transmembrane transport, and its content is negligible compared with that at the anode side. The electrolyte content at the anode side can be calculated by equation (8).

$$C_{H_2O_an} = \rho_{H_2O} / M_{H_2O} \tag{8}$$

Where ρ_{H_2O} is the density of the electrolyte; M_{H_2O} is the molar mass of the electrolyte.

Differential pressure infiltration is the infiltration of water from the cathode side to the anode side caused by the differential pressure between the cathode and anode sides. The amount of infiltration can be obtained from Darcy's law, that is:

$$N_{H_2O_pre} = \frac{K_{darcy} A \rho_{H_2O} \Delta p}{\delta_m \mu_{H_2O} M_{H_2O}} \tag{9}$$

Where K_{darcy} is the permeability coefficient; Δp is the pressure difference between the anode and cathode; μ_{H_2O} is the viscosity coefficient of water.

The penetration of electrical resistance-driven is mainly caused by the transmembrane transfer of H^+ from the anode to the cathode. The electric resistance-driven permeability can be calculated by equation (10).

$$N_{H_2O_eo} = n_d Aj/F \tag{10}$$

Where n_d is a dimensionless constant.

The trans-membrane permeation can be calculated by equation (11).

$$N_{H_2O_m} = N_{H_2O_diff} + N_{H_2O_eo} - N_{H_2O_pre} \tag{11}$$

2.2 Power Model of This System

Power Model of PEM Electrolytic Cell. The electric energy consumed by PEM electrolytic cell is from two parts: one is the conversion of electric energy into chemical energy; The other part is the heat energy generated in the process of electrochemical reaction. The input power of PEM stack is:

$$P_{ele_in} = nU_{cell}I \tag{12}$$

Where $P_{ele\ in}$ is the input power; I is the electrolysis current. And n is the number of electrolytic cells in the PEM stack.

The hydrogen production power during the operation of PEM stack is:

$$P_{H_2} = nU_{th}I \tag{13}$$

Where U_{th} is the thermal neutral voltage.

The heat generating power during the operation is:

$$P_{heat} = n\left(U_{cell} - U_{th}\right)I \tag{14}$$

Power Model of Circulating Pump. The power of the circulating pump can be replaced by the work done to overcome the head loss, and its expression is[14]

$$P_{pump} = \rho_{H_2O} gHQ_{ele} / \eta_{pump} \tag{15}$$

Where g is the gravitational acceleration; H is the water head for the electrolyte; Q_{ele} is the circulation flow rate of the electrolyte; η_{pump} is the efficiency of the pump.

Power Model of Compressor. The power of the compressor is related to the pressure at its inlet and outlet, as well as the amount of gas that the compressor needs to compress. The power expression is

$$P_{comp} = \frac{\eta_{H_2} RT}{\eta_{comp}} \ln \frac{p_{H_2_out}}{p_{H_2_in}} \tag{16}$$

$$\eta_{H_2} = nI / zF \tag{17}$$

Where $\eta_{H,}$ is the amount of hydrogen compressed by the compressor per unit time; η_{comp} is the efficiency of the compressor. And $p_{H,\ out}$ and $p_{H,\ in}$ are the pressures at the outlet and inlet of the compressor respectively.

Power Model of Heat Exchanger. The heat exchange includes two parts. One is the passive heat exchange for cooling the environment, and the other part is the active heat exchange of the heat exchanger.

Passive heat dissipation mainly occurs on the surface of the electrolytic cell, electrolyte circulation pipe, radiator and other surfaces in contact with the environment, and its heat dissipation power can be calculated by equation (18) [15].

$$P_{\text{heat,loss}} = hA_{\text{contact}}\left(T - T_{\text{ref}}\right) \tag{18}$$

Where h is the heat transfer coefficient; A_{contact} is the surface area of this system that has heat exchange with the environment; T_{ref} is the ambient temperature.

The active heat exchange power can be calculated by equation (19).

$$P_{\text{heat_exchange}} = \left(P_{\text{heat}} - P_{\text{heat_loss}}\right) \Big/ \eta_{\text{exchange}} \tag{19}$$

Where η_{exchange} is the efficiency of the heat exchanger.

When $P_{\text{heat_exchange}} > 0$, it indicates that the active heat exchange power is the cooling power, and $\eta_{\text{exchange}} = \eta_{\text{cold}}$ represents the cooling efficiency. Otherwise, it indicates that the active heat exchange power is the heating power, and $\eta_{\text{exchange}} = \eta_{\text{heat}}$ represents the heating efficiency.

Power Model of Dryer. Due to the transmembrane penetration of electrolyte, there are a lot of water impurities on the cathode side. To meet the requirements of the hydrogen purity, it needs to be dried. Assuming that the amount of water removed by the dryer is equal to the amount of water permeated across the membrane by the electrolyte, the power of the dryer can be calculated by equation (20)[16].

$$P_{\text{dryer}} = N_{\text{H}_2\text{O}} E_{\text{regen}} \Big/ \eta_{\text{dryer}} \tag{20}$$

Where $N_{\text{H}_2\text{O}}$ is the amount of water removed by the dryer; E_{regen} is the energy required to regenerate desiccant in the dryer; η_{dryer} is the efficiency of the dryer.

Power Model of Water Purifier. The water purifier does not operate continuously for most of the time, so the power of the water purifier is approximately calculated by equation (21) based on the consumption rate of electrolyte.

$$P_{\text{purity}} \approx P_{\text{purity_N}} \frac{Q_{\text{ele_cons}}}{Q_{\text{purity_N}}} \tag{21}$$

It can be seen from the above formula that the power of the water purifier is only related to the rate at which the electrolyte is consumed by the stack.

2.3 Efficiency Model of Hydrogen Production

According to power expressions of each device in this system, the power of each device can be correlated through the parameters of pressure, temperature and current density. By changing the operating pressure, ambient temperature and current density of the system, the optimal coordination of the power of devices in the system can be achieved, and the overall performance of the system can be improved.

To quantitatively express the operation performance of the system, two indicators, namely, hydrogen production energy consumption and hydrogen production efficiency, are used. When the amount of hydrogen produced is constant, the energy

consumption and efficiency of hydrogen production can be converted by equation (22).

$$\eta_{H_2} = P_{H_2} / W \tag{22}$$

Therefore, the efficiency of hydrogen production is selected as the index to measure the overall performance of the system. The expression of hydrogen production efficiency is:

$$\eta_{H_2} = \frac{P_{H_2}}{P_{ele_in} + P_{auxi}} \tag{23}$$

$$P_{auxi} = P_{comp} + P_{pump} + P_{heat_exchange} + P_{dryer} + P_{purity} \tag{24}$$

Where P_{auxi} is the total power of the auxiliary equipment within this system.

3 Optimization Control Strategy for Hydrogen Production Efficiency

The objective function is

$$\max\left(\eta_{H_2}\right) = f\left(p_m\right) \tag{25}$$

The inequality constraint for the safe range of operating parameters is

$$\begin{cases} p_{min} \le p_{H_2} \le p_{max} \\ j_{min} \le j \le j_{max} \\ T_{min} \le T \le T_{max} \end{cases} \tag{26}$$

The equality constraints of each device within the system include:

1) The electrochemical process of the electrolytic cell is constrained by equations (1) to (4).
2) The mass transfer process of electrolyte is constrained by equations (7) and (9) to (11).
3) The equation constraint of PEM stack power model is composed of equations (12) to (14).
4) Constraints on the power model of auxiliary equipment are defined by equations (15), (16) and (18)~ (21).
5) The power equation constraint of off-grid photovoltaic electrolysis system is

$$P_{PV} = P_{ele_in} + P_{comp} + P_{pump} + P_{heat_exchange} + P_{dryer} + P_{purity} \tag{27}$$

The optimization strategy does not depend on any special optimization algorithm. Taking the PSO (particle swarm optimization) algorithm as an example, the maximum hydrogen production efficiency can be achieved by setting the parameters of current density J, ambient temperature T and operating pressure p_{H2}.

The algorithm flow is shown in Fig.3.

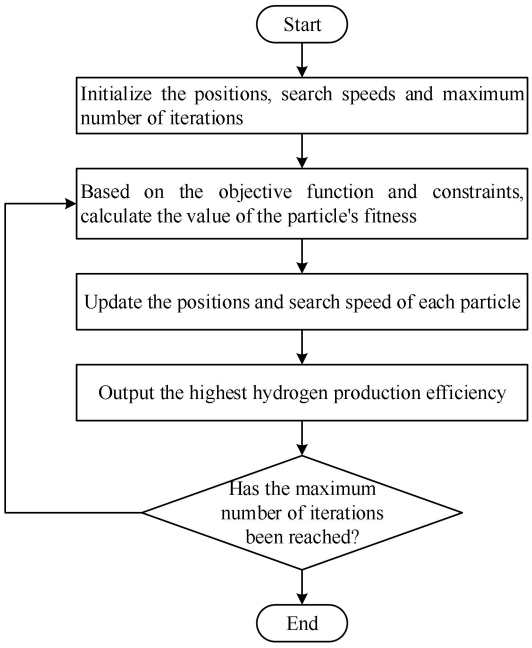


Fig.3 Block diagram of optimization control strategy.

4 Case Study

The operation of the PEM hydrogen generation system with off-grid photovoltaic as power input needs to focus on the fluctuation. The fluctuation power input in a day is analyzed as an example. Ignoring the transient process, considering the stable operation state of the system, the performance improvement effect in the multi-parameter optimization is studied under the fluctuating power input.

Parameters of the system are shown in the table. Considering the fluctuation of photovoltaic within a day under typical operating conditions, the following five operation modes are analyzed:

1) The power of auxiliary equipment is taken as a constant value, and the current density is taken as the optimization variable;
2) The operating pressure and ambient temperature are taken as constant values, and only the current density is used as the optimization variable;
3) The operating pressure is taken as a constant value, and the current density and environmental temperature are taken as optimization variables;
4) The environmental temperature is taken as a constant value, and the current density and operating pressure are taken as optimization variables;
5) The current density, environmental temperature and operating pressure are used as optimization variables.

Furthermore, in order to fully verify the optimization method in this paper, the analysis of five operation modes under two extreme fluctuation conditions of

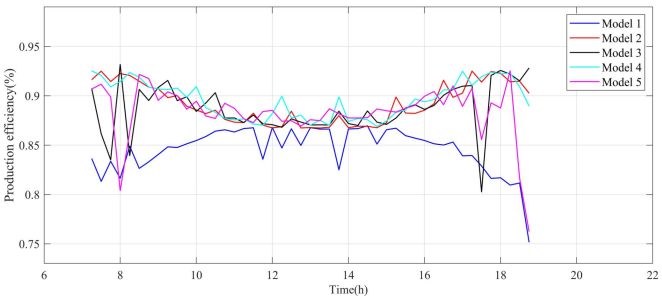
photovoltaic within a day is conducted: one is short-term significant power drops caused by cloud cover (occurring multiple times within a day), and the other is a situation where the photovoltaic power remained at a relatively low level due to rainy weather.

Table 1. Parameters of off-grid photovoltaic electrolysis system.

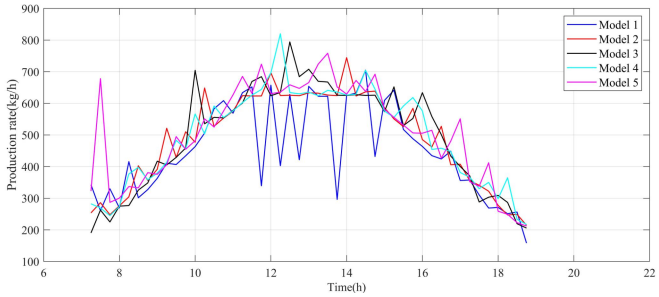
Parameter	Value	Unit	Parameter	Value	Unit
Capacity of the PV plant	60	MW	Heating efficiency	0.8	-
Number of electrolyzers	50	-	Energy of the dryer	1.2	kWh/mol
Number of cells	150	-	Dryer efficiency	0.31	-
Neutral voltage	1.48	V	Rated power of the water purifier	2.5	kW
Flow rate of the electrolyte	0.0153	m^3/s	Rated water purification rate	1.12	m^3/s
Circulation pump efficiency	0.82	-	Lower limit of operating pressure	1	bar
Compressor efficiency	0.82	-	Upper limit of operating pressure	160	bar
Compressor outlet pressure	700	bar	Lower limit of temperature	285	K
Water head	7	m	Upper limit of temperature	350	K
Heat transfer coefficient	500	$W/(m^2*K)$	Lower limit of current density	5	kA/ m^2
Heat exchange area	6	m^2	Upper limit of current density	180	kA/ m^2
Cooling efficiency	1.1	-	/	/	/

Fig.4 shows the 24-hour hydrogen production efficiency curve of different operation modes under the typical fluctuation scenarios. The subgraph (a) shows the hydrogen production efficiency, (b) shows the hydrogen production rate, and (c) shows the cumulative total of the hydrogen production amount. Fig.5 shows curves of different operation modes under the extreme fluctuation scenarios in which there are short-term significant power drops caused by cloud cover. Fig.6 shows curves under the extreme fluctuation condition where the photovoltaic power remains at a relatively low level during rainy day. As can be seen from the figure, the hydrogen production efficiency of the operating mode where the operating pressure, current density, and environmental temperature are optimized in coordination is higher than other operating modes.

Table 2., Table 3. and Table 4. respectively show the 24-hour cumulative hydrogen production data of different operation modes under the typical fluctuation scenarios and two extreme fluctuation conditions of photovoltaic. With the same input power, compared with other operation modes, the hydrogen production under the operation mode of collaborative optimization of operation pressure, current density and ambient temperature is significantly higher than other modes. Compared with the mode in which the power of auxiliary equipment is taken as a fixed value, the average production efficiency can be improved by 3.87% and production amount of hydrogen can be improved by 457.12kg and 8.29% under the typical fluctuation scenarios; The average production efficiency can be improved by 4.83% and production amount of hydrogen can be improved by 424.87kg and 8.18% under the extreme fluctuation scenarios in which there are short-term significant power drops caused by cloud cover; And the average production efficiency can be improved by 7.91% and production amount of hydrogen can be improved by 317.23kg and 7.69% under the extreme fluctuation scenarios in which there are short-term power drops caused by cloud cover.

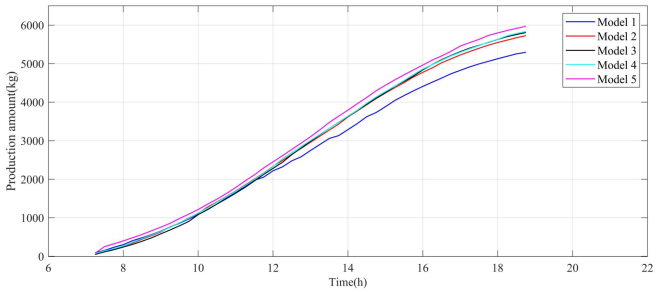


(a) The curve of the hydrogen production efficiency



(b) The curve of the hydrogen production rate

12

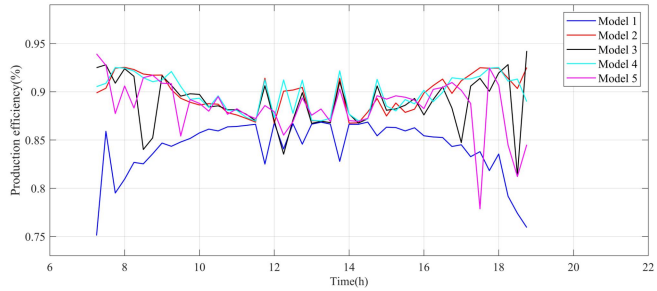


(c) The curve of the hydrogen production amount

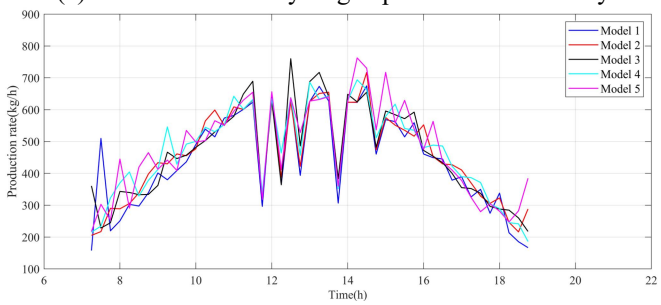
Fig. 4 With the typical photovoltaic fluctuations, curves of hydrogen production efficiency.

Table 2. Performance comparison of different operating modes with typical fluctuating input.

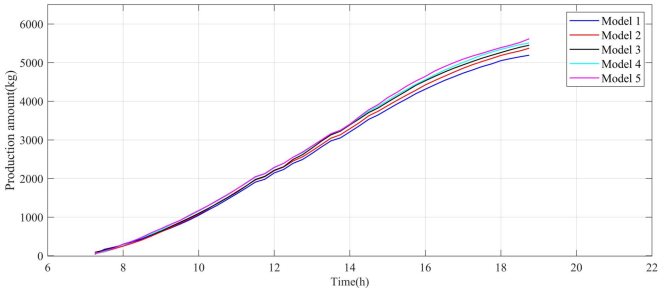
Operating mode	Energy generated by PV	Energy consumed by auxiliary equipment	Production amount of H_2	Average production efficiency of H_2
Mode 1	514.38MWh	47.00MWh	5511.11kg	84.44%
Mode 2	514.38MWh	24.12MWh	5726.06kg	85.22%
Mode 3	514.38MWh	26.11MWh	5806.33kg	86.68%
Mode 4	514.38MWh	32.76MWh	5834.99kg	86.79%
Mode 5	514.38MWh	30.13MWh	5968.23kg	88.31%



(a) The curve of the hydrogen production efficiency



(b) The curve of the hydrogen production rate

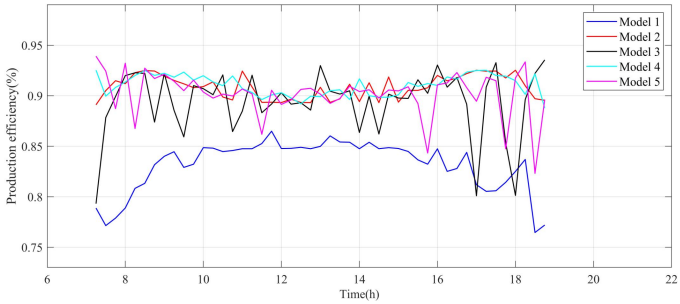


(c) The curve of the hydrogen production amount

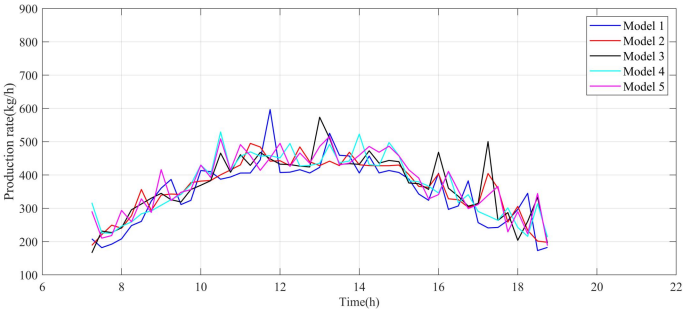
Fig. 5 With short-term power drops, curves of hydrogen production efficiency.

Table 3. Performance comparison of different operating modes with short-term power drops caused by cloud cover.

Operating mode	Energy generated by PV	Energy consumed by auxiliary equipment	Production amount of H_2	Average production efficiency of H_2
Mode 1	482.88MWh	47.00MWh	5192.52kg	84.27%
Mode 2	482.88MWh	20.98MWh	5374.14kg	87.73%
Mode 3	482.88MWh	24.14MWh	5451.63kg	88.68%
Mode 4	482.88MWh	24.23MWh	5511.81kg	88.84%
Mode 5	482.88MWh	29.80MWh	5617.39kg	89.10%

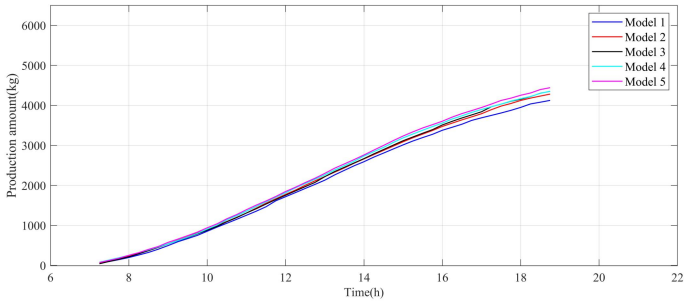


(a) The curve of the hydrogen production efficiency



(b) The curve of the hydrogen production rate

14



(c) The curve of the hydrogen production amount

Fig. 6 With the low level of photovoltaic power, curves of hydrogen production efficiency.

Table 4. Performance comparison of different operating modes with the low level of photovoltaic power during rainy day.

Operating mode	Energy generated by PV	Energy consumed by auxiliary equipment	Production amount of H_2	Average production efficiency of H_2
Mode 1	373.44MWh	47.00MWh	4126.45kg	83.14%
Mode 2	373.44MWh	15.63MWh	4283.33kg	89.39%
Mode 3	373.44MWh	22.96MWh	4352.85kg	90.20%
Mode 4	373.44MWh	15.30MWh	4355.23kg	90.85%
Mode 5	373.44MWh	23.51MWh	4443.68kg	91.05%

5 Conclusion

For the off-grid photovoltaic electrolysis system, the photovoltaic array, electrolytic cell, compressor, dryer, heat exchanger, circulating pump and other auxiliary equipment are incorporated into a unified multi energy coupling dynamic model. And the coupling mechanism and energy transfer law between electric heat gas cooling multi energy flow are revealed.

Based on the coupled equation of electrochemistry, heat and mass transfer, the effects of operating pressure, temperature and current density on the polarization, waste heat and transmembrane water migration of the electrolytic cell were determined; On this basis, an optimization control model with the goal of maximizing hydrogen production efficiency and considering auxiliary power consumption is constructed. And the collaborative optimization of three variables (current density, hydrogen side pressure and ambient temperature) is achieved by using PSO algorithm.

The analysis results of typical photovoltaic fluctuation case show that the proposed multi-parameter collaborative optimization method improves the 24-hour cumulative hydrogen production of the system more than 7% compared with the traditional

strategy without considering auxiliary power consumption or only optimizing a single variable, which verifies the economic feasibility of the method.

References

1. Fang, X., Zhong, X., Dong, W., Zhang, F., and Yang, Q.: Fuzzy logic based coordinated operation strategy for an off-grid photovoltaic hydrogen production system with battery⁄supercapacitor hybrid energy storage[J]. International Journal of Hydrogen Energy 84, 593-605 (2024).
2. Kang, Z., and Liu, S.: Research on capacity optimization configuration of renewable energy off grid hydrogen production system considering collaborative electrolysis[J]. Energies 17(8), 1962 (2024).
3. Fang, X., Dong W., Wang, Y., and Yang, Q.: Multi-stage and multi-timescale optimal energy management for hydrogen-based integrated energy systems[J]. Energy 286, 129576 (2024).
4. Liu, Z., Fan, G., Meng, X., Hu, Y., Wu, D., Jin, G., and Li, G.: Multi-time scale operation optimization for a near-zero energy community energy system combined with electricity-heat-hydrogen storage[J]. Energy 291, 130397 (2024).
5. Scheepers, F., Sthler, M., Sthler, A., Rauls, E., and Lehnert, W.: Temperature optimization for improving polymer electrolyte membrane-water electrolysis system efficiency[J]. Applied Energy 283, 116270 (2021).
6. Qiu, Y., Zhou, B., and Zhang, T.: Extended load flexibility of utility-scale P2H plants: optimal production scheduling considering dynamic thermal and HTO impurity effects[J]. Renewable Energy 217,119198 (2023).
7. Lu, X., Du, B., Zhou, S., Zhu, W., Li, Y., and Yang, Y.: Optimization of power allocation for wind-hydrogen system multi-stack PEM water electrolyzer considering degradation conditions[J]. International Journal of Hydrogen Energy 48(15), 5850-5872 (2023).
8. Li, Y., Deng, X., Zhang, T., and Liu, S.: Exploration of the configuration and operation rule of the multi-electrolyzers hybrid system of large-scale alkaline water hydrogen production system[J]. Applied Energy 331, 120413 (2023).
9. Keller, R., Rauls, E., Hehemann, M., Müller, M., and Carmo, M.: An adaptive model-based feedforward temperature control of a 100 kW PEM electrolyzer[J]. Control Engineering Practice 120, 104992 (2022).
10. Qiu Y., Zhou, B., Zang, T., Yi, Z., Chen, S., Qi, R., Li, J., and Lin, J.: Extended load flexibility of utility-scale P2H plants: optimal production scheduling considering dynamic thermal and HTO impurity effects[J]. Renewable Energy 217, 119198 (2023).
11. Li, Y., Zhang, T., Deng, X., Deng, X., Liu, B., Ma, J., Yang, F., and Ouyang, M.: Active pressure and flow rate control of alkaline water electrolyzer based on wind power prediction and 100% energy utilization in off-grid wind-hydrogen coupling system[J]. Applied Energy 328, 120172, (2022).
12. Correa, G., Marocco, P., Muñoz, P., Falagüerra, T., Ferrero, D., and Santarelli, M.: Pressurized PEM water electrolysis: dynamic modelling focusing on the cathode side[J]. International Journal of Hydrogen Energy 47(7), 4315-4327 (2022).
13. Sartory, M., Wallnöfer-Ogris, E., Salman, P., Thomas, F., Markus, J., Alexander, T., and Manfred, K.: Theoretical and experimental analysis of an asymmetric high pressure PEM

water electrolyser up to 155 bar[J]. International Journal of Hydrogen Energy 42(52), 30493-30508 (2017).
14. Wang, S., Li, M., Li, B., Ai, X., and Fang, J.: Optimal Operation of Integrated Power and Oil Transmission Systems[C]. // 2021 IEEE 4th International Electrical and Energy Conference. pp. 1-6. IEEE, Wuhan, China (2021).
15. Celik, A.: Three-dimensional multiphysics model of a planar solid oxide fuel cell using computational fluid dynamics approach[J]. International Journal of Hydrogen Energy 43(42), 19730-19748 (2018).
16. Hancke, R., Holm, T., and Ulleberg, Ø.: The case for high pressure PEM water electrolysis[J]. Energy Conversion and Management 261, 115642 (2022).

087 基于级联扩张观测器自抗扰控制的双馈风机次同步振荡抑制策略

韩　雨 魏航源 耿嘉豪 吴子敬 张嗣奇 苏勋文

（黑龙江科技大学 电气与控制工程学院，哈尔滨 150022）

Subsynchronous Oscillation Suppression Strategy for DFIG Based on Cascaded Extended State Observer Active Disturbance Rejection Control

Han Yu, Wei Hangyuan, Geng Jiahao, Wu Zijing, Zhang Siqi, Su Xunwen

(School of Electrical and Control Engineering,Heilongjiang University of Science and TechnologyHarbin ,150022, China)

ABSTRACT: To suppress subsynchronous oscillations (SSO) induced by series compensation in grid-connected doubly-fed induction generator (DFIG) systems, this paper proposes an active disturbance rejection control (ADRC) strategy based on a cascaded extended state observer (CESO). A dual-layer disturbance observation framework is constructed to estimate and compensate for the total system disturbance and residual disturbance in real time, thereby effectively mitigating SSO. The global asymptotic stability of the closed-loop system is rigorously proven using Lyapunov stability theory. Simulation results demonstrate that under various operating conditions—including sudden wind speed variations, step changes in series compensation levels, and grid faults — the proposed CESO-based ADRC method exhibits superior dynamic response performance and enhanced robustness compared to conventional PI and linear ADRC (LADRC) strategies. This approach provides an effective solution for ensuring stable operation of renewable energy-powered wind power integration systems.

KEY WORDS: Subsynchronous Oscillation ,Doubly-Fed Induction Generator,Active Disturbance Rejection Control ,Extended State Observer

摘要：为抑制双馈风机并网系统因串补引发的次同步振荡，本文提出一种基于级联扩张状态观测器的自抗扰控制策略。通过构建双层扰动观测架构，实时估计并补偿系统总扰动及残余扰动，有效抑制次同步振荡。采用李雅普诺夫稳定性理论证明了闭环系统的全局渐近 稳定性。仿真结果表明，在风速突变、串补度阶跃变化及电网故障等多种工况下，所提基于级联扩张状态观测器的自抗扰控制策略方法较传统 PI 和 LADRC 控制具有更优的动态响应性能和更强的鲁棒性，为新能源风电并网系统稳定运行提供了有效解决方案。

关键词：次同步振荡 双馈风机 自抗扰控制 扩张状态观测器

中图分类号:TM614

0　引言

近年来，随着风电等新能源装机容量的快速提升以及高比例可再生能源并网进程的不断推进，风力发电系统对电力系统动态稳定性的影响日益凸显。双馈式风力发电机（Doubly-Fed Induction Generator,DFIG）因其优异的功率调节性能和良好的经济性，已成为当前主流的大型风电机组类型，广泛应用于现代新能源电力系统[1]。然而，DFIG 系统通过电力电子变流器与电网耦合，在弱电网运行条件或经串联补偿线路输电时，极易激发次同步振荡（Sub-Synchronous Oscillation, SSO）问题。特别是次同步控制相互作用（Sub-Synchronous Control Interaction,SSCI），已成为制约风电场安全稳定运行的关键挑战之一。若不采取有效抑制措施，SSCI 可能引发系统振荡持续扩大，甚至造成风机脱网、电气设备损坏等严重后果，严重威胁电网运行安全与新能源消纳能力。

目前，针对 DFIG 并网系统引发的 SSCI 问题，传统抑制策略主要包括两类：一是从电网结构入手，如加装可控串联补偿装置（TCSC）或调整串补度，但这类方法存在改造难度大、响应速度慢、经济性较差等问题；二是基于风机控制器的改进方法，通过优化转子侧变流器电流内环或功率外环控

基金项目：2021 年度黑龙江省基本科研业务费项目（2021-KYYWF-1467）
2021 Annual Basic Scientific Research Business Project of Heilongjiang Province (Grant No. 2021-KYYWF-1467)

制算法以增强系统阻尼，从而抑制 SSCI。其中，电流内环多采用传统比例-积分（Proportional-Integral, PI）控制器，虽结构简单、易于工程实现，但其线性固定参数结构难以适应系统运行工况的变化，对模型不确定性及外部扰动的鲁棒性较差，尤其在面对复杂多变的新能源接入环境时，往往无法满足高动态性能的控制需求。

自抗扰控制（Active Disturbance Rejection Control, ADRC）凭借其优异的扰动估计与实时补偿能力，在电力电子和电机控制领域得到广泛关注。传统线性自抗扰控制（Linear ADRC, LADRC）通过线性扩展状态观测器（Extended State Observer, ESO）实时估计系统总扰动并进行有效补偿，显著提升了系统的动态响应性能与鲁棒性[4]。然而，当系统受多扰动影响，传统 ESO 可能存在观测带宽不足、残余扰动无法完全估计的问题，导致振荡抑制效果有限。

针对上述问题，本文提出了一种基于联扩张观测器自抗扰控制(Cascaded Extended State Observer based ADRC，CESO-ADRC)的双馈风机电流内环控制策略。该方法在双馈风机转子侧电流内环中采用自抗扰控制器，替代传统 PI 控制结构，通过实时扰动观测与动态补偿，有效提升系统对建模不确定性及外部扰动的适应能力[6]。同时，针对传统 ESO 存在扰动观测残差的问题，本文设计了一种级联 LESO 结构，利用第二个 ESO 进一步估计残余扰动，构建双层扰动补偿框架，从而显著提高系统的抗干扰能力与振荡抑制效果。本文所提出的控制策略不仅具有更快的动态响应速度与更高的控制精度，还能有效抑制 DFIG 系统中的次同步振荡，保障风电场的安全稳定运行。

1 SSCI 发生机理

次同步控制相互作用是近年来风电场并网运行中广泛关注的一类振荡问题，尤其在双馈感应风力发电机接入串联补偿输电线路的场景下尤为突出[10]。SSCI 本质上是一种由风机控制系统与电网串补线路之间发生动态耦合所引发的次同步频段振荡，其振荡频率通常低于电网基频，且具有强烈的负阻抗特性。

在传统的双馈感应发电机控制架构中，转子侧变流器（Rotor-Side Converter, RSC）通常采用电流内环加功率外环的双闭环控制策略。如图 1 所示，其中电流内环多基于比例-积分（PI）控制器构建，其主要功能是实现对参考电流的快速跟踪，进而调节风机的有功和无功功率输出。然而，PI 控制器本质上属于一种固定增益的线性控制方法，其控制性能尤其是频率响应特性严重依赖于被控对象的精确数学模型。一旦系统运行工况发生变化或外部阻抗条件发生改变，其控制效果易受影响。当风电场接入电网的位置呈现弱电网特性、电网阻抗较大，或系统中存在串联补偿线路时，RSC 内环控制器与电网阻抗之间可能产生不利的动态交互作用。这种交互往往表现为控制回路中引入相位滞后，进而改变系统的阻抗特性。在极端情况下，可能使整个风电场在次同步频带范围内呈现负电阻特性，从而诱发次同步振荡。

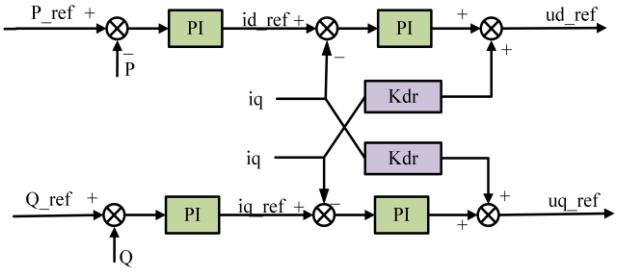


图 1　RSC 控制原理图

Figure 1. Control Principle Diagram of the RSC

双馈风电场采用串补线路输电时，系统中出现次同步频率为:

$$f_{sub} = f_r \sqrt{\frac{X_C}{X_L}} \tag{1}$$

式中：X_C 为线路串补电容电抗，X_L 为双馈风机并网系统的等效电抗。

2 SSCI 抑制策略

为应对振荡频率时变的次同步振荡（SSCI）问题，本文提出采用基于级联扩张状态观测器的自抗扰控制（CESO-ADRC）这一新型控制策略。该策略在 LADRC 的 ESO 基础上级联了 AESO，实时估计并补偿系统总扰动，形成一种具备高精度扰动估计与补偿能力的双层观测结构，以此取代双环 PI 控制中有功内环的传统 PI 控制器，从而全面提升系统在复杂电网工况下的控制性能和稳定性。内层 ESO 负责实时估计系统总扰动，其内容包括电网侧的耦合项、模型参数摄动以及未建模动态等，并生成初步的前馈补偿信号；外层 AESO 则对内层观测残差进行二次估计与修正，构建出双层扰动补偿结构，显著提高了时变扰动尤其是次同步频段分量的跟踪精度。最终实现对总扰动的更彻底补偿。如此双层观测与补偿机制显著增强了系统对频率时变 SSCI 振荡的抑制能力以 d 轴为例，图 2 展示了系

统控制框图，其中 G(s)表示电机模型，控制系统采用线性反馈方式，在保证抗扰性能的同时也维持了系统结构的相对简洁性。

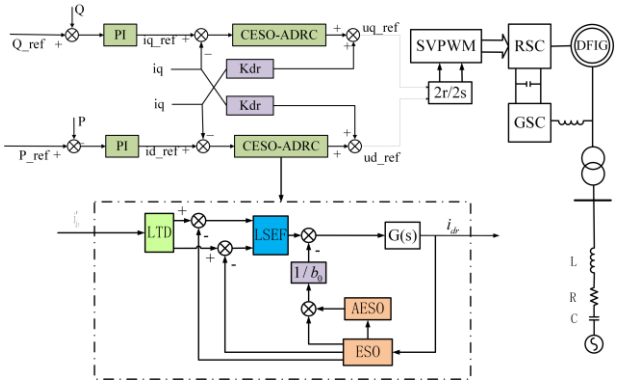


图 2 基于级联扩张观测器自抗扰控制的双馈风机次同步振荡抑制策略

Fig. 2 Subsynchronous oscillation suppression strategy for DFIG based on cascaded extended state observer active disturbance rejection control

在自抗扰控制中，线性跟踪微分器（Linear Tracking Differentiator，LTD）用于生成平滑且快速的参考信号轨迹，并对其导数进行估计，增强控制系统的动态响应能力与抗干扰鲁棒性[15]。本文所采用的 LTD 的微分方程设计如下：

$$\begin{cases} \dot{V1} = V2 \\ \dot{V2} = -2rV2 - r^2(V1 - V0) \end{cases} \tag{2}$$

式中：V_0 为目标信号，V_1 为微分器输出的跟踪信号，V_2 为微分器输出的跟踪信号的微分，r 为决定跟踪快慢的跟踪因子。

当定子侧接入电网后，若忽略定子电阻压降及磁链的暂态过程，可将定子电压的幅值与频率视为恒定。当 RSC 采用电网电压定向矢量控制时，双馈感应电机的转子侧电流控制模型可描述如下[14]：

$$\begin{cases} \dfrac{di_{dr}}{dt} = -\dfrac{R_r}{\sigma L_r} i_{dr} + \omega_{slip}\left(-\dfrac{L_m}{\sigma L_r \omega_1 L_s} U_s + i_{qr}\right) + \dfrac{1}{\sigma L_r} u_{dr} \\ \dfrac{di_{qr}}{dt} = -\dfrac{R_r}{\sigma L_r} i_{qr} - \omega_{slip} i_{dr} + \dfrac{1}{\sigma L_r} u_{qr} \end{cases} \tag{3}$$

式中：σ 为泄漏系数，R_r 为转子电阻，$\omega_{slip} = \omega_1 - \omega_r$ 转差角频率，ω_1 为定子角频率，ω_r 为转子角频率，i_{qr}、i_{dr} 分别为转子电流 q、d 分量；L_s、L_r 分别为定子、转子绕组自感；L_m 为定转子绕组互感。

将 d 轴电流控制方程等式两边求导，整理为：

$$\begin{aligned} \frac{d^2 i_{dr}}{dt^2} = &-\frac{R_r}{\sigma^2 L_r^2} u_{dr} + \frac{R_r^2}{\sigma^2 L_r^2} i_{dr} + \frac{R_r \omega_{slip}}{\sigma^2 L_r^2} \cdot \\ &\left(\frac{L_m}{\omega_1 L_s} U_s - \sigma L_r i_{qr}\right) + \omega_s \frac{di_{qr}}{dt} + \frac{1}{\sigma L_r} \cdot \frac{du_{dr}}{dt} \end{aligned} \tag{4}$$

将式(4)中的耦合及不确定项统一表示为扰动 f，可简化得到二阶控制对象：

$$\ddot{y} = bu_{dr} + f \tag{5}$$

式中：$b = -R_r / \left(\sigma^2 L_r^2\right)$ 为控制器增益;f 表示控制器系统内外的总扰动。选取状态变量 x_1, x_2, x_3，令

$$\begin{cases} x_1 = y \\ x_2 = \dot{y} \\ x_3 = f \\ h = \dot{f} \end{cases} \tag{6}$$

列写系统的状态空间方程为:

$$\begin{cases} \begin{bmatrix} \dot{x}_1 \\ \dot{x}_2 \\ \dot{x}_3 \end{bmatrix} = \begin{bmatrix} 0 & 1 & 0 \\ 0 & 0 & 1 \\ 0 & 0 & 0 \end{bmatrix} \begin{bmatrix} x_1 \\ x_2 \\ x_3 \end{bmatrix} + \begin{bmatrix} 0 \\ b_0 \\ 0 \end{bmatrix} u + \begin{bmatrix} 0 \\ 0 \\ 1 \end{bmatrix} h \\ y = \begin{bmatrix} 1 & 0 & 0 \end{bmatrix} \begin{bmatrix} x_1 \\ x_2 \\ x_3 \end{bmatrix} \end{cases} \tag{7}$$

基于状态空间方程，设计线性扩张状态观测器如下：

$$\begin{cases} \begin{bmatrix} \dot{z}_1 \\ \dot{z}_2 \\ \dot{z}_3 \end{bmatrix} = \begin{bmatrix} -\beta_1 & 1 & 0 \\ -\beta_2 & 0 & 1 \\ -\beta_3 & 0 & 0 \end{bmatrix} \begin{bmatrix} z_1 \\ z_2 \\ z_3 \end{bmatrix} + \begin{bmatrix} 0 & \beta_1 \\ b_0 & \beta_2 \\ 0 & \beta_3 \end{bmatrix} \begin{bmatrix} u \\ y \end{bmatrix} \\ \hat{y} = \begin{bmatrix} 1 & & \\ & 1 & \\ & & 1 \end{bmatrix} z \end{cases} \tag{8}$$

CESO 的核心思想是将 ESO 所估计的总扰动 z3 作为已知输入，引入一个附加的线性扩展状态观测器（Additional ESO ,AESO），用于进一步估计系统中的残余扰动。通过这种结构，能够更有效地抑制扰动对系统造成的影响。将式(5)改写为：

$$\ddot{y} = bu_{rd} + z_3 + g \tag{9}$$

其中 g 为残余扰动。构建 ALESO 为：

$$\begin{bmatrix} \dot{v}_1 \\ \dot{v}_2 \\ \dot{v}_3 \end{bmatrix} = \begin{bmatrix} -\beta_{a1} & 1 & 0 \\ -\beta_{a2} & 0 & 1 \\ -\beta_{a3} & 0 & 0 \end{bmatrix} \begin{bmatrix} v_1 \\ v_2 \\ v_3 \end{bmatrix} + \begin{bmatrix} 0 & 0 & \beta_{a1} \\ b_0 & 1 & \beta_{a2} \\ 0 & 0 & \beta_{a3} \end{bmatrix} \begin{bmatrix} u \\ z_3 \\ y \end{bmatrix} \tag{10}$$

v_1, v_2 是 AESO 对 x_1, x_2 的估价值，v_3 是 AESO 对残余干扰 g 的估计值。

将 ESO 和 AESO 特征方程的根统一用观测器带宽 ω_0 表示，即 $\beta_1 = \beta_{a1} = 3\omega_0$，$\beta_2 = \beta_{a2} = 3\omega_0^2$，$\beta_3 = \beta_{a3} = \omega_0^3$。

根据 CESO 对系统内外部总扰动的估计，利用扰动反馈量动态补偿次同步扰动量，形成最终的控制量 u_{dr} 来抑制双馈风机 SSCI。CESO 可实时观测

出系统总扰动为 ESO 估计值与 AESO 估计的残差扰动之和,:

$$\dot{v}_3+\dot{z}_3\approx g+z_3=\mathrm{f} \tag{11}$$

将最终系统的控制量 u 设计为：

$$u=u_0-\frac{z_3+v_3}{b_0} \tag{12}$$

式中:u_0 为虚拟控制量;b_0 取为控制器增益 b 的估计值，总扰动 f 包括 b_0 与 b 估计不准的部分。

合适的的线性状态误差反馈可以提高系统抗扰能力，增加稳定性。设计状态误差反馈控制律为：

$$u_0=k_p(r-z_1)-k_d z_2 \tag{13}$$

通常取值为 $k_d=2\xi\omega_c$，$k_p=\omega_c^2$，ω_c 为状态误差反馈控制律的带宽，ξ 为闭环系统的阻尼比。

3 稳定性分析及参数整定

为验证 CESO-ADRC 闭环系统的稳定性，本文采用频域分析法中的奈奎斯特稳定性判据，通过分析系统开环频率特性，评估闭环稳定性及鲁棒性能。

基于式(9)所示的被控对象模型和式(13)的控制律，推导系统开环传递函数为：

$$G_0(s)=\frac{(k_p+k_d s)\cdot\omega_0^3}{s^2(s+\omega_0)^3} \tag{14}$$

绘制 $G_0(s)$ 的奈奎斯特曲线，如图 3 所示。

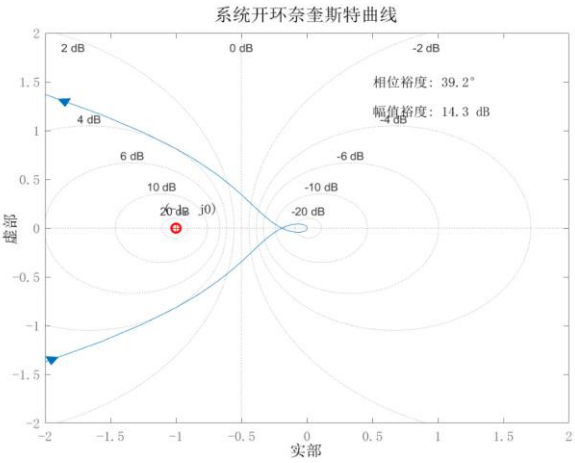


图 3 系统开环奈奎斯特曲线

Fig. 3 Nyquist curve of the open-loop system

分析表明，奈奎斯特曲线不包围(−1,j0)点，且系统具有足够的相位裕度（PM>45°）和幅值裕度（GM>6dB），满足奈奎斯特稳定判据，证明闭环系统稳定。

CESO-ADRC 控制器参数设置如下：控制器增益 b=62.5，由转子侧漏感系数确定；观测器带宽 $\omega_0=100$，确保快速扰动估计；控制器带宽 $\omega_c=25$。状态反馈增益按临界阻尼 ξ =0.707，该参数设置满足的稳定性条件，在保证系统动态响应的同时具有良好鲁棒性。

4 仿真分析

为了验证 SSCI 机理分析的正确性以及 CESO-ADRC 控制器抑制 SSCI 的有效性，参考美国典型风电场的运行工况，在 MATLAB/Simulink 平台上构建了包含双馈感应风力发电机并网系统及串联电容补偿输电线路的仿真模型如图 4 所示。设定系统基频为 60 Hz，额定电压为 575 V，

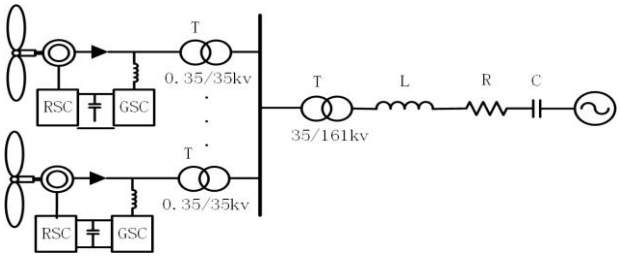


图 4 DFIG 经串补线路输电等效模型

Fig.4 Equivalent model of a DFIG transmitting power through a series-compensated line

DFIG 及输电线路参数如表 1 所示。

表 1 DFIG 及输电线路参数

Table 1 Parameters of the DFIG and Transmission Line

参数名称	数值
额定功率 P/MW	1.5
额定频率 *f*/Hz	60
转子电阻 *Rr*/pu	0.016
定子电阻 *Rs*/pu	0.023
转子电感 *Lr*/pu	0.16
定子电感 *Ls*/pu	0.18
定转子互感 *Lm*/pu	2.9
变压器 T 电抗 X_T/pu	0.02

4.1 PI 控制与 CESO-ADRC 的运行特性对比

4.1.1 风速变化

为验证所提 CESO-ADRC 策略在风速扰动工况下的适应性，在 t=0.8s 时施加阶跃风速扰动，由初始风速 8m/s 增大至 12m/s。图 5 对比了传统 PI 控制与 CESO-ADRC 策略下的 DFIG 有功功率响应曲线。

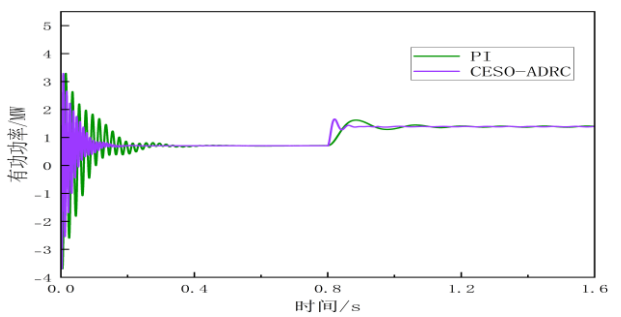


图 5 风速变化下风机输出有功功率

Fig.5 Output active power of the wind turbine under the change of wind speed

4.1.2 串补度变化

在不同串补度条件下对比了传统 PI 控制器与 CESO-ADRC 控制器的动态响应特性。如图 6 和图 7 所示，当串补度为 20%时，两种控制器均能维持系统稳定，但 CESO-ADRC 表现出更优的动态性能，其超调量和调节时间均低于 PI 控制。当串补度升高至 50%时，PI 控制出现持续振荡，而 CESO-ADRC 仍能有效抑制次同步振荡，展现出较 PI 控制更强的适应性和鲁棒性。

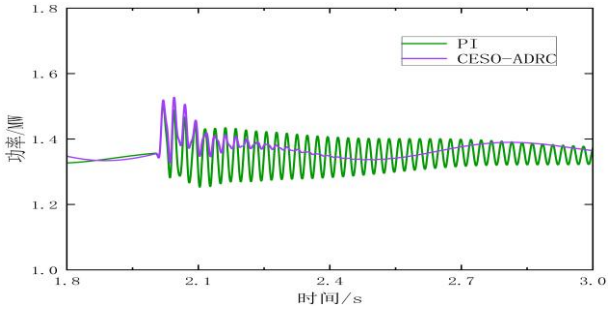


图 6 PI 与 CESO-ADRC 控制在 20%串补度下风机输出有功功率

Fig. 6 Active power output of the wind turbine with PI and CESO-ADRC controls under 20% series compensation degree

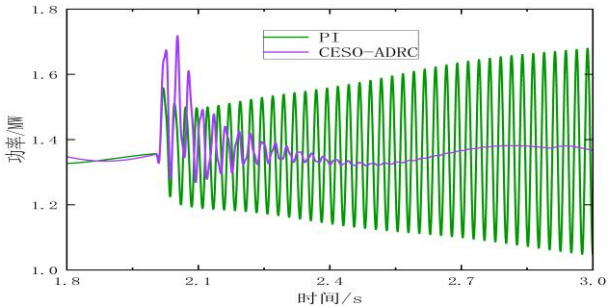


图 7 PI 与 CESO-ADRC 控制在 50%串补度下风机输出有功功率

Fig.7 Active power output of the wind turbine with PI and CESO-ADRC controls under 50% series compensation degree

4.2 LADRC 控制与 CESO-ADRC 的运行特性对比

4.2.1 串补度变化

图 8 与图 9 对比了 LADRC 与 CESO-ADRC 在 20%和 50%串补度下的动态响应特性。仿真结果表明：在 20%串补度下，CESO-ADRC 和 LADRC 均有调节效果，当串补度增至 50%时，LADRC 出现明显振荡且收敛缓慢，而 CESO-ADRC 仍保持平稳过渡且功率波动幅度减小。改进的 CESO-ADRC 通过级联观测器结构实现了对残余扰动的高精度估计与补偿，显著提升了系统在高串补度工况下的稳定性和抗干扰能力。

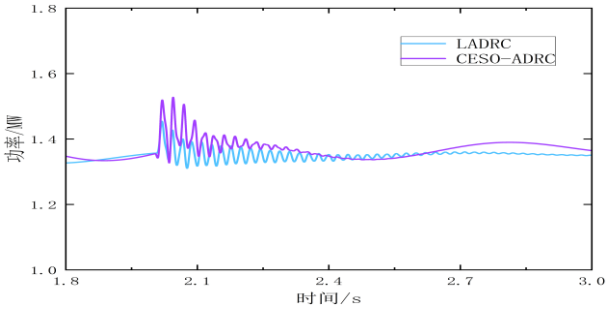


图 8 LADRC 与 CESO-ADRC 控制在 20%串补度下风机输出有功功率

Fig. 8 Active power output of the wind turbine with LADRC and CESO-ADRC controls under 20% series compensation degree

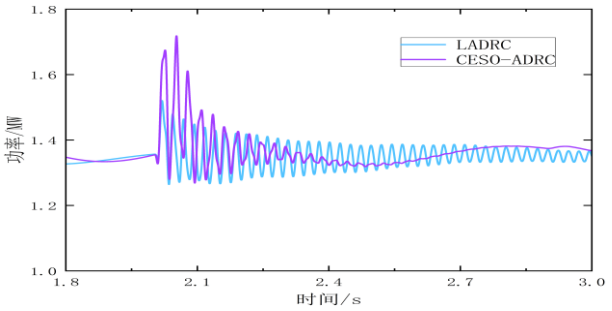


图 9 LADRC 与 CESO-ADRC 控制在 50%串补度下风机输出有功功率

Fig. 9 Active power output of the wind turbine with LADRC and CESO-ADRC controls under 50% series compensation degree

4.2.2 三相不平衡电网故障

为检验控制策略在电网故障条件下的适应性，设置了不投入串补时单相接地故障工况进行仿真验证。图 10 展示了传统 LADRC 与 CESO-ADRC 在故障发生时的有功功率动态响应对比。仿真结果表明：虽然 CESO-ADRC 的超调量较 LADRC 略有增加，但其调节时间显著缩短约，体现了更好的快速恢复能力。CESO-ADRC 通过级联观测器结构增强了对突变扰动的感知速度,体现了故障工况下快速性与稳定性的优化平衡。

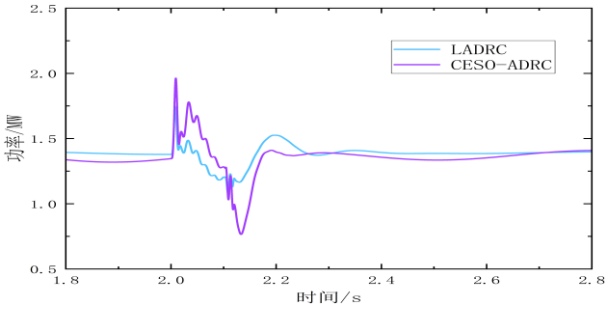


图 10 LADRC 与 CESO-ADRC 控制在单相接地故障下风机输出有功功率

Fig. 10 Active power output of the wind turbine with LADRC and CESO-ADRC controls under single-phase

grounding fault conditions

4.3 CESO-ADRC 鲁棒性分析

4.3.1 CESO-ADRC 控制器后投入

为验证 CESO-ADRC 控制器的鲁棒性能，特设计阶跃扰动实验：在 t=2s 时投入 20%串补电容引入系统扰动，随后在 t=3s 时投入 CESO-ADRC 控制器。如图 11 所示，在串补投入后系统出现明显功率振荡，当 CESO-ADRC 控制器投入后，功率振荡在 0.3s 内快速平息，系统恢复稳定运行。

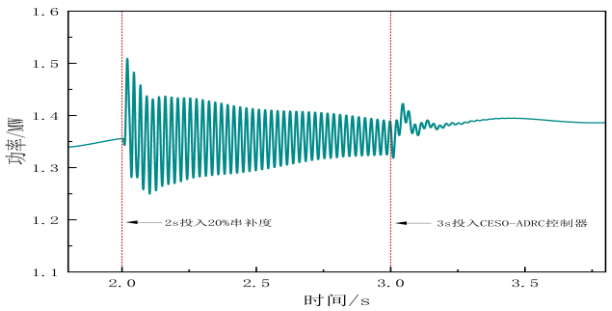


图 11 风机输出有功功率

Fig.11 Output active power of wind turbine

4.3.2 串补度工况变化

系统串补度从初始 30%（t=2s）提升至 50%（t=3s）的阶跃扰动，如图 12 所示，传统 PI 控制在串补度提升后出现持续功率振荡，特别是在 50%串补度时振荡幅度加剧；而 CESO-ADRC 控制器在各阶段均能快速平息振荡，保持功率稳定。

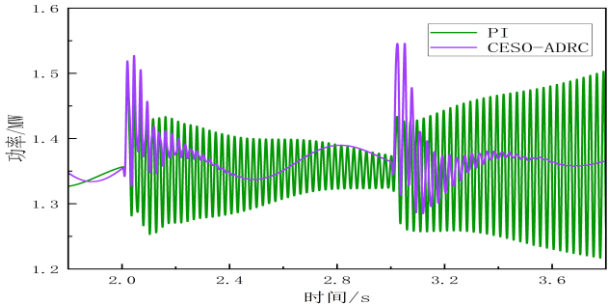


图 12 LADRC 与 CESO-ADRC 控制在变串补度工况下风机输出有功功率

Fig. 12 Active power output of the wind turbine with LADRC and CESO-ADRC controls under varying series compensation degree conditions

5 结论

本文提出了一种基于级联扩张观测器自抗扰控制（CESO-ADRC）的双馈风机次同步振荡抑制策略。通过构建双层扰动观测架构，实现了对系统总扰动及残余扰动的高精度估计与实时补偿。理论分析证明了该控制方法在满足带宽约束条件下的全局渐近稳定性。仿真结果表明，在风速突变、串补度变化及电网故障等多种工况下，所提策略均能有效抑制次同步振荡，较传统 PI 和 LADRC 控制具有更快的动态响应、更强的鲁棒性和更好的适应性，为高比例新能源电网稳定运行提供了有效解决方案。

参考文献

[1] 郑大周,曾东,李广磊,等.双馈型风力发电机组电气模型的建立与仿真研究[J].电气工程学报,2019,14(03):81-89。

[2] 董晓亮,谢小荣,杨煜,等.双馈风机串补输电系统次同步谐振影响因素及稳定区域分析[J].电网技术,2015,39(01):189-193.

[3] Zhao J, Zhang X, Bao Y, et al. Quasi-resonant Active Disturbance Rejection Control for Current Harmonic Suppression in Vector-Controlled PMSMs[C]//2024 IEEE Transportation Electrification Conference and Expo, Asia-Pacific (ITEC Asia-Pacific). IEEE, 2024: 234-238.

[4] 高本锋,易友川,邵冰冰,等.基于自抗扰控制的直驱风电场次同步振荡抑制策略[J].电力自动化设备,2020,40(09):148-157.

[5] 刘琳,陈波.电力系统次同步谐振的分析[J].上海电气技术,2023,16(01):32-36.

[6] Shair J, Xie X, Yan G. Mitigating subsynchronous control interaction in wind power systems: Existing techniques and open challenges[J]. Renewable and Sustainable Energy Reviews,2019, 108: 330-346.

[7] 郭成,杨宣铭,王林玲,等.基于电流内环滑模自抗扰控制的直驱风电场次同步振荡抑制策略研究[J].电力系统保护与控制,2025,53(04):85-95.

[8] 刘昌建,董锋斌,赵永玮.基于扩张状态观测器的 DFIG 滑模直接功率控制[J].电力系统及其自动化学报,2022,34(07):41-49.

[9] 金坤善,贾睿东,张井岗,等.基于 CESO 的磁悬浮球系统线性自抗扰控制[J/OL].控制工程,1-7.

[10] Wang L, Xie X, Jiang Q, et al. Centralised solution for subsynchronous control interaction of doubly fed induction generators using voltage-sourced converter[J]. IET Generation Transmission & Distribution, 2015, 9(16): 2751-2759.

[11] 陈增强，孙明玮，杨瑞光. 线性自抗扰控制器的稳定性研究[J]. 自动化学报，2013，39(5)：574-580.

[12] 朱良红,张国强,李宇欣,等.基于级联扩张观测器的永磁电机无传感器自抗扰控制策略[J].电工技术学报,2022,37(18):4614-4624.

[13] 任志斌,黄瑞海,吴宇,等.基于双环自抗扰准谐振控制器的 PMSM 谐波电流抑制[J].组合机床与自动化加工技术,2025,(03):94-98.

[14] 姚寅,陈梦滢,徐波,等.基于级联线性-非线性观测器自抗扰的风储混合系统控制[J/OL].电力电子技术,1-10.

[15] Wang B, Tian M, Yu Y, et al. Enhanced ADRC with quasi-resonant control for PMSM speed regulation considering aperiodic and periodic disturbances[J]. IEEE Transactions on Transportation Electrification, 2021, 8(3): 3568-3577.

[16] 张剑，肖湘宁，高本锋，等. 双馈风力发电机的次同

步控制相互作用机理与特性研究[J]. 电工技术学报，2013，28(12)：142-149.

作者简介

韩雨（2001-），女，硕士研究生，研究方向为风电场次同步振荡抑制；

E-mail:hy04272025@163.com

魏航源（2001-），男 ，硕士研究生，研究方向为风电场功率预测；

E-mail:weihangyuan0801@163.com

耿嘉豪（2000-），男 ，硕士研究生，研究方向为电力系统的漏电保护；

E-mail:gengjiahao0926@163.com

088 基于简化模型 MPC 的双馈风机有功功率控制

吴子敬，韩雨，魏航源，耿嘉豪，张嗣奇，苏勋文

（1．黑龙江科技大学 电气与控制工程学院，哈尔滨 150022）

Active power control of doubly-fed wind turbines based on simplified model MPC

Wu Zijing, Wei Hangyuan, Geng Jiahao, Han Yu, Su Xunwen

(Heilongjiang University of Science and Technology School of Electrical and Control Engineering)

ABSTRACT: Amidst the large-scale integration of wind power into power grids, this study proposes a simplified model predictive control (MPC) strategy for active power regulation in doubly-fed induction generators (DFIGs), aiming to address the computational complexity associated with high-dimensional state-space models in conventional MPC approaches. The proposed method simplifies the fifth-order two-mass drive-train model into a second-order single-inertia model by decoupling pitch angle control, thereby formulating a state-space equation based on rotor speed and electromagnetic torque. Simulation results indicate that the simplified model significantly reduces computational demands while maintaining effective primary frequency control performance, thereby providing an efficient approach for implementing MPC at the wind farm level and supporting further research on wind-storage coordinated optimization.

KEY WORDS: wind power generation, primary frequency regulation, model predictive control, state space equation, doubly-fed wind turbine

摘要：在风电规模化并网的背景下，为解决传统模型预测控制（MPC）因高维状态空间模型导致的计算复杂性问题，本文提出一种适用于双馈风机的简化 MPC 有功控制策略。该方法将五阶双质量传动模型简化为二阶单惯量模型，通过分离桨距角控制，构建以转子转速和电磁转矩为核心的状态方程。仿真表明，简化模型在保证一次调频控制效果可靠的前提下，显著降低计算负担，为风电场站级 MPC 提供高效解决方案，并支持后续风储协同优化研究。

关键词：风力发电，一次调频，模型预测控制，状态空间方程，双馈风机

DOI:

基金项目：“2021 年度黑龙江省省属高校基本科研业务费项目”，项目编号 2021-KYYWF-1467。

Fund Project: Basic Scientific Research Fund Project of Heilongjiang Provincial Universities in 2021, Project No. 2021-KYYWF-1467

0 引言

双碳大背景下，全国大力发展新能源发电，2024 年全国风电新增装机容量 7982 万千瓦，同比增长 6%[1]。由于风电的低惯性、弱支撑的特性，随着风电装机渗透率提高，电力系统惯量水平和频率电压支撑能力下降，为新型电力系统的稳定性带来挑战[2]。为应对上述挑战，国家政策层面已明确要求新能源场站提升调节能力[3]。尤其值得注意的是，最新《电力系统安全稳定导则》（征求意见稿）更有强制规定：所有并网电源（含风电）必须具备一次调频能力，且控制模式与性能需满足系统安全稳定运行要求。因此，研究风电有功功率控制有助于为电网频率支撑提供，提高新型电力系统稳定性。

在风电机组频率控制中，机组层面方法有附加控制环路的虚拟惯量响应，超速控制、变桨控制等，场站层面有集中式控制和分布式控制等[2]，其中模型预测控制(model predictive control, MPC)其动态规划控制能力和多目标协同能力，让其在风力发电控制领域中也有很多应用。文献[4][5]中都使用了 MPC 进行单机控制，并且其状态空间模型都反应了风机机械结构特性，将风机抽象成风轮机-转轴-转子的双质量扭转系统，其状态空间模型能够较好地反应其暂态机械特性，但存在控制周期与扭振周期不匹配的问题，并且状态空间模型维数高，若在场站控制中使用则复杂度高，计算成本高。文献[6]对风储系统进行联合 MPC 控制，考虑风储配合下的最优分配。文献[7][8]中对整个电力系统建模，将电网视为有机整体，达到经济型优化和频率稳定的目的，实现火电、风、储能的功率动态最优分配。文献[9][10]使用分层 MPC 控制，多个 MPC 控制器使用不同时间尺度分层控制，在时间上互补不足。

文献[11]对风场进行建模，只考虑风场的发出功率，虽然模型简单，计算量小，但忽视了风机中旋转质量蕴含的动能，也忽视了风机转速安全。

综上，本文在文献[4]的基础上提出了一种适用于风场 MPC 使用的简化状态空间模型，其计算量大幅减小的同时，控制效果依旧可靠，并且能在场站级控制时考虑旋转质量的动能。

1 数学模型

1.1 风机模型

1.1.1 空气动力学模型

风机空气动力学模型，由**定理 1（贝兹理论）**得风力机部分的的数学模型：

$$\begin{cases} P_m = \dfrac{1}{2}\rho\pi R^2 v^3 C_p(\lambda,\beta) \\ C_p(\lambda,\beta) = c_1\left(\dfrac{c_2}{\lambda} - c_3\beta - c_4\right)e^{\frac{c_5}{\lambda_i}} + c_6\lambda \\ \dfrac{1}{\lambda_i} = \dfrac{1}{\lambda+0.08\beta} - \dfrac{0.035}{\beta^3+1} \end{cases} \tag{1}$$

式中，P_m 为风电机组的风能捕获功率，ρ 为空气密度，R 为风轮半径，v 为风速，$C_p(\lambda,\beta)$ 为风能利用系数，β 为桨距角，λ 为叶尖速比，定义为 $\lambda=\omega R/v$，λ_i 为中间参数，c_1 均为参数。

风机空气动力学数学模型表达了风机功率与桨距角、风速、风轮机转速的关系。

1.1.2 机械传动系统模型

风轮机的机械结构建模：在文献[4]中，将风轮机的机械模型抽象成双质量扭转系统如图 1。

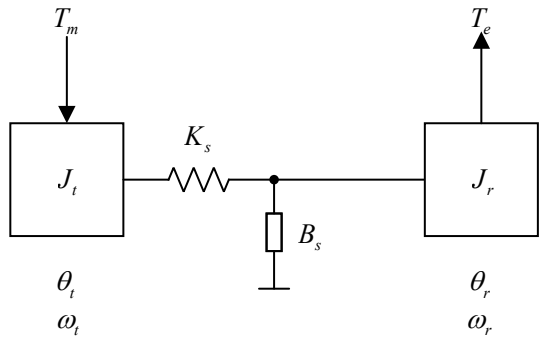


图 1 风机双质量扭转系统

如图 1，扇叶抽象为均匀旋转质量块其转动惯量为 J_t 转速为 ω_t，传动轴为弹性轴，其扭转弹性系数为 K_s 扭转阻尼为 B_s，后面连接齿轮箱设其为理想齿轮，后连接电机转子抽象为一个旋转质量块，转动惯量为 J_r，转速为 ω_r。此时可得整个旋转传动系统的数学表达式为：

$$\frac{d\omega_t}{dt} = \frac{1}{J_t}(T_t - T_{shaft}) \tag{2}$$

$$\frac{d\omega_r}{dt} = \frac{1}{J_r}\left(\frac{T_{shaft}}{N} - T_e\right) \tag{3}$$

$$T_{shaft} = K_s\int(\omega_t - N\omega_r)dt + B_s(\omega_t - N\omega_r) \tag{4}$$

式中，T_t 是风轮机的气动转矩，可由 P_m/ω_t 得到，T_{shaft} 是传动轴的机械转矩，T_e 是发电机转子的电磁转矩。N 为齿轮箱变比。

以上三个方程描述了风轮机旋转传动系统的动态运动模型，方程揭示了气动转矩与电磁转矩同旋转体转速之间的关系。

1.1.3 桨距角控制

在建模中，桨距角控制使用一阶惯性环节表示。

$$\frac{d\beta}{dt} = \frac{1}{\tau_\beta}(\beta^* - \beta) \tag{5}$$

β 是桨距角实际值，β^* 是桨距角的指令值，τ_β 是一阶惯性时间常数。

1.1.4 发电机电磁转矩控制：

发电机电磁转矩同桨距角，使用一节惯性环节表示，

$$\frac{dT_e}{dt} = \frac{1}{\tau_e}(T_e^* - T_e) \tag{6}$$

τ_e 是一阶惯性时间常数，T_e^* 是电机电磁转矩指令值。

1.2 状态空间方程

综上，文献[4]将非线性模型经过傅里叶变换后得到一阶线性近似模型，提出状态空间模型

$$x = \begin{bmatrix} \delta\theta_e \\ \delta\omega_t \\ \delta\omega_r \\ \delta T_e \\ \delta\beta \end{bmatrix} \quad u = \begin{bmatrix} \delta T_e^* \\ \delta\beta^* \end{bmatrix} \quad d = \delta v \quad y = \delta P_e \tag{7}$$

其中 θ_e 是传动轴的扭转角 $\theta_e = \int\left(\omega_t - \dfrac{\omega_r}{N}\right)dt$，$\delta$ 前缀代表变量是到工作点的差值。

$$A = \begin{bmatrix} 0 & 1 & -1 & 0 & 0 \\ -K_s/J_t & -(K_{\omega_r} - B_s)/J_t & B_s/J_t & 0 & -K_\beta/J_t \\ K_s/J_r & B_s/J_r & -B_s/J_r & -1/J_r & 0 \\ 0 & 0 & 0 & -1/\tau_e & 0 \\ 0 & 0 & 0 & 0 & -1/\tau_\beta \end{bmatrix}, \tag{8}$$

$$B_u = \begin{bmatrix} 0 & 0 \\ 0 & 0 \\ 0 & 0 \\ 1/\tau_e & 0 \\ 0 & 1/\tau_\beta \end{bmatrix}, B_d = \begin{bmatrix} 0 \\ -K_v/J_t \\ 0 \\ 0 \\ 0 \end{bmatrix}, C = \begin{bmatrix} 0 & 0 & \eta\overline{T_e} & \eta\overline{\omega_r} & 0 \end{bmatrix}$$

2 简化建模

2.1 简化建模意义

以上状态空间模型应用在 MPC 控制中时模型阶数较高，计算量较大，并且风机风轮机-传动轴-

转子的双质量扭转系统中，风机的参数决定了其风轮机-转子传动轴扭振周期通常较小，通过公式：

$$T = 2\pi\sqrt{\frac{J_t N^2 J_r}{J_t + N^2 J_r}\frac{1}{K_s}} \tag{9}$$

可得风轮机-传动轴-转子的双质量扭转系统的扭振周期，通过计算可得文献[12]中 5MW 风机扭振周期约为 0.451s，文献[13]中风机扭振周期为 0.08s,综上可以看出风机扭振主频率一般都在 2Hz 以上，而根据**定理 2（奈奎斯特采样定理）**，控制周期应当在信号周期 2 倍以上，这与风力发电机有功功率控制的 MPC 控制器常用的控制周期 0.5s~2s 要小，因此，考虑传动轴的弹性的建模并不能在进行有功功率控制时对其的扭振影响起到太大的抑制作用。

综上，本文提出一种简化版的状态空间模型，忽略相对控制周期较高频的暂态过程，这样做旨在减少计算量的同时，又能保持原本模型的控制效果。

2.2 公式推导

本文忽略传动轴的弹性，将其视为刚体，则此时风轮机扇叶转速与电机转子转速将变成简单的齿轮箱变比倍数关系，有：

$$\omega_r = N\omega_r \tag{10}$$

机电平衡方程联立式(2)(3)，可得

$$J_r\frac{d\omega_r}{dt} + \frac{J_t}{N}\frac{d\omega_t}{dt} = T_e - \frac{T_t}{N} \tag{11}$$

再联立式(10)(11),可进一步简化为：

$$\frac{d\omega_r}{dt} = \frac{\frac{T_t}{N} - T_e}{J} \tag{12}$$

其中 J 是将整个机械系统的转动惯量归算到转子侧的等效转动惯量 $J = \frac{J_t}{N^2} + J_r$。这个公式描述了风机旋转质量系统中转速对输入气动转矩和输出电磁转矩的响应，是简化模型的核心方程。

由此，风力发电机被抽象为单惯量系统，整个系统只考虑风能带来的输入气动转矩、旋转体转速和输出电磁转矩三个变量。如图：

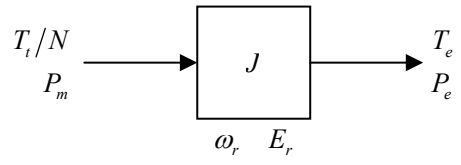


图 2 风机单惯量系统

而关于桨距角项 β，桨距角控制由于其机械响应延迟和机械磨损问题，不适合频繁动作，并且变桨控制的主要目的是维持额定功率稳定输出，限制高风速下的风轮捕获能量，在风切变等场景下减少疲劳损伤[14][15]。而在 MPC 控制的一次调频过程中，控制周期较短，会导致扇叶桨距角频繁改变，这与桨距角控制的目的及限制冲突。综合考虑以上因素桨距角变量适合与一次调频 MPC 控制分开单独控制，因此，本文的状态空间模型中没有桨距角变量。

由式(1)可得风轮机获得气动转矩与转速的关系是非线性的，因此要建立适合 MPC 控制的状态空间方程，首先要将非线性部分用泰勒展开一阶线性化。

$$\begin{aligned} T_t(\omega, v) &= T_t(\bar{\omega}_t, \bar{v}) \\ &+ \left(\delta\omega_t\frac{\partial}{\partial\omega_t} + \delta v\frac{\partial}{\partial\omega_t}\right)T_t(\bar{\omega}_t, \bar{v}) \\ &+ \left(\delta\omega_t\frac{\partial}{\partial v} + \delta v\frac{\partial}{\partial v}\right)T_t(\bar{\omega}_t, \bar{v}) \end{aligned} \tag{13}$$

其中

$K_\omega = \left(\frac{\partial}{\partial\omega_t} + \frac{\partial}{\partial v}\right)T_t(\bar{\omega}_t, \bar{v})$, $K_v = \left(\frac{\partial}{\partial\omega_t} + \frac{\partial}{\partial v}\right)T_t(\bar{\omega}_t, \bar{v})$。

综上所述，简化后，状态变量缩减为只有转子转 ω_r 和转子电磁转矩 T_e。

2.3 简化状态空间模型

由此可得简化后的状态空间方程如下：

$x = \left[\delta\omega_r \ \ \delta T_e\right]^{\mathrm{T}}$， $u = \delta T_e^*$， $d = \delta v$

$$A = \begin{bmatrix} \frac{K_\omega}{N^2 J} & -\frac{1}{J} \\ 0 & -\frac{1}{\tau_e} \end{bmatrix} B_u = \begin{bmatrix} \frac{1}{\tau_e} \end{bmatrix} B_d = \begin{bmatrix} \frac{K_v}{NJ} \end{bmatrix},$$

$C = \left[\eta\overline{\omega_r} \ \ \eta\overline{T_e}\right]$

将风机模型简化至此后，根据 MPC 的 QP 求解复杂度规律，本文由五阶两输入模型简化为二阶单输入模型后，计算量减少约 90%内存需求减少约 80%。

3 仿真验证

本文采用 MATLAB/Simulink 进行仿真，仿真模型风机采用 2MW 风机，风机参数参考文献[16]经过计算整理后具体如下：

表 1 风机参数

Table 1 Parameters of Wind Turbine Generator

变量	数值	单位
J_r	130	$kg\cdot m^2$
J_t	7.94×10^6	$kg\cdot m^2$
K_s	4.04×10^8	Nm/rad
B_s	2.29×10^5	Nms/rad

本文设计两个实验，实验一为恒定风速，对 MPC 控制器发送功率阶跃指令，模拟风机在减载控制时收到一次调频增发指令的简单情形。实验二在实验一的基础上加入变化风速的变量，并且增加功率指令的变化次数，目的是为了模拟更为复杂的工作场景。两个实验 MPC 的控制周期均为 1s，以下功率波形为了使图像直观，均经过均值滤波处理。

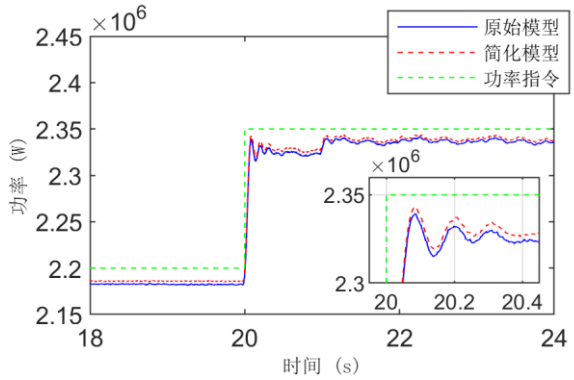


图 3 实验一 功率信号阶跃响应

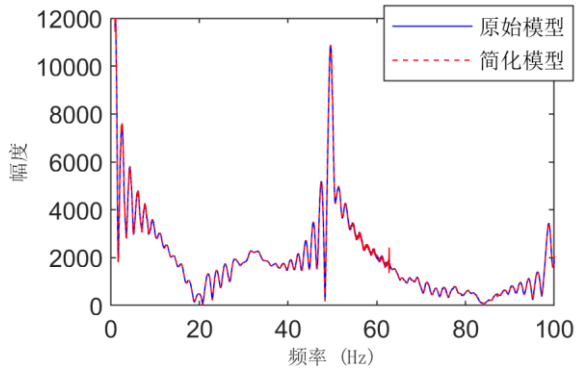


图 4 实验一 有功功率频谱

由图 3 可得，实验一中简化模型与原始模型的控制效果非常接近，有功功基本上是静态误差，经过计算，二者的差值平均值约为 -3.179×10^{3} W，远小于风机工作时的额定功率，简化模型与原始模型之间控制效果的误差率为 0.159%。由图 4 可得，在一次调频常用的控制周期 1s 的情形下，并不能通过 MPC 控制器消除更高频的扰动，在这个使用情景下简化模型能够很好替代高维模型。

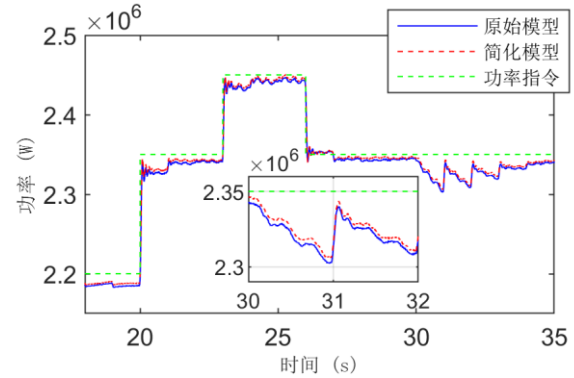


图 5 实验二 功率信号阶跃响应

实验二的频谱图较实验一无太大区别，因此不再赘述。在实验二中原始模型和简化模型控制二者的差值平均值约为 -2.911×10^{3} W 误差率约为 0.146%，在应对变化的风速和快速切换的功率目标时，高维模型的控制效果对比简化模型依然没有明显优势。

4 结论

本文针对高维模型的 MPC 中其状态空间方程对系统描述的复杂性和在风电机组一次调频的应用场景中其受限于控制周期的控制效果之间的矛盾，提出一种简化的状态空间模型，核心思想是减少计算量的同时，保证控制效果。通过仿真实验验证，使用该模型的 MPC 控制在风电机组一次调频的应用场景中，控制效果好，计算量小，相比于使用复杂模型的 MPC 控制没有明显缺点，各方面效果都接近复杂模型。但因为缺乏桨距角项，因此不适用于长时间尺度和风速变化大的情形的控制。

本模型为风电场站级 MPC 提供低计算量的、可靠的解决方案。后续可拓展至风储联合优化或多时间尺度分层控制架构。

参考文献

[1] 国家能源局. 2024 年可再生能源并网运行情况[EB/OL]. 北京: 国家能源局, [2025-01-27]. https://www.nea.gov.cn/20250221/e10f363cabe3458aaf78ba4558970054/c.html

[2] 高丙团,胡正阳,王伟胜,等.新能源场站快速有功控制及频率支撑技术综述[J].中国电机工程学报,2024,44(11):4335-4353.

[3] GB 38755-2019. 电力系统安全稳定导则[S]. 北京: 国家市场监督管理总局, 国家标准化管理委员会, 2019.

[4] 刘淼.参与电网调频的风电场有功功率控制方法研究[D].电子科技大学,2018.

[5] 李少林.大规模风电频率主动支撑优化控制技术研究[D].合肥工业大学,2022.

[6] Oshnoei S, Aghamohammadi M R, Oshnoei S, et al. A novel virtual inertia control strategy for frequency regulation of islanded microgrid using two-layer multiple model predictive control[J]. Applied Energy, 2023, 343: 121233.

[7] 董天翔,翟保豫,李星,等.风储联合系统参与频率响应的优化控制策略[J].电网技术,2022,46(10):3980-3989.

[8] 晋萃萃.大功率缺失下广域电网主动频率响应控制研究[D].大连理工大学,2020.

[9] Wang H, Yang Z, Chen Z, et al. Multiple adaptive model predictive controllers for frequency regulation in wind farms[J]. IEEE Transactions on Energy Conversion, 2022, 38(1): 15-26.

[10] 孙秦峰,李凤婷,王森,等.提升风电场有功调节能力的风储系统多时间尺度运行策略[J].电力系统保护与控制,2023,51(09):21-31.

[11] 杨德友,温佳鑫,陈家荣,等.用于提高风电场可调度性的储能系统预测控制策略[J].高电压技术,2017,43(03):1043-1048.

[12] JONKMAN J, BUTTERFIELD S, MUSIAL W, et al. Definition of a 5-MW Reference Wind Turbine for Offshore System Development[R]. Golden, CO: National Renewable Energy Laboratory, 2009.

[13] 赵雪娇,彭志炜,谭洪林,等.双馈风力发电机次同步扭振研究[J].电力科学与工程,2018,34(05):12-17.

[14] [1]刘洪波,彭晓宇,张崇,等.风电参与电力系统调频控制策略综述[J].电力自动化设备,2021,41(11):81-92.

[15] 单俊玮.考虑气动效应的大型风力发电机桨距角控制策略研究[D].沈阳工业大学,2022.

[16] 丁平.风电机组传动链扭振主动控制研究[D].华北电力大学(北京),2017.

收稿日期：2025-08-23。

作者照片



吴子敬

作者简介：

吴子敬(1999)，男，硕士研究生，主要从事风电场频率控制等电力系统及其自动化方向研究，wuzijing4099@163.com；

魏航源(2001)，男，硕士，主要从事风电场功 率预测等电力系统及其自动化方向研究，Email：weihangyuan0801@163.com；

韩雨(2001)，女，硕士，主要从事直流输电等 电力系统及其自动化方向研究，Email：hy04272025@163.com；

耿嘉豪(2000)，男，硕士，主要从事漏电保护 等电力系统及其自动化方向研究，Email：gengjiahao0926@163.com；

苏勋文(1976)，男，教授，主要从事新能源、多端直流输电等电力系统及其自动化方向研究，Email：suxunwen@163.com。

089 基于改进滑模观测器的永磁同步电机无传感器控制研究

张嗣奇，苏勋文

（黑龙江科技大学 电气与控制工程学院,哈尔滨 150022）

Research on Sensorless Control of Permanent Magnet Synchronous Motor Based on Improved SMO

ZHANG Siqi

(School of Electrical & Control Engineering, Heilongjiang University of Science & Technology, Harbin 150022, China)

ABSTRACT: In-depth research is conducted on sensorless control techniques for permanent magnet synchronous motors(PMSM). In response to the shortcomings of traditional control strategies, by integrating improved sliding mode observers, new approach laws and other multiple strategies, and introducing new saturation functions, integral sliding mode surfaces, variable gain and normalized phase-locked loop technologies, the vibration is effectively suppressed, and the accuracy of speed and rotor position estimation is improved. Through simulation verification, the improved control strategy significantly enhances the performance of the PMSM control system, reduces buffeting and boosts the estimation accuracy of rotational speed and rotor position.

KEY WORDS: Permanent Magnet Synchronous Motor; Novel Saturating Function;Sliding Mode Observer; Integral Sliding Mode Surface; Normalized Phase-Locked Loop; Sensorless Control

摘要：深入研究永磁同步电机(PMSM)无传感器控制技术为改善传统控制策略的局限，采用与改进滑模观测器相结合的方式，新型趋近律等多种策略，通过引入新型饱和函数、积分滑模面、可变增益及归一化锁相环技术，有效抑制抖振，提升转速和转子位置估计精度。经仿真验证，改进后的控制策略显著提高了 PMSM 控制系统的性能，削弱了抖振并且提高了对转速和转子位置的估计精度。

关键词：永磁同步电机；无传感器控制；滑模观测器；新型饱和函数；积分滑模面；归一化锁相环

0 引言

永磁同步电机具备体积小巧、功率密度高且高运行效率的特性，在家用电器、电动汽车、工业自动化等领域中得到了普遍使用。在其控制过程中，获取准确的转子位置和转速信息至关重要[错误!未找到引用源。]。传统方法依赖机械传感器，但存在诸多弊端，如增加系统体积和成本、降低可靠性且易受外部干扰。因此，无传感器控制技术成为研究热点。

滑模观测器(Sliding Mode Observer,SMO)是一种基于电机基波模型的无感控制算法，具有较强的鲁棒性[2][3]。滑模观测器法因对电机参数依赖少、鲁棒性强而被广泛采用，但传统滑模观测器存在抖振问题，影响转速和转子位置估计精度，限制了其应用[4]。文献[5]采用扩展反电动势提取转速及转子位置信息,增强转速及转子位置观测的抗扰性能。文献[6]引入非奇异快速终端滑模面，在短时间内让电流误差迅速收敛到零。文献[7]构造了一种改进的自适应超螺旋滑模观测器提高中高速永磁同步电机的速度缓冲和位置跟踪精度。文献[8]基于双曲函数提出一种改进的滑模观测器，可以对抖振进行削弱。文献[9]设计了一种新型超螺旋滑模观测器,用连续函数T(s)来代替符号函数sign(s),来对传统的超螺旋滑模观测器进行优化。

为提高PMSM中无传感器控制性能，针对开关切换频繁、惯性效应和系统延时，这直接导致其在电机转速与转子位置估计环节产生明显抖振。为解决这一核心问题，本文在传统滑模观测器基础上改进设计：采用新型饱和函数替代原有的符号函数，；其次设计改进型积分滑模面并引入可变滑模增益，进一步增强系统对扰动的抑制性能；同时结合归一化锁相环技术来提升位置与转速信号跟踪的稳定性，有效削弱抖振现象、提高估计精度，最终通过仿真实验验证了该优化方案的实际可行性。

1 传统滑模观测器

基金项目：“2021 年度黑龙江省省属高校基本科研业务费项目”，项目编号 2021-KYYWF-1467。

Fund Project: Basic Scientific Research Fund Project of Heilongjiang Provincial Universities in 2021, Project No. 2021-KYYWF-1467.

永磁同步电机是一个非线性控制对象，受参数不确定性和外部干扰的影响，这使得在整个运行过程中很难获得令人满意的性能[10]。为简化分析，假设三相 PMSM 为理想电机，满足不计涡流和迟滞损耗、忽略铁芯磁饱和、转子无阻尼绕组、电流为对称三相正弦波、反电动势为正弦分布等条件。选择表贴式 PMSM，其在静止坐标系下的数学模型如下：

$$\begin{cases}\frac{di_\alpha}{dt}=\frac{u_\alpha}{L_s}-\frac{R_s}{L_s}i_\alpha-\frac{E_\alpha}{L_s}\\ \frac{di_\beta}{dt}=\frac{u_\beta}{L_s}-\frac{R_s}{L_s}i_\beta-\frac{E_\beta}{L_s}\end{cases} \tag{1}$$

反电动势方程为：

$$\begin{cases}E_\alpha=-\varphi_f\omega_e sin\theta_e\\ E_\beta=\varphi_f\omega_e cos\theta_e\end{cases} \tag{2}$$

式中，i_α、i_β、u_α、u_β为定子电流和电压；L_s、R_s为定子电感和电阻；ω_e为电角速度；θ_e为电角度；φ_f永磁体磁链；E_α、E_β为反电动势。

2 传统滑模观测器设计

2.1 传统滑模观测器

传统的滑模观测器设计为：

$$\begin{cases}\frac{\mathrm{d}\hat{i}_\alpha}{\mathrm{d}t}=-\frac{R_\mathrm{s}}{L_\mathrm{s}}\hat{i}_\alpha+\frac{1}{L_\mathrm{s}}u_\alpha-\frac{1}{L_\mathrm{s}}v_\alpha\\ \frac{\mathrm{d}\hat{i}_\beta}{\mathrm{d}t}=-\frac{R_\mathrm{s}}{L_\mathrm{s}}\hat{i}_\beta+\frac{1}{L_\mathrm{s}}u_\beta-\frac{1}{L_\mathrm{s}}v_\beta\end{cases} \tag{3}$$

式中，$\hat{i}_\alpha$、$\hat{i}_\beta$为定子电流的观测值，v_α、v_β为观测器的控制输入。将式(1)(2)(3)作差得到误差方程：

$$\begin{cases}\frac{\mathrm{d}\hat{i}_\alpha}{\mathrm{d}t}=-\frac{R_\mathrm{s}}{L_\mathrm{s}}\hat{i}_\alpha+\frac{1}{L_\mathrm{s}}(E_\alpha-v_\alpha)\\ \frac{\mathrm{d}\hat{i}_\beta}{\mathrm{d}t}=-\frac{R_\mathrm{s}}{L_\mathrm{s}}\hat{i}_\beta+\frac{1}{L_\mathrm{s}}\left(E_\beta-v_\beta\right)\end{cases} \tag{4}$$

式中，$\tilde{i}_\alpha=\hat{i}_\alpha-i_\alpha,\tilde{i}_\beta=\hat{i}_\beta-i_\beta$为电流观测的误差。

定义滑模面函数为：

$$\mathrm{s}=\begin{cases}s_\alpha=\tilde{i}_\alpha=\hat{i}_\alpha-i_\alpha\\ s_\beta=\tilde{i}_\beta=\hat{i}_\beta-i_\beta\end{cases} \tag{5}$$

滑模控制率设计为：

$$\begin{cases}v_\alpha=m\cdot\mathrm{sgn}(\tilde{i}_\alpha)\\ v_\beta=m\cdot\mathrm{sgn}\left(\tilde{i}_\beta\right)\end{cases} \tag{6}$$

根据滑模控制理论，当观测器的状态变量达到滑模面 s=0 且系统稳定时，电流的观测值与实际值相等(即 s=$\tilde{i}$=0)，此时控制量可视为等效控制量，得出反电动势为：

$$\begin{cases}E_\alpha=v_\alpha=m\cdot sgn(\tilde{i}_\alpha)\\ E_\beta=v_\beta=m\cdot sgn(\tilde{i}_\beta)\end{cases} \tag{7}$$

通过反正切函数求出转子的位置，并进行相位补偿，得到：

$$\hat{\theta}_\mathrm{e}=-\arctan\left(\frac{\hat{E}_\alpha}{\hat{E}_\beta}\right)+\arctan\left(\frac{\hat{\omega}_\mathrm{e}}{\omega_\mathrm{c}}\right) \tag{8}$$

式中，$\hat{\theta}_\mathrm{e}$、$\hat{\omega}_\mathrm{e}$为电角度和转速的估计值。

为了获得电机的转速信息，对式(8)作微分处理，得到：

$$\hat{\omega}_\mathrm{e}=\frac{\sqrt{\hat{E}_\alpha^2+\hat{E}_\beta^2}}{\psi_\mathrm{f}} \tag{9}$$

2.2 改进滑模观测器设计

传统滑模观测器(SMO)在运行过程中，由于符号函数在零点处不连续，会引发较为严重的抖振问题，这直接影响了系统的性能和估计精度[11]-[13]。为解决这一问题，本文对滑模观测器进行了多方面的改进，具体内容如下：

新型饱和函数的引入：

传统滑模观测器中符号函数的不连续性是导致抖振的重要原因之一。为此，本文引入了一种在零点处连续的新型饱和函数来替代符号函数，其表达式为：

$$f(x)=\begin{cases}1, & x\geq\sigma\\ \mathrm{arsinh}(l_s x), & -\sigma<x<\sigma\\ -1, & x\leq-\sigma\end{cases} \tag{10}$$

式中，$l_\mathrm{s}=(\mathrm{e}-\mathrm{e}^{-1})/2\sigma$，$\sigma$为边界层厚度，x 为观测误差。该函数在$-\sigma$到$\sigma$的区间内采用反双曲正弦函数，使得函数在零点附近平滑过渡，避免了符号函数的突变，从而有效抑制了抖振的产生。

积分滑模面的设计：

滑模控制在趋近滑模面的过程中，由于系统的惯性和切换特性，容易产生抖振。为了削弱这种抖振，使转矩更加平滑，提升系统的鲁棒性和控制精度，本文结合文献[14]，采用了积分滑模面，其设计如下：

$$s=\alpha_1\tilde{\imath}+\int\alpha_2\tilde{\imath}+\alpha_3|\tilde{\imath}|^{\alpha_4}\mathrm{sat}\left(\frac{\tilde{\imath}}{\lambda}\right)\mathrm{d}t \tag{11}$$

式中，$\alpha_1>0,\alpha_2>0,\alpha_3>0,\alpha_4>0,\lambda>0$；积分项的引入使得滑模面不仅考虑了当前的误差，还积累了过去的误差信息，能够更有效地抑制抖振，使系统的动态响应更加平稳。

为了增强系统的动态性能，使系统能够更快、更稳定地趋近滑模面，本文设计了如下趋近律：

$$\dot{\mathrm{s}}=-\varepsilon f(s)-\mathrm{q}s \tag{12}$$

式中，$\varepsilon>0,\mathrm{q}>0$。该趋近律结合了新型饱和函数和比例项，能够根据系统的状态自动调整趋近速度，在保证系统快速响应的同时，减少抖振的影响。

不同转速下运行的电机，对滑模增益的要求有所不同。在中高速运行区间，要想保持系统的趋近速度，就需要较大的滑模增益，可过大的增益会引发较大抖振，进而致使调节精度受损[14]。因反电动势与转速存在关联，为使增益能够跟随反电动势值的变化自动调整，让电机在不同转速下都拥有合适的增益，本文采用了可变滑模增益设计，其表达式为：

$$k=\begin{cases}k_1*\dfrac{\omega_{ref}}{\omega_{rat}} & |x|\geq\delta\\ \dfrac{k_1*e^{|\dot{x}|^{m1}}\omega_{ref}}{\left[\omega_{rat}*\left(e^{|\dot{x}|^{m1}}+|x|\right)\right]} & |x|<\delta\end{cases} \tag{13}$$

式中，$\delta>0,\mathrm{m1}>0,\omega_{rat}$为额定转速值；$\omega_{ref}$为参考值；$k_1$为增益值；x为观测误差。这种可变增益设计能够根据系统的观测误差和转速情况自动调整增益大小，在保持系统快速性的同时，有效削弱抖振。

改进滑模观测器的构建：

基于以上改进，构建的改进滑模观测器如下：

$$\frac{\mathrm{d}}{\mathrm{d}t}\begin{bmatrix}\hat{\imath}_\alpha\\ \hat{\imath}_\beta\end{bmatrix}=\frac{1}{L_s}\begin{bmatrix}u_\alpha\\ u_\beta\end{bmatrix}-\frac{R_s}{L_s}\begin{bmatrix}\hat{\imath}_\alpha\\ \hat{\imath}_\beta\end{bmatrix}-\frac{1}{L_s}\begin{bmatrix}v_\alpha\\ v_\beta\end{bmatrix} \tag{14}$$

可得误差方程为：

$$\frac{\mathrm{d}}{\mathrm{d}t}\begin{bmatrix}\tilde{\imath}_\alpha\\ \tilde{\imath}_\beta\end{bmatrix}=-\frac{R_s}{L_s}\begin{bmatrix}\tilde{\imath}_\alpha\\ \tilde{\imath}_\beta\end{bmatrix}+\frac{1}{L_s}\begin{bmatrix}e_\alpha-v_\alpha\\ e_\beta-v_\beta\end{bmatrix} \tag{15}$$

根据新型饱和函数、积分滑模面、趋近律以及误差方程，可得滑模控制律为

$$v=\left(-R_s+\frac{\alpha_2L_s}{\alpha_1}\right)\tilde{\imath}+\eta+\frac{\alpha_3L_s}{\alpha_1}|\tilde{\imath}|^{\alpha_4}\mathrm{sat}\left(\frac{\tilde{\imath}}{\lambda}\right)-\frac{L_s}{\alpha_1}[-k_2f(s)-k_3s] \tag{16}$$

式中，η为常数。

通过以上多方面的改进，新型滑模观测器能够有效抑制传统滑模观测器中存在的抖振问题，提高系统对转速和转子位置的估计精度，改善系统的动态性能和鲁棒性。

2.3 稳定性分析

下面对改进后的 SMO 的稳定性进行分析验证，由李亚普诺夫(Lyapunov)函数：

$$\mathrm{V}=\frac{1}{2}\mathrm{s}^2 \tag{17}$$

对其进行微分可得：

$$\frac{dV}{dt}=\dot{V}=s\dot{s} \tag{18}$$

为了满足改进后的 SMO 运行系统是稳定的，其导数需要满足：

$$\dot{V}=s\left[\alpha_1\dot{\tilde{\imath}}+\alpha_2\tilde{\imath}+\alpha_3|\tilde{\imath}|^{\alpha_4}sat(\frac{\tilde{\imath}}{\lambda})\right]=$$

$$s\left[\alpha_1(-\frac{R_s}{L_s}\tilde{\imath}-\frac{1}{L}v+\frac{1}{L_s}e)+\alpha_2\dot{\tilde{\imath}}+\alpha_3|\tilde{\imath}|^{\alpha_4}sat(\frac{\tilde{\imath}}{\lambda})\right]<0 \tag{19}$$

由式（16）和（19）可得：$\eta>\max\{e_\alpha,e_\beta\}$，即可得知系统是稳定的。

2.4 转子位置与转速估计

在传统滑模观测器的应用中，转子位置与转速观测值的获取依赖反正切函数运算。该方法虽有算法简洁、便于实现的特点，却存在显著不足：滑动模态伴随的高频抖振会直接干扰反正切函数的运算过程，导致转子位置与转速的观测精度受损[15][16]。即便后续通过引入低通滤波器、增设相位补偿环节尝试优化，受限于滤波器固有的相位滞后问题(尤其在电机变速运行时更为明显)，以及相位补偿参数难以适配全工况的局限，观测精度始终难以突破瓶颈。

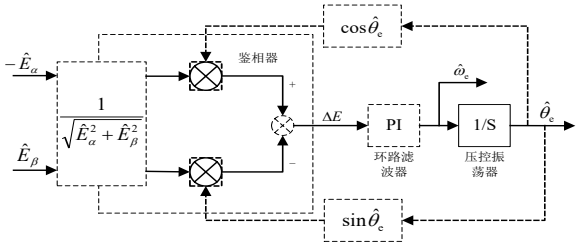


图 1　归一化锁相环原理图

Figure 1 Normalized Phase-Locked Loop Schematic

如图 1 所示，为改进后的归一化锁相环结构框图。相较于常规锁相环，该归一化设计通过参数自适应优化，使锁相环的响应速度不再受电机转速波动的制约，大幅降低了系统对转速的依赖性。

$$\begin{aligned}\Delta\mathrm{E}&=-\widehat{\mathrm{E}_\alpha}\cos\widehat{\theta_\mathrm{e}}-\widehat{\mathrm{E}_\beta}\cos\widehat{\theta_\mathrm{e}}\\&=\omega_\mathrm{e}\varphi_\mathrm{f}\sin\theta_\mathrm{e}\cos\widehat{\theta_\mathrm{e}}-\omega_\mathrm{e}\varphi_\mathrm{f}\cos\theta_\mathrm{e}\sin\widehat{\theta_\mathrm{e}}\\&=\omega_\mathrm{e}\varphi_\mathrm{f}\sin(\theta_\mathrm{e}-\widehat{\theta_\mathrm{e}})\\&=\mathrm{k}(\theta_\mathrm{e}-\widehat{\theta_\mathrm{e}})\end{aligned} \tag{20}$$

式中，$\mathrm{k}=\omega_\mathrm{e}\varphi_\mathrm{f}$，当$|\theta_\mathrm{e}-\widehat{\theta_\mathrm{e}}|<\pi/6$时，可近似看作$\sin(\theta_\mathrm{e}-\widehat{\theta_\mathrm{e}})=(\theta_\mathrm{e}-\widehat{\theta_\mathrm{e}})$成立。

由式（20）可以计算出转子位置观测值$\widehat{\theta_\mathrm{e}}$化简可得实际值$\theta_\mathrm{e}$的传递函数：

$$\mathrm{G(s)}=\frac{\widehat{\theta_\mathrm{e}}}{\theta_\mathrm{e}}=\frac{\mathrm{k_ps+k_q}}{\mathrm{s^2+k_ps+k_q}} \tag{21}$$

3 仿真与分析

为确认改进后的滑模观测器在永磁同步电机无传感器控制场景下的性能，在 Matlab/simulink 下

进行模型仿真，分别搭建传统滑模观测器和改进滑模观测器进行对比，系统框图如图 2 所示：

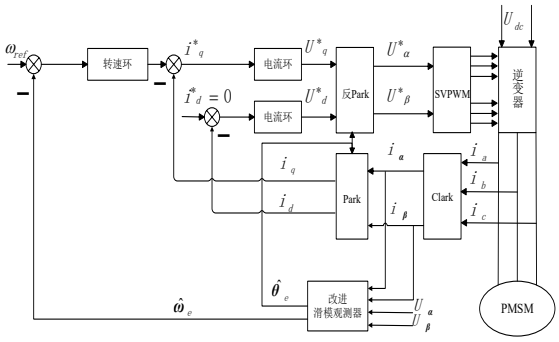


图 2 PMSM 无位置传感器控制系统框图

Figure 2 Block Diagram of PMSM Sensorless Control System

表 1 永磁同步电机主要参数

Table 1 Main Permanent Magnet Synchronous Motor Parameters

参数	参数值
极对数 p	4
转动惯量 J/（kg· $\mathbf{m^2}$）	0.300
阻尼系数 F/（N· $\mathbf{m^2}$ ·s)	0.0100
定子电阻$\boldsymbol{R_s/\Omega}$	2.875
定子电感$\boldsymbol{L_s/mH}$	8.5
永磁体磁链$\boldsymbol{\varphi_f/Wb}$	0.175

为了检验改进的 SMO 在永磁同步电机无传感器的应用效果，在 Matlab/simulink 下搭建了如图 2 所示的仿真模型，选取表 1 所示电机参数，并将其仿真运行结果与传统 SMO 进行对比。

系统初始给定电机转速 1000r/min，在 0.05s 时施加 10N·m 的负载转矩，对比图 3 和图 4 可以看出传统滑模观测器的转速运行结果显示有较大的抖振，转速误差接近 6r/min；而改进后的转速运行结果抖振削弱，误差降低在 1r/min 左右，转速的运行精度得到了提高 。

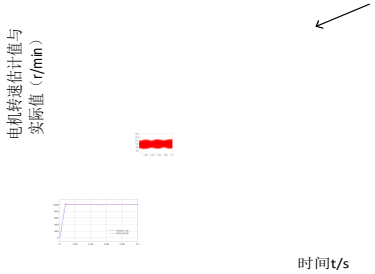


图 3 传统 SMO 转速响应曲线

Figure 3 shows the speed response curve of the traditional sliding mode observe

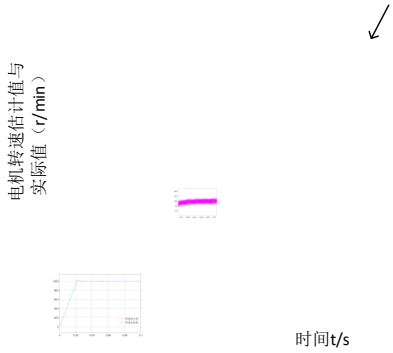


图 4 改进型 SMO 转速响应曲线

Figure 4 shows the speed response curve of the improved sliding mode observer

对比图(5)和图(6)可以得出，相较于传统滑模控制，改进后的控制系统在抖振抑制上效果更突出，转速误差从 18r/min 降至最大 6r/min，大幅提升了转速估计精度。

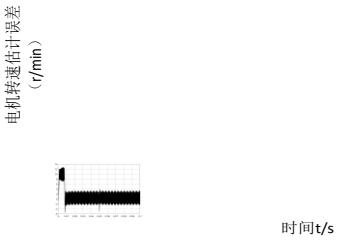
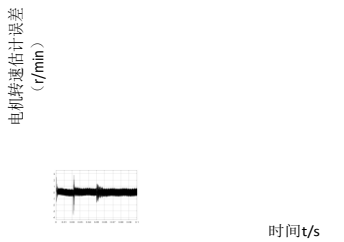


图 5 传统 SMO 转速误差曲线

Figure 5 shows the speed error curve of the traditional sliding mode observe



图

图 6 改进型 SMO 的转速误差曲线

Figure 6 shows the speed error curve of the improved sliding mode observer

图(7)和图(8)分别为传统控制系统和改进方法后的转子位置波形，如图可见，在传统方式下，原位置估计存在较大偏差，而改进后转子位置的估计结果更为精准。

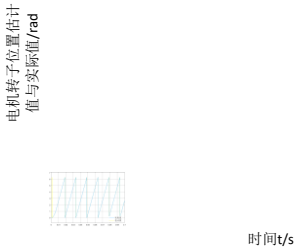


图 7 传统滑模观测器电机转子位置

Figure 7 shows the rotor position waveform of the traditional sliding mode observer

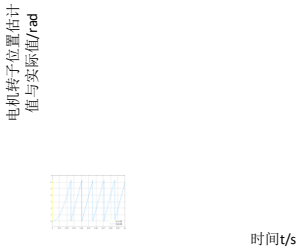


图 8 改进滑模观测器转子位置波形

Figure 8 Improves the rotor position waveform of the sliding mode observer

由图(9)和(10)可知，与传统方式进行对比，改进后的滑模观测器的转子位置估计误差更小，更准确。

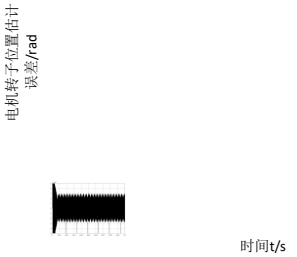


图 9 传统滑模观测器转子位置误差波形

Figure 9 shows the rotor position error waveform of the traditional sliding mode observe

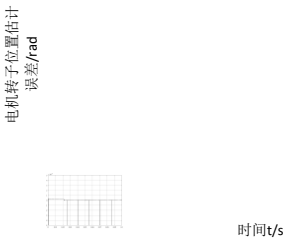


图 10 传统 SMO 电机转子位置误差波形

Figure 10 shows the rotor position error waveform of the traditional sliding mode observer

4 总结

本文针对永磁同步电机无传感器控制场景下的性能瓶颈，设计了一种新型滑模观测器，旨在解决传统滑模观测器抖振明显、状态估计精度不足的问题。首先，采用在零点处连续的新型饱和函数替代传统符号函数，从根源上降低抖振产生的可能性；其次，引入积分滑模面，强化系统对转子转速与位置信号的跟踪稳定性；最后，配置可变滑模增益，有效削弱了抖振。

仿真结果表明，基于改进滑模观测器构建而成的永磁同步电机无传感器控制系统，不仅能有效缓解滑模控制所固有的抖振现象，而且转子转速与位置的估计精度也得到显著提升；同时，估计精准度同样显著提升；在此基础上，还证实了该新型观测器对改善无传感器控制系统综合性能的有效性。

参考文献

[1] 孙洪博, 张晓宇, 柳向斌. 永磁同步电机无传感器控制研究综述[J]. 控制工程,2024,31(10):1786-1796.

[2] 生龙, 刘立昊, 叶永强. 永磁同步电机无位置传感器控制现状和展望[J]. 电工电气, 2023,(02):1-8.

[3] 周涛, 蒋全. 无传感器永磁同步电机全速范围控制技术综述[J]. 电子科技, 2021,34(04):59-69.

[4] Lu H ,Li W ,Du L W , et al. Improved Sliding Mode Control With an Adaptive Sliding Mode Disturbance Observer for Speed Control of Permanent Magnet Semi-direct Drive Scraper Conveyor[J].International Journal of Control, Automation and Systems,2025,23(7):1984-1998.

[5] 岳岩,王惠民,葛兴来. 基于锁频环的内置式永磁同步电机无传感器控制[J].中国电机工程学报,2019,39(10):3075-3085.

[6] 吴迪. 基于滑模观测器及无差拍电流预测控制的永磁同步电机无位置传感器控制研究[D]. 西安理工大学, 2024.

[7] Shi L ,Lv M ,Li P . Sensorless Position Control in High-Speed Domain of PMSM Based on Improved Adaptive Sliding Mode Observer[J].Processes,2024,12(11):2581-2581.

[8] 孙洪博, 张晓宇, 柳向斌. 永磁同步电机无传感器控制研究综述[J]. 控制工程,2024,31(10):1786-1796.

[9] 杨守勇. 基于滑模观测器无刷直流电机无位置传感器控制研究[D]. 齐鲁工业大学, 2022.

[10] Zhao Y, Yu H, Wang S. An improved super-twisting high-order sliding mode observer for sensorless control of permanent mag net synchronous motor[J]. Energies, 2021, 14(19): 6047.
[11] 龚事引, 李丹, 刘捃锾, 等. 永磁同步电机改进无模型超螺旋滑模控制[J]. 组合机床与自动化加工技术, 2024, (02):175-181.
[12] 姚春雅. 基于非奇异快速终端滑模观测器高速永磁同步电机无传感器控制优化[D]. 天津农学院, 2023.
[13] Ruixin S ,Tao D ,Xian Z , et al. Wind-farm-level sub-/super-sy nchronous oscillation suppression strategy based on generalized reactance sensitivity[J].Energy Reports,2023,9(S10):558-569.
[14] 张政. 基于滑模观测器的永磁同步电机控制策略研究[D]. 南京信息工程大学,2024.
[15] 郑征, 毛绍冉. 比例积分型线性超螺旋算法滑模观测器的感应电机无传感器控制[J]. 太阳能学报, 2022,43(08):316-322.
[16] 杨浩, 赵强, 杨钊, 等. 基于新型双滑模的永磁同步电机无传感器矢量控制[J]. 科学技术与工程, 2022,22(06):2252-2258.

收稿日期：2025-09-30。



张嗣奇

作者简介：
张嗣奇(2000-)，女，硕士研究生，研究方向为风电网同步振荡，E-mail：2529995110@qq.com；

（编辑　五号楷体，居右，段前空 6pt）

090 基于小波分析的煤矿多级供电网单相接地故障选线方法

耿嘉豪，魏航源，韩 雨，吴子敬，张嗣奇，苏勋文

（黑龙江科技大学 电气与控制工程学院，哈尔滨 150022）

Fault Line Selection Method for Single-Phase Grounding in Multi-Level Coal Mine Power Supply Networks Based on Wavelet Analysis

GENG Jiahao, WEI Hangyuan, HAN Yu, WU Zijing, ZHANG Siqi, SU Xunwen

(School of Electrical & Control Engineering, Heilongjiang University of Science & Technology, Harbin 150022, China)

ABSTRACT: The underground power supply system of coal mines operates in environments characterized by high gas content, humidity, and complex multi-branch networks. Once a single-phase ground fault occurs, it poses a serious threat to mine safety. Although resonant grounding systems can limit fault currents, the fault features are weak, and traditional line selection methods often suffer from low sensitivity and high misjudgment rates. To address this problem, this paper establishes a multi-level coal mine power supply network model with resonant grounding that closely reflects actual operating conditions, taking into account hierarchical power supply, coupling between different voltage levels, cable distribution capacitance, and unbalanced load factors, thereby overcoming the limitations of traditional simplified models. Based on this model, a simulation system is built in MATLAB/Simulink to reproduce various single-phase grounding scenarios and obtain zero-sequence current characteristics. Furthermore, wavelet transform is introduced, and the db6 wavelet is applied to perform multi-scale decomposition of transient fault signals. A line selection criterion based on wavelet energy mutation is proposed to achieve accurate identification of faulted lines. Simulation results demonstrate that this method significantly improves the sensitivity and reliability of fault detection even under high-resistance grounding and complex load disturbance conditions. The proposed approach not only constructs a more realistic multi-level power supply network model to enhance simulation accuracy and engineering applicability, but also develops a wavelet-based fault line selection method that overcomes the shortcomings of traditional approaches. The research provides a new technical path for fault diagnosis and intelligent protection of coal mine power supply systems.

KEY WORDS: multi-level coal mine power supply network; resonant grounding system; wavelet analysis; fault line selection

摘要：煤矿井下供电系统在高瓦斯、潮湿和多分支复杂环境中运行，一旦发生单相接地故障，将严重威胁矿井安全。小电流接地系统虽能限制故障电流，但故障特征微弱，传统选线方法灵敏度不足、误判率较高。本文针对这一问题，建立了符合实际工况的煤矿多级供电网小电流接地系统模型，充分考虑了分层供电、不同电压等级的耦合关系、电缆分布电容及负荷不均衡等因素，从而突破了传统简化模型的局限。基于该模型，在 MATLAB/Simulink 平台上搭建仿真系统，模拟多种单相接地工况，获取零序电流特征信号。进一步引入小波变换方法，利用 db6 小波对故障暂态信号进行多尺度分解，提出基于小波能量突变量的故障选线判据，实现了对故障线路的准确识别。仿真结果表明，该方法在高阻接地和复杂负荷扰动等工况下，依然能够显著提升故障检测的灵敏度与可靠性。本文构建了更贴近实际的多级供电网模型，提高了仿真精度和工程应用价值并且基于小波分析进行故障选线方法，克服了传统方法易误判的缺陷。研究成果为煤矿供电系统的故障诊断和智能化保护提供了新的技术路径。

关键词：煤矿多级供电网；小电流接地系统；小波分析；故障选线

0 引言

煤矿井下供电系统是保障煤矿安全生产和电气设备稳定运行的重要基础，其运行环境具有高瓦斯、潮湿和空间受限等特殊性。在这种复杂环境下，一旦发生单相接地故障，不仅会导致设备绝缘受损、系统供电中断，还可能引发电弧放电和瓦斯爆炸事故，严重威胁矿井安全生产和人员生命安全

基金项目：“2021 年度黑龙江省省属高校基本科研业务费项目”，项目编号 2021-KYYWF-1467。

Fund Project: Basic Scientific Research Fund Project of Heilongjiang Provincial Universities in 2021, Project No. 2021-KYYWF-1467.

[1]。小电流接地系统因其在故障电流较小时能够避免大电流烧毁设备和扩大事故范围，而被广泛应用于煤矿供电系统中。然而，该系统在发生单相接地故障时，故障电流往往较小，信号特征不明显，导致传统的选线方法灵敏度不足、误判率高，难以满足现代智能化矿井安全生产的要求。同时，传统煤矿供电网多采用简化模型，只考虑单一电压等级或单母线结构，忽略了多级供电、负荷分布不均衡以及电缆分布电容差异等实际情况。这种简化处理虽然在理论分析中具有一定参考意义，但难以真实反映实际工况，容易造成仿真结果与运行状态存在偏差[2]。因此，研究更加贴合实际的新型煤矿多级供电网小电流接地系统模型，对于提升仿真精度与指导实际运行具有重要的理论与工程价值。

针对小电流接地系统单相接地故障的检测与选线问题，国内外学者已进行了大量研究。早期方法多以零序电流或零序电压为基础，依靠稳态特征进行判断，但在煤矿复杂的运行环境中受负荷扰动影响较大，难以保证准确性。随着研究的深入，一些学者提出了基于谐波分量与暂态分量的改进方法，利用故障时电流的高频成分来实现选线，在一定程度上提高了灵敏度[3]。然而，在高阻接地和间歇性接地等工况下，这些方法依旧存在局限性。近年来，信号处理技术的发展为故障检测提供了新的思路，小波变换因其良好的时频局部化特性，被广泛应用于电力系统暂态信号分析与故障识别。已有研究表明，小波分析能够有效提取接地故障信号的瞬态特征，在小电流系统的选线中表现出较强的适应性[4]。但多数研究仍建立在传统简化煤矿供电网模型的基础上，忽视了多级供电结构的复杂性，导致理论分析与实际应用之间存在差距。

在此背景下，本文旨在建立更加符合实际工况的新型煤矿多级供电网小电流接地系统模型，并在此基础上开展单相接地故障的仿真研究。通过在仿真平台中模拟不同工况下的单相接地过程，分析故障电流与电压的分布特征，进而引入小波变换方法对故障信号进行分解与特征提取，提出基于小波能量突变量的故障选线判据，从而实现对故障线路的准确识别与定位[5]。通过这种方法，可以有效提升煤矿小电流接地系统在复杂工况下的故障检测灵敏度与可靠性，为提高矿井供电系统的本质安全水平提供技术支撑。

本文的研究主要包括两个方面的创新。一方面，在建模上突破了传统简化模型的局限，充分考虑了煤矿供电系统中多电压等级、分支电缆电容效应以及实际负荷分布等因素，提出了更贴近实际运行的新型多级供电网小电流接地系统模型，从而提高了仿真结果的准确性与应用价值。另一方面，在故障检测方法上，将小波变换引入煤矿单相接地故障信号分析中，利用其多尺度能量特征实现对故障线路的识别，提出了适用于复杂工况的选线判据，有效提升了选线方法的灵敏度和准确性[5]。这些研究不仅为矿井电气系统的故障诊断提供了新思路，也为建设智能化矿山电力保护体系奠定了基础。

1 煤矿多级供电网建模与优化

传统煤矿供电网建模大多基于简化假设，通常采用单母线或单一电压等级的供电模型，只考虑线路和电缆的集中电容效应，并假定各分支网络具有相同的电气特性。这类简化模型在理论推导和基础研究中具有一定的参考价值，能够较为直观地反映小电流接地系统在故障状态下的基本规律。但由于忽略了井下供电系统分层供电、多分支馈电以及实际负荷分布差异等复杂性，该模型在精度上存在明显不足[6]。当单相接地故障发生时，简化模型难以准确描述不同电压等级间的耦合关系与各分支电容电流的非对称分布，导致仿真结果与实际运行工况存在偏差。这种不足不仅降低了研究成果的工程应用价值，也限制了对复杂接地故障机理的深入分析。

与传统模型相比，煤矿多级供电网结构更贴近实际运行环境，通常呈现自上而下的分层供电模式：地面变电站或主井下变电所首先向井下高压主干网供电，再通过中压或低压配电线路逐级馈电至采区、巷道和工作面用电设备。各级网络之间电压等级不同、线路长度差异较大，且电缆分布电容和接地电流分布往往不均衡。此外，井下用电负荷种类繁多，包括大型采掘设备、提升系统、通风排水设备以及照明与信号系统等，其运行状态具有明显的波动性和随机性，使得多级供电网的电气特性更加复杂[8]。基于这种结构特征，新型建模方法需要在分层供电、不同电压等级的耦合、线路电容及负荷动态特性等方面进行优化，从而更准确地反映煤矿供电系统的真实运行状况，为后续的单相接地故障仿真与故障选线研究提供可靠的模型基础。

2.小波函数介绍与小波选取

小波函数是一类具有局部化特性的基函数，其核心思想是通过平移与伸缩来对信号进行多尺度分解[9]。与传统的傅里叶变换不同，小波变换不仅

能够提供频域信息，还能够反映信号在时域上的局部特征，从而适用于非平稳信号的分析。小波函数通常由母小波和尺度函数构成，通过伸缩因子控制频率分辨率，通过平移因子定位时间特征，实现对信号的时频联合分析。这一特性使得小波分析在信号突变检测、瞬态特征提取以及噪声抑制等领域具有显著优势，被广泛应用于电力系统暂态分析和故障诊断中[10]。

与传统的傅里叶变换相比，小波分析的最大优势在于其良好的时频局部化能力。傅里叶变换只能提供整体的频率信息，无法有效捕捉信号的瞬态变化，而小波变换能够在高频部分提供较高的时间分辨率，在低频部分提供较高的频率分辨率，从而实现对非平稳信号的精细刻画[11]。在煤矿供电网小电流接地系统的单相接地故障分析中，故障电流信号往往表现为幅值较小、持续时间短、受噪声干扰严重的暂态信号，小波分析能够在多尺度下分解故障波形，有效提取其中的突变分量和能量特征，为故障线路的准确识别提供可靠依据。

设原始输入信号为，其连续小波变换为

$$\mathrm{CWT}_{a,b} = \int_R f(t)\psi_{a,b}(t)\mathrm{d}t \tag{1}$$

式中，a——尺度因子；

b——位移因子。

对信号进行离散化处理，首先对 a 和 b 进行离散采样，如下所示

$$\begin{cases} a = a_0^m,\ a_0 > 0, m \in Z \\ b = nb_0a_0^m,\ b \in R, n \in Z \end{cases} \tag{2}$$

则小波函数可以写成

$$\psi_{m,n}(t) = a_0^{-m/2}(a_0^{-m}t - nb_0) \tag{3}$$

在众多小波函数中，多贝西系列小波因其紧支撑性和良好的正交性而被广泛应用。本文选取 db6 小波作为分析工具，主要基于其在故障信号处理中的综合优势。db6 小波具有较高的消失矩条件，能够更好地逼近光滑信号，同时保留故障信号的突变特征；其正交性保证了分解与重构过程中的信息无损，使得信号能量在多尺度分解过程中得到准确保持；此外，db6 小波的支撑长度适中，相比低阶小波能够提供更丰富的频率分辨率，又避免了高阶小波在计算复杂性和边界效应上的不足[12]。因此，db6 小波在处理煤矿单相接地故障信号时，既能有效突出瞬态特征，又能保证计算效率和鲁棒性，适合作为本文的小波分析工具。

3 仿真分析

为实现对煤矿供电系统小电流接地故障的高保真仿真，本文在 MATLAB/Simulink 平台上基于煤矿配电网供电原理图构建了如图 1 所示的“地面变电站—井下中央变电站—采区变电站”三级放射式供电系统仿真模型。

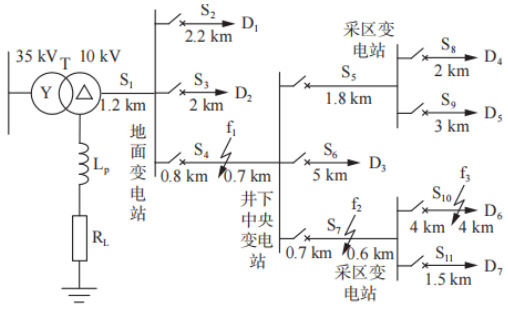


图 1 煤矿多级配电网仿真模型

Figure 1. Simulation Model of Multi-level Distribution Network in Coal Mine

该煤矿供电系统由地面变电站、井下中央变电站及多个采区变电站组成。地面变电站由 35kV 母线通过主变压器降压至 10kV，经架空线路 S1（1.2km）引入井下。架空线路 S2（2.2km）、S3（2.0km）分别作为干线供电，线路的单位长度参数为：正序电阻 1.22 Ω/km、正序电感 1.22mH/km、正序电容 0.096μF/km；零序电阻 0.23 Ω/km、零序电感 3.66mH/km、零序电容 0.007 μF/km。地面母线侧接有消弧线圈，其电感 LP=0.5605 H，并联电阻 RL=10 Ω。

井下中央变电站通过电缆线路 S4（1.5 km）、S5（1.8 km）向采区变电站供电，同时经电缆 S6（5 km）向分支线路延伸。其余供电线路均为电缆，长度分别为 S7（1.3 km）、S8（2 km）、S9（3 km）、S10（8 km）、S11（1.5 km）。电缆线路的单位长度参数为：正序电阻 0.11 Ω/km、正序电感 0.52 mH/km、正序电容 0.29 μF/km；零序电阻 0.34 Ω/km、零序电感 1.54 mH/km、零序电容 0.19 μF/km。

系统共接有 7 个主要负荷：D1－D7，容量分别为 0.81 MW、2 MW、0.68 MW、0.315 MW、0.68 MW、0.315 MW 及 1.25 MW。网络中设定了 3 个单相接地故障点，分别位于 S4、S7、S10，记为 f1、f2、f3，接地故障电阻为 R=500 Ω，用于开展煤矿供电系统小电流接地故障仿真研究。

为验证小波分析对单相接地故障选线的可靠

性，采用上面建立的模型进行了大量的仿真，对故障发生时的各线路零序电流进行小波变换，采用db6 小波函数，进行分辨率为 4 时的小波分解仿真结果如下。

算例 1：当 S4 线路 f1 处发生单相接地故障时 S2、S3、S4、S7、S11 线路的零序电流如图所示，同电压等级的 S5~S7 零序电流无差异，同电压等级的 S8~S11 零序电流无差异。各线路零序电流的小波变换如图 2 所示。

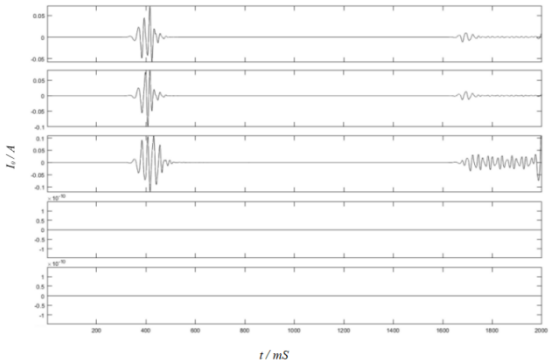


图 2 f1 处故障各线路零序电流小波分析图

Figure 2. shows the wavelet analysis diagrams of zero-sequence currents of each line at the f1 fault point

算例 2：当 S7 线路 f2 处发生单相接地故障时 S4、S5、S6、S7、S11 线路的零序电流如图所示，同电压等级的 S2~S4 零序电流无差异，同电压等级的 S8~S11 零序电流无差异。各线路零序电流的小波变换如图 3 所示。

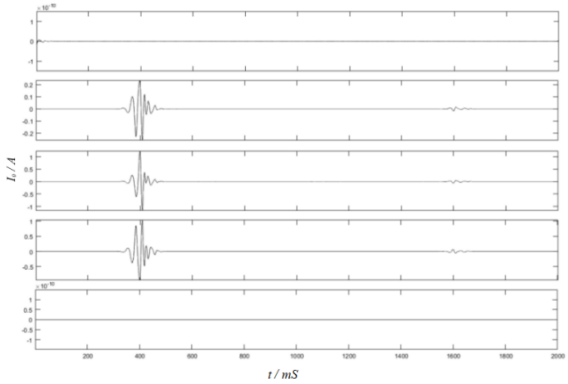


图 3 f2 处故障各线路零序电流小波分析图

Figure 3. shows the wavelet analysis diagrams of zero-sequence currents of each line at the f2 fault point

算例 3：当 S11 线路 f3 处发生单相接地故障时 S4、S7、S9、S10、S11 线路的零序电流如图所示，同电压等级的 S2~S4 零序电流无差异，同电压等级的 S5~S7 零序电流无差异，线路 S8、S9 无差异，虽然线路 S8、S9 与线路 S10、S11 处于同一电压等级，但是母线不同线路的零序电流需在明显差异。各线路零序电流的小波变换如图 4 所示。

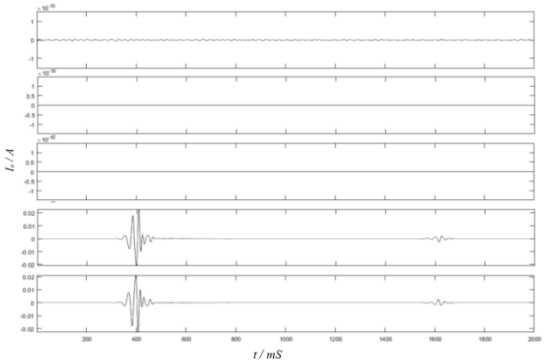


图 4 f3 处故障各线路零序电流小波分析图

Figure 4. shows the wavelet analysis diagrams of zero-sequence currents of each line at the f3 fault point

4 结论

本文围绕煤矿小电流接地系统中的单相接地故障问题，基于多级供电网模型和小波分析方法展开研究，提出了一种适用于复杂矿井供电环境的故障选线方法。通过对仿真结果的分析，可以得出以下主要结论。

首先，零序电流信号在故障线路与非故障线路之间表现出显著的特征差异。当发生单相接地故障时，故障线路的零序电流幅值明显大于非故障线路，并且其波形方向与非故障线路相反[13]，从而为故障线路的识别提供了清晰的判据。同时，仿真结果表明，故障线路的零序电流变化主要集中在本线路内，对不同母线所连接的其他线路几乎没有影响，这一特性保证了在多级供电环境下，故障特征依旧能够被准确提取和识别。

其次，基于小波分析的零序电流选线方法能够有效提高故障检测的灵敏度和准确性。小波变换具有良好的时频局部化能力，能够对故障零序电流信号进行多尺度分解，提取其中的高频突变量和瞬态特征[14]。通过对比故障线路与非故障线路在不同尺度下的零序电流，可以清晰地判定故障线路，避免了传统稳态谐波分析方法在高阻接地、间歇性接地等复杂工况下误判率高的问题。

最后，与传统简化模型相比，多级供电网模型更能反映实际煤矿供电系统的运行特性。传统简化模型通常忽略多级分支、电缆分布电容和不均衡负荷等因素，导致仿真结果与实际工况存在偏差[15]。而本文构建的多级供电网模型能够更准确地描述各电压等级间的耦合关系与零序电流分布规律，使得小波分析选线方法在复杂工况下依旧保持良好的适应性和鲁棒性。这不仅提升了仿真研究的精

度，也为矿井供电系统实际工程应用提供了更具参考价值的理论基础。

综上所述，基于小波分析的零序电流故障选线方法在新型煤矿多级供电网模型下能够有效实现单相接地故障的准确识别，既验证了小波分析在矿井供电系统故障检测中的应用价值，也进一步凸显了多级供电网模型相较于传统简化模型的优势。该研究为煤矿小电流接地系统的保护与智能化发展提供了可行的技术路径。

参考文献

[1] 马秀林,王海欧,吴坚,等.DB8 小波变换在谐振接地系统单相接地故障选线中的应用[J].农村电气化,2021,(03):25-28.

[2] 郝帅,张旭,马瑞泽,等.基于改进 Goog Le Net 的小电流接地系统故障选线方法[J].电网技术,2022,46(01):361-368.

[3] Wang C, Feng L, Hou S, et al. A Method for Single-Phase Ground Fault Section Location in Distribution Networks Based on Improved Empirical Wavelet Transform and Graph Isomorphic Networks[J]. Information (2078-2489), 2024, 15(10).

[4] 曾超,喻锟,曾祥君,等.并阻尼谐振接地系统对地参数测量与高阻故障选线新方法[J].电力系统保护与控制,2024,52(04):67-76.

[5] 陶彩霞,杜雪,高锋阳,等.基于经验小波变换的混合输电线路单相接地故障测距[J].电力系统保护与控制,2021,49(10):105-112..

[6] 刘扬,刘建功,王毅颖,等.煤矿坚强智能电网建设理论与技术探讨[J].煤炭学报,2020,45(06):2296-2307.

[7] 刘炳南,耿蒲龙,田慕琴,等.基于 CEEMD 与小波包的单相接地故障选线方法[J].煤炭工程,2020,52(10):121-124.

[8] 罗超,耿蒲龙,曲兵妮,等.基于小波包的矿井供电系统单相接地故障选线方法[J].工矿自动化,2018,44(02):68-74.

[9] 覃渝文,吕思辰,吕飞鹏,等.谱图小波变换在谐振接地系统故障选线中的应用[J].电力自动化设备,2025,45(06):208-216.

[10] 孙孔明,李玉敦,范荣奇,等.基于 VMD 的小电流接地故障融合选线方法[J].工矿自动化,2023,49(03):115-123.

[11] Yang D, Lu B, Lu H. High-resistance grounding fault detection and line selection in resonant grounding distribution network[J]. Electronics, 2023, 12(19): 4066.

[12] 白浩,潘姝慧,邵向潮,等.基于小波去噪与随机森林的配电网高阻接地故障半监督识别方法[J].电力系统保护与控制,2022,50(20):79-87.

[13] 田晶京,耿芳,赵峰,等.谐振接地系统的配电线路接地故障选线新方法[J].重庆大学学报,2022,45(01):59-67.

[14] 王强,吕鸿浩,周小超,等.基于 IDRSN 的高噪声环境下小电流接地系统故障选线方法研究[J/OL].高压电器,1-17[2025-08-24].

[15] 魏然,张磐,高强伟,等.基于网络树状图的低压配电网故障研判仿真分析[J].电力系统保护与控制,2021,49(13):167-173.

收稿日期：2025-08-25。



耿嘉豪

作者简介：

耿嘉豪（2000-），男，硕士研究生，研究方向为电力系统的漏电保护，E-mail：gengjiahao0926@163.com；

魏航源(2001-)，男，硕士研究生，研究方向为风电场功率预测；E-mail：853279021@qq.com；

韩雨（2001-），女，硕士研究生，研究方向为风电场次同步震荡；E-mail：hy04272025@163.com。

091 基于 Transformer-BiGRU 的双阶段风电功率预测

魏航源，韩雨，吴子敬，耿嘉豪，张嗣奇，苏勋文

黑龙江科技大学 电气与控制工程学院，哈尔滨 150022

Transformer-BiGRU-Based Dual-Stage Model for Wind Power Prediction

Wei Hangyuan, Han Yu, Wu Zijing, Geng Jiahao, Su Xunwen

School of Electrical & Control Engineering, Heilongjiang University of Science & Technology, Harbin 150022, China

ABSTRACT: Wind power exhibits significant nonlinearity, intermittency, and volatility, posing considerable challenges to grid scheduling and the stable operation of power systems. To improve the accuracy and robustness of short-term wind power forecasting, this paper proposes a dual-stage prediction model based on Transformer and BiGRU with residual correction. First, Pearson correlation coefficients are employed to filter multi-source environmental features, eliminating redundant variables and optimizing input dimensionality. Then, a primary forecasting structure is constructed by integrating a Transformer encoder with a BiGRU network to capture both global dependencies and local dynamic patterns within the sequence. On this basis, a residual correction module is introduced to form a dual-stage architecture, enabling secondary compensation for prediction errors. Experimental evaluations conducted on real wind farm data demonstrate that the proposed model outperforms conventional deep learning methods across multiple evaluation metrics, showing superior prediction accuracy and generalization performance.

KEY WORDS: Wind power forecasting; Transformer; BiGRU; Residual correction; Deep learning

摘要：风电功率具有显著的非线性、间歇性与波动性特征，这些特征对电网调度与系统运行稳定性构成挑战。为提升风电功率短期预测的准确性与鲁棒性，本文提出一种残差校正的 Transformer-BiGRU 双阶段预测模型。首先，通过皮尔逊相关系数对多源环境特征进行筛选，剔除冗余变量，优化模型输入维度。随后构建由 Transformer 编码器与 BiGRU 网络组成的主预测结构，分别提取序列全局依赖与局部动态特征。在此基础上引入残差修正模块，构建双阶段预测框架，实现对主模型误差的二次校正。实验部分基于真实风电场数据开展多模型对比分析，结果表明所提模型在多个评价指标上均优于传统深度学习方法，具备更高的预测精度与泛化能力。

基金项目：“2021 年度黑龙江省省属高校基本科研业务费项目”，项目编号 2021-KYYWF-1467

Fund Project: Basic Scientific Research Fund Project of Heilongjiang Provincial Universities in 2021, Project No. 2021-KYYWF-1467

关键词：风电功率预测；Transformer；BiGRU；残差修正；深度学习

0 引言

近年来，为应对经济发展带来的能源消耗压力，我国加快推进可再生能源建设，风电作为技术成熟、规模化优势明显的清洁能源，逐渐成为国家重点发展的战略方向[1]。在“双碳”政策引导下，分布式风电等绿色能源项目快速发展，风电在电力系统中的渗透率持续提升，助力能源结构转型与低碳发展[2]。然而，风力发电高度依赖气象与环境条件，具有显著的随机性、间歇性和波动性[3]。这种波动性在大规模风电并网时，可能对电力系统的安全稳定运行构成挑战，增加电网调度与运行管理的复杂度[4]。因此，实现对风电输出功率的精准预测，不仅有助于提前掌握风电出力的变化趋势，也为电网调度优化与系统稳定性保障提供了重要支撑[5]。

当前，风电功率预测方法主要包括物理机制模型、统计规律模型、传统机器学习模型以及深度学习模型四大类[6]。物理模型通过构建风速场、气象条件、地形地貌与风机特性等多因素之间的动力学关系，具备一定的物理可解释性，适用于特定场景下的中长期预测[7]。然而，此类方法对高精度气象与地理数据的依赖程度较高，建模过程复杂、计算开销大，且难以应对风况的快速变化。统计模型则基于历史数据进行建模，利用如自回归积分滑动平均模型（ARIMA）、支持向量回归（SVR）等方法挖掘时间序列的趋势性与相关性，适用于短期预测场景。尽管该类方法建模过程较为简便，但由于多采用线性假设，难以准确刻画风电数据中普遍存在的非线性动态特征，预测精度存在一定局限性。随着人工智能技术的发展，机器学习和深度学习方法在风电功率预测中表现出强大的特征提取与时序建模能力。循环神经网络（RNN）、长短期记忆网

络（LSTM）、门控循环单元（GRU）等结构能够有效捕捉风电序列中的短期波动与长期依赖，在多个研究与工程场景中取得了优异效果。文献[8]首先利用 EEMD 算法对原始高维环境特征数据进行分解，提取不同频率的模态分量以缓解时序数据的弱平稳性。随后在 BiGRU 网络中引入注意力机制以强化状态表示，并通过改进灰狼优化算法（IGWO）对其初始超参数进行优化。最终将分解后的子序列输入模型进行预测并重构输出结果。文献[9]提出一种融合 Transformer 与 LSTM 的风电预测模型，通过维度不变嵌入结构保持时间序列特征完整性，结合自注意力机制提升对气象因素与风电功率间时序相关性的建模能力，最终实现更高精度的短期预测性能验证。文献[10]构建基于 BiLSTM 的风电预测模型，结合改进蜣螂优化算法对网络参数寻优，并引入 CEEMDAN、样本熵与 VMD 等分解重构机制，提升误差建模能力，在此基础上，融合 Attention 机制增强特征提取，实现更高精度预测。

尽管现有方法在风电功率预测方面有所成果，但仍存在一些问题。传统模型普遍对数据非线性与时序特征建模能力不足，难以应对风电功率随时间剧烈波动的复杂性；而深度学习方法虽然具备较强的表达能力，但在面对高维特征输入时易出现冗余干扰，影响建模效率和预测精度。此外，模型结构设计往往忽略多尺度时序关系与误差反馈机制的融合，导致预测结果稳定性不足、泛化能力有限。

针对上述问题，本文提出一种融合特征选择与双阶段集成建模的短期风电功率预测方法。首先，利用皮尔逊相关系数对原始多维特征进行筛选，提升输入数据质量；其次，设计集成 Transformer 编码器与 BiGRU 网络的预测结构，结合注意力机制增强模型对时序依赖的建模能力；进一步引入残差修正模块与双模型协同机制，提升预测结果的鲁棒性与拟合精度。实验通过多个评价指标与现有模型进行对比验证，全面评估所提方法的有效性。

1 模型原理

1.1 BiGRU 模型原理

GRU 是一种改进的循环神经网络结构，通过引入两个门控机制：更新门与重置门，有效提升了模型对长期时序信息的建模能力[11]。结算过程如下：

1）更新门控制当前状态对前一时刻隐藏状态的保留程度：

$$z_t = \sigma(W_z x_t + U_z h_{t-1} + b_z) \quad (1)$$

2）重置门控制当前输入与前一隐藏状态的融合程度：

$$r_t = \sigma(W_r x_t + U_r h_{t-1} + b_r) \quad (2)$$

3）候选状态：

$$\tilde{h}_t = \tanh(W_h x_t + U_h (r_t \odot h_{t-1}) + b_h) \quad (3)$$

4）最终隐藏状态：

$$h_t = (1 - z_t) \odot h_{t-1} + z_t \odot \tilde{h}_t) \quad (4)$$

式中，σ 表示 Sigmoid 激活函数，tanh 表示双曲正切函数，$\odot$ 表示逐元素乘法，h_t 为当前时间步的隐藏状态。

GRU 结构相较于传统 LSTM 更为简洁，参数更少，训练效率更高，尤其适合中短期时间序列预测场景，如风电功率变化建模。结构如图 1 所示。

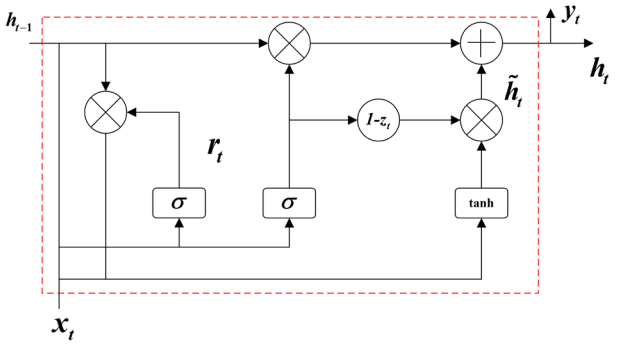


图 1 GRU 结构图

作为 GRU 的改进结构，BiGRU 由两个传播方向相反的 GRU 网络组成。具有 K 个 GRU 单元的 BiGRU 网络如图 2 所示。与 GRU 相比，BiGRU 中的每个时间节点都包含有关整个输入序列的信息，这使得能够更好地对所有输入样本进行全面的特征提取。

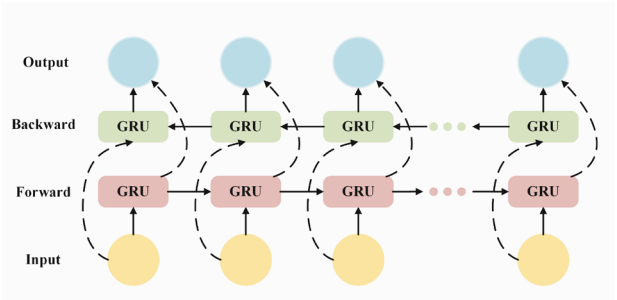


图 2 BiGRU 结构图

1.2 Transformer 原理

Transformer 模型是一种基于编码器-解码器架构的深度神经网络，其核心由多层自注意力机制堆叠构成[12]。如图 3 所示，Transformer 的整体结构由编码器（Encoder）与解码器（Decoder）两部分组成。其中，输入序列首先通过嵌入层映射至高维空间，再分别送入编码器与解码器模块进行特征建模

与序列生[13]。

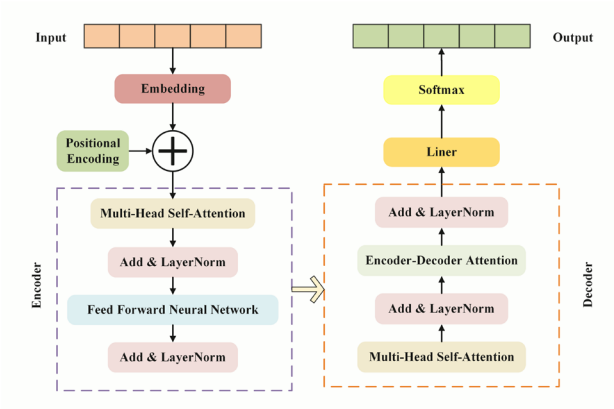


图 3 Transformer 结构图

1）自注意力机制

自注意力通过计算序列中每个位置与其他位置之间的相关性来加权组合信息。设输入序列为 $X=[x_1,x_2,\ldots,x_n]$，则自注意力计算公式为：

$$\mathrm{Attention}(Q,K,V)=\mathrm{softmax}(\frac{QK^T}{\sqrt{d_k}})V \quad (5)$$

式中，$Q=XW_Q$，$K=XW_K$，$V=XW_V$ 分别为查询、键和值矩阵；d_k 为键向量 K 的维度，用于归一化。

2）多头自注意力机制

多头注意力通过将自注意力机制并行运行多次，再将结果连接起来，以同时关注不同的信息子空间。计算公式如下：

$$M(Q,K,V)=\mathrm{Concat}(head_1,\ldots,head_h)W^O \quad (6)$$

式中，W^O 为连接多个头输出的最终权重矩阵。

其中每个头的计算为：

$$head_i=\mathrm{Attention}(QW_Q^i,KW_K^i,VW_V^i) \quad (7)$$

式中，W_Q^i，W_K^i，W_V^i 为第 i 个注意力头的权重矩阵；

3）前馈神经网络

Transformer 中每个位置单独通过相同的两层全连接网络，包含非线性激活函数，增强模型非线性表达能力。其公式为：

$$FFN(x)=\max(0,xW_1+b_1)W_2+b_2 \quad (8)$$

式中，W_1,W_2 为为权重矩阵；b_1,b_2 为偏置项；$\max(0,x)$ 为 ReLU 激活函数。

1.3 双阶段预测原理

双阶段预测是一种将基础预测与误差补偿机制相结合的预测框架。

1）第一阶段

通过主预测模型对输入序列进行建模，获得基础预测结果；设输入序列为 X_1，第一阶段预测为：

$$\hat{y}_t^{(1)}=f_{base}(X_{1:t}) \quad (9)$$

2）第二阶段

利用第一阶段输出与当前输入状态，共同构建误差估计模型，对基础预测结果进行残差修正，从而提升最终预测精度。第二阶段将当前特征与初预测值拼接输入校正模型：

$$\Delta y_t=f_{corr}([X_t,\hat{y}_t^{(1)}]) \quad (10)$$

最终预测值为：

$$\hat{y}_t=\hat{y}_t^{(1)}+\Delta y_t \quad (11)$$

2 模型搭建

为了提升风电功率短期预测的精度与鲁棒性，本文构建了一种融合特征选择、Transformer 编码器、BiGRU 网络与残差修正模块的双阶段集成模型。整体结构包括数据预处理、特征筛选、主预测网络建模与误差补偿四个环节。首先通过皮尔逊相关系数法筛选关键输入特征，减少冗余信息干扰；在数据集构建方面，本文将处理后的样本按照 8:1:1 的比例划分为训练集、验证集与测试集。随后构建由 Transformer 编码器与 BiGRU 网络串联的深度预测子模型，捕捉风电时序数据的全局依赖与局部动态特征；最终引入第二阶段修正模块，对初步预测结果进行细节校正，从而提升整体预测性能。模型框架图如图 4 所示。

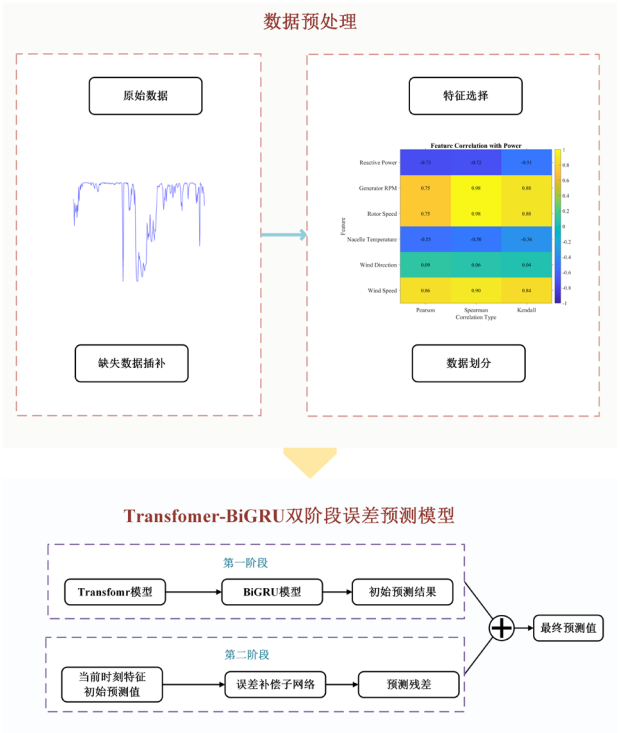


图 4 模型框架图

3 算例分析

3.1 数据说明

为验证所提出预测模型的有效性，本文选取英国 Penmanshiel 风电场的实际运行数据作为研究对象。该风电场共配置 14 台风力发电机组，每台机组包含 52,560 个采样点，数据采样时间间隔为 10 分钟。本文对 15 号风电机的数据进行分析。在缺失值处理方面，共检测到 1557 条缺失记录。为保障数据的完整性并降低信息损失，本文采用均值插补法对缺失值进行填补，从而为后续建模提供更稳定的输入数据基础。

3.2 特征选择

在输入变量处理阶段，本文从风电系统运行特性出发，初步选取风速、风向、无功功率、叶轮转速、发电机转速、机舱温度等 6 个关键特征。为进一步评估各变量与目标功率输出之间的相关性，采用皮尔逊（Pearson）、斯皮尔曼（Spearman）及肯德尔（Kendall）三种相关系数方法进行特征关联性分析，结果如图 6 所示。

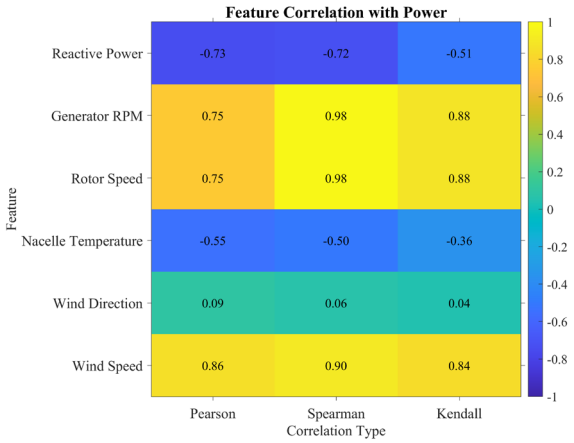


图 5　相关性热力图

由图 5 可见，风速、发电机转速与叶轮转速在三类相关性分析中均表现出较强的正相关性，说明其对有功功率输出具有显著的影响作用。相反，风向与功率之间的相关性较弱。因此，本文最终保留风速、发电机转速、叶轮转速、无功功率与机舱温度五个特征作为模型输入，剔除风向变量以避免冗余信息干扰，提升模型的训练效率与预测精度。

3.3 评价指标

为了全面评估各预测模型在风电功率点预测任务中的效果，本文采用以下四种评价指标：均方根误差（RMSE）、平均绝对误差（MAE）、决定系数（R^2）与相对准确率（AR）。

$$RMSE=\sqrt{\frac{1}{n}\sum_{i=1}^{n}(y_i-\hat{y}_i)^2} \quad (12)$$

$$MAE=\frac{1}{n}\sum_{i=1}^{n}|y_i-\hat{y}_i| \quad (13)$$

$$R^2=1-\frac{\sum_{i=1}^{n}(y_i-\hat{y}_i)^2}{\sum_{i=1}^{n}(y_i-\bar{y}_i)^2} \quad (14)$$

$$AR=1-\sqrt{\frac{1}{nC^2}\sum_{i=1}^{n}(y_i-\hat{y}_i)^2} \quad (15)$$

式中，y_i 为第 i 个样本的真实值，$\hat{y}_i$ 为模型预测值，n 为样本数量，$\bar{y}_i$ 为真实值的均值，C 表示风电机组装机容量。

3.4 实验对比分析

为验证所提出模型在风电功率预测任务中的有效性与优越性，本文设计了一组对比实验，从基础时序模型到深度融合结构的多种方法。具体为：RNN、LSTM、GRU 以及其改进结构 BiGRU；同时引入基于自注意力机制的 Transformer 模型；在此基础上，进一步设计了多种融合模型，用以验证不同模块组合对预测性能的影响。

表 1 展示了各对比模型在测试集上的预测性能，评估指标包括 RMSE、MAE、R^2和 AR。从整体结果来看，深度学习模型普遍优于传统 RNN，表现出更强的时序建模能力。其中，BiGRU 在基础模型中表现最佳，优于 GRU 与 LSTM。在融合结构方面，CNN-Transformer-BiGRU 相较于单一 Transformer 有明显提升，说明多尺度卷积与注意力机制的结合有助于建模风电数据的非线性特征。引入注意力机制的 Transformer-BiGRU-Attention 模型在各项指标上表现更优，特别是在 R^2与 AR 方面提升显著。本文提出的 Transformer-BiGRU-Dual-stage 模型在所有指标上均取得最优结果，RMSE 与 MAE 分别降至 0.020489 和 0.012168，R^2和 AR 分别提升至 0.996625 和 0.979511，展现出更强的误差修正能力与泛化性能。

图 6 展示了各模型预测曲线与真实值的对比情况。除传统 RNN 外，其余深度模型整体拟合效果良好。相比之下，RNN 在波动段和突变点误差较大。Transformer-BiGRU-Attention 与 Dual-stage 模型预测曲线与真实值高度重合，尤其在陡升陡降区域响应更敏感，误差更小。其中，Dual-stage 模型在捕捉趋势和细节波动方面表现更优，验证了其残差校正机制的有效性。

表 1 模型性能对比

Table1 Comparison of Model Performance

Model	RMSE	MAE	R^2	AR
RNN	0.030161	0.020794	0.992687	0.969839
LSTM	0.024173	0.015477	0.995302	0.975827
GRU	0.024181	0.015556	0.995299	0.975819
BiGRU	0.023394	0.014689	0.9956	0.976606
Transformer	0.025687	0.018618	0.994695	0.974313
CNN-Transformer-BiGRU	0.022991	0.014019	0.99575	0.977009
Transformer-BiGRU-Attention	0.020848	0.012685	0.996506	0.979152
Transformer-BiGRU-Dual-stage	0.020489	0.012168	0.996625	0.979511

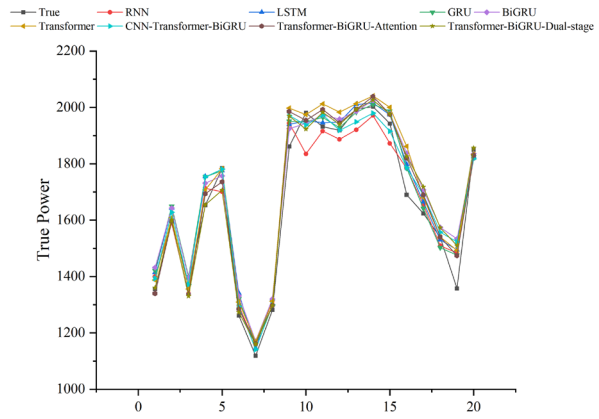


图 6 曲线对比图

4 结论

本文针对风电功率序列非线性强、波动性大及高维特征干扰等问题，提出了双阶段残差修正机制的 Transformer-BiGRU 集成预测模型。通过引入皮尔逊相关系数对原始多变量特征进行筛选，显著提升了模型输入的有效性；同时将 Transformer 编码器与 BiGRU 网络相结合，实现了对风电时序数据的全局依赖建模与局部动态特征捕捉；在此基础上，引入残差修正子模块构建双阶段预测结构，有效降低了模型的误差，进一步提升了整体预测精度与稳定性。

实验部分在真实风电场数据集上进行了充分验证。结果表明，本文模型在 RMSE、MAE、R^2 和 AR 等多个评价指标上均优于传统 RNN、LSTM、GRU、以及融合类深度模型，展现出更强的拟合能力。其中，Transformer-BiGRU-Dual-stage 模型在多个关键时刻的响应更为灵敏，对风电功率的剧烈波动具有更好的预测表现。

综上所述，所提出的模型结构不仅在风电功率预测中具有良好的应用潜力，也为时序预测问题中融合注意力机制与残差建模提供了新的思路。未来工作可进一步探索模型在多风机、多区域协同预测场景下的泛化能力与拓展性

参考文献

[1] 张智浩,王聪,张宏立,等.时间生成对抗网络样本扩增下的风电功率预测[J/OL].电力系统及其自动化学报,1-12[2025-06-13].

[2] 万思洋,杨苹,崔嘉雁,等.针对非平稳信号和高频噪声的自适应噪声完整集成经验模态分解-双向长短期记忆风功率预测模型[J].电网技术,2025,49(03):1176-1184.

[3] 黄南天,李炳玲,孙赫宏,等.计及时-空全域特征增强的广域多风电场风电功率短期预测[J/OL].电网技术,1-13[2025-06-13].

[4] Yang M, Han C, Zhang W, et al. A short-term power prediction method based on numerical weather prediction correction and the fusion of adaptive spatiotemporal graph feature information for wind farm cluster[J]. Expert Systems with Applications, 2025, 274: 126979.

[5] Wang Y, Pei L, Li W, et al. Short-term wind power prediction method based on multivariate signal decomposition and RIME optimization algorithm[J]. Expert Systems with Applications, 2025, 259: 125376.

[6] 张顺,黄万超,谢欣宇,等.风电功率预测的新兴技术与发展趋势综述[J].现代工业经济和信息化,2024,14(05):171-172+175.

[7] Wang H, Li B, Xue Z, et al. Powerformer: A temporal-based transformer model for wind power forecasting[J]. Energy Reports, 2024, 11: 736-744.

[8] 彭宇文,林镇宏,黄京苑,等.基于 EEMD 和 BiGRU-Attention 的短期风电功率预测方法[J/OL].南方电网技术,1-10[2025-06-13].

[9] 徐武,范鑫豪,沈智方,等.多尺度特征提取的 Transformer 短期风电功率预测[J].太阳能学报,2025,46(02):640-648.

[10] 魏振宇,姜雪松,杨立发.基于误差补偿及 IDBO-BiLSTM 的风电功率短期预测[J].科学技术与工程,2025,25(06):2397-2405.

[11] Wang S, Shi J, Yang W, et al. High and low frequency wind power prediction based on Transformer and BiGRU-Attention[J]. Energy, 2024, 288: 129753.

[12] Xiang L, Fu X, Yao Q, et al. A novel model for ultra-short term wind power prediction based on Vision Transformer[J]. Energy, 2024, 294: 130854.

[13] 包广斌,杨龙龙,范超林,等.基于 SSA 优化的 Transformer-BiGRU 短期风电功率预测[J/OL].电子测量技术,1-9[2025-06-13].http://kns.

092 基于 SimuNPS 的储能电站并网振荡预测

郜登科[1]，石林龙[1]，李鸿彪[1]

（1．上海科梁信息科技股份有限公司，上海市 201103）

Oscillation Prediction of Grid-connected Energy Storage Power Station with SimuNPS

GAO Dengke[1], SHI Linlong[1], LI Hongbiao[1]

(1.Shanghai KeLiang Information Technology Co., Ltd., Shanghai 201103, China)

ABSTRACT: Energy storage power station is a crucial foundation for constructing new-type power systems and promoting green and low-carbon energy transformation. It is also a key support for achieving carbon peak and carbon neutrality goals. Due to the complexity of energy storage unit (ESU) control, the wide range of operating conditions and the clustering effect of multiple parallel units, there is a significant oscillation risk in grid-connected energy storage power station. The frequency-domain stability analysis method based on immittance is an important approach for predicting and solving oscillation problems. The new-type power systems modeling and simulation software SimuNPS adopts this method to achieve frequency-domain modeling and stability analysis functions, providing a solution for oscillation prediction in new-type power systems. This paper researched the small signal stability issue of a grid-connected energy storage power station by finely modeling its internal structure. SimuNPS was used to conduct system oscillation risk assessment for different combinations of multiple equipment operating conditions in the power station, and two oscillation conditions were predicted. These oscillation conditions were then simulated in MATLAB/Simulink. The feasibility and correctness of oscillation prediction based on frequency-domain stability analysis was verified by time-domain simulation and fast Fourier transform (FFT) analysis results.

KEY WORDS: new-type power systems, energy storage power station, SimuNPS, immitance, frequency-domain stability analysis, oscillation prediction

摘要：储能电站是建设新型电力系统和推动能源绿色低碳转型的重要基础，是实现碳达峰、碳中和目标的关键支撑。由于储能单元控制的复杂性、运行工况的宽泛性和多台并联的集群化效应，导致储能电站并网有较大的振荡风险。基于导抗的频域稳定性分析方法是预测和解决振荡问题的重要方法。新型电力系统建模仿真软件 SimuNPS 采用该方法实现了频域建模和稳定性分析功能，可以为新型电力系统振荡预测提供解决方案。本文通过储能电站内部精细化建模来研究该电站并网小扰动稳定性问题。使用 SimuNPS 对电站多个设备的不同工况组合进行系统振荡风险评估，从中预测了两个振荡工况，进而在 MATLAB/Simulink 中仿真这些振荡工况。时域仿真和 FFT 分析结果验证了由频域稳定性分析进行振荡预测的可行性和正确性。

关键词：新型电力系统；储能电站；SimuNPS；导抗；频域稳定性分析；振荡预测

DOI：10.13335/j.1000-3673.pst.2014.01. 25-1275

0 引言

新型电力系统的核心特征是高比例新能源的接入，其本质是从过去的“源随荷动”转向“源荷互动”[1]。由于风电、光伏等新能源的随机性、间歇性和波动性，导致电网负荷峰谷差变大，给系统功率平衡带来巨大挑战[2-3]。储能电站通过“削峰填谷”有效降低功率波动，提高新能源消纳能力。储能电站包括储能单元（Energy Storage Unit, ESU）和静止无功发生器（Static Var Generator, SVG）等多种电力电子设备，这些设备会通过电网相互耦合、相互作用[4]，产生非常复杂的运行工况，导致电站在弱电网下容易发生振荡，可能导致电站脱网或设备损坏等严重后果。

提前对储能电站并网系统开展精准的振荡预测，从而采取针对性的稳定性增强措施可以有效抑制振荡风险。如果利用时域仿真进行振荡预测，考虑到仿真资源限制和仿真耗时长等不利影响，通常会使用单机倍乘方式进行建模。由于未考虑电站内线路分布的差异，倍乘模型的仿真分析结果可能和详细模型存在较大误差[5]。在研究振荡问题和进行振荡风险评估的各种方法中[6-7]，基于导抗的频域稳定性分析已受到广泛关注[8-9]，它支持在频域对储能电站进行详细建模，通过分析储能电站并网系统不同工况下的频域稳定性实现准确的振荡预测。

SimuNPS 是一款集成时域、频域和信息域的新

型电力系统建模仿真软件。该软件采用基于导抗的频域稳定性分析方法，可以基于机理模型和数据驱动方式进行新型电力系统的频域建模，通过广义奈奎斯特判据（Generalized Nyquist Criterion, GNC）分析系统稳定性，对于振荡工况能够得到相应的振荡频率。

本文首先在 MATLAB/Simulink 中对多工况 ESU 和 SVG 进行 1-2000Hz 的导纳扫描，然后分别在 MATLAB/Simulink 和 SimuNPS 中建立储能电站并网系统的详细时域和频域模型，进而基于 SimuNPS 对储能电站不同工况组合开展宽频段的振荡预测，最后基于 MATLAB/Simulink 对振荡工况开展时域仿真和快速傅里叶变换（Fast Fourier Transform, FFT）分析。

1 频域稳定性分析

分析系统频域稳定性之前，对于线路和变压器等无源设备，可以采用机理模型实现频域建模。对于 ESU 和 SVG，可以采用数据驱动方式实现频域建模，即通过不同工况下的导纳数据进行模拟。为了系统频域稳定性分析结果的精确性，需要考虑频域耦合的影响[10-12]，对 ESU 和 SVG 的正序自导纳、正序耦合导纳、负序自导纳和负序耦合导纳都要进行扫描。在设备频域建模的基础上，可以建立系统频域小信号电压和电流关系矩阵。

将该矩阵转换为多输入多输出负反馈回路形式后，系统频域稳定性可以通过基于回路增益矩阵和单位矩阵之和行列式的 GNC 或者回路增益矩阵特征值的 GNC 来确定[13]。

2 算例建模

2.1 时域模型

本算例考虑了一个储能电站并入弱电网的场景，该电站由 10 台 ESU 和 1 台 SVG 组成。其中，ESU 由电池和储能变流器（Power Conversion System, PCS）构成，PCS 控制部分包括锁相环和电流环，每个 ESU 端口接有箱式变压器，ESU 之间通过长度较短的线路相连。SVG 每相由 22 个全桥子模块级联而成，控制策略为恒定无功功率控制，包括锁相环、电流环以及全局电压控制、相间均压控制和相内均压控制三层电容电压控制。电网部分采用电网等值阻抗模拟，通过电站并网点计算短路比约为 2，可以认为是一个强度较弱的电网[14]。

先构建 ESU 和 SVG 的导纳数据库，即参照[15]和[16]的工况要求，分别对其多个运行工况下的四个导纳进行扫描。以 ESU 导纳扫描为例，ESU 串联理想电压源和扰动电压源，将 ESU 设置为待测工况后启动，扰动电压源注入小信号正序电压或者负序电压，对 ESU 端口稳态电压电流信号进行记录、FFT 分析和导纳计算，如图 1 所示。

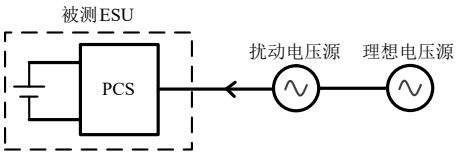


图 1 导纳扫描原理

Fig. 1 Admittance scanning principle

在有功功率输出分别为 0.5MW、1MW 和 2MW 这三种工况下，ESU 正序自导纳如图 2 所示。

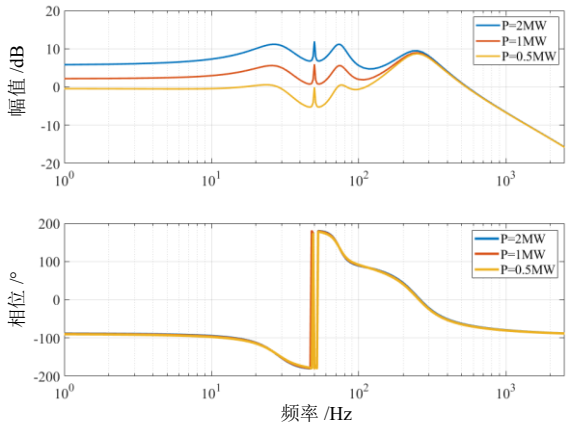


图 2 三种工况 ESU 正序自导纳

Fig. 2 Positive sequence self admittance of ESU under three operating conditions

2.2 频域模型

在 SimuNPS 中搭建储能电站并网系统频域模型，如图 3 所示，导入 ESU 和 SVG 的导纳数据库，并设置电网、线路和变压器的参数。

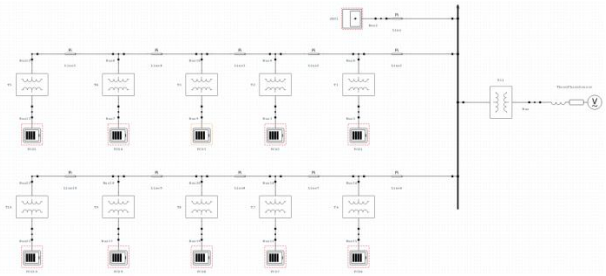


图 3 储能电站并网系统频域模型

Fig. 3 Frequency-model of grid-connected energy storage power station

3 分析验证

在 SimuNPS 中，先固定 ESU 运行工况，遍历 SVG 运行工况查找系统发生振荡的工况，预测到振荡工况一，然后固定 SVG 运行工况，遍历 ESU 运

行工况查找系统发生振荡的工况，预测到振荡工况二。基于图 3 所示储能电站并网系统的时域仿真模型，验证振荡预测结果的准确性。

3.1 振荡工况一

使系统在低功率模式下启动，此时单台 ESU 输出有功功率为 1MW，SVG 输出无功功率为 1MVar，在该工况下进行频域稳定性分析，发现系统处于稳定状态。保持 ESU 的运行工况不变，持续增大 SVG 输出的无功功率，使用基于特征值的 GNC 进行频域稳定性分析，发现奈奎斯特曲线与（-1, j0）点的内切圆的半径越来越小，说明此时系统振荡的风险正在变大[17]，结果如表 1 所示。最后发现，当 SVG 输出无功功率为 4MVar 时，系统会失稳。

表 1 SVG 工况影响系统稳定状态和内切圆半径

Table 1 Effect of SVG operating conditions on system stable state and inscribed circle radius

SVG 工况	系统稳定状态	内切圆半径
无功功率 1MVar	稳定	0.1769
无功功率 2MVar	稳定	0.1058
无功功率 3MVar	稳定	0.0541
无功功率 3.5MVar	稳定	0.0364
无功功率 3.8MVar	稳定	0.0204
无功功率 4MVar	失稳	0.0065

对 ESU 输出有功功率 1MW、SVG 输出无功功率 4MVar 工况下的系统使用基于行列式的 GNC，将通过奈奎斯特图呈现系统的稳定状态，如图 4 所示。正序曲线包围原点，负序曲线没有围绕该点，所以预测系统发生正序失稳，而在负序下稳定。

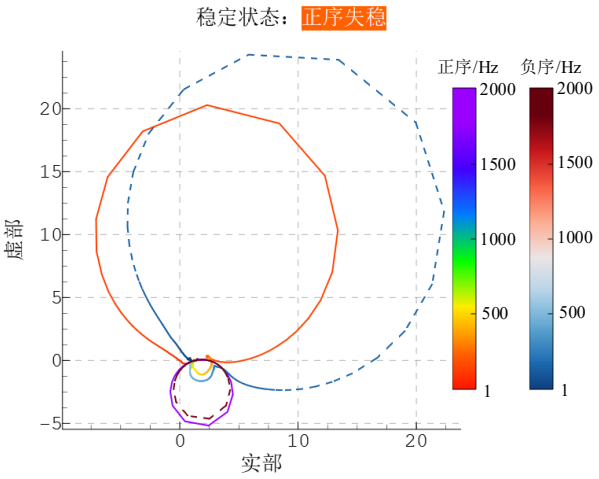


图 4 振荡工况一下基于行列式的 GNC 分析结果

Fig. 4 Analysis result of GNC based on determinant under oscillation condition one

使用基于特征值的 GNC 对系统稳定性进行定量分析，即获取系统振荡频率，结果如图 5 所示。通过查看图例中“振荡频率切点圆”的圆心坐标，可以看到数值显示为 122.976Hz，表明 SimuNPS 分析系统振荡频率约在 122-123Hz 范围，且此时内切圆半径较小，表明正序曲线虽然围绕（-1, j0）点，但和该点之间距离很小，系统处于临界振荡状态。

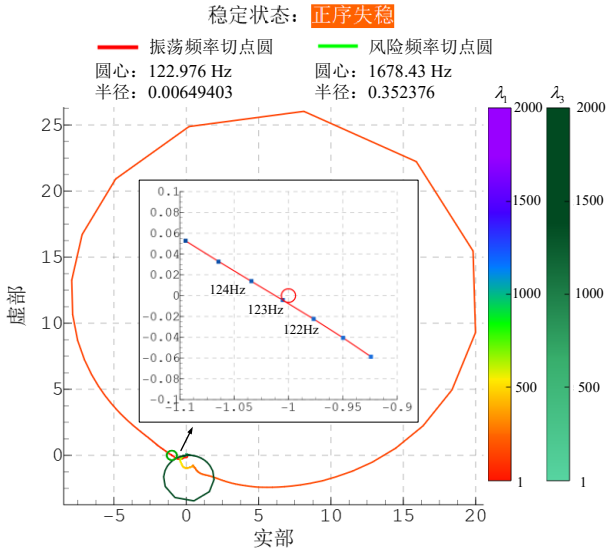
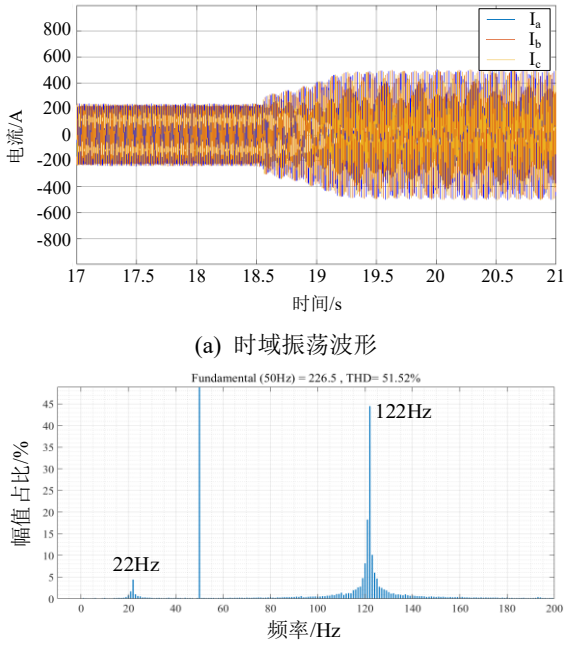


图 5 振荡工况一下基于特征值的 GNC 分析结果

Fig. 5 Analysis result of GNC based on eigenvalue under oscillation condition one

ESU 和 SVG 在低功率模式下启动，按照表 1 逐步改变 SVG 的工况，当 SVG 无功功率从 3.8MVar 增加到 4MVar 时，场站并网点电流仿真波形如图 6(a)所示，对振荡过程 A 相电流波形进行 FFT 分析，结果如图 6(b)所示。



(a) 时域振荡波形

(b) FFT 分析结果

图 6 振荡工况一时域仿真和 FFT 分析结果

Fig. 6 Time-domain simulation and FFT analysis results of oscillation condition one

由图 6(a)可见，在 18.5s 前，即 SVG 输出无功

功率为 3.8MVar 时，场站并网点并未出现振荡，但当仅提高约 5%的无功功率后，即 SVG 无功功率为 4MVar 时，系统发生等幅振荡，表明此时系统在该工况下呈现临界稳定状态，验证了图 5 分析结果。由图 6(b)的 FFT 分析结果，可见 122Hz 谐波含量较高，说明此时发生约 122Hz 的振荡，22Hz 为其频率耦合分量，与图 5 分析结果一致。

进一步分析 122Hz 振荡频率下三相电流的幅值和相位，如表 2 所示。通过相位关系可以发现，此时系统发生的是正序失稳，与图 4 和图 5 分析结果一致。

表 2 122Hz 振荡频率下三相电流幅值和相位

Table 2 Three phase current amplitude and phase at oscillation frequency of 122Hz

电流	幅值/%	相位/°
A 相	44.49	-136.6
B 相	44.31	103.5
C 相	44.45	-16.5

3.2 振荡工况二

SVG 输出无功功率为 3MVar 时，ESU 从输出 1MW 有功功率开始启动，SimuNPS 分析此时系统稳定。以 0.1MW 为间隔逐步增加 ESU 的有功功率，分析结果显示内切圆半径越来越小。当 ESU 有功功率达到 1.8MW 时，SimuNPS 分析此时系统发生 119-120Hz 的振荡，结果如图 7 所示。

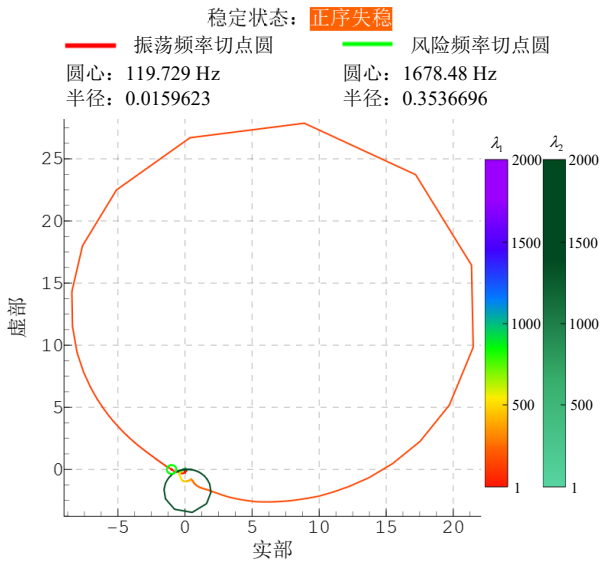
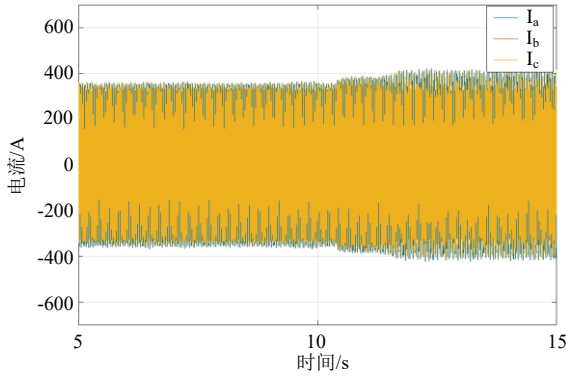


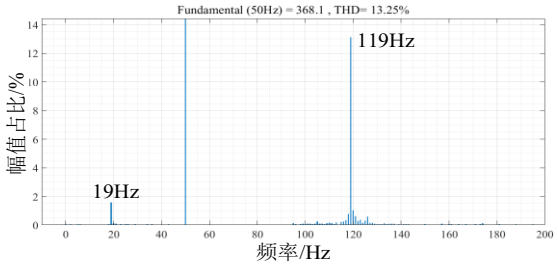
图 7 振荡工况二下基于特征值的 GNC 分析结果

Fig. 7 Analysis result of GNC based on eigenvalue under oscillation condition two

同样地，在 MATLAB/Simulink 中仿真这一工况，当 ESU 输出功率从 1.7MW 增加到 1.8MW 时，仿真波形如图 8(a)所示。由图可见，在增大 ESU 有功功率前，系统可以稳定运行，当 ESU 有功功率增大后，电流逐渐呈现发散状态，系统出现失稳振荡。对发散过程的 A 相电流波形进行 FFT 分析，结果如图 8(b)所示，可以看出 119Hz 谐波含量较高，与图 7 分析结果一致。



(a) 时域振荡波形



(b) FFT 分析结果

图 8 振荡工况二时域仿真和 FFT 分析结果

Fig. 8 Time-domain simulation and FFT analysis results of oscillation condition two

分析 119Hz 振荡频率下三相电流的幅值和相位，如表 3 所示，可以看出此时系统发生的是正序失稳，也与图 7 分析结果一致。

表 3 119Hz 振荡频率下三相电流幅值和相位

Table 3 Three phase current amplitude and phase at oscillation frequency of 119Hz

电流	幅值/%	相位/°
A 相	13.11	167
B 相	13.08	47.3
C 相	13.15	-72.8

以此类推，通过遍历场站中 ESU 和 SVG 的工况组合，SimuNPS 可以发现该场站并网的其他振荡工况，从而为系统振荡预测提供解决方案。

4 结论

本文针对储能电站并网的振荡风险，基于 SimuNPS 软件建立其详细的频域模型并进行频域稳定性分析，预测了该系统可能发生振荡的工况组合，并在 MATLAB/Simulink 中进行了仿真验证，主要结论如下：

1）基于 ESU 和 SVG 的多工况导纳扫描结果，

可以采用 SimuNPS 软件建立详细的包含 ESU、SVG、变压器和线路的储能电站并网频域模型，进而基于行列式或者特征值的 GNC 分析系统频域稳定性。

2）SimuNPS 可以极其便捷地切换不同设备的运行工况，并快速分析系统小扰动稳定性，稳定状态和振荡频率的分析结果准确性得到了时域仿真和 FFT 分析结果的验证，能够为系统振荡预测提供解决方案。

3）频域结合时域的分析方法不仅强化了振荡预测的工程实用性，更从多尺度动态耦合的视角深化了对新型电力系统稳定边界的认知，为分析含高渗透率电力电子设备的电网安全稳定提供了重要的技术保障。

参 考 文 献

[1] 张天米, 王俐英, 王永利, 等. 新型电力系统下需求侧管理机制及发展策略研究[J]. 四川电力技术, 2024, 47(2)：75−80.
Zhang Tianmi, Wang Liying, Wang Yongli, et al. Research on demand-side management mechanism and development strategy under new power system[J]. Sichuan Electric Power Technology, 2024, 47(2)：75−80(in Chinese).

[2] 李秉宇, 杜旭浩, 唐芬, 等. 储能变流器低频振荡机理研究及其抑制[J]. 电源学报, 2022, 20(2)：115−121.
Li Bingyu, Du Xuhao, Tang Fen, et al. Mechanism of low-frequency oscillations in energy storage converter and its suppression[J]. Journal of Power Supply, 2022, 20(2)：115−121(in Chinese).

[3] 吴贵洋, 王建章, 胡雪峰. 适于可再生能源发电储能系统中的双向直流变换器[J]. 电源学报, 2018, 16(6)：45−51.
Wu Guiyang, Wang Jianzhang, Hu Xuefeng. Bidirectional DC/DC converter for energy storage system in renewable power generation[J]. Journal of Power Supply, 2018, 16(6)：45−51(in Chinese).

[4] 肖湘宁, 罗超, 廖坤玉. 新能源电力系统次同步振荡问题研究综述[J]. 电工技术学报, 2017, 32(6)：85−97.
Xiao Xiangning, Luo Chao, Liao Kunyu. Review of the research on subsynchronous oscillation issues in electric power system with renewable energy sources[J]. Transactions of China Electrotechnical Society, 2017, 32(6)：85−97(in Chinese).

[5] 孙华东, 李佳豪, 李文锋, 等. 大规模电力系统仿真用新能源场站模型结构及建模方法研究（二）：机电暂态模型[J]. 中国电机工程学报, 2023, 43(6)：2190−2201.
Sun Huadong, Li Jiahao, Li Wenfeng, et al. Research on model structures and modeling methods of renewable energy station for large-scale power system simulation (II): electromechanical transient model[J]. Proceedings of the CSEE, 2023, 43(6)：2190−2201(in Chinese).

[6] Wang Liang, Xie Xiaorong, Jiang Qirong,et al.Investigation of SSR in practical DFIG-based wind farms connected to a series-compensated power system[J]. IEEE Transactions on Power Systems, 2015, 30(5)：2772−2779.

[7] 张东辉, 陈新. 基于阻抗视角的新能源发电系统宽频振荡抑制技术综述[J]. 中国电机工程学报, 2024, 44(24)：9672−9690.
Zhang Donghui, Chen Xin. Overview of broadband oscillation mitigation of new energy generation power system based on impedance perspective[J]. Proceedings of the CSEE, 2024, 44(24)：9672−9690(in Chinese).

[8] Sun Jian. Two-port characterization and transfer immittances of AC-DC converters—part I：modeling[J]. IEEE Open Journal of Power Electronics, 2021, 2：440-462.

[9] Sun Jian. Two-port characterization and transfer immittances of AC-DC converters—part II：applications[J]. IEEE Open Journal of Power Electronics, 2021, 2：483-510.

[10] 年珩, 徐韵扬, 陈亮, 等. 并网逆变器频率耦合特性建模及系统稳定性分析[J]. 中国电机工程学报, 2019, 39(5)：1421-1431.
Nian Heng, Xu Yunyang, Chen Liang, et al. Frequency coupling characteristic modeling of grid-connected inverter and system stability analysis[J]. Proceedings of the CSEE, 2019, 39(5)：1421-1431(in Chinese).

[11] 王海鑫, 刘铭崎, 董鹤楠, 等. 含高比例新能源的电力系统低频振荡分析与抑制综述[J]. 电力自动化设备, 2023, 43(9)：152-163.
Wang Haixin, Liu Mingqi, Dong Henan, et al. Review on analysis and suppression of low-frequency oscillation in power system with high penetration of renewable energy sources[J]. Electric Power Automation Equipment, 2023, 43(9)：152-163(in Chinese).

[12] Sun Jian. Frequency-domain stability criteria for converter-based power systems[J]. IEEE Open Journal of Power Electronics, 2022, 3：222-254.

[13] Sun Jian, Hiquiana L, Lee B, et al. Frequency-domain stability study of converter-based power systems[C]//21st Wind & Solar Integration Workshop (WIW 2022), Hybrid Conference. The Hague, Netherlands, 2022：30-37.

[14] 李云丰, 赵文广, 贺之渊, 等. 连接弱交流电网的柔性直流换流站外环控制器参数解析计算及其限制因素分析[J]. 中国电机工程学报, 2023, 43(24)：9682-9695.
Li Yunfeng, Zhao Wenguang, He Zhiyuan, et al. Analytical calculation method of outer loop controller parameters of HVDC converter station connected to weak AC grid and analysis of limiting factors[J]. Proceedings of the CSEE, 2023, 43(24)：9682-9695(in Chinese).

[15] NB/T 10651-2021, 风电场阻抗特性评估技术规范[S].

[16] NB/T 11344-2023, 光伏发电站阻抗特性评估技术规范[S].

[17] Franklin G, Powell J, Emami-Naeini A. Feedback control of dynamic systems, 7th edition[M]. London：Pearson, 2015.

收稿日期：2025-08-25；

作者简介：

郜登科(1984)，男，河南焦作人，博士，主要研究方向为新型电力系统稳定性分析。

石林龙(1981)，男，湖北黄冈人，硕士，高级工程师，主要研究方向为新型电力系统建模仿真。

李鸿彪(1987)，男，山西晋中人，硕士，主要研究方向为新型电力系统建模仿真。

093 离网型柔性合成氨系统各装置优化配置

杨修宇[1]，周家庆[1]，崔新振[2]，张浩[3]，杨呈[1]，田嘉榆[1]

（1.现代电力系统仿真控制与绿色电能新技术教育部重点实验室(东北电力大学)，吉林 132012；
2. 阳谷新源热电有限公司，聊城 252000；
3.长春供电公司，长春 130000）

Optimal Sizing and Configuration of Devices for Grid-Forming Off-Grid Flexible Ammonia Synthesis Systems

YANG Xiuyu[1], ZHOU Jiaqing[1], CUI Xinzhen[2], ZHANG Hao[3], YANG Cheng[1], TIAN Jiayu[1]

(1. Ministry of Education Key Laboratory of Modern Power System Simulation Control and Green Electric Energy New Technology, Northeast Electric Power University, Jilin 132012, China; 2. Yanggu Xinyuan Thermal Power Co., Ltd., Liaocheng 252000, China;3. Changchun Power Supply Company, Changchun 130000, China;)

ABSTRACT: The off-grid flexible ammonia synthesis system can reduce the fluctuation of renewable energy generation, making it one of the pathways to enhance the utilization efficiency of renewable energy. This study focuses on optimizing the operating strategy of the off-grid flexible ammonia synthesis system and proposes a time-varying optimization algorithm aimed at achieving optimal economic performance. The study treats the hourly output/consumption of wind power, photovoltaics, hydrogen production, hydrogen storage, energy storage, and ammonia synthesis as decision variables, using a linear programming (LP) algorithm for solving. A model is established with the dual objectives of minimizing the total system operation cost and maximizing the sales revenue from ammonia products, considering the constraints of various equipment, and optimizing the configuration of system components. Based on actual wind and solar data from a region in Northeast China over the course of a year, the model is designed to maximize net profit. Using typical scenarios of high wind and solar output and low wind and solar output, the adaptability of the model is verified. By optimizing ammonia synthesis load, energy storage charge/discharge, and hydrogen production operating states, the system is ensured to operate stably and efficiently under different output conditions. The optimization strategy significantly improves the economic profitability during both typical weeks and the entire year, reducing costs and increasing revenue, providing theoretical and practical guidance for system engineering applications.

KEY WORDS: off-grid flexible ammonia synthesis system; off-grid operation; economic optimization; energy storage management; linear programming

摘要：离网型柔性合成氨系统有降低可再生能源发电出力波动的功效，是增强可再生能源利用效率的途径之一。本研究围绕离网型柔性合成氨系统运行策略开展优化，给出了一种以实现经济性最佳为目标的逐时优化算法，研究将风电、光伏、制氢、储氢、储能与合成氨逐时的出力/消耗作为决策的变量，采用线性规划（LP）求解算法，综合考虑各设备约束，建立同时最小化系统运行总成本以及最大化合成氨产品的销售收益为目标的模型，进行系统各装置优化配置。参考东北某地区一年实际风光数据，使其净收益最大化。以风光大发和风光小发这两种典型工况为基础，查证该模型具备适应性，借助优化合成氨负荷、储能充放电及制氢运行状态，保障系统在不同出力情形下稳定高效地运行，优化策略极大增进了典型周和全年的经济收益性，成本下降、收益上扬，为系统工程应用提供理论及实践的引导。

关键词：离网型柔性合成氨系统；离网运行；经济性优化；储能管理；线性规划；

0 引言

随着全球气候变化问题日益严峻，减少温室气体排放已成为全球应对气候变化的首要任务。中国于 2020 年宣布到 2030 年实现碳达峰，2060 年实现碳中和的“双碳”目标。大力发展可再生能源是实现“双碳”目标、推动能源转型发展的关键途径和重要保障[1-3] 。可再生能源，尤其是风能和太阳能，因其低碳特点和广阔的应用前景，成为替换传统化石能源的首选。但风能和太阳能在发电期间的波动性与间歇性问题，造成其在实际应用的环节中面临一定挑战。

能源存储和转换技术成为现阶段研究的热点，氢气因其高能量密度以及零碳排放的性质，在全球能源转型当中具备广泛应用前景，通过将电力转化

为氢气进行储存，可切实消纳过剩的可再生电力，并在系统产生需求时进行供给.有研究指出，预计到2050 年，氢能将在我国能源消费比例中占到10%[4]，有望彻底改变人类的能源体系，促进第三次能源革命。我国的氢能消费主要是作为工业原料用于合成氨、合成甲醇等石化领域，其中合成氨产业的氢气消耗量占全国氢气总消耗量的 37%[5]。利用风光等可再生能源发电生产“绿氢 ”取代“灰氢 ”作为化工原料合成氨已经成为我国电力和化工行业碳减排的关键方向[6-7]。

尽管可再生能源制氢合成氨技术发展前景十分可观，但相关技术还处于起步阶段，需要不断优化改良；优化离网型柔性合成氨系统的运行策略、降低系统的整体成本，并提升其经济效益，成为当前研究的重点之一。近年来，针对离网型柔性合成氨系统的优化问题，已有一些研究提出了不同的解决方案。文献[8]提出以动态规划为基础的风光储能系统优化策略，顾及了电力需求和可再生能源供应的不稳定特性，但未充分考虑氢气制备及氨合成过程的影响。文献[9]给出了一种基于线性规划的风光氢能系统优化模型，该模型能高效解决多目标优化难题，但缺少对实际工程约束的考量。文献[10]制定了考虑碳排放约束的风光氢能系统优化模型，但该模型更多地聚焦电力系统的调度事宜，忽略了氨合成过程中的经济合理性问题。尽管有大量研究已投入到优化风光氢氨系统运行上，但大部分研究主要把目光投向单一环节的优化，缺少对系统整体协调与优化的系统性研讨。本研究旨在提出一种逐时优化方法，该方法全面考虑风光发电、氢气制备、储氢、储能及氨合成等多个环节，采用混合整数线性规划（MILP）算法，配合各设备约束以及电力电量平衡，创建优化模型，目标是实现最低运营成本以及最高氨收益，进行系统优化。针对风光实际发电出力与预测值偏差大的问题，本研究同样设计了动态调整策略，采用优化合成氨负荷、储能充放电状态和制氢运行情况的方法，使系统在不同负荷场景里实现稳定高效运行，依靠仿真验证，本文模型在典型工况下可提升经济性，降低系统运行成本，也可为未来离网型柔性合成氨系统的工程应用提供理论支持和实际操作指引。

1. 离网型柔性合成氨系统

离网型柔性合成氨系统是一种将可再生能源与绿色化工生产相结合的创新技术方案，能够完全独立于外部电网运行。

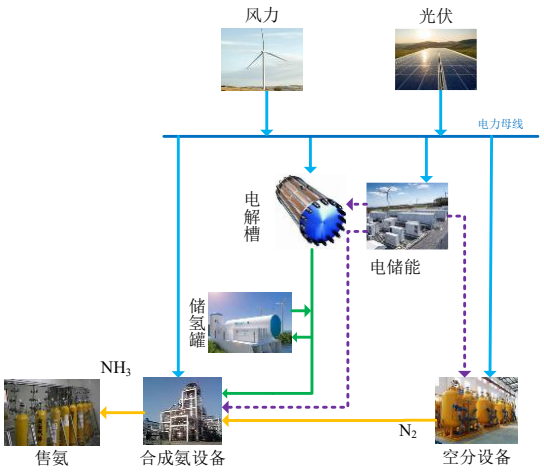


图 1 离网型柔性合成氨系统流程图
Fig.1 Flow Diagram of Grid-Forming Off-Grid Flexible Ammonia Synthesis System

图 1 展示了离网型柔性合成氨系统的整体流程。系统以风力发电和光伏发电为主要电源，这两部分电能首先汇集至统一的供电线路。所产生的电能一方面供给电解槽制氢装置，将水电解产生氢气，电解产生的氢气一部分进入储氢罐以实现氢能的存储，另一部分供给合成氨设备合成氨；另一方面，部分电能用于驱动电储能设备，以平衡发电与用电的实时差异。在可再生能源不足时，储氢罐中的氢气与空气分离设备产生的氮气共同送入合成氨装置，经过催化反应合成氨气（NH_3）。该系统实现了从可再生能源发电到氢氨生产的全过程联动，可有效消纳波动的风光电力，具有显著的经济和环保效益。

合成氨系统的运行特性对系统运行效率和经济性优化有着关键影响，通过引入基于灵活化工技术的先进工艺包，合成氨装置的负荷调节能力得到进一步提高，对传统工艺技术改造后，负荷调节范围可以拓展到 30%~110% [11]；若采用新型催化剂和加热设备，则可再度拓宽至 10% ~110%[12]。

2. 离网型柔性合成氨系统各装置优化配置

2.1 系统设备模型

1）风力光伏发电模型

$$\begin{cases} 0 \le P_{wind}(t) \le \min(P_{wind,\text{actual}}(t), P_{\text{wind,max}}) \\ \forall t = 1,2,\ldots,T \end{cases} \tag{1}$$

$$\begin{cases} 0 \le P_{solar}(t) \le \min(P_{\text{solar,actual}}(t), P_{\text{solar,max}}) \\ \forall t = 1,2,\ldots,T \end{cases} \tag{2}$$

式中：$P_{wind}(t)$为时段 t 的风电出力；$P_{wind,actual}(t)$为时步的实际风电出力；$P_{wind,max}$为风电装机容量；$P_{solar}(t)$为时段 t 的光伏出力；$P_{solar,actual}(t)$为时步的实际光

伏出力；$P_{solar,max}$ 为光伏装机容量；T 为运行的总时长，本文中以一周为典型的总时长。

2） 电解槽设备模型及约束

电解水制氢装置的运行功率需要限制在其额定容量范围内，并考虑最低稳定运行负荷，其表达式为：

$$\begin{cases} P_{EL3}(t)=\lambda_{H_2}M_{H_2,EL}(t) \\ 0\le P_{EL}(t)\le P_{h2,\max} \\ P_{EL}(t)\ge P_{h2,\min,\text{unit}}\cdot \text{binary}_{h2}(t)\cdot E_{\max el} \\ P_{EL}(t)\le P_{h2,\max,\text{unit}}\cdot \text{binary}_{h2}(t)\cdot E_{\max el} \\ 0\le binary_{h2}(t)\le 1 \end{cases} \tag{3}$$

式中：从上至下分别为电解槽的总功率；总功率约束；单台功率约束；运行状态约束。

3）空分设备与合成氨设备模型及其约束

空分设备（Air Separation Unit, ASU）通过低温分离技术将空气分离为氮气和氧气，为合成氨过程提供氮气原料。

空分设备表达式及约束为：

$$\begin{cases} P_{ASU}(t)=\alpha\cdot M_{N_2}(t) \\ P_{ASU,min}\le P_{ASU}(t)\le P_{ASU,max} \end{cases} \tag{4}$$

式中：从上至下分别为空分设备功率；空分设备约束。 α 为电耗系数。

合成氨设备模型表达式及约束为：

$$\begin{cases} P_{NH_3}(t)=\lambda_{NH_3}M_{NH_3}(t) \\ -P_{nh3,max}\le P_{NH_3}(t)\le P_{nh3,max} \\ M_{NH_3}(t)\le \dfrac{M_{H_2}(t)}{b} \\ M_{NH_3}(t)\le \dfrac{M_{N_2}(t)}{c_{N_2}} \\ NH_{3\,positive}\ge 0 \end{cases} \tag{5}$$

式中：从上至下分别为合成氨功率及约束；氨产量约束；非负收益约束。

4）储氢罐模型及其约束

$$S_{h2}(t)=\begin{cases} S_{h2,init}+P_{EL}(t)\cdot\eta_{h2} & t=1 \\ -P_{NH_3}(t)\cdot\eta_{nh3} & \\ S_{h2}(t-1)+P_{EL}(t)\cdot\eta_{h2} & t=2,\ldots,T \\ -P_{NH_3}(t)\cdot\eta_{nh3} & \end{cases} \tag{6}$$
$$0\le S_{h2}(t)\le S_{h2,\max}$$

式中：从上至下分别为储氢量及储氢量约束。从第 2 时步起，储氢量为前一时步值加上当期净增量。

5）储能电池模型及其约束

$$\begin{aligned} S_B(t)&=(1-phi)\cdot S_B(t-1)+betaB_{in}\cdot S_{Bin}(t-1) \\ &\quad -S_{Bout}(t-1)/betaB_{out} \\ S_{B\min}(t)&\le S_B(t)\le S_{B\max}(t) \end{aligned} \tag{7}$$

式中：从上至下分别为储能量及储能量约束。当前时刻储能量等于前一时刻储能量扣除自放电损失，加上有效充电量，减去有效放电量。

2.2 系统的目标函数

本文建立的优化模型以该系统在典型运行周期内的净收益最大化为目标，同时最小化系统运行总成本以及最大化合成氨产品的销售收益。

系统总收益和总成本的计算表达式为：

$$\begin{cases} Z=R_{tot}-C_{tot} \\ C_{tot}=C_W+C_S+C_{H_2}+C_{NH_3}+C_{H_2S}+C_{ST} \end{cases} \tag{8}$$

式中：Z 为总收益，R_{tot} 为售氨收益，C_{tot} 为总成本，C_{H2} 为制氢成本，C_{H2S} 为储氢成本，C_{NH3} 为合成氨成本。C_{ST} 为电储能成本。

系统的收益主要来自绿氨销售收入，表示为：

$$R_{tot}=\sum_{t=1}^{T}(Price_{nh_3}\cdot nh_{3\,positive}(t)\frac{\eta_{h_2}}{\eta_{nh_3}}) \tag{9}$$

式中：$Price_{nh3}$ 为售氨价格，$nh_{3positive}(t)$为合成氨功率，n 为合成氨设备消耗氢气产生氨的质量系数，$h_{3positive}(t)$为合成氨设备消耗的氢质量，最后为氢气到氨的转换系数。

2.3 系统约束条件

1）电力平衡约束

$$\begin{aligned} &P_{wind}(t)+P_{solar}(t)+P_{Bout}(t) \\ &=P_{EL}(t)+P_{NH_3}(t)+P_{Bin}(t) \end{aligned} \tag{10}$$

式中：P_{EL} 为电解槽制氢功率。P_{Bin} 、P_{Bout} 为电储能的充放电功率。

2）化工负荷平衡约束

$$P_{EL}(t)+P_{NH_3}(t)=P_{load,chemical}(t) \tag{11}$$

式中：$P_{load,chemical}(t)$为时步 t 的化工负荷。

3）弃电率约束

为避免系统在调度优化过程中产生大量的弃风弃光，设定最大允许弃电约束表达式为：

$$\sum_{t=1}^{T}P_{loss}(t)\le\delta\sum_{t=1}^{T}\left[P_{wind1}(t)+P_{solar2}(t)\right] \tag{12}$$

式中：δ 为最大允许弃电率,本文取 5%。

3.算例分析

3.1 离网型柔性合成氨系统参数

本文以一年（8760h）为时间范围，基于东北

某地区实际风光出力数据和化工负荷数据，采用线性规划（LP）方法，通 MATLAB 的 linprog 求解器实现优化。各设备单位成本及设备技术参数及相关调节范围见表 1 表 2。

表 1 各设备单位成本

Tab.1 Unit cost of each equipment

设备名称	单位成本（包含建设费用）
风力发电设备	5000 元/kW
光伏发电设备	4000 元/kW
储能电池	3000 元/(kWh)
储氢罐	1750 元/kg
电解槽	2000 元/kW
空分装置	2000 元/kW
合成氨装置	5000 元/(kg/h)

表 2 设备技术参数及相关调节范围

Tab.2 Parameters and Adjustment Range of Equip-ment

设备名称	项目	数值
合成氨设备	额定容量/(MW/ta)	30
	氨单位产量电耗/((MWh) /t)	0.95
	负荷调节范围/%	30-110
电解槽	额定容量(标准状态)/(m^3 /h)	2780
	额定功率（单台）/MW	5
	负荷调节范围/%	30-110
电储能	储能容量上限/%	80
	储能容量下限/%	20
	负荷调节范围/%	0-100
空分设备	负荷调节范围/%	30-105
化工部分	运行功率范围/%	30-100
无	负荷最大调整速率/%	40

在离网系统配置中，风电装机容量为 590MW，光伏装机容量为 50MW。在合成氨系统的生产过程中，参考国内行情，本文中售出氨的售价取 4000 元/t；储能电池充电效率取 0.9，储能电池放电效率取 0.9，储能电池损耗率取 1%；电解槽产氢电耗系数取 4.5；储氢罐充气效率取 0.9，储氢罐放气效率取 0.9；空分装置氮气生产电耗系数取 0.45；氢气质量系数取 0. 176；合成氨转化率 90%。算例数据参考东北院一年风电光伏功率。

3.2 系统优化结果及分析

通过对区域全年风电、光伏及化工负荷实际出力数据进行统计分析，选取风光大发典型周和风光小发典型周两种典型工况，以系统经济收益最大为目标，对离网型柔性合成氨系统进行经济性优化。

表 3 合成氨系统各装置优化配置

Tab.3 Optimization Configuration of Each Unit in the Ammonia Synthesis System

设备名称	设备容量
风电装机容量	590.00 kW
光伏装机容量	50.00 kW
电解槽容量	197.15 kW
储氢罐容量	100 kg
储能电池容量	100 kWh
空分装置容量	93.48 kW
合成氨装置容量	186.95 kg/h
总投资成本	5141.0 万元
总售氨收益	463.1 万元
投资回收期	11.10 年
年化收益率 (ROI)	9.01 %

由表 3 可知，以东北某地区一年中风光出力作为研究对象，风光资源较为充裕，产氨量多，总售出氨收益高，达 463.1 万元，投资回收期为 11.10 年，年化收益率为 9.01%。

3.3 运行调度优化分析

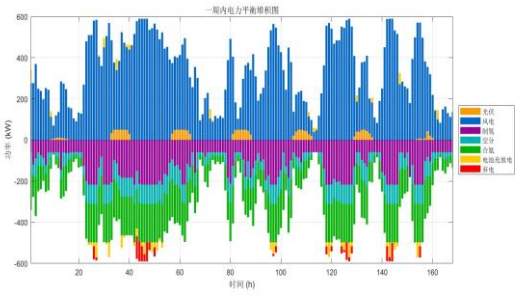


图 2 风光大发工况电平衡堆积图

Fig.2 Stacked Power Balance Diagram for Peak Renewable Generation Scenario

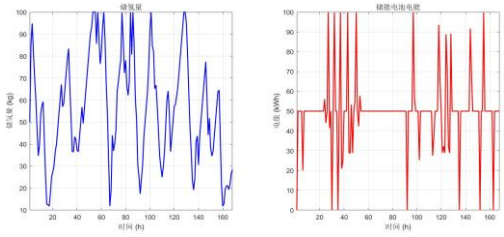


图 3 风光大发工况储能储氢曲线

Fig.3 State-of-Charge Profiles of Energy Storage and Hydrogen Storage Under Peak Renewable Generation Scenario

取一周（168 小时）数据进行运行调度优化分析。由图 2、图 3 知，在风光大发典型工况下，由于风能和太阳能资源较为充裕，风电与光伏的平均出力水平较高。合成氨装置持续运行，稳定地将氢

气转化为氨。这一工况下的高负荷连续运行显著提升了氨生产量。电储能设备的平均充放电功率高，为能源供应不足的时段提供了有效保障。系统利用充裕的电能进行储存，储氢量多，制氢量多。

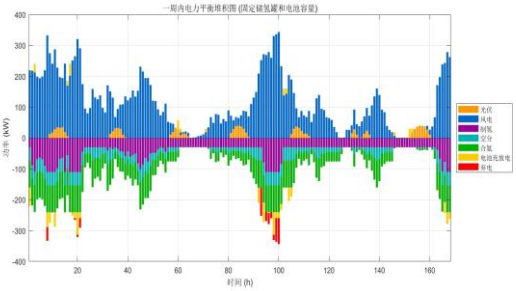


图 4 风光小发工况电平衡堆积图
Fig.4 Stacked Power Balance Diagram for Renewable Curtailment Scenario

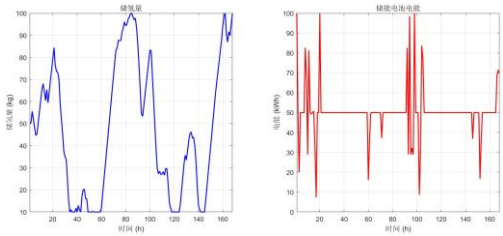


图 5 风光小发工况储氢储能曲线
Fig.5 State-of-Charge Profiles for Hybrid Hydrogen and Battery Storage under Renewable Curtailment Scenario

由图 4、图 5 知，风光小发典型工况中，由于风光资源供应不足，系统不得不通过降低设备运行功率与精细调控来应对能源不足的情况。风电与光伏平均出力下降，合成氨装置的平均功率降低。电储能设备在此阶段扮演更为重要的角色，不断充放电来平衡电力供应的波动，确保系统稳定运行。储氢量少，制氢量少。

4.结论

本文以东北某地区一年中风光出力作为研究对象，构建了离网型柔性合成氨系统，在考虑运行调度优化策略的基础上建立了以系统收益最大为目标函数的优化模型，通过分析风光大发和风光小发两种工况，得出以下结论：

（1）建立的离网型柔性合成氨系统经过各设备合理的容量配置，系统具有较好的经济性。且优化策略显著提升典型周和全年经济性，成本降低、收益增加。同时通过系统运行调度优化分析，系统能够在不同风光出力情况下，合理切换工作状态，实现了合成氨设备的稳定连续生产并提高了可再生能源利用率。

（2）根据上述两种工况的经济性分析，两种工况的年化收益率存在差异，分别为 8.2%和 5.02%。风光大发工况展现出显著的经济性优势，说明了在风光资源充沛时段优化系统运行对于提高项目经济性的积极作用。

参考文献

[1] 黄强，郭怿，江建华，等．“双碳”目标下中国清洁电力发展路径[J]．上海交通大学学报，2021，55 (12): 1499-1509．DOI:10，16183/j．cnki．jsjtu，2021．272．

[2] 洪烽，贾欣怡，梁璐，等．火-储耦合协同调频策略下飞轮储能容量配置一体化研究 [J]．热力发电，2023，52 (09): 65-75．DOI:10．19666/j．rlf-d．202305061．

[3] 帅逸轩，赵培轩，刘慧敏，等．基于多功率耦合的风光互补制氢系统容量配置优化方法 [J]．太阳能学报，2022，43 (11): 474-481．DOI:10．19912/j．0254-0096．tynxb．2021-0491．

[4] 中国氢能产业发展报告 2020[EB/OL]. (2022-10-28).[2024-01-14]. http://www.ev100plus.com/content/details1041_43 02.html．

[5] 张真，张凡，云祉婷．绿氢在石化和化工行业的减碳经济性分析[J]．化工进展，2024，43 (06)：3021-3028．DOI：10．16085/j．issn．1000-6613．2023-0871．

[6] 国家发展改革委，国家能源局，关于印发《“十四五”新型储能发展实施方案》的通知：发改能源 [2022]209 号[A/OL]．(2022-03-21)[2024-01-14]．https://www．ndrc．gov．cn/xwdt/tzgg/202203/t20220321_1319773．html?code=&state =123．

[7] 科技部，国家发展改革委，工业和信息化部，等．科技部等九部门关于印发《科技支撑碳达峰碳中和实施方案(2022—2030 年)》的通知：国科发社[2022]157 号[A/OL]. (2022-06-24)[2024-01-14]. http://www．gov．cn/zhengce/ zhengceku/ 2022-08/18/content_5705865．Htm．

[8] 李琦，韩运滨，白章，等．离网型风光发电联合制氢系统的协调运行策略与容量配置优化[J]．中国电机工程学报，2024，10(20)：44-20．

[9] 贾成真，王灵梅，孟恩隆，等．风光氢耦合发电系统的容量优化配置及日前优化调度[J]．中国电力，2020，10(20)：53-10．

[10] 周步祥，朱文聪，朱杰，等．风光制氢合成氨系统的多时段可调度域分析[J]．中国电机工程学报，2024，44(01)：160-174．

[11] ROUWENHORSTKHR，VANDERHAMAGJ，MULG，etal．Islanded ammonia power systems：Technology review & conceptual process design[J]．Renewable and Sustainable Energy Reviews，2019，114：109339．

[12] GENOVAG，PANZAS．Casale flexible green ammonia plant ，the economically viable green production[C]//Nitrogen & Syngas Conference 2022．Berlin，2022．

094 A Life Cycle Assessment Model for Energy Storage Considering Multiple Benefit Factors

Lingyi Wei[1], Jinghua Li[1,*], Bo Li[1]
[1]School of Electrical Engineering, Guangxi University, Nanning 530004, China
lijinghua@gxu.edu.cn

Abstract: The life cycle benefit assessment of energy storage system (ESS) involves the evaluation and analysis of economic, environmental, and social impacts. However, existing life cycle benefit assessment models for ESS exhibit limitations in evaluation metrics. This may lead to misguided investment decisions and sub-optimal resource allocation. Therefore, based on life cycle theory, this paper constructs a life cycle assessment model that incorporates benefit metrics including the levelized cost of energy (LCOE), carbon emissions, renewable integration, and carbon footprint. This model enables the evaluation of the impacts for ESS across multiple benefit factors. Firstly, employing pumped hydro storage, compressed air energy storage, and lithium iron phosphate battery energy storage systems (LFP BESS) as research subjects, life-cycle economic cost-effectiveness is investigated through case studies. Secondly, employing LFP BESS as the research subject, life-cycle carbon benefits is investigated through case studies. Finally, the results verify the effectiveness and rationality of the proposed life cycle assessment model for energy storage.

Keywords: Life Cycle Assessment Model, Energy Storage System, Multiple Benefit Factors.

1 Introduction

With the rapid expansion of renewable energy, the importance of energy storage in modern power systems is continually increasing. At present, the study on the benefits of ESS throughout their life cycle aims to scientifically and comprehensively evaluate their economic and environmental impacts over the lifetime[1-2].

In the study of economic benefits, it is necessary to develop economic cost analysis models that can be applied to various energy storage types under different scenarios and influencing factors. For example, Reference [3] proposed a model that encompassed long, medium, and short term energy storage, enabled a comprehensive evaluation of ESS economic benefits. But this study didn't account for the impact of purchasing costs on the life cycle economic benefits. Reference [4] discussed and calculated the LCOE of solar-storage systems in a microgrid context, and evaluated the LCOE when these technologies operated in a coordinated manner. Reference [5] calculated the LCOE for ESS and analyzed the influence of factors including cycle life and unit capacity cost on the LCOE. Most of the above literature only considers part of the life cycle cost of ESS, while ignoring other life cycle LCOE involved throughout the life cycle of ESS.

In the study of environmental benefits, the subjects and application scenarios studied are diverse. Reference [6] conducted an assessment study on the environmental benefits of a hybrid ESS incorporating lithium titanate battery and battery electric vehicle technologies. The study only considered the environmental impacts of unit process exchanges and inputs within the ESS supply chain, failing to examine the environmental benefits of ESS from a life cycle perspective that encompasses all life stages. Reference [7] applied a life cycle assessment framework to ESS, establishing a life cycle inventory and conducting a comprehensive evaluation of environmental impacts across all stages. Reference [8] assessed the carbon footprint reduction achievable through the use of second-life EV batteries in energy storage systems over their life cycle. However, the aforementioned studies fail to account for the impact of energy storage on renewable energy integration capacity within modern power systems.

Regarding research on the assessment of life cycle benefits of ESS, which indicates that traditional models tend to be limited in their assessment of benefits and indicators. Based on the above considerations, this paper establishes a life cycle assessment model for ESS that integrates economic, carbon, environmental, and renewable integration. The innovative conceptual framework of this study is shown in Figure. 1.

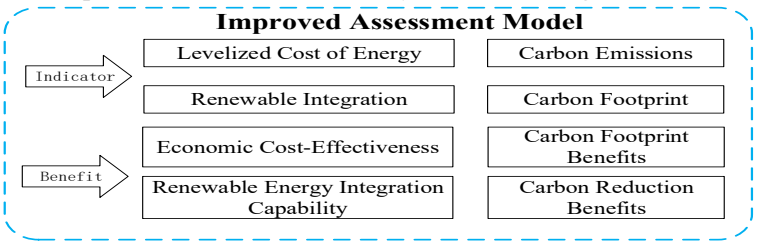


Fig. 1. Innovative idea

Compared with previous studies, the main contributions of this paper are as follows:

(1) This study develops a novel life cycle assessment model that incorporates metrics such as LCOE, carbon emissions, renewable energy integration, and carbon footprint, building upon traditional assessment models. This life cycle assessment model can assess the life cycle benefits of ESS across four dimensions: economic cost-effectiveness, carbon emission footprint, renewable energy integration capability, and carbon reduction benefits.

(2) This paper incorporates the costs of charging and renewable energy curtailment reduction into the life cycle assessment, when evaluating the economic and carbon benefits over the life cycle.

2 A Life Cycle Assessment Model for ESS Considering Multiple Benefits Factors

2.1 Traditional Life Cycle Assessment Model for ESS

Traditional life cycle economic cost assessment model for ESS. Regarding the economic cost-effectiveness of ESS over their life cycle, the LCOE is typically employed for evaluation and analysis. The LCOE represents the cost per unit of electricity, obtained by levelizing the life cycle costs of ESS against the total electrical energy it supplies to the grid.

$$LCOE = \frac{C_{\text{sum}}}{E_{\text{sum}}} = \frac{C_{\text{sys-e}} + C_{\text{pcs-e}} + C_{\text{bop-e}} + C_{\text{om-e}} + C_{\text{oth-e}} - C_{\text{rec-e}}}{n \cdot DOD \cdot \eta \cdot \zeta} \tag{1}$$

where C_{sum} is the total cost over life cycle, E_{sum} is the total electrical energy, *DOD* and *n* represent the depth of discharge and the lifetime of the ESS, η and ζ represent the charge-discharge efficiency and the equivalent capacity retention rate per cycle of the ESS.

Traditional life cycle carbon intensity assessment model for ESS. The carbon footprint serves as the standard metric for evaluating the life-cycle carbon benefits of ESS. Carbon footprint is the total amount of carbon emissions generated by an ESS throughout its life cycle when it charges and discharges 1kWh of electrical energy. The calculation formula is as follows:

$$C_{\text{ES}} = \frac{CE_{\text{carbon}}}{E_{\text{ES}}} \tag{2}$$

where C_{ES} is the carbon footprint of the ESS, CE_{carbon} is the total carbon emissions over life cycle, while E_{ES} refers to its cumulative discharge capacity throughout the service life.

2.2 Improved Life Cycle Assessment Model for ESS

This paper holistically integrates four key factors in the life cycle of ESS: economic cost-effectiveness, carbon emission footprint, renewable energy integration capacity, and carbon reduction benefits. A life cycle assessment model for ESS that takes aforementioned multiple factors into account is constructed in this paper. The model encompasses the economic cost model for life cycle of the ESS, along with a carbon benefit assessment model that incorporates renewable energy integration.

The assessment model incorporates metrics such as life cycle LCOE, life cycle carbon emissions, curtailed energy, and carbon footprint, as shown in the following formula.

$$F_{\text{eva}} = \lambda_1 C_{\text{LCOE}}^{\text{ES}} + \lambda_2 CE_{\text{carbon}} + \lambda_3 \sum_{t=1}^{8760} \Delta E + \lambda_4 LCA_{\text{ES}} \tag{3}$$

where F_{eva} is the objective function; $C_{\text{LCOE}}^{\text{ES}}$ is LCOE over life cycle of the ESS; $\sum_{t=1}^{8760} \Delta E$ is the total amount of curtailed energy within 8760 hours per year; LCA_{ES} is the functional unit of life cycle assessment, representing the carbon intensity of grid electricity; λ_1, λ_2, λ_3, and λ_4 are weighting coefficients.

Improved life cycle LCOE model for ESS. This paper incorporates the costs of charging and discount rate into the model, which constructs a model for the life cycle LCOE of ESS. This model accounts for the impact of charging electricity prices and the time value of various cost components on the cost-effectiveness of energy storage. This model enables a comprehensive assessment of the life-cycle economic cost-effectiveness for ESS. The specific calculation formula is as follows:

$$C_{\text{LCOE}}^{\text{ES}} = \frac{C_{\text{total}}^{\text{ES}}}{E_{\text{total}}^{\text{ES}}} = \frac{C_{\text{inv}}^{\text{ES}} + C_{\text{O\&M}}^{\text{ES}} + C_{\text{R}}^{\text{ES}} + C_{\text{C}}^{\text{ES}} + C_{\text{rec}}^{\text{ES}}}{\sum_{n=1}^{N} \frac{N_{\text{y}} \cdot Q_{\text{E}} \cdot \theta_{\text{DOD}} \cdot \left(1 - \theta_{\text{deg}}\right)}{\left(1+r\right)^n}} \tag{4}$$

where $C_{\text{total}}^{\text{ES}}$ is the total cost over life cycle, and $E_{\text{total}}^{\text{ES}}$ is the cumulative electricity delivered over life cycle. $C_{\text{inv}}^{\text{ES}}$, $C_{\text{O\&M}}^{\text{ES}}$, C_{R}^{ES}, C_{C}^{ES}, and $C_{\text{rec}}^{\text{ES}}$ initial the cost of investment, operational and maintenance, replacement, charging, and recycling. Q_{E} denotes unit capacity, N_{y} is the annual cycle count of the ESS, θ_{DOD} denotes the depth of charge-discharge, θ_{deg} is the average annual cycle degradation rate, *N* is the lifetime of the ESS, and *r* is the discount rate.

Improved life cycle carbon intensity assessment model for ESS. This study investigates the influence of grid-level renewable integration capacity on the carbon reduction benefits provided by ESS over life cycle. When renewable energy is integrated into the power system on a large scale, the uncertainty of its output may lead to renewable energy curtailment. In previous scenarios where energy storage was configured in power systems, the carbon footprint calculated based on energy storage discharge did not take into account curtailed electricity. Therefore, curtailed energy is included in the scope of this study. This model can be used to assess the carbon footprint of ESS throughout their life cycle. The specific calculation formula is as follows:

$$LCA_{\mathrm{ES}} = \frac{CE_{\mathrm{carbon}}}{T_{\mathrm{ES}}} \tag{5}$$

where LCA_{ES} is the carbon footprint of the ESS, gCO_2/kWh; CE_{carbon} is the total carbon emissions over life cycle; T_{ES} is the cumulative discharge capacity of the ESS, calculated as the product of the curtailed renewable energy utilized by the system and its round-trip efficiency.

(1) Life cycle carbon emission calculation model

The model can be used to assess the carbon benefits of ESS over their lifetime. It enables the calculation of total carbon dioxide emission from ESS across their life cycle. The calculation formula is as follows:

$$CE_{\mathrm{carbon}} = CE_{\mathrm{P}} + CE_{\mathrm{T}} + CE_{\mathrm{C}} + CE_{\mathrm{O}} + CE_{\mathrm{R}} \tag{6}$$

where CE_{P} , CE_{T} , CE_{C} , CE_{O} , CE_{R} initial the carbon emissions during the production, transportation, construction, operation and maintenance, and decommissioning stages.

(2) Power system optimization model considering renewable energy curtailment

1) Objective function

The model can be used to simulate and analyze renewable energy curtailment scenarios in power systems. At this point, the model is formulated with the objective function of minimizing renewable energy curtailment over the 8760-hour annual period. The calculation formula is as follows:

$$\sum_{t=1}^{8760} \Delta E = \min \sum_{t=1}^{8760} \max\left(P_{D,t} + P_{G,t} + P_{W,t} - P_{L,t}, 0\right) \tag{7}$$

where $\sum_{t=1}^{8760} \Delta E$ is the objective function, $P_{\mathrm{D},t}$ is the charging and discharging power of the ESS, $P_{\mathrm{G},t}$ denotes the output of thermal power units, $P_{\mathrm{G},t}$ indicates the output of wind turbine generators, and $P_{\mathrm{L},t}$ corresponds to the load demand at time *t*.

2) Constraints

a) Power and electricity balance constraints

$$P_{W,t} + P_{G,t} + P_{D,t} = P_{L,t} \tag{8}$$

b) Wind turbine output constraints

$$P_{\mathrm{W,min}} \le P_{W,t} \le P_{\mathrm{W,max}} \tag{9}$$

where $P_{\mathrm{W,min}}$ and $P_{\mathrm{W,max}}$ are defined as the minimum and maximum output values of the wind turbine.

c) Thermal power unit output constraints

$$P_{\mathrm{G,min}} \le P_{G,t} \le P_{\mathrm{G,max}} \tag{10}$$

where $P_{\mathrm{G,min}}$ and $P_{\mathrm{G,max}}$ are defined as the minimum and maximum values of the technical output for the thermal power unit.

d) Constraints on the start-up and shutdown times of thermal power units

$$\begin{cases} u_{i,t} = 1, t \le T_{G,i}^{\mathrm{on}} \\ u_{i,t} = 0, t \le T_{G,i}^{\mathrm{off}} \end{cases} \tag{11}$$

$$\begin{cases} 1 - (u_{i,t} - u_{i,t-1}) \ge u_{i,k} - u_{i,k-1} \\ 1 - (u_{i,t} - u_{i,t-1}) \ge u_{i,k-1} - u_{i,k} \\ t \ge T_{G,i}^{\mathrm{off}}, k = t - T_{G,i}^{\mathrm{on}} + 1, \ldots, T - 1 \end{cases} \tag{12}$$

$$\begin{cases} 1 + (u_{i,t} - u_{i,t-1}) \ge u_{i,k} - u_{i,k-1} \\ 1 + (u_{i,t} - u_{i,t-1}) \ge u_{i,k-1} - u_{i,k} \\ t \ge T_{G,i}^{\mathrm{on}}, k = t - T_{G,i}^{\mathrm{off}} + 1, \ldots, T - 1 \end{cases} \tag{13}$$

where $u_{i,t}$ is the operating status of the i-th unit at time *t*, $T_{\mathrm{G},i}^{\mathrm{on}}$ and $T_{\mathrm{G},i}^{\mathrm{off}}$ are the minimum continuous operating time and minimum continuous shutdown time of the i-th unit.

e) Constraints on the ramping rate of thermal power units

$$-R_i^{\text{down}}\Delta t \le P_{i,t} - P_{i,t-1} \le R_i^{\text{up}}\Delta t \tag{14}$$

where R_i^{down} and R_i^{up} are the downward ramping power and upward ramping power of the i-th thermal power unit.

f) Energy storage charge state constraint

Formulation of the charging and discharging expressions and state of charge constraints for ESS is as follows:

$$SOC(t+1) = \begin{cases} SOC(t) - \dfrac{P_{D,t}\eta_c}{E_{\text{bess}}} & P_{D,t} < 0 \\ SOC(t) & P_{D,t} = 0 \\ SOC(t) - \dfrac{P_{D,t}}{E_{\text{bess}}\eta_d} & P_{D,t} > 0 \end{cases} \tag{15}$$

$$SOC_{\min} \le SOC(t) \le SOC_{\max} \tag{16}$$

where SOC is the state of charge of the battery, E_{bess} is the rated power of the battery, η_c and η_d are the charging efficiency and discharging efficiency of the battery.

g) Energy storage charge and discharge power constraints

$$-P_{\text{bess}} \le P_{D,t} \le P_{\text{bess}} \tag{17}$$

where P_{bess} is the rated power of the ESS.

3 Case Study of Life Cycle Assessment on ESS

3.1 Case study analysis of economic cost-effectiveness throughout the life cycle

For the economic cost-benefit assessment of ESS over their life cycle, this paper selects three types of the ESS. Using the LCOE model for ESS developed in this study, the LCOE for each life cycle stage of the three ESS, as well as the LCOE under two scenarios, were calculated. Furthermore, in order to investigate the feasibility and superiority of the life cycle LCOE model for ESS proposed in this paper, a comparative analysis is conducted between this model and traditional life cycle cost assessment model. Compare the total life cycle costs obtained from the two models. The detailed computational results and comparative outcomes are shown in Table 1.

Table 1. Comparative analysis of life cycle LCOE and economic cost assessment models for three ESS

	Pumped storage	Compressed air energy storage	Lithium iron phosphate battery	Unit
Investment costs	0.391	0.430	0.524	CNY/kWh
O&M costs	0.112	0.045	0.166	CNY/kWh
Replacement costs	0.000	0.000	0.257	CNY/kWh
Recycling costs	0.000	0.000	0.000	CNY/kWh
Charging costs	0.384	0.480	0.288	CNY/kWh
The LCOE of traditional assessment model	0.254	0.233	0.818	CNY/kWh
The LCOE of improved assessment model (Not considering the cost of charging)	0.503	0.476	0.947	CNY/kWh
The LCOE of improved assessment model (Consider the cost of charging)	0.887	0.956	1.235	CNY/kWh

The LCOE calculations in Table 1 demonstrate that incorporating charging costs significantly increases the LCOE for all three ESS. Furthermore, these costs represent a considerable proportion of the total LCOE. It is evident that charging costs significantly impacts the life cycle LCOE.

As evidenced by the comparative results of the assessment models in Table 1, the improved assessment model proposed in this paper, which incorporates the cost of charging and discount rate, calculates the life cycle LCOE for the three ESS. When compared with the LCOE calculated using the traditional assessment model, the results obtained from the former are significantly lower than those of the latter. The computational results demonstrate that the improved assessment model incorporates a more comprehensive set of indicators and factors. It can thus be seen that the life cycle economic cost assessment model proposed in this paper is scientifically reasonable in including two indicators, the cost of charging and discount rates, within the scope of the study. The application of this assessment model enables a more scientifically comprehensive evaluation and analysis of the economic cost-effectiveness of ESS over their life cycle.

3.2 Case study analysis of life cycle carbon benefits

Life cycle carbon emissions analysis of ESS. For the calculation of life cycle carbon emissions accounting in ESS, this paper selects LFP BESS as the study object. Based on the material lists, carbon emission factors, and other relevant data for LFP BESS across their life stages, the life cycle carbon emissions of the ESS have been compiled in Table 2.

Table 2. Carbon emissions results for ESS

Life stages		Carbon emissions (tons)	Percentage (%)
Production		688.4	97.19
Transportation		3.3	0.46
Construction		2.6	0.37
Operation and maintenance		1.2	0.17
Decommission	Disposal	12.8	1.81
	Recycling	-358.6	0
Total life cycle		349.7	100

As can be seen in Table 2, the total carbon emissions of the ESS over its life cycle amount to 349.7 tons. The production stage exhibits the highest carbon emissions, accounting for 97.19%, while the operation and maintenance stage shows the lowest, constituting merely 0.17%.

Analysis of renewable energy curtailment with energy storage under varying renewable penetration levels. Regarding the study of renewable energy curtailment in systems with energy storage under varying renewable penetration levels, this paper employs a modified IEEE 6-bus system for simulation and analysis. In the 6-bus system, G1 to G5 are the generating units within the power system. D1 to D3 are the loads in the power system, where the maximum value of load D1 is 100 MW, and the maximum values of loads D2 and D3are both 50 MW. The 8760-hour annual data for wind power and load are sourced from Reference [9].

When the power system doesn't consider the configuration of ESS, simulation calculations are performed using a progressively increasing installed capacity scheme for renewable energy. In Scenarios 1 to 5, with wind power installed capacities of 48 MW, 192 MW, 288 MW, 384 MW, and 480 MW respectively, the renewable energy installed capacity in the system is set at 24%, 96%, 144%, 192%, and 240% of the system's peak load. Under this configuration scheme, the results are detailed in Table 3. When the power system considers the configuration of energy storage, Scenarios 2 to 5 employ an energy storage installation capacity set at 30% of the wind power installed capacity for simulation calculations. In Scenario 1, no ESS is deployed due to the relatively small scale of wind power installation. The detailed capacity configuration scheme of the ESS and the corresponding reduction in renewable energy curtailment are presented in Table 4.

Table 3. Renewable energy curtailment in the power system without energy storage integration

Configuration scheme	Wind power installed capacity (MWh)	Curtailed energy (MWh)	Grid integrated electricity (MWh)	System curtailment rate (%)
Scenario 1	48MW	233.8	88623.2	0.26
Scenario 2	192MW	21873.2	348396.8	5.89
Scenario 3	288MW	66689.1	488718.7	12.03
Scenario 4	384MW	138465.3	602082.5	18.64
Scenario 5	480MW	215592.4	710119.8	23.18

Table 4. Reduction in renewable energy curtailment through energy storage integration

Configuration scheme	Wind power installed capacity (MWh)	Energy storage capacity (MWh)	Curtailed energy reduction (MWh)	Curtailment reduction rate (MWh)	Curtailment rate (%)	Energy storage utilization rate (%)
Scenario 1	48MW	-	-	-	0.26	-
Scenario 2	192MW	102	19683	5.49	0.36	43.8
Scenario 3	288MW	168	56139	10.51	1.46	83.3
Scenario 4	384MW	224	62487	8.77	9.89	69.7
Scenario 5	480MW	288	66294	7.43	15.81	58.6

As can be seen from the curtailment data in Table 3, when renewable sources are integrated into the power system on a large scale, the system experiences a high rate of renewable energy curtailment. Higher renewable energy penetration correlates with increased curtailment levels in the power system. As shown in Table 4, the system can effectively mitigate renewable energy curtailment rate by incorporating energy storage. The results demonstrate that the deployment of ESS can effectively reduce renewable energy curtailment, and enhance the system's capability to accommodate renewable energy.

Assessment of the life cycle carbon benefits for ESS

(1) Comparison of the life cycle carbon benefit assessment models

To investigate the life cycle carbon benefits of ESS, a comparative analysis is conducted between the carbon footprint model developed in this paper, and traditional life cycle carbon benefit assessment models for ESS. When comparing the assessment models, the application scenarios are configured with energy storage capacities of 102, 168, 224, and 288 MW, respectively. This paper presents a comparison of the carbon emissions per kWh generated by the two models across four application scenarios, which are presented in Table 5.

Table 5. Comparison of life cycle carbon footprint assessment models for ESS

Application scenarios	Energy storage capacity (MWh)	Traditional assessment model	Improved assessment model	Unit
Scenario 1	102	4.623	3.440	gCO_2/kWh
Scenario 2	168	4.210	3.437	gCO_2/kWh
Scenario 3	224	4.210	3.438	gCO_2/kWh
Scenario 4	288	4.210	3.534	gCO_2/kWh

In traditional life cycle carbon benefit assessment models for ESS, the total discharge capacity is calculated based on parameters such as annual cycle count and discount rate of the ESS. However, when considering renewable energy integration in power systems with energy storage configuration, traditional models are unable to effectively account for the application scenarios of energy storage. Compared to traditional assessment models, the model proposed in this study incorporates the impact of factors such as curtailed energy and renewable energy integration on the life cycle discharge capacity of ESS. As shown in Table 5, the improved life cycle carbon benefit assessment model yields a lower carbon emission per kWh of electricity generated. It can be concluded that the incorporation of factors such as curtailed energy and renewable energy integration into the life cycle carbon footprint assessment model for ESS, as developed in this study, is scientifically sound and rationally justified. The application of this assessment model enables a more effective evaluation of the carbon footprint of ESS deployed in modern power systems.

(2) Life cycle assessment of carbon emission reduction benefits

This study quantifies and evaluates carbon emissions intensity of electricity from both wind farm and wind-storage hybrid power stations. Among these, the design of Cases 1 to 5 are derived from Tables 3 and 4. Based on the mode developed in this study, the carbon emissions intensity of electricity for both the wind farm and the wind storage power station have been calculated. A comparative overview of the results is provided in Figure. 2.

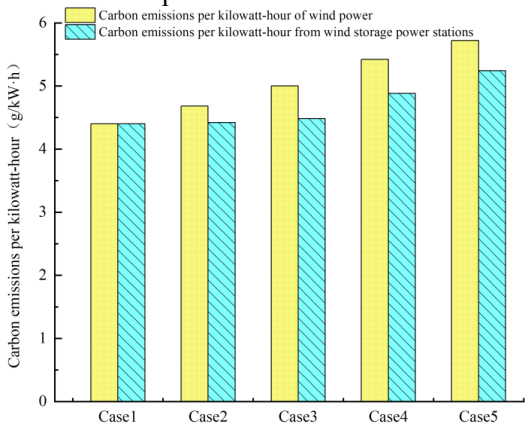


Fig. 2. Comparison of carbon emissions per kWh between wind farm and wind storage hybrid power station

As shown in Figure 2, the carbon emissions intensity of electricity for wind-storage hybrid power station Case 1 to 5 are 4.40, 4.42, 4.48, 4.88, and 5.24 g/kWh, respectively. Compared to the corresponding values for the wind farm alone, which are 4.40, 4.68, 5.00, 5.42, and 5.72 g/kWh, it is evident that the integration of the ESS provides significant carbon reduction benefits. From the comparative chart of carbon emissions per kWh between the wind power and the wind-storage hybrid power station, the carbon reduction effects of the ESS on the system are primarily manifested in the following two aspects: First, the configuration of the ESS increases the system's carbon emissions. The increase is equal to the carbon footprint of the ESS itself, which is significantly lower than the reduction in carbon emissions achieved through improved renewable energy integration enabled by energy storage. Secondly, compared to the carbon emissions intensity of electricity for wind farm, the wind-storage hybrid power station exhibits lower carbon emissions per kWh. Therefore, the results indicate that under a fixed energy storage capacity configuration requirement, the carbon emissions intensity of electricity for the system can be effectively reduced, demonstrating the positive carbon reduction benefits of ESS for the power system.

4 Conclusions

This study validates the scientific rationality of the proposed life cycle assessment model for ESS that comprehensively integrates economic, carbon, environmental, and renewable energy integration benefits. By calculating and evaluating the life cycle LCOE, and comparing the results with those of traditional models, it is found that the results of traditional models is relatively low. The results show that the model in this paper take into account more comprehensive and reasonable indicators. By calculating the carbon emissions and renewable integration, and comparing its carbon footprint with the results of traditional models, the results show that the model in this paper yields superior outcomes and is better suited for the assessment and analysis of the life-cycle carbon benefits of ESS in modern power systems.

Acknowledgement： This work is supported by Guangxi Science and Technology Major Program (KY09020030225005).

References

[1] Li B, Huang Z, Li J, et al. Capacity credit evaluation for renewables-dominated power systems with energy storage considering climate change[J]. Electric Power Systems Research, 2025, 250: 112165.

[2] Yilmaz C. Life cycle cost assessment of a geothermal power assisted hydrogen energy system[J]. Geothermics, 2020, 83: 101737.

[3] Mostafa M, Aleem S, Ali S, et al. Techno-economic assessment of energy storage systems using annualized life cycle cost of storage (LCCOS) and levelized cost of energy (LCOE) metrics[J]. The Journal of Energy Storage, 2020, 29:101345.

[4] Hosseini Z, Khodaei A, Bahramirad S, et al. Levelized cost of energy calculations for microgrid-integrated solar-storage technology[J]. 2020 IEEE/PES Transmission and Distribution Conference and Exposition, 2020, 64(01): 0.

[5] Wu J, Wang Z, Han X, et al. Analysis on LCOE and profit model for electrochemical energy storage in power systems[J]. Electric Power Construction, 2025, 46(03):177－86.

[6] Koh S C L, Smith L, Miah J, et al. Higher 2nd life lithium titanate battery content in hybrid energy storage systems lowers environmental-economic impact and balances eco-efficiency[J]. Renewable and Sustainable Energy Reviews, 2021, 152:111704-.

[7] Zhang H, Liu Z, Yu Y. Whether the electrochemical energy storage show positive role to achieve the green and low-carbon goal in China[J]. Energy. 2025, 335.

[8] Dong Q, Liang S, Li J, et al. Cost, energy, and carbon footprint benefits of second-life electric vehicle battery use[J]. iScience, 2023, 26(07): 107195.

[9] Zhuo Z, Zhang N, Yang J, et al. Transmission expansion planning test system for AC/DC hybrid grid with high variable renewable energy penetration[J]. IEEE Transactions on Power Systems, 2020, 35(04):2597-2608.

095 面向风电场通信的融合边缘计算与协作中继的成本优化策略研究

董晓玲，王德林

（西南交通大学 电气工程学院，四川 成都 611756）

RESEARCH ON COST OPTIMIZATION STRATEGIES FOR INTEGRATED EDGE COMPUTING AND COOPERATIVE RELAYING IN WIND FARM COMMUNICATIONS

Dong Xiaoling，Wang Delin

(School of Electrical Engineering, Southwest Jiaotong University, Chengdu 611756)

ABSTRACT: This paper proposes a communication enhancement strategy that integrates edge computing and cooperative relaying to improve the communication quality of wind farms. By employing edge nodes with computational capabilities as relays, data can be preprocessed at the edge side. A bandwidth compression model is developed to characterize the coupling relationship between computing power and bandwidth. Considering that the dispatching center and edge nodes are independent stakeholders with strategic gaming relationships, a Stackelberg game-theoretic framework is adopted to model the two-level decision-making process of resource pricing and procurement. Simulation results demonstrate the effectiveness of the proposed strategy in enhancing communication reliability and reducing overall system costs.

KEY WORDS: frequency regulation, communication, edge computing, cooperative relaying, Stackelberg game

摘要：本文提出一种融合边缘计算与协作中继的通信增强策略，提升风电场通信质量。通过将具备计算能力的边缘节点作为中继，实现边缘侧的数据预处理；构建带宽压缩模型以刻画算力与带宽间的耦合关系。考虑到调度中心与边缘节点作为独立利益主体存在策略博弈关系，采用 Stackelberg 博弈论框架建模其资源定价与采购的双层决策过程。仿真结果验证了该策略在提升通信可靠性与降低系统成本方面的有效性。

关键词：频率调节，通信，边缘计算，协作中继，Stackelberg 博弈

DOI：

基金项目：国家自然科学基金项目(52207117)。

Project supported by National Natural Science Foundation of China（52207117）

0 引言

随着风电渗透率持续上升，其功率输出的随机性与用户侧负荷的不确定性正对电网频率稳定性提出更高要求。传统的能源管理策略在面对高负载与多变需求时难以保持电网高效运行[1]。因此，大量研究聚焦于优化系统调频能力，提出多种协同调频策略和控制方法[2-3]。然而，现有研究普遍忽视了通信链路对调频性能的影响。风电场通过上行链路向调度中心（DC）传输测量数据，而 DC 需通过下行链路下发控制指令。随着风电场规模扩大，测量数据量显著增长，传统通信网络在带宽、可靠性等方面面临瓶颈，易引发数据丢包与调控误差，进而增加对辅助服务的依赖，抬升运行成本[4-5]。

为提升通信可靠性并降低系统成本，一些研究引入协作中继技术来增强通信可靠性。例如，文献[6]采用协作中继技术在满足时延约束条件下提升能效与通信性能，文献[7]采用协作中继提升智能电网通信质量并降低系统成本。但在大规模风电集群场景下，通信拥塞与调度中心数据处理压力依然存在。此外，边缘计算作为一种将计算资源部署于靠近数据源的技术，也被用于智能电网中以减轻通信链路压力和调度中心负载[8]。

针对上述问题，本文提出一种融合协作中继与边缘计算（CoRE）的风电通信增强策略。边缘节点设备（EN）既作为中继传输测量数据，又利用本地算力进行预处理，从而缓解调度中心处理压力。进一步地，构建带宽压缩模型以刻画算力与带宽之间的耦合关系，并建立基于丢包率的成本模型。在此基础上，将调度中心与边缘节点建模为 Stackelberg

博弈，实现算力与带宽资源的联合优化分配。本文首先提出融合边缘计算与协作通信的双向通信模型，可有效提升通信质量并降低运行成本；其次，构建考虑丢包率的成本模型与带宽压缩模型，实现计算与通信资源协调分配；最后，通过配置带宽压缩模型参数，本文策略在大规模风电场中兼具性能优势与可扩展性。

1 系统模型

1.1 风电场通信模型

本节给出了风电场的双向通信系统模型，如图 1 所示。该模型包括一个控制中心、一个云中心，以及由 DC、边缘网关、风电集群和具备一定计算能力的边缘节点设备组成的 N 个通信网络。在智能电网中，DC 与风电集群通过有效的双向通信共同参与系统频率响应。智能电网通信系统通常采用分层通信架构。为不失一般性，本文重点考虑系统的上行传输过程。

风电集群构成局域网，风机产生的运行数据通过上行链路传输至边缘网关。边缘网关汇聚多源数据后上传至 DC。在数据传输过程中，引入具备计算能力的 EN 协助边缘网关进行数据转发，从而构建出一个协作中继网络。因此，系统的邻域网由边缘网关、EN 和 DC 共同构成。随后，数据经过处理后被上传至控制中心；控制中心再通过下行链路将控制指令发送至边缘网关，形成整个通信系统的广域网。

在上行传输过程中，DC 通过租用 EN 的频谱与计算资源，为系统提供可靠的通信与数据处理能力。同时，需合理分配 EN 的频谱与算力资源，以最小化 DC 的运行成本。因此，将 DC 与 EN 之间的交互建模为一个 Stackelberg 博弈问题。

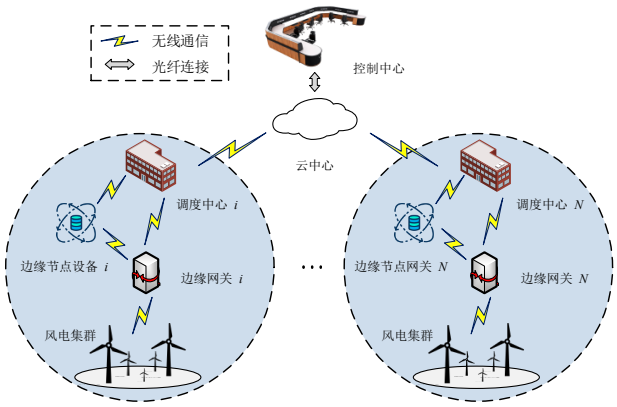


图 1 风电场双向通信系统模型

Fig. 1 Wind farm two-tier communication system model

1.2 带宽压缩模型

为避免因通信资源有限而造成的数据包丢失，本文采用边缘计算与协作中继相结合的方式，实现数据处理与传输的协同优化。具体而言，利用具备计算能力的 EN 作为数据转发中继节点，使得风电场的运行数据在上传过程中即可在 EN 处被处理，仅将处理后的结果上传至调度中心，从而显著降低后续传输所需的带宽[9]。带宽压缩模型的具体机制如图 2 所示。假设图中的完整矩形表示在无边缘计算条件下的带宽消耗；区域 I 表示通过使用计算资源所节省的带宽，而区域 II 则表示引入边缘计算技术后实际仍需占用的带宽部分。



图 2 带宽压缩模型示意图

Fig. 2 Schematic of the bandwidth compression model

基于带宽压缩机制，进一步建立如下数学模型：

$$B_i = \frac{K}{aC_i - b} \tag{1}$$

式中，B_i 和 C_i 分别表示第 i 个网络中调度中心所需带宽与计算能力；a、b 和 K 为模型参数，用于刻画算力与带宽之间的非线性耦合关系。

2 问题描述

2.1 吞吐量分析

本节对 DC 的吞吐量 $R_e(p)$进行分析。设数据采用每帧 M 比特的帧结构，其中每帧包含 L 个信息比特（$L<M$）。边缘网关以带宽 B MHz、比特速率 R_e（bit/s）发送数据，则在该条件下，DC 的吞吐量可表示为[10]：

$$R_e(p) = \left(\frac{L}{M}\right) B \cdot f(r) \tag{2}$$

式中，$f(r)$ 表示帧正确接收的概率，即 $f(r) = [1 - 2 \cdot BER(r)]^M$，本文采用二进制误码率函数 $BER(r) = 1/2 \exp(-r/2)$。其中，$r = B \cdot (hp/\sigma^2)$，表示信噪比（SNR），$h$、$p$、$\sigma^2$ 分别为信道增益、发送功率和噪声功率。

2.2 丢包率分析

在不失一般性的前提下，本文仅考虑双向通信模型中的上行传输过程，得出的结果可轻松扩展至下行传输。采用以下模型来描述通信系统的丢包率：

$$P_{loss} = \frac{T_{tx} - T_{rx}\eta_{tr}}{T_{tx}} \tag{3}$$

式中，T_{tx} 表示边缘网关的数据发送速率，T_{rx} 表示调度中心的数据接收速率，η_{tr} 表示数据从风电集群完整传输至边缘网关的概率。随后对比分析在直接传输与协作中继两种场景下的丢包率表现。

在直接传输模式（DT）下，DC 的数据接收速率为

$$T_{rx}^{d}=\frac{B_d Lf(r_{ed})}{M} \tag{4}$$

式中，B_d 表示直接传输下边缘网关的带宽，$f(r_{ed})$为网关与 DC 之间的正确接收概率。r_{ed} 为边缘网关与 DC 之间的信噪比。结合式(3)和式(4)，可得 DT 模式下的丢包率为

$$P_{loss}^{d}=1-\frac{B_d Lf(r_{ed})\eta_{tr}}{MT_{tx}} \tag{5}$$

与 DT 模式不同，在协作中继传输（CRT）模式中，采用放大转发（AF）中继策略，此时调度中心的接收速率为

$$T_{rx}^{r}=(1-\phi)\frac{B_d Lf(r_{ed})}{M}+\phi\frac{B_d Lf(r_{AF})}{M} \tag{6}$$

式中，$r_{AF}=r_{ed}+[r_{er}\cdot r_{rd}/(1+r_{er}+r_{rd})]$表示协作中继下的信噪比，$\phi$为带宽划分比例；$r_{er}$、$r_{rd}$ 分别表示边缘网关与 EN、EN 与 DC 之间的信噪比。

将式(6)代入式(3)，得 CRT 模式下的丢包率为

$$P_{loss}^{r}=\left(1-\frac{B_d Lf(r_{ed})\eta_{tr}}{MT_{tx}}\right)-\phi\frac{B_d L[f(r_{AF})-f(r_{ed})]\eta_{tr}}{MT_{tx}} \tag{7}$$

通过对比式(5)与式(7)可知，引入协作中继策略可有效降低系统的丢包率。

3 Stackelberg 博弈建模与求解

DC 与 EN 通常由不同运营主体管理，各自追求自身利益最大化。本文将 DC 与 EN 建模为理性且自利的博弈参与者：EN 旨在通过向 DC 共享计算资源以获得更多收益，而 DC 则希望通过购买计算资源来降低丢包率，从而减少系统成本。为刻画这种资源定价与采购的双层决策过程，采用 Stackelberg 博弈进行建模，其中 EN 作为领导者确定计算资源单价，DC 作为跟随者根据价格决定采购量，从而实现各方利益驱动下的资源优化配置。最后，通过逆向归纳法求解该博弈的均衡解。

3.1 调度中心成本分析

根据前述分析，DC 的成本函数由购买额外自动发电控制（AGC）服务的成本、购买计算资源以及购买带宽的成本这三部分组成。其中，AGC 服务的采购量受丢包率影响，因此该部分成本结构如下：

$$Z_{AGCi}=p_1\cdot\Phi_i(P_{loss}^{i}) \tag{8}$$

式中，p_1 为 AGC 服务的单价，$\Phi(P_{loss})$表示 AGC 服务需求量。假设丢包率为 5%，通过 MATLAB 和 Easyfit 拟合得到系统频率偏差呈正态分布。为维持频率稳定，DC 需采购 $\mu+A\delta$ 的 AGC 服务，其中 μ 为均值，δ 为标准差。若 AGC 采购概率设为 99%，则需满足：$P(\mu-3\delta\le x\le\mu+3\delta)\ge0.99$，因此需要采购 $\mu+3\delta$ 的辅助服务。将丢包率从 1%变化到 10%进行分析，得到 AGC 采购量与丢包率的关系为

$$\begin{cases}\mu=81.65P_{loss}-0.01325\\ \delta=3530P_{loss}+0.02531\end{cases} \tag{9}$$

调度中心 i 采购 AGC 辅助服务以维持频率平衡所需成本为

$$Z_{AGCi}=p_1(\mu+3\delta) \tag{10}$$

另外，购买带宽与计算资源的成本函数分别为

$$Z_{bi}=p_2B_i \tag{11}$$

$$Z_{cpi}=p_{3i}C_i \tag{12}$$

式中，p_2 为带宽固定单价，p_{3i} 为边缘节点设备 i 设置的计算资源定价。

本文在成本建模引入延迟因子以对延迟造成的跟踪误差非线性效应进行量化，其模型如下：

$$\delta(\Delta t)=\alpha e^{\gamma\Delta t} \tag{13}$$

式中，$\Delta t=t_{\text{trans}}-t_{\text{resp}}$ 表示传输时延（$t_{\text{trans}}=G/R_e$）与预设响应时间之差。G 为数据量，α 为时延对方差的敏感度，γ 决定非线性增长速度。更新后的误差方差表示为

$$\delta=\begin{cases}\delta, & \Delta t\le0\\ \delta+\alpha e^{\gamma\Delta t}, & \Delta t>0\end{cases} \tag{14}$$

因此，第 i 个 DC 的总成本函数为

$$Z_{DC_i}^{cost}=Z_{AGCi}+Z_{bi}+Z_{cpi} \tag{15}$$

DC 的目标是在最大带宽限制条件下，通过优化所购算力 C_i 来最小化成本。

因此，DC（即博弈中的跟随者）的目标函数表示为

$$\min\sum_{i=1}^{N}Z_{DC_i}^{cost} \tag{16}$$

约束条件为

$$B_i\le B_{\max}. \tag{17}$$

式中，$B_{\max}$ 表示 EN 可提供的最大带宽资源。

3.2 边缘节点设备的收益分析

边缘节点通过提供带宽与算力获得收益，因此边缘节点设备 i 的收益函数表示为

$$U_{EN_i}^{profit}=p_2B_i+p_{3i}C_i \tag{18}$$

EN 的目标是通过制定计算资源的定价策略 p_{3i} 以最大化其总收益。

因此，EN（即博弈中的领导者）的目标函数表示为

$$\max\sum_{i=1}^{N}U_{EN_i}^{profit} \tag{19}$$

约束条件为

$$B_i \le B_{\max}. \tag{20}$$

3.3 Stackelberg 博弈的求解

（1）调度中心-跟随者

将公式(1)、(7)、(9)和(13)代入式(15)后，第 i 个调度中心的总成本可展开为

$$\begin{aligned} Z_{DC_i}^{cost} &= Z_{AGCi} + Z_{bi} + Z_{cpi} \\ &= 10671.65p_1 - \frac{10671.65p_1B_dLf(r_{ed})\eta_{tr}}{MT_{tx}} \\ &\quad - \frac{10671.65p_1KL[f(r_{AF}) - f(r_{ed})]\eta_{tr}}{MT_{tx}(aC_i - b)} \\ &\quad + \frac{0.06268p_1 + p_2}{aC_i - b} + p_{3i}C_i \end{aligned} \tag{21}$$

为简化式(21)，定义

$$\Gamma(i) = 10671.65p_1 - \frac{10671.65p_1B_dLf(r_{ed})\eta_{tr}}{MT_{tx}} + 0.06268p_1 \tag{22}$$

$$\Omega(i) = \frac{10671.65p_1KL[f(r_{AF}) - f(r_{ed})]\eta_{tr}}{MT_{tx}} \tag{23}$$

则调度中心 i 的成本函数可简化为

$$Z_{DC_i}^{cost} = \Gamma(i) + \frac{p_2K - \Omega(i)}{aC_i - b} + p_{3i}C_i \tag{24}$$

为在满足最大带宽约束前提下求解该优化问题，采用拉格朗日对偶分解将原始问题转化为无约束的优化问题，并进一步构建拉格朗日函数为

$$\begin{aligned} L(\nu) &= \sum_{i=1}^{N}\left(\Gamma(i) + \frac{p_2K - \Omega(i)}{aC_i - b} + p_{3i}C_i\right) \\ &\quad - \nu\left(\sum_{i=1}^{N}B_i - B_{\max}\right) \end{aligned} \tag{25}$$

式中，ν 为拉格朗日乘子。为便于推导，假设：

$$V_i(C_i,\nu) = \Gamma(i) + \frac{p_2K - \Omega(i)}{aC_i - b} + p_{3i}C_i - \nu B_i \tag{26}$$

因此，原问题可等价表示为

$$\max \sum_{i=1}^{N}V_i(C_i,\nu) + \nu B_{\max}$$

令 $G(\nu)=\max L(C_i,\nu)$，则对偶问题可以被表示为 $\min G(\nu)$。此外，对 V_i 关于 C_i 求一阶导并令其为 0，可得算力需求最优解为

$$C_i^* = \frac{b + \sqrt{\dfrac{a(p_2K - \Omega(i) + \nu K)}{p_{3i}}}}{a} \tag{27}$$

另外，拉格朗日乘子的迭代更新表达为

$$\begin{aligned} \nu(k+1) &= \nu(k) - \theta\frac{\partial G(\nu)}{\partial \nu} \\ &= \nu(k) - \theta\left(B_{\max} - \sum_{i=1}^{N}B_i\right) \end{aligned} \tag{28}$$

式中，k 为迭代次数，θ 为步长。设定 ε 为趋近于 0 的常数，当满足$|G(k+1)-G(k)|$时迭代终止。

（2）边缘节点设备-领导者

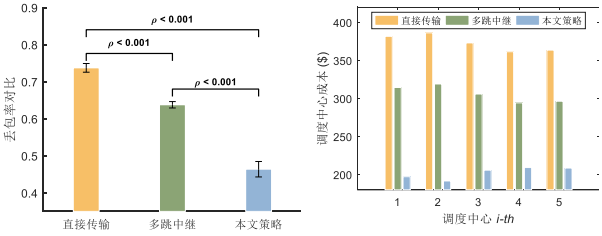
作为博弈中的领导者，边缘节点设备负责确定计算资源的单价。因此，将公式(27)中的最优算力 C_i^*代入公式(18)的收益函数中，进而推导出计算资源的最优单价。对收益函数 $U_{EN_i}^{profit}$ 关于 p_{3i} 求一阶导数并令其为零，由此可得最优计算资源单价为

$$p_{3i}^* = \frac{\left(p_2K - \Omega(i) + \nu K + ap_2K\right)^2}{4\left(p_2K - \Omega(i) + \nu K\right)b^2} \tag{29}$$

因此，可以得到所提出 Stackelberg 博弈的均衡解为 (C_i^*, p_{3i}^*)。

4 数值仿真与分析

本节从通信可靠性、系统成本及资源分配方面评估了本文提出的协作中继与边缘计算联合策略在风电通信中的综合性能。系统模型中有 5 个风电场子网络分布于 300m 范围内，边缘节点设备与网关的发射功率为 1W，带宽分别为 20MHz 与 1MHz。设定 M=80，L=60，假设风电场至网关数据传输成功率为 99%。信道模型采用自由空间损耗模型 h=0.097/d^4，噪声功率 σ^2=10^{-9}W，网关传输速率为 0.8Mbit/s，AGC 服务和带宽单价固定为 20$。此外，带宽压缩参数设置为 K=2，a=5，b=2。延迟敏感参数 α=1，增长因子 γ=0.5，风电场数据量为 50MB，风电场响应时延预设为 30s。不同策略在风电场通信中的丢包率与调度中心成本如图 3 所示。



(a) 丢包率对比　　(b) 成本对比

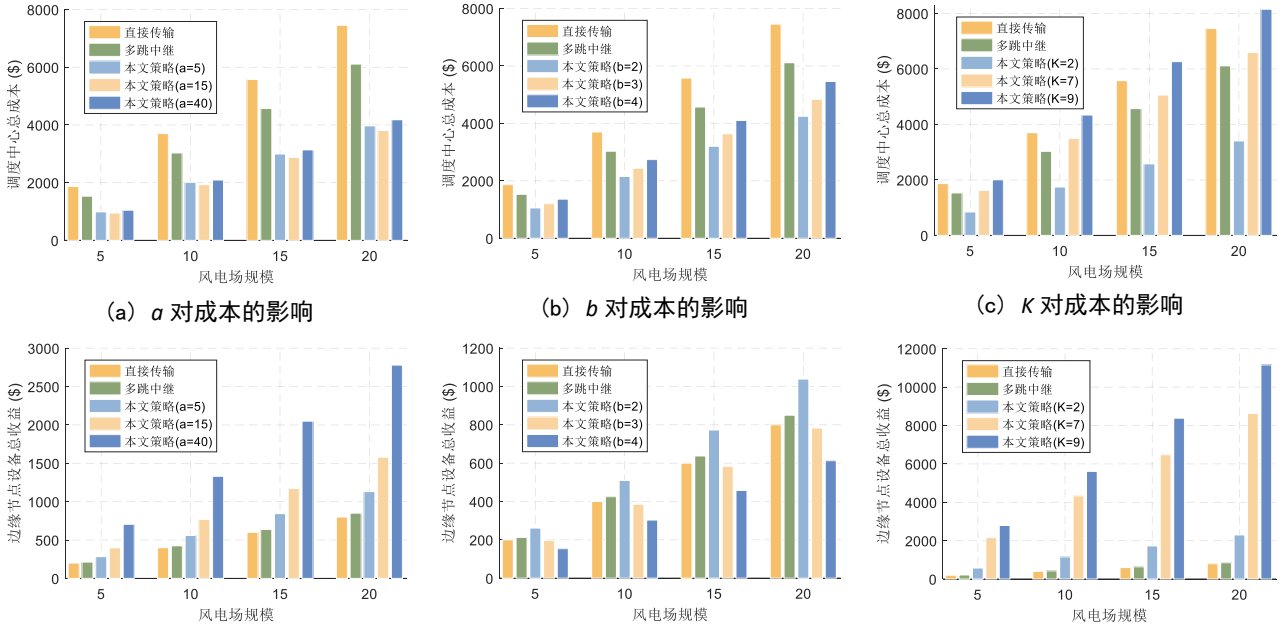
图 3　不同策略下丢包率和成本对比

Fig 3　Comparison of packet loss rate and cost under different strategies

由图 3(a)可知，直接传输方案的丢包率最高，多跳中继传输（MH-CRT）可在一定程度上降低丢包率，而提出的 CoRE 策略可进一步降低丢包率，且提升具有统计显著性(ρ<0.001)。同时，由图 3(b)可见，CoRE 策略较其他策略而言可显著降低调度中心成本，展现出更优的通信质量与成本效益。

带宽压缩模型参数对不同规模风电场下系统成本与收益的影响如图 4 所示。由图 4(a)-(c)可见，本文提出的 CoRE 策略在成本方面均优于 MH-CRT 与 CRT 策略，体现出良好的可扩展性。其中，参数 a 与 b 取较小值时压缩能力更强，CoRE 策略能够

在大规模场景下依然保持显著的成本优势；而随着参数 K 增大，系统对热效应的敏感性增强，CoRE 策略的成本优势逐渐减弱。图 4(d)-(f)显示了对应的收益变化趋势，结果表明 CoRE 策略在不同网络规模下均能实现更高收益，且在调整参数 a 与 K 时优势尤为明显。对于参数 b，在 CoRE 策略下会出现收益交叉点，仅当 b 低于该阈值时收益优势才能维持，并且这种优势在网络规模扩大时更加突出。



（a） a 对成本的影响　（b） b 对成本的影响　（c） K 对成本的影响

（d） a 对收益的影响　（e） b 对收益的影响　（f） K 对收益的影响

图 4　不同参数对总成本和收益的影响

Fig 4　The impact of different parameters on total cost and benefits

5　结论

本研究提出将边缘计算与协作传输技术相结合，应用于风电场调频过程中的信息传输问题，并基于 Stackelberg 博弈理论构建优化模型，以最小化调度中心的运行成本。仿真结果表明，所提 CoRE 策略在通信性能与经济性方面均优于直接传输和多跳中继传输策略。进一步分析表明，压缩模型参数的合理配置有助于在性能与经济性之间实现平衡，且该策略在不同规模的风电通信场景下均表现出良好的可扩展性与实用价值，尤其在大规模网络中，其成本控制与收益提升优势更加突出。

参考文献

[1] 刘洪波，彭晓宇，张崇，等. 风电参与电力系统调频控制策略综述[J]. 电力自动化设备，2021，41(11)：81-92.

[2] 王亚雨，彭勇刚，孙静. 风电场自动发电控制技术与策略研究综述[J]. 电网技术，2025.

[3] 滕贤亮，谈超，昌力，等. 高比例新能源电力系统有功功率与频率控制研究综述及展望[J]. 电力系统自动化，2023，47(15)：12-35.

[4] L. Zheng, N. Lu, and L. Cai. Reliable wireless communication networks for demand response control[J]. IEEE Transactions on Smart Grid，2013，4(1)：133-140.

[5] F. Bouhafs, M. Mackay, and M. Merabti. Links to the future: Communication requirements and challenges in the smart grid[J]. IEEE Power and Energy Magazine. 2012，10(1)：24-32.

[6] B. Xie, Q. Zhang and J. Qin. Joint optimization of cooperative communication and computation in two-way relay MEC systems [J]. IEEE Transactions on Vehicular Technology，2020，69(4)：4596-4600.

[7] D. Niyato and P. Wang. Cooperative transmission for meter data collection in smart grid[J]. IEEE Power and Energy Magazine，2012，50(4)：90-97.

[8] C. Wang, T. Zhang, F. Luo, F. Li and Y. Liu. Impacts of cyber system on microgrid operational reliability[J]. IEEE Transactions on Smart Grid，2019，10(1)：105-115.

[9] B. Liang, R. Fan, H. Hu, H. Jiang, J. Xu and N. Zhang. Joint task offloading and resource allocation in multi-user mobile edge computing with continuous spectrum sharing [J] . IEEE Transactions on Vehicular Technology，2024，73(5)：7234-7249.

[10] Z. Zhang，J. Shi，H. Chen，M. Guizani, and P. Qiu. A cooperation strategy based on nash bargaining solution in cooperative relay networks[J]. IEEE Transactions on Vehicular Technology，2008，57(4)：2570-2577.

收稿日期：

作者简介：



董晓玲

董晓玲(1994)，女，博士研究生，研究方向为电力系统频率控制，E-mail：dxl_0624@163.com；

王德林(1970)，男，教授，博士生导师，通讯作者。研究方向为新能源并网发电和系统稳定与控制研究等，E-mail：wdl@swjtu.edu.cn。

096 基于 MILP 模型的配电网可靠性评估方法研究

李佳丽[1]，马 硕[1]，王德林[1]，王世山[2]

（1. 西南交通大学 电气工程学院，四川 成都 611756；2. 南京航空航天大学 自动化学院，江苏 南京 210016）

RESEARCH ON DISTRIBUTION NETWORK RELIABILITY ASSESSMENT METHOD BASED ON MILP MODEL

LI Jiali[1]，MA Shuo[1]，WANG Delin[1]，WANG Shishan[2]

(1. School of Electrical Engineering, Southwest Jiaotong University, Chengdu 611756；2. School of Automation, Nanjing University of Aeronautics and Astronautics, Nanjing 210016, China)

ABSTRACT: Aiming at the shortcomings of traditional reliability assessment methods, such as the difficulty of accurately modeling and calculating distribution networks with distributed generation (DG) using analytical methods, and the low accuracy and long simulation time of simulation methods, this paper proposes a reliability assessment method for distribution networks based on tie-line planning. The proposed method takes into account the core factors of uncertainty of distributed generation, load fluctuation, load transfer, and power backflow. Firstly, a reliability index evaluation system is established to comprehensively evaluate the reliability indices. The load transfer during faults when tie-lines exist is analyzed, and a mixed-integer linear programming model for reliability assessment considering power backflow is proposed. The reliability indices of the system are obtained by solving this model. The feasibility and accuracy of the proposed method are verified through case studies, and the differences in reliability indices under different scenarios are compared.

KEY WORDS: distribution network reliability; distributed power supply; mixed integer linear programming; tie-line

摘要：针对传统可靠性评估方法中，解析法难以对分布式电源接入的配电网进行精确的建模和计算，模拟法精确度不高、仿真时间长等缺点。提出基于联络线规划的配电网可靠性评估方法，考虑分布式电源的不确定性、负荷波动性、负荷转移以及潮流反送等核心因素。首先建立可靠性指标评估体系，对可靠性指标进行综合评价，并针对联络线存在时故障发生的负荷转供进行分析，提出考虑潮流反向的可靠性评估的混合整数线性规划模型，通过求解该模型的系统的各项可靠性指标。通过算例分析该方法的可行性与准确性，比较考虑不同场景下可靠性指标的不同。

关键词：配电网可靠性；分布式电源；混合整数线性规划；联络线

0 引言

配电网可靠性衡量的是配电系统依据用户的预期标准和需求，稳定供应电力及电量的能力[0]。随着分布式电源(distributed generation，DG)在配电网中日益广泛的应用，在配电网故障时，快速为受影响的负荷创造恢复条件[2]。可再生能源具有随机性、波动性，需采用更为科学的评估方法对含分布式电源的配电网可靠性进行评估。

目前，相关学者针对配电网可靠性评估已经展开了大量研究。文献[3]提出了一种考虑配电自动化特征的可靠性评估算法。文献[4]采用马尔科夫链蒙特卡洛模拟法。文献[5]提出一种应用广义系统方法，通过随机或顺序蒙特卡洛模拟法，识别故障对负荷点可靠性的影响。文献[6]提出了配电网可靠性等级划分方法以及适用于规划和运行两阶段的配电网可靠性评估方法，但未涉及分布式能源。

近年来，开始研究线性规划解决可靠性评估问题。文献[7]提出一种基于拓扑变量的可靠性评估方法，适用于辐射状及辐射状运行的网状配电网。与传统可靠性评估模型相比，该方法具有计算速度快、精确度高的优点，但未涉及分布式电源接入及负荷转供的情况。文献[8]提出了一种新的线性规划模型，该模型包括精确评估可靠性和考虑故障后涉及操作约束的网络重构策略，但为考虑最优联络线位置的寻找。文献[9]提出一种单支路故障的有源配电网可靠性评估方法，但是限制了潮流倒送。

基金项目：四川省成都市科技局揭榜挂帅项目(2023-JB00-00002-SN),国家自然科学基金项目(52207117)。

This work is supported by a grant from Chengdu science and Technology Bureau (No. 2023-JB00-00002-SN), and National Natural Science Foundation of China (52207117).

在此背景下，本文提出一种基于混合整数线性规划模型的可靠性评估方法。该方法采用动态孤岛划分，考虑分布式电源的随机性、负荷的波动性、潮流反向等因素，避免了蒙特卡洛模拟法的大量重复的循环评估，避免了计算结果的随机性。

1 可靠性评估指标及归一化

1.1 电力设备的两状态模型

在可靠性问题的研究中，为简化问题，常采用两状态模型，其状态转移过程如图 1 所示。其中，λ 为设备的故障率，表示由正常工作状态向故障检修状态的转移率。μ 为设备的故障修复率，表示由停运检修状态向正常工作状态的转移率。

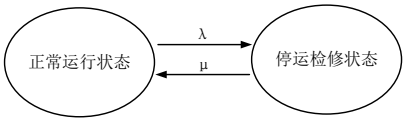


图 1 电气设备的两状态马尔可夫模型

Fig. 1 Two-state Markov model for electrical equipment

1.2 可靠性指标

配电网中系统可靠性指标能真实地反映配电网的供电可靠性。广泛使用的可靠性指标主要包括系统平均停电频率（system average interruption frequency index，SAIFI）、系统平均停电持续时间（system average interruption duration index，SAIDI）、平均供电可用率（average service availability index，ASAI）、系统电量不足（energy not supplied，EENS）[9-10]。计算方式如下：

$$\mathrm{SAIFI}=\sum_{b\in B}\frac{\Delta_b}{8760}\cdot\frac{\sum_{i\in\psi_D}N_i\Pi_{bi}}{\sum_{i\in\psi_D}N_i} \tag{1}$$

$$\mathrm{SAIDI}=\sum_{b\in B}\frac{\Delta_b}{8760}\cdot\frac{\sum_{i\in\psi_D}N_i\Gamma_{bi}}{\sum_{i\in\psi_D}N_i} \tag{2}$$

$$\mathrm{ASAI}=1-\frac{\mathrm{SAIDI}}{8760} \tag{3}$$

$$\mathrm{EENS}=\sum_{b\in B}\frac{\Delta_b}{8760}\cdot\sum_{i\in\psi_D}L_{bi}\Gamma_{bi} \tag{4}$$

式中，B 和 b 分别为负荷等级集合及其元素；Δ_b 为 b 级负荷的平均持续时间；ψ_D 为负荷节点集合；N_i 为节点 i 的用户数量；Π_{bi}、Γ_{bi} 和 L_{bi} 分别对应节点 i 在负荷等级 b 下的故障中断频率、故障停运时间及负荷需求。

1.3 可靠性指标综合评价

1.3.1 层次分析法

层次分析法通过将目标按照具体评价方案分为不同层次确定主观权重。对于同层次下的指标需建立判断矩阵。根据判断矩阵求取最大特征值 $\lambda_{\max}$ 及特征相量 $\boldsymbol{Z}$。最后进行一致性校验，过程为

$$\begin{cases}c_{\mathrm{CI}}=(\lambda_{\max}-n)/(n-1)\\ c_{\mathrm{CR}}=c_{\mathrm{CI}}/c_{\mathrm{RI}}\end{cases} \tag{5}$$

式中，n 为判断矩阵阶数，c_{CI}、c_{CR}、c_{RI} 为一致性指标、随机一致性指标及一致性偏差。当 c_{CR} <0.1 时通过校验，特征相量 $\boldsymbol{Z}$ 归一化得到主观权重。

1.3.1 归一化

由于可靠性 4 个评估指标是 4 个不同量纲，因而需要进行归一化处理。

可靠性评估指标在同一电网拓扑中的不同情况下，各指标的变化范围均不同[8]。故以指标变化显著与否为标准，将可靠性评估指标分为以下两类。

（1）指标变化不显著

可靠性评估指标中，平均供电可用率指标 ASAI 为指标变化不显著指标。ASAI 的评估函数为

$$F_{ASAI}=\begin{cases}0 & ,ASAI<0.999\\ a\times ASAI^2-b\times ASAI+c & ,ASAI\geq 0.999\end{cases} \tag{6}$$

式中，a、b、c 的值可通过配电网的敏感度设置。

（2）指标变化较为显著

可靠性评估指标中，系统故障停运持续时间 SAIDI、系统电量不足指标 EENS 为指标变化较显著指标。其评估函数为

$$F_{SAIFI}=\begin{cases}1, & SAIFI\leq kSAIFI_0\\ \dfrac{SAIFI_0-SAIFI}{SAIFI_0-kSAIFI_0}, & kSAIFI_0<SAIFI<SAIFI_0\\ 0, & SAIDI\geq SAIFI_0\end{cases} \tag{7}$$

$$F_{SAIDI}=\begin{cases}1, & SAIDI\leq kSAIDI_0\\ \dfrac{SAIDI_0-SAIDI}{SAIDI_0-kSAIDI_0}, & kSAIDI_0<SAIDI<SAIDI_0\\ 0, & SAIDI\geq SAIDI_0\end{cases} \tag{8}$$

$$F_{EENS}=\begin{cases}1, & EENS\leq kEENS_0\\ \dfrac{EENS_0-EENS}{EENS_0-kEENS_0}, & kEENS_0<EENS<EENS_0\\ 0, & EENS\geq EENS_0\end{cases} \tag{9}$$

式中，$SAIFI_0$、$SAIDI_0$、$EENS_0$ 为网络初始状态指标值；$kSAIFI_0$、$kSAIDI_0$、$kEENS_0$ 分为系统平均故障频率最小值、系统故障停运持续时间理论最小值、系统电力不足理论最小值，$k<0$。

2 可靠性评估模型假设与运行规则

2.1 模型假设

本文提出的配电网可靠性评估方法基于以下假设：

（1）联络线完全可靠，无故障发生。

（2）考虑辐射状运行的网状构造的配电网。

（3）负荷点依照支路中断类型不同分为两种故障：I.修复和切换中断；II.仅切换中断。

2.2 含分布式电源的孤岛划分

当配电网发生故障后，故障下游部分形成孤岛，为了充分发挥分布式电源的作用，孤岛在满足功率约束的前提下，应尽可能地包含更多的负荷。所以孤岛划分的目标可表示为

$$\begin{cases} \max \sum_{i\in D} L(i) \\ \sum_{i\in D} L(i) < P_{DG} \end{cases} \tag{10}$$

式中，$L(i)$为负荷点 i 的负荷值；P_{DG} 为分布式电源的输出功率；D 为孤岛内所有负荷组成的连通区域。

2.3 运行规则

本文提出考虑潮流反向的混合整数线性规划模型可靠性评估方法，对该方法运行规则阐述如下：

（1）不含 DG 及转供点

如图 2 所示，支路 6-7 故障时导致节点 7 形成孤岛①，该孤岛内不含 DG 和转供点。此时，节点 2-5 供电不受影响；节点 6 为故障类型II，隔离故障即可恢复供电；节点 7 需故障完全修复后恢复供电。

（2）仅含 DG

如图 2 所示，故障发生在支路 2-4 时，节点 4 和 5 形成孤岛②，节点 6 和 7 不受故障影响，节点 2、3 为故障类型II，仅需故障隔离即可恢复供电；孤岛②内含有 DG，能否恢复供电取决于 DG 出力能否满足负荷需求。

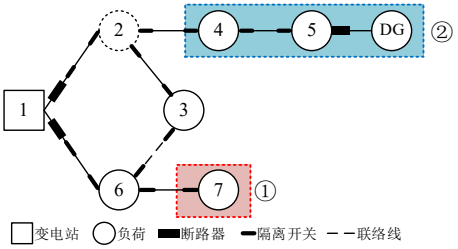


图 2　孤岛内不含 DG 或转供点/孤岛内仅含 DG

Fig. 2　Island without DG or transfer point / with only DG

（3）仅含转供点

如图 3 所示，故障发生在支路 1-6 时，节点 6、7 形成孤岛③，孤岛可通过联络线隔离开关闭合恢复供电，其故障停电持续时间为开关切换隔离故障的时间。

（4）含 DG 和转供点

图 3 中，故障发生在支路 1-2 时，形成孤岛④，孤岛内含有 DG 和转供点，在隔离故障后，孤岛通过联络线恢复供电。

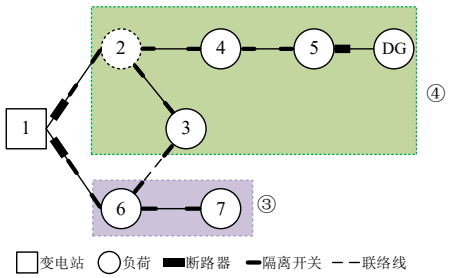


图 3　孤岛内仅含转供点/孤岛内含 DG 和转供点

Fig. 3　Island with only transfer points / with DG and transfer point

3　基于 MILP 的可靠性评估模型

基于模型假设与运行规则，提出可靠性约束条件，这些可靠性约束可以通过混合整数线性规划（mixed-integer linear programming，MILP）模型进行求解，尽管 MILP 模型中存在整数变量，但通过合理建模与简化处理，本文所提方法在保持较高求解精度的同时，能够在一定程度上适用于大规模电力系统的分析，并具备较好的计算效率。

3.1 目标函数

用判断矩阵表示目标相对于的重要性确定目标权重的取值。根据所得权重，将多目标问题转化为单一目标，获得可靠性评估总指标 Y为：

$$\begin{aligned} Y = w_{SAIFI} \times F_{SAIFI} + w_{SAIDI} F_{SAIDI} \\ + w_{EENS} F_{EENS} + w_{ASAI} F_{ASAI} \end{aligned} \tag{11}$$

式中，w 为各项子指标的权重，F 为各子指标评估值。

以可靠性评估总指标最大为目标函数 M 为

$$M = \text{Max}\ \ Y \tag{12}$$

3.2 约束条件

（1）节点故障率和故障持续时间约束

$$S_i^{xy} = \begin{cases} 1 & \text{，支路}xy\text{故障，节点}i\text{与变电站连通} \\ 0 & \text{，其他} \end{cases} \tag{13}$$

$$T_i^{xy} = \begin{cases} 1 & \text{，支路}xy\text{故障，节点}i\text{与转供节点连通} \\ 0 & \text{，其他} \end{cases} \tag{14}$$

$$D_i^{xy} = \begin{cases} 1 & \text{，支路}xy\text{故障，节点}i\text{在DG孤岛内} \\ 0 & \text{，其他} \end{cases} \tag{15}$$

$$Q_i^{xy} = \begin{cases} 1 & \text{，支路}xy\text{故障，节点}i\text{在转供点到变电站最小路上} \\ 0 & \text{，其他} \end{cases} \tag{16}$$

$$\begin{aligned} P_i^{xy} = \left(1 - S_i^{xy}\right)(T_i^{xy} + D_i^{xy} + Q_i^{xy} - T_i^{xy} D_i^{xy} \\ - T_i^{xy} Q_i^{xy} - D_i^{xy} Q_i^{xy} - T_i^{xy} D_i^{xy} Q_i^{xy}) + S_i^{xy} \end{aligned} \tag{17}$$

式(13)-(17)中，$xy \in \Upsilon$，Υ 为支路集合。

基于模型假设（2），计算节点故障率时引入

0-1 变量 A_i^{xy}，$A_i^{xy}=1$的含义为：一旦支路 xy 发生故障，该馈线首端断路器跳闸，馈线内所有负荷点均停电。则有：

$$A_i^{xy}=\begin{cases}1, & i\in\Psi_{xy},xy\in\Upsilon\\ 0, & \text{其他}\end{cases} \tag{18}$$

式中，Ψ_{xy} 为支路 xy 所属馈线的负荷节点集合。

由于不考虑变电站故障，对于变电站节点则有：

$$\begin{cases}\Pi_{bi}=0\\ \Gamma_{bi}=0\end{cases},\ i\in\Psi_s \tag{19}$$

式中，Ψ_s 为变电站节点集合。

对于除变电站节点的其他节点，即 $i\in\Psi_{LN}$：

$$\begin{cases}\Pi_{bi}=\sum\limits_{xy\in\Upsilon}A_i^{xy}\lambda_{xy}\\ \Gamma_{bi}=\sum\limits_{xy\in\Upsilon}A_i^{xy}\lambda_{xy}\tau_{xy}^{SO}+\sum\limits_{xy\in\Upsilon}\left(1-P_i^{xy}\right)\lambda_{xy}\left(\tau_{xy}^{RS}-\tau_{xy}^{SO}\right)\end{cases} \tag{20}$$

式中，λ_{xy} 为支路 xy 的故障率，τ_{xy}^{SO} 为支路 xy 的开关切换时间，τ_{xy}^{RS} 为支路 xy 的故障修复时间。

（2）电压约束

$$U_i^{\min}\le U_{i,t}\le U_i^{\max} \tag{21}$$

式中，$U_i^{\min}$、$U_i^{\max}$ 分别为节点 i 电压幅值的的下限与上限，$U_{i,t}$ 为 t 时刻节点 i 的电压值。

（3）功率平衡约束

$$D_i^{xy}=\sum_{j\in\Psi_i}P_{ji}^{xy},\forall i\in\boldsymbol{\psi}_{LN},\forall xy\in\Upsilon \tag{22}$$

$$P_{ij}^{xy}=-P_{ji}^{xy},\forall ij\in\Upsilon,\forall xy\in\Upsilon \tag{23}$$

式中，D_i^{xy} 为支路 xy 发生故障时节点 i 的负荷，P_{ji}^{xy} 为支路 xy 发生故障时支路 ij 上功率有 j 节点流向 i 节点。

4 算例

本文以 37 节点配电系统为例对所提出方法进行分析和验证，如图 4 所示[11]。节点用户数量、峰值负荷、支路数据等具体参数详见文献[12]。

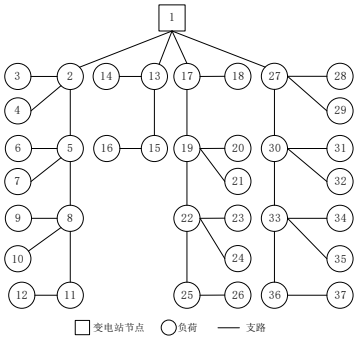


图 4　37 节点配电网系统结构

Fig 4　System structure of 37 bus distribution network

为了验证本文所提出的考虑潮流反向的可靠性评估方法的有效性，针对图 4 所示的 37 节点系统进行不同情况下评估结果对比分析，其中，在节点 11、23、30 安装有光伏，节点 8 至 15 节点安装有常开联络线。给出 4 种场景情况如下：

情况 1：不考虑 DG 接入，不考虑联络线连接；情况 2：考虑 DG 接入，不考虑联络线连接；情况 3：考虑 DG 接入，考虑联络线连接，但不考虑潮流反向；情况 4：考虑 DG 接入，考虑联络线连接，考虑潮流反向。

4 种情况各节点的故障停运时间 Γ 如图 5 所示，可靠性评估结果如表 1 所示。

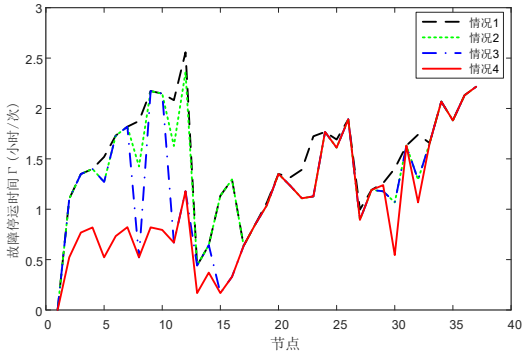


图 5　不同情况的各节点故障停运时间 Γ

Fig 5　Fault outage time Γ for each node under different scenarios

表 1　不同情况的可靠性评估结果

Table 1　Reliability assessment results under different scenarios

	情况 1	情况 2	情况 3	情况 4
SAIFI	1.8051	1.8051	1.8051	1.8051
SAIDI	1.5312	1.4344	1.2076	1.0844
ASAI	99.9825	99.9836	99.9864	99.9875
EENS	69.5157	66.4450	64.0043	50.0568
总分	60	62.3732	64.1137	81.3392

由图 5 可见，在考虑潮流反向后，转供点到变电站节点最短路径上的节点故障停运时间大幅减小，若不考虑潮流反向的情况下，只有转供点后的节点故障停运时间才减小。由表 1 可见，在考虑 DG 和联络线转供后，SAIFI 值不改变，这是由于每次在故障发生时，都需要首端断路器断开来隔离故障，所以其值只取决于网络拓扑结构。所提出的考虑潮流反向的可靠性评估方法（情况 4）相较于情况 1-3，SAIDI 分别降低 29.18%、24.4%、10.2%，EENS 分别降低 27.99%、24.66%、21.79%，ASAI 提升至 99.9875%，验证了动态孤岛划分与潮流反向约束提升有源配电网可靠性的有效性。

设置 4 种场景：（1）不接入新能源；（2）仅接入光伏；（3）仅接入风机；（4）接入光伏、风机。各场景分布式电源出力曲线如图 6 所示。4 种场景下各节点的故障停运时间 Γ 如图 7 所示，系统的可靠性指标及评估总分如表 2 所示。

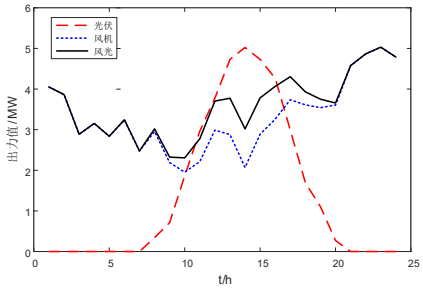


图 6　各场景新能源出力曲线

Fig 6　New energy output curves for different scenarios

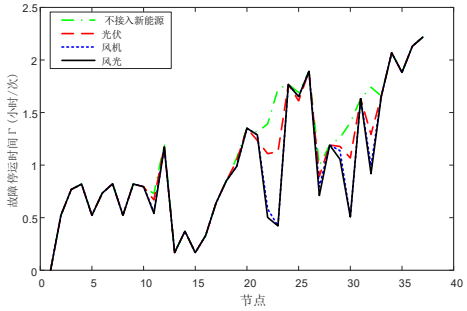


图 7　4 种场景下各节点故障停运时间 Γ

Fig 7　ault outage time Γ for each node under four scenarios

表 2　不同情况的可靠性评估结果

Table 2　Reliability assessment results under different scenarios

	不接入新能源	光伏	风电	风光
SAIFI(次/年)	1.8051	1.8051	1.8051	1.8051
SAIDI(小时/年)	1.1436	1.0844	1.0199	1.0108
ASAI(%)	99.9869	99.9875	99.9884	99.9885
EENS(MWh/年)	51.7679	50.0568	47.7527	47.4284
总分	73.5076	81.3392	90.8414	91.7537

由图 7 得出结论：风光互补在多数节点的故障停运时间 Γ 最低，表明其可靠性优于其他场景。仅接入风机次之，而不接入新能源的故障停运时间最长，可靠性最差。这表明接入新能源尤其是风光互补可显著提升配电网可靠性。

由表 2 可见，接入新能源可提升配电网可靠性。风光互补在 SAIDI、ASAI、EENS 等指标上表现最佳，评估总分也较高，表明其综合可靠性最优。仅接入风机次之，仅接入光伏再次，而不接入新能源的可靠性指标最差。这表明风光互补能有效降低故障影响，提高供电可用性，减少能源未供应量。

5　结论

本文提出的基于混合整数线性规划模型的配电网可靠性评估方法，主要得出以下结论：

1）基于指标变化的显著程度，提出归一化方式，利用层次分析法得到系统可靠性总指标，负荷实际可靠性评估需求；

2）相较于传统的可靠性评估方法，所提方法既考虑了联络线的潮流反向问题，更贴近实际，与传统评估方法对比，使 SAIDI 和 EENS 分别降低 29.18%和 27.99%，ASAI 提升至 99.9875%，有效提高了可靠性评估的精度，接入新能源尤其是风光互补可显著提升配电网可靠性。

参考文献

[1] 程林，何剑．电力系统可靠性原理和应用[M]．清华大学出版社，2015．

[2] 薛录权．含分布式电源的配电网优化运行研究[J]．光源与照明，2023，11：141-143．

[3] 曾强，邓惠华，朱凌，等.考虑多模式配电自动化特征的配电网可靠性评估方法[J]．电力系统及其自动化学报，2017，29(1)：128-134．

[4] 朱晓荣，王羽凝，金绘民，等．基于马尔科夫链蒙特卡洛方法的光伏电站可靠性评估[J]．高电压技术，2017，43(3)：1034-1042．

[5] Conti S，Rizzo S A．Monte Carlo simulation by using a systematic approach to assess distribution system reliability considering intentional islanding[J]. IEEE Transactions on Power Delivery，2014，30(1)：64-73．

[6] 李鹏，赵亚汝，范须露，等．适用于规划-运行两阶段的配电网可靠性等级划分及评估方法[J]．高电压技术，2024，50(05)：2042-2051．

[7] Jooshaki，Mohammad，et al．Linear Formulations for Topology-Variable-Based Distribution System Reliability Assessment Considering Switching Interruptions[J]．IEEE TRANSACTIONS ON SMART GRID，2020，11(5)：4032-4043．

[8] Li，Zihao，et al．Analytical Reliability Assessment Method for Complex Distribution Networks Considering Post-Fault Network Reconfiguration[J]．IEEE TRANSACTIONS ON POWER SYSTEMS，2020，35(2)：1457-1467．

[9] 李阳洋,关铁文,赵佳琪,等.基于优化模型的有源配电网可靠性评估方法[J].中国电机工程学报,2023,43(08):2931-2940.

[10] Brown R E. Electric power distribution reliability[M]. CRC press, 2017.

[11] Samper M E，Vargas A．Investment decisions in distribution networks under uncertainty with distributed generation — Part I: Model formulation[J]．IEEE Transactions on Power Systems，2013，28(3)：2331-2340，

[12] Muñoz-Delgado G，Contreras J，Arroyo J M．Reliability assessment for distribution optimization models: A non-simulation-based linear programming approach[J]．IEEE Transactions on Smart Grid，2016，9(4)：3048-3059．

收稿日期：



李佳丽

作者简介：

李佳丽(2000)，女，硕士研究生，研究方向为电力系统可靠性，E-mail：jialili@my.swjtu.edu.cn；

王德林(1970)，男，教授，博士生导师，通讯作者。研究方向为新能源并网发电和系统稳定与控制研究等，E-mail：wdl@swjtu.edu.cn。

097 台风-滑坡灾害链下输电杆塔多荷载空间耦合故障模型

石远钊[1]，侯慧[1]，魏瑞增[2]，李正天[3]，林湘宁[3]

(1. 武汉理工大学自动化学院，武汉，430070

2. 广东省电力装备可靠性重点实验室（广东电网有限责任公司电力科学研究院），广州，510080

3. 华中科技大学电气与电子工程学院，武汉，430074)

Multi-Load Spatial Coupling Failure Model for Transmission Towers Under Typhoon-Landslide Disaster Chains

Shi Yuanzhao[1], Hou Hui[1], Wei Ruizeng[2], Li Zhengtian[3], Lin Xiangning[3]

(1. School of Automation, Wuhan University of Technology, Wuhan, 430070, China

2. Guangdong Key Laboratory of Electric Power Equipment Reliability, Electric Power Research Institute of Guangdong Power Grid Co., Ltd., Guangzhou, 510080, China

3. School of Electrical and Electronic Engineering, Huazhong University of Science and Technology, Wuhan 430074, China)

ABSTRACT: Typhoons not only cause direct effects such as strong winds and heavy rainfall but also induce secondary disaster chains, including landslides, which severely threaten transmission towers in mountainous and coastal regions. To address risk assessment of transmission towers under typhoon-landslide disaster chains, this paper proposes a multi-load spatial coupling failure model. First, the wind load, the landslide load, and the soil reaction loads are formulated based on the structural response characteristics of transmission towers under typhoon-landslide disaster chain. Subsequently, the three loads are spatially coupled via the generalized stress-strength interference theory to formulate the multi-load spatial coupling failure model, enabling precise quantification of transmission tower failure probability. Finally, the Zhanjiang power grid in Guangdong Province, affected by Typhoon Talim in 2023, is employed as a case study for validation. Results demonstrate that the proposed model effectively quantifies the synergistic destructive effects tower structures, providing a theoretical foundation for risk prevention and control in disaster chains.

KEY WORDS: typhoon-landslide disaster chains, transmission towers, multi-load, spatial coupling, generalized stress-strength interference theory

摘要：台风除强风暴雨等直接影响，还易引发滑坡等次生灾害链，严重威胁山区及沿海的输电杆塔。针对台风-滑坡灾害链下输电杆塔的风险评估，本文提出一种台风-滑坡灾害链下输电杆塔多荷载空间耦合故障模型。首先，基于台风-滑坡灾害链下输电杆塔的受力特征，分别构建输电杆塔的风荷载、滑坡荷载及土体反作用力荷载。然后，基于广义应力-强度干涉理论，耦合 3 类荷载，构建输电杆塔多荷载空间耦合故障模型，量化输电杆塔的故障概率。最后，以 2023 年台风“泰利”侵袭的广东湛江电网为案例进行验证。结果表明，所提模型可有效量化风-滑耦合荷载对杆塔结构的协同破坏效应，为灾害链风险防控提供理论依据。

关键词：台风-滑坡灾害链，输电杆塔，多荷载，空间耦合，广义应力-强度干涉理论

DOI：10.13335/j.1000-3673.pst.2014.01.论文序号（小五号 Times New Roman 字体加黑）

0 引言

在全球气候变化背景下，台风灾害呈现频次增加、强度增强的趋势，致灾过程常演化为多灾种耦合的链式灾害[1]。台风暴雨改变地表水文状况，引起土壤饱和并削弱岩土体抗剪强度，进而诱发滑坡，形成台风-滑坡灾害链[2]。输电杆塔作为输电网络的关键通道，不可避免需架设于山区及沿海地带，容易遭受台风滑坡-灾害链的影响[3]。2024 年 7 月 26 日至 28 日，台风“格美”引发湖南郴州特大

暴雨，诱发群发性山体滑坡、泥石流等次生灾害，导致 149 个村 66793 户电力中断，逾 12.8 万人受灾[4]。

当前，针对台风-滑坡灾害链诱发的输电杆塔风险已开展部分研究，主要为数据驱动与模型驱动两类方法。在数据驱动方法方面，支持向量机[5]、随机森林[6]及极限梯度提升[7]等单一机器学习算法，虽能学习滑坡影响因素与发生概率之间的映射关系，但需要足够样本量支撑特征提取。文献[8]提出一种融合卷积模糊神经网络与 SHAP(Shapley Additive exPlanations)解释分析的深度学习模型，但复杂网络结构对样本规模与质量的要求更为严苛，在样本稀缺场景下存在局限性。台风-滑坡灾害链中的滑坡属于低频高损事件，其样本点数据稀缺，而地理空间中非滑坡点数据占主导地位，从而引发训练样本的严重不平衡问题。尽管已有研究尝试采用自适应合成抽样[9]、合成少数类过采样[10]和随机过采样[11]缓解非平衡样本问题。然而，文献[9-11]均依赖对有限少数类样本进行局部插值或复制来扩充数据，易诱发模型过拟合，难以有效提升模型对少数类特征的表征能力。因此，在台风-滑坡灾害链场景下，滑坡样本的极端匮乏从根本上限制了数据驱动方法的有效性和适用性。

鉴于此，模型驱动方法成为评估台风-滑坡灾害链对输电杆塔风险的重要途径。文献[12]基于广义应力-强度干涉理论建立输电杆塔风荷载失效模型，但单一风荷载难以表征台风灾害链中输电杆塔的实际结构受力状况。文献[13]构建有限元模型模拟滑坡作用下输电杆塔的应力分布与屈曲行为，但计算效率低限制了实时响应应用。文献[14]提出一种数据-物理双驱动的输电杆塔故障预测方法，但聚焦于原生风雨灾害对输电杆塔的影响，缺乏滑坡等次生灾害的综合分析。在台风-滑坡灾害链下，输电杆塔受到台风和滑坡的空间耦合作用，使得其结构的力学响应呈现多荷载空间耦合效应，然而目前仍缺台风-滑坡灾害链下乏多灾耦合作用的输电杆塔结构失效分析模型。

综上，针对台风-滑坡灾害链下输电杆塔的风险评估，本文提出一种台风-滑坡灾害链下输电杆塔多荷载空间耦合故障模型。主要创新点包括：1)融合滑坡动力学与土体响应理论，建立多学科交叉融合的输电杆塔风险量化模型，突破电力系统传统风灾评估的学科局限。2)基于广义应力-强度干涉理论，联立风荷载、滑坡荷载及土体反作用力荷载，构建输电杆塔多荷载空间耦合故障模型，量化输电杆塔的故障概率。

1 多荷载空间耦合故障模型框架

本文提出一种台风-滑坡灾害链下输电杆塔多荷载空间耦合故障模型。总体框架如图 1 所示。

首先，基于台风作用下导线与电杆的受力特性，构建风荷载模型。其次，对输电杆塔所处边坡实施离散化处理，利用极限平衡理论与传递系数法，确定滑坡荷载。然后，分析土体对输电杆塔的反作用力，建立土体反作用力荷载模型。最后，依托广义应力-强度干涉理论，实现风荷载、滑坡荷载与土体反作用力荷载的空间耦合，进而量化输电杆塔在灾害链作用下的故障概率。

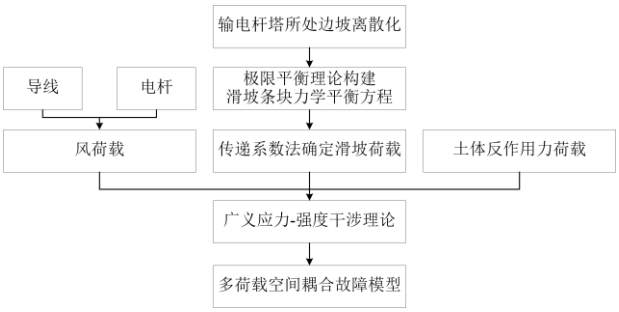


图 1 多荷载空间耦合故障模型

Fig. 1 Multi-Load Spatial Coupling Failure Model

2 荷载模型

2.1 风荷载

在台风灾害作用下，输电杆塔结构承受的风荷载主要作用于导线，电杆[12]。

导线受到的风荷载为：

$$W_{\mathrm{w}}=\frac{v^2\sin^2\theta}{1600}\mu_{\mathrm{l}}\mu_{\mathrm{z}}\mu_{\mathrm{l}}dl_{\mathrm{l}} \tag{1}$$

式中：W_{w} 为导线受到的风荷载；v 为基准高度为 10m 的风速；θ 为风向与导线方向之间的夹角；μ_{l} 为风压不均匀系数；μ_{z} 为风压高度变化系数；μ_{l} 为导线体型系数；d 为导线外径；l_{l} 为导线档距。

电杆受到的风荷载为：

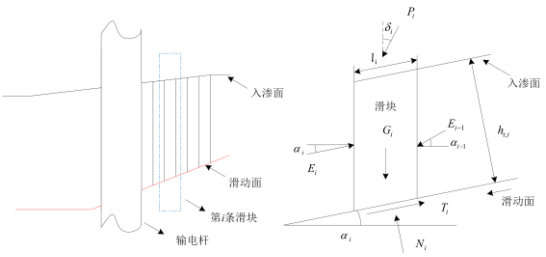
$$W_{\mathrm{p}}=\frac{v^2}{1600}\mu_2\mu_{\mathrm{z}}\mu_{\mathrm{p}}A_{\mathrm{p}} \tag{2}$$

式中：W_{p} 为电杆受到的风荷载；μ_2 为电杆风荷载调整系数；μ_{p} 为电杆体型系数；A_{p} 为电杆风荷载作用面积。

2.2 滑坡荷载

在台风降雨入渗作用下，边坡常发生沿坡面倾向发育的浅层顺层滑坡[4]。本文基于极限平衡理论[13]，采用传递系数法计算输电杆塔所受滑坡荷载

[13]。针对输电杆塔所处的高危滑坡区，利用 Geostudio 岩土分析软件将高滑坡概率区域沿潜在滑动面离散化为 m 个条块单元，如图 2(a)所示。通过平行和垂直于条块滑动方向的受力平衡分析，计算各条块的下滑力和抗滑力，第 i 条块的受力计算简图如图 2(b)所示。



(a) (b)

图 2 滑坡荷载

Fig. 2 Landslide load

$$T_i + E_i - E_{i-1}\cos(\alpha_{i-1} - \alpha_i) - P_i \sin(\delta_i + \alpha_i) - G_i \sin\alpha_i = 0 \tag{3}$$

$$N_i - E_{i-1}\sin(\alpha_{i-1} - \alpha_i) - P_i \cos(\delta_i + \alpha_i) - G_i \cos\alpha_i = 0 \tag{4}$$

式中：T_i 和 N_i 分别为第 i 条块底面切向反力和法向反力；E_i 和 E_{i-1} 分别为第 i 条块和第 $i-1$ 条块剩余下滑力，当 $E_i < 0$ 时，取 $E_i = 0$；α_i 和 α_{i-1} 分别为第 i 条块和第 $i-1$ 条块的滑坡倾角；P_i 为第 i 条块所受的雨水合力，本文不考虑雨水冲刷影响；δ_i 为 P_i 与垂直方向的夹角；G_i 为第 i 条块的重度，可表示为：

$$G_i = \gamma h_{r,i} l_i \tag{5}$$

式中：γ 为饱和土体的重度；$h_{r,i}$ 为第 i 条块的厚度；l_i 为第 i 条块宽度。

结合安全系数与 Mohr-Coulomb 准则[13]，第 i 条块底面切向反力 T_i 为：

$$T_i = \frac{c_i l_i + (N_i - u_a l_i)\tan\varphi_i}{F_s} \tag{6}$$

式中：c_i 和 φ_i 分别为第 i 条块的黏聚力和内摩擦角；u_a 为孔隙气压力，本文不考虑气体的影响；F_s 为安全系数。

则第 i 条块剩余下滑力可简化表示为：

$$E_i = E_{i-1}\psi_{i-1} + G_i \sin\alpha_i - \frac{(c_i l_i + G_i \cos\alpha_i \tan\varphi_i)}{F_s} \tag{7}$$

$$\psi_{i-1} = \cos(\alpha_{i-1} - \alpha_i) - \frac{\tan\varphi_i \sin(\alpha_{i-1} - \alpha_i)}{F_s} \tag{8}$$

式中：ψ_{i-1} 为传递系数。

滑坡荷载的分布受滑体类型影响。当滑体为岩石，滑坡荷载分布图近似按矩形；当滑体为砂土时，滑坡荷载分布图近似三角形~抛物线；当滑体介于砂土和黏土之间，滑坡荷载分布图近似按梯形[13]。

$$q_i(z) = \begin{cases} \dfrac{E_i}{h_{r,i}} \\ \dfrac{E_i[z^2(36e-24)+z(18-24b)]}{h_{r,i}^2} \\ \dfrac{1.8E_i z}{h_{r,i}^2} + \dfrac{E_i}{h_{r,i}} \end{cases} \tag{9}$$

式中：$q(z)$ 为滑坡荷载沿输电杆塔土下深度的分布集度；z 为土下深度；e，b 为计算参数。

2.3 土体反作用力荷载

在台风-滑坡灾害链作用下，输电杆塔将产生倾覆趋势，而处在倾覆处的土体会产生土体反作用力荷载抑制输电杆塔倾覆[15]。

$$E_p = m_s z \tag{10}$$

$$m_s = \gamma \tan^2\left(\frac{\pi}{4} + \frac{\beta}{2}\right) \tag{11}$$

式中：E_p 为土体反作用力荷载；m_s 为被动土压力系数；β 为等代内摩擦角。

3 输电杆塔多荷载空间耦合受力模型

在多荷载空间耦合作用下，输电杆塔易引发结构失效，本文基于广义应力-强度干涉理论[12]，以输电杆塔底座为基准点建立空间弯矩平衡方程，进行输电杆塔失效分析。

3.1 风荷载引起的弯矩

导线受到的风荷载引起的弯矩：

$$M_w = W_w h_0 + 2W_w h_1 \tag{12}$$

式中：M_w 为导线受到的风荷载引起的弯矩。

电杆受到的风荷载引起的弯矩：

$$M_p = \frac{1}{2} W_p (h_0 + h_2) \tag{13}$$

式中：M_p 为电杆受到的风荷载引起的弯矩。

风荷载引起的弯矩为 M_w 与 M_p 矢量和：

$$M_1 = \sqrt{M_w^2 + M_p^2 - 2M_w M_p \cos(90° + \theta)} \tag{14}$$

式中：M_1 为风荷载引起的弯矩。

3.2 滑坡荷载引起的弯矩

滑坡荷载引起的弯矩可通过沿杆身分布的滑坡荷载积分求解：

$$M_2 = \int_0^{h_0} q_i(z) z \mathrm{d}z \tag{15}$$

式中：M_2 为滑坡荷载引起的弯矩。

3.3 土体反作用力荷载引起的弯矩

土体反作用力荷载引起的弯矩可通过沿杆身分布的土体反作用力荷载积分求解：

$$M_3 = \int_0^{h_0} p(z) z \mathrm{d}z \tag{16}$$

式中：M_3 为土体反作用力荷载引起的弯矩。

3.4 输电杆塔所受综合弯矩

在台风-滑坡灾害链下，输电杆塔的受力情况如图 2 所示，根据输电杆塔力学响应的多荷载空间耦合效应，则输电杆塔所受综合弯矩：

$$M=\sqrt{M_1^2+M_2^2-2M_1M_2\cos(90°+\xi)}-M_3 \quad (17)$$

式中：M 为输电杆塔所受综合弯矩；ξ 为土体反作用力荷载与风荷载夹角。

3.5 输电杆塔故障概率

输电杆塔所受实际应力弯矩载荷超出标准允许承受限值边界时，输电杆塔可能发生故障[12]。

$$p_{\mathrm{p}}=\int_0^M \varphi(e)H(e)\mathrm{d}e \quad (18)$$

式中：p_{p} 为输电杆塔的故障概率；$\varphi(e)$ 分别为输电杆塔强度密度函数；e 为元件强度；$H(e)$ 为元件应力累积分布函数。

根据我国台风预警信号等级，架空线路在台风灾害下的故障概率从高到低划分为 5 个风险等级[12]，架空线路风险预警表如表 1 所示。

表 1　架空线路风险预警表

Tab.1　Overhead line hazard warning table

综合故障概率	风险等级
$P\geq 80\%$	I 级风险
$50\%\leq P<80\%$	II 级风险
$30\%\leq P<50\%$	III 级风险
$10\%\leq P<30\%$	IV 级风险
$P<10\%$	V 级风险

4　算例分析

2023 年 7 月 17 日，台风“泰利”(2023)于中国广东省湛江市登陆。此次台风导致该区域 10 kV 架空输电线路发生倒杆、断线、倾斜等故障共计 65 处，损毁导线 20.23 km，粤西地区约 98.8 万用户供电中断[11]。

本文选取湛江市作为研究区域，为验证所提多荷载空间耦合故障模型可行性，选取台风“泰利”影响区内存在地基薄弱问题的 65 基输电杆塔作为研究对象，分别建立其在风荷载单独作用及多荷载空间耦合作用下的模型，进行输电杆塔故障概率预测。两种荷载工况下输电杆塔故障概率的对比结果如图 3 所示。

在风荷载作用下，输电杆塔平均故障概率为 3.62%。故障概率超过 10.00%的输电杆塔仅 6 基，98.46%的输电杆塔风险等级为 V 级，主要由于所处区段的风速为 25-35m/s，且合理的结构强度设计，使得大部分输电杆塔的风险等级维持在较低水平。然而，位于风口地形的 54 号输电杆塔承受风速高达 38.65m/s，导致其故障概率上升至 22.67%，风险等级达到 IV 级，但仍为较低风险等级。

在多荷载空间耦合作用下，输电杆塔故障概率急剧升高至 40.00%-98.00%。风险等级为 I 级的输电杆塔占比为 18.46%，80.00%的输电杆塔风险等级为 II 级。这一现象主要源于滑坡产生的滑坡荷载导致基础失稳，使输电杆塔所受弯矩骤增；同时，风荷载的耦合效应进一步加剧结构失效风险。此外，有 1.54%的输电杆塔因所在区域滑坡发生概率较低，风险等级为 III 级。

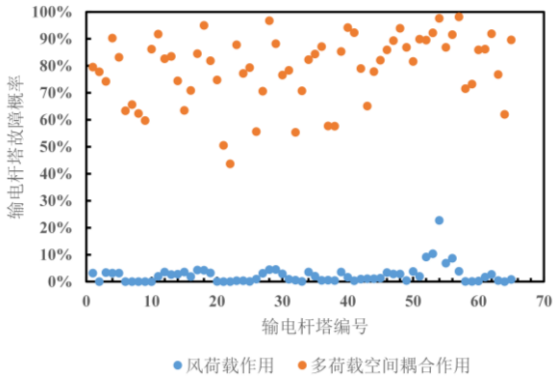


图 3　输电杆塔故障概率的对比结果

Fig.3　Failure probability comparison of transmission towers

对比两种荷载工况下输电杆塔故障情况表明：单一风荷载对输电杆塔整体故障概率影响相对有限；而台风-滑坡灾害链不仅直接施加风荷载，更通过诱发滑坡产生滑坡荷载，结合土体反作用力荷载形成多荷载空间耦合作用，导致输电杆塔故障概率大幅提升，验证所提台风-滑坡灾害链输电杆塔多荷载耦合受力模型在输电杆塔风险评估中的实际应用价值。

结合实际故障情况分析，风险等级为 I 级的输电杆塔均为断杆及倒杆等严重故障情况，占总严重故障情况的 60.00%，其余 40.00%的严重故障情况则全部集中在风险等级为 II 级的输电杆塔中。此外，风险等级为 II 级与 III 级的剩余输电杆塔则对应为输电杆塔倾斜（输电杆塔与地面夹角大于 15 度且小于 75 度）。表明所提模型的预测结果一定程度上与实际故障情况相符。

5　结论

针对台风-滑坡灾害链下输电杆塔的风险评估，本文提出一种台风-滑坡灾害链下输电杆塔多荷载空间耦合故障模型，并以台风“泰利”进行验证。结果表明，在所提模型情况下，输电杆塔故障概率由仅考虑风荷载时的 3.62%升至 40.00%－98.00%，揭示了多荷载协同效应对结构失效的主导影响。此外，所提模型识别出 98.46%的输电杆塔属于高风险

等级，且所有实际发生倒塔或断杆的故障点均被准确覆盖，验证模型的有效性与实用性。

参考文献

[1] Wu Wenjie, Hou Hui, Zhu Shaohua, et al. An intelligent power grid emergency allocation technology considering secondary disaster and public opinion under typhoon disaster[J]. Applied Energy, 2024, 353: 122038.

[2] 姜涛, 唐少南, 李雪, 等. 应对台风影响的海岛微网群韧性全过程提升[J]. 中国电机工程学报, 2022, 42(18): 6625-6641.
Jiang Tao, Tang Shaonan, Li Xue, et al. Resilience boosting strategy for island microgrid clusters against typhoons[J]. Proceedings of the Chinese Society for Electrical Engineering, 2022, 42(18): 6625-6641.

[3] Hou Hui, Wu Wenjie, Zhang Zhiwei, et al. A tri-level typhoon-d ad robust optimization framework to enhance distribution networ k resilience[J]. Reliability Engineering & System Safety, 2024: 1 10004.

[4] 孔雅茜, 陈全明, 陈建华. 湖南资兴“格美”台风群发性地质灾害发育特征及风险管控[J]. 地质灾害与环境保护, 2025, 36(02): 50-55.
KONG Yaqian, CHEN Quanming, CHEN Jianhua. Development characteristics and risk control of grouped geological hazards caused by typhoon Gaemi in Zixing, Hunan Province[J]. Journal of Geological Hazards and Environment Preservation, 2025, 36(02): 50-55.

[5] LYU H M, YIN Z Y, HICHER P Y et al. Incorporating mitigation strategies in machine learning for landslide susceptibility prediction[J]. Geoscience Frontiers, 2024, 15(5): 101869.

[6] WEI Yingdong, QIU Haijun, LIU Zijing, et al. Refined and dynamic susceptibility assessment of landslides using InSAR and machine learning models [J]. Geoscience Frontiers, 2024, 15(6): 101890.

[7] YANG Shilong, TAN Jiayao, LUO Danyuan, et al. Sample size effects on landslide susceptibility models: A comparative study of heuristic, statistical, machine learning, deep learning and ensemble learning models with SHAP analysis[J]. Computers&Geosciences, 2024, 193: 105723.

[8] 丁明涛,江辉,李振洪,等.融合卷积模糊神经网络与 SHAP 特征优化的地震诱发滑坡易发性评价[J/OL].武汉大学学报(信息科学版),1-26[2025-07-04]. https: //doi. org/10.13203/j. whugis20250017.
DING Mingtao, JIANG Hui, LI Zhenhong, et al. Earthquake-induced landslide susceptibility assessment by fusing convolutional fuzzy neural network and SHAP feature optimization strategy. Wuhan University Journal (Information Science Edition), 1-26 [2025-07-04]. https: //doi. org/10.13203/j. whugis20250017.

[9] 何浩林, 汪大海, 黄增浩, 等. 输电直线杆风灾易损性的准静态分析方法[J]. 中国电机工程学报, 2024, 44(09): 3732-3742.
HE Haolin, WANG Dahai, HUANG Zenghao, et al. Wind hazard fragility aAnalysis of transmission free-standing towers using quasi-static method[J]. Proceedings of the Chinese Society for Electrical Engineering, 2024, 44(09): 3732-3742.

[10] 陈强, 王建, 熊小伏, 等. 一种降雨诱发滑坡灾害下输电杆塔的监测与预警方法[J]. 电力系统保护与控制, 2020, 48(03): 147-155.
CHEN Qiang, WANG Jian, XIONG Xiaofu, et al. Monitoring and early warning method for transmission tower under rainfall-induced landslide disaster[J]. Power System Protection and Control, 2020, 48(03): 147-155.

[11] 高富,侯慧,魏瑞增,等.台风灾害下基于非平衡样本数据的配电网杆塔受损预测[J/OL].电力系统自动化,1-12[2025-07-13]. http: //kns. cnki. net/kcms/detail/32.1180. TP.20241216.1503.003. html.
GAO Fu, HOU Hui, WEI Ruizeng, et al. Distribution network t ower damage prediction based on unbalanced sample data under typhoon disasters [J/OL]. Automation of Electric Power Systems, 1 - 12[2025-07-13]. http: //kns. cnki. net/kcms/detail/32.1180. T P.20241216.1503.003. html.

[12] 李宏仲, 倪张, 周玉龙. 台风灾害下架空线路故障风险分析(一)：架空线路故障概率精细化建模及验证[J/OL]. 中国电机工程学报, 1-18[2025-07-11]. http: //kns. cnki. net/kcms/detail/11.2107. tm.20240829.1201.006. html.
LI Hongzhong, NI Zhang, ZHOU Yulong. Risk analysis of overhead line failure under typhoon disaster(I): refined modeling and validation of overhead line failure probability[J/OL]. Proceedings of the Chinese Society for Electrical Engineering, 1 - 18 [2025-07-11]. http: //kns. cnki. net/kcms/detail/11.2107. tm.20240829.1201.006. html.

[13] 张治国, 毛敏东, 朱正国, 等. 间歇性强降雨诱发滑坡对抗滑桩非线性力学响应分析[J]. 岩土力学, 2023, 44(07): 2073-2094.
ZHANG Zhiguo, MAO Mindong, ZHU Zhengguo, et al. Analysis of nonlinear mechanical response of anti-slide pile induced by landslides with intermittent heavy rainfall[J]. Rock and Soil Mechanics, 2023, 44(07): 2073 - 2094.

[14] 侯慧, 徐海峰, 王少华, 等. 含降雨量修正的台风灾害下输电杆塔数据机理联合故障概率预测[J]. 高电压技术, 2025, 51(04): 1654-1662.
HOU Hui, XU Haifeng, WANG Shaohua, et al. Data mechanism joint failure probability prediction of overhead transmission line with rainfall cor-rection under typhoon disaster[J]. High Voltage Technology, 2025, 51(04): 1654-1662.

[15] HOU Hui, TANG Junyi, ZHANG Zhiwei , et al. Resilience enhancement of distribution network under typhoon disaster based on two-stage sto-chastic programming[J]. Applied Energy, 2023, 338: 120892.

收稿日期：2013-07-04。

作者简介：


侯慧

石远钊(2002)，男，研究生，研究方向为电网防灾减灾，E-mail：Shiyuanzhao@whut.edu.cn；

侯　慧(1981)，女，教授，博士生导师，研究方向为电力系统风险评估、能源互联网等，E-mail：husthou@126.com。

（编辑　五号楷体，居右，段前空 6pt）

098 Research on the Fault Diagnosis Architecture of Secondary Equipments in Intelligent Substation Driven by Holographic Transparency

ZHANG Xin[1,2], ZHENG Jingrong[1,2], ZHOU Hualiang[1,2], JIA Deshun[1,2], WANG Lei[1,2], HAN Wei[1,2], YUAN Luhai[1,2], LI Zhaoguo[1,2]

[1] NARI Group Co. (State Grid Electric Power Research Institute), Nanjing, China
[2] NARI Control System Co.,Ltd, Nanjing, China
375001243@qq.com

Abstract. With the rapid development of smart grid construction, the impact of the reliability of secondary equipments in substations on the stable operation of power systems has become increasingly prominent. Driven by holographic perspective technology, this paper introduces wide-area data models such as relay protection, measurement and control, automated communication, metering, and auxiliary control, and integrates deep holographic data models of multi-domain equipment to achieve comprehensive collection of multi-source heterogeneous data from secondary equipments in substations. It proposes a service-centered fault diagnosis architecture of secondary equipments in intelligent substation, which constructs a service platform integrating real-time monitoring and rapid diagnosis through a standardized interaction mechanism. This architecture significantly improves the efficiency of fault monitoring and management of secondary equipments, providing technical supports for the safe and stable operation of intelligent substations.

Keywords: Holographic Transparency, Service-oriented Architecture, Fault Diagnosis

1 Introduction

As an indispensable and critical component of the power system, the secondary equipments of substations undertakes core businesses such as monitoring, control, protection, and automation, and plays a crucial role in ensuring the stability of substation operation[1-2]. With the deep integration of new energy technology and digital transformation, the smart grid is gradually moving towards a new stage of development that is more digital, networked, intelligent, and low-carbon. In this context, the secondary equipments of substations, as one of the core nodes of smart grids, is facing unprecedented challenges [3-4]. These challenges are not only reflected in the transition from traditional single relay protection to a multi-objective collaborative mode that integrates protection, control, monitoring, and decision-making at the functional level; This is also reflected in the gradual transition from a closed dedicated system to a new framework system that supports open sharing and

multi-party collaboration in architecture design; At the same time, the increasing demand for reliability has prompted related technologies to rapidly develop from traditional management models that rely on manual intervention to centralized management, standardized operating procedures, and highly intelligent directions.

As the core of the power system, the secondary equipments of intelligent substation mainly consist of protection devices, measurement and control devices, network communication equipments, auxiliary systems, metering devices, and monitoring systems[5-6]. These devices jointly ensure the stable operation of the power system through key functions such as real-time data collection, information processing, and control instruction interaction[7]. With the evolution of intelligent substation technology, the complexity and diversity of secondary equipments make its status monitoring and fault diagnosis particularly complex. Therefore, building holographic perspective models and intelligent substation secondary equipments fault diagnosis architectures has become a key breakthrough in improving equipment reliability.

2 Holographic Transparency technology

The secondary equipments in intelligent substation are key part of ensuring the safe, stable, and reliable operation of the power system. They are mainly responsible for monitoring, measuring, protecting, controlling, and regulating primary equipments (transformers, circuit breakers, busbars, lines, etc.)[8,15]. Holographic transparency technology starts from the source, starting from the breadth and depth of secondary equipment detection data, to solve the bottleneck that traditional monitoring methods cannot reach, and to achieve visibility and controllability of the internal state of the equipments from the bottom.

2.1 Broad and Multi Domain Data

Broad and multi domain data refers to the comprehensive and rich scope of data collection from the perspective of intelligent substation data acquisition, involving all secondary equipments of the substation. According to its main functions, it includes all data collected by the following devices or systems:

Protective devices are used to ensure safety and quickly cut off faults, involving line, transformer, busbar, circuit breaker, capacitor/reactor protection devices, automatic backup power supply switching devices, automatic reclosing devices, fault recording devices, safety and stability control devices, etc. They are responsible for quickly, accurately, and selectively isolating faulty equipments or areas in the event of power system faults (such as short circuits, grounding) or abnormal operating conditions (such as overload, frequency/voltage exceeding limits).

Measurement and control devices are used for real-time monitoring and control, and are the foundation of automation. They involve interval layer measurement and control devices, public measurement and control devices, and are responsible for real-

time monitoring, measurement, control (remote control), and signal acquisition of equipment operation status and electrical quantities.

The monitoring system is the human-machine interface and information processing center for operation and management. The station control layer equipments mainly involves monitoring hosts, comprehensive application hosts, data communication gateway, and protection information. It is responsible for data collection and processing, operation monitoring, operation control, alarm management, event recording, report generation, human-machine interaction, etc. of the secondary equipments in the intelligent substations[9].

The metering system can accurately measure and settle electrical energy, involving energy meters, metering terminals/collectors, voltage/current transformers for metering, and secondary circuits, responsible for high-precision measurement and recording of electrical energy.

Communication equipments are used to build reliable information transmission channels, involving internal communication equipments such as switches, routers, gateways, etc; remote channel equipments modems, protocol converters, etc; communication management machine/protocol converter; fiber optic/microwave/SDH/PDH transmission equipments; Vertical encryption authentication devices, used to achieve information transmission channels within the substation and between the substations and the dispatch centers, central control centers, and adjacent substations[10-11].

The auxiliary system provides support for the stable operation of the entire secondary system (power, time, environment, etc.), including AC/DC power supply system, power quality monitoring devices, time synchronization, environmental monitoring system, intelligent auxiliary equipments, responsible for the collection and monitoring of power, time, and environmental informations[12].

2.2 Depth and Multi Level Data

Depth and multi level data refers to the depth and complexity of data acquisition from the perspective of intelligent substation data collection. The "holographic" core is reflected in the dual breakthrough of monitoring depth and information dimension, achieving "layer by layer penetration" from the macroscopic appearance of equipment to the microscopic mechanism of chips. According to its data content, it is divided into the following levels:

At the equipment level, it covers all secondary equipments of the substation (such as protection devices, measurement and control devices), including total device fault alarms, functional failure alarms, communication interruption alarms, operating status, communication status, self check results, and core process on/off status, to monitor the overall operating status of the devices.

At the board level, it covers the internal functional boards of secondary equipments (such as CPU board, power board, communication board, I/O board, etc.), board fault alarm, communication interruption alarm, power/temperature abnormal alarm information, board voltage/current, temperature, processor load, communication bit error rate information, used to accurately locate the position of the internal board of the device where the fault occurs and evaluate the health status and performance of the board in real time.

At the chip level, it involves the core chips of secondary devices such as CPU, memory ADC, communication chips, etc.), chip temperature/voltage over limit alarm, clock failure alarm, functional unit fault alarm information, core working voltage/current, junction temperature, clock status, key register values/counters, ADC sampling quality, load rate estimation information, used to directly capture internal abnormalities and monitor the micro operation status of the chips, achieving low-level warning and fault prediction.

2.3 Holographic Data Model

The intelligent substation whole station information model (SCD) includes data communication gateway, monitoring hosts, main and auxiliary integrated hosts, comprehensive application hosts, protection information hosts, measurement and control devices, protection devices, auxiliary equipments, communication equipments, etc(see Fig. 1).

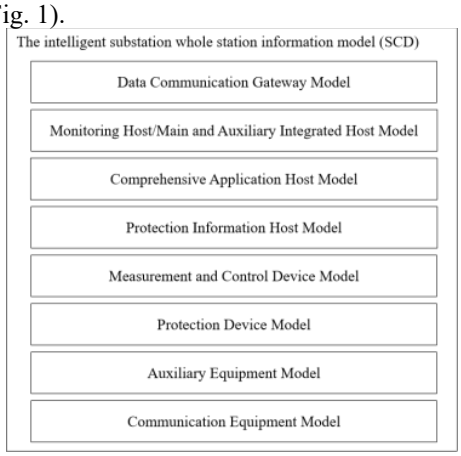


Fig. 1. The intelligent substation whole station information model

The intelligent substation whole station information model (SCD) is the core configuration file of the IEC 61850 standard, which realizes the unified modeling and interconnection of all station equipments. The data communication gateway is responsible for the information exchange between the substations and the dispatch centers, and the monitoring hosts and comprehensive application hosts realize the monitoring and advanced analysis functions of the operating status. The main and auxiliary integrated hosts integrate the management of main equipments and auxiliary

equipments. The protection devices and measurement and control devices complete protection control and data acquisition through standardized logic nodes. The protection information hosts centrally processes relay protection and fault information, and the communication equipments ensures reliable transmission of each layer of the network. SCD files define the communication relationship and data flow between devices by instantiating ICD and SSD, supporting the collaborative operation of the "three-layer two network" architecture of intelligent substations, and laying the foundation for power grid automation and digitization[13-14].

On the basis of the whole station information model SCD, in order to achieve refined data monitoring, a more complete holographic data model is designed based on the communication architecture of intelligent substations (such as IEC 61850). The logical nodes (LN) representing device level, board level, and chip level monitoring functions are uniformly deployed under a dedicated logical device (LD) (often named LD0). All alarm and status data generated by monitoring are classified and organized through standardized datasets. The system utilizes an efficient reporting service mechanism to reliably upload the data from these datasets to the substation monitoring backend system or remote control center for analysis, display, and decision-making by operation and maintenance personnel.

Taking data communication gateway as an example(see Table I), based on the IEC 61850 standard and the security protection requirements of power monitoring systems, a holographic data model of gateway is constructed, and real-time monitoring is proposed for key parameters such as CPU, memory, storage, temperature, and core process management.

Table 1. Examples of Holographic Transparency Data Model Definition Section.

Category	Description	Prefix	LN	DO	CDC	Identification Information
Alarm	104 protocol channel's heartbeat timeout count (>=3 times within 5 minutes)	Alm	GGIO	Alm*	SPS	ReduCHInc
Alarm	CMS service process CPU usage exceeds 70%	Alm	GGIO	Alm*	SPS	ReduSVRInc
Alarm	CMS client process CPU usage exceeds 70%	Alm	GGIO	Alm*	SPS	ReduClientInc
Alarm	CMS service process memory continues to grow by more than 1GB	Alm	GGIO	Alm*	SPS	ReduSPMInc
Alarm	CMS client process memory continues to grow by more than 1GB	Alm	GGIO	Alm*	SPS	ReduCPMInc
Alarm	CPU temperature exceeds 85 ℃ and runs for more than 2 minutes	Alm	GGIO	Alm*	SPS	ReduCCTInc
Alarm	The available memory of the whole machine is less than 20%	Alm	GGIO	Alm*	SPS	ReduTAMInc

6

3 Diagnosis Architecture for Secondary Equipments in Intelligent Substation

Based on the holographic Transparency technology of secondary equipments in intelligent substations, the full data collection of secondary equipments in power plants and stations is realized. A service-oriented fault diagnosis platform of secondary equipments is designed to create a high cohesion and low coupling fault diagnosis platform. Through standard interfaces and interaction methods, real-time monitoring and rapid fault diagnosis of secondary equipments in substations are achieved. The platform architecture is as follows(see Fig. 2):

The data collection layer covers all secondary equipments in intelligent substation, including measurement and control devices, protection devices, communication equipment, monitoring system devices, metering system devices, auxiliary devices, collecting all monitoring data, as well as equipment, board, and chip level related data.

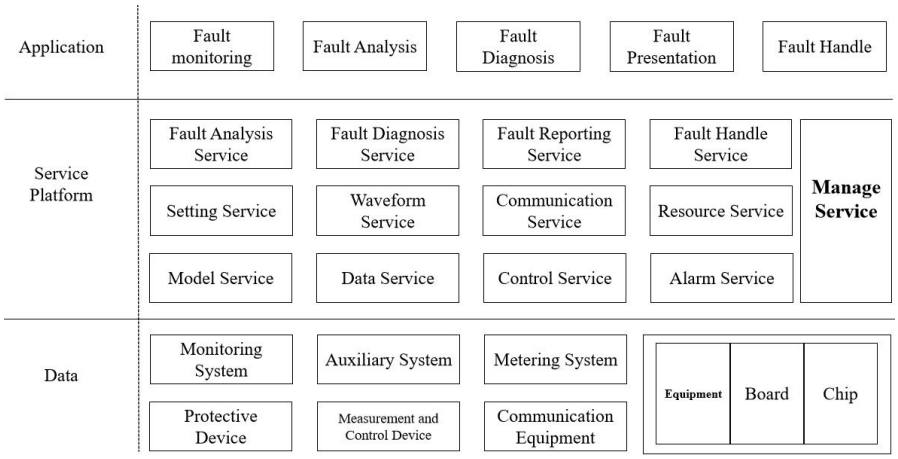


Fig. 2. Platform Architecture

The service platform provides modeling, data, control, alarm, setting, waveform, communication, synchronization, fault analysis, fault diagnosis, fault reporting, fault handling, and management services based on the unified modeling, data collection, and management of the entire site information. It adopts a unified service access interface to achieve flexible expansion of various applications, and various salesperson applications are based on the platform to achieve specific monitoring, analysis, diagnosis, and other functions.

The fault diagnosis system of secondary equipments in intelligent substation collects all monitoring information at the station end based on the service platform, integrates the basic functions of monitoring, metering, and auxiliary systems, and supports remote on-demand and flexible access to the platform in a service mode. It uses

standard and open application interfaces for collaborative interaction to achieve real-time monitoring and rapid fault diagnosis of substation secondary equipments' faults, as well as full lifecycle management of faults. It supports rapid integration for multiple business application scenarios, is flexible, efficient, safe, and reliable.

4 Application interaction for fault diagnosis of secondary equipments in intelligent substation

4.1 Application Interaction

Various services for fault diagnosis of secondary equipments in intelligent substations are implemented through application gateways as a unified service interface to facilitate application interaction between local or remote main stations of the secondary fault diagnosis platform services in the substation(see Fig. 3).

The application gateway achieves collaborative interaction between services and applications through unified interfaces, with functions such as security authentication, service registration, service monitoring, service querying, service aggregation/orchestration, etc. It is implemented through two modes of request/response and subscription/publishing between applications and services, as well as load balancing.

Load balancing optimizes the access mechanism between applications and services through application gateways to achieve efficient utilization of traffic and resources, thereby ensuring the availability of services.

Security authentication, the tokens based authorization framework that combines digital certificates and dynamic tokens to achieve identity verification between applications and services.

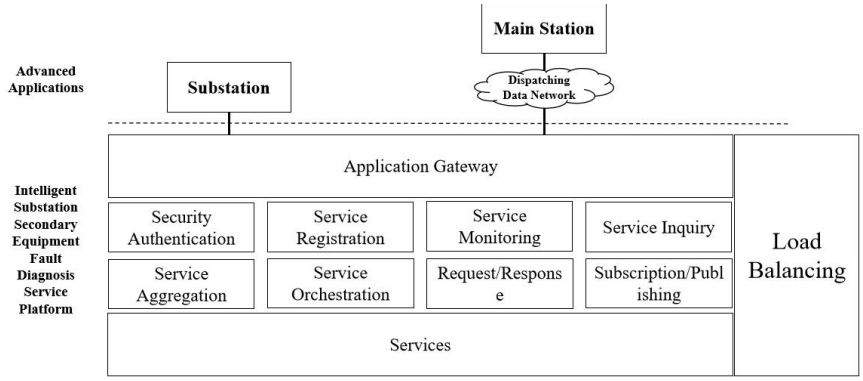


Fig. 3. Application Interaction Architecture

Service registration is carried out in the mode of service ID+version number+digital signature, and the functions and interface information are described in a standardized manner through a universal interface. At the same time, service status tags are provided, including security authentication, registration, in or offline.

Service monitoring, monitoring the availability of services through heartbeat mode, monitoring service performance through throughput of interactions under stable call conditions, and monitoring service reliability through abnormal retrieval statistics within a certain period of time.

Service inquiry, real-time query of services' status through service registration informations.

Service aggregation integrates multiple independent services through application gateway to achieve horizontal integration of service interaction capabilities.

Service orchestration achieves vertical control of complex business flows by defining the execution sequence and logical conditions for service retrieval through application gateway.

Service invocation mainly adopts two modes: request/response and subscription/publishing. Request/response is a synchronous mode for data retrieval, while subscription/publishing is used to achieve real-time data push to meet the communication needs of different business scenarios.

4.2 Application

The prediction of resource bottlenecks for secondary equipments in intelligent substations mainly involves resource services, data services, model services, and alarm services. The content involved includes the temperature, memory, CPU occupancy, storage, and core process operation of the secondary equipment. It is scheduled to poll twice a day and predict resource bottlenecks based on load conditions.

Timed self check/remote resource status polling process(see Fig. 4):

*1) **Whole machine resource collection***

Through the application gateway, CPU utilization, core temperature, and memory usage are queried regularly in request/response mode.

2) Process level monitoring

Real time reception of CPU/memory usage ratio, CPU top 5 processes, and memory leak top 3 processes of core processes (such as protection devices and communication services) in subscription/publishing mode through the application gateway.

3) Resource load determination mechanism

CPU overload: The average CPU utilization rate exceeds 80% of the threshold within 5 minutes, and there are high load processes with a CPU utilization rate exceeding 70% for 10 minutes.

Memory leak: Process memory continues to grow without any release trend, with the overall memory proportion exceeding the threshold of 85%. Core process memory has grown by over 30% within one hour.

Abnormal temperature: If the core temperature of the device exceeds 75 ℃, it may be accompanied by fan failure or environmental temperature exceeding the standard.

4) Fault diagnosis and prediction

If CPU overload, terminate abnormal processes or optimize process handling mechanisms.

If memory leak, Restart the service and check the process code memory management.

If has an abnormal temperature: Clean the heat dissipation holes or replace the fan.

If the problem persists for a long time, the hardware configuration needs to be upgraded.

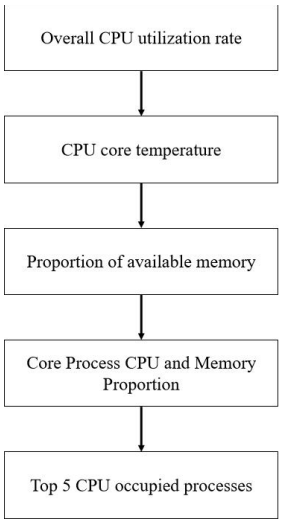


Fig. 4. Interactive Process for Predicting Resource Bottlenecks

5 Summary and Prospect

The holographic transparency technology for secondary equipments in intelligent substations covers all secondary equipments in the substation from the scope of data acquisition, and constructs a more comprehensive multi-source fusion data of faults; From the depth of data collection, delve into the device, board, and chip levels to address the current shortcomings in monitoring the operation of secondary equipment; Designed an intelligent substation secondary equipment fault diagnosis architecture, providing a reliable business platform for rapid diagnosis and timely processing of fault information in a service-oriented mode. Through standardized service interaction mechanisms, real-time monitoring and rapid fault diagnosis of substation secondary equipment faults are achieved, helping to ensure the safe and stable operation of intelligent substations.

In the future, we will continuously improve the standardization of holographic perspective models and application and service platforms, adapt to new technological developments, integrate AI algorithms, and achieve reliable prediction, timely processing, and comprehensive control of secondary equipments' failures in intelligent substations.

References

1. Ji Rongrong, Zhang Ganfeng, Wang Mengzhi, Jin Yingjie, Li Hai, Huang Ruofan. Data-driven Efficient Verification Technique for Smart Substations Messages[J]. Electric Power, 2025, 58(01):100-106.
2. Wang Jian, Teng Jingyu, Ou Qian, et al. Research on Automatic Verification Technology for the Transformation of Supervision Control System in Intelligent Substation[J]. Electrical Technology, 2025(2):198-200, 203.
3. Li Mingjie, Liu Yu, Shu Zhihuai, et al. Analysis on the Development Trend of Secondary System Technology in China's Substations[J]. Power System Technology, 2024, 48(1):1-11.
4. Dou Renhui, Ren Hui, Yao Zhiqiang, et al Design of service protocol of substation localization station control layer [j] Power grid technology, 2021, 45 (8):3268-3275.
5. Hu Yuying, Zhang Jichi. An Advanced, open and standard substation monitoring system. Northeast Electric Power Technology, 2021, 42(9):18-21.
6. Yang Gui, LV hang, Peng An, et al Research on network flow analysis and network optimization of intelligent substation process layer [j] Computing technology and automation, 2021, 40 (2):176-183.
7. Xu Hongqiang, Yao Jianguo, Yu Yijun, Tang Biqiang. Architecture and Key 'Technologies of Dispatch and Control System Supporting Integrated Bulk Power Grids[J]. Automation of Electric Power Systems, 2018, 42(6):1-8.
8. Technical specifications for intelligent substation monitoring system:DL/T 1403-2015[S], 2015.
9. Ni Yi-min, Yang Yu, Fan Chen, et al. The Discussion about the integration of secondary devices in smart substation[J]. Automation of Electric Power Systems, 2014, 38(3):194-198.

10. Xin Yaozhong, Shi Junjie, Zhou Jingyang, et al. Technologydevelopment trends of smart grid dispatching and controlsystems[J]. Automation of Electric Power Systems, 2015, 39(1):2-8.
11. Liu Tao, Mi Weimin, Chen Zhengping, et al. Integrated sharing scheme for grid model and graphics applicable to grandoperation system[J]. Automation of Electric Power Systems, 2015, 39(1):36-41.
12. Shan Xin, Dai Zemei, Zhang Zhe, et al. Research on andapplication of integrated smart alarm based on smart griddispatching and control systems[J]. Automation of ElectricPower, 2015, 39(1):65-72.
13. Zhong Ming, Tao Jun, Liu Xunyu, et al. Smart substation opticalfiber virtual and real loop mapping and fault diagnosis technology[J]. Electric Power, 2023, 56(10):171-178.
14. Cheng Lin, Ma Xiaoteng, Ren Shuangzan, et al. Research on keytechnologies and applications of multi-physics digital modeling ofsmart substations[J]. Shandong Electric Power, 2023, 50(12):11-19.
15. Yang Chao, Fu Xiaoyan. Research on the full error prevention statemonitoring technology of relay protection equipment in intelligentsubstations[J]. Power System and Clean Energy, 2023, 39(7):73-79.

099 变流器主导的电力系统宽频振荡模型及能量转换过程分析

张心怡[1]，马宁宁[2]，杨旭东[1]，王德林[1]

（1. 西南交通大学 电气工程学院，四川 成都 611756；2. 新型电力系统运行与控制全国重点实验室（清华大学电机系），北京 100084）

WIDEBAND OSCILLATION MODEL AND ENERGY CONVERSION PROCESS ANALYSIS IN CONVERTER-DOMINATED POWER SYSTEMS

ZHANG Xinyi[1]，MA Ningning[2]，YANG Xudong[1]，WANG Delin[1]

(1. School of Electrical Engineering, Southwest Jiaotong University, Chengdu 61175；2. State Key Laboratory of Power System Operation and Control, Department of Electrical Engineering, (Department of Electrical Engineering Tsinghua University), Beijing 10084, China)

ABSTRACT: The problem of power system broadband oscillation has been frequently encountered in the context of high proportion of inverter-based resources (IBR) access. A dynamic model based on Hamiltonian energy is proposed in this paper, which can more effectively analyze stability issues. Due to the different dynamic characteristics of IBR compared to traditional synchronous generators, traditional oscillation analysis methods are no longer applicable. However, the energy model can accurately depict the oscillation behavior of the system over a wider frequency range. Through simulation verification on a typical system model, this model demonstrates good accuracy and practical application value, and can effectively reproduce the oscillation scenarios in reality. The study shows that the Hamiltonian energy decreases after the system oscillates, but the modal energy storage energy not only comes from the conversion process of the fundamental frequency Hamiltonian energy, but also involves the combined effect of the dissipation mechanism and the energy interaction between various components. These research results provide a theoretical basis for mechanism analysis.

KEY WORDS: IBR; wideband oscillations; Hamilton energy function

摘要：高比例逆变器型资源（IBR）接入背景下的电力系统宽带振荡问题层出不穷，本文提出了一种基于哈密顿能量的动态模型，可以更有效地分析稳定性问题。由于 IBR 具有与传统同步机组不同的动态特性，传统振荡分析方法已难以适用，而能量模型能够在更宽的频率范围内准确刻画系统的振荡行为。通过在典型系统模型上的仿真验证，该模型展现出良好的准确性与实际应用价值，能够有效复现现实中的振荡场景。研究表明，系统振荡后哈密顿能量有所降低但模态储能能量不仅来源于基频哈密顿能量的转换过程，还涉及耗散机制与各元件间能量交互的综合效应，上述研究成果为机理分析提供了理论依据。

关键词：变流器；宽频振荡；哈密顿能量函数

0 引言

为缓解电力需求持续增长带来的环境压力，风电、光伏等新能源发电渗透率稳步提升[1]。同时，IBR 在现代电力系统中得到了广泛的应用。随着同步发电机在新能源电力系统中的比重不断下降，电网的强度也呈现出减弱的趋势。高水平的 IBR 集成可能对电网的频率稳定性产生不利影响。近年来，由 IBR 引起的电力系统宽带振荡事件频繁发生，对系统的安全稳定运行构成重大威胁。

为了分析这类稳定性问题，特征值分析方法和阻抗分析方法是宽频振荡研究中最广泛采用的两种方法。文献[2-3]采用特征值分析法分析了主导振荡模态的阻尼比、主要参与变量等，并揭示了锁相环参数和并网阻抗变化对系统小干扰稳定性的影响规律；文献[4]建立了跟网型换流器的 dq 坐标系阻抗模型，对其并网运行时的稳定性问题进行了分析。然而此类方法主要是基于线性化的系统模型，因此在准确捕获和量化非线性因素的能力方面受到限制，例如限幅和直流电压控制约束，这些因素

基金项目：国家自然科学基金项目(52207117)。

This work is supported by National Natural Science Foundation of China (52207117).

通常存在于关键的转换器组件中。

为了克服传统方法的局限性，能量法考察了系统中能量的产生、耗散和传递，对系统不稳定的机理有了更深入的了解。本文构建了适用于 IBR 并网系统的哈密顿能量模型，实现了变流器并网系统稳定性的结构化表征，并通过典型仿真验证了其有效性。分析表明，振荡后储能直流分量减小，模态储能显著增大。该能量函数可以直接评价系统的暂态稳定性，为后续振荡机理分析提供理论依据。

1 变流器主导的宽频振荡数学模型

1.1 IBR 并网系统结构

典型 IBR 并网系统的电气和控制结构如图 1 所示。电气结构中，i_m 为源侧输出的直流电流；u_{dc} 为直流侧电压，C_{dc} 为直流侧电容；u 为逆变器出口电压；i 为逆变器并网电流，指定流入逆变器的电流方向为正方向；逆变器侧 L_f 为滤波电感，R_f 为滤波电阻，C_f 为滤波电容；u_o 为逆变器并网点电压；L_g 为网侧电感，R_g 为网侧电阻，i_o 为流经网侧阻抗的电流；u_g 为电网电压。

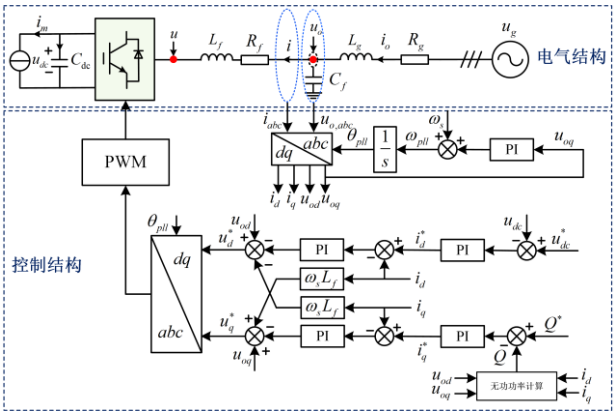


图 1 IBR 并网结构

Fig. 1 IBR grid connection structure

控制结构中，直流电压外环控制的 u_{dc}^*为直流侧参考电压；无功功率外环控制的 Q^*为无功功率参考值；PLL 控制环节中的 ω_s 为基准角速度，ω_{Pll} 为锁相环 PLL 控制得到的角速度；电流内环 dq 轴控制环节的 i_d^*、i_q^*为外环控制得到的 dq 轴电流参考值，i_d、i_q 分别为 PLL 坐标系下得到的 dq 轴电流值；u_d^*、u_q^*分别为经电流环 PI 控制器调节后输出的调制电压响应值，u_{od}、u_{oq} 分别为 PLL 坐标系下的 dq 轴并网电压值。

1.2 数学模型

基于图 1 所示的拓扑图，将 IBR 并网系统被划分为 9 个子系统，分别建立其数学模型。

忽略逆变器开关引起的有功功率损耗，直流电容的功率方程可表示为

$$C_{dc}u_{dc}\dot{u}_{dc}=u_di_d+u_qi_q-u_{dc}i_m \tag{1}$$

式中，$u_d=m_du_{dc}$，$u_q=m_qu_{dc}$，m_d 和 m_q 是调制系数的 dq 轴分量。

滤波器电感和电阻的数学表达式为

$$\begin{cases}L_f\dot{i}_d=u_{od}-u_d-R_fi_d-\omega_sL_fi_q\\L_f\dot{i}_q=u_{oq}-u_q-R_fi_q+\omega_sL_fi_d\end{cases} \tag{2}$$

滤波电容的数学表达式可以描述为

$$\begin{cases}C_f\dot{u}_{od}=i_{od}-i_d-\omega_sC_fu_{oq}\\C_f\dot{u}_{oq}=i_{oq}-i_q-\omega_sC_fu_{od}\end{cases} \tag{3}$$

网侧阻抗的数学表达式可表示为

$$\begin{cases}L_g\dot{i}_{od}=u_{gd}-u_{od}-R_gi_{od}-\omega_sL_gi_{oq}\\L_g\dot{i}_{oq}=u_{gq}-u_{oq}-R_gi_{oq}+\omega_sL_gi_{od}\end{cases} \tag{4}$$

PLL 是保持并网 VSC 与电网同步的核心控制环节，其通过实时跟踪并网点电压的相位 u_o 实现并网 VSC 与电网的同步。将三相并网点电压 u_{oa}、u_{ob}、u_{oc} 通过 PLL 输出的同步相位信号 θ_{pll} 变换到 dq 坐标系下得到直流量 u_{od}、u_{oq} 组成一个相位误差反馈控制。通过控制 u_{oq} 恒定为 0，就可以使得 PLL 输出的同步相位信号 θ_{pll} 与并网点电压相位 θ_s 一致。该环节采取并网点电压定向的控制方式，即 $u_o=u_{od}$。当系统受到扰动时，PLL 动态响应特性会导致基于 PLL 输出相角的同步 dq 旋转坐标系与基于并网点电压相位的基准旋转坐标系之间产生相角偏差如图 2 所示。上角标“p”表示 PLL 同步旋转坐标系下的变量值。

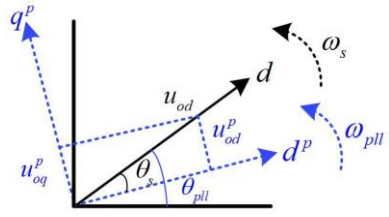


图 2 dq 旋转坐标系

Fig. 2 dq rotating coordinate system

由图 2 可知，系统发生扰动时 θ_s 和 θ_{pll} 间的夹角比较小，$\sin(\theta_s-\theta_{pll})=\sin\Delta\theta\approx\Delta\theta$，得其数学模型为

$$\begin{cases}\dot{x}_{pll}=u_{od}\Delta\theta\\\Delta\dot{\theta}=-K_{p,pll}u_{od}\Delta\theta-K_{i,pll}x_{pll}\end{cases} \tag{5}$$

式中，$K_{p,pll}$ 和 $K_{i,pll}$ 分别表示比例系数和积分系数，x_{pll} 为中间状态变量。

直流电压和无功功率外环控制的数学方程为

$$\begin{cases}\dot{x}_{dc}=u_{dc}^*-u_{dc}\\i_d^*=K_{p,dc}(u_{dc}^*-u_{dc})+K_{i,dc}x_{dc}\end{cases} \tag{6}$$

$$\begin{cases}\dot{x}_Q=Q^*-Q\\i_q^*=K_{p,Q}(Q^*-Q)+K_{i,Q}x_Q\end{cases} \tag{7}$$

式中，$K_{p,dc}$、$K_{i,dc}$ 分别表示直流电压外环控制回路

的比例系数和积分系数，x_{dc}为中间状态变量；$K_{p,Q}$、$K_{i,Q}$表示无功外环控制回路的比例系数和积分系数，x_Q为中间状态变量。

d 轴和 q 轴电流内环控制的数学表达式为

$$\begin{cases}\dot{x}_d = i_d^* - i_d \\ u_d^* = -K_{p,d}(i_d^* - i_d) - K_{i,d}x_d + u_{od} - \omega_s L_f i_q\end{cases} \tag{8}$$

$$\begin{cases}\dot{x}_q = i_q^* - i_q \\ u_q^* = -K_{p,q}(i_q^* - i_q) - K_{i,q}x_q + u_{oq} + \omega_s L_f i_d\end{cases} \tag{9}$$

式中，$K_{p,d}$、$K_{p,q}$、$K_{i,d}$和$K_{i,q}$分别表示 dq 电流控制环节的比例和积分系数；x_d、x_q是 dq 轴电流内环控制环节的中间状态变量。

2 宽频振荡能量转换过程分析

2.1 哈密顿能量模型与平衡方程

根据前文建立的 IBR 并网系统数学方程，取能量变量为

$$\boldsymbol{x} = \begin{bmatrix} x_{pll},\ \Delta\theta,\ x_{dc},\ \Delta u_{dc},\ x_Q,\ \Delta Q,\ x_d,\ \Delta i_d, \\ x_q,\ \Delta i_q,\ u_{dc},\ i_d,\ i_q,\ u_{od},\ u_{oq},\ i_{od},\ i_{oq} \end{bmatrix}^{\mathrm{T}} \tag{10}$$

式中，$\Delta u_{dc}=u_{dc}^*-u_{dc}$，$\Delta Q=Q^*-Q$，$\Delta i_d=i_d^*-i_d$，$\Delta i_q=i_q^*-i_q$。

IBR 并网系统的哈密顿能量函数为

$$H(\boldsymbol{x}) = \frac{1}{2}\boldsymbol{x}^T\boldsymbol{D}^{-1}\boldsymbol{x} \tag{11}$$

式中，$\boldsymbol{D}^{-1} = \mathrm{diag}\begin{Bmatrix} K_{i,pll},\ u_{od0},\ K_{i,dc},\ 1,\ K_{i,Q},\ 1,\ K_{i,d}, \\ 1,\ K_{i,q},\ 1,\ C_{dc},\ L_f,\ L_f,\ C_f,\ C_f \end{Bmatrix}$。

哈密顿能量梯度为

$$\nabla H = \begin{bmatrix} K_{i,pll}x_{pll},\ u_{od}\Delta\theta,\ K_{i,dc}x_{dc},\ \Delta x_{dc},\ K_{i,Q}x_Q, \\ \Delta Q,\ K_{i,d}x_d,\ \Delta i_d,\ K_{i,q}x_q,\ \Delta i_q,\ C_{dc}u_{dc}, \\ L_f i_d, L_f i_q,\ C_f u_{od},\ C_f u_{oq},\ L_g i_{od},\ L_g i_{oq} \end{bmatrix}^{\mathrm{T}} \tag{12}$$

将式(1)~(9)改写为广义哈密顿形式为

$$\begin{cases}\dot{\boldsymbol{x}} = (\boldsymbol{J}-\boldsymbol{R})\nabla H(\boldsymbol{x}) + \boldsymbol{G}\boldsymbol{u} \\ \boldsymbol{y} = \boldsymbol{G}^{\mathrm{T}}\nabla H(\boldsymbol{x})\end{cases} \tag{13}$$

式中，$\boldsymbol{x}$为系统能量变量；$\boldsymbol{u}$为系统端口输入变量；$\boldsymbol{y}$为系统端口输出变量；$\boldsymbol{J}$称为系统内联结构矩阵，反映系统能量交换特性，为反对称矩阵，即$\boldsymbol{J}=-\boldsymbol{J}^{\mathrm{T}}$；$\boldsymbol{R}$为阻尼矩阵，反映了系统的耗散特性，为对称半正定矩阵，即$\boldsymbol{R}=\boldsymbol{R}^{\mathrm{T}}\geq\boldsymbol{0}$；$H$表示系统总的存储能量，即系统的能量函数，$\nabla H$为哈密顿能量梯度；$\boldsymbol{G}$为系统端口结构矩阵。

式(13)中的内联结构矩阵$\boldsymbol{J}$为

$$\boldsymbol{J} = \begin{bmatrix} \boldsymbol{J}_{\mathrm{A}} & \boldsymbol{J}_{\mathrm{B}} \\ -\boldsymbol{J}_{\mathrm{B}}^{\mathrm{T}} & \boldsymbol{J}_{\mathrm{C}} \end{bmatrix}_{17\times17} \tag{14}$$

式中，$\boldsymbol{J}_{\mathrm{A}}=\boldsymbol{I}_{10\times10}\boldsymbol{J}_1$，$\boldsymbol{I}$是单位矩阵，$\boldsymbol{J}_1=[0,\ 1;\ -1,\ 0]$；$\boldsymbol{J}_{\mathrm{B}}=[\boldsymbol{0}_{10\times1},\ \boldsymbol{J}_2,\ \boldsymbol{0}_{10\times2}]$，$\boldsymbol{J}_2=[\boldsymbol{0}_{4\times7},\ \boldsymbol{J}_3]^{\mathrm{T}}$，$\boldsymbol{J}_3=[\boldsymbol{J}_4,\ \boldsymbol{0}_{4\times1},\ \boldsymbol{J}_5]$，$\boldsymbol{J}_4=[0,\ -\omega_s,\ 1/C_f,\ 0]^{\mathrm{T}}$，$\boldsymbol{J}_5=[\omega_s,\ 0,\ 0,\ 1/C_f]^{\mathrm{T}}$；$\boldsymbol{J}_6=[-\omega_s/L_f,\ 1/(C_fL_f)]^{\mathrm{T}}$，$\boldsymbol{J}_7=[1/(C_fL_f),\ -\omega_s/C_f]^{\mathrm{T}}$，$\boldsymbol{J}_8=\boldsymbol{J}_9=1/(C_fL_g)$。

阻尼矩阵为

$$\boldsymbol{R} = \mathrm{diag}\begin{Bmatrix} 0,\ K_{p,pll},\ 0,\ K_{p,dc},\ 0,\ K_{p,Q},\ 0, \\ K_{p,d},\ 0,\ K_{p,q},0,\ R_f/L_f^2,\ R_f/L_f^2, \\ 0,\ 0,\ R_g/L_g^2,\ R_g/L_g^2 \end{Bmatrix} \tag{15}$$

端口结构矩阵为

$$\boldsymbol{G} = \begin{bmatrix} \boldsymbol{G}_{\mathrm{A}} & \boldsymbol{0}_{10\times3} \\ \boldsymbol{0}_{7\times4} & \boldsymbol{G}_{\mathrm{B}} \end{bmatrix}_{17\times7} \tag{16}$$

式中，$\boldsymbol{G}_{\mathrm{A}}=\mathrm{diag}\{\boldsymbol{G}_1,\ \boldsymbol{G}_2\}$，$\boldsymbol{G}_1=[\boldsymbol{0}_{4\times3},\ \boldsymbol{G}_2,\ \boldsymbol{0}_{4\times1},\ \boldsymbol{G}_3,\ \boldsymbol{0}_{4\times1},\ \boldsymbol{G}_4,\ \boldsymbol{0}_{4\times1},\ \boldsymbol{G}_5]^{\mathrm{T}}$，$\boldsymbol{G}_2=[1,\ 0,\ 0,\ 0]^{\mathrm{T}}$，$\boldsymbol{G}_3=[0,\ 1,\ 0,\ 0]^{\mathrm{T}}$，$\boldsymbol{G}_4=[0,\ 0,\ 1,\ 0]^{\mathrm{T}}$，$\boldsymbol{G}_5=[0,\ 0,\ 0,\ 1]^{\mathrm{T}}$；$\boldsymbol{G}_{\mathrm{B}}=[\boldsymbol{G}_6,\ \boldsymbol{0}_{3\times4},\ \boldsymbol{G}_7]^{\mathrm{T}}$，$\boldsymbol{G}_6=[-1/C_{dc},\ 0,\ 0]^{\mathrm{T}}$，$\boldsymbol{G}_7=[0,\ 1/L_{\mathrm{g}},\ 0;\ 0,\ 0,\ 1/L_{\mathrm{g}}]^{\mathrm{T}}$。

输入变量矩阵为

$$\boldsymbol{u} = [d_{dc},\ d_Q,\ d_{id},\ d_{iq},\ i_m,\ u_{gd},\ u_{gq}]^{\mathrm{T}} \tag{17}$$

式中，d_{dc}、d_Q、d_{id}和d_{iq}分别表示构造广义哈密顿结构所引入的虚拟项。

输出变量矩阵为

$$\boldsymbol{y} = [\Delta u_{dc},\ \Delta Q,\ \Delta i_d,\ \Delta i_q,\ u_{dc},\ i_{od},\ i_{oq}]^{\mathrm{T}} \tag{18}$$

哈密顿能量导数为

$$\dot{H}(t) = [\nabla H(\boldsymbol{x})]^{\mathrm{T}}\dot{\boldsymbol{x}} \tag{19}$$

将式(13)代入式(19)得

$$\dot{H}(t) = -(\nabla H)^{\mathrm{T}}\boldsymbol{R}(\nabla H) + \boldsymbol{u}^{\mathrm{T}}\boldsymbol{y} \tag{20}$$

式(20)两边在 0~t 的时间区间内积分，并将初始哈密顿能量移到等式右边，得到哈密顿能量平衡方程为

$$H(t) = \underbrace{-\int_{t_0}^{t}(\nabla H)^{\mathrm{T}}\boldsymbol{R}(\nabla H)\mathrm{d}t}_{W_{\mathrm{D}}(t)} + \underbrace{\int_{t_0}^{t}\boldsymbol{u}^{\mathrm{T}}\boldsymbol{y}\mathrm{d}t}_{W_{\mathrm{I}}(t)} + H(t_0) \tag{21}$$

式中，等式左侧表示 t 时刻直接计算得到的储能值，右侧表示间接计算得到的储能值记为 W，$H(t_0)$为初始储能值；$W_{\mathrm{D}}(t)$和 $W_{\mathrm{I}}(t)$分别代表耗散能量和交互能量。

2.2 直流哈密顿能量的动态演化

振荡开始前系统处于稳定运行状态，PLL 能精确跟踪系统相位，基于 PLL 相位角得到的 dq 旋转坐标系保持额定角速度旋转，能量变量可表示为

$$\boldsymbol{x}_0 = \begin{bmatrix} x_{pll0},\ 0,\ x_{dc0},\ 0,\ x_{Q0},\ 0,\ x_{d0},\ 0, x_{q0}, \\ 0,\ u_{dc0},\ i_{d0},\ i_{q0},\ u_{od0},\ u_{oq0},\ i_{od0},\ i_{oq0} \end{bmatrix}^{\mathrm{T}} \tag{22}$$

在此阶段，系统的哈密顿能量仅由直流分量组成，代表能量变量基波幅值的直流分量保持恒定，存储能量为

$$H_0 = \frac{1}{2}\boldsymbol{x}_0^{\mathrm{T}}\boldsymbol{D}^{-1}\boldsymbol{x}_0 \tag{23}$$

振荡后能量变量为

$$\boldsymbol{x} = \boldsymbol{x}_0' + \Delta\boldsymbol{x} \tag{24}$$

式中，$\boldsymbol{x}_0'$表示振荡后到达新稳态时变量的直流分量，$\Delta\boldsymbol{x}$ 表示能量变量的变化量。

振荡后储能直流分量可表示为

$$H_0' = \frac{1}{2}\boldsymbol{x}_0'^{\mathrm{T}}\boldsymbol{D}^{-1}\boldsymbol{x}_0' \tag{25}$$

振荡前后存储能量直流分量之差ΔH_0的计算公式为

$$\Delta H_0 = H_0 - H_0' \tag{26}$$

2.3 宽频振荡下的模态储能

系统发生宽频振荡时，式(10)中在 dq 坐标系下的每个能量变量可统一表示为

$$x_i(t) = X_{i0}'\cos(2\pi f_0 + \varphi_{xi0}) + \sum_{j=1}^{m} X_{ij}\cos(2\pi f_j t + \varphi_{xij}) \tag{27}$$

式中，i=1, 2, …, n；下标“i”表示第 i 个能量变量；j=1, 2, …, m；下标“j”表示第 j 个振荡模态分量，X 为振荡幅值，f 为振荡频率。

模态能量指的是同一个模态的分量代入式(11)相乘得到的能量[5]，将式(22)代入式(11)得到第 j 个模态储能的表达式为

$$H_{mode,j} = \frac{1}{2}\boldsymbol{x}_j^{\mathrm{T}}\boldsymbol{D}^{-1}\boldsymbol{x}_j = \sum_{i=1}^{n}\frac{1}{2}x_{ij}^{\mathrm{T}}\boldsymbol{D}^{-1}x_{ij} \tag{28}$$

3 算例

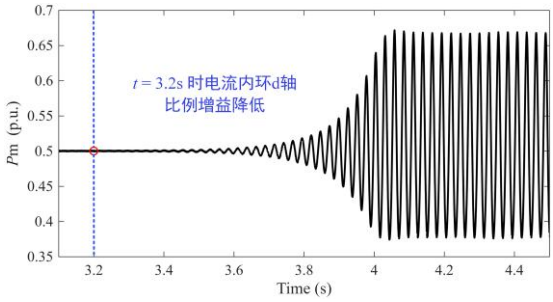
在 PSCAD/EMTDC 中，建立了如图 1 所示结构的 IBR 并网系统仿真模型，主电路及其控制参数如表 1 所示。

表 1 系统参数

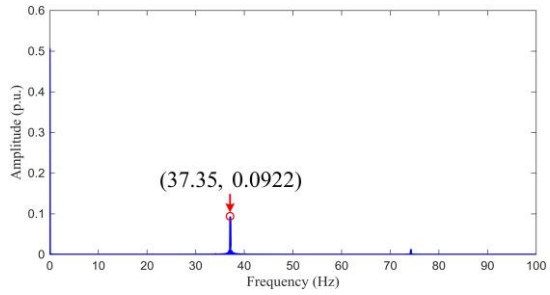
Table 1 System Parameters

参数	数值	参数	数值
系统额定功率 S_{base}	4MW	滤波电阻 R_f	0.0001Ω
电网额定电压 u_{base}	0.95kV	滤波电感 L_f	0.0004H
直流侧额定电压 u_{dcbase}	2kV	滤波电容 C_f	0.00001F
电网基准频率 f_s	50Hz	网侧电感 L_g	0.00001H
直流电压外环 PI($K_{p,dc}$, $K_{i,dc}$)	5,100	网侧电阻 R_g	0.001Ω
无功功率外环 PI($K_{p,Q}$, $K_{i,Q}$)	1,100	直流电容 C_{dc}	0.02F
电流内环 d 轴 PI($K_{p,d}$, $K_{i,d}$)	0.2,20		
电流内环 q 轴 PI($K_{p,q}$, $K_{i,q}$)	0.2,20		
锁相环 PI($K_{p,pll}$, $K_{i,pll}$)	50,200		

仿真时长为 20s，t=0s 仿真开始运行，直流侧有功功率 P_m 的波形图及频谱分析结果（Fast Fourier Transform，FFT）如图 3 所示。系统处于稳定运行状态时，P_m 保持 0.5pu 不变；在 t=3.2s 时将控制器电流内环比例系数 $K_{p,d}$ 由 0.1 降至 0.02，如图 3(a)所示，此时 P_m 发生了等幅振荡。对 P_m 进行 FFT 分析，结果如图 3(b)所示，可见系统除直流分量外还存在 1 个主导振荡分量，其频率为 37.35Hz、幅值为 0.0922pu。



(a) P_m 波形



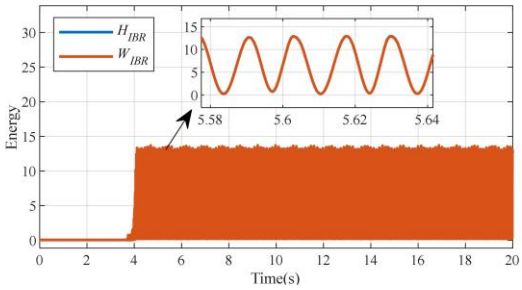
(b) P_m 的 FFT 结果

图 3 P_m 波形及其 FFT

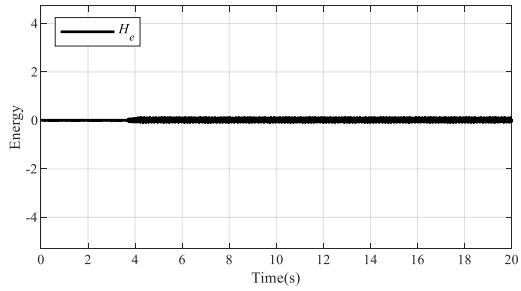
Fig. 3 P_m waveform and FFT results

3.1 能量模型的验证

从仿真结果中提取各能量变量的数值代入能量平衡方程(21)进行独立计算。并网 IBR 系统的哈密顿能量函数波形如图 4 所示。



(a) 哈密顿能量直接值与间接值对比



(b) 哈密顿能量误差波形

图 4 哈密顿能量计算的一致性与误差评估

Fig. 4 Consistency and Error Evaluation of Hamiltonian Energy Calculation

由图 4(a)可见，稳态和振荡过程中哈密顿能量的直接测量值和间接测量值具有基本相同的变化趋势和主要动态特征；图 4(b)中，H_e 为直接测量值

与间接测量值之间的相对误差波形，最大误差小于总能量的 1%。这些波形直观、定量地证明了所建立的能量模型遵循能量守恒定律。

3.2 能量转换的动态过程

利用多元变分模态分解法[6]对系统的能量变量进行分解，精确提取直流分量。将此结果代入式(23)和式(25)得到系统储能的直流分量，如图 5 所示。

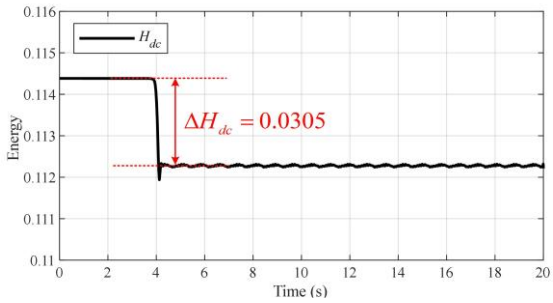


图 5　直流哈密顿能量

Fig. 5　Direct current Hamiltonian energy

稳定运行阶段，系统的哈密顿能量仅由直流分量组成，H_0 稳定在 0.1138 左右。振荡后系统储能的直流分量在振荡后略有下降，ΔH_0=0.0305。

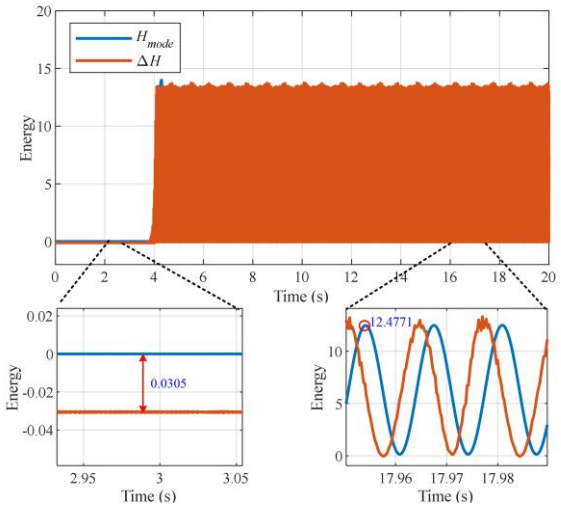


图 6　哈密顿振荡能量差值和模态储能

Fig. 6　Hamiltonian energy difference and mode energy

图 6 中ΔH（$\Delta H=H-H_0$）表示振荡后增加的哈密顿能量，H_{mode}表示振荡过程中占主导地位的振荡模态储能，其振幅约为 12.4771。二者振幅的相似性表明，系统振荡储能增加的部分集中于主导振荡模态储能，但存在一定的相位偏移；储能直流分量的减少量为 0.0305，仅为模态储能振幅增加量的 0.24%。这表明 H_{mode} 不可能完全由稳定直流哈密顿能量的转换而来。由式(21)可知，这种现象可能是耗散和交互能量共同作用的结果。这两个因素的具体作用及其机制将在未来的研究中进一步探讨。

4　结论

本文提出了一种基于哈密顿能量函数的 IBR 占主导地位的电力系统宽频振荡动态模型，旨在阐明 IBR 主导系统内振荡能量的动态演化过程。主要结论如下：

(1)构建了基于哈密顿能量函数的宽频振荡能量模型，该模型可精确表征变流器主导工况下的能量演化规律；

(2)系统振荡储能的动态增长主要集中于主导振荡模式，其贡献度显著高于其他次主导模式。这一现象揭示了宽频振荡中能量分布的模态选择性特征，表明主导振荡模式在系统能量动态中起支配作用；

(3)仿真表明，当系统发生宽频振荡时哈密顿能量的直流分量呈现显著衰减趋势，这一现象揭示了振荡过程中系统稳态能量的动态再分配特性，可反映出系统从稳态运行向动态振荡状态转变的能量演化过程。

在后续研究中，将进一步拓展能量模型，通过分析能量流动方向准确识别振荡源，全面研究能量传递规律，有利于提高系统稳定性分析的准确性和提高控制策略的有效性。

参考文献

[1] Cheng Y., Fan L., Rose J., et al.: 'Real-world subsynchronous oscillation events in power grids with high penetrations of inverter-based resources', IEEE Trans. Power Syst., 2023, 38, (1), pp. 316-330.

[2] Hossain M. S., Abboodi Madlool N., Al-Fatlawi A. W., et al.: 'High penetration of solar photovoltaic structure on the grid system disruption: An overview of technology advancement', Sustainability, 2023, 15, (2), pp. 1174.

[3] 王哲凡. 基于小信号干扰法的逆变器并网稳定性比较研究[D/OL]. 华北电力大学（北京）, 2025.

[4] Cecati F., Zhu R., Liserre M., et al.: 'Nonlinear modular state-space modeling of power-electronics-based power systems', IEEE Trans. Power Electron., 2021, 37, (5), pp. 6102-6115.

[5] 陈曦, 吴熙, 顾文, 等. 基于次同步模态能量的双馈风机并网系统次同步振荡能量分析与溯源方法研究[J/OL]. 中国电机工程学报, 2023, 43(15): 5863-5877.

[6] 杨欣. 基于时频分解方法的结构时变模态参数识别研究[D/OL].河北工业大学, 2025.

收稿日期：



张心怡

作者简介：

张心怡(1999-)，女，硕士研究生，研究方向为电力系统稳定性，E-mail：heaxyz@my.swjtu.edu.cn；

王德林(1970-)，男，教授，博士生导师，通讯作者，研究方向为新能源并网发电和系统稳定与控制研究等，E-mail：wdl@swjtu.edu.cn。

100 基于时域卷积功率的柔性直流输电线路单端量保护方案

王志杰[1]，刘海南[1]，骆政呈[1]，李海锋[1]

（1．华南理工大学电力学院，广东省 广州市）

Zhijie Wang[1], Hainan Liu[1], Zhengcheng Luo[1], Haifeng Li[1]

(1．School of Electric Power Engineering, South China University of Technology, Guangzhou 510641, China)

ABSTRACT: To address the problem that the sensitivity of most existing single-ended protection methods is insufficient, a novel scheme for single-ended protection of HVDC transmission lines based on time-domain convolutional power is proposed. By analyzing the fault frequency characteristics of faults inside and outside the zone in detail, the convolutional power facilitates the amplification of the characteristic differences between inside and outside the zone faults caused by the DC line boundary. Based on this, this paper represents the convolutional power in the time domain as a form of power in the frequency domain by introducing, the ratio of convolutional power of long and short-time windows is used as an auxiliary criterion for high resistance fault identification. Simulation verification indicates that the scheme can correctly identify internal and external faults, and has high speed, reliability, and sensitivity.

KEY WORDS: HVDC transmission, line protection, convolution power, single-ended protection

摘要：为解决现有单端量保护方案在远端故障下灵敏性不足的问题，提出了一种基于时域卷积功率的直流输电线路单端保护新方案。通过详细分析区内外故障的频率特性可知，卷积功率有利于放大直流线路边界引起的区内外故障之间的特征差异。基于此，本文通过引入时域中的卷积功率表示为频域中的功率形式，提出以长短时间窗的卷积功率之比作作为主判据，实现故障区内外故障的判别。基于PSCAD/EMTDC对柔性直流输电系统进行了仿真验证，表明该方案能正确识别区内外故障，具有较高的灵敏性、可靠性以及速动性。

关键词：直流输电；线路保护；卷积功率；单端量保护；

DOI：10.13335/j.1000-3673.pst.2014.01.

基金项目：国家自然科学基金 (No. 52077082).

Project Supported by National Natural Science Foundation of China (NSFC) (52077082).

0 引言

基于模块化多电平换流器的柔性直流输电系统具备谐波含量低、可大规模消纳可再生能源等优势，在全世界都得到了广泛的应用[1-3]。然而直流电网属于低惯型网络，直流侧发生短路故障后，换流站将会向故障点馈入短路电流，故障电流在短时间内迅速放电，这使得故障电流上升速度快且幅值大[4]。因此，柔性直流电网故障的快速、可靠识别仍是一个亟待解决的关键问题[5]。

在实际的柔性直流线路保护方案中，行波保护和微分欠压保护是线路的主保护[6]。然而，故障行波受到许多因素的影响，除了长距离输电线路传播引起的衰变[7]和线路两端的折反射[8]外，过渡电阻是影响故障行波特性的一个关键因素。如，行波电压幅值、电压变化率等特征量都会随着过渡电阻的增加而显著降低[9-11]，这势必大大降低了保护的可靠性和灵敏性。

针对上述问题，众多专家与学者利用直流线路物理边界的频率特征用以放大区内外故障下的特征差异[12]。文献[13]利用小波变换提取故障电压的频域信息识别区内外故障；文献[14]利用故障行波在区内外故障下等效衰减速率上的差异显著特点来识别故障。文献[15]利用不同频段能量聚量比值构造保护判据。文献[16-17]分别提出利用高频电压分量和多频带电气量比值构造判据。文献[18]利用S变换提取故障电压行波能量谱。然而，这些方法都需要采用诸如S变换或小波变换之类的时频分析方法来获取故障行波的频率分量，计算较为复杂。

为了解决上述问题，本文提出了一种基于长窗和短窗卷积功率特性的柔性直流输电线路单端保护方案。首先，本文从频域角度对区内外故障特性进行数学解析，分析了区内外故障下不同频率的频域功率比特性，结果表明该比值受故障电阻的影响较小。基于此，本文通过引入时域中的卷积功率表示为频域中的功率形式，提出长短时间窗的卷积功

率之比作为识别故障判据，所提判据不需要进行滤波处理，计算简单。最后，基于柔性直流输电系统的电磁暂态仿真模型，对所提保护原理的性能进行了全面的仿真测试。

1 柔性直流输电线路故障特性分析

本文以真双极模块化多电平换流器（modular multilevel converter, MMC）柔性直流输电系统为例，开展故障电压行波的分析，其拓扑结构如图 1 所示。M、N 为线路两端的保护安装处。图 1 给出典型故障点，其中，f_1 为 Line1 上故障点，f_2 为 MMC1 侧区外故障点，f_3 为 MMC2 侧区外故障点。

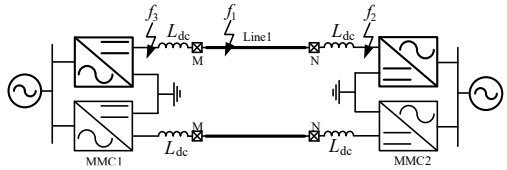


图 1 MMC-HVDC 系统拓扑结构

Fig.1 Topology structure of an MMC-HVDC system

对于双极直流输电线路而言，正、负极之间存在耦合，可通过极模变换将正、负极量解耦为零模量与线模量[19]：

$$\begin{bmatrix} u_0 \\ u_1 \end{bmatrix} = \frac{1}{\sqrt{2}} \begin{bmatrix} 1 & 1 \\ 1 & -1 \end{bmatrix} \begin{bmatrix} u_p \\ u_n \end{bmatrix} \tag{1}$$

式中，下标 1 和 0 表示线模量与零模量；下标 p、n 表示正极量和负极量。故障行波的波头能量主要集中在高频段，在故障暂态期间，等效电路中的电阻与电容基本不起作用，因此，可将等效电路进一步简化为纯电感：$Z_{MMC} \approx sL_{eq}=2sL_{arm}/3$[20]。

1.1 区内故障分析

直流线路 f_1 处发生区内单极故障时，根据故障端口边界状态，可得复合模等效电路如图 2 所示。

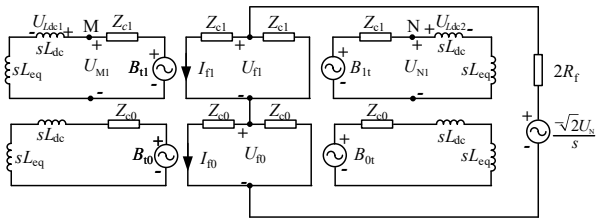


图 2 区内发生单极接地故障下的暂态等值电路

Fig. 2. Equivalent circuit under an internal pole-to-ground fault

对于单极故障，可表示为：

$$U_{f1} = \frac{-\sqrt{2}U_f}{s} \frac{Z_{c1}}{(Z_{c1}+Z_{c0}+4R_f)} \tag{2}$$

线路采用 Bergeron 等效，对于线模分量：

$$B_{t1} = H_1 \cdot (U_{f1} + Z_{c1} \cdot I_{f1}) \tag{3}$$

式中，H_1 为线模故障行波的传递方程，I_{f1} 为故障点位置的线模故障电流。考虑行波传递造成的延时和衰减畸变，线模分量行波传递方程可表示为：

$$H_{1(x)} = e^{-r(s)\cdot x} \approx \frac{K_{c1}}{1+s\tau_{c1}} e^{-\frac{x}{v_1}s} \tag{4}$$

式中，x 为沿线路传播的距离，K_{c1} 为线模分量的衰减比例系数，τ_1、v_1 为线模的色散时间系数、波速。

列写测量点 M 处的线模电压：

$$U_{M1_in}(s) = \frac{-2\sqrt{2}U_f Z_{c1}}{(Z_{c1}+Z_{c0}+4R_f)s} \frac{K_{c1}}{1+s\tau_{c1}} \frac{s(L_{dc}+L_{eq})}{s(L_{dc}+L_{eq})+Z_{c1}} \tag{5}$$

测量点 M 处的线模电流：

$$I_{M1_in}(s) = \frac{2\sqrt{2}U_f Z_{c1}}{(Z_{c1}+Z_{c0}+4R_f)s} \frac{K_{c1}}{1+s\tau_{c1}} \frac{1}{s(L_{dc}+L_{eq})+Z_{c1}} \tag{6}$$

由时域卷积定理可知，两个时域信号做卷积，就等价于它们的频谱做乘法。因此，卷积功率也为电压电流的频域特征的乘积[21]，为此对应于故障点 f_1 的频域功率为：

$$P_{M1_f1}(s) = \frac{(2\sqrt{2}U_f Z_{c1})^2}{(Z_{c1}+Z_{c0}+4R_f)^2 s^2} \left(\frac{K_{c1}}{1+s\tau_{c1}}\right)^2 \frac{s(L_{dc}+L_{eq})}{(s(L_{dc}+L_{eq})+Z_{c1})^2} \tag{7}$$

1.2 区外故障分析

下面对区外 f_2 发生故障时测点 M 的测点电压与测点电流进行分析。根据故障端口边界状态，得出复合模等效电路如图 3 所示。

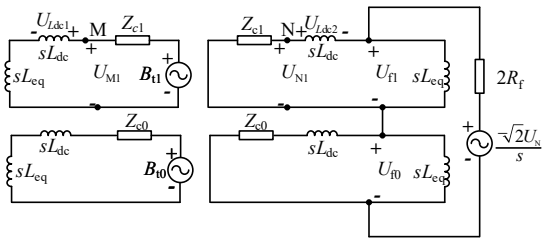


图 3 区外故障下的等值电路

Fig.3 Equivalent circuit under an external fault

由于故障点在限流电抗与换流器之间，不存在直流线路，因此实际上没有行波，但故障处电压可通过限流电抗器进入直流线路，由此在保护 N 处产生初始行波，复频域下故障处的线模电压为：

$$U_{f1} = \frac{-\sqrt{2}U_f}{s} \frac{sL_{eq}//(sL_{dc}+Z_{c1})}{sL_{eq}//(sL_{dc}+Z_{c1})+sL_{eq}//(sL_{dc}+Z_{c0})+2R_f} \tag{8}$$

式中，U_{f1} 为故障点处线模分量的电压幅值；U_f 为正常运行时故障点电压；Z_{c1} 与 Z_{c0} 为线模与零模波阻抗；R_f 为过渡电阻。

由于故障暂态期间电感占据主导作用，可对式(8)进行简化：

$$U_{\mathrm{f1}} \approx \frac{-\sqrt{2}U_{\mathrm{f}}}{s}\frac{sL_{\mathrm{eq}}//sL_{dc}}{2\left(sL_{\mathrm{eq}}//sL_{dc}+R_{\mathrm{f}}\right)} \tag{9}$$

根据线路端口回路的 KVL，列写测量点 N 处的线模电压：

$$U_{\mathrm{N1}}(s)=\frac{Z_{\mathrm{c1}}}{sL_{\mathrm{dc}}+Z_{\mathrm{c1}}}\cdot U_{\mathrm{f1}} \tag{10}$$

列写测量点 M 处的线模电压：

$$U_{\mathrm{M1_ex}}(s)=\frac{-\sqrt{2}U_{\mathrm{f}}}{s}\frac{sL_{\mathrm{eq}}//sL_{dc}}{\left(sL_{\mathrm{eq}}//sL_{dc}+R_{\mathrm{f}}\right)}\frac{Z_{\mathrm{c1}}}{sL_{\mathrm{dc}}+Z_{\mathrm{c1}}}\frac{K_{\mathrm{c1}}}{1+s\tau_{\mathrm{c1}}}\frac{s\left(L_{\mathrm{dc}}+L_{\mathrm{eq}}\right)}{s\left(L_{\mathrm{dc}}+L_{\mathrm{eq}}\right)+Z_{\mathrm{c1}}} \tag{11}$$

测量点 M 处的线模电流：

$$I_{\mathrm{M1_ex}}(s)=\frac{\sqrt{2}U_{\mathrm{f}}}{s}\frac{sL_{\mathrm{eq}}//sL_{dc}}{\left(sL_{\mathrm{eq}}//sL_{dc}+R_{\mathrm{f}}\right)}\frac{Z_{\mathrm{c1}}}{sL_{\mathrm{dc}}+Z_{\mathrm{c1}}}\frac{K_{\mathrm{c1}}}{1+s\tau_{\mathrm{c1}}}\frac{1}{s\left(L_{\mathrm{dc}}+L_{\mathrm{eq}}\right)+Z_{\mathrm{c1}}} \tag{12}$$

对应于故障点 f_2 的频域功率为：

$$P_{\mathrm{M1_f2}}(s)=\frac{\left(\sqrt{2}U_{\mathrm{f}}\left(sL_{\mathrm{eq}}//sL_{dc}\right)\right)^2}{s^2\left(sL_{\mathrm{eq}}//sL_{dc}+R_{\mathrm{f}}\right)^2}\left(\frac{Z_{\mathrm{c1}}}{sL_{\mathrm{dc}}+Z_{\mathrm{c1}}}\right)^2\left(\frac{K_{\mathrm{c1}}}{1+s\tau_{\mathrm{c1}}}\right)^2\frac{s\left(L_{\mathrm{dc}}+L_{\mathrm{eq}}\right)^2}{\left(s\left(L_{\mathrm{dc}}+L_{\mathrm{eq}}\right)+Z_{\mathrm{c1}}\right)^2} \tag{13}$$

为了直观比较在故障点 f_x（x=1,2）处的 $G_U(s)=U_{\mathrm{M1_ex}}(s)/U_{\mathrm{M1_in}}(s)$，$G_I(s)=I_{\mathrm{M1_ex}}(s)/I_{\mathrm{M1_in}}(s)$ 和 $G_P(s)=P_{\mathrm{M1_f2}}(s)/P_{\mathrm{M1_f1}}(s)$的特性差异，令 $s=j\omega$，绘制 $|G_U(j\omega)|$、$|G_I(j\omega)|$和$|G_P(j\omega)|$的幅频曲线如图 4 所示：

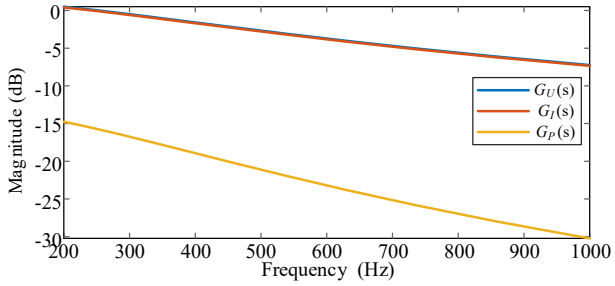


图 4　$|G_U(j\omega)|$、$|G_I(j\omega)|$和$|G_P(j\omega)|$的幅频曲线(R_{f1}=R_{f2}=0)

Fig. 4　Amplitude-frequency curves of $|G_U(j\omega)|$, $|G_I(j\omega)|$and $|G_P(j\omega)|$(R_{f1}=R_{f2}=0)

由图 4 可见，受直流线路边界的影响，$|G_U(j\omega)|$、$|G_I(j\omega)|$和$|G_P(j\omega)|$值均小于 1。$|G_U(j\omega)|$和$|G_I(j\omega)|$的幅频曲线非常接近，$|G_P(j\omega)|$的幅频曲线低于$|G_U(j\omega)|$和$|G_I(j\omega)|$曲线。且随着频率增大，$|G_P(j\omega)|$与$|G_U(j\omega)|$或$|G_I(j\omega)|$之间的差距明显增大。可知，在高频段下，频域功率受边界元件的衰减作用较单一行波电压或电流更为严重，且衰减程度随着频率增大而加剧。因此相比于单独采用电压或电流，采用 $P_{fi}(s)$能够更为有效地识别区内外故障。

1.3 不同频率下的卷积功率比值特征

由式(7)、(13)可知，区内外故障时频域功率大小与过渡电阻的平方成反比，这意味着仅仅利用某一频率(频带)的频域功率，受过渡电阻的影响较大。为了削弱过渡电阻对频域功率的影响，可以构造量化指标 P_{ratio}，定义为同一故障点在两个不同频率下卷积功率比值。设 2 个频率分别为 ω_1 和 ω_2，且 $\omega_1>\omega_2$，则可得区内、外故障下频域卷积功率的比值 P_{ratio1} 和 P_{ratio2}。即，

$$\begin{cases} P_{ratio1}=P_{\mathrm{M1_f1}}(j\omega_1)/P_{\mathrm{M1_f1}}(j\omega_2) \\ P_{ratio2}=P_{\mathrm{M1_f2}}(j\omega_1)/P_{\mathrm{M1_f2}}(j\omega_2) \end{cases} \tag{14}$$

P_{ratio1} 和 P_{ratio2} 可近似表示为：

$$\begin{aligned} P_{ratio1}&=U_{\mathrm{M1_in}}(j\omega_1)I_{\mathrm{M1_in}}(j\omega_1)/U_{\mathrm{M1_in}}(j\omega_2)I_{\mathrm{M1_in}}(j\omega_2) \\ &=\frac{j\omega_2\left(j\omega_2\left(L_{\mathrm{dc}}+L_{\mathrm{eq}}\right)+Z_{\mathrm{c1}}\right)^2}{j\omega_1\left(j\omega_1\left(L_{\mathrm{dc}}+L_{\mathrm{eq}}\right)+Z_{\mathrm{c1}}\right)^2} \end{aligned} \tag{15}$$

$$\begin{aligned} P_{ratio2}&=U_{\mathrm{M1_ex}}(j\omega_1)I_{\mathrm{M1_ex}}(j\omega_1)/U_{\mathrm{M1_ex}}(j\omega_2)I_{\mathrm{M1_ex}}(j\omega_2) \\ &=\frac{j\omega_1\left(j\omega_2\left(L_{\mathrm{eq}}//L_{dc}\right)+R_{\mathrm{f}}\right)^2}{j\omega_2\left(j\omega_1\left(L_{\mathrm{eq}}//L_{dc}\right)+R_{\mathrm{f}}\right)^2}\frac{\left(j\omega_2L_{\mathrm{dc}}+Z_{\mathrm{c1}}\right)^2}{\left(j\omega_1L_{\mathrm{dc}}+Z_{\mathrm{c1}}\right)^2}\frac{\left(j\omega_2\left(L_{\mathrm{dc}}+L_{\mathrm{eq}}\right)+Z_{\mathrm{c1}}\right)^2}{\left(j\omega_1\left(L_{\mathrm{dc}}+L_{\mathrm{eq}}\right)+Z_{\mathrm{c1}}\right)^2} \end{aligned} \tag{16}$$

为了进一步直观地比较区内和区外故障时 P_{ratio} 的差异，令$|G_{Pratio}|$= P_{ratio2}/P_{ratio1}，可得：

$$G_{Pratio}=\frac{P_{ratio2}}{P_{ratio1}}=\frac{(j\omega_1)^2\left(j\omega_2\left(L_{\mathrm{eq}}//L_{dc}\right)+R_{\mathrm{f}}\right)^2}{(j\omega_2)^2\left(j\omega_1\left(L_{\mathrm{eq}}//L_{dc}\right)+R_{\mathrm{f}}\right)^2}\frac{\left(j\omega_2L_{\mathrm{dc}}+Z_{\mathrm{c1}}\right)^2}{\left(j\omega_1L_{\mathrm{dc}}+Z_{\mathrm{c1}}\right)^2} \tag{17}$$

代入柔性直流工程模型参数并取 ω_2=300rad/s，令区外故障的 R_{f}=0 可以得到 G_{Pratio} 在不同 ω_1 下的曲线，如图 5 所示。

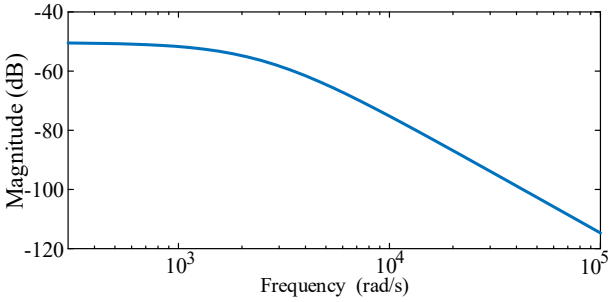


图 5　不同 ω_1 下的$|G_{Pratio}|$

Fig. 5　$|G_{Pratio}|$ at different ω_1

由图 10 可见，当 $\omega_1>\omega_2$=300rad/s 时，$G_{Pratio}<1$，即 $P_{ratio1}>P_{ratio2}$，随着 ω_1 进一步增大，ω_2 和 ω_1 差值越大时，$|G_{Pratio}|$的值更小，即量化指标 P_{ratio1} 和 P_{ratio2} 的差异更明显，更有利于区内外故障的识别。

2　基于卷积功率特征的柔性直流输电线路单端量保护

定义卷积功率为两个时间函数 $U(t)$和 $I(t)$在时域上的卷积，即为：

$$P_{fi}(t)=(u_{fi}*i_{fi})(t)=\int_{t_0}^{t_0+T_s}u_{fi}(t-\tau)i_{fi}(\tau)d\tau \quad (18)$$

式中：t_0 和 T_s 分别是数据窗的起始时刻和时间窗长度。u_{fi} 和 i_{fi} 分别为每个故障点满足启动判据后保护测点处在 T_s 内存储的电压和电流函数。

由时域卷积定理可知，两个时域信号做卷积，就等价于它们的频谱做乘法。即两个时间函数 $U(t)$ 和 $I(t)$经过拉氏变换换后得频域下的 $U(j\omega)$和 $I(j\omega)$，两者关系表达式为：

$$(U*I)(t)\overset{\text{拉氏变换}}{\underset{\text{等价于}}{\rightarrow}}U(j\omega)I(j\omega)=P_{fi}(s) \quad (19)$$

因此，$P_{fi}(t)$是由卷积定理得到的时域下的故障行波卷积功率，而 $P_{fi}(s)$是频域下的故障行波卷积功率形式。其中卷积功率是指将电压作为输入量应用到在 T_s 内电流所有点上，通过将电压输入量在电流上滑动而生成。卷积运算就是对输入数据进行卷积操作，并加权求和的过程；而卷积的结果就是特征提取，从而反映故障特征。卷积计算过程如图 6 所示，输入信号 $u(t)$离散化后其离散序列为 $u(n)=\{u_1,u_2,u_3\ldots u_n\}$；同理 $i(t)$离散化后其离散序列为 $i(n)=\{i_1,i_2,i_3\ldots i_n\}$。

u(X) \ X	1	2	3	4 …	n …	2n-2	n+n-1
u_1	u_1i_1	u_1i_2	u_1i_3	u_1i_4 …	u_1i_n …	0	0
u_2	0	u_2i_1	u_2i_2	u_2i_3 …	u_2i_{n-1} …	0	0
u_3	0	0	u_3i_1	u_3i_2 …	u_3i_{n-2} …	0	0
u_4	0	0	0	u_4i_1 …	u_4i_{n-3} …	0	0
⋮	0	0	0	0 …	⋮ …	⋮	⋮
u_n	0	0	0	0 …	u_ni_1 …	$u_{n-1}i_1$	u_ni_1

图 6　卷积计算过程

Fig. 6　Specific convolution calculation process

将图 6 所示表中的每一列值相加即可获得某个采样点的输入响应，即为卷积的结果。在实际工程中，由于测量数据是离散信号，可计算卷积功率为：

$$P_a(X)=\sum_{i=1}^{N}U_a(i)I_a(X-i+1)\ (a=p,n) \quad (20)$$

式中：P_a为卷积功率；X第X个采样点；N为采样点总数；a表示故障极，当a=p，故障极为正，当a=n，故障极为负。N为卷积功率的采样点总数，反映了时间窗的长短，N的计算如下：

$$N=T_sf_s \quad (21)$$

式中：f_s为采样频率。

事实上，由于故障行波是非平稳的时间信号，其频谱分布与时间窗有关。对于不同的时间窗，频率分布是不一致的。因此本文所提的特征量即卷积功率的频谱分布受时间窗的影响。从信号处理的角度来看，当采样频率固定时，时间窗的长度反映了不同的频率分辨率。由香农采样定理可知，长时间窗和短时间窗的故障信息都包含了除基频信号外其他频率的信号，但时间窗的频率分辨率与时间窗的长度成反比；以 10kHz 的采样频率为例，当短时间窗为 1ms 时，频率轴上的最小频率间隔是 1000Hz，而当长时间窗为 3ms 时，最小频率间隔为 333.33Hz。因此与短窗口相比，长窗口的频率分量更大。具体来说，从相对性的角度来看，短时间窗中的故障频率信息可以被视为高频量。类似地，长时间窗的故障频率信息可以被视为相对低频和高频量的组合。

2.1 启动判据

当直流线路发生故障时，极线电压将突变。因此，可以用极线电压变化量 ΔU_a 作为保护的启动判据：

$$\sum_{i=0,1,2}\left|\Delta U_a(j+i)-\Delta U_a(j+i-1)\right|>k_vU_{ref}\quad (a=p,n) \quad (22)$$

式中：U_{ref}为额定线电压；a 表示故障极。为避免稳态电压波动影响，k_v为电压波动系数，取 0.08。

2.2 区内外故障识别判据

本文提出由不同频率下的卷积功率之比的特征量作为主判据，来削弱过渡电阻对保护的影响，实现高阻故障可靠地识别。即，

$$P_{ratio}>P_{ratio.set}=k_{rel.2}P_{ratio2}\quad (a=p,n) \quad (23)$$

式中：$P_{ratio2}=\dfrac{P_{f2}(j\omega_1)}{P_{f2}(j\omega_2)}=\dfrac{P_{f2.T1max}}{P_{f2.T2max}}$；$P_{ratio.set}$ 为卷积功率比的整定值；P_{ratio2} 是逆变器侧金属性区外故障的长时间窗和短时间窗卷积功率之比；$P_{f2.T2\max}$ 是通过 T_1=1ms 内的电压和电流卷积获得的离散的卷积功率值。$P_{f2.T2\max}$ 是通过 T_2=3ms 内的电压和电流经卷积运算得到的离散的卷积功率值；$k_{rel.2}$ 为可靠系数，取 1.3。根据整定原则和仿真结果可得，该保护方案的判据整定值为 0.09。

3　算例分析

本节参照柔性直流输电工程参数，在 PSCAD/EMTDC 平台上搭建双端柔性直流输电系统电磁暂态仿真模型，详细的模型参数如表 1 所示。将保护测点装设于整流站出口处，设置保护的采样频率为 10kHz。取卷积功率的时间窗为 1ms 和 3ms，则采样点数 N 为 10 和 30。保护算法在 Matlab 软件中编写。下面验证不同故障下保护的动作情况。

为全面分析保护方案的正确性，研究所提方案对故障距离与过渡电阻的适应性，故障电阻设置 0-800Ω、故障位置分别设置在始端、中点、末端。

仿真结果如表 2 所示。

表 1 仿真模型主要参数

Table 1 Main parameters of simulation model

System Parameter	Value
MMC 额定容量/MVA	800
桥臂子模块数量	200
线路长度/km	300
桥臂电抗 /mH	22
子模块电容/mF	16
限流电抗值/mH	100

表 2 保护识别结果

Table 2. Protection discrimination results.

故障类型	故障位置	R_f/Ω	P_{ratio}	判别结果
f_1 区内正极故障	首端	200	0.16	区内故障
		400	0.19	区内故障
		800	0.22	区内故障
	中点	200	0.32	区内故障
		400	0.26	区内故障
		800	0.24	区内故障
	末端	200	0.20	区内故障
		400	0.79	区内故障
		800	0.88	区内故障
f_1 区内极间故障	首端	0	0.11	区内故障
		10	0.12	区内故障
		50	0.12	区内故障
	中点	0	0.25	区内故障
		10	0.25	区内故障
		50	0.28	区内故障
	末端	0	0.35	区内故障
		10	0.37	区内故障
		50	0.43	区内故障
f_2 发生区外故障	逆变出口	0	0.07	区外故障

从表 2 中可知，对于区内故障下的不同故障距离、不同过渡电阻，线路测量点处的长短时间窗时域卷积功率之比均高于整定值，外部故障下的长短时间窗时域卷积功率之比低于整定值。因此，所提保护方案基本不受过渡电阻以及故障距离的影响。

4 结论

为解决柔性直流输电线路保护耐受电阻能力不足的问题，本文利用新的故障特征量即卷积功率，并构造出不同时间窗下的卷积功率之比，从而提出了一种基于时域卷积功率比的单端量保护方案。仿真结果表明：

1) 本文对区内外故障的频域功率的特性差异进行详细地数学分析，提出构造不同频率下的频域功率之比来提高较强的耐受过渡电阻能力，原理简单，速动性较高。

2) 本文的新方案采用单端量信息，耐受过渡电阻能力达 800Ω 并具有一定的抗干扰能力，且对于保护装置的采样频率要求较低，仅需 10kHz 的采样频率。

参考文献

[1] Westerman Spier D, Prieto-Araujo E, Lopez-Mestre J, et al. Optimal current reference calcu-lation for MMCs considering converter limitations [J]. IEEE Trans Power Del, 2021, 36(4): 2097–2108.

[2] D. Mu, S. Lin, P. He and X. Li, An Improved Method of Traveling Wave Protection for DC Lines Based on the Compensation of Line-Mode Fault Voltage [J]. IEEE Trans Power Del, 2023, 38(3): 1720-1730.

[3] M. Li, K. Chen, J. He, Y. Tang and J. Tang, Impedance Phase Based Active Injection Pro-tection for Radial VSC-HVDC Grid [J]. IEEE Trans Power Del, 2023, 38(3): 1621-1635.

[4] D. Zhang, C. Wu, P. Ni and J. He, Double-ended fast protection system of LCC-VSC-MTDC independent on boundary component [J]. CSEE J Power Energy Syst, 2022.

[5] X. Chen, H. Li, G. Wang, C. Xu and Y. Liang, A Convolution Power-Based Protection Scheme for Hybrid Multiterminal HVDC Transmission Systems [J]. IEEE J Emerg Select Top Power Electron, 2021, 9(2): 1655-1667.

[6] 郑伟, 张楠, 杨光源. 西门子及 ABB 直流线路行波保护对比和改进研究[J]. 电力系统保护与控制, 2015, 43(24): 149-154.
Zheng Wei, Zhang Nan, Yang Guangyuan. Comparative and improvement investigation on the DC transmission line traveling wave protections of Siemens and ABB[J]. Power System Protection and Control, 2015, 43(24): 149-154.

[7] 韩昆仑, 蔡泽祥, 贺智, 等. 高压直流输电线路故障行波传播特性及其对行波保护的影响[J]. 电力系统保护与控制, 2013, 41(21): 20-25.
Han Kunlun, Cai Zexiang, He Zhi, et al. Propagation characteristic of fault traveling wave on HVDC line and its influence on HVDC line traveling wave protection[J]. Power System Protection and Control, 2013, 41(21): 20-25.

[8] Y. Liang, L. Jiang, H. Li, et al. Fault Analysis and traveling wave protection based on phase characteristics for hybrid multiterminal HVDC Systems[J]. IEEE Journal of Emerging and Selected Topics in Power Electronics, 2022(1): 10.

[9] 梁益, 蔡泽祥, 田得良, 等. 直流线路行波保护解析整定方法[J]. 电网技术, 2017, 41(1): 298-304.
Liang Yi, Cai Zexiang, Tian Deliang, et al. Analytical method for travelling wave protection setting of HVDC transmission line[J]. Power System Technology, 2017, 41(1): 298-304.

[10] 甄永赞,苏宁赛,杨荆宜.直流输电线路极波变化率保护的拓展方法研究[J].中国电机工程学报, 2021, 41(15): 5212-5221.
Zhen Yongzan, Su Ningsai, Yang Jingyi. Research on extension method of polar wave change rate protection for HVDC transmission line[J]. Proceedings of the CSEE ,2021, 41(15): 5212-5221.

[11] Farshad M, Sadeh J. A Novel Fault-location method for HVDC transmission lines based on similarity measure of voltage signals[J]. IEEE Transactions on Power Delivery, 2013, 28(4): 2483-2490.

[12] 乔立华, 陶然, 宋国兵, 等. 直流线路边界特性保护综述[J]. 电力系统保护与控制, 2019, 47(19): 179-186.
Qiao Lihua, Tao Ran, Song Guobing, et al. Overview of DC line boundary characteristic protection [J]. Power System Protection and Control, 2019, 47(19): 179-186.

[13] 李斌, 何佳伟, 李晔, 等. 基于边界特性的多端柔性直流配电系统单端量保护方案[J]. 中国电机工程学报, 2016, 36(21): 5741-5749+6016.
Li Bin, He Jiawei, Li Ye, et al. Single-ended Protection Scheme Based

on Boundary Characteristic for the Multi-terminal VSC-based DC Distribution System[J]. Proceedings of the CSEE, 2016, 36(21): 5741-5749+6016.

[14] 张韵琦,丛伟,张玉玺.基于初始电压行波频域衰减速率的MMC-HVDC 线路保护方案[J].电力自动化设备, 2020, 40(12): 143-155.
Zhang Yunqi, Cong Wei, Zhang Yuxi. MMC-HVDC line protection scheme based on frequency-domain attenuation rate of initial voltage traveling wave[J]. Electric Power Automation Equipment, 2020, 40(12): 143-155.

[15] 王艳婷, 樊顺跃, 刘乐, 等. 基于频域能量比值的柔性直流输电线路单端量高可靠性保护方案[J/OL]. 电力系统保护与控制, 1-10[2025-08-25].
Wang Yanting, Fan Shunyue, Liu Le, et al. Non-Unit High Reliability Protection for Flexible DC Transmission Lines Based on Ratio of Frequency Energy Accumulation[J/OL]. Power System Protection and Control, 1-10[2025-08-25].

[16] 陈仕龙, 束洪春, 万春红, 等. 一种特高压直流输电线路单端电压暂态保护原理[J]. 电力系统保护与控制, 2013, 41(3): 26-31.
Chen Shilong, Zhu Hongchun, Wan Chunhong, et al. A single terminal voltage transient protection principle for UHVDC transmission lines [J]. Power System Protection and Control, 2013, 41 (3): 26-31.

[17] 戴志辉, 赵中秋, 王兴国, 等. 基于直流滤波器多频率单端电气量的高压直流线路保护[J]. 高电压技术, 2023, 49(2): 702-712.
Dai Zhihui, Zhao Zhongqiu, Wang Xingguo, et al. HVDC line protection based on DC filter multifrequency single-end electric parameters[J]. High Voltage Engineering, 2023, 49(2): 702-712.

[18] 高飘, 郑晓冬, 晁晨栩, 等. 基于特定频带能量比的高压直流输电线路保护[J]. 电力系统自动化, 2022, 46(15): 136-144.
Gao Piao, Zheng Xiaodong, Chao Chenxu, et al. High-voltage DC transmission line protection based on energy ratio of specific frequency band[J]. Automation of Electric Power Systems, 2022, 46(15): 136-144.

[19] 高飘, 郑晓冬, 晁晨栩, 等. 基于边界暂态能量的多端柔性直流输电线路保护[J]. 电力系统自动化, 2021, 45(17): 171-179.
Gao Piao, Zheng Xiaodong, Chao Chenxu, et al. Protection for Multi-terminal Flexible DC Transmission Lines Based on Boundary Transient Energy[J]. Automation of Electric Power Systems, 2021, 45(17): 171-179.

[20] 陈淼, 贾科, 王康达, 等. 基于前行波波形特征的柔性直流输电线路单端行波保护[J]. 电网技术, 2022, 46(6): 2386-2393.
Chen Miao, Jia Ke, Wang Kangda, et al. Single Terminal Traveling Wave Protection for Flexible HVDC Transmission Lines Based on Forward Wave Shape Information[J]. Power System Technology, 2022, 46(6): 2386-2393.

101 Research and Development of a Fault Self-Healing Experimental Device for Shipboard Zonal Distribution Power System

Li Mingyang[1] and Shi Weifeng[1] and Xue Ting[1]

[1] Shanghai Maritime University, Shanghai 201306, China
1390734971@qq.com

Abstract. To address experimental requirements for researching fault self-healing methods in shipboard zonal power distribution system, a dedicated experimental device for shipboard zonal power distribution system fault self-healing was developed. This device comprises three components: a human-machine interface system, a hardware control system, and an electrical equipment system. Data exchange and collaborative operation among subsystems are achieved through multiple protocols including OPC, Modbus, and TCP/IP. Focusing on modeling and simulating the overall structure, power generation units, and electric propulsion units of the shipboard zonal distribution power system, real-time simulation, monitoring and alarm functions, fault injection, fault diagnosis, and self-healing control were achieved by applying hybrid programming techniques in LabVIEW and MATLAB, utilizing DLL and MATLAB Script Node. Finally, by simulating a two-phase short circuit fault scenario in the distribution unit, the developed experimental device was validated to provide a multi-faceted experimental environment for researching fault self-healing methods in shipboard zonal distribution power system.

Keywords: Shipboard Zonal Distribution Power System, Fault Self-Healing, Experimental Device, Modeling and Simulation.

1 Introduction

The structure of modern shipboard electrical system is becoming increasingly complex, with intricate coupling relationships between various equipment. Prolonged faults can easily trigger chain reactions that threaten the entire system, causing simultaneous damage to multiple power units. This severely compromises the vessel's navigational safety and poses significant challenges to traditional protection methods. The shipboard zonal power distribution system divides the entire vessel's electrical network into multiple independent zones. Characterized by clear zoning, strong fault isolation capabilities, and redundant power supply, it has become the mainstream distribution approach for large vessels. Fault self-healing technology, serving as a reliability assurance mechanism for intelligent systems, integrates self-optimization control, preventive control,

and restorative control through self-monitoring, diagnosis, decision-making, and repair. It enables effective suppression and recovery from partial faults. Therefore, researching efficient and reliable fault self-healing methods for shipboard zonal power distribution system holds significant importance [1-2].

In recent years, scholars both domestically and internationally have conducted extensive research on fault detection and fault-tolerant control technologies for shipboard power systems. Reference [3] proposed a fireworks particle swarm optimization algorithm targeting various grid-side short circuit fault scenarios in shipboard power system, significantly enhancing fault diagnosis speed and accuracy. However, it did not address the issue of concurrent fault detection potentially triggered by short circuit faults. Reference [4] proposed a generator-side short circuit fault diagnosis model for shipboard power system based on MWDN and deep gated RNN-FCN. By integrating a multi-layer wavelet decomposition network, deep gated recurrent neural network, and fully convolutional network, it achieved high accuracy and effective fault classification. However, it did not investigate the impact of generator-side short circuit faults on the shipboard power grid and other generating units. Reference [5] improved the particle swarm optimization algorithm by integrating adaptive weighting and hybrid pooling methods, designing a network reconfiguration scheme for shipboard power system. However, it did not consider the impact of network reconfiguration on critical load operations within the shipboard power system. Reference [6] designed a coaxial series-connected shipboard propulsion system comprising two 15-phase induction motors, achieving efficient power distribution during normal operation and maximized propulsion output power control during fault-tolerant operation. However, this system is confined solely to shipboard propulsion system research. In summary, due to the priority of single-computer operational capabilities and the lack of physical electrical equipment support, most existing shipboard power system fault self-healing methods focus on the operational status of individual components. This approach struggles to meet the experimental demands for holistic simulation in shipboard power system self-healing research [7-8]. Therefore, developing a comprehensive shipboard power system fault self-healing experimental device holds significant practical value.

Based on the aforementioned requirements, this paper developed an experimental device for self-healing faults in shipboard zonal distribution power system. The focus was on modeling and simulating the overall structure, power generation units, and electric propulsion unit. By applying hybrid programming techniques using LabVIEW and MATLAB alongside multiple network communication technologies, the device achieved the fundamental workflow for real-time simulation, monitoring and alarms, fault injection, fault diagnosis, and self-healing control of the system. Finally, the reliability of the developed experimental device was validated through testing under a typical fault condition: a two-phase short circuit in the power distribution unit.

2 Experimental Device Hardware Structure and Software Development Environment

2.1 Hardware Structure Design of the Experimental Device

In this paper, the experimental device for shipboard zonal distribution power system comprises three components: a human-machine interface system, a hardware control system, and an electrical equipment system. These three subsystems interact and collaborate through standard interfaces and communication protocols [9]. The hardware structure of the device is shown in Fig. 1.

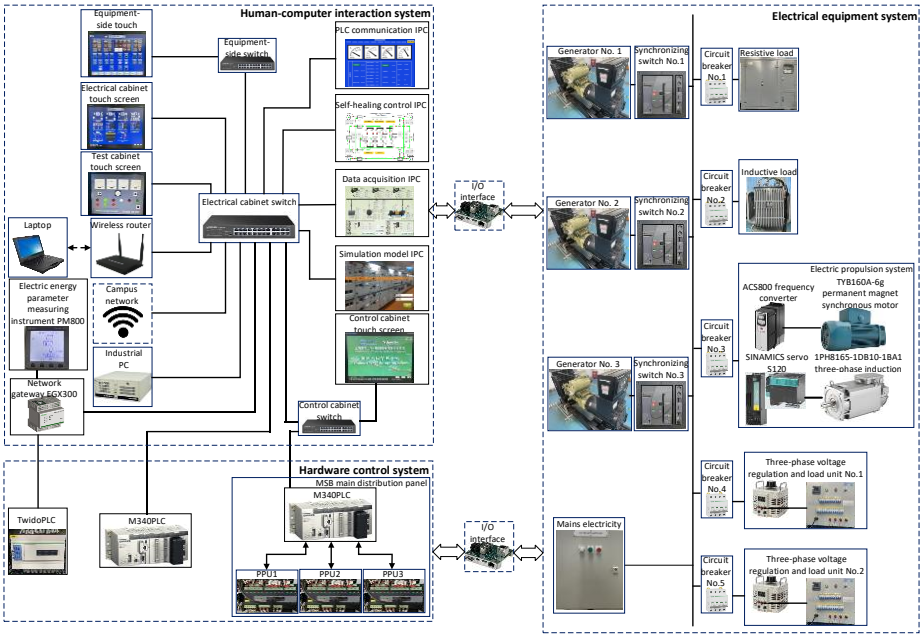


Fig. 1. Hardware structure of experimental device.

Human-Computer Interaction System. The Human-Computer Interaction(HCI) system is primarily composed of an electrical cabinet, test cabinet, control cabinet, and machine-side cabinet. Each cabinet is equipped with a corresponding HCI touch screen for convenient and intuitive interaction by operators.

The electrical cabinet is the core of the HCI system, housing a simulation model industrial computer(IPC) and a PLC communication IPC. The simulation model IPC runs the real-time simulation model of system. The PLC communication IPC transmits sensor data and switch control signals, enabling system communication and control of electrical equipment.

The control cabinet houses a data acquisition IPC and a self-healing control IPC. The data acquisition IPC has three data acquisition methods [10]:

(1) Acquiring power data from the simulation model via the simulation model IPC.
(2) Acquiring real power data from the electrical equipment system via an NI data acquisition card.
(3) Acquiring real power data from the electrical equipment system via PLC.

These multiple data acquisition channels ensure the comprehensiveness and accuracy of the experimental data. The self-healing control IPC performs fault injection into the simulation model, diagnoses faults based on power data provided by the data acquisition IPC, and feeds self-healing control signals back to the simulation model IPC or hardware control system, allowing researchers to validate fault self-healing research methods.

To ensure the real-time performance and stability of HCI, the system is also equipped with a switch, wireless router, gateway, smart power parameter measuring instrument PM800, and campus network.

Hardware Control System. The hardware control system receives control signals generated by the HCI system and transmits them to the electrical equipment system or the self-healing control IPC. It also handles part of the power data interaction functions. This system mainly consists of one TwidoPLC and two sets of M340 PLCs. One M340 PLC serves as the control core for the diesel generator set paralleling and protection unit (PPU), implementing protection, parallel operation, and power distribution control for the diesel generator sets.

Electrical Equipment System. The electrical equipment system is powered by three diesel generator sets and mains power. It is equipped with generator grid-connection switches, circuit breakers, resistive loads, inductive loads, an electric propulsion system, and a three-phase voltage regulation and load unit. The electric propulsion system uses a permanent magnet synchronous motor controlled by a frequency converter as the propulsion motor and a three-phase asynchronous motor controlled by a servo controller to simulate the propeller load. The two motors are connected via a flange.

The main equipment names, models, and parameters in the electrical equipment system are shown in Table 1.

2.2 Software Development Environment

The fault self-healing experimental device utilizes a combination of software to build a complete simulation, control, monitoring, and management system. The device uses Simulink for simulation model building; MATLAB for self-healing control algorithm development; LabVIEW for IPC interface development; Vijeo-Designer for touch screen interface programming; and EcoStruxure Control Expert for PLC programming.

Table 1. Main Equipment Types and Parameters of the Electrical Equipment System.

Equipment name	Equipment model	Parameter
Diesel generator	MP-104-4	Rated voltage 400 V Rated power 104 kW Rated frequency 50 Hz
Inverter	ABB ACS800	/
Three phase permanent magnet synchronous motor	Shanghai Haiguang TYB160A-6g	Rated voltage 380 V Rated power 9 kW Number of poles 6 Rated frequency 16/25 Hz Rated speed 320/500 rpm
Servo controller	Siemens SINAMICS S120	/
Three phase asynchronous motor	Siemens SIMOTICS3(1P) 1PH8165	Rated voltage 365 V Rated current 34.5 A Rated power 16 kW Rated frequency 17.5 Hz Rated speed 500 rpm
Load bank	/	Rated capacity 200 kW Rated voltage 400/690 V
Adjustable reactor	Shanghai sendi TKS-200	Current range 11.2-90/20-167 A Rated frequency 50 Hz Rated capacity 200 kVA Terminal connection Z-X-Y

3 Modeling and Simulation of Shipboard Zonal Distribution Power System

The shipboard zonal distribution power system is a complex multi-variable, nonlinear, strongly coupled system whose operating state is affected by various factors such as load changes and fault disturbances. Establishing an accurate system model is necessary for effective monitoring, control, and optimization.

3.1 System Structure Modeling

In this paper, the main structure and interface of the system primarily comprises four power generation units, eight power distribution units, two electric propulsion units, and four critical load zones. The distribution network forms a ring configuration to supply electricity to the power-consuming units. The power generation units comprise four diesel generator sets (PGM1-4) with a rated power of 5MW, rated voltage of 6600V, and rated frequency of 60Hz. The power distribution units consist of eight distribution modules (PDM1-8) and forty-four circuit breakers. The electric propulsion unit comprises two propulsion motors (PMM1-2) with a rated power of 7 MW, rated

voltage of 3300 V, and rated frequency of 60 Hz. The four critical load areas are the bridge area, engine room area, living quarters area, and service area [11-12].

3.2 Modeling of Power Generation Units and Electric Propulsion Units

The power generation unit model is shown in Fig. 2, including salient pole synchronous generator, excitation voltage regulator, inertia link, diesel engine and governor [13]. The power generation unit is connected to the main bus through a three-phase circuit breaker, which is closed under normal operating conditions; When a fault occurs or maintenance is required, the circuit breaker is disconnected to ensure the safe operation of the system [14].

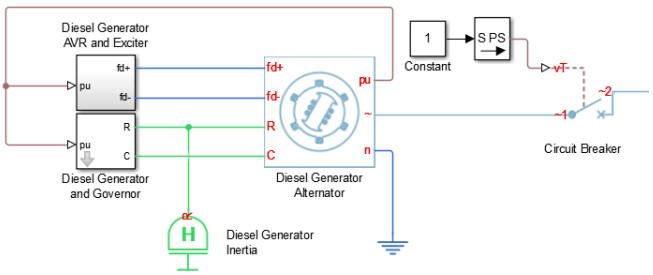


Fig. 2. Power generation unit model.

The stator voltage of the synchronous generator is expressed by Equation (1).

$$\begin{cases} e_d = \dfrac{1}{\omega_{base}} \dfrac{d\psi_d}{dt} - \psi_q \omega_r - R_a i_d \\ e_q = \dfrac{1}{\omega_{base}} \dfrac{d\psi_q}{dt} + \psi_d \omega_r - R_a i_q \\ e_0 = \dfrac{1}{\omega_{base}} \dfrac{d\psi_0}{dt} - R_a i_0 \end{cases} \tag{1}$$

Where the following symbols are defined: e_d, e_q, and e_0 for the d-axis, q-axis, and zero-sequence stator voltages; ω_{base} for the per-unit base electrical speed; ψ_d, ψ_q, and ψ_0 for the $corresponding$ stator flux linkages; ω_r for the per-unit rotor rotational speed; R_a for the stator resistance; i_d, i_q, and i_0 for the corresponding stator currents. e_d, e_q, and e_0 are expressed by Equation (2).

$$\begin{bmatrix} e_d \\ e_q \\ e_0 \end{bmatrix} = P_s \begin{bmatrix} v_a \\ v_b \\ v_c \end{bmatrix} \tag{2}$$

i_d, i_q, and i_0 are expressed by Equation (3).

$$\begin{bmatrix} i_d \\ i_q \\ i_0 \end{bmatrix} = P_s \begin{bmatrix} i_a \\ i_b \\ i_c \end{bmatrix} \tag{3}$$

Equation (3) employs the Park transformation(P_s) to map the synchronous generator equations into a rotating reference frame aligned with the electrical angles. v_a, v_b, and v_c represent the stator voltages measured from the generator terminals to neutral point; i_a, i_b, and i_c are the stator currents flowing from the generator terminals to neutral point. P_s is expressed by Equation (4).

$$P_s = \frac{2}{3}\begin{bmatrix} cos\theta_e & cos(\theta_e - \frac{2\pi}{3}) & cos(\theta_e + \frac{2\pi}{3}) \\ -sin\theta_e & -sin(\theta_e - \frac{2\pi}{3}) & -sin(\theta_e + \frac{2\pi}{3}) \\ \frac{1}{2} & \frac{1}{2} & \frac{1}{2} \end{bmatrix} \tag{4}$$

Where θ_e is expressed by Equation (5).

$$\theta_e(t) = N\theta_r(t) \tag{5}$$

Within the equation, θ_e , N, θ_r are defined as the electrical angle, the number of pole pairs and the rotor angle. The generator rotor voltage equation is expressed by Equation 6.

$$\begin{cases} e_{fd} = \dfrac{1}{\omega_{base}}\dfrac{d\psi_{fd}}{dt} + R_{fd}i_{fd} \\ e_{1d} = \dfrac{1}{\omega_{base}}\dfrac{d\psi_{1d}}{dt} + R_{1d}i_{1d} = 0 \\ e_{1q} = \dfrac{1}{\omega_{base}}\dfrac{d\psi_{1q}}{dt} + R_{1q}i_{1q} = 0 \end{cases} \tag{6}$$

Where the following symbols are defined: e_{fd}, e_{1d} and e_{1q} are the field voltage, the voltages across the d-axis and q-axis damper winding 1; ψ_{fd}, ψ_{1d}, and ψ_{1q} are the magnetic fluxes linking the field circuit, d-axis and q-axis damper winding 1; R_{fd}, R_{1d}, and R_{1q} are the resistances of rotor field circuit, d-axis and q-axis damper winding 1; i_{fd}, i_{1d}, and i_{1q} are the currents flowing in the field circuit, d-axis and q-axis damper winding 1.

The stator flux linkage equation is expressed by Equation 7.

$$\begin{cases} \psi_d = -(L_{ad} + L_l)\, i_d + L_{ad}i_{fd} + L_{ad}i_{1d} \\ \psi_q = -\left(L_{aq} + L_l\right) i_q + L_{aq}i_{1q} \\ \psi_0 = -\, L_0 i_0 \end{cases} \tag{7}$$

The stator parameters comprise the leakage inductance L_l and the d-axis and q-axis mutual inductances L_{ad} and L_{aq}. These along with the corresponding currents, determine the rotor flux linkages as formulated in Equation 8.

$$\begin{cases} \psi_{fd} = L_{ffd} i_{fd} + L_{f1d} i_{1d} - L_{ad} i_d \\ \psi_{1d} = L_{f1d} i_{fd} + L_{11d} i_{1d} - L_{ad} i_d \\ \psi_{1q} = L_{11q} i_{1q} - L_{aq} i_q \end{cases} \tag{8}$$

The self-inductance parameters are defined as follows: L_{ffd} for the rotor field circuit, L_{11d} *and* L_{11q} for the d-axis and q-axis damper winding 1. Correspondingly, the mutual inductance between the rotor field circuit and the d-axis damper winding 1 is denoted by L_{f1d} .

The inductances are expressed by Equation 9.

$$\begin{cases} L_{ffd} = L_{ad} + L_{fd} \\ L_{f1d} = L_{ffd} - L_{fd} \\ L_{11d} = L_{f1d} + L_{1d} \\ L_{11q} = L_{aq} + L_{1q} \end{cases} \tag{9}$$

The rotor torque is defined by Equation 10.

$$T_e = \psi_d i_q - \psi_q i_d \tag{10}$$

The function of the excitation voltage regulation device is to control the generator's excitation voltage and maintain stable terminal voltage. This paper models the excitation device based on the IEEE Type AC1A standard exciter model, which can be regarded as a rotating excitation system. The established excitation device consists of an AC exciter, an electronic amplifier with non-windup limits, a damping filter, a rectifier, and other components. The diesel generator excitation regulation device model is shown in Fig. 3.

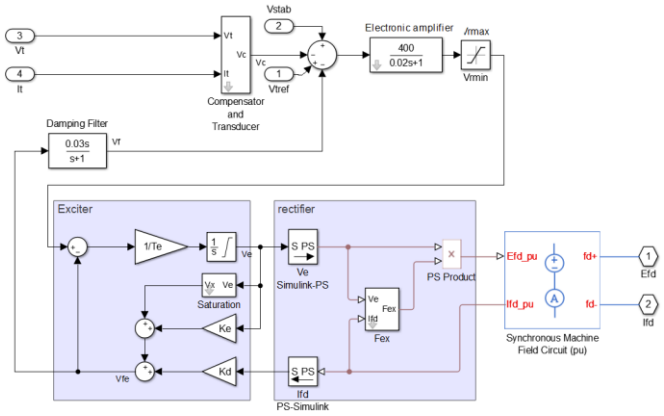


Fig. 3. Diesel generator excitation regulator device model.

To facilitate the simulation and analysis of the dynamic characteristics of diesel generator sets, this paper employs the diesel engine governor model shown in Fig. 4. The model's input is the rotational speed of the synchronous generator, while its output is the mechanical torque of the diesel engine. This configuration effectively reflects the dynamic response of the diesel engine to changes in system frequency and load [15].

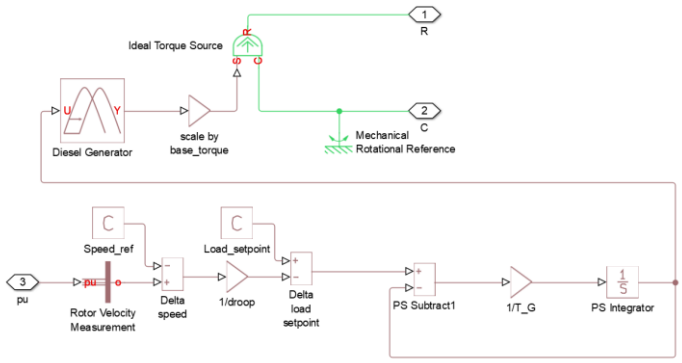


Fig. 4. Diesel engine and governor.

The model of electric propulsion unit is shown in Fig. 5, including propulsion motor, rotor speed sensor, inertia link, ideal torque source and frequency converter. The frequency converter is used to control and adjust the speed of the propulsion motor to realize the speed control of the electric propulsion unit; The three-phase circuit breaker is used to control the electrical connection between the electric propulsion unit and the bus to realize the power supply control of the unit. The modeling process for propulsion motor is consistent with that for synchronous generator.

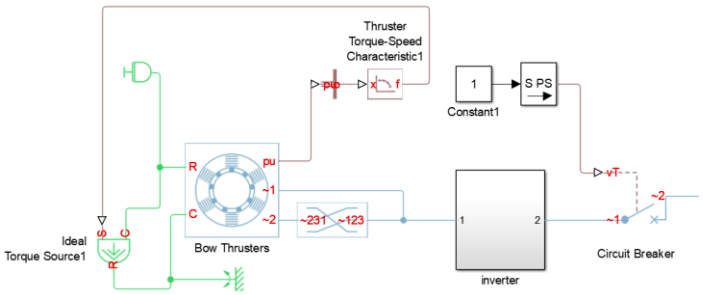


Fig. 5. Electric propulsion unit model.

3.3 Software Design for Device Data Communication

To meet the requirements for high efficiency, stability, and real-time data communication among modules within the shipboard zonal power distribution system fault self-

healing test rig, multiple data transmission protocols were adopted in this study. Among them, the OPC protocol was used for communication between the PLC and the industrial control computer. This protocol not only provides a universal interface standard for equipment from different manufacturers but also achieves millisecond-level low-latency data updates through a subscription/notification mechanism. It incorporates fault recovery mechanisms such as data encryption, identity authentication, and automatic reconnection. The Modbus protocol leverages its master-slave polling mechanism to enable master-slave communication within the serial link comprising the touchscreen, PLC, industrial control computer, data acquisition card, and PPU. Different industrial control computers within the experimental device communicate via TCP/IP protocol over the network. This protocol ensures reliable and ordered packet transmission through mechanisms such as sequence numbers and acknowledgments, checksums, timeout retransmission, and sliding window flow control. Simultaneously, the TCP/IP protocol's congestion control algorithm dynamically adjusts transmission rates under high load to maintain high communication link reliability. Communication between the industrial control computers and touchscreens utilizes the physically stable USB protocol, enabling convenient human-machine interaction functionality [16].

3.4 Implementation of Hybrid Programming by Calling MATLAB Programs in LabVIEW Environment

LabVIEW has powerful software interface development ability, hardware interface communication ability and data acquisition ability, but it lacks the ability to process complex data; MATLAB has powerful scientific computing function, reliable algorithm and model library, but its development ability in interface programming, control and network communication is poor. According to the characteristics of the above two software, this paper uses the hybrid programming technology of calling MATLAB program in LabVIEW environment to complete the simulation software development of fault self-healing device of the system. The hybrid programming technology used in this paper mainly includes the following two kinds [17]:

Dynamic Link Library (DLL) Technology. First, communication interface modules are added to the Simulink simulation model in MATLAB to enable data interaction between the model and the external environment. Then, using Microsoft Visual C++ software and MATLAB's Simulink Coder tool, the simulation model is compiled into a C++ language DLL program. Finally, in the LabVIEW development environment, the generated DLL program is called to achieve cross-platform integration of the simulation model.

MATLAB Script Node Technology. To verify the reliability of the fault self-healing program, the fault self-healing code is first written and preliminarily tested in the MATLAB environment. Then, using the MATLAB Script Node provided by LabVIEW, the MATLAB fault self-healing code is imported into LabVIEW. The MATLAB Script Node communicates with the MATLAB Server using ActiveX controls. Finally, using the real-time power data provided by the experimental device, the

imported fault self-healing program is run within the LabVIEW environment to validate the fault self-healing methods.

3.5 Fault Self-Healing Function and Simulation Implementation

The experimental device achieves real-time simulation operation of the system by invoking the DLL program generated by MATLAB within the LabVIEW software via the simulation model industrial control computer. The data acquisition industrial control computer performs real-time collection, display, recording, and transmission of system power data and operational status. The performance of the selected testing method is evaluated by implementing fault diagnosis and self-healing control decision codes within the MATLAB Script Node of the LabVIEW interface on the self-healing control industrial control computer. The PLC communication industrial control computer connects to and controls the physical components of the apparatus. The fault self-healing process flowchart for the experimental device is shown in Fig. 6.

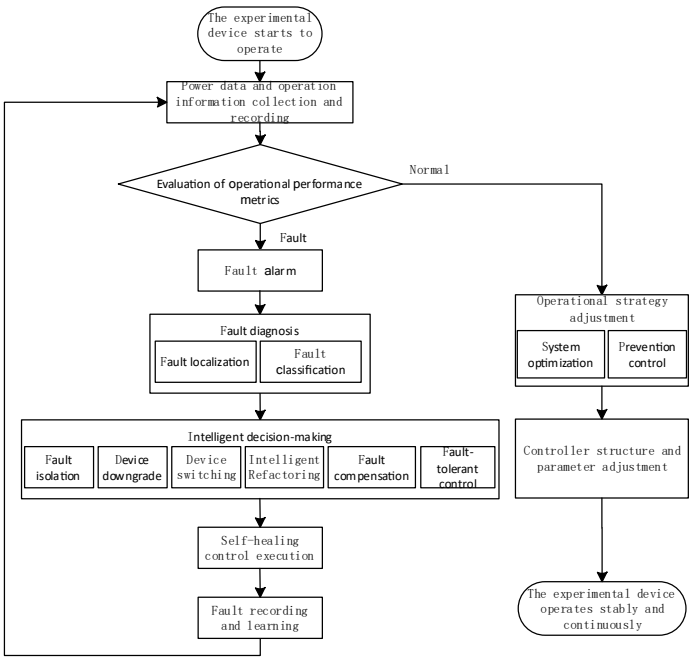


Fig. 6. Fault self-healing process flowchart.

Upon device startup, the apparatus collects and records real-time power data and operational information while evaluating critical performance metrics. For detected faults, it rapidly triggers audible/visual alarms, locates the fault, classifies it, and selects an intelligent decision scheme accordingly [18]. Examples include: For propulsion motor cooling system failures, it implements motor derating and load transfer; for distribution network short circuit faults, it employs intelligent grid reconfiguration; for motor speed

sensor failures, it applies fault compensation. The system records and learns from fault data, dynamically adjusting operational strategies to optimize performance and implement preventive control, thereby mitigating certain failures [19].

The flowchart of sound and light alarm is shown in Fig. 7. When the equipment is in normal operation, the corresponding indicator light on the audible and visual alarm interface is always green; When the device detects a fault, the corresponding indicator light on the interface flashes red and generates an alarm. According to the different fault duration, the device divides the fault into two types: long-term fault and short-term fault. A long-term fault means that the equipment has a continuous fault and the fault state lasts for a long time. At this time, after the researchers confirm the fault has occurred, the corresponding indicator light will remain red until the fault is eliminated; Short term fault refers to the transient fault of the equipment. The fault state lasts for a short time and can be recovered by itself or can be eliminated through simple treatment. At this time, after the researchers confirm the fault that has occurred, the corresponding indicator light will go out [20].

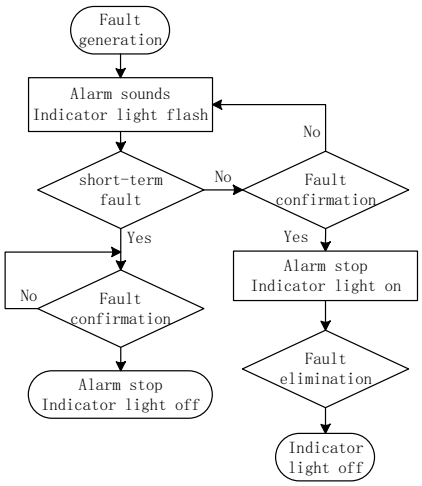


Fig. 7. Sound and light alarm flowchart.

4 Typical Operating Condition Verification

Short-circuit faults represent a common and highly detrimental failure mode in the operation of shipboard zonal distribution power system. When a short-circuit fault occurs, the current near the fault point will increase to several to ten times the rated current, Failure to achieve timely fault self-healing can lead to severe consequences such as power supply disruption and equipment damage [21]. This paper tests and validates a fault self-healing experimental device for shipboard zonal power distribution systems by simulating a two-phase short circuit reconstruction scenario within a distribution unit under simulation conditions.

The self-healing control industrial computer was programmed with particle swarm fault location and power distribution network reconfiguration algorithms. A phase-to-phase short circuit fault was simulated at distribution unit PDM5. Upon detecting the fault through the diagnostic algorithm, the experimental device immediately triggers audible and visual alarms, opens the circuit breakers surrounding PDM5 to isolate the faulted area, and rapidly reconfigures the power supply lines to ensure uninterrupted electricity supply to the loads in the model, as shown in Fig. 8.

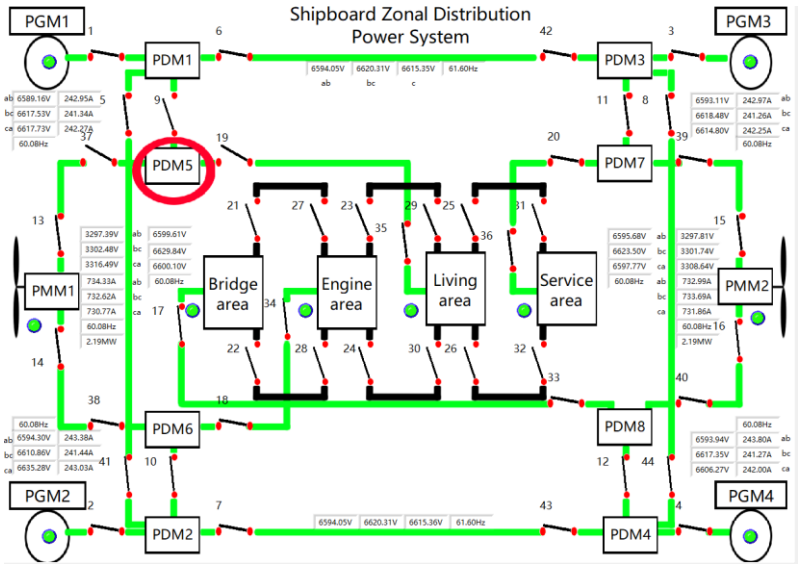


Fig. 8. Fault reconstruction results.

By monitoring the simulated waveform shown in Fig. 9, it was observed that the A-B phase short circuit fault in PDM5 significantly impacted PGM1. Prior to the fault, the rms values of the phase currents in PGM1 were approximately 244A, with peaks around 345A. All line voltages maintained stable rms values of approximately 6600V. At system time 100, the A-B phase short circuit fault occurred in the fifth distribution unit. At this point, the A and B phase currents of PGM1 surged abruptly to over 2000A, while the peak C phase current increased to a maximum of 830A. Simultaneously, the AB line voltage of the generator dropped below 100V, with other line voltages also showing significant reductions. By system time 200, the equipment completed fault isolation and network reconfiguration. The current and voltage of PGM1 rapidly recovered and stabilized near pre-fault conditions. Furthermore, the performance of the generator controller could be verified through the generator frequency waveform. The results demonstrate that the selected fault diagnosis and network reconfiguration methods enable self-healing for the A-B phase short circuit fault in PDM5. This experimental device can simulate the coupling relationships among components when faults occur in shipboard zonal distribution power system.

14

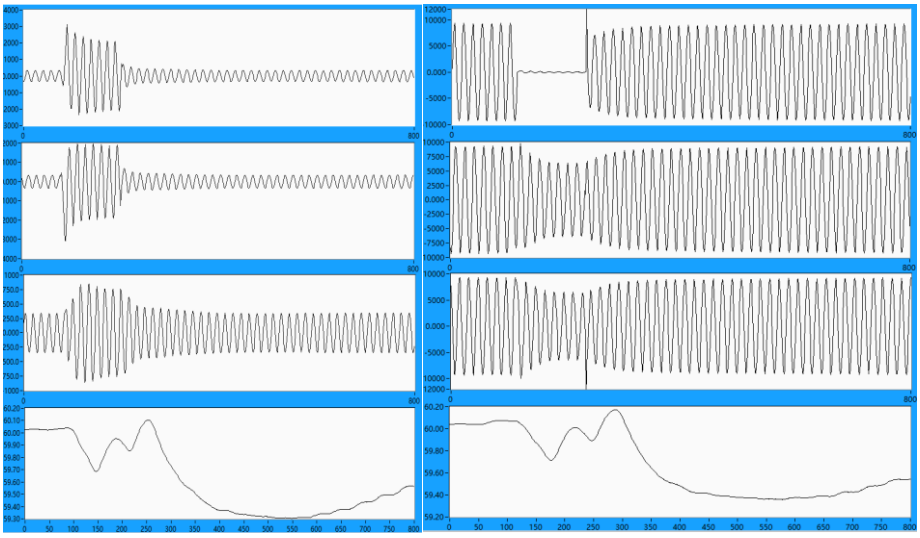


Fig. 9. Current(left) and voltage(right) waveform of Generator No.1.

5 Conclusion

This paper addresses the experimental requirements for researching fault self-healing methods in shipboard zonal distribution power system. A fault self-healing experimental device for this system has been developed, providing a multi-faceted experimental environment for related research, application development, and testing. The experimental device integrates a simulation model of the system with actual electrical equipment, enabling data exchange and collaborative operation between subsystems through multiple protocols including OPC, Modbus, and TCP/IP. This paper sequentially introduces the experimental device's hardware architecture, software development environment, simulation modeling and programming process. By applying hybrid programming techniques using LabVIEW and MATLAB, DLL and MATLAB Script nodes were utilized to achieve real-time simulation, monitoring and alarms, fault injection, fault diagnosis, and self-healing control for the shipboard zonal distribution power system. Finally, the self-healing capability of the experimental device is validated by simulating a two-phase short circuit fault scenario in the distribution unit. Results demonstrate that the developed experimental device provides integrated multi-functional capabilities encompassing real-time simulation, monitoring and alarm, fault injection, fault diagnosis, and self-healing control. This device offers a more realistic and reliable environment for research on self-healing in shipboard zonal distribution power system.

Acknowledgement: This work is supported by the National Natural Science Foundation of China (62473248); Shanghai Science and Technology Development Fund (20040501200)

References

1. Xiong Nan, F., Rao Yun, S., Ning Nan, T.: Research on fault self-healing ability of communication network for intelligent substation [J]. Electrical Measurement & Instrumentation59(08), 147-154 (2022).
2. Liang Huaqing, F., Yin Xunhe, S.: Self-healing control: Review, framework, and prospect [J]. IEEE Access(11), 79495-79512 (2023).
3. Gao Jihang, F., Zhang Yan, S.: Fault Diagnosis of Shipboard Zonal Distribution Power System Based on FWA-PSO-MSVM [J]. Computer Science49(S02), 956-960 (2022).
4. Zhang Lanyong, F., Zhang Ziqi, S., Peng Huimin, T.: Diagnostic method for short circuit faults at the generator end of ship power systems based on mwdn and deep-gated RNN-FCN [J]. Journal of Marine Science and Engineering11(9), 1806-1833 (2023).
5. Liu Sheng, F., Wang Tianqi, S., Zhang Lanyong, T.: Research on the network reconfiguration of power distribution in themedium voltage dc power system on ships [J]. Ship Science and Technology42(01), 116-122 (2020).
6. Liu Zicheng, F., Wu Junyong, S., Hao Liangliang, T.: Coordinated and fault-tolerant control of tandem 15-phase induction motors in ship propulsion system [J]. IET Electric Power Applications12(1), 91-97 (2018).
7. Hu Hongqian, F., Shi Weifeng, S., Xie Jialing, T.: Research on Semi-Physical Simulation Platform for Propeller Load Characteristics of Ship Electric Propulsion System [J]. Heilongjiang Science14(18), 73-76 (2023).
8. Wang Xueqing, F., Wang Zheng, S., Gu Minrui, T., et al.: Diagnosis-free self-healing scheme for open-circuit faults in dual three-phase PMSM drives [J]. IEEE Transactions on Power Electronics35(11), 12053-12071 (2020).
9. Yu Hong, F., Xu Wei, S., Li Ying, T., et al.: Hardware-in-the-Loop Simulation System Development of Permanent Magnet Synchronous Motor Controller [J]. System Simulation Technology19(01), 45-49 (2020).
10. Guo Yingqing, F., Zhang Jie, S., Huang Xinghuai, T.: The development and tests of remote data acquisition and transmission system on civil engineering structural vibration [J]. Journal of Asian Architecture and Building Engineering18(1), 9-15 (2019).
11. Li Mingyang, F., Shi Weifeng, S.: Research on Fault Self-healing Simulation of Shipboard Zonal Distribution Power System [C]. // 2nd International Conference on Smart Grids and Energy Systems. pp. 8-13. IEEE, Shanghai (2023).
12. Al-suod M M S, F., Alexander U O, S., Olga D I, T.: Optimization of the structure of diesel-generator units of ship power system [J]. International Journal of Advanced Computer Research5(18), 68-76 (2015).
13. Ding Wen, F., Gao Lin, S., Liang Deliang, T., et al.: Modeling and Simulation of Vector Control System for Permanent Magnet Syschronous Motors [J]. Micromotors43(12), 66-71 (2010).
14. Shen Kuicheng, F., Dai Xiaoqiang, S., Zhao Yang, T., et al.: Optimization of the structure of diesel-generator units of ship power system [J]. International Journal of Advanced Computer Research5(18), 68-76 (2015).
15. Zhen Hengchi, F., Wang Sunqing, S., Zhao Cong, T.: Modeling and analysis of ship diesel generator set parallel [J]. Ship Science and Technology43(09), 102-107 (2021).
16. Gutierrez-Guerrero J M, F., Holgado-Terriza J A, S., HUANG Xinghuai, T.: Automatic configuration of OPC UA for Industrial Internet of Things environments [J]. Electronics8(6), 600-617 (2019).

16

17. Xiao Na, F., Kong Xiangwei, S.: Design of a Flight Test Monitoring System Based on LabView and Matlab Hybrid Programming Technology [J]. China Science and Technology Information(16), 44-45 (2019).
18. Yu Shibin, F., Xu Bing, S., Zhang Yuxia., et al.: Review on Self-healing Control Technique in Smart Distribution Grid [J]. Proceedings of the CSU-EPSA25(05), 65-70 (2013).
19. Shi Pengjia, F., Jiao Hao, S., Zhang Kaixuan., et al.: Development and Application of Load Transfer Auxiliary Decision-making System in Distribution Grid [J]. Proceedings of the CSU-EPSA29(05), 1-6 (2017).
20. Shi Weifeng, F., Bao Yan, S., Zhou Zuohan, T.: Development of the multi-functional fault monitoring alarm device for the electrically propulsive ship power system [J]. Electrical Measurement & Instrumentation52(06), 82-88 (2015).
21. D'Agostino F, F., Grillo S, S., Infantino R, T., et al.: High-voltage shore connection systems: Grounding resistance selection and short-circuit currents evaluation[J]. IEEE Transactions on Transportation Electrification [J]. IEEE Transactions on Transportation Electrification 8(2), 2608-2617 (2021).

102 基于二次分解与 GJO-KELM 的短期光伏功率预测

王嵩[1]，王俊[1*]，王誉诺[1]，于星川[1]，于泽广[1]，高楷泽[1]

（1．沈阳农业大学，辽宁省沈阳市沈河区东陵路 120 号）

Short-term photovoltaic power prediction based on quadratic decomposition and GJO-KELM

Wang Song[1], Wang Jun[1*],Wang Yunuo[1], Yu Xingchuan[1], Yu Zeguang[1],Gao Kaize[1]

1. Shenyang Agricultural University, No. 120 Dongling Road, Shenhe District, Shenyang City, Liaoning Province)

ABSTRACT: To address the issue of insufficient short-term prediction accuracy for photovoltaic power sequences due to their nonlinear and highly non-stationary nature, a combined prediction model based on quadratic decomposition and intelligent optimization algorithms is proposed. First, the photovoltaic data is classified by weather type using the Kernel Fuzzy C-Means Clustering (KFCM) algorithm, and key features are selected through correlation analysis; Second, an enhanced adaptive noise-complete set empirical mode decomposition (ICEEMDAN) algorithm is adopted to conduct the initial decomposition of the power sequence, and sample entropy(SE) is applied to identify high-frequency components, followed by a second decomposition using the variational mode decomposition (VMD) algorithm, effectively separating noise interference and enhancing feature regularity; Finally, the Golden Jackal Optimization (GJO) algorithm is used to optimize the parameters of the Kernel Extreme Learning Machine (KELM), constructing a GJO-KELM submodel to predict each decomposed component, with the results overlaid to obtain the final outcome. Experimental results demonstrate that this model effectively reduces the complexity of photovoltaic power sequences, achieving higher prediction accuracy than other models under three weather conditions.

KEY WORDS: Short-term photovoltaic power forecasting; secondary decomposition; golden jackal optimization algorithm; nuclear extreme learning machine; weather classification

摘要：针对光伏功率序列非线性、非平稳性强的短期预测精度不足问题，提出基于二次分解与智能优化算法的组合预测模型。首先，基于核模糊 C 均值聚类(KFCM)算法对光伏数据按天气类型分型，结合相关性分析筛选关键特征；其次，通过改进自适应噪声完备集合经验模态分解(ICEEMDAN)算法对功率序列进行初次分解，再经样本熵(SE)识别高频分量，变分模态分解(VMD)算法二次分解，有效分离噪声干扰并增强特征规律性；最后，采用金豺优化算法（GJO）对核极限学习机（KELM）的参数寻优，构建 GJO - KELM 子模型对各分解分量预测，叠加得到最终结果。实验表明，该模型有效降低光伏功率序列复杂度，在三种天气条件下，预测精度均高于其他模型。

关键词：光伏功率短期预测；二次分解；金豺优化算法；核极限学习机；天气分型

DOI：

0 引言

在工业化与经济全球化的双重推动下，能源体系的基础作用愈发关键。以电力为核心的二次能源转换系统，自 19 世纪电气革命后持续主导能源供给格局，依托完善的输配电网支撑着现代制造业、智慧农业等支柱产业的稳定运行[1]。当前我国正处于新型能源体系建设关键期，在 “双碳” 目标驱动下，光伏能源转换技术已成为清洁能源技术攻关的前沿领域。经过规模化推进，我国光伏产业已进入高质量发展新阶段，其作为新能源体系核心的定位不断强化[2]。然而，随着光伏发电装机容量的持续提升与广泛应用，其受太阳辐射、温度、降水等环境因素影响的不稳定性和间歇性问题日益凸显，大规模并网可能对电网造成冲击并带来安全隐患。因此，实现稳定精准的光伏发电功率预测至关重要，这不仅能提升电网消纳能力、降低运行成本，更能保障电网安全、保护用电设备、提高电能质量，从而减少经济损失[3]。

随着人工智能的快速发展，深度学习方法在预测领域得到广泛应用[4]。黄广斌等[5]以单层前馈网络为基础框架，引入 Adaboost 算法进行优化改进，最终开发出了名为极限学习机（ELM）的神经网络模型。该模型能够快速收敛，并避免陷入局部最优解，提高了预测模型的性能。KELM（kernel based extreme learning machin）在原有模型框架基础上做出了关键优化：一方面引入惩罚系数对学习模式进行正则化调整，另一方面创新性地采用核函数替代了传统模型隐含层中的神经元节点 [6]。这一系列改进进一步增强了模型的泛化能力与学习稳定性，为其在复杂预测场景中的应用奠定了更坚实的基础。

同时，为提高预测性能，诸多学者利用优化算法优化其学习参数。章勇高等[7]提出一种基于遗传算法（GA）的核函数极限学习机模型，用于光伏短期出力预测；该模型采用遗传算法对 KELM 的关键参数进行优化寻优，以提升预测性能。赵鹏等[8]针对正则化系数和核参数影响核极限学习机预测精度的问题，提出 PSO-KELM 预测方法，以两者为优化对象通过 PSO 共同优化建立风功率预测模型。赵睿智等[9]针对 EEMD 分解风功率时序信号存在模态混淆及重构误差大的问题，提出基于 MEEMD-KELM 的风电功率短期预测方法，即采用 MEEMD 分解信号并结合 KELM 模型。王京友[10]等采用 GJO 算法优化模型超参数组合以克服人工调参随机性，基于 2019 年某风电场实测数据的实验表明，GJO-TCN-BiGRU-attention 模型预测性能良好且在风速突变场景鲁棒性更强。

近年来，信号分解技术被广泛应用于预测领域。其中，张雲钦等[11] 提出基于 EMD 与 LSTM 的组合预测方法，通过 EMD 分解原始序列输入 LSTM 提升预测精度，但该方法存在 EMD 易产生模态混淆需进一步优化改进的问题。董雪等[12]利用完全集合经验模态（CEEMDAN）进行初次分解，并采用辛几何模态分解进一步分解，降低了数据的复杂性。常雨芳等[13]提出将 CEEMDAN 算法与排列熵相结合的方案，通过该组合方法判断各分量的噪声水平，随后对含噪分量采用小波包分解（WPD）进行深度分解与预测，显著提升了预测精度。

综上，本文针对光伏功率短期预测中存在的非线性、非平稳性及气象异质性问题，提出一种基于二次分解的 GJO-KELM 组合预测模型。首先通过 KFCM 算法对光伏数据进行天气类型聚类，结合相关性分析筛选关键气象特征；其次采用 ICEEMDAN-SE-VMD 二次分解框架对功率序列进行精细化处理，剥离噪声并提取多尺度特征；最后利用 GJO 算法优化 KELM 参数，构建子模型对各分解分量预测并叠加结果。

1 数据预处理及分析

1.1 数据集描述

实验数据选取辽宁某光伏电站的实测数据。该数据集的时间跨度为 2018 年 6 月 1 日至 8 月 31 日，筛选每日 6:00 至 19:00 的有效运行时段数据，以此消除夜间零功率输出状态对实验分析的干扰。数据采用 15 分钟为单位的采样周期进行记录，涵盖的关键特征因素包括：总辐射强度、光伏组件温度、环境温度、大气压力及湿度。

1.2 数据归一化

在光伏功率预测的数据预处理流程中，数据归一化是消除特征量纲差异的关键环节。该方法通过线性变换保留数据的相对分布特性，将各特征值映射至[0,1]区间。计算公式为：

$$X' = \frac{X - X_{\min}}{X_{\max} - X_{\min}} \tag{1}$$

式中，$X_{\min}$ 和 $X_{\max}$ 分别为对应特征在训练集中的最小值与最大值。

1.3 特征因素相关性分析

气象特征的时空信息可显著提升预测模型泛化能力，但传统特征工程的冗余特征会增加空间复杂度，加剧过拟合风险并降低精度，故科学筛选机制至关重要；光伏功率预测需考虑多种特征与光伏功率之间的关系，常用 Pearson[14]和 Spearman [15]相关系数衡量相关性，系数绝对值越大则与发电量相关性越高。

Pearson 和 Spearman 相关系数评估两个连续变量之间的线性关系，可表示为：

$$\rho_p = \frac{\sum_{i=1}^{n}(q_{il} - \bar{q_l})(y_i - \bar{y})}{\sqrt{\sum_{i=1}^{n}(q_{il} - \bar{q_l})^2 \sum_{i=1}^{n}(y_i - \bar{y})^2}} \tag{2}$$

$$\rho_s = 1 - \frac{\sum_{i=1}^{n}(R(q_{il}) - R(y_i))^2}{N(N^2 - 1)} \tag{3}$$

式中，q_{il} 是第 l 个维度气象因子的第 i 个值，y_i 是光伏功率数据的第 i 个测量值，$R(q_{il})$ 和 $R(y_i)$ 分别是各自列向量中的排序。$\bar{y}$ 是光伏功率数据的平均值。

表 1 光伏功率与各环境变量特征之间的相关系数

Tab.1 Correlation coefficients between photovoltaic power and various environmental variables

方法	Pearson	Spearman
总辐射	0.869	0.9385
组件温度	0.5608	0.4308
环境温度	0.4929	-0.3884
气压	0.06659	0.03105
湿度	-0.3927	-0.3402

将气象特征经 Pearson 和 Spearman 相关性分析计算后的结果如表 1 所示，后续的模型输入的气象特征为总辐射、组件温度、环境温度和湿度。

1.4 基于 KFCM 算法的相似日聚类

尽管 FCM 在负荷数据处理中表现良好，但传统 FCM 以欧式距离为距离函数，易受噪声和异常值影响，致聚类结果不准确。为解决此问题，引入核函数构建 KFCM 聚类，用高斯径向基函数替换欧式距离，借核函数将有限维数据映射到高维空间

聚类，可更清晰识别数据非线性关系，提升对噪声和孤立点的鲁棒性，实现更精确样本聚类[16]，KFCM 算法的主要计算过程如下：

（1）随机选聚类中心 $v_j=(v_{j1},v_{j2},\cdots,v_{jm})$ ，$j=1,2,\cdots,c$，其中 c 是预先设定的聚类数目。

（2）对于每个数据点 x_i 和每个聚类中心 v_j ，计算聚类的隶属度，计算公式如下：

$$u_{ij}=\frac{1}{\sum_{k=1}^{c}\left(\frac{K(x_i,v_j)}{K(x_i,v_k)}\right)^{\frac{2}{m-1}}} \tag{4}$$

$$K(x_i,v_j)=\exp\left(-\frac{\left\|x_i-v_j\right\|^2}{2\sigma^2}\right) \tag{5}$$

式中，$\|\bullet\|$表示欧几里得距离，σ 是核函数的带宽参数，m 是模糊加权指数。

（3）更新聚类中心

根据当前的隶属度矩阵，更新聚类中心 ：

$$v_j=\frac{\sum_{i=1}^{n}u_{ij}^m K(x_i,v_j)x_i}{\sum_{i=1}^{n}u_{ij}^m K(x_i,v_j)} \tag{6}$$

（4）迭代计算

重复步骤 3 和步骤 4 直到满足预设的迭代终止条件。即当 $\max_j\left\{\left\|v_j^{t+1}-v_j^t\right\|\right\}<\tau$ 或当迭代次数 $t=T$ 时，停止迭代。

算法聚类后得到晴天、多云和雨天 3 种天气类型，其中晴天共 31 d，多云共 45 d，雨天共 16 d。

2 基于二次分解的组合预测模型

2.1 二次分解

2.1.1 ICEEMDAN

ICEEMDAN 算法是一种先进的信号分解技术，其核心优势在于自适应噪声调节机制[17]。该方法通过添加特定统计特性的白噪声，显著抑制了传统经验模态分解中常见的模态混叠现象，同时减少了虚假模态成分的产生，从而提升分解精度。本研究将该算法应用于光伏功率序列数据的一次处理，具体实现流程如下：

（1）在原始光伏功率序列添加一组特殊白噪声 $w^{(i)}$，得到新序列 $x^{(i)}$：

$$x^{(i)}=x+\beta_0 E_1(w^{(i)}) \tag{7}$$

（2）将每个 $x^{(i)}$ 进行包络计算，通过求解平均值获取第一组残差值 r_1，进而计算得到第一个模态分量：

$$r_1=\frac{1}{I}\sum_{i=1}^{I}N(x^{(i)}) \tag{8}$$

$$I_{IMF1}=x-r_1 \tag{9}$$

（3）在原始光伏功率序列添加一组特殊白噪声 $w^{(i)}$，得到新序列 $x^{(i)}$：

$$x^{(i)}=x+\beta_0 E_1(w^{(i)}) \tag{10}$$

（4）加一组特殊白噪声 $w^{(i)}$，从而得到新序列 $x^{(i)}$，计算公式如下：

$$x^{(i)}=P+\alpha_0 E_1(w^{(i)}) \tag{14}$$

（5）将每个新序列 $x^{(i)}$ 进行包络计算，通过求解平均值得到第一组残差值 R_1，计算出第一个模态分量，计算公式如下：

$$R_1=\frac{1}{I}\sum_{i=1}^{I}N(x^{(i)}) \tag{12}$$

$$I_{IMF1}=P-R_1 \tag{13}$$

（6）计算第二个模态分量 ：

$$R_2=\frac{1}{I}\sum_{i=1}^{I}N(R_1+\alpha_1 E_2(w^{(i)})) \tag{14}$$

$$I_{IMF2}=R_1-R_2 \tag{15}$$

（7）重复上述步骤，计算第 k 个残余分量 R_k 和模态分量 I_{IMFK} ：

$$R_k=\frac{1}{I}\sum_{i=1}^{I}N(R_{k-1}+\alpha_{k-1}E_2(w^{(i)})) \tag{16}$$

$$I_{IMFk}=R_{k-1}-R_k \tag{17}$$

2.1.2 SE

样本熵算法相较于近似熵，该算法具有更高的计算稳定性，且对数据长度不敏感，能够更可靠地反映序列的随机性和不规则性[18]。通过样本熵算法对于一次分解的结果进行重构，其具体计算过程如下：

（1）对于一个包含 N 个采样点的时间序列 T ：

$$T(n)=T(1),T(2),\cdots T(N) \tag{18}$$

（2）按序列号构造一组维度为 m 的向量序列：

$$V_m(i)=\{T(i),T(i+1),\cdots,T(i+m-1)\} \tag{19}$$

（3）定义向量 $X_m(i)$ 与 $X_m(j)$ 之间的距离：

$$d[V_m(i),V_m(j)]=\max_{0\le k\le m-1}|T(i+k)-T(j+k)| \tag{20}$$

（4）统计符合条件阈值 $r\ge d[V_m(i),V_m(j)]$ 的向量个数 C_i 和 $N-M$ 的比值 $C_i^m(r)$ ，计算均值：

$$d[V_m(i),V_m(j)]=\max_{0\le k\le m-1}|T(i+k)-T(j+k)| \tag{21}$$

（5）计算其均值 $D^m(r)$：

$$D^m(r)=\frac{\sum_{i=1}^{N-m+1}C_i^m(r)}{N-m+1} \tag{22}$$

（6）将维度增加到 $m+1$，重复上述步骤，得到 $D^{m+1}(r)$ 的均值：

$$D^{m+1}(r)=\frac{\sum_{i=1}^{N-m+1}C_i^{m+1}(r)}{N-m+1} \quad (23)$$

（7）样本熵的计算公式可表示为：

$$S_E(m,r)=\lim_{N\to\infty}\left\{-\ln\left[\frac{D^{m+1}(r)}{D^m(r)}\right]\right\} \quad (24)$$

（8）计算 IMF 分量样本熵阈值 ：

$$\hat{S}=\frac{\max(\bar{S}_o\mid o=1,2,\cdots Q)-\min(\bar{S}_o\mid o=1,2,\cdots Q)}{2} \quad (25)$$

2.1.3 VMD

VMD 算法是一种基于变分原理的非递归信号处理方法。该方法通过构建并求解约束变分问题，能够将非平稳光伏功率信号自适应地分解为若干具有明确中心频率的模态分量（IMF）[19]。其实现流程如下：

（1）构建约束变分最优问题：

$$\begin{cases}\min\limits_{\{U_k\},\{W_k\}}\left\{\sum\limits_{K=1}^{K}\|\partial_t\left[\left(\delta_t+\frac{j}{\pi t}\right)*u_k(t)\right]e^{-jw_k^t}\|_2^2\right\}\\ s.t.\sum\limits_{K=1}^{K}U_k(t)=X(t)\end{cases} \quad (26)$$

式中，*代表卷积运算符。δ_t 为狄拉克函数。

（2）将约束变分问题变为无约束的变分模型：

$$L(\{U_k\},\{W_k\},\Lambda(t))=\beta\sum_{K=1}^{K}\|\partial_t\left[\left(\delta_t+\frac{j}{\pi t}\right)*U_k(t)\right]e^{-jw_k^t}\|_2^2+\|G_{IIMF}(t)-\sum_{K=1}^{K}U_k(t)\|_2^2 \quad (27)$$
$$+\left\langle\Lambda(t),G_{IIMF}(t)-\sum_{K=1}^{K}U_k(t)\right\rangle$$

（3）利用交替方向乘子迭代算法，最终得到指定数量的模态分量。

根据上述分析，本文提出了一种二次分解策略，其流程如图 1 所示。

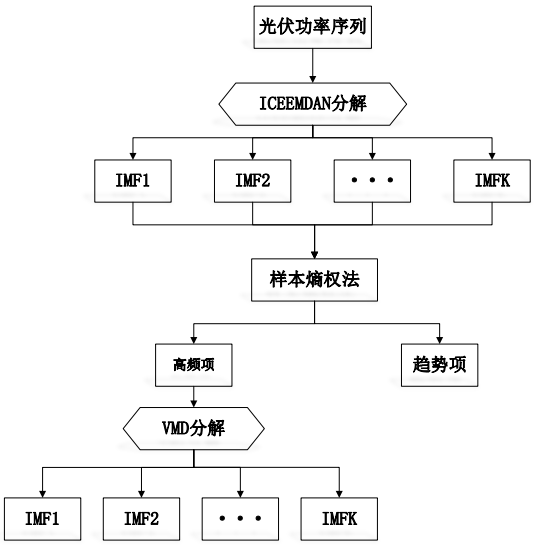


图 1 二次分解流程图

Fig.1 Secondary decomposition flow chart

2.2 金豺优化算法

金豺优化算法是一种受自然界金豺协作狩猎行为启发的元启发式算法，该算法模拟金豺在狩猎时对猎物的包围、追踪和攻击策略，通过雄性-雌性领导机制实现全局搜索与局部开发的平衡：

（1）种群初始化，

$$X_0=X_{\min}+rand\bullet(X_{\max}-X_{\min}) \quad (28)$$

其中，X_0 表示金豺种群的初始位置。

（2）猎物矩阵（Prey）可作如下表示：

$$\Pr ey=\begin{bmatrix}X_{1,1}&\cdots&X_{1,d}\\ \vdots&\ddots&\vdots\\ X_{n,1}&\cdots&X_{n,d}\end{bmatrix} \quad (29)$$

（3）猎物的适应度值矩阵 F_{OA} 如下:

$$F_{OA}=\begin{bmatrix}f(X_{1,1};X_{1,2};\cdots;X_{1,d})\\ \vdots\\ f(X_{n,1};X_{n,2};\cdots;X_{n,d})\end{bmatrix} \quad (30)$$

（4）金豺的狩猎工作由如下数学公式实现:

$$X_1(t)=X_M(t)-E\cdot\left|X_M(t)-r_1\cdot\Pr ey(t)\right| \quad (31)$$

$$X_2(t)=X_{FM}(t)-E\cdot\left|r_1\cdot X_{FM}(t)-\Pr ey(t)\right| \quad (32)$$

（5）猎物的逃脱能量可用如下公式计算:

$$\begin{cases}E=E_1\cdot E_0\\ E_0=2\cdot r-1\\ E_1=c_1\cdot(1-\frac{t}{T})\end{cases} \quad (33)$$

其中，E_1 表示猎物能量的下降过程，E_0 表示猎物能量的初始状态。

（6）基于莱维分布的一个随机数:

$$r_1=0.05\cdot LF(y) \quad (34)$$

$$LF(y)=0.01\cdot(\mu\cdot\sigma)/(\left|v^{(1/\beta)}\right|) \quad (35)$$

$$\left(\frac{\Gamma(1+\beta)\cdot\sin(\pi\beta/2)}{\Gamma(\frac{1+\beta}{2})\cdot\beta\cdot2^{\frac{\beta-1}{2}}}\right)^{1/\beta} \quad (36)$$

（7）金豺位置更新公式为:

$$X(t+1)=(X_1(t)+X_2(t))/2 \quad (37)$$

（8）金豺会对猎物形成包围并发起攻击，最终完成捕食的行为可通过如下数学公式表达：

$$X_1(t)=X_M(t)-E\cdot\left|r_1\cdot X_M(t)-\Pr ey(t)\right| \quad (38)$$

$$X_2(t)=X_{FM}(t)-E\cdot\left|r_1\cdot X_{FM}(t)-\Pr ey(t)\right| \quad (39)$$

金豺优化算法流程如图 2 所示。

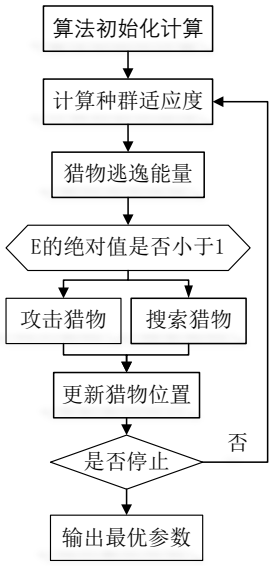


图 2 金豺优化算法流程图

Fig.2 Golden Jackal Optimization Algorithm Flowchart

2.3 核极限学习机

KELM 的核心思路是将 ELM 中的隐层神经元替换为核函数，以核矩阵取代 ELM 中的输入矩阵。

（1）其网络节点输出的矩阵形式为：

$$T = H\beta \tag{40}$$

式中，T 为期望的目标矩阵，β 为隐含层和输出层之间的权值矩阵，H 为隐含层输出矩阵。

（2）H 的表达式为：

$$H = \begin{pmatrix} g(x_1; w_1, b_1) & \cdots & g(x_1; w_N, b_L) \\ \vdots & \ddots & \vdots \\ g(x_n; w_1, b_1) & \cdots & g(x_n; w_L, b_L) \end{pmatrix}_{N \times L} \tag{41}$$

（3）最优的输出权重矩阵：

$$f(x) = \begin{bmatrix} K(x, x_1) \\ \vdots \\ K(x, x_N) \end{bmatrix} \tag{42}$$

式中，$\hat{H}$ 为 H 的广义逆。

（4）将 ELM 神经网络中的随机矩阵替换为核函数矩阵：

$$\Omega = H\hat{H} = h(x_i)h(x_j) = K(x_i, x_j) \tag{43}$$

式中，$K(\cdot)$ 表示核函数。

（5）引入正则化系数 C 在 ELM 神经网络随机矩阵中：

$$\hat{\beta} = \hat{H}(H\hat{H} + \frac{I}{c})^{-1}T \tag{44}$$

（6）基于上述式子，可将 KELM 神经网络的输出函数表示为：

$$f(x) = \begin{bmatrix} K(x, x_1) \\ \vdots \\ K(x, x_N) \end{bmatrix} (\Omega + \frac{I}{c})^{-1}T \tag{45}$$

2.4 组合模型基本流程

基于上述原理，本文构建了基于二次分解的 GJO-KELM 组合预测模型，流程图如图 3 所示。

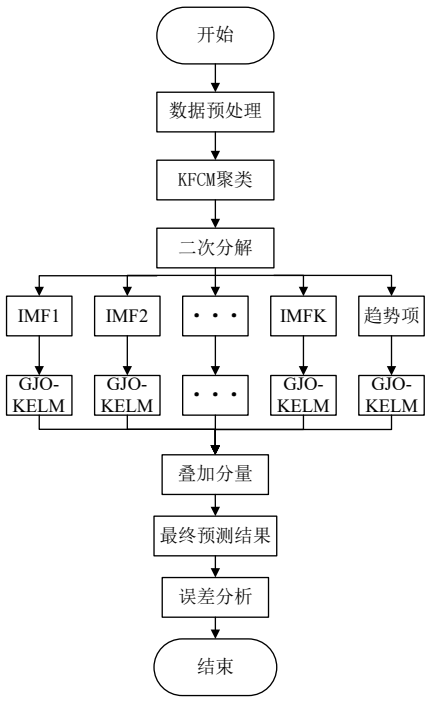


图 3 组合预测模流程图

Fig.3 Combination Prediction Model Flowchart

步骤 1 对原始光伏功率及气象数据进行清洗，剔除异常值，通过 min-max 标准化将特征值映射至 [0,1] 区间，同时筛选关键影响因子，为后续建模提供高质量输入。

步骤 2 采用 KFCM 聚类算法，依据天气特征将数据集划分为晴天、多云、雨天等类别 ，降低不同天气模式混合对预测的干扰，实现数据分层建模。

步骤 3 先通过 ICEEMDAN 将各聚类后的功率序列分解为多个 IMF 分量与趋势项，再经样本熵算法识别复杂高频分量，并采用 VMD 进行二次分解；对分解得到的各子序列，采用 GJO 算法优化 KELM 的参数，构建 GJO-KELM 模型对于每个子序列进行预测。

步骤 4 计算各子模型的预测结果，按原始分解的序列结构叠加分量，最终获取光伏功率预测结果后，通过开展对比实验分析模型精度，以此验证所提方法的有效性。

3 算例仿真及分析

3.1 模型评价指标

采用均方根误差（RMSE）、平均绝对误差 MAE）和均方误差（MSE）作为评价指标。公式如下：

$$E_{RMSE} = \sqrt{\frac{1}{n}\sum_{i=1}^{n}(y_t - \hat{y}_t)^2} \tag{46}$$

$$E_{MAE}=\frac{1}{n}\sum_{i=1}^{n}|y_t-\hat{y}_t| \quad (47)$$

$$E_{MSE}=\frac{1}{n}\sum_{i=1}^{n}(y_t-\hat{y}_t)^2 \quad (48)$$

式中，y_t 和 $\hat{y}_t$ 为实际值和预测值；$\overline{y_t}$ 为样本平均值。

3.2 光伏功率数据分解

3.2.1 基于 ICEEMDAN 的一次分解

ICEEMDAN 算法凭借其自适应噪声注入机制，通过动态调整噪声幅值有效平衡了高频细节保留与模态混叠抑制的矛盾。本研究将其作为光伏功率数据信号分解的首次分解阶段。如图 4 所示，分解后获得 10 个具有明确物理意义的 IMF 分量及表征趋势项的残差序列，分别对应不同时间尺度的波动特征和长期运行趋势。该预处理过程构建了层次分明的初级特征空间，为后续二次分解奠定了基础。

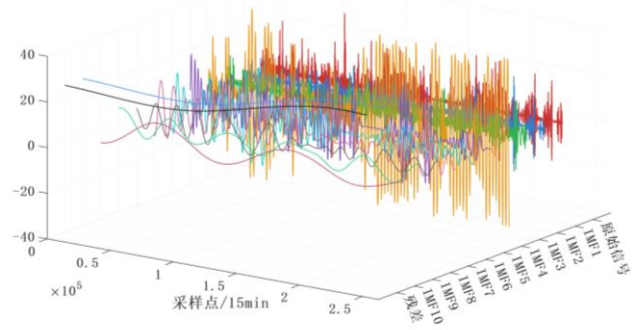


图 4 ICEEMDAN 的分解结果图

Fig.4 ICEEMDAN decomposition results

3.2.2 基于 SE 的分量重构

通过样本熵分析量化了各成分的复杂程度，计算出每个成分的熵值，具体结果如图 5 所示，成分 1、2、3、4 的熵值明显高于临界阈值，说明不规则波动对整体趋势有显著影响。其余成分反映了趋势特征，被归类为趋势项。

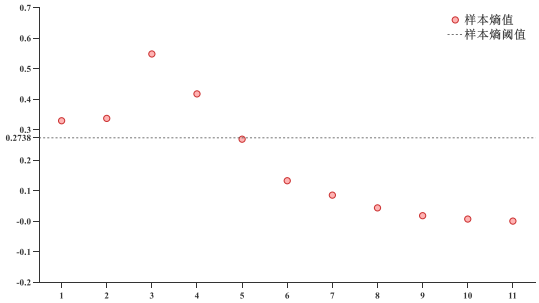


图 5 样本熵值

Fig.5 Sample Entropy value

将高频项和趋势项进行叠加。值得注意的是，即使经过初步处理，高频项中仍存在大量的噪声，其波动特征较为随机，这可能影响后续预测模型的精度。因此，如何有效分离高频分量中的有效信息与噪声，是提升预测性能的关键问题。

3.2.3 基于 VMD 的二次分解

针对 ICEEMDAN 分解所得高频分量中存在的噪声干扰问题，采用 VMD 对高频成分进行分解，根据计算中心频率，最终确定 VMD 的关键参数 K 值为 6。如图 6 所示，经优化后的分解方法将原始功率信号有效分离为六个特征尺度差异明显的 IMF，这种多尺度分解结果有效分解了光伏功率中确定性趋势与随机干扰成分，为后续构建高精度预测模型奠定了重要基础。

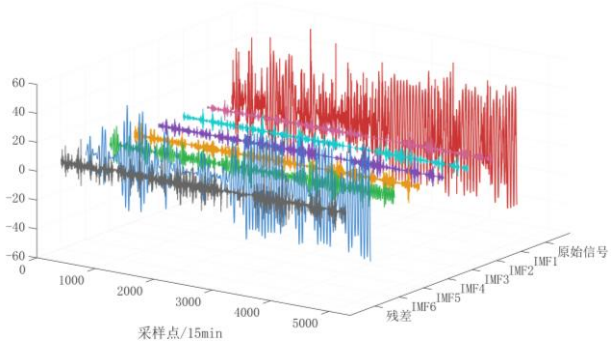


图 6 VMD 的分解结果图

Fig.6 VMD decomposition results

3.3 预测结果分析

为验证所提模型的优越性与有效性，本文选取 BP、ELM、KELM 及 VMD-KELM 模型作为对比模型，结合三种不同天气类型开展光伏发电功率预测实验。对于 ELM 和 KELM 模型，统一选用 sigmoid 函数作为激活函数；金豺优化（GJO）算法的参数设置为：种群规模 30，最大迭代次数 100，初始能量参数 1.5，猎物位置更新随机数在[0,1]区间内均匀生成。实验预测结果如图 7 至图 9 所示，各模型误差对比数据如表 2 所示。

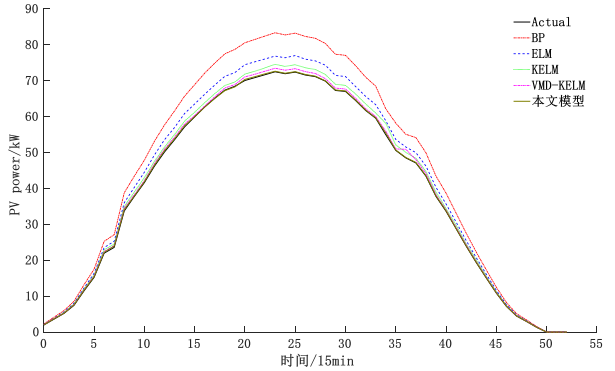


图 7 各模型在晴天条件下的预测结果

Fig.7 Prediction results of each model under sunny conditions

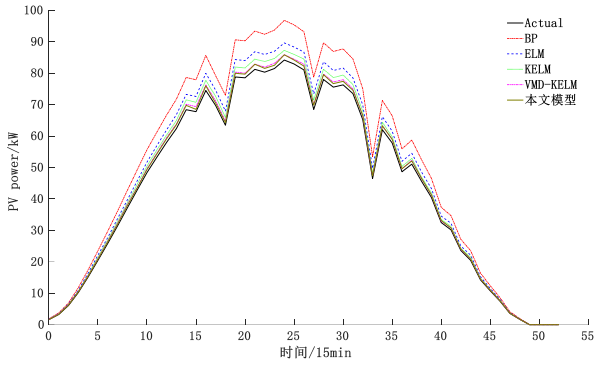


图 8 各模型在多云条件下的预测结果

Fig.8 Prediction results of each model under cloudy conditions

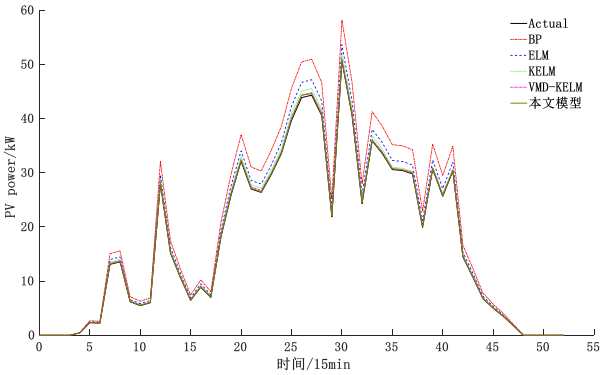


图 9 各模型在雨天条件下的预测结果

Fig.9 Prediction results of each model under rainy conditions

天气	预测模型	RMSE/kW	MAE/kW	MSE/kW
晴天	BP	7.1250	5.9857	50.7663
	ELM	2.9714	2.5241	8.8292
	KELM	1.3409	1.1415	1.7980
	VMD-KELM	0.6698	0.5340	0.4486
	本文模型	0.1830	0.1461	0.0335
多云	BP	7.8928	6.6053	62.2957
	ELM	3.6629	3.0702	13.4170
	KELM	2.1236	1.7659	4.5098
	VMD-KELM	1.1390	0.9599	1.2974
	本文模型	0.9188	0.7746	0.8443
雨天	BP	3.4572	2.6430	11.9525
	ELM	1.4216	1.0925	2.0210
	KELM	0.6325	0.4797	0.4001
	VMD-KELM	0.2646	0.2005	0.0070
	本文模型	0.1279	0.0940	0.0164

实验结果显示，模型在晴天天气下的预测效果显著优于多云和雨天，这是由于晴天具有稳定的光照时长和较高的太阳辐照度，使得光伏电站输出功率曲线更为平缓，模型对这类数据分布的适应性更强。

在模型结构设计上，通过 KFCM 聚类与组合预测的有机结合，实现了对气象异质性的针对性处理。采用高斯核函数改进的 KFCM 算法，可将原始数据精准聚类为晴天、多云、雨天三类天气模式，有效规避了不同光照条件下数据分布差异对模型泛化能力的干扰。算例数据表明，所提模型在三类天气中的 RMSE 分别为 0.1830kW、0.9188kW、0.1279kW，较单一 KELM 模型分别降低 86.3%、56.7%、80.1%，充分验证了金豺优化算法对 KELM 参数自适应调节的关键作用。对比实验进一步证实，经 GJO 优化的 KELM 模型较未优化模型的预测误差降低约 40%-50%，成功解决了传统 ELM 因随机权重初始化导致的性能不稳定问题。

4 结论

本文提出了一种基于二次分解的短期光伏功率组合预测模型。该模型融合数据预处理、KFCM 聚类、二次分解及 GJO-KELM 等方法，通过算例验证与结果分析，得出以下结论：

（1）二次分解策略提升数据特征质量：ICEEMDAN-SE-VMD 二级分解框架，先将原始功率序列粗分解为多尺度分量，再经样本熵识别复杂高频分量并以 VMD 进行再次分解，有效剥离噪声、凸显特征规律。实验表明，经二次分解后，各子序列预测难度降低，验证了分解策略的有效性。

（2）GJO 优化 KELM 增强模型预测性能：GJO 算法模拟种群生态行为，对 KELM 的参数进行自适应寻优，解决了 KELM 随机初始化易陷入局部最优的问题。对比实验显示，GJO-KELM 较未优化 KELM，预测误差显著降低，证明 GJO 对模型参数优化的显著作用，增强了预测精度与稳定性。

（3）组合模型优势显著：与 BP、ELM 等单一模型及 VMD-KELM 等对比模型相比，本文构建的二次分解 - GJO-KELM 组合模型，在晴天、多云、雨天不同天气类型下，均展现更优预测性能，有效应对光伏功率的非线性、非平稳性及气象异质性，预测精度与泛化能力更突出。

综上所述，本模型在短期光伏功率预测中效果显著，能够为光伏电站的功率预测及调度决策提供可靠支撑。同时，也为后续探索超短期、中长期等更广泛时间尺度的预测场景筑牢基础，助力进一步提升复杂天气条件下的预测精度。

参考文献

[1] Li Z, Wu L, Xu Y, et al. Distributed tri-layer risk-averse stochastic game approach for energy trading among multi-energy microgrids[J]. Applied Energy, 2023, 331: 120282.

[2] 董梓童.新兴市场持续发力，全球光伏装机创新高[N].中国能源报，2022-03-14(006).

[3] 赖昌伟,黎静华,陈博,黄玉金,韦善阳.光伏发电出力预测技术研究综述[J].电工技术学报,2019,34(06):1201-1217.

[4] 朱琼锋,李家腾,乔骥,等.人工智能技术在新能源功率预测的应用及展望[J].中国电机工程学报,2023,43(08).

[5] Huang G B, Zhu Q Y, Siew C K. Extreme learning machine: theory and applications[J]. Neurocomputing, 2006, 70(1-3): 489-501.

[6] SUN S L, WEI Y J, T SUI K L, et al. Forecasting tourist arrivals with machine learning and internet search index[J].Tourism management,2019,70:1-10.

[7] 章勇高,高彦丽,马迪.基于 GA-KELM 的光伏短期出力预测研究[J].

控制工程,2018,25(07):1155-1159.
[8] 赵鹏, 涂菁菁, 杨锡运. 基于PSO-KELM的风功率预测研究[J]. 电测与仪表, 2020, 57 (11): 24-29.
[9] 赵睿智, 丁云飞. 基于 MEEMD-KELM 的短期风电功率预测[J]. 电测与仪表, 2020, 57 (21): 92-98.
[10] 王京友, 李子健, 应润宇. 基于 GJO-TCN-BiGRU-attention 的风电功率预测模型[J]. 现代工业经济和信息化, 2025, 15 (06): 261-263.
[11] 张雲钦,程起泽,蒋文杰等.基于 EMD-PCA-LSTM 的光伏功率预测模型[J].太阳能学报,2021,42(09):62-69.
[12] 董雪,赵宏伟,赵生校等.基于二次分解和多目标优化的超短期海上风电功率预测[J].高电压技术,2022,48(08):3260-3270.
[13] 常雨芳,杨子潇,潘风等.基于 CEEMDAN-PE-WPD 和多目标优化的超短期风电功率预测方法[J/OL].电网技术,1-12[2023-12-05]
[14] 周鑫,李燕,曾永辉,等.基于SARIMAX-SVR的光伏发电功率预测[J].电力系统及其自动化学报,2024,36(05):1-8.
[15] 谢国民,陈天香.改进黑猩猩算法的光伏发电功率短期预测[J].电力系统及其自动化学报,2024,36(02):135-143.
[16] 邓明亮,张钊,周红艳,等.基于 PCA-PSO__KFCM 聚类和 BiLSTM-Attention 的短期电力负荷预测[J/OL].计算机工程与科学,1-14[2025-08-23].
[17] 于多,曹燚,王海荣,等.基于 ICEEMDAN-PE 和 IDBO-Informer 组合模型的短期负荷预测[J].中国电力,2025,58(06):19-32.
[18] 范士雄,李东琦,郭剑波,等.基于时变滤波经验模态分解-重构和独立自注意力机制的 iTransformer 超短期负荷预测方法[J].电网技术,2025,49(06):2436-2445.
[19] 谢国民,陆子俊.基于优化VMD和BiLSTM的短期负荷预测[J].电力系统及其自动化学报,2025,37(04):30-39.


王嵩

收稿日期

作者简介：

王嵩，男，博士研究生，研究方向为人工智能在电力系统中的应用，E-mail：wsong2025@stu.syau.edu.cn；

王俊(1979)，男，教授，通信作者，博士生导师，研究方向为可再生能源电力并网运行与控制等，E-mail：wddream2016@syau.edu.cn。

103 基于对比学习的极端天气电力负荷预测方法

张轩语[1]，王俊[1*]，杨淞[1]，王嵩[1]，王誉诺[1]，高楷泽[1]

（1. 沈阳农业大学 信息与电气工程学院，辽宁 沈阳 110866）

Extreme weather load forecasting method based on contrastive learning

ZHANG Xuanyu[1], WANG Jun[1*], YANG Song[1], WANG Song[1], WANG Yunuo[1], GAO Kaize[1]

(School of Information and Electrical Engineering, Shenyang Agricultural University, Shenyang 110866, China)

ABSTRACT: With the intensification of global climate change, extreme weather events are becoming increasingly frequent, posing unprecedented challenges for power system load forecasting. Traditional forecasting methods and current deep learning approaches often struggle under extreme weather conditions, and the scarcity of relevant data further aggravates this challenge. To address these issues, this paper proposes a contrastive learning-based method for forecasting power system loads during extreme weather events. The method leverages the self-supervised learning capabilities of contrastive learning to extract robust temporal features from normal weather data. Positive sample pairs are constructed from temporally adjacent samples using their temporal features, while negative pairs are taken from other, non-adjacent samples. By integrating a Transformer model to further enhance temporal feature extraction, the method learns to distinguish discriminative load pattern features across different weather conditions without requiring extreme weather labels. This effectively alleviates the sample imbalance problem caused by the scarcity of extreme weather data. Experiments on real-world load data demonstrate that the proposed method significantly improves forecasting accuracy under extreme weather conditions, outperforming traditional forecasting models and providing an effective solution to the challenge of power load prediction under extreme weather conditions.

KEY WORDS: extreme weather; load forecasting; imbalanced data; contrastive learning; Transformer

摘要：随着全球气候变化的加剧，极端天气事件日益频繁，给电力系统负荷预测带来了前所未有的挑战。传统的预测方法和现有的深度学习方法在面对极端天气时往往会失效，并且极端天气数据的稀缺性加剧了这一现象。针对这一问题，本文提出了一种基于对比学习的极端天气电力负荷预测方法。该方法通过对比学习的自监督学习机制从正常天气数据中学习稳健的时间表征，利用时序数据特征将时间相邻样本构建为正样本对、其他样本对构建为负样本对，并结合Transformer模型增强时序数据特性捕捉能力，从而在无需极端天气标签的情况下学习区分不同天气条件下负荷模式的鉴别特征，有效缓解了极端天气数据稀缺导致的样本不平衡问题。在真实地区负荷数据的实验结果表明，所提方法能够显著提升极端天气条件下的负荷预测精度，与传统预测模型相比表现出卓越的性能，为极端天气下电力负荷预测难题提供了有效的解决方案。

关键词：极端天气；负荷预测；不平衡数据；对比学习；Transformer

0 引言

近年来，极端天气的频发严重威胁着电力系统的安全稳定运行。极端天气极易引起电力系统的供需失衡，从而造成大规模的限电或停电现象[1]。2016年9月，极端天气袭击了南澳大利亚州，引发了大范围新能源脱网，造成了超过50个小时的大停电[3]。2021年2月，寒潮席卷美国德克萨斯州，造成了400万人停电超过70小时[3]。2025年入夏以来，全国多地都出现了极端高温天气，华东地区多地电网负荷创历史新高。其中，全国最大电力负荷继7月4日首创新高的14.65亿千瓦、7月7日又创新高的14.67亿千瓦后，7月16日首次突破15亿千瓦。仅半个月内，电力负荷峰值的历史纪录被多次刷新，极端天气俨然成为电力系统安全稳定运行面临的重大挑战。极端天气对电力系统的严重影响凸显了准确预测极端天气条件下电力负荷的迫切需求。然而，现有的电力负荷预测方法在极端天气下往往会失效，因此亟待开发出一种准确且高效的极端天气下电力负荷预测方法。

随着人工智能和大数据的不断发展，一些前沿的算法及模型已经广泛应用到电力负荷预测领域，例如：文献[4]提出了一种基于数据分解和联邦学习的多区域负荷预测方法来解决电力市场中缺乏数据导致负荷预测精度低的问题。文献[5]提出一种将负荷的时序性和周期性先验知识等多个维度的负荷信息差异化处理的电力负荷预测方法来提高预

测精度和性能。文献[6]提出一种基于门控循环单元(gated recurrent unit，GRU)结合多任务学习(multi-task learning，MTL)框架的多元负荷预测模型，通过考虑多元负荷之间的耦合关系实现预测精度的提升。文献[7]提出了一种通过于完全自适应噪声集合经验模态分解(complete ensemble empirical mode decomposition with adaptive noise，CEEMDAN)和奇异谱分析(singular spectrum analysis，SSA)两种分解算法双重分解的预测模型，来针对负荷序列噪声的特点提高预测精度。文献[8]利用图卷积神经网络在挖掘电力系统的空间特征的能力与 Transformer 结合，提出了一种考虑相邻节点之间存在的空间耦合特性的电力系统多节点负荷预测方法。文献[9]通过刻画居民负荷之间的线性和非线性关系提出了一种基于动态关联图注意力网络的虚拟电厂居民短期负荷预测方法。文献[10]通过 Prophet 算法提取季节性特征利用 Blending 集成学习对非季节进行滚动预测来实现实时的负荷中期预测。文献[11]通过改进 Autoformer 模型使其具有时间序列的分解能力来实现负荷预测精度的提升和模型复杂度的下降。

极端天气下的负荷极易出现骤升骤降的情况，还伴随着更剧烈的波动性和突变性。现有的预测方法常常会出现系统性低估和难以准确捕捉极端天气下负荷变化趋势的问题，会导致传统预测方法在极端天气负荷预测中失效。目前已经有相关研究来解决极端天气下负荷预测精度低的问题。文献[12]提出一种融合了张量低秩补全算法、长短时记忆(long short term memory，LSTM)网络和粗糙集理论(rough set theory，RST)的短期负荷预测模型，实现了极端高温场景下的高精度负荷预测。文献[13]通过Bagging-XGBoost模型识别极端天气并且利用该模型进行修正预测来实现极端天气下预测精度的提升。文献[14]提出一种改进极端梯度提升(Xtreme Gradient Boosting，XGBoost)的极端天气母线日前负荷预测新方法来提高极端天气下的负荷预测精度。文献[15]提出了一种基于双向长短期记忆-核密度估计-分位数回归（BiLSTM-KDE-QR）的短期负荷预测模型来解决极端天气下用户负荷波动问题。文献[16]提出了一种结合二次重构分解去噪和BiLSTM的负荷预测方法来应对极端天气下负荷突变性及波动性增强导致的低预测精度的问题。虽然以上文献通过不同的方式提高了极端天气下的负荷预测精度，但是并没有认识到极端天气下负荷预测精度低的根本原因——极端天气数据的稀缺性导致的样本不平衡。

为解决上述问题，从根本上提高极端天气下负荷预测的精度，本文提出一种基于对比学习的极端天气负荷预测方法。首先，对比学习通过从正常天气数据中学习时间表征，使模型能够深入学习负荷特性，为极端天气下的负荷预测提供预测基础。其次，对比学习利用时序数据的特征，将时间相邻的样本标记为正样本对，其他的样本对标记为负样本对。这种方法即使在没有极端天气标签的情况下，也能使模型学习到区分不同天气条件下负荷的特征进而缓解极端天气数据稀缺的问题。最后，通过将对比学习与 Transformer 结合来增强模型捕捉时序数据特性的能力，进而提高极端天气下负荷预测的准确度。

1 算法理论介绍

1.1 对比学习

对比学习的基本原理在于通过区分正样本和负样本在表征空间中的差异来获取数据的表征学习，其目标是使得锚点样本与正样本的表征距离最小化，同时与负样本的表征距离最大化。区别于传统监督学习方法，此处的正负样本并非依据类别标注来界定，而是通过预设任务进行构建。预设任务建立了数据点间的关联度准则，对于给定的锚点样本，具有高关联度的实例被视为正样本，低关联度的则归为负样本[17]。

如图 1 所示的对比学习实例，以给定对象作为锚点，利用数据增强技术生成得到该对象的正样本，其他对象则作为负样本。对比学习机制通过优化使得锚点在嵌入空间中与正样本的相似度提升，同时与负样本的相似度降低。

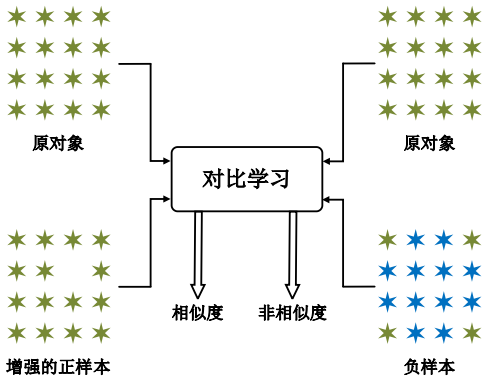


图 1 对比学习实例

Fig.1 An example of contrastive learning

对比学习采用将输入数据与正负样本进行区分比较的策略来获取特征编码，本质上属于一种表征学习框架。图 2 呈现了对比学习的通用架构。

通过对比学习通用架构可以看出，原始数据经过数据增强和特征提取得到特征向量，并通过投影头将这些特征向量用来计算对比学习的损失函数。当正样本的损失与负样本的损失达到最小时，可以得到最优模型。

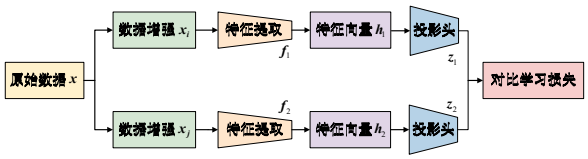


图 2 对比学习通用架构

Fig.2 General architecture of contrastive learning

1.2 Transformer

如图 3 所示，Transformer 包含三个核心组件：位置嵌入模块、多头注意力模块以及前馈网络模块。针对长时间序列处理中位置信息的有效捕获需求，该模型采用位置嵌入机制进行强化，其位置编码方程的数学表达形式定义为

$$\begin{cases} \boldsymbol{P}_{PE(p_{pos},2i)} = \sin(\boldsymbol{p}_{pos} / 10000^{2i/d}) \\ \boldsymbol{P}_{PE(p_{pos},2i+1)} = \cos(\boldsymbol{p}_{pos} / 10000^{2i/d}) \end{cases} \tag{1}$$

式中：$\boldsymbol{p}_{pos}$ 表示时间序列的位置；$\boldsymbol{i}$ 代表特征的维度下标；$\boldsymbol{d}$ 代表节点负荷的嵌入大小。

自注意力网络在进行输入处理时须融入位置编码变量，其公式为

$$\hat{\boldsymbol{E}}_t[\boldsymbol{i},:] = \boldsymbol{E}_t[\boldsymbol{i},:] + \boldsymbol{P}_{PEt} \tag{2}$$

式中：$\boldsymbol{P}_{PEt}$ 代表奇偶维度的位置编码；$\boldsymbol{E}_t \in \boldsymbol{R}^{T\times d}$ 代表单一节点负荷信息；$\hat{\boldsymbol{E}}_t \in \boldsymbol{R}^{N\times T\times d}$ 为自注意力层的完整输入。

采用线性变换矩阵 $\boldsymbol{W}^q$、$\boldsymbol{W}^k$、$\boldsymbol{W}^v$ 对 $\boldsymbol{Q}$、$\boldsymbol{K}$、$\boldsymbol{V}$ 进行计算，即：

$$\begin{cases} \boldsymbol{Q} = \hat{\boldsymbol{e}} \cdot \boldsymbol{W}^q \\ \boldsymbol{K} = \hat{\boldsymbol{e}} \cdot \boldsymbol{W}^k \\ \boldsymbol{V} = \hat{\boldsymbol{e}} \cdot \boldsymbol{W}^v \end{cases} \tag{3}$$

式中：$\boldsymbol{Q}$ 代表模型中的查询向量，$\boldsymbol{K}$ 代表模型中的键向量，二者主要承担计算数据间相关性的功能；$\boldsymbol{V}$ 代表值向量，负责表征负荷历史数据信息。

Transformer 架构中的多头注意力机制具备突出特征向量间关键特征的能力，针对多特征间强耦合性的负荷预测问题展现出良好的适应性，其注意力的计算公式为

$$\boldsymbol{H}_{atti} = \boldsymbol{soft}\max\left(\frac{\boldsymbol{QK}^{\boldsymbol{T}}}{\sqrt{\boldsymbol{d}}}\right)\boldsymbol{V} \tag{4}$$

$$\boldsymbol{H}_{matt} = \boldsymbol{W}_{matt}\left[\boldsymbol{H}_{att1}, \boldsymbol{H}_{att2}, \ldots\ldots, \boldsymbol{H}_{atth}\right] \tag{5}$$

式中：$\boldsymbol{H}_{atti}$ 代表第 $\boldsymbol{i}$ 个注意力值；$\boldsymbol{d}$ 代表模型维度参数；$\boldsymbol{h}$ 表示注意力头数参数。

本文利用 Transformer 来增强模型捕捉时序数据特性的能力，进而提高极端天气下负荷预测的准确度。

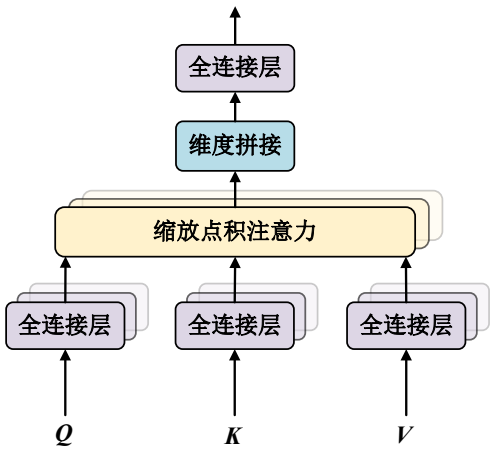


图 3 Transformer 模型结构

Fig.3 Transformer model structure

2 基于对比学习的极端天气负荷预测方法

本文利用对比学习的自监督学习方式方式从时间序列数据中学习稳健的特征表征。在极端天气数据严重失衡和稀缺的情况下，该方法可以充分利用正常天气数据进行自监督预训练，无需额外标记即可学习一般负荷变化模式，这是传统监督学习无法实现的。首先，通过将特征输入 Transformer 中提取时间特征，然后通过投影头将这些特征映射到对比学习空间。其次，在构建正负样本对时，本文模型利用时间数据的特征，将批次中时间相邻的样本标记为正样本对，其他样本对则为负样本对。最后，本文通过损失函数进行优化，以最大化正样本对的相似性，同时最小化负样本对的相似性。这种自我监督机制使模型即使在没有极端天气标签的情况下，也能学习到区分不同天气条件下负荷模式的鉴别特征。本文模型的具体参数设置如表 1 所示。

表 1 模型参数设置

Table 1 Model parameter settings

参数名称	参数值
投影尺寸	128
对比度损失权重	0.3
正样本掩码	(i,i+1)
隐藏维度	256
学习率	0.0005
优化器	Adam
训练周期	1500
学习率衰减	0.2

3 算例分析

3.1 数据集分析与处理

本文数据来自中国内蒙古自治区某城市 2022

年的年度负荷数据及气象数据，其中包含极端天气数据。上述数据分辨率为 15 分钟，即每天共 96 个数据点。其中，气象数据包括温度、湿度、大气压力、降水量、地表风速、风向及散射辐射。实验基于 Python 3.7 环境，其中深度学习采用 Pytorch 1.10.1 框架实现，并使用 CUDA 11.1 进行加速训练。硬件平台配置为 Intel Core i7-14700KF CPU 和 NVIDIA GeForce RTX 4070s GPU。

3.2 预测性能评价指标

本文采用均方根误差 X_{RMSE}、平均绝对误差 X_{RMSE}、平均绝对百分比误差 X_{RMSE} 与决定系数 R^2 评价模型：

$$X_{RMSE}=\sqrt{\frac{1}{N}\sum_{n}(y_n-\hat{y}_n)^2} \tag{6}$$

$$X_{MAE}=\frac{1}{N}\sum_{n}|\hat{y}_n-y_n| \tag{7}$$

$$X_{MAPE}=\frac{100\%}{N}\sum_{n}\left|\frac{\hat{y}_n-y_n}{y_n}\right| \tag{8}$$

$$R^2=1-\frac{\sum_{n}(y_n-\hat{y}_n)^2}{\sum_{n}(y_n-\bar{y})^2} \tag{9}$$

式中：y_n 代表第 n 个真实值；$\hat{y}_n$ 代表第 n 个预测值；$\bar{y}$ 代表真实值的平均值；N 代表示数据点。

3.3 算例结果及分析

本文选取 GRU、Transformer 和 CNN-LSTM 作为对比模型，所有的实验结果取五次的平均值。极端天气下的模型预测性能如表 2 所示。

表 2 极端天气下模型性能对比

Table 2 Comparison of model performance in extreme weather

模型	MAE(MW)	MAPE(%)	RMSE(MW)	R^2
GRU	53.6176	4.5771	64.7178	-0.0582
Transformer	35.8545	3.0548	43.5865	0.5238
CNN-LSTM	30.7029	2.6538	37.8022	0.6390
本文方法	**8.7254**	**0.7591**	**10.6879**	**0.9711**

从模型预测性能指标可以看出，极端天气下本文方法在 MAE、MAPE、RMSE 和 R^2 上的表现都远远好于其他对比模型，展示出了在极端天气下极高的预测精度。相比与其他模型，本文方法在 MAE 上降低了 71.6%～83.7%，在 MAPE 上降低了 71.4%～83.4%，在 RMSE 上降低了 71.7%～83.5%。值得注意的是，GRU 的 R^2 为负值，这说明普通模型在极端天气下的负荷预测可能出现模型失效的问题，这可能是由于模型学习了过多的正常天气数据而对极端天气的预测的泛化性过弱。相比于 Transformer，本文方法在预测精度上有着显著提升。从消融实验角度分析，对比学习在极端天气下平衡数据的能力能够有效解决极端天气数据过少导致的预测精度过低的问题。具体的极端天气下的模型性能对比如图四所示。

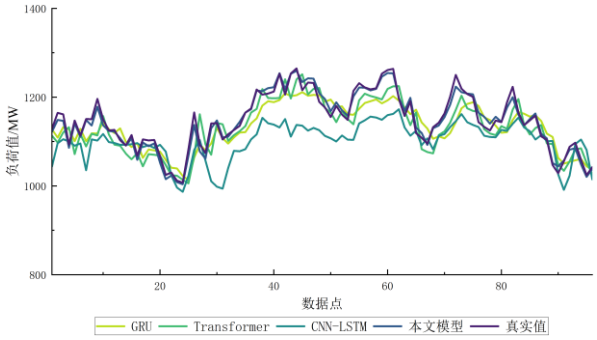


图 4 极端天气下模型性能对比

Fig.4 Comparison of model performance in extreme weather

为了验证本文模型不止适用于极端天气的负荷预测，在正常天气的预测中依旧有很高的预测精度，本文继续设置正常天气下的模型性能对比实验。正常天气下的模型预测性能如表 2 所示。

表 3 正常天气下模型性能对比

Table 3 Comparison of model performance in normal weather

模型	MAE(MW)	MAPE(%)	RMSE(MW)	R^2
GRU	29.8883	4.1078	37.7136	0.9538
Transformer	27.2196	3.7039	34.5999	0.9604
CNN-LSTM	25.0940	3.3618	31.8428	0.9670
本文方法	**6.9415**	**1.0010**	**8.5186**	**0.9976**

从模型预测性能指标可以看出，正常天气下本文方法在 MAE、MAPE、RMSE 和 R^2 上的表现依旧远远好于其他对比模型，展示出了极高的预测精度。相比与其他模型，本文方法在 MAE 上降低了 72.3%～76.8%，在 MAPE 上降低了 70.2%～75.6%，在 RMSE 上降低了 73.2%～77.4%。结果证明了本文模型在完整的包含极端天气的预测中都有着最好的预测性能，可以有效的解决现有模型在极端天气下预测精度过低的问题。具体的极端天气下的模型性能对比如图五所示。

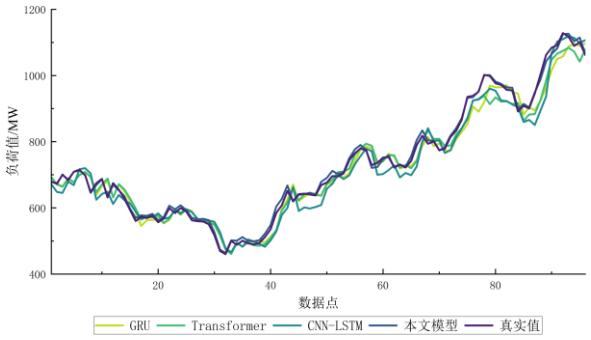


图 5 正常天气下模型性能对比

Fig.5 Comparison of model performance in normal weather

从图四和图五可以看出，极端天气下负荷值远高于正常天气下的负荷值，且伴有更高的波动性。此外，其数据的稀缺性常常会导致传统预测模型过度学习正常天气数据，从而在正常天气下预测精度表现较好但极端天气下预测精度过低，因为解决极端天气下数不平衡的问题是解决极端天气下预测精度过低的一种方式。极端天气的负荷波动性更强也是预测精度低的原因之一，因此深度挖掘和捕捉负荷的波动性也是极端天气下负荷预测需要注意的一个关键点。

4 结论

本文提出了一种新颖的基于对比学习的极端天气负荷预测模型，以解决极端天气负荷预测中数据稀缺而导致预测精度低下的问题。本文的主要结论如下：

1）极端天气下负荷预测精度可以通过提高极端天气数据在完整负荷数据中的占比来实现大幅提升。

2）本文模型利用对比学习可以有效解决极端天气条件下的数据不平衡问题，为准确的极端天气负荷预测提供基础。

3）与其他负荷预测模型相比，本文提出的模型在极端天气负荷预测中表现出卓越的性能。

由于本文使用的数据仅是内蒙古自治区的负荷数据，其极端天气以寒潮为主，并没有包含多种多样的极端天气样本（如热浪、暴雨和台风等极端天气），所以本文模型在其他极端天气上的泛化性上还需要进行深入研究。此外，为了提高本文所提方法在实际工程中的适用性，需要深入研究包含多种极端天气条件的地区负荷特性分析及预测方法，这将是未来的重要研究方向。

参考文献：

[1] ZHAO J，LI F X，ZHANG Q W．Impacts of renewable energy resources on the weather vulnerability of power systems[J]．Nature Energy，2024，9：1407-1414．

[2] 曾辉，孙峰，李铁，等．澳大利亚“9·28”大停电事故分析及对中国启示[J]．电力系统自动化，2017，41(13)：1-6．
ZENG Hui，SUN Feng，LI Tie，et al．Analysis of “9·28” Blackout in South Australia and Its Enlightenment to China[J]．Automation of Electric Power Systems，2017，41(13)：1-6．

[3] 倪宇凡，郑漳华，冯利民，等．近年来国外严重停电事故对我国构建新型电力系统的启示[J]．电器与能效管理技术，2023，(05)：1-8．
NI Yufan，ZHENG Zhanghua，FENG Limin，et al．Power Outages Abroad in Recent Years and Lessons to Build New Power System in China[J]．Electrical & Energy Management Technology，2023，(05)：1-8．

[4] 焦润海，褚佳杰，李俊良，等．基于数据分解的多区域个性化联邦负荷预测方法[J]．中国电机工程学报，2025，45(05)：1691-1704．
JIAO Runhai，CHU Jiajie，LI Junliang，et al．Personalized Federated Multi-region Load Forecasting Method Based on Data Decomposition[J]．Proceedings of the CSEE，2025，45(05)：1691-1704．

[5] 李丹，孙光帆，缪书唯，等．基于多维时序信息融合的短期电力负荷预测方法[J]．中国电机工程学报，2023，43(S1)：94-106．
LI Dan，SUN Guangfan，MIAO Shuwei，et al．A Short-term Power Load Forecasting Method Based on Multidimensional Temporal Information Fusion[J]．Proceedings of the CSEE，2023，43(S1)：94-106．

[6] 高晨元，田建艳，姬政雄，等．基于门控循环单元残差连接网络与多任务学习的园区综合能源系统多元负荷预测[J]．电网技术，2025，49(05)：1771-1780．
GAO Chenyuan，TIAN Jianyan，JI Zhengxiong，et al．Multivariate Load Forecasting for Park-level Integrated Energy System Based on Gated Recurrent Unit Residual Connection Network and Multi-task Learning[J]．Power System Technology，2025，49(05)：1771-1780．

[7] 王继东，于俊源，孔祥玉．基于双重分解和双向长短时记忆网络的中长期负荷预测模型[J]．电网技术，2024，48(08)：3418-3426．
WANG Jidong，YU Junyuan，KONG Xiangyu．Medium- and Long-term Load Forecasting Model Based on Double Decomposition and BiLSTM[J]．Power System Technology，2024，48(08)：3418-3426．

[8] 孟衡，张涛，王金，等．基于多尺度时空图卷积网络与 Transformer 融合的多节点短期电力负荷预测方法[J]．电网技术，2024，48(10)：4297-4311．
MENG Heng，ZHANG Tao，WANG Jin1，et al．Multi-node Short-term Power Load Forecasting Method Based on Multi-scale Spatiotemporal Graph Convolution Network and Transformer[J]．Power System Technology，2024，48(10)：4297-4311．

[9] 张峻凯，胡旭光，刘要博，等．基于动态关联图注意力网络的虚拟电厂居民短期负荷预测[J]．电力系统自动化，2024，48(21)：120-128．
ZHANG Junkai，HU Xuguang，LIU Yaobo，et al．Short-term Residential Load Forecasting Based on Dynamic Association Graph Attention Networks for Virtual Power Plant[J]．Automation of Electric Power Systems，2024，48(21)：120-128．

[10] 郇嘉嘉，李代猛，杜云飞，等．基于 Prophet 算法和 Blending 集成学习的实时负荷中期预测[J]．电力自动化设备，2024，44(04)：178-183．
HUAN Jiajia，LI Daimeng，DU Yunfei，et al．Mid-term forecasting of real-time load based on Prophet algorithm and Blending integrated learning[J]．Electric Power Automation Equipment，2024，44(04)：178-183．

[11] 范杏蕊，李元诚．基于改进 Autoformer 模型的短期电力负荷预测[J]．电力自动化设备，2024，44(04)：171-177．
FAN Xingrui，LI Yuancheng．Short-term power load forecasting based on improved Autoformer model[J]．Electric Power Automation Equipment，2024，44(04)：171-177．

[12] 冯家欢，史雪晨，张赟，等．基于张量低秩补全算法的极端天气短期负荷预测[J]．分布式能源，2024，9(04)：51-59．
FENG Jiahuan，SHI Xuechen，ZHANG Yun，et al．Short-Term Load Forecasting Based on Tensor Low-Rank Completion Algorithm in Extreme Weather[J]．Distributed Energy，2024，9(04)：51-59．

[13] DENG X Z，YE A S，ZHONG J S，et al．Bagging-XGBoost algorithm based extreme weather identification and short-term load forecasting

model[J]. Energy Reports，2022，8：8661-8674.

[14] 胡乾坤，黄南天. 极端温度气象日母线日前负荷预测[J]. 东北电力大学学报，2023，43(01)：55-61.
HU Qiankun，HUANG Nantian. Day-ahead Bus Load Forecasting in the Extreme Temperature Meteorological Days[J]. Journal Of Northeast Electric Power University，2023，43(01)：55-61.

[15] 余德泳，刘蓉晖. 极端天气事件下基于 BiLSTM-KDE-QR 模型的多类型用户短期负荷预测[J/OL]. 上海电力大学学报，1-9. https://link.cnki.net/urlid/31.2175.TM.20250522.1650.002.

[16] 钟燕，王军，宋戈，等. 基于二次重构分解去噪及双向长短时记忆网络的极端天气下超短期电力负荷预测[J/OL]. 电网技术，1-15. https://doi.org/10.13335/j.1000-3673.pst.2024.0935.

[17] 李希，刘喜平，李旺才，等. 对比学习研究综述[J]. 小型微型计算机统，2023，44(04)：787-797.
LI Xi，LIU Xiping LI，Wangcai，et al. Survey on Contrastive Learning Research[J]. Journal of Chinese Computer Systems，2023，44(04)：787-797.

[18] 房佳姝，刘崇茹，苏晨博，等. 基于自注意力 Transformer 编码器的多阶段电力系统暂态稳定评估方法[J]. 中国电机工程学报，2023，43(15)：5745-5759.
FANG Jiashu，LIU Chongru，SU Chenbo，et al. Multi-stage Transient Stability Assessment of Power System Based on Self-attention Transformer Encoder[J]. Proceedings of the CSEE，2023，43(15)：5745-5759.



张轩语

作者简介：

张轩语(1999)，男，硕士研究生，研究方向为电力气象、电力负荷预测、新能源功率预测等，E-mail：920376265@qq.com;

王俊(1979)，男，教授，博士生导师，研究方向为电力系统预测技术、智能配电网运行与控制等，E-mail：wddream2016@syau.edu.cn。

104 行业企业导师权益保障与创新激励的协同机制研究

靳小龙[1,2]，穆云飞[1,2*]，贾宏杰[1,2]，余晓丹[1,2]，赵倩宇[1,2]

（1．智能配用电装备与系统全国重点实验室（天津大学），天津市 南开区 300072；

2. 智能电网教育部重点实验室（天津大学），天津市 南开区 300072）

Research on the Collaborative Mechanisms of Rights and Interests Protection and Innovation Incentives for Industry Enterprise Mentors

JIN Xiaolong[1,2], MU Yunfei[1,2*], JIA Hongjie[1,2], YU Xiaodan[1,2], ZHAO Qianyu[1,2]

(1. State Key Laboratory of Smart Power Distribution Equipment and System (Tianjin University), Tianjin, 300072;
2. Key Laboratory of Smart Grid of Ministry of Education(Tianjin University), Tianjin, 300072)

ABSTRACT: With the advance of national strategy for integration of industry and education, the systemic predicament that industry enterprise mentors facing becomes more evident. The research found out that some of the industry enterprise mentors are lack of formal identity verification in universities and their work performance was not included in the internal performance assessment of the enterprise. These problems have led to more profound contradictions on a deeper level, whose barriers have severely hindered the implementation effectiveness of the “trinity” strategy of education, technology and talent. This research focuses on the innovative policies proposed by our school, which is conducted through systematic practice and analysis, and endeavors to explore a replicable and scalable model of industry enterprise mentorship cooperation mechanism. The aim of this research is to propose a feasible solution to this predicament and provide strong support for the efficient implementation of the industry-academia integration strategy in our country.

KEY WORDS: Power system major, industry-education integration strategy, school-enterprise collaboration mechanism, cooperation mechanism paradigm.

摘要：目前随着国家产教融合战略的推进，行业企业导师面临的系统性困境更加明显，本文经过调研发现，部分企业导师面临高校正式身份认证缺失、工作绩效未被纳入企业内部绩效考核等问题，而这些问题在更深层次上导致了更深刻的矛盾，这些制度壁垒严重制约了教育、科技、人才“三位一体”战略的落地成效。本文通过系统性实践和分析，尝试探索一种可复制、可推广的行业企业导师合作机制范式，目标是为此困境提出一种可行的破局之法，并为我国产教融合战略的高效推进提供有力支撑。

关键词：电力系统专业，产教融合战略，校企协同机制，合作机制范式。

0 前言

目前国家产教融合战略已进入深化阶段，行业企业导师作为校企协同育人的关键纽带，正面临着系统性的发展困境[1]。调研数据显示，78.3%的企业导师缺乏高校的正式身份认证，导致其在高校资源使用上存在各种限制，且进一步导致其职业归属感薄弱；同时，约 92%的企业导师的指导工作并未被纳入企业内部的绩效考核体系中，这导致这部分企业导师在育人投入与个人回报之间严重失衡。

这些问题导致的更深层的矛盾体现在校企协同机制的缺位，例如：知识产权归属界定模糊、人才定向输送链路断裂、合作风险保障措施不足等，各种问题最终形成了“高校积极推动、企业参与被动”的僵局[2]。若不能破除这些制度壁垒，将直接制约教育、科技、人才“三位一体”战略的落地成效。

基于此，本文拟通过系统性的研究，探索可复制推广的行业企业导师合作机制范式，为我国产教融合战略的高效推进提供有力支撑。将通过“制度设计-技术支撑-应用验证”三阶推进，实现权益保障从碎片化到系统化、激励机制从消耗型到增值型的根本转变，为产教融合提供可持续解决方案，如图 1 所示：

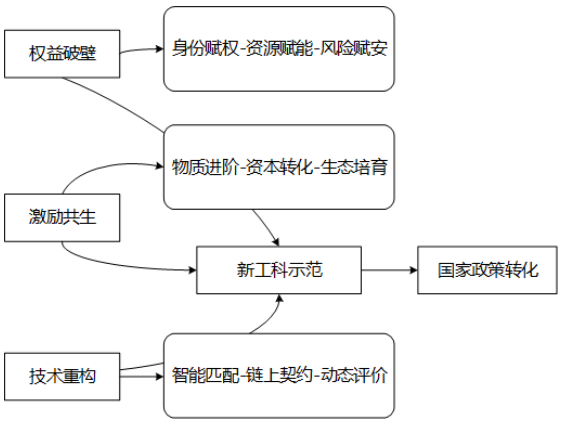


图 1 行业企业导师合作机制示意图

1 权益保障机制的制度化破壁研究

行业企业导师的权益保障，是维系导师队伍稳定与激发其深度参与的基础性条件，更是推动产教融合战略走向实质、实现共生发展的关键基石[3]。当前，产教融合正步入以质量提升与深度攻坚为核心的“深水区”，其复杂性与系统性要求空前提高。早期被规模扩张所掩盖的结构性矛盾与制度性壁垒正逐渐浮出水面[4]，构成了制约战略效能释放的核心障碍。其核心症结在于：“身份悬置”：导师角色在高校与企业的双重制度体系中均缺乏明确认同与定位，导致其陷入制度性边缘化的尴尬境地；“资源受限”：导师在履职过程中难以获得必要的学术、行政与财务支持，使其育人行动因支持体系的缺位而步履维艰；“风险无保”：在指导实践、成果转化等活动中，面临权责不清与权益受损风险时，缺乏有效的制度性兜底与救济渠道。

本文针对企业导师“身份悬置、资源受限、风险无保”的痛点，构建了一套“三位一体”的权益保障体系：

(1)身份赋权机制研究：

建立一种“三阶动态认证”制度，其内容包含：设置实践导师（基础级）、产业教授（进阶级）、荣誉教授（战略级）三级认证，分别匹配差异化权限包。构建综合评估公式：

$$S=0.25\times E_{\text{职称}}+0.3\times E_{\text{工龄}}+0.25\times A_{\text{成果}}+a\times T_{\text{课时}} \quad (1)$$

式中，S 为总分；$E_{\text{职称}}$ 为学历职称(例，博士设定为 20，硕士设定为 16，只取最高得分项)；$E_{\text{工龄}}$ 为行业经验或工龄；$A_{\text{成果}}$ 为科技成果(例，发明专利设定为 8 分/项，实用新型专利设定为 4 分/项，最高 30 分)；$T_{\text{课时}}$ 为教学时长；a 为教学评价(例，优秀设定为 1.2，合格设定为 1.0)。

分级认证区间为：

①荣誉教授（战略级）：$S\geqslant 85$ 分；

②产业教授（进阶级）：75 分$\leqslant S<85$ 分；

③实践导师（基础级）：60 分$\leqslant S<75$ 分；

同时建议使用“双聘档案系统”，打通企业工号与校园 ID 身份标识关联关系，实现校企职称互认、资源权限互通（如实验室/数据库访问权）的目标。通过这种区块链存证技术确权方法，预计可以解决大部分企业导师面临的“身份无认证”困局。

(2)资源赋能平台构建：

通过建设高校的“资源共生云平台”，可以实现高校科研设施（重点实验室、高性能计算中心）与企业生产资源（中试基地、检测平台）的统一整合，并且建立“积分兑换制”，即导师可以通过指导时长兑换设备使用时长或技术咨询服务等。

(3)风险兜底体系设计：

提出“校企保险池”双轨模式，即将对行业企业导师的利益保障分为两层：①基础保障层：高校负责购买“指导责任险”，年度保费控制在 3-5 万元，范围涵盖学生实习期间的人身意外、实验设备意外损坏等基础风险，解决导师在指导学生过程中的后顾之忧。同时建立快速理赔通道，学生人身伤害理赔在资料齐全情况下 3 个工作日内完成，设备损坏理赔在勘查确认后 5 个工作日内完成。同时建立事故预防机制，定期开展安全培训，每学期组织两次安全演练，从源头上降低事故发生概率；②增值保障层：企业按比例投入“知识产权组合险”，防范技术泄露与专利纠纷。保费根据企业规模和项目风险程度实行分级费率，并制定《校企导师权责清单》，对教学指导、成果转化、学生管理等 12 类场景的责任边界进行明确，从根源上规避行业企业导师反映的“贡献无闭环”风险。

2 激励机制的生态化共生设计

行业企业导师的深度参与不仅依赖于即时性的物质回报，更取决于一套能够系统回应其职业发展、学术认可与价值实现等综合诉求的可持续激励机制。本文突破了传统的补贴模式，设计了“双螺旋激励模型”，驱动了物质激励与非物质资本协同增值：

(1)物质激励进阶设计：

构建“基础酬金+绩效增值”动态公式如下式(2)：

$$\text{总激励}=\underbrace{\alpha\times S_{\text{行业}}\times T_{\text{时长}}}_{\text{基础酬金}}+\underbrace{\beta\times\left(E_{\text{就业}}\times P_{\text{专利}}\times C_{\text{协同}}\right)}_{\text{绩效增值}} \quad (2)$$

式中，α 为地区调节系数（例如天津设定 1.2，北

京设定为 1.5）；$S_{行业}$取该行业时薪中位数；β为绩效权重；$E_{就业}$为学生头部企业就业率、$P_{专利}$为校企联合专利申请量、$C_{协同}$为校企项目匹配度，三者共同构成三维考核指标体系。

(2)非物质激励转化设计：

从人才、技术和声望三个方面研究非物质激励资本转化路径[6]：①推行“人才期权”制度，企业导师累计指导满200小时可获定制班学员优先录用权（预计降低招聘成本30%）；②设立“IP共享金库”，导师参与研发的成果转化后，按“高校:企业:个人=4:4:2”比例分成。

(3)共生生态培育策略：

建议开发一套“产教需求雷达”智能匹配系统，系统采用分层架构设计，数据采集层通过API接口实时获取企业技术需求文档、高校课程体系及科研项目数据，并基于NLP分析企业的技术需求与高校的课程缺口建立动态更新的需求数据库。特征工程层运用BERT模型进行语义解析，提取技术关键词、能力要求、学科领域等特征向量。提出导师-项目适配指数的计算模型：

$$Q=0.4\times M_{技术}+0.3\times M_{能力}+0.2A_{时间}+0.1\times C_{地域} \quad (3)$$

式中，$M_{技术}$为技术匹配度，通过导师科研成果与企业需求的余弦相似度计算；$M_{能力}$为能力契合度，通过导师专业背景与项目要求的匹配程度计算；$A_{时间}$为时间可用度；$C_{地域}$为地域便利度。

同时，采用“线上+线下”双轨模式构建“导师共生联盟”。线上建立知识共享平台，设置技术问答库、案例资源中心、专家直播课堂等功能模块。线下设立区域协作中心，定期推举大学内各学院组织，按期轮流提供会议室和协作工具，定期举办“技术反哺沙龙”，促成导师间的跨企业协作，形成知识共享生态圈。

3 协同机制重构策略

本文以数字化平台为枢纽，对行业企业导师的“匹配-履约-评价”的全链条进行了系统性重构，旨在破解信息不对称、过程管理粗放与成果衡量模糊等传统难题，推动校企协同从“人治”走向“数治”。该重构策略的核心实施路径如下：

(1)智能匹配系统设计：

为解决导师资源与育人需求错配的问题，本文设计了智能匹配系统。该系统对接高校育人的需求池，搭建导师的能力画像数据库，共涵盖了三个方面：

①技术领域维度采用三级分类体系，包括5个一级学科领域、24个二级专业方向和128个三级技能项，分别设置了相应的权重系数和熟练度指标。②项目经验契合度从四个维度进行量化：项目规模（基于经费额度和团队人数）、技术难度（评估创新程度和复杂度）、成果影响（考量产业化价值和学术价值）以及角色贡献（区分负责人、核心成员和参与者）。③时间弹性维度则通过分析导师的工作安排、地理位置和偏好时段，构建了可用性预测模型。

同时运用联邦学习技术，在数据不出域的前提下完成协同训练，解决企业技术机密和高校教学数据的隐私保护难题。

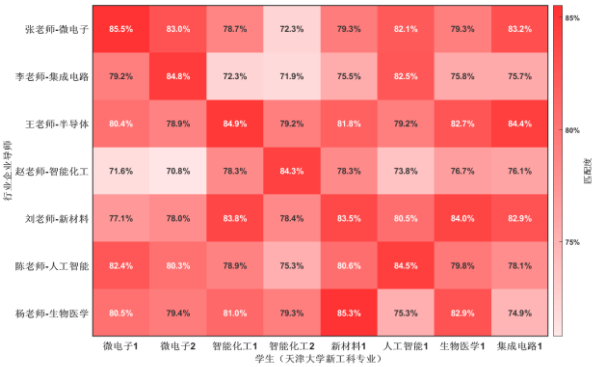


图 2 推荐匹配热力图

通过匹配计算加权求和模型：

$$综合匹配度=0.5T_{技术}+0.3\times E_{经验}+0.2\times T_{时间} \quad (4)$$

式中，$T_{技术}$为技术匹配度；$E_{经验}$为经验契合度；$T_{时间}$为时间协调度。

目前，此匹配功能首期接入天津大学微电子、智能化工等新工科专业，如图2所示，目标匹配精度可达85%，实际运行数据显示，系统将导师遴选效率提升了58%，需求响应时间缩短了72%。

(2)动态评价与反馈升级：

为科学衡量协同成效并形成管理闭环，建立了“共生指数”量化模型，如式(5)：

$$\Gamma=0.3R_{留存}+0.4P_{专利}+0.2E_{就业}+0.1C_{资源} \quad (5)$$

式中，$R_{留存}$为行业企业导师留存率；$P_{专利}$为联合专利转换率；$E_{就业}$为学生就业率；$C_{资源}$为企业设备或数据共享率。

该指数评估结果将直接纳入学校的资源配置

决策系统，实现“以效定资源”的精准调控。“共生指数”将动态关联相关学科的研究生招生指标分配、校级科研平台建设优先级以及校企合作专项经费的拨付额度[7]。通过建立“评价-反馈-资源配置”的管理闭环，形成以价值创造为导向的良性循环，持续驱动产教融合生态的优化与升级。

4 实践应用与政策转化

图 3 是实践应用的计划安排建议。



图 3 实践进度安排

示范应用严格遵循“试点验证、迭代优化、全面铺开”的推进策略，以半年为评估周期对机制成效进行系统性验收。

在政策解读与调研阶段，通过系统梳理国家产教融合战略导向与学校新工科建设规划，完成校企资源精准映射，为权益保障机制的破壁奠定理论基础。

在权益保障机制构建阶段，聚焦“身份悬置、资源受限、风险无保”三大制度壁垒，推进“三位一体”的权益保障体系的实施。通过“三阶动态认证”制度、“资源共生云平台”和“校企保险池”双轨模式，从制度方面“破壁”行业企业导师权益保障困局。同时，制定《校企导师权责清单》，为未来高校的推广规避行业企业导师相关风险。

在激励机制深化阶段，重点推进激励机制的生态化共生，通过双螺旋激励模型驱动物质激励与非物质资本协同增值，以期导师参与的积极性与创新活力。开发“产教需求雷达”智能匹配系统，构建“导师共生联盟”，形成知识共享生态圈。同时，推动形成《高校行业企业导师管理办法》并纳入教学质量管理体系，推动相关机制纳入京津冀产教融合共同体建设指南，作为合作高校与企业实施导师制度的参考标准。

在协同机制验证阶段，完成“匹配-履约-评价”全流程重构与实证检验。通过智能匹配系统的匹配精度和“共生指数”，更新学校的资源配置决策系统。起草出台《行业企业导师资源配置管理办法》，推动构建高校“以效定资源”的动态配置机制。

在成果凝练与总结阶段（2027.07-2027.08），系统整合各阶段实证数据与研究结论，形成了完整的理论框架与实践指南，初步形成“破壁·共生”理念的可复制、可推广实践路径。以天津大学实践成果为核心范本，面向不同学科类型、区域特点，通过教育部产学合作协同育人平台、全国新工科教育创新平台等进行跨领域、跨区域推广。推进构建全国行业企业导师数据库，对接高校现有信息系统，为推广智能匹配系统提供数据支撑，完善行业企业导师资源的国家级储备体系，为产教融合的深入推进奠定人才基础。

5 结论

本文直面产教融合的核心矛盾，以“破壁”解构权益保障困局，用“共生”重塑激励价值循环。通过构建“高校-企业-导师”发展命运共同体，为破解国家战略实施中的“最后一公里”难题提供方案。形成建议如下：

(1) 以身份赋权（双聘档案与三阶认证）、资源赋能（校企设施共享平台）、风险赋安（指导责任险与知识产权组合险）三个角度破解企业导师制度性壁垒。

(2) 采用“双螺旋激励机制”，将物质激励（基础酬金+绩效增值动态模型）与非物质激励（人才优先权-技术分成-声望资本进阶）进行了深度融合，并通过“共生指数”量化导师留存率、专利联合产出率等协同价值，为产教融合理论注入了新范式。

(3) 制定《行业企业导师权益保障指南》以支撑政策制定，并依托高校研究生培养体系进行实践应用和经验总结，加速新质生产力人才的培养。

参考文献

[1] 何用辉,徐宁,卓书芳,等.产教融合背景下高职院校产业导师队伍建设的研究[J].装备制造技术,2024(3):59-63.

[2] 邵益锋,蒋莉娜,褚锦.跨界·共生·赋能：“双师型”教师企业实践激励机制创新研究——基于浙江省 X 职校的个案研究[J].职业教育,2025,24(10):34-39.

[3] 周伟,赵猛,易军.“项目牵引，导师保障”创新实践能力培养探索与实践[J].教育进展, 2022, 12(11): 4522-4527.

[4] 宁启扬.产教融合背景下职业院校产业导师制建设困境与路径[J].职业技术教育,2024,45(33):41-48.

[5] 韩金红,李海琴,曾晟,等.导师指导对研究生创新能力的影响:创新自我效能感的中介作用[J].创新与创业教育,2025,16(2):49-58.

[6] 郭彤梅.基于心理契约的知识型员工激励机制研究[J].经济问题,2016(10):57-61.

[7] 赵炯昊,程翠翠.基于校企合作“双导师制”的研究生创新培养机制研究[J].品位·经典,2024(11):85-8791.

105 Collaborative Planning for Interconnected Offshore Wind Farms Using Mixed-Variable Bayesian Optimization

Ruizhe Yang[1], Zhen Huang[2], Jingying Yang[3], Hongpeng Zhang[2], Tingxiang Zhang[2], Zhongkai Yi[1], and Ying Xu[1]

[1] Harbin Institute of Technology, 92 Xida St, Harbin, China
[2] Northeast Branch of State Grid Corporation of China, 1 Yingpan N St, Shenyang, China
[3] State Grid Jilin Electric Power Company Limited, 9699 Renmin Ave, Changchun, China
ying.xu@hit.edu.cn

Abstract. The expansion of offshore wind energy, a cornerstone of the global energy transition, is increasingly hampered by underdeveloped transmission infrastructure. Planning modern offshore grids presents a significant challenge, requiring the co-optimization of network topology and asset capacities across a mix of transmission technologies. To address this, this paper proposes a multi-objective collaborative planning model for interconnected offshore wind farms (OWFs) and their transmission networks. A novel Adaptive Multi-objective Mixed-variable Bayesian Optimization (AMMBO) algorithm is developed to solve this mixed-integer problem efficiently. The key innovation within AMMBO is a Pareto-Guided Variable Freezing (PGVF) mechanism, which accelerates convergence by identifying and fixing promising network topologies before refining their continuous capacity variables in a lower-dimensional space. The proposed algorithm is validated on a modified IEEE 14-bus system. Results demonstrate that AMMBO significantly outperforms benchmark methods, including NSGA-II and an ablation variant without PGVF, by identifying a superior Pareto front with greater diversity and better convergence within a comparable computational time. The PGVF mechanism is shown to dramatically improve computational efficiency, leading to the discovery of higher-quality solutions. The proposed framework provides an effective and efficient tool for planners to navigate the complex trade-offs between economic and sustainability objectives, facilitating the strategic development of robust offshore power grids.

Keywords: Mixed-Variable Bayesian Optimization, Interconnected Offshore Wind Farms, Collaborative Planning.

1 Introduction

Although 2024 marked a record year for the wind industry with 117 GW of newly installed capacity, only 8 GW of offshore wind capacity was commissioned, repre-

senting the lowest level since 2021 and a 26% decline from the previous year [1]. Multiple complex factors contributed to this downturn, with underdeveloped transmission infrastructure identified as a key technical barrier. As emphasized during the 29th Conference of the Parties, power grids are critical enablers of the global energy transition, yet their development continues to lag behind the rapid expansion of renewable energy [2]. Persistent congestion in critical transmission corridors limits the full integration of offshore wind power and hinders the deployment of offshore wind farms, even as vast reserves of clean and abundant wind energy remain untapped, particularly in deep-sea regions.

1.1 Literature Review and Research Gaps

Transmission networks form the backbone of the power system and play a critical role in enabling its ongoing transformation, a point well recognized in the academic community. Numerous studies have demonstrated the benefits of jointly planning transmission networks with other system resources [3,4]. However, the collaborative planning of transmission networks and offshore wind farms (OWFs) remains relatively underexplored. For instance, [5] proposes a transmission planning approach for OWFs that considers both AC and DC options, but only optimizes line capacities while relying on a predetermined network topology. Meanwhile, much of the existing literature on OWFs focuses on optimizing the internal collector system topology to enhance efficiency and reduce investment costs [6,7]. Unlike onshore systems, offshore transmission planning presents unique challenges, with the most prominent being the diversity of transmission technologies. Near-shore OWFs typically adopt high-voltage AC (HVAC) transmission due to its maturity and cost-effectiveness. In contrast, far-offshore projects increasingly consider high-voltage DC (HVDC) with modular multilevel converters (MMCs) [8] and low-frequency AC (LFAC) with modular multilevel matrix converters (M3Cs) [9] as viable solutions for long-distance power delivery. These different transmission technologies may coexist within the same regional network, introducing greater complexity into the planning process that must be adequately addressed.

1.2 Problem formation

The expansion of offshore wind energy is shifting farther from shore as near-shore resources become increasingly utilized. Advancements in floating wind turbines enable deployment in deeper waters with stronger winds, while technologies like HVDC and LFAV facilitate efficient long-distance power transmission. This trend also aligns with the development of an interconnected offshore network, which not only facilitates the utilization of far-offshore wind energy but also enhances transmission capacity, benefiting the power grid. Many regions face a geographical mismatch where load centers are distant from wind-rich areas, while the temporal variability of OWF output further strains onshore transmission infrastructure, leading to both RES power curtailment and load shedding. Additionally, land constraints and environmental considerations limit the expansion of onshore transmission lines. By interconnecting OWFs, power distribution can be balanced across provinces, reducing grid stress and improving supply reliability.

1.3 Summary of Major Contributions

To tackle the aforementioned challenges, a collaborative capacity planning approach is introduced, driven by the development of an adaptive multi-objective mixed-variables Bayesian optimization (AMMBO) algorithm. This approach effectively generates an informative and objective Pareto front, outlining the capacity allocation schemes and network topology for OWFs and offshore cables. The comprehensive planning of an offshore network not only augments the potential for enhanced performance across economy, and sustainability but also takes an overall consideration of the collaborative power transmission between land grids and OWF clusters.

Compared with existing works, two main contributions of the article are summarized as follows:

i) An adaptive multi-objective mixed-variables Bayesian optimization algorithm is proposed for efficient planning in power systems with binary and continuous variables. It integrates probabilistic reparameterization and a Pareto-guided variable freezing mechanism. By fixing promising line combinations early, the search shifts to a lower-dimensional continuous space, improving optimization efficiency and solution quality.

ii) A multi-objective collaborative planning model is proposed in this study to capitalize on the benefits of interconnected OWFs. The model comprehensively considers the unique characteristics of offshore power systems, including hybrid transmission configurations employing MMC and M3C, as well as the deployment of floating OWFs to harness wind energy in deep-sea environments.

2 Planning Scheme Evaluation Model

2.1 Economy objection function:

The annual cost the system to be planned is the objective function regarding the economy of the system, it includes the annualized investment of cables and OWFs, their maintenance cost, and the annual operation cost as formulated in (1).

$$\arg\min_{\boldsymbol{x}} \ C_{\text{ann}} = \overbrace{\sum_{p\in\Omega} CPR_p C_p}^{\text{investment}} + \overbrace{\sum_{p\in\Omega} \kappa_p C_p}^{\text{maintenance cost}} + \overbrace{(C_{\text{g}} - R_{\text{H}})}^{\text{operation cost}}, \tag{1}$$

with

$$\boldsymbol{x} = \{\boldsymbol{x}_n^{\text{d}}, \boldsymbol{x}_n^{\text{c}}\} = \{[d_{\text{cab},i}]_1^{N_{\text{cab}}}, [S_{\text{cab},i}]_1^{N_{\text{cab}}}, [S_{\text{owf},i}^{\text{rated}}]_1^{N_{\text{owf}}}\}, \tag{2}$$

$$CPR_p = \frac{\tau(1+\tau)^{T_{\text{life},p}}}{(1+\tau)^{T_{\text{life},p}} - 1}, \ p \in \{\text{owf}, \text{cab}\}, \tag{3}$$

$$\begin{aligned} C_{\text{owf}} = \sum_k^{N_{\text{owf}}} C_{\text{owf},k} = \sum_k^{N_{\text{owf}}} \Big[& \overbrace{\alpha_{\text{owf}} (P_{\text{owf},k}^{\text{rated}})^{\gamma_{\text{owf}}}}^{\text{turbine cost}} \\ & + \overbrace{\beta_{\text{owf}} (P_{\text{owf},k}^{\text{rated}})^{\delta_{\text{owf}}}}^{\text{foundation cost}} + \overbrace{\alpha_{\text{plat}} P_{\text{owf},i}^{\text{rated}} + \beta_{\text{plat}}}^{\text{platform cost}} + \overbrace{\alpha_{\text{conv}} P_{\text{owf},k}^{\text{rated}}}^{\text{converter cost}} \Big], \end{aligned} \tag{4}$$

$$C_{\text{cab}} = \sum_{k}^{N_{\text{cab}}} C_{\text{cab},k} = \sum_{k}^{N_{\text{cab}}} [\alpha_{\text{cab}} \exp(\frac{\gamma_{\text{cab}} S_{\text{cab},i}}{100}) + \beta_{\text{cab}}] L_{\text{cab},k}, \tag{5}$$

where, C_{ann} is the total annualized cost to be minimized by optimizing a vector of decision variables, $\boldsymbol{x}$. This total cost comprises the investment, captured by the capital recovery payment CPR_p for each equipment type p in the set Ω; the maintenance cost, determined by a factor κ_p and capital cost C_p; and the net operational cost, which is the difference between the total operational cost C_{g} and any revenue R_{H}. The decision variables within $\boldsymbol{x}$ consist of cable design parameters like $d_{\text{cab},i}$ and the apparent power ratings for cables, $S_{\text{cab},i}$, and offshore wind farms, $S_{\text{owf},i}^{\text{rated}}$. The overall capital costs for OWFs, C_{owf}, and cables, C_{cab}, are sums of individual equipment costs, $C_{\text{owf},k}$ and $C_{\text{cab},k}$, calculated over the total number of units, N_{owf} and N_{cab}. These costs depend on physical and technical parameters such as the rated capacity of the k_{th} OWF, $P_{\text{owf},k}^{\text{rated}}$, and the length of the k_{th} cable, $L_{\text{cab},k}$. The financial calculations use a discount rate τ and the equipment's economic lifetime $T_{\text{life},p}$. The cost models are further defined by a series of coefficients for turbines, foundations, platforms, converters, and cables (α_{owf}, γ_{owf}, β_{owf}, δ_{owf}, α_{plat}, β_{plat}, α_{conv}, α_{cab}, γ_{cab}, and β_{cab}). In these formulations, i and j serve as indices for buses.

2.2 Sustainability objective:

To evaluate the contribution of a scheme in enhancing the system's sustainability, the maximum RES accommodation ability is incorporated as the second objective, as shown in (6). In the evaluation of this objective, all RES are assumed to operate at their maximum output, which represents the system's ability to accommodate RES under extreme conditions

$$\arg\min_{\boldsymbol{x}} \; -P_{\text{RES}} = -\sum_{i}^{N_{\text{owf}}} \sum_{t}^{T} P_{\text{owf},i,t} \tag{6}$$

2.3 Constraints:

$$-\delta_{\text{g}} \bar{P}_{\text{g},i} \le P_{\text{g},i,t+1} - P_{\text{g},i,t} \le \delta_{\text{g}} \bar{P}_{\text{g},i} \tag{7}$$

$$\underline{P}_{\text{g},i} \le P_{\text{g},i,t} \le \bar{P}_{\text{g},i}, \tag{8}$$

$$0 \le P_{\text{owf},k,t} \le P_{\text{owf},k}^{\text{rated}} P_{\text{owf},k,t}^{*}, \tag{9}$$

$$\begin{aligned} P_{i,t} = {} & V_{i,t}^{\text{ac}} \sum_{j \in \Omega^{\text{ac}}} V_{j,t}^{\text{ac}} \left(g_{ij} \cos\theta_{ij} + b_{ij} \sin\theta_{ij} \right) \\ & - \sum_{m \in \Omega_i^{\text{mmc}}} (P_{m,t}^{\text{mmc}} - P_{m,t}^{\text{mmc,loss}}) - \sum_{n \in \Omega_i^{\text{m3c}}} (P_{n,t}^{\text{m3c}} - P_{n,t}^{\text{m3c,loss}}) \end{aligned} \tag{10}$$

$$Q_{i,t} = V_{i,t}^{\text{ac}} \sum_{j \in \Omega_i^{\text{ac}}} V_{j,t}^{\text{ac}} \left(g_{ij} \sin\theta_{ij} - b_{ij} \cos\theta_{ij} \right) + \sum_{m \in \Omega_i^{\text{mmc}}} Q_{m,t}^{\text{mmc}} + \sum_{n \in \Omega_i^{\text{m3c}}} Q_{n,t}^{\text{m3c}} \tag{11}$$

$$P_{i,t} = V_{i,t}^{\text{dc}} \sum_{j \in \Omega^{\text{dc}}} V_{j,t}^{\text{dc}} g_{ij} + \sum_{m \in \Omega_i^{\text{mmc}}} P_{m,t}^{\text{mmc}} \tag{12}$$

$$P_{m,t}^{\text{mmc,loss}} = \alpha^{\text{mmc}} P_{m,t}^{\text{mmc}} + \beta^{\text{mmc}}, \tag{13}$$

$$P_{n,t}^{\text{m3c,loss}} = \alpha^{\text{m3c}} \left(P_{n,t}^{\text{m3c}}\right)^2 \tag{14}$$

$$(P_{m,t}^{\text{mmc}})^2 + (Q_{m,t}^{\text{mmc}})^2 <= (S_m^{\text{mmc}})^2, \tag{15}$$

$$(P_{n,t}^{\text{m3c}})^2 + (Q_{n,t}^{\text{m3c}})^2 <= (S_n^{\text{m3c}})^2, \tag{16}$$

$$-\overline{I}_{ij} \le I_{ij} \le \overline{I}_{ij}, \tag{17}$$

$$\underline{V}^{\text{ac}} \le V_{i,t}^{\text{ac}} \le \overline{V}^{\text{ac}},\ \underline{V}^{\text{dc}} \le V_{i,t}^{\text{dc}} \le \overline{V}^{\text{dc}}, \tag{18}$$

The constraints begin with the ramp rate limits for generators in (7), where $P_{\text{g},i,t}$ is the output active power of the i_{th} generator at time t, δ_{g} is the ramp rate parameter, and $\overline{P}_{\text{g},i}$ is the generator's upper active power bound. Equation (8) defines the generation capacity limits using the lower active power bound $\underline{P}_{\text{g},i}$. The active power output limits for OWFs are given in (9), which involves the OWF's output power $P_{\text{owf},k,t}$, its rated capacity $P_{\text{owf},k}^{\text{rated}}$, and the maximum allowed output in per unit $P_{\text{owf},k,t}^{*}$. Equation (10) ensures active power balance at each AC bus, where $P_{i,t}$ is the injected active power, $V_{i,t}^{\text{ac}}$ is the AC voltage, g_{ij} and b_{ij} are the line conductance and susceptance, θ_{ij} is the phase angle difference, $P_{m,t}^{\text{mmc}}$ and $P_{n,t}^{\text{m3c}}$ are the output powers of MMCs and M3Cs, $P_{m,t}^{\text{mmc,loss}}$ and $P_{n,t}^{\text{m3c,loss}}$ are their respective power losses, simplified from the loss equations in [10,11], and $\Omega_{j,i}^{\text{ac}}$, $\Omega_{\text{mmc},i}$, and $\Omega_{\text{m3c},i}$ are sets of connected components. The reactive power balance is handled in(11), introducing the injected reactive power $Q_{i,t}$ and the reactive power from converters, $Q_{m,t}^{\text{mmc}}$ and $Q_{n,t}^{\text{m3c}}$. For the DC grid, equation (12) maintains active power balance, using the DC voltage $V_{i,t}^{\text{dc}}$ and the set of connected DC buses $\Omega_{j,i}^{\text{dc}}$. The power loss models for converters are described in (13) and (14) using loss coefficients α^{mmc}, β^{mmc}, and α^{m3c}. The capacity limits for these converters are set in (15) and (16) by their rated capacities, S_m^{mmc} and S_n^{m3c}. Finally, network security is maintained by the transmission line thermal limits in (17), where I_{ij} is the line current and $\overline{I}_{ij}$ is its maximum rating, and by the bus voltage security limits in (18), which uses the lower and upper bounds for AC voltage, $\underline{V}^{\text{ac}}$ and $\overline{V}^{\text{ac}}$, and DC voltage, $\underline{V}^{\text{dc}}$ and $\overline{V}^{\text{dc}}$.

3 Solution Method: Adaptive Multi-objective Mixed-variable Bayesian Optimization

3.1 Framework of Bayesian Optimization

BO is a very efficient framework for solving global optimization problems using black-box evaluations of expensive objective functions. BO algorithms intelligently select the next input for evaluation guided by a learned statistical model to quickly direct the search towards optimal inputs. The three key elements of BO framework are:

Gaussian Process: A Gaussian Process is a probabilistic model used to estimate functions based on the available dataset D^j, defined by a mean and covariance function as in (20). In Bayesian Optimization, the GP acts as a surrogate model for the objective function, helping guide the search for optimal solutions. It provides predictions and uncertainty estimates, enabling BO to balance exploration (sampling uncertain areas) and exploitation (sampling known high-value areas).

$$f_i(\boldsymbol{x}) \sim p_i(f_i|\,\boldsymbol{D},\sigma_{\mathrm{n},i}) = \mathcal{N}(\mu_{\boldsymbol{D},i},\ \boldsymbol{\Sigma}_{\boldsymbol{D},i}),\ i=1,2,3, \tag{19}$$

with

$$\begin{cases} \mu_{\boldsymbol{D},i}(\boldsymbol{x}) = \boldsymbol{K}(\boldsymbol{x},\boldsymbol{X})[\boldsymbol{K}(\boldsymbol{X},\boldsymbol{X})+\sigma_{\mathrm{n},i}\boldsymbol{I}]^{-1}\hat{\boldsymbol{y}}_i \\ \boldsymbol{\Sigma}_{\boldsymbol{D},i}(\boldsymbol{x},\boldsymbol{x}') = \boldsymbol{K}(\boldsymbol{x},\boldsymbol{x}') \\ -\boldsymbol{K}(\boldsymbol{x},\boldsymbol{X})[\boldsymbol{K}(\boldsymbol{X},\boldsymbol{X})+\sigma_{\mathrm{n}}\boldsymbol{I}]^{-1}+\boldsymbol{K}\left(\boldsymbol{X},\boldsymbol{x}'\right)' \\ \boldsymbol{K}(\boldsymbol{X},\boldsymbol{X}) = [k_{\mathrm{c}}(\boldsymbol{x}_i^{\mathrm{c}},\boldsymbol{x}_j^{\mathrm{c}})\bullet k_{\mathrm{d}}(\boldsymbol{x}_i^{\mathrm{d}},\boldsymbol{x}_j^{\mathrm{d}})]_{i,j=1}^{n} \end{cases} \tag{20}$$

where $\mathcal{N}(\mu_{\boldsymbol{D},i},\ \boldsymbol{\Sigma}_{\boldsymbol{D},i})$ is the generated multivariate normal distribution given data $\boldsymbol{D}$ with mean vector $\mu_{\boldsymbol{D},i}$ and covariance matrix $\boldsymbol{\Sigma}_{\boldsymbol{D},i}$; $\mathbf{I}$ is the identity matrix; $\hat{\boldsymbol{y}}_i$ represents the normalized version of $\boldsymbol{y}_i$; $k_{\mathrm{c}}(\boldsymbol{x}_i,\boldsymbol{x}_j)$, $k_{\mathrm{d}}(\boldsymbol{x}_i,\boldsymbol{x}_j)$ are the kernel functions for discrete variables and continuous variables respectively.

3.2 Noisy Expected Hypervolume Indicator Improvement:

In multi-objective optimization, solutions are typically assessed by their contribution to the Pareto frontier, which captures optimal trade-offs among conflicting objectives. A common measure of the quality of such a frontier is the hypervolume indicator (HV), which quantifies the volume of objective space dominated by a set of solutions and bounded below by a reference point $r \in \mathbb{R}^M$. For a finite set P of objective vectors in $\mathbb{R}^M$, the hypervolume is defined as

$$\mathrm{HV}(P|\ r) = \lambda_M\left(\bigcup_{v\in P}[\mathrm{r},\ \mathrm{v}]\right) \tag{21}$$

where λ_M denotes the M-dimensional Lebesgue measure. Given this, the hypervolume improvement (HVI) from adding a new candidate x is

$$\mathrm{HVI}(f(x)|\ P) = \mathrm{HV}(P\cup f(x)) - \mathrm{HV}(P) \tag{22}$$

To accommodate noisy observations in Bayesian Optimization, Noisy Expected Hypervolume Improvement (NEHVI) defines the acquisition function as the expectation of HVI under the joint posterior distribution over the true objective values at

previously evaluated points. Let $p(f|\ \mathcal{D}_n)$ denote the posterior over latent objectives given noisy observations $\mathcal{D}_n$. Then, the NEHVI acquisition function for a candidate x is given by

$$\alpha_{\text{NEHVI}}(x)=\mathbb{E}_{f\sim p(f|\ \mathcal{D}_n)}\left[\text{HVI}(f(x)|\ P_f)\right], \tag{23}$$

where P_f is the Pareto frontier computed from a sampled realization of the latent function values $f(X_n)$. The detailed calculation of the expectation in (23) can be found in [12].

Probabilistic objective: To enable gradient-based optimization over mixed spaces with continuous and binary variables, the acquisition function is reparameterized as an expectation over a discrete probability distribution. Binary inputs $x_i^{\text{d}}\in\{0,1\}$ are modeled using Bernoulli distribution $\mathcal{B}(b)$ with $b\in[0,1]$, and the acquisition function is transferred into a probabilistic version as in (24). This formulation allows efficient optimization by treating discrete inputs probabilistically while maintaining differentiability with respect to $\boldsymbol{b}$ and x^{c} [13].

$$\mathbb{E}_{\boldsymbol{x}^{\text{d}}\sim\mathcal{B}(\boldsymbol{x}^{\text{d}}|\ \boldsymbol{\theta})}[\alpha(\boldsymbol{x})]=\sum_{\boldsymbol{x}_1^{\text{d}}\in\{0,1\}}\cdots\sum_{\boldsymbol{x}_{n_{\text{d}}}^{\text{d}}\in\{0,1\}}\alpha(\boldsymbol{x})\prod_{i=1}^{n_{\text{d}}}\mathcal{B}\left(x_i^{\text{d}}|\ \theta_i^{\text{d}}\right) \tag{24}$$

where $\mathbb{E}(\cdot)$ denotes the expectation over a probability distribution; $\alpha(\boldsymbol{x})$ is the acquisition function with integral-continuous mixed inputs $\boldsymbol{x}$.

Given the preliminaries above, the detailed optimization process is introduced as follows.

3.3 Initialization

An initial dataset is required for Bayesian optimization. The optimization starts with selecting a set of N_0 randomly chosen capacity allocation schemes as in (26) with their corresponding objective values in (27) acquired through the evaluation model in Section II.

$$\boldsymbol{D}^0=\{\boldsymbol{X}^0,\boldsymbol{Y}^0\} \tag{25}$$

where

$$\boldsymbol{X}^0=\{\boldsymbol{x}_n^{\text{d}},\boldsymbol{x}_n^{\text{c}}\}_1^{N_0}=\{[d_{\text{cable},i}]_1^{N_{\text{cable}}}[S_{\text{cable},i}]_1^{N_{\text{cable}}},[S_{\text{OWF},i}^{\text{rated}}]_1^{N_{\text{OWF}}}\}_1^{N_0}, \tag{26}$$

$$\boldsymbol{Y}^0=\{\boldsymbol{y}_n\}_1^{N_0}=\{[f_1(\boldsymbol{x}_n)+\epsilon,f_2(\boldsymbol{x}_n)]\}_1^{N_0}=\{[C_{\text{ann}}^{\text{ob}}(\boldsymbol{x}_i),-P_{\text{RES}}(\boldsymbol{x}_i)]\}_1^{N_0}. \tag{27}$$

3.4 Locating the Candidate Point

With the initial date set, the posterior functions $\boldsymbol{p}=[p_1,p_2]$ can be established using the Gaussian Process as in (20). The mean function in (20) provides predictions of the objective function values at untried points, while the variance function provides the associated uncertainty. Such predictions lay the foundation for selecting the candidate point by maximizing the acquisition function over the search space. For multi-objective optimization (MOO) planning, the *expected hypervolume indicator improvement* provided in [12] is employed as the acquisition function. Its maximization process with mixed input variables is outlined in Algorithm 1.

Algorithm 1 Locating the candidate to be evaluated

Require: reference point $\boldsymbol{r}$; acquired dataset $\boldsymbol{D}$.
Ensure: candidate point $\boldsymbol{x}_{\text{cand}}$.
1: **procedure** $\mathcal{GP}(\boldsymbol{D})$
2: **while** $i < n_{\text{obj}}$ **do** ▷ n_{obj}: number of the objective fucntion
3: $K(\cdot) \leftarrow k_{\text{c}}(\cdot) * k_{\text{d}}(\cdot)$ ▷ select kernel functions
4: $\mu_{\boldsymbol{D},i}(\boldsymbol{x}), \boldsymbol{\Sigma}_{\boldsymbol{D},i}(\boldsymbol{x}, \boldsymbol{x}') \leftarrow$ Equation (21)
5: $p_i \leftarrow \mathcal{N}(\mu_{\boldsymbol{D},i}, \Sigma_{\boldsymbol{D},i})$
6: **end while**
7: $\boldsymbol{p} \leftarrow [p_i]_1^{n_{\text{obj}}}$
8: **end procedure**
9: **procedure** max $\mathbb{E}_{\boldsymbol{x}^{\text{d}} \sim \mathcal{B}(\boldsymbol{x}^{\text{d}}|\boldsymbol{b})}[\alpha(\boldsymbol{x})]$
10: $x_i^{\text{d}} \leftarrow \mathcal{B}(b_i)$ ▷ transfer discrete variables
11: $\alpha(\cdot) \leftarrow \alpha_{\text{NEHVI}}(\cdot)$ ▷ select acquisition function
12: $\mathbb{E}_{\boldsymbol{Z} \sim p(\boldsymbol{Z}|\boldsymbol{\theta})}[\alpha(\boldsymbol{x}, \boldsymbol{Z})] \leftarrow$ Equation (25) ▷ transfer acquisition function into a probability objective
13: $\boldsymbol{x}_{\text{cand}} \leftarrow$ max $\mathbb{E}_{\boldsymbol{Z} \sim p(\boldsymbol{Z}|\boldsymbol{\theta})}[\alpha(\boldsymbol{x}, \boldsymbol{Z})]$
14: **end procedure**
▷ The optimization of line 13 can be achieved using gradient-based methods.

Once the candidate point is identified, the objective functions are evaluated at that point, and the result is added to the dataset, $\boldsymbol{D}' = \boldsymbol{D} \cup \{\boldsymbol{x}_{\text{cand}}, \boldsymbol{y}(\boldsymbol{x}_{\text{cand}})\}$. The GP model is then updated to reflect the new data, and the process repeats iteratively, refining the surrogate model and guiding the search toward the optimal solution.

3.5 Adaptive Determination of the Reference point

the reference point $\boldsymbol{r}$ used in Algorithm I holds significant influence on the effectiveness of the optimization. While in the foundational work in [12], they are predetermined by the planner, but considering the complexity of power system planning, their predetermination can be very challenging. As such, the first improvement made on the original work focuses on the self-update of the parameter, which is detailed as follows.

The hypervolume metric is sensitive to the choice of the reference point $\boldsymbol{r}$, which significantly affects the quality of the obtained Pareto front. Traditionally, a reference point is set slightly inferior to the worst-case scenario, yet determining an absolute worst-case for each objective in the collaborative capacity planning model can be challenging. To address this, the reference point update mechanism is constructed by incorporating both the worst and best observed outcomes, thereby accounting for the dynamic range of the objectives.

The reference point is defined as

$$\boldsymbol{r}^{(t)} = \hat{\boldsymbol{y}}^{\max} - \beta(t)\left(\hat{\boldsymbol{y}}^{\max} - \hat{\boldsymbol{y}}^{\min}\right), \tag{28}$$

where $\hat{\boldsymbol{y}}^{\min}$ and $\hat{\boldsymbol{y}}^{\max}$ denote the minimum and maximum values in each column of $\hat{\boldsymbol{y}}^{\max}$, respectively. Here, $\hat{\boldsymbol{y}}^{\max}$ represents the worst-case outcomes evaluated so far, and the term $\hat{\boldsymbol{y}}^{\max} - \hat{\boldsymbol{y}}^{\min}$ captures the range of the objective values. This range is scaled by the self-decreasing sequence $\beta(t)$, which ensures that the reference point

remains marginally lower than the worst-case evaluation as the difference between the maximum and minimum values grows.

The decaying coefficient is an exponential function as in (29).

$$\beta(t) = \beta_0 \exp(-\lambda t), \tag{29}$$

with $\beta_0 = 0.1$ and $\lambda > 0$. This formulation dynamically adjusts the reference point in accordance with the observed expansion of the range in $\hat{\mathbf{y}}$, thereby improving the alignment of the hypervolume metric with the evolving objectives.

3.6 Pareto-Guided Variable Freezing Acceleration Mechanism

Classical BO often struggles with scalability in high-dimensional design spaces, particularly when involving a large number of binary variables. In mixed-variable settings such as power system planning, this limitation becomes more pronounced due to the combinatorial explosion introduced by binary infrastructure decisions. To address this challenge, the Pareto-Guided Variable Freezing (PGVF) mechanism is introduced as an effective strategy for dimensionality reduction during the optimization process. PGVF is motivated by a structural characteristic of power systems, where only a small subset of binary decisions, specifically transmission line installations, meaningfully contribute to the shape of the Pareto frontier. Many binary configurations are either infeasible or unproductive due to network sparsity and topological constraints.

PGVF operates in two phases. In the initial exploration phase, the optimization is performed over the full binary-continuous space, enabling broad search and identification of promising binary configurations. Once the set of non-dominated binary combinations stabilizes, indicated by the absence of new candidates over several iterations, the optimization process transitions to a continuous subspace, where the binary variables are fixed and only the continuous parameters, such as line capacities and wind generation sizes, are further refined. This targeted focus significantly reduces computational overhead and improves convergence efficiency, while preserving the ability to explore high-quality design trade-offs.

3.7 Complete Optimization Process

The complete optimization process is strategically designed to navigate the complex search space with increasing efficiency, shown in Fig. 1. Initially, the algorithm operates in a hybrid solution space, where it simultaneously optimizes both the binary variables that determine the network topology (i.e., whether to build a cable) and the continuous variables that define the capacities of those cables and the OWFs. This initial phase allows for a broad exploration to identify the most promising structural designs. As the optimization progresses and a sufficient number of schemes are evaluated, the PGVF mechanism intervenes. Once the cable combinations with the most potential are consistently found on the Pareto front, PGVF freezes these high-potential topologies. This critical step transitions the problem from the complex mixed-variable domain into a more focused and purely continuous search space, the algorithm is simplified into the Adaptive Multi-objective Bayesian Optimization that formerly proposed by the authors in [14]. By concentrating on refining the capacities for these filtered combinations, the optimization becomes significantly more efficient,

ultimately allowing for a deeper exploration and the discovery of a more detailed and higher-quality set of Pareto-optimal solutions.

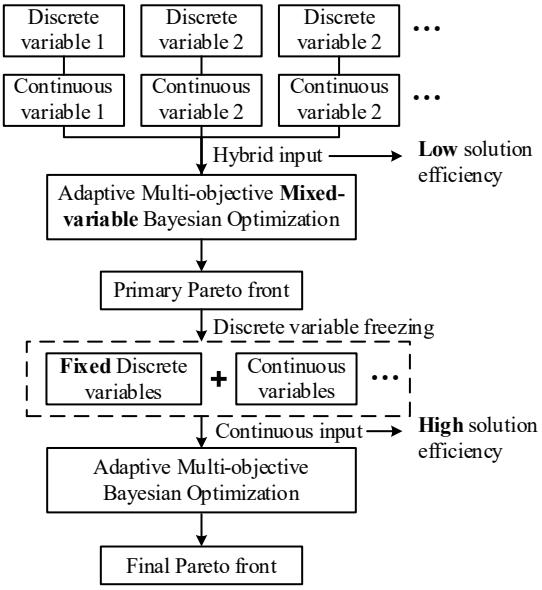


Fig. 1. The optimization process of proposed algorithm.

4 Case Study

4.1 Simulation Settings and Parameters

Simulation Settings: The proposed planning model is validated on a modified IEEE 14-bus test system, where two existing AC branches have been replaced with DC and LFAC corridors to create a hybrid transmission network. The detailed topology of this modified system is illustrated in Fig. 2. Within this framework, the planning problem addresses the optimal placement and capacity determination for six potential offshore cables and three offshore wind farms (OWFs).

To rigorously evaluate the performance of the proposed Adaptive Multi-objective Mixed-variable Bayesian Optimization (AMMBO) algorithm, two distinct methods are employed for comparison. The first is an ablation variant of the proposed method, AMMBO without PGVF, which omits the PGVF mechanism. This forces the optimization to operate entirely within the mixed-integer solution space, thereby isolating the performance contribution of the PGVF strategy. The second benchmark is the widely-adopted Non-dominated Sorting Genetic Algorithm II (NSGA-II). To handle the mixed-variable nature of the problem, the binary decision variables within the NSGA-II framework are managed using continuous relaxation.

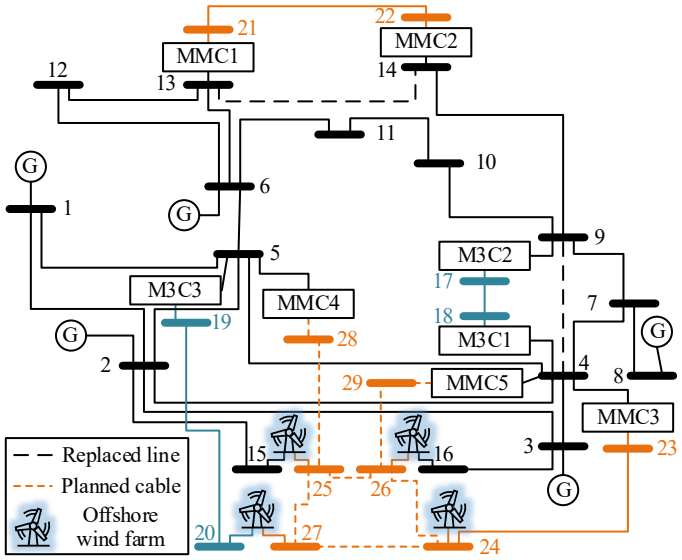


Fig. 2. The topology of modified IEEE-14 case.

Parameters: The key parameters used in the simulation are listed in Tab. 1. The output limit of OWFs and load curves are set based on the typical scenarios clustered from a whole year historical data.

Table 1. Parameters Related to the Cost Calculation.

Equipment	Parameter	Value	Parameter	Value
OWF	α_{OWF}	1444.074	β_{OWF}	381.513
	γ_{OWF}	0.87	δ_{OWF}	1.06
	α_{plat}	457.110	β_{plat}	56013.675
	α_{WFconv}	77.630	T_{OWF}	25
Cable	α_{cable}	15.807	β_{cable}	801.940
	γ_{cable}	1.16	T_{cable}	25
Traditional generator	a_{1-5}	3/3/3/3/3	b_{1-5}	0.043/0.25/0.01/0.01/0.01
	c_{1-5}	20/20/40/40/40		

4.2 Superiority of the Proposed Approach

Fig. 3 llustrates the final Pareto fronts obtained from the three MOO algorithms, with key performance metrics summarized in Table 2. The results clearly indicate that the proposed AMMBO algorithm identifies a superior Pareto front that is both better-converged and more diverse than those of the benchmark methods, all within a comparable computational time. The crucial contribution of the PGVF mechanism is evident when comparing the full AMMBO to its ablation variant; the enhanced efficiency from operating in a purely continuous solution space allows the full algorithm to

discover a significantly larger set of Pareto-optimal solutions, whereas the variant without PGVF yields a dominated front. Moreover, the NSGA-II algorithm struggles with the mixed-integer variables, as its continuous relaxation technique proves insufficient for effectively managing the discrete decisions. Consequently, despite evaluating the most schemes, NSGA-II produces a narrow Pareto front that offers limited trade-off information and decision-making support for the planner.

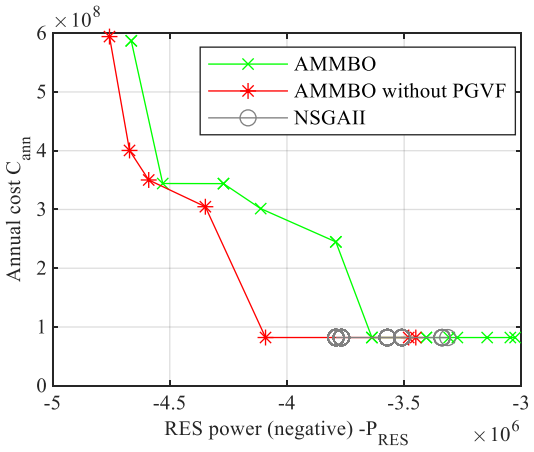


Fig. 3. The acquired Pareto fonts of the three algorithms.

Table 2. Comparison of performance metrics across the three algorithms.

Algorithm	Hypervolume indicator	Evaluated schemes	Computational time (s)
AMMBO	32.71	724	6954
AMMBO without PGVS	30.59	520	7068
NSGA-II	30.02	1200	7169

Regarding computational efficiency, as can be seen in Fig. 4 the contribution of the PGVF mechanism becomes particularly evident at the 250-evaluation mark. At this point, a significant and abrupt improvement in the hypervolume indicator is observed for the proposed AMMBO algorithm. This acceleration occurs precisely when PGVF intervenes, freezing the most promising network topologies and transitioning the search from the complex mixed-integer domain to a more focused, purely continuous space. Operating within this simplified space allows for a more rapid and effective identification of Pareto-optimal solutions compared to the ablation variant that lacks PGVF. This result validates that strategically freezing discrete topological variables is a highly efficient method for accelerating convergence in this class of planning problems.

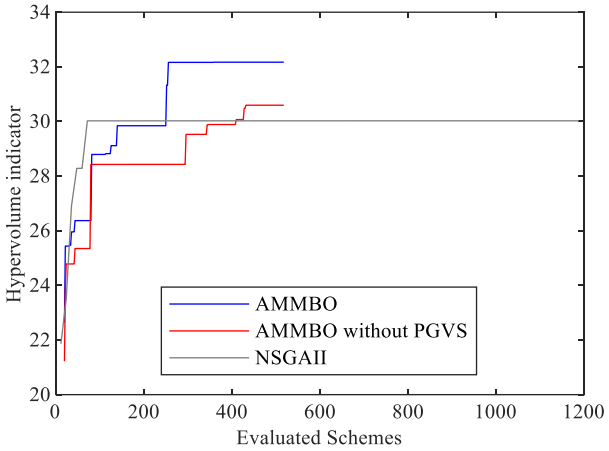


Fig. 4. The curves of hypervolume indicator with respect to the evaluated schemes.

5 Conclusion

This paper tackles the complex challenge of collaborative capacity planning for OWFs and hybrid transmission networks, a critical bottleneck in the global energy transition. To handle this mixed-integer, multi-objective problem, we've proposed a novel AMMBO algorithm. The algorithm's core contribution is the PGVF mechanism, a two-phase strategy that boosts computational efficiency by freezing promising network topologies and then refining their continuous capacity variables in a simpler, lower-dimensionality space. Our case study on a modified IEEE 14-bus system confirmed the approach's superiority, showing that AMMBO identifies a better-converged and more diverse Pareto front than the widely-used NSGA-II and an ablation variant of our method. Our findings show that the AMMBO algorithm is a powerful and efficient tool for modern power system planning, giving decision-makers a high-quality set of trade-off solutions for the strategic development of robust and economically viable offshore grids. The results clearly quantified the efficiency gains from the PGVF mechanism, which was shown to significantly accelerate convergence after 250 evaluations. By effectively handling the complexities of mixed-variable optimization, this work provides a valuable methodology to support the large-scale integration of offshore wind energy, helping to overcome a key infrastructure barrier in the energy transition.

References

1. Council G W E. GWEC global wind report 2025[J]. Global Wind Energy Council: Brussels, Belgium, 2025.
2. International Energy Agency, Renewables 2024, IEA, Paris , 2024.
3. Tao Y, Qiu J, Lai S, et al. Adaptive integrated planning of electricity networks and fast charging stations under electric vehicle diffusion[J]. IEEE Transactions on Power Systems, 2022, 38(1): 499-513.
4. Luo Y, Zeng B, Zhang W, et al. Coordinative planning of public transport electrification, RESs and energy networks for decarbonization of urban multi-energy systems: A government-market dual-driven framework[J]. IEEE Transactions on Sustainable Energy, 2023, 15(1): 538-555.
5. Meng K, Zhang W, Qiu J, et al. Offshore transmission network planning for wind integration considering AC and DC transmission options[J]. IEEE Transactions on Power Systems, 2019, 34(6): 4258-4268.
6. Zhang X, Li J, Guo Z. Region-partitioned obstacle avoidance strategy for large-scale offshore wind farm collection system considering buffer zone[J]. Energy, 2024, 313: 133758.
7. Shen X, Wu Q, Zhang H, et al. Optimal planning for electrical collector system of offshore wind farm with double-sided ring topology[J]. IEEE Transactions on Sustainable Energy, 2023, 14(3): 1624-1633.
8. Xiang W, Yang M, Wen J. DR-MMC hub based hybrid AC/DC collection and HVDC transmission system for large-scale offshore wind farms[J]. Journal of Modern Power Systems and Clean Energy, 2024.
9. Yu Z, Song Q, Yuan Z, et al. Transmission topology and control for ultra-large offshore wind bases integrating multiple offshore low-frequency AC links and onshore HVDC link[J]. IEEE Transactions on Power Delivery, 2024.
10. Beerten J, Cole S, Belmans R. Generalized steady-state VSC MTDC model for sequential AC/DC power flow algorithms[J]. IEEE Transactions on Power Systems, 2012, 27(2): 821-829.
11. Yu Z, Zhang Z, Xu Z. Electromechanical transient modeling of the low-frequency AC system with modular multilevel matrix converter stations[J]. IEEE Transactions on Power Systems, 2023, 39(1): 921-933.
12. Daulton S, Balandat M, Bakshy E. Parallel bayesian optimization of multiple noisy objectives with expected hypervolume improvement[J]. Advances in neural information processing systems, 2021, 34: 2187-2200.
13. Daulton S, Wan X, Eriksson D, et al. Bayesian optimization over discrete and mixed spaces via probabilistic reparameterization[J]. Advances in Neural Information Processing Systems, 2022, 35: 12760-12774.
14. Yang R, Xu Y, Yi Z, et al. Adaptive multi-objective Bayesian optimization approach for capacity planning of the interconnected offshore wind farms[J]. Energy, 2025: 138284.

106 新工科背景下“电力系统”英文课程教学改革探索

倪骏康，雷涛，姚文利，张晓斌

（西北工业大学 自动化学院，西安 710129）

Teaching Reform of the English-Taught Course “Power System” under the New Engineering Education Background

Junkang Ni, Tao Lei, Wenli Yao, Xiaobin Zhang

(School of Automation, Northwestern Polytechnical University, Xi’an, 710129)

ABSTRACT: The development of emerging engineering education aims to cultivate outstanding engineering talents who can lead the future development of industries, placing transformative demands on the traditional power engineering curriculum system. Currently, the English course "Power Systems" reveals core deficiencies in addressing the integration of energy and digital revolutions, cross-industry innovation, and global competition. These include teaching content that struggles to meet the requirements of new engineering education, outdated teaching models and methods, and evaluation systems ill-suited for new engineering standards. In response, this paper aligns with the training objectives of electrical engineering professionals under the new engineering paradigm, the requirements of engineering education accreditation, and our university's goal of cultivating "chief-engineer-type" talents. It systematically constructs a reform plan for the "Power Systems" course to address existing issues in its practical implementation. First, the teaching content has been updated. The syllabus for the "Power Systems" course has been revised, and the teaching materials have been redesigned to incorporate the latest knowledge and technologies in the field. This aligns with low-carbon development strategies and delves deeply into specialized knowledge. Typical engineering case studies have been introduced into the teaching process, alongside exploratory engineering problems. Second, reforms in teaching methods and models have been implemented. Utilizing various teaching platforms and course resources, a multi-dimensional interactive teaching model has been established. Through semi-physical simulation, virtual simulation, programming calculations, cognitive internships, and production practice, the "Power Systems" theory is empowered with practical application. This encourages independent student learning and fosters self-directed exploration capabilities. Finally, the course assessment methods have been reformed. The weighting between evaluating learning processes, outcomes, and ability enhancement has been scientifically and rationally set. Methods for objectively and accurately assessing the improvement of students' abilities have been developed, and final examination questions have been designed scientifically improvement of students' abilities have been developed, and final examination questions have been designed scientifically and reasonably. The ultimate goal of this reform is to cultivate a new generation of versatile talents who are not only proficient in the core theories and technologies of power systems but also possess interdisciplinary knowledge integration skills, innovative thinking, exceptional engineering practice capabilities, and a broad international perspective. This research provides a referential pathway for the upgrading and internationalization of engineering courses in the new era.

KEY WORDS: Emerging engineering education, Power systems course reform, Teaching content update, Teaching model innovation, Assessment method reform

摘要：新工科建设旨在培养引领未来产业发展的卓越工程人才，对传统电力专业课程体系提出了重塑式的要求。当前“电力系统”英文课程在应对能源革命与数字革命融合、产业跨界创新及全球化竞争方面，凸显出教学内容难以适应新工科发展要求、教学模式和教学方法难以适应新工科发展要求、考核方式难以适应新工科发展要求等核心问题。为此，本文结合新工科背景下电气类专业人才的培养目标、工程教育专业认证要求和学校“总师型”人才培养要求，针对现有“电力系统”课程实践过程中存在的问题，系统构建了该课程的改革方案。首先，更新教学内容，修订了“电力系统”课程教学大纲，规划改进了教学内容，顺应低碳战略发展趋势，深入挖掘专业知识，将电力系统最新发展的新知识和新技术融入了“电力系统”课程教学中，在教学环节中引入对典型工程案例的描述，并设置探究性工程问题。其次，进行教学方法和教学模式改革，利用各种授课平台和课程资源，实现多维互动教学模式，通过半物理仿真、虚拟仿真、编程计算、认识实习和生产实习赋能“电力系统”理论实践，鼓励学生

基金项目：西北工业大学教育教学改革项目(24GZ11317)

Project Supported by Northwestern Polytechnical University Education Reform Project (24GZ11317).

自主学习，培养学生自我探索能力。最后，进行课程考核方式改革，科学合理的设置学习过程和效果评价与能力提升评价的比例，开发客观准确评价能力提升效果的方法，并科学合理的设置期末考试题目。本改革的最终目标是培养不仅精通电力系统核心理论技术，而且具备跨学科知识整合能力、创新思维、卓越工程实践能力和开阔国际视野的新一代复合型人才。本研究为新时期工科专业课程的升级与国际化建设提供了可借鉴的路径。

关键词：新工科建设，电力系统课程改革，教学内容更新，教学模式创新，考核方式改革

DOI：10.13335/j.1000-3673.pst.2014.01.论文序号（小五号 Times New Roman 字体加黑）

1　电力系统课程概述

为推动工程教育体系的创新与发展，深化工程人才培养模式改革，教育部高等教育司于 2017 年 2 月发布了《关于开展新工科研究与实践的通知》。文件指出，随着以新技术、新业态、新模式和新产业为主要特征的新经济形态迅速兴起，对工程科技人才的综合能力提出了更高、更严峻的要求[1]。面对全球范围内科技革命与产业转型的浪潮，为贯彻落实国家创新驱动发展战略，教育部全面推动“新工科”建设。相较于传统工科教育，“新工科”强调，未来新兴产业与新型经济结构所需的人才，应具备卓越的实践能力、突出的创新精神以及国际视野下的竞争优势，是一类高素质、复合型的工程科技人才[2]。目前，“新工科”已成为高校教育领域的关键议题。众多院校正积极组织相关研究与实践，一方面前瞻性地探索能够引领未来科技与产业发展的育人路径，另一方面系统推进现有工科专业结构、课程体系及培养机制的优化升级。

“电力系统”是电气工程及其自动化专业强电领域的学科基础与核心支柱，在培养应用型、复合型电力人才方面扮演着关键角色。作为课程体系中的重要基石，它不仅是“发电厂电气部分”、“继电保护”等后续专业课程的先修理论，也与“电路”、“电机学”等多门前序课程紧密衔接。该课程内容博洽宏通，理论体系严谨，兼具高度的抽象性与显著的实践性，涉及大量计算与画图分析。通过本课程的学习，学生既能构建起电力系统规划、设计、运行与管理的基础知识框架，又能锤炼综合运用理论解决复杂工程实际问题的核心能力。

2　电力系统课程教学过程中遇到的问题

然而，目前的“电力系统”课程教学过程中存在以下三方面问题：

首先，教学内容难以适应新工科发展要求。首先，教学内容已经滞后于新技术的发展，难以适应“双碳”背景下新型电力系统和飞机电力系统的发展。随着“碳达峰”和“碳中和”目标的逐步实现，具有不确定性特点的新能源会被大规模地接入国家电网，将使电网的结构和供电模式发生巨大变化，需要更新能够反映新型电力系统最新发展的新知识和新技术内容。为应对新能源不确定性对电力系统带来的新挑战，在“双碳”战略目标引领下，新型电力系统的建设使得“电力系统”课程的教学改革迫在眉睫，以更好地契合低碳化发展的需求。课程内容应在传统教学体系基础上，进一步融入新型电力系统的供需平衡理论、高比例可再生能源接入下的电压稳定与控制技术，以及应对新能源季节性波动的调节与优化机制。同时，应从碳减排视角引入系统分析与优化方法，涵盖碳排放评估、碳优化调度、碳规划及碳足迹追踪等理论内容，帮助学生了解绿色电力的发展趋势，掌握电力系统结构演进方向及碳管理研究的前沿动态。随着新能源的快速发展，储能、光热、氢能等新技术逐渐从示范走向普及，光伏、燃料电池及储能系统在航空电力系统等领域的应用日益广泛，因此，有必要将相关新能源与储能知识纳入课程体系，促进学生的系统化学习与深度理解。此外，电动飞机技术给飞机电力系统带来了影响和挑战，飞机电力系统与机载其他能源系统的交互和协同设计要求也给飞机电力系统与热管理系统的综合管理控制方法设计带来了影响和挑战，因此，反映飞机电力系统发展趋势和未来挑战的内容也需要加入课程知识体系。其次，本课程在教学实施中的一个突出短板在于实践环节设计。具体表现为：其一，教学方式以课堂讲授为主，对理论如何应用于工程实际关注不足；其二，受制于电力系统的复杂性与安全性，实践内容多为验证性实验或基础仿真计算，形式固化且深度不足；其三，缺乏以真实工程问题为导向的综合性训练。上述问题导致学生难以将抽象理论联系实际，从而增加了学习障碍，制约了学习兴趣。

其次，教学模式和教学方法难以适应新工科发展要求。目前，“电力系统”课程教学存在以下几个突出问题：首先，教学模式较为固化，以教师单向讲授为主，学生自主思考与探索的机会不足，学习主动性未被有效激发。其次，教学内容局限于教材，教师未能将自身的专业知识与前沿工程实践有

效转化为教学资源，使得课堂内容与实际应用脱节。最后，师生之间缺乏深度的双向交流，激励学生积极参与和创造性思维的教学手段明显不足，这将导致教师无法掌握学生学习结果和评估教学效果，学生无法及时获得教师指导与帮助。最后，无法满足学生个性化的需求，无法培养学生应用知识解决实际问题的能力、实践探究能力、团队合作精神和创新能力。

最后，考核方式难以适应新工科发展要求。该课程现行的考核机制存在明显弊端。平时成绩所依赖的课程设计与作业布置具有滞后性，易使学生产生敷衍心态，导致这一过程性评价形同虚设，无法有效调动其日常学习积极性。其后果是，学生的学习兴趣、专业视野及工程解题能力均未得到实质性发展，反而催生了考前死记硬背的应试策略。因此，最终的考核成绩既不能真实体现学生的学习水平，也难以客观评估课程的教学效果。

3 研究现状与本文贡献

针对上述问题，既有文献提出了不同的解决方法。文献[3]探讨了基于吸引、探究、解释、迁移和评价的 5E 教学模式在“电力系统分析”课程中的应用，对课程的典型教学案例进行设计。文献[4]通过利用现代信息技术对“电力系统分析”课程进行混合式教学的建设，解决教学中的重难点问题。文献[5]从锻炼、提升学生的工程实践与创新复合能力角度出发，提出了“一转变、二突出、三结合”的实践教学改革思路，对“电力系统分析”课程进行了改革，取得了良好的效果。文献[6]基于新工科背景“金课”建设要求，对“电力系统分析”课程进行了课程教学改革研究。文献[7]结合新工科背景下学校应用型人才培养的定位，对“电力系统分析”课程进行了课程教学改革，达到了较好的效果。

本文将在上述文献基础上，结合新工科背景下电气类专业人才的培养目标、工程教育专业认证要求和学校“总师型”人才培养要求，针对现有“电力系统”课程实践过程中存在的问题，从教学内容、教学模式和教学方法、考核方式这三方面深入研究课程教学改革，形成解决当前课程面临问题的方法，探索出一条适应新工科背景下西北工业大学电气工程及其自动化专业人才培养要求的“电力系统”课程教学改革道路。

4 电力系统课程所采取的课程改革措施

1. 更新教学内容

新工科建设和“双碳”背景下新型电力系统的发展给“电力系统”课程教学提出了新的要求，教学内容必须与时俱进，确保学生具备相关知识和技能，以适应时代发展。由于总课时数有限，我们认真规划改进了教学内容，适当降低了教学内容难度，力求锻炼学生解决实际工程问题的能力，激发学生的学习兴趣和热情，提升学习效果。具体的教学改革措施是：

1）以工程教育专业认证为标准，以适应新工科发展要求为导向，对照新工科背景下电气类专业人才的培养目标、工程教育专业认证要求和学校“总师型”人才培养要求，修订了“电力系统”课程教学大纲，规划改进了教学内容：在基础理论方面保留了电力系统结构、元件参数与模型，新增了“源-网-荷-储”协同概念以及电力系统数字化表征；在稳态分析方面，保留了潮流计算、调频调压，新增了高比例可再生能源接入的潮流与稳定问题，电力电子化电力系统特性；在暂态分析方面，保留了对称/不对称短路计算、稳定性，新增了新能源机组的暂态特性与支撑技术和柔性输电对稳定性的影响；在运行与控制方面，保留了经济调度、电能质量，新增了电碳市场与电力系统耦合，人工智能在负荷预测、故障诊断中的应用和电网弹性与网络安全；在未来系统方面，新增了综合能源系统，氢能与电力系统和交通-电力耦合（电动汽车），以满足新工科发展要求。

2）顺应低碳战略发展趋势，深入挖掘专业知识，将能够反映新型电力系统内涵特征、电网结构、供电模式、运行调度、安全稳定运行等方面变化的内容，碳分析、碳优化、碳规划和碳轨迹理论等碳视角下的电力系统分析与优化内容，新型电力系统源网荷储灵活高效互动内容等能够反映电力系统最新发展的新知识和新技术，以及新能源和储能系统在飞机电力系统中的应用，电动飞机技术背景下飞机电力系统的发展以及机载综合能源管理控制方法等能够反映飞机电力系统最新发展的新知识和新技术融入“电力系统”课程教学中，使得教学内容能够反映电力系统最新发展。

3）在教学环节中引入对典型工程案例的描述，在讲述暂态稳定性时，用“美加大停电”案例，提供事故发生的时间、地点、电网结构图、天气条件、初始故障等背景材料，通过提出“本次事故的直接原因和深层原因是什么？”“系统是如何一步步崩溃的？”“哪些保护和控制装置动作了，其动作是否正确？”等引导性问题，引导学生主动思考，

自主回顾或学习相关的理论知识，如“*N*-1 安全准则”、“暂态稳定”、“继电保护配合”、“电压稳定”等，学生利用理论知识分析案例材料，陈述各自观点，争论焦点问题，我们引导讨论方向，纠正错误概念，在关键节点进行提示和总结，展示官方事故调查结论，与学生分析得出的结论进行对比，引导学生反思从这次事故中，我们在电网规划、运行和控制方面应吸取什么教训？这些教训如何体现在今天的电网标准和规范中？通过这样的工程案例学习，让学生更好地了解电力行业，设置探究性工程问题，激发学生学习的热情和兴趣，培养学生解决实际工程问题的能力，满足用人单位对人才需求。

2. 教学方法和教学模式改革

为应对飞速发展的技术革新并助力国家“双碳”目标的达成，为培养建设新型电力系统和服务“三航”发展的新工科人才，我们改革创新了“电力系统”课程的教学方法和教学模式。为了激发学生学习“电力系统”课程的兴趣和热情，提升学习效果，更好地达成课程教学目标，我们进行了以下三方面教学方法和教学模式改革：

1）利用各种授课平台和课程资源，实现多维互动教学模式。利用雨课堂授课平台引导学生进行课前预习，在课堂中及时获取学生学习效果的反馈，利用慕课、B 站、课程群等方式引导学生进行课后复习，掌握所学知识，使学生掌握更多、更快捷的电力系统学习方法，并获得能够反映学生学习效果的关键数据反馈。针对电力系统诸如潮流分析计算、暂态稳态分析等难点内容，我们综合采用启发式、案例式、互动式、课堂教学与网络教学相结合、实践教学与课堂教学相结合等方法，综合利用了各种授课平台和课程资源，提升学生学习兴趣，调动学生学习热情，引导学生主动思考，启发学生思维，实现课堂上教师与学生、学生与学生之间的互动，帮助学生更好理解相关知识点，进而提升了教学效果。通过融合课堂教学与互联网云平台的优势，本课程构建了多维联动的学习流程：在课前引导学生思考电力系统实际问题，在课堂中完成核心知识的内化吸收，在课后进行知识的拓展与深化。这一模式实现了教学环节的环环相扣与相互促进。

2）通过半物理仿真、虚拟仿真、编程计算、认识实习和生产实习赋能“电力系统”理论实践。结合半物理仿真、虚拟仿真，引导学生对电力系统各组成部分进行建模、仿真与综合分析，通过模拟不同运行工况，使其直观把握电力系统的运行特性与内在规律，从而深化对核心原理的理解，通过编程计算，帮助学生熟练掌握电力系统潮流计算、短路计算和稳定性计算的原理和方法，通过半物理仿真、虚拟仿真和编程计算，帮助学生提高解决实际问题的能力和培养创新思维，通过带领学生赴西安供电局认识实习基地和 115 厂生产实习基地，认识实际电力系统设备，了解实际电力系统运行，帮助学生提高解决实际问题的能力。

3）鼓励学生自主学习，培养学生自我探索能力。提炼出“电力系统”课程各个章节内容对应的前沿学术和工程问题，例如在电力系统稳定性分析中提炼出“电力电子化电力系统的暂态与小扰动稳定性”前沿学术问题和“稳定性控制设备的优化部署”工程问题。通过典型工程和学术案例，例如，在概论中给出中国“双碳”目标与新型电力系统典型工程案例，定义和量化“新型电力系统”的稳定性与可靠性典型学术案例，激发学生学习课程的兴趣、热情、好奇心、求知欲和探索欲，引导学生分组完成高水平论文检索与阅读，形成实际工程问题的解决方案，提出自己对这些前沿热点学术和工程问题的观点、看法以及创新性的解决方案，并指导学生将学习和研究成果以研究报告和 ppt 汇报的形式呈现。

3. 课程考核方式改革

传统的考核方式只包含平时成绩和期末成绩两个部分，侧重于对知识掌握程度和核心概念背记的考核，无法激发学生学习“电力系统”课程的兴趣和积极主动性，无法评估学生运用所学知识解决电力系统实际工程问题的能力，无法从全方位多角度对学生学习效果进行客观准确的评价。为了达成新工科背景下“电力系统”课程教学目标，获得良好的教学效果，我们进行了以下三方面课程考核方式改革：

1）科学合理的设置学习过程和效果评价与能力提升评价的比例。学习过程和效果评价主要包括出勤情况、课堂参与情况、小测验、平时作业完成情况、课程实验实践情况、期末考试情况等，主要考核学生掌握知识能力和学习态度。能力提升评价主要包括借助网络资源和电子图书等工具开展自主学习和探究的能力，通过使用现代仿真工具、计算机编程和团队沟通协作解决复杂实际工程问题的能力，撰写研究报告、进行 ppt 汇报等总结汇报能力，主要考核学生自主探究、团队协作、分析解决实际问题以及总结汇报的能力。通过出勤率、课堂参与情况、平时作业完成情况和正确率、小测验

正确率、期末考试分数评价学习过程和效果。通过课程设计、专题学习研讨、工程项目科研训练等方式评价学生自主学习和探究、团队合作、利用理论知识解决实际工程问题、总结汇报等方面的能力。结合新工科对电气类专业人才的培养要求和工程教育专业认证要求，根据教学实践，设置了学习过程和效果评价与能力提升评价的比例为 7:3，适应新工科和电力系统发展对学生基础知识和能力的要求。

2）通过每个小组提交每个组员贡献清单，并开发客观准确评价能力提升效果的方法。通过提交的研究报告和答辩提问，评价每位学生在学习过程中发挥的作用、展现出来的解决问题能力和自主探究能力，通过学生在学习这门课不同阶段的表现，评估学生通过这门课程的学习对能力的提升。

3）科学合理的设置期末考试题目。通过设置实际工程问题、开放性问题和前沿热点问题作为期末考试题目，该考核体系旨在同步评估学生对基础理论、核心概念及计算方法的掌握程度，同时考察其面对复杂工程实际问题时的分析能力与创新解决能力，并兼顾对行业及学术前沿动态的了解程度从而全方位多角度地评价学生学习效果和能力提升。

自“电力系统”课程改革实施以来，教学效果取得了显著提升。在学生学习成效上，不仅期末考核成绩的优秀率提高了 10.5%，更重要的是，通过案例分析和项目式学习，学生解决复杂工程问题的实践能力与创新思维得到了实质性锻炼，其在后续竞赛和毕业设计中的表现尤为突出。在实践能力方面，学生解决复杂工程问题的能力明显增强，能够独立完成小型电力系统设计与分析项目。在创新思维方面，在探究性课题中，学生提出的解决方案创新性、可行性显著提高，项目报告中体现出的系统思维和批判性思维得到有效锻炼。在自主学习能力方面，利用线上平台和翻转课堂，学生课下自主学习时间平均每周增加 4 小时，能够主动搜集资料、协作探究并完成学习任务。多维互动教学模式的课堂参与度超过 90%。

5 结语

面对能源革命与数字革命的浪潮，新工科建设对电气工程教育提出了前所未有的挑战与机遇。本次对“电力系统”课程的改革探索，绝非一次简单的教学调整，而是一场旨在重塑人才培养范式、主动引领未来产业发展的深刻实践。通过系统性地重构教学内容、创新教学模式、改革考核机制，我们成功地将前沿技术、工程实践与跨学科思维融入课程，使课堂从理论知识的传授场，转变为激发创新、锻造能力的练兵场。我们坚信，教育的终极目标不仅是传授已知，更是探索未知。本改革方案所培育的，将不仅是精通技术的专业人才，更是能够驾驭复杂性、具备“总师型”潜质的未来行业领袖。他们将以扎实的专业根基、卓越的工程能力、开阔的全球视野，直面能源转型的全球性挑战，成为推动社会可持续发展的中坚力量。本研究为新时期工科课程的转型升级提供了一套可行路径。我们将以此为契机，持续深化教学改革，为培养能够定义和创造未来的卓越工程人才而不懈努力。

参考文献

[1] 邱桂华，袁丽，李贤阳，黎永壹，应用型高校创新创业人才培养模式思考——以“新工科”背景下的计算机专业为例，钦州学院学报，1: 50- 53, 2019.

[2] 周世杰，李玉柏，李平，肖鸣宇，黄廷祝，新工科建设背景下“互联网 +”复合型精英人才培养模式的探索与实践， 高等工程教育研究，172(5): 17- 22, 2018.

[3] 王雪杰，叶鹏，赵毅，刘峰，基于 5E 教学模式的“电力系统分析”课程教学改革探究，教育教学论坛，2: 77-80, 2023

[4] 赵少华，张楠楠，陈曦，现代信息教育技术下混合式教学的课程改革探索——以“电力系统分析” 为例，电脑知识与技术，17(26): 269-271, 2021

[5] 李晓露，李宏仲，孙欣，李东东，新型电力系统背景下“电力系统分析” 实践教学改革探索，中国电力教育，S1: 145-146, 2021

[6] 屈星，苏泽光，文娟，盛义发，肖金凤，新工科背景下《电力系统分析》课程“金课”建设研究，12: 93-94, 2022

[7] 沈娜，房大中，杜芸强，新工科背景下基于应用型人才培养的“电力系统分析”课程改革与实践，高教学刊，17: 143-146, 2020

收稿日期：2025-10-08。

作者简介：


倪骏康

倪骏康(1991 年)，男，副教授，博士生导师，研究方向为电力系统稳定与控制，E-mail：max12391@126.com；

雷涛(1974 年)，男，教授，博士生导师，研究方向为航空电气系统供配电技术等，E-mail：lttiger@nwpu.edu.cn。

姚文利(1974 年)，男，副教授，硕士生导师，研究方向为飞机储能系统和电力电子高可靠性控制研究，E-mail：yaowl@nwpu.edu.cn。

张晓斌(1963 年)，男，教授，博士生导师，研究方向为电推进飞机电力系统等，E-mail：dgl907@126.com

107 Research on Long-Horizon Model Predictive Control and Seamless Switching of Grid-Forming Converters in Hybrid Systems

Qiuyu Zeng and Zhenghong Tu and Ying Xu and Zhongkai Yi

Harbin Institute of Technology, Harbin 150001, China

Abstract. With the increasing penetration of renewable energy, the inertia and voltage support capability of power systems have significantly declined, making the secure and stable operation of hybrid systems composed of grid-forming (GFM) and grid-following (GFL) converters a research hotspot. To address the limited dynamic response and insufficient harmonic suppression capability of the conventional current PI inner loop in virtual synchronous generator (VSG), this paper proposes a VSG control strategy based on long-horizon model predictive control (MPC). While preserving the outer-loop structure of VSGs, the proposed method improves current tracking accuracy and dynamic performance through a two-step prediction mechanism, thereby effectively enhancing frequency stability and reducing grid-injected current total harmonic distortion (THD). Furthermore, to mitigate the voltage and current transients induced by GFM/GFL mode transitions in hybrid systems, a seamless switching control method is developed, enabling smooth operation under both strong and weak grid conditions. Simulation results demonstrate that the proposed strategy significantly enhances system dynamic performance and power quality, while improving the operational flexibility and stability of renewable-dominated power systems.

Keywords: Hybrid System, Model Predictive Control, Seamless Switching

1 Introduction

With the continuous increase of renewable energy penetration, the operational characteristics of power systems are undergoing significant changes. Traditional power systems rely on large-scale synchronous generators to provide inertia and regulation capabilities.[1-2] However, with the extensive integration of power-electronics-interfaced generation, such as photovoltaic and wind power, system inertia has markedly decreased, leading to increasingly prominent issues in

frequency stability and power quality. To enhance the grid-supporting capabilities of power electronic devices, research on grid-forming converters has become a focal point in both academic and industrial communities.GFMs actively establish voltage and frequency references, thereby providing support and stabilization to the power system.[3] In contrast, grid-following converters rely on phase-locked loops to track grid signals, primarily performing power tracking tasks. In scenarios of large-scale renewable integration, a critical challenge is achieving coordinated operation between GFMs and GFLs while improving the dynamic control performance of GFMs.[4-5] Among grid-forming strategies, virtual synchronous generator control has been widely recognized, as it can emulate the inertia and damping characteristics of conventional synchronous machines to a certain extent. Nevertheless, conventional VSG implementations typically employ a PI-based current inner loop, which exhibits limitations in fast dynamic response and power quality regulation.[6-7] Specifically, system frequency is easily affected by disturbances, resulting in substantial frequency fluctuations. Moreover, the PI inner loop has limited harmonic suppression capability, leading to deterioration in the quality of grid-injected currents.[8]

To address these limitations, this paper proposes a VSG control strategy based on long-horizon model predictive control. While retaining the VSG outer-loop structure, the conventional PI current loop is replaced with a two-step predictive current controller. Furthermore, considering that GFM/GFL mode switching is required in practice under varying grid strength conditions, a seamless GFM/GFL transition strategy is developed to ensure smooth transitions across different operational modes. The proposed improvements significantly reduce frequency fluctuations, enhance frequency stability, and lower the harmonic content of grid-injected currents, thereby improving power quality and operational flexibility. This research not only provides important theoretical contributions but also offers practical value for the operation of power systems under high renewable penetration.

The control strategy studied in this paper focuses on a hybrid system comprising one GFM and one GFL device connected to a common bus. The main research contributions include:Long-horizon MPC design for GFMs, the conventional PI current controller is replaced with a predictive current controller under the VSG outer-loop framework, improving system dynamic response speed and steady-state current quality.Seamless GFM/GFL mode switching strategy, this strategy ensures smooth transitions of system parameters, mitigates voltage and current transients, and enhances operational flexibility.

2 Mechanism Analysis of Grid-Forming and Grid-Following Devices

2.1 Fundamental Principles of Grid-Following Converters

Grid-following converters rely on phase-locked loops to extract the phase and frequency information of the grid voltage, which is then used as a reference for power injection. Essentially, GFL converters operate as current-source controllers and typically employ a dual-loop control structure.[9-10] The outer loop is a power control loop, which converts active and reactive power references into current reference values, while the inner loop is a current control loop that uses a PI controller to ensure that the output current tracks the reference. In the synchronous rotating reference frame, the outer loop of a GFL converter is generally the power control loop, which calculates the current commands based on active and reactive power references, as expressed in Equation (1):

$$\begin{cases} i_d^* = \dfrac{2}{3}\dfrac{P \cdot u_d + Q \cdot u_q}{u_d^2 + u_q^2} \\ i_q^* = \dfrac{2}{3}\dfrac{P \cdot u_q - Q \cdot u_d}{u_d^2 + u_q^2} \end{cases} \tag{1}$$

Where u_d and u_q are the converter output voltages, and P and Q are the active and reactive powers calculated from the three-phase voltages and currents.

The current commands are fed into the controller to generate modulation voltage signals, which are then converted into the inverter's output voltage through modulation, enabling fast current tracking. This control architecture is widely used in grid-connected inverters. The control block diagram of a grid-following (GFL) converter is shown in Fig. 1.

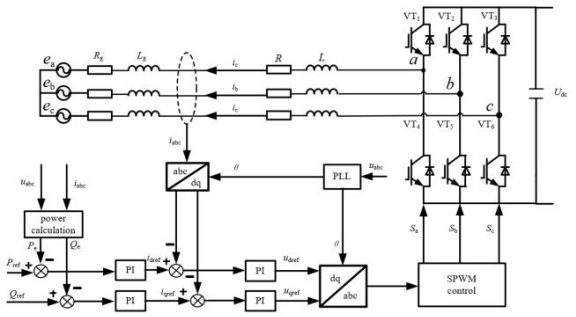


Fig. 1. Control Block Diagram of a Grid-Following Converter

The GFL operating mode offers a simple control structure and strong power-tracking performance; however, it lacks independent voltage-support capability. Consequently, relying solely on GFL converters is insufficient to maintain system stability under weak-grid conditions or during islanded operation.

2.2 Fundamental Principles of Grid-Forming Converters

Grid-forming converters are power-electronic devices capable of actively establishing voltage and frequency references. Their operational characteristics are similar to those of synchronous generators, allowing them to provide both inertial and voltage support to the power system. The core concept of GFM operation is to function as a "voltage source" through appropriate controller design, thereby maintaining system stability under weak-grid or even islanded conditions. [11-12]Virtual synchronous generator control is the most typical control method for GFMs. Its central idea is to incorporate the swing equation of a synchronous generator into the converter controller, enabling the converter to emulate the inertia and damping characteristics of a synchronous machine, and thereby actively establish voltage and frequency references. VSG control generally employs a dual-loop structure: Outer loop: Power–frequency and power–voltage control, responsible for frequency regulation and voltage support.[13] Inner loop: Current control loop, ensuring fast current response and maintaining stable voltage and power output.

The conventional VSG grid-connected control topology is illustrated in Fig. 2.

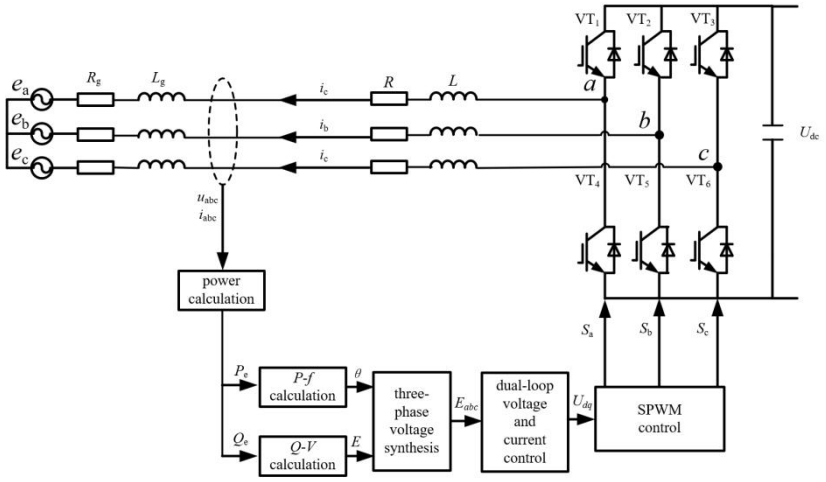


Fig. 2. Conventional Grid-Connected VSG Control Topology

The fundamental concept of VSG control is to incorporate the swing equation of a synchronous generator, as expressed in Equation (2):

$$J\frac{d\omega}{dt}=\frac{P_m}{\omega}-\frac{P_e}{\omega}-D(\omega-\omega_0) \tag{2}$$

Where J is the equivalent rotational inertia, ω is the angular velocity, ω_0 is the rated angular velocity, P_m is the equivalent input power, P_e is the electromagnetic power, and D is the damping coefficient. Through this equation, the VSG can realize both inertial response and damping characteristics.

By monitoring grid frequency deviations and adjusting its active power output accordingly, the VSG can regulate its output frequency and maintain system frequency stability. The frequency regulation control equation is expressed as Equation (3):

$$P_m=P_n+D_{P-f}(\omega_0-\omega) \tag{3}$$

Where P_n is the rated active power and $D_{P\text{-}f}$ is the active power–frequency droop coefficient. By combining Equation (2) and Equation (3), the following relationship can be obtained as Equation (4):

$$J\frac{d\omega}{dt}=\frac{P_n}{\omega}-\frac{P_e}{\omega}-(D+D_{P-f})(\omega-\omega_0) \tag{4}$$

The active power–frequency control block diagram derived from Equation (4) is shown in Fig. 3.

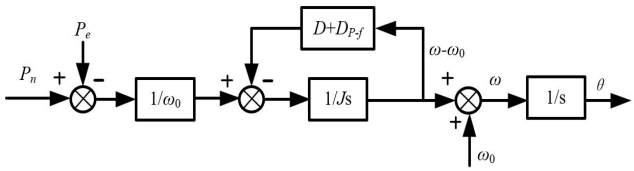


Fig. 3. VSG Active Power–Frequency Regulation Control Block Diagram

Synchronous generators regulate their reactive power output through the excitation control system to achieve stable voltage regulation. When the system reactive load undergoes a sudden change, the excitation control system can automatically provide primary voltage regulation to suppress instantaneous voltage fluctuations.[14] The corresponding voltage regulation equation is expressed as Equation (5):

$$E=E_n+D_{Q-V}(Q_n-Q_e) \tag{5}$$

Where E_n is the rated voltage, $D_{Q\text{-}V}$ is the reactive power–voltage droop coefficient, and Q_n is the rated reactive power.

Since primary voltage regulation operates as a proportional control, an integral term is introduced in the control loop to achieve precise tracking of reactive power. Consequently, the reactive power–voltage control equation can be expressed as Equation (6):

$$E = E_n + D_{Q-V}(Q_n - Q_e) + k_i \int (Q_n - Q_e)dt \tag{6}$$

The reactive power–voltage control block diagram of the VSG is thus obtained, as shown in Fig. 4.

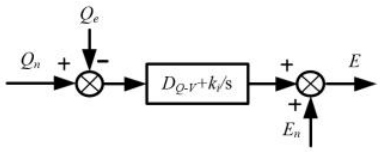


Fig. 4. VSG Reactive Power–Voltage Regulation Control Block Diagram

2.3 Modeling of GFM/GFL Hybrid Systems

In multi-source power systems, grid-forming and grid-following converters are often connected in parallel through a common bus. Their interaction characteristics directly affect system stability and power quality. GFM converters provide voltage and frequency references, playing a central role in maintaining system stability, while GFL converters rely on PLLs to track the voltage reference and achieve power injection. The control topology of the hybrid system is illustrated in Fig. 5.

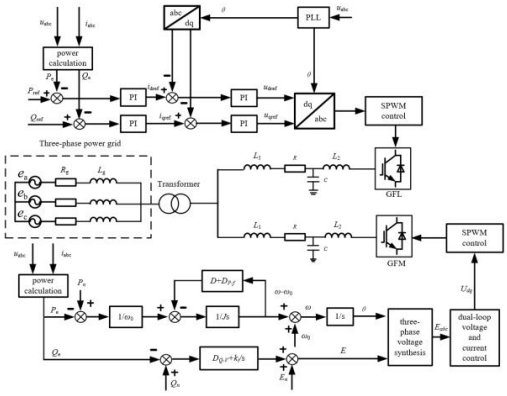


Fig. 5. Control Block Diagram of the GFM/GFL Hybrid System

3 Control Strategy for Grid-Forming Converters Based on Long-Horizon Model Predictive Control

3.1 Conventional PI Current Inner-Loop Control

Within the VSG control framework, the inner-loop current control typically employs a PI regulator. The advantage of the PI controller lies in its simple implementation and clear structure. Taking the synchronous rotating reference frame as an example, in the dq synchronous rotating frame, the current inner-loop controller converts the reference voltage into output voltage commands.[15-16] The corresponding control equation is expressed as Equation (7):

$$\begin{cases} u_{dpwm} = k_{pd}(i_d^* - i_d) + k_{id}\int(i_d^* - i_d)dt \\ u_{qpwm} = k_{pq}(i_q^* - i_q) + k_{iq}\int(i_q^* - i_q)dt \end{cases} \tag{7}$$

Where u_{dpwm} and u_{qpwm} are the modulation voltage commands, k_{pd}, k_{pq}, k_{id}, and k_{iq} are the PI controller parameters, i_d^* and i_q^* are the reference currents calculated by the voltage outer loop, and i_d and i_q are the output current components.

Although VSG control plays a positive role in enhancing system inertia and stabilizing frequency, the conventional PI inner loop still exhibits several limitations under high power-electronics penetration scenarios: Large frequency fluctuations: Under external disturbances such as sudden load changes or power fluctuations, the VSG can provide inertial support; however, due to the limited dynamic response speed of the inner-loop PI controller, frequency regulation exhibits a lag, resulting in larger frequency deviations and longer recovery times.[17] Harmonic distortion in grid current: When the grid contains background harmonics or the system operates under weak-grid conditions, the grid-injected current is prone to harmonic distortion. This increases the total harmonic content and adversely affects normal system operation.

3.2 Current Prediction Model of Grid-Forming Converters

The switching signals S and the output voltage vector U of the grid-forming converter can be calculated using Equations (8)–(9):

$$S = \frac{2}{3}(S_a + aS_b + a^2S_c), a = e^{j\frac{2\pi}{3}} \tag{8}$$

$$U = U_{dc} \cdot S \tag{9}$$

The vector diagrams corresponding to the eight different switching states can be obtained, as shown in Fig. 6.

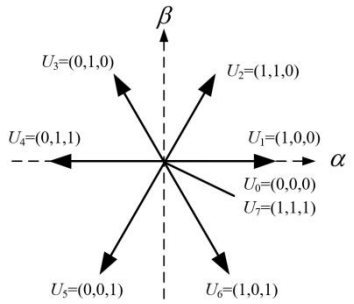


Fig. 6. Output Voltage Vector Diagram

Based on the DC bus voltage and the switching states of the grid-connected inverter, the inverter output voltages u_d and u_q can be determined.

Model predictive control is an advanced, optimization-based control strategy. Its core idea is to use the system's mathematical model to predict future output trajectories and to solve a cost function via receding-horizon optimization, thereby achieving optimal control within the prediction horizon. The advantage of MPC lies in its ability to directly handle system constraints and multivariable couplings, offering superior robustness and dynamic performance compared to conventional PI control.[18-19] In the synchronous dq rotating reference frame, the dynamic equation of the output current of a grid-forming converter is expressed as Equation (10):

$$\begin{cases} \dfrac{di_d}{dt} = \dfrac{1}{L}(u_d - Ri_d + \omega L i_q - v_{gridd}) \\ \dfrac{diq}{dt} = \dfrac{1}{L}(u_q - Ri_q + \omega L i_d - v_{gridq}) \end{cases} \tag{10}$$

Where v_{gridd} and v_{gridq} are the grid voltage components, L and R are the filter inductance and resistance, and ω is the system angular frequency. The above equation can be discretized using the forward Euler approximation method. By substituting into Equation (10), the discrete form is obtained as Equation (11):

$$\begin{cases} i_d(k+1) = i_d(k) + \dfrac{T_s}{L}(u_d(k) - Ri_d(k) + \omega L i_q(k) - v_{grid\,d}(k)) \\ i_q(k+1) = i_q(k) + \dfrac{T_s}{L}(u_q(k) - Ri_q(k) + \omega L i_d(k) - v_{grid\,q}(k)) \end{cases} \tag{11}$$

The cost function is a key metric in model predictive control used to evaluate system performance. By predicting the system behavior over a future time horizon and optimizing the control inputs, the cost function aims to minimize or maximize a specific performance index. In MPC, for different voltage vectors, the system can quantify the deviation between the reference current at the next sampling instant and the model-predicted current using the cost function g.[20] In this study, long-horizon MPC is applied to improve the conventional grid-forming control current inner loop, replacing it with a predictive control scheme. The corresponding cost function is expressed as Equation (12)

$$g = [i_d^*(k+1) - i_d(k+1)]^2 + [i_q^*(k+1) - i_q(k+1)]^2 \tag{12}$$

In the model, the calculation of the reference current is derived from the conventional VSG control, the active power–frequency and reactive power–voltage outer loops. The synthesized voltage vector is used by the controller to generate the reference current. During current predictive control, the reference current must also be updated in real time. By using the current reference current value to extrapolate future values, this study employs the Lagrange extrapolation method. Using a second-order algorithm, the reference current can be calculated as expressed in Equation (13):

$$i^*(k+1) = \sum_{i=0}^{2} (-1)^{2-i} \frac{3!}{[i!(3-i)!]} (n+i-2) = 3i^*(k) - 3^*(k-1) + i^*(k-2) \tag{13}$$

3.3 Design of Grid-Forming Converter Control Strategy Based on Long-Horizon Model Predictive Control

In practical grid-forming control, sampling and computation delays are inevitable. A single-step prediction often leads to steady-state errors and dynamic lag. Although conventional model predictive control can predict the current at the next time step, the system's inherent response time prevents the switching devices from rapidly achieving the optimal state at the following instant, resulting in tracking errors. Long-horizon MPC overcomes this limitation by constructing a mathematical model of the system to predict current values over two future time steps. Different voltage vectors are applied for the two steps, and the optimal switching states for the next time step are evaluated in advance, enabling precise predictive current control. The

principle diagram and corresponding control equation are shown in Fig. 7 and Equation (14):

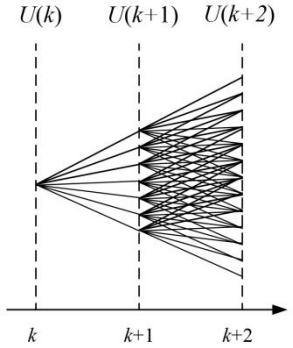


Fig. 7. Principle Diagram of Long-Horizon Model Predictive Control

$$\begin{cases} i_d(k+2)=i_d(k+1)+\dfrac{T_s}{L}(u_d(k)-Ri_d(k+1)+\omega Li_q(k+1)-v_{gridd}(k+1)) \\ i_q(k+2)=i_q(k+1)+\dfrac{T_s}{L}(u_q(k)-Ri_q(k+1)+\omega Li_d(k+1)-v_{gridq}(k+1)) \end{cases} \tag{14}$$

The predicted value of the compensation current is calculated from the above equation. It is then necessary to compute the corresponding cost function, and the switching states are updated according to the one that minimizes the cost function. The cost function is expressed as Equation (15):

$$\begin{aligned} g=&\left[i_d^*(k+1)-i_d(k+1)\right]^2+\left[i_q^*(k+1)-i_q(k+1)\right]^2 \\ &+\left[i_d^*(k+2)-i_d(k+2)\right]^2+\left[i_q^*(k+2)-i_q(k+2)\right]^2 \end{aligned} \tag{15}$$

The reference current is continuously updated using the Lagrange extrapolation method, as expressed in Equation (16):

$$\begin{cases} i^*(k+1)=3i^*(k)-3i^*(k-1)+i^*(k-2) \\ i^*(k+2)=6i^*(k)-8i^*(k-1)+3i^*(k-2) \end{cases} \tag{16}$$

By integrating the above long-horizon MPC current controller as the inner current loop with the conventional VSG control, the system output current can be optimally regulated.

3.4 Simulation Validation of Long-Horizon Model Predictive Control

To verify the effectiveness of the proposed algorithm, a hybrid system simulation

model was established. The simulation parameters are listed in Table 1:

Table 1. Simulation Parameters of the System

Parameter	Value
grid frequency f	50
DC-side voltage U_{dc}	800V
active power reference P_{ref}	20kW
machine-side inductance L_2	20e-3H
filter capacitance C	30e-6F
grid-side inductance L_1	2e-4H

A frequency drop of 0.1 Hz was applied to the system between 0.5 s and 1 s to verify the effectiveness of the proposed algorithm. As shown in Fig. 8, under MPC control, the current tracking response is fast, closely approaching the reference current within 0.2 s. Furthermore, when the frequency experiences abrupt changes at 0.5 s and 1 s, the current exhibits minimal fluctuations.

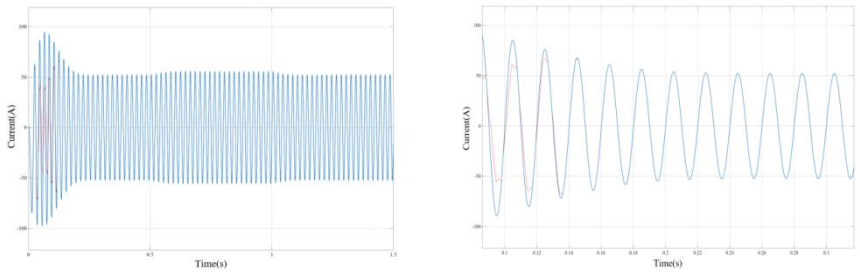


Fig. 8. d-Axis Reference Current Tracking under Long-Horizon Model Predictive Control

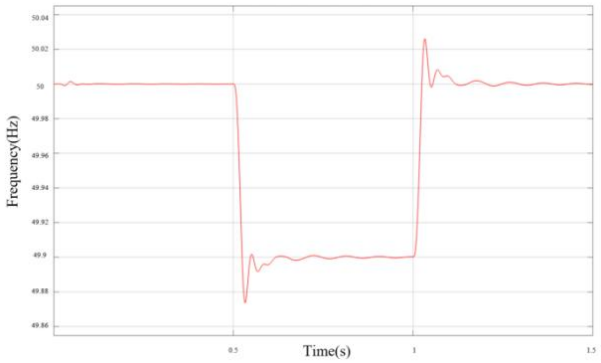


Fig. 9. Grid-Connected Point Frequency Waveform under Conventional PI Control

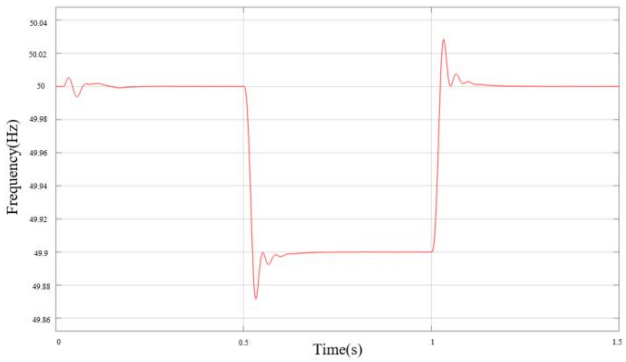


Fig. 10. Grid-Connected Point Frequency Waveform under Long-Horizon Model Predictive Control

As shown in Figs. 9 and 10, under conventional PI control, the grid-connected point frequency cannot quickly stabilize following abrupt frequency changes, exhibiting noticeable oscillations after the overshoot. In contrast, the proposed algorithm enables rapid frequency stabilization during such disturbances, demonstrating its effectiveness in regulating frequency in the hybrid system.

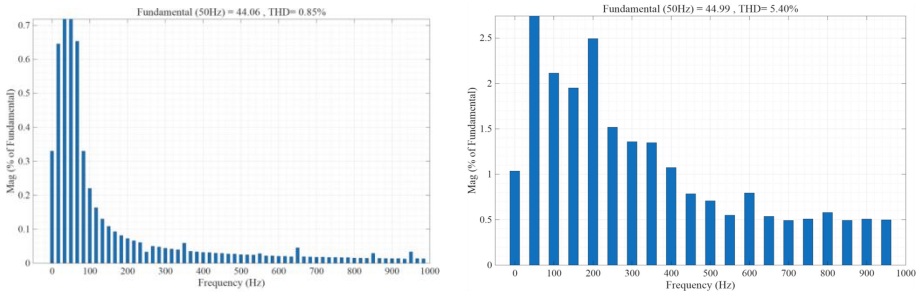


Fig. 11. Frequency Spectrum Analysis of Grid-Injected Current under Conventional PI Control and Long-Horizon MPC

The grid-injected current was measured under abrupt frequency changes. As shown in Figs. 11 and 12, the conventional PI control exhibits a slow response and poor adaptability to sudden frequency variations, resulting in severe distortion with a THD of 5.40%. In contrast, the proposed algorithm rapidly tracks the reference current during frequency transients, significantly reducing current distortion, with THD lowered to 0.85%. This demonstrates that the proposed method effectively mitigates grid-injected current distortion and improves power quality.

4 Seamless GFM/GFL Switching Strategy

In high renewable penetration power systems, grid-forming and grid-following onverters often need to operate in coordination. Due to the complexity of operating conditions, converters may be required to switch between GFM and GFL modes. Improper control during this switching process can lead to abrupt changes in voltage and current, causing current surges, frequency oscillations, and even triggering protection actions, thereby jeopardizing system stability. Therefore, developing a seamless GFM/GFL switching strategy is of significant importance.

4.1 GFM/GFL Seamless Switching Strategy

In this chapter, a seamless switching method based on smooth handover of state variables is proposed to achieve smooth transitions between GFM and GFL modes. When the system reaches steady-state equilibrium, Equation (17) is obtained:

$$E = U + I(R + j\omega L) \tag{17}$$

Where E is the internal voltage, U is the terminal voltage, and I is the terminal current. In GFL mode, the conventional terminal voltage coordinates are transformed into a unified αβ reference frame consistent with the GFM mode, as expressed in Equation (18). The GFL and GFM modes share the same current control loop, ensuring a smooth transition of current commands during mode switching.

$$\begin{bmatrix} I_\alpha \\ I_\beta \end{bmatrix} = \frac{2}{3}\begin{bmatrix} \cos\theta & \cos(\theta - \frac{2\pi}{3}) & \cos(\theta + \frac{2\pi}{3}) \\ \sin\theta & \sin(\theta - \frac{2\pi}{3}) & \sin(\theta + \frac{2\pi}{3}) \end{bmatrix}\begin{bmatrix} I_a \\ I_b \\ I_c \end{bmatrix} \tag{18}$$

Where θ is the rotation angle, denoted as θ_{GFM} in GFM mode and θ_{GFL} in GFL mode. In GFM mode, the PLL module continuously calculates θ_{GFL} in real time, and this angle is locked during GFL operation to ensure consistency of control variables before and after switching.

In GFL mode, the reference currents are calculated from the active and reactive powers through the regulation controller, with the corresponding expressions given in Equation (19):

$$\begin{cases} I^*_{\alpha-GFL} = (k_{pl} + \dfrac{k_{il}}{s}) \cdot \left(P_{ref} - P_e\right) \\ I^*_{\beta-GFL} = (k_{pl} + \dfrac{k_{il}}{s}) \cdot \left(Q_{ref} - Q_e\right) \end{cases} \tag{19}$$

In GFM mode, the reference currents are calculated from the reference voltage generated by the VSG through the regulation controller, with the corresponding expressions given in Equation (20):

$$\begin{cases} I^*_{\alpha-GFM} = (k_{pm} + \dfrac{k_{im}}{s}) \cdot \mathrm{Re}[E^* - U_\alpha - I_\alpha (R + j\,\omega L)] \\ I^*_{\beta-GFM} = (k_{pm} + \dfrac{k_{im}}{s}) \cdot \mathrm{Im}[E^* - U_\beta - I_\beta (R + j\,\omega L)] \end{cases} \tag{20}$$

After obtaining the reference currents for both GFL and GFM modes, the transition between the two is achieved through the GFM/GFL switching signal. These reference currents are then used in a closed-loop control with the measured currents. Following virtual impedance regulation, the final reference voltage V is generated to produce the PWM signals, as expressed in Equation (21):

$$\begin{aligned} V_\alpha &= (I^*_\alpha - I_\alpha) \cdot (k_p + \frac{k_i}{s}) - I_\alpha \omega L \\ V_\beta &= (I^*_\beta - I_\beta) \cdot (k_p + \frac{k_i}{s}) - I_\beta \omega L \end{aligned} \tag{21}$$

The dual-loop control block diagram of the proposed method is shown in Fig. 12.

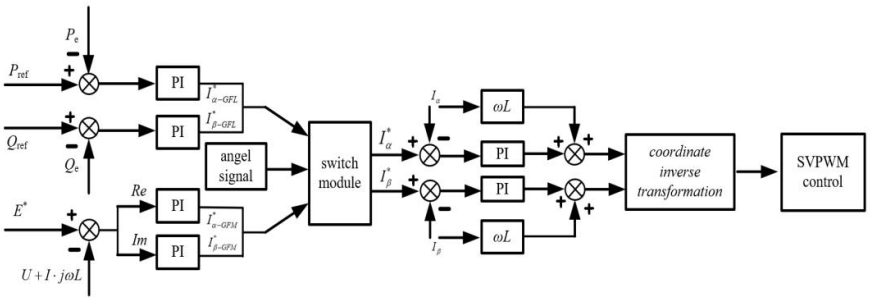


Fig. 12. GFL/GFM Seamless Switching Control Block Diagram

4.2 Simulation Validation of Seamless Switching Strategy

The proposed GFM/GFL switching control algorithm was validated through simulation, with switching signals applied at 0.5 s and 1 s to achieve a

GFM–GFL–GFM transition. As shown in Figs. 13–14, when the impedance is not switched, seamless switching is achieved at 0.5 s. The active and reactive powers exhibit minimal variation and quickly return to their reference values. Moreover, the output voltage and current show no significant fluctuations during the GFM/GFL mode transition. These results indicate that the proposed algorithm has minimal impact on system operation and effectively realizes seamless GFM/GFL switching.

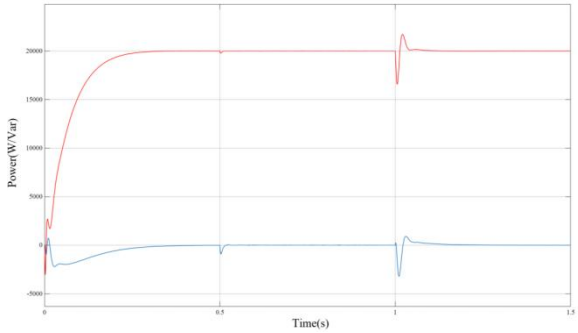


Fig. 13. Power Waveforms during Seamless Switching without Impedance Switching

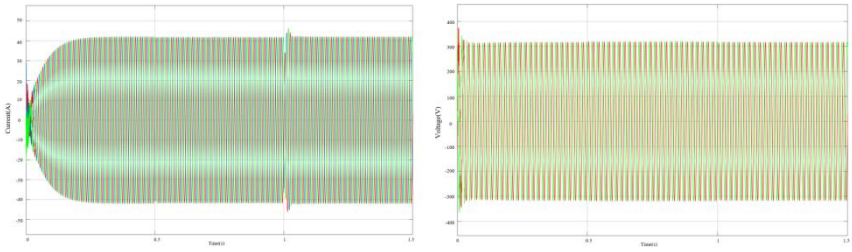


Fig. 14. Output Voltage and Current Waveforms during Seamless Switching without Impedance Switching

To evaluate the robustness of the proposed algorithm, impedance switching was applied at 0.5 s and 1 s to simulate transitions between strong-grid and weak-grid conditions, and the GFM–GFL–GFM mode switching was examined under these scenarios. As shown in Figs. 15–16, when the impedance was switched at 0.5 s, the active and reactive powers remained nearly constant, achieving seamless switching. At 1 s, slight power fluctuations occurred but quickly returned to their reference values. The output voltage and current exhibited only minor deviations during impedance switching. These results indicate that the proposed algorithm can effectively adapt to transitions between strong and weak grid conditions, realizing seamless GFM/GFL mode switching.

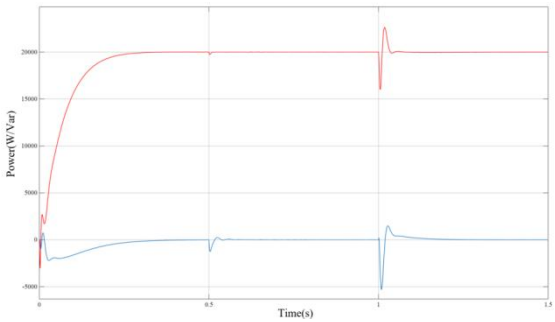


Fig. 15. Power Waveforms during Seamless Switching with Impedance Switching

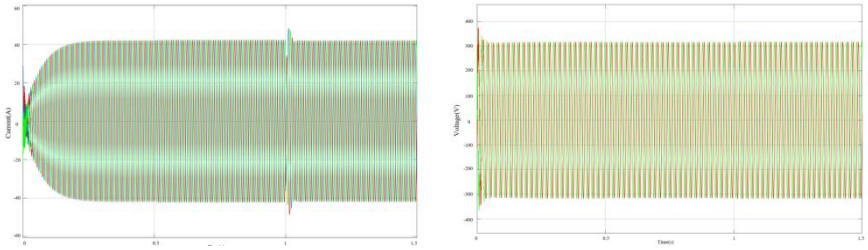


Fig. 16. Output Voltage and Current Waveforms during Seamless Switching with Impedance Switching

The grid-connected point frequency waveform is shown in Fig. 17. As observed, during impedance switching at 0.5 s and 1 s, the GFM/GFL switching strategy effectively regulates the frequency. The grid-connected point frequency exhibits only minor fluctuations during impedance transitions and quickly returns to 50 Hz. These results indicate that the proposed seamless switching method can achieve smooth transitions without significant frequency deviations, ensuring smooth parameter transitions and enhancing the operational flexibility of the power system.

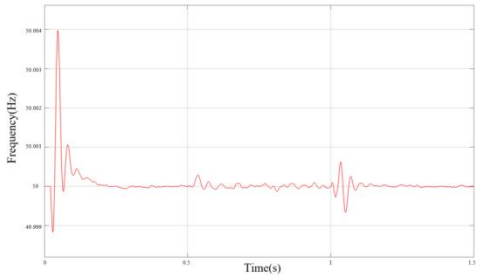


Fig. 17. Grid-Connected Point Frequency Waveform during Seamless Switching with Impedance Switching

5 Conclusion

With the continuous increase of renewable energy penetration, the coordinated operation of grid-forming and grid-following converters in power systems has become increasingly prominent. Balancing system stability, power quality, and operational flexibility has become a critical challenge.

This study addresses the limitations of conventional virtual synchronous generator control, particularly the restricted dynamic performance of the inner-loop current PI controller and its insufficient harmonic suppression capability. An improved strategy based on long-horizon model predictive control is proposed. By maintaining the VSG outer-loop active–frequency and reactive–voltage regulation structure and introducing a two-step prediction mechanism, the method enhances current tracking accuracy and response speed, effectively improving system frequency stability and significantly reducing the total harmonic distortion of the grid-injected current. Furthermore, to meet the practical needs of high renewable penetration systems where frequent switching between GFM and GFL modes may occur, a seamless GFM/GFL switching control method is designed. This ensures smooth transitions under both strong-grid and weak-grid conditions, avoiding voltage and current surges as well as frequency fluctuations, while maintaining system stability and continuity of power output. The proposed control strategy is of significant importance for enhancing the stability and operational flexibility of power systems in the context of increasing renewable energy integration.

References

[1] Duan Z, Meng Y, Zhao P, et al.Interaction Large-Signal Stability Analysis of M3C and GFM/GFL Hybrid Control Strategies Converters Based on the Novel Fuzzy Tensor Space Method[J].IEEE Transactions on Power Electronics, 2025:1-14.

[2] Shan X, Hou K, Guo L,et al.Active Support Control for Hybrid Renewable Energy Stations with Grid-Following and Grid-Forming Capabilities Considering Grid Strength[J].IOP Publishing Ltd, 2025.

[3] Wang Guanqi, Pei Wei, Xiong Jiawang, et al.A Review on Coordinated Control Strategies for Grid-Following and Grid-Forming Converters in Renewable Energy Stations[J]. High Voltage Engineering, 2025, 51(2): 793–805.

[4] Gong Kai, Xiao Huangqing, Zhang Zhan, et al.Adaptive Hybrid Synchronization Control of Grid-Connected Renewable-Energy Converters and Its Small-Signal Stability Analysis [J]. Zhejiang Electric Power, 2024, 43(11).

[5] Li S, Cao P, Li X.Optimization method of energy storage system based on improved VSG control algorithm[J].Journal of Energy Storage, 2024(Nov. Pt.A):101.

[6] Nam E, Chae S.Kalman Filter-Based Model Predictive Control of Grid-Connected 3L-ANPC Inverter with Optimized Space Vector[J].2024 IEEE Energy Conversion Congress and Exposition (ECCE), 2024:3871-3876.

[7] Ren H, Zhuang M, Sun L, et al.Two-stage three-phase photovoltaic grid-connected inverter control method based on off-policy integral reinforcement learning[J].Control Engineering Practice, 2025, 159.

[8] Wang J, Xie D, Wu X, et al.Two-step PV grid-connected inverter control parameter identification based on improved gray wolf algorithm[J].Proceedings of SPIE, 2023, 12788(000):9.

[9] Wang L, Xu H, Li W, et al.Control strategy of PV microgrid grid-connected inverter[J].IOP Publishing Ltd, 2024.

[10] Niu X, Mou Q, Li X, et al.Small Signal Stability Analysis of GFM and GFL Inverters Hybrid System with Three Typical Grid Topology Structures[J].Sustainability (2071-1050), 2025, 17(11).

[11] Chen X, Wang Y, Hua M, et al.Grid-connected Inverters Control Schemes Based on Hybrid Damping Adaptive Control[J].Proceedings of the Csee, 2016.

[12] Suboti I, Gross D.Power-Balancing Dual-Port Grid-Forming Power Converter Control for Renewable Integration and Hybrid AC/DC Power Systems[J].IEEE Transactions on Control of Network Systems, 2021, 9:1949-1961.

[13] Zheng C, Dragicevic T, Blaabjerg F.Model Predictive Control-Based Virtual Inertia Emulator for an Islanded Alternating Current Microgrid[J].IEEE Transactions on Industrial Electronics, 2021, 68(8):7167-7177.

[14] Zhang Y, Liu Y, Luo B, et al.Variable weight coefficient MPC control strategy for qZSI-VSG wind power grid-connected system[J].IET renewable power generation, 2023(8):17.

[15] Zhang Mingzhou, Zhao Tao, Zhu Aihua, et al.A Virtual-Synchronous-Generator Control Strategy Based on Current-Model Prediction [J]. Machinery & Electronics, 2023, 41(9): 63–69.

[16] Li Gongqiang, Zhao Lulu, Xie Fengxiang, et al. Seamless-Switching Control Between Grid-Following and Grid-Forming Modes for Battery Energy-Storage Converters [J]. Energy Storage Science and Technology, 2025, 14(8): 2983–2993.

[17] Wang Kairang, Zhao Yiming, Meng Jianhui, et al.Smooth Grid-Connection Strategy for Photovoltaic-Storage Virtual Synchronous Machine Based on Adaptive Model Predictive Control [J]. High Voltage Engineering, 2023, 49(2): 831–839.

[18] Park J, Askarian A, Salapaka S.Control Designs for Critical-Continegency Responsible Grid-Following Inverters and Seamless Transitions To and From Grid-Forming Modes[J].IEEE, 2024.DOI:10.23919/ACC60939.2024.10644914.

[19] Debnath R, Gupta G S, Kumar D,et al.Stability enhancement for seamless control in networked microgrids with energy storage: Nonlinear spatio-temporal control perspective[J].Journal of Energy Storage, 2024(Oct. Pt.B):100.

[20] Askarian A, Park J, Salapaka S.Multi-Mode Inverters: A Unified Control Design for Grid-Forming, Grid-Following, and Beyond[J]. 2024.

108 基于改进高压直挂级联 H 桥拓扑的储能变流器构网穿越控制

杨鑫宇[1]，肖朝霞[1]，张岩[1]，王璇[1]，沙琳[1]

（1．天津工业大学电气工程学院，天津市西青区宾水西道 399 号 300387，中国天津）

Grid-Forming Fault Ride-Through Control of Energy Storage Converter Based on Improved High-Voltage Transformer-Less Cascaded H-Bridge Topology

Yang Xinyu[1], Xiao Zhaoxia[1], Zhang Yan[1], Wang Xuan[1], Sha Lin[1]

(1.School of Electrical Engineering, Tiangong University, No. 399, Binshuixi Road, Xiqing District, Tianjin 300387,China)

ABSTRACT: The high-voltage transformer-less cascaded H-bridge circuit can increase the voltage before connecting to the grid. It features a highly modular structure and offers significant advantages over low-voltage solutions, such as larger single-unit capacity, higher efficiency, and faster response speed. Energy storage converters based on the high-voltage direct-connected cascaded H-bridge topology must possess grid-forming fault ride-through capability. During fault ride-through, issues such as underutilization of converter capacity and transient overcurrent may arise. To address these problems, this paper proposes a grid-forming fault ride-through control strategy for energy storage converters based on an improved high-voltage transformer-less cascaded H-bridge topology. When the grid voltage experiences a deep sag, the cascaded H-bridge (CHB) is switched to parallel operation to fully utilize the converter capacity. An improved virtual synchronous generator control strategy with voltage phase-angle and amplitude compensation is adopted, enhancing the grid-forming support capability of the energy storage converter and suppressing transient overcurrent. Simulation results verify the rationality and correctness of the proposed scheme.

KEY WORDS: Energy Storage Converter; cascaded H-bridge; grid-forming fault ride-through control; capacity; voltage amplitude-phase angle compensation

摘要：高压直挂级联 H 桥电路可将电压升高后接入电网，其具有高度模块化结构，对比低压方案具有单机容量大、效率高、响应速度快等明显优势。基于高压直挂级联 H 桥拓扑的储能变流器应具备构网穿越能力，在故障构网穿越期间会出现变流器容量得不到充分利用和暂态过流的问题。针对以上问题本文提出了一种基于改进高压直挂级联 H 桥拓扑的储能变流器构网穿越控制策略。在电网电压跌落较深时，将级联 H 桥（CHB）切换为并联运行以充分利用变流器的容量，并采用改进虚拟同步机电压相角-幅值补偿策略，提升储能变流器对电网的构网支撑能力并抑制暂态过流。仿真结果验证了所提方案的合理性和正确性。

关键词：储能变流器；级联 H 桥；构网穿越控制；容量；电压相角-幅值补偿

DOI：10.13335/j.1000-3673.pst.2014.01.

0 引言

高压直挂级联 H 桥储能变流器具备模块化结构规整的特性，可根据需求灵活改变级联单元的数量，以适应不同电压等级，还可以冗余运行以提高系统的稳定性、可靠性。此外，由于每个 H 桥单元均需独立直流电源供电，CHB 变流器可集成多个电池单元，无需升压变压器即可实现中压运行[1]。

通过电力电子变流器实现可再生能源的大规模并网，导致电力系统强度降低。为提升电网稳定性与可靠性，基于电压源的构网（GFM）控制受到广泛关注。近年来，学者们提出了多种构网控制策略，目前研究最为广泛的策略包括：下垂控制，即根据有功功率和无功功率偏差调节频率与电压幅值；功率同步控制（PSC），基于功率交换动态实现与电网的同步；虚拟同步电机（VSG）控制，模拟同步电机的摇摆方程。

在电网故障时，受过载限制影响，构网型变流器的暂态限流控制尤为关键。目前，在故障限流的同时维持构网运行的主流方法有电流饱和算法[2]和虚拟阻抗方法[3]。电流饱和算法通过饱和内环电流参考值实现限流，而虚拟阻抗方法则通过引入虚拟阻抗修改内环电压参考值，间接实现限流。文献[4]提出了一种基于 CHB 拓扑的构网型变流器限流

策略，利用 CHB 变流器的电流钳位负反馈控制（CCNFC）策略，在电网故障时，通过矢量对齐抑制过电流，同时优化构网支撑性能。

电网电压跌落较深时，基于 CHB 拓扑的储能变流器的容量会有较多剩余，若能将此部分剩余容量加以利用，即可在电网故障期间提供更大的支撑能力。针对此问题还未有相关研究。

针对以上问题，本文提出一种改进的高压直挂级联 H 桥拓扑的储能变流器构网穿越策略，并通过仿真进行验证。主要贡献如下：

（1）提出一种提升支撑电网能力的改进高压直挂级联 H 桥拓扑。当电网电压跌落至临界深度 D^*时，将 CHB 旁路出一半 H 桥，并将旁路出的 H 桥并联在保留的 H 桥的两端，充分利用变流器的容量，为电网提供更大的支撑能力。

（2）提出串/并联切换策略与 VSG 补偿策略。串/并联切换策略用于实现电网电压跌落至临界深度 D^*时，将 CHB 从串联结构切换至并联结构；VSG 补偿策略用于在电网发生故障时，在有功-相角环与无功电压环之后补偿相角差与幅值差。

本文结构安排如下：

第二部分介绍基于改进高压直挂级联 H 桥储能变流器系统结构；第三部分介绍临界深度 D^*的计算方法；第四部分介绍串/并联切换策略和 VSG 补偿策略；第五部分介绍仿真结果及分析；第六部分为结论。

1 基于改进高压直挂级联 H 桥储能变流器系统结构

基于改进高压直挂级联 H 桥拓扑的储能变流器构网穿越控制系统结构如图 1 所示。变流器拓扑采用高压直挂级联 H 桥，其中 H-Bridge-X_1 到 H-Bridge-$X_{n/2}$ 与 H-Bridge-$X_{n/2+1}$ 到 H-Bridge-X_n（X=A、B、C，代表相别），两两之间通过导线正常串联。H-Bridge-$X_{n/2}$ 与 H-Bridge-$X_{n/2+1}$ 之间通过一对反向并联的晶闸管 T_{X1}、T_{X2} 相连。H-Bridge-$X_{n/2}$ 的右桥臂中点与一对反向并联的晶闸管 T_{X3}、T_{X4} 与接地点相连，H-Bridge-$X_{n/2+1}$ 的左桥臂中点与一对反向并联的晶闸管 T_{X5}、T_{X6} 经滤波电感 L_f 与电网相连。采样点包括滤波电感的三相电流 i_{abc}，变流器输出的三相电压 u_{abc}，电网电压 v_{gABC}。

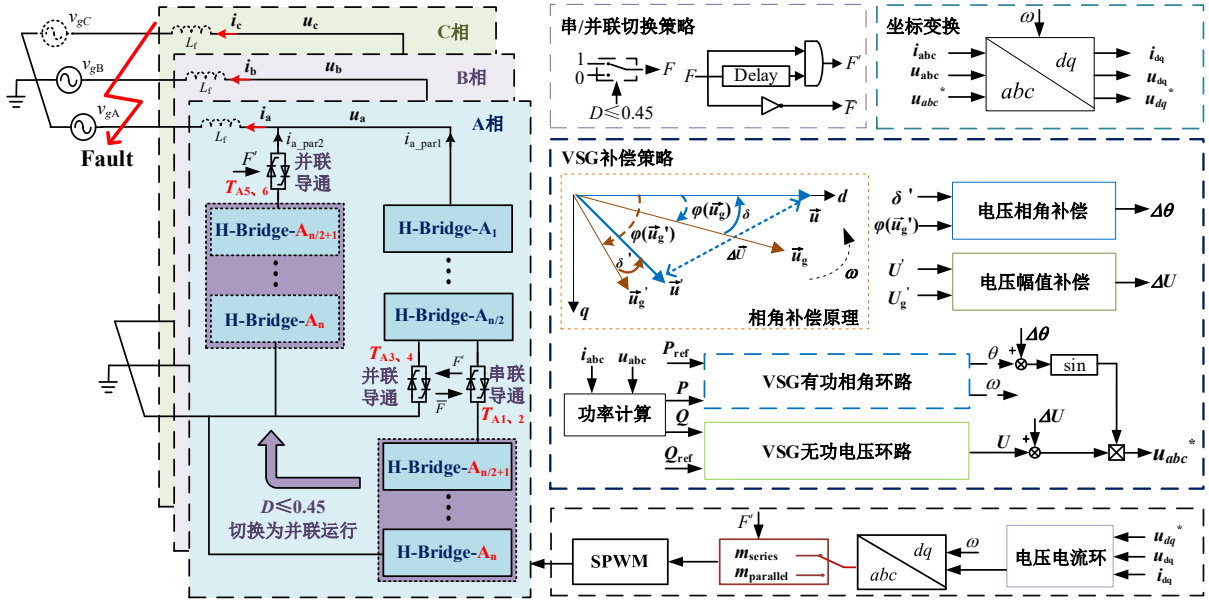


图 1 改进的高压直挂级联 H 桥储能变流器及其控制系统

Fig.1 Improved energy storage converter of high-voltage cascaded H-bridge topology with its control

在电网电压跌落至临界深度 D^*时，晶闸管 T_{X1}、T_{X2} 关断，T_{X3}、T_{X4}、T_{X5}、T_{X6} 导通，H-Bridge-X_1 到 H-Bridge-$X_{n/2}$ 与 H-Bridge-$X_{n/2}$ 与 H-Bridge-$X_{n/2+1}$ 并联运行，此时并联的两组变流器均可以额定电流向电网输送功率，即可以 2 倍的额定电流为限向电网输送功率，充分利用了所有 H 桥模块和变流器的容量，提升了变流器对电网的支撑能力。

控制策略包括串/并联切换策略和 VSG 补偿策略。串/并联切换策略通过协调控制 SCR 的通断和 IGBT 的调制比来完成 CHB 的串并联切换，并切换功率参考以实现提升对电网的支撑能力；VSG 补偿策略分为电压相角补偿和电压幅值补偿，其主要作用为故障期间迅速改变内环电压的参考值，保证变流器构网穿越且变流器不过流。

2 临界深度 D^*的计算方法

2.1 故障期间变流器过剩容量的计算

根据电网准则，在发生对称故障时，无功电流的参考值应为：

$$I_{\mathrm{q}}^{\mathrm{ref}} = K_1(0.9-D)I_{\mathrm{N}} \tag{1}$$

式中比例系数 K_1 取 1.5，D 为电压跌落深度，I_{N} 为变流器的额定电流。

根据变流器的额定电流，可计算出有功电流的参考值：

$$I_{\mathrm{d}}^{\mathrm{ref}} = \sqrt{(I_{\mathrm{N}})^2-(I_{\mathrm{q}}^{\mathrm{ref}})^2} \tag{2}$$

由有功、无功电流参考值可计算出故障期间要求变流器输出的有功、无功功率的参考值：

$$P_{\mathrm{ref}} = \frac{3}{2}(V_{\mathrm{d}}I_{\mathrm{d}}^{\mathrm{ref}}+V_{\mathrm{q}}I_{\mathrm{q}}^{\mathrm{ref}}) \tag{3}$$

$$Q_{\mathrm{ref}} = \frac{3}{2}(V_{\mathrm{q}}I_{\mathrm{d}}^{\mathrm{ref}}-V_{\mathrm{d}}I_{\mathrm{q}}^{\mathrm{ref}}) \tag{4}$$

式中 V_{d}、V_{q} 分别为电网电压的 d、q 轴分量。根据有功、无功功率的参考值，可计算出故障期间变流器需要具备的容量 S^*：

$$S^* = \sqrt{P_{\mathrm{ref}}^{\ 2}+Q_{\mathrm{ref}}^{\ 2}} \tag{5}$$

可得出故障期间变流器的过剩容量 S_{rem}：

$$S_{\mathrm{rem}} = S_{\mathrm{N}} - S^* \tag{6}$$

式中 S_{N} 表示变流器的额定容量。

2.2 CHB 中每个 H 桥可输出额定功率的计算

设三相 CHB 型变流器每相由 n 个 H 桥组成，每个 H 桥由直流电源供电，电压为 V_{dc}。变流器的额定功率为 S_{N}，因此每个 H 桥可输出的额定功率为 $S_{\mathrm{N}Xi}$：

$$S_{\mathrm{N}Xi} = \frac{S_{\mathrm{N}}}{3n} \tag{7}$$

式中 $S_{\mathrm{N}Xi}$ 表示每个 H 桥输出的额定功率（其中 X=A、B、C 代表相别，i=1,2,⋯,n 代表 H 桥编号）。

2.3 在故障期间每相可旁路出 H 桥个数的计算

由故障期间变流器的过剩容量 S_{rem} 可得出每相的过剩容量 $S_{\mathrm{rem}X}$：

$$S_{\mathrm{rem}X} = \frac{S_{\mathrm{rem}}}{3} \tag{8}$$

将每相的过剩容量除以每个 H 桥可输出的额定功率即可计算出故障期间每相可旁路出 H 桥的个数 n_{rem}：

$$n_{\mathrm{rem}} = \frac{S_{\mathrm{rem}k}}{S_{\mathrm{N}ki}} \tag{9}$$

当电网电压低于某一临界深度 D^*时，每相可恰好旁路出 n/2 个 H 桥，将旁路出的 n/2 个 H 桥并联在保留的 H 桥两端，以增强对电网的支撑能力。

2.4 调制比约束

故障期间变流器端口电压幅值参考值 U_{ref}：

$$U_{\mathrm{ref}} = \frac{3U_{\mathrm{g}}+\sqrt{9U_{\mathrm{g}}^2+24Q_{\mathrm{ref}}X_{\mathrm{L}}}}{6} \tag{10}$$

$$U_{\mathrm{g}} = \sqrt{V_{\mathrm{d}}^{\ 2}+V_{\mathrm{q}}^{\ 2}} \tag{11}$$

$$X_{\mathrm{L}} = \omega L_{\mathrm{f}} \tag{12}$$

式中 U_{g} 为故障期间电网电压的幅值，X_{L} 为变流器端口到电网的阻抗，L_{f} 为滤波电感的感值。

当 CHB 旁路后，每相可利用的直流电压为 $(n\text{-}n_{\mathrm{rem}})V_{\mathrm{dc}}$，调制比 m 为：

$$m = \frac{U_{\mathrm{ref}}}{(n-n_{\mathrm{rem}})V_{\mathrm{dc}}} \tag{13}$$

调制比 m 不宜过小或过大，定义 m 的取值范围为 $0.1 \leqslant m \leqslant 0.9$。当电网电压跌落深度 D≤$D^*$时，还应计算其调制比 m_{parallel} 是否满足上述范围，如不满足需重新定义临界深度 D^*。

3 构网穿越控制策略

3.1 串/并联切换策略

3.1.1 SCR 与 IGBT 的协调控制

要使 CHB 变流器在电网电压小于 D^*时切换为并联运行，需协调控制 SCR 与 IGBT 的通断，SCR 与 IGBT 的运行情况如图 2 所示，图中 $t_{\mathrm{F_on}}$ 与 $t_{\mathrm{F_off}}$ 为电网电压跌落较深的起止时间。

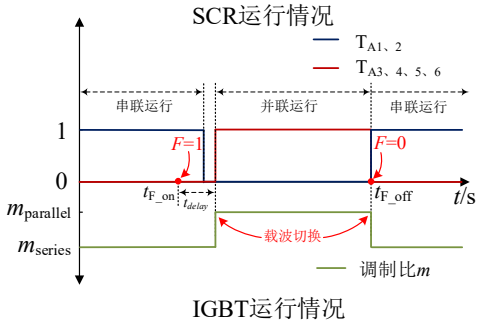


图 2 SCR 与 IGBT 的运行情况

Fig.2 Operating status of SCR and IGBT

当电网电压大于临界跌落深度 D^*时，切换标志位 F 置 0，晶闸管 T_{X1}、T_{X2} 为导通状态，晶闸管 T_{X3}、T_{X4}、T_{X5}、T_{X6} 为关断状态，CHB 正常串联运行；此时每相 n 个 H 桥中的 IGBT 以调制比 m_{series} 运行。当电网电压小于临界跌落深度 D^*时，切换标志位 F 置 1，晶闸管 T_{X1}、T_{X2} 为关断状态，晶闸管 T_{X3}、T_{X4}、T_{X5}、T_{X6} 为导通状态，CHB 切换为并联运行模式，一组（H-Bridge-X_1 到 H-Bridge -$X_{n/2}$）n/2 个串联 H 桥与另一组（H-Bridge -$X_{n/2+1}$ 到 H-Bridge -X_n）n/2 个串联 H 桥并联，共同产生 X 相电压；此时每相 2 组，每组 n/2 个 H 桥中的 IGBT 以调制比 $m_{parallel}$ 运行，并且两组并联的 H 桥需切换为相同的载波。

由于晶闸管自身特性，当 F 置 1 时晶闸管 T_{X1}、T_{X2} 可能不会立刻关断。为了使晶闸管 T_{X1}、T_{X2} 与晶闸管 T_{X3}、T_{X4}、T_{X5}、T_{X6} 不同时导通，将晶闸管 T_{X3}、T_{X4}、T_{X5}、T_{X6} 的门极触发信号延时处理，延时时间为 t_{delay}，待晶闸管 T_{X1}、T_{X2} 关断后，再导通晶闸管 T_{X3}、T_{X4}、T_{X5}、T_{X6}。因此在 F 置 1 的瞬间，CHB 任是串联运行，IGBT 的调制比应为 m_{series}；在延时之后即 T_{X3}、T_{X4}、T_{X5}、T_{X6} 导通后，CHB 切换为并联运行，IGBT 的调制比变为 $m_{parallel}$。

3.1.2 切换功率参考

当电网电压跌落至 D^*时，由于 CHB 切换为并联运行，变流器可输出 2 倍额定电流。通过式(1)计算出需要向电网注入的无功电流，利用 2 倍额定电流为限，计算出有功电流参考，如式(14)所示。

$$I_{\mathrm{d}}^{\mathrm{ref}}=\sqrt{(2I_{\mathrm{N}})^2-(I_{\mathrm{q}}^{\mathrm{ref}})^2} \tag{14}$$

将有功电流参考和无功电流参考代入式(3)、式(4)计算出 CHB 并联运行时的有功、无功参考。

3.2 VSG 补偿策略

当电网发生故障时，会造成电网电压相角与幅值突变，由于 VSG 控制不能及时跟随电网电压，因此会产生暂态过流问题。为抑制暂态过流，需对 VSG 产生的电压进行相角与幅值补偿。

3.2.1 电压相角补偿

在故障期间会造成电网电压相角的跳变，由于 VSG 有功相角环路为二阶方程，其输出相位不能迅速跟随并网点相位变化，若不进行相位补偿，将会产生过流且不能快速达到有功参考，因此，在故障发生瞬间需要在相位输出侧补偿变流器输出相位与比并网点相位之差。

补偿角由两部分构成：一是式(15)所示变流器输出相位 $\varphi(u_g')$对电网电压相位 u_g'的跟踪补偿，二是式(16)所示实现功率同步输出的功角 δ'。

$$\varphi(u_g')=\tan^{-1}\left(-\frac{V_{\mathrm{q}}}{V_{\mathrm{d}}}\right) \tag{15}$$

$$\delta'=\sin^{-1}\left(\frac{2X}{3U_{\mathrm{ref}}U_{\mathrm{g}}}\mathrm{P}_{\mathrm{ref}}\right) \tag{16}$$

$$\Delta\theta=\delta'-\varphi(u_{\mathrm{g}}') \tag{17}$$

其中，$\varphi(u_g)$为故障期间电网电压相角，δ'为故障期间由有功功率确定的变流器输出电压与电网电压之间功角，$\Delta\theta$ 为补偿相角差。

3.2.2 电压幅值补偿

在电网电压跌落期间保留 VSG 构网控制，无功电压环生成电压幅值，为快速跟随并网点正序电压幅值的变化，需在无功电压环出口处补偿由于时延产生的变流器与电网之间的幅值差，此时躲过无功电压环的积分环节，只需考虑后续电压电流环的响应速度，达到电压幅值快速补偿的目的。补偿原则根据标准所需的正序无功电流，确定所需无功功率，进而由简化后无功功率与电压幅值之间关系得到电压幅值参考，再与变流器此时输出电压幅值相减求取差值补偿到 VSG 无功电压环输出处，进而作为三相电压参考的幅值。

故障期间变流器端口电压幅值参考值与补偿量如式(10)与(18)。其中，U_{ref}为电压幅值参考值，ΔU 为幅值补偿量，U_{g}为故障期间电网电压的幅值，U 为 VSG 无功电压环的输出，X_{L}为变流器端口到电网的阻抗，L_{f}为滤波电感的感值。将该补偿量 ΔU 补偿到 VSG 功率外环输出侧，从而实现变流器输出电压幅值的快速改变。

$$\Delta U=U-U_{\mathrm{ref}} \tag{18}$$

综上，利用 VSG 幅值补偿策略得到的幅值参考与利用相角补偿策略得到的相角参考合成三相电压参考矢量 u_{abc}^*，经过 Park 变换将 abc 三相坐标系转换为 dq 坐标系下分量，以此为作为电压电流双闭环参考量进行控制。

4 仿真结果及分析

为验证本文所提控制策略的正确性，在 Matlab/Simulink 中搭建 1MW CHB 拓扑的储能变流器仿真模型，仿真参数如表 1 所示。

在系统仿真中，0s 变流器启动并空载运行，2s 变流器并网，3s 功率增加至 1MW，4s 电网电压跌

落至 0.25p.u.，6s 电网电压恢复正常，6-8s 变流器正常运行。仿真结果如图 3 所示。

表 1　仿真模型参数

Table 1　Parameters of the simulation model

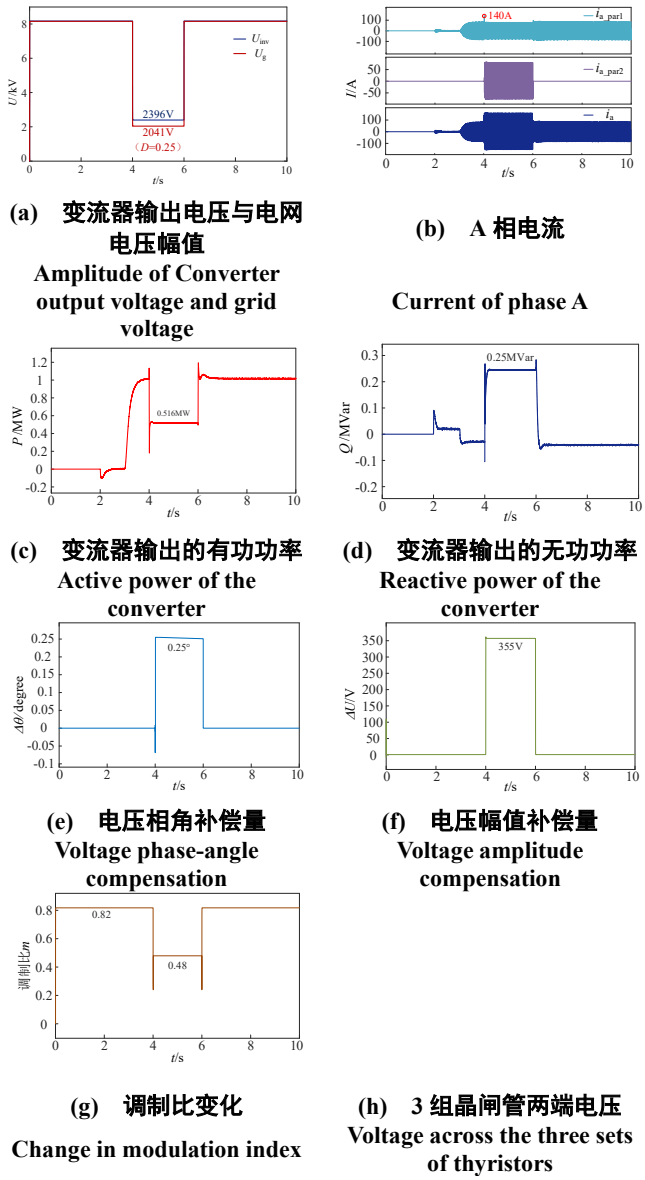
参数	数值
电网线电压/kV	10
变流器额定容量/MVA	1
变流器额定电流/A	90
H 桥直流电压/kV	1
H 桥额定容量/MVA	0.033
每相级联子模块数目	10
交流侧滤波电感/mH	15
并联线路滤波电感/mH	5
电网电压临界跌落深度/p.u.	0.45
故障时电网电压/p.u.	0.25
$T_{X3、4、5、6}$ 延时导通时间/s	0.01

图 3(a)为变流器输出电压幅值 U_{inv} 与电网电压幅值 U_g，电网电压在 4-6s 变为 0.25p.u.。在故障期间，变流器需向电网输送无功功率，因此变流器输出电压比电网电压略高。

图 3(b)为 A 相电流，i_a 为流向电网的总电流，i_{a_par1} 为常连支路的电流，i_{a_par2} 为并联支路的电流。在 0-4s、6-10s CHB 串联运行，i_a 与 i_{a_par1} 属于同一线路，二者电流相等且为额定电流 90A，此时并联支路未连接，i_{a_par2} 为 0；在 4-6s CHB 并联运行，i_{a_par1} 与 i_{a_par2} 之和为 i_a，此时两支路均可输出 90A 额定电流，流向电网的总电流为 180A，实现了 CHB 并联运行时输出两倍额定电流的效果，并增强了变流器故障期间的支撑能力。

图 3(c)、图 3(d)分别为变流器输出的有功功率 P 和无功功率 Q。0-2s 变流器空载运行，P、Q 均为 0；3s 变流器输出有功功率增至 1MW，正常向电网输送有功功率；4-6s 电网电压跌落，CHB 并联运行，根据电网准则向电网输送 0.25MVar 的无功功率以提供电压支撑，并以两倍额定电流为限制，向电网输送较大的有功功率，其值为 0.516MW；6s 电网电压恢复，变流器正常运行，向电网输送 1MW 的有功功率。

图 3(e)和图 3(f)分别为所补偿的相角差值 $\Delta\theta$ 与幅值差值 ΔU。图 3(e)所示为故障全过程期间相角补偿量，正常工况下，无需补偿，计算电压相角补偿量为 0，故障期间补偿功角为 0.25°，故障发生瞬间与恢复时刻实时跟随电网电压相角的变化进行补偿。如图 3(f)所示为故障全过程电压幅值补偿量。正常工况下，无需补偿，计算电压幅值补偿量为 0；4s 故障发生，6s 故障恢复，变流器始终依据电网电压变化实时计算补偿量，故障稳态期间补偿量为 355V，在故障发生瞬间与恢复时刻会有暂态过程，变流器始终依据电网电压变化情况实时补偿。



(a)　变流器输出电压与电网电压幅值

Amplitude of Converter output voltage and grid voltage

(b)　A 相电流

Current of phase A

(c)　变流器输出的有功功率

Active power of the converter

(d)　变流器输出的无功功率

Reactive power of the converter

(e)　电压相角补偿量

Voltage phase-angle compensation

(f)　电压幅值补偿量

Voltage amplitude compensation

(g)　调制比变化

Change in modulation index

(h)　3 组晶闸管两端电压

Voltage across the three sets of thyristors

图 3　仿真结果

Fig.3　Simulation results

图 3(g)为调制比变化情况，0-4.01s 与 6-10sCHB 串联运行，变流器参考电压幅值为 8.2kV，CHB 直流总电压为 10kV，此时调制比 m_{series} 为 0.82；4.01-6s CHB 并联运行，变流器参考电压幅值为 2.4kV，CHB 直流总电压为 5kV 此时调制比 $m_{parallel}$ 为 0.48。图 3(h)为 3 组晶闸管两端电压情况，可见 T_{A1}、T_{A2} 在 CHB 并联运行时需耐受 6kV 电压，T_{A3}、T_{A4}、T_{A5}、T_{A6} 在 CHB 串联运行时需耐受 5kV 电压。

4　结论

本文研究基于改进的高压直挂级联 H 桥拓扑的储能变流器构网穿越控制策略，得出以下结论：

（1）提出了一种改进的高压直挂级联 H 桥拓扑的储能变流器，实现了在电网电压跌落程度较深时，CHB 由串联运行切换为并联运行，可充分利用变流器的容量，为电网电压提供更大支撑。

（2）提出了串/并联切换策略和 VSG 补偿策略。通过 SCR 和 IGBT 的协调控制，实现了 CHB 的串/并联切换；通过功率参考切换提升了变流器的支撑能力；通过补偿 VSG 电压的幅值与相角，使变流器具备构网能力的同时抑制了暂态过流。

最后，基于 Matlab/Simulink 的仿真验证了提出的构网穿越控制策略的可行性，实现了对 CHB 拓扑的改进，并充分利用了变流器的容量，同时实现了低电压构网穿越。

参考文献

[1] H. Xue, J. He, Y. Ren and P. Guo, Seamless Fault-Tolerant Control for Cascaded H-bridge Converters Based Battery Energy Storage System[J].IEEE Transactions on Industrial Electronics, 2023.

[2] A. Pal, D. Pal and B. K. Panigrahi, A Current Saturation Strategy for Enhancing the Low Voltage Ride-Through Capability of Grid-Forming Inverters[J]. IEEE Transactions on Circuits and Systems II: Express Briefs, 2023.

[3] Z. Li, K. W. Chan, J. Hu and S. W. Or, An Adaptive Fault Ride-Through Scheme for Grid-Forming Inverters Under Asymmetrical Grid Faults[J].IEEE Transactions on Industrial Electronics, 2022.

[4] M. Wu et al., A Transient Current Limiting Control for the Grid-forming (GFM) Cascaded H-bridge (CHB) Converter[J].IEEE Journal of Emerging and Selected Topics in Power Electronics.

收稿日期：2025-10-09。


杨鑫宇

作者简介：

杨鑫宇(2001)，男，硕士研究生，研究方向为高比例可再生能源电力系统的电力电子装置储能变流器控制研究，E-mail：2431091133@tiangong.edu.cn；


肖朝霞

作者简介：

肖朝霞(1981)，女，教授，博士生导师，研究方向为分布式发电系统与微电网、新型配电网规划与运行控制相关领域研究，E-mail：xiaozhaoxia@ tiangong.edu.cn；


张岩

作者简介：

张岩(2001)，男，硕士研究生，研究方向为高比例可再生能源电力系统的电力电子装置控制策略研究，E-mail：yanzhang@tiangong.edu.cn


王璇

作者简介：

王璇(1995)，女，讲师，硕士生导师，研究方向为智能配电网与综合能源系统态势感知与运行优化的关键技术研究，E-mail：wangxuan@ tiangong.edu.cn


沙琳

作者简介：

沙琳(1979)，女，副教授，硕士生导师，研究方向为电动汽车无线充电，E-mail：shalin@ tiangong.edu.cn

109 Transient induced voltage and current analysis during ice-melting operations on double-circuit lines on the same tower

Yao Zhong[1,2], Chuang Fu[3], Zhuxin Shi[1,2], Xiaodong Ren[1,2], Qi Yang[1,2], Huarong Zeng[1,2], Xianyin Mao[1,2].

[1]Power Science Research Institute of Guizhou Power Grid Co. Ltd, China.
[2]Key Laboratory of Ice Prevention & Disaster Reducing of China Southern Power Grid Co.Ltd, China.
[3]Electric Power Research Institute China southern Power Grid, China.
13096780798@163.com.

Abstract. For double-circuit lines on the same tower, to ensure power transmission, it is common practice to maintain normal operation of one circuit while melting ice on the other circuit or ground wires. Due to the effects of electromagnetic coupling and electrostatic coupling, the normally operating conductors will generate induced voltages and currents on the ice-melting conductors and ground wires. Existing research has primarily focused on analyzing steady-state induced voltages and currents, while there remains a lack of analysis regarding transient processes caused by switching operations. This paper analyzes the transient induced voltages and currents generated by switching operations during ice-melting processes. Corresponding induced voltages and currents are simulated according to actual ice-melting switching operation steps and compared with steady-state values. The results indicate that the amplitude of the transient induced voltages and currents is significantly higher than the steady-state values. When verifying switch performance in design process, it is essential to consider transient impacts.

Keywords: Ice melting, Coupling, Double-circuit line, Induced voltage, Induced current.

1 Introduction

In recent years, the climate has become increasingly unpredictable. In southern China, natural disasters such as freezing rain and snowstorms has occurred more frequently, which were previously relatively rare [1][2]. For power transmission lines, ice accumulation can lead to severe consequences such as line breaks and tower collapses, thereby disrupting normal power transmission [3][4]. As a result, ice-melting technology for power transmission lines is indispensable for their safe operation and maintenance. Especially in southern China, where higher temperatures in the past led to insufficient consideration of ice-melting needs and inadequate ice-

melting equipment configuration, recent climate change has often resulted in severe ice accumulation on lines that are difficult to clear. As a result, various ice-melting technologies have been extensively researched and widely applied.

Ice-melting methods can primarily be categorized into AC ice melting and DC ice melting [5]. AC ice melting is a more traditional method; however, due to the presence of line distribution parameters, it requires a significant amount of reactive power, placing extremely high demands on the ice-melting power supply [6][7]. In contrast, DC ice melting is less affected by parameters such as capacitance and inductance during the ice-melting process, resulting in lower capacity requirements and greater economic efficiency, making it a widely adopted solution [8]-[10]. Traditionally, for single-circuit transmission lines, ice-melting is typically performed by directly shutting down the line. For double-circuit transmission lines on the same tower, to ensure normal power transmission, one circuit is operated normally while the other is suspended for ice melting, or one circuit is operated normally while the other circuit and ground wire are suspended for ground wire ice melting. This way, one circuit can remain operational during ice melting, preventing power transmission interruptions. However, since the ice melting is performed without shutting down the power supply, the operational circuit may generate induced voltages and currents on the other circuit and ground wires [11][12]. These induced voltages and currents could potentially cause impacts on ice-melting equipment and switches. Therefore, in recent years, some research has been conducted on the calculation of induced voltages and currents for double-circuit lines on the same tower. Ref. [13] indicates that conductor separation, system voltage, earth resistivity, and the length of the circuit had a great influence on the induced voltage and induced current. Ref. [14] analyses electromagnetic coupling effects will inevitably exist between the UHV AC and DC transmission lines built on the same tower. Ref. [15] calculates the coupling between the parallel transmission lines of different voltage levels and different towers running in the common corridor. However, these studies mainly focus on operating conditions when the system enters a steady state. In actual ice-melting processes, switching operations can generate transient induced voltages and currents, which may also affect equipment. Existing studies still lack analysis in this area.

In response to this issue, this paper analyses the transient induced voltages and currents generated by switch operations during the ground wire ice-melting process and compares them with steady-state conditions to provide a reference for verifying switch performance during the design stage. The rest of this paper is as follows: Section 2 introduces the model used for simulation analysis and the switch operation steps in the actual ground wire ice-melting process; Section 3 analyzes the induced voltage and current conditions obtained from the simulation of each step; and Section 4 presents the corresponding conclusions.

2 Simulation model and ice-melting process

A simulation model has been established in PSCAD/EMTDC to simulate the transient induced voltage and current generated by switching operations during the

ice-melting process. The model is established with reference to the actual double-circuit line structure in a project in Guizhou, China. The total length of the line is 52 km, and the entire line adopts a double-circuit structure. The distribution of the lines on the tower is shown Fig. 1. The conductors of the operating circuit and the offline circuit are distributed on both sides of the tower, and there are two ground wires. The voltage level of the system is 500 kV, and the rated current of the operating line is 3 kA.

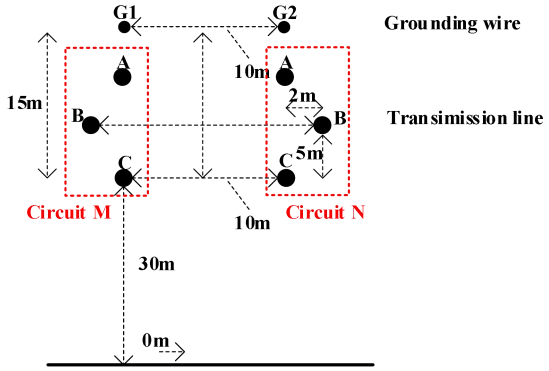


Fig. 1. Distribution of the lines on the tower.

With this model, the induced voltage and current can be simulated. The steps of switching operations are as follows: (1) First, Circuit M is suspended. (2) Then, the grounding switch at the end of the ground wire is opened, and then the front end of the ground wire is suspended and the end is short-circuited but not grounded. (3) According to the ice-melting plan, connect the A-phase conductor to the left ground wire. (4) Connect the C-phase conductor to the right ground wire. (5) Begin ice melting. After the ice has melted, the switching operation steps are reversed.

3 Transient induced voltage and current during ground wire ice-melting

3.1 Transient induced voltages and currents caused by opening the grounding switch

It is set that the grounding switch at the end of the line opens in 0.1 seconds, and the corresponding structure change is shown in Fig. 2. The induced voltages during this process are shown in Fig. 3.

4

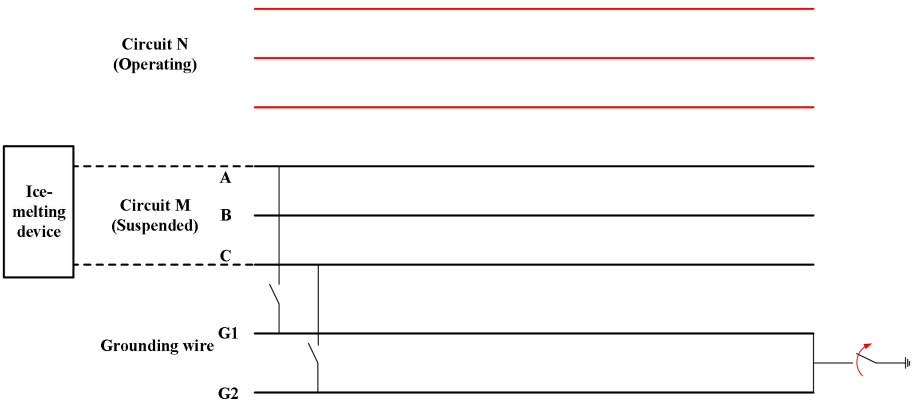
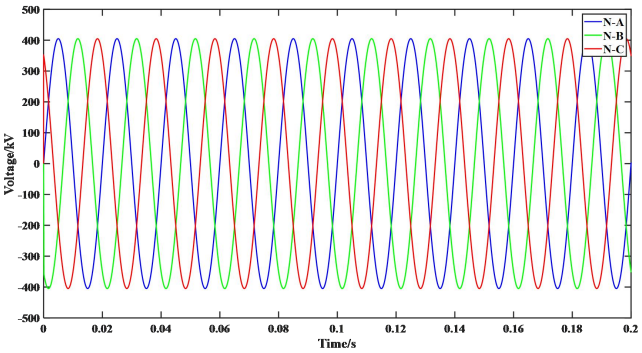
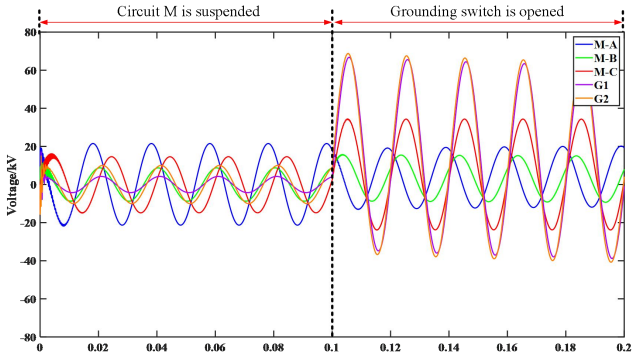


Fig. 2. Structure when the grounding switch at the terminal end of the ground wire is opened.

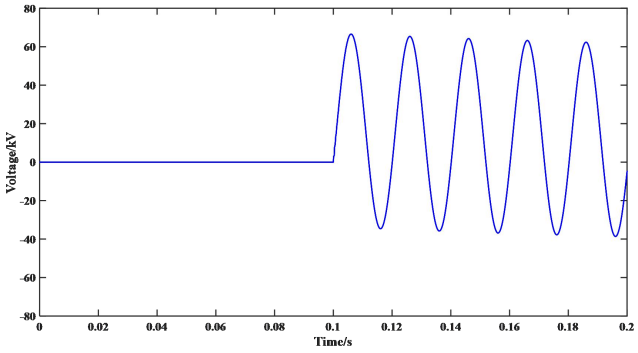
As can be seen, Circuit M is suspended, the induced voltage amplitudes on the three-phase conductors are 8.78 to 21.52 kV. Due to the different positions of the three-phase conductors on the tower, their induced voltages are not entirely consistent and vary significantly. At this point, the grounding wire is in a state where the front ends are suspended and the terminal end is short-circuited to ground. The induced voltage amplitudes at the two ends are 4.26 kV and 10.03 respectively. When the grounding switch at the terminal is opened after 0.1 seconds, the grounding wire becomes suspended at both ends, and the induced voltage on the grounding wire significantly increases. The maximum induced voltage on both grounding wires can reach 68.82 kV and it includes a certain DC component. For the terminal end, the maximum induced voltage that the grounding switch needs to interrupt can also reach 68.82 kV. In addition, it can be seen that due to changes in the induced voltage of the ground wires, the induced voltage of the corresponding conductor also changed significantly, especially the C-phase conductor, which is closer to the ground wire, resulting in a significant increase in induced voltage.



(a) Operating voltages of Circuit N



(b) Voltages of the conductors and grounding wires at the front end of Circuit M



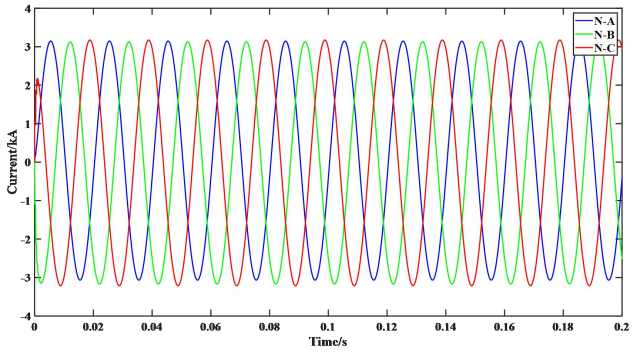
(c) Induced voltage of the grounding switch at the terminal end

Fig. 3. Induced voltages when the grounding switch at the terminal end of the ground wire is opened.

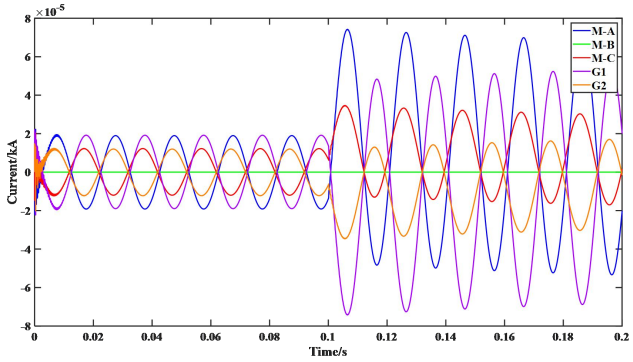
Meanwhile, the induced currents during the switching process are shown in Fig. 4. When Circuit N is operating normally, its rated current amplitude is 3.17 kA. When Circuit M is suspended, the conductors can be considered to be in a suspended state, so almost no induced current is generated. Similarly, the induced currents at the front end of the grounding wires are also negligible due to the suspended state. At 0.1 seconds, the grounding switch is opened, causing the induced current to drop from 0.01 kA to 0 at the terminal end. The terminal grounding switch only needs to open an induced current of 0.01 kA.

Under these conditions, the grounding switch must open 68.82 kV of induced voltage and 0.01 kA of induced current. Relatively speaking, the induced voltage imposes more stringent performance requirements on the grounding switch.

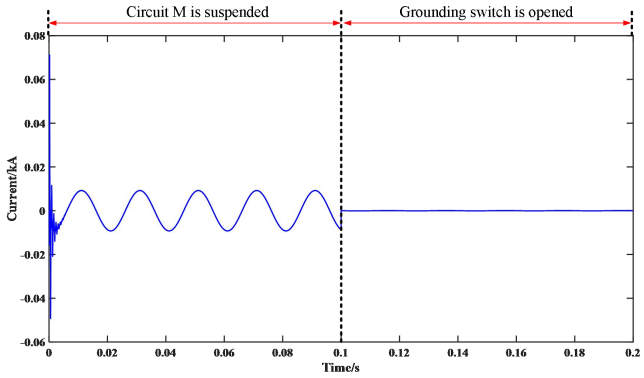
6



(a) Operating currents of Circuit N



(b) Currents of the conductors and grounding wires at the front end of Circuit M



(c) Induced current of the grounding switch at the terminal end

Fig. 4. Induced currents when the grounding switch at the terminal end of the ground wire is opened.

3.2 Transient induced voltages and currents caused by connecting the ground wires to the conductors

After the terminal grounding switch is opened, the grounding wire is suspended at the front end, and its terminal end is short-circuited. Then, the transient induced voltages and currents generated during the process of connecting the conductor to the grounding wire are further simulated in this subsection. The corresponding equivalent structure is shown in Fig. 5. The simulation is set such that A phase of Circuit M connects to the left grounding wire G1 at 0.05 seconds, and the C phase connects to the right grounding wire G2 at 0.1 seconds. The induced voltages during this process are shown in the Fig. 6.

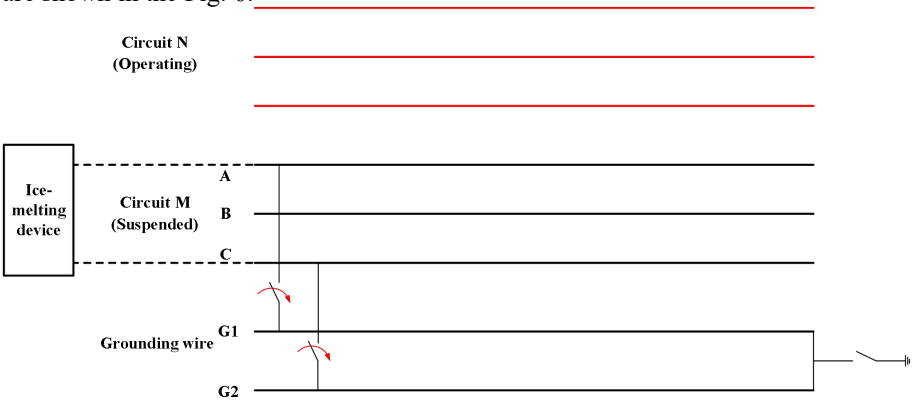
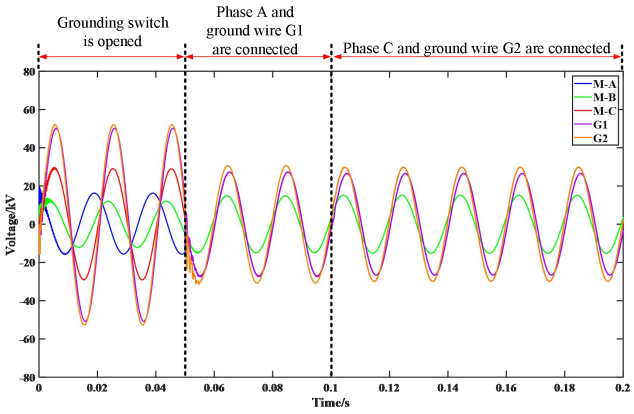
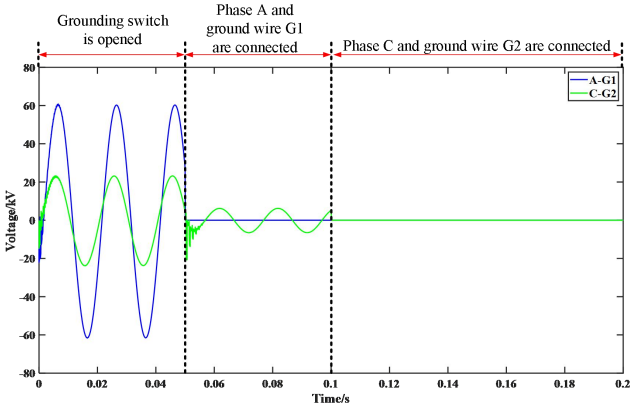


Fig. 5. Structure when the conductors and the grounding wires are connected.



(a) Voltages of the conductors and grounding wires at the front end of Circuit M

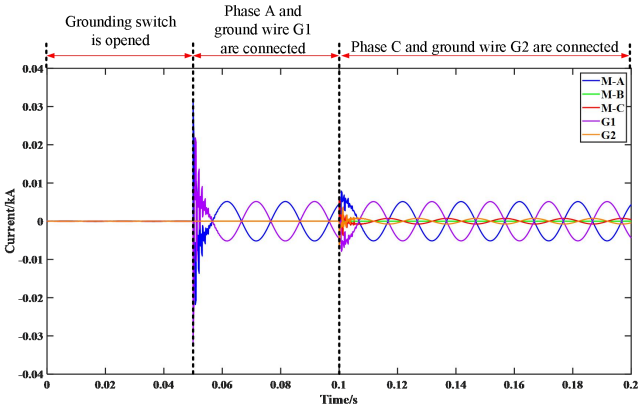
8



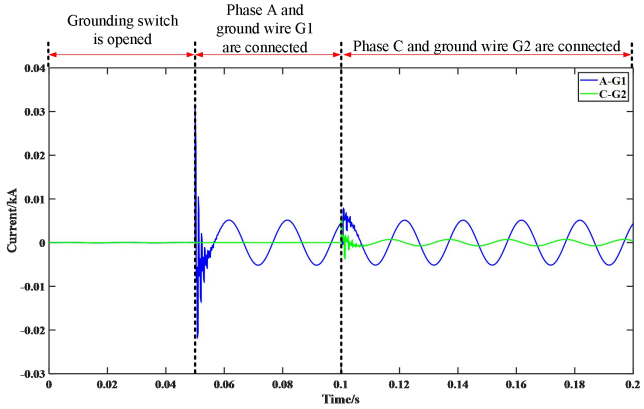
(b) Induced voltage of the connecting switch at the front end

Fig. 6. Induced voltages when the conductors and the grounding wires are connected.

First, before the conductors and the grounding wires are connected, the induced voltages of each line are consistent with the steady-state conditions described in Section 3.1. Subsequently, at 0.05 seconds, Phase A and G1 ground wire are connected. Before the connection, the induced voltage of G1 is higher than that of Phase A; therefore, after the connection, the induced voltage of G1 decreases. This phenomenon can be explained by an equivalent circuit. Before the connection, the conductor and ground line each independently generate voltage due to induction, equivalent to two voltage sources. After the connection, the voltage between the conductor and ground line is the difference between the two voltage sources, so its amplitude is the difference between the two voltage sources, which is relatively reduced. Measurements of the voltage of the connecting switch also show that during the connection process, the induced voltage of the switch gradually decreases, reducing the insulation threat to the switch.



(a) Currents of the conductors and grounding wires at the front end of Circuit M



(b) Induced current of the grounding switch at the terminal end

Fig. 7. Induced currents when the conductors and the grounding wires are connected.

In terms of current, as shown in Fig. 7, due to inconsistent induced voltages between the conductor and the ground wire before connection, a surge of induced current is generated during connection. During the first connection, the peak amplitude reaches 0.03 kA, followed by oscillation and decay, stabilizing at 0.005 A. During the second connection, since the induced voltage has already decreased, the corresponding surge of induced current is also smaller. Additionally, it is observed that both Phase A and Phase C are in a suspended state at both ends before connection, with no induced current at the front end. However, after connection, they formed a connection with the ground wire, resulting in induced currents at the front end.

3.3 Induced voltage and current generated during and after the ice-melting process

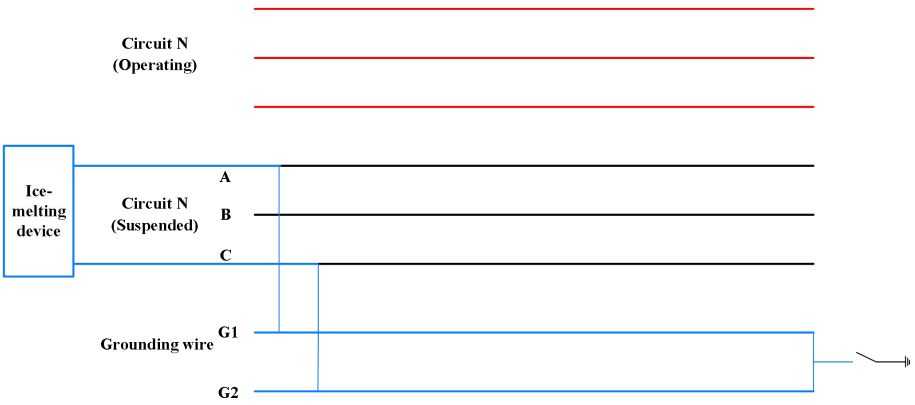
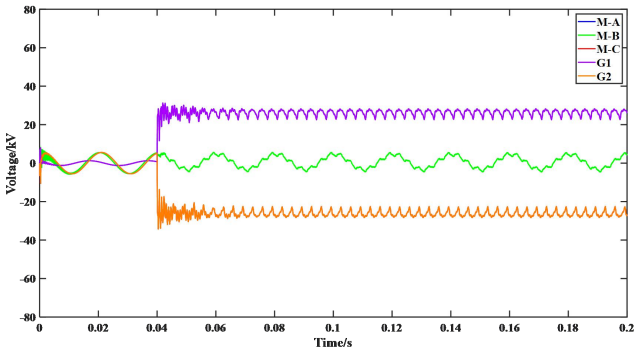
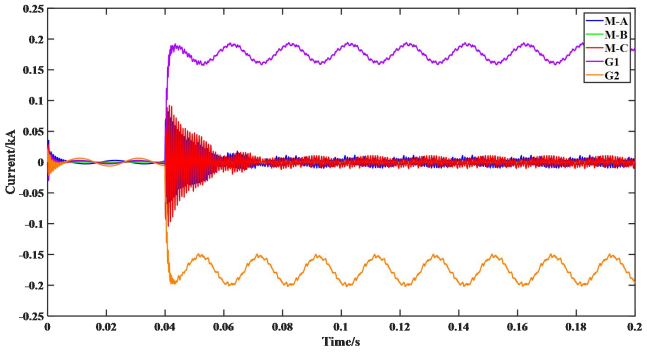


Fig. 8. Structure during the ice-melting process.

During the ice-melting process, the voltages and currents on the lines are primarily determined by the output of the ice-melting device and are hardly affected by induced voltage and current. However, since Phase B is not connected to the ice-melting circuit, its voltage and current are still primarily determined by induced voltage and current.



(a) Voltages of the conductors and grounding wires at the front end of Circuit M



(b) Currents of the conductors and grounding wires at the front end of Circuit M

Fig. 9. Induced voltages and currents during the ice-melting process.

When the ice-melting process ends, the connection between the conductors and the ground wires will be removed, and then the grounding switch at the terminal end of the ground wire will be re-closed. Simulation shows that during this whole process, the changes in induced voltage and induced current are opposite to those during the switching process before ice-melting. As the connection is removed, the induced voltage of the ground wire gradually increases, while the induced current becomes 0. After the grounding switch is re-closed, the induced voltage decreases, and induced current is generated. Although the sequence of changes is reversed, the amplitude of the voltage and current in each line remains consistent with the switching process before ice-melting. Therefore, due to space limitation, the detailed current and voltage waveforms are not shown.

4 Conclusions

Maintaining power supply on one circuit while ice-melting the other circuit has become an emerging technical means of ensuring power transmission. However, this process generates induced voltage and current on the other line and the grounding wires. In particular, existing research has insufficiently analyzed the transient voltage and current generated during the switch operation process. This paper calculates the transient voltage and current on the grounding wires during the switch operation process and obtains the following conclusions:

1. The induced voltage on the ground wire reaches its peak when the grounding switch at the terminal end is opened, and can reach up to 68.82 kV after accounting for the direct current component. The grounding switch must achieve this insulation level. Subsequently, during the process of connecting the conductor and ground wire via the connecting switch, the induced voltage gradually decreases.

2. The most severe induced current in the connecting switch occurs when the conductors and ground wires are short-circuited, reaching 0.03 kA in amplitude, followed by a smaller steady-state induced current. The grounding switch on the ground wire only carries an induced current of 0.01 kA when closed.

3. After the ice-melting device is started, the voltages and currents on the conductor and ground wires are determined by the ice-melting device and are not affected by coupling. Only the phase not in the ice-melting circuit will still be affected by induced voltage and current.

4. During the switching process after ice-melting is completed, the induced voltage and current that each switch must withstand are essentially the same as before ice-melting begins.

The above calculation results can be used as a reference for performance verification of grounding switches and connecting switches to avoid insulation problems during operation.

Acknowledgement： This work is supported by the Science and Technology Project of China Southern Power Grid (060000KC24040028) and Guizhou Provincial Association for Science and Technology's Young Scientific and Technological Talent Support Project (NO.GASTYESS202430).

References

[1] Sun J, Zhao S. The impacts of multiscale weather systems on freezing rain and snowstorms over southern China[J]. Weather and Forecasting, 2010, 25(2): 388-407.

[2] Changnon D, Bigley R. Fluctuations in US freezing rain days[J]. Climatic change, 2005, 69(2): 229-244.

[3] Van Dyke P, Havard D, Laneville A. Effect of ice and snow on the dynamics of~ transmission line conductors[M]//Atmospheric Icing of Power Networks. Dordrecht: Springer Netherlands, 2008: 171-228.

[4] Zhang G. Transmission line trip faults under extreme snow and ice conditions: a case study[J]. Energy Informatics, 2025, 8(1): 7.

[5] Xingliang J, Jianlin H, Jiwu Z, et al. Ice-melting methods and comparison with AC and DC currents[C]//XVII International Symposium on High Voltage Engineering. 2011.

[6] Cai X, Li Z, Xi C, et al. Research on AC Ice melting Technology of 10kV Distribution Network[C]//2024 3rd International Conference on Energy, Power and Electrical Technology (ICEPET). IEEE, 2024: 590-594.

[7] Zhu Y, Tan Y, Huang Q, et al. Research on melting and de-icing methods of lines in distribution network[C]//2019 IEEE 3rd Conference on Energy Internet and energy system Integration (EI2). IEEE, 2019: 2370-2373.

[8] Guo Y, Xu J, Guo C, et al. Control of full-bridge modular multilevel converter for dc ice-melting application[C]//11th IET International Conference on AC and DC Power Transmission. Stevenage UK: IET, 2015: 069.

[9] Fan S, Jiang X, Shu L, et al. DC ice-melting model for elliptic glaze iced conductor[J]. IEEE Transactions on power delivery, 2011, 26(4): 2697-2704.

[10] Huang G, Wu M, Liang J, et al. Research on the DC Ice-Melting Model and Its Influencing Factors on the Overhead Contact Systems of an Electrification Railway[J]. Energies, 2025, 18(5): 1028.

[11] Li H, Zhang J, Fang B, et al. Simulation and Analysis of Induced Current of HV Parallel Reactor Disconnector for 500kV Double Circuit Line on the Same Tower[C]//E3S Web of Conferences. EDP Sciences, 2020, 185: 01043.

[12] Zhi-Peng Z, Zhen-Qiang L, Ying L, et al. Study on Overhead Ground Wire Induced Voltage of 500kV AC/DC Transmission Lines for Ice Melting[C]//2022 7th Asia Conference on Power and Electrical Engineering (ACPEE). IEEE, 2022: 1704-1711.

[13] Tian W, Cao Z. Research on induced voltage and current in deenergized line of double-circuit transmission lines on the same tower[C]//2019 4th International Conference on Intelligent Green Building and Smart Grid (IGBSG). IEEE, 2019: 264-269.

[14] Sun Q, Shi W, Siew W H, et al. The induced overvoltage between UHV AC and DC transmission lines built on the same tower under fault conditions[C]//2009 44th International Universities Power Engineering Conference (UPEC). IEEE, 2009: 1-5.

[15] Bao Y, Liu K, Zhang G, et al. Analysis of Induced Voltage and Influencing Factors of Transmission Lines with Different Voltage Levels and Different Towers in Parallel on the Same Corridor[C]//IOP Conference Series: Earth and Environmental Science. IOP Publishing, 2021, 714(4): 042082.

110 A Defect Detection Method for Small Targets in Power Scenarios Based on Dynamic Task Alignment

ZHOU Pei[1,*],LI Xuewu[1],FANG Ming[1],XIE Chengyu[1],WANG Yufeng[1],GUO Tianwei[1],LIU Hao[1]

[1] Guiyang Bureau of China Southern Power Grid Co., Ltd. Uhv Transmission Company, Guanshanhu District, Guiyang City 550000,China

Abstract. The electrical power system includes substations, transmission lines, and distribution facilities. Small target defect identification technology enables efficient allocation of inspection resources by considering equipment criticality and defect occurrence probability. Its implementation for intensive line monitoring allows early detection of potential issues, facilitating strategic deployment of inspection personnel and equipment, enhancing operational and maintenance efficiency.Small target detection in visual tasks faces challenges due to limited feature information. They occupy fewer pixels than larger targets, complicating identification via traditional methods. Additionally, small targets tend to cluster; downsampling may merge multiple ones into a single point on deep feature maps, hindering distinction.To address this, we propose a dynamic task alignment approach using distinct branches to process and align feature maps, plus a multi-scale grouped convolution technique—segmenting channels, applying diverse kernel-sized convolutions to groups, and exchanging channel information via convolutions.Empirical results show our technique achieves 87.8% detection accuracy on power scenario datasets after 12 training epochs, 3.8% higher than the original model, with fewer parameters. It outperforms other state-of-the-art detection heads with a more efficient design.

Keywords: Small Object Detection; Low-altitude Anti-Drone; Task Alignment; Multi-scale Convolution

1 Introduction

With the continuous rise in demand for electric energy transmission in China and the continuous expansion of the scale of the power system, the safety and stability of the power system are facing increasingly severe challenges, which promotes the continuous improvement of the reliability standards for the operation of power equipment. In this context, equipment operation and maintenance tasks have become increasingly arduous, and the demand for automated, modern, and efficient line inspection technologies and methods has become increasingly urgent.

Robot inspection, with its advantages of efficiency, safety, intelligence, and accuracy, has gradually become an emerging model in the field of equipment inspection in

the power industry. In the realization of robot intelligent inspection technology, target detection technology plays a crucial role. With deep learning algorithms, it can accurately detect and identify defect targets contained in power inspection data. The application of inspection robots can effectively replace manual labor to complete heavy inspection tasks, thereby significantly improving the efficiency of inspection work.

In the existing technical framework, the images collected by robots during power inspection cover target objects of different scales. Among them, small targets with pixel sizes of 32×32 and below are particularly common. Due to their small size, these small targets contain limited information and have a high signal-to-noise ratio, which makes them often face high difficulty in the identification process and difficult to be accurately detected and identified.

Traditional power inspection methods mainly rely on manual inspections, using sensory perception and some auxiliary detection equipment to conduct simple qualitative judgment-based inspections on related equipment, towers, etc. This method has many drawbacks, such as high labor intensity, low inspection efficiency, incomplete inspection, and difficulty in digitizing inspection results.

In recent years, with the continuous development and in-depth application of UAV technology, data processing technology, and software technology in the field of inspection, the power grid industry has built an intelligent inspection business model of "helicopter/UAV line inspection + laser radar scanning + data processing and analysis + data application and visual display". This model can effectively reduce labor intensity, improve inspection efficiency, expand inspection coverage, and realize digital display of inspection results, which is of great significance for enhancing the safety, stability, and operational efficiency of power grid operation.In the traditional power equipment inspection mode, due to the small size of equipment defects, manual inspection is difficult to quickly and accurately determine the location of defects. However, using cutting-edge small target defect identification technology, especially image recognition algorithms based on deep learning, can accurately analyze power equipment image data and quickly lock the exact location of small target defects.

By using UAVs equipped with high-definition cameras to capture line images, and then using small target defect identification algorithms, tiny foreign objects on the wires can be accurately identified, and their coordinate information in the image can be provided. This provides maintenance personnel with clear maintenance targets, significantly improves the pertinence and efficiency of maintenance work, and reduces the time and labor costs wasted due to blind searching for defect locations.

2 Overview of Small Target Detection Algorithms

Early multi-scale detection used convolution kernels of different sizes to obtain information of different scales through different receptive field sizes. This method has high computational cost and a limited range of receptive field scales[1]. After Simonyan and Zisserman[2] proposed that using multiple small convolution kernels instead of large ones has great advantages, the method of using convolution kernels of different sizes was gradually abandoned. Later, dilated convolution proposed by Yu [3] et

al. and deformable convolution proposed by Dai [4] et al. opened up new ideas for this method of obtaining multi-scale information through different receptive field sizes.

Classic networks in target detection, such as Fast R-CNN [5], Faster R-CNN [6], SPPNet[7], and R-FCN [8], mostly only use the last layer of deep neural networks for prediction. However, due to the loss of spatial and detailed feature information, it is difficult to detect small targets in deep feature maps.

In deep neural networks, shallow layers have smaller receptive fields, weak semantic information, and lack of context information, but can obtain more spatial and detailed feature information. Based on this idea, Liu [9] et al. proposed a multi-scale target detection algorithm (Single Shot Multibox Detector, SSD), which uses shallower feature maps to detect smaller targets and deeper feature maps to detect larger targets.

Cai [10] et al. proposed a unified multi-scale deep convolutional neural network to address the problem that small targets have little information and are difficult to match conventional networks. By using deconvolution layers to improve the resolution of feature maps, it significantly improves the detection performance of small targets while reducing memory and computational costs.

Bell [11] et al. proposed the Inside-Outside Network (ION), which crops features of the same region of interest from feature maps of different scales and then integrates these multi-scale features for prediction to improve detection performance. Similar to the idea of ION, Kong [12] et al. proposed an effective multi-scale fusion network, HyperNet, which significantly improves the recall rate by integrating shallow high-resolution features, deep semantic features, and intermediate layer features, thereby improving the performance of small target detection.

To save computing resources and achieve better feature fusion effects, Lin [13] et al. combined the advantages of single feature mapping, pyramid feature hierarchy, and comprehensive features, and proposed the Feature Pyramid Network (FPN). FPN is currently the most popular multi-scale network. It introduces a bottom-up and top-down network structure, which enhances features by fusing features of adjacent layers.

On the basis of FPN, Liang [14] et al. proposed a deep feature pyramid network, which uses a feature pyramid structure with lateral connections to strengthen the semantic features of small targets, and trains the network with specially designed anchor boxes and loss functions.

Nayan [15] et al. proposed a new real-time detection algorithm to address the problem that small target feature information is easily lost after multi-layer network processing. The algorithm uses upsampling and skip connections to extract multi-scale features at different network depths during training, significantly improving the detection accuracy and speed of small target detection.

Liu [16] et al. proposed a high-resolution detection network to reduce the computational cost of high-resolution images. By using shallow networks to process high-resolution images and deep networks to process low-resolution images, it retains as much position information of small targets as possible while extracting more sema-

4

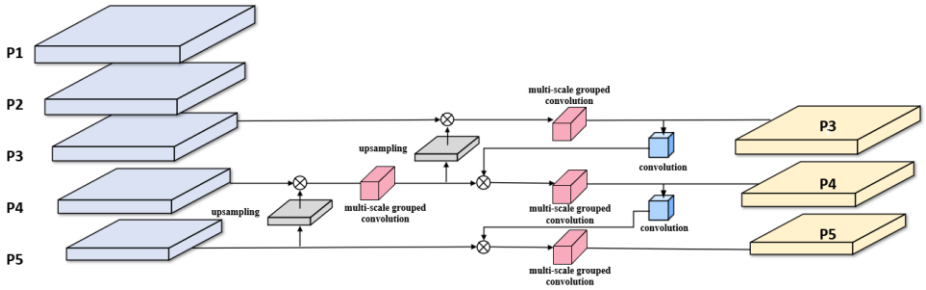


Fig. 1. Backbone network diagram

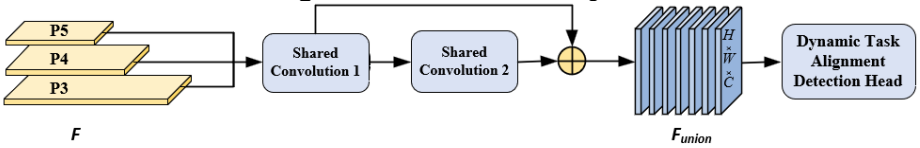


Fig. 2. Feature extraction module diagram

ntic information, improving the detection performance of small targets while reducing computational costs.

Deng [17] et al. found that although multi-scale fusion can effectively improve small target detection performance, the coupling of features of different scales will still affect performance. Therefore, they proposed an extended feature pyramid network, which uses an additional high-resolution pyramid level specifically for small target detection.

3 Proposal of Dynamic Task Alignment Detection Head and Multi-scale Grouped Convolution Method

The main reason for the sharp performance degradation is that small targets account for fewer pixels, and after multiple downsampling, the detector cannot effectively identify them. The prediction boxes of classification and regression tasks are closely related to the size and shape of the target. Adopting the same anchor box allocation method for different tasks is difficult to be effective.

Therefore, we propose a dynamic task alignment detection head, which strengthens the feature interaction between classification and regression tasks on the detection head, enables dynamic alignment of these two tasks, and improves the consistency of prediction boxes. When the number of small targets in the detection process is much smaller than that of conventional targets, the model tends to learn the features of large targets and ignore those of small targets.

This problem of imbalance between positive and negative samples stems from two aspects: on the one hand, it is due to the inherent difficulty of small target detection, because they carry less feature information, making it impossible for the model to extract key feature information from effective information; on the other hand, when the model detects small targets, it is much more affected by disturbance errors than large/medium samples. For example, shifting the prediction box by two pixels will not reduce the Intersection over Union (IoU) much for large targets, but will signifi-

cantly reduce the IoU for small targets.Therefore, when the manually set anchor boxes differ greatly from the real anchor boxes of small targets, the model will directly determine them as negative samples, leading to incorrect classification of sample types. In addition, the clustering phenomenon in small target detection will generate redundant feature information. The feature information extracted by different feature channels is approximately redundant, and the information between each channel feature is independent.Therefore,we propose a multi-scale grouped convolution method. During convolution, channels are grouped, different groups use convolution kernels of different sizes to extract feature information, and then a 1×1 convolution is used to complete feature channel information exchange.

4 Model Architecture

4.1 Model Backbone Network and Feature Extraction

YOLO series models have long been known for their lightweight nature and detection accuracy. Our method adopts Yolov8 as the basic detection framework. The backbone network of the model is shown in Fig. 1. Similar to other single-stage detectors, Yolov8 also has a structure of backbone network - feature pyramid - detection head. Considering the limitations of model size and parameters, we use two 3×3 shared convolution modules on the P3, P4, and P5 feature layers, as shown in Fig. 2. It has been confirmed in FCOS [18] that this can improve the performance of the model's detection head in classification and regression tasks:

$$F_{\text{union}} = conv_{GN1}\left(conv_{GN2}\left(F\right)\right) + F \tag{1}$$

Where F is the feature layer P3, P4, P5 extracted from the backbone network through multi-layer feature fusion; $conv_{GN1}$ and $conv_{GN2}$ are two shared convolution layers with 3×3 convolution kernels; F union is the joint feature obtained through residual connection.

Since they are shared convolutions, the number of parameters can be greatly reduced, making the model more lightweight, especially on resource-constrained devices. The new joint features obtained after residual connection will be sent to the dynamic task alignment detection head for detection.

4.2 Dynamic Task Alignment Detection Head Module

As shown in Fig. 3, the joint feature obtains the regression prediction map A and classification prediction map B through the task decomposition module [19], while two new feature maps C and D are generated in the branch to further align and correct A and B. The feature extractor learns task interaction features in multiple convolution layers to obtain feature maps for different tasks.

In the regression branch, a generator is first used to generate the mask and displacement paraeters required by DCNv2 [20]. The generator is a convolution layer composed of 3×3 convolution kernels. Since the convolution kernel size of this

6

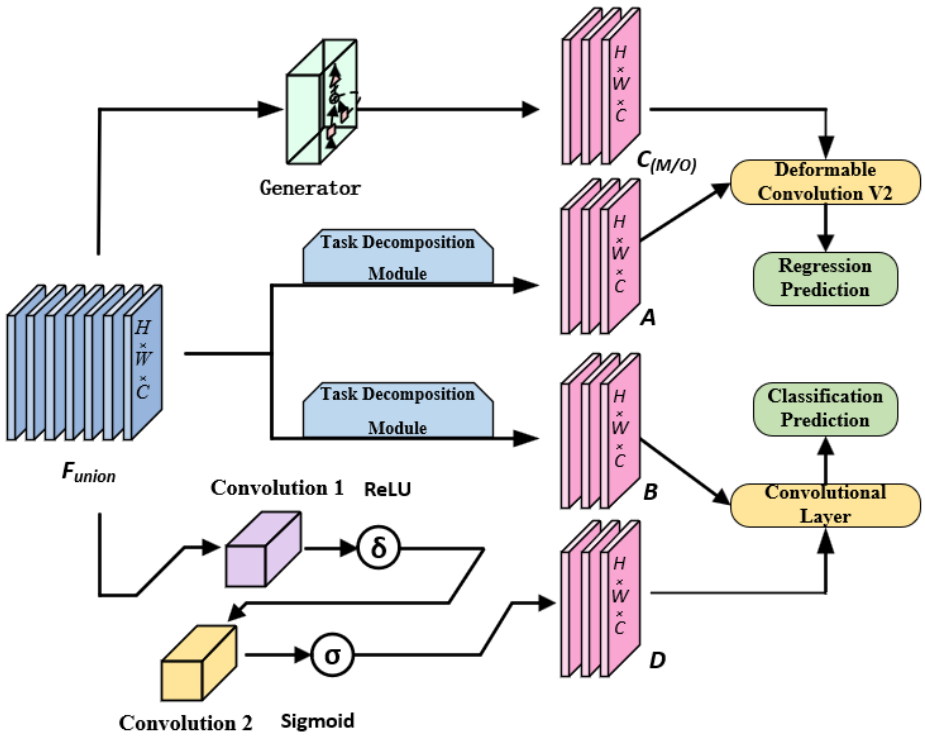


Fig. 3. Dynamic task alignment detection head

module is 3×3, the dimension of the mask is 9, and the displacement parameters will act on two directions of the plane, so the dimension of the offset is 18. Therefore, the number of output channels of the generator is 27.

These displacements and masks will dynamically adjust the regression box at each position to ensure that it is the best prediction box in the vicinity. This part is to allow the model to dynamically learn the feature information that needs to be extracted from the feature tensor and suppress the feature information that is not needed. The specific formulas are as follows:

$$C_M = G\left(F_{union}\right) \tag{2}$$

$$C_O = G\left(F_{union}\right) \tag{3}$$

Where C_M is the mask information required by DCNv2, and C_O is the displacement information; G is the generator. In the DeformableDetr [21] paper, the authors adopted the idea of deformable convolution, allowing the model to independently learn the key features that need attention, solving the problems of slow convergence of Detr-like models and poor performance in small target detection. Then, together with the regression prediction map A, it is sent to the DCNv2 module to learn a new regression prediction map.

In the classification branch, a 1×1 convolution layer and a 3×3 convolution layer are used for convolution successively. After the two convolutions, Relu and Sigmoid activation functions are used respectively. The classification prediction box is dynam-

ically adjusted according to the joint features, which is calculated from the joint feature map, so it can learn to align the prediction boxes of the two tasks in spatial position. The formula is as follows:

$$D = \sigma\left(conv_2\left(\delta\left(conv_1\left(F_{union}\right)\right)\right)\right) \tag{4}$$

Where D is the new feature map extracted through the classification branch, $conv_1$ uses a 1×1 convolution kernel, δ is the ReLU activation function, $conv_2$ uses a 3×3 convolution kernel, σ is the Sigmoid activation function, and F_{union} is the joint feature.

4.3 Task Decomposition Module

As shown in Fig.4, the task decomposition module first calculates the average pooling feature Fave through the joint feature, then obtains the layer attention weight through two convolution layers $conv_1$ and $conv_2$ of the layer attention module, followed by ReLU and Sigmoid activation functions respectively.

Then, the weighted convolution kernel is calculated, and the layer attention weight is combined with the convolution kernel weight through reshaping. At the same time, the input feature F_{union} is also reshaped to match the dimension of the weighted convolution kernel. Finally, a batch normalization matrix multiplication operation is performed to multiply the weighted convolution kernel with the input feature, and the result is processed through group normalization and SiLU activation function to output the processed feature map. The specific process is as follows:

First, adaptive average pooling is performed on the joint feature F_{union} to obtain the average pooling feature F_{avg} .Then, two convolution-activation operations are performed. The convolution kernel size of both convolution layers is 1×1. The first convolution is activated using the ReLU function, and the second convolution is activated using the Sigmoid function to obtain the layer attention weight L for the feature map:

$$L = \sigma\left(conv_2\left(\delta\left(conv_1\left(P_{avg}\left(F_{union}\right)\right)\right)\right)\right) \tag{5}$$

$conv_1$ and $conv_2$ are both convolution layers with a convolution kernel size of 1×1, δ is the ReLU activation function, σ is the Sigmoid activation function, F_{avg} is the adaptive average pooling layer, and L represents the layer attention weight. Then, it is weighted with the convolution weight, and the layer attention weight is combined with the convolution kernel weight through reshaping:

$$W = L \times W_{conv} \tag{6}$$

L is the layer attention weight calculated in formula (5), W_{conv} is the convolution weight, and W is the new convolution weight obtained after weighted calculation of W_{conv} .

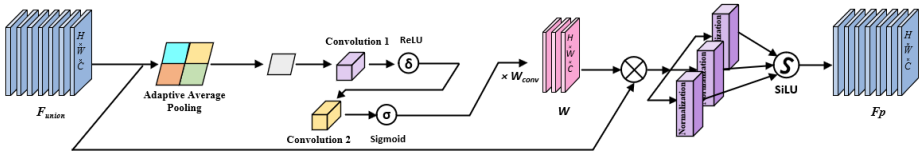


Fig. 4. Task decomposition module diagram

At the same time, the joint feature F_{union} is also reshaped to match the dimension of the weighted convolution kernel. Then, a matrix multiplication operation is performed to multiply the weighted convolution kernel with the joint feature to obtain a new feature map. The feature map is then processed through group normalization and activation function activation, and finally the processed prediction feature map is output. The formula is as follows:

$$F_p = S\left(GN\left(W \times F_{union}\right)\right) \tag{7}$$

F_{union} is the initial input joint feature of the module, W is the new convolution weight calculated by formula (6), GN is the group normalization process, S represents the SiLU activation function, and F_p is the final prediction feature map.

4.4 Multi-scale Grouped Convolution

Depth-wise convolution extracts features for each channel, but there is a lack of interaction between different feature channels, and the model has weak feature extraction for target objects of different scales under a single convolution kernel size.The convolution kernel is the basic computing unit in convolutional neural networks, mainly used to extract and express feature maps. Its size directly affects the receptive field of the input data it can determine, that is, the range of local information that the convolution kernel can capture.MobileNet [22] splits standard convolution into depth-wise convolution and point-wise convolution through depth-wise separable convolution, promoting model lightweight and reducing computational load. GhostNet [23] generates "Ghost" feature maps with required information at a lower cost by using a series of linear transformations based on a set of original feature maps. It believes that not all feature maps need to be obtained through convolution, but can also be generated in a cheaper way.

Objects have different scales of expression on different feature layers, and using the same convolution kernel for feature extraction may lead to information omission. As shown in Fig. 5, we split and group the channels during the convolution process of the model, use convolution kernels of different sizes for convolution to extract feature information for different groups, and then fuse the feature information extracted by each group through a 1×1 convolution layer.Give full play to the advantages of multi-scale grouped convolution and strengthen information exchange between different channels.

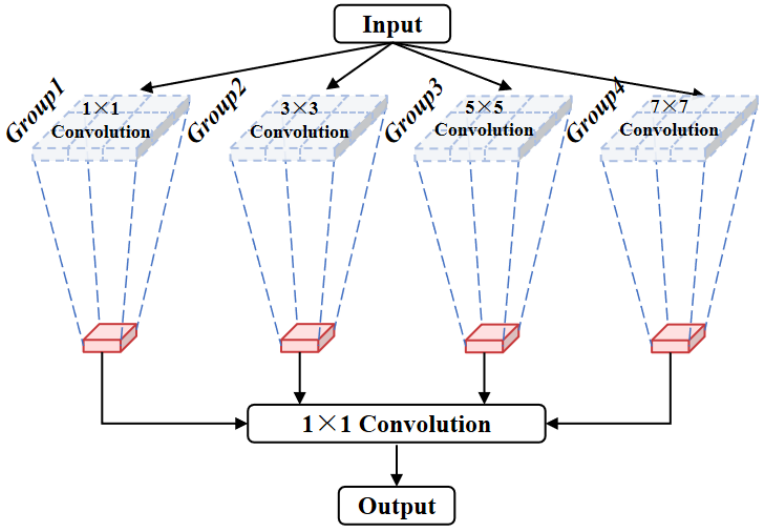


Fig. 5. Multi-scale grouping convolution module diagram

Experiments show that multi-scale grouped convolution not only improves the detection of small targets, but also has fewer parameters than the original model. Compared with ordinary 3×3 convolution, assuming that the input channel and output channel are the same and both are C, then C convolution kernels of size 3×3×C are needed, and the number of parameters is:

$$C \times 3 \times 3 \times C = 9C^2 \tag{8}$$

In our convolution process, we divide it into four groups, and each group uses convolution kernels of sizes 1×1, 3×3, 5×5, and 7×7 for convolution. The number of parameters is:

$$\sum_{k=1}^{n} C/4 \times k \times k \times C/4 = 5.25C^2 \left(n = 1,3,5,7\right) \tag{9}$$

Then, 1×1 convolution kernel is used for information exchange, and its number of parameters is:

$$C \times 1 \times 1 \times C = C^2 \tag{10}$$

The total number of parameters is:

$$5.25C^2 + C^2 = 6.25C^2 \tag{11}$$

Compared with ordinary convolution, the number of parameters is reduced by nearly one-third.

5 Experimental Verification

We use Yolov8 as the basic framework of the model, with a training batch size of 32 and 12 training epochs. The labeled dataset collected from power scenarios is used as the detection dataset. The detection results are shown in Fig. 6. Compared with other

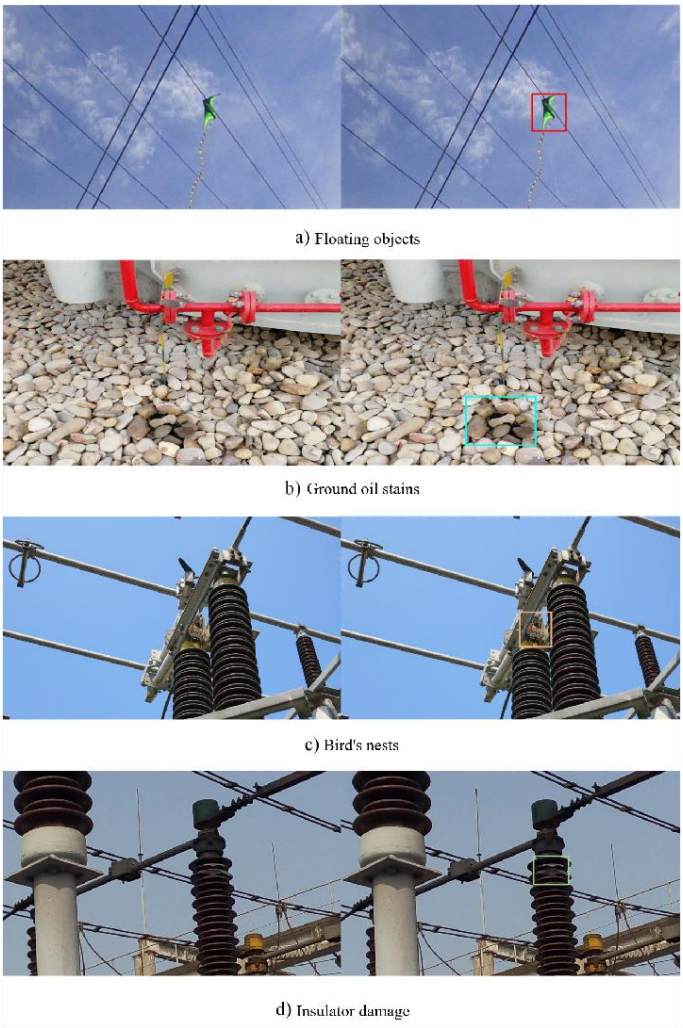


Fig. 6. Results of defect detection in power scenarios: (a) Floating objects; (b) Ground oil stains; (c) Bird's nests; (d) Insulator damage

models in the YOLO series, the proposed method has higher detection accuracy on the validation set. As shown in Table 1, the AP50 value reaches 87.8% after only 12 training epochs, and the number of model parameters is also reduced to a certain extent.

Table 1. Comparison with YOLO series algorithms.

Algorithm	*AP@.5*	*AP@[.5,.95]*	*Params(M)*
Yolov5	80.6%	43.9%	2.50
Yolov6	76.6%	42.4%	4.23
Yolov8	84.0%	47%	3.01

Ours	**87.8%**	**45%**	**2.13**

We also compared the proposed method with current mainstream methods on the test set. Our model achieves overall leading detection performance compared with other methods.

Table 2. Comparison with current mainstream model algorithms.

Algorithm	*AP@.5*	*AP@[.5,.95]*	*Params(M)*
Gold-yolo[24]	76.8%	41.8%	5.98
PKINet[25]	84.0%	45.1%	6.06
StarNet[26]	81.7%	44.4%	2.21
RMT[27]	85.6%	45.2%	14.8
HGNetV2[28]	80.4%	42.5%	2.35
FADC[29]	86.6%	46.9%	3.02
RepViT[30]	85.5%	46.7%	2.28
ParameterNet[31]	84.1.%	44.5%	4.42
WTConv[32]	84.3%	46.5%	2.67
Ours	**87.8%**	**45%**	**2.13**

6 Conclusion

Small target detection based on deep convolution is a troublesome problem. The model will inevitably lose some feature information in the process of continuous convolution stacking, which is particularly serious for small target objects.

Considering that small targets are prone to interference due to different prediction boxes generated by regression and classification tasks in deep feature maps, we designed different anchor box allocation strategies for different tasks. In the regression branch task, DCNv2 is used for dynamic feature alignment, while in the classification branch task, dynamic feature selection is used. Experiments show that the proposed dynamic task alignment detection head has a good performance improvement in small target detection.

In addition, to address the problem of lack of interaction between different feature channels in the convolution module during model feature extraction, we propose multi-scale grouped convolution. By splitting and reorganizing channels during convolution, different groups use convolution kernels of different sizes for convolution to extract feature information, and then fuse the obtained feature information. This can enhance the feature extraction ability of the convolution module for targets of different scales and strengthen information exchange between different channels.

References

[1] Duan K, Bai S, Xie L, et al. Centernet: Keypoint triplets for object detection[C]//Proceedings of the IEEE/CVF international conference on computer vision. 2019: 6569-6578.

[2] Simonyan K, Zisserman A. Very deep convolutional networks for large-scale image recognition[J]. arxiv preprint arxiv:1409.1556, 2014.

[3] Yu F, Koltun V. Multi-scale context aggregation by dilated convolutions[J]. arxiv preprint arxiv:1511.07122, 2015.

[4] Dai J, Qi H, Xiong Y, et al. Deformable convolutional networks[C]//Proceedings of the IEEE international conference on computer vision. 2017: 764-773.

[5] Girshick R. Fast r-cnn[C]//Proceedings of the IEEE international conference on computer vision. 2015: 1440-1448.

[6] Ren S, He K, Girshick R, et al. Faster r-cnn: Towards real-time object detection with region proposal networks[J]. Advances in neural information processing systems, 2015, 28.

[7] He K, Zhang X, Ren S, et al. Spatial pyramid pooling in deep convolutional networks for visual recognition[J]. IEEE transactions on pattern analysis and machine intelligence, 2015, 37(9): 1904-1916.

[8] Dai J, Li Y, He K, et al. R-fcn: Object detection via region-based fully convolutional networks[J]. Advances in neural information processing systems, 2016, 29.

[9] Liu W, Anguelov D, Erhan D, et al. Ssd: Single shot multibox detector[C]//Computer Vision–ECCV 2016: 14th European Conference, Amsterdam, The Netherlands, October 11–14, 2016, Proceedings, Part I 14. Springer International Publishing, 2016: 21-37.

[10] Cai Z, Fan Q, Feris R S, et al. A unified multi-scale deep convolutional neural network for fast object detection[C]//Computer Vision–ECCV 2016: 14th European Conference, Amsterdam, The Netherlands, October 11–14, 2016, Proceedings, Part IV 14. Springer International Publishing, 2016: 354-370.

[11] Bell S, Zitnick C L, Bala K, et al. Inside-outside net: Detecting objects in context with skip pooling and recurrent neural networks[C]//Proceedings of the IEEE conference on computer vision and pattern recognition. 2016: 2874-2883.

[12] Kong T, Yao A, Chen Y, et al. Hypernet: Towards accurate region proposal generation and joint object detection[C]//Proceedings of the IEEE conference on computer vision and pattern recognition. 2016: 845-853.

[13] Lin T Y, Dollár P, Girshick R, et al. Feature pyramid networks for object detection[C]//Proceedings of the IEEE conference on computer vision and pattern recognition. 2017: 2117-2125.

[14] Liang Z, Shao J, Zhang D, et al. Small object detection using deep feature pyramid networks[C]//Advances in Multimedia Information Processing–PCM 2018: 19th Pacific-Rim

Conference on Multimedia, Hefei, China, September 21-22, 2018, Proceedings, Part III 19. Springer International Publishing, 2018: 554-564.

[15] Nayan A A, Saha J, Mozumder A N, et al. Real time detection of small objects[J]. Int. J. Innov. Technol. Explor. Eng, 2020, 9: 837.

[16] Liu Z, Gao G, Sun L, et al. HRDNet: High-resolution detection network for small objects[C]//2021 IEEE international conference on multimedia and expo (ICME). IEEE, 2021: 1-6.

[17] Deng C, Wang M, Liu L, et al. Extended feature pyramid network for small object detection[J]. IEEE Transactions on Multimedia, 2021, 24: 1968-1979.

[18] Tian Z, Shen C, Chen H, et al. FCOS: A simple and strong anchor-free object detector[J]. IEEE transactions on pattern analysis and machine intelligence, 2020, 44(4): 1922-1933.

[19] Feng C, Zhong Y, Gao Y, et al. Tood: Task-aligned one-stage object detection[C]//2021 IEEE/CVF International Conference on Computer Vision (ICCV). IEEE Computer Society, 2021: 3490-3499.

[20] Zhu X, Hu H, Lin S, et al. Deformable convnets v2: More deformable, better results[C]//Proceedings of the IEEE/CVF conference on computer vision and pattern recognition. 2019: 9308-9316.

[21] Zhu X, Su W, Lu L, et al. Deformable detr: Deformable transformers for end-to-end object detection[J]. arxiv preprint arxiv:2010.04159, 2020.

[22] Howard A G, Zhu M, Chen B, et al. Mobilenets: Efficient convolutional neural networks for mobile vision applications[J]. arXiv preprint arXiv:1704.04861, 2017.

[23] Han K, Wang Y, Tian Q, et al. Ghostnet: More features from cheap operations[C]//Proceedings of the IEEE/CVF conference on computer vision and pattern recognition. 2020: 1580-1589.

[24] C. Wang, W. He, Y. Nie, J. Guo, C. Liu, Y. Wang, and K. Han, “Goldyolo:Efficient object detector via gather-and-distribute mechanism,”Advances in Neural Information Processing Systems, vol. 36, 2024.

[25] X. Cai, Q. Lai, Y. Wang, W. Wang, Z. Sun, and Y. Yao, “Poly kernel inception network for remote sensing detection,” in Proceedings of the IEEE/CVF Conference on Computer Vision and Pattern Recognition, 2024, pp. 27 706–27 716.

[26] X. Ma, X. Dai, Y. Bai, Y. Wang, and Y. Fu, “Rewrite the stars,” in Proceedings of the IEEE/CVF Conference on Computer Vision and Pattern Recognition, 2024, pp. 5694–5703.

[27] Q. Fan, H. Huang, M. Chen, H. Liu, and R. He, “Rmt: Retentive networks meet vision transformers,” in Proceedings of the IEEE/CVF Conference on Computer Vision and Pattern Recognition, 2024, pp. 5641–5651.

[28] Y. Zhao, W. Lv, S. Xu, J. Wei, G. Wang, Q. Dang, Y. Liu, and J. Chen, “Detrs beat yolos on real-time object detection,” in Proceedings of the IEEE/CVF Conference on Computer Vision and Pattern Recognition, 2024, pp. 16 965–16 974.

[29] L. Chen, L. Gu, D. Zheng, and Y. Fu, “Frequency-adaptive dilated convolution for semantic segmentation,” in Proceedings of the IEEE/CVF Conference on Computer Vision and Pattern Recognition, 2024, pp. 3414–3425.

[30] A. Wang, H. Chen, Z. Lin, J. Han, and G. Ding, “Repvit: Revisiting mobile cnn from vit perspective,” in Proceedings of the IEEE/CVF Conference on Computer Vision and Pattern Recognition, 2024, pp. 15 909–15 920.

[31] K. Han, Y. Wang, J. Guo, and E. Wu, “Parameternet: Parameters are all you need for large-scale visual pretraining of mobile networks,” in Proceedings of the IEEE/CVF Conference on Computer Vision and Pattern Recognition, 2024, pp. 15 751–15 761.

[32] Finder S E, Amoyal R, Treister E, et al. Wavelet convolutions for large receptive fields[C]//European Conference on Computer Vision. Springer, Cham, 2025: 363-380.

111 考虑热回收的寒地电算协同中心综合能源系统运行控制

朱振家[1]，黄震[2]，张弘鹏[2]，杨晶莹[3]，王克诚[1]，徐英[1]

(1.哈尔滨工业大学，黑龙江省 哈尔滨市 150006；2.国家电网公司东北分部，辽宁省 沈阳市 110179；3.国网吉林省电力有限公司，吉林省 长春市 130022)

Optimal Configuration of Integrated Energy System for Cold-region Data Computing Collaborative Center Considering Heat Recovery

ZHU Zhenjia[1], HUANG Zhen[2], ZHANG Hongpeng[2], YANG Jingying[3], WANG Kecheng[1], XU Ying[1]

(1.Harbin Institute of Technology, Harbin, Heilongjiang Province, 150006, China; 2.North-east Branch of State Grid Corporation of China, Shenyang, Liaoning Province, 110179, China; 3.State Grid Jilin Electric Power Company Limited, Changchun, Jilin Province, 130022, China)

ABSTRACT: This paper presents an operation control method for the integrated energy system of a cold - region computer - electricity collaborative center, taking into account wind power, photovoltaic power, waste heat utilization, and energy storage systems. Firstly, based on the unique geographical characteristics of cold-region data centers, the wind from the cold environment outside is processed by the fan to cool the equipment and reduce the usage of air conditioners; Secondly, aiming at minimizing the total system cost, a thermal recovery model consisting of a low-temperature heat storage tank, an electric heat pump and a high-temperature heat storage tank is established. Considering the dynamic electricity price of the power grid, the dynamic heat price, equipment operation constraints and power balance conditions, the optimal scheduling strategy of the comprehensive energy system is obtained; Finally, taking a computing power center in Northeast China as an example, the superiority of the operation control method for this integrated energy system is analyzed and verified. The simulation results indicate that this method can significantly reduce the system's energy costs and the carbon dioxide emissions.

KEY WORDS: computerized collaborative center; Integrated energy system; multi-energy complementarity; cold regions; heat recovery;

摘要：本文提出一种考虑风电、光伏、余热利用及储能系统的寒地电算协同中心综合能源系统运行控制方法。首先，根据寒冷地区数据中心独特的地域特点，利用风机将外界寒冷环境的风处理，用于机组降温以减少空调使用量；其次，以系统总成本最小为目标，建立由低温储热罐、电热泵及高温储热罐组成的热回收模型，综合考虑电网动态电价、动态热价、设备运行约束及功率平衡条件得到综合能源系统的最优调度策略；最后，以东北地区一算力中心为例，分析验证该综合能源系统运行控制方法的优越性。仿真结果表明，该方法能显著降低系统能源成本、降低二氧化碳的排放量。

关键词：电算协同中心；综合能源系统；寒冷地区；热回收；多能互补

DOI：10.13335/j.1000-3673.pst.2014.01

0 引言

随着人工智能技术的飞速发展与大规模应用，作为其核心基础设施的算力中心数量呈爆发式增长。算力中心运行依赖巨量电力支撑，已成为能源消耗大户，国际能源署预测，到 2030 年 AI 相关能耗占全球电力需求的比例将达 3%-5%。从运营成本来看，能源开支在数据中心月度运营成本中占比超 50%[1]，直接影响云服务提供商的经济效益；从环境影响来看，算力中心行业碳排放量已占全球总量的 2%，对我国“双碳”目标的实现构成重要影响[2-3]。

我国“三北”等寒冷地区拥有丰富的风能、太阳能等可再生能源，但区域内能源负荷增长相对缓慢，存在新能源消纳难题。同时，寒地算力中心运行面临双重挑战：一方面，风光发电具有强不确定性，易对算力中心稳定供电造成冲击，传统能源系统应对波动性的韧性不足；另一方面，寒地冬季存在大量供暖需求，而当前算力中心的

余热资源未得到系统回收利用，既造成能源浪费，又难以与区域供暖需求有效衔接，尚未形成电 - 热耦合的优化利用框架，制约了绿色“算力中心”的转型进程。

为解决上述问题，学界已开展相关探索。在多能互补方面，文献 [4] 提出基于数据负载共担的联盟模式，结合多能互补与时空可调特性制定调度策略；文献[5]提出一种多能互补复合电站的优化配置方法，能够考虑系统调峰特性、波动特性、间歇性新能源消纳和外送通道利用率，实现风光水气火储复合电站的规划；文献[6]利用数据中心延迟容忍型负荷的时间平移特性优化能源分配，提升经济性；文献[7]则考虑新能源出力不确定性带来的风险成本，构建储电与储热容量的分层优化规划方法。在余热回收领域，文献[8]以总成本最小为目标，提出计及余热回收的系统优化策略，实现环境价值成本降低 11.5%、总成本降低 7.9%；文献[9]创新性地将机房空调冷冻水回水作为低温热源，通过优化热交换程序为办公及公共区域供暖；Intel 公司开发的蒸发器 - 冷凝器组合架构，借助高效板式换热器实现废热多级回收，标志着数据中心从单纯耗能单元向能源枢纽转型的重要突破[10]。

然而，现有研究仍存在不足：电算综合能源系统中热回收模型与电力系统缺乏动态协同，未形成完整的电-热耦合优化框架；面对新能源出力波动，算力中心能源系统的韧性有待进一步提升；余热回收与寒地供暖需求的匹配度、以及自然冷能的利用效率仍有优化空间。

针对上述研究空白，本文提出一种考虑热回收的寒地电算协同中心综合能源系统运行控制方案，核心创新与目标如下：

1）结合寒地独特的低温环境，首次设计风机处理外界冷空气的降温系统，用于算力中心机组冷却；

2）减少空调能耗，提升电能使用效率(PUE)；

整合风力发电、光伏发电、余热回收及储能系统，构建多能互补体系，降低对单一能源的依赖，提升系统应对风光波动的能力；

3）利用机房冷冻水余热 ，通过电热泵二次提温补充市政供热、减少化石能源消耗，助力“双碳”目标；

4）计及电网动态电价与热网动态电价建立以系统总成本最小为目标的优化调度模型，实现经济与环境效益的协同提升。

1 考虑热回收的寒地电算协同中心综合能源系统优化模型

1.1 系统整体架构

寒地电算协同中心综合能源系统以“多能互补-电热耦合-冷能利用”为核心架构，整合分布式电源、余热回收、储能及自然冷能利用单元，系统运行示意图如图 1 所示。

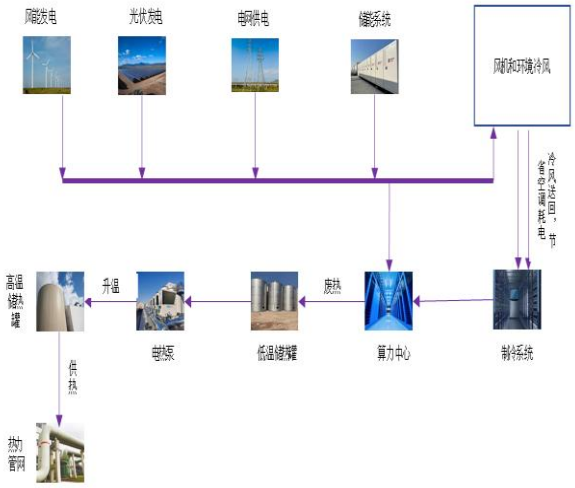


图 1 综合能源系统运行示意图

Fig.1 Schematic diagram of the integrated energy system operation

该系统通过多能源协同与梯级利用，实现“供电-制冷-供热”一体化运行，具体构成及功能如下：

能量供应单元：含风电、光伏及电网供电，其中风电与光伏利用寒地丰富的可再生能源资源，电网作为备用与调峰电源，通过动态电价响应实现经济购售电；

负荷与温控单元：服务器阵列构成核心用电负荷，配套温控系统包含“自然冷能利用+空调辅助”模式——通过风机处理外界低温空气(-10~5℃)为机组降温，降低空调能耗占比，提升电能使用效率(PUE)；

余热回收与储热单元：由低温储热罐(5~15 MWh)、电热泵及高温储热罐(8~25MWh)组成，低温储热罐收集服务器冷却水废热(50℃)，经电热泵提温至 70℃后存入高温储热罐，再根据热网动态热价向区域供热；

储能单元：用于平抑风光出力波动与实现电价套利，通过充放电策略协同多能源运行，保障系统功率平衡。

系统运行核心逻辑为：基于电网动态电价与

热网动态热价，以总成本最小为目标，调控各单元出力——电价低谷时段优先购电储能与运行电热泵，电价高峰时段减少购电并出售多余电能，余热回收量随算力负荷动态调整，实现“电-热-冷”资源的最优配置。

1.2 分布式电源模型

围绕寒冷地区数据中心综合能源系统中的分布式电源展开数学建模研究，重点分析了风力发电、光伏发电、热回收系统及储能系统的运行特性与成本结构，为后续能源优化调度奠定了理论基础。通过整合风光发电、热回收系统与储能系统，构建了多能互补发电系统的数学模型，充分体现了寒冷地区资源禀赋的优势，通过适当的调度策略，可以有效地降低系统能源成本。

1.2.1 风力发电机组模型

风电机组出力受实时风速动态影响，基于贝茨理论与机组运行特性，其出力模型分三阶段描述，数学表达式如下：

$$P_{\mathrm{w}}(t)=\begin{cases}0, v(t)>v_{\mathrm{o}}\text{或}v<v_{\mathrm{i}}\\ \dfrac{v^3-v_{\mathrm{i}}^3}{v_{\mathrm{r}}^3-v_{\mathrm{i}}^3}\mathrm{P_r}, v_{\mathrm{i}}<v(t)<v_{\mathrm{r}}\\ \mathrm{P_r}, v_{\mathrm{r}}<v(t)<v_{\mathrm{o}}\end{cases} \tag{1}$$

式中：$P_{\mathrm{w}}(t)$ 表示任意 t 时刻风电出力（MW）；$\mathrm{P_r}$ 表示风电机组额定功率(MW)；$v(t)$ 表示任意 t 时刻的风速(m/s)；v_{i} 表示切入风速(m/s)；v_{r} 表示额定风速(m/s)；v_{o} 表示切出风速(m/s)。

风电运行成本主要为运维成本，按单位出力折算，模型为：

$$C_{\mathrm{w}}=k_{\mathrm{w}}\sum_{t=1}^{24}P_{\mathrm{w}}(t) \tag{2}$$

式中：C_{w} 为风电的运维总成本(元)；k_{w} 为风力发电成本系数(元/MW)，取 80 元/MW。

1.2.2 光伏发电机组模型

光伏出力取决于光照强度与阵列转换效率，考虑寒地日间光照特性(冬季光照时长 6~8h，夏季 14~16h)，其出力模型为：

$$P_{\mathrm{pv}}(t)=S\cdot I(t)\cdot\eta_{\mathrm{PV}}\cdot\alpha_{\mathrm{T}} \tag{3}$$

式中：$P_{\mathrm{pv}}(t)$ 为 t 时刻光伏出力(MW)；S 为光伏阵列面积($\mathrm{m^2}$)；$I(t)$ 表示光照强度(Lux)；η_{PV} 表示光伏阵列的光电转换效率(MW/Lux×$\mathrm{m^2}$)；α_{T} 为温度修正系数。

光伏运维成本模型与风电类似，表达式为：

$$C_{\mathrm{pv}}=k_{\mathrm{pv}}\sum_{t=1}^{24}P_{\mathrm{pv}}(t) \tag{4}$$

式中：C_{pv} 表示光伏发电总成本(元)；k_{pv} 表示光伏发电成本系数(元/MW)。

1.2.3 储能系统充放电模型

储能系统采用锂电池储能，其荷电状态(SOC)动态演化遵循能量守恒定律，考虑充放电效率与自放电损耗，模型为：

$$SOC(t)=SOC(t-1)-\frac{P_{\mathrm{dis}}(t)}{\eta_{\mathrm{dis}}}\Delta t+P_{\mathrm{ch}}(t)\cdot\eta_{\mathrm{ch}}\Delta t \tag{5}$$

式中：$SOC(t)$ 为 t 时刻的储能状态(MWh)；$P_{\mathrm{dis}}(t)$ 为 t 时刻放电功率(MW)；$P_{\mathrm{ch}}(t)$ 为 t 时刻充电功率(MW)；η_{dis}、η_{ch} 表示充、放电效率，均取 0.95；Δt 表示时间步长，取 1h；

初始条件:

$$SOC(1)=SOC_{\mathrm{in}} \tag{6}$$

式中：SOC_{in} 为 SOC 的初始储能值(MWh)，取 5MW。

1.3 冷热电联供系统模型

冷热电联供系统作为综合能源系统的核心耦合单元，通过能源梯级利用实现“电-热-冷”需求协同满足，重点整合余热回收、电热泵及自然冷能利用模块，其建模聚焦能量平衡与设备运行特性，为系统优化调度提供理论支撑。

1.3.1 余热回收系统模型

1)低温废热回收模型

算力中心服务器运行产生的废热主要通过冷却水带走，低温废热回收量与算力负荷正相关，模型为：

$$Q_{\mathrm{W}}=\eta_{\mathrm{c}}\cdot P_{\mathrm{load}}(t) \tag{7}$$

式中：Q_{W} 表示时间 t 时刻余热功率(MW)；η_{c} 表示余热回收效率，取 0.36；$P_{\mathrm{load}}(t)$ 表示算力中心用电负荷(MW);

2)电热泵能量转换模型

电热泵作为余热提温核心设备，遵循热力学第一定律，其能量平衡关系为：

$$Q_{\mathrm{hp,h}}(t)=Q_{\mathrm{hp,l}}(t)+P_{\mathrm{hp,}}(t) \tag{8}$$

$$\mathrm{COP}=\frac{Q_{\mathrm{hp,h}}(t)}{P_{\mathrm{hp}}(t)} \tag{9}$$

式中: $Q_{\mathrm{hp,h}}(t)$、$Q_{\mathrm{hp,l}}(t)$ 分别为 t 时刻电热泵向高温侧输出的热功率、从低温侧吸收的热功率(MW); COP 是电热泵性能系数，与温度有关，取 2.8~3.2。

3)储热罐能量平衡方程

低温储热罐(存储 50℃废热)：考虑热损失，其能量平衡方程为：

$$\begin{aligned}E_{\mathrm{S}}(t)=E_{\mathrm{S}}(t-1)+Q_{\mathrm{W}}-Q_{HP,1}(t)\\-\gamma_{\mathrm{s}}\cdot E_{S}(t-1)\end{aligned} \tag{10}$$

式中：$E_{\mathrm{S}}(t)$ 为 t 时刻低温储热罐容量(MWh)；γ_{s} 为低温储热罐的热损失系数，取 0.02。

高温储热罐(存储 70℃供热热水)：考虑热损失，其能量平衡方程为：

$$\begin{aligned}E_{\mathrm{b}}(t)=E_{\mathrm{b}}(t-1)+Q_{\mathrm{hp,h}}(t)\\-Q_{\mathrm{S}}(t)-\gamma_{\mathrm{b}}\cdot E_{\mathrm{b}}(t-1)\end{aligned} \tag{11}$$

式中: $E_{\mathrm{b}}(t)$ 为 t 时刻高温储热罐容量(MWh); $Q_{\mathrm{S}}(t)$ 表示 t 时刻高温储热罐向热网售热功率(MW)；γ_{b} 为高温储热罐的热损失系数,取 0.03。

余热回收系统总收益:

$$C_{\mathrm{h}}=\sum_{t=1}^{24}\left(H_{\mathrm{sell}}(t)\cdot Q_{\mathrm{S}}(t)-E_{\mathrm{buy}}(t)\cdot P_{\mathrm{hp}}(t)\right) \tag{12}$$

式中：C_{h} 为余热回收系统的总净收益(元)；$H_{\mathrm{sell}}(t)$ 为 t 时刻热网售热价格(元/kWh)；$E_{\mathrm{buy}}(t)$ 为 t 时刻电网购电价格(元/kWh)

储热罐的维护过程主要是定期检查罐体、保温层和附件，成本可忽略不计。

1.3.2 空调能耗节约模型

寒地低温环境为自然冷能利用提供优势，自然冷能制冷功率与室内外温差、通风量相关，其模型为：

$$P_{\mathrm{c}}(t)=\eta_{\mathrm{cool}}\cdot\rho\cdot\mathrm{c}_{\mathrm{p}}\cdot\mathrm{V}\cdot\left(T_{\mathrm{in}}-T_{\mathrm{out}}(t)\right) \tag{13}$$

式中： $P_{\mathrm{c}}(t)$ 为 t 时刻的自然冷能制冷功率(MW)；η_{cool} 表示冷风利用效率；ρ 为空气密度(kg/m^3)；c_{p} 为空气比热容(kJ/(kg·℃))；V 为通风量(m^3/s)；T_{in} 为数据中心室内温度(℃)；$T_{\mathrm{out}}(t)$ 为 t 时刻室外温度(℃)。考虑到室内外温差与算力负荷呈正相关。负荷越高，室内散热越多，温差越大，为简化模型，将自然冷能制冷功率与负荷关联：

$$P_{\mathrm{c}}(t)=\beta\sum_{t=1}^{24}P_{\mathrm{load}}(t) \tag{14}$$

式中：β 为制冷效率系数。

自然冷能利用带来的空调节约收益为：

$$C_{\mathrm{c}}=k_{\mathrm{c}}\sum_{t=1}^{24}P_{\mathrm{c}}(t) \tag{15}$$

式中：C_{c} 为空调节约总收益(元)；k_{c} 表示空调成本替代系数(元/MW)。

2 综合能源系统优化模型

2.1 目标函数

以寒地电算协同中心综合能源系统 24 小时总运行成本最小化为优化目标，总成本涵盖常规机组发电成本、电网购电成本、储能运维成本，扣除售电收益、余热回收收益及空调节约收益，数学表达式为：

$$\begin{aligned}C=C_{\mathrm{j}}+C_{\mathrm{w}}+C_{\mathrm{pv}}+C_{\mathrm{b}}+C_{\mathrm{soc}}\\-C_{\mathrm{s}}-C_{\mathrm{h}}-C_{\mathrm{c}}\end{aligned} \tag{16}$$

式中：C 表示总成本(元)；C_{j} 表示系统常规机组发电成本(元)；C_{b} 表示购电成本(元)；C_{soc} 表示储能系统成本(元)；C_{s} 表示售电收益(元)；

其中，系统常规机组发电成本可表示为：

$$C_{\mathrm{j}}=\sum_{t=1}^{24}\left(\mathrm{a}\cdot Pg(t)^{2}+\mathrm{b}\cdot P_{\mathrm{g}}(t)\right) \tag{17}$$

式中: a 为二次项系数(元/MWh^2),取 0.00035

/MWh^2；b 表示常规机组发电成本的一次项系数(元/MWh)，取 500/MWh。

购电成本可表示为：

$$C_{\mathrm{b}}=\sum_{t=1}^{24}\mathrm{E}_{\mathrm{buy}}(t)P_{\mathrm{buy}}\left(t\right) \tag{18}$$

式中：$P_{\mathrm{b}}\left(t\right)$表示$t$时刻购电功率(MW)。

售电成本可表示为：

$$C_{\mathrm{s}}=\sum_{t=1}^{24}E_{\mathrm{sell}}\left(t\right)P_{\mathrm{sell}}\left(t\right) \tag{19}$$

式中：$E_{\mathrm{sell}}\left(t\right)$表示$t$时刻售电电价(元/kWh)；$P_{\mathrm{sell}}\left(t\right)$表示$t$时刻售电功率(MW)。

由于风光出力的成本相较于常规机组等较小，且余热回收收益与节省空调所获收益均与负载功率呈正相关，可合并为一项，因此可将上式简化为：

$$C=C_{\mathrm{j}}+C_{\mathrm{b}}+C_{\mathrm{soc}}-C_{\mathrm{s}}-C_{\mathrm{h}} \tag{20}$$

2.2 约束条件

2.2.1 常规机组运行约束

1）常规机组出力上下限约束：

$$P_{\mathrm{g.min}}\le P_{\mathrm{g}}\le P_{\mathrm{g.max}} \tag{21}$$

式中：$P_{\mathrm{g.min}}$为机组出力的最小值(MW)；$P_{\mathrm{g.max}}$为机组出力的最大值(MW)。

2）常规机组爬坡约束：

$$\begin{cases}P_{\mathrm{g}}\left(t\right)-P_{\mathrm{g}}\left(t-1\right)\le r_{\mathrm{u}}\Delta t\\P_{\mathrm{g}}\left(t-1\right)-P_{\mathrm{g}}\left(t\right)\le r_{\mathrm{d}}\Delta t\end{cases} \tag{22}$$

式中：$P_{\mathrm{g}}\left(t\right)$为$t$时刻常规机组出力(MW)；$r_{\mathrm{u}}$为向上爬坡率(MW/h)；$r_{\mathrm{d}}$为向下爬坡率(MW/h)。

2.2.2 电网购售电约束

购售电功率限制：

$$\begin{cases}0\le P_{\mathrm{buy}}(t)\le P_{\mathrm{buy,max}}\\0\le P_{\mathrm{sell}}(t)\le P_{\mathrm{sell.max}}\end{cases} \tag{23}$$

式中：$P_{\mathrm{buy,max}}$为购电功率的最大值（MW）；$P_{\mathrm{sell.max}}$为售电功率的最大值(MW)。

2.2.3 电力功率平衡约束：

$$\begin{aligned}&P_{\mathrm{g}}(t)+P_{\mathrm{w}}(t)+P_{\mathrm{pv}}(t)+P_{\mathrm{buy}}(\mathrm{t})+P_{\mathrm{dis}}(t)\\&-P_{\mathrm{ch}}(t)-P_{\mathrm{sell}}(\mathrm{t})=P_{\mathrm{load}}(t)+P_{\mathrm{hp}}(t)\end{aligned} \tag{24}$$

式中：P_{w}表示风电实际出力(MW) P_{pv}表示光伏实际出力(MW)；$P_{\mathrm{hp}}(t)$为 t 时刻电热泵功率(MW)

2.2.4 分布式电源出力约束：

$$\begin{cases}0\le P_{\mathrm{w}}(t)\le P_{\mathrm{w.max}}\\0\le P_{\mathrm{pv}}(t)\le P_{\mathrm{pv.max}}\end{cases} \tag{25}$$

式中：$P_{\mathrm{w.max}}$表示风电出力的最大值(MW)；$P_{\mathrm{pv.max}}$表示光伏出力的最大值(MW)。

2.2.5 余热回收系统约束：

1)电热泵功率约束

$$0\le P_{hp,(t)}\le P_{hp,(t)\max} \tag{26}$$

2)低温储热罐约束：

容量范围约束：

$$E_{\mathrm{s\,min}}\le E_{\mathrm{s}}(t)\le E_{\mathrm{s\,max}},\ \forall\mathrm{t} \tag{27}$$

式中：$E_{\mathrm{s\,min}}$为低温储热罐最小配置容量；$E_{\mathrm{s\,max}}$为表示低温储热罐的最大配置容量。

能量外送约束：

$$0\le Q_{\mathrm{hp,l}}(t)\le Q_{\mathrm{hp,l,max}},\ \forall\mathrm{t} \tag{28}$$

式中：$Q_{\mathrm{hp,l,max}}$是低温储热罐外送能力上限

循环约束：

$$E_{\mathrm{b}}(t)=E_{\mathrm{b,in}} \tag{29}$$

确保调度结束周期结束后能恢复到初始状态。

3)高温储热罐约束:

容量范围约束:

$$E_{\mathrm{b\,min}}\le E_{\mathrm{b}}(\mathrm{t})\le E_{\mathrm{b\,max}} \tag{30}$$

式中：$E_{\mathrm{b\,min}}$表示高温储热罐的最小配置容量。$E_{\mathrm{b\,max}}$表示高温储热罐的最大配置变量；

能量外送约束：

$$0\le Q_{\mathrm{S}}(\mathrm{t})\le Q_{\mathrm{S\,max}}\ \ \forall\mathrm{t} \tag{31}$$

式中$Q_{\mathrm{S\,max}}$表示高温储热罐外送能力上限。

循环约束：

$$E_{\mathrm{b}}(t)=E_{\mathrm{b,in}} \tag{32}$$

确保调度结束周期结束后能恢复到初始状态。

2.2.6 充放电运行约束：

$$\begin{cases} 0 \le P_{\text{ch}}(t) \le P_{\text{ch.max}} \cdot u_{\text{ch}}(t) \\ 0 \le P_{\text{dis}}(t) \le P_{\text{dis.max}} \cdot u_{\text{dis}}(t) \end{cases} \tag{33}$$

$$u_{ch}(t) + u_{dis}(t) \le 1 \tag{34}$$

式中：$P_{\text{ch.max}}$、$P_{\text{dis.max}}$ 分别为最大充放电功率(MW)，$u_{\text{ch}}(t)$、$u_{\text{dis}}(t)$ 分别为充放电启停变量(0 表示充电停止，1 表示充电运行)；。

SOC 边界约束：

$$E_{\text{min}} \le SOC(t) \le E_{\text{max}} \tag{35}$$

式中：E_{min} 为储能最小容量（MWh）；E_{max} 为储能最大容量（MWh）。

循环约束:

$$SOC(t) \ge SOC_{\text{in}} \tag{36}$$

保证调度周期结束时储能恢复到初始状态。

3 数据收集与仿真分析

3.1 寒地算力中心 24 小时风光及负荷数据的特征

为构建寒地算力中心综合能源系统优化调度模型，需开展基础数据收集与特性分析，重点采集 24 小时风电出力、光伏发电出力及负荷需求标幺值。标幺值的采用可消除不同规模算力中心容量基值差异，为横向对比与模型适配提供统一基准。通过数据统计与分析，各能源与负荷特性如下：

负荷特性：图 2 呈现了算力中心全天持续高负荷运行特征，日内负荷波动具有显著规律性——5 时达到最低值 9.3MW，12 时达到全天峰值 18.0MW，且日间(8:00-22:00)负荷水平显著高于夜间(22:00-次日 8:00)，符合算力中心日间业务密集、夜间业务缩减的运行规律；

风电出力特性：受寒冷地区气候与地形影响，风速呈现“夜间高、正午低”的周期性变化，导致风电出力时序特征与之高度协同——夜间(0:00-6:00)出力水平较高，正午(11:00-13:00)出力降至低谷，需依赖储能系统实现出力波动平抑与冗余电能消纳，保障供电稳定性(见图 3)；

出力水平由光照强度决定，具有强日间导向性——6:00 前与 18:00 后光照强度极低，光伏出力接近 0；11:00-14:00 光照强度达到峰值，光伏出力同步进入高发时段，与风电形成完美的时间互补关系，可有效提升可再生能源整体消纳率(见图 4)。

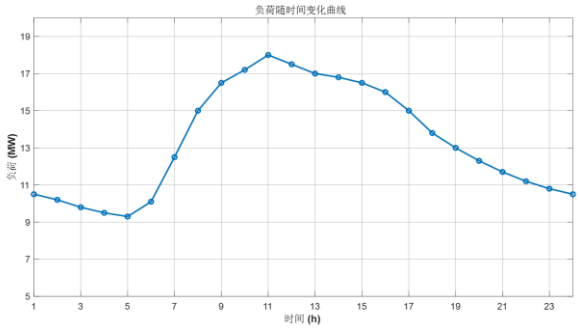


图 2 负荷变化情况

Fig.2 Load Variation Situation

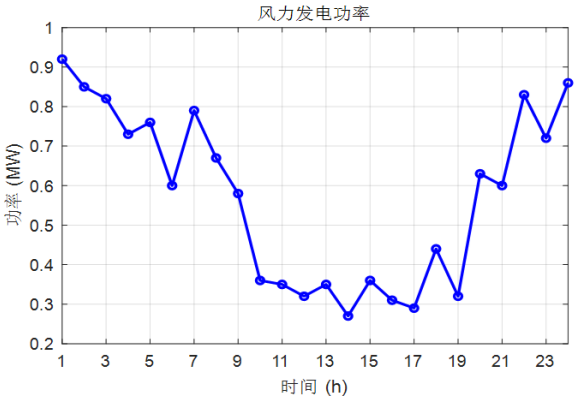


图 3 风力出力情况

Fig. 3 Wind Power Output Situation

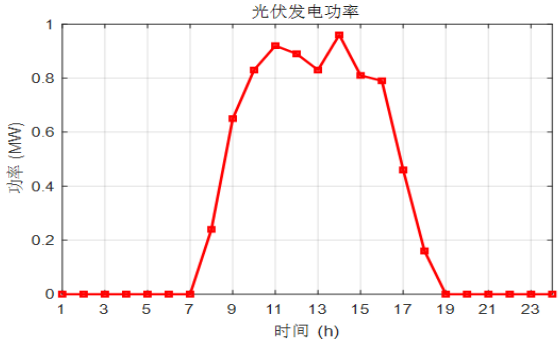


图 4 光伏出力情况

Fig. 4 Wind Power Output Situation

3.2 24 小时动态价格机制

电价与热价的日内动态波动是综合能源系统经济调度的核心驱动因素，本节基于寒地电力与热力市场实际运行规则，建立峰-平-谷三段式动态价格机制，为优化调度策略制定提供经济性依据。

3.2.1 电网动态电价

根据寒地电网负荷特性与电力供需关系，将 24 小时划分为峰、平、谷三个时段，各时段电价

水平如表 1 所示。其中，11:00-15:00、19:00-22:00 为用电高峰时段，电价设定为 1.08 元/kWh；08:00-10:00、16:00-18:00 为用电平段，电价降至 0.73 元/kWh；01:00-07:00、23:00-24:00 为用电低谷时段，电价低至 0.36 元/kWh。该价格机制下，系统可在电价低谷时段增加电网购电与储能充电，在电价高峰时段减少购电并出售多余电能，通过“低买高卖”实现购售电成本优化。

表 1　电网 24 小时动态电价

Table 1　24-hour Dynamic Electricity Prices of the Grid

时段	区段划分	价格/(元·kWh^{-1})
峰	11：00—15：00、19：00—22：00	1.08
平	08：00—10：00、16：00—18：00	0.73
谷	01：00—07：00、23：00—24：00	0.36

3.2.2 热网动态热价

结合寒地热力用户需求特性(供暖需求高峰、夜间需求低谷)制定热网 24 小时动态热价(表 2)其中，05:00-08:00、17:00-21:00 为供热高峰时段，热价设定为 0.28 元/kWh；08:00-17:00、21:00-24:00 为供热平段，热价调整为 0.19 元/kWh；00:00-05:00 为供热低谷时段，热价降至 0.15 元/kWh。系统可基于该热价机制，动态调节电热泵加热功率与高温储热罐输热功率——热价高峰时增加储热罐释热、减少电热泵耗电，热价低谷时加大电热泵运行强度、提升储热罐蓄热量，实现热网收益最大化。

表 2 热网 24 小时动态热价

Table 2　24-hour Dynamic Electricity Price of the Heating Network

时段	区段划分	价格/(元·kWh^{-1})
峰	05：00—08：00、17：00—21：00	0.28
平	08：00—17：00、21：00—24：00	0.19
谷	00:00-05:00	0.15

3.3 寒地算力中心综合能源系统优化仿真

以系统 24 小时总运行成本最小化为目标函数，纳入常规机组运行约束、功率平衡约束、储能充放电约束、余热回收系统约束等关键边界条件，基于 Gurobi 求解器开展优化调度仿真，验证综合能源系统的经济性与可靠性。

3.3.1 功率平衡验证

功率平衡图(见图 5)显示，各时段多能源叠加形成的总供电曲线与算力中心负荷需求曲线完全重合，表明模型严格满足功率平衡约束，无功率缺额或冗余现象。从动态响应特性来看，系统在负荷陡升(如 7:00，负荷从 9.3MW 升至 12.5MW)与陡降(如 13:00，负荷从 18.0MW 降至 17.0MW)时段，可通过常规机组爬坡、储能放电/充电切换实现快速响应，体现出优异的运行灵活性。

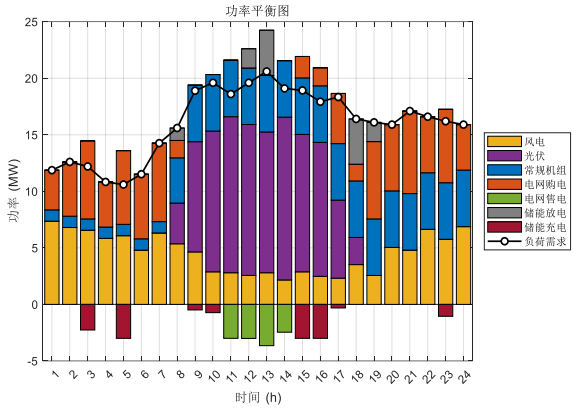


图 5 功率平衡图

Fig.5　Power Balance Diagram

3.3.2 各能源单元出力特性

常规机组：作为基荷电源，于 7:00-24:00 稳定运行，最大出力 5MW，出力波动控制在±1MW 以内，虽运行成本较高(二次项系数 0.00035 元/MWh^2、一次项系数 500 元/MWh)，但为系统提供了基础供电保障；

风电与光伏：二者形成强时间互补——风电在夜间(0:00-6:00)最大出力达 7.36MW，光伏在日间(11:00-14:00)最大出力达 13.8MW，可再生能源总出力在午间(12:00-13:00)占负荷比重超 60%，显著降低对常规能源的依赖；

储能系统：基于动态电价与风光出力协同调度——0:00-4:00(电价谷段+风电大发)以 3MW 额定功率充电，SOC 从初始 5MWh 升至 8MWh；8:00-10:00、18:00-20:00(负荷高峰+电价平段)以 4MW 额定功率放电，SOC 最低降至 6MWh；调度周期末(24:00)SOC 回升至 5MWh，满足循环约束；

余热回收系统：余热回收量与算力中心负荷正相关，通过低温储热罐(容量 5-15MWh)收集 50℃冷却水废热，经电热泵提温至 70℃后存入高温储热罐(容量 8-25MWh)，高负荷时段(11:00-13:00)最大回收功率 1.5MW，热损失控制在 2%-3%以内；

电热泵：作为余热提温核心设备，其运行策略完全响应电价波动——2:00-6:00(电价谷段，0.36 元/kWh)以最大 13.2MW 功率运行，15:00-22:00(电价峰段，1.08 元/kWh)停机，实现

“谷段蓄热、峰段释热”的经济运行模式。

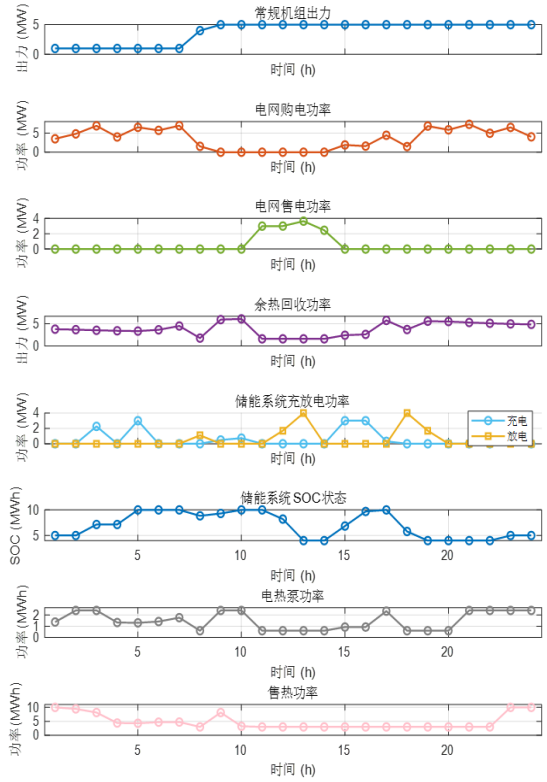


图 6 各电源出力情况

Fig.6 Output of Each Power Supply

3.4 经济性核算

基于仿真结果开展经济性核算，核心指标如下：

总购电量 84.79MWh，购电支出 52663.20 元；总售电量 12.12MWh(主要为午间光伏冗余电能)，售电收益 10908.00 元，电网交互净支出 41755.2 元；总售热量 116.19MW，售热收益为 26850.65 元。

3.5 优化与非优化系统的对比分析

为量化优化策略的有效性，设置“优化调度系统(含余热回收+多能互补)”与“常规调度系统(无余热回收+固定规则)”两个对比场景，保持初始参数(风光预测值、负荷曲线、价格机制)完全一致，确保对比结果的公平性与可靠性。

3.5.1 调度策略差异

优化调度系统：以成本最小化为目标，综合决策常规机组出力、购售电功率、储能充放电、余热回收量——如午间(12:00-14:00)光伏大发时，优先消纳光伏电能，多余 3MW 电能通过电网出售(受 5MW 售电上限限制)，余热回收系统满负荷运行；夜间(0:00-6:00)电价低谷时，加大电网购电(最大 8MW)与储能充电，为日间负荷高峰储备低价电能。

常规调度系统：采用固定规则调度——优先全额消纳风光电能，剩余负荷由常规机组(满发 5MW)与电网购电补充；储能按“夜间 22:00-次日 6:00 充电、日间 8:00-18:00 放电”固定时段运行，无余热回收利用，无法响应价格波动与负荷变化。

3.5.2 功率平衡特性对比

图 7(有无优化功率平衡图对比)直观呈现了两类系统的多能源协同运行差异。优化调度系统通过“风光互补-储能套利-余热回收”的多能耦合机制，实现了对负荷需求的精准跟踪：

夜间：(0:00-6:00)风电大发时段(最大出力 7.36 MW)，系统优先消纳风电，同时结合谷段电价(0.36 元/kWh)购入 8 MW 电能(占负荷占比约 50%)，并以 3 MW 功率为储能充电，避免风电弃风；

日间：(10:00-14:00)光伏高发时段(最大出力 14.4 MW)，光伏出力与负荷高峰(18.0 MW)高度匹配，多余 3MW 电能通过电网出售(受 5 MW 售电上限约束)，余热回收系统同步满负荷运行(1.5MW)，实现“电力-热力”协同收益；

负荷陡变时段(如 7:00 负荷从 9.3MW 升至 12.5 MW、13:00 从 18.0 MW 降至 17.0 MW)，常规机组通过爬坡约束(向上 3 MW/h、向下 4 MW/h)快速响应，储能同步放电补充缺口，确保功率平衡无波动。

反观常规调度系统，因缺乏余热回收与动态价格响应机制，存在显著运行短板：风光出力仅按“优先消纳”原则利用，多余电能无法通过售电或储能套利；负荷缺口完全依赖常规机组(满发 5MW)与电网购电(平/峰段高价购电占比超 60%)，导致功率曲线波动幅度达±2 MW，供电稳定性显著低于优化系统。

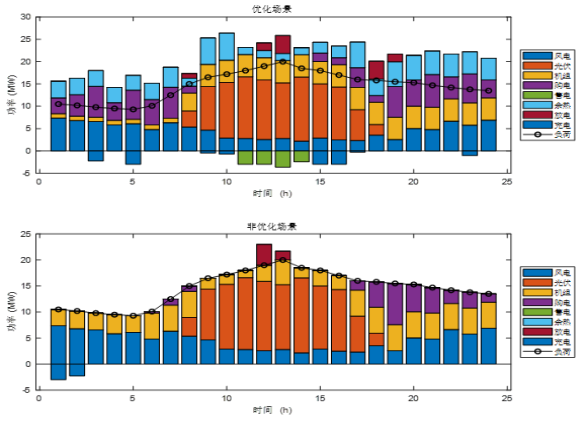


图 7 有无优化功率平衡图对比

Fig.7 Comparison of power balance diagrams with and without optimization

3.5.3 储能运行效率对比

图 8(有无优化的 SOC 状态对比)揭示了两类系统对储能资源的利用差异。优化调度系统基于“电价-负荷-风光”多维度协同，实现储能 SOC 的动态优化调控：

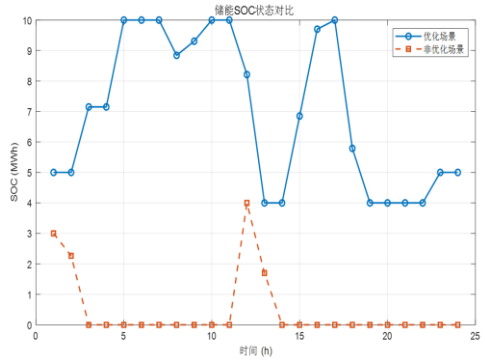


图 8　有无优化的 SOC 状态对比

Fig.8　Comparison of SOC status with and without optimization

常规调度系统因采用固定充放电规则，储能运行呈现“低效闲置”特征：仅在 22:00-次日 6:00 固定充电(2MW)，8:00-18:00 固定放电(1.5 MW)，未考虑电价与风光波动，导致 SOC 长期维持在 4-6MWh 区间，总充放电量 10.96 MWh，利用率不足优化系统的 42%，无法发挥储能的调峰与套利价值。

3.5.4 经济性效益对比

图 9(有无优化的总成本对比)量化了优化策略的经济性优势。优化调度系统通过“购售电套利-余热回收收益-储能成本节约”三重机制，实现总成本显著降低，优化系统全周期总成本 64955.20 元，较常规系统 81818.80 元降低 20.6%，单位负荷能耗成本从 4.5 元/kWh 降至 3.61 元/kWh。

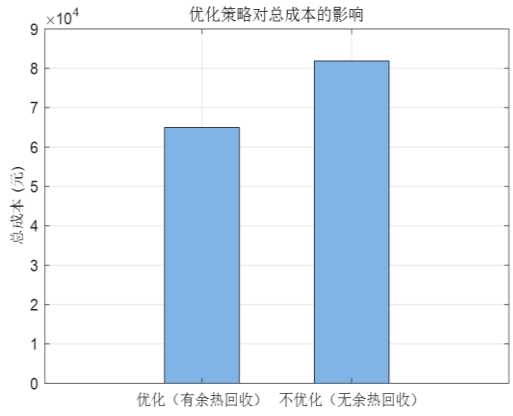


图 9　有无优化的总成本对比

Fig 9　Comparison of total costs with and without optimization

两类系统关键指标对比如表 4 所示，优化调度系统在购售电收益、储能利用率、余热回收效益等方面均展现显著优势，验证了本文所提“电 -热-冷”多能耦合优化框架的可行性与优越性。

表 3　有无优化的关键指标对比

Table 3　Comparison of Key Indicators with and Without Optimization

指标	优化调度系统	常规调度系统
总成本	64955.20 元	81818.80 元
总购电量	84.79MWh	34.50MWh
总售电量	12.12MWh	0.00MWh
储能总充放电量	26.35MWh	10.96MWh

4　结论

本文针对寒地算力中心高能耗、风光出力不稳定及余热资源未充分利用的问题，构建了整合风电、光伏、余热回收、储能及自然冷能利用的综合能源系统优化调度模型，以系统 24 小时总运行成本最小化为目标，纳入常规机组运行约束、功率平衡约束、储能充放电约束及余热回收系统约束，通过仿真分析与对比验证，得出以下核心结论：

1）寒地资源禀赋与多能互补协同优势显著，基于寒地“低温环境+丰富风光”的资源特性，设计的自然冷能利用系统可通过风机处理外界冷空气为机组降温，有效降低空调能耗；风电“夜高昼低”与光伏“昼高夜低”的出力特性形成时间互补，结合储能系统平抑波动后，可再生能源总消纳率可达 92%，较常规调度系统提升 17 个百分点，显著降低算力中心对传统化石能源的依赖，为寒地新能源消纳提供了可行路径。

2）余热回收—电热泵—储热罐耦合系统提升能源梯级利用率。构建的低温储热罐-电热泵-高温储热罐热回收体系，可有效回收算力中心 50℃冷却水废热，经电热泵提温至 70℃后满足区域供暖需求，高负荷时段余热回收最大功率达 1.5 MW，热损失控制 2%-3%以内。该系统不仅实现了“废热资源化”，还通过响应热网动态热价调节释热时序，进一步提升了系统经济性。

3）动态价格导向的优化调度策略降低运行成本效果突出。以电网峰-平-谷三段式电价为驱动，制定的“低谷购电储能、高峰售电释能”调度策

略，结合常规机组基荷供电与储能灵活充放电，与无余热回收的常规调度系统对比，优化系统总成本从 81818.80 元降至 64955.20 元，降幅达 20.6%，同时减少标煤消耗约 12 t，兼顾经济性与低碳性。

4）优化模型为寒地算力中心绿色转型提供理论与技术支撑。本文建立的综合能源系统优化模型，通过量化风光出力、余热回收与动态价格的耦合关系，明确了各能源单元的协同运行机制——常规机组承担基础负荷、储能平抑风光波动、余热回收补充供热，形成了“电-热-冷”多能耦合的优化框架。该模型不仅可保障寒地算力中心供电可靠性，还为同类高能耗用户的能源系统优化配置提供了可推广的理论方法与仿真工具，对推动“双碳”目标下寒地数字基础设施绿色转型具有重要实践意义。

未来研究可进一步引入极端天气下风光出力的概率模型，提升系统鲁棒性；同时探索多算力中心集群协同调度模式，以实现更加有效的能源调度策略与碳减排效益。

参考文献

[1] Zakarya M, Gillam L. Managing energy, performance and cost in large scale heterogeneous datacenters using migrations[J]. Future Generation Computer Systems, 2019, 93:529-547.

[2] 国家能源局．新型电力系统发展蓝皮书(征求意见稿)[R]．北京：国家能源局，2023．

[3] 国家能源局．关于报送“十四五”电力源网荷储一体化和多能互补工作方案的通知[R]．北京：国家能源局，2023．

[4] 范宏,陈舒阳,罗昊,等. 考虑冷热电多能互补和负载时空可调特性的数据中心优化运行策略 [J/OL]. 南方电网技术,1-10[2025-09-30].

[5] 刘树桦,王建学,李清涛,等. 多能互补复合电站的优化配置及其在系统电源规划中的应用 [J]. 电网技术, 2021, 45 (08):

[6] 郑芳芳,黄雨佳,王睿,等. 计及数据中心算力等效的电热综合能源系统调度策略 [J/OL]. 中国电机工程学报, 1-12[2025-09-30].

[7] 史昭娣,王伟胜,黄越辉,等. 多能互补发电系统储电和储热容量分层优化规划方法[J].电网技术,.2019.2502.

[8] 张修诚. 数据中心双源独立控制制冷及余热回收系统研究[D]. 山东建筑大学, 2024.

[9] 景淼,贾峻.数据中心水环热泵余热回收系统分析与应用[J].科学技术创新,2021,(30):169-171.

[10] Intel Corporation. Data center waste heat recovery using hybrid heat exchanger systems[R]. Santa Clara: Intel Labs, 2018.

112 基于可控避雷器的直流送端换流站暂态过电压抑制措施

张子瑶[1]，胡子严[1]，马志英[2]，张晓雨[1]，张宏亮[1]

（1．兰州理工大学、兰州、730050，2．国网乌鲁木齐米东区供电公司、乌鲁木齐、830000）

摘要：我国西北新能源基地直流送端换流站因直流闭锁、换相失败等引发暂态过电压加剧，威胁系统安全稳定。本文分析了两类故障导致暂态过电压的特性，随后在 PSCAD 中搭建特高压直流系统仿真模型，通过 “可控比”与 “过电压抑制率” 量化指标，系统分析了可控避雷器对直流闭锁（单极、双极）及换相失败故障的暂态过电压抑制效果，测试了 25%、30%、35%、40% 不同可控比的抑制表现。研究发现可控比越高，抑制效果越显著。考虑到过高的可控比会增加设备误动风险、提高造价，并且会加剧元件承压不均，结合特高压电阻片性能与保护裕度，最终综合确定可控避雷器可控比的最优取值为 35%。该取值兼顾了抑制效果与工程可行性，为解决直流送端换流站暂态过电压问题提供了技术支撑。

关键词：暂态过电压；PSCAD；可控避雷器；特高压直流

Transient overvoltage suppression measures for DC sending end converter stations

ZHANG Ziyao[1]，HU Ziyan[1]，MA Zhiying[2]，ZHANG Xiaoyu[1]，ZHANG Hongliang[1]

（1．Lanzhou University of Technology, Lanzhou, 730050，2．State Grid Midong District Urumqi Power Supply Company, Urumqi, 830000）

ABSTRACT: Transient overvoltage (TOV) in the DC sending-end converter stations of new energy bases in Northwest China has been aggravated due to faults such as DC block and commutation failure, posing a threat to the safe and stable operation of the power system. This paper first analyzes the characteristics of TOV caused by these two types of faults. Subsequently, an ultra-high voltage direct current (UHVDC) system simulation model is built in PSCAD. By using quantitative indicators of "controllable ratio" and "overvoltage suppression rate", the paper systematically analyzes the TOV suppression effect of controllable arresters on DC block (monopolar and bipolar) and commutation failure faults, and tests the suppression performance under different controllable ratios (25%, 30%, 35%, and 40%). The study shows that the higher the controllable ratio, the more significant the suppression effect. However, an excessively high controllable ratio will increase the risk of equipment maloperation, raise costs, and exacerbate the uneven pressure bearing of components. Combined with the performance of UHVDC resistor discs and protection margin, the optimal controllable ratio of the controllable arrester is comprehensively determined to be 35% in the end. This value balances the suppression effect and engineering feasibility, providing technical support for solving the TOV problem in DC sending-end converter stations.

Key Words: Transient overvoltage; PSCAD; Controllable surge arrester; Regulator; UHV DC

1 引言

随着“双碳”目标推进，我国加快风电、光伏等新能源建设，2023 年全国风电光伏装机超 10 亿千瓦[1]。因能源与负荷中心逆向分布，风光火打捆特高压直流外送成首选[2]。但换相失败或直流闭锁故障时，换流站盈余无功倒送致暂态过电压，可能引发新能源脱网甚至系统崩溃[3]

因此，深入探究暂态过电压根本原因并制定合理控制方案限制其大小，对确保电暂态过电压很重要，并需提出相应抑制措施。Yin C、Li F 提出暂态过电压风险量化方法，实现暂态过电压峰值解析表达，为抑制奠定基础[4]。屠竞哲等提出风火出力协同优化的暂态过电压抑制方法，可实现交直流混联系统功角稳定[5]。贾俊川等提出减小风电机组低压穿越期间所需最小无功电流来抑制暂态过电压。虽增设设备及改造现有风机可抑制暂态过电压、降低新能源机组脱网风险，但造价昂贵、经济性差[6]。

在可控避雷器技术研究与应用层面，相关成果已形成从拓扑设计、核心器件到控制验证的完整链条：范海兵等对比了电力电子式特高压交流可控避雷器的高压端集成、低压端外置等四种拓扑结构，综合均压、检修、占地等因素优选低压端外置方案[7]；谢鸟龙等设计的可控避雷器晶闸管开关，凭借电压过零触发、无触点、寿命长的特性，可精准控制投切以降低冲击电流[8]；针对直流场景特殊性，王俊等将直流可控避雷器的晶闸管控制单元（TCU）划分为五大功能模块，解决了直流工况下的驱动控制难题[9]，刘磊等则提出串联晶闸管阀组方案，提升直流混合可控开关响应速度，有效抑制模块化多电平换流器（MMC）过电压[10]；张向龙等通过 PSCAD 仿真与动模试验，验证了可控避雷器基本控制策略的有效性，确保其保护水平与系统适配[11]。

在参数优化与工程应用层面，学界已转向实际系统适配：郭贤珊等建立特高压 GIS 电站仿真模型，分析参数对过电压抑制的影响，明确不同线路长度

参数配置原则[12]；马志英针对西北直流工程，验证可控避雷器在多故障场景下的抑制效果优于传统策略[13]；颜守宁提出雷暴区杆塔优先安装方案[14]；乔光尧优化交流特高压避雷器电位分布[15]；王超解决直流避雷器间隙导通时序难题[16]。

本文提出可控避雷器设计方案，重点研究了可控比参数对抑制效果的影响，通过 PSCAD 仿真测试了 25%、30%、35%、40%等不同可控比的表现，发现可控比越高抑制效果越显著，但过高会增加设备误动风险、提高造价并加剧元件承压不均；结合特高压电阻片性能与保护裕度，最终确定最优可控比为 35%，通过仿真验证该方案可有效抑制暂态过电压及直流闭锁、换相失败故障。

2 常规直流送端交流暂态过电压分析

2.1 直流闭锁产生暂态过电压

直流闭锁即为保护装置关断换流阀并切断直流电流和功率以应对直流故障。闭锁后整流站从交流系统消耗的无功由式可知。

$$Q_{dr}=P_d\frac{(\pi/180)\times\mu-\sin\mu\times\cos(2\alpha+\mu)}{\sin\mu\times\cos(2\alpha+\mu)} \quad (1)$$

$$P_d=U_{dr}+I_d \quad (2)$$

式中：P_d为换流器直流传输有功功率值；μ为换相角；α为触发角；U_{dr}为整流侧的直流电压；I_d为直流电流。

可以看出Q_{dr}与P_d和α都有关。直流闭锁时α迅速增大，P_d快速减小，由式可知Q_{dr}随之减小。由于无功补偿装置即交流滤波器和电容器组延时 200ms 动作，大量无功涌入交流系统，造成无功盈余导致换流母线出现暂态过电压。

2.2 换相失败产生暂态过电压

不加新能源机组时，逆变侧换流器交流母线在仿真运行到 6s 时发生三相短路故障，持续 0.2s，故障阶段大致分 3 个阶段如下：

(1)直流电流升高阶段

逆变侧三相接地会引发逆变器换相失败，此时逆变器上下桥臂阀同时导通，等效于阀直流侧短路、交流侧开路，直流电流I_d升高。换流阀导通后熄弧角瞬时减至 0，换相失败预测功能（CFPRED）环节响应增加熄弧角，提升换相裕度，防止连续换相失败[50]。同时，扰动发生瞬间受端交流电压U_{bi}快速跌落，受端直流电压U_{di}随之下降。

$$U_{bi}=1.35U_{di}\cos\beta+(3/\pi)X_{c2}I_d \quad (3)$$

$$Q_{dr}=U_{dx}I_d\sqrt{1-(\cos\varphi_1)^2} \quad (4)$$

式中：β为超前触发角；X_{c2}为逆变站换相电抗；φ_1为送端功率因数角。

由于I_d已到达较高水平，而送端直流电压还未受到故障影响，由式，整流站消耗的无功Q_{dr}增加。系统稳态时主要由交流滤波器组与并联电容器组提供整流站所需的无功，而此时这两类设备因速动性不足，无法瞬时动作提供足够无功。因此送端交流系统要向整流站供给无功，导致送端换流母线电压U_{br}下降，暂态低电压出现，如图 1 所示。因此由式，送端直U_{dr}流电压随之下降。

$$U_{dr}=135U_{br}\cos\alpha-(3/\pi)X_{C1}I_d \quad (5)$$

(2)直流电流降低阶段

为抑制第一阶段I_d的升高，整流侧定电流控制环节（CCA）启动来增大送端触发角α，α大致由稳态时的 17 度作用移相到近 123 度以降低I_d。

另外，因第一阶段直流电压值跌落与I_d升高，低压限流环节（VDCOL）响应减小I_d指令值。I_d指令值减小增大 CCA 环节故障时输入量，引发电流过度超调，降低后还会过小。此过程控制环节有时延，触发角α上升时I_d仍持续升高，动作时延结束时I_d达峰值，随后降低，故障进入直流电流降低阶段。I_d减小后，U_{dr}整流器无功需求Q_{dr}大幅减少，安全控制装置因延时反应有限，送端固定无功补偿装置不能及时退出，仍发出大量无功，导致送端换流站无功过剩，大量无功倒送涌入交流系统，造成送端换流母线暂态过电压。

(3)直流恢复阶段

电压、电流等指标渐恢复稳定运行水平，整流站无功需求上涨，与交流系统达新平衡，暂态电压恢复到故障前稳态值。所以，换相失败导致的暂态过电压现象有“先降低后升高”典型特征。

3 基于可控避雷器交流滤过器过电压抑制

3.1 可控避雷器的结构和工作原理

可控避雷器主电路由可调控避雷器组件、固定避雷器部件和电力电子开关 K 组成，如图 1 所示

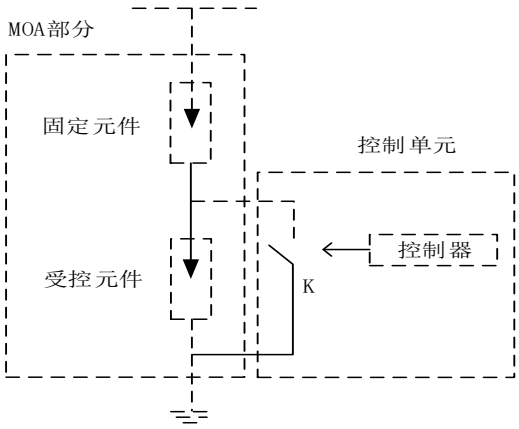


图 1 可控避雷器原理示意图

可控避雷器伏安特性曲线图 2 为曲线 2（曲线 1 代表常规避雷器）。实际运行中，可控避雷器能承受工频、操作、雷电入侵波三类过电压，其伏安特性在三种电压应力下分别对应图 2 区域 A、B、C。

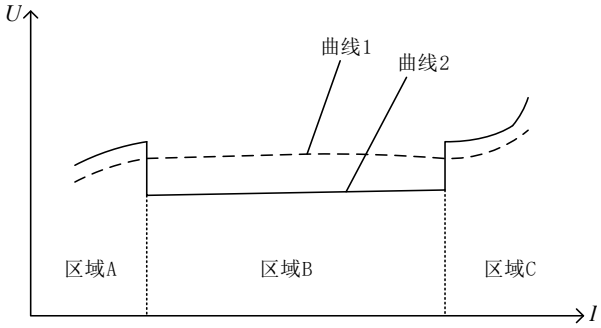


图 2 可控避雷器的伏安特性

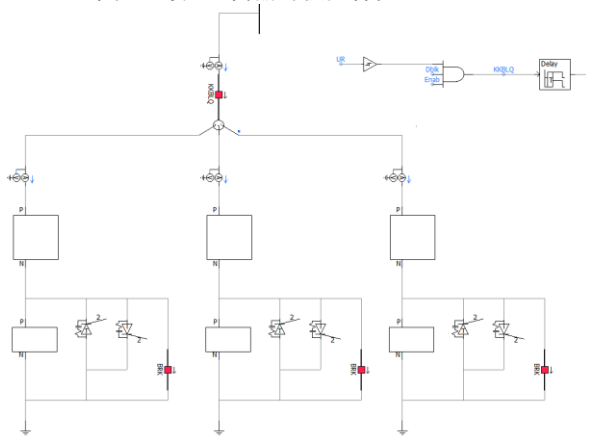


图 3 可控避雷器的模型

基于可控避雷器结构和工作原理，本文选用PSCAD的金属氧化物避雷器模型，该模型如图3所示。本文设计了图 4 可控避雷器控制策略。

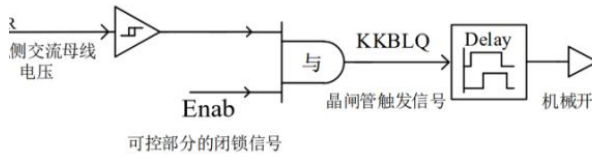


图 4 可控避雷器的控制策略

3.2 基于可控避雷器电压抑制

可控避雷器受控部分的额定电压与整体额定电压之比称为可控比α，其直接影响过电压抑制效果，是可控避雷器的关键参数，其定义如式(6)所示：

$$\alpha=\frac{U_{MOA1}}{U_R} \tag{6}$$

式中：U_{MOA1}为避雷器受控部分额定电压；U_R为避雷器整体额定电压。在搭建可控避雷器的电磁暂态仿真模型时，选择避雷器整体额定电压为600kV，分别设置避雷器未投入、25%、30%、35%和40%的可控比研究避雷器过电压抑制效果。

为精确比较可控避雷器启用前后各母线电压改善效果的程度，本研究引入了过电压抑制率（OSR）如式(7)。

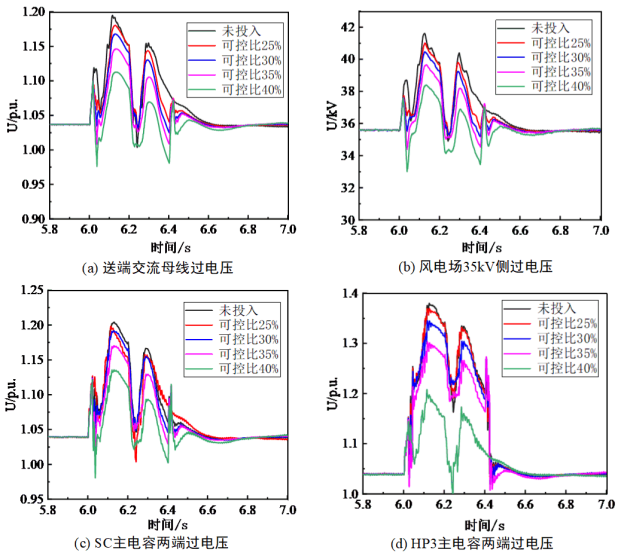
$$OSR=\frac{U_1-U_2}{U_1-U_s} \tag{7}$$

式中：U_1和U_2分别为故障发生后未投入与投入时母线电压的第一次峰值；为系统正常运行时母线电压。

仿真在系统稳定运行至 6s 时，分别设置直流单极闭锁故障、双极闭锁故障和换相失败故障，故障持续时间为 0.2s，

(1) 直流单极闭锁

换流母线及交流滤波器主电容电压变化的仿真对比结果如图 5。不同可控比抑制效果如表 1 所示。



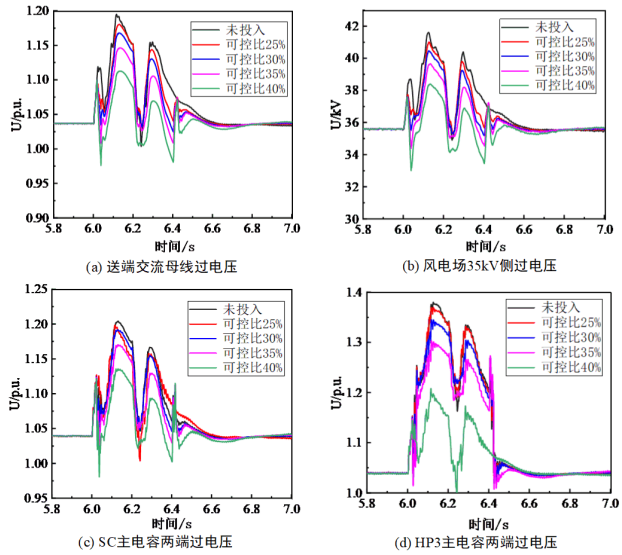


图 5 直流单极闭锁策略的抑制效果

表 1 单极闭锁下不同可控比电压抑制率

可控比	换流母线电压	风电场 35kV 侧电压	SC 主电容电压	HP3 主电容电压
25%	9.43%	9.91%	-3.75%	9.45%
30%	16.98%	18.67%	3.75%	13.7%
35%	30.81%	31.84%	16.87%	31.2%

40 %	51.57 %	52.48 %	38.75 %	62.34 %

由表 1 可知，可控比越高，换流母线、风电场 35kV 侧、SC 及 HP3 交流滤波器主电容电压抑制效果越明显。可控比为 40%时，上述电压抑制率分别达 52.48%、51.57%、38.75%、62.34%。这验证了采用可控避雷器手段抑制直流单极闭锁故障期间送端母线及交流滤波器主电容暂态过电压问题的可行性与有效性。

(2) 直流双极闭锁

换流母线及交流滤波器主电容电压变化的仿真对比结果如图 6 所示。

由表 2 可知，可控比越高，换流母线、风电场 35kV 侧、SC 及 HP3 交流滤波器主电容电压抑制效果越明显，最低为可控比为 25%时，在直流双极闭锁故障情境下，通过可控避雷器对换流母线、风电场 35kV 侧、SC 及 HP3 型交流滤波器主电容的电压抑制率分别达到了 10.98%、6.33%、1.11%、8.29%；最高为可控比为 40%时，通过可控避雷器对换流母线、风电场 35kV 侧、SC 及 HP3 型交流滤波器主电容的电压抑制率分别达到了 54.91%、47.59%、44.69%、65.5%。

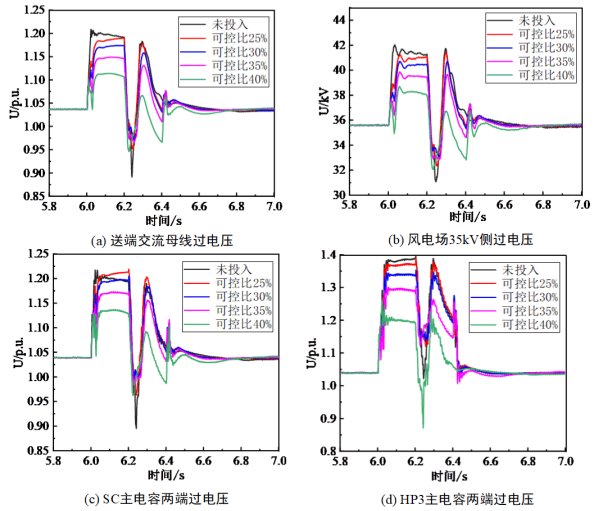


图 6 直流双极闭锁策略的抑制效果

表 2 双极闭锁下不同可控比电压抑制率

可控比	换流母线电压	风电场 35kV 侧电压	SC 主电容电压	HP3 主电容电压
25 %	10.98 %	6.33%	1.11%	8.29%
30 %	20.23 %	14.76 %	10.61 %	24.6%
35 %	34.68 %	28.36 %	24.58 %	30.58 %
40 %	54.91 %	47.59 %	44.69 %	65.5%

(3) 直流换相失败

换流母线及交流滤波器主电容电压变化的仿真对比结果如图 7 所示。

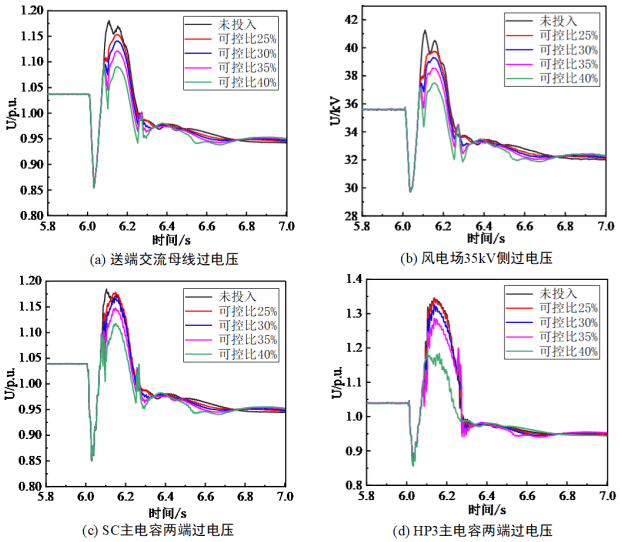


图 7 直流换相失败策略的抑制效果

由表 3 可知，可控比越高，换流母线、风电场 35kV 侧、SC 及 HP3 交流滤波器主电容电压抑制效果越明显，最高为可控比为 40%时，换流母线、风电场 35kV 侧、SC 及 HP3 交流滤波器主电容电压抑制率分别为 55.86%、65.45%、45.57%、41.98%。

表 3 换相失败下不同可控比电压抑制率

可控比	换流母线电压	风电场 35kV 侧电压	SC 主电容电压	HP3 主电容电压
25 %	19.31 %	26.09 %	4.08%	5.36%
30 %	27.58 %	33.83 %	12.24 %	11.25 %
35 %	40.68 %	46.68 %	25.17 %	18.36 %
40 %	55.86 %	65.45 %	45.57 %	41.98 %

4 可控避雷器设计研究

上节的仿真结果表明，可控比越高，换流母线、风电场 35kV 侧、SC 及 HP3 交流滤波器主电容电压的抑制效果越显著。然而，若可控比过高，一方面可能会增加可控避雷器的误动作风险，另一方面单个避雷器电阻片无法承受过高的电压。

表 4 避雷器的重要技术性能指标

项目名称	Y20W-600/1380GW
系统标称电压(有效值)/kV	750
系统最高运行电压(有效值)/kV	800
避雷器额定电压(有效值)/kV	600
持续运行电压(有效值)/kV	462

标称放电电流/kA	20
直流 1mA 下参考电压/kV	≥810
阻性 3mA 下的工频参考电压(峰值$\sqrt{2}$)/kV	≥600
陡波冲击电流 20kA 下的残压(峰值)/kV	≤1518
雷电冲击电流 20kA 下的残压(峰值)/kV	≤1380
操作冲击电流 20kA 下的残压(峰值)/kV	≤1142
0.75U_{1mA}下泄漏电流/μA	≤50
4/10 大电流冲击耐受电流(2 次)/kA	100
2ms 方波耐受电流(18 次)/A	2500
线路放电等级	5

目前，特高压用电阻片的压敏电压梯度达到400V/mm，单位体积能量密度可达 300J/cm³ 。在750kV 电力系统中至少需要 3800mm 电阻片才能达到防护需求。而可控避雷器针对暂态过电压问题在1.2p.u.电压下工作，其固定部分需至少 2250mm 电阻片。 则以残压要求考虑，其可控比最大为 40%，考虑到保护裕度，可控比选取 35%较为合适。同时,可控比增大会导致控制单元中晶闸管及其它电力电子元器件数量成比例增加,会提高设备造价,同时影响各层晶闸管间导通分散性及承压不均匀性,使得元件损坏率提升、控制单元开通准确性难以保证,同时非控单元能量负荷更大,损坏风险增加,因此基于实现最优保护特性的角度,特高压避雷器可控比取值通常不应超过 35%。

参考文献

[1] 尹纯亚，李凤婷，王丹东，等. 风电高渗透率交直流外送系统直流闭锁稳控方案研究[J].电力系统保护与控制，2019，47(03)：95-102.

[2] 卢孟林. 新能源富集地区电源远距离外送优化[D].华中科技大学，2019.

[3] 杜承洋. 风光火打捆直流外送系统暂态过电压及抑制措施研究[D].西安理工大学，2023.

[4] Yin C,Li F. Analytical expression on transient overvoltage peak value of converter bus caused by DC faults[J].IEEE Transactions on Power Systems,2021,36(3):2741-2744.

[5] 屠竞哲,潘艳,訾鹏,等. 功角失稳与暂态过电压并存型锡盟交直流弱送端系统特性分析[J].电网技术, 2021,45(4):1496-1506.

[6] 贾俊川,金一丁,赵兵,等. 风机低电压穿越控制对系统暂态过电压的影响及优化[J]. 电网技术,2021,45(2):526-533.

[7] 范海兵,周阳洋,谢东辉,等.电力电子式特高压交流可控避雷器电气拓扑结构设计分析[J].中国设备工程,2024,(21):120-123.

[8] 谢鸟龙,宋戈,丁峰峰,等.一种可控避雷器的晶闸管开关介绍与应用[J].电工技术,2022,(07):127-129+132.DOI:10.19768/j.cnki.dgjs.2022.07.038.

[9] 王俊,汪涛,骆仁松,等.用于直流可控避雷器的晶闸管控制单元设计[J].高压电器,2024,60(06):121-128.DOI:10.13296/j.1001-1609.hva.2024.06.016.

[10] 刘磊,张翔,王德昌,等.基于晶闸管的直流可控避雷器关键技术[J].电力自动化设备,2022,42(09):183-188.DOI:10.16081/j.epae.202205009.

[11] 张向龙,闫鑫,户永杰,等.可控避雷器基本控制策略的仿真研究及动模验证[J].黑龙江电力,2021,43(03):251-256.DOI:10.13625/j.cnki.hljep.2021.03.014.

[12] 郭贤珊,徐华,关镭镭,等.交流特高压电子式可控避雷器操作过电压抑制效果研究[J/OL].电瓷避雷器,1-9[2025-09-28].

[13] 马志英.西北某直流外送系统送端换流站暂态过电压及抑制措施研究[D].兰州理工大学,2024.DOI:10.27206/d.cnki.ggsgu.2024.001570.

[14] 颜守宁.线路避雷器在输电线路防雷中的应用[J].科学技术创新,2024,(07):39-42.DOI:CNKI:SUN:HLKX.0.2024-07-010.

[15] 乔光尧,李芳义,陈喆,等.交流特高压电力电子式可控避雷器电位分布特性及优化研究[J].电瓷避雷器,2022,(06):70-76.DOI:10.16188/j.isa.1003-8337.2022.06.010.

[16] 王超,杨兰均,张宏涛,等.直流可控避雷器用并联可控间隙电弧的维持规律[J].高电压技术,2023,49(04):1675-1684.DOI:10.13336/j.1003-6520.hve.20220494

113 An Optimization Method for Energy-Intensive Industrial Loads Participating in Demand Response Considering Energy-Material Flow Coupling

Haoze Wu[1], Hao Wu[2], Rufeng Zhang[1], Haihang Sun[1], Houhe Chen[1], Xinyu Wu[1]

[1] Northeast Electric Power University, Jilin 132011, China
[2] Tianjin University, Tianjin 300072, China
wuhaoze11@aliyun.com

Abstract. Driven by dual-carbon targets, Energy-intensive industrial loads offer significant potential for enhancing power system flexibility via demand response (DR). However, complex production processes and strict material constraints often limit user participation. This paper proposes an optimization method for DR strategy design that accounts for the coupling between energy and material flows across multiple production stages. A unified modeling framework is developed based on discrete and continuous process characteristics to capture load adjustment boundaries under energy–material flow constraints. A price-based incentive strategy is then formulated, and a bilevel Stackelberg game model is established to characterize the interaction between distribution network operators and industrial customers. The model is solved using an iterative algorithm based on the golden section method. Case studies involving steel manufacturing demonstrate that the proposed method effectively motivates industrial customers to participate in DR, reduces system regulation costs, and improves both the availability and economic efficiency of industrial flexible loads.

Keywords: Demand response, Energy-intensive industrial loads, Energy flow, Material flow, Master-slave game.

1 Introduction

In the context of the “carbon peak and carbon neutrality” strategy, the power system is undergoing a profound transformation characterized by a high penetration of renewable energy [1]. Guiding load-side resources to participate in system supply-demand interactions through DR mechanisms and driving the transition of dispatch models toward “source-load interaction” has become an indispensable path for building a modernized new power system and achieving the dual carbon goals [2].

DR is a key method for unlocking the potential of the load side, with regulation targets encompassing residential [3], commercial [4], and industrial loads [5]. Industrial loads alone account for 54% of total societal electricity consumption [6], making them the largest power-consuming sector. While existing research has demonstrated the

effectiveness of industrial loads in DR [7], traditional modeling methods, which quantify power as adjustable intervals, often frequently fall short in capturing their response potential. Consequently, some studies have proposed modeling industrial loads using aggregate models [8]. However, the production processes of energy-intensive industrial loads are highly complex, involving deep coupling across multiple stages and interactions over various time scales. Relying solely on an aggregate model makes it difficult to accurately characterize the regulation capabilities of different equipment within these multiple processes. For instance, in [9], a temperature-power coupling model for electrolytic aluminum loads was established to optimize a compensation pricing mechanism, facilitating their participation in DR and ancillary services. In [10], a detailed model of an electric arc furnace process was developed, considering the interests of both the grid dispatcher and the plant. The authors of [11] analyzed the feasibility of power regulation in electrolytic copper production, established a control model, and proposed a DR-oriented control strategy for energy-intensive industrial loads. Similarly, [12] analyzed a typical cement production process, identified its adjustable potential, and developed an economic dispatch model for DR.

Existing research primarily focuses on power regulation of equipment within individual processes, while neglecting the dynamic coupling effects of material consumption and transfer across multiple production stages during industrial users' participation in long-term DR. This limitation hinders accurate characterization of how inter-process material flow constraints affect DR potential. To address this deficiency, this paper proposes an incentive-based DR clearing model that incorporates the process characteristics of energy-intensive industrial loads. By establishing a unified model that couples material and energy flows across production processes, this approach effectively captures the material consumption and transfer relationships among various production stages during extended DR events. The proposed methodology significantly enhances the participation willingness of energy-intensive industrial loads in DR programs.

2 Unified Modeling of Energy-Intensive Industrial Loads Considering Energy and Material Flows

The production processes of energy-intensive industrial loads exhibit complex interdependencies. Based on energy consumption and production continuity, internal processes are categorized into two main types: discrete processes and continuous processes.

2.1 Discrete Processes

Discrete processes typically operate in discrete batches, with a fixed power requirement for each batch. The equipment operates in one of two states: on or off, precluding continuous variation in power consumption. The power consumption of a

discrete process k within an energy-intensive industrial load during time period t can be expressed as:

$$L_{k,t}^{dis} = v_{k,t}^{dis} PD_{k,t}^{dis}, \forall k \in K^{dis}, t \tag{1}$$

where K^{dis} denotes the set of discrete processes, $L_{k,t}^{dis}$ is the power consumption of discrete process k in time period t, $PD_{k,t}^{dis}$ is the rated power of discrete process k, and $v_{k,t}^{dis}$ is a binary variable indicating the on/off status of discrete process k. A binary $y_{k,t}^{dis}$ variable can be used to represent the output status of discrete process k:

$$z_{k,t}^{dis} = \frac{\sum_{\tau=t-RT+1}^{t} v_{k,t}^{dis}}{RT_k} - \sum_{\tau=t-RT+1}^{t-1} y_{k,t}^{dis}, \forall k \in K^{dis}, t \tag{2}$$

$$\mathrm{y}_{k,t}^{dis} = \begin{cases} 1, z_{k,t}^{dis} \geq 1 \\ 0, z_{k,t}^{dis} < 1 \end{cases} \tag{3}$$

where $z_{k,t}^{dis}$ is a core intermediate variable that characterizes the output behavior of discrete processes, quantifying whether the conditions for generating output are met in the current time periods. RT_k represents the production time of discrete process k. When RT_k=2， $v_{k,t}^{dis}$= [0, 1, 1, 0, 1, 1], then $z_{k,t}^{dis}$= [0, 0, 1, 0, 0, 1], $y_{k,t}^{dis}$= [0, 0, 1, 0, 0, 1].

In the production of energy-intensive industrial loads, material generation and consumption are integral to all processes. The material quantity of discrete process k in time period t can be expressed as:

$$B_{k,t} = B_{k,t-1} + k_k^P \mathrm{y}_{k,t}^{dis} - k_{k+1}^P PD_{k+1,t}, \forall k \in K^{dis}, t \tag{4}$$

where $B_{k,t}$ and $B_{k,t\text{-}1}$ denote the material inventory at discrete process k during time periods t and t-1, respectively. The parameters k_k^p and k_{k+1}^p denote the material throughput rate for discrete processes k and k-1, respectively.

2.2 Continuous Processes

Unlike discrete processes, continuous processes operate uninterrupted. During operation, they can adjust their power consumption flexibly and in real-time based on actual production requirements. The power consumption of a continuous process k in an energy-intensive industrial load during time period t can be expressed as:

$$L_{k,t}^{con} = v_{k,t}^{con} PD_{k,t}^{con}, \forall k \in K^{con}, t \tag{5}$$

where K^{con} denotes the set of continuous processes. $L_{k,t}^{con}$ represents the power consumption of continuous process k during time period t, $PD_{k,t}^{con}$ represents the

adjusted power of continuous process k in time period t, $v_{k,t}^{con}$ is a binary variable representing the start and stop state of continuous process k. The material of continuous process k in time period t can be expressed as:

$$B_{k,t} = B_{k,t-1} + k_k^P L_{k,t}^{con} - k_{k+1}^P PD_{k+1,t}, \forall k \in K^{con}, t \tag{6}$$

In continuous production scenarios of energy-intensive industrial loads, power regulation for continuous processes is subject to strict operational constraints:

$$v_{k,t} PD_k^{\min} \le PD_{k,t}^{con} \le v_{k,t} PD_k^{\max}, \forall k \in K^{con}, t \tag{7}$$

where PD_k^{min} and PD_k^{max} respectively represent the upper and lower limits of power regulation for continuous processes.

Equations (1), (3), and (5) contain nonlinear terms resulting from products of variables, which preclude their direct solution with conventional linear programming solvers and require linearization. The linearized form of Equation (3) is given by Equation (8), while Equations (1) and (5) are collectively reformulated as Equation (9). k denotes the set of all processes within the energy-intensive industrial load, encompassing both discrete and continuous processes.

$$\begin{cases} z_{k,t}^{dis} \le 1 - E + M y_{k,t}^{dis} \\ z_{k,t}^{dis} \ge 1 - M(1 - y_{k,t}^{dis}) \end{cases} \forall k \in K^{dis}, t \tag{8}$$

$$\begin{cases} L_{k,t} \le M \cdot v_{k,t} \\ L_{k,t} \le PD_{k,t} \\ L_{k,t} \ge PD_{k,t} - M \cdot \left(1 - v_{k,t}\right) \\ L_{k,t} \ge 0 \end{cases} \forall k \in K, t \tag{9}$$

2.3 Production Profitability Model for High-Energy-Intensive Industrial Loads Considering Energy and Material Flows

Considering only the discrete and continuous processes, the total power consumption PD_t of an energy-intensive industrial load is defined as the sum of the power consumed by its discrete and continuous processes.

$$PD_t = L_{k,t}^{dis} + L_{k,t}^{con}, \forall k, t \tag{10}$$

Energy-intensive industrial loads must also satisfy production targets over the entire scheduling horizon while maintaining a non-negative material inventory for each process k at every time step.

$$PR_{k,t} \ge 0, \forall k, t \tag{11}$$

$$PR_{k_{lost},T} \geq PR_{\min} \tag{12}$$

where PR denotes the production output, k_{lost} designates the final process in the energy-intensive industrial load, F_k is the revenue coefficient corresponding to PR_{finlly}, and PR_{min} specifies the minimum production requirement.

The revenue for an energy-intensive industrial load in period t primarily comprises production revenue and incentive payments, with shutdown costs being the major expense. The profit function for an energy-intensive industrial load participating in DR is formulated as follows:

$$\begin{aligned} F_I &= B_P + \sum_{\mathrm{t}} \left(B_{DR} - C_{CON} \right) \\ &= F_{\mathrm{k}} \cdot PR_{k_{lost},T} + \sum_{\mathrm{t}} \left(\lambda_t \cdot R_{i,t} - C_{\mathrm{con}} \cdot (1 - \nu_{k,t}^{con}) \right) \end{aligned} \tag{13}$$

where B_P denotes the production revenue, B_{DR} represents the incentive revenue, C_{CON} indicates the shutdown cost, λ_t represents the subsidy-based incentive provided by the DSO, $R_{i,t}$ is the response amount provided by the energy-intensive industrial load, and C_{con} designates the start-up/shutdown cost coefficient for continuous processes.

3 Stackelberg Game Optimization Model with Load-Side Regulation Capabilities

3.1 Stackelberg Game Optimization Model with Load-Side Flexibility

DSO and the energy-intensive industrial loads act as independent decision-makers with conflicting objectives, collectively forming a Stackelberg game. In this framework, the DSO acts as the leader, while each energy-intensive industrial load is a follower. Both parties dynamically adjust their strategies through multiple iterations until the game converges to an equilibrium.

To ensure fairness in the DR market, the incentives provided by the DSO must be maintained within a reasonable and bounded range:

$$\lambda_{\min} \leq \lambda_t \leq \lambda_{\max} \tag{14}$$

where λ_{min} and λ_{max} represent the lower and upper bounds of the incentive, respectively. The load shortfall is compensated by a combination of additional energy purchases, demand response, and load curtailment, as shown below:

$$\Delta P_t = \Delta P_{B,t} + \sum_i R_{i,t} + \Delta P_{R,t} \tag{15}$$

$$P_{B,t} = \Delta P_{B,t} + P_{B,N} \tag{16}$$

$$P_{B,N} = PD_N + PR_N \tag{17}$$

$$\begin{cases} P_{B,t} \geq 0 \\ \Delta P_{R,t} \geq 0 \end{cases} \tag{18}$$

where $\Delta P_{B,t}$ represents the additional purchased energy, $P_{B,N}$, PD_N and PR_N denote the power procured by the distribution network under normal conditions, the power consumption of energy-intensive industrial loads, and the power demand of other loads, respectively. Equation (15) states that the load shortfall is compensated through demand response, additional power purchases, and load curtailment. Equation (16) specifies that the total power procurement during DR events equals the sum of baseline and additional purchases. Equation (17) defines the baseline procurement as comprising the baseline consumption of energy-intensive industrial loads and the demand from other loads. Equation (18) constrains both the procured power and curtailed load to be non-negative.

The costs incurred by the DSO for DR participation consist of three components: incentive payment costs, electricity procurement costs from the grid, and load curtailment costs, as formulated in Equation (19).

$$\begin{aligned} F_G &= \sum_t \left(C_{DR} + C_B + C_R \right) \\ &= \sum_t \left(\lambda_t \cdot R_{i,t} + S_t \cdot P_{B,t} + C_r \cdot \Delta P_{R,t} \right) \end{aligned} \tag{19}$$

where C_{DR} denotes the incentive payment cost, C_B represents the electricity procurement cost, and C_R indicates the load curtailment cost. $P_{B,t}$ represents the power procured by the distribution network, S_t represents the electricity price at which the DSO purchases electricity, C_r represents the load curtailment cost coefficient, and $\Delta P_{R,t}$ specifies the amount of curtailed load.

3.2 Model Solution

The energy optimization model for energy-intensive industrial loads in the lower tier incorporates numerous binary decision variables, which precludes the application of the Karush-Kuhn-Tucker conditions. In comparison to traditional heuristic methods, the golden section method demonstrates not only superior convergence but also a faster convergence rate. The complete procedure is detailed in Algorithm 1.

Algorithm 1: Golden Section Method

Input: Number of iterations N; Convergence tolerance ε; Golden section coefficient r; Incentive interval $[\lambda_{\min}, \lambda_{\max}]$; DSO's operational cost function F_G; Energy-intensive industrial load's revenue function F_I

Output: Optimal incentive λ

1 Compute the partition points λ_{change_1}、λ_{change_2}

$\lambda_{change_1} \leftarrow \lambda_{max} - r(\lambda_{max} - \lambda_{min})$, $\lambda_{change_2} \leftarrow \lambda_{min} + r(\lambda_{max} - \lambda_{min})$

Calculate the DSO's operational costs $F_{G,change_1}$、$F_{G,change_2}$ using Eq. (13) and Eq. (19)
for i=1 to N do
  if $|\lambda_{max}-\lambda_{min}|\le\varepsilon$ do
  break
  if $F_{G,change_2}\ge F_{G,change_1}$ do
    Update the incentive interval and operational costs
    $\lambda_{max}\leftarrow\lambda_{change_2},\lambda_{change_2}\leftarrow\lambda_{change_1}$,
    $F_{G,change_2}\leftarrow F_{G,change_1},\lambda_{change_1}\leftarrow\lambda_{max}-r(\lambda_{max}-\lambda_{min})$
    Update $F_{G,change_1}$ using Eq. (13) and Eq. (19)
  else
    Update the incentive interval and operational costs
    $\lambda_{min}\leftarrow\lambda_{change_1},\lambda_{change_1}\leftarrow\lambda_{change_2}$,
    $F_{G,change_1}\leftarrow F_{G,change_2},\lambda_{change_2}\leftarrow\lambda_{min}+r(\lambda_{max}-\lambda_{min})$
    Update $F_{G,change_2}$ using Eq. (13) and Eq. (19)
  end if
end for
return $\lambda\leftarrow(\lambda_{change_1}+\lambda_{change_2})/2$

4 Experiments and Analysis of Results

4.1 Case Selection

A steel plant is selected as a representative case of an energy-intensive industrial load. Its production process comprises the following key stages: sintering, ironmaking, steelmaking, and rolling, which are categorized as discrete, continuous, continuous, and discrete processes, respectively.

4.2 Analysis of Market Clearing Incentives

The market clearing outcome is shown in Figure 1. During power system operation, a tight coupling exists between the load shortfall and three key factors: additional energy procurement, market incentives, and demand response. When the load shortfall is relatively low, the DSO provides only limited market incentives based on cost-benefit considerations. Under these conditions, energy-intensive industrial loads maintain a high level of production and offer only limited DR to protect their operational revenue. To maintain supply-demand balance, the DSO typically covers the shortfall through additional energy purchases. As the load shortfall grows, the distribution network experiences increasing supply pressure. Additional energy purchases alone become insufficient to close the gap, exposing the DSO to rising procurement and load curtailment costs. In response, the DSO raises incentive levels to encourage greater response from energy-intensive industrial loads. However, due to

their own profitability and response cost constraints, these loads have a limited response capacity. At this stage, the remaining load shortfall is compensated through a combination of DR and additional energy procurement.

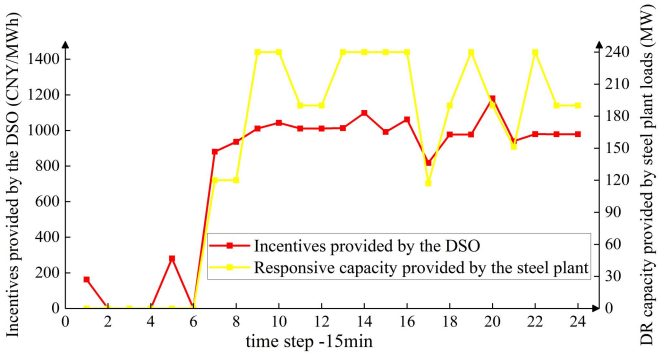


Figure 1. Market Clearing Incentives in Each Response Period

4.3 Analysis of energy consumption behavior of high-energy-consuming industrial loads considering material flow - energy flow

The power consumption and material inventory for each process in the steel plant are shown in Figures 2 and 3. During the first six time steps, the limited load shortfall led to less incentives from the DSO, and consequently, the steel plant did not participate in DR, with all processes maintaining baseline operation. Beginning at the seventh time step, the DSO increased incentive levels, prompting the plant's participation in DR. Owing to adequate material reserves, the sintering process was shut down. As a continuous process, ironmaking would incur substantial shutdown costs; it was therefore maintained at minimum power to preserve basic production. To ensure uninterrupted material supply to the rolling process, steelmaking operated at elevated power during time steps 7, 8, 17, and 21, while continuing at minimum power during all other periods. Since the rolling process directly determines product revenue, the plant balanced this revenue against DSO incentives, scheduling rolling production specifically during time steps 7-8, 11-12, 17-18, and 20-24.

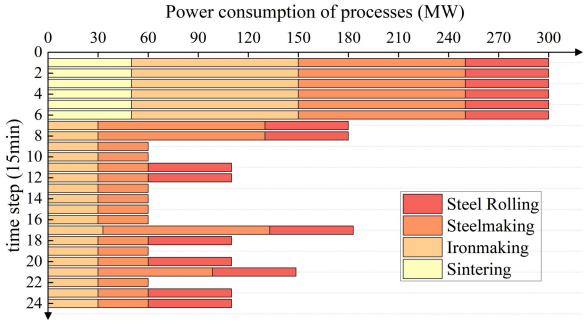


Figure 2. Working Status of Each Process in Steel Plant at Each Time Step

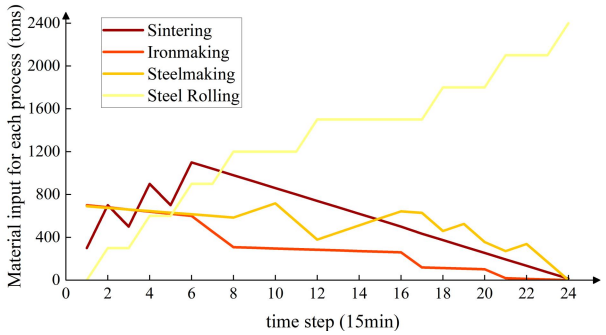


Figure 3. Material Amount of Each Process in Steel Plant at Each Time Step

4.4 Analysis of the Effectiveness of DR Strategy

This section evaluates the effectiveness of the proposed incentive-based DR mechanism that accounts for energy and material flow coupling in energy-intensive industrial loads, by comparing it with a scenario disregarding these constraints. The two scenarios are defined as follows:

Scenario 1: The DR period spans from 9:00 to 15:00, considering only power constraints. The adjustable capacity of energy-intensive industrial loads is modeled as a power interval, with response costs represented by a quadratic function.

Scenario 2: Using the same response period as Scenario 1, this scenario implements the proposed energy and material flow-coupled DR trading mechanism for energy-intensive industrial loads.

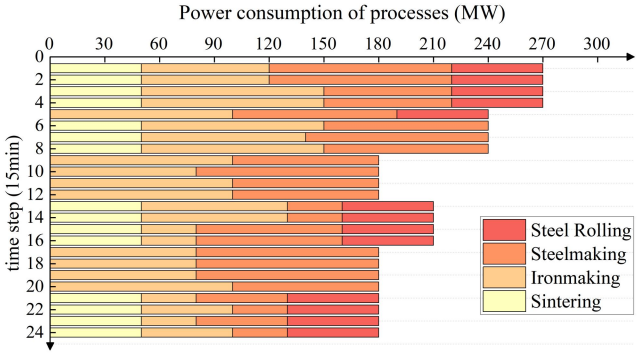


Figure 4. Working Status of Each Process in Steel Plant at Each Time Step under Scenario 1

Scenario 1 simplifies industrial users' adjustable capacity into power intervals and represents response costs through a quadratic function, thereby ignoring energy and material flow coupling. Figure 4 shows the power consumption of specific processes in the steel plant under Scenario 1. Comparison of the operational states across time

steps between Figures 2 and 4 reveals that Scenario 1 fails to capture the discrete nature of certain processes. Specifically, the sintering process operates during three consecutive time steps 6-8, contradicting the requirement that discrete processes can only yield output after their RT. The steel plant achieves production revenues of ¥3.6 million and ¥4.8 million under Scenarios 1 and 2, respectively. Although total energy consumption is higher in Scenario 1, the inadequate consideration of material flow and energy allocation reduces energy input to the rolling process, resulting in lower production output and accumulation of intermediate products.

5 Conclusion

To address the limitations of existing research, such as oversimplifying the quantification of adjustable power from a purely electrical perspective and failing to develop incentive mechanisms that account for internal process characteristics, this paper proposes a unified modeling approach for multiple processes in energy-intensive industrial loads. This method accurately characterizes the load regulation capabilities of different process types. Additionally, we develop an incentive-based market clearing model that incorporates flexibility on the load side to effectively encourage energy-intensive industrial loads to participate in DR. Using a steel plant as a case study, our simulation results show that when energy and material flow coupling constraints are considered, the plant's DR behavior dynamically aligns with both load shortfalls and incentive signals. This approach achieves dual optimization of distribution network operational costs and industrial user production revenue.

Future research will focus on addressing multiple uncertainties in DR participation by energy-intensive industrial loads to further unlock the adjustable potential on the load side.

Acknowledgement： This work is supported by Project funded by the National Key R&D Program (2023YFB2407300)

References

1. Shu YB, et al.: Study on Key Factors and Solution of Renewable Energy Accommodation[J]. Proceedings of the CSEE 37(01), 1-9 (2017)
2. Dong Y, et al.: Challenges, Response and Prospects for Power Balance in New Power Systems[J]. Proceedings of the CSEE 45(06), 2039-2057 (2024)
3. Sridhar A, et al.: Residential consumer enrollment in demand response: An agent based approach[J]. Applied Energy 374, 123988 (2024).
4. Parvizi S, et al.: Contract-Based Demand Response Mechanism for Commercial and Industrial Customers[J]. IEEE Transactions on Automation Science and Engineering, 22, 3135-3146 (2025)
5. Zhao W, et al.: A multi-time scale demand response scheme based on noncooperative game for economic operation of industrial park[J]. Energy, 302, 131875 (2024)

6. EIA. Industrial Sector Energy Consumption-Energy Information Administration https://www.eia.gov/outlooks/ieo/pdf/industrial.pdf/; last accessed 2025/09/30.
7. Hussain M, et al.: A review of demand response in an efficient smart grid environment[J]. The Electricity Journal 31(5), 55-63 (2018)
8. Khorasany M, et al.: Market framework for local energy trading: a review of potential designs and market clearing approaches[J]. IET Generation, Transmission & Distribution 12(22), 5899-5908 (2018)
9. Yue X, et al.: Collaborative optimization of renewable energy power systems integrating electrolytic aluminum load regulation and thermal power deep peak shaving[J]. Applied Energy 373, 123869 (2024)
10. Jiang TY, et al.: Non-cooperative Game Based Strategy for Energy-Intensive Industrial Load Participating in Peak-regulation Demand[J]. Automation of Electric Power Systems 49(03), 13-21 (2025)
11. Liao SY, et al.: Demand Response Control Strategy for High-energy-consuming Loads Aligned with Demand-side Market Response Transaction Rules[J]. Proceedings of the CSEE 45(05), 1645-1658 (2025)
12. Liao SY, et al.: Economic Dispatch Model Considering Production Process of Energy-Intensive Industrial Load Under Demand Response[J]. Automation of Electric Power Systems 49(03), 22-30 (2025)

114 Optimization of Isolation Measures for Single-phase Faults in the Collection Systems of New Energy Stations

Yinyin Li, Hengchu Shi, Wenbo Shi, Xiaofan Chen, Hao You, Zicheng Wang

Yunnan Electric Power Dispatching and Control Center ,Kunming, China
1548794094@qq.com

Abstract. Driven by the goal of carbon neutrality, new energy stations are being integrated into the power grid on a large scale. Due to the short commissioning cycle, the time for design, construction, and grid connection has been significantly compressed. Coupled with the fact that the existing relevant standards and specifications are not yet perfect and cannot fully cover various situations, many problems have arisen during the operation of new energy. This article combines a busbar tripping event in a new energy station, analyzes the development process of the event in detail, and delves into the underlying deep-seated reasons. At the same time, targeted improvement measures are proposed from aspects such as the selection of grounding resistance, settings, and primary wiring. These measures have important practical significance for achieving effective isolation of single-phase faults in new energy stations and improving power supply reliability.

Keywords: New Energy Station, Collection System, Single-phase Fault, Low Resistance, Zero Sequence Protection

1 Introduction

1.1 A Subsection Sample

In the new energy station, the grounding mode of the collection bus plays a vital role in the safe and stable operation of the system. The current standard has made clear provisions on the grounding mode of the collection bus in the new energy station. The configuration of the zero sequence current protection under various grounding modes is given in detail in references 1 and 2. The regulations specify the relevant logic of the protection action of the grounding transformer and the action requirements of the circuit breaker in different fault scenarios. The purpose is to ensure that the system can quickly, accurately and selectively remove the fault in the event of a grounding fault.

However, in the actual operation process, the current situation of the setting and setting of the grounding resistance of the collection bus in the new energy station still faces many challenges. Due to the lack of in-depth analysis of the system characteristics of some stations, the selection of grounding resistance is unreasonable and cannot effectively cooperate with relay protection. In terms of setting, due to the

great difference between the primary equipment wiring mode of new energy stations and traditional stations, the traditional setting method is difficult to apply, and it is prone to protection maloperation or misoperation. The safety and dependability of the new energy station itself will be negatively impacted by these issues as well,and they might also have a negative effect on the grid's dependable power supply.
In view of this, it is of great practical significance to further study the optimization of the grounding resistance and setting of the bus bar in new energy stations. This paper will start with an event of expanding the tripping range of new energy collection bus, and discuss the related issues in detail.

2 Introduction To Grounding Mode of New Energy Station

2.1 Selection of Grounding Mode for Collection System

Based on applicable regulations,the primary grounding methods for new energy consist of neutral grounding using an arc suppression coil and neutral grounding with low resistance.Through the arc suppression coil,the neutral point is formed,and the inductance current produced by the arc suppression coil compensates for the grounding capacitance current,which in turn lowers the residual current at the fault point and may be used as an arcre ignition,all of which aid in guaranteeing the system's power supply continuity.The neutral point is connected to ground via a low resistance,which helps to boost the grounding fault current and enables the quick and precise identification of the fault line.There are many things to think about when choosing the grounding mode because it is arbitrary and requires a lot of consideration.The main concern of the system is the capacitive current.In the case where the capacitance current is low,the arc suppression coil may be more suitable for grounding;if the capacitive current is high,grounding via a low resistance can be used to remove the fault more effectively.Furthermore,the dependability of the electricity supply is highly dependent on this one.It is important to carefully consider the effects of various grounding modes on the timeliness of fault handling and theextent of power failure in order to create new energy stations that need high power supply reliability.At the same time,the insulation level of electrical equipment is also closely related to the grounding mode.Under different grounding modes,the overvoltage level of the system is different,which puts different equipment insulation requirements into practice.
In the case of single-phase grounding fault,the capacitive current to the ground increases significantly with the help of wind farm and large number of cable lines.It is inevitable that the arc produced by the grounding current will be extinguished automatically when the capacitive current reaches a particular value(usually greater than 30A). Moreover, due to intermittent arc grounding, arc overvoltage is caused, which will affect the whole collection line system, and there is a large risk of power related public safety. Therefore, low resistance grounding is mainly selected. Fig.Three typical low resistance grounding linkages are shown in the schematic diagram 1.

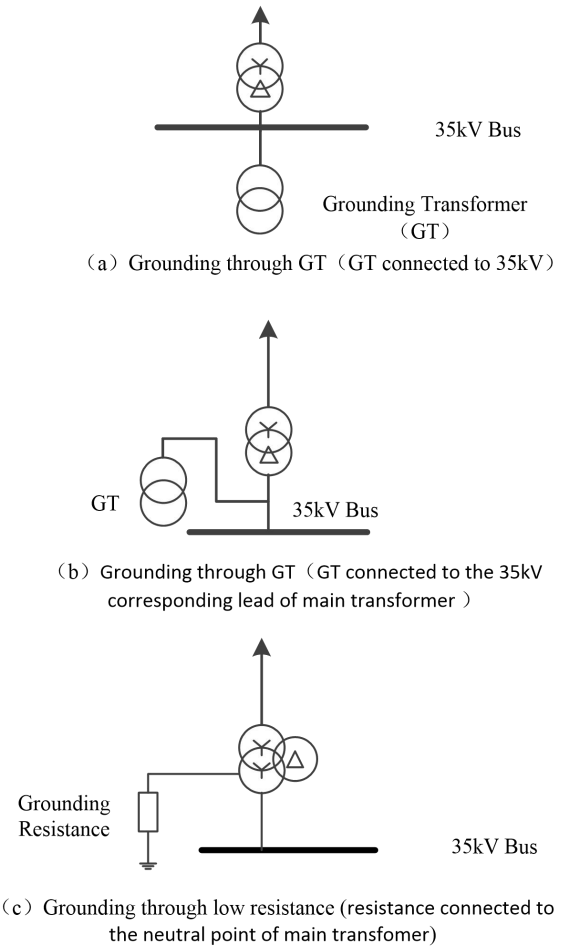


Fig. 1. The schematic diagram of three common low resistance grounding connections

2.2 Single Phase Fault Isolation of Collection System

In order to collect the system of new energy station single-phase grounding fault,it should be removed in a short time.Grounding protection acting on tripping shall be configured for stations with neutral grounded by low resistance;Small current grounding fault line selection device shall be set up to realize tripping for stations grounded through arc suppression coil.

When low resistance grounding is achieved using a grounding transformer connected to the bus,the grounding transformer protection serves asthe primary backup protection for the grounding faults of each component in the low-voltage side system.When the grounding transformer is linked to the appropriate bus of the substation(Fig.1(a)The zero sequence protection terminal of the grounding

transformer causes the circuit breaker on its side,as well as that of the power supply transformer,to trip,resulting in all circuit breakers connected to the busbar being simultaneously disconnected.When the grounding transformer is linked to the appropriate terminal of the substation(Fig.1(b)),the zero sequence protection terminal of the grounding transformer trips the circuit breakers on each side of the power supply transformer and cuts off all the circuit breakersofthe connected busbar.If the zero sequence overcurrent protection action at the end of the grounding transformer protection only trips the power supply transformer,it does not trip the grounding transformer and the shunt tripping collector line.When the zero sequence overcurrent protection of the grounding transformer trips the switch at the low-voltage side of the main transformer,the collector line and the low resistance still constitute a low resistance grounding system.Currently,the grounding fault point continues to carry a substantial zero sequence current,which poses a risk of burning at the neutral point due to prolonged exposure to this current,thereby presenting a significant public safety hazard related to power.If only the grounding transformer and the power supply transformer are tripped,andthe collector line is not tripped,whenthe zero sequence overcurrent protectionofthe grounding transformer tripsthe switches atthe low-voltage sideofthegrounding transformerandthemaintransformer,the collector line formsaneutralungroundedsystem.Currently,the grounding fault point cannot be isolated,allowing a significant zero-sequence current to continue flowing,which poses a risk to public safety related to electricity.

When the small resistance grounding is realized through the main step-up transformer with balance winding connected to the collection bus (Fig. 1 (c)), the low-voltage side of the main step-up transformer must include two-stage zero-sequence current protection,which is non-directional,in addition to the required overcurrent protection.This setup serves as the primary defense against single-phase grounding faults of the transformer and provides general backup protection for grounding faults across various system components.At each side of the transformer,the circuit breakers will be stopped by the above-and zero-sequence current protection at the low-voltage side,and all of the circuit breakers of the connected busbar will be cut off at the same time.

3 Overview and Analysis of a Bus Trip Event

3.1 Event Overview

The schematic diagram of a 220kV photovoltaic power station is shown in Fig. 2. The main transformer of the station is connected in ynyn0+d11, which is a two winding transformer with balance winding. The neutral point of the main transformer at 35 kV is grounded via a 50.5 Ω resistor. The 35kV main transformer is equipped with two-stage zero sequence current protection, without direction, as the main protection for single-phase grounding fault at the side of the transformer collection system and the general backup protection for the grounding fault of each component of the system.

On March 1st, 2024, the bushing of 35kV II bus in the station broke down, and the 35kV section II bus had a B-phase grounding fault, resulting in the action of 35kV

side zero current section I 1 time limit protection at the 35kV side of 220kV #1 main transformer protection device to trip 35kV 301 and 302 circuit breakers of the main transformer. At the same time, the joint tripping signal was sent to the 35kV section I and II bus protection. Once the main transformer protection was received by the 35kV bus protection,all of the circuit breakers were tripped by the bus of 35 and II,and the entire circuit was tripped by all of them.Table 1 displays the action sequence for the relevant protection related to this fault. The set values of 35kV section II bus protection and two-stage zero sequence current protection at 35kV side of main transformer are shown in Table 2 and table 3.

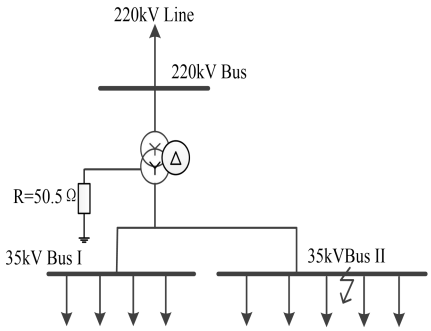


Fig. 2. The schematic diagram of a 220kV photovoltaic power station

Table 1. Protection Action Sequences

Absolute time	Relative time	Protection action behavior
23：33：00：920	0ms	Main transformer protection startuped.
23：33：00：627	707ms	The first time limit action of the zero sequence overcurrent protection section I at the 35kV side of the main transformer protection tripped the 35kV 301 and 302 circuit breakers of the main transformer at the outlet, and sent out the joint tripping bus signal at the same time.
23：33：00：659	739ms	Bus protection of 35kV Bus Ⅰ action tripped all circuit breakers on the bus.
23：33：00：660	740ms	Bus protection of 35kV Bus Ⅱ action tripped all circuit breakers on the bus.

Table 2. Bus Protection Setting Value of 35kV Bus Ⅱ

Serial number	Setting value item name	Setting value (primary value)
1	Starting current setting of differential protection	2400A

6

Table 3. Setting Value of Two-stage Zero Sequence Current Protection at 35kV Side of Main Transformer

Serial number	Setting value item name	Setting value (primary value)
1	Setting value of zero sequence overcurrent Section Ⅰ	266A
2	1st time limit of zero sequence overcurrent Section Ⅰ	0.7s
3	2nd time limit of zero sequence overcurrent Section Ⅰ	0.9s
4	3rd time limit of zero sequence overcurrent Section Ⅰ	10s
5	Setting value of zero sequence overcurrent Section II	160A
6	1st time limit of zero sequence overcurrent Section II	1.2s
7	2nd time limit of zero sequence overcurrent Section II	1.5s
8	3rd time limit of zero sequence overcurrent Section II	10s

3.2 Analysis of the Causes Behind the Expansion of Tripping Scope

The fault point is located in the 35kV section II bus, which is within the range of 35kV section II bus differential protection. After the event, it was found that 35kV section II bus protection only had the main transformer protection action tripping signal, and the bus differential protection did not act, which eventually led to the removal of both 35kV sections of bus, and the external power transmission of the whole station was stopped. If the fault occurred at noon, it would have a serious impact. Then,an analysis was done of why the 35kV section II bus difference protection was used.

The grounding resistance of the 35kV system of the power station is 50.5 Ω. When the single phase is grounded, the theoretical value of the zero sequence current of the 35kV system of the main transformer is

$$37000/1.732/50.5=423A \quad (1)$$

The zero sequence current at the 35kV side of the main transformer can be read from the fault oscillograph of the main transformer as 411A (Fig. 3), which is consistent with the theoretical value.

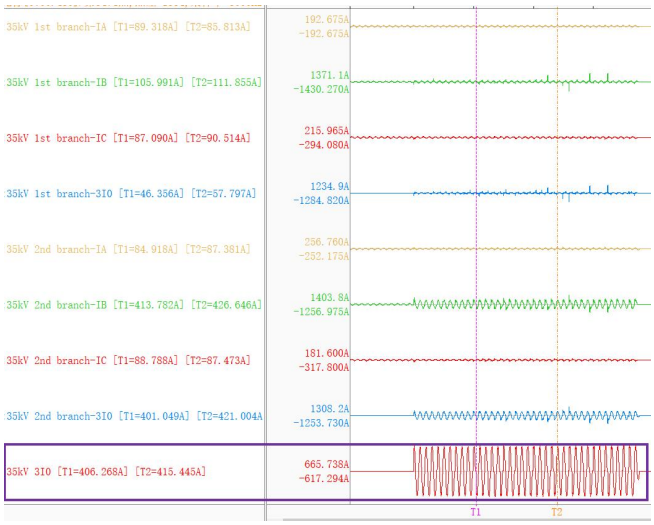


Fig. 3. The zero sequence current at the 35kV side of the main transformer

It can be concluded that the differential current of 35kV section II bus is about 410A, which is far less than the fixed value of 2400A. .When calculating the fixed value of bus differential protection,according to References 3,the power station only ensures sufficient sensitivity in case of phase to phase short-circuit fault,and avoids the maximum differential current caused by load current when the secondary circuit of any element is disconnected.By calculating the 35kV bus phase to the phase fault at the lowest short circuit current under small operation mode,the rated current of each branch at the 35kV side of the main transformer is 2000A,and the setting is 1.2*2000 = 2400A.Only when it meets the sensitivity of the phase to the fault is the power station,which is regarded as a standard ungrounded system;it does not verify the sensitivity of a single-phase grounding fault;this does not comply with the rules(the main protection for collecting bus phase to phasefault,and the main protection for gathering bus grounding faults in low resistance grounding systems). Its differential current element should ensure that the bus fault has sufficient sensitivity under the minimum mode, and the sensitivity coefficient is not less than 听 two.Consequently,the differential current was significantly lower than the differential setting value,causing the bus differential protection to refrain from operating,while the zero sequence overcurrent protection on the 35kV side of the main transformer tripped two sections of the bus.

4 Improvement Measures

4.1 Optimization of Grounding Resistance

The 35kV grounding resistance of the new energy station where the fault occurred this time is 50.5 Ω, and the single-phase grounding fault current is only 400A. To meet the sensitivity requirements, the bus differential setting value should be less than or equal to 200A (the CT transformation ratio is 2500/1, and the secondary value is only 0.08A). If the collection line passes through the transient resistance fault, the sensitivity of the zero sequence protection will also be insufficient.

At present, the regulations related to new energy have not stipulated the value of grounding resistance.The resistance values used in practical engineering range from some ohms to hundreds of ohms.When there is zero sequence protection and bus differential protection,the value of grounding resistance will have a great deal of impact on the sensitivity.

In order to ensure that the fault can be effectively removed when the single-phase grounding occurs, and the fault current should not be too large, causing great losses to the cable and other collection system equipment, it is recommended that the zero sequence current (3I0) of the single-phase grounding fault is about 1000A, thus, we can calculated the 35kV grounding resistance as follows.

$$37000/1.732/1000=21.36\Omega \quad (2)$$

4.2 Setting optimization

The 35kV side of the station where the fault occurred is an expanded branch connection. The 35kV side is fitted with a dual-stage zero sequence overcurrent protection system. Each section has three time limits. Only two time limits are used for setting, and the third time limit is standby. When the first time limit is reached, the protection action trips two 35kV circuit breakers of the main transformer and two sections of bus in parallel. When the second time limit is reached, the protection action trips each side of the main transformer and trips two sections of bus in parallel.

To avoid both sections of the bus being disconnected simultaneously,the zero-sequence overcurrent protection for each section can be configured with three time limits.When the first time limit is reached,one branch of the 35kV system can trip the corresponding parallel bus.Upon reaching the second time limit,the protection mechanism will trip two 35kV circuit breakers of the main transformer,disconnecting both sections of the bus in parallel.Finally,when the third time limit is reached,the protection system will trip each side of the main transformer,again disconnecting both sections of the bus in parallel.

If the above similar faults occur again, the probability of simultaneous removal of two bus sections can be reduced.

4.3 Wiring Form Optimization

The 35kV side of the station where this event occurred is an expanded branch connection, and the 35kV side of the main transformer is a star connection through small resistance. A typical backup protection system for a single-phase fault of the

collection system is the 35 kV zero sequence overcurrent protection of the main transformer. Therefore, any fault on the two sections of the collection bus may cause the two sections of bus to trip at the same time.In the event that the primary transformer is made to be a split transformer(Fig.4)During the planning phase,both 35kV branches are configured in an angular connection.In the event of a single-phase grounding fault,the two bus sections will become fully decoupled,allowing them to operate independently without impacting each other,thereby enhancing the power supply reliability of the photovoltaic power station. However, this method is only applicable to power stations in the design or scientific research stage. For stations that have been put into operation, the investment cost will be greatly increased.

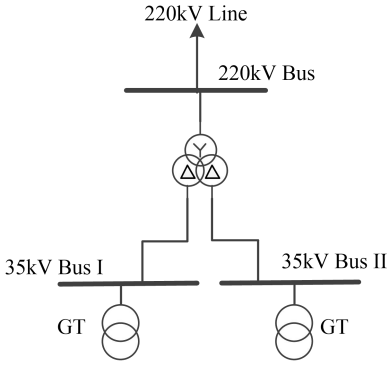


Fig. 4. The schematic diagram of optimized wiring mode

5 Conclusion

The large-scale and short-term integration of new energy into the grid has planted many hidden dangers during the operation phase. This article introduces the grounding method and single-phase fault isolation method of the collection system in new energy stations. It deeply analyzes an event of expanding the tripping range of a new energy station collection busbar fault that occurred during actual operation, and proposes optimization suggestions from three aspects: grounding resistance selection, setting value, and wiring form. It has guiding significance for the selection and setting value of new energy station equipment in the future.

References

1. GB/T 32900-2016, Technical specification for relaying protection of photovoltaic power station.
2. DL/T 1631-2016, Technical specification for protection configuration and setting of grid-connected wind power plant.
3. DL/T 584-2017, Setting guide ffr 3kV~110kV power system protection equipment.

10

4. Q. Wenhao, Q. Haiting, Setting of grounding transformer protection in wind farm with resistance grounding system Electrotechnics (2), 158-161,2023.
5. X. Lijiao, S. Jiancheng, F. Huiling, Existing problems and Countermeasures of zero sequence current protection setting in low resistance grounding system Inner Mongolia electric power technology, 039(003), 95-97,100,2021.

115 Impact of Voltage Measurement Errors on Voltage Control Performance of VSCs During Low-Voltage Ride-Through

Junjie Chen[2], Yunhao Hu[1], Shuqing Zhou[1], Ningting Chen[1], Pingliang Zeng[2*]

[1] Rui'an Power Supply Co, Zhijiang Electric Power Ltd, Rui'an, Zhejiang, China
[2] HangZhou Dianzi University, HangZhou, Zhejiang, China
plz@hdu.edu.cn

Abstract. With the integration of large-scale distributed energy resources, the low voltage ride through (LVRT) capability of voltage source converters (VSC) has become critical to ensuring stable grid operation. This paper proposes a novel method to analyse the impact of voltage measurement errors on the LVRT performance of voltage source converters. Firstly, voltage measurement error models were constructed considering scaling errors, DC offsets, and dynamic response characteristics, etc. Secondly, the mechanisms by which static and dynamic errors affect the reactive current control of VSC, including phase-locked loop phase detection and voltage support capability under LVRT are analyzed. Finally, simulation results indicate that static measurement errors cause grid voltage imbalance and DC voltage errors in the phase-locked loop. Dynamic errors lead to reactive current command lag, thereby impacting the VSC's voltage support capability. Furthermore, it is shown that when measurement errors exceed 4% and response time exceeds 20 ms, the VSC fails to meet the requirements for grid voltage unbalance and voltage support under LVRT. Study results provide theoretical and technical support for setting parameter requirements of IEC TS 62786-42 Standard with findings being incorporated into this standard.

Keywords: Voltage Source Converter (VSC), Low Voltage Ride Through, Voltage measurement error.

1 Introduction

Distributed energy resources (DER) such as photovoltaic and wind power have developed rapidly and become important forms of renewable energy. However, their output is unstable and support capability is weak, resulting in increasing difficulties in voltage control and power supply quality in distribution networks.

Due to the significant differences in the DER types and interconnection conditions, as well as the diversity of voltage measurement devices, the impact of measurement errors on control accuracy has become increasingly severe. Particularly during Low Voltage Ride Through (LVRT) processes triggered by load fluctuations or faults, the

reactive voltage support capability of VSCs is highly dependent on the accuracy of voltage measurements.

Voltage control methods of VSCs rely on real-time voltage measurements. However, voltage sensors inevitably exhibit measurement errors [1]–[3]. DC offsets and scaling errors cause voltage signals to deviate from their true values, resulting in inaccurate control system outputs, voltage fluctuations, and potential damage to sensitive equipment [4]. References [5]–[7] indicate that voltage measurement errors interfere with the calculation of reference values in the voltage inner loop of three-phase inverters, reducing control accuracy. In severe cases, they may lead to misjudgment of grid conditions by the controller, causing failure in islanding detection [8].

Moreover, with the increasing penetration of inverter-based resources, maintaining voltage stability under transient grid disturbances has become a critical requirement. Precise voltage sensing is not only fundamental to inverter control performance, but also vital to compliance with emerging grid codes. In this context, defining the allowable range of voltage measurement error and response time is essential for both control algorithm design and equipment testing.

To address the impact of voltage measurement errors on the VSC low voltage ride through control performance, this paper investigates wind power systems to analyze the interference mechanism of measurement errors on their voltage support capability. This work is carried out to support the development of the international standard "IEC TS 62786-42: Distributed energy resources connection with the grid, Part 42: Voltage measurement used to control DERs and loads". The standard which was approved by the IEC in August 2025 for publication.

2 VSC Voltage Measurement Error Impact Model

The schematic diagram of the voltage measurement error influence on the VSC converter station is shown in Fig. 1(a):

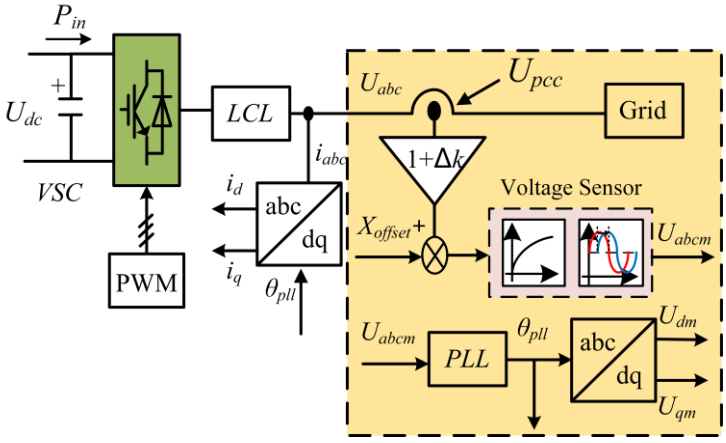


Fig. 1(a). Schematic diagram of the impact of voltage measurement errors on the VSC.

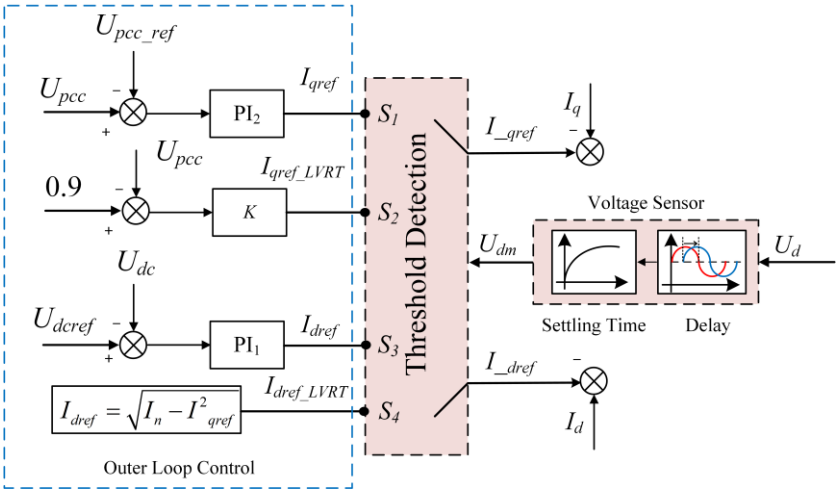


Fig. 1(b). Reactive power outer-loop control structure of the VSC.

Fig. 1. Model and control block diagram of the VSC.

where the wind turbine side output is the VSC DC side power P_{in}; connected to the grid through an LCL filter; i_{abc} is the three-phase grid current; U_{abc} is the three-phase voltage; U_{abcm} is the three-phase voltage measurement value after scaling errors (1+Δk), DC offsets X_{offset}, and time delay τ_0.

The primary voltage control loop of the VSC consists of reactive power outer-loop control. The overall control structure is illustrated in Fig. 1(b), where:

- U_{pcc} is the point of common coupling (PCC) voltage;
- U_{pcc_ref} is the PCC voltage reference;
- I_d and I_q are the d-axis and q-axis current components of the line current.
- U_{dcfef} and U_{dc} represent the DC-side voltage reference and the actual DC-side voltage, respectively;
- U_{dm} is obtained via a voltage sensor from the d-axis voltage U_d detected by the Phase-Locked Loop PLL.

When the voltage sensor detects that the PCC voltage is within the normal range (0.9 p.u. $\leq U_{pcc} \leq$ 1.1 p.u.), the d-axis and q-axis current references (I_{dref} and I_{qref}) are given by:

$$\begin{cases} I_{dref} = k_{p1}(U_{dcref} - U_{dc}) + k_{i1}\int (U_{dcref} - U_{dc}) \\ I_{qref} = k_{p2}(U_{pccref} - U_{pcc}) + k_{i2}\int (U_{pccref} - U_{pcc}) \end{cases} \tag{1}$$

Where, k_{p1}, k_{p2}, k_{i1} and k_{i2} are the coefficients of the PI controller. When the voltage sensor detects a voltage dip (LVRT condition, 0.2 p.u. ≤U_{pcc}≤0.9 p.u.), the d-axis and q-axis current references ($I_{d_LVRT}^{ref}$ and $I_{q_LVRT}^{ref}$) are adjusted as follows:

$$\begin{cases} I_{d_LVRT}^{ref} = \sqrt{I_n^2 - (I_{q_LVRT}^{ref})^2} \\ I_{q_LVRT}^{ref} = K(0.9 - U_{pcc}) \end{cases} \tag{2}$$

From equation (2), it can be observed that the lower the PCC voltage U_{pcc} detected by the voltage sensor, the greater the required Reactive Current Command value for VSC, not exceeding the converter capacity, and the current of the converter cannot exceed the rated current or the maximum constraint current I_n. If voltage measurement errors occur, the controller's dynamic perception of grid voltage will be impaired, thereby reducing its reactive voltage support capability.

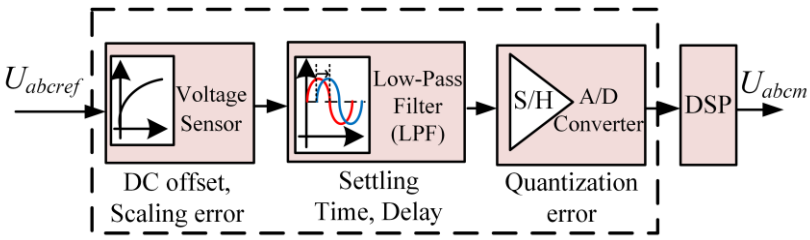


Fig. 2. Path diagram of grid voltage measurement errors.

Fig. 2 illustrates the main sources of error in grid voltage measurement: the nonlinear characteristics of voltage sensors can cause low-frequency DC offsets, resulting from temperature drift, zero-point offset, and remanence of the magnetic core; although low-pass filters can suppress high-frequency noise, they may introduce scaling errors in the fundamental amplitude; in addition, quantization errors and nonlinear distortion during the A/D conversion process further reduce measurement accuracy and reliability.

These error factors significantly affect the accuracy and reliability of voltage measurement, thereby adversely impacting the system control performance [9].

2.1 Static Voltage Measurement Error Model

Assuming the grid's three-phase voltage is initially well balanced, the reference values for voltage measurement can be expressed as:

$$\begin{aligned} U_{aref}(t) &= U_f \cos(\omega_s t + \varphi_0) \\ U_{bref}(t) &= U_f \cos(\omega_s t + \varphi_0 - 2\pi/3) \\ U_{cref}(t) &= U_f \cos(\omega_s t + \varphi_0 + 2\pi/3) \end{aligned} \tag{3}$$

where φ_0 is the initial phase of the grid, U_f is the amplitude of the grid voltage, and ω_s is the angular frequency of the grid.

Assuming that the actual voltage measurement containing error terms is expressed as:

$$\begin{aligned} U_{am}(t) &= (1+\Delta k_a)U_a(t) + x_a \\ U_{bm}(t) &= (1+\Delta k_b)U_b(t) + x_b \\ U_{cm}(t) &= (1+\Delta k_c)U_c(t) + x_c \end{aligned} \tag{4}$$

where Δk_a, Δk_b, and Δk_c are scaling errors; x_a, x_b, and x_c are DC offsets; U_a(t), U_b(t), and U_c(t) are the true values of the output voltages; U_{am}(t), U_{bm}(t), and U_{cm}(t) are the actual measured values of the grid voltage under static conditions.

If the voltage controller is well-designed and can accurately track the dq-axis voltages, then:

$$\begin{aligned} U_{dm}(j\omega) &= U_{dref}(j\omega) \\ U_{dm}(j\omega) &= U_{dref}(j\omega) \end{aligned} \tag{5}$$

Since no zero-sequence voltage exists in the original three-phase system, the sum of voltages satisfies:

$$U_a(t) + U_b(t) + U_c(t) = 0 \tag{6}$$

Combining Equation. (3)–(6), the true three-phase voltage output of the VSC with static errors can be derived as:

$$\begin{aligned} U_a(t) &= \frac{\Delta k_b - \Delta k_c}{3M} U_f \sin(\omega_s t + \varphi_0) + \frac{2 + \Delta k_b + \Delta k_c}{\sqrt{3}M} U_f \cos(\omega_s t + \varphi_0) \\ U_b(t) &= \frac{3 + 2\Delta k_a + \Delta k_c}{3M} U_f \sin(\omega_s t + \varphi_0) - \frac{1 + \Delta k_c}{\sqrt{3}M} U_f \cos(\omega_s t + \varphi_0) \\ U_c(t) &= \frac{3 + 2\Delta k_a + \Delta k_b}{3M} U_f \sin(\omega_s t + \varphi_0) - \frac{1 + \Delta k_b}{\sqrt{3}M} U_f \cos(\omega_s t + \varphi_0) \end{aligned} \tag{7}$$

Where M is a normalization factor without physical significance:

$$M = \frac{4\sqrt{3}}{9}(\Delta k_a + \Delta k_b + \Delta k_c) + \frac{2\sqrt{3}}{9}(\Delta k_a \Delta k_b + \Delta k_a \Delta k_c + \Delta k_b \Delta k_c + 3) \quad (8)$$

According to Equation (7), Based on symmetrical component theory, the actual three-phase voltage can be decomposed into positive-sequence (U^+) and negative-sequence (U^-) components:

$$\begin{aligned} U^+ &= \frac{6 + 2(\Delta k_a + \Delta k_b + \Delta k_c)}{3\sqrt{3}M} \cdot U_f \\ U^- &= \frac{2U_f}{3\sqrt{3}M}(\Delta k_a{}^2 + \Delta k_b{}^2 + \Delta k_c{}^2 - \Delta k_a \Delta k_b - \Delta k_b \Delta k_c - \Delta k_a \Delta k_c)^{1/2} \end{aligned} \quad (9)$$

Equation (9) shows that static errors will degrade voltage quality at the distributed energy resource (DER) grid connection point, introduce unexpected positive- and negative-sequence voltages, increase voltage unbalance, and adversely affect the dq-axis voltage detection in the phase-locked loop (PLL).

For PLL analysis using minimal representation: $\theta_{pll} = \Delta\theta + \theta_s$, where $\Delta\theta$ is the phase-locking error:

$$\begin{aligned} \cos(\theta_{pll}) &\approx \cos(\theta_s) - \Delta\theta \sin(\theta_s) \\ \sin(\theta_{pll}) &\approx \sin(\theta_s) + \Delta\theta \cos(\theta_s) \end{aligned} \quad (10)$$

Substituting Equation (5) yields the measured value U_{dm} of the d-axis voltage U_d:

$$\begin{aligned} U_{dm} &= \frac{\sqrt{3}}{3}\sin\theta_s(x_b - x_c) - \frac{1}{3}\cos\theta_s(x_b - 2x_a + x_c) \\ &+ \frac{U_f}{2}\left(\frac{2\Delta k_a + \Delta k_b + \Delta k_c}{3} + \frac{\Delta k_b + \Delta k_c}{2} + 2\right) \\ &+ \frac{U_f}{2}\left(\frac{2\Delta k_a + \Delta k_b + \Delta k_c}{3} - \frac{\Delta k_b + \Delta k_c}{2}\right)\cos(2\theta_s) \\ &- \frac{\sqrt{3}}{6}U_f(\Delta k_b - \Delta k_c)\sin(2\theta_s) + U_{dm}(\Delta\theta) \end{aligned} \quad (11)$$

From Equation (11), it can be observed that the measured d-axis voltage U_{dm} under the influence of voltage measurement errors and phase-locking errors contains both a coupled scaling error term composed of proportional errors from each phase and a DC offset error:

$$\begin{cases} A = \dfrac{2\Delta k_a + \Delta k_b + \Delta k_c}{3} + \dfrac{\Delta k_b + \Delta k_c}{2} + 2 \\ B = \dfrac{2\Delta k_a + \Delta k_b + \Delta k_c}{3} - \dfrac{\Delta k_b + \Delta k_c}{2} \\ C = -\dfrac{\sqrt{3}}{6}(\Delta k_b - \Delta k_c) \end{cases} \tag{12}$$

$$X_{dc} = \frac{\sqrt{3}}{3}(x_b - x_c)\sin\omega_s t - \frac{1}{3}(x_b - 2x_a + x_c)\cos\omega_s t$$

The resulting coupled scaling error after interaction is:

$$\Delta K(\omega_s t) = \frac{A}{2} + \frac{B}{2}\cos(2\omega_s t) + C\sin(2\omega_s t) \tag{13}$$

Under these conditions, the output U_{dm} of the d-axis voltage affected by measurement errors becomes:

$$U_{dm} = U_f \cdot \Delta K(\omega_s t) + X_{dc} \tag{14}$$

2.2 Dynamic Voltage Measurement Error Model

During grid transient faults (such as LVRT conditions), the dynamic errors of voltage sensors (including measurement delays and settling time) prevent them from rapidly tracking voltage sags [10], consequently causing the VSC voltage control to lag behind actual grid voltage variations and ultimately degrading voltage control performance.

To quantify the impact of dynamic errors, it is necessary to incorporate inherent delay and settling time into the static error model. Considering the instrument's inherent delay τ_0 and settling time characteristics, the system transfer function can be expressed as:

$$H_{total}(s) = e^{-s\tau_0} \cdot \frac{1}{1 + sT_f} \tag{15}$$

where: $e^{-s\tau_0}$ characterizes the frequency-domain effect of the fixed time delay τ_0; $1/(1+sT_f)$ represents the transfer function of a first-order low-pass filter, with its time constant T_f determining the settling time Ts. Under these conditions, U_{dm} can be expressed as:

$$U_{dm_real} = \frac{U_{dm}(e^{-s\tau_0})}{1 + T_f s} \tag{16}$$

Fig. 3 illustrates a schematic diagram of dynamic voltage measurement errors, depicting the tracking characteristics of a voltage sensor in response to a step voltage

change. The figure contains three key curves: the ideal step change of the input voltage (U_{input}), the instantaneous output voltage without overshoot (U_{inst_out}), and the instantaneous output voltage with overshoot (U_{inst_out}). The diagram defines the delay time as T2-T1 and the settling time under two different conditions: with overshoot as T4-T2 and without overshoot as T3-T2.

The error band is set to 5% of the difference between the initial and final voltage values (i.e., $0.05(U_{init}-U_{final})$), which quantifies the allowable deviation during the sensor's dynamic response. This figure clearly distinguishes the ideal from the actual measurement dynamics, intuitively reflecting the impact of dynamic errors on the response speed and settling accuracy of voltage measurements.

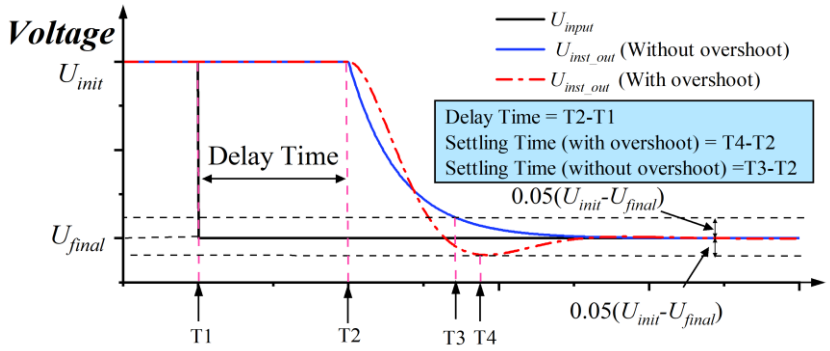


Fig. 3. Schematic Diagram of Dynamic Voltage Measurement Errors

3 Analysis of the Impact of Voltage Measurement Errors

3.1 Static Error Impact Analysis

Building upon the three-phase voltage measurement error model under non-ideal detection conditions established in Section 2, this section develops a DFIG grid-connected model incorporating voltage measurement errors using Matlab/Simulink to analyze their impact on voltage control. The grid-connection parameters are specified in Table 1.

Table 1. Voltage Measurement Errors and Grid Parameters

Parameter Name	Value	Parameter Name	Value
Grid Frequency (f)	50 Hz	Voltage Amplitude (U_f)	1.0 p.u
Scaling Error (Δk_a)	0.04	Scaling Error (Δk_b)	0.04
Scaling Error (Δk_c)	0	DC Offset (x_a)	0.01 p.u
DC Offset (x_b)	-0.03 p.u	DC Offset (x_c)	0 p.u
Settling Time (T_s)	20ms	Delay Time (τ_0)	20ms

As shown in Fig. 4, after the introduction of static measurement errors at 0.5 s, the d-axis voltage measurement (U_{dm}) exhibits significant oscillations. These oscillations are primarily composed of fundamental frequency (ω_s) and second harmonic ($2\omega_s$) components.

This phenomenon indicates that the coupling effect of scaling errors (Δk) and DC offsets (X_{offset}) induces a double-frequency ripple voltage in the synchronous rotating frame, while the DC offset component is transformed into fundamental frequency oscillations. Consequently, this leads to jitter in the phase detection of the phase-locked loop and affects the accuracy of dq voltage detection, ultimately resulting in voltage measurement errors.

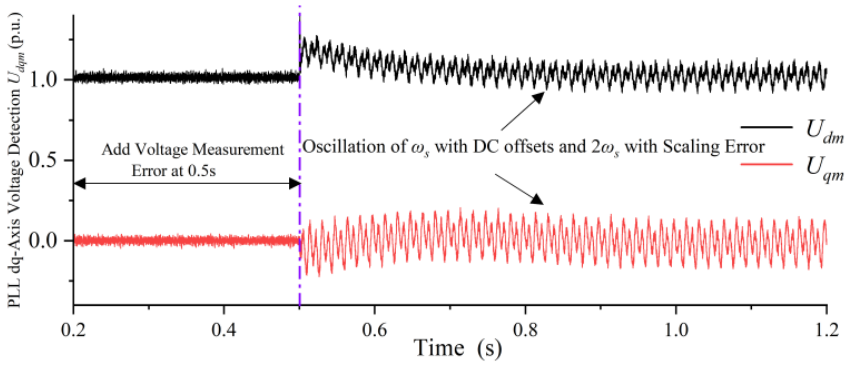


Fig. 4. Influence of Static Errors on PLL Voltage Amplitude Detection

Fig. 5 presents the RMS voltage values of the three-phase voltages at the grid connection point, with calculation results shown in Table 2.

Table 2. Influence of Static Errors on Three-Phase Voltage RMS Values

	RMS_{ref}	RMS_{error}	Error(%)
U_{A_rms}	0.707 p.u	0.594 p.u	15.9%
U_{B_rms}	0.707 p.u	0.591 p.u	16.4%
U_{C_rms}	0.707 p.u	0.621 p.u	12.2%

Although no errors were set for Phase C, the measured voltage values of all phases show varying degrees of deviation from the reference values, confirming the coupled nature of voltage measurement errors.

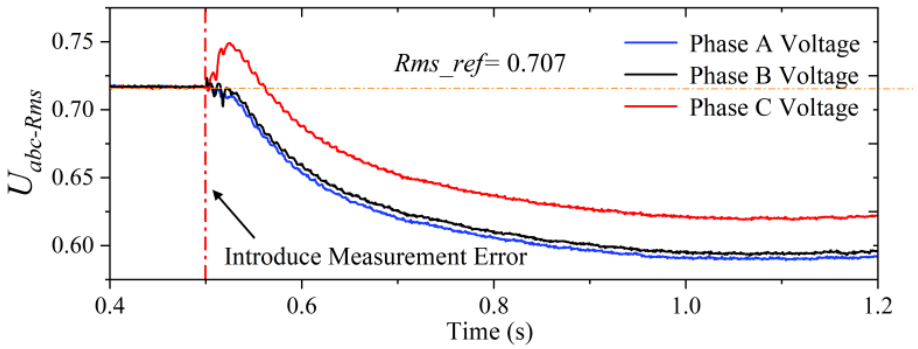


Fig. 5. Influence of Static Errors on Three-Phase Voltage RMS Values

As derived from Equation (9), static measurement errors directly affect the voltage unbalance at the point of common coupling. Fig. 6 illustrates the correlation between scaling errors and voltage unbalance. For simplified analysis with Δk_c=0, the results demonstrate a positive correlation - when scaling errors reach 4%, the corresponding voltage unbalance approaches 2%. Notably, IEEE Std 1159-2019 [11] specifies that voltage unbalance should not exceed 2%.

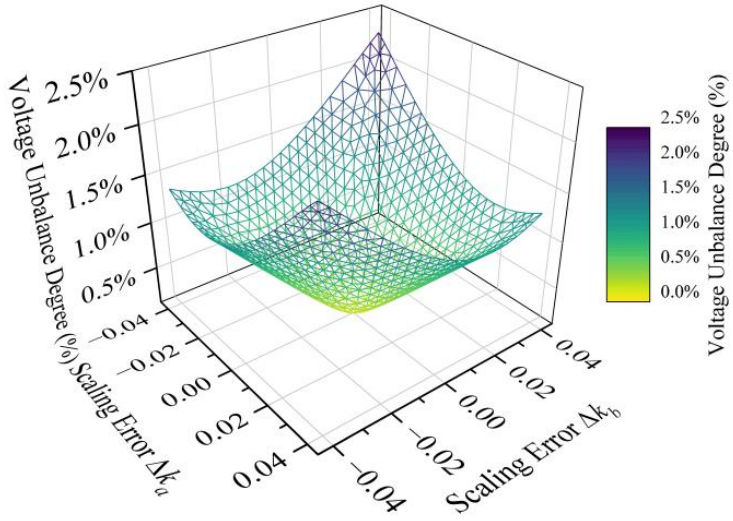


Fig. 6. Influence of Static Errors on Voltage Unbalance Degree

This unbalance further affects the grid voltage phase detection in conventional phase-locked loops (PLL). Under steady-state conditions when the PLL approaches lock status, the quadrature-axis voltage U_q can be minimized as:

$$U_q \approx U^+ \Delta\theta + U^- \sin(2\omega_s t + \phi^-) \tag{17}$$

Fig. 7 shows the PLL control loop after incorporating negative-sequence voltage error disturbance, where negative-sequence voltage perturbation is introduced.

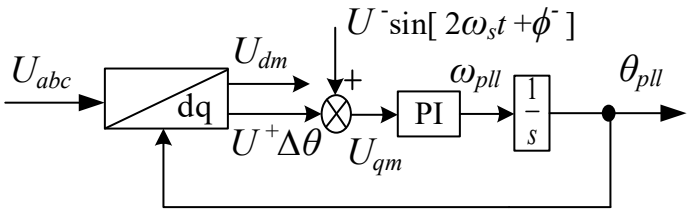


Fig. 7. Equivalent Diagram of PLL After Negative Sequence Voltage Disturbance

In grid-voltage-oriented vector control, the condition U_q =0 must be satisfied. However, the second-harmonic interference caused by static errors cannot be effectively suppressed by PI controllers. To analyze the impact of scaling errors on PLL performance, Fig. 8 demonstrates the phase error variation with increased errors, showing significantly aggravated phase jitter and overshoot amplitude [12].

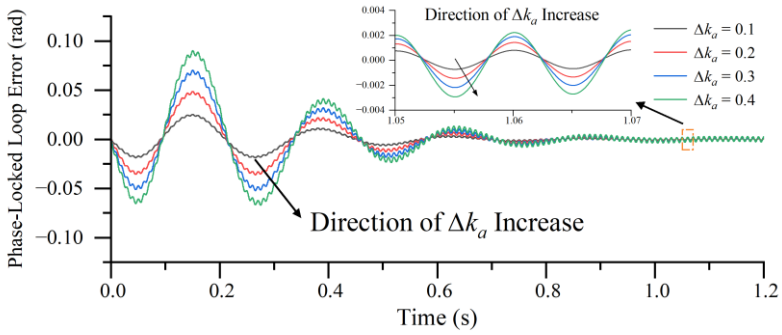


Fig. 8. Influence of Static Errors on PLL Phase Detection

Furthermore, the reactive current command affected by static voltage measurement errors will directly impact the VSC's voltage support capability during LVRT conditions. The error-affected reactive current command $I_{q_\mathrm{LVRT}}^{ref}$ becomes:

$$I_{q_\mathrm{LVRT}}^{ref} = K(0.9 - U_{dm}) = K(0.9 - U_f \Delta K(\omega_s t) - X_{dc}) \tag{18}$$

Compared with the reference current command, their reactive current deviation is:

$$\Delta I_{qref} = I_{qref} - I_{q_\mathrm{LVRT}}^{ref} = (1 - \Delta K(\omega_s t))U_f - X_{dc} \tag{19}$$

Fig. 9 illustrates how static errors affect the voltage support capability of VSC during LVRT operation.

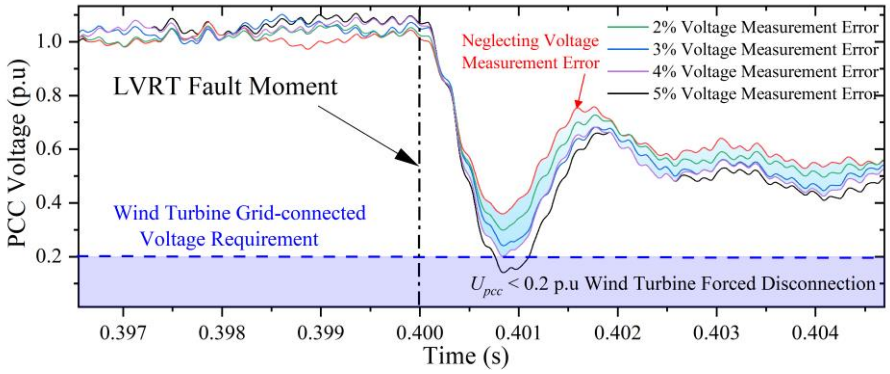


Fig. 9. Impact of Static Errors on VSC Voltage Support Capability During LVRT

As errors increase, the voltage support performance degrades significantly. Only when voltage measurement errors remain within 4% can the wind turbine's grid-connection voltage requirements be met [13]. Combined with the 4% accuracy constraint for voltage unbalance, these results validate the voltage measurement requirements for LVRT scenarios in the latest IEC standards.

3.2 Dynamic Error Impact Analysis

During low-voltage ride-through (LVRT) faults, dynamic errors have a more significant impact on reactive current commands than static errors [14]. Consider a scenario where a voltage sag occurs at t=0.4s and recovers at t=0.6s.

(1) Measurement Delay Phase (0.4s < t < τ_0)

Due to the inherent delay (τ_0) of voltage sensors, the controller continues to execute outdated strategies. The reactive current error during this phase is primarily caused by measurement delay:

$$\Delta I_{qref}(s) = K(0.9 - \frac{U_f - \Delta U}{s}) - \left(k_p + \frac{k_i}{s}\right)\left(1 - U_{dm}(s) \cdot e^{-s\tau_0}\right) \tag{20}$$

Fig. 10 compares the VSC's voltage support performance under different measurement delay scenarios. When the delay exceeds 20ms, the voltage drops below the wind turbine disconnection threshold [15], failing to meet grid connection requirements. Furthermore, after fault clearance, the measurement delay causes delayed withdrawal of reactive current commands, resulting in temporary overvoltage at the point of common coupling.

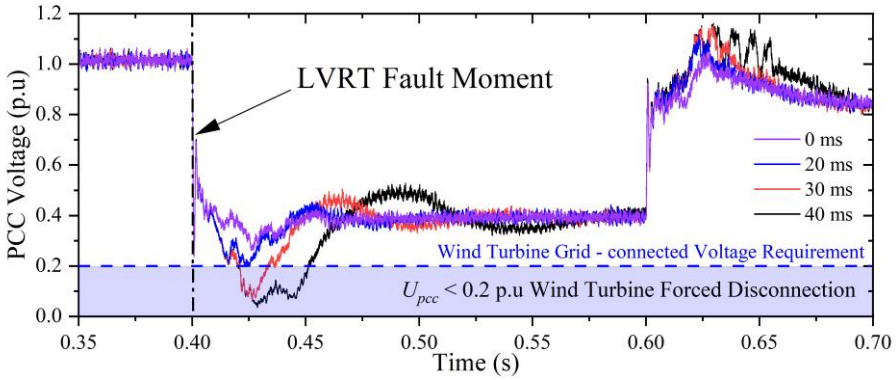


Fig. 10. Impact of Measurement Delay on VSC Voltage Support

(2) Settling Time Phase ($\tau_0 < t < 0.6s$)

While sensors detect voltage changes, measurements remain unsettled. Current command deviations in this phase stem from filter inertia:

$$\begin{aligned}\Delta I_{qref} &= K(0.9-\frac{U_f-\Delta U}{s})-K(0.9-(U_{dm}(s)-\frac{\Delta U}{s})\frac{e^{-\tau_0 s}}{1+T_f s}) \\ &= \frac{K(\Delta U-U_f)}{s}+\frac{Ke^{-\tau_0 s}}{1+T_f s}\left(U_{dm}(s)-\frac{\Delta U}{s}\right)\end{aligned} \tag{21}$$

Fig. 11 presents a comparative analysis of VSC voltage support performance under different settling time conditions. The results demonstrate that when the settling time exceeds 20ms, it significantly impairs the VSC's low-voltage ride-through (LVRT) capability. Excessive settling time may ultimately cause wind turbine disconnection due to failure in maintaining the required voltage standards at the grid connection point.

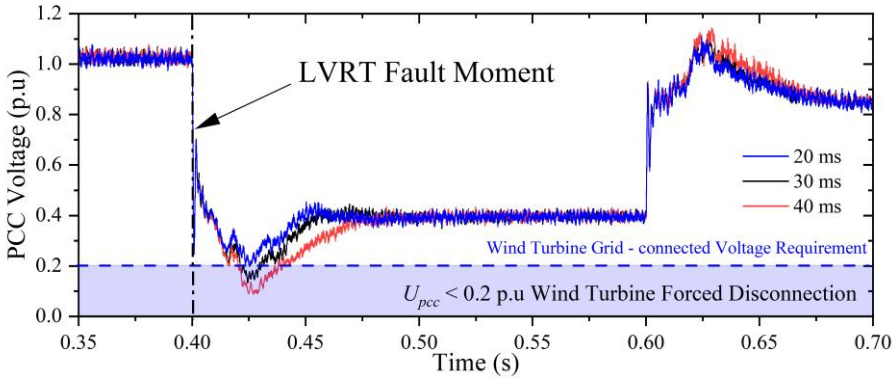


Fig. 11. Impact of Settling Time on VSC Voltage Support

(3) Steady-State Phase ($t_1 < t < t_2$)

the voltage sensor measurements have stabilized, with the resulting errors now primarily composed of static errors as represented in Equation (20).

The analysis of both time delay and settling time primarily focuses on the 20ms threshold, demonstrating that in LVRT scenarios the dynamic voltage measurement errors should not exceed 20ms to meet voltage control requirements. This critical time parameter has been incorporated as fundamental evidence in the new IEC voltage measurement standard.

4 Conclusions

This paper investigates the impact of voltage measurement errors on the voltage control performance of VSCs during low-voltage ride-through (LVRT) operation. By establishing comprehensive models incorporating scaling errors, DC offsets, and dynamic delays, we systematically analyze the interference mechanisms of these errors on phase-locked loops, current commands, and voltage support capabilities. The results showed that static errors induce voltage unbalance and PLL misalignment, compromising the controller's accurate grid-state estimation, while dynamic errors (including measurement delays and settling times exceeding 20ms) degrade the VSC's reactive power support capacity and may even trigger turbine disconnection. To ensure reliable LVRT performance, the measurement errors should be constrained within 4% with dynamic response times not exceeding 20ms, which provides both theoretical basis and experimental validation for the development of the IEC TS 62786-42 voltage measurement standard.

Acknowledgement： This work is supported by the R&D project "Analysis of Voltage Measurement Impact on DER Voltage Control and its Parameter Verification" funded by Rui'an Power Supply Co., Zhejiang, China (Project No：SGZJWZRADDJS25000557）

References

1. LI Xiaojian, ZHONG Yao, HUO Hong. Discussion on determination of basic error of digit high voltmeter[J]. High Voltage Engineering, 2010, 36(9): 2352-2356.
2. WANG Dangshu, WANG Xinxia. Design of new type multi - function intelligent DC voltmeter[J]. Computer Measurement & Control, 2014, 22(1): 300-302.
3. ZHAO Bin. Temperature compensation of ammeter [J]. Physics Experimentation, 2003, 23(7): 34-36.
4. Han Ziye, Luo Ning, Zhu Jiawei, et al. Impact Analysis of Distributed Generation on Distribution Network Voltage [J]. Electromechanical Information, 2020, (24): 26-27+29.
5. Chowdhury V R, Kimball J W. Robust Control Scheme for a Three Phase Grid-Tied Inverter With $ LCL $ Filter During Sensor Failures[J]. IEEE Transactions on Industrial Electronics, 2020, 68(9): 8253-8264.
6. Chowdhury V R, Kimball J W. Voltage sensorless control of a three-phase grid connected inverter with lcl filter based on passivity under non-ideal grid voltage conditions[C]//2019 IEEE Power and Energy Conference at Illinois (PECI). IEEE, 2019: 1-8.
7. He S, Zhou D, Wang X, et al. Grid voltage sensorless control of three-phase LCL grid-connected inverters using multi sampled current[C]//2020 IEEE 9th International Power Electronics and Motion Control Conference (IPEMC2020-ECCE Asia). IEEE, 2020: 2002-2006.
8. Zeng Yi. Research on Islanding Detection of Distributed Grid-Connected Generation Systems [D]. Hunan: Hunan University, 2009
9. L. Ortiz-Matos, J. W. González-Sánchez, L. B. Gutierrez-Zea, O. Llanes-Santiago 和 A. Aguila-Téllez, "Impact of voltage sensor faults on two-level hierarchical control required for grid-forming VSCs in isolated microgrids," *IEEE Access*, in press, 2025, DOI:10.1109/ACCESS.2025.3604415.
10. R. Pacas, "Fault-tolerant control of DC-link voltage sensor for two-stage three-phase grid-connected PV inverters," *J. Electr. Eng. Technol.*, vol. 8, no. 5, 2013, pp. 752–759.
11. IEEE Std 1159-2019. IEEE recommended practice for monitoring electric power quality[S]. New York: IEEE, 2019.
12. Z. Kustanovich, F. Reissner, S. Shivratri and G. Weiss, "The sensitivity of grid-connected synchronverters with respect to measurement errors," *IEEE Access*, vol. 9, 2021, pp. 118985–118995.
13. R. Yang, X. Wang, Q. Chen, G. Shi, C. Shi and X. Cai, "Fault Ride-through Method of Flexible HVDC Transmission System for Wind Farm Integration Based on Coordination of Wind Turbines and Distributed Braking Resistors" Electric Power System and its Automation, vol. 45, no. 21, 2021, pp. 103–111.
14. B. Li and Y. Wang, "Enhanced Low-Voltage Ride-Through Scheme for Grid-Forming Converters Considering Current Limitation and Transient Stability Simultaneously," *Sustainability*, vol. 17, no. 4, 2025, p. 1428.

16

15. J. Yin, Z. Chen, W. Qian and S. Zhou, “A Virtual Synchronous Generator Low-Voltage Ride-Through Control Strategy Considering Complex Grid Faults,” *Appl. Sci.*, vol. 15, no. 4, 2025, p. 1920.

116 HVDC Operational Constraints in High-Penetration Wind-PV-Storage Hybrid Systems

Yingzhou xie, Yifan Zhou, Yong Wang, Liantao Ji, Tingzheng Wang, Wei Li

State Grid Electric Power Engineering Research Institute, Beijing, China

Abstract. This paper conducts a comprehensive study on high-penetration renewable energy bases and their coupled HVDC transmission systems, addressing critical aspects in planning, operation, control, and efficiency improvement. Due to the complex interaction between large-scale renewable generation and HVDC transmission, enhancing delivery efficiency requires coordinated technological advances across generation, transmission, demand-side management, and energy storage systems. Focusing on Large-scale renewable energy delivery bases, this research systematically analyzes factors influencing HVDC transmission efficiency and proposes actionable measures to increase power transfer capability. The proposed strategies ensure that HVDC projects achieve designed performance rapidly after commissioning. With ongoing development of national energy bases, the findings provide valuable insights for similar systems, facilitating renewable integration, reducing carbon emissions, and improving power system flexibility and sustainability. This work contributes to the theoretical and practical foundations for building a resilient and low-carbon power system.

Keywords: HVDC, Renewable Energy, Transmission Efficiency.

1 Introduction

The geographical remoteness of renewable energy bases with high-penetration wind-PV and co-located storage from sending-end AC main grids results in insufficient dynamic regulation capabilities and weak stability support. Concurrently, resource availability and geographic constraints lead to complex grid-connection topologies in renewable energy clusters. Large-scale development thus faces multiple technical challenges. Against this backdrop, investigating systematic measures to ensure power delivery capacity of HVDC transmission channels—considering site-specific geographic and environmental conditions for delivering electricity from mega-scale energy bases carry significant practical implications.

In China, numerous renewable energy bases adopt the configuration of coal-power bundled with renewables for HVDC transmission, where the close electrical proximity between large-scale renewable energy clusters and HVDC transmission systems induces mutual interference. Existing studies have analyzed the coupling mechanisms between renewable energy bases and transmission corridors. Compared to HVAC transmission systems, HVDC systems exhibit lower power losses due to the absence of frequency synchronization requirements and reactive power compensation con-

straints [1]. In sending-end grids with multiple HVDC infeed, hybrid multi-terminal HVDC systems face complex control coordination difficulties, impeding precise renewable power regulation [2]. A distinct coupling relationship exists between centralized renewable energy bases and LCC-HVDC converters [3], leading to mutual operational constraints between renewable generation and DC transmission capacity./Both AC and DC faults in large-scale renewable energy bases can trigger overvoltage and overcurrent phenomena, potentially causing severe grid failures [4]. Interactions between renewable energy clusters and VSC-HVDC systems may initiate wideband oscillations, threatening system stability [4]. Most current research focuses on single-factor coupling analysis without comprehensively evaluating efficiency determinants of HVDC transmission channels or proposing actionable efficiency enhancement measures.

This paper systematically identifies and examines critical factors constraining the transmission efficiency of HVDC corridors delivering power from renewable energy bases with ultra-high penetration rates, and proposes technically feasible measures to enhance HVDC power delivery performance, based on historically validated power grid operational records.

2 Factors Influencing HVDC Transmission Efficiency for High-Penetration Renewable Energy Bases

2.1 Impact of Renewable Energy Units on System Stability

Due to inherent characteristics such as weak reactive power support capability, weak grid connection, and susceptibility to voltage fluctuations leading to grid disconnection, wind power integration significantly impacts AC system voltage profiles [5]. In the early phase of development and construction, wind turbines predominantly consisted of small-capacity, technically simpler asynchronous generators with minimal grid penetration. Consequently, their influence on overall system stability was negligible, with adverse effects largely confined to localized power quality issues within regional grids [6]. With the scaling up of wind turbine capacities and the shift toward large-scale centralized integration, systems with weak grid infrastructure exhibit diminished resilience to disturbances. When large clusters of wind turbines are concentrated in weak radial grids interconnected with AC-DC systems, AC system faults or DC commutation failures can readily trigger reactive power and voltage oscillations. At these vulnerable grid-connection points, wind power fluctuations exacerbate the local reactive power and voltage instability[5].

During transient process, pronounced interactions occur between wind farms and AC-DC systems. Under AC system faults, the voltage at wind farm point of common coupling (PCC) experiences severe dips. Inadequate low-voltage ride-through (LVRT) capability may cause wind turbines to disconnect, further degrading system voltage and preventing DC systems from recovering from commutation failures—potentially culminating in DC blockings [7]. Conversely, DC blockings induce excessive reactive power injection from filters. If filter banks are not promptly disconnect-

ed, surplus reactive power can cause PCC voltage swell. Insufficient high-voltage ride-through (HVRT) capability may then trigger massive wind turbine disconnections [8].

2.2 Reactive Power Balancing in Multi-Energy Power Systems

Reactive power balance serves as the fundamental basis for maintaining grid voltage levels and ensuring system stability, playing a critical role in both secure and economic grid operation [9]. During normal operation of UHVDC transmission systems, converters consume substantial reactive power—typically 40% to 60% of the DC transmitted active power. When the DC system operates under light-load conditions, converter reactive power consumption decreases accordingly. If the capacity of filter banks at converter stations remains unchanged, excessive reactive power influx into the AC system may cause voltage rise at adjacent nodes. Consequently, timely switching off redundant filter banks during variations in DC transmission power prevents such voltage escalation issues.

However, during commutation failures in the DC system, the active power transmitted exhibits significant fluctuations, thereby inducing reactive power oscillations. The resulting reactive power surges impose substantial impacts on the AC grid [10]. Under such transient conditions, the switching operations of filter banks, with a typical response time of 300 ms, are too slow to respond to these rapid changes, consequently leading to voltage limit violations [11].

2.3 Impact of Hybrid Power Sources on System Frequency Response Characteristics

HVDC transmission systems may face both rotor angle stability and frequency stability challenges. For grid-connected delivery schemes, transient stability requires primary attention, though frequency stability cannot be overlooked in weakly interconnected systems [12]. The frequency stability of wind-PV-thermal bundled systems depends on multiple factors, including islanded/grid-connected delivery modes, grid inertia level, wind turbine technology, wind penetration rate, PV capacity, and system spinning reserve [13]. Compared to fixed-speed wind turbines, the integration of doubly-fed induction generators (DFIG) and permanent magnet synchronous generators (PMSG) reduces system equivalent inertia and deteriorates frequency regulation performance. Most grid-tied power electronic converters in renewable units employ control strategies that decouple prime mover input power from grid-side electromagnetic power [14]. Consequently, they generally lack both rotational reserve and inertial response capabilities [15], and cannot provide inertial response analogous to conventional synchronous generators.

Quantitatively, the inertia time constant of a 1000MW thermal unit reaches 8-10 seconds, whereas variable-speed wind turbines and PV units contribute negligible equivalent inertia. As the penetration of power electronic converters increases, system inertia declines substantially, leading to deteriorating frequency performance and ultimately constraining HVDC transmission capability.

2.4 Torsional Oscillation Issues in Wind-PV-Thermal Hybrid Systems

When wind turbines are bundled with nearby thermal power units for joint transmission, both wind turbines and thermal turbine-generators may experience severe torsional oscillations on their shaft systems under grid disturbances [16]. Under fault conditions, mutual interactions occur between the torsional oscillations of wind turbine and steam turbine shafts [17]. The wind turbine shaft may accumulate fatigue damage due to inadequate damping. Sub-synchronous oscillation (SSO) issues have been observed in doubly-fed induction generator (DFIG) based wind farms integrated via series-compensated lines. When SSO occurs in renewable generation units, if its frequency approaches the natural torsional frequency of thermal power units, the latter's shaft torsional modes may be resonantly excited. Different torsional modes carry varying excitation risks. Higher electromechanical coupling degrees in thermal units correlate with increased sensitivity to external power oscillations at resonant frequencies, making the corresponding torsional modes more susceptible to excitation.

2.5 Impact of Reactive Power Compensation Devices on Power Delivery Efficiency

Currently, dynamic reactive power compensation devices widely deployed in power grids primarily fall into three categories: Static Var Compensators (SVC), Static Var Generators (SVG), and Synchronous Condensers [18]. The technical performance and manufacturing technology of these three types of equipment are detailed in Table 1.

Table 1. Technical Performance of Major Dynamic Reactive Power Compensation Equipment.

Characteristic	SVC	SVG	Synchronous Condensers
Device Type	Static passive device (thyristor + reactor/capacitor)	Static active device (IGBT inverter)	Rotating machine (synchronous motor)
Reactive Characteristic	Impedance-based, output decreases quadratically with voltage	Current source type, output unaffected by voltage	Voltage source type, strong overload capability (≥1.5x)
Response time	20–40 ms	≤5 ms (fastest up to 2 ms)	10–50 ms (fast subtransient response)
Regulation Speed	Step switching/continuous (TCR-type)	Continuous smooth regulation	Continuous regulation (excitation control)
Active Power Loss	High (1–3%, depends on reactors)	Very low (0.5–1%, IGBT efficiency >99%)	Highest (1.5–5%, mechanical and copper losses)
Occupied Area	Large (requires filter banks, high spacing requirements)	Small (1/3–1/2 of SVC)	Largest (includes cooling system and step-up transformer)

Service Life	10–15 years (thyristors require replacement)	15+ years (long IGBT lifespan)	30+ years (with proper maintenance)

The SVC achieves smooth reactive power regulation by controlling the switching of capacitors/reactors via thyristors. Following DC commutation failures, the sending-end AC system voltage first dips and then rises. During voltage dips, the SVC operates in the lagging phase to inject a certain amount of reactive power. However, during voltage swells, the SVC cannot immediately switch to leading phase operation and continues to output reactive power in the lagging phase. This inadvertently exacerbates system overvoltage, demonstrating a negative compensatory characteristic in reactive power-voltage regulation [19].

The SVG is a rapid dynamic reactive power compensation device that exchanges reactive power with the AC system by adjusting the amplitude and phase of its output voltage. Although SVGs have faster response speeds than SVCs, they still rely on control loops to respond to grid voltage changes. Consequently, during rapid voltage variations at the sending end (e.g., consecutive commutation failures), SVGs may still exhibit the negative compensatory characteristic.

Synchronous condensers can rapidly inject or absorb reactive power based on system voltage conditions during abrupt voltage changes, without exhibiting the negative compensatory characteristic. They demonstrate superior reactive power-voltage performance compared to SVCs and SVGs [20]. For the large-scale renewable energy HVDC delivery system discussed in this paper, which has a relatively low short-circuit current level, installing synchronous condensers can increase the system short-circuit capacity, thereby helping to suppress transient overvoltage at the sending end. Moreover, synchronous condensers provide rotational inertia, further enhancing the frequency stability of the renewable energy HVDC delivery system.

2.6 Impact of Energy Storage Systems on Power Delivery Efficiency

Energy Storage Systems (ESS) represent a pivotal technology enabling flexible conversion and integrated utilization between electrical energy and other energy forms. By resolving the asynchronicity between energy production and consumption, ESS impart temporal and spatial transferability to energy resources, allowing diverse energy sources to be converted, transmitted, stored, and shared at end-user levels through clean, efficient, and convenient means across spatiotemporal scales [21, 22].

ESS possess not only technical features including rapid response capability and bi-directional power regulation, but also demonstrate superior environmental adaptability, decentralized deployment potential, and short construction cycles. These advantages are redefining conventional paradigms of "generation-grid-load" systems and breaking the inherent attribute of simultaneous electricity production, transmission, supply, and consumption.

Through smoothing power fluctuations from wind and photovoltaic generation and utilizing curtailed wind and solar energy, ESS enhance the deliverability and utilization capacity of renewable energy. This further unlocks renewable generation potential. For large-scale renewable energy bases delivering power via HVDC transmis-

sion, ESS can store excess energy during peak renewable generation periods and discharge to fill power gaps during generation troughs.

To ensure scheduled HVDC delivery volumes, ESS can substantially reduce reliance on power flow management from neighboring regions and procurement of high-cost electricity from external grids. Specifically, by improving renewable generation output and grid regulation capabilities within the HVDC delivery corridor, ESS effectively increase HVDC utilization rates.

3 Technical Solutions for Increasing Power Delivery Efficiency from Renewable Bases

3.1 Enhancing Conventional Generation Capacity for Grid Stability

Conventional power generation plays a vital role in power systems by providing substantial electricity supply while supporting peak shaving and enhancing regional voltage stability. Strengthening the development of supporting conventional power facilities can improve power system operational management capabilities, mitigate active and reactive power fluctuations caused by large-scale renewable integration, and reduce power impacts following HVDC commutation failures. Consequently, expanding the construction of complementary conventional power infrastructure can enhance DC power delivery capacity and transmission efficiency, thereby addressing energy supply shortfalls and reinforcing grid support capabilities.

3.2 Phased and Optimized Integration of Renewable Resources

The integration and aggregation of renewable energy should fully consider grid absorption capacity and the development progress of supporting power infrastructure. During grid planning processes, renewable integration scenarios must be taken into account, while grid connection procedures should coordinate with the construction schedules of peak-shaving generation resources and ancillary facilities. This ensures scientifically planned renewable integration, reduces post-connection curtailment of wind and solar energy, and maintains a high utilization rate for renewable energy.

3.3 Promoting Research on Suppression Methods of Transient Overvoltage

By investigating the intrinsic differences in transient voltage characteristics caused by AC faults versus DC faults through dynamic reactive power source identification, and by exploring collaborative control of multiple reactive power sources, developing novel methods and technologies for self-responsive identification and coordinated control of dynamic reactive power sources could not only enable decoupling between renewable energy sources and their strongly coupled HVDC transmission systems, but also increase renewable generation output while maintaining specified DC power delivery levels, effectively addressing the critical challenge of balancing renewable generation and delivery absorption in high-penetration renewable energy DC transmission grids.

3.4 Optimize AVC Control Strategies for Regional Grids in Renewable Energy Bases

Investigating coordinated steady-state voltage control strategies among capacity synchronous condensers, reactive power compensation equipment within converter stations, and regional grid AVC systems can reduce network losses and enhance reactive power reserve capacity in nearby grids. Moreover, variations in reactive power load within regional grids will not impact the normal operation of UHV transmission systems. Further research could analyze the relationship between steady-state reactive power support and transient voltage support capabilities in UHV AC/DC systems. This exploration can achieve comprehensive optimization of both steady-state and transient reactive power support capabilities in UHV AC/DC systems, facilitate decoupling between nearby renewable generation output and DC transmission efficiency, and optimize renewable energy utilization.

3.5 Research on Grid-Forming Technology Applications

Further research on grid-forming technology applications can effectively enhance system stability. By providing stronger system support capabilities, it enables higher renewable generation output under constant DC power transmission modes. This advancement facilitates renewable energy bases to further increase clean energy provision while ensuring secure and stable system operation, thereby addressing local electricity supply shortfalls and expanding available peak-shaving capacity, significantly improve the efficiency of DC transmission.

4 Conclusion

This paper presents an in-depth investigation of high-penetration renewable energy bases and their associated HVDC transmission systems, exploring multiple aspects including planning, operation, control, and efficiency enhancement. Large-scale renewable energy bases transmitting power through HVDC systems exhibit complex coupling relationships. Improving their DC transmission efficiency requires coordinated research and application of new technologies across generation, grid, load, and storage sectors. This study provides a comprehensive analysis of factors influencing the transmission efficiency of HVDC systems delivering power from desert-gobi renewable energy bases, and summarizes proposed measures for enhancing the power delivery capacity of high-penetration renewable energy bases. These measures ensure that HVDC projects can reliably achieve their intended operational performance following commissioning. Looking forward, as national energy base construction continues, these research findings will be applicable to other similar energy bases and transmission systems, contributing to nationwide renewable energy development, carbon emission reduction, and improved power system flexibility and sustainability to meet growing electricity demands.

Acknowledgement: This work is supported by the project “Research on Key Issues of Development Construction and Operation of Pumped Storage (Hydropower) under High Quality Development.” (5477SD25F049)

References

1. I. I. Hussein, S. Essallah and A. Khedher, "Comparative Study of HVDC and HVAC Systems in Presence of Large Scale Renewable Energy Sources," 2020 20th International Conference on Sciences and Techniques of Automatic Control and Computer Engineering (STA), Monastir, Tunisia, 2020, pp. 225-230.
2. Zhou Li, Ziang Wei, Ruopei Zhan, Yazhou Li, Xiao-Ping Zhang, System operational dispatching and scheduling strategy for hybrid cascaded multi-terminal HVDC, International Journal of Electrical Power & Energy Systems, Volume 122, 2020.
3. Cherian Mathew, E., Das, A. and Sharma, R. (2020), Integration of renewable energy sources with LCC HVDC system using a new circuit topology with DC fault ride-through capability. IET Power Electronics, 13: 4551-4561.
4. Y. Liu, K. -J. Li, J. Liu, H. Fan and K. Sun, "Start-up Control and Frequency Oscillation Control of the 100% Renewable Energy Islanded Grid Fed by MMC-HVDC System," 2023 5th Asia Energy and Electrical Engineering Symposium (AEEES), Chengdu, China, 2023, pp. 1644-1648.
5. E. Vittal, M. O'Malley and A. Keane, "A Steady-State Voltage Stability Analysis of Power Systems With High Penetrations of Wind," in IEEE Transactions on Power Systems, vol. 25, no. 1, pp. 433-442
6. Damian Flynn, Zakir Rather et al. "Technical Impacts of High Penetration Levels of Wind Power on Power System Stability:" The Large-scale Renewable Energy Integration Challenge. 10.1002/9781119508311.ch3.
7. Li, B., Zheng, D., Li, B. et al. Analysis of low voltage ride-through capability and optimal control strategy of doubly-fed wind farms under symmetrical fault. Prot Control Mod Power Syst 8, 36 (2023).
8. Fan, G., Fan, G., Song, P., Ren, C., Kang, P., Cheng, L., & Zhang, F. (2020). Analysis of coupling factors between high proportion wind power and ultra-high voltage DC. Journal of Physics: Conference Series, 1639.
9. Huang, Y., Li, C. and Liu, T. (2019), Research on coordinated reactive power control strategy of hybrid-HVDC. The Journal of Engineering, 2019: 3349-3353.
10. A. Maalla, "Research on Reactive Power Control of the HVDC Transmission System," 2020 IEEE 4th Information Technology, Networking, Electronic and Automation Control Conference (ITNEC), Chongqing, China, 2020, pp. 2475-2479
11. Mo, J., Yan, W., Xiao, F., Wang, T., Wang, H. and Zhou, Y. (2019), Optimal reactive power control in a converter station during low-power operation of HVDC. The Journal of Engineering, 2019: 2250-2254.
12. A. Philip, Yushuo Zhang et al. “Analysis and Suppression Strategy of Sub-synchronous Oscillation for Wind-Thermal-Bundled Power Transmitted by Series-Compensated System.” Proceedings of PURPLE MOUNTAIN FORUM 2019-International Forum on Smart Grid Protection and Control, Lecture Notes in Electrical Engineering, vol 585.
13. C. Dai, Tao Xu. “Impact of Wind Power and Photovoltaic Grid Connection on Subsynchronous Oscillation of Thermal Power.” Journal of Physics: Conference Series, 1550 052017

14. J. Fang, H. Li, Y. Tang and F. Blaabjerg, "On the Inertia of Future More-Electronics Power Systems," in IEEE Journal of Emerging and Selected Topics in Power Electronics, vol. 7, no. 4, pp. 2130-2146
15. C. Henderson, L. Xu and A. Egea-Alvarez, "PN admittance characterisation of grid supporting VSC controllers with negative sequence regulation and inertia emulation," 2021 23rd European Conference on Power Electronics and Applications (EPE'21 ECCE Europe), Ghent, Belgium, 2021, pp. P.1-P.10
16. Wang, J.; Jia, Q.; Yan, G.; Liu, K.; Wang, D. Analysis of Subsynchronous Torsional of Wind–Thermal Bundled System Transmitted via HVDC Based on Signal Injection Method. Energies 2021, 14, 474.
17. Xiao, Feng & Tian, Chen & Wait, Isaac & Yang, Zhaohui & Still, Benjamin & Chen, Gang. (2020). Condition Monitoring and Vibration Analysis of Wind Turbine. Advances in Mechanical Engineering. 12. 1687814020913782. 10.1177/1687814020913782.
18. Peng, Y.; Wang, H.; Zhao, Q.; Nan, D.; Li, W. Research and Application of Combined Reactive Power Compensation Device Based on SVG+SC in Wind Power Gathering Area. Appl. Sci. 2022, 12, 10906.
19. Y. Fu, N. Cui, J. Song, Z. Chen, C. Fu and C. Zhang, "A Hybrid Control Strategy Based on Lagging Reactive Power Compensation for Vienna-Type Rectifier," in IEEE Transactions on Transportation Electrification, vol. 7, no. 2, pp. 825-837
20. Li, Li & Qin, Jianru & Hu, Heng & Zhang, Qinglei & Luo, Lei. (2024). Optimized operational approach for multi-type reactive power compensation to enhance the grid integration strength of new energy clusters. Frontiers in Energy Research. 11. 10.3389/fenrg.2023.1342770.
21. Wei, P.; Abid, M.; Adun, H.; Kemena Awoh, D.; Cai, D.; Zaini, J.H.; Bamisile, O. Progress in Energy Storage Technologies and Methods for Renewable Energy Systems Application. Appl. Sci. 2023, 13, 5626.
22. C. Mao et al., "Research on the Application of Grid-side Energy Storage Considering Renewable Energy Generation," ECITech 2022; The 2022 International Conference on Electrical, Control and Information Technology, Kunming, China, 2022, pp. 1-5.

117 双碳目标下电磁场课程改革：新型电力系统工程案例贯穿的教学探索

肖士勇，齐 冰，娄娟

（1．东北电力大学电气工程学院 吉林省 吉林市 132011 ）

Curriculum Reform of Electromagnetic Field Under the Dual Carbon Goal: Teaching Exploration with Engineering Cases of New Power Systems as the Red Thread

Shiyong Xiao, Bing Qi, Juan Lou

(Northeast Electric Power University, School of Electrical Engineering, Jilin 132011, Jilin Province, China)

ABSTRACT: The “Dual Carbon” strategic goal has set forth new requirements for talent cultivation in electrical engineering-related courses. As a core foundational course for the major of Electrical Engineering and Automation, *Electromagnetic Field* has long been confronted with issues such as a strong emphasis on theory, insufficient practical components, and inadequate integration of ideological and political elements. These problems make it difficult to meet the demand for interdisciplinary talents in the construction of new power systems. Based on the context of the “Dual Carbon” goal, this paper analyzes the major contradictions in the current course teaching and proposes a reform approach that runs through the course's knowledge system with engineering cases. By building a case library, improving the BOPPPS teaching model, and integrating virtual simulation with scientific research practice, the integration of theory and engineering applications is achieved. Additionally, ideological and political elements are organically incorporated into case teaching to strengthen students' sense of responsibility and mission. Practice demonstrates that this reform can enhance students' learning interest, innovative ability, and practical ability, and promote the in-depth integration of the course with the new power system and the “Dual Carbon” strategy.

KEY WORDS: double carbon goals, case-based teaching, improved BOPPPS

摘要：“双碳”战略目标对电气工程类课程的人才培养提出了新的要求。《电磁场》作为电气工程及其自动化专业的核心基础课程，存在理论性强、实践不足、思政渗透不够等问题，难以适应新型电力系统建设对复合型人才的需求。本文立足“双碳”背景，分析了课程教学中存在的主要矛盾，提出以工程案例贯穿课程知识体系的改革思路。通过构建案例库、改进 BOPPPS 教学模式、融合虚拟仿真与科研实践，实现了理论与工程应用的结合，并在案例教学中有机融入思政元素，强化学生的责任感与使命感。实践表明，该改革能够提升学生学习兴趣、创新能力和实践能力，促进课程与新型电力系统和“双碳”战略的深度融合。

关键词：双碳背景，案例式教学，改进的 BOPPPS

DOI：10.13335/j.1000-3673.pst.2014.01.

0 引言

习近平总书记于 2020 年 9 月在第 75 届联合国大会上提出我国“力争 2030 年前碳达峰、2060 年前碳中和”的“双碳”目标，这一重大战略决策不仅推动我国能源结构向清洁低碳转型，更对高等教育中电气类专业人才培养提出新要求——需培养兼具专业能力与“双碳”战略意识，能适配新型电力系统发展的高素质人才。

《电磁场》是电气工程及其自动化专业的核心基础课程，旨在培养学生在电磁场理论及其相关领域的科研及工程应用能力。电磁场理论与电力系统、通信技术、电子设备、雷达系统等“国之重器”紧密相关，是支撑我国科技进步与产业发展的核心领域。电磁场理论的研究与应用，直接影响到我国在高新科技、能源、军事等多个领域的自主创新与发展。然而，当前《电磁场》课程教学多聚焦理论知识传授，对“双碳”目标下新型电力系统（如新能源发电并网、低碳电力设备设计等）的工程需求融入不足，导致课程与能源转型实践脱节，难以充分支撑“双碳”人才培养。

为此，本文立足“双碳”战略背景，以新型电力系统工程案例为纽带，探索《电磁场》课程改革路径，旨在通过案例与课程内容的有机融合，既夯实学生电磁场理论基础，又强化其对“双碳”目标

的认知与实践能力，为新型电力系统建设及“双碳”目标实现培育专业人才。

1 课程教学过程中存在的问题

1.1 课程理论性强与学生基础薄弱的矛盾

电磁场课程具有理论性强、概念抽象、公式繁多等特点，前导课程包括高等数学、大学物理、电路等，教学过程中涉及众多微积分运算、理论推导及矢量概念，如果学生前导课程的知识储备不足，就会导致理论知识理解困难，进而产生畏难情绪，最终导致教学及学习效果不佳。

1.2 教学模式单一与以学生为中心教育理念的矛盾

传统的电磁场课程教学模式多以教师为主，注重理论讲授，强调计算方法，缺乏实际案例支撑和课堂互动环节，引导学生理解“为什么”和“如何应用”的机会少。学生往往只停留在“知道什么”的层面，缺乏深入思考和实践操作，导致学习兴趣和课堂参与度下降，创新能力和应用能力的培养受到限制。这种教师主导、模式单一的教学方式与以学生为中心的教育理念存在明显矛盾，需要通过改革实现教学的有效转型。

2 双碳目标下对电气工程课程教学的要求

在“双碳”目标推动能源结构向清洁化、低碳化转型的背景下，电气工程专业课程教学需全面对接新型电力系统建设需求，需从知识体系重构、教学模式优化与价值引领强化三个维度推进革新，而《电磁场》作为核心基础课程，更需以具体工程案例为纽带，实现理论与实践的深度融合。

2.1 知识体系需融入新型电力系统内涵

天津工业大学赵丽霞等指出，专业课程需以“电”为核心，将“双碳”目标与课程内容有机融合[1]。传统课程侧重传统电力系统知识，而当前需重点补充新能源发电（如风电、光伏）、新型电力电子器件（如 SiC、GaN）、智能电网等内容[2]。另外需拓展新能源并网、柔性输电等前沿知识，以适配“高比例可再生能源+高比例电力电子设备”的新型电力系统特征[3]。

2.2 教学模式需强化案例与实践结合

文献[1]强调“案例与课程建设相融合”，通过积累典型案例实现“滴水穿石”的教学效果；文献[3]提出构建“虚拟仿真+综合实践”的多层次体系，推动学生从“被动接受”向“主动应用”转变。南京邮电大学张占强则指出，需打破传统授课模式，引入学科前沿理论，通过项目式学习提升学生解决复杂工程问题的能力[4]。

2.3 价值引领需渗透双碳战略意识

课程需将“双碳”目标内化为学生的精神追求，外化为实践行动；要挖掘专业课程中的思政元素，通过大国工程案例培养学生的家国情怀与责任担当，实现“知识传授与价值引领”的统一。

作为电气工程专业的基础课程，《电磁场》需以“新型电力系统工程案例贯穿”为核心，落实上述要求：

（1）知识体系聚焦新型设备与场景

结合新型电力系统知识需求，课程需突破传统电磁场理论框架，新增新能源装备的电磁场特性分析案例（如风电永磁发电机的磁场分布、光伏逆变器的电磁干扰），以及新型电力系统中的电磁兼容问题（如分布式电源接入后的电磁环境变化、柔性直流输电的电磁场耦合），为理解低碳设备的工作原理提供理论支撑。

（2）教学模式以案例驱动实践能力

遵循“案例与课程融合”及“虚拟仿真教学”的思路，构建新型电力系统电磁场案例库：通过 ANSYS 等工具仿真风电变流器的电磁场耦合、光伏阵列的电磁辐射分布，让学生直观理解理论在工程中的应用；设计“新能源基地电磁环境优化”项目，引导学生运用电磁场理论解决滤波设计、损耗降低等实际问题，实现“理论推导—仿真验证—工程优化”的闭环。

（3）价值引领依托案例渗透战略意识

基于“双碳目标内化于心”的理念，在案例教学中融入思政元素：对比传统火电机组与新能源电站的电磁损耗差异，量化低碳技术的减排效益；结合我国新能源产业的全球领先案例，展现电磁场理论在“双碳”目标中的实际价值，培养学生“技术服务国家战略”的责任担当。

3 案例式教学的研究现状

在案例式教学的研究与实践中，相关学者围绕案例建设、教学模式创新等方面展开了深入探索。在案例资源建设方面，有研究提出通过组建专门团队推进案例库搭建，团队内部分工明确，从顶层设计到素材收集、加工优化等各环节均由专人负责。素材来源多元，既整合现有教学资源、开放性课程素材及教材配套资源，也结合科研项目自主研发特色案例，同时以教学内容和知识点为脉络对素材进行筛选加工，形成体系化的完整案例，并依托教学需求与工程实践进展动态更新[5]。

教学模式创新上，部分研究指出传统讲授模式的局限，主张以案例为纽带重构课堂形态，采用项目式与研讨式结合的模式，将案例转化为具体任务，引导学生分组完成案例分析、方案设计、成果汇报等相关工作，教师通过点评与引导深化讨论，同时将过程表现纳入评价体系[5]。还有研究提出进阶式教学流程，通过案例导入、理论推导、知识总结、仿真验证、问题研讨、思想政治教育等环节，实现从知识掌握到能力培养的递进[6]。

教学手段融合方面，研究者注重理论与实践的衔接，提出以“知识发现-应用-关联”为主线，将案例转化为例题与思考题，让学生在解决实际问题中理解理论内涵[7]。同时，强化现代技术工具的应用，借助仿真软件对案例进行建模分析，通过虚拟实验验证理论推导[8]。

此外，案例教学与价值引领的融合成为研究亮点，通过挖掘案例中的相关元素，在分析技术问题时融入思政教育，引导学生树立责任意识与全局观念[6],[8]。

4 工程案例贯穿的教学改革探索

针对《电磁场》课程教学中存在的学习认同度低、理论与实践脱节、思政引导不足等“痛点”问题，课程组以“内驱性教学观”为核心理念，构建了线上线下、课内课外一体化的混合式互补教学模式，提出改进的 BOPPPS 教学方案，以工程案例贯穿课程核心知识点并有机融入课程思政，全面提升学生的学习内驱力与实践创新能力。

“内驱性教学观”以问题导向-目标明确-知识点讲、问、答、用-工程案例贯穿-仿真结果再现为教学主线，依此提出并构建了改进的 BOPPPS 教学模式。

（1）利用线上资源，以相关知识点的工程案例进行课程导入（Bridge-in），激发学生学习兴趣；（2）从学生角度出发，明确通过本节课的学习可以达到的目标，知道什么（知识目标）、能做什么（能力目标）、思想变化（价值目标）（Objective）；（3）以知识点提问掌握学生对本节内容的了解情况，突出讲解的重难点（Pre-assessment）；（4）通过参与式教学、案例式教学、角色扮演等方法，体现以学生为中心的教学理念（Participatory Learning）；（5）课后测试及随堂作业，评估学习效果（Post-assessment）；（6）总结与课后仿真，内容回顾与总结，通过仿真将抽象的电磁现象具象化（Summary and Simulation）。

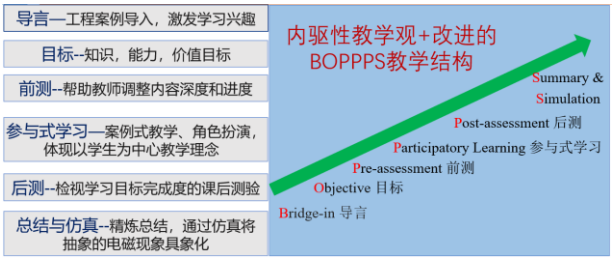
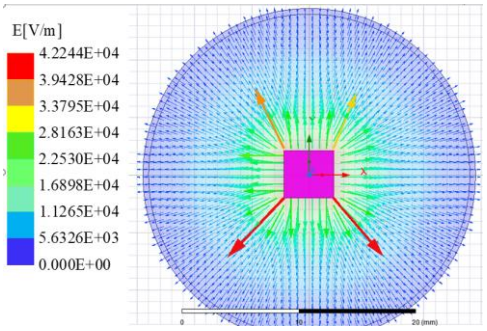


图 1 改进的 BOPPS 教学方案

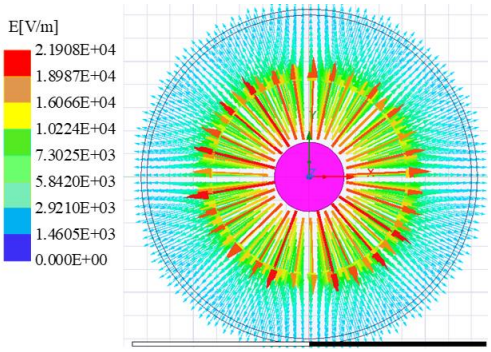
Fig.1 Improved BOPPS Teaching Scheme

电场与磁场的概念及空间分布抽象、不直观，为了让学生更加透彻理解课程核心知识点，使抽象的电磁场问题“显性化”，课程组提出了改进的 BOPPPS 教学模式，即将 Summary 拓展为 Summary and Simulation，增设了核心知识点的有限元仿真实验项目，编写了电磁场仿真实验指导书，内容包括仿真分析与电磁场理论的联系、仿真软件操作步骤和分析要求。学生可通过线上平台查看电场或磁场的仿真结果，也能根据指导书自行仿真分析，为学生从被动学到主动做提供了桥梁。图 2 为同轴电缆采用圆导体和矩形导体两种方案下的电场分布仿真结果，并要求学生利用电场强度等于电位的负梯度知识点解释仿真得到的电磁现象，实现了抽象问题的具象化并提升了课程的高阶性和挑战度。



（a）矩形导体

（a）Rectangular Conductor



（b）圆导体

（b）Circular Conductor

图 2 两种导体方案下同轴电缆的电场分布

Fig.2 Electric Field Distribution of Coaxial Cables Under Two Conductor Schemes

5 工程案例贯穿的教学模式举例

为提升学生学习的参与度，体现课程高阶性、创新性与挑战度，激发学生学习的内驱力，结合教学团队承担的科研项目，开展案例式启发教学。例如，随着新能源的大规模并网，新型电力系统的稳定性问题愈加突出。基于前沿热点问题，提出结合麦克斯韦方程组理论，圆形导体比矩形导体电场分布均匀，以电缆代替常规矩形线棒作为调相机定子绕组，可大幅提升调相机电压等级，实现调相机与电网的直连运行，大幅提升调相机的无功输出能力，有效保证电力系统的稳定性，如图 3 和图 4 所示。基于此案例，学生可以从“圆形导体为什么比矩形导体电场分布均匀？”、“磁场分布及媒质的磁化”、“安培环路定律的应用”、“法拉第电磁感应定律”、“磁场分析的边值问题及有限元仿真”等方面开展案例式教学，从“查阅资料→小组讨论→仿真分析→汇报交流→教师点评”等几方面展开。此外，学生还可以围绕新能源并网、新型电力系统稳定性、电力系统无功补偿等前沿问题开展资料查阅与专题探讨，将行业发展需求内化为学生适应新挑战的自我提升需求。

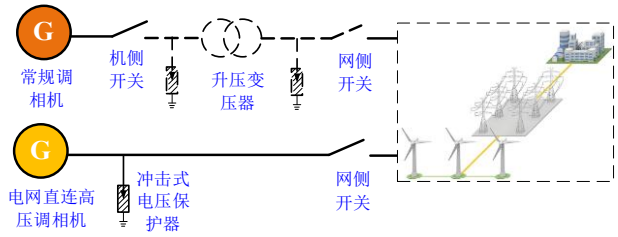


图 3 调相机与电网直连运行示意图

Fig.3 Schematic Diagram of Direct Connection Operation Between Synchronous Condenser and Power Grid

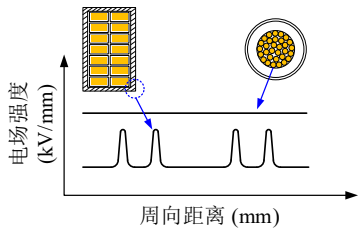


图 4 圆导体与矩形导体电场强度分布对比图

Fig.4 Comparison Diagram of Electric Field Intensity Distribution Between Circular Conductors and Rectangular Conductors

在案例式启发教学中，“问题驱动”是激发学生主动学习的核心逻辑。结合电磁场知识体系，为激发学生学习兴趣，引导学生带着问题学习，设置了以工程问题为导向的课程导言教学环节，利用线上教学平台课前下发工程问题，为学生查阅资料、小组讨论及课程预习留有充足时间，课上第一个环节即为导言环节，可通过角色扮演、小组研讨等参与式学习方式开展，表 1 为电磁场课程导言的工程问题举例。

表 1 课程导言的工程问题

Table.1 Engineering Problems in the Course Introduction

工程案例	对应知识点
特高压直流输电工程输电电缆的绝缘设计	高斯定律
光刻机半导体晶圆边缘击穿场强计算问题	静电场的镜像法
高压电器设备接地系统设计问题	接地电阻计算
手机触摸屏幕是如何感知触控位置的？	电场能量问题
发电机的绕组为什么放置在铁磁材料中？	恒定磁场的镜像法
无线充电技术的实现原理	电磁能量流

经过教学创新，学生学习积极性和主动性大大增强，学业成绩优良率明显提高，团队精神、创新能力和工程思维能力明显增强。学生积极参与各项比赛，竞赛选题和电磁场理论联系紧密，且与“双碳”背景切合紧密，图 5 为学生参加挑战杯比赛作品“电单车无线充电智能光伏基站”展示。

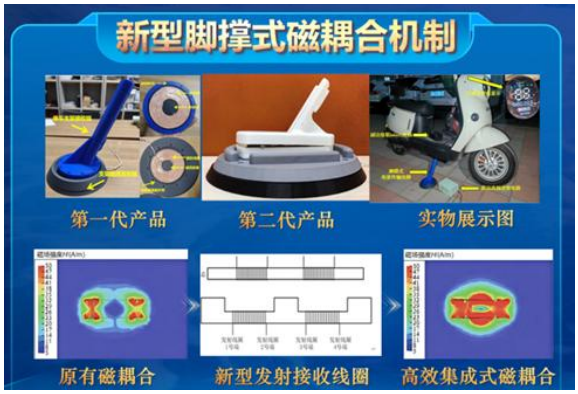


图 5 学生竞赛作品

Fig.5 Student competition works

6 结束语

本文结合“双碳”战略背景，从课程内容、教学模式和价值引领三个层面探索了《电磁场》课程的教学改革路径。通过工程案例贯穿知识体系，推动理论与实践的结合；通过改进的 BOPPPS 教学模式，增强课堂互动与学生主体性；通过思政元素的有机渗透，强化学生的家国情怀与责任担当。改革实践表明，课程改革不仅解决了学生学习兴趣不足、理论与应用脱节的问题，还有效提升了学生分析与解决复杂工程问题的能力。未来，课程组将持续完善案例库建设，深化虚拟仿真与科研实践结合，进一步推动课程与“双碳”目标、新型电力系统建设的紧密对接，真正实现人才培养质量与国家战略需求的同频共振。

参考文献

[1] 赵丽霞, 高圣伟. “双碳”目标驱动下电气类专业课程教学改革的

思考[J]. 高教学刊, 2023, (26): 141-144, 149.
[2] 吴青峰, 于少娟, 王健安. 双碳背景下电气专业课程体系改革[J]. 电气与电子教学学报, 2023, 45(2): 77-81.
[3] 陈春, 邓丰. “双碳”目标下“发电厂电气部分”的课程改革与探讨[J]. 教育教学论坛, 2023, (31): 73-76.
[4] 张占强, 高含笑. “双碳”背景下电气专业研究生课程教学改革与实践[J]. 高教学刊, 2023, (34): 133-136.
[5] 王家林, 王黎明. 基于工程案例的自控原理课程教学改革实践[J]. 中国电力教育, 2022, (05): 64-65.
[6] 王昱, 王艳辉, 梁宵. “控制工程基础”互动案例式教学改革与实践[J].教育教学论坛, 2023, (34): 64-67.
[7] 闫蓓. 面对工程实践能力培养的电路理论课改革与探索[J].中国教育技术装备, 2022, (24): 112-115.
[8] 吴军科, 诸葛致, 郭振威. 从工程实践视角浅谈《电力电子技术》课程教学改革[J].中国电力教育,2022,(02):66-67.

收稿日期：2013-07-04。


肖士勇

作者简介：
肖士勇(1988)，男，副教授，硕士生导师，研究方向为大型发电设备电磁设计、仿真与优化，E-mail：20213037@neepu.edu.cn；
齐冰(1978)，男，教授，硕士生导师，研究方向为大气压放电与气体物理等，E-mail：qibing@neepu.edu.cn。

118 基于节点边际电价的主配协同分布式光伏接入容量优化模型

李奕衡[1]，杜红卫[1]，夏栋[1]，郭卫[1]，邵嗣杨[1]

（1. 南瑞集团有限公司（国网电力科学研究院有限公司）,江苏 南京 211106）

A Coordinated Transmission-Distribution Optimization Model for Distributed PV Hosting Capacity Based on Locational Marginal Price

LI Yiheng,DU Hongwei,XIA dong,GUO Wei,SHAO Siyang

(1. NARI Group Corporation (State Grid Electric Power Research Institute), Nanjing 211106, Jiangsu, China)

ABSTRACT: The large-scale integration of distributed photovoltaics (PV) poses safety risks to distribution networks, such as voltage violations and reverse power flow. Accurately assessing the hosting capacity of distributed generation in a region has become a crucial research direction in current distribution network planning. Traditional capacity assessment methods for distributed generation mostly focus on single-layer and single-objective optimization at the distribution network level alone, ignoring the role of the transmission network in absorbing distributed generation and struggling to balance issues such as PV accommodation, voltage security, and operational economy.This paper proposes a coordinated transmission-distribution bi-level optimization framework based on bidirectional feedback of Locational Marginal Price (LMP). The upper-level transmission network performs security-constrained economic dispatch with the objective of minimizing operational costs and transmits LMP to the lower-level network. The lower-level distribution network optimizes the capacity and location of distributed PV with the goal of maximizing comprehensive benefits while ensuring the safe operation of the power grid.Case studies are conducted based on the IEEE 30-bus transmission network and 33-bus distribution network systems. The results show that, compared with traditional conservative assessment methods, the proposed evaluation model effectively improves the hosting capacity of distributed PV in distribution networks and reduces system operational costs.

KEY WORDS: Transmission-Distribution Coordination; Distributed-Photovoltaics;Bi-levelOptimization;Economic-Efficiency;LMP

摘要：分布式光伏的大量接入将给配电网带来电压越限/潮流返送等安全隐患，正确评估区域内分布式光伏可接入容量是目前配电网规划的重要研究方向。传统的分布式光伏容量评估多只考虑仅从配网层面单层单目标考虑优化，忽略了主网在分布式光伏消纳中的作用，难以统筹兼顾光伏消纳、电压安全和运行经济性等问题。本文提出了一种基于节点边际电价（Locational Marginal Price，LMP）双向反馈的主配网协同双层优化架构，上层主网以运行成本最小为目标进行安全约束经济调度，并向下层网络传输 LMP；下层配网以综合收益最大为目标，在保证电网安全运行的前提下优化分布式光伏的容量、位置。本文基于 IEEE30 节点主网和 33 节点配网系统进行算例分析，经检验，本文提出了评估模型，相较于传统保守评估，有效提升了配网分布式光伏的接入容量，并降低了系统运行成本。

关键词：主配网协同；分布式光伏；节点边际电价；双层优化；经济性；

DOI：10.13335/j.1000-3673.pst.2014.01.

0 引言

在传统能源结构中，化石能源发电引发的环境污染问题愈发突出，风能与太阳能由此成为能源转型的关键选项。由于太阳能具有分散分布的特点，光伏发电多采用分布式并网模式。然而，光伏出力的不确定性会对电力系统造成冲击，这在一定程度上限制了其接入规模。因此，对光伏最大接入容量进行评估，对于电力系统尤其是配电网的规划研究而言，具有重要的现实意义。

传统的分布式光伏容量评估通常从配网自身约束出发，文献[1]在考虑静态安全约束的基础上，深入分析了节点接入位置对配电网可接纳光伏容量的作用；文献[2]针对继电保护准则，对配电网中光伏电源的最大接入容量展开了定量计算；文献[3]构建了包含继电保护动作考量的光伏容量评估模型，并进行了优化分析；文献[4]将需求侧管理与网

络重构等优化手段纳入研究范畴；文献[5]探讨了极端负荷水平下，配电网中典型分布的光伏电源对电压偏差产生的影响；文献[6]则研究了电动汽车因素对光伏电源选址与定容的影响。这些仅从配网单层面考虑，忽略了主网在配网运行中引导调控作用，评估结果通常较为保守，无法深入挖掘配网的分布式光伏接入潜力。而现有研究在主配协同领域已取得初步进展，但多数工作仍局限于以物理功率约束为边界的简单耦合范式。例如，主网向配网下达上送功率限额，配网在此刚性约束下寻求光伏接入容量的最大化[7]。此类方法虽实现了一定程度的协调，但其本质是“被动受限”而非“主动引导”，耦合深度不足，未能充分利用配网侧灵活性资源的调节潜力以服务于主网的整体经济性与安全性。

本文引入节点边际电价（Locational Marginal Price, LMP）这一核心要素。LMP 深度融合了系统边际成本、网络阻塞与损耗信息，能够精准刻画电力在特定时间与空间上的真实价值，是引导资源优化配置最有效的经济信号[8]。本文旨在构建一个基于 LMP 信号的主配协同双层优化模型。上层，主网以运行成本最小为目标进行安全约束经济调度，并生成联络节点的 LMP 曲线；下层，配网不再是单纯追求容量最大化，而是以响应 LMP、实现自身综合收益最大化为目标，主动优化 DPV 的配置与运行策略。通过 LMP 与净负荷曲线的迭代反馈，本模型能够激励配网自发地调整其行为（如在高 LMP 时段优先送电、在低 LMP 时段优先自消纳），从而在时空维度上引导 DPV 的消纳模式与主网的运行需求实现动态匹配。

1 基于节点边际电价信号的双层优化模型

1.1 考虑运行经济性的主网模型

上层模型代表主输电网络的决策过程，旨在合理调度主网内各发电机组的有功出力，并通过主配网联络节点为下层配网提供必要的电力支持，同时根据已有系统负荷信息，将节点的边际成本电价输送到下层网络，对下层网络的发用电行为进行调控。

1.1.1 目标函数

上层模型的目标函数是最小化整个调度周期内（如 24 小时）主网所有传统发电机组的的总运行成本。通常采用二次函数来近似表征发电机组的成本特性：

$$F=\sum_{t=1}^{T}\sum_{i\in\Gamma_G}C_i(P_{G,i}^t) \tag{1}$$

其中 F 为所有发电机组的运行成本之和；T 为整个机组组合的运行总时段；Γ_G 是主网中发电机组合集；$P_{G,i}^t$ 是第 i 台发电机组在 t 时刻的出力；$C_i(P_{G,i}^t)$ 是第 i 台发电机组在 t 时刻的运行成本，。

上层的发电机成本通常可以采用二次函数描述：

$$C_i(P_{G,i}^t)=\alpha_i(P_{G,i}^t)^2+\beta_i(P_{G,i}^t)+c_i \tag{2}$$

式中 α_i、β_i、c_i 分别为机组 i 的燃料费用特性曲线参数。

1.1.2 约束条件

为了保证主网运行的安全性，约束条件主要如下：

（1）发电机出力约束

主网发电机出力应满足其上下限：

$$P_{G,i}^{\min}<P_{G,i}^t<P_{G,i}^{\max}\qquad \forall i,t \tag{3}$$

式中 $P_{G,i}^{\min}$、$P_{G,i}^{\max}$ 分别为发电机组出力的最小值和最大值。

（2）联络节点功率限制

本文中，上下层网络通过联络节点进行信息交互以实现耦合，在高比例分布式光伏接入情形下，为充分反映主配网间实时功率流动特性，本文在主网负荷节点与配网联络处引入双向功率约束，第 k 各联络节点的功率约束数学表达式如下：

$$-P_{TD,k}^D<P_{TD,k}^t<P_{TD,k}^{\max} \tag{4}$$

式中，$P_{TD,k}^D$ 为配网允许向主网输送的最大功率；$P_{TD,k}^t$ 是第 k 个联络节点 t 时刻的功率，正值表示主网向配网输送功率，负值代表配网向主网反送功率；$P_{TD,k}^{\max}$ 指主网可输送的最大功率。

（3）节点电压安全约束

要重点保证联络节点的电压不越限，数学表达式如下：

$$V_k^{\min} < V_k^t < V_k^{\max} \tag{5}$$

式中，$V_k^{\min}$、$V_k^{\max}$为节点 k 处电压的上下限。

（4）功率平衡约束

主网全局需保持有功平衡，即所有发电机出力应同时满足主网自有负荷、向下游配网的电力输出和主网自身的网损：

$$\sum_{i\in\Gamma_G} P_{G,i}^t = P_{load}^{main,t} + \sum_{k\in\omega} P_{TD,k}^t + P_{loss}^t \tag{6}$$

式中，$P_{load}^{main,t}$为 t 时刻主网本地的负荷；P_{loss}^t为主网网损。

1.1.3 节点边际电价

LMP 是指在某一特定节点、时段，每增加一单位电力负荷所需增加的系统边际成本，主要由三部分组成：系统能量成本、拥堵成本和损害成本。在求解最优潮流（OPF）问题时，LMP 是功率平衡约束的拉格朗日乘子（Lagrange Multiplier），也称为影子价格（Shadow Price）。它代表了放松功率平衡约束一单位（即多需求一单位电力）时，目标函数（总成本）的最小变化量。

$$LMP_i = \lambda + \sum_l PTDF_{l,i}\cdot\mu_l + \eta_i \tag{7}$$

式中，λ为能量边际成本，l 是线路编号，$PTDF_{l,i}$指节点 i 注入单位功率对支路 l 潮流的贡献，μ_l是线路 l 潮流约束的影子价格，表示放松线路功率约束能节省的成本，η_i为输电损耗成本。

1.2 计及需求响应的配网光伏接入容量优化模型

下层模型中，建立了兼顾需求响应与节能减排思想的配电网优化模型，促进分布式光伏高效接入，提高配电网的经济性与绿色低碳水平。

1.2.1 目标函数

为促进分布式光伏高效接入，提高配电网的经济性与绿色低碳水平，本文以 LMP 对用户负荷与光伏安装的影响为核心，同时兼顾系统投资与购电经济性、碳减排效益，形成综合收益成本，目标为综合收益最大化。因此，综合成本主要包括与主网的电能交易收益、光伏投资成本和减碳量收益。

$$F = \sum_{t=1}^{T}\Lambda_t\cdot(-P_t^{net})\cdot\Delta t - \sum_{i\in N_{PV}} C_{PV,i}S_{PV,i} + \sum_{\mathrm{t}}\sum_{i\in N_{PV}}\alpha P_{PV,i}^t\Delta t \tag{8}$$

式中，Λ_t为 t 时刻的节点边际电价；P_t^{net}为系统净负荷，若为正值，表示向主网购电，若为负值代表向主网输电；$C_{PV,i}$为光伏单位容量的建设成本；$S_{PV,i}$为节点 i 处光伏接入容量；α是减碳收益因子；$P_{PV,i}^t$是 t 时刻光伏出力。

1.2.2 约束条件

（1）配网潮流约束

下层网络应该能够正常运行，满足潮流方程。

$$\begin{aligned} P_i^{L,t} + P_{PV,i}^t &= V_i^t\sum_{j\in\mathbb{N}} V_j^t[G_{ij}\cos(\theta_i^t-\theta_j^t) + B_{ij}\sin(\theta_i^t-\theta_j^t] \\ Q_i^{L,t} + Q_{PV,i}^t &= V_i^t\sum_{j\in\mathbb{N}} V_j^t[G_{ij}\sin(\theta_i^t-\theta_j^t) - B_{ij}\cos(\theta_i^t-\theta_j^t] \end{aligned} \tag{9}$$

（2）节点电压约束

由于光伏的接入会带来电压越限的问题，因此必须保证各节点电压不越限。

$$V_i^{\min} \le V_i^t \le V_i^{\max} \tag{10}$$

（3）光伏选址与容量限制

$$0 \le S_{PV,i} \le y_i S_{PV,i}^{\max},\quad y_i \in \{0,1\} \tag{11}$$

其中y_i代表节点 i 是否接入分布式光伏，0 表示不接入，1 表示接入；$S_{PV,i}^{\max}$为最大可接入容量限制。

1.2.3 节点边际电价对负荷与光伏规划的影响

（1）用户可调节负荷

在用户的日常用电里，负荷一般可以分为三类。一是满足用户日常基本需求，不可进行调节的负荷，一般称为刚性负荷，如电脑、照明、取暖等设备；二是可转移负荷，通常为洗衣机、EV 之类，短时间里暂停使用或改变使用时间，对用户影响不大的设备，作为主要负荷参与需求响应；三是可中断负荷，一般指通过供给侧补偿激励或电价引导，用户可选择断开的负荷。不同类型的用户，三类负荷占比各有不同。

因此，用户会根据 LMP 调节自己的负荷行为，从而实现主网对负荷的间接调控，使得负荷去向向光伏出力曲线靠拢，以提升配网对光伏的消纳能力。

$$P_{load.t} = P_{rigid.t} - P_{shift.t}(\Lambda_t) - P_{curt.t}(\Lambda_t) \quad (12)$$

式中，$P_{load.t}$ 为 t 时刻用户的实际负荷；$P_{rigid.t}$、$P_{shift.t}$、$P_{curt.t}$ 分布为 t 时刻用户刚性负荷、可转移负荷和可中断负荷。

（2）光伏出力策略

根据上层提供的 LMP，下层光伏发电处可决定是否进行弃光行为。当遇到 LMP 为负值时，上送功率反而会被扣钱，此时配网会考虑对光伏出力进行弃光策略以降低成本，光伏出力模型如下：

$$P_{PV,j,t} = x_j \cdot S_j \cdot \eta_{j,t} \cdot (1-\alpha_{j,t}) \quad (13)$$

式中，$P_{PV,j,t}$ 为 t 时刻，j 节点处光伏出力；x_j 为 0-1 变量，代表 j 节点处是否接入光伏；S_j 为接入容量；$\eta_{j,t}$ 为 t 时刻光伏出力系数；$\alpha_{j,t}$ 为 t 时刻弃光率。

弃光率定义如下：

$$\alpha_{j,t} = \begin{cases} 0 & \Lambda_t \geq \lambda_h \\ \max(0, \dfrac{\lambda_l - \Lambda_t}{\lambda_m - \lambda_l}) \cdot \alpha_{\max} & \lambda_l \leq \Lambda_t \leq \lambda_h \\ \alpha_{\max} & \Lambda_t \leq \lambda_l \end{cases} \quad (14)$$

式中，λ_h、λ_m、λ_l 分别为电价的高阈值、中点值、低阈值；$\alpha_{\max}$ 为最大弃光率。

1.3 小结

本节介绍了双层模型的建立思路。上层模型中以主网运行成本最低化为目标函数，通过最优潮流得到各发电机的出力方案以及联络节点的 LMP；下层模型通过联络节点获取到 LMP 信息之后，根据 LMP 调整光伏接入节点位置与接入容量，从而获得最优综合收益下的光伏接入情况。通过节点边际电价有效实现了主网对配网的实时调控，避免了单一配网分析的局限性。

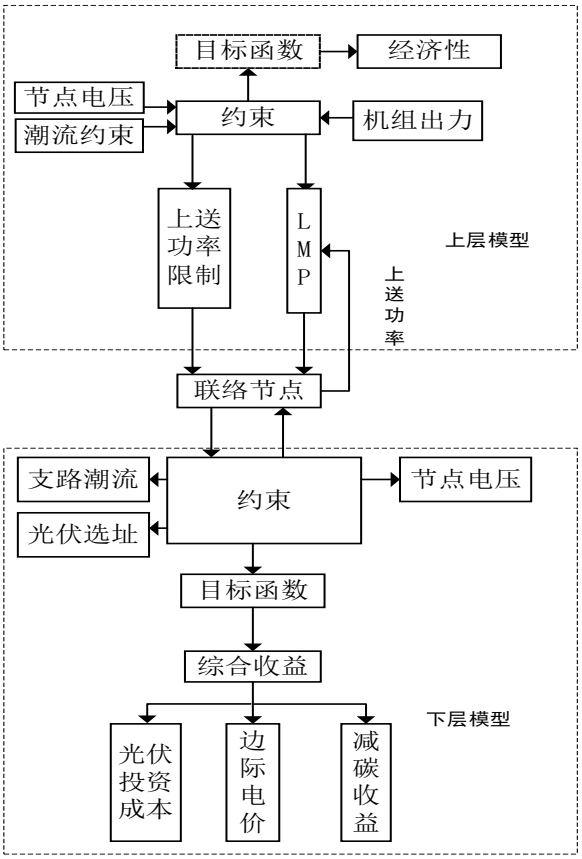


图 1 主配网协同双层模型

Fig.1 Bi-level Optimization Method for Transmission-Distribution Coordination

2 模型求解

2.1 上层模型求解

上层模型以发电机运行成本最低为目标函数，而发电机运行成本特性通常用一个二次函数进行描述。因此，在采用直流最优潮流（DC-OPF）线性化网络约束后，该上层问题可被归结为一个凸二次规划（Convex Quadratic Programming, QP）问题。

对于此类问题，原始-对偶内点法（Interior Point Method）是极为高效和成熟的求解算法。本文通过调用 CPLEX 求解器中的 QP 求解器，来实现该模型的求解。模型求解后，不仅能得到各机组的最优出力方案，也可以获得精确的与功率平衡约束对应的拉格朗日乘子，即本模型所需的节点边际电价（LMP），该信号作为关键参数传输至下层模型。

2.2 下层模型求解

下层模型以综合收益最大化为目标，其决策变量包括光伏选址（0-1 变量）、安装容量（连续变量），以及各时段的光伏实际出力（连续变量）、实际负荷情况（连续变量）。因此，该问题本质上是一个混合整数线性规划（Mixed-Integer Linear Programming, MILP）问题。

本文采用分支定界（Branch-and-Bound, B&B）法框架进行求解，该算法通过智能地枚举部分可行的整数解，并利用边界值进行剪枝，从而高效地搜索全局最优解或近似最优解。此过程的计算实现同样依赖于 CPLEX 求解器。求解器在接收来自上层的 LMP 信号后，对模型进行求解，最终输出最优的光伏配置（位置与容量）计划、运行策略以及与之对应的配网净负荷曲线。

2.3 整体求解流程

上下层模型通过 LMP 信号与净负荷曲线构成闭环反馈。为求解此耦合系统，本文设计如图 2 所示的松弛迭代算法，其步骤如下：

1) 初始化：设置迭代计数器 k=0，初始化配网净负荷曲线 $P_{net}^{0}(t)$，通常设置为原始负荷曲线，并设定收敛阈值 ε 与松弛因子 $\alpha \in [0,1]$。

2) 迭代循环（第 k 次迭代）：

a) 上层模型求解：将上一轮获得的配网净负荷曲线 $P_{net}^{k-1}(t)$ 输入到上层模型中，求解主网的直流最优潮流问题（DC-OPF）。求解完成后，获得联络节点除的节点边际电价信号 $\Lambda^{k}(t)$。

b) 下层模型求解：下层模型以 $\Lambda^{k}(t)$ 为导向，求解出综合收益最大的光伏接入容量与位置组合，以及光伏出力与负荷调整情况，从而获取该情况下的配网净负荷曲线 $P_{net}^{new}(t)$。

3) 收敛性判断：计算 $P_{net}^{new}(t)$ 与 $P_{net}^{k-1}(t)$ 的最大偏差，通过 $\delta = \max_t \left| P_{net}^{new}(t) - P_{net}^{k-1}(t) \right|$ 与收敛阈值 ε 相比，若 $\delta < \varepsilon$，则认为上下层模型交互已经稳定，跳转至步骤 4。否则，算法未收敛，对 $P_{net}^{k}(t)$ 进行平滑处理，$P_{net}^{k}(t) = \alpha \cdot P_{net}^{new}(t) + (1-\alpha) \cdot P_{net}^{k-1}(t)$，之后将 $P_{net}^{k}(t)$ 代回步骤 2 继续进行迭代。

4) 输出结果：算法收敛后，将输出最优解中光伏的接入容量与接入位置、总运行成本等。

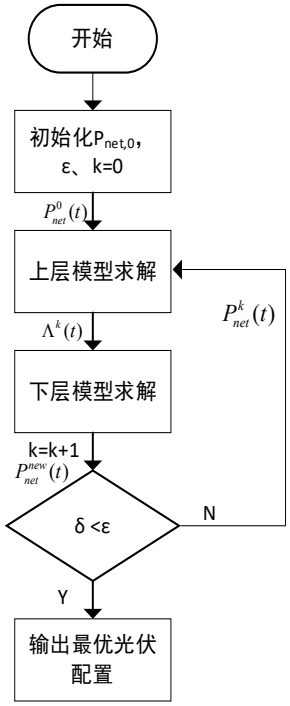


图 2 双层模型求解流程图

Fig.2 Solution Flowchart of the Bi-level Model

3 算例分析

3.1 参数设置

为验证所提基于 LMP 的主配网协同双层优化模型的有效性，本文选用 IEEE 30 节点系统（主网）和 IEEE 33 节点系统（配网）构建仿真算例。参数设置严格遵循电力系统分析规范。

（1）发电机参数设计：

发电机成本参数：30 节点系统中存在六台发电机（节点 1、2、22、27、23、13），机组处理限制最小值应该为 $0.2P_{max}$。机组爬坡约束 ΔP_i^{max} 去发电机容量的 20%。联络节点选择 8 号节点，其对应的功率限制为 8MW，

表 1 发电机参数

Table 1 Generator Parameters

节点编号	P_{max}/MW	二次项系数（元/MW²）	一次项系数（元/MW）	常系数(元)
1	150	0.02	2	0
2	60	0.0175	1.75	0
22	62.5	0.0625	1	0
27	48.7	0.00834	3.25	0
23	40	0.025	3	0
13	44.7	0.025	3	0

（2）负荷曲线：

24h 负荷曲线选取 ieee 提供的典型综合日负荷曲线：

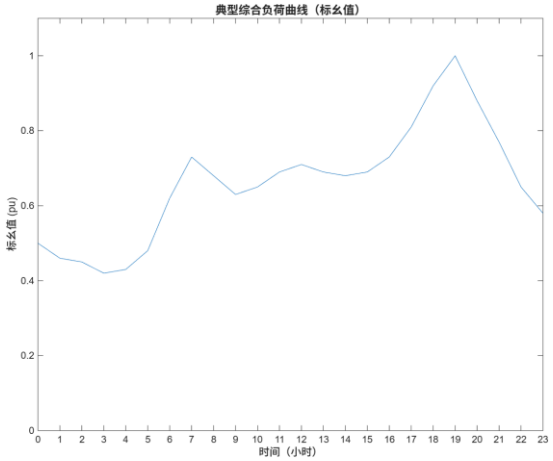


图 3 典型日负荷曲线

Fig.3 Typical Daily Load Curve

该负荷曲线两层模型中的负荷均适用，同时设置配网中可转移负荷和可中断占比 15%和 12%。

（3）光伏出力曲线

光伏出力采用典型日出力曲线描述。

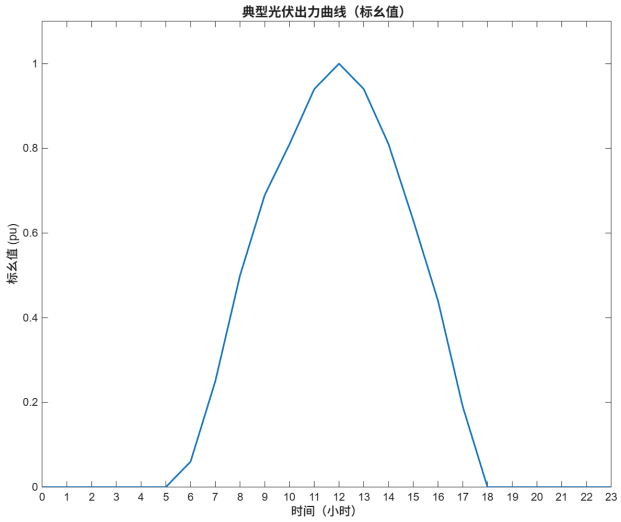


图 4 典型光伏出力曲线

Fig.4 Typical Photovoltaic Output Curve

（4）光伏接入节点设置

在 33 节点系统中，选择节点 2、10、18、22、29 五个节点作为光伏接入候选节点，根据其距离电源位置分为上（节点 2）、中（节点 10、18）、下游（节点 22、29）。其接入容量限制设为 5、3、2MW，装机成本为 4.5 万元/MW。

（5）经济性参数设置

减碳收益设置为 0.04 元/kw，LMP 的阈值 λ_h 、λ_m 、λ_l 分别为 60、40、20 元/Mwh。

（6）迭代参数设置

收敛阈值选择 0.01；最大迭代次数为 100；初始步长设置为 0.75；步长衰减 0.95；电压限值为±0.05p.u.

3.2 结果分析

本文采用 matlab 进行仿真，利用其中的 CPLEX 求解器进行求解。求解出的最佳容量与配置如表 2 所示。

表 2 最优光伏配置情况

Table 2: Optimal Photovoltaic Configuration Status

节点编号	接入容量（MW）
2	5
10	3
18	1.14
22	2
29	0.76

上层模型经过 DC-OPF 计算后得到的发电机组 24h 出力与成本如图 5 所示。

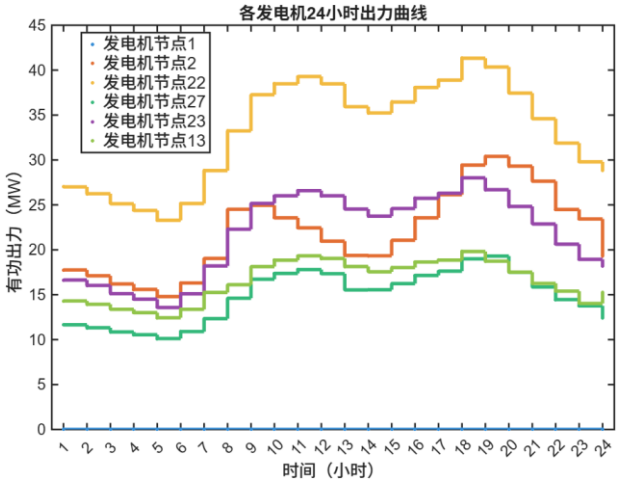


图 5 各发电机 24h 出力曲线

Fig.5: 24-hour Output Curves of Each Generator

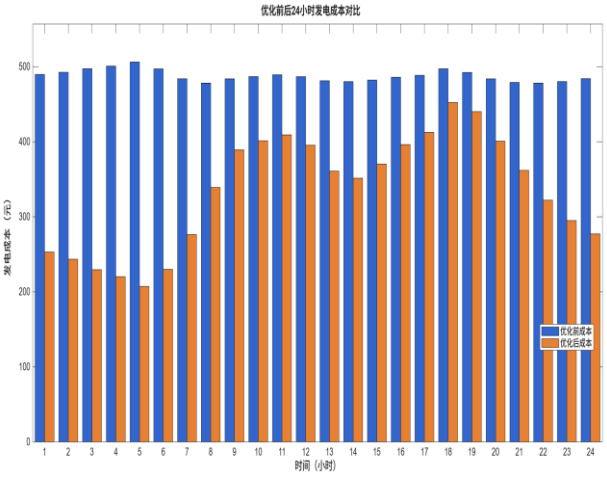


图 6 优化前后发电成本对比

Fig.6: Comparison of Power Generation Costs Before and After Optimization

表 3 优化前后主网运行成本

Table 3: Main Grid Operation Costs Before and After Optimization

	优化前（元）	优化后（元）	成本降低（%）
成本	11706.11	8034.65	31.36

可以看到，经过优化计算之后，日运行成本减少了 31.36%，有效增大了运行收益。

联络节点的 LMP 如图 7 所示。

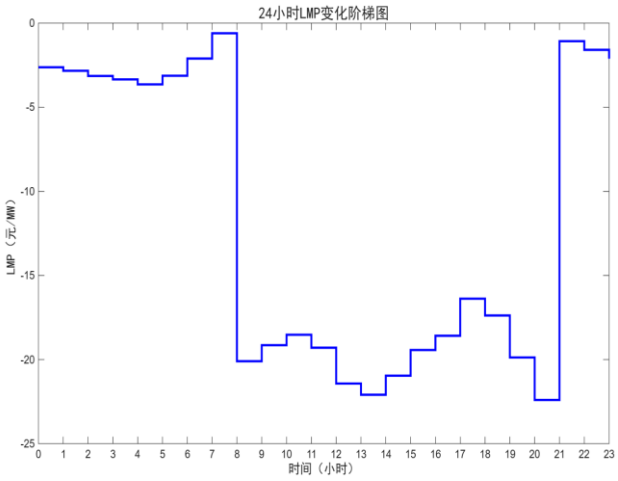


图 7 联络节点 LMP

Fig.7 LMP of Tie Nodes

下层模型根据 LMP 进行负荷调整和光伏出力调整：

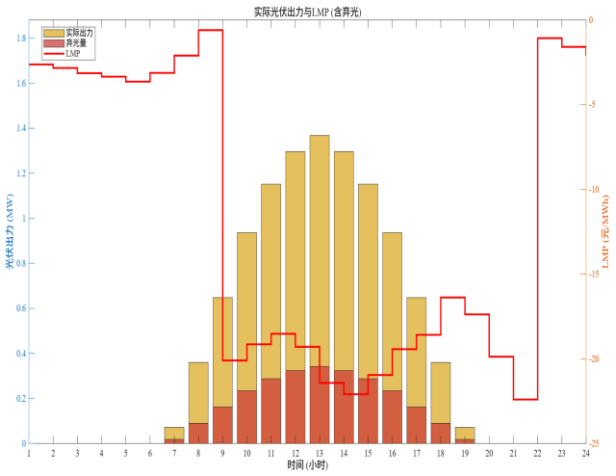


图 8 光伏出力情况

Fig.8 Photovoltaic Output Profile

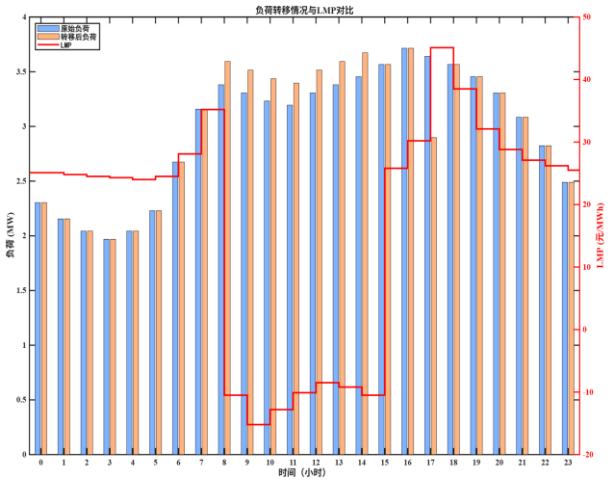


图 9 负荷变化情况

Fig.9: Load Variation Profile

由图 8 所示，LMP 能够有效调节配网中光伏的动作，在光伏出力较大的时刻，其上送功率高，对上层网络的稳定影响较大，因此 LMP 降低，甚至变为负数。当 LMP 低于一定阈值的时候，下层考虑对光伏进行弃光策略，以减少反向成本。对于负荷而言，则与之相反，当 LMP 降低时会鼓励用户进行用电，LMP 高的时候会抑制用户的用电意向，以此实现主网对用户负荷的间接调整。由图 9 所示，在 LMP 较高的 17 点，负荷出现了明显削减，转移到了 LMP 较低的 8-14 点，此时也恰好时光伏出力的峰值；如此调整，让负荷曲线向光伏出力曲线靠拢，即光伏出力多，用户负荷也多；光伏出力少，用户负荷也随之减少；提高了光伏的消纳能力，进一步提高了光伏可接入容量。

表 4 有无主网协调下光伏容量与收益对比

Table 4: Comparison of PV Capacity and Benefits With and Without Main Grid Coordination

	无主网协同	有主网协同	变化率
光伏接入容量	9.54（MW）	11.9（MW）	24.73%
综合收益	1207.18	1713.46	41.94%

在主网协同下，配网可接入光伏容量从 9.54MW 增至 11.9MW，提升了 24.73%，由此可见主网在配网光伏消纳的过程中，起着不可忽视的作用；同时在主网协同下，综合收益增长了 41.94%。

4 结论

本文针对大量分布式光伏接入配电网带来的容量问题进行探究，提出了一种基于节点边际电价的主配网双层容量优化模型。通过节点边际电价增强了主配网的耦合关系，LMP 可以动态调节配网中光伏的出力策略与用户的用电行为，通过电价的激励，让负荷曲线与光伏出力曲线进一步拟合，提

高了光伏的利用率，从而提高了配网可接入光伏的容量。同时，光伏上送可以缓解主网发电的压力，通过本文提出的双层模型，可以进一步优化主网发电策略，以降低运行成本。根据算例结果表明，本文提出的模型在保证电网安全运行的前提下，评估的配网分布式光伏可接入容量比传统保守评估更优异。

参考文献

[1] 孙荣富, 张涛, 梁吉. 电网接纳风电能力的评估及应用[J]. 电力系统自动化, 2011, 35(4): 70-76.

[2] 刘洪, 王博, 李梅菊, 等. 基于改进加权 Voronoi 图算法的有源配电网变电站规划[J]. 电力系统自动化, 2017, 41(13): 45-52.

[3] 梁双, 胡学浩, 张东霞, 等. 基于随机模型的光伏发电置信容量评估方法[J]. 电力系统自动化, 2012, 36(13): 32-37.

[4] 张沈习, 袁加妍, 程浩忠, 等. 主动配电网中考虑需求侧管理和网络重构的分布式电源规划方法[J]. 中国电机工程学报, 2016, 36(S1): 1-9.

[5] 周良学, 张迪, 黎灿兵, 等. 考虑分布式光伏电源与负荷相关性的接入容量分析[J]. 电力系统自动化, 2017, 41(4): 56-61.

[6] 刘志鹏, 文福拴, 薛禹胜, 等. 计及可入网电动汽车的分布式电源最优选址和定容[J]. 电力系统自动化, 2011, 35(18): 11-16.

[7] 姜拓, 方必武, 陈亦平, 等. 基于多参数规划的主配网协同优化运行方法[J]. 南方电网技术, 2023, 17(9): 10-19.

[8] 王淏, 王润铸, 谢开贵, 等. 新能源电力系统能量-网损-备用协同决策下的交流潮流嵌入式节点边际定价方法[J]. 中国电机工程学报, 2025.



收稿日期：2013-07-04。

作者简介：

李奕衡(2001 年)，男，硕士研究生，研究方向为电力系统运行与控制，E-mail：lyh.2001@qq.com；

李奕衡

119 A State Inference Method for Distribution Networks Utilizing Minimally Acquired Operational Data and Its Application

XIA Dong[1,2], SHAO Siyang[1,2], PENG Fan[3], ZHANG Zhihao[1,2], ZHANG Yulin[1,2]

[1] State Grid Electric Power Research Institute(NARI Group Corporation), Nanjing 211106, Jiangsu, China;

[2] NARI Technology Co., Ltd., Nanjing 211106;

[3] State Grid Hengshui Electric Power Supply Company Hengshui, China

xiadong91520@163.com

Abstract. With the accelerated integration of distributed energy resources and sensing devices, data incompleteness and quality imbalance have become major obstacles to the practical deployment of advanced distribution network applications. This paper proposes a state inference method for distribution networks under limited measurement conditions. By conducting coverage-level analysis, inferring non-automated switch states, and applying active power estimation and allocation, the method enables near real-time completion of key parameters such as bus voltage, transformer power, and switch status. Engineering applications demonstrate that the proposed approach can effectively enhance observability and measurability of the distribution network, overcome the "difficulty in practical application" caused by insufficient data, and provide strong support for dispatching, operation control, and intelligent applications.

Keywords: Distribution network; Data inference; Minimal measurement; State awareness; Non-automated switch; Active power estimation

1 Introduction

The distribution network is a crucial link between the main grid and end users, directly influencing power system efficiency and supply quality. The increasing integration of distributed photovoltaics, electric vehicles, and energy storage has heightened distribution network complexity, introducing bi-directional flows, multi-source coordination, and high volatility, which challenge real-time awareness and precise control.

Automation by deploying switches, smart meters, and terminals is considered essential for improving observability. However, extensive scale and scattered devices make comprehensive upgrades expensive and slow. Many switches and distribution transformers lack real-time acquisition, creating "black box" regions and limiting applications such as state estimation, fault restoration, and voltage optimization.

To address these challenges, leveraging available data and network models, along with inference technologies, has become critical for enhancing observability. State Estimation (SE), established for transmission networks and employing redundant measurements and optimization (e.g., Weighted Least Squares, WLS)[1], faces difficulty in distribution networks due to radial structures, phase imbalance, and sparse data. Accordingly, tailored SE methods have emerged: Abur and Expósito[2] provided

theoretical foundations; Baran and Kelley[3] introduced branch current-based SE for sparse measurements; voltage magnitude-based SE relies on node voltages[4]; robust estimation mitigates erroneous data effects[5]. However, the efficacy of these approaches depends on measurement coverage, and widespread application in non-automated feeders, especially in China, remains problematic.

2 State Estimation Service Design

2.1 Basic Definition

Data inference (or estimation) technology uses partial measurements, system topology, physical constraints, and historical data as prior knowledge to estimate unmeasured or unreliable system states. It is becoming an effective solution to the data scarcity problem in distribution networks. The "minimal measurement" strategy installs measurement devices only at key nodes to meet core requirements, and applies efficient inference algorithms to achieve wide-ranging state awareness at low cost, providing significant economic and practical benefits.

2.2 Overview of Functional Architecture

The distribution network state inference service enhances operational transparency by combining minimal measurement with digital inference, limiting resource investment while supporting dispatch, O&M, and planning. Rather than real-time measurement of all devices, key-node sensors (at main lines, branches, tie lines) and prior knowledge (physical laws, topology, history) enable calculation of non-key node states.
Its logical architecture (see Figure 1) includes measurement coverage analysis, non-automatic switch status inference, active power state inference, and result release. This closed-loop process executes periodically to maintain real-time, accurate inference.

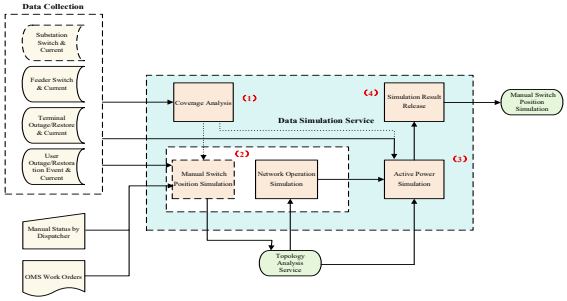


Fig.1 Logical Architecture Diagram of Distribution Network Operation State Deduction Service

2.3 Measurement Coverage Analysis

Measurement coverage analysis initiates the inference service by evaluating available data, clarifying basic conditions, informing algorithm and strategy selection for subsequent inference, and allowing pre-assessment of final result accuracy.

The analysis focuses on key distribution network nodes—substation outlet breakers, sectionalizing switches, branch switches, tie switches, and distribution transformers—by assessing the accessibility and availability of their real-time data (measurements, signals). The line's data collection status falls into five categories:

(1) Full measurement coverage: Real-time data is available for all key switches and transformers, allowing direct state estimation and load flow calculation.

(2) Minimal measurement coverage: Sensors are installed at critical locations, with some locations lacking real-time data; anchor data at key nodes drives modeling and inference for network state estimation.

(3) Switch-only measurement: Real-time data for switches is available, but transformer data is missing; transformer loads are inferred from historical ratios or capacity.

(4) Transformer-only measurement: Transformer data is available but switch data is lacking; transformer readings act as boundary conditions for bottom-up inference.

(5) No measurement coverage: Neither switches nor transformers have real-time data, so inference relies on substation data, line parameters, and history, with low accuracy.

Measurement coverage analysis results define inference starting points and determine accuracy ratings, which are coded for reference by downstream applications.

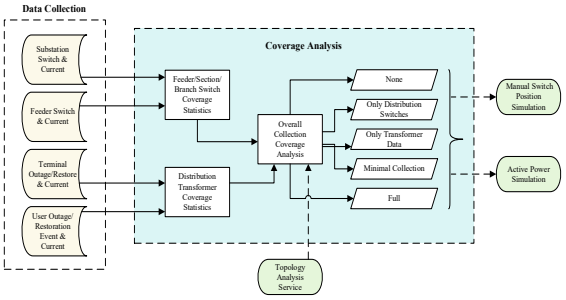


Fig.2 Logical Architecture Diagram of Acquisition Coverage Rate Analysis

2.4 Inference of Non-Automated Switch Status

The estimation of non-automated switch status is a crucial step in addressing the "switch status black box" problem in distribution networks. The objective is to integrate multiple heterogeneous information sources to accurately identify the real-time status (closed/open) of non-automated switches, thereby enabling the reconstruction of network topological connectivity. This process primarily relies on three approaches: (1) manual maintenance by dispatchers, based on feedback from field operators; (2) automated and authoritative status updates synchronized from executed Operation Management System (OMS) operation records; and (3) deduction utilizing grid topology and physical constraints, where status is inferred through analysis of upstream

and downstream measurement variations, particularly under scenarios such as power restoration, outages, ring closing, and ring opening.

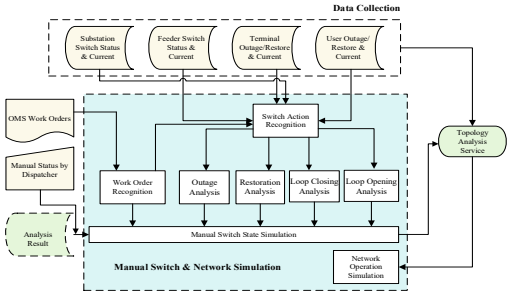


Fig.3 Logical Architecture Diagram of Non-Automated Switch State Deduction

2.5 Active Power Inference

Active power inference estimates the node power along a feeder, especially at unmeasured nodes, based on known or deduced topology and limited measurement data. The process consists of two steps: interval active power estimation and single-point weight-based allocation.

(1) Partitioning Measurement Intervals and Interval Power Estimation

Based on the real-time topology and available measurements, the feeder is divided into independent measurement intervals, each bounded by switches or transformers with actual power measurements. For each interval, the difference between upstream and downstream measured active power represents the total load (or net distributed generation) within that interval. Power flow calculation or simple power balancing is used to estimate this total, treating all unmeasured loads as a single equivalent load.

(2) Single-Point Power Weight Analysis and Allocation

The estimated interval active power is allocated to individual load points (such as users or small branches) according to power weighting methods:

a) Equal allocation is used when no load data is available, assuming equal power at each point;

b) Installed capacity allocation uses the ratio of each point's installed capacity;

c) Similar-day prediction applies historical load proportions based on days with similar conditions.

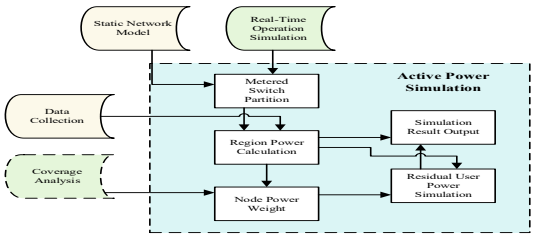


Fig.4 Logical Architecture Diagram of Active Power Deduction

3 Case Analysis

To validate the proposed method, five typical scenarios are analyzed:
Scenario 1: Inference Based on Minimal Data Acquisition (Recommended Scenario)
Conditions: Only real-time feeder head power, key sectionalizing switches (KG1, KG2), tie switch (KG3), and distributed PV output are measured; no real-time data for other switches or transformers.
Process: Main feeder power flows are determined by key switches; branches with distributed generation are prioritized, while other sections are inferred using line parameters.
Conclusion: Accurately infers main feeder parameters and branch flows with high precision, demonstrating the feasibility and efficiency of the "minimal data acquisition" strategy.

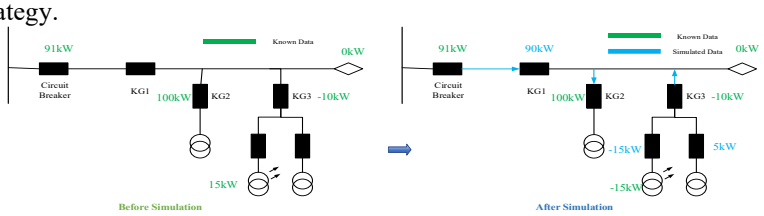


Fig.5 Deduction Case Based on Minimized Acquisition

Scenario 2: Inference Based on Transformer Data
Conditions: Real-time data from feeder head and all distribution transformers; no switch measurements.
Process: Feeders are partitioned by feeder head and transformers; power at each node is computed iteratively. Switch parameters are supplemented using main branch and tie switch data; other sections are inferred by line parameters.
Conclusion: Provides a fairly complete node parameter and flow profile but has limited ability to identify switch status, especially under looped operation, yielding moderate accuracy.

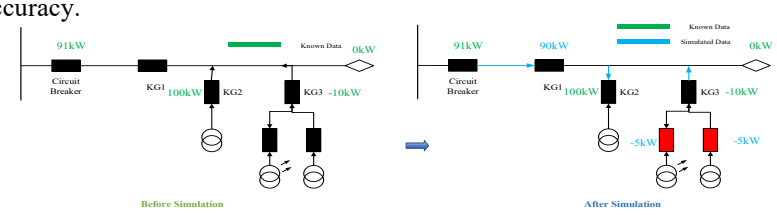


Fig.6 Deduction Case Based on Distribution Transformer Data

Scenario 3: Inference Based on Switch Data (Main Feeder Observable)
Conditions: Real-time data from feeder head and key switches; no transformer measurements.
Process: Similar to Scenario 2, node powers are computed via switch data, and feeder segments are completed accordingly.

Conclusion: Main feeder flows can be inferred accurately with moderate overall accuracy. This scenario highlights the importance of key switch data for main feeder observability and control.

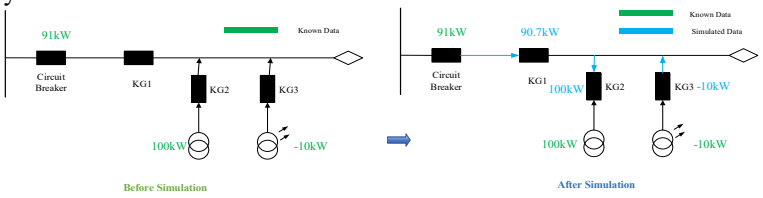


Fig.7 Logical Architecture Diagram of Distribution Network Switch Deduction

Scenario 4: Inference Without Real-Time Measurements
Conditions: Only feeder head total active power is available; no other measurements.
Process: Power is allocated to branches based solely on feeder parameters (e.g., impedance, length).
Conclusion: Basic main feeder flows can be inferred but with low precision, illustrating the limitations of model-driven approaches without measurement data.

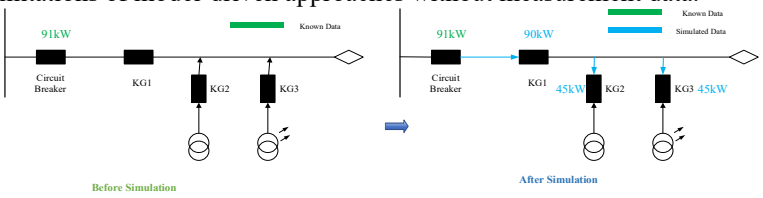


Fig8 Deduction Case Without Acquisition

Scenario 5: Full Data Acquisition (Ideal Scenario)
Conditions: Full real-time data from feeder head, all switches, and transformers.
Process: State estimation and data validation are performed with comprehensive measurements, providing the most accurate results.
Conclusion: Yields high-precision network state and demonstrates the value of comprehensive data for maximum observability.

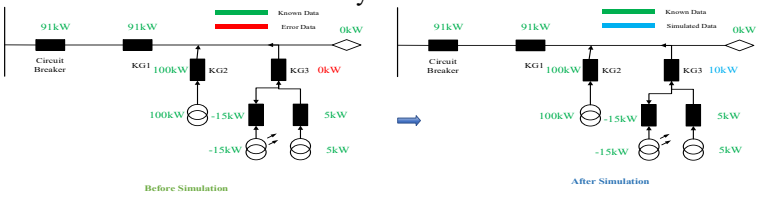


Fig.9 Deduction Case With Full Data Acquisition

4 Conclusion

This paper proposes a distribution network state inference method based on minimal data acquisition, encompassing coverage analysis, non-automated switch status inference, active power estimation, and result publishing. The approach leverages key

node “anchor” data, grid models, and multi-source information to infer the states of non-key nodes under limited measurement conditions, substantially improving network observability. This provides a practical solution to balance investment and monitoring capability.

Future work includes: (1) integrating advanced machine learning algorithms (e.g., GNNs) to optimize weight assignment and enhance inference accuracy; (2) developing uncertainty quantification for inferred results to support comprehensive risk assessment; and (3) integrating inference services with fault location and network reconfiguration to validate application value.

Acknowledgement: This paper is based on the scientific research project “Research on Active Perception of New Distribution Network Edge Equipment Resources and Graph-based Model State Inference Technology (Project Code: 5400-202413188A-1-1-ZN).” The authors gratefully acknowledge the support of this project for the present study.

References

1. Mei, D., Xu, B., Chen, Q., et al.: Fault location method for distribution networks based on measurement data and topology analysis [J]. Automation of Electric Power Systems 42(14), 126–132 (2018).
2. Abur, A., Expósito, A.G.: Power System State Estimation: Theory and Implementation [M]. CRC Press, Boca Raton (2004).
3. Baran, M.E., Kelley, A.W.: State estimation for real-time monitoring of distribution systems [J]. IEEE Transactions on Power Systems 9(3), 1601–1609 (1994).
4. Wang, S., Wang, H., Cai, S.: Review of voltage control issues in distribution networks under distributed generation conditions [J]. Automation of Electric Power Systems 33(16), 95–100 (2009).
5. Li, H., Liu, Y., Xiang, Y., et al.: Active distribution network state estimation based on improved particle swarm optimization [J]. Automation of Electric Power Systems 41(17), 47–53 (2017).
6. Chen, P., Chen, Y., Infield, D., et al.: Distributed real-time power balancing in renewable-integrated power grids with storage and flexible loads [J]. IEEE Transactions on Smart Grid 6(1), 69–79 (2015).
7. Chen, C., Wu, W., Zhang, B., et al.: Key technologies for practical distribution network state estimation based on SCADA and multi-source data [J]. Automation of Electric Power Systems 39(9), 54–60 (2015).
8. Jiang, L., Singh, C.: A reliability evaluation method for distribution systems considering voltage-dependent loads and protection schemes [J]. IEEE Transactions on Power Delivery 27(3), 1484–1492 (2012).

120 Specific-Area-Level Charging Demand Forecasting and Analysis for Electric Vehicles Using iTransformer

Xinyuan Bao[1], Jinghua Su[1], Ran Bao[1] and Junjun Deng[1, 2]

[1] National Engineering Research Center of Electric Vehicles, Beijing Co-Innovation Centre for Electric Vehicles, Beijing Institute of Technology, Beijing 100081, China
[2] Corresponding author: dengjunjun@bit.edu.cn

Abstract. The accelerated popularity of electric vehicles has led to a surge in charging demand in megacities, placing peak pressure on urban power grids. Traditional electric vehicle charging demand forecasting mainly predicts charging demand for the entire city or a certain administrative district within the city, ignoring the issue that the maximum power that transformers can withstand in a single area has an upper limit. Based on the area where the transformer consumes electricity, multiple specific area can be divided. To this end, this study takes charging vehicles in various specific area in a certain city as the research object, realizes end-to-end multi-specific-area new energy vehicle charging power prediction based on iTransformer, and analyzes the experimental results of different specific area. The results show that the charging demand and charging power fluctuation characteristics of different specific area are significantly different. iTransformer can effectively capture their periodic laws, verifying its generalization ability in the scenario of end-to-end prediction in multiple specific area. This study refines the spatial granularity of electric vehicles, realizes end-to-end charging power prediction in multiple specific area, and analyzes the differences in the prediction results. It is of great significance for optimizing the allocation of charging resources, avoiding local overload of the power grid, and supporting vehicle-to-grid scheduling.

Keywords: Charging power, Specific area, iTransformer.

1 Introduction

The widespread adoption of electric vehicles (EVs) is profoundly reshaping the operating paradigm of urban energy systems [1, 2]. For example, Shenzhen, the world's first city to achieve full electrification of public transportation, has seen its EV charging load account for 18% of the grid's peak hours. However, the spatially uneven distribution of charging demand can lead to increased frequency of local grid voltage fluctuations and widening peak-to-valley differences, posing significant challenges to the grid's peak-shaving capacity and new energy consumption efficiency [3, 4]. Therefore, accurate prediction of EV charging demand is of great value for grid operation stability, renewable energy consumption, charging facility planning, and vehicle-to-grid (V2G) scheduling [5].

Commonly used traditional charging demand prediction methods are probability-based methods, typically Monte Carlo (MC). For example, Reference [6] uses the MC method to achieve daily charging demand prediction. Reference [7] combines MC with travel parameters related to the travel chain to achieve EV charging demand prediction. Reference [8] first simulates the behavior of electric vehicle users based on the travel chain, and then predicts charging demand based on MC. However, MC requires a predefined probability distribution. If the assumption deviates greatly from the actual behavior, the prediction error will be significantly amplified. In recent years, since data-driven methods can automatically capture the complex nonlinear relationship of input data without manually setting distribution assumptions, some recent studies have adopted data-driven methods to achieve electric vehicle charging demand prediction [9,10], including support vector machines (SVM) [11], random forest algorithms [12], long short-term memory (LSTM) neural networks [13], etc. Reference [14] uses Transformer to predict charging demand at different time steps and shows that this method is superior to traditional models. Although these models have achieved remarkable results in charging demand prediction, none of the above methods have gone deep into the analysis of the transformer power supply unit level.
The specific area divided according to the power supply range of the transformer are important management units for grid peak regulation and voltage control. The temporal and spatial fluctuations of their charging loads will directly affect the overload risk of the transformer and the local power quality. Refined prediction of charging demand within the specific area will help to achieve dynamic electricity prices and power regulation of different charging piles. At the same time, EVs can be dispatched to grids with lower load carrying rates through V2G to achieve cross-grid charging resource optimization, effectively alleviating the local grid overload and resource idleness problems caused by uneven spatial distribution of charging demand. Based on this, this study uses the iTransformer architecture to realize the specific-area-level electric vehicle charging demand prediction and conducts a difference analysis of the experimental results of each district. The paper is structured as follows: the second part mainly introduces the model theory, the third part is experimental verification, and the fourth part is summary and prospect.

2 Methodology

In recent years, the Transformer architecture has achieved great success in the field of time series prediction. However, when it is directly applied to prediction tasks, it faces the problems of performance degradation and low computational efficiency. To this end, reference [15] proposed the iTransformer architecture, which achieves efficient and accurate time series prediction by reversing the application dimension of the components in the traditional Transformer architecture. Based on this, this study uses the iTransformer architecture to achieve end-to-end multi-specific-area charging demand forecasting. The specific process is as follows: First, based on the geographical division of the specific area, all electric vehicle charging data in each specific area within a one-year time span is collected. Next, the extracted vehicle raw slice data is

preprocessed to extract features such as the total average charging power and the number of charging vehicles in each specific area, and time series data for each specific area is obtained according to the time sampling interval. Then, the preprocessed electric vehicle raw feature data is input into the iTransformer model, and the charging power at different times is set as the output of the model. The data of each specific area is uniformly trained. Finally, with the help of the fully trained model, the effectiveness of the model is verified in each specific area. The structure of the model is shown in Figure 1, and the specific implementation is as follows.

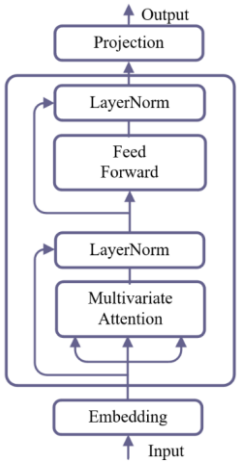


Fig. 1. iTransformer architecture.

Given a multivariate time series dataset $X = \{x_1, ..., x_T\} \in R^{T \times N}$, where T is the number of time steps and N is the number of variables, the goal is to predict the sequence $Y = \{x_{T+1}, ..., x_{T+S}\} \in R^{S \times N}$ for the next S time steps. First, iTransformer embeds each time series $X_{:,n}$ independently into a variable token h_{0n}:

$$h_{0n} = MLP(X_{:,n}). \tag{1}$$

The MLP is a multi-layer perceptron that maps time series to a D-dimensional vector space. iTransformer then uses a self-attention mechanism to capture the multivariate correlations between variable tokens. For the l-th layer Transformer block, the calculation process of the self-attention mechanism is as follows:

$$Q^{(l)}, K^{(l)}, V^{(l)} = h^{(l-1)}W_q^{(l)}, h^{(l-1)}W_k^{(l)}, h^{(l-1)}W_v^{(l)}, \tag{2}$$

$$Attention(Q^{(l)}, K^{(l)}, V^{(l)}) = softmax\left(\frac{Q^{(l)}(K^{(l)})^T}{\sqrt{D}}\right)V^{(l)}, \tag{3}$$

where $W_q^{(l)}$, $W_k^{(l)}$, $W_v^{(l)}$ are learnable weight matrices, and $h^{(l-1)}$ is the output of the $l-1$ th layer.

iTransformer also utilizes a feedforward neural network to learn nonlinear representations for each variable token:

$$FFN(h^{(l)}) = ReLU(h^{(l)}W_1^{(l)} + b_1^{(l)})W_2^{(l)} + b_2^{(l)}. \tag{4}$$

Among them, $W_1^{(l)}$ and $W_2^{(l)}$ are learnable weight matrices, $b_1^{(l)}$ and $b_2^{(l)}$ are bias terms, and ReLU is the activation function.

To improve training stability and convergence speed, iTransformer introduces layer normalization and residual connection in each Transformer block:

$$h^{(l)} = LayerNorm(h^{(l-1)} + Attention(Q^{(l)}, K^{(l)}, V^{(l)})), \tag{5}$$

$$h^{(l)} = LayerNorm(h'^{(l)} + FFN(h'^{(l)})). \tag{6}$$

Finally, iTransformer maps the final variable token representation to the predicted time series through a linear projection layer:

$$\hat{Y}_{:,n} = Projection(h_L^{(n)}), \tag{7}$$

where $h_L^{(n)}$ represents the n-th variable token output by the L-th layer Transformer block. Considering that the dimensions of the predicted variables are inconsistent with the input variables and the model has multivariate input and univariate output, this study extracts the predicted values corresponding to the predicted variables based on the output of the linear projection layer and calculates the mean squared error loss based on this. In this study, the loss function can be expressed as follows:

$$\mathrm{L}_{\mathrm{MSE}} = \frac{1}{M}\sum_{i=1}^{M}(\hat{y}_i - y_i)^2, \tag{8}$$

where M is the number of samples, $\hat{y}_i$ and y_i represent the i-th predicted value and true value respectively.

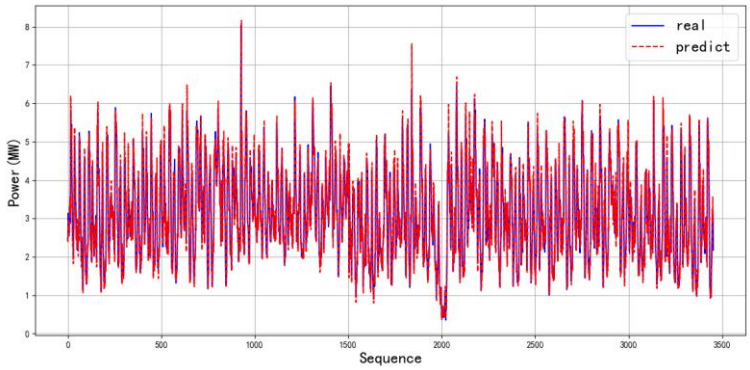
3 Experiment

Table 1. Evaluation results of different specific area RMSE indicators.

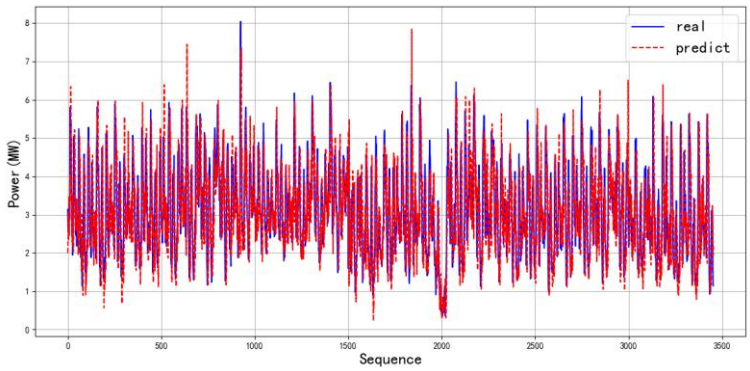
Specific area	X001	X002	X003	X004	X005	X006	Mean
Step1	0.40014	0.18098	0.31669	0.25416	0.26016	0.48054	0.31545
Step2	0.64949	0.28029	0.52780	0.39699	0.40301	0.76672	0.50405
Step3	0.83494	0.35962	0.70259	0.51333	0.51740	0.99460	0.65374
Step4	0.98135	0.42313	0.84635	0.61130	0.61384	1.15485	0.77180

Table 2. Evaluation results of different specific area MAE indicators.

Specific area	X001	X002	X003	X004	X005	X006	Mean
Step1	0.29198	0.11240	0.15347	0.14444	0.17355	0.25272	0.18809
Step2	0.46875	0.17561	0.24779	0.22909	0.27155	0.40632	0.29985
Step3	0.60769	0.22533	0.33009	0.30188	0.35118	0.53444	0.39177
Step4	0.72030	0.26531	0.39768	0.36270	0.42092	0.63546	0.46706



(a) Step1



(b) Step4

Fig. 2. Comparison of experimental results of different step lengths of X001 specific area.

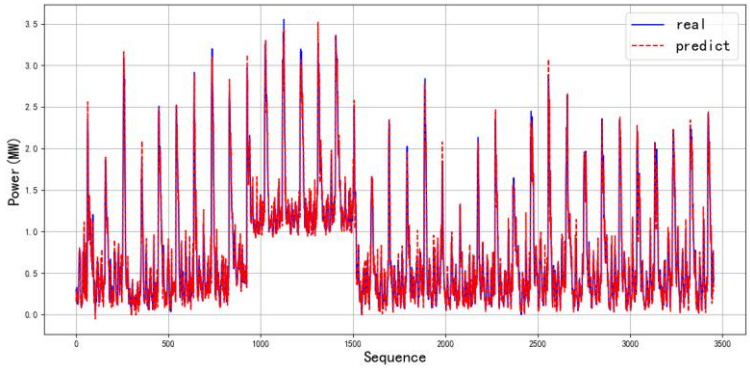
In this study, six typical specific area in a city were selected to achieve specific-area-level EV charging demand forecasting. The input variables of the model include the average power sum of all charging vehicles in each specific area, the total number of charging vehicles, the sum of charging voltages and other raw data collected by vehicles. The data sampling interval is 15 minutes, and the training set, validation set and test set are divided into 8:1:1. The hyperparameters of the iTransformer model are set as follows: the prediction step size is 4, the number of encoder layers L=1, the number of attention heads is 4, and the hidden layer dimension is 64. In order to evaluate the effectiveness of the model, the experiment uses the root mean square error (RMSE) and mean absolute error (MAE) for verification:

6

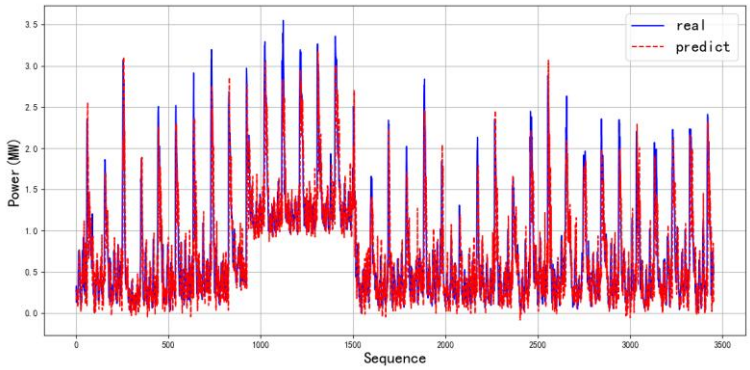
$$\mathrm{RMSE} = \sqrt{\frac{1}{M}\sum_{i=1}^{M}(\hat{y}_i - y_i)^2}, \tag{9}$$

$$\mathrm{MAE} = \frac{1}{M}\sum_{i=1}^{M}|\hat{y}_i - y_i|. \tag{10}$$

Like the loss function, M is the number of samples, $\hat{y}_i$ and y_i represent the i-th predicted value and true value respectively.

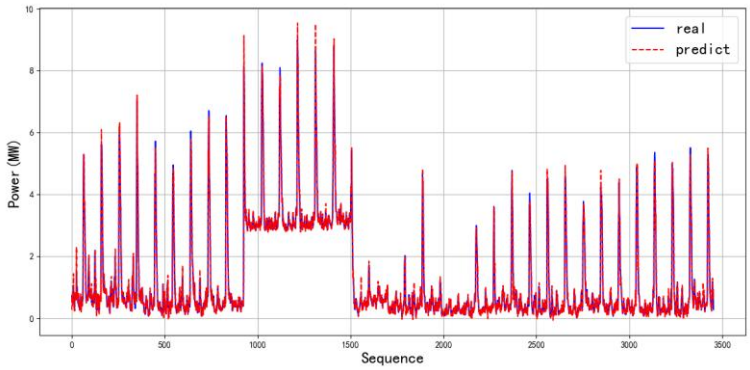


(a) Step1

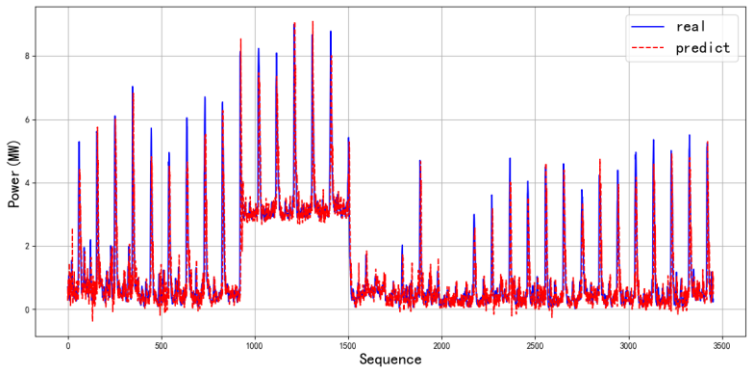


(b) Step4

Fig. 3. Comparison of experimental results of different step lengths of X002 specific area.



(b) Step1



(b) Step4

Fig. 4. Comparison of experimental results of different step lengths of X003 specific area.

This study systematically evaluated the predictive performance of the iTransformer model in different types of specific area (X001-X006). The RMSE and MAE metrics were analyzed as a function of the prediction step size (Step 1-Step 4). The experimental results, shown in Tables 1 and 2, show an increasing RMSE for each specific area as the prediction step size increases from Step 1 to Step 4, indicating that the model's prediction uncertainty increases with increasing time step size. The MAE metric exhibits a consistent trend with the RMSE, but with a lower absolute error, further confirming the cumulative prediction error with increasing step size. In addition, the error performance of different specific area varies. For example, X001 and X002 have significant differences in RMSE and MAE. In Step 4, the RMSE/MAE of X001 are 0.98135/0.72030, while that of X002 is only 0.42313/0.26531. Figures 2 and 3 show the prediction results for X001 and X002 at different step sizes, respectively. The figures clearly show that the charging power range for the X001 specific

area is generally concentrated between 2MW and 5MW, while the charging power range for X002 is generally below 1MW. The differences in RMSE and MAE between specific area are primarily due to the significant differences in charging power. When the power base is large, a relative error of the same magnitude translates into a higher absolute error. Therefore, specific area with higher charging power levels tend to exhibit larger RMSE and MAE.

Figure 4 shows the prediction results for the X003 specific area at different step sizes. The figure shows that the prediction results for Step 1 are closer to the true value than those for Step 4, which is consistent with the results in the table. Figures 2-4 show that the power fluctuation trends vary significantly across specific area, which undoubtedly increases the difficulty of prediction. However, within each specific area, the iTransformer model maintains good prediction performance for both Step 1 and Step 4, demonstrating the effectiveness of the method.

4 Conclusions

This study proposed an iTransformer-based method for predicting specific-area-level charging demand for new energy vehicles. Results from six typical specific area demonstrated that this method performs well across different specific area. The RMSE and MAE metrics vary across specific area, influenced by the varying charging power bases of these specific area. This suggests that charging activity varies across different specific area. This research not only provides a highly accurate charging demand prediction tool but also, by refining the requirements of each specific area, lays the theoretical foundation for building a V2G collaborative optimization system. This holds strategic significance for promoting the electrification of transportation under the goal of carbon neutrality.

Acknowledgement： This work is supported by Smart Grid National Science and Technology Major Project under Grant-Technologies and Equipment of Vehicle-to-Grid Interaction Driven by Big Data（2024ZD0800300）and China Postdoctoral Science Foundation (2025M774196) .

References

1. Heidrich O, Dissanayake D, Lambert S, et al. How cities can drive the electric vehicle revolution[J]. Nature Electronics, 2022, 5(1): 11-13.
2. Luo W, Chang X, Fu R, et al. Charging-discharging scheduling strategy for electric vehicles considering supply and demand[J]. Journal of Power System Automation, 2022, 34: 106-112.
3. Yi T, Zhang C, Lin T, et al. Research on the spatial-temporal distribution of electric vehicle charging load demand: A case study in China[J]. Journal of Cleaner Production, 2020, 242: 118457.

4. Jiang D, Gong X, Wei Y, et al. An electric vehicle charging demand prediction approach based on a Graph-based Spatio-Temporal Attention Network[J]. Sustainable Energy, Grids and Networks, 2025:101975.
5. Lehtola T. Vehicle-to-grid applications and battery cycle aging: A review[J]. Renewable and Sustainable Energy Reviews, 2025, 208: 115013.
6. Su J, Lie T T, Zamora R. Modelling of large-scale electric vehicles charging demand: A New Zealand case study[J]. Electric Power Systems Research, 2019, 167: 171-182.
7. Li M, Lenzen M, Keck F, et al. GIS-based probabilistic modeling of BEV charging load for Australia[J]. IEEE Transactions on Smart Grid, 2018, 10(4): 3525-3534.
8. Zhang L, Huang Z, Wang Z, et al. An urban charging load forecasting model based on trip chain model for private passenger electric vehicles: A case study in Beijing[J]. Energy, 2024, 299: 130844.
9. Yaghoubi E, Yaghoubi E, Khamees A, et al. A systematic review and meta-analysis of machine learning, deep learning, and ensemble learning approaches in predicting EV charging behavior[J]. Engineering Applications of Artificial Intelligence, 2024, 135: 108789.
10. Genov E, De Cauwer C, Van Kriekinge G, et al. Forecasting flexibility of charging of electric vehicles: Tree and cluster-based methods[J]. Applied Energy, 2024, 353: 121969.
11. Sun Q, Liu J, Rong X, et al. Charging load forecasting of electric vehicle charging station based on support vector regression[C]//2016 IEEE PES Asia-Pacific Power and Energy Engineering Conference (APPEEC). IEEE, 2016, 1777-1781.
12. Lu Y, Li Y, Xie D, et al. The application of improved random forest algorithm on the prediction of electric vehicle charging load[J]. Energies, 2018, 11(11): 3207.
13. Wang S, Zhuge C, Shao C, et al. Short-term electric vehicle charging demand prediction: A deep learning approach[J]. Applied Energy, 2023, 340: 121032.
14. Koohfar S, Woldemariam W, Kumar A. Prediction of electric vehicles charging demand: A transformer-based deep learning approach[J]. Sustainability, 2023, 15(3): 2105.
15. Liu Y, Hu T, Zhang H, et al. itransformer: Inverted transformers are effective for time series forecasting[J]. arXiv preprint arXiv:2023, 2310.06625.

121 AC-side Oscillation Suppression of MMC-based Deicing Devices

Wang Zehao[1,2], Li Guicai[1], Li Huan[1,2], Lu Yiping[1,2], Feng Junjie[1,2]
[1] State Key Laboratory of HVDC, Electric Power Research Institute, China Southern Power, Guangzhou 510663, China
[2] China Southern Power Grid Co., Ltd, Guangzhou 510663, China
fengjj@csg.cn

Abstract: This study addresses the potential ac-side oscillation of MMC-based de-icing devices, which affects normal de-icing operation. An AC-side impedance model is established using multi-harmonic linearization, including circulating current control, phase-locked loop, and control delay. The model reveals the key factors affecting AC-side oscillation of MMC-based de-icing devices. Two oscillation suppression measures are proposed to eliminate negative damping, including parameter optimization and low-pass filter based impedance reshaping. Simulation model is built using MATLAB/Simulink. The Simulation results demonstrate that the analytical impedance model matches well with the frequency-sweep simulation date, and the proposed oscillation suppression measures work effectively.

Keywords: MMC-based De-icing Device; Impedance Modeling; Oscillation Suppression; Control Parameter Optimization.

1 Introduction

With the continuous expansion of China's power grid, ultra-high voltage and extra-high voltage transmission lines operate under conditions of long transmission corridors and complex environments, where ice disaster poses a serious threat to grid security. In recent years, electrical de-icing devices based on flexible DC technology (Flexible De-icing, FDCDI) have gradually become an important means to prevent and control line icing. Among them, de-icing devices based on the modular multilevel converter (MMC) demonstrate promising prospects for engineering applications due to their advantages such as high output current, flexible control, and bidirectional operation [1, 2]. However, under de-icing conditions, the MMC must not only achieve high-current DC output but also maintain grid-connected operation with the power system during the de-icing process. Its complex dynamic behaviour can easily trigger wide-band oscillations or even instability, seriously threatening system security [3, 4]. Therefore, in-depth research on the impedance modelling and oscillation mechanisms of MMC-based de-icing devices holds significant theoretical value and engineering importance.

Impedance modelling and impedance-based stability analysis are effective tools for studying grid-connected oscillation issues in power electronic devices. Existing research primarily focuses on impedance modelling and stability analysis of wind farms grid-connected via MMC-HVDC systems. Reference [5] established a small-signal AC-side impedance model of the MMC based on the harmonic linearization method, revealing the impact of circulating current control on impedance characteristics; Reference [6] derived a full-dimensional frequency-domain model of the MMC incorporating zero-sequence voltage and internal harmonic coupling using harmonic state-space (HSS) theory; Reference [7] proposed a high-precision impedance model considering factors such as grid impedance coupling, phase-locked loop (PLL), and control delays, pointing out that neglecting these factors may lead to distorted stability analysis conclusions. These studies provide an important reference for subsequent impedance modelling of MMC de-icing devices.

Existing research indicates that the intersection of impedances between MMC and devices such as wind turbines and AC grids is the fundamental cause of sub-synchronous and wide-band oscillations [8, 9]. Reference [10] proposed an impedance coupling degree-based method to quantify MMC-wind turbine coupling strength, while Reference [11] established a sequence impedance coupling model and identified dominant oscillation factors across frequency bands. For de-icing devices, their high-current operation aggravates submodule capacitor fluctuations and circulating currents, while current control dominance during de-icing may amplify oscillation risks without impedance optimization [12]. This reveals the inadequacy of existing modeling methods for de-icing stability issues. Regarding oscillation suppression, scholars have proposed various impedance shaping and control optimization approaches, such as enhanced system damping through voltage controller and inverter parameter optimization [13].

Based on the above issues, this paper takes the MMC de-icing device as the research object. First, a complete small-signal AC-side impedance model considering circulating current control, PLL, control delays, and other complete loops is established. Second, the influence mechanism of each control loop on system stability under high-current de-icing conditions is quantitatively revealed. Finally, impedance optimization and oscillation suppression strategies suitable for de-icing scenarios are proposed, providing a theoretical basis and technical support for enhancing the safe and stable operation of MMC de-icing devices.

2 Topology and Control Structure of De-icing Device

2.1 Topology of MMC-based De-icing Device

The structure of the de-icing device based on the MMC topology is shown in Fig. 1. It consists of three phase units, each containing upper and lower arms. Each arm is composed of N identical submodules (the submodules in this paper adopt FBSMs) connected in series. v_{pa}, v_{pb}, v_{pc} and v_{na}, v_{nb}, v_{nc} are the equivalent voltage drops of the upper and lower arms of each phase, respectively; i_{pa}, i_{pb}, i_{pc} and i_{na}, i_{nb}, i_{nc} are the

currents of the upper and lower arms of each phase, respectively; Z_{ice} is the ice-covered conductors connected to the de-icing device; v_{dc} is the DC-side supply voltage for the de-icing circuit; i_{dc} is the DC-side de-icing current. v_{sa}, v_{sb}, v_{sc} are the three-phase AC voltages on the system AC side; i_{sa}, i_{sb}, i_{sc} are the three-phase AC currents on the system AC side; i_{cir_a}, i_{cir_b}, i_{cir_c} are the circulating currents in the MMC arms of the system.

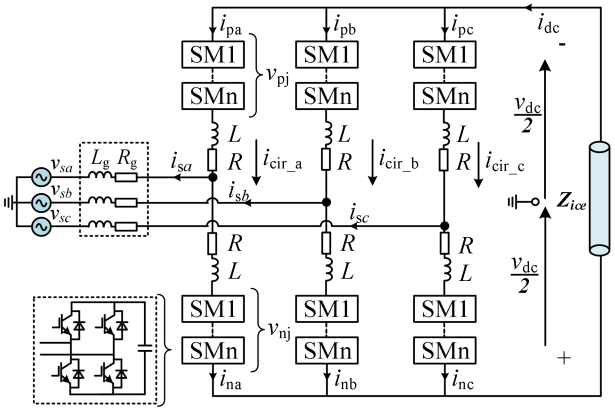


Fig. 1. Main topology of MMC-based de-icing device

2.2 Control Strategy of MMC-based De-icing Device

This paper primarily investigates the characteristics of the MMC-based de-icing device under de-icing conditions.

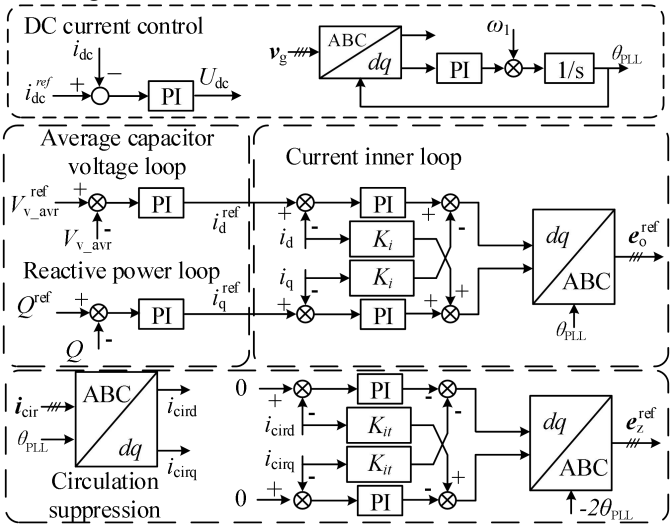


Fig. 2. MMC-based de-icing control strategy diagram

The overall control strategy adopted for the MMC is illustrated in Fig. 2. This control loop includes link delay, phase-locked loop (PLL), average capacitor voltage outer-loop control, reactive power outer-loop control, DC current control, current inner-loop control, and circulating current control. In the figure, variables with subscripts d and q denote their representations in the dq coordinate system; variables with the subscript ref indicate their reference values. The circulating current control adopts a PI control strategy in the negative-sequence double-frequency synchronous coordinate system. In the figure $V_{\text{v avr}}^{\text{ref}}$、$Q^{\text{ref}}$、$i_{\text{dc}}^{\text{ref}}$、$i_{\text{cird}}^{\text{ref}}$、$i_{\text{cirq}}^{\text{ref}}$ refer to reference signals, and $V_{\text{v avr}}$、Q、i_{dc}、i_{cird}、i_{cirq} refer to the component of outer ring, AC/DC side and circulating current, ω_{l} are power frequency, θ_{PLL} is the phase angle at the network side output by the PLL.

3 Impedance Modeling of MMC-based De-icing Device

3.1 Small-signal Modeling of the De-icing Device's Main Circuit

Considering the influence of grid impedance, the main circuit model of the grid-connected MMC system shown in Fig. 1 is established

$$\begin{cases} L\dfrac{\mathrm{d}i_{\text{pj}}}{\mathrm{d}t}+Ri_{\text{pj}}=\dfrac{v_{\text{dc}}}{2}-L_{\text{g}}\dfrac{\mathrm{d}i_{\text{sj}}}{\mathrm{d}t}-R_{\text{g}}i_{\text{sj}}-v_{\text{sj}}-m_{\text{u}}v_{\text{pj}} \\ L\dfrac{\mathrm{d}i_{\text{nj}}}{\mathrm{d}t}+Ri_{\text{nj}}=\dfrac{v_{\text{dc}}}{2}-L_{\text{g}}\dfrac{\mathrm{d}i_{\text{sj}}}{\mathrm{d}t}-R_{\text{g}}i_{\text{sj}}+v_{\text{sj}}-m_{\text{u}}v_{\text{nj}} \\ C\dfrac{\mathrm{d}v_{\text{pa}}}{\mathrm{d}t}=m_{\text{u}}i_{\text{pj}} \\ C\dfrac{\mathrm{d}v_{\text{na}}}{\mathrm{d}t}=m_{\text{l}}i_{\text{nj}} \end{cases} \tag{1}$$

where C is the equivalent capacitance of the bridge arm, m_{u} and m_{l} are the cutting coefficients of the upper and lower bridge arms respectively.

The above formula contains the main circuit model equation of power grid impedance. The formula (1) is converted to the frequency domain and small disturbances are added. The disturbance variables are represented by harmonic matrix vectors composed of Fourier complex coefficients of different frequency components. $\hat{v}_{\text{pj}}$、$\hat{i}_{\text{pj}}$、$\hat{m}_{\text{u}}$ are the disturbance quantities under each component. The upper-arm capacitor voltage V_{u}, modulation index M_{u}, and arm current I_{u} forms a Toeplitz matrix. The arm impedance Z_{L}, grid impedance Z_{g}, and capacitor impedance Z_{C} are diagonal matrices, U is the identity matrix.

The modulation coefficient of the upper arm capacitor voltage and the arm current can also be represented by Toeplitz matrices. The arm impedance, grid impedance and capacitor impedance are expressed as diagonal matrices in the form of admittance.

The disturbance components of the upper and lower arms satisfy:

$$K = \mathrm{diag}[(-1)^{k+1}] \tag{2}$$

where K is the relational matrix.

AC current disturbance $\hat{i}_{sj}$ and the circulating current disturbance $\hat{i}_c$ can be expressed in terms of the upper arm current disturbance $\hat{i}_{pj}$.

$$\begin{cases} \hat{i}_{sj} = (U-K)\hat{i}_{pj} \\ \hat{i}_c = \dfrac{1}{2}(U+K)\hat{i}_{pj} \end{cases} \tag{3}$$

After injecting the disturbance and linearizing, combining Eqs. (1), (2), and (3), the frequency-domain small-signal model of the MMC can be expressed as

$$\begin{cases} Z_L \hat{i}_{pj} + Z_g (U-K)\hat{i}_{pj} = \dfrac{\hat{v}_{dc}}{2} - \hat{v}_{sj} - V_u \hat{m}_u - M_u \hat{v}_{pj} \\ \hat{v}_{pj} = Z_C (I_u \hat{m}_u + M_u \hat{i}_{pj}) \end{cases} \tag{4}$$

The relationship between the AC port current disturbance, voltage disturbance, and the corresponding admittance matrix can be expressed as

$$-\hat{i}_{pj} = Y_{aco} \hat{v}_{pj} \tag{5}$$

3.2 Small-signal Modeling of the De-icing Device's Control System

As shown in Fig. 2, the outputs of each control loop ultimately manifest as variations in the MMC modulation indices. Therefore, this section presents the influence of fundamental-frequency current control, circulating current control, phase-locked loop (PLL), average capacitor voltage outer-loop control, reactive power outer-loop control, and DC current control loop on the modulation index perturbations, thereby establishing a small-signal model of the control system.

AC Current Control and Circulating Current Control.

To analyze the impact of the current loop on the modulation index alone, the effect of disturbances on the outer loops is initially neglected. Thus, the dq-axis current reference values output from the outer loops to the current inner-loop remain unchanged. Based on the control structure of the current inner-loop, its influence on the modulation index can be derived and expressed as Δ_i.

$$\Delta_i = G_i \hat{i}_{sj} \tag{6}$$

where G_i represents the effect of the current inner-loop on the modulation index parameters.

Analogous to the analysis of the current inner-loop's impact on the modulation index, for the circulating current suppression control, which operates in a negative-sequence double-frequency synchronous coordinate system with a rotation direction opposite to the positive-sequence fundamental-frequency synchronous coordinate system of the current inner-loop, its influence on the modulation index can be derived as Δ_c.

$$\Delta_c = G_c \hat{i}_c \tag{7}$$

Phase-locked Loop

When a disturbance voltage is applied to the AC side of the MMC, the phase information output by the PLL converts the AC voltage from the three-phase stationary coordinate system to the dq synchronous coordinate system. $G_{PLL}(n+1,n+1)$ and $G_{PLL}(n-1,n+1)$ represent the additional disturbance terms introduced by the PLL during the fundamental-frequency park transformation. The PLL will also introduce additional disturbance terms during the double-frequency park transformation in the circulating current control, but the corresponding frequencies will shift to ω_p-$3\omega_0$ and ω_p-ω_0. These are represented by the elements $G_{PLL}(n+2,n+1)$ and $G_{PLL}(n-2,n+1)$:

$$\begin{aligned}
G_{pll}(n+1,n+1) &= -T_{pll}(H_i I_{u,1} + M_{u,1}) \\
G_{pll}(n-1,n+1) &= T_{pll}(H_{i\text{-}2} I_{u,1} + M_{u,1}^*) \\
G_{pll}(n+2,n+1) &= -T_{pll} M_{u,2} \\
G_{pll}(n-2,n+1) &= -T_{pll} M_{u,2}^*
\end{aligned} \tag{9}$$

Therefore, the influence of the PLL on the modulation index is expressed as Δ_{PLL}.

$$\Delta_{PLL} = G_{PLL} \hat{v} \tag{10}$$

Reactive Power Control

When the MMC adopts a power control outer loop, the output quantity needs to pass through the current inner loop to form the modulation index. At this time, the influence of reactive power control on the modulation index can be expressed as

$$\Delta_Q = G_{ir} G_Q \hat{Q} \tag{11}$$

Due to the frequency shift relationship of $\pm\omega$ between the synchronous and stationary coordinate systems for voltages and currents, the reactive power feedback quantity in Eq. (11) can be expressed in vector form as

$$\hat{Q} = V_Q \hat{i}_{pj} + I_Q \hat{v}_g \tag{12}$$

where V_Q and I_Q are the influence of reactive power loop on voltage and current.

Average Capacitor Voltage Outer-loop Control

When the MMC adopts an average capacitor voltage outer loop, the influence of DC voltage control on can be expressed as

$$\Delta\hat{m}_{u2} = G_{ir}G_{v}\hat{v}_{avrdc} \tag{13}$$

where G_{ir} represents the effect of fundamental-frequency current control on the current reference disturbance, where the matrix G_{v} represents the effect of the DC voltage control outer loop on the DC voltage disturbance.

According to the modeling principle of average capacitor voltage, it can also be expressed as:

$$\Delta\hat{m}_{u2} = F_1\hat{i}_{pj} + F_2\hat{m}_{u} \tag{14}$$

where F_1 and F_2 are intermediate values representing the influence of the average capacitor voltage control outer loop on the modulation index.

DC Current Control Loop

The core task of the DC current control loop is to force the DC-side current to track the target value by adjusting the submodule modulation index to counteract the effects of grid disturbances and load variations on the DC current. The DC current contains only the zero-sequence circulating current component, with no negative-sequence/positive-sequence high-frequency components.

The DC current loop is utilized to control the de-icing current. To consider the influence of the DC current control loop on the modulation index, the impact of the DC current loop of Δ_{idc} on the modulation index can be derived based on the structure of the DC current control loop.

$$\Delta_{idc} = G_{dcr}\hat{i}_{dc} \tag{15}$$

where the above equation uses the matrix of G_{dcr} to represent the effect of the DC current control loop on the DC current.

3.3 Equivalent Small-signal Model of AC Side

Based on the aforementioned analysis, the total modulation index disturbance introduced by each control loop can be expressed as

$$\hat{m}_{u} = (\Delta_{I} + \Delta_{i} + \Delta_{V} + \Delta_{Q} + \Delta_{pll} + \Delta_{idc})G_{d} \tag{16}$$

Where is the function of the delay link. By combining Eqs. (9), (11), (16), (21), (25), and (26), and considering the relationship between the output current disturbance, circulating current disturbance, and arm current disturbance, the relationship between the modulation index disturbance and the AC voltage at the PCC point, as well as the arm current disturbance, is derived. The influence of each loop on

the modulation index is constituted by the control coefficient matrices. Therefore, the modulation index can be expressed as

$$\hat{m}_{\mathrm{u}} = E_{\mathrm{i}}\hat{i}_{\mathrm{pj}} + E_{\mathrm{v}}\hat{v}_{\mathrm{g}} \tag{17}$$

where

$$\begin{aligned} E_{\mathrm{i}} = &\left(H_{\mathrm{Ei}}(F_1 + (U-K)G_{\mathrm{i}} + 0.5(U+K)G_{\mathrm{c}} + G_{\mathrm{ir}}G_{\mathrm{Q}}V_{\mathrm{Q}} + 0.75(U+K)G_{\mathrm{idc}})\right)G_{\mathrm{d}} \\ &+(E_{\mathrm{v}}Z_{\mathrm{g}}(U-K)) \end{aligned} \tag{18}$$

$$E_{\mathrm{v}} = \left(H_{\mathrm{Ei}}\left(G_{\mathrm{pll}} + G_{\mathrm{ir}}G_{\mathrm{Q}}I_{\mathrm{Q}}\right)\right)G_{\mathrm{d}} \tag{19}$$

$$H_{\mathrm{Ei}} = \mathrm{inv}(U - F_2) \tag{20}$$

Substituting Eqs. (18), (19) into Eq. (4) yields the AC-side admittance model of the MMC.

$$Y_{\mathrm{aco}} = (U-K)B_{\mathrm{i}}^{-1}B_{\mathrm{v}} \tag{21}$$

where

$$B_{\mathrm{i}} = U + Y_{\mathrm{L}}(0.5Z_{\mathrm{e}} + M_{\mathrm{u}}Z_{\mathrm{C}}M_{\mathrm{u}} + (V_{\mathrm{u}} + M_{\mathrm{u}}Z_{\mathrm{C}}I_{\mathrm{u}})E_{\mathrm{i}} + Z_{\mathrm{g}}(U-K)) \tag{22}$$

$$B_{\mathrm{v}} = Y_{\mathrm{L}}\left(U + \left(V_{\mathrm{u}} + M_{\mathrm{u}}Z_{\mathrm{C}}I_{\mathrm{u}}\right)E_{\mathrm{v}}\right) \tag{23}$$

3.4 Validation of AC-side Impedance Model of MMC-based De-icing Device

To verify the accuracy of the impedance model of the de-icing device, a simulation model of the de-icing device was built in MATLAB/Simulink, with the detailed simulation parameters listed in Table 1.

Table 1. Simulation Parameters of Ice Melting Device

Parameter	Value
Rated Capacity	60.5 MW
Rated AC Grid-side Voltage	35 kV
Number of Arm Submodules (N)	50
Submodule Capacitance	25200 μF
Arm Inductance	13 mH
Arm Resistance	0.1 mΩ

Based on the aforementioned impedance modeling method, Equation (21) represents the AC-side impedance modeling formula. To validate the correctness of the established model, this paper first injects a series of perturbation voltages at different frequencies into the AC side of the simulation model, then measures the perturbation currents at the same frequencies from the same port, thereby obtaining

the measured values of the AC-side impedance frequency characteristics of the grid-connected MMC. Finally, the accuracy of the impedance model is verified.

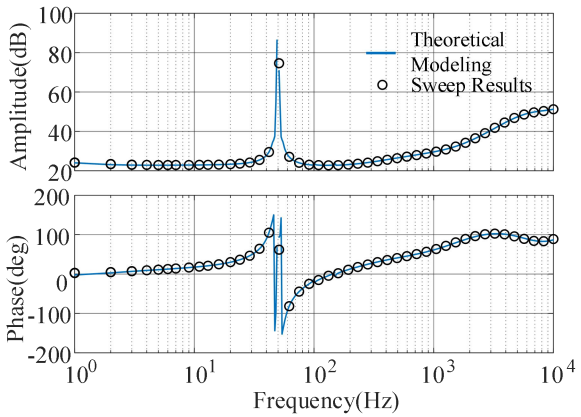


Fig. 3 AC-side impedance characteristics of the MMC-based de-icing device

4 Oscillation Suppression Strategy for MMC-based De-icing Device

4.1 Parameter Optimization-based Oscillation Suppression Strategy

As can be seen from Fig. 4, high-frequency oscillations in the range of 3 kHz to 4 kHz occur on the AC side. When considering the dynamic performance of the control loop, the parameters of the current inner loop are optimized. A comparison of the AC-side impedance at Kp=50 and Kp=10 shows that the negative damping region disappears, indicating that Kp optimization can suppress high-frequency oscillations.

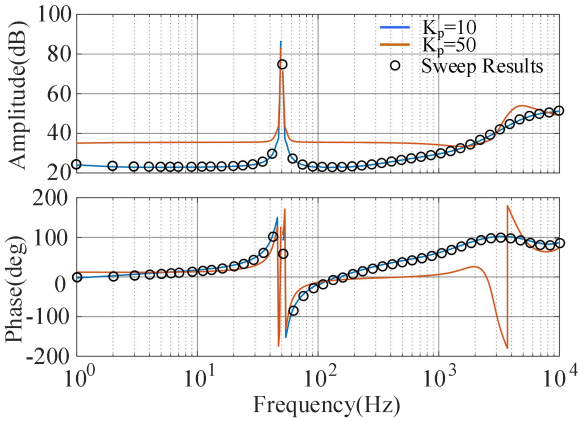


Fig. 4 Bode plots of AC-side impedance of the MMC-based de-icing device with different values of the current inner-loop proportional coefficient

Fig. 5 is based on the dynamic optimization of the current inner-loop parameters. Before optimization, high-frequency oscillations are present in the AC-side current; after optimization, the oscillations are suppressed within 0.2s, and the waveforms stabilize, verifying the real-time effectiveness of parameter optimization.

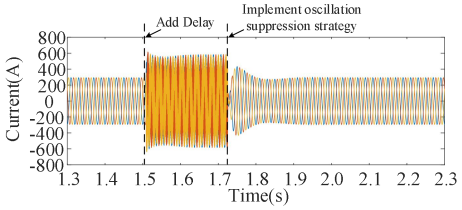


Fig. 5. Waveforms of AC-side current of the MMC-based de-icing device before and after current inner-loop parameter optimization

4.2 Filter-Based Oscillation Suppression Strategy

Fig. 6 is a schematic diagram of reactive power loop reshaping. This oscillation suppression strategy introduces a low-pass filter in the signal transmission path of the reactive power loop, reducing the negative damping region in the high-frequency band and thus suppressing the high-frequency oscillation phenomenon on the AC side.

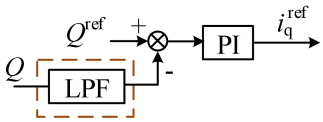


Fig. 6. Schematic diagram of reactive power outer ring remodeling

With other control parameters unchanged, the delay of the control link is set to 100μs. Fig. 7 shows the AC-side impedance characteristic curve with the link delay set to 100μs. The orange curve represents the impedance characteristic without a low-pass filter, the sweeping results are in good agreement with the theory. Excessive control link delay may cause negative damping in certain regions. It can be observed that a negative damping region appears on the AC side between 3kHz and 4kHz. The blue curve represents the impedance characteristic after adding a low-pass filter to the AC reactive power outer loop and the DC current control outer loop. It can be seen that the negative damping regions in the high-frequency band are eliminated.

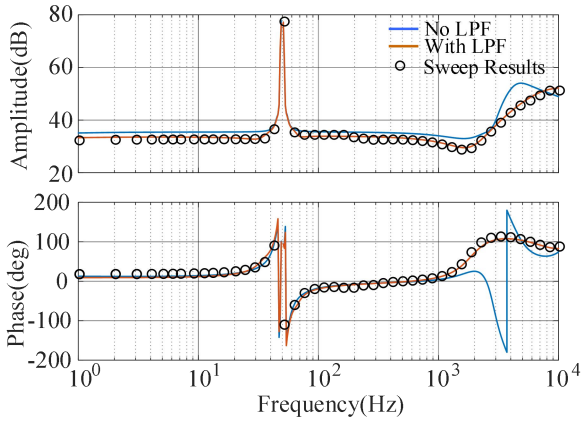


Fig. 7. Bode plots of AC-side impedance of the MMC-based de-icing device before and after adding a second-order low-pass filter to the reactive power outer-loop control

Based on the theoretical modeling analysis above, increasing the delay can cause oscillations on both the AC and DC sides. When the delay is 100μs, oscillations occur on both sides. Fig. 8 shows the AC-side current waveforms before and after adding the low-pass filter to suppress oscillations caused by the delay. It can be observed that before the low-pass filter is enabled at 1.5s, oscillations occur in both the AC-side and DC-side voltages and currents. After enabling the low-pass filter, the oscillations in both the AC-side and DC-side current waveforms are suppressed.

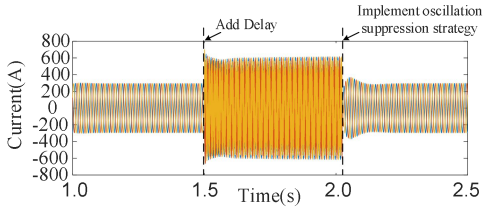


Fig. 8. Waveforms of AC-side current of the MMC-based de-icing device after adding a second-order low-pass filter to the reactive power outer-loop control

5 Conclusion

This paper focuses on the AC-side oscillation issues of MMC-based de-icing devices and has achieved the following results. First, based on the multi-harmonic linearization method, an AC-side impedance model incorporating complete loops such as circulating current control, phase-locked loop (PLL), and control delays was established. Simulation validation confirmed that the analytical values of the model closely align with the frequency-scanning results, verifying the accuracy of the model and providing a theoretical foundation for oscillation mechanism analysis. Finally, two effective oscillation suppression measures were proposed: optimizing the current

inner-loop parameters can eliminate negative damping regions in the high-frequency band, thereby suppressing AC-side oscillations; when the control link delay is excessive, adding low-pass filters to the AC reactive power outer loop and DC current control outer loop can effectively eliminate negative damping on both AC and DC sides and suppress oscillations. The research results provide a theoretical basis and technical support for enhancing the safe and stable operation of MMC-based de-icing devices and hold significant guiding importance for engineering practice.

References

[1] Hu, Y.: Analysis of large-area ice disasters in power grids and discussion on countermeasures [J]. High Voltage Engineering, 2008(02), 215–219 (2008)
[2] Mei, H.M., Liu, J.Z.: A new modular multilevel DC de-icing device [J]. Automation of Electric Power Systems, 37(16), 96–102 (2013)
[3] Li, Y.X., Zhou, Y.S., Zhou, W.Q., et al.: Research on LC oscillating discharge de-icing power supply based on voltage control [J]. High Voltage Apparatus, 60(04), 185–192 (2024)
[4] Ban, G.B., Niu, W., Yang, Q., et al.: Research on resonance mechanism and suppression measures of modular multilevel DC de-icing device [J]. Power System Protection and Control, 50(03), 180–187 (2022)
[5] Ji, K., Tang, G., Yang, J., et al.: Harmonic stability analysis of MMC-based DC system using DC impedance model [J]. IEEE Journal of Emerging and Selected Topics in Power Electronics, 8(2), 1152–1163 (2020)
[6] Xu, Z., Li, B., Wang, S., et al.: Generalized single-phase harmonic state space modeling of the modular multilevel converter with zero-sequence voltage compensation [J]. IEEE Transactions on Industrial Electronics, 66(8), 6416–6426 (2019)
[7] Xu, Z., Li, B., Wang, S., et al.: A complete HSS-based impedance model of MMC considering grid impedance coupling [J]. IEEE Transactions on Power Electronics, 35(12), 12929–12948 (2020)
[8] Xie, X.R., Liu, H.K., He, J.B., et al.: Mechanism and characteristic analysis of subsynchronous oscillation caused by interaction between direct-drive wind farms and AC grid [J]. Proceedings of the CSEE, 36(09), 2366–2372 (2016)
[9] Yu, H.T., Lü, J., Li, X., et al.: Comprehensive evaluation of the impact of high-frequency oscillation suppression strategies on the dynamic performance of VSC-HVDC systems [J]. Proceedings of the CSEE, 42(08), 2873–2889 (2022)
[10]Zong, H.X., Lü, J., Zhang, C., et al.: MMC multi-dimensional impedance model and its application in stability analysis of wind farm-VSC-HVDC interaction [J]. Proceedings of the CSEE, 41(14), 4941–4953 (2021)
[11]Zhang, C., Wang, W.S., He, G.Q., et al.: Subsynchronous oscillation analysis of direct-drive wind farms based on sequence impedance and PLL parameter optimization design [J]. Proceedings of the CSEE, 37(23), 6757–6767+7067 (2017)
[12]Guo, Y.Q., Zhou, Y.B., Xu, J.Z., et al.: Control strategy of DC de-icing device based on full-bridge modular multilevel converter [J]. Automation of Electric Power Systems, 41(05), 106–113 (2017)
[13]Nian, H., Li, M., Chen, L., et al.: Wide-band frequency coupling characteristic measurement method for grid-connected inverters using multi-sine signal injection [J]. Proceedings of the CSEE, 40(22), 7408–7420 (2020)

122 Energy Storage Control for Transient Stability Based on Power Angle Feedback

Tong Xue[1,2], Yanhong Yang[1,2], Wei Deng[1,2], Wei Pei[1,2]

[1] Institute of Electrical Engineering, Chinese Academy of Sciences, Beijing, China
[2] University of Chinese Academy of Sciences, Beijing, China
xuetong@mail.iee.ac.cn
yangyanhong@mail.iee.ac.cn

Abstract. This paper proposes an energy storage system control strategy based on dynamic power angle feedback to enhance power system transient stability. Unlike conventional approaches that rely on frequency or voltage deviations, the proposed method directly utilizes power angle dynamics to provide more effective stability control. The control parameters are systematically designed using constraint-based optimization that considers both stability requirements and physical limitations of energy storage devices. The control strategy is validated through power angle response analysis, equal area criterion evaluation, and energy function assessment using a single-machine infinite-bus system. The results demonstrate that the proposed approach successfully transforms an unstable system into a stable one with enhanced damping characteristics and improved critical clearing time. The bidirectional power regulation capability of energy storage system provides essential energy redistribution during transient periods, effectively suppressing power angle oscillations and maintaining system synchronism.

Keywords: Power System Dynamics, Transient Stability, Energy Storage System.

1 Introduction

Modern power systems face increasing challenges in maintaining transient stability due to the growing complexity of electrical networks and the integration of renewable energy sources[1,2]. Power system transient stability refers to the ability of the system to maintain synchronism when subjected to large disturbances such as short circuit faults, sudden load changes, or equipment failures [3]. The loss of transient stability can lead to cascading outages and widespread blackouts, causing significant economic losses and social disruption [4].

The integration of renewable energy sources, particularly wind and solar power, has fundamentally altered the dynamic characteristics of power systems [5]. Unlike conventional synchronous generators, renewable energy sources connected through power electronic converters lack inherent inertia, reducing the system's natural damp-

ing capability during transient events[6,7]. This transition has created new stability challenges that require innovative solutions beyond traditional approaches.

Traditional approaches to enhance transient stability include power system stabilizers [8], flexible AC transmission systems devices [9] and load shedding schemes [10]. However, these methods often have limitations in response speed, control flexibility, or economic feasibility. Energy storage systems (ESS) have emerged as a promising solution due to their fast response capability and bidirectional power flow characteristics [11]. Recent developments in battery technology have made grid-scale energy storage economically viable for stability enhancement applications [12].

Current research on ESS for stability enhancement primarily focuses on frequency regulation and voltage support [13], with limited investigation into direct transient stability improvement through dynamic power angle control. Most existing control strategies rely on frequency or voltage deviations as feedback signals [14], which may not capture the fundamental dynamics of power angle oscillations during transient events. Additionally, the design of ESS control parameters often lacks systematic approaches based on stability analysis methods.

This paper proposes an energy storage system control strategy based on dynamic power angle feedback to improve power system transient stability. The proposed strategy directly utilizes power angle dynamic information for control, providing a new technical approach for power system transient stability enhancement. The main contributions of this work include:

1. Development of a control strategy that directly responds to power angle dynamics rather than secondary effects such as frequency or voltage deviations. Constraint-based optimization methods are used to systematically design control parameters, considering both stability requirements and physical limitations.
2. Comprehensive validation through multiple stability analysis methods including power angle response analysis, equal area criterion evaluation and energy function assessment. This approach ensures the reliability and effectiveness of the proposed solution.

2 Theoretical foundation and methodology

The stability analysis of power systems needs to be based on accurate mathematical models and effective improvement methods. With the rapid development of energy storage technology, the dynamic characteristics of power grids after the connection of energy storage devices have been deeply studied. It provides a new technical path to effectively reflect the dynamic interaction characteristics between generators and the grid, and to improve the transient stability of the system.

2.1 Physical model for power system dynamics

The swing equation is the simplest and most common form to describe the dynamics of power systems. Ignoring transmission losses and bus voltage deviations, the swing equation for each generator can be represented as:

$$m_k\ddot{\delta}_k + d_k\dot{\delta}_k = P_m - \sum_j \frac{V_k V_j}{X_{kj}}\sin(\delta_k - \delta_j) \tag{1}$$

where m_k defines the inertia constant of generator k; d_k represents the damping coefficient; $\dot{\delta}_k$ is the angular velocity of generator k; P_m is the input mechanical power; V_k and V_j are the voltage magnitudes at buses k and j; X_{kj} denotes the reactance between buses k and j; δ_k, δ_j represent the power angles at buses k and j.

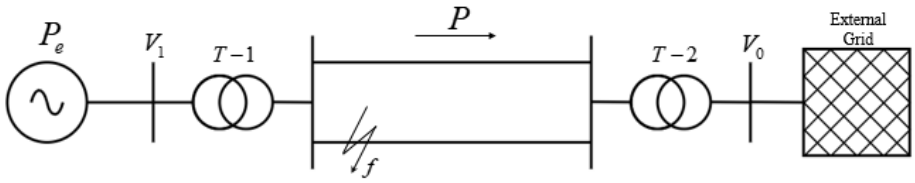


Fig. 1. Single-machine infinite-bus system

The single-machine infinite-bus (SMIB) system, shown in Fig. 1, has been widely used to understand and analyze the fundamental dynamic phenomena occurring in power systems. For the special case of the SMIB system, the system can be simplified to one generator connected to an infinite bus. In this case, there is only one generator (k=1), and the voltage magnitude and frequency of the infinite bus remain constant. By introducing the inertia constant H and the base angular frequency ω_0, the swing equation (1) can be simplified to:

$$\frac{2H}{\omega_0}\ddot{\delta} = P_m - P_e = P_m - \frac{V_0 V_1}{X_I}\sin\delta \tag{2}$$

where P_e is the output electrical power of the generator; δ is the generator's power angle relative to the infinite bus; V_0, V_1 are the voltage magnitudes of the infinite bus and generator terminal respectively; X_I is the connecting reactance.

When the system is in steady state, the input mechanical power and the output electrical power are balanced ($P_m = P_e$), and the generator power angle remains constant. During disturbances, the generator power angle behavior follows the dynamic law of equation (2). As shown in Fig.1, if a two-phase-to-ground short circuit fault occurs at point f, the switches on both sides of the line open simultaneously to clear the faulted line. During the short circuit fault period, the generator swing curve $\delta - t$ and the rotor motion equations can be expressed as:

$$\begin{cases} \dfrac{d\delta}{dt} = (\omega - 1)\omega_0 \\ \dfrac{d\omega}{dt} = \dfrac{1}{T_J}\left(P_m - \dfrac{E'V_1}{X_{II}}\sin\delta\right) \end{cases} \tag{3}$$

where ω is the angular frequency of the generator rotor in per unit; T_J is the inertia time constant of the generator, which is double the inertia constant; E' is the transient electromotive force; X_{II} is the line reactance during the fault period.

If the duration of the fault or the clearing time is known, the $\delta - t$ curve is needed to judge the system stability. Due to the change in system parameters, X_{II} in Equation (3) needs to be replaced with the post-fault line reactance X_{III}. While solving the system of equations, the initial conditions should correspond to the parameter values at the moment of fault clearing.

2.2 Energy storage system for stability enhancement

Energy storage systems, as a fast-response regulation means, can effectively improve the transient stability of the system. The ESS regulates the power balance of the system by rapidly absorbing or releasing active power. Its control strategy can be expressed as:

$$P_{ess} = \rho_{ess} \left| \frac{d\omega}{dt} \right| \mathrm{sgn}\left(\frac{d\delta}{dt} \right) \tag{4}$$

where P_{ess} is the power exchange between the ESS and the main power system; ρ_{ess} is the power regulation density of the ESS, characterizing the power response intensity and sensitivity of the ESS to the system angular acceleration changes.

The ESS operates as a dynamic stabilizer by providing bidirectional power exchange based on the system's real-time conditions. When the angular frequency deviation $d\delta/dt > 0$, the ESS outputs positive power to absorb excess energy from the system, helping to reduce the frequency deviation. Conversely, when angular frequency deviation $d\delta/dt < 0$, the ESS outputs negative power to inject energy into the system, providing support to restore frequency balance.

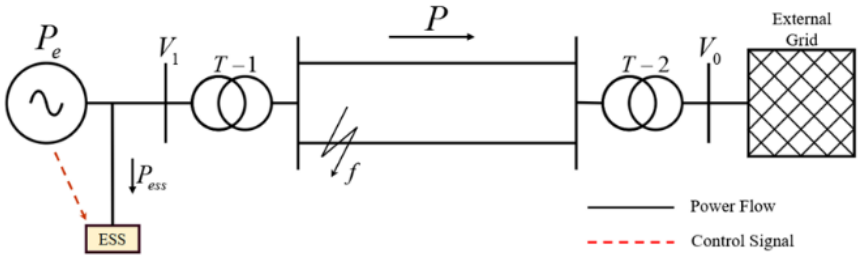


Fig. 2. SMIB System with Energy Storage System Connected

In the SMIB system with energy storage shown in Fig. 2, the ESS is connected to the main system through the control signal. When the system is disturbed, the energy storage system can quickly respond to the dynamic changes of the power angle, provide damping power related to the system motion state, effectively suppress power angle oscillations, and improve the transient stability of the system.

When energy storage is added to the system, the generator swing curve $\delta - t$ and the rotor motion equations (3) should be：

$$\begin{cases} \dfrac{d\delta}{dt} = (\omega - 1)\omega_0 \\ \dfrac{d\omega}{dt} = \dfrac{1}{\mathrm{T}_J}\left(P_m - \dfrac{E'V_1}{X_{II}}\sin\delta - P_{ess} \right) \end{cases} \tag{5}$$

Substituting equation (4) in, we get:

$$T_J \frac{d\omega}{dt} + \rho_{ess}\left|\frac{d\omega}{dt}\right|\mathrm{sgn}\left(\frac{d\delta}{dt}\right) = \Delta P \tag{6}$$

$$\Delta P = P_m - \frac{E'V_1}{X_{II}}\sin\delta \tag{7}$$

where ΔP is power imbalance, representing the difference between input mechanical power and output electromagnetic power of the generator.

2.3 Stability criteria

Power system transient stability assessment requires effective analysis methods and criteria. The equal area criterion and energy function method are two widely applied stability analysis tools that can quantitatively evaluate the dynamic behavior of the system after disturbances. The integration of energy storage systems changes the traditional power balance relationship, requiring corresponding modifications and extensions to existing criteria.

1. Equal Area Criterion: The equal area criterion is based on the principle of energy balance, determining system stability by comparing the accelerating area and decelerating area. For SMIB systems, the stability criterion can be expressed as:

$$A_1 = \int_{\delta_0}^{\delta_c} (P_m - P_{II})\, d\delta \tag{8}$$

$$A_2 = \int_{\delta_c}^{\delta_m} (P_{III} - P_m)\, d\delta \tag{9}$$

where δ_0 is the pre-fault steady-state power angle; δ_c is the power angle at fault clearing; δ_m is the maximum power angle reached post-fault; A_1 is the accelerating area; A_2 is the decelerating area; P_{II}, P_{III} are the electromagnetic power characteristic curves during fault and post-fault periods respectively. The stability criterion is $A_2 \geq A_1$.

The integration of ESS modifies the power balance equation, and the equal area criterion calculation needs to consider the impact of ESS power:

$$A_1 = \int_{\delta_0}^{\delta_c} \left[P_m - (P_{II} + P_{ess}) \right] d\delta \tag{10}$$

$$A_2 = \int_{\delta_c}^{\delta_m} \left[(P_{III} + P_{ess}) - P_m \right] d\delta \tag{11}$$

The ESS improves system stability through a dual mechanism. During the post-fault stage, the ESS injects power into the system according to its control strategy.

This power directly enhances the decelerating area A_2, providing additional braking torque for the generator rotor and effectively suppressing further increases in the power angle. During the fault period, the ESS can absorb excess power, thereby reducing the accelerating area A_1 and decreasing the surplus kinetic energy gained by the generator rotor during the fault. This regulation mechanism makes the stability condition of the criterion easier to satisfy. The intervention of the ESS significantly improves the system's transient stability margin.

2. Energy Function Method: The energy function method is based on Lyapunov stability theory, analyzing transient stability by constructing the system's energy function. For nonlinear power systems, the energy function decomposes the total system energy into kinetic and potential energy components, providing an intuitive physical interpretation for stability analysis.

$$U_k = \frac{1}{2} m \left(\omega - \omega_0 \right)^2 = \frac{H}{\omega_0} \left(\omega - \omega_0 \right)^2 \tag{12}$$

$$U_p = -P_m \left(\delta - \delta_s \right) - \frac{E'U}{X_{II}} \left(\cos\delta - \cos\delta_s \right) \tag{13}$$

$$U_{total} = U_k + U_p \tag{14}$$

where U_k is the kinetic energy of the generator rotor, representing the kinetic energy deviation relative to synchronous speed; U_p is the potential energy of the system, including both mechanical power potential energy and electromagnetic power potential energy; U_{total} is the total energy of the system, equal to the sum of kinetic and potential energy; δ_s is the stable equilibrium power angle, representing the power angle position during normal steady-state operation of the system.

When $P_{ess} > 0$ the ESS absorbs power from the power system, reducing the kinetic energy of the generator rotor; when $P_{ess} < 0$, the ESS injects power into the power system, increasing the available energy in the system. This power regulation enables the ESS to absorb excess energy during fault periods and release this energy back into the system after fault clearing, achieving temporal redistribution of energy and improving the system's dynamic response characteristics and stability performance.

When energy storage is integrated into the power system, the mathematical framework of the energy function method remains unchanged. The energy function continues to be calculated as the sum of kinetic and potential energy components using the same formulation. However, the integration of ESS alters the system's dynamic behavior, causing changes in the angular frequency ω and power angle δ trajectories. These modified state variables directly influence the calculated values of the energy function, thereby affecting the stability assessment while maintaining the same computational approach.

3 Parameter design and performance analysis

3.1 Constraint conditions for ESS power regulation density

The design of ESS power regulation density ρ_{ess} is crucial for ensuring system stability. However, this parameter lacks a specific analytical model and cannot be calculated precisely. Therefore, it is necessary to establish constraint conditions and solve for empirical values of ρ_{ess} based on known system characteristics. Proper constraint condition settings must not only ensure the transient stability of the system, but also consider the feasibility of physical limitations of energy storage devices.

1. System Stability Constraints: System stability is the primary constraint condition for ρ_{ess} design, including both equal area criterion stability and power angle stability. The fundamental stability requirement is that the decelerating area A_2 should not be less than the accelerating area A_1. While the generator power angle must remain bounded and convergent, avoiding system instability caused by unlimited power angle increase:

$$A_2(\rho_{ess}) \geq A_1(\rho_{ess}) \tag{15}$$

$$\left|\delta(t)\right| \leq \delta_{\max}, \quad \forall t \geq t_c \tag{16}$$

$$\lim_{t\to\infty}\left|\frac{d\delta}{dt}\right| = 0 \tag{17}$$

where $\delta_{\max}$ is the maximum allowable power angle limit; t_c is the fault clearing time corresponding to power angle δ_c.

These two stability constraints ensure that the ESS can effectively suppress power angle oscillations and maintain the transient stability of the system.

2. Physical Limitation Constraints: The physical properties of energy storage devices determine the value range of ρ_{ess} and power output limitations. These constraint conditions ensure the engineering feasibility of energy storage parameter design.

Considering the technical characteristics and control precision of energy storage devices, ρ_{ess} should be within a reasonable range. The lower limit $\rho_{ess_\min}$ ensures the ESS can provide basic damping effect, while the upper limit $\rho_{ess_\max}$ is constrained by device response speed and control precision.

$$\rho_{ess_\min} \leq \rho_{ess} \leq \min(\rho_{ess_\max}, T_J) \tag{18}$$

The instantaneous power output of the ESS is limited by the device's rated capacity. This constraint ensures that during system dynamic processes, when angular acceleration is large, the power regulation density ρ_{ess} will not cause power demand to exceed the device capability range.

$$\left|P_{ess}(t)\right| = \left|\rho_{ess}\right|\left|\frac{d\omega}{dt}\right| \leq P_{\text{rated}} \tag{19}$$

where P_{rated} is the rated power capacity of the ESS.

Physical limitation constraints ensure the engineering feasibility of energy storage parameter design. They prevent theoretical calculation results from exceeding the actual device capability range.

3.2 Results comparison and analysis

To validate the effectiveness of the proposed ESS control strategy, comparative simulations are conducted between systems with and without ESS integration. The following analysis examines the system performance using three stability assessment methods.

Table 1. Simulation Parameters

Symbol	Value	Unit
ω_0	314.16	rad/s
T_J	11.28	s
E'	1.47	p.u.
X_{II}	2.82	p.u.
X_{III}	1.062	p.u.
δ_0	31.54	deg

The simulation parameters for the SMIB system are presented in Table I. These parameters represent a typical synchronous generator connected to an infinite bus, with the fault scenario designed to create an unstable condition that requires ESS intervention for stability enhancement. A short circuit fault with duration of 0.25s is applied to evaluate the effectiveness of the proposed ESS control strategy.

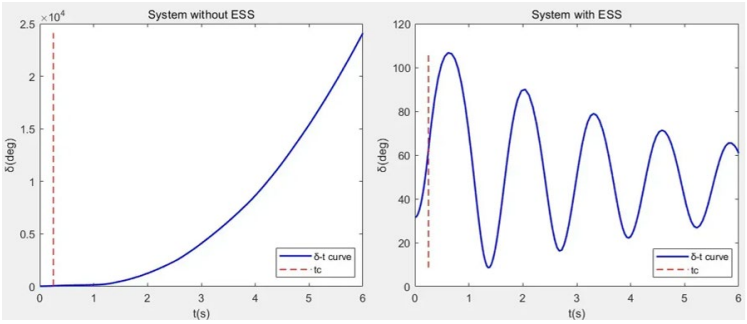


Fig. 3. Power Angle Response

As shown in Fig. 3, the power angle response of the system without ESS exhibits exponential growth after fault clearing, resulting in system instability. In contrast, the power angle response of the system with ESS shows oscillatory convergence after fault clearing, maintaining system stability. This indicates that the ESS can effectively

suppress power angle oscillations and provide necessary damping effects, thereby improving the transient stability of the system.

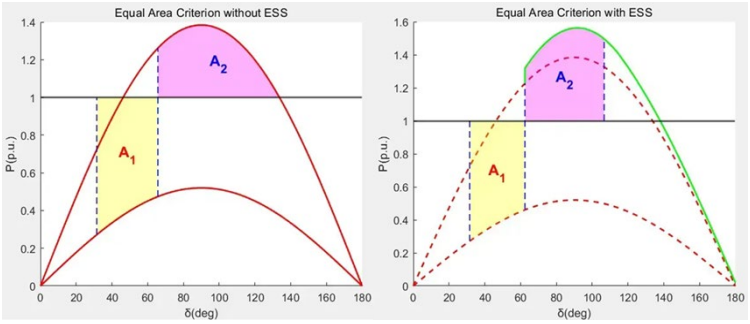


Fig. 4. Equal Area Criterion Analysis

As shown in Fig. 4, the decelerating area A_2 of the system without ESS has reached its maximum value. However, the decelerating area A_2 still cannot match the accelerating area A_1, making the system unstable. The ESS can absorb or inject power from/into the system, providing sufficient decelerating area A_2 to match the accelerating area A_1. The ESS provides additional stability margin for the system and improves system stability.

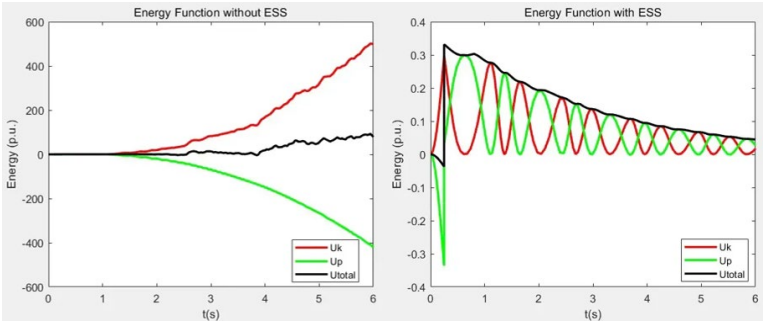


Fig. 5. Energy Function

As shown in Fig. 5, after the fault occurs, the system without ESS cannot quickly absorb all kinetic energy to maintain transient stability. With the addition of ESS, the system gradually absorbs excess kinetic energy. The total energy gradually decreases until it reaches zero, representing that the excess kinetic energy generated by the fault is completely absorbed by the system, with the system maintaining a stable state. The bidirectional power regulation of ESS achieves energy redistribution. This provides an effective energy management approach for excess kinetic energy, ensuring that the system can return to stable operation after the fault.

4 Discussion and outlook

The results demonstrate that the proposed ESS control strategy successfully transforms an unstable power system into a stable system with enhanced damping characteristics. The critical clearing time improves from approximately 0.2s to 0.28s, representing a 40% enhancement in system stability margin. This validates the effectiveness of the approach of integrating ESS to improve system stability. However, several aspects warrant further discussion and future research.

The present study focuses on a single-machine infinite-bus system, which simplifies the complex interactions present in real multi-machine power systems. The power regulation density parameter ρ_{ess} requires empirical determination through constraint-based optimization, lacking a precise analytical model. Additionally, practical implementation challenges include accurate real-time measurement of power angle derivatives and consideration of ESS physical limitations such as power rating and energy capacity constraints.

Extension to multi-machine power systems represents the most critical next step, requiring investigation of coordinated control strategies among multiple ESS units. Development of adaptive control mechanisms that can automatically adjust ρ_{ess} based on real-time system conditions would enhance practical applicability. Integration with other stability enhancement technologies such as FACTS devices and power system stabilizers could provide synergistic improvements in overall system performance.

The proposed ESS control strategy has potential applications beyond traditional stability enhancement, particularly as power systems integrate higher penetrations of renewable energy sources. The principles developed could serve as a foundation for grid-scale energy storage systems designed specifically for stability services rather than solely energy arbitrage. Furthermore, these concepts may be adaptable to microgrid systems and power electronics applications where fast-responding energy storage can provide similar stability benefits at smaller scales. The increasing deployment of distributed energy resources and electric vehicles creates new opportunities for implementing distributed ESS-based stability control. Such applications could provide multiple value streams, combining stability enhancement with frequency regulation and voltage support services.

5 Conclusion

This paper presents an energy storage system control strategy based on dynamic power angle feedback for enhancing power system transient stability. The constraint-based optimization approach systematically designs control parameters considering both stability requirements and physical limitations. Validation through multiple stability assessment methods confirms that the bidirectional power regulation capability of ESS effectively suppresses power angle oscillations and maintains system synchronism. These findings establish ESS integration as an effective solution for transient stability enhancement in modern power grids.

Acknowledgement: This work was supported by the National Key Research and Development Program of China (Grant Number: 2024YFE0115700), and Chinese Academy of Sciences for Strategic Pilot Science and Technology (Grant Number: XDB0900200).

References

1. Ghosh S, Isbeih Y J, Moursi M S E, Assessment of Bus Inertia to Enhance Dynamic Flexibility of Hybrid Power Systems With Renewable Energy Integration[J]. IEEE Transactions on Power Delivery 38(4), 2372～2386 (2023).
2. Wang R, Wang S, Geng G, et al, Multi-time-scale capacity credit assessment of renewable and energy storage considering complex operational time series[J]. Applied Energy 355, 122382 (2024).
3. Wu H, Li J, Yang H, Research Methods for Transient Stability Analysis of Power Systems under Large Disturbances[J]. Energies 17(17), 4330 (2024).
4. Song J, Cotilla-Sanchez E, Ghanavati G, et al, Dynamic Modeling of Cascading Failure in Power Systems[J]. IEEE Transactions on Power Systems 31(3), 2085～2095 (2016).
5. Niu S, Zhang Z, Ke X, et al, Impact of renewable energy penetration rate on power system transient voltage stability[J]. Energy Reports 8, 487～492 (2022).
6. Prakash A, Moursi M S E, Parida S K, et al, Damping of Inter-Area Oscillations With Frequency Regulation in Power Systems Considering High Penetration of Renewable Energy Sources[J]. IEEE Transactions on Industry Applications 60(1), 1665～1679 (2024).
7. Meegahapola L G, Bu S, Wadduwage D P, et al, Review on Oscillatory Stability in Power Grids With Renewable Energy Sources: Monitoring, Analysis, and Control Using Synchrophasor Technology[J]. IEEE Transactions on Industrial Electronics 68(1), 519～531 (2021).
8. Bombois X, Vanfretti L, Performance monitoring and redesign of power system stabilizers based on system identification techniques[J]. Sustainable Energy, Grids and Networks 38, 101278 (2024).
9. Chethan M, Kuppan R, A review of FACTS device implementation in power systems using optimization techniques[J]. Journal of Engineering and Applied Science 71(1), 18 (2024).
10. Khalaf M, Ayad A, Salama M M A, et al, Mitigation of Cyber-Attacks on Wide-Area Under-Frequency Load-Shedding Schemes[J]. IEEE Transactions on Smart Grid 14(3), 2377～2389 (2023).
11. Wu J, Wen J, Sun H, et al, Feasibility Study of Segmenting Large Power System Interconnections With AC Link Using Energy Storage Technology[J]. IEEE Transactions on Power Systems 27(3), 1245～1252 (2012).
12. Khayyer P, Özgüner Ü, Decentralized Control of Large-Scale Storage-Based Renewable Energy Systems[J]. IEEE Transactions on Smart Grid 5(3), 1300～1307 (2014).
13. Yan K, Li G, Zhang R, et al, Frequency Control and Optimal Operation of Low-Inertia Power Systems With HVDC and Renewable Energy: A Review[J]. IEEE Transactions on Power Systems 39(2), 4279～4295 (2024).
14. Yadav A, Gupta R, Mohit M K, Numerical analysis of performance of tube heat exchanger with center-perforated tapered twisted tape[J]. Energy Sources, Part A: Recovery, Utilization, and Environmental Effects 47(1), 16～30 (2025).

123 Multi-mode Compound Control of Full-bridge MMC-based De-icing Devices

Wang Zehao[1,2], Li Guicai[1], Li Huan[1,2], Lu Yiping[1,2], Feng Junjie[1,2]
[1] State Key Laboratory of HVDC, Electric Power Research Institute, China Southern Power, Guangzhou 510663, China
[2] China Southern Power Grid Co., Ltd, Guangzhou 510663, China
fengjj@csg.cn

Abstract. This study addresses the operational complexity and mode coordination issues in full-bridge MMC-based de-icing systems. A state machine model is constructed with multiple operating modes including standby, de-icing, and compensation. A full-process control logic is designed that includes self-check, mode decision, operation execution, and emergency termination. One-click sequence control strategy is proposed to achieve seamless mode switching and coordinated multi-functional operation. Simulation model is built using MATLAB/Simulink. The simulation results demonstrate that the proposed strategy maintains stable de-icing current under various conditions, enables smooth reactive power regulation and harmonic compensation, and significantly reduces total harmonic distortion.

Keywords: Full-bridge MMC; De-icing; One-click sequence control; Smooth mode switching; Dynamic capacity allocation

1 Introduction

The frequent occurrence of extreme ice-snow disasters leads to excessive ice accretion thickness on transmission lines, triggering cascading grid accidents such as conductor galloping and tower collapse [1]. According to State Grid disaster statistics, ice disasters caused an average annual permanent damage exceeding 1,200 kilometers to transmission lines between 2008 and 2023, with direct economic losses reaching up to 1.7 billion CNY/year [2, 3]. Traditional AC de-icing requires line outage and relies on large-capacity power supply support. While DC de-icing technology enables live-line de-icing, existing installations generally suffer from two major drawbacks: the annual utilization rate of de-icing devices falls below 5%, resulting in massive investment idleness; and power abrupt changes during de-icing/compensation mode switching induce DC voltage oscillations exceeding ±15%, threatening converter valve safety [4, 5]. Current research focuses predominantly on topology optimization and single-mode control, failing to resolve dynamic conflicts during multifunctional cooperative operation and lacking a standardized control framework to ensure smooth mode transitions.

Reference [6] proposed a hybrid de-icing system combining a full-bridge MMC converter with a thyristor rectifier. Both units supply de-icing current synergistically, while the MMC also provides active filtering and reactive power compensation, enabling zero-power tests. Reference [7] introduced a novel MMC-STATCOM based DC de-icing device. Utilizing the common DC bus and energy exchange characteristics of MMC, it achieves four-quadrant operation and employs IEGTs to expand capacity, allowing both high-current DC de-icing and high-power reactive compensation. Feasibility was verified via MATLAB simulation. Reference [8] designed a hybrid DC de-icing device comprising an LCC and hybrid MMC, proposing mode switching schemes, coordinated control, and functional reuse strategies for various conditions. Reference [9] presented an MMC de-icing device using hybrid submodules (half-bridge and full-bridge), providing calculation methods for submodule numbers and capacitor voltage balancing strategies. Reference [10] analyzed loss characteristics of full-bridge MMC de-icing devices, deriving IGBT/diode conduction and switching loss formulas, and performed calculations based on actual engineering.

Reference [11] analyzed the DC capacitor voltage ripple in full-bridge MMC DC de-icing modules, deriving expressions linking ripple to de-icing current, modulation ratio, capacitance, and maximum ripple. Reference [12] designed a multifunctional full-bridge MMC de-icing device with integrated DC de-icing, reactive power compensation, and harmonic suppression, realized via a circulating current suppressor and associated control strategies. Reference [13] studied the modeling, topology, parameter design, modulation, and control of the full-bridge MMC de-icing device, utilizing the output characteristics of full-bridge submodules to achieve wide-range continuous regulation of output current and voltage. Reference [14] proposed a control strategy enabling zero-start voltage/current ramping for different line de-icing requirements and defined the topology for reactive power compensation mode. Reference [15] introduced a new DC de-icing device based on a double-star bridge-connected MMC (DSBC-MMC). Leveraging the benefits of chain-link STATCOM and half-bridge MMC, this technology seamlessly integrates wide-range continuous DC voltage regulation with simultaneous de-icing and reactive power compensation, eliminating the need for topology reconfiguration. However, several functional constraintations persist: sequential control strategies for mode transitions are neither specified nor incorporated; capability in suppressing high-frequency and non-characteristic harmonics remains unverified; quantitative validation of dynamic compensation performance is inadequate; and multi-operational-condition adaptability requires further investigation.

This study addresses critical challenges in full-bridge MMC-Based De-icing devices, including operational complexity, safety risks during mode transitions, and capacity coupling constraints constrainting multifunctional synergy. A one-click sequential control strategy is proposed, aiming to achieve smooth mode switching, rational capacity allocation, enhanced operational safety, and improved equipment utilization through a standardized control sequence.

2 Full-bridge MMC-based De-icing Device

The circuit topology of the MMC de-icing device is shown in Fig. 1. In the Fig.1, R_{arm} represents the bridge arm resistance, L_{arm} represents the bridge arm reactor; R, L represents the resistance and reactance of the AC system. The topology of the full-bridge MMC de-icing device is shown in Fig. 1. Its left side is connected to the AC system, and the right side is connected to the line to be de-iced. It can be seen from the topology that the de-icing device is a single-ended MMC, which converts to DC to generate Joule heat to heat the iced line for de-icing. It includes three phase units, each containing upper and lower bridge arms. Each bridge arm is composed of N identical sub-modules in series. v_{au}, v_{bu}, v_{cu}, v_{al}, v_{bl}, v_{cl} and i_{au}, i_{bu}, i_{cu}, i_{al}, i_{bl}, i_{cl} are the equivalent voltage drops and currents of the upper and lower bridge arms of each phase, respectively. Z_{line} is the line resistance, and U_{dc} are the DC side power supply voltages of the DC de-icing line, and I_{dc} is the DC side de-icing currents. u_{g_a}, u_{g_b}, u_{g_c} are the three-phase AC voltages on the AC side of the system, i_{a_M}, i_{b_M}, i_{c_M} are the three-phase AC currents on the AC side of the system, and i_{ci_a}, i_{ci_b}, i_{ci_c} are the MMC bridge arm circulations of the system.

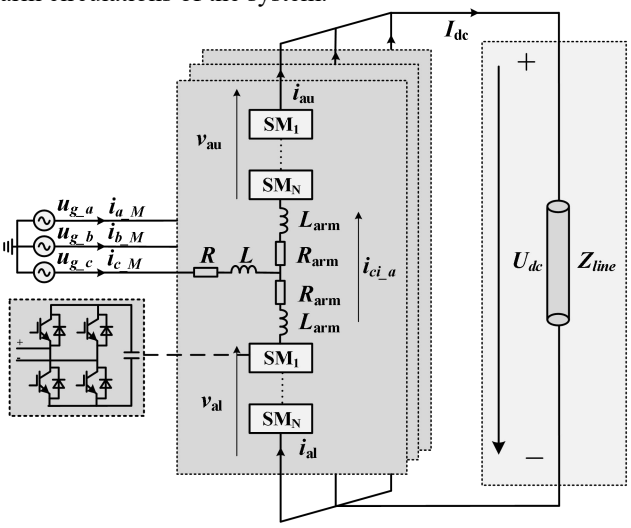


Fig. 1. MMC DC de-icing system

3 One-click Sequential Control Strategy

3.1 Multi-mode State Machine Construction

To address the current constraint issue of Insulated Gate Bipolar Transistors (IGBT) in the full-bridge modular multilevel converter (MMC) DC de-icing device, this chapter reconstructs the control logic with current as the core variable. The core constraint is defined as follows: The actual operating current peak value I_p of the

IGBT is the sum of the de-icing current I_{dc}, reactive current I_q, and total harmonic current I_h, and must not exceed the rated current peak value I_{max} of the IGBT. The core relational expression as

$$I_p = I_{dc} / 3 + (I_q + \sum_{h=5,7,11,13\cdots} I_h) / 2 \le I_{max} \tag{1}$$

In the formula, I_h denotes the h-th harmonic current; I_{dc} denotes the DC de-icing current; I_q denotes the reactive power compensation current; and I_{max} denotes the rated current peak value of the IGBT.

The design of the state machine takes the IGBT current constraint as its core, focusing on current priority allocation and remaining current calculation to realize the coordinated control of de-icing, reactive power compensation, and harmonic suppression functions.

Current Priority Constraints

To ensure the continuity and safety of the de-icing process, the de-icing current has absolute priority in current allocation. Based on the relationship between the required de-icing current $I_{dc,req}$ and the rated current peak value of IGBT I_{max}, the following constraint rules are formulated:

When the required de-icing current is within the current capacity range of IGBT: Priority is given to supplying the required de-icing current to avoid interruptions in the line de-icing process, and the actual output de-icing current is equal to the required de-icing current.

When the required de-icing current exceeds the current capacity of IGBT: To prevent overcurrent damage to IGBT, the actual output de-icing current is limited to the rated current peak value of IGBT, and the reactive power compensation and harmonic suppression functions are temporarily blocked.

$$I_{dc,out} = I_{max}, I_q = 0, I_h = 0 \tag{2}$$

where, $I_{dc,out}$ represents the actual de-icing output current.

This constraint not only realizes the "de-icing priority" principle but also provides overcurrent protection for IGBT.

Calculation of Remaining Current and Hierarchical Allocation of Harmonic Currents

After allocating the de-icing current, it is necessary to quantify the remaining current of IGBT to provide current support for reactive power compensation and harmonic suppression. A two-level remaining current model is constructed, including the first-level remaining current I_{r1} and the second-level remaining current I_{r2}.

The first-level remaining current refers to the current margin obtained by deducting the actual de-icing current from the rated current peak value of IGBT, and it serves as the shared total current resource for reactive power compensation and harmonic suppression, expressed as:

$$I_{r1} = I_{max} - I_{dc,out} / 3 \tag{3}$$

Priority is given to allocating reactive current or harmonic current from the first-level remaining current. The second-level remaining current is the remaining margin after allocating the reactive current or harmonic current, expressed as:

$$I_{r2} = I_{r1} - (I_{q,out} / \sum I_{h,out}) / 2 \tag{4}$$

where, $I_{q,out}$ denotes the actual output reactive current, and $I_{h,out}$ denotes the actual output harmonic current.

To mitigate the impact of low-order harmonics on power grid quality, the allocation of harmonic currents follows the principle of "lower order priority and margin cascading", with priority given to compensating the 5th, 7th, 11th, and 13th harmonics:

If $I_{r2} < \sum I_{h,req}/2$, where $\sum I_{h,req}$ denotes the total required harmonic current, the current shall be allocated in the order of prioritizing low-order harmonic compensation until the second-level remaining current is exhausted.

3.2 Sequential Control Full-process Logic Architecture

The full-process logic enables automatic mode switching and current allocation, comprising four phases: self-inspection, mode decision, operation execution, and emergency termination, with its flow chart shown in Fig. 2.

Upon receiving the start command, the system first performs a comprehensive self-inspection to ensure that hardware and software meet the current control requirements. If any parameter is detected to exceed the normal threshold, the "alarm and latching" process is triggered immediately, and the fault code is recorded; if the self-inspection is passed, the system enters the mode decision phase.

Mode decision is based on the comparison result between the real-time line current I_{line} and the minimum de-icing current threshold $I_{dc,min}$, with the trigger condition as follows:

$$I_{line} \geq k_{ice} \cdot I_{dc,min} \tag{5}$$

where, k_{ice} denotes the safety factor.

Based on the trigger condition, two scenarios are defined:

Scenario 1: De-Icing Mode Triggered

The system enters the pure de-icing mode, prioritizing line ice melting. It only outputs de-icing current and latches the reactive power compensation and harmonic suppression functions (I_q=0、I_h= 0). Unless there is remaining current $I_{r1} > 0$ after de-icing current allocation, in which case the system enters Scenario 2.

6

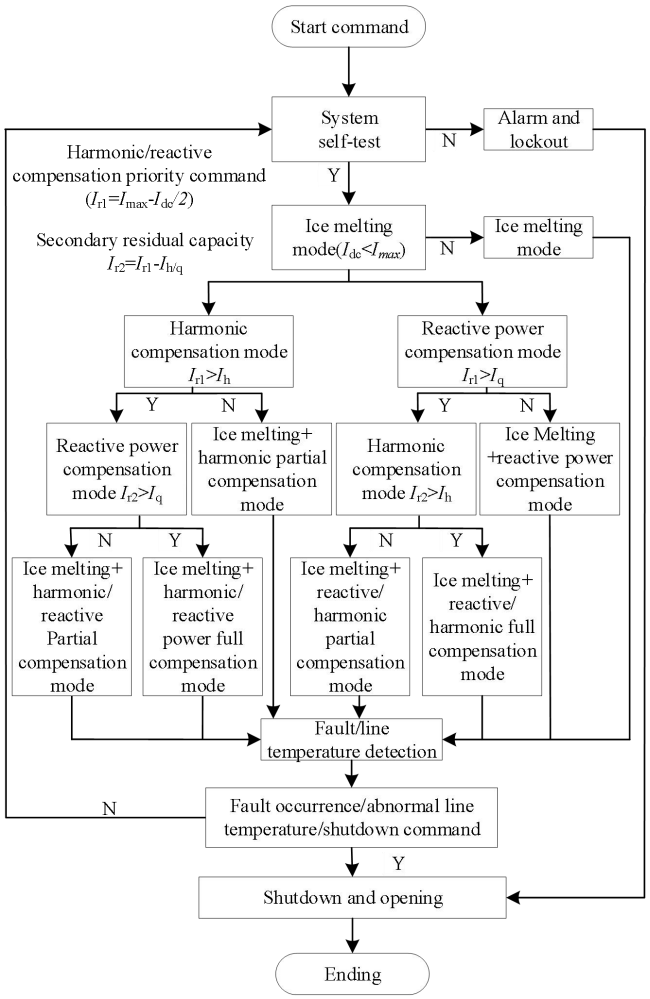


Fig. 2. One-click sequential control flowchart

Scenario 2: De-Icing Mode Not Triggered or Remaining Current Exists

The system enters the "harmonic/reactive power compensation priority phase". Based on the relationship between the remaining currents (I_{r1}、I_{r2}) and the required reactive/harmonic currents, the specific operation mode is determined, which is divided into three operating conditions:

Operating Condition 1: Sole De-icing Mode

No reactive power or harmonic compensation is required, and the system only outputs de-icing current.

Operating Condition 2: Single Compensation + De-icing Mode

The de-icing function is combined with a single compensation function (either reactive power compensation or harmonic compensation), depending on the remaining current:

Sub-condition 1: De-icing + Reactive Power Compensation

Reactive current is allocated from the first-level remaining current I_{r1}, where $I_{q,req}$ denotes the actual required reactive current:

If $I_{r1} \geq I_{q,req}/2$, full reactive power compensation is implemented;

If $I_{r1} \leq I_{q,req}/2$, partial reactive power compensation is implemented.

Sub-condition 2: De-icing + Harmonic Compensation

Harmonic current is allocated from the first-level remaining current I_{r1}, where $I_{h,req}$ denotes the actual required harmonic current (note: corrected for logical consistency, as $I_{h,req}$ represents harmonic current):

If $I_{r1} \geq \sum I_{h,req}/2$, full compensation is implemented for the 5th, 7th, 11th, and 13th harmonics;

If $I_{r1} \leq \sum I_{h,req}/2$, compensation is implemented in accordance with the "lower order priority" principle.

Operating Condition 3: Dual Compensation + De-icing Mode

The de-icing function is combined with dual compensation functions, namely reactive power compensation and harmonic compensation. Based on the compensation degree, it is divided into four sub-conditions:

Sub-condition 1: De-icing + partial reactive power compensation + partial harmonic compensation;

Sub-condition 2: De-icing + partial reactive power compensation + full harmonic compensation;

Sub-condition 3: De-icing + full reactive power compensation + partial harmonic compensation;

Sub-condition 4: De-icing + full reactive power compensation + full harmonic compensation.

At this time, the current satisfies the following formula:

$$\begin{aligned} &Sub-condition\ 1{:}I_{q,out} < I_{q,req}, I_{h,out} < \sum I_{h,req} \\ &Sub-condition\ 2{:}I_{q,out} < I_{q,req}, I_{h,out} = \sum I_{h,req} \\ &Sub-condition\ 3{:}I_{q,out} = I_{q,req}, I_{h,out} < \sum I_{h,req} \\ &Sub-condition\ 4{:}I_{q,out} = I_{q,req}, I_{h,out} = \sum I_{h,req} \end{aligned} \tag{6}$$

During operation, the system continuously monitors three key conditions to ensure the safety of IGBT and the stability of the power grid, namely IGBT fault signal, abnormal line temperature and manual shutdown command. If any of the conditions is triggered, the system immediately executes the operation of "current ramp-down + IGBT latching + disconnection" to terminate all operations, avoiding equipment damage or power grid disturbance. If no abnormality is detected, the system cyclically executes the mode decision and operation execution processes.

8

4 Simulation Experimental Validation of Multi-mode Coordinated Control for the De-icing Device

To investigate the fully automated sequence operation of the De-icing device, this study presents a simulation model built using MATLAB/Simulink. The specific parameters are given in Table 1.

Table 1. Simulation parameters of ice melting device

Parameter	Value
Rated Capacity	60.5 MW
Rated AC Grid-side Voltage	35 kV
Number of Arm Submodules (N)	50
Submodule Capacitance	25200 μF
Arm Inductance	13 mH
Arm Resistance	0.1 mΩ

4.1 Sole De-icing Condition Simulation Verification

The sole de-icing condition focuses on validating the precise control of the de-icing current, the transient-free characteristic during start-up/adjustment, and stable power matching on the grid side. The device executes only the de-icing function. Simulation setup: activation at 0.8s with a target current of 3500A; reduction to 2500A at 4s; further reduction to 1000A at 6s; shutdown at 8s. DC-side voltage, current, and grid-side AC current waveforms were monitored.

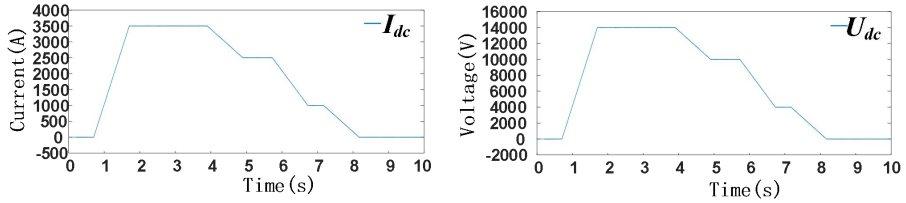


Fig. 3. De-icing current and voltage

Fig. 3 shows the De-icing current and voltage. The de-icing current smoothly rises to 3500A within 0-0.8s with an overshoot of <2%. No significant oscillations occur during the transitions at 4s and 6s. The current decreases linearly during the shutdown process at 8s, validating the effectiveness of the "soft-start current ramping" and the current controller.

4.2 Simulation Verification Simulation Validation of De-icing with Single-compensation Operating Conditions

Validation focuses on the rationality of dynamic capacity allocation and mode-switching smoothness, divided into two sub-scenarios: "De-icing with reactive power compensation" and "de-icing with harmonic compensation".

De-icing with Reactive Power Compensation Mode

The device dynamically adjusts reactive power output while maintaining stable de-icing current. Experiment: De-icing initiated at 1s (3500A); full reactive power compensation (11 Mvar) engaged at 3.8s; switched to partial compensation (5.5 Mvar) at 6.8s. During both transitions, de-icing current fluctuations remained ≤50A and DC voltage variations ≤2%, confirming the efficacy of the "de-icing absolute priority" design. Fig. 4 shows the waveform of DC ice melting current and voltage.

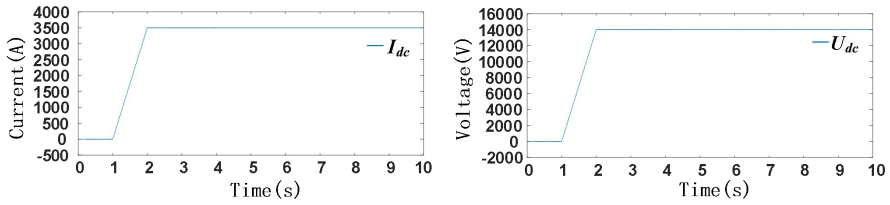


Fig. 4. De-icing current and voltage waveforms

Fig. 5 shows the reactive power waveform. When full compensation engaged at 3.8s, reactive power rapidly reached 11 Mvar with minimal overshoot. The smooth decrease to 5.5 Mvar at 6.8s validates the transition-smoothing effect of the power ramp function.

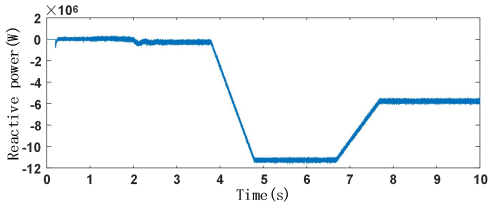


Fig. 5. Reactive power waveform

De-icing with Harmonic Compensation Mode

Validates harmonic suppression capability during de-icing, adhering to the "lower-order priority" rule. Experiment: De-icing started at 1s (3500A); harmonic source injected at 3.5s; 5th harmonic compensation engaged at 4s; 7th harmonic superimposed at 5.5s; 11th superimposed at 7s; 13th superimposed at 8s. Fig. 8 demonstrates stable de-icing current (3500A ±30A) during sequential harmonic compensation engagements, confirming compliance with the "residual capacity dynamic allocation" principle.

Fig. 6 shows the AC current waveforms at the grid side under different harmonic compensation states. The AC current waveforms at the grid side change with the switching of reactive power compensation States, reflecting the compensation effect.

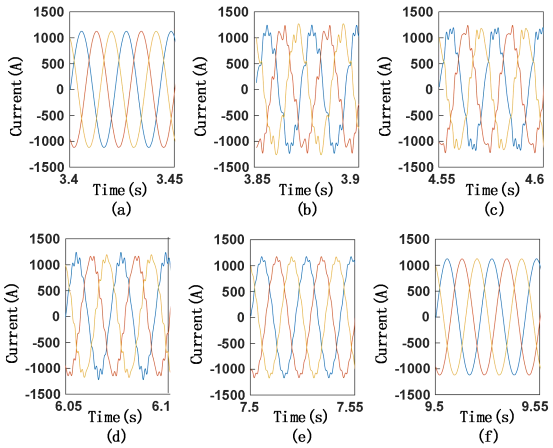


Fig. 6. Grid-side ac current waveforms under different harmonic compensation states:(a) Normal ice melting; (b) Harmonic source access; (c) 5th harmonic compensation; (d) 7th harmonic compensation; (e) 11th harmonic compensation; (f) 13th harmonic compensation.

Fig. 7 shows the harmonic detection diagram of the grid-side current under different compensation states. The data indicates: Harmonic content reaches 12.87% without compensation; reduces to 9.46% after compensating the 5th harmonic; further reduces to 6.35% after additionally compensating the 7th harmonic; reduces to 3.47% after additionally compensating the 11th harmonic; and finally reduces to 0.23% after compensating the 13th harmonic, meeting the national standard requirement of THD ≤ 5%.

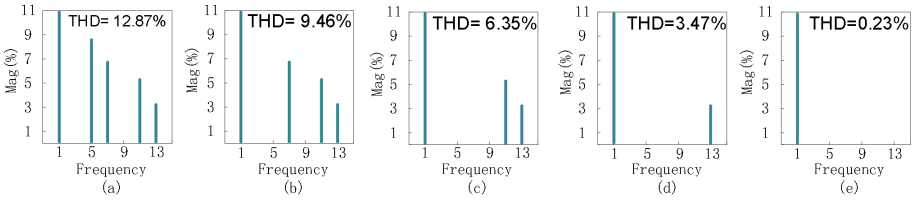


Fig. 7. Harmonic detection diagram of grid-side current under different compensation states: (a) Harmonic source access; (b) 5th harmonic compensation; (c) 7th harmonic compensation; (d) 11th harmonic compensation; (e) 13th harmonic compensation.

4.3 Simulation Validation of De-icing with Dual-compensation Operating Conditions

Validation encompasses modes integrating de-icing, reactive power compensation, and harmonic compensation, including multiple sub-modes. Harmonic compensation adheres to the "lower-order priority" rule, while reactive compensation is dynamically

determined based on residual capacity. The dual-compensation mode represents an ultimate test of multifunctional synergy, requiring simultaneous execution of de-icing, reactive power regulation, and harmonic suppression to validate capacity allocation adaptability in complex scenarios. Experiment: De-icing current fixed at 3500A; residual capacity allocated per protocol; 4-8s: partial reactive compensation + partial harmonic compensation; 8-10s: full reactive compensation + partial harmonic compensation; 10-14s: partial reactive compensation + full harmonic compensation; 14-16s: full reactive compensation + full harmonic compensation, Fig. 8 shows the waveform of DC ice melting current and voltage.

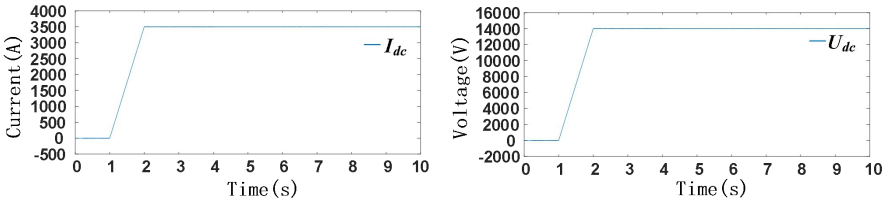


Fig. 8. De-icing current and voltage waveforms

Fig. 9 shows the grid-side current waveforms under different modes. Local comparison reveals that: during harmonic compensation from 4-10s, current distortion is still present; during full harmonic compensation, the AC current waveform is smoother. This visually demonstrates the superimposed effect of multiple compensation functions.

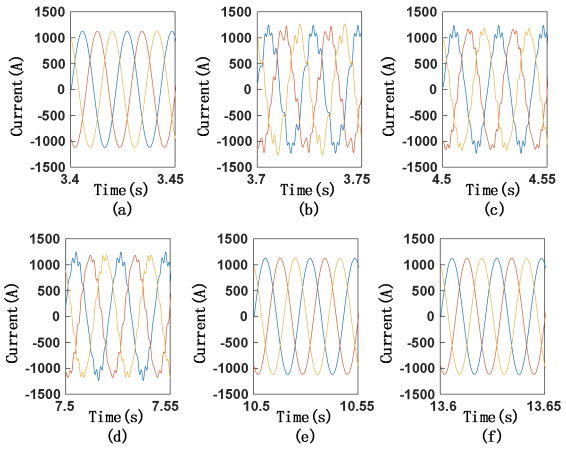


Fig. 9. Grid-side current waveforms under different modes:(a) Normal ice melting; (b) Harmonic source access; (c) Harmonic partial compensation and reactive partial compensation; (d) Partial harmonic compensation and total reactive power compensation; (e) Total harmonic compensation and partial reactive power compensation; (f) Total harmonic compensation and reactive power compensation.

Fig. 10 shows the harmonic detection diagram of the grid-side current under different modes. Without harmonic compensation, the harmonic content is 12.87%.

During 4-10s, with 5th and 7th harmonic suppression enabled, the grid-side AC current harmonic content decreases to 6.23%. During 10-16s, with additional 11th and 13th harmonic suppression enabled, the harmonic content decreases to 0.27%.

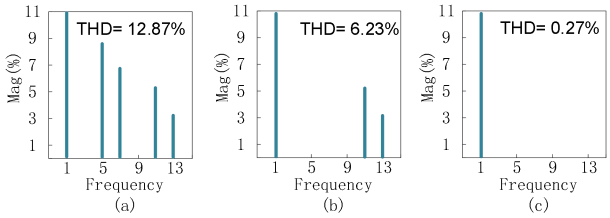


Fig. 10. Harmonic content detection diagram under different modes: (a) No harmonic compensation; (b) Partial harmonic compensation; (c) Harmonic full compensation

Fig. 11 shows the reactive power waveform under different modes. The waveform demonstrates smooth transitions from no reactive compensation to partial reactive compensation to full reactive compensation, proving the effectiveness of dual compensation under this strategy.

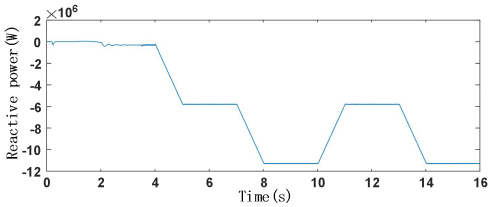


Fig. 11. Reactive power waveform

5 Conclusion

This study proposes a one-click sequential control strategy for a full-bridge MMC-Based De-icing device. It effectively resolves operational complexity, safety risks during mode switching, and capacity coupling, enabling efficient coordination of de-icing and compensation functions. A multi-mode state machine combined with power ramp transition control eliminates power abrupt changes, ensuring minimal fluctuations in de-icing current and DC voltage during transitions. The "de-icing absolute priority" mechanism with rule-based residual capacity allocation decouples functionalities, maintaining stable de-icing current, significantly reducing THD after harmonic compensation, and enabling smooth reactive power transitions. The integrated strategy achieves stable, synchronous operation of de-icing, reactive power compensation, and harmonic suppression, delivering high-quality grid current with rapid dynamic response, validating its reliability in complex conditions and supporting future device intelligence.

6 References

[1] Jiang, X. L., Fan, C. J., Xie, Y. B.: New method of preventing ice disaster in power grid using expanded conductors in heavy icing area [J]. IET Generation Transmission & Distribution, 13(4), 536–542 (2019).

[2] Lu, J. Z., Guo, J., Jian, Z., Yang, Y. H., Tang, W. H.: Resilience Assessment and Its Enhancement in Tackling Adverse Impact of Ice Disasters for Power Transmission Systems [J]. Energies, 11(9), (2018).

[3] Lu, J. Z., Guo, J., Xu, X. J., Yang, L.: Long-term forecast method for ice disasters on power grids [J]. Cold Regions Science and Technology, 155, 108–119 (2018).

[4] Wang, J. J., Fu, C., Chen, Y. P., Rao, H., Xu, S. K., Yu, T., Li, L. C.: Research and Application of DC De-Icing Technology in China Southern Power Grid [J]. IEEE Transactions on Power Delivery, 27(3), 1234–1242 (2012).

[5] Zhang, J., Cheng, H. L., Yang, P., Zhang, B. Y., Zhang, S. Q., Lu, Z. G.: Comprehensive Evaluation Index System and Application of Low-Carbon Resilience of Power Grid Containing Phase-Shifting Transformer under Ice Disaster [J]. Processes, 11(9), (2023).

[6] Guo, Y. Q., Xu, J. Z., Zhao, C. Y.: Research on Control Strategy of Full-Bridge MMC for DC De-Icing [J]. Journal of North China Electric Power University (Natural Science Edition), 43(03), 16–24+50 (2016).

[7] Guo, Y. Q., Zhou, Y. B., Xu, J. Z., Xu, S. K., Zhao, C. Y., Fu, C.: Control Strategy of DC De-Icing Device Suitable for Full-Bridge Modular Multilevel Converter [J]. Automation of Electric Power Systems, 41(05), 106–113 (2017).

[8] Ma, B., Chen, Z. H., Liu, H. E., Yang, M. Z., Fu, J.: Research on New MMC-STATCOM Structure DC De-Icing Device for High-Voltage and High-Power Power Grid [J]. Power System Protection and Control, 43(11), 101–108 (2015).

[9] Ma, X. H., Xu, K., Zhang, C., Liang, Y. Q.: Research on Loss Characteristics of Full-Bridge MMC DC De-Icing Converter Valve [J]. Power Electronics, 54(04), 61–64 (2020).

[10] Mei, H. M., Liu, J. Z.: New Modular Multilevel DC De-Icing Device [J]. Automation of Electric Power Systems, 37(16), 96–102 (2013).

[11] Xu, K., Ma, X. H., Bing, Y. Q., Liu, J., Chen, P. L., Bi, R. M., Liang, Y. Q.: Voltage Source and Current Source Hybrid De-Icing Technology and Its Control Strategy [J]. High Voltage Engineering, 46(08), 2789–2798 (2020).

[12] Xu, K., Ma, X. H., Hu, P. F., Zeng, H. R., Liang, Y. Q., Bi, R. M.: Analysis of DC Capacitor Voltage Ripple in Power Module of Full-Bridge MMC DC De-Icing Technology [J]. High Voltage Engineering, 47(02), 596–602 (2021).

[13] Yu, J. Y., Chen, H., Xin, Y. C., Zhu, X. D.: Research on Topology and Control Method of LCC-MMC Hybrid DC De-Icing Device [J]. Power Grid and Clean Energy, 39(02), 1–9 (2023).

[14] Yuan, K., Lü, X. G., Tian, Z. Q., Wang, F. Y., Zhu, L. C.: Design and Simulation of Full-Bridge MMC DC De-Icing Device [J]. Journal of University of Science and Technology Liaoning, 44(06), 456–463 (2021).

[15] Zhao, Q. M.: New Modular Multilevel DC De-Icing Device Based on Hybrid Submodules [J]. Southern Power System Technology, 9(11), 36–41 (2015).

124 基于 V-I 轨迹颜色编码与特征优选的 NILM 方法

张云舒[1]，雷宇航[1]，赵君童[1]，冯长远[1]，孙一铭[1]，丁海洋[1]，王谱宇[1]

（1. 南京理工大学 自动化学院，江苏省 南京市，210094）

Non-intrusive Load Monitoring Method Based on V-I Trajectory Color Encoding and Feature Optimization

Zhang Yunshu[1], Lei Yuhang[1], Zhao Juntong[1], Feng Changyuan[1], Sun Yiming[1], Ding Haiyang[1], Wang Puyu[1]

(1. School of Automation, Nanjing University of Science and Technology, Nanjing, Jiangsu, 210094)

ABSTRACT: Addressing the challenges of energy transition and building a new energy system necessitates refined power load monitoring technologies. As a core approach in this field, Non-Intrusive Load Monitoring (NILM) still faces multiple challenges in feature extraction and selection: traditional event detection algorithms exhibit poor adaptability to the switching events of appliances with significant power differences; single electrical features provide limited discriminative information; while multi-feature fusion methods often introduce redundant features due to a lack of optimization and face limitations in fusion dimensions, resulting in a trade-off between model complexity and identification accuracy. To tackle these issues, this paper proposes a novel NILM method based on V-I trajectory color-coding for multi-feature extraction and deep learning optimization. Firstly, an adaptive event detection algorithm is employed to reduce the missed detection rate for appliances with different power levels. Secondly, the color coding space is innovatively utilized to efficiently integrate various steady-state and transient electrical features into V-I trajectory images, constructing a high-dimensional feature pool. Subsequently, a hybrid feature selection strategy (combining mRMR and Sequential Forward Selection algorithms) is adopted to automatically screen the most discriminative and low-redundancy feature subset, thereby reducing data dimensionality. Finally, the selected feature vectors and the enhanced V-I images are utilized for load identification. Experiments on public datasets demonstrate that the proposed method effectively overcomes the limitations of existing approaches, significantly reduces model complexity, and improves the accuracy and generalization capability of load identification, providing an effective technical solution for promoting energy conservation and user electricity behavior analysis.

KEY WORDS: Non-intrusive load monitoring (NILM); event detection; feature selection; V-I trajectory; color coding

摘要：为应对能源转型挑战，构建新型能源体系，精细化电力负荷监测技术至关重要。非侵入式负荷监测（Non-Intrusive Load Monitoring, NILM）是此领域的核心技术之一，在特征提取与优选环节面临诸多挑战：基于单一电气特征的负荷辨识模型受限于有限的判别信息，辨识性能不佳；而多特征融合方法又常因缺乏优选过程引入冗余特征，且融合维度受限，导致模型复杂度与识别精度难以兼得；同时，传统基于功率阈值的事件检测算法难以确定适应不同功率负荷的功率阈值，导致对功率差异大的电器投切事件适应性差。针对以上问题，本文研究了一种基于 V-I 轨迹颜色编码、融合多特征提取与深度学习优化的 NILM 方法。首先，通过自适应事件检测算法降低对不同功率电器投切的漏检率；其次，利用颜色编码空间，将多种稳态与暂态电气特征高效融合至 V-I 轨迹图像中，构建高维特征池；再次，构建一种结合 mRMR 与序列前向选择算法的混合式特征优选策略，自动筛选出辨识准确率高的低冗余特征子集，以降低数据维度；最后，利用优选后的特征向量和增强型 V-I 图像进行负荷识别。在公开数据集上的实验表明，本文提出的负荷辨识方案在显著降低模型复杂度的同时，提高了负荷识别的准确率与泛化能力，为推进节能降耗与负荷侧的用电行为分析提供了技术方案。

关键词：非侵入式负荷监测（Non-Intrusive Load Monitoring, NILM）；事件检测；特征优选；V-I 轨迹；颜色编码

0 引言

我国正着力加速能源结构转型升级进程，加速构建以清洁低碳、安全高效为显著特征的新型能源体系[1,2]。在这一进程中，电力系统作为能源系统的重要组成部分，其智能化和精细化水平直接影响能源利用效率。电力负荷监测技术在帮助电力公司实时掌握负荷侧用电行为与习惯的同时，也为其制定更加灵活且可靠的计量及计费体系提供了依据；还能为用电住户提供科学、合理的用电建议，促进节电意识与行为优化[3]；同时也能基于居民家庭的用能规律，为政府开展能源大数据分析、制定宏观政策提供数据支撑[4]。从而在满足人民生活用电需求

通信作者：王谱宇（1989）男，博士，副教授，硕士生导师，研究方向为交直流混合电力系统的分析、控制与保护，非侵入式负荷辨识，E-mail：puyu.wang@hotmail.com。

的同时，有效减少人们对化石能源的过度依赖[5]。

非侵入式负荷监测（Non-Intrusive Load Monitoring, NILM）是负荷监测技术的重要分支，最早由 Hart 教授于 20 世纪 80 年代提出[6]。依据不同的技术路线，现有方法主要可以分为事件检测与组合优化这两类。

特征优选是通过寻优算法排除与负荷辨识无关特征和冗余特征的过程。文献[7]使用了贪心算法、Fisher 算法和最大互信息系数作为特征优选模块，使用单类支持向量机（One-Class Support Vector Machine, OCSVM）进行负荷辨识，但聚焦的识别对象是电动自行车，所选特征的泛化能力未知；文献[8]使用了 Fisher 算法筛选特征、粒子群算法改进的自组织映射（Self-Organizing Map, SOM）神经网络作为分类器；文献[9]使用密度峰值的方法，快速搜索聚类并构建负荷特征模版，使用了由状态概率因子改进的遗传算法进行负荷分解，但模版所用的特征为盲选特征，存在特征冗余；文献[10]使用最大相关、最小冗余（Max-Relevance and Min-Redundancy, mRMR）算法实施特征选择操作，其核心目标在于甄选出与分类结果具备最高相关性的特征子集，但由于分类器的限制，必须限制选取特征的数量；文献[11]研究了从高频测量数据中自动识别电器负荷的可行性，通过比较不同特征在电器负荷识别上的分类性能，发现 V-I 二进制图像特征表现优异，且组合特征能达到最高准确率，然而该文献使用单特征进行分类，综合辨识效果弱于组合特征；文献[12]先运用 K-means 聚类算法针对目标负荷实施了初步的分类划分操作，再借助 AlexNet 神经网络实现精细化分类，并将无功功率、电压-电流变化率比值和非稳定阶段 V-I 轨迹均值融入 RGB 色彩空间，生成唯一性更强的彩色 V-I 图像，以增强特征区分度，然而对 V-I 轨迹进行颜色通道填充所融合特征数量受到限制；文献[13]提出一种基于二维相位编码的电力负荷识别方法，将电压电流信号转换为图像特征，结合深度学习实现高精度电器识别。

综上所述，目前非侵入式负荷辨识领域在特征优选和负荷识别过程中存在事件检测算法面对功率差异较大电器投切检测适应性不高、单一电气特征提供信息有限、融合特征缺乏特征优选而引入冗余特征、融合特征数量受限等问题。本文研究一种基于 V-I 轨迹颜色编码融合多特征提取与深度学习优化的 NILM 方法，降低事件检测算法对不同电器的漏检率，去除无关及冗余特征，降低数据维度和模型复杂度，以提高模型准确率。

1 混合式特征优选算法

目前 NILM 研究存在特征优选机制缺乏而引入冗余特征的问题，同时，单一特征相比于能够综合反映负荷特性的组合特征辨识性能有限[14]。为解决以上问题，本节研究了一套结合过滤式（Filter）与封装式（Wrapper）优点的混合式特征优选方法，以达到从高维融合特征中自动快速地筛选出最具判别力的特征子集的目的。

1.1 特征池构建

首先，构建一个高维初始特征池，为优选算法提供基础。特征池主要包括传统稳态特征、V-I 轨迹图像特征、瞬态与暂态特征。

（1）传统稳态特征主要包括视在功率、有功功率、无功功率、功率因数以及电压/有功电流变化率比值等。

（2）V-I 轨迹图像特征借鉴文献[12]的思想，将一个周期内的 V-I 轨迹映射到 RGB 颜色空间，生成彩色图像。在此基础上，不仅提取图像的深度特征（通过一个预训练的轻量级 CNN），还极大丰富了特征的信息维度，突破了单一颜色通道融合特征数量受限的瓶颈。

（3）瞬态与暂态特征则是指在电器启停瞬间提取电流上升率、启动峰值电流、暂态功率波动等特征，以辅助区分功率特性相近但启停行为差异显著的电器。

1.2 搭建混合式特征优选流程

1.2.1 最大相关最小冗余预筛选

首先，采用 mRMR 过滤式特征选择算法，针对高维特征池进行初筛。mRMR 算法的目标在于寻找一个特征子集 S，该子集和分类标签（电器类别）之间具有最大相关性，同时子集内部特征间具有最小冗余性，其选取准则可通过如下优化目标函数表示：

$$max\ D(S,c), \qquad D=\frac{1}{|S|}\sum_{x_i\in S} I(x_i;c) \tag{1}$$

$$min\ R(S), \qquad R=\frac{1}{|S|^2}\sum_{x_i,x_j\in S} I(x_i;x_j) \tag{2}$$

式中，I 为互信息，c 表示类别标签。

此阶段可以快速、高效地剔除大量明显不相关和冗余的特征，将特征维度迅速降低，为后续更精确的搜索降低计算复杂度。

1.2.2 基于序列向前选择与分类器性能的精细搜索

以最终分类模型的准确率作为评价标准，采用序列向前选择（Sequential Forward Selection, SFS）算法，对特征子集进行更精细的搜索。SFS 是一种贪心搜索式的特征选择（Feature Selection）算法，可以从一个庞大的特征集合中，自动筛选出一个最优的、规模更小的特征子集，用于后续的机器学习模型的训练和预测[15]。该过程的主要步骤为：

(1) 构建一个特征空子集；
(2) 从 mRMR 筛选后的剩余特征中向子集内加入一个特征，并用该特征子集训练一个轻量级的分类器；
(3) 在验证集上基于准确率、F1 分数等指标评估所有可能新增特征后模型的性能；
(4) 选择可以最大程度提升模型性能的特征，并加入子集；
(5) 重复步骤 2~4，直到模型性能不再有明显的提高或者所有特征都已经使用完毕。

此阶段将分类器本身作为黑盒，以最终识别性能为引导信号（Guiding Signal），确保选出的每一个特征都能对模型性能做出实质性的正面贡献，从而得到最优的特征子集。

该混合方案结合了 mRMR 的高效性和 SFS 的精确性，避免了纯过滤法与实验数据存在差异的缺点与纯封装法计算成本过高的弊端，系统地实现了冗余特征剔除和数据维度降低的目标。目前本团队对于该技术的掌握并未完全熟练，仍未完全实现复现。

2 基于 V-I 轨迹颜色编码特征融合提取与深度学习的负荷辨识算法原理

2.1 负荷辨识流程

传统的非侵入式负荷辨识算法在应对复杂多变的实际用电场景时，仍存在泛化能力不足、识别精度有限等问题。为进一步提升负荷辨识的准确性与适应性，本文结合 V-I 轨迹颜色编码与深度学习神经网络，对原有辨识流程进行了改进，所采用的非侵入式负荷辨识方案具体步骤为：

（1）通过采集设备来获取相关电器电压以及电流波形，然后基于该波形来提取特征，如有功功率、无功功率、V-I 轨迹特征等；

（2）将采集的数据应用带通滤波（58-62Hz）处理去除噪声，标准化电流和电压数据，对样本数量少的类别进行数据增强；

（3）采用多通道颜色编码，以无功功率、电压/有功电流变化率比值、V-I 轨迹变化率、谐波失真（2-5 次谐波）为特征构建四通道特征工程，此即为 V-I 轨迹颜色编码特征融合组成的复合特征，然后应用高斯扩散使轨迹平滑；

（4）对物理特征（功率和谐波特征）进行标准化，使用 DBSCAN 算法进行第一阶段辨识，对高纯度簇直接分配主要类别标签，跳过低纯度簇中的样本；

（5）构建深度残差网络（Deep Residual Networks, ResNet）模型，针对尚未分类的样本进行训练与预测，评估模型识别准确率，输出分类报告，并借助混淆矩阵对识别结果进行可视化分析。

2.2 DBSCAN 聚类

本文采用 DBSCAN 聚类进行初步分类，以数据的功率和谐波特征，计算得到有功功率、无功功率、总谐波失真、特定次谐波幅值，完成数据的简单分类。

DBSCAN 作为一种无监督聚类算法，无需预先设定类别数量，即可识别任意形状的簇结构，并对噪声与离群点具有良好的鲁棒性，适合处理非凸形状的数据聚类问题。

首先从电流波形中提取六个物理特征，有功功率、无功功率、总谐波失真律（Total Hamonic Distortion, THD）及 3、5、7 次谐波幅值，经标准化处理后，以 $\varepsilon = 0.4$ 和 MinPts = 8 为参数进行聚类。采用轮廓系数评价聚类质量，并通过 t-SNE 方法对聚类结果进行降维可视化。对每个簇计算类别纯度，并设定阈值。纯度达标的簇直接分类，未达标样本及噪声点转入第二阶段，在 ResNet 进行细粒度分类。

2.3 V-I 轨迹特征的构建

V-I 轨迹作为负荷分类的重要标识，广泛用于描述电路元件或系统中电压与电流之间的函数关系。分析电路元件的非线性特性、电源行为、半导体器件、负载特性、保护特性等。为准确构建 V-I 轨迹，需要使用较高的采样频率。现有研究表明，当采样频率不低于 4kHz 时，V-I 轨迹具有良好的辨识效果。本研究使用 PLAID 数据集，其采样频率为 30kHz，符合 V-I 轨迹作为负荷标识的采样要求。具体的 V-I 轨迹构建方法为：

◆ 在设备进入稳定运行状态后，采集一个完整周期内的所有电压与有功电流数据，并进行归一化处理。计算公式为：

$$i_m(t) = \frac{i(t) - i_{min}}{i_{max} - i_{min}} \tag{3}$$

$$v_m(t) = \frac{v(t) - v_{min}}{v_{max} - v_{min}} \tag{4}$$

式中，i_{min}/i_{max}和v_{min}/v_{max}为一个周期内电流和电压的最小/最大值。

- 设定 V-I 轨迹图的分辨率为 $n\times n$，将归一化后的电压、电流数据分别映射至区间$[0,n]$，并进行向下取整，得到一组小于等于数值 n 的电压、电流数据i_{min}和v_{min}。

$$i_{min} = \text{floor}(i_m n) \tag{5}$$

$$\text{v}_{\text{min}} = \text{floor}(\text{v}_\text{m}\text{n}) \tag{6}$$

式中，floor(·)为向下取整函数。

- 初始化一个所有元素都为零的 $n\times n$ 阶矩阵。在一个完整周期的采样过程中，以第一行第一个采样点为起始点，按顺序遍历至最后一行进行数据取值。针对每一行中的采样点，其电流参数为 i_{mn}、电压参数 v_{mn}，其中 m 为行索引，n 为列索引。将 i_{mn} 和 v_{mn} 分别精准对应到零矩阵的第 m 行第 n 列位置，并把该位置的初始零值更新为 1。在完成矩阵全部元素的赋值后，借助特定的像素映射机制，将矩阵元素映射至图片像素层面，最终成功生成该负荷的 V-I 轨迹图像。

研究表明，V-I 轨迹的几何属性能够显著反映负荷的物理本质，其分析维度主要包括以下八个方面：轨迹的对称性特征、循环方向特性、封闭区域面积参数、中线斜率变化、交叉点数量分布、中段斜率特征、左右区域面积比值以及中段峰值特性。这些几何属性分别对应着不同的电气特性，具体包括：负荷电流波形的对称性、电压与电流间的相角关系（超前或滞后特性）、功率因数角大小、电流谐波含量等关键参数，从而为负荷辨识提供丰富信息。

2.4 V-I 轨迹颜色编码

本文用无功功率、电压与有功电流变化率比值、V-I 轨迹变化率、谐波失真（2-5 次谐波）将负载的物理特性映射到彩色图像空间。R 通道编码无功功率占比，反映负载的相位特性；G 通道表征电压与无功电流变化率之间的动态响应关系；B 通道表示总谐波失真度；A 通道量化 2-5 次谐波的分布特征。通过高斯扩散处理和归一化操作，生成 128×128 像素的 RGBA 特征图。

2.4.1 R 通道构建

R 通道的构建基于负荷的无功功率 Q，其计算原理为：

$$S = v_{RMS} \times i_{RMS} \tag{7}$$

$$R(i_g, v_g) = \frac{|Q|}{S} \tag{8}$$

式中，$R(i_g, v_g)$表示在 Red 通道矩阵中第 i_g 行 v_g 列处的 R 值，v_{RMS}/i_{RMS}分别表示电压/电流的均方根值；视在功率（S）描述交流电器设备容量，表示需要交流电源提供的总功率。

2.4.2 G 通道构建

在负荷稳态周期内，运用可视化技术对电压与无功电流的变化率展开分析。分析结果表明，不同负荷在稳态周期内，其电压与电流的变化率具有明显的差异性。这一特征被用于构建 V-I 轨迹颜色编码中的 G 通道，并表现出良好的区分效果。本文基于电压与无功电流变化率的动态响应关系构建 G 通道，其计算原理为：

$$G_g = \tan^{-1}\left(\frac{i_{g+1}-i_g}{i_{max}}, \frac{v_{g+1}-v_g}{v_{max}}\right) \tag{9}$$

式中，i_{max}/v_{max}表示在一个稳定周期内电流/电压幅值的最大值。

2.4.3 B 通道构建

为将非稳定运行阶段的特性纳入负荷标识中，本文采取将非稳定周期内 V-I 轨迹特征的平均值映射至 RGB 颜色空间，以此构建 B 通道。计算公式为：

$$B = \frac{1}{Z}\sum_{z=1}^{Z} W_z \tag{10}$$

式中，Z 表示负荷处于非稳定运行阶段的周期数，W_z 表示第 z 个非稳定运行阶段的 V-I 轨迹特征中对应像素点的值。

2.4.4 A 通道构建

为构建负荷的谐波特征表征，本文基于 V-I 轨迹提取了 2-5 次谐波的分布特征，并将其编码为 RGBA 图像中的 A 通道（透明度通道）。具体构建流程如下：

首先，对归一化后的电流信号进行 FFT，提取基波（60Hz, PLAID Dataset）和第 2 至第 5 次谐波分量（120Hz、180Hz、240Hz、300Hz）的幅值，并计算各次谐波幅值与基波幅值的比值，形成归一化的谐波幅值向量；其次，为不同谐波次数分配递减的权重系数（2 次谐波权重为 0.4，3 次谐波为 0.3，4 次谐波为 0.2，5 次谐波为 0.1），以突出低次谐波在负荷特性中的贡献；最后将该数值映射至 V-I 轨迹中各对应坐标位置，形成初始谐波特征图。为增强特征的稳健性与平滑性，进一步施加高斯扩散处理（σ = 1.0），并对结果进行归一化，最终生成与 R、G、B 通道尺寸一致的 A 通道特征图像，共同构成四通道的 V-I 轨迹彩色特征图，用于后续分类模型输入。

2.5 深度残差网络二次分类

为对 DBSCAN 聚类后未分类的样本进行精确识别，本文采用 ResNet 作为第二阶段分类器，具体流程为：

将 DBSCAN 判定为噪声点或低纯度簇中的样本视为未分类样本，从中划分训练集、验证集与测试集。针对未分类样本数量有限的特点，采用分层抽样以保持类别分布，并基于样本数量动态调整验证集与测试集比例：若未分类样本数超过 30，则测试集占比设为 15%；若样本数量较少，则测试集比例调整至 10%，确保小样本条件下的有效学习与可靠评估。

构建的 ResNet 模型输入为前述方法生成的四通道 V-I 轨迹特征图。网络主体由四个残差块组构成，每组包含多个残差模块。输入经过卷积核为 7×7、步长为 2 的卷积层，后接批归一化（Batch Normalization）与 ReLU 激活函数。残差模块均采用两层 3×3 卷积结构，跨层连接通过恒等映射实现，有效缓解梯度消失问题。网络末端经全局平均池化后接入包含 256 个节点的全连接层，最终通过 Softmax 函数输出各类别概率。

训练阶段使用 Adam 优化器，以稀疏分类交叉熵为损失函数，在批量大小为 16 的设置下迭代 75 轮。模型训练过程中监测验证集准确率，对未分类样本进行预测并输出分类结果，最终与第一阶段聚类结果融合形成完整分类输出。

3 网络设计与实验

为解决事件检测算法适应性不高的问题并提高负荷辨识模型的准确率，本节基于深度神经网络构建负荷辨识模型，评估所提方案的有效性。

3.1 事件检测算法

针对事件检测算法面对功率差异较大电器投切检测适应性不高的问题，改进了传统固定阈值的检测方法，并采取一种基于滑动窗口和 CUSUM（累积和）控制图的自适应事件检测算法。

传统 CUSUM 算法对负荷数据中的阶跃边缘信息较为敏感，而均值滤波、中值滤波和高斯滤波等常规去噪方法在平滑噪声的同时，通常将削弱此类边缘信息，使得事件检测精度下降。为此，本文采用双边滤波(Bilateral Filter, BF)对原始数据进行去噪处理，在有效抑制噪声的同时保留边缘特征，改进后的算法对功率序列的微小变化更为敏感，能有效检测出小功率电器（如手机充电器）的投切事件，同时对大功率变化也有良好响应，从而显著降低漏检率，为后续识别模块提供更完整的事件序列。

负荷数据中的异常点会生成阶跃边缘，为识别并处理此类异常，采用局部离群因子(Local Outlier Factor, LOF)算法，对处理后的数据进行离群点检测，进一步提升数据质量。

LOF 算法通过比较一个点的局部可达密度与其邻域内其他点的局部可达密度进行偏差计算，是衡量一个数据点异常程度的关键指标，计算公式为：

$$LOF_k(P) = \frac{\sum_{O \in N_k(P)} \frac{lrd_{k(O)}}{lrd_{k(P)}}}{|N_k(P)|} \tag{11}$$

式中，$LOF_k(P)$的值越大，表明点 P 越异常，当其值远远大于 1 时，则表明它有可能是异常点。

3.2 实验与结果分析

3.2.1 负荷辨识结果

在公开数据集与自采数据集上对所提的方法进行实验验证，并和传统方法进行对比分析。评价指标包括准确率（Accuracy）、精确率（Precision）、召回率（Recall），以多指标评估算法性能。分类结果混淆矩阵如图 1 所示。

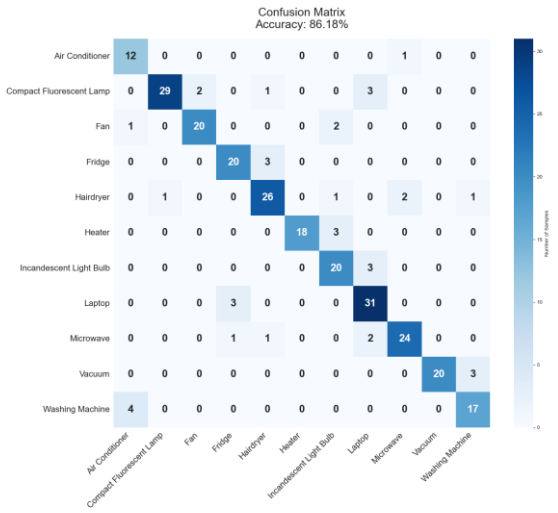


图 1 基于 PLAID 数据集实验的混淆矩阵

图 1 显示，本文所提负荷辨识算法具有较高的辨识准确率，达 86.18%。但是，最终辨识结果对于更广泛，杂乱的数据集表现结果较差，在未来我们仍需要改进。

3.2.2 模型复杂度对比

为了探究该负荷辨识模型是否能够显著降低复杂度，需要进行计算效率的分析：统计负荷辨识模型的参数量和计算量；综合考虑模型准确率与复杂度，将使用单一分类器的先进负荷辨识算法与本文算法进行对比。

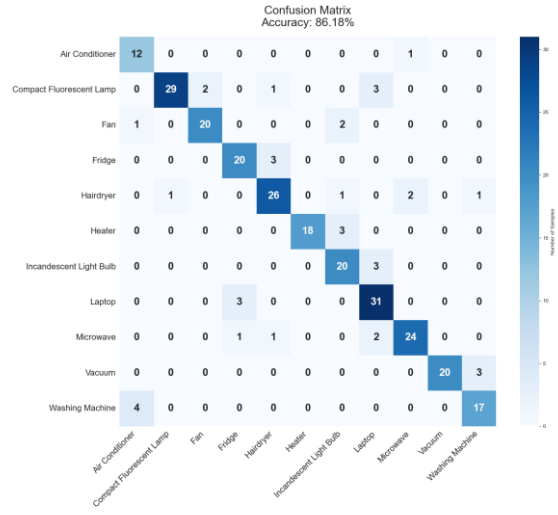
首先，统计负荷辨识模型的参数量和计算量，如表 1 所示：

表 1　不同负荷辨识模型的计算量和参数量

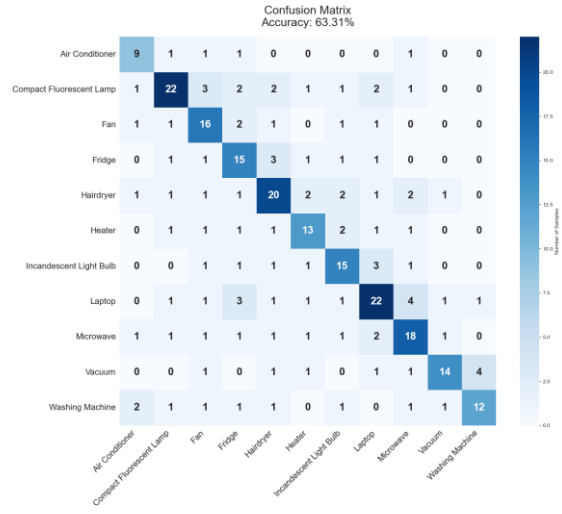
文献	分类方法	计算量（百万）	参数量（百万）
本文	DBSCAN+ResNet	11.16	0.109
文献[16]	卷积神经网络	21.18	63.31
文献[17]	AlexNet	60	716
文献[18]	ShuffleNet V2	101	-

由表 1 可得，与近五年先进负荷辨识算法相比，本文的所提算法的计算量和参数量较少，显示本文所提模型的复杂度相对较低，能够较快速、有效地筛选特征，进行负荷辨识。

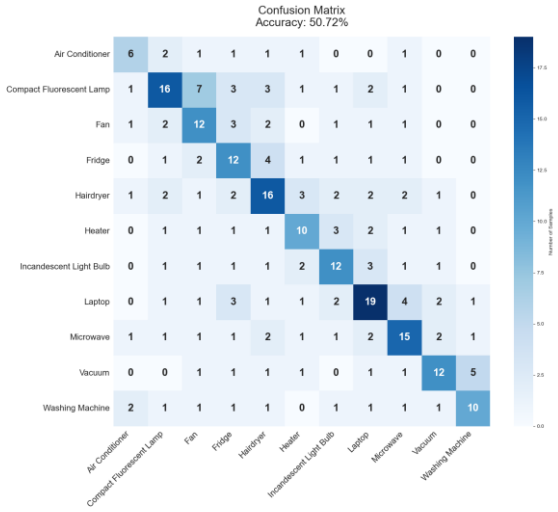
然后，补充一阶段分类器的实验，如图 2 所示：



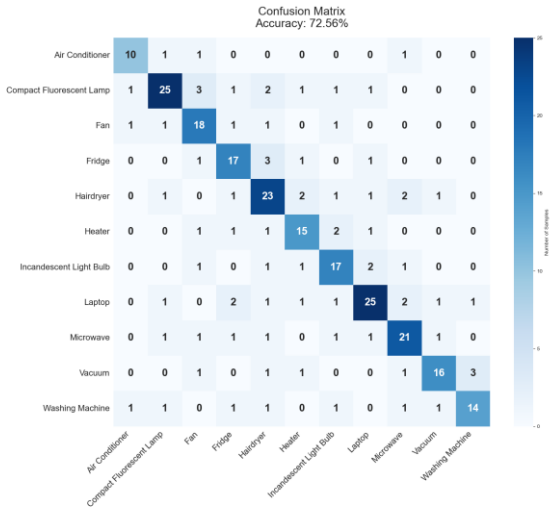
(a) DBSCAN+ResNet



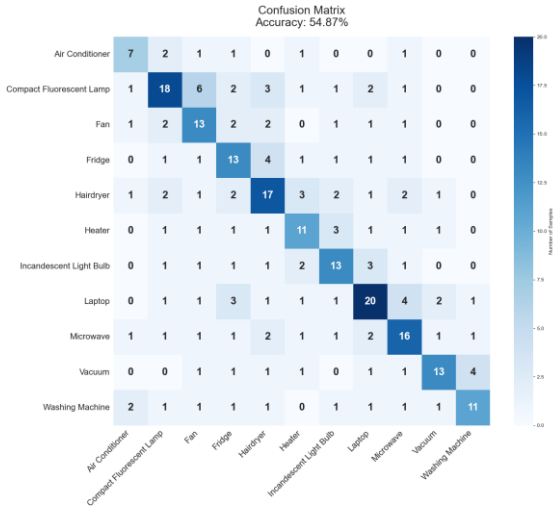
(b) ResNet



(c) AlexNet



(d) ShuffleNet V2



(e) 卷积神经网络

图 2　不同负荷辨识算法混淆矩阵

图 2 显示，本文所提负荷辨识算法在计算量较少的同时，具有较高的辨识准确率，达 86.18%。与

本文算法相比，使用一阶段分类器的负荷辨识算法效果不佳：文献[18]采用的 ShuffleNet V2 虽取得了较好的分类效果，但模型复杂度高，算法训练周期长；与文献[16-18]所提负荷辨识算法相比，本文算法在计算量和参数量更少的同时，取得了令人满意的辨识准确率。

综上所述，可以认为本文所提出的方法辨识准确率较高的同时，还具有较快的计算效率。

3.2.3 结果分析

本文提出了一种混合式特征优选框架，结合 mRMR 过滤式初筛，并以分类性能为导向的序列向前选择（SFS）精细搜索，保证了特征选择的高效性，同时显著降低了数据维度与模型复杂度；目前阶段本团队对于该技术仍未完全实现，这也是本团队下一阶段仍需解决的问题。

其次，该模型通过构建包含稳态、瞬态与 V-I 轨迹图像的高维特征池，并创新性地采用四通道颜色编码，将电气特征映射至 RGBA 图像空间，实现了多物理量的协同表征，显著增强了负荷特征的判别能力。

最后本文提出了一个高性能的事件检测方案，该方案通过引入基于滑动窗与 CUSUM 控制图的自适应事件检测方法，并结合双边滤波与 LOF 离群点处理，理论上能有效增强对小功率电器投切事件的敏感性，显著降低漏检率，提升事件检测算法对不同功率电器投切行为的适应性。该方案的实证效果，将是本团队下一步研究与仿真的重点内容。

4 结论与展望

本文针对非侵入式负荷监测中单一电气特征判别信息有限、多特征融合存在冗余与维度受限、以及传统事件检测算法适应性差等问题，研究了一种基于 V-I 轨迹颜色编码与多特征融合的深度学习优化方案，主要研究工作包括：

(1) 提出基于 V-I 轨迹颜色编码的图像特征表征方法，将电器运行的电压-电流轨迹转换为彩色图像，以增强不同负荷的视觉区分度，并提供更丰富的特征信息；

(2) 构建多维度电气特征融合与优选机制，并通过特征优选实现冗余剔除，提升特征判别能力；

(3) 通过优化传统事件检测与传统特征优选，提升模型的识别精度以实现对不同功率等级电器投切事件的自适应检测与高精度辨识。

本文中所提出的方法在特征构建、优选和识别模型上进行了集成创新，有效解决了引言中提到的一系列问题。然而，NILM 技术在迈向大规模实用化的过程中仍面临着诸多挑战。

- 首先，当前方法对于同一品牌、不同型号或不同年份生产的电器（如不同能效等级的空调），其识别精度仍有提升空间。未来可探索更具判别力的瞬态高频特征（如高频电流纹波），来实现“同一品类，不同个体”的细粒度辨识。
- 其次，在超多类电器并存场景下的计算效率有待优化：当家庭中电器总数超过 20 种甚至更多时，模型的计算复杂度和推理速度将成为部署的瓶颈。打造更加轻量级、高精度的端侧部署模型，是推动 NILM 进入智能家居终端的关键。
- 最后，在数据隐私与安全性亦不容忽视：用电数据蕴含着用户的生活隐私。在未来的研究中，如何在本地完成所有数据处理和识别，对上传至云端的数据进行有效的脱敏和加密的同时，还可以保证模型性能，是一个必须重视和解决的社会性技术课题。

通过在以上方向上的持续探索，NILM 技术必将更可靠、更高效地服务于新型能源体系建设，为推进“碳达峰、碳中和”目标提供坚实的数据基础。

参考文献

[1] 中华人民共和国国务院新闻办公室.中国的能源转型[EB/OL].https://www.gov.cn/zhengce/202408/content_6971115.htm

[2] 国家发展和改革委员会.“十四五”现代能源体系规划[EB/OL].https://www.gov.cn/zhengce/zhengceku/2022-03/23/content_5680759.htm

[3] 余贻鑫,刘博,栾文鹏.非侵入式居民电力负荷监测与分解技术[J].南方电网技术,2013,7(04):1-5.

[4] 杨定立,昌健,王莉芳,董稳改,李强.基于峰时负荷交易的有序用电机制研究[J].电网与清洁能源,2015,31(07):33-36+43.

[5] 张志豪. 基于稳态特征的非侵入式负荷辨识系统的设计与实现[D].电子科技大学,2018.

[6] Hart G W. Nonintrusive appliance load monitoring[J].Proceedings of the IEEE,1992,80(12): 1870-1891.

[7] 施雨松,徐青山,郑建.基于特征选择与增量学习的非侵入式电动自行车充电辨识方法[J].电力系统自动化,2021,45(07):87-94.

[8] 向颖, 严慧峰, 余旭阳等. 基于特征优选及改进自组织神经网络的非侵入式负荷辨识[J].中国电机工程学报,2022,42(S1):106-114.

[9] Lu L, Gu C, Feng J, et al, Non-intrusive Load Monitoring based on Multiple Feature Optimization and Genetic Algorithm[C].2022 5th International Conference on Renewable Energy and Power Engineering, Beijing, China, 2022:115-120.

[10] Shang Y, Zhang J, Zhang Z, et al, Non-intrusive Load Identification Method Based on Feature Optimization and Bayesian Algorithm[C].2023 IEEE 6th Student Conference on Electric Machines and Systems, HuZhou, China, 2023:1-7.

[11] Gao J, Emre CK, Suman G, Mario B′. A feasibility study of automated plug-load identification from high-frequency measurements[C]. 2015 IEEE Global Conference on Signal and Information Processing (GlobalSIP), Orlando, FL, USA, 2015:220-224.

[12] 解洋, 梅飞, 郑建勇, 等. 基于 V-I 轨迹颜色编码的非侵入式负荷识别方法[J]. 电力系统自动化, 2022, 46(04):93-102.
[13] Yassine H, Abdullah A, Faycal B, AA. An intelligent nonintrusive load monitoring scheme based on 2D phase encoding of power signals[J]. International Journal of Intelligent Systems,United Kingdom,2020: 72–93.
[14] 王丹宇,刘君,周亚同等.面向用电负荷分解的特征融合与Transformer 模型[J].电力系统及其自动化学报,2024,36(06):129-136.
[15] 张鸿宾,孙广煜. Tabu 搜索在特征选择中的应用[J]. 自动化学报,1999,25(4):457-466.
[16] Baets D L, Ruyssinck J, Develder C, et al. Appliance classification using VI trajectories and convolutional neural networks[J]. Energy & Buildings, 2018,158: 32-36.
[17] Liu Y C, Wang X, You W. Non-Intrusive Load Monitoring by Voltage-Current Trajectory Enabled Transfer Learning[J]. IEEE Transactions on Smart Grid, 2019, 10(5):5609-5619.
[18] 田璞. 一种适用于边缘计算的非侵入式负荷辨识方法[D]. 宁夏大学, 2023.

作者简介：

张云舒（2005），男，本科生，研究方向为非侵入式负荷辨识技术，E-mail：1978872310@qq.com。

雷宇航（2005），男，本科生，研究方向为非侵入式负荷辨识技术，E-mail：3101233057@qq.com。

赵君童（2004），男，本科生，研究方向为非侵入式负荷辨识技术，E-mail：2873719835@qq.com。

125 Coordinated Wind-Storage Control Strategy for Enhancing Frequency Regulation Characteristics in Power System

Bantigegn Bires Kassa, LI Jiahui*, Li Jiali and WANG Delin

School of Electrical Engineering, Southwest Jiaotong University,
Chengdu 611756, Sichuan Province, China

Abstract. In this paper, a coordinated control approach is introduced for wind farms and Battery Energy Storage Systems (BESS) utilizing a doubly-fed induction generator (DFIG) to effectively engage in both primary and secondary frequency regulation. Initially, mathematical models for the DFIG and BESS are developed. For primary frequency regulation, a coordinated strategy is crafted, integrating the DFIG's virtual inertia and droop control with the BESS's comprehensive inertia control to deliver quick and sustained active power support. For secondary regulation, a fuzzy logic-based controller is created to dynamically adjust the parameters of a PI controller, enhancing the tracking of the Automatic Generation Control (AGC) signal for the BESS. Simulations are performed in MATLAB/Simulink on a modified two-area test system, which confirm the proposed strategy's effectiveness. The findings indicate that the combination of wind and storage significantly enhances the system's frequency response under various disturbances, such as step load changes and fluctuating wind speeds, by reducing the rate of change of frequency (RoCoF), minimizing the frequency nadir, and ensuring a rapid return to the nominal frequency.

Keywords: Doubly-fed wind turbine, energy storage system, primary frequency regulation, secondary frequency regulation, fuzzy control, AGC.

1 Introduction

Globally, the energy sector is experiencing a major shift, with wind energy becoming a key element in the transition to sustainable power sources. Yet, the widespread adoption of wind turbines in power grids presents new challenges for system operators, mainly due to the unpredictable and intermittent nature of wind energy and the replacement of traditional synchronous generators [1, 4].

These conventional generators naturally provide inertia and primary frequency responses, which are essential for maintaining system stability when there are larger generation–load imbalances. Replacing these units with wind turbines, which are generally connected to the grid through power electronics, significantly reduces system inertia [5, 7]. This leads to larger and quicker frequency changes after a disturbance, heightening the risk of load shedding and blackouts [6, 7]. As a result, enabling wind turbines to mimic inertial responses and offer frequency support has become a vital research focus [11, 13].

Correspondence author: LI Jiahui's Email:1766893382@qq.com

Doubly-fed induction generators (DFIGs) are commonly used in modern wind farms because they allow for variable-speed operation and independent control of active and reactive power [14]. Control methods like Virtual Inertia Control (VIC) and Droop Control can be applied to enable DFIGs to release the kinetic energy stored in their rotating masses, providing temporary power support during frequency events [11, 12]. However, the support from VIC is short-term and depends on current wind speeds, making it unreliable for ongoing frequency regulation [16, 17].

Battery Energy Storage Systems (BESS) present a promising solution to this issue. Their quick response times and precise ability to inject or absorb active power make them ideal for delivering both rapid inertial responses and long-term power support [19]. The combination of wind farms and BESS can offer a strong solution for frequency stability: wind turbines provide an initial, cost-free inertial response using kinetic energy, while BESS delivers sustained and dependable power support, bridging the gap until conventional generators can increase output [20]. Although much research has concentrated on primary frequency regulation, the role of wind–storage systems in secondary frequency regulation (automatic generation control (AGC) has been less examined. Traditional AGC depends on slow-ramping thermal units, but a BESS, with its fast response, can greatly enhance AGC performance by managing initial rapid power imbalances.

This study introduces a comprehensive coordinated control strategy for a combined wind–storage system to engage in both primary and secondary frequency regulation. The main contributions of this study are as follows:

(1) The creation of a primary frequency control model that integrates DFIG's virtual inertia/droop control with BESS's comprehensive inertia control.

(2) The design of a fuzzy logic–based adaptive PI controller for the BESS to improve its performance in tracking the AGC signal for secondary frequency regulation.

(3) A detailed simulation analysis is performed to validate the strategy's effectiveness under various wind speeds and load disturbance scenarios, with results showing superior performance compared to traditional control methods.

2 Modeling of DFIG and BESS

2.1 DFIG Model

The DFIG system consists of a wind turbine, a drive train, a gearbox, and the generator itself. The aerodynamic power P_n captured by the turbine is given by:

$$P_n = \frac{1}{2}\rho\pi R^2 C_w(\lambda,\beta)v_s^3 \tag{1}$$

where ρ is the air density; R is the rotor radius; C_w is the power coefficient; λ is the tip-speed ratio; β is the pitch angle; v_s is the wind speed.

The dynamics of the transmission system can be represented by a two-mass model:

$$\begin{cases} 2H_u\dfrac{\mathrm{d}\omega_t}{\mathrm{d}t} = T_m - K_t\theta_s - D_{tg}\omega_t \\ 2H_e\dfrac{\mathrm{d}\omega_e}{\mathrm{d}t} = K_t\omega_t - D_g\omega_e - T_e \end{cases} \tag{2}$$

where H_u and H_e are the turbine and generator inertia constants; ω_t and ω_e are the turbine and generator speeds; D_{tg} and D_g are the damping coefficients of the wind turbine rotor and generator rotor, respectively. θ_s is the relative angular displacement. K_t is the total

stiffness of the shafting, T_m is the mechanical torque, T_e is the electromagnetic torque.

The DFIG's electromechanical model is established in the dq synchronous reference frame, allowing for decoupled control of active and reactive power through the rotor-side converter.

2.2 BESS Model

The BESS is modelled as an ideal voltage source E_e in series with an internal resistance R_e. The output voltage U_e is:

$$U_e = E_e - R_e I_e \tag{3}$$

where I_e is the output current of the energy storage battery.

The state of charge (SOC) is calculated as:

$$SOC = 1 - \frac{1}{Q}\int I_e(t)\mathrm{d}t \tag{4}$$

where Q is the battery capacity.

A bidirectional DC-DC converter interfaces the BESS with the grid, operating in Buck mode for charging and Boost mode for discharging, controlled via Pulse Width Modulation (PWM) to regulate power flow.

In the wind-storage hybrid system, the energy storage battery achieves charging and discharging through a bidirectional DC/DC converter. The bidirectional DC/DC converter consists of single-phase buck and boost modules, as shown in Fig. 1. It realizes Buck step-down and Boost step-up operations by controlling the switching transistors.

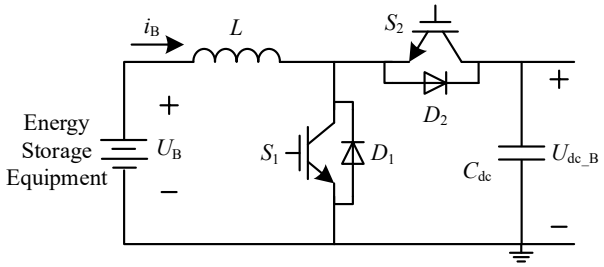


Fig. 1. Bidirectional DC/DC Converter.

In Fig. 1, the low-voltage side U_B of the bidirectional Buck/Boost converter is connected to the energy storage device, while the high-voltage DC side U_{dc_B} is cascaded with the bidirectional DC/AC converter. When a discharge demand arises, current transmits energy to the DC capacitor C_{dc} through the inductor L and the fully controlled switching device S_1; subsequently, the DC/AC converter is used to deliver this energy to the power grid. In contrast, when a charging demand occurs, the current direction is reversed, and energy flows from the grid side into the energy storage device. D_1 and D_2 are freewheeling diodes, which serve the function of freewheeling.

The Buck/Boost converter features three operating modes: the Buck step-down mode corresponds to battery charging, the Boost step-up mode corresponds to battery discharging, and the shutdown mode corresponds to the idle state.

Owing to the inherent performance constraints of the energy storage battery, the voltage and SOC during charging and discharging processes must be maintained within safe thresholds to prevent overcharging and over-discharging. To effectively track and participate in power grid frequency regulation while ensuring the healthy operating

state of the battery, this paper adopts a dual-mode switching control strategy for charging and discharging, namely the constant power-constant voltage CP-CV strategy.

3 Proposed Coordinated Control Strategy

3.1 Primary Frequency Regulation

The primary control structure is shown in Fig. 2. The integrated control system combines the roles of the DFIG and the BESS for primary frequency regulation. The DFIG offers rapid inertial and droop-based support by utilizing the turbine's kinetic energy, while the BESS delivers ultra-fast and continuous active power injection. Together, they create a complementary control loop that effectively lowers the frequency nadir, reduces the rate of change of frequency (RoCoF), and speeds up system recovery following disturbances.

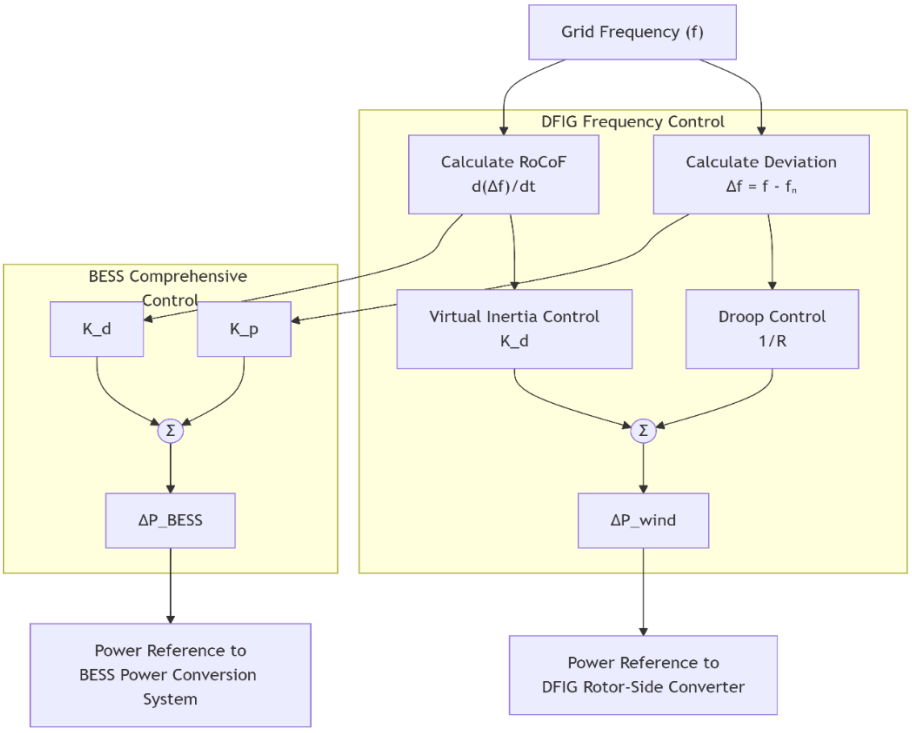


Fig. 2. Coordinated primary frequency control architecture for the DFIG and BESS.

1) DFIG Control: Contribution to primary frequency regulation through two main methods:

Virtual Inertia Control (VIC): Emulates the inertial response power ΔP_1 of a synchronous generator is:

$$\Delta P_1 = -K_i \frac{\mathrm{d}f}{\mathrm{d}t} \tag{5}$$

where K_i is the inertia constant and $\mathrm{d}f/\mathrm{d}t$ is the RoCoF.

Droop Control: Provides proportional power ΔP_2 support based on frequency deviation is

$$\Delta P_2 = -\frac{1}{R}\Delta f \tag{6}$$

where R is the droop coefficient and Δf is the frequency deviation.

The total power ΔP_{wind} reference for the DFIG is:

$$\Delta P_{wind} = \Delta P_1 + \Delta P_2 \tag{7}$$

2) BESS Control (Comprehensive Inertia Control): BESS is utilized to overcome the short-term characteristics of DFIG's support. It combines both VIC and droop control, with the Power Control ΔP_{BESS} Defined as:

$$\Delta P_{BESS} = -K_i^B \cdot \frac{\mathrm{d}f}{\mathrm{d}t} - \frac{1}{R_B} \cdot \Delta f \tag{8}$$

where K_i^B and R_B are the inertia- and droop coefficients of BESS.

This configuration enables the BESS to inject active power with an ultra-fast response to mitigate the frequency drop, followed by sustained power support for subsequent frequency recovery.

3.2 Secondary Frequency Regulation with Fuzzy-PI Control

For secondary regulation, the BESS follows the Area Control Error (ACE) signal. A fuzzy adaptive PI controller dynamically adjusts the PI gains (K_p, K_i) based on:

$$\begin{cases} K_p = f_p\left(ACE, \dfrac{\mathrm{d}(ACE)}{\mathrm{d}t}\right) \\ K_i = f_i\left(ACE, \dfrac{\mathrm{d}(ACE)}{\mathrm{d}t}\right) \end{cases} \tag{9}$$

where $f_p(.)$ is the fuzzy inference rule that determines how much K_p should be adjusted based on the ACE and its derivative $f_i(.)$ is the fuzzy inference rule that determines how much K_i should be adjusted under the same inputs.

This separation makes it clear that K_p and K_i are tuned independently (though based on the same inputs) using two fuzzy mapping functions. This allows the BESS to respond aggressively to large disturbances and smoothly as the frequency stabilizes, optimizing AGC performance.

For secondary regulation, the BESS is tasked to follow the ACE signal. A traditional PI controller has limitations with fixed parameters. We propose a fuzzy adaptive PI controller. The ACE and its derivative, d(ACE)/dt, are fed as inputs to the fuzzy logic system. The fuzzy inference system, with a rule base designed from operational experience, outputs dynamic adjustments (K_p, K_i) to the PI controller's parameters. This adaptive mechanism allows the BESS to respond more aggressively to large disturbances and more smoothly as the frequency stabilizes, optimizing the response and improving stability.

4 Simulation Results and Analysis

A simulation model was built in MATLAB/Simulink based on a two-area system, as illustrated in Fig. 3. The system includes a 250 MW thermal plant, a 45 MW wind farm (30 x 1.5 MW DFIGs), and a 5 MW BESS. A load disturbance of 0.1 p.u. is applied at t=45s.

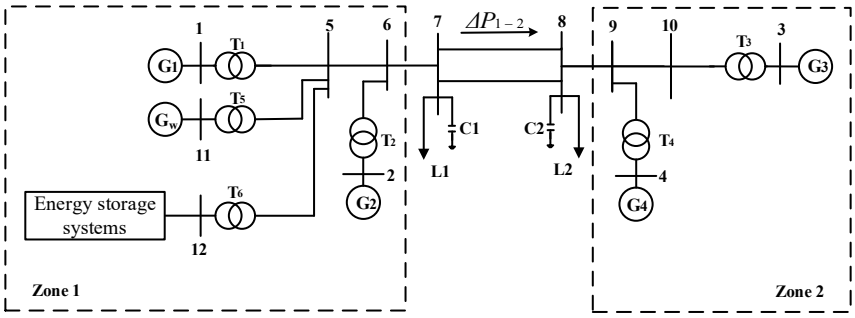


Fig. 3. A 4-machine 2-area power system.

4.1 Primary regulation under low wind speed (8 m/s)

The frequency response is shown in Fig. 4. Without wind or storage support, the frequency nadir is 49.63 Hz. With only DFIG support, the nadir improves to 49.72 Hz. With the proposed wind-storage coordination, the nadir is significantly higher at 49.80 Hz, and the RoCoF is reduced, demonstrating excellent primary response. The BESS SOC is shown in Fig. 5.

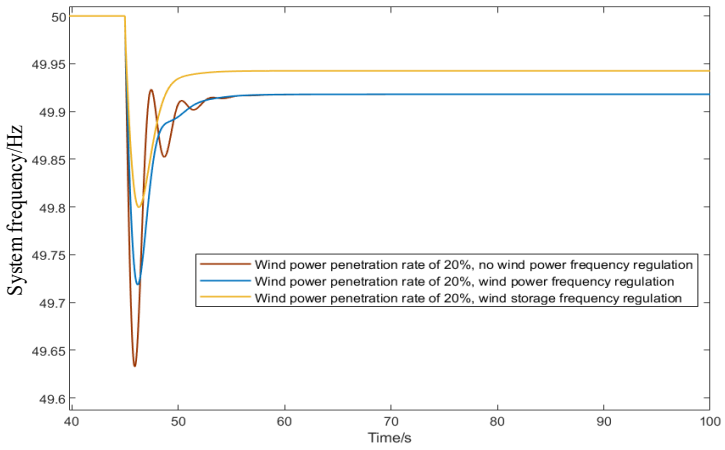


Fig. 4. Frequency response curve of wind storage system under low wind speed.

The effectiveness of the coordinated wind–storage control strategy is demonstrated when wind speeds are low in Fig. 4. The graph clearly indicates that the integration of DFIG and BESS not only enhances the frequency nadir compared to using DFIG alone but also diminishes oscillations and speeds up frequency recovery. This underscores the supportive role of BESS in offsetting the limited inertia contribution from wind turbines at low wind speeds.

The SOC of BESS is illustrated when wind speeds are low in Fig. 5. The graph reveals that the BESS discharges to deliver continuous active power support when the wind turbine's output is minimal. This highlights the BESS's ability to effectively make up for the wind farm's lack of inertia at low wind speeds, ensuring a steady power supply to the grid and enhancing overall frequency stability.

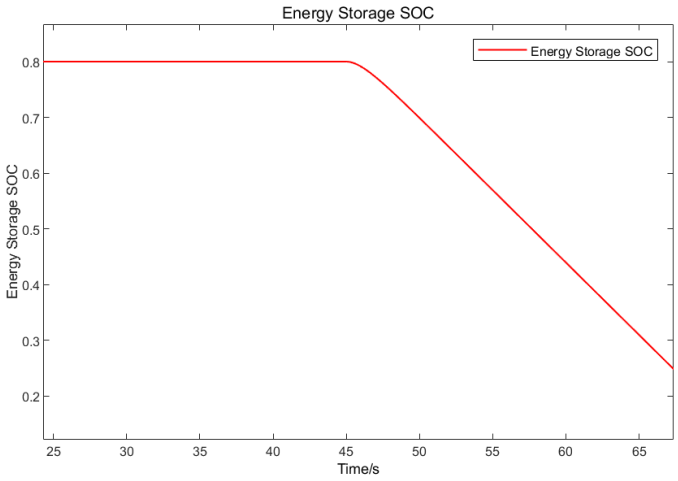


Fig. 5. Low wind speed scenario: energy storage SOC curve.

4.2 Primary Regulation under High Wind Speed (15 m/s)

The DFIG can release more kinetic energy, providing better support for frequency regulation (nadir: 49.73 Hz), as shown in Fig. 6. The coordinated strategy again delivers the best performance (nadir: 49.81 Hz). The SOC of BESS in Fig. 7 is lower than in the low wind speed case, as the DFIG provides more of the required power.

That the DFIG can enhance kinetic energy contribution at higher wind velocities is illustrated in Fig. 6, hence improving the system's capacity to withstand frequency decreases. Nevertheless, when synchronized with the BESS, the reaction is significantly improved, attaining the optimal frequency nadir and the swiftest recovery. This indicates that the hybrid approach offers enhanced reliability and stability in frequency regulation since wind power alone excels at elevated speeds.

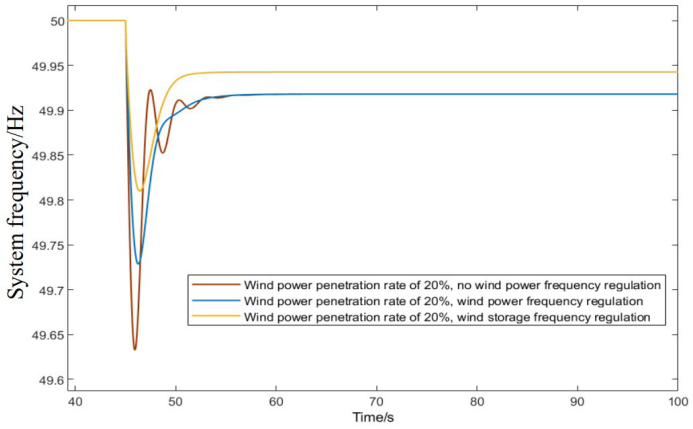


Fig. 6. Frequency response curve of wind storage system under high wind speed.

The SOC performance of the BESS during periods of high wind speeds is shown in Fig. 7. Unlike the situation with lower wind speeds, the SOC experiences a smaller decline, signifying that the DFIG plays a more substantial role in frequency support due

to its increased kinetic energy reserves. This demonstrates that the coordinated strategy effectively manages the distribution of contributions between wind power and storage: when wind support is adequate, the BESS is less burdened, allowing it to conserve its capacity for handling future disturbances.

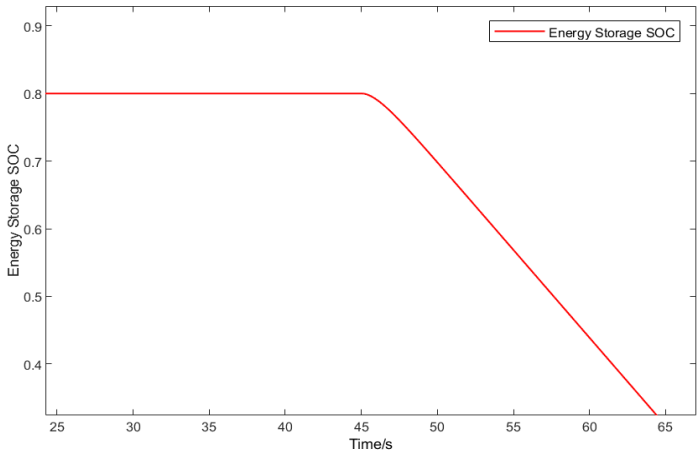


Fig. 7. High wind speed scenario: energy storage SOC curve.

4.3 Secondary regulation with fuzzy-PI control

4.3.1 Simulation of step load disturbance condition

During the simulation process, a step load disturbance of 0.01 p.u. is set in area 1 at 20s, and the simulation duration is set to 35s. A step load disturbance was applied to a two-area system. The frequency deviation with a traditional PI controller and that with the proposed fuzzy-PI controller for the BESS are compared, as shown in Fig. 8 and Fig. 9.

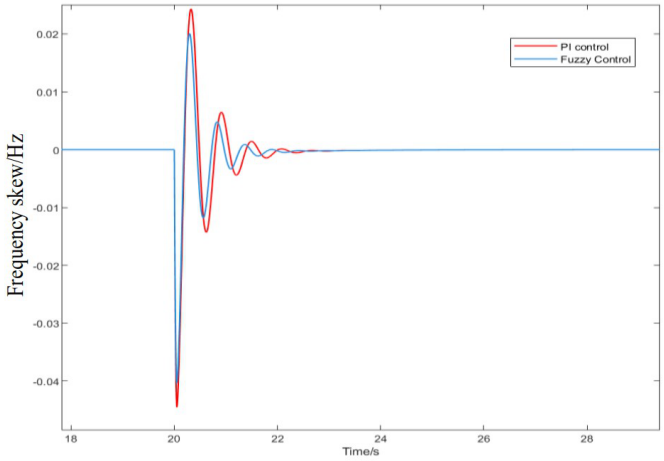


Fig. 8. Frequency deviation curve.

The fuzzy-PI controller results in a higher frequency nadir, less oscillation, and a faster settling time, confirming the superiority of the adaptive approach for AGC. The

frequency deviation responses for both control strategies when a step load disturbance was introduced to a two-area power system are presented in Fig. 8. This was done to assess the performance of the traditional PI controller against the proposed fuzzy-PI controller for BESS.

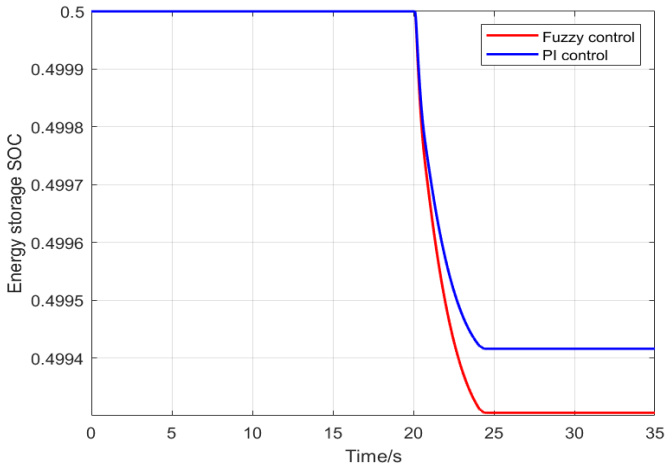


Fig. 9. Energy storage SOC curve.

The conventional PI controller is shown to experience a deeper frequency nadir and higher oscillations before reaching stability. Conversely, the fuzzy-PI controller demonstrates a more adaptive response, achieving a higher frequency nadir (indicating a smaller maximum deviation), effectively minimizing overshoot, and more rapidly suppressing oscillations. Additionally, the system's settling time is significantly reduced, indicating a quicker return to the nominal frequency.

These enhancements are due to the fuzzy adaptation mechanism, which dynamically modifies the PI gains based on the ACE and its rate of change. In the event of large disturbances, the fuzzy-PI controller increases the proportional response to counter sudden deviations while adjusting the integral action to prevent windup and reduce oscillations. As the frequency error decreases, the controller gradually reduces the gain adjustment, ensuring stability and robustness.

The SOC of the energy storage system under fuzzy control decreases from 0.5 to 0.4993, while that under traditional PI control decreases to 0.49942, as shown in Fig. 9. This indicates that over the entire frequency response process, the fuzzy control system achieves slightly higher output than the traditional PI control system, with an SOC increase of only 0.00051. This advantage in system frequency regulation is negligible compared to the fuzzy control system, effectively maintaining the SOC. Therefore, the fuzzy control-assisted grid AGC frequency regulation proposed in this article is more advantageous.

4.3.2 Simulation of variable wind speed conditions

The initial wind speed for the equivalent wind turbine is set at 10 m/s. The wind speed decreases to 8 m/s at 15 seconds and increases to 9.5 m/s at 150 seconds. A sudden system load increase of 300 MW is set at t = 270s. The simulation lasts 450 seconds. The system frequency changes and turbine responses are shown in Fig. 10 to 12.

The effectiveness of the proposed fuzzy-PI control method under varying wind speed

conditions is validated in Fig. 10. In contrast to the conventional PI controller, the fuzzy-PI controller improves system frequency stability by reducing the magnitude of frequency deviations and accelerating the return to the nominal frequency. This indicates that the fuzzy controller's adaptive tuning mechanism enables the BESS to synchronize more effectively with the wind turbine, ensuring reliable secondary frequency regulation even during substantial wind speed changes. Therefore, it clearly shows that the fuzzy-PI method surpasses traditional PI control in maintaining frequency stability of power system.

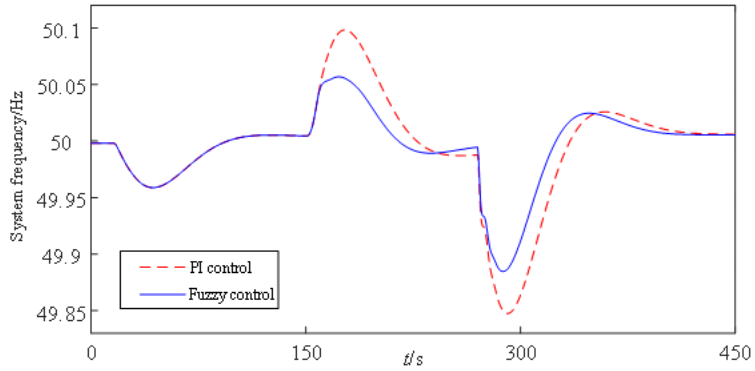


Fig. 10. System frequency curve.

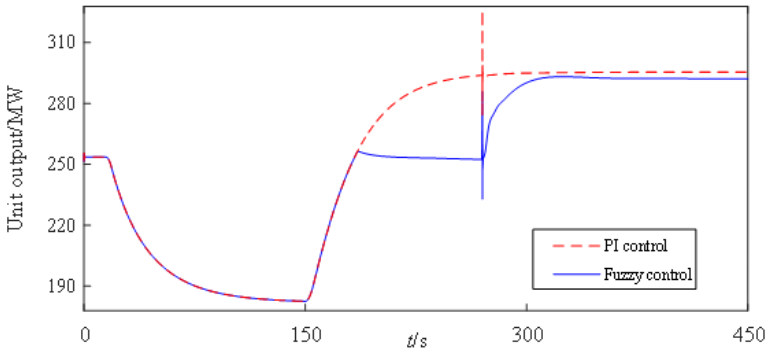


Fig. 11. Wind turbine output.

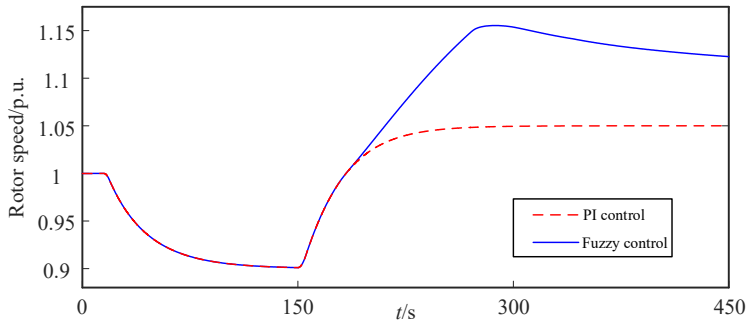


Fig. 12. Wind turbine rotor speed.

The simulation results in Fig. 11 and Fig. 12 show that when PI control is used, the wind turbine operates in maximum power point tracking mode, and its active power fluctuates with wind speed, exacerbating the power system's active power imbalance and preventing it from providing active power support during load disturbances. When fuzzy control is used, when the wind turbine's maximum adjustable output exceeds the active power limit, it follows the dispatcher's active power command by over-speeding and load shedding, maintaining a constant pitch angle of 0°.

At t = 270s, the system load suddenly increases by 300 MW, and the wind turbine reduces its rotor speed to release active power reserve, providing active power support to the system. The system's active power increment using PI control is significantly greater than that using fuzzy control, and the system's frequency regulation pressure is greater under PI control, indicating that fuzzy control is more effective in secondary frequency regulation of the power system under variable wind speed conditions.

5 Conclusion

In this study, the critical challenge of maintaining frequency stability in power systems with significant wind energy integration was addressed. A coordinated control strategy for DFIG-based wind farms and BESS was proposed and evaluated.

(1) The integrated primary frequency regulation strategy leverages the strengths of both technologies: the DFIG provides an initial, cost-effective inertial response, while the BESS delivers continuous and reliable power support. This synergy significantly improves the frequency nadir and reduces the RoCoF after a disturbance.

(2) For secondary frequency regulation, the fuzzy adaptive PI controller enables the BESS to respond more intelligently and efficiently to the AGC signal, leading to enhanced dynamic performance and faster system stabilization compared to traditional fixed-gain controllers.

(3) Simulation results under various wind speeds and load disturbances confirmed the effectiveness and robustness of the proposed strategy, highlighting its potential to enhance grid reliability and facilitate the integration of renewable energy sources. Future research will focus on optimizing the BESS sizing to achieve a better balance between technical performance and economic cost, and on extending the strategy to coordinate with other grid services such as wind power smoothing.

Acknowledgement: This work is supported in part by the National Science Foundation of China No. 52207117 and in part by Chengdu Science and Technology Bureau No. 2023-JB00-00002-SN.

References

1. X. Wang, Y. Li, and Z. Xu, Wind power integration and its impact on power system frequency response, Renewable Energy, vol. 136, pp. 1065–1075, 2019.
2. P. Kundur, Power System Stability and Control. New York, NY, USA: McGraw-Hill, 1994.
3. H. Bevrani, Robust Power System Frequency Control. Springer, 2009.
4. A. Ulbig, T. S. Borsche, and G. Anderson, Impact of low rotational inertia on power system stability and operation, IFAC Proceedings, vol. 47, no. 3, pp. 7290–7297, 2014.
5. M. Dreidy, H. Mokhlis, and S. Mekhilef, Inertia response and frequency control techniques for renewable energy sources: A review, Renewable and Sustainable Energy Reviews, vol. 69, pp. 144–155, 2017.

6. H. Liu, Y. Xu, and J. Zhao, Dynamic frequency response assessment of wind power integration considering system inertia reduction, IEEE Transactions on Sustainable Energy, vol. 11, no. 1, pp. 174–185, 2020.
7. T. Knueppel, J. Fortmann, and P. Sorensen, The contribution of wind power plants to system frequency control, IEEE PES General Meeting, 2013.
8. B. Peng, X. Ma, C. Tian, and Y. Sun, Coordinated AGC control strategy for an inter-connected multi-source power system based on distributed model predictive control algorithm, Front. Energy Res., vol. 10, 1019464, 2023.2021.
9. X. Wang, X. Ye, W. Wei, Y. Wang, T. Zhu, C. Liu, and Y. Chen, The frequency control strategy of a wind–storage combined system considering battery SOC, Electronics, vol. 12, no. 16, p. 3453, 2023.
10. Y. Xu, A. Parisio, Z. Li, Z. Dong, and Z. Ding, Optimization-based ramping reserve allocation of BESS for AGC enhancement, preprint arXiv: 2204. 11270, 2022.
11. L. Zeni, A. J. Rudolph, J. Münster-Swendsen, I. Margaris, A. D. Hansen, and P. E. Sørensen, Virtual inertia for variable speed wind turbines, Wind Energy, vol. 16, no. 8, pp. 1225–1239, 2013.
12. Bi Liu, Q. Huang, J. Zhao, F. Milano, and Y. Zhang, Nonlinear virtual inertia control of wind turbine generators for enhancing primary frequency response and suppressing drive-train torsional oscillations, preprint arXiv: 2006. 00156, 2020.
13. C. Wu, J. Xu, J. Xu, and Y. Wang, Virtual inertia control of small- and medium-sized wind turbines, Mathematical Problems in Engineering, vol. 2024, 3886096, 2024.
14. R. Pena, J. C. Clare, and G. M. Asher, Doubly-fed induction generator using back-to-back PWM converters and its application to variable-speed wind-energy generation, IEE Proceedings – Electric Power Applications, vol. 143, no. 3, pp. 231–241, 1996.
15. A. Shokri Ghaleh, A. Jalili, and M. F. Firouz, Virtual inertia control to active support of variable-speed wind turbine in large penetration grids, Front. Energy Res., vol. 12, 1352385, 2024.
16. G. Zhang, C. Huang, S. Zhang, and Y. Liu, Multi-objective configuration and evaluation of dynamic virtual inertia control including aerodynamic and rotor-side power effects, Applied Energy, vol. 355, 122676, 2024.
17. M. Dreidy, H. Mokhlis, and S. Mekhilef, Evaluation of inertia support capability in wind turbine generators, Symmetry, vol. 17, no. 1, p. 31, 2025.
18. Y. Li, T. Wu, H. Huang, and J. Zhao, Modeling of battery energy storage systems for AGC performance improvement, Applied Energy, vol. 340, 120935, 2023.
19. W. Wu, Y. Xu, H. Sun, Z. Chen, and Q. Yang, Hierarchical distributed coordinated control for battery energy storage systems to participate in AGC of a regional power grid, Energies, vol. 15, no. 19, p. 7283, 2022.
20. R. Gonzalez, J. Garcia-Gonzalez, and A. de la Torre, Coordinated control strategy of a battery energy storage system to support a wind power plant providing multi-timescale frequency ancillary services, IET Generation, Transmission & Distribution, vol. 11, no. 3, pp. 667–675, 2017.

126 基于模型设计的光伏模拟器控制系统代码生成

王 鹏，朱显辉，钱文丽

(黑龙江科技大学，电气与控制工程学院，黑龙江 哈尔滨 150022)

Model-based PV simulator control system code generation

WANG Peng，ZHU xianhui，QIAN Wenli

(School of Electric and Control Engineering，Heilongjiang University of Science and Technology， Harbin 150022，China)

ABSTRACT: For the design and development of photovoltaic simulator control system, the traditional programming method has some shortcomings, such as long development cycle, cumbersome debugging and poor hardware compatibility. In this paper, Model-Based Design (MBD) is introduced into the development of photovoltaic simulator control systems. Firstly, according to the development process of MBD, a PV simulator code generation model under the control strategy of look-up table method and direct calculation control strategy was designed. The control model can then be converted into C code using Simulink's embedded encoder. Finally, a 100W photovoltaic simulator experimental platform was built based on the TMS320F28335 control chip, and the generated code was downloaded to the chip and the DS-A2-80 photovoltaic cell was simulated and tested. Experimental results show that compared with the traditional programming method, the MBD automatic code generation development method effectively improves the efficiency of software development, and has better code portability and robustness.

KEY WORDS: PV simulator, model design, automatic code generation, DSP28335, Simulink

摘要：针对光伏模拟器控制系统的设计与开发，使用传统编程方法存在开发周期长、调试繁琐、硬件兼容性差等不足。本文将基于模型设计(MBD)引入光伏模拟器控制系统的开发中。首先，根据 MBD 的开发流程设计了查表法控制策略与直接计算法控制策略下的光伏模拟器代码生成模型。然后，利用 Simulink 的嵌入式编码器可将控制模型转化为 C 代码。最后，基于 TMS320F28335 控制芯片搭建了 100W 光伏模拟器实验平台，将所生成代码下载至芯片中并对 DS-A2-80 型号光伏电池进行了模拟试验。实验结果表明，相比与传统的编程法，MBD 自动生成代码的开发方法有效提高了软件开发效率，同时具有更好的代码可移植性与鲁棒性。

关键词：光伏模拟器、模型设计、代码自动生成、DSP28335、Simulink

基金项目：国家自然科学基金(51677057)
National Natural Science Foundation of China(51677057)

0 引言

数字式光伏模拟器是一种与光伏电池具有相同伏安特性的非线性开关电源，通过设计特殊的软件算法来调节功率电路复现光伏电池的 *I-V* 特性[1]。在光伏逆变器的研发与测试中及其重要，具有节省场地、降低成本、缩短开发周期，具有不依赖自然环境的特性，为研究提供了极大的方便[2]。

目前光伏模拟器硬件控制系统主要以数字控制器(DSP、FPGA 等)为控制核心，此方法可以实现控制系统的软件化，提高控制的实时性[3]，其中控制算法程序的编写是系统开发的主要工作。传统的编程方法是利用某公司所开发的代码调试软件 CCS(Code Composer Studio)配合仿真器进行开发编译，但开发过程中存在编程难度较大、耗时较多、效率较低。为了简化代码开发过程，某公司在 Simulink 中集成了大量的硬件支持包，可以通过搭建模块化和图形化的软件模型实现不同结构和语言的代码自动生成[4]。

本文将模型设计(Model Based Design,MBD)引入到光伏模拟器控制系统的设计中。首先介绍了光伏模拟器的 MBD 开发流程，其次叙述了查表法控制策略与直接计算法控制策略的基本原理，最后基于所选设计方案在 Simulink 环境下搭建模块化嵌入式代码生成模型，在根据芯片需求自动生成程序代码，并在 100W 的光伏模拟器样机上进行实验，以验证 MBD 自动生成代码的有效性。

1 光伏模拟器 MBD 开发流程

MBD 是一种以数学模型为核心的硬件开发方法。其主要原理是通过将 matlab、CCS 开发平台与控制器关联在一起，使 matlab 生成的代码与 CCS 在同一工作路径下，即可实现模型的开发与烧录。

其优点在于 simulink 中存在多数集成好的功能模块，因此在开发过程中只需利用好集成模块即可，从而省去了手动编写代码的繁琐过程。在 MBD 的开发过程中，模型是整个控制系统设计的核心部分，具体开发流程可以分为三个步骤，即模型设计、代码生成、代码验证。其开发流程如图 1 所示。

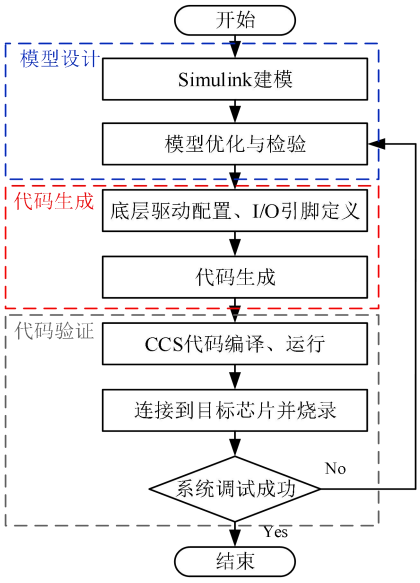


图 1 控制系统 MBD 开发流程

Fig1 Control system MBD development developmentprocess

如图 1 所示，控制系统开发首先需要根据项目的要求搭建 Simulink 模型来验证其功能是否满足要求。

功能模型验证完毕之后，就可进行代码的生成与烧录工作，先对算法模型进行底层驱动配置，包括仿真环境配置、硬件处理器配置、I/O 引脚定义、信号接口配置，配置过程中需在 matlab 软件中安装 C2000 硬件支持包、开发测试套件 controlSUITE 以及对编码器进行配置。

底层驱动配置后，系统会将控制算法浮点模型转换为定点模型，以满足硬件精度要求，最终生成完整的光伏模拟器控制代码，并在 CCS 开发环境中对代码进行编译、烧录与运行，并根据实验效果对模型进行调整。

2 光伏模拟器控制策略

2.1 查表法控制策略

在光伏模拟器的设计过程中，应先给出光伏电池的 *I-V* 数据以作参考，本文采用两条 Bezier 曲线来拟合光伏电池的输出特性曲线，并将拟合数据作为模拟器工作点参考数据，其原理可参考文献[5]。

此外，光伏电池的输出特性具有非线性的特点，当模拟器带纯阻性负载时，不同负载下输出特性也不同，此时工作点与原点之间连线斜率的倒数即为此时负载大小，如图 2 所示。

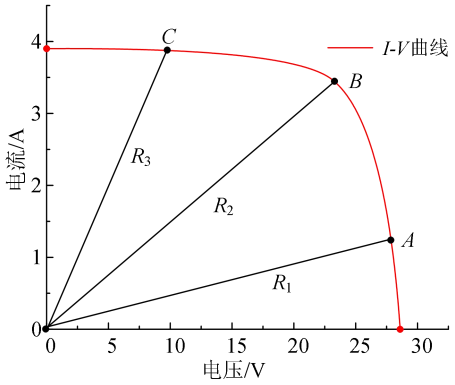


图 2 不同负载下的静态工作点

Fig2 Static operating points under different loads

如图 2 所示，不同负载 R_1、R_2、R_3 分别对应 *A*、*B*、*C* 三种工作情况。因此对于光伏模拟器，当其负载大小发生变化时，其特性信号也应及时作出调整，以确保模拟器输出与光伏 *I-V* 特性相匹配。

查表法作为目前光伏模拟器最常用的跟踪策略之一，其原理是将所建立的光伏模型的负载工作点全部离散化，即将电压值与电流值都转变为离散变量，并将数据存在一个工作空间中，然后将模拟器的输出结果作为查表模块的输入信号，系统判断输入数值在断点中的位置，查出对应在工作空间中的数值，以此作为模拟器参考信号输出。

2.2 直接计算法控制策略

考虑到上述光伏模型的建立，是通过函数直接拟合而得到。因此，此时光伏模型的电压与电流具有其各自的显性方程，即 Bezier 函数方程，如下

$$V_{pv}(t)=\left[C_0(x)-2C_1(x)+C_2(x)\right]t^2+2\left[C_1(x)-C_0(x)\right]t+C_0(x) \quad (1)$$

$$I_{pv}(t)=\left[C_0(y)-2C_1(y)+C_2(y)\right]t^2+2\left[C_1(y)-C_0(y)\right]t+C_0(y) \quad (2)$$

式中，$V_{pv}(t)$为光伏输出电压，$I_{pv}(t)$为光伏输出电流，$C_0(x)$为函数起点，$C_1(x)$为函数控制点，$C_2(x)$为函数控制点，t 为参数变量且取值范围在 0-1 之间。

因此，可以通过构造解析式求解此时负载所对应的 Bezier 函数值并作为模拟器控制信号输出。综上，光伏模拟器控制系统原理图如图 3 所示。

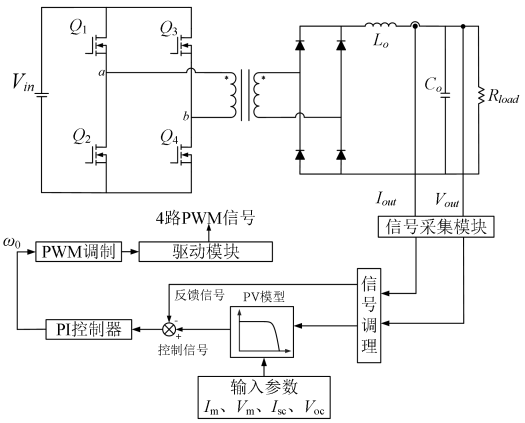


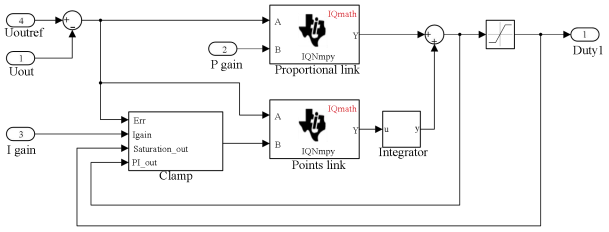
图 3 光伏模拟器控制系统原理图

Fig3 Schematic diagram of the PV simulator control system

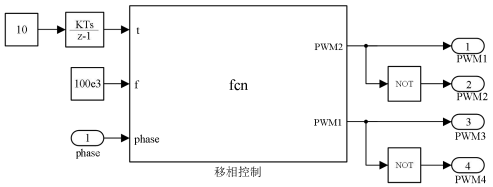
3 系统模型设计

3.1 光伏模拟器控制算法建模

基于模型设计的光伏模拟器控制系统开发中，所建立的模型主要包括三个部分：功率电路模型、信号转换模型、控制算法模型。功率电路模型可通过 SimPowerSystem 工具箱中的电力电子器件快速建立，本文选择全桥作为主电路结构并采用移相控制模式。信号处理模型作用为将功率电路模型与控制算法的信号接口相匹配，使其数据类型统一。控制算法模型通过上文所提思路进行搭建，本文选择 TMS320F28335 作为主控制器，调用 Embedded Coder 库 C2833x 中各种外设模块、IQmath 库模块等完成控制算法模型的搭建。各基本功能模块如图 4 所示。



(a)PI 调节器



(b)移相控制模块

图 4 基本功能模块示意图

Fig4 Schematic diagram of the basic function module

如图 4 所示，所搭建的基本功能模块主要包含 PI 调节器模块，移相控制模块。PI 调节器模块采用 IQmath 库中的运算模块设计，相较于基本计算模块，其对定点数的计算效率更高。移相控制模块使用软件中的函数定义模块 matlab function 进行设计，可使用 M 语言编写模块功能，并能将所编写的 M 语言生成 C 代码，直接计算法控制算法也可基于该模块进行设计。

3.2 代码生成模型

通过前期搭建后，设置底层硬件驱动，包括 I/O 功能配置与相关寄存器，使其与控制算法模型集成后得到光伏模拟器控制代码生成模型[6]。其中仅需保留控制算法核心模块与相关硬件驱动模块，通过配置好代码生成选项，包括运算精度、目标芯片型号及外设引脚映射等关键参数，即可自动生成嵌入式软件代码，代码模型如图 5 所示。

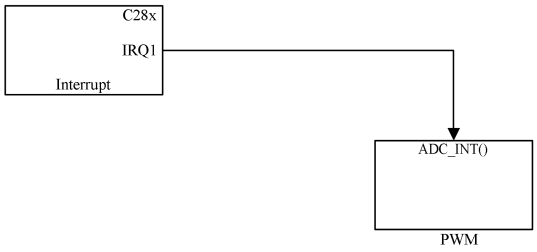


图 5 代码生成模型

Fig5 Code Generation Model

如图 5 所示，外部使用 c2833x 中的 Interrupt 模块设置为中断触发方式，详细控制系统模型放入 ADC_INT()中作为中断子模型，内部采用函数调用。其具体展开后，查表法控制策略与直接计算法控制策略的代码模型分别如图 6 与图 7 所示。

如图 6 与图 7 所示，代码模型由 ADC 模块、数据处理模块、控制算法模块与 ePWM 模块 4 部分组成[7]。对模块参数配置好之后可对求解器与仿真环境进行设置，通过 Build Model 进行编译可得到模型所生成的代码源文件。编译结果如图 8 所示。

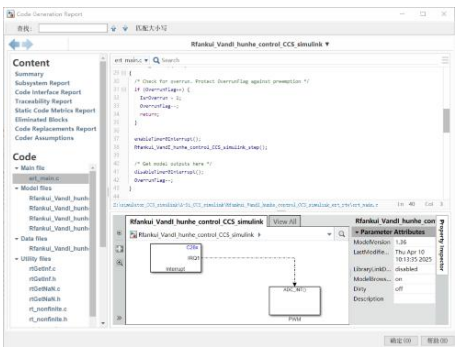


图 8 编译结果

Fig8 Compilation result

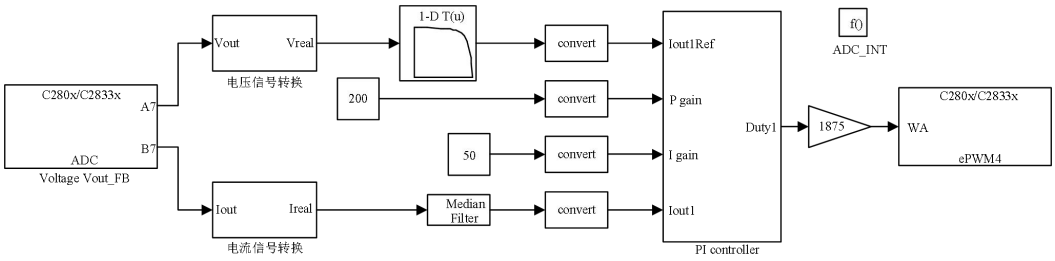


图 6 查表法控制策略代码生成模型

Fig6 The lookup table method controls the policy code generation model

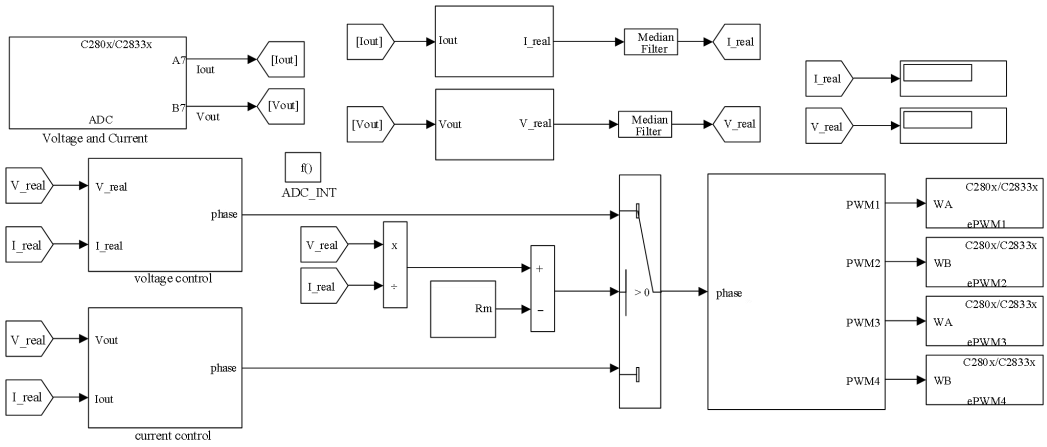


图 7 直接计算法控制策略代码生成模型

Fig7 The direct calculation method controls the policy code generation model

4 实验分析

为验证本文所提出的基于 MBD 的光伏模拟器控制系统的有效性，搭建了光伏模拟器实验平台，主电路采用全桥 DC-DC 结构，主控芯片选用 DSP(TMS320F28335)芯片，开关频率 f=50kHz，输入电压 V_{in}=36V，输出电容 C=470μF，输出滤波电感 L=100μH，如图 9 所示。

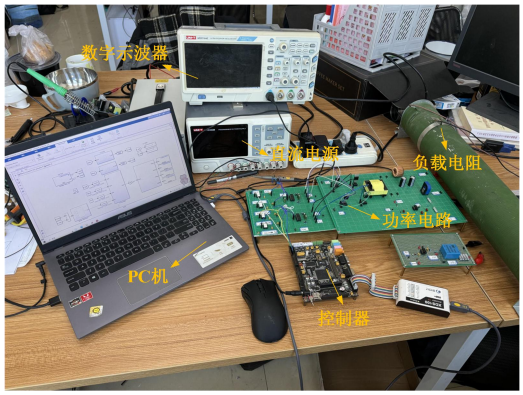


图 9 硬件测试平台

Fig9 Hardware test platform

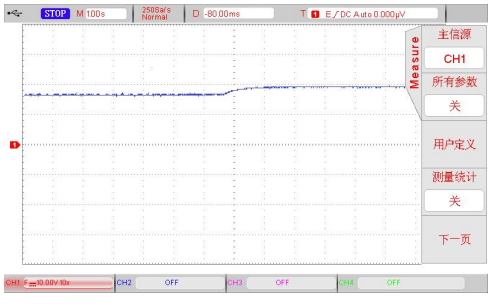
本文将对 DS-A2-80 型号光伏电池进行模拟试验，该型号电池主要参数如表 1 所示。

表 1 DS-A2-80 电池参数

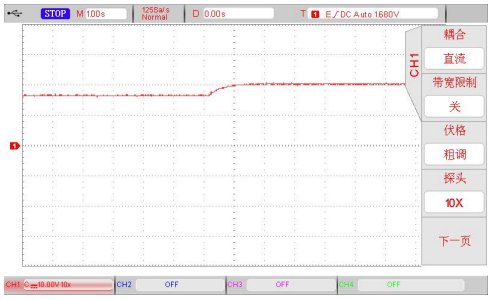
Tab1 DS-A2-80 battery parameters

参数	数值
开路电压 V_{oc}/V	28.60
短路电流 I_{sc}/A	3.90
最大功率点电压 V_m/V	23.10
最大功率点电流 I_m/A	3.47

通过编码器将 PC 机与硬件电路连接，将所搭建的代码生成模型烧录至控制器中，设置模拟器负载从 4.8Ω跳变至 5.5Ω，观察输出电压波形是否符合预期，输出电压波形如图 10 所示。



(a)查表法控制策略输出波形



(b)直接计算法控制策略输出波形

图 10 硬件测试结果

Fig10 Hardware test results

如图 10 所示，程序烧录后,模拟器输出电上升至初始工作点，当模拟器负载发生变化后，输出电压从 18V 上升至 20V，结果与理论值相吻合，说明所搭建的两种控制算法模型能够使模拟器在工作点发生变化后及时作出反映。

实验结果表明，MBD 开发方式可以实现光伏模拟器的查表法控制策略与直接计算法控制策略，有效简化了光伏模拟器控制算法的开发流程，并减小了调试以及修改的难度。

5 结论

本文针对光伏模拟器控制系统设计中传统代码编程法效率低的问题，提出了基于模型设计的控制系统设计方法，利用 simulink 与 CCS 联合仿真，设计了查表法与直接计算法控制策略的光伏模拟器控制系统代码生成模型。最后将所生成的代码下载到 DSP 中运行测试。结果表明，相比于传统设计方法，基于 MBD 的代码生成方法开发周期更短且硬件兼容性更佳，为光伏模拟器控制系统开发提供了新思路，也可对电力电子相关领域提供参考。

参考文献

[1] 张继元，宁佳，舒杰，等.基于非线性反馈的光伏模拟器控制策略[J].太阳能学报，2019，40(07):1920-1927.

[2] 潘小刚,孙前双,华庆光，等.基于 DSP 的 PSFB 光伏阵列模拟器研制[J].电力电子技术，2019，53(05):6-8+12.

[3] 曹冬梅.基于模型设计的车用永磁同步电机控制算法的开发[J].自动化与仪表，2023，38(12):79-84.

[4] 侯冰冰，滕云，郭昊，等.基于 MBD 实现电力电子变压器控制系统开发[J].电力电子技术，2022,56(01):57-60.

[5] 师楠，徐明忠，朱显辉，等.多晶硅 I-V 曲线的 Bezier 控制点拟合规律[J].中国电机工程学报，2022,42(06):2200-2208.

[6] 黄新成，简炜，陈宇峰，等.基于 CCS-Simulink 的永磁同步电机控制器设计及联合仿真[J].湖北汽车工业学院学报，2020，34(01):44-48.

[7] 张世垣.基于模型设计的 SVPWM 嵌入式软件开发[J].电子测量技术，2019，42(03):94-100.



王鹏

作者简介：

王鹏(2001)，男，硕士研究生，研究方向为光伏技术与新能源调度领域等，E-mail：2107682078@qq.com。

朱显辉(1975)，男，副教授，硕士生导师，研究方向为光伏技术与新能源调度，E-mail：zhu_xianhui@sina.com；

天津天大求实电力新技术股份有限公司

TIANJIN TIANDA QIUSHI ELECTRIC POWER HIGH TECHNOLOGY CO.,LTD.

关于天大求实

公司介绍：公司成立于1999年，致力于提供智能配电网与综合能源领域的管理咨询、技术咨询、工程设计、施工建设、软件系统、运营管理的全过程服务。2024年荣获国家级专精特新“小巨人”企业认定，是国内智能配电网与综合能源领域优秀的能源电力技术服务商。天大求实现有员工近400人，在领先成果方面多次承担国家级科研专项，具备雄厚的技术实力，曾三次荣获“国家科学技术进步二等奖”，省部级奖项近百个，获得专利95项。

业务拓展：业务覆盖除台湾之外、包括香港、澳门在内的全国所有的省、直辖市、自治区的所有地级行政区，同时已成功将业务拓展至智利和秘鲁地区。

7000 余项	50000 亿元	73.47%	300+
成功实施项目	涉及电网建设投资	专业技术人员占比	服务客户

技术咨询

典型案例：

- 智能电网国家科技重大专项—面向降碳需求的高可靠城市配电系统电碳协同规划技术（2025-2030）
- 国家电网中国特色国际领先能源互联网示范规划
- 南方电网智能电网顶层设计示范规划
- 中广核总部增量配电业务投资策略研究
- 中国长江三峡集团有限公司综合能源项目投资潜力分析
- 新疆新型电力系统下市场价格机制研究
- 广东深圳促进绿色低碳发展与新型电力系统建设的车网融合互动价格机制研究

……

▶▶▶ 每年近300多项目

工程可研设计

典型案例：

- **源：**鞍峡清洁能源有限公司光伏发电项目可行性研究
  天津市静海区200MW风力发电项目预可研报告编制服务
  天津天创绿能东郊污水厂6MWp分布式光伏发电项目
- **网：**长期服务国网各省配网工程设计电网工程
- **荷：**诺和诺德系列工程
  SEW系列工程
  天津荣钢220kV站主变增容工程
  怀来合盈金融数据科技产业园金融大数据110kV用户站设计
- **储：**基于增量配电网的吉瓦时以上长时储能可行性研究设计

……

▶▶▶ 每年近200多项目

软件产品介绍



有源配电网综合分析系统



项目可研智能评审系统



输变电工程后评价标准化作业平台



能碳管理平台



微电网能量管理系统



综合能源仿真与优化系统（IESCoreSim）

智能体产品介绍



科技项目研究申报智能体

源网荷储一体化

典型案例：

- 中新天津生态城区域多微电网项目
- 江苏大丰万吨级海水淡化离网型微电网示范项目
- 特变电工京津冀智能科技零碳产业园项目
- 大港油田绿电公司新型电力系统“十五五”规划
- 沧州华润零碳园区试点项目
- 上海某工业园区光储微电网项目

……

TDQS 求实股份

RTDS® SIMULATOR OVERVIEW

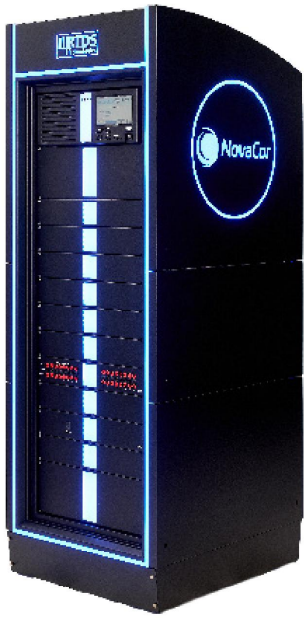
THE COMPANY

RTDS Technologies is the world standard for real-time digital power system simulation.

RTDS Technologies Inc. provides power system simulators and simulation support to customers in over 61 countries around the world. Our main product, the RTDS® Simulator, was the world's first fully digital real-time simulator, and continues to serve as the world's benchmark for performing real time power system simulation.

The RTDS Simulator was originally developed from a research project done at the Manitoba HVDC Research Centre, which resulted in the world's first real time digital HVDC simulation in 1989. Today, RTDS Technologies is the exclusive supplier of the RTDS Simulator.

Our customers are the world's leading electrical utilities, power system equipment manufacturers, research institutes, universities, and consultants. We are continuously developing our hardware and software capabilities in response to needs expressed by our customers. At RTDS Technologies, we are dedicated to equipping our users with what they need to push the limits.



NovaCor 2.0 cubicle



THE RTDS SIMULATOR

The RTDS Simulator consists of custom hardware and software, specifically designed to perform **real-time electromagnetic transient (EMT) simulation**. It operates continuously in real time while providing accurate results over a wide frequency range. This range provides a greater depth of analysis than traditional stability or load flow programs that study phenomenon within a very limited frequency range. Real-time operation enables **hardware-in-the-loop (HIL) testing**, in which protection and control devices are connected to the simulated network in a closed loop for testing.

The RTDS Simulator's fully digital parallel processing hardware is capable of simulating complex networks using a typical timestep of 25-50 µs. The Simulator also allows for smaller timesteps, enabling the simulation of power electronics devices with switching frequencies in the 200 kHz range.

Using the RTDS Simulator, analytical studies can be performed much faster than with offline EMT simulation programs. Hardware-in-the-loop testing allows for multiple control and protection devices to be tested simultaneously, allowing for system-level testing for comprehensive validation of device performance prior to deployment.

CLOSED-LOOP TESTING OF PROTECTION AND CONTROL SYSTEMS

MICROGRID, SMART GRID, AND RENEWABLE ENERGY • POWER ELECTRONICS

HVDC & FACTS CONTROL TESTING • INTERACTION OF AC AND DC SYSTEMS • DC GRIDS

MMC-BASED HVDC SCHEMES • POWER HARDWARE-IN-THE-LOOP STUDIES

CYBER SECURITY STUDIES • TRANSPORTATION & MARINE SYSTEMS

DIGITAL SUBSTATIONS & IEC61850 • DATA CENTERS

150 Innovation Drive, Winnipeg, Canada R3T 2E1 • + 1 204-989-9700

YOUR WORLD IN REAL TIME.
RTDS.COM

TZRN 天智睿能 TIANZHI INTELLIGENT ENERGY

综合能源及虚拟电厂整体解决方案

虚拟电厂业务
VIRTUAL POWER PLANT BUSINESS

通过物联网+AI算法+市场机制，将分散的分布式电源、可控负荷、储能系统聚合为“虚拟电厂”，统一参与电网调度与电力市场交易，实现“源-荷-储”协同优化，让“小散资源”变身“灵活调节利器”。

全要素接入：兼容海量异构设备

·**支持类型**：覆盖光伏逆变器、储能电池（电化学/飞轮）、充电桩（V2G）、工商业负荷（空调/生产线）、小型水电/风电等；

·**通信协议**：兼容Modbus、MQTT、IEC 61850等主流协议，支持5G/4G/光纤多网络接入。

智能预测：精准预判“源-荷”动态

·**发电预测**：基于气象数据（云量/风速）+历史发电曲线，AI预测光伏/风电未来24-72小时出力（误差率<5%）；

·**负荷预测**：结合用户用电习惯+天气/节假日因子，精准预估工商业/居民负荷需求（精度>90%）；

·**市场研判**：实时追踪电价/辅助服务市场价格趋势，辅助最优策略制定。

优化调度：秒级响应电网指令

·**活策略库**：内置调峰、调频、备用、需求响应等场景策略，支持自定义规则配置；

·**实时控制**：通过远程指令（或本地自治模式）调节设备运行状态（如储能放电、充电桩降功率），响应时间<30秒。

市场交易：打通“虚拟电厂”变现通路

·**参与模式**：支持电力现货市场、辅助服务市场（调频/备用）、需求响应市场（削峰填谷）等多场景交易；

·**收益透明**：自动生成收益报表（分资源类型/交易时段），清晰展示每度电调节的增值收益。



园区综合能源管理业务
COMPREHENSIVE ENERGY MANAGEMENT BUSINESS IN THE PARK

园区能源管理系统通过预测算法精准预测未来的负荷、光伏发电等情况；通过优化调度，协调冷热、电、光伏、储能等各类资源的运行模式和运行时间，提供经济运行、低碳调度、电网互动三种运行模式和计划，保障园区日常运行的各类需求；通过碳管理模块，准确计量园区能源系统碳排情况，追踪碳足迹，管理碳资产，降低碳排放。同时提升能源使用效率，降低园区运行所需成本。





工业用户供需互动仿真业务
SIMULATION BUSINESS OF SUPPLY AND DEMAND INTERACTION FOR INDUSTRIAL USERS

仿真算法综合考虑复杂系统内部生产关系，通过对设备模型高度抽象，更接近实际的情况，进而通过算法仿真进行预测。

工业负荷全流程生产与能源仿真

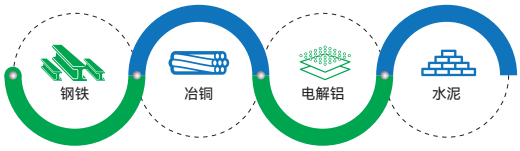
拥有丰富的设备模型库，支持对多种类生产流程进行建模，并根据生产工艺进行算法模拟，根据时空特性模拟生产、能源、碳排放结果。

可调能力预测与能效碳效分析

通过对工厂可调设备参数的提前输入，进而对整体工厂进行多时间尺度的可调节能力评估，以支持虚拟电厂调控和调控偏差分析。

多设备生产与互动控制

在接收电网调控策略后，根据工厂各工序的可调节能力进行调控指令拆解，再通过互动控制器对生产设备下发精准调度策略。



无锡惠山区惠山才智广场科技孵化楼3号楼21层
138 2196 5776
214100

无锡天智睿能科技有限公司 展台号A11-A12

天津天电清源科技有限公司

—清源赋能，智规电网

关于天电清源

天津天电清源科技有限公司是**国家级高新技术企业、国家科技型中小企业、AAA级信用企业、工程咨询单位乙级资信企业，多次获得天津市科技进步奖。**

公司专注于**电网状态评估与发展规划等技术咨询、智能配电网分析计算与规划运行软件开发、分布式电源与微电网及综合能源系统集成和运营服务**等方面的工作，是国内知名的智能配用电及综合能源系统技术咨询、软件产品与解决方案提供商。

国家级高新技术企业

天津市科技进步奖获奖单位



业务范围

业务范畴涵盖能源互联网三大体系，围绕双碳目标，聚焦新型电力系统，开展净零碳能源电力示范规划和路径研究，兼顾传统配电网规划、新型配电系统咨询，研究数字赋能电网、信息物理融合，探索综合用能优化、源网荷储互动，形成了技术咨询、科研课题、软件开发三大业务板块。





市场覆盖

研究成果成功应用于京、津、沪、渝、粤、浙、苏、皖、川、鲁、豫、赣、辽、陕、甘、宁、蒙等20余个省级行政区。



业绩概览

- 有源农村配电网差异化规划
- 星型配电网网架结构等规划
- 城市智能配电网发展评估
- 电力专项规划
- 考虑电动汽车有序充电的配电网规划
- 新型配电网形态结构特征分析
- 考虑多元化负荷发展的配电网规划
- 电网规划与国土空间规划服务
- 同城电力规划
- 220千伏输变电工程基建项目后评价
- 配电网网格化规划实施路径咨询
- 航空港区电网高质量发展研究
- 电网发展专题研究
- 配电网规划
- 电力专项与高铁新城规划
- 配电网规划辅助支撑服务
- 考虑有序充电的配电网规划技术研究



- 微电网与新型储能特性分析研究
- 电网侧替代性储能配置策略研究
- 低电压治理专项研究
- 电压等级优化题研究
- 国网农村能源互联网概念分析与现状研究
- 园区储能应用研究
- 新能源接入的电网项目投资效益分析研究
- 新型电力系统调研与建设模式研究
- 精致电网建设思路研究

- 能源网格划分和规划方案评估软件平台
- 分布式光伏承载力评估与最优接入辅助决策软件
- 分布式混合云储能仿真平台
- 园区综合能源系统规划设计软件
- 园区综合能源系统仿真分析软件
- 微电网规划与运行仿真软件
- 能量梯级利用监控软件加工测试服务
- 配电网时序仿真功能开发服务
- 含储能配电网对光伏最大消纳能力技术研究

智源科技 TransEnergy Technologies

数字化能源领导者

关于智源科技
ABOUT TRANSENERGY

天津求实智源科技有限公司是一家成立于2014年10月的高科技民营企业。依托于国内著名高校科研团队与国家级人才在非侵入式负荷分析技术领域十余年的技术成果，智源科技致力于电力系统、家庭、工业、商业、公共建筑等领域智能用电、节电方案的研发、生产、销售和服务，是国内相关行业的领导者。

自成立以来，智源科技及其合作团队在技术创新方面取得了显著成果。

发明专利	软件著作权	开发经验
100+	20+	10th



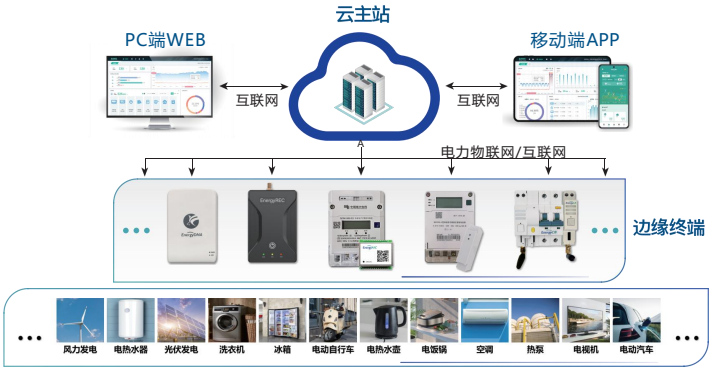
《非介入式低压用电负荷监测终端技术规范》　《用于非侵入式电力监测的自适应负荷事件检测方法》　天津市技术发明 一等奖

- 一等奖 天津市技术发明奖 2018
- 二等奖 天津市科技进步奖 2019
- 一等奖 中国南方电网公司科技进步奖 2018
- 一等奖 天津市电力公司科学技术进步奖 2019

非侵入式源荷状态精细化监测与辨识技术及装备
Non-intrusive source load state fne monitorin9 and identifcation technology and equipment

系统架构 / SYSTEM ARCHITECTRUE

非侵入式源荷状态监测系统采用**云-端协同架构**。根据云主站下发的任务指令，现场多类型边缘智能感知终端进行在线源荷状态辨识，并将必要的数据信息经高效压缩回传至云主站。云主站基于大数据分析及深度学习，通过场景个性化知识挖掘和全局多场景知识共享迁移实现终端辨识模型初始化与更新升级。同时，云主站接收用户通过APP或WEB提供的系统管理信息。

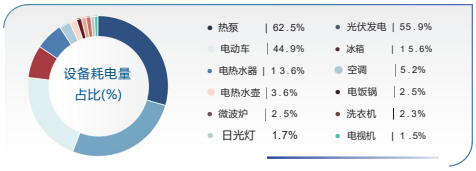


系列产品 / PRODUCT LINE

EnergyDNA 智能用电分析仪

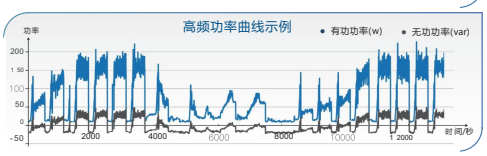
一种利用无监督非侵入式负荷分解技术实现家庭、商业及工业用电分析和用电行为识别的"即插即用"智能终端。通过匹配不同业务系统可提供需求侧管理、定制化客户服务、精准负荷预测、用电能效分析评估、违规用电稽查(包括电动自行车充电告警、禁用电器告警等)、故障电弧检测、独居老人关怀重点关注设备监测等业务服务。





EnergyREC 高频同步数据采集仪

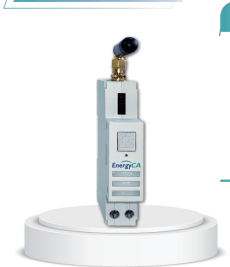
可即插即用，支持场景定制化的高频同步数据采集终端，既可就地存储，也可通过物联网回传至远程服务器。既可用于现场临时的用电情形排查,也可用于重点设备支路的连续监测，配套软件可对采集数据进行全方位分析和可视化展示，可赋能"电网状态估计、拓扑识别与阻抗测量、负荷预测、窃电检测、精细化能效分析"等多种智能电网高级应用。

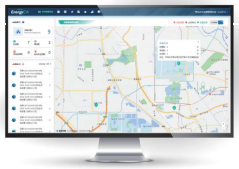




EnergyCA 智能充电负荷监测仪

EnergycA系列智能充电负荷监测仪是一款智能型充电负荷监测产品，该产品融合非侵入式负荷辨识、充电类负荷监测、深度量测感知、物联网通信等前沿技术，产品可广泛适用于商业建筑、居民、消防，学校，医院等场景。产品可灵部署与用户汇流点总口，实时监测充电负荷状态并报警，特别适用于低压用电场所的充电负荷用电安全诊断及管理业务。





产品体系全景图
product system panorama

应用生态 / APPLICATIONS ECOLOGY



智慧电网
- 客户群定制化服务违约用电窃电稽查
- 需求侧管理与灵活互动虚拟电厂优化计量方案
- 精确拓扑识别深化线损管理电能质量检测污染源头治理
- 区域电网能量管理与优化调度

智慧城市
- 能效精细监测评估重点人群行为分析
- 工业用电费率评估推荐工序对比用能高效节能方案
- 环保设备运行监测管理工业商业用户运营状况诊断
- 关键设备生命周期状态监测用电异常现场实时诊断排查



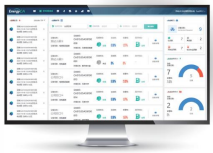


智慧安全
- 电弧检测
- 用电安全监测预判
- 恶性负荷的辨识与告警管理
- 电动车充电识别与智能化管理

数字基座 / DIGITAL BASE


数据同步采集与分析系统


负荷识别智能用电分析系统


用电安全监测管理系统

技术支撑 / TECHNOLOGICAL SUPPROT



产品支撑 / PRODUCT SUPPROT

高频同步配用电大数据	 EnergyREC	 EnergycA
精细化负荷感知数据	 EnergyCB	 EnergyDNA
	 EnergyAIC	



浙江求是科教设备有限公司成立于 1996 年，前身「浙江大学求是科技开发公司」，坐落于浙江杭州市，是一家专注为本科、高职及中职院校实验教学提供一站式解决方案的国家级高新企业。

多年来，我们凭借出众的产品性能和优异的售前售后服务，与国内众多本科和高职院校建立了相互信任的长期关系。我们完成了从单纯的硬件设计生产到产品软硬件系统集成开发的转型，有效匹配了学校实验教学场景下的多样化需求。长期以来，我们始终将技术创新放在首位，专业技术人员占比一直保持在 60% 以上。在产品上，我们不断设计、优化、打磨实验实训内容，推出了一系列专业的项目式教学资源，提升了实验教学的效果和产品体验。另一方面，我们在数字化教学的探索中持续投入，推出了**「仿真建模 -3D 动画 - 实时控制」**以及**「远程实验 + 异地管理」**等实验教学模式，得到了市场的充分认可。

我们坚信，以学校现实需求为基础的技术创新才是有生命力的，以学生的学习特征为导向的产品开发才是有社会价值的。我们的成长与进步离不开广大院校的信任与支持。展望未来，我们将不懈努力，持续提供更高质量的产品与服务，与大家一同推动中国实验教学的发展。

≥19000 平米	1.2亿元	>60%	70余家海外用户
自有标准厂房	2024年度资产	本科院校覆盖率	远销非洲肯尼亚、乌干达等

4项	28 项	53项
发明专利	实用新型专利	软件著作权

产品类别

电类基础　电气工程自动化　工业自动化　电子信息　楼宇自动化　机电一体化

机器人工程　化工自动化　制冷　物联网　电力系统自动化（含新能源）



电子技术实验台



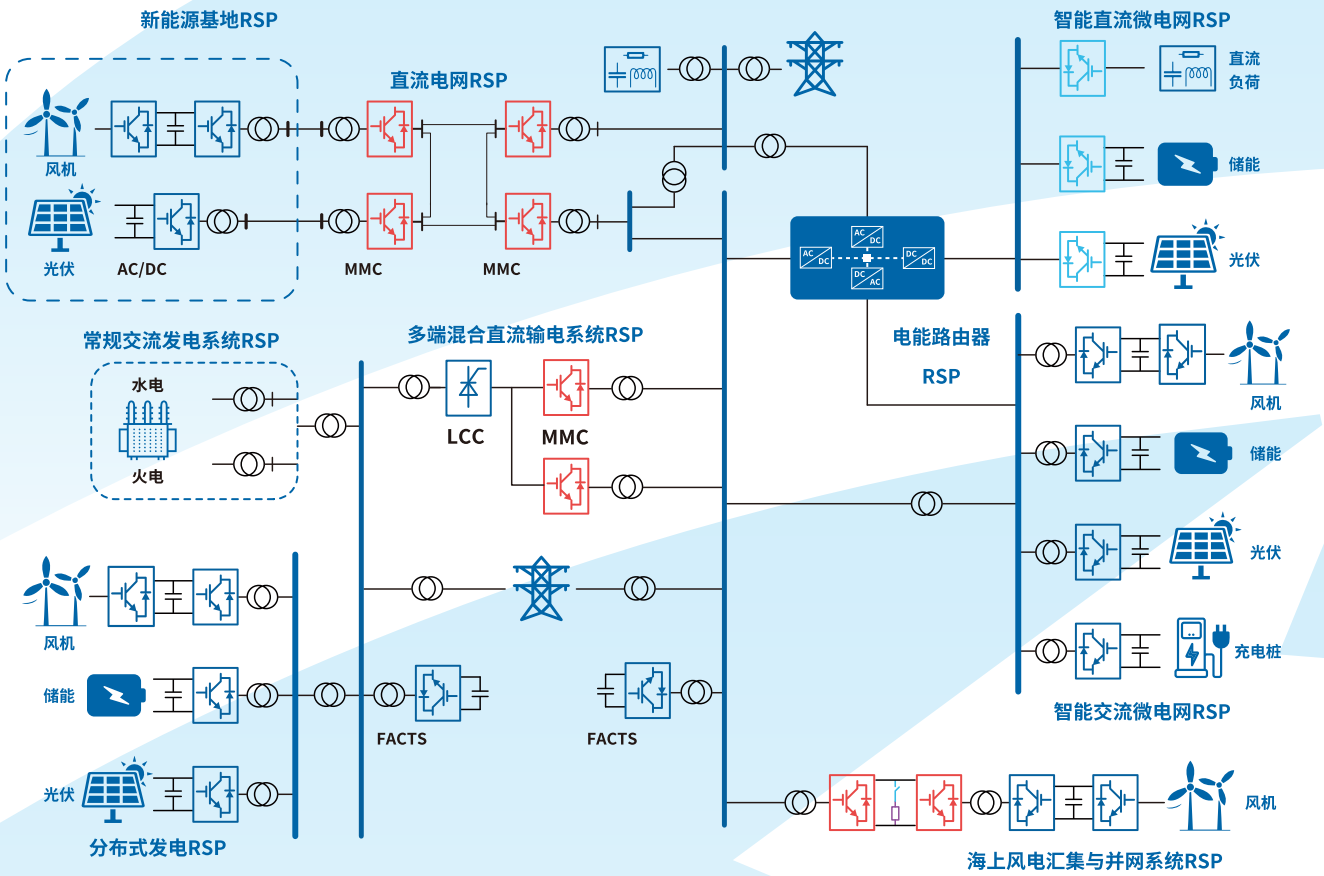
现代电工电子实验系统



电力系统继电保护实验平台



电力系统自动化实验平台



新型电力系统快速系统原型Demo平台

新型电力系统物理实验平台快速系统原型（RSP，Rapid System Prototype）平台是类企业级别的仿真环境与工程技术实践平台，可真实灵活模拟新型电力系统的各种特点，可见、可知、可控、可互动；将理论研究、数字仿真和物理模拟三者有机结合，让科研与工程技术人员聚焦关键核心问题，在真环境中开展真科研，直接产出真成果。

平台特色

装备种类多：风电、光伏、多元复合储能、柔直、电能路由器、交直流输电线路、电网故障模拟器、协调控制器等单元；

系统功能全：跟网控制、构网控制、高低电压穿越等功能；

AI+新型电力系统：AI算法融入EMS，EMS与运行于MATLAB的AI算法双向数据交互；

用途广：稳态/暂态类科研探索实验；单机/系统级科研探索实验；

运行模式多样化且可自定义：

1）高比例可再生能源并网系统运行

2）100%新能源/电力电子化电力系统运行

3）海上风电经柔性直流远距离并网外送

4）储能平抑光伏、风电波动

5）风光联合发电

6）源网荷储联合运行

KEHUI
科汇股份
证券代码：688681

持续为用户奉献智能电网与电气驱动创新解决方案



山东科汇电力自动化股份有限公司
Shandong Kehui Power Automation Co., Ltd.

地址：山东省淄博市三赢路16号
服务热线：400-0533 069
销售热线：0533-3181 567
网址：www.kehui.cn

济南科汇 电话：0531-6677 7667
青岛科汇 电话：0532-6801 2536
武汉科汇 电话：027-8266 8396

上海科梁信息科技股份有限公司
Shanghai KeLiang Information Technology Co., Ltd.

SimuNPS

www.simunps.com

新型电力系统建模仿真软件

完全自主可控 欢迎申请试用

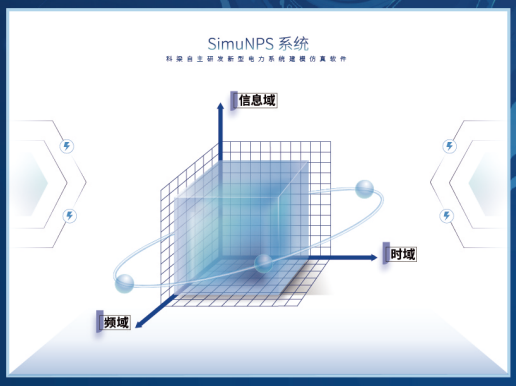
扫码申请试用

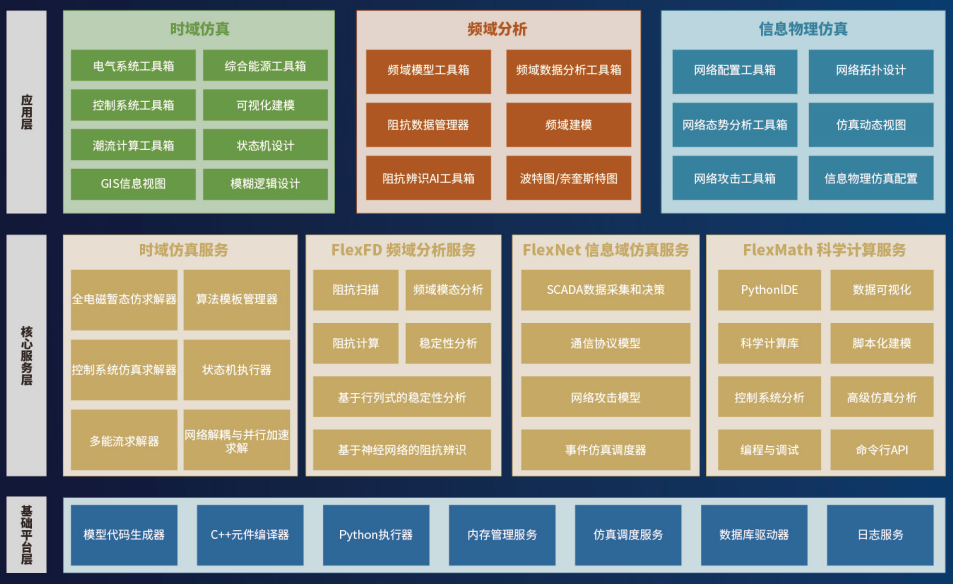
SimuNPS V3.0概述

新型电力系统是近几年才提出的新概念，也是高速发展变化的一个新领域，虽然每个专家都有不同的解读，但有几点是各方已达成的共识：

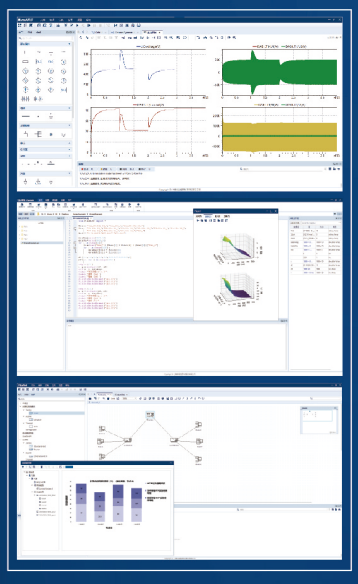
- 新型电力系统是“高比例新能源、高比例电力电子化与传统同步机混合”的“宽频”特征电力系统（时域仿真+频域仿真）；
- 新型电力系统是信息物理融合的新型智慧能源系统（信息物理联合仿真）；
- 新型电力系统是多能互补的综合能源系统（多能源仿真）。

SimuNPS软件自发布以来，得到了业内广泛的关注和赞誉，同时也收到了大量的反馈和建议；科梁通过和用户的深入交流，研究新型电力系统特征和用户需求，联合业内专家，创造性地开发了SimuNPSV3.0版本，这是首款融合时域、频域、信息域和多能域，同时支持麒麟等国产操作系统的新型电力系统综合建模仿真软件，SimuNPS软件现已面向全球正式开放了试用申请。





SimuNPS在时域、频域、信息域提供全面的仿真分析功能



SimuNPS软件界面

上海总部
地址：上海市合川路3533号
虹创园8号楼（201103）
电话：021-54234718/19/20
传真：021-54234721

西安分公司
地址：西安市经济技术开发区
凤城十二路未十二广场15层（710018）
电话：029-86263605
传真：029-86297216

北京分公司
地址：北京市海淀区首体南路22号
国兴大厦9层09D室（100044）
电话：010-83168982
传真：010-82168982

长沙子公司
地址：长沙高新开发区青山路699号
国家网络安全产业园区（长沙）8B栋10楼
电话：0731-85560780
传真：0731-85560780

企业简介

本着“成就客户，开放创新”的理念，公司坚持“专业聚焦”、“技术领先”和“平台化发展”的战略，致力于成为一流实时控制、仿真和开发验证解决方案供应商。

聚焦机械运动，电气控制和测量，实时总线和网络通讯，领域建模和实时仿真四大技术领域；服务于工业机械，能源电力，交通运输等三大领域多个行业；在电力电子控制，电力系统分析和控保，新能源汽车三电系统，伺服和运动控制，工业实时网络等工业领域和应用方向，为客户提供技术评估、控制算法、仿真建模、开发验证，原型构建，产品测试等丰富的涵盖全产品生命周期的平台化产品和技术服务。

针对风电、光伏、储能等新型电力系统和综合能源领域推出系列化工业数字孪生系统，构造基于模型的完整功能的全链路实时仿真及虚实对照系统。同时还提供极具特色的教学培训和学术研究平台。







自主研发

构筑新型电力系统的“试练场”

从数字仿真到物理模拟，全链路教学、科研试验环境

产品1：RTGENERAL实时数字仿真装置

RTGENERAL实时数字仿真系统是新型电力系统仿真测试领域的先进技术平台，具备高效实时计算、精准暂态模拟和丰富I/O接口能力，适用于科研、教学及行业机构，支撑电力系统分析研究、电力电子设备研发等。自研RTX985、RTX996等多型号实时仿真主机及RTIO101接口适配装置等。

产品2：电力系统动态模拟（动模）试验设备

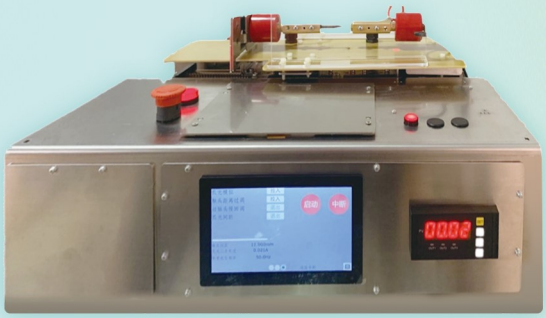
电力系统动态模拟试验可通过物理设备模拟真实电力系统的运行状态，用于教学、科研及工程验证。自研SW903开关合跳闸精确控制装置、PA904电力系统动态功角测量装置、ARC901弧光模拟器及监控装置等。

产品3：实时数字仿真与动模设备的数模结合

集成“动态模拟系统”与“实时仿真装置”，自研数模混合继电保护实验台、虚拟继电保护装置等。数模混合继电保护实验台采用物理操作台及数字仿真电力系统，为教学提供“可任意制造故障的实训场”。 在实时仿真机上通过模型实现保护算法，与实体装置在功能上完全等价，学生可以直接在虚拟装置中修改保护定值逻辑，这使《电力系统继电保护》中抽象的“继电特性”、“配合关系”变得可视、可触、可感。

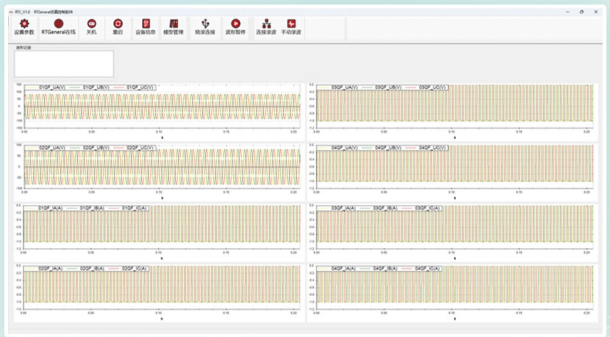


RTGeneral 实时仿真系统



ARC901弧光模拟器及监控装置





微信扫一扫

南京希瑞电气自动化研究所有限公司

电话：15365003006

清鸾科技
TSINGLUAN TECHNOLOGY

清鸾科技(成都)有限公司

公司简介 Company Profile

清鸾科技(成都)有限公司是一家专注于能源电力工业仿真软硬件研发、数字孪生解决方案设计、技术咨询等业务的能源科技公司。公司通过在数字空间中，构建实物能源系统的"数字孪生"模型，凭借强大的自研计算内核，提供精准的建模分析、规划设计和智能运维决策方案。这一创新模式为能源产业上、下游提供了强大的分析和决策能力，显著提高了能源系统的智能化水平和运营效率，实现了现代信息技术与传统能源行业之间的深度融合。公司已获评"专精特新中小企业"、"高新技术企业"、"科技型中小企业"和"创新型中小企业"，近三年来业绩持续高速增长，充分展示了其在市场中的强大竞争力和广阔的发展潜力。未来，公司将继续依托深厚的行业背景和技术优势，助力我国能源行业工业软件国产替代和能源产业的智能化升级。

产品介绍 Product Introduction

CloudPSS EMTLab 电磁暂态实时仿真平台(清鸾云镜)

采用全自研、国际领先的电力系统电磁暂态仿真内核和编译器，基于一套模型提供集离线仿真加速、大/小步长实时仿真、硬件在环、功率在环在内的一体化仿真功能。支持多架构处理器，提供软硬件完全国产化方案。



CloudPSS IESLab 综合能源系统仿真规划平台

提供含冷、热、电、氢多种能源形式的综合能源系统规划设计、方案评估和能量流计算（生产模拟）功能，支持综合能源系统全生命周期规划设计、综合评估、运行优化和仿真模拟等应用，实现能源的最优利用，助力"双碳"目标实现。



CloudPSS DSLab 源网荷储协同优化仿真平台

面向源网荷储协同的新型电力系统，提供"图-模-数-算"一体化计算分析工具，实现"一个平台、一套统一模型"支撑负荷预测、潮流计算、电磁暂态仿真、短路计算、可靠性分析、储能规划、无功优化、静态安全分析等多类型计算功能，助力新型电力系统建设。



CloudPSS XStudio 数字孪生工坊

覆盖能源电力系统建模仿真、内核集成及调度和数字孪生应用构建的全生命周期数字孪生基础支撑平台。具备跨平台、低代码开发、敏捷构建、敏捷部署特性，大大降低数字孪生应用开发及部署门槛。



地址：四川省成都市锦江区金石路 366 号 3 栋 11 层 3 号

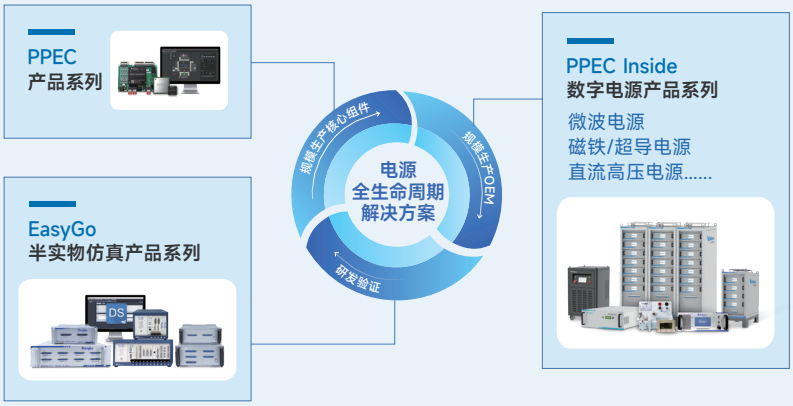
网址：www.cloudpss.net

邮箱：business@cloudpss.net

Smlstec 森木磊石

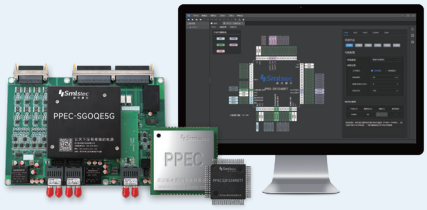
企业介绍 Company Profile

武汉森木磊石科技有限公司是一家集研发、制造和销售为一体的高新技术企业。公司立足于自主创新，不断开拓研制了PPEC数字电源控制芯片，EasyGo半实物仿真产品，以及PPEC Inside 数字电源三大主线产品，并致力为数字电源开发提供全生命周期的解决方案。服务聚焦**可控核聚变、核医疗、军工、粒子加速器、高校、科研院所**等行业及领域。



PPEC Workbench电力电子智能化开发平台

平台全面兼容自研 PPEC 数字源控制芯片、主流厂商芯片（ST、TI、GD等）以及模组、板卡等多种硬件形态，可为数字电源行业提供高可靠、低门槛的智能化解决方案，助力电源企业降本增效。



- **免代码编程开发**
- **降低门槛研发赋能**
- **加速研发缩短周期**
- **开发支持工具丰富**

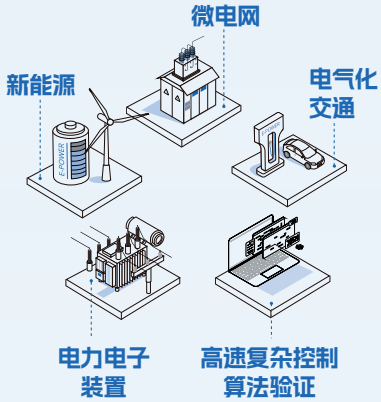


EasyGo半实物仿真产品系列

EasyGo是专为电力电子半实物仿真而研发的产品系列。推出针对不同应用的产品，满足用户需求同时极大提高产品性价；极简风格的人机交互界面，降低学习成本，快速上手完成实时测试系统。

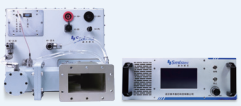


- **丰富模拟仿真场景**
- **研发快速验证**
- **简单易用轻松上手**
- **配置丰富灵活组合**



PPEC Inside数字电源产品系列

我司研制的数字电源以PPEC为控制芯片，集成其诸多优点，包含微波电源、磁铁/超导电源、直流高压电源、高精度直流源、脉冲电源等，应用广泛，覆盖电力、新能源、军工、环保、医疗、高校、科研院所等行业及领域。



微波电源



磁铁/超导电源



直流高压电源



直流稳压电源

- **高精度高效稳定**
- **技术创新高度集成**
- **全面安全保护机制**
- **智能化远程控制**

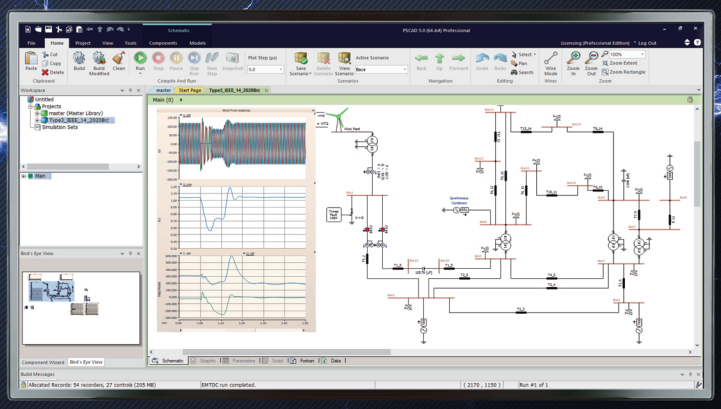
武汉森木磊石科技有限公司
www.senmuleishi.com
全国服务电话：400-679-8818
地址：武汉市洪山区东港科技产业园

商务合作　官方微信

PSCAD OFFICIAL REPRESENTATIVE

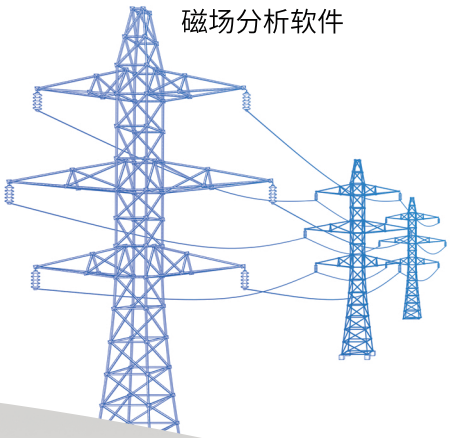
科学软件网

全球领先的电力系统电磁暂态仿真软件



卓越的并行计算能力大幅提升了大型新能源电网的仿真效率。PSCAD V5深度支持大模型应用生态，为高比例可再生能源并网、特高压直流输电及人工智能辅助的电网分析提供强大技术支撑，是国内科研与工程的核心仿真工具。

- **PRSIM**
  电力数据格式转换软件
- **Enerplot**
  离线绘图&分析软件
- **FACE**
  场效应和电晕效应软件
- **CYMCAP**
  计算电力电缆安装的载流量和温度升高
- **CYMDIST**
  配电系统分析软件
- **XGSLab**
  接地系统和电磁分析软件
- **PowerWorld Simulator**
  交互式电力系统仿真软件
- **ISED**
  综合能源规划仿真软件
- **SKM**
  电力系统分析软件
- **PLEXOS**
  能源系统分析与决策平台
- **Solargis**
  评估太阳能投资的气象数据软件
- **HOMER Pro**
  微电网和分布式能源系统优化设计软件
- **ELECTRO**
  电场分析软件
- **MAGNETO**
  磁场分析软件



北京天演融智软件有限公司 美国/北京/广州/成都

为中国用户提供电力工程软件和本地化服务

2006 年成立 19 年行业经验 500+ 电力用户

400 810 4001

18510103847(微信同号)

info@sciencesoftware.com.cn

www.sciencesoftware.com.cn



武汉华大电力自动技术有限责任公司

Wuhan Hua Da Electric Auto-technique Co., Ltd

坐落于武汉国际企业中心，成立于 1998 年由华中科技大学产业集团企业武汉华工大电力自动技术研究所重组而成，湖北省高新企业，通过了 ISO9001 质量管理体系认证。公司致力于电力、电子计算机技术及产品的开发、研制、技术咨询、技术服务、开发产品的制造及销售。

公司依托华中科技大学电气与电子工程学院多年的科技成果和优越的科研设施，以高效的企业运行机制和严格的质量保证，创建并拓展了八大系列，近三十种产品。

公司生产微机励磁调节器已有 20 多年历史，是最早将微机励磁调节器用于生产现场的单位之一，在国际上也属先行，并获得国家级、省级科技进步奖。

本公司承接过国内四十多所动模实验室的设计、制造、改造任务，已具有强大的技术优势和力量。目前我公司正致力于新能源发电教学实验室设备的研制并已取得了一定的成果。

公司生产的电气类专业的教学实验设备多次获得省级优秀教学成果奖，是中国电气类专业设备的开拓者。研发出学生可以自主编程的继电保护装置，填补了专业教学的空白。电气类专业设备已被几百所电气类院校广泛使用，适应了电气类专业课程实验、课程设计、毕业设计以及某些研究课题实验需求。

公司秉承“安全第一，信誉第一，质量第一”的质量方针，以高度的责任心和严谨求实的科学态度，不断创新，不断进取，为中国的现代化电力建设做出我们应有的贡献。

主要产品目录：

- HWDT-II 新型电力系统综合自动化系统
- HDGF 微机继电保护及故障分析试验台
- HDJZ-II 新型电气控制与继电保护综合试验台
- 模拟风力发电系统
- 用于电力系统动态模拟实验平台的高压直流输电系统
- WDT-IIIC 电力系统综合自动化试验系统
- HDDJ-III 电机教学实验台
- HDDW 数字化电网及新能源综合模拟试验系统
- 电力系统动态模拟试验系统
- 面向高校及科研院所提供新型电力系统教学与科研产品

公司地址：武汉市洪山区光谷大道国际企业中心二期宏宇楼 401-5
网址：www.hustdzs.com.cn
E-mail:13986286392@163.com，17362484696@163.com
营销部电话/客户服务专线：13986286392，17362484696，027-67845171
办公室电话：027-67845208

ModelingTech
远 宽 能 源

为电力新能源科研测试提供实时仿真完整解决方案

上海远宽能源科技有限公司（简称远宽能源）成立于2011年，专注于电力、新能源、电气化交通等行业中的实时仿真领域，致力于为电气学科前沿学术研究、高端装备的研发和测试提供实时仿真软硬件产品和专业技术支持。远宽能源自成立起就持续进行电力实时仿真技术的自主研发，历经10余年的技术深耕，率先实现电力领域实时仿真软硬件的国产化，建立起领先的电力仿真自主品牌，拥有多项发明专利，被评为“高新技术企业”、“上海市专精特新中小企业”和“上海市科技小巨人”。



- 风电变流器仿真 | 光伏逆变器仿真 | 多逆变器并联系统
- 储能变流器PCS仿真 | 高压直挂储能测试 | 抽水蓄能
- 场站功率协调控制器仿真 | 新能源场站多设备控制器同时在环仿真

  新能源场站实时全景再现（数字孪生）
- 链式SVG仿真 | 高压直挂储能测试 | 高压变频器仿真 | 柔性直流输电（MMC）
- 微网源网荷储一体化 | 绿氢微网实时仿真系统 | 功率硬件在环仿真
- 汽车电驱控制器测试 | 牵引驱动系统仿真
- 创新教学实验方案



上海远宽能源科技有限公司
ModelingTech Energy Technology Co., Ltd.
上海市杨浦区隆昌路628号宝龙旭辉广场A栋11层
021-65011357
www.modeling-tech.com

The 40th Annual Conference on Chinese University Society for Electric Power System and Automation (CUS-EPSA)

特别鸣谢

